OHBM 2024
JUNE 23~27, SEOUL, KOREA

ABSTRACTS

Sunday, June 23 – Thursday, June 27
COEX CONVENTION & EXHIBITION CENTER | SEOUL

30TH ANNUAL MEETING OF THE
ORGANIZATION FOR HUMAN BRAIN MAPPING

Poster No 1506

A Connectional Gradient of Individual Variability across Functional Connectome Edges

Hang Yang[1], guowei wu[1,2], Yaoxin Li[1,3], Xiaoyu Xu[1,4], Yiyao Ma[1], Runsen Chen[5], Adam Pines[6], Ting Xu[7], Valerie Sydnor[8], Theodore Satterthwaite[9], Zaixu Cui[1]

[1]Chinese Institute for Brain Research, Beijing, China, [2]University of Chinese Academy of Sciences, Beijing, China, [3]Michigan Neuroscience Institute, University of Michigan, Ann Arbor, MI, [4]State Key Laboratory of Cognitive Neuroscience and Learning, Beijing Normal University, Beijing, China, [5]Vanke School of Public Health, Tsinghua University, Beijing, China, [6]Psychiatry and Behavioral Sciences, Stanford School of Medicine, Stanford University, Stanford, CA, [7]Child Mind Institute, New York, NY, [8]University of Pittsburgh, Pittsburgh, PA, [9]UPenn, Philadelphia, PA

Introduction: The regional functional connectivity (FC) variability exhibits a cortical gradient, increasing from the primary sensorimotor to higher-order association areas (Mueller et al. 2013; Sydnor et al. 2021). This inter-individual variability in FC matures throughout development (Tooley, Bassett, and Mackey 2021; Teeuw et al. 2019). However, the organization of individual FC variability at the edge level remains unclear. In this study, we identified a connectional gradient in the edge-level FC variability and investigated its maturation during youth.

Methods: We utilized the Human Connectome Project (HCP)-development (HCP-D, n = 415, aged 8–21) dataset (Somerville et al. 2018) and unrelated HCP-young adult (HCP-YA, n = 245, aged 22–35) dataset (Van Essen et al. 2013) to assess edge-level FC variability. The minimally preprocessed fMRI data were post-processed with the extensible connectivity pipelines (XCP-D), including nuisance regression (36P), filtering (0.01–0.08 Hz), and smoothing (FWHM = 6 mm). We obtained 45- and 58-min fMRI data from the HCP-D and HCP-YA datasets and equally divided them into 12 and 8 sessions, respectively. We extracted regional BOLD timeseries using the Schaefer atlas with 400 regions (Schaefer et al. 2018) and calculated FC between each pair of cortical regions using Pearson correlation. A linear mixed-effects model estimated inter- and intra-individual variability for each FC edge (Xu et al. 2022). The intra-class coefficient (ICC) measured adjusted inter-individual variability, considering intra-individual variability (Mueller et al. 2013). Finally, a 400×400 inter-individual variability matrix was generated, with each element representing the variation in connection strength for an edge across all participants. Then, we explored the FC variability gradient maturation in youth by employing a sliding-window method (Vasa et al. 2018) to sort HCP-D participants by age (length = 50, step = 5), resulting in 74 groups (Fig. 2a). First, we assessed whether FC variability matured towards an adult-like pattern during youth. Using FC variability in the HCP-YA dataset as a reference, we estimated the alignment between each of the 74 HCP-D variability matrices and the reference using Spearman's rank correlations (Fig. 2b). We used a general additive model (GAM) to measure associations between variability gradient alignment and age while controlling for sex and in-scanner motion. Next, we introduced a gradient slope to quantify the connectional gradient through linear regression on the 21 ranked network-level variability values (Fig. 2d), and assessed the development of the variability gradient slope using the same GAM.

Results: We observed high variability in association network connections in both HCP-YA and HCP-D datasets (Fig. 1a–f). We averaged FC variabilities at the network level and ranked them for each network separately, and defined this as the 'connectional variability gradient'. The ranking revealed decreasing individual variability from within-network edges to those between association networks and further to sensorimotor-association connections (Fig. 1g–h). Next, we examined the whole-brain connectome by ranking the FC variability of all network-level connections. Within-association network edges peaked on this gradient, while sensorimotor-other network edges were at the base (Fig. 1i–j). Additionally, we found a significant positive correlation between age and variability gradient alignment (partial R2 = 0.29, P = 1.23×10-6, Fig. 2c), and the slope of the network-level FC variability gradient significantly declined during youth (partial R2 = -0.82, P = 1.78×10-67, Fig. 2e).

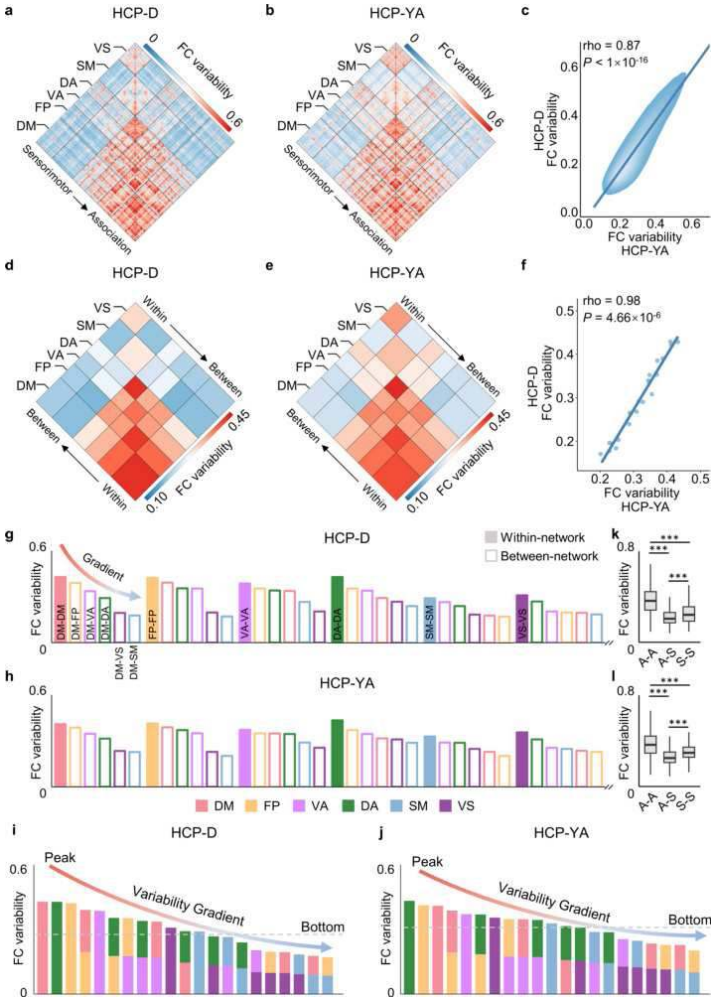

a | The development of variability gradient in youth

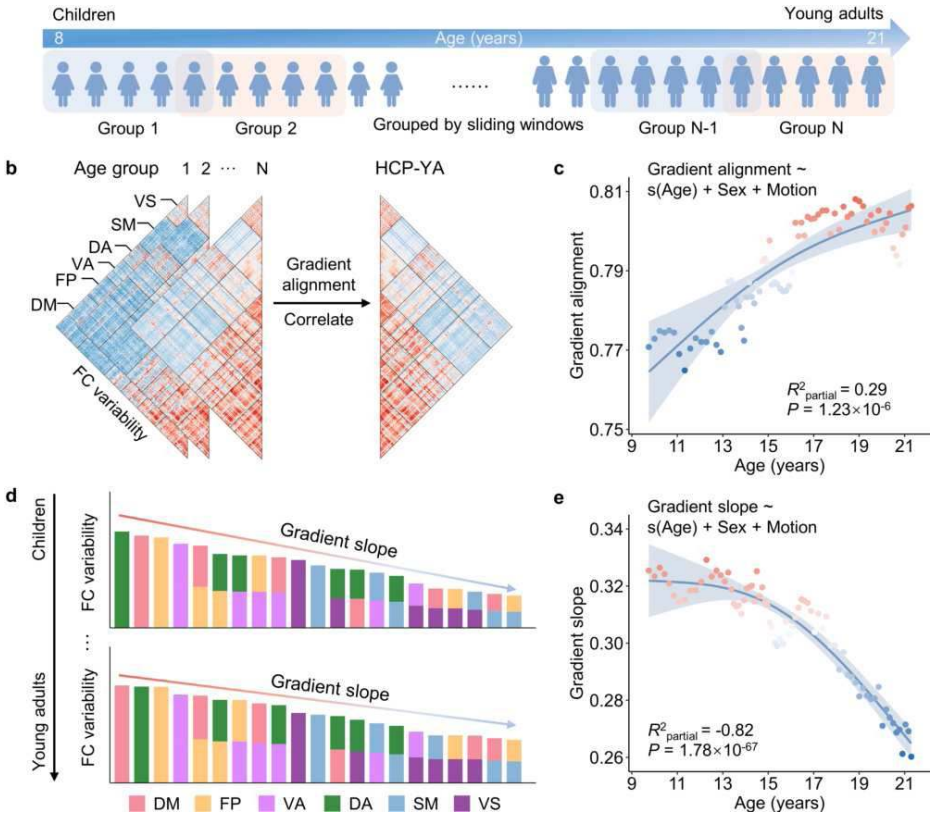

Conclusions: We identified a connectional gradient in the edge-level FC variability which declined continuously along an axis from the edges among association networks to those that connect the sensorimotor and association networks. Furthermore, the connectional variability gradient matured into an adult-like pattern with a flatter gradient slope during youth.

References

1. Mueller, S., D. Wang, M. D. Fox, B. T. Yeo, J. Sepulcre, M. R. Sabuncu, R. Shafee, J. Lu, and H. Liu. 2013. 'Individual variability in functional connectivity architecture of the human brain', Neuron, 77: 586-95.
2. Schaefer, A., R. Kong, E. M. Gordon, T. O. Laumann, X. N. Zuo, A. J. Holmes, S. B. Eickhoff, and B. T. T. Yeo. 2018. 'Local-Global Parcellation of the Human Cerebral Cortex from Intrinsic Functional Connectivity MRI', Cereb Cortex, 28: 3095-114.
3. Somerville, L. H., S. Y. Bookheimer, R. L. Buckner, G. C. Burgess, S. W. Curtiss, M. Dapretto, J. S. Elam, M. S. Gaffrey, M. P. Harms, C. Hodge, S. Kandala, E. K. Kastman, T. E. Nichols, B. L. Schlaggar, S. M. Smith, K. M. Thomas, E. Yacoub, D. C. Van Essen, and D. M. Barch. 2018. 'The Lifespan Human Connectome Project in Development: A large-scale study of brain connectivity development in 5-21 year olds', NeuroImage, 183: 456-68.
4. Sydnor, V. J., B. Larsen, D. S. Bassett, A. Alexander-Bloch, D. A. Fair, C. Liston, A. P. Mackey, M. P. Milham, A. Pines, D. R. Roalf, J. Seidlitz, T. Xu, A. Raznahan, and T. D. Satterthwaite. 2021. 'Neurodevelopment of the association cortices: Patterns, mechanisms, and implications for psychopathology', Neuron, 109: 2820-46.
5. Teeuw, J., R. M. Brouwer, Jpoft Guimaraes, P. Brandner, M. M. G. Koenis, S. C. Swagerman, M. Verwoert, D. I. Boomsma, and H. E. Hulshoff Pol. 2019. 'Genetic and environmental influences on functional connectivity within and between canonical cortical resting-state networks throughout adolescent development in boys and girls', NeuroImage, 202: 116073.
6. Tooley, U. A., D. S. Bassett, and A. P. Mackey. 2021. 'Environmental influences on the pace of brain development', Nat Rev Neurosci, 22: 372-84.
7. Van Essen, D. C., S. M. Smith, D. M. Barch, T. E. Behrens, E. Yacoub, K. Ugurbil, and W. U-Minn HCP Consortium. 2013. 'The WU-Minn Human Connectome Project: an overview', NeuroImage, 80: 62-79.
8. Vasa, F., J. Seidlitz, R. Romero-Garcia, K. J. Whitaker, G. Rosenthal, P. E. Vertes, M. Shinn, A. Alexander-Bloch, P. Fonagy, R. J. Dolan, P. B. Jones, I. M. Goodyer, Nspn consortium, O. Sporns, and E. T. Bullmore. 2018. 'Adolescent Tuning of Association Cortex in Human Structural Brain Networks', Cereb Cortex, 28: 281-94.
9. Xu, Ting, Jae Wook Cho, Gregory Kiar, Eric W Bridgeford, Joshua T Vogelstein, and Michael P Milham. 2022. 'A Guide for Quantifying and Optimizing Measurement Reliability for the Study of Individual Differences', bioRxiv: 2022.01. 27.478100.

Poster No 1507

Assessing the Generalizability of an HCP Connectome Harmonization Model

Jagruti Patel[1], Yasser Alemán-Gómez[1], Sebastien Tourbier[1], Mikkel Schöttner[1], Thomas Bolton[1], Patric Hagmann[1]

[1]Department of Radiology, Lausanne University Hospital and University of Lausanne (CHUV-UNIL), Lausanne, Switzerland

Introduction: Data harmonization (DH) is crucial to mitigate heterogeneity in multi-site neuroimaging studies and thereby enhance statistical power and generalizability[9]. A factor contributing to such heterogeneity is the variability in acquisition parameters (APs) of the data collected across sites[10]. While there is no gold standard in designing a DH model[5], information regarding APs makes valuable prior knowledge to improve performance[3]. In this work, we have designed such a model to harmonize structural connectomes (SCs)[4].

Methods: Our training dataset included the minimally preprocessed T1-weighted imaging (T1W) and diffusion-weighted imaging (DWI) data of 150 subjects from the Human Connectome Project Young Adult (HCP-YA) dataset[8]. The DWI data was resampled to have two factors of variation: resolution (res, 1.25 [original] and 2.3 [downsampled] mm isotropic) and b-value (bval, 1000 and 3000 s/mm2), mimicking a training scenario with 150 "traveling subjects"[7] and 4 acquisition sites. Then, SCs were derived by parcellating the T1W data into 274 regions and performing deterministic tractography on the DWI data to infer the numbers of fibers linking them[6]. Linear regression (LR) was performed independently on each structural connection: $\hat{y} = \beta0 + \beta1\ bval + \beta2\ res + \beta3\ bval*res$, where $\hat{y}$ is an estimated structural connection across subjects and AP combinations, and $[\beta0, \beta1, \beta2, \beta3]$ is the estimated weight vector for the connection at hand. Our independent validation dataset consisted of the T1W and DWI data of 11 healthy subjects from the Lausanne Psychosis Cohort[1,2]. The DWI data included diffusion tensor imaging (DTI), bval = 0 and 1000 s/mm2, res = 2 x 2 x 3 mm3 or 2 x 2 x 3.3 mm3 depending on the subject, as well as diffusion spectrum imaging (DSI), maximum (max) bval = 8000 s/mm2, res = 2.2 x 2.2 x 3 mm3. The DSI data was resampled to have max bval as a factor of variation (3000, 5000 and 8000 s/mm2). SCs were derived as above except that fiber orientation distribution functions were estimated using constrained spherical deconvolution (order 6) for DTI and simple harmonic oscillator-based reconstruction and estimation (order 6) for DSI. The above LR model was used to harmonize DTI-derived SCs to DSI-derived SCs at the three modeled max bval settings. Mean L1 distances across connections were calculated between the DSI SCs of different subjects, and between the DTI and DSI SCs of the same subjects before and after DH (Fig. 1). DTI vs DSI cross-subject distance matrices were also calculated before and after DH (Fig. 2). Since DTI and DSI data resolutions were not isotropic, a cube root of the volume of each voxel was used as res in the above model.

Results: For DSI at max bval = 3000 and 5000 s/mm2, intra-subject distances decreased after DH and became smaller than inter-subject distances (Fig. 1). However, the opposite was observed for max bval = 8000 s/mm2. Intra-subject distances (diagonal entries in Fig. 2 matrices) decreased after DH and were the lowest for all but one subject for DSI data at max bval = 3000 and 5000 s/mm2, denoting that subject-specific features required for fingerprinting were not removed by our method. However, at max bval = 8000 s/mm2, differences between inter-subject and intra-subject distances were less pronounced.

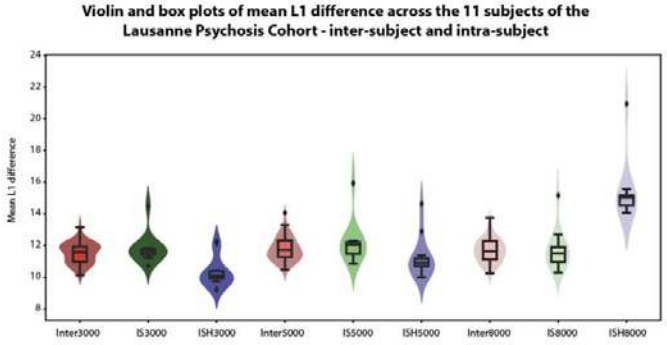

Fig. 1: L1 difference averaged across connections, between pairs of SCs (for the Lausanne Psychosis Cohort) when both SCs are from different subjects acquired with DSI
(max bval 3000 s/mm²//res 2.2 x 2.2 x 3 mm³, labelled as Inter3000;
max bval 5000 s/mm²//res 2.2 x 2.2 x 3 mm³, labelled as Inter5000;
max bval 8000 s/mm²//res 2.2 x 2.2 x 3 mm³, labelled as Inter8000),
from the same subject acquired with DSI max bval 3000 s/mm²//res 2.2 x 2.2 x 3 mm³ and DTI bval 1000 s/mm²//res 2 x 2 x 3 mm³ or 2 x 2 x 3.3 mm³ before and after harmonization (labelled as IS3000 and ISH3000, respectively),
from the same subject acquired with DSI max bval 5000 s/mm²//res 2.2 x 2.2 x 3 mm³ and DTI bval 1000 s/mm²//res 2 x 2 x 3 mm³ or 2 x 2 x 3.3 mm³ before and after harmonization (labelled as IS5000 and ISH5000, respectively),
and from the same subject acquired with DSI max bval 8000 s/mm²//res 2.2 x 2.2 x 3 mm³ and DTI bval 1000 s/mm²//res 2 x 2 x 3 mm³ or 2 x 2 x 3.3 mm³ before and after harmonization (labelled as IS8000 and ISH8000, respectively).
All the harmonizations have been done with the LR model trained on 150 traveling subjects of the HCP-YA dataset (600 SCs).

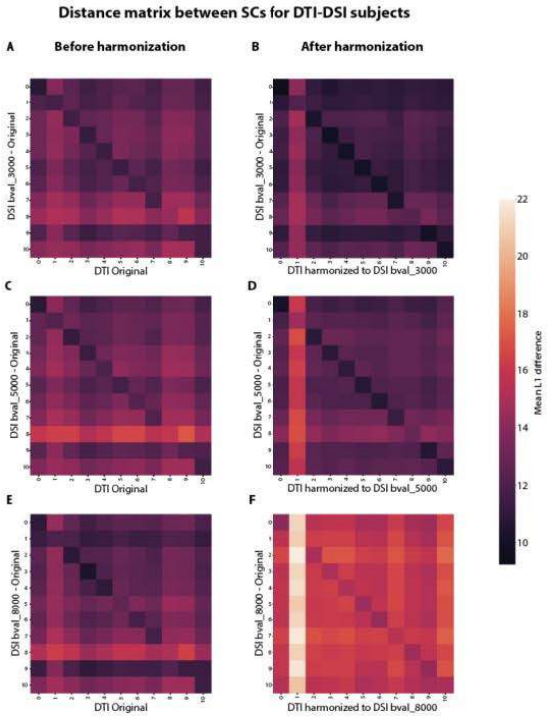

Fig. 2 : Distance matrix between DTI vs DSI SCs for Lausanne Psychosis Cohort with L1 difference averaged across connections as a metric.
A : DSI (max bval 3000 s/mm²//res 2.2 x 2.2 x 3 mm³) vs DTI (bval 1000 s/mm²//res 2 x 2 x 3 mm³ or 2 x 2 x 3.3 mm³)
B : DSI (max bval 3000 s/mm²//res 2.2 x 2.2 x 3 mm³) vs DTI (bval 1000 s/mm²//res 2 x 2 x 3 mm³ or 2 x 2 x 3.3 mm³) harmonized to DSI (bval 3000 s/mm²//res 2.2 x 2.2 x 3 mm³)
C : DSI (max bval 5000 s/mm²//res 2.2 x 2.2 x 3 mm³) vs DTI (bval 1000 s/mm²//res 2 x 2 x 3 mm³ or 2 x 2 x 3.3 mm³)
D : DSI (max bval 5000 s/mm²//res 2.2 x 2.2 x 3 mm³) vs DTI (bval 1000 s/mm²//res 2 x 2 x 3 mm³ or 2 x 2 x 3.3 mm³) harmonized to DSI (bval 5000 s/mm²//res 2.2 x 2.2 x 3 mm³)
E : DSI (max bval 8000 s/mm²//res 2.2 x 2.2 x 3 mm³) vs DTI (bval 1000 s/mm²//res 2 x 2 x 3 mm³ or 2 x 2 x 3.3 mm³)
F : DSI (max bval 8000 s/mm²//res 2.2 x 2.2 x 3 mm³) vs DTI (bval 1000 s/mm²//res 2 x 2 x 3 mm³ or 2 x 2 x 3.3 mm³) harmonized to DSI (bval 8000 s/mm²//res 2.2 x 2.2 x 3 mm³)
All the harmonizations have been done with the LR model trained on 150 traveling subjects of the HCP-YA dataset (600 SCs).

Conclusions: Although our simple LR model was trained on the high-quality HCP-YA dataset, it generalized to a different clinical dataset. While it was trained to harmonize DTI data from bval = 1000 to 3000 s/mm2, it also efficiently harmonized DTI data at bval = 1000 s/mm2 to DSI data until a max bval of 5000 s/mm2, demonstrating generalizability and robustness. Hence, simple models should not be disregarded completely for more complex ones, especially when it comes to clinical applications.

References

1. Alemán-Gómez, Y., et al. (2023), 'Multimodal Magnetic Resonance Imaging Depicts Widespread and Subregion Specific Anomalies in the Thalamus of Early-Psychosis and Chronic Schizophrenia Patients', Schizophrenia Bulletin, vol. 49, no.1, pp. 196-207
2. Baumann, P.S., et al. (2013), 'Treatment and Early Intervention in Psychosis Program (TIPP-Lausanne): Implementation of an Early Intervention Programme for Psychosis in Switzerland', Early Intervention in Psychiatry, vol. 7, no.3, pp. 322- 328
3. Borges, P., et al. (2019), 'Physics-Informed Brain MRI Segmentation', Simulation and Synthesis in Medical Imaging, pp. 100-109
4. Contreras, J.A., et al. (2015), 'The Structural and Functional Connectome and Prediction of Risk for Cognitive Impairment in Older Adults', Current Behavioral Neuroscience Reports, vol. 2, pp. 234-245
5. Gebre, R.K., et al. (2023), 'Cross–Scanner Harmonization Methods for Structural MRI may Need Further Work: A Comparison Study', Neuroimage, vol. 269, pp. 119912
6. Patel, J., et al. (2022), 'Quantifying the Impact of Scanner Bias on the Construction of Structural Connectomes', Organization for Human Brain Mapping Annual Meeting, abstract #2928, poster #WTh205
7. Tian, D., et al. (2022), 'A Deep Learning-Based Multisite Neuroimage Harmonization Framework Established with a Traveling-Subject Dataset', Neuroimage, vol. 257, pp. 119297
8. Van Essen, D.C., et al. (2012), 'The Human Connectome Project: A Data Acquisition Perspective', Neuroimage, vol. 62, no. 4, pp. 2222–2231
9. Yu, M., et al. (2018), 'Statistical Harmonization Corrects Site Effects in Functional Connectivity Measurements from Multi-Site fMRI Data', Human Brain Mapping, vol. 39, no. 11, pp. 4213-4227
10. Zhu, A.H., et al. (2019), 'Challenges and Opportunities in dMRI Data Harmonization', Medical Image Computing and Computer-Assisted Intervention, pp. 157–172

Poster No 1508

Decoding short- and long-range structural connectivity using manifold learning techniques

Seulki Yoo[1], Sunghyoung Hong[2,3], Seok-Jun Hong[2,3,4], Bo-yong Park[5,6,3]

[1]Convergence Research Institute, Sungkyunkwan University, Suwon, Republic of Korea, [2]Department of Biomedical Engineering, Sungkyunkwan university, Suwon, Republic of Korea, [3]Center for Neurosciene and Imaging Research, Sungkyunkwan University, Suwon, Republic of Korea, [4]Center for the Developing Brain, Child Mind Institute, New York, NY, United States, [5]Department of Data Science, Inha University, Incheon, Republic of Korea, [6]Department of Statistics and Data Science, Inha University, Incheon, Republic of Korea

Introduction: The human brain consists of billions of neurons and organizes networks through complex physical connections between brain regions. The structural connectivity estimated via diffusion magnetic resonance imaging (MRI) tractography represents the physical architecture of the brain. Investigation of short- and long-range connectivity is intriguing because these patterns reflect brain hierarchy, where the unimodal regions are mainly characterized by short-range connections, while the heteromodal association areas by a large number of long-range connections.[1] However, quantitative differences between short- and long-range structural connections and their role in explaining brain function have not been investigated. In this study, we aim to unravel the underlying characteristics of short- and long-range structural connectivity by employing manifold learning techniques.

Methods: We obtained diffusion MRI data of 86 healthy young adults (male/female = 35/51; mean ± standard deviation [SD] age = 28.77 ± 3.33 [range = 22-36]) from the Q3 release of the Human Connectome Project database.[2] Diffusion MRI data were preprocessed using MRtrix3[3], and structural connectome was constructed based on the sub-parcellation of the Desikan-Killiany atlas with 400 parcels[4] and log-transformed to adjust for the scale.[5] For each individual, the streamlines with a connection length below 30% of the maximum length were defined as short-range connections, while those above 30% were considered long-range connections.[6] We then estimated low-dimensional representations of the structural connectivity (i.e., gradients) for both short- and long-range connections using nonlinear dimensionality reduction techniques.[7] Furthermore, we associated the short- and long-range connectivity-based gradients with multiple task activation maps obtained from the BrainMap database to assess distinct structure-function coupling strategies according to the connection lengths.

Results: We generated five gradients (G1-G5) for short- and long-range structural connectivity, as well as the whole connectivity (Figure 1). Although the order of the gradients was slightly different (G3 and G4), their spatial patterns based on the whole connectivity were largely explained by those based on the short-range connectivity (spatial correlations: FDR-corrected p-values < 0.001). For the long-range connectivity, the gradients of the anterior-posterior axis (G2) and sensorimotor-transmodal axis (G4) showed similar spatial patterns with those based on the whole connectivity. However, we could not find

the left-right and dorsal-ventral patterns seen in the whole connectivity-based gradients. When we associated the gradients with task-evoked functional activation patterns, the anterior-posterior and sensorimotor-transmodal axes were closely associated with emotions and actions, regardless of connection lengths (Figure 2). On the other hand, the interoception was dominantly related to the short-range gradients, while perception was associated with the long-range gradients.

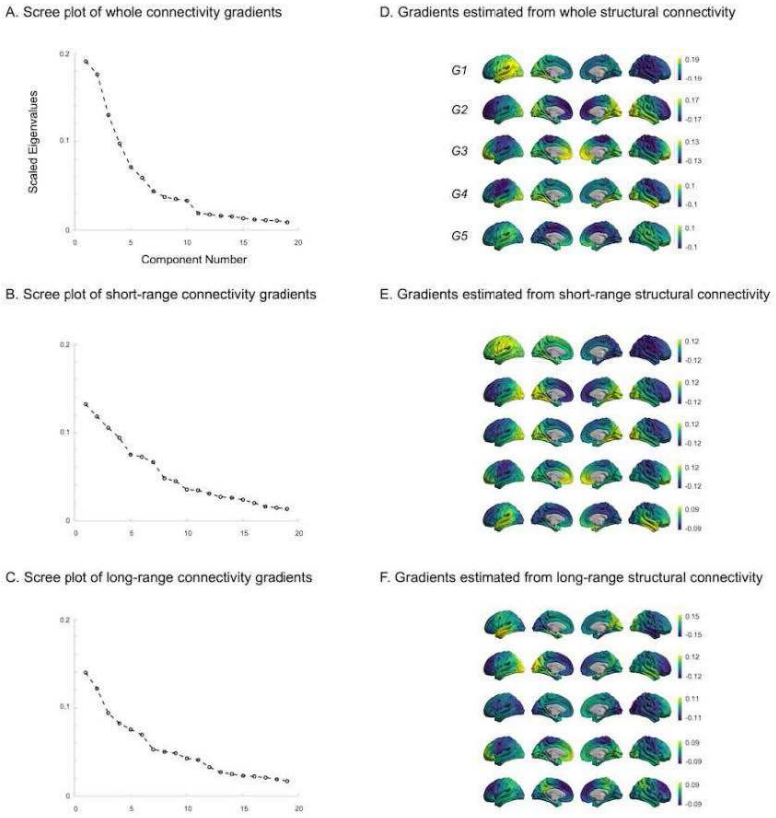

Figure 1. Structural connectome gradients. Cortex-wide structural connectivity gradients for whole, short-range and long-range connections. (A)-(C)The scree plots show the scaled eigenvalues of estimated eigenvectors. (D)-(E) Spatial patterns of the estimated gradients are shown on brain surfaces.

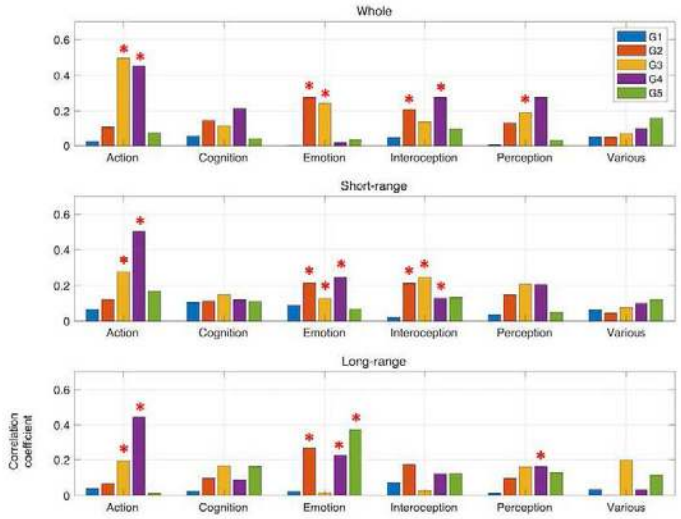

Figure 2. Correlations between the structural connectivity gradients and multiple task activation maps. The bar plot represent the absolute values of the correlation coefficients, and the asterisks indicate the ones passed for the significance level.

Conclusions: By estimating principal gradients of short- and long-range structural connectomes[8,9], we found that short-range connections may dominate the whole-brain structural connectome organization. Associations with task maps revealed a distinct relationship between short- and long-range connections. Although defining the threshold level should be explored further, our work offered a novel insight for the principle of structural connectome organization with respect to physical connection lengths.

References
1. Oligschläger, S. (2017), 'Gradients of connectivity distance are anchored in primary cortex', Brain Structure and Function, vol. 222, pp. 2173-2182
2. WU-Minn, H. C. P. (2017), '1200 subjects data release reference manual', (https://www. humanconnectome. org)
3. Tournier J-D. (2019), 'MRtrix3: A fast, flexible and open software framework for medical image processing and visualisation', Neuroimage, vol. 202, pp. 116137
4. Desikan, R. S. (2006), 'An automated labeling system for subdividing the human cerebral cortex on MRI scans into gyral based regions of interest', Neuroimage, vol. 31, no.3, pp. 968-980
5. Fornito, A. (2016), 'Fundamentals of brain network analysis', Academic press.
6. Betzel, RF. (2019), 'Distance-dependent consensus thresholds for generating group-representative structural brain networks', Network neuroscience, vol.3, pp.475-496
7. Vos de Wael, R (2020), 'BrainSpace: a toolbox for the analysis of macroscale gradients in neuroimaging and connectomics datasets', Communications biology, vol.3, no.1, pp.103
8. Margulies, D. S. (2016), 'Situating the default-mode network along a principal gradient of macroscale cortical organization' Proceedings of the National Academy of Sciences, vol.113, no.44, pp.12574-12579
9. Huntenburg, J. M. (2018), 'Large-scale gradients in human cortical organization', Trends in cognitive sciences, vol.22, no.1, pp.21-31

Acknowledgements
Funding: National Research Foundation of Korea (NRF-2021R1F1A1052303; NRF-2022R1A5A7033499), Institute for Information and Communications Technology Planning and Evaluation (IITP) funded by the Korea Government (MSIT) (No. 2022-0-00448, Deep Total Recall: Continual Learning for Human-Like Recall of Artificial Neural Networks; No. RS-2022-00155915, Artificial Intelligence Convergence Innovation Human Resources Development (Inha University); No. 2021-0-02068, Artificial Intelligence Innovation Hub), Institute for Basic Science (IBS-R015-D1).

Poster No 1509

Mapping the subcortical connectome in Parkinson's disease patients undergoing deep brain stimulation

Alaa Taha[1], Jason Kai[2], Mohamad Abbass[3], Brendan Santyr[1], Greydon Gilmore[3], Bradley Karat[1], Arun Thurairajah[4], Ali Khan[1], Jonathan Lau[5]

[1]University of Western Ontario, London, Ontario, [2]Imaging Research Laboratories, Robarts Research Institute, Western University, London, Ontario, [3]Department of Clinical Neurological Sciences, Division of Neurosurgery, London, Ontario, [4]Department of Clinical Neurological Sciences, Division of Neurosurgery, Western University, London, ON, [5]Department of Clinical Neurological Sciences, Division of Neurosurgery, London, ON

Introduction: Deep brain stimulation (DBS) involves surgical implantation of electrodes to modulate aberrant brain networks[1]. DBS is a focal therapeutic option, while also offering a unique window to understand underlying mechanisms of targeted neural circuits. The most common application of DBS is to manage Parkinson's disease (PD)[1], specifically targeting the subthalamic nucleus (STN), a lens-like basal ganglia (BG) structure spanning ~10 millimeters[2]. The STN serves as an integrative hub that spatially compresses information projected from the cortex, BG, and thalamus[2]. As a result, DBS electrodes placed in the STN can modulate large brain networks, although the exact connections to cortical and subcortical structures remain poorly understood. Most studies employing tractography seek to understand cortical connections (i.e. within the cortex or between the subcortex and cortex)[3]. However, recapitulating the short-range subcortical connections (e.g., within or between the BG and thalamus), important for motor control, cognition, and emotion[4,5] is crucial to understanding PD progression and DBS mechanisms. In this work, we 1) recapitulate literature validated subcortical connectivity in-vivo via 7-Tesla (7T) MRI, comparing PD and healthy controls (HC) and 2) employ patient-specific subcortical connectivity to predict DBS outcomes.

Methods: A total of 60 participants were included in this study, 26 were diagnosed with PD and underwent STN-DBS (age: 60.19 ± 7.08, median = 62.5; 11 female; 12 ± 2 years since diagnosis) and the rest are HCs (age: 45.48 ±13.66, median = 47.5; 15 female). The following sequences were employed: 1) 3D T1w MP2RAGE, 2) 3D optimized T2w fast-spin echo (T2 SPACE), and 3) Whole-brain dMRI, 1.5 mm isotropic, with B-values 1000/2000 and 95 directions. Minimal preprocessing was performed on all MRI modalities. This included gradient non-linearity distortion correction and FreeSurfer. Deep brain region of interest (ROI) segmentations were generated from FreeSurfer combined with the BigBrain subcortical atlas[6] propagated back to subject space, all ROIs were combined via Labelmerge[7]. Mrtrix3[8] was employed for probabilistic tractography by generating an average group response from HC to estimate the fibre orientation distribution maps. Twenty million streamlines were generated per participant with terminating criteria being a 2 voxel radius from ROI. Apparent fibre density (AFD) was investigated in literature defined[9] motor, limbic, and associative circuits across HC and PD. Lead-DBS[10] was employed for DBS electrode localization and stimulation volume modeling. We leverage the motor section of the Unified Parkinson's Disease Rating Scale (UPDRS) to capture clinical outcomes 1 month post-DBS device turn on. Patient subcortical connectome was

filtered based on tracts traversing DBS electrode stimulated volumes which yielded best clinical improvement. Using leave-one-out cross validation, we predicted UPDRS improvement (%) from filtered patient subcortical connectome.

Results: All individual circuits (i.e., motor, limbic, and associative) were highly correlated ($r > 0.8$, $p < 0.0001$) between HC and PD, indicating that the same circuits between the two groups were recapitulated (Figure 1A). We identified significant differences in tract density across 8 subcortical connections between HC and PD (Figure 1B). All DBS electrodes were localized successfully and visualized in a common space (Figure 2). Connectivity strength between subcortical node tracts traversing DBS stimulated volumes predicted UPDRS improvement with an average error of 31%.

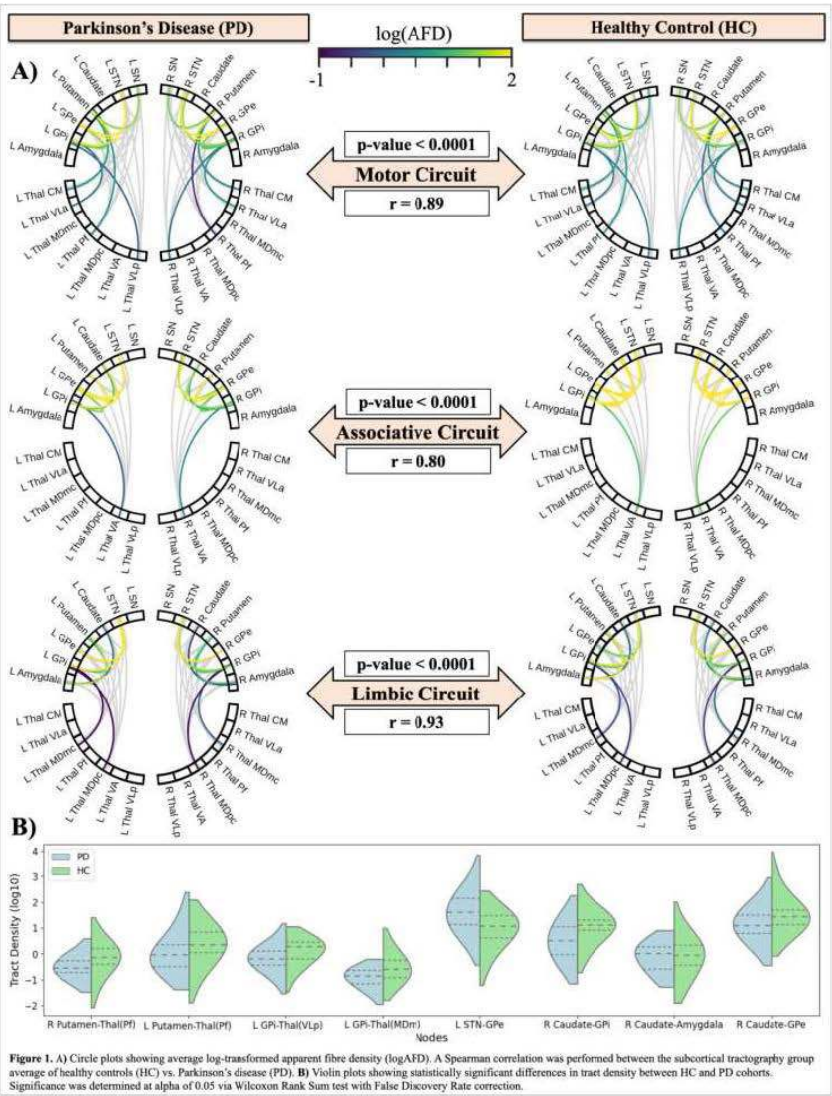

Figure 1. A) Circle plots showing average log-transformed apparent fibre density (logAFD). A Spearman correlation was performed between the subcortical tractography group average of healthy controls (HC) vs. Parkinson's disease (PD). **B)** Violin plots showing statistically significant differences in tract density between HC and PD cohorts. Significance was determined at alpha of 0.05 via Wilcoxon Rank Sum test with False Discovery Rate correction.

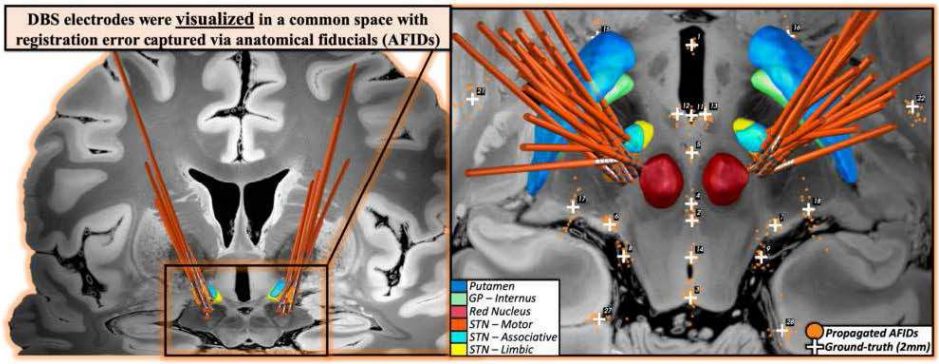

Conclusions: We employ a suite of open software for neuroimaging, tractography, DBS analysis, and ML to investigate patient specific subcortical structures and their connections including in the context of DBS electrode implantation.

References
1. Lozano, A. M. et al. Deep brain stimulation: current challenges and future directions. Nat. Rev. Neurol. 15, 148–160 (2019)
2. Horn, A., Al-Fatly, B., Neumann, W.-J. & Neudorfer, C. Chapter 1 - Connectomic DBS: An introduction. in Connectomic Deep Brain Stimulation (ed. Horn, A.) 3–23 (Academic Press, 2022)
3. Kai, J., Khan, A. R., Haast, R. A. & Lau, J. C. Mapping the subcortical connectome using in vivo diffusion MRI: Feasibility and reliability. Neuroimage 262, 119553 (2022)
4. Gallay, M. N., Jeanmonod, D., Liu, J. & Morel, A. Human pallidothalamic and cerebellothalamic tracts: anatomical basis for functional stereotactic neurosurgery. Brain Struct. Funct. 212, 443–463 (2008)
5. de Hollander, G., Keuken, M. C. & Forstmann, B. U. The subcortical cocktail problem; mixed signals from the subthalamic nucleus and substantia nigra. PLoS One 10, e0120572 (2015)
6. Xiao, Y. et al. An accurate registration of the BigBrain dataset with the MNI PD25 and ICBM152 atlases. Sci Data 6, 210 (2019)
7. Kai, J, Kuehn, T., Taha, A., Karat, B. (2023). khanlab/labelmerge: 0.2.1 (v0.2.1). Zenodo. https://doi.org/10.5281/zenodo.7523035
8. Tournier, J.-D., Calamante, F. & Connelly, A. MRtrix: Diffusion tractography in crossing fiber regions. Int. J. Imaging Syst. Technol. 22, 53–66 (2012)
9. McGregor, M. M. & Nelson, A. B. Circuit Mechanisms of Parkinson's Disease. Neuron 101, 1042–1056 (2019)
10. Neudorfer, C. et al. Lead-DBS v3.0: Mapping deep brain stimulation effects to local anatomy and global networks. Neuroimage 268, 119862 (2023)

Poster No 1510

An investigation of changes in motor and memory networks in patients with transient ischemic attack

Truc Chu[1,2], Seonjin Lee[1,2], Il-Young Jung[3], Youngkyu Song[4], Hyun Ah Kim[5], Anh Nguyen[1,2], Jong Wook Shin[6], Sungho Tak[1,2]

[1]Research Center for Bioconvergence Analysis, Korea Basic Science Institute, Cheongju, Chungcheongbuk, Korea, Republic of, [2]Graduate School of Analytical Science and Technology, Chungnam National University, Daejeon, Chungcheongnam, Korea, Republic of, [3]Department of Rehabilitation Medicine, Chungnam National University Sejong Hospital, Sejong, Chungcheongnam, Korea, Republic of, [4]Bio-Chemical Analysis Team, Korea Basic Science Institute, Cheongju, Chungcheongbuk, Korea, Republic of, [5]Department of Rehabilitation Medicine, Chungnam National University Hospital, Daejeon, Chungcheongnam, Korea, Republic of, [6]Department of Neurology, Chungnam National University Sejong Hospital, Sejong, Chungcheongnam, Korea, Republic of

Introduction: Transient ischemic attack (TIA) is a temporary episode of neurological dysfunction resulting from focal brain ischemia. Although TIA symptoms are transient, patients with TIA have a high risk of stroke and persistent impairments in various motor and cognitive functions (Coull et al., 2004). This study aims to explore the changes in task-residual effective connectivity of TIA during motor and working memory tasks. Additionally, this study seeks to associate these altered connectivity of patients with TIA with the risk of stroke.

Methods: This study involved 15 patients with TIA and 28 age-matched healthy subjects (HC). The subjects underwent scanning using a 7T MRI system while performing motor and working memory experiments. During the motor task, the subjects performed right or left fist-closing movements synchronized with a 1Hz visual cue. In the working memory assessment, subjects performed the n-back task, involving 0-, 1-, and 2-back conditions. We applied spectral dynamic causal modeling (DCM) (Razi et al., 2015) to task-residual BOLD time series, to estimate effective connectivity among regions of interest (ROI). Specifically, based on the general linear model (GLM) results across all participants, ROIs for motor task included the primary motor cortex (M1), premotor cortex (PMC), supplementary motor area (SMA), and inferior parietal lobule (IPL). The ROIs for the n-back task comprised various regions such as the prefrontal cortex (PFC), parietal cortex (PAR), and cingulate cortex (CC). The task-residual time series within the ROIs were obtained by regressing out the task-related signal and systemic confounds from the fMRI signal. The parameters of effective connectivity were then estimated from the task-residual time series using spectral DCM.

Results: Compared to HC, stronger excitatory connections from the left PMC to the ipsilateral M1 were observed in patients with TIA, during both right- and left-hand movement. Moreover, during right-hand movement, patients with TIA exhibited a stronger excitatory influence from the contralateral M1 to the ipsilateral M1. Regarding the SMA region, the effective connectivity to the SMA was decreased in patients with TIA, compared with HC during both right- and left-hand movement. Regarding the PMC regions, patients with TIA had higher suppressive influence to the PMC during right hand movement than HC. These results were shown in Figure 1. During the n-back task, patients with TIA exhibited higher connectivity strength compared to the HC group, as shown in Figure 2. Specifically, patients with TIA consistently showed increased effective connectivity among the ROIs of the PAR and CC in both hemispheres, in contrast to the HC group. Moreover, there was a reduction in connectivity to the right PFC in patients with TIA.

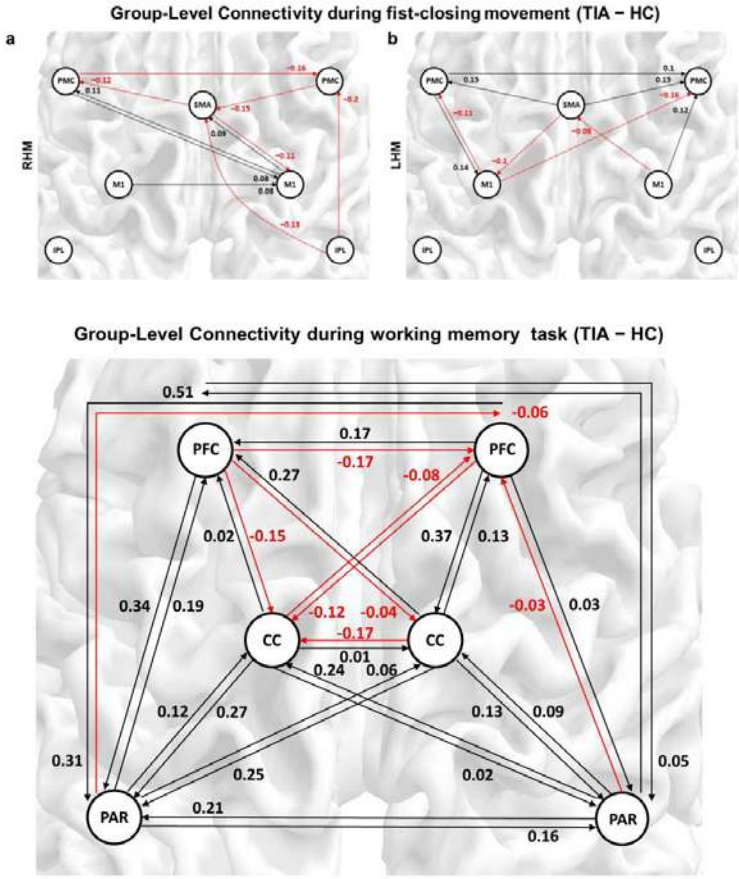

Conclusions: This study showed that while performing fist-closing movements according to the visual stimuli of flickering circles, patients with TIA had greater connections to the ipsilateral M1 and lower connections to the SMA and PMC than the HC (Chu et al., 2023). These results may reflect the disruptions in the information processing (visual cue to action) and controls of voluntary movement, and decreased efficiency of primary motor function M1 in patients with TIA. We also found that patients with TIA had higher excitatory connections between the PAR and CC, and lower connections toward the right PFC during working memory task, compared with HC. It has been shown that the PAR is involved in the storing and retrieving information, and the CC plays a role in performance adjustment during working memory task (Owen et al., 2005). Therefore, although further investigation may be required, these results suggest that patients with TIA would have an increased recruitment of interaction between the storing-retrieving information and its adjustment for supporting the short-term memory function, and the reduced neural capacity of information controls.

References

1. Chu, T. (2023), 'Task-residual effective connectivity of motor network in transient ischemic attack', Communications Biology, vol. 6, no. 1, pp. 843.
2. Coull, A. (2004), 'Population based study of early risk of stroke after transient ischaemic attack or minor stroke: implications for public education and organisation of services', BMJ, vol. 328, no. 7435, pp. 326.
3. Owen, A. M., (2005), 'N-back working memory paradigm: a meta-analysis of normative functional neuroimaging studies', Human brain mapping, vol. 25, no. 1, pp. 46–59.
4. Razi, A. (2015), 'Construct validation of a DCM for resting state fMRI', Neuroimage, vol. 106, pp. 1-14.

Poster No 1511

Harmonizing connectome-wise statistics across different atlases

Qingyuan Liu[1], Yongbin Wei[1], Koen Helwegen[2], Long-Biao Cui[3], Yong Liu[1], Martijn van den Heuvel[2]

[1]School of Artificial Intelligence, Beijing University of Posts and Telecommunications, Beijing, China, [2]Vrije Universiteit Amsterdam, Amsterdam, the Netherlands, [3]The First Affiliated Hospital of Xi'an Jiaotong University, Xi'an, Shanxi

Introduction: Recent studies using multi-site data show that more reproducible connectome-wise alterations[1] can be reported when summary data is combined across multiple studies. This surge in the accumulation of vast amounts of neuroimaging

data brings the need for new methods to incorporate summary statistics of connectome studies. This requires particularly new methods to combine data processed using multiple reconstruction pipelines, in particular concerning variations in atlas selection. Here, we introduce a novel computational framework to remap structural network-based t-statistics across brain atlases.

Methods: T1-weighted MRI and diffusion-weighted imaging (DWI) of 1053 subjects from the Human Connectome Project (HCP)[2] were used. T1-weighted MRI data were processed using FreeSurfer (v7.2) with six atlases used for cortical parcellation, including the Desikan-Killiany (DK) atlas (N = 68)[3], the 114-/219-region subdivisions of the DK atlas (DK-114/DK-219; N = 114/219), the Brainnetome (BN) atlas (N = 210)[4], the HCP-MMP atlas (N = 360)[5], and the Schaefer atlas (N = 200)[6]. DWI data were processed using CATO (v3.2.1), with white matter streamlines reconstructed through deterministic fiber tractography. Next, we propose a framework comprising two consecutive modules to remap network-based t-statistics from a source atlas to a target atlas. The first module uses linear models to map connections from the source to corresponding connections in the target atlas. Coefficients in the linear models are deduced according to the overlap ratios of streamlines between the two atlases, by going through all reconstructed streamlines in each subject from the HCP data. The second module transposes the network-based t-statistic maps by means of derivations of t values incorporating parameters derived from the group-wise overlap ratios generated by the first module and variance maps for the disease and control groups under the source atlas. 369 schizophrenia patients and 418 healthy controls from five data cohorts, including the open-access COBRE[7], UCLA_UNP[8], MCICShare (9), and two in-house datasets[10], were used to examine how the framework could be applied to real network-based statistics and downstream meta-analysis.

Results: We started by simulating network-based statistics by randomly generating two groups using the HCP dataset, with a total of 1000 simulations performed in order to evaluate the framework. Taking the DK-114 atlas as a reference, we show the results of remapping originating from the rest of the atlases in Fig. 1A. Empirical t-statistic maps in the DK-114 atlas show high spatial correlations with the predicted t-statistic maps originated from the rest of the five atlases (r=0.53~0.95). Permutation testing further shows that the correlation achieved in each simulation significantly exceeded null distributions derived from correlations to the rest of the simulations (all p<.001). Furthermore, we show our framework's utility in a meta-analysis, with the effect sizes from five schizophrenia cohorts being combined. The real network-based Cohen's d maps in the DK-114 atlas show high spatial correlations with the predicted Cohen's d maps originating from the five referenced atlases (r=0.56~0.94) (Fig. 2A). Cohen's d maps based on different atlases were selected independently and again revealed a high correlation (r=0.74). Furthermore, we set a range of thresholds of effect sizes and showed 66%±16% (mean ± SD) connections with a certain real effect size could be identified according to predicted effect sizes (Fig. 2B).

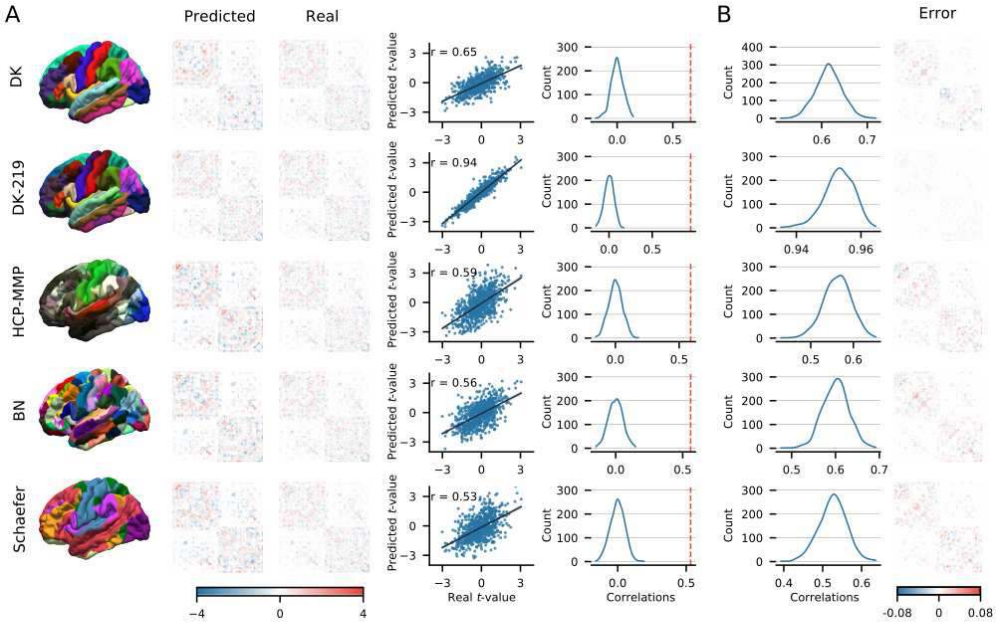

Figure 1. Performance using the simulated network-based statistics derived from the HCP dataset. **(A)** Examples of conversions from DK (N=68), DK-219 (N=219), HCP-MMP (N=360), BN (N=210) and Schaefer (N=200) atlases to DK-114 atlas (N=114) for one simulation. The predicted connection-wise *t* values, the real *t* values and their correlations are shown. Permutation tests show correlations between the predicted and real *t* values (red dashed line) to exceed null distributions of correlations generated using the predicted *t* values from the rest of the simulations (all $p < 0.001$). **(B)** The distribution of correlation coefficients and the sum of error maps of 1000 simulations for all six atlases.

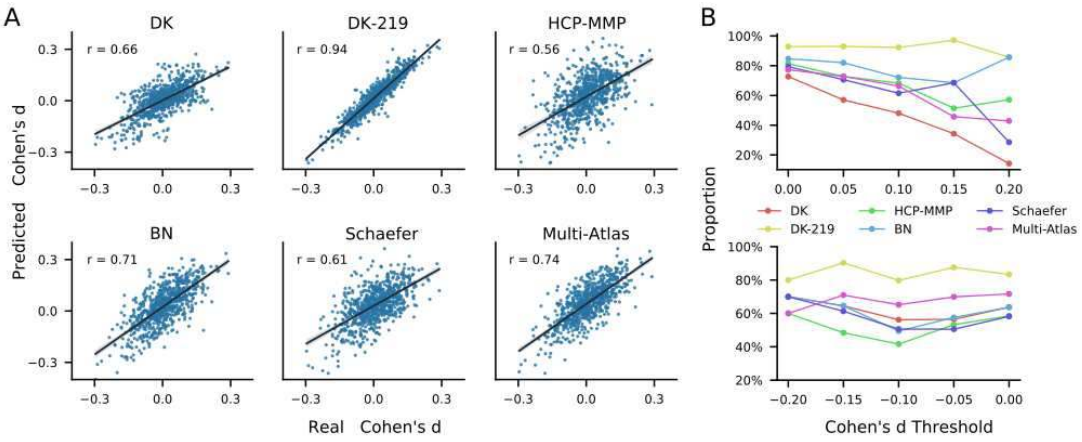

Figure 2. Application of the conversion framework to meta-analysis using the schizophrenia cohorts. **(A)** Scatterplots for correlations of the network-based Cohen's d maps in DK-114 atlas with the predicted Cohen's d maps originated from the five atlases, separately, and from a random mixture of multiple atlases. **(B)** The proportion of connections, among those with a true effect size exceeding a given Cohen's d threshold, being reserved when using the predicted effect size with the same threshold. Top: positive effect sizes; Bottom: negative effect sizes.

Conclusions: We present a powerful framework to remap network-based t-statistics across structural connectomes in various brain atlases. This tool harmonizes connectome-wise summary statistics obtained from different atlases, thereby enhancing the ability to uncover disease heterogeneity within the brain connectome by combining connectome summary statistics across studies.

References

1. Crossley, N. A. et al. (2016), Altered hub functioning and compensatory activations in the connectome: a meta-analysis of functional neuroimaging studies in schizophrenia. Schizophrenia bulletin 42, 434-442.
2. Glasser, M. F. et al. (2016), The human connectome project's neuroimaging approach. Nature neuroscience 19, 1175-1187.
3. Desikan, R. S. et al. (2006), An automated labeling system for subdividing the human cerebral cortex on MRI scans into gyral based regions of interest. NeuroImage 31, 968–980.
4. Fan, L. et al. (2016), The Human Brainnetome Atlas: A New Brain Atlas Based on Connectional Architecture. Cereb Cortex 26, 3508–3526.
5. Glasser, M. F. et al. (2016), A multi-modal parcellation of human cerebral cortex. Nature 536, 171–178.
6. Schaefer, A. et al. (2018), Local-Global Parcellation of the Human Cerebral Cortex from Intrinsic Functional Connectivity MRI. Cerebral Cortex 28, 3095–3114.
7. Cetin, M. S. et al. (2014), Thalamus and posterior temporal lobe show greater inter-network connectivity at rest and across sensory paradigms in schizophrenia. NeuroImage 97, 117–126.
8. Poldrack, R. A. et al. (2016), A phenome-wide examination of neural and cognitive function. Sci Data 3, 160110.
9. Gollub, R. L. et al. (2013), The MCIC Collection: A Shared Repository of Multi-Modal, Multi-Site Brain Image Data from a Clinical Investigation of Schizophrenia. Neuroinform 11, 367–388.
10. Cui, L.-B. et al. (2019), Connectome-Based Patterns of First-Episode Medication-Naïve Patients With Schizophrenia. Schizophrenia Bulletin 45, 1291–1299.

Poster No 1512

Development of Segregation and Integration of Functional Connectomes during the First 1000 Days

Qiongling Li[1,2,3], Mingrui Xia[1,2,3], Debin Zeng[4], Yuehua Xu[1,2,3], Lianglong Sun[1,2,3], Xinyuan Liang[1,2,3], Zhilei Xu[1,2,3], Tengda Zhao[1,2,3], Xuhong Liao[5], Huishu Yuan[6], Ying Liu[6], Ran Huo[6], Shuyu Li[1], Yong He[1,2,3,7]

[1]State Key Laboratory of Cognitive Neuroscience and Learning, Beijing Normal University, Beijing, China, [2]Beijing Key Laboratory of Brain Imaging and Connectomics, Beijing Normal University, Beijing, China, [3]IDG/McGovern Institute for Brain Research, Beijing Normal University, Beijing, China, [4]Beihang university, Beijing, China, [5]School of Systems Science, Beijing Normal University, Beijing, China, [6]Peking University Third Hospital, Beijing, China, [7]Chinese Institute for Brain Research, Beijing, China

Introduction: The first 1000 days, from conception to the first 3 postnatal years[1], are critical periods during which the human brain undergoes a remarkable process of growth and reorganization[2]. One of the most important aspects of this process is to unravel the developmental rules of segregation and integration of functional connectomes. Understanding how these processes mature during this critical period is a crucial step in elucidating the mechanisms underlying typical and atypical development. Here, we investigated the continuous, longitudinal developmental process of functional segregation and integration during the first 1000 days and the potential genetic contributions underlying connectome growth.

Methods: Participants. This study used two publicly available longitudinal imaging datasets- the dHCP[3] and the BCP[4], comprised 930 scans from 665 infants. These infants underwent task-free functional MRI (tf-fMRI) scans at different ages, ranging from 28 post-conceptional weeks to 3 postnatal years. All MRI data were publicly available and anonymized. Connectomic analysis. To capture the continuous maturational process of functional segregation and integration during the first 1000 days, we used a generalized additive mixed model (GAMM) with age as a smooth term and subject ID as a random effect. Linear covariates such as gender, head motion within scanners, and site were included in the model. By applying the GAMM to each brain voxel, we aimed to model the non-linear growth trajectories across the cortex. We also investigated whether the developmental trajectory of functional segregation and integration exhibited spatio-temporal heterogeneity across the cortex, indicating non-uniform maturation patterns. We also investigated the potential influence of differential spatio-temporal gene transcription on the development of the functional connectome.

Results: Significant age-related changes in FCS during the first 1000 days were primarily observed in the primary cortical regions, and regions within default mode and executive control systems (Gaussian random field corrected, voxel-level $p<0.001$, cluster-level $p<0.05$). To illustrate the developmental trajectory of different functional systems, six seeds were selected from brain regions with significant changes (colored circles in Fig 1A). Perinatally, hubs were concentrated in the sensorimotor system shifting to the dorsal attention and visual systems postnatally, transitioning to the default mode at two years, potentially reorganizing by three years (Fig 1B). Specifically, the hub voxel ratio in the sensorimotor system initially decreased then increased. The dorsal attention system showed an increasing and then decreasing trajectory, while the default mode and visual systems continued to increase, with the default mode having a higher ratio (all $p<0.001$). Functional segregation and integration followed distinct developmental trajectories, spatially heterogeneous across the cortex and aligned with the A-P axis (Fig 1C). Module assignment across age is shown in Fig 1D revealing finer changes in the sensorimotor and occipital visual cortices, contrasting with minimal changes in the prefrontal cortex. Additionally, the sensorimotor and occipital visual cortices exhibited greater flexibility in module assignment compared to other regions (Fig 1E). Distinct transcriptomic trajectories between significant and non-significant regions in key neuronal metabolic pathways and dendritic development process were observed (Fig 2), with gene expression differences focusing on aerobic glycolysis ($p<0.001$, FDR-corrected) and dendritic development ($p=0.02$, FDR-corrected).

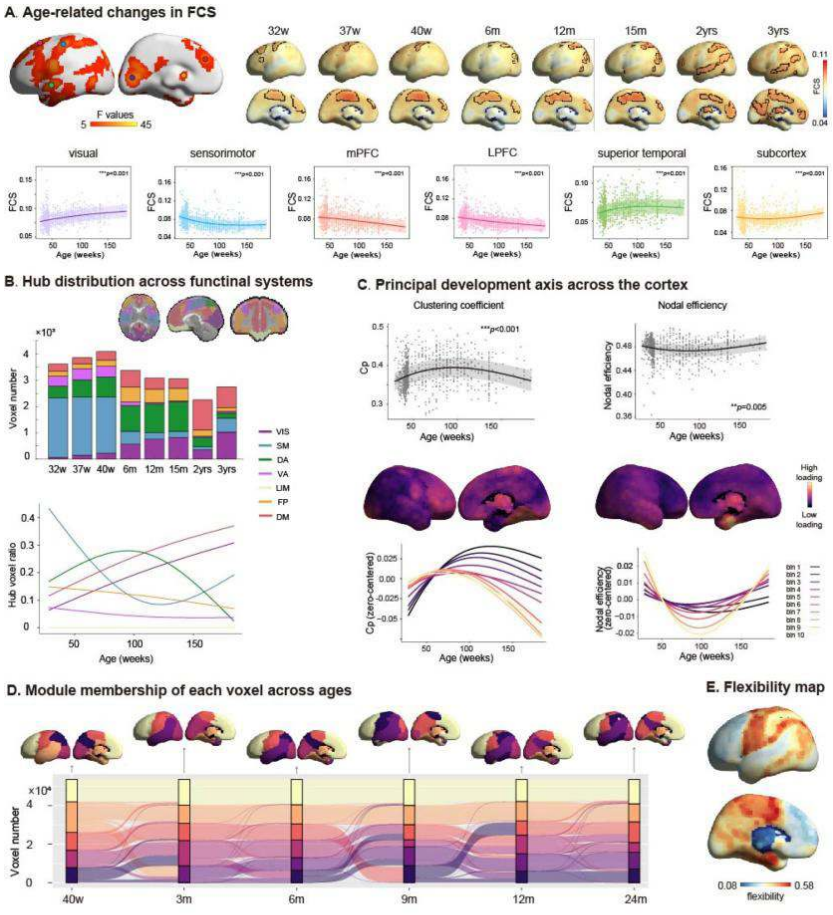

Fig 1. (A) Voxel-wise developmental changes of functional connectivity strength. (B) Hub distribution across different functional systems. (C) The developmental trajectories of mean clustering coefficient and nodal efficiency and the principal developmental axis for clustering coefficient and nodal efficiency respectively. (D) Module membership of each voxel across ages and the flexibility of module assignment of each voxel. w post-conceptional week; m postnatal month; y postnatal year.

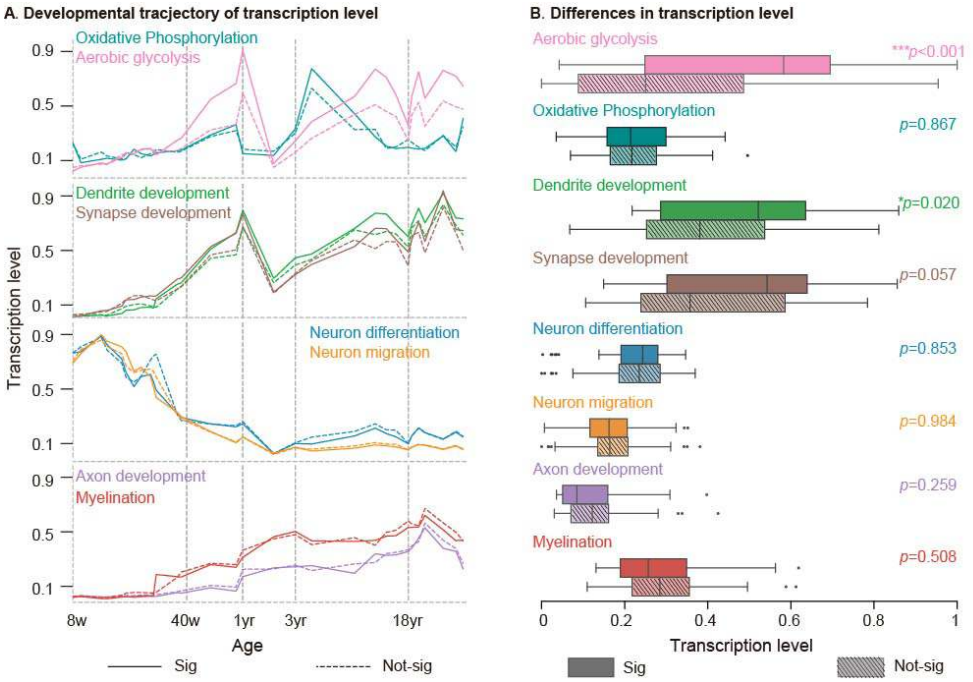

Fig 2. (A) Transcriptomic trajectories of significantly and non-significantly changed FCS regions. (B) Gene expression differences between significant and non-significant FCS regions. w post-conceptional week; m postnatal month; y postnatal year.

Conclusions: Our analysis revealed a priority development of local segregation and hub relocation from primary to higher-order cortex. Regional developmental trajectories of functional segregation and integration diverged in a continuous manner across the A-P axis. The underlying mechanism may be the regulation of genes related to aerobic glycolysis and dendritic development.

References

1. Cusick, S.E.. (2016). The role of nutrition in brain development: the golden opportunity of the “first 1000 days.” The Journal of pediatrics 175, 16–21.
2. Gilmore, J.H., (2018). Imaging structural and functional brain development in early childhood. Nat. Rev. Neurosci. 19, 123–137. 10.1038/nrn.2018.1.
3. Edwards, A.D., (2022). The Developing Human Connectome Project Neonatal Data Release. Front. Neurosci. 16.
4. Howell, B.R., (2019). The UNC/UMN Baby Connectome Project (BCP): An overview of the study design and protocol development. NeuroImage 185, 891–905. 10.1016/j.neuroimage.2018.03.049.

Poster No 1514

Differential contributions of functional and structural connectivity to chronic stress symptoms

David O’Connor[1], Charbel Gharios[2], Mandy Van Leent[1], Helena Chang[1], Shady Abohashem[2], Michael Osborne[2], Cheuk Tang[1], Audrey Kaufman[1], Philip Robson[1], Sarayu Ramachandran[1], Claudia Calcagno[1], Venkatesh Mani[1], Maria Giovanna Trivieri[1], Antonia Seligowski[2], Sharon Dekel[2], Willem Mulder[3], James Murrough[1], Lisa Shin[4], Ahmed Tawakol[2], Zahi Fayad[1]

[1]Icahn School of Medicine at Mount Sinai, New York, NY, [2]Massachusetts General Hospital, Boston, MA, [3]Radboud University Medical Center, Nijmegen, Netherlands, [4]Tufts University, Boston, MA

Introduction: Chronic stress is a long-standing health concern. Its effects are particularly evident in post-traumatic stress disorder (PTSD). PTSD symptoms include intrusive recollections of traumatic events, hypervigilance, and elevated physiological arousal. Individuals with chronic stress have poorer health outcomes overall. In this study we investigate the effects of chronic stress on the brain using functional and structural MRI connectivity estimates.

Methods: MR imaging of the brain was performed in 70 participants (19 with PTSD, 35 Trauma-exposed controls without PTSD, and 16 Healthy controls). Task (face-matching, (Hariri et al., 2000; Swartz et al., 2015)) and resting state fMRI (rs-fMRI), diffusion MRI and T1 images were collected. Questionnaire data were collected to assess chronic stress, resilience, anxiety, and trauma, including the Perceived Stress Scale (PSS), Conor Davidson Resilience Scale (CDRISC), State-Trait Inventory for Cognitive and Somatic Anxiety (STICSA), and PTSD checklist for DSM-5 (PCL-5). MR data were preprocessed using Freesurfer, fMRIPrep and QSIPrep (Cieslak et al., 2021; Esteban et al., 2019; Fischl, 2012). Functional (task and rs-fMRI) and structural connectivity

matrices were generated using the Shen 368 atlas. The network-based statistic (NBS) was used to identify functional and structural connections which discriminate participants with PTSD and controls (Zalesky et al., 2010). NBS was run for varying t value thresholds from 0.5 up to 4. Functional and structural network mean connectivity, within each of the respective discriminating networks, were then related to questionnaire summary scores using linear regression, with adjustment age and sex. The cross-modality generalization of the connections was also assessed. The functional task connections which successfully discriminated subgroups were applied to the rs-fMRI data, and structural data, and then in each case related to the set of four questionnaires. The structural connections which successfully discriminated subgroups was then applied to each set of functional data and similarly related to the questionnaires.

Results: A task-based functional network of 92 edges was found at t = 3.5, p = 0.063 (Figure 1, panel A), which discriminated PTSD subjects from controls. A structural network of 238 edges was also found at t = 3, p = 0.078, Figure 1, panel B. For rs- fMRI, no discriminating network was found. The mean connectivity of the task fMRI network and structural network were negatively associated with CDRISC scores, and positively associated with the PSS, PCL, and STICSA. Figure 2 shows a table of beta values and confidence intervals. The brain regions most represented in the task network were the left fusiform gyrus, secondary visual areas, primary motor area, cerebellum, and frontal eye fields. This result likely reflects differences in how the task was processed, with individuals with PTSD documented as having disrupted visual processing (Mueller-Pfeiffer et al., 2013). The brain regions most represented in the structural network were the left and right amygdala, pars orbitalis, insula, and secondary visual area. The amygdala is a classical feature in structural findings in PTSD (Logue et al., 2018). The results of the cross-modality comparisons are also shown in Figure 2, where the structural network could be applied to the task data, and the task network to the rest data, with some success.

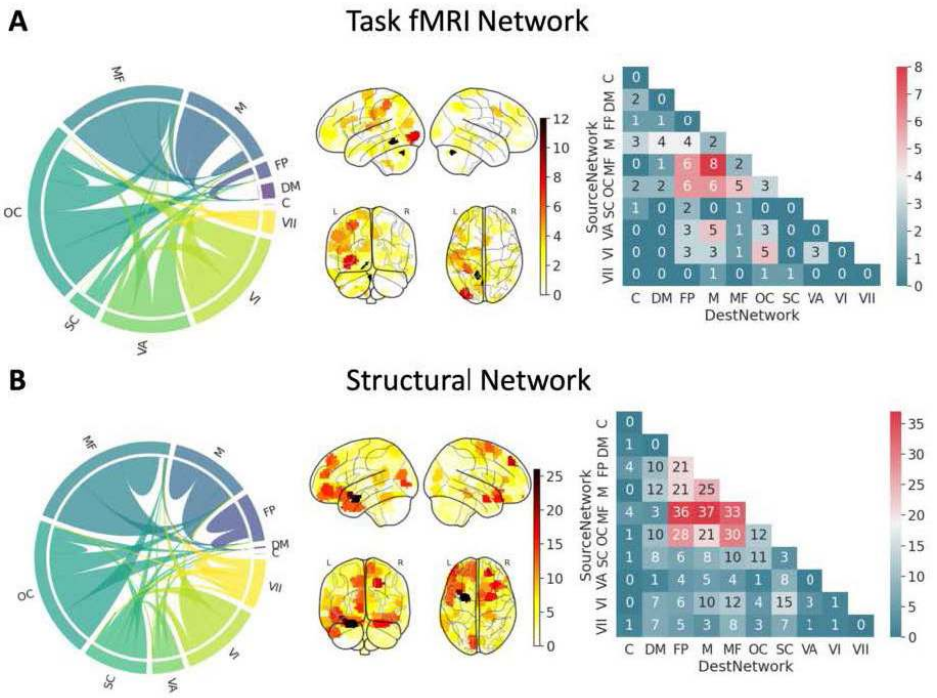

Figure 1 – Task based functional network (A) and structural network (B) which discriminate PTSD and controls. First column is a network level chord plot, second column shows which brain regions are most involved in the network, third column shows a heatmap of connections by network. C = Cerebellum. DM = Default Mode, FP = Frontal Parietal, M = Motor, MF = Medial Frontal, OC = Other Cortical, SC = Subcortical, VA = Visual Association, VI = Visual 1, VII = Visual 2

Explanatory variable		Beta	95% Conf Int	p
PSS	Mean task fMRI Network Connectivity	64.75	45.79, 83.70	<0.001
STICSA		80.43	59.57, 101.28	<0.001
CDRISC		-79.94	-120.72, -39.15	<0.001
PCL		160.84	101.33, 220.33	<0.001
PSS	Mean Structural Network Connectivity	48.79	29.96, 67.62	<0.001
STICSA		62.14	40.82, 83.45	<0.001
CDRISC		-69.33	-103.65, -34.99	<0.001
PCL		140.58	90.26, 190.88	<0.001
PSS	Mean rest fMRI connectivity within task network	23.83	-14.15,61.80	0.214
STICSA		54.42	7.23,101.60	0.025
CDRISC		-68.38	-134.82,-1.92	0.044
PCL		79.69	-74.82,234.19	0.300
PSS	Mean structural connectivity within task network	0.09	-39.39,39.56	0.997
STICSA		11.08	-31.93,54.09	0.608
CDRISC		-32.30	-97.92,33.33	0.328
PCL		18.50	-101.12,138.11	0.755
PSS	Mean task fMRI connectivity within structural network	41.15	8.68,73.61	0.014
STICSA		41.14	2.96,79.32	0.035
CDRISC		-42.10	-103.34,19.15	0.175
PCL		75.99	-48.25,200.24	0.223
PSS	Mean rest fMRI connectivity within structural network	-7.86	-37.84,22.12	0.601
STICSA		16.29	-22.09,54.66	0.398
CDRISC		-16.39	-70.10,37.32	0.543
PCL		-4.45	-127.55,118.66	0.942

Figure 2 – Associations between functional and structural connectivity estimates and mental health questionnaires, adjusting for age and sex.

Conclusions: We were able to find functional and structural connectivity networks which are sensitive to commonly used scales for assessing resilience, stress, trauma, and anxiety. The results suggests that task fMRI is more salient than rest, as is the structural data. There was some concordance between task and structural data in the features extracted. These results highlight the benefit of multimodal approaches to investigating brain-behavior relationships.

References

1. Cieslak, M., Cook, P. A., He, X., Yeh, F.-C., Dhollander, T., Adebimpe, A., Aguirre, G. K., Bassett, D. S., Betzel, R. F., Bourque, J., Cabral, L. M., Davatzikos, C., Detre, J. A., Earl, E., Elliott, M. A., Fadnavis, S., Fair, D. A., Foran, W., Fotiadis, P., … Satterthwaite, T. D. (2021). QSIPrep: An integrative platform for preprocessing and reconstructing diffusion MRI data. Nature Methods, 18(7), Article 7. https://doi.org/10.1038/s41592-021-01185-5
2. Esteban, O., Markiewicz, C. J., Blair, R. W., Moodie, C. A., Isik, A. I., Erramuzpe, A., Kent, J. D., Goncalves, M., DuPre, E., Snyder, M., Oya, H., Ghosh, S. S., Wright, J., Durnez, J., Poldrack, R. A., & Gorgolewski, K. J. (2019). fMRIPrep: A robust preprocessing pipeline for functional MRI. Nature Methods, 16(1), 111–116. https://doi.org/10.1038/s41592-018-0235-4
3. Fischl, B. (2012). FreeSurfer. NeuroImage, 62(2), 774–781. https://doi.org/10.1016/j.neuroimage.2012.01.021
4. Logue, M. W., van Rooij, S. J. H., Dennis, E. L., Davis, S. L., Hayes, J. P., Stevens, J. S., Densmore, M., Haswell, C. C., Ipser, J., Koch, S. B. J., Korgaonkar, M., Lebois, L. A. M., Peverill, M., Baker, J. T., Boedhoe, P. S. W., Frijling, J. L., Gruber, S. A., Harpaz-Rotem, I., Jahanshad, N., … Morey, R. A. (2018). Smaller Hippocampal Volume in Posttraumatic Stress Disorder: A Multisite ENIGMA-PGC Study: Subcortical Volumetry Results From Posttraumatic Stress Disorder Consortia. Biological Psychiatry, 83(3), 244–253. https://doi.org/10.1016/j.biopsych.2017.09.006
5. Mueller-Pfeiffer, C., Schick, M., Schulte-Vels, T., O'Gorman, R., Michels, L., Martin-Soelch, C., Blair, J. R., Rufer, M., Schnyder, U., Zeffiro, T., & Hasler, G. (2013). Atypical visual processing in posttraumatic stress disorder. NeuroImage : Clinical, 3, 531–538. https://doi.org/10.1016/j.nicl.2013.08.009
6. Zalesky, A., Fornito, A., & Bullmore, E. T. (2010). Network-based statistic: Identifying differences in brain networks. NeuroImage, 53(4), 1197–1207. https://doi.org/10.1016/j.neuroimage.2010.06.041

Poster No 1515

Attenuated reconfiguration of functional networks in extremely preterm-born children and adolescents

Maksym Tokariev[1], Virve Vuontela[1], Anton Tokariev[2], Piia Lönnberg[2], Sture Andersson[2], Helena Mäenpää[2], Marjo Metsäranta[2], Aulikki Lano[2], Synnöve Carlson[1]

[1]Aalto University, Espoo, Finland, [2]Helsinki University Hospital and University of Helsinki, Helsinki, Finland

Introduction: Large-scale brain networks undergo significant structural and functional developments since the third trimester of gestation and continue to mature into adulthood. These networks support a broad repertoire of higher cognitive functions, and their functional organization also reconfigures in response to external sensory stimuli and task performance. Extremely preterm birth (< 28 weeks of gestation) poses a high risk for the proper formation of the brain networks which can be reflected in altered functional connectivity (FC). We collected functional magnetic resonance imaging (fMRI) data from extremely preterm-born and term-born children and adolescents during two brain-states, resting-state and performance of visuospatial n-back tasks, to investigate whether the FC of cognitive networks differs between the two groups. We aimed to identify

networks that reconfigure FC between the brain-states differently between the groups. We also evaluated whether the FC strength of the networks associates with task performance.

Methods: Participants were extremely preterm-born (n=24, 15 males, mean age at fMRI 10.3 ± SD 3.2 y) and healthy term-born (n=22, 11 males, mean age 9.5 ± SD 2.5 y) children and adolescents with normal global cognitive performance. The fMRI data were preprocessed using a volume-based pipeline from CONN 21a toolbox, which included realignment, slice-time correction, and indirect normalization of functional and structural images to standard MNI152 space. The confounding effects, including motion parameters, were regressed out from the timeseries, and band-pass filtration within frequency band of 0.01-0.15 Hz was performed. The Schaefer atlas was used to parcellate the brain into 400 regions that were assigned to seven networks including the default mode (DMN), frontoparietal (FPN), visual (VN), dorsal attention (DAN), ventral attention, somatomotor, and limbic networks. For each subject, the matrices of resting-state and task FC were computed as pairwise Pearson's correlations between time courses of all regions. Differences in FC between the groups and brain-states, and the associations between FC strength and n-back task performance were analyzed using network-based statistics (significance level 0.05, followed by FWE-correction).

Results: Statistical analysis produced a significant group-by-state interaction in DMN ($p = 0.016$, $\eta 2 = 0.22$), DAN ($p = 0.016$, $\eta 2 = 0.23$), and VN ($p=0.022$, $\eta 2 = 0.21$). Controls had stronger FC during resting-state compared to tasks in both DMN ($t21 = 14.54$, $p < 0.001$) and VN ($t23 = -0.72$, $p = 0.45$), while in preterms the FC strength did not differ between the brain-states. In DAN, controls had stronger FC during tasks than during resting-state ($t21 = -5{,}79$, $p < 0.001$), while the opposite was observed in preterms ($t23 = 3.18$, $p = 0.02$). Controls exhibited significant associations between task performance and network FC strength during tasks. Fewer incorrect responses were associated with stronger FC in DAN ($R = -0.708$, $p = 0.026$) and VN ($R = -0.751$, $p = 0.028$). Shorter response times associated with stronger FC in FPN ($R = -0.848$, $p = 0.037$) and weaker FC in DAN ($R = 0.583$, $p = 0.017$) and VN ($R = 0.607$, $p = 0.034$). No significant associations between performance and FC were observed in preterms.

Conclusions: We found that in preterms, the FC strength during task performance was either reduced or comparable to that during resting-state in several networks supporting cognitive performance. Moreover, preterms did not show significant associations between network FC and task performance. Controls, on the other hand, had a larger change in FC strength between the brain-states, and the FC strength of several networks during tasks was associated with better performance. Together these results suggest that flexible reconfiguration of network FC is important for successful performance of tasks that require attention and working memory, and this ability is reduced in extremely preterm-born children and adolescents.

References

1. Cole, M.W. (2014), 'Intrinsic and task-evoked network architectures of the human brain', Neuron, vol. 83, no. 1, pp. 238-251
2. Kostović, I. (2006), 'The development of cerebral connections during the first 20-45 weeks' gestation', Seminars in Fetal & Neonatal Medicine, vol. 11, no. 6, pp. 415-422
3. Schaefer, A. (2018), 'Local-global parcellation of the human cerebral cortex from intrinsic functional connectivity MRI', Cerebral Cortex, vol. 28, no. 9, pp. 3095-3114
4. van den Heuvel, M.P. (2015), 'The neonatal connectome during preterm brain development', Cerebral Cortex, vol. 25, no. 9, pp. 3000-3013
5. Whitfield-Gabrieli, S. (2012), 'Conn: A functional connectivity toolbox for correlated and anticorrelated brain networks', Brain Connectivity, vol. 2, no. 3, pp. 125-141
6. Yeo, B.T.T. (2011), 'The organization of the human cerebral cortex estimated by intrinsic functional connectivity', Journal of Neurophysiology, vol. 106, no. 3, pp. 1125-1165

Poster No 1516

An Effective "Traffic Map" of the Human Brain via Unified Structural and Functional Connectivity

Arzu C Has Silemek[1,2], Haitao Chen[2], Pascal Sati[1,2], Wei Gao[2]

[1]Department of Neurology, Cedars-Sinai Medical Center, Los Angeles, CA, [2]Biomedical Imaging Research Institute (BIRI), Cedars-Sinai Medical Center, Los Angeles, CA

Introduction: Conventional studies of the human brain connectome utilize either structural or functional connectivity measure, but few studies have combined them for a better understanding of how the brain is effectively wired (Zamani Esfahlani, Faskowitz et al. 2022). In this study, we viewed structural connections (SC) as the brain's "road" system, with strong SC representing efficient "road segments" over short distances and weaker SCs indicating greater "cost" over longer distances. Functional connections (FC) were considered as "effective traffic" between different pairs of regions. To bridge the two, each "traffic"/FC would choose to use the most efficient "route" defined by one of more steps of direct SCs that collectively have the least "cost" (i.e., anatomical distance/SC). By unifying structural and functional connectivity (USFC) and defining

all structural “routes” that support most efficient functional communication, we created an effective “traffic map” of the human brain. The mostly used routes/road segments of this traffic system were highlighted and we further characterized the relationship between SC and FC in these routes as well as their global efficiency properties.

Methods: Data from a cohort of 394 subjects [59% female, age range: 22 – 36] from the Human Connectome Project were used. After constructing SC and FC measures based on the AAL template(Jeurissen, Tournier et al. 2014, Fenske, Liu et al. 2023), the most “efficient” pathway for each FC in each subject was identified by summing the cost of each “step” (i.e., the Euclidean distance divided by the strength of direct SC between a pair of regions) along all potential routes (up to 4 steps were searched) and choosing the one with the least “cost”. A USFC value for each “road segment”/direct FC was then calculated as the sum of all FC values that use this segment in their respective routes, essentially quantifying the amount of “traffic” on this “road segment”. Next, we examined nodal-level functional-structural coupling at the group level across all routes, focusing on those that are consistent in over 50% of the subjects. Finally, global efficiency of the whole brain system was calculated and compared across each metric (i.e., FC, SC and USFC) via Dijkstra algorithm.

Results: The effective “traffic map”/ “route system” of the human brain was shown in Fig. 1A while the top 10 “most heavily used” segments were shown in Fig. 1b. These segments concentrate on the default mode network, the salience network, along with subcortical and visual regions (Fig. 1B). For SC-FC relationships across all routes, slightly positive (for 1-step routes) (Fig. 1D) or non-significant correlations (for 2 and 3-step routes) (Fig. 1F & Fig. 1H) were observed for routes supporting positive FCs, which is consistent with previous findings. Intriguingly, more significant, and stronger negative associations were identified for routes underlying negative FCs for all routes raging from 1 to 3 steps (Fig. 1C, Fig. 1E & Fig. 1G), which has never been reported. Note no common patterns (i.e., shared by >50% of subjects) emerged for 4-step connections so they were not evaluated. When the global efficiencies were quantified for the whole brain connectome, those supported by USFC were significantly higher than those based on either FC or SC alone ($p < 0.001$) (Fig. 1I).

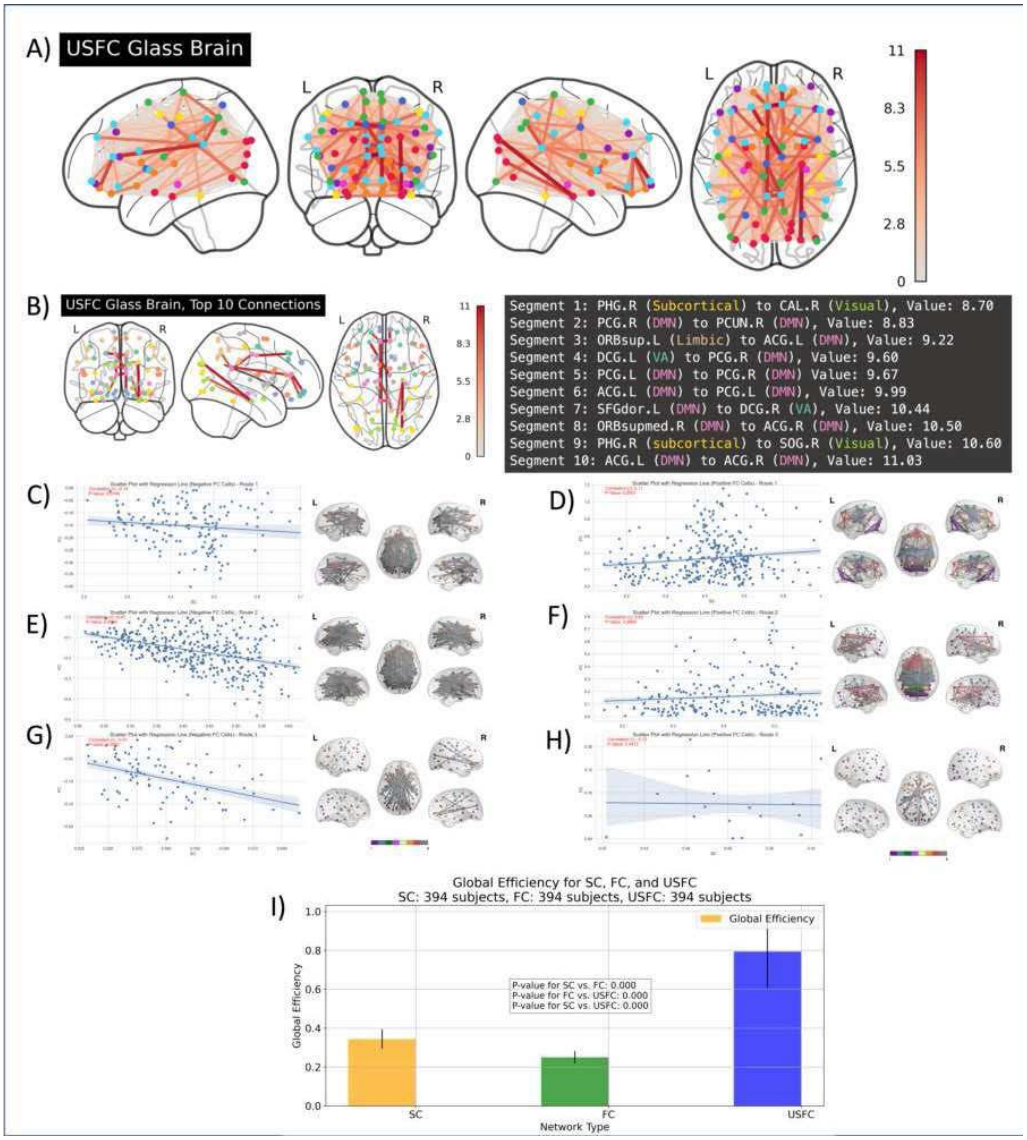

Conclusions: Overall, we introduced USFC as a novel approach and created the brain's first effective "traffic map" highlighting most heavily used "road segments" from the brain's default-mode network, salience network, and visual/subcortical regions. Our analysis revealed a notable negative correlation between negative FC and underlying SC for the first time, suggesting that stronger negative FC needs support from stronger structural connectivity. Finally, the USFC system showed much elevated global efficiency of the whole brain connectome compared to FC or SC alone, underscoring the brain's better efficiency when characterized by this novel effective "traffic map".

References

1. Fenske, S. J., J. Liu, H. Chen, M. A. Diniz, R. L. Stephens, E. Cornea, J. H. Gilmore and W. Gao (2023). "Sex differences in resting state functional connectivity across the first two years of life." Dev Cogn Neurosci 60: 101235.
2. Jeurissen, B., J. D. Tournier, T. Dhollander, A. Connelly and J. Sijbers (2014). "Multi-tissue constrained spherical deconvolution for improved analysis of multi-shell diffusion MRI data." Neuroimage 103: 411-426.
3. Zamani Esfahlani, F., J. Faskowitz, J. Slack, B. Misic and R. F. Betzel (2022). "Local structure-function relationships in human brain networks across the lifespan." Nat Commun 13(1): 2053.

Poster No 1517

The Primary Sensation Network Drives Time-resolved Functional Fluctuation Patterns during Resting

Dezhi Jin[1], Ye He[1]

[1]School of Artificial Intelligence, Beijing University of Posts and Telecommunications, Beijing, China

Introduction: A recent study developed a temporal unwrapping method to decompose functional connectivity (FC) into frame-by-frame co-fluctuation patterns based on edge timeseries (ETS)[1,2]. The investigation revealed that moments ("events") characterized by high-amplitude co-fluctuation contained more brain network information that might drive FC than low-amplitude moments[3]. However, other studies found that a range of co-fluctuation amplitudes synchronized across subjects during movie watching[4], and could predict cognitive performance[5]. This suggests that a broad range of co-fluctuation moments may hold specific neural significance other than only the high-amplitude events are important[6]. Therefore, it is worth systematically exploring how the co-fluctuation patterns differ in encapsulating brain network information and what causes variations in whole-brain co-fluctuation across timeseries.

Methods: We preprocessed resting-state fMRI data from 100 unrelated subjects from the Human Connectome Project. Followed the previous approach[2], we computed the element-wise product of the z-scored BOLD timeseries between pairs of brain regions, which generated a co-fluctuation matrix at each time point. Then, we calculated root sum square (RSS) of the co-fluctuation values across region pairs at each time point, quantifying the co-fluctuation amplitude(Fig. 1A). The timepoints were ranked based on their RSS and divided into 20 bins. FC matrices were derived by averaging co-fluctuation matrices either across the entire timeseries (static FC networks) or within each bin (bin FC networks), which recovers the Pearson correlation coefficient. Various network topological properties were calculated for each bin FC network. To evaluate the contribution of each subnetwork to the whole-brain co-fluctuation amplitudes, we defined the ratio of subnetwork-specific RSS to the whole-brain RSS, which was normalized by the number of edges in each subnetwork. We constructed a null model by applying the cyclic shift operator to ETS to examine the significance.

Results: Compared to static FC network, high-amplitude FC networks exhibited stronger connectivity in primary sensation networks (visual, somatomotor, dorsal attention, and ventral attention networks) while low-amplitude FC networks displayed the opposite pattern (Fig. 1D,F,G). It emphasized the role of primary sensation networks in the disparity of FC networks across different co-fluctuation amplitudes. Examining the global topological properties, we observed that the brain network became more integrated and less segregated as the co-fluctuation amplitude decreased in Fig 2A. In local topological properties, the clustering coefficient of all regions decreased with decreasing co-fluctuation amplitude in Fig 2B. The clustering coefficient and degree findings revealed a pattern of separation between primary and high-level networks. Within the control and default mode network, regions exhibited higher degrees in low-amplitude bins compared to high-amplitude bins (Fig 2C). Fig. 2D illustrates the contribution of subnetworks to the whole-brain co-fluctuation. The results indicated that the visual, somatomotor and dorsal attention networks drove the co-fluctuation in the high-amplitude bins, while the limbic network influenced low-amplitude bins (Fig 2D). This suggests that the events were predominantly driven by the primary sensation networks.

Conclusions: Our study systematically examined the functional organization patterns of the brain across varying states of co-fluctuation amplitudes and revealed that the primary sensation network drove the high amplitude of whole-brain co-fluctuation. These findings provided new insights into understanding the mechanism underlying functional connectivity and establishing a solid foundation for further exploring time-resolved functional fluctuations.

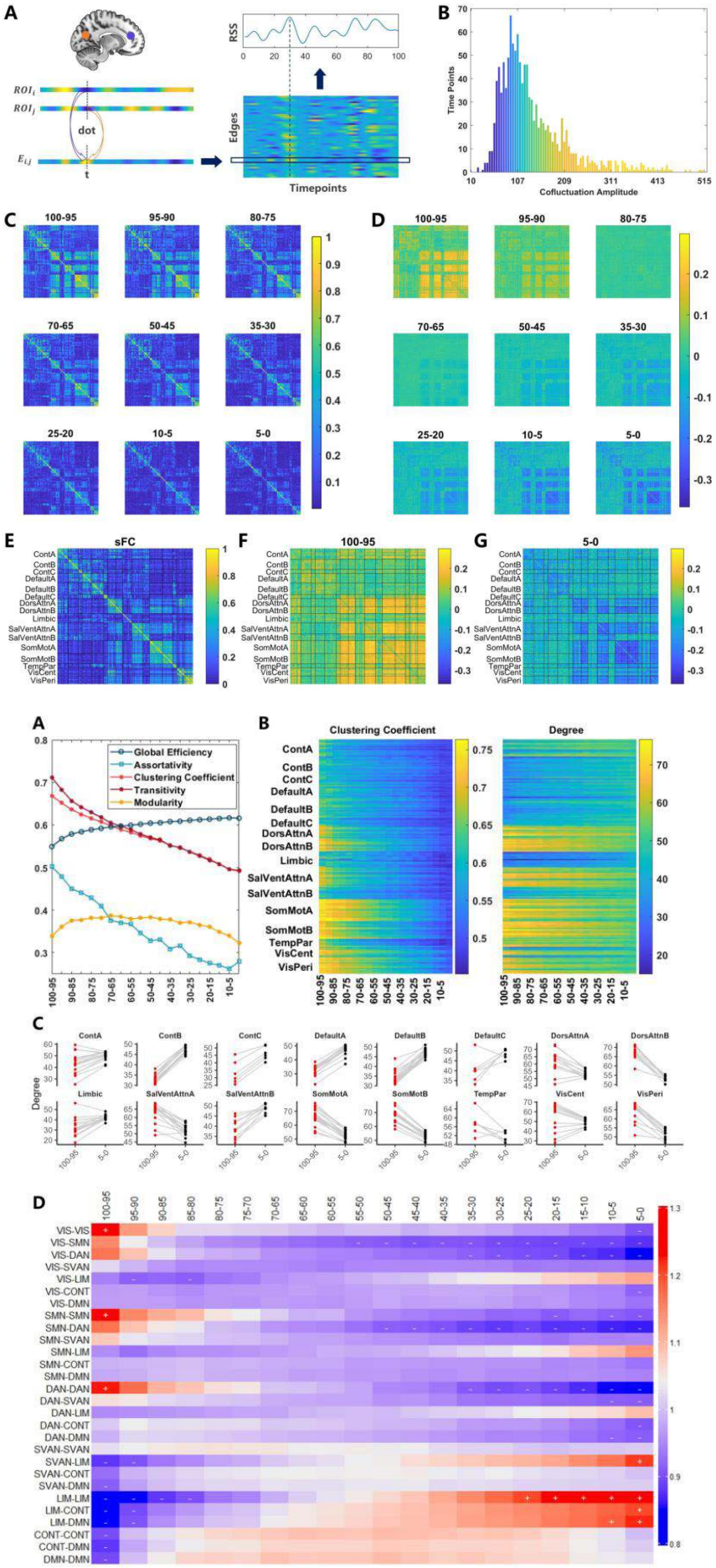
A
RSS
Edges
Timepoints
dot
B
Time Points
Cofluctuation Amplitude
C
100-95
95-90
80-75
70-65
50-45
35-30
25-20
10-5
5-0
D
E
sFC
F
100-95
G
5-0
ContA
ContB
ContC
DefaultA
DefaultB
DefaultC
DorsAttnA
DorsAttnB
Limbic
SalVentAttnA
SalVentAttnB
SomMotA
SomMotB
TempPar
VisCent
VisPeri
A
Global Efficiency
Assortativity
Clustering Coefficient
Transitivity
Modularity
B
Clustering Coefficient
Degree
C
Degree
D
VIS-VIS
VIS-SMN
VIS-DAN
VIS-SVAN
VIS-LIM
VIS-CONT
VIS-DMN
SMN-SMN
SMN-DAN
SMN-SVAN
SMN-LIM
SMN-CONT
SMN-DMN
DAN-DAN
DAN-SVAN
DAN-LIM
DAN-CONT
DAN-DMN
SVAN-SVAN
SVAN-LIM
SVAN-CONT
SVAN-DMN
LIM-LIM
LIM-CONT
LIM-DMN
CONT-CONT
CONT-DMN
DMN-DMN

References
1. Faskowitz, J. (2020), 'Edge-centric functional network representations of human cerebral cortex reveal overlapping system-level architecture', Nature Neuroscience, vol. 23, no. 12, pp. 1644-1654
2. Betzel, R.F. (2022), 'Individualized event structure drives individual differences in whole-brain functional connectivity, NeuroImage, vol. 252, p. 118993
3. Zamani Esfahlani, F. (2020), 'High-amplitude cofluctuations in cortical activity drive functional connectivity', Proceedings of the National Academy of Sciences, vol. 117, no. 45, pp. 28393-28401
4. Tanner, J.C. (2023), 'Synchronous high-amplitude co-fluctuations of functional brain networks during movie-watching', Imaging Neuroscience, vol. 1
5. Wehrheim, M.H. (2022), 'Few temporally distributed brain connectivity states predict human cognitive abilities', NeuroImage, vol. 277, p. 120246
6. Ladwig, Z. (2022), 'BOLD cofluctuation 'events' are predicted from static functional connectivity', NeuroImage, vol. 260, p. 119476

Poster No 1518

Disrupted brain subnetworks in early demyelinating clinically isolated syndrome

Michael Foster[1], Ferran Prados[1,2], Sara Collorone[1], Baris Kanber[1], Indran Davagnanam[1], Done-Helen Dogan[1], Niamh Cawley[1], Marios Yiannakas[1], Lola Ogunbowale[3], Ailbhe Burke[3], Fulvia Palesi[4], Frederik Barkhof[1,5], Claudia Gandini Wheeler-Kingshott[1,6], Olga Ciccarelli[1], Wallace Brownlee[1], Ahmed Toosy[1]

[1]University College London, London, United Kingdom, [2]Universitat Oberta de Catalunya, Barcelona, Spain, [3]Moorfields Eye Hospital NHS Foundation Trust, London, United Kingdom, [4]Univerista di Pavia, Pavia, Italy, [5]Amsterdam University Medical Centre, Amsterdam, Noord-Holland, [6]Universita di Pavia, Pavia, Italy

Introduction: Here we assess the relationship of brain subnetwork connectomes with disability in the demyelinating clinically isolated syndrome (CIS).

Methods: 73 people with early CIS (pwCIS) were assessed for motor, visual and cognitive performance. Multi-shell diffusion-weighted imaging (DWI) was acquired alongside conventional brain MRI sequences. 28 healthy controls (HC) underwent the same protocol. Brain lesion masks were created with Jim software on PD/T2-weighted images. 3D T1-weighted images were filled[1] and segmented[2] into cortical, white and deep grey matter regions, and registered to diffusion space after distortion correction. Activation maps of motor, visual and default mode networks derived from task-based functional MRI meta-analysis[3] were applied to participants' native DWI space. Constrained spherical deconvolution was performed with MRtrix3[4] and fibre orientation distributions generated with multi-shell multi-tissue response functions. Anatomically-constrained probabilistic tractography generated tractograms with 3x107 streamlines, re-weighted with SIFT2[5] to produce connectomes. Graph metrics were calculated with Brain Connectivity Toolbox.[6,7] Statistical analysis was performed with R 4.3.1. Significance levels were set at $P<0.05$. Linear regression models compared graph metrics in each network between pwCIS and HC. Using 'glmulti'[8] to identify linear regression models, graph metrics were independently and in combination assessed for association with clinical outcomes, and the combination of conventional MRI metrics that best correlated with clinical outcomes was identified. Graph metrics were added to the best MRI models. Resulting coefficients were examined to determine if the relationship of each graph metric to disability was preserved after adjusting for conventional MRI; log-likelihood ratio tests compared nested model performance.

Results: Global efficiency (GE), local efficiency (LE), clustering coefficient (CC), transitivity (TS) and node strength (NS) were all increased ($P=0.010$, 0.028, 0.033, 0.047 and 0.020 respectively) in motor networks of pwCIS; the assortativity coefficient (AC) and betweenness centrality (BC) were preserved. No differences between pwCIS and HC were found in visual or cognitive networks. No significant clinical relationships were seen in motor networks. In visual networks, low-contrast letter acuity (LCLA) 2.5% had an inverse relationship with TS ($P=0.034$), and Farnsworth-Munsell 100-hue (FM-100) outcomes had a positive association with NS ($P=0.049$). In cognitive networks, symbol-digit modality testing (SDMT) had an inverse relationship with AC ($P=0.026$). Structural MRI models of clinical outcomes are in Table 1. For T25FW, addition of AC improved model performance ($P=0.033$, $\Delta R2$ 5.3%); no other MRI models of motor outcomes were improved by graph metrics. In visual networks, addition of GE and NS to the MRI model for LCLA 2.5% improved performance ($P=0.001$, $\Delta R2$ 15.1%), and GE, NS and BC together strengthened models of LCLA 1.25% ($P<0.001$, $\Delta R2$ 20.4%). In cognitive networks, adding CC and NS to a model for brief visuospatial memory testing (BVMT-R) appeared to improve the MRI model, but did not reach significance ($P=0.078$, $\Delta R2$ 4.5%).

Clinical outcome	Structural MRI metrics	R^2 (%)
EDSS	BPF + lesion proportion	10.2
T25FW	BPF + WMF + GMF + lesion proportion	7.4
9HPT	none	n/a
HCLA	BPF + lesion proportion	5.8
LCLA 2.5%	BPF + lesion proportion	10.2
LCLA 1.25%	none	n/a
FM-100	BPF + lesion proportion	8.3
SDMT	none	n/a
CVLT-II	WMF	11.7
BVMT-R	GMF	7.7
PASAT	none	n/a

Table 1: The best-performing linear regression models of each clinical outcome according to structural MRI metrics. BPF = brain parenchymal fraction; BVMT-R = brief visuospatial memory test; CVLT-II = California verbal learning test; EDSS = extended disability status scale; FM-100 = Farnsworth-Munsell 100-hue test; GMF = grey matter fraction; HCLA = high-contrast letter acuity; LCLA = low-contrast letter acuity; PASAT = paced auditory serial addition test; SDMT = symbol-digit modality test; T25FW = timed 25-foot walk; WMF = white matter fraction; 9HPT = nine-hole peg test

Conclusions: The motor network was most disrupted against HC; no differences were seen in visual or cognitive networks. However, the relationship of graph metrics with clinical outcomes was stronger in visual and cognitive networks compared with motor; worse clinical outcomes were associated with increased graph metric values. Additionally, graph metrics strengthened MRI models of T25FW and LCLA. The results suggest motor network disruption occurs earlier in the demyelinating disease course; the increase in graph metrics indicates compensatory reorganisation, but clinical associations suggest it is either inadequate or maladaptive. Altogether, the results demonstrate the utility of graph metrics in varied brain networks in CIS.

References

1. Prados F, Cardoso MJ, Kanber B, et al. A multi-time-point modality-agnostic patch-based method for lesion filling in multiple sclerosis. Neuroimage. 2016;139:376–84.
2. Cardoso MJ, Modat M, Wolz R, et al. Geodesic Information Flows: Spatially-Variant Graphs and Their Application to Segmentation and Fusion. IEEE Trans Med Imaging. 2015;34:1976–88.
3. Yarkoni T, Poldrack RA, Nichols TE, et al. Large-scale automated synthesis of human functional neuroimaging data. Nat Methods. 2011;8:665–70.
4. Tournier J-D, Smith RE, Raffelt D, et al. MRtrix3: A fast, flexible and open software framework for medical image processing and visualisation. Neuroimage. 2019;202:116137.
5. Smith RE, Tournier J-D, Calamante F, et al. SIFT2: Enabling dense quantitative assessment of brain white matter connectivity using streamlines tractography. Neuroimage. 2015;119:338–51.
6. Rubinov M, Sporns O. Complex network measures of brain connectivity: Uses and interpretations. Neuroimage. 2010;52:1059–69.
7. Humphries MD, Gurney K. Network 'Small-World-Ness': A Quantitative Method for Determining Canonical Network Equivalence. PLoS One. 2008;3:e0002051.
8. Calcagno V, de Mazancourt C. glmulti: An R Package for Easy Automated Model Selection with (Generalized) Linear Models. J Stat Softw. 2010;34:1–29.

Poster No 1519

Disrupted graph theory properties of resting-state networks in young APOEe4 carriers

Ludmila Kucikova[1], Adam Brass[1], Jianmin Zeng[2], Graciela Muniz-Terrera[3,4], Craig Ritchie[4,5], John O'Brien[6], Li Su[1,6]

[1]University of Sheffield, Sheffield, United Kingdom, [2]Southwest University, Chongqing, China, [3]Ohio University, Athens, OH, [4]University of Edinburgh, Edinburgh, United Kingdom, [5]Scottish Brain Sciences, Edinburgh, United Kingdom, [6]University of Cambridge, Cambridge, United Kingdom

Introduction: Alzheimer's Disease (AD) is defined by a prolonged preclinical period during which brain changes occur without producing overt clinical symptoms. Understanding the relationship between biomarkers, potential risk factors, and related clinical symptoms is crucial to capture different stages of this phase reliably. Middle-aged carriers of risk factors for AD show disturbances in brain structure and microstructure (reviewed in Mak et al., 2017) and brain function (reviewed in Habib et al., 2017), specifically in functional connectivity of large-scale networks of APOEe4-carriers (reviewed in Kucikova et al., 2021). Mapping the trajectory of connectivity differences in young adulthood is still inconclusive. However, our recent research indicates decreased connectivity in the youngest sample of adults with APOEe4 gene that has been previously looked at (Kucikova et al., 2023). The aim of present study is to extend these findings by examining the graph theoretical properties of functional connectivity.

Methods: We analysed the effects of one of the most important genetic risk factors for AD, specifically the APOEe4, on resting-state functional connectivity in a sample of 129 cognitively healthy young adults (aged 17-22). Seven resting-state networks of interest included the DMN, executive, salience, sensorimotor, dorsoattentional, visual, and language networks. Graphs were constructed from single subject correlation matrix. To threshold connectivity within the graphs, we initially used a standard z-scores method. However, recognising the impact of methodological choices on outcomes, we sought to comprehensively investigate the sensitivity of different analytical pipelines. Hence, the second part of this study involved calculating graph properties using alternative thresholding methods (i.e., correlation coefficient, cost) and employing three different types of brain parcellation (i.e., ICA, Oxford-Harvard atlas, Power's atlas) to compare the reliability of the findings across different methodological choices.

Results: The APOEe4-carriers consistently showed decreased functional connectivity in multiple resting-state networks compared to non-carriers. Specifically, we observed decreased degree (T=-3.3, pFDR<0.01; Fig1A1) and global efficiency (T=-2.85, pFDR<0.01; Fig1A2) and increased betweenness centrality (T=2.92, pFDR<0.05; Fig1A3) within the salience network; decreased global efficiency (T=-2,73, pFDR<0.05; Fig1B1) and decreased average path length (T=-529, p<0.0001; Fig1B2) within the sensorimotor network; and increased betweenness centrality (T=2.6, pFDR<0.05; Fig1C1), degree (T=2.82, pFDR=0.01; Fig1C2), and global efficiency (T=3.08, pFDR<0.01; Fig1C3) within dorsoattentional network. Findings in other networks were more sensitive to parcellation and/or thresholding methods used.

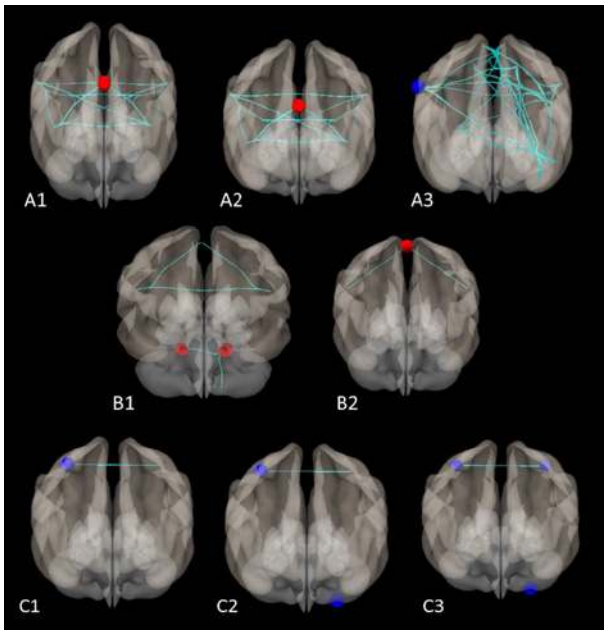

Conclusions: Our results demonstrate that APOEe4 allele alters functional connectivity of multiple networks in cognitively healthy young adults. Functional connectivity was consistently disturbed in salience, sensorimotor, and dorsoattentional networks, reflecting alterations in graph theory properties crucial for communication and information flow within these networks. These results carry implications for our understanding of brain vulnerability related to genetic risk for AD in young adulthood. While our findings were mostly reproducible across different thresholding methods which emphasises the internal validity, the choice of parcellation methods yielded less consistent results. This may be explained by the brain atlas concordance problem (Bohland et al., 2009). In the realm of clinical applications, our study underscores the critical role of methodological choices, particularly in the selection of a brain parcellation method, which can enhance the interpretability and applicability of neuroimaging findings in clinical contexts, potentially informing early diagnostic strategies or intervention approaches for individuals at risk of AD.

References

1. Bohland, J. W., Bokil, H., Allen, C. B., & Mitra, P. P. (2009). The brain atlas concordance problem: quantitative comparison of anatomical parcellations. PloS one, 4(9), e7200.
2. Habib, M., Mak, E., Gabel, S., Su, L., Williams, G., Waldman, A., ... & O'Brien, J. T. (2017). Functional neuroimaging findings in healthy middle-aged adults at risk of Alzheimer's disease. Ageing research reviews, 36, 88-104.
3. Mak, E., Gabel, S., Mirette, H., Su, L., Williams, G. B., Waldman, A., ... & O'Brien, J. (2017). Structural neuroimaging in preclinical dementia: from microstructural deficits and grey matter atrophy to macroscale connectomic changes. Ageing research reviews, 35, 250-264.
4. Kucikova, L., Goerdten, J., Dounavi, M. E., Mak, E., Su, L., Waldman, A. D., ... & Ritchie, C. W. (2021). Resting-state brain connectivity in healthy young and middle-aged adults at risk of progressive Alzheimer's disease. Neuroscience & Biobehavioral Reviews, 129, 142-153.
5. Kucikova, L., Zeng, J., Muñoz-Neira, C., Muniz-Terrera, G., Huang, W., Gregory, S., ... & Su, L. (2023). Genetic risk factors of Alzheimer's Disease disrupt resting-state functional connectivity in cognitively intact young individuals. Journal of Neurology, 1-10.

Poster No 1520

Enhanced contralateral hand learning through virtual reality-induced sensorimotor mismatch training

Elisabeth Jochmann[1], Alexander Schmidt[1], Thomas Jochmann[2], Maximilian Weber[1], Matthias Nürnberger[1], Carsten Klingner[1]

[1]Jena University Hospital, Jena, Germany, [2]Technische Universität Ilmenau, Ilmenau, Germany

Introduction: Current rehabilitation strategies often insufficiently mitigate motor deficits following a stroke. Early post-stroke, patients experience a sensitive period with enhanced motor learning capabilities, which is crucial for regaining motor functions (Zeiler, 2019). However, this period of rapid recovery diminishes substantially over time (Coleman, 2017). During that sensitive period of enhanced motor learning, patients typically suffer from a mismatch between intended and executed movements. Our study posits that this mismatch may be a key driver in motor learning. We hypothesize that artificially inducing a similar sensorimotor mismatch could reactivate the sensitive period for motor learning, particularly in elderly subjects. To explore this, we evaluated motor learning in volunteers subjected to a virtual reality (VR)-induced sensorimotor mismatch. We used resting state functional magnetic resonance imaging (rs-fMRI) to investigate how this mismatch affects the brain's functional networks responsible for motor learning.

Methods: We recruited 69 healthy right-handed participants, aged 19-82 years (mean = 54.1 ± 19.2 years). Participants were randomized into two groups: mismatch (intervention) and errorless (control) (Fig. 1). Participants underwent fMRI scans (3T, Siemens Trio, resting state) before and after a 10-minute VR ball-throwing task with their right hand (Oculus Rift S VR headset, in-house developed game software, performed outside the scanner). The task consisted of picking up a ping pong ball from a table and throwing it at a target. For the mismatch group, the VR system introduced varying sensorimotor discrepancies, such as axis inversion, amplitude changes, or simulated tremors. The target size was reduced or increased to constantly maintain a moderate success rate. The errorless group performed the task without artificial sensorimotor disturbances and the target size adaptation was programmed to a higher success rate. Afterwards, a second round of the VR task was performed, followed by a motor learning task on a laptop: This task required participants to click on transient round targets using a computer mouse, structured into 12 blocks of 30 seconds each, with 30-second rest intervals, first using the right hand and then the left. The objective was to maximize target hits. Rs-fMRI pre- and post-intervention were compared using parametric multivariate statistics (Jafri, 2008), comparing ROI-to-ROI evaluations centered on the somatomotor regions from the Schaefer 2018 atlas (Schaefer, 2018), using the CONN toolbox for SPM (Whitfield-Gabrieli and Nieto-Castanon, 2012). Motor learning performance was derived from the scores in the computer mouse-based target clicking task using a generalized estimating equation (GEE) in R (Liang, 1986; Højsgaard, 2006).

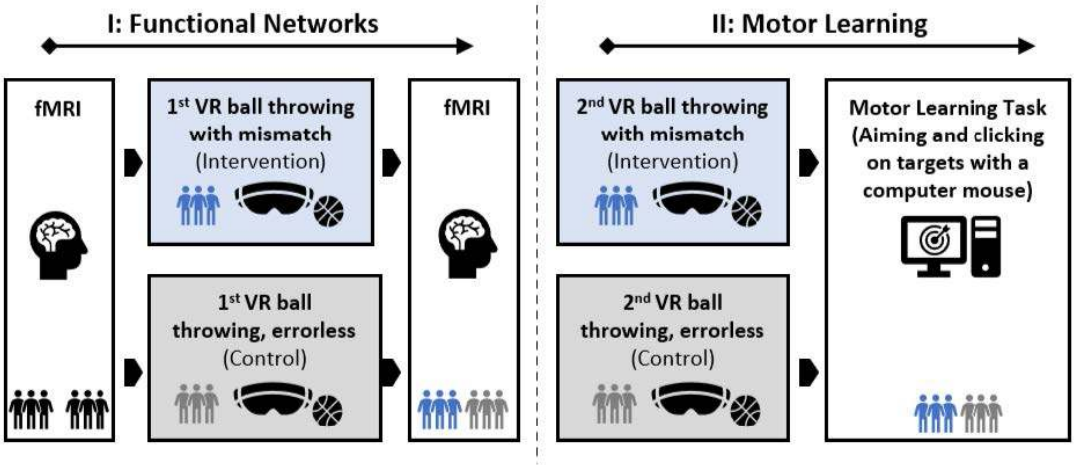

Fig. 1: **Experiment setup**. Participants were randomized to an intervention and a control group. They underwent the shown steps from left to right: first fMRI, VR ball-throwing task, second MRI, VR ball-throwing task, motor learning task. Thus, changes in functional networks (I) and motor learning (II) could be evaluated.

Results: Rs-fMRI analysis: Focusing on participants aged 60 and above (mismatch: n=15; errorless: n=16), the mismatch group displayed enhanced functional connectivity in comparison to the errorless group. These changes were primarily observed in the right somatomotor areas, between the left and right somatomotor regions interhemispherically, and within the left somatomotor regions (Fig. 2). Across the entire cohort, no significant changes in resting state connectivity were observed. Behavioral task: The mismatch group demonstrated a significant increase in the learning rate of the left hand versus the right hand in the mismatch group compared to the errorless group for an adjusted age of 60 years (p=0.039).

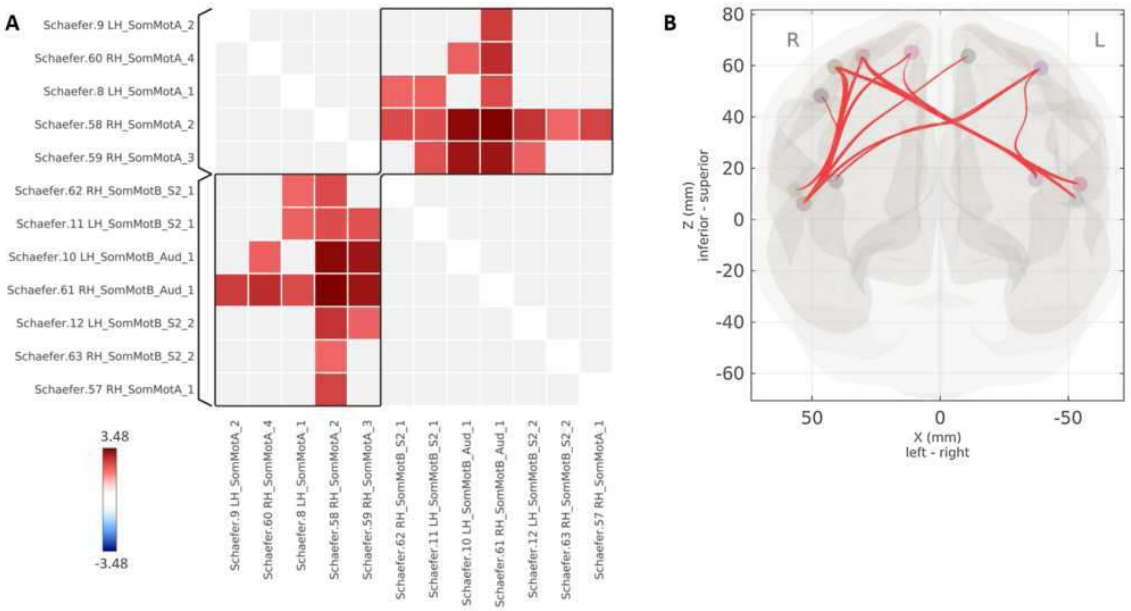

Fig. 2: **RS-fMRI results**. Enhanced functional connectivity in the mismatch group in comparison to the errorless group following the virtual reality (VR) ball-throwing task, relative to baseline measurements. Red denotes enhanced ROI-to-ROI connectivity. The color bar represents the T statistics of the connectivity matrix.

Conclusions: VR-induced artificial sensorimotor mismatch training enhances the functional connectivity in both the contralateral and ipsilateral somatomotor cortex. This training method also improves the learning rate of the contralateral hand in subsequent motor tasks. The next phase involves applying these findings to clinical settings, specifically examining functional connectivity and learning improvements in chronic stroke patients after VR mismatch training.

References

1. Coleman, E.R. (2017) 'Early Rehabilitation After Stroke: a Narrative Review', Current atherosclerosis reports, 19(12), p. 59. Available at: https://doi.org/10.1007/s11883-017-0686-6.
2. Højsgaard, S. (2006) 'The R Package geepack for Generalized Estimating Equations', Journal of Statistical Software, 15, pp. 1–11. Available at: https://doi.org/10.18637/jss.v015.i02.
3. Jafri, M.J. (2008) 'A method for functional network connectivity among spatially independent resting-state components in schizophrenia', NeuroImage, 39(4), pp. 1666–1681. Available at: https://doi.org/10.1016/j.neuroimage.2007.11.001.
4. Liang, K.-Y. (1986) 'Longitudinal data analysis using generalized linear models', Biometrika, 73(1), pp. 13–22. Available at: https://doi.org/10.1093/biomet/73.1.13.
5. Schaefer, A. (2018) 'Local-Global Parcellation of the Human Cerebral Cortex from Intrinsic Functional Connectivity MRI', Cerebral Cortex (New York, NY), 28(9), pp. 3095–3114. Available at: https://doi.org/10.1093/cercor/bhx179.
6. Whitfield-Gabrieli, S. (2012) 'Conn: A Functional Connectivity Toolbox for Correlated and Anticorrelated Brain Networks', Brain Connectivity, 2(3), pp. 125–141. Available at: https://doi.org/10.1089/brain.2012.0073.
7. Zeiler, S.R. (2019) 'Should We Care About Early Post-Stroke Rehabilitation? Not Yet, but Soon', Current Neurology and Neuroscience Reports, 19(3), p. 13. Available at: https://doi.org/10.1007/s11910-019-0927-x.

Poster No 1521

CCEP Inpainting: A Computer Vision-Based Method to Predict Cortico-Cortical Evoked Potentials

Rachel June Smith[1], Arie Nakhmani[1], Kyle Evans-Lee[2], Helen Brinyark[1], Joshua LaRocque[3], Erin Conrad[3]

[1]University of Alabama at Birmingham, Birmingham, AL, [2]Systems and Technology Research, Woburn, MA, [3]University of Pennsylvania, Philadelphia, PA

Introduction: Single-pulse electrical stimulation (SPES) elicits cortico-cortical evoked potentials (CCEPs) that reflect effective connectivity in the human brain. Though SPES is gaining popularity in the epilepsy research community, SPES is not part of routine clinical care because the stimulation procedure is time-consuming and can be tedious to perform. Computational methods to infer the full effective connectivity network from a sampled subset would reduce the need to stimulate all brain areas during testing and lower the barrier to routine use in clinical epilepsy investigations. Using inspiration from computer vision, we present "CCEP inpainting", where we predict the effective connections of missing network nodes by minimizing the Dirichlet energy over the missing data domain.

Methods: We gathered intracranial EEG data collected during SPES from ten epilepsy patients treated for drug-resistant epilepsy at the University of Pennsylvania Hospital. Brief biphasic pulses of electrical stimulation were administered in adjacent pairs of contacts at 1 Hz for 30 trials, and responses were captured in all other contacts. The root-mean-square values of the trial-averaged waveforms in the fast transient (10-50 ms after stimulus) time interval were computed and organized as a matrix with stimulation channels as columns and response channels as rows (Figure 1A). We hid varying percentages of columns (simulating the effective network if specific sites were never stimulated) and then predicted those hidden columns with the inpainting algorithm (Figure 1B). We computed the root-mean-squared error (RMSE) of the difference between the predicted and the original matrix. We also randomized the selection of channels and selected blocked subsets of channels to measure the robustness of the algorithm.

Results: We used the harmonic image inpainting algorithm to impute the hidden columns of the CCEP matrix for all ten patients. A mean RMSE value of 35.4 +/- 12.2 uV resulted when every other column (50% of the full matrix) was hidden. We found that the RMSE increased on average by 0.94 with the addition of one hidden column in the CCEP matrix. The blocked and randomized subsets of hidden channels were more difficult for the algorithm to predict than the regularly spaced hidden channels.

Conclusions: We proposed a novel application of image inpainting to CCEP matrices computed from epilepsy patients. The technique demonstrates that some of the effective connections that would have been directly measured from stimulating a specific site in the brain can be accurately predicted from the stimulation of surrounding areas. These results may indicate that only a subset of sites needs to be stimulated to accurately estimate the full true effective connectivity network as defined by SPES. Increased efficiency of the SPES procedure may invite its adoption into routine clinical procedures for epilepsy investigations.

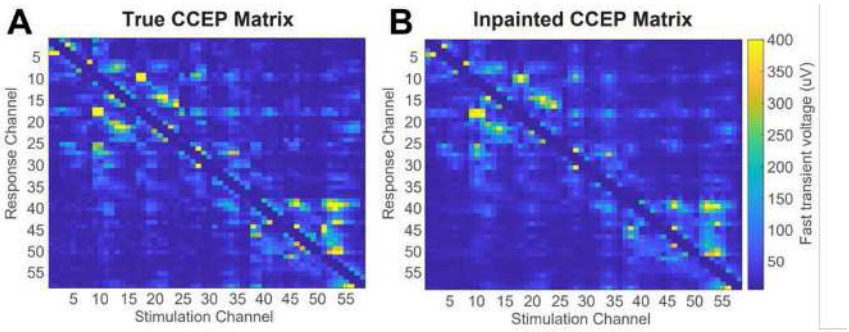

Figure 1. CCEP inpainting for a representative patient with 50% hidden columns. A) The true CCEP matrix is defined by the RMS values of the average fast transient (10-50 ms after stimulus) response waveform in response to electrical stimulation. The matrix is organized such that the response of each channel is an element along the column for each stimulation channel. B) Every other column in the matrix was hidden and then imputed using the harmonic image inpainting algorithm. The color scale is equivalent in both panels.

Poster No 1522

Multi-modal Analysis Show Distinct Covariance Network Patterns Between FTLD Proteinopathies

Hyung Seok Roh[1], Daniel Ohm[1], Jeffrey Phillips[1], Noah Capp[1], Alejandra Bahena[1], Philip Sabatini[1], Lauren Massimo[1], David Wolk[1], Edward Lee[1], Murray Grossman[1], Corey McMillan[1], James Gee[1], David Irwin[1], Min Chen[1]

[1]University of Pennsylvania, Philadelphia, PA

Introduction: Frontotemporal dementia (FTD) is a common form of early-onset dementia with diverse clinical syndromes[1] associated with Frontotemporal Lobar Degeneration (FTLD) mainly caused by tau (FTLD-Tau) or TDP-43 (FTLD-TDP) proteinopathies[2]. Despite evidence relating specific proteinopathies to FTD clinical syndromes, there is still considerable heterogeneity of clinical syndromes and proteinopathies [3]. We perform a multi-modal network-based analysis incorporating both antemortem MR structural imaging and histopathological sampling of FTLD. We construct structural covariance networks from MR volume measurements at regions with histopathological sampling to reveal distinct network patterns between FTLD-Tau and FTLD-TDP. These networks are then compared to postmortem covariance networks from histopathology measurements of disease burden.

Methods: Digital Histopathology Our cohort included 76 FTLD-Tau and 103 FTLD-TDP subjects. Each subject was sampled bilaterally at up to 20 regions in each hemisphere. Staining and percentage of area occupied (%AO) calculation of each

pathology inclusions follow methods described in[4]. MR Data 56 autopsy-confirmed patients (26 FTLD-Tau, 30 FTLD-TDP), and 54 healthy controls (HCs) from Penn Integrated Neurodegenerative Disease Database were used. Volume was measured at cortical regions of interest from T1-weighted MR scans follow methods described in[5]. Volume measurements matching pathology regions were converted to W-scores[6], corrected for both age and sex, to account for healthy variation. Covariance Networks Postmortem log %AO and antemortem T1 MR volume W-score covariance networks for the FTLD-Tau and FTLD-TDP groups were constructed with nodes representing sampled regions and edges weighted by group-level Pearson's correlation coefficient. Group-level differences were evaluated using z-tests after Fisher's Z-transformation[7], focusing on the 5% most significant edges in the networks. Node Strength Node strength was calculated as sum of all connected edge weights at each node. To test if regions with greater pathology act as epicenters, correlation between node strength and log %AO of postmortem group difference networks was measured. To show that increased covariance reflects greater atrophy, we measured correlation between node strength and volume W-score of antemortem group difference networks. Lastly, to test that increased covariance reflects greater pathology, correlation between node strength of antemortem group difference networks and log %AO was measured. Goodness of Fit Graph distance metrics (Hamming Distance, Frobenius Distance, Jaccard Distance, and Graph Diffusion[8]) were used to measure the goodness of fit between postmortem and antemortem group-level difference networks.

Results: Node Strength Positive correlations between postmortem node strength and log %AO for FTLD-Tau and FTLD-TDP groups were observed. Statistically significant negative correlations were found between antemortem node strength and volume W-score for both groups. Positive correlations between antemortem node strength and log %AO were observed for both groups, with statistical significance in the FTLD-Tau group (Figure 1) establishing that increased covariance among nodes of both modalities was associated with greater neurodegeneration. Goodness of Fit Similar network characteristics within each FTLD-Tau and FTLD-TDP group were observed between postmortem and antemortem networks, with distinct patterns between the two groups. Quantitively, we consistently observe a smaller graph distance between postmortem and antemortem networks for both FTLD-Tau and FTLD-TDP groups than between pathology groups across all metrics (Figure 2).

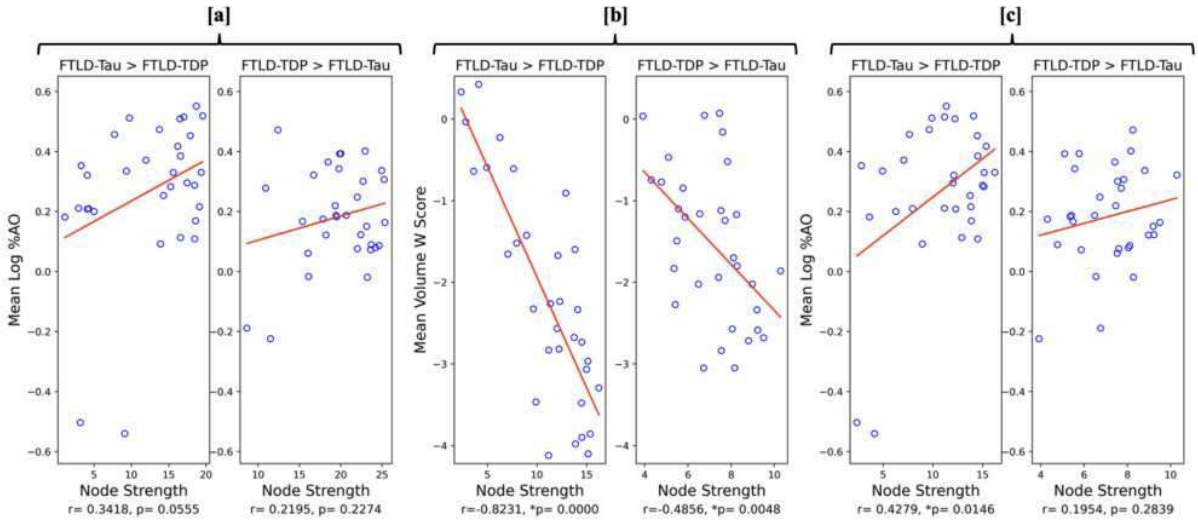

Figure 1. Shown in [a] are the correlation between node strength and mean log %AO of postmortem group-level difference networks. Shown in [b] are the correlation between node strength and mean volume W-score of antemortem group-level difference networks. Shown in [c] are the correlation between node strength of antemortem group-level difference networks and mean log %AO of postmortem group-level difference networks. Blue circles represent the nodes of the group-level difference network, with the linear regression line depicted in red for all plots.

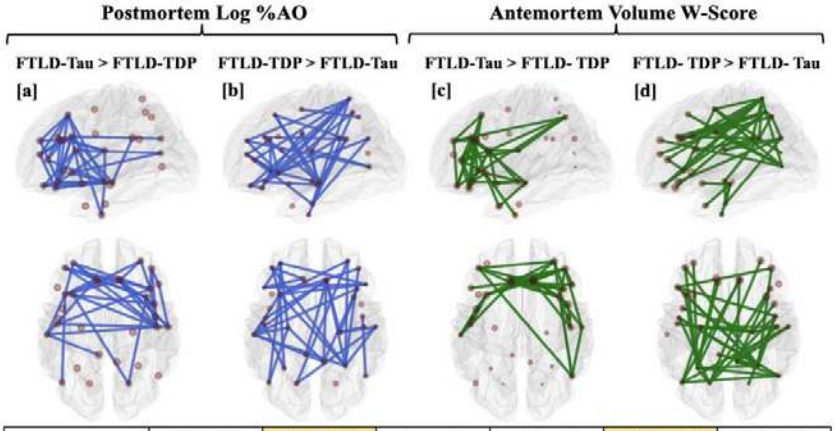

	[a] vs [b]	[a] vs [c]	[a] vs [d]	[b] vs [c]	[b] vs [d]	[c] vs [d]
Hamming Distance	0.161	0.133	0.161	0.153	0.137	0.161
Frobenius Distance	12.649	11.489	12.649	12.329	11.662	12.649
Jaccard Distance	1.0	0.904	1.0	0.974	0.919	1.0
Graph Diffusion	3.622	2.732	3.633	3.819	3.149	4.079

Figure 2. Postmortem log %AO group-level difference networks are shown in [a] and [b]. The size of nodes in the network illustrates the relative pathological burden, with edges (blue) showing the top 5% significant group-level differences. Antemortem volume W-Score group-level difference networks are shown in [c] and [d]. The size of the nodes in the network illustrates the relative cortical atrophy, with edges (green) showing the top 5% significant group-level differences. The table displays the graph distances between all networks. Graph distance between postmortem and antemortem networks for FTLD-Tau and FTLD-TDP groups are highlighted in yellow.

Conclusions: Our results suggest there exist distinct network patterns of disease between FTLD-Tau and FTLD-TDP that are consistent across different modalities. In future work, we plan to assess the goodness of fit through more intricate methodologies, such as motif analysis and stochastic block model.

References

1. Irwin, D.J., Cairns, N.J., Grossman, M., McMillan, C.T., Lee, E.B., Van Deerlin, V.M., Lee, V.M., Trojanowski, J.Q. (2015). "Frontotemporal lobar degeneration: defining phenotypic diversity through personalized medicine." Acta Neuropathol, 129, 469–491.
2. Mackenzie, I.R., Neumann, M., Bigio, E.H., Cairns, N.J., Alafuzoff, I., Kril, J., Kovacs, G.G., Ghetti, B., Halliday, G., Holm, I.E., Ince, P.G., Kamphorst, W., Revesz, T., Rozemuller, A.J., Kumar-Singh, S., Akiyama, H., Baborie, A., Spina, S., Dickson, D.W., Trojanowski, J.G., Mann, D.M. (2010). "Nomenclature and nosology for neuropathologic subtypes of frontotemporal lobar degeneration: an update." Acta Neuropathol, 119, 1–4.
3. Murley, A.G., Coyle-Gilchrist, I., Rouse, M.A., Jones, P.S., Li, W., Wiggins, J., Lansdall, C., Rodríguez, P.V., Wilcox, A., Tsvetanov, K.A., Patterson, K., Lambon Ralph, M.A., Rowe, J.B. (2020). "Redefining the multidimensional clinical phenotypes of frontotemporal lobar degeneration syndromes." Brain, 143, 1555–1571.
4. Chen, M., Ohm, D.T., Phillips, J.S., McMillan, C.T., Capp, N., Peterson, C., Xie, E., Wolk, D.A., Trojanowski, J.Q., Lee, E.B., Gee, J., Grossman, M., Irwin, D.J. (2022). "Divergent Histopathological Networks of Frontotemporal Degeneration Proteinopathy Subtypes." Journal of Neuroscience, 42(18), 3868–3877.
5. Chen, M., Burke, S., Olm, C.A., Irwin, D.J., Massimo, L., Lee, E.B., Trojanowski, J.Q., Gee, J.C., Grossman, M. (2023). "Antemortem network analysis of spreading pathology in autopsy-confirmed frontotemporal degeneration." Brain Communications, 5(3), fcad147.
6. La Joie, R., Perrotin, A., Barré, L., Hommet, C., Mézenge, F., Ibazizene, M., Camus, V., Abbas, A., Landeau, B., Guilloteau, D., de La Sayette, V., Eustache, F., Desgranges, B., Chételat, G. (2012). "Region-specific hierarchy between atrophy, hypometabolism, and β-amyloid (AB) load in Alzheimer's disease dementia." The Journal of Neuroscience, 32(46), 16265–16273.
7. Fisher, R.A. (1915). "Frequency distribution of the values of the correlation coefficient in samples from an indefinitely large population." Biometrika, 10, 507–521.
8. McCabe, S., Torres, L., LaRock, T., Haque, S., Yang, C.-H., Hartle, H., Klein, B. (2021). "Netrd: A library for network reconstruction and graph distances." Journal of Open Source Software, 6(62), 2990.

Poster No 1523

Unconscious processing networks by combining simultaneous EEG-fMRI data using optimal transport

Julia Schräder[1,2], Damin Kühn[3], Lennard Rompelberg[3], Han-Gue Jo[4], Thilo Kellermann[1,2], Michael Schaub[3], Lisa Wagels[1,2]

[1]Department of Psychiatry, Psychotherapy and Psychosomatics, Faculty of Medicine, RWTH Aachen, Aachen, Germany, [2]Institute of Neuroscience and Medicine: JARA-Institute Brain Structure Function Relationship (INM 10), Research Center Jülich, Jülich, Germany, [3]Department of Computer Science, RWTH Aachen University, Aachen, Germany, [4]Kunsan National University, Gunsan, Jeollabuk-do

Introduction: MRI compatible EEG systems enable simultaneous EEG-fMRI data assessment, which provides high spatial and high temporal resolution of neural signaling data underlying experimentally defined cognitive processes. This allows

us to determine (network) models for the same process based on two modalities using either EEG-informed fMRI analysis or dynamic causal modeling (DCM) (Friston et al., 2003). However, methods to construct dynamic network models using the information of both recording modalities jointly are still in their infancy. As a proof of principle, we use the mathematical framework of optimal transport (OT) to align multimodal DCMs in the form of multiplex networks. OT has shown promising results in many application domains including Neuroscience (Bazeille et al., 2019; Gramfort et al., 2015; Thual et al., 2022). Here, we interpret and formalize the unimodal DCMs as distributions over nodes of brain regions and compute mappings that minimize the distances between the distributions of different modalities. Subsequently, a shared multimodal representation (barycenter) is computed from these mappings.

Methods: We use simultaneously recorded EEG-fMRI data of 66 healthy participants (HC) and 60 patients with major depressive disorder (MDD) undergoing a priming task, in which an unconsciously presented prime stimulus may influence the participants' decision. This task ensured emotional conflict trials (primer emotion × target emotion) as well as non-conflict trials at conscious (150 ms primer presentation time) or unconscious level (16.7 ms primer presentation time). As a first step, we are using EEG-informed fMRI analysis in a multiple regression including the individual N170 EEG values for each condition (happy / sad / neutral primer × conscious / unconscious) as regressor. As a second step, we are using DCM to describe stimulus-related changes in neurophysiological networks and formalize these as multiplex networks, a special case of multilayer networks. Lastly, we apply OT to derive a multimodal barycenter that optimally matches to both neuronal networks inferred through DCM from EEG- and fMRI-data respectively. To obtain a suitable distance measure for such optimizations, we extend the definition of OT to directed multiplex networks and provide an efficient numerical solution. To test for behavioral differences between groups, mean reaction times (RT) were compared between groups in incongruent trials via two-tailed t-tests.

Results: MDD showed significantly higher mean RT compared to HC ($t = 7.80$, $p < 0.001$; HC mean RT = 0.62 s; MDD mean RT = 0.69 s). Multiple regression of N170 amplitudes and BOLD signal revealed significant negative correlations ($pFWE\text{-}corr = 0.005$) in several grey matter clusters. The larger the N170 amplitude, the higher the brain activity in cortical regions such as the fusiform gyrus ($k = 137$), middle/inferior temporal ($k = 137$), middle/superior frontal gyrus ($k = 28$ and 20), as well as middle cingulate & paracingulate gyri ($k = 15$) the cerebellum ($k = 10$) and the right amygdala ($k = 18$). Alignment of EEG-DCM and fMRI-DCM using OT showed group differences in the bottom-up processing of emotional facial expressions similar to behavioral differences (slower processing of happy facial expressions in MDD). We show that the barycenter is a more accurate model of neural connectivity than those inferred solely through either modality.

Conclusions: In this study, we demonstrated that performance in emotion detection is decreased in MDD compared to HC. Additionally, EEG-informed fMRI analysis showed correlation of face sensitive N170 values and face / emotion sensitive brain areas (e.g. fusiform gyrus and amygdala). We demonstrate that the optimal transport method enables us to align EEG and fMRI data effectively. This synchronization facilitates the development of more precise neural networks.

References

1. Bazeille, T., Richard, H., Janati, H., & Thirion, B. (2019). Local Optimal Transport for Functional Brain Template Estimation. In A. C. S. Chung, J. C. Gee, P. A. Yushkevich, & S. Bao (Eds.), Information Processing in Medical Imaging (Vol. 11492, pp. 237–248). Springer International Publishing. https://doi.org/10.1007/978-3-030-20351-1_18
2. Friston, K. J., Harrison, L., & Penny, W. (2003). Dynamic causal modelling. Neuroimage, 19(4), 1273–1302.
3. Gramfort, A., Peyré, G., & Cuturi, M. (2015). Fast Optimal Transport Averaging of Neuroimaging Data. In S. Ourselin, D. C. Alexander, C.-F. Westin, & M. J. Cardoso (Eds.), Information Processing in Medical Imaging (Vol. 9123, pp. 261–272). Springer International Publishing. https://doi.org/10.1007/978-3-319-19992-4_20
4. Thual, A., Tran, H., Zemskova, T., Courty, N., Flamary, R., Dehaene, S., & Thirion, B. (2022). Aligning individual brains with Fused Unbalanced Gromov-Wasserstein. https://doi.org/10.48550/ARXIV.2206.09398

Poster No 1524

Longitudinal mapping of structural disconnection and morphometric similarity in Multiple Sclerosis

Mario Tranfa[1], Alessandra Scaravilli[1], Maria Petracca[2], Marcello Moccia[1], Mario Quarantelli[3], Sirio Cocozza[1], Arturo Brunetti[1], Giuseppe Pontillo[1]

[1]University of Naples "Federico II", Naples, Italy, [2]Sapienza University of Rome, Rome, Italy, [3]National Research Council, Naples, Italy

Introduction: Multiple sclerosis (MS) can be conceptualized as a network disorder. The accumulation of white matter (WM) demyelinating lesions leads to structural disconnection between gray matter (GM) regions (Rise et al. 2022), adding to other pathological processes that directly and indirectly damage the GM (i.e., microglial activation and cortical demyelination) (Calabrese et al. 2015). The resulting neurodegeneration (Tsagkas et al. 2020) disrupts the morphometric similarity patterns,

ultimately subverting the hierarchical organization of the brain (Sebenius et al. 2023). Network-based approaches may represent a tool to overcome the “clinico-radiological paradox”, that is the gap between the clinical status and the radiological severity assessed through conventional MRI biomarkers, such as WM lesion load and brain atrophy (Barkhof 2002). However, these methods require advanced MRI sequences that are not routinely acquired and long processing times, hampering their application in clinical practice. Here, using conventional MRI and publicly available software, we assessed cross-sectional and longitudinal alterations of structural disconnection and morphometric similarity networks in MS, and tested whether they are sensitive to disease status and progression over time, and whether they could explain disease-related physical and cognitive disability.

Methods: We retrospectively collected 3T structural brain MRIs of 461 MS patients (age=37.2±10.6y;F:M=324:137), corresponding to 1235 visits (mean follow-up time=1.9±2.0y, range=0.1-13.3y), and 55 healthy controls (age=42.4±15.7y;F:M=25:30). From 3D-T1w and FLAIR-T2w scans, WM lesions were automatically segmented and the brain was parcellated into 100 cortical (Schaefer atlas) and 14 subcortical (Aseg atlas) regions. For MS patients, subject-level WM masks were registered to the MNI space and used to compute networks of structural disconnection: using the Lesion Quantification Toolkit (Griffis et al. 2021), based on the HCP842 tractography atlas, disconnection between pairs of regions was estimated as the proportion of connecting streamlines passing through WM lesions. Likewise, with the Morphometric Inverse Divergence (MIND) method (Sebenius et al. 2023), we computed networks of morphometric similarity between cortical regions from 3D-T1w derived FreeSurfer outputs for both groups. Physical and cognitive disability were assessed with the expanded disability status scale (EDSS) and the symbol digit modalities test (SDMT), respectively. Via network-based statistics, the effect of time and clinical disability (and group, for MIND networks) were tested with linear mixed-effects models. Five-thousands permutations were used and statistical significance was set at $p<0.05$ (FWER-corrected). Statistical analyses were carried out using R (version 4.1.2).

Results: We identified a subnetwork of significant progressive structural disconnection (82 edges, pFWE=0.04), mainly comprising cortico-subcortical tracts. MIND networks were sensitive to disease status and progression over time, with distributed effects of decreased morphometric similarity in large subnetworks of 431 and 509 edges, respectively (pFWE<0.01). We observed associations of EDSS with structural disconnection and MIND subnetworks of 960 and 670 edges, respectively (pFWE<0.01, Figure 1). Similarly, SDMT was associated with structural disconnection and MIND subnetworks of 988 and 202 edges, respectively (pFWE<0.01, Figure 2).

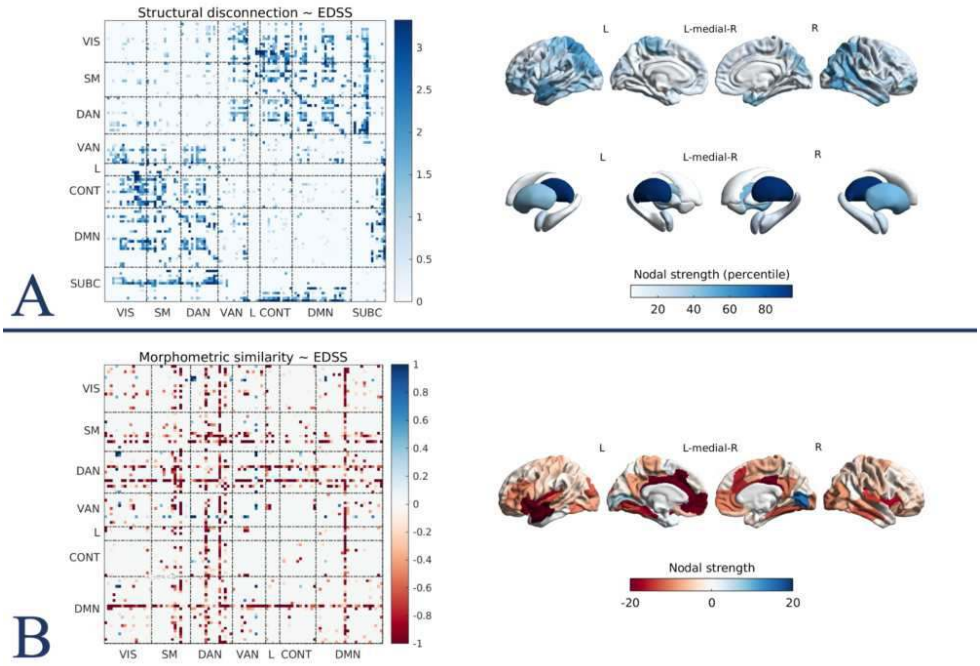

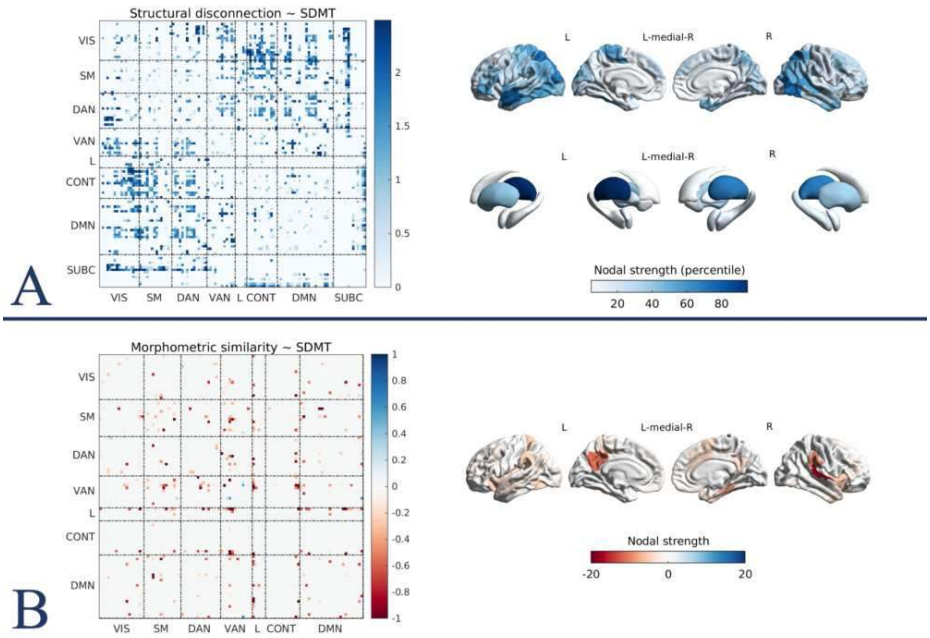

Conclusions: We have shown that structural disconnection and morphometric similarity networks, as assessed through conventional MRI, are sensitive to MS-related brain damage and its evolution over time. Moreover, they proved to be sensitive to physical and cognitive disability, potentially adding to established conventional MRI-derived measures as biomarkers of disease severity and progression. Extracting network measures from conventional MRI holds the potential for driving brain connectomics towards applicability in everyday clinical practice.

References

1. Barkhof, F. (2002). «The Clinico-Radiological Paradox in Multiple Sclerosis Revisited»: Current Opinion in Neurology 15 (3): 239–45. https://doi.org/10.1097/00019052-200206000-00003.
2. Calabrese, M. (2015). «Exploring the Origins of Grey Matter Damage in Multiple Sclerosis». Nature Reviews Neuroscience 16 (3): 147–58. https://doi.org/10.1038/nrn3900.
3. Griffis, J. C., (2021). «Lesion Quantification Toolkit: A MATLAB Software Tool for Estimating Grey Matter Damage and White Matter Disconnections in Patients with Focal Brain Lesions». NeuroImage: Clinical 30: 102639. https://doi.org/10.1016/j.nicl.2021.102639.
4. Rise, H. H., (2022). «Brain Disconnectome Mapping Derived from White Matter Lesions and Serum Neurofilament Light Levels in Multiple Sclerosis: A Longitudinal Multicenter Study». NeuroImage: Clinical 35: 103099. https://doi.org/10.1016/j.nicl.2022.103099.
5. Sebenius, I., (2023). «Robust Estimation of Cortical Similarity Networks from Brain MRI». Nature Neuroscience 26 (8): 1461–71. https://doi.org/10.1038/s41593-023-01376-7.
6. Tsagkas, C. M. (2020). «Longitudinal Patterns of Cortical Thinning in Multiple Sclerosis». Human Brain Mapping 41 (8): 2198–2215. https://doi.org/10.1002/hbm.24940.

Poster No 1525

Cingulate and prefrontal cortex effective connectivity during emotion inhibition in bipolar disorder

Jacqueline Quirke[1], Leila Nabulsi[2], Genevieve McPhilemy[1], Fiona Martyn[1], Brian Hallahan[1], Colm McDonald[1], Maria Dauvermann[3], Dara Cannon[1]

[1]University of Galway, Galway, Ireland, [2]University of Southern California, Marina Del Rey, United States, [3]University of Birmingham, Birmingham, United Kingdom

Introduction: Emotion inhibition deficits are a core feature in bipolar disorder (BD), greatly affecting quality of life. Prefrontal regions, including the dorsolateral and ventrolateral prefrontal cortex (dlPFC and vlPFC respectively) and cingulate cortices, are involved in emotion processing and inhibition (Wessa & Linke, 2009). They are differentially connected in BD (Wessa & Linke, 2009) and may underlie emotional dysregulation. Dysconnectivity in prefrontal regions may correspond to deficits in attention, salience attribution, and inhibition of emotional information, especially negatively valenced stimuli (Nabulsi et al., 2022; Hummer et al., 2013). Few effective connectivity studies exist with regards to BD and emotion inhibition, yet they may increase our understanding of altered networks underlying emotion inhibition deficits in BD. Here, we used Dynamic Causal Modeling (DCM) for functional Magnetic Resonance Imaging (fMRI) (Friston et al., 2003) and assessed modulatory connection

strengths during an emotion inhibition task (Lisiecka et al., 2012) using negatively valenced stimuli in BD and healthy controls (HC).

Methods: Participants with BD met DSM-V criteria for type-I or -II BD. Subjects underwent 3T fMRI scanning during an emotion inhibition task (Lisiecka et al., 2012). Blood oxygen level-dependent (BOLD) responses during the emotion inhibition task have been reported previously (Nabulsi et al., 2022). Bilinear DCM analysis was conducted (SPM12 v7771, DCM 12.5, Matlab R2022b) across eight models including the right anterior cingulate cortex (ACC), posterior cingulate cortex (PCC), dlPFC, and vlPFC (Figure 1). Bayesian Model Selection (BMS) at the group level was performed to compare models between BD and HC. Individual effective connectivity measures for the modulatory connection of the optimal model were extracted and compared between groups. A post-hoc Pearson correlation assessed the relationship between the modulatory effective connectivity strengths and the behavioral accuracy scores on the emotion inhibition task (SPSS v27, IBM).

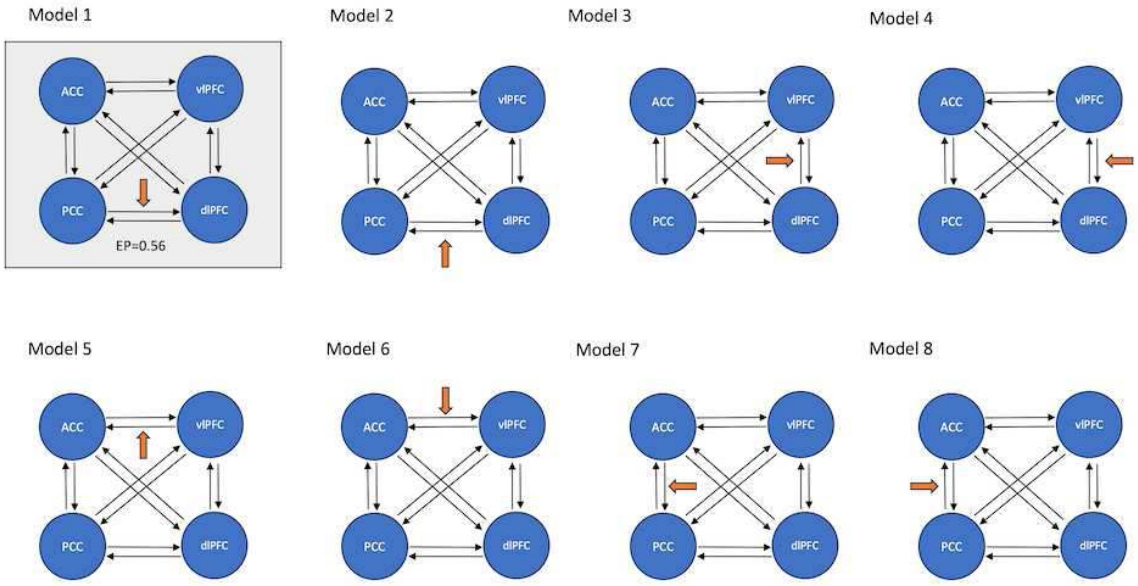

Figure 1. Model space of bilinear emotion inhibition models and optimal model exceedance probability.
All models have bidirectional endogenous connections (black arrows) between ACC, PCC, vlPFC, and dlPFC regions (blue circles) and modulatory inputs which differentiate between models (orange arrows). EP = exceedance probability, ACC = anterior cingulate cortex, PCC = posterior cingulate cortex, dlPFC = dorsolateral prefrontal cortex, vlPFC = ventrolateral PFC

Results: The BD (n=33, age mean years±standard deviation=40.58±11.47) and HC (n=49, 39.71±13.42) groups did not differ in age (U=790.50, p=0.87) or gender ($\chi 2$=0.35, 0.56). Subjects with BD performed more poorly on the emotion inhibition task (U=507, p=0.02). Across groups, during inhibition of negatively valenced stimuli, Model 1 was the optimal model with a modulation on the connection from the PCC to the dlPFC (Exceedance probability (EP)=0.56; Figure 1). This model explained the given fMRI data with the highest probability in both BD (EP=0.54) and HC (EP=0.55) groups. We did not observe a significant difference in modulatory connection strength between groups (U=758, p=0.63). Post-hoc analyses found no significant relationship between connection strength and emotion inhibition task accuracy across subjects (r(77)=0.01, p=0.97) or between groups (BD: r(29)=0.19, p=0.31; HC: r(46)=-0.14, p=0.36).

Conclusions: Overall, the model with modulatory effective connectivity between the PCC and dlPFC was the best model to explain the fMRI data across all individuals when inhibiting negatively valenced stimuli. Some effective connectivity studies have found reduced effective connectivity from the dlPFC to the amygdala during emotion processing in depressed BD (Radaelli et al., 2015; Perry et al., 2018). However, consistency of optimal models across groups may point to similar effective connectivity of emotion inhibition regions during BD euthymia compared with controls. This work adds directional, mechanistic insight implicating prefrontal and cingulate effective connectivity during emotion inhibition in BD, corroborating PCC and dlPFC involvement in emotion processing (Maddock et al., 2003; Wessa & Linke, 2009), which appears to persist during periods of remission.

References

1. Friston, K.J. (2003), 'Dynamic Causal Modeling', Neuroimage, vol. 19, no. 4, pp. 1273-1302.
2. Hummer, T.A. (2013), 'Emotional response inhibition in bipolar disorder: a functional magnetic resonance imaging study of trait- and state-related abnormalities', Biological Psychiatry, vol. 73, no. 2, pp. 136-43.
3. Lisiecka, D.M. (2012), 'Altered inhibition of negative emotions in subjects at family risk of major depressive disorder', Journal of Psychiatric Research, vol. 46, pp. 181–8.
4. Maddock, R.J. (2003), 'Posterior cingulate cortex activation by emotional words: fMRI evidence from a valence decision task', Human Brain Mapping, vol. 18, pp. 30-41.

5. Nabulsi, L. (2022), 'Normalization of impaired emotion inhibition in bipolar disorder mediated by cholinergic neurotransmission in the cingulate cortex', Neuropsychopharmacology, vol. 47, pp. 1643–1651.
6. Perry, A. (2018), 'Connectomics of Bipolar Disorder: A Critical Review, and Evidence for Dynamic Instabilities within Interoceptive Networks', Molecular Psychiatry, vol. 24, no. 9, pp. 1296–1318.
7. Radaelli, D. (2015), 'Fronto-limbic disconnection in bipolar disorder', European Psychiatry, vol. 30, no. 1, pp. 82-88.
8. Wessa, M. (2009), 'Emotional processing in bipolar disorder: Behavioural and neuroimaging findings', International Review of Psychiatry, vol. 21, no. 4, pp. 357-367.

Poster No 1526

Intra-hemishperic functional reorganization in ischemic stroke

Cemal Koba[1], Joan Falco-Roget[2], Alessandro Crimi[2]

[1]Sano Centre for Computational Personalized Medicine, Krakow, Lesser Poland, [2]Sano Center for Computational Personalized Medicine, Krakow, Lesser Poland

Introduction: Ischemic stroke is a case of lack of or interrupted blood flow to arteries in the brain. If the abnormality lasts long enough, neural death is unavoidable. The region that suffers from the lack of blood flow will be infarcted, and there is a chance that the surrounding region will be swollen. The change in the metabolism of the brain is associated with a wide range of neural and behavioral dysfunctions e.g. motor dysfunction and hemispheric imbalance in the motor activity during the relevant behavioral task. There are also many functional connectivity differences reported in resting-state fMRI. Neural dynamics from the damaged regions are naturally affected by stroke, due to the structural and metabolic changes. However, functional change in the intact hemisphere can be a more accurate indicator of neural plasticity. In this study, we examine the functional-structural organization of the intact hemispheres, for the right and left hemispheres separately.

Methods: Methods: 104 stroke patients in the acute stage (within 2 weeks after the stroke) and 26 healthy controls were included in this study. Each subject went through a resting-state fMRI scan of 256 scans 1-7 times. In total, 130 subjects and their 875 resting state scans were used in the study. Each run was preprocessed with fmriprep (Esteban et al., 2019), and the regressors of no interest were removed with the 36P strategy described in Satterwaite et al. (2013). In addition, mean framewise displacement and a linear trend were acquainted. After band-passing the time series between 0.01 and 0.1 Hz, mean time series were extracted based on Schaefer's 400 region parcellation. The mean time series were used to generate the correlation matrices between the regions. The mean correlation matrix for each subject was calculated, resulting in one matrix for each subject (104 for stroke subjects and 26 for controls). The functional-structural organization was calculated via the functional connectivity gradients method explained in Marguiles et al.(2016). For each subject, the first 3 gradients that explain the most variance in connectivity both within the right and left hemispheres were calculated separately. For stroke subjects, this procedure included only the intact hemispheres, leaving 48 stroke subjects for within-left hemisphere connectivity maps (due to their damage on the right hemisphere) and 56 within-right connectivity maps. The connectivity gradients approach represents the functional distribution of the regions in the embedding space, thanks to the positions of the first 3 gradients. Leveraging this advantage, for each stroke subject, the Euclidean distance between the position of each region to the mean control distribution in both hemispheres was calculated. The mean Euclidean distance for each subject was saved. Mean Euclidean distances for the right and left hemispheres were compared via an independent sample t-test. The same analysis was repeated by calculating the Euclidean distances for each 3 gradients separately in order to identify their contribution.

Results: The comparison between the Euclidean distances of the intact right and left hemispheres to their corresponding control distribution in 3D space showed a higher mean Euclidean distance value in the right hemisphere ($t(398)=-3.43$, $p=0.0006$). Repeating the same analysis by using the Euclidean distances of each 3-gradient separately showed that the difference is specific to the second gradient (Difference for the 1st, 2nd, and 3rd gradients respectively: $t(398)=-0.88, -2.39, -1.61$, $p=0.37, 0.01, 0.11$). Relaying the mean distance on the surface showed that the highest difference on the 2nd gradient is placed on the visual and sensorimotor areas.

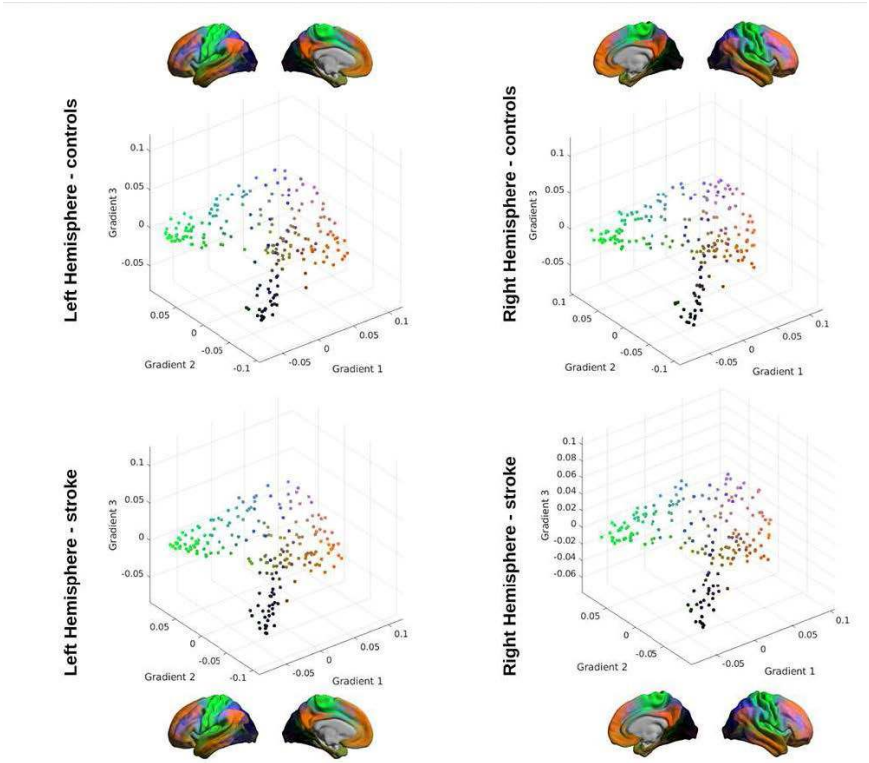

Figure 1: Functional distribution of the regions in 3D space for separate hemispheres of the control and stroke subjects.

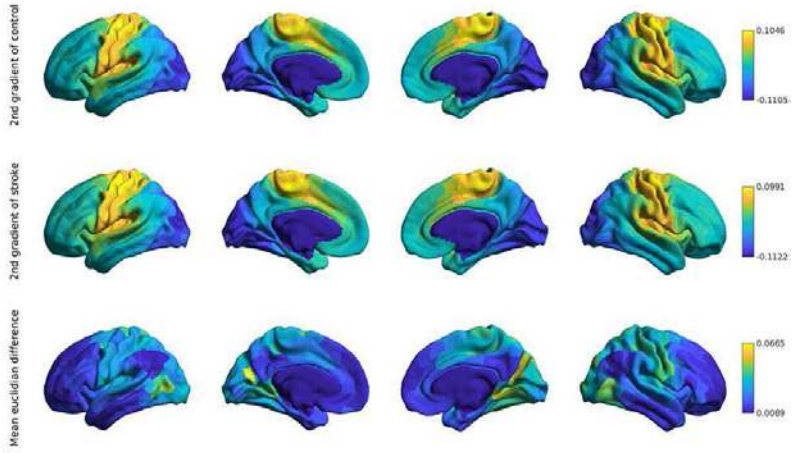

Figure 2: Distribution of the 2nd gradient for control and stroke subjects and the mean distance between them.

Conclusions: The right hemisphere is more sensitive to ischemic stroke damage on the contralateral hemisphere. This difference is the sensitivity comes from the second gradient, where the brain function is clustered between visual and sensorimotor areas.

References

1. Esteban, O., Markiewicz, C. J., Blair, R. W., Moodie, C. A., Isik, A. I., Erramuzpe, A., ... & Gorgolewski, K. J. (2019). fMRIPrep: a robust preprocessing pipeline for functional MRI. Nature methods, 16(1), 111-116.
2. Margulies, D. S., Ghosh, S. S., Goulas, A., Falkiewicz, M., Huntenburg, J. M., Langs, G., ... & Smallwood, J. (2016). Situating the default-mode network along a principal gradient of macroscale cortical organization. Proceedings of the National Academy of Sciences, 113(44), 12574-12579.
3. Satterthwaite, T. D., Elliott, M. A., Gerraty, R. T., Ruparel, K., Loughead, J., Calkins, M. E., ... & Wolf, D. H. (2013). An improved framework for confound regression and filtering for control of motion artifact in the preprocessing of resting-state functional connectivity data. Neuroimage, 64, 240-256.

Poster No 1527

Comparing network configurations of Schizophrenia and Autism Spectrum Disorders using CovSTATIS

Ju-Chi Yu[1], Colin Hawco[1,2], Lindsay Oliver[1], Maria Secara[1,2], Iska Moxon-Emre[1], Fariah Sandhu[3], Zara Khan[4], Peter Szatmari[1,2], Meng-Chuan Lai[1,2], Miklos Argyelan[5], James Gold[6], Sunny Tang[5], George Foussias[1,2], Robert Buchanan[6], Anil Malhotra[5], Aristotle Voineskos[1,2], Stephanie Ameis[1,2], Erin Dickie[1,2]

[1]Centre for Addiction and Mental Health, Toronto, Ontario, [2]University of Toronto, Toronto, Ontario, Canada, [3]York University, Toronto, Ontario, [4]McMaster University, Hamilton, Ontario, [5]Zucker Hillside Hospital, Glen Oaks, NY, [6]Maryland Psychiatric Research Center, Baltimore, MD

Introduction: Schizophrenia Spectrum Disorder (SSD) and Autism Spectrum Disorder (autism) are both characterized by social cognitive deficits, of which the severity and impact on everyday life vary substantially within diagnoses, with overlap across diagnoses. To understand such heterogeneity, we aimed to identify group-specific and shared functional network configurations present during a social processing functional magnetic resonance imaging (fMRI) empathic accuracy (EA) task.

Methods: We included fMRI data during the EA social cognition task from 67 autism (35 females; mean age = 20.78, age range = [15, 33]), 174 SSD (121 females; mean age = 30.95, age range = [18, 54]), and 170 Healthy Controls (HC; 92 females; mean age = 31.47, age range = [17, 55]). Background functional connectivity of the EA task was extracted from parcellated connectomes (Ji et al., 2019) and analyzed by CovSTATIS (i.e., multi-table multidimensional scaling, or DiSTATIS, for covariance matrices) (Abdi et al., 2012). CovSTATIS is a multivariate method that analyzes multiple correlation matrices by creating a compromise that best captures the shared pattern. This compromise is a linear combination of all matrices, weighted by their similarity to the common pattern. This compromise is then decomposed by the singular value decomposition to extract latent dimensions characterizing prominent EA-associated network configurations. The factor score of each region of interest (ROI) illustrates the network configuration on each dimension with proximity indicating a close association. Mean factor scores of each network are then computed to examine network segregation. Furthermore, CovSTATIS projects individual connectivity matrices to compute partial factor scores, which illustrate each individual's network configuration in the same dimension space. These partial factor scores were averaged based on networks and participant groups to examine group differences in network segregation (See Figure 1 for details). Bootstrap procedures (1000 iterations) were used to estimate the 95% bootstrap confidence intervals of network and group means and were illustrated by ellipses in Figures 1-2. Bootstrap tests were used to examine configuration and group differences with two non-overlapping ellipses indicating a significant difference at α = .05.

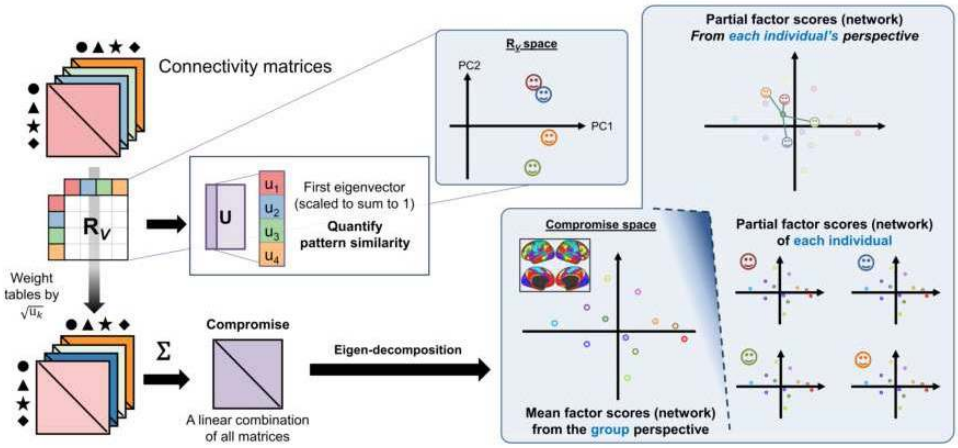

Figure 1.

Results: From CovSTATIS, we considered all dimensions that contribute <1% of the variance being noise and the others as signal dimensions. Two orthogonal latent dimensions of EA task-associated activity were identified across all groups. The first dimension's configuration (explaining 14.98% of signal dimensions; x-axis in Figure 2A) was characterized by differentiation between language (LAN), and default mode networks versus visual (VIS), and dorsal attention networks (DAN). The second dimension's configuration (explaining 11.97% of the signal dimensions; y-axis in Figure 2A) was characterized by differentiation between auditory, and somatomotor versus frontoparietal networks. On group-wise comparison, HC showed significant differentiation between primary VIS and DAN (bootstrap $p < .05$; Figure 2B) that was absent in autism and SSD. Autism showed differentiation between LAN and ventral-multimodal network (Figure 2C), while HC and SSD groups did not (bootstrap $p < .05$). Finally, while HC and autism showed significant differentiation between primary and secondary VIS, SSD did not (bootstrap $p > .05$; Figure 2D).

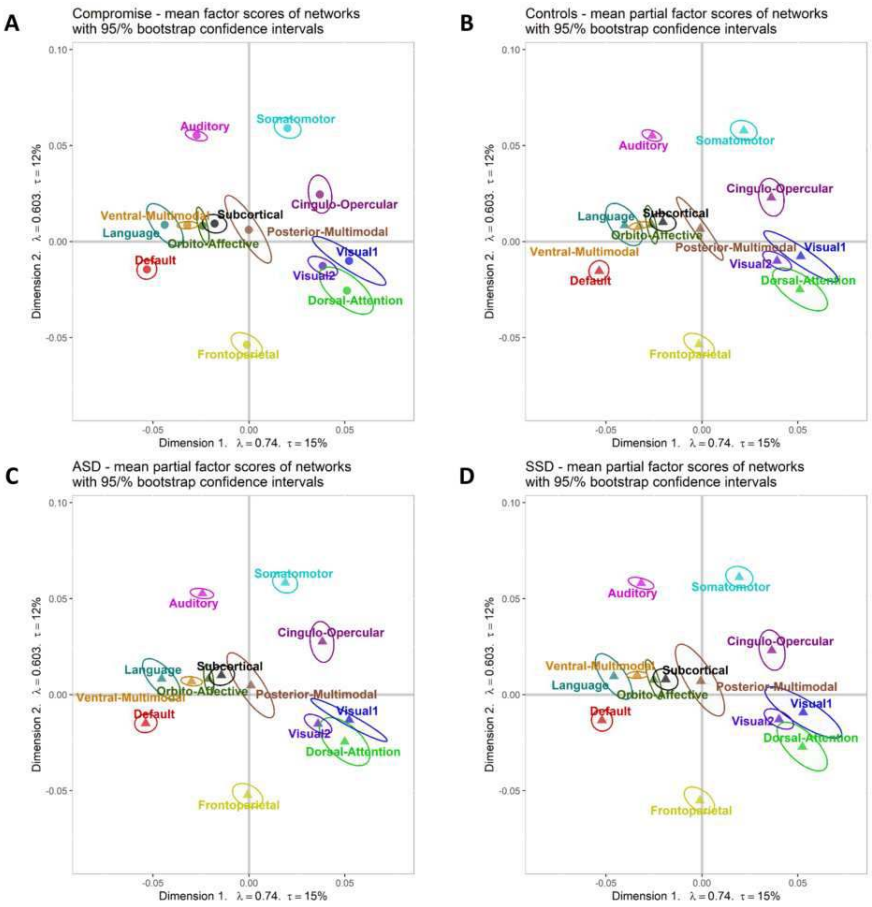

Figure 2.

Conclusions: In the EA task, prominent configurations that characterize the latent dimensions did not differ significantly across groups. Divergent patterns were found between all groups with specific configurations for autism group (in LAN) and SSD group (in VIS). The associations of these latent dimensions to cognition and clinical outcomes can help identify potential biomarkers for social cognitive deficits in autism and SSD.

References

1. Ji, J.L. (2021), 'Mapping brain-behavior space relationships along the psychosis spectrum', eLife, vol. 10, pp. E66968
2. Abdi, H. (2012), 'STATIS and DISTATIS: optimum multitable principal component analysis and three way metric multidimensional scaling', Wiley Interdisciplinary Reviews: Computational Statistics, vol. 4, pp. 124–167

Poster No 1528

Calculating dynamic connectivity around EEG seizure onset based on nonlinearity and nonstationarity

Iris Soare-Nguyen[1,2], Shima Abdullateef[3], Afreen Islam[4], Javier Escudero[1,2]

[1]Institute for Imaging, Data and Communications, School of Engineering, University of Edinburgh, Edinburgh, Midlothian, [2]Muir Maxwell Epilepsy Centre, Edinburgh, Midlothian, United Kingdom, [3]Usher Institute, University of Edinburgh, Edinburgh, Midlothian, [4]Control and Robotics Group, Dep. of Electrical and Electronic Engineering, University of Manchester, Manchester, Greater Manchester

Introduction: Seizures represent abnormal brain activity due to unregulated synchronization. Connectivity can measure spatiotemporal interaction between brain network nodes to characterize such synchronization. Brain activity transitions between emergent patterns that can be locally characterized as linear or stationary, interrupted by nonlinear bursts (Roberts et al. 2019; Breakspear et al. 2006). Supplementarily, seizures are known to be strongly nonlinear (Lancaster et al. 2018) and nonstationary (Manuca et al. 1998). Thus, testing linearity and stationarity of epileptic electroencephalograms (EEGs) in the context of connectivity is of interest (Zhang et al. 2020), as shifts in signal properties introduce errors in connectivity estimation. Changes in nonlinearity signify shifts in emergence (Roberts et al. 2019), and segments may also exhibit local stationarity changes around seizures (Borgnat et al. 2010). To explore epileptogenic network evolution, we compute delta

band dynamic effective connectivity (dEC) on human epileptic EEGs. By adopting a piecewise first order approximation across multiple points in the system's trajectory (Leith and Leithead 1999), we inspect the changes in linearity and stationarity to differentiate states. We summarize the signal and connectivity properties we found.

Methods: We studied 20 human epileptic EEG recordings (Detti 2020) consisting of five minutes of preictal and then ictal activity. We preprocessed the data with a low-pass Butterworth filter with cut-off at 45 Hz and removing blinks and saccades. We tested stationarity separately on every channel by computing the Euclidean distance of spectrograms between every 1s segment pair. We computed the cumulative median absolute deviation (MAD) z-score across each channel (Edwards et al. 2020). Segments with a lower MAD than 1 were considered stationary. To test linearity for each 1s segment, we created 40 iterative amplitude adjusted Fourier transform (IAAFT2) surrogates (Lancaster et al. 2018), then computed the nonlinear measure of Lyapunov exponent (LE) of the signal and surrogates. We considered all segments with a lower LE than 97.5% of the surrogates as linear. Finally, we fed the stationarity and linearity scores into k-medoids clustering to obtain consecutive signal segments with comparable properties. For each cluster of segments, we computed dEC using spectrally resolved Granger causality. We obtained proof-of-concept delta band dynamic connectivity for each seizure.

Results: As Fig. 1A and 1C show, we consistently found a change in stationarity with seizure onset. However, the median value of all previous Euclidean distances introduced a delay in identifying the change in channel signal stationarity. The linearity results indicate complex dynamics: nonlinear segments are spread across every seizure; at any moment, certain channels show nonlinear LE scores while others do not. This confirms that brain activity is mostly linear with intermittent nonlinear fluctuations (Breakspear et al. 2006). By taking the linear fit of the mean LE scores we also show that ictal activity displays either decreasing or increasing nonlinearity compared to preictal activity, as Fig. 1D shows. This variability between seizures represents future work. Our k-medoids results indicate a trend of faster network reorganization before than during seizure with a p-value of 0.061. This is in agreement with (Khambhati et al. 2015), as Fig. 2 shows. Unlike them, we were not able to distinguish three ictal network reconfigurations, which requires further investigation.

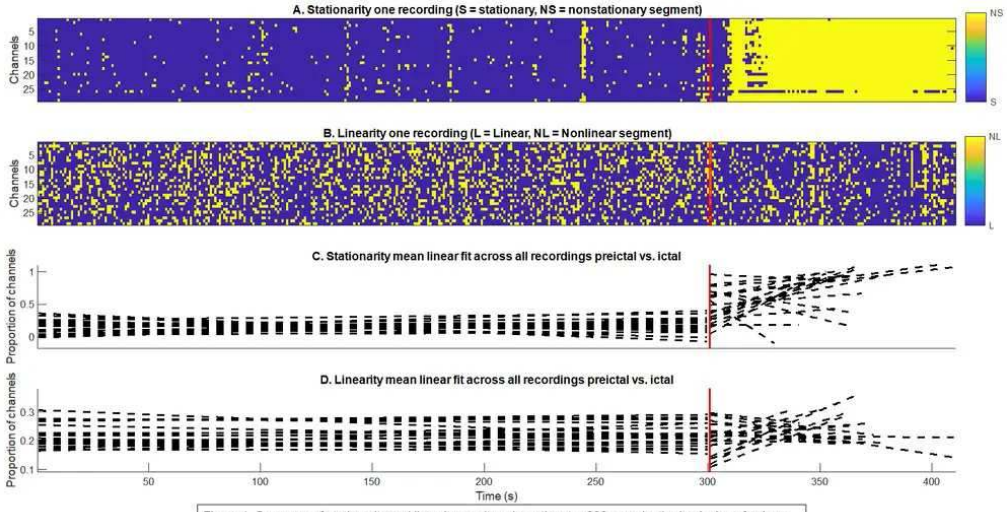

Figure 1. Summary of stationarity and linearity results, where time t = 300 s marks the beginning of seizure.

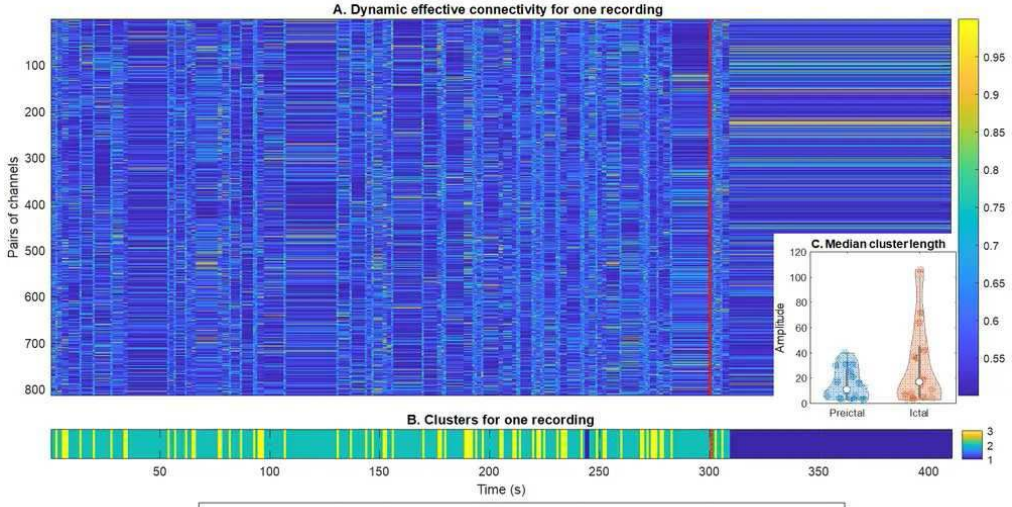

Figure 2. Summary of clustering and connectivity results,where time t = 300 s marks the beginning of the seizure.

Conclusions: We computed dEC of human epileptic EEG activity by clustering signal segments in terms of changes in stationarity and linearity. The signal segmentation suggests that the epileptogenic network changes more rapidly and displays different behavior in terms of linearity and stationarity around seizures. We will use the obtained dynamic connectivity to study linear time-variant network control strategies.

References

1. Borgnat, P., P. Flandrin., P. Honeine, C. Richard., and J. Xiao.. 2010. "Testing Stationarity With Surrogates: A Time-Frequency Approach." IEEE Transactions on Signal Processing 58 (7): 3459–70. https://doi.org/10.1109/TSP.2010.2043971.
2. Breakspear, M., J. A. Roberts, J. R. Terry, S. Rodrigues, N. Mahant, and P. A. Robinson. 2006. "A Unifying Explanation of Primary Generalized Seizures Through Nonlinear Brain Modeling and Bifurcation Analysis." Cerebral Cortex 16 (9): 1296–1313. https://doi.org/10.1093/cercor/bhj072.
3. Detti, P.. 2020. "Siena Scalp EEG Database." PhysioNet. https://doi.org/10.13026/5D4A-J060.
4. Edwards, M. C., P. Maturana-Russel, R. Meyer, J. Gair, N. Korsakova, and N. Christensen. 2020. "Identifying and Addressing Nonstationary LISA Noise." Physical Review D 102 (8): 084062. https://doi.org/10.1103/PhysRevD.102.084062.
5. Khambhati, A. N., K. A. Davis, B. S. Oommen, S. H. Chen, T. H. Lucas, B. Litt, and D. S. Bassett. 2015. "Dynamic Network Drivers of Seizure Generation, Propagation and Termination in Human Neocortical Epilepsy." PLOS Computational Biology 11 (12): e1004608. https://doi.org/10.1371/journal.pcbi.1004608.
6. Lancaster, G., D. Iatsenko, A. Pidde, V.a Ticcinelli, and A. Stefanovska. 2018. "Surrogate Data for Hypothesis Testing of Physical Systems." Physics Reports, Surrogate data for hypothesis testing of physical systems, 748 (July): 1–60. https://doi.org/10.1016/j.physrep.2018.06.001.
7. Leith, D J, and W. E. Leithead. 1999. "Input-Output Linearisation by Velocity-Based Gain-Scheduling." International Journal of Control 72 (3). https://www.hamilton.ie/doug/1998-3.pdf.
8. Manuca, R., M. C. Casdagli, and R. S. Savit. 1998. "Nonstationarity in Epileptic EEG and Implications for Neural Dynamics." Mathematical Biosciences 147 (1): 1–22. https://doi.org/10.1016/S0025-5564(97)00055-2.
9. Roberts, J. A., L. L. Gollo, R. G. Abeysuriya, G. Roberts, P. B. Mitchell, M. W. Woolrich, and M. Breakspear. 2019. "Metastable Brain Waves." Nature Communications 10 (1): 1056. https://doi.org/10.1038/s41467-019-08999-0.
10. Zhang, Y., D. Lai, J. Han, X. Wang, Q. Lin, X. Zhao, and Z. Hu. 2020. "Testing Nonlinearity in Topological Organization of Functional Brain Networks." " European Journal of Neuroscience 52 (9): 4185–97. https://doi.org/10.1111/ejn.14882.

Poster No 1529

Brain connectivity and microstructure in COVID-19 patients with cognitive or olfactory dysfunction

Alberto Arrigoni[1], Mattia Previtali[1], Sara Bosticardo[2], Giulio Pezzetti[3], Sofia Poloni[1], Serena Capelli[1], Angela Napolitano[3], Andrea Remuzzi[4], Rosalia Zangari[3], Ferdinando Lorini[3], Maria Sessa[3], Alessandro Daducci[2], Anna Caroli[1], Simonetta Gerevini[3]

[1]Istituto di Ricerche Farmacologiche Mario Negri IRCCS, Bergamo, Italy, [2]University of Verona, Verona, Italy, [3]ASST Papa Giovanni XXIII, Bergamo, Italy, [4]University of Bergamo, Bergamo, Italy

Introduction: The global impact of the COVID-19 pandemic has resulted in mortality and multi-organ morbidity affecting millions of individuals. Notably, significant neurological complications, such as cognitive impairment and the most common olfaction disorder, have been reported. While previous MRI studies have identified structural changes in the brains of COVID-19 patients, there is still a limited comprehension of alterations in brain microstructure and connectivity [Davis et al., 2021; Guo et al., 2022]. This study aimed to examine changes in brain structure, microstructure, and connectivity in individuals with COVID-19-related neurological issues using multi-directional diffusion-weighted MRI (DW-MRI).

Methods: The study included 16 COVID-19 patients with cognitive and memory deficits (COVID-CM, 56[51-61] years, 69% females), 35 COVID-19 patients with olfaction disorder (COVID-OD, 40[31-53] years, 71% females), and 14 normal controls (62[45-70] years old, 57% females). All patients underwent a T1-weighted MRI scan and a 32-direction DW-MRI scan at 264[208-313] days after the disease onset. A state-of-the-art processing pipeline was developed for this study. This pipeline first involved MRI pre-processing to address potential issues such as noise, artifacts, and distortions. Subsequently, the corrected DW-MRI scan was employed to compute the diffusion tensor image with the pertinent mean diffusivity (MD) and fractional anisotropy (FA) maps, offering insights into the brain microstructure's condition. The application of constrained spherical deconvolution (CSD) generated the fiber-orientation distribution image (FOD), which allowed the whole brain tractography via a probabilistic algorithm (iFOD2). The COMMIT2 filtering model was employed to enhance the biological accuracy of the reconstructed fibers before evaluating connectivity. The process also involved registering the pre-processed T1 scan to the DWI-b0 scan and brain segmentation into gray matter (GM) and white matter (WM). Brain tissue masks were combined with GM and WM anatomical atlases to classify the brain into distinct tissues and areas, allowing regional investigation.

Results: Compared to controls, COVID-CM patients showed overall gray matter atrophy (age and sex corrected $p=0.004$), and both COVID-19 patient groups showed regional atrophy and cortical thinning (corrected $p<0.001$). Both groups showed a significant increase in gray matter mean diffusivity (corrected $p=0.001$), and COVID-CM patients also showed an overall

increase in white matter diffusivity (p=0.022) and a decrease in white matter anisotropy (corrected p=0.038). Graph-based analysis revealed reduced network modularity in both groups (corrected p=0.024 and p=0.010, respectively), with an extensive pattern of connectivity increase in conjunction with a more localized reduction in a few connections, mainly located in the left hemisphere. In both groups, connection impairment mainly involved the left cingulate, anterior cingulate, and insula. In COVID-CM patients, the left postcentral cortex and the right frontal and anterior cingulate cortex were also affected, while in COVID-OD patients, the left nucleus accumbens and the frontal, supramarginal, and occipital left cortex were further concerned.

Conclusions: In line with earlier findings [Douaud et al., 2022; Kas et al., 2021], this study revealed notable changes in the brain's structure, microstructure, and connectivity among individuals with COVID-19 who experienced either olfactory or cognitive disorders. Current findings indicate possible underlying neurodegeneration and neuroinflammation alongside compensatory mechanisms. It would be crucial to perform additional longitudinal studies to provide definitive evidence of brain changes in response to COVID-19 pathology, explore brain impairment evolution over time, and ultimately determine its temporary or permanent nature.

References

1. Davis HE, Assaf GS, McCorkell L, Wei H, Low RJ, Re'em Y, Redfield S, Austin JP, Akrami A (2021): Characterizing long COVID in an international cohort: 7 months of symptoms and their impact. eClinicalMedicine 38. https://www.thelancet.com/journals/eclinm/article/PIIS2589-5370(21)00299-6/fulltext.
2. Douaud G, Lee S, Alfaro-Almagro F, Arthofer C, Wang C, McCarthy P, Lange F, Andersson JLR, Griffanti L, Duff E, Jbabdi S, Taschler B, Keating P, Winkler AM, Collins R, Matthews PM, Allen N, Miller KL, Nichols TE, Smith SM (2022): SARS-CoV-2 is associated with changes in brain structure in UK Biobank. Nature 604:697–707.
3. Guo P, Benito Ballesteros A, Yeung SP, Liu R, Saha A, Curtis L, Kaser M, Haggard MP, Cheke LG (2022): COVCOG 2: Cognitive and Memory Deficits in Long COVID: A Second Publication From the COVID and Cognition Study. Frontiers in Aging Neuroscience 14. https://www.frontiersin.org/articles/10.3389/fnagi.2022.804937.
4. Kas A, Soret M, Pyatigoskaya N, Habert M-O, Hesters A, Le Guennec L, Paccoud O, Bombois S, Delorme C, on the behalf of CoCo-Neurosciences study group and COVID SMIT PSL study group (2021): The cerebral network of COVID-19-related encephalopathy: a longitudinal voxel-based 18F-FDG-PET study. Eur J Nucl Med Mol Imaging 48:2543–2557.

Poster No 1530

Coming up short: generative network models fail to accurately capture long-range connectivity

Stuart Oldham[1], Gareth Ball[1]

[1]Murdoch Children's Research Institute, Melbourne, VIC

Introduction: Generative network models (GNMs) are used to create synthetic networks which aim to capture key properties of human brain connectomes. GNMs are parameterised using simple wiring-rules, commonly a trade-off between minimising connection cost and promoting advantageous features, such as topological value or the connection of biologically similar regions[1-3]. Differences in GNM parameters and wiring-rules may give insight into the mechanisms that shape brain connectivity. Indeed, GNM wiring constraints vary among individuals and are linked to cognition and psychopathology[4-6]. Drawing biological insight from GNMs rests on their ability to accurately model human brain networks. While GNMs capture connectome topology–including long-tailed degree distributions, clustering, and small-world properties[1-6]–they are less able to reproduce connectome topography (spatial embedding of network properties)[3]. Such embedding is critical for enabling brain dynamics, thus is a key property GNMs should capture[7,8]. Therefore, we aimed to evaluate the ability of GNMs to reproduce the topography of human brain networks.

Methods: Diffusion tractography from 326 participants of the Human Connectome Project was used to construct a consensus 200 cortical region empirical network in the left hemisphere[9]. The GNM was formulated as a trade-off between connection cost and regional similarity of cortical metrics (Fig. 1A). Free parameters were fit using an optimisation procedure that maximised the topological similarity of the model networks to the empirical data. Networks produced using the best fit parameters were evaluated based on topological similarity, overlapping connections, and degree sequence similarity with the empirical data (Fig. 1B). Nine different GNMs, each using different cortical features[9], were evaluated (Fig. 1C).

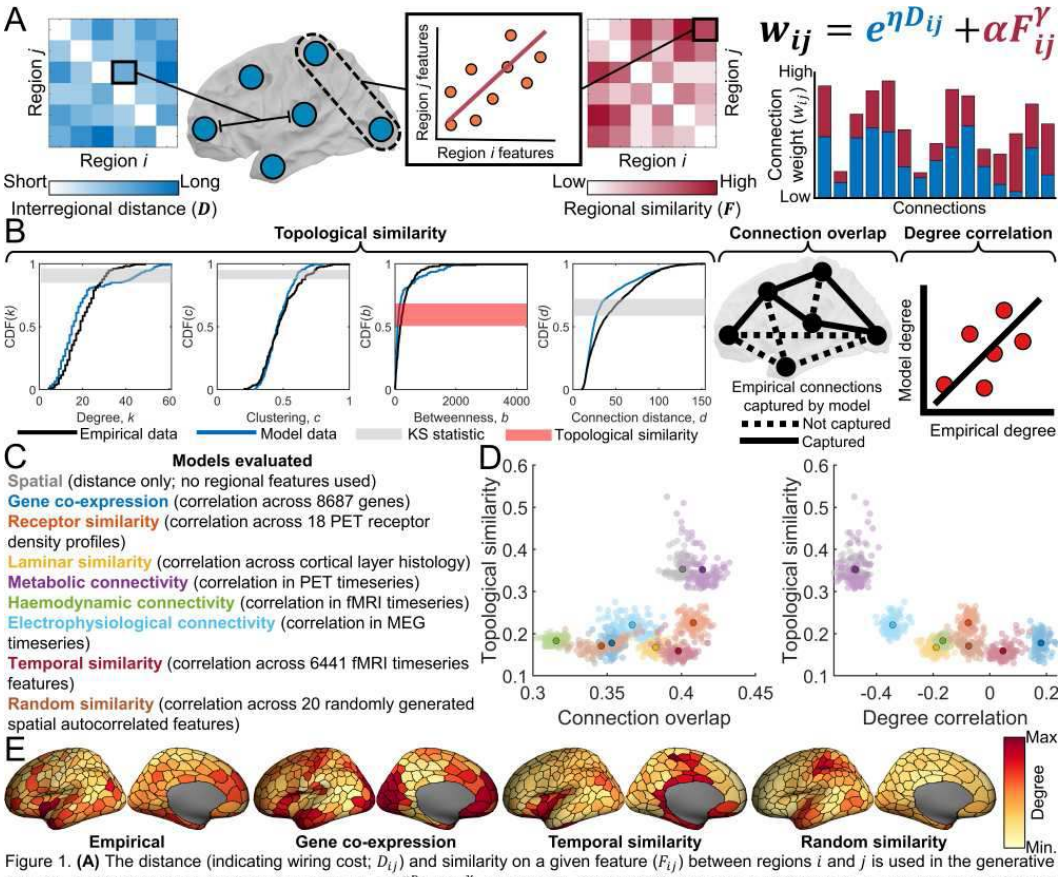

Figure 1. **(A)** The distance (indicating wiring cost; D_{ij}) and similarity on a given feature (F_{ij}) between regions i and j is used in the generative network model according to the wiring-rule $w_{ij} = e^{\eta D_{ij}} + \alpha F_{ij}^{\gamma}$. The model probabilistically adds connections to a network based on the w_{ij} values (higher values more likely). η, γ, and α are free parameters that are estimated via an optimisation procedure[1,2]; optimal parameters were used to generate 100 networks for each model to use for further evaluation **(B)** Topological similarity is defined as the maximum Kolmogorov–Smirnov (KS) statistic (i.e., the maximum difference in cumulative distribution functions) across four topological distributions (shaded area indicates where the KS is calculated). Connection overlap (proportion of empirical connections captured by the model) and degree correlation (correlation between empirical and model network degree) assess topographical similarity **(C)** The different features used in the generative network models[9] **(D)** Scatter plots of the relationship between topological similarity, connection overlap, and degree correlation for model networks. The darker point indicates the average across model runs **(E)** The spatial embedding of degree in the empirical and selected model network data (model degree is the average across the 100 iterations).

Results: Overall, GNMs showed high topological similarity to empirical networks (maximum dissimilarity:0.16–0.35) but reproduced only 36–44% of empirical connections and showed weak correlations with the empirical degree sequence (r=-0.48–0.18), highlighting the mismatch between synthetic and empirical topographies (Fig. 1C-1D). To isolate the underlying cause of this mismatch, we examined the overlap between connections of different lengths. GNMs were able to capture 51–84% of empirical short-range connections (<30mm), but this accuracy dropped to 2–20% for mid-range (30–90mm) and 0–10% for long-range (>90mm) connections (Fig. 2A). Empirical degree topography is mainly determined by connections >30mm (Fig. 2B). The discrepancies in spatial embedding therefore arise from GNMs' inability to accurately capture these connections. Importantly, no cortical feature was able to mitigate this error (Fig. 2C). Indeed, using a random similarity matrix achieves similar model performance to neurophysiological metrics, suggesting that the formation of long connections in GNMs is largely invariant to model input.

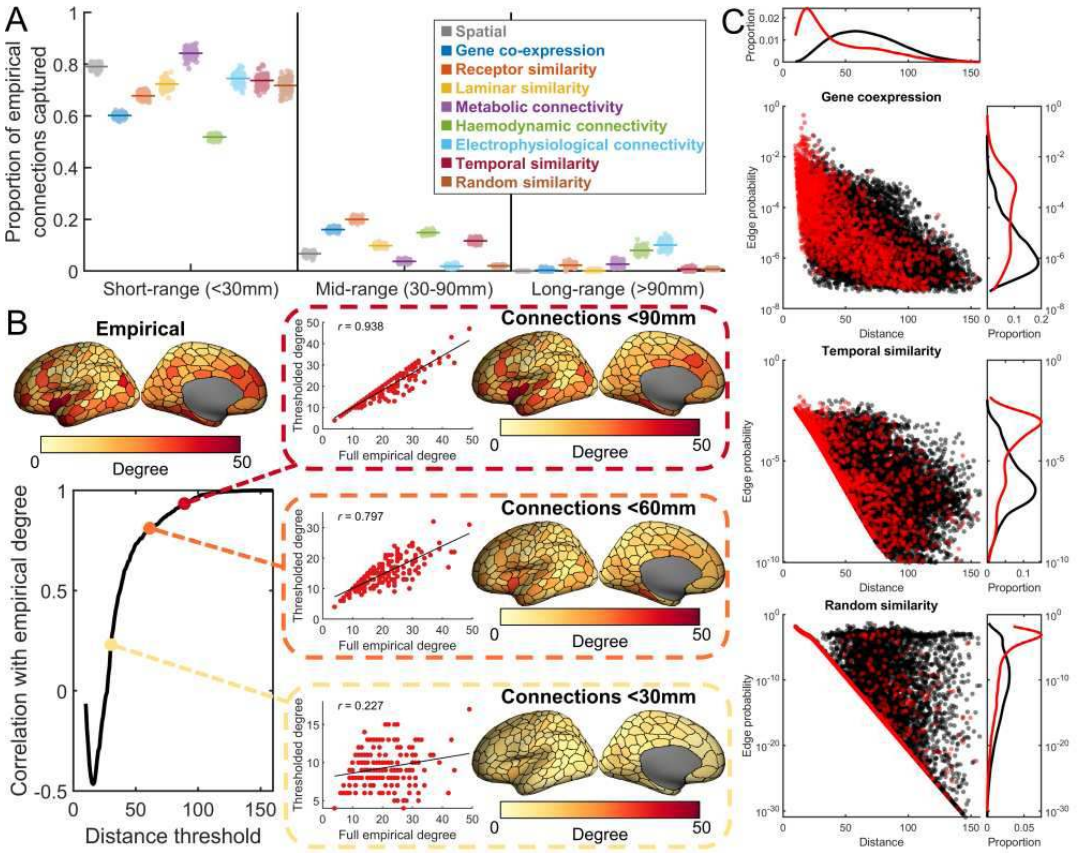

Figure 2. **(A)** Proportion of empirical short-range, mid-range, and long-range connections captured by the best fitting generative network models. The coloured line indicates the average overlap, while each point indicates the result for an individual model network **(B)** Similarity of the empirical degree sequence at different distance thresholds. Degree is calculated only using connections with a length less than the current distance threshold. The thresholded degree is then correlated with the full empirical degree (i.e., degree calculated when using all empirical connections). Degree is largely shaped by connections >30mm (particularly mid-range connections), meaning that these specific connections need to be captured to obtain the empirical spatial embedding of nodal degree **(C)** The probability of a given connection being selected in the best fitting networks as a function of distance for exemplar models. Red points/lines correspond to connections that exist in the empirical data while black points/lines correspond to non-existing connections. A kernel density plot of the distance distributions of empirical connections/non-connections is shown at the top. Kernal density plots of the probabilities for both connection types are shown on the axis right. Many empirical connections are improbable and/or cannot be distinguished from non-connections at longer distances. Thus, given the input features used, the generative network model cannot successfully capture specific connections in the empirical data.

Conclusions: We show that GNMs, while matching brain network topological features, fail to capture topography due to inaccurate reconstruction of mid/long-range connections. GNMs can induce topologically-similar empirical networks by mapping most short-range connections and promoting a few long-range connections, even at random. Specific long-range connections enable topographic properties that are essential to brain dynamics/function[7,8]. Drawing conclusions based on GNMs' ability to reproduce topology–but not topography–is likely to lead to an incomplete or inaccurate understanding of the mechanisms and constraints which shape brain networks. To improve GNMs, mechanisms which are preferentially biased towards long-range connectivity should be explored. Factors like connection timing may be relevant, as evidence suggests that long-range connections between hubs form earlier than other connection types[10]. Investigating these ways to improve GNMs is required so they can be used to explore the underpinning developmental mechanisms of the connectome.

References

1. Betzel, R. F., Avena-Koenigsberger, A., Goñi, J., He, Y., De Reus, M. A., Griffa, A., ... & Sporns, O. (2016). Generative models of the human connectome. Neuroimage, 124, 1054-1064.
2. Vértes, P. E., Alexander-Bloch, A. F., Gogtay, N., Giedd, J. N., Rapoport, J. L., & Bullmore, E. T. (2012). Simple models of human brain functional networks. Proceedings of the National Academy of Sciences, 109(15), 5868-5873.
3. Oldham, S., Fulcher, B. D., Aquino, K., Arnatkevičiūtė, A., Paquola, C., Shishegar, R., & Fornito, A. (2022). Modeling spatial, developmental, physiological, and topological constraints on human brain connectivity. Science advances, 8(22), eabm6127.
4. Zhang, X., Braun, U., Harneit, A., Zang, Z., Geiger, L. S., Betzel, R. F., ... & Tost, H. (2021). Generative network models of altered structural brain connectivity in schizophrenia. Neuroimage, 225, 117510.
5. Akarca, D., Vértes, P. E., Bullmore, E. T., & Astle, D. E. (2021). A generative network model of neurodevelopmental diversity in structural brain organization. Nature communications, 12(1), 4216.
6. Carozza, S., Holmes, J., Vértes, P. E., Bullmore, E., Arefin, T. M., Pugliese, A., ... & Astle, D. E. (2023). Early adversity changes the economic conditions of mouse structural brain network organization. Developmental Psychobiology, 65(6), e22405. doi:10.1126/sciadv.abm6127
7. Betzel, R. F., & Bassett, D. S. (2018). Specificity and robustness of long-distance connections in weighted, interareal connectomes. Proceedings of the National Academy of Sciences, 115(21), E4880-E4889.

8. Gollo, L. L., Roberts, J. A., Cropley, V. L., Di Biase, M. A., Pantelis, C., Zalesky, A., & Breakspear, M. (2018). Fragility and volatility of structural hubs in the human connectome. Nature Neuroscience, 21(8), 1107-1116.
9. Hansen, J. Y., Shafiei, G., Voigt, K., Liang, E. X., Cox, S. M., Leyton, M., ... & Misic, B. (2023). Integrating multimodal and multiscale connectivity blueprints of the human cerebral cortex in health and disease. Plos Biology, 21(9), e3002314.
10. Oldham, S., & Fornito, A. (2019). The development of brain network hubs. Developmental cognitive neuroscience, 36, 100607.

Poster No 1531

The hippocampus as a network epicentre for distant cortical thinning in neurocognitive aging

Charly Billaud[1], Junhong Yu[1]

[1]Nanyang Technological University, Singapore

Introduction: Multimodal neuroimaging studies on neurocognitive disorders, such as Alzheimer's disease (AD) and mild cognitive impairment (MCI) have highlighted associations between gray matter structures and white matter integrity (Cauda et al., 2018; Sui et al., 2015). AD has been suggested to follow a degeneration model where pathology affects widespread brain structures through network propagation across axonal tracts (Brier, Thomas & Ances, 2014; Pandya et al., 2017; Raj & Powell, 2018). Across neurocognitive disorders including AD, co-alterations in grey matter volumes have been associated both with fMRI functional connectivity (FC) and diffusion tensor imaging (DTI) measured structural connectivity (SC, Cauda et al., 2018), which suggests disrupted connections in both modalities may explain widespread atrophy. The medial temporal lobe, in particular the hippocampal formation, has been identified as a potential epicentre of connectivity disruption as well as of distant alterations (Cauda et al., 2020, Mallio et al., 2015; Manuello et al., 2018). The present study tested the effect of SC and FC to the hippocampus on the cortical thickness (CT) of areas connected to the same hippocampus.

Methods: T1, DTI and resting state fMRI images were obtained and preprocessed in 26 participants with AD, 150 with MCI, 15 with subjective memory complaint and 228 cognitively normal from the Alzheimer's Disease Neuroimaging Initiative (ADNI*) dataset (N=419; Age=73±8; 223F:196M). A composite memory score was defined using learning, immediate, delay, recognition scores from the Rey Auditory Verbal Learning Test (RAVLT) and used to define clusters where the score was significantly associated with CT in the sample. Two structural equation models (SEM, for SC and FC respectively) were fitted including cortical thickness of the clusters were identified previously; regressors were SC (shortest weighted path length with Dijkstra's algorithm) and FC (correlation) between the bilateral hippocampi and the parcellations.

Results: The SEM for SC (CFI=.951, RMSEA = 0.042, SRMR = .092) showed that the weighted length of the shortest path to the left hippocampus negatively predicted CT in the temporal poles/parahippocampal cortices (left CT: β = -0.150, p = <.001), so did the shortest path length to the right hippocampus (left CT: β = 0.139, p = <.001; right: β = -0.191, p = <.001). Shortest path length to the left hippocampus also predicted CT in the right fusiform/parahippocampal cortex (β = -0.104, p = .011) and right intraparietal sulcus/superior parietal lobule (β = 0.101; p = .028). The SEM for FC (CFI=.996, RMSEA = 0.012, SRMR = .092) showed that the connectivity with the hippocampi predicted right fusiform/parahippocampal CT (left: β = -0.97; p = .023) and the left parietal operculum/inferior parietal lobule (right: β = 0.375; p = .042).

Conclusions: The present findings show that both SC and FC from the bilateral hippocampi, especially from the left hippocampus, are associated with the grey matter thickness of temporal and parietal regions they connect to. The more "costly" it is for information to travel to these regions (longer path length, less white matter streamlines) from the hippocampus, the greater the atrophy can be observed in these regions. Association are also found between CT and FC from the left hippocampus. This gives support to the idea that the hippocampus is an epicentre for distant brain alterations and that its disrupted connections affect distant brain structures. Such network phenomenon may explain neurodegenerative spread processes in AD and MCI.

References

1. *Data used in preparation of this article were obtained from the Alzheimer's Disease Neuroimaging Initiative (ADNI) database (adni.loni.usc.edu). As such, the investigators within the ADNI contributed to the design and implementation of ADNI and/or provided data but did not participate in analysis or writing of this report.
2. A complete listing of ADNI investigators can be found at:
3. http://adni.loni.usc.edu/wp-content/uploads/how_to_apply/ADNI_Acknowledgement_List.pdf
4. Brier, M. R. (2014). Network dysfunction in Alzheimer's disease: refining the disconnection hypothesis. Brain Connectivity, 4(5), 299–311.
5. Cauda, F. (2020). Hubs of long-distance co-alteration characterize brain pathology. Human Brain Mapping, 41(14), 3878.
6. Cauda, F. (2018). Brain structural alterations are distributed following functional, anatomic and genetic connectivity. Brain : A Journal of Neurology, 141(11), 3211–3232.
7. Mallio, C. A. (2015). Epicentral Disruption of Structural Connectivity in Alzheimer's Disease. CNS Neuroscience & Therapeutics, 21(10), 837.

8. Manuello, J. (2018). The pathoconnectivity profile of Alzheimer's disease: A morphometric coalteration network analysis. Frontiers in Neurology, 8(JAN), 289568.
9. Pandya, S. (2017). The Brain's Structural Connectome Mediates the Relationship between Regional Neuroimaging Biomarkers in Alzheimer's Disease. Journal of Alzheimer's Disease : JAD, 55(4), 1639–1657. https://doi.org/10.3233/JAD-160090
10. Raj, A. (2018). Models of Network Spread and Network Degeneration in Brain Disorders. Biological Psychiatry. Cognitive Neuroscience and Neuroimaging, 3(9), 788–797.
11. Sui, X. (2015). Sparse canonical correlation analysis reveals correlated patterns of gray matter loss and white matter impairment in Alzheimer's disease. Proceedings - International Symposium on Biomedical Imaging, 2015-July, 470–473. https://doi.org/10.1109/ISBI.2015.7163913

Poster No 1532

Structural Connectivity Network in Human Brain in Relation to Transgenderism

Ye Wu[1], Yifei He[1], Tao Zhou[1], Xiaoming Liu[2]

[1]Nanjing University of Science and Technology, Nanjing, China, [2]Department of Radiology, Union Hospital, Tongji Medical College, Huazhong University of Science and, Wuhan, China

Introduction: Gender identity and sexual orientation are among the most fascinating aspects of human biology[1–4]. However, the mechanisms that underlie them are still unknown. Both transgenderism and homosexuality are aspects of human biology that are believed to arise from different sexual differentiation of the brain, leading to differences in the structural network of the brain. The purpose of this study is to investigate the relationship between gender identity, sexual orientation, and structural white matter connections as measured by length. A hypothesis suggests that transgender individuals, regardless of their sexual orientation, may differ from cisgender individuals in terms of the transitivity of structural connections in the network involved in their body perception in the context of self.

Methods: T1-weighted and pre-processed dMRI of 928 healthy subjects from the publicly accessible Amsterdam Open MRI Collection[5] were used in this study. The acquisition parameters of the images, as well as the pre-processing, are described in the original publications of each dataset. The restricted diffusion was quantified using restricted diffusion imaging[6]. A deterministic fiber tracking algorithm[7] was used with augmented tracking strategies[8] to improve reproducibility. Shape analysis[8] was conducted to derive shape metrics for tractography. HCP-MMP[9] was used as the brain parcellation, and the connectivity matrix was calculated by using the mean length of the connecting tracks. The connectivity matrix and graph theoretical analysis were conducted using DSI Studio (http://dsi-studio.labsolver.org). The global structural connectivity was assessed with measures such as global efficiency, small-worldness index, and transitivity was investigated with the measure including betweenness centrality. To test whether gender identity or sexual orientation correlated with either structural connectivity or its derived metrics, we conducted Bayesian correlation analyses[10]. All Bayesian tests used a non-informative prior and a medium-sized distribution (conjugate distributions on either side). The network metrics and sex distribution were compared using separate independent samples t-tests. Neuroimaging results are presented as the mean ± standard error of the mean. Statistical analyses were conducted using a 0.05 alpha level. All of the statistical analysis was implemented using JASP[11].

Results: The Bayesian correlation between transgenderism, which includes both gender identity and sexual orientation, and the transitivity of structural connectivity is depicted in Fig. 1. These results provide evidence that suggests a correlation between transgenderism and structural connectivity. Furthermore, the Bayes factor comparing the predictions of the two hypotheses shows that the data are ultra-high times more likely under the alternative hypothesis H+ than under H0. Fig. 2 shows the results of independent samples t-tests with sex grouping on three network properties derived by structural connectivity. The results show that males have significantly higher values ($p<.001$) of transitivity, small worldness, and global efficiency when compared to females. Fig. 3 explores the partial correlation between agreeableness personality (NEO-A) and the transitivity of structural connectivity while controlling for the effect of transgenderism. The results indicate a significant negative relationship ($p<.001$) between them. Additionally, a robustness analysis using a different value for the Cauchy scale parameter confirms the high robustness of this correlation to different prior specifications.

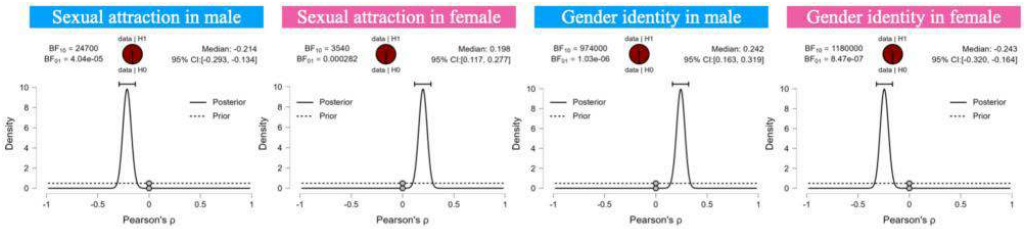

Figure 1. The results of the Bayesian correlation between transgenderism (gender identity or sexual orientation) and the transitivity of structural connectivity.

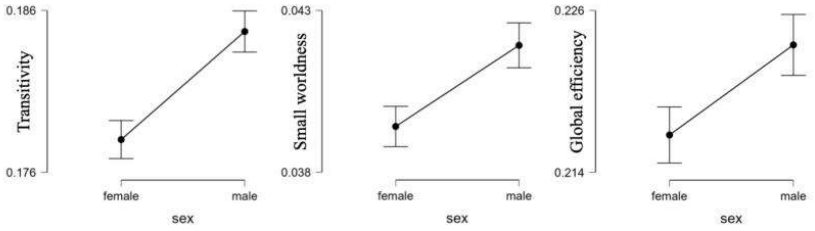

Figure 2. The results of the independent samples t-tests with sex grouping on three network properties derived by structural connectivity.

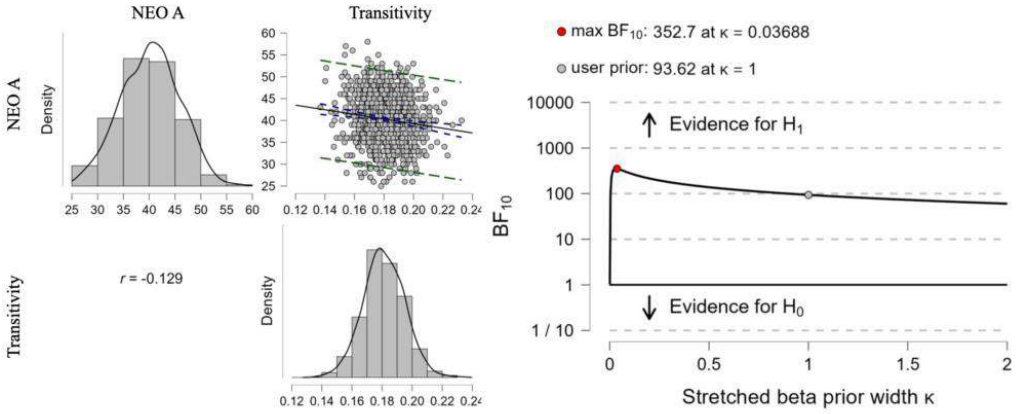

Figure 3. Left: The results of the partial correlation between agreeableness personality (NEO-A) and the transitivity of structural connectivity while controlling for the effect of transgenderism. Right: The results of the corresponding robustness analysis.

Conclusions: Using structural connectivity, the present study investigates whether and how brain networks are related to gender identity and sexual orientation, revealing sex-atypical brain network properties in transgender individuals. The present findings support the idea of a distinction and partial overlap between the brain network underlying sexual orientation and transgenderism.

References

1. Burke, S. M. (2017). Structural connections in the brain in relation to gender identity and sexual orientation. Scientific Reports, 7(1), 17954.
2. Gilmore, J. H. (2007). Regional Gray Matter Growth, Sexual Dimorphism, and Cerebral Asymmetry in the Neonatal Brain. Journal of Neuroscience, 27(6), 1255–1260.
3. Glasser, M. F. (2016). A multi-modal parcellation of human cerebral cortex. Nature, 536(7615), 171–178.
4. Hahn, A. (2015). Structural connectivity networks of transgender people. Cerebral Cortex, 25(10), 3527–3534.
5. Love, J. (2019). JASP: Graphical statistical software for common statistical designs. Journal of Statistical Software, 88, 1–17.
6. Snoek, L. (2020). The Amsterdam Open MRI Collection, a set of multimodal MRI datasets for individual difference analyses. Neuroscience.
7. Uribe, C. (2023). A gendered brain perspective from structure to brain interactions. In Principles of Gender-Specific Medicine (pp. 39–59). Elsevier.
8. Wagenmakers, E.-J. (2018). Bayesian inference for psychology. Part II: Example applications with JASP. Psychonomic Bulletin & Review, 25(1), 58–76.
9. Yeh, F.-C. (2017). Mapping immune cell infiltration using restricted diffusion MRI. Magnetic Resonance in Medicine, 77(2), 603–612.
10. Yeh, F.-C. (2020). Shape analysis of the human association pathways. NeuroImage, 223, 117329.
11. Yeh, F.-C. (2013). Deterministic diffusion fiber tracking improved by quantitative anisotropy. PloS One, 8(11), e80713.

Poster No 1533

Estimating Connectional Brain Templates with Augmented Federated Learning

Geng Chen[1], Qingyue Wang[1], Abid Ali[1], Islem Rekik[2]

[1]Northwestern Polytechnical University, Xi'an, China, [2]Imperial College, London, United Kingdom

Introduction: Federated learning of Connectional Brain Templates (CBTs) estimates a central brain connectivity across datasets collected by different hospitals[1]. Despite its progress, it suffers from the non-Independent and Identically Distributed (non-IID) issue of multiple domains, where the data distribution varies across hospitals. This issue degrades the centeredness of the learned CBT. To this end, we propose a novel augmented federated learning framework for robust CBT learning across diverse domains. The key innovation lies in generalizing the model by augmenting the data diversity of each hospital, which is achieved through a custom brain connectivity generator. Extensive experiments demonstrate the superiority of our method in learning cross-hospital CBTs from multi-view morphological brain networks.

Methods: An overview of the proposed method, called AugFedCBT, is shown in Figure 1. We build upon FedCBT[1], which combines FedAvg[2] with the DGN[3] for federated CBT learning. Our improvement involves the integration of the Multigraph Generator Network (MGN)[4] for local domain augmentation. Specifically, each hospital is equipped with a pretrained MGN-based generator, which generates brain connectivities from subject-specific CBTs obtained with DGN. During the federated learning, local model DGNk, trained with brain connectivities Sk at hospital k, updates its network weights wk for the t-th round via:

$$\mathbf{w}_k^{t+1} = \mathrm{DGN}_k(\mathbf{w}_k^t, \mathbf{S}_k).$$

After updating weights across all hospitals, the global DGN on the server is updated by computing the weighted average weights according to the proportion of local samples to the total samples as follows:

$$\mathbf{w}^{t+1} = \sum_{k=1}^{K} \frac{N_k}{N} \mathbf{w}_k^{t+1}.$$

Next, a post-federated-learning procedure generalizes the domain by augmenting new brain connectivities from a set of subject-specific CBT Ck perturbed by the same random Gaussian noise matrix nk via MGNk:

$$\mathbf{A}_k = \mathrm{MGN}_k(\mathbf{n}_k, \mathbf{C}_k).$$

The network weight learning is then improved by including the augmented domain data Ak as follows:

$$\mathbf{w}_k^{t+1} = \mathrm{DGN}_k(\mathbf{w}_k^t, \hat{\mathbf{S}}_k); \hat{\mathbf{S}}_k = \mathbf{S}_k \bigcup \mathbf{A}_k.$$

The DGN model is trained with an enhanced DGN Loss[3], which considers data Sk and Ak from both source and augmented domains.

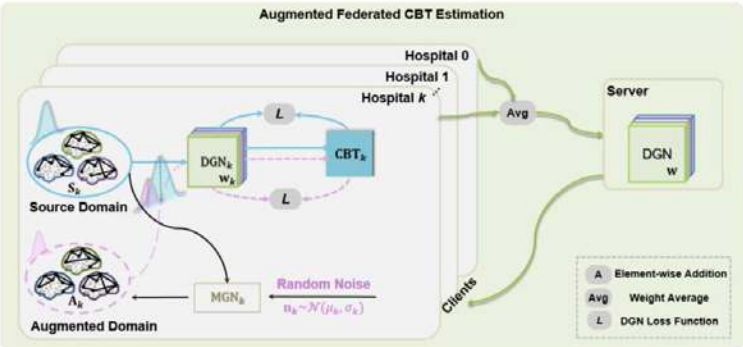

Figure 1: An overview of AugFedCBT: For each local learning round of hospital k, we randomly generate a symmetric Gaussian noise matrix $\mathbf{n}_k \sim \mathcal{N}(\mu_k, \sigma_k)$ to increase disturbance on the source multi-view dataset $\mathbf{S}_k$. This facilitates the generation of the augmented domain $\mathbf{A}_k$ through the MGN_k for subsequent local learning. Next, the local model DGN_k is trained on an enhanced DGN loss. Finally, following the federated learning approach in FedCBT [1], the model weights are updating round-by-round between the hospitals and the server.

Results: Dataset: We evaluate our method using right hemisphere morphological brain networks of 186 normal subjects from the ABIDE-I dataset[5]. Using FreeSurfer[6], we generate cortical surfaces from T1-weighted MR images and further construct six morphological networks based on the Desikan-Killiany Atlas. These networks encode shape relationships between cortical regions in terms of different attributes. Experimental Results: We compare our AugFedCBT with state-of-the-art (SOTA) models[1,3] and its non-federation-learning ablated version (AugDGN). To obtain stable results, we conduct 10 random data simulations and report the average results. The CBT centeredness results, shown in Figure 2(a), indicate that AugFedCBT significantly ($p<0.0001$) outperforms the SOTA models and achieves the minimum Frobenius distance in all hospitals. Additionally, it surpasses its ablated version, demonstrating the effectiveness of combining connectivity augmentation with federated CBT learning to overcome the non-IID issue. Figure 2(b) further confirms the superior CBT-centeredness performance of our AugFedCBT, aligning with the observations in Figure 2(a).

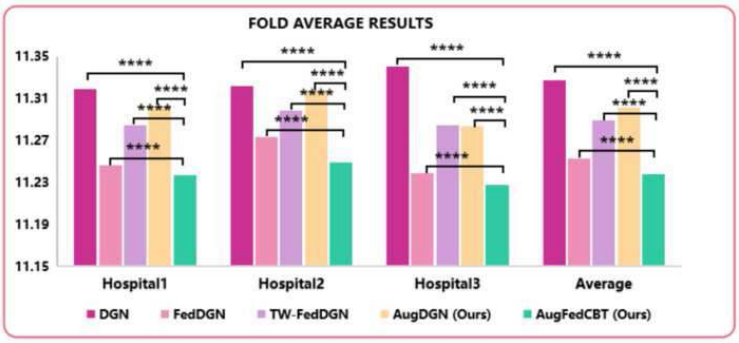

a. Cross-hospital CBT centerednes comparison

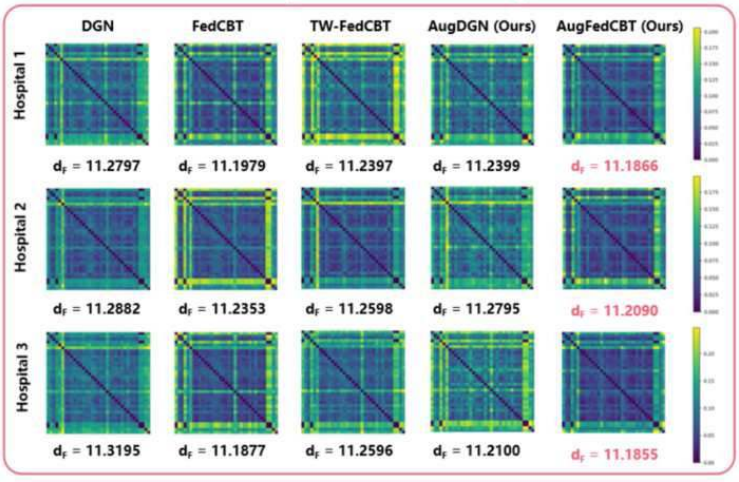

b. Cross-hospital CBT Visual comparison

Figure 2: Experimental Results. (a) Quantitative comparison of the centeredness of CBTs given by AguFedCBT and the comparison models, inlcuding the ablated version. The Frobenius distance is adopted for evaluation. Experiments are performed with the NC RH dataset. We also report the *p*-values using a two-tailed paired t-test between AugFedCBT and each comparison method. The *p*-value less than 0.0001 is flagged with (****). **(b)** Visual comparison of CBTs given by AugFedCBT and the comparison models. Results are based on fold one of the NC RH dataset.

Conclusions: We proposed AugFedCBT, an effective CBT learning model to tackle non-IID brain graph data through connectivity augmentation. The effectiveness of AugFedCBT is demonstrated qualitatively and quantitatively by extensive experiments.

References

1. Bayram H C. (2021), 'A federated multigraph integration approach for connectional brain template learning', in International Workshop on Multimodal Learning for Clinical Decision Support, pp. 36–47, Springer
2. McMahan B. (2017), 'Communication-efficient learning of deep networks from decentralized data', in Artificial intelligence and statistics, pp. 1273-1282, PMLR
3. Gurbuz M B. (2020), 'Deep graph normalizer: a geometric deep learning approach for estimating connectional brain templates', in Medical Image Computing and Computer Assisted Intervention, pp. 155–165, Springer
4. Pala F. (2022), 'Predicting Brain Multigraph Population from a Single Graph Template for Boosting One-Shot Classification', in International Workshop on PRedictive Intelligence In MEdicine, pp. 191-202, Springer
5. Di Martino A. (2014), 'The autism brain imaging data exchange: towards a large-scale evaluation of the intrinsic brain architecture in Autism', Molecular Psychiatry, Molecular psychiatry, vol. 19, no. 6, pp. 659–667
6. Fischl B. (2012), 'FreeSurfer', NeuroImage, vol. 62, no. 2, pp. 774–781

Poster No 1534

Mouse fMRI with optogenetic silencing reveals neural interactions underlying resting-state fMRI

Hyun Seok Moon[1], Thanh Vo[1,2,3], Seong-Gi Kim[1,2,3]

[1]Center for Neuroscience Imaging Research (CNIR), Institute for Basic Science (IBS), Suwon, Korea, Republic of, [2]Department of Biomedical Engineering, Sungkyunkwan University, Sungkyunkwan University, Suwon, Korea, Republic of, [3]Department of Intelligent Precision Healthcare Convergence, Sungkyunkwan University, Suwon, Korea, Republic of

Introduction: Resting-state (RS) fMRI is a potent tool for mapping brain-wide functional connectivity (FC), yet its mechanism remains not fully understood. RS FC only partially corresponds to monosynaptic structural connectivity (SC) while exhibiting strong interhemispheric connections, implicating polysynaptic or indirect connectivity (Honey et al. 2009, Grandjean et al. 2017). However, a causal link between spontaneous neural interactions and FC has yet to be established. Optogenetic fMRI may resolve this question by mapping changes in neural activity induced by precise spatiotemporal neural manipulation (effective connectivity; EC). Notably, optogenetic activation of local excitatory neurons revealed predominantly ipsilateral connections resembling SC (Bauer et al. 2018, Kim et al. 2023). We hypothesized that this discrepancy arises because the upregulation of neural activity does not account for spontaneously occurring connectivity. To address this, we employed optogenetic silencing to assess ongoing interactions during RS. Our study investigated (de)activation patterns resulting from excitatory and inhibitory neuron-specific optogenetic EC and their relationship with SC and FC (Figure 1A).

Methods: For optogenetic fMRI, VGAT-ChR2-EYFP and Thy1-ChR2-EYFP mice were used for specific modulation of inhibitory/excitatory neurons. We prepared a thinned-skull cranial window covering the entire dorsal cortex for cortex-wide patterned optogenetics (Kim et al. 2023). Optogenetic CBV-weighted fMRI data were acquired at 9.4T (Bruker Biospec). Resting state BOLD fMRI data were acquired at 15.2T (Bruker Biospec) in eight C57BL/6N mice. Mice were anesthetized under a continuous infusion of dexmedetomidine (0.05 mg/kg/h) with 0.3% isoflurane during experiments. All fMRI data were preprocessed and normalized to the Allen mouse brain atlas (Wang et al. 2020). Whole-brain SC dataset was obtained from a previous study (Coletta et al. 2020), which contains a full connectivity matrix among 15,314 parcels across the brain. To match the SC resolution, our RS fMRI dataset was resampled to this parcellation, and an FC matrix was generated by pairwise correlation between parcels. For ROI-level analysis, SC and FC were further computed in 86 atlas-based bilateral cortical ROIs.

Results: Optogenetic fMRI data were acquired by stimulating 6 cortical areas (Figure 1B). Overall, FC exhibited more extensive connectivity than SC. Notably, optogenetic activation induced localized responses in structurally connected areas, while optogenetic silencing led to more widespread responses. Quantifying connectivity strengths in 86 bilateral cortical ROIs (Figure 1C), we found a stronger association between FC strengths and optogenetic silencing-induced responses, compared to optogenetic activation (Figure 2A). We further examined intra- and inter-hemispheric connections separately, since interhemispheric connectivity is a hallmark of FC (Figure 2B, C). Optogenetic silencing exhibited extensive connections to contralateral regions, implying that interhemispheric FC may arise from neural interactions via indirect structural pathways. We also found a strong linear relationship between the strength of intrahemispheric connections and their contralateral counterparts (Figure 2D), while the slope of linear regression was highest (~0.5) for FC and optogenetic silencing, followed by optogenetic activation (~0.3), and lowest for SC (~0.1) (Figure 2E).

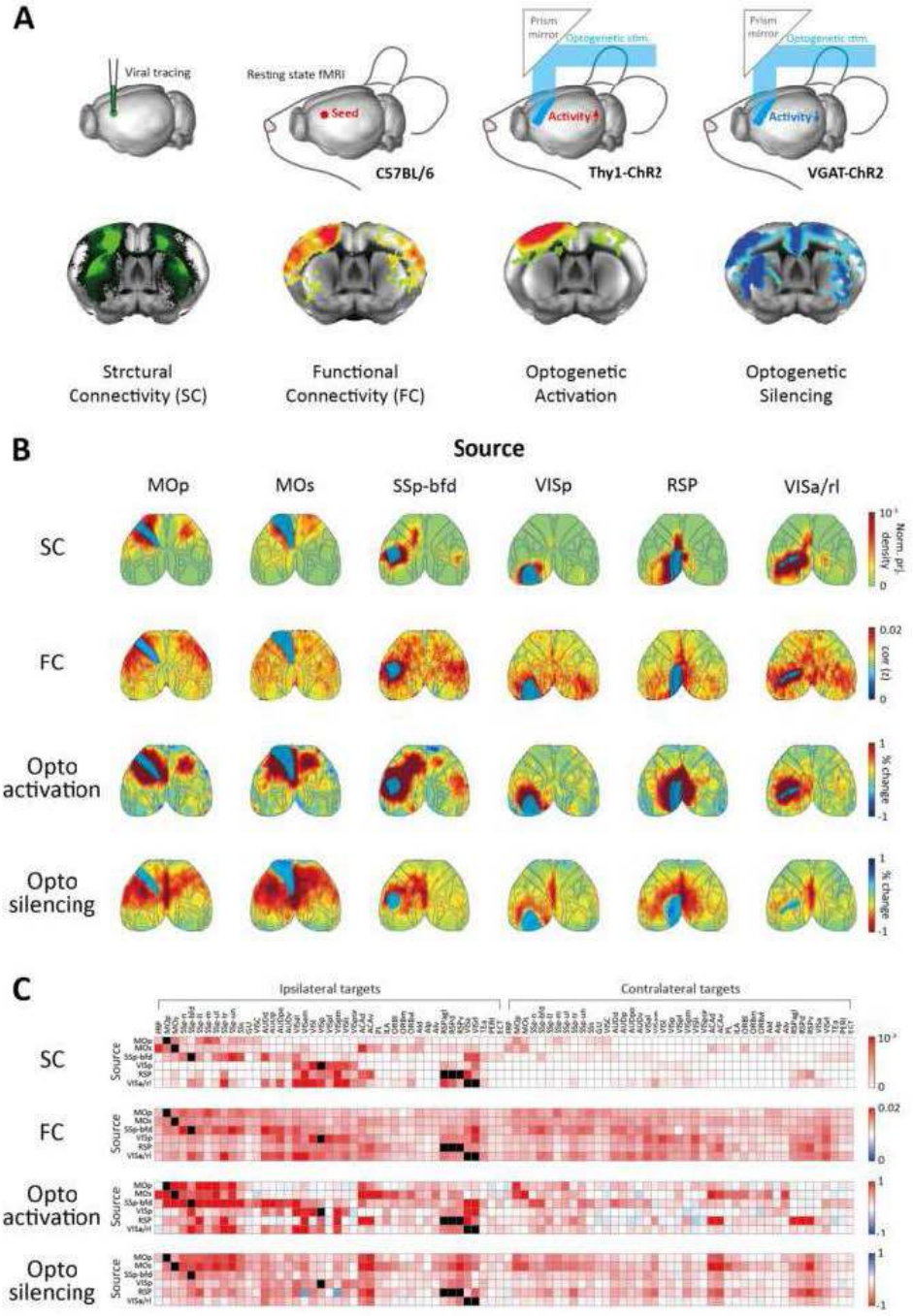
A
Viral tracing
Resting state fMRI
Seed
C57BL/6
Prism mirror
Optogenetic stim.
Activity ↓
Thy1-ChR2
Activity ↑
VGAT-ChR2
Strctural Connectivity (SC)
Functional Connectivity (FC)
Optogenetic Activation
Optogenetic Silencing
B
Source
MOp
MOs
SSp-bfd
VISp
RSP
VISa/rl
SC
FC
Opto activation
Opto silencing
Norm. prj. density
corr (r)
% change
C
Ipsilateral targets
Contralateral targets
Source
SC
FC
Opto activation
Opto silencing

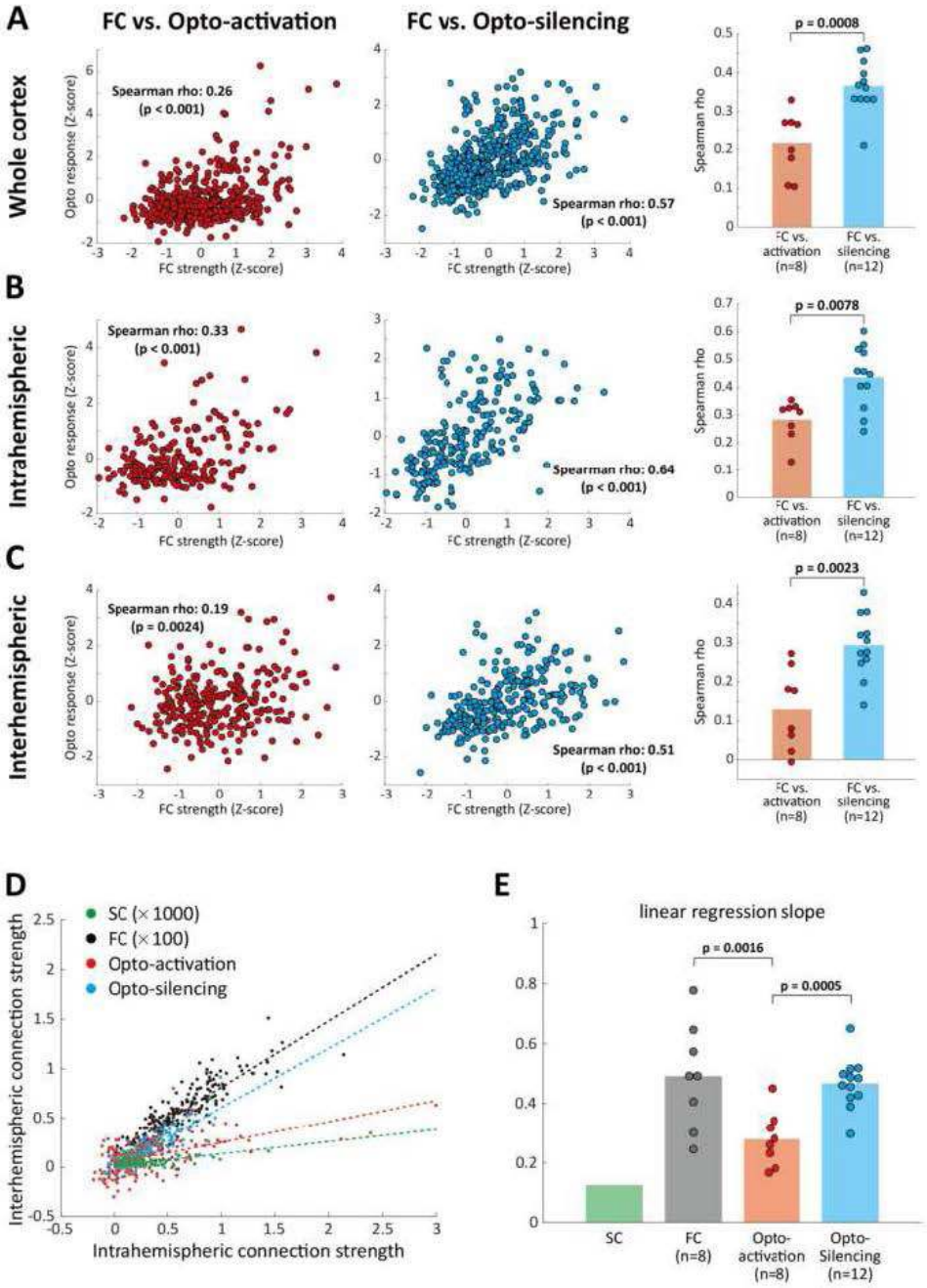

Conclusions: Our study has several important implications. First, the connectivity patterns by optogenetic silencing were highly correlated with FC, implying that FC depends more on spontaneous activity than evoked activity. Second, we revealed that cortical regions have resting-state interactions not only with contralateral homotopic regions but also with heterotopic regions, possibly via polysynaptic structural pathways. The results suggest that FC originates, at least partially, from neural interaction during RS.

References

1. Honey, C.J. (2009), Predicting human resting-state functional connectivity from structural connectivity. Proceedings of the National Academy of Sciences 106, 2035-2040.
2. Grandjean, J. (2017), Structural basis of large-scale functional connectivity in the mouse. Journal of Neuroscience 37, 8092-8101.
3. Bauer, A.Q. (2018), Effective Connectivity Measured Using Optogenetically Evoked Hemodynamic Signals Exhibits Topography Distinct from Resting State Functional Connectivity in the Mouse. Cerebral Cortex 28, 370-386.
4. Kim, S. (2023), Whole-brain mapping of effective connectivity by fMRI with cortex-wide patterned optogenetics. Neuron 111, 1732-1747.
5. Wang, Q. (2020), The Allen mouse brain common coordinate framework: a 3D reference atlas. Cell 181, 936-953. e920.
6. Coletta, L. (2020), Network structure of the mouse brain connectome with voxel resolution. Science Advances 6, eabb7187.

Poster No 1535

Eigenvector centrality functional connectivity patterns indicate age and APOE4 carrier status

Aïda Fall[1], Maria Preti[1], Mohamed Eshmawey[2], Sonja Kagerer[3], Dimitri Van De Ville[4], Paul Unschuld[5]

[1]University of Geneva, Geneva, Geneva, [2]Geneva university hospitals, Geneva, Geneva, [3]Institute for Regenerative Medicine (IREM), Zurich, Zurich, [4]École Polytechnique Fédérale de Lausanne, Lausanne, Switzerland, [5]Geneva university hospitals, Geneva, Geneva

Introduction: Age and Apolipoprotein E4 (APOE4) are the greatest risk factors for Alzheimer's disease (AD) (Yin et al., 2018) but the fundamental processes underlying the onset of the pathology remains unclear. Functional brain change in AD, as revealed by functional magnetic resonance imaging (fMRI), is characterized by disruption of brain networks (Sperling et al., 2010). Carrier-status of the ApolipoproteinE4 (ApoE4) allele is associated with faster progression of AD, and therefore a potentially more pronounced disintegration of brain functional connectivity (FC). Here, we investigated functional connectivity changes associated with aging and the presence of APOE4 allele, to link individual brain network properties with AD risk.

Methods: We included in the study 128 individuals from the Alzheimer's Disease Neuroimaging Initiative database (ADNI). This sample includes 54 APOE4 carriers and 74 non-carriers. 76 were non-symptomatic (39 Cognitive Normal (CN), 37 with Subjective Memory Complaint (SMC)) and 52 were symptomatic (39 with Mild Cognitive Impairment (MCI), 13 with AD). Resting-state fMRI images were preprocessed with conventional in-house pipelines including realignment, regression of nuisance signals (motion, cerebrospinalfluid and white matter signals), spatial smoothing. Regional time courses were then obtained by parcellation into 379 brain regions (360 from Glasser parcellation (Glasser et al., 2016) and 19 subcortical ones (Fischl et al., 2002)), and band-pass filtered within the range [0.01-0.15 Hz]. Functional connectomes (FC) were obtained as pairwise Pearson's correlation between regional timecourses, and eigenvector centrality was computed as the first eigenvector of FC. We investigated the relationship between eigenvector centrality, aging and the presence of APOE4 with Partial Least Square Correlation (PLSC) analysis (Krishnan et al., 2011), where the brain data matrix X included eigenvector centrality for each subject, and behavioral matrix Y included z-scored age of each subject and symptomatic index (1 for symptomatic and 0 for non-symptomatic). By eigendecomposition of the covariance matrix between these two sets of variables, we are able to extrapolate sets of variables that maximize the correlation between brain and behavior.

Results: PLSC analysis yielded one significant latent component (p-val<0.001). By looking at brain and behavioral scores (Fig. 1 and 2, respectively), we can highlight which brain / behavioral variables contribute the most to the multivariate correlation. We found a significant relationship between centrality, aging, the presence of APOE4 and disease progression in brain regions in both parietal and frontal lobes. In particular, decreased centrality in the dorsal somatomotor and visuospatial attention networks (Fig. 1, blue nodes) is associated with aging, cognitive impairment, and the presence of the genetic risk factor for AD, APOE4. The presence of FC alterations in aging is largely explored in literature, with results concordant with our findings (Dennis et al., 2014). However, our analysis suggests that the same pattern of FC alterations which is associated with aging is acerbated by the presence of not only cognitive impairment but also APOE4, possibly accelerating the degeneration process in carrier individuals. This opens a window for further insights into the exploration of pathological mechanisms in APOE4 carriers, with the perspective of an early diagnosis.

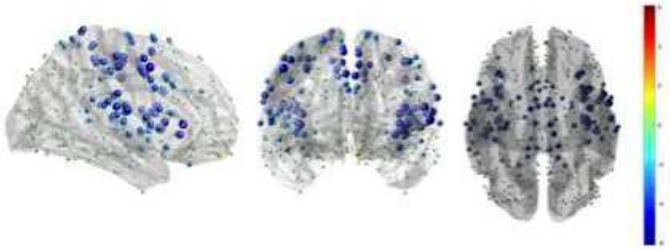

Figure 1. **Brain plot representing the PLS brain salience pattern of correlation driven by aging, the presence of APOE4 and cognitive impairment.** One sphere represents one brain region, and their size represents the degree of connection. The relative strength of the connections is illustrated either in red for positive or blue for negative. Most of the significant regions are located in the lower part of both parietal and frontal lobes.

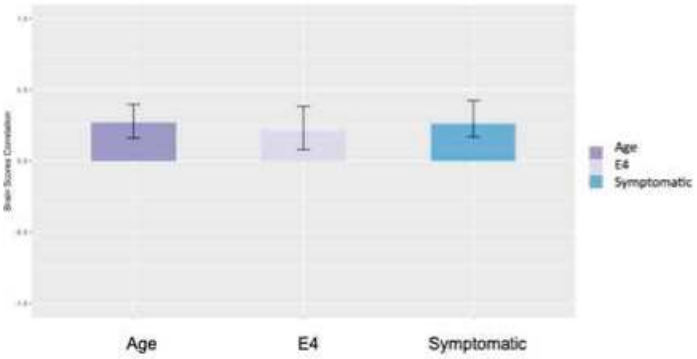

Figure 2. Bar plot representing the PLS behavioral salience, capturing multivariate correlation between the three behavioral variables (age, the presence of APOE4 and cognitive symptoms) and the eigenvector centrality in the brain salience pattern shown in Fig. 1. The bars correspond to the confidence interval 95%.

Conclusions: In this work, we explored the impact of aging on brain functional connectivity and the potential mediation of this effect by the presence of the genetic risk factor for AD. We found a signature brain pattern associated with aging, but acerbated by the presence of APOE4, corroborating evidence of earlier degeneration in these subjects. Future longitudinal studies will allow to further validate these findings and advance towards an early diagnosis of AD based on multiple markers.

References

1. Yin, Y., Wang, Z. (2018). ApoE and Neurodegenerative Diseases in Aging. In: Wang, Z. (eds) Aging and Aging-Related Diseases. Advances in Experimental Medicine and Biology, vol 1086. Springer, Singapore. https://doi.org/10.1007/978-981-13-1117-8_5
2. Sperling RA, Dickerson BC, Pihlajamaki M, Vannini P, LaViolette PS, Vitolo OV, Hedden T, Becker JA, Rentz DM, Selkoe DJ, Johnson KA. (2010) Functional alterations in memory networks in early Alzheimer's disease. Neuromolecular Med. 2010 Mar;12(1):27-43. doi: 10.1007/s12017-009-8109-7. PMID: 20069392; PMCID: PMC3036844.
3. Glasser MF, Coalson TS, Robinson EC, Hacker CD, Harwell J, Yacoub E, Ugurbil K, Andersson J, Beckmann CF, Jenkinson M, Smith SM, Van Essen DC. (2016) A multi-modal parcellation of human cerebral cortex. Nature. 2016 Aug 11;536(7615):171-178. doi: 10.1038/nature18933. Epub 2016 Jul 20. PMID: 27437579; PMCID: PMC4990127.
4. Fischl B, Salat DH, Busa E, Albert M, Dieterich M, Haselgrove C, van der Kouwe A, Killiany R, Kennedy D, Klaveness S, Montillo A, Makris N, Rosen B, Dale AM. (2002) Whole brain segmentation: automated labeling of neuroanatomical structures in the human brain. Neuron. 2002 Jan 31;33(3):341-55. doi: 10.1016/s0896-6273(02)00569-x. PMID: 11832223.
5. Krishnan A, Williams LJ, McIntosh AR, Abdi H. Partial Least Squares (PLS) methods for neuroimaging: a tutorial and review. Neuroimage. 2011 May 15;56(2):455-75. doi: 10.1016/j.neuroimage.2010.07.034. Epub 2010 Jul 23. PMID: 20656037.
6. Dennis EL, Thompson PM. Functional brain connectivity using fMRI in aging and Alzheimer's disease. Neuropsychol Rev. 2014 Mar;24(1):49-62. doi: 10.1007/s11065-014-9249-6. Epub 2014 Feb 23. PMID: 24562737; PMCID: PMC4109887.

Poster No 1536

An fMRI Study on Symptom Subtypes of Obsessive Compulsive Disorder

Harah Kwon[1], Minji Ha[2], Sunah Choi[2], Sunghyun Park[3], Moonyoung Jang[3], Minah Kim[3], Jun Soo Kwon[4]

[1]Seoul National University Hospital, Seoul, Seoul, [2]Seoul National University, Seoul, Seoul, [3]Department of Neuropsychiatry, Seoul National University Hospital, Seoul, Seoul, [4]Department of Brain and Cognitive Sciences, Seoul National University College of Natural Sciences, Seoul, Seoul

Introduction: While intrusive thoughts and repetitive actions are the hallmarks of Obsessive-Compulsive Disorder (OCD), new research has shown that the disorder can include a variety of symptom categories. Distinct etiology, treatment responses, and prognoses are demonstrated by unique dimensions such as contamination, symmetry/order, and pure obsessions. Research aiming at understanding the underlying causes has revealed differences in the amygdala according to symptom dimensions, suggesting a relationship between modifications in amygdala function and symptom presentation. The amygdala is a key region for emotional assessment and fear reactions. While the basolateral amygdala is an input area that controls fear learning, the centromedial amygdala, acting as an output area, plays a critical role in fear expression. Recognizing social value is related to the superficial amygdala. The variability of OCD is partly explained by the different functions that amygdala subregions play in fear processing. Studies show that prognosis varies according to functional connectivity (FC) of particular amygdala subregions at rest. The ventromedial prefrontal cortex and basolateral amygdala show less connection in OCD patients who are responding well to cognitive behavioral therapy. Different amygdala subregions are active in relation to different aspects of OCD symptoms. However, there hasn't been much research done on the connections between amygdala subregions and cortical areas, which are necessary for different function and can explain why symptoms vary in size. By analyzing the functional connectivity between amygdala subregions and the whole brain in a group of OCD patients who do not take medication, this study aims to decipher the heterogeneity of OCD. The hypothesis is that in the compulsion-focused symptom dimension, there is less connection between the frontal brain and the centromedial amygdala. In addition, the obsession-focused symptom dimension is predicted to show a decrease in connection between the sensorimotor cortex and the basolateral amygdala.

Methods: 110 healthy controls (HCs) and 107 OCD patients had their resting-state functional magnetic resonance imaging taken. Using seeds from the amygdala's centromedial, laterobasal, and superficial subregions, whole-brain FC was compared between OCD patients and HCs as well as between the various OCD symptom aspects.

Results: The three OCD subgroups and the overall OCD and HC groups did not differ significantly in terms of sex, handedness, age, IQ, or years of education. The Y-BOCS total and compulsion scores of patients with contamination/washing-type OCD were greater than those of individuals with the other two OCD subtypes. When compared to healthy controls, individuals with symmetry/ordering/counting/checking-type OCD demonstrated hypoconnectivity between the bilateral superior frontal gyri and left centromedial amygdala. Additionally, when compared to individuals with contamination/washing-type OCD, there was hypoconnectivity between the left frontal cortex and left centromedial amygdala.

Conclusions: The results indicate that the compulsion-focused presentation of OCD may be caused by a defect in the control of behavioral responses to emotion processing resulting from hypoconnectivity between the centromedial amygdala and frontal cortex. Our findings highlight the potential importance of comprehending the brain bases of various OCD manifestations, which may open the door to future treatment approaches that are more individualized and focused.

References

1. Abramowitz, J.S. et al. (2010), 'Assessment of obsessive-compulsive symptom dimensions: development and evaluation of the Dimensional Obsessive-Compulsive Scale', Psychological Assessment, vol. 22, no. 1, pp. 180-198
2. Bellia, F. et al. (2021), 'Genetic and epigenetic architecture of Obsessive-Compulsive Disorder: In search of possible diagnostic and prognostic biomarkers', Journal of Psychiatric Research, vol. 137, pp. 554-571
3. Bzdok, D. et al. (2013), 'An investigation of the structural, connectional, and functional subspecialization in the human amygdala', Human Brain Mapping, vol. 34, no. 12, pp. 3247-3266
4. Davis, M. (1997), 'Neurobiology of fear responses: the role of the amygdala', Journal of Neuropsychiatry and Clinical Neurosciences, vol. 9, no. 3, pp. 382-402
5. Goodman, W.K. et al. (1989), 'The Yale-Brown Obsessive Compulsive Scale. I. Development, use, and reliability' Archives of General Psychiatry, vol. 46, no. 11, pp. 1006-1011
6. Graybiel, A.M. et al. (2000), 'Toward a neurobiology of obsessive-compulsive disorder', Neuron, vol. 28, no. 2, pp. 343-347
7. Jhung, K. et al. (2014), 'Distinct functional connectivity of limbic network in the washing type obsessive-compulsive disorder', Progress in Neuropsychopharmacology & Biological Psychiatry, vol. 53, pp. 149-155
8. Kim, M. et al. (2019), 'Functional connectivity of the raphe nucleus as a predictor of the response to selective serotonin reuptake inhibitors in obsessive-compulsive disorder', Neuropsychopharmacology, vol. 44, no. 12, pp. 2073-2081
9. Kwak, S. et al. (2020), 'Defining data-driven subgroups of obsessive-compulsive disorder with different treatment responses based on resting-state functional connectivity', Translational Psychiatry, vol. 10, no. 1, p. 359
10. Leckman, J.F. et al. (2005), 'Symptom dimensions in OCD: Developmental and evolutionary perspectives', In Concepts and controversies in obsessive-compulsive disorder, Springer: 3-25
11. van den Heuvel, O.A. et al. (2009), 'The major symptom dimensions of obsessive-compulsive disorder are mediated by partially distinct neural systems', Brain, vol. 132, Pt 4, pp. 853-868
12. Via, E. et al. (2014), 'Amygdala activation and symptom dimensions in obsessive-compulsive disorder', British Journal of Psychiatry, vol. 204, no. 1, pp. 61-68

Poster No 1537

Assortative mixing in micro-architecturally annotated brain connectomes

Vincent Bazinet[1], Justine Hansen[1], Reinder Vos de Wael[1], Boris Bernhardt[1], Martijn van den Heuvel[2], Bratislav Misic[1]

[1]McConnell Brain Imaging Centre, Montréal Neurological Institute, Montreal, Quebec, [2]Vrije Universiteit, Amsterdam, N/A

Introduction: The wiring of the brain connects micro-architecturally diverse neuronal populations. These neuronal populations have distinct anatomical and cellular makeups and thanks to modern technological advances, this heterogeneity in the brain's micro-architecture can be imaged with unprecedented detail and depth. The conventional graph model, however, encodes brain connectivity as a network of nodes and edges, and abstracts away the rich biological detail of each node[1].

Methods: In this work, we investigated the systematic arrangement of brain network connections with respect to a range of molecular, cellular, and genetic attributes. More specifically, we used the assortativity coefficient[2] to ask whether brain regions with similar annotations (i.e. biological attributes) are more likely to be connected with each other (Fig. 1a). To disentangle the relationships between the brain's connectivity, regional heterogeneity, and spatial embedding, we implemented novel null models that control for the spatial autocorrelation of nodal attributes (Fig. 1b)[3]. We performed all experiments using four brain network datasets from three different species (human, macaque, and mouse; Fig. 1c). This allowed us to uncover universal principles of organization across network reconstruction techniques, species, spatial scales, and attributes.

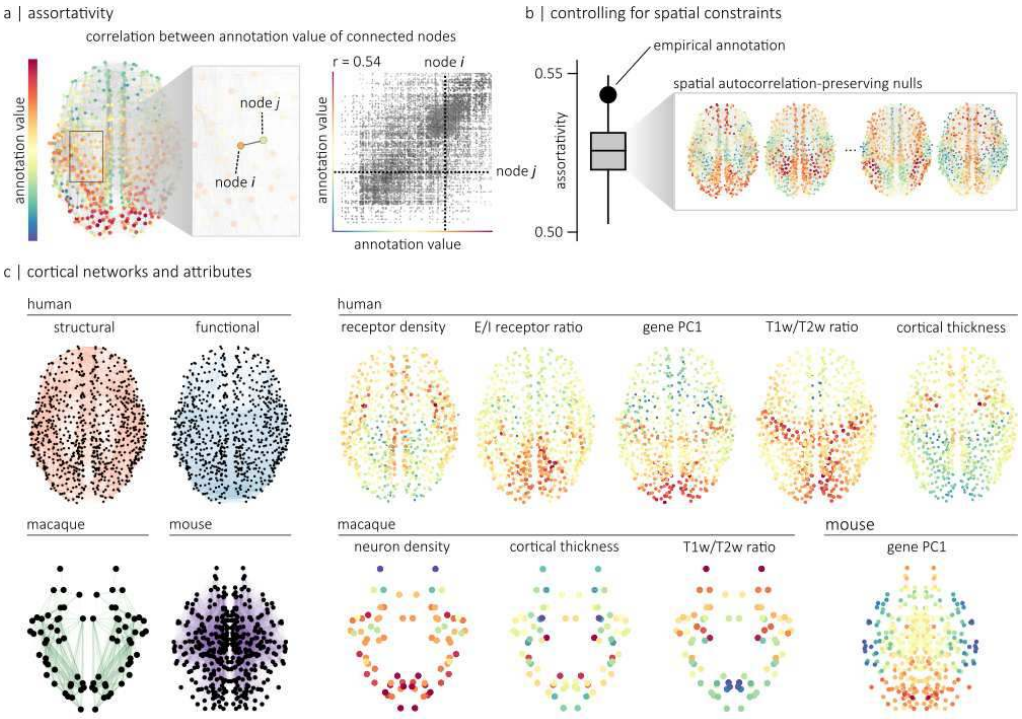

Figure 1 | (a) Given an annotated network where each node has a local annotation value, we quantify the tendency for nodes with similar values to be connected using the assortativity coefficient, defined as the Pearson correlation between the values of connected nodes. This relationship between the values of connected nodes can be visualized with a scatterplot of a network's edges where the position of each edge is determined by the annotation values of its two endpoints. (b) To control for spatial constraints, the assortativity coefficient of an empirical annotation is compared to the assortativity coefficients of null annotations that preserve the spatial autocorrelation of the empirical one. (c) Connectomes include a human structural and a human functional connectome reconstructed using data from the HCP, a macaque connectome generated using data from the CoCoMac database and a mouse connectome reconstructed using data from the Allen Mouse Brain Connectivity Atlas. Human connectomes are annotated with measures of neurotransmitter receptor density, the ratio of excitatory-to-inhibitory neurotransmitter receptors, the principal axis of gene expression (gene PC1), T1w/T2w ratio and cortical thickness. The macaque connectome is annotated with neuron density (neuron-to-cell ratio), cortical thickness and T1w/T2w ratio. The mouse connectome is annotated with the principal axis of gene expression (gene PC1).

Results: While we find that all annotations are positively assortative (i.e., connected brain regions tend to have similar annotations), we find that only a few are significantly assortative when compared to spatial autocorrelation-preserving null annotations (Fig. 2a). These are gene PC1, T1w/T2w ratio and cortical thickness for the functional connectome, and neuron density and T1w/T2w ratio for the macaque connectome. To explore how the mixing properties of our annotations vary as we consider connections of different lengths, we computed the assortativity of our annotations in thresholded connectomes where a given percentile of the shortest connections are removed. As short-distance connections are removed, leaving behind the longest connections, the standardized assortativity of all annotations in all four connectomes decreases (Fig. 2b). This result suggests that long-distance connections increase the diversity of a region's inputs and outputs and support the integration of information between micro-architecturally dissimilar regions[4]. We next asked if the heterogeneous distribution

of pairs of attributes from multi-member classes of annotation – neurotransmitter receptor profiles and laminar differentiation – is reflected in the connectivity of the brain. We find that laminar thicknesses of layers III, V and VI are assortative with respect to each other, but disassortative with respect to layer IV. For neurotransmitter receptors, we find evidence of disassortative mixing for pairs of receptors and transporters predominantly expressed in brain regions on opposite ends of the functional hierarchy as well as a significant assortative relationship between VaChT and NAT (Fig. 2c). This supports the idea that the cholinergic and norepinephrine systems interact with each other and with the brain's topology to influence large-scale dynamical processes[5]. Finally, using meta-analytic decoding[6], we find that the arrangement of connectivity patterns with respect to biological attributes shape patterns of regional functional specialization. Specifically, regions that connect to biologically similar regions are associated with executive function while regions that connect with biologically dissimilar regions are associated with memory function (Fig. 2d).

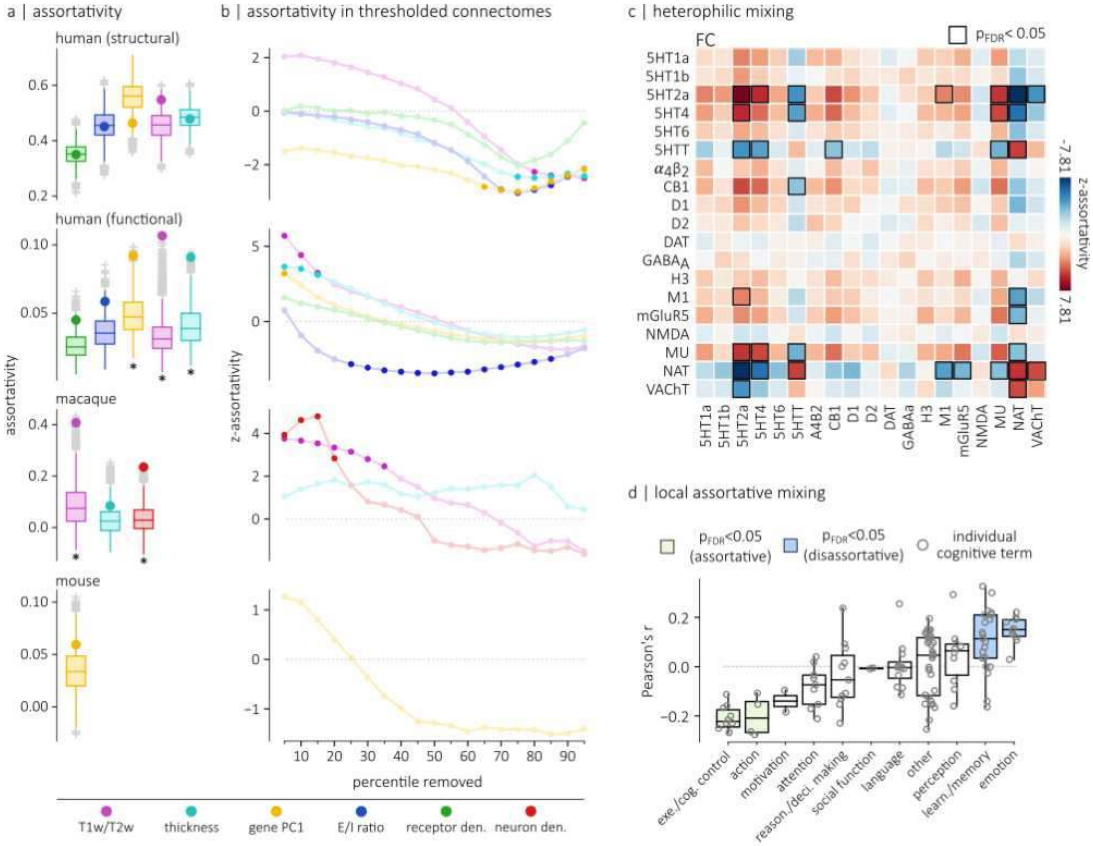

Figure 2 | **(a)** Assortativity of empirical annotations (circles) were compared to n = 10,000 null annotations with preserved spatial autocorrelation (boxplots). Asterisks denote significance (p_{FDR}<0.05) **(b)** Assortativity coefficients were computed in thresholded connectomes where a percentile of the shortest connections are removed. Scores are standardized with respect to a null distribution of spatial autocorrelation-preserving nulls. Standardized assortativity scores (z-assortativity) for each annotation are displayed as a function of the percentile of connections removed in the network. Highlighed circles denote significance (p_{FDR}<0.05). **(c)** To quantify heterophilic mixing, we extend the concept of assortativity to pairs of annotations. In other words, we compute the assortativity coefficient for pairs of annotations such that the annotation at endpoint *i* represents an attribute **x** and the annotation at endpoint *j* represents a different attribute **y**. Here, we show the heterophilic mixing matrix of the functional connectome for the receptor densities of 19 different neurotransmitter receptors and transporters. Black squares highlight statistically significant relationships (p_{FDR}<0.05) **(d)** We quantified the extend to which individual regions connect to other regions with similar attributes and obtained a brain maps of local homophilic preferences which we then correlated with 123 brain maps of probabilistic associations between functional keywords and individual voxel activations. These keywords were separated into 11 different cognitive categories. Highlighted boxes denote significantly large or significantly small correlations (averaged).

Conclusions: In summary, the present work bridges microscale attributes and macroscale connectivity. While carefully controlling for the background effect of the brain's spatial embedding, we systematically assessed how connectivity is interdigitated with a broad range of micro-architectural attributes and empirically tested multiple theories about the wiring of cortical brain networks.

References

1. Bazinet, V. (2023). Towards a biologically annotated brain connectome. Nature Reviews Neuroscience, 1-14.
2. Newman, M. E. (2003). Mixing patterns in networks. Physical review E, 67(2), 026126.
3. Markello, R. D., & Misic, B. (2021). Comparing spatial null models for brain maps. NeuroImage, 236, 118052.
4. Betzel, R. F. (2018). Specificity and robustness of long-distance connections in weighted, interareal connectomes. Proceedings of the National Academy of Sciences, 115(21), E4880-E4889.
5. Shine, J. M. (2019). Neuromodulatory influences on integration and segregation in the brain. Trends in cognitive sciences, 23(7), 572-583.
6. Yarkoni, T. (2011). Large-scale automated synthesis of human functional neuroimaging data. Nature methods, 8(8), 665-670.

Poster No 1538

The impact of early life stress on whole-brain functional connectivity during emotion regulation

Seda Sacu[1], Tobias Banaschewski[1], Martin Gerchen[2], Nathalie Holz[1]

[1]Department of Child and Adolescent Psychiatry and Psychotherapy, Central Institute of Mental Health, Mannheim, Germany, [2]Department of Clinical Psychology, Central Institute of Mental Health, Mannheim, Germany

Introduction: Early life stress (ELS) alters brain development and increases the risk of developing psychopathology later in life. Previous literature suggested that ELS is associated with alterations in brain function and connectivity during emotion processing, especially in the fronto-limbic pathway [VanTieghem and Tottenham, 2018]. However, most of the previous connectivity studies were limited to a small set of priori-selected regions of interest. Recent findings suggest the involvement of several large-scale brain networks in emotion processing and regulation beyond the fronto-limbic pathway [Morawetz et al., 2020]. Thus, investigating whole-brain connectivity via large-scale brain networks rather than a small set of regions of interest can bring new insights into the neural embedding of ELS. However, this approach requires a selection of a brain parcellation map, which could further introduce heterogeneity [Hallquist and Hillary, 2018] and affect the interpretation of results [Bryce et al., 2021].

Methods: Using data from a longitudinal birth cohort study (n=161, 87 females), we investigated the associations between stressful life events and task-based whole-brain functional connectivity by taking into account parcellation map choice. All participants completed an fMRI-based emotion regulation task at the age of 33 years. We measured stressful life events using a modified version of the Munich Event List [Maier-Diewald et al., 1983] from prenatal period to 19 years via seven assessment waves. Whole-brain functional connectivity was calculated for the emotion regulation contrast (i.e., regulate negative > look negative) using the whole-brain generalized psychophysiological interactions [Gerchen et al., 2014] using three commonly used brain parcellation maps: Automated Anatomical Labeling [Rolls et al., 2020], Brainnetome [Fan et al., 2016], and Schaefer Atlas [Schaefer et al., 2018]. The association between life stress and connectivity was investigated within the multiple regression framework with and without network-based statistics [Zalesky et al., 2010] correction for multiple comparisons.

Results: Our results showed that ELS (i.e., stress during infancy and childhood) was mainly associated with lower connectivity during emotion regulation between frontal, temporal and subcortical brain regions covering dorsal attention, frontoparietal, and limbic networks. Those alterations were identifiable across all parcellation maps. However, each parcellation map was also related to distinct alterations that could be explained by their specific features (e.g., more elaborate parcellation of some brain regions). In addition, applying a correction for multiple comparisons affected the extent of shared and distinct connection patterns. We did not find a significant association between life stress that occurred during adolescence and whole-brain functional connectivity during emotion regulation.

Conclusions: Our results showed that ELS is related to the connectivity alterations between attention and limbic networks, which take part in emotion processing and regulation. We identified these ELS-related alterations across different parcellation schemes, however, similarities were more pronounced before the correction for multiple comparisons. These results suggest that using different parcellation schemes and reporting shared and distinct patterns could help to alleviate the heterogeneity induced by parcellation map choice and increase the generalizability of the findings.

References

1. Bryce N V., Flournoy JC, Guassi Moreira JF, Rosen ML, Sambook KA, Mair P, McLaughlin KA (2021): Brain parcellation selection: An overlooked decision point with meaningful effects on individual differences in resting-state functional connectivity. Neuroimage 243.
2. Fan L, Li H, Zhuo J, Zhang Y, Wang J, Chen L, Yang Z, Chu C, Xie S, Laird AR, Fox PT, Eickhoff SB, Yu C, Jiang T (2016): The Human Brainnetome Atlas: A New Brain Atlas Based on Connectional Architecture. Cereb Cortex 26.
3. Gerchen MF, Bernal-Casas D, Kirsch P (2014): Analyzing task-dependent brain network changes by whole-brain psychophysiological interactions: A comparison to conventional analysis. Hum Brain Mapp 35:5071–5082.
4. Hallquist MN, Hillary FG (2018): Graph theory approaches to functional network organization in brain disorders: A critique for a brave new small-world. Netw Neurosci 3.
5. Maier-Diewald W, Wittchen H-U, Hecht H, Werner-Eilert K (1983): Die Münchner Ereignisliste (MEL) - Anwendungsmanual. München.
6. Morawetz C, Riedel MC, Salo T, Berboth S, Eickhoff SB, Laird AR, Kohn N (2020): Multiple large-scale neural networks underlying emotion regulation. Neuroscience and Biobehavioral Reviews. Elsevier Ltd.
7. Rolls ET, Huang CC, Lin CP, Feng J, Joliot M (2020): Automated anatomical labelling atlas 3. Neuroimage 206.
8. Schaefer A, Kong R, Gordon EM, Laumann TO, Zuo X-N, Holmes AJ, Eickhoff SB, Yeo BTT (2018): Local-Global Parcellation of the Human Cerebral Cortex from Intrinsic Functional Connectivity MRI. Cereb Cortex 28.
9. VanTieghem MR, Tottenham N (2018): Neurobiological programming of early life stress: Functional development of amygdala-prefrontal circuitry and vulnerability for stress-related psychopathology. In: . Current Topics in Behavioral Neurosciences. Springer Verlag. Vol. 38, pp 117–136.
10. Zalesky A, Fornito A, Bullmore ET (2010): Network-based statistic: Identifying differences in brain networks. Neuroimage 53.

Poster No 1539

Structural and functional connectivity predicts MRgFUS thalamotomy outcome in Parkinson's disease

Alberto Cacciola[1], Gianpaolo Basile[1], Giuseppe Acri[1], Lilla Bonanno[2], Augusto Ielo[2], Silvia Marino[2], Amelia Brigandì[2], Chiara Sorbera[2], Rosa Morabito[2], Giuseppe Di Lorenzo[2], Antonio Cerasa[3,4,5], Angelo Quartarone[2]

[1]University of Messina, Messina, Italy, [2]IRCCS Centro Neurolesi "Bonino Pulejo", Messina, Italy, [3]S. Anna Institute, Crotone, Italy, [4]Institute for Biomedical Research and Innovation (IRIB), National Research Council of Italy, Messina, Italy, [5]University of Calabria, Rende, Italy

Introduction: Magnetic Resonance-guided Focused UltraSound (MRgFUS) thalamotomy has been demonstrated to effectively reduce tremor symptoms in Parkinson's disease (PD). Emerging evidence suggests that its efficacy may depend on the connectivity between the target and other brain areas, more than the choice of the target site itself. However, evidence demonstrating whether brain connectivity can predict clinical outcomes in tremor-dominant PD patients is still missing. Herein, we characterize the structural and functional connectivity associated with successful focused ultrasound ablation of the Ventral intermediate thalamic nucleus (Vim) and assess its potential to predict treatment outcome.

Methods: Twelve tremor-dominant PD patients were retrospectively included in this study. All patients underwent unilateral MRgFUS thalamotomy and received preoperative and 24-hour postoperative structural MRI. Treatment outcome was measured as the percentage change in motor score of the Unified Parkinson Disease Rating Scale (UPDRS-III) assessed one week after the treatment. Segmentation of the ablation core was performed on each subject postoperative images by two independent raters and the Dice coefficient was computed to assess accuracy segmentation. To identify the spatial relationship between the ablation site and the Vim, each patient's thalamus was segmented into thalamic nuclei through the THOMAS automated segmentation using White-Matter null images synthesized from preoperative T1w images. We examined how different ablation features (ablation volume, Vim-ablation overlap, Euclidean distance between ablation core and Vim centroids and, Euclidean distance between Vim-ablation overlap and Vim centroids) correlated with clinical outcome. We then combined our PD dataset with publicly available normative human connectome data (diffusion tractography and resting state functional connectivity) to identify connectivity patterns reliably associated with clinical improvement. The structural and functional connectivity profiles were then independently employed to predict clinical outcome in a leave-one-patient-out cross-validation design.

Results: We found no significant correlations between standard ablation features (ablation volume, Vim-ablation overlap, Euclidean distance between ablation and Vim centroids and, Euclidean distance between Vim-ablation overlap and Vim centroids) and 1-week post-treatment clinical outcome (all $p>0.05$). In contrast, connectivity between the area of ablation and a distributed network of brain regions correlated with clinical improvement including structural connectivity to pre-supplementary, supplementary motor area, superior frontal gyrus, and cerebellum. Similar patterns of functional connectivity, and anticorrelation between the ablation area and primary somatosensory cortex and the most lateral part of primary motor cortex, were correlated with clinical outcome. Finally, leave-one-patient-out cross-validation showed that both structural ($R2 = 0.53$; $R = 0.73$; $p = 0.002$) and functional connectivity ($R2 = 0.23$; $R = 0.48$; $p = 0.007$) fingerprints are predictive of clinical improvement within the cohort. The prediction errors were on average 5.58±13.95 and 5.40±10.35 from actual UPDRS-III improvements, for structural and functional connectivity respectively.

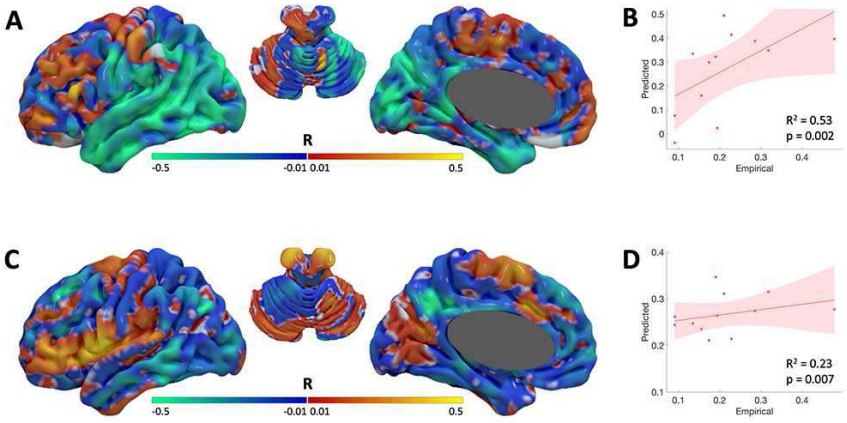

Figure 1. Structural and functional connectivity predictive of clinical improvement in the tremor-dominant PD dataset. Results from analyses using publicly available connectome of age- and sex-matched matched PD subjects are shown. Structural (A) and functional connectivity (C) associated with clinical improvement were identified using correlation with clinical outcome. Using the correlation map derived from structural and functional connectivity, clinical outcome was predicted for each patient using a leave-one-patient-out design (B and D, respectively).

Conclusions: While neither target volume- nor distance-based measures correlated with clinical outcome, our results suggest that both target structural and functional connectivity are independent predictors of clinical improvement in tremor-dominant MRgFUS-thalamotomized PD patients. Being based on publicly available normative connectome, this predictive approach did not require advanced diffusion and functional imaging that may be not routinely available in the clinical setting. The present pilot study suggests the future potential for patient-specific connectomics surgical targeting, while warranting future work to test and validate the present findings in independent cohorts.

References

1. Ewert, S. (2018), 'Toward defining deep brain stimulation targets in MNI space: A subcortical atlas based on multimodal MRI, histology and structural connectivity', Neuroimage, vol. 170, pp. 271-282.
2. Horn, A. (2017), 'Probabilistic conversion of neurosurgical DBS electrode coordinates into MNI space', Neuroimage, vol. 150, pp. 395-404.
3. Marek, K. (2011), 'The Parkinson Progression Marker Initiative (PPMI)', Progress in Neurobiology, vol. 96, pp. 629-635.
4. Setsompop, K. (2013), 'Pushing the limits of in vivo diffusion MRI for the Human Connectome Project', Neuroimage, vol. 80, pp. 220-233.
5. Su, J. H. (2019), 'Thalamus Optimized Multi Atlas Segmentation (THOMAS): fast, fully automated segmentation of thalamic nuclei from structural MRI', Neuroimage, vol. 194, pp. 272-282.
6. Vidal, J. P. (2023), 'Robust thalamic nuclei segmentation from T1-weighted MRI', arXiv, https://doi.org.10.48550/arXiv.2304.07167.

Poster No 1540

Evidence for a monosynaptic connection between A1 and V1 in the human brain

Samuel Paré[1], James Lubell[2], Sylvain Baillet[3], Ron Kupers[1], Maurice Ptito[1]

[1]Université de Montréal, Montréal, Quebec, [2]University of Aarhus, Aarhus, Jutland, [3]Montreal Neurological Institute, Montreal, Quebec

Introduction: The conventional view of the visual cortex as a stimulus-driven, unimodal system with a hierarchical organization has been recently challenged (Qin & Yu, 2013). Both animal (Rockland & Ojima, 2003) and human (Ghazanfar & Schroeder, 2006) studies have demonstrated that the visual cortex responds to non-visual stimuli. However, the question as through which neural pathways non-visual information reaches the visual cortex is still a matter of debate. For instance, recent studies showed that tactile information can reach the visual cortex via a polysynaptic pathway between cortices (Ioannides et al., 2013; Müller et al., 2019). There is also evidence that auditory information may reach the occipital cortex (refs you showed before) but it is unclear whether this also involves a polysynaptic, or a monosynaptic, pathway. We took advantage of the millisecond time resolution of magnetoencephalography (MEG) to disentangle this question.

Methods: Eighteen normal sighted control subjects participated in a MEG study in which we measured response latencies to monaural auditory stimulation in primary auditory cortex (A1), primary visual cortex (V1) and posterior thalamus, corresponding to the purported location of the lateral geniculate nucleus (LGN). Each trial began with an auditory cue (simple tone) presented to either the left or right ear, indicating participants to focus their attention on their left or right index finger, respectively. One second later, an electro-tactile stimulus was delivered to the left or right index finger (figure 1) and participants had to indicate as quickly as possible which hand had been stimulated. A part of the MEG data come from the Müller et al., (2019) study but we focus here on the time-locked responses to the preparatory auditory cue instead of the electro-tactile stimulus. We used Brainstorm to preprocess the MEG data (Tadel et al., 2011). For source reconstruction, individual scalp and cortical surfaces were segmented from 3-D MRI data, using Freesurfer (Fischl, 2012). We used MEG forward and inverse modeling steps for source reconstruction that were subsequently completed with multi-sphere analytical approximation for head modeling and weighted minimum-norm estimation (wMNE) with unconstrained source orientation. Individual source data were then projected to the Colin27 brain template. To examine the time series of neural activity associated with auditory-visual connections, we used a multiple linear regression model that has increased sensitivity and consistency in detecting subcortical activity with MEG but is restricted to 3 or 4 ROIs (Coffey et al., 2016; Müller et al., 2019) which in our case, were posterior thalamus, A1 and V1.

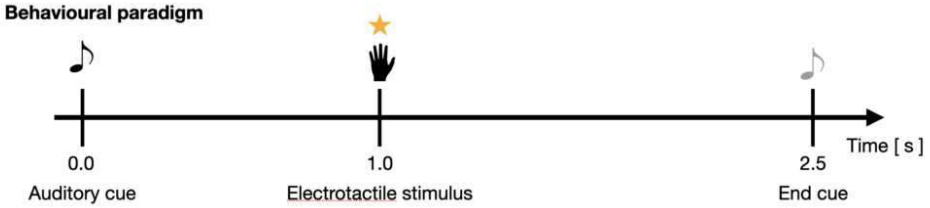

Results: We found evidence for a distinct sequential activation pattern following a monaural auditory cue starting from the thalamus between 10-20 ms, followed by activity in A1 as early as 35 ms, and culminating in V1 10 to 15 ms later (50 ms post auditory cue) in both contralateral and ipsilateral hemispheres relative to the auditory cue.

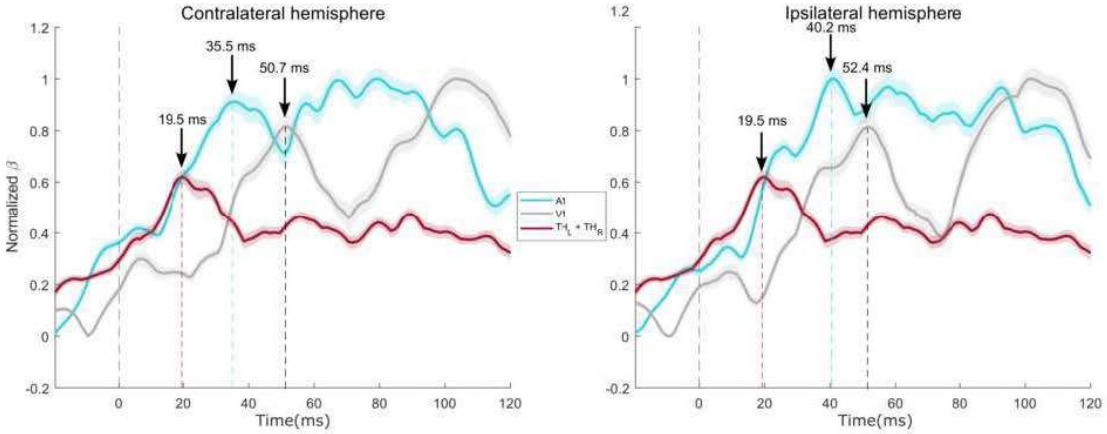

Conclusions: Considering that the monosynaptic transmission of information from one cortical area to another typically occurs within a time frame of approximately 10–15 ms (Molholm et al., 2002), this sequence of events suggests that in the human brain, auditory inputs reach the visual cortex via a monosynaptic A1-V1 connection. This is clearly distinct from our previous data which showed that tactile information is funneled to the occipital cortex via a polysynaptic pathway. Supported by the Canadian Institutes of Health Research (CIHR 163014-2019).

References

1. Coffey, E. B., Herholz, S. C., Chepesiuk, A. M., Baillet, S., & Zatorre, R. J. (2016). Cortical contributions to the auditory frequency-following response revealed by MEG. Nature communications, 7(1), 1-11.
2. Fischl, B. (2012). FreeSurfer. Neuroimage, 62(2), 774-781.
3. Ghazanfar, A. A., & Schroeder, C. E. (2006). Is neocortex essentially multisensory? Trends in cognitive sciences, 10(6), 278-285.
4. Ioannides, A. A., Liu, L., Poghosyan, V., Saridis, G. A., Gjedde, A., Ptito, M., & Kupers, R. (2013). MEG reveals a fast pathway from somatosensory cortex to occipital areas via posterior parietal cortex in a blind subject. Frontiers in human neuroscience, 7, 429.
5. Molholm, S., Ritter, W., Murray, M. M., Javitt, D. C., Schroeder, C. E., & Foxe, J. J. (2002). Multisensory auditory–visual interactions during early sensory processing in humans: a high-density electrical mapping study. Cognitive Brain Research, 14(1), 115-128.
6. Müller, F., Niso, G., Samiee, S., Ptito, M., Baillet, S., & Kupers, R. (2019). A thalamocortical pathway for fast rerouting of tactile information to occipital cortex in congenital blindness. Nature communications, 10(1), 1-9.
7. Qin, W., & Yu, C. (2013). Neural pathways conveying novisual information to the visual cortex. Neural plasticity, 2013.
8. Rockland, K. S., & Ojima, H. (2003). Multisensory convergence in calcarine visual areas in macaque monkey. International Journal of Psychophysiology, 50(1-2), 19-26.
9. Tadel, F., Baillet, S., Mosher, J. C., Pantazis, D., & Leahy, R. M. (2011). Brainstorm: a user-friendly application for MEG/EEG analysis. Computational intelligence and neuroscience, 2011.

Poster No 1541

Dynamic functional connectivity in mouse widefield calcium activity relates to future learning rates

Giuseppe de Alteriis[1], Matthew Harvey[1], Adil Khan[1], Dafnis Batalle[2]

[1]King's College London, London, Greater London, [2]King's College London, London, N/A

Introduction: A key property of brain-wide networks is the dynamic nature of the interactions between their nodes (Hutchison et al., 2013). While functional connectivity has been studied using correlation-based approaches, the dynamical properties of functional connectivity are poorly understood and their relation to behaviour and cognition are largely unknown. Here we extend methods used for the analysis of dynamic functional connectivity (dFC) in fMRI (Allen et al., 2014; Cabral et al., 2017), to widefield calcium imaging of mouse cortex. This allows 1) to seek a more mechanistic understanding of dFC patterns in widefield calcium imaging, given its higher temporal resolution (Ts=36 ms) 2) to apply dFC to investigate the properties of brain dynamics during different behavioural states (stationary vs. locomotion), and their association with learning rates in a visual discrimination task.

Methods: We performed widefield calcium imaging of mouse dorsal cortex expressing GCaMP7f. We characterised dFC in n=12 mice (6 wildtype mice and 6 mice with a knockout of the Neurexin 1-alpha gene, which is associated with cognitive impairments and autism). We selected a 1s-long sliding window and obtained time-varying sliding correlation matrices (dFC matrices). We reduced the large dimensionality of pixel-wise dFC matrices by approximating each dFC matrix by its

leading eigenvector (i.e., performing Leading Eigenvector Dynamics Analysis -LEiDA, Fig 1A). The LEiDA signal indicates how much a brain area engages in interactions with others. Using k-means clustering of the LEiDA signal we identified 7 connectivity patterns (transient brain states) that all mice exhibit (Fig 1B). For each state we computed Fractional Occupancy (FO, percentage of time in a particular state), Dwelling Time (DT, average duration of a state bout), and metastability (the variability of dFC, i.e. standard deviation of LEiDA for each state), a metric of brain dynamic flexibility. Mice were considered in a locomotion condition if the speed of the wheel was higher than 5 cm/s, otherwise, they were considered in a stationary condition.

Results: The 7 brain states that we identified involve brain areas that are homologous to those found in human fMRI (Fig 1B). We found distinct dFC patterns between stationary and locomotion conditions, with multiple DT and FO state features (but not metastability) correlated with the animals' running speed. Locomotion was characterized by increased FO and DT of the olfactory and somatosensory states and decreased in motor states (Fig 2A). Furthermore, the landscape of dFC was atypical in the Neurexin 1-alpha KO mice when compared with wildtype mice. We found decreased metastability during stationary conditions in the knockout mice in the global, olfactory and motor states (Fig 2B). Multiple distinct dFC patterns were also identified when comparing wildtype and knockout mice (Fig 2B). Finally, after the recordings, mice were trained on a visual discrimination task. Metastability in the stationary condition before behavioural training was correlated with the learning rate in the visual discrimination task (Fig 2C).

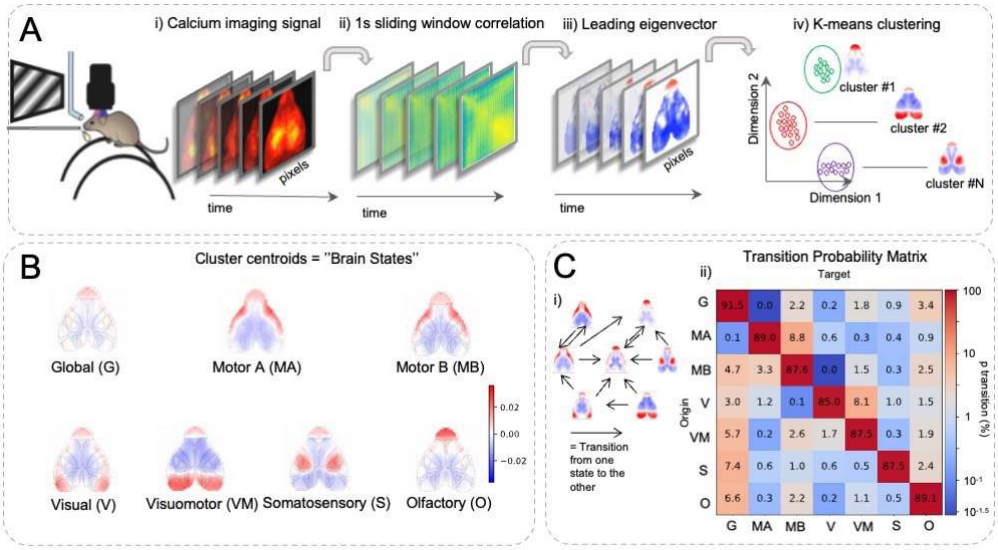

A. Pipeline of dynamic functional connectivity applied to widefield calcium imaging (i) acquisition of widefield calcium imaging from a dorsal view of the cortex (ii) computation of the sliding window correlation matrix (iii) extraction of its leading eigenvector (LEiDA) (iv) clustering of the leading eigenvectors. B. We identified 7 biologically relevant brain states C. (i) Schematic representing the transitions from one state to the other. Arrows represent the most likely transitions (p>2.5%). (ii) Transition probability matrix (TPM).

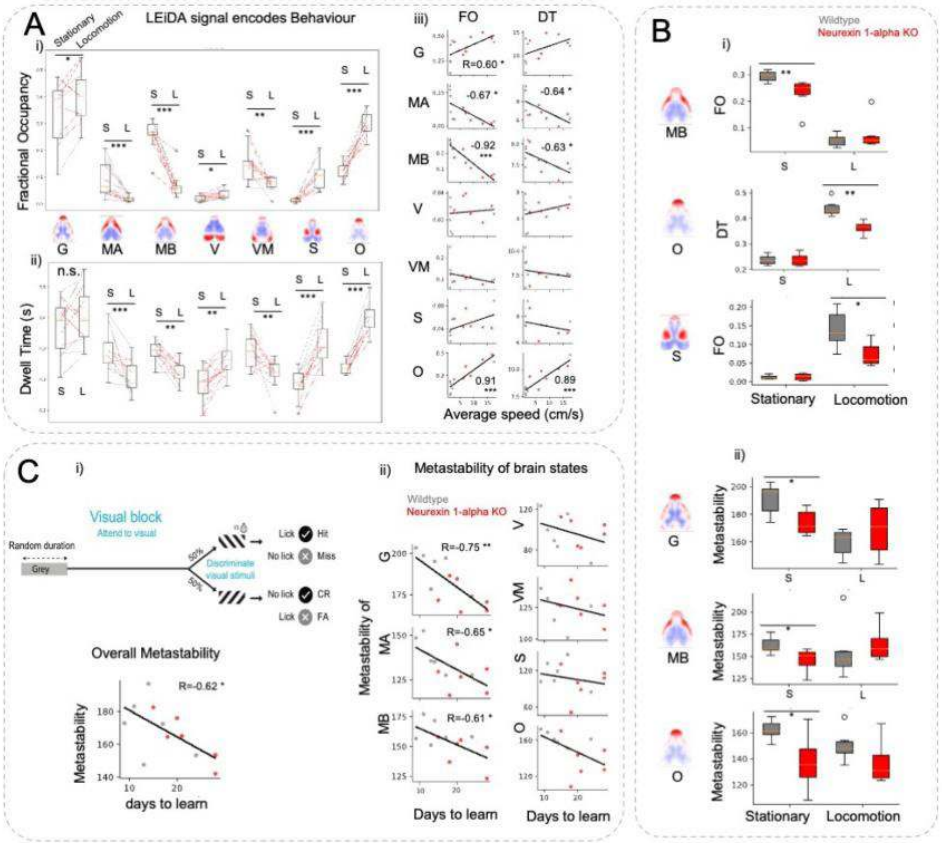

A. (i) Fractional Occupancy (FO) and (ii) Dwelling Time (DT) of the brain states in the stationary (S) vs locomotion (L) conditions. (iii) correlation of these measures with average running speed of the mouse. B. (i) FO and DT in some of the states, comparing wildtype and KO mice (ii) metastability in wildtype vs KO mice. C (i) Top, the visual discrimination task. CR= Correct Rejection; FA= False Alarm. Bottom, correlation of overall metastability with number of days to learn the task. (ii) Correlation of metastability of the specific states during the stationary condition with number of days to learn the task.

Conclusions: The differences in locomotion versus stationary conditions validate the ability of our method to distinguish the underlying patterns of brain-wide interactions supporting different behavioural states. This also suggests a behavioural relevance of the LEiDA patterns, which up to now have been mainly studied in resting-state fMRI. Our results also support the role of metastability as a promising neuromechanistic biomarker of psychiatric disorders (Hancock et al., 2023). Additionally, our results suggest that metastability is linked to cognitive abilities, being predictive of learning performance, and highlight the central role of brain-wide dynamics in cognition and flexible behaviour.

References

1. Allen, E. A., Damaraju, E., Plis, S. M., Erhardt, E. B., Eichele, T., & Calhoun, V. D. (2014). Tracking Whole-Brain Connectivity Dynamics in the Resting State. Cerebral Cortex, 24(3), 663–676. https://doi.org/10.1093/cercor/bhs352
2. Cabral, J., Vidaurre, D., Marques, P., Magalhães, R., Silva Moreira, P., Miguel Soares, J., Deco, G., Sousa, N., & Kringelbach, M. L. (2017). Cognitive performance in healthy older adults relates to spontaneous switching between states of functional connectivity during rest. Scientific Reports, 7(1), Articolo 1. https://doi.org/10.1038/s41598-017-05425-7
3. Hancock, F., Rosas, F. E., McCutcheon, R. A., Cabral, J., Dipasquale, O., & Turkheimer, F. E. (2023). Metastability as a candidate neuromechanistic biomarker of schizophrenia pathology. PLOS ONE, 18(3), e0282707. https://doi.org/10.1371/journal.pone.0282707
4. Hutchison, R. M., Womelsdorf, T., Allen, E. A., Bandettini, P. A., Calhoun, V. D., Corbetta, M., Della Penna, S., Duyn, J. H., Glover, G. H., Gonzalez-Castillo, J., Handwerker, D. A., Keilholz, S., Kiviniemi, V., Leopold, D. A., de Pasquale, F., Sporns, O., Walter, M., & Chang, C. (2013). Dynamic functional connectivity: Promise, issues, and interpretations. NeuroImage, 80, 360–378. https://doi.org/10.1016/j.neuroimage.2013.05.079

Poster No 1543

Potent DWI connectome markers of verbal and non-verbal functions in children with unilateral lesions

Min-Hee Lee[1], Jeong-Won Jeong[1], Nore Gjolaj[1], Hiroshi Uda[1], Michael Behen[1], Aimee Luat[1], Eishi Asano[1], Csaba Juhasz[1]

[1]Wayne State University, Detroit, MI

Introduction: Unilateral brain lesions in children longitudinally affect neural plasticity mechanisms of neurocognitive functions including verbal IQ (VIQ) and non-verbal IQ (NVIQ).[1-3] This study aims to develop an imaging marker that can accurately differentiate two DWI connectomes (DWICs) related to VIQ and NVIQ from children with unilateral brain lesions, such as lesional epilepsy and Sturge-Weber syndrome (SWS; a venous vascular disorder), by using a deep learning tract classification approach with clinically acquired DWI tractography.

Methods: Three cohorts: 6 healthy children with typical development (TD, 12.3±3.8 years old, 3 boys), 52 children with epilepsy (11.7±3.5 years old, 25 boys; 21/13/18 left/right/non-lesional epilepsy), and 11 children with SWS (13.3±2.7 years old, 5 boys; 3/8 left/right-hemisphere involved SWS) were recruited and completed 3T DWI tractography and neuropsychological language assessments including VIQ and NVIQ tests. 3T DWI tractography scans were also collected from 29 TD (11.6±3.3 years old, 14 boys) as baseline data. To ensure reproducibility of DWIC, our previous DCNN-based tract classification[4], which effectively removes false-positive tracts (e.g., wiggly shaped tracts), was extended to the iFOD2-ACT whole-brain tractography[5,6] of individual subjects. This approach yields a whole-brain backbone DWIC, Si,j, in which each element defines an average factional anisotropy (FA) value of true-positive tract classes, Ck=1,2,...,1477, consisting of a series of tracts connecting i and j regions in the AAL atlas. Briefly, for each tract of the training Ck, our DCNN model was designed to learn 3-D coordinates of 100 equal-number tract segments by minimizing focal and center loss. Each VIQ and NVIQ network comprises specific axonal connectivity edges derived from Si,j of 69 subjects (i.e., 6 TD, 52 epilepsy patients, and 11 SWS patients), with elements of Si,j that significantly correlate with VIQ and NVIQ scores across subjects (p-value of correlation coefficient<0.001 after controlling for age and sex). Global efficiency (GE)[7], which measures efficiency of parallel information flow in a network, was calculated for each VIQ and NVIQ intra-hemispheric network. To assess how far the GE marker value deviates from baseline, Z-scores of GE values were calculated. A non-parametric ANOVA test was applied after controlling for age and sex to assess the difference in Z-scores of GE values between ipsilateral and contralateral intra-hemispheric network. To explore the potential of this imaging marker to assess neurocognitive outcomes, the strength of the linear relationship between the Z-scores of GE values and IQ scores was evaluated by Pearson's correlation.

Results: We could successfully differentiate the VIQ network with 24 key nodes and the NVIQ network with 22 key nodes (Fig. 1). Figure 2A presents that Z-scores of GE in the ipsilateral IQ network were lower than those in contralateral IQ network. Specifically, the Z-score of GE in right VIQ and NVIQ networks in right epilepsy (n=21) was significantly lower than that of left epilepsy (n=13) (p=0.04 and p=0.03). The VIQ score was significantly correlated with the Z-score of GE in the left VIQ network (r=0.36, p=0.03) across all subjects (Fig. 2B). Additionally, the NVIQ score was significantly correlated with the Z-score of GE in the right NVIQ network (r=0.37, p=0.05) across all subjects (Fig. 2B), while there was no significant correlation between VIQ/NVIQ scores and Z-scores of GE for separate cohorts (Fig. 2C).

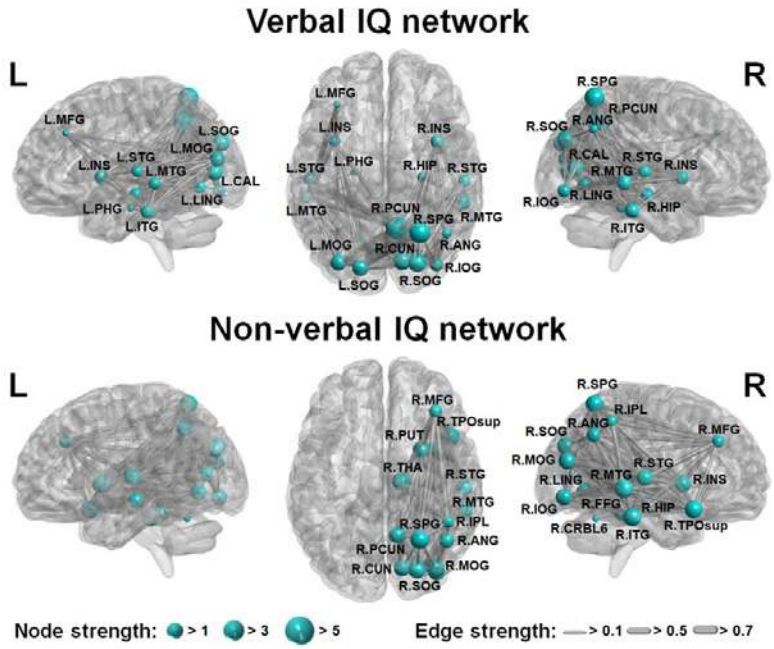

Figure 1. DCNN-based whole-brain backbone DWIC networks for verbal IQ and non-verbal IQ that were constructed using all pair-wise connections of S_{ij} that exhibited statistically significant cross-subject correlations with the corresponding verbal and non-verbal IQ scores. At the threshold of p-value < 0.001 after correction for age and sex, a total of 24 and 22 AAL nodes were identified as key nodes of VIQ network, and NVIQ network, respectively. To construct IQ networks, 69 subjects were included. Anatomical locations and labels of individual nodes are available at https://neurovault.org/images/14257/.

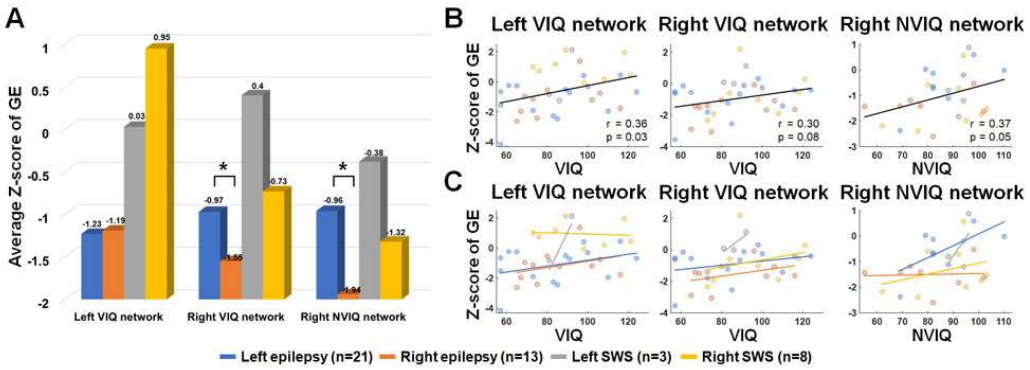

Figure 2. A. Average Z-scores of global efficiency (GE) obtained from verbal IQ (VIQ) and non-verbal IQ (NVIQ) intra-hemispheric networks of 34 epilepsy patients and 11 SWS patients. B. Correlation between the Z-score of GE for each intra-hemispheric network and IQ scores for all subjects. C. Correlation between the Z-score of GE for each intra-hemispheric network and IQ scores for each cohort. To assess the lesional effect on IQ networks, 18 non-lesional epilepsy patients were excluded from these analyses. An asterisk (*) indicates significant difference in Z-score of GE.

Conclusions: We provided preliminary evidence that lower efficiency of neural information flow in the ipsilateral VIQ and NVIQ networks can be used as potential markers for assessing lower verbal and non-verbal functions via effectively differentiating VIQ and NVIQ networks disrupted by the ipsilateral lesions in children with unilateral lesions. The reproducibility of this finding should be further evaluated in a larger cohort.

References

1. Aram, D.M. (1994), 'Intellectual stability in children with unilateral brain lesions, Neuropsychologia, vol. 32, no. 1, pp. 85-95.
2. Behen, M.E. (2011), 'Brain damage and IQ in unilateral Sturge-Weber Syndrome: Support for a "fresh start" hypothesis', Epilepsy & Behavior, vol. 22, no. 2, pp. 352-357.
3. Chugani, H.T. (1996), 'Functional brain reorganization in children', Brain and Development, vol. 18, no. 5, pp.347-356.
4. Lee, M.H. (2019), 'Improving reproducibility of diffusion connectome analysis using deep convolutional neural network model', Proceedings of the International Society for Magnetic Resonance in Medicine, vol. 27, pp. 3578.
5. Tournier, J.D. (2010) Improved probabilistic streamlines tractography by 2nd order integration over fibre orientation distributions', Proceedings of the International Society for Magnetic Resonance in Medicine, vol. 18, pp. 1670.
6. Smith, R.E. (2012), 'Anatomically-constrained tractography: Improved diffusion MRI streamlines tractography through effective use of anatomical information', NeuroImage, vol. 62, no. 3, pp. 1924-1938
7. Latora, V. (2001), 'Efficient behavior of small-world networks', Physical Review Letters, vol. 85, no. 19, pp. 198701.

Poster No 1544

Amount and Localisation of Non-Linearity in rs-fMRI Functional Connectivity

Giulio Tani Raffaelli[1], Jaroslav Hlinka[1], Jakub Kopal[2]

[1]Institute of Computer Science of the Czech Academy of Sciences, Prague, Czech Republic, [2]McGill University, Montreal, Quebec

Introduction: The last 20 years have shown a growth in interest towards research and clinical applications for Functional Connectivity (FC). Along with the interest in FC, there is increasing attention to alternatives to Pearson's correlation in the connectivity estimate. While the correlation accounts only for linear relationships between regions or electrodes, a common alternative is Mutual Information (MI), which accounts for non-linearities. As the application of MI increases, despite a previous study (Hlinka, 2011) pointing at a marginal role of non-linearity, new evidence shows there might be more (Motlaghian, 2022). We follow up on Hlinka's study and leverage a twenty times larger cohort to quantify and localise the non-linearity in rs-fMRI BOLD signal and assess the dependency on the atlas.

Methods: In this study, we use rs-fMRI BOLD data from 242 healthy subjects from the publicly available dataset associated with (Kopal, 2020). From this, we selected data subject to stringent preprocessing. We chose parcellation with the AAL atlas with 90 regions and the Craddock atlas with 10 to 950 regions. To ensure that the observed non-linearity comes from the relationship between time series and not from their marginal distribution, we applied a monotonic transformation to ensure normally distributed marginals. We computed the total MI via the equiquantal binning method and corrected for its bias. To evaluate the amount of non-linearity, we generated 99 Fourier-transform multivariate surrogates, preserving the covariance matrix of the data. For each subject, we evaluate the amount of MI not justified by correlation as the relative difference between all regions' total MI and the average MI in surrogates. We then assess non-linearities' localisation by checking for regions whose total MI, across all subjects, was significantly higher than surrogate MI. We controlled for bias in the whole non-linearity estimation by repeating the entire analysis on a shadow dataset generated by surrogation of the original one.

Results: We obtain a consistent presence of non-linearity for the different region sizes from the Craddock atlas. The amount of MI not explained by the covariance (Fig. 1) sits stable at around 4% for all region sizes except for very small (single voxel) and large regions. At the same time, the non-linearity observed in the shadow dataset remains lower than 1%. We observe that regions with relationships with MI consistently higher than surrogates are grouped primarily on the occipital lobe (Fig. 2). For comparison, the number of such connections in the shadow dataset is lower by two-thirds, and the non-linearities localisation is more sparse.

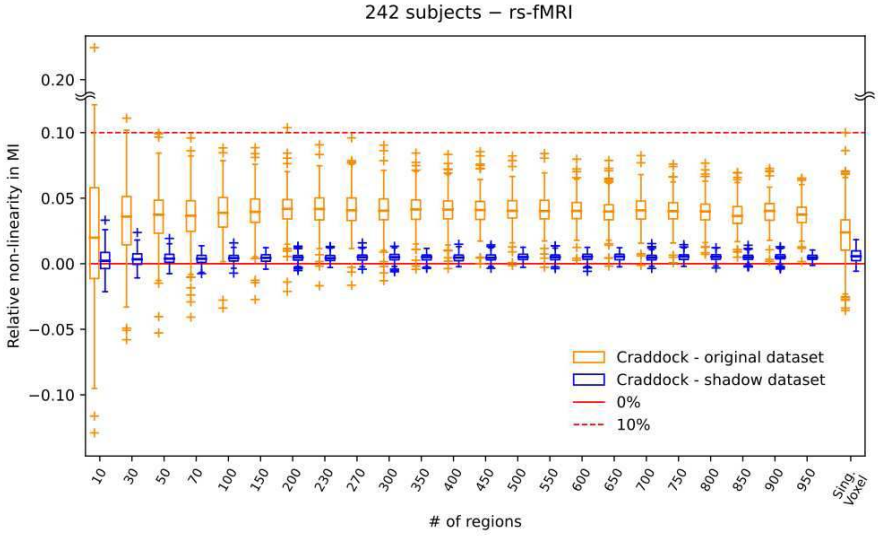

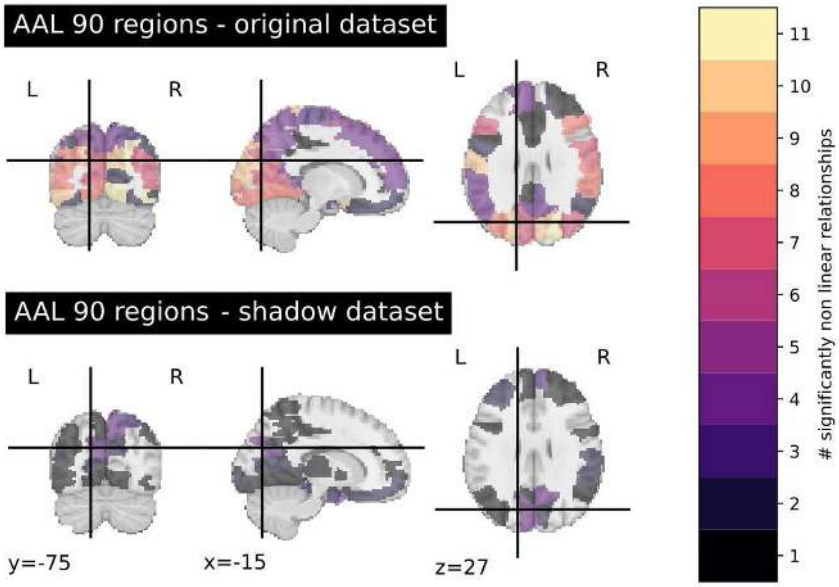

Conclusions: This study confirms that the non-linearity in the rs-fMRI BOLD signal is measurable above the bias in the estimation. Furthermore, we show that non-linearities are consistent, independent of the atlas of choice. This study also shows the localisation of such non-linearities and agrees with the independent findings from (Motlaghian, 2022). At the same time, the non-linearity is minor, even in the most non-linear regions. Observing it reliably at the individual level will present a future challenge due to the effect of noise.

References

1. Hlinka, J. (2011), 'Functional connectivity in resting-state fMRI: is linear correlation sufficient?', Neuroimage, vol. 54, no. 3, pp. 2218-2225.
2. Kopal, J. (2020), 'Typicality of functional connectivity robustly captures motion artifacts in rs-fMRI across datasets, atlases, and preprocessing pipelines', Human Brain Mapping, vol. 41, no. 18, pp. 5325-5340.
3. Motlaghian, S. M. (2022), 'Nonlinear functional network connectivity in resting functional magnetic resonance imaging data', Human brain mapping, vol. 43, no. 15, pp. 4556-4566.

Poster No 1545

Eigenvector Dynamics Analysis (EiDA): a mathematical framework for dynamic Functional Connectivity

Giuseppe de Alteriis[1], Oliver Sherwood[2], Alessandro Ciaramella[3], Robert Leech[4], Federico Turkheimer[5], Paul Expert[6]

[1]King's College London, London, Greater London, [2]Kings College London, London, London, [3]Scuola Superiore Sant'Anna, Pisa, Toscana, [4]King's College London, London, United Kingdom, [5]King's College London, London, London, [6]University College London, London, Greater London

Introduction: A key property of brain-wide networks is the dynamic nature of the interactions between their nodes. This is what the field of dynamic Functional Connectivity (dFC) investigates (Hutchison et al., 2013). dFC is, in general terms, the analysis of a matrix that evolves with time dFC(t). Commonly used dFC(t) matrices are the sliding window correlation/ covariances (Allen et al., 2014), coactivations (Esfahlani et al. 2020), or instantaneous Phase Locking (Cabral et al., 2017). It is also common to then extract the eigenvectors of dFC(t), perform clustering on dFC(t) and/or calculate parameters such as average connectivity or entropy. However, different dFC approaches lack a unified mathematical framework, in which to perform the operations mentioned above. We introduce here Eigenvector Dynamics Analysis (EiDA) which is a unified mathematical framework that allows theoretically sound and fast analysis of dFC(t) data and exact calculations of derived dynamic parameters.

Methods: All the dFC(t) matrices are ultra low-ranked, positive semidefinite and symmetric. We propose a new formula for computing the EVD (eigenvector decomposition) of dFC(t), which does not require building the dFC(t) matrices but takes advantage of the ultra-low-rankedness to operate in a low-dimensional space without loss of information. We also introduce a common set of basic operations for dFC which are general enough to be applied to correlation, covariance, phase locking, and coactivation matrix, and rely on their EVD. We then show that a) the norm of dFC(t) is a proxy for the overall amount of connectivity b) the distance between two matrices is the norm of their difference and c) the reconfiguration speed is the distance between dFC(t) and the lagged dFC(t-τ). As a measure of entropy, we propose the Von Neumann Entropy, which

quantifies the diversity of the eigenvalue spectrum. We showcase the method using a simulated dataset. We generated an i.i.d. Gaussian multivariate signal and multiplied it by the Cholesky decomposition of a known covariance matrix. We used this approach to generate a multivariate time series with 5 time-varying underlying covariance patterns. (simulated brain states), see Fig 2.i. See https://github.com/Mimbero/MEIDAS_MAIN for more details on the formulas and the software. (both MATLAB and Python available).

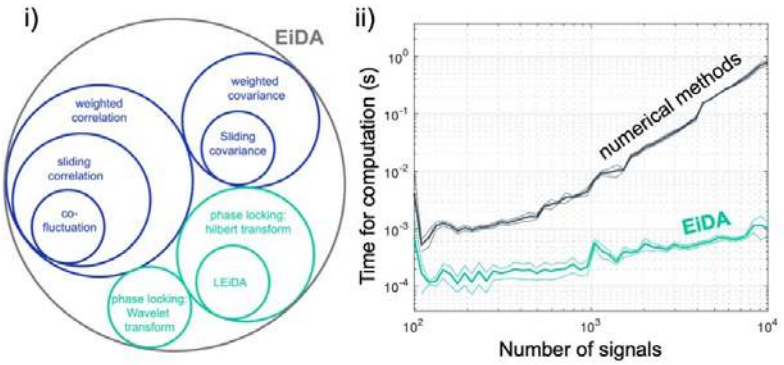

i) The EiDA framework proposes a unified approach and comprehensive set of measures for a wide variety of dynamic Functional Connectivity approaches. Moreover, it proposes a unique algorithm for their eigenvector decomposition (EVD). ii) Comparison of computational speed of the EiDA EVD algorithm with previous numerical methods. We repeated the experiment 20 times. Thick lines represent the mean computation time, on an Apple M2 CPU, thin lines mean +- variance.

Results: As in Fig 1.ii, the EiDA algorithm outperforms the standard numerical algorithms for eigenvector decomposition by up to 1000x in practical applications. For example, in an HCP voxelwise fMRI timeseries (Van Essen et al. 2013), with a window of 30 frames, the computation of sliding window covariance matrices dFC(t) would be extremely demanding with standard algorithms. EiDA recovered the full information of dFC(t) from 29 eigenvectors (rank=window size-1) and then all the measures of interest, without rebuilding the matrices (in ~3s on an Apple M2 CPU). In the simulated dataset, EiDA correctly recovered the underlying covariance patterns (Fig. 2.ii). The reconfiguration speed peaks in the time frames where the covariance patterns switch from one state to the other (Fig. 2.iii). K-medoids clustering with the EiDA matrix distance (Distance 2) recovers the 5 underlying covariance patterns, (Fig 2.iv). The Functional Connectivity Dynamics plot (time-to time distance matrix) shows that, with all three possible dFC EiDA distances, it is possible to recover the simulated brain states (Fig. 2.v).

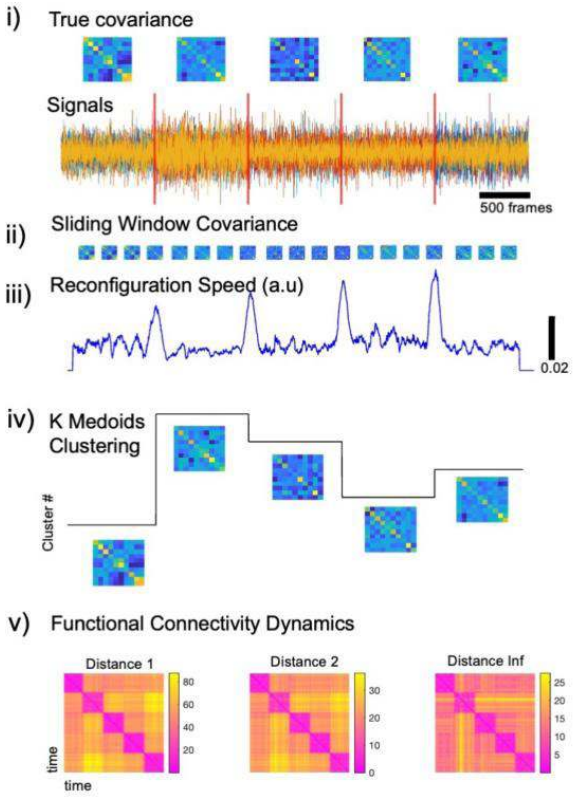

Application of EiDA in a simulated dataset. i) simulated signals (N=10 signals) and the five underlying covariance patterns (brain states) ii) The sliding window covariance matrix computed using the EiDA formula iii) Reconfiguration speed with a lag of 100 frames shows peaks corresponding to the switches between brain states iv) K Medoids Clustering using the EiDA Distance 2 fully recovers the 5 underlying brain states v) Functional Connectivity Dynamics matrices (FCD_{ij} is the distance between the matrix at time t_i and the matrix at time t_j) using the three possible distances of the EiDA framework.

Conclusions: We have introduced a generalizable theoretical framework for dFC analyses. The first benefit is that it unifies most of the main dFC approaches (Fig 1.i). The second is the gain in computational speed so that otherwise uncomputable matrices can be represented losslessly and all the quantities of interest (norm, distance, entropy) recovered efficiently. This paves the way for parcellation-free analyses and real-time algorithms, where computational efficiency is a stringent requirement.

References

1. Allen, E. A., Damaraju, E., Plis, S. M., Erhardt, E. B., Eichele, T., & Calhoun, V. D. (2014). Tracking Whole-Brain Connectivity Dynamics in the Resting State. Cerebral Cortex, 24(3), 663–676. https://doi.org/10.1093/cercor/bhs352
2. Cabral, J., Vidaurre, D., Marques, P., Magalhães, R., Silva Moreira, P., Miguel Soares, J., Deco, G., Sousa, N., & Kringelbach, M. L. (2017). Cognitive performance in healthy older adults relates to spontaneous switching between states of functional connectivity during rest. Scientific Reports, 7(1), Articolo 1. https://doi.org/10.1038/s41598-017-05425-7
3. Hutchison, R. M., Womelsdorf, T., Allen, E. A., Bandettini, P. A., Calhoun, V. D., Corbetta, M., Della Penna, S., Duyn, J. H., Glover, G. H., Gonzalez-Castillo, J., Handwerker, D. A., Keilholz, S., Kiviniemi, V., Leopold, D. A., de Pasquale, F., Sporns, O., Walter, M., & Chang, C. (2013). Dynamic functional connectivity: Promise, issues, and interpretations. NeuroImage, 80, 360–378. https://doi.org/10.1016/j.neuroimage.2013.05.079
4. Zamani Esfahlani, F., Jo, Y., Faskowitz, J., Byrge, L., Kennedy, D. P., Sporns, O., & Betzel, R. F. (2020). High-amplitude cofluctuations in cortical activity drive functional connectivity. Proceedings of the National Academy of Sciences, 117(45), 28393-28401.
5. Van Essen, D. C., Smith, S. M., Barch, D. M., Behrens, T. E., Yacoub, E., Ugurbil, K., & Wu-Minn HCP Consortium. (2013). The WU-Minn human connectome project: an overview. Neuroimage, 80, 62-79.

Poster No 1546

Tackling the challenges of group network inference from intracranial EEG data

Anna Pidnebesna[1], Pavel Sanda[1], Adam Kalina[2], Jiri Hammer[2], Petr Marusic[2], Kamil Vlcek[3], Jaroslav Hlinka[1]

[1]Institute of Computer Science of the Czech Academy of Sciences, Prague, Czech Republic, [2]Charles University, [2]nd School of Medicine, University Hospital Motol, Prague, Czech Republic, [3]Institute of Physiology of the Czech Academy of Sciences, Prague, Czech Republic

Introduction: Effective connectivity, or the causal relationships between brain areas, is an important tool for understanding information flow in the brain. However, it can be difficult to estimate accurately due to various challenges. In this study, we address these challenges specifically in inferring group networks from intracranial EEG recordings of epileptic patients during a visual task. These challenges include low and heterogeneous brain coverage, nonlinear signals, the influence of unobserved variables, a limited number of patients, a large amount of time-series data, and difficulties in statistical inference. We present a group network estimation pipeline that deals with these difficulties[1].

Methods: Data. iEEG was recorded in 15 patients with a sampling frequency of 512 Hz. Recorded time series were normalised to their pre-stimulus standard deviation. Bipolar montage was used to reduce the influence of distant sources. For the connectivity network exploration, 7 ROI were identified as parts of ventral/dorsal pathways[2]. Task. A set of pictures was presented to the subjects on a computer monitor. Brain responses to three types of images were studied (scenes, faces, objects) with 200 trials of each type. Every trial included 200 ms of baseline, 300 ms of stimulus, and 600 ms of reaction time. The trials were aligned on stimulus presentation yielding the event-related potentials (ERPs). Only those contacts with significantly more pronounced responses to scenes than objects were analysed. Methods. We present a pipeline for group network estimation using an example of a Directed Transfer Function (DTF). We propose to compute the dynamical connectivity for a filtered signal for a set of frequency bands, evaluating the statistical significance via the multivariate Fourier surrogates. Further, binary maps of significant connectivity values are collected among all patients to a heatmap per pair of ROIs. To evaluate the connectivity presence, we compute an average entry of a heatmap for a reaction time, corrected to the average heatmap entry during the baseline. This value is compared to the distribution obtained from the surrogates; FWE correction ($p<0.05$) is applied in the last step of the analysis (Fig.1).

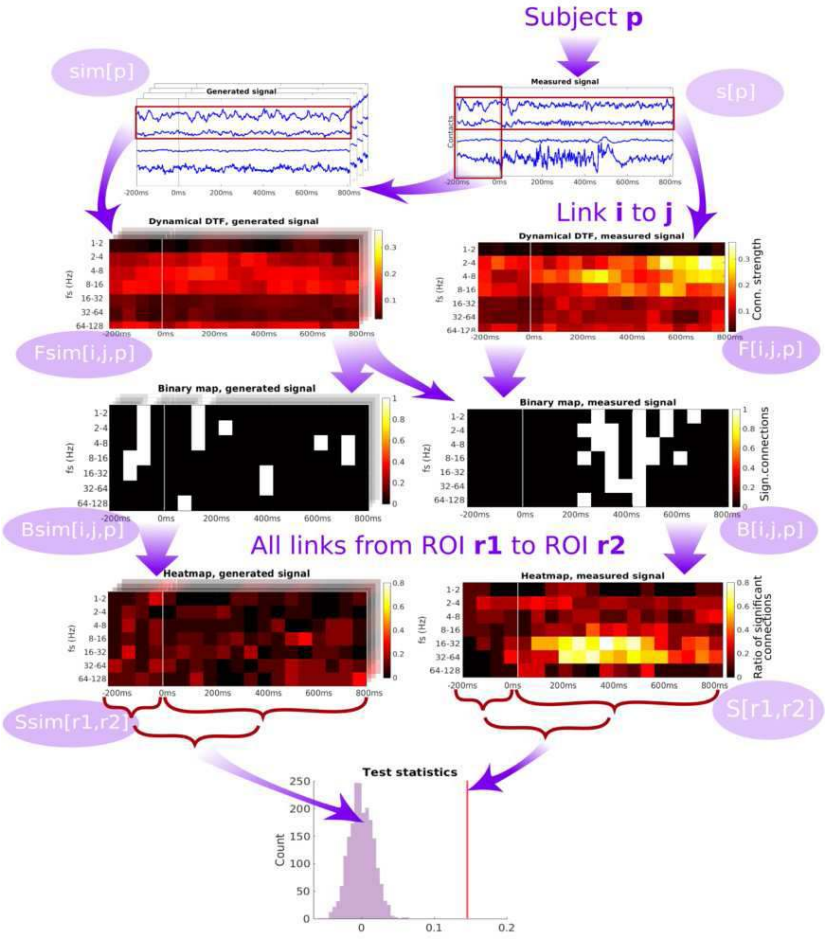

Results: Although the specific application was not the main rationale of this study, the utilisation of the developed pipeline provided interesting results. Our data show that the indirect pathway connecting the parietal lobe with locations in the medial temporal lobe via the retrosplenial complex is active during static visual scene processing in humans.

Conclusions: Based on the discussion of the possible ways to tackle challenges named in the introduction, we have made a range of methodological decisions to build up a pipeline allowing robust statistical inference of the alterations of the brain connectivity network during processing visual stimuli. The application of the pipeline was demonstrated on an example dataset, giving rise to a group-level network in terms of functional and effective connectivity.

References

1. Pidnebesna, A. (2022). Tackling the challenges of group network inference from intracranial EEG data. Frontiers in Neuroscience, 16. https://doi.org/10.3389/fnins.2022.1061867
2. Vlcek, K. (2020). Mapping the Scene and Object Processing Networks by Intracranial EEG. Frontiers in Human Neuroscience, 14. https://doi.org/10.3389/fnhum.2020.561399

Poster No 1547

Inter-subject synchrony of edge centric connectivity during naturalistic viewing

Yulia Nurislamova[1], Susanne Weis[2], Richard Betzel[3], Simon Eickhoff[1], Xuan Li[2]

[1]Institute for Systems Neuroscience, Medical Faculty, Heinrich-Heine University Düsseldorf, Düsseldorf, Germany, [2]Institute of Neuroscience and Medicine (INM-7), Research Centre Jülich, Jülich, Germany, [3]Department of Psychological and Brain Sciences, Indiana University, Bloomington, IN, United States

Introduction: Naturalistic viewing (NV) paradigms, namely movie watching, have shown great promise for facilitating our understanding of brain functions[1]. Inter-subject synchrony (ISS) is a commonly used approach to study evoked brain activity in NV studies[2]. Previous studies have observed ISS in not only brain activity[2] but also functional connectivity (FC)[3], suggesting that processing of complex naturalistic stimuli requires integration of information over different networks. However, it remains largely unknown to what degree shared NV stimuli induce coherent network dynamics over subjects. In this study, we investigated changes in ISS of FC patterns over time during NV.

Methods: Data for this analysis was obtained from the Human Connectome Project[4], specifically the 7T fMRI dataset, containing recordings of 178 subjects watching 14 different movie clips. The mean signal was derived for each parcel (node) as defined by the Schaefer 400 parcellation[5] and z-scored within each subject (Fig. 1A). For each participant, dynamic FC patterns were computed as edge time series[6], reflecting the co-fluctuation of signals between all pairs of parcels (nodes) at each time point. (Fig. 1B). Higher ISS indicates that the dynamic FC at the given TR is more consistent across subjects. Here, ISS was measured by the variance explained by the first principal component (PC1)[7], with PC1 reflecting the edge co-fluctuation pattern shared across subjects. For the whole-brain level, principal component analysis was performed on all z-scored ETS across all subjects for each time point separately (Fig. 1C). The analysis was repeated for each TR of all movie clips. Next, we investigated how the ISS changes at a finer spatial scale. Specifically, whole-brain ETS were assigned according to the functional 7-network atlas[8], resulting in 28 pairs: 7 within- and 21 between-network. ISS was calculated for each TR and pair of networks independently. We repeated the entire procedure on 900 TRs of the resting state data, generating a null-distributions to determine the statistical significance of each ISS value to identify TRs where brain states are reliably shared between subjects.

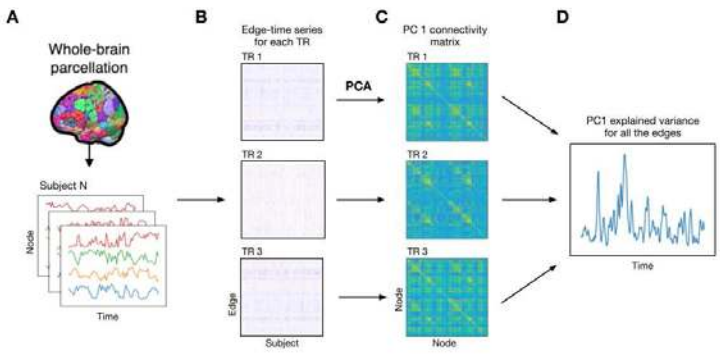

Figure 1. Schematics of the analysis pipeline. **A.** For each subject whole-brain parcellation was applied, resulting in 400 nodes with averaged fMRI BOLD time courses. **B.** Edge time series was calculated (i.e., the edge-by-subject matrix) for each timepoint and z-scored. **C.** The first principal component (PC1) across subjects for each time-point, reflecting shared spatial edge patterns across subjects. **D.** Explained variance of PC1 over time for one movie clip defined as inter-subject synchrony (ISS)

Results: Firstly, ISS values were not correlated to the subject's head motion (r=-0.05, p=0.54). Further, our results indicate that the ISS of the whole-brain connectivity patterns varies at a single TR resolution through the movie presentations (Fig. 2A-B). Here, we will focus on two clips, illustrating extreme cases of unique ISS profiles, possibly due to different movie content. 'Inception' showed the largest mean-ISS (0.066±0.03; Fig. 2C), while 'Dreary' achieved the lowest (0.033±0.004; Fig. 2C). At a finer spatial scale, our network analysis revealed TRs with significant ISS fluctuations that were not observed at the whole-brain level. For instance, ISS within the visual network in response to 'Dreary' displays periods of significant fluctuations over the course of the movie. As expected for a NV, the most prominent ISS fluctuations were observed between visual and all other networks for all movie clips (Fig 2D). Interestingly, in the case of 'Inception', ISS fluctuations were not limited to the interactions with the visual network: dorsal attentional network interactions exhibited prominent ISS dynamics with somatomotor, default mode, and other networks (Fig 2E).

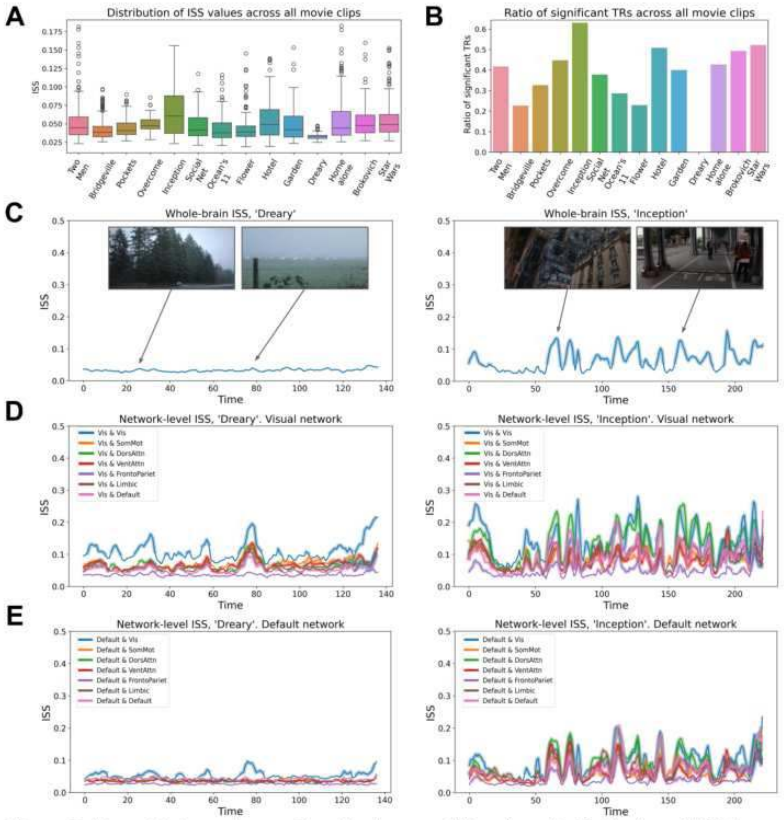

Figure 2. Inter-subject synchrony of functional connectivity values. **A.** Distribution of ISS for each movie clip. **B.** The ratio of statistically significant TRs (p<0.005) for each movie clip on a whole-brain level. Significance was determined by comparing ISS value at each TR to the resting-state null-distribution. **C.** Whole-brain ISS values over time for 2 movie clips: 'Dreary' and 'Inception'. Movie frames provided as examples of the movie content. Statistically significant TRs (p<0.005) are outlined. **D.** Example of network-level ISS of visual network and its integration with the other (6) networks for both movies. Vis - Visual, SomMot - Somatomotor, DorsAttn - Dorsal Attentional, VentAtt - Ventral Attentional, FrontoPariet - FrontoParietal, Limbic and Default mode networks. Statistically significant TRs (p<0.005) were determined for each network pair separately. **E.** Example of network-level ISS of dorsal attentional network and its integration with the other (6) networks for both movies.

Conclusions: Overall, we observed highly dynamic fluctuations of inter-subject synchrony of FC patterns over time for all movie clips, suggesting that rapidly changing movie content heavily influences brain connectivity at a fine temporal scale. Furthermore, network-level analysis revealed nuanced influence of the movie content on FC, where ISS is observed beyond sensory areas, including dorsal attentional, somatomotor, and default networks related to the processing complex movie stimuli. This study provides fundamental insights for future research into complex brain activity induced by specific features of movie stimuli.

References

1. Sonkusare, S., Breakspear, M., & Guo, C. (2019). Naturalistic stimuli in neuroscience: critically acclaimed. Trends in cognitive sciences, 23(8), 699-714.
2. Hasson, U., Nir, Y., Levy, I., Fuhrmann, G., & Malach, R. (2004). Intersubject synchronization of cortical activity during natural vision. science, 303(5664), 1634-1640.
3. Simony, E., Honey, C. J., Chen, J., Lositsky, O., Yeshurun, Y., Wiesel, A., & Hasson, U. (2016). Dynamic reconfiguration of the default mode network during narrative comprehension. Nature communications, 7(1), 12141.

4. Van Essen, D.C. (2013), The WU-Minn Human Connectome Project: An overview, Neuroimage 80, 62–79.
5. Schaefer, A., Kong, R., Gordon, E.M., Laumann, T.O., Zuo, X.N., Holmes, A.J., Eickhoff, S.B. and Yeo, B.T. (2018). Local-global parcellation of the human cerebral cortex from intrinsic functional connectivity MRI. Cerebral cortex, 28(9), 3095-3114.
6. Faskowitz, J., Esfahlani, F. Z., Jo, Y., Sporns, O., & Betzel, R. F. (2020). Edge-centric functional network representations of human cerebral cortex reveal overlapping system-level architecture. Nature neuroscience, 23(12), 1644-1654.
7. Li, X., Friedrich, P., Patil, K. R., Eickhoff, S. B., & Weis, S. (2023). A topography-based predictive framework for naturalistic viewing fMRI. NeuroImage, 120245.
8. Yeo, B.T., Krienen, F.M., Sepulcre, J., Sabuncu, M.R., Lashkari, D., Hollinshead, M., Roffman, J.L., Smoller, J.W., Zöllei, L., Polimeni, J.R. and Fischl, B. (2011). The organization of the human cerebral cortex estimated by intrinsic functional connectivity. Journal of neurophysiology.

Poster No 1548

M-RBM: A Spatially Informed Model for Individual Brain Parcellation

Da Zhi[1], Ladan Shahshahani[2], Caroline Nettekoven[3], Ana Luisa Pinho[4], Danilo Bzdok[5], Jörn Diedrichsen[6]

[1]University of Western Ontario, London, Ontario, [2]Brown University, Providence, RI, [3]University of Western Ontario, London, MT, [4]Western University, London, Ontario, [5]McConnell Brain Imaging Centre (BIC), Montreal Neurol, McGill Universityogical Institute (MNI), Montreal, Quebec, [6]The Brain and Mind Institute, University of Western Ontario, London, Ontario

Introduction: Understanding individual variability becomes a significant challenge in brain parcellation studies. A major concern for building accurate individual parcellation is the intrinsic spatial dependence between nearby brain locations, which are more likely connected to each other than far-away ones. As a consequence, the neighboring brain locations tend to exhibit a higher functional similarity. However, most parcellation methods do not utilize this intrinsic smoothness, which leads to a poor and noisy reconstruction. Here, we present a new computational model, multinomial-restricted Boltzmann machine (m-RBM), that models the spatial co-dependency between brain locations. We then integrated this model into our Bayesian parcellation framework (Zhi et al., 2023) to learn individual cortical parcellations. The experiments on both synthetic and task-based fMRI data show the performance of individual parcellations derived by m-RBM model are improved compared to the ones by spatially independent model.

Methods: The m-RBM model imposes spatial dependence between brain locations (voxels) on the group probability measure p(U), which defines how likely a certain location belongs to a functional region across population. This was modeled through a modified three-layer RBM parameterized by a connectivity weights w_(i,j) connecting the parcellation layer U with the hidden layer H, and a temperature parameters θ_w to control the overall strength of this connection (Fig. 1). Compared to Markov Random Fields (Ryali et al., 2013; Schaefer et al., 2018), the new model is computationally faster, using layer-wise Gibbs sampling and variational approximation. In contrast to traditional RBMs, the units in each layer of the m-RBM model are now multinomial variables, rather than binary Bernoulli variables, thereby making it possible to learn the parcellation into K regions. The individual parcellations (for each subject s) are then estimated by integrating the spatially informed group map p(U) with data likelihood of the observed data given the individual parcellation p(Y^s|U^s) under the Bayesian framework (Zhi et al., 2023). Here, we applied a stochastic maximum likelihood algorithm with mini-batch learning to train the m-RBM model. The parameters update then follow the gradients of the un-normalized likelihood calculated by contrastive divergence between positive and negative phase. We first validate this new model on an exhaustive simulation. Then, we applied this new model to a task-based dataset that covers many functional domains (Pinho et al., 2018) to generate individual cortical atlas. We evaluated the parcellations using the distance-controlled boundary coefficient (DCBC, Zhi et al., 2022).

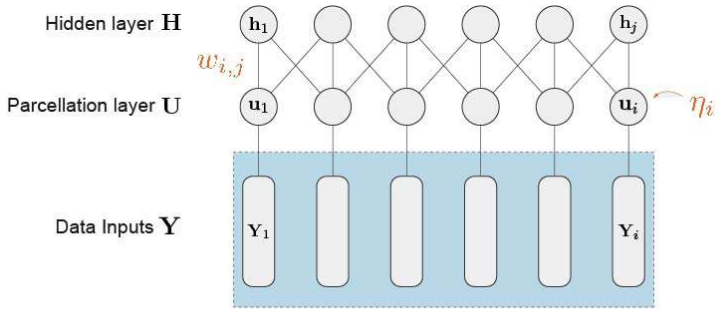

Figure 1: The multinomial-restricted Boltzmann machine (m-RBM) spatial arrangement model.

Results: We first ran a simulation by training either a m-RBM or a spatially independent model on a synthetic dataset with true spatial dependence (Fig. 2a). The evaluation on three evaluation metrics showed that the m-RBM model was able

to reconstruct the true individual parcellation better than the spatially independent model (Fig 2b,c,d). We then estimate individual parcellations using the m-RBM model on real task fMRI data (Pinho et al., 2018) with different connection strength θ_w within range 0.1 to 5. We then tested the performance of the resultant maps on test set, and found that the individual parcellations from m-RBM model with θ_w between 2 to 4 show significant better performance than the ones trained by the independent model (Fig. 2e).

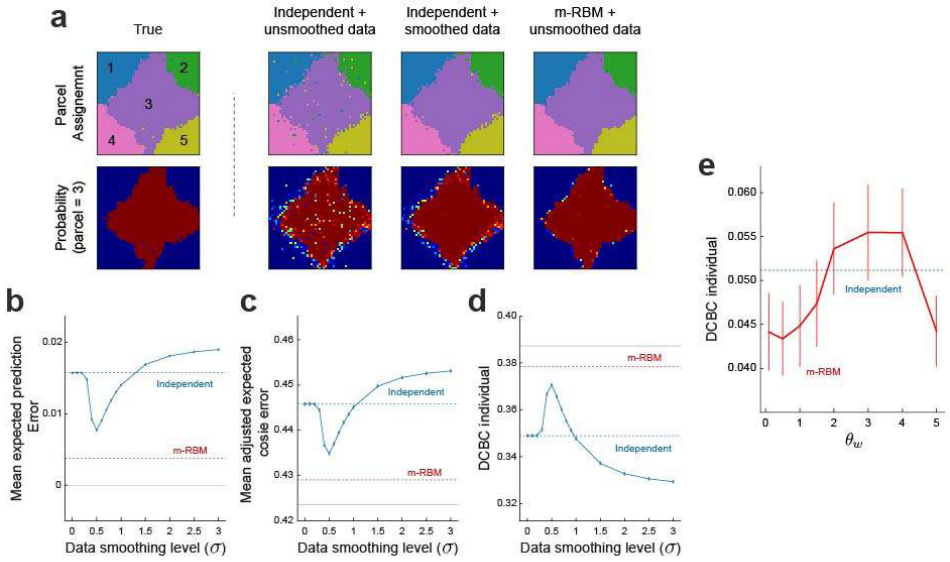

Figure 2: (a) The comparison of reconstructed individual parcellation (top row) and probability map of parcel 3 (bottom row) to the true map when it leaned from independent model with or without the smoothed data, and m-RBM model. (b) The mean reconstruction error (lower=better), (c) the mean expected weighted cosine error (lower=better), and (d) the DCDC (higher=better) of the individual parcellation derived from the independent model (blue dotted line) and m-RBM model (red dotted line) with unsmoothed data, or by the independent model with smoothed data (blue solid line). As reference the performance of the noise floor (gray solid line) is shown. The error bar indicates the SEM across 100 simulations. (e) The DCBC evaluation of individual parcellations using the IBC task fMRI data, using the spatially independent model (blue dotted line) or the m-RBM model with different temperature parameters θ_w from 0.1 to 5 (red line).

Conclusions: In this work, we proposed a novel computational architecture, called m-RBM, which is designed to capture the intrinsic spatial dependence between brain locations while accounting for individual variations. Both simulation and real data results showed the m-RBM model has significant advantages in estimating individual parcellations in the presence of spatial dependencies. Altogether, the proposed model may have promising applications in understanding variations of brain functional organizations by accurate individual parcellations.

References

1. Pinho, A. L. (2018). 'Individual Brain Charting, a high-resolution fMRI dataset for cognitive mapping', Scientific Data, 5.
2. Ryali, S. (2013). 'A parcellation scheme based on von Mises-Fisher distributions and Markov random fields for segmenting brain regions using resting-state fMRI', Neuroimage, 65, 83–96.
3. Schaefer, A. (2018). 'Local-global parcellation of the human cerebral cortex from intrinsic functional connectivity MRI', Cerebral Cortex, 28(9), 3095–3114.
4. Zhi, D. (2022). 'Evaluating brain parcellations using the distance-controlled boundary coefficient', Human Brain Mapping, 43(12), 3706-3720
5. Zhi, D. (2023). 'A hierarchical Bayesian brain parcellation framework for fusion of functional imaging datasets', BioRxiv

Poster No 1549

Transforming Structural Networks into Functional Networks: A Physics-Guided Deep Learning Approach

Ayush Kanyal[1], Vince Calhoun[2], Dong Hye Ye[1]

[1]Georgia State University, Atlanta, GA, [2]GSU/GATech/Emory, Decatur, GA

Introduction: Schizophrenia (SZ) is a severe mental condition that has an impact on an individual's thoughts, feelings, and behavior. The use of deep learning in MRIs and medical imaging has opened new avenues for research into techniques to detect SZ. SZ patients have been shown to have changes in their brain morphology and often exhibit unusual functional connectivity[2]. This validates the use of deep learning approaches on fractional anisotropy (FA) maps and functional MRI data. A variety of strategies, particularly those based on computational models, have been developed to better understand the link between structural connectivity (SC) and functional connectivity (FC). In this work, we use a physics-guided dynamical model

that is based on the Kuramoto model of synchronization along with a deep learning architecture to better understand the relationship between SC and FC.

Methods: Fig. 1 depicts our overall approach. FA, or fractional anisotropy maps, are a type of output from diffusion tensor imaging (DTI) scans[4]. Diffusion tensor imaging (DTI) provides quantitative information about the directional organization, integrity, and structural properties of white matter tracts in the brain. High FA values indicate highly organized fiber bundle orientations, while low FA values suggest disorganized or damaged fibers[6]. Once we have the structural connectivity from the FA maps, we apply the Kuramoto simulation to get the estimated FC matrices. Kuramoto simulation[7] refers to a physics model that simulates the synchronization of many interacting oscillators, such as groups of neurons in the brain. With a dynamic model derived from the Kuramoto model, our approach treats each brain region as an individual oscillator with distinct dynamics. Li et al.[8] used the Kuramoto dynamic model to calculate the phase information. (See the equation in Fig. 1, where Θ_i is the i-th brain region's phase state. ω_i is the intrinsic frequency of the i-th brain region. λ is the global coupling strength. A_ij is the coupling strength from the j-th to the i-th region, and α denotes the phase shift.) We then use the Balloon-Windkessel hemodynamics model to get the simulated FC matrices. We then use a U-Net to predict FC matrices from physics-guided input.

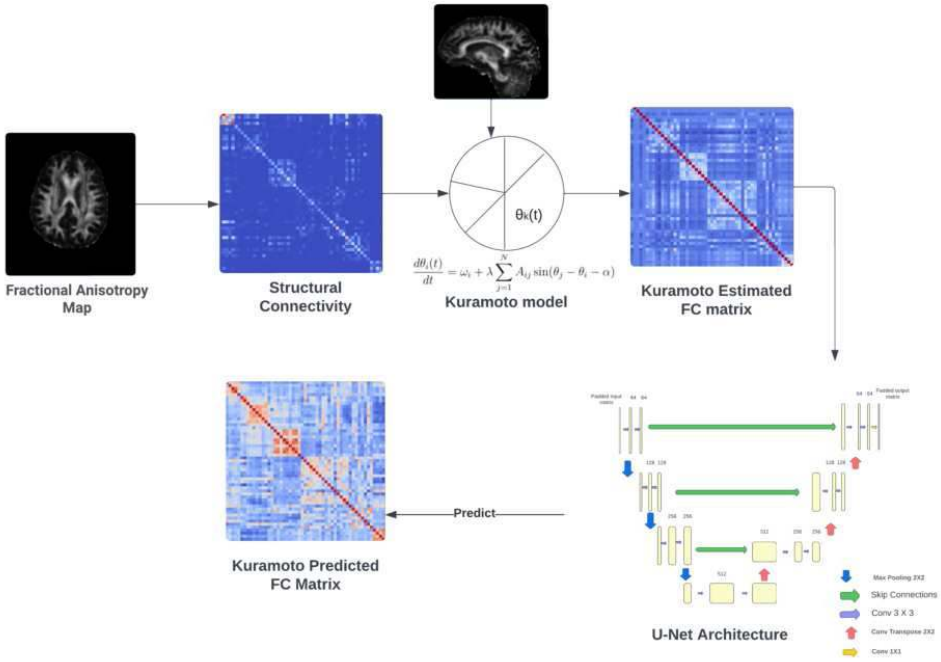

Fig. 1. Proposed Method Overview: We use FA maps to generate the SC (structural connectivity) matrix. We then apply the Kuramoto simulation to the SC matrices to get an estimated FC (functional connectivity matrix). This is further enhanced by using a U-Net to predict the FC matrix. We also used the U-Net directly on the SC matrices and compared the predicted FC matrices from the two approaches with the empirical FC matrices.

Results: We used a subset of the FBIRN[9] dataset, consisting of 278 patients, of whom 137 are SZ and 141 are healthy. We performed five-fold cross-validation to gauge the performance of our methods, and the results are summarized in Fig 2 b. We used correlation and mean square error as our metrics. Also, we ran the U-Net with an identical architecture with the same 150 epochs and a learning rate of 0.001 directly on the structural connectivity matrix to have a baseline for our comparison. The U-Net consists of a downsampling and an upsampling path. In downsampling, there are a series of convolutional layers followed by ReLU activation functions. Similarly, in the upsampling path, we use transposed convolution. The empirical FNC is derived from fMRI. fMRI measures blood oxygenation to determine connections between various brain regions. Spatial Independent Component Analysis (ICA) studies functional connections between brain regions at the network level. These connections are referred to as functional network connectivity[9]. The physics-guided model achieved a lower mean square error (0.0490) and higher correlation (0.748) than the SC-only model (0.1106 and 0.4253).

a)

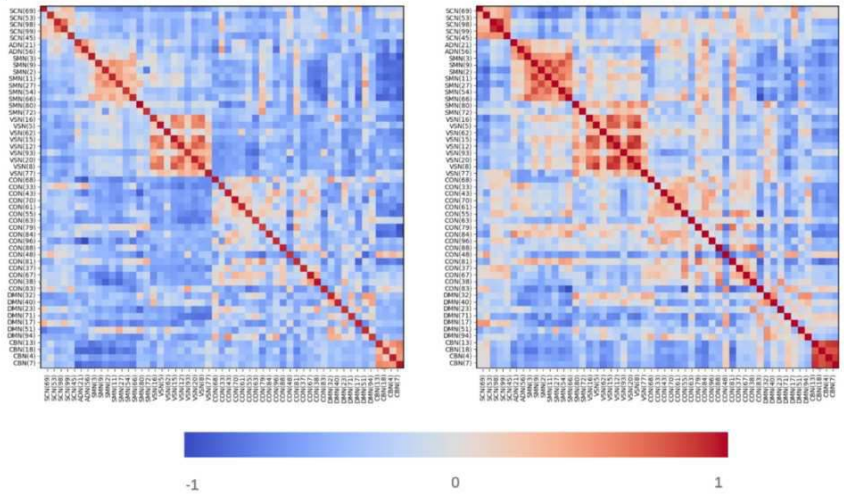

b)

U-Net with Kuramoto 5 Folds		U-Net without Kuramoto 5 folds		Kuromoto on SC
Mean Square Error	Correlation	Mean Square Error	Correlation	Correlation
0.0490 ± 0.002	0.748 ± 0.012	0.1106 ± 0.012	0.4253 ±0.2154	0.5613

Fig. 2. Results: a) Figure: FC plot for a single patient. Left: Kuramoto simulation-predicted FC matrix using a U-Net. Right: empirical FC matrix.
b) Table: Comparison of correlation and mean square error across different approaches.

Conclusions: We propose a physics-guided approach for predicting FCs from SCs. We performed a comparative study between the Kuramoto model with the U-Net and just using the U-Net on SC. The experimental results on clinical datasets demonstrated enhanced predictions in the case of using a physics-guided model with higher correlation and lower mean square error when the predicted outputs are compared to the empirical FC matrices.

References

1. Haukvik, Unn Kristin, Cecilie Bhandari Hartberg, and Ingrid Agartz. “Schizophrenia–what does structural MRI show?.” Tidsskrift for Den norske legeforening (2013).
2. Ronneberger, Olaf, Philipp Fischer, and Thomas Brox. “U-net: Convolutional networks for biomedical image segmentation.” In Medical Image Computing and Computer-Assisted Intervention–MICCAI 2015: 18th International Conference, Munich, Germany, October 5-9, 2015, Proceedings, Part III 18, pp. 234-241. Springer International Publishing, 2015.
3. Kimura, Mitsuhiro, Hidetake Yabuuchi, Ryoji Matsumoto, Koji Kobayashi, Yasuo Yamashita, Kazuya Nagatomo, Ryoji Mikayama, Takeshi Kamitani, Koji Sagiyama, and Yuzo Yamasaki. “The reproducibility of measurements using a standardization phantom for the evaluation of fractional anisotropy (FA) derived from diffusion tensor imaging (DTI).” Magnetic Resonance Materials in Physics, Biology and Medicine 33 (2020): 293-298.
4. Glenn, G. Russell, L-W. Kuo, Y-P. Chao, C-Y. Lee, Joseph A. Helpern, and Jens H. Jensen. “Mapping the orientation of white matter fiber bundles: a comparative study of diffusion tensor imaging, diffusional kurtosis imaging, and diffusion spectrum imaging.” American Journal of Neuroradiology 37, no. 7 (2016): 1216-1222.
5. Le Bihan, Denis, Jean-François Mangin, Cyril Poupon, Chris A. Clark, Sabina Pappata, Nicolas Molko, and Hughes Chabriat. “Diffusion tensor imaging: concepts and applications.” Journal of Magnetic Resonance Imaging: An Official Journal of the International Society for Magnetic Resonance in Medicine 13, no. 4 (2001): 534-546.
6. Acebrón, Juan A., Luis L. Bonilla, Conrad J. Pérez Vicente, Félix Ritort, and Renato Spigler. “The Kuramoto model: A simple paradigm for synchronization phenomena.” Reviews of modern physics 77, no. 1 (2005): 137.
7. Li, Bai, Xue Chen, Yue Yuan, and Yanjiang Wang. “Analyzing the Relationship Between Human Brain Structural and Functional Connectivity Using Kuramoto Model.” In 2018 14th IEEE International Conference on Signal Processing (ICSP), pp. 774-779. IEEE, 2018.
8. Keator, David B., et al. “The function biomedical informatics research network data repository.” Neuroimage 124 (2016): 1074-1079.
9. Jafri, Madiha J., Godfrey D. Pearlson, Michael Stevens, and Vince D. Calhoun. “A method for functional network connectivity among spatially independent resting-state components in schizophrenia.” Neuroimage 39, no. 4 (2008): 1666-1681.

Poster No 1550

Disrupted development of cortical-amygdala functional connectivity following childhood maltreatment,

Yu Mao[1]

[1]*Yu Mao, Postdoctor, Southwest University, Chongqing, GA*

Introduction: Childhood maltreatment (CM) is characterized by significant impairment in emotion processing and regulation, through the dysregulation of the cortical-limbic pathway, however, there is little longitudinal evidence on the neurobiological influence of CM. This study is designed to explore the influence of CM on cortical-amygdala functional connectivity (FC) and further reveal the longitudinal changes cortical-amygdala FC following CM.

Methods: First, the relationship between CM and cortical-amygdala FC was tested in two independent datasets of healthy young adults, controlling for the current life stress. Then, a linear mixed effects model was used test the interaction of time and CM score on the longitudinal changes in cortical-amygdala FC, using a dataset with resting-state fMRI data acquired at two different time points (mean time interval = 725 days). Finally, we explored the associations between disrupted developed pattern following CM experience and the latent vulnerability of emotional problem, using a moderated mediation analysis.

Results: We herein report three main findings. First, our results support the hypothesis that CM is characterized by reduced cortical-amygdala FC, in a reliable and reproducible manner. Second, the longitudinal results revealed individuals with higher level of CM demonstrated higher level of increase in cortical-amygdala connectivity, compared with individuals with lower level of CM. Third, among individuals with higher level of CM, higher level of increase of cortical-amygdala connectivity was associated with higher risk of emotional problem risk under stressful life events.

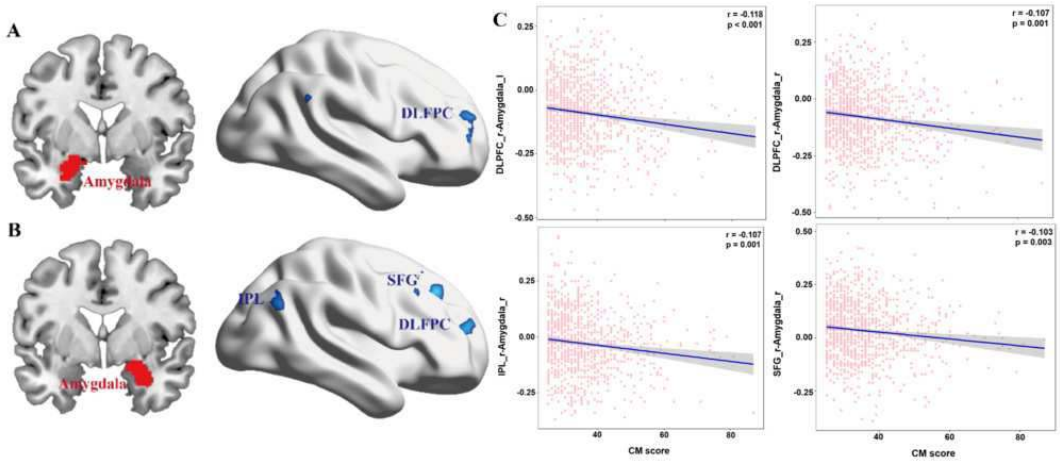

Figure 1. The relationship between CM and amygdala related functional connectivity.

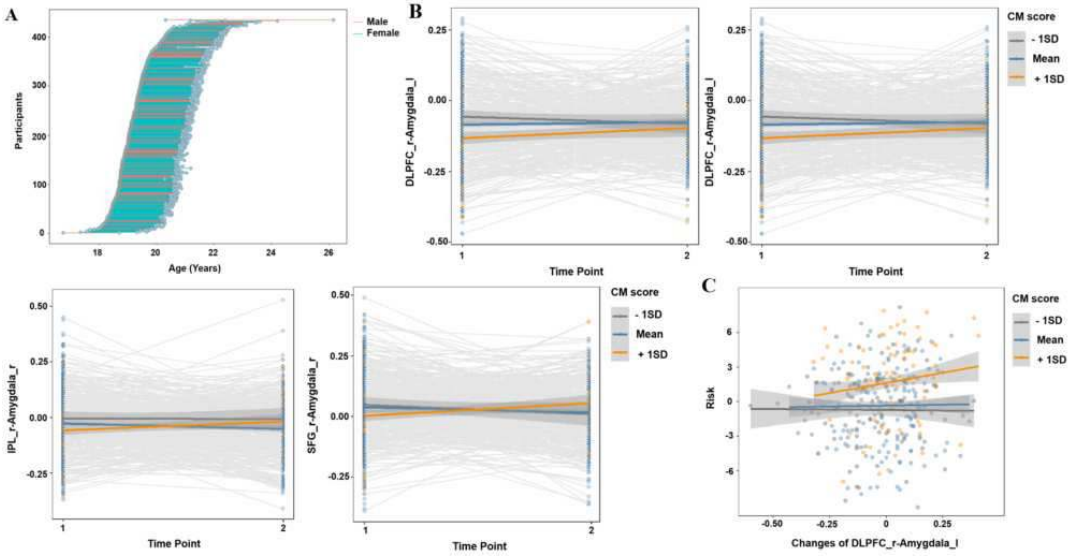

Figure 2. Longitudinal changes of DLPFC-amygdala FC various across different CM groups.

Conclusions: These results suggested that CM was associated with reduced amygdala connectivity with brain regions involving cognitive control and emotion regulation. Furthermore, these atypical development of cortical-amygdala FC in individuals with higher level of CM might symbolize the latent vulnerability for future risk of emotional problems.

References

1. Ajilian Abbasi, M. (2015). Child maltreatment in the world: a review article. International Journal of Pediatrics, 3(1.1), 353–365.
2. Dannlowski, U. (2012). Limbic scars: long-term consequences of childhood maltreatment revealed by functional and structural magnetic resonance imaging. Biological Psychiatry, 71(4), 286–293.
3. Ghashghaei, H. T. (2007). Sequence of information processing for emotions based on the anatomic dialogue between prefrontal cortex and amygdala. Neuroimage, 34(3), 905–923.
4. Jedd, K. (2015). Long-term consequences of childhood maltreatment: Altered amygdala functional connectivity. Development and Psychopathology, 27(4 0 2), 1577.
5. McCrory, E. J. (2011). Heightened neural reactivity to threat in child victims of family violence. Current Biology, 21(23), R947–R948.
6. Teicher, M. H. (2016). Annual research review: enduring neurobiological effects of childhood abuse and neglect. Journal of Child Psychology and Psychiatry, 57(3), 241–266.
7. Varese, F. (2012). Childhood adversities increase the risk of psychosis: a meta-analysis of patient-control, prospective-and cross-sectional cohort studies. Schizophrenia Bulletin, 38(4), 661–671.

Poster No 1551

Differences in the Modulation of Functional Connectivity by Positive and Negative Self-Talk in Anxio

Hyejeong Jo[1], Hesun Kim[2], Byung-Hoon Kim[3], Chanmi Park[4], Jaejin Kim[3], Joohan Kim[5], Jinwoo Kim[4]

[1]Department of Cognitive Sciences, Yonsei School of Medical Science, Brain Korea 21 Project, Seoul, Korea, Republic of, [2]Institute of Behavioral Sciences in Medicine, Yonsei University College of Medicine, Seoul, Korea, Republic of, [3]Department of Psychiatry, Gangnam Severance Hospital, Yonsei University College of Medicine, Seoul, Korea, Republic of, [4]HCI Lab, Yonsei School of Business, Yonsei University, Seoul, Korea, Republic of, [5]Department of Communication, Yonsei University, Seooul, Korea, Republic of

Introduction: Individuals who experience high levels of anxiety often struggle to manage their emotions due to their heightened self-focused attention, which can lead to various problems. Consequently, individuals with high anxiety struggle to fully benefit from positive events and are significantly affected by negative events due to excessive analytical rumination. However, there is a lack of neuroimaging investigation into how this self-focused attention occurs based on positive and negative emotions. Thus, the current study aimed to elucidate the effect of positive and negative self-talks on functional connectivity in highly anxious individuals.

Methods: Thirty-four individuals with high level of anxiety (HA, n= 18; BAI, mean=24.3, SD=6.07) and low level of anxiety (LA, n= 16; BAI, mean=6.56, SD=1.90) were scanned using functional magnetic resonance imaging at 5-min self-respect and self-criticism tasks. A seed-to-voxel analysis was conducted using the seeds in the posterior cingulate cortex (PCC) for the default mode network and self-referential processes, the anterior cingulate cortex (ACC) for emotion regulation, and the nucleus accumbens (NAcc) and insula for the reward-motivation network. We conducted 2 (group: HA and LA) X 2 (task: self-respect and self-criticism) mixed ANOVA to identify the main effect of group and the interaction effect of group x task. Identified brain activities were correlated with psychological scales including the Level of Self-Criticism Scale and the Connor Davidson Resilience Scale.

Results: In the self-respect task, the HA group showed significantly higher connectivity strength between the insula and left supramarginal gyrus, as well as between the insula and left cerebellum, whereas the LA group showed significantly higher connectivity strength between the ACC and left frontal pole. In the self-criticism task, the HA group showed significantly higher connectivity strength between the PCC and right middle frontal gyrus, and between the insula and left supramarginal gyrus, whereas the LA group showed significantly higher connectivity strength between the ACC and left middle frontal gyrus. Moreover, the group x task interaction effect was identified in the connection between the insula and right cerebellum, as well as between the NAcc and left pallidum. Lastly, connectivity between the insula and left cerebellum in the self-respect task, connectivity between the PCC and right middle frontal gyrus, and connectivity between the insula and left supramarginal gyrus in the self-criticism task were correlated with some psychological scale scores.

Conclusions: This study was conducted to elucidate differences in the modulation of functional connectivity by positive and negative self-talk in highly anxious individuals compared to low-anxious individuals. Our findings suggest that, regardless of the task, highly anxious participants exert more effort to activate the reward-motivation network and default mode network, whereas they may not adequately regulate their emotions when exposed to both self-respect and self-criticism. Furthermore,

correlations with psychological variables imply that the neuronal mechanisms of anxious individuals might affect other basic psychological needs, such as resilience.

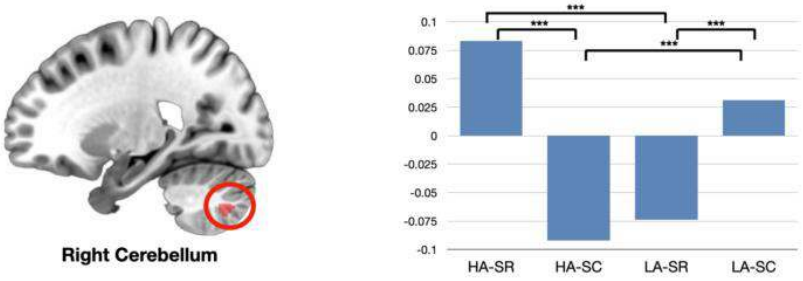

Fig 1. Insula- based functional connectivity showing the group x task interaction effect in the right cerebellum. Abbreviation: HA, high anxiety; LA, low anxiety; SR, self-respect; SC, self-criticism.

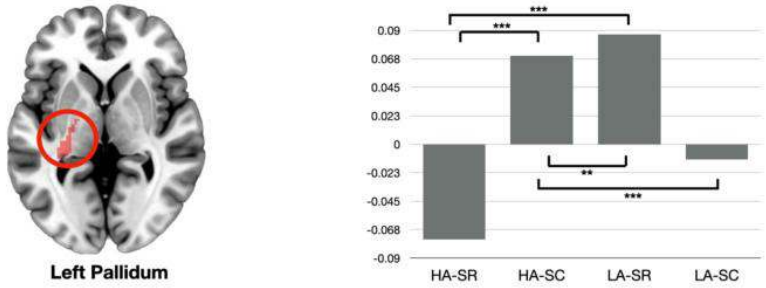

Fig 2. Nucleus accumbent (NAcc)- based functional connectivity showing the group x task interaction effect in the Left Pallidum. Abbreviation: HA, high anxiety; LA, low anxiety; SR, self-respect; SC, self-criticism.

References

1. Ingram, R. E. (1990). Self-focused attention in clinical disorders: review and a conceptual model. Psychological bulletin, 107(2), 156.
2. Boehme, S., Miltner, W. H., & Straube, T. (2015). Neural correlates of self-focused attention in social anxiety. Social Cognitive and Affective Neuroscience, 10(6), 856-862.
3. Morin, A. (1993). Self-talk and self-awareness: On the nature of the relation. The Journal of Mind and Behavior. 223-234
4. Kross, E., Bruehlman-Senecal, E., Park, J., Burson, A., Dougherty, A., Shablack, H., ... & Ayduck, O. (2014). Self-talk as a regulatory mechanism: How you do it matters, Journal of personality and social psychology, 106(2).
5. Kyeong, S., Kim, J., Kim, D. J., Kim, H. E., & Kim, J. J. (2017). Effects of gratitude meditation on neural network functional connectivity and brain-heart coupling. Scientific reports, 7(1), 5058.

Poster No 1552

Exploring Default Mode Network Association with Naturalistic Stimuli Using Topological Data Analysis

Iqra Ejaz[1], Sadia Shakil[2]

[1]BiCoNeS lab, Department of Electrical Engineering, Institute of Space Technology, Islamabad, Pakistan, [2]Department of Biomedical Engineering, The Chinese University of Hong Kong, Hong Kong

Introduction: The Default Mode Network (DMN) is a sense-making network of the brain influenced by naturalistic stimuli such as movies, stories, and music. Understanding the relation between DMN and naturalistic stimuli can assist in comprehension of such stimuli and our thought process. This study utilizes topological data analysis (TDA) from algebraic topology to extract significant DMN and demographic covariates for distinguishing between a) modalities, and b) contents of the incoming stimuli.

Methods: The dataset (Zadbood, 2017) consisted of fMRI data of listening (to narration) and watching of two movies (Merlin and Sherlock). Out of 36 participants, 18 listened to the narration of Merlin and watched Sherlock; and the other 18 listened to the narration of Sherlock and watched Merlin. We pre-processed the data using statistical parametric modelling (SPM) and then extracted DMN's regions-of-interest (ROIs) from (Raichle 2015)(Hospital and Chase 2008), consisting of five cortices (posterior cingulate, anterior cingulate and medial prefrontal, inferior parietal, hippocampal formation, lateral temporal). Pairwise correlation between the DMN cortices was estimated using Pearson correlation coefficient. Mean correlation (mCorr) value of each matrix was computed and TDA was implemented on the correlation matrices to extract the betti-curves for each matrix (Gracia-Tabuenca, 2020). TDA extracts the shape and structure of data by identifying patterns and features such as loops and holes. Betti curves represents the transition of these topological features from being isolated nodes to a single connected component. From these betti curves features such as (area under curve (AUC), slope and kurtosis) were extracted. Binary logistic regression was implemented to extract covariates association with modalities (listening vs. watching) and contents (Merlin vs. Sherlock). Three demographic (Age, sex, recall score) and four data driven (mCorr, AUC, slope, kurtosis)

covariates were used for each participant. Best covariates model selection was based upon lowest AIC (Akaike information criterion) values and covariates with significant association were with p-values <=0.05 (Annas, Aswi, and Abdy 2022). Using significant covariates, similar analysis was performed on the cortices of DMN to get the information about cortex having positive or negative association with the modalities/contents.

Results: Fig. 1(a) shows the lowest AIC value (left) for mCorr and AUC and significant p-values (right) with positive association of these covariates with the watching data relative to listening data. Fig. 1(b) shows lowest AIC value (left) for ACMP and IP and significant p-values (right) for ACMP (mCorr + AUC) with positive association and IP (AUC only) with negative association with the watching data. Fig. 2(a) shows lowest AIC (left) for AUC, slope, kurtosis and significant p-values (right) for AUC and slope with positive and negative association respectively with Sherlock. Fig. 2(b) shows lowest AIC value (left) for IP but no significant p-values for it, hence showing no significant association. Positive association of mCorr with the watching data shows overall high mean correlation among the regions of DMN but does not provide information about the correlations of individual regions. However, higher AUC shows segregation of DMN regions providing information about individual regions. ACMP and IP were found to play a significant role in distinguishing different modalities of the incoming stimuli. AUC and slope being significantly associated with the Sherlock movie shows more segregated activations in the regions of DMN.

Conclusions: We used combination of TDA and logistic regression in a novel manner to explore association of different demographic and data-driven covariates with the modalities and contents of the naturalistic stimuli. Our results suggest that our approach provides a meaningful and deep insight about the relationship of DMN activity with the modalities/contents of the incoming stimuli.

Model selection (Modalities)

Model No	Combinations	AIC value
Model 1	Sex + Age + Recall + mCorr + AUC + slope + Kurtosis	68.49798389450811
Model 2	Age + Recall + mCorr + AUC + slope + Kurtosis	68.16802504213275
Model 3	Sex + mCorr + AUC + slope + Kurtosis	65.49979087610701
Model 4	Sex + AUC + slope + Kurtosis	67.26391508247036
Model 5	mCorr + AUC + slope + Kurtosis	64.86128618331443
Model 6	AUC + slope + Kurtosis	67.81611882763147
Model 7	Sex + Recall + AUC	66.22703435627216
Model 8	Sex + Recall + slope	67.61272379157711
Model 9	Sex + Recall + mCorr	69.33084970015759
Model 10	Sex + mCorr + AUC	61.54251422611995
Model 11	Age + mCorr + AUC	62.67746413571709
Model 12	Age + Recall + mCorr	71.51763293617945
Model 13	**mCorr + AUC**	**60.95976898039725**
Model 14	Age + mCorr	69.60637758582486
Model 15	Age + AUC	66.19841777295088
Model 16	slope + Kurtosis	67.51227711853157
Model 17	Recall + mCorr	69.52036721495725
Model 18	Recall + AUC	66.14386452595828
Model 19	Recall + slope	67.91055771492509
Model 20	AUC + slope	68.16802504213275
Model 21	Sex + mCorr	67.33534629797303
Model 22	Sex + AUC	64.23469867900863
Model 23	Sex + slope	65.61926146277241
Model 24	mCorr	67.62368732414917
Model 25	AUC	64.20404414795996

Covariates p-values for best model (Modalities)

	Coefficient	Std error	Z value	P value
Constant	0.0421	0.327	0.129	0.897
mCorr	1.4193	0.665	2.134	**0.033**
AUC	1.9575	0.782	2.505	**0.012**

(a)

Model selection (Modalities (DMN Cortex-wise))

Model No	Combinations	AIC value
Model 1	PCC + ACMP + IP + HPH + LTC	62.50342863233187
Model 2	PCC + ACMP + IP + LTC	64.34351528007433
Model 3	PCC + ACMP + HPH + LTC	64.15257111341651
Model 4	ACMP + IP + LTC	60.927361657113714
Model 5	ACMP + HPH + LTC	60.662803939811006
Model 6	PCC + IP + LTC	71.05713637288005
Model 7	PCC + ACMP + LTC	65.98099614629108
Model 8	PCC + ACMP + HPH	62.037114569937 72
Model 9	IP + HPH + LTC	72.83473532080637
Model 10	IP + HPH	69.57826850712544
Model 11	PCC + ACMP	63.96097626728449
Model 12	PCC + IP	67.42694553385638
Model 13	PCC + HPH	68.73855873976498
Model 14	PCC + LTC	72.2049397689117
Model 15	**ACMP+ IP**	**59.40636843015413**
Model 16	ACMP + LTC	62.646480652632505
Model 17	IP + LTC	72.66893157697035
Model 18	ACMP + LTC	59.52474776907871
Model 19	HPH + LTC	69.91802947846668
Model 20	PCC	64.34351528007433
Model 21	ACMP	60.755551985728364
Model 22	IP	69.00989147495653
Model 23	HPH	67.10503850637159
Model 24	LTC	69.63084644298063

Covariates p-values for best model (Modalities (DMN cortex-wise))

	Coefficients	Std error	Z value	P value
Constant	0.0109	0.313	0.035	0.972
ACMP (mCorr)	2.8281	1.065	2.656	**0.008**
ACMP (AUC)	3.4180	1.096	3.118	**0.002**
IP (mCorr)	-1.4483	0.767	-1.888	0.059
IP (AUC)	-1.7104	0.822	-2.080	**0.037**

(b)

Fig 1. (a) AIC values for different models (combination of covariates) and p-values for best selected model for the case of modalities. (b) AIC values for different models (combination of DMN cortices) and p-values for best selected model for the case of modalities (DMN cortex-wise)

Model selection (Contents)		
Model No.	**Combinations**	**AIC value**
Model 1	Sex + Age + Recall + mCorr+ AUC + slope + Kurtosis	64.85033883963632
Model 2	Age + Recall + mCorr + AUC + slope + Kurtosis	64.02507510213763
Model 3	Sex + mCorr + AUC + slope + Kurtosis	61.19102024921956
Model 4	Sex + AUC + slope + Kurtosis	59.25324182190188
Model 5	mCorr + AUC + slope + Kurtosis	60.731044086256O8
Model 6	**AUC + slope + Kurtosis**	**58.880315O1001743**
Model 7	Sex + Recall + AUC	69.8620338825352
Model 8	Sex + Recall + slope	62.481818250397566
Model 9	Sex + Recall + mCorr	70.65649081475183
Model 10	Sex + mCorr + AUC	69.15846252699279
Model 11	Age + mCorr + AUC	69.57835916222045
Model 12	Age + Recall + mCorr	71.21128841553957
Model 13	mCorr + AUC	67.60207932641026
Model 14	Age + mCorr	69.21335624240302
Model 15	Age + AUC	68.36534603148112
Model 16	slope + Kurtosis	61.23891449080363
Model 17	Recall + mCorr	69.33206967283432
Model 18	Recall + AUC	68.49066022397082
Model 19	Recall + slope	61.17210406857796
Model 20	AUC + slope	64.02507510213763
Model 21	Sex + mCorr	68.68441727056081
Model 22	Sex + AUC	67.90470296090933
Model 23	slope	59.25468892613769
Model 24	mCorr	67.3344721810889
Model 25	AUC	66.49075253248523

Covariates p-values for best model (Contents)				
	Coefficients	**Std error**	**Z value**	**P value**
Constant	-0.4634	0.327	-1.418	0.156
AUC	1.5436	0.771	2.001	**0.045**
Slope	-1.5084	0.504	-2.992	**0.003**
Kurtosis	1.2260	0.698	1.755	0.079

(a)

Model selection (Contents (DMN Cortex-wise))		
Model No	**Combinations**	**AIC value**
Model 1	PCC+ ACMP + IP + HPH + LTC	73.61019541279421
Model 2	PCC + ACMP + IP + LTC	70.984203425132
Model 3	PCC + ACMP + HPH + LTC	72.41135781949497
Model 4	ACMP + IP + LTC	68.88986167000257
Model 5	ACMP + HPH + LTC	70.30553336959446
Model 6	PCC + IP + LTC	70.31823239150108
Model 7	PCC + ACMP + LTC	70.75572822808664
Model 8	PCC + ACMP + HPH	73.03903616130475
Model 9	IP + HPH + LTC	69.84353746743955
Model 10	IP + HPH	69.22287204254242
Model 11	PCC + ACMP	70.80625412937076
Model 12	PCC + IP	70.10502239331612
Model 13	PCC + HPH	71.58288755370253
Model 14	PCC + LTC	70.47602521742516
Model 15	ACMP + IP	68.88371989070237
Model 16	ACMP + LTC	69.32664083284828
Model 17	IP + LTC	67.82170715495916
Model 18	ACMP + LTC	69.83335593942911
Model 19	HPH + LTC	69.61243570272387
Model 20	PCC	70.984203425132
Model 21	ACMP	68.02575457391478
Model 22	IP	67.55006133423868
Model 23	HPH	68.18951630375503
Model 24	**LTC**	**67.21820682706715**

Covariates p-values for best model (Contents (DMN cortex-wise))				
	Coefficient	**Std error**	**Z value**	**P value**
Constant	0.0005	0.303	0.002	0.999
LT (AUC)	0.8351	0.625	1.336	0.182
LT (Slope)	-0.9806	0.635	-1.545	0.122

(b)

Fig 2. (a) AIC values (left) for different models (combinations of covariates) and p-values (right) for the best model for the case of contents. (b) AIC values (left) for different models (combinations of DMN cortices) and p-values (right) for the best model for the case of contents (DMN cortex-wise)

References

1. Annas, Suwardi, Aswi Aswi, and Muhammad Abdy. 2022. “Binary Logistic Regression Model of Stroke Patients : A Case Study of Stroke Centre Hospital in Makassar *.” 6(1): 161–69.
2. Hospital, Massachusetts General, and Chevy Chase. 2008. “The Brain ’ s Default Network Anatomy, Function, and Relevance to Disease.” 38: 1–38.
3. Raichle, Marcus E. 2015. “The Brain ’ s Default Mode Network.”
4. Gracia-Tabuenca, Z. a.-P. (2020). Topological data analysis reveals robust alterations in the whole-brain and frontal lobe functional connectomes in attention-deficit/hyperactivity disorder. eneuro.
5. Zadbood, A. a. (2017). How we transmit memories to other brains: constructing shared neural representations via communication. Cerebral cortex, 4988--5000.

Poster No 1553

Effects of excessive smartphone use on sensory processing and developing brain

Ji Hyeong Ro[1], Yong Jeon Cheong[1], Seonkyoung Lee[1], Jihyun Bae[1], Minyoung Jung[1]

[1]Korea Brain Research Institute, Daegu, Korea, Republic of

Introduction: Does increased exposure to smartphone affect child development? If then, how? Considering smartphone simultaneously provides strong multisensory inputs (Cho, 2021), excessive use of smartphone is highly thought to be associated with sensory processing problems (Harrison, 2019). Accordingly, recent research has demonstrated that excessive use of smartphone is associated with changes in the brain among developing children (Horvath, 2020; Montag, 2023; Pomper, 2014). In line, this study aims at investigating the role of excessive use of smartphone in brain structure of children in terms of sensory processing.

Methods: This study includes 128 child participants (70 boys, 58 girls, mean age [SD] = 7.86[0.08]). We assessed the levels of excessive use of smartphone and behavior response to sensory information using Children Sensory Profile (CSP) and Children’s Smartphone Overdependence index (SO), respectively. Using 3T magnetic resonance imaging (MRI) scanner we

collected structural MRI data. The institutional boards of the Korea Brain Research Institute granted ethical approval for this study (KBRI-202206-HR-001). Using FreeSurfer, we computed values of 68 parcellated surface area of children's brain. We conducted partial correlation analyses 1) between CSP and SO scores, and 2) between SO score and values of each surface area after adjusting age, sex, handedness, and intracranial volume. P-values for significant correlations are corrected at FDR q = 0.05. Next, we performed mediation analysis to identify directionality between CSP, SO, and the cortical feature with a 95% confidence interval using 5000 bootstrapping.

Results: We found significant correlations: (1) between SO and two CSP subscales ('Sensitivity': r = 0.3; 'Auditory processing': r = 0.3) and (2) between SO and area of the right superior temporal sulcus (STS) (r = -0.31). Indirect mediating effects of SO were observed in two models: (1) the relationship between 'Sensitivity' and the right STS area was mediated by SO (path a = .31, p = 0.000; path b = -0.35, p = 0.000, path c' = 0.22, p = 0.013, path c = 0.11 p = 0.2) and (2) the relationship between 'Auditory processing' and the right STS area was mediated by SO (path a = 0.3, p = 0.001; path b = -0.35, p = 0.000, path c' = 0.22, p = 0.014, path c = 0.12 p = 0.2).

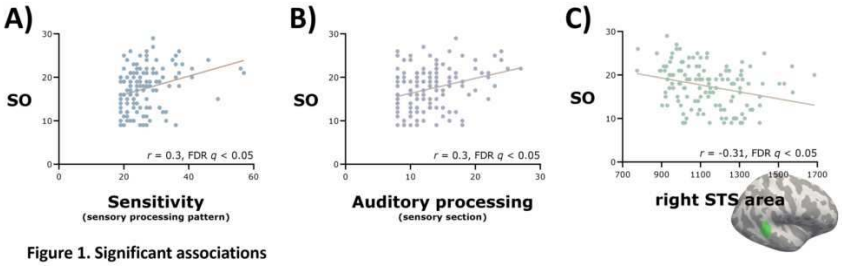

Figure 1. Significant associations

A) between Smartphone-Overdependence(SO) and Sensitivity;

B) between SO and Auditory processing;

C) between SO and right Superior temporal sulcus(STS) area.

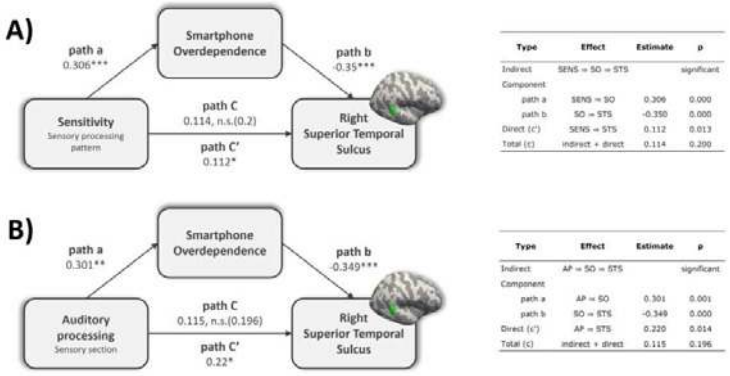

Type	Effect	Estimate	p
Indirect	SENS → SO → STS		significant
Component			
path a	SENS → SO	0.306	0.000
path b	SO → STS	-0.350	0.000
Direct (c')	SENS → STS	0.112	0.013
Total (c)	indirect + direct	0.114	0.200

Type	Effect	Estimate	p
Indirect	AP → SO → STS		significant
Component			
path a	AP → SO	0.301	0.001
path b	SO → STS	-0.349	0.000
Direct (c')	AP → STS	0.220	0.014
Total (c)	indirect + direct	0.115	0.196

Figure 2. Mediation models and summary tables:

A) Smartphone-Overdependence mediates Sensitivity and right Superior Temporal Sulcus;

B) Smartphone-Overdependence mediates Auditory processing and right Superior Temporal Sulcus.

Conclusions: Previous studies have demonstrated negative effects of excessive use of smartphone on various aspects of children development including psychological factors and brain structure. The present study added new aspects of excessive use of smartphone in terms of sensory processing in association with developing brain : We showed 1) excessive smartphone use is associated not only with sensory processing but with the right STS area. It was interesting that both 'Sensitivity' and 'Auditory processing' of CSP subscales lead to changes in right STS area, which confirms the role of STS in auditory processing. Our finding proposed that excessive use of smartphone may link both sensory processing and the STS in a sophisticated way, which requires further investigation.

References

1. Cho, I. H. (2021), 'Reduced Volume of a Brainstem Substructure in Adolescents with Problematic Smartphone Use', Journal of the Korean Academy of Child and Adolescent Psychiatry, vol. 32, no. 4, pp.137-143
2. Harrison, K. (2019), 'Rude or shrewd? Reframing media devices as care structures and child use as accommodation', Journal of Children and Media, vol. 13, no. 3, pp. 367–375.
3. Horvath, J. (2020), 'Structural and functional correlates of smartphone addiction', Addictive Behaviors, vol. 105, no. 106334, 10.1016/J.ADDBEH.2020.106334
4. Montag, C. (2023), 'Neuroimaging the effects of smartphone (over-)use on brain function and structure—a review on the current state of MRI-based findings and a roadmap for future research', Psychoradiology, vol. 3, 10.1093/PSYRAD/KKAD001
5. Pomper, U. (2014), 'Taking a Call Is Facilitated by the Multisensory Processing of Smartphone Vibrations, Sounds, and Flashes', PLOS ONE, vol. 9, no. 8, 10.1371/JOURNAL.PONE.0103238

Poster No 1554

White matter connectivity is organized by cytoarchitecture from birth

Emily Kubota[1], Xiaoqian Yan[2], Mareike Grotheer[3], Bella Fascendini[4], Sarah Tung[1], Christina Tyagi[1], Vaidehi Natu[5], Kalanit Grill-Spector[6]

[1]Stanford University, Stanford, CA, [2]Institute of Science and Technology for Brain-Inspired Intelligence, Fudan University, Shanghai, Shanghai, [3]University of Marburg - Philipps-Universität Marburg, Marburg, Hesse, [4]Princeton, Princeton, NJ, [5]Psychology Department, Stanford University, Stanford, CA, [6]Psychology Department, Stanford University, Stanford, CA

Introduction: High-level visual areas are organized consistently across individuals, and in blind participants, high level visual areas respond to their preferred categories presented in other modalities (van den Hurk, Van Baelen, and Op de Beeck 2017; Murty et al. 2020). This phenomenon has led researchers to ask: what determines where functionally specialized regions emerge? One hypothesis is that innate white matter connectivity determines the functional specialization of ventral temporal cortex (VTC). In recent work, however, we found that white matter connectivity is organized by cytoarchitecture rather than functional specialization in children (Kubota et al. 2023). Are white matter connections organized by functional specialization or cytoarchitecture from birth? Using diffusion magnetic resonance imaging, we test these two hypotheses in newborns, 3 month-olds, 6 month-olds, and adults.

Methods: Our final sample included N=88 sessions from 42 infants (21 longitudinal) and 21 adults ((n=23 newborns (M=28.56 days, SD= 10.21days), n=23 3-month-olds (M=106.91 days, SD=19.33 days), n=21 6-month-olds (M=189.05 days, SD=15.77 days), n=21 adults (M=28.21 years, SD=5.51 years)). We collected dMRI data in all infants and adults, and generated a whole brain tractogram in each participant. We projected adult maximum probability map (MPM) regions of interest (ROI) of six category-selective regions in ventral temporal cortex (VTC) to individual participant brains. For each participant, we intersected the whole brain tractogram with each of the MPM ROIs (see Fig 1). We then projected the endpoints of the intersected connectome to the cortical surface to see how the endpoints connect to the rest of the brain. Finally, we quantified the endpoint density at each Glasser Atlas ROI (Glasser et al. 2016) to determine the connectivity profile of each ROI. We used principal component analysis to reduce the dimensionality of the connectivity profiles and found that the first 10 principal components explain 98% of the variance in connectivity. We used a leave-one-out cross-validated classifier to test if we could classify from the connectivity profile of the ROI its cytoarchitectonic area (FG2/FG3/FG4), category selectivity(word/face/body/place), or age group (0 months/3 months/6 months/adult) in a held out subject.

Results: We found that from the white matter connectivity profiles we can classify cytoarchitecture (Fig 2C) and category (Fig 2D) above chance. The odds of correct classification of cytoarchitecture was significantly higher compared to category (odds ratio= 5.97, 95% CI [3.99, 8.94], binomial logistic regression). There was no significant difference in the odds of correct classification or for newborns, 3-month-olds, and 6-month-olds compared to adults (newborns: odds ratio =1.20, 95% CI [0.77, 1.89], 3-months: odds ratio =1.01, 95% CI [0.65, 1.56], 6-months: odds ratio =1.05, 95% CI [0.67, 1.65], binomial logistic regression). These results demonstrate that cytoarchitecture was classified better than category across all age groups. In addition, from white matter connectivity we could classify age group above chance (Fig 2E), suggesting development of connectivity profiles. Examination of the endpoint connectivity profiles across the brain reveals that connections from VTC to lateral prefrontal cortex increase over development, whereas connections from VTC to orbitofrontal cortex and the parietal lobe decrease over development.

Conclusions: Our results indicate that white matter connectivity and cytoarchitecture in VTC are linked from birth, providing evidence for innate organization of white matter connectivity. However, white matter connectivity also changes over development: connections from VTC to lateral frontal cortex increase from infancy to adulthood, whereas connections from VTC to the parietal lobe decrease. These results suggest that white matter connectivity has both innate scaffolding and the capacity to change over development.

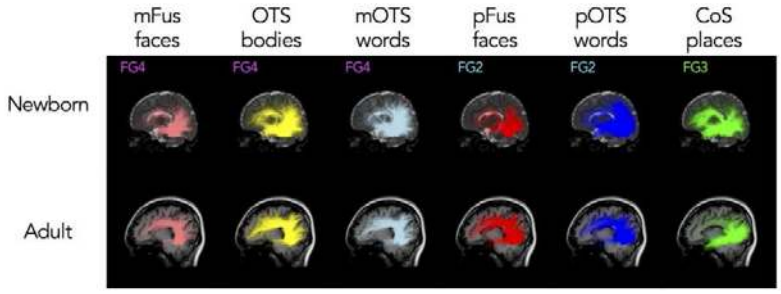

Figure 1. Example white matter connectivity of MPM ROIs in an example newborn (top) and adult (bottom). The names of the functional ROIs include their anatomical location and functional selectivity (mFus-faces: mid fusiform face-selective area, OTS-bodies: occipito-temporal sulcus body-selective area, mOTS-words: mid occipito-temporal sulcus word-selective area, pFus-faces: posterior fusiform face-selective area, pOTS-words: posterior occipitotemporal sulcus word-selective aes, CoS-places: collateral sulcus place selective area). The cytoarchitectonic area of each functional ROI is in the upper left corner.

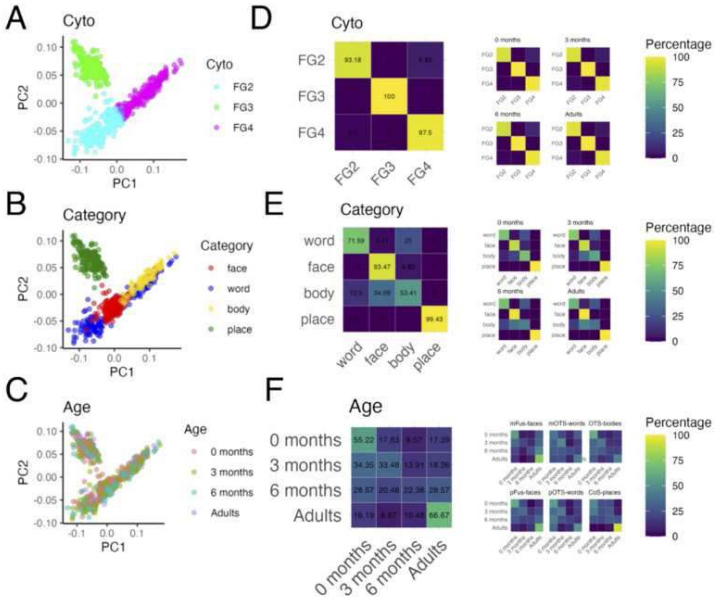

Figure 2. White matter connectivity is organized by cytoarchitecture from birth. A) Principal component 1 (PC1) vs principal component 2 (PC2) colored by cytoarchitectonic area (cyan: FG2, green: FG3, magenta: FG4). B) PC1 vs PC2 colored by category-selectivity (red: face, blue: word, green: place, body: yellow). C) PC1 vs PC2 colored by participant age (pink: 0 months, green: 3 months, teal: 6 months, purple: adults). (A,B,C) Each dot represents a single connectivity profile (connections of one functional ROI in a single subject). (D,E,F) Confusion matrices for classification of cytoarchitecture (D), category (E), and age (F) with leave-one-out cross validation. Color of the square indicates the percentage of classifications for each true value (y) for each predicted value (x). On diagonals depict correct classification.

References

1. Glasser, Matthew F., Timothy S. Coalson, Emma C. Robinson, Carl D. Hacker, John Harwell, Essa Yacoub, Kamil Ugurbil, et al. 2016. "A Multi-Modal Parcellation of Human Cerebral Cortex." Nature 536 (7615): 171–78.
2. Hurk, Job van den, Marc Van Baelen, and Hans P. Op de Beeck. 2017. "Development of Visual Category Selectivity in Ventral Visual Cortex Does Not Require Visual Experience." Proceedings of the National Academy of Sciences of the United States of America 114 (22): E4501–10.
3. Kubota, Emily, Mareike Grotheer, Dawn Finzi, Vaidehi S. Natu, Jesse Gomez, and Kalanit Grill-Spector. 2023. "White Matter Connections of High-Level Visual Areas Predict Cytoarchitecture Better than Category-Selectivity in Childhood, but Not Adulthood." Cerebral Cortex 33 (6): 2485–2506.
4. Murty, N. Apurva Ratan, Santani Teng, David Beeler, Anna Mynick, Aude Oliva, and Nancy Kanwisher. 2020. "Visual Experience Is Not Necessary for the Development of Face-Selectivity in the Lateral Fusiform Gyrus." Proceedings of the National Academy of Sciences 117 (37): 23011–20.

Poster No 1555

Assessing Reliability and Geometric Influence in Organization of Structural Brain Connectivity

Sunghyoung Hong[1], Seulki Yoo[2], Bo-yong Park[3], Seok-Jun Hong[4]

[1]Sungkyunkwan University, Suwon, Republic of Korea, [2]Convergence Research Institute, Sungkyunkwan University, Suwon, Republic of Korea, [3]Inha University, Incheon, Republic of Korea, [4]IBS Center for Neuroscience Imaging Research, Suwon, Republic of Korea

Introduction: Understanding the functional mechanism of human cognitive systems prerequisites a precise mapping of underlying physical brain networks. Structural connectivity (SC) based on diffusion tractography has been instrumental in this purpose, as it allows to grasp the configuration of whole-brain physical connections in a single matrix form. However, the prohibitively high dimensionality of SC matrices, together with inconsistent results depending on the tractography-related parameters (e.g. tractography method, parcellation, filtering strategy) have hindered the effort to use this technique in capturing the principles of structural brain organization[1]. Here, we sought to address these issues by applying a low-dimensional connectome mapping approach on SC[2,3], which provides a smooth transition of connectivity profiles across the whole brain (also known as "connectome gradient"). Moreover, inspired by a recent study demonstrating a significant role of gross cortical geometry on human brain function[4], we further tested the association between this SC gradient and cortical geometry to investigate a fundamental constraint in the manifestation of the structural brain organization.

Methods: We analyzed structure and diffusion MRI of 86 young-adult subjects from the Q3 release of the Human Connectome Project (HCP)[5] (51 females; age range: 22-36). To generate SC matrices, we used three different tractography algorithms (FACT and SD STREAM: both for deterministic; iFOD2 for probabilistic)[6], three parcellations (Schaefer 400[7], Glasser 360[8], and sub-parcellation of Desikan-Killiany 400[3,9]), and two filtering methods (SIFT2[6] and COMMIT2[10]). Gradients were then generated from these SCs using Brainspace, specifically based on the diffusion map algorithm for non-linear dimensionality reduction with zero sparsity[3]. To compare this gradient with cortical geometry, we also calculated eigenmodes from a group-averaged mid-thickness cortical surface using the Laplace-Beltrami operator[4]. Next, gradients and SC were reconstructed by cumulatively adding geometric eigenmodes weighted by their corresponding coefficients.

Results: We profiled the gradients of SC from 18 different combinations of tractography algorithms (3 tractography methods×3 parcellations×2 filtering algorithms). Among these, we found that the gradient showed high reproducibility, particularly in the 1st-4th components, between different algorithmic combinations (Fig1A). When we examined the variance explained by each principal component, however, it turned out that the first 3 components account for the majority of connectome data (~44% on average; Fig1B). These 3 principal components showed 1) the left to right, 2) the anterior to posterior, and 3) the sensory to transmodal axes (Fig1C). This suggests that even if the original SC matrices were seemingly complex, their underlying structures could be recapitulated by a parsimonious set of low-dimensional bases. Notably, as hypothesized, when we visualized the tractography results at each gradient, all of them seemed greatly affected by cortical geometric effects (Fig1D). Our post-hoc analysis confirmed this visual inspection that there are strikingly similar patterns between the eigenmodes of cortical surface and SC gradients (Fig2A,1C). Indeed, when we reconstructed the SC gradient based on cortical eigenmodes, >95% of accuracy was achieved with a minimal number of eigenmodes (Fig2B,2D). This strong geometric effect was also observed in the SC matrix (Fig2C,2D).

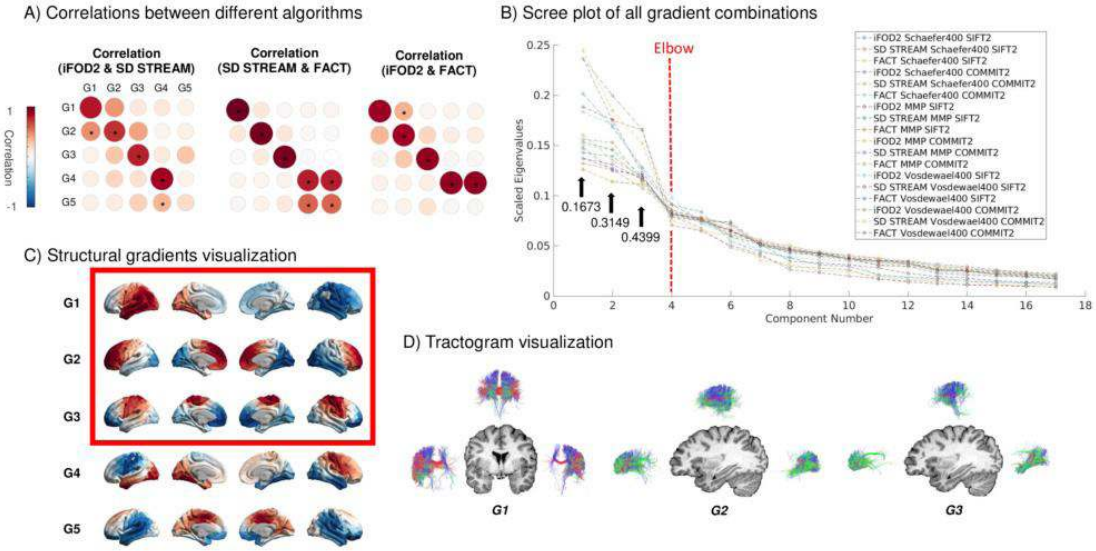

Fig 1. Consistency of structural gradients, their principal components and tractography visualization. A) Gradients 1st-4th between different tractography algorithms have a high correlation. B) Scree plot of all gradient combinations shows that the first three gradients which are determined by an elbow point have, on average, a fairly high explanatory power of more than 0.43. C) Among five principal gradients, the first gradient appears to be the left to right, the second gradient looks like the anterior to posterior, and the third gradient seems to be the sensory to transmodal axes. This gradient was made of iFOD2, sub-parcellation of Desikan-Killiany 400, SIFT2, diffusion map, and sparsity 0. Based on A) and B), we decided to focus on the first three gradients of the analysis after it. D) It shows seed-based tractography along the progress of each gradient. Seed points are parcels with the largest, the medium, and the smallest value.

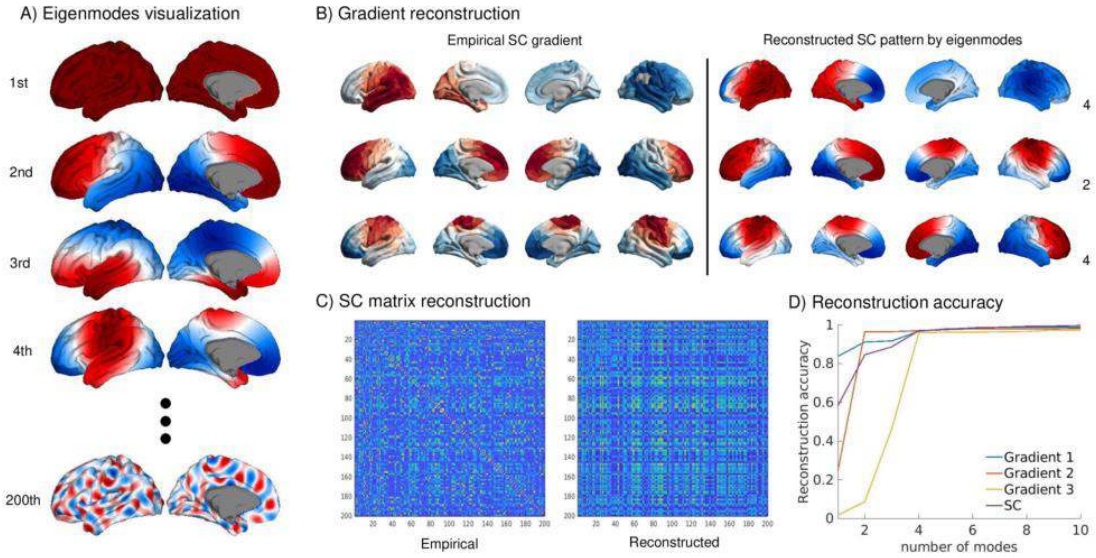

Fig 2. Eigenmodes and reconstruction of structural gradient and connectivity with them. A) Total 200 geometric eigenmodes were generated of group-averaged mid-thickness cortical surface. 1st, 2nd, and 4th eigenmodes are very similar with 1st, 2nd, and 3rd gradients, respectively. B) Each gradient was reconstructed by cumulatively adding eigenmodes multiplied by each coefficient. The numbers in the lower right of each gradient are the minimum number of eigenmodes to achieve reconstruction accuracy of more than 95%. C) Group-averaged left hemisphere structural connectivity was reconstructed in the same way. Only 4 eigenmodes were needed to reconstruct more than 95% accuracy. D) It is shown that the graph of the reconstruction accuracy is saturated using more than four eigenmodes in both gradient and structural connectivity.

Conclusions: Here, our study systematically investigated the principles of SC organization using a non-linear dimensionality reduction approach. Our main finding, i.e. a strong geometric effect on SC gradients, suggests that the topology of structural brain networks may be predominantly determined by the connectivity from the adjacent cortical areas (e.g., a short-range U fibers), a potential signature of evolutionarily shaped brain organization that prioritizes energy efficiency.

References

1. Klein, J., Grötsch, A., Betz, D., Barbieri, S., Friman, O., Stieltjes, B., ... & Hahn, H. K. (2010, March). Qualitative and quantitative analysis of probabilistic and deterministic fiber tracking. In Medical Imaging 2010: Image Processing (Vol. 7623, pp. 720-727). SPIE.
2. Margulies, D. S., Ghosh, S. S., Goulas, A., Falkiewicz, M., Huntenburg, J. M., Langs, G., ... & Smallwood, J. (2016). Situating the default-mode network along a principal gradient of macroscale cortical organization. Proceedings of the National Academy of Sciences, 113(44), 12574-12579.
3. Vos de Wael, R., Benkarim, O., Paquola, C., Lariviere, S., Royer, J., Tavakol, S., ... & Bernhardt, B. C. (2020). BrainSpace: a toolbox for the analysis of macroscale gradients in neuroimaging and connectomics datasets. Communications biology, 3(1), 103.
4. Pang, J. C., Aquino, K. M., Oldehinkel, M., Robinson, P. A., Fulcher, B. D., Breakspear, M., & Fornito, A. (2023). Geometric constraints on human brain function. Nature, 1-9.
5. WU-Minn, H. C. P. (2017). 1200 subjects data release reference manual. URL https://www. humanconnectome. org, 565.

6. J.-D. Tournier, R. E. Smith, D. Raffelt, R. Tabbara, T. Dhollander, M. Pietsch, D. Christiaens, B. Jeurissen, C.-H. Yeh, and A. Connelly. MRtrix3: A fast, flexible and open software framework for medical image processing and visualisation. NeuroImage, 202 (2019), pp. 116–37.
7. Schaefer, A., Kong, R., Gordon, E. M., Laumann, T. O., Zuo, X. N., Holmes, A. J., ... & Yeo, B. T. (2018). Local-global parcellation of the human cerebral cortex from intrinsic functional connectivity MRI. Cerebral cortex, 28(9), 3095-3114.
8. Glasser, M. F., Coalson, T. S., Robinson, E. C., Hacker, C. D., Harwell, J., Yacoub, E., ... & Van Essen, D. C. (2016). A multi-modal parcellation of human cerebral cortex. Nature, 536(7615), 171-178.
9. Desikan RS, Ségonne F, Fischl B, et al. An automated labeling system for subdividing the human cerebral cortex on MRI scans into gyral based regions of interest. Neuroimage 2006;31:968-980.
10. Schiavi, S., Ocampo-Pineda, M., Barakovic, M., Petit, L., Descoteaux, M., Thiran, J. P., & Daducci, A. (2020). A new method for accurate in vivo mapping of human brain connections using microstructural and anatomical information. Science advances, 6(31), eaba8245.

Poster No 1556

Generative model of the human connectome: a geometric approach

Francis Normand[1], James Pang[2], Trang Cao[3], Jace Cruddas[2], Alex Fornito[1]

[1]Monash University, Clayton, Victoria, [2]Monash University, Melbourne, Victoria, [3]Monash University, Clayton, VIC

Introduction: In what follows, the connectome refers to the structural connectivity matrix (SC) representing the large-scale network of physical connections (white-matter fiber tracts) between it's nodes (brain regions). The cortex is usually parcellated between 100 and 1000 brain regions. The connectome is a weighted and undirected network, where the weights (strengths of the connections) represent the total number or the density of fiber tracts between the regions. The interest in generating realistic connectome models stems from the desire to compress its complex network description (its connectivity matrix) to a few simple wiring rules, with a few parameters that are optimized to fit the empirical connectome. The current best generative models usually incorporate two rules that dictate the formation of connections, i.e., a spatial and a topological rule. The topological rule is usually the matching index, which assigns greater probability of connection to nodes who already share common neighbors. This family of generative models can successfully capture the topology of the empirical connectome, based on the four network measures of node degree, betweenness centrality, clustering coefficient and edge length distribution. On the other hand, these models fail to capture the topography of the empirical connectome, for e.g., the location of the hubs. In this work, we propose a generative model of the connectome based entirely on the geometry of the cortex, i.e., using the geometric modes and eigenvalues of the cortical surface mesh. The geometric modes, analogous to the resonant frequencies on a guitar string, represent the fundamental modes of vibrations of the cortical surface mesh representation, i.e., in the linear regime, any pattern of vibration can be decomposed into a combination of the geometric modes. Therefore, the basis of geometric modes is a tool of interest to describe the process through which brain anatomy shapes its function.

Methods: The spectral theorem tells us that we can reconstruct the connectome (SC) using its eigenvectors (connectome eigenmodes and eigenvalues. Reconstructing the connectome in this way is trivial, since the connectome itself is used as an input. In this work, we posit that we can approximate SC using instead the geometric modes as a starting point. The geometric modes are obtained by solving the Helmholtz equation using the Laplace-Beltrami operator (LBO) of the mesh. The starting point is to consider what we term the geometric contribution to the functional connectivity matrix (FC). We posit that the geometric contribution to FC is given by a truncated LBO. From this hypothesis, our framework lends itself well to the one proposed by Robinson (2012) that relates different representations of connectivity (SC and FC) together through neural field theory (NFT). This framework allows us to reconstruct SC with remarkable precision.

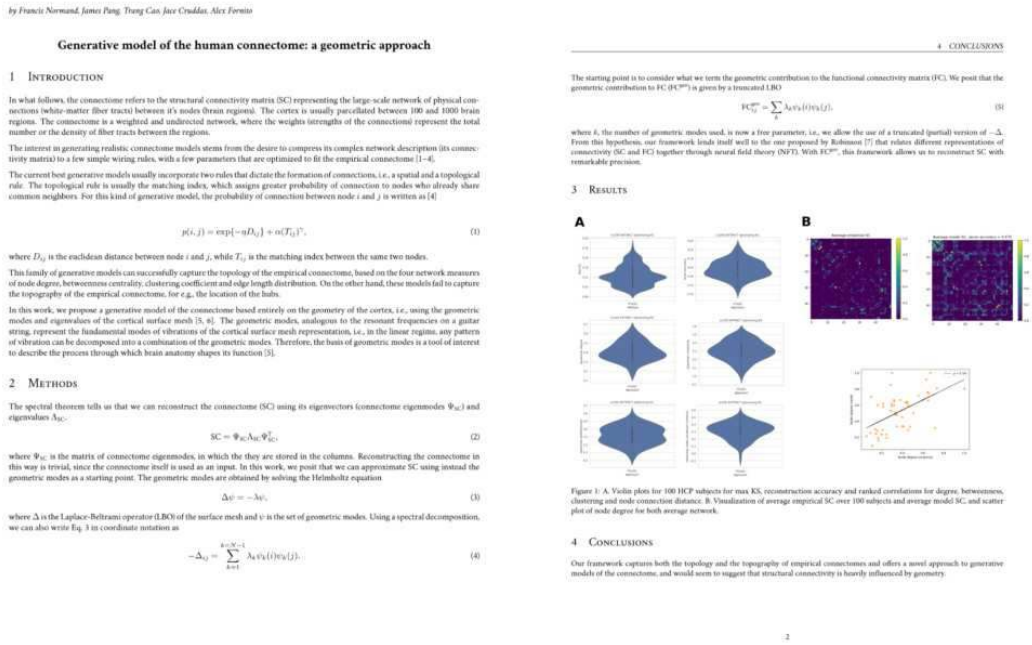

by Francis Normand, James Pang, Trang Cao, Jace Cruddas, Alex Fornito

Generative model of the human connectome: a geometric approach

1 Introduction

In what follows, the connectome refers to the structural connectivity matrix (SC) representing the large-scale network of physical connections (white-matter fiber tracts) between it's nodes (brain regions). The cortex is usually parcellated between 100 and 1000 brain regions. The connectome is a weighted and undirected network, where the weights (strengths of the connections) represent the total number or the density of fiber tracts between the regions.

The interest in generating realistic connectome models stems from the desire to compress its complex network description (its connectivity matrix) to a few simple wiring rules, with a few parameters that are optimized to fit the empirical connectome [1–4].

The current best generative models usually incorporate two rules that dictate the formation of connections, i.e., a spatial and a topological rule. The topological rule is usually the matching index, which assigns greater probability of connection to nodes who already share common neighbors. For this kind of generative model, the probability of connection between node i and j is written as [4]

$$p(i,j) = \exp(-\eta D_{ij}) + \alpha(T_{ij})^{\gamma}, \quad (1)$$

where D_{ij} is the euclidean distance between node i and j, while T_{ij} is the matching index between the same two nodes.

This family of generative models can successfully capture the topology of the empirical connectome, based on the four network measures of node degree, betweenness centrality, clustering coefficient and edge length distribution. On the other hand, these models fail to capture the topography of the empirical connectome, for e.g., the location of the hubs.

In this work, we propose a generative model of the connectome based entirely on the geometry of the cortex, i.e., using the geometric modes and eigenvalues of the cortical surface mesh [5, 6]. The geometric modes, analogous to the resonant frequencies on a guitar string, represent the fundamental modes of vibrations of the cortical surface mesh representation, i.e., in the linear regime, any pattern of vibration can be decomposed into a combination of the geometric modes. Therefore, the basis of geometric modes is a tool of interest to describe the process through which brain anatomy shapes its function [5].

2 Methods

The spectral theorem tells us that we can reconstruct the connectome (SC) using its eigenvectors (connectome eigenmodes Ψ_{SC}) and eigenvalues Λ_{SC}.

$$SC = \Psi_{SC}\Lambda_{SC}\Psi_{SC}^{T}, \quad (2)$$

where Ψ_{SC} is the matrix of connectome eigenmodes, in which the they are stored in the columns. Reconstructing the connectome in this way is trivial, since the connectome itself is used as an input. In this work, we posit that we can approximate SC using instead the geometric modes as a starting point. The geometric modes are obtained by solving the Helmholtz equation

$$\Delta\psi = -\lambda\psi, \quad (3)$$

where Δ is the Laplace-Beltrami operator (LBO) of the surface mesh and ψ is the set of geometric modes. Using a spectral decomposition, we can also write Eq. 3 in coordinate notation as

$$-\Delta_{ij} = \sum_{k=1}^{k<N-1} \lambda_k \psi_k(i)\psi_k(j). \quad (4)$$

4 Conclusions

The starting point is to consider what we term the geometric contribution to the functional connectivity matrix (FC). We posit that the geometric contribution to FC (FC^{geo}) is given by a truncated LBO

$$FC_{ij}^{geo} = \sum_{k} \lambda_k \psi_k(i)\psi_k(j), \quad (5)$$

where k, the number of geometric modes used, is now a free parameter, i.e., we allow the use of a truncated (partial) version of $-\Delta$. From this hypothesis, our framework lends itself well to the one proposed by Robinson [7] that relates different representations of connectivity (SC and FC) together through neural field theory (NFT). With FC^{geo}, this framework allows us to reconstruct SC with remarkable precision.

3 Results

A B

Figure 1: A. Violin plots for 100 HCP subjects for max KS, reconstruction accuracy and ranked correlations for degree, betweenness, clustering and node connection distance. B. Visualization of average empirical SC over 100 subjects and average model SC, and scatter plot of node degree for both average network.

4 Conclusions

Our framework captures both the topology and the topography of empirical connectomes and offers a novel approach to generative models of the connectome, and would seem to suggest that structural connectivity is heavily influenced by geometry.

2

Results: The results presented in the figure show the violin plots for 100 HCP subjects for max KS, reconstruction accuracy and ranked correlations for degree, betweenness, clustering and node connection distance. We also show a visualization of average empirical SC over 100 subjects and average model SC, and scatter plot of node degree for both average network.

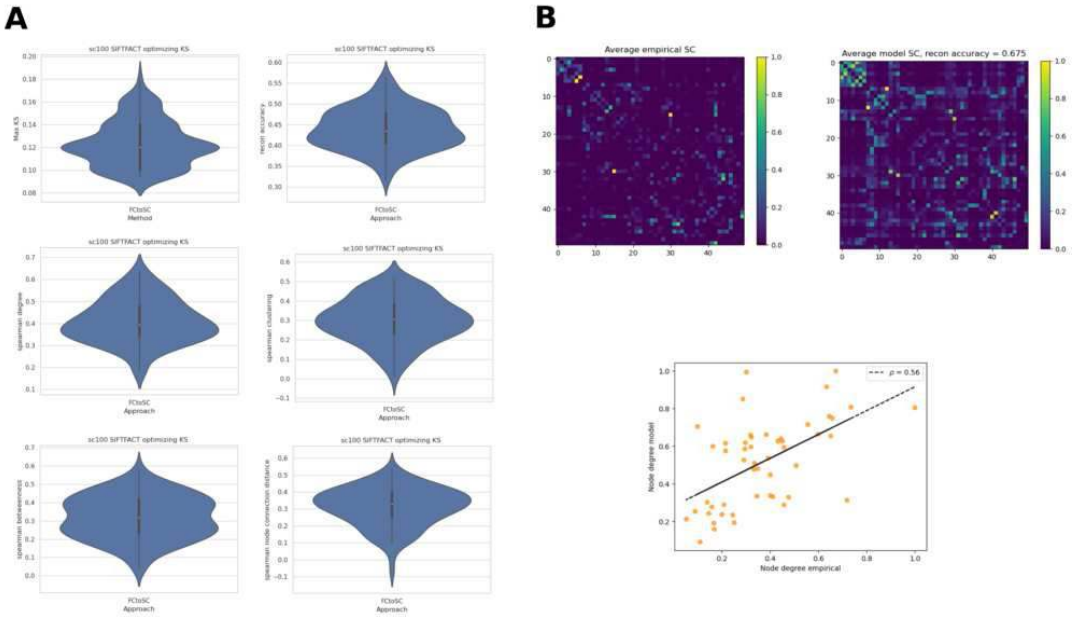

Conclusions: Our framework captures both the topology and the topography of empirical connectomes and offers a novel approach to generative models of the connectome, and would seem to suggest that structural connectivity is heavily influenced by geometry.

References

1. Akarca, D.et al (2021). A generative network model of neurodevelopmental diversity in structural brain organization. Nature communications 12, 1–18
2. Betzel, R. F. et al. (2016) Generative models of the human connectome. NeuroImage 124, 1054–1064.
3. Oldham, S. et al. Modeling spatial, developmental, physiological, and topological constraints on human brain connectivity. (2022) Science Advances 8, eabm6127.
4. Pang, J. C. et al. Geometric constraints on human brain function. Nature, 1–9 (2023).
5. Robinson, P. et al.(2016 Eigenmodes of brain activity: Neural field theory predictions and comparison with experiment. NeuroImage 142, 79–98. issn: 1053-8119
6. Robinson, P. A. (2012) Interrelating anatomical, effective, and functional brain connectivity using propagators and neural field theory. Physical Review E 85, 011912

Poster No 1557

Exploring the Influence of Structural Topology on Brain Dynamic Fluctuations

Dongmyeong Lee[1], Yelim Lee[2], Hae-Jeong Park[1]

[1]Yonsei University College of Medicine, Seoul, Korea, Republic of, [2]Yonsei University College of Medicine, Seoul, Korea, Republic of

Introduction: It is widely recognized that the human brain reveals a myriad of cognitive functions through the segregation and integration of brain areas over time, a phenomenon illuminated by the fluctuations of correlation between these areas (Kucyi 2017). Despite extensive research on the relationship between functional connectivity, derived from average correlations, and underlying structural connectivity (Suárez 2020), there is a significant lack of studies exploring how the characteristics of structural connectivity topology shape the manifestation of fluctuations in brain dynamics. Functional correlations research is predominantly conducted based on data acquired from fMRI. However, data obtained from fMRI primarily represents the average signals of neuronal populations. As a result, there is a limited understanding of how characteristics of network topology at the single-neuronal connectivity influence macroscopic brain dynamics and correlations. In this study, we simulated the neuron signals from various structural networks to investigate the relationship between the characteristics of topology and the fluctuations of brain dynamics. Moreover, by analyzing calcium imaging data from zebrafish and comparing it with computationally simulated brain dynamics at the single-neuron level, we revealed a striking similarity between the computational simulation and the information processing occurring in the real brain.

Methods: The anatomical connections in the brain can exhibit various network topology characteristics, such as small-world or scale-free features (He 2010). In this study, we simulated neuronal dynamics based on various structural connectivity to investigate how the characteristics of topology shape functional networks and influence brain dynamic fluctuations. To efficiently simulate the activity of thousands of neurons, we developed parallel GPU-based code, utilizing the Izhikevich neuron model for large-scale spiking neural network simulations. We used public calcium imaging data (Chen 2018). Zebrafish, known for easy genetic manipulation and real-time tracking of individual neuron activity, offer the advantage of providing activity at the single-neuron level for thousands of neurons.

Results: We created various modules and connected them, each with different topology characteristics, such as a random network, a scale-free network, or a small-world network. We observed how spiking patterns were segregated and integrated under various topologies. To measure segregation, coherence of spikes within each module was measured, while for integration, entropy between modules was measured. The results revealed that in small-world and random networks, coherence within modules was low, and entropy values were not particularly high. However, in the scale-free network, both coherence and entropy values maintained a high level across coupling constants. The results were consistently confirmed through mathematical stability analysis. We showed that functional networks in actual zebrafish data exhibited scale-free network topology characteristics, and brain dynamic fluctuations of zebrafish are highly close to that, which is simulated scale-free network properties. Furthermore, when simulating the brain dynamics based on zebrafish structural connection data with scale-free network properties, it showed the highest similarity between empirical and simulated functional networks.

Conclusions: Conclusively, through this study, we showed that connectivity properties at the individual neuron level, exhibiting scale-free topology characteristics, could lead to high brain dynamic fluctuations, which are related to brain information processing. Additionally, we believe that this research could contribute to the development of new neural chips by presenting a novel topology. This work was supported by the National Research Foundation of Korea(NRF) grant funded by the Korea government(MSIT) (NO. 2023R1A2C200621711)

References

1. Chen, X. (2018). Brain-wide organization of neuronal activity and convergent sensorimotor transformations in larval zebrafish. Neuron, 100(4), 876-890
2. He, B. J. (2010). The temporal structures and functional significance of scale-free brain activity. Neuron, 66(3), 353-369
3. Kucyi, A. (2017). Dynamic brain network correlates of spontaneous fluctuations in attention. Cerebral cortex, 27(3), 1831-1840
4. Suárez, L. E. (2020). Linking structure and function in macroscale brain networks. Trends in cognitive sciences, 24(4), 302-315.

Poster No 1558

Altered neural connectivity of Somatosensory and Motor cortex in patients with Atopic Dermatitis

Da-Eun Yoon[1], Seoyoung Lee[1], Jundong Kim[1], Kyuseok Kim[1], Hi-Joon Park[1], In-Seon Lee[1], Youn Byoung Chae[1]

[1]Kyung Hee University, Seoul, Korea, Republic of

Introduction: As Atopic dermatitis (AD) patients experience chronic itch and pain, it's been hypothesized that their intrinsic brain networks are different from healthy controls (HC). Acupuncture treatment was reported as a safe intervention which can be effective at improving AD. We aimed to explore the alterations of functional connectivity (FC) patterns of resting-state (rs) functional magnetic resonance imaging (fMRI) data and further investigate the effects of acupuncture on clinical and neural changes in patients with AD.

Methods: This study investigates changes in brain function among patients with AD through a combined randomized controlled trial and a cross-sectional component. Healthy subjects were recruited for comparison with patients. AD patients were randomly assigned to either verum acupuncture (VA) (n=28) or sham acupuncture (SA) (n=13) groups. Symptom assessments and neuroimaging scans were conducted at pre-treatment and post-treatment stages. Symptom severity was measured using the SCORAD scale, with responders defined as those showing an improvement of more than 8.7 in SCORAD score. Seed-based functional connectivity was calculated with forty functional regions of interest (ROIs) of the pre-defined regions of the default mode network and somatosensory-motor network. The two-sample t-test was performed to identify the differences in FC between HC and pre-treatment AD patients. Paired t-tests of FC were performed to compare the changes of before and after acupuncture treatment in VA and SA group, and also in responder and non-responder group. Pearson's correlation analyses were performed to examine the correlations between the severity of symptoms and neural indices of pre-treatment AD patients.

Results: Forty HC and forty-one AD patients participated in the study. Among twenty patients who finished the treatment, nine were defined as responders. Major differences in AD patients compared with HC were found in the right somatosensory and motor processing regions. The significant differences were observed in five seeds including right primary motor cortex (M1), primary somatosensory cortex (S1), inferior temporal gyrus (ITG), left S1 and superior parietal area (SPL) (Figure 1). No significant difference was observed in the pre- and post-treatment FC of AD patients in either VA and SA groups at the significance level of $\alpha < 0.05$ (error-corrected). However, decreased connectivity was observed between the seed of right S1 and the regions of bilateral supplementary motor area (SMA), precuneus, middle cingulate cortex (MCC) and right postcentral gyrus at the significance level of $\alpha < 0.08$ (error-corrected) in the responder group only after the treatment (Figure 2A). Correlation analyses revealed a significant positive correlation ($r= 0.65$, $p=0.0068$, Bonferroni-corrected) between the mean FC of the right S1 and the left SMA with the SCORAD score in pre-treatment patients. After the treatment, positive correlation was observed in the changes of FC between the right S1 and left SMA and the changes of SCORAD value in patients ($r=0.41$, $p=0.028$, uncorrected) (Figure 2B). This indicate that the patients with more severe symptom have greater connectivity between the right S1 and left SMA, and this connectivity has decreased as the symptoms have improved.

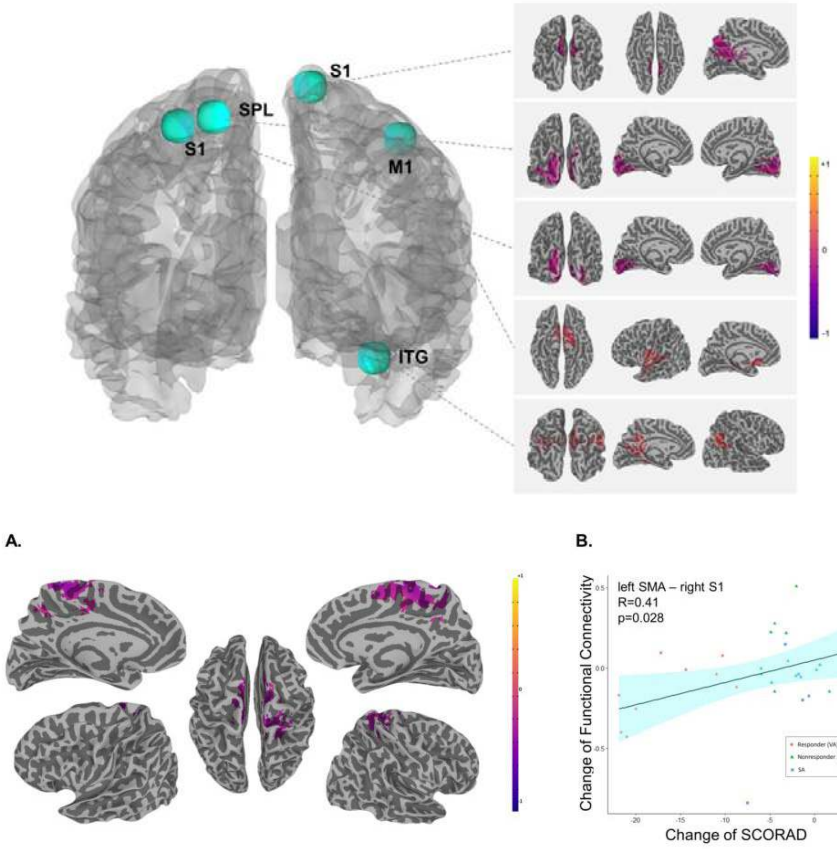

Conclusions: In summary, the study identified significant differences in functional connectivity between AD patients and healthy controls, particularly in somatosensory and motor regions. While there was no significant change in connectivity before and after acupuncture treatment, the responder group exhibited decreased connectivity in S1 seed with lower level of significance. Correlation analyses revealed associations between symptom severity and changes in functional connectivity in AD patients. Our findings underscore altered patterns of functional connectivity and suggest potential clinical significance for somatosensory regions in AD patients.

References

1. Jiao, Ruimin, et al (2020), "The effectiveness and safety of acupuncture for patients with atopic eczema: a systematic review and meta-analysis." Acupuncture in Medicine 38.1 (2020): 3-14.
2. Schram, M. E., et al (2012), "EASI,(objective) SCORAD and POEM for atopic eczema: responsiveness and minimal clinically important difference." Allergy 67.1 (2012): 99-106.
3. Power, Jonathan D., et al (2011), "Functional network organization of the human brain." Neuron 72.4 (2011): 665-678.

Poster No 1559

Clocks or clouds: movie functional connectivity as a combination of intrinsic and evoked components

Ahmad Samara[1], Samuel Nastase[2], Tamara Vanderwal[3]

[1]University of British Columbia, Vancouver, BC, [2]Princeton University, Princeton, NJ, [3]Department of Psychiatry, University of British Columbia, Vancouver, BC

Introduction: Human brain activity is driven in part by external stimuli and in part by intrinsic fluctuations. Can we decompose this activity into the relative contributions of external and internal events[1,2]? In this reductionist view, a timeseries is more like a clock that can be understood by examining its pieces than a cloud that defies a simple additive understanding. The same concept has been applied to FC by viewing its coupling pattern as arising from invariant constraints and dynamic properties encouraged by the task state[3,4]. We have previously hypothesized that movie-watching causes whole-brain shifts in signal-to-noise ratios[5], such that processing rich, dynamic, multimodal stimuli may yield a "brain state" that is more than the sum of its parts (i.e., it is more cloud than clock). Here, we ask if movie-watching FC could be modeled using a combination of resting-state intrinsic FC and stimulus-driven FC (via intersubject FC, or ISFC). We predict that much of the variance in movie FC would not be explained by this model, but that perhaps more primary visual and auditory regions could be captured l with stronger weightings of the ISFC components.

Methods: All data are from the minimally preprocessed 7T release of the Human Connectome Project (n=174, 104 females, mean age 29.4±3.3). Specifically, we used 4 movie-watching and 4 resting-state runs, each around 15 minutes. Subjects were scanned in 4 sessions over 2 days. Vertex timeseries were averaged within Schaefer-1000 atlas[6] parcels for each condition (concatenated) and subject, and a functional connectivity (FC) matrix was computed for each condition and subject as the pair-wise Pearson's correlations of parcel timeseries. ISFC matrices were computed as the Pearson's correlation between the timeseries of one parcel from a given subject n and the timeseries of another parcel averaged across all subjects excluding subject n for all pairs or parcels. Since the resulting matrix is asymmetric, each pair of off-diagonal values was replaced by its average. At each edge, a simple linear model was fitted to predict the edge strength during movie-watching using an intrinsic component (i.e., the rest edge strength) and an evoked component (i.e., the ISFC edge strength) as follows: $Y = \beta0 + \beta1X1 + \beta2X2 + \varepsilon$, where Y is movie edge strength, X1 is rest edge strength, X2 is ISFC edge strength, β0, β1, and β2 are the intercept, X1 weight, and X2 weight, respectively, and ε is a random error term. Additionally, two partial models were fitted at each edge to predict movie edge strength using intrinsic edge strength in partial model 1 or the evoked edge strength in partial model 2.

Results: Linear modeling of movie FC using intrinsic resting state and movie-evoked connectivity values at each edge explained more than 50% of the variance at 26.4% of edges. The amount of R2 across all edges followed the first movie gradient hierarchy[7], with models at edges involving dorsal attention, frontoparietal, and default networks demonstrating the highest amounts of explained variance and sensorimotor network edges demonstrating the lowest. Intrinsic edge strength explained more variance in higher-order association cortex, whereas ISFC explained more variance in visual and auditory regions. The variability (i.e.standard deviation) of movie-FC edge strength itself increased along the cortical hierarchy and was strongly correlated with explained variance across subjects ($r = 0.71$, $p < 0.001$).

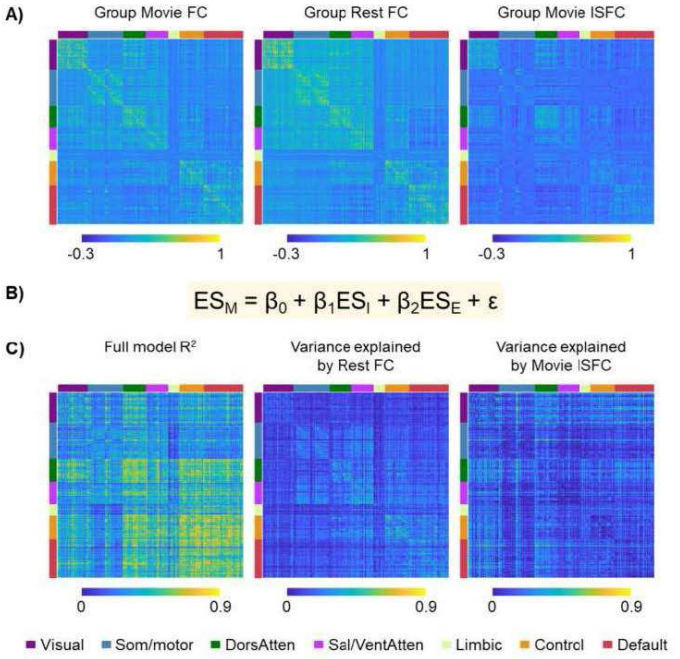

Figure 1. Movie FC as a linear combination of Rest FC and Movie ISFC. (A) Group Movie FC matrix (left) computed from four 15-min concatenated movie-watching fMRI runs, group Rest FC matrix (middle) computed from four 15-min concatenated resting-state fMRI runs, and group Movie ISFC matrix (right) computed from the same concatenated movie-watching runs used to compute movie FC. **(B)** A linear model was fitted at each edge with movie FC edge strength (ES_M) as the output and rest, or intrinsic, edge strength (ES_I) and ISFC, or evoked, edge strength (ES_E) as inputs: $ES_M = \beta_0 + \beta_1 ES_I + \beta_2 ES_E + \varepsilon$. **(C)** The models' variance (adjusted R^2) values are visualized on the left. Two partial models with either ES_I (partial model 1) or ES_E (partial model 2) as the input were also fitted. The proportions of variance explained by Rest FC (middle) and Movie ISFC (right) are computed as the difference in R^2 between the full model and partial model 1 and 2, respectively.

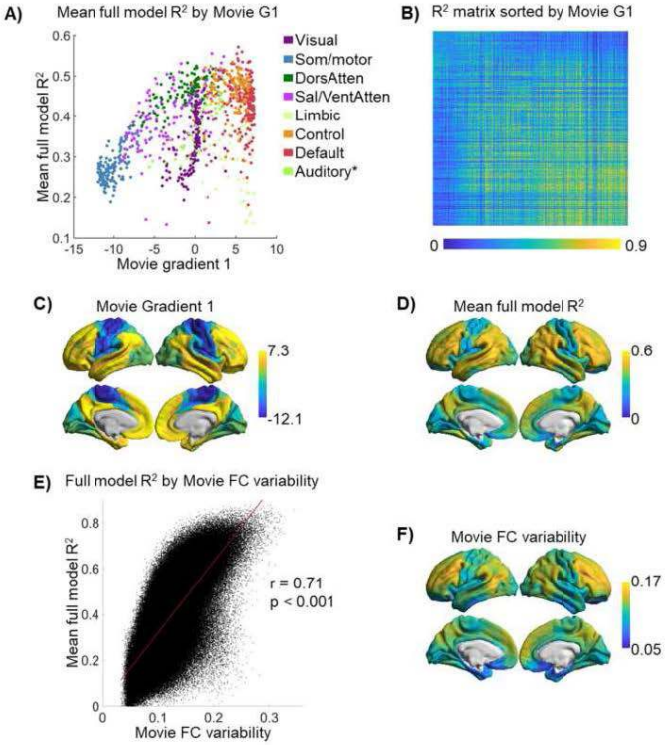

Figure 2. Full model R^2 values vary with movie FC variability and along the functional hierarchy. (A) Scatter plot of movie FC gradient 1 scores and mean R^2 of the full model, with each data point representing a cortical parcel color-coded by its network assignment. **(B)** Full model R^2 matrix reorganized by parcel movie FC gradient 1 score. **(C)** For each parcel, full model R^2 was averaged across all its edges and projected on the cortical surface. **(D)** Movie gradients 1 scores projected on the cortical surface. **(E)** Scatter plot of movie FC variability (computed as the standard deviation of FC across all subjects) and R^2 of the full model, with each data point representing a single edge. Red line represent the best fit line. **(F)** For each parcel, FC variability scores were averaged across all its edges and projected on the cortical surface.

Conclusions: In 1/4 of the edges in the brain, a basic linear model combining rest FC and movie-based ISFC can predict more than half the variance observed in a movie FC matrix. Intersubject variability of movie-FC inherently constrains the variance explained, and both variability of movie-FC and R2 of the model follow hierarchical brain organization during movie-watching. - Ongoing work is testing these findings across time within a movie, and against task-based FC matrices.

References

1. Simony, Erez et al. “Dynamic reconfiguration of the default mode network during narrative comprehension.” Nature communications vol. 7 12141. 18 Jul. 2016, doi:10.1038/ncomms12141
2. Nastase, Samuel A et al. “Measuring shared responses across subjects using intersubject correlation.” Social cognitive and affective neuroscience vol. 14,6 (2019): 667-685. doi:10.1093/scan/nsz037
3. Buckner, Randy L et al. “Opportunities and limitations of intrinsic functional connectivity MRI.” Nature neuroscience vol. 16,7 (2013): 832-7. doi:10.1038/nn.3423
4. Lynch, Lauren K et al. “Task-evoked functional connectivity does not explain functional connectivity differences between rest and task conditions.” Human brain mapping vol. 39,12 (2018): 4939-4948. doi:10.1002/hbm.24335
5. Vanderwal, Tamara et al. “Individual differences in functional connectivity during naturalistic viewing conditions.” NeuroImage vol. 157 (2017): 521-530. doi:10.1016/j.neuroimage.2017.06.027
6. Schaefer, Alexander et al. “Local-Global Parcellation of the Human Cerebral Cortex from Intrinsic Functional Connectivity MRI.” Cerebral cortex (New York, N.Y. : 1991) vol. 28,9 (2018): 3095-3114. doi:10.1093/cercor/bhx179
7. Samara, Ahmad et al. “Cortical gradients during naturalistic processing are hierarchical and modality-specific.” NeuroImage vol. 271 (2023): 120023. doi:10.1016/j.neuroimage.2023.120023

Poster No 1560

How to shape connectivity in task-evoked functional MRI data: An examination

Alice Giubergia[1,2], Sara Mascheretti[3], Valentina Lampis[1], Tommaso Ciceri[1,2], Martina Villa[4], Chiara Andreola[5], Filippo Arrigoni[6], Alessandra Bertoldo[2], Denis Peruzzo[1]

[1]Scientific Institute IRCCS Eugenio Medea, Bosisio Parini (LC), Italy, [2]University of Padova, Padova, Italy, [3]University of Pavia, Pavia, Italy, [4]University of Connecticut, Storrs, CT, [5]Université Paris Cité, Paris, Paris, [6]V. Buzzi Children’s Hospital, Milan, Italy

Introduction: Functional connectomics, which maps functional associations among brain regions, typically relies on resting-state fMRI (Biswal 2010). However, due to practical constraints, many studies lack sufficient resting-state data (Elliott 2019) and resort to inferring a “pseudo-resting” state through task-modulated connectivity (Bhandari 2020). Task connectivity allows for examining broader brain region involvement beyond task activation (Di 2019). This study aims to assess the feasibility of inferring “pseudo-resting” state connectivity from task data and explore its impact on subsequent behavioral trait analysis.

Methods: Seventy-seven subjects (age 9-18 years, M/F: 49/28), 39 Typical Readers – TR and 38 with Developmental Dyslexia – DD) underwent two visual tasks, Sinusoidal Gratings (SG) and Coherent Motion (CM), using fMRI. BOLD time-series were processed with FreeSurfer to obtain task (i.e., without task regression) and “pseudo-resting” (i.e., after task regression) conditions for both tasks across 200 cortical and 18 deep Grey Matter (dGM) regions of interest (ROIs). Various task regression setups were tested varying the number of derivatives in the GLM’s HRF function, and connectomes were derived using ROI-wise Pearson correlation of each subject’s time series, resulting in 218×218 matrices. Spurious connections were addressed through thresholding (He 2010) and multiple task-classification experiments were conducted using different Cross-Validated (CV) machine learning algorithms. Figure 1 reports SG Vs. CM classification metrics. After that, we set the sparsity level (50%) and the derivatives for task regression (d=0), and performed a classification experiment with the aim of investigating the impact of task regression in the characterization of DD and TR. In each fold of each experiment accuracy, AUC score, and the connections selected for the classification were saved to dig in the discriminative process. Connections selected in at least 5 folds out of 6 were identified as discriminative and compared between the 4 SVM experiments (i.e., task SG, task CM, “pseudo-resting” SG and “pseudo-resting” CM). All connections were grouped by the belonging macro-ROIs as defined in the Schaefer atlas to get an overview of the areas devoted to the discrimination of DD and TR.

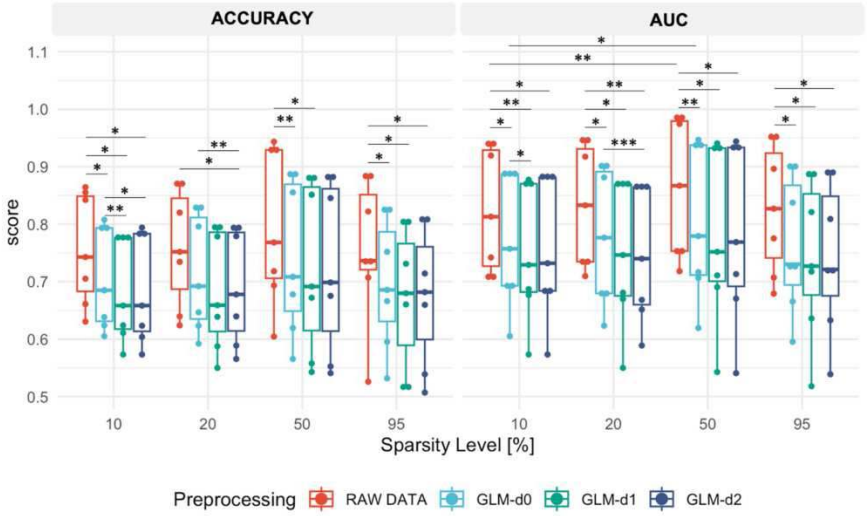

Figure 1. Stimulus inference from connectomes. Task discrimination (SG Vs CM) performances from connectome matrices among the different pre-processing techniques: applying different GLM derivatives (i.e., no derivatives – RAW DATA, 0 derivative – GLM-d0, 1 derivative – GLM-d1, or 2 derivatives – GLM-d2) and levels of graphs' sparsity (i.e., 10%, 20%, 50%, 95%). Levels of significance (Bonferroni corrected): p<0.05 (*), p<0.01 (**), p <0.001 (***).

Results: All task classification experiments provided significant classification performances, with a classification accuracy and AUC larger than 50%. Task regression did remove task-related content from fMRI signals, but the stimulus could still be inferred from derived connectomes irrespective of preprocessing. SVM experiments demonstrated successful classification between Typical Readers (TR) and children with Developmental Dyslexia (DD) in both task and "pseudo-resting" conditions ($p<0.001$). Circular plots of Figure 2 display the preprocessing-modulated connections. No connections were commonly selected between SG and CM tasks, both in task and "pseudo-resting" states (intra-processing and inter-task). However, over 50% of connections were commonly selected when comparing task and "pseudo-resting" conditions for SG and CM (intra-task and inter-processing). Macro-ROI analysis highlighted the involvement of regions known to be associated with DD, while task-related differences aligned with distinct networks elicited by each task.

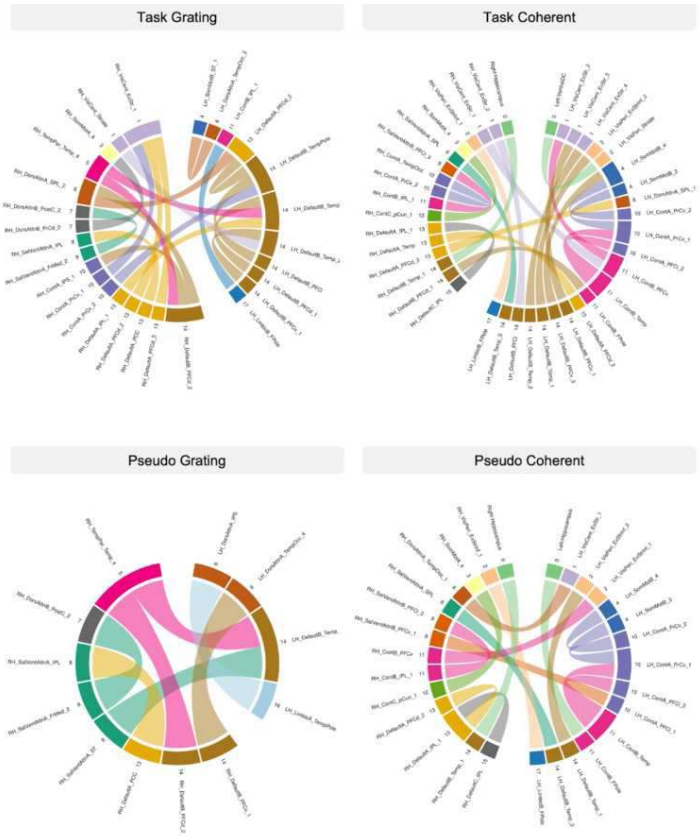

Figure 2. Chord Diagrams of relevant connections in the 4 classification experiments. Each graph portrays the relevant connections selected as features by the classifier in the SVC experiments. Connections were intended as relevant if they were selected by the CV-classfiier at least 80% of the times (i.e., in 5 folds over 6). ROIs were divided between left and right sided and colour-grouped by their belonging macro-ROI. 20 were the connections selected in the "task" SG experiment, 7 in the "pseudo-resting" experiment, 22 in the "task" CM, and 16 in the "pseudo-resting" CM.

Conclusions: Task fMRI data preprocessing was examined to understand the impact of task information on connectomics. Successful discrimination in "pseudo-resting" conditions suggests that connectomes retain task information even after GLM regression. This implies that a task-free "pseudo-resting" state cannot be reliably inferred from task fMRI. Discriminative connections depend on the task type, influencing how classifiers differentiate between groups. Despite task-related differences, signal preprocessing does not significantly affect classification rule inference, indicating similar evaluation of significant features in both tasks.

References

1. Bhandari R. (2020). 'Does higher sampling rate (multiband + SENSE) improve group statistics - An example from social neuroscience block design at 3T', Neuroimage, 213, 116731. https://doi.org/10.1016/j.neuroimage.2020.116731
2. Biswal BB. (2010). 'Toward discovery science of human brain function', Proceedings of the National Academy of Sciences of the United States of America, 107(10), 4734–4739. https://doi.org/10.1073/pnas.0911855107
3. Di X. (2019). 'Toward Task Connectomics: Examining Whole-Brain Task Modulated Connectivity in Different Task Domains', Cerebral Cortex (New York, N.Y. : 1991), 29(4), 1572–1583. https://doi.org/10.1093/cercor/bhy055
4. Elliott ML. (2019). 'General functional connectivity: Shared features of resting-state and task fMRI drive reliable and heritable individual differences in functional brain networks', Neuroimage, 189, 516–532. https://doi.org/10.1016/j.neuroimage.2019.01.068
5. He Y. (2010). 'Graph theoretical modeling of brain connectivity', Current opinion in neurology, 23(4), 341–350. https://doi.org/10.1097/WCO.0b013e32833aa567

Poster No 1561

Modelling subject variability in dynamic functional brain networks using embedding vectors

Rukuang Huang[1], Chetan Gohil[2], Mark Woolrich[3]

[1]OHBA, Department of Psychiatry, University of Oxford, Oxford, Oxfordshire, [2]University of Oxford, Oxford, Oxford, [3]University of Oxford, Oxford, Oxfordshire

Introduction: With recent studies, data driven models like the Hidden Markov Model (HMM, Baker et al., 2014) are getting more attention due to their ability to infer fast temporal dynamics in functional networks in an unsupervised manner. However, these dynamic network models are limited by only giving a group-level description, e.g. of the brain regions and spectral content in each brain network. Whilst it is possible to post-hoc estimate the subject-specific networks, this does not allow the model to discover and benefit from subject-wise structure in the population, e.g. sub-groupings of subjects. We propose an extension to the HMM model that incorporates embedding vectors (c.f. word embedding in Natural Language processing) into the group model. Applying this model to resting-state and task MEG data, we show the learnt embedding vectors capture meaningful sources of variation across a population. This includes sub-groupings related to demographics and systematic differences, such as scanner types or measurement sites.

Methods: We assume that the data is generated by a HMM generative model, but each subject has their own set of state covariances which are generated by our novel subject encoding block. The subject encoding block groups together subjects with similar covariances with a combination of Bayesian hierarchical modelling and embedding vectors. Inference is done with a variant of the EM algorithm. Datasets: We demonstrate the usecases of the proposed model with 3 publicly available MEG datasets, including two resting-state and one visual task dataset. The datasets are preprecessed, source- reconstructed and parcellated to 38 regions with the osl toolbox. The first resting-state dataset (the Cam-CAN dataset, Taylor et al., 2017) contains eyes-closed data of 612 healthy participants. These data were collected using an Elekta scanner. In the visual task MEG dataset ([Wakeman and Henson, 2015]), each of the 19 health participants were scanned 6 times, during which 3 types of visual stimuli were shown to the participants. The data were also collected using an Elekta scanner. The second resting-state dataset (Nottingham) was collected suing a CTF scanner. It contains eyes-closed data of 64 healthy participants, collected at Nottingham University, UK as part of the MEGUK partnership.

Results: In Figure 1, we show results of SE-HMM trained on the visual task data and assign each session an embedding vector. The session-pairwise distances of embedding vectors are plotted in a), which shows a clear block diagonal structure - sessions for a subject are more similar than those for different subjects. Session-pairwise distance of inferred covariances from SE-HMM is compared with dual estimation in b) and c), where we see that SE-HMM infers covariances that form better-separated clusters. In Figure 2, we train SE-HMM on data which combines the Nottingham and Cam-CAN datasets. In a), we see that dataset and age information are encoded in different directions in the embedding space. In b), we again see a block diagonal structure in the pairwise distances of embedding vectors. In c), we show that both SE-HMM and HMM dual estimated covariances form well-defined clusters. But with 3 metrics, we show SE-HMM better separates scanner types in d). SE-HMM can also summarise the differences in state-specific spectral content between scanner types. Shown in e) are the group-level power, FC for each state, as well as the difference in power and PSD between the datasets.

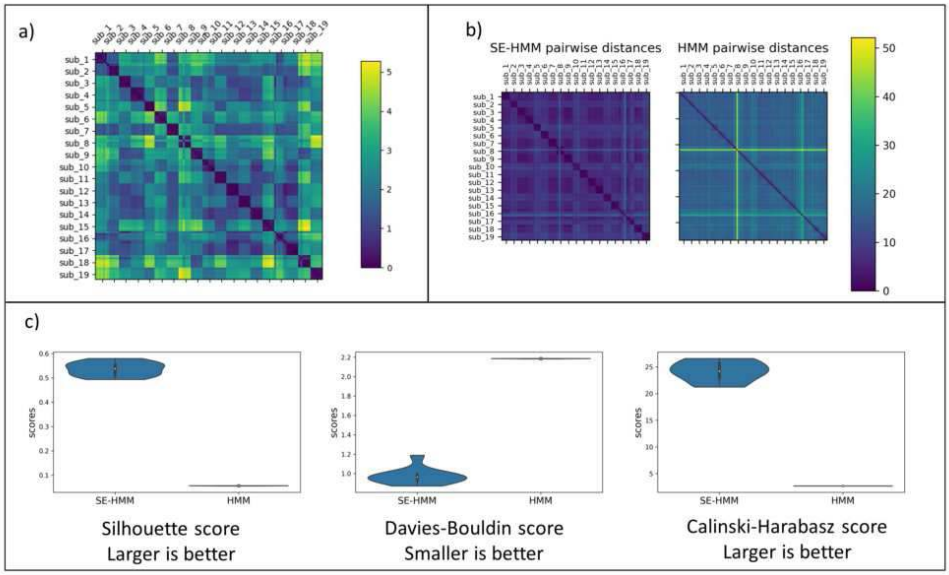

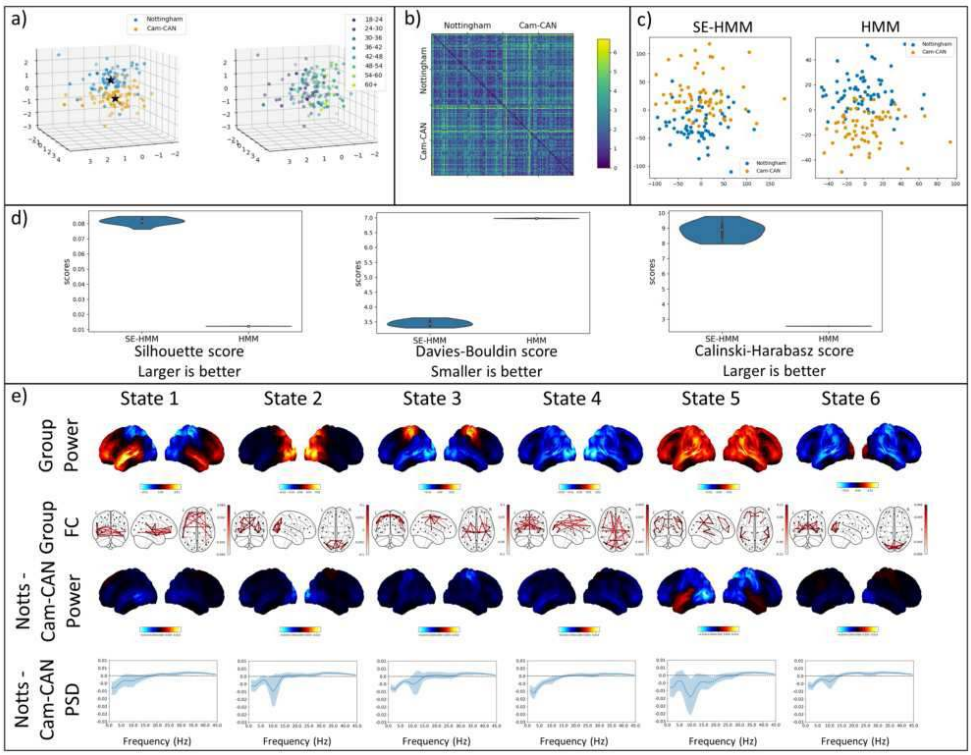

Conclusions: We proposed a novel generative model that explicitly models subject variability in a principled way and provided a way to perform efficient inference. With a Bayesian prior, the model pools information across individuals for how they may deviate from the group average. The additional feature of embedding vectors allows the model to group together similar data and help the interpretation of more details in a population. Source code is available at the osl-dynamics toolbox (Gohil et al., 2023).

References

1. Baker A.P. (2014). Fast transient networks in spontaneous human brain activity. elife, 3:e01867.
2. Wakeman, D. G. (2015). A multi-subject, multi-modal human neuroimaging dataset. Scientific data, 2(1):1–10.
3. Taylor, J. R (2017). The cambridge centre for ageing and neuroscience (cam-can) data repository: Structural and functional mri, meg, and cognitive data from a cross-sectional adult lifespan sample. neuroimage, 144:262–269.
4. Gohil, C. (2023). osl-dynamics: A toolbox for modelling fast dynamic brain activity. bioRxiv, pages 2023–08.

Poster No 1562

Intrinsic dynamic effective connectivity analysis of the resting-state network in COPD

Jinho Bae[1], Kyung-Il Han[2], Tae Hyung Kim[2], Hang Joon Jo[3]

[1]Hanyang Univ., Seoul, Korea, Republic of, [2]College of Medicine, Hanyang, Seoul, Korea, Republic of, [3]Hanyang University, Seoul, AK

Introduction: A common chronic respiratory disease known as chronic obstructive pulmonary disease (COPD) is characterized by persistent respiratory symptoms and irreversible airflow limitation, and cognitive impairment is a frequent and essential comorbidity in COPD patients. Although functional connectivity (FC) can be beneficial for describing abnormal patterns of brain activity, it cannot be used to infer the underlying effective connectivity (EC), which is defined as the directional causal relationships among brain regions. The purpose of this study was to explore the dynamic changes in the intrinsic effective connectivity of the resting-state (RS) network and their relationship with cognitive impairment in COPD patients.

Methods: At the time of the study, 50 COPD patients over the age of 60 without a precise diagnosis of cognitive dysfunction or depression were asked to take part. Healthy controls with no respiratory symptoms who were matched for sex and age with the patients were recruited. Of the 50 COPD patients participating in the study, 38 were chosen as the patient group. Twelve patients who were excluded had severe brain shrinkage or infarction. Thus, this study included 38 patients with COPD and 30 healthy controls. For all subjects, anatomy images were acquired by a T1-weighted MRRAGE pulse sequence. Then, RS fMRI data were acquired with a gradient echo-planar pulse sequence, and they were preprocessed by an automatic pipeline of AFNI (afni_proc.py). Networks of 14 functional regions of interest (ROIs) were used as a mask from the atlas of 90 functional ROIs created by Stanford Greicius Lab. We conducted three types of smoothing processes: (i) without smoothing, (ii) gaussian smoothing, and (iii) smoothing within the ROI mask, and we extracted the mean time series, 95% principal component (PC), and first PC time series for each functional ROI network. Vector auto-regression (VAR) is a multivariate forecasting algorithm that can be used when two or more time series influence each other. We performed VAR (1) modeling, which contained up to one lag of each predicted time series, with 90 observed time series influencing each other as input. Through this model, a coefficient matrix was estimated to determine how the past value of each time series affects the current value of the other time series. To identify the directionality, strength, and lag effect of EC within each group (normal and patient groups), a 1-sample t-test was performed on the coefficient matrix estimated in the VAR (1) model. Through this, it was evaluated whether the relationship between time series within each region was statistically significant. In addition, a 2-sample t-test was performed on the coefficient matrix of each group to evaluate the difference in time series between the normal group and the patient group. Through this, it was evaluated whether there was a statistically significant difference in the dynamic interaction of time series between the two groups. In addition, the correlation between networks with differences between groups, and cognitive assessment was analyzed in COPD patients.

Results: Compared to normal groups, there were significant differences among COPD patients between and within networks (fig. 1). In addition, there was a significant correlation with some essential clinical indicators (FEV1%_ac) in COPD patients. The significance threshold was set at Bonferroni-corrected $p < 0.05$ (fig. 2).

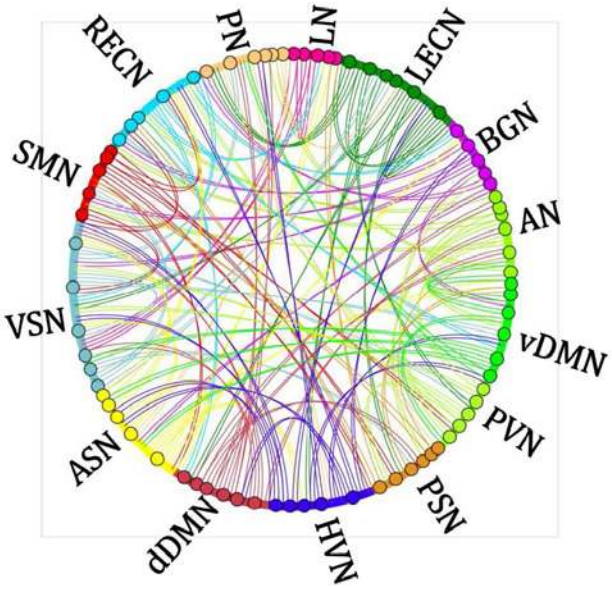

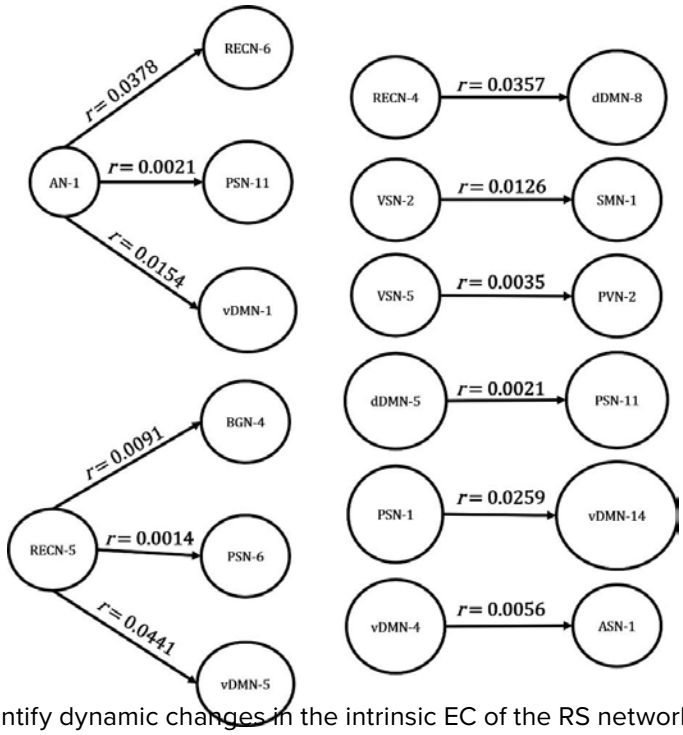

Conclusions: We attempted to identify dynamic changes in the intrinsic EC of the RS network. For this purpose, the VAR model was used, and the analysis was conducted on the premise that, due to the nature of the VAR model, mutual influences must exist between all input time series data. It is necessary to check whether all-time series data affect each other and whether their connectivity is statistically significant. In addition, the normality of the time series data should be verified to have the same number of observations.

References

1. Dana DeMaster. (2022), 'Effective connectivity between resting-state networks in depression', Journal of Affective Disorders, vol.307, pp. 79-86
2. Gang Chen. (2011), 'Vector autoregression, structural equation modeling, and their synthesis in neuroimaging data analysis', Computers in Biology and Medicine, vol. 41, no. 12, pp. 1142-1155

Poster No 1563

Differential impact of sleep deprivation conditions on resting-state effective connectivity

Edoardo Bettazzi[1], Alexander Silchenko[1], David Elmenhorst[2,3], Simon Eickhoff[1,4], Masoud Tahmasian[1,3,4], Felix Hoffstaedter[1,4]

[1]Institute of Neuroscience and Medicine (INM-7), Research Centre Jülich, Jülich, NRW, Germany, [2]Institute of Neuroscience and Medicine (INM-2), Research Centre Jülich, Jülich, NRW, Germany, [3]Department of Nuclear Medicine, University Hospital and Medical Faculty, University of Cologne, Cologne, NRW, Germany, [4]Institute for Systems Neuroscience, Medical Faculty, Heinrich-Heine University Düsseldorf, Düsseldorf, NRW, Germany

Introduction: Sleep loss affects the human brain at multiple levels and leads to various cognitive dysfunctions, including attention lapses, impaired working memory and emotional hyperreactivity. Experimentally induced sleep deprivation (SD) is an interventional approach to investigate how the brain responds to sleep loss. SD affects the functional connectivity of the intrinsic neural networks of the brain, including the Salience Network (SN) and Central Executive Network (CEN). A previous neuroimaging meta-analysis identified reduced activity in the right intraparietal sulcus (rIPS). Thus, we investigated the influences of SD on the effective connectivity (EC) of SN and CEN, each with the rIPS.

Methods: We included resting-state fMRI across three conditions of SD: Stockholm SleepyBrain dataset (N=40, age 20-30 yrs; TR 2.5s, 193 volumes), acute partial SD (3-hours sleep); PETcoffee dataset (N=36, age 22-37 yrs; TR 2.29s, 262 volumes), chronic partial SD (5-hours sleep, 5 nights); Somnosafe dataset (N=35, age 20-39 yrs; TR 2s, 146 volumes), total SD (0-hours sleep). fMRI data was preprocessed using fMRIPrep in the FAIRly big workflow with Datalad, before time-series extraction based on Nilearn (version 0.9.2) and deploying DCM in SPM12 (version 7912) with Matlab, implemented in a custom-built pipeline (Fig.1). AROMA denoised first eigenvariate time series were extracted 12 SN and 13 CEN nodes from the Schaefer100 parcellation and the rIPS region, for SD and normal sleep (NS). The Spectral DCM framework was used to model EC of (1.) the SN with rIPS as well as (2.) the CEN with rIPS. Parametric Empirical Bayes (PEB) was then applied to estimate the effects of SD in contrast to NS. For each SD condition, we quantified EC patterns of each sleep state and their differences, which were filtered for significant state effects, excluding connectivity differences not present in either SD or NS. Resulting state-informed difference matrices were tested for pairwise correlations between the 3 SD conditions, yielding coefficients of <0.1 for all pairs. Finally, for heuristic comparison between SD conditions, two network-level metrics were computed: the absolute sum over connectivity values, to quantify the impact of treatment (i.e. the amount of change in EC); and the sum over connectivity values, to evaluate the network balance after treatment (i.e. overall increase/decrease in EC).

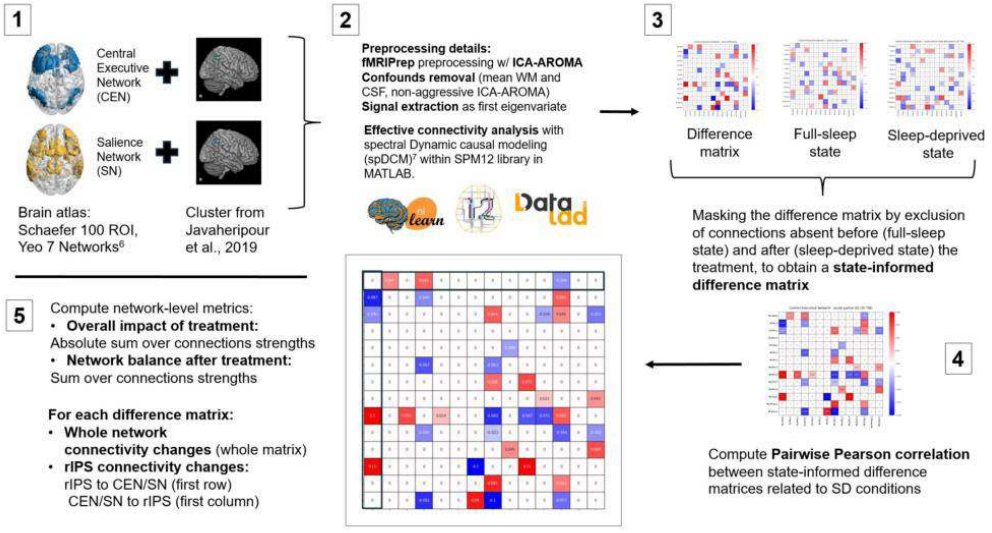

Fig. 1 | Workflow of the methods applied: (1.) Production of custom brain masks for ROI-specific signal extraction; (2.) fMRIPrep preprocessing, removal of confounds and extraction of signals, effective connectivity analysis (spDCM and PEB); (3.) filtering of PEB matrices; (4.) pairwise Pearson correlation; (5.) Network-level metrics.

Results: PEB reveals altered EC patterns in both neural networks after all SD conditions (Fig. 2). Regarding SN, the impact of SD on the network and the resulting balance were the following, acute partial SD: 0.84/+0.23; chronic partial SD: 0.24/+0.09; total SD: 0.89/+0.26. Effects observed in CEN were acute partial SD: 2.52/+0.11; chronic partial SD: 0.91/+0.04; total SD: 1.35/-0.22. The chronic partial SD treatment with 5h of sleep for 5 nights induced the smallest change in connectivity strength for both networks. The most impactful treatment was partial acute SD, with 3 hours of sleep, on the CEN, while the SN was altered generally less and similarly by acute partial and total SD. Finally, in total deprivation, EC of the rIPS to nodes of both

CEN (-0.097) and SN (-0.043) is decreased, while EC toward the rIPS is increased with only 3h of sleep time. Overall, CEN to rIPS connections show the biggest change in EC for acute (0.362), chronic partial (0.155) and total SD (0.093).

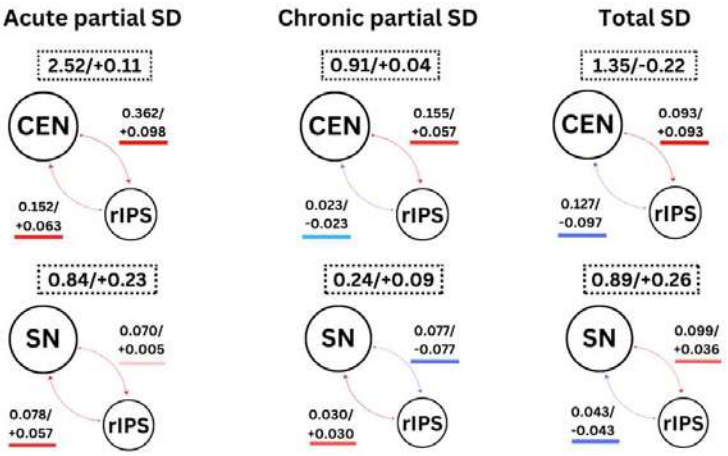

Fig. 2 | Changes in EC of Central Executive (above) and Salience (below) networks with the rIPS. Impact of treatment/network balance for the entire network are reported in dotted boxes. Blue hue: decrease in EC, red hue: increase in EC; arrows: directed connectivity from/to.

Conclusions: SD differentially impacts resting-state networks depending on the amount of sleep, with acute (total and partial) SD showing more impact than chronic partial SD. As expected from previous reports of rIPS hypoactivity, PEB reveals a decreasing influence of rIPS on both networks in total SD. Since the rIPS is regarded as an attentional hub, the observed changes in EC from and to this region could disrupt communication between networks and impair the allocation of attentional resources.

References

1. Balderston N. L. (2017), "Threat of Shock Increases Excitability and Connectivity of the Intraparietal Sulcus", eLife, vol. 6.
2. Chu C. (2023), "Total Sleep Deprivation Increases Brain Age Prediction Reversibly in Multisite Samples of Young Healthy Adults", Journal of Neuroscience, vol. 43.12, pp. 2168–2177.
3. Esteban O. (2019), "fMRIPrep: A Robust Preprocessing Pipeline for Functional MRI", Nature Methods, vol. 16.1, pp. 111–116.
4. Friston K. J. (2016), "Bayesian Model Reduction and Empirical Bayes for Group (DCM) Studies", NeuroImage, vol. 128, pp. 413–431.
5. Javaheripour N. (2019), "Functional Brain Alterations in Acute Sleep Deprivation: An Activation Likelihood Estimation Meta-Analysis", Sleep medicine reviews, vol. 46, pp. 64–73.
6. Krause A. J. (2017), "The Sleep-Deprived Human Brain", Nature Reviews Neuroscience, vol. 18.7, pp. 404–418.
7. Razi A. (2015), "Construct Validation of a DCM for Resting State fMRI", NeuroImage, vol. 106, pp. 1–14.
8. Schaefer A. (2018), "Local-Global Parcellation of the Human Cerebral Cortex from Intrinsic Functional Connectivity MRI", Cerebral Cortex, vol. 28.9, pp. 3095–3114.
9. Wagner, A. S. (2022), "FAIRly big: A framework for computationally reproducible processing of large-scale data", Scientific Data, vol. 9, issue 1.
10. https://gin.g-node.org/Edoardo96/DCM_sleep_project.git

Poster No 1564

Intra- and inter-hemispheric connectivity in lateralized brain areas associated with autism symptoms

Junesung Yoon[1], Hang Joon Jo[2], Taeyeop Lee[1], Yong-Wook Shin[3]

[1]Asan Medical Center, Seoul, Korea, Republic of, [2]Hanyang University, Seoul, AK, [3]Department of Psychiatry, University of Ulsan College of Medicine, Asan Medical Center, Seoul, Korea, Republic of

Introduction: Brain lateralization, the functional specialization of the human brain's two hemispheres, is notably significant in autism spectrum disorder (ASD). Many studies indicate reduced lateralization in ASD, emphasizing its relevance in understanding the disorder[1,2]. This study employed the novel laterality index3 to investigate the relationship between brain lateralization and autism spectrum disorder. This index consists of two components: Segregation and Integration. Segregation measures the tendency for greater within-hemisphere than across-hemisphere communication, and Integration measures a sum of within- and across-hemisphere communication. As the left hemisphere mainly engages in Segregation while the right hemisphere shows Integration[3-5], we hypothesized that intra-hemispheric functional connectivity in the left-lateralized segregation network and the inter-hemispheric functional connectivity in right-lateralized integration network are associated with symptoms of autism spectrum disorder (ASD).

Methods: We used rs-fMRI data from the ABIDE I and II dataset, including 127 ASD and 134 control subjects from NYU Langone Medical Center. After preprocessing with afni_proc.py in AFNI, time-series data at each node was correlated with the activity at every other node within and across hemispheres, averaging these correlations separately per location to quantify intra- and inter-hemispheric cortical interactions. Thus, each node was assigned with two values: left hemispheres with LL (meaning average correlation of the "left" hemisphere seed node with every node in "left" hemisphere as target nodes) and LR, and right hemispheres with RR and RL. Segregation was computed as LL-LR (left) and RR-RL (right), while Integration was calculated as LL+LR (left) and RR+RL (right). To identify networks of interest, paired t-tests were applied separately to the segregation and integration metrics across participants. By clustering brain regions with significantly greater laterality index than their homotopic locations, we identified left-lateralized segregation networks and right-lateralized integration networks (Fig.1). For each ASD subject, we calculated the average LL score to quantify functional intra-hemispheric interaction in the left-lateralized regions. We also calculated the average RL score for the right-lateralized regions to measure inter-hemispheric connections. To examine relationships between patterns of intra- and inter-hemispheric connectivity and autism symptom severity, the Pearson correlation between ADOS scores and these averaged scores was calculated.

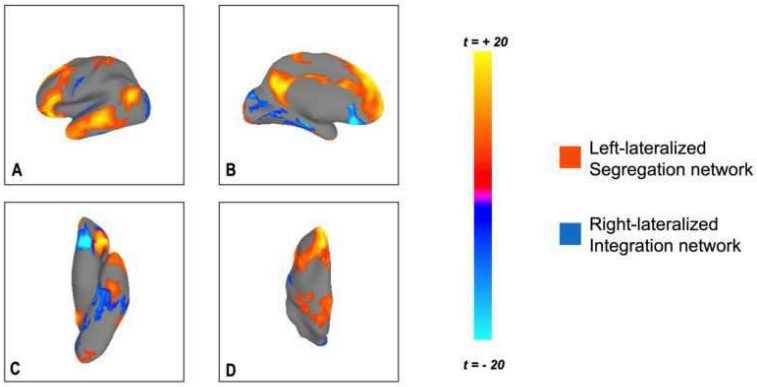

Fig 1. **Networks of interest mapped onto left hemisphere.**
Applying paired t tests to laterality index in every node across participants with P < 0.001, false discovery rate (FDR) to q < 0.01 revealed our networks of interest. Left-lateralized segregation networks are colored as red, and right lateralized integration networks as blue. Left-lateralized networks consist of left inferior frontal gyrus, middle temporal gyrus and posterior cingulate gyrus whose functions are involved in social processing and communication. Right-lateralized network regions include occipital cortex, fusiform gyrus and para-hippocampal gyrus and orbifrontal cortex, which is involved in visuospatial network and sensory integration.

Results: The averaged LL and RL scores in the networks of interest showed a statistically significant correlation with the ADOS scores (Fig. 2). To illustrate, averaged LL score in the left-lateralized regions were found to be negatively correlated with ADOS total score (r=-0.307, P=0.0014), ADOS social interaction score (r=-0.309, P = 0.0012) and ADOS communication score (r=-0.2573, P=0.008), but not with ADOS restricted and repetitive behavior score (r=0.0557, P=0.5723). In addition, averaged RL score in the right-lateralized regions showed negative correlation with ADOS total score (r=-0.3247, P=0.0007), ADOS social interaction score (r=-0.3162, P=0.001) and ADOS communication score (r=-0.2781, P=0.004) but no significant correlation with ADOS restricted and repetitive behavior score (r=0.0332, P=0.7371).

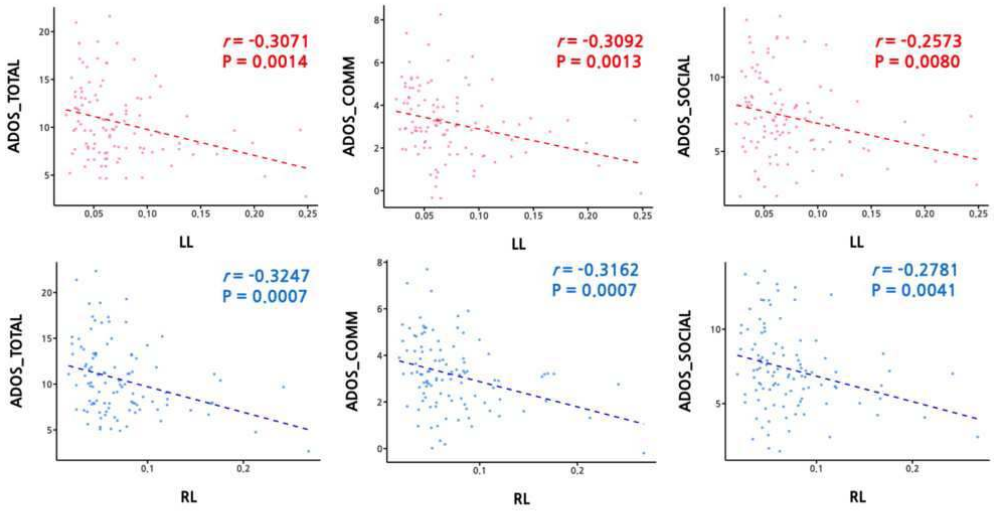

Fig 2. **Correlation between laterality index in our network of interest and ADOS total, communication and social scores.**
Upper row shows the correlation between averaged LL scores from left lateralized network and ADOS scores. Lower row shows the correlation between averaged RL scores from right lateralized network and ADOS scores. Degree of Inter-, Intrahespheric connectivity in left and right lateralized network is correlated with lower ADOS scores. Overlapping dots have been minimally jittered for visualization.

Conclusions: In conclusion, our results suggest that functional intra-hemispheric connectivity in left lateralized brain regions and inter-hemispheric connectivity in right lateralized brain regions are negatively correlated with ADOS total score, social interaction score, and communication score. Our study highlights the complex relationship between functional brain connectivity in lateralized brain areas and ASD symptom severity, particularly how different patterns of left and right hemispheres correlate with ASD symptoms.

References

1. Jouravlev, O. et al. (2020), 'Reduced Language Lateralization in Autism and the Broader Autism Phenotype as Assessed with Robust Individual-Subjects Analyses'. Autism Res, vol.13, pp.17461761
2. Knaus, T. A. et al. (2010), 'Language laterality in autism spectrum disorder and typical controls: A functional, volumetric, and diffusion tensor MRI study', Brain Lang, vol.112, pp. 113120 .
3. Gotts, S. J. et al. (2013), 'Two distinct forms of functional lateralization in the human brain', Proc. Natl. Acad. Sci., vol.110, pp. E3435E3444 .
4. Corbetta, M. & Shulman, G. L. (2011), Spatial Neglect and Attention Networks. Annu. Rev. Neurosci. 34, 569599.
5. Poeppel, D. (2003), 'The analysis of speech in different temporal inte

Poster No 1565

Effect of Multiband Imaging on temporal dynamics of functional connectivity in typical aging

Himanshu Singh[1], S. Senthil Kumaran[1]

[1]*All India Institute of Medical Sciences, New Delhi, India*

Introduction: The analysis of brain function using resting-state functional magnetic resonance imaging (rsfMRI) is associated to underlying synchronization of neuronal activity[1]. Majority of imaging studies incorporate conventional (single band) scan for the resting data[2–4]. Recent advances in parallel imaging using multiband (MB) have shown to improve the Blood oxygenation level dependent (BOLD) sensitivity[5]. Aging is a crucial aspect of lifespan and its effect related to brain function using rsfMRI is a common approach in connectome studies[6,7]. Most of such studies use single band rsfMRI which is limited by the temporal resolution of the MR scanner. Employing multiband method and increasing/optimizing the acquisition time may allow for hemodynamic signal enhancement[5]. The increase in time of acquisition via multi session approach can improve temporal resolution, and have reduced effects of the physiological noise (such as respiratory and cardiac rhythm)[5]. In the current study, we looked at the effect of MB and multisession in understanding how the global hemodynamic signal change with increase in temporal resolution and acquisition time specifically for typical aging population above 60 years.

Methods: Study was conducted on healthy subjects with typical aging (n=12, mean age 75 (range: 63-86) years), after IEC approval, on a 3T MR scanner (Ingenia 3T, M/s Philips). The rs-fMRI was carried out using multiband factor of 4 with repetition time (TR) 1.4s and TE: ms, in two sessions of 300 dynamics each, resulting in a total acquisition time of 14 minutes. Data was preprocessed using a default pipeline and Denoising method using Compcor of conn toolbox[8,9]. Local/global correlation (LCor/GCor), Intrinsic/interhemispheric connectivity (ICC/IHC), Amplitude of Low Frequency Fluctuations (ALFF), fractional Amplitude of Low Frequency Fluctuations (f/ALFF) and ROI functional connectivity were computed to estimate changes. Group level covariates (with first session considered as "short" and two sessions concatenated considered as "long") were the input for statistical inference through General Linear Model. All computed analysis were tested for significance with a cluster threshold of p FDR corrected <0.05.

Results: The ROI and IHC connectivity across the two conditions remained the same, with no significant difference in the connectivity matrices between the two. Inferior/Superior temporal gyrus (r) and Superior frontal gyrus (l) revealed a significant difference in short session when compared to long acquisitions in ALFF. Cerebellar signal change was also observed in short condition when compared to long, with precuneus having significant f/ALFF signal for long condition (Figure 1). Global correlation change (Figure 2) was observed in frontal pole right and local correlation change were observed in inferior temporal gyrus, posterior (r). Intrinsic connectivity (Figure 2) for long temporal condition exhibited signal in postcentral/supramarginal Gyrus's (r).

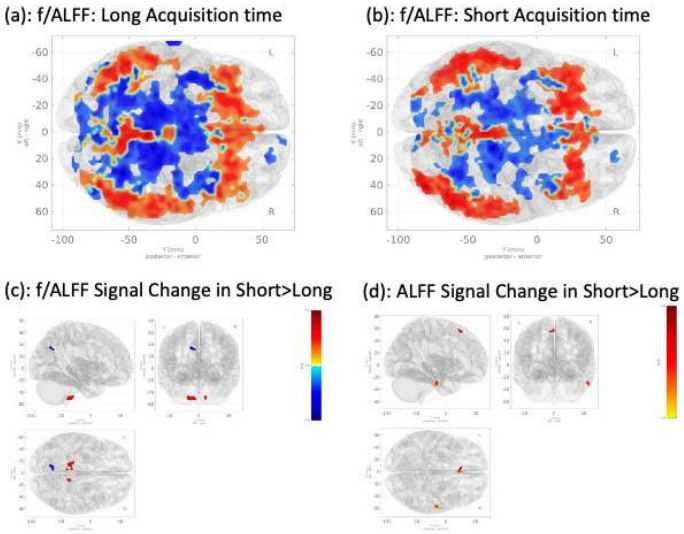

Figure 1: ALFF and f/ALFF percentage signal change in rs-fMRI through acquisition time window short and long condition.

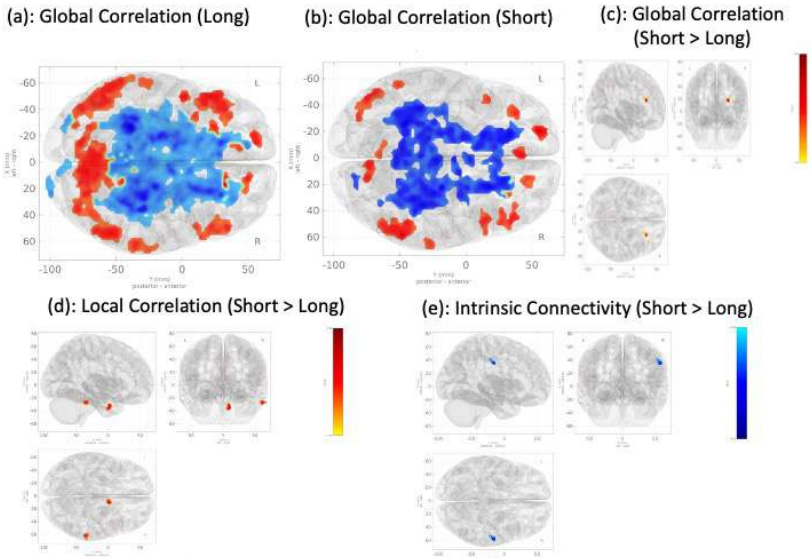

Figure 2: Global/Local Correlation and intrinsic connectivity change in rs-fMRI through acquisition time window short and long condition.

Conclusions: The multiband acquisition exhibited an improvement in sensitivity across in intrinsic connectivity in typical agers. The local coherence and voxel level interaction revealed f/ALFF signal enhancement associated with longitudinal acquisition. Aging is generally associated to the decline in executive function[2,6]. However, current result shows an improvement in the temporal hemodynamics in frontal pole and supramarginal gyrus activity on rs-fMRI. More studies employing the multiband reference and acquisition time frame need to be carried out to develop well informed cognitive connectome model for aging.

References

1. Kajimura, S., et al. (2023), Frequency-specific brain network architecture in resting-state fMRI. Sci Rep 13, 2964.
2. Baeuchl, C. et al. (2023), Dopamine differentially modulates medial temporal lobe activity and behavior during spatial navigation in young and older adults. Neuroimage 273, 120099 .
3. Courtney, S. M. & Hinault, T. (2021), When the time is right: Temporal dynamics of brain activity in healthy aging and dementia. Progress in Neurobiology vol. 203, 102076.
4. Li, A. W. Y. & King, J. (2019), Spatial memory and navigation in ageing: A systematic review of MRI and fMRI studies in healthy participants. Neuroscience and Biobehavioral Reviews 103, 33-49..
5. Risk, B. B. et al. (2021), Which multiband factor should you choose for your resting-state fMRI study? Neuroimage 234, 117965.
6. Dennis, E. L. & Thompson, P. M. (2014), Functional brain connectivity using fMRI in aging and Alzheimer's disease. Neuropsychology Review 24, 49-62..
7. Ren, P. et al. (2023), Enhanced putamen functional connectivity underlies altered risky decision-making in age-related cognitive decline. Sci Rep 13, 6619.
8. Behzadi, Y.et al. (2007), A component based noise correction method (CompCor) for BOLD and perfusion based fMRI. Neuroimage 37, 90-101.
9. Nieto-Castanon, A. (2020), Handbook of functional connectivity Magnetic Resonance Imaging methods in CONN.

Poster No 1566

Reveal Global Interconnected Functional Tree in the Human Brain

Wei Zhang[1], Yu Bao[2]

[1]Augusta University, Augusta, GA, [2]James Madison University, Harrisonburg, VA

Introduction: Functional connectivity networks (FCNs) portray variance in deoxyhemoglobin concentration consequent to spontaneous or task-evoked modulation of neural metabolism in Blood Oxygen Level Dependent (BOLD) functional Magnetic Resonance Imaging (fMRI)[1,2]. Since deoxyhemoglobin concentration changes in normal and abnormal brain regions are distinctive, FCNs have been increasingly noticeable to be conducted as a clinically actionable biomarker in order to benefit neurological disorders diagnostics[3-5]. Notably, a single or individual FCN might be more dynamic than structural biomarkers and perhaps unreliable which impairs its application to neurological disease diagnostics. But the unique advantage of FCNs is to reflect the earliest functional variation through various functional regions in the brain before significant irreversible structural impairments happen[6]. In the foreseeable future, a concrete biomarker built on FCNs for early and reliable diagnostics of neurological and psychiatric diseases is desirable. Recent works suggested that understanding the communication of FCNs in nervous systems is a crucial goal in neuroscience and communication of multiple FCNs could be reliable[7]. Thus, we plan to propose a global interconnected functional tree (GIFT) in the normal human brains to represent the functional hierarchy and interconnections across all involved FCNs, which integrates functional interconnection and hierarchy across FCNs.

Methods: We propose an innovative deep learning framework named Deep Matrix Approximate Nonlinear Decomposition (DEMAND) to discover reproducible GIFT at the individual level. The following Figure 2 describes a computational framework of DEMAND and Deep Independent Component Analysis (DICA)[8] for validation since ICA is one of the most computational approaches to identify FCNs[8]. In general, the fundamental framework of DEMAND to identify FCNs is to decompose input fMRI signal as a product of time series and canonical or meta-FCNs and plus sub-FCNs. Canonical and meta-FCNs are usually revealed at shallow and deeper layers, as shown in Figure 1 (c2) and (e2), respectively. In addition, since sub-FCNs are usually weak/minor patterns, we treat sub-FCNs as background patterns in Figure 1 (e2). Moreover, to identify hierarchical FCNs, we employ identified FCNs at the previous layer as input to continuously reveal high-level FCNs, such as the decomposition of all identified FCNs at previous layer to the product of time series and FCNs adding sub-FCNs, which is homologous to other layer-stack computational frameworks, shown in Figure 1 (h1).

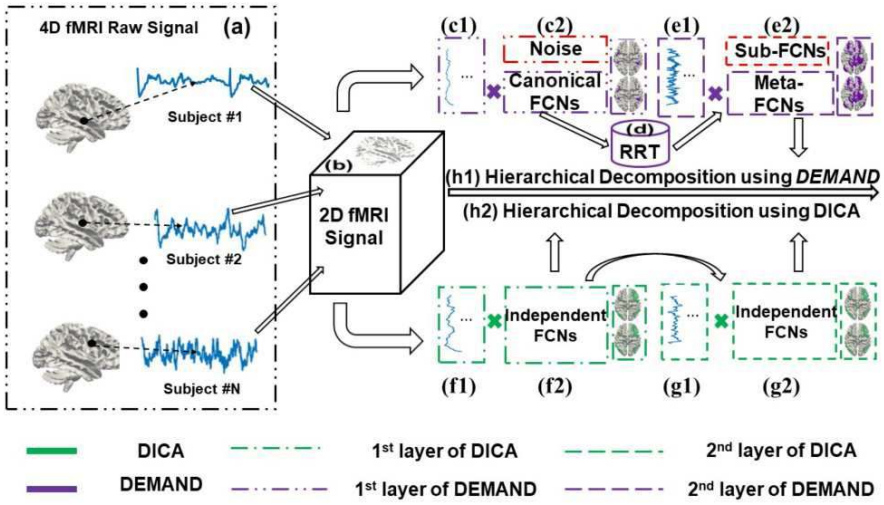

Results: We validate the proposed DEMAND via employing publicly released Multiband Multi-echo (MBME) fMRI data[9], including test and retest fMRI scans from 70 augmented subjects. In general, a large identifiability indicates that the difference between test and retest is not significant[10]. Therefore, we present the quantitative results to validate the proposed DEMAND with DICA. Considering identified canonical FCNs, the identifiability of DEMAND ranges from 0.40-0.50. On the contrary, identifiability of canonical FCNs extracted via DICA is lower than 0.38. Meanwhile, the identifiability of meta-FCNs derived via DEMAND is between 0.60-0.70, demonstrating a considerable reproducibility on augmented 70 subjects[9]. The identifiability of meta-FCNs identified via DICA is between 0.35-0.56. The identifiability of sub-FCNs revealed via DEMAND varies from 0.28-0.35 which is relatively small compared to canonical and meta-FCNs. Unfortunately, DICA cannot identify consistent sub-FCNs based on 70 subjects. In Fig. 2, we present a group-wise GIFT on 70 subjects identified via DEMAND.

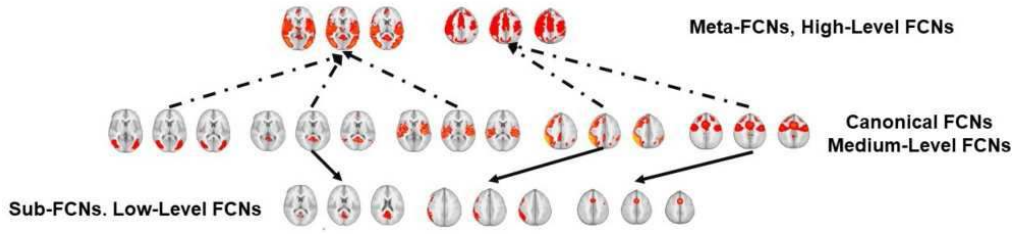

Conclusions: In a word, the superiority of GIFT is to deliver a global connection abstracted as a graph and more reliable architecture to benefit further understanding of brain functional connectivity and early diagnostics of neurological disorders.

References

1. Van Den Heuvel, M. P., & Pol, H. E. H. (2010). Exploring the brain network: a review on resting-state fMRI functional connectivity. European neuropsychopharmacology, 20(8), 519-534.
2. Peng, L., Luo, Z., Zeng, L. L., Hou, C., Shen, H., Zhou, Z., & Hu, D. (2023). Parcellating the human brain using resting-state dynamic functional connectivity. Cerebral Cortex, 33(7), 3575-3590.
3. Fiorenzato, E., Strafella, A. P., Kim, J., Schifano, R., Weis, L., Antonini, A., & Biundo, R. (2019). Dynamic functional connectivity changes associated with dementia in Parkinson's disease. Brain, 142(9), 2860-2872.
4. Franzmeier, N., Rubinski, A., Neitzel, J., Kim, Y., Damm, A., Na, D. L., ... & Alzheimer's Disease Neuroimaging Initiative. (2019). Functional connectivity associated with tau levels in ageing, Alzheimer's, and small vessel disease. Brain, 142(4), 1093-1107.
5. Wingrove, J., Makaronidis, J., Prados, F., Kanber, B., Yiannakas, M. C., Magee, C., ... & Batterham, R. L. (2023). Aberrant olfactory network functional connectivity in people with olfactory dysfunction following COVID-19 infection: an exploratory, observational study. EClinicalMedicine, 58.
6. Zamani Esfahlani, F., Jo, Y., Faskowitz, J., Byrge, L., Kennedy, D. P., Sporns, O., & Betzel, R. F. (2020). High-amplitude cofluctuations in cortical activity drive functional connectivity. Proceedings of the National Academy of Sciences, 117(45), 28393-28401
7. Daws, R. E., Timmermann, C., Giribaldi, B., Sexton, J. D., Wall, M. B., Erritzoe, D., ... & Carhart-Harris, R. (2022). Increased global integration in the brain after psilocybin therapy for depression. Nature Medicine, 28(4), 844-851.
8. Wylie, K. P., Kronberg, E., Legget, K. T., Sutton, B., & Tregellas, J. R. (2021). Stable Meta-Networks, Noise, and Artifacts in the Human Connectome: Low-to High-Dimensional Independent Components Analysis as a Hierarchy of Intrinsic Connectivity Networks. Frontiers in Neuroscience, 15.
9. https://openneuro.org/datasets/ds000216/versions/00001.
10. Finn ES, Shen X, Scheinost D, Rosenberg MD, Huang J, Chun MM, Papademetris X, Constable RT. Functional connectome fingerprinting: identifying individuals using patterns of brain connectivity. Nat Neurosci. 2015 Nov;18(11):1664-71.

Poster No 1567

Feeling drowsy? Brain structure-function coupling dynamics track alertness during resting-state

Maria Giulia Preti[1], Dimitri Van De Ville[2]

[1]EPFL / UNIGE, Geneva, Switzerland, [2]École Polytechnique Fédérale de Lausanne, Lausanne, Switzerland

Introduction: Resting-state functional magnetic resonance imaging (fMRI) is a well-established methodology to probe brain organization. However, previous evidence showed that different levels of drowsiness, or even sleep, might occur especially in later phases of the resting-state session (i.e., after 8-10 minutes)[1]. While it has been shown that such variations of conscious state are reflected by changes of specific functional network activity[2], it remains an open question whether and how the coupling between brain activity with the underlying structure is affected. By leveraging graph signal processing (GSP), we previously introduced a quantitative method to measure structure-function coupling through the structural decoupling index (SDI), whose temporal fluctuations have not yet been fully investigated. Here, we introduce a new time-resolved measure of SDI, and investigate its changes across the first and second half of the acquisition.

Methods: The 100 unrelated healthy participants from the Human Connectome Project (HCP) were considered[3]. Diffusion weighted images as well as two sets of fMRI datasets were considered during resting-state and motor task, with test and retest sessions. Conventional preprocessing pipelines[4] were adopted to obtain regional fMRI timecourses and structural connectomes, using a parcellation with 379 brain regions (360 from Glasser parcellation[5] and 19 subcortical[3]). The GSP pipeline outlined in[4] was used to filter individual fMRI signals into a liberal and a structurally aligned portion. A new metric of temporally resolved SDI was calculated as the instantaneous difference dt in amplitude between the structurally liberal and aligned portion. K-means clustering (k=[5,..,15] were tested, k=5 retained) was then applied to the patterns of dynamic SDI, temporally demeaned. For each subject, the percentage of occurrence of each cluster during the first and second half of the acquisition was computed and compared with a paired two-sample t-test. The intraclass correlation coefficient (ICC) was used to measure the reliability of cluster occurrences across test-retest sessions.

Results: Fig. 1 shows the obtained cluster centroids Ck, ordered by their occurrence percentages along the resting-state acquisition. Given the temporal demeaning operation performed on dt before clustering, these can be interpreted as brain patterns of change in structure-function decoupling with respect to the average pattern (across time). A significant difference between occurrences in the first and second half of the session was found for all the clusters (paired t-tests corr. for multiple comparisons, pcorr < 0.5). We found that a pattern of decoupling (globally in C1 and for somatomotor/visual networks in C4) is most characteristic for the first part, while a significant trend towards increased coupling both globally (C2), and in sensory networks (C3, and C5) occurs in the second half (Fig. 2). This finding indicates higher decoupling for higher level of alertness, presumable at the beginning of the session, versus increased coupling for higher drowsiness. The same coupled networks, in fact, were found in previous work to emerge in resting-state later stages of the acquisition, more prone to falling asleep[1]. The results appear reliable across test-retest sessions (ICC> 0.8 for C1, C2 and C5, C> 0.6 for C3 and C4). As further support of this interpretation, the same analysis didn't lead to any significant differences when applied to motor task session, which are reasonably less subject to changes in alertness by the participants.

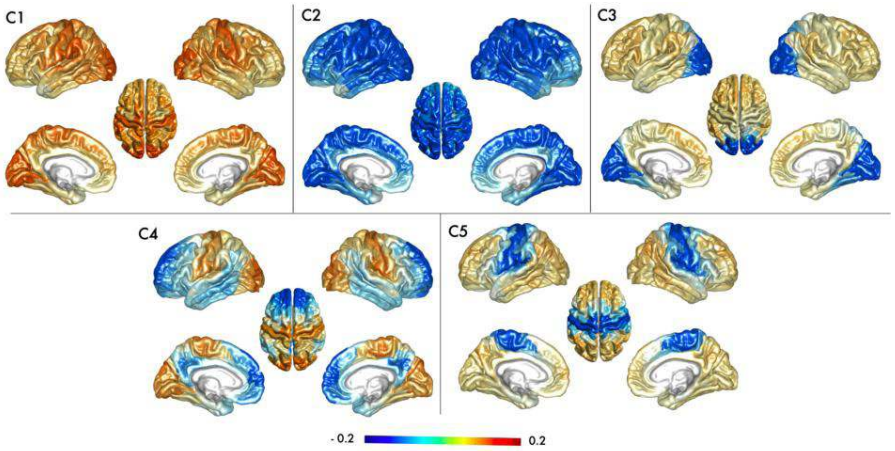

Fig. 1 - Brain patterns representing the five cluster centroids C1-C5, ordered by decreasing temporal occurrence percentages.

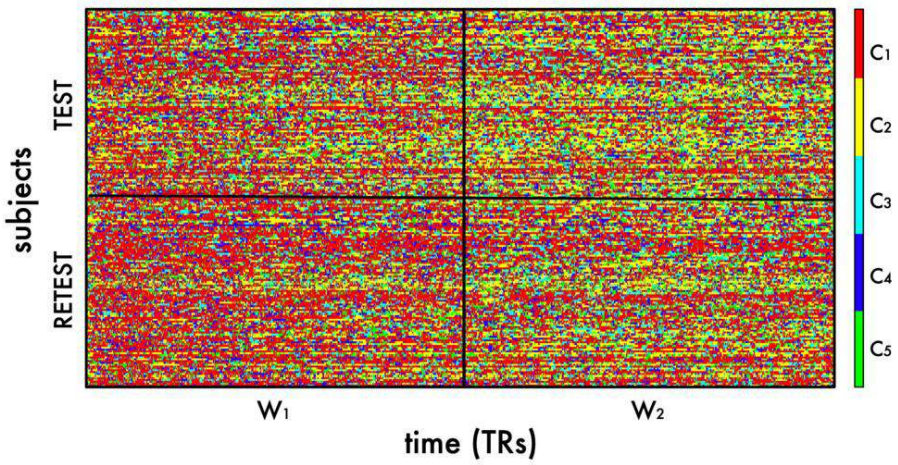

Fig. 2 - Temporal occurrences of the five recurrent brain patterns C_1-C_5 along the resting-state session. Each session (one row) lasts a total of 1200 time points, split into the two temporal windows W_1 and W_2 of 600 time points each (the split is indicated by the black vertical line). The whole sample constitutes of 100 subjects repeating the session twice. Test-retest sessions are separated by the black horizontal line.

Conclusions: We showed for the first time that structure-function coupling can track changes during resting-state, opening the avenue to characterizing different states of consciousness through the structure-function coupling dynamic. Additional analyses on datasets annotated for drowsiness level and/or sleep stages will be conducted to further confirm the association between coupling/decoupling and drowsiness/alertness.

References

1. Enzo Tagliazucchi and Helmut Laufs (2014), "Decoding Wakefulness Levels from Typical fMRI Resting-State Data Reveals Reliable Drifts between Wakefulness and Sleep," Neuron, vol. 82, no. 3, pp. 695–708.
2. Eva M.M. Strijbis, Yannick S.S. Timar, Deborah N. Schoonhoven, Ilse M. Nauta, Shanna D. Kulik, Lodewijk R.J. de Ruiter, Menno M. Schoonheim, Arjan Hillebrand, and Cornelis J. Stam (2022), "State Changes Durlng Resting-State (Magneto)encephalographic Studies: The Effect of Drowsiness on Spectral, Connectivity, and Network Analyses," Frontiers in Neuroscience, vol. 16, no. June

3. Matthew F. Glasser, Stamatios N. Sotiropoulos, J. AnThony Wilson, Timothy S. Coalson, Bruce Fischl, Jesper L. Andersson, Junqian Xu, Saad Jbabdi, Matthew Webster, Jonathan R. Polimeni, David C. Van Essen, and Mark Jenkinson (2013), "The minimal preprocessing pipelines for the Human Connectome Project," NeuroImage, vol. 80, pp. 105–124, oct.
4. Maria Giulia Preti and Dimitri Van De Ville (2019), "Decoupling of brain function from structure reveals regional behavioral specialization in humans," Nature Communications, vol. 10, no. 1, pp. 4747, dec
5. Matthew F. Glasser, Timothy S. Coalson, Emma C. Robinson, Carl D. Hacker, John Harwell, Essa Yacoub, Kamil Ugurbil, Jesper Andersson, Christian F. Beckmann, Mark Jenkinson, Stephen M. Smith, and David C. Van Essen (2016), "A multi-modal parcellation of human cerebral cortex," Nature, vol. 536, no. 7615, pp. 171–178

Poster No 1568

Functional brain modularity as a metric of cognitive function in neuroPASC

David O'Connor[1], Shams Rashid[1], Jacqueline Becker[1], Sera Saju[1], Claudia Kirsch[1], Yael Jacob[1], Laurel Morris[1], Alan Seifert[1], Priti Balchandani[1]

[1]Icahn School of Medicine at Mount Sinai, New York, NY

Introduction: Post-acute sequelae of COVID-19 (PASC) refers to a group of persistent symptoms occurring after acute SARS-CoV-2 infection (Proal & VanElzakker, 2021). Neurological manifestations of PASC include cerebrovascular, neurodegenerative, and mental health symptoms, as well as impaired cognitive function (Douaud et al., 2022). The potential burden of neuroPASC on the health system is significant. Our understanding of how COVID-19 infections lead to neuroPASC, and subsequent symptoms is poor. In this study we attempt to characterize the post-acute effects of COVID-19 on neural networks and cognitive function. A well validated functional MRI (fMRI) marker of cognitive function is the modularity of functional connectivity matrices. We sought to investigate the relationship between functional brain modularity and cognitive functioning in a long covid cohort.

Methods: 7T MR imaging of the brain was performed in 49 subjects (35 neuroPASC [24F, 11M], 14 controls [7F, 7M]). Multi echo resting state fMRI (rs-fMRI) and anatomical MP2RAGE were collected. Cognitive measures assessed all domains . MR data were preprocessed using multi-echo independent component analysis (MEICA) implemented in AFNI (Kundu et al., 2013). Functional connectivity matrices were generated using the Desiken-Killiany atlas (Desikan et al., 2006). Graph theory metrics including community membership and modularity were generated from the FC matrices using the Brain Connectivity Toolbox (Rubinov & Sporns, 2010). These metrics were then related to the cognitive functioning scores using linear regression, correcting for age and sex. Following this analysis, cooccurrence of brain regions in communities across subjects was generated for each subgroup.

Results: Functional brain modularity was marginally higher in controls vs neuroPASC (median 0.34 vs 0.33, Mann Whitney U = 227, p = 0.65). Semantic fluency (Mean Z = -0.21 vs -0.55) and number span backwards (Mean Z = 0.34 vs 0.3) were also marginally higher in controls. Despite the non-significant relative differences, modularity exhibited a significant association with semantic fluency (ß = 2.7, 95% CI [0.3, 5.1], p = 0.03) and working memory (ß = 2.96, 95% CI [0.04, 5.88], p = 0.047), which attenuated with correction for age and sex (Semantic fluency: ß = 2.24, 95% CI [-0.28, 4.77], p = 0.08, working memory: ß = 2.71, 95% CI [-0.28, 5.71], p = 0.075), as shown in Figure 1. Other cognitive domains including memory, attention, executive functioning, and processing speed were non-significant. A within subgroup analysis of community membership of brain regions revealed the most common divergences between neuroPASC and health controls. Figure 2 shows the regions which differentially associated more often (>35% of the time) in neuroPASC (red), and in healthy controls (blue). The regions which differentially associated most often (>40% of the time) in healthy controls were the left thalamus and right putamen, right thalamus and left putamen, and the left inferior temporal cortex and right inferior temporal cortex. In neuroPASC the regions which associated more often were the left caudal middle frontal area and left inferior temporal area, the left medial temporal orbitofrontal cortex, and left pars triangularis, and the left frontal pole and left pars triangularis.

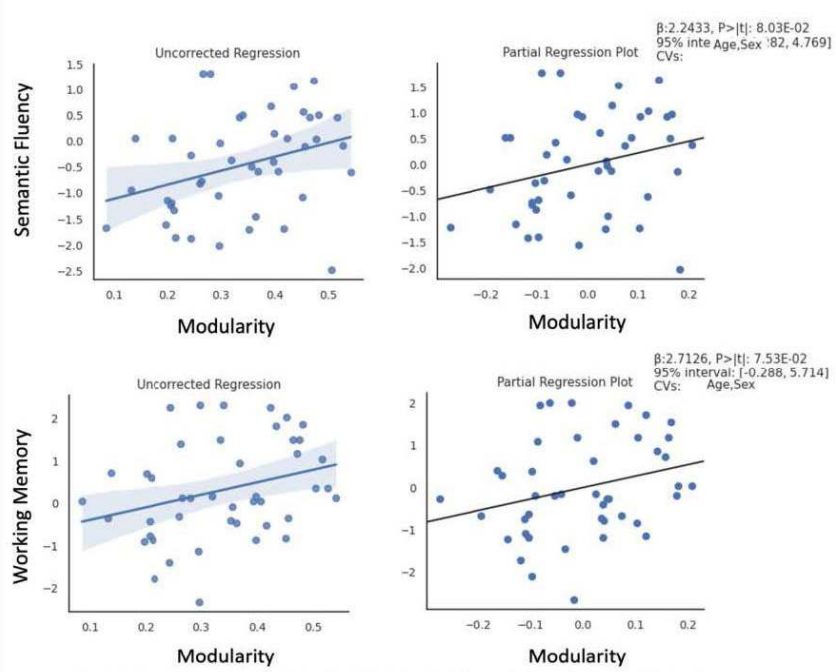

Figure 1: Association between functional brain modularity and semantic fluency (top) and working memory (bottom). Left column is uncorrected association, right column is corrected for age and sex.

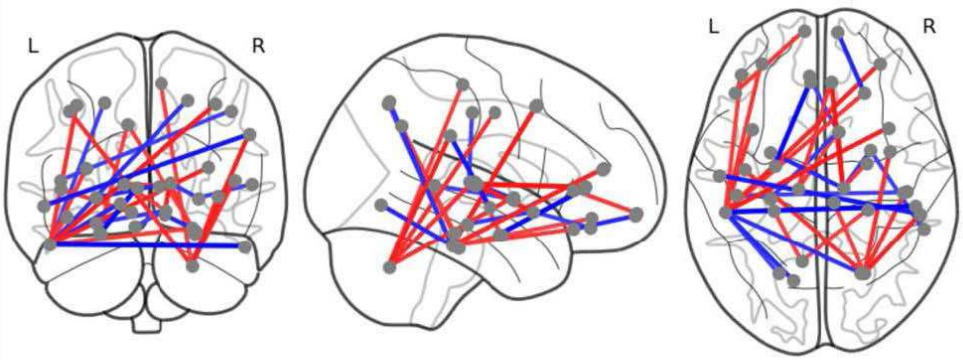

Figure 2: Functional connections which are more likely to be in the same community (more connected) for those with neuroPASC (Red), and those which are more likely to be in the same community in the control group (blue).

Conclusions: Our results suggest that while there were non-significant differences in functional brain modularity and cognitive measures in our cohort, perhaps due to sample size, an association was exhibited between modularity and each of semantic fluency and working memory. These results suggest that functional brain modularity may be sensitive to cognitive function and could help shed light on the brain regions whose function are most impacted in neuroPASC.

References

1. Desikan, R. S., Ségonne, F., Fischl, B., Quinn, B. T., Dickerson, B. C., Blacker, D., Buckner, R. L., Dale, A. M., Maguire, R. P., Hyman, B. T., Albert, M. S., & Killiany, R. J. (2006). An automated labeling system for subdividing the human cerebral cortex on MRI scans into gyral based regions of interest. NeuroImage, 31(3), 968–980. https://doi.org/10.1016/j.neuroimage.2006.01.021
2. Douaud, G., Lee, S., Alfaro-Almagro, F., Arthofer, C., Wang, C., McCarthy, P., Lange, F., Andersson, J. L. R., Griffanti, L., Duff, E., Jbabdi, S., Taschler, B., Keating, P., Winkler, A. M., Collins, R., Matthews, P. M., Allen, N., Miller, K. L., Nichols, T. E., & Smith, S. M. (2022). SARS-CoV-2 is associated with changes in brain structure in UK Biobank. Nature, 604(7907), Article 7907. https://doi.org/10.1038/s41586-022-04569-5
3. Kundu, P., Brenowitz, N. D., Voon, V., Worbe, Y., Vértes, P. E., Inati, S. J., Saad, Z. S., Bandettini, P. A., & Bullmore, E. T. (2013). Integrated strategy for improving functional connectivity mapping using multiecho fMRI. Proceedings of the National Academy of Sciences of the United States of America, 110(40), 16187–16192. https://doi.org/10.1073/pnas.1301725110
4. Proal, A. D., & VanElzakker, M. B. (2021). Long COVID or Post-acute Sequelae of COVID-19 (PASC): An Overview of Biological Factors That May Contribute to Persistent Symptoms. Frontiers in Microbiology, 12. https://www.frontiersin.org/articles/10.3389/fmicb.2021.698169
5. Rubinov, M., & Sporns, O. (2010). Complex network measures of brain connectivity: Uses and interpretations. NeuroImage, 52(3), 1059–1069. https://doi.org/10.1016/J.NEUROIMAGE.2009.10.003

Poster No 1569

State modulation of hippocampal functional topography supports memory across the adult lifespan

Kristin Nordin[1], Robin Pedersen[2], Farshad Falahati[3], Saana Korkki[1], Jarkko Johansson[4], Filip Grill[5], Anna Rieckmann[6], Alireza Salami[7]

[1]Karolinska Institutet, Solna, Stockholm, [2]Umeå University, Umeå, Västerbotten, [3]Karolinska Institutet, Stockholm, Sweden, [4]Department of Radiation Sciences, Umeå, [5]Donders Centre for Cognitive Neuroimaging, Nijmegen, Gelderland, [6]University of the Bundeswehr Munich, Munich, Bayern, [7]Karolinska Institutet & Umeå University, Stockholm, Stockholm

Introduction: Characterizing age-related alterations in hippocampal (HC) function is key to understanding age-related memory decline. Compared to task-free rest, naturalistic viewing more closely resembles our everyday experience and is reported to modulate HC activity in a manner that predicts memory; differs across the HC's extent; declines in aging [Reagh et al., 2020]. Compared to rest, it may enhance inter-individual differences in functional connectivity (FC), benefitting predictions of behavior [Greene et al., 2018]. Neocortical FC varies along multiple overlapping gradients within the HC [Nordin et al., 2023], the topography of which declines in aging and supports memory [Nordin et al., 2023; Przeździk et al., 2019]. Yet, it is unknown how naturalistic viewing modulates this multidimensional organization and contributes to individual differences in memory across the adult lifespan.

Methods: Analyses included data from the DopamiNe, Age, connectoMe, and Cognition (DyNAMiC) study (N=180 healthy adults; 20-79 years; mean age=49.8±17.4; 90 women) [Nordin et al., 2022]. Functional MRI data were collected during resting state and naturalistic viewing, equal in duration and acquisition parameters. During naturalistic viewing, participants watched a sequence from the Swedish movie "Cockpit". For evaluation against HC gradients previously derived from the resting-state data [Nordin et al., 2023], gradients of HC-neocortical FC were computed for naturalistic viewing by connectopic mapping [Haak et al., 2018]. This method applies non-linear manifold learning to the similarity across voxel-wise FC fingerprints within a region. Gradients were computed at group-level and subject-level using left and right HC masks from FreeSurfer's automated segmentation [Fischl et al., 2002] of a sample-mean T1-wieghted anatomical image. Fine-scale topographic properties of gradients were parameterized through trend-surface modelling [Haak et al., 2018], for each participant and gradient yielding a set of variables used in subsequent analyses.

Results: At a coarse scale, naturalistic-viewing gradients resembled those identified during rest [Nordin et al., 2023] (Figure 1A). We previously showed that resting-state topography of left-hemisphere G2 (separating the middle from the anterior/posterior HC), specifically, predicted episodic memory across the adult lifespan, and that older age was linked to decreased FC change across its extent [Nordin et al., 2023]. Here, analyses of gradients' topographic parameters revealed that left-hemisphere G2, specifically, displayed behaviorally relevant state-dependent modulation. Its topography differed between rest and naturalistic viewing, and its topography during naturalistic viewing significantly added to predicting episodic memory over its topography at rest. Modulation entailed an anterior-medial shift in its middle-HC anchor, indicating closer integration of uncal areas with medial posterior parietal, anterior temporal, and ventromedial prefrontal cortical areas at naturalistic viewing (Figure 1B). Older adults exhibiting a youth-like HC gradient profile during rest – and superior memory – compared to age-matched adults with dedifferentiated gradient topography, displayed a youth-like G2 also during naturalistic viewing. Importantly, older sub groups were consistently youth-like and aged in their functional modulation of G2 between states (Figure 1C).

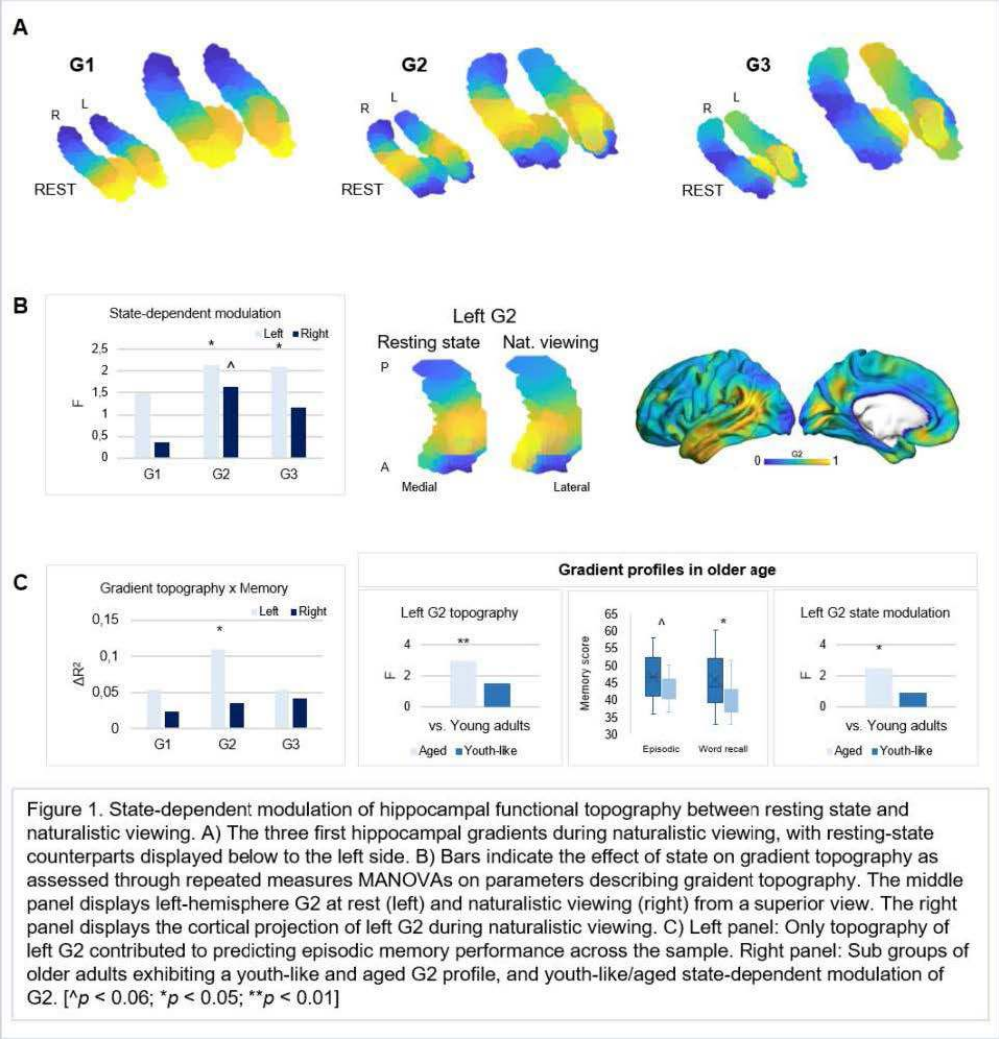

Figure 1. State-dependent modulation of hippocampal functional topography between resting state and naturalistic viewing. A) The three first hippocampal gradients during naturalistic viewing, with resting-state counterparts displayed below to the left side. B) Bars indicate the effect of state on gradient topography as assessed through repeated measures MANOVAs on parameters describing graident topography. The middle panel displays left-hemisphere G2 at rest (left) and naturalistic viewing (right) from a superior view. The right panel displays the cortical projection of left G2 during naturalistic viewing. C) Left panel: Only topography of left G2 contributed to predicting episodic memory performance across the sample. Right panel: Sub groups of older adults exhibiting a youth-like and aged G2 profile, and youth-like/aged state-dependent modulation of G2. [^$p < 0.06$; *$p < 0.05$; **$p < 0.01$]

Conclusions: Our results reveal that naturalistic viewing modulates HC functional organization in a manner that magnifies behaviorally relevant inter-individual differences. Furthermore, the specific link between memory and state-dependent modulation of G2 emphasizes the importance of not restricting functional analyses to the conventional, linear, anteroposterior understanding of HC organization. Critically, we provide novel evidence for maintenance of youth-like modulation of HC function between states as a determinant of preserved memory function in aging.

References

1. Fischl B, Salat DH, Busa E, Albert M, Dieterich M, Haselgrove C, van der Kouwe A, Killiany R, Kennedy D, Klaveness S, Montillo A, Makris N, Rosen B, Dale AM (2002): Whole brain segmentation: Automated labeling of neuroanatomical structures in the human brain. Neuron 33:341–355.
2. Greene AS, Gao S, Scheinost D, Constable RT (2018): Task-induced brain state manipulation improves prediction of individual traits. Nat Commun 9:2807.
3. Haak KV, Marquand AF, Beckmann CF (2018): Connectopic mapping with resting-state fMRI. NeuroImage 170. Segmenting the Brain:83–94.
4. Nordin K, Gorbach T, Pedersen R, Panes Lundmark V, Johansson J, Andersson M, McNulty C, Riklund K, Wåhlin A, Papenberg G, Kalpouzos G, Bäckman L, Salami A (2022): DyNAMiC: A prospective longitudinal study of dopamine and brain connectomes: A new window into cognitive aging. J Neurosci Res:1–25.
5. Nordin K, Pedersen R, Falahati F, Johansson J, Grill F, Andersson M, Korkki S, Backman L, Zalesky A, Rieckmann A, Nyberg L, Salami A (2023): Two long-axis dimensions of hippocampal cortical integration support memory function across the adult lifespan. bioRxiv. https://www.biorxiv.org/content/10.1101/2023.03.24.534115v1.
6. Przeździk I, Faber M, Fernández G, Beckmann CF, Haak KV (2019): The functional organisation of the hippocampus along its long axis is gradual and predicts recollection. Cortex 119:324–335.
7. Reagh ZM, Delarazan AI, Garber A, Ranganath C (2020): Aging alters neural activity at event boundaries in the hippocampus and Posterior Medial network. Nat Commun 11:3980.

Poster No 1570

Integrative Role of Attention Networks in Multi-Frequency Modular Organization of Human Brain

Hüden Neşe[1], Ahmet Ademoğlu[1], Tamer Demiralp[2]

[1]Boğaziçi University, Istanbul, Uskudar, [2]Istanbul University, Istanbul, Fatih

Introduction: Even though there is converging evidence of hierarchical organization in the cerebral cortex, with sensory-motor and association regions at opposite ends, the mechanism of such hierarchical interactions remains elusive (Mesulam, 1998). This organization was primarily investigated in terms of the spatiotemporal dynamics of intrinsic connectivity networks (ICNs); however, more effort is needed to investigate network dynamics in the frequency domain. Network science has a powerful tool, multilayer modularity analysis, to examine frequency-dependent changing patterns in brain connectivity (Betzel & Basset, 2017). It also gives us the opportunity to determine the flexibility and the topological roles (hub/connector) of individual brain regions. In this study, we used the help of network theory to investigate the integrative role of brain regions.

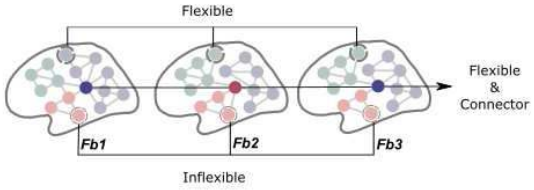

Figure 1. Representation of flexible and/or connector nodes. Flexibility expresses the extent to which a node can exhibit variability in associating itself with different modules through different network layers. Hubs are densely connected with other nodes within the same module and can be considered as central regions facilitating functional specialization. On the other hand, connector nodes with numerous links to different modules play essential roles in functional integration. Fb1: 0.011 - 0.038Hz, Fb2: 0.043 - 0.071Hz, and Fb3: 0.076 - 0.103Hz.

Methods: We used resting-state fMRI data (96 participants) from the HCP dataset with 400-parcel 7-network parcellation (Van Essen et al., 2013; Schaefer et al., 2018). We calculated connectivity matrices in three frequency bands (0.011 - 0.038Hz, 0.043 - 0.071Hz, and 0.076 - 0.103Hz) via a phase-based connectivity estimation approach. We performed multilayer modularity analysis, considering the connectivity matrices at each frequency band as a layer (Mucha et al., 2010). At the subject level, we calculated the flexibility of each brain region. Then, we checked the significance of estimated flexibility values with a Wilcoxon rank sum test by comparing them to the ones obtained from 100 randomized networks. Moreover, two graph metrics, Normalized Participation Coefficient (PCnorm) and Within Module Degree z-score (WMz), were calculated for each brain region to investigate parcels' node roles in the network (Guimera & Amaral, 2005). We identified the hubs and connectors with high WMz and PCnorm, respectively. At the group level, we applied consensus clustering algorithm to find group-level modular organization robust to intersubject variability (Lancichinetti & Fortunato, 2012). We identified main modules and regions with frequency-domain flexibility.

Results: At the group level, three large modules were consistent over frequency bands; one dominated by VN, one dominated by SMN, and one cognitive module covering LN, CN, and DMN. Attention networks were distributed to these three main modules. Our results indicated that most of the group-level flexible parcels, which we called integrative regions, belonged to attention networks, especially the salience ventral attention network. At subject level, a Wilcoxon rank sum test indicated that most of the flexibility values of real connectivity networks, except some parcels belonging to limbic, were significantly different from the randomized networks (p-fdr<0.05). When we compared ICNs in terms of their flexibility, we observed that ICNs were clustered into two groups: somatosensory networks with lower flexibility and attention and cognitive networks with higher flexibility. When we investigated connectors that were common in three frequency bands, 16 out of 26 belonged to SVAN and 7 out of 26 belonged to DAN. Therefore, we concluded that attention networks play an important role in integration not only by simultaneously participating in different modules via different frequency bands but also by connecting various modules at each frequency band.

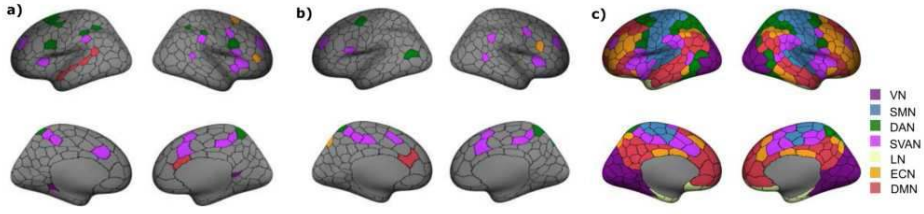

Figure 2. (a) Group-level flexible parcels. (b) Connector nodes common in three frequency bands. (c) Schaefer's parcellation with 400 parcels assigned to seven ICNs. VN, visual network; DAN, dorsal attention network; DMN, default mode network; ECN, executive control network; LN, limbic network; SMN, somatomotor network; SN/VAN, salience/ventral attention network.

Conclusions: We proposed that the decomposition of the conventional BOLD frequency band into sub-bands may allow for the observation of simultaneous, parallel processes, which can provide a mechanistic perspective on the integration among modular structures. Given the proposed hierarchical organization among ICNs, it was consistent with our expectations to find those integrative regions predominantly in attention networks that connect the two ends of the hierarchy. Our multi-frequency modularity analysis results emphasize the integrative role of attention networks and the importance of multiband frequency analysis of brain networks.

References

1. Betzel, R. F., & Bassett, D. S. (2017). Multi-scale brain networks. Neuroimage, 160, 73-83.
2. Guimera, R., & Amaral, L. A. N. (2005). Cartography of complex networks: modules and universal roles. Journal of Statistical Mechanics: Theory and Experiment, 2005(02), P02001.
3. Lancichinetti, A., & Fortunato, S. (2012). Consensus clustering in complex networks. Scientific reports, 2(1), 336.
4. Mesulam, M. M. (1998). From sensation to cognition. Brain: a journal of neurology, 121(6), 1013-1052.
5. Mucha, P. J., Richardson, T., Macon, K., Porter, M. A., & Onnela, J. P. (2010). Community structure in time-dependent, multiscale, and multiplex networks. science, 328(5980), 876-878.
6. Schaefer, A., Kong, R., Gordon, E. M., Laumann, T. O., Zuo, X. N., Holmes, A. J., ... & Yeo, B. T. (2018). Local-global parcellation of the human cerebral cortex from intrinsic functional connectivity MRI. Cerebral cortex, 28(9), 3095-3114.
7. Van Essen, D. C., Smith, S. M., Barch, D. M., Behrens, T. E., Yacoub, E., Ugurbil, K., & Wu-Minn HCP Consortium. (2013). The WU-Minn human connectome project: an overview. Neuroimage, 80, 62-79.

Poster No 1571

A PET study on raphe connectivity alteration in Parkinson disease depression

Seunggyun Ha[1], Yeongjoo Lee[2], Sang-Won Yoo[2], Joo Hyun O[2], Ie Ryung Yoo[2], Joong-Seok Kim[2]

[1]The Catholic University of Korea, Seoul, Seocho-gu, [2]The Catholic University of Korea, Seoul, Korea, Republic of

Introduction: While understanding brain networks based on specific neurotransmitters, which may be deficient or imbalanced, can be crucial for certain diseases, research in this area is lacking. Depression is a significant non-motor symptom in early Parkinson's disease (PD), often associated with the serotonergic system. However, its pathophysiology remains unclear. This study explores the relationship between metabolic connectivity and serotonergic connectivity in patients with Parkinson's disease, and investigates abnormalities in serotonergic connectivity that contribute to depressive mood.

Methods: We used bimodal imaging with early phase [18F]Florbetaben positron-emission tomography (PET) for perfusion and [18F]FP-CIT PET for extrastriatal serotonergic transporter (SERT) imaging to explore the relationship between the raphe-associated serotonergic system and metabolic connectivity in both depressive and non-depressive PD groups. Preprocessing of spatial normalization and smoothing for PET imaging was carried out using Statistical Parametric Mapping version 8. Intensity normalization of [18F]FP-CIT uptake was conducted by calculating the Standardized-Uptake-Value-Ratio (SUVRFP-CIT) using the reference region of a composite occipital regions-of-interest (ROI). Intensity normalization of e[18F]FBB PET scan was carried out by calculating SUVReFBB, with the reference region being the whole cerebellum. The normalized PET images were parcellated by the extrastriatal ROIs using the AAL3 atlas. To extract group-wise raphe-associated ROI connectivity, we designated each of dorsal and median raphe nuclei as seed ROIs. Raphe-associated metabolic connectivity was derived from perfusion information on e[18F]FBB PET, based on the principle of brain perfusion-metabolism coupling. We assessed serotonergic connectivity by examining the synchronization of raphe-extrastriatal SERT-availability on [18F] FP-CIT PET. Connectivity was measured via a partial correlation coefficient for the mean SUVR of the ROIs, while controlling for age, sex, mH&Y stages, and amyloid deposition. The Pearson correlation test were applied to assess the linear association between raphe-associated serotonergic connectivity and metabolic connectivity. A paired t-test was used to compare gross tone of raphe-serotonergic transporter connectivity, calculated for each region over the gross brain, between the depressive and non-depressive groups. A permutation test with 20,000 randomizations was used to compare ROI-based raphe-associated serotonergic transporter connectivity between the depressive and non-depressive groups.

Results: Raphe-associated serotonergic connectivity had a significant linear correlation with raphe-associated metabolic connectivity across the extrastriatal cortex for both depressive and non-depressive groups (seed: dorsal raphe r 0.502, $p < 0.0001$ & r 0.642, $p < 0.0001$, respectively; seed: median raphe, r 0.494, $p < 0.0001$ & r 0.348, $p = 0.0005$, respectively). The depressive group had grossly lower tone of connectivity than the non-depressive group (r, 0.153 ± 0.220 vs. 0.242 ± 0.255, $p = 0.0004$ for dorsal raphe seed; 0.125 ± 0.172 vs. 0.312 ± 0.280, $p < 0.0001$ for median raphe seed). Specifically, median raphe-associated serotonergic connectivity was significantly weakened in the right inferior frontal gyrus pars orbitalis, right anterior orbital gyrus, and left lateral orbital gyrus (all Bon-ferroni adjusted $p < 0.05$).

Conclusions: Raphe-associated metabolic connectivity is linearly associated by underlying serotonergic connectivity. Weakening of raphe-associated serotonergic connectivity in the frontal lobe may contribute to depressive mood in Parkinson's disease.

References

1. Kim, J-S. (2008), 'Practical approach for the clinical use of dopamine transporter imaging', Nuclear Medicine and Molecular Imaging, vol. 42, no. 6, pp.425-34

Poster No 1572

How much is enough? Optimizing data collection for pediatric functional connectivity research

Shefali Rai[1], Kirk Graff[1], Kate Godfrey[1], Shelly Yin[1], Daria Merrikh[1], Ryann Tansey[1], Tamara Vanderwal[2], Signe Bray[1]

[1]University of Calgary, Calgary, Alberta, [2]Department of Psychiatry, University of British Columbia, Vancouver, BC

Introduction: Functional MRI functional connectivity (fMRI-FC) is used to understand how brain network organization changes as children mature, and how networks are impacted in children with neurodevelopmental conditions. However, acquiring sufficient low-motion data presents a challenge to obtaining reliable individual measures of the functional connectome[1-3]. How much data is 'enough'? And how do design choices – using movies to increase compliance – impact data quantity and quality[4-7]? Here we used a repeated-sampling approach to investigate the impact of scan duration and viewing condition on test-retest reliability in adults and children.

Methods: We recruited 25 parent-child pairs (adults 33.8-47.1 years, 12 female; children 6.6-8.9 years, 13 female) that underwent four MRI scans, each including one T1-weighted (TR = 7.29ms, TE = 2.66ms, voxels = 1mm isotropic) and six multi-echo fMRI runs (TR = 2000ms; TEs = 13ms, 32.33ms, 51.66ms; flip angle = 70°, MB factor=2), each lasting ~6.5 minutes. fMRI data was collected during three viewing conditions: 1) narrative movie (sequential clips from the film Dora and the Lost City of Gold), 2) low-demand videos (similar in concept to Inscapes 6 and 3) popular and child-friendly non-narrative video clips (accessed from YouTube.com), totaling ~40 minutes per participant, per session. T1-weighted images were processed via FreeSurfer 6.08, and functional images were preprocessed with Python and MATLAB scripts. Functional preprocessing included slice time correction, multi-echo denoising (Tedana[9]), strict motion censoring (FD threshold > 0.15mm), bandpass filtering (0.01-0.08), and global signal regression. Surface-projected functional runs were created using Ciftify10, and connectomes were generated by Pearson correlating time series from each parcel, using the Schaefer 200 parcel 17-network atlas. Excluding one child with <30 minutes of censored data, analysis included in 24 children (median = 120 min; range = 72.9 – 160.4 min) and 24 adults (median = 150 min; range = 60.5 – 161.4 min). Connectome split-half reliability was computed using test-retest correlation (FC-TRC11), using ANOVAs to compare across groups and tasks with matched amounts of data.

Results: Concatenating all conditions, test-retest correlation reached a maximum of r=0.77 for adults and r=0.75 for children (with >50 minutes per split; Figure 1). Up to 30 minutes, adults had significantly higher reliability at 5-minute increments (paired t-tests, all ps<0.001). Adults reached test-retest r>0.7 with 19 minutes of post-censored data and children at 26 minutes. The pre-censored median was 20.7 minutes (range = 20.3 – 54.2 min) for adults and 35.6 minutes (range = 26.6 – 58.5 min) for children, indicating ~72% more data was acquired to achieve comparable reliability in children. In the low-demand condition, both adults and children retained the least data, with significant differences in head motion between viewing conditions and groups (ANOVA, p<0.05). No interaction was found between condition and group (p>0.05). For each condition, adults consistently had higher reliability than children, up to 10 min of post-censored data (ANOVA, p<0.001; Figure 2). At 10 min of post-censored data, there was no significant effect of condition, or condition * group interaction (ANOVA, p>0.05), on reliability.

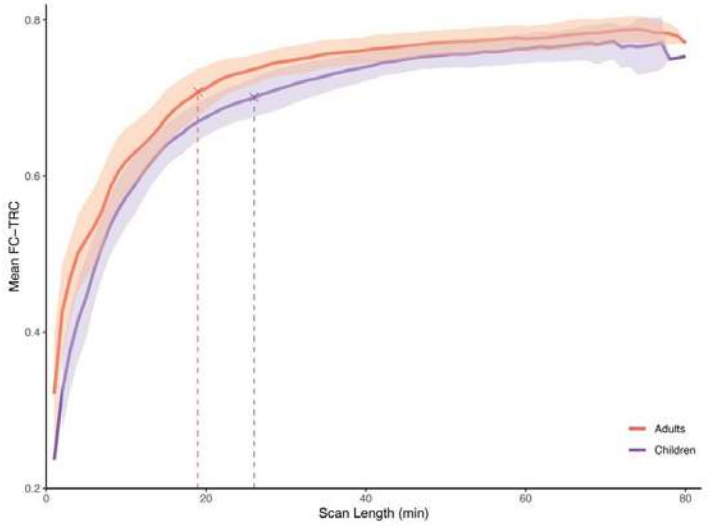

Figure 1. Mean test-retest reliability (FC-TRC) steadily increases with scan length, reaching r>0.7 at 19 minutes for adults and 26 minutes for children.

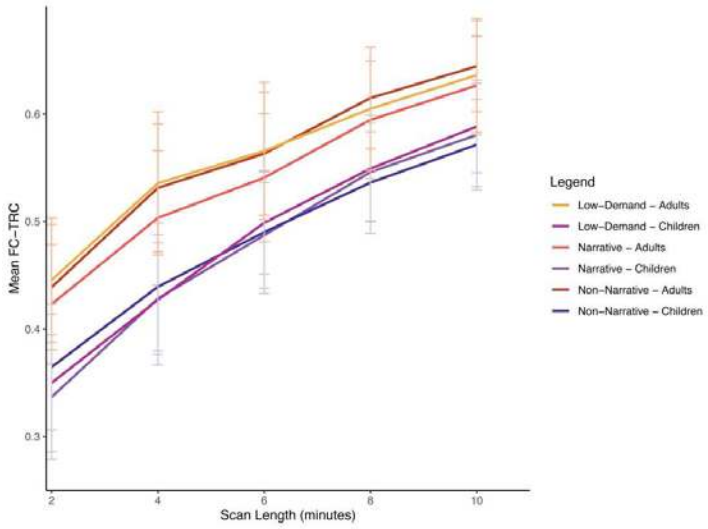

Figure 2. Mean test-retest reliability (FC-TRC) varies by age group, but not by viewing conditions.

Conclusions: Our findings suggest pediatric studies may require >50% longer data collection for comparable reliability to adults and that reliability can match across age groups with sufficient data (e.g., 1h post-censoring). Our study found video type does not impact whole-connectome FC-TRC, but significantly influences data retention. Together our results underscore the need for careful pediatric study design for desired test-retest reliability, aligning with literature supporting movie fMRI in children[6,12,13].

References

1. Dale, A. M. (1999),'Cortical Surface-Based Analysis', NeuroImage, vol. 9, no. 2, pp. 179–194.
2. Davis, B. R. (2022),'Key considerations for child and adolescent MRI data collection', Frontiers in Neuroimaging, vol. 1, pp. 981947.
3. DuPre, E. (2021),'TE-dependent analysis of multi-echo fMRI with tedana', The Journal of Open Source Software, vol. 6, no. 66.
4. Emerson, R. W. (2015),'Network-Level Connectivity Dynamics of Movie Watching in 6-Year-Old Children', Frontiers in Human Neuroscience, vol. 9.
5. Glasser, M. F. (2013),'The minimal preprocessing pipelines for the Human Connectome Project', NeuroImage, vol. 80, pp. 105–124.
6. Gordon, E. M. (2017),'Precision Functional Mapping of Individual Human Brains', Neuron, vol. 95, no. 4, pp. 791-807.e7.
7. Luna, B. (2010),'Methodological approaches in developmental neuroimaging studies', Human Brain Mapping, vol. 31, no. 6, pp. 863–871.
8. Meer, J. N. V. D. (2020),'Movie viewing elicits rich and reliable brain state dynamics', Nature Communications, vol. 11, no. 1, pp. 5004.
9. Power, J. D. (2012),'Spurious but systematic correlations in functional connectivity MRI networks arise from subject motion', NeuroImage, vol. 59, no. 3, pp. 2142–2154.
10. Satterthwaite, T. D. (2012),'Impact of in-scanner head motion on multiple measures of functional connectivity: Relevance for studies of neurodevelopment in youth', NeuroImage, vol. 60, no. 1, pp. 623–632.
11. Vanderwal, T. (2021),'Stability and similarity of the pediatric connectome as developmental measures', NeuroImage, vol. 226, pp. 117537.
12. Vanderwal, T. (2015),'Inscapes: A movie paradigm to improve compliance in functional magnetic resonance imaging', NeuroImage, vol. 122, pp. 222–232.
13. Yeo, B. T. T. (2011),'The organization of the human cerebral cortex estimated by intrinsic functional connectivity', Journal of Neurophysiology, vol. 106, no. 3, pp. 1125–1165.

Poster No 1573

Wiener-Granger "Causality" recovers the flow of information during simple unimanual processing

Minha Gil[1], John Kopchick[2], Phillip Easter[1], David Rosenberg[1], Jeffrey Stanley[2], Vaibhav Diwadkar[1]

[1]Wayne State University, Detroit, MI, [2]Wayne State University, Department of Psychiatry, Detroit, MI

Introduction: Brain network interactions can be characterized using undirected (functional relations between nodes) and directed models (Silverstein et al., 2016). The latter class of models can provide some insights into the vivid nature of the "flow" of information across brain networks (Bressler and Seth, 2011). Classes of directional models include DCM (Stephan and Friston, 2010) and the more flexibly applied Wiener-Granger Causality (WGC)(Bressler and Kelso, 2016). It has been hypothesized that the "flow" of information may be affected in conditions like obsessive-compulsive disorder (OCD), which has been associated with connectivity loss in frontal, striatal and thalamic (FST) circuits which is thought to be exacerbated by repetitive motor behaviors (Burguière, 2015). Thus, here, we provide the first application of WGC applied to task-based data collected in OCD participants (and healthy controls, HC), where the task, a basic motor control paradigm (Morris et al., 2018) was likely to evoke posterior to anterior information flow across the cerebrum. After extracting fMRI time series in a functionally defined 246-region cerebral atlas (Fan et al., 2016), WGC was used to estimate directed functional graphs (246 nodes, 60,270 unique edges) in each participant, which allows for the quantification of directional dominance across various lobes of the brain.

Methods: 67 subjects (37 OCD, ages: 14-21 yrs.) engaged in a visuo-motor integration task (finger tap in response to green or red probes) during fMRI (Siemens Verio 3T). fMRI data were preprocessed using SPM12 (typical methods). After extracting averaged time-series from each of the 246 nodes (organized into seven "lobes") WGC (lag 1) across all pairs (and in both directions) was estimated from in-house scripts in R. For each pair, the estimated WGC coefficients were used as the dependent variable in mixed model Analyses of Variance, with Group (OCD vs HC) modeled as between-subjects factor, and Direction (Node1 to Node2 vs. Node2 to Node1) modeled as within-subjects factor.

Results: While we did not observe substantial main effects of group or of interactions, a large corpus of pairs of nodes evinced main effects of direction (Figure 1A). As seen, the asymmetric significance map highlights the direction in which the effects were significant for observed main effects (Vertical Axis: Source; Horizontal Axis: Target). The effects are distilled into circular frequency bars for each node (Figure 1B). For each node, we represent the source frequency (outward radiating bars) and target frequency (inward radiating bars). As seen, occipital lobes tend to have very high source frequencies, whereas frontal lobes tend to have very high target frequencies.

Figure 1

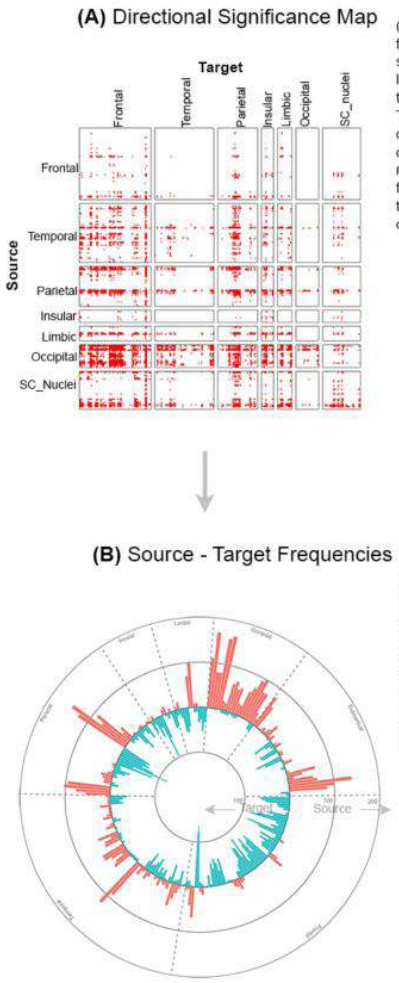

(a) This is a visual representation of a binary map produced from results computed through ANOVA analysis, depicting significant effects of direction. The 246 nodes are organized by lobes. The regions on the vertical axis represent the "source" in the pair, while regions on the horizontal axis represent the "target". The highlighted cells signify a higher WGC in the source - target direction (note that the map is by definition asymmetric). As seen, occipital nodes appear to frequently be sources where the other member of the node pair is within the frontal lobe. Conversely, frontal nodes are only infrequently present as sources. To quantify this observation, for each node, the frequency of it being a source or target were computed (see below).

(b) The circular barplot displays the source or target frequencies for each of the 246 cerebral nodes that were part of a pair where we observed a significant effect of direction. Source frequencies are depicted on the outwardly radiating bars, whereas target frequencies are depicted on the inwardly radiating bars. As seen, the source frequencies of occipital nodes is very high, but the target frequencies of frontal nodes is conversely high. We also observed high source frequencies for thalamic nodes ("subcort--ical lobe") and for select parietal nodes. This figure provides a lucid summary of how the application of WGC recovers the direction of information "flow" in the context of the task.

Conclusions: While we did not observe notable effects of group or any interactions, our analyses revealed widespread effects of directionality on WGC coefficients. When summarized, these data recover the putative directional flow of information in the context of this visually driven motor paradigm. As seen, the direction flow appears to recapitulation a posterior (occipital, parietal, thalamic) to frontal flow of information. These results are consistent with the sensorial role of thalamic and occipital regions in "feeding" information up the cortex (Kody and Diwadkar, 2022), the parietal regions for supplementing this sensory processing (Kobayashi, 2016), and the . Due to the nature of the visuo-motor task, the high ratios in occipital and subcortical nuclei regions may be attributed to their roles in visual information processing and motor control, respectively. While further fractionation of the task into its different conditions is ongoing, our results provide a lucid demonstration of the value of WGC in recovering task-driven directional effects in large networks.

References

1. Bressler, S.L., Kelso, J.A., 2016. Coordination Dynamics in Cognitive Neuroscience. Frontiers in neuroscience 10, 397.
2. Bressler, S.L., Seth, A.K., 2011. Wiener-Granger causality: a well established methodology. NeuroImage 58(2), 323-329.
3. Burguière, E., 2015. Striatal circuits, habits, and implications for obsessive-compulsive disorder. Current Opinion in Neurobiology 30, 59-65.
4. Fan, L., Li, H., Zhuo, J., Zhang, Y., Wang, J., Chen, L., Yang, Z., Chu, C., Xie, S., Laird, A.R., Fox, P.T., Eickhoff, S.B., Yu, C., Jiang, T., 2016. The Human Brainnetome Atlas: A New Brain Atlas Based on Connectional Architecture. Cereb Cortex 26(8), 3508-3526.
5. Kobayashi, Y., 2016. [Neuroanatomy of the Parietal Association Areas]. Brain Nerve 68(11), 1301-1312.
6. Kody, E., Diwadkar, V.A., 2022. Magnocellular and parvocellular contributions to brain network dysfunction during learning and memory: Implications for schizophrenia. J Psychiatr Res 156, 520-531.
7. Morris, A., Ravishankar, M., Pivetta, L., Chowdury, A., Falco, D., Damoiseaux, J.S., Rosenberg, D.R., Bressler, S.L., Diwadkar, V.A., 2018. Response Hand and Motor Set Differentially Modulate the Connectivity of Brain Pathways During Simple Uni-manual Motor Behavior. Brain Topogr 31(6), 985-1000.
8. Silverstein, B., Bressler, S., Diwadkar, V.A., 2016. Inferring the dysconnection syndrome in schizophrenia: Interpretational considerations on methods for the network analyses of fMRI data. Frontiers in psychiatry 7, 132.
9. Stephan, K.E., Friston, K.J., 2010. Analyzing effective connectivity with functional magnetic resonance imaging. Wiley Interdiscip Rev Cogn Sci 1(3), 446-459.

Poster No 1574

How does structure inform the function of the nucleus accumbens in the context of chronic pain?

Paul Bautin[1], Marc-Antoine Fortier[1], Monica Sean[1], Graham Little[1], Pascal Tétreault[1]

[1]*Université de Sherbrooke, Sherbrooke, Quebec*

Introduction: Chronic pain (CP) is a pervasive condition with increasing implications for public health, affecting approximately 1 in 5 people globally. Recent human neuroimaging studies, complemented by behavioral and animal investigations, have begun to elucidate the role of the brain corticolimbic system in chronic pain across various clinical populations. Notably, abnormalities in the nucleus accumbens (NAc) structure and function have consistently been reported[1,2]. However, due to the challenges it presents, the NAc white matter connectivity has rarely been investigated in the context of CP. This study employs diffusion MRI to explore the link between structure and function of the NAc in the context of CP.

Methods: As presented in figure 1, we evaluate and compare the NAc structural and functional projections in both chronic low back pain (CLBP) participants (n=27) and healthy controls (n=25) at 3 time points (0, 2 and 4 months) with fully automated pipelines. Structural connectomes were reconstructed using Tractoflow[3] and Connectflow, BOLD images were processed using fMRIprep[4] and RapidTide[5] and seed based functional connectivity was performed with Nilearn. The NAc projections to the cortex were first reconstructed using an atlas free approach to generate an average heatmap of the regions where NAc projected the most across subjects (figure 1A). Then in an attempt to benchmark the link between structure and function projections of the NAc projections, structural and functional connectivity surface projections were correlated and compared between groups (control and CLBP) – significance was measured with neuromaps[6] spatial null spin tests (figure 1D).

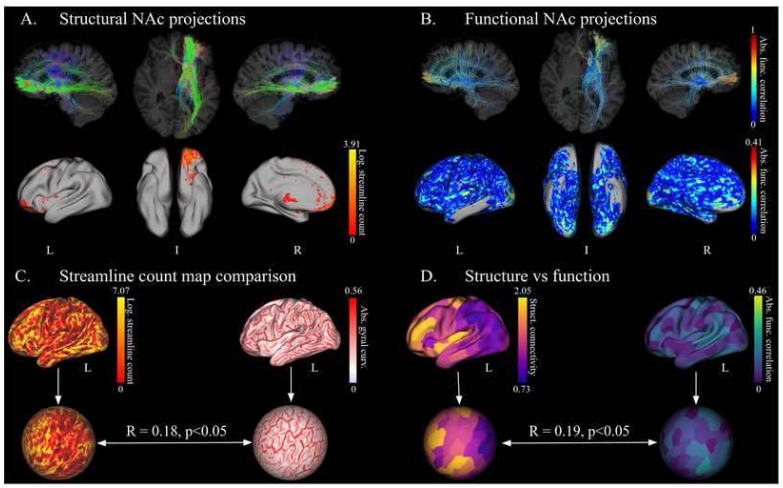

Figure 1. Overview of the comparison between structural and functional projections of the nucleus accumbens (NAc) in the human brain. A) Top: structural NAc PFT tractography streamline projections. Below: surface representation showing regions with highest streamline density in yellow B) Top: Functional NAc signal projected on streamline endpoints, correlated and projected on streamlines. Bottom: brain surfaces showing areas with highest signal correlation in red, gray represents regions outside nilearn EPI mask. C) Comparison of surface streamline density maps with the absolute value of the gyral curvature map using spatial null spin test. D) Comparison of structural NAc projections using communication models with functional NAc projections on the surface using the Schaefer 200 atlas.

Results: Figure 2) presents the results of the comparison of structural NAc projections using communication models with functional NAc projections on the cortical surface using the Schaefer 200 atlas. Different structural connectivity metrics (streamline count, COMMIT2[7] and fiber length) associated with communication models (inverse shortest path, inverse mean first passage time, search information) present different capacities to represent the functional connectivity. In the preliminary results, correlation between structure and function was on average across subjects highest using COMMIT2 associated with shortest path. That said, the results have a large inter-subject variability and unexpected negative correlations appear. As seen in figure 1B (bottom) in grey, a signal dropoff due to susceptibility artifacts in the orbitofrontal cortex could explain the negative correlations as these regions are also the most structurally connected to the NAc. Figure 1A) presents the cortex surface streamline count heatmap measured on 1 subject reconstructed with PFT tracking and connectome spatial smoothing (CSS)[8] to show the cortical regions most structurally connected to the NAc. The nucleus accumbens projections fall reliably in the mPFC regions which is aligned with prior results showing the segmentation of the accumbofrontal tract[9]. Figure 1C, presents the results of the investigation to determine if the streamline count is dependent on the cortex geometry. Absolute value of the gyral curvature map was significantly correlated to streamline count for this subject (aligned with the known tractography gyral bias).

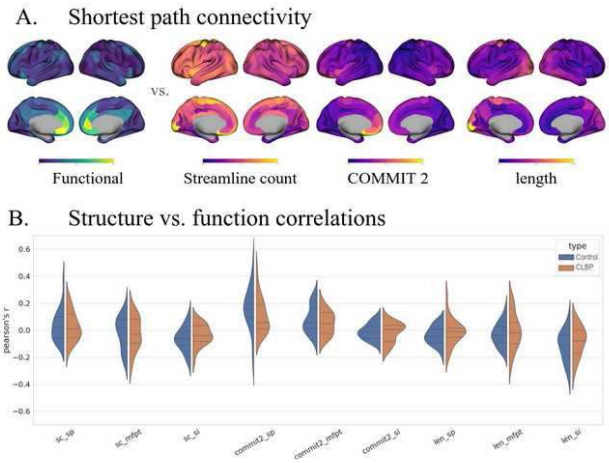

Figure 2. Comparison of structural NAc projections using communication models with functional NAc projections on the surface using the Schaefer 200 atlas. A) Example of across subject average structural connectivity metrics using shortest path communication model. B) Comparison of the structure/function correlation between controls (in blue) and chronic low back pain patients (CLBP in orange). "sc_" is streamline count – number of streamlines reconstructed between regions, "commit2" is the COMMIT2 weights, "len_" is the average streamline length between regions, "_sp" is the inverse shortest path length from the NAc, "_mfpt" is the inverse mean first passage time from the NAc and "_si" is the search information from the NAc.

Conclusions: The aim of the project is to investigate if the functional connectivity differences, described in the CP literature, could be attributed to underlying structural white matter connectivity. Whilst investigating the link between structure and function of specific ROIs is promising, linking tractography reconstructions to fMRI bold images remains challenging. Therefore, we plan to further validate these results by: i) using age/sex matched subjects from the the human connectome project (HCP) dataset[10]; ii) investigating potential biases of high resolution connectomes; iii) and exploring the definition of the mPFC ROI to individualize segmentation of the accumbofrontal tract.

References

1. Baliki, M. N. (2010). Predicting value of pain and analgesia: nucleus accumbens response to noxious stimuli changes in the presence of chronic pain. Neuron, 66(1), 149-160.
2. Makary, M. M. (2020). Loss of nucleus accumbens low-frequency fluctuations is a signature of chronic pain. Proceedings of the National Academy of Sciences, 117(18), 10015-10023.
3. Theaud, G. (2020). TractoFlow: A robust, efficient and reproducible diffusion MRI pipeline leveraging Nextflow & Singularity. Neuroimage, 218, 116889.
4. Esteban, O. (2019). fMRIPrep: a robust preprocessing pipeline for functional MRI. Nature methods, 16(1), 111-116.
5. Tong, Y. (2019). Low frequency systemic hemodynamic "noise" in resting state BOLD fMRI: characteristics, causes, implications, mitigation strategies, and applications. Frontiers in neuroscience, 13, 787.
6. Markello, R. D. (2022). Neuromaps: structural and functional interpretation of brain maps. Nature Methods, 19(11), 1472-1479.
7. Schiavi, S. (2020). A new method for accurate in vivo mapping of human brain connections using microstructural and anatomical information. Science advances, 6(31), eaba8245.
8. Seguin, C. (2022). Connectome spatial smoothing (CSS): Concepts, methods, and evaluation. Neuroimage, 250, 118930.
9. Karlsgodt, K. H. (2015). The accumbofrontal tract: diffusion tensor imaging characterization and developmental change from childhood to adulthood. Human Brain Mapping, 36(12), 4954-4963.
10. Van Essen, D. C. (2013). The WU-Minn human connectome project: an overview. Neuroimage, 80, 62-79.

Poster No 1575

Post-natal development of the rat connectome and the impacts of early life and adult stress

Rachel Smith[1,2], Lena Dorfschmidt[3], Stephen Sawiak[2], Ethan Dutcher[4], Francis McMahon[1], Armin Raznahan[1], Jeffrey Dalley[2], Petra Vértes[2], Edward Bullmore[2]

[1]National Institute of Mental Health, Bethesda, MD, [2]University of Cambridge, Cambridge, United Kingdom, [3]The Children's Hospital of Philadelphia, Philadelphia, PA, [4]University of California, San Francisco, San Francisco, CA

Introduction: Structural similarity networks are a useful tool for characterizing the coordinated development of brain regions in individuals. However, these networks have been primarily explored in humans, thus limiting mechanistic insights. Rats are a valuable model organism in neuroscience due to their complex behaviors and biological similarities to humans. We present the first characterization of individual structural similarity networks in rats, generated using a magnetic resonance (MR)-derived proxy for myelination, elucidating developmental patterns and environmental susceptibility.

Methods: In the normative development cohort, 46 male rats underwent MRI scanning at post-natal day (PND) 20 (n = 41), ~PND 63 (n = 41), and ~PND 230 (n = 44; Fig 1A). These timepoints roughly correspond to infancy, late adolescence/early adulthood, and adulthood in humans. No experimental manipulation was performed during this time. In the early life stress (ELS) cohort, male and female rats were allocated to either the repeated maternal separation (RMS; = 30) or control (n = 28) condition. From PND 5 through PND 19, RMS pups were separated from their dam for 6 hours a day. Beginning around PND 270, all animals (control and RMS groups) underwent a foot shock stress, for a total of 20 shocks per animal across 19 days. All animals were scanned around PND 63 and PND 290 (Fig 1B). MRI data were registered to the Waxholm rat brain atlas (1), and magnetization transfer ratio (MTR) of each voxel was calculated. Individual gray matter myelination networks were calculated using the MIND toolkit (2) and voxel-based MTR. Linear mixed effects models were used to identify control-RMS differences in weighted degree, and modular edge connectivity in adulthood (PND 63) and following adult stress (PND 290).

Results: The adult rat structural connectome was defined as the median edge weight across PND 230 animals in the normative development cohort (Fig 1C). This network is highly modular in structure, composed of seven functionally relevant modules: (1) cognition and sensory integration, (2) limbic system and sensory integration, (3) auditory and somatosensory processing, (4) motor control and sensory relay, (5) olfactory and reward processing, (6) limbic and stress regulation, (7) higher cognitive function (Fig 1D & 1E). Network hubs, many of which are thalamic nuclei, fell in modules 4 and 6. Across regions of interest (ROIs), weighted degree tended to decrease in early development (PND 20 to 63), with more posterior ROIs demonstrating a steeper decline. The connectome was highly conserved between the normative cohort adults and ELS cohort control adults (r = 0.96). Furthermore, the rat connectome was sensitive to environmental stress. In the ELS cohort, RMS animals largely demonstrated increases in ROI weighted degree compared to controls. Following adult stress, this relationship was reversed, with RMS animals showing decreased weighted degree compared to controls (Fig 2A). Thalamic nuclei were particularly impacted both pre- and post-adult stress, though the degree effect size maps were not correlated. Patterns of modular connectivity were also perturbed by stress, with adult RMS animals demonstrating increased intermodular connectivity and decreased intramodular connectivity compared to controls. This relationship was also reversed following adult stress, indicating divergent response to adult stress depending on exposure to ELS (Fig 2B). Connections between modules 4 and 7 were notably affected both pre- and post-adult stress, strongly implicating thalamocortical connectivity.

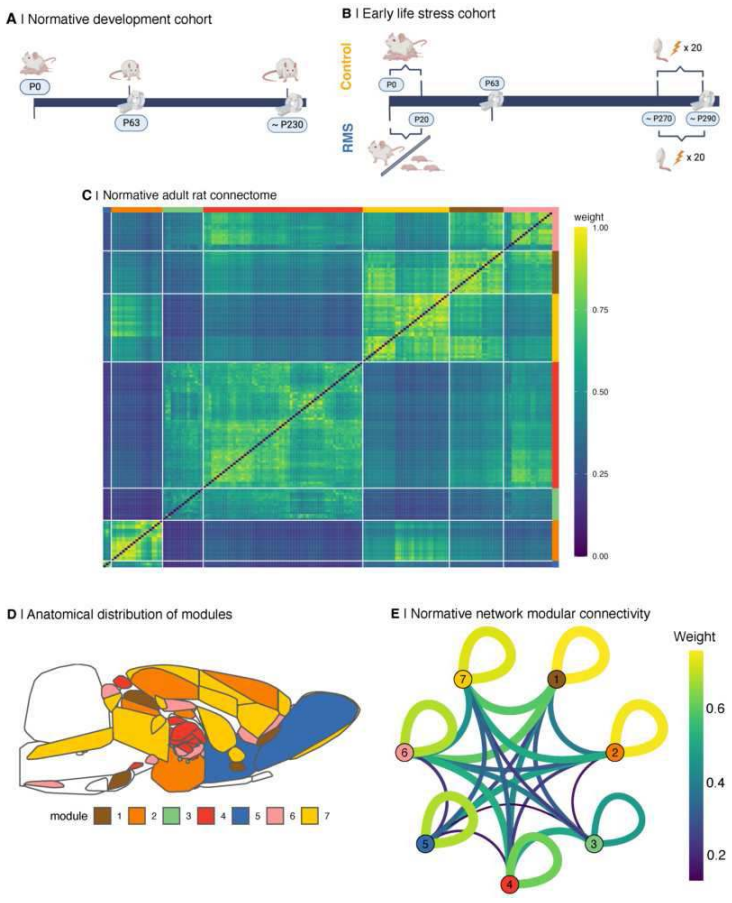

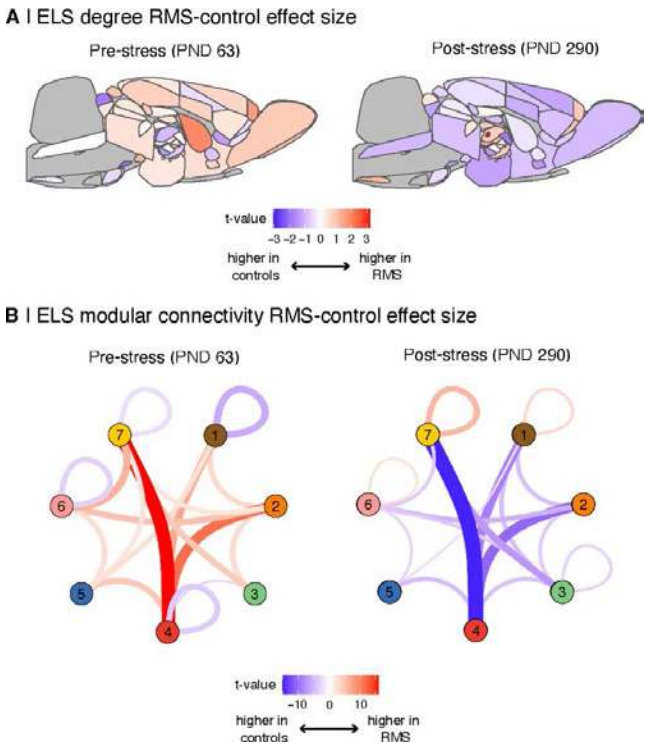

Conclusions: Our study unveils the normative development of the rat structural connectome, describing its reproducibility, functional significance, and environmental sensitivity, with a specific focus on the pivotal role of the thalamus. Importantly, this work establishes a foundation for furthering our understanding of human neurodevelopment, particularly in investigating the impact of environmental stressors.

References

1. Kleven H. (2023), 'Waxholm Space atlas of the rat brain: a 3D atlas supporting data analysis and integration', Nature Methods, vol. 20, no. 11, pp. 1822–1829.
2. Sebenius I.S. (2023), 'Robust estimation of cortical similarity networks from brain MRI', Nature Neuroscience, vol. 26, no. 8, 1461–1471.

Poster No 1576

Brain functional connectivity predicts emotional awareness

Quentin Dessain[1], Laurence Dricot[1], Nicolas Delinte[1], Benoît Macq[1], Philippe de Timary[1], Ron Kupers[2,1]

[1]Université Catholique de Louvain, Louvain-La-Neuve, Belgium, [2]University of Copenhagen, Copenhagen, Denmark

Introduction: The aim of this study was to use brain functional connectivity at rest to predict emotional awareness. Emotional awareness is part of interoceptive awareness and refers to the awareness of certain bodily sensations associated with emotions. Deficiencies in emotional awareness may lead to psychopathology, such as alexithymia. The literature on the cerebral underpinnings of emotional awareness is rather limited. Whereas some studies point to a role of the (anterior) insula (Simmons et al., 2013), other studies report evidence of the involvement of the posterior superior temporal sulcus (Andò et al., 2021, Silani et al., 2008).

Methods: Participants. A total of 86 normal healthy control subjects participated in the study. Average age of the participants was 43.6 ± 6.6 years (47F, 39M). Psychological testing. Participants completed the Multi-dimensional Assessment of Interoceptive Awareness (MAIA) which consists of 32 questions probing different aspects of interoceptive awareness. The scale provides both an overall measure of interoceptive awareness, as well as subscores of eight components, including emotional awareness (Mehling et al. 2012). MRI scanning. We used a 3T Philips Achieva with a 32-channel phased array head coil. The MRI session included one anatomical sequence (T1-weighted) and one eyes-closed rsfMRI scan (RS). T1-weighted images are obtained with a gradient-echo sequence with an inversion prepulse acquired in the sagittal plane with TR=9.1ms, TE=4.6ms, flip angle=8°, 150 slices, slice thickness=1mm, in-plane resolution reconstructed in 0.75x0.75 mm2. RS MRI T2*-weighted sequence was collected with echo-planar imaging: in-plane resolution=3.438*4.348, TE=30 msec, TR=2000ms, FA=90°, 35 slices (ascending), slice thickness=3.44mm. The whole brain slices were scanned 200 times per run. RS MRI Preprocessing. This consisted of linear trend removal to exclude scanner-related signal drift, a temporal high-pass

filter to remove frequencies below 0.005 Hz and correction for head movements using a rigid body algorithm for rotating and translating each functional volume in 3D space. Data were also corrected for time differences in the acquisition of the slices. Regression analyses were performed to remove artefacts due to residual motion and changes in ventricles. Data were smoothed in the spatial domain (Gaussian filter, FWHM–5mm). Anatomical and functional volumes were spatially normalised in MNI space. We used BrainVoyager and a customized Matlab code to calculate cross-correlations between the average time-course signals, extracted from 280 regions (Fan et al. 2016, Diedrichsen, 2006). Using connectome-based predictive modeling (CPM), we tested for predictive models of brain–emotional awareness relationship from connectivity data using cross-validation (Shen et al., 2007). This implies four consecutive steps: 1) feature selection, 2) feature summarization, 3) model building, and 4) assessment of prediction significance. This produces a generalizable model with as input brain connectivity data and that generates predictions of behavioral measures in novel subjects, accounting for a large amount of the variance in these measures.

Results: Connectome-based predictive modeling revealed that emotional awareness could be predicted from the RS data. The correlation between the predicted and actual emotional awareness was 0.258 (p=0.016) (Fig.1). The prediction significance of this correlation, based on 2.000 permutations, resulted in a p value of 0.01. The two highest degree nodes were right and left parahippocampus. The connections with the highest correlation value with emotional awareness were from left STS to bilateral thalamus, right subgenual cingulate and CrusI, cerebellum (Fig.2).

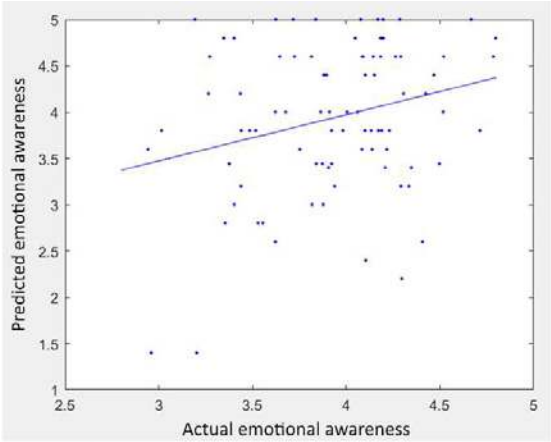

Figure 1. Correlation between actual and predicted emotional awareness based on CPM.

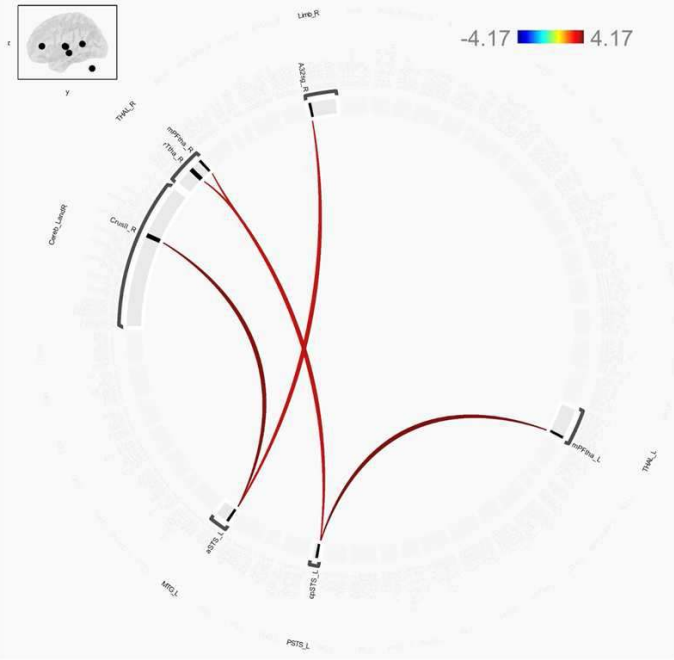

Figure 2: Highest significant connections best correlating with emotional awareness.

Conclusions: The current data point to a role of the parahippocampus and the left posterior superior temporal sulcus in emotional awareness. These data also provide new insights in the cerebral correlates of interoceptive awareness as measured by the MAIA (Smith et al., 2022).

References

1. Simmons, W. K., Avery, J. A., Barcalow, J. C., Bodurka, J., Drevets, W. C., & Bellgowan, P. (2013). Keeping the body in mind: insula functional organization and functional connectivity integrate interoceptive, exteroceptive, and emotional awareness. Human brain mapping, 34(11), 2944-2958.
2. Andò, A., Vasilotta, M. L., & Zennaro, A. (2021). The modulation of emotional awareness using non-invasive brain stimulation techniques: a literature review on TMS and tDCS. Journal of Cognitive Psychology, 33(8), 993-1010.
3. Silani, G., Bird, G., Brindley, R., Singer, T., Frith, C., & Frith, U. (2008). Levels of emotional awareness and autism: an fMRI study. Social neuroscience, 3(2), 97-112.
4. Mehling, W. E., Price, C., Daubenmier, J. J., Acree, M., Bartmess, E., & Stewart, A. (2012). The multidimensional assessment of interoceptive awareness (MAIA). PloS one, 7(11), e48230.
5. Fan, L., Li, H., Zhuo, J., Zhang, Y., Wang, J., Chen, L., ... & Jiang, T. (2016). The human brainnetome atlas: a new brain atlas based on connectional architecture. Cerebral cortex, 26(8), 3508-3526.
6. Diedrichsen, J. (2006). A spatially unbiased atlas template of the human cerebellum. Neuroimage, 33(1), 127-138.
7. Shen, X., Finn, E. S., Scheinost, D., Rosenberg, M. D., Chun, M. M., Papademetris, X., & Constable, R. T. (2017). Using connectome-based predictive modeling to predict individual behavior from brain connectivity. nature protocols, 12(3), 506-518.
8. Smith, S. D., Nadeau, C., Sorokopud-Jones, M., & Kornelsen, J. (2022). The relationship between functional connectivity and interoceptive sensibility. Brain Connectivity, 12(5), 417-431.

Poster No 1577

Effects of combined physiotherapy and acupuncture treatment on RSFC in ischaemic stroke patients

Soné Fouché[1], Hai Lu[2], Fleur Warton[1], Frances Robertson[3], Yu Wang[4], Sebnem Er[1], Jiu Chen[2], Nelleke Langerak[1], Marc Combrinck[1], Xuesheng Ma[5], Xuesong Ren[4], Ernesta Meintjes[1], Chunhong Zhang[4], Jia Fan[1]

[1]University of Cape Town, Cape Town, Western Cape, [2]Nanjing University, Nanjing, Jiangsu, [3]Cape Universities Body Imaging Centre, University of Cape Town, Cape Town, South Africa, [4]First Teaching Hospital of Tianjin University of Traditional Chinese Medicine, Tianjin, Tianjin, [5]University of the Western Cape, Cape Town, Western Cape

Introduction: Stroke patients often have lasting physical and cognitive impairments. Acupuncture has been reported to stimulate the central nervous system as well as promote functional recovery[1] and is recommended by the WHO as an adjunctive treatment after stroke[2]. However, the exact mechanisms of acupuncture remain unknown[3] and brain changes following an extended rehabilitation programme have not been established. Rs-fMRI is a non-invasive technique used to identify brain regions that are temporally correlated when the subject is not performing any explicit task[4]. Resting state functional connectivity (RSFC) therefore measures the connectedness and functional integration of the brain and has been used as a measure of disease burden[5]. In the present study we compared treatment-related changes in brain RSFC in ischaemic stroke patients with unilateral limb dysfunction randomised to receive either 1) True Acupuncture (TA), 2) TA and Physiotherapy (PT), or 3) PT and Sham Acupuncture (SA).

Methods: Participants were recruited from the Tianjin University of Traditional Chinese Medicine, including 23 stroke patients (58.5±8.0 yr) and 9 healthy controls (53.9±6.9 yr). Stroke patients were assigned to one of the three treatment arms mentioned above and received either 5 TA or 5 SA sessions per week for 3 weeks. Rs-fMRI scans were performed on a 3T Skyra Scanner (Siemens, Erlangen, Germany) using a gradient echo EPI sequence both before commencing and after completing the 3-week rehabilitation programme; healthy controls were scanned only once and did not receive any treatment. T1-weighted structural images were acquired using an MPRAGE sequence. Pre-processing was conducted using afni_proc.py in AFNI. All images were registered to a 3x3x3 mm3 Talairach-Tournoux (TT) standard space. Independent component analysis (ICA) and dual regression were performed in FSL. Eleven resting-state networks (RSNs) were identified from 20 group components using FSL-MELODIC in data from the 9 healthy controls. FSL-randomise was used to find clusters within the identified resting state networks (RSNs) showing treatment-related differences (at $p<0.01$; cluster size threshold $\alpha<0.05$) on the post-treatment scans of the stroke patients. Values for mean z-scores were obtained in each cluster on both the pre- and post-treatment scans of each patient to assess for differences before treatment for these clusters.

Results: Higher RSFC were seen after the 3-week rehabilitation treatment, in 5 regions within 3 RSNs in patients who received TA and PT compared to patients receiving TA alone or PT and SA (Fig 1). These regions include the right (R) Cingulate Gyrus and medial (M) precuneus within the default mode network (DMN), left (L) orbitofrontal cortex within the executive control network, and R lingual gyrus and R cuneus within the visual network. Cluster size, peak coordinates, and location of each region of interest (ROI) are shown in Table 1. There were no significant differences in RSFC between groups in these 5 regions before treatment.

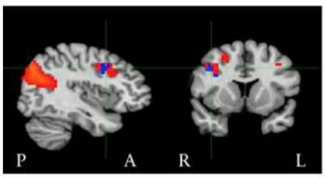

(a) R Cingulate Gyrus

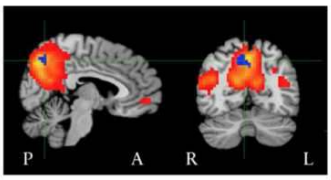

(b) M Precuneus

Default Mode Network

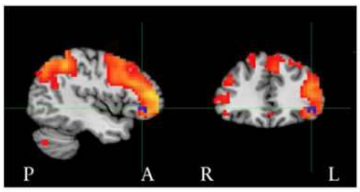

(c) L Orbitofrontal Cortex

Executive Control Network

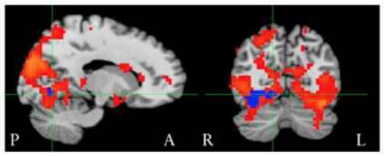

(d) R Lingual Gyrus

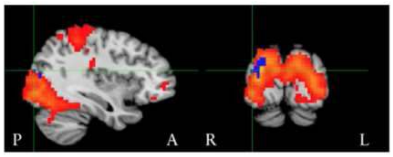

(e) R Cuneus

Visual Network

Figure 1: Each panel shows the group ICA map of a resting state network thresholded at z>3 (hot colours) and clusters where RSFC was higher in patients who received TA+PT compared to others who received TA or PT+SA (in blue). Crosshairs indicate the peak coordinates.

ICA= independent component analysis. RSFC=resting state functional connectivity. TA+PT= True acupuncture and physiotherapy. TA=True acupuncture. PT+SA = Physiotherapy and sham acupuncture. R=right. M=medial. L=left.

Table 1: Cluster sizes and peak coordinates (in TT standard space) of regions where RSFC was higher in patients receiving TA+PT compared to others who received TA or PT+SA. The significantly higher RSFC is highlighted in yellow.

Network Location Peak coordinates (mm)	Cluster Size (mm^3)	Scan	Group averaged (SD) mean z-scores within the cluster			
			TA	TA+PT	SA+PT	F (p)
DMN						
R Cingulate Gyrus 37.5, 7.5, 38.5	756	AT	0.22(0.23)	0.70(0.40)	0.13(0.20)	8.90 (0.002)
		BT	0.20(0.25)	0.10(0.10)	0.15(0.25)	0.296 (0.747)
M Praecuneus 4.5, -61.5, 41.5	594	AT	0.79(0.20)	1.57(0.46)	0.83(0.20)	15.37(<.001)
		BT	1.03(0.45)	0.75(0.26)	1.06(0.35)	1.535(0.240)
Executive Control						
L Orbitofrontal Cortex -40.5, 31.5, -3.5	702	AT	0.06(0.37)	0.87(0.19)	0.29(0.19)	16.76(<.001)
		BT	0.50(0.35)	0.42(0.25)	0.43(0.32)	0.134(0.875)
Visual						
R Lingual Gyrus 13.5, -64.5, -6.5	3240	AT	0.62(0.21)	0.99(0.52)	0.27(0.14)	10.953(<.001)
		BT	0.62(0.39)	0.32(0.19)	0.53(0.37)	1.253(0.307)
R Cuneus 34.5, -82.5, 17.5	1026	AT	0.52(0.21)	1.55(0.83)	0.56(0.20)	10.979(<.001)
		BT	0.49(0.35)	0.43(0.27)	0.79(0.53)	1.705(0.207)

R = Right. M = Medial. L = Left. DMN = Default Mode Network. SD = Standard Deviation. TA = True Acupuncture. TA+PT = True Acupuncture and Physiotherapy. SA+PT = Sham Acupuncture and Physiotherapy. AT = After Treatment. BT = Before Treatment. RSFC= Resting-State Functional Connectivity. TT = Talairach-Tournoux.

Conclusions: Greater RSFC increases in the DMN suggests that TA and PT combined may lead to improved information-processing, memory, self-awareness, and cognitive, language, and motor function[6]. This is consistent with studies showing

acupuncture improves depression symptoms and cognitive deficits of stroke patients, to improve recovery[7]. Greater FC increases in the executive control network may contribute to improved attention and working memory[8]. TA has previously been shown to improve alertness and attention of stroke survivors[9,10]. Greater RSFC increases in the visual network point to improved alertness, visual processing, and visual-motor control such as visually guided movements[9]. Specifically, the cuneus controls the vestibular-ocular reflex, and the lingual gyrus, which is involved in locating objects in space to determine their positions relative to body parts, plays a role in vision-motion coordination.

References

1. Y. Huang et al., "Acupuncture for ischemic stroke: cerebellar activation may be a central mechanism following Deqi," Neural Regeneration Research, vol. 10, no. 12, p. 1997, 201
2. L. Chen et al., "Acupuncture treatment for ischaemic stroke in young adults: protocol for a randomised, sham-controlled clinical trial," BMJ Open, vol. 6, no. 1, p. e010073, Jan. 2016
3. Q. Lv et al., "Effect of Acupuncture on Neuroplasticity of Stroke Patients with Motor Dysfunction: A Meta-Analysis of fMRI Studies," Neural Plasticity, vol. 2021, no. 1, p. e8841720, Jun. 2021
4. C.-H. Fu et al., "Altered effective connectivity of resting state networks by acupuncture stimulation in stroke patients with left hemiplegia," Medicine, vol. 96, no. 47, p. e8897, Nov. 2017
5. E. Canario, D. Chen, and B. Biswal, "A review of resting-state fMRI and its use to examine psychiatric disorders," Psychoradiology, vol. 1, no. 1, pp. 42–53, Mar. 2021
6. R. Luerding, T. Weigand, U. Bogdahn, and T. Schmidt-Wilcke, "Working memory performance is correlated with local brain morphology in the medial frontal and anterior cingulate cortex in fibromyalgia patients: structural correlates of pain–cognition interaction," Brain, vol. 131, no. 12, pp. 3222–3231, Sep. 2008
7. J. Hua et al., "Electroacupuncture ameliorating post-stroke cognitive impairments via inhibition of peri-infarct astroglial and microglial/macrophage P2 purinoceptors-mediated neuroinflammation and hyperplasia," BMC Complementary and Alternative Medicine, vol. 17, no. 1, Oct. 2017
8. a. Blanke and S. Arzy, "The Out-of-Body Experience: Disturbed Self-Processing at the Temporo-Parietal Junction," The Neuroscientist, vol. 11, no. 1, pp. 16–24, Feb. 2005
9. H. Liu et al., "Scalp Acupuncture Enhances the Functional Connectivity of Visual and Cognitive-Motor Function Network of Patients with Acute Ischemic Stroke," Evidence-Based Complementary and Alternative Medicine, vol. 2020, p. e8836794, Dec. 2020
10. G. Liu et al., "Effects of painful stimulation and acupuncture on attention networks in healthy subjects," Behavioral and Brain Functions, vol. 9, no. 1, Jun. 2013

Poster No 1578

Brain Networks Involved in Raven's Standard Progressive Matrices (RSPM) and their Functions

Riley Zurrin[1], Samantha Wong[2], Meighen Roes[1], Chantal Percival[1], Abhijit Chinchani[3], Leo Arreaza[1], Mavis Kusi[4], Maiya Rasheed[1], Zhaoyi Mo[1], Vina Goghari[4]

[1]University of British Columbia, Vancouver, British Columbia, [2]McGill, Montreal, Quebec, [3]The University of British Columbia (UBC), Vancouver, British Columbia (BC), [4]University of Toronto, Toronto, Ontario

Introduction: A non-verbal estimate of fluid intelligence (Gf) is provided by the Raven's Standard Progressive Matrices (RSPM). Duncan and Owen proposed a neuroanatomical basis of Gf called the multiple demand system (MD system; Duncan & Owen, 2000) based on univariate functional magnetic resonance imaging (fMRI) analysis methodology. However, a network-based approach can provide (1) the anatomical configuration of the full set of brain networks involved, and (2) the task-induced BOLD signal changes associated with each anatomical configuration, which when combined with differential responses to task conditions, provide a neurological function for each network. In the current study we achieved this using carried out a dimensional, FIR-based analysis of the RSPM task, which utilized the smallest available anatomical measurement (i.e., voxels as opposed to parcels or a-priori regions of interest), and isolated task-timing-estimable variance prior to the dimension reduction.

Methods: N = 56. Please see Figure 1 for task description). Constrained principal component analysis for fMRI (fMRI-CPCA) was used to extract the whole-brain task-based BOLD networks. It uses multivariate multiple regression to separate out task-timing-predictable variance in the BOLD signal from task-timing-unpredictable variance, and then PCA is applied to the former. Dominant sets of voxel-based component loadings are then interpreted spatially, alongside statistical assessment of temporal information in the task-induced BOLD changes. This method produces networks (task-timing dependent spatial patterns) that are common across all subjects, and allows the researcher to examine how each network's task-induced BOLD changes respond to subject and task/condition variables.

Figure 1. A (left): timeline of one block of stimulus presentations in the Raven's Standard Progressive Matrices (RSPM) task. A matrix was presented for five seconds, after which there was an 8s response period whereby an answer was highlighted in red, and the participants responded whether the highlighted answer was correct or incorrect via a button press with their index or middle finger, respectively. One block consisted of ten matrix problems. The block shown displays medium difficulty RSPM problems. B (right): timeline of entire RSPM task. After participants finished reading the instructions, 15s of fixation were presented at the beginning of each block. One second of fixation was presented before each thirteen second trial. The task concluded with 15s of fixation. One easy block, one medium block, and one hard block were presented to each participant.

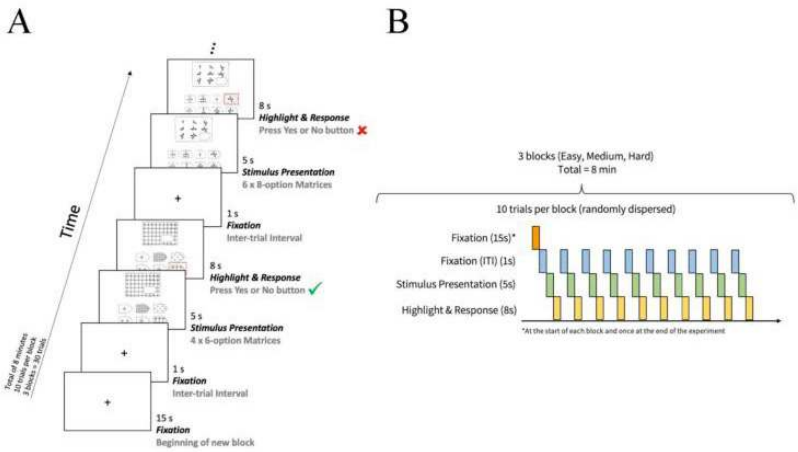

Results: Components were classified as Default Mode Network (DMN), Motor Responding Network (RESP), Multiple Demand Network (MDN), Multiple Demand Network and Default Mode Network (MDN/DMN), and Re-evaluation Network (RE-EV). We focus on the RESP, MDN, and (RE-EV) network here. The anatomical depiction of RESP is presented in Figure 2A, and Figure 2B displays the estimated task-induced BOLD change pattern. The peak time point fell within approximately 11-14s for all conditions. The anatomical depiction of MDN is presented in Figure 2C, and Figure 2D displays the estimated task-induced BOLD change pattern for MDN. The peak time point fell at approximately 9s for all conditions. The anatomical depiction of RE-EV is presented in Figure 2E, and Figure 2F displays the estimated task-induced BOLD change pattern. The peak time point was the latest of all networks, falling within approximately 16-21s for all conditions. A significant difficulty × time interaction was caused by a more fluctuating curve for the medium condition, including the highest peak (see Figure 7B, 16-19s). The Pearson correlations for the predictor weights averaged over the trial were computed between DMN, RESP, MDN, MDN/DMN, and RE-EV. The only correlations to achieve significance after correction were the positive correlations between MDN and RE-EV; namely, RE-EV Hard × MDN Medium (r = .43), and RE-EV Hard × MDN Hard (r = .44).

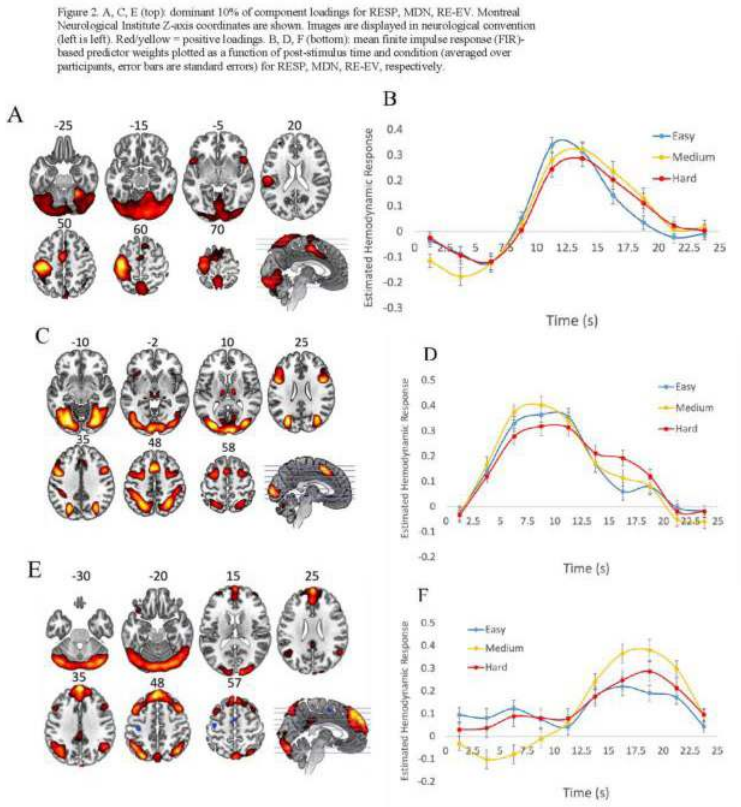

Figure 2. A, C, E (top): dominant 10% of component loadings for RESP, MDN, RE-EV. Montreal Neurological Institute Z-axis coordinates are shown. Images are displayed in neurological convention (left is left). Red/yellow = positive loadings. B, D, F (bottom): mean finite impulse response (FIR)-based predictor weights plotted as a function of post-stimulus time and condition (averaged over participants, error bars are standard errors) for RESP, MDN, RE-EV, respectively.

Conclusions: The MDN for solution searching peaked early in the trial (~9s peak), followed by RESP for response selection (~12s peak), and RE-EV for solution checking (~18s peak), (2) high activity in the MDN is correlated with high activity in the later-peaking RE-EV network, proposed to underpin cooperative searching (MDN) and checking (RE-EV) processes, supported by past work on other tasks (Lavigne, Menon, Moritz, & Woodward, 2020; Lavigne, Menon, & Woodward 2020; Lavigne et al., 2015), and provide overlap with the proposed abstraction/elaboration (MDN solving) and hypothesis testing (RE-EV checking) phases of the P-FIT (Jung & Haier, 2007; Colom et al., 2010).

References

1. Duncan, J., & Owen, A. M. (2000). Common regions of the human frontal lobe recruited by diverse cognitive demands. Trends in Neurosciences, 23(10), 475-483. https://doi.org/10.1016/S0166-2236(00)01633-7
2. Lavigne, K. M., Menon, M., Moritz, S., & Woodward, T. S. (2020). Functional brain networks underlying evidence integration and delusional ideation. Schizophrenia research, 216, 302-309. https://doi.org/10.1016/j.schres.2019.11.038
3. Lavigne, K. M., Menon, M., & Woodward, T. S. (2020). Functional brain networks underlying evidence integration and delusions in schizophrenia. Schizophrenia bulletin, 46(1), 175-183. https://doi.org/10.1093/schbul/sbz032
4. Lavigne, K. M., Metzak, P. D., & Woodward, T. S. (2015). Functional brain networks underlying detection and integration of disconfirmatory evidence. NeuroImage, 112, 138–151. https://doi.org/10.1016/j.neuroimage.2015.02.043
5. Jung, R. E., & Haier, R. J. (2007). The parieto-frontal integration theory (P-FIT) of intelligence: Converging neuroimaging evidence. Behavioral and Brain Sciences, 30(2), 135-154. https://doi.org/10.1017/S0140525X07001185
6. Colom, R., Karama, S., Jung, R. E., & Haier, R. J. (2010). Human intelligence and brain networks. Dialogues in Clinical Neuroscience, 12(4), 489-501. https://doi.org/10.31887/DCNS.2010.12.4/rcolom

Poster No 1579

Moderation of persistent homology-based functional connectivity on cognitive decline in AD

Seonjoo Lee[1], Pei Liu[2], Xi Zhu[3], Yaakov Stern[4]

[1]Columbia University Irving Medical Center, Columbia University, and The New York, New York, NY, [2]Columbia University, New York, NY, [3]New York State Psychiatric Institute, New York, NY, [4]Columbia University Irving Medical Center, New York, NY

Introduction: Network analysis has been widely used to understand the complex interactions and organization of the human brain. Resting-state functional networks, often studied for cognition and aging, are analyzed through network analysis with modular assumption. However, it is more plausible to assume a core-periphery or rich club structure accounts for brain functions where the hubs are tightly interconnected to allow for integrated processing[1]. To address this, we introduced

persistent homology-based functional connectivity (PHFC) indices, including backbone strength (BS), backbone dispersion (BD), and cycle strength (CS), to quantify integrated processing patterns. BS reflects overall functional integration, BD indicates differences in critical information flow, and low CS suggests strong information flow through the backbone rather than additional cycles to study cognitive aging[2]. Using large public data, our study investigates the role of PHFC indices in Alzheimer's disease pathology, revealing their potential advantages beyond traditional measures.

Methods: Sample included 503 adults (mean age 74.53 [age range 56-96], 50.5% female) from the ADNI. Amyloid positivity was measured using av45 PET SUVR with cut point 1.1. Resting-state functional magnetic resonance imaging (rs-fMRI) data was obtained from 3T scanners. The time series data were extracted using Power's atlas, functional connectivity was computed using Pearson's correlation coefficients, and the PHFC indices were calculated as implemented in the PHFconn R package (https://github.com/hyunnamryu/PHfconn). We performed separate mixed effect regression for each executive function and episodic memory composite scores as dependent variables. Each mixed effect model included PH-based functional connectivity indices, years from baseline, amyloid positivity and their two-way and three-way interactions as fixed effects, and subject intercepts and years from baseline slopes as random effects. We also included baseline age, sex, and education as covariates for all models.

Results: There was a significant three-way interaction between BD, days from baseline, and amyloid positivity (=-0.05, CI=-0.09 to -0.02, p=.005) for executive function. For episodic memory, significant three-way interactions were found for BD (=-0.04, CI=-0.08 to -0.01, p=.008), BS (=-0.04, CI=-0.08 to -0.01, p=.006), and CS (=-0.03, CI=-0.06 to -0.00, p=.034) with days from baseline and amyloid positivity. These results indicate that the patterns of information integration in functional connectivity moderate the effect of amyloid burden on the speed of cognitive decline. Specifically, in the amyloid positivity group, higher BD is associated rapid cognitive decline, while lower BD is associated with faster decline in the absence of amyloid.

Figure1: The slope of EF over time as a function of BD and amyloid positivity.

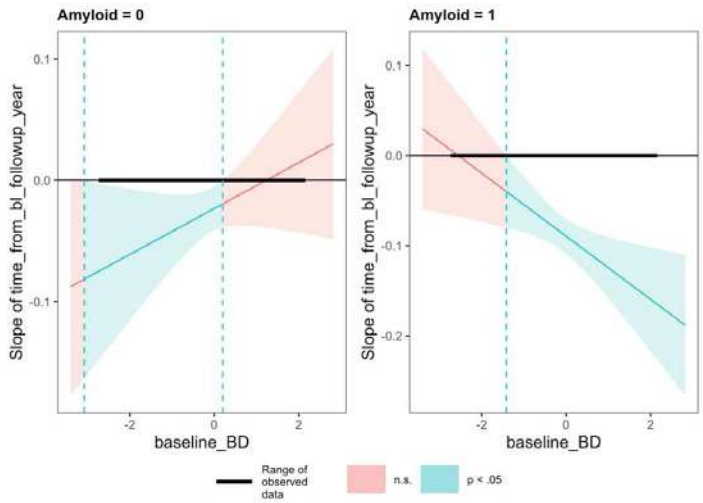

Figure2: The slope of episodic memory over time as a function of BD and amyloid positivity.

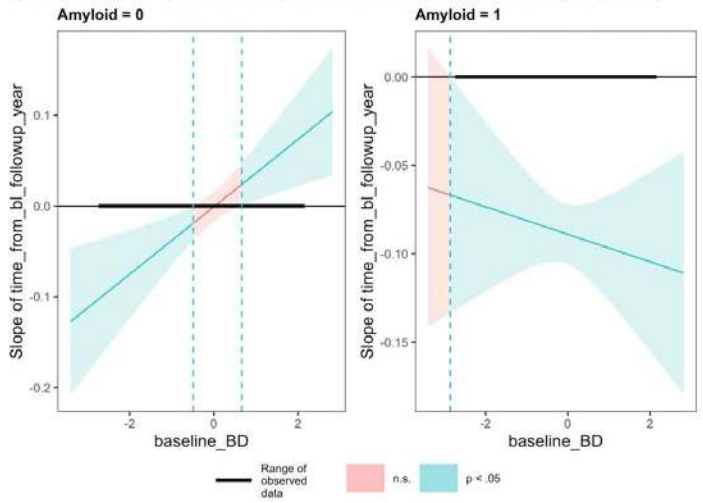

Conclusions: By employing the PHFC indices, we have uncover intricate patterns of information integration with the functional networks. These patterns of information integration patterns play a crucial role in moderating the relationship between Alzheimer's disease related amyloid burden on cognitive decline.

References
1. M. A. Bertolero, B. T. T. Yeo, and M. D'Esposito, "The diverse club," Nat. Commun., vol. 8, no. 1, p. 1277, Nov. 2017, doi: 10.1038/s41467-017-01189-w.
2. H. Ryu, C. Habeck, Y. Stern, and S. Lee, "Persistent homology-based functional connectivity and its association with cognitive ability: Life-span study," Hum. Brain Mapp., vol. 44, no. 9, pp. 3669–3683, 2023, doi: 10.1002/hbm.26304.

Poster No 1580

Effects of physiotherapy and acupuncture treatment on basal ganglia network in stroke rehabilitation

Jia Fan[1], Soné Fouché[1], Hai Lu[2], Fleur Warton[1], Frances Robertson[1], Yu Wang[3], Sebnem Er[1], Jiu Chen[2], Nelleke Langerak[1], Xuesong Ren[3], Xuesheng Ma[4], Marc Combrinck[1], Chunhong Zhang[3], Ernesta Meintjes[1]

[1]University of Cape Town, Cape Town, Western Cape, [2]Nanjing University, Nanjin, Jiangsu, [3]First Teaching Hospital of Tianjin University of Traditional Chinese Medicine, Tianjin, Tianjin, [4]University of the Western Cape, Cape Town, Western Cape

Introduction: Stroke occurs when blood supply to an area of the brain is interrupted by either occlusion or haemorrhage. Typically, a multidisciplinary team comprising a physiotherapist, occupational therapist, and/or speech therapist will be involved in stroke rehabilitation depending on the patient's needs[1]. The benefits of physiotherapy are widely recognised[2]. Acupuncture on particular acupoints may be excitable muscle/skin-nerve complexes containing a high density of nerve endings and activates afferent fibres that send signals to the spinal cord[3]. Therefore, acupuncture may have effect on regulation of cerebral blood flow via angiogenesis and modulation of vasoactive mediators[4]. However, the exact mechanisms of acupuncture in the treatment of stroke remain unclear. Resting-state functional MRI (rs-fMRI) allows us to identify brain regions that are temporally correlated when the subject is not performing any explicit task. The current study aims to compare treatment-related changes in resting state function connectivity (RSFC) within the basal ganglia (BG) network in ischaemic stroke patients with unilateral limb dysfunction.

Methods: Twenty-three right-handed stroke patients with unilateral limb dysfunction (mean±sd age: 58.5±8.0 yr) were recruited from the First Teaching Hospital of Tianjin University of Traditional Chinese Medicine. These participants were assigned to three different treatment arms: (1) True Acupuncture (TA), (2) TA and Physiotherapy (PT), and (3) PT and Sham Acupuncture (SA). MRI scans were performed on a 3T Skyra Scanner (Siemens, Erlangen, Germany) after stroke patients who received 5 TA or 5 SA sessions per week with/without PT for 3 weeks, including a gradient echo EPI sequence (TR=2000 ms, TE=30 ms, flip angle=90˚, FOV=220 mm, voxel size 3.4×3.4×3.0 mm3) and an MPRAGE sequence (TR=2000 ms, TE=1.97 ms, flip angle=8˚, FOV=256 mm, voxel size 1.0×1.0×1.0 mm3). Pre-processing was conducted using afni_proc.py in AFNI including the following standard procedures: realignment, regression, and blurring. All images were registered to a 3x3x3 mm3 Talairach-Tournoux (TT) standard space. BG seeds were spherical regions of interest (ROIs) (radius = 3 mm, coordinates (+/- 3.5, 4, -0.3)) bilaterally in the caudate putamen[5]. The average ROI time series of the seed was used to perform whole-brain correlation analysis. FSL-randomise was used to find clusters within the identified resting state networks (RSNs) showing treatment-related differences. We only report results that survived at a cluster threshold of $p<0.01$ and $\alpha<0.05$.

Results: Patients who received TA and PT (TA+PT) showed higher RSFC between the seed in the left (L) caudate putamen and clusters in the left (L) and right (R) anterior cingulate, and between the seed in the R caudate putamen and clusters in the R anterior cingulate and L Thalamus compared others who received TA or SA and PT (SA+PT) (Figure 1). The 2 clusters in the R Anterior cingulate were overlapped. The cluster size, peak coordinate, and location of each region of interest (ROI) are shown in Table 1.

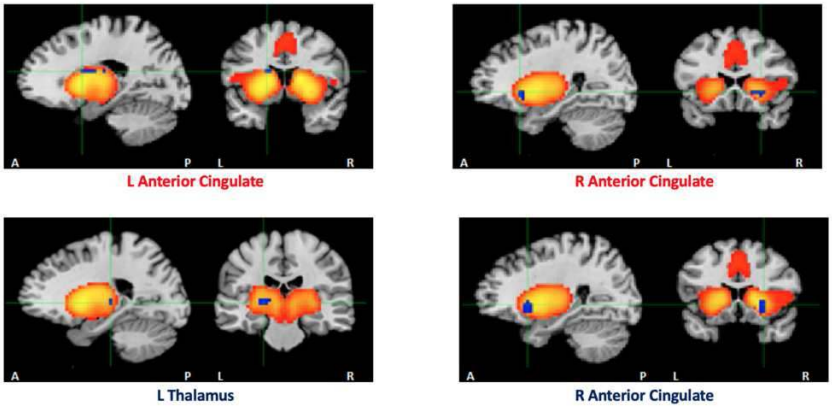

Figure 1. Each panel shows the basal ganglia network (hot colours) and clusters where RSFC was higher in patients who received TA+PT compared to others who received TA or PT+SA (in blue). Crosshairs indicate the peak coordinates. RSFC=resting state functional connectivity. TA+PT= True acupuncture and physiotherapy. TA=True acupuncture. PT+SA = Physiotherapy and sham acupuncture. R=right. L=left.

Table 1. Cluster sizes and peak coordinates (in TT standard space) of regions where RSFC were higher in patients who received TA+PT compared to others who received TA or PT+SA. The significantly higher RSFC is highlighted in yellow.

Seed (coordinates) Location Peak coordinates (mm)	Cluster Size (mm^3)	Group averaged (SD) mean z-scores within the cluster			
		TA	TA+PT	SA+PT	F (p)
R caudate putamen (3.5, 4, -0.3)					
L Anterior Cingulate -16.5, 4.5, 17.5	405	0.42(0.42)	1.25(0.43)	0.90(0.41)	6.37(0.007)
R Anterior Cingulate 25.5, 16.5, -0.5	324	0.63(0.26)	1.46(0.47)	0.82(0.35)	9.26(0.001)
L caudate putamen (-3.5, 4, -0.3)					
R Anterior Cingulate 25.5, 13.5, -0.5	459	0.53(0.22)	1.41(0.33)	0.74(0.45)	10.09 (<.001)
L Thalamus -19.5, 22.5, 2.5	297	0.17(0.11)	1.04(0.67)	0.22(0.14)	12.60(<0.001)

TA+PT= True acupuncture and physiotherapy. TA=True acupuncture. PT+SA = Physiotherapy and sham acupuncture.
TT = Talairach-Tournoux. RSFC= resting state functional connectivity. SD = Standard Deviation. R = right. L = left.

Conclusions: This study examined the potential benefits of combined TA and PT treatment on RSFC in the BG network in stoke patients with unilateral limb dysfunction compared to others who received either TA alone or SA + PT. Higher RSFC in bilaterally in anterior cingulate and L thalamus were found in stroke patients who received TA+PT. Anterior cingulate is responsible for emotional expression, attention allocation, and mood regulation, and mediates reward-based behaviors together with orbital frontal cortex[6]. Previously, higher RSFC in the anterior cingulate were seen in palsy patients who received acupuncture treatment[7]. Thalamus can be segregated into discrete loops for motor, oculomotor, prefrontal, and limbic functions[8]. Greater RSFC in thalamus may suggest better motor behaviors where better thalamus activation was seen in individuals who received TA[9] or PT[10].

References

1. Langhorne P, Bernhardt J, Kwakkel G (2011). Stroke rehabilitation. The Lancet, 377(9778): 1693-1702.
2. Verbeek J, Senger MJ, Riemens, L Haafkens J (2004). Patient expectations of treatment for back pain: a systematic review of qualitative and quantitative studies. Spine, 29:2309-18.
3. Zhao F, Williams M, Meng X, Welsh DC, Coimbra A, Crown ED, Cook JJ, Urban MO, Hargreaves R, Williams DS (2008). BOLD and blood volume-weighted fMRI of rat lumbar spinal cord during non-noxious and noxious electrical hindpaw stimulation. Neuroimage, 40(1): 133-147.
4. Chavez LM, Huang SS, MacDonald I, Lin JG, Lee YC, Chen YH (2017). Mechanisms of Acupuncture Therapy in Ischemic Stroke Rehabilitation: A Literature Review of Basic Studies. Int J Mol Sci,18(11): e2270.
5. Sierakowiak A, Monnot C, Aski SN, Uppman M, Li T, Damberg P, Brené S (2015). Default Mode Network, Motor Network, Dorsal and Ventral Basal Ganglia Networks in the Rat Brain: Comparison to Human Networks Using Resting State-fMRI. PLOS One, 10(3):e0120345.
6. Hadland KA, Rushworth MFS, Gaffan D, Passingham RE (2003). The anterior cingulate and reward-guided selection of actions. J Neurophysiol., 89(2):1161-1164.
7. Wu H, Kan H, Li C, Park K, Zhu Y, Mohamed AZ, Xu C, Wu Y, Zhang W, Yang J (2015). Effect of acupuncture on functional connectivity of anterior cingulate cortex for bell's palsy patients with different clinical duration. Evid Based Complement Alternat. Med., e646872.
8. Alexander GE, Crutcher MD (1990). Functional architecture of basal ganglia circuits: Neural substrates of parallel processing. Trends Neurosci., 13:266-271.
9. Song Y, Yang W, Guo H, Han Y (2006). Clinical observation on acupuncture combined with medicine for treatment of infantile febrile convulsion. Zhongguo ZhenJiu, 26:561-562.
10. Müller K, Bacht K, Prochnow D, Schramm S, Seitz RJ (2013). Activation of thalamus in motor imagery results from gating by hypnosis. Neuroimage, 66: 361-367.

Poster No 1581

Tracing neuronal synchronized slow oscillations with simultaneous fMRI and optical imaging in mice

Wen-Ju Pan[1], Lauren Daley[1], Harrison Watters[1], Lisa Meyer-Baese[1], Shella Keilholz[1]

[1]Emory University/Georgia Institute of Technology, Atlanta, GA

Introduction: Resting state fMRI functional connectivity (FC) has been widely used to study the functional network organization of the brain with the assumption that it reflects underlying slow synchronized neuronal activity[1-3]. However, little is known about the correspondence between fMRI FC and the spatial and temporal properties of the slow neuronal oscillations due to the challenges of obtaining of concurrent neuronal FC during fMRI[4]. In our studies, we combined a conventional wide-field cortical optical imaging method with ZTE fMRI in mice to investigate the concurrent neuronal fluorescent signals across cortical areas during whole brain fMRI. Using our setup, the FC of neuronal calcium signals (GCaMP) or membrane voltage signals (VSFPB or JEDI) from infraslow bands to 25Hz were examined from one side of the upper limb area during fMRI. The concurrent BOLD EPI signals or ZTE signals and FCs were evaluated from different cortical layers.

Methods: Five mice were examined under two anesthesia conditions, (1% isoflurane (iso) and 0.5% iso mixed with 0.05mg/kg/hr Dexmedetomidine (iso-dex)) with simultaneous fMRI and optical imaging setup, 3 with neuronal calcium fluorescence (GCaMP 6f) and 2 with neuronal voltage indicators (VSFPB or JEDI). All mice were imaged on the recently upgraded Bruker BioSpin 9.4T scanner with AVANCE NEO console and Paravision360 v3.4. ZTE fMRI was set with ~ 345um isotropic voxels and whole brain coverage and temporal sampling rate of 2s per brain volume scan. TR: 0.673 ms, flip angle 3.7°, bandwidth 187.5 kHz, oversampling 4, matrix size 72 × 72 × 72, field-of-view 25 × 25 × 25 mm3, polar under sampling factor 5.64, and number of projections 2460. The 10 min resting state scan sessions were conducted in iso or iso-dex anesthesia. The optical imaging system was designed to fit inside the magnet with a long tube lens[5]. The wavelength was 466/40nm for fluorescence excitation, and the emitted 525/50nm were detected in a camera at 50Hz in 16bit with image matrix 110 by 110. Meanwhile, the green light pulses were illuminated alternatively at 50Hz and the reflection signals were detected with the same camera. The raw fluorescent signals were purified to represent neuronal signals by regression of simultaneous green reflection imaging of total hemoglobin absorption. All data were preprocessed and registered to Allen mouse atlas for FC analysis from left side upper limb area, Figure 1.

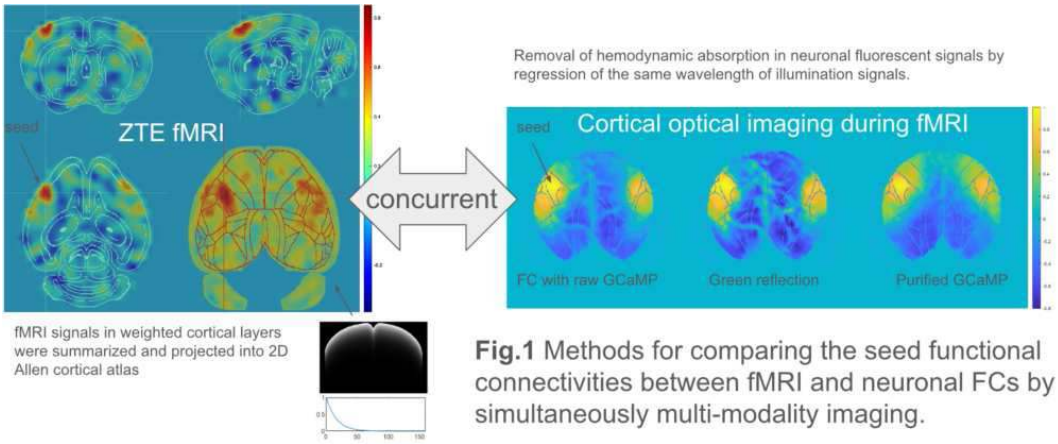

Fig.1 Methods for comparing the seed functional connectivities between fMRI and neuronal FCs by simultaneously multi-modality imaging.

Results: Neuronal FCs across hemisphere were detected in slow frequency bands but not in high frequencies > 1Hz or >0.5Hz (example in Figure 2). The neuronal voltage FCs exhibited relatively narrow frequency bands, 0.1-0.5 Hz, comparing with calcium FCs, 0.01-1 Hz. The fMRI FCs were evaluated over the conventional 0.01-0.1Hz band for different layers of left upper limb area, layers 1, 2/3, 4, 5 and 6. The localized FCs observed mostly in top and middle layers across scans of ZTE fMRI with varied anesthesia conditions.

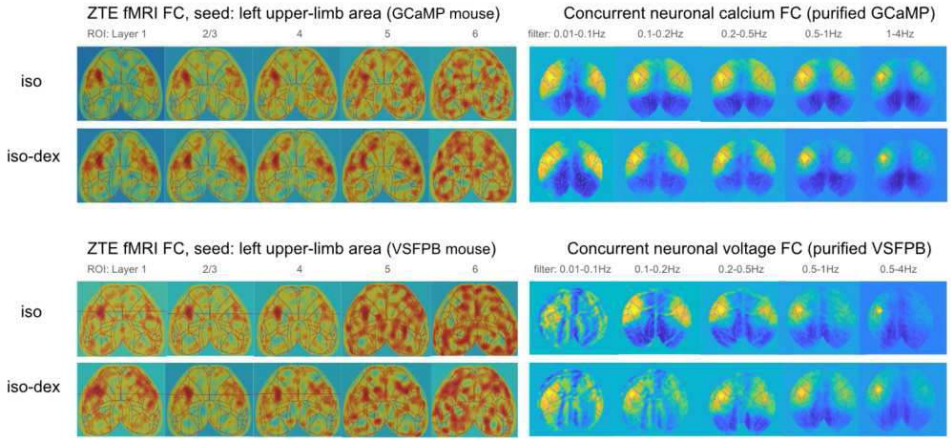

Fig. 2 Layer-dependent FC in fMRI and Frequency band-dependent FC in neuronal optical imaging.

Conclusions: In this report, we demonstrated the concurrent measurement of neuronal and fMRI FCs in anesthetized mice. Under both anesthesia conditions, iso or iso-dex, the neuronal FCs came from slow oscillations but not high frequencies. The neuronal voltage FCs may be in a relatively narrow band of the slow oscillations. The neuronal calcium FCs of the slow oscillations included infraslow bands additionally. The corresponding fMRI FCs in a primary somatosensory cortex, were mostly from top and middle layers. The present methods and the initial examination may pave a way for a wide application in the future.

References

1. Li, J. M., Bentley, W. J., Snyder, A. Z., Raichle, M. E. & Snyder, L. H. Functional connectivity arises from a slow rhythmic mechanism. Proceedings of the National Academy of Sciences of the United States of America 112, E2527–E2535 (2015).
2. Pan, W. J., Thompson, G. J., Magnuson, M. E., Jaeger, D. & Keilholz, S. Infraslow LFP correlates to resting-state fMRI BOLD signals. NeuroImage 74, 288–297 (2013).
3. Schwalm, M. Cortex-wide BOLD fMRI activity reflects locally-recorded slow oscillation-associated calcium waves. eLife 6, e27602 (2017).
4. Lake, E. M. R. et al. Simultaneous cortex-wide fluorescence Ca2+ imaging and whole-brain fMRI. Nature Methods 17, 1262–1271 (2020).
5. Pan, W.-J. et al. (ISMRM 2022) Optimization of wide-field optical imaging method towards fMRI integration in mice. https://archive.ismrm.org/2022/3331.html.

Poster No 1583

Learning and dysfunctional higher order functional connectivity in schizophrenia

Hady Saad[1], John Kopchick[2], Patricia Thomas[2], Usha Rajan[2], Dalal Khatib[2], Caroline Zajac-Benitez[1], Luay Haddad[2], Alireza Amirsadri[2], Jeffrey Stanley[2], Vaibhav Diwadkar[1]

[1]Wayne State University, Detroit, MI, [2]Wayne State University, Department of Psychiatry, Detroit, MI

Introduction: Traditional methods for assessing second order functional connectivity (FC) rely on the quantification of bivariate relationships between pairs of nodes (Silverstein, Bressler, & Diwadkar, 2016). These pairwise characterizations typically rely on zero log correlations that can then be used in the service of understanding connectivity and dysconnectivity in conditions like schizophrenia (SCZ)(Meram et al., 2023). In a large connectomic space, these pairwise characterizations bely relationships between individual nodes and all other nodes in the network. Thus, in a connectivity matrix (of size k), the connectivity vector of any node i consists of k elements. Between any two nodes i and j, it is possible to estimate their Higher Order Functional Connectivity (HOFC) in the network from their vector cross product (Zhang et al., 2016). This measure captures similarities (or dissimilarities) in the cross-matrix similarity of the connectivity profiles of nodes. Here, we provide the first application of HOFC to recover dysfunctional learning induced profiles in SCZ (compared to Healthy Controls, HC).

Methods: fMRI data (Siemens Verio 3T) were acquired in 88 participants (49 SCZ) while they engaged in object-location learning (Stanley et al., 2017) separated into epochs for Encoding (objects shown in their associated locations) and Retrieval (locations cued for retrieving object identity). fMRI data were processed in SPM 12 (standard methods). In preparation for HOFC analyses, in each participant, time series were extracted from 246 functionally defined cerebral parcels (Fan et al., 2016) for the computation of pairwise functional connectivity in each of Encoding and Retrieval (30,135 pairs). Next, HOFC was computed between each of the 246 FC vectors for data in each participant and condition. Finally, inter-group differences in HOFC in each condition were identified ($p<.05$) and separated by direction (HC > SCZ, SCZ > HC).

Results: The results are depicted for each of Encoding (Figure 1) and Retrieval (Figure 2). In each figure, the central brain maps are frequency maps where the shading indicates the frequency with each that region is part of a pathway with a significant HOFC differences (Red: HC greater; Blue: SCZ greater). These frequencies are redundantly depicted in the surrounding circular bar plots. The chord diagrams in the satellites break down the observed effects by lobe (frontal, temporal, parietal, insular, limbic, visual and sub-lobar nuclei). Here, each chord connects a pair with significant differences in HOFC. As seen, during Encoding SCZ are characterized by decreased HOFC involving frontal, temporal, parietal and visual regions, but a converse (and presumably compensatory) increase in HOFC involving sub-lobar nuclei. This pattern largely repeats itself for Retrieval.

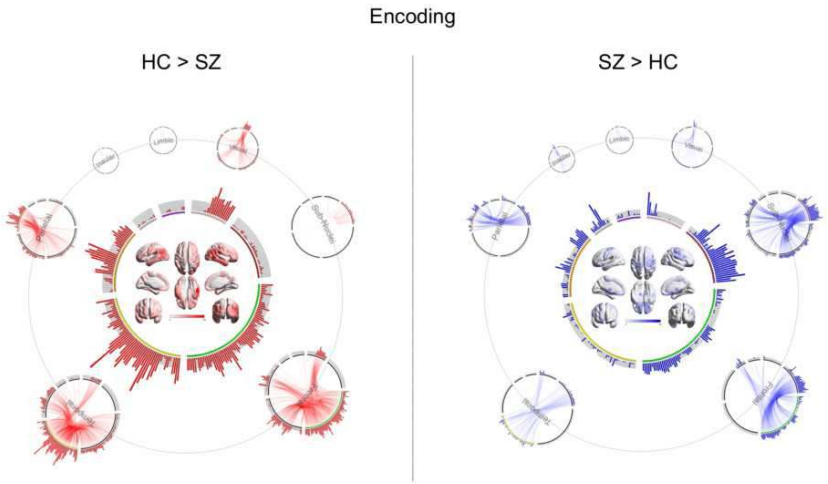

Figure 1: The figure reveals pairs of regions with significant inter-group differences in HOFC during Encoding (Red: HC Greater; Blue: SCZ Greater). The central brain map is a frequency map. The color indicates the frequency with each any region is involved in a pathway with a significant difference in HOFC (these frequencies are redundantly depicted in the surrounding circular bar plots with the brain image providing location information). The chord diagrams in the satellites break down the observed effects by lobe (frontal, temporal, parietal, insular, limbic, visual and sub-lobar nuclei). As seen, in HC (compared to SCZ) there is increase in HOFC involving frontal, temporal, parietal and visual regions. However, in SCZ we observe (a presumably compensatory) an increase in HOFC involving sub-lobar nuclei, the visual lobe, and the insular lobe.

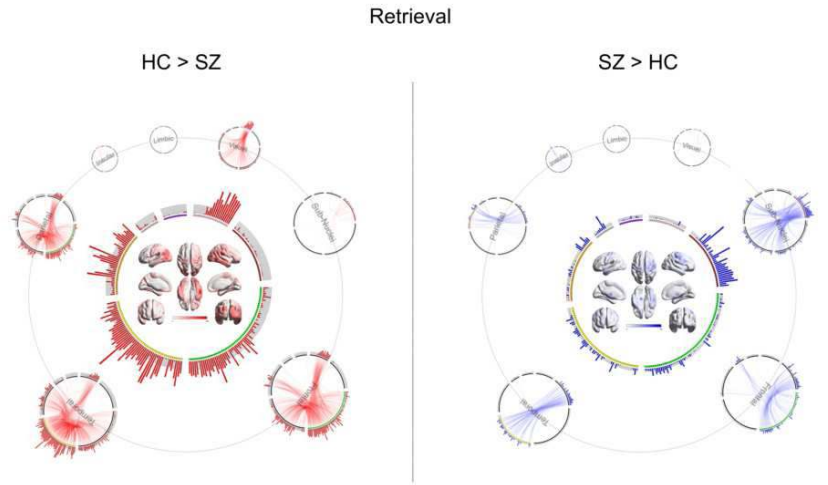

Figure 2. The figure reveals pairs of regions with significant inter-group differences in HOFC during Retrieval (Red: HC Greater; Blue: SCZ Greater). The central brain map is a frequency map. The color indicates the frequency with each any region is involved in a pathway with a significant difference in HOFC (these frequencies are redundantly depicted in the surrounding circular bar plots with the brain image providing location information). The chord diagramsin the satellites break down the observed effects by lobe (frontal, temporal, parietal, insular, limbic, visual and sub-lobar nuclei). As seen, in HC (compared to SCZ) there is increase in HOFC involving frontal, temporal, parietal and visual regions. However, in SCZ we observe (a presumably compensatory) an increase in HOFC involving sub-lobar nuclei, a part of the visual lobe that does not see a decrease during Encoding or Retrieval, and in small regard the insular lobe.

Conclusions: HOFC focuses on the correlation of spatial or topographical FC properties rather than actual temporal correlations, and while the neuronal correlates are obscure HOFC applied to resting state has captured salient differences between patients with autism (Zhao, Zhang, Rekik, An, & Shen, 2018) and mild cognitive impairment (Zhang et al., 2019). The current application in task-based fMRI data in schizophrenia is unique in terms of both the class of fMRI data (task-based) and the target population (schizophrenia). In our ongoing work, we are attempting to clarify the level of information embedded in HOFC that exceeds that embedded in conventional second order FC data.

References

1. Fan, L., Li, H., Zhuo, J., Zhang, Y., Wang, J., Chen, L., . . . Jiang, T. (2016). The Human Brainnetome Atlas: A New Brain Atlas Based on Connectional Architecture. Cereb Cortex, 26(8), 3508-3526. doi: 10.1093/cercor/bhw157
2. Meram, E. D., Baajour, S., Chowdury, A., Kopchick, J., Thomas, P., Rajan, U., . . . Diwadkar, V. A. (2023). The topology, stability, and instability of learning-induced brain network repertoires in schizophrenia. Network Neuroscience, 7(1), 184-212. doi: 10.1162/netn_a_00278
3. Silverstein, B., Bressler, S., & Diwadkar, V. A. (2016). Inferring the dysconnection syndrome in schizophrenia: Interpretational considerations on methods for the network analyses of fMRI data. Front Psychiatry, 7, 132. doi: 10.3389/fpsyt.2016.00132
4. Stanley, J. A., Burgess, A., Khatib, D., Ramaseshan, K., Arshad, M., Wu, H., & Diwadkar, V. A. (2017). Functional dynamics of hippocampal glutamate during associative learning assessed with in vivo 1H functional magnetic resonance spectroscopy. Neuroimage, 153, 189-197. doi: 10.1016/j.neuroimage.2017.03.051
5. Zhang, H., Chen, X., Shi, F., Li, G., Kim, M., Giannakopoulos, P., . . . Shen, D. (2016). Topographical Information-Based High-Order Functional Connectivity and Its Application in Abnormality Detection for Mild Cognitive Impairment. J Alzheimers Dis, 54(3), 1095-1112. doi: 10.3233/JAD-160092
6. Zhang, H., Giannakopoulos, P., Haller, S., Lee, S. W., Qiu, S., & Shen, D. (2019). Inter-Network High-Order Functional Connectivity (IN-HOFC) and its Alteration in Patients with Mild Cognitive Impairment. Neuroinformatics, 17(4), 547-561. doi: 10.1007/s12021-018-9413-x
7. Zhao, F., Zhang, H., Rekik, I., An, Z., & Shen, D. (2018). Diagnosis of Autism Spectrum Disorders Using Multi-Level High-Order Functional Networks Derived From Resting-State Functional MRI. Front Hum Neurosci, 12, 184. doi: 10.3389/fnhum.2018.00184

Poster No 1584

Higher-order interaction of brain microstructural and functional connectome

Hao Wang[1], Hui-jun Wu[2], Yang-Yu Liu[3], Linyuan Lü[4]

[1]School of Physics and Optoelectronic Engineering, Hainan University, Haikou, Hainan, [2]School of Media & Communication, Shanghai Jiao Tong University, Shanghai 200240, P. R. China., Shanghai, Shanghai, [3]Brigham and Women's Hospital and Harvard Medical School, Boston, MA, [4]University of Science and Technology of China, Hefei, Anhui

Introduction: Despite a relatively fixed anatomical structure, the human brain can support rich cognitive functions, triggering particular interest in investigating structure-function relationships (Honey, Sporns et al. 2009). Myelin is a vital brain microstructure marker; however, most myelin studies have constructed a structural covariance network at the population level, making individual cognitive or behavioral predictions impossible. Therefore, examining the myelin microstructural and functional relationship at the individual level is urgently needed but is still elusive. Recently, higher-order representations (beyond the node or edge level) emerged, including simplicial complexes (Giusti, Pastalkova et al. 2015), persistent homology (Liang and Wang 2017), neural network (Suárez, Richards et al. 2021), subgraphs (Przulj 2007), and motifs (Benson, Gleich et al. 2016), which have proven to be extremely useful in understanding and comparing complex networks. Nevertheless, few studies have examined individual myelin microstructure-function relationships using higher-order representations. Here, we quantify the individual-level microstructure-function relationship using a higher-order framework and explore the microstructure-function higher-order relationship across individual cognitive scores, development and network scale.

Methods: MRI data. Dataset: We downloaded unprocessed MR data of 213 participants from the Human Connectome Project (HCP) "S1200" new subjects release (Van Essen, Smith et al. 2013). We excluded eight participants who met any of the following criteria: (a) mean of framewise displacement (mFD) > 0.25 mm; (b) more than 20% of the FDs were above 0.2 mm; and (c) if any FDs were greater than 5 mm (Parkes, Fulcher et al. 2018). Seven participants aged > 36 years were excluded from the study. Finally, we obtained quality-controlled resting-state fMRI (rfMRI), T1-weighted, and T2-weighted images of 198 participants (108 males and 90 females). Here, we constructed the individual level myelin (T1w/T2w) structural network using probability distribution function (PDF)-based morphological methods (Wang, Jin et al. 2016) with Gordon parcellation of 333 brain regions (Gordon, Laumann et al. 2016), and constructed functional networks with the same parcellation as the myelin-structural network. Exploring the brain microstructure-function relationships using a higher-order framework, derived from 2- to 4-node subgraphs (Figure. 1)

Results: Global (network-level) higher-order microstructure-function relationships were negatively correlated with male participants' personality scores and declined with age ($P = 0.005$). Nodal (node-level) higher-order microstructure-function relationships are not aligned uniformly throughout the brain, being stronger in association cortices and lower in sensory cortices (Figure 2a-b), showing gender differences ($P < 0.001$, FDR correction), see Figure 2c. Notably, higher-order microstructure-function relationships are maintained from the whole-brain to local circuits, which uncovers a compelling and straightforward principle of brain structure-function complex interactions (Figure. 2d-f). Additionally, targeted artificial attacks can disrupt these higher-order relationships. The main results are robust against several factors, including (I) effect of sparsity thresholding; (II) effect of sample size; (III) split-half reliability for nodal higher-order interactions; (IV) higher-order relationships on other types of networks.

Conclusions: Our results advance our understanding of higher-order structural-function similarity that underlies cognition, individual differences, and aging, as well as provide a framework for measuring the similarity between complex systems.

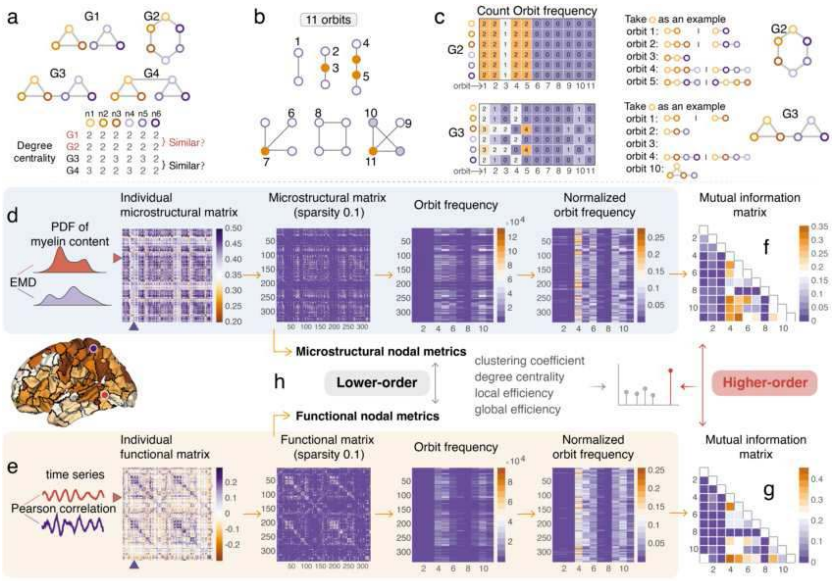

Figure 1 | Lower- and higher-order frameworks. **(a)** Schematic representation of four simple networks with six nodes represented by different colors, G1 and G2 have the same number of nodes and edges, G1 and G2 have identical nodal degree centrality but exhibit different topological structures, G1 consists of two triangles and G2 is a connected circle. G3 and G4 own identical topological structures; they both consist of two triangles and one path, while their nodal degree centrality is different. Thus, the lower-order depiction cannot capture the whole fact. **(b)** 11 non-redundant orbits from 2- and 4-node graphlet, each orbit is derived on their unique position within a graphlet. We used 11 non-redundant orbits to depict the network's higher-order property. **(c)** Take the G2 and G3 as an example; we give a toy example to depict how to count the frequency of 11 orbits for each node. **(d)** Construct the individual microstructural network based on the similarity of probability distribution function (PDF) of any paired regions' myelin content, then thresholding the network with sparsity value 10%, and calculating the orbit frequency matrix (333×11) for each network and normalizing orbit frequency matrix using logarithm (10-base) transformation. **(e)** Construct the individual functional network by calculating the Pearson correlation between the median time series of any paired brain regions, same with the structural network, we obtain the normalized orbit frequency matrix. **(f-g)** Mutual information (MI) matrix is obtained by calculating the similarity between the 11 orbits. We term the Pearson correlation between the MI matrix of the myelin-based microstructural and functional network as their higher-order relationship or interaction. **(h)** Lower-order framework, we term the Pearson correlation between the microstructural and functional brain network's nodal metrics as the lower-order similarity.

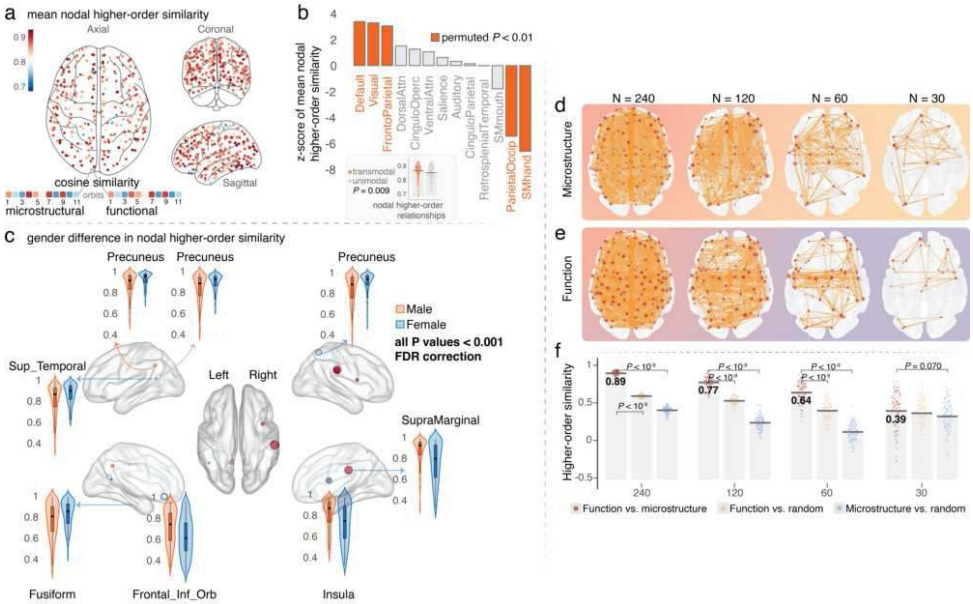

Figure 2 | **Nodal (node-level)** and **local (circuit-level)** higher-order microstructure-function relationship. **(a)** Nodal (regional) higher-order relationships were defined by the cosine similarity between the frequency of 11 orbits of each node in the functional and microstructural network. **(b)** Z-score of nodal higher-order relationships. **(c)** Gender difference in nodal higher-order relationships. **(d)** We randomly sample 100 times with different resolutions (network size) to extract the microstructural circuits (subnetworks); Here, the schematic shows the results for only 240,120, 60, and 30 nodes for one-time sampling. **(e)** The node index is consistent between the microstructural and functional network; the functional circuits (subnetworks) are also shown for only 240,120, 60, and 30 nodes. **(f)** After random sampling, we calculate the higher-order relationships between the microstructure-function subnetwork and their relationships with the random networks.

References

1. Benson, A. R., D. F. Gleich and J. Leskovec (2016). "Higher-order organization of complex networks." Science 353(6295): 163-166.
2. Giusti, C., E. Pastalkova, C. Curto and V. Itskov (2015). "Clique topology reveals intrinsic geometric structure in neural correlations." Proc Natl Acad Sci U S A 112(44): 13455-13460.
3. Gordon, E. M., T. O. Laumann, B. Adeyemo, J. F. Huckins, W. M. Kelley and S. E. Petersen (2016). "Generation and Evaluation of a Cortical Area Parcellation from Resting-State Correlations." Cereb Cortex 26(1): 288-303.
4. Honey, C. J., O. Sporns, L. Cammoun, X. Gigandet, J. P. Thiran, R. Meuli and P. Hagmann (2009). "Predicting human resting-state functional connectivity from structural connectivity." Proc Natl Acad Sci U S A 106(6): 2035-2040.
5. Liang, H. and H. Wang (2017). "Structure-Function Network Mapping and Its Assessment via Persistent Homology." PLoS Comput Biol 13(1): e1005325.
6. Parkes, L., B. Fulcher, M. Yucel and A. Fornito (2018). "An evaluation of the efficacy, reliability, and sensitivity of motion correction strategies for resting-state functional MRI." Neuroimage 171: 415-436.
7. Przulj, N. (2007). "Biological network comparison using graphlet degree distribution." Bioinformatics 23(2): e177-183.
8. Suárez, L. E., B. A. Richards, G. Lajoie and B. Misic (2021). "Learning function from structure in neuromorphic networks." Nature Machine Intelligence 3(9): 771-786.
9. Van Essen, D. C., S. M. Smith, D. M. Barch, T. E. Behrens, E. Yacoub, K. Ugurbil and W. U.-M. H. Consortium (2013). "The WU-Minn Human Connectome Project: an overview." Neuroimage 80: 62-79.
10. Wang, H., X. Jin, Y. Zhang and J. Wang (2016). "Single-subject morphological brain networks: connectivity mapping, topological characterization and test-retest reliability." Brain Behav 6(4): e00448.

Poster No 1585

Predicting micro-structure from low-dimensional embeddings of brain networks

Vincent Bazinet[1], Bratislav Misic[1]

[1]McGill University, Montreal, Quebec

Introduction: The human brain is a complex system of heterogeneous regions that interact with each other. At the micro-scale, individual brain regions have unique genetic, cellular, laminar and chemoarchitectural properties, and understanding how this local architecture varies across the cortex is one of the fundamental goals of neuroscience. Their main axes of variation can indeed provide valuable information about the development and function of individual brain regions and ultimately help characterise their role in different psychopathologies[1]. Here, we demonstrate that brain connectivity can be used to characterize variations in a wide range of micro structural properties.

Methods: In this work, we explored the relationship between micro-structure and brain connectivity by asking (i) which type of brain connectivity (structural or functional) best predict variations in micro-structure, (ii) which type of embedding best summarize these variations, and (iii) what are the main distinctions between the spatial embedding of the brain and network-based embeddings of the brain? We first reconstructed structural and functional connectomes using diffusion and functional MRI data from the Human Connectome Project (HCP; Fig. 1a)[2], which were parcellated into 800 brain regions[3]. The micro structural attributes studied included T1w/T2w ratio and cortical thickness information from the HCP, transcriptional information from the Allen Human Brain Atlas[4] and regional receptor profiles from publicly available positron emission tomography tracer studies (Fig. 1b)[5]. We next generated three different low-dimensional representations of the structural and functional connectomes using diffusion map embeddings[6], dynamical embeddings[7], and principal components (Fig. 2a). Then, we trained regression models to predict the micro-structural properties of each region of the brain, using the components of our embeddings as features. Half of the nodes in our networks were used to train our models, and the remaining half was used to evaluate their performance.

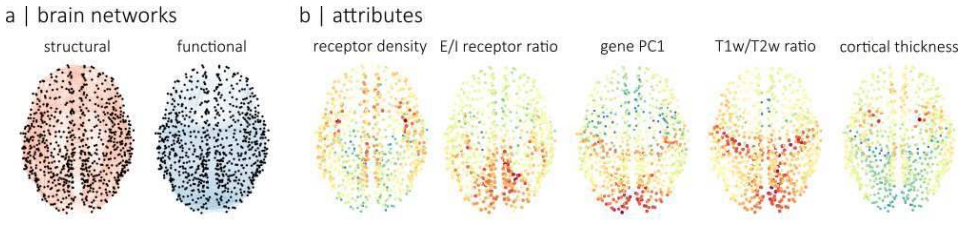

Fig. 1 Dataset description | (a) Brain networks include a group-averaged consensus structural connectome and a group-averaged consensus functional connectome, respectively generated using diffusion and fMRI data from the Human Connectome Project. (b) Micro-structural attributes include the average density of neurotransmitter receptors in each brain region (receptor density), the ratio of excitatory-to-inhibitory neurotransmitter in each brain region (E/I receptor ratio), the principal axis of variance in gene expression (gene PC1), T1w/T2w ratio and cortical thickness.

Results: We evaluated the performances of each low-dimensional representation using the coefficient of determination (R2). The best results were obtained, on average, with models relying on diffusion map embeddings of the structural connectome (mean R2=0.59; Fig. 2b, bottom-left panel). This is in line with recent work demonstrating that communication models

unfolding on the structural connectome can unveil important features of brain organization[8]. For the functional connectome, models relying on linear representation of connectivity (i.e. principal components) outperformed models relying on diffusion or dynamical embeddings (Fig. 2b, top-left panel) We also explored whether connectivity information can enhance modelsthat rely on information about the spatial relationship between brain regions (the Euclidean distance between them). We hence trained models using a low-dimensional representation of the distance relationships between brain regions and compared the accuracy of their predictions to those of models combining low-dimensional representations of both the spatial and topological relationships between brain regions. These models combining spatial and topological information outperformed the models relying solely on spatial information by a significant margin ($p<0.001$; Fig. 2c). This result shows that the information provided in structural and functional brain networks can enhance predictions of micro-structure variations made using the spatial information between brain regions.

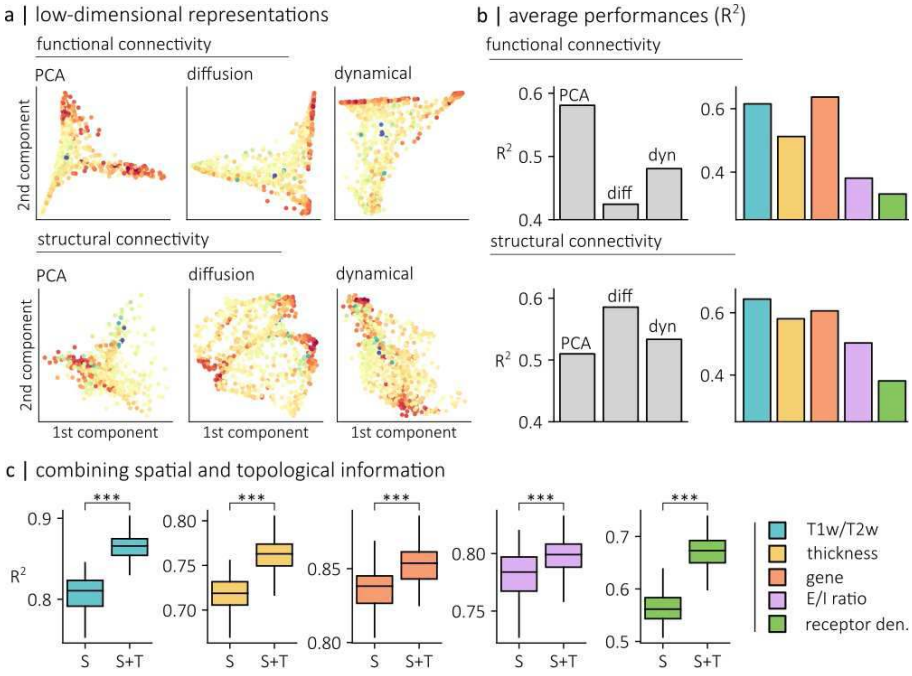

Fig. 2 Model performances | (a) Low-dimensional embeddings of functional (top) and structural (bottom) connectivity generated using principal component analysis (PCA; left), diffusion map embedding (middle) and dynamical embeddings (right). For each network and embedding type, we show the position of each node along the first and second components and color the nodes according to their T1w/T2w ratio. **(b)** The performance of each regression model was evaluated using the coefficient of determination (R^2). R^2 scores, are presented for each type of low-dimensional representation (averaged across attributes; left), and for each micro-structural attribute (averaged across low-dimensional representations; right). **(c)** The performance of models relying solely on spatial relationship between brain regions (S) were compared to models relying on both spatial and topological relationships between brain regions (S+T). Across all five attributes, S+T models significantly outperform S models ($p<0.001$).

Conclusions: In summary, the present work shows that brain connectivity provides valuable information about how the local boundaries and non-uniformities in the topographic distribution of micro-structural properties arise. Importantly, it also shows that the information retrieved from brain connectivity is fundamentally different from the background information provided by the spatial relationship between brain regions.

References

1. Sydnor, V. J. (2021). Neurodevelopment of the association cortices: Patterns, mechanisms, and implications for psychopathology. Neuron, 109(18), 2820-2846.
2. Van Essen, D. C. (2013). The WU-Minn human connectome project: an overview. Neuroimage, 80, 62-79.
3. Schaefer, A. (2018). Local-global parcellation of the human cerebral cortex from intrinsic functional connectivity MRI. Cerebral cortex, 28(9), 3095-3114.
4. Hawrylycz, M. J. (2012). An anatomically comprehensive atlas of the adult human brain transcriptome. Nature, 489(7416), 391-399.
5. Hansen, J. Y. (2022). Mapping neurotransmitter systems to the structural and functional organization of the human neocortex. Nature Neuroscience, 25, 1569-1581
6. Coifman, R. R. (2005). Geometric diffusions as a tool for harmonic analysis and structure definition of data: Diffusion maps. Proceedings of the national academy of sciences, 102(21), 7426-7431.
7. Schaub, M. T. (2019). Multiscale dynamical embeddings of complex networks. Physical Review E, 99(6), 062308.
8. Avena-Koenigsberger, A. (2018). Communication dynamics in complex brain networks. Nature reviews neuroscience, 19(1), 17-33.

Poster No 1586

Investigating the properties of hippocampal subfield networks

Samuel Berry[1], Marie-Lucie Read[2], Jiaxiang Zhang[3], Kim Graham[4], Andrew Lawrence[4], John Aggleton[2], Carl Hodgetts[5]

[1]Royal Holloway University of London, London, London, [2]Cardiff University, Cardiff, United Kingdom, [3]Swansea University, Swansea, United Kingdom, [4]The University of Edinburgh, Edinburgh, United Kingdom, [5]Royal Holloway University of London, London, United Kingdom

Introduction: Studies in animal models suggest that the subicular complex of the hippocampus (HC) may act as a hub within an extended event memory system, serving as the primary source of HC outputs to several key regions in this network, including retrosplenial cortex, mammillary bodies and anterior thalamic nuclei[1]. Despite its privileged position in this system, we have limited knowledge of subicular network properties in the human brain. Addressing this, we applied network analysis approaches to both structural and functional 7T MRI data, comparing subiculum connectivity to CA1 and CA2/3. A key challenge for MRI network analysis (particularly with diffusion-based tractography) is the proliferation of false positives. Therefore, we contextualise our results with regards to historical anatomical tract-tracing data. This cross-modality and cross-species approach helps us to interrogate this network whilst understanding the anatomical validity of these MRI-constructed connectomes.

Methods: Subjects were 50 adults from the Young Adults Human Connectome Project. All samples had 7T task-free functional, diffusion, and sub-millimetre structural scans. Fourteen extended HC network ROIs were defined with reference to a comprehensive review of HC tract-tracing data by Aggleton & Christiansen, 2015. Human HC segmentation was performed using the automated segmentation of hippocampal subfields (ASHS)[2] tool, with the other human ROI's defined using freesurfer[3,8,9]. Registrations were performed using FS(4)L flirt, fnirt and ANTs[5] syn algorithms. Functional connectivity (FC) was measured via BOLD correlations and structural connectivity (SC) was estimated using anatomically constrained probabilistic tractography analysis via MRTRIX[6]. SC and FC connectivity measures were then used as inputs for GT analysis via the brain connectivity toolbox[7], in Matlab. Descriptive network statistics (such as connectivity strength) were calculated. Additionally, we performed a series of 'virtual lesions' by iteratively removing and HC ROIs and re-calculating global efficiency scores.

Results: Tractography results demonstrated that the subiculum had the highest connectivity strength, followed by CA1 (vs subiculum d = 0.56, p = 0.01) and CA2/3 (vs subiculum d = 3.13, p <0.0001) (figure 1). Differences with CA1 were mostly driven by connections to the entorhinal cortex (t = 11.76, p <0001). Structural virtual lesion analysis showed that removing CA1 had the greatest effect on the network (d = 0.27, p < 0.001), followed by subiculum (d = 0.16, p <0.001), whereas CA2/3 removal increased network efficiency (d = 0.21, p < 0.001)(figure 1). All statistical comparisons between the ROIs were statistically significant (p<0.001, Bonferroni corrected). Functional connectivity results showed CA1 to have the highest connectivity strength, followed by the subiculum (vs CA1 d = 1.56, p < 0.001), and CA2/3 (vs subiculum d =4.48, p < 0.001) (figure 2). Functional virtual lesion analysis showed that removing the subiculum had a significantly larger effect (d = 0.47, p < 0.001) than CA1 (d = 0.22, p < 0.001) and CA2/3 (0.42, p<0.001 (figure 2).

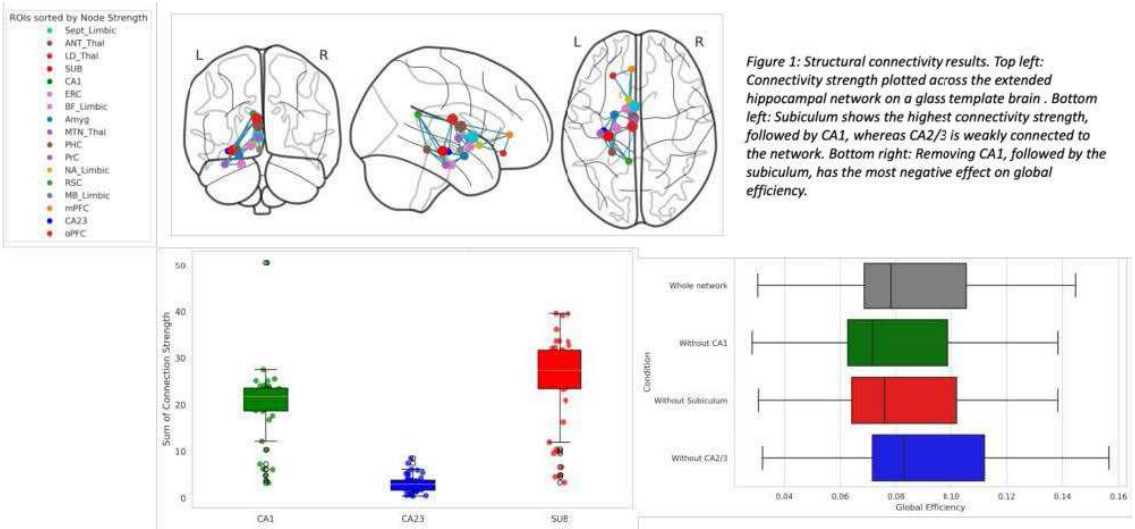

Figure 1: Structural connectivity results. Top left: Connectivity strength plotted across the extended hippocampal network on a glass template brain . Bottom left: Subiculum shows the highest connectivity strength, followed by CA1, whereas CA2/3 is weakly connected to the network. Bottom right: Removing CA1, followed by the subiculum, has the most negative effect on global efficiency.

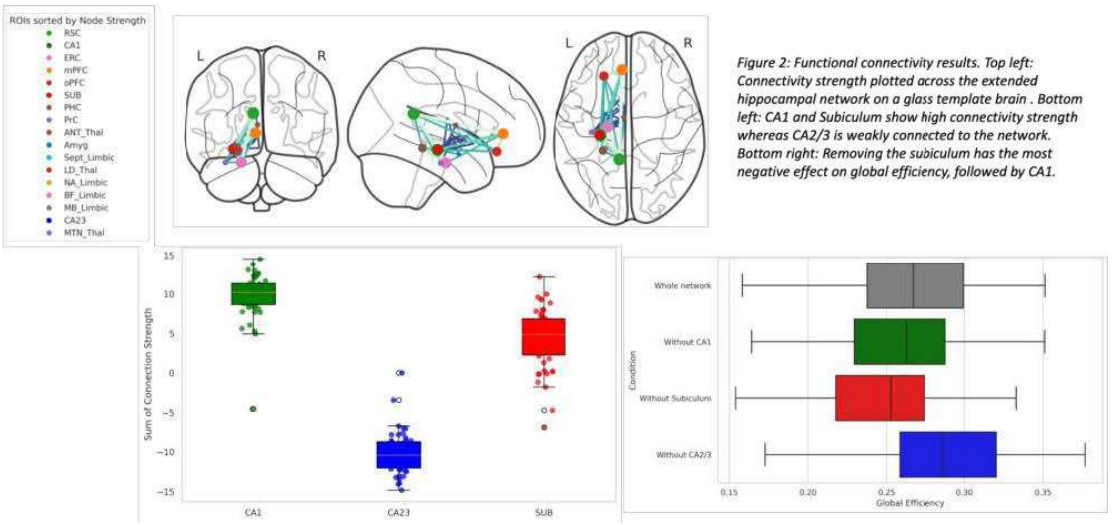

Figure 2: Functional connectivity results. Top left: Connectivity strength plotted across the extended hippocampal network on a glass template brain . Bottom left: CA1 and Subiculum show high connectivity strength whereas CA2/3 is weakly connected to the network. Bottom right: Removing the subiculum has the most negative effect on global efficiency, followed by CA1.

Conclusions: We provide novel high resolution structural and functional evidence for the subiculum, and CA1's, role as key regions within the extended HC network. This work largely corroborates previous anatomical tract-tracing studies in animal models, endorsing the role of the subiculum as a key HC hub. Interestingly, while our findings align with expectations regarding the subiculum's role as the principal structural output region of the hippocampus, they reveal a higher degree of functional connectivity with CA1 than anticipated based solely on anatomical data. Future work will focus on the interrogation of specific tracts generated through the diffusion analysis with direct comparisons to macaque MRI data.

References

1. Aggleton, J. P., & Christiansen, K. (2015). The subiculum: the heart of the extended hippocampal system. Progress in brain research, 219, 65-82.
2. Yushkevich, P. A., Pluta, J. B., Wang, H., Xie, L., Ding, S. L., Gertje, E. C., ... & Wolk, D. A. (2015). Automated volumetry and regional thickness analysis of hippocampal subfields and medial temporal cortical structures in mild cognitive impairment. Human brain mapping, 36(1), 258-287.
3. Fischl, B. (2012). FreeSurfer. Neuroimage, 62(2), 774-781
4. Jenkinson, M., Beckmann, C. F., Behrens, T. E., Woolrich, M. W., & Smith, S. M. (2012). Fsl. Neuroimage, 62(2), 782-790.
5. Avants, B. B., Tustison, N., & Song, G. (2009). Advanced normalization tools (ANTS). Insight j, 2(365), 1-35.
6. Tournier, J. D., Calamante, F., & Connelly, A. (2012). MRtrix: diffusion tractography in crossing fiber regions. International journal of imaging systems and technology, 22(1), 53-66.
7. Rubinov, M., Kötter, R., Hagmann, P., & Sporns, O. (2009). Brain connectivity toolbox: a collection of complex network measurements and brain connectivity datasets. NeuroImage, 47, S169.
8. Greve, D. N., Billot, B., Cordero, D., Hoopes, A., Hoffmann, M., Dalca, A. V., Fischl, B., Iglesias, J. E., & Augustinack, J. C. (2021). A deep learning toolbox for automatic segmentation of subcortical limbic structures from MRI images. NeuroImage, 244, 118610.
9. Iglesias, J. E., Insausti, R., Lerma-Usabiaga, G., Bocchetta, M., Van Leemput, K., Greve, D. N., van der Kouwe, A., Alzheimer's Disease Neuroimaging Initiative, Fischl, B., Caballero-Gaudes, C., & Paz-Alonso, P. M. (2018). A probabilistic atlas of the human thalamic nuclei combining ex vivo MRI and histology. NeuroImage, 183, 314–326.

Poster No 1587

Modularity of Human Brain Asymmetric Network Revealed by 40,000 Healthy Individuals from sMRI

Sifeng Wang[1], Suyu Zhong[1]

[1]Beijing University of Posts and Telecommunications, Beijing, Beijing

Introduction: Brain asymmetry has been a predominant perspective to unravel the mapping from structural morphology to functions and complex behaviors of human. Great efforts have been made depicting the wiring between brain structure and function where network analysis approaches are widely used to measure similarity and discrepancy between structural and functional networks[4]. Following the footsteps, we construct highly modulated networks of brain asymmetry index derived from regional morphology including regional area and grey matter volume. Especially, a consistent module decomposition across gender subgroups is observed in the regional grey matter volume network, demonstrating the potential of asymmetrical networks to bridge brain structure and function.

Methods: Brain imaging phenotypes of 42800 (Female: 22584) and 43063 (Female: 22684) cross-sectional T1-weighted MRIs in UK Biobank dataset[5] were selected to construct asymmetrical networks on regional grey matter volume (rGMV, 65 paired regions) and white surface area (rWSA, 74 paired regions) respectively. Age of subjects were ranged from 44 to 86.

Brain asymmetric networks were defined based on correlation matrices across all cerebral regional Asymmetry Index (AI) in corresponding parcellations. A linear regression was performed to alleviate impact of age and gender before calculating AI following a simple definition: AI(X)=(L(X)-R(X))/2(L(X)+R(X))[6]. Empirical interregional correlations were then calculated on normalized AI[2]. Pearson's R with FDR correction are applied to reject insignificant connections. Additional gender-specific correlations were constructed independently on gender subsets following same steps as above, except that linear regression was only performed on age. Regional pairs survived from significance test in each dataset formed a weighted undirected graph. That is, brain regions were treated as nodes and correlations as edges. Modularity Q is optimized with greedy algorithm by maintaining a matrix of ΔQ proposed by Clauset[1]. We used Clauset's greedy-based algorithm encapsulated in Gretna toolbox[7] (v2.0.0) to perform modularity analysis of our lateralization networks. Significance of network modularity were then tested with 1,000 randomly generated networks with the same number of nodes and degree distribution as the brain network to compare with.

Results: rGMV asymmetrical networks showed strong modularity in overall dataset (Q=0.27, z=7.95, p<0.001) and gender-specific subsets (Male: Q=0.28, z=12.56, p<0.001, Female: Q=0.28, z=12.24, p<0.001), with a consistent five-module composition across gender (Fig. 1). Five nonoverlapping modules were characterized by subcortical necli and cerebellum subdivisions, temporal regions, frontal regions, and parieto-occipital regions respectively. rWSA asymmetrical networks exhibited even stronger modularity compared to rGMV in both overall dataset (Q=0.32, z=13.97, p<0.001) and gender-specific subsets (Male: Q=0.34, z=23.01, p<0.001, Female: Q=0.33, z=19.84, p<0.001). However, slight permutations in module composition were observed that causes significant difference in modularity analysis results (Number of modules. Overall: 4, Male: 4, Female: 5). The majorities in modules were central and parietal regions, frontal regions and occipito-temporal regions respectively (Fig. 2).

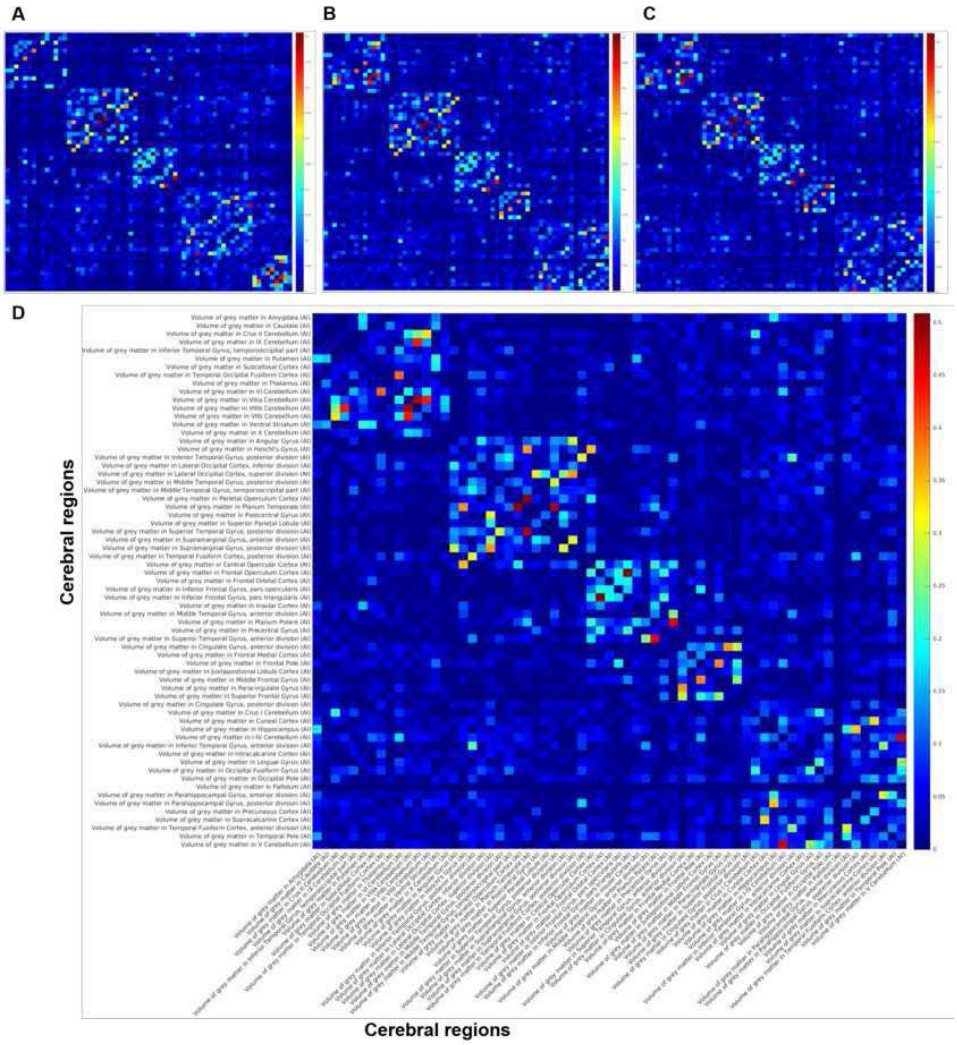

Figure 1. Asymmetry Index Network of rGMV. (A) Female subgroup network. (B) Overall network. (C) Male subgroup network. (D) Overall network with region names. A consistent five-module was observed in rGMV Asymmetry Index networks across gender. (Edge weights are absolute interregional correlations)

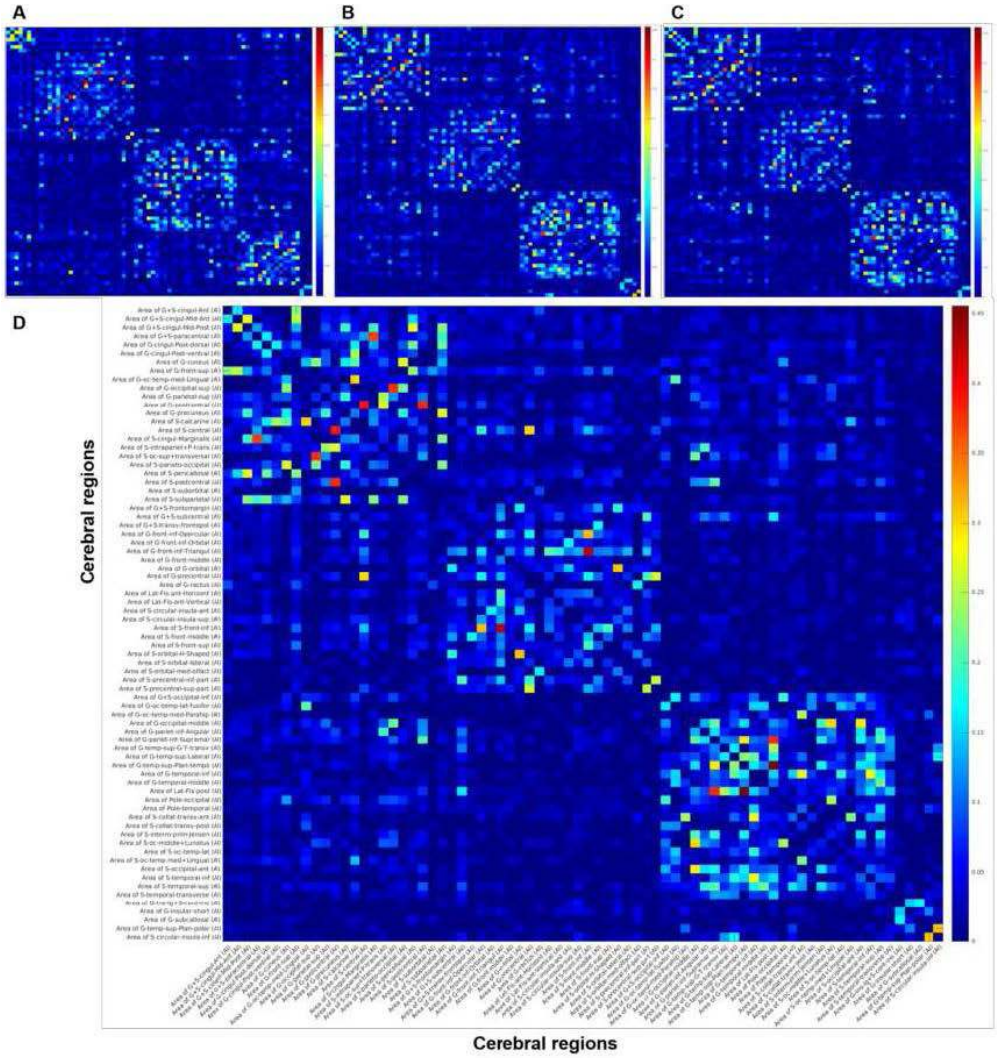

Figure 2. Asymmetry Index Network of rWSA. (A) Female subgroup network. (B) Overall network. (C) Male subgroup network. (D) Overall network with region names. A four-module partitioning of overall and male-specific network was observed while female-specific network yielded a five-module partitioning. (Edge weights are absolute interregional correlations)

Conclusions: We provided a brand new perspective of analyzing human brain connectivity simply by constructing a region-wise cerebral network of Asymmetry Index. Asymmetrical networks derived from regional grey matter volume and white surface area demonstrate outstanding modularity properties. Networks of regional grey matter volume were perfectly aligned across gender, while some of the modules of in white surface area network altered across gender. Future studies are needed to testify genetic and behavioral associations of individual asymmetrical networks.

References

1. Clauset, A., Newman, M.E. and Moore, C. (2004) 'Finding community structure in very large networks', Physical review E, 70(6), p.066111.
2. He, Y., Chen, Z.J. and Evans, A.C. (2007) 'Small-World Anatomical Networks in the Human Brain Revealed by Cortical Thickness from MRI', Cerebral Cortex, 17(10), pp. 2407–2419.
3. Newman, M.E.J. (2006) 'Modularity and community structure in networks', Proceedings of the National Academy of Sciences, 103(23), pp. 8577–8582.
4. Park, H.-J. and Friston, K. (2013) 'Structural and Functional Brain Networks: From Connections to Cognition', Science, 342(6158), p. 1238411.
5. Sudlow, C. et al. (2015) 'UK Biobank: An Open Access Resource for Identifying the Causes of a Wide Range of Complex Diseases of Middle and Old Age', PLOS Medicine, 12(3), p. e1001779.
6. Toga, A.W. and Thompson, P.M. (2003) 'Mapping brain asymmetry', Nature Reviews Neuroscience, 4(1), pp. 37–48.
7. Wang, J. et al. (2015) 'GRETNA: a graph theoretical network analysis toolbox for imaging connectomics', Frontiers in Human Neuroscience, 9.

Poster No 1588

Improving Brain-Behavior Associations in Functional Connectivity with Selection of Movie Timeframes

Sarah Cutts[1], Jacob Tanner[1], Caio Seguin[2], Richard Betzel[1], Olaf Sporns[1]

[1]Indiana University, Bloomington, IN, [2]Department of Psychological and Brain Sciences, Indiana University, Bloomington, IN

Introduction: Past work has shown that identifiability and behavioral signatures in functional connectivity (FC) vary within a scan session[1-4]. This work suggests that multiple levels of variation exist within resting state scans based on the behavior or network property of interest. Movie data has been shown to be promising for assessing FC because it is both more engaging and easier to collect data. It has been shown to enhance behavioral prediction from FC[5] suggested due to similarities in stimuli enhancing notable differences between subjects[6]. It remains unclear whether subject-variability in behavioral measures reveal stronger relationships to specific time points within movies. We optimize the selection of the top 10% of time points within multiple movies that enhance brain-behavioral correlations across 58 separate behaviors.

Methods: We analyzed fMRI movie data of 126 healthy subjects from the Human Connectome Project[7]. Four scan sessions of movie clips were shown, and each participant performed a battery of out-of-scanner behavioral assessments. Resting-state blocks between movie clips were accounted for by removing 10 TRs at the start of each clip and retaining 5 TRs into resting blocks. An implementation of the Metropolis-Hastings algorithm and simulated annealing[2] was used to find moments within movies that improved correlations with 58 distinct behavioral measures (Fig 1A). Initial timestamps for each movie were randomly generated to select for 80 TRs (~10% of each movie) and these time points were shifted at each step of the optimization to determine which selection of moments improved behavioral correlations. At each step, selected time points were made into functional connectivity components (FCc)[2,8] by computing the agreement matrix across the binarized nodal time series of the selected frames[9]. Magnitude of overall brain-behavior correlations was used as the cost function in the optimization. This was done by computing correlations between each edge of the FCc across subjects with the behavior, then taking the mean absolute value of the correlations across all edges. Selection of time points was then either accepted or rejected based on improvements to the cost function. Timestamps were then altered on 1-3 frames and the process was repeated over 10,000 iterations until the selection of time points converged. One-hundred optimizations were performed on each of the 58 behaviors with separate random selections of 80/20 (101 training / 25 testing subjects) cross validations. Improvements in magnitude of brain-behavior correlations and similarity of brain-behavior correlation edge maps between training and testing groups were assessed by comparing FCc from optimized timestamps to randomly initialized timestamps. Similarities between selected timestamps across behaviors were assessed with Jaccard distance.

Results: Improvements in brain-behavior correlations and similarity between correlation maps of training and testing groups are shown in Fig 1B for all behaviors of each movie. Multiple behaviors showed significantly ($p < 0.05$) improved train-test transfer over initialization in the held-out testing subjects and certain behaviors showed significant improvements in brain-behavior correlations or in both measures. Optimizations consistently converged onto similar time points within each of the movies over multiple cross validations (Fig 2A). Notably, the selection of time points and brain-behavior correlation maps differed across behavioral measures (Fig 2B) but shared similar timestamps between some of the behaviors (Fig 2C). Optimized timestamps selected moments that improved variability across subjects (mean standard deviation across edges) for each behavior compared to initial timestamps (Fig 2D).

Conclusions: Optimizing time point selection in movies to improve behavioral correlations showed consistent convergence onto similar moments within the same behavior and selection of unique moments across unrelated behaviors.

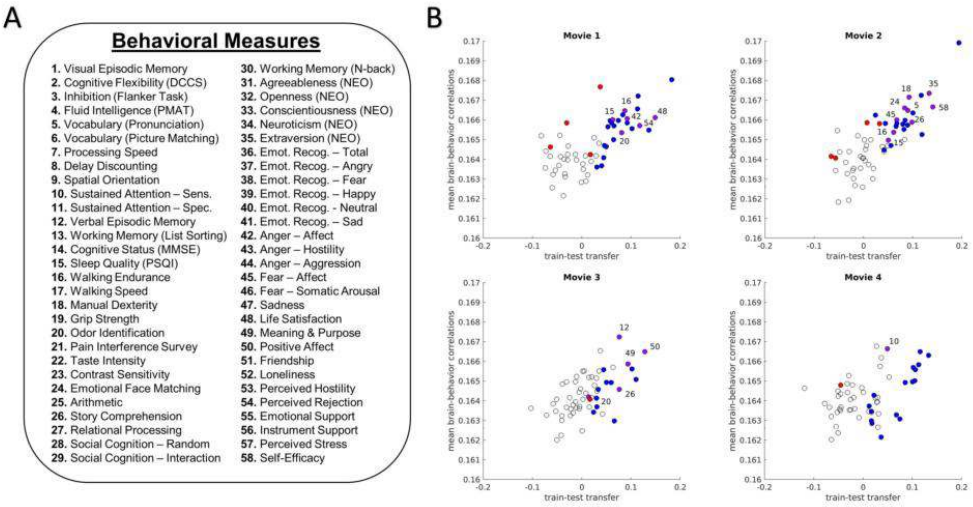

Figure 1. Summary of Behavior Optimizations. (A) List of 58 behaviors selected based on [10] for high subject compliance and distribution across cognitive, social, and emotional measures. Age, sex, frame-wise displacement (FD), DVARS, body mass index, and total brain volume were regressed from behaviors prior to all procedures and analyses. **(B)** Summary results show mean absolute brain-behavior correlations by similarity of brain-behavior correlation maps between training and testing groups (train-test transfer) for each of the 4 movies. Colored behaviors show instances where optimized values were significantly greater ($p < 0.05$) than the initial random time points across the 100 cross validations of the held-out test subjects. Behaviors with both significantly greater brain-behavior correlations and train-test transfer are listed and displayed in purple. Behaviors with only significantly greater train-test transfer are shown in blue and only significantly greater brain-behavior correlations are in red. Results from test subjects were averaged across all 100 cross validations for each of the 58 behaviors. Behavioral labels were included for behaviors that maintained across all categories.

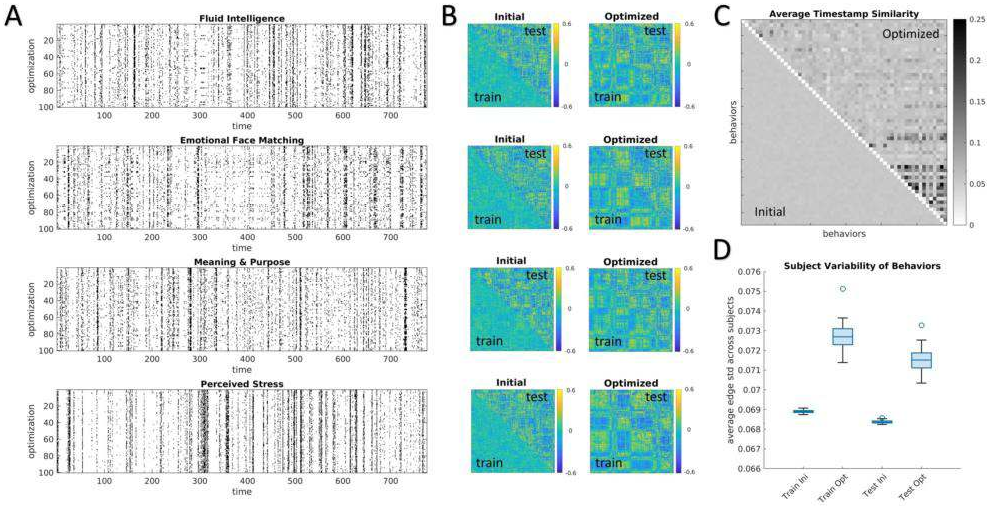

Figure 2. Temporal Variability in Brain-Behavior Correlations. (A) Timestamps optimized for 4 separate example behaviors from movie 1. Eighty time points (~10% of each movie) were selected across 100 separate 80/20 (training/testing set) cross validations over the course of 10,000 iterations of simulated annealing optimizations using mean absolute value of brain-behavior correlations as the cost function. **(B)** Brain-behavior correlation maps for randomly selected initial time points (left) and their corresponding optimized maps (right) of the behaviors directly adjacent in (A). Brain-behavior correlation maps are displayed of an example cross validation from the training set (lower triangle) with results from the held-out testing set (upper triangle). **(C)** Timestamps were compared between each behavior using Jaccard distance and averaged across cross validations for both the initial randomly selected time points (lower triangle) and the optimized time points (upper triangle). **(D)** Standard deviation across subjects were computed for each edge of the FCc created from selected time points. Results were averaged across all edges and cross validations separately for each behavior. All behavior values of average standard deviation of FC edges are shown for both training and testing subject groups as well as initial and optimized timestamps.

References

1. Van De Ville, D., Farouj, Y., Preti, M. G., Liégeois, R., & Amico, E. (2021). When makes you unique: temporality of the human brain fingerprint. Science advances, 7(42), eabj0751.
2. Peña-Gómez, C., Avena-Koenigsberger, A., Sepulcre, J., & Sporns, O. (2018). Spatiotemporal network markers of individual variability in the human functional connectome. Cerebral Cortex, 28(8), 2922-2934.
3. Cutts, S. A., Faskowitz, J., Betzel, R. F., & Sporns, O. (2023). Uncovering individual differences in fine-scale dynamics of functional connectivity. Cerebral Cortex, 33(5), 2375-2394.
4. Cutts, S. A., Chumin, E. J., Betzel, R. F., & Sporns, O. (2023). Temporal Variability of Brain-Behavior Relationships in Fine-Scale Dynamics of Edge Time Series. bioRxiv, 2023-09.
5. Finn, E. S., & Bandettini, P. A. (2021). Movie-watching outperforms rest for functional connectivity-based prediction of behavior. NeuroImage, 235, 117963.
6. Finn, E. S., Scheinost, D., Finn, D. M., Shen, X., Papademetris, X., & Constable, R. T. (2017). Can brain state be manipulated to emphasize individual differences in functional connectivity?. Neuroimage, 160, 140-151.

7. Van Essen, D. C., Smith, S. M., Barch, D. M., Behrens, T. E., Yacoub, E., Ugurbil, K., & Wu-Minn HCPConsortium. (2013). The WU-Minn human connectome project: an overview. Neuroimage, 80, 62-79.
8. Chumin, E. J., Cutts, S. A., Risacher, S. L., Apostolova, L. G., Farlow, M. R., McDonald, B. C., ... & Sporns, O. (2023). Edge time series components of functional connectivity and cognitive function in Alzheimer's disease. Brain Imaging and Behavior, 1-13.
9. Sporns, O., Faskowitz, J., Teixeira, A. S., Cutts, S. A., & Betzel, R. F. (2021). Dynamic expression of brain functional systems disclosed by fine-scale analysis of edge time series. Network Neuroscience, 5(2), 405–433.
10. Kong, R., Li, J., Orban, C., Sabuncu, M. R., Liu, H., Schaefer, A., Sun, N., Zuo, X. N., Holmes, A. J., Eickhoff, S. B., & Yeo, B. T. (2019). Spatial topography of individual-specific cortical networks predicts human cognition, personality, and emotion. Cerebral Cortex, 29(6), 2533-2551.

Poster No 1589

A Copula Linked Parallel ICA for sMRI and 4D-fMRI fusion

Oktay Agcaoglu[1], Rogers F. Silva[2], Deniz Alacam[2], Vince Calhoun[3]

[1]Tri-Institutional Center for Translational Research in Neuroimaging and Data Sci, Atlanta, GA, [2]TReNDS, Atlanta, GA, [3]GSU/GATech/Emory, Decatur, GA

Introduction: Current multimodal fusion methods are primarily confined to using second-level 3D fMRI features, such as fALFF, regional homogeneity, or FNC, often neglecting the temporal information in the full 4D fMRI data. To overcome this, we introduce a novel method, Copula Linked Parallel ICA (CLiP-ICA). This method uniquely estimates an unmixing matrix for each modality independently while synchronizing sources through a copula model. We evaluated CLiP-ICA's effectiveness in both a simulation study and a real-world application using fMRI and sMRI data from the Alzheimer's Disease Neuroimaging Initiative (ADNI) study. To our knowledge, this is the inaugural study capable of jointly estimating independent components of fMRI and sMRI while preserving crucial temporal information.

Methods: Preprocessed fMRI and sMRI datasets are reduced to the dimensions specified by the model order using separate Principal Component Analysis (PCA). CLiP-ICA aims to find two unmixing matrices that maximize the likelihood of a 2D joint distribution, which is implemented as the 1D marginal distribution of each modality and a copula to link them[1]. The marginal distribution can vary between modalities, and the copula can be of any type, such as a Gaussian copula[2]. In this paper, we focus on illustrating the use of Gaussian copulas. During training, batches contain data from corresponding voxels in both modalities

Results: We generated 4 spatially independent components using a simulation toolbox[3], and later, we used custom MATLAB scripts to generate a second set of 4 components that are linked to the first set with Pearson correlations of 0.05, 0.8, 0.5, and 0.2, while preserving the independency between components and the blob-like structure in the components. Subsequently, we generated two 4x4 mixing matrices and the observed data. To make the simulation more representative of real data scenarios, we ensured that the corresponding rows of the first and second mixing matrices were highly correlated, with correlations of [0.91, 0.96, 0.94, 0.93], resulting in highly similar but not identical mixtures. We then attempted to retrieve sources using both conventional JICA and our proposed CLiP-ICA. CLiP-ICA was able to retrieve the original sources almost perfectly (correlation of 0.99), while JICA only achieved partial retrieval (correlation of 0.53). We also tested CLiP-ICA on 864 fMRI and sMRI scans from ADNI. The fMRI data were reduced to 30 PCA (45 at the subject level and 30 at the group level), and the gray matter images were also reduced to 30 PCA. Then, we ran CLiP-ICA with a Gaussian copula, where linkage parameters ranged linearly from 0.95 to 0.65. After training, we compared the sMRI and fMRI components. Figure 2 shows the aggregated structural FNC results. Subsequently, utilizing back reconstruction enabled the calculation of subject-specific FNC for both fMRI and structural FNC.

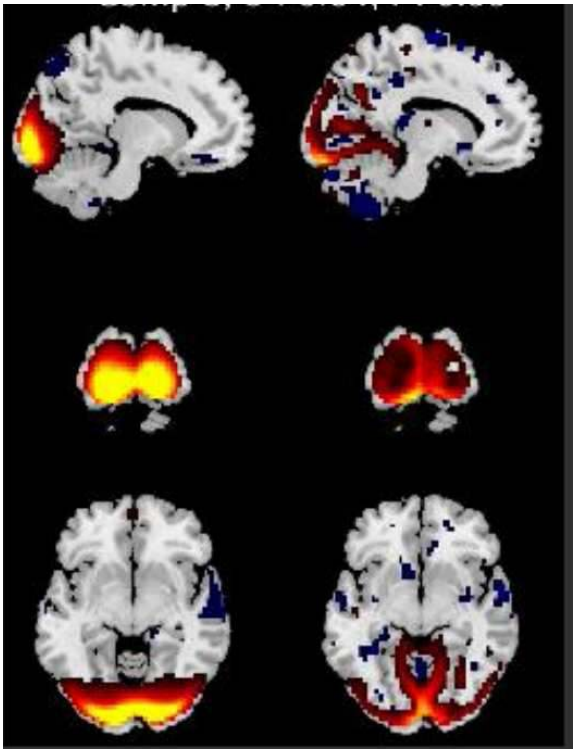

Fig. A component pair: on the left, an fMRI component; on the right, the corresponding linked sMRI component.

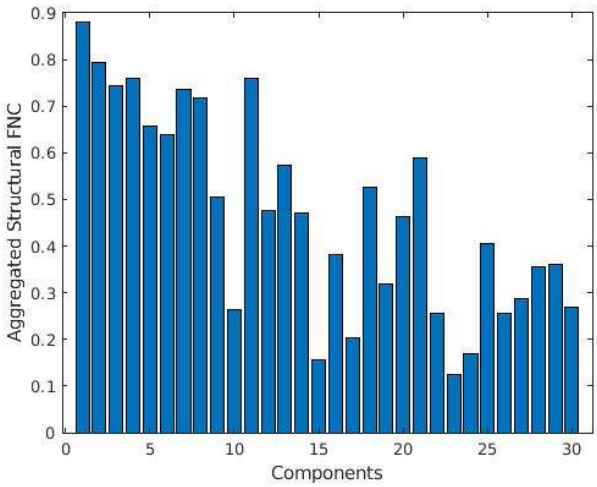

Table. Aggregated structural FNC between each fMRI and sMRI components

Conclusions: In conclusion, this study introduces a groundbreaking algorithm, designed to fully leverage the complete 4D fMRI dataset in the fusion of fMRI and sMRI, thereby enabling enhanced linked independent component analysis. Our comprehensive simulations have demonstrated the superior performance of our proposed CLiP-ICA algorithm over the traditional Joint ICA (JICA) approach. Furthermore, the application of our method to real medical imaging datasets has validated its effectiveness in harnessing valuable information, marking a significant advancement in medical imaging analysis

References

1. O. Agcaoglu, R. F. Silva, D. Alacam, and V. D. Calhoun, “A MULTI-DIMENSIONAL JOINT ICA MODEL with GAUSSIAN COPULA,” presented at the International Conference on Image Analysis and Processing, Multi-Modal Medical Imaging Processing Workshop, 2023, 2023

Poster No 1590

An analysis of sleep quality and resting state global transition energy in young adults

Anthony Villegas[1], Amy Kuceyeski[2], Parker Singleton[3], Keith Jamison[2]

[1]Weill Cornell Medicine, Maspeth, NY, [2]Weill Cornell Medicine, New York City, NY, [3]Weill Cornell Medicine, New York, NY

Introduction: Approximately 1 in 3 adults in the United States report insufficient rest or sleep, a widespread issue with significant public health implications. Poor sleep quality extends beyond fatigue, impacting cognitive processes and contributing to mental health disorders. Inadequate sleep is linked to adverse effects on working memory, executive function, and decision-making (Zavecz 2020), and with anxiety and depression (Abdelhack 2023; Dietch 2016). The complex relationship between sleep quality and brain functionality necessitates innovative approaches for characterization and diagnosis. Heterogeneity in outcomes among those with poor sleep quality underscores the limitations of conventional measures, emphasizing the need for novel biological markers.

Methods: We used high-resolution, preprocessed MRI data from the Human Connectome Project – Young Adult S1200 dataset (van Essen 2013). Regional time-series and structural connectomes were extracted from 958 HCP subjects using the 268-region Shen atlas and deterministic tractography. K-means clustering and network control theory-based transition energy (TE) calculations were employed to characterize brain states. TE represents the minimum energy input within the structural connectome needed for transitioning between brain activity states (Gu 2015). Average TE quantified overall energy requirements for transitions across four brain states. The Pittsburgh Sleep Quality Index (PSQI) assessed sleep quality, and ordinary least squares regression explored the relationship between average TE and sleep quality, accounting for age, sex, and mean framewise displacement as covariates.

Results: Significant main effects of PSQI scores on average global transition energy were found, with interactions between PSQI scores and age and framewise displacement.

	coef	std err	t	P>|t|	[0.025	0.975]
Intercept	5.372e+04	6011.079	8.938	0.000	4.19e+04	6.55e+04
PSQI	3429.9747	1107.052	3.098	0.002	1257.425	5602.524
Age	−403.1616	212.084	−1.901	0.058	−819.370	13.046
Sex	1228.1965	1596.054	0.770	0.442	−1904.002	4360.395
Mean_FD	−2.231e+04	1.4e+04	−1.599	0.110	−4.97e+04	5075.611
PSQI:Age	−138.1623	39.951	−3.458	0.001	−216.564	−59.760
PSQI:Sex	−196.6987	293.201	−0.671	0.502	−772.095	378.698
PSQI:Mean_FD	4955.5149	2201.076	2.251	0.025	635.983	9275.047

Conclusions: This study provides evidence of the influence of sleep quality, as assessed by the PSQI, on resting-state global transition energy among young adults. Our findings suggest that individuals with poorer sleep quality may exhibit alterations in brain activity, reflecting a less dynamic system characterized by reduced complexity and higher energetic barriers. In contrast, those with better sleep quality may demonstrate a more robust and intricate neural network, highlighting the potential implications of sleep quality on the overall dynamism of the brain. These insights contribute to our understanding of the neurobiological underpinnings of sleep quality and underscore the importance of considering sleep-related factors in assessing brain dynamics.

References

1. Abdelhack, M. (2023), 'Opposing brain signatures of sleep in task-based and resting-state conditions', Nat Communications, 14, 7927
2. Dietch JR (2016), 'Psychometric Evaluation of the PSQI in U.S. College Students', Journal of Clinical Sleep Medicine, vol. 12, no. 8
3. Cornblath EJ (2020), 'Temporal sequences of brain activity at rest are constrained by white matter structure and modulated by cognitive demands', Communications Biology, 22;3(1):261.
4. Gu S (2015), 'Controllability of structural brain networks', Nature Communications, 1;6:8414.
5. Singleton, S.P (2022), 'Receptor-informed network control theory links LSD and psilocybin to a flattening of the brain's control energy landscape', Nature Communications, 13, 5812
6. Van Essen DC (2013), 'The WU-Minn Human Connectome Project: an overview', Neuroimage. 15;80:62-79.
7. Zavecz Z (2020), 'The relationship between subjective sleep quality and cognitive performance in healthy young adults: Evidence from three empirical studies', Sci Rep, 10(1):4855.

Poster No 1591

Evaluating the impact of denoising on diffusion MRI-based tractometry on glaucoma patients

Daiki Taguma[1,2], Shumpei Ogawa[3], Hiromasa Takemura[1,2,4]

[1]National Institute for Physiological Sciences, Okazaki, Japan, [2]The Graduate Institute of Advanced Studies, SOKENDAI, Hayama, Japan, [3]The Jikei University School of Medicine, Tokyo, Japan, [4]Center for Information and Neural Networks (CiNet), Advanced ICT Research Institute, NICT, Suita, Japan

Introduction: Diffusion MRI (dMRI)-based tractometry is the sole method available for measuring tissue properties of white matter tracts in living humans (Jones et al., 2005; Yendiki et al., 2011; Yeatman et al., 2012). While this method offers high test-retest reliability (Kruper et al., 2021), dMRI data often suffers from measurement noise such as thermal noise limiting image quality. Several methods have been proposed to reduce noise in dMRI data (Veraart et al., 2016; Fadnavis et al., 2020). However, while these denoising methods improve overall image quality, it is unclear how much it affects the sensitivity of the tractometry-based measurement to identify tissue changes caused by disorders, without evaluating the empirical dataset. To address this, we assessed the impact of denoising on dMRI measurements along the optic tract of patients with glaucoma, a disorder that damages the retinal ganglion cells (RGCs) and likely affects tissue properties of the optic tract, which is composed of axons from RGCs (Quigley et al., 1989). Additionally, we also examined the effects of denoising on tractometry results for the optic radiation, which is not a part of RGCs but is often reported to be affected by glaucoma (Ogawa et al., 2022).

Methods: We re-analyzed the dMRI dataset presented in previous work (Ogawa et al., 2022), including 17 glaucoma patients and 30 healthy controls. We compared dMRI data with and without denoising, which is implemented as the “dwidenoise” command in MRTrix3 (Veraart et al., 2016). dMRI data is then corrected for susceptibility-induced and eddy-current distortion using FSL. We identified the optic tract and optic radiation from preprocessed dMRI data using tractography methods described in previous work (Ogawa et al., 2022) and then evaluated tissue properties along these tracts using the AFQ MATLAB toolbox (Yeatman et al., 2012). Specifically, we evaluated the impact of denoising for intra-cellular volume fraction (ICVF), which is a dMRI-based measurement of microstructural properties (Zhang et al., 2012). Finally, we evaluated scan-rescan reproducibility of ICVF along the optic tract and optic radiation, to assess the impact on denoising for tractometry reproducibility.

Results: Based on a visual inspection of the images, denoising improved the image quality of dMRI data, making tissue borders between gray matter and white matter more distinct. In addition, we found that glaucoma patients showed significantly lower ICVF compared with controls along the optic tract and optic radiation in both the data with and without denoising. Importantly, we found that denoising has no or little impact on the tractometry results. We found that the degree of abnormality in ICVF of glaucoma patients did not significantly differ between data with and without denoising, in both the optic tract and optic radiation (Figure 1; BF10 ≃ 0.3, 0.6 in each case). Finally, we also found that scan-rescan reproducibility of ICVF is comparable between data with and without denoising in both the optic tract and optic radiation (Figure 2).

Conclusions: While denoising improved image quality, we found that it had minimal or no impact on sensitivity to identify tissue changes caused by glaucoma and on measurement reproducibility. These results are consistent with a recent study evaluating the impact of denoising in dMRI data of the spinal cord (Schilling et al., 2023). One possibility is that denoising may improve the fitting accuracy of voxelwise models to the dMRI signal by reducing measurement noise, however, resulting tissue properties measurement, such as ICVF, remain unchanged. Consequently, tractometry results do not seem to be affected. Therefore, we conclude that at present, we did not find evidence that denoising makes an actual impact on tractometry results on tissue changes caused by the retinal disorder.

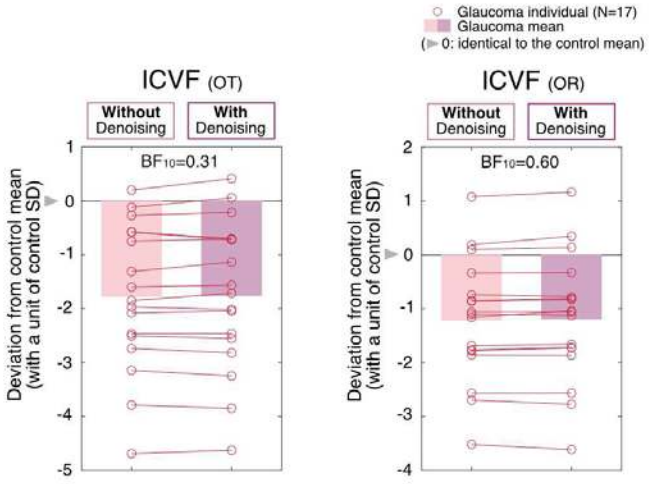

Figure 1. Tractometry results of the ICVF along the optic tract (OT, left panel) and the optic radiation (OR, right panel) in data without (light purple) and with denoising (dark purple) by showing normalized differences from controls. Dots depict the data of individual glaucoma patients. The unit of the vertical axis represents a degree of deviation from the control mean, with a unit of the standard deviation in controls.

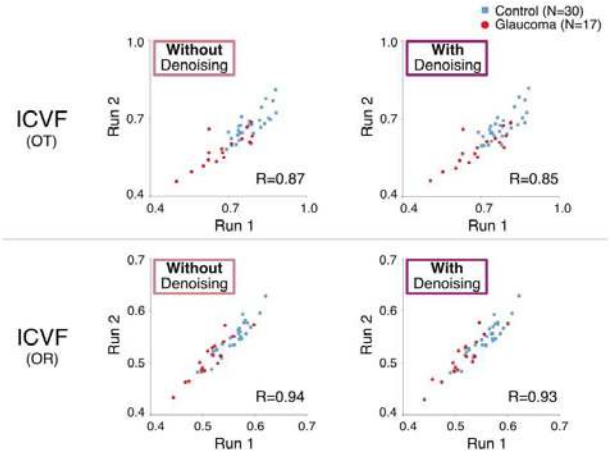

Figure 2. Scan-rescan reproducibility of the ICVF along the OT (top panel) and the OR (bottom panel) in data without (left) and with (right) denoising. Each dot depicts the data from each participant (blue, control; red, glaucoma).

References

1. Fadnavis et al. (2020) arXiv: 2011.01355.
2. Jones et al. (2005) Magn Reson Med., 53(6), 1462-1467.
3. Kruper et al. (2021) Aperture Neuro,1(1).
4. Ogawa et al. (2022) Invest. Ophthalmol. Vis. Sci., 63(2), 29.
5. Quigley et al. (1989) Am. J. Ophthalmol., 107(5), 453-464.
6. Schilling et al. (2023) NeuroImage, 266, 119826.
7. Veraart et al. (2016) NeuroImage, 142, 394-406.
8. Yeatman et al. (2012) PLOS ONE, 7(11), e49790.
9. Yendiki et al. (2011) Front. Neuroinf., 5, 10815.
10. Zhang et al. (2012) NeuroImage, 61(4), 1000-1016.

Poster No 1592

Hierarchical modelling of crossing fibres in the white matter

Hossein Rafipoor[1], Frederik Lange[1], Christoph Arthofer[1], Michiel Cottaar[1], Saad Jbabdi[1]

[1]*Oxford University, Oxford, United Kingdom*

Introduction: Fixel-based analyses aim to extract fibre-specific parameters from single voxels using diffusion MRI data. To compare fibre-specific parameters across subjects, it is necessary to identify equivalent fibre populations. This task is

complicated by variations in the number of crossing fibres and fibre orientations per voxel among subjects. Conventionally, fixel-based analyses resolve these correspondences after fitting crossing fibre models to each individual. In this work, we introduce a hierarchical framework to fit crossing fibre models to diffusion MRI data, ensuring consistent and comparable fibre-specific parameters across subjects. We employ an Expectation-Maximisation (EM) method for scalability. Additionally, we introduce a modified version of Threshold Free Cluster Enhancement (TFCE) applied to fixel data for family-wise error correction. As an example application, we applied our method to the UK biobank dataset to investigate changes in white matter through ageing.

Methods: The ball and sticks model posits that the diffusion MRI signal arises from intra-axonal water diffusing along fibres (sticks) and extracellular water diffusing isotropically (ball) (Figure 1A). Traditionally, this model is fitted to single voxels and single subjects independently. Here we extend the model with a hierarchical structure, where we assume that each subject's model parameter is drawn from a population distribution, which ensures consistent fibre labelling across subjects (Figure 1B). Fitting the entire hierarchical model necessitates optimization in a high dimensional space, increasing linearly with the number of subjects. For scalability, we adopt an EM approach. During maximisation, subject parameters are estimated while keeping group parameters fixed, enabling parallel processing across subjects. In the expectation step, subject parameters are fixed while group parameters are estimated. These steps are iterated until convergence. To determine the number of fibres in each voxel, we fit models with one to three fibres. The optimal number is then determined by evaluating the enhancement in the likelihood function upon the addition of extra fibres (Figure 1C). For multiple comparison corrections for fixel statistics, we adjusted the original TFCE approach to accommodate the structure of the fixel neighbourhood (Figure 1D). We employ the Oxford Multimodal (OMM-1) template as the structural reference space. For each voxel within this space, we extract data from the corresponding voxels in each subject's native diffusion space using the nearest neighbour sampling technique, utilising nonlinear transformations created by FSL MMORF.(https://doi.org/10.1101/2023.09.26.559484)

Results: Our EM algorithm was used to create a white matter fibre template using T1 and diffusion images from 100 HCP young adult dataset. (Figure 2A) This template contains the group means and variances for the ball and sticks model parameters within each white matter voxel. Using this template, we fitted the hierarchical model to 400 subjects from the UK biobank dataset and estimated fibre signal fractions to study age-related alterations in white matter. Figure 2B illustrates the resulting t-statistics from the GLM analysis, using fixel signal fractions as the dependent variable and age as the independent variable, while adjusting for head size and sex as confounding variables. We can observe fibre-specific changes in the sample region. Subsequently, our modified TFCE was used to identify fixels with significant age-related changes, set at an alpha threshold of 0.05 after family-wise error correction (Figure 2C).

Conclusions: This work presents a hierarchical Bayesian framework to extract fibre-specific parameters from diffusion MRI data that are comparable across subjects. This facilitates the application of Fixel-Based Analysis techniques for models with a discrete fibre orientation distribution. Such integration can pave the way for fibre-level comparisons of biophysically meaningful parameters.

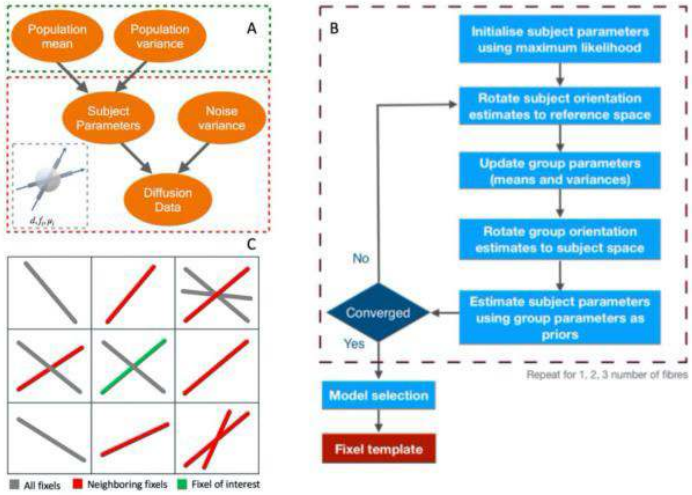

Figure 1. A) Illustration of the hierarchical structure. In this framework, we assume that the subject parameters are sampled from a population distribution. The population distributions of all scalar parameters are assumed to be Gaussians, while orientation parameters are assumed to be drawn from a Watson distribution. We assume uniform priors for all the group mean parameters. For the group variance we use a power-law distribution to penalise the group variance converging to zero. Inset: Schematic for the ball and stick model parameters. B) Template creation pipeline. Firstly, the diffusion data is fitted with models for each subject independently using maximum likelihood estimation. We then use the parameters from all subjects to estimate the population distribution for each parameter. The population parameters (mean and variance) are then utilised as prior distributions to re-fit the subject parameter to the diffusion data. This process is repeated until convergence, and for models with 1, 2, and 3 fibres. During this process the fibre orientations are rotated between subject space and reference space using rotations implied by the warp field. C) 2D section of fixel neighbourhood for TFCE. The neighbours of a fixel (green fixel) are all the fixels that are located in an adjacent voxel (at least one corner is shared, in total 27 voxels) and make angles smaller than a threshold (red fixels). Multiple fixels in a neighbouring voxel may be taken into account as neighbours of the same fixel.

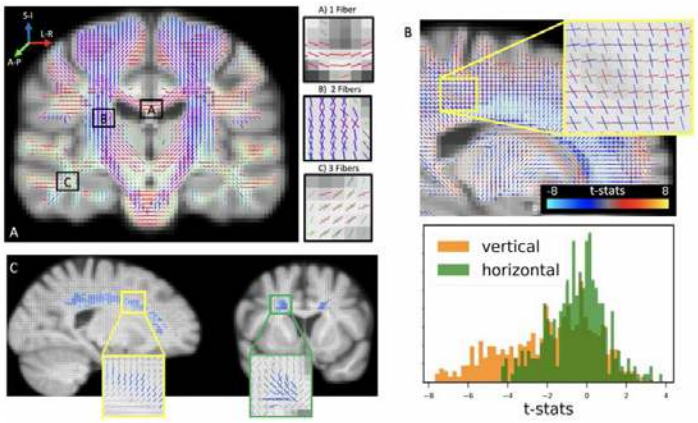

Figure 2. A) White matter fibre template. The fibres that are present in each voxel are shown with sticks, colour-coded with orientation. The patches show sample regions with 1, 2 or 3 fibres in the majority of voxels. B) (Top) A sample slice of t-statistics for fixels. Colour of lines in this map indicate correlation with age (blue for negative, red for positive correlations). (Bottom). Histogram of the t-statistics for horizontal and vertical fixels in the magnified region and 5 slices parallel to it. In this region both positive and negative changes are observable. Notably, the majority of horizontal (anterior-posterior) fibres exhibited positive changes, while most vertical (superior-inferior) fibres showed negative changes. C) Statistically significant changes. Fixel-specific threshold-free cluster enhancement is applied to the t-stats derived from the GLM analysis on fixel signal fractions versus age. Permutation tests with 5000 repetitions on the TFCE values are used to estimate p-values for each fixel. The maps depict the significant fixels (colour-coded based on the t-statistics) with corrected $p < 0.05$. We observe that only the negative changes in signal fractions reached statistical significance, and these were exclusively located in the same tract, the body of the corpus callosum, in both hemispheres.

References

1. Arthofer, Christopher et al. (2021). “Multimodal MRI template construction from UK Biobank: Oxford-MM-0”. In: Organisation for Human Brain Mapping (OHBM).
2. Dhollander, Thijs et al. (2021). “Fixel-based Analysis of Diffusion MRI: Methods, Applications, Challenges and Opportunities”. en. In: NeuroImage 241, p. 118417. issn: 10538119.

3. Lange, Frederik J. et al. (2020). “A Symmetric Prior for the Regularisation of Elastic Deformations: Improved anatomical plausibility in nonlinear image registration”. en. In: NeuroImage 219, p. 116962. issn: 10538119.
4. Miller, Karla L et al. (2016). “Multimodal population brain imaging in the UK Biobank prospective epidemiological study”. In: Nature Neuroscience 19.11. Publisher: Springer Science and Business Media LLC, pp. 1523–1536.
5. Raffelt, David A., J.-Donald Tournier, et al. (2017a). “Investigating white matter fibre density and morphology using fixel-based analysis”. In: NeuroImage 144.0. Publisher: Elsevier BV, pp. 58–73.
6. Smith, S and T Nichols (2009). “Threshold-free cluster enhancement: Addressing problems of smoothing, threshold dependence and localisation in cluster inference”. In: NeuroImage 44.1. Publisher: Elsevier BV, pp. 83–98.
7. Van Essen, David C. et al. (2013). “The WU-Minn Human Connectome Project: An overview”. In: NeuroImage 80. Publisher: Elsevier BV, pp. 62–79.

Poster No 1593

Microstructural Differences in diffusion MRI in tinnitus population

Cristina Tobias Figuerola[1], Carine Signoret[1], Josefine Andin[1], Emil Holmer[1], Marta Topor[1], Rina Blomberg[1], Åsa Elwér[1], Lina Homman[1], Mikael Skagenholt[1], Kenny Skagerlund[1], Mattias Ekberg[1], Örjan Dahlström[1]

[1]Linköpings Universitet, Linköping, Östergötland

Introduction: Tinnitus is defined as a phantom sound experienced by the individual as a ringing, hissing, or buzzing sound, even though there is no such sound in the external world[3,4]. This condition has been explained by deterioration at the peripheral level, which induces changes at the central neural level. At a neural level, it has been reported that increased connectivity between auditory areas could explain the prevalence of tinnitus symptoms. This study aims to examine microstructural differences in diffusion MRI for normal-hearing (NH) individuals with or without tinnitus, and between individuals with low and high tinnitus severity.

Methods: Forty participants were included in the study (15 NH -7F and 8M, 25 TIN, 11F and 14M, mean age = 39.08) but only thirty-three participants (16 males and 17 females) with a mean age of 39.30 years (SD = 14.22 years) were eligible for diffusion tensor imaging (DTI). Twenty participants presented with a diagnosis of tinnitus (9 males and 11 females) and a mean tinnitus duration of 12.65 years (SD = 7.95 years). Participants with diagnosed tinnitus symptoms were recruited from the clinical population at the Department of Technical Audiology, Linköping University Hospital, Sweden. A correlational tractography analysis was performed to compare the tinnitus group with the control; the tinnitus group was then divided into two groups according to their severity and compared. The study involved 33 MRI scans integrated into a connectometry database using a diffusion tensor imaging (DTI) scheme with 32 sampling directions, an 800 s/mm^2 b-value, 1.75 mm in-plane resolution, and 2 mm slice thickness. B-table accuracy was verified against a population-averaged template[10]. Restricted diffusion was quantified using restricted diffusion imaging[9], and data were reconstructed with generalized q-sampling imaging[6]. Tensor metrics were derived using DWI with a b-value below 1750 s/mm^2, and dti_fa values were employed in the connectometry analysis. Correlational tractography was performed using diffusion MRI connectometry[8], correlating diffusion metrics with the group. A nonparametric Spearman correlation, a T-score threshold of 2.5, and a deterministic fiber tracking algorithm[7] were applied, excluding the cerebellum. Tracks were filtered using topology-informed pruning with 16 iterations. The selection criteria included an FDR threshold of 0.05 and a track coverage threshold of 5%, validated through 4000 randomized permutations for false discovery rate estimation.

Results: We obtained significantly correlated regions in fractional anisotropy (FA), mean diffusivity (MD) and axial diffusivity (AD) for the tinnitus vs control tractography (Fig 1). The severity comparison tractography yielded significant results (fig 2) for FA, MD, AD and radial diffusivity (RD). For tinnitus vs control: the decrease in FA seems to indicate a demyelination[1,5] in regions correlated with emotional regulation and integration of sensory information (e.g., the anterior and posterior regions of the corpus callosum (CC) respectively)[2], with the CC tapetum also showing signs of axonal loss (increase in MD). The increase in MD and AD in the left hemisphere seems to suggest a reorganization of the brain white matter for tinnitus individuals which has been the subject of study in recent years[2]. For low vs high severity: CC tapetum, forceps major, and the fornix from both sides showed increased AD, MD, RD and decreased FA which could be indicators of axonal injuries and inflammation.

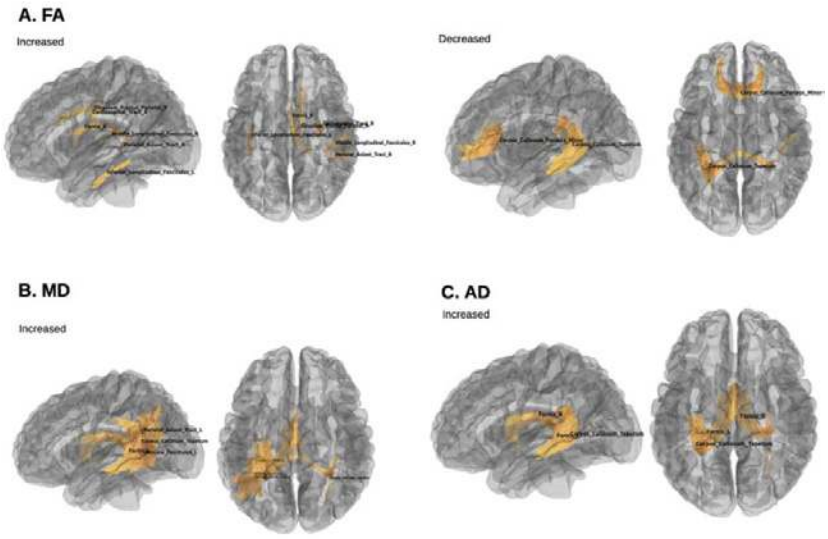

Figure 1: Comparison between tinnitus and control in different metrics. A) increased fractional anisotropy (Left) and decreased fractional anisotropy (Right) . B) Increased mean diffusivity. C) Increased axial diffusivity

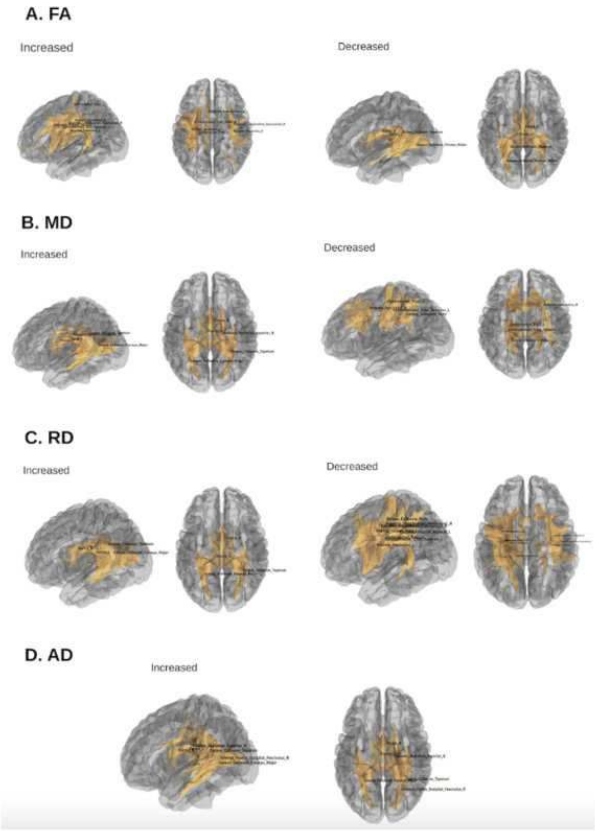

Figure 2: Comparison between low severity and high severity tinnitus in different metrics. A) increased (Left) and decreased (Right) fractional anisotropy. B) increased (Left) and decreased (Right) mean diffusivity. C) increased (Left) and decreased (Right) radial diffusivity. D) increased axial diffusivity

Conclusions: Our study found significant results in two different comparisons (tinnitus vs control; low severity and high severity) for correlational tractography analysis. The results suggest a potential demyelination in emotional regulation and sensory integration regions and a white matter reorganization in the left hemisphere. An increase in the perceived severity of the tinnitus condition might be correlated with injuries in the posterior parts of the CC and the fornix.

References

1. Budde, M. D., Kim, J. H., Liang, H. F., Schmidt, R. E., Russell, J. H., Cross, A. H., & Song, S. K. (2007). Toward accurate diagnosis of white matter pathology using diffusion tensor imaging. Magnetic Resonance in Medicine: An Official Journal of the International Society for Magnetic Resonance in Medicine, 57(4), 688-695.
2. Chen, Q., Lv, H., Wang, Z., Wei, X., Liu, J., Liu, F., ... & Wang, Z. (2022). Distinct brain structural-functional network topological coupling explains different outcomes in tinnitus patients treated with sound therapy. Human Brain Mapping, 43(10), 3245-3256.
3. Hoare, D. J., Stacey, P. C., & Hall, D. a. (2010). The efficacy of auditory perceptual training for tinnitus: a systematic review. Annals of Behavioral Medicine : A Publication of the Society of Behavioral Medicine, 40(3), 313–24. doi:10.1007/s12160-010-9213-5
4. Lanting, C. P., de Kleine, E., Eppinga, R. N., & van Dijk, P. (2010). Neural correlates of human somatosensory integration in tinnitus. Hearing Research, 267(1-2), 78–88. doi:10.1016/j.heares.2010.04.006
5. Song, S. K., Sun, S. W., Ramsbottom, M. J., Chang, C., Russell, J., & Cross, A. H. (2002). Dysmyelination revealed through MRI as increased radial (but unchanged axial) diffusion of water. Neuroimage, 17(3), 1429-1436.
6. Yeh, F. C., Wedeen, V. J., & Tseng, W. Y. I. (2010). Generalized ${q} $-sampling imaging. IEEE transactions on medical imaging, 29(9), 1626-1635.
7. Yeh, F. C., Verstynen, T. D., Wang, Y., Fernández-Miranda, J. C., & Tseng, W. Y. I. (2013). Deterministic diffusion fiber tracking improved by quantitative anisotropy. PloS one, 8(11), e80713.
8. Yeh, F. C., Badre, D., & Verstynen, T. (2016). Connectometry: a statistical approach harnessing the analytical potential of the local connectome. Neuroimage, 125, 162-171.
9. Yeh, F. C., Liu, L., Hitchens, T. K., & Wu, Y. L. (2017). Mapping immune cell infiltration using restricted diffusion MRI. Magnetic resonance in medicine, 77(2), 603-612.
10. Yeh, F. C., Panesar, S., Fernandes, D., Meola, A., Yoshino, M., Fernandez-Miranda, J. C., ... & Verstynen, T. (2018). Population-averaged atlas of the macroscale human structural connectome and its network topology. Neuroimage, 178, 57-68.

Poster No 1594

Microstructural Characterization of Network-Based Neurodegeneration in Multiple Sclerosis

Florence Chiang[1], Eva Krijnen[1], Hansol Lee[1], Hong-Hsi Lee[1], Peter Fox[2], Eric Klawiter[1], Susie Huang[1]

[1]Athinoula A. Martinos Center for Biomedical Imaging, Massachusetts General Hospital, Boston, MA, [2]Research Imaging Institute, The University of Texas Health Science Center at San Antonio, San Antonio, TX

Introduction: Neurodegeneration is a key component of clinical disability in multiple sclerosis (MS). However, the underlying mechanism of localized gray matter (GM) atrophy in MS remains unknown. More recently, a network-based etiology has been postulated, which may be associated with clinical progression (Schoonheim, Broeders, and Geurts 2022; Chard and Miller 2016; Chiang et al. 2021). The goal of this study was to assess network behavior of microstructural alteration in atrophy-prone GM (Chiang et al. 2021; 2019). We leveraged high gradient diffusion MRI (dMRI) to probe GM at the mesoscopic scale by using the SANDI (Soma and Neurite Density Imaging) method, a novel biophysical modeling approach (Palombo et al. 2020). Our hypothesis was that cell body density of atrophy-prone GM will be decreased in MS which will correlate with disease severity and that these regions will exhibit microstructural covariation. Findings of this study would clarify the microstructural substrate of network-based GM atrophy and improve current understanding of network concepts in MS.

Methods: Whole-brain dMRI was obtained for all participants on the 3T Connectome MRI scanner with 300 mT/m maximum gradient strength (MAGNETOM Connectom, Siemens Healthineers)(Huang et al. 2020). dMRI was acquired with a multi-shell diffusion protocol using a diffusion time Δ = 19 ms, 8 b-values (b = 50-350-800-1500 s/mm2 in 32 directions, and b = 2400-3450-4750-6000 s/mm2 in 64 directions), and an isotropic resolution of 2 mm. A short diffusion time was used to minimize the potential confound of intercompartmental exchange (Jelescu et al. 2022). After all imaging data were preprocessed using an established pipeline (Tian et al. 2022), SANDI model fitting was performed using AMICO (Daducci et al. 2015). SANDI metrics were computed including the intra-soma signal fraction (fis), which reflects cell body density. Nodes in the Atrophy-based Functional Network (AFN) model was used to define regions-of-interest (ROIs; Figure) (Chiang et al. 2021; 2019). ROIs were binarized and transformed from standard (Montreal Neurological Institute) to the diffusion space of each participant with nonlinear registration. ROIs were then used to sample the fis map of each participant. Statistical analyses included group-wise comparisons of the average fis of each ROI and for the nodal aggregate using independent samples t-tests with FDR-correction. Association of AFN nodal aggregate fis with the Expanded Disability Status Scale (EDSS) score and disease duration were assessed using Spearman's rank-order correlation. Pearson's correlation coefficients were computed for all ROIs pairs to generate a covariance matrix.

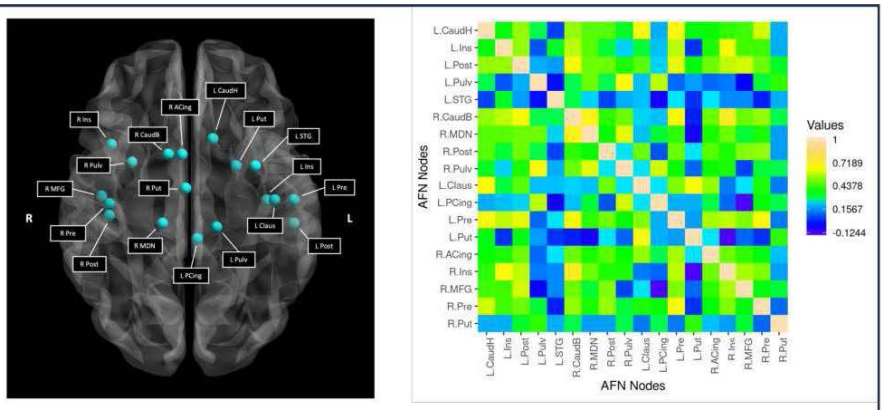

Figure. Atrophy-Prone Gray Matter Demonstrates Microstructural Covariation in in Multiple Sclerosis. Meta-analytically defined nodes in the Atrophy-based Functional Network (AFN) Model represent cortical and subcortical gray matter prone to atrophy in multiple sclerosis (Chiang et al. *Radiology* 2021). The average intra-soma signal fraction of AFN nodes was used to generate a heatmap, which demonstrates network behavior and microstructural covariation. Pearson's correlation coefficients were computed between every nodal pair, and medium to large effect sizes were detected.
AFN, Atrophy-based Functional Network model; L, left; R, right; CaudH, caudate head; Ins, insula; Post, postcentral gyrus; Pulv, pulvinar; STG, superior temporal gyrus; CaudB, caudate body; MDN, mediodorsal nucleus; Claus, claustrum; PCing, posterior cingulate gyrus; Pre, precentral gyrus; Put, putamen; ACing, anterior cingulate gyrus; MFG, middle frontal gyrus.

Results: Participants included 38 MS (M/F: 11/27; age 44 ± 11 years; EDSS 2.8 ± 1.7, 1 - 7.5; disease duration 9.5 ± 6.6 years) and 35 age-matched healthy controls (HC; M/F: 15/20; age 39 ± 15 years; p = 0.13). fis was decreased between MS and HC for the aggregate average of all AFN atrophy nodes. fis of both cortical and subcortical nodes including in the basal ganglia, thalamus, and precentral gyrus remained significantly decreased at the individual nodal level (Table). The aggregate nodal fis demonstrated a strong association with the EDSS score (ρ = -0.543, p < 0.001) and a relatively weaker correlation with disease duration (ρ = -0.317, p = 0.056). Correlations between all nodes were computed and displayed in a heatmap, which demonstrated presence of medium to large effect sizes (Figure).

Intra-soma Signal Fraction (f_{is})	MS Mean (SD)	HC Mean (SD)	P-value	Effect Size
Aggregate f_{is}	0.48 (0.04)	0.51 (0.04)	0.002*	0.68
Nodal f_{is}				
L CaudH	0.59 (0.07)	0.64 (0.06)	0.002*	0.69
L Ins	0.42 (0.08)	0.40 (0.07)	0.196	0.20
L Post	0.52 (0.09)	0.53 (0.06)	0.290	0.13
L Pulv	0.48 (0.05)	0.52 (0.05)	<0.001*	0.83
L STG	0.59 (0.05)	0.62 (0.05)	0.005*	0.61
R CaudB	0.43 (0.07)	0.48 (0.07)	0.003*	0.66
R MDN	0.33 (0.06)	0.37 (0.06)	<0.001*	0.75
R Post	0.47 (0.08)	0.50 (0.07)	0.065	0.36
R Pulv	0.43 (0.06)	0.47 (0.05)	<0.001*	0.85
L Claus	0.55 (0.05)	0.58 (0.06)	0.048	0.39
L PCing	0.44 (0.09)	0.47 (0.06)	0.136	0.26
L Pre	0.47 (0.07)	0.51 (0.06)	0.013*	0.53
L Put	0.59 (0.05)	0.61 (0.04)	0.066	0.35
R ACing	0.47 (0.07)	0.50 (0.07)	0.082	0.33
R Ins	0.39 (0.06)	0.40 (0.08)	0.167	0.23
R MFG	0.48 (0.09)	0.51 (0.07)	0.053	0.38
R Pre	0.43 (0.06)	0.47 (0.06)	0.005*	0.62
R Put	0.49 (0.04)	0.52 (0.05)	0.005*	0.62

Table. Groupwise Comparisons of f_{is}. Nodes in the AFN model demonstrate decreased cell body density in multiple sclerosis compared to healthy controls for the aggregate nodal average f_{is} and individual nodal average f_{is}. *Effect sizes were computed as Hedges' g.*
**P-values <0.05 after FDR correction.*

Conclusions: In conclusion, decreased cell body density was observed in atrophy-prone GM of MS which correlated with clinical disability. Further, covariance of localized GM microstructural alteration suggests that neuronal loss may relate in part to network-based effects. Network-based microstructural measures may provide the foundation for future development of quantitative non-invasive methods to help achieve more sensitive monitoring of disease progression in MS, which would enable prompt clinical intervention.

References

1. Chard, Declan T, and David H Miller. 2016. 'What Lies beneath Grey Matter Atrophy in Multiple Sclerosis?' Brain 139 (1): 7–10. https://doi.org/10.1093/brain/awv354.
2. Chiang, Florence L., Max Feng, Rebecca S. Romero, et al. 2021. 'Disruption of the Atrophy-Based Functional Network in Multiple Sclerosis Is Associated with Clinical Disability: Validation of a Meta-Analytic Model in Resting-State Functional MRI'. Radiology 299 (1): 159–66. https://doi.org/10.1148/RADIOL.2021203414.
3. Chiang, Florence L., Qian Wang, Fang F Yu, Rebecca Romero, Susie Y. Huang, P M Fox, B Tantiwongkosi, and P T Fox. 2019. 'Localised Grey Matter Atrophy in Multiple Sclerosis Is Network-Based : A Coordinate-Based Meta-Analysis'. Clinical Radiology 74 (10): 816.e19-816.e28. https://doi.org/10.1016/j.crad.2019.07.005.
4. Daducci, Alessandro, Erick J. Canales-Rodríguez, Hui Zhang, Tim B. Dyrby, Daniel C. Alexander, and Jean Philippe Thiran. 2015. 'Accelerated Microstructure Imaging via Convex Optimization (AMICO) from Diffusion MRI Data'. NeuroImage 105 (January): 32–44. https://doi.org/10.1016/j.neuroimage.2014.10.026.
5. Huang, Susie Y., Qiyuan Tian, Qiuyun Fan, Thomas Witzel, Barbara Wichtmann, Jennifer A. McNab, J. Daniel Bireley, et al. 2020. 'High-Gradient Diffusion MRI Reveals Distinct Estimates of Axon Diameter Index within Different White Matter Tracts in the in Vivo Human Brain'. Brain Structure and Function 225 (4): 1277–91. https://doi.org/10.1007/s00429-019-01961-2.
6. Jelescu, Ileana O., Alexandre de Skowronski, Françoise Geffroy, Marco Palombo, and Dmitry S. Novikov. 2022. 'Neurite Exchange Imaging (NEXI): A Minimal Model of Diffusion in Gray Matter with Inter-Compartment Water Exchange'. NeuroImage 256 (August). https://doi.org/10.1016/j.neuroimage.2022.119277.
7. Palombo, Marco, Andrada Ianus, Michele Guerreri, Daniel Nunes, Daniel C. Alexander, Noam Shemesh, and Hui Zhang. 2020. 'SANDI: A Compartment-Based Model for Non-Invasive Apparent Soma and Neurite Imaging by Diffusion MRI'. NeuroImage 215 (July). https://doi.org/10.1016/j.neuroimage.2020.116835.
8. Schoonheim, Menno M., Tommy A.A. Broeders, and Jeroen J.G. Geurts. 2022. 'The Network Collapse in Multiple Sclerosis: An Overview of Novel Concepts to Address Disease Dynamics'. NeuroImage: Clinical 35 (January). https://doi.org/10.1016/j.nicl.2022.103108.
9. Tian, Qiyuan, Qiuyun Fan, Thomas Witzel, Maya N. Polackal, Ned A. Ohringer, Chanon Ngamsombat, Andrew W. Russ

Poster No 1595

Exploring the Links Between Lexical Production and Track-Weighted Imaging in Middle-Aged Adults

Clément Guichet[1], Arnaud Attyé[2], Elise Roger[3,4], Sophie Achard[5], Martial Mermillod[1], Monica Baciu[1]

[1]Univ. Grenoble Alpes, LPNC, CNRS UMR 5105, Grenoble, France, [2]GeodAIsics, Grenoble, France, [3]Institut Universitaire de Gériatrie de Montréal, Communication and Aging Lab, Montreal, Quebec, Canada, [4]Faculty of Medicine, University of Montreal, Montreal, Quebec, Canada, [5]Univ. Grenoble Alpes, LJK, UMR CNRS 5224, Grenoble, France

Introduction: Cognitive aging manifests as a gradual deterioration in lexical retrieval and generation, referred to as lexical production (LP), beginning in middle age[1]. Previous research showed that LP decline is not solely attributed to domain-specific mechanisms (e.g., language), but also involves domain-general factors like executive functioning[2]. While disruptions in functional connectivity have been linked to age-related LP decline[3], the structural correlates remain unclear. Therefore, this study aims to investigate structural modifications in conjunction with cognitive scores to elucidate LP decline among middle-aged adults.

Methods: We analyzed 7 cognitive scores and diffusion MRI data obtained from 155 healthy adults aged 45 to 60 in the CAMCAN cohort[4]. T1w MR images were preprocessed using FreeSurfer's recon-all command. The standard mrtrix3 pipeline was applied for diffusion MR preprocessing and whole-brain tractography (SIFT2;[5]). We quantified structural modifications with Track-Weighted Imaging (TWI;[6]). To establish voxel-wise correspondence across subjects, each subject's tractogram was first registered to a study-based population template and a TW-FA map was built with the subject's fractional anisotropy (FA) image previously warped to template space. Structure-cognition links were modeled using Partial Least Square Correlation (PLSC) contrasted across three age groups (45-50; 51-55; 56-60). This contrast ensured that covariance effects were isolated from absolute age-related differences in either modality[7]. To start the PLSC, TW-FA maps were vectorized and stacked across subjects. This TW-FA matrix was cross-correlated with the matrix containing cognitive scores, yielding a covariance matrix that was submitted to singular value decomposition (Figure 1).

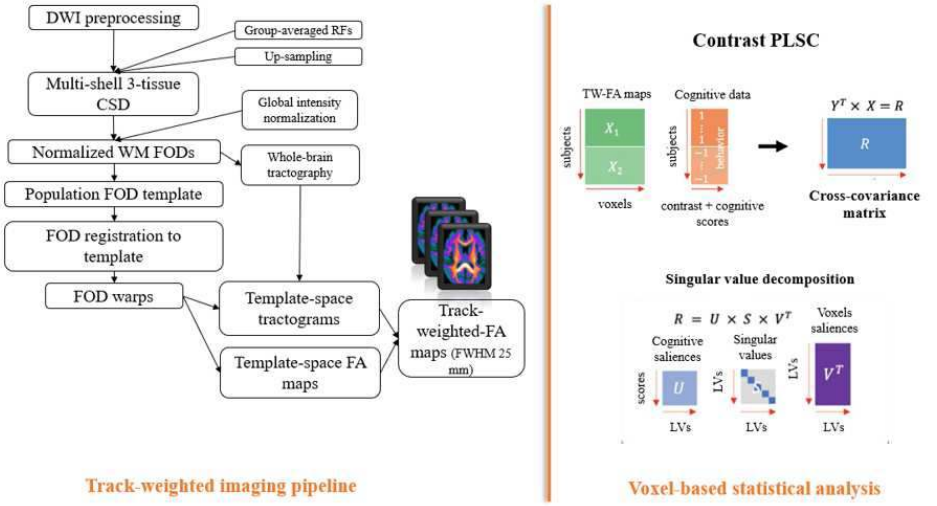

Figure 1 illustrates the workflow of the study. *Abbreviations:* RF (response function), CSD (constrained spherical deconvolution), FOD (fiber orientation distribution), TW (track-weighted), FA (fractional anisotropy), PLSC (partial least square correlation); and LV (latent variable).
Note 1. Track-weighted imaging (TWI) maps were generated using a 70 mm Full Width at Half Maximum (FWHM) Gaussian kernel to examine variations in short-to-mid range tracts. Comparable results were achieved when using a coarser 70 mm kernel for investigating longer range variations.
Note 2. PLSC was implemented with myPLS toolbox (github.com/MIPLabCH/myPLS). Before SVD, gender, handedness, MMSE scores, and intracranial volume were regressed out. Quantile normalization was applied to all 7 cognitive variables (Cattell/fluid intelligence, Naming, Tip-of-the-tongue, Sentence comprehension, Proverb task, and Verbal Fluency) to enhance Gaussianity. Statistical significance of the singular values was assessed with 1000 permutations, and the robustness of saliences was evaluated using 500 bootstrap resamples. For resampling statistics purposes (Zimmerman et al., 2018), voxels with null TW-FA values for >5% of subjects were excluded. The model produced consistent results regardless of whether cognitive age was included as meta-information.

Results: One latent component, capturing 32% of the covariance between TW-FA values and cognitive scores (singular value = 6,845.4, p = .01), distinguished individuals aged 56 and above from the other two groups (BSR56-60>45-55 = 20.7, BSR51-55>45-50 = 0.9; Figure 2A). This component was associated with lower cognitive performances (tip-of-the-tongue = -8.3; naming = -8.9; sentence comprehension = -7.8, proverb = -2.7, Cattell = -8.4), and lower TW-FA values predominantly in clusters located in the right inferior fronto-temporal white matter (WM; Figure 2B). Surprisingly, increased TW-FA in the WM adjacent to the right temporo-parietal junction (TPJ) also contributed to the cognitive decline pattern described above. Exploratory analysis showed that salient voxels (BSR >= 2.58) in the right TPJ are crossed by bundles with different orientations: association (52.2% of the right middle longitudinal fascicle, MLF; 27.3% of the right arcuate fasciculus: AF), callosal (34.8% of the isthmus, CC6), and to a lesser extent by fibers originating from the striatum (21.8%), thalamus (20.2%), and occipital lobe (16.9%) (Figure 2C).

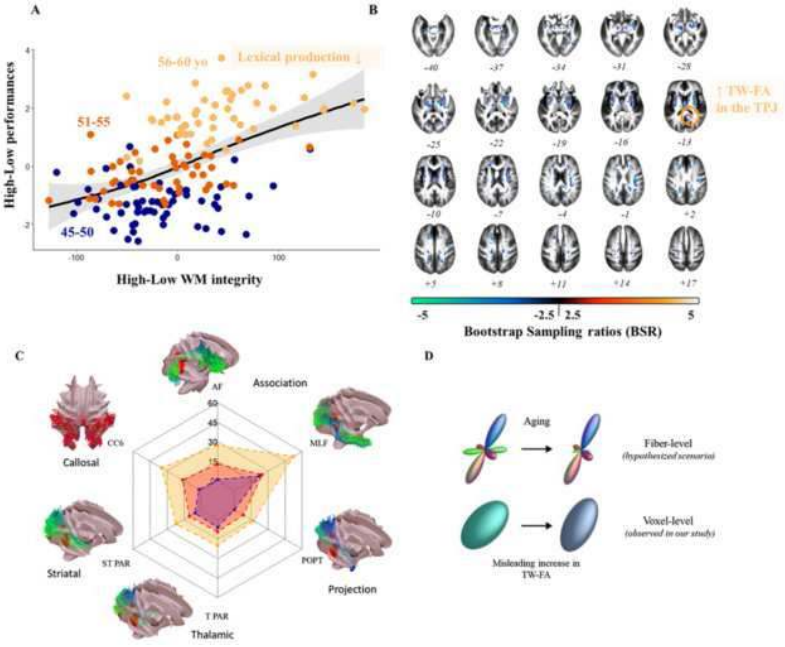

Figure 2 showcases the pattern of structure-cognitive covariance in middle-aged adults.

(A) Depicts the latent variables of the first latent component. Age exhibits a nonlinear alignment with multivariate associations between structure and cognition. The decline in language-related performances accelerates notably beyond age 56.

(B) Illustrates voxels that contribute robustly to the covariance presented in panel A. Presented in template space with LAS coordinates, the FOD template is based on 35 subjects with mean/std age matching that of the population (ε = 1%). Bootstrap ratios (BSR) quantify the contribution of each voxel and cognitive variable to the latent component. High BSR (± 2.58 corresponds to CI 99%) indicates a substantial singular vector weight coupled with a small standard error.

(C) Depicts the crossing fiber architecture at the right TPJ . The largest cluster of salient voxels (i.e., around the right TPJ) is defined as the two largest connected components (211/164 voxels, convex volume 637/537 voxels with peak maxima at x=37.4; y=-9.2;z=-30.4). On the radarplot, red indicates the contribution of a bundle to the total transit via the cluster; orange indicates the percentage of bundle fibers crossing the cluster; blue indicates the proportion of the mid-range fibers (min/max length 25/70 mm). For example, the MLF right accounts for 24% of the total transit (red) with 52% of its fibers traversing the cluster (orange), of which 22% are midrange fibers (blue). Bundles were segmented with TractSeg (Wasserthal et al., 2018) from the study FOD template. Tractograms are filtered to retain only of the fibers traversing the cluster. Displayed on study template mesh of an averaged TW-FA map. *Abbreviations:* AF (Arcuate Fascicle), CC (Corpus Callosum), MLF (Middle Longitudinal Fascicle), POPT (Parieto-Occipital Pontine), ST_PAR (Striato-Parietal), T_PAR (Thalamo-Parietal).

(D) Illustrates the limitations of voxel-based analysis. Adapted from Mito et al (2018). Age-related increase in TW-FA observed in the cluster (right TPJ) is likely due to a limitation of voxel-based analysis. Amid a complex fiber architecture, fiber-specific degeneration can result in a misleading increase in TW-FA in perpendicular fibers.

Conclusions: Our study reveals a pattern of covariance between brain structure and lexical production which distinguishes middle-aged adults before and after 56 yo. Although reduced WM integrity around fronto-temporal regions is mainly predictive of lower LP performances, the same alterations also contribute to the age-related decline in domain-general processes. Interestingly, the degree of TW-FA in the right TPJ could be a potential structural biomarker for LP performance in middle-aged adults. Notably, a recent work argues that increased TW-FA during aging, as reported in our study, is not related to better WM integrity but to selective fiber degeneration[8]. This hypothesis is supported by our study's identification of the bundles converging to the right TPJ, which have been reported to form a bottleneck region of crossing fibers along an anterior-posterior axis[9]. However, we acknowledge that our voxel-based analysis is insufficient for distinguishing fiber differences in WM alterations in this bottleneck region. Further research to validate these findings is planned.

References

1. Baciu, M. (2021), 'Strategies and cognitive reserve to preserve lexical production in aging'. GeroScience 43, 1725–1765
2. Roger, E. (2022), 'Missing links: The functional unification of language and memory (LuM)'. Neuroscience & Biobehavioral Reviews 133, 104489
3. Guichet, C. (2023), 'Modeling the Neurocognitive Dynamics of Language across the Lifespan'. http://biorxiv.org/lookup/doi/10.1101/2023.07.04.547510
4. Cam-CAN. (2014), 'The Cambridge Centre for Ageing and Neuroscience (Cam-CAN) study protocol: a cross-sectional, lifespan, multidisciplinary examination of healthy cognitive ageing'. BMC Neurol 14, 204
5. Tournier, J.-D. (2019), 'MRtrix3: A fast, flexible and open software framework for medical image processing and visualisation'. NeuroImage 202, 116137
6. Calamante, F., et al. A generalised framework for super-resolution track-weighted imaging. NeuroImage 59, 2494–2503 (2012).
7. Zöller, D. (2017), 'Disentangling resting-state BOLD variability and PCC functional connectivity in 22q11.2 deletion syndrome'. NeuroImage 149, 85–97
8. Schilling, K. G. (2022), 'Prevalence of white matter pathways coming into a single white matter voxel orientation: The bottleneck issue in tractography'. Human Brain Mapping 43, 1196–1213
9. Han, A. (2023), 'Fiber-specific age-related differences in the white matter of healthy adults uncovered by fixel-based analysis'. Neurobiology of Aging 130, 22–29

Poster No 1596

Linking psychotic-like experiences and brain white matter microstructure in young women

Rikka Kjelkenes[1], Sara Fernandez-Cabello[1], Irene Voldsbekk[2], Madelene Bukhari[1], Andreas Dahl[1], Ingvild Sandø Lofthus[1], Henning Hoel Rise[1], Ivan Maximov[3], Lars Westlye[4]

[1]University of Oslo, Oslo, Oslo, [2]Norwegian Centre for Mental Disorders Research, Oslo, Oslo, [3]Western Norway University of Applied Sciences, Bergen, Bergen, [4]Norwegian Centre for Mental Disorders Research (NORMENT), Oslo University Hospital, Oslo, Norway

Introduction: Mental health issues in adolescence and young adulthood co-occurs with a complex interplay of psychosocial factors and neurobiological processes. Psychosis-like experiences have been viewed as a risk factor for psychosis, but it has also been suggested as a general severity marker for mental health. Sex differences in psychotic disorders have long been reported, yet little research has been carried out in female only samples. A better understanding of individual differences in vulnerability to psychotic-like experiences is highly relevant for identifying targets for prevention and intervention.

Methods: We analyzed cross-sectional diffusion magnetic resonance imaging (dMRI) data and online questionnaires assessing mental health symptoms and social factors from 661 females aged 9-42 years. Self-administered questionnaires were used to measure Psychotic-like experiences as well as other domains of psychopathology. Linked independent component analysis (LICA) was used to decompose the voxel-wise data from 24 dMRI metrics from 4 different diffusion models, resulting in 10 spatially independent components and corresponding subject weights. Next, we examined the association between the components and age. Using Bayesian statistics, we tested for associations between the LICA subject weights and both total and subscales of psychotic-like experience.

Results: The LICA analysis revealed that LICA component 6 appeared to capture protracted neurodevelopment. We found evidence for an association between LICA component 7 and Psychotic-like experiences. The evidence of this effect was the strongest for the subscale capturing persecutory ideations.

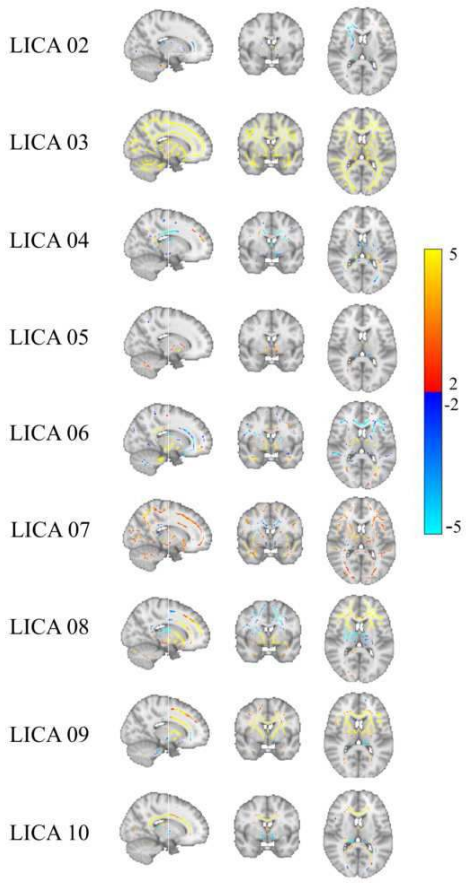

Conclusions: These results show that LICA can be a valuable tool in fusing different modalities to decompose and sort out shared and unique variance across different advanced dMRI models to identify patterns of protracted white matter development, as well as patterns that can be linked to psychopathology.

Poster No 1597

Studying new axial diffusion properties at high diffusion-weighting for the at-risk aging brain

Carson Ingo[1], Thomas Barrick[2], Farzaneh Sorond[1]

[1]Northwestern University, Chicago, IL, [2]St. George's, University of London, London, United Kingdom

Introduction: Diffusion MRI (dMRI) is an emerging modality to study aging in the brain aside from classical FLAIR for white matter hyperintensities (WMH)[1]. In this study, we utilize a generalized mathematical expression for diffusion signal decay, the Mittag-Leffler function (MLF), with α as an index to encode heterogeneous, power-law behavior, $0<\alpha\leq1$[2]. As α decreases, diffusion becomes more heterogeneous, and is indicative of an increasingly complex diffusion environment[3]. Here, we use tract-based spatial statistics (TBSS)[4] to study the sensitivity of α to white matter microstructure in an aging cohort that is at risk of stroke[5]. We also evaluated the behavior of α at ultra-high b-values in an excised mouse brain.

Methods: 72 participants (57.0(3.4) years, 35 female) had vascular risk information collected since 1985[5]. Within this cohort, an at-risk sub-group was identified (57.1(3.42) years, 26 participants, 14 female) with significantly increased systolic blood pressure exposure of 124.3(16.3) mmHg compared to the control sub-group of 112.4(13.2) mmHg (p=0.02). dMRI data were collected on a 3T Siemens Prisma scanner for all participants with the following using SE-EPI: TE/TR=76.8/3000ms, resolution=1.5x1.5x1.5mm3, b-values=0,1000,2000,3000s/mm2, b=0s/mm2 averages=9, gradient directions=60. FLAIR data were acquired with the following: TE/TR/TI=289/6000/2200ms, flip=120°, resolution=1x1x1mm3 in order to identify visible white matter hyperintensities (WMH). Open source dMRI data of a mouse brain was made available[6] and was acquired on a 9.4T Bruker Biospec scanner with the following using a PGSE-EPI: TE/TR=36.8/4000ms, resolution=120x120x400um3, b-values=0,1000,2500,4000,5500,7000,8500,10000,12500s/mm2, gradient directions=40. All dMRI data were preprocessed as previously described[7]. For both human and mouse data, the classical DTI parameters were calculated from 0 and 1000s/mm2 b-value shells to generate FA, MD, RD, and AD maps. α was estimated using all b-value shells the MLF[7,8]. Akin to classical

DTI which computes the tensor of the apparent diffusion coefficient (D), the tensor elements of α can also be computed with an analogous form as Fractional Anisotropy of α (FAα), Mean α (Mα), Radial α (Rα), and Axial α (Aα)[7,8]. TBSS was performed using the DTI and α metrics to identify for potential sensitivity to the sub-group with increased vascular risk versus the control sub-group not at-risk. The t-tests were adjusted for age, sex, and WMH volumes as covariates.

Results: Fig.1 shows significantly decreased FAα, Mα, and Aα for the at-risk sub-group compared to the control sub-group not at-risk, however Rα did not reach significance. None of the classical DTI metrics (FA, MD, RD, AD) reached significance in the same group comparison. Decreased FAα and Mα were primarily driven by widespread decreased Aα for the at-risk sub-group, which demonstrated the greatest number of significantly different voxels out of all tested parameters (71.5% of TBSS skeleton voxels). Fig.2a shows a coronal slice through an excised mouse brain for FA and FAα and magnification in the corpus callosum of their associated primary eigenvector orientations with a 9.48(0.89)° vector difference, which demonstrates good agreement with respect to orientation along the primary fiber direction. Fig.2b shows the dMRI signal fits in each direction along all ultra-high b-values demonstrating high quality fitting with low residual sum of square error of 0.29(0.03).

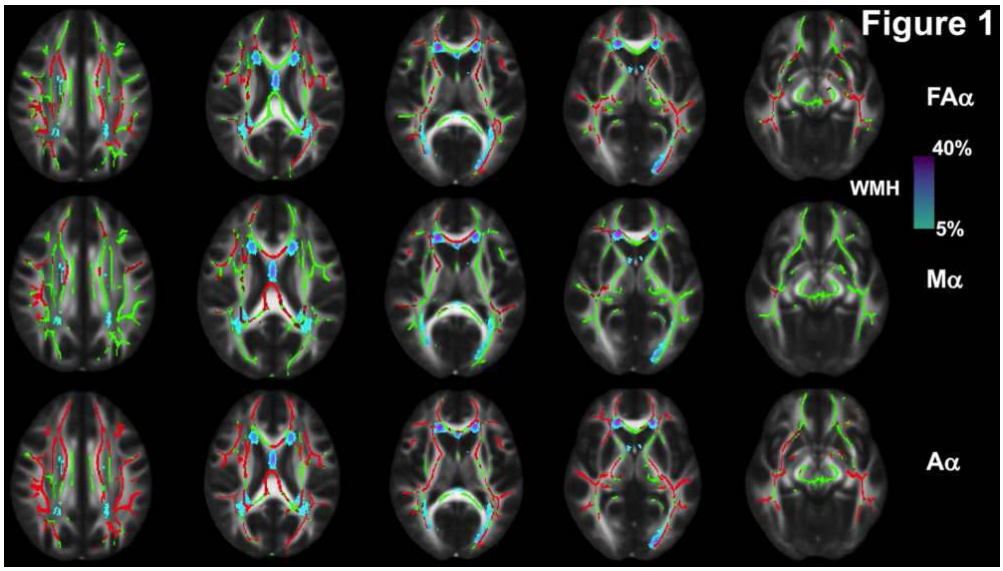

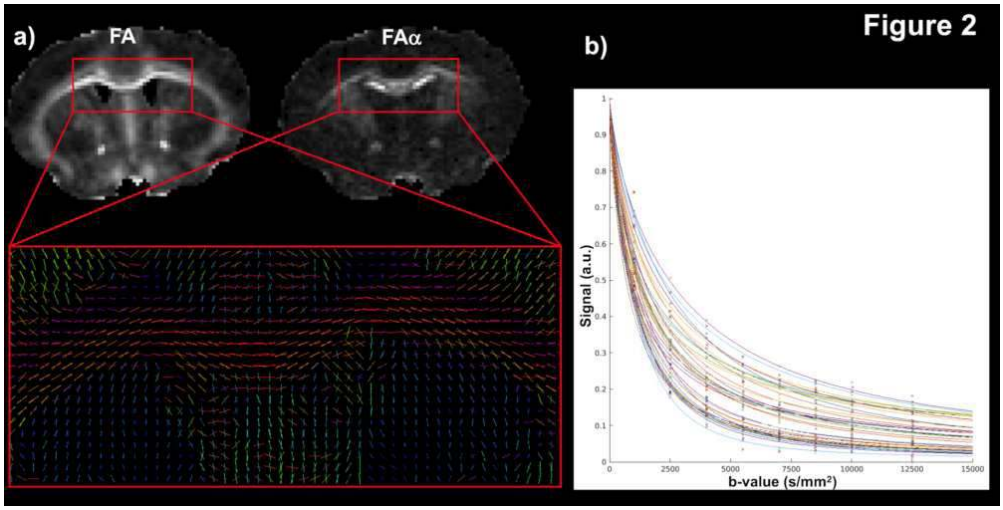

Conclusions: Prior work is supportive of increased cellular heterogeneity in the presence of disease[9]. In this study of white matter using human and mouse dMRI data, our results suggest that Aα and its well aligned eigenvector may be early biomarkers of axonal disruption, increased inflammation, and increased glial proliferation parallel to the primary fiber direction in white matter, prior to changes in classical DTI metrics[10].

References

1. Vernooij MW, Ikram MA, Vrooman HA, et al. (2009). White matter microstructural integrity and cognitive function in a general elderly population. Arch Gen Psychiatry. 66(5):545-53. doi:10.1001/archgenpsychiatry.2009.5.
2. Mittag-Leffler G. (1905). Sur la representation analytique d'une branche uniforme d'une fonction monogene. Acta Mathematica. 29(1):101-181.
3. Metzler R, Klafter J. (2000). The random walk's guide to anomalous diffusion: a fractional dynamics approach. Phys Rep. 339(1):1-77. doi: 10.1016/S0370-1573(00)00070-3.

4. Smith SM, Jenkinson M, Johansen-Berg H, et al. (2006). Tract-based spatial statistics: voxelwise analysis of multi-subject diffusion data. NeuroImage. 31(4):1487-505. doi:10.1016/j.neuroimage.2006.02.024.
5. Hughes GH, Cutter G, Donahue R, et al. (1987). Recruitment in the Coronary Artery Disease Risk Development in Young Adults (Cardia) Study. Control Clin Trials. 8(4 Suppl):68S-73S. doi:10.1016/0197-2456(87)90008-0.
6. Ianuş, A., Carvalho, J., Fernandes, F. F., Cruz, R., Chavarrias, C., Palombo, M., & Shemesh, N. (2022). Soma and Neurite Density MRI (SANDI) of the in-vivo mouse brain and comparison with the Allen Brain Atlas. Neuroimage. 254, 119135.
7. Barrick TR, Spilling CA, Ingo C, et al. (2020). Quasi-diffusion magnetic resonance imaging (QDI): A fast, high b-value diffusion imaging technique. NeuroImage. 211:116606. doi:10.1016/j.neuroimage.2020.116606.
8. Spilling CA, Howe FA, Barrick TR. (2022). Optimization of quasi-diffusion magnetic resonance imaging for quantitative accuracy and time-efficient acquisition. Magn Reson Med. 88(6):2532-2547. doi:10.1002/mrm.29420.
9. Gatto RG, Ye AQ, Colon-Perez L, et al. (2019). Detection of axonal degeneration in a mouse model of Huntington's disease: comparison between diffusion tensor imaging and anomalous diffusion metrics. Magn Reson Mater Phy. 32(4):461-471.
10. Walhovd KB, Johansen-Berg H, Karadottir RT. (2014). Unraveling the secrets of white matter--bridging the gap between cellular, animal and human imaging studies. Neuroscience. 276:2-13. doi:10.1016/j.neuroscience.2014.06.058.

Poster No 1598

White matter changes in healthy aging revealed by fixel-based analysis

Feliberto de la Cruz[1], Andy Schumann[1], Katrin Rieger[1], Daniel Güllmar[1], Jürgen R. Reichenbach[1], Karl- Jürgen Bär[1]

[1]*Jena University Hospital, Jena, Germany*

Introduction: The healthy aging process is a multifaceted phenomenon involving numerous physiological, psychological, and neurobiological changes. With advancing age, individuals experience a series of white matter (WM) changes that contribute to alterations in cognitive processing, sensory perception, and motor function. However, most studies on WM changes in aging have mainly employed diffusion tensor imaging (DTI). While DTI performs well in regions characterized by a dominant fiber direction, its efficacy diminishes in regions with complex fiber geometry and various fiber populations. In contrast, a recently developed analytical framework known as fixel-based analysis (FBA) introduces a novel avenue for assessing WM characteristics. This methodology enables the statistical examination of quantitative measures in complex fiber geometry. Here, we aimed to characterize age-related WM changes across the entire brain using FBA. We complemented our study by exploring the relationship between potential risk factors contributing to WM alterations, such as pulse pressure, alcohol consumption, and frequency of physical activities and how these WM changes correlate with cognitive performance.

Methods: We recruited 120 healthy volunteers, divided into 60 younger and 60 older adults. DWI parameters: TR/TE = 3318/87 ms, voxel size = 1.5x1.5x1.5 mm^3, 96 axial slices, and a multiband acceleration factor = 4. Three diffusion-weighted shells: b = 800 s/mm^2 (16 volumes), b = 1600 s/mm^2 (32 volumes), and b = 2500 s/mm^2 (48 volumes), along with 8 non-diffusion-weighted volumes (b=0 s/mm^2). Three fixel-based metrics were derived: fiber density (FD), fiber cross-section (FC) and a combined measure of FD and FC (FDC). All statistical analyses were conducted in the study-specific template space, controlled by total intracranial volume and gender. Pulse pressure was computed as the difference between systolic and diastolic blood pressure. Participants completed a self-reported questionnaire and reported the frequency of physical activity and alcohol consumption per week, as well as the number of glasses of alcohol consumed per day. Cognitive performance was evaluated using the neuropsychological Trail Making Test (TMT-A/B).

Results: The whole-brain FBA comparing younger and older adult participants revealed substantial WM changes at pFWE < 0.05 (Fig. 1A and B). These changes mainly encompassed reduced FD, FC and FDC in older participants. Specifically, reductions were evident across multiple fixels within the anterior thalamic radiation, corticospinal tract, body of the corpus callosum, forceps minor, fornix and middle cerebellar peduncle (Fig. 1A). Though to a lesser extent, the opposite contrast also identified a set of WM regions where FBA metrics were greater in older participants than their younger counterparts (Fig. 1B). These group differences were driven by greater FD and included fixels within the bilateral anterior thalamic radiation, superior portion of bilateral corticospinal tracts, and superior cerebellar peduncles. We did not find any significant association between changes in FBA metrics in older participants and the examined risk factors. However, we observed significant associations between greater FBA metrics and cognitive performance in several major tracts, as depicted in Fig. 1C for the left corticospinal tract. Notably, the relationship between FBA and TMT was mainly influenced by the relationship between FD and TMT-A.

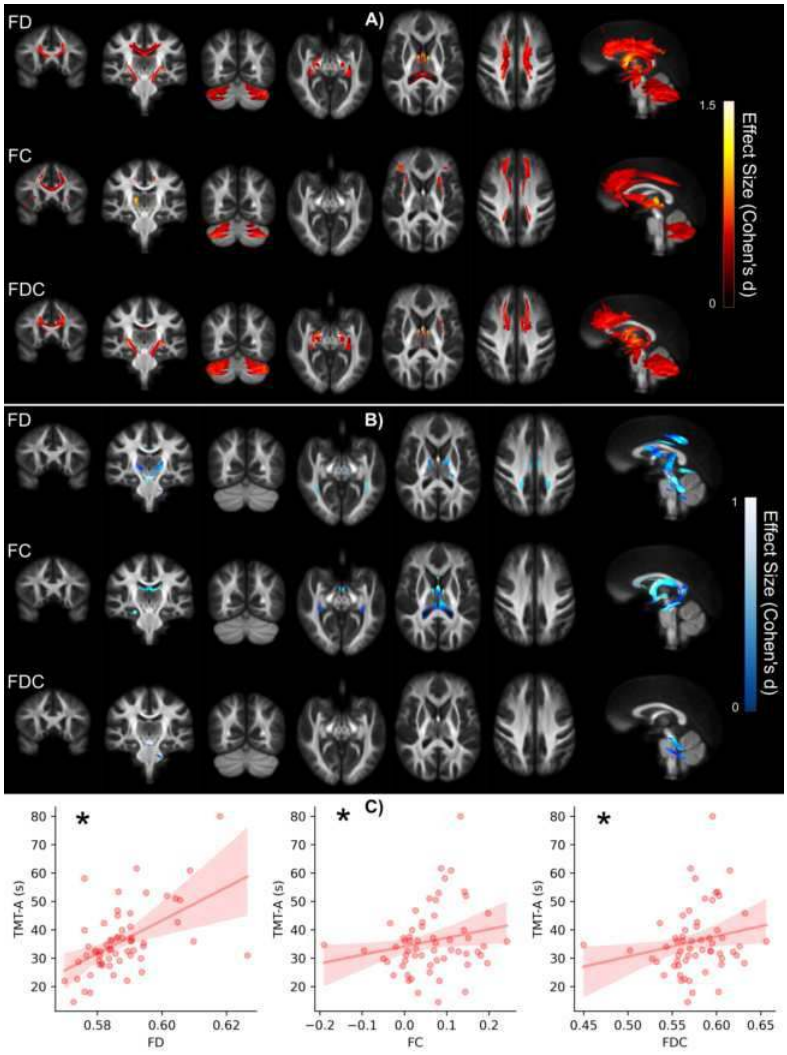

Fig. 1: A) WM areas with lower fiber density (FD), fiber bundle cross-section (FC), and fibre density and cross-section (FDC) in older subjects.
B) WM areas with greater FD, FC and FDC in older subjects. The sagittal view on the right side shows all fixels that met the threshold of $p_{FWE} < 0.05$.
C) A representative association of FD, FC and FDC in the corticospinal tract with TMT-A in older participants. * $p_{FWE} < 0.05$.

Conclusions: Our study provides additional insights into white matter alterations that occur with aging, utilizing a precise and interpretable approach known as fixel-based analysis. These findings highlight the complexity of age-related changes, involving both microstructural and macrostructural effects associated with variations in fiber density, cross-section, and FDC. This study demonstrates that fixel-based analysis could be valuable for exploring the white matter correlates of cognitive decline in older individuals.

References

1. Gunning-Dixon, F.M. (2000). The cognitive correlates of white matter abnormalities in normal aging: A quantitative review. Neuropsychology 14, 224–232.
2. Jeurissen, B. (2014). Multi-tissue constrained spherical deconvolution for improved analysis of multi-shell diffusion MRI data. Neuroimage, 103, 411–426.
3. Kelley, S. (2021). Age-Related Differences in White Matter: Understanding Tensor-Based Results Using Fixel-Based Analysis. Cereb. Cortex 31, 3881–3898.
4. Raffelt, D.A. (2017). Investigating white matter fibre density and morphology using fixel-based analysis. Neuroimage 144, 58–73.

Poster No 1599

Optimizing Diffusion MRI Strategies: Gradient Sampling Schemes and b-Values for Infants

Yajuan Zhang[1], Rui Zhou[1], Lin Zhang[2], Mingwen Yang[2], Zuozhen Lan[2], Ying Lin[3], Lixuan Zhu[1], Guoqiang Cheng[4], Xianghui Huang[3], Jungang Liu[2], Han Zhang[1,5]

[1]School of Biomedical Engineering, ShanghaiTech University, Shanghai, China, [2]Department of Radiology, Xiamen Children's Hospital, Children's Hospital of Fudan University, Xiamen, Fujian, China, [3]Fujian Key Laboratory of Neonatal Diseases, Children's Hospital of Fudan University (Xiamen Branch), Xiamen, Fujian, China, [4]Department of Neonatology,Children's Hospital of FudanUniversity, National Children's Medical Center, Shanghai, China, [5]Shanghai Clinical Research and Trial Center, Shanghai, China

Introduction: Multi-shell dMRI with simultaneous multi-slice imaging technique allows for characterizing complex diffusion signals with the help of advanced models such as neurite orientation dispersion and density imaging (NODDI) (Zhang et al., 2012) and constrained spherical deconvolution (CSD) (Jeurissen et al., 2014). However, the significantly prolonged acquisition time poses potential challenges, especially for infant where the available acquisition time for non-sedated healthy infants is limited. Furthermore, the infant brain consists of more water and less myelin; adult protocol cannot be directly applied. For large-scale infant brain development cohort (age 0-6 years), it is very critical and necessary to develop and valid a dMRI protocol balancing image quality, scanning time, and the dramatically changed macro-/micro-structure and connectomic attributes during early development. Taken together, this study did not only refer the existing infant cohorts (e.g., dHCP and BCP) (Bastiani et al., 2019; Howell et al., 2019) but also proposed modifications to the gradient sampling protocol and b-values, aiming to establishing infant dMRI protocol that offers accurate modeling while maintaining flexibility, quality, success rate across 0-6 years of age.

Methods: The infant dMRI protocol optimization is carried out for the China Baby Connectome Project (CBCP) as a pilot study. In this study, 5 subjects were recruited at 1 wk, 1 mo, 2 mo, 3 yrs, and 5 yrs, respectively. Multi-shell dMRI (TR/TE=3016/77.1ms, FOV=210×210 mm2, slices number=92, slice thickness=1.5 mm, multiband factor=4) were acquired with a 3.0T scanner (uMR890, United Imaging). To assess various candidate multi-shell schemes and establish an optimal one for infant dMRI longitudinal cohort, two experiments were conducted. Experiment 1: Comparing two gradient encoding schemes: 1) complete acquisitions of three-shell scheme (500, 1000, 3000 s/mm^2) with 9, 12, and 48 directions, respectively, at both AP and PA phase encoding (PE) directions (8min24s); 2) single acquisition of six b-value shells (500, 1000, 1500, 2000, 2500, 3000 s/mm^2) with 9, 12, 17, 24, 34, and 48 directions, respectively, with PA PE directions, and b=0 for AP PE (8min44s). Experiment 2: Determine best b-value combinations for infants using three sampling schemes (blow=500 s/mm^2, bmid=1000 s/mm^2, bhigh=2000, or 2500, or 3000 s/mm^2) with the same b-vectors. We systematically compared the derived DTI and NODDI indices and CSD-based orientation distribution function (ODF) for an optimized protocol.

Results: In preschoolers (3 and 5 yrs old), Schemes 1 and 2 generated very similar results. In three infants (1 wk, 1 mo, 2 mo old) with immature myelination, only the main fibers were detectable by both schemes. Nevertheless, compared to Scheme 2, Scheme 1 provided more accurate fiber orientations and enhanced sensitivity to crossing fibers (Fig 1). Compared to the schemes with bhigh of 2000 and 2500 s/mm^2, the scheme with bhigh of 3000 s/mm^2 exhibited greater sensitivity in ODF estimation to crossing fibers, while maintaining comparable performance using DTI and NODDI (Fig 2).

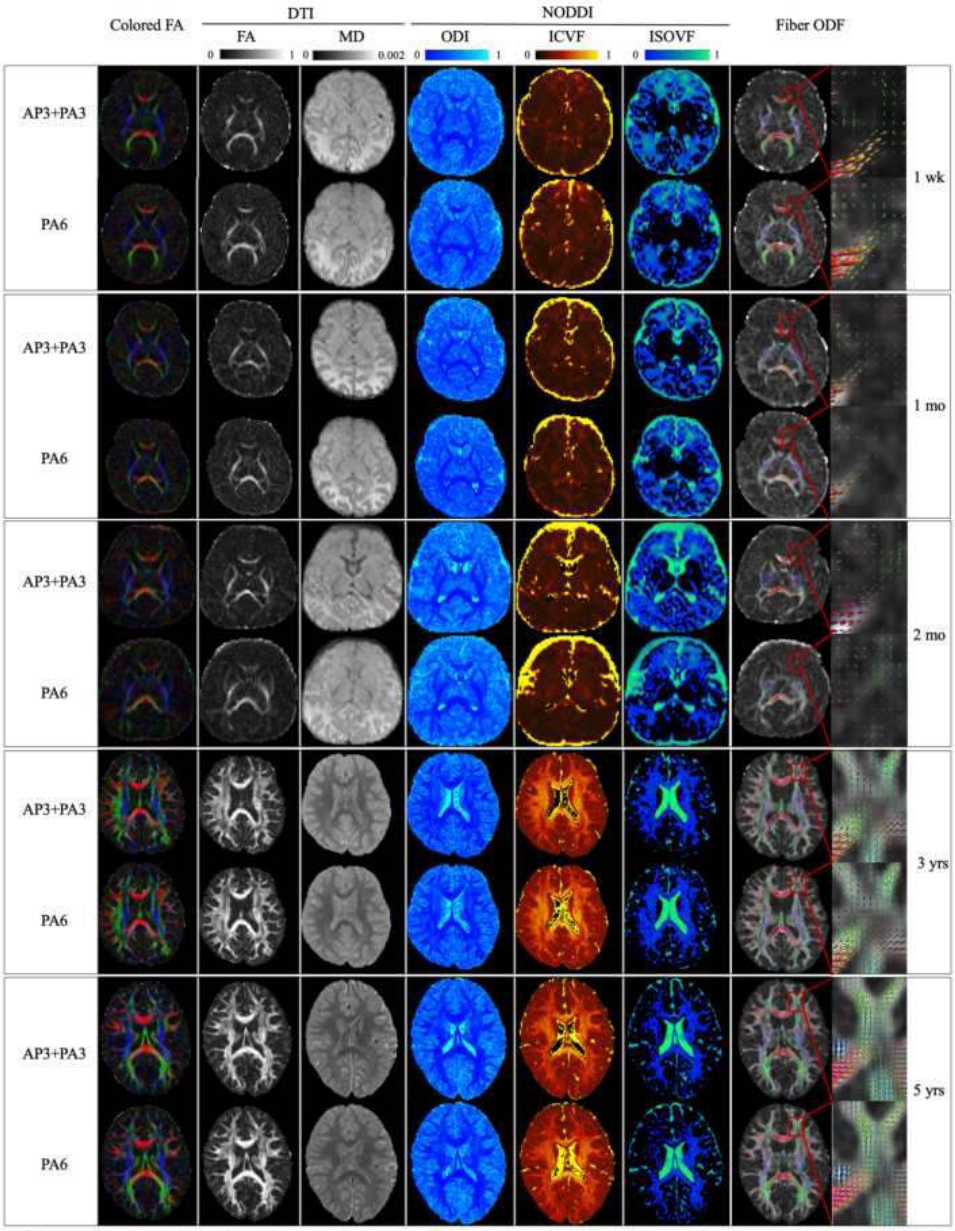

Fig 1 Qualitative evaluation of two gradient encoding schemes in five subjects. The figure displays results for the dominant orientation map, DTI (Fractional Anisotropy: FA; Mean Diffusivity: MD), NODDI (Orientation Dispersion Index: ODI; Intra-cellular Volume Fraction: ICVF; Cerebral Spinal Fluid Volume Fraction: ISOVF), and ODF. AP3+PA3: 3-shell scheme with both AP and PA PE; PA6: 6 b-value shells only with PA PE.

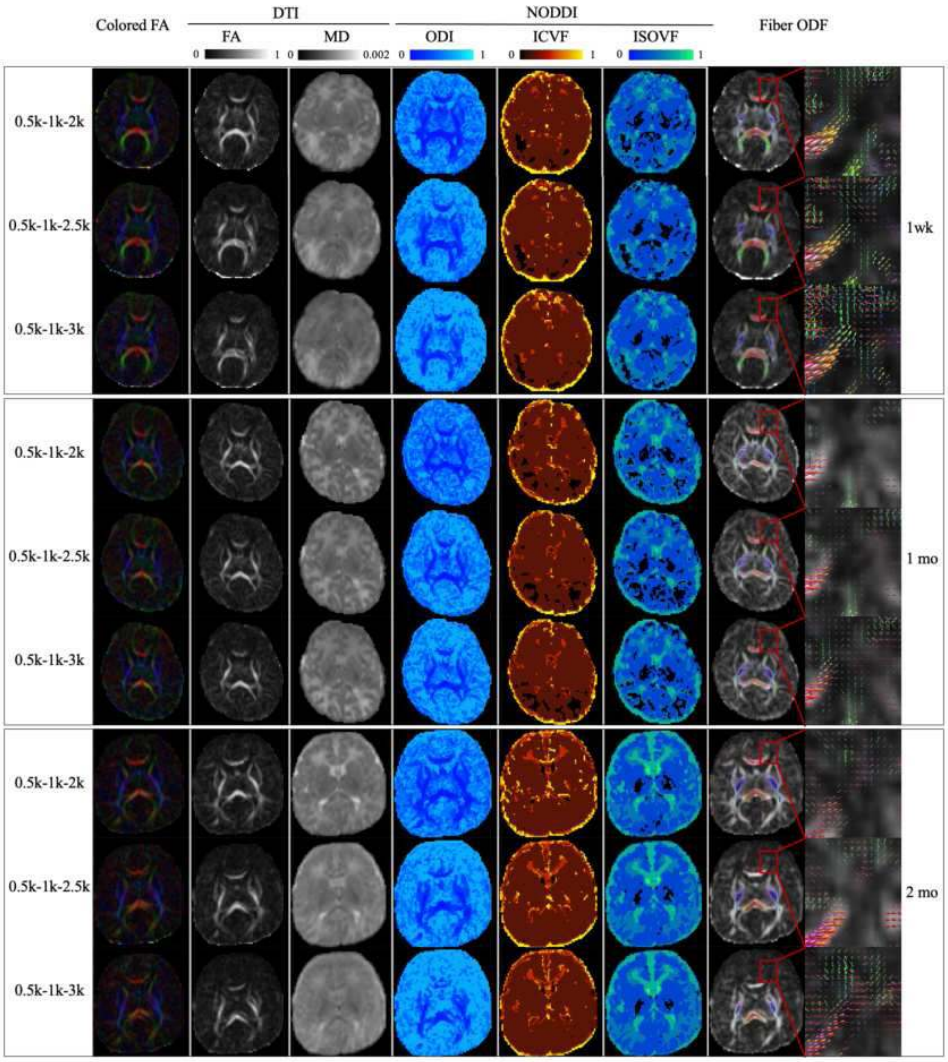

Fig 2 Qualitative evaluation of suitable maximal b-values for infants. The figure displays results for the dominant orientation map, DTI metrics (FA, MD), and NODDI metrics (ODI, ICVF, ISOVF)

Conclusions: This study established the optimal multi-shell infant dMRI acquisition scheme: three shells (500, 1000, 3000 s/mm^2) with 9, 12, and 48 directions, respectively, and a complete acquisition with both AP and PA PE directions. Additionally, all b-vectors and b-shells should be optimally ordered to ensure incremental acquisition within each shell and across all the shells. A blow of 500 s/mm^2 ensures compatibility to low myelination and high-water content in neonates, a bhigh of 3000 s/mm^2 enhances sensitivity to microstructures and the crossing fibers. Combining information from both full AP and PA PE acquisitions with 3 shells improves the quality of the infant dMRI derivatives without significantly prolonging acquisition time or local distortion. Our optimized dMRI provides suitable imaging protocol for infant studies with balanced data quality and acquisition time.

References

1. Bastiani, M. (2019). Automated processing pipeline for neonatal diffusion MRI in the developing Human Connectome Project. Neuroimage, 185, 750-763.
2. Howell, B. R. (2019). The UNC/UMN Baby Connectome Project (BCP): An overview of the study design and protocol development. Neuroimage, 185, 891-905.
3. Jeurissen, B. (2014). Multi-tissue constrained spherical deconvolution for improved analysis of multi-shell diffusion MRI data. Neuroimage, 103, 411-426.
4. Zhang, H. (2012). NODDI: practical in vivo neurite orientation dispersion and density imaging of the human brain. Neuroimage, 61(4), 1000-1016.

Acknowledgements

This work is partially supported by the STI 2030—Major Project (2022ZD0209000, 2021ZD0200516), Shanghai Pilot Program for Basic Research—Chinese Academy of Science, Shanghai Branch (JCYJ-SHFY-2022-014), Open Research Fund Program of National Innovation Center for Advanced Medical Devices (NMED2021ZD-01-001), Shenzhen Science and Technology Program (No. KCXFZ20211020163408012), and Shanghai Pujiang Program (No. 21PJ1421400).

Poster No 1600

A mesoscale ex vivo macaque white matter atlas using high-performance computing global tractography

Simon Legeay[1,2], Maëlig Chauvel[3], Fanny Darrault[4], Guillaume Dannhoff[4], Bastien Herlin[1], Felix Matuschke[5,2], Christophe Destrieux[4,6], Markus Axer[5,7,2], Ivy Uszynski[1,2], Frédéric Andersson[4], Igor Lima Maldonado[4,6], Cyril Poupon[1,2]

[1]BAOBAB, NeuroSpin, Université Paris-Saclay, CNRS, CEA, Gif-Sur-Yvette, France, [2]AIDAS Joint Institute, Research Centre Jülich, CEA, Jülich, Germany, Gif-sur-Yvette, France, [3]Department of Neurophysics, Max Planck Institute for Human Cognitive and Brain Sciences, Leipzig, Germany, [4]UMR 1253, iBrain, Université de Tours, Inserm, Tours, France, [5]Institute of Neuroscience and Medicine (INM-1), Research Centre Jülich, Jülich, Germany, [6]CHRU de Tours, Tours, France, [7]Department of Physics, University of Wuppertal, Wuppertal, Germany

Introduction: While global tractography offers enhanced accuracy and reliability compared to standard streamline tractography methods[1], it comes at the cost of substantial computational resources in terms of both time and memory. This approach simultaneously generates and optimizes the trajectories of virtual axonal white matter (WM) fibers (represented as connected spin-glasses), considering the local orientation distribution derived from diffusion MRI (dMRI) data. Leveraging this method on extensive datasets poses significant challenges, leading to the creation of ExaTract[2], a novel High-Performance Computing (HPC) global tractography approach. In this study, we demonstrate the ability of ExaTract to reconstruct numerous brain connections and robustly identify deep WM bundles from a very high resolution (250µm) dataset in a reasonable time.

Methods: Ex vivo brain: The brain of a 3-year-old female Macaca fascicularis was collected by the iBrain Unit (University of Tours, France). Imaging protocol: The sample was scanned using a Bruker Biospin 11.7 T MRI system equipped with a 60mm volume coil. The imaging protocol included a 3D T2-weighted (T2w) MSME 100µm scan, a 180µm 2D T2w MSME scan, and 250µm multishell dMRI scans using 3D segmented EPI PGSE sequences at b=1500/4500/8000s/mm2 along 25/60/90 directions (TE/TR=24/250ms, 33 segments)[3]. Pre-processing: After noise correction, dMRI data were used to compute an ODF map based on the analytical Q-ball model. A tractography mask was manually delineated by 2 independent neuroanatomists from the T2w MRI previously matched to the dMRI dataset using ANTs[4]. The mask was split into 160 partitions using METIS[5] to distribute global tractography optimization across supercomputer nodes while minimizing partition interfaces for communication cost preservation. Global tractography: According to the previous partitioning, ExaTract was launched on 20 nodes of the Joliot-Curie HPC cluster, with 160 MPI[6] processes, each with 16 multithreaded CPU cores, totaling 2560 CPU cores. The tractography framework was largely inspired by the works of[7,8] and used the following parameters: 4 initial spin-glasses/voxel, spin-glass length of 120um, connection maximum aperture angle 20°, ratio of connection/motion/creation/deletion=1/4/0.8/0.05, 1 simulated annealing cycle of initial/final temperature 0.1/0.03K, energy: connection likelihood L=4, αextern/αintern=1/3. Post-processing: A hierarchical fiber clustering algorithm[9] was applied using the Ginkgo toolbox[10] to classify fibers with close geometries into fasciculi. Deep WM bundle-contributing fasciculi were selected using identified ROIs at the crossroads of the target bundle.

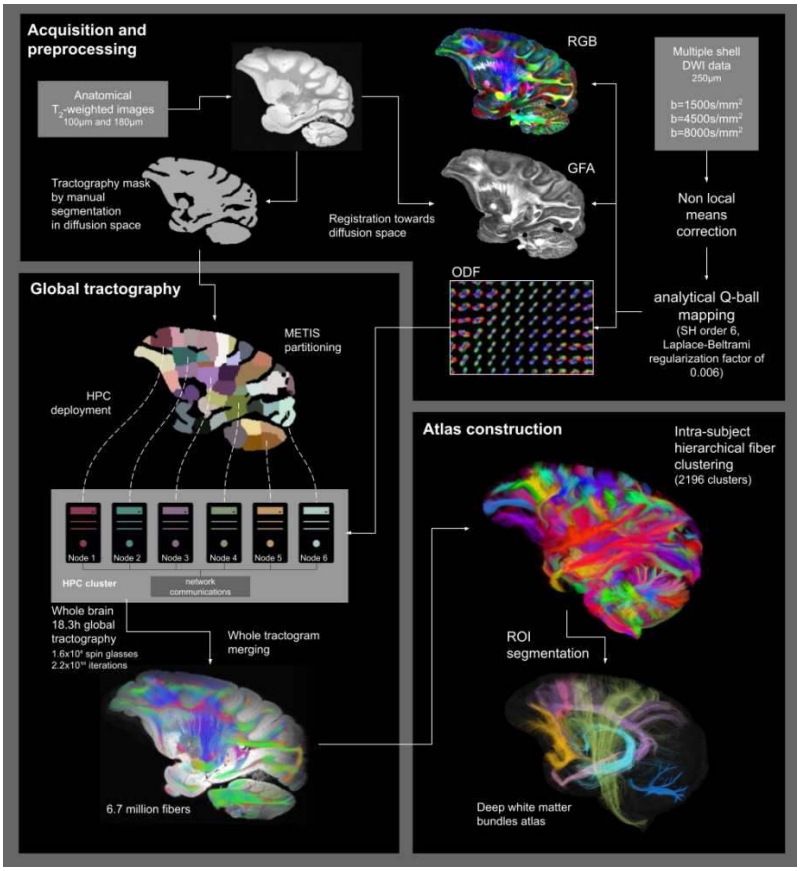

Results: The global tractography optimization took 18.3 hours to produce 6.7 million fibers by connecting 1.6x108 spin glasses through 2.2x1010 iterations. Tools like MRTrix or MITK face memory constraints:[8] generated 80.000 fibers from 2.5 million connected spin-glasses after 5x108 iterations within 12 to 24 hours on a single workstation. This fell short when representing the structural connectivity of the human brain. With ExaTract, we optimized 100 more spin-glasses through 100 more iterations in a comparable time frame, resulting in 84 times more fibers. We successfully recovered deep WM clusters, including the cingulum, fornix, CST, frontal aslant, uncinate bundles, corpus callosum, optical radiations, pontocerebellar fibers, anterior and posterior commissures (Fig2).

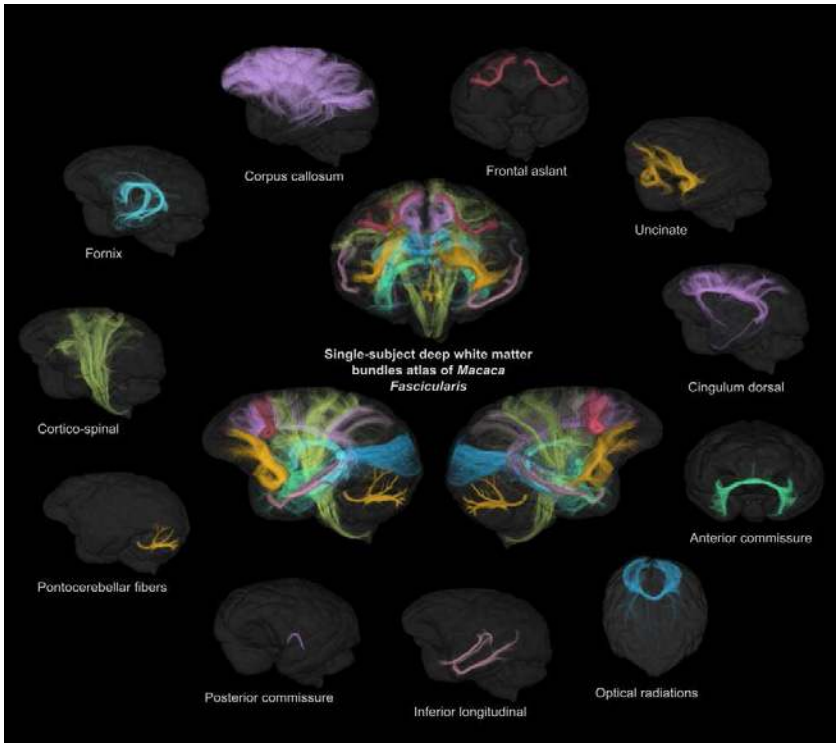

Conclusions: ExaTract, designed for HPC and compatible with upcoming exascale supercomputers, introduces a global tractography framework free from computational constraints. It enables fast and robust fiber tracking from ultra-high resolution datasets like ex vivo mesoscale diffusion MRI but also microscale PLI datasets in the coming future. It allowed the development of a novel mesoscopic WM atlas of the Macaca fascicularis.

References

1. Mangin, J.-F. (2013), 'Towards global tractography', NeuroImage, vol. 80, pp. 290-296
2. Legeay, S. (2023) 'High-Performance Computing global tractography for ultra-high resolution diffusion MRI and 3D-PLI', proceedings of OHBM 2023
3. Chauvel, M. (2022), 'Investigation of the inferior fronto-occipital fasciculus in the macaque fascicularis brain using ultra-high field MRI at 11.7 T', proceedings of OHBM 2022
4. Avants, B. B. (2009), 'Advanced normalization tools (ANTS)', Insight journal, 2(365), 1-35
5. Karypis, G. (1997), 'METIS: A Software Package for Partitioning Unstructured Graphs, Partitioning Meshes, and Computing Fill-Reducing Orderings of Sparse Matrices', retrieved from the University of Minnesota Digital Conservancy
6. Clarke, L. (1994), 'The MPI Message Passing Interface Standard', in Decker KM, Rehmann RM, eds. Programming Environments for Massively Parallel Distributed Systems. Monte Verità. Birkhäuser, pp. 213-218
7. Fillard, P. (2009), 'A Novel Global Tractography Algorithm Based on an Adaptive Spin Glass Model', Medical Image Computing and Computer-Assisted Intervention – MICCAI 2009, pp. 927-934
8. Reisert, M. (2009), 'Global reconstruction of neuronal fibres', In proceeding of MICCAI Diffusion Modelling Workshop 2009
9. Chauvel, M. (2023), 'In vivo mapping of the deep and superficial white matter connectivity in the chimpanzee brain', NeuroImage, vol. 282
10. https://framagit.org/cpoupon/gkg

Poster No 1601

Enhancing Tractometry Robustness with Streamline and Bundle-Specific Nonlinear Registration

Bramsh Chandio[1], Sophia Thomopoulos[2], Jaroslaw Harezlak[3], Eleftherios Garyfallidis[4], Paul Thompson[5]

[1]University of Southern California, Los Angeles, CA, [2]USC, Marina del Rey, CA, [3]Indiana University School of Public Health, Bloomington, IN, [4]Indiana University Bloomington, Bloomington, IN, [5]USC, Marina Del Rey, CA

Introduction: In tractometry, the goal is to analyze microstructural measures projected on specific segments along white matter tracts. Registration is used to establish correspondences between these segments across subjects, enabling segment-specific analyses. We incorporate BundleWarp[1] nonlinear streamline-specific bundle registration into BUndle ANalytics (BUAN)[2] tractometry pipeline to ensure that white matter tracts are accurately aligned and can be effectively analyzed and compared across individuals, enhancing the reliability and interpretability of results. We evaluate the effects of BundleWarp registration on group statistics using Alzheimer's Disease Neuroimaging Initiative Phase 3 (ADNI3) data[3].

Methods: We add BundleWarp registration into the BUAN tractometry pipeline, as shown in Figure 1. BUAN extracts bundles from populations and analyzes the microstructural measures (e.g., FA) projected onto the bundles along the length of the tracts to test for significant group differences. BUAN creates N horizontal segments along the length of the tracts to be analyzed. Horizontal segments are created based on points on the streamlines of a bundle belonging to the closest model bundle centroid point. Here, we add a partially deformable BundleWarp registration to nonlinearly align subjects' bundles with model bundles before creating the horizontal segments to find better segment correspondences among populations. Linear Mixed Models are applied to 6 WM bundles with group, age, and sex modeled as fixed effects and subject as a random effect term, the response variable being each DTI metric. We corrected for multiple comparisons using the FDR method. Note that the nonlinearly moved bundles are only used to assign segment numbers to points on the streamlines in the bundles. The actual statistical analysis always takes place in the native space of diffusion data. This step uses bundles of the original shape and microstructural measures in the native space, using segment labels given during the assignment step for segment-specific group analysis.

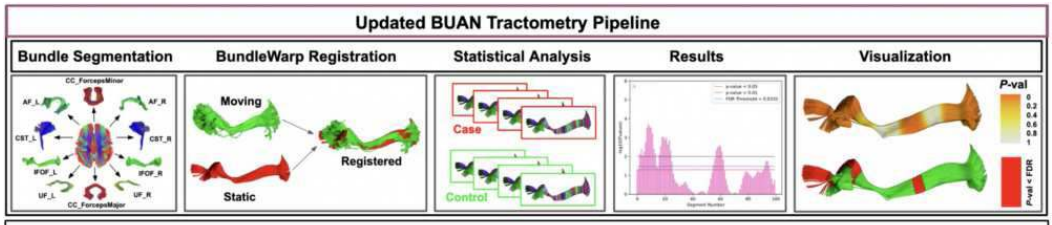

BUAN tractometry with BundleWarp registration: The pipeline starts with bundle segmentation from whole brain tractograms using a method called 'auto-calibrated *RecoBundles*'. Extracted bundles are then nonlinearly registered to atlas bundles using *BundleWarp*. *N* segments are created along the length of the bundles. Linear mixed models are run per segment along the length of the tracts. Results can be plotted as a graph or as *p*-values projected along the length of the tracts. Note that the nonlinearly moved bundles are only used to assign segment numbers to points on the streamlines in the bundles. The actual statistical analysis always takes place in the native space of the diffusion data. This step uses bundles of the original shape and microstructural measures in the native space, using segment labels given during the assignment step for segment-specific group analysis.

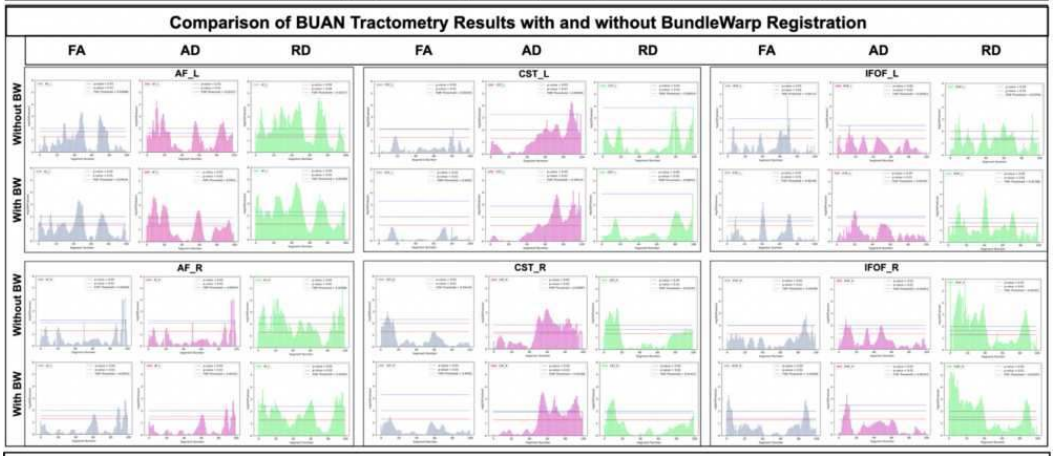

Figure 1: Six panels showing results of six bundles, bilateral arcuate fasciculus (AF_L, AF_R), corticospinal tract (CST_L, CST_R,) and inferior frontal occipital fasciculus (IFOF_L, IFOF_R) on three microstructural measures, FA, AD, and, RD. One bundle per panel. In each panel, the first row shows BUAN results without BundleWarp (BW) registration and the second row shows BUAN results with BW included in the tractometry pipeline. Plots have segment numbers along the length of the tract on the *x*-axis and negative logarithm of *p*-values on the *y*-axis. The third row shows qq-plots of *p*-values comparing the results of plots from the first two rows.

Results: Fig. 2 shows BUAN results (with and without BundleWarp) on the AF_L bundle using the FA metric. Fig.1 bottom panel, overall, from the results on six bundles (AF_L, AF_R, CST_L, CST_R, IFOF_L, and IFOF_R), BundleWarp made BUAN robust to outliers due to misaligned segments across groups and subjects . It enhanced the sensitivity for detecting group differences by mitigating errors from anatomical misregistration across subjects. However, in specific instances, a decrease in significance indicates that certain confounding effects may have been corrected that were due to disparities in tract alignment within each group. Moreover, adding nonlinear registration did not cause artifacts that substantially alter results relative to those obtained without BundleWarp.

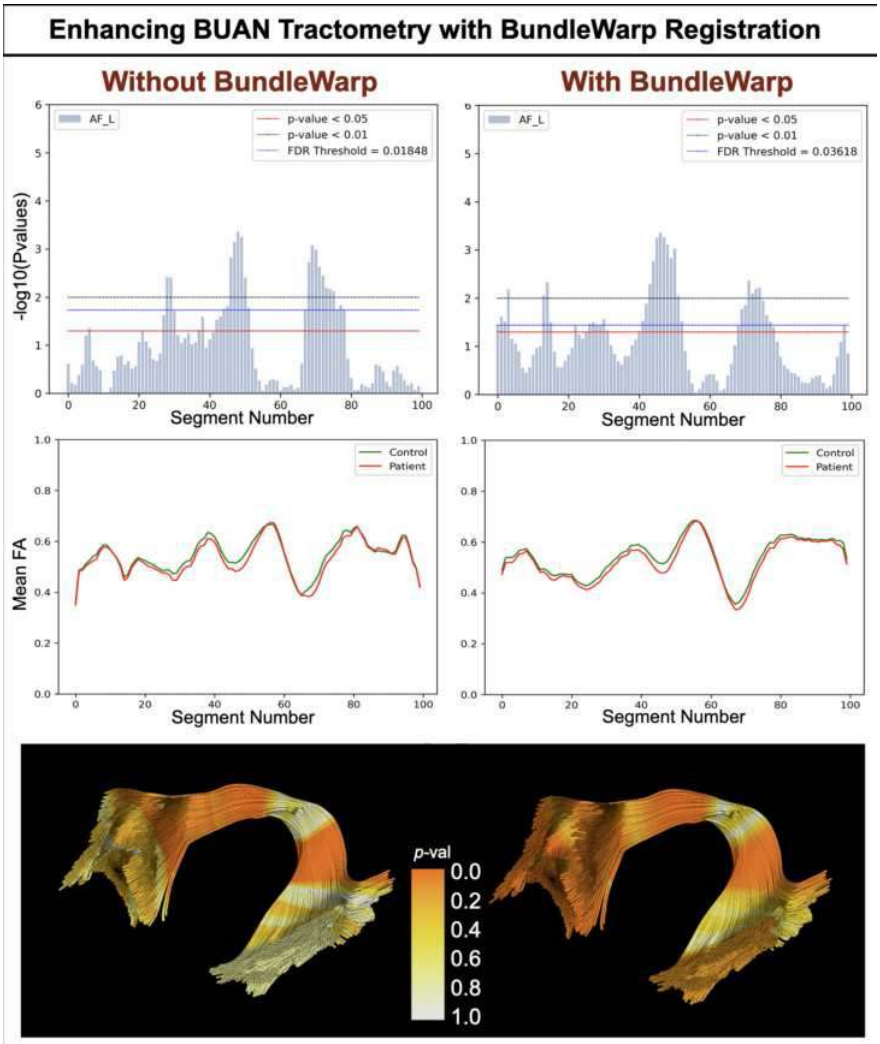

Figure 2: BUAN results without (*first column*) and with BundleWarp (*second column*) are presented for the left arcuate fasciculus (AF_L) bundle for the FA metric. Plots in the first row show the segment number on the *x*-axis and the negative logarithm of the *p*-values on the *y*-axis. We find stronger effects (lower *p*-values) in most segments with BundleWarp registration as compared to those without. Higher numbers of segments typically pass FDR. Plots in the second row show the mean FA of the MCI group in red and the mean FA of the control group in green. Adding BundleWarp registration provides smoother mean estimates. The last row visualizes *p*-values projected along the length of the AF_L bundle. *Darker orange* colors indicate lower *p*-values and greater group differences. We find more highly significant group differences (great effect sizes) with BundleWarp registration.

Conclusions: BundleWarp is a valuable addition to the BUAN tractometry pipeline for robust tractometric analysis. Nonlinearly aligning subjects' WM bundles with model bundles improves along-tract segment correspondence, increasing the sensitivity of group statistical analyses by eliminating errors due to misalignment across subjects.

References

1. Chandio, B.Q., Olivetti, E., Romero-Bascones, D., Harezlak, J. and Garyfallidis, E., 2023. BundleWarp, streamline-based nonlinear registration of white matter tracts. bioRxiv.
2. Chandio, B.Q., Risacher, S.L., Pestilli, F., Bullock, D., Yeh, F.C., Koudoro, S., Rokem, A., Harezlak, J. and Garyfallidis, E., 2020. Bundle analytics, a computational framework for investigating the shapes and profiles of brain pathways across populations. Scientific Reports, 10(1), pp.1-18.
3. Zavaliangos-Petropulu, A., Nir, T.M., Thomopoulos, S.I., Reid, R.I., Bernstein, M.A., Borowski, B., Jack Jr, C.R., Weiner, M.W., Jahanshad, N. and Thompson, P.M., 2019. Diffusion MRI indices and their relation to cognitive impairment in brain aging: the updated multi-protocol approach in ADNI3. Frontiers in Neuroinformatics, 13, p.2.
4. Thomopoulos, S.I., Nir, T.M., Villalon-Reina, J.E., Zavaliangos-Petropulu, A., Maiti, P., Zheng, H., Nourollahimoghadam, E., Jahanshad, N., Thompson, P.M., for the Alzheimer's Disease Neuroimaging Initiative. Diffusion MRI Metrics and their Relation to Alzheimer's Disease Severity: Effects of Harmonization Approaches. SIPAIM 2021, Campinas, Brazil. 2021.
5. Tournier, J.-D., Calamante, F. & Connelly, A. Robust determination of the fibre orientation distribution in diffusion MRI: non-negativity constrained super-resolved spherical deconvolution. NeuroImage 35, 1459–1472 (2007).
6. Girard, G., Whittingstall, K., Deriche, R., & Descoteaux, M. Towards quantitative connectivity analysis: reducing tractography biases. NeuroImage, 98, 266-278, 2014.
7. Garyfallidis, E., Brett, M., Amirbekian, B., Rokem, A., van der Walt, S., Descoteaux, M. and Nimmo-Smith, I., "Dipy, a library for the analysis of diffusion MRI data," Front. Neuroinform. 8, 8 (2014).
8. Garyfallidis, E., Côté, M.A., Rheault, F., Sidhu, J., Hau, J., Petit, L., Fortin, D., Cunanne, S. and Descoteaux, M., 2018. Recognition of white matter bundles using local and global streamline-based registration and clustering. NeuroImage, 170, pp.283-295.

Poster No 1602

Advanced diffusion modeling classifies FLAIR white matter hyperintensity types in an aging cohort

Kelly Chang[1], Luke Burke[2], Nina LaPiana[1], Bradley Howlett[1], David Hunt[1], Margaret Dezelar[2], Jalal Andre[1], James Ralston[2], Ariel Rokem[1], Christine Mac Donald[1]

[1]University of Washington, Seattle, WA, [2]Kaiser Permanente Washington Health Research Institute, Seattle, WA

Introduction: White matter hyperintensities (WMH) in fluid-attenuated inversion recovery (FLAIR) imaging are used as an indicator of clinical conditions ranging from multiple sclerosis to cerebrovascular disease (Ferris et al., 2022; Preziosa et al., 2023). However, the biophysics underlying FLAIR WMH is only partially understood, and current diagnostic standards rely on cumbersome visual inspection. In contrast, advanced diffusion MRI (dMRI) modeling, such as multi-shell and high angular resolution imaging, provides biophysically interpretable tissue properties. To study the relationships between biophysical tissue properties and FLAIR WMH in aging, we used a combination of unsupervised and supervised machine learning to classify the distribution of tissue properties within WMH regions of interest (ROI) in a sample from the Adult Changes in Thought (ACT) study (Kukull et al., 2002).

Methods: 143 participants (ages 70 - 103, mean age = 80.23; 80 females) underwent T1-weighted (T1w), T2-weighted (T2w), and FLAIR structural imaging as well as multi-shell diffusion MRI. We used a neural network (Forooshani et al., 2022) to automatically segment WMH voxels from FLAIR images. WMH regions of interest (ROIs) were defined to be a cluster of contiguous WMH voxels. The WMH ROIs were then categorized as periventricular if the ROI was adjacent to the lateral ventricles – taking care to exclude voxels immediately adjacent (within 1 mm) to the ventricles to avoid partial volume effects – or as deep otherwise. The remaining white matter volume was categorized as normal-appearing white matter (NWM). Diffusion modeling was performed on the QSIprep-0.18.1 (Cieslak et al., 2021) preprocessed data. Diffusional kurtosis imaging (DKI; Jensen et al., 2005), free-water diffusion tensor imaging (FWDTI; Hoy et al., 2014) and mean apparent propagator MRI (MAPMRI; Özarslan et al., 2013) models were fit using the Diffusion Imaging in Python (DIPY) software library. The neurite orientation dispersion and density imaging (NODDI) model (Zhang et al., 2012) was fit using the accelerated microstructure via convex optimization (AMICO) library. We derived several metrics from these models (and T1w/T2w), which were normalized to each participant's average within their white matter volume.

Results: We found that periventricular WMH were characterized by greater mean diffusivity and extracellular water content, and less myelination (quantified as T1w/T2w ratio) than NWM (Figure 1A). Whereas deep WMH was more similar to NWM, except for a slightly greater mean diffusivity and a large decrease in myelination as indicated by the T1w/T2w ratio (Figure 1B). We performed a principal components analysis (PCA) on the biophysical metrics, where the first two components explained 83.28% of the variance in the dataset (Figure 2A). A logistic regression classifier was trained on the first two PCs was able to classify periventricular and deep WMH ROIs with an average cross-validation accuracy of 77.84% (± 0.71%). We confirmed the classification performance by training a separate logistic regression classifier on the biophysical metrics, while controlling for age (refer to Figure 2B for model coefficients). The biophysical logistic regression had an average cross-validation classification accuracy of 80.64% (± 0.89%).

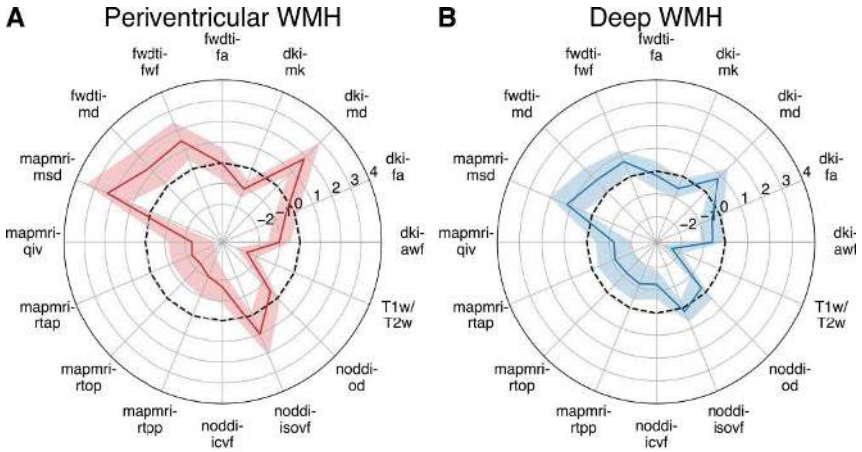

Figure 1. Normalized biophysical metrics of periventricular and deep white matter hyperintensities (WMH). (A) Biophysical metrics within periventricular WMH. (B) Biophysical metrics within deep WMH. The biophysical metrics were normalized to participant's overall white matter. The solid line represents the average and the shared regions represents ± 1 standard deviation.

Model Abbreviations: dki = Diffusional Kurtosis Imaging; fwidti = Free-water diffusion tensor imaging; mapmri = Mean apparent propagator MRI; noddi = Neurite orientation dispersion and density imaging. *Metric Abbreviations*: awf = Axonal water fraction; fa = Fractional anisotropy; md = Mean diffusivity; mk = Mean kurtosis; fwf = Free-water fraction; msd = Mean squared displacement; qiv = Q-space inverse variance; rtap = Return to axis probability; rtop = Return to origin probability; rtpp = Return to plane probability; icvf = Intracellular volume fraction; isovf = Isotropic volume fraction; od = Orientation dispersion; T1w/T2w = T1w / T2w ratio.

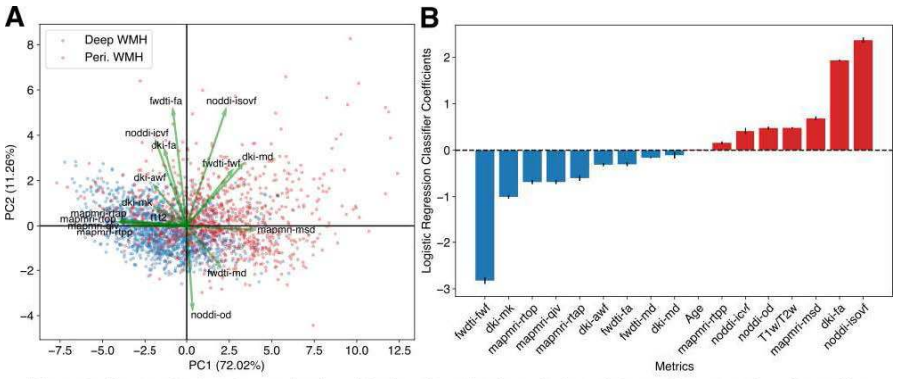

Figure 2. Unsupervised and supervised machine learning of periventricular and deep white matter hyperintensities (WMH). (A) Periventricular and deep WMH along the first two principal components. The green vectors reflect the projection of biophysical metric axes into PC space. (B) Coefficients of the logistic regression classifier trained to classify periventricular and deep WMH. Error bars represent ± 1 SEM across cross-validation folds.

Conclusions: This study highlights the potential of advanced dMRI modeling in characterizing the biophysical properties of periventricular and deep WMH. The biophysical metric patterns indicate that periventricular and deep WMH tissue begins to resemble ventricles more than NWM, particularly in the case of periventricular WMH. Furthermore, the high classification accuracy achieved by the linear SVM emphasized the differences in underlying tissue properties of periventricular and deep WMH, suggesting pathological differences between the two WMH types.

References

1. Cieslak, M. (2021). "QSIPrep: An integrative platform for preprocessing and reconstructing diffusion MRI data", Nature Methods, vol. 18, no. 7, pp. 775-778
2. Ferris, J. K. (2022). "In vivo myelin imaging and tissue microstructure in white matter hyperintensities and perilesional white matter", Brain communications, vol. 4, no. 3, fcac142
3. Forooshani, P. M. (2022). "Deep Bayesian networks for uncertainty estimation and adversarial resistance of white matter hyperintensity segmentation", Human Brain Mapping, vol. 43, no. 7, pp. 2089-2108
4. Hoy, A. R. (2014). "Optimization of a free water elimination two-compartment model for diffusion tensor imaging", NeuroImage, vol. 103, pp. 323-333.
5. Jensen, J. H. (2005). "Diffusional kurtosis imaging: The quantification of non-gaussian water diffusion by means of magnetic resonance imaging", Magnetic Resonance in Medicine, vol. 53, no. 6, pp. 1432-1440
6. Kukull, W. A. (2002). "Dementia and Alzheimer disease incidence: A prospective cohort study", Archives of neurology, vol. 59, no. 11, pp 1737-1746
7. Özarslan, E. (2013). "Mean apparent propagator (MAP) MRI: A novel diffusion imaging method for mapping tissue microstructure", NeuroImage, vol. 78, pp. 16-32
8. Preziosa, P. (2023). "NODDI, diffusion tensor microstructural abnormalities and atrophy of brain white matter and gray matter contribute to cognitive impairment in multiple sclerosis", Journal of neurology, vol. 270, no. 2, pp. 810–823
9. Zhang, H. (2012). "NODDI: Practical in vivo neurite orientation dispersion and density imaging of the human brain", NeuroImage, vol. 61, no. 4, pp. 1000-1016

Poster No 1603

Age-Related Variations in Glymphatic System Captured by Perivascular Diffusivity

Chao-Hsin Ding[1], Chih-Chin Heather Hsu[1], Shin Tai Chong[1], Ching-Po Lin[1,2]

[1]Institute of Neuroscience, National Yang Ming Chiao Tung University, Taipei, Taiwan, [2]Department of Education and Research, Taipei City Hospital, Taipei, Taiwan

Introduction: The glymphatic system plays a crucial role in brain waste clearance. In recent years, research has delved into understanding the relationship between aging and the glymphatic system functionality[1]. In this system, the influx of CSF into the perivascular space (PVS) plays an important role in clearing brain waste, enabling fluid and solute exchange in the brain, and supporting overall brain health. Previous studies have suggested that the dysfunction of PVS influx may contribute to various neurological diseases[2]. Capturing the PVS diffusivity may serve as a biomarker for evaluating glymphatic system performance. However, methods for animal studies are usually invasive[3], while human studies, though effective in capturing glymphatic function in disease or aging, rely on indirect, region-specific measures[4]. In this study, we aim to directly quantify the diffusivity within the PVS area. We utilized the T1-weighted (T1w) images for PVS segmentation[5] and pseudo diffusion tensor images (pDTI)[6] for quantifying the diffusivity within the PVS area. We examined the relation between PVS volume fraction (PVSVF) and the diffusivity within the PVS in adult group to evaluate its potential as a biomarker of glymphatic function.

Methods: Eighty-nine healthy participants (age range: 20-50, median: 27.9±6.15) underwent T1w and diffusion-weighted imaging (DWI) scans on a 3T MRI scanner at National Yang Ming Chiao Tung University. DWIs were acquired at two b-values (300 and 500) with 20 directions in each shell. For PVS mapping, T1w images were preprocessed by following steps: image alignment, bias correction, and denoising via ANTs, FSL, and an adaptive non-local means filter developed by José V. Manjón[7], respectively. After preprocessing, Frangi filter was used for PVS segmentation with a threshold of t -=2.3[5,8]. Finally, we calculated the PVSVF by dividing the voxel count within the PVS area by the total intracranial volume. On the other hand, DWIs were preprocessed via iDIO and the pDTI was calculated by MRtrix . The PVS regions were then overlaid on the pDTI map to investigate their diffusivity characteristics.

Results: Figure 1 shows the T1w image, PVS area map, and the pseudo-diffusivity (D*) map from a representative participant. Across participants, the median PVSVF was 0.002±3.67×10-4. The scatter plot in Figure 2a showed no clear correlation among PVSVF, D*, and age. K-mean clustering categorized participants into four subgroups. The Kruskal-Wallis's test didn't indicate a statistically significant difference in age across groups (p=0.09), yet a trend of increasing PVSVF with age was noted. The youngest participants (G4) had lower PVSVF and higher D* (median age=25.6±5.30), whereas the oldest participants (G3) demonstrated higher values in both measures (median age=32.9±6.63) (Figure 2b and 2d). Moreover, when aggregating the data by PVSVF, G1+G3, with higher PVSVF, corresponded to an older age profile (median age=29.4±6.08), while G2+G4, with lower PVSVF, had a younger demographic (median age=26.8±6.14) (Figure 2c). Similarly, when groups were combined based on D*, participants with lower D* (G1+G2) were older (median age=29.3±6.11) compared to those with higher D* (group G3+G4) who were younger (median age=26.1±6.07) (Figure 2e).

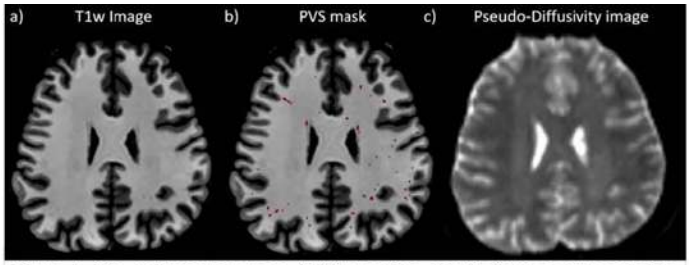

Figure 1. The perivascular space (PVS) mapping results from a representative participant. a) T1w image of the representative participant. b) Perivascular space. The red area represents the perivascular space (PVS) in the white matter. c) Pseudo-diffusivity image.

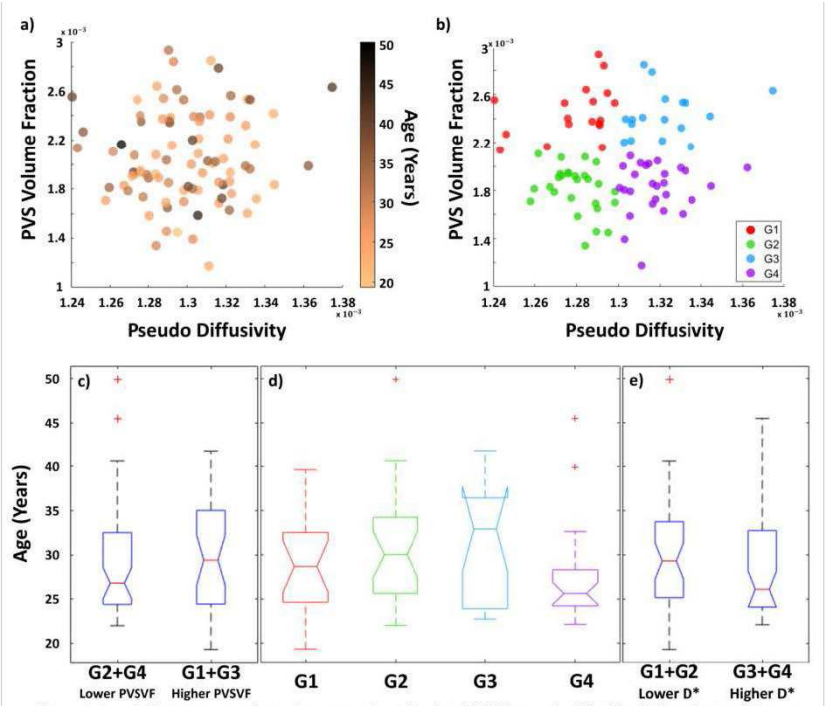

Figure 2. Associations among perivascular space volume fraction (PVSVF), pseudo diffusivity (D*), and age. a) Scatter plot correlating PVSVF and D*, with each point representing the median value of individual participants' PVSVF and D*, color-coded by age. b) participants were clustered into four groups by the k-mean algorithm. G1(red): N=18; Median age: 28.7±5.48. G2(green): N=27; Median age: 30±6.47. G3(blue): N=17; Median age: 32.9±6.63. G4(purple): N=27; Median age: 25.6±5.30. c, d, e) The box plots of the age distribution of different groups. The outliers were shown in red plus symbol. In c), groups were merged by PVSVF. G2+G4: N=54; Median age: 26.8±6.14. G1+G3: N=35; Median age: 29.4±6.08. in e), groups were merged by D*. G1+G2: N=45; Median age: 29.3±6.11. G3+G4: N=44. Median Age: 26.1±6.07. The unit of D* is mm^2/s.

Conclusions: Despite the absence of a clear correlation between PVSVF, D*, and age in the overall sample, the application of the K-mean clustering revealed distinct age-related patterns within specific subgroups. Our findings suggest an association of lower PVSVF and higher D* with younger individuals. Conversely, in the aggregated groups, participants with higher PVSVF and lower D* tended to be older. These patterns underline the potential of PVSVF and D* as indicators for assessing glymphatic function across age demographics. Future research could benefit from expanding the age range and sample size or incorporating longitudinal data to substantiate the reliability and clinical relevance of these measures.

References

1. Bohr, Tomas et al. (2022). "The glymphatic system: Current understanding and modeling". iScience, vol. 25, no. 9, pp. 104987.
2. Kaur, Jasleen et al. (2020). "Magnetic Resonance Imaging and Modeling of the Glymphatic System." Diagnostics (Basel, Switzerland), vol. 10, no. 6, pp. 344.
3. Iliff, Jeffrey J et al. (2012). "A paravascular pathway facilitates CSF flow through the brain parenchyma and the clearance of interstitial solutes, including amyloid β." Science translational medicine, vol. 4, no. 147. pp. 147ra111
4. Taoka, Toshiaki et al. (2017). "Evaluation of glymphatic system activity with the diffusion MR technique: diffusion tensor image analysis along the perivascular space (DTI-ALPS) in Alzheimer's disease cases." Japanese journal of radiology, vol. 35, no. 4, pp. 172-178.
5. Sepehrband, Farshid et al. (2019). "Image processing approaches to enhance perivascular space visibility and quantification using MRI." Scientific reports vol. 9, no. 1, pp. 12351.
6. Harrison, Ian F et al. (2018) "Non-invasive imaging of CSF-mediated brain clearance pathways via assessment of perivascular fluid movement with diffusion tensor MRI." eLife vol. 7, no. e34028.
7. Manjón, José V et al. (2010) 'Adaptive non-local means denoising of MR images with spatially varying noise levels." Journal of magnetic resonance imaging: JMRI vol. 31, no. 1, pp. 192-203.
8. Cabeen, R. P. et al. (2018). 'Quantitative Imaging Toolkit: Software for Interactive 3D Visualization, Data Exploration, and Computational Analysis of Neuroimaging Datasets '. Proceedings of the International Society for Magnetic Resonance in Medicine (ISMRM), no. 2854.

Poster No 1604

Assessing substantia nigra pars compacta connections with 3T and 7T multi-shell diffusion MRI

Federica Franza[1], Giuseppina Caiazzo[1], Giovanni Cirillo[1], Michele Papa[1], Mario Cirillo[1], Fabrizio Esposito[1]

[1]University of Campania "Luigi Vanvitelli", Naples, Italy

Introduction: Structural connections through the substantia nigra pars compacta (SNc) could be disrupted at the early stages of Parkison's disease[1]. High angular resolution diffusion imaging (HARDI) tractography from multi-shell (MS) HARDI MRI series allows investigating whole-brain structural connections non-invasively in humans[2,3] but its application to the quantitative analysis of subcortico-subcortical connections is still limited[4]. Here we compared the relative percentages of connections through SNpc terminating in the striatum or the thalamus across three different data sets, acquired at 3T and 7T in healthy human adults, using 3-shell protocols derived from ADNI (https://adni.loni.usc.edu) and HCP (https://www.humanconnectome.org) initiatives.

Methods: Two MS-HARDI MRI data sets were serially acquired on a 3 T scanner at 1.5 mm isotropic resolution using ADNI (MS1) and HCP (MS2) protocols in 10 healthy human subjects (5 males, mean age ± std. 23.8 ± 3.65 years, age range: 25-30 years). Additional HCP 7T data sets from 10 age- and sex-matched healthy subjects, acquired at 1.0 mm isotropic resolution, were retrieved from the public HCP database[5]. Whole-brain tractograms were reconstructed via MRtrix (www.mrtrix.org) using the inverse fiber orientation distribution algorithm ver. 2[6] within the anatomical constrained tractography framework[7]. Binary masks for subcortical regions of inclusion/exclusion were taken from validated anatomical atlases. Starting from the full set of streamlines through SNc, only those terminating in the striatum or thalamus were selected, after excluding those encompassing nearby structures according to previous knowledge[4]. The streamline counts were normalized to the total number of SNc streamlines, obtaining a relative connection index (%). Wilcoxon signed rank and rank sum tests were used to compare median estimates from MS1 vs. MS2 data sets (same subjects) and from MS1/MS2 vs. HCP-7T data sets (different subjects).

Results: For the left (right) nigrostriatal pathway (figure 1), the median connection index (± IQR) was 7.20 ± 1.26 (6.56% ± 1.21) for MS1, 5.79% ± 1.35 (4.95% ± 1.98) for MS2, and 4.91% ± 1.91 (7.47% ± 3.28) for HCP (figure 2a). For the left (right) nigrothalamic pathway, the median connection index (± IQR) was 13.17% ± 5.74 (9.05% ± 3.62) for MS1, 10.99% ± 3.26 (7.86% ± 2.89) for MS2, and 9.66% ± 3.45 (6.12% ± 3.27) for HCP (figure 2b). The median index of the SNc-striatum connection was significantly higher for MS1 (ADNI-3T), compared to MS2 (HCP-3T) (left: $p = 0.0020$, right: $p = 0.0039$) and, for the left hemisphere, to HCP-7T ($p = 0.0073$), data sets. The median index of SNc-Thalamus connection was not significant different between MS1 and MS2 (3T) data sets and between MS1/MS2 (3T) and HCP 7T datasets.

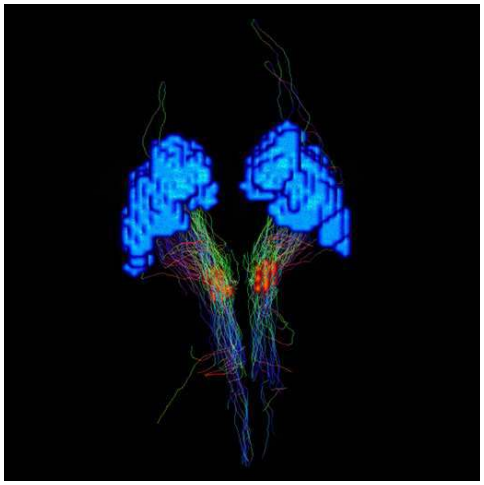

Figure 1. 3D visualization of the streamlines between SNc and the striatum for one representative subject acquired with MS1 (ADNI-3T).

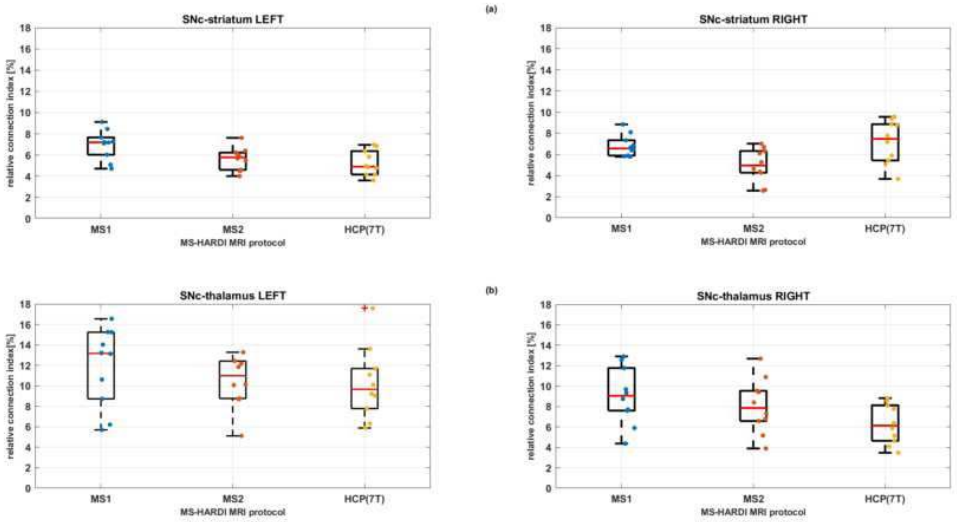

Figure 2. Relative connection index estimated from MS1 (ADNI-3T) , MS2 (HCP-3T) and HCP-7T datasets for both hemispheres: (a) target region: striatum; (b) target region: thalamus.

Conclusions: MS-HARDI protocols derived from ADNI and HCP initiatives identified non-zero putative nigro-striatal and nigro-thalamic connections. A significantly higher SNc-Striatum connectivity was obtained from MS1 (ADNI-3T), compared to MS2 (HCP-3T) data sets, on the same subjects, despite MS1 having less directions. Most likely, the shorter acquisition time of MS1 data sets might have reduced the impact of motion artifacts. MS1 (3T) data sets also revealed relatively more SNc-Striatum connections than HCP (7T) data sets in the left hemisphere despite the lower spatial resolution. A larger intersubject variability was observed for the putative SNc-Thalamus connections with no significant differences between datasets. Nevertheless, these estimates should be taken more carefully since there is no current evidence in humans for direct nigro-thalamic pathways. Furthermore, the estimates did not expressly account for volumes of, or distances between, the regions, making it not appropriate to compare estimates between different target regions[8].

References

1. Y. Zhang et al., «Diffusion tensor imaging of the nigrostriatal fibers in Parkinson's disease.», Mov Disord, vol. 30, fasc. 9, pp. 1229–1236, ago. 2015, doi: 10.1002/mds.26251.
2. F. Trojsi et al., «High angular resolution diffusion imaging abnormalities in the early stages of amyotrophic lateral sclerosis», Journal of the Neurological Sciences, vol. 380, pp. 215–222, set. 2017, doi: 10.1016/j.jns.2017.07.039.
3. B. Jeurissen et al., «Multi-tissue constrained spherical deconvolution for improved analysis of multi-shell diffusion MRI data», NeuroImage, vol. 103, pp. 411–426, dic. 2014, doi: 10.1016/j.neuroimage.2014.07.061.
4. A. Quartarone et al., «New insights into cortico-basal-cerebellar connectome: clinical and physiological considerations.», Brain, vol. 143, fasc. 2, pp. 396–406, feb. 2020, doi: 10.1093/brain/awz310.
5. A. T. Vu et al., «High resolution whole brain diffusion imaging at 7T for the Human Connectome Project.», Neuroimage, vol. 122, pp. 318–331, nov. 2015, doi: 10.1016/j.neuroimage.2015.08.004.

6. J.-D. Tournier et al., «Improved probabilistic streamlines tractography by 2nd order integration over fibre orientation distributions», Proc. Intl. Soc. Mag. Reson. Med. (ISMRM), vol. 18, gen. 2010.
7. R. E. Smith et al., «Anatomically-constrained tractography: improved diffusion MRI streamlines tractography through effective use of anatomical information.», Neuroimage, vol. 62, fasc. 3, pp. 1924–1938, set. 2012, doi: 10.1016/j.neuroimage.2012.06.005.
8. Y.-N. Chang et al., «Distance-dependent distribution thresholding in probabilistic tractography.», Hum Brain Mapp, vol. 44, fasc. 10, pp. 4064–4076, lug. 2023, doi: 10.1002/hbm.26330.

Poster No 1605

Mapping White Matter Anomalies in Parkinson's Disease Progression using Deep Normative Tractometry

Yixue Feng[1], Conor Owens-Walton[1], Bramsh Chandio[1], Julio Villalón-Reina[1], Corey McMillan[2], Peter Opriessnig[3], Petra Schwingenschuh[3], Duygu Tosun[4], Sophia Thomopoulos[1], Ysbrand van der Werf[5], Neda Jahanshad[1], Paul Thompson[1]

[1]University of Southern California, Los Angeles, CA, [2]University of Pennsylvania, Philadelphia, PA, [3]Medical University of Graz, Graz, Austria, [4]University of California, San Francisco, San Francisco, CA, [5]Vrije Universiteit Amsterdam, Amsterdam, Netherlands

Introduction: Normative models (NM) can be applied to brain metrics derived from structural, functional, and diffusion MRI to quantify individual deviations from the statistical distribution observed in a reference population, with applications in neurology and psychiatry. NMs have recently been extended to tractometry, using deep autoencoders (AE) to detect individual anomalies in white matter (WM) microstructure from diffusion MRI. While traditional NMs are typically estimated for single brain measures (e.g. hippocampal volume), AEs can encode statistical distributions of complex features such as 3D tract geometry as well as continuously varying measures along tracts. We have shown in our prior work that a Variational Autoencoder (VAE), the generative counterpart of AE, is able to capture structural features of tracts and can be used for anomaly detection in AD when trained on data from healthy controls (HC). In this work, we extend our framework to jointly model the 3D geometry of WM tracts and their microstructures, and show its ability to identify along-tract abnormalities across different stages of Parkinson's Disease (PD) in a multi-site cohort.

Methods: dMRI data from 112 HC and 437 participants with PD (age range: 31-87; 197 F/352 M) collected at 4 sites were preprocessed using the ENIGMA-DTI pipeline. Constrained spherical deconvolution reconstruction and the deterministic EuDX tracking method were used to generate whole-brain tractograms; 30 WM bundles were extracted using BUAN pipeline. To leverage a larger sample of HC, the VAE model was first pre-trained on 30 WM tracts from 198 HC of the TractoInferno dataset. Input features to the model contained 3D coordinates and fractional anisotropy (FA) mapped to 128 points per streamline in the native space. We then created 100 bootstrap samples from 50 HC participants for fine-tuning and calculated anomaly scores (mean absolute error, MAE) along 100 segments of each bundle for the remaining 62 HC and 437 PD subjects averaged across all the bootstrap sets (Fig. 1). ComBat harmonization was applied on along-tract MAE to adjust for site effects and linear regression was used to correct for age and sex effects. Group comparisons between HC and Hoehn-Yahr (HY) stage 1, 2, and 3 participants were conducted using a cluster-based permutation test on the t-statistic at alpha=0.05 to account for correlation between neighboring segments.

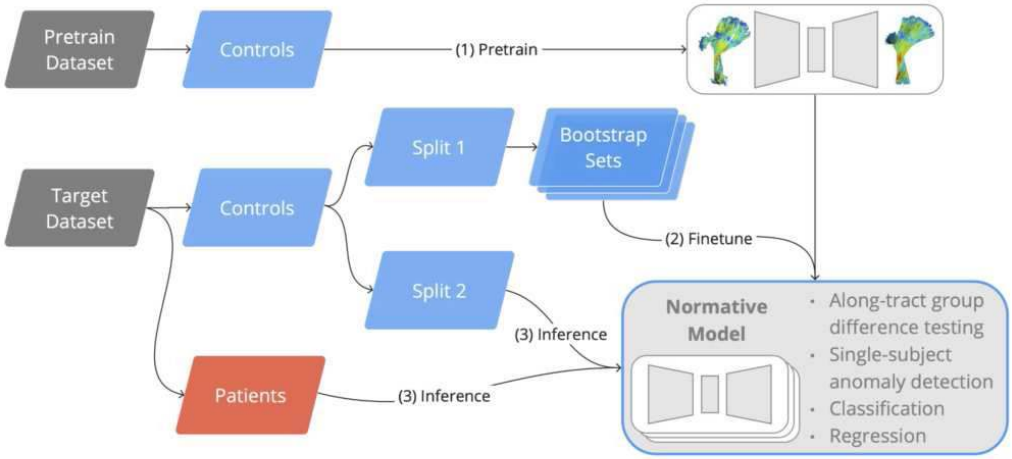

Figure 1. Schematic diagram of our deep normative tractometry framework. The Variational Autoencoder (VAE) model is first pretrained on a public dataset of young healthy controls (HC), then fine-tuned on a target dataset. Pre-training utilizes a larger sample size, allows for public sharing of the model, and reduces the computational cost of creating the normative model. Fine-tuning is meant to calibrate the model for specific cohort, in this case data from healthy older adults processed differently, compared to the pre-training dataset. The final normative model can be used for not only group difference testing as shown in the current study, but also single-subject anomaly detection, disease classification and regression tasks.

Results: Since the VAE model was trained on HC participants, we expect to see larger deviations from the norm quantified using MAE scores in the PD participants. The cluster-based permutation test revealed significant group differences - in segments 89-100 in the right optic radiation (OR_R) between HC and HY2, segments 81-97 in the left uncinate fasciculus (UF_L), and segments 76-92 in the right inferior fronto-occipital fasciculus (IFOF_R) between HC and HY3 - with a medium effect calculated using Cohen's d (Fig. 2). While significant differences are detected in HY2 and HY3, the anomaly patterns emerge in earlier stages, most notable in IFOF_R at stage HY2.

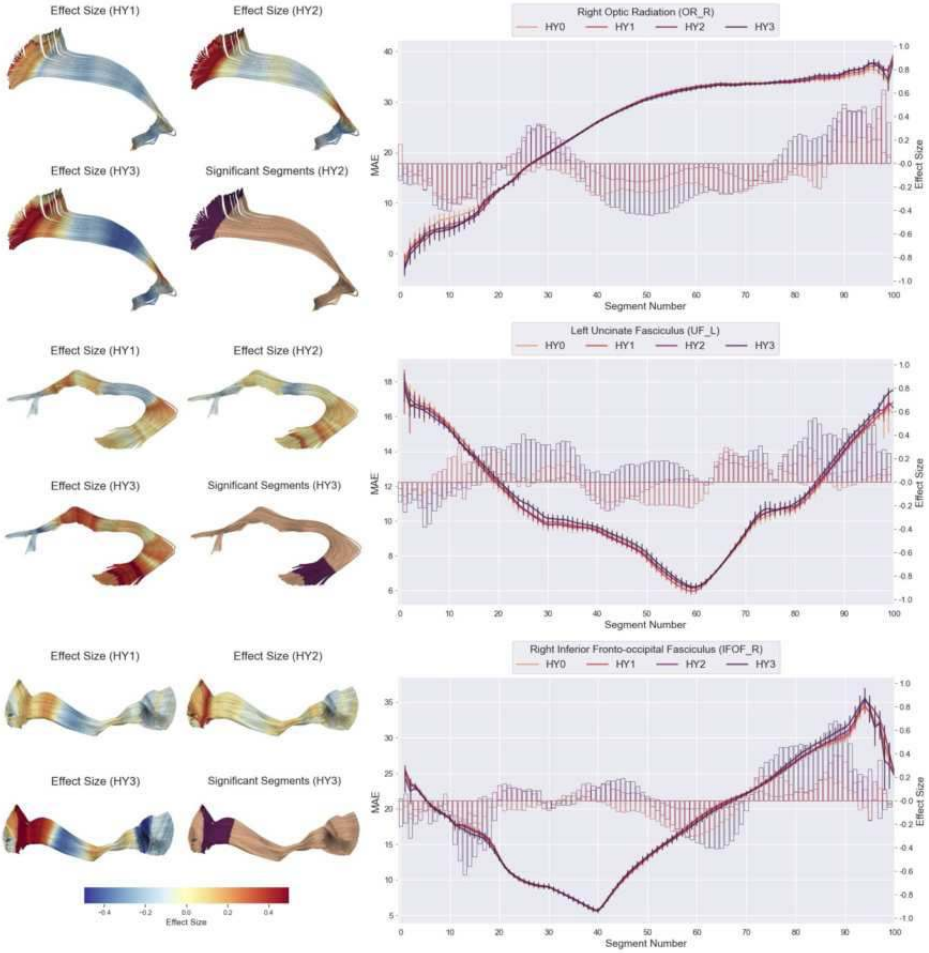

Figure 2. Along-tract anomalies in three WM tracts detected using our framework. *Left*: Effect sizes, measured by Cohen's d are plotted along 100 tract segments for each comparison, and segments with significant differences revealed by the cluster-based permutation tests are colored in dark purple. *Right*: Anomaly score, measured by mean absolute error (MAE) for HY stage 0-3 are shown as line plots with their 95% confidence interval. The effect sizes for HY stage 1-3 plotted on the left are also shown in the barplot. *Key*: HY: Hoehn-Yahr stage; MAE: mean absolute error; OR_R: Right optic radiation (segment increasing from right to left); UF_L: left uncinate fasciculus (segment increasing from left to right); IFOF_R: right inferior fronto-occipital fasciculus (segment increasing from right to left).

Conclusions: Our normative tractometry framework based on VAE can encode both the WM macro- and micro-structures from HC participants. Given the limited sample size typical in this and other studies, our framework uses a public independent dataset for pretraining, and supports multi-site harmonization for along-tract statistics. In a multi-site PD cohort, our framework identified along-tract anomalies, supporting the notion that structural WM changes may be coupled with microstructural changes in PD. Future work will examine additional dMRI and shape metrics, along with the effect of the size, inclusion criteria and diversity of the reference population.

References

1. Chamberland, M. (2021). Detecting microstructural deviations in individuals with deep diffusion MRI tractometry. Nature Computational Science, 1(9), 598–606.
2. Chandio, B. Q. (2020). Bundle analytics, a computational framework for investigating the shapes and profiles of brain pathways across populations. Scientific Reports, 10(1), 17149.
3. Feng, Y. (2023). Learning optimal white matter tract representations from tractography using a deep generative model for population analyses. In M. G. Linguraru, L. Rittner, N. Lepore, E. Romero Castro, J. Brieva, & P. Guevara (Eds.), 18th International Symposium on Medical Information Processing and Analysis (p. 48). SPIE.
4. Jahanshad, N. (2013). Multi-site genetic analysis of diffusion images and voxelwise heritability analysis: A pilot project of the ENIGMA–DTI working group. NeuroImage, 81, 455–469.
5. Kingma, D. P., & Welling, M. (2014). Auto-Encoding Variational Bayes. arXiv:1312.6114 [Cs, Stat].
6. Langkammer, C. (2016). Quantitative Susceptibility Mapping in Parkinson's Disease. PLOS ONE, 11(9), e0162460.

7. Parkinson Progression Marker Initiative. (2011). The Parkinson Progression Marker Initiative (PPMI). Progress in Neurobiology, 95(4), 629–635.
8. Pinaya, W. H. L. (2021). Using normative modelling to detect disease progression in mild cognitive impairment and Alzheimer's disease in a cross-sectional multi-cohort study. Scientific Reports, 11(1), 15746.
9. Poulin, P. (2022). TractoInferno—A large-scale, open-source, multi-site database for machine learning dMRI tractography. Scientific Data, 9(1), 725.
10. Toledo, J. B. (2014). A platform for discovery: The University of Pennsylvania Integrated Neurodegenerative Disease Biobank. Alzheimer's & Dementia, 10(4), 477.

Poster No 1606

Deep Learning-Based Segmentation of Brainstem White Matter Using Tractographic Guidance

Mark Olchanyi[1,2], Schreier David[1,2,3,4], Hannah Kinney[5,3], Juan Eugenio Iglesias[6,2,3], Emery Brown[1,2,3], Brian Edlow[6,2,3]

[1]Massachusetts Institute of Technology, Cambridge, MA, [2]Massachusetts General Hospital, Boston, MA, [3]Harvard Medical School, Boston, MA, [4]University of Bern, Bern, Switzerland, [5]Boston Children's Hospital, Boston, MA, [6]Athinoula A. Martinos Center for Biomedical Imaging, Charlestown, MA

Introduction: Diffusion MRI (dMRI) provides a non-invasive way of studying white matter that connects regions of interest (ROIs) in the brain (Basser, 2000) (Mori, 2001). Reliably reconstructing brainstem white matter bundles (WMB) in dMRI is crucial to the study and treatment of diseases of the central nervous system (CNS) with subcortical pathology. However, brainstem WMB segmentation methods are lacking due to the brainstem's small size and architectural complexity. We present an automated brainstem WMB segmentation method, the BrainStem Bundle Tool (BSB). BSB segmentation is performed on a tract intensity map (SIM) that is formed by passing WM streamlines between regions that are structurally adjacent to the rostral brainstem and are readily segmentable. For the segmentation model, we utilize a Convolutional Neural Network (CNN) architecture that is modified with two distinct elements that emphasize small-structure segmentation: an attention gate and a semi-dense conditional random field (CRF) attached to the CNN output, which inflates posterior probabilities around high WMB probability regions.

Methods: We identified seven candidate brainstem WMB that are visualizable across both ex vivo and clinical-resolution in vivo dMRI volumes. A U-Net CNN (Ronneberger, 2015) with a fine attention gate (Schlemper, 2019) positioned between the highest-resolution encoder and decoder layers is used, which inputs low-b, fractional anisotropy, and SIM volumes. Each SIM volume is created via probabilistically propagating streamlines between four ROIs adjacent to the ponto-mesencephalic component of the brainstem: the medulla, cerebellar grey matter, thalamus, and ventral diencephalon (Figure 1 A/B). All inputs are resampled to 1mm isotropic resolution and centered around the center-of-mass of a pontine mask. The SoftMax CNN layer dilutes posteriors of thin WMB in low-resolution and ex vivo dMRI modalities, therefore we employ label posterior refinement via a semi-dense CRF (Figure 1C). The CNN was trained on 30 subjects from the WU-Minn Human Connectome Project dMRI dataset (Van Essen, 2013). The training set is aggressively augmented to mimic multiple dMRI modalities, including shell dropout randomization, resampling, noise injection, and local deformation. We tested BSB segmentation accuracy on 10 HCP subjects at 1.25mm isotropic resolution, 7 ex vivo specimens scanned at 0.75mm isotropic resolution, and 15 control subjects from the Alzheimer's Disease Neuroimaging Initiative 3 (ADNI3) dataset at 2mm isotropic resolution (Wiener, 2017) (Figure 2A). We then proceeded to assess the translatability of BSB via an along-tract diffusivity metric classification task between ADNI3 Alzheimer's (AD) patients and control subjects (Figure 2B/C).

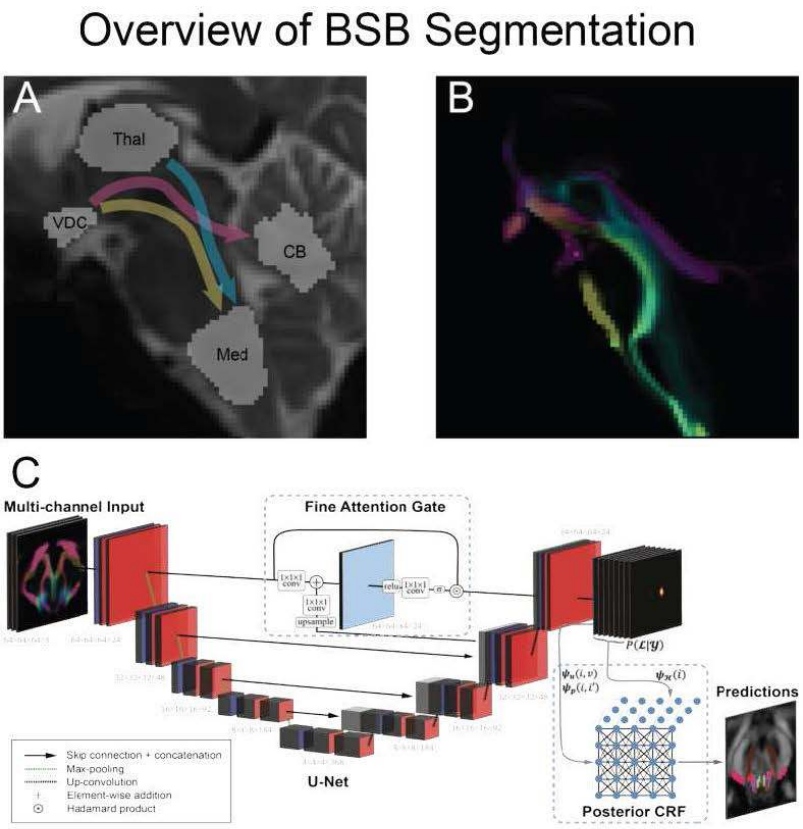

Figure 1: (**A**) Low-B volume with dilated Freesurfer ventral diencephalon (VDC), cerebellar grey matter (CB), thalamus (Thal) and Medulla (Med) segmentations, along with color-encoded streamline seeding directions. The SIM generated from probabilistic tract seeding between the extra-brainstem ROIs is shown in (**B**). Rostral brainstem WBM segmentations are generated from the SIM channel, as well as the the fractional anisotropy and Low-B channels with a U-Net CNN endowed with an attention gate and a semi-dense CRF that is directly conditioned on the WMB label posterior distributions from the U-Net *SoftMax* layer as shown in (**C**).

Results: BSB displayed robust WMB segmentation accuracy across all three datasets (HCP, ex vivo, and ADNI3) (Figure 1A). Furthermore, inclusion of the attention gate, CRF, and the SIM channel yielded significantly higher accuracies across both the ADNI3 control and ex vivo datasets. In AD classification, BSB WMB showed a similar discriminatory power to cortical WMB, and superior discriminatory power to a cortical white matter mask and the whole brainstem in when assessing average along-tract mean diffusivity classification between cognitively normal controls and AD/mildly cognitively impaired subjects in the ADNI3 dataset (Figure 2B/C).

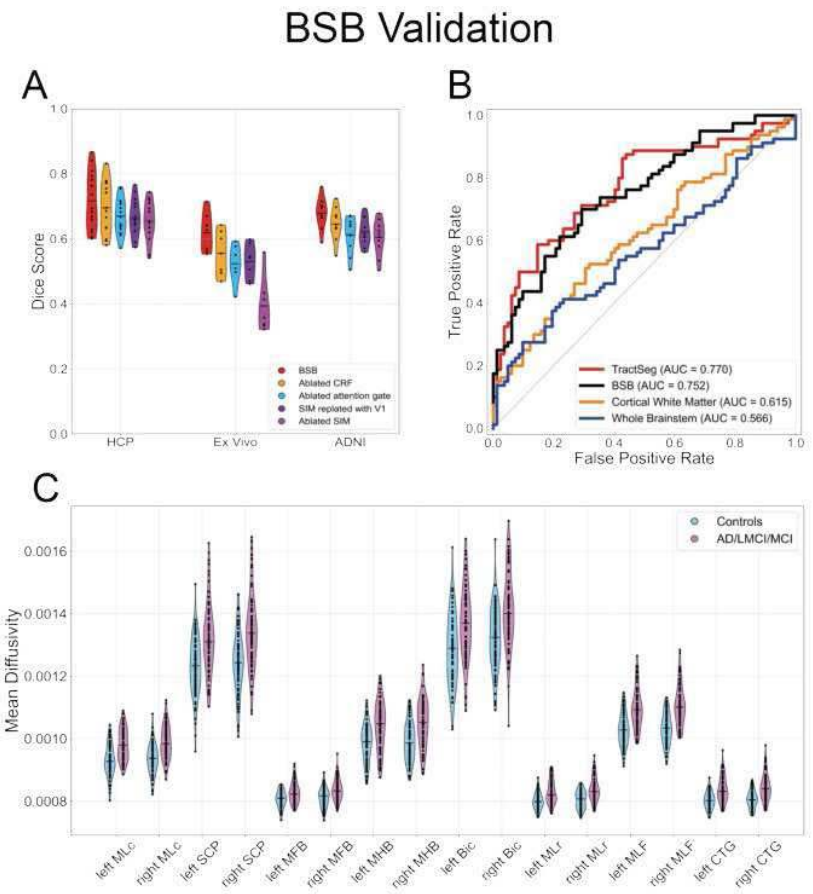

Figure 2: (**A**) Dice coefficents (averaged across WMB) between manual annotations and BSB predictions for fifteen in vivo HCP cases, seven ex vivo cases, and ten in vivo ADNI3 control cases. Ablations include the removal of the semi-dense CRF, removal of the attention gate, replacement of the SIM with a primary eigenvector (V1) volume, and U-Net training only performed on the low-b and FA volumes. (**B/C**) The translatibility of BSB is assessed via its classification performance of an ADNI3 AD, mild cognitive impairment (MCI), and late MCI (LMCI) cohort compared to cognitively-normal controls. Discriminatory comparison is performed by comparing leave-one-out linear discriminant analysis classifiers applied to all BSB WMB, seventeen segmented cortical WMB where alterations are historically known to be correlated with AD progression, left/right cortical white matter masks from FreeSurfer, and the whole brainstem, is shown in the ROC curve in **B**. Shown in **C** are average along-tract mean diffusivity metrics for each BSB WMB for ADNI3 controls and AD/LMCI/MCI subjects. *MLc*: caudal medial lemniscus, *SCP*: superior cerebellar peduncle, *MFB*: medial forebrain bundle, inferior division, *MHB*: mesencephalic homeostatic bundle, *Bic*: brachium of the inferior colliculus *MLr*: rostral medial lemniscus, *MLF*: medial longitudinal fasciculus, *CTG*: central tegmental tract.

Conclusions: We present BSB, a tool that creates a tractographic mapping of streamline intensities corresponding to brainstem WMB from extra-brainstem regions and provides candidate WMB segmentations from those mappings. BSB accurately segments brainstem WMB in both high-resolution ex vivo and low-resolution in vivo dMRI data. We show that one translational application of BSB is in Alzheimer's disease classification via assessment of brainstem WMB diffusivity metrics. We anticipate that subcortical WMB segmentation with BSB can be used to elucidate subcortical white matter pathology in a broad spectrum of CNS diseases.

References

1. Basser, P.J. (2000) 'In vivo fiber tractography using DT-MRI data.', Magnetic Resonance in Medicine, vol. 44, no. 4, pp. 625-632
2. Mori, S. (2001) 'Three-dimensional tracking of axonal projections in the brain by magnetic resonance imaging.', Annals of Neurology, vol. 45, no. 2, pp. 265-269
3. Ronneberger, O. (2015) 'Convolutional Networks for Biomedical Image Segmentation.', arXiv, no. 1505.04597
4. Schlemper, J. (2019) 'Attention gated networks: Learning to leverage salient regions in medical images.', Medical Image Analysis, vol. 53, pp. 197-207
5. Van Essen, D.C. (2013) 'The WU-Minn Human Connectome Project: An overview.', NeuroImage, vol. 80, pp. 62-79
6. Weiner, M.W (2017) 'The Alzheimer's Disease Neuroimaging Initiative 3: Continued innovation for clinical trial improvement.', Alzheimer's & Dementia, vol. 13, no. 5, pp. 561-571

Poster No 1607

White matter alterations in cannabis users using Diffusion MRI: a Fixel-Based Analysis study

Arush Honnedevasthana Arun[1], Suraya Dunsford[2], Adam Clemente[1], Thijs Dhollander[3], Nadia Solowij[2], Lisa Greenwood[4], Valentina Lorenzetti[1]

[1]Australian Catholic University, Melbourne, Victoria, [2]University of Wollongong, Wollongong, Wollongong, New South Wales, [3]Murdoch Children's Research Institute, Melbourne, Victoria, [4]The Australian National University, Canberra, ACT

Introduction: Cannabis use disorders (CUD) affect > 60 million people globally and have significant adverse psychosocial outcomes (inability to quit, cravings, operating machinery/driving while intoxicated). Such outcomes have been attributed to altered brain integrity but this notion is yet to be tested in people with a DSM-5 diagnosis of CUD and using advanced measures of white-matter microstructure such as Fixel-based analysis on diffusion MRI data.

Methods: A sample of 109 participants aged 18-32 years, comprised of 79 cannabis users stratified by CUD severity (22 mild,26 moderate, 31 severe, according to the DSM-V criteria and 30 non-using controls participated in the study. Participants underwent diffusion MRI scan on a 3T GE Architect scanner with a 48-channel head coil. All the DWI data analysis was conducted using MRtrix3(www.mrtrix3.org) (Tournier, Smith et al. 2019). Firstly, the DWI data was denoised (Veraart, Novikov et al. 2016), Gibbs ringing artifacts were removed (Kellner, Dhital et al. 2016), motion and distortion correction was performed using the flipped DWI dataset (Andersson and Sotiropoulos 2016). All the DWI data were upsampled to an isotopic voxel size of 1·25 mm in order to increase contrast and improve template construction (Raffelt, Tournier et al. 2017). FODs were calculated using constrained spherical deconvolution (Tournier, Calamante et al. 2007) utilising group averaged response functions for white matter, grey matter and CSF(Dhollander, Raffelt et al. 2016). FOD images were globally normalised to correct for image intensity differences between subjects. All the subject FOD images were spatially registered and normalized to a create a symmetric study-specific template (Raffelt, Tournier et al. 2017). Fibre density (FD) was computed from the integral of each FOD lobe. Fibre cross-section (FC) for each subject is calculated by using the warp information derived from the registration process. Fibre density and cross-section (FDC) measure is a combined (product) measure of FD and FC. General Linear Model (GLM) was utilized to compare FD, FC and FDC between cannabis and control groups, controlling for age, gender, ICV, standard drinks/year. We compared cannabis users vs control users and cannabis user individual classification (mild, moderate and severe) groups with controls.

Results: Cannabis users and controls were found to differ significantly in education ($p=0·009$), IQ ($p<0·001$), and alcohol dependence (AUDIT scores; p=0·0)04, the control group had significantly higher IQ and more years of education, and lower alcohol dependence than the cannabis users. Cannabis users had significantly higher scores than controls in STAI-T ($U=647$ $p<0·001$), BDI ($U= 429$, $p<0·001$), CAPE_P ($U=328.5$, $p<0·001$), CAPE_N ($U=526$, $p<0·0001$and PSS ($U= 480.5$, $p=<0·001$). We found no significant differences between cannabis users with controls. In summary, Figure 1 shows significant fixels (FWE-corrected p-value < 0·05) overlaid on a FOD template in mild users vs controls for the FD, FC and FDC metric in Superior Longitudinal Fasciculus (SLF) and Fornix regions. We found that parts of SLF in mild users have lower FD and FDC compared to controls. We also found lower FC in Fornix within mild cannabis users compared to controls.

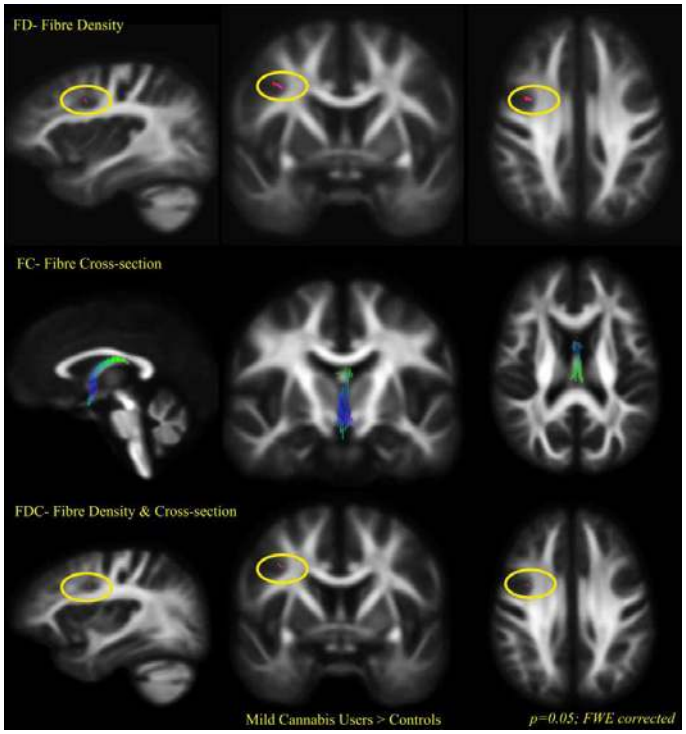

Fig. Significant fixels (p=0.05, FWE corrected) displayed for mild cannabis users > controls in Fibre density (first row), Fibre cross-section (middle row) and Fibre density & cross-section (last row)

Conclusions: We explored if group differences are associated with CUD severity and cannabis exposure. CUD and control groups were not significantly different. Both mild and moderate CUD groups vs controls, had lower FD in the superior longitudinal fasciculus connecting parietal and striatal-cingulate tracts implicated in addictive behavior (eg disinhibition), and this was correlated with the age of cannabis use onset. Mild CUD compared to controls had lower FC in a fornix region connecting the hippocampus to the subcortex. Different white matter integrity in mild and moderate CUD might reflect transient neuroplastic changes at the initial stages of addiction, which may normalize with the transition to severe CUD.

References

1. Andersson, J. L. R. and S. N. Sotiropoulos (2016). "An integrated approach to correction for off-resonance effects and subject movement in diffusion MR imaging." NeuroImage 125: 1063-1078.
2. Dhollander, T., D. Raffelt and A. Connelly (2016). Unsupervised 3-tissue response function estimation from single-shell or multi-shell diffusion MR data without a co-registered T1 image.
3. Kellner, E., B. Dhital, V. G. Kiselev and M. Reisert (2016). "Gibbs-ringing artifact removal based on local subvoxel-shifts." Magnetic Resonance in Medicine 76(5): 1574-1581.
4. Raffelt, D. A., J. D. Tournier, R. E. Smith, D. N. Vaughan, G. Jackson, G. R. Ridgway and A. Connelly (2017). "Investigating white matter fibre density and morphology using fixel-based analysis." NeuroImage 144(Pt A): 58-73.
5. Tournier, J. D., F. Calamante and A. Connelly (2007). "Robust determination of the fibre orientation distribution in diffusion MRI: Non-negativity constrained super-resolved spherical deconvolution." NeuroImage 35(4): 1459-1472.
6. Tournier, J. D., R. Smith, D. Raffelt, R. Tabbara, T. Dhollander, M. Pietsch, D. Christiaens, B. Jeurissen, C.-H. Yeh and A. Connelly (2019). "MRtrix3: A fast, flexible and open software framework for medical image processing and visualisation." NeuroImage 202: 116137.
7. Veraart, J., D. S. Novikov, D. Christiaens, B. Ades-Aron, J. Sijbers and E. Fieremans (2016). "Denoising of diffusion MRI using random matrix theory." NeuroImage 142: 394-406.

Poster No 1608

Body Mass Index Relates to Regional White Matter Microstructure in Sex-Specific Manners

Tiril Pedersen Gurholt[1], Dani Beck[2], Irene Voldsbekk[3], Nadine Parker[4], Daniel Askeland-Gjerde[1], Ann-Marie de Lange[5], Dennis van der Meer[4], Ivan Maximov[6], Ida Sønderby[7], Lars Westlye[8], Ole Andreassen[9]

[1]Oslo University Hospital, Oslo, Oslo, [2]Diakonhjemmet Hospital, Oslo, Oslo, [3]Norwegian Centre for Mental Disorders Research, Oslo, Oslo, [4]University of Oslo, Oslo, Oslo, [5]University of Lausanne, Lausanne, Switzerland, [6]Western Norway University of Applied Sciences, Bergen, Bergen, [7]Oslo University Hospital, Oslo, Norway, [8]Norwegian Centre for Mental Disorders Research (NORMENT), Oslo University Hospital, Oslo, Norway, [9]NORMENT, Oslo, Norway

Introduction: Sex differences are observed in brain disorders [Arnold et al., 2023], white matter microstructure [Ritchie et al., 2018], and body shape and fat distribution [Tchernof and Després, 2013]. Indications of sex-related differences in how obesogenic traits (e.g., body mass index (BMI)) relate to white matter microstructure exists [Kroll et al., 2020], including higher brain age in men than women at higher body fat [Subramaniapillai et al., 2021]. Yet, our knowledge of sex-related differences between obesogenic traits and regional white matter remains limited. Here, we investigate whether and how BMI relates to white matter microstructure in sex-specific patterns to enhance our understanding of the role of sex in somatic and brain health.

Methods: We included n=40,517 UK Biobank participants (52.1% women) with diffusion magnetic resonance imaging (MRI), clinical, and demographic data. On average, women were slightly younger (aged 63.7±7.6 years) than men (aged 64.9±7.9 years) and had lower cardiometabolic risk, including lower BMI (women: 25.9±4.7; men: 26.9±3.8). We used an optimized pipeline to process raw diffusion MRI scans, derive diffusion maps of fractional anisotropy (FA), radial diffusivity (RD), axial diffusivity (AD), and mean diffusivity (MD), extract FSL tract-based spatial statistics diffusion metrics, and for quality control [Maximov et al., 2019; Maximov et al., 2021]. We included 27 regions of interest (ROIs) from the Johns Hopkins University atlas [Mori et al., 2008] (Fig. 1). We performed statistical analyses in R (v-4.2.1). We used multiple linear regression to investigate sex differences in how BMI relates to regional white matter by (i) investigating for BMI-by-sex interaction effects (adjusted for main BMI effect), followed by (ii) sex-stratified analyses while adjusting for age, age2, sex, self-identified ethnic ancestry (European/non-European), self-reported cardiometabolic factors, and assessment site. We derived r effect sizes from t-statistics and used Bonferroni correction ($p \leq 0.0005$).

Figure 1: Extracted regions of interest.

	Abbreviation	Full name
Brainstem tracts	CST*	Corticospinal tract
	ML*	Medial lemniscus
	P	Pontine
	MCP	Middle cerebellar peduncle
	ICP*	Inferior cerebellar peduncle
	SCP*	Superior cerebellar peduncle
Projection fibers	CP*	Cerebral peduncle**
	ACR*	Anterior corona radiata
	PCR*	Posterior corona radiata
	SCR*	Superior corona radiata
	ALIC*	Anterior limb of the internal capsule
	PLIC*	Posterior limb of the internal capsule
	RLIC*	Retrolenticular part of internal capsule
	PTR*	Posterior thalamic radiation
Commissural fibers	GCC	Genu of corpus callosum
	BCC	Body of corpus callosum
	SCC	Splenium of the corpus callosum
	TAP*	Tapetum
Association fibers	FX	Fornix
	FXST*	Fornix stria-terminalis
	CGC*	Cingulum cingulate gyrus
	CGH*	Cingulum (hippocampal portion)
	EC*	External capsule
	SFO*	Superior fronto-occipital fasciculus
	SLF*	Superior longitudinal fasciculus
	SS*	Sagittal stratum
	UNC*	Uncinate fasciculus

*Bilateral structure

Results: The analyses revealed significant BMI-by-sex interaction effects on regional white matter phenotypes for 12.5% FA, 45.8% AD, 58.3% RD, and 68.8% MD ROIs (|r| effect sizes [0.02, 0.06] and p-values [0.0005, 1.4e-32]). The main effect of BMI was also significant for 68.8% FA, 68.8% AD, 39.6% RD, and 62.5% MD ROIs (|r| effect sizes [0.02, 0.15] and p-values [0.0003, 5.5e-202]). Additionally, the main effect of sex was significant for most ROIs: 83.7% FA, 89.6% AD, 85.4% RD, and 91.7% MD ROIs (|r| effect sizes [0.02, 0.26] and p-values [0.0002, 0]). Stratified by sex, we observed distinct sex-specific association patterns between BMI and white matter phenotypes (Fig. 2). The pattern for women and men was similar for FA but differed significantly for AD, RD, and MD, reflecting the above interaction analysis. Women showed lower negative effect sizes across AD, RD, and MD at higher BMI for brainstem tracts than men. For multiple non-brainstem tracts, men showed higher positive effect sizes across AD, RD, and MD at higher BMI than women. Overall, BMI was significantly associated with white matter in women for 68.8% FA, 83.3% AD, 45.8% RD, and 64.6% MD ROIs (|r| values [0.03, 0.19] and p-values [0.0003, 6.9e-196]). For men, BMI was significantly associated with white matter for 75.0% FA, 66.7% AD, 66.7% RD, and 60.4% MD ROIs (|r| values [0.03, 0.18] and p-values [0.0004, 1.1e-136]).

Figure 2: Significant sex differences in how BMI relates to white matter microstructure

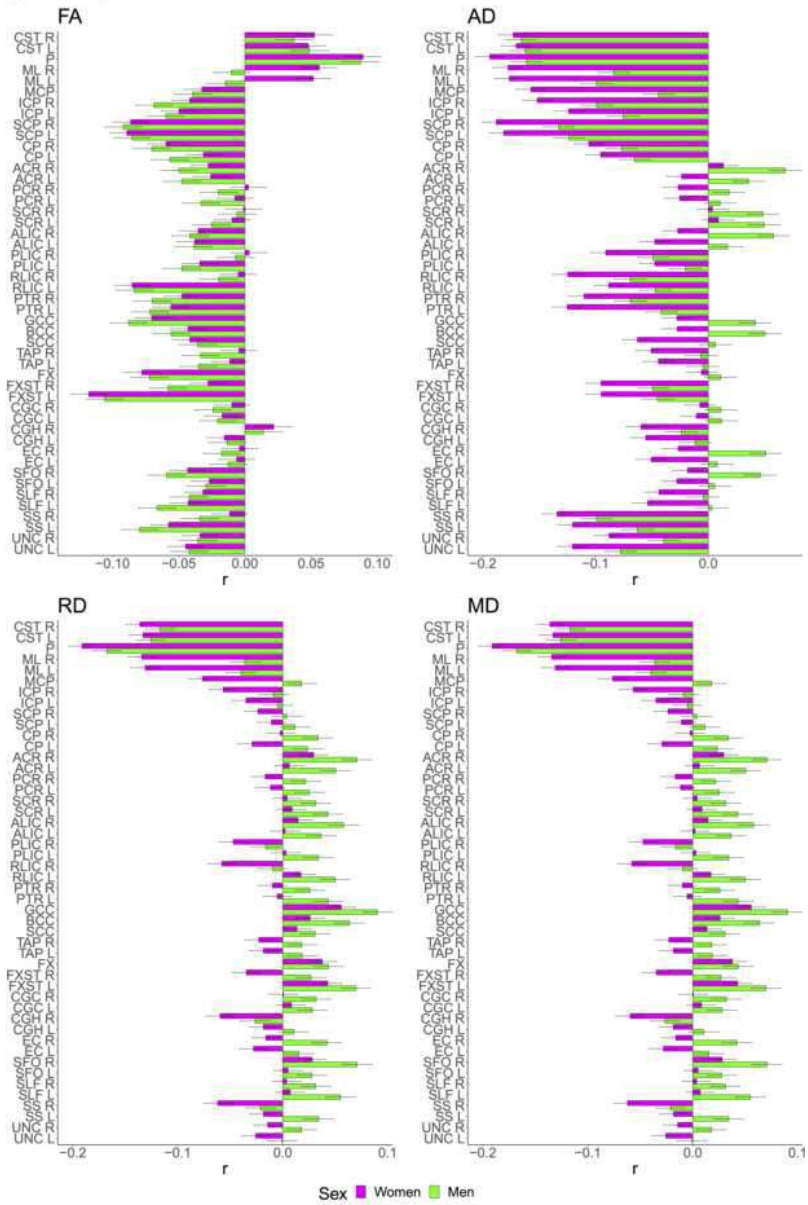

Notes: See Figure 1 for white matter tracts abbreviation details. Abbreviations: FA - fractional anisotropy; AD - axial diffusivity; RD - radial diffusivity; MD - mean diffusivity; BMI - body mass index.

Conclusions: Our results show that sex is an essential factor when investigating obesogenic traits with white matter microstructure. The results indicate that sex-related body shape and fat distribution differences are reflected in sex-related white matter differences. It is also insufficient only to study FA as AD, RD, and MD better capture regional sex-related variation. Understanding the observed sex differences in how BMI relates to white matter microstructure might be important for disentangling sex-specific brain and somatic disease risk and outcomes.

References

1. Arnold AP, Abdulai-Saiku S, Chesselet M-F, Dubal DB, Gold SM, McCullough LD, Shaw CK, Werling DM (2023): Chapter 51 - Sex differences in neurological and psychiatric diseases . In: Zigmond, MJ, Wiley, CA, Chesselet, M-F, editors. Neurobiology of Brain Disorders (Second Edition). Academic Press. pp 933–952. https://www.sciencedirect.com/science/article/pii/B9780323856546000344.
2. Kroll DS, Feldman DE, Biesecker CL, McPherson KL, Manza P, Joseph PV, Volkow ND, Wang G-J (2020): Neuroimaging of Sex/Gender Differences in Obesity: A Review of Structure, Function, and Neurotransmission. Nutrients 12:1942.
3. Maximov II, Alnæs D, Westlye LT (2019): Towards an optimised processing pipeline for diffusion magnetic resonance imaging data: Effects of artefact corrections on diffusion metrics and their age associations in UK Biobank. Hum Brain Mapp 40:4146–4162.
4. Maximov II, van der Meer D, de Lange A-MG, Kaufmann T, Shadrin A, Frei O, Wolfers T, Westlye LT (2021): Fast qualitY conTrol meThod foR derIved diffUsion Metrics (YTTRIUM) in big data analysis: U.K. Biobank 18,608 example. Hum Brain Mapp 42:3141–3155.
5. Mori S, Oishi K, Jiang H, Jiang L, Li X, Akhter K, Hua K, Faria AV, Mahmood A, Woods R, Toga AW, Pike GB, Neto PR, Evans A, Zhang J, Huang H, Miller MI, van Zijl P, Mazziotta J (2008): Stereotaxic white matter atlas based on diffusion tensor imaging in an ICBM template. NeuroImage 40:570–582.

6. Ritchie SJ, Cox SR, Shen X, Lombardo MV, Reus LM, Alloza C, Harris MA, Alderson HL, Hunter S, Neilson E, Liewald DCM, Auyeung B, Whalley HC, Lawrie SM, Gale CR, Bastin ME, McIntosh AM, Deary IJ (2018): Sex Differences in the Adult Human Brain: Evidence from 5216 UK Biobank Participants. Cereb Cortex N Y N 1991 28:2959–2975.
7. Subramaniapillai S, Suri S, Barth C, Maximov I, Voldsbekk I, Meer D van der, Gurholt T, Beck D, Draganski B, Andreassen OA, Ebmeier KP, Westlye LT, Lange A-MG de (2021): Sex- and age-specific associations between cardiometabolic risk and white matter brain age in the UK Biobank cohort. PsyArXiv. https://psyarxiv.com/7xcun/.
8. Tchernof A, Després J-P (2013): Pathophysiology of Human Visceral Obesity: An Update. Physiol Rev 93:359–404.

Poster No 1609

Increasing the realism of in silico cortex substrates for diffusion MRI simulation

Anas Bachiri[1], Alexis Brullé[1], Ivy Uszynski[1], Cyril Poupon[1]

[1]BAOBAB, NeuroSpin, Paris-Saclay University, CNRS, CEA, Gif-sur-Yvette, France

Introduction: Numerical simulations have provided an interesting approach to studying and validating brain microstructure models[1]. For this purpose, many methods to generate virtual brain cells have been proposed. However, these methods target only the generation of substrates with specific brain cells of a given type. For example, generating a virtual scene populated only by axons[2,3] or neurons of multiple types[4]. To the best of our knowledge, no method was proposed to synthesize virtual microstructure scenes combining neurons with white matter cells such as axons. This work aims to close the modeling gap of virtual brain microstructure by extending the MEDUSA framework[5] to allow the generation of hybrid virtual substrates. The presented method allows the synthesis of volume of interests (VOIs) combining neurons with axons with similar volume fractions to values reported on human brain gray matter microstructure[6].

Methods: Dataset: The NEUROMORPHO dataset[7,8] has been used to reconstruct virtual neurons of the human brain in the ".SWC" format. Cell Reconstruction: The reconstruction method creates spheres from the provided cell ".SWC" file which are then interpolated to represent synapses and to fill the gaps between different connected parts of the neuron. Thus providing the same sphere-atom representation used in MEDUSA. The reconstruction code is available at the repository[9]. Generation of neuron populations: Four different substrate types with VOI of 100x100x100µm3 were considered. For each substrate type, ten different samples have been generated. The first substrate type a) comprises axons with an 85% volume fraction (VF). Second type b) contains a population of axons with 44% VF and a population of pyramidal neurons with 6% VF. The substrate type c) is similar to b) with a more dense population of neurons of 12% VF. Finally, the type d) has only a neuron population with 15% VF. The VF values in substrates b) and c) are comparable to those reported from human brain samples scanned with electron microscopy[6]. The MEDUSA framework was used to generate the substrates and to perform cell de-overlapping to minimize intersections between different cells. Diffusion MRI simulations: Diffusion MRI simulations were performed on the generated substrate samples. For each sample type, the diffusion MRI signals were orientation-averaged, and an average signal for all samples of the same type was calculated. The diffusivity used is D0=3x10-9 m^2/s with 500k walkers initialized in both intra and extracellular space and a time step of 15µs.

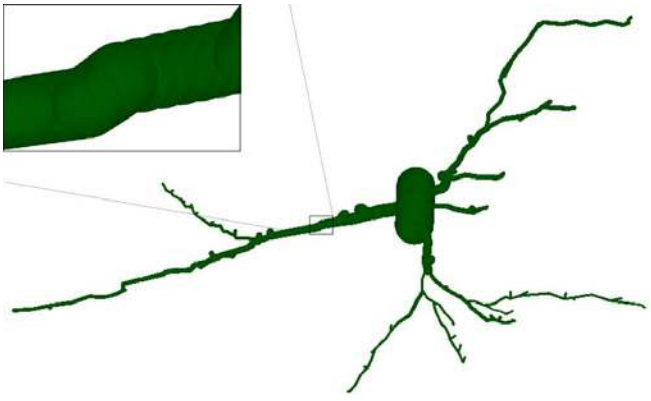

Results: Figure 1 illustrates a reconstructed pyramidal neuron cell from the NEUROMORPHO dataset using the reconstruction code9, the spheres used to represent the neuron highly overlap to ensure a high quality representation of the cell. Figure 2 upper panel shows four samples representing each substrate type generated in a VOI of 100x100x100µm3. The sparse representation of these substrates with sphere atoms allows to keep the memory required for each sample below 60 Mbytes. Finally, the simulated diffusion MRI signals in the bottom part of Figue 2 show a clear distinction between signal attenuations in the four different substrate types. The diffusion process parameters were chosen such that the diffusion is in the short time limit (td < 20 ms) and the cells were considered to be impermeable.

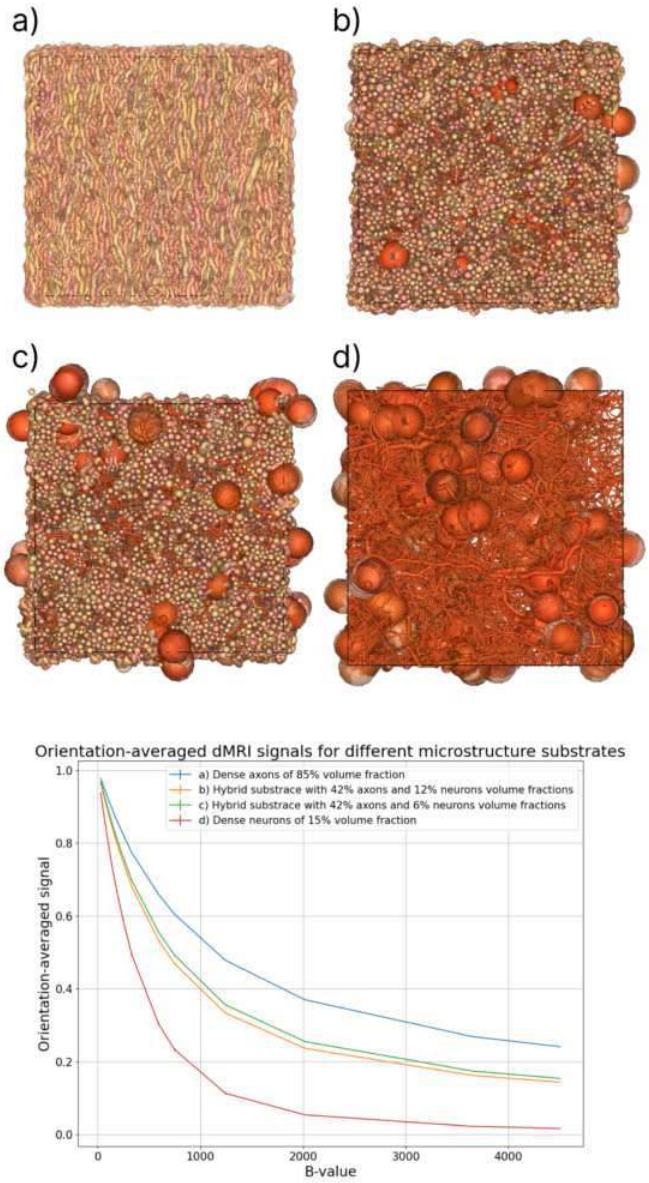

Conclusions: This work demonstrates a proof of concept for synthesizing virtual substrates with hybrid cells mixing neurons and axons, thus increasing the modeling realism of synthetic gray microstructure. Future work directions include large-scale simulation of microstructure and exploring the ability to add more components in the synthetic substrates such as blood vessels and glial cells, which were not included in this study.

References

1. Novikov, Dmitry S., et al. (2019), "Quantifying brain microstructure with diffusion MRI: Theory and parameter estimation." NMR in Biomedicine.
2. Callaghan, R., Alexander, D. C., Palombo, M., & Zhang, H. (2020). ConFiG: Contextual Fibre Growth to generate realistic axonal packing for diffusion MRI simulation. NeuroImage, 220, 117107. https://doi.org/10.1016/J.NEUROIMAGE.2020.117107.
3. Villarreal-Haro, J. L., Gardier, R., Canales-Rodriguez, E. J., Gomez, E. F., Girard, G., Thiran, J.-P., & Rafael-Patino, J. (2023). CACTUS: A Computational Framework for Generating Realistic White Matter Microstructure Substrates. https://doi.org/10.3389/fninf.2023.1208073.
4. Palombo, M., Alexander, D. C., & Zhang, H. (2019). A generative model of realistic brain cells with application to numerical simulation of the diffusion-weighted MR signal. NeuroImage, 188, 391–402. https://doi.org/10.1016/j.neuroimage.2018.12.025
5. Ginsburger, K., Matuschke, F., Poupon, F., Mangin, J. F., Axer, M., & Poupon, C. (2019). MEDUSA: A GPU-based tool to create realistic phantoms of the brain microstructure using tiny spheres. NeuroImage, 193, 10–24. https://doi.org/10.1016/j.neuroimage.2019.02.055
6. Shapson-Coe, A., Januszewski, M., Berger, D. R., Pope, A., Wu, Y., Blakely, T., Schalek, R. L., Li, P., Wang, S., Maitin-Shepard, J., Karlupia, N., Dorkenwald, S., Sjostedt, E., Leavitt, L., Lee, D., Bailey, L., Fitzmaurice, A., Kar, R., Field, B., ... Lichtman, J. W. (2021). A connectomic study of a petascale fragment of human cerebral cortex. BioRxiv, 2021.05.29.446289. https://doi.org/10.1101/2021.05.29.446289.
7. Akram MA, Nanda S, Maraver P, Armañanzas R, Ascoli GA (2018) An open repository for single-cell reconstructions of the brain forest. Sci Data. 5:180006. doi: 10.1038/sdata.2018.6.
8. https://neuromorpho.org/ (November 2023).
9. https://framagit.org/cpoupon/gkg/-/tree/master/python/simulation?ref_type=heads (November 2023).

Poster No 1611

Along-tract analysis of DTI parameters in patients with gliomas and neuropsychological impairment

Francesco Latini[1], Sadia Mirza[1], Åsa Munkhammar[2], Maria Zetterling[1], Markus Fahlström[3]

[1]Department of medical Sciences, Neurosurgery. Uppsala University Hospital, Uppsala, Sweden, [2]Rehabilitative medicine, Uppsala University Hospital, Uppsala, Sweden, [3]Department of Surgical sciences, Radiology, Uppsala University, Uppsala, Sweden

Introduction: Diffuse gliomas(DG) grade 2-3 show extensive infiltration through white matter(WM) tracts. Diffusion tensor tractography(DTI) with along-tract analysis (ATA) has been used to assess the microstructural integrity of WM pathways. The published results have been inconsistent, warranting further exploration into accuracy and possible limitation of this technique. We aimed to use ATA analysis to compare DTI parameters in DG and correlate them with preoperative neuropsychological assessment of patients with DG.

Methods: Fourteen patients with IDH-mutated DG grade 2-3 were included. Tumour volumes were manually segmented on 3D-FLAIR images, spatially normalised to MNI space. DTI was acquired using a single-shot echo-planar sequence on a 3T with 48 sampling directions. DTI data was reconstructed within MNI space using q-space diffeomorphic reconstruction(QSDR) in DSI studio. Five bilateral sets of WM pathways(Frontal Aslant tract; Arcuate fasciculus; Inferior Fronto-Occipital Fasciculus; Cortico-spinal tract; and Cingulum), were reconstructed based on the HCP-1065 template. All WM pathways were stretched to the same length of 100 indices and FA, RD, AD, MD and QA were sampled for each index. An overlay of tumour 3D reconstruction was used to detect contact with WM pathways. Contralateral and not affected WM pathways were considered normal and included as normal data. WM pathways were compared individually and per index to the normal data using a z-test. False discovery rate was controlled using the Benjamini-Hochberg procedure with Q = 10%. Preoperative neuropsychological assessment (attention and working memory, processing speed, learning and long-term memory both verbal and visual, visuospatial construction, and executive functioning) was performed in all the subjects and correlated to results from ATA.

Results: Eleven (78.6%) of the patients presented epilepsy and 6 (42.9%) presented preoperative neuropsychological impairment. When tumour was in contact with the WM pathways abnormalities were detected in infiltrated bundles at z-test in 13 patients. AD and FA were the most sensitive DTI parameters. Tumour volume (Tv), the tumour infiltration per voxel (TIv) and tumour extension (Te) along the pathway were successfully displayed with topographical details on the each graph together with DTI parameter. Abnormal AD, RD, MD and FA correlated with Tv, TIv and Te (p <.001). The presence of preoperative neuropsychological impairment was correlated with higher AD (p .04), lower QA (p .005), higher TIv (p .01) and Te (p .03).

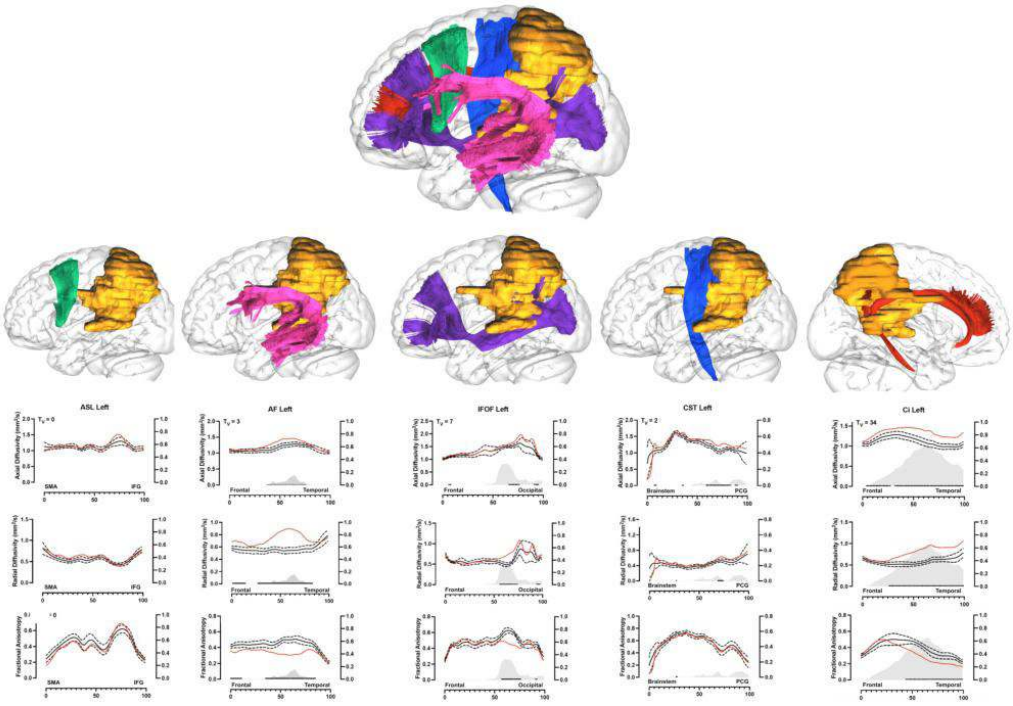

Figure 1: The picture illustrates the case of patient n°5. In the upper part the 3-D tumor reconstruction (in orange) and its relationship with the five WM pathways recontructed with different colours (FAT, green; AF, magenta; IFOF, purple; CST, blue, CI, dark red) within a 3-D "glass-brain" of the left hemisphere.In the lower part each WM pathway is displayed separately in the first row with its relatio ship with the tumour. The graphs on the second, third and fourth rows display the ATA analysis of each WM pathway for all the DTI indices. The red line represents the patient's white matter index, the continous black line represents the normal values with standard deviation (balck dotted lines). The black dots on the lower part show the areas of significant difference between the patient's index and the normal values. Tumor volume (Tv) is displayed in ml on the top left of the first graph. The gray area on the lower part of the graph shows the tumor overlay for each WM pathway. Within each graph the scale on the left shows DTI values, while the scale on the right Y axis shows the tumor infiltration per voxel of white matter (TI-V, between 0 and 1). Tumor extension along the X axis is shown on a scale from 0 to 100. Major lobar or anatomical locations are displayed on the X axis to better locate the DTI index abnormalities and the direction of potential white matter damage.

SMA: Supplementary motor area; IFG: inferior frontal gyrus; PCG: Precentral gyrus.

Conclusions: ATA analysis is a sensitive and reliable method to detect DTI abnormalities but also the extension of WM infiltration in patients with DG. Quantitative and qualitative DTI abnormalities were correlated with preoperative neuropsychological impairment. ATA may be valuable for longitudinal controls after the preoperative assessment, surgical planning or for implementing tailored radiotherapy treatment.

References

1. Celtikci P, et al.,(2018) 'Generalized q-sampling imaging fiber tractography reveals displacement and infiltration of fiber tracts in low-grade gliomas'. Neuroradiology. 60(3):267-80.
2. D'Souza S, et al.,(2019) 'Fiber-tract localized diffusion coefficients highlight patterns of white matter disruption induced by proximity to glioma'. PLoS One. 14(11):e0225323
3. Latini F, et al.,(2022) 'Can diffusion tensor imaging (DTI) outperform standard magnetic resonance imaging (MRI) investigations in post-COVID-19 autoimmune encephalitis?' Upsala Journal of Medical Sciences..20;127(1)
4. Latini F, et al.,(2021) 'White matter abnormalities in a patient with visual snow syndrome: New evidence from a diffusion tensor imaging study'. Eur J Neurol. ;28(8):2789-2793
5. Leroy HA, et al.(2020) 'Radiological correlation between diffusion tensor imaging and histologic analyses of glial tumors: a preliminary study'. Acta Neurochir (Wien);162(7):1663
6. Pieri V., et al, (2021) 'Along-tract statistics of neurite orientation dispersion and density imaging diffusion metrics to enhance MR tractography quantitative analysis in healthy controls and in patients with brain tumors'.Hum Brain Mapp ;42(5):1268-1286.
7. Yeh FC, et al.,(2011) 'NTU-90: a high angular resolution brain atlas constructed by q-space diffeomorphic reconstruction'. Neuroimage.;58(1):91-9
8. Zoli M, et al.(2021) 'From Neurosurgical Planning to Histopathological Brain Tumor Characterization: Potentialities of Arcuate Fasciculus Along Tract Diffusion Tensor Imaging Tractography Measures'. Front Neurol;12:633209.

Poster No 1612

Network-Based White Matter Microstructure Measures Using b-Tensor Encoding and Cognition in HIV

Md Nasir Uddin[1], Abrar Faiyaz[1], Chase Figley[2], Xing Qiu[1], Miriam Weber[1], Giovanni Schifitto[1]

[1]University of Rochester, Rochester, NY, [2]University of Manitoba, Winnipeg, MB

Introduction: Despite receiving combination antiretroviral therapy (cART), individuals infected with HIV (HIV+) persistently contend with chronic inflammation, consequently elevating the risk of brain injury[1,2]. Diffusion MRI is highly sensitive to microstructural damage, but standard read-outs such as DTI are hindered by factors like regional fiber orientation dispersion (e.g., crossing fibers), impeding the detection of specific regional or network-based pathology[3,4]. Recently introduced, b-tensor encoding serves as a method capable of mapping microscopic fractional anisotropy (μFA) independently of intricate fiber architecture, including crossing and bending fibers[5-7]. Moreover, the b-tensor protocol estimates tissue heterogeneity via the anisotropic kurtosis (MKa) and isotropic kurtosis (MKi). Prior studies in HIV have shown relationships between cognitive performance and resting state functional connectivity in several brain networks[8]. In this work, we examine the relationships between b-tensor metrics throughout the functionally defined brain networks with neurocognitive scores

Methods: Fifty-five participants were evaluated (24 HIV+: mean age=55±15years, female=8; and 31 HIV- controls: mean age=55±10years, female=7). After obtaining written informed consent, all participants underwent scanning using a 3T Siemens MRI. The MRI protocol included: 3D MPRAGE and FLAIR (1mm isotropic resolution); diffusion weighted imaging (DWI) using 2D SE-EPI (1.5mm isotropic resolution, 128 gradients with b=1000 and 2000 and 7 b=0 s/mm2); 4) b-tensor encoding using a free waveform encoding sequence with linear and spherical tensor encodings for four b-values (i.e., 100,700,1400,2000 s/mm2), 80 non-colinear directions with resolution=2×2×4 mm3. DWI data were preprocessed using FSL[9]. The b-tensor data were preprocessed using Multidimensional diffusion MRI toolbox[12]. The UManitoba-JHU functionally defined human white matter (WM) atlases[13,14] and b-tensor maps were nonlinearly transformed to DWI native space using ANTs[15]. We then extracted ROI means in WM pathways underlying 12 previously-reported intrinsic functional brain networks[16]. These include – dorsal and ventral Default Mode Network, left and right Executive Control Network, anterior and posterior Salience Network, Precuneus Network, Language Network, Basal Ganglia Network, Higher Visual Network, Visuospatial Network, and Sensorimotor Network. Two-sample t-tests were used for group comparisons. All cognitive testing was performed using a neuropsychological battery that included tests of attention and working memory, processing speed, executive function, fine motor skills, verbal and visual learning, verbal and visual memory and language. The effects of HIV status on cognitive impairment and their interactions with imaging metrics were investigated via two-way analysis of variance (ANOVA). In addition, Pearson partial correlations were used to examine linear associations between cognitive performance and imaging metrics, with age as a covariate. All statistical analyses were performed in Python, and $p<0.05$ was considered significant.

Results: We observed lower μFA and MKa, along with higher MKi, in the HIV+ group compared to the HIV- group; however, these differences did not reach statistical significance. A two-way ANOVA examining HIV status and its interaction with

imaging metrics revealed that the basal ganglia network (BGN) is the most affected among the 12 functionally defined networks investigated. µFA in BGN was strongly positively associated with cognitive function, especially in HIV- participants. This association is particularly pronounced and statistically significant in subdomains such as processing speed and executive function (Table 1, Fig. 1).

Table 1: Two-way ANOVA to assess the effect of imaging metrics, HIV status and their interactions on cognitive scores.

µFA vs. SPE score					µFA vs. EXE score				
	β	SE	t	P>|t|		β	SE	t	P>|t|
Intercept	-2.54	0.82	-3.09	***0.003***	**Intercept**	-4.61	1.51	-3.05	***0.004***
BGN	3.68	1.20	3.07	***0.003***	**BGN**	6.64	2.21	3.01	***0.004***
HIV Status	2.52	1.01	2.49	***0.016***	**HIV Status**	3.48	1.86	1.87	0.067
Interaction	-4.16	1.50	-2.79	***0.008***	**Interaction**	-5.12	2.75	-1.87	0.068
FA vs. SPE score					**FA vs. EXE score**				
Intercept	-1.53	0.79	-1.95	0.057	**Intercept**	-2.92	0.81	-3.61	***0.001***
BGN	4.63	2.41	1.92	0.06	**BGN**	3.74	1.05	3.57	***0.001***
HIV Status	1.23	0.99	1.25	0.217	**HIV Status**	2.01	1.01	1.98	0.053
Interaction	-4.72	3.01	-1.57	0.123	**Interaction**	-2.68	1.32	-2.03	***0.048***
MKi vs. SPE score					**MKi vs. EXE score**				
Intercept	0.82	0.41	1.99	0.052	**Intercept**	2.12	0.70	3.02	***0.004***
BGN	-2.46	1.16	-2.13	***0.038***	**BGN**	-6.40	1.98	-3.23	***0.002***
HIV Status	-0.86	0.58	-1.48	0.144	**HIV Status**	-1.02	0.99	-1.03	0.308
Interaction	1.66	1.60	1.04	0.303	**Interaction**	2.96	2.73	1.08	0.284
MKa vs. SPE score					**MKa vs. EXE score**				
Intercept	-1.38	0.46	-3.00	***0.004***	**Intercept**	-2.54	1.44	-1.77	0.083
BGN	1.78	0.60	2.99	***0.004***	**BGN**	7.57	4.40	1.72	0.092
HIV Status	1.12	0.58	1.95	0.057	**HIV Status**	1.07	1.80	0.60	0.554
Interaction	-1.88	0.75	-2.51	***0.015***	**Interaction**	-3.48	5.50	-0.63	0.53
MD vs. SPE score					**MD vs. EXE score**				
Intercept	0.77	0.44	1.76	0.085	**Intercept**	1.47	0.80	1.84	0.072
BGN	-0.75	0.40	-1.88	0.066	**BGN**	-1.46	0.73	-2.00	0.051
HIV Status	-1.39	0.57	-2.43	***0.019***	**HIV Status**	-1.02	1.05	-0.97	0.335
Interaction	1.01	0.51	1.99	0.052	**Interaction**	0.95	0.93	1.02	0.313

Figure 1: Relationships between cognitive domain scores and diffusion (b-tensor and DTI) metrics in basal ganglia network (BGN). SPE: processing speed; EXE: executive function; HIV+: HIV infected individuals, HIV-: Healthy controls.

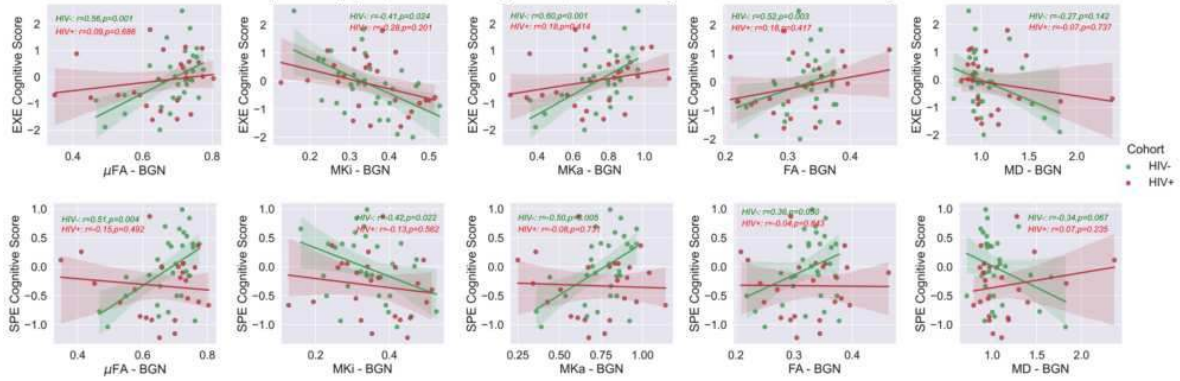

Conclusions: b-tensor metrics can be used to evaluate abnormalities associated with HIV infection in white matter networks (particularly the basal ganglia network) and may overcome certain limitations of traditional DTI with regard to fiber architecture.

References

1. Su, T., et al., AIDS, 2016. 30(15): p. 2329-2339.
2. Haddow, L.J., et al., AIDS research and human retroviruses, 2019.
3. Figley, C.R., et al., Front in Neuro, 2022. 15: p. 799576.
4. Jeurissen, B., et al., HBM, 2013. 34(11): p. 2747-2766.
5. Szczepankiewicz, F., et al. PloS one, 2019. 14(3): p. e0214238.
6. Nilsson, M., et al. MRM 83.2 (2020): 608-620.
7. Szczepankiewicz et al., Data in brief, 2019. 25:104208.
8. Zhuang, Y., et al., Journal of neurovirology, 2017. 23(5): p. 704-712.
9. Zhang, H., et al., Neuroimage, 2012. 61(4): p. 1000-16.
10. Klein, S., et al., IEEE transactions on medical imaging, 2009. 29(1): p. 196-205.
11. Nilsson, M., et al., PloS one, 2015. 10(11): p. e0141825.
12. Nilsson, M., et al., in Proc Intl Soc Mag Reson Med. 2018.
13. Figley, T.D., et al., Frontiers in human neuroscience, 2017. 11: p. 306.
14. Figley, T.D., et al., Frontiers in human neuroscience, 2015. 9: p. 585.
15. Avants, B.B., et al., Neuroimage, 2011. 54(3): p. 2033-2044.
16. Shirer, W.R., et al., Cerebral cortex, 2012. 22(1): p. 158-165.

Poster No 1613

Bootstrapped disconnection-symptom mapping and decoding in stroke patients with motor deficits

Ardalan Aarabi[1], Maedeh Khalilian[1], Martine Roussel[1], Olivier Godefroy[1]

[1]*University of Picardy Jules Verne, Amiens, Picardie*

Introduction: Focal structural damage to white matter tracts can lead to functional deficits in stroke patients. Traditional voxel-based lesion-symptom mapping (VLSM) is susceptible to issues such as lesion frequency and collinearity between neighboring voxels (Godefroy et al., 1998). The statistical power of VLSM is also hindered by patient heterogeneity in terms of lesion locations, volumes, and neurological symptoms, especially when lesions are situated in critical areas with a significant impact on structural connectivity between brain regions associated with functional deficits (Boes et al., 2015). In this study, we present a bootstrapped multivariate structural disconnection-symptom mapping (SVR-DSM) and decoding method based on support vector regression (DeMarco et al., 2018) to identify brain structures associated with motor deficits in stroke patients.

Methods: Structural imaging data were acquired from 340 stroke patients (mean age 63.9 ± 10.5 years) with left/right motor deficits as part of the GRECogVASC study cohort[4] conducted at Amiens University Hospital. Clinical and neuropsychological examinations, along with MR imaging, were performed six months post-stroke. Among these patients, 64 displayed motor impairment in upper and lower limb items in the NIHSS (32 with left and 29 with right motor deficits, and 3 with both). Lesions for each patient were manually segmented on 3D T1 MRI data using MRIcron and normalized into the MNI152 template with SPM12. For disconnection-symptom mapping, a probabilistic structural disconnection map was created for each patient by utilizing streamlines passing through the patient's lesion. This was estimated through fiber tracking from diffusion-weighted imaging data obtained from over 400 healthy controls (mean age 62.87 ± 13.47 years) from the Cambridge Centre for Ageing and Neuroscience repository (CamCAN, Stage 2)[5]. In these probabilistic maps, each voxel represented a disconnection probability (ranging from 0 to 1) based on the number of healthy subjects exhibiting a disconnection in that specific voxel[6]. For the left and right motor deficit, 100 bootstrapped bags of disconnection maps were then generated from all 340 patients to balance patients with (32 with left, 29 with right and 3 with both) motor deficits compared to 276 without motor deficits. Multivariate SVR regression analysis was then used to obtain a β-map for each bag using logistic regression and permutation testing ($p<0.005$, 1000 permutations) for left/right motor deficits. Statistical comparison of β-maps (SPM's second level, $p<0.005$, FWER corrected) using permutation testing produced a t-statistic map of voxels with significant associations with left/right motor deficits across all bags. Finally, a decoding model was constructed to predict right-left motor scores on a voxel-by-voxel basis using a searchlight strategy[7] and the leave-one-out cross-validation strategy across the bags.

Results: The statistical maps obtained using SVR-DSM were more effective in identifying brain structures, including the corticospinal tract, shown to be associated with left/right motor deficits (Arnoux et al., 2018). In comparison with VLSM, for the right motor deficit, no lesioned voxels survived with $p<0.005$ in the left hemisphere after correction for multiple comparisons. SVR-DSM also demonstrated high sensitivities (0.87 and 0.79) in identifying patients with left and right motor deficits, respectively. The decoding model based on bootstrapped SVR maps achieved high accuracies (up to 100%) for disconnected voxels in identifying patients with motor deficits.

Conclusions: Our results showed that for patient datasets with imbalanced data the bootstrapped bagging could significantly improve the performance of structural disconnection-deficit mapping compared to lesion-symptom mapping methods for identifying brain structures associated with motor deficits in stroke patients with relatively low false positive rates when dealing with unbalanced data

References

1. Godefroy, O. (1998). Brain-behaviour relationships. Some models and related statistical procedures for the study of brain-damaged patients. Brain, 121 (Pt 8), 1545-1556.
2. Boes, A. D. (2015). Network localization of neurological symptoms from focal brain lesions. Brain, 138(Pt 10), 3061-3075.
3. DeMarco, A. T. (2018). A multivariate lesion symptom mapping toolbox and examination of lesion-volume biases and correction methods in lesion-symptom mapping. Hum Brain Mapp, 39(11), 4169-4182.
4. Barbay, M. (2018). Prevalence of Poststroke Neurocognitive Disorders Using National Institute of Neurological Disorders and Stroke-Canadian Stroke Network, VASCOG Criteria (Vascular Behavioral and Cognitive Disorders), and Optimized Criteria of Cognitive Deficit. Stroke, 49(5), 1141-1147.
5. Taylor, J. R (2017). The Cambridge Centre for Ageing and Neuroscience (Cam-CAN) data repository: Structural and functional MRI, MEG, and cognitive data from a cross-sectional adult lifespan sample. Neuroimage, 144(Pt B), 262-269.
6. Thiebaut de Schotten, M. (2011). Atlasing location, asymmetry and inter-subject variability of white matter tracts in the human brain with MR diffusion tractography. Neuroimage, 54(1), 49-59.
7. Hebart, M. N. (2014). The Decoding Toolbox (TDT): a versatile software package for multivariate analyses of functional imaging data. Front Neuroinform, 8, 88.
8. Arnoux, A. (2018). Is VLSM a valid tool for determining the functional anatomy of the brain? Usefulness of additional Bayesian network analysis. Neuropsychologia, 121, 69-78.

Poster No 1614

The Relationship Between DTI-ALPS, Sleep Quality, and WM Integrity in Patients with Focal Epilepsy

En-Chi Tsui[1], Siew-Na Lim[2], Yi-Ping Chao[1]

[1]Department of Computer Science and Information Engineering, Chang Gung University, Taoyuan, Taiwan, [2]Chang Gung Memorial Hospital, Linkou, Taiwan

Introduction: The glymphatic system has recently attracted heightened attention due to its potential implications for brain health and disease. Substantial evidence supports the glymphatic system's role in facilitating the extracellular drainage of waste within the cerebrospinal fluid (CSF), and disruptions in this system may be associated with neuroinflammation and functional impairments. Utilizing diffusion tensor imaging (DTI)-derived indices of ventricular diffusion velocity along the perpendicular planes of the projection and association fiber white matter pathways, a technique referred to as DTI-based analysis along the perivascular space (DTI-ALPS) has been applied to investigate the glymphatic system. Here, we aimed to investigate the glymphatic system function using DTI-ALPS and its relationship with sleep quality and tract-based white matter integrity in patients with focal epilepsy.

Methods: In this study, 54 patients with focal epilepsy (mean age: 37.5±13.4, 25 males) and 39 healthy controls (HCs) (mean age: 32.7±8.8, 19 males) were recured. The 54 patients could be classified into four subgroups, including temporal lobe epilepsy (TLE, 8), frontal lobe epilepsy (FLE, 10), Mesial temporal lobe epilepsy (MTLE, 25), and MTLE with hippocampal sclerosis (MTLE with HS, 11). All DTI data were collected using Siemens 3T Trio scanners at Chang Gung Memorial Hospital at Linkou, Taiwan. DTI was conducted using spin-echo single-shot EPI sequences with 64 different diffusion directions on each shell (b-values = 1000 and 2000 s/mm2). DSI Studio software was utilized for data preprocessing and DTI reconstruction. Manual regions of interest (ROIs) were delineated to obtain the fiber orientation and diffusivities of the three directions along the x-, y-, and z-axes as voxel levels within the ROIs. Subsequently, the DTI-ALPS index was calculated using the formula shown in Figure 1 The tract-based white matter integrity was assessed using the PANDA (Pipeline for Analyzing braiN Diffusion imAges) toolbox, and sleep quality for all subjects was evaluated using the Pittsburgh Sleep Quality Index (PSQI) score.

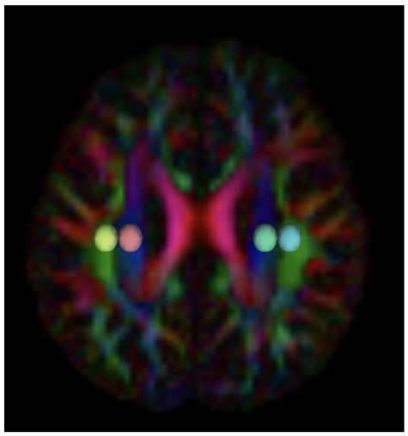

Figure 1. Calculation of diffusion tensor imaging analysis along the perivascular space index (DTI-ALPS). The blue, green, and red regions of interest in the DTI color map represent the locations of projection fibers, association fibers, and subcortical fibers, respectively.

Results: The results indicate that there is no statistically significant difference in ALPS values between patients with focal epilepsy and HCs (1.60 vs. 1.57, p=0.52). Even though the patients are divided into four subgroups, there is still no significant difference observed among the subgroups or between the subgroups and NCs. Moreover, there is still no significant difference observed when the right and left ALPS indices were calculated in both hemispheres. In the correlation analysis between clinical characters and ALPS, a significant negative correlation was observed between PSQI score and ALPS in both NCs and the MTLE group (r=-0.387 with $p<0.05$ and r=-0.521 with $p<0.01$).

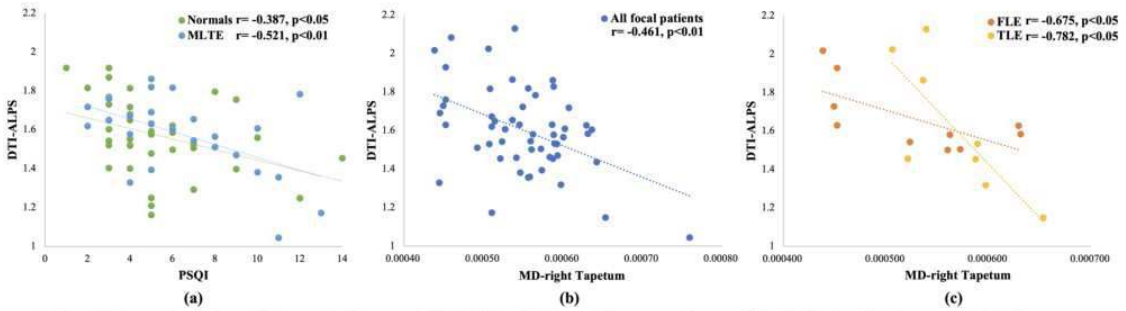

Figure 2. The results of the correlation analysis between DTI-ALPS and PSQI, as well as averaged mean diffusivity in the right Tapetum.(a) A significant negative correlation is observed between DTI-ALPS and PSQI scores in the NCs and MTLE groups.(b) A significant negative correlation is observed between DTI-ALPS and the averaged mean diffusivity (MD) in the right Tapetum in the entire focal patient group.(c) A significant negative correlation is also observed between DTI-ALPS and the averaged mean diffusivity (MD) in the right Tapetum in the FLE and TLE groups.

Conclusions: However, no significant correlation was found in the other three groups and all focal patients. Furthermore, in the correlation analysis between ALPS and the diffusion characteristics of white matter tracts, the results indicate a significant negative correlation between the mean diffusivity in the right Tapetum and ALPS in the all focal patients group (r=-0.461 with p<0.01). Additionally, within the sub-groups, both FLE and TLE also exhibit a significant negative correlation (r=-0.675 and -0.782, p<0.05). The results of correlation analyses were shown in Figure 2. These findings align with previous research, suggesting no significant DTI-ALPS differences between patients and HCs. ALPS correlated negatively with the PSQI in HCs and MTLE groups, indicating a glymphatic function-sleep duration relationship. Ipsilateral atrophy of the tapetum was found in both TLE-HS and TLE, suggesting a common lateralized effect of focal seizures. Ongoing recruitment efforts are planned to increase the number of participants in the future. This will allow for a more comprehensive understanding of the effects of ALPS on the sleep quality of focal epilepsy patients and white matter integrity.

References

1. A. M. Goodman and J. P. Szaflarski, "Recent Advances in Neuroimaging of Epilepsy," Neurotherapeutics, vol. 18, no. 2, pp. 811-826, 2021/04/01 2021, doi: 10.1007/s13311-021-01049-y.
2. D. A. Lee et al., "Glymphatic system function in patients with newly diagnosed focal epilepsy," (in eng), Brain Behav, vol. 12, no. 3, p. e2504, Mar 2022, doi: 10.1002/brb3.2504.
3. Y. Saito et al., "Glymphatic system impairment in sleep disruption: diffusion tensor image analysis along the perivascular space (DTI-ALPS)," (in eng), Jpn J Radiol, vol. 41, no. 12, pp. 1335-1343, Dec 2023, doi: 10.1007/s11604-023-01463-6.
4. T. Taoka et al., "Evaluation of glymphatic system activity with the diffusion MR technique: diffusion tensor image analysis along the perivascular space (DTI-ALPS) in Alzheimer's disease cases," (in eng), Jpn J Radiol, vol. 35, no. 4, pp. 172-178, Apr 2017, doi: 10.1007/s11604-017-0617-z.
5. D. N. Vaughan et al., "Tract-specific atrophy in focal epilepsy: Disease, genetics, or seizures?," (in eng), Ann Neurol, vol. 81, no. 2, pp. 240-250, Feb 2017, doi: 10.1002/ana.24848.
6. X. Zhao et al., "The asymmetry of glymphatic system dysfunction in patients with temporal lobe epilepsy: A DTI-ALPS study," Journal of Neuroradiology, vol. 50, no. 6, pp. 562-567, 2023/11/01/ 2023, doi: https://doi.org/10.1016/j.neurad.2023.05.009.

Poster No 1615

Fixel Based Analysis on Diffusion MRI of COVID-19 Survivors

Sapna Mishra[1], Tapan Gandhi[1], Bharat Biswal[2]

[1]Indian Institute of Technology Delhi, New Delhi, Delhi, [2]New Jersey Institute of Technology, Newark, NJ

Introduction: Even after recovery from the COVID-19 infection, there have been a multitude of reports of post-COVID sequelae like memory loss, inattention, brain fog, and fatigue across the world (Badenoch et al. 2022). The neurological underpinnings of these cognitive disruptions remain to be fully characterized. Therefore, we conducted a cross-sectional study to investigate the microstructural changes in the nervous tissue of COVID survivors using Fixel-Based Analysis (FBA) on Diffusion MRI (dMRI).

Methods: We acquired dMRI (1×1×2 mm3, 30 encoding directions (b=1000s/mm2), 4 B0 volumes (b=0s/mm2)) and T1-weighted MRI (1×1×1 mm3 voxel) scans of 35 COVID-recovered participants (CRPs) (11 females, 35.26 ± 11.17 years) and 29 Healthy Controls (HCs) (5 females, 33.76 ± 9.25 years). The CRPs were scanned within six months of recovery. The T1-w MRI was pre-processed by performing bias-field correction using FSL (fsl.fmrib.ox.ac.uk/fsl) followed by cortical surface reconstruction with Freesurfer (surfer.nmr.mgh.harvard.edu). Pre-processing of dMRI involved denoising, warping artifacts removal, and Gibbs ringing artifact correction using MRtrix (Tournier et al. 2019). We corrected for susceptibility induced distortions using the Synb0-DISCO (Schilling et al. 2019) and FSL's TOPUP algorithms. Finally, Eddy current correction was performed. The FBA on

dMRI included the following steps (Raffelt et al, 2017). The population average response function was estimated, followed by upsampling to 1.5 mm isotropic voxels and brain masking. The fiber orientation distributions (FODs) were determined using the multi-shell, multi-tissue Constrained Spherical Deconvolution (MSMT-CSD) algorithm. Next, a study specific template was created by averaging the FOD images and the subject FOD maps were warped to the template. The subject and template FODs were segmented to obtain discrete fixels, followed by reorientation of subject fixels. To aid group-level comparisons of CSD-derived metrics, correspondence was established between fixels in subject scans and the template. Finally, CSD-derived metrics: Log-scaled Fiber Cross-section (log-FC), Fiber Density (FD), and a combined measure of fiber density and cross-section (FDC), were calculated. A fixel-derived whole brain tractogram was filtered to 2 million streamlines using SIFT (Spherical-deconvolution Informed Filtering of Tractograms)and a sparse fixel-to-fixel (f2f) connectivity matrix was obtained which was used to smooth the fixel maps. The FD, log-FC, and FDC maps were statistically compared across cohorts using permutation tests with 2500 iterations. Family-wise error was controlled (p FWE < 0.05) using the Connectivity-based fixel enhancement method (Raffelt et al. 2015).

Results: Upon statistical comparison of the FBA metrics, the log-FC values showed significant differences between the CRPs and HCs in the corpus callosum, caudate nucleus, forceps major, inferior fronto-occipital fasciculus (IFOF), and the anterior cingulum cingulate (ACC) (CRP > HC, see Figure 1). No significant changes were observed in the FD and FDC measure.

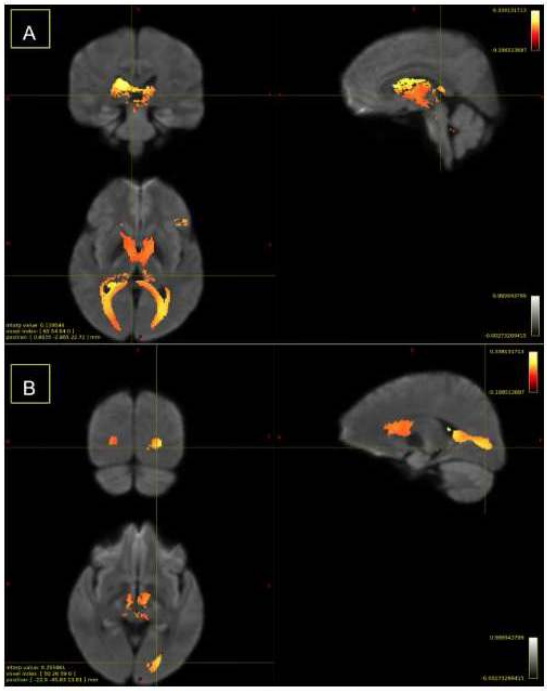

Figure 1. Regions that exhibit significant change in log-scaled Fiber cross-section between the COVID-recovered and Healthy control groups (p_{FWE}<0.05). **(A)** Corpus callosum, caudate nucleus, and the forceps major. **(B)** Forceps major, inferior fronto-occipital fasciculus (IFOF), and anterior cingulum cingulate (ACC).

Conclusions: An increase in FC with insignificant changes in FD suggests a potential rise in axon number, hinting at compensatory neural mechanisms in white matter post-COVID-19 recovery (Andica et al, 2021). The clusters in Figure 1(A) encompass the corpus callosum, caudate nucleus, and the forceps major. Clusters shown in Figure 1(B) cover occipital white matter areas like the forceps major and the inferior fronto-occipital fasciculus along with the anterior cingulum cingulate. Overall, the identified regions are involved in regulatory control of behaviour, working memory, executive control and visual attention (Grahn et al. 2008). Notably, these functions align closely with the reported behavioral symptoms in individuals who have recovered from COVID-19. We expect that this study shall help us in understanding the neurological underpinnings of COVID-19.

References

1. Andica, Christina. (2021), “Fiber-specific white matter alterations in early-stage tremor-dominant Parkinson’s disease.” npj Parkinson’s Disease, 7.1, 51.
2. Badenoch, James B. (2022), “Persistent neuropsychiatric symptoms after COVID-19: a systematic review and meta-analysis.” Brain Communications, 4.1.
3. Grahn, Jessica A. (2008), “The cognitive functions of the caudate nucleus.” Progress in neurobiology 86.3, 141-155.
4. Raffelt, David A. (2017), “Investigating white matter fibre density and morphology using fixel-based analysis.” Neuroimage, 144, 58-73.
5. Raffelt, David A. (2015) “Connectivity-based fixel enhancement: Whole-brain statistical analysis of diffusion MRI measures in the presence of crossing fibres.” Neuroimage, 117, 40-55.
6. Schilling, Kurt G. (2019) “Synthesized b0 for diffusion distortion correction (Synb0-DisCo).” Magnetic resonance imaging, 64, 62-70.

Poster No 1616

Intravoxel incoherent motion and cerebrovascular reactivity in acute stroke and clinical follow-up

Astrid Cancino[1,2], Pablo Muñoz[3], Pablo Cox[4,5], Lilian Acevedo[4], Sebastian Castillo[4], Aldo Letelier[4], Sebastian Espinoza[6], Alejandro Veloz[7], Maria Rodriguez-Fernandez[8,9], Stéren Chabert[10,9]

[1]Millennium Institute for Intelligent Healthcare Engineering, iHEALTH, Santiago, Chile, [2]PhD Program in Sciences and Engineering for Health. Universidad de Valparaíso, Valparaíso, Chile, [3]Center for Applied Neurological Sciences, Faculty of Medicine, Universidad de Valparaíso, Valparaíso, Chile, [4]Hospital Carlos Van Buren, Valparaíso, Chile, [5]Radiology Department, Universidad de Valparaiso, Valparaíso, Chile, [6]Universidad de Valparaíso, Valparaíso, Chile, [7]School of Biomedical Engineering, Universidad de Valparaíso, Valparaíso, Chile, [8]Institute for Biological and Medical Engineering, Pontificia Universidad Católica de Chile, Santiago, Chile, [9]Millenium Institute for Intelligent Healthcare Engineering iHealth, Santiago, Chile, [10]School of Biomedical Engineering, Universidad de Valparaíso, Valparaíso, Chile

Introduction: An ischemic stroke is a perfusion impairment, and it ranks as the second-leading cause of death globally and the third-leading cause when death and disability are combined (Feigin 2022). The imaging management of stroke involves the gold standard diffusion-weighted imaging (DWI) and/or perfusion MRI with or without contrast agents (Powers 2018). Intravoxel Incoherent motion (IVIM) explores the biexponential decay of the DWI signal obtained with multiple b-values. The pseudo-perfusion (D*) and the free water diffusion of free water (D) coefficients have been related to the microperfusion (Chabert 2020). IVIM has been suggested as an alternative technique for stroke assessment (Falk 2019 ; Pavila 2023). Cerebrovascular reactivity (CVR) is traditionally evaluated with a CO2 challenge to induce vasodilation (Gupta 2012). In the past year, an alternative method has been proposed for measuring CVR (Yang 2007) in a resting state fMRI (Frank 2023). These two MRI methods could provide a better understanding of the microvascular status during ongoing ischemia and their correlation with motor outcomes six months later

Methods: 23 volunteers enrolled with an ischemic stroke in the first 48 hours. Indication of thrombolysis or thrombectomy was an exclusion criterion. This study received full approval from the local ethics committee. All patients, or legal representatives, gave informed consent to participate. The severity of symptoms was assessed by NIHSS. The fMRI was acquired in a 1.5 Tesla. We used the task residual fMRI to explore the background connectivity as a resting state (rs) signal to generate the ALFF mapping as an approximation of CVR. DWI with 16 b values was used for the IVIM parameters fitting according to the biexponential model in two steps (Chabert 2020). All The analyses were undertaken in Regions of Interest (ROI) from the ischemic ROI and the contralateral non-ischemic ROI. Clinical follow-up at 6 months was realized with clinical scales: Barthel Index and Functional Independence Measure (FIM) for motor and functional Independence performance. The clinical data, CVR, and IVIM (D and D*) parameters were averaged over all patients. The ischemic and non-ischemic ROI were reported as mean ± standard deviation. The paired student t-test was used to compare the mean or U Mann Whitney in non-normal distribution. The Pearson correlation analysis was performed for all the subjects to explore relationships between the MRI parameters and clinical assessment

Results: The mean age of participants was 66.7 years (±12.8), with 21.7% (n=5) being female. The median NIHSS score at admission was 4 (1-21) The DWI lesions at admission was 12.9 ml (± 28.4), with a median volume of 1.85 ml. The CVR values in ischemic and non ischemic do not present differences in the mean values. A significant difference for the D ($Z = 3.7$, $p < .001$) and D*values ($W+ = 131$, $p = 0.048$). in ischemic and non ischemic ROI. Qualitative in Figure 1.B Dmaps and D*maps of 3 participants., the reduction of D values in the ischemic region is evident. The ischemic CVR value correlates with ischemic volume -0.6 (0.03); The ischemic D value correlates with the Delta CVR (non ischemic – ischemic) 0.78 (0.005). Concerning the motor outcome, the ischemic D* value correlated with FIM outcome -0.71 (0.006).

	Age	Vol isch. (mL)	NIHSS	Isch_CVR (a.u.)	Non_isch_CVR (a.u.)	DeltaCVR %	Isch_D* (10-3 mm2/s)	Non_isch_D*	Isch_D	Non_isch_D
Mean	66.65	12.9	5.65	0.93	0.94	0.68	3.98	5.58	0.52	0.87
Std. Dev.	12.59	28.42	5.54	0.17	0.18	14.06	4.2	5.56	0.1	0.23

Table. Characterization of variables of interest. Vol.isch = Ischemic volume; NIHSS = National Institutes of Health Stroke Scale. Isch_CVR = Ischemic CVR value in ROI ; Non_isch_CVR = Non ischemic CVR value

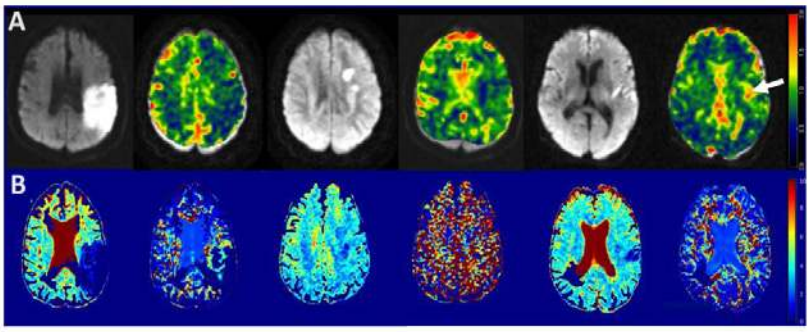

Fig. A. Example of DWI at b=1000 to identify the ischemic ROI and CVR maps, first participant (P25) has decreased CVR value and the third participant (P11) has increased CVR value. B. Maps of diffusion

Conclusions: This work shows a promising approach as it provides a quantitative measure of vascular flow dysfunction and establishes a strong correlation with motor outcomes six months later. This vascular impairment is supported by data in the literature. However, the main limitation of this study was the heterogeneous presentation of the stroke, along with the loss of data due to technical issues. More questions are still open and involve the ischemic neuroinflammatory cascade and its impact on the hemodynamic response function.

References

1. Chabert, S., (2020). Impact of b-Value Sampling Scheme on Brain IVIM Parameter Estimation in Healthy Subjects. Magnetic resonance in medical sciences: MRMS: an official journal of Japan Society of Magnetic Resonance in Medicine, 19(3), 216–226
2. Falk, D.A.,(2019) 'Diagnostic value of alternative techniques to gadolinium-based contrast agents in MR neuroimaging—a comprehensive overview'. Insights Imaging. 10:84.
3. Frank, L.E., (2023), Evaluating methods for measuring background connectivity in slow event-related functional magnetic resonance imaging designs. Brain Behavior. 2023 Jun;13(6):e3015.
4. Feigin, V. L. (2022), World Stroke Organization (WSO): Global Stroke Fact Sheet 2022. International journal of stroke: official journal of the International Stroke Society, 17(1), 18–29.
5. Gupta, A., 'Cerebrovascular reserve and stroke risk in patients with carotid stenosis or occlusion: a systematic review and meta-analysis. ' Stroke 2012;43:2884-2891.
6. Pavilla, A., (2023). Intravoxel incoherent motion and diffusion kurtosis imaging at 3T MRI: Application to ischemic stroke. Magnetic resonance imaging, 99, 73–80.
7. Powers, W.J. (2018), ' Guidelines for the early management of patients with acute ischemic stroke: a guideline for healthcare professionals from the American Heart Association/American Stroke Association ' . Stroke. 49:e46–e110.
8. Yang, H. (2007), ' The amplitude of low-frequency fluctuation within visual areas revealed by resting-state functional MRI ', Long XY, Yang Y, Yan H, Zhu CZ, Zhou XP, Zang YF, Gong QY. Neuroimage. May 15;36(1):144-52.

Poster No 1617

Tractometry-based Harmonization of Scanner Effects for White Matter Tract Analysis

Bramsh Chandio[1], Julio Villalón-Reina[1], Talia Nir[2], Sophia Thomopoulos[3], Yixue Feng[4], Neda Jahanshad[5], Jaroslaw Harezlak[6], Eleftherios Garyfallidis[7], Paul Thompson[8]

[1]University of Southern California, Los Angeles, CA, [2]University of Southern California Keck School of Medicine, Marina del Rey, CA, [3]USC, Marina del Rey, CA, [4]University of Southern California, Marina Del Rey, CA, [5]USC Keck School of Medicine, Marina Del Rey, CA, [6]Indiana University School of Public Health, Bloomington, IN, [7]Indiana University Bloomington, Bloomington, IN, [8]Imaging Genetics Center, Keck School of Medicine of University of Southern California, Los Angeles, CA

Introduction: In neuroimaging research, the harmonization of data acquired from different imaging sites and scanners is paramount to ensure the reliability, comparability, and accurate interpretation of the findings. ComBat[1,2] is a harmonization method often used to model variations arising from site-specific and scanner-specific effects when analyzing multi-site datasets. It has mostly been applied at the voxel or region of interest level for harmonizing morphometric or microstructural measures when analyzing the measures in group statistics. Here, we add the ComBat method to our BUndle ANalytic (BUAN)[3] tractometry pipeline. We use ADNI3[4] (Alzheimer's Disease Neuroimaging Initiative) data from 7 diffusion MRI protocols to correct for scanner acquisition protocol effects examining the effects of mild cognitive impairment (MCI) and dementia on 38 white matter tracts. We compare results with and without harmonization using different statistical approaches.

Methods: Data from 730 ADNI3 participants (age: 55-95, 349M/381F, 214 MCI, 69 dementia, 447 cognitively healthy controls (CN)) scanned with 7 acquisition protocols (GE36, GE54, P33, P36, S127, S31, S55) were included. Tables 1 and 2 detail

demographic and acquisition protocol information. Data was preprocessed using the ADNI3 protocol[5,6], robust and unbiased model-based spherical deconvolution[7], with particle filtering tractography[8] applied to generate tractograms using DIPY[9]. We used BUAN to extract 38 bundles and create their bundle profiles for 4 microstructural metrics, FA, MD, AD, and RD (see Fig. 1 for full names). Bundle profiles consist of 100 segments along the length of the tract with microstructural metrics associated with them. The average of each segment's points is calculated resulting in 100 microstructural values per bundle profile. For each tract and metric, we first pool together bundle profiles of all subjects across CN, MCI, and dementia groups. Pooled bundle profiles consisting of 100 segments modeled as features are then fed to ComBat for scanner protocol effect correction with group, age, and sex modeled as covariates. Due to limited subjects scanned with specific protocols at some sites in ADNI3, we chose not to model site nested within protocol, as the modeling would not be robust. ComBat corrected data is then used to run a linear regression with group, age, and sex modeled as fixed effects and the response variable being microstructural measure, and protocol is incorporated as a random effect in linear mixed models (LMM) to find group differences between MCI and CN and dementia and CN.

Table 1. Participant demographics. 'Site N' denotes the number of sites across North America using the dMRI acquisition protocol specified (protocols are further detailed in **Table 2**). * NB: some sites collected data with more than one protocol, so the total number of sites is less than the sum of the final column.

Protocol	Total N	Diagnosis			M	F	Age (Mean±SD)	CDR-sob (Mean±SD)	Amyloid		Site N*
		CN	MCI	Dementia					Aβ+	Aβ-	
S55	270	175	71	24	120	150	74.4±7.9	0.93±2.0	103	117	18
S31	96	59	27	10	39	57	72.0±8.5	0.96±1.8	26	49	10
S127	112	68	36	8	53	59	73.7±7.6	0.78±1.5	35	58	14
P36	46	20	23	3	24	22	73.1±6.9	0.84±1.1	12	27	5
P33	56	37	14	5	34	22	75.7±7.7	1.03±2.1	19	21	6
GE36	42	21	17	4	24	18	72.2±7.1	1.29±2.7	13	22	4
GE54	108	67	26	15	55	53	76.1±8.1	1.16±2.0	37	57	10
Total	730	447	214	69	349	381	74.1±7.9	0.97±1.9	245	351	58

Table 2. ADNI3 dMRI acquisition protocols.

Protocol	Scanner		Volumes			Matrix	Acquisition Time (min:sec)
	Vendor	Model	b_0	DWI	Total		
GE36	GE	Basic Widebore 25x	4 b=0 s/mm^2	32 b=1000 s/mm^2	36	256x256	9:52
GE54	GE	Basic 25x	6 b=0 s/mm^2	48 b=1000 s/mm^2	54		7:09
P33	Philips	Basic Widebore	1 b=0 s/mm^2	32 b=1000 s/mm^2	33	128x128	7:32
P36	Philips	Basic Widebore R3	1 b=0 s/mm^2 3 b=2 s/mm^2	32 b=1000 s/mm^2	36		6:54
S31	Siemens	Basic VB17	1 b=0 s/mm^2	30 b=1000 s/mm^2	31	116x116	7:02
S55	Siemens	Basic Skyra E11 & Prisma D13	7 b=0 s/mm^2	48 b=1000 s/mm^2	55		9:18
S127	Siemens	Advanced Prisma VE11C	13 b=0 s/mm^2	6 b=500 s/mm^2 48 b=1000 s/mm^2 60 b=2000 s/mm^2	127		7:25*

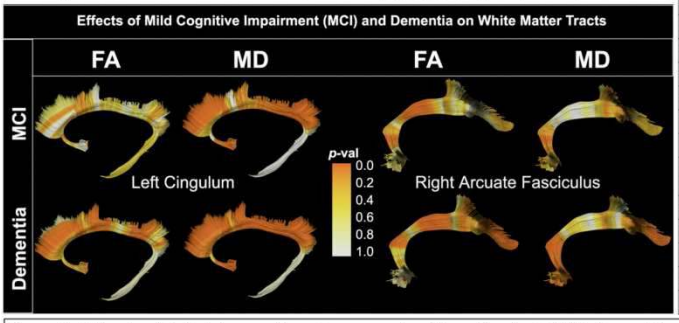

Abbreviation
Left/Right (L/R)
Corticospinal Tract (CST)
Fornix (F)
Optic Radiation (OR)
Frontopontine Tract (FPT)
Occipitopontine Tract (OPT)
Cingulum (C)
Arcuate Fasciculus (AF)
Extreme Capsule (EMC)
Inferior Fronto Occipital Fasciculus (IFOF)
Inferior Longitudinal Fasciculus (ILF)
Middle Longitudinal Fasciculus (MdLF)
Superior Longitudinal Fasciculus (SLF)
Uncinate Fasciculus (UF)
Anterior Commissure (AC)
Corpus Callosum Mid (CCMid)
CC Forceps_Minor
CC Forceps_Major
Posterior Commissure (PC)
Cerebellum (CB)
Vermis (V)
Medial Lemniscus (ML)
Medial Longitudinal Fasciculus (MLF)
Spinothalamic Tract (STT)
Fractional Anisotropy (FA)
Mean Diffusivity (MD)
Axial Diffusivity (AD)
Radial Diffusivity (RD)

Figure 1. Tables 1 and 2 detail demographic and scanner protocol information about ADNI3 data used in our experiments (data from Thomopoulos et al, 2021). The abbreviation table on the right shows the names of 38 white matter tracts and four microstructural measures analyzed in this work. The bottom panel shows the effects of MCI and Dementia using the harmonized BUAN tractometry approach on the left cingulum (C_L) and right arcuate fasciculus (AF_R) bundles on fractional anisotropy (FA) and mean diffusivity (MD) metrics.

Results: After ComBat harmonization, group differences were more sensitively detected, as compared to linear regression and LMM applied without scanner correction. However, we also find comparable results when using LMM with scanner protocol modeled as a random effect aligned with our previous work[4,5]. While harmonization enhances the significance of the group effect for most tracts, it also decreases the group difference effect for some tracts, suggesting the removal of site-specific confounds that are correlated with the disease effect. We also visualize the results of harmonized BUAN mapping effects of MCI and Dementia, for the left cingulum and right arcuate fasciculus (Fig. 1, bottom panel). Adding different scanner protocols in the analysis boosts disease sensitivity, and harmonization further boosts power, as shown before and after harmonization in Fig. 2f-g.

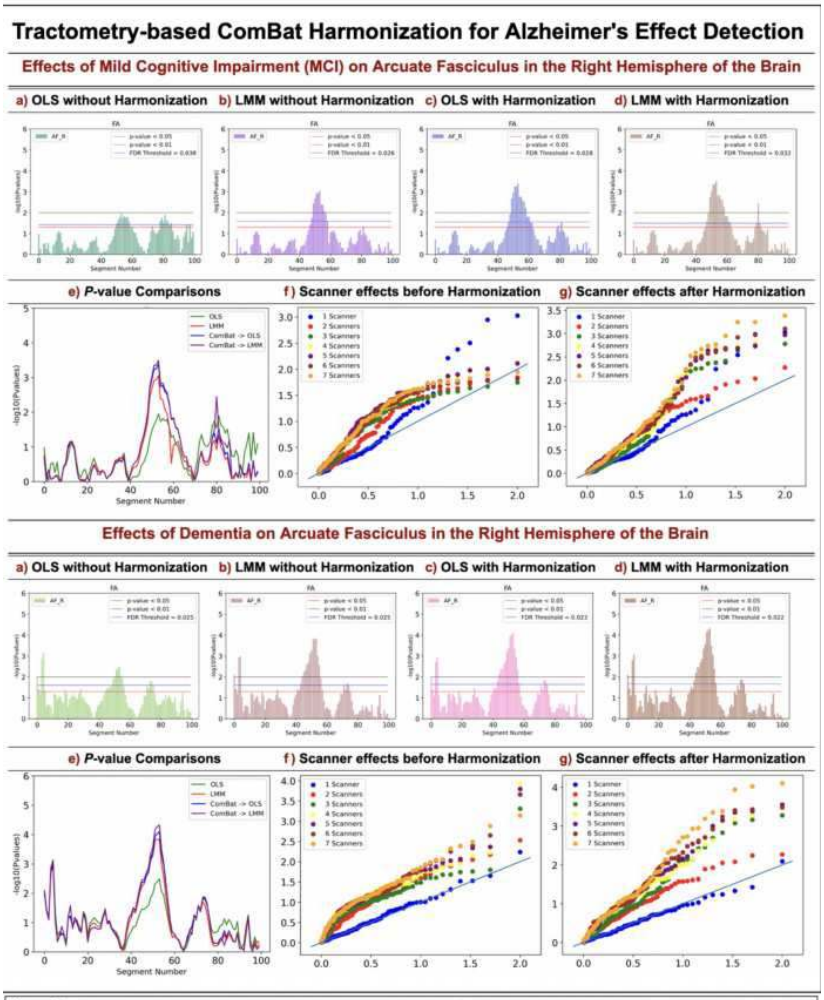

Figure 2: The top and bottom panels show the results for the right arcuate fasciculus (AF_R) bundle on the fractional anisotropy (FA) measure for MCI vs CN and Dementia vs CN group comparisons, respectively. In all four statistical experiments, group, age, and sex were modeled as fixed effects. In both panels' plots, the *x*-axis has segment numbers along the length of the tracts and the *y*-axis shows the negative logarithm of the *p*-values. FDR corrected threshold is plotted as a blue horizontal line in the plots. a) Linear regression on unharmonized data, b) Linear Mixed Models (LMM) with scanner protocol modeled as a random effect on unharmonized data, c) linear regression on harmonized data, and d) LMM with scanner protocol modeled as a random effect on harmonized data. e) shows comparisons of *p*-values obtained from the four experiments. We find that linear regression and LMM on harmonized data yields higher significance (smaller nominal *p*-values), while LMM on unharmonized data with scanner protocol modeled as random term gives comparable results. Note that we did not correct for site effects in these experiments as most sites scan N<10 people (each scan protocol is used at several sites). When modeling a site as a random term in LMM, we obtain similar results to those presented here. Plots f) and g) present the effects of adding data acquired from different acquisition protocols on unharmonized and harmonized data, respectively. With each new protocol added to analyses, statistical power increases in both f) and g). While the N increases, and this should boost power, it is possible that the protocol effect could reduce power, but this is shown to be mitigated. Harmonization in g) further helps to boost the power of analysis.

Conclusions: Integrating ComBat into the BUAN tractometry can merge data from different scanning protocols. By incorporating ComBat harmonization, we model site-specific and scanner-specific effects, ensuring the reliability and comparability of results by mitigating confounding variables. To the best of our knowledge, this is the first time harmonization has been applied to tractometry analysis. Future work will explore varied ComBat versions and advanced deep-learning approaches.

References

1. Johnson, W.E., Li, C. & Rabinovic, A., 2007. Adjusting batch effects in microarray expression data using empirical Bayes methods. Biostatistics, 8(1), pp.118-127.
2. Fortin, J.P., Cullen, N., Sheline, Y.I., Taylor, W.D., Aselcioglu, I., Cook, P.A., Adams, P., Cooper, C., Fava, M., McGrath, P.J. & McInnis, M., 2018. Harmonization of cortical thickness measurements across scanners and sites. Neuroimage, 167, pp.104-120.
3. Chandio, B.Q., Risacher, S.L., Pestilli, F., Bullock, D., Yeh, F.C., Koudoro, S., Rokem, A., Harezlak, J. & Garyfallidis, E., 2020. Bundle analytics, a computational framework for investigating the shapes and profiles of brain pathways across populations. Scientific Reports, 10(1), pp.1-18.
4. Zavaliangos-Petropulu, A., Nir, T.M., Thomopoulos, S.I., Reid, R.I., Bernstein, M.A., Borowski, B., Jack Jr, C.R., Weiner, M.W., Jahanshad, N. & Thompson, P.M., 2019. Diffusion MRI indices and their relation to cognitive impairment in brain aging: the updated multi-protocol approach in ADNI3. Frontiers in Neuroinformatics, 13, p.2.
5. Thomopoulos, S.I., Nir, T.M., Villalon-Reina, J.E., Zavaliangos-Petropulu, A., Maiti, P., Zheng, H., Nourollahimoghadam, E., Jahanshad, N., Thompson, P.M., for the Alzheimer's Disease Neuroimaging Initiative. Diffusion MRI Metrics and their Relation to Alzheimer's Disease Severity: Effects of Harmonization Approaches. SIPAIM 2021, Campinas, Brazil. 2021.
6. Jahanshad, N., Kochunov, P.V., Sprooten, E., Mandl, R.C., Nichols, T.E., Almasy, L., Blangero, J., Brouwer, R.M., Curran, J.E., de Zubicaray, G.I. & Duggirala, R., 2013. Multi-site genetic analysis of diffusion images and voxelwise heritability analysis: A pilot project of the ENIGMA–DTI working group. Neuroimage, 81, pp.455-469.

7. Canales-Rodríguez, E.J., Daducci, A., Sotiropoulos, S.N., Caruyer, E., Aja-Fernández, S., Radua, J., Yurramendi Mendizabal, J.M., Iturria-Medina, Y., Melie-García, L., Alemán-Gómez, Y. & Thiran, J.P., 2015. Spherical deconvolution of multichannel diffusion MRI data with non-Gaussian noise models and spatial regularization. PloS one, 10(10), p.e0138910.
8. Girard, G., Whittingstall, K., Deriche, R., & Descoteaux, M. Towards quantitative connectivity analysis: reducing tractography biases. NeuroImage, 98, 266-278, 2014.
9. Garyfallidis, E., Brett, M., Amirbekian, B., Rokem, A., van der Walt, S., Descoteaux, M. & Nimmo-Smith, I., "Dipy, a library for the analysis of diffusion MRI data," Front. Neuroinform. 8 8 (2014).

Poster No 1618

Evaluating Accuracy and Reliability of Brain-Behavior Models Using Diffusion MRI

McKenzie Hagen[1], John Kruper[1], Keshav Motwani[1], Eardi Lila[1], Jason Yeatman[2], Ariel Rokem[1]

[1]University of Washington, Seattle, WA, [2]Stanford University, Stanford, CA

Introduction: Diffusion MRI measures tissue properties of white matter, which contains long-range connections between different brain regions. A variety of methods for processing raw dMRI data create distinct sets of features for subsequent analyses. One such method, tractometry, results in "tract profiles", which describe tissue properties along the length of major white matter tracts (Yeatman et al. 2012; Kruper et al. 2021). Another is the "local connectome", or connectivity within neighboring regions of cerebral white matter (Yeh et al. 2016). While these features originate from the same raw data, they have distinct characteristics that can be exploited by different types of predictive models. With these models, we can quantify the relation between white matter microstructure and various phenotypes and identify which aspects of the microstructure are most influential. However, in high-dimensional settings, where there are many more features than subjects, such as in neuroimaging data, high model variance across resamples can complicate model interpretation.

Methods: To address high-dimensional problems, regularized regression methods have been used, which perform model selection by removing non-predictive features from the model. In the case of the Least Absolute Shrinkage and Selection Operator (LASSO) regularization, a linear model fit with ordinary least squares (OLS) is penalized by the absolute value of the coefficient assigned to each feature in the model. This results in non-informative features being removed from the model by assigning them a coefficient of zero. An alternative model is sparse group LASSO (SGL), which can be used with feature sets that have inherent groups, such as tract profiles (Richie-Halford et al. 2021). SGL regularizes by and within each group of features, resulting in uninformative groups of features being removed, as well as individual features within groups. Using both local connectome and bundle profiles from the Human Connectome Project as input features, we compared the accuracy and reliability of predictive models, with age and a subset of behavioral phenotypes as prediction targets. A LASSO model was fit separately for both local connectome and bundle profiles, and an SGL model was fit to bundle profiles with each bundle forming a separate group. Nested 5-fold cross validation with each family assigned to the same fold was used to fit and evaluate models, and bootstrapping by family was used to create 95% confidence intervals (CIs) to evaluate the stability of models.

Results: Results: We found that both feature sets are slightly predictive of behavioral phenotypes when modeled with LASSO, with no significant difference between local connectome and bundle profiles (Fig 1). Interestingly, endurance, which was operationalized by how far an individual can walk in 2 minutes, is the most predictable after age. Across prediction targets, the average R... value ranges between .001 and .17 for local connectome, and .001 and .14 for bundle profiles, showing that both diffusion feature sets predict some phenotypes better than others, replicating previous work (Rasero et al. 2021). A comparison of SGL and LASSO bundle profile models predicting cognitive ability shows that while the predictive accuracy of either model isn't significantly different (Fig 1), the stability of model coefficients is. Across all nodes, the standard deviation of the model coefficients for 35 bootstraps for LASSO is .06 and SGL is 0.007 (Fig 2).

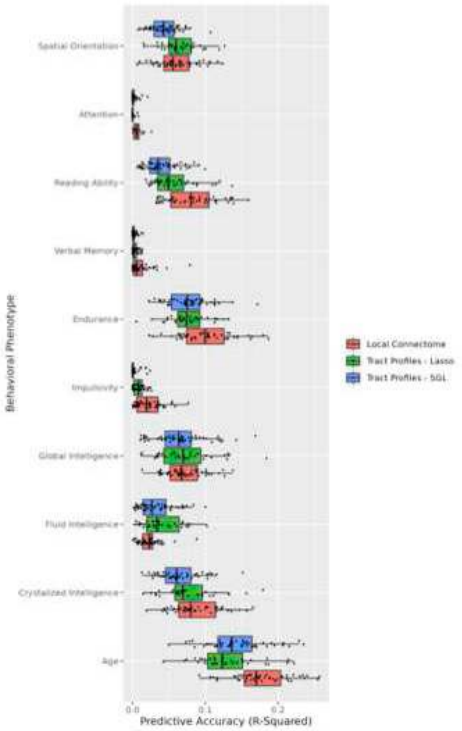

Figure 1. Across phenotypes, there is no significant difference in the predictive accuracy of LASSO regularized models between feature sets. Error bars represent a 95% CI calculated with repeated bootstrap resampling (dots indicate 35 individual boot samples). Between phenotypes, there is considerable variation in the predictive ability of both local connectome and tract profiles.

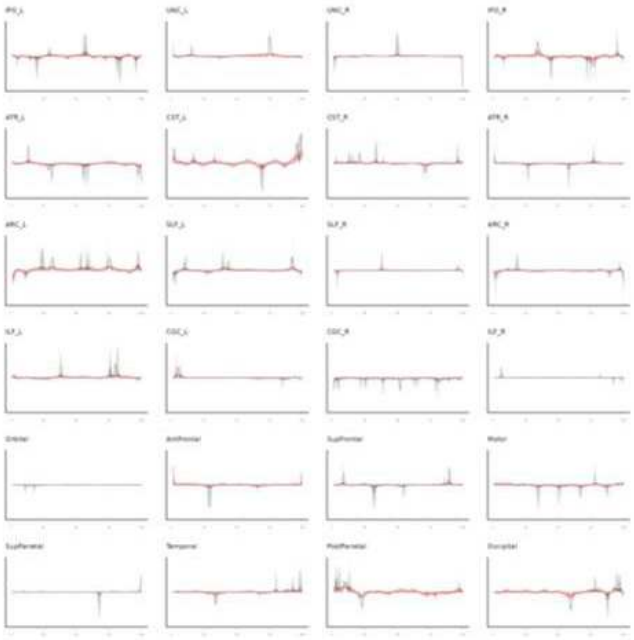

Figure 2. Model coefficients for each tract node plotted by bundle, with shaded 95% CIs. SGL models (red) favor selecting a range of nodes with small coefficients, rather than a single node with a large coefficient in the case of a LASSO model (black). The CIs also show that the SGL models are more stable, with narrower CIs.

Conclusions: These results show that characteristics of diffusion feature sets can be leveraged with different predictive models, to improve inferences by increasing model stability. While local connectome and bundle profiles perform equally well predicting behavioral phenotypes, the instability of the LASSO regularized local connectome model challenges inference from the coefficients. In contrast, using SGL with the inherently grouped bundle profiles leads to more interpretable and stable models.

References

1. Kruper, John, Jason D. Yeatman, Adam Richie-Halford, David Bloom, Mareike Grotheer, Sendy Caffarra, Gregory Kiar, et al. 2021. "Evaluating the Reliability of Human Brain White Matter Tractometry." Aperture Neuro 1 (1). https://doi.org/10.52294/e6198273-b8e3-4b63-babb-6e6b0da10669.
2. Rasero, Javier, Amy Isabella Sentis, Fang-Cheng Yeh, and Timothy Verstynen. 2021. "Integrating across Neuroimaging Modalities Boosts Prediction Accuracy of Cognitive Ability." PLoS Computational Biology 17 (3): e1008347.
3. Richie-Halford, Adam, Jason D. Yeatman, Noah Simon, and Ariel Rokem. 2021. "Multidimensional Analysis and Detection of Informative Features in Human Brain White Matter." PLoS Computational Biology 17 (6): e1009136.
4. Yeatman, Jason D., Robert F. Dougherty, Nathaniel J. Myall, Brian A. Wandell, and Heidi M. Feldman. 2012. "Tract Profiles of White Matter Properties: Automating Fiber-Tract Quantification." PloS One 7 (11): e49790.

Poster No 1619

Effect of adjunctive acupuncture on the white matter tract integrity in ischemic stroke patients

Pearly Joubert[1], Jia Fan[1], Frances Robertson[1], Hai Lu[2], Fleur Warton[1], Yu Wang[3], Sebnem Er[1], Jiu Chen[2], Nelleke Langerak[1], Marc Combrinck[1], Xuesheng Ma[4], Xuesong Ren[3], Ernesta Meintjes[1], Chunhong Zhang[3]

[1]University of Cape Town, Cape Town, Western Cape, [2]Nanjing University, Nanjin, Jiangsu, [3]First Teaching Hospital of Tianjin University of Traditional Chinese Medicine, Tianjin, Tianjin, [4]University of the Western Cape, Cape Town, Western Cape

Introduction: Stroke is the second leading cause of mortality and the third leading cause of disability, worldwide[1]. Rehabilitation is necessary for reducing disability in stroke patients[2]. Acupuncture is an alternative and complementary strategy for the rehabilitation of stroke patients[3]. However, the mechanism of acupuncture on stroke rehabilitation is poorly understood. This study evaluated the effects of adjunctive acupuncture treatment on white matter (WM) integrity in ischemic stroke patients using diffusion tensor imaging (DTI), which allows the characterization of water diffusion in voxels[4].

Methods: Twenty-three right-handed stroke patients with unilateral limbs dysfunction (mean ±sd: 58.8 ±8.1 yr) were recruited from the First Teaching Hospital of Tianjin University of Traditional Chinese Medicine. Participants were randomized into three treatment groups: 1) True Acupuncture (TA), 2) TA and Physiotherapy (PT), and 3) PT and Sham Acupuncture (SA, a placebo or non-acupoint acupuncture). The patients were imaged on a 3T Skyra MRI (Siemens, Erlangen, Germany). DTI and T1-weighted images were acquired on participants after receiving five acupuncture sessions per week for 3 weeks. Distortion correction and co-registration were done in FSL[5]. Unweighted (b0) images were co-registered to their own T1-weighted structural image using linear and nonlinear co-registration algorithms. T1 images were co-registered to 1x1x1 mm3 Montreal Neurological Institute (MNI) standard space. Fractional anisotropy (FA) images were warped using the same transforms from co-registration to achieve intra- and inter-subject alignment. A threshold of FA > 0.2 was applied to ensure that only WM was included in the analysis. F-tests in FSL-randomise were used to determine clusters showing significant group differences in FA. 3dFWHMx and 3dClustSim from AFNI[6] were used to identify the clusters that survived a cluster threshold of $p<0.01$ and $\alpha<0.05$. One-way ANOVA with LSD post-hoc was employed to assess significance among three treatment groups regarding mean FA values within clusters. Fugl-Meyer Assessment (FMA) was performed to measure the sensorimotor stroke recovery and to evaluate the impact of various treatments[7], subsequently, was associated with the mean FA conducted in SPSS[8].

Results: Higher FA was seen in both TA+PT and SA+PT group in R VIIb compared to the TA group. where higher FA in the TA group were seen in the L MCP compare to other groups. Cluster size, peak coordinates, and location of each region of interest (ROI) are shown in Table 1. The FMA increased for all three groups in the middle of treatment and after treatment compared to before treatment (Figure 1. C). There was a significant increase in FMA after treatment compared to before treatment for all the groups (Figure 1. D). The mean FA values within the ROIs were not significantly correlated with the FMA.

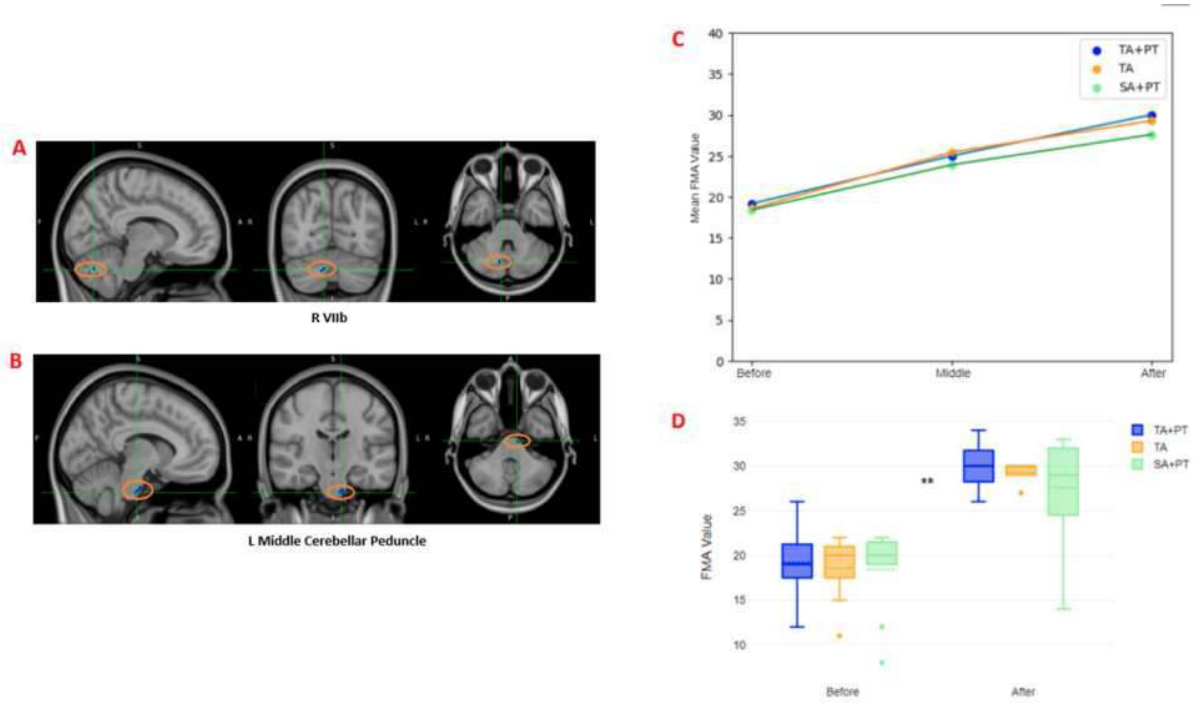

Figure 1: Each panel (A-B) shows clusters where significant group differences were seen in FA (in blue), including R VIIb, and L Middle Cerebellar Peduncle. Green crosshairs indicate the peak coordinates. C) Scatterplot shows the mean FMA before treatment, during 2nd week treatment and after treatment for the three groups. D) Boxplots show the FMA before and after treatment for the three groups. Significant improvement (P<0.01) in FMA score after treatment vs before treatment for all three treatment groups. L=left. R=right.**

Table 1: Size and peak coordinates (in MNI standard space) of two brain regions where the mean FA clusters survived thresholds of p<0.01 and α<0.05 and had a cluster size greater than 100 mm^3 for three different treatment groups: 1) TA+PT, 2) TA and 3) SA+PT. Correlation analysis of mean FA with FMA after treatment, is shown. [5]

Region Peak Coordinates (mm)	Cluster size (mm^3)	Group Mean FA (SD)			F	Correlation of Mean FA with FMA r (p)
		TA+PT	TA	SA+PT		
R VIIb						
10, -70, -34	143	0.31 (0.02)	0.27 (0.02)	0.32 (0.03)	10.24***	-0.11 (0.63)
L Middle Cerebellar Peduncle						
-8, -20, -39	112	0.47 (0.03)	0.61 (0.05)	0.49 (0.04)	22.064***	0.062 (0.78)

[5] Values are mean (SD); SD = standard deviation; R = right; *** P<0.001; FA = Fractional Anisotropy; FMA = Fugal-Meyer Assessment; TA = True Acupuncture; PT = physiotherapy; SA = Sham acupuncture. L=left. R = right

Conclusions: Higher FAs in R VIIb in both TA+PT and SA+PT groups might suggest that combined treatment have no added benefit on WM within the region compared to physiotherapy alone. Higher FA in the L MCP suggest acupuncture alone is beneficial for this brain region. Additionally, the mean FA and FMA was not significantly correlated and might suggest that motor performance could improve despite WM disruption or it might be as a result of the small sample size. Interestingly, patients with basal ganglia infarcts have delayed visual memory. The Right VIIb, a cerebellar lobule, is functionally connected with the visual dorsal attention network, important for working memory[9]. Furthermore, the MCP is associated with planning of motor movements[10]. Taken together, the acupuncture and physiotherapy might affect motor planning and visual memory in ischemic stroke patients, respectively, independent of WM integrity.

References

1. Haupenthal, D., Kuramatsu, J.B., Volbers, B., Sembill, J.A., Mrochen, A., Balk, S., Hoelter, P., Lücking, H., Engelhorn, T., Dörfler, A., et al.: Disability-adjusted life-years associated with intracerebral hemorrhage and secondary injury. JAMA Network Open 4(7), e2115859–e2115859 (2021)
2. Lynch, E.A., Labberton, A.S., Kim, J., Kilkenny, M.F., Andrew, N.E., Lannin, N.A., Grimley, R., Faux, S.G., Cadilhac, D.A.: Out of sight, out of mind: long-term outcomes for people discharged home, to inpatient rehabilitation and to residential aged care after stroke. Disability and rehabilitation 44(12), 2608–2614 (2022)
3. Chavez, L.M., Huang, S.S., MacDonald, I., Lin, J.G., Lee, Y.C., Chen, Y.H.: Mechanisms of acupuncture therapy in ischemic stroke rehabilitation: a literature review of basic studies. International journal of molecular sciences 18(11), 2270 (2017)
4. Soulard, J., Huber, C., Baillieul, S., Thuriot, A., Renard, F., Broche, B.A., Krainik, A., Vuillerme, N., Jaillard, A., et al.: Motor tract integrity predicts walking recovery: a diffusion mri study in subacute stroke. Neurology 94(6), e583–e593 (2020)
5. Beckmann, C.F., DeLuca, M., Devlin, J.T., Smith, S.M.: Investigations into resting-state connectivity using independent component analysis. Philosophical Transactions of the Royal Society B: Biological Sciences 360(1457), 1001–1013 (2005)
6. Cox, R.W.: Afni: software for analysis and visualization of functional magnetic resonance neuroimages. Computers and Biomedical research 29(3), 162–173 (1996)
7. Gladstone, D.J., Danells, C.J., Black, S.E.: The fugl-meyer assessment of motor recovery after stroke: a critical review of its measurement properties. Neurorehabilitation and neural repair 16(3), 232–240 (2002)
8. Masuadi, E., Mohamud, M., Almutairi, M., Alsunaidi, A., Alswayed, A.K., Aldhafeeri, O.F., Almutairi, M.B.: Trends in the usage of statistical software andtheir associated study designs in health sciences research: A bibliometric analysis. Cureus 13(1) (2021)
9. Brissenden, J.A., Somers, D.C.: Cortico–cerebellar networks for visual attention and working memory. Current opinion in psychology 29, 239–247 (2019).
10. Zhou, C., Fan, H., Chen, H., Wang, H., Li, Z., Xu, N., Sun, R., Zhu, Y., He, Y.: Evaluation of clinical features and stroke etiology in patients with bilateral middle cerebellar peduncle infarction. European Neurology 83(3), 271–278 (2020).

Poster No 1621

Localized Microstructural Alterations of the Dentatorubrothalamic Tract in Dystonia

Elizabeth Haddad[1], Xenos Mason[1], Iyad Ba Gari[1], Siddharth Narula[1], Neda Jahanshad[1]

[1]University of Southern California, Los Angeles, CA

Introduction: Dystonia is a movement disorder characterized by sustained or intermittent muscle contractions which presents as abnormal movements and/or postures. Dystonia may involve widespread physiological, structural, and functional changes in the cerebello-thalamic networks, beyond well-documented neurophysiologic alterations in the basal ganglia[1]. Nonspecific DTI measures, including FA, have been implicated in Dystonia[2], yet NODDI may better inform specific microstructural tissue changes[3]. Tractography methods have been developed to characterize along-tract changes; these could help guide the targeting of surgical interventions including deep brain stimulation (DBS). Here, we used the UK Biobank[4] to interrogate location-specific white-matter properties along the dentatorubrothalamic tract (DRTT), in individuals with dystonia compared to controls, using advanced dMRI methods.

Methods: 19 subjects with dystonia (63.8±7.5 years old; 14F) and 65 controls (64.3±7.3; 46F) matched on age, sex, medical comorbidities and scan site were included (Figure 1a). Raw dMRI were downloaded, corrected for noise, Gibbs ringing, EPI distortion, eddy currents, and bias field inhomogeneity. The following NODDI maps were generated: orientation dispersion (OD), extracellular (ECVF), intracellular (ICVF), and isotropic (ISOVF) volume fraction. ISOVF maps were thresholded with an upper limit of 0.5 to ensure CSF cancellation. Coregistration was performed between subject T1w MRI and dMRI, as well as between subject T1w MRI and the MNI152 template in order to propagate labels to diffusion space. We used a multi-shell multi-tissue constrained spherical deconvolution reconstruction for probabilistic tractography in MRTrix[5]. The DRTT was generated by reconstructing the cerebello-thalamic (CTT) and the thalamo-cortical (TCT) components separately. First, the dentate, fastigial, and interposed nuclei were combined and dilated and then used as a seed ROI to track to either the ipsilateral or contralateral thalamus. Second, seed termination points of both the ipsilateral and contralateral segments were combined and used as a probabilistic seed map to track motor cortex targets. The resulting TCT tract was parcelleted into either the premotor, primary, or supplementary motor cortices. See details in Figure 1b. NODDI metrics were sampled across all tracts. Robust means were calculated for all bilaterally averaged tracts. Along tract analysis was performed using Automated Fiber Quantification[6], where each individual tract component was divided into 10 segments. Linear regression models were run with dystonia, age, and sex as independent variables on all bilaterally averaged measures. The bilateral averages with the strongest associations then underwent along tract analysis on lateralized tracts to localize differences. Multiple comparisons correction was performed on (1) all bilateral averages across all measures and (2) all segments across all tracts which were significant in 1.

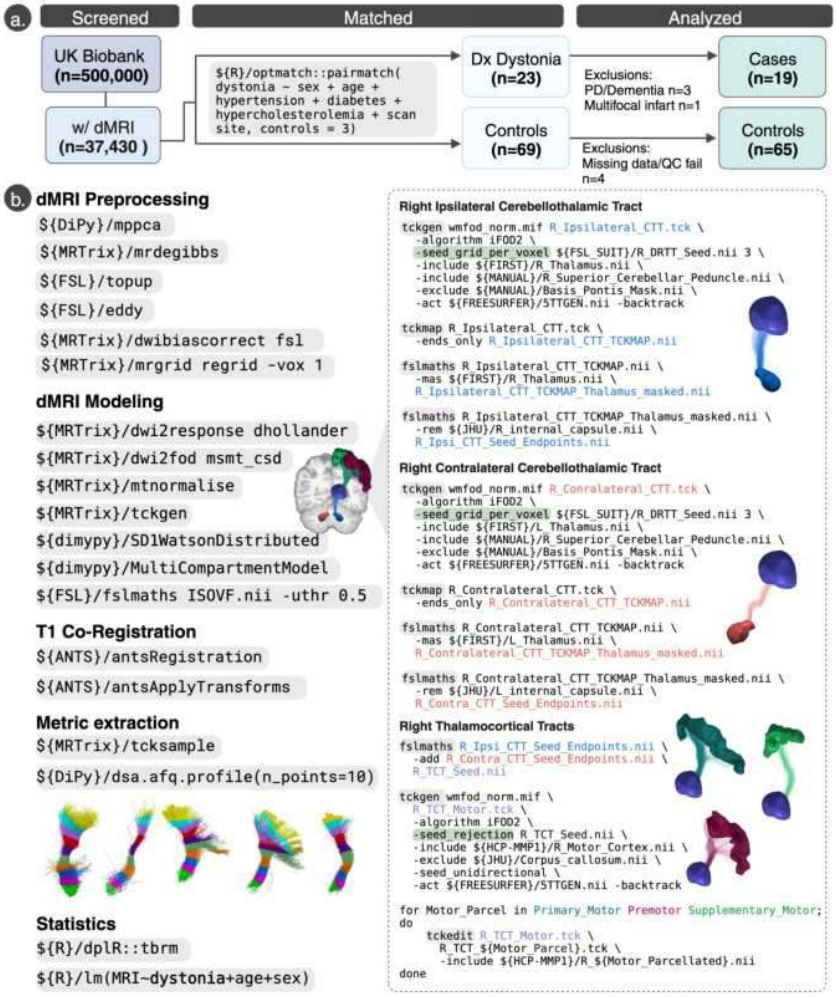

Figure 1. (**a**) Subjects with dMRI were screened for dystonia. A 3:1 ratio of controls were matched on age, sex, hypertension, diabetes, hypercholesterolemia, and scan site. Following neurological disease and QC fail exclusions, a total of 84 subjects were used for analysis. (**b**) Processing steps along with associated packages are listed. In brief, raw dMRI data was downloaded and corrected for noise, Gibbs ringing, EPI distortion, eddy currents, and bias field inhomogeneities. A multi-shell multi-tissue CSD reconstruction was performed for tractography generation. Co-registration between subject T1w and dMRI was performed, as well as between subject T1w and the MNI152 template in order to propagate anatomical labels to diffusion space. Specific tractography generation steps are provided in pseudocode for the right hemisphere. NODDI metrics were sampled for the whole tract and along tract metrics were extracted using Automated Fiber Quantification (AFQ), where each individual tract component was divided into 10 segments. We ensured that all tracts across subjects were oriented in the same way and that they all originated from their respective seed regions. Ipsilateral and contralateral CTT were trimmed such that the start of the tract was in the seed regions and only propagated to the next "include" ROI.

Results: For all bilateral tracts assessed, we find lower ISOVF to be significantly associated with dystonia. The strongest component was found in the ipsilateral CTT component (standardized β=-0.67; p=0.008; q=0.14) although none of these associations survived multiple testing correction (Figure 2a). Several segments along this tract and others were significantly associated with dystonia, although these did not survive multiple testing correction (Figure 2b).

a.

MRI Measure ~ Dystonia	Standardized β	95% CI[1]	p-value	q-value[2]
Ipsi Cerebello-thalamic ECVF	0.42	-0.09, 0.94	0.110	0.300
Contra Cerebello-thalamic ECVF	0.28	-0.25, 0.80	0.300	0.600
Thalamocortical (Premotor) ECVF	0.43	-0.08, 0.94	0.100	0.300
Thalamocortical (Primary motor) ECVF	0.40	-0.11, 0.91	0.120	0.300
Thalamocortical (Supplementary motor) ECVF	0.46	-0.05, 0.96	0.077	0.300
Ipsi Cerebello-thalamic ICVF	-0.05	-0.57, 0.46	0.800	>0.9
Contra Cerebello-thalamic ICVF	0.03	-0.45, 0.51	>0.9	>0.9
Thalamocortical (Premotor) ICVF	-0.02	-0.50, 0.46	>0.9	>0.9
Thalamocortical (Primary motor) ICVF	-0.06	-0.55, 0.42	0.800	>0.9
Thalamocortical (Supplementary motor) ICVF	0.01	-0.47, 0.48	>0.9	>0.9
Ipsi Cerebello-thalamic OD	0.01	-0.51, 0.53	>0.9	>0.9
Contra Cerebello-thalamic OD	-0.13	-0.65, 0.40	0.600	>0.9
Thalamocortical (Premotor) OD	0.00	-0.46, 0.46	>0.9	>0.9
Thalamocortical (Primary motor) OD	0.02	-0.45, 0.49	>0.9	>0.9
Thalamocortical (Supplementary motor) OD	0.09	-0.37, 0.56	0.700	>0.9
Ipsi Cerebello-thalamic ISOVF	-0.67	-1.2, -0.18	**0.008**	0.140
Contra Cerebello-thalamic ISOVF	-0.54	-1.1, -0.04	**0.036**	0.200
Thalamocortical (Premotor) ISOVF	-0.53	-1.0, -0.06	**0.027**	0.200
Thalamocortical (Primary motor) ISOVF	-0.50	-0.99, 0.00	**0.049**	0.200
Thalamocortical (Supplementary motor) ISOVF	-0.60	-1.1, -0.13	**0.014**	0.140

[1] CI = Confidence Interval

[2] Benjamini & Hochberg correction for multiple testing

b.

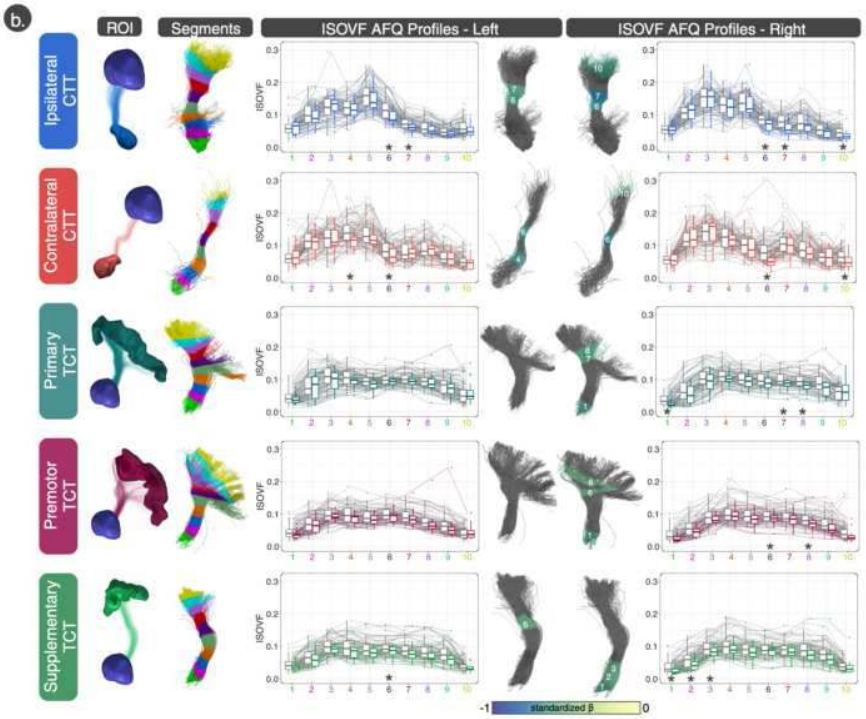

Figure 2. (**a**) Linear regression results of bilateral robust means of the whole tract across all 4 NODDI measures. ISOVF was significant across all tracts. The strongest component was found in the ipsilateral CTT component (standardized β=-0.67; p=0.008; q=0.14) (**b**) Lateralized AFQ profiles for all tract's ISOVF measures. The strongest local effect was in the right ipsilateral CTT in segment 7 (standardized β=-0.77; p=0.002; q=0.19)

Conclusions: We find trends of lower ISOVF along the DRTT in individuals with dystonia. These findings support the hypothesis that changes in cerebellar networks contribute to dystonia, a rare condition with otherwise limited characterization of white matter microstructure. Neuroimaging can be leveraged to inform underlying microstructural tissue properties contributing to disease pathogenesis and possibly to guide treatment. Larger studies are needed for better powered analyses to capture such effects.

References

1. Horn, A., Reich, M. M., Ewert, S., Li, N., Al-Fatly, B., Lange, F., Roothans, J., Oxenford, S., Horn, I., Paschen, S., Runge, J., Wodarg, F., Witt, K., Nickl, R. C., Wittstock, M., Schneider, G.-H., Mahlknecht, P., Poewe, W., Eisner, W., … Kühn, A. A. (2022). Optimal deep brain stimulation sites and networks for cervical vs. generalized dystonia. Proceedings of the National Academy of Sciences of the United States of America, 119(14), e2114985119.
2. Sondergaard, R. E., Rockel, C. P., Cortese, F., Jasaui, Y., Pringsheim, T. M., Sarna, J. R., Monchi, O., Sadikot, A. F., Pike, B. G., & Martino, D. (2021). Microstructural Abnormalities of the Dentatorubrothalamic Tract in Cervical Dystonia. Movement Disorders: Official Journal of the Movement Disorder Society, 36(9), 2192–2198.
3. Zhang, H., Schneider, T., Wheeler-Kingshott, C. A., & Alexander, D. C. (2012). NODDI: practical in vivo neurite orientation dispersion and density imaging of the human brain. NeuroImage, 61(4), 1000–1016.
4. Miller, K. L., Alfaro-Almagro, F., Bangerter, N. K., Thomas, D. L., Yacoub, E., Xu, J., Bartsch, A. J., Jbabdi, S., Sotiropoulos, S. N., Andersson, J. L. R., Griffanti, L., Douaud, G., Okell, T. W., Weale, P., Dragonu, I., Garratt, S., Hudson, S., Collins, R., Jenkinson, M., … Smith, S. M. (2016). Multimodal population brain imaging in the UK Biobank prospective epidemiological study. Nature Neuroscience, 19(11), 1523–1536.

5. Jeurissen, B., Tournier, J.-D., Dhollander, T., Connelly, A., & Sijbers, J. (2014). Multi-tissue constrained spherical deconvolution for improved analysis of multi-shell diffusion MRI data. NeuroImage, 103, 411–426.
6. Yeatman, J. D., Dougherty, R. F., Myall, N. J., Wandell, B. A., & Feldman, H. M. (2012). Tract profiles of white matter properties: automating fiber-tract quantification. PloS One, 7(11), e49790.

Acknowledgements
Funding: R01AG059874, U01AG068057, P41EB05922. UK Biobank Resource under Application Number '11559'.

Poster No 1622

Healthy Brain Aging is Associated with Decreased White Matter Tract Integrity

Kauê Duarte[1], Abhijot Sidhu[1], Cheryl McCreary[2], Marina Saluzzi[2], Louis Lauzon[2], Richard Frayne[2]

[1]University of Calgary, Calgary, AL, [2]University of Calgary, Calgary, Alberta

Introduction: The functional gray matter regions of the brain are interconnected by white matter (WM) fiber tracts that across between various regions of the central nervous system. These fibers enable communication between regions that is vital for sensory and associative functions. Diffusion imaging studies suggest that the integrity of WM tracts follows an inverted "U-shaped" trajectory across adulthood, where WM maturation peaks occur in middle age, plateaus, and then decreases in late adulthood[1,2]. This study examines the aging trajectories of 31 major WM tracts. We hypothesize WM tract integrity fractional anisotropy (FA) follows an inverse "U-shape" increases until middle age, plateaus, and subsequently declines in older adulthood (i.e., "inverted U-shaped" trajectory). Conversely, mean diffusivity (MD), axial diffusivity (AD), and radial diffusivity (RD) are hypothesized to follow a "U-shaped" trajectory.

Methods: Cross-sectional DWI data of 263 presumed healthy individuals (48.7±18.4y, 55% female) from the Calgary Normative Study were acquired on a 3-T MR system with b-value = 1000 s/mm2 with 30 non-colinear diffusion directions[3]. Diffusion data were processed using MRtrix3 with standard BATMAN and included denoising, Gibbs artifact removal, brain extraction, eddy current and motion correction, and diffusion tensor estimation. Rigid transformation (six degrees of freedom) was applied to transform the images to MNI152 space. Tractseg[4] was used to generate WM tract masks which were visually inspected. Preprocessed diffusion, FA masks, and WM tracts were visually inspected. Mean FA, MD, RD, and AD were computed for these tracts. Corresponding left and right WM tract masks were merged into a single mask file, the fornix was excluded due to poor segmentation results, and the corpus callosum was analyzed as one tract rather than as multiple subsegments. Linear models were fit to investigate the FA, MD, RD, and AD as response variables and age, age2, sex, and age×sex interaction for each tract. Results were adjusted for multiple comparisons using Holm-Bonferroni correction.

Results: Age2 exhibited a significant effect on average FA, MD, and RD for all 31 examined tracts, as shown in Figure 1 and summarised in Table 1. Age2 also exhibited a significant effect on average AD for 28 tracts with age2 effects not surviving multiple comparisons correction for MCP, ICP and SCP. FA displayed an "inverted U-shaped" trajectory, where FA increases from young adulthood and peaks, on average, around 45.2±3.1 y, plateaus, and then declines in older adulthood across all 31 tracts. MD and RD displayed a "U-shaped" trajectory, where MD and RD both increase from young adulthood, reach a minimum, on average, at 34.7±5.3 y and 36.2±5.1 y, respectively, and then increases into older adulthood across all 31 tracts. Except in 3 tracts, AD displayed a "U-Shaped" trajectory, where AD increases from young adulthood, reaches a minimum, on average, at 30.2±6.1 y, plateaus, and then increases into older adulthood across all tracts. No significant sex or age×sex interactions effects were found.

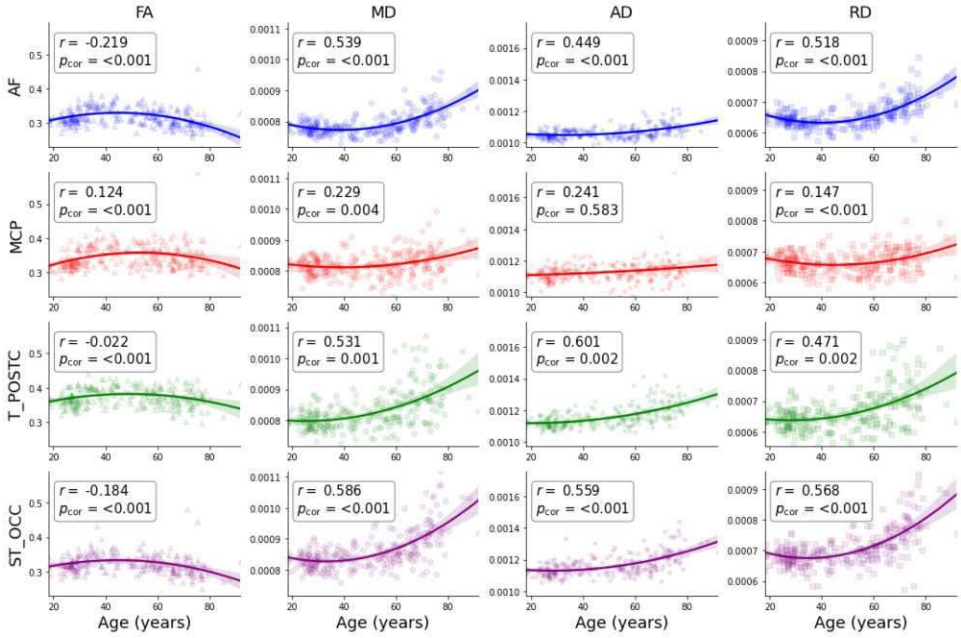

Tract Name (Abbreviation)	Beta (p value)				Inflection Age, years			
	FA	MD	RD	AD	FA	MD	RD	AD
Anterior thalamic radiation (ATR)	-3.45 x 10e-5*	7.89 x 10e-8*	8.45 x 10e-8*	6.77 x 10e-8*	42.0	34.5	32.3	35.3
Arcuate fascicle (AF)	-3.24 x 10e-5*	4.60 x 10e-8*	5.54 x 10e-8*	2.71 x 10e-8*	45.0	38.3	32.3	39.8
Cingulum left (CG)	-3.75 x 10e-5*	4.70 x 10e-8*	5.83 x 10e-8*	2.44 x 10e-8(0.001)	44.2	39.8	36.0	40.5
Commissure anterior (CA)	-2.95 x 10e-5*	6.41 x 10e-8*	7.10 x 10e-8*	5.03 x 10e-8*	44.9	37.9	35.0	38.6
Corpus callosum (CC)	-2.92 x 10e-5*	5.61 x 10e-8*	6.04 x 10e-8*	4.73 x 10e-8*	43.5	28.6	24.1	30.8
Corticospinal tract (CST)	-1.74 x 10e-5(0.001)	5.39 x 10e-8*	4.73 x 10e-8*	6.70 x 10e-8*	50.9	40.5	40.5	41.2
Fronto-pontine tract (FPT)	-2.23 x 10e-5*	6.73 x 10e-8*	6.34 x 10e-8*	7.51 x 10e-8*	42.7	39.0	39.8	39.0
Inferior cerebellar peduncle (ICP)	-3.21 x 10e-5*	2.76 x 10e-8*	3.69 x 10e-8*	8.86 x 10e-9(0.303)	51.7	47.2	33.8	NA
Inferior longitudinal fascicle (ILF)	-3.23 x 10e-5*	4.64 x 10e-8*	5.53 x 10e-8*	2.86 x 10e-8(0.006)	45.0	36.0	27.8	38.3
Inferior occipito-frontal fascicle (IFO)	-2.44 x 10e-5*	5.82 x 10e-8*	6.31 x 10e-8*	4.85 x 10e-8*	44.2	32.3	27.8	33.8
Middle cerebellar peduncle (MCP)	-3.05 x 10e-5*	2.28 x 10e-8(0.004)	3.05 x 10e-8*	7.36 x 10e-9(0.583)	53.1	39.0	18.2	NA
Middle longitudinal fascicle (MLF)	-3.25 x 10e-5*	5.02 x 10e-8*	5.92 x 10e-8*	3.22 x 10e-8(0.014)	45.0	30.8	19.7	33.8
Optic radiation (OR)	-2.23 x 10e-5*	6.84 x 10e-8*	7.00 x 10e-8*	6.51 x 10e-8*	44.2	33.1	30.8	34.5
Parieto-occipital pontine (POPT)	-2.44 x 10e-5*	4.95 x 10e-8(0.001)	5.07 x 10e-8(0.001)	4.72 x 10e-8(0.003)	43.5	25.6	22.6	27.1
Striato-fronto-orbital (ST_FO)	-2.46 x 10e-5*	5.78 x 10e-8*	6.03 x 10e-8*	5.26 x 10e-8*	40.5	36.0	36.0	36.0
Striato-occipital (ST_OCC)	-2.72 x 10e-5*	5.87 x 10e-8*	6.50 x 10e-8*	4.60 x 10e-8*	45.0	33.1	27.8	35.3
Striato-parietal (ST_PAR)	-2.78 x 10e-5*	5.63 x 10e-8*	6.03 x 10e-8*	4.84 x 10e-8(0.002)	44.2	25.6	19.7	27.8
Striato-postcentral (ST_POSTC)	-2.59 x 10e-5*	4.29 x 10e-8*	4.48 x 10e-8*	3.89 x 10e-8(0.001)	46.4	28.6	23.4	30.1
Striato-precentral (ST_PREC)	-2.83 x 10e-5*	5.84 x 10e-8*	5.98 x 10e-8*	5.57 x 10e-8*	45.7	35.3	33.8	36.0
Striato-prefrontal (ST_PREF)	-3.18 x 10e-5*	6.57 x 10e-8*	7.03 x 10e-8*	5.64 x 10e-8*	42.7	34.5	32.3	35.3
Striato-premotor (ST_PREM)	-4.15 x 10e-5*	8.48 x 10e-8*	9.04 x 10e-8*	7.36 x 10e-8*	44.2	38.6	36.4	39.3
Superior thalamic radiation (STR)	-2.23 x 10e-5*	6.77 x 10e-8*	6.26 x 10e-8*	7.79 x 10e-8*	44.2	39.0	39.8	39.0
Superior cerebellar peduncle (SCP)	-2.41 x 10e-5*	3.81 x 10e-8(0.002)	4.09 x 10e-8*	3.25 x 10e-8(0.084)	53.1	39.8	30.8	NA
Superior longitudinal fascicle (SLF_I)	-3.44 x 10e-5*	4.50 x 10e-8*	5.33 x 10e-8*	2.86 x 10e-8(0.029)	43.5	31.6	24.9	33.8
Thalamo-occipital (T_OCC)	-2.20 x 10e-5*	6.52 x 10e-8*	6.78 x 10e-8*	6.01 x 10e-8*	45.0	32.3	29.3	33.8
Thalamo-parietal (T_PAR)	-2.56 x 10e-5*	6.09 x 10e-8*	6.28 x 10e-8*	5.70 x 10e-8(0.001)	43.5	24.1	20.4	26.4
Thalamo-postcentral (T_POSTC)	-2.35 x 10e-5*	3.80 x 10e-8(0.001)	3.90 x 10e-8(0.002)	3.61 x 10e-8(0.002)	48.7	24.9	18.9	27.8
Thalamo-precentral (T_PREC)	-2.62 x 10e-5*	6.07 x 10e-8*	6.03 x 10e-8*	6.16 x 10e-8*	45.7	36.8	35.3	37.5
Thalamo-prefrontal (T_PREF)	-3.32 x 10e-5*	7.50 x 10e-8*	7.93 x 10e-8*	6.64 x 10e-8*	42.0	35.3	33.8	36.0
Thalamo-premotor (T_PREM)	-3.61 x 10e-5*	8.37 x 10e-8*	8.67 x 10e-8*	7.76 x 10e-8*	44.2	38.6	37.1	39.3
Uncinate fascicle (UF)	-2.64 x 10e-5*	4.71 x 10e-8*	5.26 x 10e-8*	3.62 x 10e-8*	43.5	39.3	36.4	40.0

Conclusions: This work investigated in a large group aging effects on four diffusion tensor measures (FA, MD, AD, RD) for 31 WM tracts across the healthy adult lifespan. FA exhibited an “inverted U-shaped” trajectory across adulthood, whereas MD, and RD displayed a “U-shaped trajectory” for all 31 tracts. Similarly, AD also displayed a “U-shaped” trajectory, however, this effect was observed in 28 of 31 tracts after multiple comparisons correction. These trajectories possibly indicate underlying age-associated changes in WM integrity. The homogeneity of our results suggests that age-associated differences in WM integrity reflect more global or whole-brain mechanism rather than region-specific changes. The absence of significant sex differences or age by sex interaction effects also suggests that the observed patterns are consistent across both sexes.

References

1. Liu H, Yang Y, Xia Y, Zhu W, Leak RK, Wei Z, Wang J, Hu X. (2017) Aging of cerebral white matter. Ageing Res Rev. Mar;34:64-76. doi: 10.1016/j.arr.2016.11.006.
2. Westlye L, Walhovd K, Dale A, et al (2010) Life-Span Changes of the Human Brain White Matter: Diffusion Tensor Imaging (DTI) and Volumetry, Cerebral Cortexm Volume 20, Issue 9, Pages 2055–2068, https://doi.org/10.1093/cercor/bhp280.
3. McCreary, C. (2020), Calgary normative study: Design of a prospective longitudinal study to characterise potential quantitative MR biomarkers of neurodegeneration over the adult lifespan, BMJ Open, vol. 10, no. 8.
4. J Wasserthal, P Neher, K Maier-Hein (2018) TractSeg - Fast and accurate white matter tract segmentation, NeuroImage, Volume 183, Pages 239-253,https://doi.org/10.1016/j.neuroimage.2018.07.070.

Poster No 1623

Identifying epileptogenic abnormality by decomposing intracranial EEG and MEG power spectra

Csaba Kozma[1], Gabrielle Schroeder[1], Thomas Owen[1], John Duncan[2], Yujiang Wang[1], Peter Taylor[1]

[1]Newcastle University, Newcastle, United Kingdom, [2]UCL Queen Square Institute of Neurology, London, United Kingdom

Introduction: Improved EEG biomarkers of the epileptogenic zone are important, as around half of individuals have recurrent seizures after surgical treatment. Substantial research has focused on interictal EEG biomarkers using normative maps of power in different frequencies. This approach involves outlining the spatial characteristics and ranges of the feature of interest in a healthy context and comparing patient data to identify abnormalities. Recent studies proposed using patient iEEG data from regions outside the epileptogenic zone to create normative maps. The band power of different frequency bands can be used to infer expected healthy spatial profiles of EEG activity. This approach showed promising results to identify abnormalities and classify patient outcomes across different modalities. It is unclear what spectral features drive the observed band power abnormalities. One way to explore these features is to decompose the power spectra into rhythmic (periodic) and non-rhythmic (aperiodic) components. The aperiodic component can be described by its offset and exponent, while periodic components form peaks in the power spectra. Both components should be considered, as power changes observed in specific frequency bands can be attributed to either changes in the peak or the offset. Despite the growing interest in decomposing power spectra, previous studies have not investigated which power spectrum components contribute to abnormal interictal brain activity. Here we investigate if interictal abnormality is driven by periodic components, aperiodic components, or a combination of both components.

Methods: Using iEEG data from 234 subjects, we constructed a normative map and compared this with a separate cohort of 63 patients with refractory focal epilepsy being considered for neurosurgery. The normative map was computed using three approaches: (i) relative complete band power, (ii) relative band power with the aperiodic component removed (iii) the aperiodic exponent. Corresponding abnormalities were also calculated for each approach in the separate patient cohort. We investigated the spatial profiles of the three approaches, assessed their localising ability, and replicated our findings in a separate modality using MEG (HC=70, patients=33).

Results: The normative maps of relative complete band power and relative periodic band power had similar spatial profiles. In the aperiodic normative map, exponent values were highest in the temporal lobe. Abnormality estimated through the complete band power robustly distinguished between good and bad outcome patients (AUC=0.71, p$<$0.01; MEG AUC=0.69, p=0.03). Neither periodic band power nor aperiodic exponent abnormalities distinguished seizure outcome groups. Combining periodic and aperiodic abnormalities improved performance, similar to the complete band power approach (iEEG AUC=0.64, p=0.05; MEG AUC=0.69, p=0.039).

Conclusions: Our findings suggest that sparing cerebral tissue that generates abnormalities in either periodic or aperiodic activity may lead to a poor surgical outcome. Both periodic and aperiodic abnormalities are necessary to distinguish patient outcomes, with neither sufficient in isolation. Future studies could investigate whether periodic or aperiodic abnormalities are affected by the cerebral location or pathology.

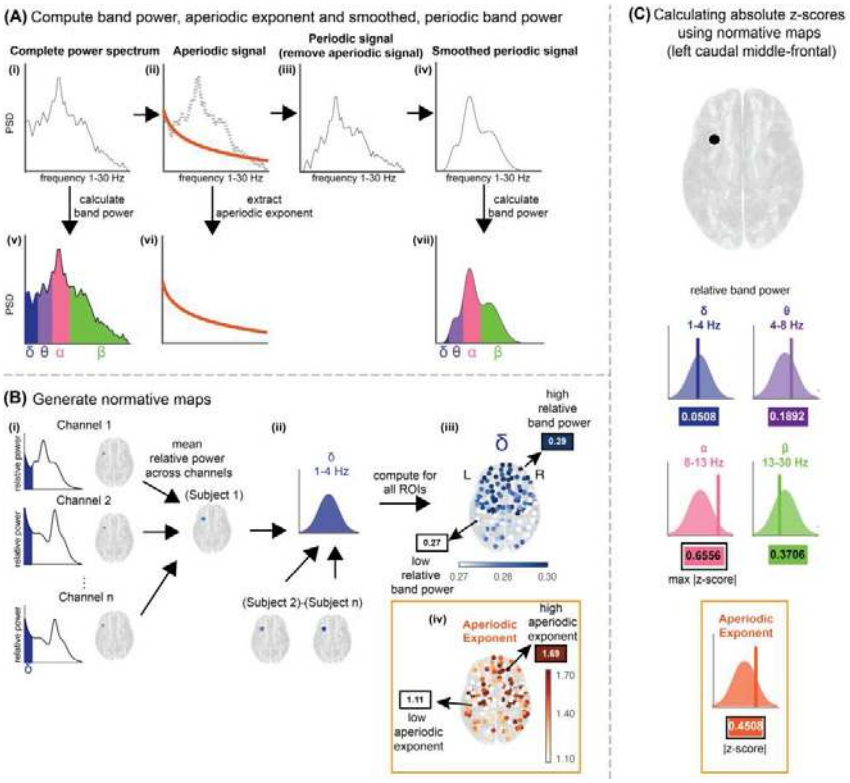

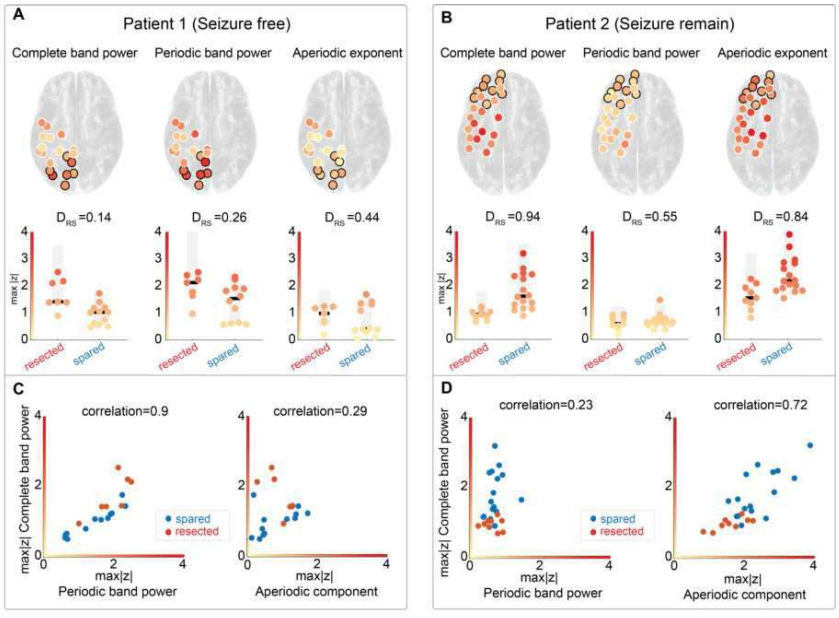

References

1. Bernabei et al. (2022).: Normative intracranial eeg maps epileptogenic tissues in focal epilepsy. Brain. 145:1949–1961. doi: 10.1093/368brain/awab480.
2. Taylor et al. (2022).: Normative brain mapping of interictal intracranial eeg to localize epileptogenic tissue. Brain. 145:939–949. doi: 10.1093/brain/awab380.501.
3. Owen et al. (2023).: Meg abnromalities and mechanisms of surgical failure in neocortical epilepsy. Epilepsia. 64:692–704. doi: 10.1111/epi.17503.
4. Donoghue T. (2020). Parameterizing neural power spectra into periodic and aperiodic components. Nature Neuroscience, 23:1655–1665. doi: 10.1038/s41593-020-00744-x.

Poster No 1624

Signal propagation tracking unveils Distinct Properties of Resting-State Network Dynamics

Davide Momi[1], Zheng Wang[1], Sara Parmigiani[2], Ezequiel Mikulan[3], Sorenza Bastiaens[1], Mohammad Oveisi[1], Kevin Kadak[1], Allison Waters[4], Sean Hill[1], Andrea Pigorini[3], Corey Keller[2], John Griffiths[1]

[1]Centre for Addiction and Mental Health, Toronto, Ontario, [2]Stanford University, Palo Alto, CA, [3]Università degli Studi di Milano, Milan, N/A, [4]Icahn School of Medicine at Mount Sinai, New York, NY

Introduction: The human brain comprises distinct resting-state networks (RSNs) characterized by spontaneous activity patterns[1]. Prior research has revealed a hierarchical organization of these networks, ranging from high-order multimodal networks to low-order networks[2,3]. A critical inquiry for both fundamental and clinical studies on brain dynamics is whether this topographical organization influences how different brain regions engage in information processing based on their network affiliation. Furthermore, if such differences exist, do they manifest in distinct propagation patterns, governed by local versus global processes?

Methods: To address these questions, we employed a dataset where simultaneous sEEG and hd-EEG was recorded following intracortical single pulse electrical stimulation on 36 patients (Figure 1A). We identified the Schaefer's parcel[4] that overlapped with the intracranial electrode responsible for delivering the stimulus, ultimately enabling us to determine the stimulated network (Figure 1B). After exploring empirical results, we used a computation connectome-based whole-brain model we developed recently[5] to present new insights into the role of recurrent feedback activity in stimulation-evoked brain responses (Figure 1C). We employed a virtual lesion approach[6] to isolate and prevent the stimulated network from receiving feedback input from the rest of the other non-stimulated RSNs (Figure D). This procedure allows us to evaluate the extent to which model-generated stimulation-evoked patterns relied on recurrent incoming connections from downstream brain areas that belong to the not stimulated networks. We hypothesized that for the condition where the stimulation was delivered to low-order networks the late responses will be relatively unchanged indicating that the activity observed in the empirical data highly depends on the intrinsic network dynamics. Conversely, for high-order networks we expect a progressive suppression of the late responses meaning that their propagation dynamics in the empirical data reflects an overall integrated pattern where feedback connections are necessary.

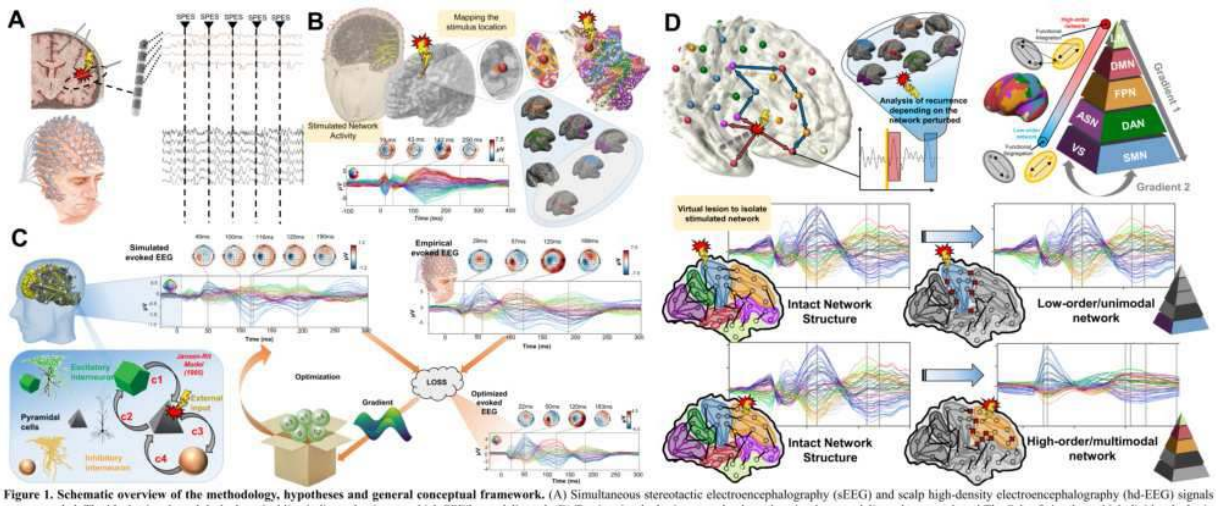

Figure 1. Schematic overview of the methodology, hypotheses and general conceptual framework. (A) Simultaneous stereotactic electroencephalography (sEEG) and scalp high-density electroencephalography (hd-EEG) signals were recorded. The black triangle and dashed vertical line indicate the time at which SPES was delivered. (B) To pinpoint the brain network where the stimulus was delivered, we employed The Schaefer's atlas, which divides the brain into 1000 regions across seven distinct RSNs. We then mapped this atlas to the individual's FreeSurfer parcellation. Subsequently, we identified the parcellation region that overlapped with the intracranial electrode responsible for delivering the stimulus, ultimately enabling us to determine the stimulated network. (C) To model-individual stimulus-evoked timeseries, the Jansen-Rit model , a neural mass model comprising pyramidal, excitatory interneuron, and inhibitory interneuron populations was embedded in every parcel of the 200-parcel Schaefer atlas for simulating and fitting neural activity time series. The connectivity between parcel was model using the diffusion-weighted MRI tractography computed from a sample of healthy young individuals from the Human Connectome Project Dataset and then averaged to give a grand-mean anatomical connectome. The quality of fit (loss) was quantified by calculating the cosine similarity between the simulated and empirical stimulus-evoked time series. Optimization of model parameters was accomplished by leveraging the autodiff-computed gradient between the objective function and the model parameters, employing the ADAM algorithm. Ultimately, the optimized model parameters were utilized to generate the fitted, simulated stimulus-evoked hd-EEG activity, and we present comparisons with the empirical data. (D) Single Pulse Electrical Stimulation applied to an intracortical target region generates an early response (evoked potential waveform component) at scalp hd-EEG channels sensitive to that region and its immediate neighbors (red arrows). This also appears in more distal connected regions after a short delay due to axonal conduction and polysynaptic transmission. Subsequently, second and sometimes third late evoked components are frequently observed (blue arrows). By identifying the stimulated network, we aim to untangle the extent to which this second component relies on intrinsic network activity versus recurrent whole-brain feedback activity. On the right side, a schematic of the spatial relationships of canonical resting-state networks as demonstrated in (2). This hierarchy spans from separate unimodal regions distinguished by functional segregation to high-order transmodal regions characterized by integrative processes. (E) Our aim was to investigate the nature of each evoked response and understand how they varied depending on the perturbed network. Specifically, we seek to distinguish the extent to which a response is influenced by the internal dynamics of the stimulated network versus its dependence on multimodal connections. In order to answer this question, precisely communication interruptions or 'virtual lesions' are introduced into an accurately fitting individual subject computational model of stimulus-evoked responses, and the resulting changes in the propagation pattern are evaluated. We anticipate that propagation dynamics will remain relatively stable when the stimulus is applied to a low-order unimodal network, suggesting that the measured empirical activity is predominantly internally generated. Conversely, for high-order multimodal networks, we hypothesize a suppression of late responses, indicative of their significant reliance on functional integration processes.

Results: Both the sEEG and the hd-EEG Global Mean Field Power (GMFP) shows a significantly stronger propagation pattern when the stimulus targeted high-order multimodal networks particularly for the late evoked responses (Figure 2A). This findings mirror the identical hierarchy previously reported in the literature through the analysis of functional and anatomical MRI data[2,3,7]. Our connectome-based neurophysiological model of stimulus-evoked responses achieves robust and accurate recovery (Figure 2B bottom). The analysis using a virtual lesion approach reveals that the late responses are highly dependent

on whole-brain integrity for high-order networks and mainly restricted to intrinsic network properties when the stimulus is delivered to low-order networks. The GMFP for model-generated hd-EEG data run with the lesioned structural connectome reveals a change in the propagation dynamics compared to both empirical and standard simulated data, where this time larger evoked responses were recorded for the unimodal (Figure 2C). A significant response reduction was found for late responses of Frontoparietal and Default Mode networks compared to Somatomotor network (Figure 2D). This indicates that in the case of the unimodal network, the lesion does not significantly impact the evoked potentials (Figure 2E top/right) while for the high-order network a substantial reduction or disappearance of evoked components was observed (Figure 2E bottom/right).

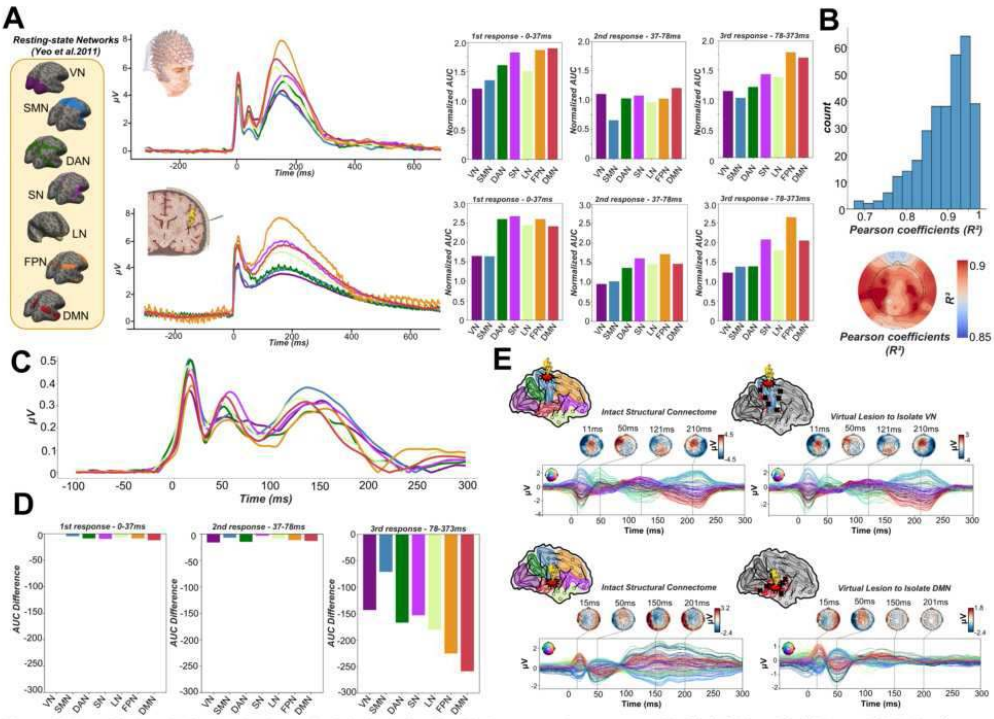

Figure 2. Empirical and simulated electrophysiological signals global propagation pattern. (A) Global Mean Field Power (GMFP) of every stimulated network for hd-EEG (top row) and sEEG (bottom row). Our analysis, focusing on the Area under the curve (AUC) of the three clusters, revealed a significantly stronger propagation pattern when the stimulus targeted high-order multimodal networks, such as the Default and Frontoparietal networks, particularly for the late evoked responses (third clusters). Notably, our findings mirror the identical hierarchy previously reported in the literature through the analysis of functional and anatomical MRI data (2). This hierarchy encompasses a spectrum from discrete unimodal regions characterized by functional segregation to high-order transmodal regions marked by integrative processes (3). (B) Histogram and Topomaps plots showing the Pearson correlation coefficients between simulated and empirical time series for each subject and session. (C) GMFP for every stimulated network for model-generated hd-EEG data run with the lesioned structural connectome. Compared to both empirical and standard simulated data, a change in the propagation dynamics was reported where larger evoked responses were recorded for the unimodal SMN instead of multimodal FPN. (D) AUC differences comparing the simulation run with the intact vs the lesioned structural connectome. A significant reduction in the AUC was found for late responses of LBN, FPN and DMN compared to SMN. (E) Demonstration of the network recurrence-based theory for two representative sessions. Simulation of evoked dynamics runs using the intact (left) and lesioned (right) anatomical connectome. In the latter case, the connections were removed to isolate the stimulated networks for SMN (top) and DMN (bottom). In the case of the unimodal network, this lesion does not significantly impact the evoked potentials, while for the high-order network, a substantial reduction or disappearance of evoked components was observed. These findings indicate that, for high-order networks, the propagation dynamics depend on multimodal whole-brain integration while for low-order networks they are mainly driven by intrinsic network reverberation.

Conclusions: Overall, these novel discoveries pinpoint the presence of an RSN hierarchy based on information processing within the human brain, shedding light on the distinct propagation patterns shaped by either local or global dynamics. These findings have implications for understanding brain function in health and pathology, with potential applications in personalized interventions and therapeutic strategies.

References

1. M. E. Raichle, A. Z. Snyder, A default mode of brain function: a brief history of an evolving idea. NeuroImage 37, 1083–1090; discussion 1097-1099 (2007).
2. D. S. Margulies, S. S. Ghosh, A. Goulas, M. Falkiewicz, J. M. Huntenburg, G. Langs, G. Bezgin, S. B. Eickhoff, F. X. Castellanos, M. Petrides, E. Jefferies, J. Smallwood, Situating the default-mode network along a principal gradient of macroscale cortical organization. Proc. Natl. Acad. Sci. 113, 12574–12579 (2016).
3. C. Seguin, A. Razi, A. Zalesky, Inferring neural signalling directionality from undirected structural connectomes. Nat. Commun. 10, 4289 (2019).
4. A. Schaefer, R. Kong, E. M. Gordon, T. O. Laumann, X.-N. Zuo, A. J. Holmes, S. B. Eickhoff, B. T. T. Yeo, Local-Global Parcellation of the Human Cerebral Cortex from Intrinsic Functional Connectivity MRI. Cereb. Cortex N. Y. N 1991 28, 3095–3114 (2018).
5. D. Momi, Z. Wang, J. D. Griffiths, TMS-evoked responses are driven by recurrent large-scale network dynamics. eLife 12, e83232 (2023).
6. H. Aerts, W. Fias, K. Caeyenberghs, D. Marinazzo, Brain networks under attack: robustness properties and the impact of lesions. Brain 139, 3063–3083 (2016).
7. M. J. Veit, A. Kucyi, W. Hu, C. Zhang, B. Zhao, Z. Guo, B. Yang, C. Sava-Segal, C. Perry, J. Zhang, K. Zhang, J. Parvizi, Temporal order of signal propagation within and across intrinsic brain networks. Proc. Natl. Acad. Sci. 118, e2105031118 (2021).

Poster No 1625

A Century of the Alpha Rhythms: A Unified Description of Alpha, Mu, and Tau at Last

Peter Robinson[1], Rawan El-Zghir[1], Natasha Gabay[1]

[1]*University of Sydney, Sydney, NSW*

Introduction: Berger first recorded human EEG on 6 July 1924, noting the ~10 Hz alpha rhythm to be the most prominent brain activity[1]. Alpha is concentrated over visual cortex, sometimes displays two frequency peaks, and is suppressed by visual inputs[2]; the beta rhythm occurs at its harmonic. Later, the ~10 Hz mu rhythm was discovered, concentrated over sensorimotor cortex, suppressed by motor activity, and sometimes associated with ~20 Hz activity[2]. The ~10 tau rhythm is concentrated over auditory cortex and is suppressed by sound. Early theories argued that separate groups of neurons fire at ~10 Hz at the relevant locations, but these were ad hoc and lacked explanatory power[3]. More recently, the alpha rhythm was argued to be a natural mode of activity in the cortex[3] or of the corticothalamic (CT) system[4,5], and has been analyzed using neural field theory (NFT), whose predictions for the basic 10 Hz alpha frequency and its relationship to beta have been confirmed experimentally[8]. So far, however, no unified theory of the alpha, mu, and tau rhythms has been proposed that would account for their frequency structure, scalp topography, and reactivity to stimuli. The present work advances such a unified description, shows that it is consistent with experimental data, and makes predictions for future experimental test and analysis.

Methods: NFT averages over the activity of large numbers of neurons to predict mean quantities such as firing rates and their effects on EEG. The NFT equations predict the existence of natural modes of activity, each associated with a characteristic spatial pattern on the cortex and resonant frequencies; these are analogous to the notes of a violin string and their associated spatial patterns. The first few NFT modes dominate activity and its spatial and frequency structure, so we employ them to explain the main characteristics of the alpha, mu, and tau rhythms in a unified way. The results are compared with data published over the last 100 years on frequency structure, topography, and reactivity of the rhythms, while additional predictions are made for cases in which observations are not yet available.

Results: We show that: (i) The first 4 CT activity eigenmodes suffice to explain the key features of alpha, mu, and tau rhythms, including their frequency structure and topography. CT loop delays account for the basic 10 Hz frequency of alpha-band rhythms, for observed alpha-beta correlations, and for observations of harmonic activity associated with the mu rhythm. Additionally, we predict the existence of activity at the harmonic of the tau rhythm. (ii) Frequency splitting arises from the differential effects of cortical folding on various CT modes, consistent with prior observations of split-alpha and split-beta rhythms. We also predict the existence of splitting in the mu and tau rhythms and their harmonics. (iii) Strong suppression, or blocking, of each rhythm and its harmonic occurs when CT loop gains decrease by as little as 10%. This is consistent with positive correlations between alpha and beta peak power. (iv) Spatial peaks of rhythms are due to constructive interference of modes in the relevant sensory region, supported by enhanced CT gains and are suppressed when gains are reduced by attention, consistent with prior work[6].

Conclusions: The theory provides the first unified description of the alpha, mu, and tau rhythms and accounts for their main spectral, spatial, and reactivity properties. Several predictions remain to be confirmed experimentally and fits of theory to data will enable brain states to be probed in real time, as is the case for the basic alpha rhythm[7]. NFT links these results to work on attention[6] and other phenomena such as evoked responses, opening the way to much richer analyses than have previously been possible.

References

1. Berger, H, (1929) Ueber das elektroenkephalogramm des menschen, Archiv f. Psychiatrie, vol. 9, pp. 527-570.
2. Niedermeyer, E and Lopes da Silva F. H (1999). Electroencephalography (Philadelphia: Lippincott).
3. Nunez P. L and Srinivasan R (2006). Electric Fields of the Brain (New York: Oxford Univ. Press).
4. Robinson, P. A, Rennie, C. J, and Rowe, D. L (2002). Dynamics of large-scale brain activity in normal arousal states and epileptic seizures. Phys. Rev. E. Vol. 65, Art. 041924.
5. El Zghir, R. K, Gabay, N. C, and Robinson, P. A (2023). NFT of Alpha-Band Rhythms via Eigenmodes of Brain Activity, submitted.
6. Babaie-Janvier, T and Robinson, P. A (2020). NFT of evoked response potentials with attentional gain dynamics. Front. Human Neurosci. Vol. 14, Art. 293.
7. Abeysuriya, R. G, Rennie, C. J, and Robinson, P. A (2015). Physiologically based arousal state estimation and dynamics. J. Neurosci. Meth. Vol. 253, pp. 55-69.
8. van Albada, S. J. and Robinson, P. A. (2013). Relationships between EEG spectral peaks across frequency bands, Front. Hum. Neurosci., 7, Art. 56.

Poster No 1626

Extracting EEG Features of Dyadic Cooperation Skill Using an Explainable Deep Learning Approach

Kazumasa Uehara[1,2,3], Kenta Matsuoka[2], Keiichi Kitajo[2,4]

[1]Toyohashi University of Technology, Toyohashi, Aichi, [2]National Institute for Physiological Sciences, Okazaki, Japan, [3]JST PRESTO, Tokyo, Japan, [4]The Graduate Institute for Advanced Studies, SOKENDAI, Okazaki, Japan

Introduction: Cognitive and motor actions cooperated between individuals play crucial roles in not only social interactions, but also team sports and musical performance. In the past decade, the development of hyper-scanning brain activity has allowed us to explore neural mechanisms involving dyadic cooperation (Kawasaki et al. 2018; Abe et al. 2019). While our understanding of some neural mechanisms has advanced, there is a possibility that a strong hypothesis-driven approach and excessive data preprocessing that has been taken for granted may overlook hidden neural mechanisms. To overcome these potential limitations, we adopted a data-driven approach based on deep learning to identify the success and failure of cooperative actions from hyper-scanning EEG data. Subsequently, we used a technique for producing visual explanations to extract spatial and temporal features of EEG that have the highest impact on classification decisions. Furthermore, another open question is whether the data-driven approach can detect individual neural features. To explore this, the present study recruited musicians and non-musicians. This is because musicians exhibit a higher level of behavioral synchronization with others when playing their instruments compared to non-musicians. We aimed at identifying the potential of a data-driven deep learning approach in musicians and non-musicians who may differ in the dyadic cooperation skills. In addition, we addressed how the visualization of the classification decision can contribute to elucidating functional relationships between previously unseen neural features and behavioral performance.

Methods: A total of twenty-three dyads were formed. Twenty-four of these individuals had daily musical experience. The remaining individuals had no intensive musical experience throughout their lives. During an experimental task, hyperscanning EEG was performed using two-32-channel EEG acquisition systems. Our experimental task was a dyadic visuo-motor cursor tracking task using a joystick controller per person. Each dyad was asked to repeat a total of 100 trials. For the behavioral data analysis, we computed the displacement value between the cursor and the target throughout the target trajectory for each trial. We then annotated the data with information regarding the success or failure of the cooperative actions for every trial. For the EEG data analysis, band-pass filtered EEG data (1-50Hz) were then fed into convolutional neural network (CNN) with the success or failure annotations. In this study, we were more interested in the individual brain activity that generates the cooperative actions rather than the person-to-person brain connectivity. We, therefore, used Intra-individual brain activity for CNN classifications. For the CNN analysis, using the EEGNet architecture (Lawhern et al. 2018), we addressed the binary-classification problem of assigning success and failure to the cooperative actions. To explore what kind of neural features have a strong impact on the model's classification decision, we adapted gradient-weighted class activation mapping (Grad-CAM) as a visualization approach (Selvaraju et al. 2017).

Results: The classification accuracy was 75.6% for the musician's group and 65.5% for the non-musician's group. Furthermore, the Grad-CAM approach for the visualization of the classification decision revealed that preparatory EEG signals in the frontal and occipital brain areas showed the highest impact on the classification decision in musicians, whereas EEG signals in the frontal and occipital brain areas immediately before and after the onset of cooperative actions contributed to the classification decision in non-musicians.

Conclusions: Our findings demonstrate the potential for a fusion of neurophysiology and artificial intelligence. This result may bring an entirely new dimension for validation and further development of cognitive and motor control theory and traditional neurophysiology studies.

References

1. Abe M, Koike T, Okazaki S, Takahashi K, Watanabe K, Sadato N (2019) Neural correlates of online cooperation during joint force production. Neuroimage. :150–161.
2. Kawasaki M, Kitajo K, Yamaguchi Y.(2018) Sensory-motor synchronization in the brain corresponds to behavioral synchronization between individuals. Neuropsychologia. 119:59–67.
3. Lawhern VJ, Solon AJ, Waytowich NR, Gordon SM, Hung CP, Lance BJ (2018) EEGNet: A compact convolutional neural network for EEG-based brain-computer interfaces. J Neural Eng. 15(5).
4. Selvaraju RR, Cogswell M, Das A, Vedantam R (2017) Visual explanations from deep networks via gradient-based localization. Proceedings of the 2017 IEEE.

Poster No 1627

Communication with Surprise – Computational and Neural Mechanisms of Non-verbal Human Interactions

Tatia Buidze[1], Jan Gläscher[1], Yuanwei Yao[1]

[1]*Institute for Systems Neuroscience, University Medical Center Hamburg-Eppendorf, Germany*

Introduction: Conventionally, violating expectations signals a need to refine predictions through learning[1]. Yet in communication, surprise can have a different role: guiding the Receiver's focus towards key information. In language-driven communication, attention is captured using standout verbal and prosodic cues[2]. But how do we effectively communicate without a common language in novel situations? Here, we propose that the intentional use of surprise can effectively communicate information by defying expectations.

Methods: We explore this in the Tacit Communication Game (TCG)[3], a non-verbal game where the Sender directs the Receiver to a goal on a grid board using "messages" (Fig.1a). The Receiver then deduces his goal based on these messages. We developed a surprise model (SM), for the Sender's message design. SM uses intuitive priors based on principles of movement kinetics(Fig.1h) and goal orientation (Fig.1i) and constructs messages step by step by maximizing surprise at the Receiver's goal state. We compared SM against a belief-based model (BBM)[4], which selects messages through exhaustive search and updates beliefs based on the Receiver's success, but lacks step-by-step predictions. Furthermore, aiming to substantiate the SM, we explored physiological and neural responses to surprise, employing model-based analysis of Pupillary Dilation Responses (PDR) and Electroencephalogram (EEG) data. For analysis of PDR data, we employed a mixed-effect model[5]. In the model, to predict PDR, we included model-derived surprise values as the fixed effects and random intercepts for each participant. For analysis of EEG data, We again used the step-by-step estimated surprise values as a predictor for EEG power in a model-informed EEG analysis. Specifically, for each Receiver, we performed a regression at each electrode and time points, and subsequently we analyzed the regression weights obtained.

Results: The results revealed that The SM accurately reproduces Sender's behavior, while also showed a better fit to the behavioral data compared to BBM (Fig.1e-g). Furthermore, in examining receivers' physiological reactions as they process messages, we found a direct correlation between PDRs and model-derived surprise values (Fig. 2a-b). This indicates that Senders, significantly impact the physiological states of Receivers by creating surprise. An analysis of the neural encoding of surprise via EEG data unveiled two prominent time-space clusters over frontal and frontal-central electrodes. Positioned above the Anterior Cingulate Cortex (ACC), the electrophysiological activity in the observed cluster (Fig.2c, yellow markers) likely reflects the neural processing within this region. This cluster, presumably reflecting ACC activity, can be associated with the Receiver detecting the prediction error, grounded in the anticipated intention of the Sender[6,7]. The second cluster is positioned over the anterior prefrontal cortex (Fig.2c, pink markers), can be linked to action programming[8]. As the senders formulates a message for optimal surprise, they delve into intricate action planning. After both parties align on a successful approach, the receiver possibly fine-tunes their understanding of the sender's planned intent. Temporal aspects of these clusters also hold significance. If, as postulated, the receiver's frontal cluster corresponds to a high-level representation of the sender's strategy, we would anticipate its emergence early in the epoch. This would likely be followed by activations associated with the ACC, which is predominantly implicated in error detection.

Conclusions: In summary, the SM showcases the effectiveness of utilizing surprise in communication without a shared language, a phenomenon explored through the TCG. Not only did the SM exhibit a notable alignment with human sender behaviors, but it also substantiates its influence through both physiological and neural markers, affirming the crucial role of surprise in novel communication.

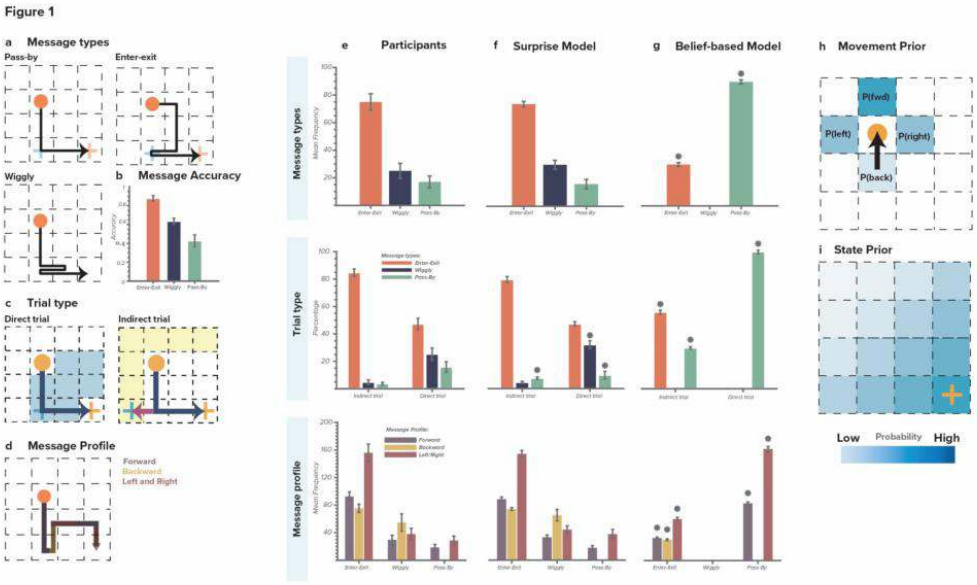

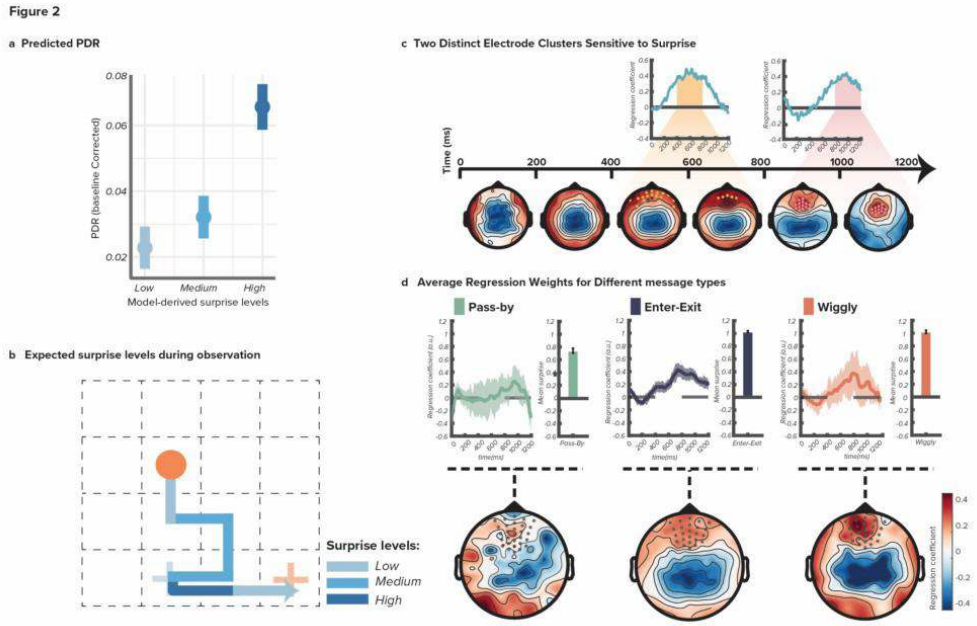

References

1. Sutton, R. S. & Barto, A. G. Reinforcement Learning, second edition: An Introduction. (MIT Press, 2018).
2. Dahan, D. Prosody and language comprehension. Wiley Interdiscip. Rev. Cogn. Sci. 6, 441–452 (2015).
3. Blokpoel, M. et al. Recipient design in human communication: simple heuristics or perspective taking? Front. Hum. Neurosci. 6, 253 (2012).
4. de Weerd, H., Verbrugge, R. & Verheij, B. Higher-order theory of mind in the Tacit Communication Game. Biologically Inspired Cognitive Architectures 11, 10–21 (2015).
5. Luke, S. G. Evaluating significance in linear mixed-effects models in R. Behav. Res. Methods 49, 1494–1502 (2017).
6. Kolling, N., Behrens, T., Wittmann, M. K. & Rushworth, M. Multiple signals in anterior cingulate cortex. Curr. Opin. Neurobiol. 37, 36–43 (2016).
7. Rushworth, M. F. S., Kolling, N., Sallet, J. & Mars, R. B. Valuation and decision-making in frontal cortex: one or many serial or parallel systems? Curr. Opin. Neurobiol. 22, 946–955 (2012).
8. Badre, D. & Desrochers, T. M. Hierarchical cognitive control and the frontal lobes. Handb. Clin. Neurol. 163, 165–177 (2019).

Poster No 1628

Novel Cyclic Homogeneous Oscillation Detection Method for Neural Oscillatory Mapping

Hohyun Cho[1,2], Markus Adamek[1,2], Jon Willie[1,2], Peter Brunner[1,2]

[1]Washington University School of Medicine in St. Louis, St. Louis, MO, [2]National Center for Adaptive Neurotechnologies, St. Louis, MO

Introduction: Temporal and spectral nuances of neural oscillations are pivotal for decoding complex rhythms underlying large-scale brain activity. Traditional methods, which discern these oscillations through frequency peaks above 1/f-sloped background activity, are often constrained to the frequency domain and fail to precisely determine the onset and offset of oscillations. They cannot distinguish the fundamental frequencies of non-sinusoidal oscillations from their harmonics.

Methods: Our novel cyclic homogeneous oscillation detection method (CHO) distinguishes oscillations as peaks above the 1/f-sloped noise across time and frequency domains. CHO requires neural oscillations to complete at least two full cycles to ensure their validity and rejects false positives commonly generated by non-sinusoidal waveforms and their harmonics.

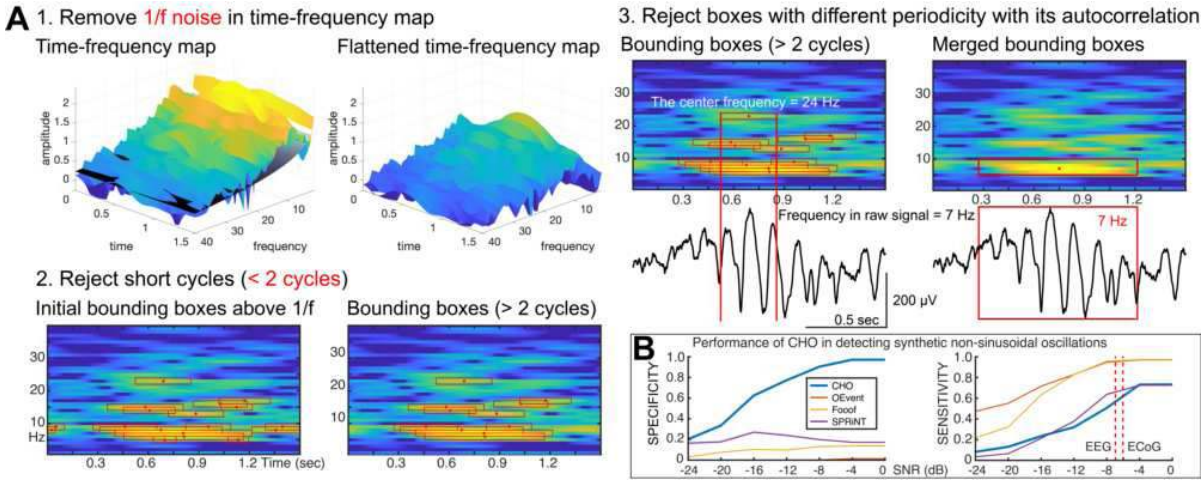

Results: We verified the ability of CHO to isolate simulated oscillatory patterns, both sinusoidal and non-sinusoidal, amidst the prevalent 1/f noise. We applied CHO on a wide range of electrophysiological datasets, including ECoG, EEG, and SEEG recordings, across different cognitive states and tasks. For each of these datasets, CHO accurately detected peak frequencies in task-relevant brain regions, identifying oscillations of specific fundamental frequency in areas such as primary auditory cortex, primary motor cortex, Broca's area, and the hippocampus, both during rest and task engagement. CHO identified characteristic oscillations in ECoG and EEG signals in an auditory reaction-time task; and detected a significant decrease in the initiation of 7 Hz oscillations in the hippocampus, during a memory task.

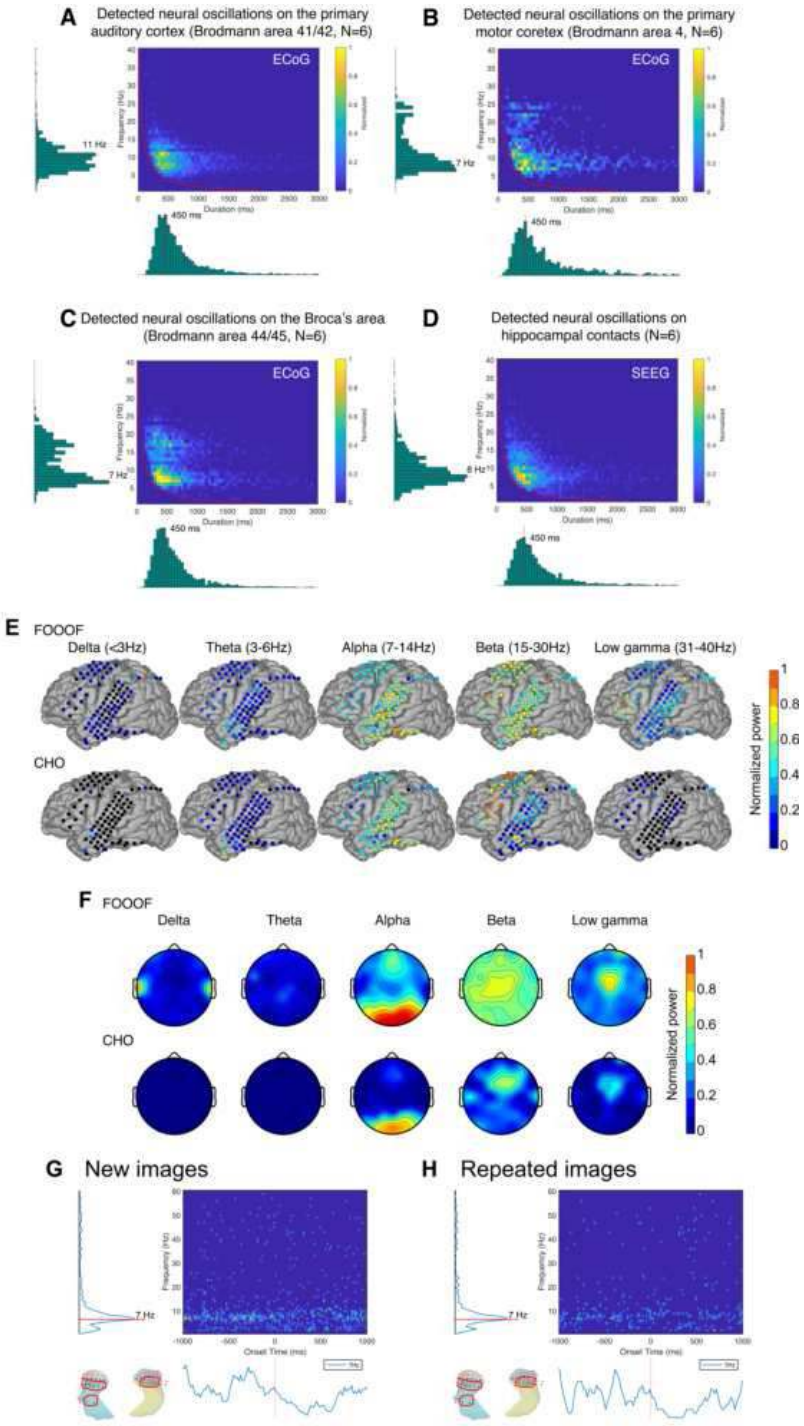

Conclusions: In summary, our results show that CHO stands out as an exceptionally precise and specific instrument for neural oscillation detection, and that it can be used to elucidate the spectro-temporal dynamics of neural oscillations that govern human cognition. CHO considers non-sinusoidal oscillation attributes, such as waveform asymmetry and shape. With this, CHO has the potential to become an important tool in investigating the role of neural oscillations within the brain's circuitry and identifying unique oscillatory biomarkers that may indicate unusual brain functions.

References

1. Annas, G.J. (1997a), 'New Drugs for Acute Respiratory Distress Syndrome', New England Journal of Medicine, vol. 337, no. 6, pp. 435-439

Poster No 1629

The correlation between Subjective Well-Being and EEG Frontal Asymmetry in different frequency bands

Betty Wutzl[1], Kenji Leibnitz[2], Masayuki Murata[3]

[1]Osaka University, Suita,Japan, [2]National Institute of Information and Communication Technology, Suita, Japan, [3]Osaka University, Suita, Japan

Introduction: A correlation between frontal alpha asymmetry, measured via electroencephalography (EEG), and Subjective-Well Being (SWB) has been reported in several papers, e.g., (Urry et al. 2004; Xu et al. 2018). In our previous work (Wutzl et al. 2023), we showed that such a correlation even holds when SWB is not changed by long-term psychological or psychiatric interventions, but also when it is changed on short time scales (60 or 30 seconds). We focused on the asymmetry of the most frontal EEG sensors (AF3 and AF4) and analyzed the influence of the specific time intervals on the calculation of frontal alpha asymmetry. Then, we focused on the asymmetry between different frontal sensors, as these sensor locations were reported to influence the asymmetry scores (Metzen et al. 2022). Here, we expand this research to include the asymmetries between all frontal sensors, as well as different EEG frequency bands.

Methods: We performed this experiment in 2022. In order to measure SWB on small time intervals, we changed the experimental room's temperature and humidity, and we recorded EEG with an Emotiv EPOC X headset (EMOTIV, San Francisco, USA) for up to nine minutes for six sets of different temperature-humidity settings. During each EEG recording, the participants were asked to orally report their SWB every 30 s on a scale from 1 (worst) to 10 (best). The EEG dataset for each subject was preprocessed following HAPPE (Gabard-Durnam et al. 2018), using EEGLAB (Delorme and Makeig 2004) and MARA (Winkler, Haufe, and Tangermann 2011; Winkler et al. 2014). Then, the data was filtered into one of the frequency bands: delta (0.5–3 Hz), theta (4–7 Hz), alpha (8–13 Hz), beta (14-30 Hz), or gamma (31-100 Hz). We also used the unfiltered signal as "non" (0.5-100 Hz). We calculated the power spectrum of two channels ch_1 and ch_2 and determined their asymmetry Asym by subtracting the natural logarithm of the power densities of ch_1and ch_2. Asym was then combined with the reported SWB value as tuple (Asym_band (ch_1,ch_2), SWB) for each subject and band. Participants tend to report mid-ranged SWB values SWB (6–8) more frequently than very low or very high SWB values (1–3, 10). Hence, we balanced the data set for each participant using SMOTE (Chawla et al. 2002) to have an equal number of samples per SWB, and we performed a linear regression with Asym as the independent and SWB as the dependent variable. We did this for each subject and then used a one-sided t-test to determine the statistical significance that the mean of the slopes of the linear regression from each subject is greater than zero. Figure 1 shows a graphical representation of the workflow and EEG sensor layout.

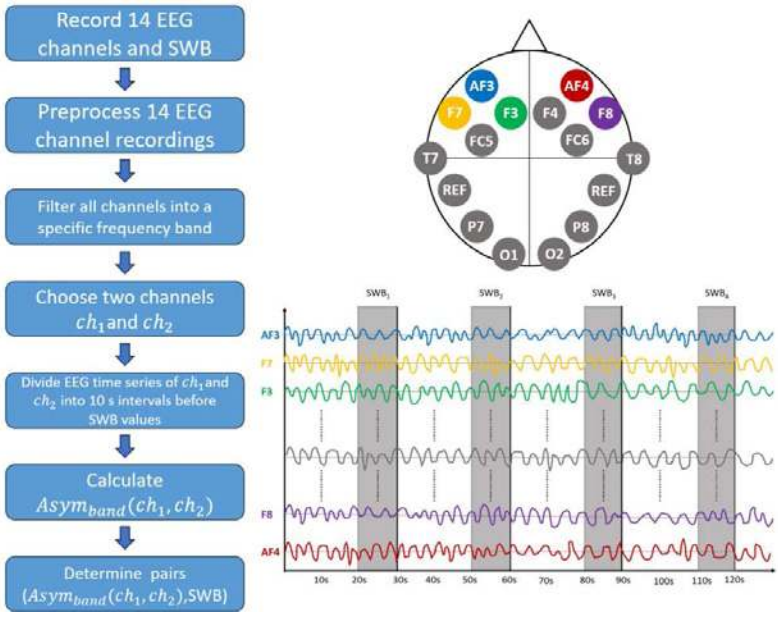

Results: We acquired EEG and SWB data from 30 students (28 right-handed, 2 left-handed, 16 males, 14 females, ages 22.3 ± 4.2 years). Results with p-values of less than 0.01 are shown in Table 1. As expected from reports in the literature and our previous results, the alpha frequency band shows statistically significant results. However, filtering into the delta or theta bands, or not filtering at all (non), also yields a positive linear correlation between frontal sensors from contralateral brain hemispheres and SWB.

Table 1: The columns titled "band" show the frequency band considered. Entries ch_1 and ch_2 give the EEG channels in the calculation of $Asym_{band}(ch_1, ch_2)$. The columns p-value and CI specify the one-sided t-test and the confidence interval (CI) of the slope of the linear correlation. The results marked in bold are the ones with a p-value < 0.001.

band	*ch₁*	*ch₂*	p-value	CI	*band*	*ch₁*	*ch₂*	p-value	CI
Delta	AF3	AF4	0.002	[0.40, Inf)	**Alpha**	**FC5**	**AF4**	**<0.001**	**[0.45, Inf)**
Delta	**F7**	**AF4**	**<0.001**	**[0.39, Inf)**	Beta	F7	AF4	0.002	[0.34, Inf)
Delta	FC5	AF4	0.001	[0.30, Inf)	Gamma	AF3	AF4	0.003	[0.55, Inf)
Theta	**AF3**	**AF4**	**<0.001**	**[0.46, Inf)**	Gamma	F3	AF4	0.006	[0.38, Inf)
Theta	F7	F8	0.008	[0.17, Inf)	Gamma	FC5	AF4	0.004	[0.25, Inf)
Theta	**F7**	**AF4**	**<0.001**	**[0.41, Inf)**	Non	AF3	AF4	0.006	[0.54, Inf)
Alpha	AF3	AF4	0.002	[0.50, Inf)	**Non**	**F7**	**AF4**	**<0.001**	**[0.68, Inf)**
Alpha	**F7**	**AF4**	**<0.001**	**[0.47, Inf)**	Non	FC5	AF4	0.003	[0.34, Inf)

Conclusions: In our previous work, we focused on the alpha frequency band and the relationship between FAA and short-term SWB changes. Here, we present that also other frequency bands, i.e., delta or theta, or not filtering at all into a specific frequency band show similar results. Thus, we conclude that alpha is not the only EEG frequency band that should be investigated when focusing on short-term SWB changes.

References

1. Chawla, N. V., et al. 2002. "SMOTE: Synthetic Minority Over-Sampling Technique." Journal of Artificial Intelligence Research 16 (June): 321–57. https://doi.org/10.1613/jair.953.
2. Delorme, A., et al 2004. "EEGLAB: An Open Source Toolbox for Analysis of Single-Trial EEG Dynamics Including Independent Component Analysis." Journal of Neuroscience Methods 134 (1): 9–21. https://doi.org/10.1016/j.jneumeth.2003.10.009.
3. Gabard-Durnam, L.J., et al. 2018. "The Harvard Automated Processing Pipeline for Electroencephalography (HAPPE): Standardized Processing Software for Developmental and High-Artifact Data." Frontiers in Neuroscience 12. https://doi.org/10.3389/fnins.2018.00097.
4. Metzen, D., et al. 2022. "Frontal and Parietal EEG Alpha Asymmetry: A Large-Scale Investigation of Short-Term Reliability on Distinct EEG Systems." Brain Structure & Function 227 (2): 725–40. https://doi.org/10.1007/s00429-021-02399-1.
5. Urry, H.L., et al., 2004. "Making a Life Worth Living: Neural Correlates of Well-Being." Psychological Science 15 (6): 367–72. https://doi.org/10.1111/j.0956-7976.2004.00686.x.
6. Winkler, I., et al. 2014. "Robust Artifactual Independent Component Classification for BCI Practitioners" 11 (3): 035013. https://doi.org/10.1088/1741-2560/11/3/035013.
7. Winkler, I., 2011. "Automatic Classification of Artifactual ICA-Components for Artifact Removal in EEG Signals." Behavioral and Brain Functions 7 (1): 30. https://doi.org/10.1186/1744-9081-7-30.
8. Wutzl, B., et al. 2023. "Analysis of the Correlation between Frontal Alpha Asymmetry of Electroencephalography and Short-Term Subjective Well-Being Changes." Sensors 23 (15): 7006. https://doi.org/10.3390/s23157006.
9. Xu, Y-Y, et al. 2018. "Frontal Alpha EEG Asymmetry Before and After Positive Psychological Interventions for Medical Students." Frontiers in Psychiatry 9. https://doi.org/10.3389/fpsyt.2018.00432.

Poster No 1630

Predicting subject traits from EEG spectral signatures: an application to brain age

Cecilia Jarne[1], Ben Griffin[2], Diego Vidaurre[3]

[1]Aarhus University CFIN /Universidad Nacional de Quilmes/ CONICET, Aarhus, Aarhus C, [2]Oxford University, Oxford, Oxford, [3]Aarhus University, Aarhus, Aarhus C

Introduction: We address the prediction of behavioural or cognitive traits from brain EEG spectral data. To predict from individual channels, we proposed a novel method based on interpreting the EEG spectrogram as a probability distribution. Specifically, without predefining frequency bands or relying on manual feature engineering, the proposed approach uses so-called Kernel Mean Embeddings (KME) to represent EEG spectrograms in a high-dimensional feature space (Smola et. al, 2007; Iyer et. al, 2014; Borgwardt et. al, 2006). Our method, Kernel Mean Embedding Regression (KMER), utilises Maximum Mean Discrepancy (MMD) as a distance metric on the space of probability measures, together with kernel ridge regression(Smola et. al, 2007; Saunders et al., 1998). As an example, we focus on age prediction, which can be used to explore how an individual's brain appears to have aged relative to the population average (Franke and Gaser, 2019; Smith et al, 2019. We demonstrate the effectiveness of KMER in age prediction using a multi-site resting-state EEG dataset spanning a wide age range.

Methods: This study utilises EEG data from the HarMNqEEG dataset (Li et. al, 2022), where subjects were scanned across 14 sites, to predict individuals' age using three regression methods: Ridge Regression (RR), Kernel Ridge Regression (KRR), and Kernel Mean Embedding Regression (KMER) (See Fig 1 for an illustration of how they work). In KMER, the Maximum Mean Discrepancy (MMD) is employed as a distance metric, interpreting EEG spectrograms as probability distributions. The MMD is

estimated using different kernel functions to create a distance matrix. The predictive models KRR and KMER both incorporate the kernel trick for age prediction. We evaluated prediction performance using explained variance (R^2) and mean absolute error (MAE). The open-source code for this analysis is available on GitHub (Jarne et. al 2023).

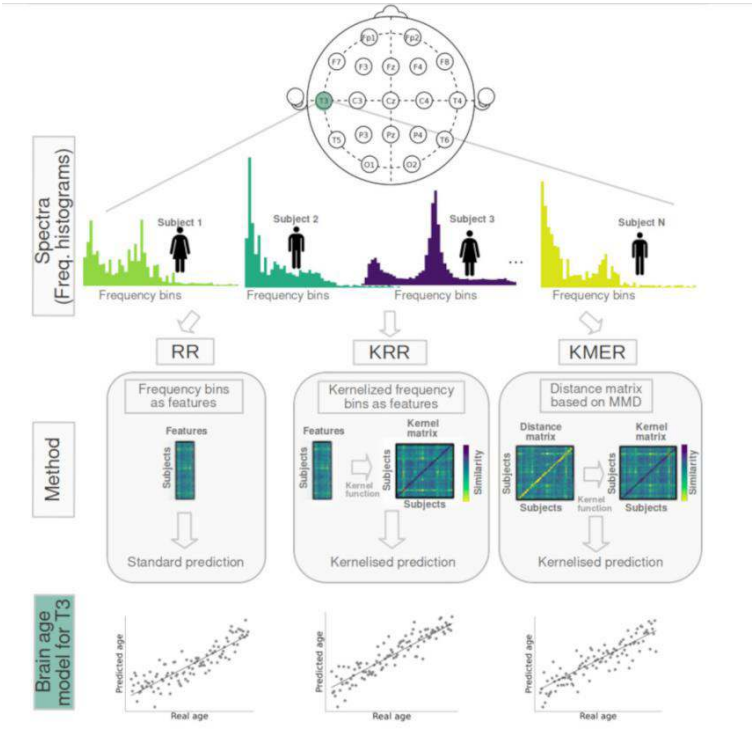

Figure 1: General workflow of the analysis. We used the HarMNqEEG dataset, which contains (adequately normalized) power densities per sensor and participant, as well as information on gender, age and scanning batch (acquisition site). We considered three prediction approaches, which we run separately per EEG sensor: (i) Ridge Regression (RR) using the power estimates at each frequency bin of the spectrogram as features; (ii) Kernel Ridge Regression (KRR), a kernelised version of RR (based on a non-linear Gaussian kernel) also based on the power estimates per bin; and (iii) our Kernel Mean Embedding Regression (KMER) approach, where we interpreted the power spectral estimates across bins as probability distributions so that we can leverage the mathematical machinery of kernel learning on probability measures for prediction.

Results: KMER resulted in superior age prediction from EEG spectrograms compared to RR and KRR. KMER outperformed alternatives across all EEG channels, likely because of its capacity to capture non-linearities effectively (See Fig 2). KMER revealed that parietal sensors are the most accurate in predicting age. When predicting separately by sex, females demonstrated slightly higher prediction accuracy, suggesting a closer alignment of biological changes with chronological age. Predicting across 14 sites was harder than within site due to the wide range of age distributions. KMER, however, exhibited good accuracy and robust results even in this case.

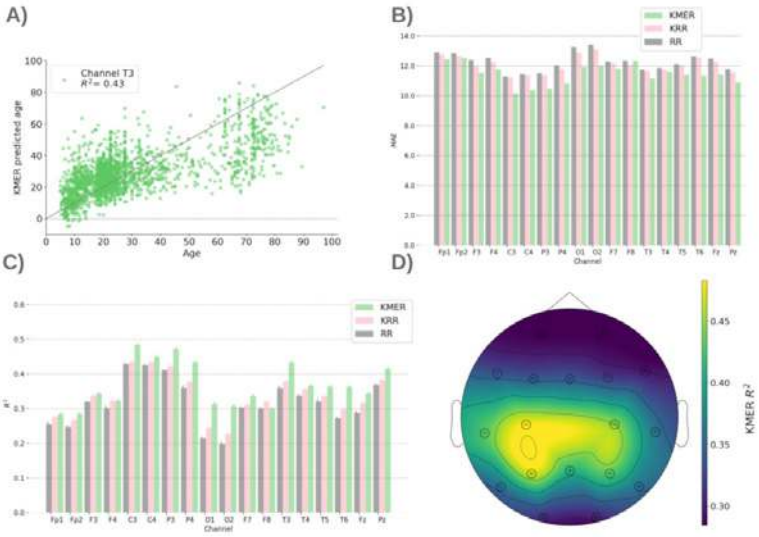

Figure 2: KMER shows lower errors and higher accuracies than standard alternatives, RR and KRR. **A)** Illustration of predicted vs. real age for channel T3 for KMER. **B)** Mean Absolute Error (MAE) per channel for KMER, RR and KRR. **C)** Explained variance R^2 per channel for the three methods. **D)** Explained variance projected on sensor space for KMER.

Conclusions: KMER was introduced as a method for predicting individual traits from EEG spectral information. Interpreting EEG channel spectrograms as probability distributions, leverages mathematical principles from kernel learning. KMER is straightforward to implement, computationally efficient, and broadly applicable. Despite the challenge of predicting age across sites with very different age distributions and other potential differences, the presented results showcase notable performance in age prediction in comparison to previous EEG studies. Beyond its success in age prediction from EEG data, KMER can be used in other modalities, including MEG and fMRI, and to predict other subject traits besides age. Although here we restricted ourselves to the polynomial, Gaussian, and linear kernels, the method can be further optimised through the exploration of different kernel functions and hyperparameters.

References

1. Borgwardt, K. M., Gretton, A., Rasch, M. J., Kriegel, H.-P., Schölkopf, B., and Smola, A. J. (2006). Integrating structured biological data by Kernel Maximum Mean Discrepancy. Bioinformatics, 22(14):e49–e57.
2. Franke, K. and Gaser, C. (2019). Ten years of brain age as a neuroimaging biomarker of brain aging: What insights have we gained? Frontiers in Neurology, 10(JUL).
3. Iyer, A. S., Jagarlapudi, S., and Sarawagi, S. (2014). Maximum mean discrepancy for class ratio estimation: Convergence bounds and kernel selection. International Conference on Machine Learning.
4. Jarne, C., Griffin, B., and Vidaurre, D. [8] (https://github.com/katejarne/Kernel_Max_mean_discrepancy_EEG_Age)
5. Li, M., Wang, Y., Lopez-Naranjo, C., Hu, S., Reyes, R. C. G., Paz-Linares, D., Areces-Gonzalez, A., Hamid, A. I. A., Evans, A. C., Savostyanov, A. N., Calzada-Reyes, A., Villringer, A., Tobon-Quintero, C. A., Garcia-Agustin, D., Yao, D., Dong, L., Aubert-Vazquez, E., Reza, F., Razzaq, F. A., Omar, H., Abdullah, J. M., Galler, J. R., Ochoa-Gomez, J. F., Prichep, L. S., Galan-Garcia, L., Morales-Chacon, L., Valdes-Sosa, M. J., Tröndle, M. Zulkifly, M. F. M., Abdul Rahman, M. R. B., Milakhina, N. S., Langer, N., Rudych, P., Koenig, T., Virues-Alba, T. A., Lei, X., Bringas-Vega, M. L., Bosch-Bayard, J. F., and Valdes-Sosa, P. A. (2022). Harmonized-multinational qeeg norms (harmnqeeg). NeuroImage, 256:119190.
6. Saunders, C., Gammerman, A., and Vovk, V. (1998). Ridge regression learning algorithm in dual variables. In Proceedings of the Fifteenth International Conference on Machine Learning, pages 515–521. Morgan Kaufmann. Edited by J.Shavlik.
7. Smola, A., Gretton, A., Song, L., and Schölkopf, B. (2007). A Hilbert space embedding for distributions. In Hutter, M., Servedio, R. A., and Takimoto, E., editors, Algorithmic Learning Theory, pages 13–31, Berlin, Heidelberg. Springer Berlin Heidelberg.
8. Smith, S. M., Vidaurre, D., Alfaro-Almagro, F., Nichols, T. E., and Miller, K. L. (2019). Estimation of brain age delta from brain imaging. NeuroImage, 200:528–539.

Poster No 1631

Neural Evidence for Disrupted Predictive Coding in First Episode Psychosis

Angela Wang[1], Eric Rawls[2], Collin Teich[2], Angus MacDonald[1], Scott Sponheim[3]

[1]Department of Psychology, University of Minnesota, Minneapolis, MN, [2]Department of Psychiatry and Behavioral Sciences, University of Minnesota, Minneapolis, MN, [3]Minneapolis Veteran Affairs HealthCare System, Minneapolis, MN

Introduction: Predictive coding is a theoretical framework that suggests our brain constantly attempts to predict sensory inputs based on past experiences to guide our learning and behavior. Prediction error (PE), the mismatch between our priors (predictions) and our actual sensory input, allows the brain to update these sensory predictions for the future. In patients with psychosis, maladaptive inferences and behavior are theorized to result from atypical updating of priors following PEs. However, few studies have tested this proposition directly. Using a three armed-bandit task with EEG, we sought to understand the impact of neural PEs on subsequent sensory updating in patients with first episode psychosis (PwP) and healthy controls (HC). Our goal was to directly test for links between neural PEs (reward positivity [RewP], P300) and subsequent sensory updating (P1, N1). This link is hypothesized to be present in HC, but not in PwP, implying that predictive coding partially underlies reinforcement learning deficits in PwP.

Methods: We collected 32-channel EEG simultaneously with 3T fMRI from 36 HC and 34 PwP. We employed a 3-armed bandit task, which instructed participants to select one out of three options, resulting in a win of +1 points or an omission of +0 points. We separated feedback trials, and the immediately following stimulus trials, according to Outcome (win/omission) and PE (low/high). Thus, event-related potentials for the following feedback conditions were extracted: Win-HighPE, Win-LowPE, Lose-HighPE, and Lose-LowPE. A mixed model approach was used to calculate main effects of Group (HC/PwP), Outcome (win/omission), and PE (low/high), as well as interactions between Group and the within-subject factors of Outcome and PE. Pearson correlations were calculated between feedback-locked potentials (RewP, P300) and the immediately subsequent stimulus-locked potentials (P1, N1), separately for HC and PwP. Furthermore, correlations between stay/switch choices and ERP components were also analyzed.

Results: Within our analysis of feedback-locked potentials, the RewP displayed significantly greater activity to wins versus losses ($t = 3.14$, $p < 0.01$) and to highPE versus lowPE ($t = 4.53$, $p < 0.001$), as well as an interaction indicating that the greatest RewP amplitudes were for Win-highPE trials. P300 showed significantly greater activity in highPE versus lowPE ($t = 5.37$, $p <$

0.001). We found no group differences between HC and PwP in the RewP or P300. We then directly tested for links between neural PEs and subsequent sensory updating. This analysis revealed significant correlations in HC between RewP/P300 amplitudes with the subsequent visual P1, in Lose-HighPE condition (rs > 0.51, ps < 0.001). This correlation was absent in PwP. Moreover, in HC, switch behavior was correlated with RewP and P300 in the Lose-LowPE condition (rs > 0.35, ps < 0.03). However, in PwP, switch behavior was correlated with P1 in the Lose-LowPE condition (r = -0.52, p < 0.01), and N1 in the Win-HighPE and Win-LowPE conditions (rs > 0.39, ps < 0.02).

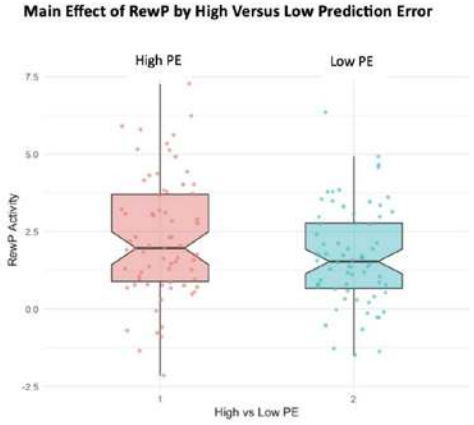

Figure 1. Main Effect of RewP by Prediction Error
Boxplot showing significant activity in the RewP feedback-locked potential across healthy controls and patients with psychosis for high PE versus low PE ($t = 4.53$, $p < 0.001$).

Correlation Table of Feedback and Stimulus Locked Potentials

Healthy Controls (HC)

	P1 Component			
	Win-HighPE	Win-LowPE	Lose-HighPE**	Lose-LowPE
RewP	-0.18	0.11	**0.57****	0.12
P300	0.35*	0.18	**0.52****	0.38*

Patients with Psychosis (PwP)

	P1 Component			
	Win-HighPE	Win-LowPE	Lose-HighPE	Lose-LowPE
RewP	0.08	0.24	-0.15	-0.03
P300	0.17	0.14	-0.10	-0.03

** p < 0.001
* p < 0.05

Figure 2. Correlation Table of Feedback and Stimulus Locked Potentials
Table showing Pearson correlations between feedback potentials (RewP/P300) and sensory component (P1) in HC and PwP. In HC, highly significant correlations (p < 0.001) are present in the Lose-HighPE condition for both RewP and P300 components. No correlations are present in PwP.

Conclusions: Our findings provide evidence that both HC and PwP experience PE, indicating that PE signaling itself is not disrupted in PwP. However, in HC, reward processing (RewP, P300) modulates subsequent sensory inputs (P1). This modulation is absent in PwP, suggesting a dysfunctional link between PE signaling and sensory updating. In addition, within HC, neural reinforcement processing predicts reinforcement learning behaviors, while for PwP, these behaviors are instead predicted by sensory components. Overall, our results support the hypothesis that PEs should drive sensory updating, and that dysfunctions in this predictive coding impact maladaptive learning and behavior in psychosis. Future research will incorporate simultaneously recorded fMRI data to directly localize brain regions underlying predictive coding deficits, which could be later targeted for brain-based interventions such as neuromodulation.

References

1. Adams, R. A. (2013). The computational anatomy of psychosis. Frontiers in Psychiatry, 4, 47.
2. Adams, R. A. (2018). Chapter 7 - Bayesian Inference, Predictive Coding, and Computational Models of Psychosis. In A. Anticevic & J. D. Murray (Eds.), Computational Psychiatry (pp. 175-195). Academic Press. ISBN 9780128098257.
3. Hager, N. M. (2021). Win, lose, or draw: Examining salience, reward memory, and depression with the reward positivity. Psychophysiology, 59, e13953.
4. Rawls, E. (2020). Feedback-Related Negativity and Frontal Midline Theta Reflect Dissociable Processing of Reinforcement. Frontiers in Human Neuroscience, 13, 452.
5. Rawls, E. (2021). The aversion positivity: Mediofrontal cortical potentials reflect parametric aversive prediction errors and drive behavioral modification following negative reinforcement. Cortex, 140, 26-39.
6. Sterzer, P. (2018). The Predictive Coding Account of Psychosis. Biological Psychiatry, 84(9), 634-643.
7. Sterzer, P. (2019). Decision-making in schizophrenia: A predictive-coding perspective. NeuroImage, 190, 133-143.
8. Wu, Y. (2009). The P300 and reward valence, magnitude, and expectancy in outcome evaluation. Brain Research, 1286, 114-122.

Poster No 1632

Problem of vertical microstate topography in simultaneous EEG/fMRI data

Tomáš Jordánek[1,2], Radek Marecek[2], Martin Lamos[2]

[1]Brno, Masaryk University, Faculty of Medicine, Brno, South Moravia, [2]Brain and Mind Research Program, CEITEC Masaryk University, Brno, South Moravia

Introduction: Simultaneous recording of electroencephalography (EEG) and functional magnetic resonance (fMRI) is connected with strong artifacts mainly in EEG. Analysis of EEG microstates (MS) (Lehmann et al., 1987) as a method for spatio-temporal analysis of the EEG is very sensitive to residual artifacts in the data and its results can be affected. Analyzing simultaneous EEG/fMRI data with MS analysis reveals a specific left-right topography with strong vertical line in the middle – we call it vertical topography (VT). It can be found in papers analyzing EEG/fMRI data (Agrawal et al., 2022; Bréchet et al., 2019), as well as analyzing EEG recorded in a shielded room (Custo et al., 2017). Here we show that the VT cannot be considered as a manifestation of neural activity. Rather, we propose that it represents artificial variability in a data introduced mainly by movements of sensitive parts of EEG system during data acquisition.

Methods: We collected resting state EEG data from 77 healthy controls acquired during fMRI (Dataset A) and in shielded cabin (Dataset B). Further, we performed several testing measurements with spherical MR phantom covered with a wet towel and an EEG cap attached: EEG/fMRI with same protocol as used for humans (Dataset C) and cabin EEG data (Dataset D). All EEG recordings were done with MR-compatible HD-EEG cap (EGI 256-channel), sampling frequency 1 kHz, reference at Cz. After standard gradient artifacts and cardiobalistogram (CB) removal (Allen et al., 2000), the EEG data were revised and marked for large artifacts, filtered to 1–40 Hz, and processed by ICA to remove eye artifacts (and ECG in cabin data). Finally, bad channels were interpolated. Correction of CB and ICA was omitted in phantom data. For each individual subject and phantom dataset, we extracted topomaps at global field power (GFP) peaks that were 100 times clustered with modified k-means algorithm to reveal most stable topographies. Resulting maps were 200 times clustered (k-means) in group analyses and optimal number of MS was based on metacriterion (Bréchet et al., 2019). Resulting maps were back fitted to the data.

Results: Dataset A: 6 MS as optimum, VT is present (1A) and is explaining 13,5 % of variance and covering 18,1 % of signal. We have revealed significant correlation (Pearson's) between amount of movement of subject (framewise displacement) and parameters of map 1A – GEV (r= 0.355; p=0.0015), Mean duration (r=0.293; p=0.0097), Time coverage (r=0.340; p=0.0077), Occurrence (r=0.302; p=0,0025). Dataset B: 4 MS as optimum – so-called canonical MS, VT is not present (VT is present after segmentation to 6 clusters explaining 3,3 % of GEV and covering 8,0 % of EEG.) Dataset C: 8 MS as an optimum, four of them (map 2C, 4C, 6C and 8C) are VTs and map 6C is the most dominant, explaining 60,1 % of GEV and covering 61,7 % of the signal. Dataset D: 7 MS as an optimum, no VT is present even after segmentation up to ten clusters. 99 % of the EEG is unlabeled, data have no structure and represent noise only.

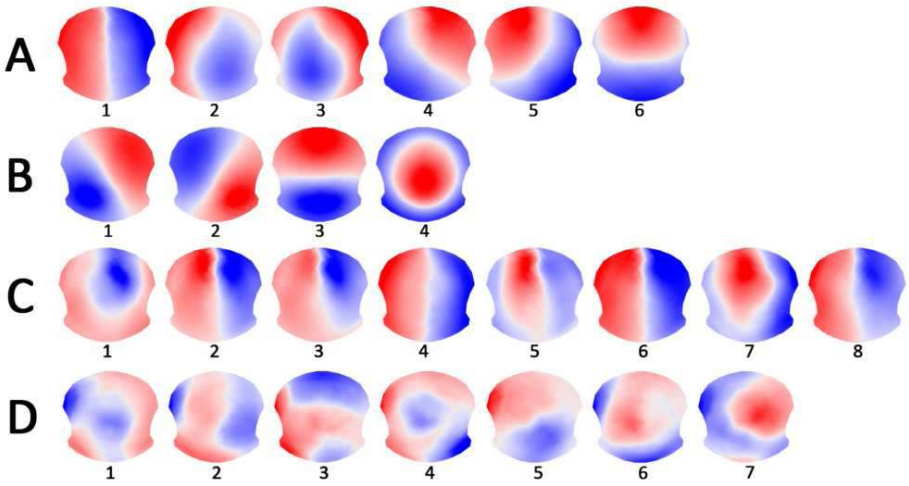

Figure 1 - Resulting microstate topographies for each dataset A-D

Conclusions: Vertical topography affects analysis of MS with its very presence and also changes spatio-temporal parameters of canonical MS A and B (during fitting part VT can be falsely marked as A or B and conversely). Based on our analyses we suppose that VT is connected with movement of EEG cap and wires: - In MR environment the VT is present in both human and phantom data – movement of subject, vibrations, heart activity; effect is increased by strong magnetic field - Significant correlation between parameters of VT and amount of movement - Presence of VT in human cabin EEG – subject's movement,

heart activity; effect is lower without strong magnetic field - VT is not present in cabin phantom EEG – phantom lies stationary VT is very likely artificial topography, does not represent physiological activity - it is present in phantom data and it is absolutely dominant topography there.

References

1. Agrawal, S., 2022. Hemodynamic functional connectivity optimization of frequency EEG microstates enables attention LSTM framework to classify distinct temporal cortical communications of different cognitive tasks. Brain Informatics 9, 25. https://doi.org/10.1186/s40708-022-00173-5
2. Allen, P.J., 2000. A Method for Removing Imaging Artifact from Continuous EEG Recorded during Functional MRI. NeuroImage 12, 230–239. https://doi.org/10.1006/nimg.2000.0599
3. Bréchet, L., 2019. Capturing the spatiotemporal dynamics of self-generated, task-initiated thoughts with EEG and fMRI. NeuroImage 194, 82–92. https://doi.org/10.1016/j.neuroimage.2019.03.029
4. Custo, A., 2017. Electroencephalographic Resting-State Networks: Source Localization of Microstates. Brain Connectivity 7, 671–682. https://doi.org/10.1089/brain.2016.0476
5. Lehmann, D., 1987. EEG alpha map series: brain micro-states by space-oriented adaptive segmentation. Electroencephalography and Clinical Neurophysiology 67, 271–288. https://doi.org/10.1016/0013-4694(87)90025-3

Poster No 1633

Dynamic functional brain network of rsEEG to predict antidepressant responses in patients with MDD

Taegyeong Lee[1], Kang-min Choi[1,2], Seung-Hwan Lee[2,3], Chang-Hwan Im[1,4]

[1]School of Electronic Engineering, Hanyang University, Seoul, Republic of Korea, [2]Clinical Emotion and Cognition Research Laboratory, Inje University, Goyang, Korea, Republic of, [3]Department of Psychiatry, Ilsan Paik Hospital, Inje University College of Medicine, Goyang, Korea, Republic of, [4]Department of Biomedical Engineering, Hanyang University, Seoul, Korea, Republic of

Introduction: Several patients with major depressive disorder (MDD) do not respond to the antidepressant. Prediction of antidepressant response is regarded as one of the necessary issues because pharmacotherapy for treatment-resistant patients could cause unnecessary side effects. For several years, numerous neuroimaging studies have demonstrated the feasibility that characteristics of functional brain networks could serve as predictors for pharmacotherapeutic responses in patients with MDD. Most of these studies have assumed that the brain would maintain a functionally static state; however, as well known, functional brain networks indeed dynamically fluctuate even in the resting state[1]. Electroencephalography (EEG) has comparative advantages for exploring dynamic functional brain networks over the other modalities, due to its excellent temporal resolution. In this study, we compared the dynamic patterns of the resting-state EEG-derived functional brain networks between patients with non-remitted MDD (nrMDD) and remitted MDD (rMDD).

Methods: Forty-nine drug-naïve patients with MDD (aged 45.47 ± 12.00, W 46) and twenty-two healthy controls (HC, aged 44.05 ± 13.80, W 18) participated in this study. After receiving vortioxetine treatment for 8 weeks, patients were divided into two subgroups based on Hamilton Depression Rating Scales: (i) nrMDD (Ham-Dw8 ≥ 8) and rMDD (otherwise). EEG signals were acquired during the resting state while participants closed their eyes for 3 min. After signal pre-processing, a 30-s noise-free segment was manually selected individually. To construct the dynamic functional brain network, the 30-s segments were divided into 2-s time bins with 95 % overlap. Thirty-one regions of interest were determined as nodes. For edges, functional connectivity was dynamically evaluated for each time bin using the weighted phase-lag index (wPLI), for 6 frequency bands, including theta, low alpha, high alpha, low beta, high beta, and gamma bands. The k-means clustering was implemented to identify the states of the reoccurring functional network (FN). For clustering each network derived from the time bin, the L1 norm-based distance was employed for the clustering analysis. The number of states, k, was determined by the elbow method. It is noted that the clustering was conducted using all networks for the participants, including nrMDD, rMDD, and HC. The fraction time (FT) and dwell time (DT) of each state were evaluated to assess the dynamic characteristics of the FN states. To compare the dynamic FN indices between the nrMDD and rMDD, the permutation test was conducted, with the significance level adjusted by the number of frequency bands (i.e., $\alpha = 0.05/6$).

Results: The optimal k values were determined to be 4, except for the high-alpha band (k = 5). In the high alpha band, nrMDD exhibited decreased FT (nrMDD = 0.18 vs. rMDD = 0.24, p = 0.0060) and DT (nrMDD = 2.93 vs. rMDD = 3.48, p = 0.0034) in the state 3, which is characterized with overall hypoconnectivities particularly for the right hemispheric temporo-parieto-occipital regions: right visual primary cortex, right intraparietal sulcus, right angular gyrus, right inferior parietal lobule, right middle temporal gyrus, and right supramarginal gyrus.

Conclusions: In this study, we suggested that aberrant dynamicity in the resting-state functional brain networks could predict the treatment efficacy of antidepressants in patients with MDD. Non-remitted patients tended to spend less time and escape

earlier for the functional state in which the right hemispheric temporo-parieto-occipital regions are suppressed in the high-alpha band.

References

1. Fox, Michael D. (2005), 'The human brain is intrinsically organized into dynamic, anticorrelated functional networks', Proceedings of the National Academy of Sciences, vol. 102, no. 27 pp. 9673-9678.

Poster No 1634

Multiverse analysis on depression biomarkers from EEG

Yasmin Hollenbenders[1], Christoph Maier[2], Alexandra Reichenbach[1]

[1]Heilbronn University, Heilbronn, Baden-Württemberg, [2]Medical Informatics, Heilbronn University, Heilbronn, Baden-Wuerttemberg

Introduction: Major depressive disorder (MDD) is one of the most common mental disorders (GBD 2019 Mental Disorders Collaborators, 2022) but diagnosis is rather subjective (Cai et al., 2018). A method to gain objective biomarkers is based on electroencephalography (EEG). Studies show that those distinguish between MDD patients and healthy controls (HC) but with contradictory results regarding discriminatory features (De Aguiar Neto & Rosa, 2019). One substantial problem is that EEG data acquisition and processing is not standardized (Kołodziej et al., 2021). However, to support clinical decision-making, biomarkers need to be robust against variations. This multiverse analysis (Steegen et al., 2016) systematically investigates the effect of processing steps on the performance of α-band depression biomarkers in diagnostic classification.

Methods: We used a public dataset with 5 min resting-state eyes closed EEG (HC:28/MDD:30) (Mumtaz, 2016). 13 channels were chosen for analysis: frontal (Fp1/2, F3/4, F7/8, Fz), central (C3/4), parietal (P3/4), and occipital (O1/2). Data was bandpass filtered (1-40 Hz) and artifacts were removed with ICLabel (Li et al., 2022). The effect of processing steps on biomarker performance was investigated with a multiverse analysis constructing 720 paths over the processing step (Fig. 1). A) Data normalization (3 level): None, z-normalization over all channels of each subject, and z-normalization for each channel of each subject. B) Window length (4 level): non-overlapping windows of 5-, 10, 15, and 20 sec. Subjects with less than 10 windows were excluded from further analyses. This left 41/36/23 subjects for 5, 10/15/20 sec windows from whom we sub-sampled 10 windows each. C) Feature extraction (9 features + combination (all)): absolute and relative α band power, α peak frequency (αpf), and from the upper signal envelope (env) kurtosis (kurt), skewness (skew), median, interquartile range, variance, and range. D) Aggregation (2 level): 10 individual values or median. E) Classification algorithm (3 level): Logistic Regression, Random Forest, and Support Vector Machine. The classification models were trained with six-fold cross-validation. With resulting accuracies, we conducted an ANOVA for comparison of processing steps and t-tests against chance-level for statistical robustness of the models.

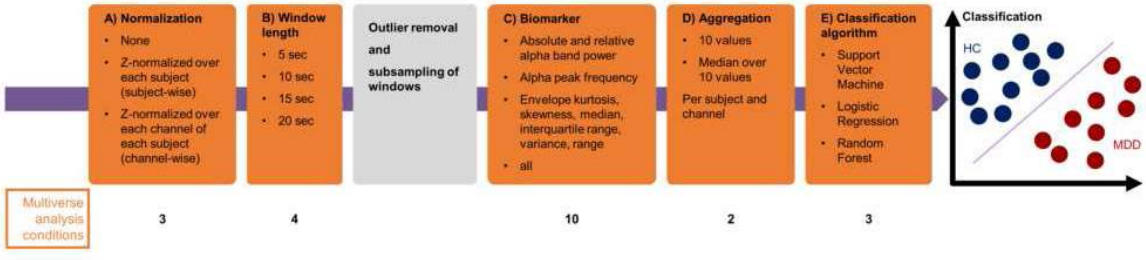

Figure 1: Multiverse analysis with preprocessing and classification.

Results: All processing steps but normalization have a sign. influence on diagnostic accuracy (all p<.001). For further analysis, we used subject-wise normalization to keep the regional information of electrodes. Aggregating to the median (63.4±17.0%) achieves higher accuracy than individual values ($F(1,3600)=59.467$, p<.001). However, the latter yields more statistically robust models (15 vs 7). 15-sec windows (65.7±13.5%) achieve sign. higher accuracies (all $t(2158)>5.288$, p<.001), while 10-sec windows yield most statistically robust models (8). Random Forest performs sign. better (all $t(2878)>3.243$, p<.001), yet Logistic Regression yields most statistically robust models (8). Env skew scores the highest accuracies (8/9, $t(862)>3.737$, p<.001), followed by all (7/9, $t(862)>4.847$, p<.001), αpf (6/9, $t(862)>4.519$, p<.001), and env kurt (6/9, $t(862)>7.337$, p<.001). However, the order of the most statistically robust markers differs: env kurt (7), αpf (5), env skew (4), and all (2).

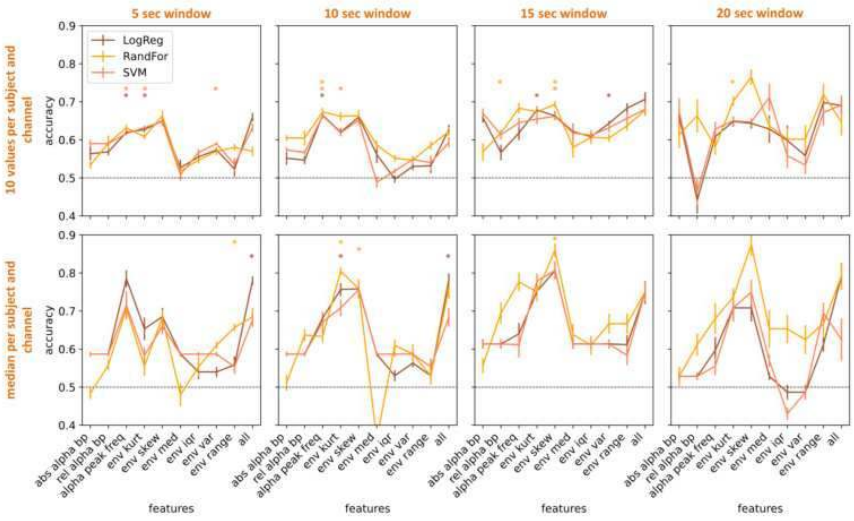

Figure 2: Classification results of multiverse analysis for subject-wise normalization. Errorbars denote 95%-CI. Dotted line represents classification at chance-level. Stars depict t-tests vs. chance-level on $\alpha = 0.001$. Abbreviations: abs alpha bp (absolute alpha bandpower), rel alpha bp (relative alpha bandpower), alpha peak freq (alpha peak frequency), env kurt (envelope kurtosis), env skew (envelope skewness), env med (envelope median), env iqr (envelope interquartile range), env var (envelope variance), env range (envelope range)

Conclusions: We demonstrate the effect of processing on the performance of biomarkers for depression diagnosis with a multiverse analysis. Biomarkers used in clinical settings need high discriminatory value as well as robustness. The biomarkers of this study achieved neither. Furthermore, none of the variations of the processing steps yield a clear advantage. We can thus neither recommend a set of methods nor biomarkers. This study is restricted by the choice of biomarkers and additional EEG features need to be considered. Nonetheless, we demonstrate the relevance of systematic work on the influence of data processing methods to resolve contradictory results in biomarker research.

References

1. Cai, H.(2018), 'A Pervasive Approach to EEG-Based Depression Detection', Complexity, vol. 2018, pp. 1–13
2. De Aguiar Neto, F. S. (2019), 'Depression biomarkers using non-invasive EEG: A review', Neuroscience & Biobehavioral Reviews, vol. 105, pp. 83-93
3. GBD 2019 Mental Disorders Collaborators, G. (2022), 'Global, regional, and national burden of 12 mental disorders in 204 countries and territories, 1990–2019: a systematic analysis for the Global Burden of Disease Study 2019', The Lancet Psychiatry, vol. 9, no. 2, 137-150
4. Kołodziej, A. (2021), 'No relationship between frontal alpha asymmetry and depressive disorders in a multiverse analysis of five studies', eLife, vol. 10
5. Li, A. (2022), 'MNE-ICALabel: Automatically annotating ICA components with ICLabel in Python', Journal of Open Source Software, vol. 7, no. 76, p. 4484
6. Mumtaz, W. (2016), 'MDD Patients and Healthy Controls EEG Data (New)', figshare Dataset
7. Steegen, S. (2016), 'Increasing Transparency Through a Multiverse Analysis', Perspectives on Psychological Science, vol. 11, no. 5, pp. 702–712

Poster No 1635

Altered Macroscale Topography of Gamma Oscillations in Parkinson's Disease

Hao Ding[1], Jens Volkmann[2], Muthuraman Muthuraman[3]

[1]Würzburg, Wurzburg, Bavaria, [2]Universitätsklinikum Würzburg, Würzburg, Bavaria, [3]Universitätsklinikum Würzburg, Würzburg, Germany

Introduction: In Parkinson's disease (PD), reduced gamma oscillations disrupt the functional connectivity between brain regions, affecting macroscale brain function. Entraining the gamma rhythm through neural modulation can help restore the cortical plasticity related to motor function. However, the macroscale functional topography at specific neural oscillations is not well characterized. This study aims to examine the macroscale functional reorganization in PD, with a particular focus on the gradient topography associated with gamma oscillations.

Methods: Thirty-five PD patients (in the medication-On state) and 35 sex and age-matched healthy seniors were studied. A 5-minute resting state was recorded using high-density EEG. The forward solution was estimated using the finite element method, and cortical brain activity was reconstructed using a beamformer as the inverse solution. Functional connectivity in the source space was calculated using Pearson correlation based on HCP-MMP1 parcellation. Cortical gradients were

analysed using a normalized angle kernel to capture connectivity profile similarities. Primary gradient components at gamma band (60-90Hz) were identified using diffusion map embedding. Network-wise analysis was performed on the Cole-Anticevic brain-wide network parcellation. A surface-based linear model on z-transformed gradients was used to identify gradient differences between groups. Significant clusters were functionally decoded using the Neurosynth meta-database. Finally, clinical measures were correlated with these clusters to provide meaningful clinical interpretations.

Results: An examination of the primary gradient components revealed alterations in gamma oscillation in PD. Further exploration through Euclidean space analysis identified an additional cluster in PD patients compared to healthy individuals. Notably, global histograms also showed a noticeable contraction of the two gradient anchors in PD patients. A network-wise analysis highlighted increased gradient values in the Cingulo-Opercular network (p = 0.032). Surface-based linear models revealed differences on the first gradient component in the middle temporal cortex (p=0.018). Importantly, gradients in this region showed a significant negative correlation with UPDRS-III scores (p=0.03), highlighting their clinical importance. Functional annotation of brain regions suggested their significance in the motor network, as interpreted from meta-analytic maps.

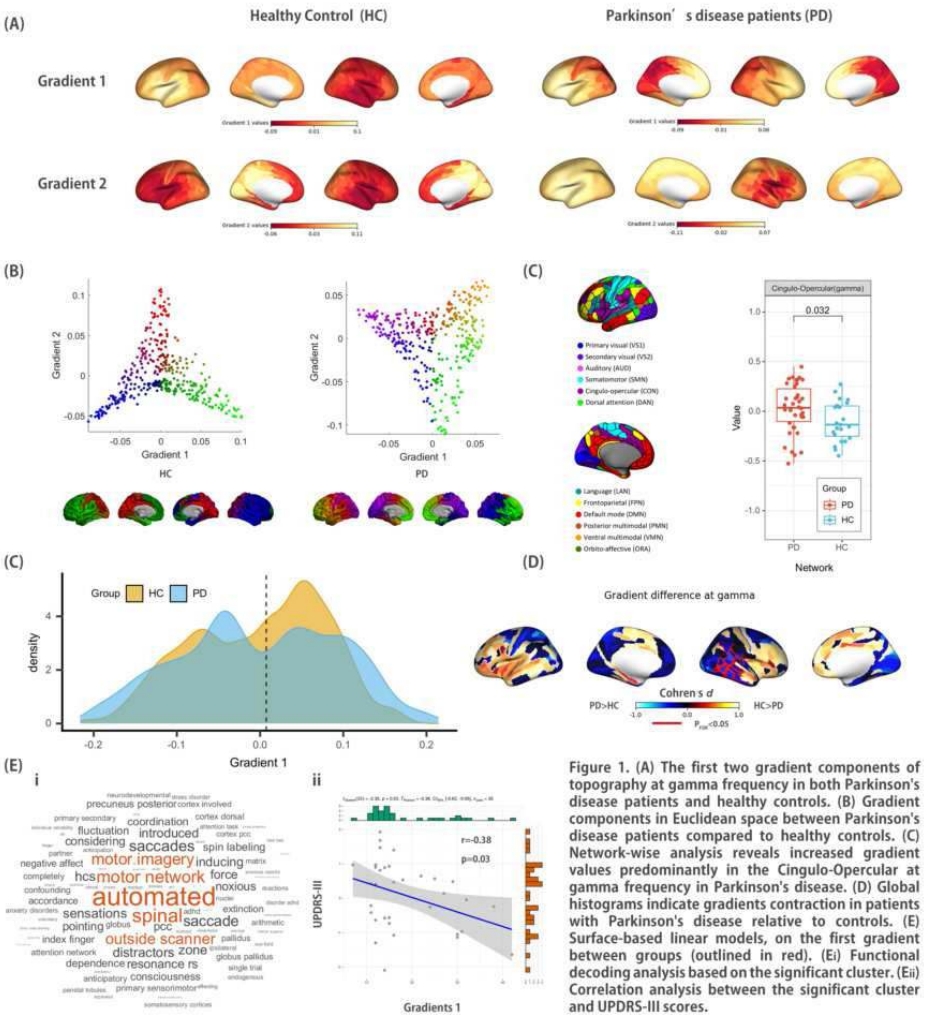

Figure 1. (A) The first two gradient components of topography at gamma frequency in both Parkinson's disease patients and healthy controls. (B) Gradient components in Euclidean space between Parkinson's disease patients compared to healthy controls. (C) Network-wise analysis reveals increased gradient values predominantly in the Cingulo-Opercular at gamma frequency in Parkinson's disease. (D) Global histograms indicate gradients contraction in patients with Parkinson's disease relative to controls. (E) Surface-based linear models, on the first gradient between groups (outlined in red). (Ei) Functional decoding analysis based on the significant cluster. (Eii) Correlation analysis between the significant cluster and UPDRS-III scores.

Conclusions: In conclusion, our investigation has revealed disruptions in the macroscale hierarchy, which affect the processes of integration and segregation within unimodal and transmodal networks in PD patients. These findings provide valuable insights into the subtle changes associated with PD at both macroscopic and clinical levels. Future research on the topography of gradients in other canonical neural oscillations could provide deeper insights into the pathology of PD.

References

1. Guerra, Andrea, et al. “Enhancing gamma oscillations restores primary motor cortex plasticity in Parkinson’s disease.” Journal of Neuroscience 40.24 (2020): 4788-4796.
2. Glasser, Matthew F., et al. “A multi-modal parcellation of human cerebral cortex.” Nature 536.7615 (2016): 171-178.
3. Ji, Jie Lisa, et al. “Mapping the human brain’s cortical-subcortical functional network organization.” Neuroimage 185 (2019): 35-57.
4. Vos de Wael, Reinder, et al. “BrainSpace: a toolbox for the analysis of macroscale gradients in neuroimaging and connectomics datasets.” Communications biology 3.1 (2020): 103.

Poster No 1636

Global brain function is predicted by the brain's anatomical connectivity and myelination

Parul Verma[1], Benjamin Sipes[2], Joline Fan[1], Srikantan Nagarajan[1], Ashish Raj[1]

[1]University of California San Francisco, San Francisco, CA, [2]University of California, San Francisco, San Francisco, CA

Introduction: Understanding how the dynamic brain functional patterns arise despite the brain's structural constraints is a prevailing question in neuroscience. We address this question by quantifying brain function in terms of spectral patterns and the alpha frequency band (8-13 Hz) spatial patterns as observed in magnetoencephalography (MEG). The brain structural constraints are quantified in terms of the anatomical connectivity and regional myelination. Subsequently, we investigate how the spectral and spatial patterns arise in different states of consciousness.

Methods: We use whole-brain biophysical modeling that incorporates the brain's anatomical connectivity and regional myelination to predict the spectral and spatial patterns as observed with MEG. It is a global analytic model that describes the coupled excitatory and inhibitory activity of local neuronal subpopulations, and the long-range excitatory macroscopic activity, for every brain region. The local neuronal excitatory and inhibitory time constants are modulated by the extent of myelination in that region. The model is parameterized by a small set of global parameters that we inferred for two healthy cohorts (N=36, 18). We investigate the following three different states of consciousness: wakefulness, non-rapid eye movement sleep (N2 stage), and propofol-induced anesthesia.

Results: We show that the spectral and spatial patterns are predictable from the brain's anatomical connectivity and regional myelin map in the resting wakefulness state, using the biophysical model (Fig 1A and B). We confirm this finding in two healthy cohorts (N=36, 18; figures shown only for the N=18 cohort). Further, the model can capture the transition of the spectral peak in the alpha band in wakefulness to the delta band in the N2 stage (Fig 1A). Simultaneously, it can capture the disappearance of the alpha band spectral power's posterior-anterior spatial gradient when transitioning from wakefulness to N2 stage (Fig 1B). Comparing the model parameters show that the overall global coupling is increased in N2, in addition to changes in the excitatory signals (not shown). Last, increasing the inhibitory neuronal time constant to simulate the effect of propofol anesthesia in the model results in arousal of delta waves, as observed in empirical EEG-based studies previously (Fig 1C). Simultaneously, it results in an anteriorization of the alpha band's spatial patterns, as observed in prior empirical studies.

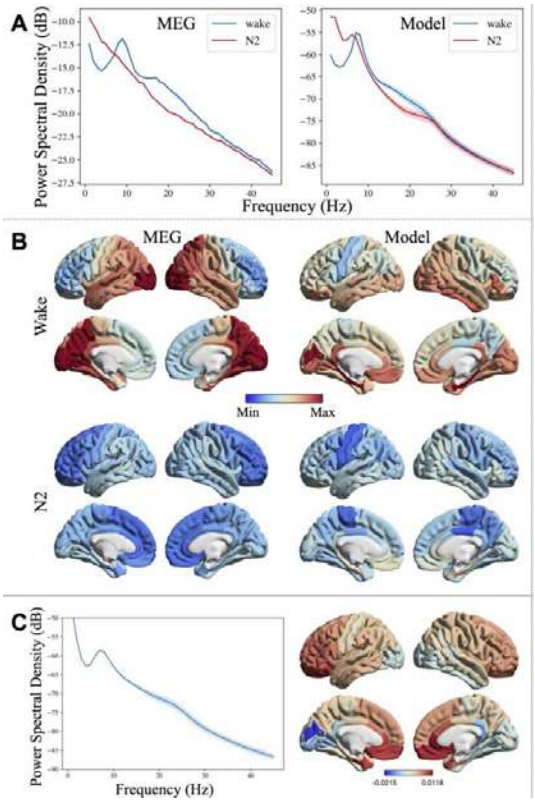

A: Power spectral density for subjects under wakefulness (blue) and N2 sleep stage (red) from MEG (left) and model (right).

B: Spatial pattern of alpha frequency band (8-13 Hz) spectral power for wakefulness (top) and N2 (bottom) from MEG (left) and model (right).

C: Power spectral density obtained by increasing the inhibitory time constant in the model to simulate the effect of propofol anesthesia (left). Difference in alpha band spectral power between model simulation after increasing inhibitory time constant and model simulation for wakefulness.

Conclusions: Together, these results suggest a parsimonious explanation for the spectral and spatial patterns in wakefulness, N2 sleep, and general anesthesia. In addition, comparing the biophysical parameters when transitioning from resting state to N2 sleep allows us to infer the biophysical mechanisms underlying this transition.

References
1. Raj, Ashish, et al. “Spectral graph theory of brain oscillations.” Human brain mapping 41.11 (2020): 2980-2998.
2. Purdon, Patrick L., et al. “Clinical electroencephalography for anesthesiologists: part I: background and basic signatures.” Anesthesiology 123.4 (2015): 937-960.

Poster No 1637

Alpha Oscillations During Speech Information Encoding

Ehsan Eqlimi[1,2,3], Heather Read[1]

[1]Sensory Perception & Neuroscience Lab, Department of Biomedical Engineering, University of Connecticut, Storrs, CT, USA, [2]WAVES Research Group, Department of Information Technology, Ghent University, Ghent, Belgium, [3]Data Science Team, Department of Process and Quality, AZORG Hospital (formerly OLV), Aalst, Belgium

Introduction: Brain alpha oscillations, central to cognitive processes, face evolving interpretations. In the auditory context, uncertainty arises from auditory alpha’s existence, EEG measurability, and potential visual alpha dependence. A pivotal 1999 finding challenged expectations, suggesting alpha’s inhibitory role as a neural cyclic ‘brake’ during mental activity. The causality of this relationship remains debated. Research distinguishes lower and upper alpha frequencies, crucial for identifying peaks in diverse brain regions during cognitive tasks. Alpha oscillations play a key role in parsing sensory information, emphasizing power, frequency, and phase in tasks requiring perceptual parsing and temporal binding. EEG studies on alpha oscillations focus on parsing brain responses into components, offering insight into short-term information processing. Yet, understanding prolonged behaviors, especially in goal-oriented tasks with continuous and complex information, remains a gap. Our HD-EEG study addresses this, investigating alpha oscillation modulations during attentive listening to 5-minute speeches with and without multitalker noise. We explore their predictive role in memory and retention performance, aiming to enhance comprehension of alpha oscillations’ extended cognitive engagement.

Methods: 23 listeners underwent 4 speeches without and 3 with multitalker background noise, covering diverse Belgian culture topics. The 64-channel EEG data was recorded continuously during attentive listening, followed by a written exam 45 minutes later to assess scores for all 7 speeches. After preprocessing, three alpha oscillation features were extracted: alpha peak frequency, alpha peak power, and long-range temporal correlations (LRTC). Linear mixed-effect modeling analyzed multitalker noise impact and its linear relationship with exam scores. Time-frequency analysis using a GAMM compared topics and background noise effects. Nonparametric cluster-based permutation testing assessed channel influence on alpha manifestation.

Results: Despite a significant decline in exam scores with background noise, no difference in alpha peak power and frequency was observed. However, alpha LRTC increased during multitalker noise, correlating negatively with exam scores, suggesting a role in speech perception and memory in noise. Increased synchronization of alpha peak frequency occurred in temporal lobes, contrasting with higher alpha peak power mainly in occipital lobes and less in temporal, central, and frontal areas. Nonparametric tests showed no significance, but alpha LRTC changed significantly with background noise, increasing in occipital and temporal regions and decreasing in the frontal region. This suggests enhanced suppression of task-irrelevant input in occipital and temporal regions, with increased task-vigilance in frontal areas. In theory, increased LRTC in occipital and temporal regions could facilitate suppression of task-irrelevant background audio and visual input. Conversely, decreased LRTC in frontal executive control areas could facilitate task-vigilance. Overall, LRTC increased across channels in the noisy condition. Analyzing the modulated alpha changes over time, measured by LRTC, inspired us to examine the evolving alpha power pattern between conditions. Although no significant difference was found in average alpha power, temporal progression analysis using GAMM uncovered a significant increase in noisy conditions in the second part of the trend (after the first minute).

Conclusions: Results emphasize alpha oscillations’ role in top-down speech attention, highlighting temporal dynamics during distractions. Heightened cognitive effort is reflected in increased alpha LRTC, suggesting implications for focused attention and speech information encoding. The two-stage alpha trend reveals initial sensory processes and a subsequent increase in effort for higher-level cognitive engagement, including mnemonic binding and memory encoding, especially evident in multitalker noise.

References
1. Haegens, S. (2011). Alpha oscillations in the monkey sensorimotor network influencing discrimination performance by rhythmical inhibition of neuronal spiking. Proceedings of the National Academy of Sciences, 108(48), 19377–19382.
2. Klimesch, W., Doppelmayr, M., Schwaiger, J., Auinger, P., & Winkler, T. (1999). ‘Paradoxical’ alpha synchronization in a memory task. Cognitive Brain Research, 7(4), 493–501.

3. Peylo, C., Hilla, Y., & Sauseng, P. (2021). Cause or consequence? Alpha oscillations in visuospatial attention. Trends in Neurosciences, 44(9), 705–713.
4. VanRullen, R. (2016). Perceptual cycles. Trends in Cognitive Sciences, 20(10), 723–735.

Poster No 1638

Correspondence of dynamic resting-state networks in source space EEG and MEG

SungJun Cho[1], Chetan Gohil[1], Mats van Es[1], Mark Woolrich[1]

[1]University of Oxford, Oxford, United Kingdom

Introduction: The resting state networks (RSNs) in EEG and MEG have been pivotal for understanding the oscillatory dynamics underlying various cognitive functions and clinical conditions[1-3]. While most studies have focused on static RSNs, analysing network activities averaged over time, the dynamic aspect of these networks, especially in EEG, has received less attention. Traditional methods like microstates, sliding window correlation, and temporal independent component analysis have explored EEG-based dynamic RSNs before, but with limitations inherent to their assumptions[4-6]. The Hidden Markov Model (HMM)[7,8] has advanced the study of dynamic RSNs in MEG, but their comparability to EEG remains underexplored. Our study addresses this gap, demonstrating that dynamic RSNs can be reliably inferred in source space EEG and showing similar group-level effects in both EEG and MEG.

Methods: In this study, we utilized the Leipzig Study for Mind-Body-Emotion Interactions EEG dataset[9] and the Cambridge Centre for Ageing and Neuroscience MEG dataset[10]. To facilitate comparative analyses, we age-matched these data, resulting in 96 healthy subjects per dataset, each consisting of 60 young (20-35 years) and 36 older (55-80 years) adults. The sensor signals were projected onto the source space using a beamformer. Next, we employed the Time-Delay Embedded HMM[8] to segment source reconstructed data into eight distinct dynamic RSNs, each described by a unique multivariate Gaussian model and associated oscillatory profiles. Using the inferred state activation time courses, three state-specific brain network features were extracted at the individual level: power spectral densities (PSDs), power maps, and functional connectivity (i.e., coherence) maps[11]. To contrast the ability of M/EEG in resolving the effects of interest, we investigated group-level differences between two age groups by fitting each network feature to a General Linear Model[12], with sex and head size as covariates. The statistical significance of age-related effects in network features was determined using nonparametric max-t or cluster permutation tests. The alpha significance threshold was set to 0.05.

Results: Our analysis revealed that dynamic RSNs display comparable subject-averaged PSDs and wide-band (1-45 Hz) power maps across both modalities in source space. Wide-band coherence maps of EEG exhibited slightly more noise compared to MEG. Overall, canonical RSNs, such as the anterior and posterior default mode networks, visual network, and sensorimotor network, were consistently identified in both modalities (Fig. 1). This aligns with the previous study that found similar spatial signatures in wide-band (3-40 Hz) power maps between EEG and MEG in sensor space[13]. Regarding age-related effects in dynamic RSNs, MEG demonstrated more pronounced age effects in PSDs, while both EEG and MEG reported similar age-related changes in narrow-band power and coherence maps. Specifically, delta (1-4 Hz) and theta (4-8 Hz) power maps indicated reduced activity in frontotemporal, parietal, and sensorimotor cortices with aging across HMM states, whereas beta (13-30 Hz) power maps showed increased activity in these regions. These age-related changes conformed to those reported in previous research[14,15]. Age-dependent changes in coherence generally mirrored those in power but with more globally widespread activations.

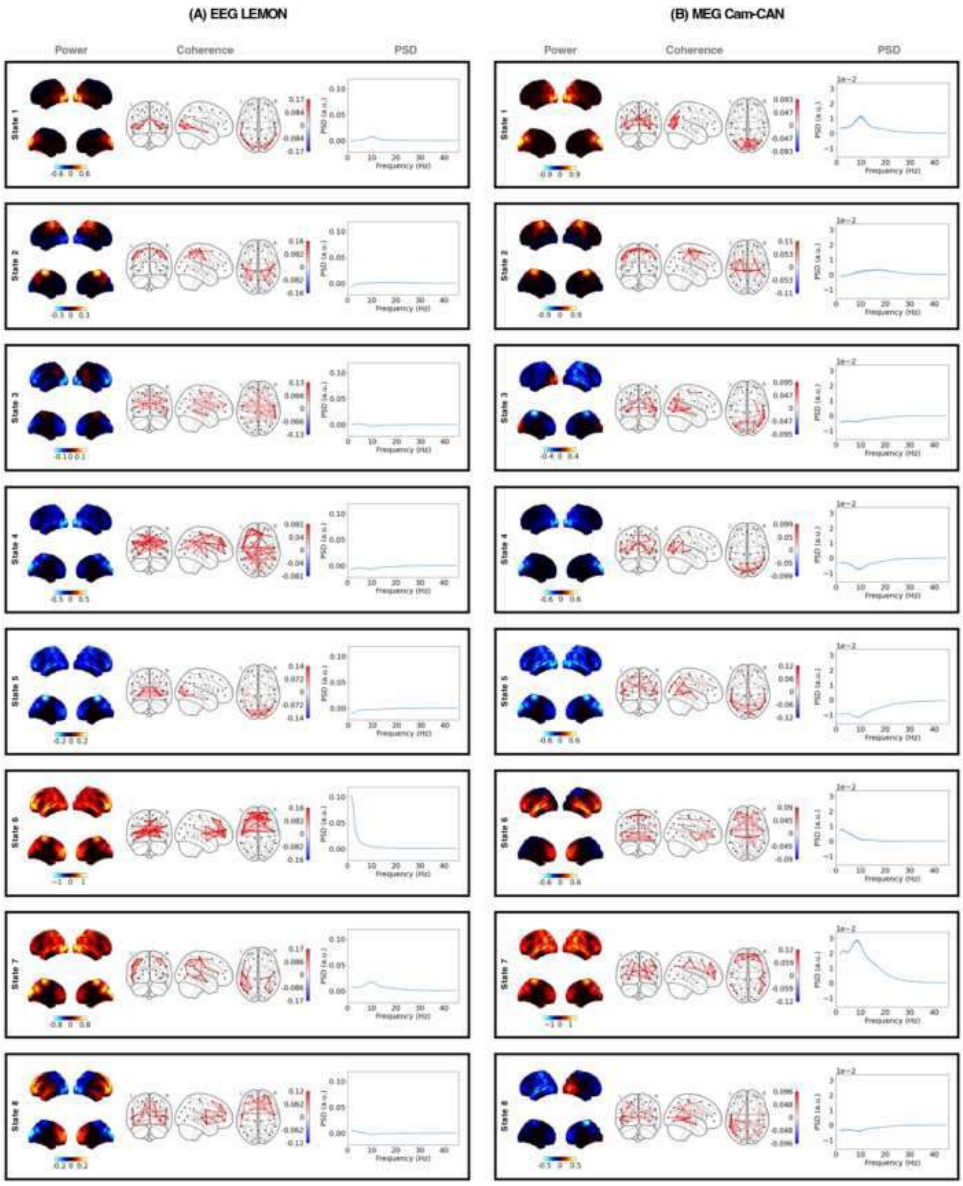

Figure 1: HMM resting-state network states inferred from the EEG and MEG datasets. (A) Each box shows the power map (left), FC network (middle), and parcel-averaged PSD (right) of each HMM state for 96 EEG subjects. The power maps show lateral surfaces at the top and medial surfaces at the bottom. The FC networks illustrate connections with the top 3% coherence values. The shaded areas of the PSDs represent the standard error of the mean. The power maps, FC networks, and PSDs are visualized relative to their average across all states. **(B)** The plots follow the same format as (A), showing the RSNs computed from 96 MEG subjects. EEG and MEG states were ordered and labelled by manually pairing the power maps.

Conclusions: In summary, our findings demonstrate that dynamic RSNs can be reliably estimated from EEG, as in MEG. The brain network features derived from these RSNs robustly replicate previously reported age effects, which were comparable across modalities. These results validate the use of current methodologies and generative models in EEG analysis, corroborating the existence of canonical RSNs in EEG akin to those in MEG and fMRI. Consequently, this supports the broader application of these techniques to clinical and cognitive datasets obtained through EEG.

References

1. Higgins C et al. (2021). Replay bursts in humans coincide with activation of the default mode and parietal alpha networks. Neuron, 109:882-893.
2. Sitnikova TA et al. (2018). Short timescale abnormalities in the states of spontaneous synchrony in the functional neural networks in Alzheimer's disease. NeuroImage:Clinical, 20:128-152.
3. Nour MM et al. (2023). Reduced coupling between offline neural replay events and default mode network activation in schizophrenia. Brain Communications, 5(2):fcad056.
4. Custo A et al. (2017). Electroencephalographic Resting-State Networks: Source Localization of Microstates. Brain Connectivity, 7(10):671-682.
5. Zink N et al. (2021). Resting-state EEG Dynamics Reveals Differences in Network Organization and its Fluctuation between Frequency Bands. Neuroscience, 453:43-56.

6. Chen J et al. (2013). Dynamic Changes of ICA-Derived EEG Functional Connectivity in the Resting State. Human Brain Mapping, 34:852-868.
7. Baker AP et al. (2014). Fast transient networks in spontaneous human brain activity. eLife, 3:e01867.
8. Vidaurre D et al. (2018). Spontaneous cortical activity transiently organises into frequency specific phase-coupling networks. Nature Communications, 9(1):2987.
9. Babayan A et al. (2019). A mind-brain-body dataset of MRI, EEG, cognition, emotion, and peripheral physiology in young and old adults. Scientific Data, 6:180308.
10. Shafto MA et al. (2014). The Cambridge Centre for Ageing and Neuroscience (Cam-CAN) study protocol: a cross-sectional, lifespan, multidisciplinary examination of healthy cognitive ageing. BMC Neurology, 14:204.
11. Gohil C et al. (2022). Mixtures of large-scale dynamic functional brain network modes. NeuroImage, 263:119595.
12. Quinn AJ et al. (2022). The GLM-Spectrum: A multilevel framework for spectrum analysis with covariate and confound modelling. bioRxiv:2022.11.14.516449.
13. Coquelet N et al. (2022). Microstates and power envelope hidden Markov modeling probe bursting brain activity at different timescales. NeuroImage, 247:118850.
14. Rossini PM et al. (2007). Clinical neurophysiology of aging brain: From normal aging to neurodegernation. Progress in Neurobiology, 83(6):375-400.
15. Babiloni C et al. (2006). Sources of Cortical Rhythms in Adults During Physiological Aging: A Multicentric EEG Study. Human Brain Mapping, 27:162-172.

Poster No 1639

Neurovascular Coupling During Task Engagement and Resting State in Concurrent EEG and MRI

Yi-Chia Kung[1], Chia-Wei Li[2], Ai-Ling Hsu[3], Chi-Yun Liu[4], Changwei Wu[4,5], Wei-Chou Chang[1], Ching-Po Lin[6]

[1]Department of Radiology, Tri-service General Hospital, National Defense Medical Center, Taipei, Taiwan, [2]Department of Radiology, Wan Fang Hospital, Taipei Medical University, Taipei, Taiwan, [3]Chang Gung University, Taoyuan, Taiwan, [4]Graduate Institute of Mind, Brain and Consciousness, Taipei Medical University, Taipei, Taiwan, [5]Research Center of Sleep Medicine, Taipei Medical University Hospital, Taipei, Taiwan, [6]Institute of Neuroscience, National Yang Ming Chiao Tung University, Taipei, Taiwan

Introduction: Neurovascular coupling constitutes a pivotal neurophysiological mechanism within functional neuroimaging, which traditionally posited to exhibit robustness across physiological states, encompassing both task engagement and resting states. However, recent evidence suggests that neurovascular may exhibit state-dependent variability in humans[1]. By employing concurrent EEG and fMRI or neurovascular coupling, we investigated the cross-frequency spectral correspondence in two distinct states: Eyes-Open-Eyes-Close (EOEC) task and resting.

Methods: The simultaneous EEG-fMRI data were collected from 14 young participants (7 females; mean age=25.6±3.9) using 3T SIEMENS Trio MRI with a 32-channel MRI-compatible system (Brain Products, Gilching, Germany). The functional data (TR/TE/FA=2500ms/30ms/80°, FOV=220, matrix size=64x64, 35 slices with 3.4 mm thickness) were collected under EOEC task and a resting state. The EOEC protocol comprised three blocks, each featuring a 30-second epoch of both eye-open and eye-closed states. We used Hilbert-Huang Transformations (HHT) with amplitude-amplitude coupling (AAC) and phase-amplitude coupling (PAC) analysis to explore neurovascular coupling. The HHT[2] entailed: (1) decomposition of the dataset into intrinsic mode functions (IMFs), (2) calculating the instantaneous frequency in IMFs, and (3) presenting spectral information through Hilbert spectral analysis (HSA). PAC was calculated via cross-frequency correlations between the IMFs of fMRI signals and the HSAs of EEG signals, while AAC was determined through correlations across HSA maps. Group-level PAC/AAC across IMFs or frequency bands was evaluated using one-sample t-tests.

Results: For EOEC task, as shown in Figure 1, the activated cluster in the occipital lobe was selected from fMRI signal for neurovascular coupling analysis with EEG-Oz signal. In the PAC between EEG and fMRI, significant negative correlation (Bonferroni-corrected $p < 0.05$) emerged between theta/alpha-bands of EEG and the IMFs (0.008-0.031 Hz) of fMRI signal during the EOEC task. In the AAC between EEG and fMRI, beta- and gamma-bands of EEG showed significant positive correlation with fMRI signal in 0.025-0.05 and 0.1-0.125 Hz frequency ranges, respectively, during the EOEC-task performed. In resting-state, as shown in Figure 2, no significant PAC correlation was found between EEG signal from the Oz channel and fMRI signals. However, fMRI signal in the relative higher frequency band (0.15-0.25 Hz) displayed a significant positive AAC with the gamma band of the EEG-Oz channel (Bonferroni corrected $p<0.05$).

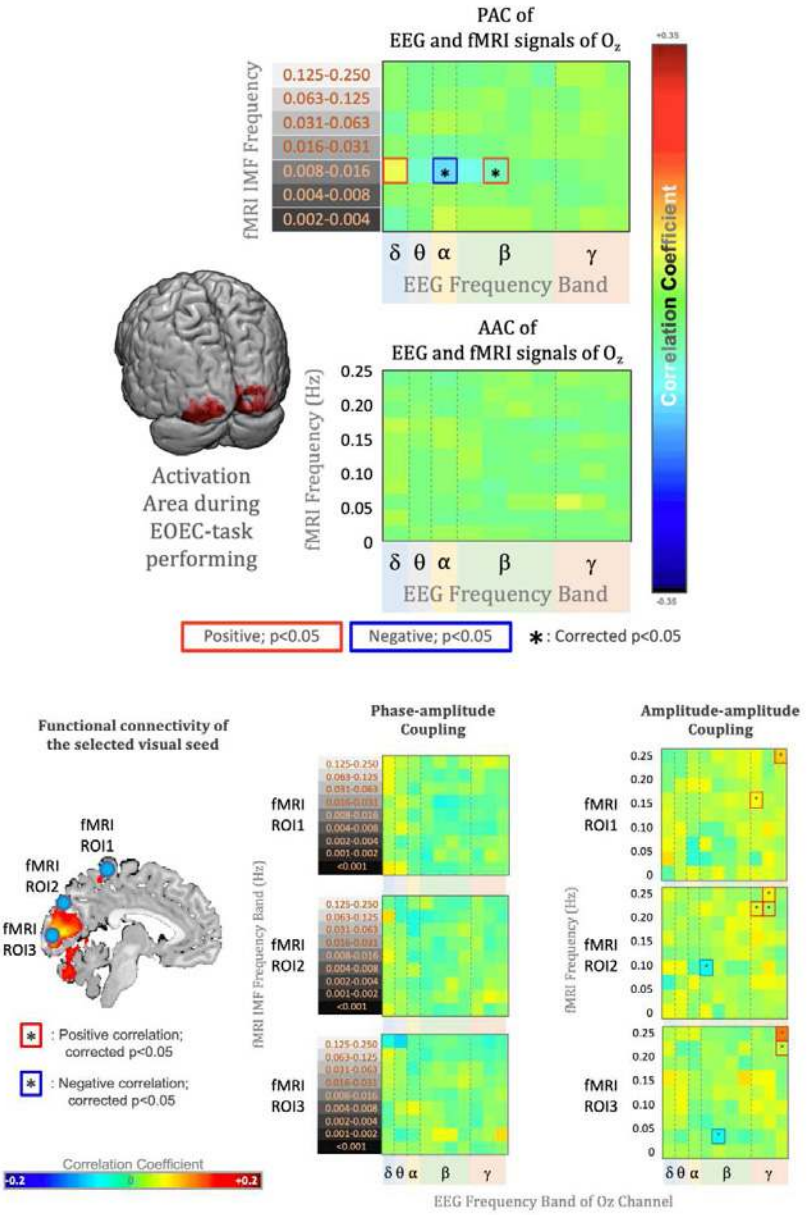

Conclusions: Our study examined the neurovascular coupling through the EEG-fMRI spectral correspondence in both EOEC and resting conditions. During the EOEC task, we observed a negative PAC between alpha-band EEG oscillations and the relevant fMRI fluctuation of visual activation. In the resting state, AAC of EEG-fMRI was present between gamma-band of EEG-Oz and the high-frequency band fMRI signals within the visual network. This dichotomy may stem from the nonlinear characteristic of resting-state fluctuations, distinct from those observed in task engagement[3]. Further, PAC affords insight into the temporal dynamics of neural oscillations, while AAC provides insight into the intensity relationship between different rhythms[4]. To sum, the divergent findings between EOEC and resting states intimate that neurovascular coupling via EEG-fMRI synchronization may be contingent on cognitive or physiological states rather than representing a static relationship. These revelations hold significant import for the comprehension of brain functionality and the refinement of neuroimaging data interpretation.

References

1. Wu, C. W. (2019). 'Indication of Dynamic Neurovascular Coupling from Inconsistency between EEG and fMRI Indices across Sleep–Wake States.' Sleep and Biological Rhythms, vol. 17, no.4, pp. 423–31.
2. Huang, N. E. (1998), 'The Empirical Mode Decomposition and the Hilbert Spectrum for Nonlinear and Non-Stationary Time Series Analysis.' Proceedings of the Royal Society of London. Series A: Mathematical, Physical and Engineering Sciences, vol. 454, no. 1971, pp. 903–95.
3. Gultepe, E., and Bin H. (2013). 'A Linear/Nonlinear Characterization of Resting State Brain Networks in fMRI Time Series.' Brain Topography, vol. 26, no. 1, pp. 39–49.
4. Bruns, A. and Reinhard E. (2004), 'Task-Related Coupling from High- to Low-Frequency Signals among Visual Cortical Areas in Human Subdural Recordings.', International Journal of Psychophysiology, vol. 51, no. 2, pp. 97–116.

Poster No 1640

Decoding Depth of Meditation: Neurophysiological Insights from Expert Vipassana Practitioners

Nicco Reggente[1], Tracy Brandmeyer[1], Ninette Simonian[1], Christian Kothe[2]

[1]Institute for Advanced Consciousness Studies, Santa Monica, CA, [2]Intheon, Inc., San Diego, CA

Introduction: This project's overarching objective is to develop a personalized, multivariate neurofeedback tool to assist meditation, addressing the limitations of generic models in the face of neurodiversity and compensatory mechanisms (Brandmeyer & Reggente, 2024). In pursuit of this goal, we first conducted an EEG study with expert Vipassana practitioners (n=40), leveraging the standardized nature of Vipassana and the experts' ability to discern subtle gradations of meditative depth. Recognizing the challenges posed by self-reports (e.g., the "observer phenomenon" where reporting can disrupt the meditative state), we used these expert-defined self-reports as a gold standard. Across two sessions (held 2 weeks apart), we leveraged machine learning (deep neural nets) to predict meditative depth across sessions, aiming to identify implicit neural markers that track meditative depth. We also included a passive auditory oddball task to identify if oddball ERPs varied as a function of depth. The goal of this current project is to refine these implicit, predictive markers, facilitating non-intrusive tracking of meditation in future studies without the need for explicit self-reports.

Methods: Participants Expert Vipassana practitioners were recruited based on the following criteria: a minimum of 5 years of consistent practice, participation in at least one 3-day silent retreat, and a report of meditating at least 20 minutes for a minimum of 5 days per week. Procedure Upon arrival, participants completed pre-experiment questionnaires. They were then fitted with a 64-channel EEG and peripheral monitoring devices to record heart rate, respiration rate, EMG, and GSR. Participants underwent two 35-minute meditation blocks (additional blocks and tasks beyond the scope of this report were also conducted). Post-meditation, participants filled out subsequent questionnaires. The entire process was repeated in a follow-up session 2 weeks later. During the four meditation blocks, participants were either exposed to a passive auditory oddball tone sequence they were instructed to ignore. Meditation blocks were characterized by one of two types: Probed Trials: Participants were instructed to report their meditative depth on a scale of 1-5 using a finger-attached presentation clicker in response to an auditory probe presented approximately every 4 minutes. Emergence Trials: Participants reported their meditative depth organically, only when they perceived a change from a deeper state since their last report. Data Analysis Event-related potential (ERP) analyses were conducted to ascertain changes in response to the oddball tone contingent on meditative depth. Deep neural networks employing FIR-type filter kernels (Bouallegue et al., 2020) were applied to the EEG time series between reporting periods across all channels. Two cross-validation methods were adopted: Eight-fold Cross-validation: This was executed across participants, amalgamating data from all sessions and participants. Leave-one-session-out Cross-validation: This was conducted within individual participants. Predictive models aimed to discern meditation depth at either all 5 levels or as a binary classification (shallow[1,2] vs. deep[4,5]). Performance metrics included mean square error for the 1-5 classification and area under the curve (AUC) for the binary classification.

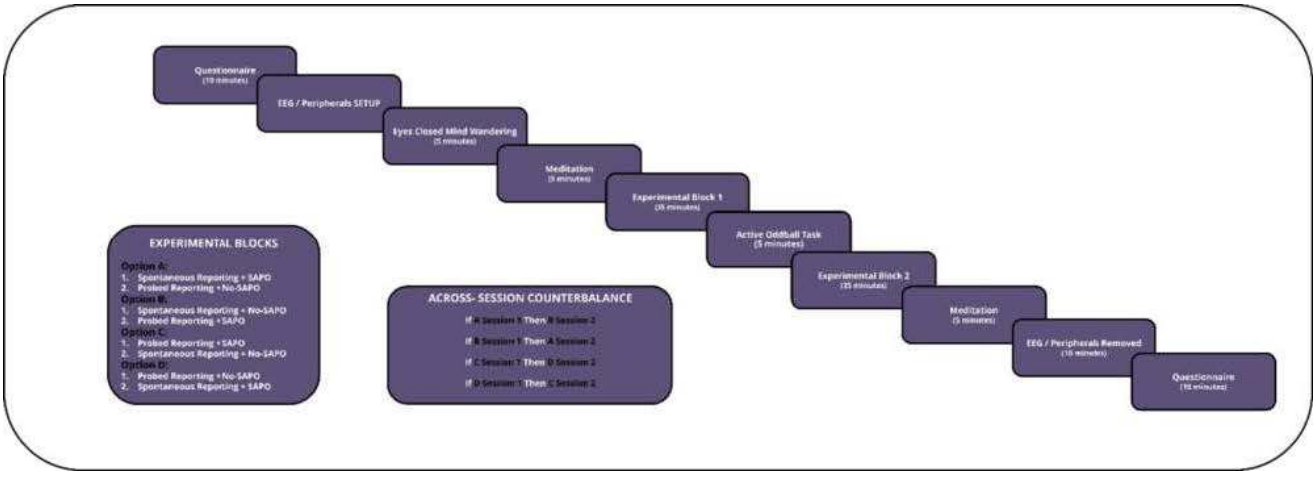

Results: Significant ERP differences were noted by depth, with increased frontal midline theta and parietal beta values. ERP scaled linearly with depth, predicting it in meditation with 1.2 MAE (5-way) and .81 AUC (deep vs. shallow). Cross-validation showed similar results (1.1 MAE, .76 AUC). A real-time metric, ranging 0-1 at 33Hz, measured the qualia distance to an ideal meditation state.

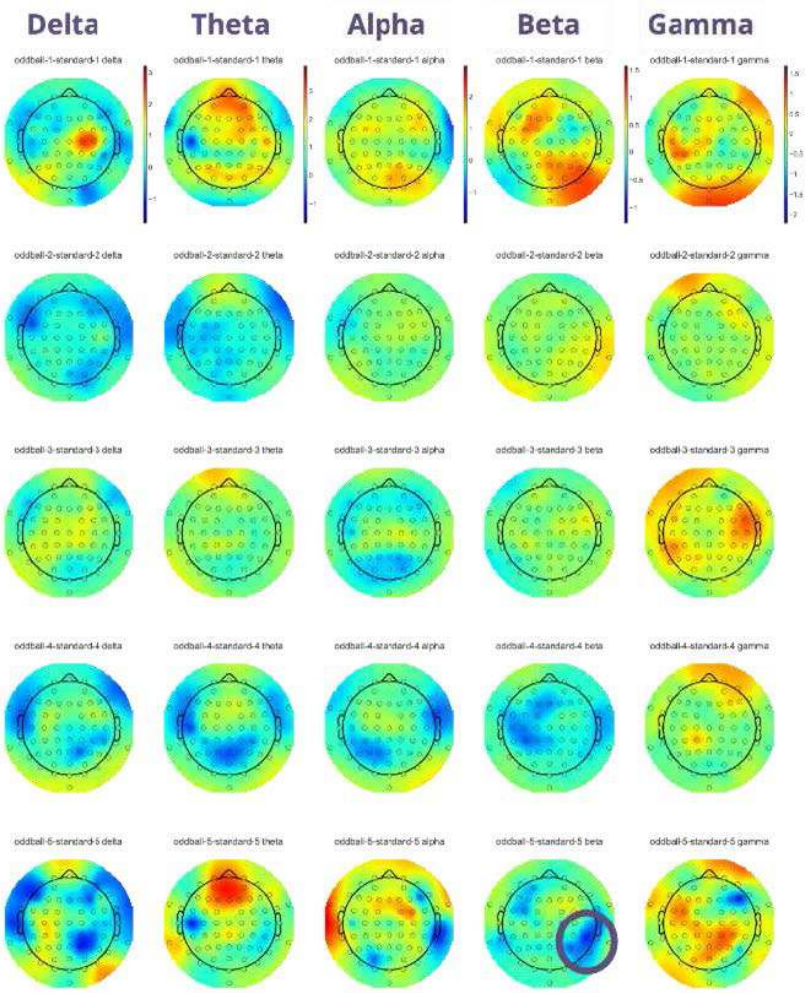

Conclusions: Expert meditators show amplified ERPs to oddballs as a function of meditative depth. Meditatiive depth can also be implicitly decoded in ways that promote personalized neurofeedback systems.

References

1. Brandmeyer, T., & Reggente, N. (2024). Navigating the 'Zen Zeitgeist': The potential of personalized neurofeedback for meditation assistance. Psychological Bulletin. (Under review)
2. Bouallegue, G., Djemal, R., Alshebeili, S. A., and Aldhalaan, H. (2020). A Dynamic Filtering DF-RNN Deep-Learning-Based Approach for EEG-Based Neurological Disorders Diagnosis. IEEE Access 8, 206992–207007. doi: 10.1109/ACCESS.2020.3037995.
3. Debener, S., Kranczioch, C., Herrmann, C. S., and Engel, A. K. (2002). Auditory novelty oddball allows reliable distinction of top–down and bottom–up processes of attention. International Journal of Psychophysiology 46, 77–84. doi: 10.1016/S0167-8760(02)00072-7.

Poster No 1641

A Novel Spatio-Temporal Event Network Information Mining Method for Resting-state EEG

Qiwei Dong[1,2,3], Runchen Yang[2,4], Zongwen Feng[2,4], Li Dong*[2,4], Qi Xu[1,3], Dezhong Yao[2,3,4]

[1]Institute of Basic Medical Sciences (IBMS), Chinese Academy of Medical Sciences & Peking Union, Medical College (CAMS & PUMC), Beijing, China, [2]The Clinical Hospital of Chengdu Brain Science Institute, MOE Key Lab for Neuroinformation, University of Electronic Science and Technology of China, Chengdu, China, [3]Research Unit of NeuroInformation, Chinese Academy of Medical Sciences, Chengdu 2019RU035, China, [4]Sichuan Institute for Brain Science and Brain-Inspired Intelligence, Chengdu, China

Introduction: In face of the complex brain information, it is necessary to explore the spatiotemporal dimension in order to elucidate the precise temporal coordination and spatial connectivity patterns (Iraji et al., 2022; Park and Friston, 2013). However, there is presently a significant shortfall in the development of EEG-based method for mining spatiotemporal information of brain activity. This study introduces a novel framework, named EEG Spatio-Temporal Event Network Analysis (ESENA), to map rhythmic activity related events into a network structure according to their temporal sequence to mine

spatiotemporal patterns of the brain. The purpose of this study was to introduce ESENA for validating the mapping and interpretation of dynamic brain activity patterns during resting-state condition.

Methods: Data were collected from 50 subjects (age range = 18-22 years) during a resting-state with their eyes closed. All data were preprocessed and analyzed using the WeBrain toolbox (Dong et al., 2021). The main procedures included: filtering (1-60Hz), quality assessment, artifacts removal using ICA, re-referencing to REST and bad channels interpolating. Based on the extraction of recurrent spatiotemporal patterns from EEG data (Ferreira et al., 2020), the ESENA analysis contains following steps: 1) segmenting clean EEG data into epochs of equal length, 2) calculating the relative power spectrum (Delta: 1-4Hz, Theta: 4–8 Hz, Alpha: 8–12.5 Hz, Beta: 12.5–30 Hz, Gamma: 30–60 Hz) for each epoch, 3) defining events of channels that exceed a given threshold (event threshold) are identified as detected events for each epoch, and 4) constructing network by accumulating links of adjacent epoch channels with events and normalizing to 0-1. The parameters of event threshold and data length were investigated, and a one-sample T-test is conducted on all the links (FDR<0.05). After testing, connections that are consistently present in 60% of the dataset are retained as the final connections.

Results: As shown in Figure 1, the optimal parameter of event threshold was set at 1 standard deviation, and data length was set at 90s. In the delta band, links are mainly located in the fronto-parietal regions. The theta band networks are main links between central frontal and parietal areas. The alpha band network shows links in the inferior parietal-occipital regions. For the beta and gamma band, the ESENA highlights connections predominantly between the bilateral temporal lobes. In addition, the links of those networks are mainly located in the regions of relative power spectrum.

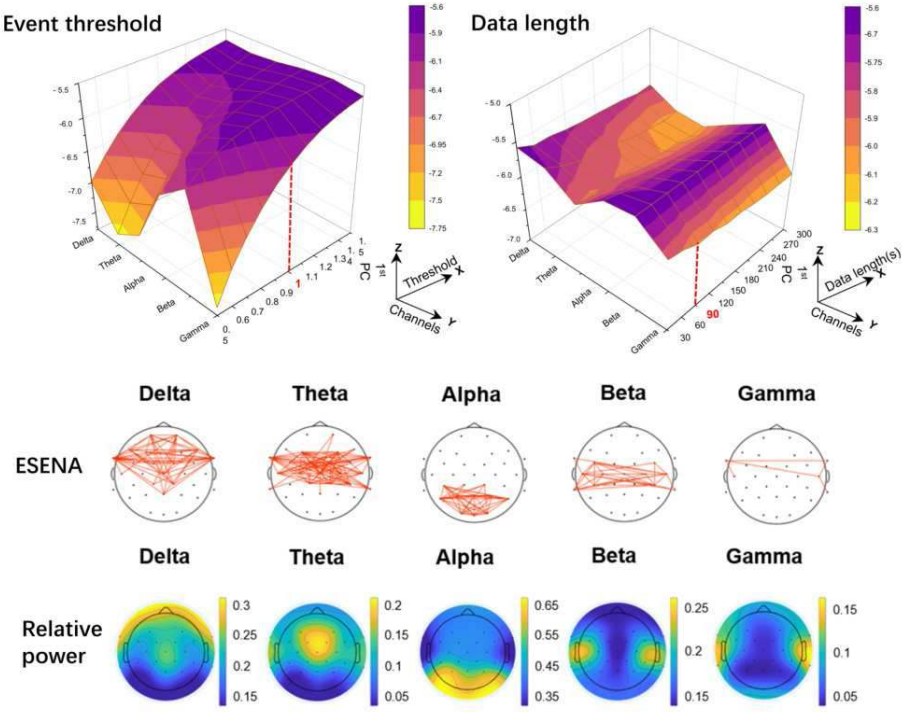

Figure 1. The first principal component of the event thresholds (mean relative power + 0.5-1.5*standard deviation of relative power) and data length (30-300s) of ESENA; ESENA analysis and relative power of eyes-closed resting state.

Conclusions: ESENA perhaps is a promised method to mine the spatio-temporal network information for resting-state EEG data. This method may provide new insight for enhancing our understanding of brain activity patterns.

References

1. Dong, L. (2021),' WeBrain: A web-based brainformatics platform of computational ecosystem for EEG big data analysis', Neuroimage. vol. 245, pp. 118713.
2. Ferreira, L.N. (2020), 'Spatiotemporal data analysis with chronological networks', Nature Communications, vol. 11, no.1, pp. 4036.
3. Iraji, A. (2022), 'Moving beyond the 'CAP' of the Iceberg: Intrinsic connectivity networks in fMRI are continuously engaging and overlapping', Neuroimage, vol. 251, pp. 119013.
4. Park, H.J. (2013), 'Structural and functional brain networks: from connections to cognition', Science, Vol. 342, no. 6158, pp. 1238411.

Poster No 1642

EEG-based emotion recognition in VR using functional brain networks and graph theoretical measures

Hyejeong Jo[1], Won Hee Lee[1]

[1]*Kyung Hee University, Yongin*

Introduction: Affective computing research using electroencephalography (EEG) data has traditionally used 2D displays, such as images or videos, to evoke emotional responses. However, this approach has limitations, especially when transitioning into 3D settings, as it often overlooks spatial differences in emotional responses and neural mechanisms (Suhaimi, Yuan et al. 2018; Tian, Hua et al. 2021). To address these limitations, virtual reality (VR) has emerged as a powerful tool for eliciting emotions in controlled laboratory environments, primarily due to its capability to create an immersive sense of presence in users (Alcañiz, Baños et al. 2003). Recent studies have explored the use of VR to establish highly immersive environments for emotion recognition (Suhaimi, Mountstephens et al. 2022; Yu, Xiao et al. 2022). In this work, we aim to improve the accuracy of emotion recognition using EEG data collected within VR environments. Specifically, we employ a machine learning-based approach that leverages functional brain networks and graph theoretical measures to differentiate between positive and negative emotional states.

Methods: We used the VREED dataset consisting of high-density (59-channel) EEG data collected from 19 healthy participants immersed in a VR environment (Yu, Xiao et al. 2022). We constructed functional connectivity (FC) matrices between pairs of EEG electrodes using coherence (Bowyer 2016) for each emotional stimulus (positive/negative) across six different frequency bands (delta, theta, alpha, beta, gamma, and high gamma) (Figure 1A). We applied the minimum spanning tree algorithm to transform each FC matrix into an undirected binary graph (Tewarie, van Dellen et al. 2015). We then computed graph theoretical properties of the binarized FC, including characteristic path length, global efficiency, clustering coefficient, local efficiency, betweenness centrality, node degree, and eigenvector centrality (Vecchio, Miraglia et al. 2017). We focused on the binary emotion classification of negative and positive emotional states by using FC and graph theoretical measures as features. We identified significant FC features between positive and negative states using a network-based statistic approach (Zalesky, Fornito et al. 2010). Significant graph theoretical measures were determined using ANOVA, followed by post-hoc pairwise comparisons using the Games-Howell test (Figure 1B). To assess the classification performance, we employed six commonly used machine learning algorithms (SVM, random forest, XGBoost, MLP, extra trees, kNN). We employed nested 10-fold cross-validation to evaluate the performance of our models (Figure 1C).

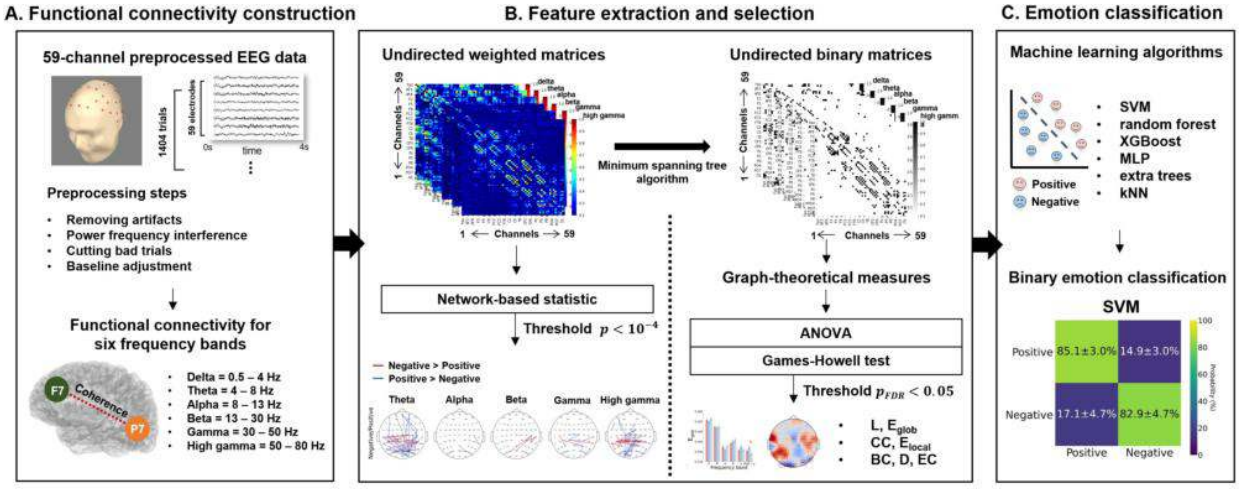

Figure 1. Workflow for EEG-based emotion recognition. (A) Preprocessed 59-channel VREED EEG dataset recorded in a virtual reality environment. Functional connectivity is constructed using coherence between EEG time-series on the scalp for six frequency bands (delta = 0.5 – 4 Hz, theta = 4 – 8 Hz, alpha = 8 – 13 Hz, beta = 13 – 30 Hz, gamma = 30 – 50 Hz, and high gamma = 50 – 80 Hz). (B) Feature extraction and selection process. Network-based statistic with threshold $p < 10^{-4}$ is applied to identify significant weighted network connections. Undirected weighted matrices are transformed to undirected binary matrices using the minimum spanning tree algorithm. Graph theoretical measures are calculated from undirected binary matrices, and significant graph theoretical features are determined using ANOVA, followed by post-hoc pairwise comparisons using the Games-Howell test. (C) Six different machine learning algorithms are evaluated for emotion classification to differentiate between positive and negative emotional states using a nested 10-fold cross-validation strategy. Abbreviations: L, characteristic path length; E_{glob}, global efficiency; CC, clustering coefficient; E_{local}, local efficiency; BC, betweenness centrality; D, node degree; EC, eigenvector centrality; SVM, support vector machine; XGBoost, extreme gradient boosting; MLP, multi-layer perceptron; kNN, k-nearest neighbors.

Results: Figure 2 shows the confusion matrices, illustrating the binary emotion classification results for the six different machine learning algorithms. Among these algorithms, random forest achieved the lowest classification accuracy of 71.6% (recall = 67.7%, f1-score = 70.5%, precision = 73.8%, AUC = 71.6%), while support vector machine demonstrated the highest classification accuracy of 84.0% (recall = 85.1%, f1-score = 84.3%, precision = 83.6%, AUC = 84.0%).

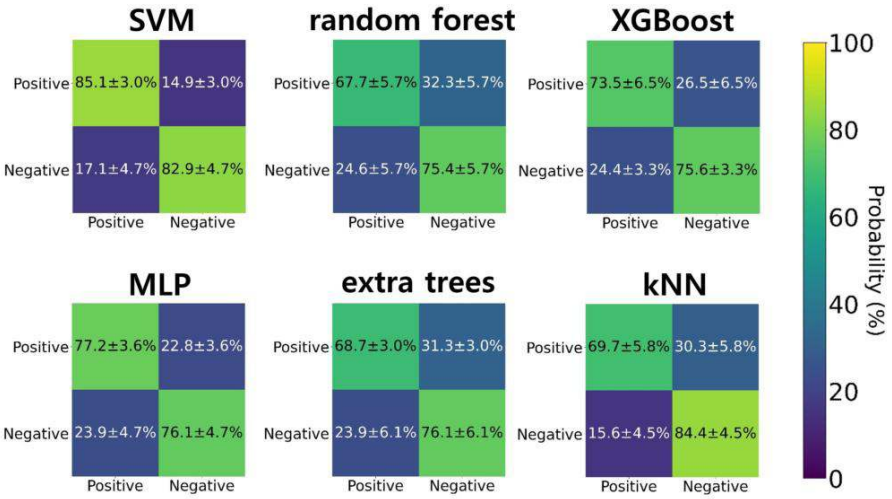

Figure 2. Classification performance. Confusion matrices of the binary emotion classification (positive/negative) from nested 10-fold cross-validation for each machine learning algorithm.

Conclusions: We conducted a comprehensive evaluation of six machine learning algorithms for emotion recognition using EEG recorded during emotional experiences in a VR environment. Our results revealed that SVM achieved the highest classification accuracy of 84.0% in binary emotion recognition. Our approach outperformed the existing literature, establishing state-of-the-art performance on the VREED dataset (Uyanık, Ozcelik et al. 2022; Yu, Xiao et al. 2022). These results suggest the potential of using functional brain networks and graph theoretical measures as effective features for EEG-based emotion recognition, as they capture local brain activities responsive to emotional states and reveal interactions among different brain areas.

References

1. Alcañiz, M., Baños, R., Botella, C. and Rey, B. (2003). 'The EMMA Project: Emotions as a determinant of presence', PsychNology Journal, vol. 1, no.2, pp. 141-150.
2. Bowyer, S. M. (2016). 'Coherence a measure of the brain networks: past and present', Neuropsychiatric Electrophysiology, vol. 2, no.1, pp. 1-12.
3. Suhaimi, N. S., Mountstephens, J. and Teo, J. (2022). 'A dataset for emotion recognition using virtual reality and EEG (DER-VREEG): emotional state classification using low-cost wearable VR-EEG headsets', Big Data and Cognitive Computing, vol. 6, no.1, pp. 16.
4. Suhaimi, N. S., Yuan, C. T. B., Teo, J. and Mountstephens, J. (2018). Modeling the affective space of 360 virtual reality videos based on arousal and valence for wearable EEG-based VR emotion classification. 2018 IEEE 14th International Colloquium on Signal Processing & Its Applications (CSPA), IEEE.
5. Tewarie, P., van Dellen, E., Hillebrand, A. and Stam, C. J. (2015). 'The minimum spanning tree: an unbiased method for brain network analysis', Neuroimage, vol. 104, pp. 177-188.
6. Tian, F., Hua, M., Zhang, W., Li, Y. and Yang, X. (2021). 'Emotional arousal in 2D versus 3D virtual reality environments', PloS one, vol. 16, no.9, pp. e0256211.
7. Uyanık, H., Ozcelik, S. T. A., Duranay, Z. B., Sengur, A. and Acharya, U. R. (2022). 'Use of differential entropy for automated emotion recognition in a virtual reality environment with EEG signals', Diagnostics, vol. 12, no.10, pp. 2508.
8. Vecchio, F., Miraglia, F. and Rossini, P. M. (2017). 'Connectome: Graph theory application in functional brain network architecture', Clinical neurophysiology practice, vol. 2, pp. 206-213.
9. Yu, M., Xiao, S., Hua, M., Wang, H., Chen, X., Tian, F. and Li, Y. (2022). 'EEG-based emotion recognition in an immersive virtual reality environment: From local activity to brain network features', Biomedical Signal Processing and Control, vol. 72, pp. 103349.
10. Zalesky, A., Fornito, A. and Bullmore, E. T. (2010). 'Network-based statistic: identifying differences in brain networks', Neuroimage, vol. 53, no.4, pp. 1197-1207

Poster No 1643

Inferring laminar origins of MEG signals with optically pumped magnetometers (OPMs)

Saskia Helbling[1]

[1]Ernst Strungmann Institute for Neuroscience, Frankfurt am Main, Germany

Introduction: Magnetoencephalography (MEG) is a non-invasive technique that measures the tiny magnetic fields generated by neural currents in the brain. Conventional MEG operates with superconducting SQUID magnetometers that must be immersed in liquid helium for cooling, which introduces a substantial gap between the sensors and the scalp. Optically-pumped magnetometers (OPMs) are new, highly sensitive magnetometers that operate without the need for cryogenic cooling and can be placed close to the scalp, substantially improving sensitivity to cortical sources (Boto et al., 2016, Iivanainen et al., 2017). The typical spatial resolution achieved by conventional MEG is not sufficient for laminar inference. One strategy to

distinguish between deep and superficial sources is to use high-precision forward models that exploit the small variations in the so-called lead fields between deep and superficial sources (Bonaiuto et al., 2018a and 2018b). On-scalp OPM-MEG has been suggested to further improve the discriminability of laminar sources. To investigate this, we simulate cortical sources at deep and superficial layers and infer their laminar origin using OPM sensor arrays with varying numbers of sensors and measurement axes.

Methods: We simulated OPM array designs with sampling distances between 25 and 55 mm in 10 mm increments and single, dual and triaxial sensor configurations, following Tierney et al. (2020). Current dipole sources were added to vertices of the white and the pial surface meshes reconstructed by FreeSurfer. For each surface, we randomly selected 60 vertices as cortical source locations. At each source location, a 20 Hz sinusoidal dipolar source patch was added to each of the 200 trials modelled per cortical source location. The dipolar sources were active for 400 ms. We determined the laminar origin of the simulated sources using a whole-brain and an ROI-based analysis, equivalent to those described in Bonaiuto et al. (2018), and used empirical Bayes beamformer (EBB) and multiple sparse priors (MSP) source reconstruction approaches. We compared the classification accuracy and bias of each analysis and source inversion algorithm using two-sided binomial tests and used logistic regression to evaluate changes in classification performance across sampling densities, number of axes and co-registration errors.

Results: We find that for an OPM-MEG sensor array with an inter-sensor distance of 35 mm we are able to achieve highly accurate laminar inferences at SNRs of -30 dB or higher. However, at high SNRs, we observed a bias towards the deep surface for the whole-brain analysis when combined with the EBB source reconstruction approach. For the EBB approach, classification accuracy significantly increased with decreasing inter-sensor distances and increasing number of measurement axes at moderate to high SNRs. The MSP approach exhibited classification performance close to ceiling levels for SNRs of -30 dB or higher. We note that laminar inference was possible at a low sensor counts of 32 at sufficiently high SNRs. We observed a steep decrease in classification accuracy with increasing co-registration errors for the EBB approach, where laminar inference was not feasible anymore at a co-registration error of 4 mm. For the MSP approach, classification accuracy remained high across co-registration errors but still decreased significantly with increasing co-registration errors.

Conclusions: Overall, we find that laminar inference with OPM arrays is possible at relatively low sensor counts at moderate to high SNRs. Laminar inference improved with increasing spatial sampling densities and number of measurement axes. Challenges persist in dealing with biases at very low SNRs and a distinct bias toward the deep surface when combining EBB source reconstruction with the free energy whole-brain analysis. Adequate SNR through appropriate trial numbers and shielding, as well as precise co-registration, is crucial for reliable laminar inference with OPMs.

References

1. Boto, E. et al. (2016), 'On the Potential of a New Generation of Magnetometers for MEG: A Beamformer Simulation Study', PLOS ONE, vol. 11, e0157655
2. Iivanainen, J. et al. (2017), 'Measuring MEG closer to the brain: Performance of on-scalp sensor arrays', NeuroImage, vol. 147, pp. 542–553
3. Bonaiuto, J.J. et al. (2018a), 'Non-invasive laminar inference with MEG: Comparison of methods and source inversion algorithms', NeuroImage, vol. 167, pp. 372–383
4. Bonaiuto, J.J. et al. (2018b), 'Lamina-specific cortical dynamics in human visual and sensorimotor cortices', eLife, vol. 7, e33977
5. Tierney, T.M. et al. (2020), 'Pragmatic spatial sampling for wearable MEG arrays', Scientific Reports, vol. 10, 21609

Poster No 1644

Benchmarking M/EEG inverse solutions to noise level misspecifications

Anuja Negi[1,2], Stefan Haufe[1,2,3,4], Alexandre Gramfort[5], Ali Hashemi[1,6]

[1]Technical University Berlin, Berlin, Germany, [2]Bernstein Center for Computational Neuroscience Berlin, Berlin, Germany, [3]Charité – Universitätsmedizin Berlin, Berlin, Germany, [4]Physikalisch - Technische Bundesanstalt Institute Berlin, Berlin, Germany, [5]Inria, Université Paris-Saclay, Paris, Paris, [6]The Berlin Institute for the Foundations of Learning and Data (BIFOLD), Berlin, Germany

Introduction: Magneto- and electroencephalographic (M/EEG) are non-invasive techniques that can measure electrical activity in the brain. Brain source imaging (BSI) is used to infer the underlying brain activity from the M/EEG signals. However, this is a challenging ill-posed inverse problem. BSI methods are susceptible to inaccurate source localization, some more than others. This can result from small degrees of under- or overfitting that heavily depend on the choice of modeling parameters. To compare the feasibility of inverse estimators at varying regularization strengths or estimated noise levels, we benchmark their performance to study the ranges of noise misspecification within which different BSI approaches can still localize well.

Methods: We conduct extensive simulations in realistic MEG volume conductor models based on the CamCan dataset[5]. One to five dipolar sources with orientation normal to the cortex are randomly positioned and are assigned a Gaussian random time course of length 10. Sources are then mapped to MEG channels, where Gaussian white noise is added to yield varying signal-to-noise ratios (SNR) ranging from -20 to 40 dB. Sources are reconstructed using smooth linear inverse solutions and sparse non-linear learning solutions[1-4,6-8] for predefined choices of noise variance for each SNR.

Results: For each reconstruction, performance is evaluated using earth-mover's distance (Fig. 1) and other metrics like euclidean distance, mean squared error, etc. Further, we also assess how noise learning and cross-validation (CV) approaches approximate the "sweet spot" leading to optimal localization. It is observed that most methods work best at high SNR levels and have varying SNR points at which their performance begins to drop. For a fixed SNR, best performance is usually observed with a moderate degree of underfitting. Furthermore, noise variance picked by spatial CV fitting results in a reconstructed SNR close to the ground truth SNR and near-optimal localization performance.

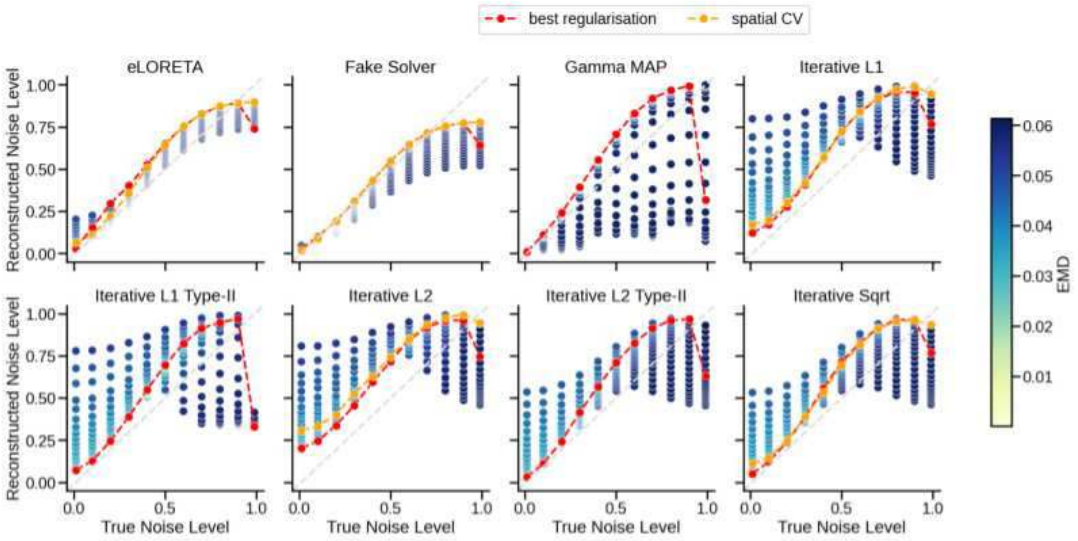

Fig. 1: EMD performance of several smooth linear inverse solutions and sparse non-linear learning solutions. For each method, source reconstruction is benchmarked for 20 predefined choices of noise variance for each noise level.

Conclusions: This work allows for a unified and principled framework to compare the performance of BSI methods. Our results contribute to the understanding of BSI techniques by providing a comprehensive evaluation of different inverse estimators and their performance under varying conditions and highlights the importance of carefully selecting modeling parameters in BSI methods. All methods and experiments are publicly available within the "BSI zoo" (github.com/braindatalab/BSI-Zoo) python package, to facilitate further investigation of novel BSI techniques.

References

1. Cai, C. (2021). Robust estimation of noise for electromagnetic brain imaging with the champagne algorithm. NeuroImage, 225, 117411.
2. Hashemi, A. (2021). Unification of sparse Bayesian learning algorithms for electromagnetic brain imaging with the majorization minimization framework. NeuroImage, 239, 118309.
3. Haufe, S. (2008). Combining sparsity and rotational invariance in EEG/MEG source reconstruction. NeuroImage, 42(2), 726-738.
4. Pascual-Marqui, R. D. (2007). Discrete, 3D distributed, linear imaging methods of electric neuronal activity. Part 1: exact, zero error localization. arXiv preprint arXiv:0710.3341.
5. Shafto, M. A. (2014). The Cambridge Centre for Ageing and Neuroscience (Cam-CAN) study protocol: a cross-sectional, lifespan, multidisciplinary examination of healthy cognitive ageing. BMC neurology, 14, 1-25.
6. Strohmeier, D. (2016). The iterative reweighted mixed-norm estimate for spatio-temporal MEG/EEG source reconstruction. IEEE transactions on medical imaging, 35(10), 2218-2228.
7. Wipf, D. (2010). Iterative reweighted $\ell_1 $ and $\ell_2 $ methods for finding sparse solutions. IEEE Journal of Selected Topics in Signal Processing, 4(2), 317-329.
8. Wipf, D. (2010). Robust Bayesian estimation of the location, orientation, and time course of multiple correlated neural sources using MEG. NeuroImage, 49(1), 641-655.

Poster No 1645

Pro-ictal brain state marked by global critical slowing and local gamma power increase

Isa Dallmer-Zerbe[1,2], Jakub Kopal[3,1], Anna Pidnebesna[1,4], Jonathan Curot[5,6], Marie Denuelle[5], Jean-Christophe Sol[5], Luc Valton[5], Emmanuel Barbeau[6], Jaroslav Hlinka[1,4]

[1]Institute of Computer Science of the Czech Academy of Sciences, Prague, Czech Republic, [2]Second Faculty of Medicine, Charles University, Prague, Czech Republic, [3]McGill University, Montreal, Quebec, [4]National Institute of Mental Health, Klecany, Czech Republic, [5]Brain electrophysiology, Epilepsy and Sleep Unit, Neurology Department, University Hospital, Toulouse, France, [6]Centre de Recherche Cerveau et Cognition (CerCo), Toulouse, France

Introduction: The clinical workup during the pre-surgical evaluation for epilepsy relies on the electrophysiological recording of seizures. The interval until first seizure occurrence is characterized by an increase in seizure likelihood caused by progressive drug dose decreases, during which the epileptic brain transitions from a state of low to a state of high seizure likelihood, so-called pro-ictal state (Baud et al., 2020). This study aimed to identify and characterize the dynamic brain changes characteristic of this transition.

Methods: We analyzed 386 ten-minute segments of intracranial EEG recordings of 29 patients with drug-refractory temporal lobe epilepsy, irregularly sampled between electrode implantation and first seizure. As measures of brain dynamics we studied the mean phase coherence (gMPC; Mormann et al., 2000) and the relative power (gPR; Panagiotopoulou et al., 2022) in gamma frequency band, as well as the autocorrelation function width (ACFW; Maturana et al., 2020). We further investigate the interaction of those brain dynamics with various susceptibility factors, such as the rate of interictal spikes and high frequency oscillations (Roehri et al., 2018), circadian and multi-day cycles (Schroeder et al., 2020), and clinical outcomes.

Results: We observe a significant increase in relative gamma power in the epileptogenic zone between the beginning and the end of the measured interval ($Z = 2.998$, $pFDR = .008$, Cohen's $d = .678$), and an increase in critical slowing in both the epileptogenic zone ($Z = 1.992$, $pFDR = .046$, $d = -.545$) as well as the healthy cortex ($Z = 2.757$, $pFDR = .009$, $d = -.680$). These brain dynamic changes were linked with increases in spike and high frequency oscillations rate. While the brain dynamic changes occurred on the slow time scale - from the beginning to the end of the multi-day interval - they did not change in the short-term during the pre-ictal interval.

Conclusions: We highlight gamma power and critical slowing as markers of pro-ictal (as opposed to pre-ictal) brain states, as well as their potential to track the seizure-related brain mechanisms during the presurgical evaluation of epilepsy patients.

References

1. Baud, M. O., Proix, T., Rao, V. R., & Schindler, K. (2020). 'Chance and risk in epilepsy.' Current Opinion in Neurology, vol. 33, no. 2, pp. 163–172.
2. Maturana, M. I., Meisel, C., Dell, K., Karoly, P. J., D'Souza, W., Grayden, D. B., Burkitt, A. N., Jiruska, P., Kudlacek, J., Hlinka, J., Cook, M. J., Kuhlmann, L., & Freestone, D. R. (2020). 'Critical slowing down as a biomarker for seizure susceptibility.' Nature Communications, vol. 11, no. 1, p. 2172.
3. Mormann, F., Lehnertz, K., David, P., & E. Elger, C. (2000). 'Mean phase coherence as a measure for phase synchronization and its application to the EEG of epilepsy patients.' Physica D: Nonlinear Phenomena, vol. 144, no. 3–4, pp. 358–369.
4. Panagiotopoulou, M., Papasavvas, C. A., Schroeder, G. M., Thomas, R. H., Taylor, P. N., & Wang, Y. (2022). 'Fluctuations in EEG band power at subject-specific timescales over minutes to days explain changes in seizure evolutions.' Human Brain Mapping, vol. 43, no. 8, pp. 2460–2477.
5. Schroeder, G. M., Diehl, B., Chowdhury, F. A., Duncan, J. S., de Tisi, J., Trevelyan, A. J., Forsyth, R., Jackson, A., Taylor, P. N., & Wang, Y. (2020). 'Seizure pathways change on circadian and slower timescales in individual patients with focal epilepsy.' Proceedings of the National Academy of Sciences, vol. 117, no. 20, pp. 11048-11058.

Poster No 1646

Exploring Heterogeneity in Neurodevelopmental Disorders Using EEG-based Normative Modeling

Aida Ebadi[1], Sahar Allouch[1], Aya Kabbara[1,2,3], Judie Tabbal[4,1], Nadia Chabane[5], Borja Rodríguez-Herreros[5], Ahmad Mheich[6], Mahmoud Hassan[1]

[1]MINDIG, Rennes, France, [2]Lebanese Association for Scientific Research (LaSeR), Tripoli, Lebanon, [3]Lebanese International University, Tripoli, Lebanon, [4]Institut des Neurosciences Cliniques de Rennes (INCR), Rennes, France, [5]CHUV Lausanne, Lausanne, Vaud, [6]Lausanne University Hospital (CHUV), Lausanne, Vaud

Introduction: Developing data-driven biomarkers in clinical neuroscience, particularly in psychiatry, faces major challenges due to the heterogeneous nature of mental disorders. Conventional case-control methods tend to overlook individual differences assuming homogeneity within groups and clear demarcations between groups. However, these assumptions do

not accurately represent the complexity and the diversity within the population. To overcome this limitation, recent studies have embraced a more individualized, patient-centric approach using Normative Modeling (NM). It involves estimating reference trajectories for a brain phenotype and measuring individual deviations. NM's focus on individual rather than average patient profiles allows for the exploration of potential overlaps in brain activity between healthy individuals and patients, as well as among patients with different disorders. In this study, we explore the potential of using EEG-based normative models to investigate heterogeneity in Autism Spectrum Disorder.

Methods: The study pipeline involves several key steps: EEG preprocessing, extraction of power spectral features, normative modeling, and subsequent analysis of the results. We used resting state EEG from the Healthy Brain Network initiative led by the Child Mind Institute (N=3055, age: [5-22]). The dataset included a myriad of neurodevelopmental disorders with the majority being Attention deficit hyperactivity disorder (ADHD), Autism Spectrum Disorder (ASD), and Anxiety Disorder. EEG preprocessing and artifact removal were accomplished using a fully automated algorithm. The Power Spectrum Density (PSD) for each channel was computed using Welch's method. Generalized Additive Models for Location, Scale, and Shape (GAMLSS) models were fitted to the relative power of each channel and frequency band (delta, theta, alpha 1, alpha 2, beta, gamma). Afterward, using an independent dataset (age: [5-10]) consisting of 13 subjects diagnosed with ASD and 31 Typically Developing (TD) subjects, we computed the deviation scores (Z-scores) from the reference trajectory for each individual (Figure 1). The Z-scores were further condensed for each group (TD and ASD) into percentages of positive/negative extremely deviant subjects (Z<-2, Z>2) per EEG channel (Figure 2).

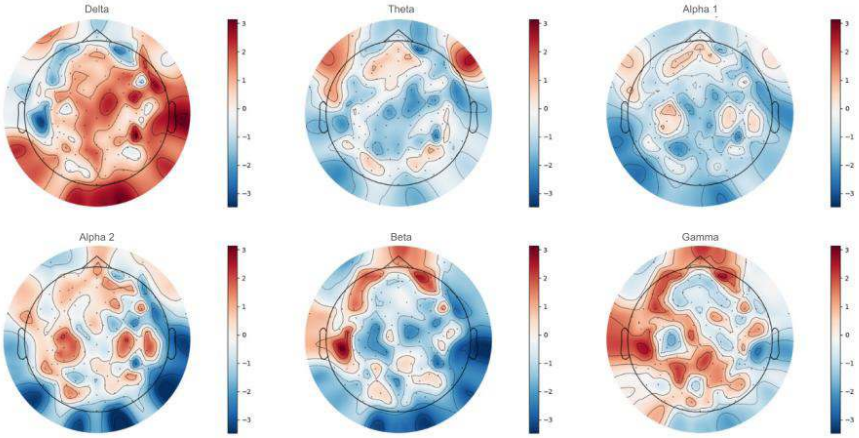

Figure 1. Deviation maps for a sample subject across different frequency bands showing that the delta and gamma bands have high deviation scores over extensive regions. In contrast, the alpha1 band shows the lowest deviation scores from the reference trajectory.

Results: Figure 2 shows higher percentages in TD as compared to ASD across the delta, alpha 2, beta, and gamma frequency bands. Notably, within the TD group, positive deviations in TD are consistently more prevalent across subjects in alpha 2, beta, and gamma bands, while negative deviations appear to exhibit higher consistency across subjects in the delta band. Furthermore, the percentage of extreme deviations in the theta band seems to be higher for the ASD compared to the TD group.

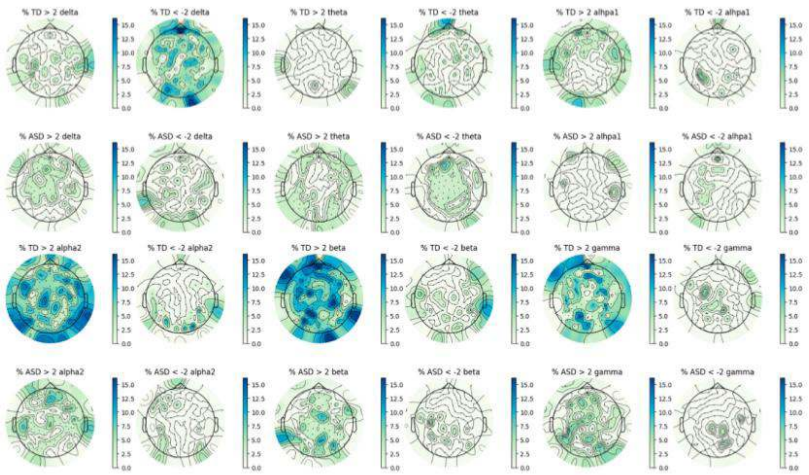

Figure 2. Topographical distribution of the percentage of subjects having extreme regional deviations (Z>2; Z<-2) within TD and ASD groups.

Conclusions: The percentage of subjects with extreme regional deviations summarizes the consistency of individual regional deviations across TD and ASD cohorts. In the delta, alpha 2, beta, and gamma, no more than 15% of the individuals in the TD group deviate from the normative trajectory of the patients' group. In contrast, approximately 85% of the subjects closely align with the reference patient cohort. This highlights the nuanced difference between healthy controls and patients and provides evidence that case-control studies may be flawed when making significant distinctions between groups. Moreover, the low percentages of subjects exhibiting extreme regional deviations reflect the non-consistency of deviation topographical patterns across subjects, hence, corroborating the notion of heterogeneity within clinical and healthy cohorts. To summarize, we developed normative curves for the relative power in EEG and demonstrated the possibility of quantifying the heterogeneity of neurodevelopmental disorders using NM.

References

1. Alexander, L. M., et al. 2017. "An open resource for transdiagnostic research in pediatric mental health and learning disorders." Scientific Data, 4(1), 1–26.
2. Bethlehem, R. A. I., et al. 2022. "Brain charts for the human lifespan." Nature, 604(7906), 525–533.
3. Marquand, A. F., et al. 2019. "Conceptualizing mental disorders as deviations from normative functioning." Molecular Psychiatry, 24(10), 1415–1424.
4. Marquand, A. F., et al. 2016. "Understanding heterogeneity in clinical cohorts using normative models: beyond case-control studies." Biological Psychiatry, 80(7), 552–561.
5. Rutherford, S., et al. 2022. "Charting brain growth and aging at high spatial precision." eLife, 11, e72904.
6. Rutherford, S., et al. 2022. "The normative modeling framework for computational psychiatry." Nature Protocols, 17(7), 1711–1734.
7. Stasinopoulos, D. M., & Rigby, R. A. 2008. "Generalized additive models for location scale and shape (GAMLSS) in R." Journal of Statistical Software, 23, 1–46.
8. Verdi, S., et al. 2021. "Beyond the average patient: how neuroimaging models can address heterogeneity in dementia." Brain, 144(10), 2946–2953.

Poster No 1647

A Taxonomy of Explainability Methods for Deep Learning Models Applied to Raw Electroencephalograms

Charles Ellis[1], Robyn Miller[1], Vince Calhoun[2]

[1]Center for Translational Research in Neuroimaging and Data Science (TReNDS), Atlanta, GA, [2]Center for Translational Research in Neuroimaging and Data Science (TReNDS), Decatur, GA

Introduction: Deep learning is being increasingly applied to raw electroencephalograph (EEG) data for automated neuropsychiatric disorder diagnosis. Unfortunately, while these methods can boost model performance, they can also reduce explainability, which has led to the development of a variety of explainability (XAI) methods uniquely adapted to raw EEG data. In this study, we taxonomize existing approaches (Figure 1) and present a new XAI approach. Existing raw EEG XAI approaches generally fall within the categories of spatial (i.e., identifying key channels) (Pathak et al., 2021), spectral (i.e., identifying key frequency bands) (Nahmias and Kontson, 2020), or temporal (i.e., identifying key waveforms) (Ellis et al., 2022) explainability approaches, and among each of these categories can be found both local (i.e., providing insight into the classification of an individual sample) and global (i.e., providing insight into how a model generally behaves) explainability approaches. The categories can be further subdivided based upon the characteristics of the approaches (e.g., perturbation (Nahmias and Kontson, 2020), activation maximization (Ellis et al., 2021b), or gradient-based methods (Ellis et al., 2021a)). However, while many approaches have been developed for identifying EEG spatial, spectral, and temporal importance, it is also important to identify interactions uncovered by models between channels and frequency bands, so in this study, we develop a model for major depressive disorder (MDD) diagnosis and present a novel raw EEG XAI approach that identifies spatiospectral interactions between frequency bands in a given channel and other channels.

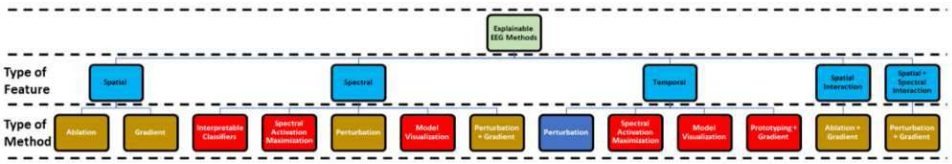

Figure 1. Taxonomy of XAI Approaches for Deep Learning Models Using Raw EEG Data. The taxonomy has 3 levels that are each separated by black horizontal dashed lines: (1) the overall field of EEG XAI methods, (2) the types of features into which the XAI methods provide insight, and (3) the types of XAI approaches that provides insight into the different feature types. Light blue boxes correspond to specific types of features. Note that the type of method or XAI approach generally corresponds to methods that were first developed outside the domain of EEG analysis and then adapted to the domain. Dark blue, red, and gold boxes show methods that provide local, global, and both local and global explanations.

Methods: We used 19 channels of resting-state EEG data from 30 individuals with MDD (MDDs) and 28 healthy controls (HCs). The data is available at: https://figshare.com/articles/dataset/EEG_Data_New/4244171. We segmented the data into 25-second samples and downsampled to 200 Hz. We trained a 1-dimensional convolutional neural network with 10-fold subject-wise cross-validation to classify between the two classes. In our XAI analysis, we applied layer-wise relevance propagation (LRP) (Bach et al., 2015) with an αβ-relevance rule (α=1, β=0) to identify the relative importance of each channel. We then converted the data to the frequency domain, successively zeroed out canonical frequency bands (δ, θ, α, β, γlow, γhigh) in each channel, converted the perturbed data back to the time domain, reapplied LRP, and applied t-tests with false discovery rate correction (α=0.001) to identify significant interactions between frequency bands and channels (i.e., whether a channel's relevance changed after a frequency band was perturbed in another channel). We analyzed the model from the fold with the highest test performance and performed separate analyses for MDDs, HCs, and all samples.

Results: Our model performance was relatively high, particularly when compared to other papers that used robust subject-wise cross-validation approaches. The mean and standard deviation of our model accuracy, balanced accuracy, sensitivity, and specificity were 85.00 ± 7.82, 86.52 ± 8.14, 90.33 ± 11.68, and 82.70 ± 16.82, respectively. As shown in Figure 2, for HCs, our model identified widespread interactions between parietal electrodes and electrodes in most other regions. In contrast, for MDDs, our model identified interactions primarily between frontal and central electrodes and electrodes in other regions, which fits with other MDD studies that have identified frontal connectivity effects (Movahed et al., 2021).

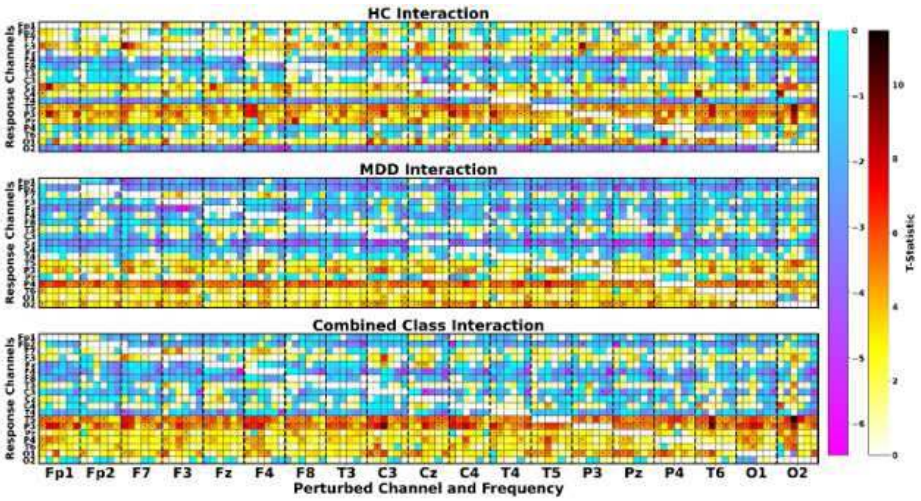

Figure 2. Spatio-Spectral Interaction Results. The top, middle, and bottom panels show heatmaps of the t-statistics from the two-sample, two-tailed, paired t-tests comparing the amount of relevance in a channel before versus after the perturbation of frequency bands in other channels for HCs, MDDs, and both classes, respectively. Perturbed channels and frequency bands are arrayed along the x-axis. Perturbed channels are separated by thick vertical dashed lines, and from left to right within each set of vertical dashed lines are shown results for the perturbation of δ (0 – 4 Hz), θ (4-8 Hz), α (8 – 12 Hz), β (12 – 25 Hz), γ_{low} (25 – 45 Hz), and γ_{high} (55 – 100 Hz) frequency bands. Channels in which a change in relevance was measured are arrayed along the y-axis (i.e., response channels). The color bars to the right of the figure are shared by all panels and indicate the value of the t-statistics in the heatmaps. Black dots indicate channel and frequency band combinations in which there was a significant change in the relevance of a channel after perturbation following FDR correction ($\alpha = 0.001$).

Conclusions: In this study, we presented a taxonomy of existing EEG XAI approaches and further expanded it by contributing a new XAI approach that identifies spatiospectral interactions between different EEG frequency bands and electrodes. We used our approach within the context of automated MDD diagnosis and identified patterns comparable to those identified in traditional connectivity-based analyses in MDD.

References

1. Bach, S., Binder, A., Montavon, G., Klauschen, F., Müller, K.R., Samek, W., 2015. On pixel-wise explanations for non-linear classifier decisions by layer-wise relevance propagation. PLoS One 10. https://doi.org/10.1371/journal.pone.0130140
2. Ellis, C.A., Miller, R.L., Calhoun, V.D., 2022. A Systematic Approach for Explaining Time and Frequency Features Extracted by Convolutional Neural Networks From Raw Electroencephalography Data. Front. Neuroinform. 16, 1–11. https://doi.org/10.3389/fninf.2022.872035
3. Ellis, C.A., Miller, R.L., Calhoun, V.D., Wang, M.D., 2021a. A Gradient-based Approach for Explaining Multimodal Deep Learning Classifiers, in: 2021 IEEE 21st International Conference on Bioinformatics and Bioengineering (BIBE). IEEE, pp. 0–5.
4. Ellis, C.A., Sendi, M.S.E., Miller, R., Calhoun, V., 2021b. A Novel Activation Maximization-based Approach for Insight into Electrophysiology Classifiers, in: 2021 IEEE International Conference on Bioinformatics and Biomedicine (BIBM).
5. Movahed, R.A., Jahromi, G.P., Shahyad, S., Meftahi, G.H., 2021. A major depressive disorder classification framework based on EEG signals using statistical, spectral, wavelet, functional connectivity, and nonlinear analysis. J. Neurosci. Methods 358, 109209. https://doi.org/10.1016/j.jneumeth.2021.109209
6. Nahmias, D.O., Kontson, K.L., 2020. Easy Perturbation EEG Algorithm for Spectral Importance (easyPEASI): A Simple Method to Identify Important Spectral Features of EEG in Deep Learning Models, in: Proceedings of the 26th ACM SIGKDD International Conference on Knowledge Discovery & Data Mining. ACM, New York, NY, USA, pp. 2398–2406. https://doi.org/10.1145/3394486.3403289
7. Pathak, S., Lu, C., Nagaraj, S.B., van Putten, M., Seifert, C., 2021. STQS: Interpretable multi-modal Spatial-Temporal-seQuential model for automatic Sleep scoring. Artif. Intell. Med. 114, 102038. https://doi.org/10.1016/j.artmed.2021.102038

Poster No 1648

Large scale network modelling of the effect of sensory and electric brain stimulation

Mónica Otero Ferreiro[1,2], Felipe Torres[3], Caroline Lea-Carnall[4], Alejandro Weinstein[3], Joana Cabral[5], Wael El-Deredy[6]

[1]Universidad San Sebastián, Santiago de Chile, RM. Metropolitana, [2]Centro Basal Ciencia & Vida, Santiago de Chile, Chile, [3]Universidad de Valparaíso, Valparaíso, Valparaíso, [4]University of Manchester, Manchester, Manchester, [5]University of Minho, Braga, Portugal, [6]Universidad de Valparaíso, Valparaíso, Valparaíso

Introduction: The phenomenon referred to as neural entrainment, characterized by the synchronization of neural oscillations with external stimulus frequencies, is considered a potential mechanism explaining the impact of external sensory and electric stimulation on the brain. This entrainment occurs as ongoing oscillations align their phases with the driving stimulus. Yet, the interaction between stimulation parameters and ongoing brain network dynamics is poorly understood.

Methods: In this research, we use the concepts of resonance and loosely coupled oscillators to model the emergence of oscillatory networks in the brain which exhibit a preference for specific frequencies of incoming stimulation. A large-scale model of coupled oscillators was implemented using a partially forced Kuramoto Model (FKM)[1] with realistic connectivity structure and connection delays[2], to generate a realistic frequency spectrum comparable to real EEG[3,4]. Structural connectivity information was computed from the human connectome, based on the AAL atlas[5]. Intrinsic frequencies of nodes (brain regions) were set to 40Hz as in[3,4]. As it has been previously demonstrated in[4], the addition of delays to the Kuramoto model promotes the emergence of multi-state metastability in the system, which has been associated with the capacity of the brain to transition between network configurations and has been related to cognitive flexibility. We identify the parameters of FKM in which we obtained maximal spectral entropy of the model as a proxy for multi-state metastability. Using this set of parameters, we investigated the effect of the structural information of the node stimulated (brain region) and the frequency of stimulation in the propagation of this external stimulation. The activation of nodes due to stimulation was computed using the power spectrum and phase locking value of the signals during stimulation compared to the ongoing simulated signals.

Results: Simulated signals with similar spectral features to those from EEG recordings were obtained using the FKM model. Moreover, spectral profiles of the simulated signals were found to be different depending of the parameters of coupling and mean delay of the FKM. Different patterns of propagation emerge when different nodes are stimulated with varied frequencies. In figure1, we can observe that nodes activation changed depending on the driver node (node stimulated) (see figure 1a), but also depending on the frequency of stimulation (see figure 1b). Furthermore, we found that spectral profiles of nodes changed as a result of the stimulation depending on the frequency of stimulation. In figure 2a) is shown the spectral profile of several nodes in resting state (ongoing activity); in figure 2b and 2C is shown the effect of the stimulation at one location (brain region) and two different frequencies 43Hz and 13Hz respectively. Our findings suggest that structure information of the stimulated node (degree and strength of connections) determined the number of nodes that can be activated through the repetitive stimulation. Furthermore, we found a selective preference of different neural networks for

specific stimulation frequencies, and this preference is dependent on the stimulated node (brain area), but also the state of metastability of the system. Additionally, we observed that new functional subnetworks, different to those existing in simulated ongoing signals, emerge as the result of the stimulation at specific locations and using specific frequencies.

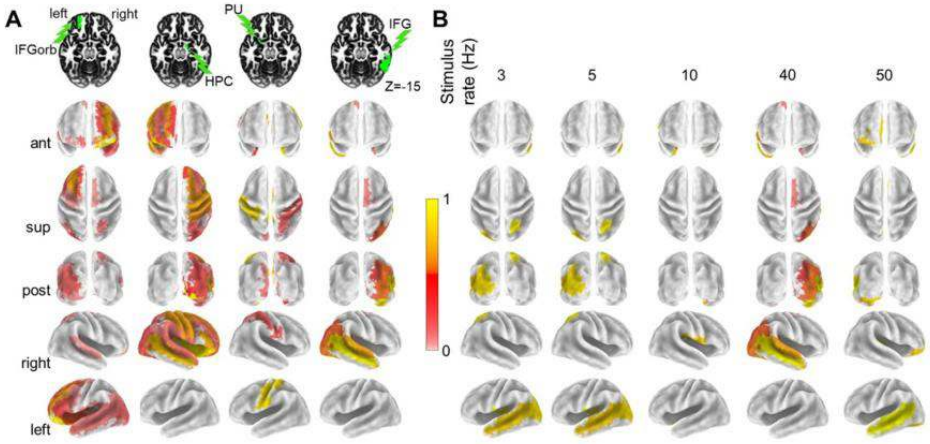

Fig.1 *Cortical activation elicited by external stimulation of specific nodes in a model of 90 coupled oscillators of phase interactions.* ***A)*** *Cortical activation as a function of the target node. Stimulated nodes are highlighted with a lightning symbol: IFGorb, inferior frontal gyrus (pars orbitalis); HPC, hippocampus; PU, putamen, and ITG, inferior temporal gyrus. All nodes were stimulated with a 40-Hz sinusoid.* ***B)*** *Cortical activation as a function of the stimulation frequency when the target node was the right inferior temporal gyrus.*

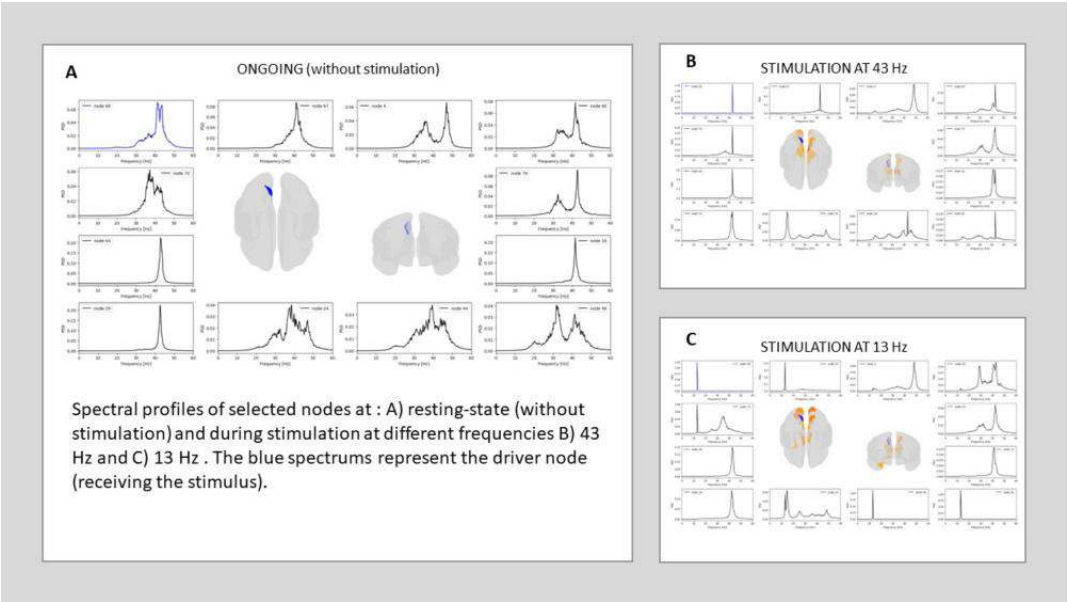

Conclusions: Our findings suggest that FKM is suitable for the simulation of the effect of external stimulation in the brain. This study corroborates the importance of using computational models to guide the selection of the parameters of stimulation to selectively activate specific neuronal networks.

References

1. Sakaguchi, H. (1988). Cooperative phenomena in coupled oscillator systems under external fields. Progress of theoretical physics, 79(1), 39-46.
2. Yeung, M. S. et al. (1999). Time delay in the Kuramoto model of coupled oscillators. Physical review letters, 82(3), 648.
3. Cabral, J. et. al. (2014). Exploring mechanisms of spontaneous functional connectivity in MEG: how delayed network interactions lead to structured amplitude envelopes of band-pass filtered oscillations. Neuroimage, 90, 423-435.
4. Cabral, J. et al. Metastable oscillatory modes emerge from synchronization in the brain spacetime connectome. Commun Phys 5, 184 (2022). https://doi.org/10.1038/s42005-022-00950-y.
5. Tzourio-Mazoyer et. al. (2002). Automated anatomical labeling of activations in SPM using a macroscopic anatomical parcellation of the MNI MRI single-subject brain. Neuroimage, 15(1), 273-289.

Poster No 1649

Functional Connectivity in Aperiodic Brain Activity at Rest

Luc Wilson[1], Jason da Silva Castanheira[1], Sylvain Baillet[1]

[1]Montreal Neurological Institute, Montreal, Quebec

Introduction: Macroscopic brain signals comprise aperiodic and periodic components (Donoghue et al., 2020). Neurophysiological brain activity is thought to covary across the brain in a region- and frequency-specific manner (Brookes et al., 2011). This connectivity has been shown to predict age and fluid intelligence test performance (Jauny et al., 2022). However, conventional measures of functional connectivity cannot resolve the unique contributions of periodic and aperiodic components. Here, we separate dynamic periodic and aperiodic brain signals from resting-state magnetoencephalography (MEG) to identify their unique functional networks. We find aperiodic features of brain signals occupy their own unique functional connectivity profiles (separate from alpha-band activity), and that the aggregate strength of several within- and across-network connections of resting-state aperiodic features are significant predictors of age and fluid intelligence test performance.

Methods: We used 2.5 minutes of clean resting-state MEG recordings from 603 participants (298 females; age range = 18 – 88) from the CamCAN dataset (Taylor et al., 2017). Data were preprocessed using Brainstorm (Tadel et al., 2011) before generating cortical source estimates at 15,000 locations through linearly constrained minimum-variance beamforming. From these estimates, we extracted the mean time-series for 200 predefined cortical regions of interest (ROIs) according to the Schaefer-200 atlas, 17-network variant (Schaefer et al., 2018). We identified the time-varying aperiodic and periodic spectral components of the neural time series at 1-s intervals (2-s windows, 50% overlap) using Spectral Parameterization Resolved in Time (SPRiNT; Wilson et al., 2022). At each time point, we measured the mean alpha-band (8-13 Hz) power and aperiodic-corrected alpha power by subtracting the aperiodic component from the spectrogram. We quantified aperiodic dynamics using spectral parameters (exponent, offset). To measure functional connectivity across ROIs, we computed Pearson's correlation coefficients between time-varying periodic and aperiodic regional features. We estimated periodic connectivity using mean alpha-band power (before and after removing aperiodic activity), while aperiodic connectivity used spectral exponent and offset parameters resolved in time. We combined within- and across- network edge strengths according to their 17-network designations. For each edge of the aperiodic networks, we tested whether participant age and Cattell test score were related to edge strength using linear regression models. We corrected for multiple comparisons using a Bonferroni procedure ($\alpha = 0.05$; N=153).

Results: We observed that alpha-band connectivity (mean r = 0.38) decreased after correcting for aperiodic activity (mean r = 0.24), while aperiodic offset and exponent connectivity remained low (mean r = 0.17, 0.13, respectively) but distinct from the alpha band (Figure 1). Several combined within- and across-network edges in aperiodic connectivity significantly predicted participant age (highest R2 = 0.09) and Cattell test score (highest R2 = 0.04; Figure 2). Of note, few edges were associated with Dorsal Attention network A or Visual Central network, while a large number of edges were associated with Default Mode network B.

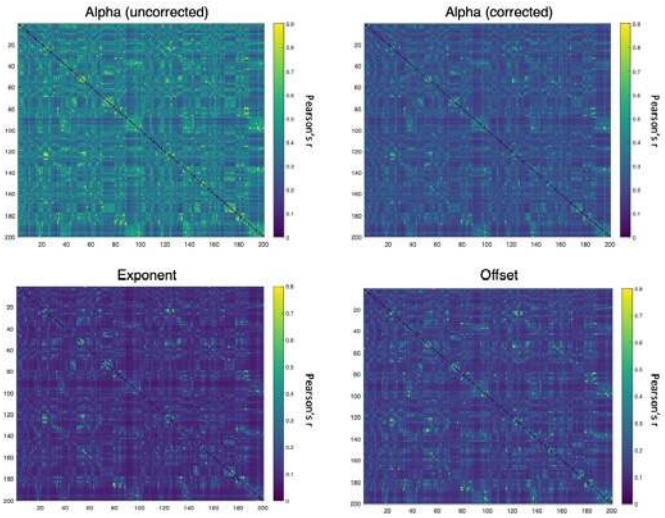

Figure 1. Correlation matrices for alpha (uncorrected), alpha (aperiodic-corrected), aperiodic exponent, and aperiodic offset. Rows and columns are organized such that the first 100 represent data from the left hemisphere and the last 100 represent data from the right hemisphere. Within each hemisphere, data appears in the following order of networks: Control, Default Mode, Dorsal Attention, Limbic, Salient Ventral Attention, Somatomotor, Temporal Parietal, Visual.

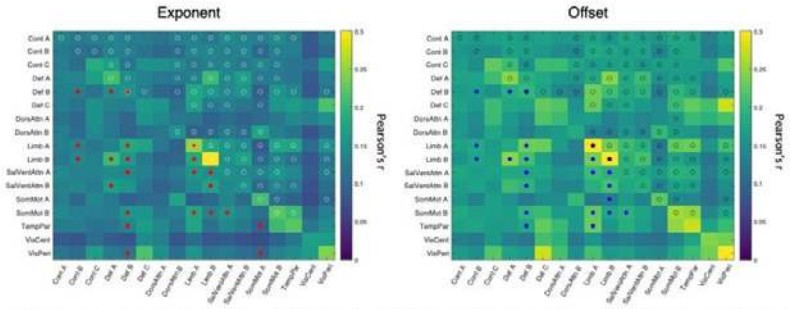

Figure 2. Correlation matrices for aperiodic exponent and offset, averaged by network. Diagonal pairings reflect within-network connectivity strength (except connections to self), while off-diagonal pairings reflect across-network connectivity strength, for each network averaged across network ROIs. White/black outlined circles reflect network edges that significantly predict participant age, while red/blue filled dots reflect network edges that significantly predict participant Cattell score.

Conclusions: The present study explores the respective contributions of periodic and aperiodic brain signal features to functional connectivity. Aperiodic exponent and offset are thought to reflect excitation-inhibition balance (Gao et al., 2017) and aggregate population spiking (Voytek et al., 2015), respectively. Therefore, functional networks could reflect regional co-fluctuations of these physiological phenomena. Future studies should explore the links between the respective connectivity patterns of a/periodic activity to the topography of meaningful cortical features such cortical thinning with age and neurotransmitter receptor densities.

References

1. Brookes, M.J. (2011), 'Investigating the Electrophysiological Basis of Resting State Networks using Magnetoencephalography', PNAS, vol. 108, no. 40, pp. 16783-16788
2. Donoghue, T. (2020), 'Parameterizing Neural Power Spectra into Periodic and Aperiodic Components', Nature Neuroscience, vol. 23, no. 12, pp. 1655-1665
3. Gao, R. (2017), 'Inferring Synaptic Excitation/Inhibition Balance from Field Potentials', NeuroImage, vol. 158, pp. 70-78
4. Jauny, G. (2022), 'Connectivity dynamics and cognitive variability during aging', Neurobiology of Aging, vol. 118, pp. 91-105
5. Schaefer, A (2018), 'Local-Global Parcellation of the Human Cerebral Cortex from Intrinsic Functional Connectivity MRI', Cerebral Cortex, vol. 28, no. 9, pp. 3095-3114
6. Tadel, F. (2011), 'Brainstorm: A User-Friendly Application for MEG/EEG Analysis', Computational Intelligence and Neuroscience, p. 879716
7. Taylor, J.R. (2017), 'The Cambridge Centre for Ageing and Neuroscience (Cam-CAN) Data Repository: Structural and functional MRI, MEG, and Cognitive Data from a Cross-Sectional Adult Lifespan Sample', NeuroImage, vol. 144, pp. 262-269
8. Voytek, B. (2015), 'Age-Related Changes in 1/f Neural Electrophysiological Noise', The Journal of Neuroscience, vol. 35, no. 38, p. 13257
9. Wilson, L.E. (2022), 'Time-Resolved Parameterization of Aperiodic and Periodic Brain Activity', eLife, 11:e77348

Poster No 1650

How to Detect the Depth of Anesthesia in Human Brain Waves Utilizing Relative Phase Dynamics

Youngjai Park[1,2], Joon-Young Moon[1,2]

[1]Center for Neuroscience Imaging Research, Institute for Basic Science (IBS), Suwon, Republic of Korea, [2]Sungkyunkwan University, Suwon, Republic of Korea

Introduction: The human brain shows emergent states such as consciousness and unconsciousness and dynamic transition between them. However, after many years of research, the search to understand the mechanism of conscious to unconscious transition and to correctly measure the level of consciousness still remains elusive. In recent years, researchers have found that the phase dynamics of low-frequency brain waves are related to the level of consciousness[1]. In this study, we further pursue to study the relationship between the phase dynamics of brain waves and the level of consciousness in anesthesia: we analyze the relative phase patterns of brain waves across the whole brain network and its relationship with conscious to unconscious state transitions using the electroencephalogram (EEG) recordings over anesthesia. We aim to understand how the phase dynamics of cortical brain waves differ between conscious and unconscious states, and what mechanism can account for such differences.

Methods: We analyze the EEG of 18 human participants covering the whole brain (128 channels) where 9 of them undergo general anesthesia and recover. We first band pass-filtered the brain wave signals from each channel and separate frequency bands (i.e., delta:1-4, theta:4-8, alpha:8-12, low-beta:12-18, and high-beta:18-30 Hz bands). We then define the relative phase of each channel at the specific frequency band by subtracting the global mean phase of the brain waves from the phase of

the wave from each channel. By subtracting the global mean phase, we can gather the information on which part of the brain leads or lags behind the phase of the others.

Results: We find that there are two robust and dominant modes of global phase patterns: parietal area phase-leading or lagging the frontal area. The brain dynamically transitions between these two dominant modes during various conscious states (e.g., resting states, and general anesthesia states). As the participants undergo general anesthesia, the dominance of these two modes begins to disappear and in deep anesthesia, these patterns themselves disappear: the global phase pattern becomes almost random (see Fig. 1). Front-to-back pattern, which is the frontal area leading the phase, is related to the depth of anesthesia in the K-mean cluster result. In the transition matrix in eyes open (conscious) and suppression (unconscious) states, the deeper the level of consciousness is, the more random the relative phase patterns become. Consistently, the distribution of the eigenvalues becomes homogeneous when the depth of anesthesia is deeper in the principal component analysis (PCA). As a result, the relative phase patterns can be a measurement to detect the level of consciousness. We further study the functional connectivity from the brain wave dynamics, by constructing whole brain networks where each channel becomes a network node and the connection between nodes is given by the similarity between the waves from respective channels. The parietal area becomes hubs (i.e., the nodes with many connections). Therefore, two dominant modes of phase patterns (i.e., parietal phase-lead or -lag) can be identified as either the hub area phase-leading or -lagging.

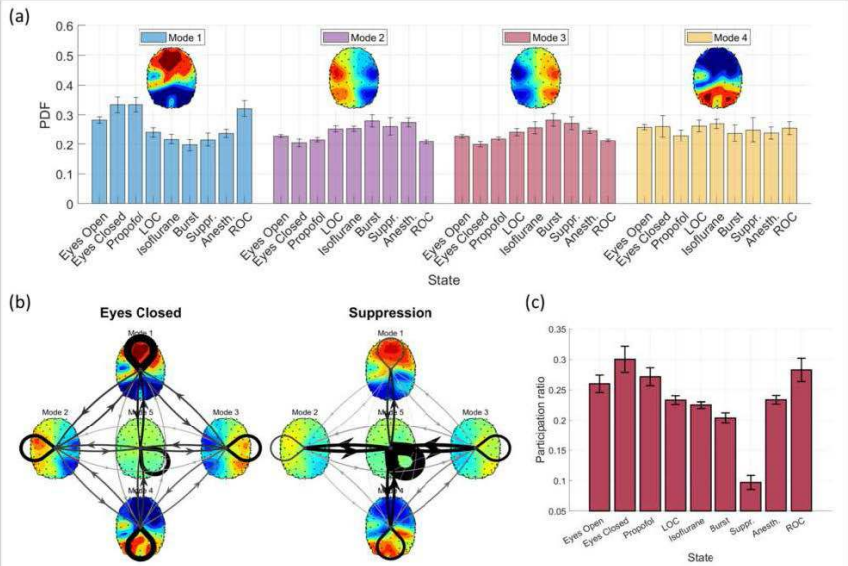

Figure 1. Relative phase patterns over the depth of anesthesia. (a) Distributions of each mode. Mode 1, which is the frontal area leading the phase, is related to the depth of anesthesia in the K-mean cluster result. (b) Transition schematic between each mode. Here, arrows represent the transition probability between each mode and the self-loop within each mode represents the probability to stay in each mode. Mode 5 represents random patterns which could not be classified to the other modes. In the suppression (unconscious) states the relative phase patterns become more random. (c) Participation Ratio (PR) across each state. The ratio is defined as the summation of the squared eigenvalues over the square of the summation of the eigenvalues in the principal component analysis (PCA). The higher PR is, the narrower the eigenvalue distribution is. The distribution of the eigenvalues becomes homogeneous when the depth of anesthesia is deeper. Overall, the relative phase patterns can be a measurement to detect the level of consciousness.

Conclusions: Altogether, we find that the hub phase-leading and -lagging patterns are the robust and dominant modes in conscious states while the pattern becomes random in unconscious states. These patterns can be interpreted as information flow patterns (the hub being either the source or the sink) which dominantly exist during the conscious state[2], disappearing in the unconscious state. Therefore, the action of the anesthetics is to disturb the dominant information flow patterns existing in the conscious state.

References

1. Moon, J. Y., Lee, U., Blain-Moraes, S., & Mashour, G. A. (2015). 'General relationship of global topology, local dynamics, and directionality in large-scale brain networks', PLoS computational biology, 11(4), e1004225.
2. Moon, J. Y., Kim, J., Ko, T. W., Kim, M., Iturria-Medina, Y., Choi, J. H., ... & Lee, U. (2017). 'Structure shapes dynamics and directionality in diverse brain networks: mathematical principles and empirical confirmation in three species', Scientific reports, 7(1), 46606.

Poster No 1651

The effects of personalized tPBM based on Machine Learning-based QEEG phenotypes

Juhee Ko[1], Ukeob Park[2], Boeun Choi[3], Seung Wan Kang[3]

[1]iMediSync Inc., Seoul, Seoul, [2]iMediSync, Inc., Seoul, seoul, [3]iMediSync, Seoul, Seoul

Introduction: Over the past 40 years, numerous studies have clustered Quantitative Electroencephalogram(QEEG) into phenotypes for clinical and research purposes.[1,2,3,4] Particularly, phenotypes based on the alpha band are notable.[5,6] Furthermore, recent research has been actively conducted using QEEG and Transcranial photobiomodulation(tPBM) for the treatment and diagnosis of various brain diseases.[7,8] However, it remains unclear how the effects of tPBM manifest in terms of EEG, cognitive function, and emotions based on the power spectral density(PSD) pattern of the occipital lobe. In this study, clustering was performed using a machine learning algorithm(ML)(Gaussian Mixture Method(GMM)+Support Vector Machine(SVM)) based on the PSD phenotype of the occipital lobe. Subsequently, a suitable tPBM protocol was applied on a case-by-case basis according to the characteristics of each cluster, and we provide insights into the altered QEEG pattern and the effects on cognitive function and emotions after tPBM.

Methods: We utilized EEG data measured at 19 channels on the 10-20 system in the resting state from a total of 104 subjects. Both eyes-closed and eyes-open data were employed as the dataset for the clustering model. As QEEG features used in the model, we utilized spectrum power and power ratio from the occipital lobe. Additionally, the participants include both normal and abnormal data. Among these 104 data, 80% were used as the train set, and the remaining 20% were used as the test set. We applied the Clustering Method (GMM) to select meaningful features for forming clusters, and subsequently trained the model using those features previously chosen as features for the Classification Method (SVM).The features of each cluster classified by the clustering model were used as criteria for labeling, and subsequently, these labels were employed as criteria for evaluating the performance of the classification model. The labels used were based on the commonly used QEEG phenotype criteria[1]. Cluster 1 corresponds to Persistent eyes-open alpha in the occipital lobe, Cluster 2 represents Low-voltage fast alpha in the occipital lobe during eyes-closed states, Cluster 3 includes complex abnormal patterns, and Cluster 4 denotes normal patterns (presence of alpha in the occipital lobe during eyes-closed states, and more than a 50% decrease in alpha during eyes-open states).Using the trained model, we classified 58 subjects into four groups and applied personalized tPBM protocols for each group over 8 weeks (3 sessions per week, 10 minutes per session). Subsequently, we evaluated the personalized tPBM effects on individualized changes in EEG, cognitive functions (comprehensive memory, inference ability, executive function, processing speed), and emotions (depression, stress, trait anxiety, state anxiety) through EEG examinations and questionnaires.

Results: The accuracy of the classification model on the training set exhibited an F1 score of 0.88, Precision of 0.88, and Recall of 0.88. On the test set, the model showed an F1 score of 0.86, Precision of 0.86, and Recall of 0.88. Furthermore, the effects of tPBM for each cluster based on the results of the trained model showed a significant increase (p-value < 0.01) in processing speed and executive function among cognitive function indicators. Additionally, among emotional indicators, a significant decrease (p-value < 0.05) was observed in depression, state anxiety, trait anxiety, and stress.

Conclusions: This study, through a machine learning-based clustering model using QEEG phenotypes as a foundation, identified meaningful clusters and demonstrated significant positive effects on cognitive function and emotions through the implementation of personalized tPBM based on these clusters. Such personalized tPBM can be more effectively utilized for the treatment of cognitive function and emotions. Further development of diverse QEEG phenotypes is expected to broaden its application as a biomarker for brain diseases.

References

1. Johnstone, J. (2005a, September), 'QEEG patterns: Subgroups, profiles, phenotypes', Paper presented at the 13th annual meeting of the International Society for Neuronal Regulation, Denver, CO.
2. Johnstone, J. (2005), 'Clinical database development: characterization of EEG phenotypes', Clinical EEG and Neuroscience, 2005 Apr;36(2):99-107. doi: 10.1177/155005940503600209.
3. Walker JE. (2010), 'Recent advances in quantitative EEG as an aid to diagnosis and as a guide to neurofeedback training for cortical hypofunctions, hyperfunctions, disconnections, and hyperconnections: improving efficacy in complicated neurological and psychological disorders', Applied Psychophysiology and Biofeedback, Mar;35(1):25-7. doi: 10.1007/s10484-009-9107-0.
4. Robertson C. (2022), 'Quantitative EEG (qEEG) guided transcranial magnetic stimulation (TMS) treatment for depression and anxiety disorders: An open, observational cohort study of 210 patients', Journal of Affective Disorders, 2022 Jul 1;308:322-327. doi:10.1016/j.jad.2022.04.076.
5. McVoy M. (2019), 'Resting-State Quantitative Electroencephalography Demonstrates Differential Connectivity in Adolescents with Major Depressive Disorder', Journal of Child and Adolescent Psychopharmacology, Jun;29(5):370-377. doi: 10.1089/cap.2018.0166.
6. Pérez-Elvira R. (2021), 'Individual Alpha Peak Frequency, an Important Biomarker for Live Z-Score Training Neurofeedback in Adolescents with Learning Disabilities', Brain Sciences, Jan 28;11(2):167. doi: 10.3390/brainsci11020167.

7. Baik JS. (2021), 'Effects of Photobiomodulation on Changes in Cognitive Function and Regional Cerebral Blood Flow in Patients with Mild Cognitive Impairment: A Pilot Uncontrolled Trial', Journal of Alzheimer's Disease, 2021;83(4):1513-1519. doi: 10.3233/JAD-210386.
8. Dole M. (2023), 'A systematic review of the effects of transcranial photobiomodulation on brain activity in humans', Reviews in The Neurosciences, 2023 Mar 17;34(6):671-693. doi: 10.1515/revneuro-2023-0003.

Poster No 1652

Classification of Mindfulness Experiences from EEG-Gamma Effective Connectivity

Ai-Ling Hsu[1], Chun-Yu Wu[1], Hydra Ng[2], Chi-Yun Liu[3], Chih-Mao Huang[4], Changwei Wu[3], Chun-Hsiang Chuang[2], Yi-Ping Chao[1]

[1]Chang Gung University, Taoyuan, Taiwan, [2]National Tsing Hua University, Hsinchu, Taiwan, [3]Taipei Medical University, New Taipei, Taiwan, [4]National Yang Ming Chiao Tung University, Hsinchu City, Taiwan

Introduction: Mindfulness refers to a transient shift of the mental process with interoceptive awareness. Previous literature has highlighted that practicing mindfulness reduces mental stress and alters the brain function or structure, along with the practice time[1,2]. However, there is lack of effective biomarkers to differentiate the mindfulness state from a mind-wandering state[3]. Based on the reported changes of electroencephalography (EEG) markers under mindfulness, a wearable neurofeedback system may enable the prediction of one's mindfulness experiences. Therefore, this study aims at probing EEG-based brain functionality to classify whether the participants had prior history of mindfulness-based stress reduction (MBSR) training.

Methods: The dataset comprises behavioral and simultaneous EEG-fMRI recordings of 33 healthy participants aged between 20 and 80 years, same as the protocol by Ng et al[4]. All participants completed two EEG experiments, spaced eight weeks apart, and were blindly assigned to either the MBSR intervention group (n=18, mean age=47.50) or the waiting-list control group (n=15, mean age=45.87), resulting in 46 pre-intervention and 18 post-intervention EEG data. Each EEG experiment consisted of three recording sessions: resting state, focus breathing, and body scan, where each session lasted 5 minutes. Recorded 32-channel EEG data were preprocessed with standard protocol (artifact removal, bandpass filter, ICA and re-reference) of EEGLab toolbox on MATLAB 2018a. After preprocessing, gamma-band (30–40 Hz) effective connectivity between channels were calculated using the direct Directed Transfer Function (dDTF)[5]. Due to computational load, we only selected 19 channels out of 32 to calculate effective connectivity. Subsequently, WEKA workbench (v3.8.5) was employed to perform seven machine-learning analysis, and we employed principal component analysis (PCA) implemented in WEKA to transform the initial 342-dimensional data onto a new subspace. The predictive performance of each algorithm was calculated using leaving-one-out cross validation (LOOCV). Accuracy, sensitivity, and specificity were calculated to evaluate the models' performance. The statistical significance of cross-validated accuracy was set at $p < 0.05$, determined through a comparison with the random chance estimated by the binomial distribution (Fig.1).

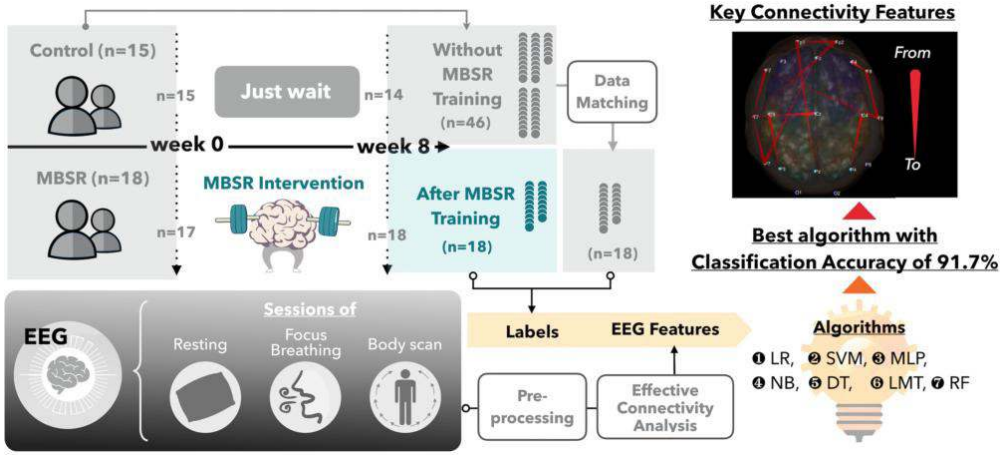

Results: Table 1 lists the performance measures of the seven classification algorithms in resting-state, focus-breathing, and body-scan sessions. The performance varied extensively across models and task sessions. Across all task sessions, the average accuracy of algorithms in the resting-state session (73.4%) outperformed those in the other two sessions of mindfulness practices (69.0% for focus-breathing and 64.3% for body-scan). Compared to sensitivity, the specificity contributed more to the accuracy in all three sessions. In the resting-state session, the algorithms of LR, SVM, NB, DT, LMT, and RF showed significantly higher accuracy of 69.4%, 75.0%, 69.4%, 91.7%, 69.4%, and 72.2%, respectively, compared to the random chance of 66.6% estimated from the binomial probability. In the focus-breathing session, four algorithms of SVM, MLP, NB, and LMT exhibited significant accuracies of 72.2%, and the RF algorithm showed a significant accuracy of 69.4%.

Compared to the resting-state and focus-breathing sessions, algorithms of SVM, MLP, and NB achieved significantly higher accuracies of 72.2%, 69.4%, and 72.2% in the body-scan session above the chance level.

Table 1: Performance measures of dDTF-based binary classifiers in three task sessions.

	Resting State			Focus Breathing			Body Scan		
Algorithms	Acc.	Sen.	Spe.	Acc.	Sen.	Spe.	Acc.	Sen.	Spe.
LR	*69.4	50.0	88.9	66.7	66.7	66.7	63.9	50.0	77.8
SVM	*75.0	50.0	100.0	***72.2**	50.0	94.4	***72.2**	44.4	100.0
MLP	66.7	44.4	88.9	***72.2**	50.0	94.4	*69.4	44.4	94.4
NB	*69.4	50.0	88.9	***72.2**	50.0	94.4	***72.2**	50.0	94.4
DT	***91.7**	88.9	94.4	58.3	55.6	61.1	47.2	33.3	61.1
LMT	*69.4	72.2	66.7	***72.2**	50.0	94.4	63.9	38.9	88.9
RF	*72.2	61.1	83.3	*69.4	61.1	77.8	61.1	61.1	61.1
Mean	73.4	59.5	87.3	69.0	54.8	83.3	64.3	46.0	82.5

Note: The cross-validated performance of classifiers is represented in percentage. The algorithm with the best accuracy within each session is boldfaced. The * denotes that the accuracy is significantly higher than the random chance. LR = Logistic Regression, SVM = Support Vector Machine, MLP = Multilayer Perceptron, NB = Naïve Bayes, DT = Decision Tree, LMT = Logistic Model Trees, RF = Radom Forest, Acc=Accuracy, Sen = Sensitivity, Spe = Specificity.

Conclusions: Automatic classification of mindfulness experiences was disclosed based on the gamma-band dDTF. We found the decision tree algorithm reached the highest prediction accuracy of 91.7% with the resting state, compared to the classification accuracies of other two mindful states. By testing different algorithms and providing the effective brain features for prediction, we initiated a milestone how to objectively detect the mindfulness experience from the brain functions.

References

1. J. Kabat-Zinn, An outpatient program in behavioral medicine for chronic pain patients based on the practice of mindfulness meditation: Theoretical considerations and preliminary results, Gen Hosp Psychiat. 4 (1982) 33–47.
2. S.F. Santorelli, F. Meleo-Meyer, L. Koerbel, J. Kabat-Zinn, Mindfulness-Based Stress Reduction (MBSR): Authorized Curriculum Guide, Center for Mindfulness in Medicine, Health Care, and Society, 2017.
3. J. Gao, J. Fan, B.W.Y. Wu, Z. Zhang, C. Chang, Y.-S. Hung, P.C.W. Fung, H.H. Sik, Entrainment of chaotic activities in brain and heart during MBSR mindfulness training., Neuroscience Letters. 616 (2016) 218–223.
4. H.-Y.H. Ng, C.W. Wu, F.-Y. Huang, Y.-T. Cheng, S.-F. Guu, C.-M. Huang, C.-F. Hsu, Y.-P. Chao, T.-P. Jung, C.-H. Chuang, Mindfulness Training Associated With Resting-State Electroencephalograms Dynamics in Novice Practitioners via Mindful Breathing and Body-Scan, Front. Psychol. 12 (2021) 748584.
5. A. Delorme, T. Mullen, C. Kothe, Z.A. Acar, N. Bigdely-Shamlo, A. Vankov, S. Makeig, EEGLAB, SIFT, NFT, BCILAB, and ERICA: New Tools for Advanced EEG Processing, Comput. Intell. Neurosci. 2011 (2011) 130714.

Poster No 1653

Beyond log-normal: Exploring variability of MEG signals with theoretical probability distributions

Hayyan Liaqat[1], Vasily Vakorin[2], Sam Doesburg[2], Sylvain Moreno[2]

[1]Simon Fraser University, Burnaby, British Columbia, [2]Simon Fraser University, Vancouver, British Columbia

Introduction: Neurophysiological parameters characterizing brain organization at various levels of functional and structural hierarchies are commonly observed as following skewed distributions (Buzsáki & Mizuseki, 2014; Roberts et al., 2015). Skewed distributions can take many shapes, but in general, resemble a logarithmic-normal (log-normal) distribution (Koch, 1966). The log-normal distribution has been used to model firing rates of individual neurons (Shafi et al., 2007), spike transmission probability (Mizuseki & Buzsáki, 2013), axon diameters, conduction velocity (Wang et al., 2008). While studies commonly assume that the logarithmic-normal distribution is a suitable model for describing brain parameters, we still have a limited understanding of how accurate this assumption is (Buzsáki & Mizuseki, 2014). In our study, we aimed to compare probability distribution models to determine what models can accurately describe the temporal variability of MEG signals. This can reveal the specific brain mechanisms responsible for the observed variability and guide the use of more accurate statistical tools to compare experimental groups.

Methods: We analyzed MEG data from the Cambridge Centre for Ageing and Neuroscience (Cam-CAN) Stage 2 cohort study (Shafto et al., 2014). The Cam-CAN study is a population-based, cross-sectional investigation that spans the adult lifespan (18–89 years old). We included 646 healthy adults, dividing them into three age groups: younger (18-45 years old), middle-aged (45-66 years old), and older (66-89 years old) adults, with males and females considered separately. We analyzed the variability of frequency-specific MEG power fluctuations at five frequencies: 2 Hz, 6 Hz, 12 Hz, 24 Hz, and 48 Hz. For each participant and frequency, we randomly selected a MEG channel from the MEG gradiometers and then randomly selected

a 30-second segment. We then modeled the variability of MEG signals power across time by fitting their corresponding empirical distributions to a large pool of theoretical probability distribution models with a maximum likelihood criterion. In total, we evaluated the goodness of fit for 72 statistical models applied to each empirical distribution. We then ranked the best-performing models. To distinguish the performance of each theoretical distribution model, we performed a pairwise comparison of the goodness of fit between each pair of models.

Results: Our results revealed that two models, the Generalized Gamma and Exponentiated Weibull distributions, provided the best fit of the temporal variability of MEG signals, with undistinguishable performance irrespective of age, sex, and frequency. In comparison, the log-normal distribution showed moderate performance, being out-performed by the power logarithmic-normal distribution. Across frequencies, we observed that the goodness of fit becomes more diverse across distribution models at higher frequencies. That is, as the frequency of brain oscillations increases, we could better distinguish models that showed similar performance. Conversely, at lower frequencies, more models demonstrated equal performance.

Conclusions: We sought to determine which theoretical probability distribution models could best describe the temporal variability of neurophysiological signals. The Generalized Gamma and Exponentiated Weibull distributions consistently outperformed the other 70 models tested, suggesting that they may be the most appropriate models for describing the temporal variability of neurophysiological signals across different populations and types of oscillations. Our analysis also demonstrated that neither power-law scaling alone, nor exponential decay accurately describes the temporal dynamics of brain signals recorded at the level of large neuronal ensembles. Instead, our results suggest that the extreme value theory may offer a more sensitive framework for discriminating between neural states or predicting clinical, behavioral, or cognitive measures from neurophysiological signals.

References

1. Buzsáki, G. (2014), 'The log-dynamic brain: How skewed distributions affect network operations', Nature Reviews Neuroscience, 15(4), Article 4
2. Koch, A. L. (1966), 'The logarithm in biology 1. Mechanisms generating the log-normal distribution exactly', Journal of Theoretical Biology, 12(2), 276–290
3. Mizuseki, K. (2013), 'Preconfigured, skewed distribution of firing rates in the hippocampus and entorhinal cortex', Cell Reports, 4(5), 1010–1021
4. Roberts, J. A. (2015), 'The heavy tail of the human brain', Current Opinion in Neurobiology, 31, 164–172
5. Shafi, M. (2007), 'Variability in neuronal activity in primate cortex during working memory tasks', Neuroscience, 146(3), 1082–1108
6. Shafto, M. (2014), 'The Cambridge Centre for Ageing and Neuroscience (Cam-CAN) study protocol: A cross-sectional, lifespan, multidisciplinary examination of healthy cognitive ageing', BMC Neurology, 14(1), 204
7. Wang, S. S.-H. (2008), 'Functional Trade-Offs in White Matter Axonal Scaling', Journal of Neuroscience, 28(15), 4047–4056

Poster No 1654

Stimulus-related modulation in the 1/f slope suggests an impaired inhibition in people with multiple

Fahimeh Akbarian[1,2], Chiara Rossi[1,2], Lars Costers[3], Marie D'hooghe[4], Miguel D'Haeseleer[4,5], Guy Nagels[2,5,6], Jeroen Van Schependom[1,2]

[1]Department of Electronics and Informatics (ETRO), Vrije Universiteit Brussel, Brussels, Belgium, [2]AIMS lab, Vrije Universiteit Brussel, Center for Neurosciences, Brussels, Belgium, [3]icometrix, Brussels, Belgium, [4]National MS Center Melsbroek, Melsbroek, Belgium, [5]UZ Brussel, Department of Neurology, Brussels, Belgium, [6]St Edmund Hall, University of Oxford, Oxford, UK

Introduction: Multiple sclerosis (MS), an inflammatory and neurodegenerative disease characterized by inhibitory and excitatory synaptic loss[1], imposes a cognitive burden on people with MS (pwMS) with a significant effect on information processing speed and working memory (WM). It has been computationally demonstrated that the balance between excitation and inhibition (E/I) is essential for efficient information processing and WM maintenance. The non-oscillatory or 1/f-like component of the power spectrum of neuronal activity has been hypothesized to provide an accessible marker of E/I balance. The steepness of this 1/f power-law component (denoted as "x" in (1/f)∧x), has been associated with the E/I ratio[2], where a steeper slope indicates a higher level of inhibition[2–4]. Gyurkovics et al[5] were the first to report an immediate and possibly transient increase in 1/f slope following an oddball auditory stimulation. In this study, we examine the 1/f slope during a visual-verbal n-back task. We hypothesize that the 1/f slope will be steeper post vs. pre-stimulus during the n-back task, similar to what has been observed in recent studies[5,6]. In addition, we hypothesize that an impaired E/I balance – as suggested in pwMS1 - will lead to reduced inhibition during distractor trials. Finally, we will explore to which extent the level of 1/f modulation can be associated with offline cognitive performance.

Methods: MEG data were recorded from 38 HCs, 19 pwMS treated (pwMS(BZDp)) and 60 pwMS not treated (pwMS(BZDn)) with benzodiazepines, during a visual-verbal n-back task[7] which included 240 target and distractor stimuli with three level of WM loads (0, 1 and 2-back). Data were preprocessed using the OSL library and source reconstructed using an LCMV beamformer[8] and then parceled into 42 parcels. We computed and compared the steepness of the 1/f spectral slope through the FOOOF algorithm[9] in the time windows [-1 0] and [0 1] second peristimulus time for both target and distractor stimulus, for each brain parcel, and different working memory loads. To estimate the periodic alpha power, we corrected the power spectrum density for the fitted aperiodic component. After subtraction of the 1/f component, the periodic alpha power was defined as the average alpha power in the [8-12] Hz band.

Results: Besides the expected alpha suppression, we observed a steeper 1/f slope after both target and distractor trials suggesting an increase in inhibition following stimulus onset. Importantly, while we observed that higher alpha power is associated with a steeper 1/f slope, the changes of alpha power and 1/f slope after stimulus onset occurred in opposite directions. In line with our hypothesis, pwMS(BZDn) had a flatter 1/f slope after distractor stimuli compared to HCs (p0-back= 0.043, p1-back = 0.02, p2-back = 0.042). We observed a significant positive Pearson correlation between 1/f slope and reaction time, particularly pronounced in the 2-back condition. Our findings corroborate a recent computational study[10] which demonstrated that a higher E/I ratio is associated with a longer reaction time. We also observed a significant Pearson correlation between 1/f slope modulation and visuospatial working memory performance measured by the Brief Visuospatial Memory Test (Revised; BVMT-R). In HCs, a weaker 1/f slope modulation during a WM task correlated with increased spatial working memory, whereas the opposite effect was observed in pwMS.

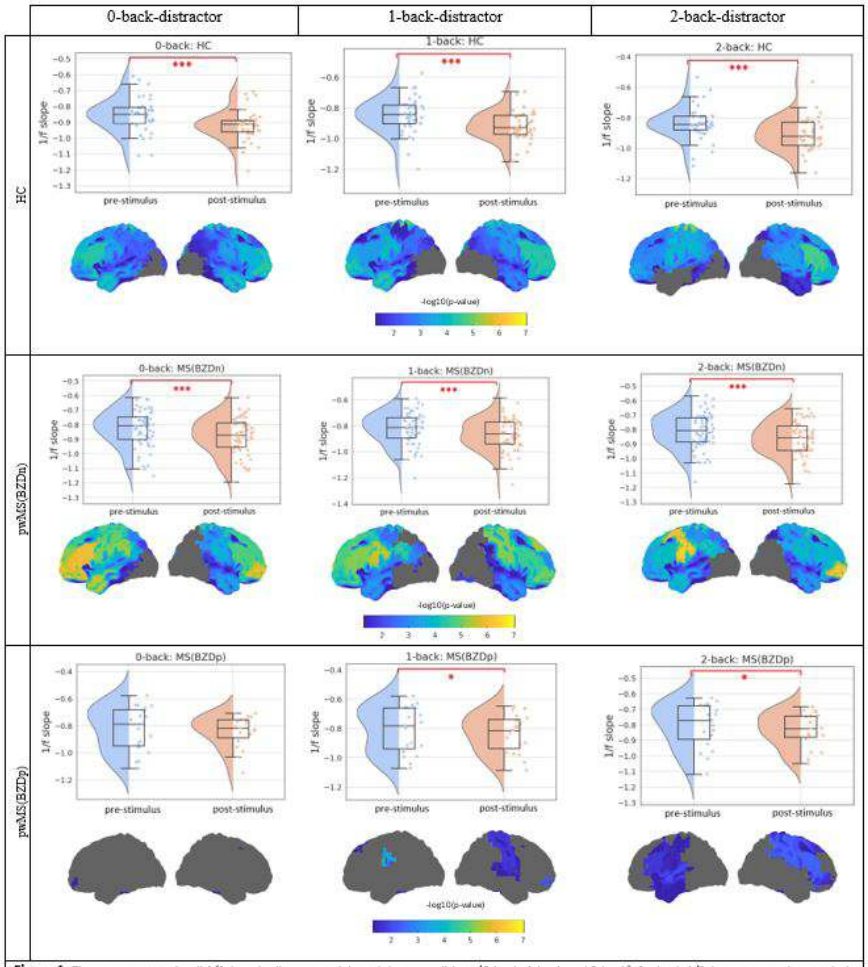

Figure 1. The pre- vs post-stimuli 1/f slope in distractor trials and three conditions (0-back, 1-back and 2-back), for both 1/f slope averaged over whole brain and in parcel level. Note that the -log10(p-value)>1.3 indicated the significant values and that p-values have been corrected for multiple comparison across the 42 parcels. The Wilcoxon signed-rank test was used to compare the pre- and post-stimuli 1/f slope. First row: HC subjects, second row: pwMS(BZDn), third row: pwMS(BZDp). *:0.001<p<0.05, **: 0.0001<p<0.001, ***: 0.00001<p<0.0001.

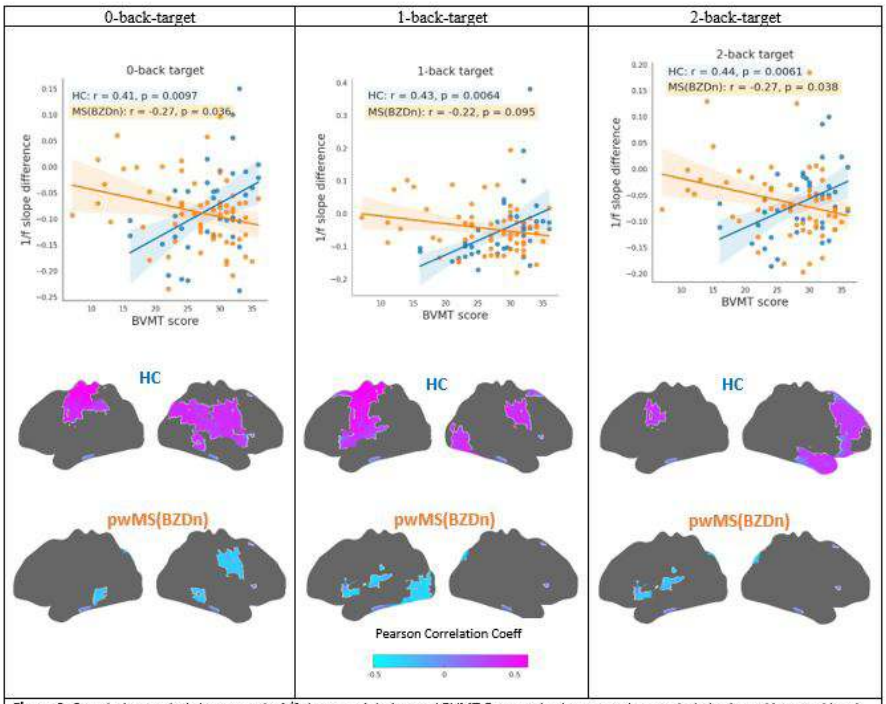

Figure 2. Correlation analysis between the1/f slope modulation and BVMT-R scores both averaged over whole brain and in parcel level for HC and pwMS (BZDn) groups in three conditions (0-back, 1-back and 2-back) in target trials. Only the parcels with significant correlations are shown.

Conclusions: Our findings are consistent with an increase in inhibition following stimulus onset. In pwMS(BZDn), this increase is reduced after distractor stimuli compared to healthy controls, suggesting a less pronounced inhibition of irrelevant information in pwMS in all three conditions. The association of 1/f slope modulation with behavioral and visuospatial WM performance, underscoring the potential significance of the 1/f spectral slope as a valuable marker for task analysis in clinical applications.

References

1. Huiskamp, M. et al. (2022), 'Inhibitory synaptic loss drives network changes in multiple sclerosis: An ex vivo to in silico translational study', Multiple Sclerosis Journal 28, 2010–2019.
2. Gao, R. et al. (2017), 'Inferring synaptic excitation/inhibition balance from field potentials', `NeuroImage 158, 70–78.
3. Chini, M. et al. (2022), 'An increase of inhibition drives the developmental decorrelation of neural activity', eLife 11.
4. Akbarian, F. et al. (2023), 'The spectral slope as a marker of excitation/inhibition ratio and cognitive functioning in multiple sclerosis', Human Brain Mapping, 44(17), 5784–5794
5. Gyurkovics, M. et al. (2022), 'Stimulus-Induced Changes in 1/ f -like Background Activity in EEG', The Journal of Neuroscience 42, 7144–7151.
6. Virtue-Griffiths, S. et al. (2022), 'Task-related changes in aperiodic activity are related to visual working memory capacity independent of event-related potentials and alpha oscillations', bioRxiv 2022.01.18.476852. doi:10.1101/2022.01.18.476852.
7. Costers, L. et al. (2020), 'Spatiotemporal and spectral dynamics of multi-item working memory as revealed by the n-back task using MEG', Human Brain Mapping 41, 2431–2446.
8. Woolrich, M. et al. (2011), 'MEG beamforming using Bayesian PCA for adaptive data covariance matrix regularization', NeuroImage 57, 1466–1479.
9. Donoghue, T. et al. (2020), 'Parameterizing neural power spectra into periodic and aperiodic components'. Nature Neuroscience 23, 1655–1665.
10. Calvin, O. L. & Redish, A. D. (2021), 'Global disruption in excitation-inhibition balance can cause localized network dysfunction and Schizophrenia-like context-integration deficits', PLOS Computational Biology 17, e1008985.

Poster No 1655

Normalized connectome explains frequency-dependent cortical activity in MEG

Spase Petkoski[1], Marmaduke Woodman[1], Viktor Jirsa[1]

[1]Inst Neurosci Syst (INS), INSERM, Univ Amu, Marseille, France

Introduction: Network theory significantly advanced our understanding of brain activity (Bassett & Sporns, 2017), and their perturbations lead to psychiatric disorders and brain disease. Brain networks are characterized by their connectomes, which comprise the totality of all connections, and are commonly described by graph theory. In a recent work (Petkoski &

Jirsa, 2022), however, we demonstrated that the traditional graph theory is deeply rooted in a particle view of information processing, and we extend it to a dual, particle-wave, perspective that is a necessity for the study of brain rhythms. Frequency and time delays become inseparable properties of the network and together with the connectome determine the synchronization and nodal activity (Petkoski & Jirsa, 2019). When applied to the database of the Human Connectome Project, normalized connectome robustly explains the emergence of frequency-specific network cores in MEG recordings during rest, including the visual and default mode networks. We also showed that the predictive value of the metrics is further improved by incorporating time-delays derived from cortico-cortical evoked potentials (CCEP) (Lemarechal et al., 2022).

Methods: Connectomes were derived from the first release of diffusion tractography imaging of 100 healthy subjects part of the Human Connectome Project (Van Essen et al., 2013). Time delays were derived from 780 patients with epilepsy (387 females; age at evaluation from 2 to 61years old; mean age 24 ± 14) explored with SEEG included in the F-TRACT protocol (Trebaul et al., 2018). Only significant CCEPs with a peak latency comprised in the first 80 ms were selected, in order to limit the analysis to the early N1 component. (Lemarechal et al., 2022). To compare the empirical with the predicted activation patterns at different frequencies of MEG, we compared the similarities between the vectors of normalized activity in both cases. The same procedure was repeated for the regions with the strongest activity only, where the threshold was set at different levels.

Results: We integrated time delays due to finite transmission speeds, and derive a normalization of the connectome for communication through coherence (Fries, 2015). For weak couplings, dynamics of the oscillatory system are captured by phase models, of which the simplest and the most elaborate is the Kuramoto model (Kuramoto, 1984). We use the insight that the impact of the direct link in the phase difference between oscillators can be separated from the rest of the network leading to a normalization of network weights wij by the term cosΩτij, where Ω is the frequency and τij is the time-delay due to axonal propagation over the link between the nodes i and j (Petkoski & Jirsa, 2022). We compare empirical and predicted relative activation patterns of all the brain regions for the frequencies of 1 - 80 Hz. For the time-delays of the normalized connectome in the first case we assume homogeneous propagation velocity, which is often used as a first approximation, resulting in time delays being defined by the lengths of the links (Sanz Leon et al., 2013). Then, we use the time-delays from the stimulation and we quantify the improved predictive value of spectral strength and capacity.

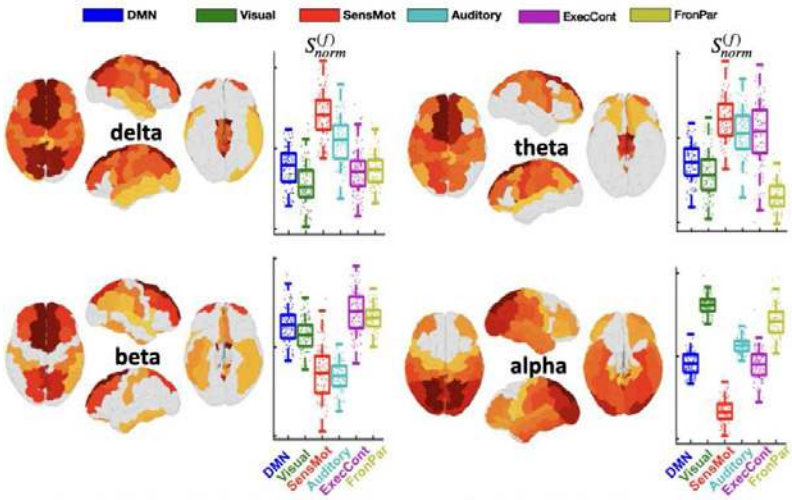

Predicted cortical activation patterns using tract length for the time-delays
Mean spectral strength over 100 subjects is shown for different cortical regions (higher for warmer colors) and frequency bands. The activation of resting-state networks (RSNs) is projected in the frequencies and the boxplots contain the scatterplots of all 100 subjects. The values per given RSN and lobe are normalized by the number of regions in that subnetwork.

Conclusions: The incorporation of signal transmission delays in the connectome's metrics completes the characterization of the spatiotemporal skeleton, within which oscillatory brain activity can be amplified by the properties of the medium supporting it, i.e., it provides a corpus resonantiae. We propose that the activation of certain parts of the brain, that are related to different tasks, can be explained as being anatomically prewired. We have demonstrated that the connectome has such properties and allows for selective, frequency-dependent information processing that could support the differentiation of brain activity for various processes and frequency bands.

References

1. Bassett, D. S. (2017). Network neuroscience. Nature Neuroscience, 20(3), 353–364. https://doi.org/10.1038/nn.4502

2. Fries, P. (2015). Rhythms for Cognition: Communication through Coherence. Neuron, 88(1), 220–235. https://doi.org/10.1016/j.neuron.2015.09.034
3. Kuramoto, Y. (1984). Chemical Oscillations, Waves, and Turbulence (Vol. 19). Heidelberg: Springer Berlin Heidelberg. https://doi.org/10.1007/978-3-642-69689-3
4. Lemarechal, J. D. (2022). A brain atlas of axonal and synaptic delays based on modelling of cortico-cortical evoked potentials. Brain, 145(5), 1653–1667. https://doi.org/10.1093/brain/awab362
5. Petkoski, S. (2019). Transmission time delays organize the brain network synchronization. Philosophical Transactions of the Royal Society A: Mathematical, Physical and Engineering Sciences, 377(2153), 20180132. https://doi.org/10.1098/rsta.2018.0132
6. Petkoski, S. (2022). Normalizing the brain connectome for communication through synchronization. Network Neuroscience, 6(3), 1–23. https://doi.org/10.1162/netn_a_00231
7. Sanz-Leon, P. (2015). Mathematical framework for large-scale brain network modeling in The Virtual Brain. Neuroimage, 111, 385–430. https://doi.org/10.1016/j.neuroimage.2015.01.002
8. Trebaul, L.. (2018). Probabilistic functional tractography of the human cortex revisited. NeuroImage, 181(June), 414–429. https://doi.org/10.1016/J.NEUROIMAGE.2018.07.039
9. Van Essen, D. C. (2013). The WU-Minn Human Connectome Project: An overview. NeuroImage, 80, 62–79. https://doi.org/10.1016/j.neuroimage.2013.05.041

Poster No 1656

The virtual multiple sclerosis patient: on the clinical-radiological paradox

Pierpaolo Sorrentino[1], Anagh Pathak[2], Abolfazl Ziaeemehr[1], Emahnuel Troisi Lopez[3], Lorenzo Cipriano[4], Antonella Romano[5], Simona Bonavita[6], Mario Quarantelli[7], Arpan Banerjee[8], Giuseppe Sorrentino[5], Meysam Hashemi[1], Viktor Jirsa[9]

[1]Aix-Marseille University, Marseille, Please Select, [2]National Brain Research Centre, Gurgaon, Haryana, [3]National Research Council of Italy, Naples, NA, [4]Parhtenope university of Naples, Naples, Italy, [5]Parthenope university of Naples, Naples, Italy, [6]University of Naples L Vanvitelli, Naples, Italy, [7]National Research Council, Naples, Naples, [8]National Brain Research Centre, Manesar, India, [9]nstitut de Neurosciences des Systèmes, Marseille, N/A

Introduction: Multiple sclerosis (MS) is typically diagnosed based on the clinical presentation, the presence of structural MRI lesions, and a “no better explanation” criterion. The structural lesions, disseminated in time and space, are a consequence of autoimmune processes leading to the damage of the myelin sheath in the central nervous system. As such, one would expect that more lesions would relate to higher clinical disability. However, a conflicting scenario is often present, with a high lesion load related to mild clinical impairment, and vice versa, a phenomenon referred to as the “clinico-radiological paradox”. The myelin damage in MS is widespread, which is likely mirrored in a widespread slowing of conduction velocities. However, conduction velocities are typically measured on selected white-matter tracts (e.g., visual evoked potentials), which do not directly relate to clinical impairment. In this paper, we hypothesize that the overall slowing of conduction velocities (i.e., across all brain tracts) is a better predictor of clinical disability. However, estimating the whole-brain average velocities is challenging.

Methods: To overcome this obstacle, we estimated patient-specific conduction velocities in MS patients by merging multimodal data (i.e., DTI and source-reconstructed magnetoencephalography) to inform large-scale brain models, fitted on each individual patient. We started from the known reduction of the power of the alpha frequency band, as well as the shift in its peak, observed in MS patients. We then reproduced these individual spectral features in silico using large-scale models based on the individual connectomes. We then used state-of-the-art deep neural networks for Bayesian model inversion to estimate the most likely average conduction velocity in each patient, given the observed spectral features (and the connectomes). Finally, we used the inferred conduction velocities to predict the individual clinical disability.

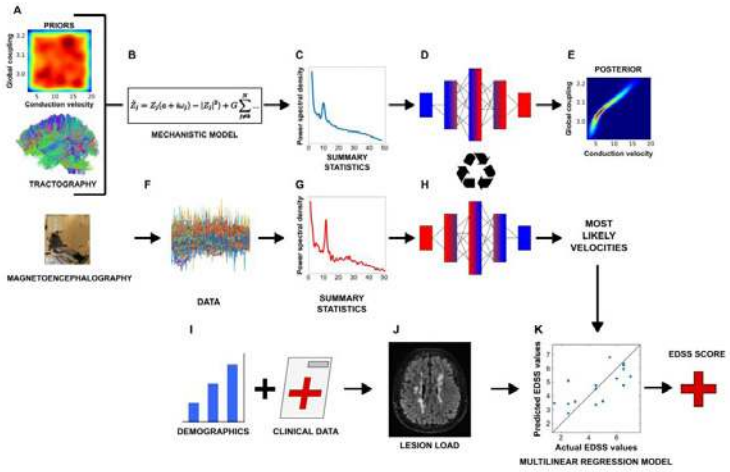

Results: We find that the conduction velocities inferred for patients are significantly lower than those inferred for controls and that they are predictive of individual clinical disability, well above the predictive power of demographic and clinical variables and lesion load.

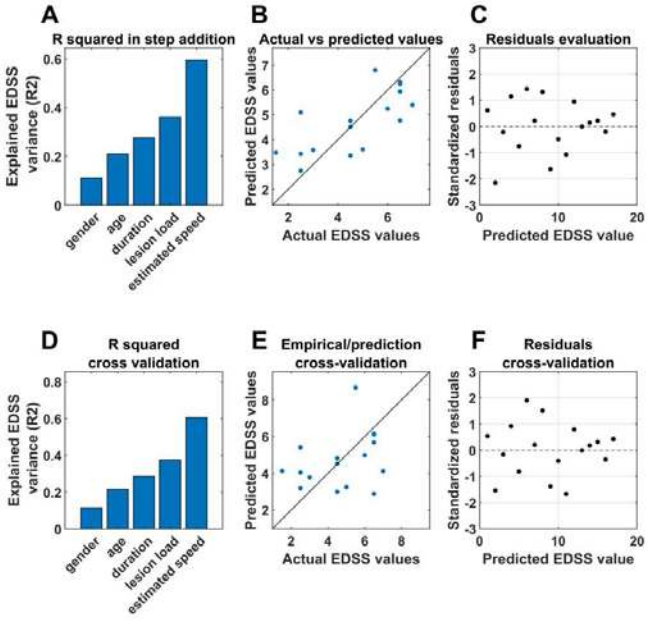

Conclusions: Our results suggest a biologically and physically plausible solution to the "clinico-radiological" paradox, where the inferred, individual changes in conduction velocities across the whole networks are proposed as causative to the clinical disability.

References

1. F. Barkhof, The clinico-radiological paradox in multiple sclerosis revisited: Curr. Opin. Neurol. 15, 239–245 (2002).
2. P. Sorrentino, C. Seguin, R. Rucco, M. Liparoti, E. Troisi Lopez, S. Bonavita, M. Quarantelli, G. Sorrentino, V. Jirsa, A. Zalesky, The structural connectome constrains fast brain dynamics. eLife. 10, e67400 (2021).
3. J. Cabral, F. Castaldo, J. Vohryzek, V. Litvak, C. Bick, R. Lambiotte, K. Friston, M. L. Kringelbach, G. Deco, Metastable oscillatory modes emerge from synchronization in the brain spacetime connectome. Commun. Phys. 5, 1–13 (2022).
4. A. Pathak, V. Sharma, D. Roy, A. Banerjee, Biophysical mechanism underlying compensatory preservation of neural synchrony over the adult lifespan. Commun. Biol. 5, 1–12 (2022).
5. M. Hashemi, A. N. Vattikonda, V. Sip, M. Guye, F. Bartolomei, M. M. Woodman, V. K. Jirsa, The Bayesian Virtual Epileptic Patient: A probabilistic framework designed to infer the spatial map of epileptogenicity in a personalized large-scale brain model of epilepsy spread. NeuroImage. 217, 116839 (2020).
6. P. Sorrentino, R. Rucco, F. Baselice, R. De Micco, A. Tessitore, A. Hillebrand, L. Mandolesi, M. Breakspear, L. L. Gollo, G. Sorrentino, Flexible brain dynamics underpins complex behaviours as observed in Parkinson's disease. Sci. Rep. 11, 4051 (2021).

Poster No 1657

Group-level current source reconstruction of the MNI iEEG atlas

Ying Wang[1], Min Li[2], Deirel Paz-Linares[1], Ariosky Areces-Gonzalez[1], Jorge Bosch-Bayard[3], Maria Bringas-Vega[1], Pedro Valdes-Sosa[1]

[1]University of Electronic Science and Technology of China, Chengdu, Sichuan, [2]Hangzhou Dianzi University, Hangzhou, Zhejiang, [3]McGill University, Chengdu, Quebec

Introduction: Multichannel imaging tools, such as fMRI and EEG/MEG, capture brain functional activity. However, these measures rely on indirect physical responses or face limitations in spatial/temporal resolution. iEEG offers direct observation but exhibits heterogeneous coverage due to invasiveness. This paper addresses the incomplete observation problem by proposing a method for whole-brain activity construction. Our approach reconstructs activity in uncovered regions and corrects amplitude differences across patients, enabling the generation of a comprehensive activation map across the entire brain. This method is compatible with other imaging modalities.

Methods: We employ Electrophysiological Source Imaging (ESI) for whole-brain activity reconstruction. Due to electrode number and position limitations, individual brain activity is often reconstructed in nearby patches. Instead of Monte-Carlo

simulations for confidence intervals, this paper opts for the screening method (Fan and Lv 2008) for high-dimensional regression. Individual target regions are obtained by truncating the cumulative correlation between a smooth simulation and its inverse solution, in which the correlation is sorted by leadfield gain. Selected patches per subject are small; most cannot estimate the entire brain individually. A group-level approach is necessary to create a whole-brain activation map due to individual differences and system deviations. Scaling each subject's data to the same level is crucial. In scalp EEG analysis, the Global Scale Factor (GSF) (Hernández et al., 1994) normalizes amplitudes, facilitating population metrics analysis (e.g., spatial patterns, norms (Li et al. 2022)). GSF, however, falls short for sEEG and ECoG due to randomly distributed electrodes. Our method estimates the scale factor for sEEG and ECoG by assuming energy distribution fluctuates from a similar spatial pattern across subjects. The aligned space for this scale estimation is the group-averaged cortex or volume space, exemplified by the MNI cortical space. The leadfield, obtained from Denuro FEM via the Brainstorm (Medani et al. 2023), was converted from bipolar to unipolar montage. Activation in selected regions for each subject was estimated using the eLORETA (Pascual-Marqui 2007) estimator. In this group-level space, we address the scale issue between subjects by modeling the source log spectrumlog10(s^_jj (i)) for each subject using IOLMM (Incomplete Observation Linear Mixed Effect Model) outlined in Eq (1) in the figure. The X(i) is a binary selection matrix for each subject, choosing confident sources based on the above criteria for reconstruction. The population mean log10(s^_jj) is modeled with the fixed effect. The observation scale problem is addressed with a univariate random effect, where z(i) is 1 and b(i) is the scalar scale factor for each subject in the log scale. The additive independent error ε(i) is modeled with Gaussian noise N(0,σ^2). The problem is solved by maximizing the likelihood with the EM (Expectation Maximization) algorithm (McLachlan and Krishnan 2008). The scale factor for the original signal is obtained as c(i)=√(10^b(i)), along with the group pattern s^_jj. The figure with a bipolar colormap illustrates the entire process.

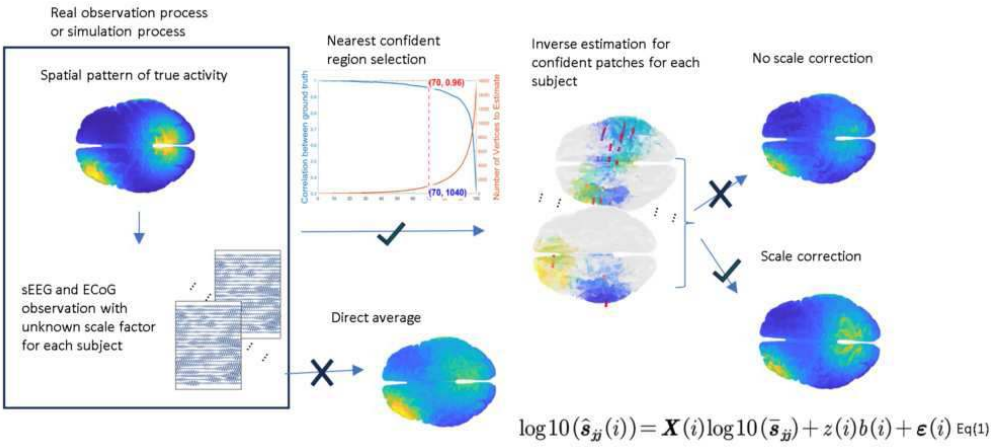

Fig. The procedures and model for the reconstruction.

Results: Utilizing the MNI atlas dataset (Frauscher et al. 2018), our figure displayed rescaled data results. The left map reveals a global energy pattern congruent with EEG source localization of alpha rhythm in the eye-closed condition, with heightened occipital lobe activation. On the right, a measure of signal nonlinearity, max bicoherence, demonstrating the generalized nonlinearity of iEEG courses. This nonlinearity is particularly prominent in the parietal lobe.

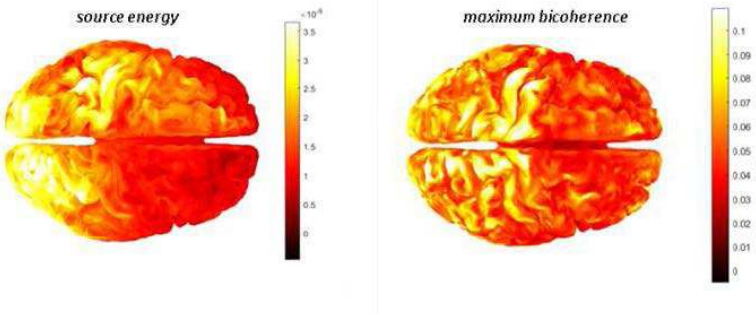

Fig. The left figure is the energy (0-80Hz) distribution estimated from 105 patients. The right figure is the maximum bicoherence (0-80Hz panel) distribution estimate from 105 subjects.

Conclusions: We offer a robust tool for constructing group-level intracranial activation from iEEG data across various subjects. This approach facilitates the integration and comparison of direct biophysical measurements of neural activity with other brain imaging modalities.

References

1. Birkelund, Y., A. Hanssen, and E.J. Powers. 2001. “Multitaper Estimation of Bicoherence.” In 2001 IEEE International Conference on Acoustics, Speech, and Signal Processing. Proceedings (Cat. No.01CH37221), 5:3085–88 vol.5. https://doi.org/10.1109/ICASSP.2001.940310.
2. Fan, Jianqing, and Jinchi Lv. 2008. “Sure Independence Screening for Ultrahigh Dimensional Feature Space.” Journal of the Royal Statistical Society: Series B (Statistical Methodology) 70 (5): 849–911. https://doi.org/10.1111/j.1467-9868.2008.00674.x.
3. Frauscher, Birgit, Nicolas von Ellenrieder, Rina Zelmann, Irena Doležalová, Lorella Minotti, André Olivier, Jeffery Hall, et al. 2018. “Atlas of the Normal Intracranial Electroencephalogram: Neurophysiological Awake Activity in Different Cortical Areas.” Brain 141 (4): 1130–44. https://doi.org/10.1093/brain/awy035.
4. Li, Min, Ying Wang, Carlos Lopez-Naranjo, Ronaldo Cesar Garcia Reyes, Aini Ismafairus Abd Hamid, Alan C. Evans, Alexander N. Savostyanov, et al. 2022. “Harmonized-Multinational qEEG Norms (HarMNqEEG).” NeuroImage, April, 119190. https://doi.org/10.1016/j.neuroimage.2022.119190.
5. McLachlan, Geoffrey J., and Thriyambakam Krishnan. 2008. The EM Algorithm and Extensions. 2nd edition. Hoboken: Wiley-Interscience.
6. Medani, Takfarinas, Juan Garcia-Prieto, Francois Tadel, Marios Antonakakis, Tim Erdbrügger, Malte Höltershinken, Wayne Mead, et al. 2023. “Brainstorm-DUNEuro: An Integrated and User-Friendly Finite Element Method for Modeling Electromagnetic Brain Activity.” NeuroImage 267 (February): 119851. https://doi.org/10.1016/j.neuroimage.2022.119851.
7. Pascual-Marqui, Roberto D. 2007. “Discrete, 3D Distributed, Linear Imaging Methods of Electric Neuronal Activity. Part 1: Exact, Zero Error Localization,” October. http://arxiv.org/abs/0710.3341.

Poster No 1658

EEG-ExPy: Democratizing the Cognitive Neuroscience Experiment

John Griffiths[1,2], Taha Morshedzadeh[3], Sorenza Bastiaens[3], Parsa Oveisi[4], Ore Ogundipe[5], Erik Bjäreholt[6], Daniele Marinazzo[7], Yannick Roy[8], EEG-ExPy Team .[9]

[1]Departments of Psychiatry, Medical Sciences, & Biomedical Engineering, University of Toronto, Canada, [2]Krembil Centre for Neuroinformatics, Centre for Addicton and Mental Health, Canada, [3]Institute of Medical Sciences, University of Toronto, Canada, [4]Institute of Biomedical Engineering, University of Toronto, Canada, [5]Fusion Research Inc., Canada, [6]Lund University, Sweden, [7]University of Ghent, Belgium, [8]University of Montreal, Canada, [9]Github, The World

Introduction: Cognitive neuroscience experiments using EEG and other neuroimaging techniques have traditionally been restricted to lab settings, with dedicated (typically university or hospital) spaces, expensive hardware, manned by professional technical and academic staff. Fortunately however, recent years have seen alternatives to these conventions begin to emerge. It is now becoming possible to run a wide range of classic experimental paradigms in a highly affordable fashion with minimal specialist equipment and expertise. This shift represents to many a democratizaton of the cognitive neuroscience experiment. It is in this spirit that we introduce here EEG-ExPy - A Python-based platform for cognitive neuroscience experimentation and education. Formerly known as eeg-notebooks (and before that muse-lsl), the EEG-ExPy project (github.com/NeuroTechX/EEG-ExPy) is an international open science initiative, driven by members of the NeuroTechX community. EEG-ExPy allows sophisticated visual, auditory, and other experimental paradigms to be run using a standard personal computer and a minimal, affordable, consumer-grade mobile EEG device.It is also fully compatible and usable with research-grade EEG systems in a traditional lab setting. EEG-ExPy’s ease of use makes it attractive for a wide audience, including research scientists, clinicians, educators, and hobbyists. Use cases to date span a wide range of settings, from high school outreach programs, hackathons, hands-on university-level cognitive neuroscience teaching, brain stimulation clinical trials in psychiatry, and bedside recordings in neurology patients. Here we describe the motivation, design, and usage of EEG-ExPy, demonstrating example data from several featured experiments.

Methods: EEG-ExPy contains functionality for the three main pieces of an eeg experiment: data streaming, stimulus presentation, and analysis. It is an installable Python package that can be run from an OS command line, a Python command line, or via Python scripts and jupyter notebooks, on a Windows, Mac, or Linux laptop/desktop. The primary use case is with wireless mobile EEG devices such as the InteraXon Muse, Neurosity Crown, OpenBCI Cyton, and G.tec Unicorn. These are handled by a Device Class, which initiates a bluetooth data stream using third-party libraries such as BrainFlow. If data streaming is to be handled by external software, triggers can be delivered via internal or external hardware ports. After initiating a streaming connection with the EEG device, experiments are launched. Currently all featured experiments use PsychoPy for visual and auditory stimulus presentation, key press recognition, and instruction presentation; although this is not required. Featured experiments that have been tested extensively include N170 RSVP w/ faces, P300 RSVP w/ animals, auditory oddball, SSVEP, SSAEP, visual cueing, rest. Analyses draw primarily on the MNE-Python library, focusing on computing and visualizing ERPs, frequency-domain responses, and ML-based trial classification. An automated analysis report tool generates HTML files for fast inspection of data.

Results: Usage examples and key software elements are shown in Figure 1. Figure 2 shows results from the faces vs. houses and SSVEP experiments, showing the face-selective N170 ERP component and flicker-frequency peaks in the power spectrum. These two examples demonstrate clearly the ability to reproduce canonical experimental findings from the EEG cognitive neuroscience literature with mobile EEG systems.

Conclusions: In conclusion, EEG-ExPy is a powerful tool for the amateur and expert-trained cognitive neuroscientist alike, lowering the barrier-to-entry for conducting meaningful research with established paradigms, reducing the cost and time for setup, iteration, and implementation of new ideas and initiatives, from education through research to clinical monitoring.

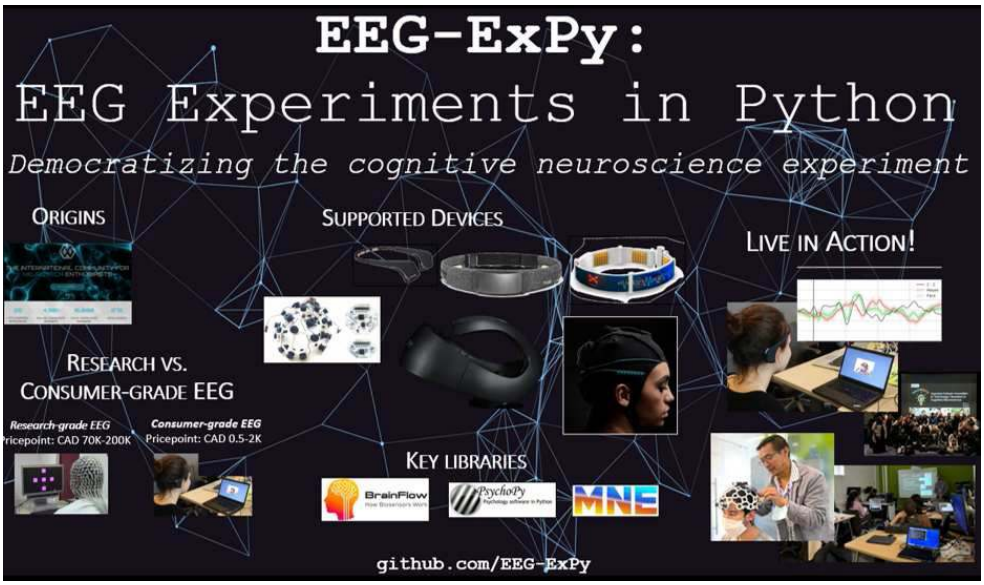

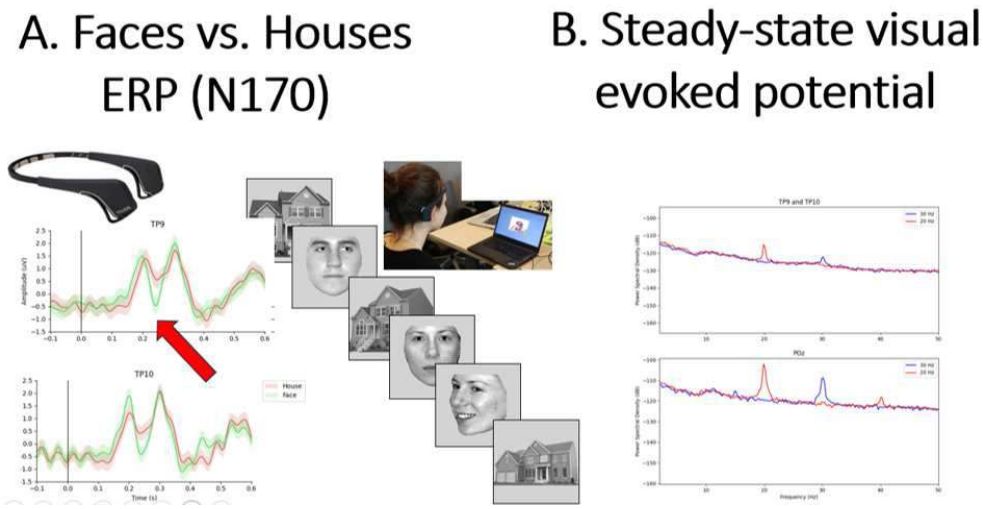

Poster No 1659

Global nonlinear approach for mapping parameters of neural mass models

Dominic Dunstan[1], Mark Richardson[2], Eugenio Abela[2], Samantha Chan[3], Alexander Shaw[1], Alessia Caccamo[1], Marc Goodfellow[1]

[1]University of Exeter, Exeter, United Kingdom, [2]King's College London, London, United Kingdom, [3]University College London, London, United Kingdom

Introduction: Neural mass models (NMMs) are a useful tool for interpreting observations of brain dynamics. By incorporating assumptions about how neuronal populations (excitatory and inhibitory) interact, they provide a means to understand data by examining model parameters as a proxy for underlying mechanisms. To interpret data using NMMs we need to quantitatively compare the output of NMMs with data, and thereby find parameter values for which the model can produce the observed dynamics. Though abstract, NMMs still comprise of many parameters that are difficult to constrain a priori. Existing approaches to model fitting make assumptions to simplify a particular optimisation scheme. These include exploring only a subset of the

parameter space by fixing the values of many parameters a priori (Wendling 2005; Nevado-Holgado 2012), and, in the case of dynamical causal modelling (Friston 2012), linearising models and assuming Gaussian distributions. Therefore, we still have little knowledge of how different regions of parameter space of NMMs can yield dynamics that approximate data, how nonlinearities in models can affect parameter mapping or how best to quantify similarities between model output and data. Here, we take a global nonlinear approach for mapping parameters of NMMs. We use evolutionary algorithms to explore large regions of parameter space and to demonstrate how using different objective functions can affect the inferences made. We demonstrate some advantages of using multiobjective evolutionary algorithms (MOEA), combining the weighted horizontal visibility graph with spectral properties to quantify similarities between model and data. We illustrate the usefulness of this approach in two applications: (i) understanding the slowing of the alpha rhythm in epilepsy (Abela 2019); and (ii) understanding why children with epilepsy have altered EEG during slow wave sleep (Eriksson 2022).

Methods: To explore the former application, we recorded EEG alpha activity during the eyes closed resting state from 20 healthy individuals and 20 people with focal epilepsy. For the latter application, EEG polysomnography was acquired from 15 children with drug naïve epilepsy. We then compared the slow wave sleep obtained from the frontal electrodes to 16 healthy age-matched controls. In both cases, we used the MOEA to optimise the dynamics of an NMM to the data and were able to accurately recreate properties of the data in the time and spectral domain.

Results: We found that the mean excitatory gain parameter had the largest effect in explaining the shift in alpha power observed (Dunstan 2023). Counterintuitively, this parameter was reduced in people with epilepsy compared to control. By mapping the differences in slow-wave sleep seen in children with epilepsy to an NMM, we found enhanced neuronal firing rate (excitability) in model excitatory and inhibitory populations, which comes predominantly from enhanced excitatory synaptic currents. Furthermore, using the model to infer mechanisms underpinning a classical epileptiform spike-wave rhythm reveals that these differences in currents place patients closer to seizure dynamics than controls.

Conclusions: These results demonstrate that the MOEA framework proposed is a potentially useful tool to map differences seen in EEG recordings to underlying mechanisms. In particular, we found that mechanisms of epilepsy are manifested in non-seizure states and that patient EEG can be mapped to specific synaptic deficits which are causative for epilepsy.

References

1. Abela, E. (2018), 'Slower alpha rhythm associates with poorer seizure control in epilepsy', Annals of Clinical and Translational Neurology, vol. 6, no. 2, pp. 333-343.
2. Dunstan, D.M. (2023), 'Global nonlinear approach for mapping parameters of neural mass models', PLOS Computational Biology, vol. 19, no. 3, e1010985.
3. Eriksson, M.H. (2023), 'Sleep homeostasis, seizures, and cognition in children with focal epilepsy', Developmental Medicine & Child Neurology, vol. 65, no. 5, pp. 701-711.
4. Friston, K.J. (2012), 'DCM for complex-valued data: cross-spectra, coherence and phase-delays', Neuroimage, vol. 59, no. 1, pp. 439-455.
5. Nevado-Holgado, A.J. (2012), 'Characterising the dynamics of EEG waveforms as the path through parameter space of a neural mass model: Application to epilepsy seizure evolution', NeuroImage, vol. 59, no. 3, pp. 2374-2392.
6. Wendling, F. (2005), 'Interictal to ictal transition in human temporal lobe epilepsy: insights from a computational model of intracerebral EEG', Journal of Clinical Neurophysiology, vol. 22, no. 5, pp. 343-356.

Poster No 1660

Modelling dynamic functional brain networks during sleep

Hongyu Qian[1], Mark Woolrich[1], Chetan Gohil[2]

[1]University of Oxford, Oxford, Oxfordshire, [2]University of Oxford, Oxford, Oxford

Introduction: One major task of understanding brain networks is building computational methods that automatically (via unsupervised learning) learn how the brain's dynamics are organised into recurrent activations of transient brain networks. Recent studies have revealed the brain networks during resting state. However, limited work has been done to investigate the dynamics of such brain networks during sleep. Researchers have proposed a new approach DyNeMo (Dynamic Network Modes) that uses a new generative model for electrophysiological data and a Bayesian framework to learn model parameters from the observed data. This approach has been proven to be effective in analysing both resting-state and task M/EEG data. This study therefore set out to assess the performance of DyNeMo on sleep EEG data. DyNeMo was able to identify reasonable networks in sensor space. Finally, it is concluded that DyNeMo is a reliable tool to analyse sleep EEG data and the study can now extend to source space.

Methods: Researchers have proposed a new method that builds on recent advances in deep learning to capture the rich spatio-temporal content of brain network dynamics that underpins cognition. The current approach models brain networks as a time-varying linear mixture of spatially distributed modes. The temporal evolution of this mixture is governed by a recurrent

neural network (RNN), which enables the model to generate data with a rich temporal structure. This approach of Dynamic Network Modes called DyNeMo is proposed by Gohil et al. in “Mixtures of large-scale dynamic functional brain network modes”. Data from the research of Schreiner et al. was used in this study. Twenty participants (age: 20.75±0.35; 17 female) took part in two experimental sessions and we received data for nineteen subjects. In both sessions, they performed an episodic learning task, with memory performance being assessed before and after taking a 120-min nap. A Brain Products 64-channel EEG system was used to record electroencephalography (EEG) throughout the experiment. Impedances were kept below 10 kΩ. EEG signals were referenced online to electrode FCz and sampled at a rate of 1000 Hz. Furthermore, electromyogram (EMG) and electrocardiogram (ECG) were recorded for polysomnography. Sleep architecture was determined offline according to standard criteria by two independent raters.

Results: In Figures 1, we show topographic power maps and PSDs of 8 modes inferred by DyNeMo when trained on the sleep dataset. A General Linear Model (GLM)-based approach was used on a spectrogram directly calculated from the data to calculate mode and region-specific PSDs.Mode 1 appears to be a low-power background mode, whereas modes 2-8 show high power with different frequency bands at different locations. Figure 3 shows more detailed topographic maps for each mode in different frequency bands. We can observe that mode 4 shows clear alpha activity at occipital regions and has the strongest beta activity across the modes. Mode 8 is the only mode with significant sigma power and the power is stronger near the F3 and F4 electrodes. Modes 2 and 3 show high power in the low-delta band at the centralposterior region and frontal region respectively, while mode 7 shows low-delta power near a specific electrode. Modes 2,3,4 and 8 parallel the characteristic patterns observed in typical sleep EEG results. This correlation supports the relevance and validity of the DyNeMo modes. The classifier achieved an average accuracy of 68.2% and only made few blatant errors, for example, mislabelling N2 and N3 to wake or REM.This indicates their potential for furthering our understanding of dynamic functional brain networks during sleep.

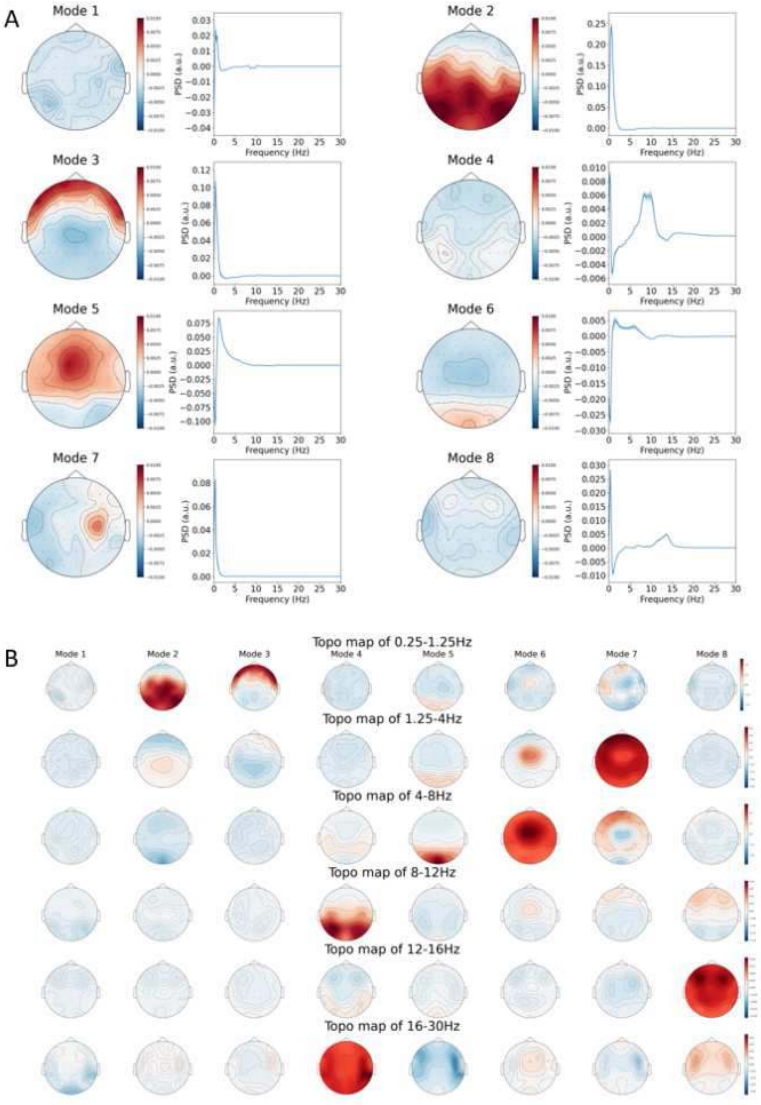

Conclusions: This study has used DyNeMo to identify distinct modes that are broadly in line with previous EEG studies The application of DyNeMo to sleep EEG data reveals modes that could relate to sleep spindles and slow oscillation, suggesting that it remains a novel and complementary tool for studying sleep data.

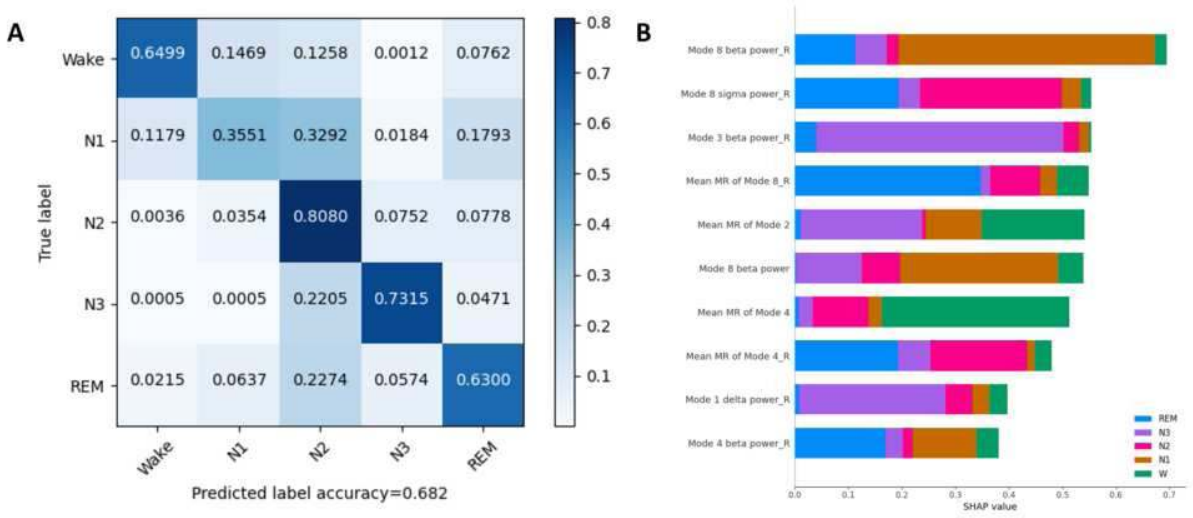

References

1. osl: OHBA Software library. https://github.com/OHBA-analysis/osl. Accessed:25/09/2023.
2. Baker, A. P. (2014). Fast transient networks in spontaneous human brain activity. eLife, 3:e01867.
3. Carskadon, M. (1989). Normal human sleep: An overview. principles and practice of sleep medicine. m.h. kryger (ed.). W.B. Saunders, Philadelphia, pages 3–13.
4. Friston, K. (2006). A free energy principle for the brain. Journal of physiology, Paris, 100:70–87.
5. Gohil, C. (2023). osl-dynamics: A toolbox for modelling fast dynamic brain activity.
6. Gohil, C. (2022). Mixtures of large-scale dynamic functional brain network modes. NeuroImage, 263:119595
7. Greicius, M. (2003). Functional connectivity in the resting brain: A network analysis of the default mode hypothesis. Proceedings of the National Academy of Sciences of the United States of America, 100:253–8.
8. Kaulen, L.(2022). Advanced sleep spindle identification with neural networks. Scientific Reports, 12:7686.
9. Lacourse, K. (2018). A sleep spindle detection algorithm that emulates human expert spindle scoring. Journal of Neuroscience Methods, 316.
10. Quinn, A. (2022). The glm-spectrum: A multilevel framework for spectrum analysis with covariate and confound modelling.
11. Schreiner, T. (2021). Endogenous memory reactivation during sleep in humans is clocked by slow oscillation-spindle complexes. Nature Communications, 12.

Poster No 1661

Effects of diet on the neurodevelopment of 2- and 6-month-old infants determined by EEG Microstates

Dylan Gilbreath[1,2], Darcy Hagood[2], Heather Downs[2], Linda Larson-Prior[1,2]

[1]University of Arkansas for Medical Sciences, Little Rock, AR, [2]Arkansas Children's Nutrition Center, Little Rock, AR

Introduction: Infant diet plays a critical role in shaping the developing nervous system by providing essential nutrients that effect myelination, neurogenesis, synaptogenesis, and cognitive development. These developing neuronal processes are sensitive to various nutrient deficiencies throughout infancy, and these insults often produce enduring effects. However, little research has been done exploring how different healthy infant diets may effect neuromaturation. While breastmilk is widely regarded as being the optimal source of nutrients, little is known of its actual effect on the function and maturation of the brain. Recent advances in neuroimaging have expanded our conceptualization of dynamic neuronal function. Electroencephalography (EEG) is a non-invasive, direct measure of neuronal activity, and can be used to measure microstates – transiently stable scalp potentials that occur on the order of milliseconds. These microstates have distinct topologies referred to as classes, with each class indicating a different pattern of global neuronal activity thought to be necessary for cognitive experiences. Currently, it is unknown the extent to which infant and adult microstates are comparable, and whether these microstates can be used as an indicator of neuronal maturation. We hypothesize that infant microstates will be spatially similar to the adult microstates, and that children fed breastmilk (BF) will demonstrate the most similarity due to a higher degree of neuronal maturation than their dairy (MF) or soy (SF) formula counterparts for each age group.

Methods: Resting state, eyes open EEGs were collected from infants at 2 months (n = 316; BF = 109, MF = 102, SF = 105) and 6 months (n = 419; BF = 135, MF = 143, SF = 141) using a 128-sensor net. The Harvard Automated Processing Pipeline for EEG was used to preprocess EEG data. Data were band-pass filtered (.5-45 Hz), referenced to a global mean using REST, and Morlet wavelet filtered to remove artifacts. EEGs were then rejected for the following criteria: >70% bad channels or segments, or an R Pre/Post wavelet thresholding value below .2 for frequencies in our range of interest. 10 artifact free, 10 second segments were then averaged for each subject, and this average was used for further analysis. Microstates were calculated for each individual using k-means clustering (k = 5, repetitions = 20), before being calculated for the grand average, sorted by class based upon an adult template, and backfit to the individual. Significance was tested using a TANOVA to determine topographical differences between dietary groups for each age group and microstate class. Microstate analysis and statistical testing was conducted using the MICROSTATELAB toolbox for EEGLAB.

Results: While significance was not achieved for the dietary groups in 2-month-olds in any microstate class, microstates at this age as well as in the 6-month-olds were found to closely resemble adult microstates, with a high spatial correlation ranging from 85-97% (Fig1). In the 6-month-olds, microstate C was found to be significantly different between groups (p = .014), with topographic differences being largely prefrontal (Fig2). Because of the high fidelity to the adult maps, we believe that these significant differences are due to the subtle changes in neuromaturation between the dietary groups, manifesting in divergent global neuronal activity.

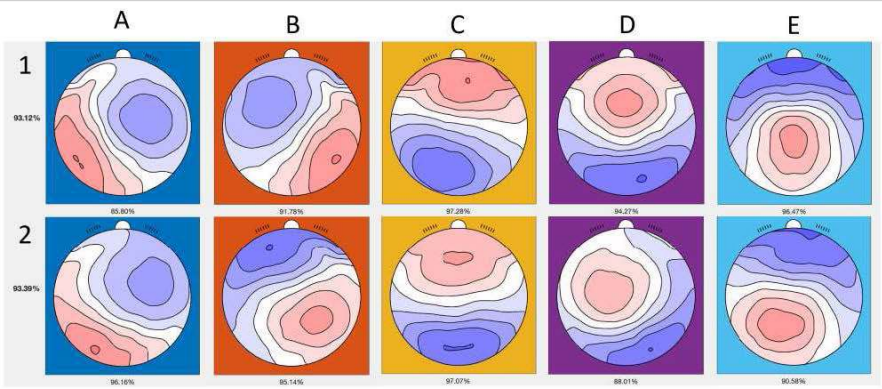

Figure 1. Infant microstate classes sorted by topological similarities to adult classes. Microstates were averaged across dietary groups for each age group with row 1 designating the 2-month-olds and row 2 being the 6-month-olds. Topologies were sorted into classes (A-E) based on their similarity to the adult template. Shared variance with the adult template for each class is given below each topological plot.

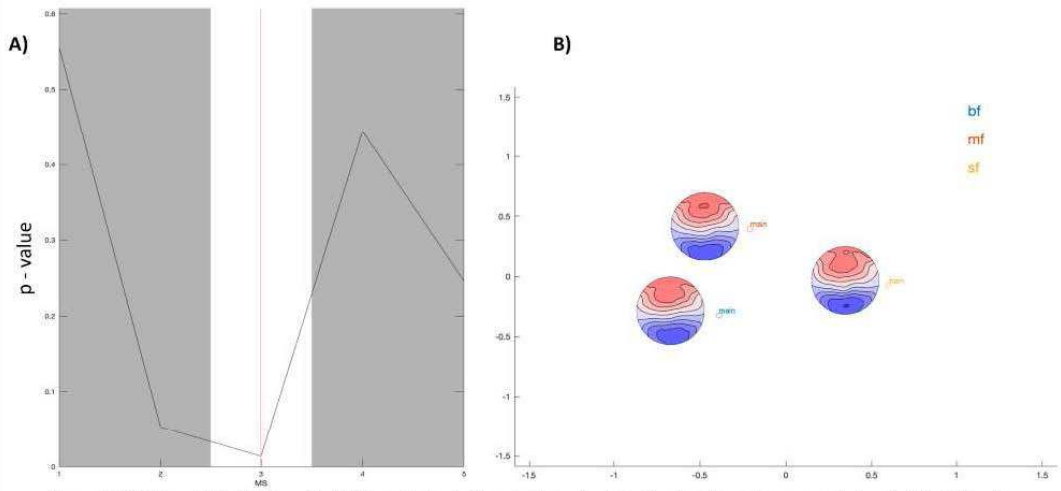

Figure 2. TANOVA results for the 6-month-old infants. **A)** Graph of p-values for each microstate class; the y axis corresponds to each distinct class (1 = class A, 2 = class B, etc). Significance was found across all groups for microstate C which was further explored in **B)**. Each microstate topography was scaled down to one point using multidimensional scaling (MDS) to visualize the difference between BF, MF, and SF groups. The average topology of each group at microstate C is presented to the left of their respective MDS points.

Conclusions: Despite undergoing massive neuronal changes during infancy, resting state networks and their microstate correlates seem not only present at this early time point, but to also closely resemble the adult microstates. This is one of the first studies demonstrating this similarity between adults and infants, and the first study exploring the effects of diet on these microstates. Future studies will assess more specific metrics of these microstates such as duration and transition probability of each class to gain a better understanding of the subtle changes infant diet has on neuromaturation.

References
1. Custo, Anna (2017), "Electroencephalographic Resting-State Networks: Source Localization of Microstates." Brain Connectivity 7 (10): 671–82. https://doi.org/10.1089/brain.2016.0476.
2. Fransson, Peter. (2007), "Resting-State Networks in the Infant Brain." Proceedings of the National Academy of Sciences of the United States of America 104 (39): 15531–36. https://doi.org/10.1073/pnas.0704380104.
3. Gabard-Durnam, Laurel J. (2018), "The Harvard Automated Processing Pipeline for Electroencephalography (HAPPE): Standardized Processing Software for Developmental and High-Artifact Data." Frontiers in Neuroscience 12 (February): 1–24. https://doi.org/10.3389/fnins.2018.00097.
4. Habermann, Marie. (2018), "A Student's Guide to Randomization Statistics for Multichannel Event-Related Potentials Using Ragu." Frontiers in Neuroscience 12 (JUN): 1–20. https://doi.org/10.3389/fnins.2018.00355.
5. Meek, Joan. (2022), "Policy Statement: Breastfeeding and the Use of Human Milk." Pediatrics 150 (1): 1–15. https://doi.org/10.1542/peds.2022-057988.
6. Michel, Christoph M. (2018), "EEG Microstates as a Tool for Studying the Temporal Dynamics of Whole-Brain Neuronal Networks: A Review." NeuroImage 180 (May): 577–93. https://doi.org/10.1016/j.neuroimage.2017.11.062.
7. Nagabhushan Kalburgi, Sahana. (2023), "MICROSTATELAB: The EEGLAB Toolbox for Resting-State Microstate Analysis." Brain Topography, no. 0123456789. https://doi.org/10.1007/s10548-023-01003-5.
8. Yao, D. (2001), "A Method to Standardize a Reference of Scalp EEG Recordings to a Point at Infinity." Physiological Measurement 22 (4): 693–711. https://doi.org/10.1088/0967-3334/22/4/305.

Poster No 1662

Predicting upper limb motor prognosis in stroke patients with a graph embedding model using EEG sign

Seoyeon Kim[1], Yunjeong Jang[2], Yunhee Kim[3], Minji Lee[4]

[1]Department of Artificial Intelligence, The Catholic University of Korea, Bucheon, South Korea, Bucheon, Seoul, [2]Department of Biomedical Software Engineering, The Catholic University of Korea, Bucheon, South Kore, Seoul, Seoul, [3]Department of Physical and Rehabilitation Medicine, Sungkyunkwan University School of Medicine, Suwo, Seoul, Seoul, [4]Department of Biomedical Software Engineering, The Catholic University of Korea, Bucheon, South Kore, Bucheon, Gyeonggi

Introduction: Stroke is increasingly occurring in modern society, and its severity is getting worse day by day. Patients suffer from poor motor and cognitive functions, which are directly related to the quality of life of survivors. Therefore, in order to present proper rehabilitation training, a system that predicts the motor and cognitive function of patients is needed. Recent studies have notably illuminated the intricate relationship between electroencephalography (EEG) signal patterns and motor recovery in stroke patients[1,2]. However, few studies have used these patterns to present prediction of motor recovery as a biomarker from a machine learning perspective. In this study, we proposed the deep learning framework in subacute stroke patients to predict the upper limb motor function.

Methods: Ten chronic stroke patients (60.6 ± 7.9 years; Female = 5; Infarction = 8) were participated in this study. In the motor function using an Fugl-Meyer upper extremity (FMA-UE), they had 38.0 ± 11.4 scores in subacute phase, and 55.3 ± 5.78 scores after two months. As a result, we proposed to predict the prognosis of motor function by dividing the improvement score of FMA-UL into good recovery group and low recovery group based on 20 points[3,4]. The good group (class 0) changed from 30.0 ± 8.0 to 55.6 ± 5.0, whereas the low group (class 1) changed from 46.0 ± 11.2 to 55.0 ± 6.4. In summary, each group was assigned five subjects. EEG data were measured at rest-state with eyes closed for 5 min and the sampling rate was 4,000 Hz. The 27 channels using 10-20 international system were used. Continuous data were downsampled to 500 Hz and segmented into 5-sec epochs. In addition, bandpass filtering was performed from 1 to 45 Hz in preprocessing step. The feature used the normalized mutual information (NorMI)[5], and as a result, the matrix of 27×27 was calculated. To achieve subject-balance while preserving the characteristics of each subject, generative adversarial networks symmetry was used. Pairwise subjects from each class are considered in the wasserstein distance calculation to account for the influence of multiple subjects on each other and the individual characteristics of each subject. We utilized the 3-layer neural network to classify the masked training and test sets (Figure 1). We performed leave-one-subject-out cross-validation, because of independence on a specific stroke patient.

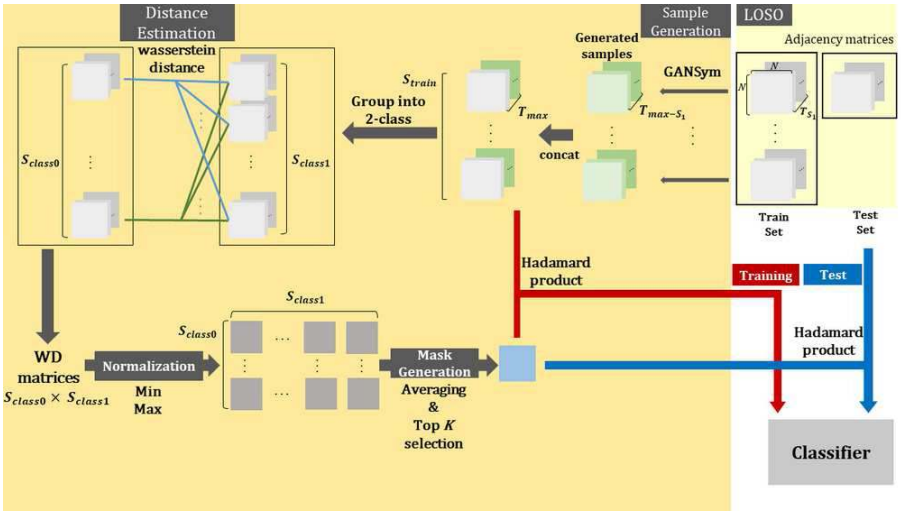

Results: The mean accuracy was approximately 0.93±0.07 excluding when test subject was 8 and 10, whereas 0.78±0.23 including them. A significant decrease was observed with the case when test subject is 8 and 10. The t-distributed stochastic neighbor embedding (t-SNE) result show the feature distribution of NorMI matrices. Subject 8 and 10 show similar distributions and these are mixed at the boundary of the classes. If one of them falls into the test set, the class boundary may not fit the test set (Figure 2). We designed another framework to evaluate the effectiveness of our approach. When training the designed model, wasserstein distance was calculated with all subjects in each class at once. In results, when test subject was in class0, the mean accuracy was 0.74±0.27, but for subjects in class 1, the accuracy was 0. In the cases where the subject in class 0 as test set, the highest accuracy was 1.0 and the lowest was 0.28. In other words, due to some strong subject NorMI pattern, subject independence was reduced.

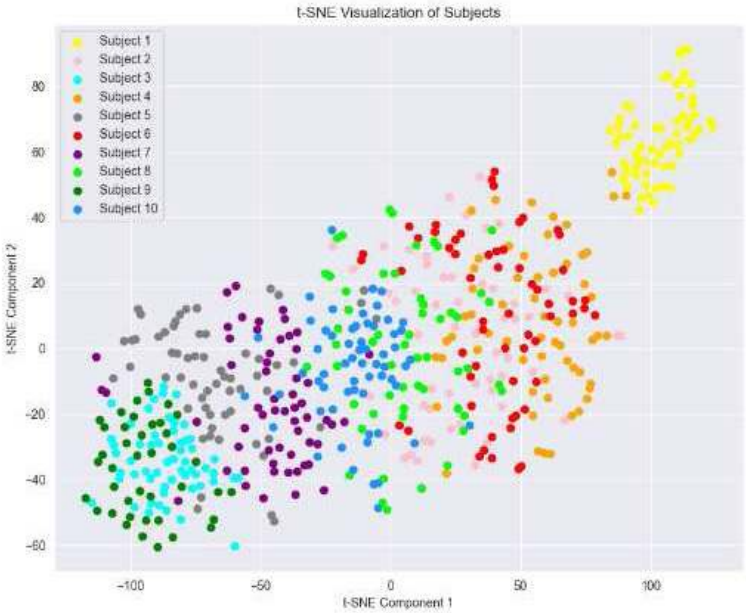

Conclusions: In this study, we proposed the classification framework using normalized mutual information for predicting upper limb motor prognosis. These results would be of great help in guiding rehabilitation training based on stroke prognosis, and should be challenged not only in the motor function but also in the cognitive function.

References

1. Mane, R., Chew, E., Phua, K.S., Ang, K.K., Vinod, A. P., Guan, C. (2018), 'Quantitative EEG as Biomarkers for the Monitoring of Post-Stroke Motor Recovery in BCI and tDCS Rehabilitation', 2018 40th Annual International Conference of the IEEE Engineering in Medicine and Biology Society (EMBC), pp.3610-3613
2. Milani, G., Antonioni, A., Baroni, A., Malerba, P., and Straudi, S. (2022), 'Relation Between EEG Measures and Upper Limb Motor Recovery in Stroke Patients: A Scoping Review', Brain Topography, vol 35, no. 5-6, pp. 651-666.
3. Gladstone, D.J., Danells, C.J., and Black, S.E. (2002), 'The Fugl-Meyer Assessment of Motor Recovery after Stroke: A Critical Review of Its Measurement Properties', Neurorehabil Neural Repair, vol. 13, pp. 232–240.

4. Fugl-Meyer, A.R., Jääskö, L., Leyman, I., Olsson, S., Steglind, S. (1975), 'The post-stroke hemiplegic patient. 1. a method for evaluation of physical performance', Scandinavian Journal of Rehabilitation Medicine, vol. 7, no. 1, pp. 13-31.
5. Jin, J., Sun, H., Daly, I., Li, S., Liu, C., Wang, X., and Cichocki, A. (2022), 'A Novel Classification Framework Using the Graph Representations of Electroencephalogram for Motor Imagery Based Brain-Computer Interface', IEEE Transactions on Neural Systems and Rehabilitation Engineering, vol.30, pp.20-29.

Poster No 1663

Different Electroencephalographic Profiles of Remimazolam and Propofol after Anesthesia

Yeji Lee[1], Youngjai Park[1], Hyoungkyu Kim[1], Sujung Park[2], Bon-Nyeo Koo[2], Joon-Young Moon[1]

[1]Sungkyunkwan University/Institute for Basic Science, Suwon, Republic of Korea, [2]Department of Anesthesiology and Pain Medicine, Yonsei University College of Medicine, Seoul, Republic of Korea

Introduction: Understanding the dynamic changes of EEG characteristics after emergence from anesthesia (AE) is crucial for distinguishing the risk of postoperative neurocognitive disorder. Previous research has found that changes of alpha-oscillatory activity (8-12 Hz) is a decisive factor for detecting such disorder at risk[1]. Remimazolam is a newly introduced ultra-short-acting benzodiazepine anesthetic, and few studies have compared its changes of EEG patterns with Propofol after AE. Recent studies of clinical trials have reported delayed emergence in Remimazoalm versus Propofol[2], but the underlying mechanism remains elusive. Hence, we compare the characteristics of EEG patterns between Remimazolam and Propofol after AE. By applying various phase measures, we aim to understand the underlying mechanism of differing EEG characteristics between the two anesthetic drugs. Ultimately, we aim to suggest these measures as alternative indicators for assessing the anesthetic depth, the quality of recovery, and the disorder at risk.

Methods: Various phase measures were applied to four-channel electroencephalogram (EEG) data (sampling rate 178 Hz), which were recorded from Sedline device at Yonsei Severance Hospital. The data includes 50 patients undergoing laparoscopic cholecystectomy who were randomly assigned to the remimazolam group (n = 25) and the propofol group (n = 25). We upsampled the data to 200 Hz. Specifically, we applied phase lag entropy (PLE), coherence, phase coherence, and the absolute value of relative phase, as described in the Measurements section below, at specific frequency bands (i.e., delta: 0.5-4, theta: 4-8, alpha: 8-12, beta: 12-20, gamma: 20-40, and broad: 6-25 Hz). We considered a broad frequency band in our analysis following the evidence from the literature that rhythmic activity induced by propofol starts in the broad band[3]. Preprocessing As EEG characteristics are distinctly exhibited in different anesthetic states, the data were divided into 6 states: (1) baseline eyes closed (BEC), defined as 3 minutes after eyes closed; (2) baseline eyes open (BEO), defined as 3 minutes after eyes open; (3) after intubation (AI), defined as 15 minutes after the intubation point; (4) recovery of consciousness (ROC), defined as 15 minutes before the extubation point; (5) eyes closed (EC), defined as 3 minutes after eyes closed; (6) eyes open (EO), defined as 3 minutes after eyes open.

Results: (a) PLE measures the pattern diversity of phase lag difference between two channels. 0 indicates simplicity of patterns, thus lead/lag relationship is predictable; 1 indicates diversity of patterns, thus lead/lag relationship is unpredictable[3]. (b) Coherence measures the coherency of phase magnitude and the degree of synchronization between two channels. 0 indicates an absence of coherence; 1 indicates the presence of coherence[4]. (c) Phase coherence measures the degree of phase locking between the two channels. 0 indicates an absence of phase locking; 1 indicates complete phase locking[5]. (d) |relative phase| measures the magnitude of phase relationship between two channels. 0 indicates the absence of lead/lag relationship between the channels; 1 indicates the presence of lead/lag relationship[6]. In our analysis, we observed a significant group difference after AE from the four selected phase measures at the broad frequency band (Fig. 1). From all four measures, we found that the Propofol group recovered up to the baseline states faster than the Remimazolam group. Especially, the group difference was observed in PLE, where the phase relationship patterns were highly unpredictable in the Propofol group than the Remimazolam group after AE.

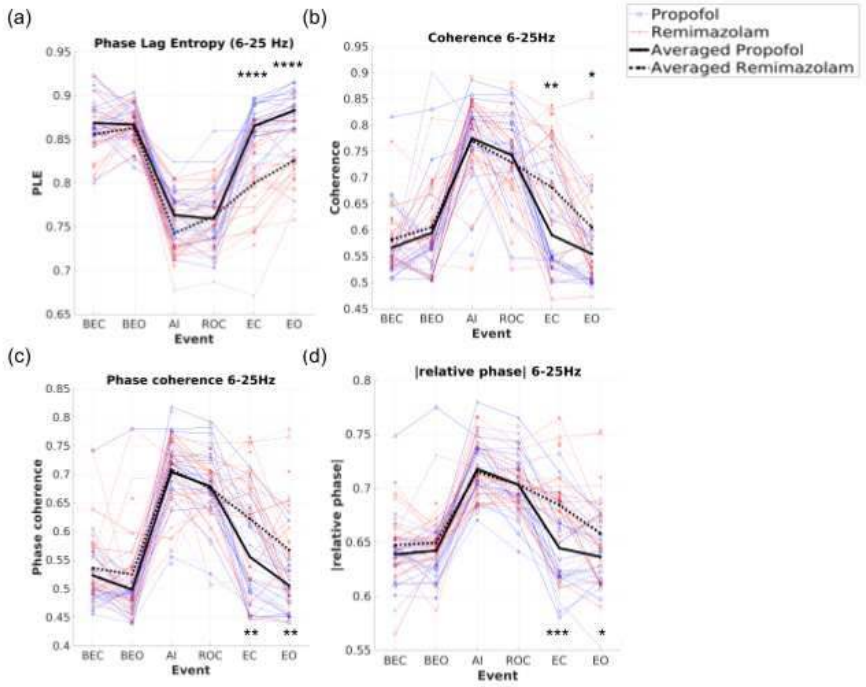

Figure 1. Results of phase measures at the frequency band 6-25Hz. Bold line indicates the average of participants with remimazolam anesthesia and the bold dotted line indicates the average of participants with propofol anesthesia. Blue line represents the propofol group and red line represents the remimazolam group. All measures show group difference in the eyes closed (EC) and eyes open (EO) states. (a) In phase lag entropy, Propofol group exhibited higher entropy patterns compared to the remimazolam group. (b) In coherence, Propofol group exhibited higher degree of synchronization in the Propofol group compared to the Remimazolam group. (c) In phase coherence, Propofol group exhibited reduced phase locking compared to the Remimazolam group. (d) In |relative phase|, Propofol group exhibited lower phase lead/lag relationship between channels than the Remimazolam group. Across all measures, participants with Propofol anesthesia exhibited measured values similar to the baseline state.

Conclusions: These findings were in accordance with the previous study[2], indicating delayed emergence after general anesthesia with Remimazolam. Our observation suggests that this delayed emergence is linked with the residual effects observed after recovery from Remimazolam anesthesia.

References

1. Lutz, R. et al. (2022), 'The absence of dominant alpha-oscillatory EEG activity during emergence from delta-dominant anesthesia predicts neurocognitive impairment- results from a prospective observational trial', Journal of clinical anesthesia, vol. 82, 110949.
2. Takemori, T. et al. (2022), 'Long-term delayed emergence after remimazolam-based general anesthesia: a case report', JA Clinical Reports, vol. 8, no. 86.
3. Lee, H. et al. (2017), 'Diversity of functional connectivity patterns is reduced in propofol-induced unconsciousness', Human Brain Mapping, vol. 38, no. 10, pp. 4980-4995.
4. Nunez, P.L. (2006), 'Electric fields of the brain: the neurophysics of EEG', Oxford: Oxford University Press.
5. Mormann, F. et al. (2000), 'Mean phase coherence as a measure for phase synchronization and its application to the EEG of epilepsy patients', Physica D: Nonlinear Phenomena, vol. 144, no. 3-4, pp. 358-369.
6. Moon, J.Y. et al. (2017), 'Structure shapes dynamics and directionality in diverse brain networks: mathematical principles and empirical confirmation in three species', Science Reports, vol. 7, 46606.

Poster No 1664

Multiscale Neural Processing of Visual Stimuli

Richa Richa[1], Bryan Paton[2], Peter Robinson[3], Michael Breakspear[4]

[1]The University of Newcastle, Australia, North Lambton, NSW, [2]University of Newcastle, New Lambton Heights, New South Wales, [3]University of Sydney, Sydney, NSW, [4]University of Newcastle, Newcastle, N/A

Introduction: Periodic photic stimulation of human volunteers at 10 Hz is known to entrain their Electroencephalography (EEG) signals. This entrainment manifests as an increment in power at 10, 20, 30 Hz. We observed that sub-harmonics' emergence accompanies this entrainment, but only at specific frequencies and higher intensities of the stimulating signal. Neural Mass models and Neural Field Theories have previously been used to explore the dynamics underlying the emergence of such

behavior. In our work, we focus on the bifurcation structure of the Jansen and Rit NMM to explore the behavior at a single electrode level and the NFT to further explore the spatial behavior/patterns corresponding to our experimental results.

Methods: Healthy adult participants were exposed to visual stimuli at two distinct forcing frequencies and intensities while their EEGs were recorded. We also record the resting state EEG to get a contrast or baseline to assess the effects of stimulation. Following this, Neural Mass Models (NMMs) were used to emulate the experimental findings and to provide a mesoscale perspective on the entrainment phenomena observed on the occipital electrodes. We then probe further into the spatial distribution of these subharmonics with Neural Field Theory.

Results: Our results indicate that stimulation with high-intensity 10 Hz frequency resulted in a pronounced increase in EEG power at 5 Hz, an effect not seen with low-intensity stimulation at the same frequency. Subsequent experiments done with a 6 Hz stimulation did not significantly alter power at 3 Hz, regardless of the intensity. Simulated Neural Mass Models (NMMs) recapitulate these phenomena and provide a plausible mesoscale explanation for the observed experimental results, laying a framework for a deeper understanding of the underlying neural mechanisms. Building on these mesoscopic explanations, we subsequently look at the spatial patterns underlying cortical entrainment with the help of neural field theory simulations.

Conclusions: Our results suggest that the brain's response to rhythmic visual stimuli is intricately dependent on both the intensity and frequency of the stimulation. The bifurcation structure of the Jansen and Rit NMM provides a plausible mesoscopic explanation for these results. This suggests that the bifurcation properties of the NMM mirror similar features possessed by the actual neural masses producing the EEG dynamics. Our more recent NFT simulations provide further insights into large-scale brain dynamics, and highlight the potential for a unifying theoretical framework to understand the brain's complex responses to external stimuli.

References

1. Breakspear M.(2006), A unifying explanation of primary generalized seizures through nonlinear brain modeling and bifurcation analysis, Cerebral Cortex, vol. 16 no. 9, pp. 1296-1313.
2. Pang J. C. (2023), Geometric constraints on human brain function, Nature, pp. 1-9.
3. Phogat R. (2022), Intensity dependence of sub-harmonics in cortical response to photic stimulation, Journal of Neural Engineering, vol. 19 no. 4, pp. 046026.
4. Rennie C. J. (1999), Effects of local feedback on dispersion of electrical waves in the cerebral cortex, Physical Review E, vol. 59 no. 3, pp. 3320.
5. Robinson P. A. (2016), Eigenmodes of brain activity: Neural field theory predictions and comparison with experiment, NeuroImage, vol. 142, pp. 79-98.

Poster No 1665

Connectome spectrum electromagnetic tomography: application in focal epilepsy source localization

Nino Herve[1], Joan Rué-Queralt[2], Yasser Alemán-Gómez[1], Jonathan Wirsich[3], Bernd Vorderwülbecke[4], Laurent Spinelli[3], Margitta Seeck[3], Serge Vulliemoz[3], Patric Hagmann[1]

[1]Department of Radiology, Lausanne University Hospital and University of Lausanne (CHUV-UNIL), Lausanne, Switzerland, [2]Center for Imaging, École Polytechnique Fédérale de Lausanne, Lausanne, Switzerland, [3]EEG and Epilepsy Unit, University Hospitals and Faculty of Medicine University of Geneva, Geneva, Switzerland, [4]Epilepsy Center Berlin-Brandenburg, Department of Neurology, Charité-Universitätsmedizin Berlin, Berlin, Germany

Introduction: To avoid invasive procedures, scalp-recorded EEG can be used to solve inverse problems for localizing focal epileptic sources. Connectome spectrum electromagnetic tomography (CSET) is an innovative EEG source reconstruction method that considers structural connections by imposing sparsity on the connectome spectrum (Rué-Queralt 2022). In this work, CSET was tested and compared to weighted minimum norm estimation (WMNE) using one patient from the dataset in Vorderwülbecke 2022. The patient achieved epilepsy-free status after the surgical removal of the epileptic source.

Methods: Multimodal processing pipeline is illustrated in Figure 1. MRI: Pre/post-surgical structural 3T MRI were acquired with 0.7/1.0 mm slice thickness. T1-MPRAGE images were re-sampled to 1mm3 isotropic resolution through cubic interpolation using Connectome Mapper 3, and artifacts were removed using Cartool. Post-surgical MRI data was acquired three months after surgery and linearly co-registered to pre-surgical MRI using FSL5.0. EEG: Pre-surgical 256-channel (EGI) EEG was recorded for around 20 minutes. Interictal discharges were identified visually by a trained specialist, high-pass filtered at 0.3-1 Hz and low-pass filtered at 30-100 Hz. Epochs were centered on the discharge peak before being averaged and downsampled to 250 Hz. The time point at 50% of the averaged discharge's rising phase is utilized for source reconstruction. Forward model: Brain, skull and skin surfaces were extracted from pre-surgery T1 MRI using the watershed algorithm implemented in Freesurfer 7.2.0. Python MNE 1.5.0 library was used to construct the boundary element model, sampling cortical brain sources at ~5 mm

intervals (~11000 cortical sources) and the computation of the lead field matrix. Connectome: The source connectome was created from the probabilistic connectome atlas (Alemán-Gómez 2022). The patient's brain underwent the same parcellation as the atlas to associate each source to one of the 446 cortical regions. Each source inside a region is connected to all the sources in another region if the regions exhibit consistency in connectivity higher than 75%. We expanded the network by including geodesically close connections to accommodate grey matter interactions. Inverse Problem: The task involves finding the brain activity distribution, denoted as x, that minimizes the optimization problem: argminx {1/2 ||b-Ax||22+||Fx||1}. b represents EEG measurements, A is the lead field matrix, and F is the graph Fourier transform of the connectome. Fx is the connectome spectrum, and minimizing ||Fx||1 enforces sparsity according to the user-defined parameter λ. The solution was obtained using proximal gradient descent implemented through Pyxu (Simeoni 2023).

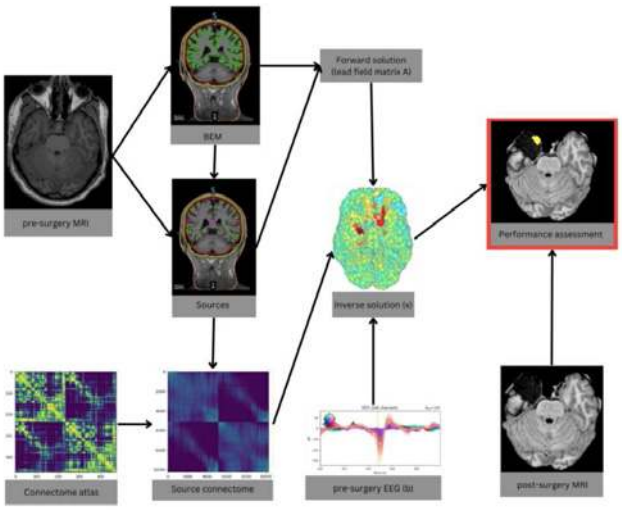

Figure 1: Source Reconstruction Pipeline: The pipeline involves several steps. First, data acquisition includes collecting pre/post-surgery MRI and EEG. Next, defining the forward problem includes computing the boundary element model (BEM) and sampling sources from the pre-surgery MRI. If using WMNE, the inverse problem is then defined with EEG data and the lead field matrix. For CSET, a connectome for sources is required, inferred from a connectome atlas. Finally, the source reconstruction results (inverse solution) are compared with post-surgery MRI to check the superposition with the resected area (performance assessment).

Results: Figure 2 shows reconstructed brain activity, where the last column projects peak activity into the voxel space, estimating spike origins in the right temporal pole for CSET and the left rectus and medial orbitofrontal gyri for WMNE. While WMNE showed a diffuse result, CSET had focused targets, aligning peak activity precisely with the surgically resected region where focal epilepsy was clinically localized.

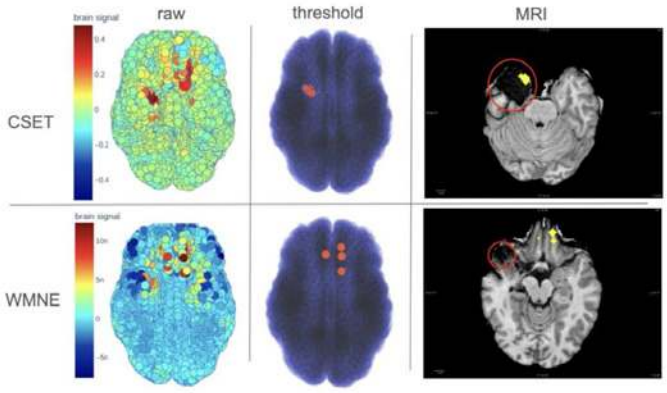

Figure 2: Source Reconstruction Results: The first row displays the outcomes of source reconstruction using CSET, while the second row employs WMNE. The first column presents the raw reconstruction results. It is evident that WMNE results are dispersed, whereas CSET defines two distinct regions of activity. In the second column, we emphasize the four sources with the highest activity, which are then projected into the voxel space to observe the superposition between the peak activity and the resection area (circled in red - third column). It is notable that CSET estimated the peak activity within the resection, while WMNE is slightly off target.

Conclusions: In conclusion, the CSET method successfully identified the source of epilepsy within the resected area, a capability not achieved by WMNE. Incorporating the connectome into source reconstruction aims to discern a more fitting regularizer for the inverse problem, drawing insights from the previously unveiled structural-functional relationships (Glomb 2020). The dataset (including 44 more patients) allowed us to test reconstruction outcomes using actual data rather than simulations, providing a more realistic assessment of method efficacy.

References
1. Alemán-Gómez, Y. (2022). A multi-scale probabilistic atlas of the human connectome. Scientific Data, 9(1):516
2. Glomb, K, (2020). Connectome spectral analysis to track EEG task dynamics on a subsecond scale. NeuroImage, vol 221, pp. 117-137.
3. Rué-Queralt, J. (2022). Connectome spectrum electromagnetic tomography: a method to reconstruct electrical brain source-networks at high-spatial resolution. BioRxiv. [online] doi:https://doi.org/10.1101/2022.07.26.501544.
4. Simeoni, M, matthieumeo/pyxu: pyxu. [online] GitHub. Available at: https://github.com/matthieumeo/pyxu.
5. Vorderwülbecke, B. J. (2020) High-density Electric Source Imaging of interictal epileptic discharges: How many electrodes and which time point? Clinical Neurophysiology vol. 131, pp. 2795-2803

Poster No 1666

Exploring the link between EEG metastability and autistic traits in neurotypical adults

Mebuki Izumiya[1,2], Keiichi Kitajo[2,1]

[1]Department of Physiological Sciences, The Graduate University for Advanced Studies, SOKENDAI, Okazaki, Aichi, Japan, [2]National Institute for Physiological Sciences, Okazaki, Aichi, Japan

Introduction: EEG phase synchronization networks mediate the integration and segregation of information among brain regions that are pertinent to the ongoing task[1]. The capacity of the phase synchronization network to smoothly transition between different network states is crucial for optimizing cognitive functions. It is suggested that this transient property allows the brain to effectively execute various cognitive processes[1]. We focus on metastable EEG phase synchronization networks and hypothesize that they are associated with individual psychological traits. “Metastability” refers to the temporal transitions occurring between states with relatively weak attraction within a dynamical system[2]. Far from being random activity, these transitions indicate the complexity and nonlinear nature of brain function[3]. The metastable nature of the brain may have implications for understanding the psychological traits of individuals[4,5]. Therefore, the objective of this study is to establish metastability indices and investigate potential connections between these indices for EEG phase synchronization and psychological tendencies such as autistic spectrum disorder (ASD).

Methods: The subjects were 88 neurotypical adults (24.4 ± 5.6 years old). Among them, 32 subjects went for the follow-up second recording with an average interval of 101 day s. Subjects sat at rest with their eyes closed. The EEG signals were recorded for 180 sec using an EEG amplifier (BrainAmp MR+, Brain Products GmbH, Gilching, Germany) and a 63-channel EEG cap (Easycap, EASYCAP GmbH, Herrsching, Germany) placed on the scalp in accordance with the International 10/10 system. The sampling rate was set to 1000 Hz, and the band-pass filter was 0.016-250 Hz. In EEG preprocessing,current source density (CSD) transformation was used to obtain more localized topography and to reduce the negative impact of spurious synchrony caused by volume conduction. After extracting the time series, the temporal variation pattern of the phase synchronization network is calculated. Next, the metastability of the phase synchronization network between brain regions is compared between subjects using Synchrony Coalition Entropy (SCE) and Metastability Index (MSI). Here, SCE is an information-theoretic measure of the diversity of spatiotemporal synchrony patterns per electrode, whereas MSI is a measure of the fluctuations of the degree of global phase synchronization across brain regions[6,7]. Therefore, we focused on the association between these indicides and autistic traits using the Autism Spectrum Quotient (AQ).

Results: The test-retest reliability between twice measurements per subject was assessed using Spearman and interclass correlation coefficients (Figure 1). The results showed that both MSI and SCE exhibited test-retest reproducibility, with individual spatial patterns observed in the SCE values per channel. The association between the SCE values and AQ total scores was analyzed. We observed a positive correlation between the degree of metastability and autistic tendency in the delta (1-4 Hz) and theta (4-8 Hz) bands, although, we found that the alpha (8-14 Hz) and beta (14-30 Hz) bands showed different tendencies.

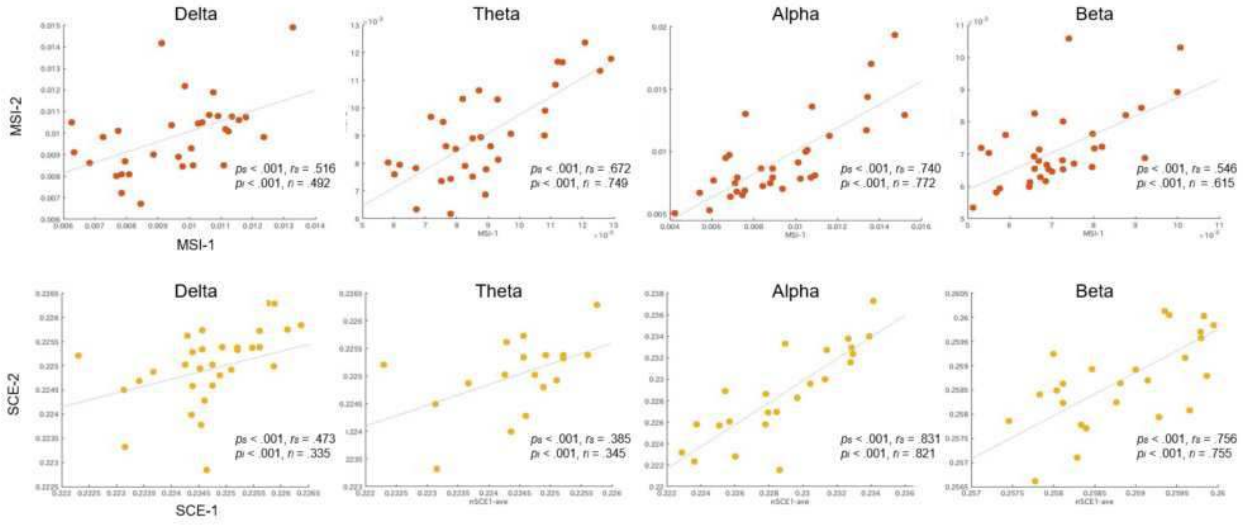

Figure 1. Test-retest reliability of MSI and SCE. The figure displays individual MSI and SCE values measured on two separate days and correlation coefficients.

Conclusions: These findings suggest that the SCE and MSI exhibit test-retest reliability. Notably, the spatial patterns of SCE for each electrode display individual characteristics. These results demonstrate that these metastability indices effectively capture individual brain dynamics robustly. Furthermore, the correlation results between SCE and AQ suggest a connection of metastability with ASD traits. It appears that the metastability of EEG phase synchronization networks is linked to psychological traits. In the future, this research is poised to shed light on the mechanisms that underlie intricate human cognitive processes, such as creative thinking, as well as contribute to our understanding of brain disorders.

References

1. Tognoli E. & Kelso J. A. S. (2014), 'The metastable brain', Neuron, 8; 81(1): 35-48.
2. Heitmann S. & Breakspear M. (2018), 'Putting the "dynamic" back into dynamic functional connectivity', Network Neuroscience, 2(2): 150–174.
3. Deco G. et al. (2017), 'The dynamics of resting fluctuations in the brain: metastability and its dynamical cortical core', Scientific Reports, 7, 3095
4. Gili T. et al. (2018), 'Metastable states of multiscale brain networks are keys to crack the timing problem', Frontiers Computational Neuroscience, 12:75.
5. Sase T. & Kitajo K. (2021), 'The metastable brain associated with autistic-like traits of typically developing individuals', PLoS Computational Biology, 17(4): e1008929.
6. Shanahan M. (2010), 'Metastable chimera states in community-structured oscillator networks', Chaos, 20, 013108.
7. Schartner M. et al. (2015), 'Complexity of multi-dimensional spontaneous EEG decreases during propofol induced general anaesthesia', PLoS ONE, 10(8): e0133532.

Poster No 1667

Quantitative Electroencephalography Reveals Regional Brain Alteration in Mild Traumatic Brain Injury

Caerwen Beaton[1,2,3], Andre Avila[1,2,3], Melissa Papini[1,2,3], Jacinta Thorne[1,2], Aleksandra Gozt[1,2], Francesca Buhagiar[4], Elizabeth Thomas[5,6], Alexander Ring[7,8], Glenn Arendts[9,10], John Iliff[3,11,12,13], Antonio Celenza[14,15], Sjinene Van Schalkwyk[16], Philip Brooks[3,17,18], Dan Xu[3,5,19], Stephen Honeybul[20,21], Gill Cowen[1,3], Carmela Pestell[1,4], Daniel Fatovich[10,22,23], Ben Smedley[24], Ashes Mukherjee[25,23], Michael Bynevelt[26], Melinda Fitzgerald[1,2], Sarah Hellewell[1,2]

[1]Curtin Health Innovation Research Institute, Faculty of Health Sciences, Curtin University, Perth, WA, Australia, [2]Perron Institute of Neurological and Translational Science, Perth, WA, Australia, [3]Curtin Medical School, Curtin University, Perth, WA, Australia, [4]School of Psychological Science, The University of Western Australia, Perth, WA, Australia, [5]School of Population Health, Curtin University, Perth, WA, Australia, [6]School of Medicine, The University of Western Australia, Perth, WA, Australia, [7]Institute for Immunology and Infectious Diseases, Murdoch University, Perth, WA, Australia, [8]School of Physiotherapy and Exercise Science, Faculty of Health Sciences8 School of Physiotherapy and Exercise Science, Faculty of Health Sciences, Perth, WA, Australia, [9]Emergency Department, Fiona Stanley Hospital, Perth, WA, Australia, [10]Centre for Clinical Research in Emergency Medicine, Harry Perkins Institute of Medical Research, Perth, WA, Australia, [11]Emergency Department, Saint John of God Hospital Murdoch, Perth, WA, Australia, [12]Emergency Department, Royal Perth Hospital, Perth, WA, Australia, [13]Royal

Flying Doctor Service- Western Operations, Perth, WA, Australia, [14]Emergency Department, Sir Charles Gairdner Hospital, Perth, WA, Australia, [15]Division of Emergency Medicine, School of Medicine, The University of Western Australia, Perth, WA, Australia, [16]Emergency Department, Joondalup Health Campus, Perth, WA, Australia, [17]Emergency Department, Saint John of God Midland Public Hospital, Perth, WA, Australia, [18]School of Medicine, The University of Notre Dame, Perth, WA, Australia, [19]The First Affiliated Hospital, Sun Yat-Sen University, Guangzhou, China, [20]Department of Health, Government of Western Australia, Perth, WA, Australia, [21]Sir Charles Gairdner Hospital, Royal Perth Hospital and Fiona Stanley Hospital, Perth, WA, Australia, [22]Emergency Medicine, Royal Perth Hospital, Perth, WA, Australia, [23]The University of Western Australia, Perth, WA, Australia, [24]Emergency Department, Rockingham General Hospital, Perth, WA, Australia, [25]Emergency Department, Armadale Health Service, Perth, WA, Australia, [26]The Neurological Intervention & Imaging Service of Western Australia at Sir Charles Gairdner Hospita, Perth, WA, Australia

Introduction: Mild Traumatic Brain Injury (mTBI) results from a direct impact or rapid acceleration and deceleration of the head, which can alter brain function. Following mTBI, patients may experience varied signs and symptoms which may be broadly classed as physical, cognitive or emotional. However, the relationship between brain alterations and presence of symptoms is complex and poorly understood. Quantitative electroencephalography (qEEG) utilises digital EEG signals that are processed, transformed and analysed using mathematical algorithms. qEEG is rapid to acquire and could provide insight into brain dysfunction after injury. This study used qEEG to detect regional brain dysfunction following mTBI and investigated whether qEEG findings were associated with reporting of mTBI signs and symptoms, including those related to emotion.

Methods: 24 adult participants aged 36.56±12.87 years (10 female) with medically diagnosed mTBI were recruited from major metropolitan emergency departments in Perth, Western Australia as part of the Concussion REcovery STudy (CREST) (Gozt, et al., 2021). 30 age and sex-matched healthy controls were also recruited (33.88±12.15 years; 14 female). Within 7 days of injury, participants completed the Post-Concussion Symptom Scale (PCSS) and Depression Anxiety Stress Scale (DASS-21) questionnaires. qEEG scans (resting-state, eyes-open condition) were acquired using a 19-channel Electro-cap (Electro-cap International Inc., Eaton, USA) with a standardised 10-20 electrode placement, and a MITSAR-EEG-BT amplifier (Mitsar, Ltd., St. Petersburg, Russia). Analysis was performed using NeuroGuide and NeuroNavigator software (Applied Neuroscience, Inc., St. Petersburg, USA). Five minutes of activity were recorded with linked-ears montage, using a sampling rate of 500 Hz, with impedance <10 kΩ and a low pass filter of 50 Hz. At least one minute of artifact-free data from the recording was selected in NeuroGuide and imported into NeuroNavigator to generate current source density (CSD) for Brodmann areas (BA). Data from mTBI and control participants were expressed as Z-scores and compared using t-tests for each BA to determine the effects of mTBI on CSD. Pearson correlations were performed separately for mTBI and control groups to assess the relationship to PCSS and DASS-21 scores.

Results: Substantial bilateral increases in CSD (Z-score >1.65) were detected within the cingulate (BAs 23, 31) and retrosplenial cortices (BAs 26, 29) ($p < 0.05$) across multiple bands: delta (1-3 Hz), theta (4-7 Hz), beta (12-24 Hz) and high beta (25-30 Hz). mTBI participants had higher mean PCSS symptom (10.63±4.49 vs. 4.57±4.04; $p<0.0001$) and severity scores (30.25±18.99 vs.7.93±9.2; $p<0.0001$); as well as DASS-21 depression subscale scores (3.5±3.69 vs. 1.77±2.25; $p<0.05$) compared to controls. In the mTBI group, increased CSD in the delta band within the left cingulate (BA 29) was moderately associated with PCSS total score ($r = -0.48$, $p<0.05$) and symptom severity ($r = -0.53$, $p<0.05$). In the beta band, bilateral increases in CSD in the cingulate (BAs 23, 31) and retrosplenial cortex (BAs 26, 29) were moderately to highly correlated with DASS-21 anxiety and stress subscale scores in each hemisphere (all $r>0.44$; $p<0.05$), while unilateral CSD increases correlated with depression subscale scores: right BA 23, $r=0.47$, $p<0.05$; left BA 26, $r=0.52$, $p<0.05$; right BA 29, $r=0.63$, $p<0.001$.

Conclusions: These findings suggest that the cingulate and retrosplenial cortices are vulnerable to the effects of mTBI. These regions have known associations with anxiety, depression and stress (Straube, et al., 2009; Duval, et al., 2013; Hellewell, et al., 2019; Lin, et al., 2021). Given the relationships observed between CSD alteration in these brain regions and symptom scores, altered functioning following mTBI may contribute to the development of emotional symptoms of PPCS (Corcoran, et al., 2018).

References

1. Corcoran, K. A., Yamawaki, N., Leaderbrand, K., & Radulovic, J. (2018), 'Role of Retrosplenial Cortex in Processing Stress-Related Context Memories', Behavioral Neuroscience, vol. 132, no. 5, pp. 388–395.
2. Duval, E. R., Hale, L. R., Liberzon, I., Lepping, R., N. Powell, J., Filion, D. L., & Savage, C. R. (2013), 'Anterior cingulate cortex involvement in subclinical social anxiety', Psychiatry Research: Neuroimaging, vol. 214, no. 3, pp. 459–461.
3. Gozt, A. K., Hellewell, S. C., Thorne, J., et al. (2021), 'Predicting outcome following mild traumatic brain injury: Protocol for the longitudinal, prospective, observational Concussion Recovery (CREST) cohort study', BMJ Open, vol. 11, no. 5.
4. Hellewell, S. C., Welton, T., Maller, J. J., Lyon, M., Korgaonkar, M. S., Koslow, S. H., Williams, L. M., Rush, A. J., Gordon, E., & Grieve, S. M. (2019). 'Profound and reproducible patterns of reduced regional gray matter characterize major depressive disorder', Translational Psychiatry, vol. 9, no. 1, pp. 176.

5. Lin, I.M., Yu, H.E., Yeh, Y.C., Huang, M.F., Wu, K.T., Ke, C.L. K., Lin, P.Y., & Yen, C.F. (2021), 'Prefrontal Lobe and Posterior Cingulate Cortex Activations in Patients with Major Depressive Disorder by Using Standardized Weighted Low-Resolution Electromagnetic Tomography', Journal of Personalized Medicine, vol. 11, no. 11, pp. 1054.
6. Straube, T., Schmidt, S., Weiss, T., Mentzel, H.-J., & Miltner, W. H. R. (2009), 'Dynamic activation of the anterior cingulate cortex during anticipatory anxiety'. NeuroImage, vol. 44, no. 3, pp. 975–981.

Poster No 1668

Decoding Newly Learned Sound Categories from Neuroimaging Signals: Towards an Optimal Pipeline

Naishi Feng[1], Gangyi Feng[1]

[1]The Chinese University of Hong Kong, Hong Kong SAR, China

Introduction: Machine learning (ML) techniques have been successfully applied to neuroimaging data for decoding a diverse set of mental information. Most of the stimuli to be decoded are well-learned and familiar, such as common object categories[1], native language[2], and speech[3]. However, it is often challenging to decode unfamiliar or newly learned knowledge from noisy neuroimaging signals. This decoding task becomes even more challenging when decoding novel auditory categories with only brief training and exposure to the exemplars. The temporal fleet and multidimensional properties of acoustic signals also pose a significant challenge for machine learning algorithms to learn complex patterns. Therefore, a new signal processing and machine learning pipeline is required to overcome these challenges and increase neural decodability, which could also provide insights into how learning shapes neural responses. Here, we used Magnetoencephalography (MEG) to record neural signals of novel artificial sounds when participants learned to categorize these sounds into categories. We applied various ML algorithms to decode the newly learned sound categories to determine an optimal algorithm and analysis pipeline.

Methods: Thirty-five healthy right-handed participants were recruited for the auditory category learning study. Participants listened to the sounds and learned to categorize them into two categories based on feedback in a 40-minute session. The MEG signals were recorded by an Elekta Neuromag machine. We selected three types of machine learning algorithms: linear discriminant analysis (LDA), support vector machine (SVM), and artificial neural networks (ANN) to test their neural decoding performances. For SVM, we used both linear and nonlinear SVM. ANN includes a three-layer fully connected neural network (FNN) and a shallow ConvNet (SC)[4]. These algorithms are chosen because of their ability to extract useful information from neural signals and effectively learn complex patterns with relatively small training samples. ANN algorithms may require more training data to reveal their decoding power. FNN has two layers that can learn and store mapping relations between neural data and targets, whereas SC has two convoluted layers capable of capturing information abstracting from the raw data. In addition to the overall decoding performances, we evaluated the decoding abilities of these algorithms based on their performance for successful (top 15) and less successful (bottom 15) learners, different training blocks, and across different brain locations and time windows of sound presentation.

Results: Among all the algorithms tested, the linear-SVM combined with PCA dimension reduction and SC was found to be more effective in decoding newly learned categories than others when using all the available data. Neural decoding accuracies gradually increased as the training blocks progressed for all the methods, which is similar to the patterns of behavioral learning. The decoding performances of the linear classifiers (LDA and linear-SVM) can achieve better performances than others when applied to subgroups of the learners (i.e., successful and less successful learners). We further demonstrated that the best performance in decoding sound categories across the time and location of the neuroimaging signals is mainly at the time windows of 200-300 and 400-500 ms after sound presentation and located at the bilateral temporal and parietal channels.

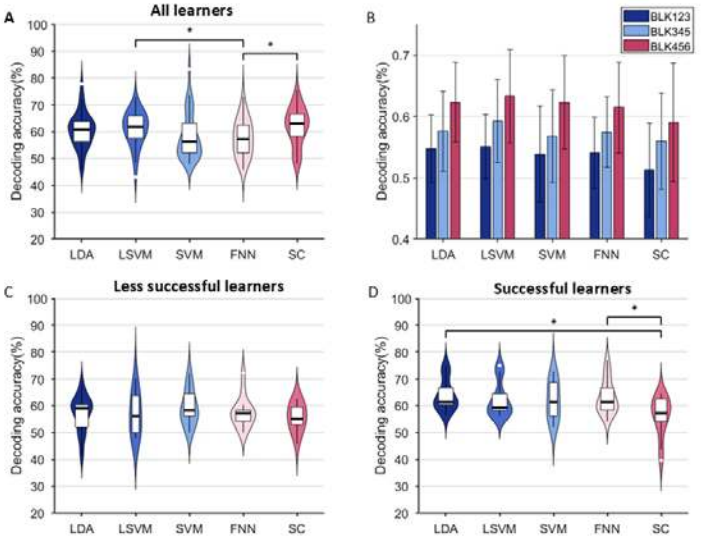

Fig.1. Neural decoding performances with five machine-learning algorithms. A, overall decoding performances using all available neuroimaging data and with a leave-two-subject-out cross-validation procedure. B, neural decoding across three training sessions (session 1 = training block 1 to 3; session 2 = training block 3-5; session 3 = training block 5-7). C & D, neural decoding accuracy for less-successful and successful learners. These two subgroups of learners were determined by their behavioral sound categorization performances after training.

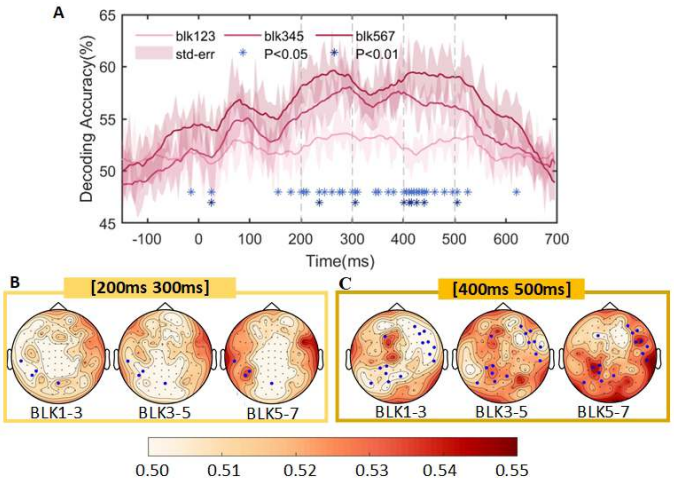

Fig.2. Neural decoding accuracy across time and space. A, the temporal searchlight approach was used for neural decoding. It was found that two time windows (200-300 ms and 400-500 ms) were significantly better than chance and revealed learning-related increases in decoding performance. B & C , neural decoding performances across MEG sensors for the two time windows were analyzed. It was found that left hemisphere (e.g., left temporal and parietal regions) involvement increased as learning progressed.

Conclusions: Although decoding newly learned knowledge is a challenging task, we demonstrate that the linear-SVM with dimension reduction procedure and SC algorithms could be a promising technical solution to uncover the hidden neural signals related to the new knowledge with brief learning experience and exposure. This pipeline could potentially capture the useful and core temporal and spatial neural information for decoding and provide novel insights into the neural mechanisms of auditory learning.

References

1. Liu, C. (2022), 'SincNet-Based Hybrid Neural Network for Motor Imagery EEG Decoding', IEEE Transactions on Neural Systems and Rehabilitation Engineering, vol. 30, pp. 540–549. Available at: https://doi.org/10.1109/TNSRE.2022.3156076.
2. Lin, Y. (2022), 'Neural decoding of speech with semantic-based classification', Cortex, vol. 154, pp. 231–240. Available at: https://doi.org/10.1016/j.cortex.2022.05.018.
3. Cooney, C. (2020), 'Evaluation of hyperparameter optimization in machine and deep learning methods for decoding imagined speech eeg', Sensors (Switzerland), vol. 20, no. 16, pp. 1–22. Available at: https://doi.org/10.3390/s20164629.
4. Schirrmeister, R.T. (2017), 'Deep learning with convolutional neural networks for EEG decoding and visualization', Human Brain Mapping, vol. 38, no.11, pp. 5391–5420. Available at: https://doi.org/10.1002/hbm.23730.

Poster No 1669

Improvement of MEG source localization performance by Bayesian-based greedy sensor selection

Shunsuke Ota[1], Kai Miyazaki[1], Chihaya Abe[2], Keigo Yamada[2], Taku Nonomura[3], Yoichi Miyawaki[1]

[1]The University of Electro-Communications, Chofu, Tokyo, [2]Tohoku University, Sendai, Miyagi, [3]Nagoya University, Nagoya, Aichi

Introduction: Magnetoencephalography (MEG) can acquire brain activity at a high temporal resolution, but its spatial resolution is not enough to identify the active source location precisely. To resolve this issue, previous studies attempted to develop various source localization methods but it suffers from ill-posedness caused by insufficiency of the number of MEG sensors relative to the potential number of source locations in the brain. However, the increase in the number of sensors is technically difficult in terms of their placement in the limited space, and more importantly, it might not help to improve source localization accuracy because added sensors might provide signals similar to existing sensors. A recent study proposed a method to reconcile this problem by selecting a limited number of sensors with determinant-based greedy-least squares (DG-LS) model[1], showing that MEG signals acquired by full sensors were reconstructed by the small number of selected sensors, though the sensor selection was biased toward near-source locations. Yamada et al. (2021) showed that their Bayesian determinant-based greedy-Bayesian estimation (BDG-BE) can reduce this bias[2]. In this study, we further examined whether the Bayesian-based sensor reduction is also beneficial for achieving better performance in source estimation.

Methods: We used BDG-BE model to reconstruct MEG signals based on the data from the reduced number of sensors, applied the source estimation model to the reconstructed signals, and compared the results with DG-LS model. Proper orthogonal decomposition was performed to decompose MEG signals into signal (rank: r (< the number of all sensors, n)) and noise components. DG-LS model used the greedy algorithm for selecting sensor locations based on the signal components and then used least-squares estimation with the QR algorithm for MEG signal reconstruction. On the other hand, BDG-BE model considered the noise components and Bayesian prior in addition to the signal components. It selected the sensor locations based on the greedy algorithm and then applied Bayesian estimation for signal reconstruction. In this study, we used two types of Brainstorm tutorial data: the phantom data containing an electrically activated single current dipole out of 32 possible locations, and the real brain activity data obtained while the human subject performed the oddball task. The current dipole was estimated from the reconstructed MEG signals while varying the rank order and the number of sensors using the dipole scanning method provided by Brainstorm software. For the phantom data, source localization accuracy was evaluated by spatial displacement from the true source location for the phantom data and that from the source location estimated using the full MEG signals for the oddball standard stimuli without sensor reduction for the real data at 90 ms after stimulus onset.

Results: BDG-BE model outperformed DG-LS model in MEG signal reconstruction using a fewer number of sensors. For the phantom data, source localization accuracy was better when using the MEG signals reconstructed from the reduced number of sensors than using the full MEG signals for both models. For the real data, BDG-BE model showed better source localization performance with a fewer number of sensors than DG-LS model when the number of sensors was less than the number of signal modes (Fig. 1, 2).

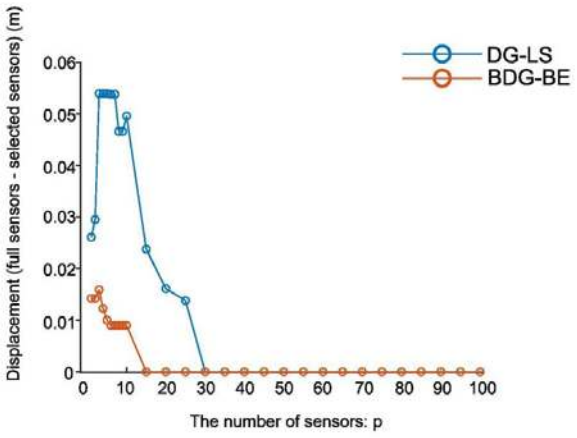

Fig. 1: Spatial displacement of localized sources using the real data. The MEG signals were reconstructed with r (mode) = 30.

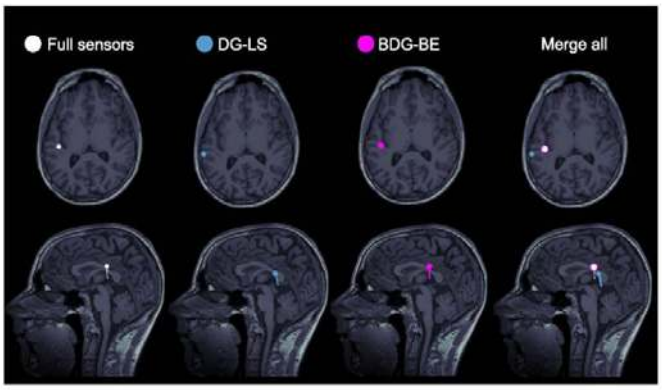

Fig. 2: An example of the mapping of a localized source using the real data. The positions of the localized source were estimated from full-sensor MEG signals, MEG signals reconstructed by DG-LS, and BDG-BE model (r (mode) = 30, p (number of sensors) = 15). All results are merged in the rightmost column for comparison.

Conclusions: We demonstrated that MEG signals can be reconstructed even after the number of sensors is reduced, and the sensor reduction might be even useful to improve the source localization accuracy. Source localization with sensor reduction further showed that BDG-BE model outperformed DG-LS model for the real data that might have complex signal components, which probably reflected in the number of signal modes, than the simple phantom data. These results suggest that the proper MEG sensor selection can improve source localization accuracy and is particularly useful for analyzing complex brain activity patterns.

References

1. Wan-Jin, Y., Samu, T. and J. Nathan, K. (2022), 'Efficient magnetometer sensor array selection for signal reconstruction and brain source localization', arXiv:2205.10925.
2. Yamada, K., Saito, Y., Nankai, K., Nonomura, T., Asai, K. and Tsubakino, D. (2021) 'Fast greedy optimization of sensor selection in measurement with correlated noise', Mechanical Systems and Signal Processing, vol. 158, article 107619.

Poster No 1670

Investigating the Use of Raw EEG Data Augmentation Methods in Neuropsychiatric Disorder Diagnosis

Charles Ellis[1], Robyn Miller[1], Vince Calhoun[2]

[1]Center for Translational Research in Neuroimaging and Data Science (TReNDS), Atlanta, GA, [2]Center for Translational Research in Neuroimaging and Data Science (TReNDS), Decatur, GA

Introduction: While the application of deep learning methods to raw electroencephalogram (EEG) data is becoming more common, the development of reliable models can be challenging due to the small size of many EEG datasets. One potential solution is data augmentation, wherein synthetic training data is generated by duplicating and modifying the training data. While multiple data augmentation approaches have been developed for raw EEG data, their utility for the diagnosis of neuropsychiatric disorders remains underexplored. Moreover, it is unclear if existing approaches boost model performance because they increase the number of training samples or because they introduce augmentations that help the model learn better representations. In this study, we train a baseline convolutional neural network for automated major depressive disorder (MDD) diagnosis, train a second baseline model with duplicate training data (i.e., two identical copies), and compare performance to 6 models that are each trained with a different data augmentation approach that doubles the training set size (i.e., original data + augmented data).

Methods: We used a publicly available resting-state EEG dataset (Mumtaz et al., 2017) with 5-10-minute recordings from 30 individuals with MDD and 28 healthy controls (HCs). We trained our model with 19 channels: Fp1, Fp2, F7, F3, Fz, F4, F8, T3, C3, Cz, C4, T4, T5, P3, Pz, P4, T6, O1, and O2. We downsampled the data to 200 Hz, channel-wise z-scored each recording separately, and separated the data into 25-second samples with a sliding window approach (2.5-second step size) that yielded 2,942 MDD samples and 2,950 HC samples. We trained 8 models: a baseline model with no duplicate data (M1.1), a baseline model with 2 copies of identical unmodified training data (M1.2), 6 models trained with 1 copy of unmodified training data and a copy of data augmented with Gaussian noise (M2) (Ellis et al., 2022), time reverse (M3) (Rommel et al., 2022), smooth time masking (M4) (Mohsenvand et al., 2020), Fourier surrogate (M5) (Schwabedal et al., 2019), frequency shift (M6) (Rommel et al., 2022), or channel dropout (M7) (Saeed et al., 2021) augmentation. For M1.1, we began with an architecture from (Oh et al., 2019)

and optimized it with the Hyperband algorithm in Keras-Tuner. We used M1.1 as a starting point for M1.2-7 and optimized the learning rate of each model with Hyperband and the data augmentation parameters. We trained for 25 folds with subject-wise cross-validation and tested performance for each fold via accuracy, balanced accuracy, sensitivity, and specificity. We lastly compared the performance of each model with pair-wise t-tests and false discovery rate correction.

Results: Table 1 shows our model test performance, which is fairly high. Most data augmentation approaches improved model performance by 2-2.5% compared to M1.1 but not M1.2. Also, our statistical testing did not identify any significant changes in accuracy, balanced accuracy, and sensitivity and only a couple significant changes in specificity.

Table 1. Model Performance Results

Model	Accuracy	Balanced Accuracy	Sensitivity	Specificity
M1.1	86.30 ± 12.28	85.84 ± 15.94	92.79 ± 16.99	78.89 ± 15.94
M1.2	88.75 ± 10.90	88.23 ± 14.66	92.67 ± 11.51	83.80 ± 26.99
M2	88.66 ± 10.30	88.61 ± 12.96	91.62 ± 12.24	85.60 ± 22.98
M3	84.68 ± 13.34	84.27 ± 16.50	91.57 ± 17.45	76.97 ± 29.30
M4	88.27 ± 11.56	89.23 ± 11.26	92.55 ± 14.72	85.91 ± 20.55
M5	88.39 ± 11.02	88.13 ± 13.16	91.27 ± 13.98	84.99 ± 22.82
M6	88.82 ± 10.89	88.53 ± 13.40	92.34 ± 12.26	84.72 ± 23.46
M7	89.05 ± 11.14	87.96 ± 15.05	90.74 ± 19.46	85.18 ± 24.30

Conclusions: Our results suggest that the benefits of existing EEG data augmentation approaches may mainly result from increased training set size and not necessarily from the introduction of helpful augmentations. As such, it may be beneficial to compare new augmentation methods to a baseline model with duplicate training data to see if their augmentations are helpful. It is also possible that future studies might benefit from an "augmentation by duplication" approach in which models are simply trained on two identical copies of the training data. We hope that our findings will provide helpful guidance as the field seeks to develop more robust models on small EEG datasets. Moreover, we would also like to stress that absolute rules cannot be derived from our findings. It is possible that other architectures or datasets might yield different conclusions on the efficacy of the data augmentation approaches we examined.

References

1. Ellis, C.A., Sattiraju, A., Miller, R., Calhoun, V., 2022. Examining Effects of Schizophrenia on EEG with Explainable Deep Learning Models, in: 2022 IEEE 22nd International Conference on Bioinformatics and Bioengineering (BIBE). IEEE, pp. 301–304. https://doi.org/10.1109/BIBE55377.2022.00068
2. Mohsenvand, M.N., Maes, P., Alsentzer, E.E., Mcdermott, M.B.A., Falck, F., Sarkar, S.K., 2020. Contrastive Representation Learning for Electroencephalogram Classification. Proc. Mach. Learn. Res. 136, 238–253.
3. Mumtaz, W., Xia, L., Yasin, M.A.M., Ali, S.S.A., Malik, A.S., 2017. A wavelet-based technique to predict treatment outcome for Major Depressive Disorder. PLoS One 12, 1–30. https://doi.org/10.1371/journal.pone.0171409
4. Oh, S.L., Vicnesh, J., Ciaccio, E.J., Yuvaraj, R., Acharya, U.R., 2019. Deep convolutional neural network model for automated diagnosis of Schizophrenia using EEG signals. Appl. Sci. 9. https://doi.org/10.3390/app9142870
5. Rommel, C., Moreau, T., Paillard, J., Gramfort, A., Paris-saclay, U., 2022. CADDA : Class-wise Automatic Differentiable Data Augmentation for EEG Signals, in: International Conference on Learning Representations (ICLR).
6. Saeed, A., Grangier, D., Pietquin, O., Zeghidour, N., 2021. Learning from heterogeneous EEG signals with differentiable channel reordering, in: IEEE International Conference on Acoustics, Speech and Signal Processing - Proceedings. pp. 1255–1259. https://doi.org/10.1109/ICASSP39728.2021.9413712
7. Schwabedal, J.T.C., Snyder, J.C., Cakmak, A., Nemati, S., Clifford, G.D., Jan, S.P., 2019. Addressing Class Imbalance in Classification Problems of Noisy Signals by using Fourier Transform Surrogates 1–8.

Poster No 1671

Two-brain EEG microstates: a novel method for quantifying task-driven interbrain asymmetry

Qianliang Li[1], Marius Zimmermann[2], Ivana Konvalinka[1]

[1]Technical University of Denmark, Kgs. Lyngby, Denmark, [2]University of Regensburg, Regensburg, Germany

Introduction: To fully understand social cognition between individuals interacting together, it has been argued that it is inadequate to only measure neural processes in single individuals. Instead, a second-person approach should be employed to capture both the neural processes within individuals, but also dynamical interactions between individuals (Schilbach et al. 2013). The simultaneous measurement of brain activity from multiple individuals has been coined hyperscanning (Montague et al. 2002) and been around for two decades; however, interbrain analysis methods remain underdeveloped with no clear standard in the field (Zamm et al. 2023). Previously, we reported unique individual behavioral and neural signatures of performing actions when observed by others during a mirror-game paradigm (Zimmermann, Lomoriello, and Konvalinka

2022). Here, we explore interbrain synchronization during the mirror-game using a novel approach employing two-brain EEG microstates.

Methods: The mirror-game is an experimental paradigm designed for examining the dynamics of two interacting individuals (Noy, Dekel, and Alon 2011), where the two individuals have to improvise motion either alone, together with a partner, or while observed by the partner. Hyperscanning EEG (n = 42 participants, corresponding to 21 pairs) was recorded while the individuals were performing the mirror-game. The EEG was recorded and pre-processed as described in (Zimmermann, Lomoriello, and Konvalinka 2022). Briefly, two synchronized 64-channel Biosemi EEG set-ups were recorded at a 2kHz sampling frequency, followed by bandpass filtering 1-40 Hz and downsampled to 256 Hz. Manual visual inspection was performed to clean the data and independent component analysis (ICA) was used to detect eye movements and eye blinks. The cleaned EEG was subjected to microstate analysis. Microstates are quasi-stable configurations of brain activity that have been reliably replicated across studies, and proposed to be basic buildings blocks for mental processing (Michel and Koenig 2018). Expanding the microstate methodology to dyads of interacting participants (two-brain microstates) enables us to investigate quasi-stable moments of interbrain synchronous activity. Specifically, the two-brain microstates were estimated using a modified K-means algorithm (polarity invariant) on the synchronized EEG from the pairs. The number of clusters were chosen based on the cross-validation criteria (Pascual-Marqui, Michel, and Lehmann 1995).

Results: We found that conventional microstates fitted to individuals (single-brain microstates) were not related to the different task conditions; however, the dynamics of the two-brain microstates were changed for the observed actor-observer condition, compared to all other conditions where participants had more symmetric task demands (rest, individual, joint). The topographies of the two-brain microstates were relatable to the conventionally found resting-state microstates determined from single individuals (Tarailis et al. 2023), and our source localized two-brain microstates (Figure 1) also had cortical activities similar to previous findings relating the microstates to the Default Mode Network (Pascual-Marqui et al. 2014).

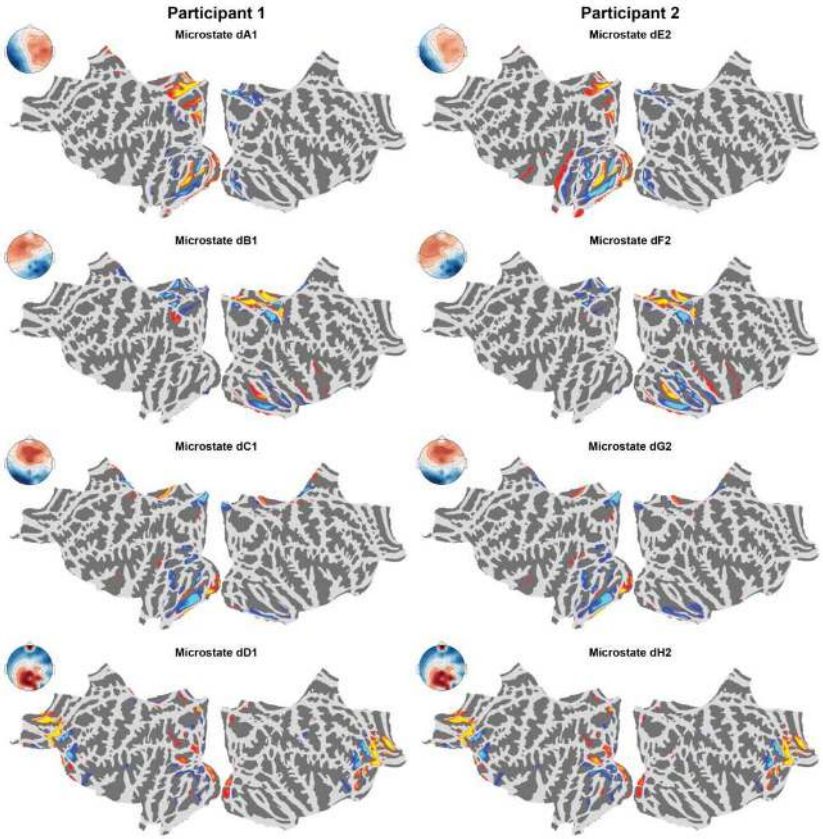

Conclusions: These results suggest that two-brain microstates might serve as a method for identifying asymmetric interbrain states during real-time social interaction.

References

1. Michel, Christoph M., and Thomas Koenig. 2018. "EEG Microstates as a Tool for Studying the Temporal Dynamics of Whole-Brain Neuronal Networks: A Review." NeuroImage 180 (October): 577–93. https://doi.org/10.1016/j.neuroimage.2017.11.062.
2. Montague, P. Read, Gregory S. Berns, Jonathan D. Cohen, Samuel M. McClure, Giuseppe Pagnoni, Mukesh Dhamala, Michael C. Wiest, et al. 2002. "Hyperscanning: Simultaneous fMRI during Linked Social Interactions." NeuroImage 16 (4): 1159–64. https://doi.org/10.1006/nimg.2002.1150.

3. Noy, Lior, Erez Dekel, and Uri Alon. 2011. “The Mirror Game as a Paradigm for Studying the Dynamics of Two People Improvising Motion Together.” Proceedings of the National Academy of Sciences of the United States of America 108 (52): 20947–52. https://doi.org/10.1073/pnas.1108155108.
4. Pascual-Marqui, Roberto D., Dietrich Lehmann, Pascal Faber, Patricia Milz, Kieko Kochi, Masafumi Yoshimura, Keiichiro Nishida, Toshiaki Isotani, and Toshihiko Kinoshita. 2014. “The Resting Microstate Networks (RMN): Cortical Distributions, Dynamics, and Frequency Specific Information Flow.” arXiv. https://doi.org/10.48550/arXiv.1411.1949.
5. Pascual-Marqui, Roberto D., Christoph M. Michel, and Dietrich Lehmann. 1995. “Segmentation of Brain Electrical Activity into Microstates; Model Estimation and Validation.” IEEE Transactions on Biomedical Engineering 42 (7): 658–65. https://doi.org/10.1109/10.391164.
6. Schilbach, Leonhard, Bert Timmermans, Vasudevi Reddy, Alan Costall, Gary Bente, Tobias Schlicht, and Kai Vogeley. 2013. “Toward a Second-Person Neuroscience.” Behavioral and Brain Sciences 36 (4): 393–414. https://doi.org/10.1017/S0140525X12000660.
7. Tarailis, Povilas, Thomas Koenig, Christoph M. Michel, and Inga Griškova-Bulanova. 2023. “The Functional Aspects of Resting EEG Microstates: A Systematic Review.” Brain Topography, May. https://doi.org/10.1007/s10548-023-00958-9.
8. Zamm, Anna, Janeen D. Loehr, Cordula Vesper, Ivana Konvalinka, Simon L. Kappel, Ole Adrian Heggli, Peter Vuust, and Peter E. Keller. 2023. “A Practical Guide to EEG Hyperscanning in Joint Action Research: From Motivation to Implementation.” PsyArxiv. https://doi.org/10.31234/OSF.IO/FY4KN.
9. Zimmermann, Marius, Arianna Schiano Lomoriello, and Ivana Konvalinka. 2022. “Intra-Individual Behavioural and Neural Signatures of Audience Effects and Interactions in a Mirror-Game Paradigm.” Royal Society Open Science 9 (2). https://doi.org/10.1098/rsos.211352.

Poster No 1672

Connectome-Based Modelling Reveals Ketamine’s Modulatory Effects on Thalamocortical Connectivity

Andreea Diaconescu[1], Zheng Wang[2], Milad Soltanzadeh[1], Davide Momi[3], Andrew Clappison[4], André Schmidt[5], Franz Vollenweider[6], John Griffiths[1]

[1]University of Toronto, Toronto, Ontario, [2]Centre for Addiction and Mental Health, Toronto, Ontario, [3]CAMH, Toronto, Ontario, [4]University of Ottawa, Ottawa, Ontario, [5]University of Basel, Department of Clinical Research (DKF), University Psychiatric Clinics (UPK), Tr, Basel, Basel, [6]University Hospital of Psychiatry, Zurich, Ontario

Introduction: Ketamine, an NMDA receptor antagonist, is a pharmacological model for schizophrenia as it induces schizophrenia-like cognitive impairments at subanesthetic doses in healthy individuals[1]. Its antagonism of NMDA receptors, especially in the prefrontal cortex, indirectly boosts dopamine release[2]. The increase in dopamine levels following ketamine administration can enhance the activity of D1 receptors, which are predominantly excitatory. This can affect various cognitive processes and is particularly relevant in the context of schizophrenia spectrum disorders (SSD), where D1 receptor dysregulation is implicated[3]. To understand ketamine’s effect on D1/D2 receptors and thalamocortical connectivity, we modelled the effects of ketamine during sensory learning using the auditory mismatch negativity (MMN) paradigm.

Methods: To assess ketamine’s effect on brain dynamics in an auditory MMN, we re-analyzed a previously published EEG dataset using a placebo-controlled, crossover design[4]. We employed a neural mass model[5] in a cortico-striato-thalamo-cortical (CSTC) circuit framework. This incorporated the 7 Yeo networks with 200 subdivisions[6] as a structural prior. The CSTC circuit (Fig. 1) included subcortical and cortical-subcortical connections. Each node comprised three neuronal populations: pyramidal, excitatory, and inhibitory, modeled using the Jansen-Rit (JR) approach. We simulated auditory responses by introducing a step stimulus into auditory-related regions and running the JR neural mass model with the CSTC circuit to generate EEG signals using a leadfield matrix. The model was implemented in the WhoBPyT Python library, allowing optimization to empirical EEG data using mean-square error as a cost function and PyTorch for automatic gradient calculation, updating node and population connections, and the leadfield matrix until parameter convergence[7]. The optimized parameters, particularly connection gains within nodes and across the CSTC circuit, were evaluated to compare ketamine’s effects against placebo during the MMN paradigm.

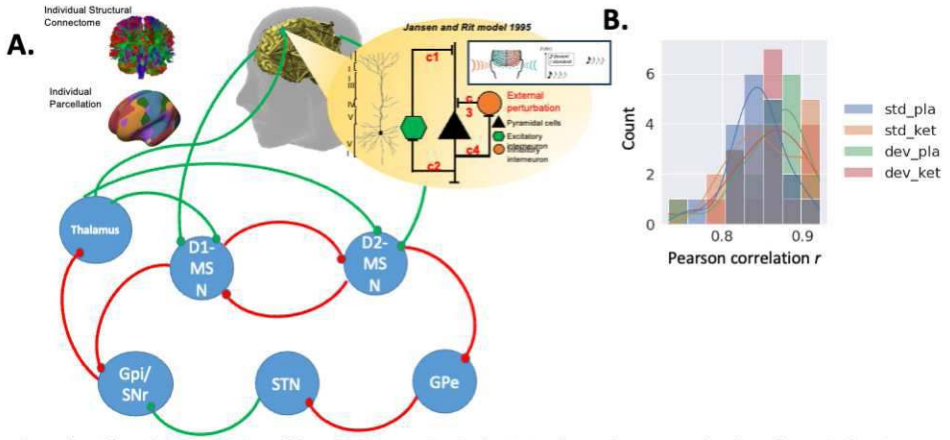

Figure 1| A. Schematic representations of the synaptic connections in the CSTC pathway. The two most abundant cell types in the striatum, D1- and D2-MSN, receive glutamatergic inputs from the cortex and the thalamus and inhibit each other via GABAergic synaptic connections. D1- and D2-MSNs send GABAergic signals to other basal ganglia nuclei via direct and indirect connections to the substantia nigra (SNr), respectively. Abbreviations: GPe (globus pallidus external part), GPi (globus pallidus internal part), STN (sub-thalamic nucleus), SNs (substantia nigra pars compacta), MSN (Medium Spiny Neuron). **B. Model fitting performance across conditions.**

Results: Partial least squares (PLS) analysis was used to assess condition-by-drug interactions based on these model-derived parameters. Firstly, we found significant group differences (p=0.03) between the ketamine and placebo conditions in the "standard tone" response. Specifically, the connection gain from the pyramidal (P) to inhibitory (I) populations (C3) in the JR model and the thalamus to D1 connection gain were notably higher in the placebo condition. This implies more pronounced inhibition within nodes and stronger thalamic inhibition across nodes in the placebo compared to the ketamine condition. Secondly, PLS analysis showed a significant difference (p=0.04) in "deviant tone" responses between the ketamine and placebo conditions, with the ketamine condition exhibiting increased D2 connection gains in temporal, cingulate, and medial prefrontal regions, but decreased gains in parietal and dorsal middle cingulate areas (Fig 2A). Additionally, a substantial difference (p=0.0002) was found in thalamocortical connectivity during "standard tone" responses, with the posterior cuneus and anterior cingulate showing higher connectivity following ketamine administration, while the temporal, parietal, and medial prefrontal regions had increased connectivity under placebo (Fig. 2B).

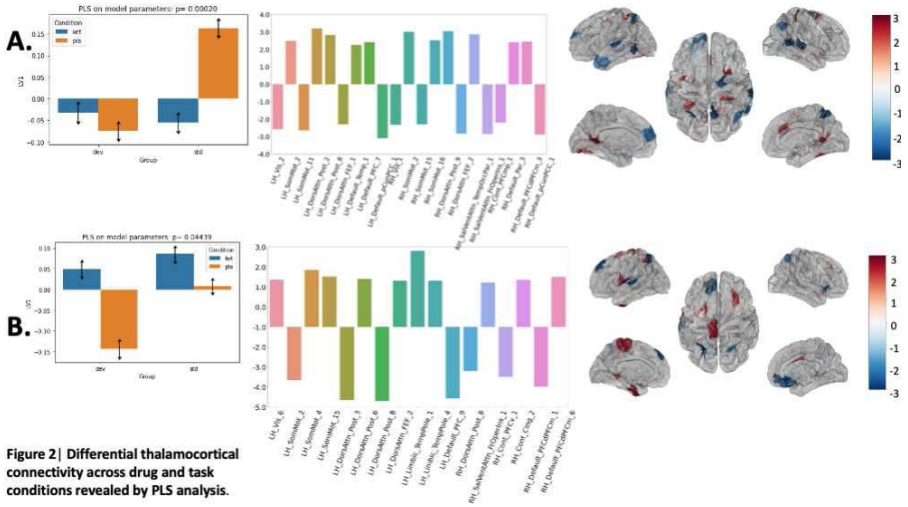

Figure 2| Differential thalamocortical connectivity across drug and task conditions revealed by PLS analysis.

Conclusions: These findings underscore significant changes in brain connectivity patterns, specifically in thalamus to D1 and cortex to D2 connections, under the influence of ketamine compared to placebo. This indicates that ketamine markedly alters neural pathways, especially influencing cortical intra-connections and those between the cortex and thalamus, providing understanding into the neural underpinnings of schizophrenia spectrum disorders.

References

1. Kokkinou, M., Ashok, A. H. & Howes, O. D. (2018) 'The effects of ketamine on dopaminergic function: meta-analysis and review of the implications for neuropsychiatric disorders'. Mol. Psychiatry 23, 59–69.
2. Krystal, J. H. et al. (1994) 'Subanesthetic Effects of the Noncompetitive NMDA Antagonist, Ketamine, in Humans: Psychotomimetic, Perceptual, Cognitive, and Neuroendocrine Responses'. Arch. Gen. Psychiatry 51, 199–214.
3. Stone, J. M., Morrison, P. D. & Pilowsky, L. S. (2007) 'Glutamate and dopamine dysregulation in schizophrenia–a synthesis and selective review'. J Psychopharmacol 21, 440–52 .
4. Schmidt, A. et al. (2012) 'Mismatch Negativity Encoding of Prediction Errors Predicts S-ketamine-Induced Cognitive Impairments'. Neuropsychopharmacology 37, 865–875.

5. Jansen, B. H. & Rit, V. G. (1995) 'Electroencephalogram and visual evoked potential generation in a mathematical model of coupled cortical columns'. Biol. Cybern. 73, 357–66.
6. Yeo, B. T. et al. (2011) 'The organization of the human cerebral cortex estimated by intrinsic functional connectivity'. J. Neurophysiol. 106, 1125–1165.
7. Griffiths, J. D. et al. (2022) 'Deep Learning-Based Parameter Estimation for Neurophysiological Models of Neuroimaging Data'. bioRxiv. Preprint at https://doi.org/10.1101/2022.05.19.492664.

Poster No 1673

Neurophysiological gradient of cortical traveling waves

Xiaobo Liu[1], Sylvain Baillet[2]

[1]McGill University, Montreal, Quebec, [2]Montreal Neurological Institute, Montreal, Quebec

Introduction: Identifying the spatiotemporal structure of macroscopic brain dynamics remains a challenge to understand the mechanisms of human brain functions and their dysfunctions. Traveling waves are recurrent and consistent observations at multiple spatial scales and in diverse preparations, including animal models and noninvasive human brain data collected with time-resolved techniques. However, practical tools for characterizing these phenomena of cortical flow in a quantitative manner are only currently fledging. We proposed to use 3-D optical flow decompositions of time-resolved cortical activity, which enable the rigorous delineation of various spatiotemporal elements of propagation patterns such as sources and sinks and translational components (Lefèvre & Baillet, 2008 & 2009 ; Khan et al., 2011). Here we expand this toolkit to test whether intrinsic activity of the human brain showcases a predominant spatiotemporal structure of propagation across the cortex.

Methods: Our data analysis pipeline is summarized in Fig.1. We used resting-state MEG and structural MRI (T1) data from the Open MEG Archive (OMEGA). The MEG data were analyzed using Brainstorm with default parameters, unless specified. Preprocessed-MEG data were resampled at 368 Hz, based on the observation that 95% of the sensor signal power spectrum density (PSD) was contained below 92 Hz across participants. We used Brainstorm's default overlapping-spheres and minimum-norm imaging method for mapping sensor data on the cortical surface of the participants. To characterize the dynamics of cortical activity, we derived the optical flow of cortical activity at each time point and ran the Helmholtz-Hodge decomposition (HHD ; Khan et al., 2011) of this vector field, which yielded propagation patterns into elemental diverging and curling components. We further assigned local minima of diverging components as sources and local maxima as sinks of cortical activity, respectively. All inferential statistics were run using two-sample t-tests with false discovery rate (FDR) correction.

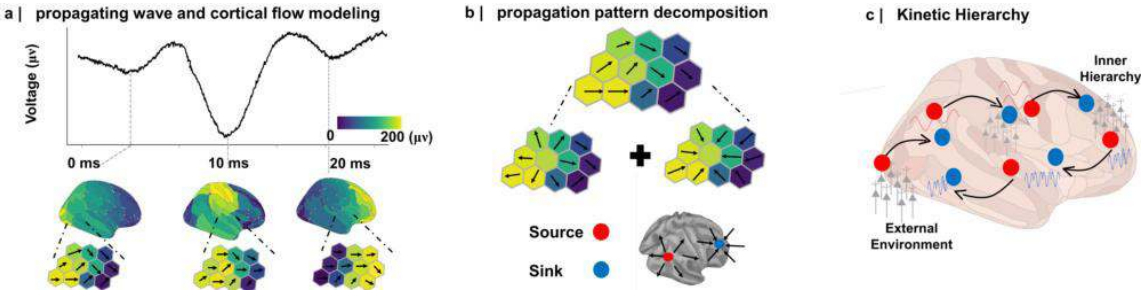

Results: We observed a consistent gradient of cortical flow dynamics along the cortical anatomy (Fig. 2): frontal cortical sources were significantly stronger than cortical sinks strength in occipital regions ($P_{fdr} < 0.05$). We also observed that the sinks in the limbic network have greater strength than the sources of the sensorimotor network. These observations were systematic along the antero-posterior sagittal ($R = -0.60$, $P < 0.0001$) and the dorso-ventral axial direction ($R = 0.38$, $P < 0.0001$). These results suggest that spontaneous, task-free brain activity propagates according to a marked spatiotemporal structure consistent with the grand traits of neuroanatomy.

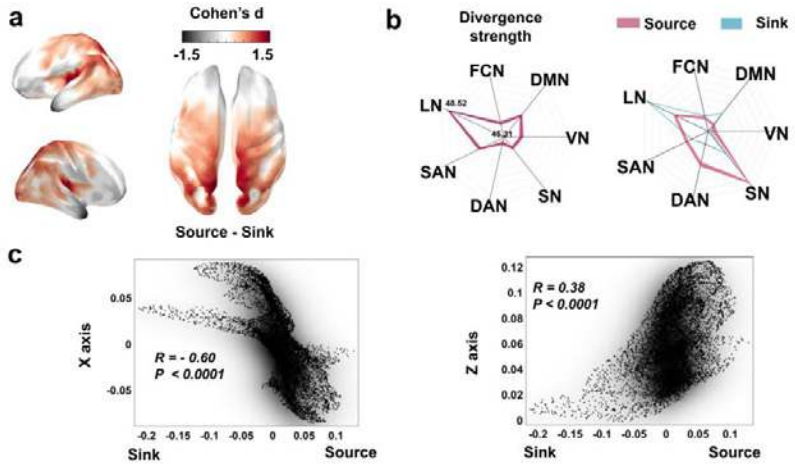

Conclusions: Our study implements a novel framework for quantifying cortical propagation patterns, to delineate the spatio-temporal organization of cortical activity. The results of our investigation indicate that spontaneous neurophysiological activity displays a high degree of organization within a kinetic cortical framework, showcasing a discernible trajectory from sensation to cognition.

References

1. Khan, S., et. al (2011). Feature detection and tracking in optical flow on non-flat manifolds. Pattern recognition letters, 32(15), 2047-2052.
2. Lefèvre, J., et. al (2008). Optical flow and advection on 2-Riemannian manifolds: a common framework. IEEE Trans Pattern Anal Mach Intell, 30(6), 1081-1092.
3. Niso, G., et. al (2016). OMEGA: the open MEG archive. NeuroImage, 124, 1182-1187.

Poster No 1674

Exploring the Interplay of EEG and BOLD Signals: Insights from Neural Mass Modeling

Shih-Cheng Chien[1], Stanislav Jiříček[2], Thomas Knösche[3], Jaroslav Hlinka[2], Helmut Schmidt[1]

[1]Institute of Computer Science, The Czech Academy of Sciences, Prague, Prague, [2]Institute of Computer Science of the Czech Academy of Sciences, Prague, Czech Republic, [3]Max Planck Institute, Leipzig, Saxony

Introduction: Studies investigating the relationship between electrophysiology (EEG) rhythms and blood-oxygen-level-dependent (BOLD) activity have revealed intriguing correlations, such as the negative correlation between EEG alpha power and BOLD signal in occipital areas during eyes-closed resting states. Conversely, positive correlations have been observed in various other brain regions[1]. Additionally, studies have identified positive correlations between EEG gamma power and the BOLD signal during sensory stimulation[2]. A possible interpretation for these diverse findings may lie in the involvement of distinct types of inhibitory neurons, known for their differential effects on EEG rhythm generation[3] and varied neural-vascular coupling properties[4].

Methods: This study employs a cortical column model to simulate EEG and BOLD signals, encompassing excitatory (E) and inhibitory (PV, SOM, and VIP) populations across cortical layers (L2/3, L4, and L5/6). Various conditions are simulated, with the model initially driven by constant inputs to induce either PV-dominant or SOM-dominant states[5]. Subsequently, a combination of pink noises serves as thalamic input (to E and PV populations) and cortico-cortical input (to E populations). The EEG signals are approximated by the weighted sum of simulated excitatory and inhibitory postsynaptic potentials (EPSPs and IPSPs) of the E populations. BOLD signals are simulated using the Balloon-Windkessel model[6], where the input is the sum of simulated EPSPs of the E, PV, SOM, and VIP populations. Simulated EEGs and BOLDs undergo typical analysis procedures employed in investigating the EEG-BOLD relationship in experimental studies.

Results: In the PV-dominant state, our simulations reveal a positive correlation between the EEG and BOLD signals, denoted by a significant correlation coefficient. Conversely, the simulated EEG and BOLD signals exhibit a negative correlation under the SOM-dominant state. These findings highlight the influence of inhibitory neuron dominance on the observed correlation patterns between EEG and BOLD signals.

Conclusions: This preliminary exploration delves into the potential factors contributing to the observed (anti-)correlation between EEG and BOLD signals in EEG-fMRI experiments. We identify instances that give rise to the observed anti/correlation phenomena by systematically examining model configurations across the parameter space. These configurations are linked

to dynamic factors, such as variations in input sets, and static factors, including intra-column connectivity and the ratio of PV/SOM cell counts. The nuanced interplay of these factors provides valuable insights for future investigations into the underlying dynamic columnar states in simultaneous EEG/fMRI studies.

References
1. Gonçalves, Sonia I. (2006), 'Correlating the alpha rhythm to BOLD using simultaneous EEG/fMRI: inter-subject variability', Neuroimage 30.1, 203-213.
2. Niessing, Jorn (2005), 'Hemodynamic signals correlate tightly with synchronized gamma oscillations', science 309.5736, 948-951.
3. Whittington, Miles A. (2003), 'Interneuron diversity series: inhibitory interneurons and network oscillations in vitro', Trends in neurosciences 26.12, 676-682.
4. Cauli, Bruno (2004), 'Cortical GABA interneurons in neurovascular coupling: relays for subcortical vasoactive pathways', Journal of Neuroscience 24.41, 8940-8949.
5. Hertäg, Loreen (2019), 'Amplifying the redistribution of somato-dendritic inhibition by the interplay of three interneuron types', PLoS computational biology 15.5, e1006999.
6. Friston, Karl J. (2000), 'Nonlinear responses in fMRI: the Balloon model, Volterra kernels, and other hemodynamics', NeuroImage 12.4, 466-477.

Poster No 1675

EEG microstate repertoire & dynamics captured by linear statistics or Gaussian stationary twin

Jaroslav Hlinka[1], Nikola Jajcay[2]

[1]Institute of Computer Science of the Czech Academy of Sciences, Prague, Czech Republic, [2]National Institute of Mental Health, Klecany, Czech Republic

Introduction: One of the interesting aspects of EEG data is the presence of temporally stable and spatially coherent patterns of activity, known as microstates (Pascual-Marqui et al., 1995), which have been linked to various cognitive and clinical phenomena. However, various clustering algorithms have been used for microstate computation, and there is still no general agreement on the interpretation of microstate analysis. This study addresses two gaps in the literature. Firstly, by applying several state-of-the-art microstate algorithms to a large dataset of EEG recordings, we aim to characterize and describe relations of various microstate algorithms. Secondly, we aim to test the hypothesis that dynamical microstate properties might be, to a large extent, determined by the linear characteristics of the underlying EEG signal, in particular, by the cross-covariance and autocorrelation structure of the EEG data, paving way to more efficient estimation (Pascual-Marqui, 2022; Jajcay, 2023).

Methods: Data: For the experimental part of our study, we used the publicly available EEG data that are part of the Max Planck Institut Leipzig Mind-Brain-Body Dataset (LEMON) dataset (Babayan et al., 2019). The dataset consists of 228 healthy participants comprising a young (N = 154, 25.1 +/-3.1 years, range 20–35 years, 45 female) and an elderly group (N = 74, 67.6 +/- 4.7 years, range 59–77 years, 37 female) acquired cross-sectionally in Leipzig, Germany, between 2013 and 2015. Among other neuroimaging modalities, participants completed a 62-channel EEG experiment at rest (rsEEG hereafter) using two paradigms: eyes open and eyes closed. We used directly the preprocessed EEG data (total N = 204) provided as EEGLAB .set and .fdt files. The complete description can be found in (Babayan et al., 2019). Briefly, all EEG data have a sampling frequency of 250 Hz, are low-pass-filtered with a 125 Hz cutoff frequency, and are ~8 min long. Simulations: We generated a Fourier transform surrogate of the EEG signal to compare microstate properties. Alternatively, we treated the EEG data as a vector autoregression process, estimated its parameters, and generated surrogate stationary and linear data from fitted VAR. Microstate algorithms: We compared 6 different algorithms that can be used for the clustering stage of the microstate analysis: (Topographic) atomize and agglomerate hierarchical clustering, Modified K-means, Principal component analysis, Independent component analysis, and Hidden Markov model. Microstate measures: apart from comparing directly the extracted microstates topographies, we assess a number of standard summary statistics to describe the temporal characteristics of inferred sequences from various clustering algorithms: average lifespan, coverage, occurrence; as well as selected dynamic statistics: mixing time, entropy, entropy rate, and the first peak of auto-mutual information function.

Results: In terms of relations of the algorithms, we show theoretically why the three ''classically'' used algorithms ((T)AAHC and modified K-Means) yield virtually the same results, while HMM algorithm gives the most dissimilar results. By simulations, we show that microstate statistics of data (Fig. 1) and its Fourier surrogates (Fig. 2) are largely similar, hinting that microstate properties depend to a very high degree on the linear covariance and autocorrelation structure of the underlying EEG data. Similarly, for a linear VAR data model we observed that it generates microstates highly comparable to those estimated from real EEG data, potentially providing even higher reliability of microstate repertoire and dynamics estimation due to robustness of the linear estimates.

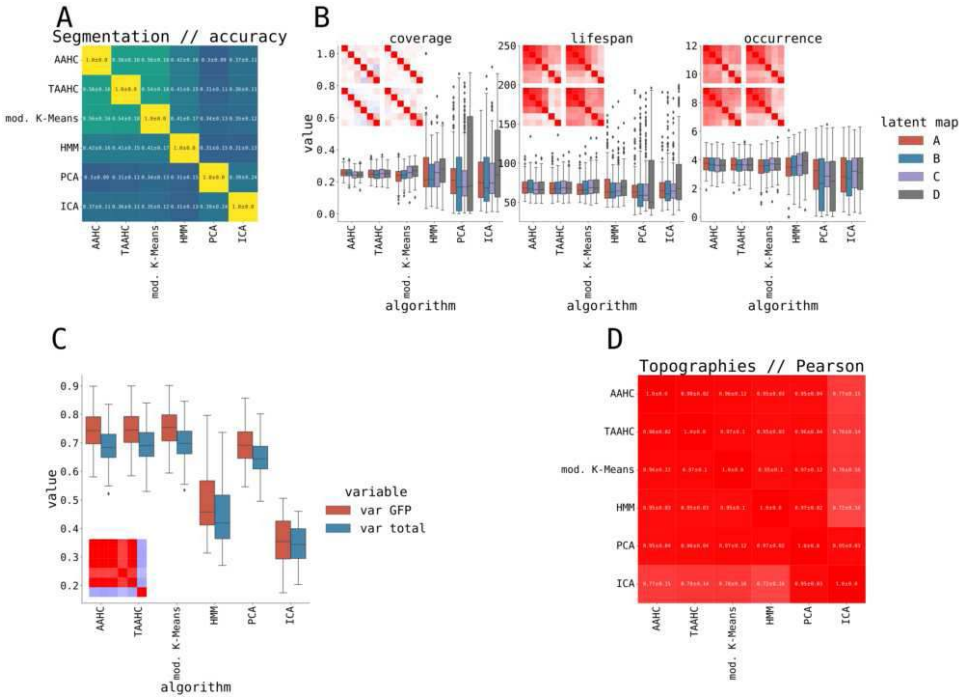

Fig. Overview of microstate properties of a LEMON dataset in the eyes-closed resting state EEG paradigm.

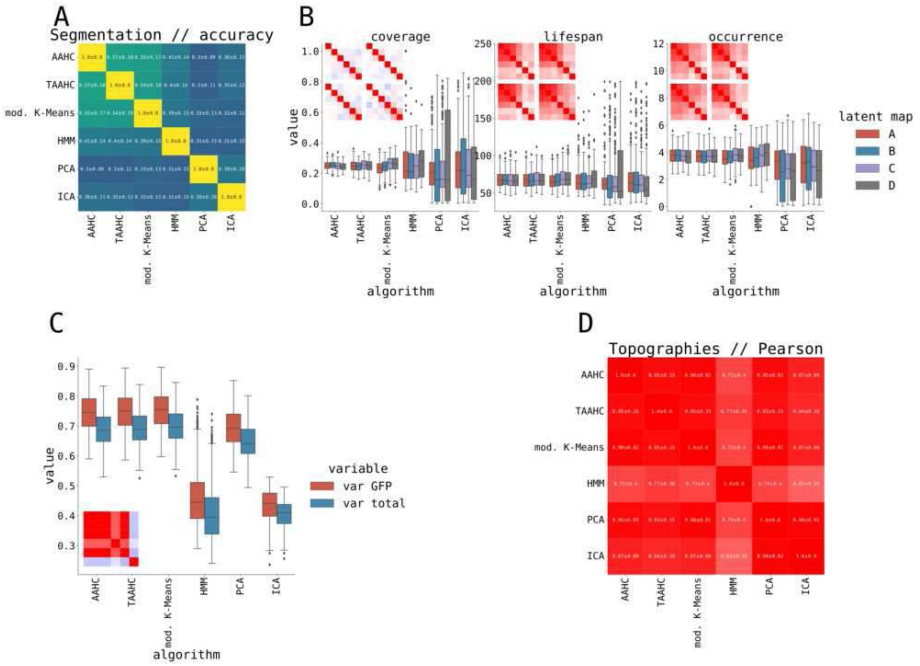

Fig. Overview of microstate properties of a Fourier Transform surrogate data generated from the LEMON dataset in the eyes-closed resting state EEG paradigm.

Conclusions: The observation of high reproducibility of the microstates properties from the linear models, particularly Fourier surrogates and VAR model, support the conclusion that a linear EEG model can help with methodological and clinical interpretation of both static and dynamic human brain microstate properties.

References

1. Babayan, A. (2019). Data descriptor: A mind-brain-body dataset of MRI, EEG, cognition, emotion, and peripheral physiology in young and old adults. Scientific Data, 6, 1–21. https://doi.org/10.1038/sdata.2018.308
2. Jajcay, N. (2023). Towards a dynamical understanding of microstate analysis of M/EEG data. NeuroImage, 281(September), 120371. https://doi.org/10.1016/j.neuroimage.2023.120371
3. Pascual-Marqui, R. D. (1995). Segmentation Of Brain Electrical-activity Into Microstates - Model Estimation And Validation. IEEE Transactions On Biomedical Engineering, 42(7), 658–665. https://doi.org/10.1109/10.391164
4. Pascual-Marqui, R. D. (2022). On the relation between EEG microstates and cross-spectra. 1–15. http://arxiv.org/abs/2208.02540

Poster No 1676

Corticothalamic circuit parametrization of spatial variations in resting-state alpha activity

Sorenza Bastiaens[1,2], Davide Momi[1], Taha Morshedzadeh[1,2], Parsa Oveisi[1,3], Kevin Kadak[1,2], John Griffiths[1,2,3,4]

[1]Krembil Centre for Neuroinformatics, Centre for Addiction and Mental Health (CAMH), Toronto, Canada, [2]Institute of Medical Science, University of Toronto, Toronto, Canada, [3]Institute of Biomedical Engineering, University of Toronto, Toronto, Canada, [4]Department of Psychiatry, University of Toronto, Toronto, Canada

Introduction: Understanding the underlying mechanisms driving resting-state alpha oscillations is of major importance due to their role in a number of neurocognitive processes and pathologies. This study aims to compare and contrast current prominent alpha rhythmogenesis theories within a novel framework. The approach involves identifying large-scale resting-state spatial feature variations associated with the alpha rhythm. Subsequently, a corticothalamic model is fitted, and parameters are explored to elucidate the key circuits believed to shape alpha rhythms. The rationale for examining spatial variations arises from the hypothesis that alpha oscillations in rostral and caudal regions originate from distinct neural processes[1].

Methods: Using the publicly available Cam-CAN dataset[2] (N=631, ages 18-88), resting-state MEG source analysis resulted in time series from 8196 source locations per subject, from which the power spectrum was computed. Periodic features (alpha peak frequency and power) and aperiodic components (low and high-frequency slope), were estimated using the FOOOF toolbox[3]. Cortical parcellation into 200 regions-of-interest with the Schaefer brain atlas[4] facilitated the investigations of spatial variations within different age groups. Finally, the significance of the spatial and age-related empirical feature variations were determined with pearson correlations and linear mixed models. Source power spectra from occipital and frontal regions were then fitted with the BrainTrak toolbox[5], which estimates the Robinson corticothalamic model[6] parameters, including cortico-cortical, corticothalamic and intrathalamic connection strengths (gains).

Results: A significant Pearson correlation with the MNI y coordinate value, indicating a posterior-anterior gradient, was observed in 73.81% of subjects for alpha peak frequency, 96.98% for alpha power, 89.37% for the high-frequency aperiodic slope, and 80.79% for the low-frequency aperiodic exponent (all $p<0.005$). Subject-averaged feature values within each decile (18-27, 28-37,..., 78-88) also showed a posterior-anterior gradient, with significant negative correlations observed in all age groups between y and alpha peak frequency ($r=-0.8877$ to $r=-0.5382$, $p<0.0001$), alpha power ($r=-0.9583$ to $r=-0.9105$, $p<0.0001$), high-frequency aperiodic exponent ($r=-0.8388$ to -0.5417, $p<0.0001$), and low-frequency exponent ($r=-0.5534$ to -0.8659, $p<0.0001$). Within these, the strength of correlation with y was weaker in older subjects for the high-frequency aperiodic exponent, and stronger for the low-frequency aperiodic exponent. These consistent variations over space were observed for all spectral features, but markedly stronger in alpha power. Furthermore, linear mixed model results found a significant effect of space and a significant effect of age for the alpha peak (ROI coeff.=-4.199, $z=-54.373$, $p<0.0001$; Age coeff.=-0.006, $z=-5.490$, $p<0.0001$; ROI:Age coeff.=0.052, $z=38.187$, $p<0.0001$). Between the anterior vs posterior regions, our physiological model parameter fitting results indicated a higher cortico-cortical activity in frontal areas than occipital regions ($t=19.1398$, $p<0.0001$), but a greater corticothalamic ($t=-9.0176$, $p<0.0001$) and intrathalamic ($t=-12.0461$, $p<0.0001$) activity in occipital regions.

Conclusions: Our results confirm previously-reported spatial and age-related variations in oscillatory brain activity[7,8,9], separating out the contribution of different spectral features with greater precision than earlier work. Moreover, physiologically-based modelling of these data was able to capture these effects - suggesting that activity in occipital areas is more strongly driven by corticothalamic interactions than frontal areas, and conversely that the observed frontal features reflect relatively stronger cortico-cortical interactions than in occipital areas.

References

1. Hoshi, H. (2020), 'Age-and gender-specific characteristics of the resting-state brain activity: a magnetoencephalography study', Aging, vol. 12(21), pp. 21613-21637
2. Taylor, J.R. (2017), 'The Cambridge Centre for Ageing and Neuroscience (Cam-CAN) data repository: Structural and functional MRI, MEG, and cognitive data from a cross-sectional adult lifespan sample', NeuroImage, vol. 144, pp.262-269
3. Donoghue T (2020). 'Parameterizing neural power spectra into periodic and aperiodic components'. Nature Neuroscience, vol. 23, pp. 1655-1665
4. Schaefer, A. (2018), 'Local-global parcellation of the human cerebral cortex from intrinsic functional connectivity MRI', Cerebral cortex, vol. 28(9), pp. 3095-3114
5. Abeysuriya R.G. (2016), 'Real-time automated EEG tracking of brain states using neural field theory', Journal of Neuroscience Methods, vol 258, pp. 28-45
6. Roberts, J. A. (2012), 'Corticothalamic dynamics: structure of parameter space, spectra, instabilities, and reduced model', Physical Review E, vol. 85(1), pp. 011910.
7. Mahjoory, K. (2020), 'The frequency gradient of human resting-state brain oscillations follows cortical hierarchies', Elife, vol. 9, pp. e53715.

8. Lew, B. J. (2021), 'Three-year reliability of MEG resting-state oscillatory power', NeuroImage, vol. 243, pp. 118516
9. Donoghue, T. (2020), 'Parameterizing neural power spectra into periodic and aperiodic components', Nature neuroscience, vol. 23(12), pp. 1655-1665

Poster No 1677

Electroencephalography-targeted Graph Attention Network Model to Extract Spatiotemporal Features

Jae-eon Kang[1], Changha Lee[1], Jong-Hwan Lee[1]

[1]Department of Brain and Cognitive Engineering, Korea University, Seoul, Korea, Republic of

Introduction: Brain-computer interface (BCI) enhances our lives by bridging brains to external devices and deepens our understanding of the human brain. Utilizing electroencephalography (EEG), BCI studies have strived to develop algorithms that facilitate daily life improvements while unraveling the characteristics of brain activities in various tasks. Within this realm, deep learning-based BCI studies have demonstrated remarkable performance[1], albeit with challenges in interpreting their underlying brain mechanisms. In addressing this interpretability gap, our paper proposes a novel deep learning model, EEG-Graph Attention Network (EEGAT), leveraging the graph structure and attention mechanism of the Graph Attention Network (GAT)[2] to enhance interpretability.

Methods: Fig. 1 illustrates the architecture of the EEGAT model, comprising the Feature Extraction Block and the Graph Learning Block. The Feature Extraction Block incorporates both temporal and spatial convolution kernels. Temporal convolution kernels discern temporal features from raw EEG signals, followed by spatial convolution kernels extracting spatial features. These spatiotemporal features serve as node features in the subsequent graph construction process. In the Graph Learning Block, the graph is structured using the k-nearest neighbor (kNN) algorithm. GAT modules with residual connections are applied to update node features to enhance interpretability. Following the GAT layers, features undergo flattening and pass through a linear layer, culminating in a softmax activation function, generating the final output of the EEGAT model. Our study employed three distinct datasets for evaluation-fatigue dataset[3], DEAP[4], and BCI Competition IV 2a[5]. The fatigue dataset involved EEG signals from 27 subjects engaged in a 90-minute virtual reality driving task. Preprocessing of the recorded 30 EEG channels included band-pass filtering (1-50 Hz), eye blink removal, and downsampling to 128 Hz. Fatigue levels, determined by reaction time during lane-departure events, were labeled as fatigue and non-fatigue states. DEAP, a multimodal human emotion states dataset, employed 40 emotional music videos to evoke emotions in 32 subjects. EEG signals (32 channels) underwent downsampling to 128 Hz, EOG removal, band-pass filtering (4-45 Hz), and re-referencing. Trials, segmented into 4-second nonoverlapping windows, facilitated model training. Valence ratings were chosen as the classification thresholds (5 for two classes, 3 and 6 for three classes). The BCI Competition IV 2a dataset encompassed nine subjects performing four motor imagery tasks. EEG signals (22 electrodes) underwent preprocessing: bandpass filtering (4-40 Hz), downsampling to 128 Hz, and exponential moving standardization. Recorded across two sessions, each consisting of six runs with 48 trials, tasks included left hand (class 1), right hand (class 2), both feet (class 3), and tongue (class 4). Leave-one-subject-out (LOSO) validation utilized the three datasets to evaluate model performance, demonstrating the reliability of learned features. Additionally, we compared EEGAT against EEGNet[6] models with 4 and 8 temporal kernels, assessing the effectiveness of the proposed model.

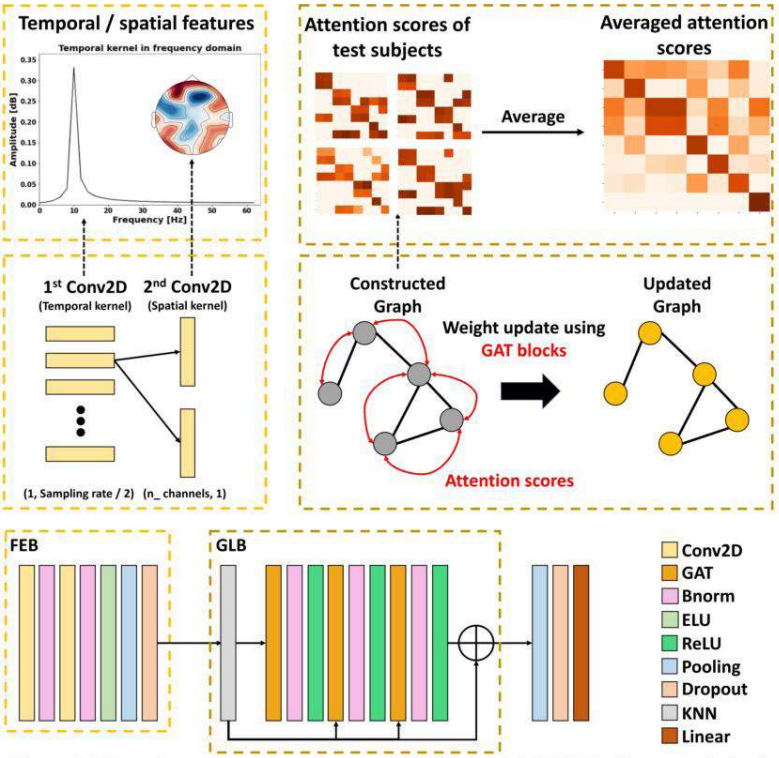

Figure 1. Schematic representation of proposed EEGAT model. EEGAT utilizes convolutional kernels to extract temporal and spatial features from the raw EEG data. The extracted features are then employed to construct a graph using a k-nearest neighbor (kNN) algorithm, and node features are updated through Graph Attention Network (GAT) layers. The features derived from the convolutional kernels identify crucial frequencies and electrodes for each task. In addition, average attention scores from test subjects are presented to elucidate the relationship between the extracted features.

Results: Fig. 2 demonstrates the overall performance of the models. EEGAT achieved higher accuracy on the three datasets. Especially on the fatigue dataset and DEAP, EEGAT achieved significantly higher accuracy than EEGNet models ($p<0.05$). The attention weights revealed relationships between the trained weights of the temporal and spatial kernels representing specific spatiotemporal patterns captured by the model.

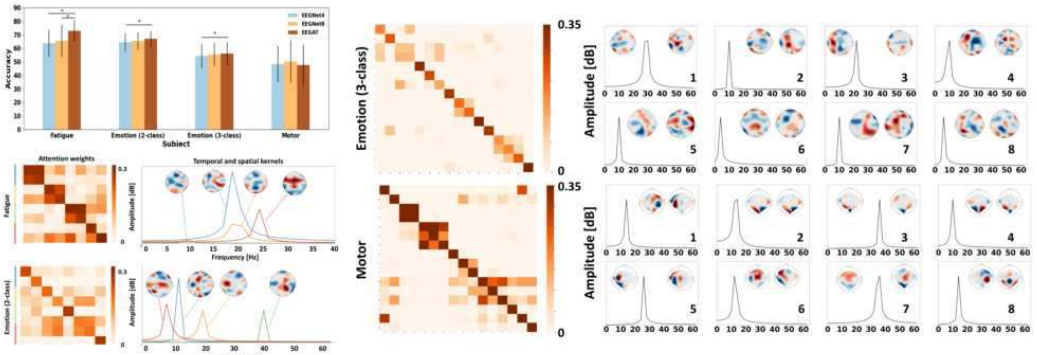

Figure 2. LOSO cross-validation results and extracted features from trained EEGAT model. The EEGAT model showed significantly higher accuracy (73.0%) than the EEGNet models (63.8% and 65.4%) in the Fatigue dataset, extracting alpha and beta frequency components around frontal and posterior electrodes. In emotion classification tasks, the EEGAT model performed slightly better than others. In the motor imagery task, EEGAT did not significantly outperform others in accuracy but extracted central electrode features in mu rhythm activity. * in the first row, $p < 0.05$. LOSO, leave-one-subject-out.

Conclusions: Our proposed EEGAT outperforms previous models in accuracy, particularly on the fatigue dataset and DEAP. In addition, the graph structure and the attention weights of each node provide insights into complex relationships among spatiotemporal patterns of diverse BCI tasks, with an improvement in model interpretability.

References

1. Khademi Z, Ebrahimi F and Kordy H M 2023 A review of critical challenges in MI-BCI: From conventional to deep learning methods J. Neurosci. Methods 383 109736
2. Veličković P, Cucurull G, Casanova A, Romero A, Lio P and Bengio Y 2017 Graph attention networks ArXiv Prepr. ArXiv171010903
3. Cao Z, Chuang C-H, King J-K and Lin C-T 2019 Multi-channel EEG recordings during a sustained-attention driving task Sci. Data 6 19

4. Koelstra S, Muhl C, Soleymani M, Lee J-S, Yazdani A, Ebrahimi T, Pun T, Nijholt A and Patras I 2011 Deap: A database for emotion analysis; using physiological signals IEEE Trans. Affect. Comput. 3 18–31
5. Brunner C, Leeb R, Müller-Putz G, Schlögl A and Pfurtscheller G 2008 BCI Competition 2008–Graz data set A Inst. Knowl. Discov. Lab. Brain-Comput. Interfaces Graz Univ. Technol. 16 1–6
6. Lawhern V J, Solon A J, Waytowich N R, Gordon S M, Hung C P and Lance B J 2018 EEGNet: a compact convolutional neural network for EEG-based brain–computer interfaces J. Neural Eng. 15 056013
7. Acknowledgment: This work was supported by the National Research Foundation (NRF) grant funded by the Korea government (MSIT) (NRF-2021M3E5D2A01022515, No. RS-2023-00218987), and in part by the Electronics and Telecommunications Research Institute (ETRI) grant funded by the Korean government. [23ZS1100, Core Technology Research for Self-Improving Integrated Artificial Intelligence System].

Poster No 1678

Consolidation of Interictal HFOs Produces Superior fMRI Localization

Daniel Pittman[1], William Wilson[2], Perry Dykens[2], Victoria Mosher[2], Laura Gill[3], Paolo Federico[2]

[1]University of Calgary, Calgary, AL, [2]University of Calgary, Calgary, Alberta, [3]Univeristy of Calgary, Calgary, Alberta

Introduction: Electroencephalography (EEG) has been the dominant diagnostic modality for the clinical evaluation of patients with epilepsy. Recordings acquired during the inter-ictal period, from either scalp or intracranially implanted electrode arrays (iEEG), are visually appraised by epileptologists, to identify characteristic morphological events. The most common are inter-ictal epileptiform discharges (IEDs), recognized as markers of the seizure onset zone (SOZ), where epileptic seizures arise. More recently, alternate markers have been employed, comprised of brief periods of activity of low-amplitude high-frequency oscillations (HFOs). These may be superior SOZ markers, but there has been debate surrounding whether they are more indicative of true pathology, or rather normal physiological brain behaviors. EEG can be recorded simultaneously during functional magnetic resonance imaging (fMRI), which measures oxygenation level changes within the brain over time, reflective of local neural metabolism, and thus neural activity levels. The EEG event timings are included to produce 3D brain volumes whose locations are scored according to the statistical significance of the synchronicity of the brain's oxygenation with the EEG events. This localization process has been used to identify brain regions systematically related to the EEG events, which are considered a surrogate marker of the SOZ. The low amplitude HFOs are difficult to detect on scalp EEG, but the combination of using more sensitive iEEG, simultaneously with functional MR (fMRI), greatly improves their utility. Even so, a challenge frequently arising is that HFOs may occur very often or almost continually, which does not produce a sequence of events with discriminatory value as an input for fMRI analyses. It is suggested that physiological HFOs occur independently and individually, whereas pathological HFOs occur simultaneously across several contacts of an iEEG electrode. Consolidating such co-occurring HFOs (cHFOs), and removing independent HFOs (iHFOs), would reduce the analysis to presumed pathological events, and improve localization of the SOZ.

Methods: Eleven epilepsy patients undergoing EEG monitoring for pre-surgical evaluation were recruited to undergo a 60-minute simultaneous iEEG/fMRI exam. The EEG data was cleaned of MRI signal contamination, filtered (80-125Hz) and converted to within-electrode bipolar montages. The channels of the electrode identified as being implanted closest to the suspected SOZ underwent processing to algorithmically identify HFOs (6 contiguous half-cycles whose absolute amplitude exceeded 3.1 standard deviations from the mean). An additional process was applied wherein the HFOs of an electrode were identified as being temporally overlapping for >50% of their duration, and as being more than 90% in phase. Such qualifying clusters of HFOs constituted a consolidated HFO (cHFO), spanning the interval across its constituents, and non-qualified events classified as iHFOs fMRI analyses were performed using as inputs the timings of a) all iHFOs on the SOZ electrode, and b) just the cHFOs. The resultant statistical volumes were compared by simple mathematical analysis of all supra-threshold voxels, evaluated according to their degree of overlap and their average distance to the SOZ electrode.

Results: The cHFO fMRI results had overall fewer supra-threshold voxels than the iHFO results. They also had shorter average distance to the SOZ electrode contacts. Consolidation of the iHFOs resulted in an average event count reduction of 80%.

Conclusions: Consolidated HFOs produced better localization than iHFOs, indicating their greater likelihood of being pathological HFOs. This was likely due to the greater statistical design efficiency of the significantly fewer cHFO events.. The substantial reduction of events also significantly reduces the workload for visual review.

References

1. Engel Jr, J., Bragin, A., Staba, R., & Mody, I. (2009). 'High-frequency oscillations: What is normal and what is not?', Epilepsia, 50(4), 598–604.
2. Jacobs, J., LeVan, P., Chander, R., Hall, J., Dubeau, F., & Gotman, J. (2008). 'Interictal high-frequency oscillations (80–500 Hz) are an indicator of seizure onset areas independent of spikes in the human epileptic brain', Epilepsia, 49(11), 1893–1907.

Poster No 1679

Brain Network Hypersensitivity Underlies Pain Crises in Sickle Cell Disease

Pangyu Joo[1], Uncheol Lee[1], Richard Harris[2], Ying Wang[3]

[1]Center for Consciousness Science, University of Michigan, Ann Arbor, MI, [2]University of California at Irvine School of Medicine, Irvine, CA, [3]Indiana University School of Medicine, Indianapolis, IN

Introduction: Sickle cell disease (SCD) is a genetic disorder characterized by abnormally deformed red blood cells that block blood flow in small blood vessels and cause acute pain episodes, referred to as vascular occlusion crises (VOCs). The frequent and repeated pain episodes lower the pain threshold, resulting in increased pain hypersensitivity. In addition, the occurrence of VOC is repetitive and unpredictable, making timely implementation of preventive strategies challenging. Therefore, these raise two crucial questions: Is there a brain mechanism responsible for the pain hypersensitivity in SCD? Can we predict the upcoming VOCs? In a previous study, we proposed explosive synchronization (ES), a universal phenomenon wherein a small perturbation can abruptly trigger global synchronization within a network, as the hypersensitivity of fibromyalgia. Here we hypothesize that ES may also underlie the pain hypersensitivity of SCD. In light of the temporal progression of VOC, we expect that the condition of ES may develop progressively until VOC onset and diminish afterward.

Methods: To test the hypotheses, we analyzed the EEG of SCD and developed a computational model. We recruited 24 SCD patients and 18 healthy control subjects for the EEG analysis. EEG recordings were acquired at rest and during painful pressure cuff application to the left calf. We examined the relationship between ES strength, measured by frequency disassortativity of the alpha EEG band (7-13Hz), patient-reported outcome measures (PROMs), and VOCs. Frequency disassortativity (FDA), a measure reflecting the proximity of a network to ES, indicates a tendency of higher frequency EEG channels linking to lower frequency EEG channels. Additionally, we designed a computational model with an anatomically informed human brain network structure and neural-mass models to simulate the interplay between ES strength in the brain network, brain sensitivity, and the occurrence of VOCs.

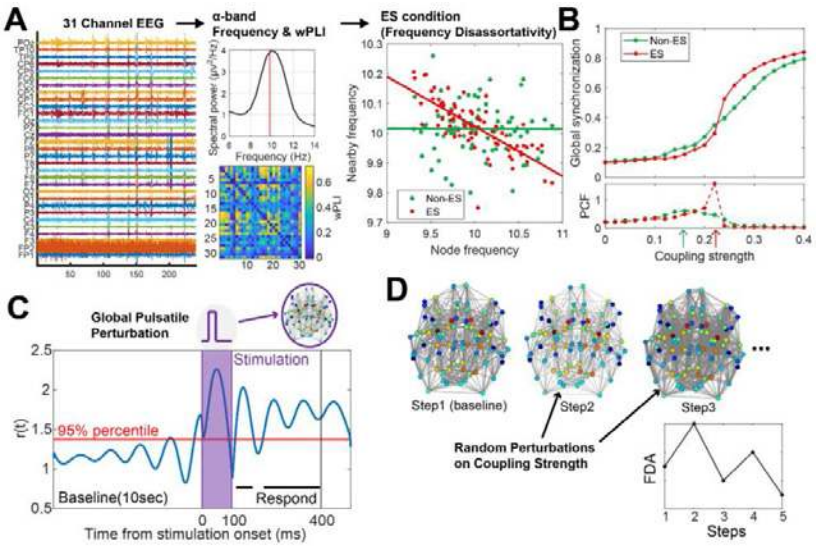

Figure 1. Schematic diagram of the study. (EEG analysis): A) wPLI matrix and median frequency of the alpha band (7-13Hz) were calculated from 31-channel EEG. Frequency disassortativity (FDA), a measure of ES, was obtained from the wPLI network and median alpha frequencies. B) Examples of state transitions (fast and slow) in the brain networks with different proximities to ES are shown. These networks exhibit different FDA values and state transition patterns (fast and slow, represented by red and green lines). (Computational modeling study): C) An anatomically informed brain network and neural mass model were employed to investigate the relationship between ES strength, brain sensitivity, and the occurrence of VOC. Global Pulsatile perturbation was applied for 100 milliseconds, and the response was measured by the subsequent perturbed brain activities for 300 milliseconds. D) The occurrence of VOC was simulated by determining how often the brains with different ES strengths cross a threshold of FDA, set as the indicator of VOC based on the SCD's EEG, under a noisy environment.

Results: (EEG analysis) The SCD group exhibited a significantly lower median alpha frequency (9.01±0.09Hz) compared to the control group (9.83±0.13Hz) in the eyes-closed resting state. Under pain stimulation, the FDA of the alpha EEG band (measured by Spearman correlation between the median alpha frequencies of 31 EEG channels) for the SCD significantly correlated with three pain scores (PROMs): BPI Pain Interference score (R=-0.451, p=0.031), PROMISE29 Physical Function (R=-0.620, p=0.002), and HADS Depression (R=-0.482, p=0.020). These findings suggest that patients with greater pain, depression, and poor physical function displayed a stronger ES in the EEG network. Furthermore, patients with more frequent

VOCs in the preceding 12 months presented with a larger ES strength (i.e., a larger FDA, R=-0.595, p=0.001). Importantly, the occurrence of the VOCs relative to the time of EEG recordings (within 30 days) was significantly correlated with the ES strength: the closer the occurrence of VOCs, the stronger the ES (i.e., a larger FDA) in EEG. (Computational model) Consistent with the EEG analysis results, increasing the FDA in the brain network model resulted in a higher brain network sensitivity to external perturbation, as measured by the responsivity and complexity of the perturbed signals. Additionally, the brains more frequently crossed over a threshold of FDA (set by the EEGs of VOC) under noisy environments.

Conclusions: In summary, we presented first-hand evidence supporting ES as the underlying mechanism of pain hypersensitivity in SCD and proposed the frequency disassortativity (FDA) of median alpha frequencies, a measure of ES strength in EEG, as a promising indicator for assessing pain scores and predicting the occurrence of VOCs. Further research should focus on developing a mechanism-based brain modulation method to preempt VOCs.

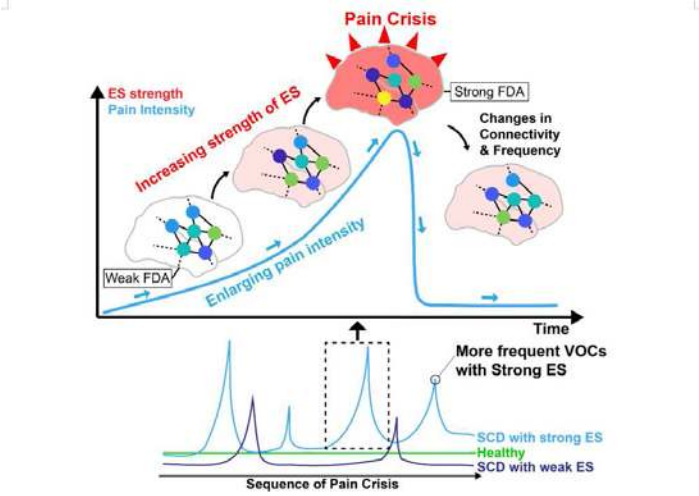

Figure 2. Hypothesis on the network mechanism of pain and VOCs in SCD. The effect of SCD may gradually accumulate within the brain network, strengthening frequency disassortativity (FDA), a measure of ES. The cumulative effect on ES can enhance the sensitivity of the brain network, potentially triggering a pain crisis, upon reaching a critical threshold.

References

1. Beggs, J.M. (2007) 'The criticality hypothesis: how local cortical networks might optimize information processing', Philosophical Transactions of the Royal Society A: Mathematical, Physical and Engineering Sciences, 366(1864), pp. 329–343.
2. Boccaletti, S. et al. (2016) 'Explosive transitions in complex networks' structure and dynamics: Percolation and synchronization', Physics Reports, 660, pp. 1–94.
3. Case, M. et al. (2019) 'Graph theory analysis reveals how sickle cell disease impacts neural networks of patients with more severe disease', NeuroImage: Clinical, 21, p. 101599.
4. Darbari, D.S. et al. (2015) 'Frequency of Hospitalizations for Pain and Association With Altered Brain Network Connectivity in Sickle Cell Disease', The Journal of Pain, 16(11), pp. 1077–1086.
5. Gómez-Gardeñes, J. et al. (2011) 'Explosive Synchronization Transitions in Scale-Free Networks', Physical Review Letters, 106(12), p. 128701.
6. Kim, M. et al. (2022) 'Explosive Synchronization-Based Brain Modulation Reduces Hypersensitivity in the Brain Network: A Computational Model Study', Frontiers in Computational Neuroscience, 16, p. 815099.
7. Kim, M. et al. (2020) 'Alpha oscillation, criticality, and responsiveness in complex brain networks', Network Neuroscience, 4(1), pp. 155–173.
8. Lee, U. et al. (2018) 'Functional Brain Network Mechanism of Hypersensitivity in Chronic Pain', Scientific Reports, 8(1), p. 243.
9. Skardal, P.S. et al. (2015) 'Frequency assortativity can induce chaos in oscillator networks', Physical Review E, 91(6), p. 060902.

Poster No 1680

Inhibitory tDCS stimulation to the bilateral DLPFC disrupts implicit emotional control

Agnieszka Adamczyk[1,2], Miroslaw Wyczesany[3,2]

[1]Jagiellonian University, Krakow, malopolskie, [2]Institute of Psychology, Krakow, Poland, [3]Jagiellonian University, Krakow, MLP

Introduction: Effective emotional control is central to well-being. Recently, it has been shown that emotional control processes can be initiated automatically, i.e., without conscious and deliberate attempts, and that such implicit emotional control relies on cognitive control brain networks (Adamczyk & Wyczesany, 2023) and, at least partly, shares neuronal mechanisms with explicit forms of emotional control (e.g., reappraisal; Wyczesany et al., 2021). The aim of the present study was to further our understanding of the role of the (left and right) DLPFC, the crucial hub of the frontoparietal cognitive control brain

network, in instigating top-down downregulatory effects on emotional and attentional systems after implicit induction of emotional control.

Methods: To this end, we inhibited activity of the left and right DLPFC using cathodal transcranial direct current stimulation (tDCS) before implementation of emotional control in a double-blind, sham-controlled, within-subject study design. Thirty-five participants unscrambled sentences of either neutral (no-regulation condition) or neutral and self-control-related content (implicit emotional control condition) before passively viewing negative pictures (see Wyczesany et al., 2021, Adamczyk & Wyczesany, 2023). EEG source-based effective connectivity (based on Granger causality) was measured in the frontoparietal and cinguloopercular cognitive control networks and the perceptual/attentional brain networks during the implementation of emotional control. Late Positive Potential (LPP) amplitude was measured to verify the effects on emotional arousal.

Results: Replicating previous findings, implicit emotional control decreased the LPP amplitude, indicating successful emotion downregulation, and increased connectivity within both cognitive control networks compared to the no-regulation condition in the sham session. Enhanced connectivity was observed in the theta frequency band (3–7 Hz) from the right DLPFC to the left intraparietal sulcus (IPS; frontoparietal network) and from the dorsal anterior cingulate cortex to the right insula/frontal operculum (cingulo-opercular network). Moreover, implicit emotional control increased downstream influence from the frontoparietal network towards the visual system in the beta band (15–30 Hz). Increased connectivity was observed from the left IPS to the right primary visual cortex and the left precuneus. All these effects were abolished after stimulation of both right and left DLPFC.

Conclusions: Our study shows the causal role of the bilateral DLPFC in automatic control of emotions. By revealing connectivity profile of successful emotional control, our findings provide mechanistic targets for stimulation-based therapies that could enhance effectiveness of implicit emotion regulation in psychopathologies.

References

1. Adamczyk, A. K. (2023), 'Theta-band connectivity within cognitive control brain networks suggests common neural mechanisms for cognitive and implicit emotional control', Journal of Cognitive Neuroscience, vol. 35, no. 10, pp. 1656–1669. https://doi.org/10.1162/jocn_a_02034
2. Wyczesany, M. (2020), 'Implicit induction of emotional control. A comparative fMRI investigation of self-control and reappraisal goal pursuit', Emotion, vol. 21, no. 7, pp. 1379–1391. https://doi.org/10.1037/emo0000852

Poster No 1681

Affective Response Modeling Leveraging EEG and Deep Learning Toward Mental Health Assessment

Woojae Jeong[1], Takfarinas Medani[1], Hamzeh Alturk[2], Colin McDaniel[2], Idan Blank[3], Dani Byrd[4], Assal Habibi[2], Baruch Cahn[2], Shrikanth Narayanan[1], Richard Leahy[1]

[1]Ming Hsieh Department of Electrical and Computer Engineering, University of Southern California, Los Angeles, CA, [2]Brain and Creativity Institute, University of Southern California, Los Angeles, CA, [3]Department of Psychology and Department of Linguistics, University of California, Los Angeles, Los Angeles, CA, [4]Department of Linguistics, University of Southern California, Los Angeles, CA

Introduction: Mental health is critical in determining one's overall health, quality of life, and functional status. After the COVID-19 pandemic, we witnessed a significant increase in the global prevalence of depression and suicide rates[1]. Accurate and timely assessment of depression and suicide risk is one the most effective ways to support mental healthcare. Current methods for assessing individual mental health and potential risk factors predominantly rely on self-reports or behavioral interviews through questionnaires. However, these approaches are often incomplete and unreliable. With advances in neuroscience and machine learning, recent studies have shown promising results in emotion recognition with high accuracy by decoding distinctive features from emotionally evoked electroencephalogram (EEG) time-frequency representations using different convolutional neural network (CNN) architectures[2,3]. Here, we seek to develop a reliable means to objectively assess and classify mental states by identifying biomarkers from EEG signals evoked by four different emotional stimuli in an Emotional Strop paradigm using deep neural networks and machine learning classifiers.

Methods: Participants were pre-screened and grouped into control, depressed, and suicide risk groups based on their performance on PHQ-9[4] and SIS (Suicidal Ideation Scale) scores[5]. Participants were asked to perform an Emotional Stroop task[6] with four groups of 60 emotional stimuli words related to happy, neutral, sad, and suicidality designed and developed to trigger an emotional response. Participants were to identify the color of the word while instructed to ignore the meaning of the word. Differential interference in color by emotional versus neutral words implicates excess attention deployed to stimuli related to underlying emotional processing, taking attentional resources away from color identification. We collected EEG

using a 64-channel active electrode system (Brain Products) sampled at 1 kHz. The EEG signal was preprocessed using the standard Brainstorm pipelines[7]. We performed a preliminary analysis of the behavioral data and event-related potential (ERP) on data from 31 participants (healthy control: 17, depressed: 8, suicide risk: 6). We computed the average reaction time (time from stimulus onset to the participant's response) for each emotional category in each group. The ERP was computed by averaging across trials for each emotional category and averaged across the 9 selected channels in the fronto-central area, where we expected to capture signals originating from the Anterior Cingulate Cortex (ACC) and Dorsolateral Prefrontal Cortex (DLPFC)[8].

Results: The overall reaction time of the healthy control group showed a faster trend than the depressed and the suicide risk groups (Figure 1). Our preliminary analysis suggests that, in comparison to the healthy control group, which exhibits similar neural responses to both affective and non-affective stimuli, the neural processing in response to affective stimuli appears to differ in the groups with depression and suicidal tendencies (Figure 2).

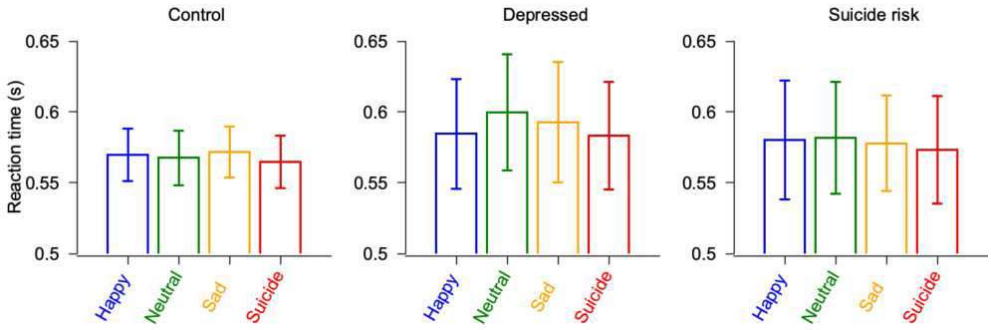

Figure 1. Average reaction time for each group and emotional category.

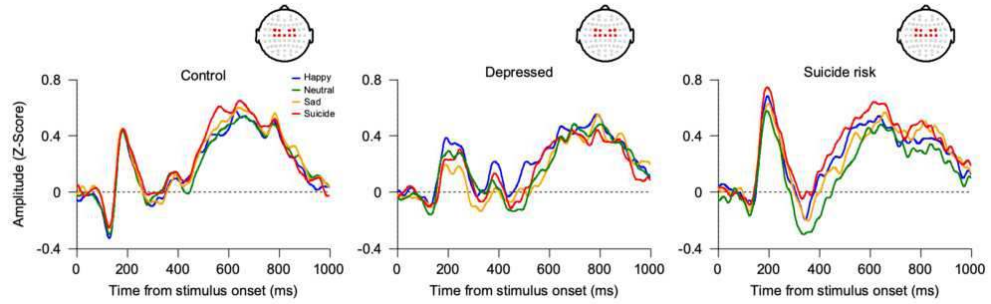

Figure 2. Average ERP from fronto-central channels (red dots in the topography) for each group and emotional category.

Conclusions: Our initial findings indicate that the emotionally aroused neural responses exhibit distinct characteristics across different groups both on reaction time and the underlying neural mechanisms, although larger samples will be required to verify statistical significance. We aim to collect 150 participants (control: 74, depressed: 38, suicide risk 38) and extend our analysis of these subjects. Future analysis will include extracting discriminative underlying features from the EEG time-frequency representations at the source level[7,9,10] by a deep convolutional neural network (CNN)[2]. By employing this approach, we aim to deepen our understanding of the neural responses that underlie different mental states and elaborate our capability to assess mental health with greater objectivity.

References

1. Panchal, N., Kamal, R., Orgera, K., Cox, C., Garfield, R., Hamel, L., and Chidambaram, P. (2020), 'The implications of COVID-19 for mental health and substance use', Kaiser family foundation, 21, 1-16.
2. Zali-Vargahan, B., Charmin, A., Kalbkhani, H., and Barghandan, S. (2023), 'Deep time-frequency features and semi-supervised dimension reduction for subject-independent emotion recognition from multi-channel EEG signals', Biomedical Signal Processing and Control, 85, 104806.
3. Khare, S. K., and Bajaj, V. (2020), 'Time-frequency representations and convolutional neural network-based emotion recognition', IEEE transactions on neural networks and learning systems', 32(7), 2901-2909.
4. Kroenke, K., Spitzer, R. L., and Williams, J. B. (2001), 'The PHQ-9: validity of a brief depression severity measure', Journal of general internal medicine', 16(9), 606-613.
5. Rudd, M. D. (1989), 'The prevalence of suicidal ideation among college students', Suicide and Life-Threatening Behavior, 19, 173-183.
6. Wells, A., Mathews, G. (1996), 'Modelling cognition in emotional disorder: the S-REF model', Behaviour Research and Therapy, 34, 881-888.
7. Tadel, F., Baillet, S., Mosher, J. C., Pantazis, D., and Leahy, R. M. (2011), 'Brainstorm: a user-friendly application for MEG/EEG analysis', Computational intelligence and neuroscience, 1-13.

8. Ergen, M., Saban, S., Kirmizi-Alsan, E., Uslu, A., Keskin-Ergen, Y., and Demiralp, T. (2014), 'Time-frequency analysis of the event-related potentials associated with the Stroop test', International Journal of Psychophysiology, 94(3), 463-472.
9. Baillet, S., Mosher, J. C., and Leahy, R. M. (2001), 'Electromagnetic brain mapping', IEEE Signal processing magazine, 18(6), 14-30.
10. Mosher, J. C., Leahy, R. M., and Lewis, P. S. (1999), 'EEG and MEG: forward solutions for inverse methods', IEEE Transactions on biomedical engineering, 46(3), 245-259.

Poster No 1682

Dynamics brain-state allocation using echo state network

Yolanda Vives-Gilabert,[1], Felipe Torres[2], Andre Gómez-Lombardi[3], Wael El-Deredy[4]

[1]Universitat de València, Valencia, Spain, [2]Universidad de Valparaíso, Valparaíso, Valparaíso, [3]Universidad de Valparaíso, Valparaíso, Chile, [4]Universidad de Valparaíso, Valparaíso, Valparaíso

Introduction: Transiently stable and recurrent patterns of activity in the spontaneous EEG are thought to represent fundamental computational properties of the brain shaping behavior and brain function, transitioning between various states or modes of activity based on the ongoing cognitive demands, environmental stimuli, and internal processes [Trujillo-Barreto et al, 2019]. The identification of the brain states and their transitioning is an area of active research [Woolrich et al 2013; Baker et al 2014 ;Honcamp et al 2022] . Of particular interest are brain state allocation methods that can handle the natural non-linear dynamics of the brain, in a manner that affords subsequent biological interpretability [Trujillo-Barreto et al, 2019]. Here we explore the potential of Echo State Network (ESN) modeling for dynamical brain state allocation based on neuroimaging data. ESN is a recurrent neural network with randomly connected neurons, and it acts as a nonlinear dynamic system, Jaeger (2002) and Lukoševičius (2012). The state of the reservoir captures the network's response to the temporal patterns and dynamics present in the input signals. When feeding EEG data into an ESN and train the network to predict the same EEG data at the output, the internal states of the ESN capture relevant temporal patterns, dependencies, and information present in the input EEG signals, reproducing its nonlinear dynamics. By using a compact representation inside the ESN [the reservoir], the states would encode the temporal dynamics of the EEG signals, and reflect how the EEG signals have evolved over time.

Methods: An Echo State Network is a type of recurrent neural network with a specific architecture characterized by a fixed random reservoir of recurrently connected neurons, comprising three layers Jaeger (2002) and Lukoševičius (2012): An input layer that receives the incoming data [EEG] and communicates it to the reservoir. A reservoir layer comprising large number of recurrently connected neurons. The connections between neurons in the reservoir are randomly assigned and usually remain fixed during training [here we adapt the reservoir connections using Hebbian learning rule]. Finally, the Output (Readout) Layer) is the trainable part of the network usually using linear methods. We followed this convention to training the output layer of the ESN, with the output predicting the input, as in autoencoders, while training the internal reservoir connections using Hebbian learning (Yusoff,et al 2016). Hebbian learning adjusts the weights based on the (temporal) correlations between the activities of connected neurons. To test the method's capture of the non-linear dynamics, we simulated an EEG like time series with non-linear interaction between two frequencies [Figure 1a].

Results: The unsupervised training of the reservoir connections, leads to robust internal state that represent the temporal dynamics of the time-series [Figure 1B]. The internal state trace a the evolution of the oscillatory modes that emerge due to the frequency interactions.

Conclusions: Echo State Networks offer a simple non-parametric machine learning model of nonlinear EEG type data that affords subsequent feature extraction, classification and regression analyses.

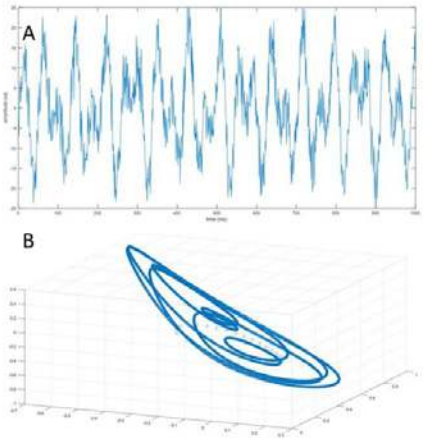

References
1. Baker, A. P., Brookes, M. J., Rezek, I. A., Smith, S. M., Behrens, T., Probert Smith, P. J., & Woolrich, M. (2014). Fast transient networks in spontaneous human brain activity. elife, 3, e01867.
2. Honcamp, H., Schwartze, M., Linden, D. E., El-Deredy, W., & Kotz, S. A. (2022). Uncovering hidden resting state dynamics: A new perspective on auditory verbal hallucinations. Neuroimage, 255, 119188.
3. Jaeger, H. (2002). Adaptive nonlinear system identification with echo state networks. Advances in neural information processing systems, 15.
4. Lukoševičius, M. (2012). A practical guide to applying echo state networks. In Neural Networks: Tricks of the Trade: Second Edition (pp. 659-686). Berlin, Heidelberg: Springer Berlin Heidelberg.
5. Trujillo-Barreto, N. J., Araya, D., & El-Deredy, W. (2019). The discrete logic of the Brain-Explicit modelling of Brain State durations in EEG and MEG. BioRxiv, 635300.
6. Woolrich, M. W., Baker, A., Luckhoo, H., Mohseni, H., Barnes, G., Brookes, M., & Rezek, I. (2013). Dynamic state allocation for MEG source reconstruction. Neuroimage, 77, 77-92.
7. Yusoff, M. H., Chrol-Cannon, J., & Jin, Y. (2016). Modeling neural plasticity in echo state networks for classification and regression. Information Sciences, 364, 184-196.

Poster No 1683

Longitudinal EEG and fMRI Measures of Excitation:Inhibition Ratio after Traumatic Brain Injury

Ana Radanovic[1], Samuel Louviot[2], Keith Jamison[3], Sudhin Shah[2], Amy Kuceyeski[3]

[1]Weill Cornell Graduate School of Medical Sciences, New York, NY, [2]Department of Radiology, Weill Cornell Medicine, New York, NY, [3]Weill Cornell Medicine, New York City, NY

Introduction: Traumatic brain injury (TBI) is associated with persistent symptoms and incomplete recovery, and is a leading cause of long-term disability worldwide (Ahsman et al., 2006). Acute TBI is known to begin with a period of high excitotoxicity, however, the mechanisms of injury and recovery long-term remain unknown. Examining neurobiological mechanisms via neuroimaging is crucial for gaining insights into the processes of recovery, prognostic assessment, and potential treatment targets. The excitation to inhibition (E:I ratio) is thought to play an important role in pathophysiological mechanisms of autism, schizophrenia, and other intellectual disabilities (eg. Molina et. al, 2020). In addition, alterations in connectivity that occur after TBI are associated with changes in excitatory targets (dopamingergic and nornoradrenergic; Woodrow et. al, 2023). Thus, investigating the E:I ratio after TBI could reveal important information regarding injury and recovery mechanisms after TBI. There are noninvasive proxy markers of E:I in both electrophysiological (electroencephalography, EEG) and functional neuroimaging (functional Magnetic Resonance Imaging, fMRI). A measure of E:I in EEG, namely the aperiodic signal of the power spectral density (PSD) known as 1/f, has gained much interest. A proxy marker for E:I ratio identified in fMRI is the Hurst exponent (H) or, similarly, fALFF (fractional amplitude of low-frequency fluctuations). Both 1/f and fALFF have been independently validated, correlated, and shown to be clinically relevant (Gao et. al, 2017; Maschke et. al, 2023; Molina et. al, 2020; Trakoshis et al., 2020).

Methods: Longitudinal resting state fMRI and EEG data were collected from TBI patients and non-injured healthy controls (HC). TBI patients were measured at 2 timepoints: 4-6 months and 1 year after injury. EEG analyses were conducted on 29 TBI subjects (6 females, aged 18-82 mean 43 years) and 45 HC (13 females, aged 18-76 mean 41 years). EEG signals at rest were preprocessed using standard pipelines and aperiodic exponents were extracted using the specparam toolbox (Donoghue et al, 2020). fMRI analyses were conducted on 32 TBI subjects (8 females, aged 24-83 mean 53 years) and 14 HC (6 females, aged 23-86 mean 56 years). fMRI resting state data was processed using standard pipelines and fALFF was calculated for each of the FreeSurfer atlas's 86 regions. Between session analysis was conducted using a paired t-test. Analysis of differences between TBI and HC measurements were conducted using an ANCOVA, considering age and sex. The number of subjects used for each analysis is mentioned per figure.

Results: The TBI subjects' average exponent values decreased on frontal channels over time ($p=0.05$) (Fig 1c). Frontal regions of the scalp show the most change over time in exponent values in TBI subjects, and these same channels tend to differ when compared with healthy controls (Fig1a), indicating a change in the TBI subjects over time that brought them closer to controls. Frontal fALFF values do not show the same significant trend over time (Fig 2b). Average frontal fALFF values seem to be higher in TBI subjects compared to healthy controls (Fig 2a., controlled for Age, Sex; $p<0.1$) but decrease over time to be closer to control values (although this was not significant).

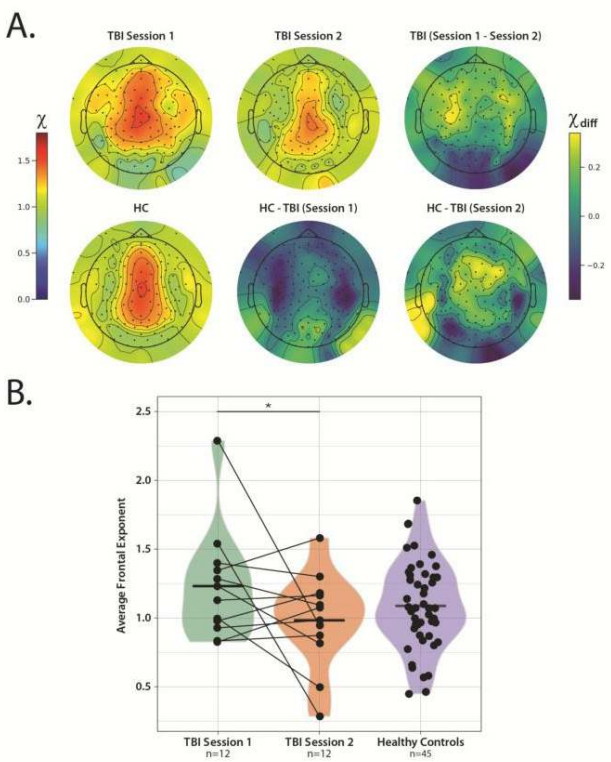

Figure 1. TBI and healthy control (HC) aperiodic exponents. (A.) Top row: Topoplots of average exponent values at each of the 129 channels for TBI subjects at session 1 and session 2, and the difference between these values. Bottom row: Topoplots show average exponent values per channel in healthy controls at each of the 129 channels. Difference topoplots show change in exponent value per channel in healthy controls and TBI at session 1, and healthy controls and TBI at session 2. Colorbars to the left indicate exponent value (slope of PSD) and colorbars on the right indicate exponent value change. (B.) Exponent values from slope of PSD from averaged frontal channels for TBI session 1, TBI session 2, and healthy controls. Lines track individual subjects' change between sessions. Bar and "*" indicates significance at p=0.05.

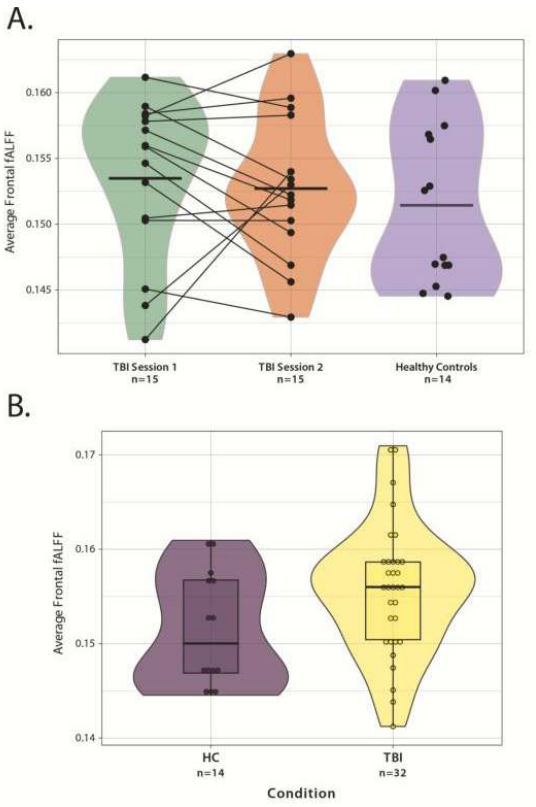

Figure 2. fALFF values for TBI and healthy controls (HC) and changes in fALFF over 2 sessions in TBI. (A.) fALFF values from all frontal regions averaged per subject in TBI and healthy controls. Difference between groups is not significant (p<0.1). (B.) fALFF values from all frontal regions averaged between session 1 and session 2 in TBI, and healthy controls. Lines track individual subject's change between session 1 and session 2.

Conclusions: With the aperiodic exponent as a proxy measure of E:I ratio, TBI subjects have a decreased aperiodic exponent (increased excitation) through recovery. This change is significant in the frontal and frontal midline regions, which are known

to be important for executive attention (Kim et al, 2023). fALFF in the frontal regions seems to be higher (decreased excitation) compared to healthy controls at the first time point, and trends towards decreasing over time toward healthy control levels. This work suggests E:I ratio changes over time during TBI recovery, and understanding this progression could hint towards biomarkers of chronic pathology or recovery.

References

1. Ashman TA, Gordon WA, Cantor JB, Hibbard MR. Neurobehavioral consequences of traumatic brain injury. Mt Sinai J Med. 2006 Nov;73(7):999-1005. PMID: 17195886.
2. Donoghue T, Haller M, Peterson EJ, Varma P, Sebastian P, Gao R, Noto T, Lara AH, Wallis JD, Knight RT, Shestyuk A, Voytek B (2020). Parameterizing neural power spectra into periodic and aperiodic components. Nature Neuroscience, 23, 1655-1665. DOI: 10.1038/s41593-020-00744-x
3. Gao R, Peterson EJ, Voytek B. Inferring synaptic excitation/inhibition balance from field potentials. Neuroimage. 2017 Sep;158:70-78. doi: 10.1016/j.neuroimage.2017.06.078. Epub 2017 Jul 1. PMID: 28676297.
4. Kim N, Jamison K, Jaywant A, Garetti J, Blunt E, RoyChoudhury A, Butler T, Dams-O'Connor K, Khedr S, Chen CC, Shetty T, Winchell R, Hill NJ, Schiff ND, Kuceyeski A, Shah SA. Comparisons of electrophysiological markers of impaired executive attention after traumatic brain injury and in healthy aging. Neuroimage. 2023 Jul 1;274:120126. doi: 10.1016/j.neuroimage.2023.120126. Epub 2023 Apr 30.
5. Maschke C, Duclos C, Owen AM, Jerbi K, Blain-Moraes S. Aperiodic brain activity and response to anesthesia vary in disorders of consciousness. Neuroimage. 2023 Jul 15;275:120154. doi: 10.1016/j.neuroimage.2023.120154. Epub 2023 May 19. PMID: 37209758.
6. Molina, J. L. et al. Memantine effects on electroencephalographic measures of putative excitatory/inhibitory balance in schizophrenia. Biol. Psychiatry Cogn. Neurosci. Neuroimaging 5, 562–568 (2020).
7. Trakoshis S, Martínez-Cañada P, Rocchi F, Canella C, You W, Chakrabarti B, Ruigrok AN, Bullmore ET, Suckling J, Markicevic M, Zerbi V; MRC AIMS Consortium; Baron-Cohen S, Gozzi A, Lai MC, Panzeri S, Lombardo MV. Intrinsic excitation-inhibition imbalance affects medial prefrontal cortex differently in autistic men versus women. Elife. 2020 Aug 4;9:e55684. doi: 10.7554/eLife.55684.
8. Woodrow RE, Winzeck S, Luppi AI, Kelleher-Unger IR, Spindler LRB, Wilson JTL, Newcombe VFJ, Coles JP; CENTER-TBI MRI Substudy Participants and Investigators; Menon DK, Stamatakis EA. Acute thalamic connectivity precedes chronic post-concussive symptoms in mild traumatic brain injury. Brain. 2023 Aug 1;146(8):3484-3499. doi: 10.1093/brain/awad056. PMID: 36811945

Poster No 1684

An optimized pipeline for Topup geometric distortion correction

Maeve McGowan[1], Jack Grinband[1]

[1]Columbia University, New York, NY

Introduction: Echo planar imaging (EPI) sequences suffer from image distortion due to B0 magnetic field inhomogeneities, susceptibility changes across tissue types, eddy currents, gradient coil nonlinearities, and cardiovascular pulsations[1,2], particularly in the phase-encode (PE) plane due to lower acquisition bandwidth per pixel. In fMRI, these distortions in brain geometry can lead to poor spatial normalization between functional and structural images, incorrect placement of regions of interest, incorrect tissue segmentation, incorrect localization of brain activity, and increased noise in group averages of brain activity. While there are methods for correcting geometric distortion in real time during scan acquisition[3], most corrections are performed retrospectively. FSL's Topup tool, a widely-used method for unwarping distorted EPI data, estimates magnetic susceptibility by computing the field that maximizes similarity between images acquired in opposite PE-directions[4,5] and uses it to unwarp distorted data. However, Topup relies on good linear registration between the opposite PE-direction images to estimate the distortion accurately. Importantly, greater distortion means greater potential for misregistration between the two opposite PE-direction images and subsequent errors in the Topup-estimated B0 field. Further, in practice, the field map estimate is noisy, resulting in less than perfect unwarping in the PE plane[6,7]. Finally, while Topup can significantly reduce distortion in the PE plane, it has no effect in the two orthogonal planes. We propose a new pipeline (Downunder) that reduces these three sources of error by applying standard distortion correction tools recursively, using outputs of each loop as reference information for the subsequent loop, implementing Topup unwarping in the slice encode direction, and applying nonlinear registration to the structural T2w image to account for any remaining distortions.

Methods: The first round of Topup correction used one of the SE images as the reference for registration, identical to standard Topup preprocessing. However, in subsequent rounds, a reference mask of the undistorted image was used for registration. The mask was computed by taking the average of the undistorted opposite-PE images from the prior iteration. The mask was then brain extracted, and binarized, and thresholded, using only voxels with displacements less than 80% of maximum displacement for calculating the cost function for registration (reference weighting: weighting = 1 for displacements < 80%; weighting = 0 for displacements ≥ 80%). This approach further minimized the effect of PE distortion on the cost function. After iterative Topup correction, the B0 field estimate from Topup was used to create a shift map in the slice-direction using the slice-encode bandwidth. The undistorted SE image was corrected in the slice-direction and subsequently linearly (FLIRT) and non-linearly (FNIRT) co-registered to the T2w image.

Results: The resulting Downunder-corrected data (healthy subjects, n = 27) showed increased geometric similarity to the T2w structural image. The mean correlation ratio between distortion-corrected SE-AP and T2w images across subjects decreased with each iterative Topup application and the addition of slice-encode correction (Fig 1A), indicating improved structural similarity to the T2w image. The addition of FNIRT as a final step produced lower correlation ratio values than the respective Topup-only images (data not shown). To determine how much Downunder improves the geometric distortion over Topup alone, a 3mm isotropic ROI seed was placed in MNI space and the geometric errors were simulated for each subject. Fig 1B shows the effect of distortion and blur of the ROI across subjects with a peak percent overlap of only 31% and a blur diameter of about 12mm.

Conclusions: Our results suggest that Downunder significantly reduces errors in structural geometry, registration, and localization of brain activity.

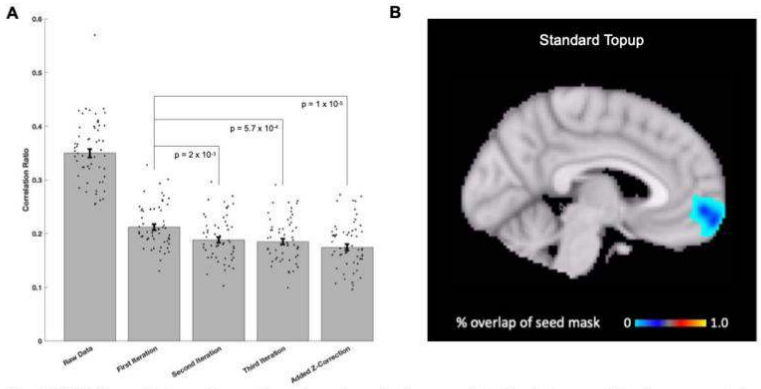

Fig. 1. FLIRT correlation ratio cost function values for linear registration between distortion-corrected SE-AP and T2w images. The cost function is minimized such that lower values indicate better registration. **(A)** Correlation ratio degreases with each application of Topup, and further with correction in the slice-encode directions; p-values are relative to a single Topup. The black dots represent individual subjects. **(B)** Percent of overlap between orbital frontal ROI seed masks between subjects for standard Topup distortion correction. There is a diameter of ~12mm in the distribution spread of a 3mm isotropic seed mask when transformed from original subject space to MNI space after standard distortion correction.

References

1. Andersson, J.L., Skare, S., Ashburner, J., 2003. How to correct susceptibility distortions in spin-echo echo-planar images: application to diffusion tensor imaging. Neuroimage 20, 870-888.
2. Embleton, K.V., Haroon, H.A., Morris, D.M., Ralph, M.A., Parker, G.J., 2010. Distortion correction for diffusion-weighted MRI tractography and fMRI in the temporal lobes. Hum Brain Mapp 31, 1570-1587.
3. Hutton, C., Bork, A., Josephs, O., Deichmann, R., Ashburner, J., Turner, R., 2002. Image distortion correction in fMRI: A quantitative evaluation. Neuroimage 16, 217-240.
4. Jezzard, P., Clare, S., 1999. Sources of distortion in functional MRI data. Human Brain Mapping 8, 80-85.
5. Juchem, C., Nixon, T.W., McIntyre, S., Boer, V.O., Rothman, D.L., de Graaf, R.A., 2011. Dynamic multi-coil shimming of the human brain at 7 T. J Magn Reson 212, 280-288.
6. Smith, S.M., Jenkinson, M., Woolrich, M.W., Beckmann, C.F., Behrens, T.E., Johansen-Berg, H., Bannister, P.R., De Luca, M., Drobnjak, I., Flitney, D.E., Niazy, R.K., Saunders, J., Vickers, J., Zhang, Y., De Stefano, N., Brady, J.M., Matthews, P.M., 2004. Advances in functional and structural MR image analysis and implementation as FSL. Neuroimage 23 Suppl 1, S208-219.
7. Wu, M., Chang, L.C., Walker, L., Lemaitre, H., Barnett, A.S., Marenco, S., Pierpaoli, C., 2008. Comparison of EPI distortion correction methods in diffusion tensor MRI using a novel framework. Med Image Comput Comput Assist Interv 11, 321-329.

Poster No 1685

Microstate-metric test-retest reliability to assess simultaneous EEG-fMRI noise reduction methods

Toshikazu Kuroda[1], Takeshi Ogawa[2], Reinmar Kobler[3], Mizuki Tsutsumi[1], Tomohiko Kishi[1], Motoaki Kawanabe[1]

[1]Advanced Telecommunications Research Institute International, Soraku-gun Seika-cho, Kyoto, [2]Advanced Telecommunications Research Institute International, Kyoto, Japan, [3]ATR, Seika-cho, Soraku-gun, Kyoto

Introduction: Electroencephalography (EEG) and functional magnetic resonance imaging (fMRI) are two major noninvasive approaches for measuring brain activity. Their simultaneous recording has an advantage in examining how EEG is associated with fMRI. Although promising, the simultaneous recording suffers from serious contamination of noise in EEG. Moreover, it remains difficult to evaluate noise reductions due to the absence of ground truth in EEG. One remedy is the use of EEG recorded outside MR scanners as a reference (van der Meer et al., 2016). This approach implicitly assumes high test-retest reliability, however: EEG should be similar between inside and outside the scanner if noise reductions are sufficient. EEG

microstates could be a useful alternative for the evaluation of noise reductions in the context of simultaneous recording with fMRI. Briefly, the microstates are extracted by clustering EEG spatial maps, typically resulting in four to five templates (Michel et al., 2018). Backfitting the templates to raw EEG provides several metrics such as duration, occurrence, and coverage, and transition probability of each microstate. Moreover, the test-retest reliability of the first three metrics generally is high at least for EEG recorded outside the MR scanner (Kleinert et al., 2023).

Methods: Here we introduce a new evaluation method for noise reduction in the context of EEG-fMRI simultaneous recording taking advantage of EEG microstate metrics. We assumed that, if EEG recorded outside an MR scanner on two different days has high test-retest reliability in terms of microstate metrics, then it would be reasonable to consider that the reliability should also be high for EEG recorded inside and outside the scanner on the same day. This led us to the notion that the scanning noise should be reduced in a way that the reliability would increase. Taking this approach, we recorded EEG during an 8-min resting state both inside and outside the scanner on two separate days per participant (n=25). For EEG recorded outside the scanner, artifacts were reduced in a similar way to the previous study (Kleinert et al., 2023). EEG recorded inside the scanner was also processed in the same way but with additional steps for reducing scanning-specific artifacts. In particular, residual ballistocardiogram (BCG) artifacts were reduced with an extension of optimal basis set (OBS; de Cheveigné et al., 2014; Niazy et al., 2005) in which a threshold was set for the ratio between EEG power time-locked to heartbeats and the power during randomly selected periods. Using intraclass correlation coefficient (ICC) as an index, test-retest reliability of microstate metrics was assessed 1) between a pair of recordings on Days 1 and 2 outside the scanner, 2) between a pair of recordings on the same day inside and outside the scanner, 3) and between a pair of recordings on Days 1 and 2 inside the scanner.

Results: We obtained moderately high test-retest reliability (ICCs > .50 on average) for duration, occurrence, and coverage in all the three cases (see Figure 1). Moreover, the ICCs were higher with than without the new method for reducing residual BCG.

Microstate Templates

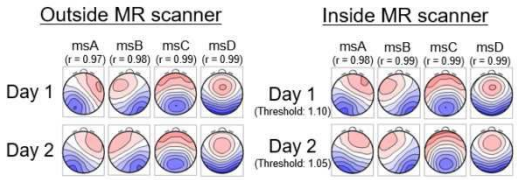

Intraclass Correlation Coefficients

Comparisons	Duration	Occurrence	Coverage	Transition Probability
Outside (Day 1) Outside (Day 2)	.83	.81	.77	.56
Outside (Day 1) Inside (Day 1)	.66	.63	.57	.48
Outside (Day 1) Inside (Day 1) without reducing residual BCG	.41	.43	.27	.24
Outside (Day 2) Inside (Day 2)	.50	.53	.54	.41
Outside (Day 2) Inside (Day 2) without reducing residual BCG	.10	.17	.11	.10
Inside (Day 1) Inside (Day 2)	.54	.58	.58	.48

Figure 1. (Top) Microstate templates extracted from EEG recorded outside and inside an MR scanner. "msA-D" represent microstate A-D. "r" stands for spatial correlation between templates across Days 1 and 2. "Threshold" is the threshold for reducing residual ballistocardiogram (BCG) artifacts with an extension of optimal basis set (OBS). (Bottom) Z-transformed means of intraclass correlation coefficients, averaged across microstate templates, based on the templates above.

Conclusions: We demonstrated that scanning noise can be reduced to a level that EEG microstate metrics reached moderately high test-retest reliability between a pair of EEG recorded on the same day inside and outside an MR scanner and also between a pair of EEG recorded on different days inside the scanner. Still lower reliability for EEG recorded inside than outside the scanner suggest a room for further improvement in noise reduction.

References

1. de Cheveigné, A. (2014), 'Joint decorrelation, a versatile tool for multichannel data analysis', NeuroImage, vol. 98, pp. 487-505.
2. Kleinert T. (2023), 'On the reliability of the EEG microstate approach', Brain Topography, DOI: 10.1007/s10548-023-00982-9

3. Michel, C.M. (2018), 'EEG microstates as a tool for studying the temporal dynamics of whole-brain neuronal networks: A review', NeuroImage, vol. 180, pp. 577-593.
4. Niazy, R.K. (2005), 'Removal of fRMI environment artifacts from EEG data using optimal basis sets', NeuroImage, vol. 28, pp. 720-737.
5. van der Meer, J.N. (2016), 'Carbon-wire loop based artifact correction outperforms post-processing EEG/fMRI corrections – A validation of a real-time simultaneous EEG/fMRI correction method', NeuroImage, vol. 125, pp. 880-894.

Poster No 1686

Harmonizing T1-weighted MRI via disentangled information bottleneck while preserving brain anatomy

Seonggyu Kim[1], Hanyeol Yang[2], Yongseon Yoo[2], Jihwan Min[2], Jong-Min Lee[1,2,3]

[1]Department of Electronic Engineering, Hanyang University, Seoul, Korea, Republic of, [2]Department of Artificial Intelligence, Hanyang University, Seoul, Korea, Republic of, [3]Department of Biomedical Engineering, Hanyang University, Seoul, Korea, Republic of

Introduction: Recently, many deep learning models, such as ChatGPT, have been applied to various industrial fields, leveraging their outstanding performance. Despite being an early focus of AI research, the medical field has seen limited utilization of AI models compared to other sectors. One significant factor contributing to this issue is the challenge posed by insufficient data, leading to suboptimal model performance. For instance, transformer models, widely used today, struggle to learn effectively with limited datasets. Additionally, the variation in image value across cohorts, stemming from differences in data collection methods, hinders the robustness of AI in healthcare applications. A clear and effective solution to these challenges is the construction of large-scale datasets. While it may sound cliché, there are generally two approaches to building such datasets. One involves standardizing data collection protocols for all images, which could include standardizing scanners or simply unifying imaging parameters. The other approach is data harmonization through post-processing of collected images. Even after protocol standardization, the need for data harmonization often arises. Harmonization techniques can be broadly categorized into feature level and image level, with methods like ComBat being prevalent at the feature level and generative models at the image level.

Methods: Liu et al.[1] employed conditional variational autoencoders (VAE) and adversarial learning for MRI harmonization. They interpreted their model from the perspective of information bottleneck theory, enhancing a traditional information bottleneck-based VAE by introducing assumptions such as the global Markov property of latent variables (beta and theta) given the input and the shared anatomy of T1 weighted and T2 weighted images within the same subject. However, the optimization of such approaches often fails to guarantee maximum compression of latent variables in the information bottleneck, and the assumption that T1 and T2 weighted images share anatomy may be inaccurate for some slices. In this study, we introduce a disentangled information bottleneck[2] loss to ensure maximum compression of the latent variable beta and train a more interpretable harmonization model through simulation.

$$\min_{\mathbb{P}_s,\mathbb{P}_c}\max_{\text{disc}}\ \mathbb{E}_{\mathbb{P}_s(s)\mathbb{P}_c(c)}[log(disc(s,c))]+\mathbb{E}_{\mathbb{P}_{sc}(s,c)}[1-log(disc(s,c))]$$

$$+\max_{\mathbb{P}_c,\text{dec}}\frac{1}{N}\sum_{i=1}^{N}\mathbb{E}_{c\sim\mathbb{P}_c(c|x_i)}[log(p_{\text{dec}}(y_i|s,c)]$$

$$+\max_{\mathbb{P}_s,\text{cdec}}\frac{1}{N}\sum_{i=1}^{N}\mathbb{E}_{s\sim\mathbb{P}_s(s|x_i)}[log(p_{\text{cdec}}(x_i|s_i,y_i))]$$

Results: Our approach, which maps images from the source cohort and target cohort to the same space during harmonization, demonstrates higher structural similarity index (SSIM) scores than traditional methods, indicating improved performance compared to images from the source and target cohorts.

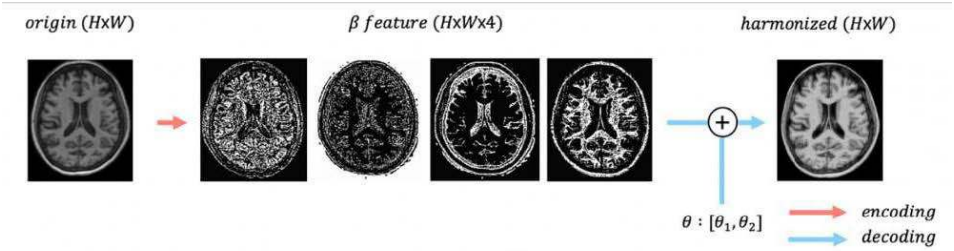

SSIM score

	Cohort source 1 , Corhot target		Cohort source 2, Cohort target	
origin	0.6732		0.7176	
Harmonized	**0.6784** (source space -> target space)	**0.6926** (source,target -> common space)	0.7149 (source space -> target space)	**0.7227** (source,target -> common space)

Conclusions: Using this methodology, we successfully validated the creation of a more robust harmonization model, maintaining individual anatomical information while accommodating contrast variations. Nevertheless, there remain several intricate facets regarding the interpretation of latent variable, which may be addressed in the future through the development of explainable encoding methods. Moreover, it is crucial to assess whether these harmonization methods indeed improve the efficacy of diverse downstream tasks.

References

1. Zuo, L., Dewey, B. E., Carass, A., Liu, Y., He, Y., Calabresi, P. A., & Prince, J. L. (2021, June). Information-based disentangled representation learning for unsupervised MR harmonization. In International Conference on Information Processing in Medical Imaging (pp. 346-359). Cham: Springer International Publishing.
2. Pan, Z., Niu, L., Zhang, J., & Zhang, L. (2021, May). Disentangled information bottleneck. In Proceedings of the AAAI Conference on Artificial Intelligence (Vol. 35, No. 10, pp. 9285-9293).
3. This work was supported by the Korea Medical Device Development Fund grant funded by the Korea government (the Ministry of Science and ICT, the Ministry of Trade, Industry and Energy, the Ministry of Health & Welfare, the Ministry of Food and Drug Safety) (Project Number: 1711196790, RS-2023-00247272)

Poster No 1687

Evaluation of Respiratory and Cardiac Peak Detection Using Interactive AFNI Tools

Joshua Dean[1], Daniel Handwerker[1], Paul Taylor[1], Peter Lauren[1], Daniel Glen[1], Peter Bandettini[1]

[1]National Institute of Mental Health, Bethesda, MD

Introduction: Physiological regressors are useful for denoising fMRI data, as the fMRI signal contains physiological (non-neuronal) sources, such as respiration and cardiac pulsations[1,2]. The efficacy of the regressors is directly related to how well these fluctuations are characterized. Multiple public and in-house programs generate physiological regressors from the data, but methods to identify and fix errors are tedious, rarely done, and never reported. AFNI programs have been developed in step with the growth of quality control (QC) of fMRI data[3]. AFNI's[4] new physio_calc.py estimates respiration volume per time (RVT)[2], respiratory, and cardiac regressors. This program includes a manual correction option and generates QC reports automatically. We evaluated the quality of physio_calc.py's results in real respiratory and cardiac traces in an effort to improve physio_calc.py's algorithms and interactive QC tools. We also highlight common corrections to benefit other researchers and to provide feedback to tool developers.

Methods: 24 healthy participants performed 2 cued-breathing tasks and 1 event-related audiovisual task during a multi-echo fMRI acquisition, typically completing 2-3 runs per task. Complete task descriptions can be found here (https://github.com/nimh-sfim/ComplexMultiEcho1) and were conducted for a more extensive multi-echo fMRI study. Respiration and cardiac traces were acquired using a respiratory belt and pulse oximeter, respectively. In total, 147 respiratory and 160 cardiac traces were analyzed. RVT and cardiac regressors were generated per run using physio_calc.py, which was also used for manual inspection and correction of each run. We report on our manual review of the traces, identifying and removing artifactual peaks and troughs, with both referred to as extrema.

Results: When reviewing the estimated respiratory trace's extrema, we removed an average of 7.56 extrema, added 5.13 extrema, and adjusted in temporal position 0.38 extrema per run (Fig. 1A). 5.95% of the total extrema required editing, but 50% of the total changes were performed in just 10 of the 147 respiratory traces. Most respiratory datasets required minimal editing, and 39 datasets required no editing (Fig. 1B). Fig. 2A shows a portion of a representative good quality respiratory trace

without artifactual extrema. Fig. 2B depicts examples of artifactual extrema encountered in respiratory traces, which required manual corrections. The respiratory trace required more manual changes than the cardiac trace. For the cardiac traces, the most prevalent issue encountered by physio_calc.py was noisy extrema, likely due to finger motion lasting for a few seconds (Fig. 2C). Across all cardiac datasets, 0.60 ± 1.14 occurrences of disruptive extrema were observed per run, with 13 out of 160 runs contributing to 50% of the changes and 108 runs requiring no changes. Because these noisy extrema prevent true peak detection, functionality is currently being added to physio_calc.py to interpolate peak times or censor noisy parts of oximetry traces. Including time taken to manually edit extrema, generation of RVT and cardiac regressors for all 307 traces were completed in 6.08 hours (1.2 min/trace), with editing contributing to less than half of that time.

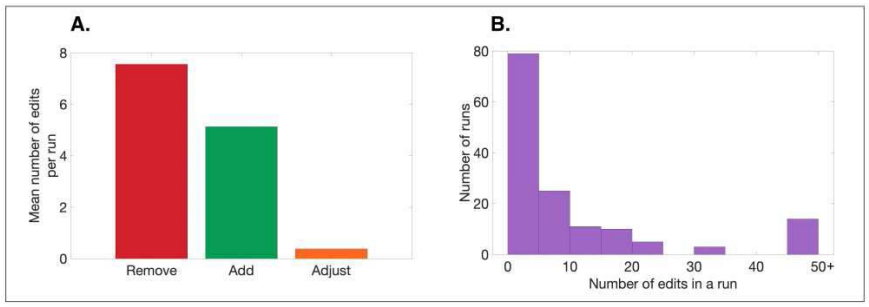

Figure 1. Edit Rates. (A) Average counts of the manual corrections made on respiration traces per run, considering which peaks and troughs were chosen to be removed (red, based on incorrectly placed peaks or troughs), added (green, based on true peaks or troughs in the trace not selected by the program), or adjusted in position (orange, based on peaks or troughs that were near true extrema in the trace but did not ideally represent their temporal position). **(B)** Number of edits chosen to be made per dataset. Rightmost bar corresponds to 50 or more edits. Manual corrections were made based on physiological signal amplitude and peak-to-peak or trough-to-trough interval distances.

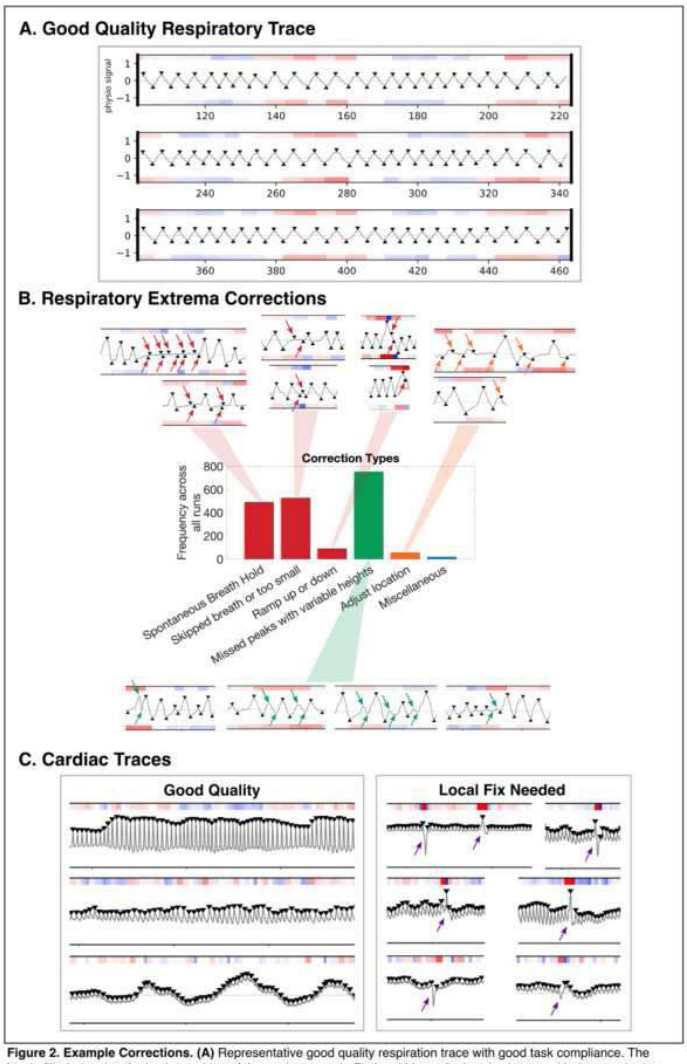

Figure 2. Example Corrections. (A) Representative good quality respiration trace with good task compliance. The black, filled triangles depict the position of the peak or trough. Red and blue color bands above and below respiration traces highlight longer and shorter peak-to-peak intervals, respectively, in relation to the median peak-to-peak or trough-to-trough interval. **(B)** Classification of manual corrections made on respiration traces. Brief representative examples of respiration traces highlight the types of changes that were made. Red arrows indicate peaks and troughs that were chosen to be removed, green arrows indicate additions, and orange arrows indicate adjustments in position. **(C)** Representative examples of good quality cardiac traces (left) and poor quality cardiac traces (right) with noisy extrema (purple arrow). The segments of poor quality cardiac traces are likely due to finger motion.

Conclusions: It is necessary to check the quality of all physiologic traces to appropriately model physiological fluctuations. Bad data, such as extrema due to finger motion with pulse oximetry, will cause problems for many algorithms and benefit from human inspection and correction. Efficient methods for interactive fixing of issues are necessary. Already, this QC evaluation has led to improvements in physio_calc.py's accuracy by identifying types and frequency of errors encountered, and the program's underlying assumptions have been improved. This work is an example of how QC tools (particularly visual ones) provide useful feedback to improve algorithms.

References

1. G. H. Glover, T.-Q. Li, and D. Ress (2000). "Image-based method for retrospective correction of physiological motion effects in fMRI: RETROICOR," Magn. Reson. Med., vol. 44, no. 1, pp. 162–167.
2. R. M. Birn, J. B. Diamond, M. A. Smith, and P. A. Bandettini (2006). "Separating respiratory-variation-related fluctuations from neuronal-activity-related fluctuations in fMRI," NeuroImage, vol. 31, no. 4, pp. 1536–1548.
3. P. A. Taylor, D. R. Glen, R. C. Reynolds, A. Basavaraj, D. Moraczewski, and J. A. Etzel (2023). "Editorial: Demonstrating quality control (QC) procedures in fMRI," Front. Neurosci., vol. 17.
4. R. W. Cox (1996). "AFNI: software for analysis and visualization of functional magnetic resonance neuroimages," Comput. Biomed. Res. Int. J., vol. 29, no. 3, pp. 162–173.

Poster No 1688

Applying Neural Style Transfer in Generative Adversarial Nets for Multi-site MRI Harmonization

Yongseon Yoo[1], Seonggyu Kim[2], Hanyeol Yang[1], Jihwan Min[1], Jong-Min Lee[1,2]

[1]Department of Artificial Intelligence, Hanyang University, Seoul, Korea, Republic of, [2]Department of Electronic Engineering, Hanyang University, Seoul, Korea, Republic of

Introduction: MRI brain scans are essential for diagnosing neurological diseases, and deep learning models trained on data from multiple sites face performance issues due to differences in MR images, known as "scanner effect." To mitigate this, "harmonization" techniques are used, with recent advances in generative models showing better performance in minimizing these variations compared to traditional methods[9,8]. We plan to apply the Style Transfer technique using GANs for the brain MRI harmonization task across different sites. In GAN models, the AdaIN (Adaptive Instance Normalization)[4] method is used for applying style[6], which changes the first order statistics to impart style. We have enhanced our generative model (GAN) to better learn the style of target MRI images by incorporating the loss function technique from Neural Style Transfer (NST)[2] that considers second order statistics[5] using the Gram Matrix. This approach allows our model to consider both first and second order statistics in the process of learning and applying style. Additionally, to preserve the anatomical structure of the original MRI images, we have incorporated a loss function that reduces the difference in feature maps between the original and generated images, in addition to the existing cycle consistency loss. Our method applies Neural Style Transfer to GANs for performing cross-site brain MRI harmonization, offering an enhanced style application approach compared to existing methods.

Methods: We propose a method to enhance GANs by adding loss functions from Neural Style Transfer[2]. We employ the StarGANv2[1,7] model for this purpose. To calculate NST's style and content loss, we integrate a pre-trained VGG19[3] into the existing GAN model structure. The style loss is computed by passing the reference image and the generated target image through VGG19, creating Gram Matrices from the feature maps obtained after the first convolution in each layer, and then minimizing the difference between these two matrices. The content loss is determined by passing the source image and generated target image through VGG19, then reducing the difference between the feature maps produced after the second convolution. Figure shows our network. The architecture is composed as follows: a generator that creates images, a mapping network that converts latent code z into a style code, a style encoder that converts an image into a style code, discriminator and Pre-trained VGG19. The training involves several loss functions: an adversarial loss (L_adv) responsible for the training of a generator and discriminator; a style reconstruction loss (L_sty) responsible for the training of a style encoder; a style diversification loss (L_ds) ensuring a style encoder produces various style codes; and a cycle consistency loss (L_cyc) that regenerates an original image from a generated image for comparison. Additionally, there is a NST style loss (L_(NST-S)) comparing the reference image's gram matrix with the generated target image's gram matrix, and a NST content loss (L_(NST-C)) comparing the reference image's feature map with the generated target image's feature map.

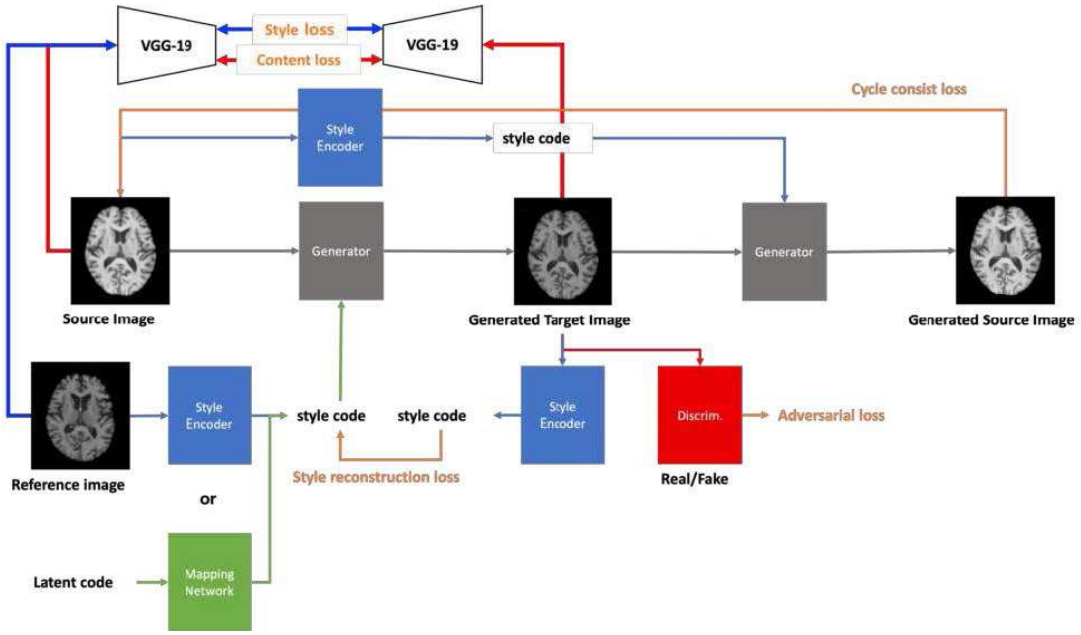

Results: Our cross-site brain MRI harmonization method was assessed using quantitative metrics, namely Peak Signal-to-Noise Ratio (PSNR) and Structural Similarity Index Map (SSIM) scores.

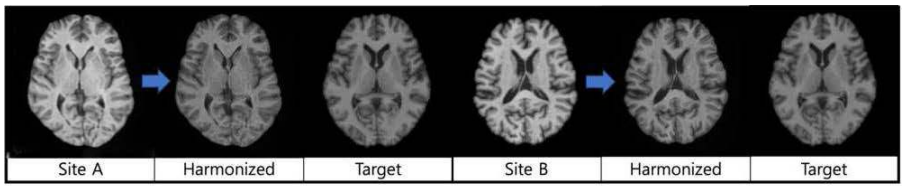

	Site A → Target	Harmonized → Target	Site B → Target	Harmonized → Target
PSNR	15.629	**21.738**	16.251	**19.402**
SSIM	0.534	**0.597**	0.524	**0.570**

Conclusions: In conclusion, our novel approach to cross-site brain MRI harmonization, integrating Neural Style Transfer with Generative Adversarial Networks, demonstrated improvements in two scores. Our methodology, incorporating both first and second-order statistics, offers a comprehensive solution for style transfer and preserving anatomical structure.

References

1. Choi, Yunjey, Youngjung Uh, Jaejun Yoo and Jung-Woo Ha. "StarGAN v2: Diverse Image Synthesis for Multiple Domains." 2020 IEEE/CVF Conference on Computer Vision and Pattern Recognition (CVPR) (2019): 8185-8194.
2. Gatys, Leon A., Alexander S. Ecker and Matthias Bethge. "Image Style Transfer Using Convolutional Neural Networks." 2016 IEEE Conference on Computer Vision and Pattern Recognition (CVPR) (2016): 2414-2423.
3. Geirhos, Robert, Patricia Rubisch, Claudio Michaelis, Matthias Bethge, Felix Wichmann and Wieland Brendel. "ImageNet-trained CNNs are biased towards texture; increasing shape bias improves accuracy and robustness." ArXiv abs/1811.12231 (2018): n. pag.
4. Huang, Xun and Serge J. Belongie. "Arbitrary Style Transfer in Real-Time with Adaptive Instance Normalization." 2017 IEEE International Conference on Computer Vision (ICCV) (2017): 1510-1519.
5. Julesz, Béla. "Visual Pattern Discrimination." IRE Trans. Inf. Theory 8 (1962): 84-92.
6. Karras, Tero, Samuli Laine and Timo Aila. "A Style-Based Generator Architecture for Generative Adversarial Networks." 2019 IEEE/CVF Conference on Computer Vision and Pattern Recognition (CVPR) (2018): 4396-4405.
7. Liu, M., et al. "Style Transfer Using Generative Adversarial Networks for Multi-site MRI Harmonization." In: Medical Image Computing and Computer Assisted Intervention – MICCAI 2021, edited by M. de Bruijne, et al., Lecture Notes in Computer Science, vol. 12903. Springer, Cham, 2021. https://doi.org/10.1007/978-3-030-87199-4_30.
8. Shinohara, Russell T., Elizabeth M. Sweeney, Jeff Goldsmith, Navid Shiee, Farrah J. Mateen, Peter A. Calabresi, Samson Jarso, Dzung L. Pham, Daniel S. Reich and Ciprian M. Crainiceanu. "Statistical normalization techniques for magnetic resonance imaging." NeuroImage : Clinical 6 (2014): 9 - 19.
9. Wrobel, Julia, M. L. Martin, Rohit Bakshi, Peter A. Calabresi, Mark Elliot, David R. Roalf, Ruben C. Gur, Raquel E. Gur, Roland G. Henry, Govind Nair, Jiwon Oh, Nico Papinutto, Daniel Pelletier, Daniel S. Reich, William D. Rooney, Theodore Daniel Satterthwaite, William Stern, Karthik Prabhakaran and Jeff Goldsmith. "Intensity warping for multisite MRI harmonization." NeuroImage 223 (2019): n. pag.

Poster No 1689

Characterizing the inter-subject variability of physiological response functions

Shiyu Wang[1], Roza Bayrak[2], Jingyuan Chen[3,4], Catie Chang[2,5]

[1]Department of Biomedical Engineering, Vanderbilt University, Nashville, TN, USA, [2]Department of Computer Science, Vanderbilt University, Nashville, TN, USA, [3]Athinoula A. Martinos Center for Biomedical Imaging, Massachusetts General Hospital, Charlestown, MA, USA, [4]Department of Radiology, Harvard Medical School, Boston, MA, USA, [5]Department of Electrical and Computer Engineering, Vanderbilt University, Nashville, TN, USA

Introduction: Low-frequency fluctuations in respiration volume and heart rate contribute to functional magnetic resonance imaging (fMRI) blood-oxygen level dependent (BOLD) signals across the brain[1]. Understanding the variability of how physiological factors associate with BOLD signals across subjects could help us better model their relationship. People have studied the inter-regional variability of the physiological response functions (PRFs) averaged across young adults[1] and the inter-subject differences of PRFs fitted to the global signal[2], but inter-subject differences in the full spatiotemporal pattern of PRFs remain to be quantified. Here, we characterized the range of whole-brain physiological response patterns that can be obtained across resting-state autonomic activities, using data that includes a variety of spontaneous breathing behaviors and heart rate levels.

Methods: We included 1500 3T resting-state fMRI scans (375 subjects, each with 4 scans) from the Human Connectome Project (HCP) under the HCP Minimal Preprocessing pipeline (TR=720ms; 1200 frames; voxel size=2mm isotropic). In addition, we detrended the signal, applied band-pass filtering (0.01–0.15Hz), downsampled by a factor of 2, extracted 497 cortical and subcortical ROIs using 4 atlases[3-6], and z-normalized the time courses. Respiratory variation (RV) was defined as the standard deviation of a 6 s window of the respiratory belt recording centered at each time point. Heart rate (HR) was 1/(mean inter-beat-interval) of the pulse oximeter signal within the same windows. RV and HR were z-normalized, detrended, each convolved with 5 pre-defined basis functions[1], and fitted to each ROI's time course to obtain PRFs. Specifically, RRFs (respiratory response functions) and CRFs (cardiac response functions) were defined by multiplying the convolved RV or HR with their fitted β. We used modularity detection to obtain whole-brain PRF patterns across scans. We concatenated the 497×2 PRFs (both RRFs and CRFs) for each scan and correlated the concatenated PRFs, forming a 1500×1500 correlational matrix. Next, we applied modularity detection on the correlational matrix using the brain connectivity toolbox[7]. The goal was to derive modules that maximize the within-cluster similarity while minimizing the across-cluster similarity[8]. A resolution parameter γ was introduced to overcome the resolution limit of modularity[9]. We tested γ values ranging from 0.9 to 1.2 with an increment of 0.01, with γ > 1 encouraging smaller clusters. The optimal γ was decided by selecting the most stable clustering results across all γ, where stability was measured by mean normalized mutual information[10].

Results: The correlational matrix among the 1500 scans' PRFs were shown in Fig 1. The optimal γ value was 1.05, giving 11 clusters in total. There were 3 large clusters, 3 medium-sized clusters and 5 small clusters. Among the 375 subjects, at least 3 out of 4 PRFs from 4 scans were assigned the same cluster for 252 subjects, with only 12 subjects for whom all 4 PRFs were assigned to different clusters. Fig 2 shows the centroids of the whole-brain RRFs from 2 of the biggest clusters. The major difference between them was that cluster #8 had an initial dip before an increase in the RRFs, whereas cluster #10 peaked immediately after the physiological onset, which was more consistent with the previous population-level spatiotemporal dynamics of RRFs[1].

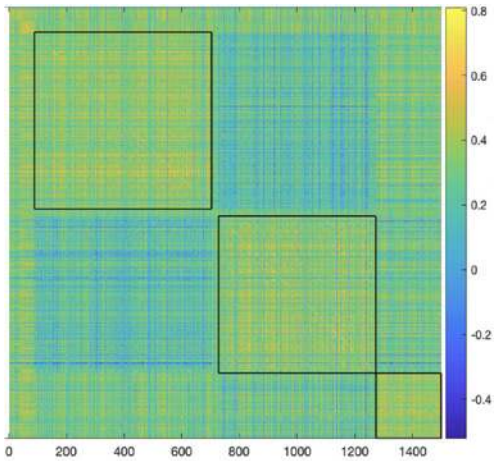

Figure 1. Correlational matrix among 375*4 scans (correlation was calculated between the PRFs concatenated among all ROIs). The matrix is ordered by cluster index and the 3 large clusters are marked.

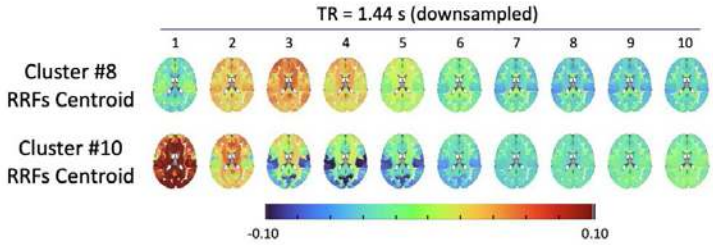

Figure 2. The centroids of the whole-brain RRFs from 2 of the biggest clusters. Cluster #8 had an initial dip and then response started to go up, whereas the cluster #10 peaked directly after the RV onset.

Conclusions: We observed several whole-brain PRF patterns that were shared across groups of subjects. Further, the cluster assignment of different scans within a given subject was relatively consistent. The observed inter-subject differences may arise, to some extent, from differences in subjects' breathing patterns during the scans. Our future steps include comparing PRFs across scans with matched breathing patterns, modeling respiratory and cardiac effects separately, and examining different physiological basis sets.

References

1. Chen, J. E., Lewis, L. D., Chang, C., Tian, Q., Fultz, N. E., Ohringer, N. A., Rosen, B. R., & Polimeni, J. R. (2020). Resting-state "physiological networks." NeuroImage, 213, 116707.
2. Kassinopoulos, M., & Mitsis, G. D. (2019). Identification of physiological response functions to correct for fluctuations in resting-state fMRI related to heart rate and respiration. NeuroImage, 202, 116150.
3. Schaefer, A., Kong, R., Gordon, E. M., Laumann, T. O., Zuo, X.-N., Holmes, A. J., Eickhoff, S. B., & Yeo, B. T. T. (2018). Local-Global Parcellation of the Human Cerebral Cortex from Intrinsic Functional Connectivity MRI. Cerebral Cortex, 28(9), 3095–3114.
4. Tian, Y., Margulies, D. S., Breakspear, M., & Zalesky, A. (2020). Topographic organization of the human subcortex unveiled with functional connectivity gradients. Nature Neuroscience, 23(11), 1421–1432.
5. Hansen, C. B., Yang, Q., Lyu, I., Rheault, F., Kerley, C., Chandio, B. Q., Fadnavis, S., Williams, O., Shafer, A. T., Resnick, S. M., Zald, D. H., Cutting, L. E., Taylor, W. D., Boyd, B., Garyfallidis, E., Anderson, A. W., Descoteaux, M., Landman, B. A., & Schilling, K. G. (2021). Pandora: 4-D White Matter Bundle Population-Based Atlases Derived from Diffusion MRI Fiber Tractography. Neuroinformatics, 19(3), 447–460.
6. Edlow, B. L., Takahashi, E., Wu, O., Benner, T., Dai, G., Bu, L., Grant, P. E., Greer, D. M., Greenberg, S. M., Kinney, H. C., & Folkerth, R. D. (2012). Neuroanatomic Connectivity of the Human Ascending Arousal System Critical to Consciousness and Its Disorders. Journal of Neuropathology & Experimental Neurology, 71(6), 531–546.
7. Rubinov, M., & Sporns, O. (2010). Complex network measures of brain connectivity: Uses and interpretations. NeuroImage, 52(3), 1059–1069.
8. Sporns, O., & Betzel, R. F. (2016). Modular Brain Networks. Annual Review of Psychology, 67(1), 613–640.
9. Fortunato, S., & Barthélemy, M. (2007). Resolution limit in community detection. Proceedings of the National Academy of Sciences, 104(1), 36–41.
10. Bassett, D. S., Porter, M. A., Wymbs, N. F., Grafton, S. T., Carlson, J. M., & Mucha, P. J. (2013). Robust detection of dynamic community structure in networks. Chaos: An Interdisciplinary Journal of Nonlinear Science, 23(1).

Poster No 1690

New in AFNI's physio_calc.py (for FMRI physio regressors): QC images, reports and interactive mode

Peter Lauren[1], Daniel Glen[2], Richard Reynolds[1], Joshua Dean[1], Daniel Handwerker[3], Paul Taylor[1]

[1]National Institute of Mental Health, Bethesda, MD, [2]NIMH, Bethesda, MD, [3]Section on Functional Imaging Methods, NIMH, Bethesda, MD

Introduction: FMRI's BOLD signal includes both neuronal and non-neuronal contributions. Breathing and heart rate both have strong influences on blood oxygenation levels, and these sources are unlikely to be turned off during any in vivo scan. Therefore, it can be helpful to include measures of these biological phenomena within an FMRI model to more fully account for underlying signal contributions. The AFNI software package[1] has recently developed the physio_calc.py program[2] to take physiological time series (such as breathing and heart rate measures) acquired during a scan session and create regressors for single subject analysis, such as within afni_proc.py or other pipeline tools. The program estimates both slicewise RETROICOR regressors[3], as well as respiration volume per time (RVT)[4]. These estimates depend on several time series analysis steps, such as peak and trough estimation across the curve, as well as local phase and amplitude. We describe new features in physio_calc.py that allow users to: reduce the effects of outliers and bad values in the time series; efficiently check and interactively correct initial estimates; see useful quality control (QC) images; and have quantitative reviews to help validate and check the underlying calculations.

Methods: The physio_calc.py program is written in Python and distributed within AFNI's afnipy module. It contains several automatic checks for corrupted data within input time series, such as NaN and missing values. Outlier checks, as well as replacement of potential "bad" values such as zeros that might be recorded erroneously, can also be enabled. A multistep algorithm is used to estimate peak and trough locations, including bandpassing, filtering and local refinement. A set of slicewise regressors for an accompanying FMRI time series is calculated, as well as RVT measures derived from the phases of the respiratory peaks and troughs.

Results: Fig 1A shows an example of the QC output for respiratory time series processing, where estimated peaks and troughs (triangles) are shown with the input physio time series. The time interval over which the FMRI dataset was collected has a white background, and the remaining regions are helpful as boundary conditions. The top of each subplot contains color-coded rectangles for each interpeak interval: near-median values are white, while shorter ones are bluer and longer ones are redder. These can highlight either physio-based patterns within the time series, or potential QC issues (e.g., an erroneous or missing peak). The same appears at the bottom of each panel when troughs have been estimated. The user can add a "do_interact" option to have an interactive window open, to easily add, remove or shift points. All changes are saved immediately. Fig 1B shows part of the review output text for each physio time series. This can easily be combined using AFNI into a spreadsheet, and queried to find outliers. This quantitative QC is helpful in summarizing group properties and/or finding data issues. Fig 2 shows QC images of the computed physio regressors, for slicewise RETROICOR estimates and volume-wise RVT regressors. These regressors can be added directly into an FMRI processing pipeline stream, e.g., using afni_proc.py.

A) QC plot of estimated peaks and troughs for respiratory time series

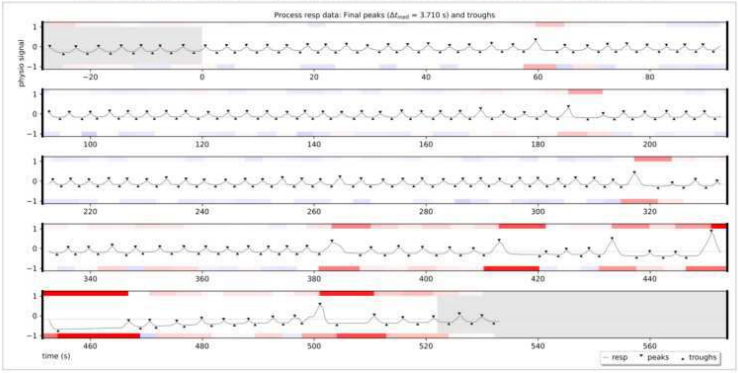

B) Part of final review summary text file, which can be compared across subjects

```
read_in sampling freq              : 2000.0
prefilt mode                       : median
prefilt window, sec                : 0.25
is user interact on?               : True
num peaks changed                  : 0
num troughs changed                : 0

ts_orig sampling freq              : 50.0
ts_orig sampling rate              : 0.02
ts_orig num points                 : 28023
ts_orig start time                 : -27.392
ts_orig end time                   : 533.068
ts_orig duration                   : 560.46

dset tr                            : 1.500000
dset start time                    : 0.000000
dset end time                      : 522.000000
dset duration                      : 522.000000

peak num total                     : 139
peak ival min max                  : 3.100000 15.880000
peak ival mean std                 : 4.037826 1.377283
peak ival q25 q50 q75              : 3.480000 3.710000 4.060000

peak num over dset                 : 130
peak ival over dset min max        : 3.100000 15.880000
peak ival over dset mean std       : 4.036899 1.420773
peak ival over dset q25 q50 q75    : 3.480000 3.660000 4.040000
```

Figure 1. Qualitative and quantitative QC output from AFNI's physio_calc.py. A) A QC image of estimated peaks and troughs (triangles) for the respiratory time series. The time series interval overlapping the FMRI acquisition has a white background. Each interpeak/intertrough interval ("ival") is color-coded by a box at the top/bottom of each subplot: intervals close to the median are white, shorter ones are bluer and longer ones are redder. The interactive peak/trough window looks the same as this window, to help guide the researcher to check particular features. B) A text table of dataset properties is output. This can be combined into a single spreadsheet across all subjects and compared/queried using AFNI's gen_ss_review_table.py. This can help detect outlier subjects, as well as help summarize properties across the group.

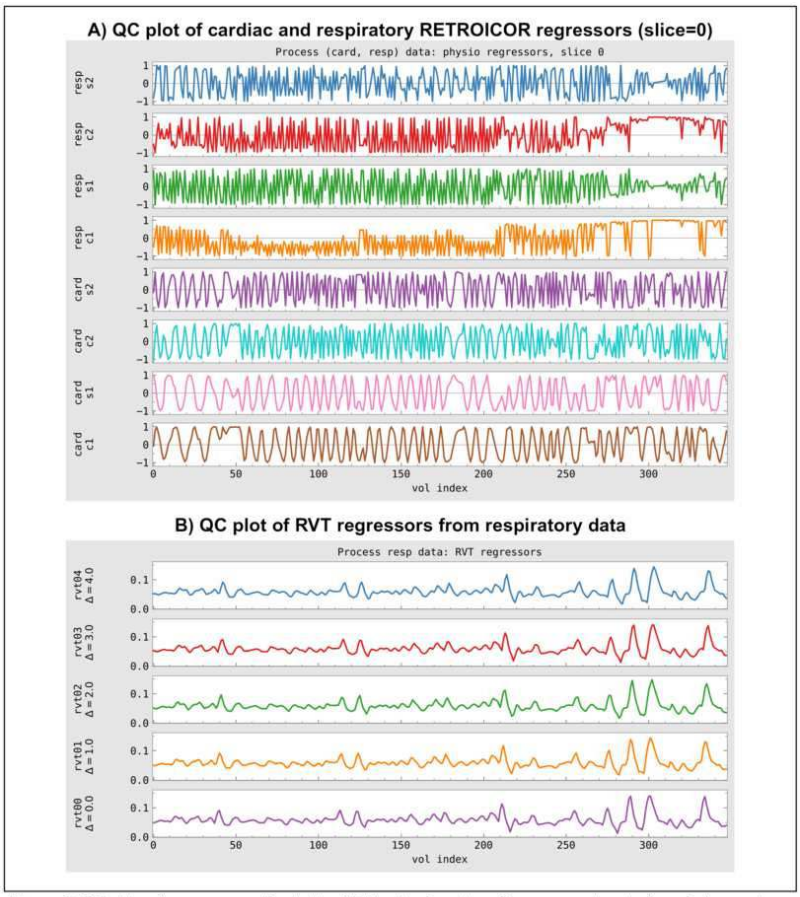

Figure 2. QC plots of regressors estimated by AFNI's physio_calc.py for an example set of respiratory and cardiac time series. A) Slicewise regressors are estimated for each physio time series, following the RETROICOR approach which contain sine- and cosine-derived terms related to phases; in the QC image, only the regressors at slice=0 are shown. B) Volume-wise regressors of respiration volume per time (RVT) are estimated at different time shifts (here, the default unshifted, and then shifts of 1, 2, 3 and 4s).

Conclusions: Physio regressors can play an important part in FMRI processing, but they rely heavily on how they are processed. To date, little formal attention has been paid to the QC of these physio inputs and their computed regressors. They are highly susceptible to noise and distortion (e.g., due to pulse oximeter finger movement), and must be checked for accuracy. AFNI's physio_calc.py contains several features to provide efficient QC images and quantitative reporting. It also has a simple interface for fixing any features within the estimates. Careful QC of all processing steps (both visual and quantitative) is key to all FMRI processing and sub-step processing[5], so these features should be considered vital in all analyses.

References

1. Cox RW (1996). AFNI: software for analysis and visualization of functional magnetic resonance neuroimages. Comput Biomed Res 29(3):162-173.
2. Lauren PD, Glen DR, Reynolds RC, Taylor PA (2023). physio_calc.py: New program to model cardiac & respiratory contributions to BOLD signal in AFNI. Presented at the 29th Annual Meeting of the Organization for Human Brain Mapping.
3. Glover GH, Li T-Q and Ress D (2000). Image-Based Method for Retrospective Correction of Physiological Motion Effects in fMRI: RETROICOR. Magnetic Resonance in Medicine 44:162-167.
4. Birn RM, Diamond JB, Smith MA, Bandettini PA (2006). Separating respiratory-variation-related fluctuations from neuronal-activity-related fluctuations in fMRI. Neuroimage 31(4):1536-48.
5. Taylor PA, Glen DR, Reynolds RC, Basavaraj A, Moraczewski D, Etzel JA. Editorial: Demonstrating quality control (QC) procedures in fMRI. Front Neurosci. 2023 May 31;17:1205928.

Poster No 1691

Improving skullstripping and nonlinear warping in AFNI: sswarper2

Paul Taylor[1], Richard Reynolds[1], Daniel Glen[2]

[1]National Institute of Mental Health, Bethesda, MD, [2]NIMH, Bethesda, MD

Introduction: Nonlinear alignment (or registration, or spatial "normalization") is a common processing step in FMRI analysis. While it is computationally expensive and can require on the order of hours to complete, it allows for individual datasets to be

correspond across a common space. As more similar structures are brought into closer alignment, the accuracy and statistical power of the final results should increase. However, no alignment algorithm is perfect. Mathematically, estimated "warps" between the source and reference datasets are generally constrained to be smooth, invertible and diffeomorphic. But even among healthy populations, anatomical variability exists (e.g., numbers of sulci/gyri can differ locally), and warps are typically unable to overcome such differences. Moreover, datasets can have distortion, low contrast, etc., possibly decreasing quality of alignment. As a result, algorithms can get stuck in local minima or produce distortions or other inaccuracies. Here we describe "sswarper2," a new nonlinear alignment program in AFNI[1] that both skullstrips (SS) a T1w volume and aligns (warps) it to a reference dataset. We show its improvements to predecessor @SSwarper, which had similar dual roles.

Methods: The primary nonlinear alignment program in AFNI is 3dQwarp[2]. @SSwarper wraps around 3dQwarp and also includes removal of nonbrain material ("skullstripping"), since warping and skullstripping are each complicated processes that improve when the other is done well. If the skull+nonbrain region of a subject's anatomical dataset has been exactly removed, alignment to a template is much easier; or if a dataset has been well aligned to a template, one can use the latter to "punch away" the skull of the former. @SSwarper makes use of this by iterating between these steps with increasing accuracy, improving each. During alignment, it uses a local Pearson cost to drive early stages of alignment[3]. It also saves snapshots of initial and final stages of overlap, to provide quality control (QC) checks. Similarly, sswarper2 iterates between (local Pearson) alignment to a template and skullstripping, but it does so in smaller steps, more finely interleaved with skull removal, increasing stability. Additionally, sswarper2 saves a detailed history of snapshots of intermediate processing steps, to facilitate any troubleshooting. To compare overall robustness of the programs, we tested each on a set of 169 anatomical T1w datasets from 8 different sites from 3 continents, with a wide subject age range (8-70 yrs)[4], aligning to the MNI 2009c asymmetric template[5]. We compare individual and group-wide results both qualitatively and quantitatively.

Results: In many cases, @SSwarper and sswarper2 yield quite similar results, providing accurate skullstripping and nonlinear registration to the MNI template. However, in a small number of cases, @SSwarper had inaccurate final skullstripping, resulting in localized misalignment. Fig 1 shows two examples of datasets in which the warped subject anatomy extends 2-3 mm outside the brain locally. In each case, sswarper2 provides more accurate alignment and skullstripping. Fig 2A shows the mean of all warped datasets (each had been unifized to similar brightness values per tissue class) for each program. There is overall good alignment to the template in both cases. Fig 2B shows the voxelwise standard deviation across the group for each program. Again, overall patterns are similar, but sswarper2 results are uniformly more tightly aligned within the brain volume and at major tissue boundaries, while the effect of the small fraction of stretched @SSwarper results can be seen around the brain edge.

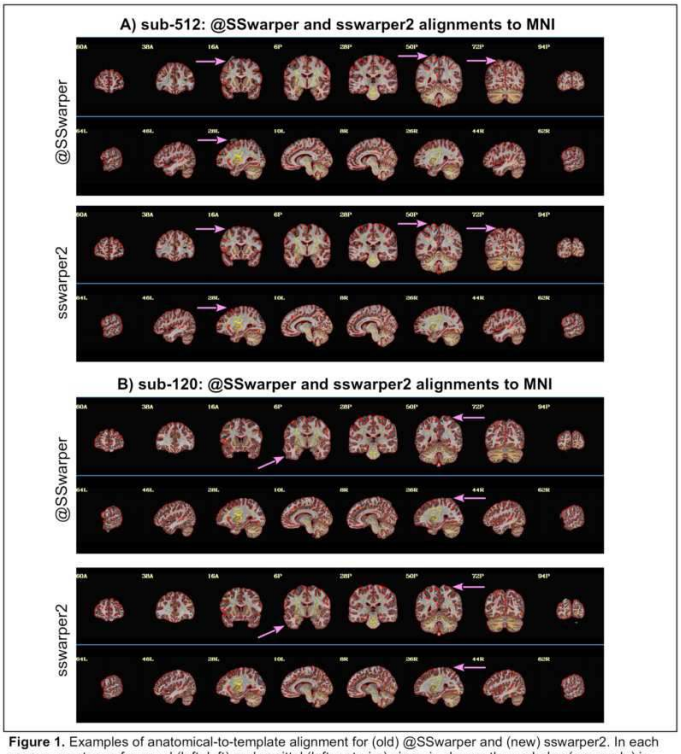

Figure 1. Examples of anatomical-to-template alignment for (old) @SSwarper and (new) sswarper2. In each case, a montage of coronal (left=left) and sagittal (left=anterior) views is shown: the underlay (grayscale) is the warped anatomical volume, and the overlay shows the edges of the MNI template dataset. Each panel shows the results of warping from @SSwarper (top) and sswarper2, for different subjects. In each case, pink arrows highlight local misalignments from @SSwarper, while the same arrows show how sswarper2 provides correct alignments in each case. While @SSwarper typically produces good alignment, outlier misalignments such as shown occur in a small fraction of cases. The sswarper2 program is much more robust against these kinds of errors.

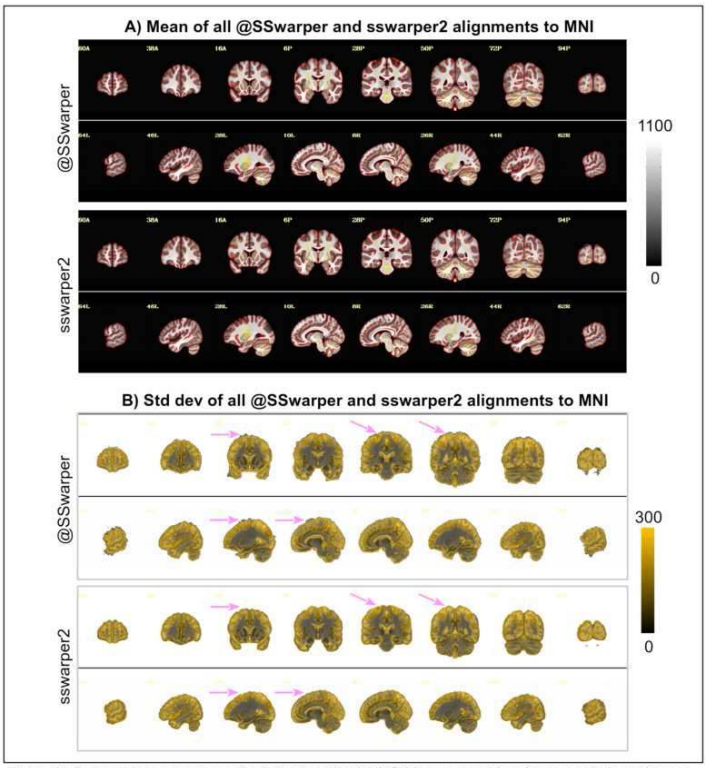

Figure 2. Group-wide summary results of alignment for (old) @SSwarper and (new) sswarper2. In each case, a montage of coronal (left=left) and sagittal (left=anterior) views is shown. A) The mean of all warped anatomical datasets is shown for both @SSwarper (top) and sswarper2 (bottom); the edges of the reference MNI template are overlaid for structural comparison. In each case, the mean shows a fairly uniformly accurate alignment to the template. B) The standard deviation of all warped anatomical datasets (amber) for both @SSwarper (top) and sswarper2 (bottom). For @SSwarper, pink arrows highlight some nonzero values outside the brain, due to the local misalignment of a small fraction of subjects (see Fig 1); the same show how sswarper2 has avoided such issues. Within the brain, results are similar, with sswarper2 having slightly lower values in several regions of gyral gray matter.

Conclusions: While both programs typically produce warped anatomicals that closely match the template structure, the new sswarper2 provides more robust alignment across a broader range of datasets. The sswarper2 results can also be integrated directly into afni_proc.py and other FMRI pipeline tools.

References

1. Cox RW (1996). AFNI: software for analysis and visualization of functional magnetic resonance neuroimages. Comput Biomed Res 29(3):162-173. doi:10.1006/cbmr.1996.0014
2. Cox RW, Glen DR (2013). Nonlinear warping in AFNI. Presented at the 19th Annual Meeting of the Organization for Human Brain Mapping.
3. Saad ZS, Glen DR, Chen G, Beauchamp MS, Desai R, Cox RW (2009). A new method for improving functional-to-structural MRI alignment using local Pearson correlation. Neuroimage 44 839–848.
4. Taylor PA, Glen DR, Reynolds RC, Basavaraj A, Moraczewski D, Etzel JA (2023). Editorial: Demonstrating quality control (QC) procedures in fMRI. Front. Neurosci. 17:1205928.
5. Fonov V, Evans AC, Botteron K, Almli CR, McKinstry RC, Collins DL, et al. (2011). Unbiased average age-appropriate atlases for pediatric studies. Neuroimage 54, 313–327.

Poster No 1692

SDCFlows: convergent formalization of MRI field mappings for reliable distortion correction

Oscar Esteban[1], Matthew Cieslak[2], Mathias Goncalves[3], Eilidh MacNicol[4], Russell Poldrack[5], Christopher Markiewicz[3]

[1]Lausanne University Hospital and University of Lausanne, Lausanne, VD, [2]UPenn, Philadelphia, PA, [3]Stanford University, Stanford, CA, [4]Neuroimaging, Institute of Psychiatry, Psychology and Neuroscience, King's College London, London, United Kingdom, [5]Stanford University, Palo Alto, CA

Introduction: Echo-planar imaging (EPI) allows very fast acquisition of whole-brain data enabling standard functional and diffusion MRI. However, small deviations in parts-per-million from the nominal B_0 caused by steps in magnetic susceptibility at tissue interfaces introduce misplacements in the registered location of voxels of up to centimeters. Geometrical distortions of the imaged specimen become apparent along the phase-encoding direction. In humans, geometrical distortions are prominent near the ventromedial prefrontal cortex and temporal lobes due to the proximity of air in the nasal sinuses and

ear canals. The expected voxel shifts can be estimated by mapping B_0 deviations (so-called fieldmaps). Abundant literature has supported the consolidation of a few families of estimation: using ad-hoc B_0 inhomogeneity mapping with specific MRI schemes[1] (most often called "phase-difference"), measuring the point spread function[2], acquiring two or more short EPI schemes with varying phase-encoding polarity and/or direction[3] (called "pepolar" in the following), and by image registration to an undistorted reference such as T_2-weighted image[4] (often referred to as "fieldmapless"). Here, we introduce a BIDS-App to execute SDCFlows (Susceptibility Distortion Correction Flows), an open-source utility that leverages BIDS[5] and several existing software tools to provide standardized, best-effort B_0 inhomogeneity map estimates and corresponding distortion correction.

Methods: Data. The development of the core libraries employed several datasets openly available at OpenNeuro[6]. Bugfixes and debugging were mostly based on minimally viable datasets provided by users of fMRIPrep[7], which is the principal mode of distribution and deployment of SDCFlows. To evaluate the new BIDS-App, we employed the Human Connectome PHantom (HCPh) dataset[8]. Implementation. The new BIDS-App implementation is based on the NiPreps framework, akin to fMRIPrep. Therefore, the user interface follows the corresponding specifications and requires the input dataset to be BIDS-compliant. At the output, preprocessed fieldmaps ready to correct EPI volumes are generated under BIDS-Derivatives conventions. The software first processes the input with PyBIDS[9], and identifies the estimable field maps leveraging the BIDS metadata. These estimable maps are represented by FieldmapEstimation objects. Then, the get_workflow() member is called on each object, which generates the corresponding processing and estimation workflow depending on the type of fieldmap. All the workflows are then loaded into a NiPype[10] computational graph, which can be executed in parallel and distributable through a number of platforms.

Results: Single representation model for all estimation methodologies. SDCFlows represents all map estimations with a B-Spline basis, ensuring the smoothness of the solution, easier to manipulate (e.g., map onto a target image), and a compressed representation with fewer parameters than the corresponding dense field. We generated 131 fieldmap estimations corresponding to 50 phase-difference and 81 pepolar estimators, amounting to all the available estimable fieldmaps in the dataset. By sharing a common basis, different estimation strategies can be compared and combined. The single representation model also enabled the implementation of a B0FieldTransform object that permits head-motion correction and susceptibility distortion correction with a single interpolation step (Fig. 1). A BIDS-Apps interface and the NiPreps transparency principles. SDCFlows can easily be integrated into the neuroimaging pipeline thanks to its BIDS-Apps compliance and generates comprehensive diagnostic figures (Fig. 2) for their aggregation within other tools such as fMRIPrep.

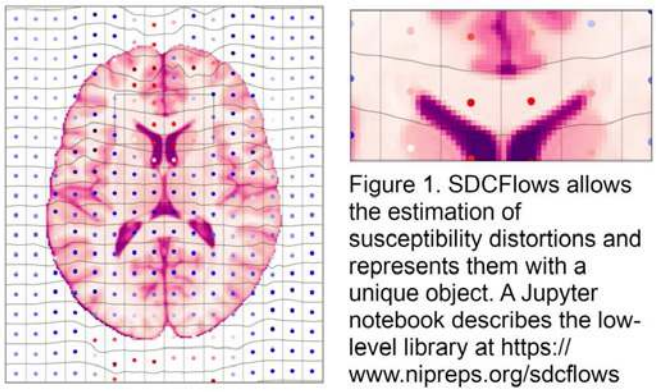

Figure 1. SDCFlows allows the estimation of susceptibility distortions and represents them with a unique object. A Jupyter notebook describes the low-level library at https://www.nipreps.org/sdcflows

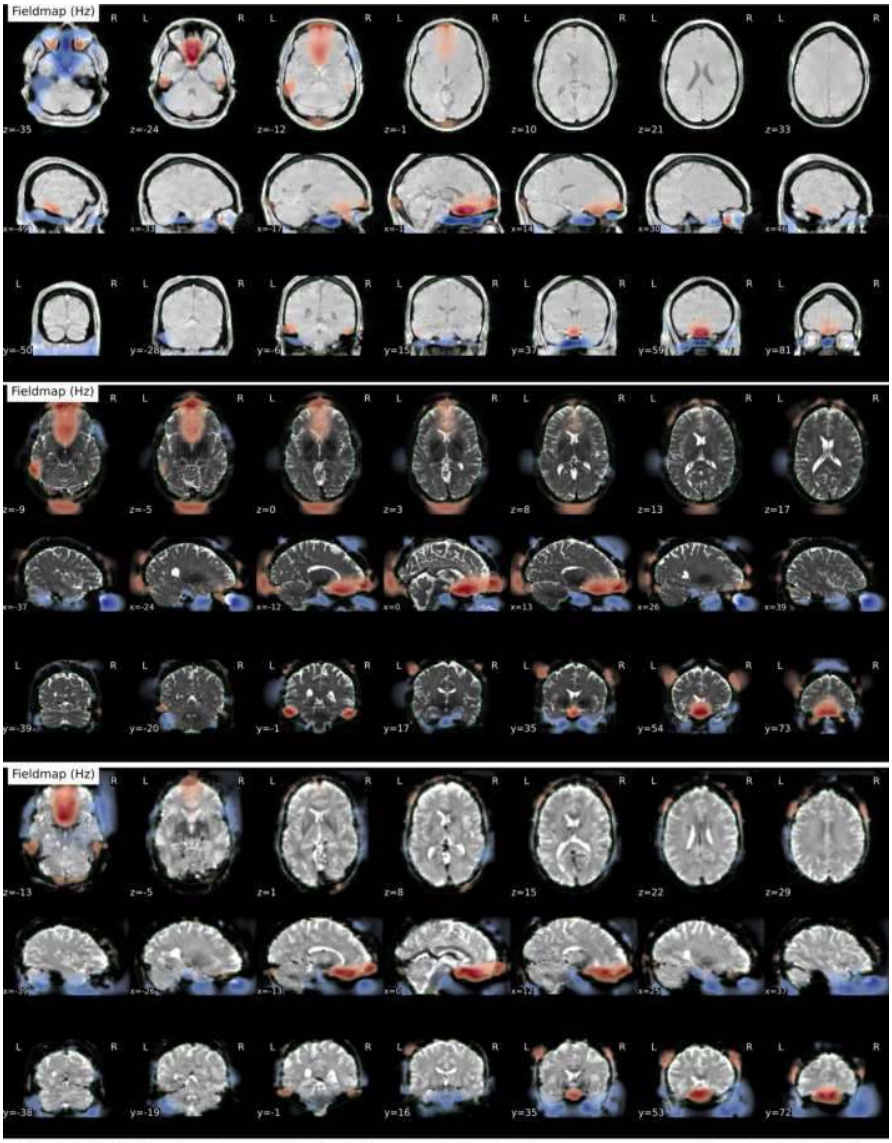

Figure 2. SDCFlows generates a reportlet showing the estimated fieldmap in Hz. The three panels show the mosaic of a fieldmap estimation of session 007 of the HCPh dataset. First mosaic corresponds to a "phase-difference" approach, second is a "pepolar" fitting with three low-b (b = 0 s/mm2) phase-encoding directions (left-right, LR; RL; and anterior-posterior, AP), third is a "pepolar" fitting with four single-band BOLD phase-encoding directions (LR, RL, AP, PA). The three estimates showcase similar qualitative results across all sessions.

Conclusions: The standardization of distortion estimation and correction offered by SDCFlows will equip researchers with a reliable, off-the-shelf solution to solidify their neuroimaging workflow.

References

1. Hutton, C. et al. Image Distortion Correction in fMRI: A Quantitative Evaluation. NeuroImage 16, 217–240 (2002).
2. Zaitsev, M., Hennig, J. & Speck, O. Point spread function mapping with parallel imaging techniques and high acceleration factors: Fast, robust, and flexible method for echo-planar imaging distortion correction. Magn. Reson. Med. 52, 1156–1166 (2004).
3. Chiou, J. Y. & Nalcioglu, O. A simple method to correct off-resonance related distortion in echo planar imaging. in Proc. Intl. Soc. Mag. Reson. Med. vol. 8 1711 (2000).
4. Studholme, C., Constable, R. T. & Duncan, J. S. Accurate alignment of functional EPI data to anatomical MRI using a physics-based distortion model. IEEE Trans. Med. Imaging 19, 1115–1127 (2000).
5. Poldrack, R. A. et al. The Past, Present, and Future of the Brain Imaging Data Structure (BIDS). Preprint at https://doi.org/10.48550/arXiv.2309.05768 (2023).
6. Markiewicz, C. J. et al. The OpenNeuro resource for sharing of neuroscience data. eLife 10, e71774 (2021).
7. Esteban, O. et al. fMRIPrep: a robust preprocessing pipeline for functional MRI. Nat. Methods 16, 111–116 (2019).
8. Provins, C. et al. Reliability characterization of MRI measurements for analyses of brain networks on a human phantom. Nat. Methods (Stage 1 accepted-in-principle), (2023).
9. Yarkoni, T. et al. PyBIDS: Python tools for BIDS datasets. J. Open Source Softw. 4, 1294 (2019).
10. Gorgolewski, K. et al. Nipype: a flexible, lightweight and extensible neuroimaging data processing framework in python. Front. Neuroinformatics 5, 13 (2011).

Poster No 1693

Background R2* correction for χ-separation (chi-separation)

Kyeongseon Min[1], Jongho Lee[1]

[1]*Seoul National University, Seoul, Seoul*

Introduction: χ-separation (chi-separation) is an advanced quantitative susceptibility mapping (QSM) technique that jointly utilizes tissue phase and transverse relaxation rate (R2* and R2) maps to separate paramagnetic (χpara) and diamagnetic susceptibility (χdia) contributions in QSM (Shin, 2021). Inaccurate tissue field or R2* (or R2) maps may result in erroneous χpara and χdia maps. When creating a tissue field map, background field from susceptibility difference (e.g. air-tissue interface) and incomplete shimming is removed by applying background field removal techniques (Liu, 2011) to the phase of gradient-echo data. Background field variation also causes intravoxel dephasing, resulting in magnitude modulation of gradient-echo data and overestimation of R2* (Ordidge, 1994). Therefore, this additional R2*, named as background R2*, should be corrected when conducting χ-separation to prevent potential bias in χpara and χdia maps. In this study, we demonstrated that background R2* correction can reduce artifactual overestimation of χpara and χdia. Moreover, we examined the effect of background R2* correction under varying k-space filtering, confirming that background R2* correction leads to consistent χ-separation maps across different k-space filtering.

Methods: A healthy volunteer was scanned using Siemens 3 T MRI with a 3D multi-echo gradient-echo sequence and a 2D multi-echo spin-echo sequence. The effect of intravoxel field gradient on 3D multi-echo gradient-echo data was modelled using voxel spread function method (Yablonskiy, 2013). In this model, the modulated signal from a voxel by linearly varying intravoxel field can be expressed as multiplication with a shifted sinc function in k-space, where the shift is proportional to the intravoxel field gradient. The voxel spread function can be calculated by inverse Fourier transform of this shifted sinc function. When k-space data is filtered with a windowing function, the effect of windowing can be accommodated by multiplying the shifted sinc function with the windowing function. The schematic flowchart of background R2* correction for χ-separation is presented in Fig. 1. First, the field gradient was estimated from the numerical gradient of combined phase of multi-echo gradient-echo data. The voxel spread function was calculated from the field gradient map. Using this voxel spread function, the magnitude modulation by the field gradient was estimated, and utilized to generate a background-corrected R2* map. For χ-separation, a tissue field map was prepared by removing background field from the combine phase map (Wu, 2012). The R2 map were derived from the multi-echo spin-echo data. Finally, χpara and χdia maps were acquired with χ-sepnet (Kim, 2022) utilizing the corrected or uncorrected R2*, R2, and tissue field maps as inputs.

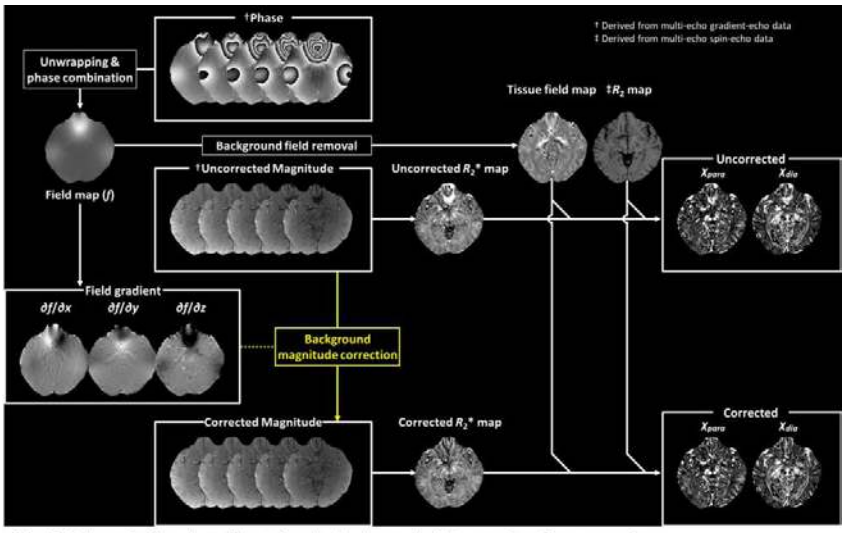

Fig. 1. Schematic flowchart illustrating the background R_2* correction for χ-separation.

Results: In Fig. 2A, the effect of background R2* correction on χpara and χdia maps were examined at the regions close to air cavities. While uncorrected χpara and χdia maps exhibited overestimation at regions marked with cyan lines, corrected χpara and χdia values were in normal ranges, as confirmed by the χpara, χdia, and R2* profile, which was plotted along cyan lines. Overall, the χpara and χdia bias from background R2* at regions close to nasal, frontal, and tympanic cavities were properly reduced in the corrected χpara and χdia maps. In Fig. 2B, the same k-space data was reconstructed after Tukey-windowing with different low-pass level. By applying background R2* correction, the overestimation in χpara and χdia was corrected, providing more consistent χpara and χdia maps across different low-pass levels.

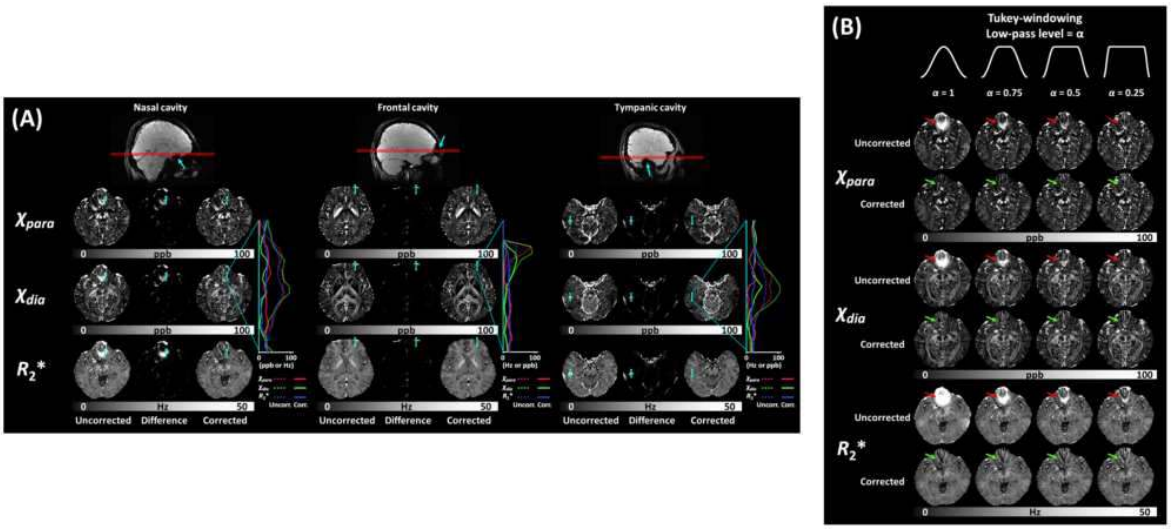

Fig. 2. (**A**) The effect of background R_2* correction on χ_{para} and χ_{dia} maps at regions close to air cavities (cyan arrows). The χ_{para} (red), χ_{dia} (green), and R_2* (blue) profiles along cyan lines are plotted on the right of each set of imaging slices, demonstrating successful correction of overestimated χ_{para} and χ_{dia}. (**B**) Background R_2* and overestimation in χ_{para} and χ_{dia} (red arrows) at different levels of low-pass filtering in *k*-space. The background R_2* intensifies when effective voxel size increases by higher level of low-pass filtering. The overestimation χ_{para} and χ_{dia} successfully removed by background R_2* correction (red arrows), providing consistent χ_{para} and χ_{dia} maps across different low-pass levels.

Conclusions: Background R2* correction for χ-separation successfully reduced overestimation in χpara and χdia maps. As MRI vendors provide reconstructed images at different low-pass levels, the background R2* differs vendor-to-vendor. Therefore, applying background R2* correction is crucial for consistent χ-separation maps across venders.

References

1. Kim, M. (2022). "Chi-sepnet: Susceptibility source separation using deep neural network." Proceedings of International Society of Magnetic Resonance in Medicine 30: 2464.
2. Liu, T. (2011). "A novel background field removal method for MRI using projection onto dipole fields (PDF)." NMR in Biomedicine 24: 1129-1136.
3. Ordidge, R.J. (1994). "Assessment of relative brain iron concentrations using T2-weighted and T2*-weighted MRI at 3 tesla." Magnetic Resonance in Medicine 32: 335-341.
4. Schweser, F. (2011). "Quantitative imaging of intrinsic magnetic tissue properties using MRI signal phase: An approach to in vivo brain iron metabolism?" NeuroImage 54: 2789-2807.
5. Shin, H.-G. (2021). "χ-separation: Magnetic susceptibility source separation toward iron and myelin mapping in the brain." NeuroImage 240: 118371.
6. Wu, B. (2012). "Whole brain susceptibility mapping using compressed sensing." Magnetic Resonance in Medicine 67: 137-147.
7. Yablonskiy, D.A. (2013). "Voxel Spread Function Method for Correction of Magnetic Field Inhomogeneity Effects in Quantitative Gradient-Echo-Based MRI." Magnetic Resonance in Medicine 70(5): 1283-1292.

Poster No 1694

Localizing Hallucination-Driven Individual Differences with Eigenvector Centrality

Theresa Marschall[1], Remco Renken[1], Frans Cornelissen[1], Teus van Laar[1]

[1]*University Medical Center Groningen, Groningen, Groningen*

Introduction: In neurological research comparing individual cases with publicly available data can pose significant challenges, especially when scanning parameters vary. We introduce a method to detect individual differences in brain connectivity, employing rank scores on eigenvector centrality to overcome these challenges. To address discrepancies in scanning parameters across datasets, we employed a ranking system and interquartile range (IQR) normalization. Our focus on rank differences, rather than raw eigenvector centrality coefficients, allows for a more widely applicable comparison between individual cases and extensive sets of norm data.

Methods: We applied this method to neuroimaging data from a male Parkinson's Disease (PD), with frequent visual hallucinations (VH) comparing it with two distinct datasets. The patient held a button box (for a subsequent task) which was unique to these data. All data consisted of a T1-weighted reference scan and a 10-minute resting-state fMRI. The patient's data were collected using a Siemens 3T scanner implementing online motion correction. Dataset 1, comprising 9 PD individuals without VH (3 females), was collected on the same scanner with a comparable protocol but without online motion correction. Dataset 2 included 20 male PD patients without VH, sourced from the PPMI database (Brumm et al., 2023) and collected using a different protocol and scanner. All data underwent preprocessing with fMRIPrep 23.0.1 (Esteban et al., 2019), high-pass

filtering and confound regression (WM and CSF), followed by eigenvector centrality computation for 232 ROIs (Power et al. 2011) using the fECM toolbox (Wink et al., 2012). The eigenvector centrality coefficients were sorted and differences in rank between the patient and each subject, i.e. delta rank differences, were calculated. For each dataset we normalized the delta rank differences by dividing the median per ROI by its IQR.

Results: The normalized delta rank differences between each dataset and the patient can be seen in Figure 1 and a linear regression analysis between the normalized delta ranks revealed a significant correlation ($p < 0.01$), with a regression coefficient of 0.656. This indicates a strong linear association between the changes in centrality ranking of the patient compared to either dataset.

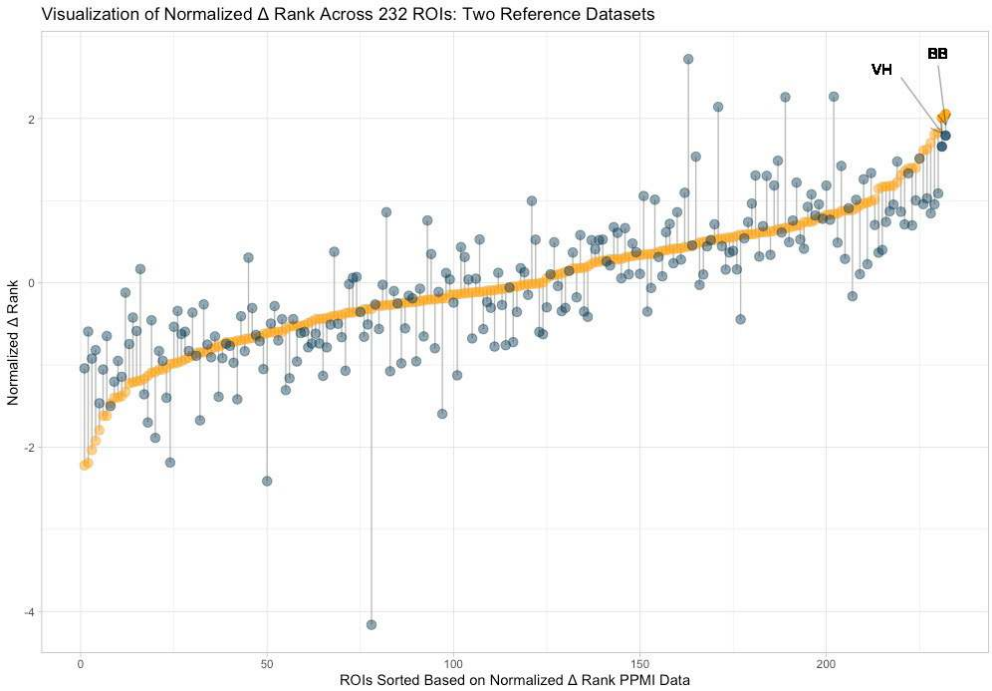

Conclusions: Notably, our method identified multiple regions in which the patient's connectivity deviated from that of both comparison datasets. These included a region associated with hand movements (annotated as BB in Figure 1), possibly associated with the patient's task of holding a button box. Of note was also a region in the visual cortex which may potentially be linked to his visual hallucinations (annotated as VH in Figure 1). We expect that our approach will facilitate personalized treatment planning and offers potential for broader applications in detecting interindividual differences, with scalability for incorporating more extensive data. Our study demonstrates the ability to reliably compare a single patient's data with different datasets, despite variations in data acquisition. This is crucial for personalized treatment strategies, such as targeted rTMS interventions, which requires the detection of brain regions that deviate from normal.

References

1. Brumm, M. C., Siderowf, A., Simuni, T., Burghardt, E., Choi, S. H., Caspell-Garcia, C., Chahine, L. M., Mollenhauer, B., Foroud, T., Galasko, D., Merchant, K., Arnedo, V., Hutten, S. J., O'Grady, A. N., Poston, K. L., Tanner, C. M., Weintraub, D., Kieburtz, K., Marek, K., & Coffey, C. S. (2023). Parkinson's Progression Markers Initiative: A Milestone-Based Strategy to Monitor Parkinson's Disease Progression. Journal of Parkinson's Disease, 13(6). https://doi.org/10.3233/JPD-223433
2. Esteban, O., Markiewicz, C. J., Blair, R. W., Moodie, C. A., Isik, A. I., Erramuzpe, A., Kent, J. D., Goncalves, M., DuPre, E., Snyder, M., Oya, H., Ghosh, S. S., Wright, J., Durnez, J., Poldrack, R. A., & Gorgolewski, K. J. (2019). fMRIPrep: a robust preprocessing pipeline for functional MRI. Nature Methods, 16(1). https://doi.org/10.1038/s41592-018-0235-4
3. Power, J. D., Cohen, A. L., Nelson, S. M., Wig, G. S., Barnes, K. A., Church, J. A., Vogel, A. C., Laumann, T. O., Miezin, F. M., Schlaggar, B. L., & Petersen, S. E. (2011). Functional Network Organization of the Human Brain. Neuron, 72(4). https://doi.org/10.1016/j.neuron.2011.09.006
4. Wink, A. M., de Munck, J. C., Van Der Werf, Y. D., Van Den Heuvel, O. A., & Barkhof, F. (2012). Fast Eigenvector Centrality Mapping of Voxel-Wise Connectivity in Functional Magnetic Resonance Imaging: Implementation, Validation, and Interpretation. Brain Connectivity, 2(5). https://doi.org/10.1089/brain.2012.0087

Poster No 1696

Reconsidering reliability for brain-wide association studies under normative modeling

Zi-Xuan Zhou[1], Xi-Nian Zuo[1]

[1]Beijing Normal University, Beijing, China

Introduction: Evidence indicated that effect sizes observed in brain-wide association studies (BWAS) are generally very small (Marek et al., 2022), and improving measurement reliability alone is not sufficient to boost effect sizes (thus reduce the required sample size) to meet the real effect sizes and the expectations of current practices. We aim to re-evaluate the reliability issues in BWAS under normative modeling with age as the predictor variable, i.e., brain charts (Bethlehem et al., 2022). We will dive into the reliability/validity of brain charts, investigate the reliability in cross-sectional and longitudinal BWAS under chart-derived scores, and reveal a hidden space in longitudinal BWAS that could enhance effect sizes by orders of magnitude.

Methods: Mathematical derivations, simulations, and analysis are combined to demonstrate the utility of our methods to the ABCD datasets. The essence of the mathematical derivations will be covered in the Results section, with detailed derivations/explanations provided in the poster/video. For simulations, we established parameter spaces based on the evidence of longitudinal changes and reliabilities of structural MRI phenotypes from the literature (Bethlehem et al., 2022; Biase et al., 2023; Madan et al., 2017; Hedges et al., 2022) and from the analysis of ABCD data. We repeatedly sampled the space and build developmental brain charts to derive variability and bias in the modeling and assessed the impact of measurement noise on chart-based inferences. Finally, the global structural MRI phenotypes of all samples from ABCD Data Release 5.0 that passed quality control were evaluated. To establish benchmarks for their longitudinal changes, in some cases, paired samples (two measurements from an individual) were selected for the evaluations.

Results: Accurate brain charts require sample sizes in the tens of thousands, appropriate methodologies, and significant population-level longitudinal changes of the phenotypes over the age span. Poor reliability increases observed inter-individual variabilities and reduces relative population-level changes, thus necessitating a larger sample size for accurate models. It also significantly alters the estimated distribution (which is more spread out due to noise) and leads to bias in statistical inferences. Fortunately, the bias can be derived and corrected given the reliability value. For cross-sectional BWAS under chart-derived scores, the reliability can be reduced as individual differences related to covariates such as age/sex are removed. For longitudinal BWAS, which we defined here as studies linking intra-individual longitudinal brain changes to non-brain measures, this effectively eliminate confounds related to, e.g., massive innate and early-life random factors. Removing population-level changes with chart-derived scores allows better exploration of more subtle person-specific changes. However, despite population-level changes can be accurately mapped with large-scale samples, measured intra-individual changes are drowned by measurement noise that is much larger than the population-level changes. Observed longitudinal changes in chart-derived scores in ABCD data align with the noise-driven changes (Fig. 1) and are very weakly associated with the interscan intervals, suggesting that time-independent noise-like changes dominate the changes and longitudinal BWAS face severe challenges of measurement reliability: noise can be orders of magnitude larger than true person-specific changes, burying the validity of research by sharply reducing effect sizes and reproducibility.

Conclusions: Our findings suggest a clear path to substantially boosting effect sizes in BWAS, especially longitudinal BWAS, by simply improving reliability under chart-derived scores. This indicates the priority of improving measurement reliability and the prospect of lifting innovative small-scale studies with a priori information from population imaging data, such as lifespan brain charts.

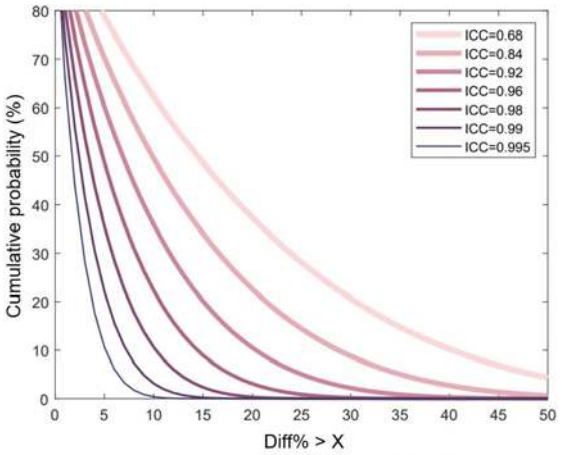

Fig. 1 Noise-driven cumulative distribution curves of the difference in centile scores between two measurements. The horizontal axis, X, represents the event that the difference exceeds X, while the vertical axis represents the probability of that event. Different curves correspond to varying levels of reliability, simulated and highly consistent with mathematical derivation. It is evident that longitudinal changes in centile scores are extremely sensitive to reliability. Even with very high reliability (ICC = 0.995), there is still about a 10% chance that the noise-driven difference in centile scores between two measurements exceeds 5.

References

1. Bethlehem, R.A.I. (2022), 'Brain charts for the human lifespan', Nature, vol. 604, pp. 525-533.
2. Biase, M.A.D. (2023), 'Mapping human brain charts cross-sectionally and longitudinally', Proceedings of the National Academy of Sciences of the United States of America, vol. 120, no. 20, p. e2216798120.
3. Hedges, E.P. (2022), 'Reliability of structural MRI measurements: The effects of scan session, head tilt, inter-scan interval, acquisition sequence, FreeSurfer version and processing stream', NeuroImage, vol. 246, p. 118751.
4. Madan, C.R. (2017), 'Test–retest reliability of brain morphology estimates', Brain Informatics, vol. 4, pp. 107-121.
5. Marek, S. (2022), 'Reproducible brain-wide association studies require thousands of individuals', Nature, vol. 603, pp. 654-660.

Poster No 1698

Hydra Nordic: A thermal-noise removal strategy for multi-echo fMRI

Marco Flores-Coronado[1], Cesar Caballero-Gaudes[2]

[1]Basque Center on Cognition, Brain and Language, Donostia-San Sebastián, Guipuzkoa, [2]Basque Center of Cognition, Brain and Language, San Sebastián, Spain

Introduction: During MRI acquisition, artifacts (e.g., body movement, and respiratory effects)(Satterthwaite et al., 2019) and noise sources (e.g., thermal noise from the scanners)(Wald & Polimeni, 2017) hinder signal fidelity. Multi-echo fMRI techniques (ME), in turn, have demonstrated superior data quality compared to conventional single-echo acquisitions. ME combines signals from different echo times (TEs) to amplify the contrast-to-noise ratio(Poser et al., 2006). Complementing this, multi-echo independent component analysis (ME-ICA) refines signal quality by removing components that do not follow BOLD assumptions(Community et al., 2023; DuPre et al., 2021; Kundu et al., 2017). Additionally, Nordic has emerged as an effective method in reducing thermal noise during single-echo acquisition(Vizioli et al., 2021). Yet, an integrated approach leveraging the advantages of both ME and Nordic remains unformulated. Here, we investigate the optimal use of thermal-noise reduction using Nordic and ME-based techniques (e.g., optimal combination and ME-ICA). Our proposed method, named Hydra Nordic, explores the simultaneous use of these techniques for an enhancement in signal quality.

Methods: Five healthy volunteers (3 women) were scanned in a 3T Siemens PrimaFit MAGNETOM MR scanner using a 64-channel head at the Basque Center on Cognition, Brain and Language. Multi-echo fMRI data was collected during two resting state runs with different voxel resolutions (2.4 mm isotropic voxels: TR=1.2s, TE= 11.2/28.1/45/61.9 ms, and 2 mm isotropic voxels: TR=1.7s, TE=13.4/36.1/58.8/81.5 ms, both runs with SMS=5, GRAPPA=2, 65/75 whole-head sagittal slices respectively). Single-band reference (SBRef) images were acquired for each TE. T1-weighted MP2RAGE and T2-weighted Turbo Spin Echo images were collected at 1 mm voxel resolution in each subject. ME-fMRI data was minimally preprocessed with AFNI, including the removal of the 10 first volumes to achieve a steady-state magnetization, image realignment of the first echo to the SBRef and applying this transformation to the other echoes, and T2*-weighed linear (optimal) combination of the echoes using TEDANA (ME-OC). Before this standard ME-fMRI preprocessing, two versions of the Nordic denoising

approach were also applied to reduce thermal noise: applying Nordic to each echo dataset independently (NORDIC-OC), and applying Nordic on the spatial concatenated dataset (3dZcat) from all the echoes and then separating them (3dZcutup) for subsequent preprocessing (HYDRA-OC). Both Nordic approaches used the noise-only scans (i.e., no RF excitation) acquired at the end of each run to estimate the hyper-parameters of the Nordic algorithm. Temporal signal-to-noise ratio (TSNR) maps (i.e. voxelwise mean divided by its standard deviation) were computed on the ME-OC, NORDIC-OC and HYDRA-OC datasets. We hypothesize that reducing thermal noise from echoes simultaneously would better capture thermal noise because we assume it to be similar between echoes

Results: Temporal Signal-to-Noise Ratio (T-SNR) maps were computed from OC maps -TSNR=mean(OC)/sd(OC)- As previously reported, we found that Nordic reduced overall signal variance. Moreover, we found an positive increase in overall tSNR values between HYDRA-OC TSRN values as compared both to ME-OC, and NORDIC-OC. In FIgure 1, scatterplots from a representative subject show a positive increment in overall TSNR values (2.4mm isotropic voxel). In FIgure 2, scatter plots from the same individual inform that with lower voxel size, there is a greater increment in TSNR values between methods.

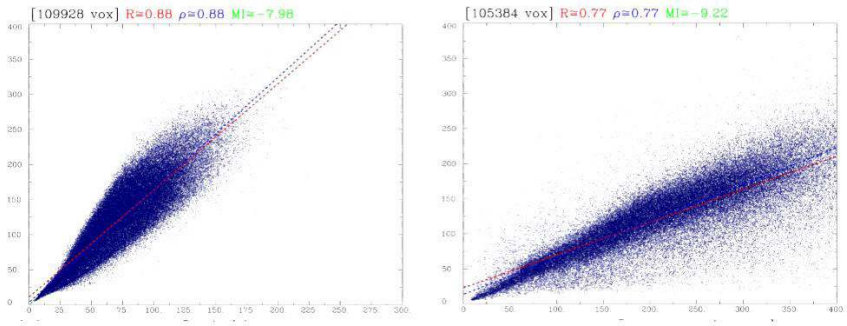

FIgure 1. Scatterplots comparing hydra OC tsnr values (y-axis), against Nordic OC (left x-axis) and OC (right x-axis) with a 2.4 mm isotropic voxel

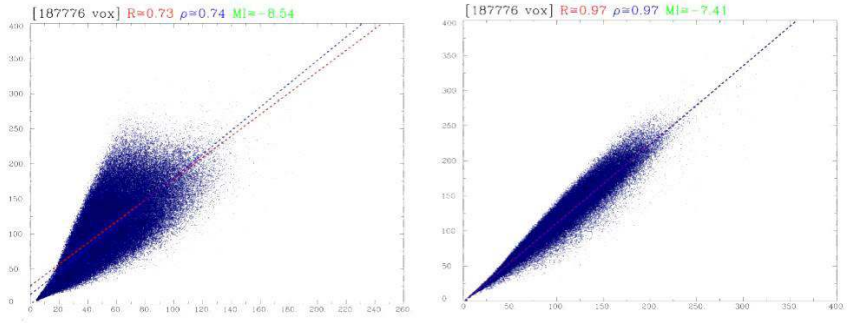

FIgure 2. Scatterplots comparing hydra OC tsnr values (y-axis), against Nordic OC (left x-axis) and OC (right x-axis) with a 2 mm isotropic voxel

Conclusions: We argue that, concatenating the echo-time-series volumes let us better approach the thermal noise distribution. Furthermore, me found evidence that such estimation improves if voxel size decrease.

References

1. Community, T. tedana, Ahmed, Z., Bandettini, P. A., Bottenhorn, K. L., Caballero-Gaudes, C., Dowdle, L. T., DuPre, E., Gonzalez-Castillo, J., Handwerker, D., Heunis, S., Kundu, P., Laird, A. R., Markello, R., Markiewicz, C. J., Maullin-Sapey, T., Moia, S., Molfese, P., Salo, T., Staden, I., … Whitaker, K. (2023). ME-ICA/tedana: 23.0.1 (23.0.1) [Computer software]. Zenodo. https://doi.org/10.5281/zenodo.7926293
2. DuPre, E., Salo, T., Ahmed, Z., Bandettini, P., Bottenhorn, K., Caballero-Gaudes, C., Dowdle, L., Gonzalez-Castillo, J., Heunis, S., Kundu, P., Laird, A., Markello, R., Markiewicz, C., Moia, S., Staden, I., Teves, J., Uruñuela, E., Vaziri-Pashkam, M., Whitaker, K., & Handwerker, D. (2021). TE-dependent analysis of multi-echo fMRI with tedana. Journal of Open Source Software, 6(66), 3669. https://doi.org/10.21105/joss.03669
3. Kundu, P., Voon, V., Balchandani, P., Lombardo, M. V., Poser, B. A., & Bandettini, P. A. (2017). Multi-echo fMRI: A review of applications in fMRI denoising and analysis of BOLD signals. NeuroImage, 154, 59–80. https://doi.org/10.1016/j.neuroimage.2017.03.033
4. Poser, B. A., Versluis, M. J., Hoogduin, J. M., & Norris, D. G. (2006). BOLD contrast sensitivity enhancement and artifact reduction with multiecho EPI: Parallel-acquired inhomogeneity-desensitized fMRI. Magnetic Resonance in Medicine, 55(6), 1227–1235. https://doi.org/10.1002/mrm.20900
5. Satterthwaite, T. D., Ciric, R., Roalf, D. R., Davatzikos, C., Bassett, D. S., & Wolf, D. H. (2019). Motion artifact in studies of functional connectivity: Characteristics and mitigation strategies. Human Brain Mapping, 40(7), 2033–2051. https://doi.org/10.1002/hbm.23665
6. Vizioli, L., Moeller, S., Dowdle, L., Akçakaya, M., De Martino, F., Yacoub, E., & Uğurbil, K. (2021). Lowering the thermal noise barrier in functional brain mapping with magnetic resonance imaging. Nature Communications, 12(1), Article 1. https://doi.org/10.1038/s41467-021-25431-8

7. Wald, L. L., & Polimeni, J. R. (2017). Impacting the effect of fMRI noise through hardware and acquisition choices – Implications for controlling false positive rates. NeuroImage, 154, 15–22. https://doi.org/10.1016/j.neuroimage.2016.12.057

Poster No 1699

A method for inclusion of high-motion underrepresented youth for robust brain-behaviour relationship

Jivesh Ramduny[1], Lucina Uddin[2,3,4], Tamara Vanderwal[5,6], Eric Feczko[7,8], Damien Fair[7,8,9], Clare Kelly[10,11,12], Arielle Baskin-Sommers[1,13,14]

[1]Department of Psychology, Yale University, New Haven, CT, USA, [2]Department of Psychiatry and Biobehavioral Sciences, University of California Los Angeles, Los Angeles, CA, USA, [3]Department of Psychology, University of California Los Angeles, Los Angeles, CA, USA, [4]Semel Institute for Neuroscience and Human Behavior, University of California Los Angeles, Los Angeles, CA, USA, [5]Department of Psychiatry, University of British Columbia, Vancouver, BC, Canada, [6]BC Children's Hospital Research Institute, Vancouver, BC, Canada, [7]Masonic Institute for the Developing Brain, University of Minnesota Medical School, Minneapolis, MN, USA, [8]Department of Pediatrics, University of Minnesota Medical School, Minneapolis, MN, USA, [9]Institute of Child Development, University of Minnesota Medical School, Minneapolis, MN, USA, [10]School of Psychology, Trinity College Dublin, Dublin, Ireland, [11]Department of Psychiatry, School of Medicine, Trinity College Dublin, Dublin, Ireland, [12]Trinity College Institute of Neuroscience, Trinity College Dublin, Dublin, Ireland, [13]Department of Psychiatry, Yale University, New Haven, CT, USA, [14]Wu Tsai Institute, Yale University, New Haven, CT, USA

Introduction: Consortia datasets provide an unprecedented opportunity for the neuroimaging community to estimate the true effect sizes of brain-behaviour associations with sufficient statistical power. However, in part due to the variation in data acquisition across consortia sites, researchers tend to apply strict data quality control to mitigate the impact of head motion. This practice typically excludes a disproportionate number of participants who belong to minioritised backgrounds and from lower socioeconomic status[1,2]. Here, we proposed a resampling strategy known as bagging[3] to rescue high-motion underrepresented youths to maximise sample inclusivity for establishing robust and inclusive brain-behaviour associations from the Adolescent Brain Cognitive Development (ABCD) Study[4].

Methods: Structural and resting-state fMRI data were obtained from the ABCD Study Baseline Release (9-10 years). Participants were categorised into 3 racial/ethnic groups: White (N=3,864), Black (N=910), and Hispanic (N=1,342). Asian participants were not included due to their limited sample size. Standard data preprocessing was performed using the ABCD-BIDS Community Collection[5]. For each youth, the fMRI data was parcellated[5,6] and functional connectivity (FC) was computed between each pair of ROIs to construct a 352x352 FC matrix. Partial Spearman's Rank correlation (R) was computed at the edge level to assess the relationships between FC and externalising behaviours [CBCL] and cognitive performance [NIH Toolbox] while adjusting for participant sex and head motion. For each behaviour, the edge showing the strongest R was selected after correcting for multiple comparisons (~61K edges; $P < 0.05$ FDR). To establish the robustness of R across sample sizes[7], N was bootstrapped across 500 iterations, and the mean R and 95% CI was plotted as a function of N. Scrubbing was applied to estimate the FC matrices based on the participants' least motion-corrupted timepoints whose framewise displacement (FD) < 0.20 mm[8,9] (Fig.1A). Bagging was then performed to select subsets of the participants' least motion-corrupted timepoints with replacement over 500 iterations and compute their FC matrices[3,10] (Fig.1A). Finally, bagging was repeated without discarding the high-motion participants based on their motion-limited timepoints[3]. To include as many youth as possible, a minimum of 100 least motion-corrupted timepoints were bootstrapped for bagging.

Results: Underrepresented youth exhibited significantly greater head motion relative to White youth (Fig.1B&C). Low-motion youth were retained (mean FD < 0.20 mm). This disproportionally reduced the size of the Black and Hispanic groups by 49.1% and 52.5%, respectively. The variability in R decreased with increasing sample sizes using a standard procedure (full timeseries; 33K correlations; Fig.2A) and bagging (16.5 million correlations; Fig.2B). The differences in CIs (computed by AUC) between the two approaches were 0.2-21% for NIH Toolbox and 2-5% for CBCL, with bagging producing tighter CIs around R in most cases. Bagging retained 99.97% of all White, 99.78% Black, and 100% Hispanic youth for brain-behaviour relationships (Fig.2C). When the high-motion youth were included, the differences in CIs between the two approaches were 2-5% for NIH Toolbox and 0.2-2% for CBCL, with bagging producing tighter CIs in almost all correlations.

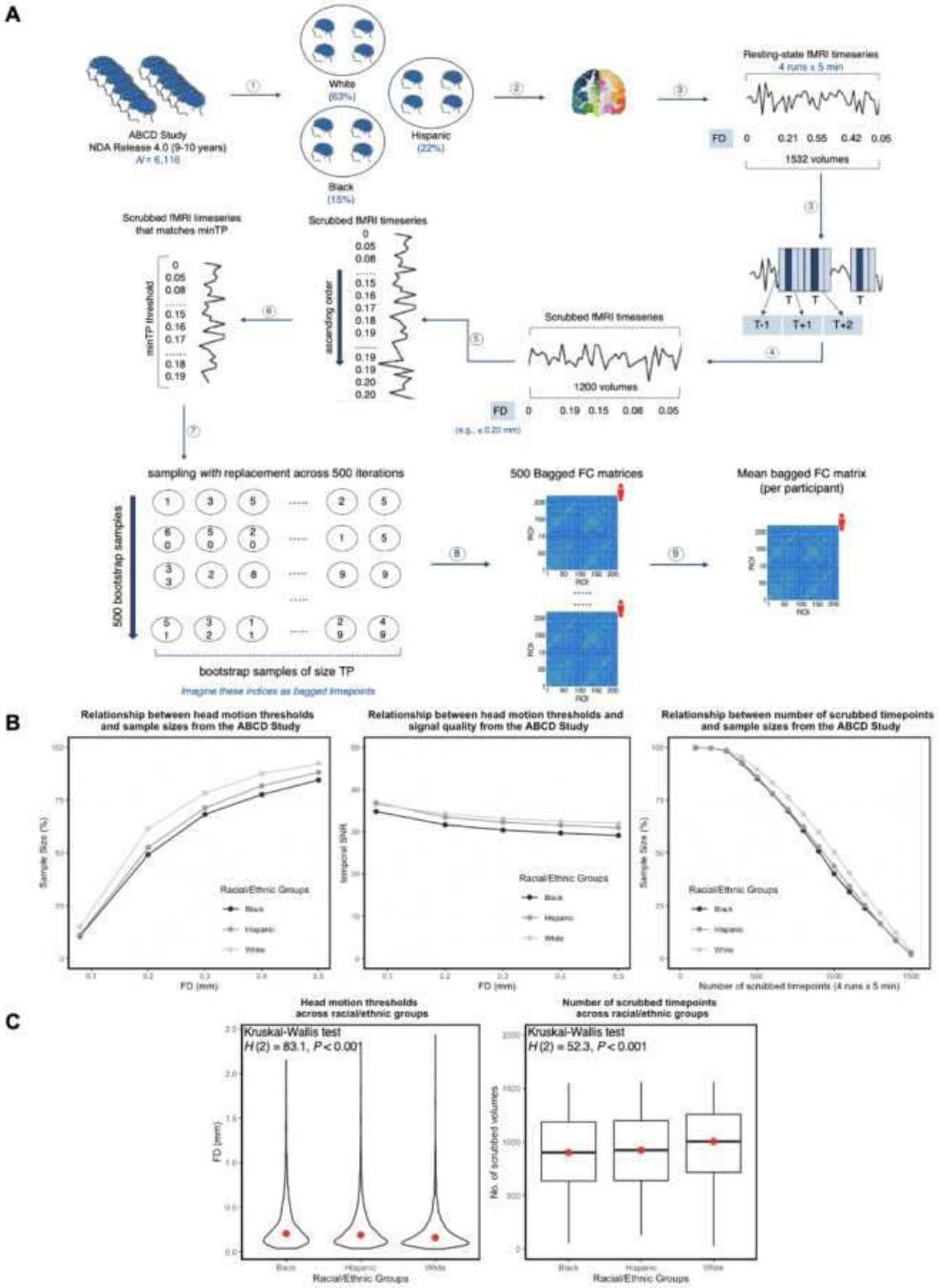

Fig.1. Framework to rescue high-motion underrepresented youths for robust and inclusive brain-behaviour relationships. A. The resting-state fMRI data was parcellated to extract the fMRI timeseries. Scrubbing was employed to identify and censor each motion-corrupted timepoint whose FD > 0.20 mm in addition to removing their preceding and two succeeding timepoints in the fMRI timeseries. Bagging was performed to salvage high-motion participants based on the participants' scrubbed timeseries. We selected the top 100 least contaminated timepoints (minTP) from the scrubbed timeseries of all participants across the 3 groups during which 100 timepoints (TP) were bootstrapped *with* replacement over 500 iterations to construct the FC matrices (Fisher z-transformed). **B.** Effects of head motion thresholds and number of scrubbed timepoints on sample size across the 3 racial/ethnic groups. **C.** There was a tendency to exclude a greater number of underrepresented youths with stricter head motion thresholds to improve signal quality.

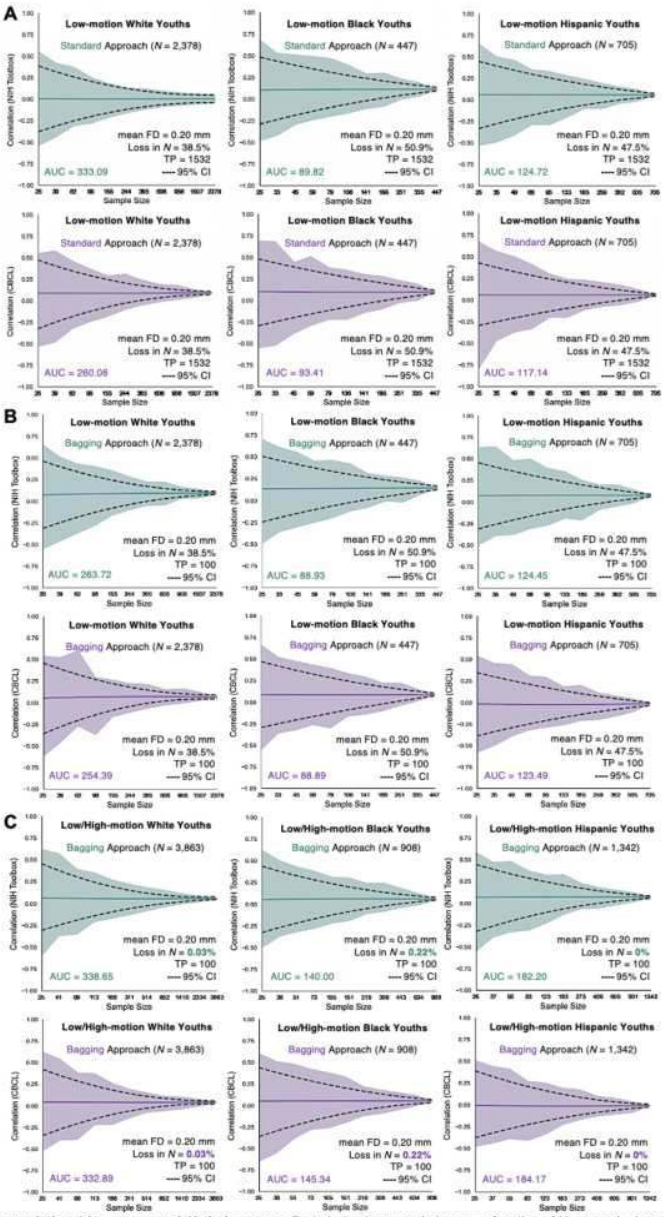

Fig.2. Brain-behaviour relationships across racial/ethnic groups. Brain-behaviour correlations as a function of *N* across the low-motion youths in each group using **(A)** a standard approach (full timeseries), **(B)** bagging, and **(C)** including the "high-motion" youths with bagging. AUC: Area under curve.

Conclusions: Bagging shows merit in (1) maximising sample inclusivity by permitting inclusion of fMRI data from high-motion underrepresented youth, and (2) generating robust and inclusive brain-behaviour relationships from those who typically are excluded using traditional low-motion criteria. Bagging enhances the representation of individuals and serves to fulfil the promise of consortia data to produce generalisable effect sizes across races and ethnicities.

References

1. Ricard, J.A. (2022), 'Confronting racially exclusionary practices in the acquisition and analyses of neuroimaging data', Nature Neuroscience, vol. 26, pp. 4–11.
2. Kopal, J. (2023), 'The end game: Respecting major sources of population diversity', Nature Methods, vol. 20, pp. 1122–1128.
3. Ramduny, J. (2023), 'Delineating the Functional Brain as Fingerprints to Predict Reproducible Brain-Behaviour Relationships in Developmental Youths', Biological Psychiatry, vol. 93, pp. S120.
4. Casey, B.J. (2018), 'The Adolescent Brain Cognitive Development (ABCD) study: Imaging acquisition across 21 sites', Developmental Cognitive Neuroscience, vol. 32, pp. 43-54.
5. Feczko, E, 'Adolescent Brain Cognitive Development (ABCD) Community MRI Collection and Utilities', bioRxiv, 2021.07.09.451638.
6. Seitzman, B.A. (2020), 'A set of functionally-defined brain regions with improved representation of the subcortex and cerebellum', Neuroimage, vol. 206, pp. 116290.
7. Marek, S. (2022), 'Reproducible brain-wide association studies require thousands of individuals', Nature, vol. 603, pp. 654-660.
8. Power, J.D. (2014), 'Methods to detect, characterize, and remove motion artifact in resting-state fMRI', Neuroimage, vol. 84, pp. 320-341.
9. Power, J.D. (2012), 'Spurious but systematic correlations in functional connectivity MRI networks arise from subject motion', Neuroimage, vol. 59, no. 3, pp. 2142-2154.
10. Biswal, B.B. (2001), 'Use of jackknife resampling techniques to estimate the confidence intervals of fmri parameters', Journal of Computer Assisted Tomography, vol. 25, no. 1, pp. 113-120.

Poster No 1700

When There Are No Better Solutions: Characterizing Optimal Communication in the Human Brain Network

Kayson Fakhar[1], Fatemeh Hadaeghi[1], Caio Seguin[2], Shrey Dixit[1], Arnaud Messé[1], Bratislav Misic[3], Claus Hilgetag[1,4]

[1]University-Hospital of Hamburg (UKE), Hamburg, Germany, [2]Department of Psychological and Brain Sciences, Indiana University, Bloomington, Indiana, [3]McGill University, Montreal, Quebec, [4]Department of Health Sciences, Boston, MA

Introduction: Addressing the human brain as a network unveils its complex connectivity pattern. This network shows a multitude of properties, including an abundance of short-range connections to minimize wiring cost while allowing a small set of long-range connections (Sporns et al., 2004). This set of costly long-range connections provides a shorter network-wide average path-length allowing efficient communication, hence striking a balance between cost and efficiency (Bullmore & Sporns, 2012). However, communication efficiency in this context presupposes brain regions communicate via the shortest path, a notion demanding nodes' global network knowledge (Avena-Koenigsberger et al., 2018). Consequently, alternative communication models (CMs), envisioning signaling via various mechanisms such as random walking and broadcasting have been developed (Seguin et al., 2023). There is yet to be a consensus over how to define communication among brain regions and measure if it is indeed optimal given the structural constraints.

Methods: Game theory is a branch of mathematics that studies the strategic interactions of players in a game, assuming that each player aims at maximizing its payoff. For instance, when a buyer and a seller bargain over an item, they both start with extreme proposals that maximize their profit, but their constraints (buyer's budget and the item's selling price) force them to compromise and find a solution that satisfies both parties. Theoretically, for every such a game, there exists a unique equilibrium point where no player can unilaterally increase its payoff. The exact payoff of every player given that division scheme is their "Shapley values" (Gul, 1989; Shapley, 1953). Through multi-perturbation Shapley value Analysis (MSA) (Keinan et al., 2004), we computed the optimal influence (OI) matrix, detailing exact nodal influences at the mentioned equilibrium point. In brief, MSA finds this unique point by exhaustively perturbing every possible combination of nodes and comparing the outcome of each perturbation with others (See Fig1 for more details; Fakhar & Dixit, 2021). Here, we define the game as a large-scale computational model of the human brain dynamics. Specifically, we used the consensus structural connectivity with 219 parcels from the Lausanne dataset and simulated the activity profile of each region by various computational models (linear and nonlinear, including an oscillatory neural mass model). Lastly, to identify which conceptualization of CMs best captures optimal interactions in brain networks, we compared them with the OI matrix using Pearson's correlation.

Results: First, we found that the OI is largely model-independent, as all of our computational models result in the same equilibrium point. This finding suggests that complex neural mass models do not provide extra information compared to simple linear models of information propagation, which are the backbone of graph-theoretical metrics. Second, among the putative CMs, communicability is the most reliable predictor of OI, with r=0.94. By incorporating a broadcasting strategy, communicability considers all path-lengths while exponentially discounting longer walks. However, we found that the exponential discount is too strict for long path-lengths as communicability results in the underestimation of their actual influence. Consequently, we employed a simple analytical model with the same strategy but using a linear discount. This model predicts OI with R2=0.99 (Fig2).

Conclusions: In this work, we employed a game-theoretical framework to, first, provide an intuitive and model-agnostic definition of communication, and, second, to find the optimal point where no node can unilaterally increase its influence over others given the imposed structural constraints. We then compared how much nodes influence each other at this point with other CMs and found that the best fitting ones follow a broadcasting conceptualization that utilizes not only the shortest path but the longer ones as well.

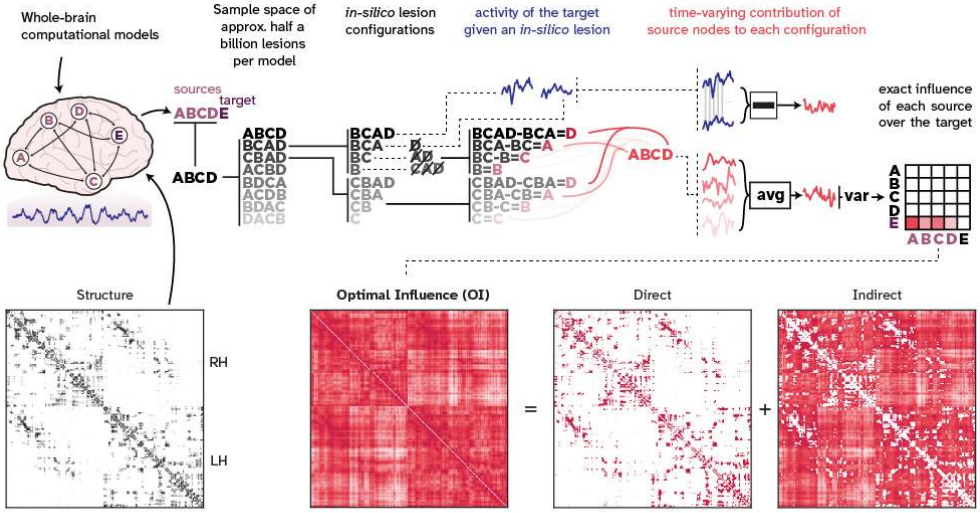

Fig1. Visual explanation of how MSA derives the equilibrium state of OI: MSA is a systematic lesioning framework built on Shapley values. The Shapley value is a game-theoretical measure that provides a unique and stable allocation of contributions among agents forming a coalition (not to be confused with the explainable machine learning toolbox SHAP). Briefly, for each target node, MSA forms coalitions of source nodes and computes the average contribution of each source node by adding them to all possible different coalitions. More precisely, the configurations are formed by systematically lesioning coalitions of nodes, *e.g.,* all single nodes, all pairs, all triplets, ... The contribution of each node to that particular configuration is then calculated as the difference between when the node was included in the coalition and when it was excluded. The state of OI for each source over the target is calculated as the average contribution of the source node to all configurations formed. Here the game is defined as an arbitrary computational model of whole-brain dynamics. We explored three models with increasing complexity: a linearized Wilson-Cowan model (linear), the linear model but wrapped in a nonlinear function of tanh (nonlinear) and an oscillatory neural mass model known as Hopf/Stuart-Landau at its critical point (Hopf). This amounts to a total of approximately 1.5 billion multi-site lesion configurations.

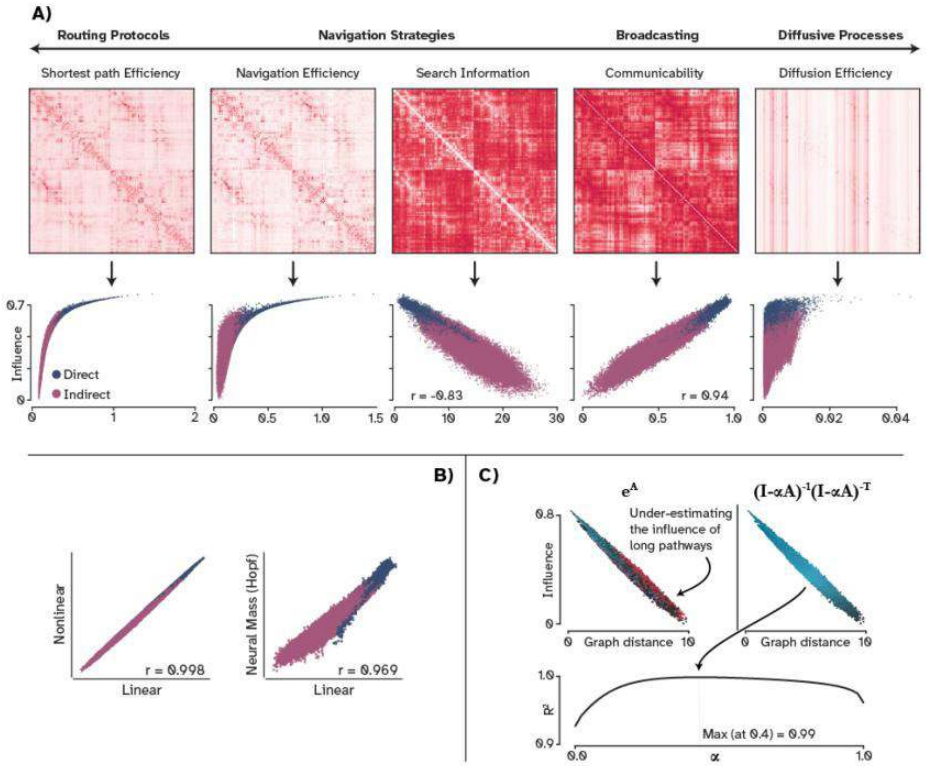

Fig2. Summary of the findings: A) shows the network communication measures derived from the same structural connectivity and their relationship with the influence matrix under the OI state. *The shortest path efficiency* assumes that nodes influence each other exclusively via the shortest path. Thus, the longer the shortest path between them, the less efficient the communication will be. *Navigation efficiency* assumes that the signal propagates as a geometrically greedy random walker, where, at every step, the walker aims to minimize its distance to the target node. *Search information* quantifies the amount of information required to bias a random walker to travel via the shortest path, where more information means less accessibility of the shortest path. *Communicability* conceptualizes signal propagation as a broadcasting process in which communication takes place via multiple paths. However, longer pathways contribute exponentially smaller to communication efficiency. *Diffusion efficiency* counts the number of steps that an unbiased random walker takes to reach the target node. We found communicability to have the best linear relationship with the signal propagation under the OI state. **B)** shows that information flow under the OI state is largely dictated by the connectivity instead of model dynamics as increasing model complexity introduces almost no change in the equilibrium state. **C)** shows that the communicability penalizes the influence of topologically distant nodes too harshly. Our proposed model *Spatial Autoregressive model* (SAR; the righ hand side) follows the linear attenuation of influence proposed by Katz in 1953. Switching from an exponential attenuation (communicability) to a linear attenuation (SAR) not only captures the influence of these pathways accurately but also completely recovers the communication matrix under the OI state. in the equation, *I* represents the identity matrix, *alpha* is the spatial decay, *A* represents the connectome, and *-T* denotes the inverse of the transposed matrix. Here we fitted *alpha* to the OI matrix, however, as depicted, the range of *alpha* values that can provide a high performance is relatively broad (from 0.2 to 0.8) relaxing the need to fit an exact value.

References

1. Avena-Koenigsberger, A., Misic, B., & Sporns, O. (2018). Communication dynamics in complex brain networks. Nature Reviews. Neuroscience, 19(1), 17–33. https://doi.org/10.1038/nrn.2017.149
2. Bullmore, E., & Sporns, O. (2012). The economy of brain network organization. Nature Reviews. Neuroscience, 13(MAY), 336–349. https://doi.org/10.1038/nrn3214
3. Fakhar, K., & Dixit, S. (2021). MSA: A compact Python package for Multiperturbation Shapley value Analysis. https://doi.org/10.5281/zenodo.5636435
4. Gul, F. (1989). Bargaining Foundations of Shapley Value. Econometrica: Journal of the Econometric Society, 57(1), 81–95. https://doi.org/10.2307/1912573
5. Keinan, A., Sandbank, B., Hilgetag, C. C., Meilijson, I., & Ruppin, E. (2004). Fair attribution of functional contribution in artificial and biological networks. Neural Computation, 16(9), 1887–1915. https://doi.org/10.1162/0899766041336387
6. Seguin, C., Sporns, O., & Zalesky, A. (2023). Brain network communication: concepts, models and applications. Nature Reviews. Neuroscience. https://doi.org/10.1038/s41583-023-00718-5
7. Shapley, L. S. (1953). A value for n-person games. In H. W. Kuhn & A. W. Tucker (Ed.), Contributions to the theory of games (Vol. 2, pp. 307–317). Princeton, NJ:Princeton University Press.
8. Sporns, O., Chialvo, D. R., Kaiser, M., & Hilgetag, C. C. (2004). Organization, development and function of complex brain networks. Trends in Cognitive Sciences, 8(9), 418–425. https://doi.org/10.1016/j.tics.2004.07.008

Poster No 1702

Distance-Based Metrics of Time-Varying Functional Connectivity

Omar Shafik[1], Myar Sayed[1], Hussien Al Asi[2], Ansam El Shikh[1]

[1]British University in Egypt, Cairo, Egypt, [2]Cairo University, Cairo, Egypt

Introduction: Sliding-window methods of estimating time-varying functional connectivity (tvFC) are limited by their recommended window size (Leonardi, 2015), and their ability to distinguish null from significant functional connectivity dynamics (Laumann, 2017; Hindriks, 2016). The sum of absolute distances between BOLD signals have been previously shown to produce similar statistics to static correlation-based FC (Minati, 2014). Here, we introduce a distance-based sliding-window method for computing tvFC estimates with high temporal resolution, and argue using complementary test statistics for the method's ability to distinguish significant from null-modeled FC estimates.

Methods: To obtain tvFC estimates, we compute absolute distances between z-scored signals and between z-scored first-order derivatives of the signals. Then, distances are averaged for each time point, inverted, log-transformed, and sequentially sampled using a sliding-average window. We use window sizes spanning from 9 to 69 time points. To evaluate the interpretability of tvFC estimates, we employ 3 null hypotheses: H0,1 interrogating the estimates' variability from the global (null-hypothesized) mean using their z-scores, H0,2 interrogating the variability of static estimates using spectrally constrained Gaussian noise, and H0,3 interrogating the variability of edges' variances using spectrally and covariance constrained Gaussian noise. We use empirical resting-state fMRI data from the HCP database (Van Essen, 2013). Significance levels of 0.05 were used.

Results: We found that the sampling distributions for all used window sizes are consistently normal around a mean that corresponds to computed estimates from white noise signals. We found that the global mean and variance are stationary for all analyzed time points using Augmented Dickey–Fuller test. Moreover, Inter-subject variations were found insignificant. Although distribution tails of empirical estimates were similar to null-modeled surrogates, empirical edge statistics diverged from nulls for H0,2 and H0,3. We found that more than 35% of empirical edges are statistically significant to H0,2, and more than 14% of empirical edges are statistically significant to H0,3. In total, more than 38% of empirical edges are significant to H0,2 and H0,3. Third, we found that between 1.4% and 4% of tvFC estimates have significant z-scores to H0,1 and belong to significant edges.

Figure 1

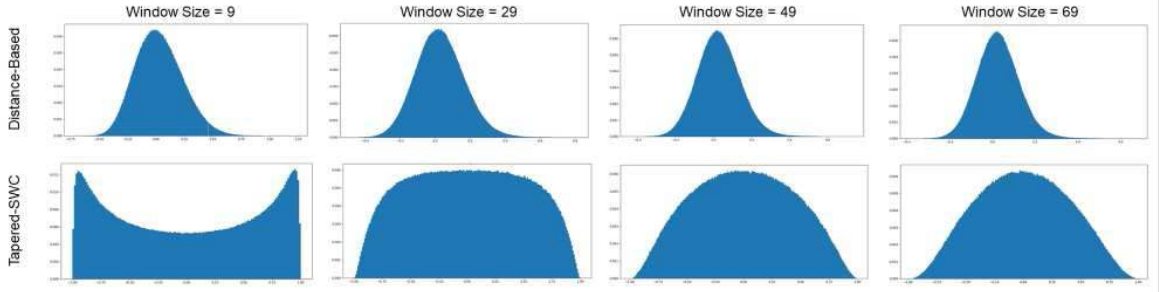

Sampling Distributions of tvFC Estimates. The plots contrast the sampling distributions of distance-based (top) and tapered-SWC (bottom) tvFC estimates using window sizes of 9, 29, 49, and 69 (columns). Distance-based estimates are stable and approximately normally distributed for all window sizes. Distributions of SWC estimates exhibit bi-/uni-modality and uniformity for different window sizes.

Figure 2

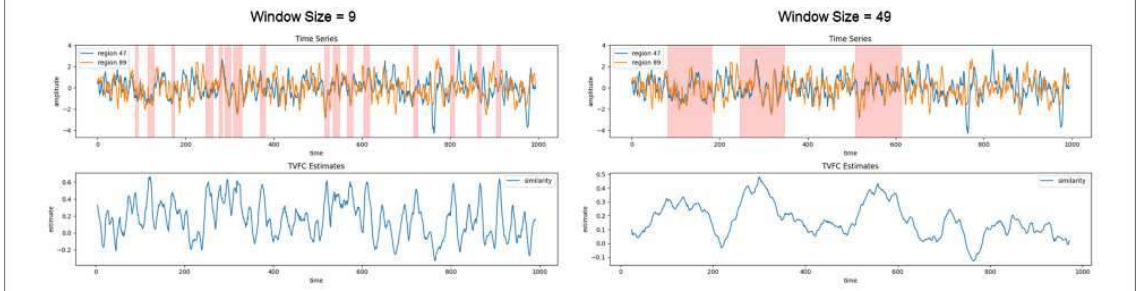

Time-Resolved FC Statistics. We compute z-statistics for one edge using two window/sample sizes: 9 (left), and 49 (right). After computing tvFC estimates (bottom), we compute each estimate's z-score using the sampling population mean and variance. We find and highlight frames of the z-normalized BOLD time series that belong to significant estimates (top). We observe a visible overlap between significant frames using the short and long windows. However, fast and infrequent significant co-fluctuations are averaged out by the long window.

Conclusions: The proposed method offers a sliding-window alternative that overcomes limitations of temporal resolution and interpretability. Estimates are computed with window sizes as short as 9 time points while maintaining within-session and intersubject stability of the ensemble parameters. Although empirical estimates were replicated in randomly-driven estimates, we were able to discern interesting time-resolved observations and dynamics by investigating mechanistic effects in edgewise statistics. Diverging from the null space of H0,1 and H0,2 suggests that time-resolved estimates from a specific edge are driven by an underlying mechanism. Diverging from the null space of H0,1 and H0,3 suggests that estimates from a specific edge are driven by a dynamic underlying mechanism. These interpretations do not infer anything about the weight, directness, or directionality of hypothesized connectivity. They merely suggest that an observed effect is mechanistic rather than random. All procedures are implemented in Python and will be available on GitHub.

References

1. Hindriks, Rikkert. (2016). "Can sliding-window correlations reveal dynamic functional connectivity in resting-state fMRI?." Neuroimage 127, 242-256.
2. Laumann, Timothy O. (2017). "On the stability of BOLD fMRI correlations." Cerebral cortex 27, no. 10, 4719-4732.
3. Leonardi, Nora. (2015). "On spurious and real fluctuations of dynamic functional connectivity during rest." Neuroimage 104, 430-436.
4. Minati, Ludovico. (2014). "Fast computation of voxel-level brain connectivity maps from resting-state functional mri using l1-norm as approximation of pearson's temporal correlation: Proof-of-concept and example vector hardware implementation." Medical Engineering & Physics 36, no. 9.
5. David C. Van Essen. (2013). "The WU-Minn Human Connectome Project: An overview." NeuroImage 80(2013):62-79.

Poster No 1703

An open-source Julia package for estimating whole-brain effective connectivity

Imre Kertesz[1], Stefan Fraessle[1], Jakob Heinzle[1], Klaas Stephan[1,2]

[1]Translational Neuromodeling Unit (TNU), University of Zurich & ETH Zurich, Zurich, Switzerland, [2]Max Planck Institute for Metabolism Research, Cologne, Germany

Introduction: Mapping effective (directed) connectivity in whole-brain networks is a key challenge in Computational Neuroscience and Computational Psychiatry. Using neuroimaging data, dynamic causal modeling (DCM) is a popular framework to estimate brain connectivity. Due to its computational complexity, analysis is restricted to small networks with few

regions. A novel approach called regression DCM (rDCM) overcomes those computational limitations, rendering inference on effective connectivity in whole-brain networks feasible.

Methods: In order to turn the novel approach into a beneficial tool in the context of computational assays, it is indispensable to have computational runtimes that are compatible within clinical practice. Motivated by this desideratum, we present an open-source software package in Julia that implements the rDCM framework. The new Julia language endorses the development of highly efficient code, resulting in minimal resource usage. The robust and user-friendly implementation allows to perform whole-brain analysis with only few lines of code. With Julia being a freely available open-source project, we hope to reach a large audience.

Results: Here we illustrate the utility of the package, present runtime and memory consumption comparison between the Julia and Matlab implementation. Furthermore, we outline the typical workflow when using the new tool and demonstrate it in application to concrete examples.

Conclusions: Using the new Julia language, we implemented a package that allows to perform whole-brain effective connectivity analysis in the order of seconds to minutes on standard hardware. This new tool is part of the Translational Algorithms for Psychiatry-Advancing Science (TAPAS) software package (https://translationalneuromodeling.github.io/tapas/) – an open-source collection of building blocks for computational assays in psychiatry developed at the Translational Neuromodeling Unit (TNU).

References

1. Fraessle, S. (2017), 'Regression DCM for fMRI', NeuroImage, vol. 155, pp. 406-421
2. Fraessle, S. (2018), 'A generative model of whole-brain effective connectivity', NeuroImage, vol. 179, pp. 505-529
3. Fraessle, S. (2021), 'TAPAS: An Open-Source Software Package for Translational', Neuromodeling and Computational Psychiatry, vol. 12
4. Friston, K. (2003), 'Dynamic causal modelling', NeuroImage, vol. 19, no. 4, pp. 1273-1302

Poster No 1704

Analytical estimation of the network statistics of the Hopf whole-brain model

Adrián Ponce-Alvarez[1], Gustavo Deco[2]

[1]Polytechnic University of Catalonia, Barcelona, Spain, [2]Pompeu Fabra University, Barcelona, Spain

Introduction: Whole-brain models are useful to understand the emergence of collective activity among brain regions. These models combine connectivity matrices (connectomes) with local node dynamics, noise, and transmission delays. Diverse choices for the local dynamics have been proposed. Among them, nonlinear oscillators corresponding to a Hopf bifurcation have been used to study collective phase and amplitude dynamics in different brain states (e.g. Deco et al., 2017; López-González et al., 2021). However, estimating the network statistics of such system requires long simulations, impeding the exploration of different model parameters. Here, we studied the linear fluctuations of this model to analytically estimate its stationary statistics, i.e. the covariances in the temporal and frequency domains.

Methods: Hopf network: The whole-brain dynamics are obtained by coupling the local dynamics of N nodes interconnected through a coupling matrix C representing anatomical connections. Here, we used a publicly available human diffusion MRI connectome from the Human Connectome Project (HCP) (Smith et al. 2013). The state variables of the network, zj (for j=1,...,N), are given by the complex stochastic differential equations: $dz_j/dt = F_j(z_1,z_2,...,z_N) = (a_j + i\omega_j)z_i - |z_j|^2 + g\Sigma_k C_{jk}(z_k-z_j) + \eta_j$, where i is the complex unit, g is a global scaling of connectivity C, ωj is the intrinsic frequency of node j, ηj represents noise, and aj is the bifurcation parameter of node j. In isolation, a node undergoes noise-driven oscillations if $a_j < 0$ or self-sustain oscillations if $a_j > 0$. Node parameters can be homogenous (same for all nodes) (Deco et al. 2017) or heterogeneous (different for different nodes, i.e., hierarchy) (López-González et al. 2021). In the case of delayed interactions, the coupling term becomes: $g\Sigma_k C_{jk}[z_k(t-d_{kj})-z_j(t)]$, where dkj is the time-delay of the interaction between nodes j and k. Linearization: In the case of weak noise and small non-linearities, one can estimate the network statistics using a linear approximation, without the need of long, computationally-costly stochastic simulations. For this, we studied the linear fluctuations δz around the fixed point $(z_1,...,z_N) = (0,...,0)$, which dynamics are governed by the Jacobian matrix J, given by the partial derivatives of the system at the fixed point: $J_{jk} = \partial F_j/\partial z_k$. We showed that the Jacobian matrix determines the statistics of the system and that delays can be treated in the Fourier space.

Results: We showed that the stationary instantaneous and lagged covariance matrices, the cross-spectrum, and the power spectral densities (PSDs) of the model can be obtained through algebraic operations including the Jacobian matrix. This can be done both in the homogeneous and the heterogeneous cases, and also in the presence of time delays. We illustrated the method by fitting human rs-fMRI signals from the HCP in the model's parameter space.

Conclusions: Using a linear approximation, we derived the network statistics of the Hopf whole-brain model. This can be done in the most general form of the model, namely in the delay-coupled heterogeneous case (allowing to study temporal and spatial hierarchies). The estimated statistics can be used to track changes in brain state, e.g.,low-level states of consciousness, anesthesia, sleep, etc., or to evaluate the effect of lesions in the connectome. Finally, the linear approximation of delay-coupled model derived here can represent a valuable tool to study the PSDs and cross-spectrum of MEG, which are well-stablished methods for FC analysis in the frequency domain.

References

1. Deco, G. et al. (2017). 'Single or multiple frequency generators in on-going brain activity: A mechanistic whole-brain model of empirical MEG data', NeuroImage, vol. 152, pp. 538–550.
2. López-González, A. et al. (2021) 'Loss of consciousness reduces the stability of brain hubs and the heterogeneity of brain dynamics', Communications Biology, vol. 4, p. 1037.
3. Smith, S. M. et al. (2013), 'Resting-state fMRI in the Human Connectome Project', NeuroImage, vol. 80, pp. 144–168.

Poster No 1705

Functional network integration mediates arousal effects on naturalistic recall

Jadyn Park[1], Jin Ke[1], Kruthi Gollapudi[1], Ioannis Pappas[2], Yuan Chang Leong[1]

[1]The University of Chicago, Chicago, IL, [2]Keck School of Medicine, University of Southern California, Los Angeles, CA

Introduction: A consistent finding in memory research is that arousing stimuli are more likely to be remembered than neutral ones. Yet, the neural mechanisms underlying how arousal supports memory are not fully understood. Fluctuations in arousal have been found to covary with functional network integration across the entire brain (Shine et al., 2016), which, in turn, is associated with memory encoding performance (Keerativittayayut et al., 2018). Here, we tested whether increases in functional network integration is a mechanism by which events with higher arousal are more strongly encoded and better remembered.

Methods: We used two publicly available fMRI datasets: "Sherlock" (n=17; Chen et al., 2017) and "FilmFest" (n=15; Lee & Chen, 2022). In both studies, participants watched hour-long movie clips immediately followed by a free verbal recall session in the scanner. For analysis, we identified 48 and 68 events from each respective dataset. We parcellated the cortical and subcortical regions into 216 ROIs by combining the Schaefer and the Melbourne subcortical atlas. We then constructed an unweighted, undirected graph from functional connectivity matrices for each participant and event. Metrics of functional network integration (global efficiency, participation coefficient) and segregation (modularity) were extracted to examine how the dynamic reorganization of their structure during encoding supports memory. To obtain a continuous measure of recall performance, we converted movie annotations and transcriptions of participants' recall to text embeddings using Google's Universal Sentence Encoder. We then calculated the memory fidelity as the cosine similarity between the movie and recall embeddings for each event--the higher the fidelity score, the better the participants recalled the event with accuracy and detail. To estimate the arousal level for each event, we used an open-access Large Language Model (LLM), StableBeluga-13B. We provided the model with detailed annotations on each event and prompted it to rate the arousal level of the event on a scale of 1 to 10. The model-generated ratings were validated against human ratings (n=30 for each experiment).

Results: LLM-generated arousal ratings were correlated with human ratings (Sherlock: r=.37, p=.02; FilmFest: r=.41, p=.006), demonstrating the model's consistency with human subjective ratings. Across both datasets, global efficiency at encoding was positively associated with subsequent recall fidelity (Sherlock: β=.19, SE=.03, t(809)=5.66, p<.001; FilmFest: β=.16, SE=.03, t(1017)=5.26, p<.001), suggesting that events associated with greater functional network integration were more likely to be remembered with greater accuracy and detail (Fig.1). Arousal was associated with both global efficiency and recall fidelity, such that highly arousing events coincided with greater network integration (Sherlock: β=.22, SE=.04, t(796)=4.91, p<.001; FilmFest: β=.21, SE=.04, t(1004)=5.33, p<.001) and higher recall fidelity (Sherlock: β=.20, SE=.04, t(796)=4.57, p<.001; FilmFest: β=.19, SE=.04, t(1004)=4.65, p<.001). Functional network integration mediated the effects of arousal on recall (Sherlock:β=.04, 95%CI=[.02, .06], p<.001; FilmFest: β=.03, 95%CI=[.02, .05], p<.001) (Fig.2). Importantly, the effects of brain-wide integration on recall fidelity were driven by inter-modular integration across multiple networks (e.g., DMN, attention, control) (Sherlock: β=.11, SE=.03, t(808.3)=3.16, p<.01; FilmFest: β=.10, SE=.03, t(1017)=3.14, p<.01). Conversely, modularity was not associated with recall fidelity, indicating that network segregation was not related to memory performance.

Conclusions: The study establishes arousal-dependent biases in memory to dynamic changes in the integration of functional brain networks. Combining the approaches from systems and affective neuroscience, our work contributes to building a theoretical framework that bridges affective states, ongoing cognition, and functional network topology.

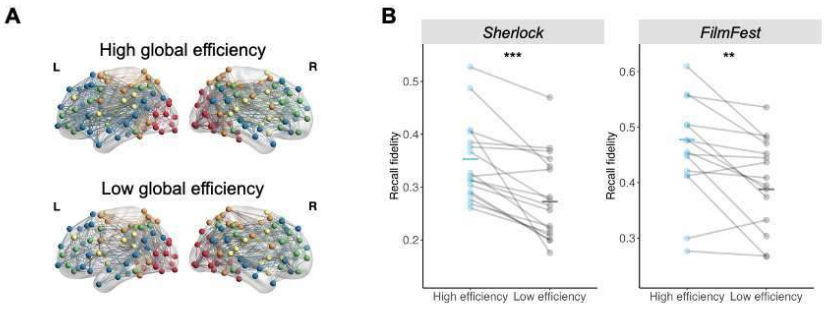

Figure 1. Memory benefits from whole-brain functional network integration
(A) Global efficiency, calculated as the inverse of the average shortest path length between all node pairs, reflects the efficiency of the network's information transfer. Higher global efficiency indicates greater functional network integration. For clarity, only 5 networks are shown in the illustration. **(B)** Across both datasets, higher global efficiency was associated with better recall fidelity. For visualization purposes, global efficiency values were split based on the median; however, all analyses were performed on a continuous scale. Each dot on the plot represents an individual participant. The figure illustrates paired t-tests comparing recall fidelity during periods of low vs. high global efficiency (*Sherlock:* $t(16)=4.85$, ***$p<.001$, *FilmFest:* $t(16)=3.43$, **$p<.01$).

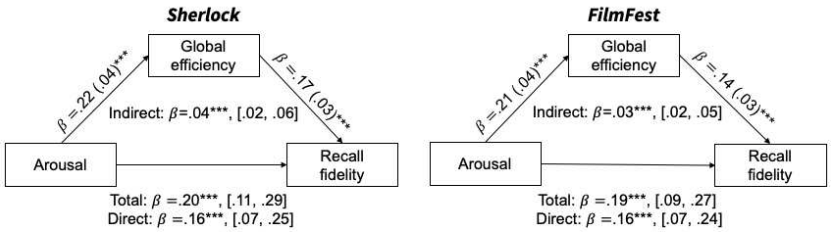

Figure 2. Functional network integration mediates effects of arousal on recall fidelity
The figure presents mediation models from *Sherlock* (left) and *FilmFest* (right). A formal mediation analysis revealed that global efficiency mediates arousal effects on recall. Indirect effects were computed for each of the 1,000 bootstrapped samples. Values in parentheses indicate standard error (***$p<.001$); values in brackets indicate 95% confidence interval.

References

1. Chen, J., Leong, Y. C., Honey, C. J., Yong, C. H., Norman, K. A., & Hasson, U. (2017). Shared memories reveal shared structure in neural activity across individuals. Nature Neuroscience, 20(1), Article 1. https://doi.org/10.1038/nn.4450
2. Keerativittayayut, R., Aoki, R., Sarabi, M. T., Jimura, K., & Nakahara, K. (2018). Large-scale network integration in the human brain tracks temporal fluctuations in memory encoding performance. eLife, 7, e32696. https://doi.org/10.7554/eLife.32696
3. Lee, H., & Chen, J. (2022). Predicting memory from the network structure of naturalistic events. Nature Communications, 13(1), 4235. https://doi.org/10.1038/s41467-022-31965-2
4. Shine, J. M., Bissett, P. G., Bell, P. T., Koyejo, O., Balsters, J. H., Gorgolewski, K. J., Moodie, C. A., & Poldrack, R. A. (2016). The Dynamics of Functional Brain Networks: Integrated Network States during Cognitive Task Performance. Neuron, 92(2), 544–554. https://doi.org/10.1016/j.neuron.2016.09.018

Poster No 1706

Comparing dynamic functional connectivity models in fMRI

Yiming Wei[1], Stephen Smith[1], Mark Woolrich[1], Rezvan Farahibozorg[1], Stanislaw Adaszewski[2], Stefan Fraessle[2]

[1]University of Oxford, Oxford, Oxfordshire, [2]F. Hoffmann-La Roche AG, Basel, Basel-Stadt

Introduction: Functional connectivity (FC) measures how different brain regions interact with each other. Recent research has increasingly focused on dynamic functional connectivity, which explores how these interactions change over time[1]. Despite various dynamic functional connectivity models in the literature, a comprehensive comparison of these approaches is absent. Here we conducted a systematic comparison of three models: Hidden Markov Modeling (HMM)[2], Dynamic network modeling (DyNeMo)[3,4] and Sliding Window Correlation (SWC)[5]. Our analysis encompassed a range of hyperparameters (number of input channels and number of distinct dynamic states), examining reproducibility and model goodness.

Methods: We utilized rfMRI data from the Human Connectome Project (HCP) S1200 release (N = 1003 subjects, four 15-min scans per subject)[6,7]. Processing included ICA-FIX denoising, surface alignment by MSMAll[8] and group-level spatial Independent Component Analysis (ICA)[9]. This process yielded spatial maps and the N_channels associated time series which are the input channels to dynamic modelling. The time series were z-scored for each 15min run. We then fitted HMM[2]

and DyNeMo[3,4] (Fig 1) on these data via stochastic variational inference using the osl-dynamics repository[10]. The range of hyperparameters was specified as N_channels = {15, 25, 50, 100} and N_states = {4, 8, 12, 16, 20}. For SWC[5], we first applied a Butterworth filter (order = 16, high-pass cut-off frequency = 0.25 Hz), set the window_length = 143, step_size = 118 to calculate functional connectivity, and finally employed K-means clustering to determine the centroids of these matrices in FC space. To assess model reproducibility, we divided all 4012 sessions randomly into two halves and trained our models on both splits, computed Fisher-z transformed correlation coefficients to quantify the similarity of states' functional connectivity matrices, and used the Hungarian algorithm to pair the model states obtained from different splits. Finally, the mean diagonal value of pair-reordered Fisher-z transformed correlation served as the measure of reproducibility. To evaluate model goodness, we conducted five separate model training sessions on the entire dataset and computed the average free energy.

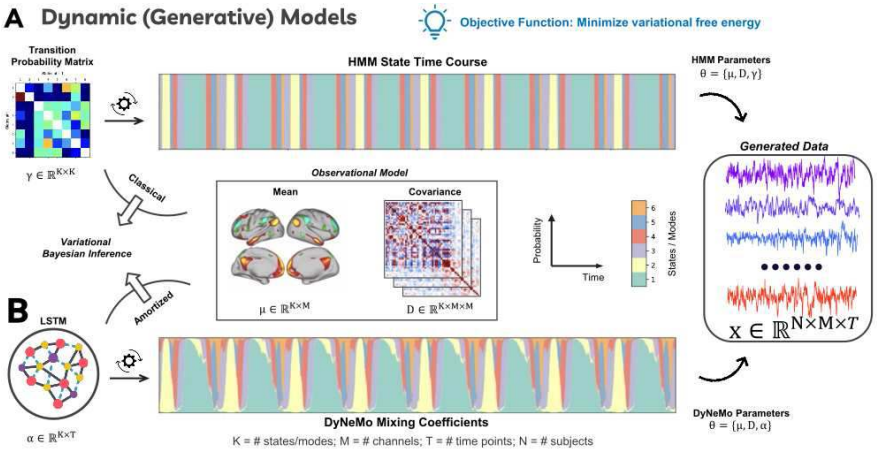

Figure 1. Dynamic (generative) functional connectivity models. (A) Hidden Markov Modelling (HMM) assumes the existence of a finite set of brain states, with each state corresponding to a mean activation and covariance pattern. The brain transitions between different states according to transition probability matrix (TPM). Given the observed data, it fits the model parameters (mean activation, covariance and TPM) via classical variational Bayesian method. **(B)** Dynamic Network Modes (DyNeMo) extends the HMM in two ways. First, it posits that the brain operates in a mixing combination of "modes" rather than mutually exclusive "states", and each mode has a mean activation and covariance matrix. Second, DyNeMo allows for long-range temporal dependencies by modelling the mixing coefficients with a Long Short-Term Memory (LSTM) network. The model then infers these parameters (mean activation, covariance matrix and LSTM weights) using amortized variational Bayesian inference. **This figure is adapted from Sungjun Cho's dissertation.**

Results: As shown in Fig 2A-C, the reproducibility of FC matrices from HMM and SWC is satisfactory, while FCs in DyNeMo exhibit poorer reproducibility across all hyperparameter settings. For example, with N_channels = 50, N_states = 12 (Fig 2B, left), state 0 in the first half of DyNeMo displays a low correlation with all other states from the second half. Comparison across different numbers of channels and states in Fig 2A-C also demonstrates a trend: larger N_channels and smaller N_states yield better reproducibility. Free energy decreases in the HMM as more states are introduced (Fig 2D). However, in DyNeMo, the free energy fluctuates as N_states increase (Fig 2E). This suggests the possibility of an optimal number of states for the free energy metric. It is also possible that there is instability in DyNeMo inference (for these rfMRI data). Moreover, the varying magnitudes of free energy across different models suggest that free energy may not be a reliable metric to select model type (HMM and DyNeMo) and N_channels. It should be noted that free energy is only available for generative models, and thus is not applicable to the SWC approach.

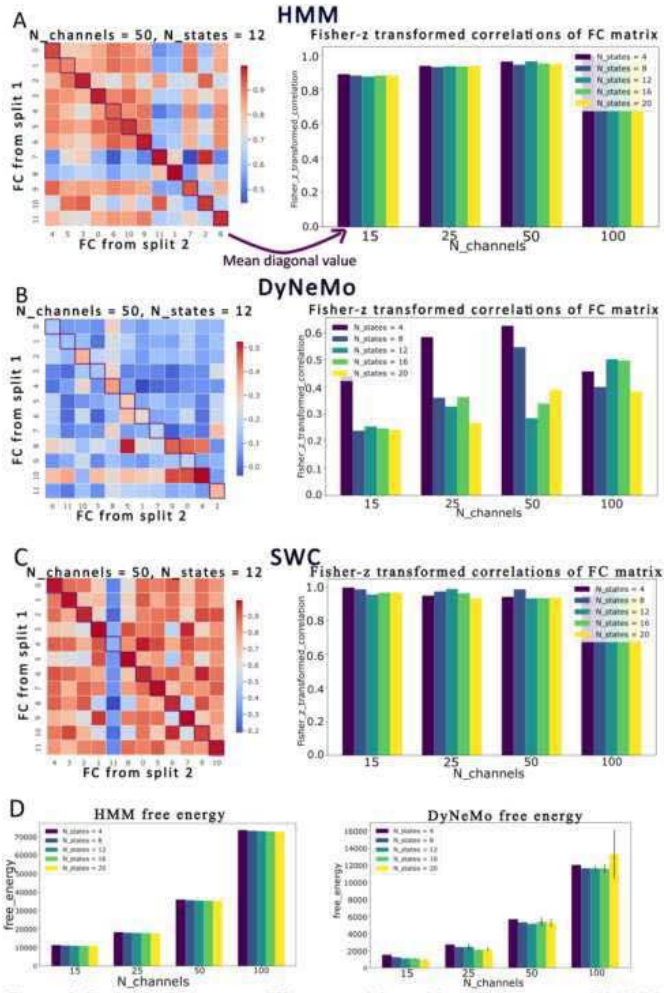

Figure 2. Performance across different models and hyperparameters. (A) HMM **(B)** DyNeMo **(C)** SWC reproducibility analysis. The entire dataset was randomly split into two halves, on which different models were trained. The functional connectivity matrices of states/modes from the first and second split were analyzed. On the left panel, the Fisher-z transformed correlation of these matrices were calculated and plotted, and these matrices were paired using Hungarian algorithm. We used the mean value of diagonal elements as a metric to measure the reproducibility and plotted it across different models and hyperparameters. **(D)** HMM **(E)** DyNeMo model goodness. Each model was trained on the entire dataset for five times, and the free energy was plotted across different models and hyperparameters. The heights represent the average free energy while the error bar is the standard deviation.

Conclusions: Our findings reveal that both HMM and SWC tend to produce states that are similar (within-method) to each other and exhibit superior reproducibility. Conversely, DyNeMo yields networks that are more distinct from each other and demonstrate greater representation capacity. As expected, larger numbers of states tend to explain the data better in different models, but this can come at the cost of lowering reproducibility.

References

1. Calhoun, V. D., Miller, R., Pearlson, G., & Adalı, T., 2014. The Chronnectome: Time-Varying Connectivity Networks as the Next Frontier in fMRI Data Discovery, Neuron, 84(2), 262–274.
2. Vidaurre, D., Smith, S. M., & Woolrich, M. W., 2017. Brain network dynamics are hierarchically organized in time, Proceedings of the National Academy of Sciences of the United States of America, 114(48), 12827– 12832.
3. Gohil, C., Roberts, E., Timms, R., Skates, A., Higgins, C., Quinn, A., Pervaiz, U., van Amersfoort, J., Notin, P., Gal, Y., Adaszewski, S., & Woolrich, M., 2022. Mixtures of large-scale dynamic functional brain network modes, NeuroImage, 263, 119595.
4. Pervaiz, U., Vidaurre, D., Gohil, C., Smith, S. M., & Woolrich, M. W., 2022. Multi-dynamic modelling reveals strongly time-varying resting fMRI correlations, Medical Image Analysis, 77, 102366.
5. Sakoglu, u., Pearlson, G. D., Kiehl, K. A., Wang, Y. M., Michael, A. M.,& Calhoun, V. D., 2010. A method for evaluating dynamic functional network connectivity and task-modulation: application to schizophrenia, Magnetic Resonance Materials in Physics, Biology and Medicine, 23(5), 351–366.

6. Van Essen, D. C., Smith, S. M., Barch, D. M., Behrens, T. E. J., Yacoub, E., & Ugurbil, K., 2013. The WU-Minn Human Connectome Project: An overview, NeuroImage, 80, 62–79.
7. Glasser, M. F., Sotiropoulos, S. N., Wilson, J. A., Coalson, T. S., Fischl, B., Andersson, J. L., Xu, J., Jbabdi, S., Webster, M., Polimeni, J. R., Van Essen, D. C., & Jenkinson, M., 2013. The minimal preprocessing pipelines for the Human Connectome Project, NeuroImage, 80, 105–124.
8. Robinson, E. C., Jbabdi, S., Glasser, M. F., Andersson, J., Burgess, G. C., Harms, M. P., Smith, S. M., Van Essen, D. C., & Jenkinson, M., 2014. MSM: A new flexible framework for Multimodal Surface Matching, NeuroImage, 100, 414–426.
9. Smith, S. M., Hyvärinen, A., Varoquaux, G., Miller, K. L., & Beckmann, C. F., 2014. Group-PCA for very large fMRI datasets, NeuroImage, 101, 738–749.
10. Gohil, C., Huang, R., Roberts, E., Es, M. W. J. v., Quinn, A. J., Vidaurre, D., & Woolrich, M. W., 2023. osl-dynamics: A toolbox for modelling fast dynamic brain activity, Pages: 2023.08.07.549346 Section: New Results.

Poster No 1707

Characterizing the Relationship Between Cortical Gradients and Cognitive Traits in Children

Mia Zwally[1], Dustin Moraczewski[1], Ka Chun Lam[2], Adam Thomas[1]

[1]National Institute of Mental Health, Data Science and Sharing Team, Bethesda, MD, [2]National Institute of Mental Health, Machine Learning Team, Bethesda, MD

Introduction: Cortical gradients, or axes of variance in cortical structure, provide a novel perspective on understanding brain functional connectivity, and while previous work has reached a consensus that the primary gradient in adults displays a unimodal to transmodal axis (Margulies et al., 2016), comparatively less work has investigated the development of functional gradients and their associations with behavioral and cognitive measures. In a developmental sample, Dong et al. found that the primary and secondary gradients of children before the age of 12 were flipped compared to their adult counterparts, with the unimodal to transmodal gradient being the secondary contributor in children while ranking as primary in adults (Dong et al., 2021). This study aims to replicate the findings of the flipped primary-secondary gradient within the larger (11,000 subjects) and more heterogeneous Adolescent Brain Cognitive Development dataset (ABCD) which was collected at 21 different sites across the United States. We also initiate the investigation of the complex, multidimensional relationship between functional gradient profiles and behavioral and cognitive traits in youth. Prior to beginning the analysis, we filed a pre-registration on OSF: https://doi.org/10.17605/OSF.IO/T9DHK

Methods: All code used in the creation of this abstract is publicly available in this repository: https://github.com/MIZwally/gradients-and-behavior This study uses the baseline resting state fMRI data from the ABCD dataset preprocessed with fMRIPrep 20.2.0 (Esteban et al., 2018) and 25 measures of behavior and cognition distributed in ABCD Annual Release 5. For comparisons with adult gradients, we used the Human Connectome Project (HCP) connectivity matrices distributed in the BrainSpace toolbox (Vos de Wael et al., 2020). After quality control, our ABCD sample consisted of 7,179 children. Using the 400-region, 17-network Schaefer atlas (Schaefer et al., 2018) we constructed a pairwise connectivity matrix for every participant, on which we calculated the top 10 gradients using the BrainSpace toolbox. Group gradients for both datasets were created from a connectivity matrix resulting from the average of all individual matrices. To investigate the relationship between gradient profiles and cognitive traits, we first calculated individual differences from the group via the Spearman's correlation of each individual's gradient to the group gradient (Mckeown et al., 2020). We then conducted a sparse PCA on the behavior and cognition measures, retaining the top 8 components that account for 95% of the variance. The individual to group correlations and the PCA components were entered into a canonical correlation analysis (CCA). Confidence intervals for all tests were created using 1000 bootstrap samples.

Results: Confirming previous findings, the correlation comparing the ABCD child primary and the HCP adult secondary was 0.418, 99% CI [0.416, 0.421], and the child secondary to adult primary 0.724, 99% CI [0.719, 0.728]. These primary-secondary correlations were greater than the primary-primary and secondary-secondary correlations of -0.011, 99% CI [-0.024, -0.001] and 0.168, 99% CI [0.162, 0.177], respectively. See Figures 1 and 2 for hemisphere visualizations of primary and secondary gradients from both ABCD and HCP samples. In addition, we found that the primary mode from the CCA had a correlation value of 0.220, 95% CI [0.206 0.240], suggesting that there is indeed a complex, multidimensional relationship between gradient profiles and measures of behavior and cognition.

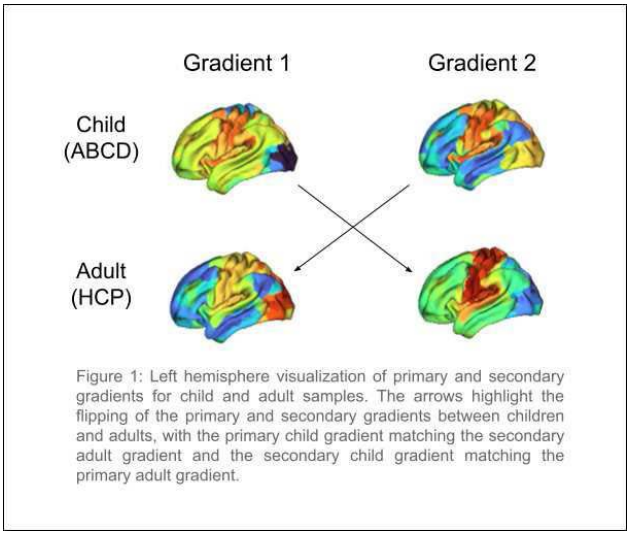

Figure 1: Left hemisphere visualization of primary and secondary gradients for child and adult samples. The arrows highlight the flipping of the primary and secondary gradients between children and adults, with the primary child gradient matching the secondary adult gradient and the secondary child gradient matching the primary adult gradient.

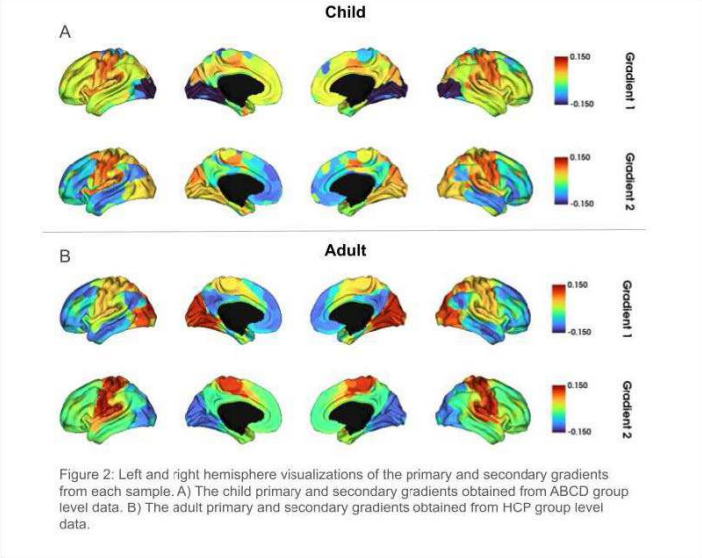

Figure 2: Left and right hemisphere visualizations of the primary and secondary gradients from each sample. A) The child primary and secondary gradients obtained from ABCD group level data. B) The adult primary and secondary gradients obtained from HCP group level data.

Conclusions: Our results show strong support for the flipping of the primary and secondary gradients in children through the replication of Dong et al. (2021) in a larger, more heterogeneous sample. In addition, we show that there is a complex, multidimensional relationship between functional gradient profiles and measures of behavior and cognition. Future work should focus on examining the nature of this relationship in greater detail.

References

1. Dong, H.-M., Margulies, D. S., Zuo, X.-N., & Holmes, A. J. (2021). Shifting gradients of macroscale cortical organization mark the transition from childhood to adolescence. Proceedings of the National Academy of Sciences, 118(28). https://doi.org/10.1073/pnas.2024448118
2. Esteban, O., Markiewicz, C. J., Blair, R. W., Moodie, C. A., Isik, A. I., Erramuzpe, A., Kent, J. D., Goncalves, M., DuPre, E., Snyder, M., Oya, H., Ghosh, S. S., Wright, J., Durnez, J., Poldrack, R. A., & Gorgolewski, K. J. (2018). fMRIPrep: A robust preprocessing pipeline for functional MRI. Nature Methods, 16(1), 111–116. https://doi.org/10.1038/s41592-018-0235-4
3. Goyal, N., Moraczewski, D., Bandettini, P. A., Finn, E. S., & Thomas, A. G. (2022). The positive–negative mode link between brain connectivity, demographics and behaviour: A pre-registered replication of Smith et al. (2015). Royal Society Open Science, 9(2). https://doi.org/10.1098/rsos.201090
4. Margulies, D. S., Ghosh, S. S., Goulas, A., Falkiewicz, M., Huntenburg, J. M., Langs, G., Bezgin, G., Eickhoff, S. B., Castellanos, F. X., Petrides, M., Jefferies, E., & Smallwood, J. (2016). Situating the default-mode network along a principal gradient of macroscale cortical organization. Proceedings of the National Academy of Sciences of the United States of America, 113(44), 12574–12579. https://doi.org/10.1073/pnas.1608282113
5. Mckeown, B., Strawson, W. H., Wang, H.-T., Karapanagiotidis, T., Vos de Wael, R., Benkarim, O., Turnbull, A., Margulies, D., Jefferies, E., McCall, C., Bernhardt, B., & Smallwood, J. (2020). The relationship between individual variation in macroscale functional gradients and distinct aspects of ongoing thought. NeuroImage, 220, 117072. https://doi.org/10.1016/j.neuroimage.2020.117072
6. Schaefer, A., Kong, R., Gordon, E. M., Laumann, T. O., Zuo, X.-N., Holmes, A. J., Eickhoff, S. B., & Yeo, B. T. (2017). Local-global parcellation of the human cerebral cortex from intrinsic functional connectivity MRI. Cerebral Cortex, 28(9), 3095–3114. https://doi.org/10.1093/cercor/bhx179
7. Vos de Wael, R., Benkarim, O., Paquola, C., Lariviere, S., Royer, J., Tavakol, S., Xu, T., Hong, S.-J., Langs, G., Valk, S., Misic, B., Milham, M., Margulies, D., Smallwood, J., & Bernhardt, B. C. (2020). BrainSpace: A toolbox for the analysis of macroscale gradients in neuroimaging and Connectomics datasets. Communications Biology, 3(1). https://doi.org/10.1038/s42003-020-0794-7

Poster No 1708

Using a SSVAE to Predict Antidepressant Treatment Response Among Older Adults with Depression

Linghai Wang[1], Jihui Diaz[1], Akiko Mizuno[1], James Wilson[2], Andrew Gerlach[1], Carmen Andreescu[1], Minjie Wu[1], Howard Aizenstein[1]

[1]University of Pittsburgh, Pittsburgh, PA, [2]University of San Francisco, San Francisco, CA

Introduction: Late-life depression (LLD) represents a significant concern in geriatric mental health due to its association with heightened risks of suicide, cardiovascular disease, and cognitive impairment including dementia[1]. The effectiveness of antidepressants for LLD is modest, typically achieving only a 50% remission rate for the first trial[2]. Resting-state functional magnetic resonance imaging (fMRI) is frequently used to understand responses to antidepressant treatment in LLD[3]. However, the analysis of such data often relies on aggregate measures due to challenges in interpreting raw data, which are characterized by noise, nonlinearities, and high dimensionality. Recent advancements in deep learning have demonstrated considerable promise for data-driven analysis of complex datasets, harnessing more nuanced information. In this study, we tested the performance of an analytic strategy integrating baseline resting-state fMRI functional connectivity data using a semi-supervised variational autoencoder (SSVAE) to predict depression remission of driven by standard antidepressant medication.

Methods: In this study, remission was encoded as a binary variable, defined by a final MADRS score of 10 or less for two consecutive weeks following 12 weeks of treatment, with assessments by a clinician blinded to the treatment conditions. A total of 80 resting-state fMRI scans were analyzed (mean±SD age 66.2±6.8 years; baseline MADRS 24.2.2±6.8). The image acquisition and processing details were outlined in the study by Wilson et al.[4]. Region-to-region functional connectivity (FC) was calculated for each scan using the Shen50 atlas. For the main model, demographic, and clinical factors, such as age, race, education, cumulative illness burden, baseline MADRS, and FC were used as inputs for an SSVAE[5], which was modified to predict remission status at the end of treatment (Fig. 1). The SSVAE combines an autoencoding network with a prediction network to efficiently learn information relevant for prediction while minimizing overfitting. The SSVAE was trained for an average of 22 epochs with early stopping at three epochs and a learning rate of 0.00001. The hyperparameters were selected using a held-out validation set comprising 10% of the data. Monte Carlo cross-validation over 30 repetitions was used to evaluate the model performance, with 20% of the data reserved for testing. The SSVAE's results were compared to a random forest classifier using the same cross-validation methods and evaluating the area under the curve (AUC). To evaluate the predictive significance of FC, we trained both SSVAE and random forest models with an identical set of input variables, excluding FC, as a secondary model for each.

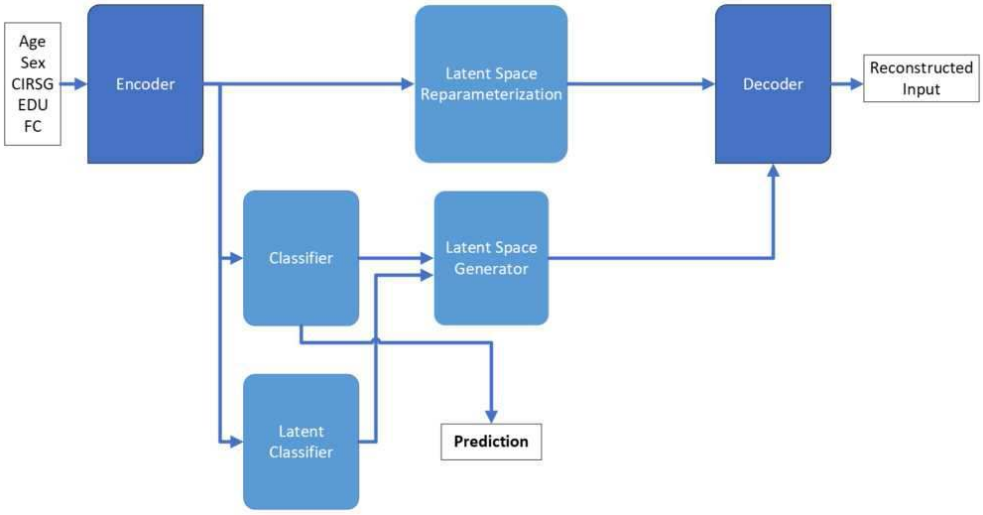

Results: These results are promising, indicating that a pretreatment scan can predict the treatment response. From our testing, the SSVAE outperformed the random forest model when including pre-treatment FC but performed worse when it was excluded. This indicates the ability of the SSVAE to effectively handle a larger number of variables in the prediction. This is consistent with the ability of neural networks to scale effectively for complex inputs. However, further work is needed to refine the interpretation of these predictions.

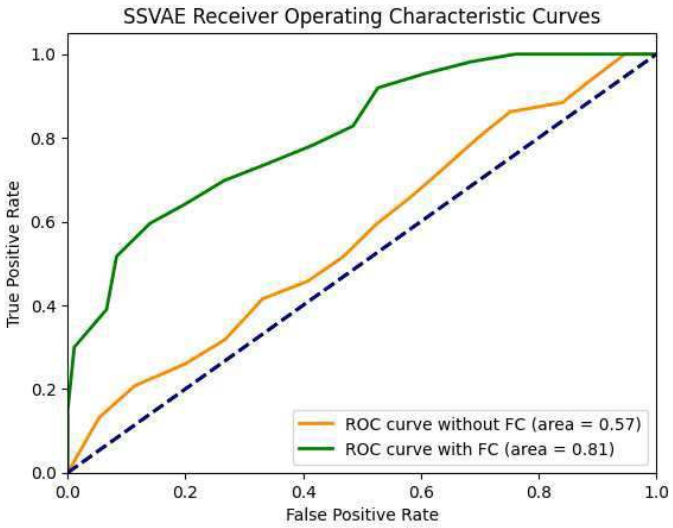

Conclusions: These results are promising, indicating that a pretreatment scan can predict the effectiveness of first-line antidepressant treatments. From our testing, the SSVAE outperformed the random forest model when including pre-treatment FC but performed worse when it was excluded. This indicates the ability of the SSVAE to effectively handle a larger number of variables in the prediction. This is consistent with the ability of neural networks to scale effectively for complex inputs. However, further work is needed to refine the interpretation of these predictions.

References

1. Sekhon S., Patel J., Sapra A. (2023), 'Late-Life Depression' StatPearls. https://www.ncbi.nlm.nih.gov/books/NBK551507/
2. Trivedi, M. H., Rush, A. J., Wisniewski, S. R., et al. (2006), 'Evaluation of outcomes with citalopram for depression using measurement-based care in STAR*D: implications for clinical practice', The American journal of psychiatry, vol. 163, pp. 28–40. https://doi-org.pitt.idm.oclc.org/10.1176/appi.ajp.163.1.28
3. Dichter G.S., Gibbs D., Smoski M.J. (2012), 'A systematic review of relations between resting-state functional-MRI and treatment response in major depressive disorder', Journal of Affective Disorders, vol. 172, pp. 8-17, https://doi.org/10.1016/j.jad.2014.09.028.
4. Wilson, J.D., Gerlach, A.R., Karim, H.T. et al. (2023), 'Sex matters: acute functional connectivity changes as markers of remission in late-life depression differ by sex', Molecular Psychiatry, https://doi.org/10.1038/s41380-023-02158-0
5. Zhuang, Y., Zhou Z., Alakent B., et al. (2022), 'Semi-supervised Variational Autoencoder for Regression: Application on Soft Sensors', arXiv, https://doi.org/10.48550/arXiv.2211.05979

Poster No 1709

Investigation into the Dynamic Repertoire and Functional Connectivity in Focal Epilepsy

Oliver Sherwood[1], David Carmichael[2], Joel Winston[3], Robert Leech[2]

[1]Kings College London, London, United Kingdom, [2]King's College London, London, United Kingdom, [3]Kings College London, London, United Kingdom

Introduction: Epilepsy is a neurological disorder characterised by abnormally coordinated brain activity which leads to seizures. Treatment for epilepsy is managed with anti-seizure medication that is effective in 70% of patients; however, there is still a large proportion of people unable to achieve seizure freedom[1]. Our current understanding of epilepsy is as a network disorder, largely due to imaging findings that demonstrate focal and generalised epilepsy being characterised by macroscopic network perturbations. However, an improved understanding of network dynamics and their perturbation in epilepsy could provide new diagnostic and therapeutic avenues[2]. This study aims to investigate the dynamic repertoire of patients with focal epilepsy (FE) using Leading Eigenvector Dynamic Analysis (LEiDA) to describe functional network dynamics in BOLD (Blood Oxygen Level Dependent) fMRI[3]. Specifically, we aimed to determine the occurrence and stability of FC brain states in a group of FE patients compared to healthy controls (HC).

Methods: This study used 55 participants consisting of patients with Focal Epilepsy (35 drug-resistant children aged 7-18 years) and healthy controls (20 children without Epilepsy aged 7-17 years). First, BOLD phase coherency connectivity is used to obtain a time-resolved dynamic Functional Connectivity (dFC) matrix for each run. A Hilbert transform is used to calculate phase of the acquired BOLD signal, and the phase coherence is calculated at each time point (t) between each of the 90 brain regions (n, p) of the AAL atlas parcellation. We consider only the leading eigenvector of each dFC(t). We next apply k means clustering analysis of all the leading eigenvectors across time-points and subjects (varying the k values between 2

and 20 clusters and obtain k centroid clusters each representing an Nx1 vector of the recurrent FC state). We next compare our obtained FC states to 7 a-priori resting state networks (RSN's) defined by Yeo et al[4] as well as delving into the FC state trajectory amongst the participants (achieved by calculating: mean fractional occupancy, dwell time and the transition probability of the FC states). Statistical validity was assessed using a Monte Carlo Permutation test which functions by calculating a test statistic (in this case Levene's t-test) for the obtained group assignments, before reshuffling the data and thus group assignments and recalculating the test statistic.

Results: Following analysis, the optimal clustering was obtained using the Dunn index at k = 13 (figure 1). Fractional occupancy of brain states resembling limbic and visual network were significantly different between the two groups ($p<0.05$). In dwell time, a significant difference between groups was only seen in one brain state (brain state = 9, visual network) ($p<0.05$) (figure 2). The transition matrix showed a significant difference in transitions from FC state 3 (visual) to FC state 9 (visual) as well as from FC state 8 (frontal parietal) to FC state 13 (unlabelled).

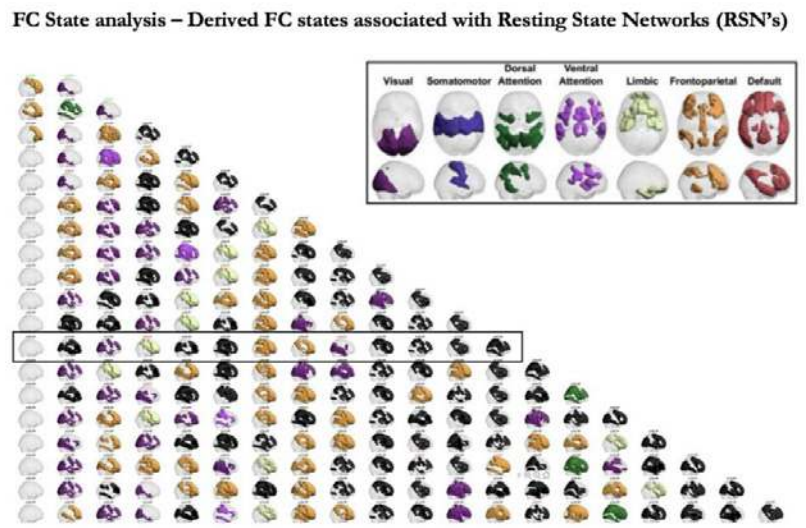

Figure 1 - Shows each of the derived brain states from the LEiDA analysis, each row represents a k numbers (2-20) from the clustering and columns represent discrete FC states associated with the 7 resting state networks. The rectangle on row 13 corresponds to the optimal cluster solution (k=13) from the Dunn's score.

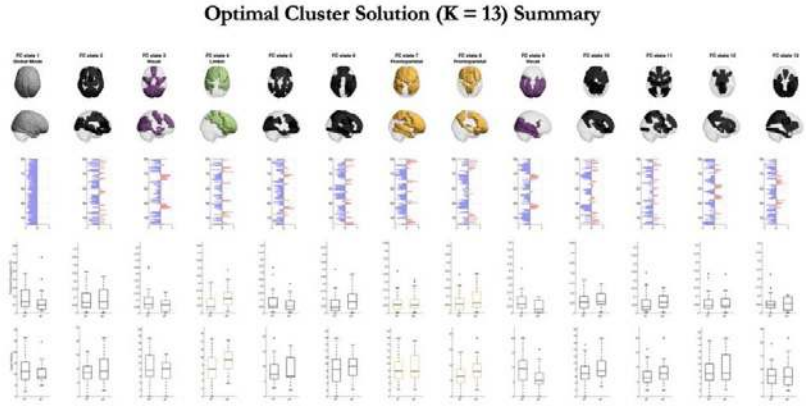

Figure 2 - Shows a summary of the clustering analysis for k=13. The Top layer represents the RSN centroids for each of the brain states. The second layer shows which brain areas are involved with each FC state. The 3rd layer contains boxplots which describe the mean fractional occupancy for each of the FC states. The 4th layer contains boxplots which illustrate the dwell time for each FC state. The boxplots are colour coded based on a p-value threshold described above whereby: Red= p1, green = p2, Blue= p3.

Conclusions: From these results it appears that FE patients are less likely to engage the limbic network than HCs but more likely to dwell in the visual network. It is interesting to note that there is no observed propensity for FE patients to reside within the DMN as has been observed in other research[5]. While it is imprudent to draw significant inferences from these preliminary results, it is clear that this method of analysis may prove vital in unpicking the variations in functional repertoire and transitions in patients with epilepsy compared to healthy controls. Further improvement of the analysis methods, to overcome limitations and diversify the dataset are required to fully investigate this. Some of these limitations include reliance on the AAL parcellation, heterogeneity within the FE group and unwanted decomposition of important signals from the data.

References
1. G. L. Krauss and M. R. Sperling, 'Treating patients with medically resistant epilepsy', Neurol. Clin. Pract., vol. 1, no. 1, p. 14, Dec. 2011.
2. M. Centeno and D. W. Carmichael, 'Network Connectivity in Epilepsy: Resting State fMRI and EEG-fMRI Contributions', Front. Neurol., vol. 5, 2014.
3. J. Cabral et al., 'Cognitive performance in healthy older adults relates to spontaneous switching between states of functional connectivity during rest', Sci. Reports 2017 71, vol. 7, no. 1, pp. 1–13, Jul. 2017.
4. B. T. Thomas Yeo et al., 'The organization of the human cerebral cortex estimated by intrinsic functional connectivity', J. Neurophysiol., vol. 106, no. 3, pp. 1125–1165, Sep. 2011.
5. N. B. Danielson, J. N. Guo, and H. Blumenfeld, 'The default mode network and altered consciousness in epilepsy', Behav. Neurol., vol. 24, no. 1, p. 55, Jan. 2011.

Poster No 1710

Harmonizing Structural and Functional Brain Connectivity: A Graph Neural Network Approach

Gang Qu[1], Aiying Zhang[2], Yu-Ping Wang[3]

[1]Tulane University, Metairie, LA, [2]University of Virginia, Charlottesville, VA, [3]Tulane University, New Orleans, LA

Introduction: The fusion of multimodal neuroimaging data is essential for advancing neuroscience, offering a comprehensive perspective on the brain dynamics. Structural connectivity (SC) defines the anatomical network of neuronal pathways (Hagmann2010), while functional connectivity (FC) reflects the transient neural activity patterns associated with cognitive functions (Zhang2022). The concurrent analysis of these modalities is challenging, necessitating the reconciliation of SC's static precision with the variable nature of FC to obtain a holistic understanding of the brain's functionality (Damoiseaux2009,Yan2022). Harmonizing these modalities is further complicated by the high-dimensional nature of neuroimaging data, which necessitates sophisticated methods to maintain the integrity of the intricate topology of neural networks (Qu2021). By meticulously integrating SC and FC data within a unified topological context and enriching it with anatomical statistics (AS), our endeavor represents a substantial step forward in multi-modal brain network analysis, promising to enrich the understanding and interpretation of complex neural interactions.

Methods: The HCP-D maps the connectome in individuals aged 5 to 21, encompassing 1,300 participants (Somerville2018). Scanning protocols, consistent across multiple sites, include sMRI, d-MRI, and rs-fMRI. We applied HCP minimal preprocessing to rs-fMRI data to employ smoothing and motion regression based on FD (Power2012). fMRI was assessed using Glasser360 atlas (Glasser2016), and d-MRI data were preprocessed with MRtrix, facilitating SC measurement with the same ROIs. AS from cortical parcellation complemented these data, offering a detailed view of brain structure and connectivity during development (Cruces2022). To address the significant disparities in the values of SC and anatomical metrics, we employed normalization techniques. To address the significant disparities in the values, SC were standardized by the square root of the product of gray matter volumes in the interconnected regions. To refine the representation of brain networks, we implemented a Graph Convolutional Network (GCN), operating on a sparsified binary adjacency matrix to capture the intricacies of the brain's network structure. FC and SC serve as primary features in the GCN, ensuring the preservation of topological accuracy and inter-regional connectivity patterns. AS are introduced as supplementary features for a comprehensive architectural analysis of the brain. Subsequent to the embedding of SC and FC, the embeddings are concatenated with AS, preceding the readout stage that entails graph pooling and final predictive model formulation, as illustrated in the Fig.1.

Results: The model was applied to estimate age-adjusted Crystal Cognition Composite (CCC) and Fluid Cognition Composite (FCC) Scores using multimodal neuroimaging data. Preliminary analyses assessed the efficacy of individual and combined data modalities. The model's predictive performance was then benchmarked against established models, including LR, MLP, and graph-based deep learning architectures such as GIN and GAT, with results delineated in Table 2. The integration of FC, SC, and AS markedly enhanced performance compared to single or dual-modality analyses. Additionally, the GCN architecture surpassed all comparison models in predictive accuracy, as quantified by RMSE with associated mean and standard deviation.

Conclusions: Our integrative framework synthesizes functional and structural connectivity with AS, enhancing neuroimaging analytics. Validation on the HCP-D demonstrates a significant enhancement in cognitive score predictions, outstripping established analytical models. The empirical evidence attests to the GNN's adeptness in modeling the brain's elaborate topology, indicating its utility in augmenting the fidelity of multimodal neuroimaging investigations and contributing to a more nuanced comprehension of cerebral connectivity dynamics.

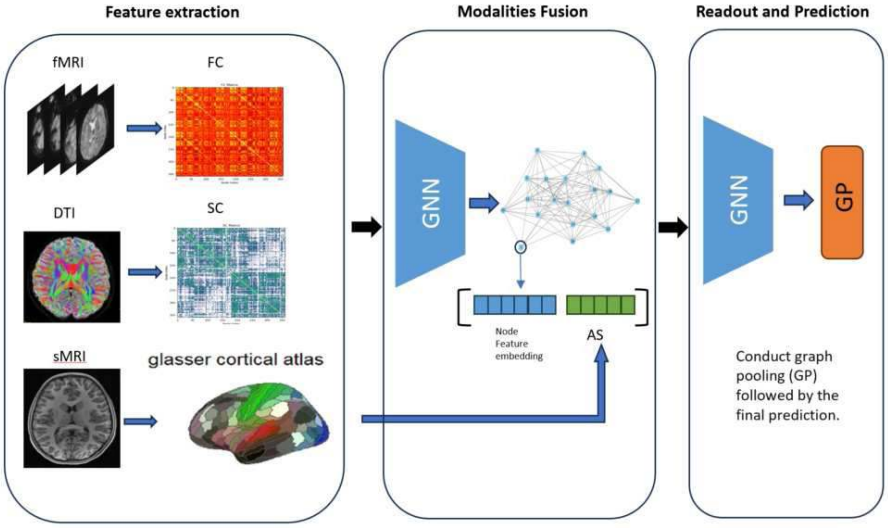

Table 1: Notations and GGT forward propagation.

Notation	Description
$H^{(l)}$	Features at the l-th layer
$\hat{A}$	Augmented adjacency matrix
Θ	Weight matrix
AS	anatomical statistics matrix
E	GCN-embedded features
$\hat{D}$	Degree matrix of $\hat{A}$
$W^{(l)}$	Weight matrix for the l-th layer
σ	Non-linear activation function
SC normalization	$SC_{normalized}(i,j) = \frac{SC_{raw}(i,j)}{\sqrt{v_{GM}(i) \cdot v_{GM}(j)}}$
GCN	$H^{(l+1)} = \sigma\left(\hat{D}^{-\frac{1}{2}}\hat{A}\hat{D}^{-\frac{1}{2}}H^{(l)}W^{(l)}\right)$
Propagation	$H^{(1)} = \mathrm{GCN}(H^{(0)}; \Theta^{(0)})$ $H^{(1)} = \mathrm{Concatenate}(H^{(1)}, AS)$ $\hat{y} = \mathrm{Readout}(H^{l})$

Table 2: Prediction Performance.

Model	Modalities	CCC RMSE	P-value	FCC RMSE	P-value
GCN	FC	17.168 ± 0.003	<0.001	16.987 ± 0.017	<0.001
GCN	SC	19.224 ± 0.000	<0.001	16.622 ± 0.000	<0.001
GCN	FC+SC	16.994 ± 0.520	0.006	16.573 ± 0.480	0.008
GCN	**FC+SC+AS**	**16.374 ± 0.004**	-	**16.032 ± 0.001**	-
GAT	FC+SC+AS	17.211 ± 0.317	<0.001	17.441 ± 0.209	<0.001
GIN	FC+SC+AS	16.947 ± 0.716	0.040	17.675 ± 0.707	<0.001
Linear	FC+SC+AS	17.492 ± 0.387	<0.001	17.737 ± 0.386	<0.001
MLP	FC+SC+AS	17.014 ± 0.010	<0.001	17.508 ± 0.010	<0.001

[a] Each deep learning model is constructed with a base two-layer architecture, followed by a dense readout layer for making predictions.
[b] Hyperparameters are optimized for each distinct model, while L2 regularization is applied to mitigate overfitting across all models.
[c] The dataset underwent random partitioning into training, validation, and test subsets at a ratio of 70:10:20.
[d] Model efficacy was evaluated using bootstrap analysis with 10 repeated experiments, supplemented by paired t-tests for statistical significance assessment of performance variations.

References

1. Cruces, R. R. (2022). 'Micapipe: A pipeline for multimodal neuroimaging and connectome analysis', NeuroImage, vol. 263, 119612.
2. Damoiseaux, J. S. (2009). 'Greater than the sum of its parts: A review of studies combining structural connectivity and resting-state functional connectivity', Brain Structure and Function, vol. 213, pp. 525–533.
3. Glasser, M. F. (2016). 'A multi-modal parcellation of human cerebral cortex', Nature, vol. 536, no. 7615, pp. 171–178.
4. Hagmann, P. (2010). 'White matter maturation reshapes structural connectivity in the late developing human brain', Proceedings of the National Academy of Sciences, vol. 107, no. 44, pp. 19067–19072.
5. Power, J. D. (2012). 'Spurious but systematic correlations in functional connectivity MRI networks arise from subject motion', NeuroImage, vol. 59, no. 3, pp. 2142–2154.
6. Qu, G. (2021). 'Ensemble manifold regularized multi-modal graph convolutional network for cognitive ability prediction', IEEE Transactions on Biomedical Engineering, vol. 68, no. 12, pp. 3564–3573.
7. Somerville, L. H. (2018). 'The lifespan human connectome project in development: A large-scale study of brain connectivity development in 5–21 year olds', NeuroImage, vol. 183, pp. 456–468.
8. Yan, W. (2022). 'Deep learning in neuroimaging: Promises and challenges', IEEE Signal Processing Magazine, vol. 39, no. 2, pp. 87–98.
9. Zhang, A. (2022). 'Decoding age-specific changes in brain functional connectivity using a sliding-window based clustering method', Neuroscience. Preprint.

Poster No 1711

Intraindividual variability in functional cortical organization relates to hormone levels and stress

Bianca Serio[1], Deniz Yilmaz[2], Laura Pritschet[3], Hannah Grotzinger[3], Emily Jacobs[3], Simon Eickhoff[4], Sofie Valk[5]

[1]Max Planck School of Cognition, Leipzig, Germany, [2]Palo Alto High School, Palo Alto, USA, [3]University of California Santa Barbara, Santa Barbara, USA, [4]Institute for Systems Neuroscience, Medical Faculty, Heinrich-Heine University Düsseldorf, Düsseldorf, Germany, [5]Max Planck Institute for Human Cognitive and Brain Sciences, Leipzig, Germany

Introduction: Open science initiatives and study consortia allow the field of neuroscience to conduct population-level research, with large samples in the order of thousands of subjects aiming to yield more generalizable effects (Marek et al., 2022). However, generalizability implies focusing on inter-individual similarities to detect group-level effects, and large

samples require the collection of unspecific data that answers general questions. We thus lack studies focusing on intra-individual variability through fine-grained data, designed to mechanistically probe neurocognitive processes such as the neuromodulatory role of hormones (Pritschet et al., 2021) or the physiological and neurocognitive influence of stress (Harrewijn et al., 2020). Here, we used densely sampled and deeply phenotyped data to investigate intra-individual variability in functional organization, exploring hormone levels and self-reported stress as potential underpinnings.

Methods: One female (23 years) and one male (26 years) were respectively tested for 29 and 20 consecutive days in time-locked study sessions including brain imaging, venipuncture/salivary sampling and self-report questionnaires. We computed the sensory-association (S-A) axis as our measure of functional organization as it represents a key macroscale organizational principle. For this, we used diffusion map embedding to reduce the dimensionality of functional connectivity matrices (Margulies et al., 2016) at each timepoint for both subjects (Fig. 1A-B). We tested inter-individual differences in intra-individual variability along the S-A axis over time with Levene's test for equality of variances, quantifying variability as the standard deviation (STD) of parcel loadings on the S-A axis, and differences in variability by subtracting male from female STD. We used linear models to test local effects of hormone levels (serum estradiol and progesterone in the female, salivary testosterone and cortisol in the male), as well as self-reported stress, on the S-A axis. We used Spearman's rank correlation to test for associations between patterns in these local effects and patterns of inter-individual differences in variability. We also used linear models to test system-level effects of hormones and stress on measures of network topography, namely within- (WN) and between- (BN) network dispersion, quantifying the spread of functional networks along the S-A axis. False discovery rate correction was used on linear model local-level results, and Bonferroni correction was used on linear model system-level results (7 networks for WN dispersion, 21 pairwise network comparisons for BN dispersion), in addition to spin permutation testing (1000 permutations) to control for spatial autocorrelation.

Results: Inter-individual differences in variability were found along the S-A axis, predominantly in association areas belonging to the default mode network (Fig. 1C-D). In fact, statistically significant greater local variability was found exclusively in the male subject. Except for testosterone (Fig. 1E), there were no local-level effects of hormones or stress on the S-A axis, and except for cortisol, there were no associations between patterns of local effects and patterns of inter-individual differences in variability. However, stress and the hormones assessed per subject all revealed some intra-individual system-level effects on WN dispersion (Fig. 1F-G). There were no effects on BN dispersion.

Conclusions: Using a dense sampling approach, we showed daily variations in human functional organization in two healthy subjects. Interestingly, we found extensive intra-individual system-level effects of hormone levels and perceived stress on WN dispersion, whereas local-level effects on the S-A axis were only subtle. Further research in larger samples is required to generalize endocrine and cognitive diurnal effects on intra-individual variability and to probe sex differences as well as limits to reliability in such effects.

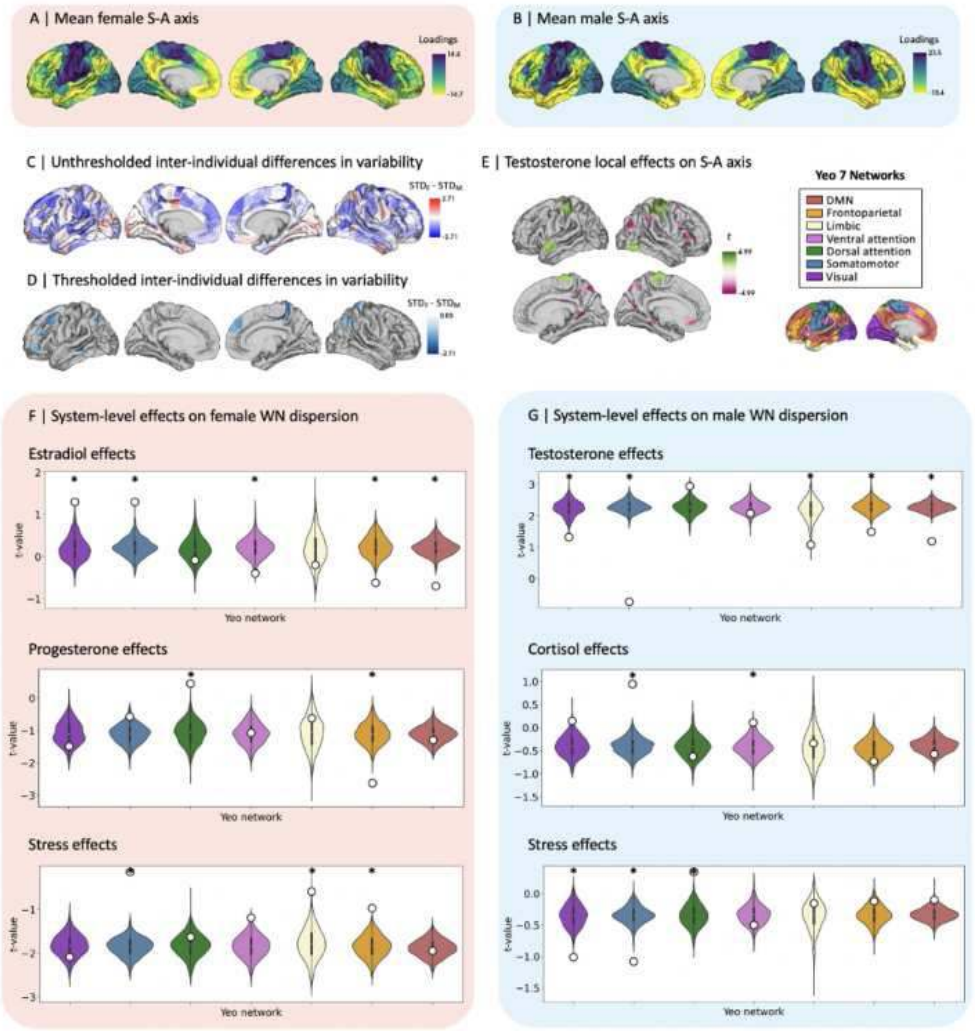

Figure 1. Inter- and intra-individual variability on the sensory-association (S-A) axis, with local- and system-level hormonal and stress effects. Mean S-A axis loadings (spanning from visual to default mode network (DMN) regions) on hemispheric surfaces (across time) in **A** | female subject and **B** | male subject; **C** | Unthresholded inter-individual differences in variability, calculated by locally (i.e., per parcel) subtracting male from female standard deviation (STD) of S-A axis loadings across time; **D** | Thresholded inter-individual differences in variability, i.e., only displaying statistically significant inter-individual differences established by Levene's test for equality of variances following false discovery rate (FDR) correction ($q < 0.05$); **E** | FDR-corrected statistically significant testosterone local effects on male subject's S-A axis, established by linear regression; **F** | female subject and **G** | male subject *t*-values for system-level effects on within-network (WN) dispersion for each Yeo network (displayed as white dots), plotted on null distributions of *t*-statistics derived from 1000 spin permutations. * indicates Bonferroni-corrected ($p_{spin} < .004$) statistical significance of the sex contrast.

References

1. Harrewijn, A. (2020). Associations between brain activity and endogenous and exogenous cortisol–a systematic review. Psychoneuroendocrinology, 120, 104775.
2. Marek, S. (2022). Reproducible brain-wide association studies require thousands of individuals. Nature, 603(7902), 654-660.
3. Margulies, D. S. (2016). Situating the default-mode network along a principal gradient of macroscale cortical organization. Proceedings of the National Academy of Sciences, 113(44), 12574-12579.
4. Pritschet, L. (2021). Applying dense-sampling methods to reveal dynamic endocrine modulation of the nervous system. Current opinion in behavioral sciences, 40, 72-78.

Poster No 1712

Resilience in Juvenile Fibromyalgia: Links with Symptoms, Affective Distress, and Brain Connectivity

Maria Suñol[1], Jon Dudley[2], Michael Payne[3], Han Tong[2], Tracy Ting[2], Susmita Kashikar-Zuck[2], Robert Coghill[2], Marina López-Solà[1]

[1]University of Barcelona, Barcelona, Catalunya, [2]Cincinnati Children's Hospital Medical Center, Cincinnati, OH, [3]Cincinnati Children's Hospital Medical Center, Cincinnati, OH

Introduction: Juvenile fibromyalgia (JFM) is a chronic pain syndrome predominantly affecting adolescent females[1,2]. In JFM, resilience has been associated with reduced pain, disability, symptom severity, and suicidality, and with increased energy levels and quality of life[3,4]. Thus, resilience may be a protective factor in coping with pain, reducing affective burden, and promoting a positive outlook. We study, for the first time, differences between higher vs. lower resilience JFM adolescents on core disease symptoms, affective traits, and brain functional connectivity.

Methods: We recruited 41 adolescent females with JFM and 40 matched pain-free adolescent females. Participants completed a resting-state fMRI exam and validated questionnaires on resilience (Shift-and-Persist Scale), core JFM symptoms (Fibromyalgia Symptom Severity Questionnaire, Widespread Pain index, Functional Disability Inventory), and affective traits (Children's Depression Inventory, Screen for Child Anxiety-Related Disorders, Self-Compassion Scale). Based on Shift-and-Persist scores, we performed a hierarchical clustering analysis in the JFM group, which landed two patient subgroups (higher vs lower resilience). We performed two principal component analyses (varimax rotation and component' eigenvalues>1) to reduce the dimensionality of 1) core JFM symptom-related variables, and 2) affective traits. Next, using two-sample t-tests, we assessed differences in the principal components of core JFM symptoms and affective traits between JFM patients with higher vs. lower resilience. Imaging data were preprocessed and denoised using MATLAB-R2021a and the CONN Toolbox-20.b. We estimated resting-state functional connectivity strength with the Intrinsic Connectivity Contrast Approach[5] and computed average path length and clustering coefficient across the nodes of the cortical CONN network atlas. Connectivity strength and network topology differences between higher vs. lower resilience JFM groups were assessed with two-sample t-tests. For completion, we compared these subgroups of patients with pain-free controls in terms of clinical and connectivity measures.

Results: JFM patients with higher vs. lower resilience did not differ in the principal component summarizing core JFM symptoms (T=1.02; p=.314). In contrast, the groups differed in the component summarizing affective traits (T=4.03; p<.001). Considering component loadings, the higher resilience JFM group showed less depressive and anxiety symptoms and higher self-compassion. The high resilience JFM group (vs. the low resilience JFM group) showed increased connectivity strength in the posterior cingulate cortex (T=6.22; pFDR=.025), angular gyri (T's>3.9; pFDR's<.024), superior frontal (T>5.2, pFDR's<.017) and inferior temporal cortices (T's>4.7; pFDR<.015) (Figure 1). They also showed lower average path length (i.e., higher efficiency) in nodes of the visual, dorsal attention, and default-mode networks (T's>2.6, pFDR's<.041). We found no differences in clustering coefficient. Compared to controls, JFM patients with higher resilience had reduced connectivity strength in a single cluster located in the paracentral lobule (T=4.18; pFDR=.013), whereas JFM patients with lower resilience had a broader pattern of reduced connectivity encompassing sensorimotor, visual, attentional, and self-referential regions (T's>4 ; pFDR's<.04) (Figure 2).

Figure 1. Voxel-based Connectivity Differences: JFM Higher vs Lower Resilience

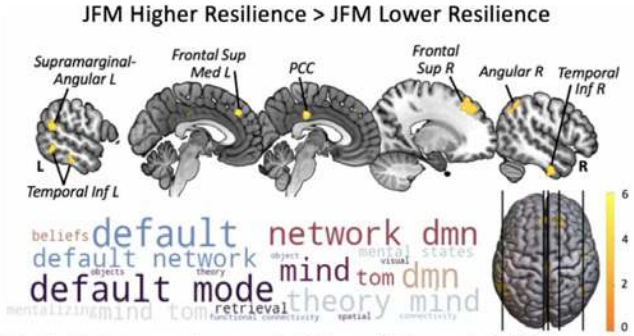

*Note: **Top**: Clusters in warm colors represent global connectivity increases in the JFM subgroup with higher resilience compared to the lower resilience subgroup. These findings survive a voxel-level threshold of p<.001 and an FDR cluster-level corrected pFDR<.05. The color bar indicates T-values. Inf: Inferior; L: Left; Med: Medial; PCC: Posterior cingulate cortex; R: Right; Sup: Superior; **Bottom**: Display of the 20 functional terms most associated with the unthresholded t-map based on the Neurosynth Database. Wordcloud was computed with Python. The size of the word is based on the correlation coefficient between each specific term and the connectivity t-map. The color of words is for aesthetic purposes.*

Figure 2. Voxel-based Connectivity Differences: JFM subgroups vs Healthy Controls

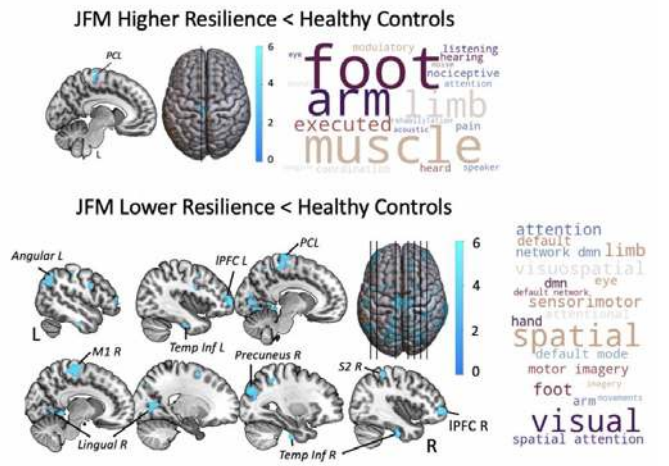

*Note: **Top** : Clusters in blue represent global connectivity decreases in the JFM subgroup with higher resilience compared to healthy controls. **Bottom**: Clusters in blue represent global connectivity decreases in the JFM subgroup with lower resilience compared to healthy controls. All findings survive a voxel-level threshold of p<.001 and an FDR cluster-level corrected pFDR<.05. The color bar indicates T-values. Inf: Inferior; L: Left; R: Right; IPFC: lateral prefrontal cortex; PCL: Paracentral Lobule; R: Right; S2: Secondary somatosensory cortex. **On the right**, we display of the 20 functional terms most associated with the unthresholded t-maps based on the Neurosynth Database. Wordcloud were computed with Python. The size of the word is based on the correlation coefficient between each specific term and the connectivity t-map. The color of words is for aesthetic purposes.*

Conclusions: Our results emphasize the clinical relevance of resilience in mitigating affective suffering and shaping neural networks, particularly the default-mode network. The higher resilience JFM group (vs. lower resilience JFM group) had similar levels of core JFM symptoms, reduced affective suffering, increased connectivity strength in key nodes of the DMN, and lower average path lengths in cortical networks. We found that the connectivity strength pattern of higher resilience JFM patients resembled that of pain-free controls more than the pattern observed in the lower resilience JFM group.

References

1. Kashikar-Zuck, S., & Ting, T. V. (2014). Juvenile fibromyalgia: current status of research and future developments. Nature reviews. Rheumatology, 10(2), 89–96. https://doi.org/10.1038/nrrheum.2013.177
2. Kashikar-Zuck, S., King, C., Ting, T. V., & Arnold, L. M. (2016). Juvenile Fibromyalgia: Different from the Adult Chronic Pain Syndrome?. Current rheumatology reports, 18(4), 19. https://doi.org/10.1007/s11926-016-0569-9
3. Gmuca, S., Xiao, R., Urquhart, A., Weiss, P. F., Gillham, J. E., Ginsburg, K. R., Sherry, D. D., & Gerber, J. S. (2019). The Role of Patient and Parental Resilience in Adolescents with Chronic Musculoskeletal Pain. The Journal of pediatrics, 210, 118–126.e2. https://doi.org/10.1016/j.jpeds.2019.03.006
4. Gmuca, S., Sonagra, M., Xiao, R., Miller, K. S., Thomas, N. H., Young, J. F., Weiss, P. F., Sherry, D. D., & Gerber, J. S. (2021). Suicidal risk and resilience in juvenile fibromyalgia syndrome: a cross-sectional cohort study. Pediatric rheumatology online journal, 19(1), 3. https://doi.org/10.1186/s12969-020-00487-w
5. Martuzzi, R., Ramani, R., Qiu, M., Shen, X., Papademetris, X., & Constable, R. T. (2011). A whole-brain voxel based measure of intrinsic connectivity contrast reveals local changes in tissue connectivity with anesthetic without a priori assumptions on thresholds or regions of interest. NeuroImage, 58(4), 1044–1050. https://doi.org/10.1016/j.neuroimage.2011.06.075

Poster No 1713

Comparison of neuroimaging topological properties of Meige's syndrome with hemifacial spasm

Hao Chen[1], Ying Wang[2], Kexue Deng[2], Yingxing Zhang[3]

[1]The First Affiliated Hospital of USTC, Hefei, Hefei, [2]The First Affiliated Hospital of USTC, Hefei, Anhui, [3]Anhui Hospital Affiliated to Children's Hospital of Fudan University/Anhui Children's Hospital, Hefei, China

Introduction: Meige's syndrome is one of the focal dystonic movement disorders, mainly characterized by bilateral blepharospasm and symmetrical and irregular contraction of oral and facial muscles (Hirono et al. 2014). Hemifacial spasm (HFS) is another kind of dystonia disorder with different clinical manifestations, which is often characterized by a unilateral twitch of the face (Brimley and Sampath 2021). Microvascular decompression is a commonly used method for the radical treatment of HFS (Joo et al. 2022), but there is no ideal treatment for Meige. Investigation of the differences in the neural basis of the two forms of dystonia might give us the inspiration to understand these diseases, which might further help with improving the treatment. Based on previous findings on the neural basis of both diseases, we hypothesized changed role of the frontal regions in the motor network might be related to the etiology of Meige and the main difference between these two

disorders. The present study aimed to estimate the differences in terms of functional connectivity between Meige's syndrome and the HFS.

Methods: Nineteen unilateral HFS patients (57.26±4.17 years, 13 females) and 15 Meige's syndrome patients (58.67±6.89 years, 10 females) were recruited in this study. All participants were right-handed with no major psychiatric disorders or neurological illnesses. All participants underwent MRI scanning on a GE 3.0T magnetic resonance scanner (GE, 750W). Resting-state MRI data with 242 frames were acquired with a T2*-weighted echo-planar imaging sequence (TE=30ms, TR=2000ms, FOV=240mm, matrix=64×64, flip angle=85°) with 33 axial slices (no gaps, voxel size: 3.6×3.6×3.6mm ^{3}) covering the whole brain. Corresponding high-resolution T1-weighted three-dimensional gradient-echo (for stereotaxic transformation) images were also collected (TR=1900ms; TE=2.26ms; TI=900ms; 1mm isotropic voxel; 250mm field of view). Resting-state fMRI data processing was conducted with AFNI (version AFNI_19.0.24, pre-compiled binary linux_ubuntu_16_64). To analyze the rsFC, we adopted the Anatomical Automatic Labeling (AAL) template, a brain atlas system including 90 regions of interest (ROIs) covering all the brain regions of cerebral cortex (Tzourio-Mazoyer et al. 2002). For each participant, the time-course of each ROI was extracted, and the corresponding degree centrality(Cd) and betweenness centrality(BC) of each ROI were computed. BC refers to the ratio of the shortest path that passes through a point and connects the two points to the total number of shortest path lines between the two nodes in the network (Verbavatz and Barthelemy 2022). Cd is a simple count of the total number of connections linked to a vertex, which is the most direct measure to describe node centrality in network analysis (Telesford et al. 2011). For either BC or Cd of all the 90 ROIs, we conducted a group t-test between Meige's patients and the HFS patients. And ROIs with p values were FDR corrected (with mafdr function embedded with Matlab R2022a,) and FDR less than 0.05 were considered as ROIs with significant between-group differences.

Results: There was no significant difference in age (t=−0.69, ρ=0.49) or gender distribution between the HFS and the Meige's syndrome patients, as shown in Fig. 1. As shown in Fig. 2, Meige's syndrome patients showed higher BC of the right superior frontal cortex and higher Cd of the left superior frontal cortex, the left superior medial frontal cortex, the right superior medial frontal cortex, and the left cerebellum cortex than the HFS patients (FDR correction with FDR value less than 0.05, whose uncorrected ρ< 0.005).

Conclusions: Higher centrality of the frontal and cerebellum cortex might be the topological property difference between Meige's syndrome and HFS, which may help to preliminarily understand the mechanism of and abnormal functional connection in Meige's patients, and further explore better treatment.

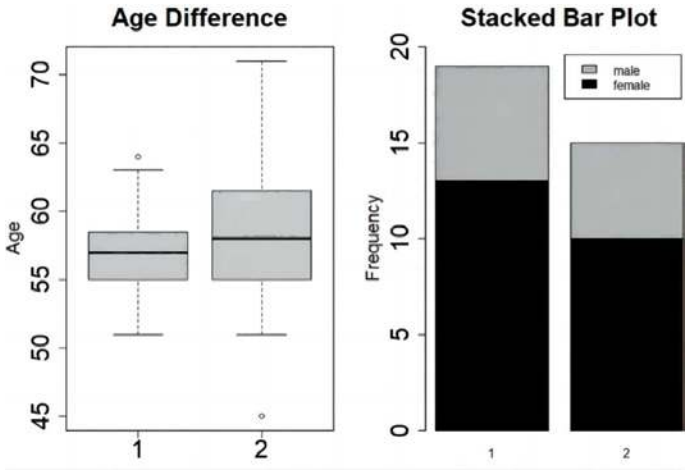

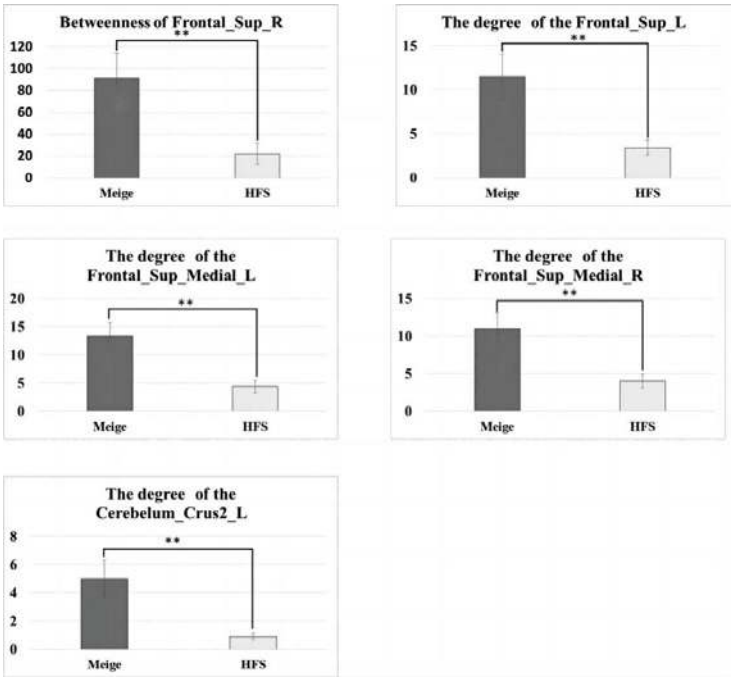

References

1. Brimley, CJ (2021) Hemifacial Spam: Endoscopic Assistance in Facial Nerve Decompression With Lateral Spread Response Corroboration: 2-Dimensional Operative Video. Operative Neurosurgery (Hagerstown, Md.), 20(2), E128. doi:10.1093/ons/opaa301.
2. Hirono, S (2014) Continuous intraoperative monitoring of abnormal muscle response in microvascular decompression for hemifacial spasm; a real-time navigator for complete relief. Neurosurgical Review, 37(2), 311–319; discussion 319-320. doi:10.1007/s10143-013-0507-5.
3. Joo, B-E (2022) Advances in Intraoperative Neurophysiology During Microvascular Decompression Surgery for Hemifacial Spasm. Journal of Clinical Neurology (Seoul, Korea), 18(4), 410–420. doi:10.3988/jcn.2022.18.4.410.
4. Telesford, QK (2011) The brain as a complex system: using network science as a tool for understanding the brain. Brain Connectivity, 1(4), 295–308. doi:10.1089/brain.2011.0055.
5. Tzourio-Mazoyer, N (2002) Automated anatomical labeling of activations in SPM using a macroscopic anatomical parcellation of the MNI MRI single-subject brain. NeuroImage, 15(1), 273–289. doi:10.1006/nimg.2001.0978.
6. Verbavatz, V (2022) Betweenness centrality in dense spatial networks. Physical Review. E, 105(5–1), 054303. doi:10.1103/PhysRevE.105.054303.

Poster No 1714

Integrating brainstem and cortical functional architectures

Justine Hansen[1], Simone Cauzzo[2], Kavita Singh[2], Maria Guadalupe Garcia-Gomar[2], James Shine[3], Marta Bianciardi[2], Bratislav Misic[4]

[1]McGill University, Montreal, QC, [2]Harvard Medical School, Boston, MA, [3]University of Sydney, Sydney, NA, [4]McGill University, Montreal, Quebec

Introduction: The brain is a network of functionally interacting neural populations. Studying the functional architecture of the brain in awake humans is possible with multiple imaging technologies, although these technologies are often biased towards the cortex where signal quality is highest[1]. Perhaps the biggest missing piece of modern in vivo brain network reconstruction is the brainstem. This early evolutionary structure is crucial for survival and consciousness, and integrates signals from throughout the nervous system. Furthermore, multiple neurotransmitter systems originate in brainstem nuclei and project throughout the cortex, shaping cortical activity[2]. However, knowledge about brainstem function primarily comes from either lesion studies or studies in model organisms, and these studies are often limited to specific nuclei or pathways. Exciting recent imaging advances have improved the feasibility of measuring brainstem activity, making it now possible to augment the cortical functional connectome with an anatomically comprehensive representation of the brainstem[3-5].

Methods: Here we study how functional activity throughout the brainstem aligns with cortical function. We use high-resolution 7 Tesla resting-state fMRI, via a novel brainstem-optimized acquisition protocol and processing pipeline, to image the whole-brainstem across 58 anatomically-defined nuclei spanning midbrain, pons and medulla[3-5]. First we identify hubs of brainstem-cortex functional connectivity (FC) and link brainstem-cortex FC with cytoarchitectonic classes, laminar differentiation, and

electrophysiological signatures of neural oscillations. Next, we cluster brainstem nuclei with respect to their cortical FC. Using meta-analytic cortical functional activation patterns from NeuroSynth, we derive a psychological signature for each brainstem community[6]. Furthermore, we use PET-estimated brain maps for 18 neurotransmitter receptors and transporters to determine whether neurotransmitter systems are mediating the link between neuromodulatory brainstem nuclei and cortical functional activation patterns[7]. Finally, we identify cortical regions that are similarly functionally connected with the brainstem, as well as the brainstem nuclei with which these cortical regions are connected. To ensure all findings are robust, we replicate the analyses using 3 Tesla data acquired in the same individuals, using an alternative parcellation resolution, and in the subcortex.

Results: We identify a compact set of brainstem-cortex hubs, including the periaqueductal grey, dorsal raphe, laterodorsal tegmental nucleus, and inferior medullary reticular formation (Figure 1a). On the other hand, cortical regions are functionally connected with the brainstem following an anterior-posterior gradient that is correlated with cellular architecture and MEG-derived oscillatory dynamics (Figure 1b-e). Next, we identify five modules of brainstem nuclei with distinct patterns of cortical FC related to memory, cognitive control, multisensory coordination, perception and movement, and emotion. Furthermore, we find that neuromodulatory nuclei within each module are likely mediating the link between brainstem module and cortical activation pattern. Finally, we find that cortical regions are functionally connected with the brainstem along a unimodal-transmodal hierarchy, indicating that the putative cortical functional gradient can be traced back to the brainstem (Figure 2a, b). Unimodal cortex is connected with caudal brainstem, and transmodal cortex with rostral brainstem (Figure 2c).

Conclusions: Altogether, using simultaneous in vivo human imaging of brainstem and cortical functional activity, this study extends our perspective of cortical function---including dynamics, cognitive function, and the unimodal-transmodal cortical functional gradient---to the brainstem, demonstrating how cortical functional architecture consistently reflects the brainstem.

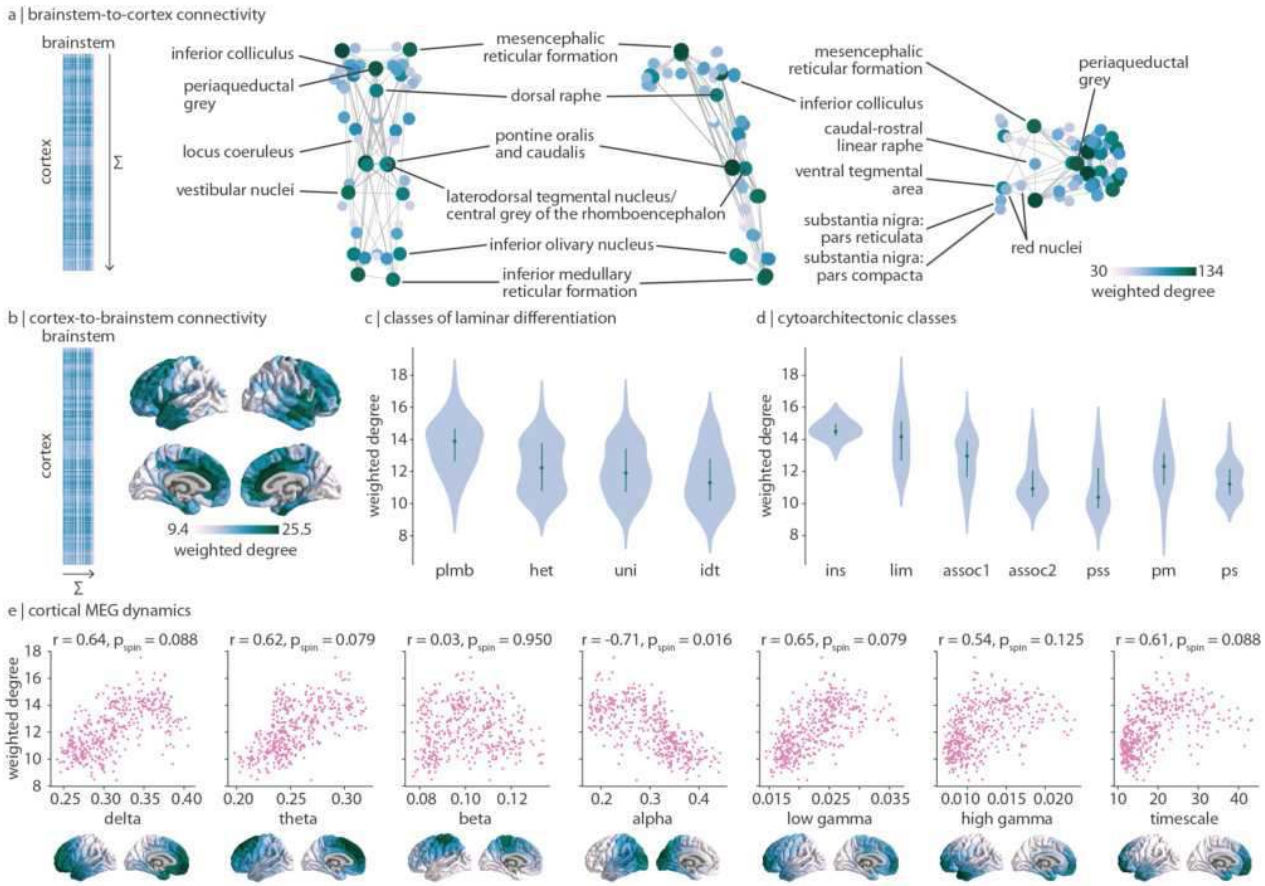

Figure 1. Dominant patterns of brainstem-cortex functional connectivity | **(a)** Brainstem-to-cortex weighted degree is calculated by summing a brainstem nucleus' functional connectivity across all cortical regions. Coronal (posterior view), sagittal, and axial perspectives of brainstem nuclei are shown. Node size and colour reflect weighted degree, and edges are plotted for the 5% strongest functional connections within the brainstem. Key brainstem nuclei are labelled. **(b)** Cortex-to-brainstem weighted degree is calculated by summing a cortical region's functional connectivity across all brainstem nuclei. **(c)** Cortex-to-brainstem weighted degree binned according to classes of laminar differentiation (one-way ANOVA $F=18.5$, $p=2.8\times10^{-11}$); plmb = paralimbic; het = heteromodal; uni = unimodal; idt = idiotypic. **(d)** Cortex-to-brainstem weighted degree binned according to classes of cytoarchitecture (one-way ANOVA $F=35.6$, $p=2.0\times10^{-34}$); ins = insular; lim = limbic; assoc1 = association network 1; assoc2 = association network 2; pss = primary/secondary sensory; pm = primary motor; ps = primary sensory. **(e)** Scatter plots are shown for the correlation between cortex-to-brainstem weighted degree and seven metrics of MEG dynamics: power spectrum distributions for six canonical frequency bands and the intrinsic timescale (temporal memory of a neural element); each point is a brain region (N=400). Cortical distributions of MEG measures are shown on the brain surface below each plot and are derived from data in the HCP.

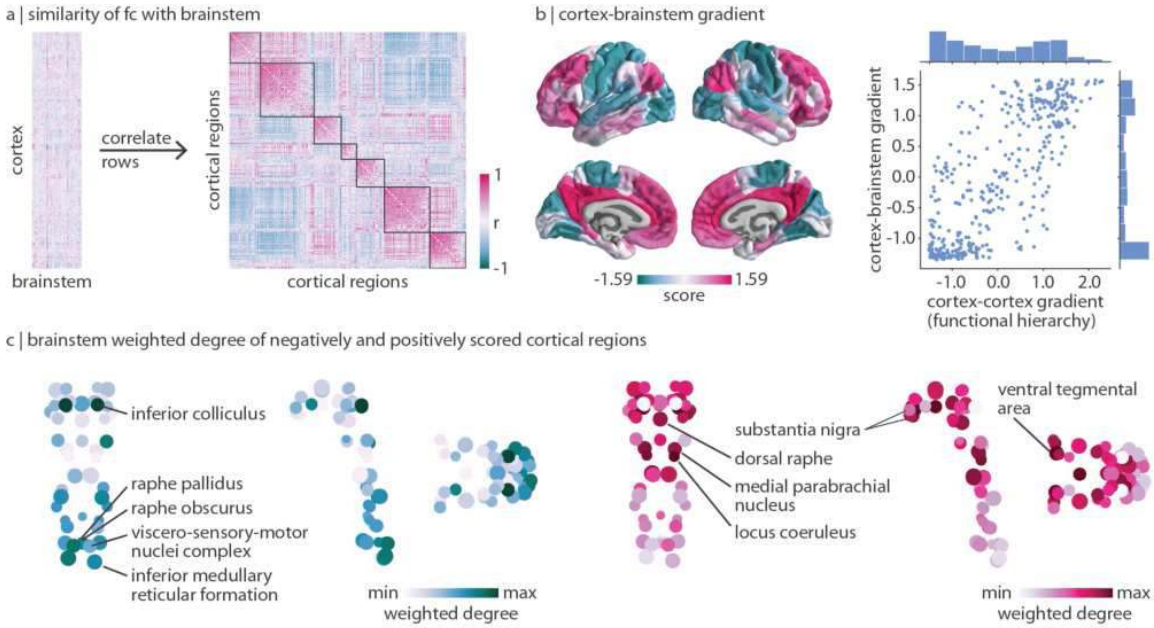

Figure 2. Brainstem nuclei delineate unimodal and transmodal cortical regions | **(a)** Correlation matrix represents how similarly (Spearman's r) two cortical regions are functionally connected with the brainstem above and beyond the dominant pattern of brainstem-cortex connectivity. Outlines are shown around the seven Yeo-Krienen resting-state networks (order: control, default mode, dorsal attention, limbic, ventral attention, somato-motor, visual). **(b)** Diffusion map embedding was applied to the matrix shown in panel (a). Left: the first gradient of cortex-brainstem functional connectivity. Right: correlation between the first gradient of cortex-brainstem connectivity and the first gradient of cortex-cortex functional connectivity (also called the cortical functional hierarchy, the unimodal-transmodal axis, and the sensory-association axis; $r = 0.77$, $p_{spin} = 0.0001$). Distribution of gradient values are shown for both gradients. **(c)** Brainstem weighted degree patterns are calculated as the sum of a brainstem nucleus' functional connectivity with all negatively- (left) or positively- (right) scored regions of the cortical gradient shown in panel (b). Coronal (posterior view), sagittal, and axial perspectives of brainstem nuclei are shown. Node size is proportional to weighted degree of brainstem-cortex functional connectivity.

References

1. Beissner, F. (2015). Functional MRI of the brainstem: common problems and their solutions. Clinical neuroradiology, 25(Suppl 2), 251-257.
2. Shine, J. M., Breakspear, M., Bell, P. T., Ehgoetz Martens, K. A., Shine, R., Koyejo, O., ... & Poldrack, R. A. (2019). Human cognition involves the dynamic integration of neural activity and neuromodulatory systems. Nature neuroscience, 22(2), 289-296.
3. Bianciardi, M., Toschi, N., Edlow, B. L., Eichner, C., Setsompop, K., Polimeni, J. R., ... & Wald, L. L. (2015). Toward an in vivo neuroimaging template of human brainstem nuclei of the ascending arousal, autonomic, and motor systems. Brain connectivity, 5(10), 597-607.
4. Cauzzo, S., Singh, K., Stauder, M., García-Gomar, M. G., Vanello, N., Passino, C., ... & Bianciardi, M. (2022). Functional connectome of brainstem nuclei involved in autonomic, limbic, pain and sensory processing in living humans from 7 Tesla resting state fMRI. Neuroimage, 250, 118925.
5. Singh, K., Cauzzo, S., García-Gomar, M. G., Stauder, M., Vanello, N., Passino, C., & Bianciardi, M. (2022). Functional connectome of arousal and motor brainstem nuclei in living humans by 7 Tesla resting-state fMRI. NeuroImage, 249, 118865.
6. Yarkoni, T., Poldrack, R. A., Nichols, T. E., Van Essen, D. C., & Wager, T. D. (2011). Large-scale automated synthesis of human functional neuroimaging data. Nature methods, 8(8), 665-670.
7. Hansen, J. Y., Shafiei, G., Markello, R. D., Smart, K., Cox, S. M., Nørgaard, M., ... & Misic, B. (2022). Mapping neurotransmitter systems to the structural and functional organization of the human neocortex. Nature neuroscience, 25(11), 1569-1581.

Poster No 1715

Mapping the Brain's Core Network for High-Order Cognition via Machine Learning

Guowei Wu[1,2], Xiuyi Wang[1,2], Yi Du[1,2,3]

[1]CAS Key Laboratory of Behavioral Science, Institute of Psychology, Chinese Academy of Sciences, Beijing, China, [2]Department of Psychology, University of Chinese Academy of Sciences, Beijing, China, [3]Chinese Institute for Brain Research, Beijing, China

Introduction: Understanding the role of functional connectivity (FC) between brain regions in facilitating complex cognitive functions is a fundamental question in the field of neuroscience. Researchers have shown that machine learning models can predict cognitive abilities by utilizing FC with moderate accuracy (Kong et al., 2021a, 2023b; Tian & Zalesky, 2021). However, these models have primarily focused on specific cognitive behaviors, failing to comprehensively reveal how FC networks support the complexity of human cognition. Although evidence suggests that FC networks exhibit higher accuracy in predicting cognitive ontology than single-task performance (Dubois et al., 2018), it remains uncertain whether specific subsets of FC, crucial for predicting cognitive ontology, can effectively represent various high-order cognitive functions. Furthermore,

understanding the relationship between the FC connectome, structural connectivity and gene expression patterns is crucial for unraveling the mechanisms underlying cognitive processing.

Methods: To investigate the FC underpins of cognitive functions, we developed a machine learning framework using HCP Young Adult (HCP-YA) and Lifespan Development datasets. We derived a cognitive ontology factor from HCP-YA data and identified the key FC edges via ridge regression. Our proposed 'Cognitive Ontology Prediction Model' (COMP), comprising the most influential 10% of edges, was compared against two models - a full FC model (F-F) and a ridge regression-based connectome predictive model (rCPM) with the same number of edges as COMP. We evaluated the predictive accuracy of these models across 25 behavioral tasks and calculated the 'cognitive loading' through Spearman correlations between ontology score and behavioral scores. To examine whether the COPM model more precisely predict behaviors closely related to the cognitive ontology score compared to the F-F model and rCPM, we computed the Spearman correlation between cognitive loading and the prediction accuracy for the 25 behavioral metrics for each model. We then validated the COPM model on the HCP-D dataset to assess its predictive accuracy for high-order cognitive functions across different dataset. Furthermore, we examine the association between the FC edges' coefficients and biological markers like FC strength variability and gene co-expression. The robustness of our approach was confirmed by replicating the analyses using different brain atlas parcellations and edge selection criteria.

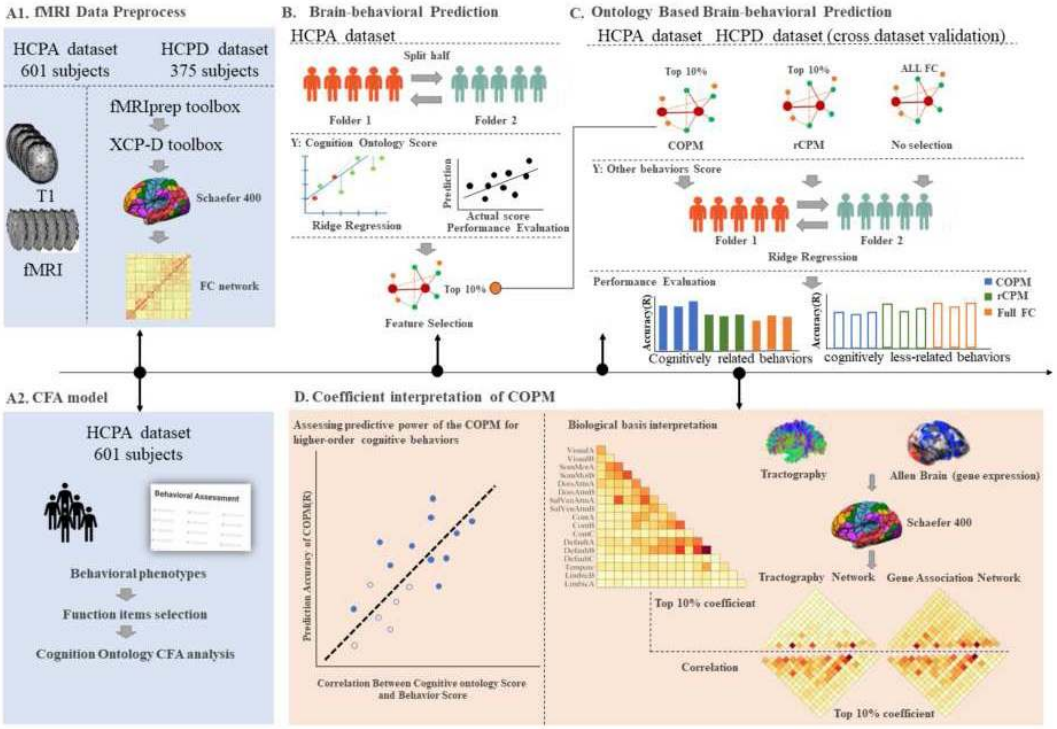

Results: Using a second-order CFA model on HCP-YA dataset tasks, we derived a cognitive ontology factor emcompassing diverse cognitive functions, revealing a robust hierarchical structure (CFI = 0.95, RMSEA = 0.07). We then assessed the prediction accuracy of FC edges associated with this factor using ridge regression on the Schaefer 400 atlas-based FC matrix, achieving a median accuracy of 0.39. Furthermore, we correlated the cognitive loading of 25 behavioral tasks with prediction accuracy in the COPM, F-F, and rCPM models. Notably, COPM exhibited a superior correlation ($r = 0.64$, $p < 0.001$), significantly outperforming F-F and rCPM models. The validation of the COPM's predictive performance using the HCP-D dataset further substantiated its efficacy, particularly for high-order cognitive tasks. Additionally, we found a significant positive correlation between FC strength variability, white matter connectivity, gene co-expression, and absolute beta weights from the cognitive ontology prediction model. These edges predominantly resided within association networks like the Default Mode and Frontal-Parietal Networks. Our replication study using the Glasser 360 atlas and various edge selection thresholds reaffirmed the robustness of our findings.

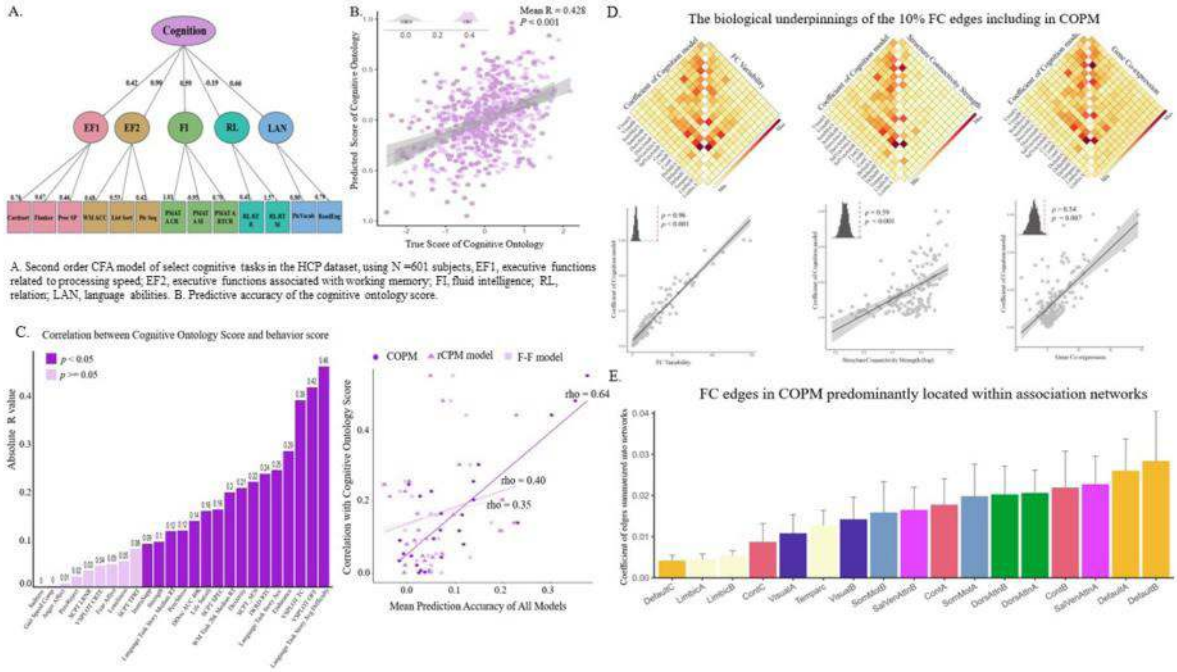

Conclusions: Our investigation delved into the FC networks underpinning cognitive ontology and their broader implications for high-order cognitive functions. Brain's cognitive task reliance is influenced by structural connectivity, and genetics.

References

1. Dubois, J., Galdi, P., Paul, L. K., & Adolphs, R. (2017). A distributed brain network predicts general intelligence from resting-state human neuroimaging data. https://doi.org/10.1098/rstb.2017.0284
2. Kong, R., Tan, Y. R., Wulan, N., Ooi, L. Q. R., Farahibozorg, S. R., Harrison, S., Bijsterbosch, J. D., Bernhardt, B. C., Eickhoff, S., & Thomas Yeo, B. T. (2023). Comparison between gradients and parcellations for functional connectivity prediction of behavior. NeuroImage, 273. https://doi.org/10.1016/j.neuroimage.2023.120044
3. Kong, R., Yang, Q., Gordon, E., Xue, A., Yan, X., Orban, C., Zuo, X. N., Spreng, N., Ge, T., Holmes, A., Eickhoff, S., & Yeo, B. T. T. (2021). Individual-Specific Areal-Level Parcellations Improve Functional Connectivity Prediction of Behavior. Cerebral Cortex, 31(10), 4477–4500. https://doi.org/10.1093/cercor/bhab101
4. Tian, Y., & Zalesky, A. (2021). Machine learning prediction of cognition from functional connectivity: Are feature weights reliable? NeuroImage, 245(May), 118648. https://doi.org/10.1016/j.neuroimage.2021.118648

Poster No 1716

Functional connectivity changes across the whole brain in newborns and children

Yali Huang[1], Xiaoxu Na[1], Xiawei Ou[1,2]

[1]1. Department of Radiology, University of Arkansas for Medical Sciences, Little Rock, AR, [22]. Department of Pediatrics, University of Arkansas for Medical Sciences, Little Rock, AR

Introduction: Functional magnetic resonance imaging (fMRI) has been widely used to depicts neural activity in the brain and understand the human brain function. Functional connectivity (FC) is defined as the temporal correlation between brain areas, and it undergoes complex transformation through the life span. Previous studies have shown that functional brain networks undergo a progressive change from isolated local regions to distributed networks until adolescence in the gray matter (Edde et al. 2021). However, such changes in white matter functional connectivity remain unknown. Here, we investigated and explored the differences in white matter brain functional connectivity between infants and 8-year-old children, offering new insights into the development of brain networks. We also compared that with the development of gray matter functional connectivity in these cohorts.

Methods: Three set of fMRI data were divided into 16 independent components using the GIFT, respectively (Calhoun et al. 2001, Allen et al. 2014). These 16 components were then defined as 16 functional networks. Subsequently, we performed an in-depth analysis of functional connectivity, exploring both intra-network and inter-network connections within these 16 identified functional networks. Intra-network FC: For each functional network, we assessed intra-network FC by computing

the mean Pearson correlation coefficient across the voxel time courses within the network, excluding diagonal elements. This computation yields 16 intra-network FC metrics per participant, corresponding to the identified functional networks. We further average these metrics across participants within each dataset, obtaining 16 mean intra-network FC values for Newborn group 1 (N=40), Newborn group 2 (N=107), and the 8-year-old children's group (N=43) respectively. Inter-network FC: For each participant, we compute the inter-network FC by evaluating the Pearson correlation coefficient matrix among all pairs of the 16 functional networks, again omitting diagonal elements. This process provides us with distinct inter-network FC values for each individual and for the group average: N=40 for Newborn group 1, 107 for Newborn group 2, and 43 for the 8-year-old children's group.

Results: Intra-network and inter-network FC within white matter. Fig. 1 displays the results of intra-network and inter-network functional connectivity within white matter across the three datasets. It is evident that intra-network functional connectivity is greater in newborns than in 8-year-old children, whereas inter-network functional connectivity is higher in 8-year-old children compared to newborns. T-tests performed on the inter-network functional connectivity results show no significant differences between the two newborn groups; however, significant differences exist between the 8-year-old children and both newborn groups, with both p-values smaller than 0.001, for both intra- and inter- network FC measures. Intra-network and inter-network FC within gray matter. Fig. 2 depicts the results of intra-network and inter-network FC within grey matter across the three datasets. Intra-network functional connectivity decreases with age, while inter-network functional connectivity increases with age, similar to the patterns observed in white matter functional networks. T-tests on the inter- and intra- network functional connectivity results reveal no significant differences between the two newborn groups, but significant differences are present between the 8-year-old children and both newborn groups, with both p-values smaller than 0.001, for both intra- and inter-network FC measures.

Conclusions: Our study uncovers a pivotal aspect of neurodevelopment, demonstrating that with brain maturation from infancy to young childhood, there is a marked increase in the connectivity among distinct functional networks, while connectivity within individual networks decreasing. This phenomen is evident not only in grey matter but also in white matter.

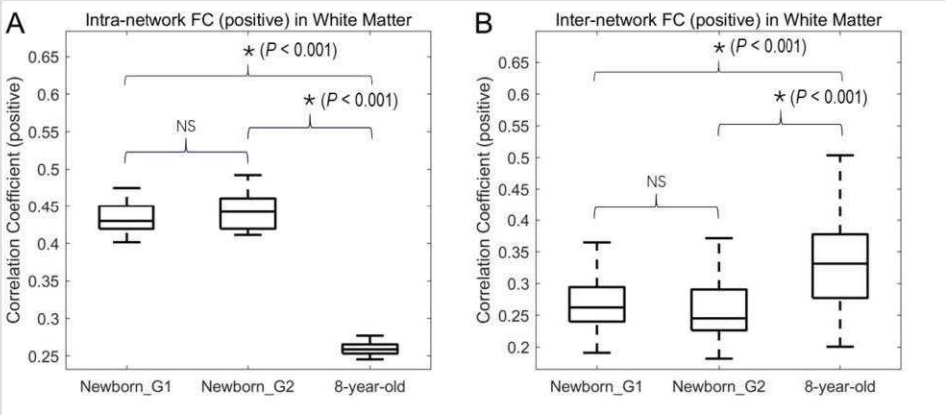

Fig. 1. Intra-network and inter-network FC within white matter.

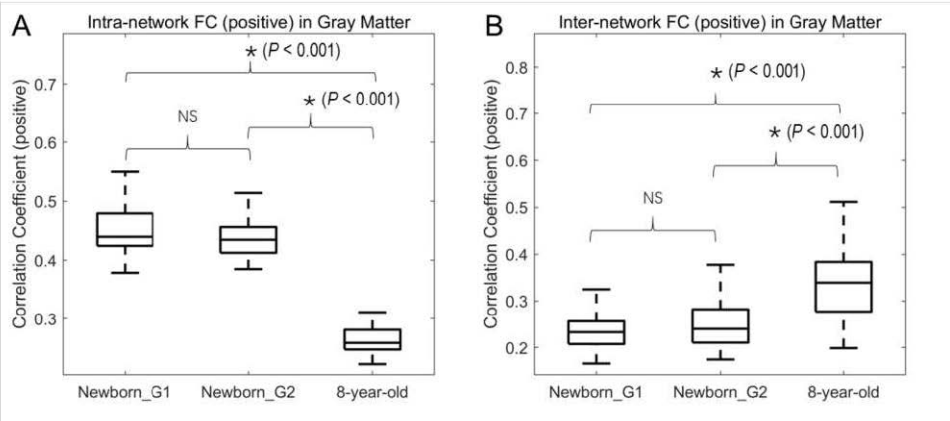

Fig. 2. Intra-network and inter-network FC within gray matter.

References
1. Allen, E. A., E. Damaraju, S. M. Plis, E. B. Erhardt, T. Eichele and V. D. Calhoun (2014). "Tracking whole-brain connectivity dynamics in the resting state." Cerebral cortex 24(3): 663-676.
2. Calhoun, V. D., T. Adali, G. D. Pearlson and J. J. Pekar (2001). "A method for making group inferences from functional MRI data using independent component analysis." Human brain mapping 14(3): 140-151.
3. Edde, M., G. Leroux, E. Altena and S. Chanraud (2021). "Functional brain connectivity changes across the human life span: From fetal development to old age." Journal of neuroscience research 99(1): 236-262.

Poster No 1717

Neurodynamic Impacts of Meditation Combined with Ayahuasca Constituents DMT and Harmine

Klemens Egger[1,2,3], Daniel Meling[1], Firuze Polat[1], Mihai Avram[4], Milan Scheidegger[1,2]

[1]Psychiatric University Hospital Zurich, Zurich, Switzerland, [2]Neuroscience Center Zurich (ZNZ), Zurich, Switzerland, [3]Inselspital Bern, Bern, Switzerland, [4]University of Lübeck, Lübeck, Germany

Introduction: Meditation and psychedelic substances, such as psilocybin, LSD, or DMT, exert profound effects on human consciousness. Current models of biological mechanisms of action of both meditation and psychedelics hint toward synergistic effects on brain functioning when the two are combined. Building on a prior study exploring the effects of meditation combined with psilocybin [Smigielski et al., 2019], we conducted a double-blind, placebo-controlled between-subject study, investigating the combined impact of meditation and a novel ayahuasca-derived formulation containing N,N-Dimethyltryptamine (DMT) and harmine. Functional brain scans (fMRI) were conducted before and after a three-day psychedelic-enhanced meditation retreat, and changes in resting-state fMRI data were compared between the two groups.

Methods: Forty trained meditators (22 m, 18 f) participated in one of two three-day meditation retreats, receiving either DMT and harmine (120 mg each) or placebo on day two of the retreat. Resting-state fMRI scans (7.5 minutes, closed eyes) were acquired one day before and one day after the retreat, i.e., two days pre- and two days post-drug administration. Functional data were preprocessed using the nipype-based fMRIprep pipeline (v23.0.2) and analyzed with the Conn Toolbox (v22.a) in Matlab. Denoising involved 24 head motion parameters [Friston et al., 1996], component-based noise reduction (aCompCor), and scrubbing (FD<0.5 mm). Analyses included seed-to-voxel analyses of seven resting-state networks (RSN), as defined by Yeo and colleagues [Yeo et al., 2011], between- and within-network changes, and global connectivity. For between- and within-network changes, mean timeseries of each network were extracted and correlated with each voxel of the brain (between-network approach) or with each voxel of the network (within-network approach). The full GLM design matrix included both conditions (verum-placebo) and both timepoints (post-pre). We also analyzed pre to post changes in the placebo and verum group independently, as well as changes between the two groups in the post-intervention scans. Global correlation maps were used to calculate network centrality at each voxel and analyzed with a GLM at the second level using the approach from above. All voxel-thresholds were set to $p < 0.001$, cluster-thresholds were set to $p < 0.05$, FDR-corrected.

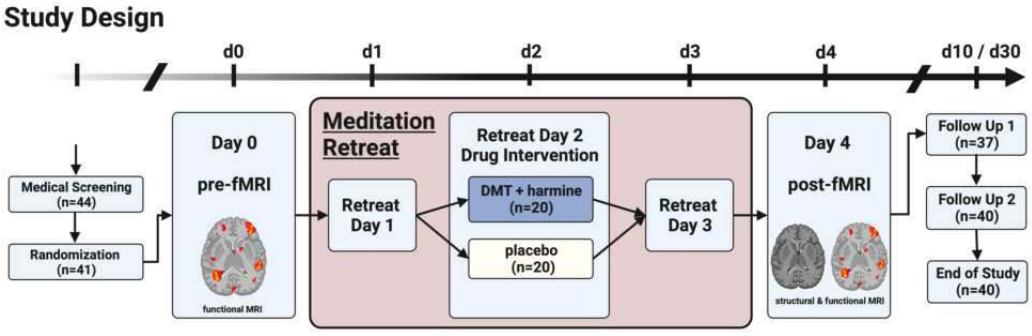

Results: The comparison of post-pre scans for the placebo condition revealed significantly reduced connectivity changes between 5 out of 7 (except the sensory-motor and limbic networks) RSNs and other clusters in the brain. Within-network analyses did not yield significance. Global correlation analysis revealed three clusters with decreased connectivity for the post-pre contrast of placebo scans in the precentral gyrus, the inferior frontal gyrus and the precuneus. Post-pre comparisons of the verum group revealed significantly increased connectivity from the visual, dorsal attention and salience network to the left occipital pole. Within-network and global correlation analyses did not yield significance. No differences were found between the two groups' pre-intervention scans for any measure. Regarding the verum-placebo post-pre contrast, we observed significantly increased salience network connectivity to bilateral occipital poles, bilateral cuneal cortex and lateral occipital cortex, while the visual network showed increased functional connectivity to left and right insula.

Conclusions: Our findings suggest that subacute effects of combining DMT and harmine in a meditation retreat setting enhance connectivity between various brain networks, in contrast to the opposing effects observed without pharmacological intervention. Furthermore, subacute effects of the psychedelic did not alter within-network or global connectivity. This underscores distinctions in neurodynamics between altered states induced by the psychedelic ayahuasca-derived formulation and contemplative practice alone.

References

1. Friston KJ, (1996), 'Movement-Related effects in fMRI time-series', Magnetic Resonance in Medicine, vol. 35, no.3, pp. 346–355.
2. Smigielski L, (2019), 'Psilocybin-assisted mindfulness training modulates self-consciousness and brain default mode network connectivity with lasting effects', Neuroimage, vol. 196, pp. 207–215.
3. Yeo BTT, (2011), 'The organization of the human cerebral cortex estimated by intrinsic functional connectivity', Journal of Neurophysiology, vol. 106, no. 3, pp. 1125–65.

Poster No 1718

Simulated brain networks reflecting severity of Parkinson's disease

Kyesam Jung[1,2], Simon Eickhoff[1,2], Julian Caspers[3], Oleksandr Popovych[1,2]

[1]Institute of Neuroscience and Medicine - Brain and Behaviour (INM-7), Forschungszentrum Jülich, Jülich, Germany, [2]Institute of Systems Neuroscience, Medical Faculty, Heinrich Heine University, Düsseldorf, Germany, [3]Department of Diagnostic and Interventional Radiology, Medical Faculty, Heinrich Heine University, Düsseldorf, Germany

Introduction: Brain connectome of patients with Parkinson's disease (PD) showed different network properties compared to healthy participants (Zuo et al. 2022), which is supposed to develop in time with PD progression and motor impairment (Holden et al. 2018). Empirical investigation of such changes of the brain networks is mostly restricted to longitudinal data, which limits the evaluation of the disease effects on the network properties of the human brains in vivo. Here we suggest an alternative approach and consider the resting-state brain dynamics simulated by whole-brain dynamical models, which allows us to probe network changes using brains in silico. Accordingly, we performed whole-brain simulations and investigated network modularity (segregation) and global efficiency (integration) of the simulated brain networks for behavioral model fitting to clinical measures. As a result, we demonstrate significant enhancements of correlation between simulated network properties and disease severity, which was not observed in empirical cross-sectional neuroimaging PD data used for model derivation.

Methods: This study included 51 (30 males) healthy controls and 60 (43 males) PD patients. Empirical functional connectivity (eFC) and empirical structural connectivity (eSC) were calculated using the resting-state blood oxygenation level-dependent (BOLD) signals and streamlines from whole-brain tractography, respectively. We used two parcellation schemes based on functional (Schaefer et al. 2018) and structural (Desikan et al. 2006) brain properties. We performed whole-brain simulations using a network of the Jansen-Rit type models (Jansen and Rit 1995) informed by eSC and the model parameters on a dense 64 coupling × 43 delay parameter grid. The obtained simulated BOLD signals were used to calculate the simulated functional connectivity (sFC). Subsequently, we calculated network properties (modularity and efficiency) of all connectivities (1 eFC, 1 eSC, and 2752 sFCs for each subject and parcellation). We applied a behavioral model fitting (optimizing the whole-brain model to fit to target variables) for group comparison between healthy controls and PD patients and correlation with disease severity based on the unified PD rating scale (UPDRS) (Goetz et al. 2008). We searched for the optimal parameter points corresponding to the largest effect size of the network properties of sFC between healthy controls and PD patients as well as the optimal parameter points corresponding to the strongest correlation between the simulated network properties and the disease severity from 60 patients.

Results: The applied model fitting for the network properties of sFC showed significant group differences between healthy controls and PD patients in network modularity and efficiency (Fig. 1a-b), which was not the case for the empirical data. The largest effect size was 0.19 for eFC and 0.12 for eSC as compared with the largest effect size of 0.38 for sFC. Furthermore, the behavioral network-based model fitting showed that sFC network properties significantly correlate with the disease severity (Fig. 1c-e and Fig. 2e-g), which was again not significant for the empirical connectomes (Fig. 2a-d). Remarkably, efficiency of sFC exhibited two local optima of negative and positive correlations with disease severity (Fig. 1d-e) in contrast to weak and non-significant correlation with the network properties of empirical connectomes (Fig. 2b, d).

Conclusions: Our results indicate that functional segregation (modularity) and integration (efficiency) of simulated brain networks can exhibit an enhanced group difference between healthy subjects and PD patients and significant correlations with severity of motor impairment in patients with PD as compared with empirical data. With this, we suggest using the

network-based model fitting of the whole-brain dynamical models to find dynamical regimes closely related to clinical measures of PD for further investigations of disease onset and progression.

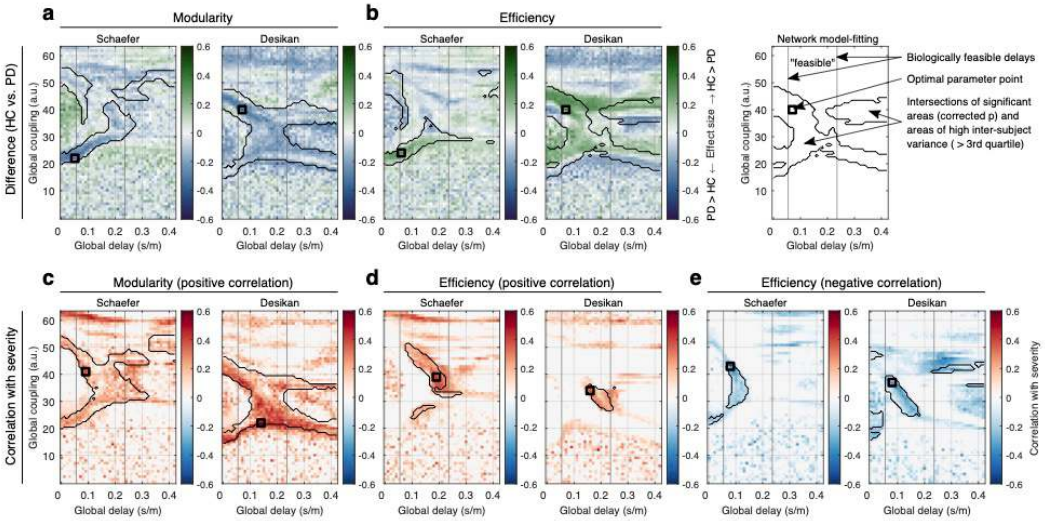

Figure 1. Parameter landscapes of behavioral model fitting of the whole-brain dynamical model of the Jansen-Rit type. The network modularity (functional segregation) and network efficiency (functional integration) of simulated FC were used to calculate **(a-b)** landscapes of the effect size of group difference between healthy controls (HC) and patients with Parkinson's disease (PD) and **(c-e)** landscapes of Pearson's correlation (across PD patients) between simulated network properties and severity of the disease as given by the unified PD rating scales (UPDRS III medication On). The calculations were performed for the Schaefer and the Desikan-Killiany (Desikan) brain atlases indicated in the titles of the plots together with the respective network properties. The color depicts the effect size and correlation in plots (a-b) and (c-e), respectively. The vertical lines bound an approximate range of biologically feasible delays, the black squares indicate optimal parameter points of the largest effect size or correlation in the parameter domain bounded by the black contour curves of intersection of significant areas thresholded by the random-field theory for multiple tests and areas of high inter-subject variance of the respected network properties (> 3rd quartile), see the rightmost plot in the upper row.

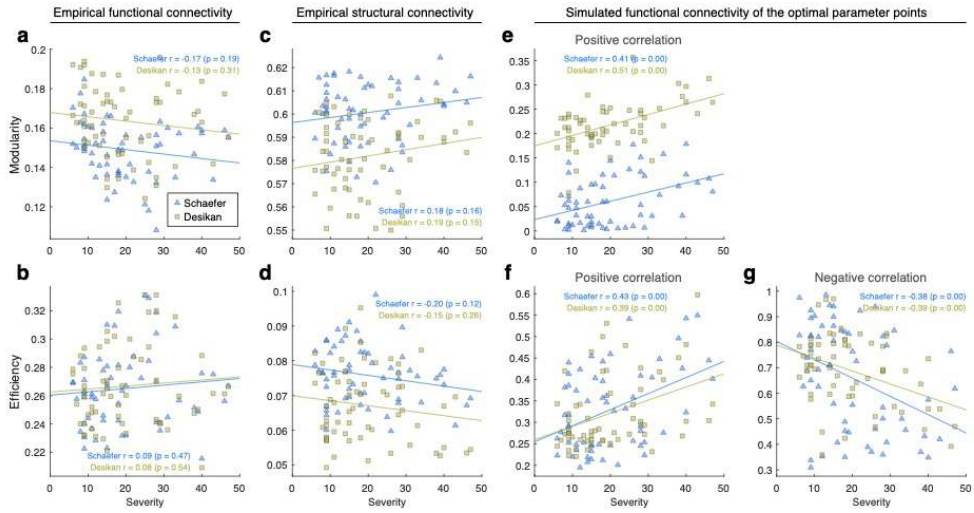

Figure 2. Correlation between severity of the disease as given by the unified Parkinson's disease rating scales (UPDRS III medication On, horizontal axes) and modularity and efficiency network properties (vertical axes) of empirical and simulated and brain connectomes for **(a-b)** empirical FC, **(c-d)** empirical SC and **(e-g)** simulated FC calculated for the optimal parameters denoted by the squares in Fig. 1c-e. The used brain parcellation, calculated Pearson's correlation coefficient and its statistical test (*p*-value) are indicated in the legends.

References

1. Desikan, R. S. (2006), 'An automated labeling system for subdividing the human cerebral cortex on MRI scans into gyral based regions of interest', Neuroimage, 31: 968-80.
2. Goetz, C. G. (2008), 'Movement Disorder Society-sponsored revision of the Unified Parkinson's Disease Rating Scale (MDS-UPDRS): scale presentation and clinimetric testing results', Movement Disorders, 23: 2129-70.
3. Holden, S. K. (2018), 'Progression of MDS-UPDRS Scores Over Five Years in De Novo Parkinson Disease from the Parkinson's Progression Markers Initiative Cohort', Movement Disorders Clinical Practice, 5: 47-53.
4. Jansen, B. H. (1995), 'Electroencephalogram and visual evoked potential generation in a mathematical model of coupled cortical columns', Biological Cybernetics, 73: 357-66.
5. Schaefer, A. (2018), 'Local-Global Parcellation of the Human Cerebral Cortex from Intrinsic Functional Connectivity MRI', Cerebral Cortex, 28: 3095-114.
6. Zuo, C. (2022), 'Global Alterations of Whole Brain Structural Connectome in Parkinson's Disease: A Meta-analysis', Neuropsychology Review.

Poster No 1719

How Spontaneous Exploration of the Dynamic Repertoire at Rest Shapes Behavioural Performance

John Sampaio[1], Norman Farb[1], Stephen Strother[1]

[1]*University of Toronto, Toronto, Ontario*

Introduction: Resting-state brain activity exhibits structured spatiotemporal patterns known as resting state networks in human fMRI research. The strength of resting state functional connectivity (rs-FC) may reveal individual differences in brain activity, and seem to be predictive of spatial brain activation patterns during task performance (Tavor, 2016). The study of these networks has focused on static structures, i.e., a consistent set of networks derived from resting state data. Yet resting state networks are not static. They dynamically reconfigure over time; shifting between many different transient network configurations, termed "brain states." Recent studies have begun to explore the dynamic nature of these resting state networks and their potential role in shaping aspects of human cognition. One proposed function is that the exploration of different configurations during rest allows the brain to rehearse brain states and optimize neural networks in anticipation of future stimulation (Deco, 2011). The dynamic repertoire hypothesis suggests that spontaneous engagement in distinct brain states during rest could predict the frequency of engaging these brain states during cognitive tasks to predict behavioural performance. Using a sliding time window approach, we tested the dynamic repertoire hypothesis. We predicted that performance on a given task would be correlated with the frequency of entering certain brain states. Additionally, the brain state most correlated with task performance was also expected to be most similar to the functional connectivity participants exhibited while performing said task.

Methods: We analyzed the fMRI data of 250 participants collected by Ohio State University. In addition to 5 minutes of resting state, participants completed a series of neurocognitive tasks while in the MRI scanner. We examined the go-nogo and 2-back tasks, which were designed to measure inhibitory control and working memory, respectively. Neuroimaging data were preprocessed using the in-house developed PreProcessing Resting Imaging Data with Scrubbing pipeline (Eusebio, 2023). We extracted region of interest (ROI) time courses using a sliding time window. ROIs were defined using the 246 ROI Brainnetome atlas (Fan, 2016). We used K-means clustering to cluster rs-FC matrices into k brain states. Static task FC was computed across the entire task fMRI time course. Participants' performance metrics were correlated with time spent in each brain state to determine which brain state was associated with better performance. We used Manhattan distance to determine the similarity between each resting brain state and task FC. Shorter Manhattan distances mean the matrices were more alike.

Results: The results were partially consistent with the hypothesis. As expected, the resting brain state most associated with go-nogo task performance also had the shortest Manhattan distance from the task-based go-nogo FC matrix. However, this was not the case for the 2-back task, as the brain state most correlated with task performance did not have the shortest Manhattan distance from the task-based go-nogo FC matrix.

Conclusions: The results of this study provide tenuous support for the hypothesis that brain state exploration during rest allows the brain to prepare for future stimulation. While our go-nogo results were consistent with this, the 2-back results were not. Still, the 2-back results were somewhat consistent since the brain state most correlated with 2-back performance did have the second-lowest Manhattan distance. Future studies may expand these findings using a wider variety of neurocognitive tasks. It could be that some neural circuits benefit more from this spontaneous rehearsal than others.

References

1. Deco, G. (2011), 'Emerging concepts for the dynamical organization of resting-state activity in the brain', Nature Reviews. Neuroscience, vol. 12, no. 6, pp. 43–56
2. Eusebio, J. (2023), 'PreProcessing Resting Imaging Data with Scrubbing (PPRIDS) [Linux]', https://github.com/johneusebio/PPRIDS-pipeline
3. Fan, L. (2016), 'The Human Brainnetome Atlas: A New Brain Atlas Based on Connectional Architecture', Cerebral Cortex, vol. 26, no. 8, pp. 3508–3526
4. Tavor, I. (2016), 'Task-free MRI predicts individual differences in brain activity during task performance', Science, vol. 352, no. 6282, 216–220

Poster No 1720

Neonatal network topography predicts brain maturation and neurodevelopmental outcomes

Jianlong Zhao[1,2,3], Tengda Zhao[1,2,3], Yuehua Xu[1,2,3], Hongming Li[4,5], Lianglong Sun[1,2,3], Xinyuan Liang[1,2,3], Meizhen Han[1,2,3], Zilong Zeng[1,2,3], Yong He[1,2,3,6]

[1]State Key Laboratory of Cognitive Neuroscience and Learning, Beijing Normal University, Beijing, China, [2]Beijing Key Laboratory of Brain Imaging and Connectomics, Beijing Normal University, Beijing, China, [3]IDG/McGovern Institute for Brain Research, Beijing Normal University, Beijing, China, [4]Center for Biomedical Image Computing and Analytics, University of Pennsylvania, Philadelphia, PA, [5]Department of Radiology, University of Pennsylvania, Philadelphia, PA, [6]Chinese Institute for Brain Research, Beijing, China

Introduction: The neonatal human brain lays a critical neural foundation for establishing wide cognitive and behavioral abilities that last a lifetime[1-3]. However, how the individualized functional topography at birth evolves with age and supports later neurodevelopmental outcomes remain largely unclear. Here, we investigated the variability pattern of neonatal brain functional topography by combining individualized functional network and machine learning predictive models in neonatal large sample resting fMRI datasets.

Methods: Based on 367 term-born neonates from the Developing Human Connectome Project[4], we firstly employed a regularized NMF approach to derive individualized functional networks for each neonate[5](Fig. 1A). Then we quantify the overall variability of functional topography across subjects based on median absolute deviations (Fig. 1B) and a fine-grained description of variability within each functional network (position, size, overlap, and region homogeneity) (Fig. 1C). Finally, we proposed a network-based SVR approach to delineate how individual functional topography of neonatal brain could predict brain maturation and cognitive, language, and motor function at 18 months (Fig. 1D). The network-wise feature weights were evaluated to understand the network contribution for predicting brain maturity and various behavior abilities. Cognitive, language, and motor development were assessed using the Bayley Scales of Infant and Toddler Development, 3rd Edition (BSID-III).

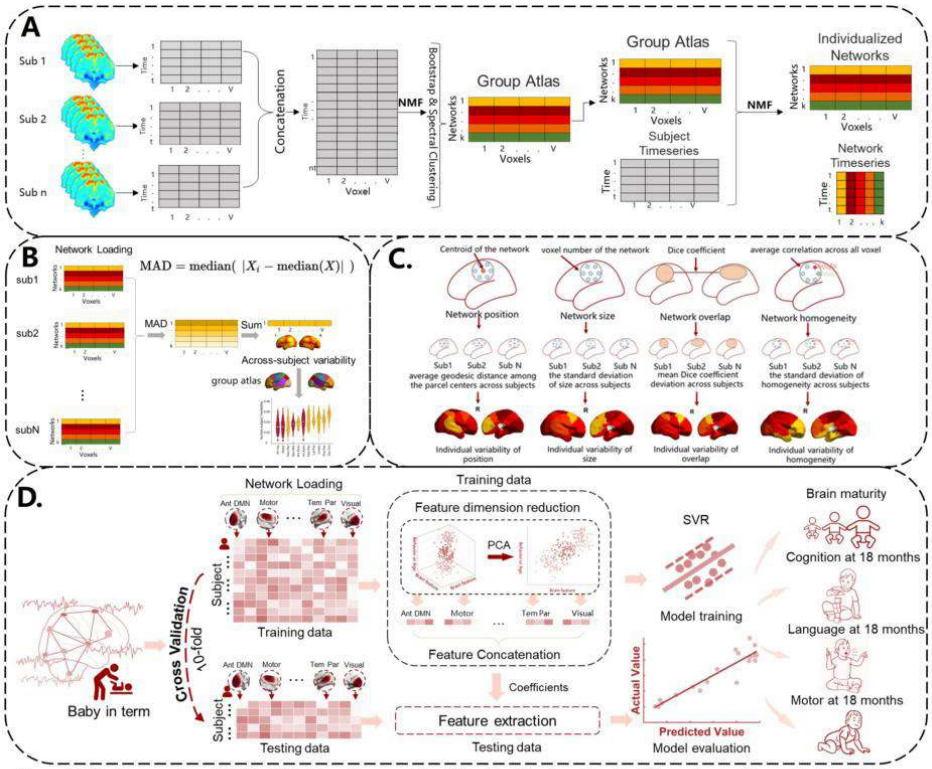

Figure 1. Study overview. (A) Identification of personalized functional brain networks. We used sparsity regularized NMF and high spatial-temporal resolution of neonates to obtain a typical group-level functional network. Then we used group network as initialization to generate individualized functional networks. Eleven functional networks were obtained for each neonate. (**B**) We quantitatively assessed neonatal brain functional topography's overall individual variability by calculating a voxel-wise index based on median absolute deviations of probabilistic loadings across individuals for each network and average across all eleven networks. Then we categorized into primary or association systems to examine whether individual variability constraints by the fundamental primary-to-heteromodal brain organization. (**C**) To describe the intricate heterogeneity of each functional networks between neonates, we calculate the size, position, overlap, and region homogeneity of each network and evaluate the individual variability of each indicator. (D) we proposed the network-based SVR model to evaluate whether individual's functional networks could predict brain maturity and individual difference in later cognition, motor, and language at 18 months.

Results: We identified 11 functional networks for each neonate (Fig. 2A left). The highest between-subject variance is mainly located in association cortex while the lowest variance is located in primary cortex (Fig. 2A middle, right, Pspin < 0.05). The fine-grained description of variability pattern of the size, position, overlap, region homogeneity was similar to the voxel-level pattern (all index: Pspin < 0.05, Fig. 2B). However, there exist some indicator-specific distributions especially within the association system, such as the medial prefrontal cortex and temporal-parietal junction cortex. The network-based SVR model achieved a significant prediction for brain maturity and later cognition, language and motor performance at 18 months (age: r = 0.46; cognition: r = 0.39, language: r = 0.29, motor: r = 0.37; all Pperm < 0.001, Fig. 2C). To assess the effect of random fold assignment, we repeated this procedure 100 times by newly classifying all neonates into 10 subsets each time, which yielded highly consistent results (age: mean r = 0.51; cognition: mean r = 0.34; language: mean r = 0.27; motor: mean r = 0.34; all Pperm < 0.001, Fig. 2D). Finally, for predicting brain maturity and various behavior abilities, we found that high contributing networks are located consistently at primary motor networks and heterogeneous within association networks (Fig. 2E).

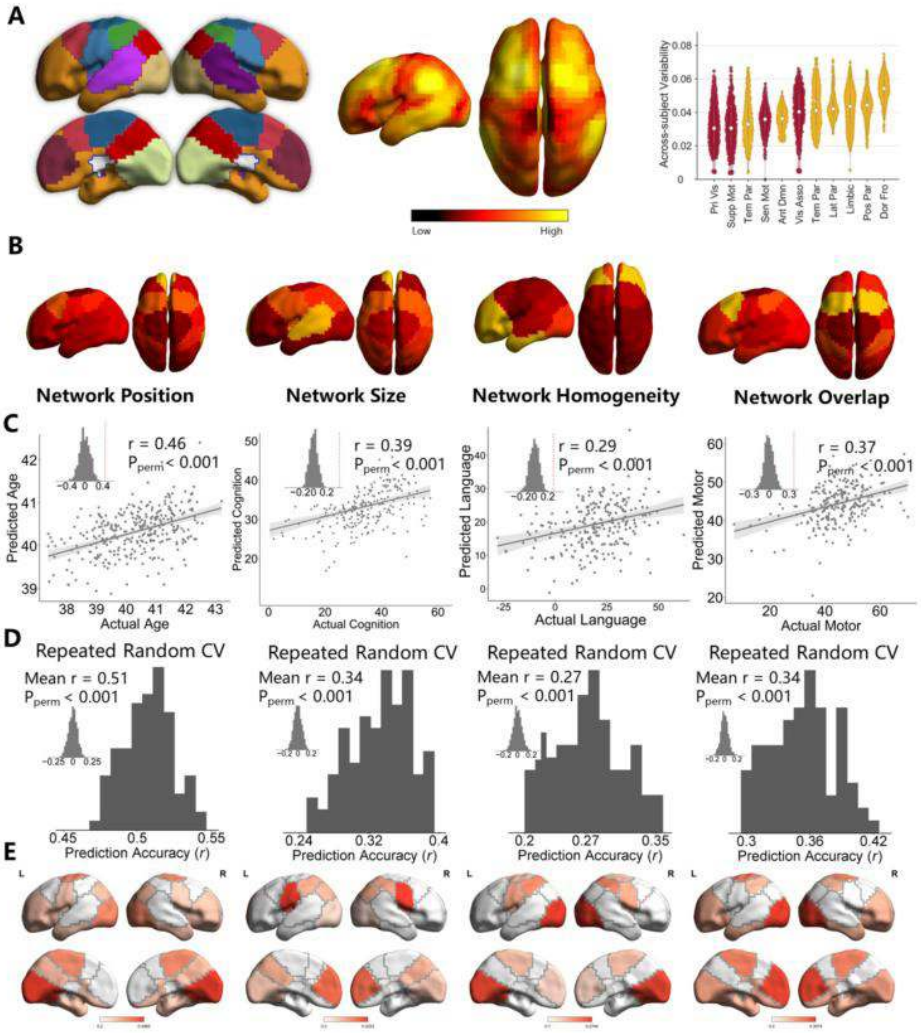

Figure 2. Study overview(A) The left panel shows group-level functional network. The middle and right panel shows overall individual variability of functional network topography. (B) Fine-grained description of variability pattern of functional network topography. (C) The complex pattern of functional topography could be used to predict brain maturity and neurodevelopmental outcomes at 18 months including cognition, language, and motor. Data points represent predicted brain maturity of subjects in a model trained on independent data; the inset histogram represents the null distribution of prediction accuracy from a permutation test. (D) By conducting repeated random 10-F CV (100 runs), we have provided strong evidence of stable prediction accuracy, which significantly outperformed the null distribution generated using permuted data (inset). (E) High contributing regions are primarily located at primary visual and motor networks and heterogeneous within association networks.

Conclusions: The results suggest that the variation pattern of neonatal primary networks is discernible from that of association networks. Critically, we demonstrated that individual variation of neonatal primary networks brain supports the accurate prediction of brain maturity and later cognition, language, and motor performance at 18 months. Individual variation of association networks contributes differentially to brain maturation and behavior prediction. Our results have implications for understanding how functional neuroanatomy at birth matures and supports the early establishment of neurodevelopmental outcomes.

References
1. Bressler, S. L. (2010). Large-scale brain networks in cognition: emerging methods and principles. Trends in Cognitive Sciences, 14(6), 277-290.
2. Cui, Z. (2020). Individual Variation in Functional Topography of Association Networks in Youth. Neuron, 106(2), 340-353.e348.
3. Gilmore, J. H. (2018). Imaging structural and functional brain development in early childhood. Nature Reviews Neuroscience, 19(3), 123-137.
4. Laumann, T. O. (2015). Functional system and areal organization of a highly sampled individual human brain. Neuron, 87(3), 657-670.
5. Li, H. (2017). Large-scale sparse functional networks from resting state fMRI. NeuroImage, 156, 1-13.

Poster No 1721

Higher integration of reward, cognitive, and attention networks in people with Opioid Use Disorder

Danielle Kurtin[1], Katherine Herlinger[1], Alexandra Hayes[2], Lexi Hand[1], Leon Fonville[1], Anne Lingford-Hughes[1], Louise Paterson[1]

[1]Imperial College London, London, United Kingdom, [2]Kings College London, London, United Kingdom

Introduction: The cycles of relapse and remittance characterising Opioid Use Disorder (OUD) are driven by drug-induced changes in reward circuitry and incentive drives, which in turn effect decision making. This can be characterised as a disrupted relationship between reward circuitry (the VentroMedial Network (VMN)) and the functional networks associated with visualisation of drug consumption (Default Mode Network (DMN)), planning/strategizing to acquire the drug (Control/Cognitive networks), attention to drug-related stimuli and impulsive use (Salience Network) (Dunlop et al., 2017).

Methods: To characterise how the neural correlates of reward processing are disrupted in OUD we collected fMRI data in Methadone Dependent participants (MD, n=22) and healthy controls (HC, n=22) during Monetary Incentive Delay (MID) and Cue Reactivity tasks. These tasks reliably show blunted VMN activity during non-drug, monetary rewards and heightened VMN responses to drug-related cues respectively (Hayes et al., 2020). Functional connectivity was captured via mutual information (miFC). Cortical regions were defined by transforming the 200-region Schaefer atlas to subject space; Freesurfer parcellation defined 14 subcortical regions. Since fMRI-based measures of brain function are linked to neurotransmitter receptor availability (Hansen et al., 2022), we additionally evaluated the relationship between group differences in miFC and MOR and D2 receptor density, given the importance of these receptors in the development of addiction (Volkow et al., 2011).

Results: During the MID task, MD participants showed higher miFC in VMN regions (Ventral Striatum, medial prefrontal cortex (mPFC), and orbitofrontal cortex) to regions in attention (Frontal Eye Fields and Insula) and cognitive/control networks (PFC, Superior Parietal Lobule). HCs showed higher miFC between attentional networks to Visual and Somatomotor networks, as well as the DMN and thalamus, in line with two recent studies (Nestor et al., 2020; Nestor and Ersche, 2023) (Fig 1). These results indicate stronger integration among VMN, attention, and cognitive networks in MD participants, whereas connectivity among regions in attentional networks to visual, somatomotor, and DMN networks is lessened. Given the self-referential and interoceptive functions of the DMN, decreased integration of the DMN may result in a weakened ability to integrate reward-related outcomes, which is associated with the development of habitual consumption (Nestor and Ersche, 2023). The results from the Cue Reactivity task provide further evidence that MD participants exhibit a strong neural framework supporting automatic responses to drug-related stimuli, since MD participants showed higher miFC in the same VMN regions to regions in attention and cognitive/control networks (Fig 1). These results suggest the relationship between drug-related cues and decision-making processes are driven by compulsive, automatic processes. This is supported by two studies in alcohol-dependent participants showing higher FC among VMN, attention, and cognitive/control networks was significantly correlated with markers of increased impulsivity (Zhu et al., 2017) and compulsivity (Strosche et al., 2021). We found significant, positive relationships between the magnitude of higher miFC in MD vs HC participants and the sum of MOR and D2 receptor density during the Cue Reactivity task (Fig 2). This accords with the role of D2 receptors in the incentive salience of drug cues (Everitt and Robbins, 2016; Koob and Volkow, 2010).

Conclusions: In summary, the higher integration among reward, attentional, and cognitive networks in MD participants during both non-drug and drug-related tasks suggests maladaptive, drug-induced changes in reward circuitry influences other processes affected by addiction, such as attention and cognition. These mechanistic insights provide a foundation for future research to further characterise the relationship between the neural and behavioural correlates of addiction.

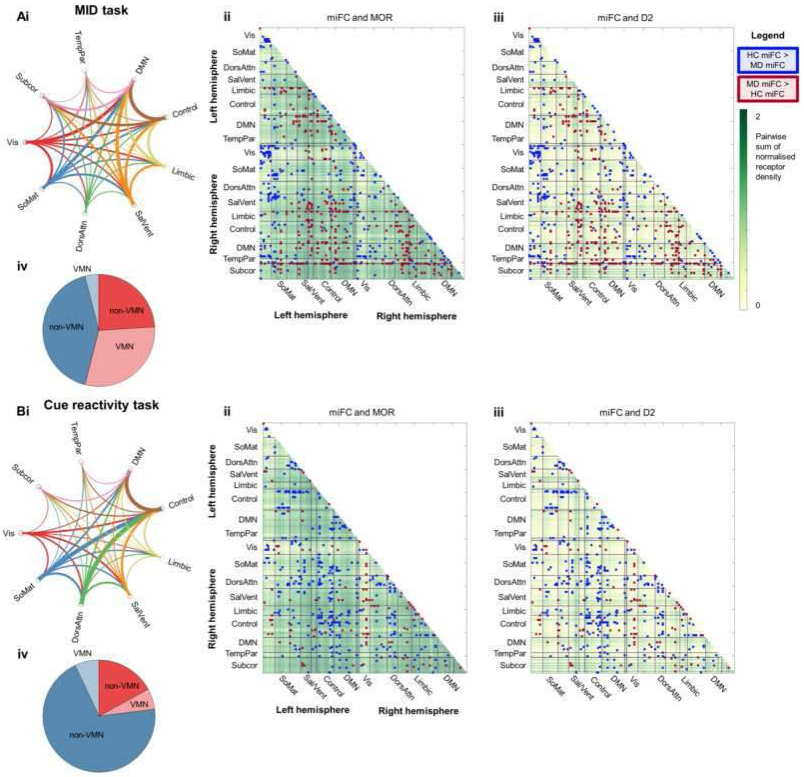

Fig 1: There were significant differences in miFC between HC and MD participants during **(A)** the MID and **(B)** Cue Reactivity tasks. **(Ai, Bi)** Circle plots show regions with differences in miFC grouped by functional network. The thickness of the lines between networks is proportional to the number of significant edges between the networks. Connectivity matrices showing edges that were significantly higher in MD participants vs HC (red points), and vice versa (blue points) during the **(Aii-iii)** MID and **(Bii-iii)** Cue Reactivity task. Connectivity matrices are visualised over heatmaps of the sum of **(Aii, Bii)** MOR and **(Aiii, Biii)** D2 receptor density. Pie charts show the percent of significant edges that were or were not within the VMN during the MID **(Aiv)** and Cue Reactivity task **(Biv)**. Network abbreviations: Vis=Visual; SoMat=Somatomotor; DorsAttn=Dorsal Attention; Sal/Vet=Salience/Ventral Attention; TempPar=Temporal Parietal; Subcor=subcortical regions.

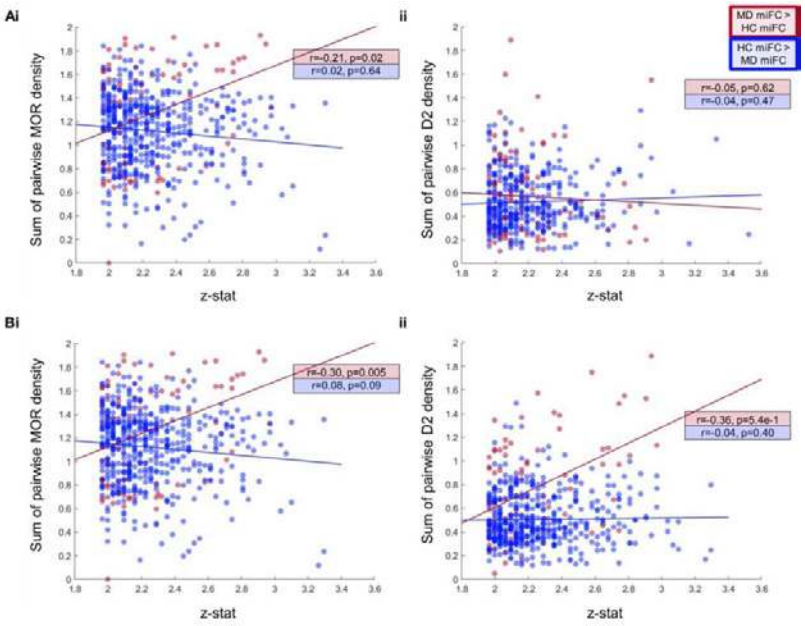

Fig 2: Relationships between the strength of the difference in miFC between MD and HC participants and the sum of pairwise receptor density. For both the **(A)** MID and **(B)** the Cue Reactivity task, two sets of z-stats are plotted against the pairwise sum of **(Ai, Bi)** MOR and **(Aii, Bii)** D2 receptors. The first set of z-stats are in red and are from the Wilcoxon sign rank tests with significantly higher miFC in MD participants compared to HC, whereas blue points show edges where HC participants had significantly higher miFC than MD participants. For each group of results, least-squared lines are added to aid visualisation of the relationship between the receptor density and z-stats, and the r- and p-values from Spearman's correlations assessing the strength of the relationship for each group of results are displayed in the bottom right corner of each plot. P-values are significant if lower than the alpha adjusted for Bonferroni correction for multiple comparisons (p=0.025).

References
1. Dunlop, K., Hanlon, C.A., Downar, J., 2017. Noninvasive brain stimulation treatments for addiction and major depression. Annals of the New York Academy of Sciences 1394, 31–54.
2. Everitt, B.J., Robbins, T.W., 2016. Drug Addiction: Updating Actions to Habits to Compulsions Ten Years On. Annual Review of Psychology 67, 23–50.
3. Hansen, J.Y., Shafiei, G., Markello, R.D., Smart, K., Cox, S.M.L., Nørgaard, M., Beliveau, V., Wu, Y., Gallezot, J.-D., Aumont, É., Servaes, S., Scala, S.G., DuBois, J.M., Wainstein, G., Bezgin, G., Funck, T., Schmitz, T.W., Spreng, R.N., Galovic, M., Koepp, M.J., Duncan, J.S., Coles, J.P., Fryer, T.D., Aigbirhio, F.I., McGinnity, C.J., Hammers, A., Soucy, J.-P., Baillet, S., Guimond, S., Hietala, J., Bédard, M.-A., Leyton, M., Kobayashi, E., Rosa-Neto, P., Ganz, M., Knudsen, G.M., Palomero-Gallagher, N., Shine, J.M., Carson, R.E., Tuominen, L., Dagher, A., Misic, B., 2022. Mapping neurotransmitter systems to the structural and functional organization of the human neocortex.
4. Koob, G.F., Volkow, N.D., 2010. Neurocircuitry of Addiction. Neuropsychopharmacol 35, 217–238.
5. Nestor, L.J., Ersche, K.D., 2023. Abnormal Brain Networks Related to Drug and Nondrug Reward Anticipation and Outcome Processing in Stimulant Use Disorder: A Functional Connectomics Approach. Biological Psychiatry: Cognitive Neuroscience and Neuroimaging 8, 560–571.
6. Nestor, L.J., Suckling, J., Ersche, K.D., Murphy, A., McGonigle, J., Orban, C., Paterson, L.M., Reed, L., Taylor, E., Flechais, R., Smith, D., Bullmore, E.T., Elliott, R., Deakin, B., Rabiner, I., Hughes, A.-L., Sahakian, B.J., Robbins, T.W., Nutt, D.J., 2020. Disturbances across whole brain networks during reward anticipation in an abstinent addiction population. NeuroImage: Clinical 27, 102297.
7. Strosche, A., Zhang, X., Kirsch, M., Hermann, D., Ende, G., Kiefer, F., Vollstädt-Klein, S., 2021. Investigation of brain functional connectivity to assess cognitive control over cue-processing in Alcohol Use Disorder. Addiction Biology 26, e12863.
8. Volkow, N.D., Wang, G.-J., Fowler, J.S., Tomasi, D., Telang, F., 2011. Addiction: Beyond dopamine reward circuitry. Proceedings of the National Academy of Sciences 108, 15037–15042.
9. Zhu, X., Cortes, C.R., Mathur, K., Tomasi, D., Momenan, R., 2017. Model-free functional connectivity and impulsivity correlates of alcohol dependence: a resting-state study. Addiction Biology 22, 206–217.

Poster No 1722

Evaluating the repeatability and validity of community detection in functional brain networks

Makoto Fukushima[1], Ryusuke Nakamura[2], Kazushi Ikeda[2,3]

[1]Graduate School of Advanced Science and Engineering, Hiroshima University, Hiroshima, Japan, [2]Graduate School of Science and Technology, Nara Institute of Science and Technology, Nara, Japan, [3]Data Science Center, Nara Institute of Science and Technology, Nara, Japan

Introduction: Network analysis methods have been widely used to characterize complex connectivity patterns in functional networks in the brain. One such method is community detection, which decomposes the entire network into communities (or modules) consisting of brain regions whose activity time series are positively correlated (Sporns and Betzel, 2016). These functional communities are often detected by maximizing the modularity with the resolution parameter that controls the spatial size of the detected communities (Reichardt and Bornholdt, 2006; Rubinov and Sporns, 2011). Optimal resolution parameters were chosen so that the detected communities were repeatable across multiple trials of modularity maximization (Mišić et al., 2016) or were valid and similar to known intrinsic connectivity networks (ICNs) (Hilger et al., 2020). However, how the repeatability and validity of detected functional communities change with resolution parameters has not been comprehensively investigated. In this study, we systematically evaluated these repeatability and validity across the spectrum of resolution parameters using multiple criteria and parcellation scales with/without global signal regression (GSR) (Murphy and Fox, 2017).

Methods: Group-averaged functional brain networks were derived from resting-state fMRI data of the 100 unrelated subjects downloaded from the public database of the WU-Minn Human Connectome Project (Van Essen et al., 2013). The fMRI data of 15 high motion subjects and 1 subject categorized as age ≥ 36 were excluded in this study. Nodes in the functional brain networks were defined based on two multiscale parcellation atlases, Lausanne (Cammoun et al., 2012) and Schaefer (Schaefer et al., 2018). The functional brain networks were constructed with or without GSR. Communities in the functional brain networks were detected by modularity maximization and the consensus clustering approach (Sporns and Betzel, 2016). The repeatability of community detection was evaluated by quantifying the similarity of initial and consensus partitions and the similarity of consensus partitions in different sessions. The validity of community detection was evaluated by quantifying the similarity of consensus communities to the seven canonical ICNs (visual, somatomotor, dorsal attention, ventral attention, limbic, frontoparietal, and default mode) (Yeo et al., 2011), visualizing their spatial overlap, and checking the existence of tiny communities.

Results: We found that when the repeatability of detected communities over resolution parameters was highest, the number of detected communities was around three or four in most cases. (Fig. 1). The similarity of these most repeatable communities to the seven ICNs was not as high as in cases where a larger number of communities were detected (Fig. 2A). When the similarity to the seven ICNs was the highest, the number of communities detected was in most cases around eight, with a few

tiny communities often appearing when finer parcellation scales were used (Fig. 2A). From low to high resolution parameters, communities corresponding to the visual, somatomotor, and default mode networks appeared first, followed in most cases by the ventral attention network and then the remaining ICNs (Fig. 2B). With GSR, communities corresponding to the limbic and frontoparietal networks rarely appeared until the entire network was decomposed into about 30 communities (Fig. 2B).

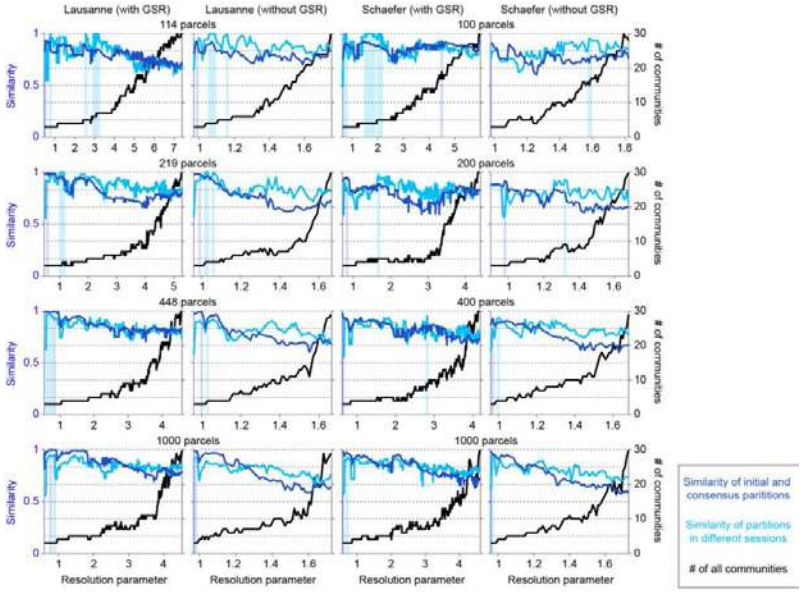

Figure 1. Repeatability of detected communities. Partition similarity was quantified using adjusted mutual information. The resolution parameters with the highest similarity are marked with vertical lines.

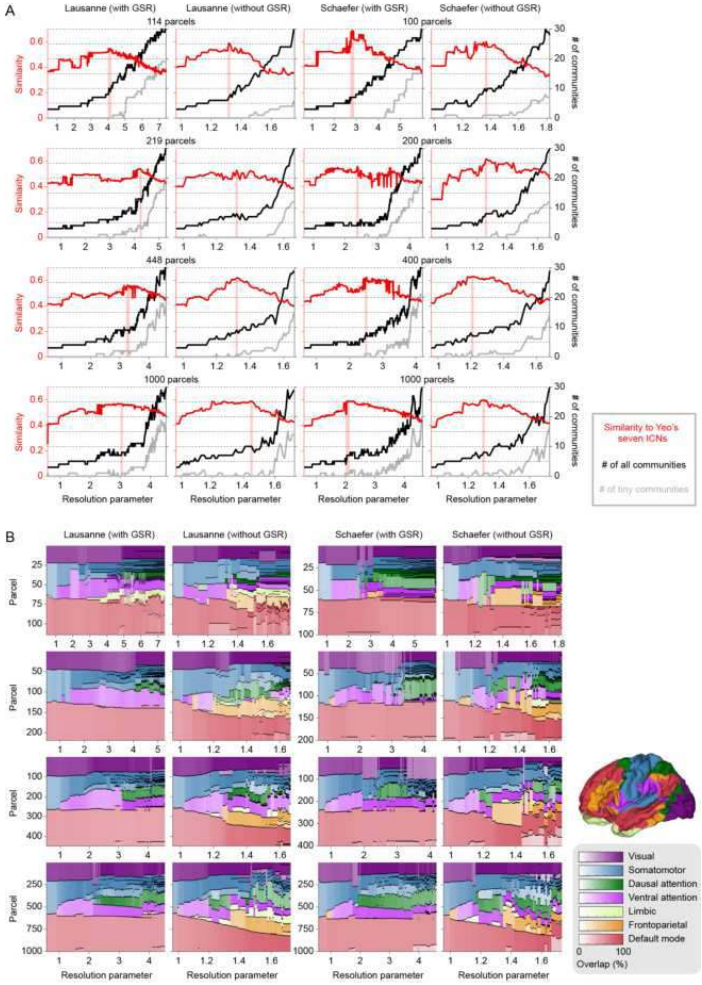

Figure 2. Validity of detected communities. (A) Similarity to the seven ICNs quantified using adjusted mutual information. The resolution parameters with the highest similarity are marked with vertical lines. A tiny community was defined as one in which the number of nodes was less than or equal to 1% of the total number of nodes (parcels) in the entire network. (B) Spatial overlap of detected communities with the ICNs.

Conclusions: Using multiple parcellation scales, we evaluated the repeatability and validity of functional brain network communities detected by modularity maximization across resolution parameters. Our results illustrate how the repeatability and validity of detected communities vary with resolution parameters and depend on the use of parcellation scales and GSR. These results may help users choose resolution parameters, parcellation scales, and whether or not to use GSR when applying modularity-based community detection to functional brain networks.

References

1. Cammoun, L. et al. (2012) 'Mapping the human connectome at multiple scales with diffusion spectrum MRI', Journal of Neuroscience Methods, vol. 203, no. 2, pp. 386-397
2. Hilger, K. et al. (2020) ' Temporal stability of functional brain modules associated with human intelligence', Human Brain Mapping, vol. 41, no. 2, pp. 362-372
3. Mišić, B. et al. (2016) 'Network-level structure-function relationships in human neocortex', Cerebral Cortex, vol. 26, no. 7, pp. 3285-3296
4. Murphy, K and Fox, M. D. (2017) ' Towards a consensus regarding global signal regression for resting state functional connectivity MRI', NeuroImage, vol. 154, pp. 169-173
5. Reichardt, J. and Bornholdt, S. (2006) 'Statistical mechanics of community detection', Physical Review E, vol. 74, no. 1, 016110
6. Rubinov, M. and Sporns, O. (2011) 'Weight-conserving characterization of complex functional brain networks', NeuroImage, vol. 56, no. 4, pp. 2068-2079
7. Schaefer, A. et al. (2018) ' Local-global parcellation of the human cerebral cortex from intrinsic functional connectivity MRI', Cerebral Cortex, vol. 28, no. 9, pp. 3095-3114
8. Sporns, O. and Betzel, R.F. (2016) 'Modular brain networks', Annual Reviews of Psychology, vol. 67, pp. 613-640
9. Yeo B.T.T., et al. (2011) 'The organization of the human cerebral cortex estimated by intrinsic functional connectivity', Journal of Neurophysiology. vol. 106, no. 3, pp. 1125-1165

Poster No 1723

Targeted Time-Varying Functional Connectivity

Sonsoles Alonso[1], Luke Hearne[2], Luca Cocchi[3], James Shine[4], Diego Vidaurre[1]

[1]Aarhus University, Aarhus C, Aarhus, [2]QIMR Berghofer Medical Research Institute, Herston, Queensland, [3]QIMR Berghofer Medical Research Institute, Brisbane, Queensland, [4]University of Sydney, Sydney, New South Wales

Introduction: Current methods for time-varying functional connectivity (FC) often model the overall dynamics of the entire network. This inherent approach results in symmetric FC measures where all possible pairwise connections need to be modelled, hampering the modelling of specific connections. To overcome this limitation, our study introduces a novel approach, Targeted Time-Varying FC (TTVFC), which explicitly models the temporal dynamics of specific connections of interest rather than the entire brain network. TTVFC facilitates the exploration of the relationship between two sets of brain time series, X and Y, rigorously testing the statistical significance of their fluctuations throughout ongoing tasks.

Methods: In this study, we applied this novel methodology to explore the dynamic relationship between thalamic and cortical activity. The analysis involved 7T fMRI data with a repetition time of 0.58 seconds, obtained from 60 participants across three 10-minute task sessions. The data were originally presented in Hearne et al. (2017). Specifically, we utilized preprocessed timeseries extracted from the cortex using the atlas by Gordon et al. (2016) and from the thalamus, employing the Morel atlas (Niemann et al., 2000), as detailed in Shine et al. (2019). The experimental task was deliberately designed to systematically manipulate reasoning complexity while minimizing working memory demands (Birney et al., 2006). Implementing TTVFC involves utilizing a variant of the Hidden Markov Model (HMM; Vidaurre et al., 2017). This variant derives a discrete sequence of sequential states, each characterized by a distinct set of beta coefficients obtained from regressing Y time series on X time series. State time courses, indicating the probability of a given state being active at each time point, were also estimated. To understand the variations in state fluctuations, each representing a specific pattern of thalamocortical connections, we examined their changes in response to cognitive complexity. The statistical significance of these fluctuations over time was determined by employing a clustered-based permutation t-test (Maris and Oostenveld 2007), assessing the differences across levels of complexity.

Results: Our findings reveal that thalamocortical dynamics are intricately linked to distinct problem-solving patterns. Remarkably, TTVFC, without prior knowledge of task timings, effectively describes fluctuations in the interaction of targeted brain regions in response to different cognitive processes induced by the task. Importantly, the application of a conventional HMM approach, where states represent matrices of connectivity across all elements in X and Y, proved inadequate in capturing distinctions in problem-solving tasks.

Conclusions: This suggests that emphasizing specific connections, rather than relying on the whole-brain FC approach, more effectively elucidates certain cognitive processes. The study underscores the utility of TTVFC in understanding and modelling targeted brain dynamics, extending its applicability beyond fMRI data to various neuroimaging data modalities.

References
1. Birney, D. P., Halford, G. S., & Andrews, G. (2006). Measuring the Influence of Complexity on Relational Reasoning: The Development of the Latin Square Task. Educational and Psychological Measurement, 66(1), 146-171.
2. Gordon, E. M., Laumann, T. O., Adeyemo, B., Huckins, J. F., Kelley, W. M., & Petersen, S. E. (2016). Generation and evaluation of a cortical area parcellation from resting-state correlations. Cerebral Cortex, 26(1), 288-303.
3. Hearne, L. J., Cocchi, L., Zalesky, A., & Mattingley, J. B. (2017). Reconfiguration of Brain Network Architectures between Resting-State and Complexity-Dependent Cognitive Reasoning. Journal of Neuroscience: The Official Journal of the Society for Neuroscience, 37(35), 8399-8411.
4. Maris, E., & Oostenveld, R. (2007). Nonparametric statistical testing of EEG- and MEG-data. Journal of neuroscience methods, 164(1), 177–190.
5. Niemann, K., Mennicken, V. R., Jeanmonod, D., & Morel, A. (2000). The Morel stereotactic atlas of the human thalamus: atlas-to-MR registration of internally consistent canonical model. NeuroImage, 12(5), 601-616.
6. Shine, J. M., Hearne, L. J., Breakspear, M., Hwang, K., Müller, E. J., Sporns, O., Poldrack, R. A., Mattingley, J. B., & Cocchi, L. (2019). The Low-Dimensional Neural Architecture of Cognitive Complexity Is Related to Activity in Medial Thalamic Nuclei. Neuron, 104(5), 849-855.E3.
7. Vidaurre, D., Smith, S. M., & Woolrich, M. W. (2017). Brain network dynamics are hierarchically organized in time. Proceedings of the National Academy of Sciences, 114(48), 12827-12832.

Poster No 1724

Motion Effects in Procrustes Aligned Individual-Level Gradients

Leonard Sasse[1], Casey Paquola[2], Simon Eickhoff[1], Kaustubh Patil[2]

[1]Institute of Systems Neuroscience, Medical Faculty and University Hospital Düsseldorf, Düsseldorf, Germany, [2]Institute of Neuroscience and Medicine, Brain and Behaviour (INM-7), Research Centre Jülich, Jülich, Germany

Introduction: Functional connectivity (FC) is a cornerstone of fMRI research for unraveling human brain organization (Biswal et al. 1995). One widely employed technique involves the extraction of FC gradients from FC matrices using dimensionality reduction (Margulies et al. 2016; Vos de Wael et al. 2020). However, as the sign and the ordering of gradients can be different between subjects, they need to be aligned to make them comparable. Procrustes alignment is often employed for this purpose (Vos de Wael et al. 2020). This study aims to investigate the impact of varying the number of gradients used in Procrustes alignment on the aligned principal gradient, and its use in subject-level downstream analyses.

Methods: We used rs-fMRI data from the Human Connectome Project (HCP) for 395 unrelated subjects (192 female, 203 male), aged 22-37 (M=28.71, SD=3.82) (Van Essen et al. 2013). Specifically, we used data that has undergone the HCP's ICA-FIX procedure, which also included removal of Friston 24 motion parameters (Glasser et al. 2013; Salimi-Khorshidi et al. 2014). In addition, we regressed out white matter (WM), cerebro-spinal fluid (CSF), and global (GS) signals, their squared terms, and temporal derivatives. The data was bandpass filtered at 0.01 - 0.08 Hz and aggregated using the Schaefer 400 parcellation. FC was calculated as Pearson's correlation. Gradients were extracted using the BrainSpace toolbox, which also provides Procrustes alignment to find the optimal transformation matrix to minimise the sum of squared errors of a source matrix to a reference matrix (Fig. 1a). We split subjects into an analysis and a holdout reference dataset for alignment (Fig. 1b). We performed identification (Finn et al. 2015) and calculated differential identifiability (Amico and Goñi 2018) to test the impact of the alignment on downstream subject-level analyses. To quantify similarity of the aligned principal gradient with the unaligned gradients, we calculated the ratio of the maximum to the sum of absolute values in the first column of the transformation matrix ("Correspondence"; Fig. 1c). Motion was characterized using average framewise displacement (FD) for each subject.

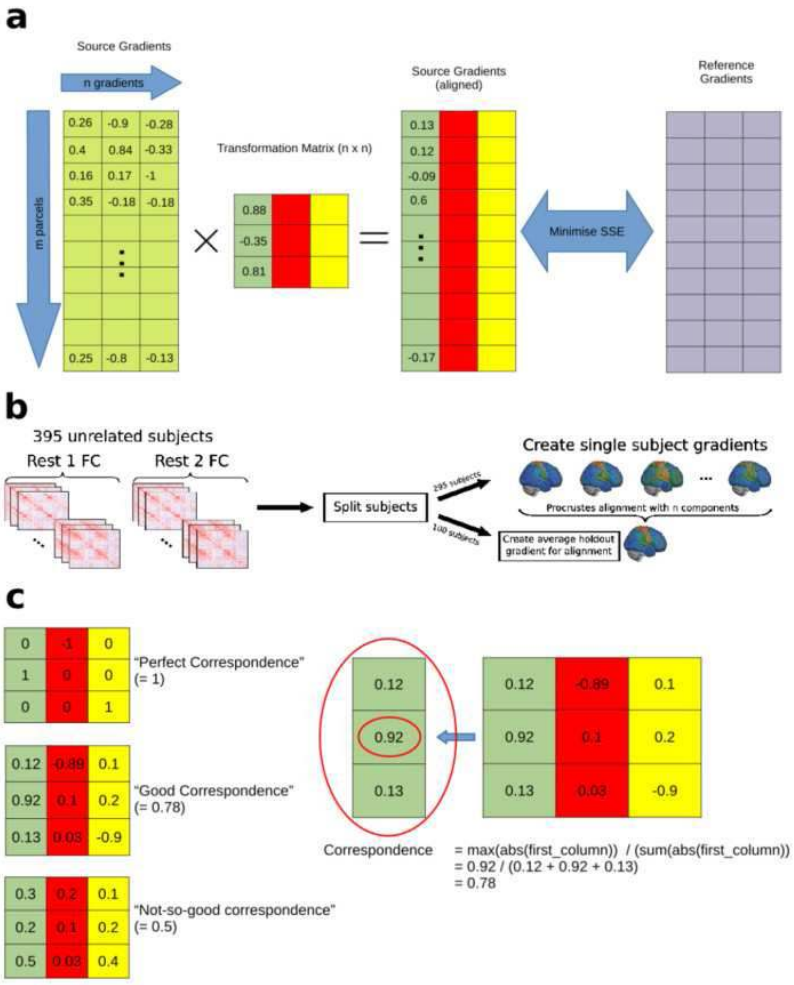

Figure 1. Illustration of the main methods used. **a)** Procrustes alignment finds a transformation matrix to align the source gradients to the holdout reference gradients such that the sum of squared errors between them is minimised. **b)** The sample is split into a main dataset of 295 subjects and a holdout dataset of 100 subjects to be used as a reference in alignment. **c)** Correspondence is defined as the ratio of the maximum to the sum of absolute values in the first column of the transformation matrix and quantifies the degree to which one of the unaligned, original gradients corresponds to the aligned principal gradient of a subject.

Results: Identification accuracy substantially increased (Fig. 2a), whereas differential identifiability decreased (Fig. 2b) when using more gradients for alignment. In addition, correspondence of the aligned gradient decreased with increasing number of gradients, indicating that the principal gradient takes on an increasingly mixed character, including more information from lower gradients (Fig. 2c). This result suggests that higher distinctiveness of individuals is not due to simply re-ordering of the gradients, but rather due to global subject-specific information being introduced into the aligned principal gradient. One candidate for such subject-specific global information is motion. We found that average FD was correlated with the magnitude of the transformation (Fig. 2d-e), and this correlation increased with increasing number of gradients used in alignment. Additionally, motion signal as indicated by typicality of the FC matrices (Kopal et al., 2020) was correlated to the total transformation (Fig. 2f). Finally, using more gradients in alignment improved prediction of FD based on the aligned principal gradient, indicating an increased presence of motion signal after alignment (Fig. 2g-i).

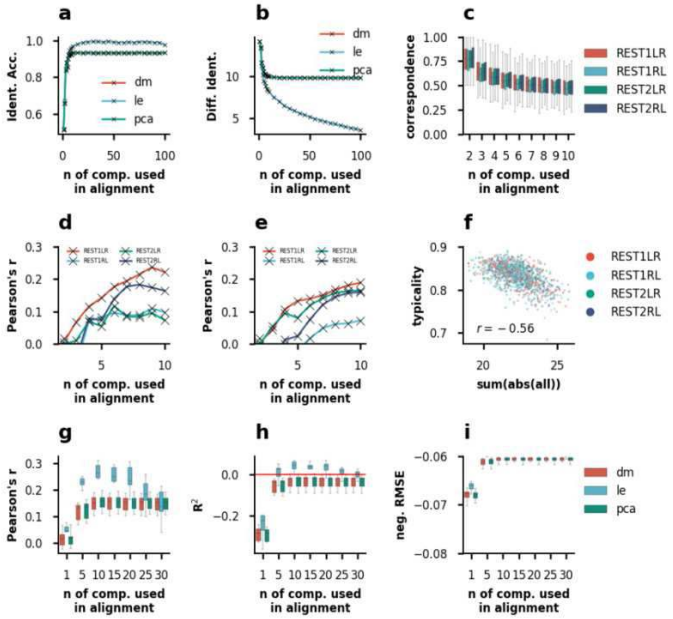

Figure 2. a) Mean Identification accuracy and **b)** differential identifiability using principal gradients from day 1 and day 2 of HCP-YA resting state data. **c)** Correspondence: The degree to which aligned principal gradients correspond to one of the original gradients. **d)** Correlation between the sum of absolute values in subjects' transformation matrices with FD as a measure of motion and **e)** Correlation between the sum of absolute values in the first column of subjects' transformation matrices and FD. **f)** Typicality of subjects' FC matrices correlated with the sum of absolute values in subjects' transformation matrices. **g)** Pearson's correlation between predicted and observed values when predicting FD in a 5-Fold CV with 10 repeats, **h)** R^2 when predicting FD in a 5-Fold CV with 10 repeats, and **i)** negative root mean squared error when predicting FD in a 5-Fold CV with 10 repeats.

Conclusions: We observed that the number of components used for Procrustes alignment plays a substantial role in downstream analyses. Specifically, we found that as more gradients are utilized in alignment, identification accuracy increases while differential identifiability decreases. Additionally, our results indicate that Procrustes alignment, especially when using many gradients, introduces information from lower-order information into the principal gradient. Notably, we identified that motion effects are introduced in the alignment procedure.

References

1. Amico, E. (2018), 'The Quest for Identifiability in Human Functional Connectomes'. Scientific Reports 8 (1)
2. Biswal, B. (1995), 'Functional Connectivity in the Motor Cortex of Resting Human Brain Using Echo-Planar Mri'. Magnetic Resonance in Medicine 34 (4): 537–41.
3. Finn, E.S. (2015), 'Functional Connectome Fingerprinting: Identifying Individuals Using Patterns of Brain Connectivity'. Nature Neuroscience 18 (11): 1664–71.
4. Glasser, M.F. (2013), 'The Minimal Preprocessing Pipelines for the Human Connectome Project'. NeuroImage 80 (October): 105–24.
5. Kopal, J. (2020), 'Typicality of Functional Connectivity Robustly Captures Motion Artifacts in rs-fMRI across Datasets, Atlases, and Preprocessing Pipelines'. Human Brain Mapping 41 (18): 5325–40.
6. Margulies, D.S. (2016), 'Situating the Default-Mode Network along a Principal Gradient of Macroscale Cortical Organization'. Proceedings of the National Academy of Sciences 113 (44): 12574–79.
7. Salimi-Khorshidi, G. (2014), 'Automatic Denoising of Functional MRI Data: Combining Independent Component Analysis and Hierarchical Fusion of Classifiers'. NeuroImage 90 (April): 449–68.
8. Van Essen, D.C. (2013), 'The WU-Minn Human Connectome Project: An Overview'. NeuroImage 80 (October): 62–79.
9. Vos de Wael, R. (2020). 'BrainSpace: A Toolbox for the Analysis of Macroscale Gradients in Neuroimaging and Connectomics Datasets'. Communications Biology 3 (1): 1–10.

Poster No 1725

Thalamic BOLD States Explain Visual Response Variability and Changes in Occipital Alpha Power

Brandon Ingram[1], Stephen Mayhew[2], Andrew Bagshaw[1]

[1]University of Birmingham, Centre for Human Brain Health, Birmingham, West Midlands, [2]Aston University, Institute of Health and Neurodevelopment (IHN), Birmingham, West Midlands

Introduction: The thalamus is the largest subcortical structure in the human brain and is widely involved in sensory processing, with visual, auditory, somatosensory, and gustatory signals all passing through their associated thalamic nuclei

before being relayed to their respective cortical areas. Due to this, the thalamus has often been viewed as a simple sensory relay station, and as a result has been understudied within human neuroscience research (Shine et al., 2023). However, the region has since been associated with more complex functions, including visual attention (Rees, 2009) and the generation and regulation of the alpha rhythm (Becker et al., 2015; Suffczynski et al., 2001). One such function is the modulation of visual responses, with recent animal literature demonstrating that the pulvinar nucleus modulates the firing rate of V1 neurons during visual perception (De Souza et al., 2020). In addition, fMRI research in humans has shown that the thalamus, as well as other subcortical regions such as the putamen, exhibit unique BOLD patterns when different resting-state networks are active (Greene et al., 2020), suggesting a link with the control of resting-state networks (Hwang et al., 2017). This demonstrates that the thalamus is implicated in a wide range of functions and that the relay station hypothesis represents an oversimplification of the region. This study employed EEG-fMRI to investigate the dynamics of the thalamus and their involvement with visual response modulation and the occipital alpha rhythm.

Methods: Thirty control participants were displayed full contrast visual checkerboards to the left visual field to evoke a lateralised visual BOLD response, VEP and alpha ERD/S. EEG (BrainProducts) and fMRI (Siemens Prisma, TR=1010 ms, 2.5 × 2.5 × 2.5 mm) were recorded simultaneously. The thalamus was masked, and a group-level ICA (10 components) performed to obtain a functional parcellation of the thalamus. This was used as input within a Hidden Markov Model (HMM-MAR toolbox) (Vidaurre et al, 2016). We evaluated the impact of thalamic states when they were active at the time of visual stimulation on subsequent BOLD, VEP and alpha ERD/S responses. Additionally, we investigated the relationship between the thalamic states and occipital alpha power by calculating an alpha power time course and correlating it with the thalamic state time courses.

Results: Hidden Markov Modelling identified a total of six thalamic states. Thalamic state at pre-stimulus baseline significantly impacted the magnitude of subsequent BOLD responses and the amplitude of the P250 component of the VEP. Two of the thalamic states exhibited a specific temporal relationship with occipital alpha power, with alpha power increasing or decreasing approximately six to eight seconds after the onset of the thalamic state.

Conclusions: This study demonstrates that the thalamus exhibits complex BOLD dynamics during a visual task, with different states showing specific relationships with the rest of the brain and with posterior alpha power. Further, these thalamic states significantly modulated responses to visual stimuli when they were active at pre-stimulus baseline, influencing the amplitude of the visual BOLD response peak and the amplitude of the P250 VEP component. The results presented here confirm the complex role of the thalamus, beyond what would be expected of a simple sensory relay. HMM is able to identify multiple thalamic BOLD states, with strong relationships with the rest of the brain and posterior alpha power. These states modulate visual responses, highlighting the involvement of the thalamus in both the generation of the alpha rhythm and visual attention.

References

1. Becker, R. et al. (2015). Relating alpha power and phase to population firing and hemodynamic activity using a thalamo-cortical neural mass model. PLoS computational biology, 11(9), e1004352.
2. de Souza, B. O. F. et al. (2020). Pulvinar modulates contrast responses in the visual cortex as a function of cortical hierarchy. Cerebral Cortex, 30(3), 1068-1086.
3. Greene, D. J. et al. (2020). Integrative and network-specific connectivity of the basal ganglia and thalamus defined in individuals. Neuron, 105(4), 742-758.
4. Hwang, K. et al. (2017). The human thalamus is an integrative hub for functional brain networks. Journal of Neuroscience, 37(23), 5594-5607.
5. Rees, G. et al. (2009). Visual attention: the thalamus at the centre?. Current biology, 19(5), R213-R214.
6. Shine, J. M., et al. (2023). The impact of the human thalamus on brain-wide information processing. Nature Reviews Neuroscience, 1-15.
7. Suffczynski, P. et al. (2001). Computational model of thalamo-cortical networks: dynamical control of alpha rhythms in relation to focal attention. International Journal of Psychophysiology, 43(1), 25-40.
8. Vidaurre, D. et al. (2016). Spectrally resolved fast transient brain states in electrophysiological data. Neuroimage, 126, 81-95.

Poster No 1726

Brain-wide modeling of causal circuit dynamics in human working memory

Byeongwook Lee[1], Louis Rouillard[2], Luca Ambrogioni[3], Srikanth Ryali[1], Demian Wassermann[2], Vinod Menon[1]

[1]Stanford University, Palo Alto, United States, [2]Université Paris-Saclay, Inria, CEA, Paris, France, [3]Donder's Institute of Cognition, Radboud University, Nijmegen, Netherlands

Introduction: Working memory, a fundamental component of human cognition, encompasses the ability to retain and manipulate information in the mind for various cognitive tasks, a function central to all reasoning, comprehension, and learning[1,2]. While previous research has made significant strides in identifying key brain regions and probing interactions

within limited sets of brain regions, a comprehensive understanding of brain-wide dynamic orchestration of distributed brain regions during working memory has remained elusive. This gap in knowledge is particularly notable in the context of analyzing causal control circuits at the whole-brain level, which are crucial for understanding how specific brain nodes or networks assert control in human working memory through asymmetric influences.

Methods: Here we bridge this gap by developing a novel Multivariate Dynamic Systems Identification[3]-hybrid Variational Bayes (MDSI-hVB) technique. This novel computational framework is tailored to capture whole-brain asymmetric directed interactions, addressing pivotal challenges in dynamic causal modeling within cognitive neuroscience. These challenges encompass the development of computational methods for large-scale network analysis, modeling regional variations in the hemodynamic response function (HRF), and deciphering context-dependent brain-wide causal interactions. We analyzed brain-wide dynamic causal interactions in a large (N=737) sample of participants from the Human Connectome Project[4] who performed a n-back working memory task during fMRI scanning. DiFuMo atlas[5] was used to extract task fMRI time series for subsequent analyses as it offers fine-grained brain-wide functional modes for both cortical and subcortical areas and features multi-dimensional functional networks. We utilized time series data obtained from 128 dimensions for the main analyses and employed time series data extracted from both 64 and 256 dimensions to assess the scalability and robustness of MDSI-h-VB in estimating whole-brain causal interactions.

Results: Utilizing MDSI-hVB, we explored intricate brain-wide dynamic causal and asymmetric interactions during working memory. A key aspect of our approach was capturing the heterogeneity of the HRF across different brain regions. This capability allowed our MDSI-hVB model to more accurately represent latent neural activity, reflecting underlying neural dynamics rather than mere blood flow changes. Our MDSI-h-VB model identified asymmetric connectivity patterns exhibiting significant dynamic causal interactions under both the 0-back and 2-back task conditions ($p<0.01$, FDR-corrected, two-side paired t-test). Notably, load-dependent causal interactions distinguished the task conditions (2-back vs. 0-back) with remarkable accuracy (classification accuracy=98%, $p<0.01$, permutation test). This high level of accuracy underscores the effectiveness of our approach in capturing brain-wide load-dependent causal circuit dynamics during working memory. Additionally, our MDSI-h-VB model reliably predicted brain-behavior relationships. A critical finding of our study was the identification of directed causal outflows during the working memory task. We discovered that the anterior insula (AI) and the middle frontal gyrus (MFG) function as pivotal outflow and inflow nodes, respectively, at the whole-brain level. This discovery is significant, as it highlights the specific roles individual brain regions play in orchestrating the complex dynamics of working memory processes. Lastly, our methodological framework demonstrated remarkable scalability, successfully extending the analysis to encompass multiple dimensions encompassing 64, 128, and 256 regions.

Conclusions: Our study not only unravels brain-wide dynamic circuit mechanisms underpinning human working memory but also opens new avenues for exploring context-dependent dynamic causal networks at the whole-brain level, offering deeper insights into dynamic networks that drive human cognition.

References

1. Menon, Vinod, and Mark D'Esposito. "The role of PFC networks in cognitive control and executive function." Neuropsychopharmacology 47.1 (2022): 90-103.
2. D'Esposito, Mark, and Bradley R. Postle. "The cognitive neuroscience of working memory." Annual review of psychology 66 (2015): 115-142.
3. Ryali, Srikanth, et al. "Multivariate dynamical systems models for estimating causal interactions in fMRI." Neuroimage 54.2 (2011): 807-823.
4. Van Essen, David C., et al. "The WU-Minn human connectome project: an overview." Neuroimage 80 (2013): 62-79.
5. Dadi, Kamalaker, et al. "Fine-grain atlases of functional modes for fMRI analysis." NeuroImage 221 (2020): 117126.

Poster No 1727

Precision Functional Brain Mapping after Methamphetamine Administration

Wililam Hoffman[1,2], Robert hermosillo[3,2,4,5], Laura Dennis[1,2], Anita Randolph[3], Holly McCready[1], Daniel Smith[2], Meghan Oswald[6], Milky Kohno[1,2], Gracie Grimsrud[7], Heba Abuad[3], Eric Feczko[8,4], Damien Fair[8,4,5]

[1]Portland VA Health Care System, Portland, OR, [2]Oregon Health & Science University, Portland, OR, [3]Masonic Institute for the Developing Brain, University of Minnesota, Minneapolis, MN, [4]Department of Pediatrics, University of Minnesota, Minneapolis, MN, [5]Institute of Child Development, University of Minnesota, Minneapolis, MN, [6]Zucker School of Medicine/Northwell Health at Mather Hospital, Port Jefferson, NY, [7]Masonic Institute for the Developiing Brain, University of Minnesota, Minneapolis, MN, [8]Masonic Institute for the Developing Brain, University of Minnesota Medical School, Minneapolis, MN

Introduction: Precision functional mapping (Gordon et al., 2018) can reliably identify the resting state functional connectivity network structure of individual brains. The method offers important advantages for producing individual steady state functional connectivity networks will more precise borders between regions. We used this method to investigate the effect of orally administered methamphetamine (MA) or placebo (PBO) on network connectivity in healthy control subjects (CS).

Methods: Participants were recruited through the Veterans Affairs Portland Health Care System (VAPORHCS) and Oregon Health & Science University (OHSU) (Portland, Oregon, USA). The research was approved by a joint Institutional Review Board at OHSU and VAPORHCS. Participants (n=8, age = 37.75 ± 13.06, 5 female) CS completed 2 separate sessions in a double-blind cross-over study. Either MA, 0.3 mg/kg or a matching PBO were orally administered in two sessions separated by at least 3 days to allow for drug washout. Subjective experience (euphoria) was rated hourly on the Addiction Research Center Inventory (ARCI) morphine-benazadrine group (MBG) subscale. Subjects received a baseline scan and then a scan initiated 1.5 h after receiving double blind MA or PBO (Figure 1). MA serum levels were measured from saliva collected before and after the scan. Scanning was performed on a 3.0-T Siemens Prisma Scanner using a 32-channel head coil at OHSU. During each scan, high resolution T1w and T2w images and field maps were obtained. BOLD data (TR: 800 ms, TE: 0.03, slice thickness: 2.4mm, flip angle: 52°) for RSFC were collected in 5 minute blocks FIRMM software in real-time to collect 30 to 45 min worth of low motion (FD<0.2mm) volumes. BOLD data for each participant was processed similarly to the ABCD-BIDS pipeline (Feczko et al. 2021). Time series data from each session were treated as separate tasks to ensure that BOLD data was registered to an identical surface mesh generated from a common T1w image. Motion censoring was performed to reduce the influence of motion artifacts (Power 2014). Network templates were produced from 164 participants in a separate study using the template matching procedure, described in Hermosillo et al. (2022). This resulted in 14 different network templates identified in Figure 2. Precision functional maps were constructed for each participant in the present study. The spatial similarity (eta^2) at each grayordinate was calculated to each of the network templates and, in each individual participant, the grayordinate was assigned to the network template that had the highest eta^2 value. Group connectivity matrices (Figure 2) were obtained by assigning each grayordinate to a network if it occurred in that network in at least 7 individuals.

Results: Post scan MA levels were 389 ± 209 ng/mL (range 145 – 780). There was a consistent subjective response after MA administration (Fig 1), with subjects reporting maximum subjective effects at 12 to 15 on the MBG scale. Inspection of the individual correlation maps. pre and post drug in the MA condition, found robust, consistent decreased within network connectivity in the SMd, SMl, AUD, VIS networks and, less consistently, in the DMN (Figure 2). There were minimal changes in the PBO condition.

Conclusions: Precision functional mapping is a feasible method for the study of acute drug administration by accounting for differences in functional topography. The method produces individual maps that approach a steady state and allow detection of precise borders between networks with increased confidence. The method can yield stable group maps in modest subject cohorts. In this study, MA administration induced widespread decreased within network connectivity in primary sensorimotor networks in healthy controls.

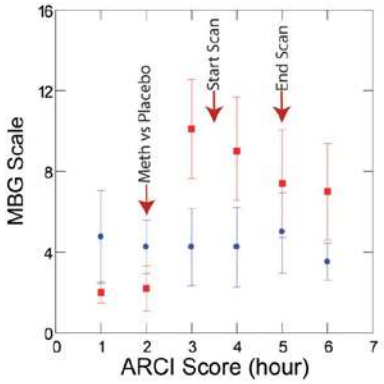

Figure 1: Morphine-Benzadrine Group (MBG) subscale (euphoria) vs time. Termination time for resting state scans varied from 1 to 1.5 hours to meet criterion for minimal motion volumes.

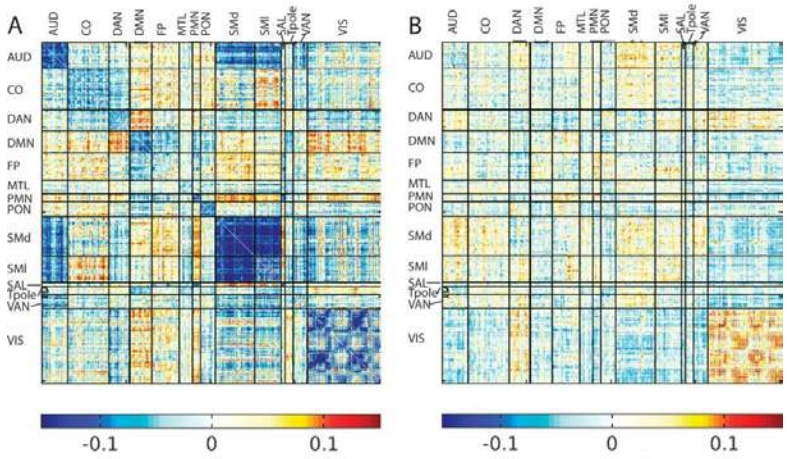

Figure 2: Post - Pre differences in RSFC (A) after MA administration and (B) after PBO administration. AUD - auditory network, CO - cingulo-opercular network, DAN - dorsal attention network, DMN -default mode network, FP - fronto-parietal network, MTL - medial temporal network, PMN - parietal medial network, PON - parieto-occipital network, SMd - dorsal somatomotor, SMl - lateral somatomotor, SAL - salience, Tpole - temporal pole, VAN - ventral attention network, VIS - visual network.

References

1. Feczko, E et al. (2021), Adolescent Brain Cognitive Development (ABCD) Community MRI Collection and Utilities, bioRxiv 2021, doi: https://doi.org/10.1101/2021.07.09.451638.
2. Gordon, E et al., (2017), Precision functional mapping of individual human brains, Neuron 96(4), 791-807.
3. Hermosillo, RJM et al. (2022), A Precision Functional Atlas of Network Probabilities and Individual-Specific Network Topography, bioRxiv 2022.01.12.475422; doi: https://doi.org/10.1101/2022.01.12.475422.
4. Power, JD et al. (2014), Methods to Detect, Characterize and Remove Motion Artifact in Resting State fMRI, Neuroimage 84, 320-341.

Poster No 1728

Perturbation of intrinsic oscillatory modes by ischemic stroke in rats

Rita Alves[1], Joana Cabral[1,2], Noam Shemesh[1]

[1]Champalimaud Research, Champalimaud Foundation, Lisbon, Portugal, [2]Life and Health Sciences Research Institute, University of Minho, Braga, Portugal

Introduction: Disruption of functional networks is a hallmark of numerous brain disorders (Fornito, 2015). In stroke, loss of interhemispheric functional connectivity (FC) has been reported at the acute stages, possibly followed by renormalization (van Meer, 2010). However, the biophysical mechanisms underlying these changes in FC remain to be elucidated. Recently, a repertoire of intrinsic oscillatory modes exhibiting stationary wave pattern features were discovered in healthy animal brains (Cabral, 2023) and humans (Pang, 2023), and provided insight into the organizing principles underpinning spontaneous long-range FC. Here, we investigated how disrupting a specific and well-localized cortical area modulates these intrinsic modes.

Methods: All experiments received proper ethical approvement. Stroke induction: A photothrombotic stroke (Watson, 1985) was induced unilaterally in Long-Evan rats. N = 10 stroked animals were imaged 1w poststroke along with N = 10 healthy controls (under medetomidine). MRI: Ultra-fast rs-fMRI data were acquired with a GE-EPI sequence in a 9.4T scanner: TR/TE = 90/16ms, FOV = 21x21mm2, resolution = 250x250µm2, slice = 1.2mm, tacq = 24min, flip angle = 20°, Nreps = 16000, 2 scans per animal, BW = 277kHz axial and coronal. Data analysis: The first 2000 frames were removed due to significant gradient temperature drift during this time. Correlation analyses: fMRI signals within the brain mask were bandpass filtered between 0.1-0.3Hz, and ROI seed-based correlation maps were performed (Pearson's). Spectral analysis of data: Power spectra were computed voxelwise, after aligning (Guizar-Sicairos, 2008) and detrending. Spectral power was taken as the integral under the peaks in each bin. Extracting intrinsic modes from Principle Component Analysis: For each scan, the fMRI signals in N = 1263 (coronal) and N = 2007 (axial) brain voxels were band-pass filtered (0.01-0.3Hz) and the N×N covariance matrix was computed and averaged across the 20 scans in each group. The first 10 eigen vectors were extracted and mapped.

Results: Fig.1C-D shows a conventional seed-based functional connectivity analysis. The healthy group seeds show higher degree of correlation compared to the stroke group. Particularly, when the contralesional cortex served as a seed, the stroked area showed nearly no connectivity (ROI 1). A more distant contralateral cortical area exhibited low correlation values (ROI 2). Finally, the contralesional striatum showed relatively stronger interhemispheric correlation to ROI 3 in stroke compared to the

healthy group. In Fig 1D, the axial slices revealed similar trends, with stronger cortico-cortical correlations in healthy controls, and weaker correlations near the lesion. Fig.2A-D show the averaged spatial maps of spectral power in 7 frequency bands (0.05-0.4Hz). Higher power was observed in the cortex in the healthy group only until 0.2 Hz. Figure 2E shows the first 10 intrinsic modes detected for the coronal slice. Modes were similar between animals in every group but their spatial features were clearly different between groups. For instance, ψ1 and ψ2 show strong cortical oscillations in the healthy controls, while in stroke the oscillations strongly involve striatal areas. Figure 2F shows the first 10 intrinsic modes for the axial slice. Multiple spatial wave patterns are disturbed due to the lesion.

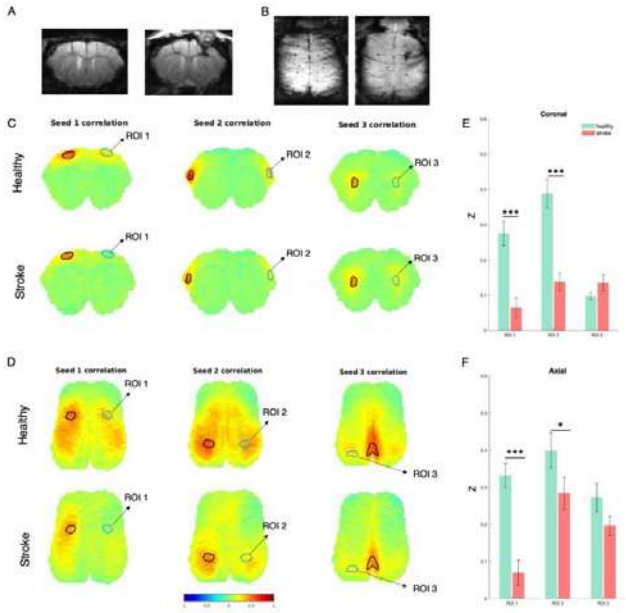

Figure 1. Conventional seed-based functional connectivity analysis
A-B. Raw GE-EPI coronal **(A)** and axial **(B)** data from the healthy (left) and stroke (right) groups. **C-D**. Seed-based correlation maps and statistical analysis are presented for three different seed ROIs (black), where each voxel is coloured according to its degree of correlation with the seed. Coronal seeds: 1- contralesional (cl) cortical ROI, 2-distant cl cortical ROI, 3- cl striatum ROI. Axial seeds: 1- cl somatosensory ROI, 2- cl visual cortex ROI, 3- retrosplenial ROI. **E-F.** Correlation values between seed ROIs and respective contralateral ROIs were calculated for healthy and stroke groups, followed by a statistical analysis to account for differences between groups. Results of t-test for both groups (corrected for multiple comparisons) are presented. Statistically significant differences were observed between groups in ROIs 1 and 2, for both coronal and axial slices (*p < 0.05; *** p < 0.001).

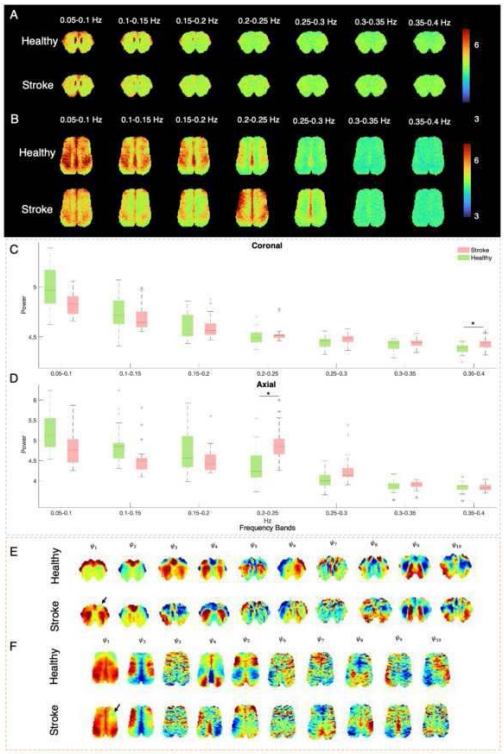

Figure 2. Spatial maps of spectral power and intrinsic oscillatory modes.
A-B. Spatial maps of spectral power in 7 non-overlapping frequency bands, averaged across the 20 fMRI scans per group, for the coronal **(A)** and axial **(B)** slices. **C-D.** Boxplots of the measured spectral power results for all frequency bands averaged across all brain voxels in the coronal and axial slices. Results of t-test for both groups (corrected for multiple comparisons) are presented (*p < 0.05). **E-F**. The first 10 intrinsic modes detected in both groups for the coronal **(C)** and axial **(D)** slices. Modes were similar between individual animals in every group (not shown) but the spatial patterns of these waves were clearly different between the healthy and stroked animals.

Conclusions: Our findings likely reflect reorganization of activity in networks in the stroked brain. In ischemia, weaker FC is observed in the cortico-cortical network. Interestingly, there is an increase in inter-hemispheric striatal connectivity, in line with the stronger oscillatory patterns observed in the striatal areas. The inter-hemispheric asymmetry observed in both axial and coronal slices in the stroke group's intrinsic modes may indicate that the contralesional hemisphere is more involved in compensatory mechanisms for the connection breakdown driven by the lesion.

References

1. Cabral, J. (2023), 'Intrinsic macroscale oscillatory modes driving long range functional connectivity in female rat brains detected by ultrafast fMRI', Nature Communications, vol. 14, 375
2. Fornito, A. (2015), 'The connectomics of brain disorders', Nature Reviews Neuroscience, vol. 16, no.3, pp.159–172
3. Guizar-Sicairos, M. (2008), 'Efficient subpixel registration', Optics Letters, vol. 33, pp. 156–158
4. Pang, J. (2023), 'Geometric constraints on human brain function', Nature, vol. 618, pp. 566–574
5. van Meer, M. P. (2010), 'Recovery of sensorimotor function after experimental stroke correlates with restoration of resting-state interhemispheric functional connectivity', The Journal of Neuroscience, vol. 30, pp. 3964–3972
6. Watson, B.D. (1985), 'Induction of reproducible brain infarction by photochemically initiated thrombosis', Annals of Neurology., vol. 17, no. 5, pp. 497–504

Poster No 1729

Single Scan, Subject-Specific component extraction in dynamic functional connectivity using COBE

Pratik Jain[1], Anil Sao[2], Bharat Biswal[3]

[1]New Jersey Institute of Technology, Newark, NJ, [2]Indian institute of Technology Bhilai, Bhilai, Chhattisgarh, [3]New Jersey Institute of Technology, Newark, NJ

Introduction: The study of individual differences in healthy controls can provide precise descriptions of individual brain activity. Subject-specific (SS) information can be utilized to map individual brains to individual behaviors which can elucidate the mechanistic understanding of how neural events give rise to cognition and action[2]. However, the use of FC at the individual level has been a challenge due to the heterogeneity in the data acquired multiple times from the same subject (within subject variation). In our previous work, we attempted to extract the SS components using multiple scans of the same subject[3]. However, acquiring multiple scans of a subject is difficult, hence in this work we propose to extract the SS components using a single scan of the subject.

Methods: Publicly available Human connectome project (HCP) dataset consisting of 100 unrelated subject's (54 m, mean age 29.1±3.7 yrs) data was used. The minimally preprocessed HCP resting-state data was used for this study. Additionally, the mean white matter, cerebrospinal fluid the motion regressors and their derivatives were regressed as mentioned by[1]. Moreover, different brain regions were identified using the Schaefer 400 atlas and for completeness 16 subcortical regions and 3 cerebellar regions were added using the HCP atlas ("Atlas_ROI2.nii.gz"). The voxel timeseries belonging to each of the 419 regions were averaged and a mean timeseries for every region was formed. Furthermore, a dynamic functional connectivity (dFC) matrix was formed using the sliding window technique. We used the window size of 576 sec out of the other explored window sizes (7.2, 36, 72, 144, 288 s) and stride was fixed at 7.2 s as it gave the best dynamic differential identifiability dIdiff score. To extract the SS information from dFC, Common Orthogonal Basis Extraction (COBE) algorithm was used. COBE attempts to find out common components (CC) in the dFC matrix and then the difference between the original dFC and the CC gives the SS components. To quantify the SS components and show that it is better than the original dFC we use the metric proposed by[1] called (dIdiff). It assumes that dFC should be more similar between visits of the same subjects than between different subjects. It represents how accurately one can identify a new scan that belongs to a particular subject from a pool of subjects. The higher the dIdiff the more the intra-subject similarity and lesser the inter-subject similarity. dIdiff can be anywhere between 0 to 100, where a score of 100 signifies the best SS dFC that one could get. dIdiff gives a value for every time frame in the dFC, so we show only the max value here. COBE algorithm must be first trained using the training data to get the basis that can obtain the CC (using which we obtain the SS components). We used single scans from 50 subjects to get the basis. Later during the test phase, the SS components were extracted from multiple scans of subjects that were not used during training phase (Note that the multiple scans were only used to quantify the SS using the dIdiff metric).

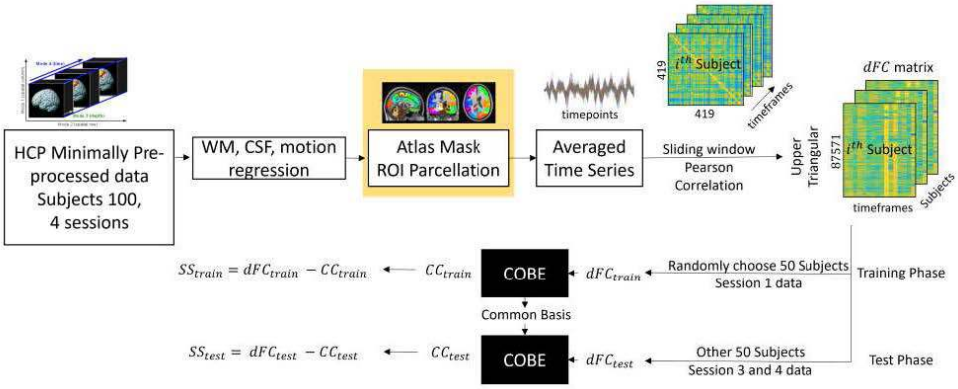

Figure 1 Processing pipeline is shown. Minimally processed HCP data is first regressed with the White matter (WM), cerebrospinal fluid (CSF) and motion parameters. Schaefer 400 atlas along with 19 sub-cortical regions is used to extract the region timeseries and then the dynamic FC matrix is created. Randomly chosen 50 subjects are used in the training phase to get the COBE common basis. Using the COBE common basis the data from other 50 subjects is decomposed into common components (CC) and subject-specific (SS) components

Results: Single scans of 50 subjects were randomly selected for training the COBE algorithm and the other 50 subjects were used for test. This process was repeated 100 times to see any variability due to training subjects. We observed that the SS dFC computed by COBE gave a significantly high value of dIdiff as compared to that of original dFC (Paired sample t-test, t(99) = 295.78, p<0.001).

Conclusions: Results show that COBE algorithm gives robust SS components when trained using only single subject dFC matrices. On average the max dIdiff score improves from 27.47 to 44.70 when COBE is used. This shows that the COBE algorithm has the potential to extract the SS components from dFC only by using single scan data which can be used for a variety of individual differentiability applications such as behavior prediction.

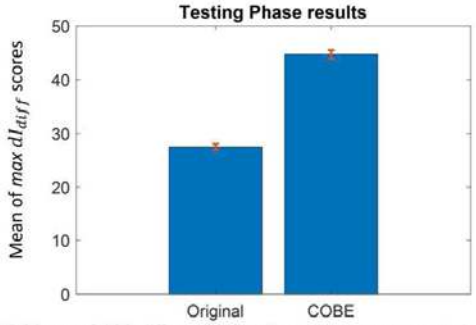

Figure 2 Mean of 100 different max dI_{diff} scores computed using original dFC and SS-dFC extracted from COBE (trained on 50 randomly chosen training subjects) during test phase. (Error bars represent ± 1 SD)

References

1. Dimitri V., et al. (2021), 'When makes you unique: Temporality of the human brain fingerprint', Science Advances, 42.
2. Finn, E. S., et al. (2017), 'Can brain state be manipulated to emphasize individual differences in functional connectivity?', NeuroImage, 160, 140-151.
3. Jain P., et al. (2023), 'Enhancing the network specific individual characteristics in rs-fMRI functional connectivity by dictionary learning'. Human Brain Mapping, 8, 3410-3432.

Poster No 1730

Structural and functional alterations in young adult presymptomatic C9orf72 expansion carriers

Jolina Lombardi[1], Liwen Zhang[1], Taru Flagan[1], Andrea Gorham Vargas[1], Maria Luisa Mandelli[1], Jesse Brown[1], Howard Rosen[1], Kejal Kantarci[2], Eliana Ramos[3], John van Swieten[4], Lize Jiskoot[4], Harro Seelaar[4], Jonathan Rohrer[5], Arabella Bouzigues[5], Lucy Chisman-Russell[5], Phoebe Foster[5], Eve Ferry-Bolder[5], Raquel Sanchez-Valle[6], Maria Carmela Tartaglia[7], Mario Masellis[8], Barbara Borroni[9], James Rowe[10], Elizabeth Finger[11], Matthis Synofzik[12], Robert Laforce[13], Daniela Galimberti[14], Rik Vandenberghe[15], Pietro Tiraboschi[16], Isabelle Le Ber[17], Bruce Miller[1], Maria Luisa Gorno-Tempini[1], William Seeley[1], Suzee Lee on behalf of the ALLFD Consortia & the Frontotemporal Dementia Prevention Initiative[1]

[1]Memory and Aging Center, Department of Neurology, Weill Institute for Neurosciences, UCSF, San Francisco, USA, [2]Department of Radiology, Division of Neuroradiology, Mayo Clinic Rochester, Rochester, USA, [3]Department of Neurology, David Geffen School of Medicine, UCLA, Los Angeles, USA, [4]Department of Neurology, Erasmus Medical Centre, Rotterdam, Netherlands, [5]Dementia Research Centre, UCL Queen Square Institute of Neurology, London, United Kingdom, [6]Alzheimer's disease and Other Cognitive Disorders Unit, Neurology Service, Hospital Clínic, Institut, Barcelona, Spain, [7]Tanz Centre for Research in Neurodegenerative Diseases, University of Toronto, Toronto, Canada, [8]Sunnybrook Health Sciences Centre, Sunnybrook Research Institute, University of Toronto, Toronto, Canada, [9]Neurology Unit, Department of Clinical and Experimental Sciences, University of Brescia, Brescia, Italy, [10]Dept. of Clinical Neurosciences & Cambridge University Hospitals NHS Trust, University of Cambridge, Cambridge, United Kingdom, [11]Department of Clinical Neurological Sciences, University of Western Ontario, London, Canada, [12]Department of Neurodegenerative Diseases, Hertie-Institute for Clinical Brain Research and Center of, Tuebingen, Germany, [13]Clinique Interdisciplinaire de Mémoire, CHU de Québec & Faculté de Médecine, Université Laval, Quebec, Canada, [14]Fondazione Ca' Granda, IRCCS Ospedale Policlinico, Milan, Italy, [15]Laboratory for Cognitive Neurology, Department of Neurosciences, KU Leuven, Leuven, Belgium, [16]Fondazione IRCCS Istituto Neurologico Carlo Besta, Milan, Italy, [17]Sorbonne Université, Paris Brain Institute – Institut du Cerveau – ICM, Inserm U1127, CNRS UMR 7225, Paris, France

Introduction: Presymptomatic C9orf72 expansion carriers as young as their thirties display gray matter (GM) deficits and alterations in connectivity networks targeted during the symptomatic phase (Lee et al. 2017; Bertrand et al. 2018; Finger et al. 2023). These studies raise the question of a neurodevelopmental role of the C9orf72 expansion, yet sufficient research in young adults (ages 18-30) is lacking.

Methods: Leveraging 3T MRI scans from Frontotemporal Dementia Prevention Initiative sites in Europe, Canada, and the United States, we identified 28 presymptomatic C9orf72 expansion carriers [PreSx-C9, mean age: 25.8±3.4] and 55 demographically-matched healthy controls [HC; mean age: 26.0±2.8] with T1-weighted (T1w) and T2*-weighted echo-planar imaging sequence. Preprocessing: For preprocessing, structural MRI (sMRI) data were visually inspected for quality and manually reoriented before segmentation, normalization, and smoothing (8mm full width at half maximum (FWHM) isotropic Gaussian kernel) in SPM12. Task-free functional MRI (tf-fMRI) data were preprocessed using fmriprep. After coregistration to the T1w reference, blood-oxygen level dependent (BOLD) data were corrected for slice-timing, head motion, and susceptibility distortions, then smoothed (6mm FWHM Gaussian kernel) and regressed for motion-related artifacts before linear detrending, bandpass filtering (0.008-0.08 Hz), and nuisance regression (including global signal). Harmonization: To control for batch-effects, we applied a post-acquisition data harmonization approach: ComBat for structural (Fortin et al. 2018) and functional (Yu et al. 2018) data. Using a customized approach, ComBat parameters were estimated from a sample of 329 HC (55 young adult HC and 274 additional HC) and administered to harmonize study cohort data. ComBat was applied on individual smoothed gray matter maps (sMRI) and seed-based intrinsic connectivity network maps (tf-fMRI) prior to group comparisons. Analyses: We performed voxel-based morphometry (VBM) to compare GM volume between groups (HC > PreSx-C9 and PreSx-C9 > HC) using a 2-sample t-test (SPM12), thresholded at $p<0.001$ uncorrected and $p<0.05$ familywise error corrected ($pFWE<0.05$). Seed-based tf-fMRI analysis examined salience network (SN), sensorimotor network (SMN), and default mode network (DMN) connectivity. To create intrinsic connectivity networks, a 4mm radius sphere ("seed") was set on peak atrophy coordinates in patients for the SN, SMN, and DMN (Seeley et al. 2008; Seeley et al. 2009; Zielinski et al. 2010). Connectivity was assessed using bivariate regression between the mean BOLD time series within each seed and the time series in the remaining voxels per subject. Single-subject connectivity maps were compared between groups using 2-sample t-tests, thresholded at a joint height and extent of $p<0.05$ and masked to the relevant network. For all analyses, nuisance covariates included age, sex, education, handedness, TIV (sMRI only), and eyes-open/closed status (tf-fMRI only).

Results: At an uncorrected threshold, PreSx-C9 carriers had low gray matter intensity vs. HC within the right medial pulvinar thalamus and within small clusters of frontotemporoparietal and insular cortices ($p<0.001$, uncorrected). No significant GM differences were detected between PreSx-C9 carriers and HC at $pFWE<0.05$. PreSx-C9 carriers displayed regions of SN (right

frontal and parietal lobe) and SMN (bilateral supplementary motor area) hypoconnectivity alongside DMN hyperconnectivity (parietal lobe) compared with HC.

Conclusions: Despite a lack of significant GM deficits in adult presymptomatic C9orf72 expansion carriers ages 18 to 30, tf-fMRI analyses detected alterations in the SN, SMN, and DMN, suggesting that network abnormalities appear early in the lifespan. These findings indicate that C9orf72 expansions might play a crucial role in neurodevelopment.

References

1. Bertrand, A. (2018), 'Early cognitive, sturctural, and microstructural changes in presymptomatic C9orf72 carriers younger than 40 years', JAMA Neurology, vol. 75, no. 2, pp. 236-245
2. Finger, E. (2023), 'Neurodevelopmental effects of genetic frontotemporal dementia in young adult mutation carriers', Brain, vol. 146, no. 5, pp. 2120-2131
3. Fortin, J.-P. (2018), 'Harmonization of cortical thickness measurements across scanners and sites', Neuroimage, vol. 167, pp. 104–120
4. Lee, S.E. (2017), 'Network degeneration and dysfunction in presymptomatic C9ORF72 expansion carriers', NeuroImage Clinical, vol. 14, pp.286-297
5. Seeley, W. W (2008), 'Frontal paralimbic network atrophy in very mild behavioral variant frontotemporal dementia', Archives of Neurology, vol. 65, no. 2, pp. 249–255
6. Seeley, W. W. (2009), 'Neurodegenerative diseases target large-scale human brain networks', Neuron, vol. 62, pp. 42–52
7. Yu, M. (2018), 'Statistical harmonization corrects site effects in functional connectivity measurements from multi-site fMRI data', Human Brain Mapping, vol. 39, pp. 4213–4227
8. Zielinski, B. A. (2010), 'Network-level structural covariance in the developing brain', PNAS, vol. 107, pp. 18191–18196

Poster No 1731

Biophysical models reveal distinct role of parietal lobe and sensory regions in the emergence of FC

Songjun Peng[1], Xinran Wu[1], Yunman Xia[1], Jie Zhang[1]

[1]Institute of Science and Technology for Brain-inspired Intelligence, Fudan University, Shanghai, China

Introduction: Brain function emerges from the complex multi-scale neural networks(Suárez et al., 2020). However, how neural dynamics characteristics (such as excitation-inhibition balance of neural networks) at the micro-scale shape the non-linear dependence between structural connectivity and functional connectivity(FC) at the macro-scale, and eventually lead to the emergence of functional activities from structural connectivity, is still unclear.

Methods: To explore the role of excitation-inhibition balance in the emergence of resting-state whole-brain functional connectivity patterns, we built brain network models based on group-averaged structural connectivity(Kong et al., 2021) and dynamic mean field models(Deco et al., 2014) to predict group-averaged resting-state functional connectivity, and then conducted modulations of global and local excitation-inhibition ratios on the models. The group-averaged connectivities were derived from MRI data of the Human Connectome Project (HCP) S1200 release(Van Essen et al., 2013)

Results: Simulations found that changes of global excitation-inhibition ratio can lead to significant changes in whole-brain functional connectivity. In this process, two core subnetworks distributed in frontal and parietal lobes respectively, consisting of rich-club nodes(Heuvel & Sporns, 2011) and high-weighted edges, play a dominant role. Analysis of local excitation-inhibition ratio modulations shows that the emergence of resting-state functional connectivity relies on the levels of excitation in parietal lobe (superior parietal lobe, inferior parietal lobe and precuneus) and sensory regions. Specifically, when the parietal lobe is in the intermediate state between excitation and inhibition, which is sensitive to external perturbations, and the sensory regions is in the excited state, the brain network models can better simulate resting-state functional connectivity. In addition, meta-analysis based on neurosynth(Yarkoni et al., 2011) showed that activities in parietal lobe are related to higher-order cognitive functions of top-down processing.

Conclusions: The study demonstrates the significant impact of the excitation-inhibition balance of local neural circuits on the patterns of resting-state whole-brain function under the topological constraints of structural connectivity, and the selective dependence of the emergence of resting-state functional connectivity on different dynamic states in higher-order brain regions and sensory regions. It provides a reference for further understanding the mechanisms of emergence of resting-state functional connectivity and the underlying cognitive processes.

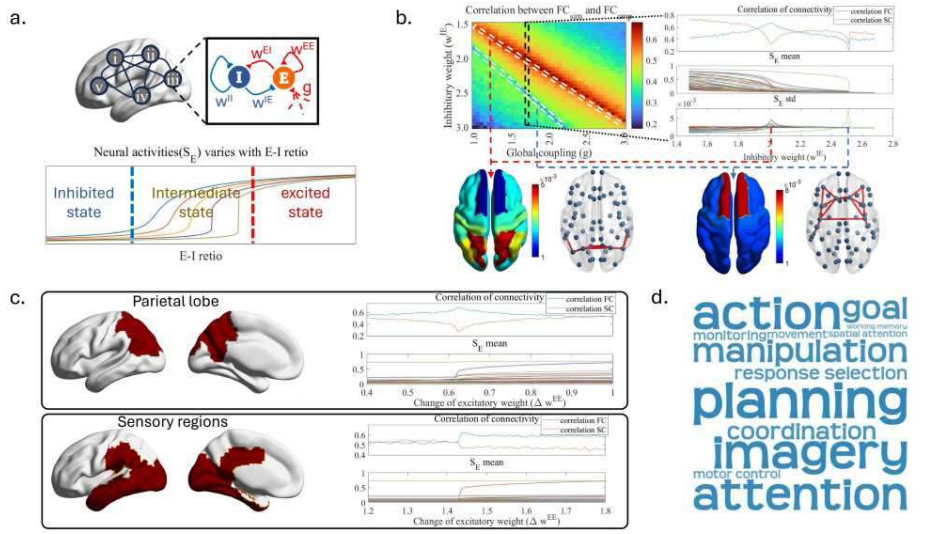

Figure 1. (a.) In brain network models, each node of the structure connectivity is modeled as coupled excitatory and inhibitory neuronal populations. The average activity of the excitatory population follows an S-shaped curve with the change of the excitation-inhibition(E-I) ratio. We divide this S-shaped curve into inhibited state, intermediate state, and excited state. **(b.)** A grid search for parameters g and w^{IE} reveals that changes in global E-I ratio can lead to two types of changes in whole-brain functional connectivity patterns dominated by high fluctuations of neural activities in the frontal and parietal lobes respectively. The brain regions with high fluctuations are aligned with two core subnetworks in the structural connectivity. **(c.)** Modulation of local E-I ratio reveals that when the parietal lobe(superior parietal lobe, inferior parietal lobe and precuneus) is in the intermediate state and sensory regions is in the excited state, the similarity between simulated functional connectivity and empirical functional connectivity increases. **(d.)** Cognitive terms from Neurosynth that are related to fluctuations of neural activities dominated by the parietal lobe.

References

1. Deco, G., Ponce-Alvarez, A., Hagmann, P., Romani, G.L., Mantini, D. & Corbetta, M. (2014) 'How Local Excitation–Inhibition Ratio Impacts the Whole Brain Dynamics', Journal of Neuroscience, 34(23), pp. 7886–7898.
2. Heuvel, M.P. van den & Sporns, O. (2011) 'Rich-Club Organization of the Human Connectome', Journal of Neuroscience, 31(44), pp. 15775–15786.
3. Kong, X., Kong, R., Orban, C., Wang, P., Zhang, S., Anderson, K., Holmes, A., Murray, J.D., Deco, G., van den Heuvel, M. & Yeo, B.T.T. (2021) 'Sensory-motor cortices shape functional connectivity dynamics in the human brain', Nature Communications, 12(1), p. 6373.
4. Suárez, L.E., Markello, R.D., Betzel, R.F. & Misic, B. (2020) 'Linking Structure and Function in Macroscale Brain Networks', Trends in Cognitive Sciences, 24(4), pp. 302–315.
5. Van Essen, D.C., Smith, S.M., Barch, D.M., Behrens, T.E.J., Yacoub, E. & Ugurbil, K. (2013) 'The WU-Minn Human Connectome Project: An overview', NeuroImage, 80pp. 62–79.
6. Yarkoni, T., Poldrack, R.A., Nichols, T.E., Van Essen, D.C. & Wager, T.D. (2011) 'Large-scale automated synthesis of human functional neuroimaging data', Nature Methods, 8(8), pp. 665–670.

Poster No 1732

Reduced functional connectivity in autoimmune encephalitis is explained by BOLD pattern incongruency

Amy Romanello[1,2], Stephan Krohn[1,2], Carsten Finke[1,2]

[1]Charité - Universitätsmedizin Berlin, Berlin, Germany, [2]Berlin School of Mind and Brain, Humboldt-Universität zu Berlin, Berlin, Germany

Introduction: Patients with anti-N-methyl-D-aspartate receptor encephalitis (NMDARE) present with a complex neuropsychiatric syndrome, yet clinical MRI sequences often show no abnormalities. Interestingly, resting-state functional MRI (rs-fMRI) studies in NMDARE have consistently found reduced functional connectivity (FC) between the hippocampus and default mode network (DMN). Given the mathematical definition of FC, an explanation for these findings must be present in the BOLD patterns themselves. However, it remains unclear what underlying signal property drives these FC alterations. Against this background, we here leverage two recently introduced methodologies - a time-resolved signal complexity approach as in Krohn et al. (2023) combined with the edge time-series framework as in Esfahlani et al. (2020) - to compute a novel, pairwise measure that quantifies differences in BOLD-signal pattern distributions, yielding an "index of pattern incongruency" (IPI).

Methods: Resting-state fMRI data from 75 healthy controls (HCs) and 75 patients with NMDARE were preprocessed and parcellated into 244 regions of interest (ROIs) using the Human Brainnetome Atlas. Static FC was calculated as the product-moment correlation coefficient between every pair of ROI time-series. Time-resolved signal complexity was calculated as weighted permutation entropy (WPE) with a sliding-window approach, resulting in a set of 244 ROI-wise complexity time-series

for each participant. WPE estimates the irregularity of a time-series based on a symbolic encoding framework that is sensitive to both amplitude information and frequency content of a signal. Importantly, WPE is agnostic to which individual pattern drives the signal and instead computes Shannon entropy on the distribution across all possible patterns. Thus, it is possible for two different pattern distributions to have equal WPE values. The calculation of IPI rests first on the application of the edge time-series framework to compute the moment-to-moment synchronization between each pair of complexity time-series, resulting in a continuous measure of complexity cofluctuation at the resolution of windows. We then isolated the windows with the highest 10% complexity cofluctuation, within which we examined the individual BOLD pattern distributions that underlie the WPE calculation. IPI was then calculated as the Euclidean distance between the pattern frequency distributions of two ROI time-series in each window. Metrics were calculated on the regional level with the hippocampus as well as the global level as distributions over all within- and between-network connections. ROI-wise between group differences were calculated using permutation-based T-tests and group differences in distributions using Wilcoxon rank-sum tests.

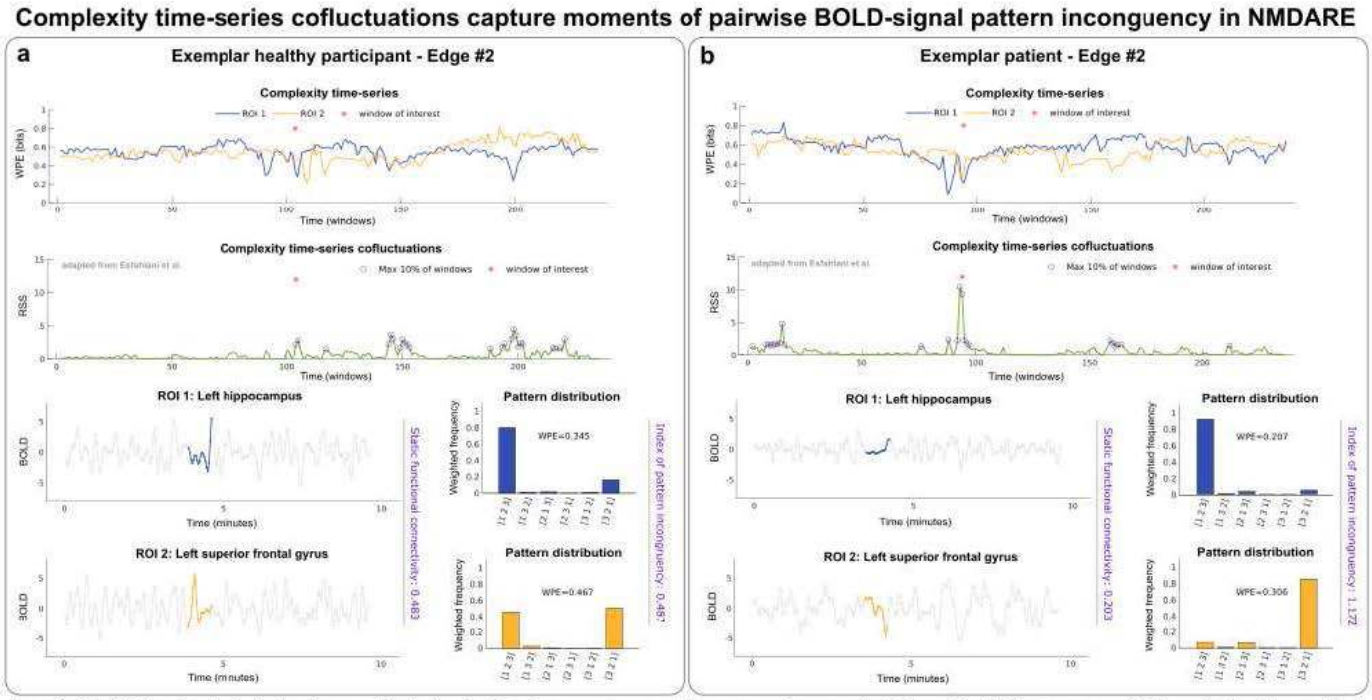

Figure 1. Visualization of analysis pipeline for computing index of pattern incongruency measure for one exemplar connection between the left hippocampus and left superior frontal gyrus. Panel (a) shows analysis steps for an exemplar healthy control participant and panel (b) shows that for an exemplar patient with anti-NMDA receptor encephalitis. Within each panel (top to bottom): top: complexity time-series for each region of interest (ROI) resulting from the calculation of WPE using a sliding window (window size = 20 TR, slide by 1 TR). The red star indicates the selected window used in subsequent plots; middle: complexity time-series cofluctuations calculated using the edge time-series framework applied to the two complexity time-series that are plotted in the above panel. This step is calculated by taking the root sum square (RSS) of the element-wise product of the two z-scored complexity time-series. Purple circles denote windows with the highest 10% amplitudes of complexity cofluctuation; bottom-left: BOLD time-series for each ROI. Colored portion of time-series corresponds to the selected window of interest. Static functional connectivity strength between the two BOLD time-series is shown on the right side of the plot; bottom-right: Pattern distributions for the window of interest for each ROI time-series. Corresponding weighted permutation entropy (WPE) value is shown. The index of pattern incongruency is calculated as the Euclidean distance between the plotted pattern distriputions and is displayed on the right side of the plot.

Results: In line with previous work, we found that patients with NMDARE show significantly reduced FC between the hippocampus and several DMN regions, including medial frontal and cingulate cortices (all $p < 0.05$). Analysis of BOLD-signal patterns revealed that decreases in FC are explained by higher IPI in patients (correlation of FC and IPI test statistics: rho = -0.451, $p < 0.001$). In between-network connections, patients had significantly reduced FC ($Z = 14.40$, $p < 0.001$), increased complexity cofluctuation ($Z = -17.90$, $p < 0.001$), and increased IPI ($Z = -27.69$, $p < 0.001$). Within-network analyses revealed a similar trend with weaker effects: patients trended towards reduced FC ($Z = 1.01$, $p = 0.31$) and showed significantly increased complexity co-fluctuation ($Z = -4.50$, $p < 0.001$) and increased IPI ($Z = -2.52$, $p = 0.01$).

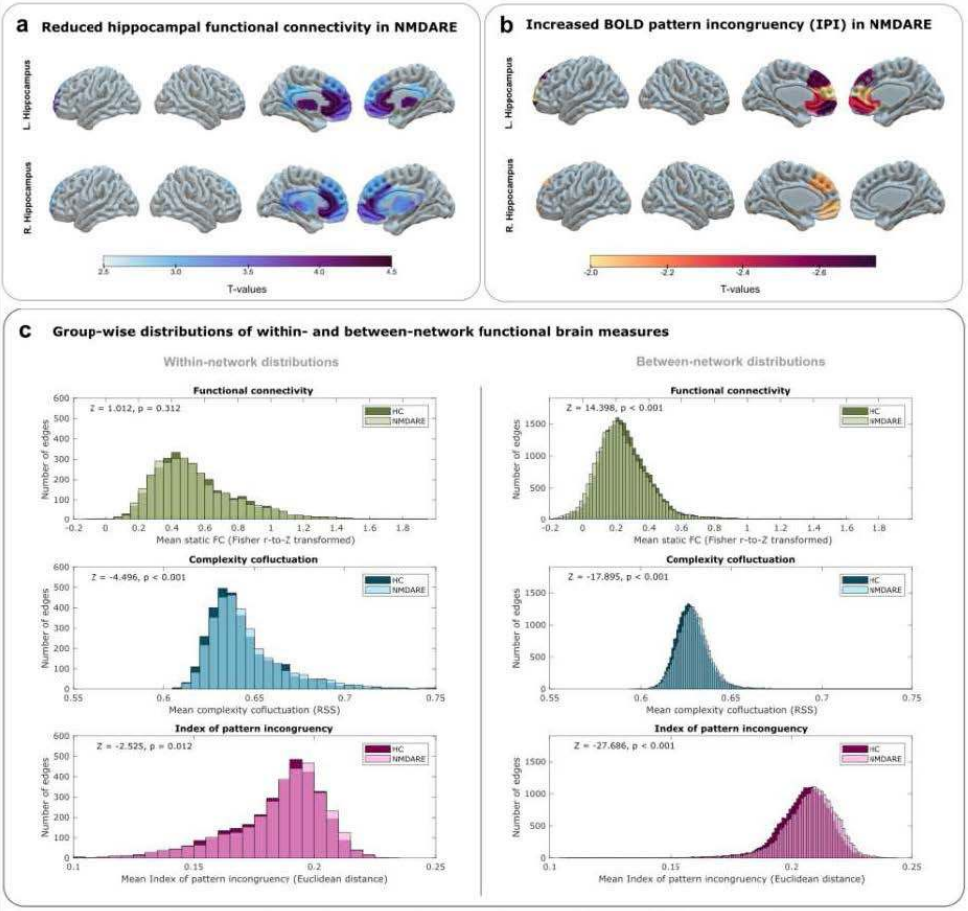

Figure 2. Hippocampal and network-wise differences in functional connectivity, complexity coflucuations, and BOLD pattern incongruency (IPI). Panel (a): Results of between group tests for differences in hippocampal static functional connectivity (FC) with the rest of the brain; Panel (b) Results of between group tests for differences in hippocampal BOLD pattern incongruency calculated as the novel index of pattern incongruency (IPI); Panel (c) Distributions of group average functional connectivity, complexity coflucuation, and index of pattern incongruency for within- and between-network connections according to the Human Brainnetome Atlas and Yeo 7-network resting-state network assignments.

Conclusions: Reduced functional connectivity between the hippocampus and DMN in NMDARE is explained by an increased incongruency of the underlying symbolic patterns in individual BOLD signals. The novel IPI metric links the covariance structure of BOLD signals to the underlying pattern variability within each signal and is sensitive to differences in functional brain dynamics that are undetected by WPE alone.

References

1. Esfahlani, F.Z. (2020), "High-Amplitude Cofluctuations in Cortical Activity Drive Functional Connectivity", Proceedings of the National Academy of Sciences 117 (45): 28393–401.
2. Fadlallah, B. (2013), "Weighted-Permutation Entropy: A Complexity Measure for Time Series Incorporating Amplitude Information", Physical Review E 87 (2): 022911.
3. Fan, L. (2016), "The Human Brainnetome Atlas: A New Brain Atlas Based on Connectional Architecture", Cerebral Cortex 26 (8): 3508–26.
4. Finke, C. (2013), "Functional and Structural Brain Changes in Anti-N-Methyl-D-Aspartate Receptor Encephalitis", Annals of Neurology, Vol 73 No 6, June
5. Krohn, S. (2023), "A Spatiotemporal Complexity Architecture of Human Brain Activity", Science Advances 9 (5).

Poster No 1733

Hierarchical communities of high-amplitude co-fluctuations in extremity disuse

Youngheun Jo[1], Haily Merritt[2], Joshua Faskowitz[1], Richard Betzel[2]

[1]Indiana University Bloomington, Bloomington, IN, [2]Indiana University, Bloomington, IN

Introduction: Edge time series (eTS) decompose static functional connectivity into its exact time-varying contributions[1,2]. Studies have shown that global, instantaneous, high-amplitude co-fluctuations in eTS – "events" – originate from modules of structural connectivity[3], synchronize with naturalistic stimuli[4], and improve both brain-behavior correlations[2] and subject

identifiability[5]. Recently, high-amplitude region-level pulses in fMRI activation have been reported in motor areas during a disuse period of the upper extremities[6,7]. However, it is unknown whether such regional pulses and global events are related, and whether clusters of events reflect changes in extremity disuse. Here, we investigate events and their hierarchical community structure in extremity disuse and investigate instantaneous global changes at various organizational scales[8]. We find that pulses in the motor cortices are aligned with, but do not equate to global events. Events have been found to have distinct patterns with local change in disuse and global changes with cast removal.

Methods: We detected motor cortex-specific activation peaks (a node-level measurement) and global co-fluctuation events (an edge-level measurement) using the casting dataset[6]. Specifically, we detected motor cortex-specific peaks by calculating the root mean squared (RMS) from nodal time series in only the motor regions and using only the peaks with positive activations. Events were found by using the RMS across all brain regions and thresholding the global peaks against a null circularly shifted surrogate time series[2]. Next, we applied a hierarchical clustering algorithm across all events for each subject, to extract hierarchical communities of events[8]. We then investigated the large (> 100 events) found at the coarsest level of hierarchy (level 2) and derived the community centroid for the pre-casting, casting, and post-casting periods. We compared whether there are significant system-level differences between the casting and pre-casting, casting and post-casting periods compared to a scan randomized and nodal-permutation null. We note that all analyses were performed on each subject's fMRI time series data, individually due to different TRs.

Results: First, we found that motor pulses and events are significantly more temporally aligned than chance (Fig.1a, d) but that their activation patterns are not highly correlated (Fig. 1b). Also, events were found to be significantly more variable than motor pulses (Fig. 1c). We then identified the brainwide activation patterns of global events and positive motor pulses (Fig.1e, f). After establishing that motor pulses and events are not identical, and that events are more variable than motor pulses, we identified the hierarchical organization of event clusters for each subject (Fig.2a, f, k). In each subject there were 4 ~ 6 large communities at level 2 (Fig.2b, g, l). Our results show that the largest community which constitutes ~50 percent of all events in level 2 are similar upon visual inspection across subjects and when creating brain plots using the cluster's first principal component (Fig.2c, h, m). Lastly, we investigated whether this cluster changes between paradigms - pre-casting, casting, and post-casting periods (Fig.2d, e, i, j, m, o). Overall, these results suggest that there are local and global changes in events throughout the disuse paradigm.

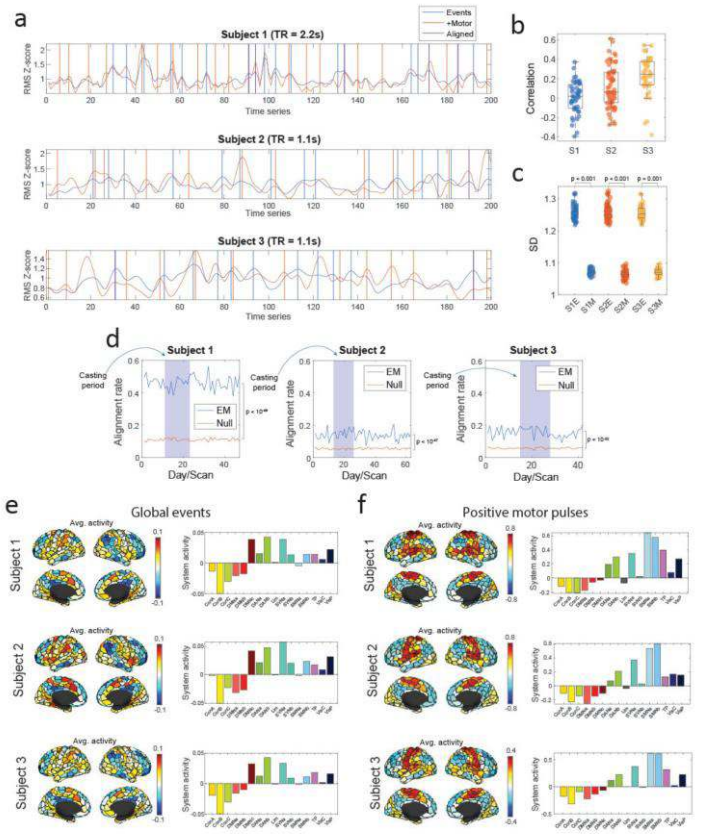

Figure 1: (a) Example of root mean squared (RMS) Z-scores of global high-amplitude co-fluctuations (blue horizontal line) and RMS Z-scores of nodal activation patterns in only the motor cortices (orange horizontal line). Blue vertical lines indicate time points at which have been identified as global events , orange vertical lines represent positive motor pulses, and purple vertical lines represent moments of co-activation of events and pulses. (b) Correlation of event and pulse patterns for each scan. (c) Standard deviation within event patterns and within pulse patterns. (d) Rate of global event and motor pulse temporal alignment (blue line) compared to that of a circshift statistical null (orange line). (e) Average activation pattern of all events across all scans for each subject, plotted on the Schaefer 400 parcellation (left) and averaged into 17 Yeo networks (right). (f) Average activation pattern of all positive motor pulses across all scans for each subject, plotted on the Schaefer 400 parcellation (left) and averaged into 17 Yeo networks (right).

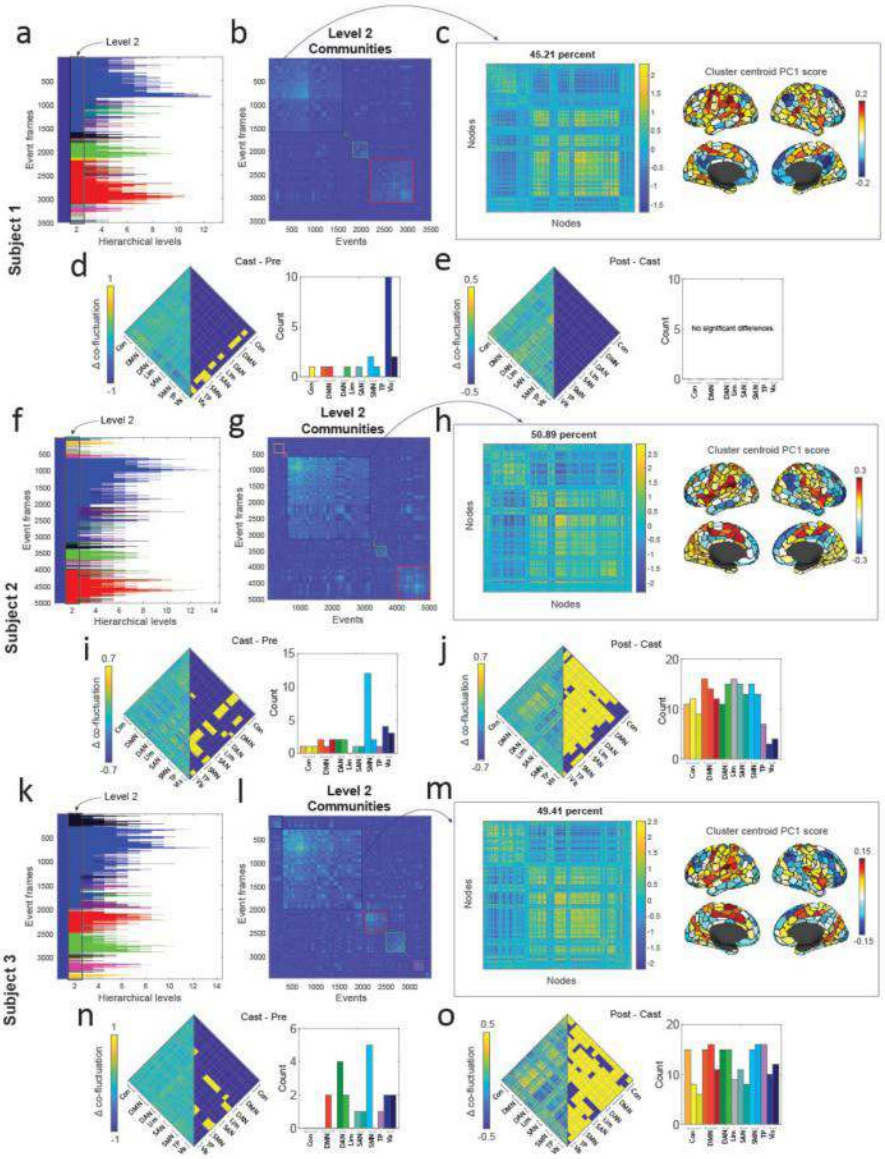

Figure 2: (a, f, k) Hierarchical organization of event communities reordered by optimal sorting based on community membership. (b, g, l) Visualizing the concordance of communities in the second hierarchical level. Communities with more than 100 member events have been boxed. (c, h, m) The averaged co-fluctuation pattern of events assigned to the largest cluster in level 2 (left) and the first principal component score of this cluster centroid (right). (d, i, n) Difference of event co-fluctuation patterns between casting and pre-casting periods (left) and the count of significant systems (right). (e, j, o) Difference of event co-fluctuation patterns between post-casting and casting periods (left) and the count of significant systems (right).

Conclusions: Our results demonstrate that peaks of motor cortex-specific activations are not identical to that of global events which change systematically with the casting paradigm. Shifting the focus to global events of various organizational scales may allow further understanding of changes occurring in the disuse paradigm. Also, the dataset includes multiple scans of each subject, allowing for precise, individualized investigation of disuse-induced changes in the brain's functional organization[9,10].

References

1. Faskowitz, J., Esfahlani, F.Z., Jo, Y., Sporns, O. and Betzel, R.F. (2020). Edge-centric functional network representations of human cerebral cortex reveal overlapping system-level architecture. Nature Neuroscience, 23(12), pp.1644–1654. doi:10.1038/s41593-020-00719-y.
2. Esfahlani, F.Z., Jo, Y., Faskowitz, J., Byrge, L., Kennedy, D.P., Sporns, O. and Betzel, R.F. (2020). High-amplitude cofluctuations in cortical activity drive functional connectivity. Proceedings of the National Academy of Sciences, [online] 117(45), pp.28393–28401. doi:10.1073/pnas.2005531117.
3. Pope, M., Fukushima, M., Betzel, R.F. and Sporns, O. (2021). Modular origins of high-amplitude cofluctuations in fine-scale functional connectivity dynamics. Proceedings of the National Academy of Sciences, 118(46). doi:10.1073/pnas.2109380118.
4. Tanner, J.C., Faskowitz, J., Byrge, L., Kennedy, D.P., Sporns, O. and Betzel, R.F. (2022). Synchronous high-amplitude co-fluctuations of functional brain networks during movie-watching. bioRxiv. doi:10.1101/2022.06.30.497603.
5. Jo, Y., Faskowitz, J., Esfahlani, F.Z., Sporns, O. and Betzel, R.F. (2021). Subject identification using edge-centric functional connectivity. NeuroImage, 238, p.118204. doi:10.1016/j.neuroimage.2021.118204.

6. Newbold, D. J., Laumann, T. O., Hoyt, C. R., Hampton, J. M., Montez, D. F., Raut, R. V., ... & Dosenbach, N. U. (2020). Plasticity and spontaneous activity pulses in disused human brain circuits. Neuron, 107(3), 580-589.
7. Newbold, D. J., Gordon, E. M., Laumann, T. O., Seider, N. A., Montez, D. F., Gross, S. J., ... & Dosenbach, N. U. (2021). Cingulo-opercular control network and disused motor circuits joined in standby mode. Proceedings of the National Academy of Sciences, 118(13), e2019128118.
8. Betzel, R. F., Cutts, S. A., Tanner, J., Greenwell, S. A., Varley, T., Faskowitz, J., & Sporns, O. (2023). Hierarchical organization of spontaneous co-fluctuations in densely sampled individuals using fMRI. Network Neuroscience, 7(3), 926-949.
9. Gordon, E. M., Laumann, T. O., Gilmore, A. W., Newbold, D. J., Greene, D. J., Berg, J. J., ... & Dosenbach, N. U. (2017). Precision functional mapping of individual human brains. Neuron, 95(4), 791-807.
10. Gratton, C., Kraus, B. T., Greene, D. J., Gordon, E. M., Laumann, T. O., Nelson, S. M., ... & Petersen, S. E. (2020). Defining individual-specific functional neuroanatomy for precision psychiatry. Biological psychiatry, 88(1), 28-39.

Poster No 1734

Assessing Frequency-Dependent Behavior Predictability via Coherence-based Fingerprinting

Wenjun Bai[1], Okito Yamashita[1], Junichiro Yoshimoto[1]

[1]CBI, ATR, Kyoto, Kyoto

Introduction: Leveraging vast resting-state functional MRI (rsfMRI) data and machine learning, individual-level rsfMRI-based brain connectivity, especially the functional connectome, serves as reliable brain features in capturing individual behavioral differences (Finn et al. 2015, Beaty et al. 2018, Nostro et al. 2018). Despite its limited frequency bandwidth (0.01-0.20Hz (Niazy et al. 2011, Yuen et al. 2019)), rsfMRI signals show a diverse spectral distribution in the human cortex (Fox&Raichle2007), prompting the question of whether these spectral differences influence intrapersonal behavior prediction. To answer this question, we propose the coherence-based predictive modeling (CoPM), using spectrally rich functional coherence features to explore this spectral-behavior relationship. Our application of CoPM to Human Connectome Project rsfMRI data (Van Essen et al. 2013) reveals that the behavior predictability of functional coherence features is frequency-dependent, highlighting a strong spectral-behavior relationship.

Methods: The proposed coherence-based predictive model (CoPM) aims to evaluate the predictive performance of frequency-specialized coherence features across various behavioral items and domains. The methodology of CoPM is structured into a three-stage pipeline as follows: (A) brain-wide coherence feature extraction (including Table 1 embedded in Figure 1), (B) frequency-dependent coherence profiling (including Table 2 embedded in Figure 1), and (C) predictive model construction. A graphical representation of this pipeline is illustrated in Figure 1. (For a complete demonstration of the proposed CoPM, please refer to the OHBM2024_complete.pdf file at https://github.com/LeonBai/Rhythmic_Cortex.)

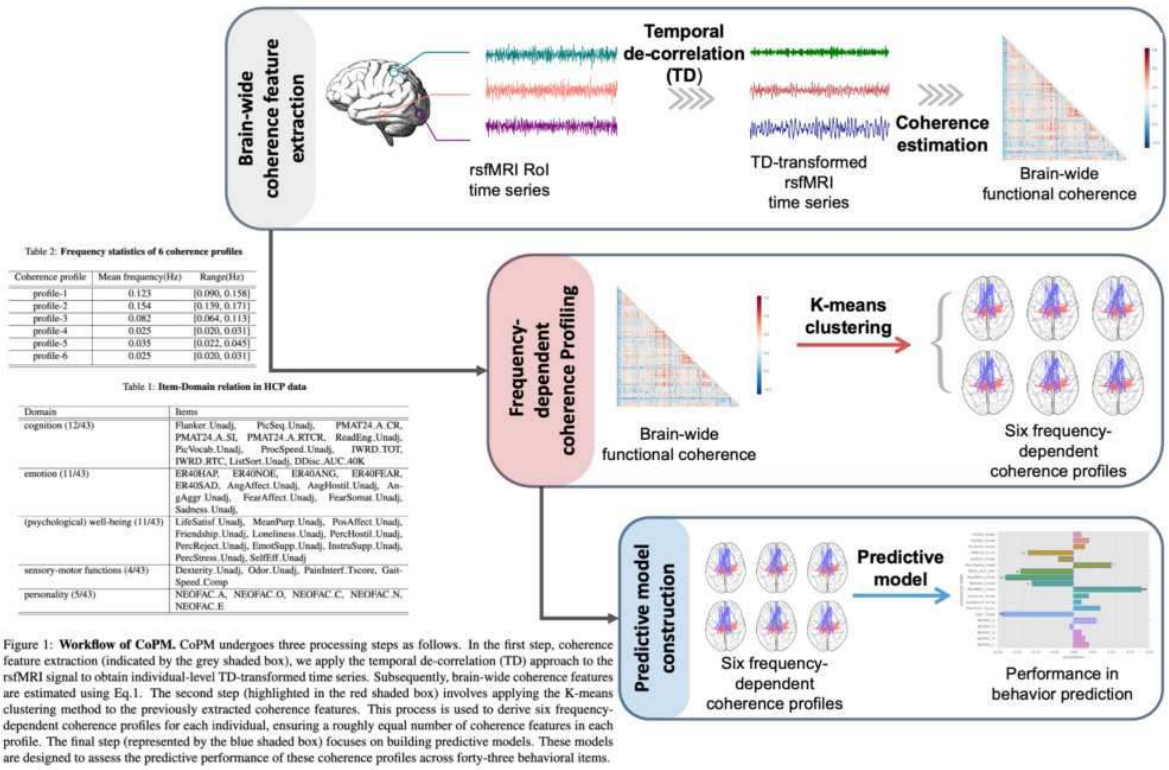

Table 2: **Frequency statistics of 6 coherence profiles**

Coherence profile	Mean frequency(Hz)	Range(Hz)
profile-1	0.123	[0.090, 0.158]
profile-2	0.154	[0.139, 0.171]
profile-3	0.082	[0.064, 0.113]
profile-4	0.025	[0.020, 0.031]
profile-5	0.035	[0.022, 0.045]
profile-6	0.025	[0.020, 0.031]

Table 1: **Item-Domain relation in HCP data**

Domain	Items
cognition (12/43)	Flanker_Unadj, PicSeq_Unadj, PMAT24_A_CR, PMAT24_A_SI, PMAT24_A_RTCR, ReadEng_Unadj, PicVocab_Unadj, ProcSpeed_Unadj, IWRD_TOT, IWRD_RTC, ListSort_Unadj, DDisc_AUC_40K
emotion (11/43)	ER40HAP, ER40NOE, ER40ANG, ER40FEAR, ER40SAD, AngAffect_Unadj, AngHostil_Unadj, AngAggr_Unadj, FearAffect_Unadj, FearSomat_Unadj, Sadness_Unadj,
(psychological) well-being (11/43)	LifeSatisf_Unadj, MeanPurp_Unadj, PosAffect_Unadj, Friendship_Unadj, Loneliness_Unadj, PercHostil_Unadj, PercReject_Unadj, EmotSupp_Unadj, InstruSupp_Unadj, PercStress_Unadj, SelfEff_Unadj
sensory-motor functions (4/43)	Dexterity_Unadj, Odor_Unadj, PainInterf_Tscore, Gait-Speed_Comp
personality (5/43)	NEOFAC_A, NEOFAC_O, NEOFAC_C, NEOFAC_N, NEOFAC_E

Figure 1: **Workflow of CoPM.** CoPM undergoes three processing steps as follows. In the first step, coherence feature extraction (indicated by the grey shaded box), we apply the temporal de-correlation (TD) approach to the rsfMRI signal to obtain individual-level TD-transformed time series. Subsequently, brain-wide coherence features are estimated using Eq.1. The second step (highlighted in the red shaded box) involves applying the K-means clustering method to the previously extracted coherence features. This process is used to derive six frequency-dependent coherence profiles for each individual, ensuring a roughly equal number of coherence features in each profile. The final step (represented by the blue shaded box) focuses on building predictive models. These models are designed to assess the predictive performance of these coherence profiles across forty-three behavioral items.

Results: Upon applying the proposed CoPM to the HCP rsfMRI data, our initial observation highlighted the discriminative capability of functional coherence features in identifying intrapersonal behavioral differences, regardless of their frequency. Notably, within the predicted behavior domains, psychological well-being emerged as the consistent domain that was successfully predicted across all six coherence profiles. This suggests that brain signatures related to well-being may encompass a broad spectral range. Similarly, the personality behavior domain also showed predictions across a wide frequency bandwidth, expect for the low-frequency profile-6. In contrast, successful predictions for the emotion domain were predominantly associated with the median-frequency coherence features (as shown in Figure 2(a)). The predictive performance varied among the six profiles, with high-frequency profile-2 showing the least success, and median-frequency profiles (profile-3, 4, and 5) demonstrating broader and more accurate predictions. This frequency-dependent prediction was further evident when the similarity between profile-wise rhythmic (e.g., frequency) characteristics and the prediction patterns were observed in terms of a strong positive correlation (Pearson's r = 0.606,p < 0.001; Figure 2(b)).

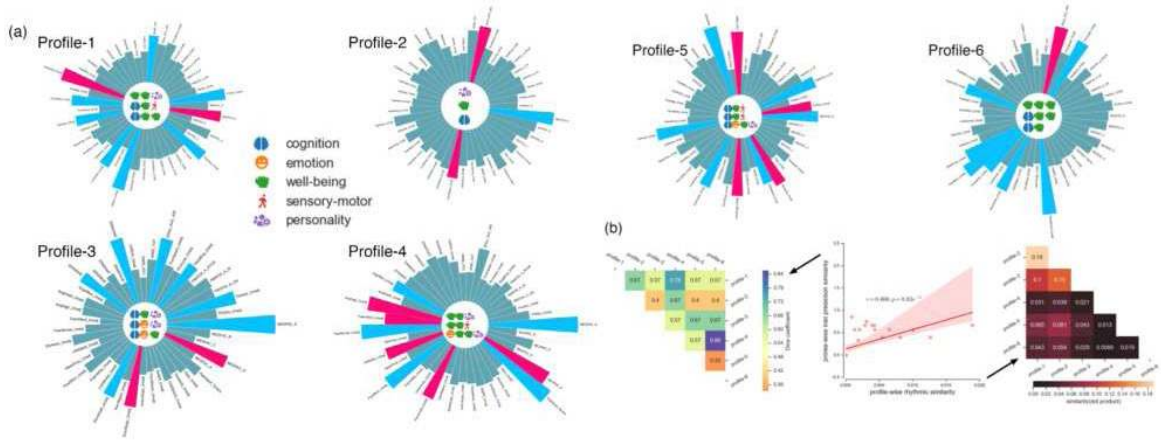

Figure 2: **Frequency-dependent coherence profiles in predicting behavior items and domains.** (a) Varied performance of 6 coherence profiles in predicting intra-personal behavior domains. The highlighted bars in each of 6 circular bar-plots (profiles) indicate the significantly predicted behavior items, which red and blue colors represent the statistical significant positive and negative correlations $p < 0.05$. The icons that fill the inner circles of 6 circular bar-plots represent the predicted behavior domains. (b) The revealed correlational relation between the profile-wise resemblance in prediction patterns and the spectral similarity between profile-wise coherence features. Differences in prediction patterns are quantified in terms of their pair-wise dice coefficient, whereas the profile-wise spectral similarity is computed via the dot product (cosine similarity) between mean frequencies of profiles.

Conclusions: The widespread use of rsfMRI recordings and machine learning advancements have enabled individual-level cortico-cortical connections, like the functional connectome, to serve as crucial brain signatures for identifying intrapersonal behavioral differences. As cortical regions show varied spectral distributions, exploring their spectral bias in behavior prediction is gaining interest. Our study introduces coherence-based predictive modeling (CoPM), a novel approach leveraging spectrally rich coherence features to explore their frequency-dependent behavior predictability. Applied to HCP rsfMRI data, CoPM effectively discerns individual behavioral differences using frequency-dependent coherence features. It demonstrates that behavioral predictability is frequency-dependent, offering valuable insights for future CoPM applications in diverse neuroimaging contexts, such as exploiting the use of functional coherence features in computational psychiatry.

References

1. Beaty, R. E., Kenett, Y. N., Christensen, A. P., Rosenberg, M. D., Benedek, M., Chen, Q., Fink, A., Qiu, J., Kwapil, T. R., Kane, M. J. et al. (2018), 'Robust prediction of individual creative ability from brain functional connectivity', Proceedings of the National Academy of Sciences 115(5), 1087–1092.
2. Finn, E. S., Shen, X., Scheinost, D., Rosenberg, M. D., Huang, J., Chun, M. M., Papademetris, X. &Constable, R. T. (2015), 'Functional connectome fingerprinting: identifying individuals using patterns of brain connectivity',Nature Neuroscience 18(11), 1664–1671.
3. Fox, M. D. & Raichle, M. E. (2007), 'Spontaneous fluctuations in brain activity observed with functional magnetic resonance imaging', Nature Reviews Neuroscience 8(9), 700–71 1.
4. Niazy, R. K., Xie, J., Miller, K., Beckmann, C. F. &Smith, S. M. (2011), Spectral characteristics of resting state networks, in 'Progress in Brain Research', Vol. 193, Elsevier, pp. 259–276.
5. Nostro, A. D., Muller, V. I., Varikuti, D. P., Plaschke, R. N., Hoffstaedter, F., Langner, R., Patil, K. R. &Eickhoff, S. B. (2018), 'Predicting personality from network-based resting-state functional connectivity', Brain Structure and Function 223(6), 2699–2719.
6. Van Essen, D. C., Smith, S. M., Barch, D. M., Behrens, T. E., Yacoub, E., Ugurbil, K., Consortium, W.-M. H. et al. (2013), 'The wu-minn human connectome project: an overview', Neuroimage 80, 62–79.
7. Yuen, N. H., Osachoff, N. & Chen, J. J. (2019), 'Intrinsic frequencies of the resting-state fMRI signal: The frequency dependence of functional connectivity and the effect of mode mixing', Frontiers in Neuroscience13.

Poster No 1735

Changes of Intrinsic Connectivity in Autistic Adults After Social Skills Training

Yi-Ling Chien[1], Chi Chen[1], Wen-Hao Chen[1]

[1]National Taiwan University Hospital, Taipei, Taiwan

Introduction: Evidence-based social skills training programs improve social communication skills in autistic adults. However, most effectiveness studies measured the intervention outcomes by questionnaires or clinical assessment. Whether the clinical improvement in social communication skills can reflect on changes in the brain connectivity waits to be examined. This study aims to investigate whether social skills training alters intrinsic connectivity in autistic adults.

Methods: This study recruited 34 autistic adults (mean age 24.3 years; female n = 6, 17.6%) who were diagnosed with autism spectrum disorder accordingly to the Diagnostic Statistical Manual of Mental Disorders Fifth version. All participants have a full-IQ above 70 and are motivated to enhance their social skills. They completed 16-week social skills training program (the Program for the Education and Enrichment of Relational Skills, PEERS®) with their social coaches. Resting-state functional connectivity was examined by the 3T MRI before and after the training.

Results: Using seed-based analysis to analyze intrinsic connectivity, we found decreased functional connectivity of several brain regions after the PEERS social skills training. First, using default mode network as a seed, we found that the precuneus had a decreased functional connectivity to right putamen, and that the medial prefrontal cortex had a decreased functional connectivity to right later occipital cortex after PEERS training. Using planum temporale of the auditory network as a seed, we found a decreased functional connectivity to frontal pole, middle frontal gyrus and precuneus after PEERS training. While using the right posterior superior temporal gyrus as a seed, there was a decreased functional connectivity to the middle frontal gyrus after PEERS social training. In addition, we tried independent component analysis. After PEERS social training, functional connectivity between the salience network and the right superior frontal gyrus decreased; whereas, functional connectivity between the sensorimotor network and the left lateral occipital cortex increased.

Conclusions: In summary, decreased functional connectivity was found in several brain networks connecting to default mode network, auditory network, and salience network. In contrast, sensorimotor network had an increased functional connectivity to the left lateral occipital cortex. Social skills training may change the specific intrinsic connectivity in autism. Our preliminary findings worth further investigation and validation.

References

1. Chien YL, Tsai WC, Chen WH, Yang CL, Gau SS, Soong WT, Laugeson E, Chiu YN. Effectiveness, durability, and clinical correlates of the PEERS social skills intervention in young adults with autism spectrum disorder: the first evidence outside North America. Psychological Medicine. 2023 Feb;53(3):966-976.

Poster No 1736

Common Optimal Network Between Laser Interstitial Thermal Therapy and Thalamic DBS for Temporal Lobe

Min Jae Kim[1], Frederic Schaper[2], Rob Rouhl[3], Yasin Temel[3], Michael Fox[2], Kathryn Davis[1], H. Isaac Chen[1], Ramya Raghupathi[1], Joon-Yi Kang[4], William Anderson[4]

[1]Perelman School of Medicine, University of Pennsylvania, Philadelphia, PA, [2]Brigham and Women's Hospital, Harvard Medical School, Boston, MA, [3]Maastricht University Medical Center, Maastricht, Maastricht, [4]Johns Hopkins School of Medicine, Baltimore, MD

Introduction: Laser interstitial thermal therapy (LiTT) and thalamic deep brain stimulation (DBS) are both widely accepted surgical therapies for patients with temporal lobe epilepsy (TLE). LiTT is used to ablate the seizure onset zone in the temporal lobe, while DBS is used to modulate the anterior thalamus (ANT) and its connected network to reduce seizures. While both therapies have shown significant clinical promise for TLE, postoperative seizure outcomes are variable across patients, presumably due to a lack of understanding of their mechanisms of action. Identifying which brain circuits are involved in improved clinical outcome after both therapies may increase our understanding of their seizure suppressive mechanisms. In this study, we first explore the network-level effect of LiTT and ANT-DBS by studying functional connectivity patterns associated with improved seizure outcome, and second by identifying a common brain network that may predict seizure reduction.

Methods: 27 TLE patients who underwent unilateral amygdalohippocampal LiTT were classified into two cohorts (14 patients with left and 13 patients with right TLE) based on one-year postoperative seizure outcome. Seizure outcome was measured as either seizure-free (ILAE Class I) or seizures-present (ILAE Class II – VI). Individual ablation volumes were segmented from the intraoperative MRI sequence. From another cohort of TLE patients who underwent bilateral ANT-DBS, their volumes of tissue activated (VTA) were generated based on active electrode contact. Segmented ablation volumes and VTA were then seeded into a normative functional connectome (Brain Genomics Superstruct Project, n=1000) to extract functional connectivity (FC) profiles associated with respective ablation volumes or VTA. For LiTT patients, functional connections associated with seizure freedom were identified by comparing FC patterns between the two cohorts, resulting a voxel-wise "T-map". For ANT-DBS patients, FC patterns were correlated with a percentage degree of reduction (%) relative to preoperative seizure frequency to create a voxel-wise "R-map".

Results: For the LiTT dataset, 10 TLE patients achieved complete seizure freedom. Seizure free patients had right LiTT ablation volumes that were more functionally connected to bilateral calcarine area, cuneus, and thalamic anterior and medial pulvinar nucleus compared to non-seizure free patients. (Figure 1B). The spatial similarity between the "T-map" produced from right-side ablation and each patients' connectivity profiles was highly associated with seizure outcomes by fitting a logistical regression model (log-likelihood ratio = 10.25, p = 0.0014**) as shown in Figure 1C. In the "R-map" produced from ANT-DBS, DBS sites associated with increased seizure control were more functionally connected to right cuneus and thalamic medial dorsal nucleus and medial pulvinar nucleus (Figure 2B). Finally, "T-map" produced from right-side LiTT and "R-map" from ANT-DBS was positively correlated (r = 0.29, p < 0.0001), suggesting that the predictive functional maps from the two procedures for TLE are highly similar.

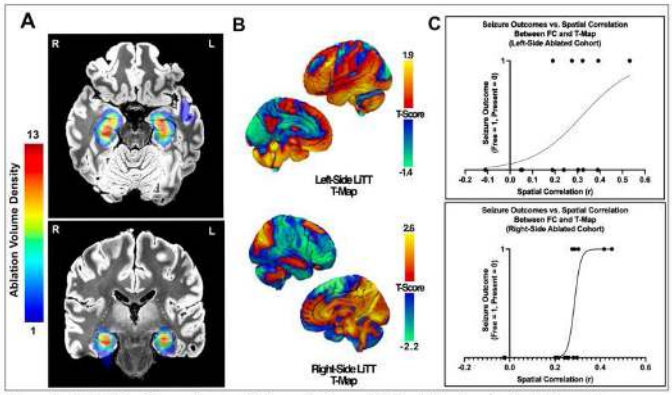

Figure 1. LiTT T-Map Generation and Seizure Outcome (A) Population density of ablation volumes on each side suggests that ablation was made mostly in mesial temporal areas. **(B).** Once ablation volumes were seeded into a normative functional connectome, extracted functional connectivity (FC) profiles of each patient were stratified based on postoperative outcomes (seizure-free or present), followed by a voxel-wise t-test to produce T-map for each ablation side. Regions with positive t-scores (yellow-red) correspond to areas where increased connectivity is associated with more seizure freedom, and negative t-score (blue-green) with seizure presence. T-maps produced from right (top row) or left (bottom row) ablations were spatially correlated with individual FC maps. **(C)** Correlation coefficients were logistically regressed against seizure outcomes. For the right side ablation, the model fit was significant (log-likelihood ratio = 10.25, p = 0.0014**) where high spatial similarity between T-map and FC profiles within the same cohort was more associated with seizure freedom.

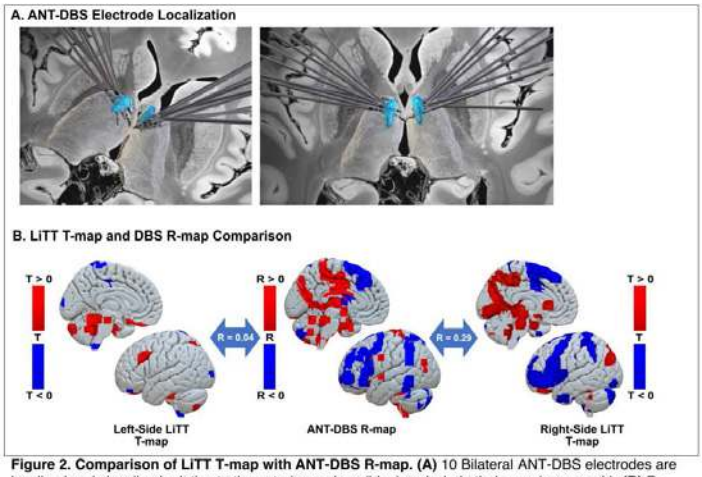

Figure 2. Comparison of LiTT T-map with ANT-DBS R-map. (A) 10 Bilateral ANT-DBS electrodes are localized and visualized relative to the anterior nucleus (blue) and whole thalamus (grey mesh). **(B)** R-map was compared between T-maps (both maps thresholded to only show statistically significant voxels) derived from left and right-side LiTT respectively. Regions with positive R values (red) represent regions where increased connectivity with VTA is associated with seizure reduction, and negative R-value (blue) with seizure worsening. ANT-DBS R-map were spatially similar to the right-side LiTT T-map (r = 0.29, p < 0.0001), especially within cuneus gyrus and anterior and medial pulvinar nucleus of the thalamus.

Conclusions: In this study, we identified a common brain network connected to laser ablation and thalamic DBS sites associated with improved seizure outcome. This common network included functional connections to the cuneus and medial pulvinar nucleus, which may potentially improve surgical targeting and DBS programming to control seizures in TLE. Specifically, with more evidence of medial pulvinar nucleus playing a larger role in seizure propagation in TLE[1,2], our study further proposes medial pulvinar nucleus as an alternative target for controlling seizures through its networks engaged from neuromodulatory or ablative procedures.

References

1. Guye, M (2006), 'The Role of Corticothalamic Coupling in Human Temporal Lobe Epilepsy', Brain, vol. 129, pp. 1917–1928
2. Rosenberg, D.S (2006), 'Involvement of Medial Pulvinar Thalamic Nucleus in Human Temporal Lobe Seizures', Epilepsia, vol. 47, pp. 98-107

Poster No 1737

Prenatal Distress and Longitudinal Infant Functional Brain Development in a COVID-19 Pandemic Cohort

Aliza Jaffer[1], Kathryn Manning[1], Gerald Giesbrecht[1], Lianne Tomfohr-Madsen[2], Catherine Lebel[1]

[1]University of Calgary, Calgary, Alberta, [2]University of British Columbia, Vancouver, British Columbia

Introduction: Prenatal maternal psychological distress (i.e., anxiety and depression) can disrupt infant brain development and impact behaviour. During pregnancy, around 9-11% of individuals experience depression, while 18-25% experience elevated anxiety. The in-utero environment is directly influenced by prenatal distress. Such disruptions during critical periods of brain development may compromise developmental trajectories, potentially leading to lifelong consequences for cognitive, behavioural, and emotional functions in some children. Rates of psychological distress were substantially higher during the COVID-19 pandemic, raising concerns about its effect on infant development. We studied a cohort of pandemic-born infants and aimed to relate functional connectivity within brain networks across the first 2 years of life to prenatal distress and infant behaviour.

Methods: Mother-infant pairs were recruited from the Pregnancy during the COVID-19 Pandemic (PdP) study. Eligibility for the PdP study were being <35 weeks pregnant, living in Canada, ≥17 years of age, and able to read and write in English or French. Prenatal maternal distress was quantified using a combined factor of the Edinburgh Postnatal Depression Scale (EPDS) and the Patient Reported Outcomes Measurement Information System (PROMIS) Anxiety. Infant magnetic resonance imaging (MRI) was obtained at 3 months (n=63), 1 year (n=9), and 2 years (n=43) of age at the Alberta Children's Hospital using a GE 3T MR750w scanner with a 32-channel head coil (TR=2000 ms, TE=30 ms, voxel 3.6x3.6x3.6 mm3, flip angle=60°, 37 slices). 17 infants had scans for at least two timepoints. Parents assessed behaviour at 2 years using the Ages & Stages Questionnaire. MRI were preprocessed using FSL. MELODIC independent component analysis was used to remove volumes with excessive motion. Multi-session temporal concatenation was run using 3-month data to construct common spatial components and identify default mode (DMN), left frontoparietal (LFP), and executive control (EC) networks. Two regions of interest (ROIs) were defined in each network using 5 mm radii spheres placed at the hubs or peaks of connectivity networks (Figure 1): ROIs were in the anterior and posterior cingulate gyri (DMN), left angular gyrus and left precentral gyrus (LFP), and left and right superior frontal gyri (EC). Masks were generated using age-appropriate AAL atlases, where average time series were extracted and correlated for each subject to quantify functional connectivity within networks. Trajectories of connectivity and their relationship with prenatal distress were investigated using linear mixed effects models, including an interaction term between infant age and prenatal distress. Regression models were run to test relationships between distress, connectivity, and behaviour. Models were corrected for multiple comparisons using FDR.

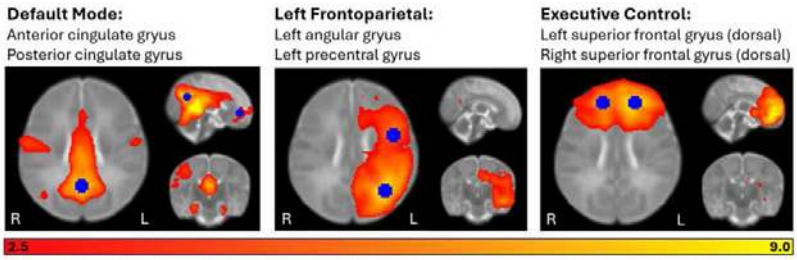

Figure 1. Seed regions (blue) within the default mode, left frontoparietal, and executive control brain networks of 3-month infants used to inform corresponding AAL atlas-defined brain regions for connectivity analysis. Functional connectivity (red/yellow) was quantified between pairs of brain regions within each network. Brain maps display brain networks identified from common spatial components generated through multi-session temporal concatenation in FSL using 3-month infant data.

Results: Functional connectivity in the LFP network was significantly related to the interaction between age and prenatal distress (T=2.6, p=0.01, q=0.03, df=112) (Figure 2). Younger infants exposed to higher prenatal distress had weaker connectivity than infants exposed to lower prenatal distress; older infants exposed to higher prenatal distress had stronger connectivity than infants exposed to lower prenatal distress. At 2 years of age, higher prenatal distress was related to stronger LFP network connectivity (T=2.8, p=0.008, q=0.024, df=39), and DMN connectivity was negatively associated with fine motor scores (T=-3.4, p=0.002, q=0.006, df=32).

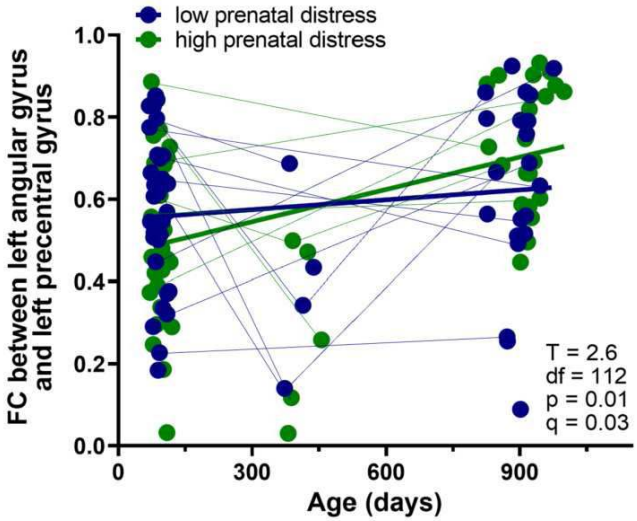

Figure 2. A significant age-prenatal maternal distress interaction related to functional connectivity between the left angular gryus and left precentral gryus of the left frontoparietal brain network (T=2.6, p=0.01, q=0.03, df=112).

Conclusions: Higher order cognitive networks, including the frontoparietal network, typically display immature connectivity patterns at birth that mature over time. Our findings reveal distinct patterns of functional connectivity within the LFP network, suggesting that infants exposed to higher prenatal distress have faster development. DMN connectivity may also affect fine motor ability, motivating the need for continued monitoring of these infants through childhood.

References

1. Agarwal, P.K. (2020), 'Evaluation of the Ages and Stages Questionnaire (ASQ 3) as a developmental screener at 9, 18, and 24 months', Early Human Development, vol 147, e105081.
2. Bergink, V. (2011), 'Validation of the Edinburgh Depression Scale during pregnancy', Journal of Psychosomatic Research, vol. 70, no. 4, pp. 385–389.
3. Cella, D. (2019), 'PROMIS® Adult Health Profiles: Efficient Short-Form Measures of Seven Health Domains', Value in Health, vol. 22, no. 5, pp. 537–544.
4. Dennis, C.L. (2017), 'Prevalence of antenatal and postnatal anxiety: systematic review and meta-analysis', British Journal of Psychiatry, vol. 210, no. 5, pp. 315–323.
5. Gao, W. (2015), 'Development of human brain cortical network architecture during infancy', Brain Structure & Function, vol. 220, no. 2, pp. 1173-1186.
6. Gao, W. (2017), 'Functional Connectivity of the Infant Human Brain: Plastic and Modifiable', Neuroscientist, vol. 23, no. 2, pp. 169–184.
7. Gavin, N.I. (2005), 'Perinatal depression: a systematic review of prevalence and incidence', Obstetrics and Gynecology, vol. 106, no. 5, pp. 1071–1083.
8. Giesbrecht, G.F. (2021), 'Protocol for the Pregnancy During the COVID-19 Pandemic (PdP) Study', JMIR Research Protocols, vol. 10, no. 4, e25407.
9. Jenkinson, M. (2012), 'FSL', NeuroImage, vol. 62, no. 2, pp. 782–790.
10. Lebel, C. (2020), 'Elevated depression and anxiety symptoms among pregnant individuals during the COVID-19 pandemic', Journal of Affective Disorders, vol. 227, pp. 5–13.

Poster No 1738

A generalized epilepsy network derived from brain abnormalities and deep brain stimulation

Gong-Jun Ji[1], Michael Fox[2], Mae Morton-Dutton[2], Yingru Wang[3], Jinmei Sun[4], Panpan Hu[5], Xingui Chen[5], Zhiqiang Zhang[6], Haya Akkad[2], Janne Nordberg[7], Juho Joutsa[7], Cristina Torres Diaz[8], Sergiu Groppa[7], Gabriel Gonzalez-Escamilla[7], Linda Dalic[9], John Archer[10], Aaron Warren[2], Melissa Chua[2], Alexander Cohen[2], Sara Larivière[2], Clemens Neudorfer[2], Andreas Horn[2], Rani Sarkis[2], Ellen Bubrick[2], Robert Fisher[11], John Rolston[2], Kai Wang[4], Frederic Schaper[2]

[1]Anhui Medical University, Hefei, Anhui Province, [2]Brigham and Women's Hospital, Harvard Medical School, Boston, MA, [3]Anhui Medical University, Hefei, Anhui, [4]Anhui Medical University, Hefei, Anhui, [5]The First Affiliated Hospital of Anhui Medical University, Anhui Medical University, Hefei, Anhui, [6]Jinling Hospital, the First School of Clinical Medicine, Southern Medical University, Nanjing, Jiangsu, [7]Department of Clinical Neurophysiology, Turku University Hospital, Turku, Pori, [8]Hospital Universitario La Princesa, Universidad Autónoma de Madrid, Madrid, Madrid, [9]The University of Melbourne, Victoria, Victoria, [10]The University of Melbourne, Victoria, Victoria, [11]Stanford University School of Medicine, Palo Alto, California

Introduction: Patients with idiopathic generalized epilepsy (IGE) show distributed subtle brain abnormalities. However, it is unknown if these abnormalities occur within a common brain network and whether they can inform network therapies such as deep brain stimulation (DBS).

Methods: We performed a systematic search and retrieved all published coordinates of brain abnormalities (atrophy or fMRI hyperactivity) associated with IGE (n = 21 studies, including 540 IGE patients and 778 healthy controls). We computed the functional connections of these abnormal coordinates on the healthy connectome of 652 Asian adults (validated by Western connectome and pediatric connectome) using a novel technique termed coordinate network mapping. The resulting coordinate networks were overlapped to identify a common IGE network across all studies. Voxel-wise statistical analyses were performed using the PALM function in FSL (V6.0.4). We considered an FDR-corrected two-sided $P<0.05$ as significant.

Results: The coordinates of brain abnormalities in IGE are highly heterogeneous between studies, but their functional connectivities were highly overlapped in a common brain network (Fig. 1A) with positive connectivity to the somato-cognitive action network (SCAN) regions and negative connectivity to the default mode regions. This overlapping network was specific to IGE as compared to coordinates in neurodegenerative disease (n=49, from Darby et al., 2019, Brain) or random coordinates (n=63) ($P < 0.05$, Fig. 1B). Hereafter, we termed the overlapping map as IGE network. To further validate the IGE network, we searched the literature for simultaneous EEG-fMRI studies in generalized and focal epilepsies reported coordinates activated by (inter)ictal discharges. We found 7 studies with generalized epilepsy and 6 studies with focal epilepsy. Brain regions activated with (inter)ictal discharges in generalized epilepsy overlapped more with our IGE network than regions activated in focal epilepsy ($t = 2.83$, $P = 0.017$, Fig. 1C). To explain the involuntary movements of the whole body rather than any single hand or leg during generalized seizures, we tested whether our IGE network affected the (inter)effector regions in the primary motor area more than the effector regions of leg, hand, and mouth as defined by Gordon et al. (2023, Nature). This hypothesis was supported by the comparison between inter-effector and effector regions ($t = 3.96$, $P = 0.003$, Fig. 1D). To test the therapeutic relevance of our IGE network, we analyzed two independent datasets of DBS sites from 27 patients with generalized seizures who received thalamic centromedian (CM)-DBS. Thalamic centromedian (CM)-DBS electrode locations differed between patients (Fig. 2A), as did the magnitude of seizure control after DBS. The IGE network involved functional connectivity to the CM, and more specifically peaked at the anterolateral part of the CM bordering the ventral lateral posterior (ventral subdivision, VLPv) thalamic nucleus (Fig. 2B-C). Higher CM-DBS stimulation site (i.e., volume of activated tissue [VAT]) overlap with our IGE network was associated with better seizure control (Spearman $R = 0.44$, $P = 0.019$, Fig. 2D). In contrast, no association was found between seizure control and VAT volume, VAT overlap with the CM or ALE results.

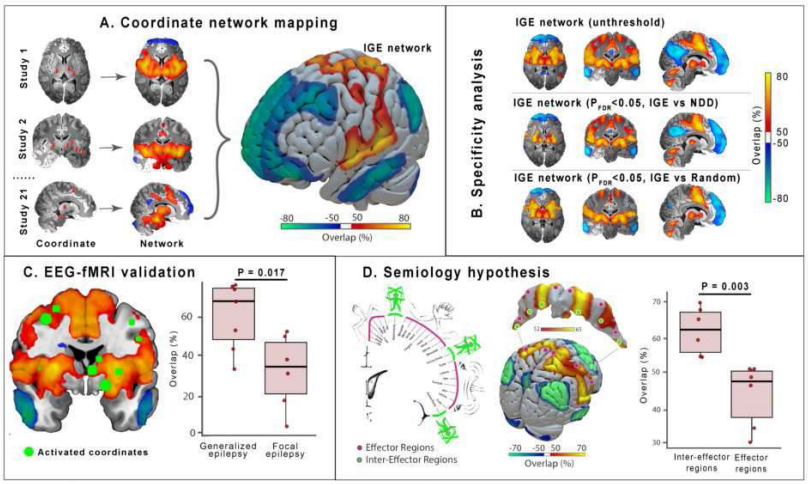

Figure 1 IGE network mapping. Networks of coordinates in each IGE study were threhsolded and overlapped to get common connections (A). This common connections are specific to IGE (B) and validated by EEG-fMRI findings. Thus, it is termed as IGE network (C). Higher involvment of inter-effector regions than effector regions in the IGE network (D) explains the whole body convulsion during generalized seizures NDD = NeuroDegeneration Disorder.

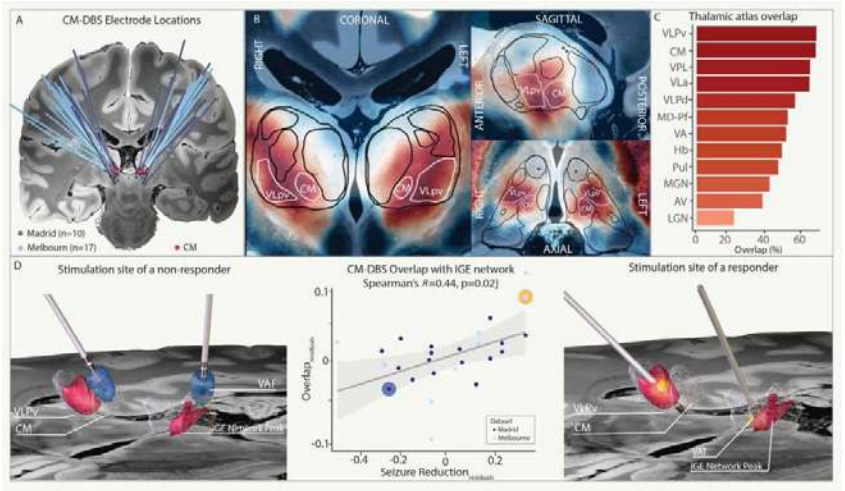

Figure 2. Relevance for deep brain stimulation. DBS electrode locations implanted at the thalamic centromedian (CM) to treat drug resistant generalized seizures differed slightly between patients (A). The IGE network included functional connectivity to the CM, peaked at its antero-lateral border between the CM and VLPv (B), and showed variable involvement of different thalamic nuclei (C). DBS sites of patients that had less seizure control after CM-DBS (D, left) co-localized less to our IGE network (D, middle) than DBS sites of patients with better seizure control (D, right).

Conclusions: This generalized epilepsy network could be a novel network target and guide clinical trials of (non)invasive brain stimulation to control generalized seizures.

References

1. Darby, R.R., (2019), 'Network localization of heterogeneous neuroimaging findings', Brain, vol. 142, no. 1, pp. 70-79.
2. Gordon, E.M., (2023), 'A somato-cognitive action network alternates with effector regions in motor cortex', Nature, vol. 617, no. 7960, pp. 351-359.

Poster No 1739

Evaluation of Structural-Functional Coupling Mechanism on Human Connectome Project Using HoloBrain

Huan Liu[1], Tingting Dan[1], Defu Yang[1], Won Hwa Kim[2], Minjeong Kim[3], Paul Laurienti[4], Guorong Wu[1]

[1]University of North Carolina at Chapel Hill, Chapel Hill, NC, [2]Pohang University of Science and Technology (POSTECH), Pohang, Korea, Republic of, [3]University of North Carolina at Greensboro, Greensboro, NC, [4]Wake Forest School of Medicine, Winston Salem, NC

Introduction: Human brain is a complex wiring system in which diverse behaviors are supported by ubiquitous functional fluctuations. Although striking efforts have been made to investigate the association between brain structure connectivity (SC) and function connectivity (FC), the SC-FC coupling mechanism is largely elusive. Recently, we have developed a novel analytic

approach, called HoloBrain (Liu, Dan et al. 2023), to characterize the interference patterns formed by the BOLD signals modulated by a collection of harmonic wavelets (stemming from wirings of white matter fibers) across a widespread graph spectrum. In this work, we have applied our HoloBrain technique to task-fMRI data from HCP-YA. Compared to conventional network analysis methods, HoloBrain offers a new window to investigate the task-specific footprint of SC-FC coupling through the lens of cross-frequency coupling (CFC), demonstrating great potential in discovering novel neurobiological biomarkers for resting-state fMRI studies.

Methods: Method overview of HoloBrain. First, we construct harmonic wavelets from the Laplacian matrix of SC by (1) calculating harmonic waves based on the Laplacian matrix, (2) localizing each harmonic wave to each brain region and form region-specific (indexed by i) and frequency-specific (denoted by s) harmonic wavelet ψis using graph signal processing techniques (Hammond, Vandergheynst et al. 2011). Second, we modulate the snapshot of BOLD signal f(t) at time t with each harmonic wavelets and generate a time series of harmonic power pis. Third, we construct a collection of local CFC patterns CFCijsr by the inner product of harmonic power between i-th and j-th brain regions and across frequencies s and r. Supposing we break down the whole graph spectrum into four frequency bands (Fig. 1(c)), the output of HoloBrain is a 4×4 CFC matrix for each node/edge. Neuroscience insight of HoloBrain. Following the concept of wave-to-wave interference (Gabor 1948), we have developed a proof-of-concept approach to computationally "record" the CFC of time-evolving interference patterns that are formed by superimposing the harmonic wavelets on the subject-specific neural activities. Group comparison using HoloBrain. For each CFC value, we apply a linear regression model to examine whether the underlying CFC manifests significant difference between two cognitive tasks, where age and gender are confounders.

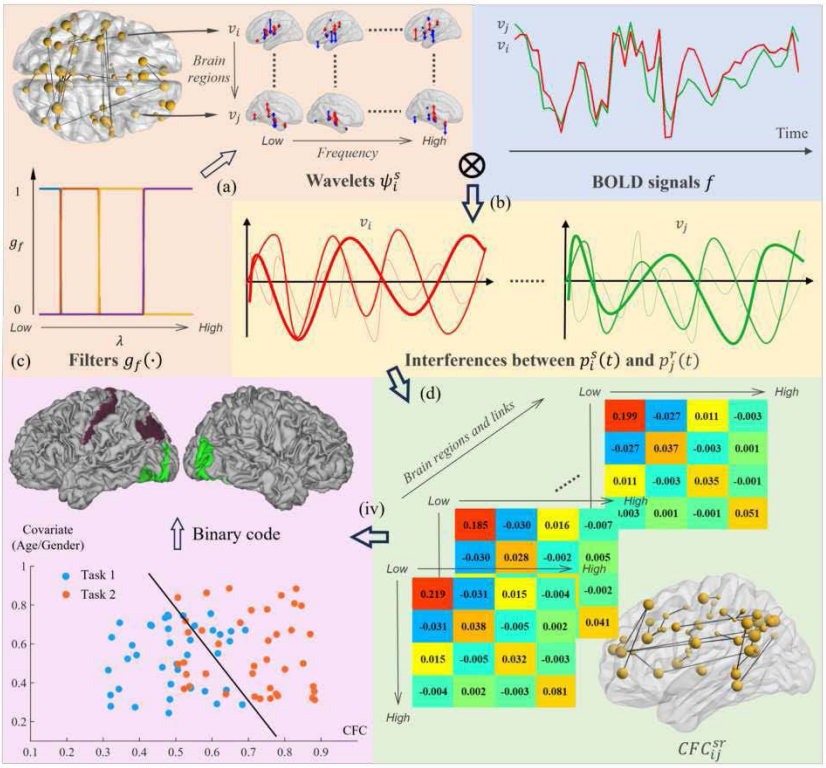

Fig. 1. The overall framework of *HoloBrain*. It is mainly divided into three steps: (i) construct harmonic wavelets from SC, (ii) calculate time series of harmonic power, and (iii) calculate CFC across brain regions and frequencies.

Results: We evaluate the statistical power of HoloBrain on task-based fMRI of HCP-YA dataset, where each subject is partitioned into 360 brain regions (HCP atlas). In the following experiments, we only show the significant motor (1) vs. language (0) result at the significance level of 10-8, along with the effect size greater than 0.2 and adjusted R2>0.2. In Fig. 2 top, it is evident that the identified brain regions and connections are aligned with current findings in the neuroscience field (Glasser, Coalson et al. 2016), which are located at the somatosensory, motor cortex, and Auditory Association cortex. Compared to the conventional network analysis using FC matrix only (Fig. 2(a)), HoloBrain provides a new dimension of brain connectome in the frequency domain. Furthermore, we apply the same analysis to the re-test scans (shown in Fig. 2 bottom). In terms of replicability, the group comparison results by HoloBrain are more consistent than conventional FC analysis, as indicated by circles.

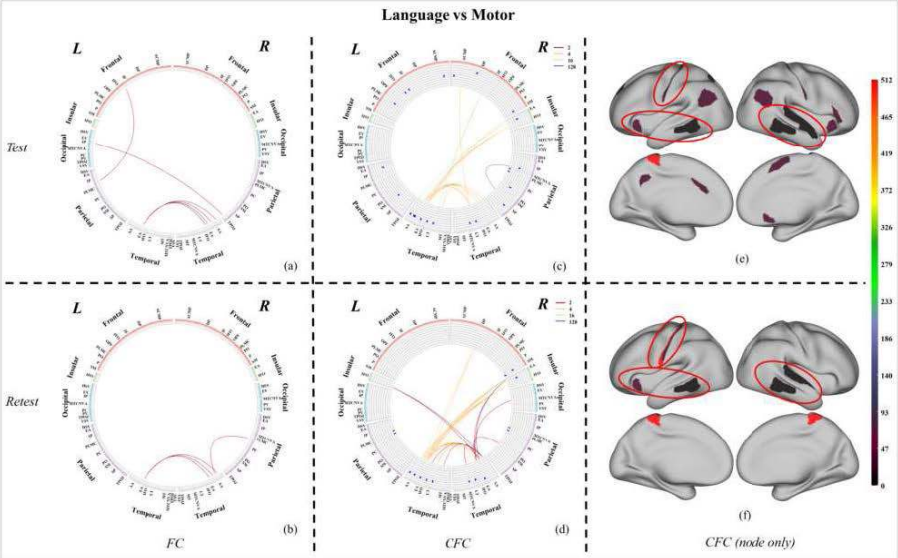

Fig. 2. Top: The significant brain nodes and links that manifest SC-FC CFC difference between the Motor task and Language task using test fMRI scans. (a) Group comparison using conventional FC matrix only. (c) SC-FC CFC with significant difference between motor and language. To summarize the statistical results in multiple frequencies in one brain mapping plot, we use binary index trick to code each possible combination of frequencies, where each frequency (from low to high) corresponds to a unique bit in the binary code (from small to large bit position). Each possible combination of cross-frequency coupling is binary-coded and associated with a unique decimal value. The marked spots in the ring plot indicate the same-region cross-frequency SC-FC CFC exhibits significant group differences, where each layer corresponds to particular frequency-to-frequency coupling. The curved links indicate the cross-region cross-frequency SC-FC CFC exhibits significant group difference, where the color is in line with the decimal value of binary code. (e) Following the same notion of colormap, we display the brain mapping of regionwise motor vs language significance of CFC. Bottom: Same data analysis based on re-test fMRI scans.
The abbreviations around the circle stand for different cortexes: "ACMP: Anterior_Cingulate_and_Medial_Prefrontal, DP: Dorsolateral_Prefrontal, IF: Inferior_Frontal, IFO: Insular_and_Frontal_Opercular, OPF: Orbital_and_Polar_Frontal, PLMC: Paracentral_Lobular_and_Mid_Cingulate, PO: Posterior_Opercular, P: Premotor, SM: Somatosensory_and_Motor, DSV: Dorsal_Stream_Visual, EA: Early_Auditory, IP: Inferior_Parietal, MTCNVA: MT+_Complex_and_Neighboring_Visual_Areas, PC: Posterior_Cingulate, PV: Primary_Visual, TPOJ: Temporo-Parieto_Occipital_Junction, VSV: Ventral_Stream_Visual, SP: Superior_Parietal, AA: Auditory_Association, EV: Early_Visual, LT: Lateral_Temporal, MT: Medial_Temporal".

Conclusions: We evaluate the statistical power and replicability performance of our recently developed HoloBrain technique on task-fMRI data in HCP-YA. Since HoloBrain characterizes the SC-FC coupling mechanism via the interference between SC-modulated BOLD signals, we are able to examine the groupwise SC-FC coupling differences on both brain regions and connections across the graph spectrum.

References

1. Gabor, D. (1948). "A new microscopic principle." Nature 161(4098): 777.
2. Glasser, M. F., T. S. Coalson, E. C. Robinson, C. D. Hacker, J. Harwell, E. Yacoub, K. Ugurbil, J. Andersson, C. F. Beckmann, M. Jenkinson, S. M. Smith and D. C. Van Essen (2016). "A multi-modal parcellation of human cerebral cortex." Nature 536(7615): 171-178.
3. Hammond, D. K., P. Vandergheynst and R. Gribonval (2011). "Wavelets on graphs via spectral graph theory." Applied and Computational Harmonic Analysis 30(2): 129-150.
4. Liu, H., T. Dan, Z. Huang, D. Yang, W. H. Kim, M. Kim, P. Laurienti and G. Wu (2023). HoloBrain: A Harmonic Holography for Stereotyped Brain Function. Information Processing in Medical Imaging 2023. N. Navab and D. Wassermann. Argentina, LNCS.

Poster No 1740

Systematically comparing properties of local dynamics and pairwise coupling in the brain

Annie Bryant[1], Kevin Aquino[1,2], Linden Parkes[3,4], Alex Fornito[4], Ben Fulcher[1]

[1]The University of Sydney, Sydney, NSW, [2]Brain Key Incorporated, San Francisco, CA, [3]Rutgers University, Piscataway, NJ, [4]Monash University, Clayton, VIC

Introduction: Dynamical structures of brain activity can be quantified from functional magnetic resonance imaging (fMRI), like local regional activity and functional connectivity (FC) between pairs of regions (Fig 1A). To date, most studies use only one of the two representations with a limited set of statistics, like the fractional amplitude of low-frequency fluctuations (fALFF) for regional dynamics and the Pearson correlation coefficient for FC[1]. Emerging work using comprehensive libraries of interdisciplinary time-series features[2,3] suggests that alternative statistics may be more suitable for a given application[3,4], though there is currently no unifying framework for comparing across multiple features and representation types simultaneously. Here, we introduce a systematic approach to quantify diverse types of local and pairwise dynamical structure from fMRI data, comparing the ability of multiple feature-based representations to capture meaningful differences in neuropsychiatric case–control datasets.

Methods: We formulated five analyses (depicted in Fig 1B) to investigate different representations of fMRI temporal structure: i) multiple time-series features measured within one region; ii) one property of local dynamics measured across the entire brain; iii) brain-wide maps of all local properties; iv) individual FC metrics across all brain pairs; and (v) each FC metric plus all brain-wide local dynamics. We investigated how well each of these representations captured salient case–control differences using cross-validated linear support vector machine (SVM) classification applied to resting-state fMRI time series from participants with schizophrenia (SCZ, N=48), bipolar I disorder (BP, N=49), attention-deficit hyperactivity disorder (ADHD, N=39), and autism spectrum disorder (ASD, N=513; Fig 1C)[5–7]. For each participant, we computed 25 univariate time-series features and 14 pairwise interaction statistics (representing subsets of broad interdisciplinary libraries[2,3]), which formed the basis for all classifiers (Fig 1D).

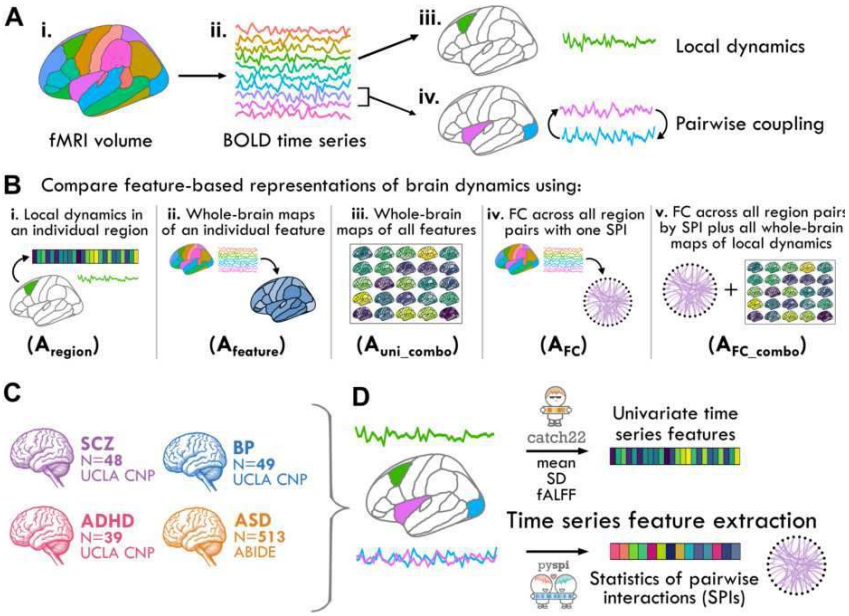

Figure 1. **A** For a given resting-state fMRI volume (i), the cortex and subcortex were parcellated into individual regions from which the voxel-averaged BOLD signal time series is extracted (ii). Two key ways of quantifying dynamical patterns from these data are to: (iii) measure properties of the dynamics of individual brain regions (green); or (iv) statistical dependencies between pairs of regions (pink and blue). **B** We systematically compared five distinct representations of resting-state fMRI dynamics: (i) Localized properties of activity within an individual region, A_{region}; (ii) Whole-brain maps of an individual time-series feature, $A_{feature}$; (iii) whole-brain maps of multiple univariate time-series features, A_{uni_combo}; (iv) FC matrices across all region pairs using a given statistic of pairwise interactions (SPI), A_{FC}; and (v) Each FC matrix plus multiple univariate time-series features computed from all brain regions (Auni_combo), termed A_{FC_combo}. **C** As an exemplary case study, we investigated the ability of each of the five representations to capture disease-relevant changes in neural activity across four neuropsychiatric disorders: SCZ (*N*=48), BP (*N*=49), ADHD (*N*=39), and ASD (*N*=513), with control subjects also included from the two open-access dataset cohorts. **D.** To additionnally compare temporal properties within each representation, we computed 25 univariate time-series features and 14 SPIs -- representative subsets of the *hctsa* and *pyspi* libraries, respectively. These features form the basis for case--control classification for each disorder, evaluated using linear SVMs.

Results: Strikingly, dynamical signatures of many brain regions significantly distinguished cases from controls across all four disorders, visualized as spatial maps of disorder-specific localized alterations (Fig 2A). Combining the brain-wide spatial maps from all 25 univariate time-series features generally improved classification performance relative to either representation on their own in SCZ and BP (Fig 2B), suggesting there are complex alterations to brain activity in these disorders that are incompletely captured by a singular brain region or singular time-series feature. Many individual FC metrics also significantly distinguished cases from controls, supporting the continued use of coupling statistics to quantify brain dynamics. However, classification performance was improved when FC was combined with brain-wide maps of local, region-specific dynamical properties (Fig 2C). Importantly, this demonstrates that regional activity and functional connectivity provide complementary and relevant information about disorder-specific brain dynamics. Moreover, we found that time-series features tailored to stochastic, linear, Gaussian processes are well suited for resting-state fMRI time series (Fig 2D), which are typically noisy with low temporal resolution.

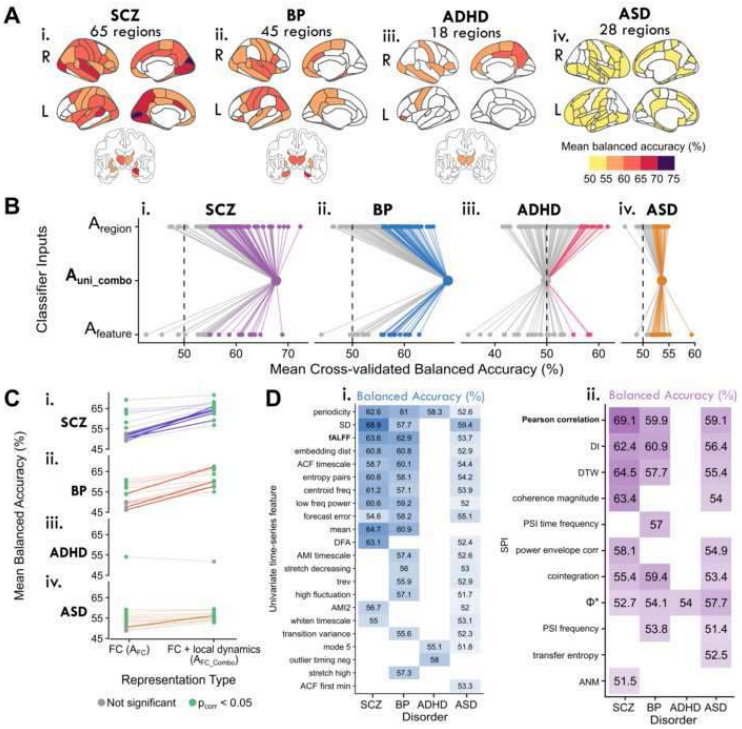

Figure 2. A To visualize the spatial distribution of regional classification performance, the mean case--control classification balanced accuracies are depicted for each brain region by disorder. Only regions that yielded a statistically significant balanced accuracy ($P_{corr} < 0.05$, Holm-Bonferroni corrected across 82 brain regions for SCZ, BP, and ADHD, 48 brain regions for ASD) are shaded, and the total number of significant brain regions per disorder is indicated above each brain map. **B** To compare performance of the combined region times feature classifier to that of individual regions and time-series features, the mean balanced accuracy is shown for all brain regions (upper row, labeled 'A_{region}'), the combination classifier (middle row, labeled 'A_{uni_combo}'), and time-series features (bottom row, labeled '$A_{feature}$'). Lines are included as a visual guide to aid comparison, while dot color indicates whether the corresponding classifier yielded a significant balanced accuracy ($P_{corr} < 0.05$, colored in) or not (shaded in gray). **C** For each FC metric (SPI), the mean balanced accuracy is shown for the FC matrix on its own (left, A_{FC}) and with the inclusion of all univaraite region times feature data (right, A_{FC_combo}). Points are colored to indicate whether the corresponding balanced accuracy was significant (green, $P_{corr} < 0.05$) or not (gray). Each line maps to one SPI to visually guide comparison across representation types. Lines are shaded darker to indicate $P_{corr} < 0.05$ based on a T-test corrected for repeated resampling for each SPI between the two representation types. **D** Classification results are shown as a heatmap, with rows representing univariate time-series features (i) or pairwise SPIs (ii) that yielded significant balanced accuracy ($P_{corr} < 0.05$) in at least one disorder, with columns mapping to each of the four disorders.

Conclusions: Here, we present the first comprehensive, data-driven comparison of five statistical representations of dynamical structures in resting-state fMRI time series, using interdisciplinary libraries of time-series analysis methods to quantify both univariate time-series structure and pairwise coupling strengths. Our results identified multiple types of disruptions to localized activity and pairwise coupling across multiple neuropsychiatric disorders. The systematic approach presented herein is highly generalizable to myriad applications and imaging modalities, in which complex dynamical systems like the brain are analyzed.

References

1. Noble, S., Scheinost, D., & Constable, R. T. (2019). A decade of test-retest reliability of functional connectivity: A systematic review and meta-analysis. NeuroImage, 203, 116157. https://doi.org/10.1016/j.neuroimage.2019.116157
2. Fulcher, B. D., & Jones, N. S. (2017). hctsa: A Computational Framework for Automated Time-Series Phenotyping Using Massive Feature Extraction. Cell Systems, 5(5), Article 5. https://doi.org/10.1016/j.cels.2017.10.001
3. Cliff, O. M., Bryant, A. G., Lizier, J. T., Tsuchiya, N., & Fulcher, B. D. (2023). Unifying pairwise interactions in complex dynamics. Nature Computational Science, 1–11. https://doi.org/10.1038/s43588-023-00519-x
4. Markicevic, M., Fulcher, B. D., Lewis, C., Helmchen, F., Rudin, M., Zerbi, V., & Wenderoth, N. (2020). Cortical Excitation:Inhibition Imbalance Causes Abnormal Brain Network Dynamics as Observed in Neurodevelopmental Disorders. Cerebral Cortex (New York, N.Y.: 1991), 30(9), Article 9. https://doi.org/10.1093/cercor/bhaa084
5. Poldrack, R. A., Congdon, E., Triplett, W., Gorgolewski, K. J., Karlsgodt, K. H., Mumford, J. A., Sabb, F. W., Freimer, N. B., London, E. D., Cannon, T. D., & Bilder, R. M. (2016). A phenome-wide examination of neural and cognitive function. Scientific Data, 3(1), 160110. https://doi.org/10.1038/sdata.2016.110
6. Di Martino, A., Yan, C.-G., Li, Q., Denio, E., Castellanos, F. X., Alaerts, K., Anderson, J. S., Assaf, M., Bookheimer, S. Y., Dapretto, M., Deen, B., Delmonte, S., Dinstein, I., Ertl-Wagner, B., Fair, D. A., Gallagher, L., Kennedy, D. P., Keown, C. L., Keysers, C., … Milham, M. P. (2014). The autism brain imaging data exchange: Towards a large-scale evaluation of the intrinsic brain architecture in autism. Molecular Psychiatry, 19(6), 659–667. https://doi.org/10.1038/mp.2013.78
7. Di Martino, A., O'Connor, D., Chen, B., Alaerts, K., Anderson, J. S., Assaf, M., Balsters, J. H., Baxter, L., Beggiato, A., Bernaerts, S., Blanken, L. M. E., Bookheimer, S. Y., Braden, B. B., Byrge, L., Castellanos, F. X., Dapretto, M., Delorme, R., Fair, D. A., Fishman, I., … Milham, M. P. (2017). Enhancing studies of the connectome in autism using the autism brain imaging data exchange II. Scientific Data, 4, 170010. https://doi.org/10.1038/sdata.2017.10

Poster No 1741

Quantitative Assessment of ML-Based Feature Attribution Methods for ASD Biomarker Discovery in fMRI

Lucas Mahler[1], Klaus Scheffler[2,3], Gabriele Lohmann[3]

[1]Max-Planck-Institute for Biological Cybernetics, Tübingen, Baden-Württemberg, [2]University of Tübingen, Tübingen, Germany, [3]Max-Planck-Institute for Biological Cybernetics, Tübingen, Baden-Württemberg, Germany

Introduction: Mental disorders are a pressing global health concern, highlighting the critical need for reliable biomarkers, particularly in conditions such as autism spectrum disorder (ASD). Despite its prevalence, affecting 1 in 160 children worldwide, the lack of objective biomarkers hinders timely and accurate diagnosis, relying solely on behavioral observations. This study explores the convergence of deep learning, explainable AI, and ASD diagnostics. We aim to evaluate the potential of extracting meaningful biomarkers from the learned representations of deep learning models applied to rs-fMRI data. In line with recent advances in explainable AI, our focus is on quantitatively evaluating different methods for interpreting machine learning predictions. The goal is to identify the method that produces the highest quality explanations, thereby improving our understanding of the decision-making process in the model. Beyond prediction, this study undertakes a quantitative exploration of brain imaging-based biomarkers. Using the selected explainable AI method, we aim to uncover biomarkers that contribute to a deeper understanding of ASD, with implications for refining diagnostic strategies and advancing our understanding of psychiatric disorders.

Methods: In our investigation, we use METAFormer (Mahler et al. 2023), a multi-atlas transformer model for ASD classification, trained on the ABIDE-I (DiMartino et al., 2013) dataset (406 ASD, 476 TC subjects) and preprocessed using the PCP-DPARSF pipeline. METAFormer achieves 83.7% accuracy with functional connectomes from the AAL, CC200, and DOS160 atlases. To identify critical input ROIs, we use common feature attribution methods - Integrated Gradients, DeepLIFT, Feature Ablation, Gradient SHAP, and DeepLIFT-SHAP (Lundberg & Lee, 2017). Each method provides insight into feature contributions. For quantitative evaluation, we use two metrics (Yeh et al., 2019): 1) Infidelity, measured by the mean squared error between the influence of input perturbations on explanations and corresponding changes in the prediction function, assesses the accuracy of explanations under significant perturbations. 2) Sensitivity measures how attribution is affected by insignificant perturbations from a test point. We randomly sample training, validation, and test sets for model training and attribution generation, calculating infidelity and sensitivity for each data point and attribution method. Since many attribution methods require a manual choice of baseline, we examine its effect on explanation quality by evaluating methods over a baseline range of [-1, 1].

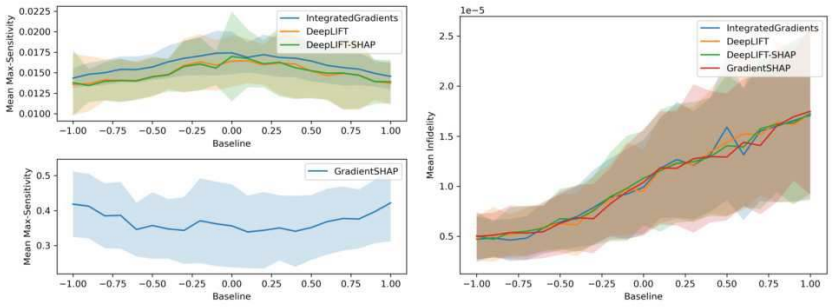

(a) METAFormer Sensitivity (b) METAFormer Infidelity

Figure 1: Comparison of Sensitivity and Infidelity for explanations provided by different feature attribution methods on METAFormer. The inputs to the model are normalized connectomes of the AAL, CC200 and DOS160 atlases where −1 represents strongest anticorrelation and 1 strongest correlation between given ROIs for a subject.

Results: From Figure 1 we can see that DeepLIFT provides the optimal trade-off between infidelity and sensitivity. It can also be seen that a baseline choice of 0, representing the mean correlation for a given subject, does not yield optimal explanations for all methods except for Integrated Gradients. To minimize infidelity and sensitivity a baseline value of -1, representing strongest anticorrelation for a given subject, provides the most robuts and faithful explanations. When looking at the most important features, as shown in Figure 2 and Table 1, the attributions provided by DeepLIFT are very consistent with existing autism literature. The influence of the default mode network, cerebellum, frontal and occipital regions in discriminating between ASD and controls is very prominent.

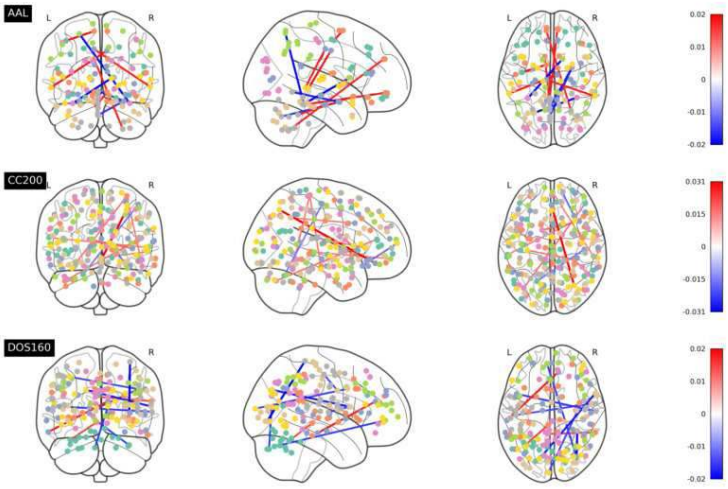

Figure 2: Visualization of the top 10 features with the highest absolute attribution scores for the ASD class in METAFormer. Positive attribution scores indicate that the feature's value is contributing to increasing the model's output from the baseline value and vice versa for negative scores.

# ↓	AAL Connections	DOS160 Connections
1.	Fusiform L ↔ Caudate R	Post Occipital ↔ TPJ
2.	Fusiform R ↔ Parietal Sup L	Post Cingulate ↔ Inf Cerebellum
3.	Supp Motor Area L ↔ Precentral L	Precentral Gyrus ↔ Thalamus
4.	Cingulum Mid R ↔ Temporal Mid L	aPFC ↔ Lat Cerebellum
5.	Amygdala R ↔ Vermis 4 5	Mid Insula ↔ Post Occipital
6.	Vermis 1 2 ↔ Frontal Med Orb R	Temporal ↔ mPFC
7.	Cingulum Mid L ↔ Temporal Mid R	IPL ↔ occipital
8.	Frontal Sup Medial L ↔ Cerebelum 8 R	vFC ↔ Vent aPFC
9.	Olfactory L ↔ Vermis 10	Occipital ↔ Med Cerebellum
10.	Amygdala R ↔ Vermis 8	dFC ↔ Parietal

Table 1: Top 10 connections for the AAL and DOS160 atlases as determined by extracting the features with highest absolute attribution scores using DeepLIFT for METAFormer. Connections are sorted descending by their importance. Names of the connections correspond to the labels from the respective atlas.

Conclusions: We have shown that DeepLIFT is able to extract ROIs from the trained METAFormer model best in terms of explanation sensitivity and fidelity. The explanations provided are very consistent with existing literature. The demonstrated influence of the default mode network, cerebellum, frontal and occipital regions in discriminating between ASD and controls could be a significant step towards the development of model-based imaging biomarkers. This opens further avenues for quantitatively guided deep learning-based imaging biomarker discovery.

References

1. Mahler, L. et al. (2023). Pretraining is All You Need: A Multi-Atlas Enhanced Transformer Framework for Autism Spectrum Disorder Classification. In: Abdulkadir, A., et al. Machine Learning in Clinical Neuroimaging. MLCN 2023. Lecture Notes in Computer Science, vol 14312. Springer, Cham.
2. Lundberg, S., & Lee, S. (2017). A unified approach to interpreting model predictions. Neural Information Processing Systems, 30, 4768–4777. https://papers.nips.cc/paper/7062-a-unified-approach-to-interpreting-model-predictions.pdf
3. Yeh, C. K., Hsieh, C. Y., Suggala, A., Inouye, D. I., & Ravikumar, P. K. (2019). On the (in) fidelity and sensitivity of explanations. Advances in Neural Information Processing Systems, 32.
4. Di Martino, A., Yan, C. G., Li, Q., Denio, E., Castellanos, F. X., Alaerts, K., ... & Milham, M. P. (2014). The autism brain imaging data exchange: towards a large-scale evaluation of the intrinsic brain architecture in autism. Molecular psychiatry, 19(6), 659-667.

Poster No 1742

Maintaining spatially fine-grained connectivity gradients improves brain-behavior predictions

Karl-Heinz Nenning[1], Ting Xu[2], Arielle Tambini[1], Alexandre Franco[1], Daniel Margulies[3], Stanley Colcombe[1], Michael Milham[2]

[1]Nathan Kline Institute, Orangeburg, NY, [2]Child Mind Institute, New York, NY, [3]Université Paris Cité, CNRS, Paris, France

Introduction: Dimensionality reduction techniques are increasingly utilized to characterize meaningful organizational principles within high-dimensional brain connectivity data. The dimensions of such low-dimensional representations - connectivity gradients - capture topographical patterns of intrinsic brain organization (Margulies et al., 2016; Bernhardt et al., 2022). Their calculation usually relies on a n-by-n affinity matrix that is constructed by pairwise connectivity between n nodes. The computational cost increases exponentially with the number of nodes, and for high-resolution data spaces such as the

90,000 grayordinates of the Human Connectome Project, more than 100GB of memory is required for the calculation. This renders voxel-wise calculation of gradients often intractable on consumer hardware, typically requiring users to downsample the data, e.g. through a parcellation strategy. While parcellation and the entailed data averaging can increase signal-to-noise ratio, concerns about the loss of detail and the appropriate choice of parcellation remain.

Methods: Here, we propose Fast Connectivity Gradient Approximation (FCGA), a computationally efficient approach to establish high-resolution connectivity gradients, leveraging consumer-grade hardware. At its core, the approach uses a subset of connectivity targets to approximate the underlying connectivity structure at full scale (Figure 1a). We evaluated our approach on the group and individual level, using two different datasets: the Human Connectome Project (HCP; Glasser et al., 2013) and the Enhanced Nathan Kline Institute - Rockland Sample (NKI-RS; Nooner et al., 2010). We evaluated the performance of different connectivity targets based on parcellations and individual vertices, randomly and uniformly distributed across the cortex. We quantified the spatial similarity (Spearman's ρ) between approximated gradients (G_fcga) and gradients based on the full connectivity matrix (G_fullfc). Furthermore, we studied the practical implications of gradients based on parcellated data by comparing the predictive performance (age and intelligence) to parcellated fine-scale gradients.

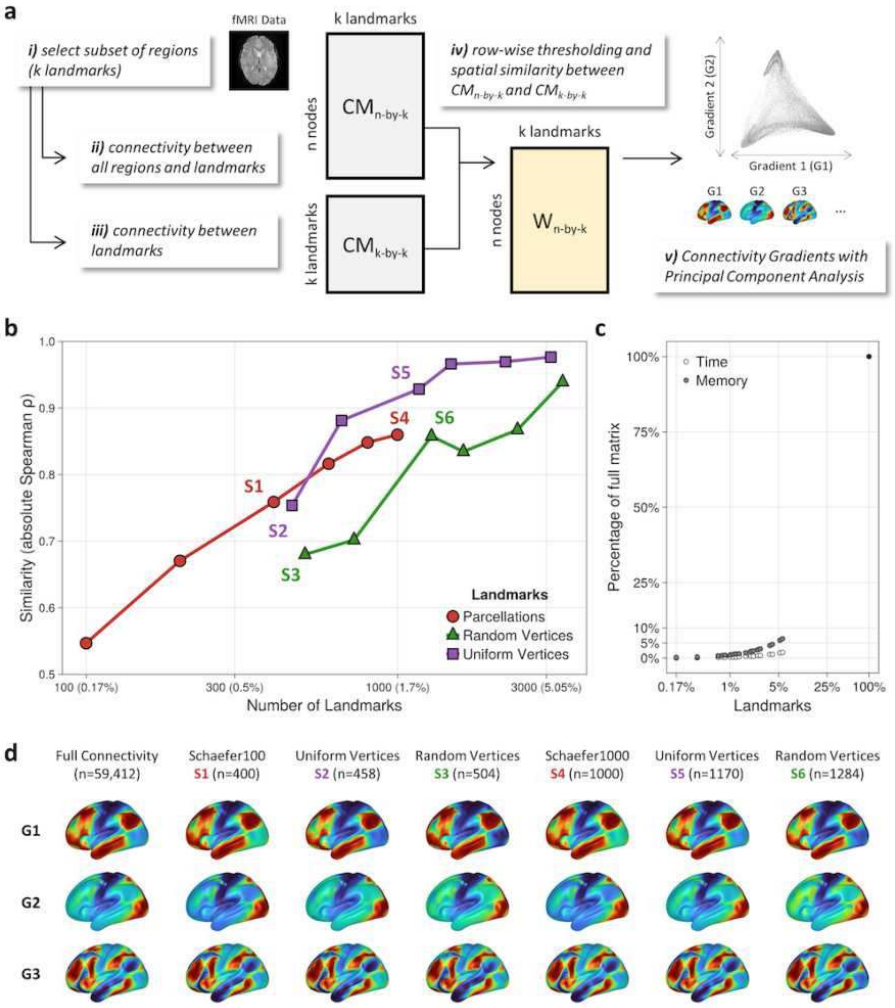

Results: The spatial similarity between G_fcga and G_fullfc increased with the number of connectivity targets used to calculate the approximated gradients (Figure 1b). Remarkably, when using 1000 Schaefer parcels as connectivity targets (~1.7% of the full connectivity matrix), the average spatial similarity across 25 connectivity gradients was $\rho > 0.85$. Increasing the number of targets further to 3000 uniformly sampled vertices (~5% of the full matrix), an average spatial similarity $\rho > 0.98$ was achieved with <10% computational time and memory usage, compared to the calculation of G_fullfc (Figure 1c). On the individual level (HCP, n=100), reliability and discriminability analysis confirmed the repeatability and the preservation of individual features for G_fcga (Figure 2ab). Importantly, in brain-behavior prediction using a lifespan cohort (NKI-RS, n=313, age 6-86y), averaged fine-scale gradients G_fcga with parcels outperformed gradients calculated from parcellated time series (Figure 2c). This was observed for both age and intelligence across various parcellations.

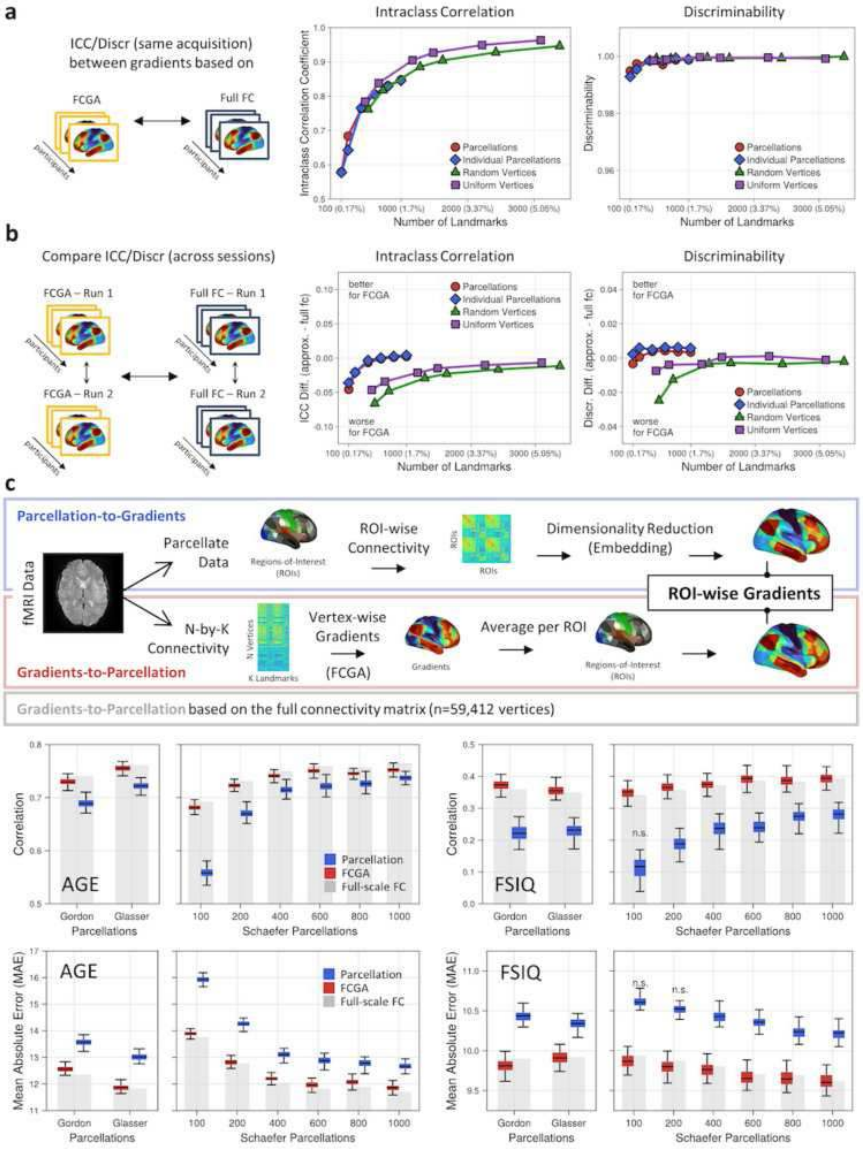

Conclusions: Overall, approximation of full-scale connectivity gradients is computationally efficient, feasible on commodity hardware, showing a $\rho > 0.98$ spatial similarity with the full gradient results at a fraction (~10%) of the computational costs. Importantly, calculating large-scale gradients preserves more relevant information for predicting age and intelligence as gradients calculated from parcellated data. The high fidelity with gradients based on the full connectivity matrix paired with its ability to run on consumer hardware can both democratize this powerful approach and advance new insights across a range of applications.

References

1. Bernhardt, B.C. (2022). 'Gradients in brain organization'. Neuroimage. vol. 251, 118987.
2. Glasser, M.F. (2013), 'The minimal preprocessing pipelines for the Human Connectome Project', Neuroimage, vol. 80, pp.105-124.
3. Margulies, D.S. (2016), 'Situating the default-mode network along a principal gradient of macroscale cortical organization', Proceedings of the National Academy of Sciences, vol. 113, no. 44, pp. 12574-12579.
4. Nooner, K.B. (2012). 'The NKI-Rockland Sample: A Model for Accelerating the Pace of Discovery Science in Psychiatry', Frontiers in Neuroscience, vol. 6, 152.

Poster No 1743

Movie Content Influence Relation Between Connectome Similarities and Metastability in fMRI

Tiago Pereira[1], André Cravo[2], Claudinei Biazoli[2]

[1]Federal University of ABC, São Bernardo do Campo, São Paulo, [2]Center of Mathematics, Computing and Cognition. Federal University of ABC, São Bernardo do Campo, São Paulo

Introduction: Better characterizing brain dynamics, particularly in fMRI, is a crucial step to advancing neuroscience[1]. A promising approach models the brain as a metastable system that alternates between integration and segregation of regions.[2] Recent work with MEG links non-linear features of the signal with brain FC identification (i.e. connectome brain fingerprinting).[3,4] Movie stimuli provide technical, methodological, cognitive and affective advantages.[5,6] However, each film has a specific narrative and different range of low and high features that must be considered. This work intends to investigate the correlation between metastability, identifiability at the global and large-scale functional network levels with naturalistic fMRI. Moreover, we sought to investigate how this relation is modulated by movie content.

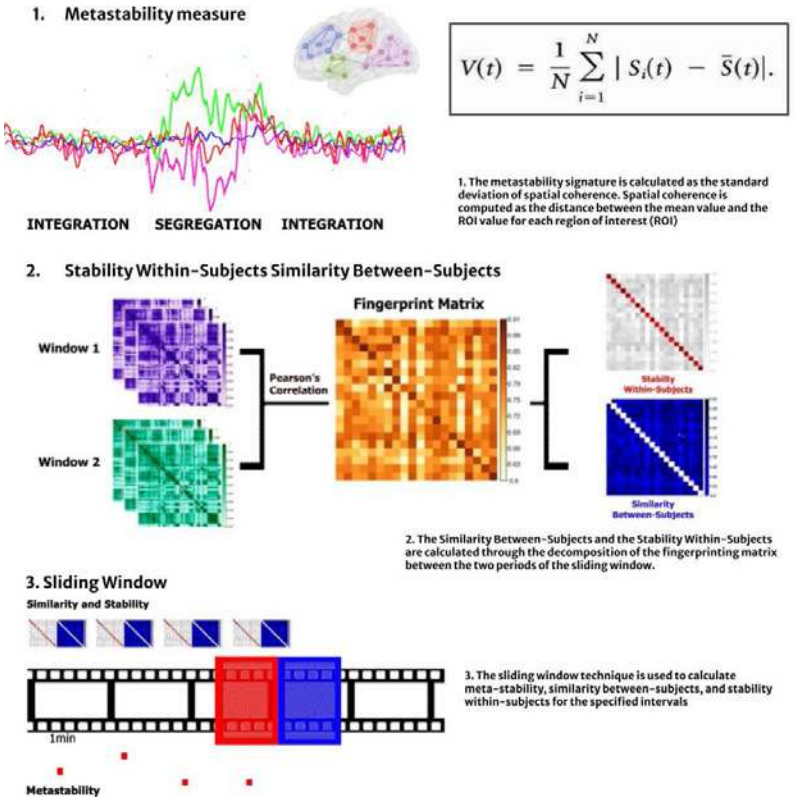

Methods: The Naturalistic Neuroimaging Database, comprising 86 participants (42 females, 18–58 years, M=26.81, SD=10.09 years, TR =1s, 10 movies stimuli), was used. The spatial coherence was calculated as the distance between each ROI value at each timepoint and the standard deviation (metastability) was based on a specific time window.[7] The Similarity Between-Subjects and Stability Within-Subjects were respectively defined as the mean of the correlation's values of the FC matrix in 333 regions between (86 pairs) and within subjects (7310 pairs), on the same time window as the metastability for the whole-brain and for 8 functional networks (>23 ROIs). Both measures were calculated throughout 91 minutes (shortest film) merging the 10 movies, and then separately for two movies, a romantic-comedy (500 Days of Summer, 91 minutes, 5470 timepoints) and a documentary (Citizenfour, 113 minutes, 6780 timepoints).

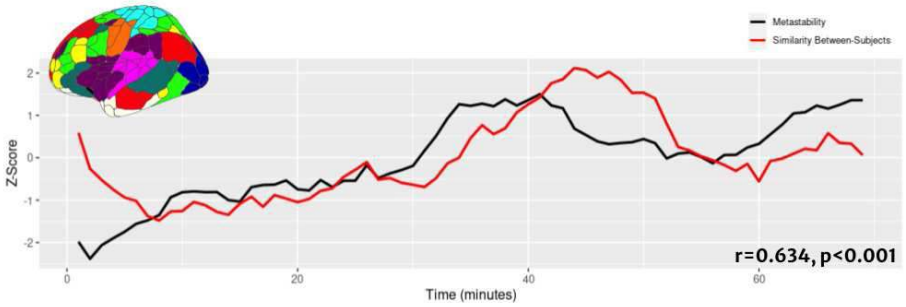

Figure 1. Correlation between the metastability measure (standard deviation of spatial coherence) and the similarity between-subjects for the whole brain of 86 subjects across 10 films in a sliding window of 11 minutes covering 90 minutes, and in a parcellation of 333 ROIs.

NETWORKS	ROIs	r	p
Auditory	24	-0.416	0.001
Motor	38	0.315	0.008
Visual	39	0.522	0.001
DMN	41	0.535	0.001
Cingulo Opercular	40	0.658	0.001
Dorsal Attentional	32	0.710	0.001
Frontoparietal	24	0.866	0.001

Table.1 Correlation between the metastability measure (standard deviation of spatial coherence) and similarity between-subjects at network levels, where attentional networks exhibit a stronger link with the relationship of the measures.

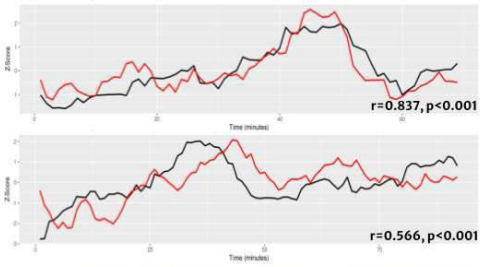

Figure 2. Correlation between the meta-stability measure (standard deviation of spatial coherence) and similarity between-subjects at network levels, where attentional networks exhibit a stronger link with the relationship of the measures.

NETWORKS	ROIs	r	p
Ventral Attentional	23	-0.252	0.029
Auditory	24	-0.343	0.004
Visual	39	0.404	0.001
Frontoparietal	24	0.425	0.001
Dorsal Attentional	32	0.496	0.001
Motor	38	0.560	0.001
DMN	41	0.740	0.001
Cingulo Opercular	40	0.770	0.001

NETWORKS	ROIs	r	p
Ventral Attentional	23	-0.052	0.668
Auditory	24	-0.227	0.059
Visual	39	0.022	0.854
DMN	41	-0.126	0.298
Dorsal Attentional	32	0.101	0.406
Motor	38	0.209	0.083
Frontoparietal	24	0.323	0.006
Cingulo Opercular	40	0.601	0.001

Table.2 Correlation between the whole-brain metastability (standard deviation of spatial coherence) and the similarity between-subjects. The Hollywood movie showed a significant correlation in all networks, while the documentary exhibited correlation only in the Frontoparietal and Cingulo Opercular networks.

Results: For the whole brain, metastability and the similarities between subjects were moderately correlated (r = 0.634, p<0.001) at a 11-minute sliding-window. At the network level, 7 out of the 8 networks analyzed presented moderate to strong correlations between these measures, with the highest values observed for the networks related with attentional process: Fronto Parietal (r = 0.866, p<0.001), Dorsal Attentional (r = 0.710, p<0.001) and Cingulo Opercular (r = 0.658, p<0.001). On the other hand, evidence for coupling between metastability and Stability Within-Subjects was found only for Primary Motor (0.534, p<0.001) and Auditory (0.428, p<0.001) networks. In the 2 films separately, the romantic-comedy showed a much higher correlation (r=0.837, p<0.001) between metastability and Similarity Between-Subjects compared to the documentary (r=0.566, p<0.001). When correlating global metastability with the Similarity Between-Subjects of each network for each movie, all the 8 networks presented a correlation in the first movie while the documentary only correlated in 2 networks.

Conclusions: In this work and for this sample, a significant correlation was found between metastability levels and Similarity Between-Subjects during movie watching for the whole-brain and at network levels, more distinctly in attentional networks. Furthermore, metastability and Stability Within-Subjects correlated only for primary sensory-motor cortical networks. These results expand the finding of a relation between identifiability and non-linear dynamics observed in MEG. The results also match with developmental processes, with sensory-motor networks that stabilized earlier in brain development showing greater Stability Within-Subjects while attentional networks are more strongly shaped by environmental stimuli. Finally, the relation between identifiability and metastability varied with the content of the stimuli, suggesting that different features of the movies are related with fMRI nonlinear dynamics.

References

1. Finn, (2023), “Functional neuroimaging as a catalyst for integrated neuroscience”, Nature, vol. 623, pp. 263-273.
2. Hancock, (2022), “Metastability, fractal scaling, and synergistic information processing: What phase relationships reveal about intrinsic brain activity”, Neuroimage, vol 259, pp. 119433.
3. Sorrentino, (2023), “Brain fingerprint is based on the aperiodic, scale-free, neuronal activity”, Neuroimage, vol 277, pp. 120260.
4. Tepper, (2023), “Intra and inter-individual variability in functional connectomes of patients with First Episode of Psychosis”, NeuroImage: Clinical, vol 38, pp. 103391.
5. Frew, (2022), “Getting the nod: Pediatric head motion in a transdiagnostic sample during movie- and resting-state fMRI”, PLOS One, vol. 17, pp. e0265112.
6. Eickhoff, (2020), “Towards clinical applications of movie fMRI”, Neuroimage, vol 217, pp. 116860.
7. Hellyer, (2014), ‘The Control of Global Brain Dynamics: Opposing Actions of Frontoparietal Control and Default Mode Networks on Attention’, Journal of Neuroscience, vol. 34, pp. 451-466.

Poster No 1744

Altered Expression of Brain Network Dynamics in Affective and Psychotic Illnesses

Carrisa Cocuzza[1], Sidhant Chopra[1], Ashlea Segal[1], Rowena Chin[1], Avram Holmes[2]

[1]Yale University, New Haven, CT, [2]Department of Psychiatry, Brain Health Institute, Rutgers University, Piscataway, NJ

Introduction: Emerging evidence suggests that spatiotemporal shifts in brain network interactions enable the adaptive recruitment of processing resources, a property of brain functioning which may be impaired in psychiatric illness[1,2]. Despite the importance of linking such brain dynamics to behavior, research has largely examined static brain connectivity patterns exhibited during resting-state. Thus, the clinical relevance of across-state network dynamics remains unclear. Further, a longstanding barrier in linking neurobiology to psychopathology is the insufficient explanatory power of discrete diagnostic boundaries[3]. Thus, investigating transdiagnostic data with densely measured symptomatology is critical for the advancement of clinical neuroscience.

Methods: We examined neuroimaging and behavioral data from the Transdiagnostic Connectome Project[4], which used the Human Connectome Project's processing pipelines[5]. N=203 participants (129 with affective/psychotic diagnoses, 74 without diagnoses) whole-brain functional connectomes from resting- and task-state (Stroop; emotional face matching) fMRI were decomposed using nonnegative matrix factorization (NMF) to identify dynamical constraints ("motifs") on network interactions across states[6]. We applied dimensional phenotyping[3] to 94 subscale measures given by 28 self-report and clinician-assessed tests that span psychopathology. We used agglomerative clustering on individual difference correlations of all pairs of measures and the elbow method to optimize the number of clusters. Probabilistic principal component (PC) analysis estimated each participant's expression of each cluster; expression patterns can be considered phenotypic fingerprints.

Results: We found five phenotypic clusters with the following ontology: cluster (1) represents internalizing traits; (2) externalizing traits; (3) negative valence constructs; (4) positive valence constructs; (5) cognitive ability (Fig 1). This pattern is consistent with two prominent frameworks: the Hierarchical Taxonomy of Psychopathology[7] and the Research Domain Criteria[8]. Phenotypic fingerprints were variably expressed across participants, suggesting that cognitive features vary along a continuum of health and disease. We used NMF results in a preliminary case-control analysis (Fig 2). In patients, motif expression was less variable across task contexts, suggesting that dedifferentiated (i.e., flattened) network dynamics are linked with failures to meet varied cognitive demands. We extended this to dimensional phenotypes, and found that internalizing and externalizing traits were positively and negatively correlated with across-state variability in expression of motif one, respectively. Motif one also exhibited the greatest network efficiency[9], suggesting that the extent that motif one confers information flow is a dynamical constraint that is dissociably linked with internalizing/externalizing traits. Individual differences in negative valence were positively linked with variability in motif five; positive valence with motif four; and cognitive ability with motif three. This provides novel evidence that dynamical constraints upon across-state network interactions are differentiably linked to the phenotypic hierarchy.

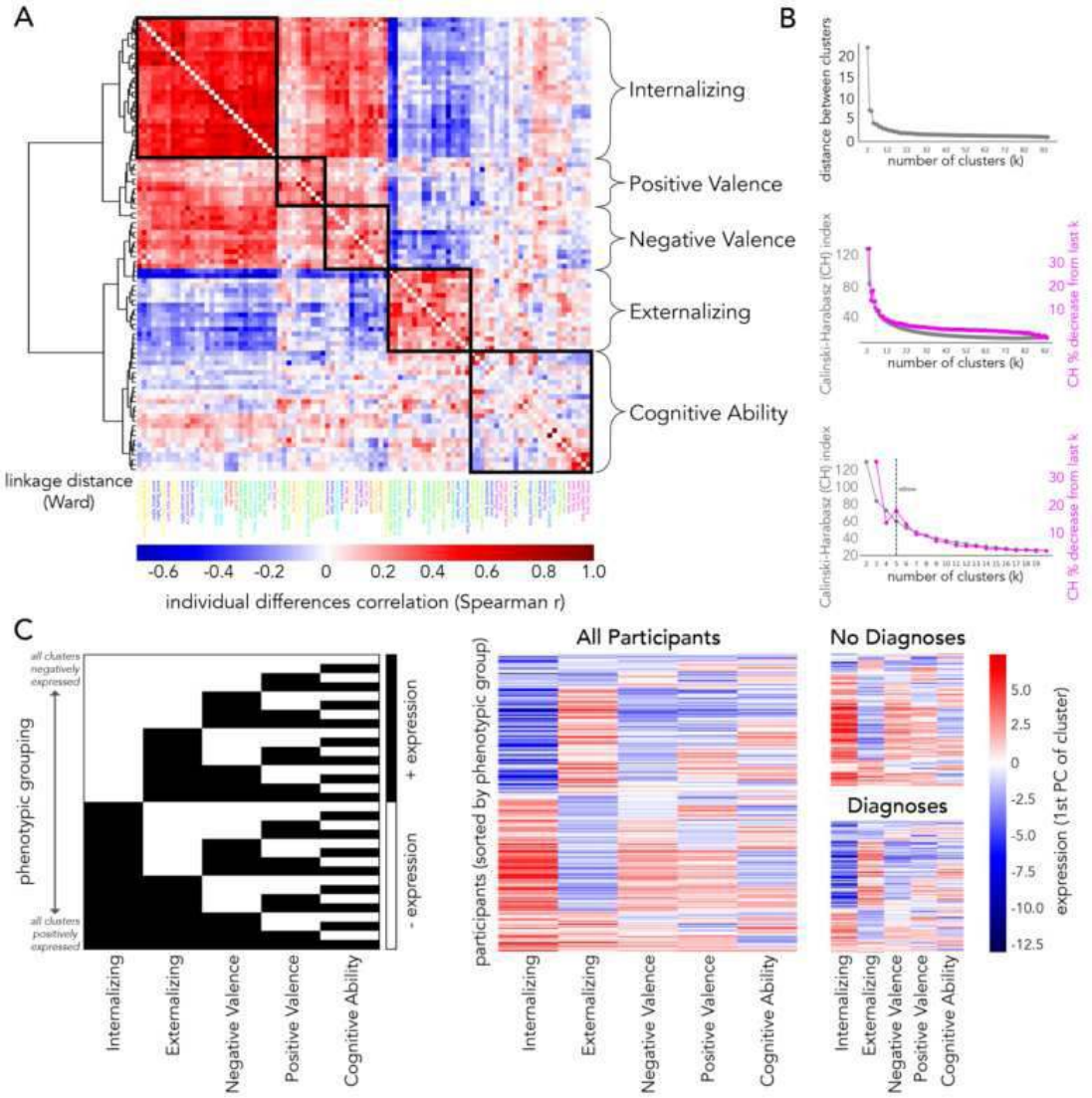

Figure 1. Dimensional phenotyping reveals hierarchically-expressed clinical fingerprints across health and disease. (**A**) Individual difference correlations (Spearman r) of 94 behavioral measures (pre-normalized via min-max feature scaling). Higher r-values indicate two measures were similarly expressed across participants. This distance array was hierarchically clustered via Ward linkage. Clusters are outlined by black boxes. (**B**) *Top*: As expected, the linkage distance between clusters monotonically decreased as the number of clusters (k) increased. *Middle and bottom*: Following a popular heuristic for agglomerative clustering, the optimal number of clusters (k=5) was chosen based on the presence of an "elbow" (black dashed line) when comparing the Calinski-Harabasz (CH) index (gray) and percent decrease in CH index from the last choice of k (magenta). (**C**) To uncover phenotypic fingerprints expressed by each participant, we first performed probabilistic principal component (PC) analysis on the set of variables loaded onto each cluster. The first PC for each cluster (projected back onto the original data space) provided an estimate of the extent that each participant expressed each cluster. We binarized these by positive/negative expression, revealing 32 unique phenotypic groupings (*left*). We sorted participants by these 32 groupings (*middle*), demonstrating a continuum of phenotypic fingerprints across the entire dataset, which included participants with and without mental health diagnoses. When partitioning phenotypic fingerprints by participants with and without diagnoses (*right*), patients expressed externalizing traits more than healthy controls.

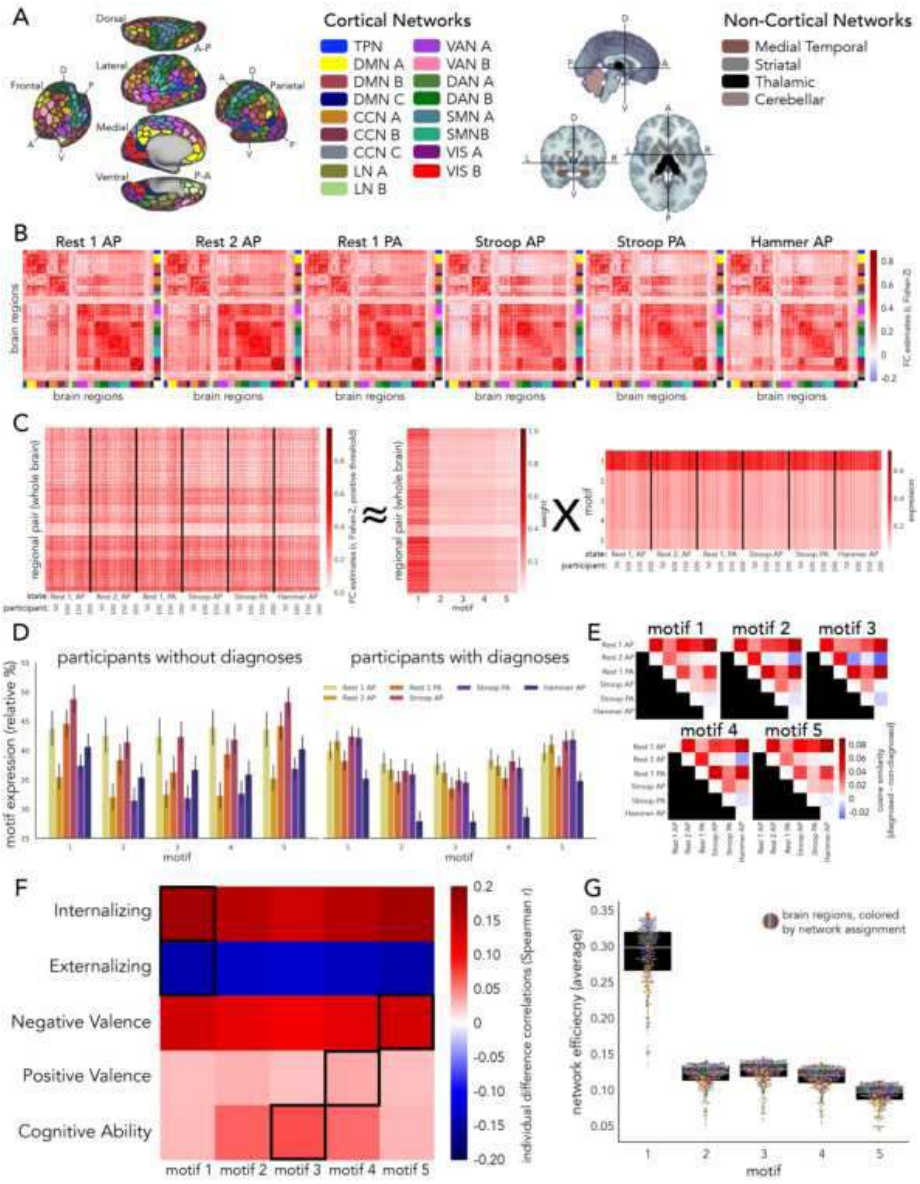

Figure 2. Dynamic constraints upon across-state shifts in brain network interactions link with phenotypic fingerprints. (A) Whole-brain regional parcellation (black borders, 432 regions) and network partition (filled in colors, 21 networks) across the cortex (*left*) and non-cortex (*right*). TPN: temporal parietal network, DMN: default mode network, CCN: cognitive control network, LN: limbic network, VAN: salience/ventral attention network, DAN: dorsal attention network, SMN: somatomotor network, VIS: visual network. (B) Functional connectivity (FC) estimates for 6 neurocognitive states (across-participant averages). (C) Non-negative matrix factorization (NMF) pipeline, following Khambhati et al., (2018). Upper triangles of each functional connectome were vectorized into 93,096 regional pairs, and stacked by state and participant (i.e., across-state configuration matrix, *left*). Split-half cross-validation was performed over 100 permutations to optimize the number of motifs (k=5), a regularization parameter (alpha=0.2), and a loss parameter (beta=1.2). With these parameters, NMF decomposed the configuration matrix into a motif weight matrix (*middle*) and a motif expression matrix (*right*). (D) Preliminary case-control analysis comparing the motif expressions of participants without and with mental health diagnoses. (E) To quantify the extent that patients exhibited dedifferentiation of network dynamics, we computed the cosine similarity of each state-to-state expression (across participants in each group), per motif. Then, we subtracted non-diagnosis similarities from diagnosis similarities. Across the majority of state-to-state pairs, patients had more similar motif expression patterns. (F) We extended the observations in panel E using variance of across-state motif expression to quantify dedifferentiation (i.e., low variance) at the individual participant level. Individual difference correlations with each phenotypic cluster revealed a pattern of unique linkage between each cluster and each motif. (G) Motifs in panel C (*middle*) were reorganized into region-by-region network architectures, allowing us to apply a network metric that quantifies efficiency for each region's connectivity patterns. Motif one exhibited the greatest efficiency, suggesting that it constrains FC dynamics by allowing efficient exchange of information. Generally, regions in subcortical networks and cortical LNs exhibited the lowest efficiencies; cortical CCNs, VANs, DANs, SMNs, VIS', and TPN exhibited the highest; and cortical DMNs exhibited medium efficiency.

Conclusions: Brain network dynamics were dedifferentiated transdiagnostically, suggesting there is a failure to flexibly recruit and coordinate processing resources to meet increased task demands in patients. The motifs constraining these dynamics were linked in a distinct manner across phenotypic dimensions. Interestingly, dedifferentiated network dynamics were associated with externalizing traits, suggesting that failures to coordinate dynamic processes are linked with individual differences in a specific set of psychiatric features, including disinhibition, dysregulated attention, and noncooperation[10]. Our findings emphasize the importance of uncovering the dynamical constraints upon brain network reconfigurations in health and disease.

References
1. Yin, D., & Kaiser, M. (2021). Understanding neural flexibility from a multifaceted definition. NeuroImage, 235, 118027.
2. Reinen, JM., Chén, OY., ... Holmes, AJ. (2018). The human cortex possesses a reconfigurable dynamic network architecture that is disrupted in psychosis. Nature Communications, 9(1), 1157.
3. Parkes, L., Satterthwaite, TD., & Bassett, DS. (2020). Towards precise resting-state fMRI biomarkers in psychiatry: synthesizing developments in transdiagnostic research, dimensional models of psychopathology, and normative neurodevelopment. Current Opinion in Neurobiology, 65, 120–128.
4. Chopra, S., Dhamala, E., Lawhead, ... Holmes, AJ. (2022). Reliable and generalizable brain-based predictions of cognitive functioning across common psychiatric illness. In medRxiv (p. 2022.12.08.22283232).
5. Glasser, MF., Sotiropoulos, SN., Wilson, JA., Coalson, TS., Fischl, B., Andersson, JL., Xu, J., Jbabdi, S., Webster, M., Polimeni, JR., Van Essen, DC., Jenkinson, M., & WU-Minn HCP Consortium. (2013). The minimal preprocessing pipelines for the Human Connectome Project. NeuroImage, 80, 105–124.
6. Khambhati, AN., Medaglia, JD., Karuza, EA., Thompson-Schill, SL., & Bassett, DS. (2018). Subgraphs of functional brain networks identify dynamical constraints of cognitive control. PLoS Computational Biology, 14(7), e1006234.
7. Kotov, R., Krueger, RF., ... Zimmerman, M. (2017). The Hierarchical Taxonomy of Psychopathology (HiTOP): A dimensional alternative to traditional nosologies. Journal of Abnormal Psychology, 126(4), 454–477.
8. Sanislow, CA., Ferrante, M., Pacheco, J., Rudorfer, MV., & Morris, SE. (2019). Advancing Translational Research Using NIMH Research Domain Criteria and Computational Methods. Neuron, 101(5), 779–782.
9. Wang, L., Wu, L., Lin, X., Zhang, Y., Zhou, H., Du, X., & Dong, G. (2016). Altered brain functional networks in people with Internet gaming disorder: Evidence from resting-state fMRI. Psychiatry Research. Neuroimaging, 254, 156–163.
10. Krueger, RF., Hicks, BM., Patrick, CJ., Carlson, SR., Iacono, WG., & McGue, M. (2009). Etiologic connections among substance dependence, antisocial behavior, and personality: Modeling the externalizing spectrum. In G. A. Marlatt (Ed.), Addictive behaviors: New readings on etiology, prevention, and treatment, (pp (Vol. 778, pp. 59–88). American Psychological Association, xii.

Poster No 1745

The Effect Of Ketamine on Brain Functional Dynamics

Nooshin Javaheripour[1], Zümrüt Duygu Sen[1], Frederick Lange[2], Meng Li[3], Lena Danyeli[1], Carina Heller[4], Lejla Colic[5], Habib Ganjgahi[6], Martin Walter[7]

[1]Department of Psychiatry and Psychotherapy, Jena University Hospital, Jena, Thuringen, [2]Wellcome Centre for Integrative Neuroimaging University of Oxford, Oxford, Oxfordshire, [3]Jena University Hospital, Jena, Thuringia, [4]Friedrich Schiller University Jena, Jena, Germany, [5]Jena University Hospital, Jena, Germany, [6]University of Oxford, Oxford, United Kingdom, [7]Department of Psychiatry and Psychotherapy, Jena University Hospital, Jena, Germany

Introduction: A single sub-anaesthetic dose of ketamine induces transient alterations in cognitive functions and sensory perception. This study aims to comprehensively examine ketamine's impact on brain dynamics, particularly its brief dissociative effects, using the hidden Markov model (HMM). Functional dynamics during intravenous esketamine and 24 hours post-infusion in resting-state fMRI are investigated, along with the association of dynamic features with subjective experiences measured by the Altered States of Consciousness Scale (5D-ASC).

Methods: A double-blinded randomized placebo-controlled crossover study was designed on 34 healthy participants (mean ± SD = 25.1 ± 4.2 years). The participants were randomized into two groups by treatment order (ketamine-placebo and placebo-ketamine) for two periods (day 1: baseline and infusion and day 2: 24h post-infusion) in each treatment arm (ketamine and placebo) with a three-week washout period. On day 1, participants underwent MR scanning (ultra-high field 7T scanner, Siemens) before and during the infusion of either esketamine (at a dose of 0.33 mg/kg body weight, brand name "Ketanest S Pfizer") or 0.9% saline solution. On day 2, the same neuroimaging protocol was used. MRI data were preprocessed by the FSL pipeline, and artefacts were removed using ICA-FIX. To obtain time series for cortical regions, we used Yeo 2011 parcellation scheme with seven functional networks (DMN, FPN, SN, DAN, SMN, VN, and LN). The HMM-Multivariate Autoregressive (HMM-MAR) toolbox was employed for variational Bayes inversion in dynamic brain analysis. The HMM ran for 500 cycles with 4 to 16 states, and the optimal number was determined based on the minimum free energy criterion, balancing accuracy and complexity. Temporal measures included fractional occupancy (FO), averaged lifetime (ALT), and switching rate (SR). we compared dynamic features between ketamine and placebo arms using the linear mixed-effect model (LME), adjusting for within-subject variability and treatment order. We defined the contrast to examine changes from baselines in infusion and 24-hour post-infusion (ketamine arm [infusion – baseline] vs. placebo arm [infusion – baseline]) and (ketamine arm [24-hour post-infusion - baseline] - placebo arm [24-hour post-infusion-baseline]), respectively, using "emmeans" in R.

Results: The LME results showed significant differences of FO and ALT occur between two arms in infusion sessions, where the FO and ALT of state #2 are lower during ketamine compared to placebo and higher in state #7 (state #2 ketamine infusion < placebo infusion: FO: estimate = -0.05, p = 0.002; ALT: estimate = -1.62, p-value (p) = 0.005; state #7 ketamine infusion > placebo infusion: FO: estimate = 0.05, p = 0.001; ALT: estimate = 1.37, p = 0.002) (Fig2). The findings on contrasts indicate

that in state #2 (DAN+), the FO and ALT of Δ (Infusion – baseline) ketamine were significantly lower compared to Δ placebo (state #2; FO: ketamine < placebo; t-value = -3.19, p = 0.0017; ALT: ketamine < placebo; t-value = -2.81, p = 0.0054). In contrast, in state #7 (SN+), the FO and ALT of Δ ketamine exhibited higher values compared to Δ placebo (state #7; FO: ketamine > placebo; t-value =3.45, p < 0.001; ALT: ketamine > placebo; t-value = 3.09, p = 0.002). In state #3 (FPN+), the ALT of Δ ketamine is lower than Δ placebo (state #3: ALT: ketamine < placebo; t-value = -2.33, p = 0.02). For partial correlations between ASC-5D subscales and the dynamic metrics, we calculated the relative changes (ketamine [infusion – baseline] - placebo [infusion – baseline]). The association between disembodiment and Δ FO of state #7 was significant (t-value = 2.5, p = 0.017) but not with FO or ALT of state #2.

Figure 1: Brain parcellation and averaged functional activity of brain networks in eight brain spatial states

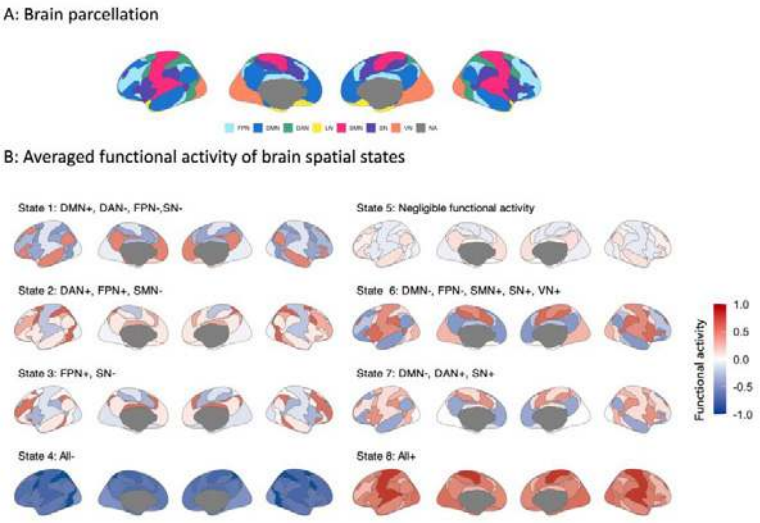

A) This figure illustrates the locations of seven brain networks as defined by Yeo et al. in 2011, which we utilized for extracting the rs-fMRI time series. Abbreviations: Default mode network (DMN), Frontoparietal network (FPN), Dorsal attention network (DAN), Salience network (SN), Somatosensory motor network (SMN), Visual network (VN). B) This figure depicts the averaged functional activity (AFA) of each brain network for each of the eight brain spatial states. The AFA values, ranging from -1 to 1, are represented using a gradient from blue to red. A negative sign (-) indicates that the AFA is less than 0, while a positive sign (+) signifies an AFA greater than 0. White indicates that the AFA is approximately zero, as seen in all networks in state 5. These states reoccur across time and we calculated the Fractional occupancy (FO) and averaged lifetime (ALT) and switching rate to compare the dynamic characteristics of these states between ketamine and placebo arms.

Figure 2: Ketamine impacts on functional brain dynamics

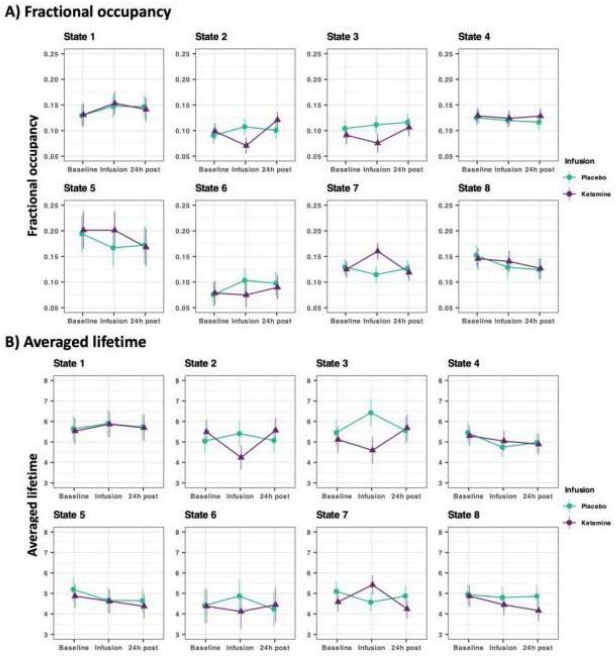

Fractional occupancy (A) and averaged lifetime (B) of eight states across sessions (baseline, infusion and 24h pos-infusion) in ketamine (purple) and placebo arms (green).

Conclusions: These findings highlight the potential of brain dynamic models to investigate the neuropharmacological impacts of ketamine on brain functional activity dynamics associated with subjective experiences.

References

1. Walter, M., Li, S. & Demenescu, L. R. Multistage drug effects of ketamine in the treatment of major depression. Eur Arch Psychiatry Clin Neurosci 264, 55–65 (2014).
2. Daly, E. J. et al. Efficacy of Esketamine Nasal Spray Plus Oral Antidepressant Treatment for Relapse Prevention in Patients With Treatment-Resistant Depression: A Randomized Clinical Trial. JAMA Psychiatry 76, 893–903 (2019).
3. Danyeli, L. V. et al. Association of the delayed changes in glutamate levels and functional connectivity with the immediate network effects of S-ketamine. Transl Psychiatry 13, 60 (2023).
4. Vidaurre, D., Smith, S. M. & Woolrich, M. W. Brain network dynamics are hierarchically organized in time. PNAS 114, 12827–12832 (2017).
5. Cabral, J. et al. Cognitive performance in healthy older adults relates to spontaneous switching between states of functional connectivity during rest. Scientific Reports 7, 1–13 (2017).
6. Li, M. & Walter, M. Chapter 64 - The Acute and Chronic Effects of Ketamine as Revealed by Noninvasive Brain Imaging. in Neuropathology of Drug Addictions and Substance Misuse (ed. Preedy, V. R.) 689–702 (Academic Press, 2016). doi:10.1016/B978-0-12-800212-4.00064-9.
7. Thomas Yeo, B. T. et al. The organization of the human cerebral cortex estimated by intrinsic functional connectivity. J Neurophysiol 106, 1125–1165 (2011)

Poster No 1746

Structure-function decoupling in genetic frontotemporal dementia

Kamen Tsvetanov[1], Simon Jones[2], Maura Malpetti[2], Timothy Rittman[3], Arabella Bouzigues[4], John van Swieten[5], Lize Jiskoot[6], Harro Seelaar[7], Barbara Borroni[8], Enrico Premi[8], Raquel Sanchez-Valle[9], Fermin Moreno[10], Robert Laforce Jr[11], Caroline Graff[12], Matthis Synofzik[13], Daniela Galimberti[14], Mario Masellis[15], Maria Tartaglia[16], Elizabeth Finger[17], Rik Vandenberghe[18], Alexandre de Mendonça[19], Fabrizio Tagliavini[20], Isabel Santana[21], Simon Ducharme[22], Chris Butler[23], Alexander Gerhard[24], Johannes Levin[25], Markus Otto[26], Sandro Sorbi[27], Lucy Russell[28], Jonathan Rohrer[28], James Rowe[29]

[1]University of Cambridge, Cambridge, Cambridgeshire, [2]University of Cambridge, Cambridge, [3]Department of Clinical Neurosciences, University of Cambridge, Cambridge, Cambridgeshire, [4]University College London, London, [5]Erasmus Medical Center, Rotterdam, [6]Erasmus Medical Center, Rotterdam, Netherlands, [7]Erasmus Medical Center, Rotterdam, United Kingdom, [8]University of Brescia, Brescia, Italy, [9]University of Barcelona, Barcelona, Spain, [10]Hospital Universitario Donostia, San Sebastian, Spain, [11]Université Laval, Quebec, Canada, [12]Karolinska Institutet, Stockholm, Sweden, [13]German Center for Neurodegenerative Diseases (DZNE), Tübingen, Germany, [14]University of Milan, Milan, Italy, [15]Sunnybrook Research Institute, Toronto, ., [16]Tanz Centre for Research in Neurodegenerative Disease, Toronto, ., [17]University of Western Ontario, London, ON, [18]UZ Leuven, Leuven, Belgium, [19]University of Lisbon, Lisbon, Portugal, [20]Istituto Neurologico Carlo Besta, Milan, Italy, [21]University of Coimbra, Coimbra, Portugal, [22]McGill University, Montreal, ., [23]University of Oxford, Oxford, United Kingdom, [24]University of Manchester, Manchester, United Kingdom, [25]Department of Neurology, LMU University Hospital, LMU Munich, Munich, Bavaria, [26]University Hospital Halle/Saale, Halle/Saale, Sachsen-Anhalt, [27]University of Florence, Florence, Italy, [28]University College London, London, United Kingdom, [29]Department of Clinical Neurosciences and Cambridge University Hospitals NHS Trust, Cambridge, United Kingdom

Introduction: Functional network integrity is important for maintaining cognitive performance during the 10-20 year presymptomatic period of frontotemporal dementia (FTD), conferring resilience to advancing neuropathology and atrophy[1]. The extent to which functional integrity relies on preserved structural connectivity is unclear. Here, we test the relationship between functional connectivity and structural connectivity, termed structure-function coupling, against genetic risk for FTD and disease progression.

Methods: We studied 56 symptomatic and 165 pre-symptomatic FTD-mutation carriers, and 141 family members without mutations from the GENFI cohort[2]. Diffusion weighted imaging and functional magnetic resonance imaging were acquired and analysed using established approaches (Siemens MR platforms)[3,4] to quantify participant-level structural and functional connectomes (Figure 1-(1)). Connectomes were defined in the Brainnetome Atlas[5] and re-mapped onto a subcortical network and seven resting-state networks based on the Yeo Networks[6] (Figure 1-(2)). An inter-subject regularized canonical correlation analysis (CCA) with permutation-based cross-validation was used to jointly analyse the structural and functional connectomes (Figure 1-(3-4)). Second-level analysis with robust multiple linear regression models[1] tested for differences between non-carriers, pre-symptomatic carriers and symptomatic carriers in the strength of association between structural and functional CCA subject scores. Age, sex, head motion and scanner site were included as covariates.

Results: Canonical correlation analysis identified significant components linking structural and functional connectivity patterns. The first component ($r=0.656$, $p<0.001$) reflected a structural connectivity pattern with high within- and between-

networks loadings (Figure 1-(5)) with strong within-networks functional connectivity and weak-to-negative between-network functional connectivity (Figure 1-(6)). This component associated structural integrity with function segregation, whereby individuals with high structural connectivity within and between networks exhibit greater functional network segregation as shown by strong within-network functional connectivity and weak between network connectivity[7]. The strength of this structure-function coupling was greater for non-carriers compared to pre-symptomatic carriers (Figure 1-(7)). Symptomatic carriers showed minimal relationship between structural and functional scores, indicating structure-function decoupling, consistent with the hypothesis that cognitive decline is triggered by critical decoupling of previously synergistic neural systems.

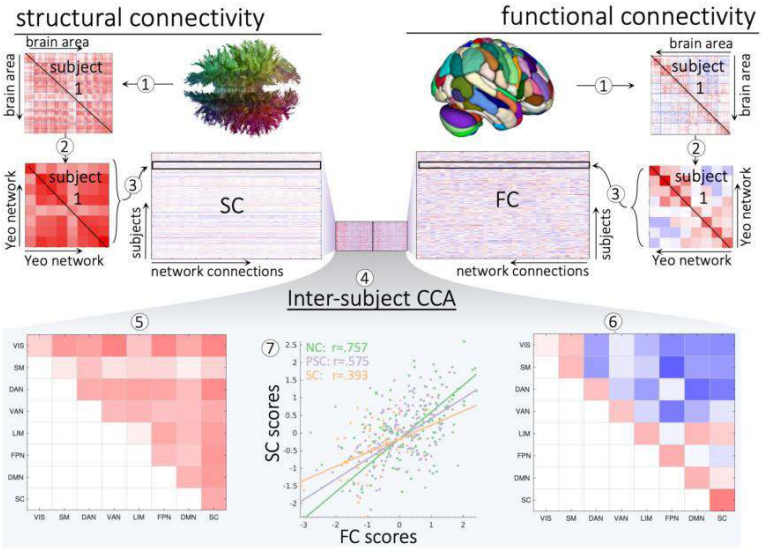

Analytical strategy (top panel) and Results (lower panel). Individuals' estimates of the structural and functional connectivity (1-2, SC, FC) are re-mapped to Yeo networks (2) and concatenated (3, subjects by FC across networks and subjects x SC across networks) as inputs to canonical correlation analysis (4, CCA). CCA identifies sources of signal in SC and FC that are related across individuals in terms of connectivity patterns (5 and 6) and subject scores. The correlation between FC-SC subject scores is stronger for non-carriers (green in 7) versus pre-symptomatic carriers (purple in 7). There is minimal relationship in symptomatic carriers (orange in 7). VIS – visual network; SM – sensorimotor network; DAN – dorsal attention network; VAN – ventral attention network; LIM – limbic network; FPN – frontoparietal network; DMN – default mode network; SC – subcortical network; SC – structural connectivity; FC – functional connectivity; NC – non-cariers; PSC – pre-symptomatic carriers; SC (orange colour) – symptomatic carriers

Conclusions: Our findings demonstrate progressive de-coupling between structural connectivity and functional segregation over the course of genetic frontotemporal dementia. These results have implications for designing pre-symptomatic disease-modifying 'preventative' trials, supported by imaging-based surrogate markers of neural system dynamics.

References

1. K. A. Tsvetanov et al., "Brain functional network integrity sustains cognitive function despite atrophy in presymptomatic genetic frontotemporal dementia," Alzheimer's & Dementia, 2020, doi: 10.1002/alz.12209.
2. J. D. Rohrer et al., "Presymptomatic cognitive and neuroanatomical changes in genetic frontotemporal dementia in the Genetic Frontotemporal dementia Initiative (GENFI) study: a cross-sectional analysis," Lancet Neurol, vol. 14, no. 3, pp. 253–262, 2015, doi: 10.1016/S1474-4422(14)70324-2.
3. J. D. Tournier et al., "MRtrix3: A fast, flexible and open software framework for medical image processing and visualisation," Neuroimage, vol. 202, p. 116137, Nov. 2019, doi: 10.1016/J.NEUROIMAGE.2019.116137.
4. L. Geerligs, K. A. Tsvetanov, Cam-Can, and R. N. Henson, "Challenges in measuring individual differences in functional connectivity using fMRI: The case of healthy aging," Hum Brain Mapp, 2017, doi: 10.1002/hbm.23653.
5. L. Fan et al., "The Human Brainnetome Atlas: A New Brain Atlas Based on Connectional Architecture," Cerebral Cortex, vol. 26, no. 8, pp. 3508–3526, 2016, doi: 10.1093/cercor/bhw157.
6. B. T. Yeo et al., "The organization of the human cerebral cortex estimated by intrinsic functional connectivity," J Neurophysiol, vol. 106, no. 3, pp. 1125–1165, 2011, doi: 10.1152/jn.00338.2011.
7. O. Sporns, "Network attributes for segregation and integration in the human brain," Curr Opin Neurobiol, vol. 23, no. 2, pp. 162–171, 2013, doi: 10.1016/j.conb.2012.11.015.

Poster No 1748

Higher Criticism—an optimal test for sparse and weak effects in connectomics

Andrew Gerlach[1], Helmet Karim[1], Carmen Andreescu[1], Robert Krafty[2]

[1]University of Pittsburgh, Pittsburgh, PA, [2]Emory University, Atlanta, GA

Introduction: Connectome approaches to analyze MRI data have gained increasing popularity[1]. This comes at the cost of increased dimensionality and sparse/weak effects[2]. Machine learning and graph theory have been popular choices for connectome analysis, though their interpretation is challenging.

Methods: We introduce Higher Criticism (HC)[3] as a flexible and intuitive tool for connectome analysis. HC is an omnibus test optimal in the rare-and-weak regime that can be applied to mass univariate testing at the edge level. The primary constraints are that the test must be univariate with respect to the connectome and associated with a valid p-value. HC compares the empirical distribution of p-values with the null using a modified Kolmogrov-Smirnov statistic to quantify the deviation (Figure 1). Importantly, this procedure can be carried out at various levels of the connectome (e.g., whole-brain, network, node). We propose that analysis should begin with a whole-brain HC test, which provides no information on localization, but strong motivation for further testing at a more refined level if the result is positive. This procedure can then be repeated for increasing levels of precision, with multiple comparisons correction for only the number of subunits analyzed at a particular level. We demonstrate HC with data comparing resting state functional connectivity (FC) between 39 never-depressed (ND) and 72 recently remitted depressed (RD) older adults. FC matrices are generated by parcellation of the processed scans with the Schaefer400 atlas[4]. Nodes are grouped into seven canonical Yeo networks[5]. We conduct whole-brain edge-wise independent sample t-tests to differentiate remitters from healthy controls to generate the p-values for HC. We begin with a whole-brain HC test and proceed to network then node levels.

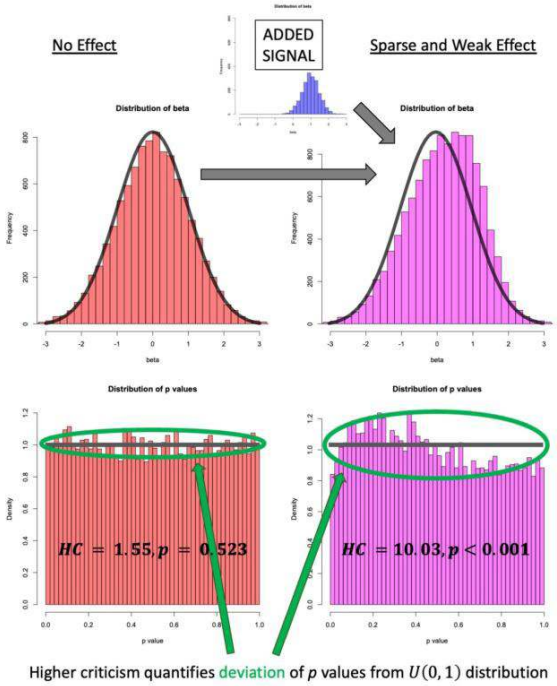

Figure 1. Overview of higher criticism (HC) demonstrated with simulated data for $k = 1000$ tests. Left column shows null case; right column shows case with added signal (90% sparse, effect size equal to 1 standard deviation). The top row shows distribution of simulated beta coefficients; bottom row shows the resulting distribution of p values, which is expected to be uniform in the null case. To calculate the HC statistic, tests are ordered as ascending p values and compared to the uniform expectation with HC as the maximum value of the range of tests. Resulting HC statistics demonstrate the expected effect: non-significant deviation in the null case, strong deviation in the added signal case.

$$HC = \max_{1 \le i \le k} \sqrt{k} \frac{i/k - p_{(i)}}{\sqrt{p_i(1-p_i)}} \text{ for } k \text{ tests}$$

Results: We show how HC can be applied to connectome analysis to detect rare and weak effects, and discuss considerations specific to connectome analysis, specifically: sample size, p-value calculation, and HC variants. Further, we show that HC naturally gives rise to a hierarchical testing procedure through increasing levels of regional specificity that do not require a pre-defined level of analysis and allows for a principled reduction of the multiple comparisons burden. In our example analysis (Figure 2), we show that the RD and ND groups differ at the whole-brain level. We then use HC to compare each intra- and internetwork block of the FC matrices with Bonferroni correction (m = 28), where we observe 12 network pairs with differing connectivity between RD and ND. Finally, we applied HC to individual rows/columns of the intra- and internetwork blocks to identify nodes with aberrant FC with Bonferroni correction for the number of nodes in each block, resulting in the identification of 154 unique nodes with connectivity differences between groups.

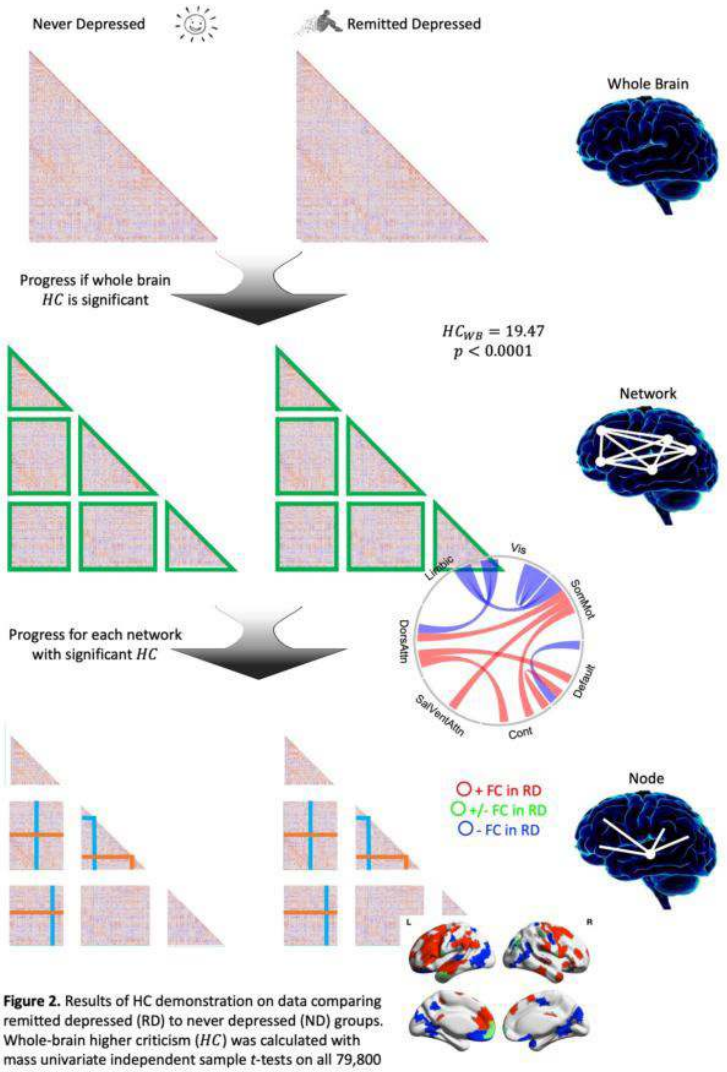

Figure 2. Results of HC demonstration on data comparing remitted depressed (RD) to never depressed (ND) groups. Whole-brain higher criticism (HC) was calculated with mass univariate independent sample t-tests on all 79,800 entries in the functional connectivity (FC) matrix and showed a significant group difference. Next, HC was applied to the tests in each intra- and internetwork block of the FC matrix, as visualized with 3 networks for simplicity, blocks outlined in green. Network pairings with significant differences are shown in the chord diagram with red for greater FC in the RD group, blue for lower FC in the RD group. Finally, HC was applied at the node level to the individual columns and rows network pairings with significant differences, represented with the orange and light blue lines. Nodes with significant FC differences between groups are highlighted in the brain map with red for greater FC in the RD group, blue for lower FC in the RD group, and green for mixed results (e.g., node shows lower within Default FC but greater Default to Control FC).

Conclusions: Higher criticism is a powerful and flexible tool that can be used to exploit the spare and weak signals inherent in connectome-based analysis. HC can naturally be applied in a hierarchical fashion which does not require a strong a priori hypothesis, allows for an optimal balance between regional specificity and power, and reduces the multiple comparisons burden in a principled manner. Thus, interpretable inferences can be made in connectome analysis with reasonable sample sizes. Further, HC allows for relevant, translational interpretations that provides a complementary approach to graph theoretic measures. We demonstrate application of HC with a dataset comparing remitted depressed and never depressed older adults, showing altered connectivity at the whole-brain, network, and node levels. Given the intuitiveness of HC, we suggest a larger applicability in the neuroimaging field. Further use may lead to methodological improvements accounting for the idiosyncrasies of neuroimaging, especially if the inherent correlation structure can be harnessed.

References

1. Smith, S. M. et al. Functional connectomics from resting-state fMRI. Trends Cogn Sci 17, 666–682 (2013).
2. Marek, S. et al. Reproducible brain-wide association studies require thousands of individuals. Nature 603, 654–660 (2022).
3. Donoho, D. & Jin, J. Higher Criticism for Large-Scale Inference, Especially for Rare and Weak Effects. Statistical Science 30, 1–25 (2015).
4. Schaefer, A. et al. Local-Global Parcellation of the Human Cerebral Cortex from Intrinsic Functional Connectivity MRI. Cereb Cortex 28, 3095–3114 (2018).
5. Thomas Yeo, B. T. et al. The organization of the human cerebral cortex estimated by intrinsic functional connectivity. J Neurophysiol 106, 1125–1165 (2011).

Poster No 1749

Impact of Individualized Parcellation on State and Network Specific Brain-Behavior Relationships

Nevena Kraljević[1,2], Robert Langner[1,2], Federico Raimondo[1,2], Kaustubh Patil[1,2], Ru Kong[3], Leon Ooi[3], B. T. Thomas Yeo[3], Simon Eickhoff[1,2], Veronika Müller[1,2]

[1]Institute of Systems Neuroscience, Medical Faculty, HHU Düsseldorf, Düsseldorf, Germany, [2]Institute of Neuroscience and Medicine (INM-7: Brain and Behaviour), Research Centre Jülich, Jülich, Germany, [3]National University of Singapore, Singapore, Singapore

Introduction: Behavior prediction based on brain data can contribute to our understanding of human brain functioning and even to personalized neuroscience. Various approaches have been developed to improve brain-behavior prediction: using task-based functional connectivity (FC) rather than resting-state FC[1]; using feature-reduction methods[2–5]; or individualizing brain features[4-6]. In our previous work, we explored how the correspondence of fMRI state and network priors with predicted target behavior (i.e. state and network specificity) influences behavioral prediction. Despite overall weak predictions, we observed a tendency for state specificity in working memory (WM), but none for theory-of-mind cognition (SOCIAL) or emotion matching (EMO). Employing an algorithm to individualize functional networks[6], we here assessed systematically if stronger brain-behavior relationships for states and networks that fit with the predicted behavioral domain can be found when using individualized brain features for prediction.

Methods: We used openly available behavioral and fMRI data from the Human Connectome Project - Young Adult S1200[7] (340 participants, 186 women, mean age = 28.7 years) dataset. A multi-session hierarchical Bayesian model was employed on resting-state data, factoring in group functional and spatial network information, to estimate individual-specific cortical network parcellations[6]. To obtain the FC features, minimally preprocessed fMRI data was used regressing out age, sex and motion. FC matrices were generated for two parcellation schemes (non-individualized vs. individualized), and two connectome representations (whole brain 400-Schaefer atlas[8] vs. three task-related networks[9]) each from four task fMRI states (resting/WM/SOCIAL/EMO). In a machine-learning approach applying partial least squares regression, the FC matrices were used as features to predict (z-transformed) performance of three tasks performed in the scanner: WM, SOCIAL, and EMO. Prediction performance was evaluated by coefficient of determination (COD) and mean root mean squared error (RMSE) between predicted and observed score and from the cross-validation.

Results: Task states predicted WM performance better than resting state (lower RMSE, see Fig 1A), while for SOCIAL and EMO it was the other way around (Fig. 1B-C). Whole-brain FC patterns predicted WM and EMO a bit better than did task-based networks (Fig. 2). However, none of those differences were significant. Generally, the prediction models showed a poor fit with low prediction performance (COD of 0.17). Prior individualization didn't lead to better prediction performance and did in particular not reveal stronger state and network specificity as none of the parcellation schemes (individualized, non-individualized) indicated a benefit of network correspondence.

Fig. 1) Specificity of FC state in general (solid columns) and individualized (hatched columns) parcels.

Fig. 2) Specificity of network in general (solid columns) and individualized (hatched columns) parcels. Yellow: resting state, green: WM, blue: SOCIAL, red: EMO, white: whole-brain 400 Schaefer parcels.

Conclusions: In conclusion, predicting behavior based on FC remains a significant challenge. However, in line with previous results[1] task-specific FC patterns seem to provide more information about individual behavior in WM performance than do resting-state FC patterns but this does not generalize to socio-affective behaviors. Calculation of FC within individualized networks did not enhance the expected state and network specificity, indicating that the use of individual functional markers does not necessarily capture more task-specific variance than do nodes from group-averaged maps. However, this might be due to the rather small amount of participants and the fact that the individualization was based on resting-state data[6], while individualization on task-fMRI data specific to the target domain might improve prediction and reveal specific effects of state and network. Notably, given the limitations and the generally low prediction accuracies, the observed absence of differences in prediction performance between state and network conditions as well as the lack of impact of individualization need to be viewed with caution and invite further investigations.

References

1. Finn, E. S. 'Is it time to put rest to rest?', Trends in Cognitive Sciences, 25, 1021–1032 (2021).
2. Finn, E. S. et al. 'Functional connectome fingerprinting: identifying individuals using patterns of brain connectivity', Nature Neuroscience, 18, 1664–1671 (2015).
3. Pläschke, R. N. et al. 'On the integrity of functional brain networks in schizophrenia, Parkinson's disease, and advanced age: Evidence from connectivity-based single-subject classification', Human Brain Mapping, 38, 5845–5858 (2017).
4. Shen, X. et al. Using connectome-based predictive modeling to predict individual behavior from brain connectivity. Nat. Protoc. 12, 506–518 (2017).
5. Chen, J. et al. 'Intrinsic Connectivity Patterns of Task-Defined Brain Networks Allow Individual Prediction of Cognitive Symptom Dimension of Schizophrenia and Are Linked to Molecular Architecture', Biological Psychiatry, 89, 308–319 (2021).
6. Kong, R. et al. 'Spatial Topography of Individual-Specific Cortical Networks Predicts Human Cognition, Personality, and Emotion', Cerebral Cortex, 29, 2533–2551 (2019).
7. Van Essen, D. C. et al. 'The WU-Minn Human Connectome Project: An overview', NeuroImage, 80, 62–79 (2013).
8. Schaefer, A. et al. 'Local-Global Parcellation of the Human Cerebral Cortex from Intrinsic Functional Connectivity MRI', Cerebral Cortex, 28, 3095–3114 (2018).
9. Kraljević, N. et al. 'Network and State Specificity in Connectivity-Based Predictions of Individual Behavior', http://biorxiv.org/lookup/doi/10.1101/2023.05.11.540387 (2023).
10. The work was supported by: Helmholtz Portfolio Theme "Supercomputing and Modeling for the Human Brain"; European Union's Horizon 2020 Research and Innovation Programme under Grant Agreement No. 945539 (HBP SGA3); fellowship of the German Academic Exchange Service (DAAD).

Poster No 1750

Time-varying causal interactions in the functional brain networks: Modeling and Validation

Nan Xu[1], Xiaodi Zhang[1], Wen-Ju Pan[2], Jeremy Smith[2], Jason Allen[3], Vince Calhoun[4], Shella Keilholz[1]

[1]Georgia Institute of Technology, Atlanta, GA, [2]Emory University, Atlanta, GA, [3]Indiana University School of Medicine, Indianapolis, IN, [4]GSU/GATech/Emory, Decatur, GA

Introduction: The fMRI BOLD brain dynamic processes have served as a sensitive indicator for various brain disorders[1]. Most work in characterizing brain dynamics evaluates temporal variability among functional brain networks e.g.,[2],[3]. There has been less focus on dynamic analysis to capture the brain's causal interactions[4],[5], which may play a key role in understanding clinical outcomes in conditions like post-concussive visual motion sensitivity (PCVMS). To overcome this, we propose a new computational method to reveal time-varying causal dynamics in brain networks. The model's reliability was validated through concurrent LFP-BOLD measurements in rodents, assessing if causal interactions stem from deeper neuronal layers. Further validation was achieved by observing brain state shifts in the vestibular networks of PCVMS patients.

Methods: The model integrates the sliding-window technique with a validated static causal model prediction correlation[6],[7] to analyze time-varying causal interactions in brain networks. It operates in two main steps within each window [t, t+L] (Fig 1): (1) using a linear time-invariant model to predict output y from input x and determine the duration of information transfer D_yx[t], and (2) estimating directed functional connectivity strength (ρ_yx[t]=corr(ý[t], y[t]), where ý[t] is the prediction of y[t] from x[t] in step (1)). This method called SWpC dynamically predicts connectivity strength and duration using inputs from current and previous windows, distinguishing between forward and backward connections (ρ_yx[t]≠ρ_xy[t] and D_yx[t] ≠D_xy[t] for any t). SWpC was first validated with 22 concurrent LFP-BOLD scans (500s/scan) from two regions of the rat somatosensory cortex (S1L and S1R) under 1-2% dexmedetomidine[8], assessing the reliability of signal strength and duration. Band-limited power (BLP) signals across six frequency bands (δ, θ, α, low β, high β, and γ) was calculated from downsampled LFP using a 2TR-sliding window[9], matching BOLD's sampling rate (TR=0.5s). SWpC was then applied to both BOLD and BLP signals of S1L and S1R, contrasting with sliding window correlation (SWC) results. Following[10], a 50s sliding window was used in SWpC and SWC analysis. Second, SWpC assessed alterations in brain states, both in strength and duration, using fMRI recordings (420s/scan,

TR=0.7s) of the vestibular networks[11] in patients with varying severity of PCVMS (37 healthy controls, 25 subacute, 15 chronic). Following previous human study[2], a 44s sliding window was implemented and brain states identified by strength and duration were obtained by k-mean clustering.

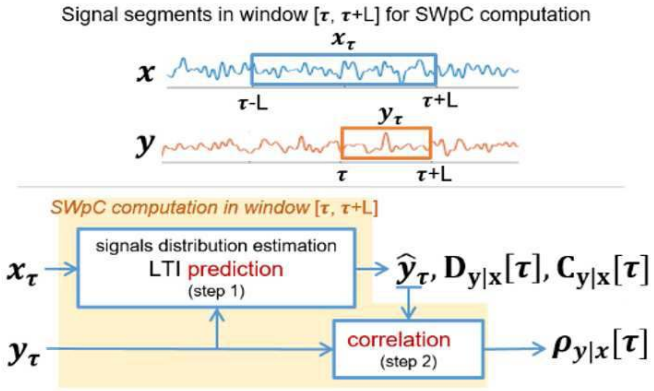

- window-specific duration: $\mathbf{D}_{\mathbf{y|x}}[\boldsymbol{\tau}]$
  - $\hat{y}_\tau[n] = x_\tau[n] * h_\tau[n] = \sum_{m=0}^{\mathbf{D}_{\mathbf{y|x}}[\boldsymbol{\tau}]-1} h_\tau[m]x[n-m]$ for $n \in [\tau, \tau + L]$
- window-specific strength: $\boldsymbol{\rho}_{\mathbf{y|x}}[\tau]$=corr($\hat{y}_\tau$, y_τ)

Results: First, strength and duration of SWpC were reliably predicted in both BLP and BOLD signals from S1L and S1R, exhibiting symmetries between the two regions as their directional asymmetry is consistently < scan variability (Fig 2A). SWpC strength reflects LFP-BOLD correlations akin to those uncovered by SWC[9], showing high BLP-BOLD correlates within the θ, low β, and upper bands, while SWpC duration lacks significant LFP-BOLD correlation (Fig 2BC). Second, four SWpC brain states in strength and duration were identified in PCVMS patients. Severity influenced time spent in strength-based states, with subacute similar to controls and chronic showing more deviation, consistent with known patterns of the disorder. However, less variation was noted in duration-based states (Fig 2D).

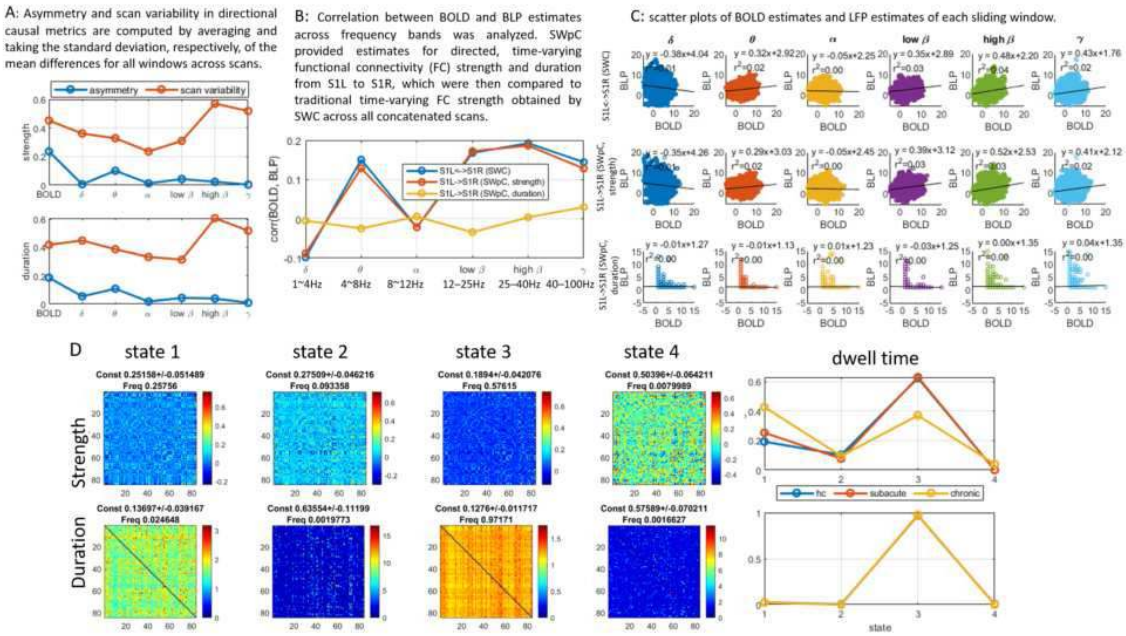

Conclusions: A computational framework was developed to reliably estimate the dynamic strength and duration of information transfer in neural and BOLD signals. BOLD strength estimates reflect causal dynamics in LFP at θ, low β and upper bands, but BOLD estimates in temporal influence do not tie to neural activity. This aligns with prior findings of LFP-BOLD correlates using SWC[9] and expands such correlates to include causal factors. Furthermore, SWpC estimations offer fresh perspectives on the dynamic nature of neurological disorders like PCVMS.

References

1. V. D. Calhoun, R. Miller, G. Pearlson, and T. Adali, "The chronnectome: time-varying connectivity networks as the next frontier in fMRI data discovery," Neuron, vol. 84, no. 2, pp. 262–274, Oct. 2014, doi: 10.1016/J.NEURON.2014.10.015.

2. E. A. Allen, E. Damaraju, S. M. Plis, E. B. Erhardt, T. Eichele, and V. D. Calhoun, "Tracking whole-brain connectivity dynamics in the resting state," Cereb Cortex, vol. 24, no. 3, pp. 663–676, 2012, doi: 10.1093/cercor/bhs352.
3. S. Shakil, C. H. Lee, and S. D. Keilholz, "Evaluation of sliding window correlation performance for characterizing dynamic functional connectivity and brain states," Neuroimage, vol. 133, pp. 111–128, 2016, doi: 10.1016/j.neuroimage.2016.02.074.
4. K. J. Friston, "Functional and Effective Connectivity: A Review," Brain Connect, vol. 1, no. 1, pp. 13–36, 2011, doi: 10.1089/brain.2011.0008.
5. A. Mitra, A. Z. Snyder, T. Blazey, and M. E. Raichle, "Lag threads organize the brain's intrinsic activity," Proc Natl Acad Sci U S A, vol. 112, no. 17, pp. E2235-44, 2015, doi: 10.1073/pnas.1503960112.
6. N. Xu, P. C. Doerschuk, S. D. Keilholz, and R. N. Spreng, "Spatiotemporal functional interactivity among large-scale brain networks," Neuroimage, vol. 227, p. 117628, Feb. 2021, doi: 10.1016/j.neuroimage.2020.117628.
7. N. Xu, R. N. Spreng, and P. C. Doerschuk, "Initial validation for the estimation of resting-state fMRI effective connectivity by a generalization of the correlation approach," Front Neurosci, vol. 11, no. MAY, p. 271, May 2017, doi: 10.3389/fnins.2017.00271.
8. W. ju Pan, G. Thompson, M. Magnuson, W. Majeed, D. Jaeger, and S. Keilholz, "Broadband local field potentials correlate with spontaneous fluctuations in functional magnetic resonance imaging signals in the rat somatosensory cortex under isoflurane Anesthesia," Brain Connect, vol. 1, no. 2, pp. 119–131, Aug. 2011, doi: 10.1089/brain.2011.0014.
9. X. Zhang, W. J. Pan, and S. D. Keilholz, "The relationship between BOLD and neural activity arises from temporally sparse events," Neuroimage, vol. 207, p. 116390, Feb. 2020, doi: 10.1016/j.neuroimage.2019.116390.
10. G. J. Thompson et al., "Neural correlates of time-varying functional connectivity in the rat," Neuroimage, vol. 83, no. 0, pp. 826–836, 2013, doi: 10.1016/j.neuroimage.2013.07.036.
11. J. L. Smith et al., "The 'vestibular neuromatrix': A proposed, expanded vestibular network from graph theory in post-concussive vestibular dysfunction," Hum Brain Mapp, 2021

Poster No 1751

On the features of spiking connectivity

Joshua Faskowitz[1], Javier Gonzalez-Castillo[1], Daniel Handwerker[1], Peter Bandettini[1]

[1]Section on Functional Imaging Methods, NIMH, Bethesda, MD

Introduction: The concept of functional connectivity is pervasive in modern fMRI research. Resting state and task-based correlation has been applied in a litany of neuroimaging contexts, to demonstrate how discrete regions of the brain might be in or out of sync, potentially modulated by state[1], task context[4], or even clinical condition. The connectivity measure commonly used for fMRI analysis-Pearson or product-moment correlation-can be mathematically unwrapped into a series of values that record instantaneous similarity[3]. These data, which we call edge time series, record a dynamic pattern that when averaged, equals the time-averaged correlation. A longstanding finding in fMRI connectivity analysis is the identification that punctuated moments in time[7], identified via methods like co-activation maps[5], point processes[9], or high-amplitude edge events[10], contribute disproportionally to the time-averaged connectivity[2], such as modularity. These findings prompt us to further explore the characteristics of these punctuated moments using edge time series, which render connectivity patterns at the same temporal resolution as the collected data. Here, we simplify high-amplitude edge events as binary spikes and compare measures of these spikes to conventionally defined functional connectivity and its derivatives. Further, by examining the length of spikes, we seek to characterize how distinct regions of the brain correlate in different manners.

Methods: Resting-state fMRI data (14.4 minutes; 0.72 TR) was obtained from 50 random selected low-motion subjects from the Human Connectome Project. Preprocessed data included steps for motion correction, distortion correction, high-pass filtering, and ICA-FIX noise removal. The data were nuisance regressed further using traces from both CSF and WM masks. Time series were obtained for 400 nodes of the Schaefer parcellation[8] plus 55 subcortical and cerebellar nodes. Edge time series are constructed by taking the element-wise product between two z-score node time series. Enumerating this operation between all pairs of nodes renders the edge time series matrix. Edge times series were converted into spike time series (i.e., binary points) using a threshold of 2 (arbitrary units of co-fluctuation). Spikes were defined as contiguous above-threshold events, meaning that the length of each spike could be binned (short: 0.72-2.88 sec, medium: 2.88-5.76 sec, long > 5.76 sec).

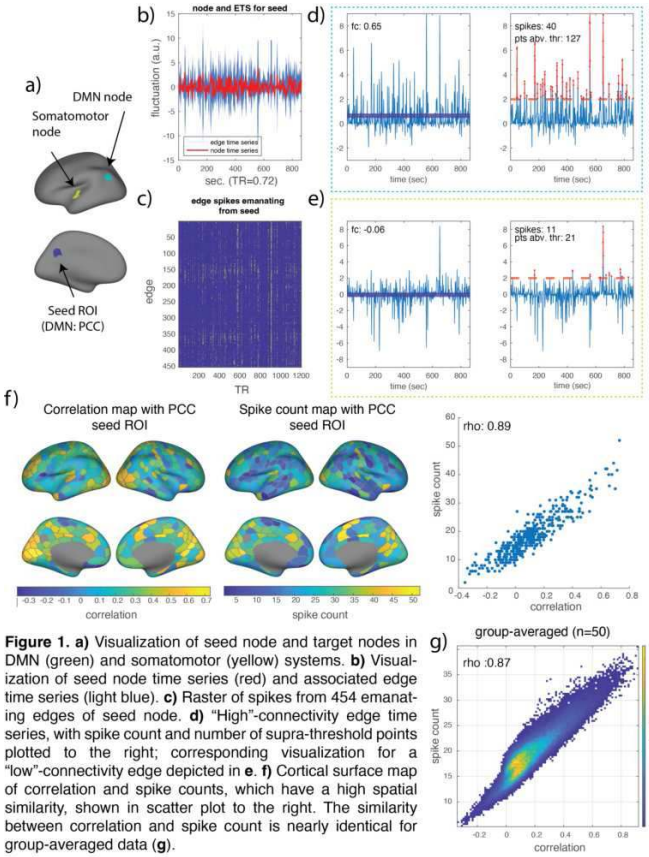

Figure 1. a) Visualization of seed node and target nodes in DMN (green) and somatomotor (yellow) systems. **b)** Visualization of seed node time series (red) and associated edge time series (light blue). **c)** Raster of spikes from 454 emanating edges of seed node. **d)** "High"-connectivity edge time series, with spike count and number of supra-threshold points plotted to the right; corresponding visualization for a "low"-connectivity edge depicted in **e**. **f)** Cortical surface map of correlation and spike counts, which have a high spatial similarity, shown in scatter plot to the right. The similarity between correlation and spike count is nearly identical for group-averaged data (**g**).

Results: First, a posterior cingulate cortex node was highlighted in a single subject to demonstrate its edge time series with another highly correlated node (also in the DMN) and an uncorrelated node (in the somatomotor system; Fig 1a-e). In this example, we observe that spike counts recapitulate functional connectivity, despite the loss of continuous co-fluctuation information (Spearman's rho: 0.88; Fig 1f). This pattern is replicated when using group-average data (rho: 0.87; Fig 1g). Next, we asked if different systems have different characteristic edge spike durations (Fig 2a). We observed that edges within the visual, somatomotor, and dorsal attention systems displayed the greatest counts of long spiking, whereas short spikes were generally pervasive. However, edges of the DMN to other systems displayed fewer short spikes. Finally, we compared nodes long and short spike counts at the node level (Fig 2b-c). Notably regions along the cingulate emanate short spiking edges and regions in the posterior temporal lobe emanate long spiking edges. This pattern did not relate to the principal gradient, a marker of hierarchical organization[6].

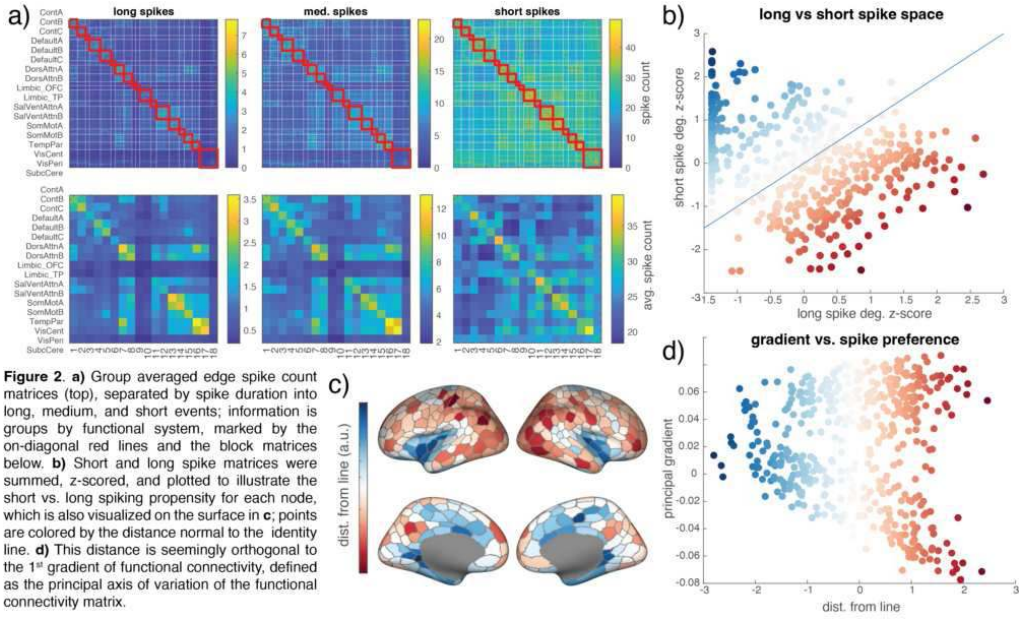

Figure 2. **a)** Group averaged edge spike count matrices (top), separated by spike duration into long, medium, and short events; information is groups by functional system, marked by the on-diagonal red lines and the block matrices below. **b)** Short and long spike matrices were summed, z-scored, and plotted to illustrate the short vs. long spiking propensity for each node, which is also visualized on the surface in **c**; points are colored by the distance normal to the identity line. **d)** This distance is seemingly orthogonal to the 1st gradient of functional connectivity, defined as the principal axis of variation of the functional connectivity matrix.

Conclusions: By virtue of unwrapping correlation, edge time series reveal the manner in which correlation values are realized. Some edges are marked by brief intermittent spikes whereas other edges have longer, more infrequent spikes. Future work should examine if distinct spiking profiles correspond to different cognitive processes, and if deviation from normal ranges can prove to be clinically relevant.

References

1. Allen, E. A. (2014). Tracking whole-brain connectivity dynamics in the resting state. Cerebral cortex, 24(3), 663-676.
2. Cifre, I. (2020). Further results on why a point process is effective for estimating correlation between brain regions. Papers in physics, 12, 120003-120003.
3. Faskowitz, J. (2020). Edge-centric functional network representations of human cerebral cortex reveal overlapping system-level architecture. Nature neuroscience, 23(12), 1644-1654.
4. Gonzalez-Castillo, J. (2015). Tracking ongoing cognition in individuals using brief, whole-brain functional connectivity patterns. Proceedings of the National Academy of Sciences, 112(28), 8762-8767.
5. Liu, X. (2013). Time-varying functional network information extracted from brief instances of spontaneous brain activity. Proceedings of the National Academy of Sciences, 110(11), 4392-4397.
6. Margulies, D. S., (2016). Situating the default-mode network along a principal gradient of macroscale cortical organization. Proceedings of the National Academy of Sciences, 113(44), 12574-12579.
7. Petridou, N. (2013). Periods of rest in fMRI contain individual spontaneous events which are related to slowly fluctuating spontaneous activity. Human brain mapping, 34(6), 1319-1329.
8. Schaefer, A., (2018). Local-global parcellation of the human cerebral cortex from intrinsic functional connectivity MRI. Cerebral cortex, 28(9), 3095-3114.
9. Tagliazucchi, E. (2012). Criticality in large-scale brain fMRI dynamics unveiled by a novel point process analysis. Frontiers in physiology, 3, 15.
10. Zamani Esfahlani, F. (2020). High-amplitude cofluctuations in cortical activity drive functional connectivity. Proceedings of the National Academy of Sciences, 117(45), 28393-28401.

Poster No 1752

Capturing cortical hierarchy and dual stream architecture with precision functional MRI at 7T

Yezhou Wang[1], Jordan DeKraker[2], Raúl Rodriguez-Cruces[2], Donna Gift Cabalo[1], Bin Wan[3], Casey Paquola[4], Sofie Valk[3], Seok Jun Hong[5], Alan Evans[6], Boris Bernhardt[2]

[1]McGill University, Montreal, Quebec, [2]Montreal Neurological Institute and Hospital, Montreal, Quebec, [3]Max Planck Institute for Human Cognitive and Brain Sciences, Leipzig, Germany, [4]INM-7, Jülich, Jülich, [5]Center for Neuroscience Imaging Research, Institute for Basic Science, Suwon, Gyeonggi-do, [6]McGill Centre for Integrative Neuroscience (MCIN), Montreal, Quebec

Introduction: Understanding the functional processing hierarchy of the human cerebral cortex is a longstanding challenge in neuroscience. Foundational hierarchical models of the cortex, formulated in non-human primates, presume the interaction of feedforward and feedback processes[1-3]. There is increasing support for a dual stream architecture, in which the laminar origin of projection patterns determines feedback vs feedforward signaling, especially for long-range connectivity patterns. Here, we expand this research to the human cortex, capitalizing on ultra-high-resolution 7 Tesla magnetic resonance imaging (7T MRI)[4]. Combining directional functional connectivity modelling with geodesic distance mapping across cortex, we specifically tested whether feedback signalling to primary sensory systems derives from deeper layers with increasing anatomical distance between different cortical areas.

Methods: We analyzed 7T MRI data of 10 unrelated healthy adults (age: 26.80±4.61 years, 5 females). Each participant underwent three separate sessions, during which structural (resolution 0.5mm) and resting-state functional MRI (rs-fMRI; 1.9mm) scans were acquired. MRI data were processed using micapipe[5]. We constructed 14 equivolumetric surfaces between the pial and white matter boundaries based on structural MRI and registered them to the rs-fMRI data to sample deep- and superficial-layer timeseries. Timeseries from the three sessions were concatenated and mapped to a parcellation[6]. Regression dynamic causal models (rDCM)[7] were applied to these timeseries, resulting in effective connectivity matrices. To evaluate patterns of feedback streams, we defined the deep source ratio (DSR). For area V1, we assessed DSR of the feedback stream from regions in visual network (VN), dorsal attention network (dAN), and default mode network (DMN). For each region, we calculated Spearman's correlation coefficients between its DSR and its geodesic distance to the regions of interest (ROI). We performed similar analyses for primary somatosensory cortex (S1) within the somatomotor network (SMN) and for A1 within the auditory network (AN). We integrated all ROIs together and examined associations by controlling inter-ROI differences using a mixed linear model. To further enhance the precision of defining superficial and deep layers, we reconstructed the effective connectivity matrix by incorporating cortical layer information from a histological dataset (Figure 2.A)[8]. Subsequently, we reran all main analyses based on the updated effective connectivity matrix. Spatial autocorrelation permutation tests were conducted for all correlations.

Results: We derived effective connectivity matrices for each participant (Figure 1.A). Individual matrices were averaged to obtain the group-level matrix for subsequent analyses. Our initial investigation focused on V1, revealing a significant association between DSR and geodesic distance, especially in VN+dAN+DMN (r=0.45, p=0.002; Figure 1.B). Similar findings were observed for S1 in SMN+dAN+DMN (r=0.37, p=0.042; Figure 1.C) and for A1 in AN (r=0.60, p=0.034; Figure 1.D). Combining all regions using a mixed model revealed significant associations (r=0.49, p<0.001; Figure 1.E). Finally, we cross-validated findings after adjusting definitions of deep and superficial surfaces by incorporating cortical layer information from a histological dataset[8] (Figure 2.A). We repeated the main analyses and obtained similar results in VN (r=0.43, p=0.002), SMN (r=0.43, p=0.016), AN (r=0.62, p=0.027), and all regions together (r=0.46, p<0.001; Figure 2.B).

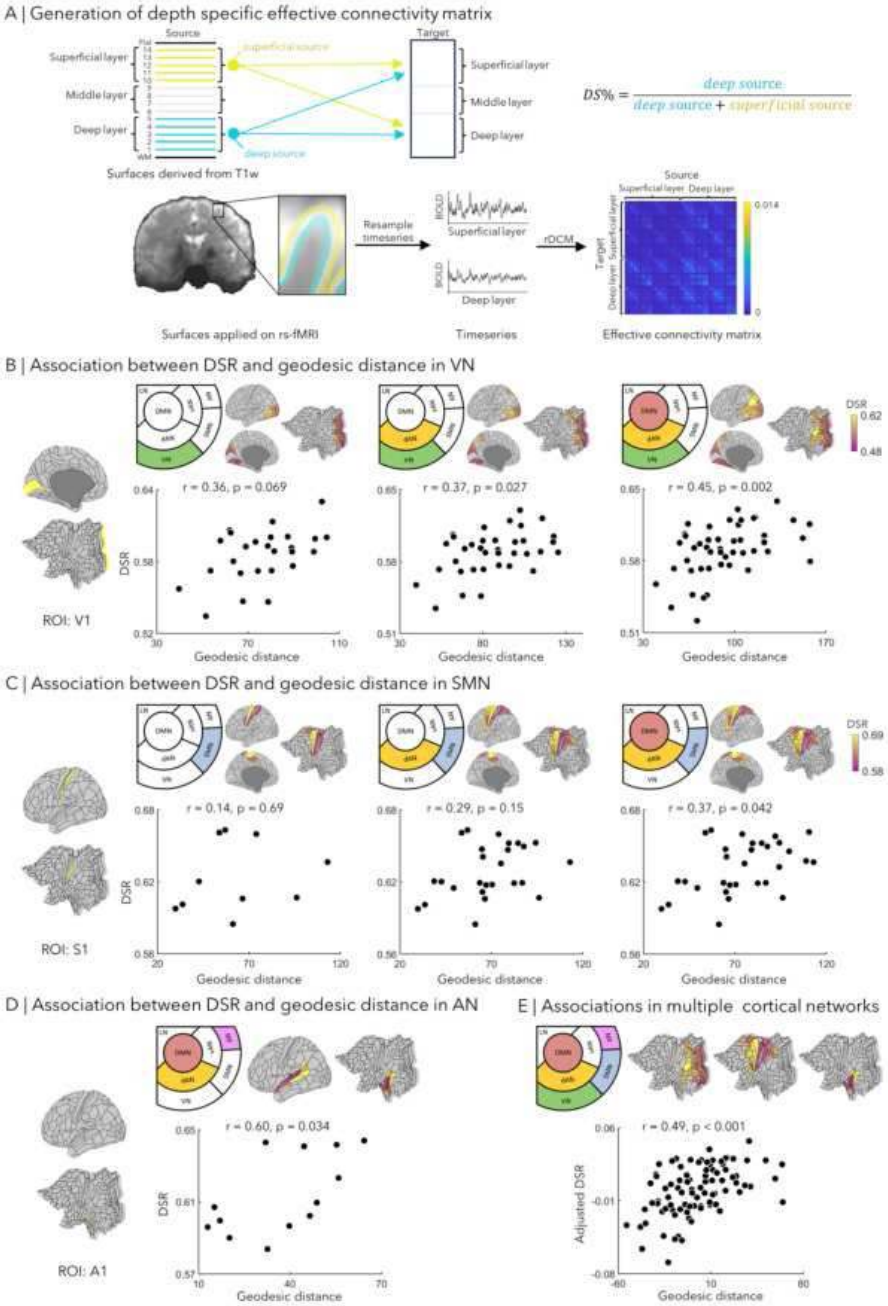

Figure 1. **A) Generation of depth specific effective connectivity matrix.** 14 equivolumetric intracortical surfaces were generated from high resolution structural MRI, and divided into superficial, middle and deep cortical depths. Following cross-modal registration, rs-fMRI timeseries of deep and superficial depths were resampled and were used as input of rDCM to generate effective connectivity matrix. DSR was defined as shown in the formulation, following the theory proposed in prior study [9]. **B) Association between DSR and GD in VN.** DSR and GD of each region to the ROI V1 was computed in VN, and additional regions in dAN and DMN. Spearman's correlation coefficients between DSR and GD were estimated. **C) Association between DSR and GD in SMN.** DSR and GD of each region to the ROI S1 was computed in SMN, dAN and DMN. Spearman's correlation coefficients were also estimated. **D) Association between DSR and GD in AN.** DSR and GD of each region to the ROI A1, and Spearman's correlation coefficients between them were computed in AN. **E) Associations in multiple cortical networks.** Associations between DSR and GD in VN, SMN, AN, dAN and DMN were estimated. **Abbreviation**: GD: geodesic distance; VN: visual network; SMN: somatomotor network; AN: auditory network; dAN: dorsal attention network; vAN: versal attention network; DMN: default mode network; LN: limbic network.

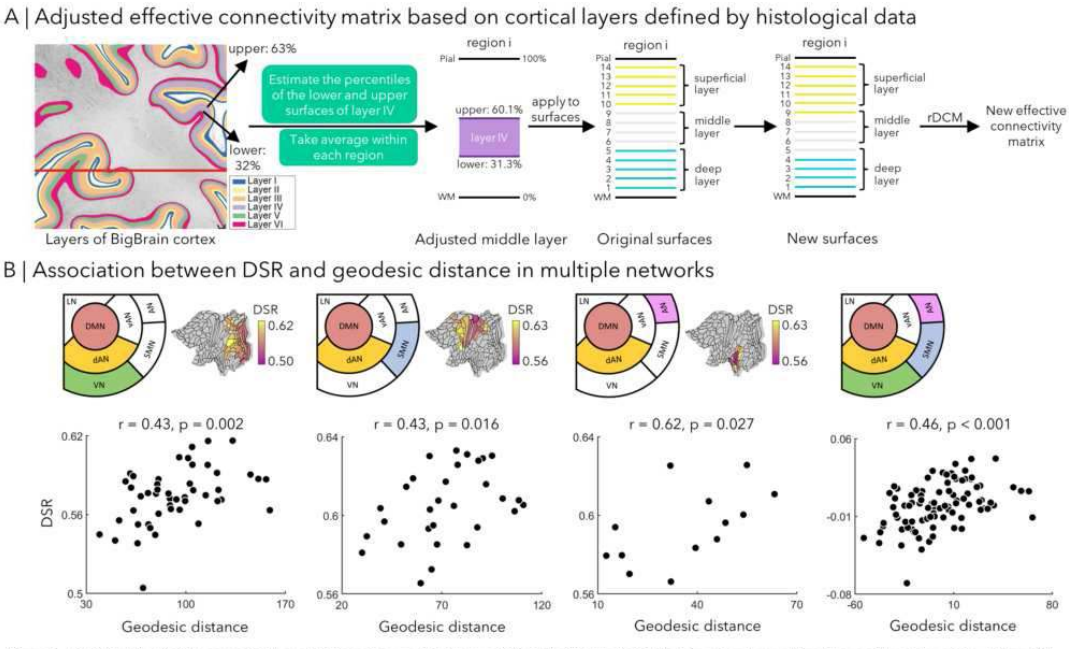

Figure 2. **A) Adjusted effective connectivity matrix based on cortical layers defined by histological data.** For region i, we utilized the position information of layer IV from the BigBrain dataset [8] to refine the middle layer, resulting in new surfaces. This process improved the precision of defining the superficial and deep layers of the cortex. Subsequently, we resampled timeseries using these new surfaces and reran rDCM to generate the adjusted effective connectivity matrix. **B) Associations between DSR and GD in multiple networks.** We evaluated the associations between DSR and GD in VN, SMN and AN using a new effective connectivity matrix. **Abbreviation**: GD: geodesic distance; DS: deep source.

Conclusions: Our findings reveal a clear hierarchical organization within the human cortex, particularly in the feedback stream from unimodal and heteromodal association cortex to V1, S1, and A1. These results indicate the presence of well-defined, distance-dependent feedback pathways in both the superficial and deep layers, consistent with the notion of feedback connections providing a generative network[9].

References

1. Felleman DJ, Van Essen DC. (1991), Distributed Hierarchical Processing in the Primate Cerebral Cortex. Cereb Cortex. 1(1):1-47. doi: 10.1093/cercor/1.1.1-a.
2. Mesulam MM. (1998), From sensation to cognition. Brain. 121(6):1013-52. doi: 10.1093/brain/121.6.1013.
3. Pascal B, Alexandre B, Kenneth K, Henry K. (2000), Laminar Distribution of Neurons in Extrastriate Areas Projecting to Visual Areas V1 and V4 Correlates with the Hierarchical Rank and Indicates the Operation of a Distance Rule. J Neurosci. 20(9):3263. doi: 10.1523/JNEUROSCI.20-09-03263.2000.
4. van der Kolk AG, Hendrikse J, Zwanenburg JJM, Visser F, Luijten PR. (2013), Clinical applications of 7T MRI in the brain. Eur J Radiol. 82(5):708-18. doi: https://doi.org/10.1016/j.ejrad.2011.07.007.
5. Cruces RR, Royer J, Herholz P, Larivière S, Vos de Wael R, Paquola C, et al. (2022), Micapipe: A pipeline for multimodal neuroimaging and connectome analysis. Neuroimage. 263:119612. doi: https://doi.org/10.1016/j.neuroimage.2022.119612.
6. Glasser MF, Coalson TS, Robinson EC, Hacker CD, Harwell J, Yacoub E, et al. (2016), A multi-modal parcellation of human cerebral cortex. Nature. 536(7615):171-8. doi: 10.1038/nature18933.
7. Frässle S, Lomakina EI, Razi A, Friston KJ, Buhmann JM, Stephan KE. (2017), Regression DCM for fMRI. Neuroimage. 155:406-21. doi: https://doi.org/10.1016/j.neuroimage.2017.02.090.
8. Wagstyl K, Larocque S, Cucurull G, Lepage C, Cohen JP, Bludau S, et al. BigBrain 3D atlas of cortical layers: (2020),Cortical and laminar thickness gradients diverge in sensory and motor cortices. PLoS Biol. 18(4):e3000678. doi: 10.1371/journal.pbio.3000678.
9. Vezoli J, Magrou L, Goebel R, Wang X-J, Knoblauch K, Vinck M, et al. (2021), Cortical hierarchy, dual counterstream architecture and the importance of top-down generative networks. Neuroimage. 225:117479. doi: https://doi.org/10.1016/j.neuroimage.2020.117479.

Poster No 1753

Continuous axes of individual variability in big data: enhanced fMRI biomarkers for traits & health

Seyedeh-Rezvan Farahibozorg[1], Mark Woolrich[1], Stephen Smith[1]

[1]*University of Oxford, Oxford, UK*

Introduction: Functional MRI from thousands of individuals, e.g., as made available by UK Biobank, allows to examine the brain function at population-scale[1]. This holds great promise for addressing fundamental questions in brain health: can differences in brain function be used to predict cognition and brain disorders? To leverage this potential, there is an increasing need for functional connectivity techniques that can extract accurate and clinically relevant brain features[2,3]. Here we characterised a high-dimensional embedding space built on cross-subject similarities in the brain's resting state networks (RSNs) across

20,000 individuals in UK Biobank. This embedding space captures continuous axes of subject variability, where the most similar individuals will be placed close together along axes of variation. We demonstrate that this simple and flexible modelling of continuous variations across the population substantially improved cross-validated prediction accuracies for a wide range of phenotypes (>1000) in UK Biobank.

Methods: RSNs were modelled using stochastic Probabilistic Functional Modes (PFMs) (Fig1a), which estimates RSNs in population and individuals simultaneously[4]. PFMs decompose subject fMRI data (D) into a set of functional modes, represented by spatial maps (P), time courses (A), amplitudes (H) and noise (E): D=PHA+E. Subject-specific models are regularised hierarchically using group-level priors[4,5]. P_concat (size N_subject x N_voxel x N_RSN), the subject-specific spatial configuration of RSNs across brain voxels, was used to estimate summary features in two ways: 1- Conventional Feature extraction (Fig1a): P_ concat was dimension-reduced to X1: N_subject x 500 feature space using Dictionary Learning and linked ICA, as described in our previous work[4]. 2- Continuous Axes of Individual Variability (Fig1b): Cross-subject similarities were computed based on X1 and PCA was applied, while treating 'subjects' as variables, obtaining X2: N_ subject x 500. X1 and X2 were used separately to predict phenotypes using ElasticNet regression and repeated 5-fold nested cross-validation. Imaging confounds were regressed out[6]. Phenotypes included: age (1), sex (1), region-wise cortical area (148 phenotypes) and thickness (148), White Matter (WM) tracts and microstructure (453), cognitive (68), alcohol (37), tobacco (19), health metrics related to blood/heart (77), bone (93) and mental health (142).

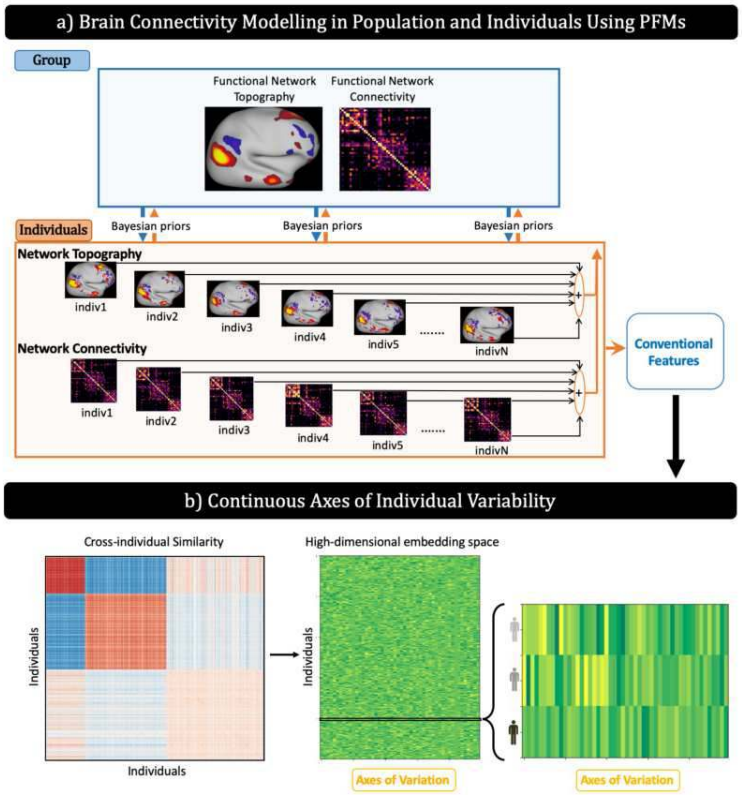

Figure 1 a) Schematic of the framework of Probabilistic Functional Modes (PFMs). PFMs are modelled using a hierarchical Bayesian Model with two levels: population and individuals, where population is used for top-down regularisation of individuals and evidence across individuals is iteratively fed back to update the group. Subject-specific network topography and connectivity are estimated. We used the former, after applying dimension-reduction, as conventional feature space (X1). **b) Continuous axes of population variation were identified** by applying subject PCA (X2) to cross-subject similarity matrices in spatial brain organisation.

Results: First, we found that modelling continuous axes of individual variability substantially improved prediction accuracies for all the categories of phenotypes (Fig2a), with the following average accuracies (r): age: 0.61 -> 0.75; sex: 0.72 -> 0.79; cortical area: 0.37 -> 0.45; cortical thickness: 0.22 -> 0.28; WM: 0.30 -> 0.38; Cognition: 0.03 -> 0.05 ; Alcohol: 0.04 -> 0.07 ; Tobacco: 0.06 -> 0.08; Heart health: 0.12 -> 0.16; Bone Health: 0.28 -> 0.34; Mental Health: 0.02 -> 0.03. Second, we computed the projection of the 500 axes of individual variability (i.e., columns of X2) onto the original voxel space of each RSN, yielding 500 X2_based spatial maps per RSN. We next computed phenotype-informed RSNs: 500 maps were weighted by their contribution in ElasticNet prediction of a specific phenotype (e.g., age) and averaged to obtain phenotype-informed maps, e.g., age-informed Default Mode Network in Fig2b. These can be used to examine age related population variations in each RSN.

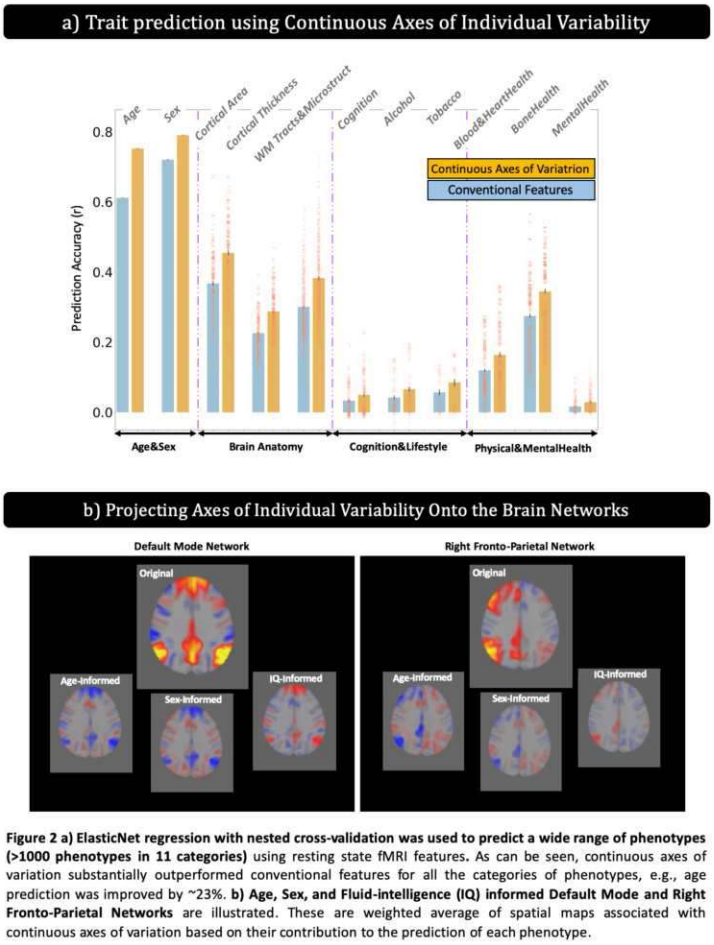

Figure 2 a) ElasticNet regression with nested cross-validation was used to predict a wide range of phenotypes (>1000 phenotypes in 11 categories) using resting state fMRI features. As can be seen, continuous axes of variation substantially outperformed conventional features for all the categories of phenotypes, e.g., age prediction was improved by ~23%. **b) Age, Sex, and Fluid-intelligence (IQ) informed Default Mode and Right Fronto-Parietal Networks** are illustrated. These are weighted average of spatial maps associated with continuous axes of variation based on their contribution to the prediction of each phenotype.

Conclusions: We characterised continuous axes of individual variability in brain function using a flexible data-driven approach for modelling subpopulation continua in large human populations. This new representation yielded clearly enhanced fMRI biomarkers for a wide range of traits related to cognition, health and substance use. Additionally, we used these axes of variability to compute phenotype-informed RSNs, which can be used as new population priors for RSN modelling in future studies.

References

1. K. L. Miller et al., “Multimodal population brain imaging in the UK Biobank prospective epidemiological study,” Nat. Neurosci., vol. 19, no. 11, pp. 1523–1536, 2016.
2. T. He et al., “Meta-matching: a simple framework to translate phenotypic predictive models from big to small data,” bioRxiv, p. 2020.08.10.245373, 2020.
3. Vidaurre D, Ilera A, S. M. Smith, and M. W. Woolrich, “Behavioural relevance of spontaneous, transient brain network interactions in fMRI,” Neuroimage, vol 229, p 117713, 2021.
4. S.-R. Farahibozorg et al., “Hierarchical modelling of functional brain networks in population and individuals from big fMRI data,” Neuroimage, 2021.
5. S. J. . Harrison et al., “Modelling subject variability in the spatial and temporal characteristics of functional modes,” Neuroimage, vol. 222, p. 117226, 2020.
6. F. Alfaro-Almagro et al., “Confound modelling in UK Biobank brain imaging,” Neuroimage, vol. 224, p. 117002, 2020.

Poster No 1754

Music/Dance Training Improve Empathy by Enhancing the Mirror Neurons System Connectivity

Yayun Liu[1,2,3], Gujing Li[1,2,3], Hui He[1,2,3], Lupeng Yue[4], Kexin Gao[1,2,3], Yuanyuan Yu[1,2,3], Cheng Luo[1,2,3], Dezhong Yao[1,2,3]

[1]School of life Science and technology, University of Electronic Science and Technology of China, Chengdu, Sichuan, China, [2]MOE Key Lab for Neuroinformation, Center for Information in Medicine, Chengdu, Sichuan, China, [3]The Clinical Hospital of Chengdu Brain Science Institute, Chengdu, Sichuan, China, [4]Education Center for Students Cultural Qualities, University of Electronic Science and Technology of China, Chengdu, Sichuan, China

Introduction: Music and dance are expressive arts of affection and prolonged artistic training might induce enhanced emotional understanding and empathy (Foster Vander Elst, Foster et al. 2023). Previous studies proved that the amygdala was the central subcortical mirror neurons system which constantly assigns sensory information appropriate values of emotional dimensions and is highly involved in the empathy process (Decety 2011, Messina, Caraci et al. 2023). Besides, the basal ganglia is another subcortical area within the mirror neurons system, playing a key role in emotion recognition. Essentially, the amygdala and basal ganglia integrate information and project back to the cortex that subserve social, affective, and motivational functions, which are highly involved in the domains of the empathy process (Haris, Bryant et al. 2023). However, very few studies explored the relationship between subcortical and cortical structure within basal ganglia and amygdala after prolonged artistic training. As a result, this study recruited the within-module degree (WMD) in order to know how the subcortical regions related to emotions interact with cortical functional networks in music/dance group and whether various WMD could induce improved empathy (Hwang, Bertolero et al. 2017).

Methods: A total of 94 right-handed participants (32 dancers, 29 musicians and 33 healthy control) underwent resting-state fMRI scans and fulfilled the Interpersonal Reactivity Index (IRI) scale (Davis 1980). The Brainnetome Atlas was used to parcellate the whole brain into 246 regions (Fan, Li et al. 2016). Pearson correlation was used to establish functional connections between regions. This correlation matrix was then binarized across a range of thresholds (0.1– 0.15, increments of 0.001). Amygdala and basal ganglia were selected as ROIs to calculate WMD between ROI and seven functional networks (Yeo, Krienen et al. 2011), and the WMD of each region was averaged across thresholds. The differences of WMD among groups were evaluated using one-way ANOVA and post-hoc analyses. Finally, the different WMD was correlated with IRI scale.

Results: Significant differences in WMD were observed in the amygdala and putamen among groups. Post-hoc analysis revealed that WMD between the right medial amygdala and ventral attention network significantly increased in the dance and music groups. The increased WMD between the bilateral ventromedial putamen and the limbic network was only found in the music group. Correlation analysis showed that the WMD of the amygdala and attention network had a significant positive correlation with the PT subscale, while the WMD of the putamen and the limbic network was correlated with the PT or FS subscale.

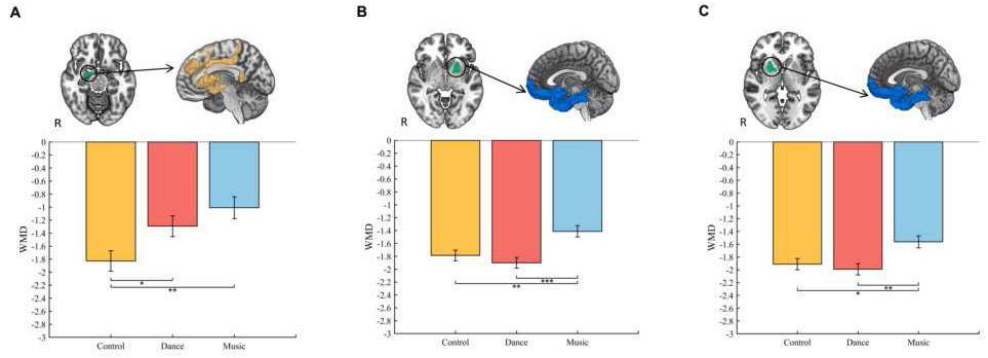

Fig.1 WMD of subcortical regions to cortical networks among three groups. A, different WMD between the right medial amygdala and ventral attention network. B and C, WMD of bilateral ventromedial putamen and limbic network. (*p<0.05,**p<0.01,***p<0.001)

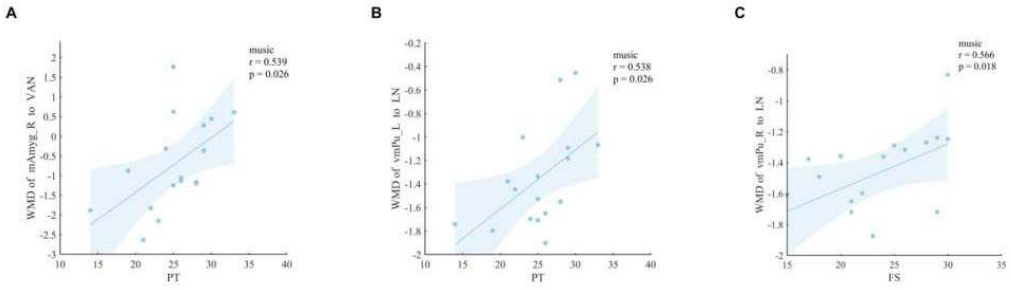

Fig.2 Relationship between WMD and empathy. Only the music group has significant results.

Conclusions: The results showed increased connections between the subcortical mirror neuron system and cortical regions associated with emotion in the music/dance group. Increased WMD of the putamen indicate long-term music training might intensively recruit ventromedial putamen and limbic network to participate in emotional perception (Hooker, Verosky et al. 2010). Increased amygdala connectivity to the ventral attention network revealed that music/dance training enhanced a bottom-up process of the amygdala in affective arousal while the ventral attention network contributes to emotion regulation

by a top-down approach (Decety 2010). In addition, behavioural results indicated that the communication of the amygdala and putamen with the cortex was highly correlated with empathic capacity. These findings suggested that music training might have broader effects on facilitating cortico-subcortical interaction, which increased the capacity for empathy, particularly in the cognitive domain.

References

1. Davis, M. H. (1980), 'A Multidimensional Approach to Individual Differences in Empathy'. Journal of Personality and Social Psychology.
2. Decety, J. (2010), 'The Neurodevelopment of Empathy in Humans', Developmental Neuroscience, vol. 32, no. 4, pp. 257-267.
3. Decety, J. (2011), 'The neuroevolution of empathy', Annals of the New York Academy of Sciences, vol. 1231, no. 1, pp. 35-45.
4. Fan, L. (2016), 'The Human Brainnetome Atlas: A New Brain Atlas Based on Connectional Architecture', Cerebral Cortex, vol. 26, no. 8, pp. 3508-3526.
5. Foster Vander Elst, O. (2023), 'The Neuroscience of Dance: A Conceptual Framework and Systematic Review', Neuroscience & Biobehavioral Reviews, vol. 150, pp. 105197.
6. Haris, E. M. (2023), 'Functional connectivity of amygdala subnuclei in PTSD: a narrative review', Mol Psychiatry.
7. Hooker, C. I. (2010), 'Neural activity during social signal perception correlates with self-reported empathy', Brain Research, vol. 1308, pp. 100-113.
8. Hwang, K. (2017), 'The Human Thalamus Is an Integrative Hub for Functional Brain Networks', The Journal of Neuroscience, vol. 37, no. 23, pp. 5594-5607.
9. Messina, A. (2023), 'Catatonia-like behavior and immune activation: a crosstalk between psychopathology and pathology in schizophrenia', Annals of General Psychiatry, vol. 22, no. 1.
10. Yeo, B. T. (2011), 'The organization of the human cerebral cortex estimated by intrinsic functional connectivity', J Neurophysiol, vol. 106, no. 3, pp. 1125-1165.

Poster No 1755

Functional connectivity predicts speech perception activation around the primary auditory cortex

Junhao Luo[1], Gaolang Gong[1]

[1]State Key Laboratory of Cognitive Neuroscience and Learning & IDG/McGovern Institute for Brain Resea, Beijing, China

Introduction: The relationship between connectivity patterns and brain functions is crucial in neuroscience. Previous studies have demonstrated that connectivity patterns can predict functional activation in various brain regions, with considerable individual differences in prediction scores[1],[2]. However, such individual difference and its neurobiological underpinnings are largely overlooked. This study applied the resting-state functional connectivity (rsFC) from the primary auditory cortex (PAC) to predict its speech perception activation and further explored the individual difference of the prediction score.

Methods: Participants. Following quality assurance, 766 subjects with high-quality magnetic resonance imaging (MRI) from the Human Connectome Project (HCP) dataset were included. The defined PAC. For each subject, the PAC is determined as the combination of the planum temporale (PT) and Heschl's gyrus (HG). These two structures were manually delineated by two trained raters. Vertex-level rsFC. For each vertex on the PAC, 1\times400 rsFC vector was obtained with each element as the Pearson's correlation between its resting-state time series and the averaged time series of a parcel from the "Kong400" parcellation[3]. Functional activation. Four task functional MRI scans from the HCP S1200 dataset were utilized, including language, gambling, social, and emotion. The activation was represented by the t-value. Given the high correlation, the "story - baseline" and "math - baseline" contrasts of the language task were averaged, representing the speech perception. The "story - math" contrast was derived to represent speech comprehension[4]. Predictive framework. The ridge regression algorithm with a nested five-fold cross-validation was applied (Fig. 1). In addition, an independent dataset[5] was used to further evaluate model generalizability. Prediction score (PS). For each subject, the prediction score was defined as the Pearson's correlation between the actual and predicted activation across all PAC vertices. Statistical analyses. A general linear model was applied to investigate the associations of prediction score with structural measures and functional activation with the PAC, while controlling for age, sex, and PAC vertex number.

Results: As shown in Fig. 2A, the predicted PAC activation pattern from the rsFC highly resembles the actual activation pattern in selected subjects. Particularly, the model trained from all HCP subjects can be applied to well predict the activation of speech perception for most subjects from an independent validation dataset, indicating robust generalization (Fig. 2C-D). For both speech perception and comprehension, there exist substantial individual difference in the prediction score for both left and right PAC across HCP subjects. As shown, the prediction scores of speech perception are significantly higher than the ones from both speech comprehension and other fMRI contrasts, suggesting a greater and specific rsFC predictive capability to the activation of speech perception within the PAC (Fig. 2B). Finally, the prediction scores for speech perception only showed a significant positive correlation with both peak value and variation of functional activation within the PAC (Fig. 2E,

All related r > 0.3, p < 2.2×10-16), but no correlation with any of the PAC structural measures (Fig. 2E). In addition, there was a significant correlation between the prediction score of the left PAC and reading decoding score (r = 0.11, p = 0.003).

Conclusions: Our study demonstrated a robust and specific rsFC-based model of individually predicting the activation pattern of speech perception within the PAC. This predictive model showed individual difference in prediction performance, which correlates with specific individual and therefore is biologically meaningful.

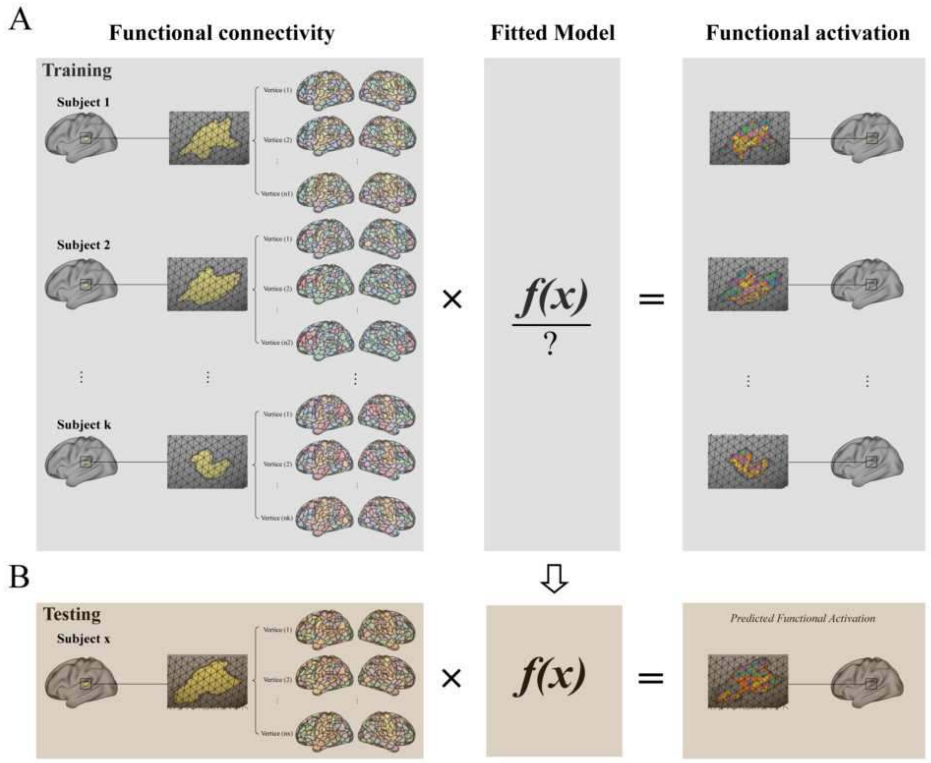

Fig. 1. Schematic of the predictive framework. The prediction paradigm for both left and right PAC (encapsulated in yellow within the black square). The rsFC (illustrated in the left panel) was constructed as the predictive feature, and the corresponding functional activation (t-value, delineated in the right panel) was utilized as the response variable. The ridge regression algorithm with a nested 5-fold cross validation framework was performed, with the the inner loop to determine the optimal model hyperparameter, and the outer loop to acquire their predicted activation for the unseen subjects. **(A)** Model training. The rsFC and corresponding functional activation for all vertices in the PAC of all subjects in the training set were concatenated, respectively. The folds for cross validation were divided at the subject-level, while the predictive model f(x) was trained at the vertex-level, using the concatenated rsFC and functional activation. **(B)** Model Testing. For each subject in the testing set, the resulting f(x) was applied to all vertices in the PAC to predict their functional activation. The performance of f(x) was evaluated by Pearson's correlation (prediction score, PS) between the actual and predicted activation across all vertices in the PAC. This train-and-predict procedure was iteratively conducted 100 times under varying fold divisions. The average of the 100 prediction scores was used as the final prediction score for the subject.

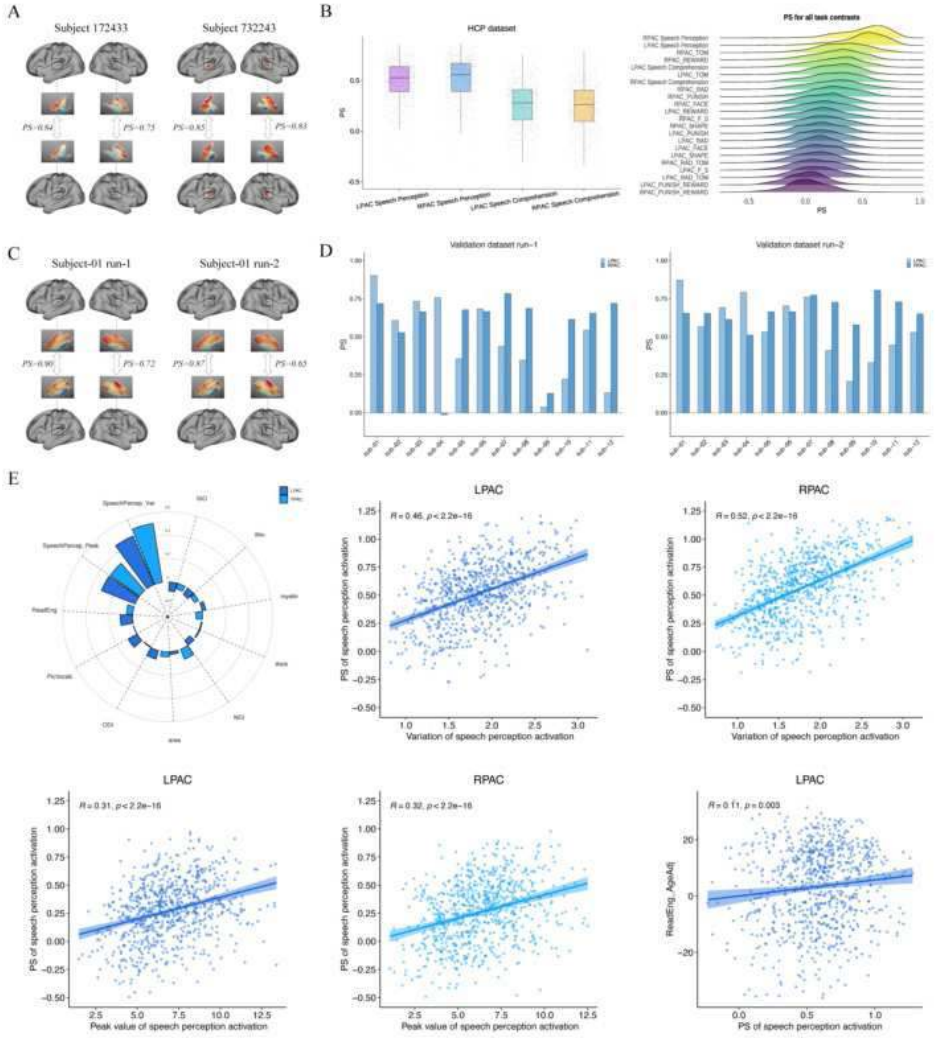

Fig. 2. Predicted results for the four tasks and statistical results of the individual differences in prediction scores of speech perception activation. (A) The actual and predicted speech perception activation for representative subjects in the HCP dataset. Brain map above the arrow is the actual activation and brain map below the arrow is the predicted activation. The "PS" is the prediction score, determined by the Pearson's correlation between them. **(B)** The boxplots in the left side are the prediction scores for speech perception and comprehension activation of all subjects in the HCP dataset. The ridge charts in the right side are the prediction scores for all task (language, emotion, social, and gambling) contrasts in the HCP dataset. More details about these task contrasts please refer to Barch et al., (2013) [6]. LAPC/RPAC indicates left/right PAC. **(C)** The predicted results for a selected subject in the validation dataset, using the model of speech perception activation from the HCP dataset. The meanings of the brain map and the "PS" are the same as above. **(D)** The prediction scores for all the 12 subjects in the validation dataset, using the model of speech perception from the HCP dataset. **(E)** The relationship of prediction scores of speech perception activation and brain measures in the PAC as well as the speech-related behavior scores. SpeechPercep_Peak and SpeechPercep_Var indicate the peak and variation of speech perception activation in the PAC. ReadEng, PicVocab, and Win denote reading decoding, picture word naming, and word-in-noise behavior scores respectively. The average cortical area, thickness, myelin content, axon density, orientation dispersion, and water molecule content of the PAC are represented by area, thick, myelin, NDI, ODI, and ISO, respectively. The circular bar shows the partial correlations, where '*' denotes the significant results after Bonferroni correction. The significant partial correlations were also illustrated in the corresponding scatter plots.

References

1. Tavor, I. et al. (2016), "Task-free MRI predicts individual differences in brain activity during task performance", Science, vol. 352, no. 6282, pp. 216–220
2. Saygin, Z. M. et al. (2012), "Anatomical connectivity patterns predict face selectivity in the fusiform gyrus", Nature Neuroscience, vol. 15, no. 2, pp. 321-327
3. Kong, R. et al. (2021), "Individual-Specific Areal-Level Parcellations Improve Functional Connectivity Prediction of Behavior", Cerebral Cortex, vol. 31, no. 10, pp. 4477–4500
4. Binder, J. R. et al. (2011), "Mapping Anterior Temporal Lobe Language Areas with FMRI: A Multi-Center Normative Study", NeuroImage, vol. 54, no. 2, pp. 1465–1475
5. Wang, S. et al. (2022), "A synchronized multimodal neuroimaging dataset for studying brain language processing", Scientific Data, vol. 9, no. 1, pp. 590
6. Barch D. M. et al. (2013), "Function in the human connectome: task-fMRI and individual differences in behavior", NeuroImage, vol. 80, pp. 169–189

Poster No 1756

Systematic Mapping of Functional Interactions in Human Brain Dynamics

Zhen-Qi Liu[1], Andrea Luppi[1], Ye Tian[2], Ben Fulcher[3], Bratislav Misic[1]

[1]McGill University, Montreal, Quebec, [2]University of Melbourne, Carlton South, Victoria, [3]The University of Sydney, Sydney, NSW

Introduction: The human brain consists of anatomically connected regions that exhibit rich functional interactions at the macroscale. Intrinsic functional connectivity (FC), often estimated as zero-lag Pearson correlation between pairs of resting-state fMRI time series, stands as the most popular measure for studying pairwise relationships between brain regions' activities over time. However, this methodological choice is largely arbitrary, and numerous other methods could potentially be used to define FC. Here we profile pairwise functional associations between brain regions using a large library of interaction statistics. We then systematically benchmark multiple features of FC across these measures, including: 1) spatial & geometrical organization; 2) structural & biological associations; 3) fingerprinting and brain–behavior relationships; and 4) information-dynamics flow patterns.

Methods: Using resting-state functional MRI (rsfMRI) time series of N=326 unrelated subjects from the Human Connectome Project, we adapted the recently developed pyspi toolkit to systematically estimate 239 statistics from 49 pairwise interaction measures across 6 major categories. Group consensus and similarity matrices were calculated. Multimodal neurophysiological networks were used to contextualize the pairwise interactions across 100 cortical regions. Fingerprinting was implemented as the identifiability index, and brain-behavior predictions were carried out using kernel ridge regression with nested cross-validation. Finally, Integrated Information Decomposition (ΦID) was used to understand the specific information flow patterns captured by each pairwise measure.

Results: The present report broadly surveys pairwise interactions between rsfMRI time series across the neocortex using a library of 239 interaction statistics. We first found that the interaction statistics are highly organized and form meaningful clusters at the group level. Covariance estimators, the most widely used FC measures, are most (anti-)correlated to precision, distance, mutual information, and entropy estimators, confirming the analytical relationship, and most unrelated to spectral estimators. Precision and coherence estimators show the greatest structure–function coupling, while precision and mutual information estimators exhibit higher correlation with multiple inter-regional similarity networks, including gene co-expression and receptor similarity networks. Moving into individual differences, we consider the capacity of pairwise measures to capture individual fingerprints and behavior phenotypes. The precision estimator shows superior performance in uniquely identifying individuals. Covariance, distance, and information-theoretic measures show the greatest predictive accuracy across multiple behavior domains. Finally, we related our findings to finer-scaled information-flow patterns using the novel ΦID framework. We found that commonly used covariance estimators only emphasize the preservation of redundant information ("information storage"); in contrast, some spectral coupling measures also capture unique ("migration") or synergistic ("encryption") information flows.

Conclusions: In summary, we provide a comprehensive benchmark of pairwise interactions for resting-state haemodynamics in the human brain. We find that many interaction statistics capture distinct aspects of the underlying topological, neurophysiological, and population-level organization. Our analyses reveal some consensus and, at the same time, substantial differences coming from choice of pairwise interaction statistics. Interestingly, precision estimators show greater ability to capture meaningful individual variability, suggesting a relook into classic partial correlation methods. Overall, our project highlights the importance of studying methodological variability and their downstream implications, calling for tailored adoption of analysis methods in both basic and clinical phenotyping studies.

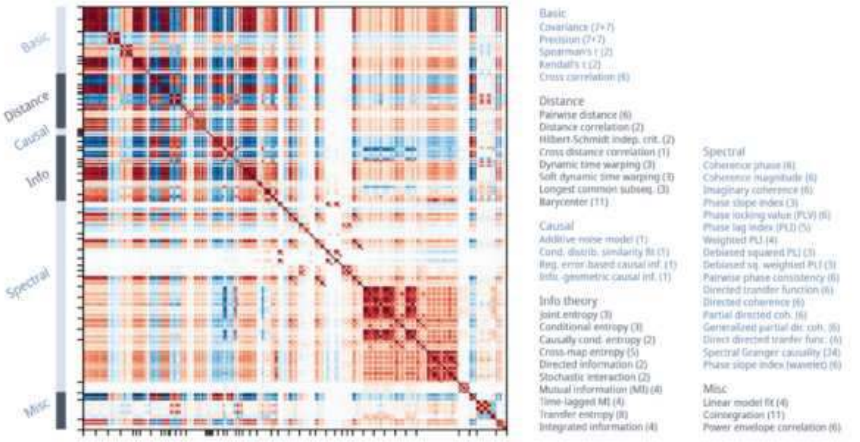

Figure 1 | **Overview of pairwise interaction statistics across the brain** Interaction statistics for functional time series were estimated between macroscopic brain regions across the brain. **(Upper left)** Group-level similarity profile between the 239 statistics. **(Lower left)** Group average matrices for some exemplar statistics. **(Right)** List of 49 pairwise interaction measures across 6 major categories, following the convention from *pyspi*. Numbers in parentheses represent specific variants of statistics calculated for the measure.

[figure truncated to fit submission requirements]

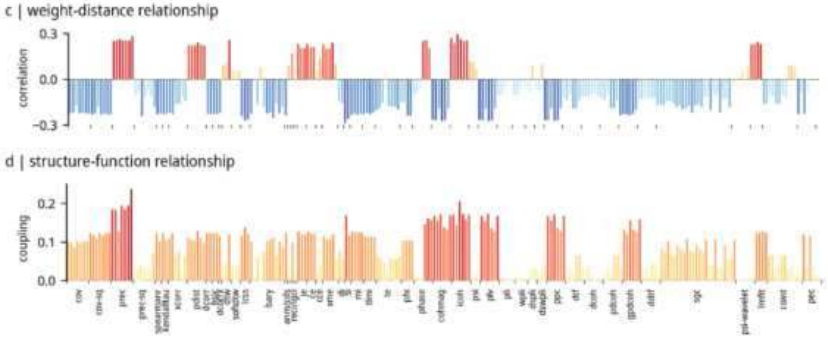

Figure 2 | **Benchmarking spatial and geometrical organization (a)** Heatmap of value distribution for each interaction statistic. **(b)** Heatmap showing weighted degree for each cortical region. Regions are ordered by intrinsic functional networks for left and right hemispheres separately. VIS: visual, SM: somatomotor, DA: dorsal attention, VA: ventral attention, LIM: limbic, FP: fronto-parietal, DMN: default mode network. **(c)** Spearman correlation of each interaction statistic with inter-regional Euclidean distance. Colors represent the extent of correlation. **(d)** Coupling between matrices of interaction statistics and predictor matrices derivd from structural connectivity, quantified as coefficient of determination (adjusted R-squared) of multilinear regression models that takes into account Euclidean distance and a set of communication measures generated from structural connectivity matrix, including shortest path length, navigation efficiency, search information, communicability, and diffusion efficiency. Colors represent the extent of coupling.

[figure truncated to fit submission requirements]

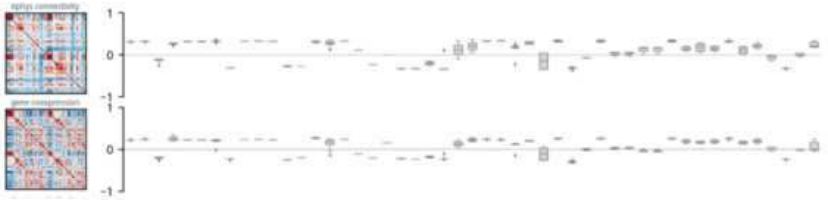

Figure 3 | **Aligning with multimodal neurophysiological networks (Left)** Inter-regional similarity networks generated from resting-state MEG (electrophysiology connectivity), microarray transcriptional expression (gene co-expression), histology-derived cytoarchitecture distribution (laminar similarity), FDG PET (metabolic connectivity), and PET tracer images for 18 neurotransmitter receptors and transporters (receptor similarity). **(Right)** Spearman correlation between the group average interaction statistics matrices and the corresponding network.

[figure truncated to fit submission requirements]

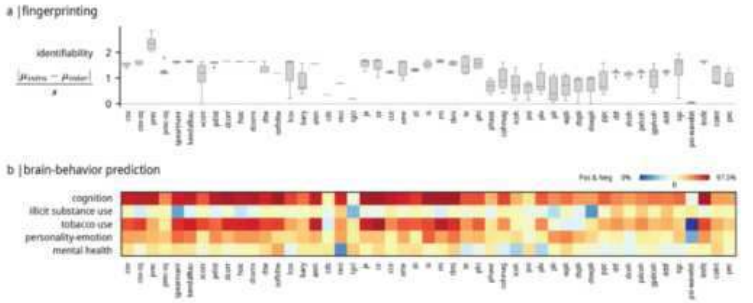

Figure 4 | **Quantifying individual differences (a)** Individual fingerprints quantified using identifiability index, calculated from the 4 fMRI runs for each subject. **(b)** Prediction of 5 major components derived from 109 HCP behavior terms using kernel ridge regression under a nested 10-fold cross-validation setting. Colors show average Pearson correlation between empirical and predicted behavior scores across the test folds.

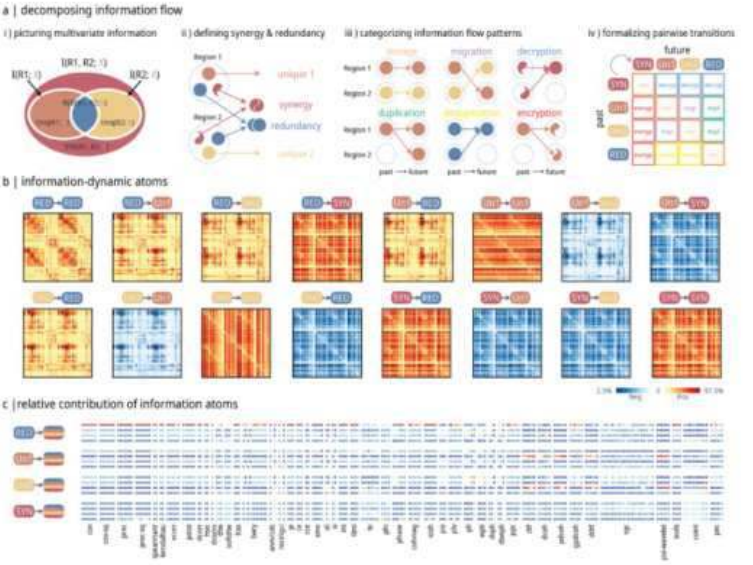

Figure 5 | **Decomposing information-dynamic flow with Integrated Information Decomposition (a)** Schematics of Integrated Information Decomposition (ΦID), showing the basic definitions of information atoms, information-dynamic atoms, and their descriptions. **(b)** Information-dynamic atoms calculated from the functional time series. **(c)** Relative contribution of the 16 information-dynamic atoms for each interaction statistic, quantified with relative importance estimated using dominance analysis.

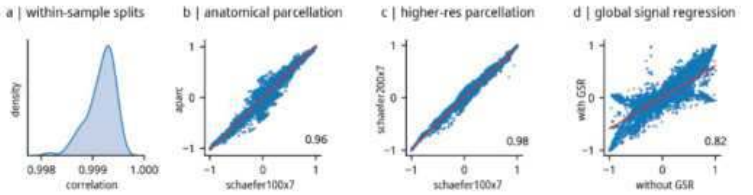

Figure 6 | **Sensitivity analyses** The upper left matrix in Fig. 1 is reproduced under different scenarios. **(a)** Distribution of Spearman correlation with the empirical matrix for 100 random discovery-validation spits. **(b)** Spearman correlation between the functionally-derived atlas (Schaefer 100-node 7-network, Schaefer100×7) used in the main analyses and an anatomically-derived atlas (Desikan-Killany; aparc). **(c)** Spearman correlation between the 100-node atlas (Schaefer 100-node 7-network, Schaefer100×7) used in the main analyses and a higher-resolution atlas (Schaefer 200-node 7-network, Schaefer200×7). A subset of 179 interaction statistics were used in this panel for faster calculation. **(d)** Spearman correlation between functional time series without global signal removal used in the main analyses and with global signal removal. GSR: global signal regression.

References

1. Cliff, O. M., Bryant, A. G., Lizier, J. T., Tsuchiya, N., & Fulcher, B. D. (2023). Unifying pairwise interactions in complex dynamics. Nature Computational Science, 1-11.
2. Smith, S. M., Miller, K. L., Salimi-Khorshidi, G., Webster, M., Beckmann, C. F., Nichols, T. E., ... & Woolrich, M. W. (2011). Network modelling methods for FMRI. Neuroimage, 54(2), 875-891.
3. Pervaiz, U., Vidaurre, D., Woolrich, M. W., & Smith, S. M. (2020). Optimising network modelling methods for fMRI. Neuroimage, 211, 116604.
4. Suárez, L. E., Markello, R. D., Betzel, R. F., & Misic, B. (2020). Linking structure and function in macroscale brain networks. Trends in cognitive sciences, 24(4), 302-315.
5. Tian, Y., Margulies, D. S., Breakspear, M., & Zalesky, A. (2020). Topographic organization of the human subcortex unveiled with functional connectivity gradients. Nature neuroscience, 23(11), 1421-1432.
6. Bazinet, V., Hansen, J. Y., & Misic, B. (2023). Towards a biologically annotated brain connectome. Nature Reviews Neuroscience, 1-14.
7. Luppi, A. I., Mediano, P. A., Rosas, F. E., Holland, N., Fryer, T. D., O'Brien, J. T., ... & Stamatakis, E. A. (2022). A synergistic core for human brain evolution and cognition. Nature Neuroscience, 25(6), 771-782.

Poster No 1757

Clustintime: a python toolbox for spatio-temporal clustering of fMRI data

Cristina Tobias Figuerola[1], Eneko Uruñuela[2], Fernando Pérez-Bueno[3], Itxaso Aizpurua[4], Laura De Frutos[5], Lucia Manso[5], Sylvia Yang[5], Vicente Ferrer[5], Cesar Caballero-Gaudes[5]

[1]Linköpings Universitet, Linköping, Östergötland, [2]Basque Center on Cognition, Brain and Language, Donostia - San Sebastián, Gipuzkoa, [3]Universidad de Granada, Granada, Spain, [4]Independent researcher, Barcelona, Spain, [5]Basque Center of Cognition, Brain and Language, San Sebastián, Spain

Introduction: The identification of synchronous BOLD fMRI signals is usually done through spatial clustering, allowing researchers to identify functional brain networks or parcellations[9]. There is an increasing interest in employing clustering algorithms in the temporal domain to identify instances of BOLD activity sharing similar spatial patterns[2]. For that purpose, we created Clustintime in 2022 and present here its latest release[1]. Clustintime stands as an open-source toolboxto automatically identify spatio-temporal patterns of neuronal activity in fMRI data. With a GPL-3.0 license, coded in python[3] and based on Scikit-learn[3], infomap[4], and networkx. Comprising 5 modules, it offers a range of tools for diverse time-clustering analyses, meeting various user needs. This release introduces the capability to cluster multiple datasets simultaneously, while offering the possibility of consensus clustering across all algorithms.

Methods: In this release, Clustintime maintains its user-friendly 3-step pipeline (matrix computation-clustering-visualization), now improved with an optional 4th feature for consensus clustering. Internally, all the modules have been modified to achieve a better performance. The main module underwent significant changes, absorbing mandatory features previously within the processing module (i.e: choosing a positive, negative or whole-signal analysis anddistance matrix computation with or without the sliding window approach). Additionally, it now supports simultaneous loading of data from multiple files, enabling researchers to employ clustering methods for studying groups and/or multiple run analyses. The processing module has evolved into an optional feature, providing users with an additional choice rather than a compulsory step. These updates transformed the toolbox into a more modular tool, with improved code readability and facilitated collaboration for new contributors. Further, a newly integrated consensus module enriches user experience with more robust outcomes than a singular execution of an algorithm on the entire dataset, especially if said algorithm employs heuristic methods. If selected, the clustering algorithm will be applied to, at least, 100 random subsamples of the data until it converges into a common solution.

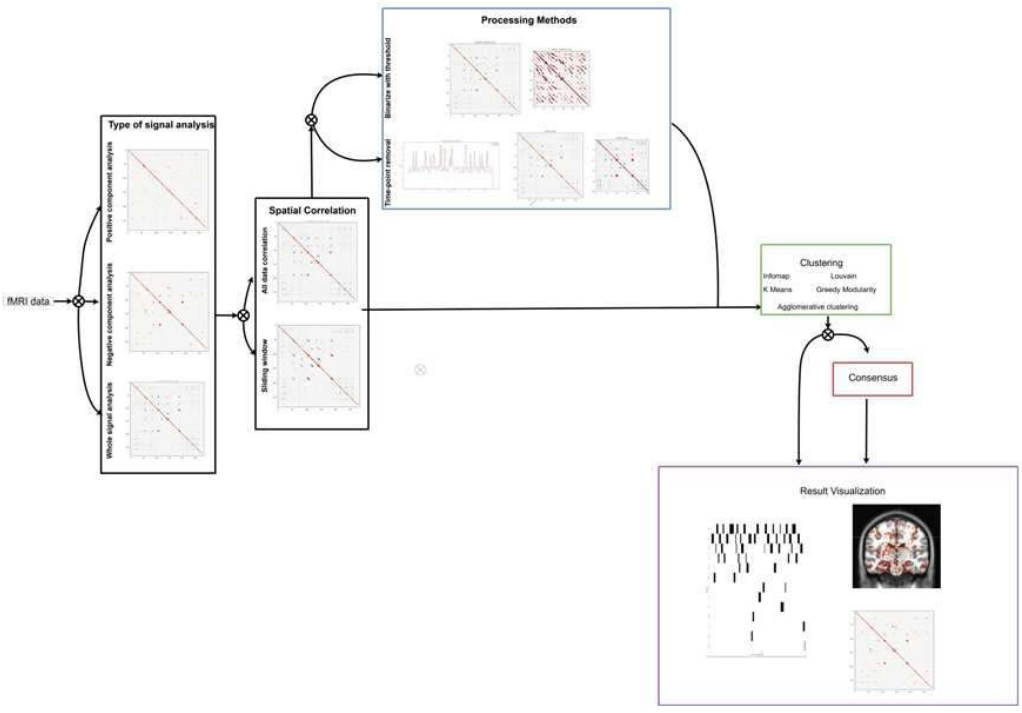

Figure 1: Clustintime is organized in 5 modules: Black) the main pipeline module for selection of type of input signal, computation of the distance between frames with spatial correlation. Blue) Processing module with time-point removal possibility. Green) Clustering module with different clustering algorithms to select. Pink) Consensus module. Purple) Visualization module, which depicts time-series corresponding to each cluster and associated cluster maps

Results: As an example, we applied Clustintime to a motor task of a single subject (100206) from the Human Connectome Project (HCP)[6] using the Infomap algorithm. The images were already preprocessed using a standard HCP pipeline including

realignment, coregistration, spatial normalization and smoothing and had been previously analyzed with multivariate sparse Paradigm Free Mapping using stability-selection[5]. Clustintime grouped the BOLD data volumes into multiple clusters (Figure 2A), automatically revealing activation maps (Figure 2B-E) associated with the tasks. Among the 13 clusters, a temporal pattern can be identified when observing the first 4 clusters. Figure 2B illustrates cluster 1, displaying activation in the region responsible for left foot movement. Figure 2C depicts cluster 2 with activation on the regions responsible for finger tapping. Figure 2D depicts cluster 3 showing activation inregions associated with tongue movement. Figure 2E portrays cluster 4 indicating activation in regions linked to left finger-tapping.

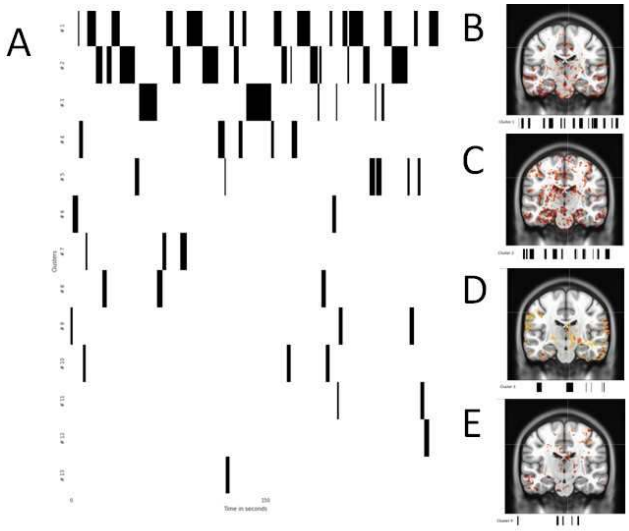

Figure 2: Results for 100206 HCP dataset. (A) Time-series for each cluster. (B) Infomap cluster 1 depicts PMC activation relevant to left-foot movement task. (C) Infomap cluster 2 depicts PMC activation relevant to finger-tapping task. (D) Infomap cluster 3 depicts PMC activation relevant to tongue movement task. (E) Infomap cluster 4 depicts PMC activation relevant to left-hand finger-tapping task

Conclusions: Clustintime, an open-source tool, empowers researchers to seamlessly integrate diverse tools for temporal clustering analyses of fMRI data. Its latest release enables the performance of these analyses across multiple fMRI volumes and introduces a consensus clustering feature. This toolbox gathers processing, clustering, and visualization methods to help researchers exploring events shaping the dynamics of brain function or identifying instances of artifact data. Backed by an open and expanding community, this project embraces contributions of any kind.

References

1. Clustintime (2023) “Cristina-Tobias/clustintime: v0.0.2”. Zenodo. doi: 10.5281/zenodo.10184455.
2. Jo, Y. (2021). ‘The diversity and multiplexity of edge communities within and between brain systems’. Cell reports, 37(7), 110032. https://doi.org/10.1016/j.celrep.2021.110032
3. Pedregosa, F (2011) ‘Scikit-learn: Machine learning in Python’, the Journal of machine Learning research, 12, 2825-2830.
4. Thirion, B. (2014), ‘Which fMRI clustering gives good brain parcellations?’, Front. Neurosci. 8:167.
5. Uruñuela, E., Gonzalez-Castillo, J., Zheng, C., Bandettini, P., & Caballero-Gaudes, C. (2023). Whole-brain multivariate hemodynamic deconvolution for functional MRI with stability selection. Medical Image Analysis, 103010.
6. Van Essen, D. C (2013), ‘The WU-minn human connectome project: An overview.’, NeuroImage, 80, 62–79. doi:10.1016/j.neuroimage.2013.05.041.

Poster No 1758

Noninvasive brain stimulation augments and stabilizes dynamic functional connectivity

Timothy Jordan[1], Michael Apostol[1], Nicole Petersen[1]

[1]*University of California, Los Angeles, Los Angeles, CA*

Introduction: Repetitive transcranial magnetic stimulation (rTMS) is an emerging tool for treating neuropsychiatric conditions -- including most recently, Tobacco Use Disorder – however, the mechanism by which rTMS achieves its therapeutic effects is still in the process of being explored, and biomarkers of rTMS efficacy remain elusive. Using resting-state fMRI, previous studies have examined the effects of rTMS on static functional connectivity (FC), however the results have been varied, pointing towards no specific mechanism (Beynel et al., 2020). Dynamic FC is an alternative to static FC with a few potential

advantages that could provide more insight into the attributes of FC that explain the effects of rTMS. We sought to examine the effects of rTMS on dynamic connectivity and stability and variance, two properties of dynamic connectivity.

Methods: In this study, we examined the effects of single-session rTMS (3,000 pulses at 10Hz over 15 minutes) delivered to the left dorsolateral prefrontal cortex (dlPFC) and a control region (visual cortex, v5) on craving and withdrawal symptoms, and on both static and dynamic FC in people who smoke cigarettes. Cigarette craving and withdrawal were measured by self-report before and after stimulation to determine effectiveness of stimulation to each region on their relief. To access functional connectivity, resting state functional imaging data (EPI, TR= 0.8 sec, Slice Thickness= 2mm, Voxel size 2 x 2 x 2mm) was collected from participants before and after stimulation. After preprocessing imaging data in FSL, data was denoised using a trained data set in FIX, and time series extracted into nodes defined by the Schaefer 400 atlas parcellation with subcortical regions added from the Human Connectome Project atlas. Static FC was calculated by taking the full scan time series from each parcel and calculating the Pearson correlation coefficient for each pair, creating a 419 x 419 matrix. Dynamic FC was calculated using the sliding window method with a window length of 60 seconds, creating 513 FC values per connection. For each functional time series, the average FC, the stability as measured by sample entropy, and the variance was calculated. Sample entropy was calculated using the Brain Entropy Mapping Toolbox (BENtbx).

Results: Significant decreases were found in participant-reported cigarette craving and withdrawal after stimulation to dlPFC only; v5 stimulation did not significantly change craving or withdrawal. Similarly, stimulation to v5 did not significantly change any functional connection or properties of connections. For stimulation to dlPFC, we found brain-wide changes in FC, stability and variance (FDR-correct $p < 0.01$). Functional connectivity was found to significantly increase for both static and dynamic measures of FC. Stability of connectivity was also found to significantly increase, decrease in entropy, as well as increases in variance were observed in more than 70% of node-node connections. Of the nodes found to have significant changes for each calculated measure, approximately 75% of node-node connections had medium or greater effects in all three. The majority of changes for these connections showing changes in FC, stability, and variance were seen between the default-mode network and both the somatomotor and dorsal attention networks as well as visual network to somatomotor network.

Conclusions: These results are consistent with previous findings describing widespread effects of rTMS on connections outside the stimulated regions, (reviewed by Beynel et al.) The findings show that effective rTMS stimulation not only alters FC values, but also the properties of those connections that can be examined through a dynamic approach. The finding that variance increases and the stability of the connections also increases may indicate that rTMS increases connectivity strength in a less sporadic and more consistent manner, which allows nodes to and transition more fluidly between states of high and low connectivity.

References

1. Beynel L. (2020), “Effects of repetitive transcranial magnetic stimulation on resting-state connectivity: A systematic review”, Neuroimage, doi: 10.1016/j.neuroimage.2020.116596.
2. Wang Z, Li Y, Childress AR, Detre JA (2014) “Brain Entropy Mapping Using fMRI”, PLoS ONE 9(3): e89948. https://doi.org/10.1371/journal.pone.0089948

Poster No 1759

Thalamic Network Controllability Changes and Cognitive Impairment in Multiple Sclerosis

Yuping Yang[1], Anna Woollams[1], Ilona Lipp[2], Zhizheng Zhuo[3], Valentina Tomassini[4], Yaou Liu[3], Nelson Trujillo-Barreto[1], Nils Muhlert[5]

[1]University of Manchester, Manchester, Manchester, [2]Max Planck Institute for Human Cognitive and Brain Sciences, Leipzig, Leipzig, [3]Beijing Tiantan Hospital, Beijing, Beijing, [4]G. d’Annunzio University of Chieti-Pescara, Chieti, Chieti, [5]University of Manchester, Manchester, UK

Introduction: Multiple sclerosis is a neuroinflammatory and neurodegenerative disease commonly associated with cognitive impairment. Understanding brain mechanisms of cognitive impairment in multiple sclerosis is crucial for early diagnosis and developing effective interventions to improve the quality of life in patients. Recent studies indicate that individuals with multiple sclerosis who develop cognitive impairment display changes in network activity in the brain, such as altered transitions between network states (activity patterns). Particularly, regions within the subcortical network, like the thalamus, show abnormalities early in multiple sclerosis, possibly driving the subsequent changes in the rest of the brain.

Methods: In this study, we investigated whether there are brain regions specifically involved in driving network changes throughout the brain in multiple sclerosis, and assessed how this relates to cognitive impairment in patients. To this end, we constructed functional brain networks based on resting-state functional MRI data from 102 multiple sclerosis patients and 27

healthy controls. Then we applied network controllability analysis using the most commonly used controllability measures to quantify the effect that brain networks or regions have on driving network changes and state transitions in multiple sclerosis. Furthermore, we compared network controllability changes between patients with different cognitive status. Finally, we tested the reproducibility of our main results using a separate dataset of 95 multiple sclerosis patients and 45 healthy controls.

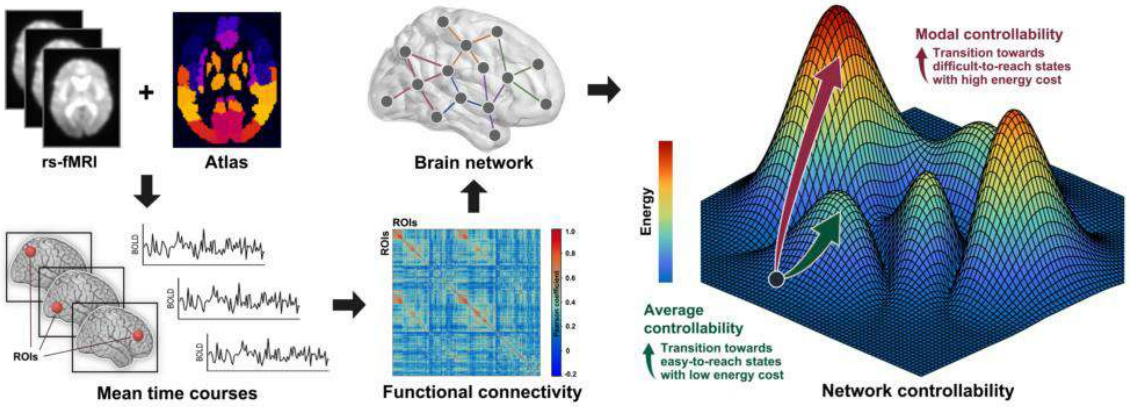

Results: We found significant global, cortical, and subcortical controllability changes in multiple sclerosis, as indicated by increased average controllability while decreased modal controllability and decreased activation energy in patients compared to controls. These changes predominately concentrated in the subcortical network, particularly the thalamus, and were further confirmed in the replication dataset. Moreover, both cognitively impaired and cognitively preserved patients showed increased average controllability while decreased modal controllability and decreased activation energy in the subcortical network, as well as increased average controllability in the thalamus. However, cognitively impaired patients additionally showed decreased modal controllability and decreased activation energy in the thalamus compared to the healthy controls. Besides, the thalamus in cognitively impaired patients showed significantly greater increase in average controllability than cognitively preserved patients.

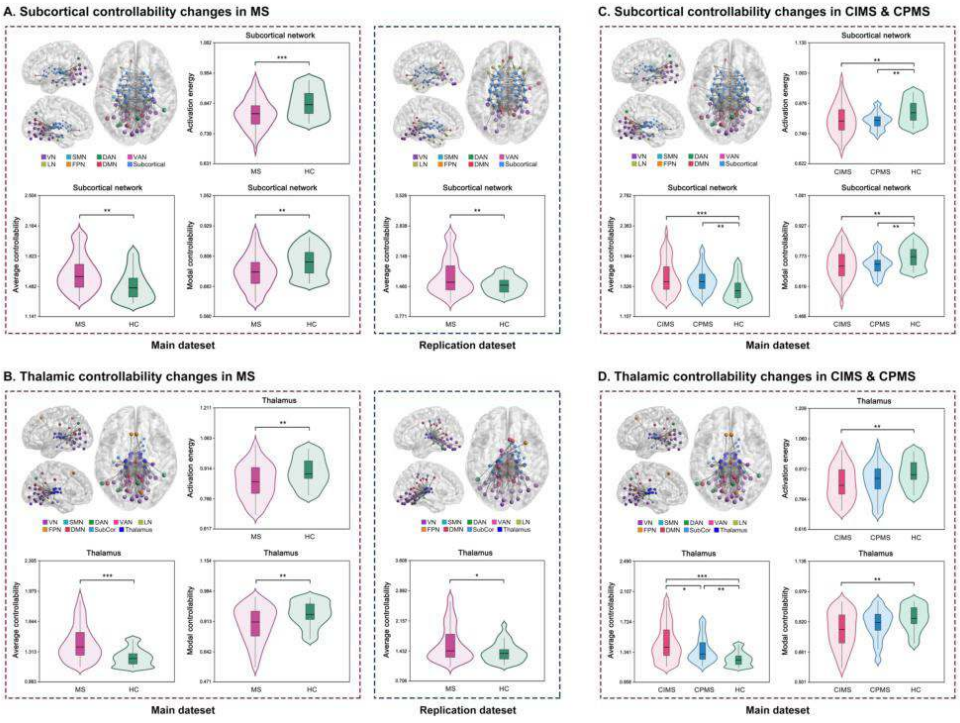

Conclusions: This study shows the specific effects that the subcortical network and the thalamus have on driving network changes and their association with cognitive impairment in multiple sclerosis. Our results emphasize the crucial role of the subcortical network and the thalamus in preserving brain transitions towards easy-to-reach network states while relinquishing brain transitions towards difficult-to-reach network states in multiple sclerosis, especially in those cognitively impaired patients, suggesting a possible brain mechanism underpinning the emergence of cognitive impairment in individuals with this disease.

References
1. Chiaravalloti, N. D. (2008). Cognitive impairment in multiple sclerosis. The Lancet Neurology, 7(12), 1139–1151. https://doi.org/10.1016/S1474-4422(08)70259-X
2. Coupé, P. (2023). Lifespan neurodegeneration of the human brain in multiple sclerosis. Human Brain Mapping, n/a(n/a). https://doi.org/10.1002/hbm.26464
3. d'Ambrosio, A. (2020). Reduced dynamics of functional connectivity and cognitive impairment in multiple sclerosis. Multiple Sclerosis Journal, 26(4), 476–488. https://doi.org/10.1177/1352458519837707
4. Eshaghi, A. (2018). Progression of regional grey matter atrophy in multiple sclerosis. Brain, 141(6), 1665–1677. https://doi.org/10.1093/brain/awy088
5. Hidalgo de la Cruz, M. (2021). Dynamic Functional Connectivity in the Main Clinical Phenotypes of Multiple Sclerosis. Brain Connectivity, 11(8), 678–690. https://doi.org/10.1089/brain.2020.0920
6. Jandric, D. (2022). A Systematic Review of Resting-State Functional MRI Connectivity Changes and Cognitive Impairment in Multiple Sclerosis. Brain Connectivity, brain.2021.0104. https://doi.org/10.1089/brain.2021.0104
7. Tozlu, C. (2023). The sequence of regional structural disconnectivity due to multiple sclerosis lesions. bioRxiv, 2023.01.26.525537. https://doi.org/10.1101/2023.01.26.525537

Poster No 1760

From Geometry to Hierarchy: Charting the Dominant Modes of Human Cortical Function in Development

Alexander Holmes[1], James Pang[1], Alex Fornito[2]

[1]Monash University, Melbourne, Victoria, [2]Monash University, Clayton, Victoria

Introduction: Low-dimensional representations of brain-wide inter-regional functional coupling (FC) offer a powerful tool for uncovering dominant organizational motifs of the cerebral cortex. Neural field theory, a well-validated, biophysically constrained framework for modelling large-scale brain activity, predicts that the dominant spatial eigenmodes of cortical dynamics should correspond to the modes of cortical geometry, under the assumption that neural dynamics are dominated by distance-dependent wave-like propagation (Robinson et al., 2016). In line with this view, recent work has shown that eigenmodes of cortical geometry offer a parsimonious explanation for how anatomy constrains diverse aspects of brain function (Pang, et al., 2023), but a precise alignment between these geometric modes and the dominant modes of dynamics is lacking. For instance, the first non-global mode of geometry follows an anterior-posterior (A-P) gradient, whereas the dominant mode of inter-regional FC estimates is organized along a sensorimotor-association (S-A) axis that reflects classically described cortical processing hierarchies (Margulies et al., 2016; Mesulam, 1998). Notably, while this discrepancy is apparent in adult brains, it is less salient in neonates, where geometric and functional modes show greater alignment (Lariviere et al., 2020), suggesting that maturation of complex patterns of connectivity that perturb simple distance-dependent processes may lead to the gradual emergence of an S-A axis from a functional organization that is initially dominated by geometry. Here, we tested this hypothesis using three independent fMRI datasets spanning age ranges from birth to 21 years.

Methods: We obtained fMRI data from 282 individuals in the UNC/UMN Baby Connectome Project (BCP; aged 1-60 months), 650 individuals in the Human Connectome Project – Development cohort (HCP-D; aged 6-21 years), and 347 individuals in the Nathan Kline Institute – Rockland Sample (NKI-RS; aged 6-21 years). Across 1,279 total participants, we computed low-dimensional connectivity manifolds via diffusion map embedding using FC matrices extracted from 11,524 cortical surface vertices, with group average manifolds also obtained across representative age bands. Geometric eigenmodes were calculated using the Laplace-Beltrami operator of a downsampled, left–right symmetric version of FreeSurfer's fsaverage population-averaged template (Pang et al., 2023). We then evaluated how well the age-specific FC modes correlated with either the canonical S-A axis obtained via diffusion map embedding in the Human Connectome Project S1200 group average FC matrix (Margulies et al., 2016), or a general linear model predicting the FC mode using the first three non-global geometric eigenmodes, which correspond to A-P, dorsal-ventral, and medial-lateral spatial patterns.

Results: The dominant functional mode in infancy reflected an A-P pattern that transitioned towards a hierarchical S-A axis in later development (Fig. 1). The coefficient of determination of the geometric model (r2) peaked in early infancy, with a maximum value of 0.95 at 6-9 months in the BCP dataset, and declined throughout adolescence, suggesting that the proportion of variability in FC modes explained by geometric eigenmodes decreases with age (Fig. 2). The r2 eventually reached a minimum value of 0.24 at 19-21 years old in the HCP-D cohort. Conversely, the r2 between the S-A axis and each age-specific gradient map increased with age, peaking at 0.94 at 19-21 years old in the HCP-D cohort.

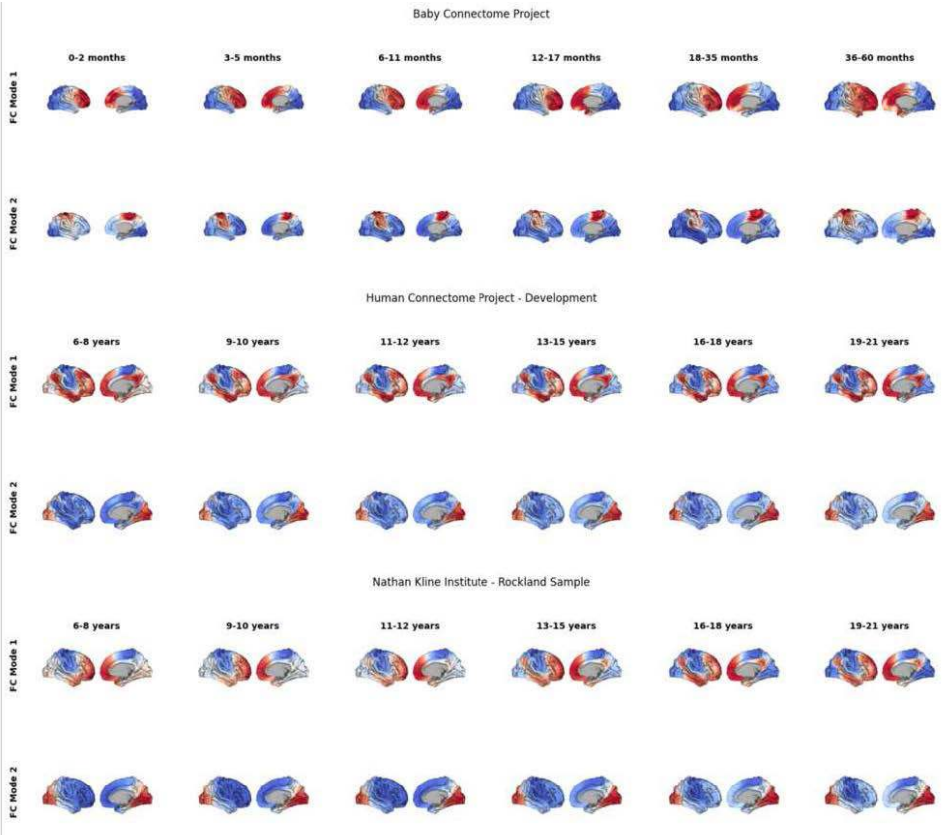

Figure 1. Spatial maps of the first two functional connectivity modes across development. The first functional connectivity mode in the Baby Connectome Project demonstrates an anterior-posterior gradient, while the later stages of development reflect a sensorimotor-association axis of organization in the brain.

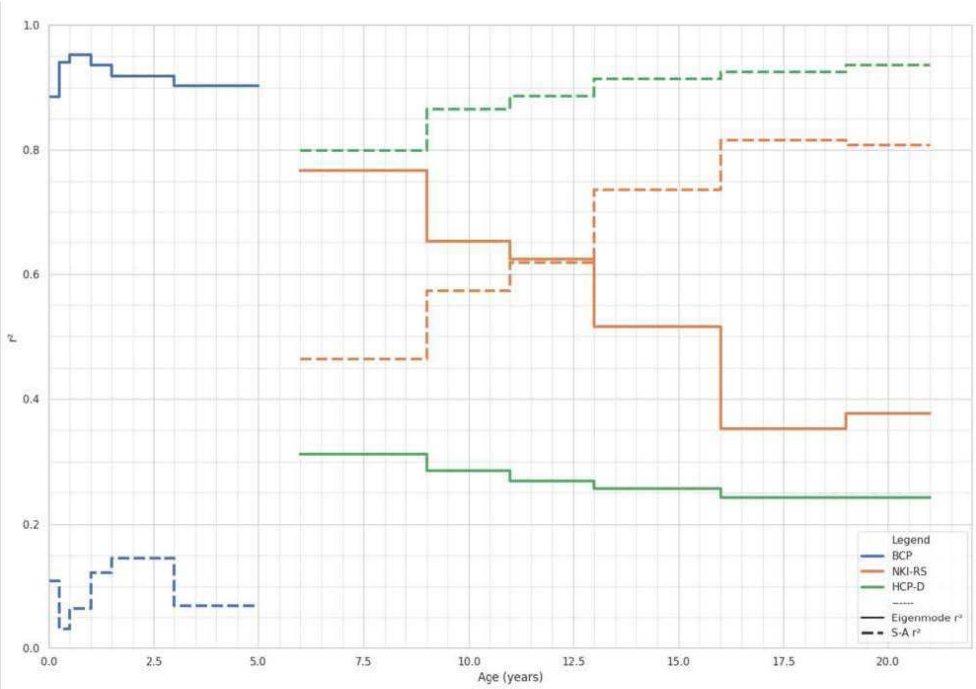

Figure 2. Correspondence between the dominant functional mode, the sensorimotor-association (S-A) axis, the first three non-global geometric eigenmodes across the Baby Connectome Project (BCP; Blue), the Nathan Kline Institute – Rockland Sample (NKI-RS; Orange), and the Human Connectome Project – Development (HCP-D; Green). The r^2 between the functional mode and the three geometric eigenmodes (solid line) peaks in infancy and declines with age, while the r^2 between the functional mode and the S-A axis (dashed line) peaks in later adolescence.

Conclusions: The functional organization of the infant cortex is strongly dominated by geometry and is patterned predominantly along an A-P gradient. As development progresses, this organization transitions towards a hierarchical S-A axis. These shifts may be driven by the maturation of long-range cortico-subcortical or cortico-cortical fibers.

References

1. Larivière, S., Vos de Wael, R., Hong, S. J., Paquola, C., Tavakol, S., Lowe, A. J., ... & Bernhardt, B. C. (2020). Multiscale structure–function gradients in the neonatal connectome. Cerebral Cortex, 30(1), 47-58.
2. Margulies, D. S., Ghosh, S. S., Goulas, A., Falkiewicz, M., Huntenburg, J. M., Langs, G., ... & Smallwood, J. (2016). Situating the default-mode network along a principal gradient of macroscale cortical organization. Proceedings of the National Academy of Sciences, 113(44), 12574-12579.
3. Mesulam, M. M. (1998). From sensation to cognition. Brain: a journal of neurology, 121(6), 1013-1052.
4. Pang, J. C., Aquino, K. M., Oldehinkel, M., Robinson, P. A., Fulcher, B. D., Breakspear, M., & Fornito, A. (2023). Geometric constraints on human brain function. Nature, 1-9.
5. Robinson, P. A., Zhao, X., Aquino, K. M., Griffiths, J. D., Sarkar, S., & Mehta-Pandejee, G. (2016). Eigenmodes of brain activity: Neural field theory predictions and comparison with experiment. NeuroImage, 142, 79-98.

Poster No 1761

Integrated Effective Connectivity Reveals Mesulam's Cortical Hierarchy in the Human Brain

Younghyun Oh[1,2,3], Yejin Ann[1,4], Takuya Ito[5], Sean Froudist-Walsh[6], Boris Bernhardt[7], Casey Paquola[8], Michael Milham[9,10], Choong-Wan Woo[1,2,3], Seok-Jun Hong[1,2,4,3,10]

[1]IBS Center for Neuroscience Imaging Research, Sungkyunkwan University, Suwon, South Korea, [2]Department of Biomedical Engineering, Sungkyunkwan University, Suwon, South Korea, [3]Life-inspired Neural Networks for Prediction and Optimization (LNPO) Group, Suwon, South Korea, [4]Department of Intelligence Precision Health Care, Sungkyunkwan University, Suwon, South Korea, [5]T.J. Watson Research Center, IBM Research, Yorktown, United States, [6]Bristol Computational Neuroscience Unit, Faculty of Engineering, University of Bristol, Bristol, United Kingdom, [7]McConnell Brain Imaging Centre, Montreal Neurological Institute and Hospital, McGill University, Montreal, Canada, [8]Institute of Neuroscience and Medicine, Forschungszentrum Jülich, Jülich, Germany, [9]Nathan S. Kline INstitute for Psychiatric Research, New York, United States, [10]Center for the Developing Brain, Child Mind Institute, New York, United States

Introduction: Identifying macro-scale directed functional flows between the brain regions, i.e. effective connectivity (EC), is key to understanding the emergence of our complex behaviors. However, reliable EC mapping remains as a daunting task, due to a lack of consensus across existing EC algorithms. This absence of methodological integration hinders a deeper investigation of neural dynamics along the brain architectures. Here, we sought to address these issues by introducing a new analytical framework, "integrated EC" (iEC), which combines the strengths of individual EC algorithms to create synergistic effects on sensitivity and reliability. Our framework revealed distinct connectome profiles across large-scale cortical hierarchy, demonstrating the utility of iEC as a robust tool for network neuroscience.

Methods: To implement the iEC framework, we first selected the major EC algorithms based on their mathematical uniqueness (Fig 1a). The iEC was then obtained by linear combination of the individual algorithms via Bayesian optimization (Fig 1b). We validated the inferred EC by assessing whether it could recover a FC pattern from rs-fMRI (Fig 1e). Next, we investigated the connectome profile, signal flows, and functional hierarchy using iEC to elucidate the organization of the human brain. For connectome profile, we assessed in-/out-degree and computed the ratio of their positive/negative connections. We further mapped the signal flow along the iEC by solving an equation 'x(t)=e^At x_0', where x_0 is a binary vector initialized with ones at seed brain regions and A is a the iEC matrix. Finally. the cortical hierarchy was determined based on the established method1, which involved conducting a general linear model in the form g(E[EC_ij])=θ_i-θ_j, with θ_i representing the hierarchical level of brain region i.

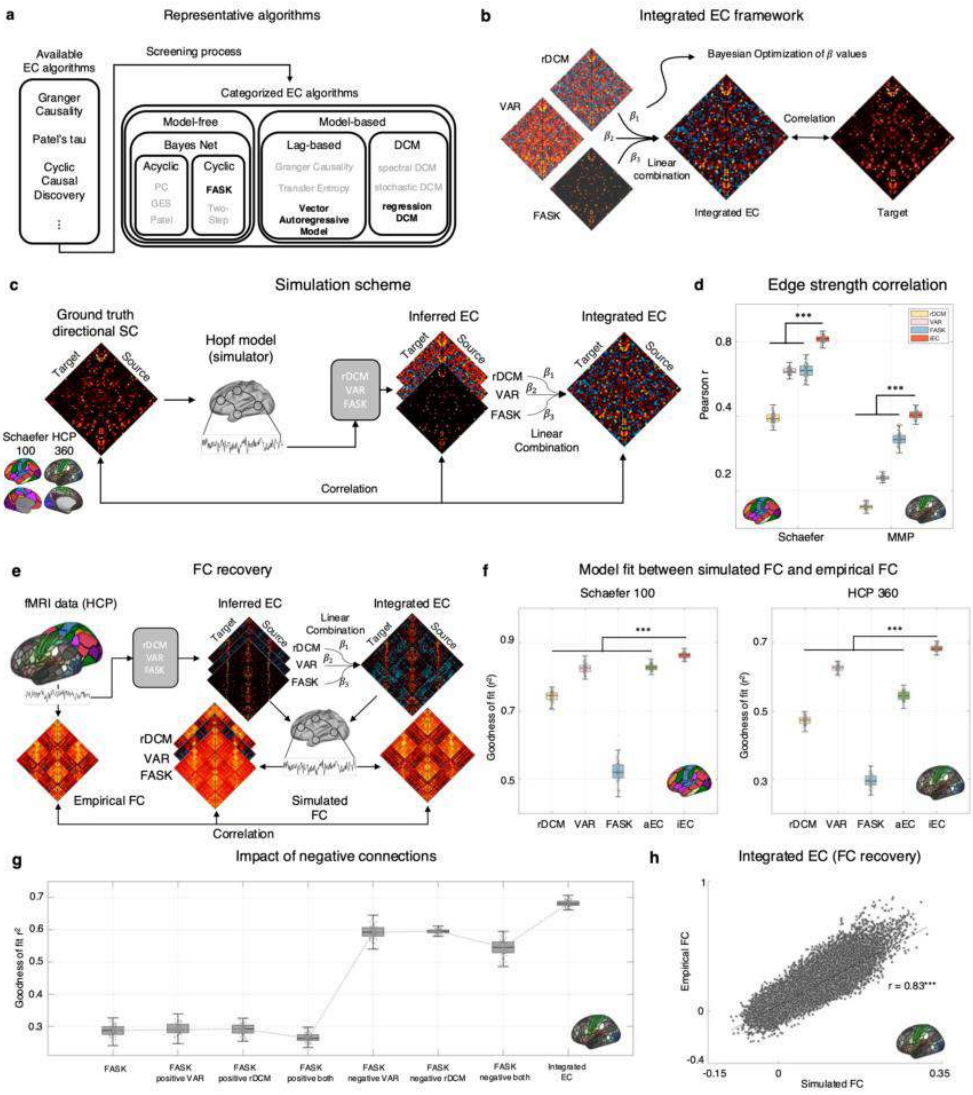

Results: Prior to implementing the iEC framework, we first assessed face validity of EC algorithms using Hopf model2 based on the ground-truth directed connectivity (Fig 1c). Across different network resolutions, iEC showed a superior performance over individual algorithms, showing mean correlation values of 0.82 and 0.41 with ground-truth networks of 50 and 180 nodes, respectively (Fig 1d). This validity was confirmed by a subsequent analysis based on experimental rs-fMRI data, in which we recovered FC from EC and tested the model fit between simulated and empirical FCs (Fig 1e). Again, the iEC showed better FC recovery compared to individual algorithms (Fig 1f; model fit r=0.83, Fig 1h), with a notable improvement by the inclusion of negative connections (Fig 1g). The connectome profile of iEC showed two distinct network characteristics (Fig 2a, b): i) generally higher in/out-degree in the default mode network (DMN) and ii) a clear positive-negative connection ratio along the sensory-fugal axis. This distinct topology informs the observed signal propagation pattern (Fig 2c, d): Positive signals predominantly originated from lower sensory regions, whereas negative signals propagated mostly from the higher association areas. Building on these findings, we posited that the positive/negative connections might correspond with feedforward/feedback connections, respectively, enabling us to deduce a cortical hierarchy from the discerned iEC. (Fig 2e). Our hierarchy map diverged from the established principal gradient4, particularly by positioning interoceptive regions at the top of hierarchy, instead of DMN (Fig 2f-g), which fully reflects the original concept of cortical diagram proposed by Mesulam4 (Fig 2h).

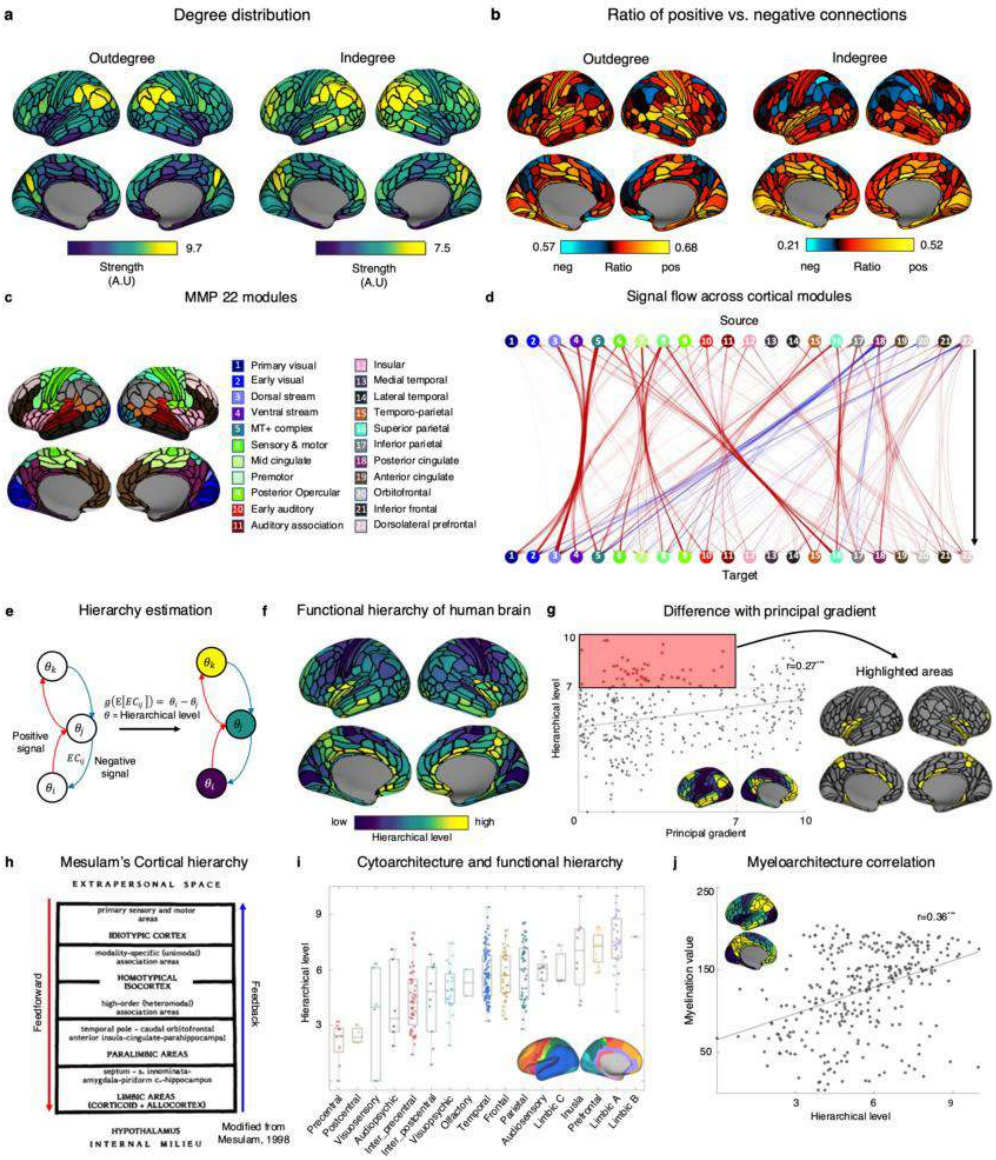

Conclusions: The iEC approach we introduce aims to overcome the current challenges in neuroimaging related to inferring the directionality of connectomes. By integrating existing methods, we have enhanced both accuracy and validity of EC mapping, which we believe the two key factors in uncovering novel principles of the human brain organization.

References

1. Markov, N. T. et al. Anatomy of hierarchy: feedforward and feedback pathways in macaque visual cortex. J. Comp. Neurol. 522, 225–259 (2014).
2. Deco, G., Kringelbach, M. L., Jirsa, V. K. & Ritter, P. The dynamics of resting fluctuations in the brain: metastability and its dynamical cortical core. Sci. Rep. 7, 3095 (2017).
3. Margulies, D. S. et al. Situating the default-mode network along a principal gradient of macroscale cortical organization. Proc. Natl. Acad. Sci. U. S. A. 113, 12574–12579 (2016).
4. Mesulam, M. M. From sensation to cognition. Brain 121 (Pt 6), 1013–1052 (1998).

Poster No 1762

Tracking Frequency Specific Instantaneous Brain Connectivity Dynamics in Resting State fMRI

Muchen Li[1], Zirui Song[1], Yuyang Xu[1], Yang Zhou[1], Yanxi Wang[1], Zhao Qing[1]

[1]*Southeast University, Nanjing, JiangSu*

Introduction: Typical resting-state functional magnetic resonance imaging (fMRI) studies measured brain functional connectivity (FC) and brain networks based on calculating the correlations between fMRI time series within a typical frequency

band, typically 0.01-0.1Hz, which was supposed to represent neural activities. However, these process implicated assumptions of the temporal stationarity throughout the measurement period, as well as no frequency specificity within this 0.01-0.1Hz band. There were amounts of studies reported fMRI signal have frequency-specific features even within 0.01-0.1Hz. Moreover, lots of studies have already investigated the "dynamic FC" and showed the importance temporal variation of FC. However, the parameters used to divide fMRI signal is often chosen arbitrarily, and limited the generalizability and comparability across these studies. The Hilbert Huang Transform (HHT) method is an adaptive iterative algorithm widely used in engineering. HHT decomposes signals into intrinsic model functions (IMFs) and define instantaneous phase, amplitude, and frequency for each IMF. Therefore, we apply HHT on fMRI to achieve adaptive frequency decomposition and high temporal resolution synchronization measurement based on instantaneous phase difference.

Methods: We downloaded one subset of the public database "Consortium for Reliability and Reproducibility, CORR," which is named"BNU1". 50 healthy young subjects (male/female: 30/20; age: 19–30 years) were included in the current study. The fMRI data here have 200 time points with TR=2s, voxel size=3.125×3.125×4.2 mm, matrix = 64×64, 33 slices. The preprocessing was performed by in DPABI, including realignment, slice-timing, covariates regression and spatial normalization. After preprocessing the time series were extracted for each Brainnetome atlas region. Then HHT was applied on each fMRI time series and instantaneous FC between each two regions for different frequency bands were decided by the following steps: 1). Using empirical model decomposition subdivided signals from two regions into different IMFs. 2). Instantaneous phase, amplitude, and frequency for each IMF were calculated. 3). Hilbert weighted frequency (HWF) was calculated from each IMF. 4). IMFs with HWF out of 0.01-0.1Hz were excluded, and the remaining IMFs from two brain regions were coupled based on the similarity of their HWF. 5). The Cosine values of the difference of the coupled IMFs' instantaneous phases were defined as instantaneous FC value at the frequency corresponded to the IMFs used. Similarly, we extend such steps and generated FC matrices among all 246 Brainnetome regions Then, similar to previous studies measured brain states using dynamic FC by K-means and further compared the results across different frequency bands.

Results: As shown in Figure.1, the IMFs from all brain regions and subjects have similar frequency distribution. There were 3 typical IMFs have HWF within 0.01-0.1Hz for all subjects and regions, which mean HWF were 0.01Hz, 0.02Hz and 0.05Hz, while the IMFs have higher frequency have larger HWF variation among regions and subjects. We further investigated brain states based on these 3 frequency bands. As shown in Figure. 2, in each band, there were 5 brain states. No matter to which frequency, there was one state which have longest duration, and showing that brain was organized into clusters: default mode, attention related and primary regions (visual, auditory and sensorimotor). A Chi-square test showed this main brain states across 3 bands significantly (P<0.001) to occur at the same time points. Besides, the Chi-square test also showed some of the minor states in different bands were temporal coupled across frequencies.

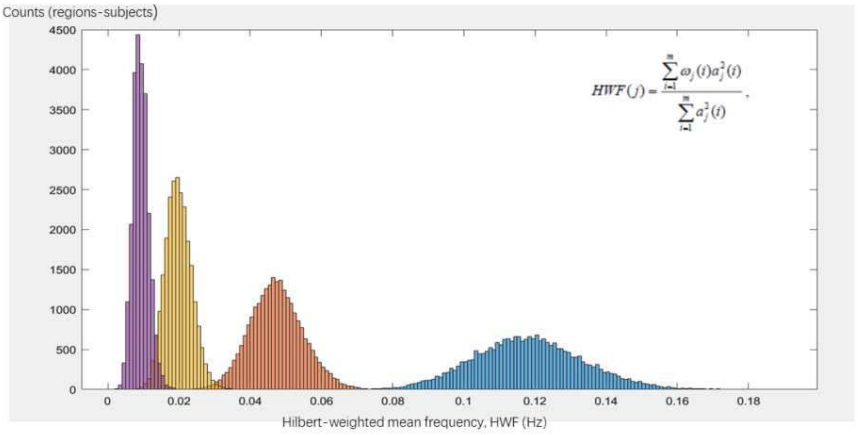

Figure.1. The Hilbert weighted frequency (HWF) distribution of all IMFs from all the regions and subjects. The definition of HWF was shown on the upper right where j is time points and ω is instantaneous frequency, a is instantaneous amplitude. All IMFs can be divided into 6 clusters by K-means and here we excluded the 2 clusters with lowest HWF which is below 0.01Hz, the HWF distribution of the IMFs in remaining 4 clusters were shown in this figure by different colors.

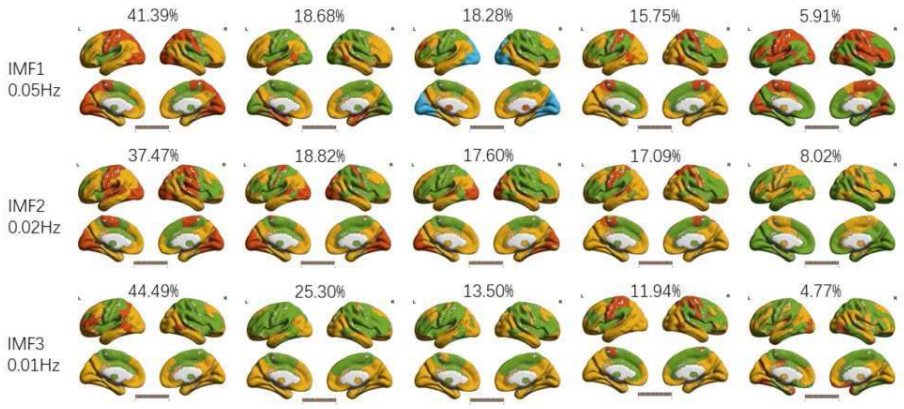

Figure.2. The connectivity model of all brain states in different frequency bands. For each IMFs, the instantaneous FC matrices of all time points were defined by Hilbert's instantaneous phase difference, and then divided into different brain states by K-means. The connectivity modularity (By Newman''s algorithm) for each states and their time proportion was shown in this figure.

Conclusions: The current study applied HHT on fMRI and reveal brain network dynamics at instantaneous level and also among different frequency. Moreover, brain dynamics have 3 characteristic frequency bands while the brain network dynamics showed coupling across bands.

References

1. Allen, E. A.(2014). "Tracking whole-brain connectivity dynamics in the resting state." Cereb Cortex 24(3): 663-676.
2. Kringelbach, M. L. (2020). "Brain States and Transitions: Insights from Computational Neuroscience." Cell Rep 32(10): 108128.
3. Schumacher, J. (2019). "Dynamic functional connectivity changes in dementia with Lewy bodies and Alzheimer's disease." Neuroimage Clin 22: 101812.
4. Yang, H.(2022). "Frequency-specific coactivation patterns in resting-state and their alterations in schizophrenia: An fMRI study." Hum Brain Mapp 43(12): 3792-3808.

Poster No 1763

Homotopic Functional Affinity Unraveling Regional Specialization and Cross-Cultural Diversity

Li-Zhen Chen[1], Xi-Nian Zuo[1]

[1]Beijing Normal University, Beijing, CN

Introduction: The integration/specialization of the two brain hemispheres can be characterized by the functional similarity of homotopic areas, providing important perspectives for the neural correlates of cognition and behavior. Despite the decisive role of spatial geometric constraints and homophilic attachment on the human connectome (Betzel et al., 2016), traditional practices in mapping functional homotopy only considered the correlations of functional timeseries between homotopic areas, disrespecting homophily factors and interactions between non-homotopic brain areas. Here, we proposed a new method on functional homotopy analysis, namely Homotopic Functional Affinity (HFA), depicted a new prospect for studies investigating hemispheric integration/specialization through the lens of functional homotopy.

Methods: HFA evaluates the affinity between the full-brain Functional Connectivity Profiles (fbFCP) of homotopic areas, simultaneously captures geometric constraints (homotopic location) and homophily (fbFCP affinity) (Fig.1). Using high-precision resting state fMRI data from the Human Connectome Project (HCP, Van Essen et al., 2013) and the Chinese Human Connectome Project (CHCP, Ge et al., 2023), we constructed the human HFA map and evaluated its test-retest reliability with Intraclass Correlation Coefficient (ICC). Next, we validated HFA through ROI-based analysis, including ROIs' fbFCP comparison, meta-analysis of cognitions involved in ROIs, and the correlation analysis between activations of ROIs under different tasks and their HFA. Finally, we validated HFA at global level by calculating the correlation between the HFA map and multimodal brain maps of evolution, gene expression, myelination, functional gradient and cognitive association.

Results: The HFA maps were highly similar to the principal functional gradient map (Margulies et al., 2016), with an ICC of the global mean greater than 0.5, and vertex-level ICCs generally greater than 0.4, while some vertices with almost perfect reliability (Fig.1). Low HFA of the Inferior Parietal Lobule (IPL) and their clear differentiable subregions were observed. Based on the HFA map of HCP, three adjacent IPL subregions were defined as ROIs, namely aIPL, mIPL, and pIPL. The fbFCP of aIPL and pIPL showed cross-dataset consistency. The left aIPL strongly connected with the default mode network (DMN), while the right aIPL tended to connect with attention networks. Importantly, the right aIPL negatively connected with the

DMN. The left pIPL also had the strongest connectivity with DMN, but many negative connectivity appeared in the attention networks, while the right pIPL had fewer negative connectivity globally. The fbFCP of mIPL displayed transition between aIPL and pIPL. The fbFCP of left mIPL was similar to that of the left aIPL, and the fbFCP of right mIPL was similar to that of the right pIPL (Fig.2). Compared with the connectivity in HCP, the left mIPL in the CHCP had more negative connectivity with the ventral attention network. The results of meta-analysis showed a gradual functional shift from attention to social cognition, and then to language between aIPl, mIPL, and pIPL. Functional specialization of ROIs in left hemisphere was stronger, and their right counterparts engaged in more extensive cognitions. The results of task activation correlation were consistent with those of the meta-analysis. Notably, there were significant differences across datasets in social cognition tasks. Furthermore, multimodal brain maps' correlation analysis illustrated a close relationship between HFA map and multimodal brain maps (Fig.2).

Conclusions: The consistency of results in different analyzes demonstrated the feasibility of using HFA to explore the rs-fMRI and t-fMRI associations and the sensitivity of HFA in detecting brain functional specialization mechanisms underlying cultural-related differences. This new method will provide a reliable and effective tool for future population neuroscience research.

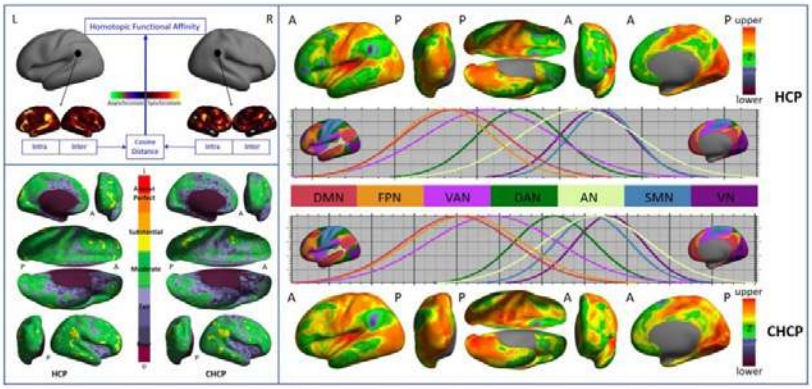

Fig.1 HFA diagram. The upper left panel shows the calculation procedure of HFA for a pair of homotopic areas. HFA is the cosine distance between homotopic areas' full-brain functional connectivity profiles. The lower left panel displays the test-retest reliability of HFA. The right panel shows the HFA maps of different datasets and their distribution in seven networks. HFA: Homotopic Functional Affinity; L: Left; R: Right; A: Anterior; P: Posterior; DMN: Default Mode Network; FPN: Frontoparietal Network; VAN: Ventral Attention Network; DAN: Dorsal Attention Network: AN: Auditory Network: SMN: Somatomotor Network: VN: Visual Network.

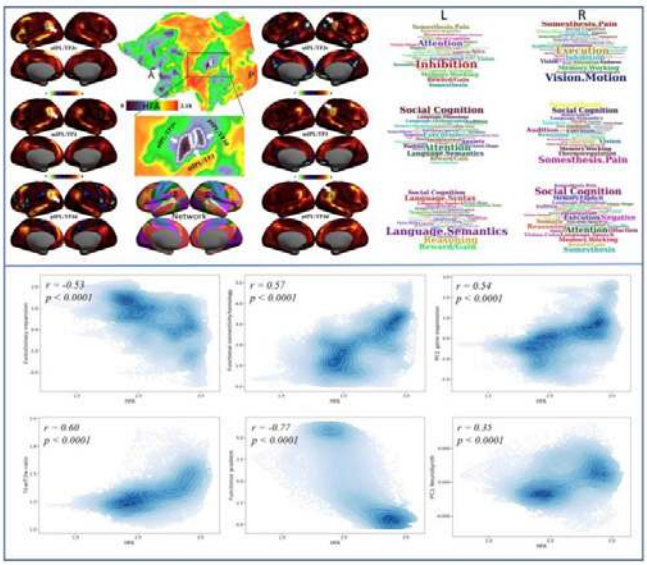

Fig.2 Validation of HFA from HCP dataset at ROI level and global level. The first panel displays three ROIs (aIPL/TPJv, mIPL/TPJ, and pIPL/TPJd) defined according to HFA map from HCP dataset, and their bilateral full-brain functional connectivity profiles. They are significantly different across hemispheres, and there are gradual transitions between regions. The right side of this panel exhibits the cognitive and behavioral meta-analysis results of bilateral ROIs. The second panel shows strong correlations between global HFA map of HCP and multimodal brain maps. HFA: Homotopic Functional Affinity; IPL: Inferior Parietal Lobule; TPJ: Temporoparietal Junction; L: Left; R: Right; A: Anterior; P: Posterior.

References
1. Betzel, R.F. (2016), 'Generative models of the human connectome', Neuroimage, vol. 124, Pt A, pp. 1054-1064.
2. Ge, J. (2023), 'Increasing diversity in connectomics with the Chinese Human Connectome Project', Nature Neuroscience, vol. 26, no. 1, pp. 163-172.
3. Margulies, D.S. (2016), 'Situating the default-mode network along a principal gradient of macroscale cortical organization', Proceedings of the National Academy of Sciences of the United States of America, vol. 113, no. 44, pp. 12574-12579.
4. Van Essen, D.C. (2013), 'The WU-Minn Human Connectome Project: an overview', Neuroimage, vol. 80, pp. 62-79.

Poster No 1764

CNN Hippodeep AI volumetry correlated with rs-fMRI networks FC in predicting Alzheimer's disease

Nur Shahidatul Nabila Ibrahim[1], Subapriya Suppiah[2], Buhari Ibrahim[3], Nur Hafizah Mohad Azmi[3], Vengkatha Priya Seriramulu[3], Mazlyfarina Mohamad[4], Hakimah Mohamad Sallehuddin[3], Rizah Mazzuin Razali[5], Nor Harzana Harrun[6], Marsyita Hanafi[2]

[1]KPJ Healthcare University, Nilai, Negeri Sembilan, [2]Universiti Putra Malaysia, Serdang, Selangor, [3]Universiti Putra Malaysia, Serdang, Selangor, [4]Universiti Kebangsaan Malaysia, Kuala Lumpur, Wilayah persekutuan, [5]Hospital Kuala Lumpur, Kuala Lumpur, Kuala Lumpur, [6]Klinik Kesihatan Pandamaran, Klang, Selangor

Introduction: Minor alterations in the size of the hippocampus can happen during normal and abnormal ageing in the human brain. Evaluating hippocampal volumes by manual or even semi-automated means is a laborious process, necessitating the development of fully automated segmentation techniques that are efficient and consistent across time. Artificial intelligence technology using deep convolutional neural networks (CNN) are now being used as effective algorithms for segmenting images in big longitudinal neuroimaging investigations for Alzheimer's Disease (AD). Nevertheless, in order for these innovative algorithms to have practical use in clinical research, it is imperative to verify their accuracy and repeatability by using various datasets.

Methods: In this study, we assess the effectiveness of a CNN method called Hippodeep, which was created by Thyreau et al., for segmenting the hippocampus. We conducted a comparative analysis of its segmentation outputs with semi-automated segmentation using Voxel-based morphometry (VBM). This analysis was performed on a sample of 15 healthy controls (HC) and 15 AD participants who underwent structural MRI and resting-state functional MRI as well as neuropsychological test questionnaires.

Results: Findings of (15 AD and 15 HC) showed reduced functional connectivity for resting-state networks such as Default Mode Network (DMN) and Salience Network (SN). HippoDeep model shows higher correlation in assessing hippocampal volume compared to VBM method. Diagnosis accuracy test using ROC curve shows improved sensitivity 93.33% and specificity of 80.00% and AUC 0.927 while right hippocampal volume with sensitivity 80.00%, specificity of 100.00% and AUC 0.91 using HippoDeep model in detecting AD compared to VBM method and ability of HippoDeep model to predict early detection of AD.

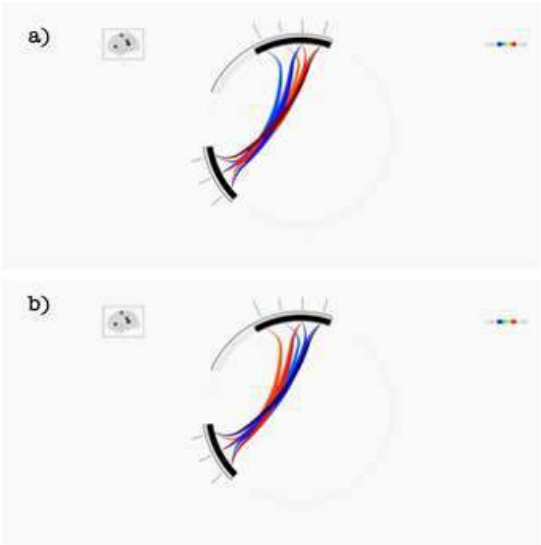

Figure 1: a) Comparison network difference in HC > AD b) Comparison network difference in AD > HC

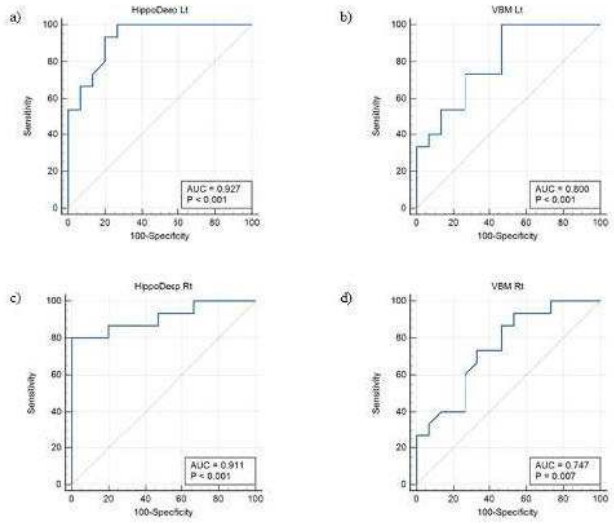

Figure 2: ROC curve of the accuracy of the HippoDeep compared to the VBM model for classifying Alzheimer's disease based on the measurements of bilateral hippocampal volumes.

Conclusions: Decreased functional connectivity in resting-state networks can serve as a biomarker, along with HippoDeep, to predict the early onset of Alzheimer's disease.

References

1. Thyreau, B., Sato, K., Fukuda, H., Taki,Y (2018), 'Segmentation of the hippocampus by transferring algorithmic knowledge for large cohort processing'. Med Image Anal vol.4, pp.214. doi: 10.1016/j.media.2017.11.004. Epub 2017 Nov 10. PMID: 29156419.
2. Ibrahim, N.S.N, Suppiah, S.,Ibrahim, B.,Mohad Azmi, N. H., Seriramulu, V.P., Mohamad, M.,Hanafi, M., Sallehuddin, H., Razali R. M.,Harrun, N. H. (2023). Validation of automated hippocampus volume assessment using deep learning convolutional neural networks in patients with Alzheimer's disease medRxiv 2023.04.11.23288432; doi: https://doi.org/10.1101/2023.04.11.23288432
3. Islam, J., & Zhang, Y. (2019). Understanding 3D CNN Behavior for Alzheimer's Disease Diagnosis from Brain PET Scan. ArXiv, abs/1912.04563.
4. Liu, L., Zhao, S., Chen, H., Wang, A.: A new machine learning method for identifying alzheimer's disease. Simulation Modelling Practice and Theory 99, 102023 (2020)

Poster No 1766

Multi-Scale Analysis Framework Integrating Brain Functional Connectivity and Activity

Xiangxiang Cui[1], Min Zhao[2], Dongmei Zhi[1], Weizheng Yan[3], Vince Calhoun[4], Chuanjun Zhuo[5], Jing Sui[6]

[1]Beijing Normal University, Beijing, Beijing, [2]Institute of Automation, Chinese Academy of Sciences, Beijing, China, Beijing, Beijing, [3]Lab of Neuroimaging, National Institutes of Health, Bethesda, MD, [4]GSU/GATech/Emory, Decatur, GA, [5]Tianjin Mental Health Center, Nankai University Affiliated Anding Hospital, Beijing, Tianjin, [6]Beijing Normal University, Beijing, China

Introduction: In the field of psychiatric diagnosis, despite some research advancements, challenges persist in accurately classifying and understanding mental illnesses. Notably, current methodologies have limitations in capturing and analyzing the complexities of brain functional networks, especially in handling the multiscale spatiotemporal features of brain activity. Our study aims to overcome these limitations by utilizing multiscale information to enhance the accuracy of psychiatric disorder classification and to delve deeper into the role of spatiotemporal characteristics of brain functional networks in disease identification.

Methods: Our research methodology integrates strategies of both multiscale modeling and multiscale features. 1) Firstly, in terms of feature multiscale, we conducted variable step-length analysis on time series (TC) to extract functional network connectivity (FNC) and dynamic functional network connectivity (dFNC), revealing the brain network's activity characteristics across different temporal scales. Additionally, through multiscale entropy analysis of TC features, we further uncovered the hierarchical organization patterns of brain network states. 2) Secondly, in terms of model multiscale, we first proposed Neural Connection Search (NCS) to optimize network connections, and applied multiscale dilated convolution to further enhance network architecture. This approach not only mimics the brain's long and short connection mechanisms but also significantly improves the performance of psychiatric disorder classification.

Results: In in-house dataset, our method achieved an accuracy rate (ACC) of 87.9%, surpassing advanced algorithms. Our method also realized a specificity (SPE) of 88.7%, indicating its robust capability in accurately identifying negative samples. Moreover, our method excelled in sensitivity (SEN) and F1 score, reaching 87.3% and 88.0%, respectively, further proving its ability to maintain high sensitivity for positive samples while also ensuring high precision. These results consistently indicate that our method provides more accurate and reliable predictions when dealing with complex datasets, which is essential for practical applications. Overall, by integrating traditional features (FNC) with time series characteristics (TCs) and their derived features (dFNC), our multi-scale analysis method not only stands out in individual metrics but also exhibits balanced and superior performance across all evaluated metrics.

Conclusions: By combining multiscale feature analysis and multiscale modeling, our study effectively analyzes the spatiotemporal features of brain functional networks, thereby enhancing the accuracy of psychiatric disorder classification. These findings represent a important technical advancement and offer a new perspective for a deeper understanding of the complex dynamics of brain networks, holding substantial scientific significance and practical value for the diagnosis of mental illnesses.

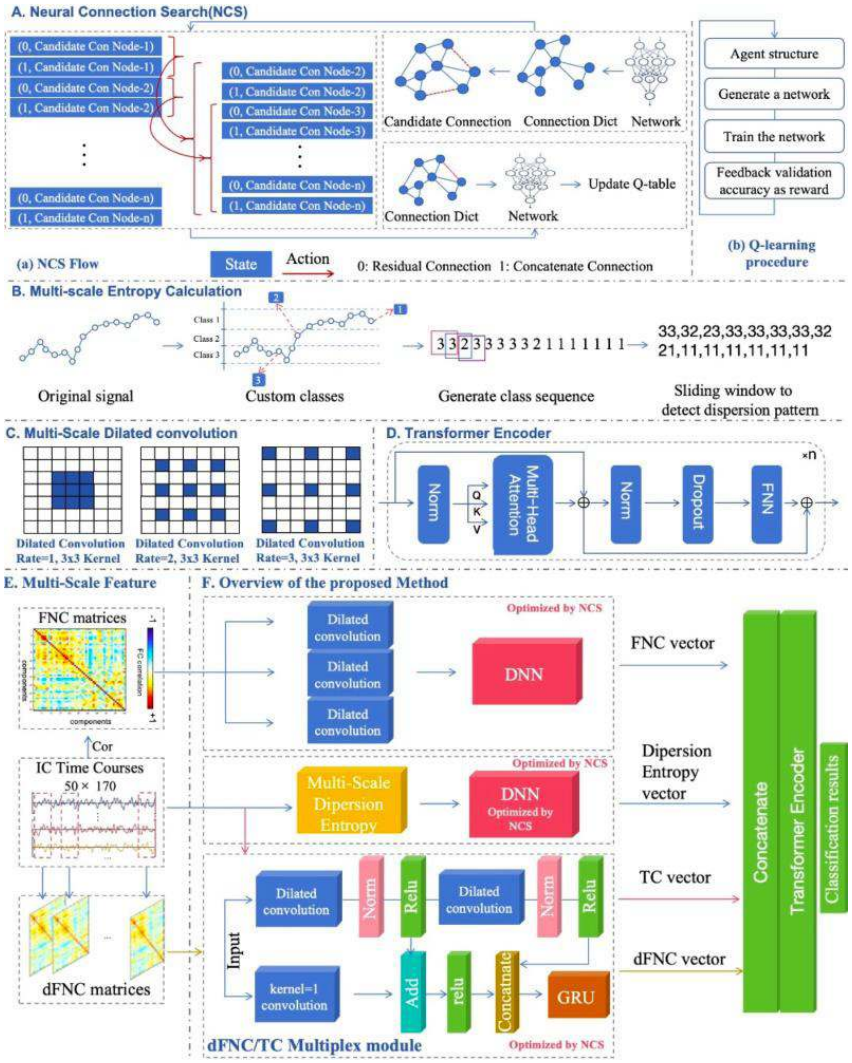

Table I. Comparative experimental results on the internal dataset

Methods	Feature	ACC	SPE	SEN	F1	AUC
RF	FNC	76.4 ± 0.8	72.3 ± 1.8	80.4 ± 0.5	77.6 ± 0.5	84.6 ± 0.2
AdaBoost	FNC	77.0 ± 0.2	75.6 ± 0.2	78.3 ± 0.3	77.6 ± 0.2	81.8 ± 0.3
SVM	FNC	81.5 ± 0.3	80.0 ± 0.8	83.0 ± 0.5	82.6 ± 0.2	88.4 ± 0.2
BrainNetCNN	FNC	80.1 ± 0.8	77.2 ± 1.5	82.9 ± 1.2	80.1 ± 0.9	87.7 ± 0.5
DNN	FNC	80.9 ± 0.4	80.6 ± 1.2	81.3 ± 0.7	81.3 ± 0.4	88.8 ± 0.3
C-RNN	FNC	82.5 ± 0.9	80.8 ± 1.1	84.2 ± 0.9	83.1 ± 0.8	90.8 ± 0.4
C-RNN	FNC	83.5 ± 0.6	81.5 ± 0.9	85.4 ± 0.5	84.0 ± 0.5	91.4 ± 0.3
cGCN	FNC+TCs	78.3 ± 0.6	77.2 ± 1.2	78.6 ± 1.1	78.4 ± 0.8	81.2 ± 0.5
HDLFCA	FNC+TCs	85.3 ± 0.4	83.4 ± 0.6	87.1 ± 0.5	85.8 ± 0.3	92.4 ± 0.2
Ours	FNC+TCs+dFNC	87.9 ± 0.5	88.7 ± 0.5	87.3 ± 0.3	88.0 ± 0.3	93.1 ± 0.2

References

1. Liu, Mianxin, et al. “Assessing spatiotemporal variability of brain spontaneous activity by multiscale entropy and functional connectivity.” NeuroImage 198 (2019): 198-220.
2. Yan, Weizheng, et al. “Discriminating schizophrenia using recurrent neural network applied on time courses of multi-site FMRI data.” EBioMedicine 47 (2019): 543-552.
3. Yan, Weizheng, et al. “Deep chronnectome learning via full bidirectional long short-term memory networks for MCI diagnosis.” Medical Image Computing and Computer Assisted Intervention–MICCAI 2018: 21st International Conference, Granada, Spain, September 16-20, 2018, Proceedings, Part III 11. Springer International Publishing, 2018.
4. Zhao, Min, et al. “An attention-based hybrid deep learning framework integrating brain connectivity and activity of resting-state functional MRI data.” Medical image analysis 78 (2022): 102413.
5. Zoph, Barret,, et al.”Neural architecture search with reinforcement learning.” arXiv preprint arXiv:1611.01578 (2016).
6. Zhong, Zhao, et al. “Practical block-wise neural network architecture generation.” Proceedings of the IEEE conference on computer vision and pattern recognition. 2018.

Poster No 1767

A Common Space for Human-Macaque Brain Comparison Constructed by Graph Convolutional Neural Network

Haiyan Wang[1], Yuheng Lu[1], Yumeng Xin[2], Luqi Cheng[3], Yufan Wang[1], Weiyang Shi[1], Deying Li[1], Congying Chu[1], Lingzhong Fan[1], Ning Liu[2], Tianzi Jiang[1]

[1]Brainnetome Center, Institute of Automation, Chinese Academy of Sciences, Beijing, China, [2]Institute of Biophysics, Chinese Academy of Sciences, Beijing, China, [3]School of Life and Environmental Sciences, Guilin University of Electronic Technology, Guilin, China

Introduction: Cross-species comparative research on primates plays a crucial role in understanding the unique high-order cognitive functions that distinguish humans from non-human primates. Given the variations in brain scale, morphology, and function across different species, it is essential to define a common space when conducting cross-species comparisons[1]. Currently, the common space definition is mainly based on known homologous landmarks and relies on single-modality images. In this study, we proposed a novel data-driven approach to create a common space using a graph convolutional neural network (GCN), effectively integrating both structural connectivity and resting-state functional connectivity information.

Methods: For humans, data from Human Connectome Project[2] was used. For macaques, data was collected in a 3T Siemens Prisma MRI scanner at Beijing MRI Center for Brain Research (N=8, Anesthetic: T1, T2, and DTI, Awake: resting-state fMRI). For macaques, structural data was processed with HCP-NHPpipelines[3], resting-state fMRI data was processed using afni_proc.py. Vertex-to-vertex functional connectivity was calculated for both humans and macaques. The preprocessing of DTI data was conducted using FSL for both humans and macaques, and each vertex’s blueprint was calculated using XTRACT[4]. Each of the blueprint feature was homogenous between humans and macaques[5]. The data of humans and macaques was separately mapped to a 10k surface. In this study, we constructed a common space for cross-species comparison between humans and macaques using GCN (Fig. 1). Specifically, we used cortical vertices as the nodes of the graph. The edges of the graph were derived from the triangular facets of the surface or the vertex-to-vertex functional connection. We selected the 10, 20, 30, and 40 strongest nodes associated with each cortical vertex for the functional connections. The blueprints were used as features for the graph nodes. The model consisted of two Chebyshev convolutional layers and a linear layer. Since each convolutional layer integrated the features of connected nodes, the final output of the linear layer formed a feature space that combined both structural and functional connections. Finally, an attention mechanism was employed to map from human to macaque.

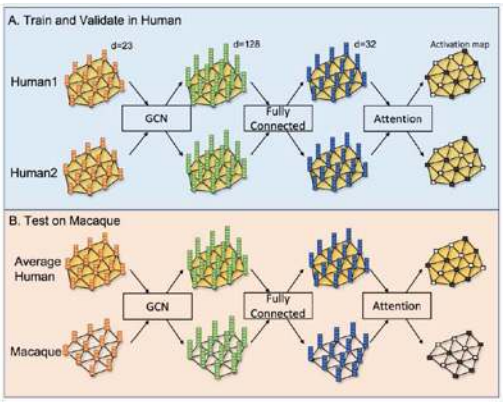

Figure 1. The graph convolutional neural network used to construct the brain common space between humans and macaques. (A) The training and validation processes in humans. (B) The testing process in macaques.

Results: Taking myelin map projection as an example, Fig. 2 shows the prediction performance of macaque myelin maps based on the GCN model. The best prediction results were obtained using the 20 strongest nodes associated with each cortical vertex as edges (Fig. 2A). Fig. 2B shows the training, validation, and testing processes for both the left and right hemispheres. As the number of training epochs increased, the loss gradually decreased, and the correlation between the true and predicted maps increased. Fig. 2C presents a comparison with existing methods, where 'BPregister' represents the projection based on the KL divergence of blueprint features[5], and 'Joint-embedding' refers to the gradient method based on functional connectivity[6]. It can be observed that the GCN-based method outperforms the other two methods under different numbers of subjects. Specifically, when we use 600 human subjects, the accuracies are: BPregister, L=0.592, R=0.615, mean=0.604; Joint-embedding, L=0.552, R =0.648, mean=0.600; GCN, L=0.631, R=0.652, mean=0.641.

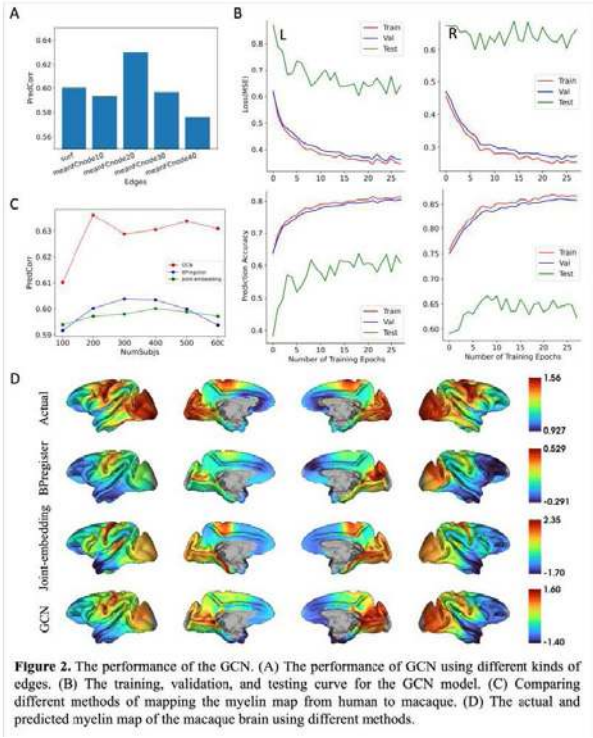

Figure 2. The performance of the GCN. (A) The performance of GCN using different kinds of edges. (B) The training, validation, and testing curve for the GCN model. (C) Comparing different methods of mapping the myelin map from human to macaque. (D) The actual and predicted myelin map of the macaque brain using different methods.

Conclusions: In the present study, we employed a GCN-based approach to integrate both structural and functional connectivity, constructing a novel data-driven common space for cross-species comparisons between humans and macaques. By using this common space, the projection of human myelin maps onto macaques can be improved. Notably, when training this model for projecting different task-based activations simultaneously, a more comprehensive common space can be constructed. Furthermore, since DTI and resting-state fMRI can be more easily acquired compared to task-based fMRI, this method can also be applied to newborns and other species.

References

1. Mars, R. B. (2021), 'A common space approach to comparative neuroscience', Annual Review of Neuroscience, vol. 44, pp. 69-86.
2. Glasser, M. F. (2013), 'The minimal preprocessing pipelines for the Human Connectome Project', Neuroimage, vol. 80, pp. 105-124.
3. Donahue, C. J. (2016), 'Using diffusion tractography to predict cortical connection strength and distance: a quantitative comparison with tracers in the monkey', Journal of Neuroscience, vol. 36, pp. 6758-6770.
4. Warrington, S. (2020), 'XTRACT-Standardised protocols for automated tractography in the human and macaque brain', Neuroimage, vol. 217.
5. Mars, R. B. (2018), 'Whole brain comparative anatomy using connectivity blueprints', eLife, vol. 7.
6. Xu, T. (2020), 'Cross-species functional alignment reveals evolutionary hierarchy within the connectome', Neuroimage, vol. 223.

Poster No 1768

Quantifying multiplexing in the brain using functional connectivity embedding

Nicole Eichert[1], Saad Jbabdi[2]

[1]University of Oxford, Oxford, Oxfordshire, [2]Oxford University, Oxford, United Kingdom

Introduction: The cerebral cortex is composed of over one hundred distinct functional regions[1]. However, these areas are not homogenous as they can contain various sources of functional heterogeneity. These different functional patterns can

overlap within the same region. E.g., primary visual cortex contains a retinotopic 2D map, but also ocular dominance columns. Dorsal parietal lobe contains retinotopic maps as well as body maps. We posit that overlapping patterns of function relate to overlapping patterns of connections, and reflect the rich array of functions that a brain area participates in[2]. We refer to this as multiplexing[3]. Overlapping patterns may also interact, via short-range connections, to enable more complex functions. Despite this, the dominant paradigm in macroscopic brain connectivity represents brain areas as single, discrete, and homogenous nodes, and falls short of capturing within-area diversity. Here we introduce a method for characterising the diversity of within-area functional patterns, a.k.a. multiplexing. We use low-dimensional embedding of functional connectivity to extract within-area overlapping patterns of connections from pairwise regional connections. We quantify multiplexing through assessing the diversity of overlapping connectivity patterns. Finally, we show that these overlapping patterns are associated with task-relevant networks.

Methods: To extract overlapping patterns of connectivity from a brain area, we consider its pairwise connections with an extended set of other areas throughout the brain. We implemented an extension of spectral embedding to bipartite graphs to identify the dominant pattern of pairwise connectivity (Fig1A). For each pair of parcels, the connectivity matrix is reduced to a 1-dimensional embedding space (Fig1B). Resting-state scans from 100 HCP subjects were used to build the connectivity matrix C at group level. By changing the target area (amongst a set of 316 uniform parcels), we can build up a matrix summarising the dominant spatial modes within a given region. We quantify the diversity of these modes using hierarchical clustering with a range of cut-off thresholds. Utility of the metric was evaluated by simulating mixtures from multivariate distributions whilst systematically varying the number of non-overlapping clusters (Fig2B). We derived the diversity metric for each parcel and averaged the result across 5 random parcellations, produced by randomly rotating the original parcellation (Fig2C). Finally, we ask whether the spatial modes are associated with brain activity and accessed 300 task-fMRI maps from neurovault[4] (Fig2D,E). Since the spatial modes are related to the connectivity of a brain area with a set of external regions throughout the cortex, we hypothesise that evoked brain activity within a region would reflect this association.

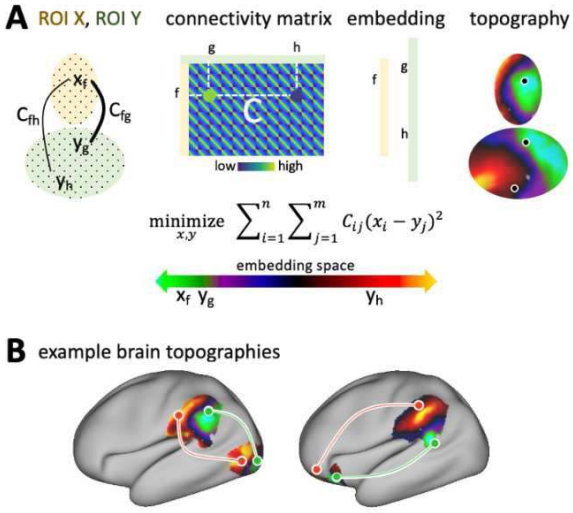

Fig 1. Connectivity embedding. **A**: A set of n points in ROI X maps to a set of m points in ROI Y resulting in the connectivity matrix C (in this example: $C_{fg} > C_{fh}$). We define a low-dimensional (here one-dimensional) embedding space that maps points with high connectivity close to each other, as formulated in the cost function. Applying a spectral embedding algorithm to C to optimise the cost function, reveals a spatial topography within the ROIs: Similar colours in the two ROIs indicate high connectivity. **B**: Example topographies obtained from connectivity embedding of group-level rs-fMRI data with connectivity patterns highlighted with coloured lines. Importantly, the same temporo-parietal ROI exhibits different topography depending on the second target area (here occipital vs. prefrontal).

Results: The clustering-based diversity metric robustly scales with the number of true clusters, independent of the parcellation resolution (Fig2B). Across the cortex, highest diversity in spatial topographies was observed in the insula, the medial frontal lobe and the medial temporal lobe. These regions are often considered part of the multiple-demand network (Fig2C). We found significant assoications between spatial modes within a region and their corresponding external regions during task (Fig2E). The association between spatial modes and task activations is robust across the whole cortex.

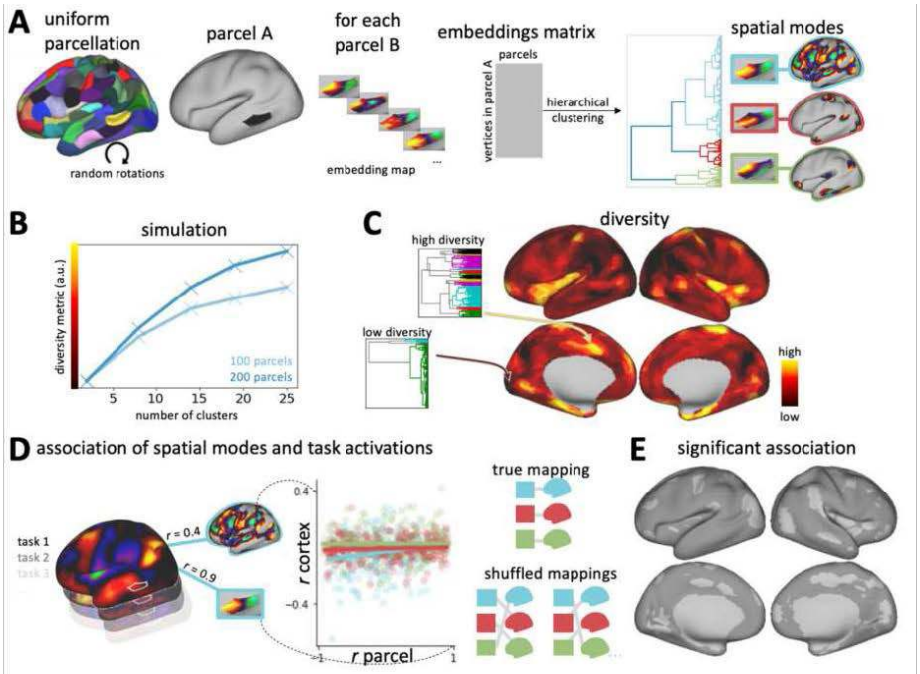

Fig 2. Quantifying multiplexing. A: Workflow to quantify multiplexing based on embedding of resting-state functional MRI inter-parcel connectivity data. The principal embedding map is computed for parcel A with every other parcel B, as described in Fig 1A. We applied clustering to derive spatial modes of parcel A with the associated cortical parcels (here 3 modes). **B**: From the embeddings matrix, we derived a diversity metric based on hierarchical clustering with a range of cluster thresholds. The utility of the metric was confirmed using simulations. **C**: Highest diversity in connectivity topographies is observed in insular and medial frontal areas. **D**: Workflow to test for association of spatial modes with task activation: We correlate task-based activity within a region to each of its spatial modes (*r* parcel), and we also correlate activity outside the region with the corresponding set of areas associated with said mode (*r* cortex). If the two are interrelated, the two correlation coefficients should show an association. For comparison, we also computed the association when shuffling the spatial mode used within and outside the parcel. **E**: Areas with a significant relationship between spatial modes and task activations are highlighted dark ($r>0$, $p<0.05$, $n=900$, exceeding shuffled mappings).

Conclusions: We present an algorithm to define and measure regional spatial topographies across the cortex using connectivity embedding. We developed a framework to detect topographic diversity from resting-state data, which serves as a marker for the multiplexing ability of a brain region. We showed that topographically organised connectivity is abundant in the brain and relevant for task activity and that multiplexing is highest in the multiple-demand network.

References

1. Glasser, M. F. et al. A multi-modal parcellation of human cerebral cortex. Nature 536, 171–178 (2016).
2. Jbabdi, S., Haak, K. & Behrens, T. Separating functional modes using spectral methods applied to resting-state FMRI. in OHBM 2013 Conference proceedings.
3. Jbabdi, S., Sotiropoulos, S. N. & Behrens, T. E. The topographic connectome. Curr. Opin. Neurobiol. 23, 207–215 (2013).
4. Gorgolewski, K. J. et al. NeuroVault.org: a web-based repository for collecting and sharing unthresholded statistical maps of the human brain. Front. Neuroinform. 9, 8 (2015).

Poster No 1769

BrainMap Community Portal: Meta-analytic Connectivity Modeling in an HPC Environment

Peter Fox[1], William Allen[2], Mickle Fox[3], Angela Uecker[3], Michaela Robertson[3], Jonathan Towne[4], Mohamad Habes[5], Simon Eickhoff[6]

[1]The University of Texas Health Science Center at San Antonio, San Antonio, TX, [2]University of Texas, Austin, TX, [3]University of Texas Health Science Center at San Antonio, San Antonio, TX, [4]UT Health San Antonio, San Antonio, TX, [5]University of Texas Health San Antonio, San Antonio, TX, [6]Institute for Systems Neuroscience, Medical Faculty, Heinrich-Heine University Düsseldorf, Düsseldorf, North Rhine–Westphalia Land

Introduction: Meta-analysis offers powerful approaches for synthesis of neuroimaging findings across laboratories, subject cohorts, and imaging modalities. Coordinate-Based Meta-Analysis (CBMA) computes between-study, effect-location replicability from atlas-referenced, 3-D coordinates. The preponderance of CBMA studies to date are mass univariate, computing 3-D meta-analytic maps. Multivariate CBMA methods, by contrast, identify the neural network architectures

underlying task performance and brain disorders. Disorder-network modeling, in particular, is underutilized, as current evidence suggests that the vast majority of neurolologic, psychiatric and developmental disorders are network based. Cardinal limitations to wider adoption of multivariate CBMA ("meta-connectomics") for task and disorder network modeling are computational demand, pipeline availability, and data availability. The BrainMap Community Portal addresses these limitations by providing three online databases of coordinate-reporting task and disorder data sets in a high performance computing environment with multivariate and univariate CBMA applications.

Methods: The BrainMap Community Portal applies the community-portal (science gateway) architecture (Lawrence et al. 2015). Data, pipelined applications and HPC access are provided in an integrated environment as a standalone deployment of the Texas Advanced Computing Center (TACC) "Core Experience Portal" codebase. Computation is provided by TACC resources: Stampede2, Lonestar6, Maverick2, Frontera and Longhorn. Data and meta-data are accessed via mirrored instances of three BrainMap Databases (DBs), implemented in Oracle®. These are: Task-Activation (TA DB; Fox et al. 2005), Voxel-Based Morphometry (VBM; DB Vanasse et al. 2018), and Voxel-Based Physiology (VBP DB). Containerized implementations of BrainMap tools are provided in both graphical and command line formats. Sleuth 3.0.4 performs data retrieval filtered by the meta-data taxonomy to create an editable workspace. GingerALE 3.0.2 performs mass-univariate CBMA on the workspace using the latest implementation of the alteration-likelihood estimation (ALE) algorithm (Turkeltaub et al., 2002, 2012) with best-practices default settings (Eickhoff et al. 2016; Frahm L et al., 2023). Mango provides data visualization and regional interpretation of output by anatomy, function and disease. For multivariate analysis, five algorithms are implemented as pipelined, script-controlled, command-line applications. Meta-analytic connectivity modeling (MACM; Robinson et al., 2010) is implemented de novo as mass-multivariate application of ALE, using a novel cooccurrence architecture. Connectivity-based parcellation (CBP; Bzdok et al. 2013) is implemented in an ALE-specific manner using shared code (Reuter et al., 2020) and the MACM co-occurrence architecture. ICA is implemented as a containerized instance of MELODIC (Beckmann et al. 2004) as adapted for CBMA (Smith et al., 2009). GTM (Cauda et al., 2018) and Author-topic modeling (Yeo et al. 2015; Ngo et al. 2019) are implemented in an ALE-specific format using code shared by the originators.

Results: In-house and beta testing of the BrainMap Community Portal confirms that the portal interface, the BrainMap database, CBMA applications are operational and ready for community access.

Conclusions: The BrainMap Community Portal is ready for access at: portal.brainmap.org. We invite the community to explore this new resource and provide feedback Brainmap.org/forum). We encourage users to expand this resource by: 1) coding CBMA-compliant articles for entry; 2) sharing CBMA workspaces and other work products; 3) implementing new CBMA pipelines within the community portal (Yeung et al., 2023).

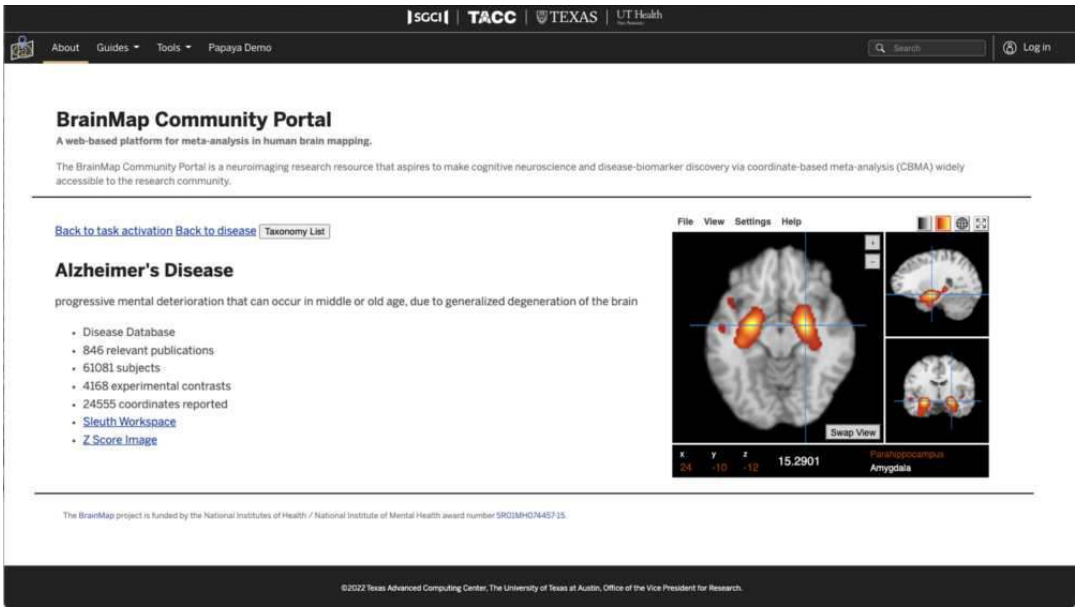

References

1. Beckmann CF (2004) Probabilistic Independent Component Analysis for Functional Magnetic Resonance Imaging. IEEE Transaction on Medical Imaging Vol 23 (2) 137-152.
2. Bzdok D (2013) An investigation of the structural, connectional and functional subspecialization in the human amygdala. Hum Brain Mapp 34(12_:3247-3266.
3. Eickhoff SB (2016) Behavior, sensitivity, and power of activation likelihood estimation characterized by massive empirical simulation. Neuroimage 137:70-85.
4. Fox PT (2005) BrainMap Taxonomy of Experimental Design: Description and Evaluation. Hum Brain Mapp 25:185-198.

5. Fox PT (2014) Meta-Analysis in Human Neuroimaging: Computation Modeling of Large-Scale Databases. Annual Review of Neurosciences 37:409-34.
6. Frahm L (in review) ALE meta-analysis of voxel-based morphometry Studies: Parameter validation via largescale simulation.
7. Lawrence KA Science gateways today and tomorrow: positive perspective of nearly 5000 members of the research community. Concurrency Computat: Pract. Exper. 2015: 27:4252-4268.
8. Ngo G (2019) Beyond consensus: Embracing heterogeneity in curated neuroimaging meta-analysis. NeuroImage 300:142-158.
9. Reuter N (2020) CBPtools: a Python package for regional connectivity-based parcellation. Brain Structure & Function 225:1261-1275.
10. Robinson JR (2010) Meta-analytic connectivity modeling: Delineating the Functional Connectivity of the Human Amygdala. Hum Brain Mapp 31:173-184.
11. Smith SM (2009) The functional architecture of the human brain: Correspondence between resting FMRI and task-activation studies. Proc Natl Acad Sci USA 106:13040-13045.
12. Towne J (in review) BrainMap VBP: a resource for meta-analysis of voxel-based physiological literature.
13. Turkeltaub P (2002) Meta-analysis of the functional neuroanatomy of single-word reading: Method and Validation. NeuroImage 16: 765-780.
14. Vanasse T (2018) BrainMap VBM: An environment for structural meta-analysis. Human Brain Mapp 39(8) 3308-3325.
15. Yeo BTT (2015) Functional specialization and flexibility in human association cortex. Cerebr Cortex 25:3654-3672.
16. Yeung AWK et al. (2023) Trends in the sample size, statistics, and contributions to the BrainMap database of activation likelihood estimation meta-analyses: An empirical study of 10-year data. Human Brain Mapp (in press).

Poster No 1770

Networks in nonlinear fMRI connectivity are present during infancy and exhibit associations with age

Spencer Kinsey[1], Masoud Seraji[1], Sarah Shultz[2], Vince Calhoun[1], Armin Iraji[1]

[1]Tri-Institutional Center for Translational Research in Neuroimaging and Data Science (TReNDS), Atlanta, GA, [2]Emory University School of Medicine, Atlanta, GA

Introduction: Independent component analysis (ICA) is often used to estimate brain intrinsic connectivity networks (ICNs) from functional magnetic resonance imaging (fMRI) time series. Although such analyses are typically designed to extract ICNs that reflect linear (LIN) functional connectivity (FC), we previously showed that ICNs can be extracted from voxel-wise distance correlation patterns that move beyond signed Pearson correlation patterns (i.e., from explicitly nonlinear (ENL) whole-brain FC (ENL-wFC)) (Iraji et al., 2023; Kinsey et al., 2023). Here, we extend our connectivity domain (Iraji et al., 2016) ICA framework by estimating ICNs from distance correlation patterns that move beyond Pearson correlation magnitudes. We find that ICNs are reliably extracted from infant resting-state fMRI (rsfMRI) data using our approach. Moreover, we show that the LIN and ENL estimates of many canonical ICNs exhibit spatial variation during infancy, and that some ENL estimates show associations with age that are missed by LIN counterparts.

Methods: We analyzed 442 rsfMRI scans collected from infants during a study conducted by Marcus Autism Center, Atlanta, GA, i/o CHOA. Subjects were classified as low-likelihood (LL) or elevated likelihood (EL) for autism spectrum disorder (ASD). The subject pool included 94 LL infants and 59 EL infants (n = 153). Data were collected with Siemens TIM Trio (TR = 720ms; TE = 33ms) and Siemens MAGNETOM Prisma (TR = 800ms; TE = 37ms) scanners. Preprocessing involved 1) discarding the first ten scans, 2) head motion, distortion, and slice timing correction, 3) normalization to MNI 152 space, 4) spatial smoothing with a 6mm FWHM Gaussian kernel, 7) motion regression, detrending, and despiking, 8) temporal resampling to TR = 720ms, and 9) time series Z-scoring. We constructed LIN whole-brain FC (LIN-wFC) and ENL-wFC matrices for each scan (Fig. 1A). We calculated the voxel-wise Pearson correlation coefficient (PCC), which is a conventional linear FC estimator, to construct LIN-wFC. Then, we calculated the voxel-wise distance correlation (Székely et al., 2007) to construct nonlinear whole-brain FC (NL-wFC). To extract ENL-wFC, we removed the effect of the absolute value of LIN-wFC on NL-FC by estimating a value of $\propto$ which minimized the sum of squared errors between NL-wFC and |LIN-wFC| for each scan. The top 30 components from principal component analysis were used as input to group-level spatial independent component analysis via Group ICA of fMRI Toolbox (GIFT v4.0). A component was identified as an ICN if and only if 1) it exhibited peak weight in and high overlap with gray matter, 2) it passed visual inspection, and 3) it exhibited ICASSO stability > .80. ICNs were matched based on spatial similarity. ICNs reconstructed from LL infant scans via group information-guided ICA (Du & Fan, 2013) were statistically analyzed. Voxel-wise GLMs were constructed to assess spatial variation between LIN and ENL ICNs. Voxel-wise GLMs were also constructed to determine LIN and ENL ICN associations with age.

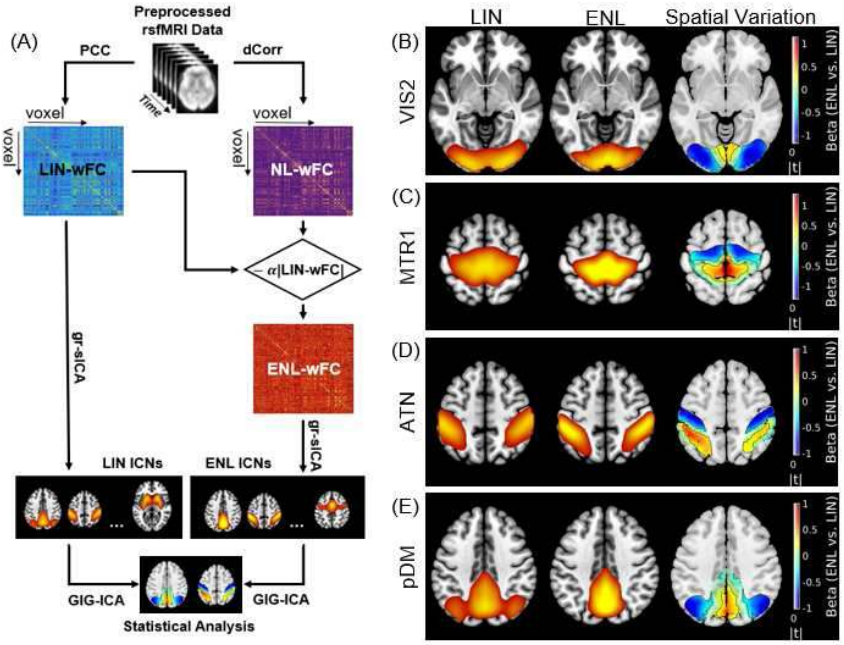

Fig. 1. (A) Schematic of the analysis pipeline. (B-E) Non-comprehensive display of group-level linear (LIN) and explicitly nonlinear (ENL) secondary visual (VIS2) (Z = -5.5 mm), primary sensorimotor (MTR1) (Z = 59.5 mm), dorsal attention (ATN) (Z = 52 mm), and posterior default mode (pDM) (Z = 39.5 mm) intrinsic connectivity networks (ICNs) and their spatial variation. For spatial variation, contours indicate FDR corrected statistical significance ($q < 0.05$); warmer hues: ENL> LIN; cooler hues: LIN > ENL.

Results: Our analysis uncovered 11 common ICNs (similarity > .80) and 1 ICN unique to each dataset (similarity < .40). GLM statistics revealed that matched LIN and ENL counterparts exhibit unique spatial variation during infancy (Fig. 1B-E). For instance, the posterior default mode (pDM) ICN exhibits a visible ENL-LIN gradient between the precuneus and bilateral angular gyri. GLM testing also revealed distinct age association patterns, with many ENL voxels showing associations with age that are missed by LIN (Fig.2).

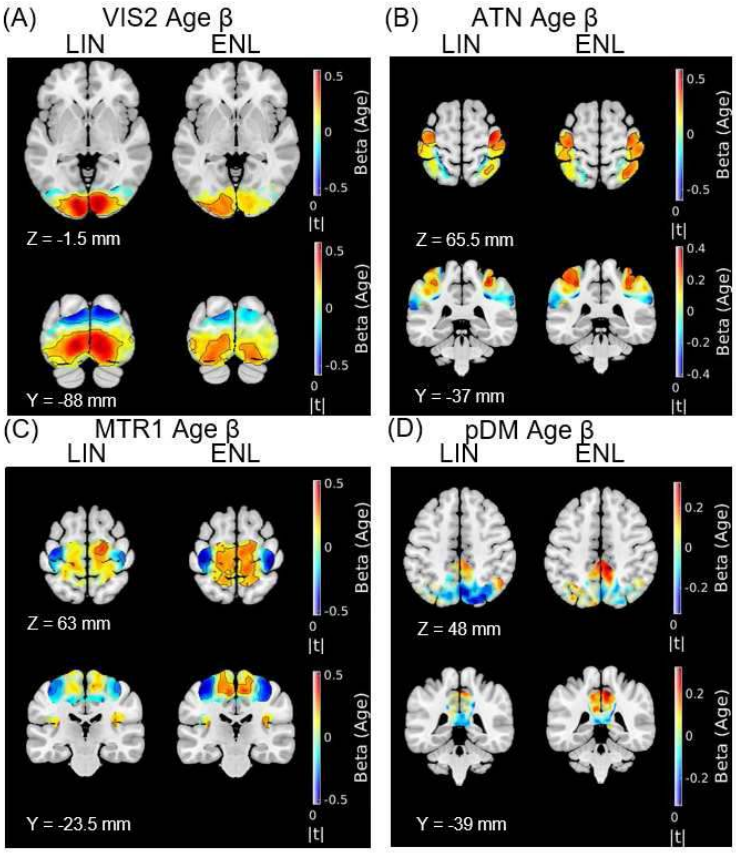

Fig. 2. Non-comprehensive display of (A) secondary visual (VIS2), (B) dorsal attention (ATN), (C) primary sensorimotor (MTR1), and (D) posterior default mode (pD) intrinsic connectivity network (ICN) associations with age. Contours indicate FDR corrected statistical significance ($q < 0.05$). Age association patterns differ between LIN and ENL: while LIN VIS2 (A) and pDM (D) ICNs show larger numbers of voxels associated with age, ENL ATN (B) and MTR1 (C) ICNs exhibit sizable clusters of significant voxels missed by LIN counterparts.

Conclusions: Here, we leveraged connectivity domain ICA to estimate ICNs from ENL-wFC patterns within infant rsfMRI data. Our results show that the ENL counterparts of many large-scale canonical ICNs are present during early postnatal life, are differentiated via their spatial distributions, and show associations with age that may provide valuable insight into typical and atypical early life brain development.

References

1. Du, Y., & Y. Fan, Y. (2013), "Group information guided ICA for fMRI data analysis," NeuroImage, vol. 69, pp. 157-197. https://doi.org/10.1016/j.neuroimage.2012.11.008
2. Iraji, A., et al. (2016), "The connectivity domain: Analyzing resting state fMRI data using feature-based data-driven and model-based methods," NeuroImage, vol. 134, pp. 494-507. https://doi.org/10.1016/j.neuroimage.2016.04.006
3. Iraji, A., et al. (2023), 'The nonlinear brain: towards uncovering hidden brain networks using explicitly nonlinear functional interaction,' IEEE International Symposium on Biomedical Imaging.
4. Kinsey, S., et al. (2023), "Networks extracted from nonlinear fMRI connectivity exhibit unique spatial variation and enhanced sensitivity to differences between individuals with schizophrenia and controls," bioRxiv. https://doi.org/10.1101/2023.11.16.566292
5. Székely, G. J., et al. (2007), "Measuring and Testing Dependence by Correlation of Distances," The Annals of Statistics, vol. 35, no. 6, pp. 2769-2794. 35(6), 2769–2794. http://www.jstor.org/stable/25464608

Poster No 1771

Brain Large-scale Networks and Language Modeling during Spoken Narrative Listening

Marianna Chianese[1], Federica Di Nardo[1], Maria Agnese Pirozzi[1], Mario Cirillo[1], Francesco Di Salle[2], Fabrizio Esposito[1]

[1]University of Campania "Luigi Vanvitelli", Naples, Italy, [2]University of Salerno, Baronissi, Salerno, Italy

Introduction: Understanding the spatio-temporal dynamics of large-scale brain networks during narrative listening might benefit from the application of language models. As different recurrent patterns of large-scale inter-network functional connectivity (FC) are usually linked to distinct brain states, a static (sFC) and dynamic (dFC) FC analysis of whole-brain fMRI time-series is presented where sFC and dFC changes are correlated to word suprisal, a linguistic metric previously used to link the narrative text to fMRI neural activity in language-related regions[1,2].

Methods: Preprocessed fMRI data sets from two runs of a previous 3 Tesla MRI study[1,2], acquired in 31 healthy subjects during task-free listening to a 12-minute audiobook, played in both original (forward, FW) and reversed (backward, BW) versions, were re-analyzed via group independent component analysis (gICA) using the GIFT toolbox[3]. Seven gICA components were labelled to major large-scale networks and back-projected to individual time-courses (per subject, network, condition). These were entered into linear mixed-effects (LME) models to estimate the significance of each network temporal correlation to the word surprisal predictor after correction with false discovery rate (FDR) while accounting for the variance explained by the acoustic envelope of the sound and the frequency and duration of single words[1]. Clusters of recurring patterns of inter-network correlations across 660 consecutive time windows of 90 sec were extracted via K-means and silhouette methods and identified as dFC brain states. Frequency of occurrence and mean dwell time of each state were estimated across subjects, compared between playing conditions and correlated to mean word surprisal across time windows.

Results: Somato-motor network (SMN) time-course was positively correlated (FDR<0.05) to the surprisal predictor during both BW and FW conditions while the default-mode network (DMN) time-course was positively correlated only during BW condition. Visual (VIS), dorsal (DAN) and ventral (VAN) attention and limbic (LN) network time-courses were all positively correlated, while fronto-parietal network (FPN) time-course was negatively correlated, to the surprisal predictor, during FW, but not BW, condition. Six dFC states were identified (Figure 1): States 1, 3 and 5 were dominated by DAN-VAN interactions, whereas states 2, 4 and 6 variably involved VIS, SMN, FPN and LN (mainly interacting with VAN and DAN). The frequency of occurrence and mean dwell time of state 1 were significantly higher during FW, compared to BW, while the opposite was observed for states 3 and 5 (Wilcoxon signed-rank test, FDR<0.05). No significant differences between conditions were observed for states 2, 4 and 6. The average percentage of subjects found in the same state across time windows was significantly correlated (Spearman correlation coefficient, FW: $|\rho| > 0.21$, $P < 0.05$, BW: $|\rho| > 0.18$, $FDR < 0.05$) to the average surprisal of the words within the same windows for four (1, 3, 4, 6) and five (1, 2, 3, 4, 6) states respectively during BW and FW conditions. For state 3 this correlation switched from positive (BW) to negative (FW) whereas the opposite was observed for state 4 (Figure 2).

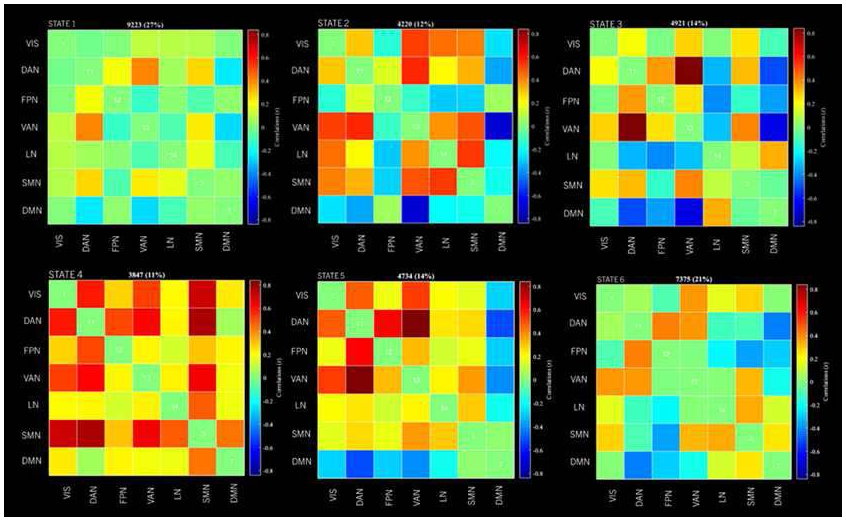

Figure 1. Inter-network correlations matrices for each cluster (dFC state).

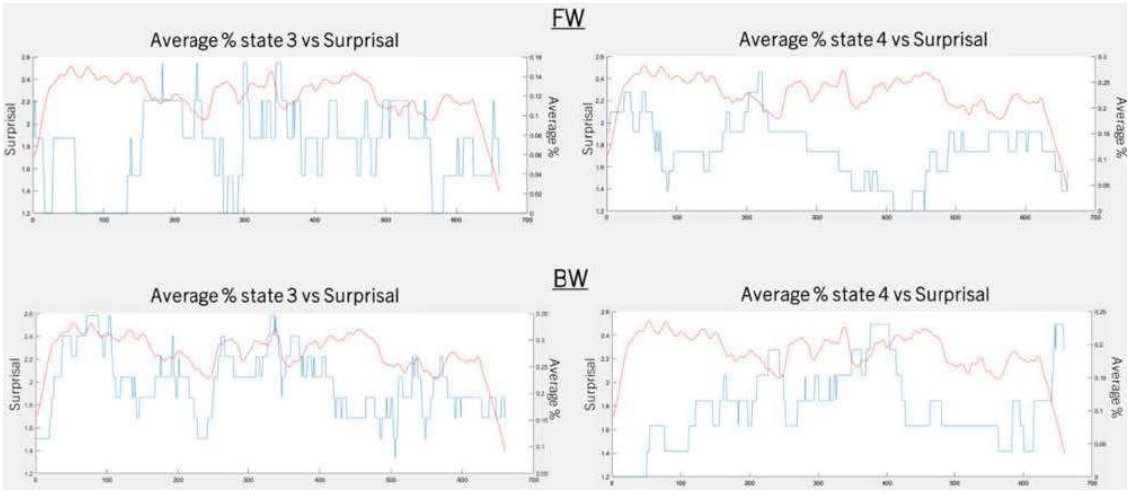

Figure 2. The average percentage of subjects found in the same state across time windows (blue), average surprisal of the words within the same time windows (red) in FW and BW conditions.

Conclusions: These results illustrate the usefulness of surprisal for explaining sFC and dFC effects across large-scale brain networks during natural listening conditions. The interaction between DAN and VAN networks was found dominant in specific states for which (i) the number of occurrences and mean dwell time were significantly changed when the listened words were understandable to (and could be put in narrative context by) the same subjects and (ii) the co-occurrence of the same dFC state was correlated to the average surprisal across all words listened during intervals as long as 90s. These findings might have implications for future naturalistic fMRI studies and for probing language comprehension during narrative listening.

References

1. A. G. Russo et al., «Semantics-weighted lexical surprisal modeling of naturalistic functional MRI time-series during spoken narrative listening», NeuroImage, vol. 222, p. 117281, nov. 2020, doi: 10.1016/j.neuroimage.2020.117281.
2. A. G. Russo, A. Ciarlo, S. Ponticorvo, F. Di Salle, G. Tedeschi, e F. Esposito, «Explaining neural activity in human listeners with deep learning via natural language processing of narrative text.», Sci Rep, vol. 12, fasc. 1, p. 17838, ott. 2022, doi: 10.1038/s41598-022-21782-4.
3. V. D. Calhoun, T. Adali, G. D. Pearlson, e J. J. Pekar, «A method for making group inferences from functional MRI data using independent component analysis.», Hum Brain Mapp, vol. 14, fasc. 3, pp. 140–151, nov. 2001, doi: 10.1002/hbm.1048.

Poster No 1772

A Systematic Review connecting Functional Connectivity and Alcohol Use Disorder with Relevance Maps

Marco Bottino[1], Natálie Bočková[1], Nico Poller[1], Michael Smolka[2], Justin Böhmer[3], Henrik Walter[4], Michael Marxen[1]

[1]Technische Universität Dresden, Dresden, Saxony, [2]Department of Psychiatry and Psychotherapy, Technische Universität Dresden, Dresden, Germany, [3]Charité – Universitätsmedizin Berlin, Berlin, Brandenburg, [4]Division of Mind and Brain Research, Department for Psychiatry, Charité–Universitätmedizin Berlin, Berlin, Germany

Introduction: Alcohol use disorder (AUD) has been associated consistently with aberrations in brain functional connectivity. To provide an overview of current findings, we systematically reviewed the literature linking resting-state functional MRI (rs-fMRI) to AUD. However, studies and methodologies are very heterogeneous. We devised an algorithm to deal with this heterogeneity and create quantitative relevance maps for regions as well as connections that can be used to formulate hypotheses in future studies.

Methods: We identified 248 papers with a systematic search across PubMed, Scopus, and Web of Science using the query "alcohol" AND "connectivity" AND ("resting" OR "rest"). After screening and excluding studies, as shown in Fig. 1, 50 papers with 95 separate analyses remained for detailed analysis. Potential biases, especially in studies linking alcohol use disorder (AUD) to specific seeds, prompted the decision to prioritize whole-brain analyses (40/95) in creating relevance maps. The Automated Anatomical Atlas version 3.1 (AAL, Rolls et al., 2020) was employed to standardize results. All significant results concerning rs-fMRI and AUD were collected in a table, which we used to create two outputs: 1) a relevance matrix counting all studies that reported a correlation with AUD for a particular connection between regions, accounting for the direction of the effect; 2) a ranking of the regions, counting the number of whole-brain analyses citing a particular region, independently of the direction of the effect. We also categorized the most common methods and results in the field.

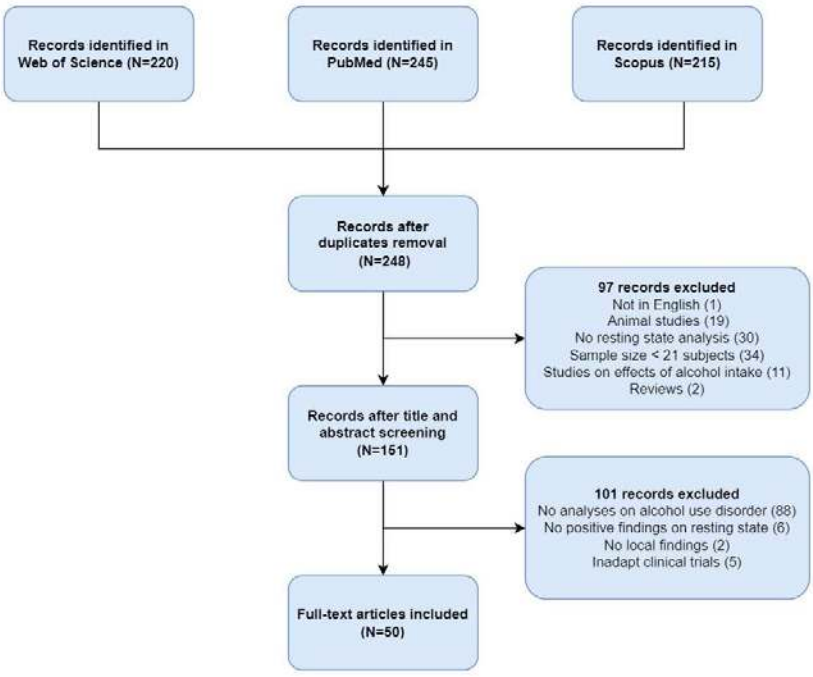

Figure 1: Flowchart with information on papers selection

Results: As a general overview, most of the studies have a sample size of less than 100 subjects and use a group comparison approach, where standard divisions are healthy controls vs. AUD, binge vs. light drinkers, and, in longitudinal studies, relapsers vs. abstainers. Methodologically, two main brain parcellations are employed: atlas-based (e.g., AAL or Harvard-Oxford from Desikan et al., 2006) or data-driven independent component analysis. The subsequent rs-fMRI connectivity analyses typically involve generating subject-specific statistical maps (e.g., through dual regression) or functional connectivity matrices through Pearson's correlation. Analyses fall into three main types: group statistical comparisons, correlation/regression models predicting addiction severity measures, and machine learning for binary classification of AUD against controls. Severity measures include structured clinical interviews and scores on different aspects of the disorder, e.g., AUDIT score (Saunders et al., 1993). The relevance matrix in Figure 2a includes connection scores from -2 to 2: 8.4% of all scores are

not zero. Noteworthy, positive associations include a triangle involving the insula, anterior cingulate cortex, and left superior temporal cortex. Negative associations include connections between the middle temporal cortex and precuneus, as well as between the superior temporal cortex and the right lingual gyrus. The region ranking (Fig. 2b) highlights the most cited brain regions in whole-brain analyses: dorsolateral prefrontal cortex (PFC), dorsal anterior cingulate cortex, dorsomedial PFC, insula, putamen, and left precuneus are on top of the list . Despite being a common seed, the amygdala has significant results in only one analysis.

Conclusions: While the literature linking rs-fMRI connectivity and AUD is substantial, it is also very heterogeneous and partially biased toward particular brain regions. Our methodological approach aimed to address potential biases and to ensure a comprehensive analysis of the diverse findings. The resulting relevance maps summarize our current knowledge of which regions and connections of the brain are associated with AUD. Additionally, they provide a basis to formulate more precise and unbiased hypotheses in future projects and interpret new data .

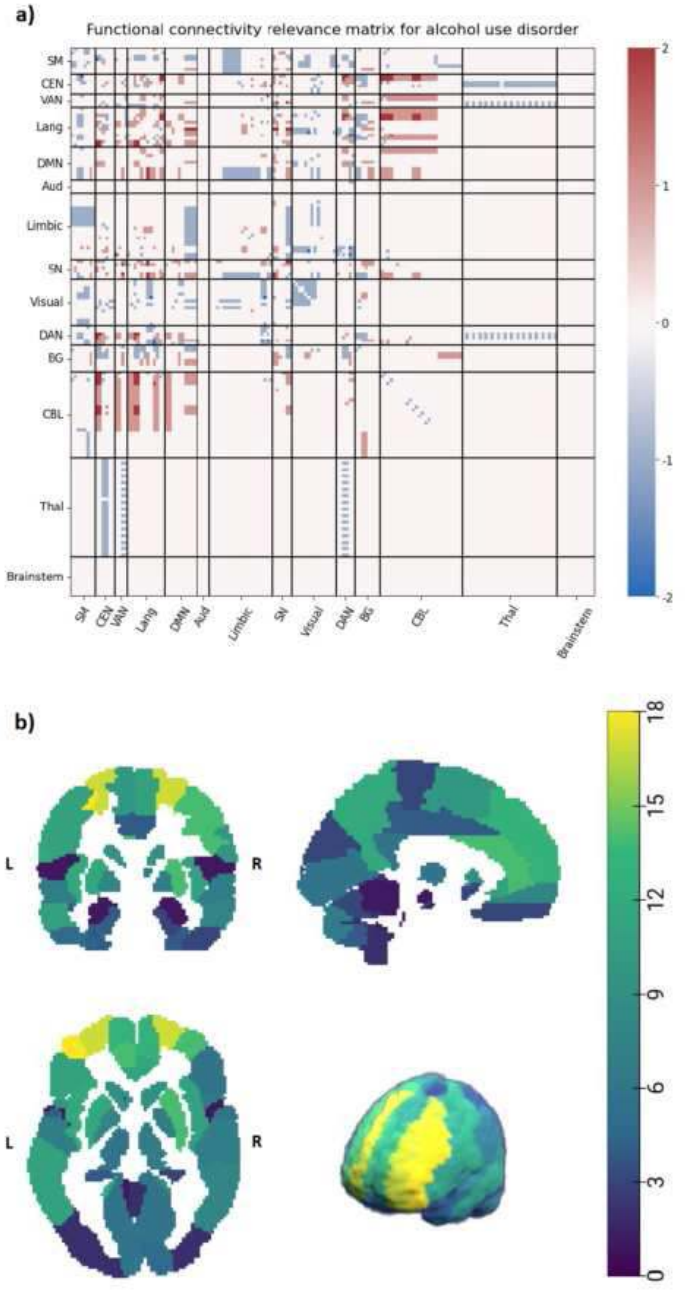

Figure 2: a) Relevance matrix showing associations of between-region connections with alcohol use disorder, sorted and labelled according to the most common functional networks. b) Map of the brain colored according to the number of whole-brain analyses citing each region with AAL3 parcellation (X=-4, Y=0, Z=0); SM=Sensorimotor, CEN=Central Executive Network, VAN=Ventral Attention Network, Lang=Language, DMN=Default mode network, Aud=Auditory, SN=Salience network, DAN=Dorsal attention network, BG=Basal ganglia, CBL=Cerebellum, Thal=Thalamus

References

1. Desikan, R. S., Ségonne, F., Fischl, B., Quinn, B. T., Dickerson, B. C., Blacker, D., Buckner, R. L., Dale, A. M., Maguire, R. P., Hyman, B. T., Albert, M. S., & Killiany, R. J. (2006). An automated labeling system for subdividing the human cerebral cortex on MRI scans into gyral based regions of interest. NeuroImage, 31(3), 968–980. https://doi.org/10.1016/j.neuroimage.2006.01.021
2. Rolls, E. T., Huang, C.-C., Lin, C.-P., Feng, J., & Joliot, M. (2020). Automated anatomical labelling atlas 3. NeuroImage, 206, 116189. https://doi.org/10.1016/j.neuroimage.2019.116189
3. Saunders, J. B., Aasland, O. G., Babor, T. F., La Fuente, J. R. de, & Grant, M. (1993). Development of the Alcohol Use Disorders Identification Test (AUDIT): Who Collaborative Project on Early Detection of Persons with Harmful Alcohol Consumption--II. Addiction (Abingdon, England), 88(6), 791–804. https://doi.org/10.1111/j.1360-0443.1993.tb02093.x

Poster No 1773

Brain Lesion Parcellation Using a Precomputed Human Brain Connectome Improves Symptom Localization

William Drew[1], Alexander Cohen[2], Amy Brodtmann[3], Maurizio Corbetta[4], Natalia Egorova-Brumley[5], Sophia Gozzi[3], Jordan Grafman[6], Andrew Naidech[6], Joel Voss[7], B. T. Thomas Yeo[8], Michael Fox[9], Shan Siddiqi[9]

[1]Brigham and Women's Hospital, Harvard Medical School, Boston, MA, [2]Boston Children's Hospital, Harvard Medical School, Boston, MA, [3]Monash University, Melbourne, Victoria, Australia, [4]Clinica Neurologica, Department of Neuroscience, University of Padova, Padova, Italy, [5]University of Melbourne, Melbourne, Victoria, Australia, [6]Northwestern University, Chicago, IL, [7]University of Chicago, Chicago, IL, [8]National University of Singapore, Singapore, [9]Brigham and Women's Hospital, Harvard Medical School, Boston, MA

Introduction: Lesion network mapping (LNM) uses brain lesions to causally link symptoms to functional brain networks. However, there are two main limitations of this method. First, LNM is computationally inefficient, inhibiting the use of large connectome datasets like the 40,000+ subject UK Biobank. Second, LNM assumes that a brain lesion is connected to a single functional brain network. However, lesions may span multiple functionally distinct brain regions, potentially introducing noise. Here, we attempt to resolve these limitations by developing a method to parcellate brain lesions using resting-state functional connectivity into regions connected to functionally distinct networks and a method to compute lesion network maps rapidly and efficiently. We also apply these methods to improve lesion-symptom prediction of depression.

Methods: First, we generated a precomputed human brain connectome (PHBC) by computing the mean whole-brain functional connectivity of each voxel across 1,000 healthy individuals. Next, to address LNM's first limitation, we developed the "precomputed" LNM method. Using the PHBC, a weighted average of the functional connectivity maps associated with the ROI's voxels is computed, and a scaling factor is applied to account for differences between individual voxel BOLD signal strengths. Weights are computed as the standard deviation of a voxel's BOLD signal amplitude. To address LNM's second limitation, we used the PHBC to parcellate stroke lesions into distinct regions that share common patterns of functional connectivity. For each lesion, we extract a connectivity matrix that consists of connectivity measures between every pair of voxels in the lesion. Next, the connectivity matrix is thresholded to remove weak connections between voxels. The thresholded connectivity matrix is then clustered using Infomap, a modular community detection algorithm that is commonly used for resting-state network parcellation, to group voxels into clusters with similar connectivity profiles. For each lesion, we used the largest parcel as a seed to generate functional connectivity maps and compared these maps to depression outcomes in five lesion datasets (n=449), yielding a map of connectivity of lesion parcels associated with depression. The largest parcel was selected as a simple metric for the optimal component. We hypothesized that LNM using lesion parcels would explain more variance in post-lesion depression than whole lesions.

Results: Functional connectivity maps of whole lesions generated using both the "precomputed" and conventional LNM methods were similar (spatial r=0.997) and were far more efficiently computed (~7X faster) when using a 1,000-subject normative functional connectome. In a leave-one-dataset-out cross-validation, lesion network maps derived from the largest parcel of each lesion from four datasets predicted depression outcomes in the fifth ($r=0.155$, $p<0.001$). This was significantly stronger ($p=0.0011$) than the predictive value of whole lesions.

Conclusions: The PHBC and the "precomputed" LNM method accelerate LNM, enabling functional connectivity analyses of even single voxel lesions in a computationally efficient manner. The PHBC also enables functional parcellation of lesions, potentially removing noise from lesion analyses. This parcellation method significantly improved lesion-symptom localization when using each lesion's largest parcel compared to whole lesions. If lesion-symptom localization can be improved even when using a simple size metric to pick the optimal parcel, we hypothesize that further improvements in LNM can be achieved by using a more specialized parcel selection method that could include selecting multiple relevant lesion parcels to consider their interacting network effects. The PHBC enables functional brain network analysis with a higher level of granularity than

conventional LNM, making it possible to discriminate between the interacting network effects of a functionally heterogeneous brain lesion.

References
1. Alfaro-Almagro, F. (2018), 'Image processing and Quality Control for the first 10,000 brain imaging datasets from UK Biobank', NeuroImage 166, 400–424.
2. Fox, M.D. (2018), 'Mapping Symptoms to Brain Networks with the Human Connectome', New England Journal of Medicine, 379(23), 2237–2245.
3. Gordon, E.M. (2017), 'Precision Functional Mapping of Individual Human Brains', Neuron, 95(4), 791-807.e7.
4. Sanchez-Rodriguez, L.M. (2021), 'Detecting brain network communities: Considering the role of information flow and its different temporal scales', NeuroImage, 225, 117431.
5. Siddiqi, S.H. (2021), 'Brain stimulation and brain lesions converge on common causal circuits in neuropsychiatric disease', Nature Human Behaviour, 5(12), Article 12.

Poster No 1774

Dynamics of functional modes represent behavior during task fMRI

Ikko Kimura[1], Janine Bijsterbosch[2], Matthew Glasser[2], Takuya Hayashi[1]

[1]Laboratory for Brain Connectomics Imaging, RIKEN Center for Biosystems Dynamics Research, Kobe, Hyogo, [2]Department of Radiology, Washington University in St Louis, St Louis, MO

Introduction: Several methods have been proposed to decompose fMRI data into a small number of networks[1]. Among them, PRObabilistic FUnctional MOdes (PROFUMO)[2] utilizes bayesian modeling and better characterizes the individual traits of the resting-state networks than conventional approaches with independent component analysis (ICA)[3]. While the previous studies used PROFUMO for resolving mode at rest[2–5], it is not well known whether it is applicable to evaluate modes during tasks. Here, we examined whether the modes (1) can be reproducibly estimated from task fMRI data and (2) are sensitive to the conditional differences or the individual variability in task performance during the scan.

Methods: We obtained fMRI data during working memory tasks (tfMRI) and at rest (rsfMRI) of 50 unrelated participants from Human Connectome Project Young Adult database. Both data were denoised with multi-run FIX, re-applied manually reclassified noise components, surface registered with multi-modal surface matching algorithm[6], de-drifted, and resampled to 32k standard mesh surfaces. PROFUMO was applied separately to tfMRI and rsfMRI data (dimension: 50) to extract the spatial maps and time signal of each mode. We chose five major modes for further analysis (i.e., dorsal attention [DA], left fronto-parietal [left FP], right fronto-parietal control [right FP], default mode network [DMN] and posteromedial cortex, inferior parietal lobule [PMPL]) reported in the previous study[2]. Similar functional networks were also extracted using group spatial ICA and dual regression (ICA-DR)[7] for comparison. The similarity of the spatial maps derived from tfMRI to those from rsfMRI data was assessed by cosine similarity. A general linear model (GLM) was applied to evaluate the degree of differences in the time signal of the modes across conditions (i.e., 2-back tasks [2bk], 0-back tasks [0bk], and at rest). Dynamic functional connectivity (dyFC)[8] between modes was calculated using a sliding window method (timepoint window: 15, sliding steps: 1) to test whether interactions between modes changed across conditions. We also tested whether the accuracy of the WM task was correlated with the metrics derived from PROFUMO with Pearson's correlation coefficient.

Results: Figure 1 shows the spatial maps derived from PROFUMO (Fig. 1A) and ICA-DR (Fig. 1B), highlighting that more widespread brain regions were positively involved in PROFUMO than in ICA-DR (red arrows). Modes from tfMRI showed high spatial cosine similarity with those from rsfMRI (0.78–0.89). Figure 2 depicts the group-averaged time signal of each mode in tfMRI (Fig. 2A) and the estimated contrasts with GLM analysis (Fig. 2B). While task-related signal increase (2bk vs. 0bk) was clearly found in both PROFUMO and ICA-DA (right FP and DA), the resting-related signal change (rest vs. task) was relatively small in PROFUMO compared to ICA-DR (DA, left FP, DMN, PMPL; red arrows in Fig. 2A). In PROFUMO, the task-related contrast of DMN (2bk vs. 0bk) showed a negative correlation with the task accuracy (rho = -0.43, FWE-corrected P = 0.023) but not in ICA-DR. Figure 2C illustrates the Z statistics (thresholded with FWE-corrected $P < 0.05$) comparing the dyFC between 2bk and the others. The dyFCs from PROFUMO revealed conditional differences in a larger number of modes than those from ICA-DR. Moreover, the task accuracy was positively correlated with the temporal variability of dyFC between right FP and DMN (rho = 0.41, FWE-corrected P = 0.031) and between right FP and PMPL (rho = 0.47, FWE-corrected P = 0.0064) in PROFUMO while not in ICA-DR.

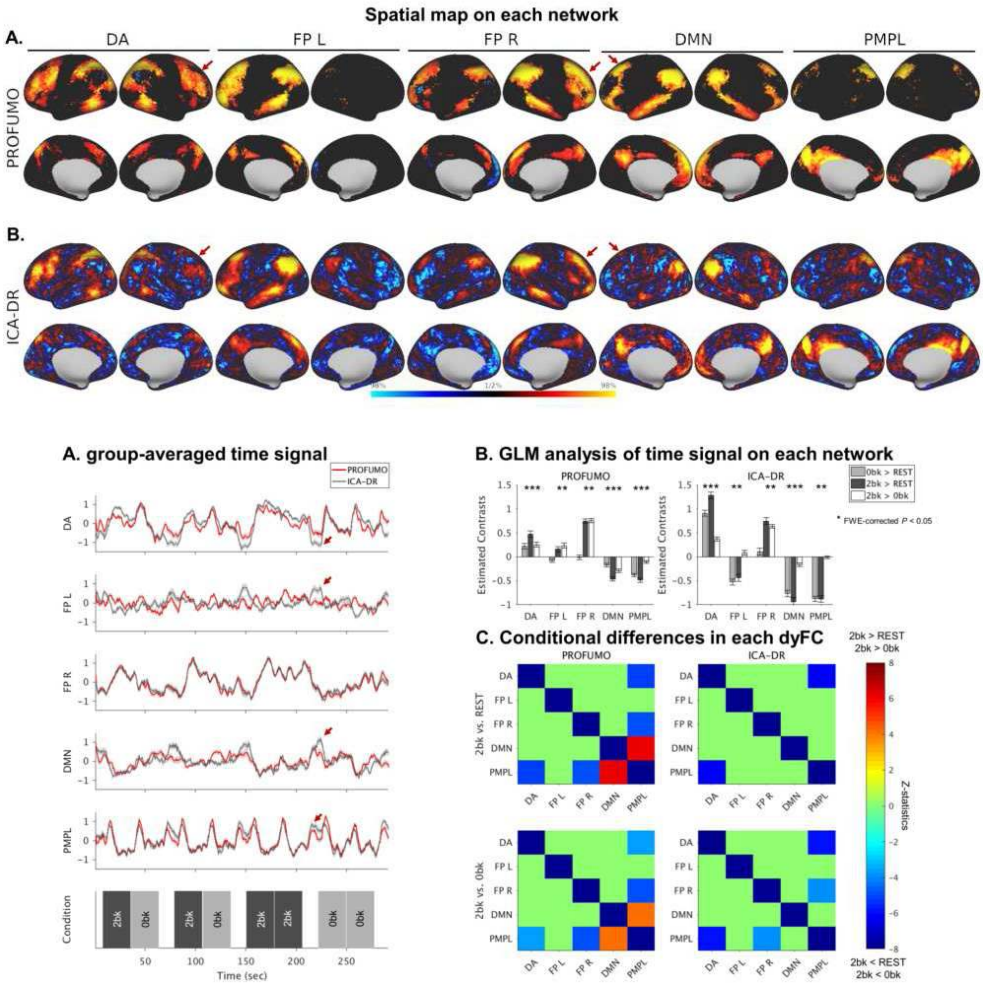

Conclusions: PROFUMO can reliably extract the spatial maps of the major modes from tfMRI as from rsfMRI. While both PROFUMO and ICA-DR depicted a distinct pattern of time signal across conditions, PROFUMO was sensitive to the differences in the interactions of modes across conditions and to the individual variability in task performance.

References

1. Bijsterbosch, J. D., Valk, S. L., Wang, D. & Glasser, M. F. (2021), Recent developments in representations of the connectome. Neuroimage 243, 118533.
2. Harrison, S. J. et al. (2015), Large-scale probabilistic functional modes from resting state fMRI. Neuroimage 109, 217–231.
3. Harrison, S. J. et al. (2020), Modelling subject variability in the spatial and temporal characteristics of functional modes. Neuroimage 222, 117226.
4. Bijsterbosch, J. D. et al. (2018), The relationship between spatial configuration and functional connectivity of brain regions. Elife 7, e32992.
5. Bijsterbosch, J. D., Beckmann, C. F., Woolrich, M. W., Smith, S. M. & Harrison, S. J. (2019), The relationship between spatial configuration and functional connectivity of brain regions revisited. Elife 8.
6. Robinson, E. C. et al. (2018), Multimodal surface matching with higher-order smoothness constraints. Neuroimage 167, 453–465.
7. Nickerson, L. D., Smith, S. M., Öngür, D. & Beckmann, C. F. (2017), Using Dual Regression to Investigate Network Shape and Amplitude in Functional Connectivity Analyses. Front. Neurosci. 11, 115.
8. Hutchison, R. M. et al. (2013), Dynamic functional connectivity: promise, issues, and interpretations. Neuroimage 80, 360–378.

Poster No 1775

The impact of functional connectivity on task information coding

Takuya Ito[1], John D. Murray[2]

[1]IBM Research, Yorktown Heights, NY, [2]Dartmouth College, Hanover, NH

Introduction: The brain is a complex system with dynamic network changes. Functional connectivity – the measurement of correlated brain activity – is a commonly-used approach to characterizing brain network changes. Despite the wealth of

neuroscience studies that have reported reliable state-dependent changes to macroscale brain network organization (Cole et al., 2014), there is no widely accepted theory or understanding of what these functional connectivity changes are for. However, theoretical work in systems neuroscience (at the level of local spiking neurons) has demonstrated that state-dependent neural correlations can be understood from a neural coding framework (Panzeri et al., 2022). Prior theory posits that noise correlations (NC) — idiosyncratic with functional connectivity — can be interpreted only if the underlying signal correlation (SC) — similarity of task tuning (or task co-activations) between pairs of neural units — is known. Here we investigate whether the theoretical framework used to study neural coding in neuronal spikes can account for macroscale brain network changes (Ito and Murray, 2022).

Methods: We analyzed a publicly available fMRI data set – the Multi-Domain Task Battery – that contained a diverse set of 26 cognitive tasks collected per participant (n=24) (King et al., 2019). Data were collected across four imaging sessions, enabling within-subject test-retest reliability of analyses across task conditions. SCs were estimated by measuring the correlation of mean task activations across tasks (e.g., cross-task co-activations; Fig. 1a-c). NCs, which are statistically analogous to background functional connectivity (Al-Aidroos et al., 2012) or functional connectivity estimated with a beta series regression (Rissman et al., 2004), were measured using the block-to-block covariability (Fig. 1d-g). We measured the signal-noise differential matrix – the element-wise multiplication of task-state NC changes (NC) (Fig. 2e) with the SC matrix – to determine which sets of brain regions were likely to have a positive impact on information decoding based on prior theory (Fig. 2f). To test the hypothesis that negative signal-noise differentials enhanced coding of task information (Fig. 2a-c), we randomly subsampled networks of brain regions with exclusively negative signal-noise differentials. We assessed task coding ability by decoding multitask activations from brain regions with negative (or positive) signal-noise differentials (Fig. 2h,i).

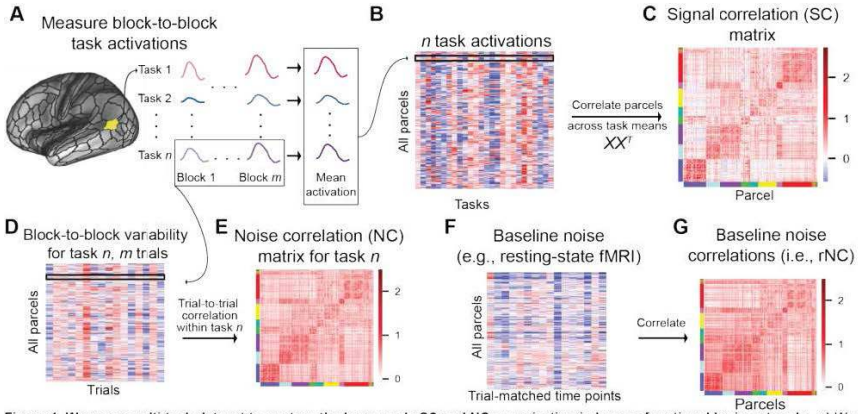

Figure 1. We use a multi-task dataset to capture the large-scale SC and NC organization in human functional brain networks. a) We estimated the block-to-block task activation amplitude in fMRI data for each brain region in the Glasser et al. (2016) atlas for each of the 26 tasks. **b,c)** To estimate the SC matrix, we compute the correlation between all pairs of brain parcels using the cross-trial mean activation of many tasks. **d,e)** In contrast, NC matrices for a given task is computed as the correlation of trial-to-trial variability between pairs of parcels within a single task. **f,g)** The NC for a task can be compared to the well-studied baseline rNC using resting-state fMRI activity. SCs and NCs are computed for each participant separately, and then averaged to produce a group-level matrix estimate.

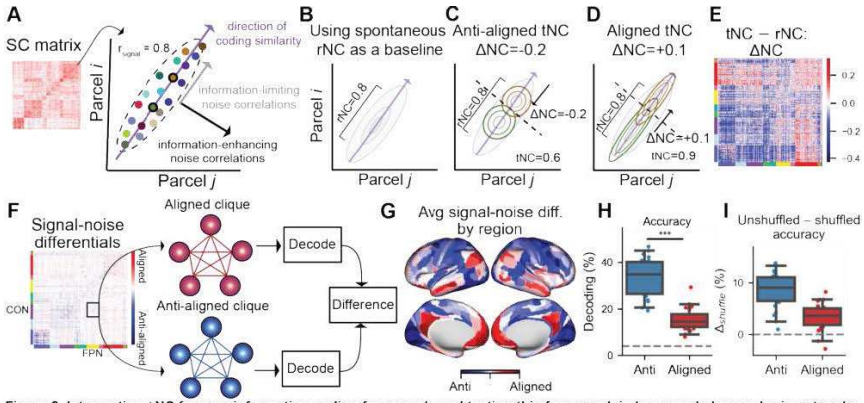

Figure 2. Interpreting ΔNC from an information coding framework, and testing this framework in large-scale human brain networks. a)) For a pair of brain regions, the SC captures the direction of correlation of the tuning curves across many tasks. tNCs, on the other hand, capture within-task covariability (across events) **b-d)** We modify prior theories to assess how the task-state correlation (tNC) impacts information coding relative to the **b)** baseline rNC estimate (i.e., the ΔNC). Baselining tNCs against rNCs addresses: Are the task correlation changes limit (aligned) or limit (anti-aligned) information coding? **c)** An anti-aligned ΔNC, whereby the ΔNC is the opposite sign of the SC, thereby reducing noise interference along the SC axis. **d)** An aligned ΔNC, whereby the ΔNC is the same sign of the SC, thereby increasing noise interference along the SC axis. **e)** The ΔNC matrix, as estimated in empirical fMRI data for all pairs of cortical regions. **f-i)** Brain regions with anti-aligned ΔNCs have improved information decoding over aligned ΔNCs. **f)** We identified network-matched sets of aligned or anti-aligned ΔNCs by identifying cliques (sub-networks of entirely aligned or anti-aligned ΔNCs). **g)** The average of the signal-noise differential matrix for each region (i.e., averaging across columns for each row in panel **f**). **h)** The decoding accuracy for the anti-aligned versus aligned ΔNC cliques with the greatest signal-noise differnetials. **i)** We computed the difference in decoding performance between unshuffled and shuffled conditions. Shuffling task blocks impacted the decoding performance for anti-aligned cliques significantly more than aligned cliques.

Results: We characterized the SC and NC organization of macroscale brain networks. We found that task-state NC changes did not typically change in the same direction as their underlying SC (e.g., task coactivation structure). In other words, task-

state NC changes typically decreased between similarly tuned regions. Crucially, NCs that changed in the opposite direction as their SC (i.e., anti-aligned correlations) improved information coding of these brain regions (Fig. 2h,i). In contrast, NCs that changed in the same direction (aligned NCs) as their SC did not. Interestingly, these aligned NCs were primarily correlation increases, suggesting that most functional correlation increases across fMRI networks actually degrade information coding.

Conclusions: We found that regions with opposite SCs and NCs (i.e., negative signal-noise differentials) could better decode multitask activations. This provides empirical evidence that theories developed to study the neural code in local spiking circuits can be extended to understand the structure of correlated brain activity at the level of whole-brain functional networks. We conclude that state-dependent NCs shape information coding of macroscale functional brain networks, with interpretation of correlation changes requiring knowledge of underlying SCs.

References

1. Al-Aidroos, N., Said, C.P., Turk-Browne, N.B., 2012. Top-down attention switches coupling between low-level and high-level areas of human visual cortex. Proc. Natl. Acad. Sci. 109, 14675–14680. https://doi.org/10.1073/pnas.1202095109
2. Cole, M.W., Bassett, D.S., Power, J.D., Braver, T.S., Petersen, S.E., 2014. Intrinsic and task-evoked network architectures of the human brain. Neuron 83, 238–251. https://doi.org/10.1016/j.neuron.2014.05.014
3. Ito, T., Murray, J.D., 2022. Large-scale signal and noise correlations configure multi-task coding in human brain networks. https://doi.org/10.1101/2022.11.23.517699
4. King, M., Hernandez-Castillo, C.R., Poldrack, R.A., Ivry, R.B., Diedrichsen, J., 2019. Functional boundaries in the human cerebellum revealed by a multi-domain task battery. Nat. Neurosci. 22, 1371–1378. https://doi.org/10.1038/s41593-019-0436-x
5. Panzeri, S., Moroni, M., Safaai, H., Harvey, C.D., 2022. The structures and functions of correlations in neural population codes. Nat. Rev. Neurosci. 1–17. https://doi.org/10.1038/s41583-022-00606-4
6. Rissman, J., Gazzaley, A., D'Esposito, M., 2004. Measuring functional connectivity during distinct stages of a cognitive task. NeuroImage 23, 752–763. https://doi.org/10.1016/j.neuroimage.2004.06.035

Poster No 1776

From Rest to Digest: A Large-Sample fMRI Exploration of Brain-Stomach Coupling

Ignacio Rebollo[1], Leah Banellis[2], Niia Nikolova[3], Micah Allen[4]

[1]German Institute of Human Nutrition, Potsdam-Rebrücke, Nuthetal, [2]Aarhus University, Aarhus C, Midtjylland, [3]Aarhus University, Aarhus, DK, [4]Aarhus University, Lystrup, Denmark

Introduction: Signals from the gastro-intestinal tract are constantly relayed to subcortical, cortical and neuromodulatory structures, interacting with spontaneous brain activity and its underlying organization into resting state networks (Azzalini et al., 2019). The stomach, produces its own slow electrical rhythm (~0.05 Hz, i.e., every 20 seconds), and multiple studies have shown that fMRI activity continuously waxes and wanes with the pace of this gastric rhythm (Levakov et al., 2023; Müller et al., 2021; Rebollo et al., 2018; Rebollo & Tallon-Baudry, 2022), albeit with sample sizes limited to 30-60 participants. In this study, we aimed to replicate, compare and extend these findings in a larger sample, while performing strict control for cardiac and physiological artifacts.

Methods: We simultaneously recorded brain activity with fMRI (3 Tesla, TR=1.4 secs, 600 volumes), stomach activity with the electrogastrogram (EGG, (Wolpert et al., 2020)) in 247 human participants at rest with eyes open. fMRI preprocessing included fMRIPrep minimal pipeline, spatial smoothing with a 3mm FWHM kernel, and regressing out six motion parameters, six aCompCor parameters, as well as 12 RETROICOR components reflecting cardiac and respiratory physiological noise. After bandpass filtering the EGG and BOLD time series at individual EGG peak frequencies, we measured the phase coupling between the two (Lachaux et al., 1999). Each voxel coupling was compared to a chance level, estimated by shifting in time the EGG time series. We used FSL randomize algorithm to extract significant coupled voxels at the group level, correcting for multiple comparisons by using the null distribution of the max cluster mass (Strict threshold t = 5.4, liberal threshold = 2.7).

Results: We found an extended network of cortical and subcortical regions significantly coupled to the stomach at the group level. Using a more liberal threshold as in previous studies, we found that significant gastric coupling spans virtually the whole cortex. Using a more stringent threshold, the so-called gastric network (Figure 1) is more salient in sensory motor as well as transmodal regions, with largest overlap with the sensory-motor network followed by the default mode network, in line with previous studies using smaller sample sizes.

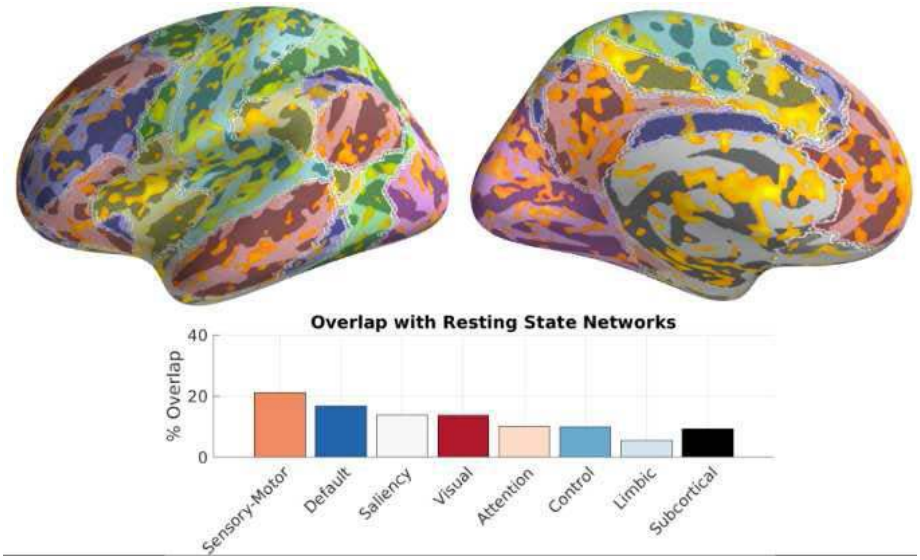

Conclusions: We found that coupling between the brain and the stomach during resting state is pervasive across the cortex, despite strict corrections for physiological noise from the heart and respiration. The large sample size of the current study allowed thus to reveal the full extent of the gastric network, which is in line with the multiple neuromodulatory pathways that are recruited by afferents from the stomach.

References

1. Azzalini, D., Rebollo, I., & Tallon-Baudry, C. (2019). Visceral Signals Shape Brain Dynamics and Cognition. Trends in Cognitive Sciences. https://doi.org/10.1016/j.tics.2019.03.007
2. Lachaux, J.-P., Rodriguez, E., Martinerie, J., Varela, F. J., & others. (1999). Measuring phase synchrony in brain signals. Human Brain Mapping, 8(4), 194–208.
3. Levakov, G., Ganor, S., & Avidan, G. (2023). Reliability and validity of brain-gastric phase synchronization. Human Brain Mapping, 44(14), 4956–4966. https://doi.org/10.1002/hbm.26436
4. Müller, S., Teckentrup, V., Rebollo, I., Hallschmid, M., & Kroemer, N. B. (2021). Vagus nerve stimulation increases stomach-brain coupling via a vagal afferent pathway (p. 2021.10.07.463517). https://doi.org/10.1101/2021.10.07.463517
5. Rebollo, I., Devauchelle, A.-D., Béranger, B., & Tallon-Baudry, C. (2018). Stomach-brain synchrony reveals a novel, delayed-connectivity resting-state network in humans. eLife, 7, e33321. https://doi.org/10.7554/eLife.33321
6. Rebollo, I., & Tallon-Baudry, C. (2022). The sensory and motor components of the cortical hierarchy are coupled to the rhythm of the stomach during rest. Journal of Neuroscience. https://doi.org/10.1523/JNEUROSCI.1285-21.2021
7. Wolpert, N., Rebollo, I., & Tallon-Baudry, C. (2020). Electrogastrography for psychophysiological research: Practical considerations, analysis pipeline, and normative data in a large sample. Psychophysiology, e13599. https://doi.org/10.1111/psyp.13599

Poster No 1777

Prenatal chronic inflammation impacts fetal brain functional connectivity

Iris Menu[1], Lanxin Ji[1], Amyn Majbri[2], Mark Duffy[1], Christopher Trentacosta[3], Adam Eggebrecht[4], Muriah Wheelock[5], Suzanne Jacques[3], Faisal Qureshi[3], Moriah Thomason[6]

[1]NYU Langone Health, New York, NY, [2]New York University Medical Center, New York, NY, [3]Wayne State University School of Medicine, Detroit, MI, [4]Washington University School of Medicine, St. Louis, MO, [5]Washington University in St. Louis, St. Louis, MO, [6]NYU Langone Medical Center, New York, NY

Introduction: Strong evidence suggests that prenatal inflammation significantly increases the risk of neurodevelopmental or psychotic disorders in offspring (Brown et al., 2004; Werenberg Dreier et al., 2016). The belief is that inflammation during pregnancy can disrupt fetal brain development, leading to long-term impacts on the health and development of the offspring. Prior studies have shown that newborns born to mothers with elevated levels of prenatal interleukin-6 and C-reactive protein, biological indicators of maternal inflammation, exhibit differences in functional connectivity in salience, dorsal attention, medial temporal, and subcortical networks (Graham et al., 2018; Rudolph et al., 2018; Spann et al., 2018). However, to date, if and how prenatal inflammation is related to the fetal brain is still unknown.The current study aims to fill this gap.

Methods: Pregnant mothers (N = 102; 89% racial/ethnic minority) were recruited during the second and third trimester of pregnancy. Instead of measuring a single cytokine at one time point in maternal blood, we assessed chronic inflammation based on placental histology. Expert pathologists examined the placental tissues and scored them for chronic placental

inflammatory lesions, including chronic chorioamnionitis, villitis of unknown etiology, and chronic deciduitis. Resting-state imaging data were acquired in fetuses between 24.14 and 37.86 weeks of gestation using two sets of Multi-Echo Functional Magnetic Resonance Imaging (ME-fMRI). Each set comprised of a 12-minute ME-fMRI scan (360 volumes) and the scanning parameters were as follows: for dataset a) TR = 2000ms; TE = 18, 31.07, 44.14ms (3 echoes); flip angle: 83 degrees; voxel size: 3.5 x 3.5 x 3.5 mm^3, and for dataset b) TR = 2000ms; TE = 18, 34, 50ms (3 echoes); flip angle: 83 degrees; voxel size: 3.487 x 3.487 x 3.5 mm^3. We first applied a consensus procedure (infomap) to develop an optimal model consisting of 15 distinct fetal networks distributed across cortical and subcortical regions of interest (Figure 1). Once networks defined, we conducted an enrichment analysis (Eggebrecht et al., 2017) to examine differences associated with chronic inflammation in each within- and between-network pair. We used the Kendall-tau rank correlation, followed by enrichment permutation Wilcoxon tests (10,000 permutations), to determine if the number of significant connections (edges) affected by prenatal inflammation within each network pair exceeded what would be expected by chance.

Results: Our findings revealed that prenatal chronic inflammation disrupted connectivity in frontal, visual, motor, and subcortical networks (Figure 1). Specifically, chronic inflammation led to reduced connectivity within the prefrontal network (network 5, in cyan) and between the fronto-parietal (network 6, in yellow) and subcortical networks (network 13, in light pink) (Figure 2).

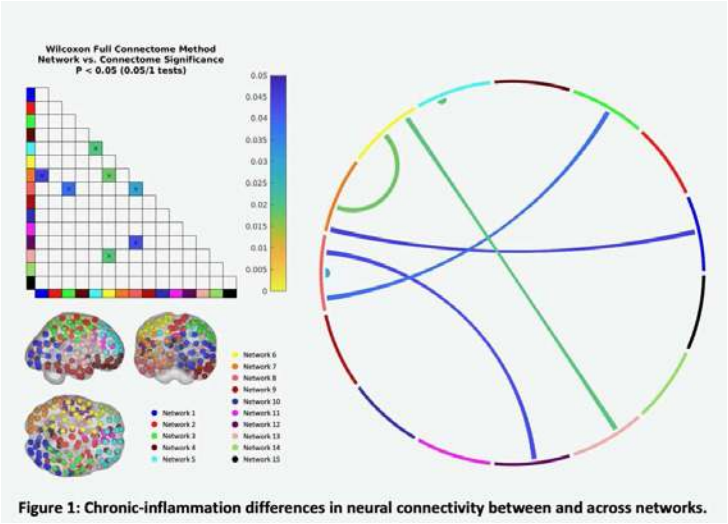

Figure 1: Chronic-inflammation differences in neural connectivity between and across networks.

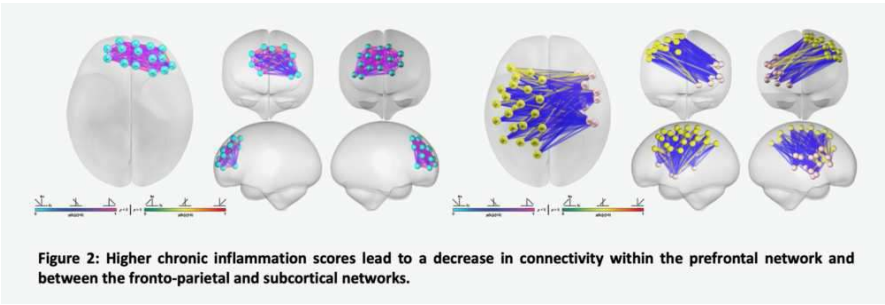

Figure 2: Higher chronic inflammation scores lead to a decrease in connectivity within the prefrontal network and between the fronto-parietal and subcortical networks.

Conclusions: These results support the idea that the neural regions most susceptible to prenatal chronic inflammation are those associated with behavioral impairments based on existing literature (Morgan et al., 2020; Rudolph et al., 2018). Overall, this suggests that the heightened risk of developmental disorders in children exposed to chronic inflammation before birth may be a result of neuroinflammatory events that occur while they are still in the womb.

References

1. Brown, A. S., et al. (2004). Elevated Maternal Interleukin-8 Levels and Risk of Schizophrenia in Adult Offspring. American Journal of Psychiatry, 161(5), 889–895. https://doi.org/10.1176/appi.ajp.161.5.889
2. Eggebrecht, A. T., et al. (2017). Joint Attention and Brain Functional Connectivity in Infants and Toddlers. Cerebral Cortex (New York, N.Y.: 1991), 27(3), 1709–1720. https://doi.org/10.1093/cercor/bhw403
3. Graham, A. M., et al. (2018). Maternal Systemic Interleukin-6 During Pregnancy Is Associated With Newborn Amygdala Phenotypes and Subsequent Behavior at 2 Years of Age. Biological Psychiatry, 83(2), 109–119. https://doi.org/10.1016/j.biopsych.2017.05.027
4. Morgan, J. E., et al. (2020). Prenatal maternal C-reactive protein prospectively predicts child executive functioning at ages 4–6 years. Developmental Psychobiology, 62(8), 1111–1123. https://doi.org/10.1002/dev.21982
5. Rudolph, M. D., et al. (2018). Maternal IL-6 during pregnancy can be estimated from newborn brain connectivity and predicts future working memory in offspring. Nature Neuroscience, 21(5), 765–772. https://doi.org/10.1038/s41593-018-0128-y

6. Spann, M. N., et al. (2018). Maternal Immune Activation During the Third Trimester Is Associated with Neonatal Functional Connectivity of the Salience Network and Fetal to Toddler Behavior. The Journal of Neuroscience: The Official Journal of the Society for Neuroscience, 38(11), 2877–2886. https://doi.org/10.1523/JNEUROSCI.2272-17.2018
7. Werenberg Dreier, J., et al. (2016). Fever and infections in pregnancy and risk of attention deficit/hyperactivity disorder in the offspring. Journal of Child Psychology

Poster No 1778

Dose-Dependent Alcohol Effects on Adult vs. Adolescent Brain Functional Connectivity in Rats

Sung-Ho Lee[1,2,3,4], Tatiana Shnitko[1,2,3], LiMing Hsu[1,2,3], Margaret Broadwater[1,2,3,4], Mabelle Sardinas[1,2,3], Tzu-Wen Wang[5,2,3], Donita Robinson[6,7], Ryan Vetreno[6,7], Fulton Crews[6,7,8], Yen-Yu Shih[1,2,3,4]

[1]Center for Animal MRI, University of North Carolina, Chapel Hill, NC, [2]Biomedical Research Imaging Center, University of North Carolina, Chapel Hill, NC, [3]Department of Neurology, University of North Carolina, Chapel Hill, NC, [4]Bowles Center for Alcohol Studies University of North Carolina, Chapel Hill, NC, [5]University of North Carolina at Chapel Hill, Chapel Hill, NC, [6]Bowles Center for Alcohol Studies, University of North Carolina, Chapel Hill, NC, [7]Department of Psychiatry, University of North Carolina, Chapel Hill, NC, [8]Department of Pharmacology, University of North Carolina, Chapel Hill, NC

Introduction: Alcohol abuse, a significant cause of premature mortality, is notably prevalent among adolescents, increasing risks for alcohol use disorder (AUD) (Crews et al., 2000; Squeglia et al., 2015; Sohi et al., 2021; Miech et al., 2023). Early alcohol exposure disrupts critical neurodevelopmental, hormonal, and cognitive processes, particularly affecting the frontal cortex during pivotal adolescent brain changes (Walker et al., 2022). This period coincides with maturing executive functions and inhibitory control (Saito et al., 2022; Broadwater et al., 2018). This study investigates the impact of acute alcohol intoxication on functional connectivity (FC), taking into account variables including sex and age. Despite evolutionary distinctions, rodent models provide valuable insights into neural mechanisms of addiction. We employed a rat fMRI protocol to investigate the "triple-network" model, analogous to human brain networks, in the context of addiction (Menon et al., 2019; Lee et al., 2021). We examined the age, sex, and alcohol dose-dependent effects on intra- and inter-network connectivity in rats, including the lateral cortical network (LCN), default mode network (DMN), and salience network (SN) (Lee et al., 2021; Mandino et al., 2022).

Methods: This study employed 38 in-house bred Wistar rats, categorized by sex and age (P45, P80). Each rat underwent a single resting-state fMRI (rs-fMRI) session that included both baseline and post-injection scans using saline and varying alcohol doses (0, 1, 2, 4 g/kg). Anesthesia and imaging protocols were conducted as described in Lee et al., 2021. For data preprocessing, we implemented several steps: slice timing correction, motion correction, skull-stripping, spatial normalization, removal of nuisance signals, and band-pass filtering. A Pearson's correlation coefficient matrix was generated for each subject using our in-house rat brain atlas. To assess the effects of sex, age, alcohol exposure, and dose, we conducted a non-parametric factorial ANOVA. Additionally, a moderation analysis was performed to evaluate the influences of sex and age on alcohol-induced changes in FC.

Results: The rs-fMRI matrix from baseline data in this study aligned with prior rat rs-fMRI datasets (Lee et al., 2021), attesting to our FC assessments' reproducibility, shown in Figure 1. The experimental design, in Figure 2A, sets a framework for fMRI sessions, capturing dynamic FC changes post-alcohol administration. Figure 2B reveals sex, age, and alcohol dose effects on FC. Sex differences were evident in FC patterns among intra-network FC within LCN, DMN, SN, and inter-network FC between DMN and other networks. Age altered FC within and between the DMN and SN. Alcohol exposure led to a dose-responsive FC increase across networks. Acute alcohol administration caused significant changes, especially in intra-network FC within LCN and inter-network FC between LCN, DMN, SN. The moderation analysis in Figure 2D highlights age as a more significant factor than sex in alcohol-induced FC alterations, with older subjects showing greater increases in LCN-related FC due to alcohol.

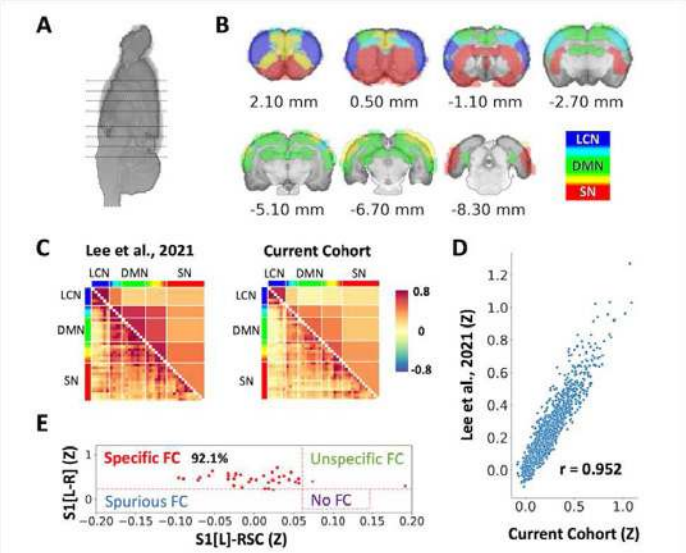

Figure 1. Triple networks of the rat brain and reproducibility of functional connectivity measures. **(A, B)** Triple networks are color-coded and mapped on coronal brain slices with locations indicated in **(A)**. Lateral cortical network (LCN): blue; Default mode network (DMN): green; Salience network (SN): red. **(C)** Comparison of functional connectivity patterns between cohorts. Left: 87 subjects reported in Lee at al., 2021. right: the baseline of current cohort of 38 subjects prior to alcohol administration. Color-bar indicates Fisher's Z score. **(D)** High spatial correlation of functional connectivity patterns between two cohorts. **(E)** Functional connectivity specificity analysis supports the quality of the current dataset.

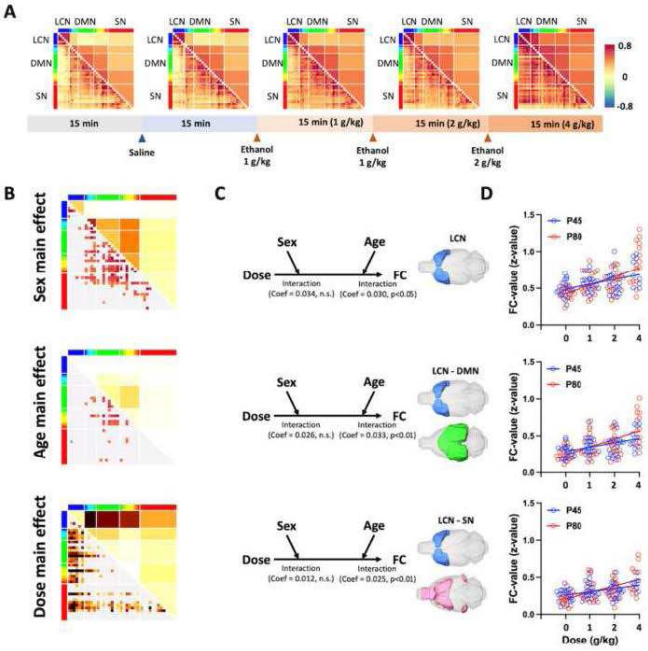

Figure 2. Experimental paradigm and population-level functional connectivity changes (A) An overall increase in functional connectivity was observed after cumulative injections of ethanol. The horizontal bar on the bottom shows the protocol of ethanol dosing. The colorbar on the right indicates Fisher's Z score. **(B)** Main effect of sex (top), age (middle), alcohol dose (bottom) on connectivity revealed by the GLM analysis. Functional connectivity (lower left) and fraction of significant edges (upper right) highlight statistically significant differences between sexes ($p < 0.05$) **(C)** The three models use EtOH dose, as independent variables, sex and age as moderators, and three network-level FC changes as dependent variables: (top) within LCN, (middle) between LCN and DMN, and (bottom) between LCN and SN. In all three models, main effect of alcohol dose on LCN-related FC was dependent on age (a significant interaction effect, all $p < 0.05$) but not sex (all $p > 0.05$). **(D)** Dose-dependent increase in LCN-related FC in P45 and P80 groups of rats. Circles indicate data for individual subjects color-coded according to age group. Red and blue lines indicate linear regression slopes.

Conclusions: This study used rs-fMRI to examine the effects of acute alcohol on functional connectivity in rat brains, specifically focusing on the DMN, SN, and LCN. Reproducibility was confirmed by comparing with previous datasets. The research revealed sex- and age-dependent differences in connectivity. Notably, acute alcohol exposure increased connectivity within the LCN and between LCN, DMN, and SN. Age was a significant moderator in alcohol-induced FC changes, aligning with prior findings on age-related behavioral responses to alcohol. This work supports the utility of rs-fMRI in studying alcohol's acute effects on brain networks and suggests a mechanism for adolescent insensitivity to alcohol intoxication.

References
1. Broadwater M.A. et al., (2018), 'Adolescent alcohol exposure decreases frontostriatal resting-state functional connectivity in adulthood', Addiction Biology, 23(2), 810-823.
2. Crews F.T. et al., (2000), 'Binge ethanol consumption causes differential brain damage in young adolescent rats compared with adult rats', Alcoholism: Clinical and Experimental Research, 24(11), 1712-1723.
3. Lee S. et al., (2021), 'An isotropic EPI database and analytical pipelines for rat brain resting-state fMRI', NeuroImage, 243:118541.
4. Mandino F. et al., (2022), 'A triple-network organization for the mouse brain', Molecular Psychiatry, 27(2), 865-872.
5. Menon B., (2019), 'Towards a new model of understanding - The triple network, psychopathology and the structure of the mind', Medical Hypotheses, 133:109385.
6. Miech R.A. et al., (2023). 'Monitoring the Future National Survey Results on Drug Use, 1975–2022: Secondary School Students', Ann Arbor: Institute for Social Research, The University of Michigan.
7. Saito D.N. et al., (2022), 'Development of attentional networks during childhood and adolescence: A functional MRI study', Neuropsychopharmacology Reports, 42(2), 191-198.
8. Sohi I. et al., (2021), 'The global impact of alcohol consumption on premature mortality and health in 2016', Nutrients, 13(9).
9. Squeglia L.M. et al., (2015), 'Brain development in heavy-drinking adolescents', American Journal of Psychiatry, 172(6), 531-542.
10. Walker C.D. et al., (2022), 'Diverging Effects of Adolescent Ethanol Exposure on Tripartite Synaptic Development across Prefrontal Cortex Subregions', Cells, 11(19), 11193111.

Poster No 1779

Benchmarking 200+ pairwise similarity measures for resting-state functional connectivity estimation

Connor Lane[1], Florian Rupprecht[2], Michael Milham[1], Gregory Kiar[3]

[1]Child Mind Institute, New York, NY, [2]Child Mind Institute, Brooklyn, NY, [3]Child Mind Institute, Montreal, Quebec

Introduction: A long term goal in brain imaging is to leverage fMRI to inform clinical practice. The current dominant approach for relating fMRI to clinical behavior leverages features based on resting-state functional connectivity[1]. However, the poor reliability of these features is a major barrier to clinical usefulness[2]. Recent efforts to improve functional connectivity based prediction have emphasized the importance of choosing a good brain parcellation and downstream prediction algorithm[3,4]. In this work, we evaluate the measure of functional connectivity itself. Using the Python Toolkit of Statistics for Pairwise Interactions (PySPI)[5], we evaluate 215 measures for computing generalized functional connectomes. Our goal is to determine whether any of these metrics should replace Pearson correlation as the standard functional connectivity measure used in behavior prediction.

Methods: We included six publicly available datasets with multi-session resting state fMRI: BNU-2, HNU-1, NYU-1, and NKI test-retest from the CoRR initiative[6], HCP S1200 test-retest[7], and MSC[8]. Each dataset consists of 10–61 subjects each scanned for 2–10 sessions, across a range of sites, scanner manufacturers, and protocols. We pre-processed each dataset using two analysis pipelines: fMRIPrep using XCP-D and the Glasser parcellation[9-10], and C-PAC using the Schaefer-400 parcellation[11]. After pre-processing, we computed generalized functional connectivity matrices using 215 statistics of pairwise interactions (SPIs) from the PySPI toolkit[5]. While PySPI contains 250+ metrics, the current analysis includes only computationally tractable methods from the "fast" config. Furthermore, we impose time and memory constraints (5 min, 16 GB). We evaluated the 215 SPIs in terms of two notions of reliability. First, we computed standard within-subject inter-session reliability using ICC. This measure, which we refer to as ICC_ses, measures the reliability of each connectivity edge across sessions for the same subject. Second, to assess how well each SPI captures "meaningful" structure, we also report a measure we call ICC_sub, which measures the consistency of the overall connectome across subjects.

Results: Of the 215 statistics of pairwise interaction (SPI) considered, we find that only 102 compute successfully under the imposed time and memory constraints (Figure 1). The Pearson correlation baseline is among the most resource efficient methods, with some SPIs requiring an order of magnitude more memory and four orders more run time. Among the 102 SPIs that compute successfully, we observe substantial variability in both inter-session and inter-subject reliability (Figure 2). For both metrics, the Pearson correlation baseline is among the top 10 most reliable SPIs. Furthermore, the numerical differences between the most reliable SPIs are small. However, there appears to be a small numerical advantage under both reliability metrics for regularized covariance estimation methods (OAS, Ledoit-Wolf) and robust correlation statistics (Spearman, Kendall's Tau). We also observe substantial variability between datasets, which is expected considering the variety of data collection conditions. Variation due to pre-processing pipeline is also present, particularly in inter-subject ICC, although to a smaller degree compared to dataset variation.

Conclusions: In this work, we performed a benchmark of 215 measures for estimating functional connectivity over 6 datasets and 2 pre-processing pipelines. Our initial results suggest that none of the measures considered convincingly outperform the de facto standard Pearson correlation measure. Although we do observe weak support for more robust covariance and

correlation measures. In continuing work, we plan to add evaluations of downstream behavior prediction performance, as well as expand the set of evaluated measures.

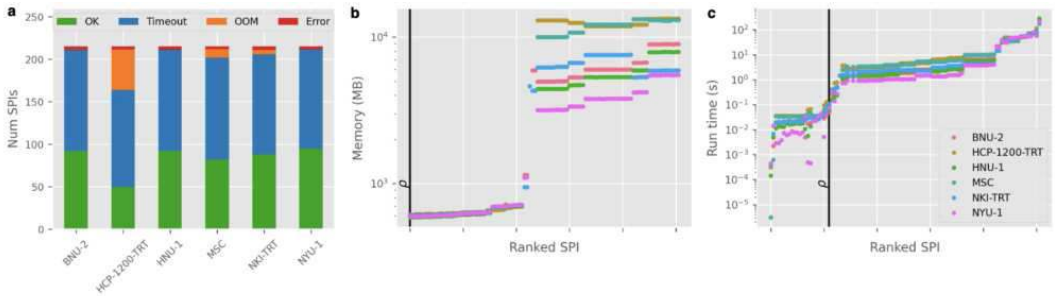

Figure 1. Completion and resource usage statistics for 215 Statistics of Pairwise Interactions (SPIs) for the fMRIPrep-based preprocessing pipeline. **(a)** Completion status counts across all 215 SPIs. We ran each SPI with a 5 minute time budget and 16GB memory budget. Counts are averaged across dataset, subject, and session. **(b)** Sorted memory usage **(c)** run time across all 102 SPIs with a successful execution. Black vertical lines indicates rank of the Pearson correlation baseline (memory: 1/102, run time: 23/102). Resource usage statistics are averaged across subject and session within dataset.

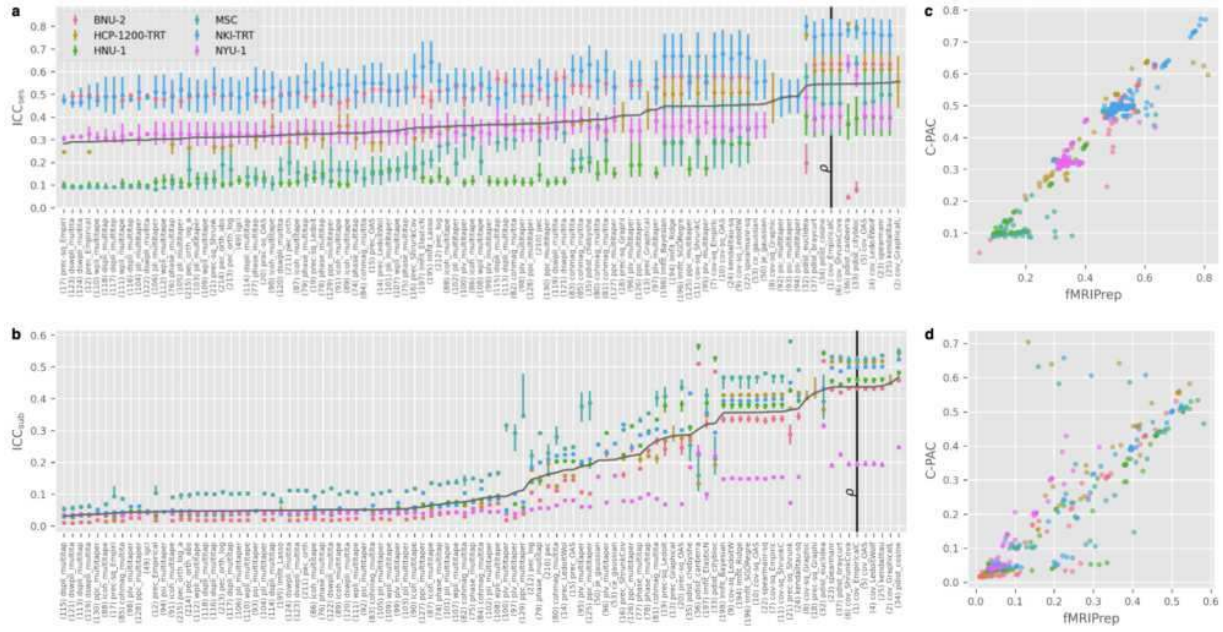

Figure 2. Inter-session and inter-subject reliability of 100+ SPIs across 6 datasets and 2 pre-processing pipelines. **(a)** Inter-session and **(b)** inter-subject intraclass correlation coefficients (ICCs) for all successful SPIs (median +/- IQR). Inter-session ICC measures the reliability of an individual subject's SPI connectome across sessions. Inter-subject ICC measures the reliability of the group average SPI connectome across subjects. SPIs are sorted by mean ICC (dark gray line). Black vertical line indicates the Pearson correlation baseline. **(c)** Cross-pipeline agreement for inter-session and **(d)** inter-subject ICC.

References

1. Chen, J., et al. (2022). Shared and unique brain network features predict cognitive, personality, and mental health scores in the ABCD study. Nature communications.
2. Milham, M. P., Vogelstein, J., & Xu, T. (2021). Removing the reliability bottleneck in functional magnetic resonance imaging research to achieve clinical utility. JAMA psychiatry.
3. Kong, R., et al. (2021). Individual-specific areal-level parcellations improve functional connectivity prediction of behavior. Cerebral Cortex.
4. Dadi, K., et al. (2019). Benchmarking functional connectome-based predictive models for resting-state fMRI. NeuroImage.
5. Cliff, O. M., Bryant, A. G., Lizier, J. T., Tsuchiya, N., & Fulcher, B. D. (2023). Unifying pairwise interactions in complex dynamics. Nature Computational Science.
6. Zuo, X. et al. (2014). An open science resource for establishing reliability and reproducibility in functional connectomics. Scientific data.
7. Van Essen, D. C., et al. (2013). The WU-Minn human connectome project: an overview. Neuroimage.
8. Gordon, E. M., et al. (2017). Precision functional mapping of individual human brains. Neuron.
9. Esteban, O., et al. (2019). fMRIPrep: a robust preprocessing pipeline for functional MRI. Nature methods.
10. Adebimpe, A., et al. (2023). XCP-D: A Robust Postprocessing Pipeline of fMRI data.
11. Craddock, C., et al. (2013). Towards automated analysis of connectomes: The configurable pipeline for the analysis of connectomes (c-pac). Front Neuroinform.

Poster No 1781

An fMRI study on Long-Term Brain Function in Youth with a Previous Enterovirus-71 Infection

Jasmine I Ali-Gami[1], Susan Shur-Fen Gau[2], Jung-Chi Chang[3], Wen-Yih Tseng[4], Luan-Yin Chang[3], Hsiang-Yuan Lin[5]

[1]University of Toronto, Toronto, Ontario, [2]National Taiwan University College of Medicine, Taipei, Taiwan, [3]National Taiwan University Hospital, Taipei, Taiwan, [4]Institute of Medical Device and Imaging, College of Medicine, National Taiwan University, Taipei, Taiwan, [5]Centre for Addiction and Mental Health, Department of Psychiatry, University of Toronto, Toronto, Ontario

Introduction: An Enterovirus (EV) infection, particularly the EV-71 strain, is a common pediatric infectious disease. EV-71 is known to cause illnesses ranging from a low-grade fever, and hand-foot-and-mouth disease, to a severe central nervous system (CNS) disease.[5] With a global presence, this life-altering infection poses a serious public health threat across the Asia-Pacific region and beyond.[6] Among the manifestations and sequelae, the long-term impact of an EV CNS infection remains a critical concern with neuropsychiatric sequelae.[3,2] Specifically, numerous studies have shown the correlation between an EV-71 CNS infection and the development of attention-deficit/hyperactivity disorder (ADHD) and associated emotional-behavioural problems later in life.[3,1] However, no published evidence has studied the longitudinal brain development in this unique population of youth who are at a three times greater risk of developing ADHD following an EV-71 CNS infection earlier in life (will be referred to as EVA, henceforth). Our research investigated the longitudinal brain features of youth with a pediatric EV-71 CNS infection earlier in life. Specifically, our research aimed to address the following questions: "Are there abnormalities in functional connectivity of the midbrain and striatum that would link to the increased risk of developing ADHD?", and "Are there functional network connectivity-based differences in youth who have had an enterovirus infection with later ADHD development in comparison to idiopathic ADHD and Control groups".

Methods: This cohort study included 31 youth with a previous EV-71 CNS infection 6-18 years ago. Sixteen of them developed ADHD later in life. Additionally, this study included 53 age- and sex-matched youth with idiopathic ADHD, and 37 matched neurotypical youth as the control groups. Our methods utilized multi-echo resting-state functional magnetic resonance imaging (rs-fMRI) to examine the functional connectivity in two approaches. For the first approach, we took on a seed-based analysis of dopamine-associated structures within the midbrain and striatal regions.[4] Following, our second approach utilized a whole brain functional connectome-based statistical approach to examine any atypical findings in neural networks across the groups.

Results: Compared to youth who had an EV-71 CNS infection and did not develop ADHD, the group that developed ADHD showed lower functional connectivity between the right substantia nigra pars compacta, right ventral tegmental area, the left dorsal caudate and the left calcarine. Additionally, our connectome analysis showed that in comparison to the idiopathic ADHD group, the EVA group showed reduced functional connectivity in the subcortical, salience and default mode networks. In comparison to the neurotypical developing group, EVA subjects showed greater functional connectivity in the default mode and salience networks.

Conclusions: This is the first study investigating longitudinal functional brain patterns following a severe EV-71 CNS infection. We found that generally, youth with Enterovirus-facilitated ADHD had a similar intrinsic functional connectivity pattern at cortical and striatal levels. Altered midbrain functional connectivity is unique in Enterovirus-facilitated ADHD. Our study suggests a possible avenue for future studies, being dopamine dysregulation within the midbrain and striatal regions contributing to ADHD symptomology, which may facilitate the development of targeted intervention and rehabilitation strategies to enhance the quality of life and reduce disabilities in infected youth.

References

1. Chang L.Y. (2007), 'Neurodevelopment and cognition in children after enterovirus 71 infection', New England Journal of Medicine, vol. 356, no. 12, pp. 1226-1234
2. Huang H.I. (2015), 'Neurotropic Enterovirus Infections in the Central Nervous System', Viruses, vol. no. 11, pp. 6051-6066
3. Lin H.Y (2022), 'Long-term psychiatric outcomes in youth with enterovirus A71 central nervous system involvement'. Brain Behaviour & Immunity-Health, vol. 23, no.
4. Messacar, K. (2020) 'Clinical characteristics of enterovirus A71 neurological disease during an ou in children in Colorado, USA, in 2018: an observational cohort study', The Lancet Infectious Diseases, vol. 20, no. 2, pp. 230-239
5. Sawyer M.H. (2002), ' Enterovirus infections: diagnosis and treatment', Seminars in Pediatric Infectious Disease, vol. 13, no. 1, pp. 40-47
6. Solomon T (2010), 'Virology, epidemiology, pathogenesis, and control of enterovirus 71', The Lancet Infectious Disease, vol. 10, no. 11, pp. 778-790

Poster No 1782

Brain functional connectivity asymmetry: Left hemisphere not necessarily more modular

Lucia Jajcay[1,2,3], David Tomeček[1,2,3], Jiří Horáček[1,4], Filip Španiel[1,4], Jaroslav Hlinka[1,2]

[1]National Institute of Mental Health, Klecany, Czech Republic, [2]Institute of Computer Science, The Czech Academy of Sciences, Prague, Czech Republic, [3]Faculty of Electrical Engineering, Czech Technical University in Prague, Prague, Czech Republic, [4]Third Faculty of Medicine, Charles University, Prague, Czech Republic

Introduction: Recently, we examined brain functional connectivity (FC) asymmetry in terms of modularity – a statistic that quantifies the degree to which a graph (network) may be subdivided into clearly delineated groups of nodes (modules) [Newman, 2004] – and reported that the left hemisphere is more modular [Jajcay, 2022; 2023]. The finding appeared to be in line with morphological studies of the human brain and promising for studying aberrant hemispheric lateralization and its functional relevance in neuropsychiatric disorders. Here, we thus extend the original analysis (performed on healthy controls) to patients with schizophrenia. We also examine its robustness with respect to different preprocessing pipelines. Moreover, since the previous finding could potentially be due to the fact that the Automated Anatomical Labeling (AAL) atlas is not symmetrical, we further extend the analysis to additional brain parcellations.

Methods: Using a Siemens Trio 3T MRI scanner, we measured the resting-state brain activity of 90 healthy subjects (40M – mean age 28.15 ± 6.90 years, 36 right-handed; 50F – 27.54 ± 6.82, 46) and 100 patients with schizophrenia (58M – 26.42 ± 5.05, 45; 42F – 31.75 ± 7.75, 35). Functional T2*-weighted images with blood oxygenation level-dependent (BOLD) contrast (GE-EPIs; TR/TE = 2000/30 ms, flip angle = 70°, 48×64 voxels, voxel size = 3×3×3 mm3, FOV = 192 mm, 400 volumes, 35 axial slices covering the entire cerebrum), as well as high-resolution 3D T1-weighted images (for anatomical reference), were acquired. Using SPM12 and CONN running under MATLAB, three different data preprocessing pipelines were applied – "stringent", "moderate" (both described in Kopal [2020]), and "default" ("stringent" without linear detrending). Individual FC matrices were computed by linear (Pearson's) correlation [Hlinka, 2011; Hartman, 2011] from – initially – the mean BOLD time series of 90 regions of interest of the AAL atlas ("AAL-90"). Using the Brain Connectivity Toolbox, the subgraphs of each hemisphere were then thresholded by preserving a proportion of the strongest weights (5–95%, in increments of 5), binarized, their modularity was computed and, finally, compared across subjects using the Wilcoxon signed-rank test. We then repeated the analysis using additional parcellations (with "default" preprocessing). First, we created three symmetrized versions of AAL-90 by mirroring the left ("AAL-90_L") and the right ("AAL-90_R") hemispheres and by using the intersection of the mirrored masks ("AAL-90_LR"), respectively. Second, we used the gray matter areas from the MNI152 template resampled to 4284 cubes of size 6×6×6 mm^3 ("cubes") as a less computationally demanding alternative to using individual voxels. Finally, since the newly created parcellations are perfectly symmetrical yet not anatomically meaningful, we also used two homotopic atlases – v2 of the volumetric AICHA which consists of 384 regions [Joliot, 2015] and the surface-based atlas by Yan et al. [2023] projected to MNI152 space, at two different resolutions ("Yan-100" and "Yan-400").

Results: For a detailed overview of results across parcellations, preprocessing pipelines, and subject groups, see Table 1. Notably, the results reported previously (using AAL-90 and stringent preprocessing on healthy controls) also hold for an analogous analysis on patients with schizophrenia. However, using the more symmetrical ('artificial' or homotopic) parcellations, the results are generally not statistically significant.

Parcellation	Preprocessing	Healthy Controls				Patients			
		Modularity		z	p	Modularity		z	p
		Left	Right			Left	Right		
AAL-90	stringent	0.231	0.224	2.05	0.040	0.232	0.223	2.88	0.004
AAL-90	moderate	0.213	0.201	4.83	<0.001	0.224	0.213	3.49	<0.001
AAL-90	default	0.233	0.233	-0.46	0.642	0.237	0.233	0.69	0.487
AAL-90_L	default	0.232	0.230	1.21	0.225	0.235	0.232	1.10	0.273
AAL-90_R	default	0.229	0.232	-1.70	0.090	0.231	0.233	-2.30	0.021
AAL-90_LR	default	0.225	0.227	-0.36	0.722	0.227	0.227	-1.29	0.197
cubes	default	0.130	0.130	-0.75	0.455	0.126	0.124	0.94	0.348
AICHA	default	0.215	0.219	-1.54	0.124	0.213	0.216	-1.67	0.095
Yan-100	default	0.245	0.241	2.11	0.035	0.245	0.240	2.57	0.010
Yan-400	default	0.225	0.220	0.96	0.337	0.224	0.217	2.14	0.032

Table 1. Comparison of modularity (median ranks across subjects, averaged across the entire range of thresholds) of the left and the right hemispheres with corresponding *z*-values and *p*-values, for both healthy controls and patients with schizophrenia, for each version of the analysis (different parcellations and preprocessing pipelines). Whenever the difference between the two hemispheres is statistically significant, the higher value of modularity is highlighted in colour (blue for the left hemisphere, red for right).

Conclusions: We have replicated our recent finding of the left hemisphere being more modular on patients with schizophrenia. However, the result appears to be sensitive to both preprocessing pipelines and brain parcellations. As a next step (in progress), we will replicate the analyses on a larger dataset (HCP) to elucidate the effect of these variables, and the nature of the asymmetry of modularity across the two hemispheres – which, for now, remains ambiguous.

References

1. Hartman, D. (2011), 'The role of nonlinearity in computing graph-theoretical properties of resting-state functional magnetic resonance imaging brain networks', Chaos, vol. 21, no. 1, 013119.
2. Hlinka, J. (2011), 'Functional connectivity in resting-state fMRI: Is linear correlation sufficient?', NeuroImage, vol. 54, no. 3, pp. 2218–2225.
3. Jajcay, L. (2022), 'Brain functional connectivity asymmetry: Left hemisphere is more modular', Symmetry, vol. 14, no. 4, 833.
4. Jajcay, L. (2023, July 22–26) 'Brain functional connectivity asymmetry: Left hemisphere is more modular' [Poster no. 1511], OHBM 2023 – 29th Annual Meeting of the Organization for Human Brain Mapping, Montreal, Canada.
5. Joliot, M. (2015), 'AICHA: An atlas of intrinsic connectivity of homotopic areas', Journal of Neuroscience Methods, vol. 254, pp. 46–59.
6. Kopal, J. (2020), 'Typicality of functional connectivity robustly captures motion artifacts in rs-fMRI across datasets, atlases, and preprocessing pipelines', Human Brain Mapping, vol. 41, no. 18, pp. 5325–5340.
7. Newman, M.E.J. (2004), 'Finding and evaluating community structure in networks', Physical Review E, vol. 69, no. 2, 026113.
8. Yan, X. (2023) 'Homotopic local-global parcellation of the human cerebral cortex from resting-state functional connectivity', NeuroImage, vol. 274, 120010.

Poster No 1783

Whole-Brain States Explain Variability in Visually Evoked BOLD Responses and P100 Component

Brandon Ingram[1], Stephen Mayhew[2], Andrew Bagshaw[1]

[1]University of Birmingham, Centre for Human Brain Health, Birmingham, West Midlands, [2]Aston University, Institute of Health and Neurodevelopment, Birmingham, West Midlands

Introduction: Functional magnetic resonance imaging (fMRI) is one of the most widely applied methods for non-invasively investigating human brain function. Unlike other neuroimaging techniques, fMRI can measure changes in the BOLD signal across the entirety of the human brain at millimetre resolution. Thus, with fMRI, it is possible to investigate the functions of deeper brain structures (e.g. the thalamus) and to identify large-scale networks (Biswal et al., 1995; Smith et al., 2009). Research has demonstrated that the BOLD signal exhibits a large amount of variability within individuals, between sessions (Aguirre et al., 1998) and within sessions, with the BOLD response varying to repeated presentations of the same stimulus (Bianciardi et al., 2009; Duann et al., 2002; Schölvinck et al., 2012; Mayhew et al., 2013). A proportion of this variability in BOLD responses results from the ongoing BOLD dynamics within the region, with the baseline activity becoming linearly summated with the evoked BOLD activity (Fox & Raichle, 2007; Fox et al., 2006). However, these studies generally focussed on the spontaneous BOLD signal within the sensory cortex associated with the stimulus, neglecting the impact of BOLD signals within more distal brain regions. Recent research in rodents has demonstrated that spontaneous BOLD activity across the whole brain (including areas that do not respond to the stimulus) explained approximately 30% of the variability in visual BOLD responses, indicating that the spontaneous activity across the whole brain also explains a large amount of the variance in visually evoked responses (Zhang et al., 2022). Therefore, this study applied Hidden Markov Modelling to EEG-fMRI data with the goal of identifying whole-brain states, and evaluating their impact on visually evoked BOLD responses, visually evoked potentials (VEPs) and alpha synchronisation / desynchronisation (alpha ERD/S).

Methods: Thirty control participants were displayed full contrast visual checkerboards to the left visual field to evoke a lateralised visual BOLD response, VEP and alpha ERD/S. EEG (BrainProducts) and fMRI (Siemens Prisma, TR=1010 ms, 2.5 × 2.5 × 2.5 mm) were recorded simultaneously. A group level ICA (20 components) was performed to obtain a functional parcellation of the resting state networks. This was used as input within a Hidden Markov Model (HMM-MAR toolbox) (Vidaurre et al, 2016). We then evaluated how whole-brain states influenced visual BOLD responses, VEPS and alpha ERD/S responses when the states were active at the time of visual stimulation.

Results: The HMM approach found five whole-brain states, with three significantly modulating the amplitude of subsequent BOLD responses and the P100 VEP component when active at the time of visual stimulation. Specifically, whole-brain states associated with high BOLD activity within visual cortex resulted in smaller BOLD responses and P100 component amplitudes (and vice versa for whole-brain states associated with low BOLD activity in visual cortex). Additionally, the amplitude of the visual BOLD responses was significantly increased when a DMN state was active at the time of visual stimulation. The ERD/ERS was not impacted significantly by pre-stimulus brain state.

Conclusions: Overall, the results of this study demonstrated that the active whole-brain state during the pre-stimulus baseline period significantly influences BOLD responses and P100 amplitudes. This finding shows that baseline BOLD activity defined across the whole brain affects subsequent BOLD responses and electrophysiological responses to visual stimuli, highlighting the importance of accounting for baseline BOLD activity within neuroimaging research. HMMs are an effective way of identifying brain states to examine their impact on stimulus responses.

References

1. Aguirre, G. K. et al. (1998). The variability of human, BOLD hemodynamic responses. Neuroimage, 8(4), 360-369.
2. Bianciardi, M. et al. (2009). Modulation of spontaneous fMRI activity in human visual cortex by behavioral state. Neuroimage, 45(1), 160-168.
3. Biswal, B. et al. (1995). Functional connectivity in the motor cortex of resting human brain using echo-planar MRI. Magnetic resonance in medicine, 34(4), 537-541.
4. Duann, J. R. et al. (2002). Single-trial variability in event-related BOLD signals. Neuroimage, 15(4), 823-835.
5. Fox, M. D. et al. (2006). Spontaneous neuronal activity distinguishes human dorsal and ventral attention systems. Proceedings of the National Academy of Sciences, 103(26), 10046-10051.
6. Fox, M. D., & Raichle, M. E. (2007). Spontaneous fluctuations in brain activity observed with functional magnetic resonance imaging. Nature reviews neuroscience, 8(9), 700-711.
7. Mayhew, S. D. et al. (2013). Spontaneous EEG alpha oscillation interacts with positive and negative BOLD responses in the visual–auditory cortices and default-mode network. Neuroimage, 76, 362-372.
8. Schölvinck, M. L. et al. (2012). The influence of spontaneous activity on stimulus processing in primary visual cortex. Neuroimage, 59(3), 2700-2708.
9. Smith, S. M. et al. (2009). Correspondence of the brain's functional architecture during activation and rest. Proceedings of the national academy of sciences, 106(31), 13040-13045.
10. Vidaurre, D. et al. (2016). Spectrally resolved fast transient brain states in electrophysiological data. Neuroimage, 126, 81-95.
11. Zhang, Q. et al. (2022). Brain-wide ongoing activity is responsible for significant cross-trial BOLD variability. Cerebral Cortex, 32(23), 5311-5329.

Poster No 1784

Impact of removing global signals on functional connectivity associated to state and trait anxiety

Kimberly Rogge-Obando[1], Caroline Martin[1], Terra Lee[1], Sarah Goodale[1], Shiyu Wang[1], Ruogi Yang[1], Richard Song[1], Jeremy Hogeveen[2], Catie Chang[1]

[1]Vanderbilt University, Nashville, TN, [2]University of New Mexico, Albuquerque, NM

Introduction: The functional connectivity between anxiety and the default mode, central executive, and salience networks have been well established.[1,2] However, full-brain fluctuations that stem from arousal states and physiological influences such as heart rate have also been shown to influence functional connectivity. This has led a portion of the field choosing to remove these influences using global signal regression (whole-brain average BOLD signal). However, recent studies indicate that the global signal holds valuable information about psychiatric disorders.[3] Here, we determine the amount and extent to which regressing out the global signal, related measures of arousal, and heart rate impacts the relationship between functional connectivity and measures of anxiety. Additionally, we examine the spatial distribution of these global effects correlated to anxiety across the brain.

Methods: Resting-state fMRI and psychometrics data from the Nathan Kline Institute (NKI-Rockland Sample,[4] was analyzed for this study. A total of 481 subjects that had State and Trait Anxiety Inventory scores greater than 30 were included in the analysis (F=328, M=153). FSL MELODIC ICA was used to derive five networks of interest: ventral-default mode (VDMN), dorsal-default mode (DDMN), salience (SAL), left-central executive (LCEN), and right-central executive (RCEN). Dual regression was used to extract subject-specific time series of each network. After motion regression, functional connectivity was computed between all pairs of networks and correlated to psychometrics, covarying for age and gender. This analysis was repeated after separately regressing out the global signal, a low-frequency heart rate signal, and an fMRI-derived arousal signal.[5] Lastly, spatial maps reflecting the association of global signal, arousal, and heart rate variability to fMRI signals across the brain were also constructed. FSL randomise was used to relate these spatial maps to anxiety measures while covarying for age, gender, and ethnicity and correcting for multiple comparisons.

Results: Before global signal regression, the connectivity between the VDMN-SAL and SAL-RCEN was significant for state anxiety and SAL-RCEN connectivity was significant for trait anxiety. The regression of global signal and full-brain arousal fluctuations removed any significant network connections. However, when regressing heart rate related fluctuations, these functional connectivity values remained significant. For our arousal spatial maps, areas of the para hippocampal, intra parietal lobe and visual cortex were related to state anxiety but not to trait anxiety. There was no relationship between anxiety measures and either global signal maps or heart rate variation maps.

Conclusions: Our results show that global signal regression impacted the significance of resting-state network functional connectivity and their relationship with anxiety. These results were replicated when regressing out an fMRI-derived arousal metric but not for heart rate. These results suggest that global fMRI signals, including arousal effects, may hold valuable information related to anxiety. This notion is further supported by our observation that key regions of the brain demonstrated arousal-related BOLD signals that were related to state anxiety.

References

1. Saviola, F. et al. (2020),' Trait and state anxiety are mapped differently in the human brain', Scientific Reports 2020
2. Menon, V. (2011),' Large-scale brain networks and psychopathology: a unifying triple network model' Trends Cogn Sci
3. Hahamy, A. et al.(2014)' Save the Global: Global Signal Connectivity as a Tool for Studying Clinical Populations with Functional Magnetic Resonance Imaging', Brain Connect
4. Tobe, R. H. et al.(2022), 'A longitudinal resource for studying connectome development and its psychiatric associations during childhood',Scientific Data
5. Goodale, S. E. et al.(2021) 'Fmri-based detection of alertness predicts behavioral response variability', Elife

Poster No 1785

A principled approach to predict functional connectivity from age and sex for normative modelling

Janus Kobbersmed[1], Diego Vidaurre[1]

[1]Aarhus University, Aarhus, Aarhus C

Introduction: Many neurological and psychiatric diseases lack measures of brain functioning as indicators of brain pathology. The search for such biomarkers is complicated by the fact that many brain diseases and disorders, like e.g. autism or ADHD, affect multiple brain regions and their interplay. Furthermore, these conditions are often described as a spectrum from normal to abnormal rather than a sick-healthy dichotomy (Marquand et al. 2016). Recently, normative modelling of brain structure and function has gained increasing popularity (Rutherford et al. 2023). This approach seeks to characterize the distributions of population brain measures to identify the range of normal brain measures. Normative modelling of brain function requires data from a large population of healthy subjects as well as a method to predict normal brain functioning from sex and age. In fMRI studies, brain functioning is often assessed via functional connectivity (FC) which is the matrix of covariances between brain regions (Smith et al. 2013). However, predicting FC from sex and age is challenging because of the mathematical structure and high dimensionality of the FC matrix (Hoff and Niu 2012). Current normative modelling studies have mainly focused on predicting the individual elements of the FC matrix rather than the FC matrix as a whole and its structure (e.g. (Looden et al. 2022)). To address this gap, we investigate a newly developed method for covariance matrix regression in a normative modelling setting. Using resting fMRI data from the Human Connectome Project (HCP), we adapt this method to predict FC from sex and age for characterization of normal brain functioning.

Methods: FC was derived from a set of resting fMRI scans from 1000 subjects from the HCP. The parcellation was an overlapping, spatial parcellation with 50 ICA parcels. In order to predict FC from sex and age, we used a newly developed method called covariate-assisted principal regression (CAPR), which was found in literature (Zhao et al. 2021). The method finds a transformation of the subjects' covariance matrices by identifying projections that depend on chosen covariates. We first assessed the consistency and scalability of the method and how it depended on the parcellation, covariates, and number of subjects and timepoints. We then adapted the method to our normative modelling framework and identified 2 age-dependent projections for each sex category in a training set of 800 healthy subjects. This allowed us to find the distribution of the transformed FC in the training set. Each of 200 healthy out-of-sample test subjects were then assigned a Z-score of their FC given sex and age. The whole process was repeated using 5-fold cross-validation to validate the model's capability of defining normal functioning in a healthy population.

Results: Having established the consistency of the CAPR method, we adapted it for use in normative modelling and identified relevant transformations of the FC data in the HCP dataset. This reduced dimensionality of the data to summarize individual FC in 2 age-dependent derived values (Figure 1). The prediction of the derived brain measures allowed assigning Z-scores for each of 200 out-of-sample test subjects (4 examples shown in Figure 1). The distribution of the Z-scores obtained from cross-validation showed that we were able to characterize brain functioning in the healthy population. Bootstrapping revealed that this method was computationally scalable to larger datasets (>20000 subjects).

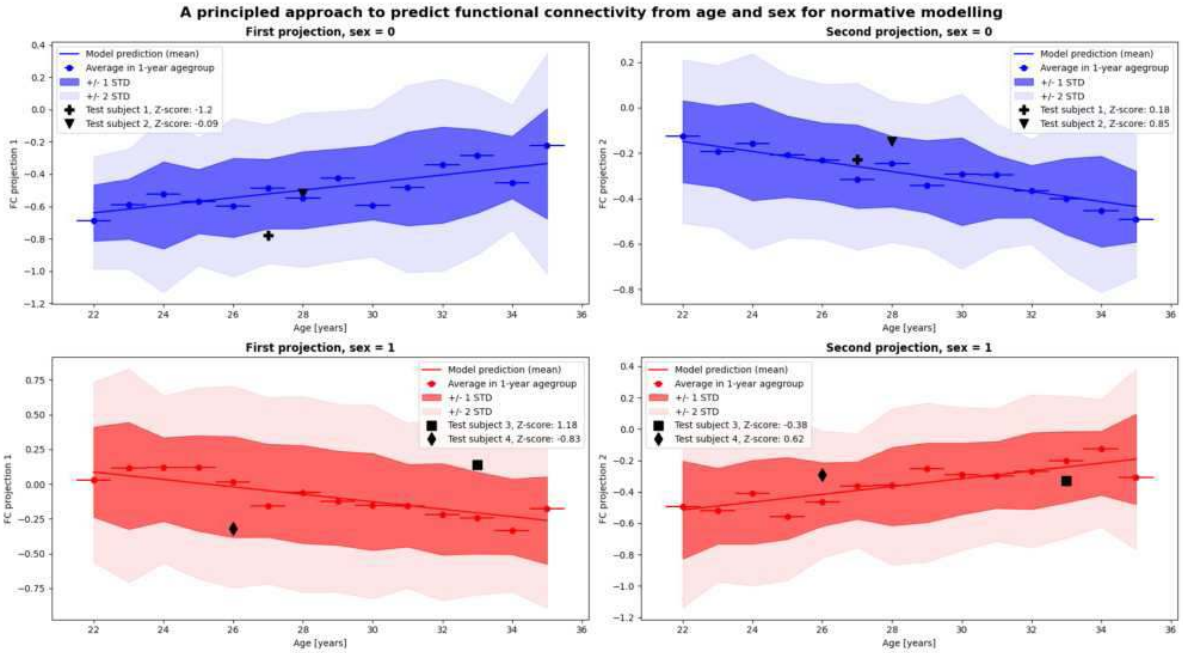

Conclusions: Taking advantage of a large, publicly available brain dataset, this work suggests a useful method to extract relevant age- and sex-related characteristics in FC and use these to predict normal brain functioning. The method successfully characterizes the FC in a healthy population and is scalable. This paves the way for normative modeling using larger datasets as well as identification of brain functioning pathology.

References

1. Hoff, Peter D. (2012), 'A Covariance Regression Model', Statistica Sinica, 22.
2. Looden, T. (2022), 'Patterns of connectome variability in autism across five functional activation tasks: findings from the LEAP project', Mol Autism, 13: 53.
3. Marquand, A. F. (2016), 'Understanding Heterogeneity in Clinical Cohorts Using Normative Models: Beyond Case-Control Studies', Biol Psychiatry, 80: 552-61.
4. Rutherford, S. (2023), 'Evidence for embracing normative modeling', Elife, 12.
5. Smith, S. M. (2013), 'Functional connectomics from resting-state fMRI', Trends Cogn Sci, 17: 666-82.
6. Zhao, Y., B. (2021), 'Covariate Assisted Principal regression for covariance matrix outcomes', Biostatistics, 22: 629-45.

Poster No 1786

Inter-network correlations between white-matter networks measured using BOLD fMRI

Nayana Menon[1], Jonathan Polimeni[2], J. Jean Chen[3]

[1]University of Toronto, Oakville, Ontario, [2]Athinoula A. Martinos Center for Biomedical Imaging, Massachusetts General Hospital, Charlestown, MA, [3]Baycrest Health Sciences, Toronto, Ontario

Introduction: Detecting brain activation white matter (WM) using blood-oxygenation level-dependent (BOLD) fMRI data is a topic of growing interest[1-2]. Recent work using BOLD has demonstrated that BOLD activity in WM corresponds to task demands[3]. Additionally, the detection of functional networks in the WM was demonstrated using BOLD fMRI (REF). It has also been found that signals in WM networks correlate with signals in functional gray matter (GM) networks, which have established connections[4]. Furthermore, inter-network connections have been established amongst GM functional networks[4]. While these findings fill gaps in the knowledge around the interpretation of WM fMRI signals and networks, they also highlight that little is known about whether inter-network connections exist in the WM. This work aims to determine whether WM networks display spatial clusters of inter-network correlations in the same way that GM networks do.

Methods: Participants Here we report findings from the 10 youngest healthy participants (equal males and females) selected from the Human Connectome Project's Aging dataset (mean age = 36.6 years)[5]. fMRI Data Acquisition 10 youngest participants from the HCP Aging study (HCP-A) were chosen. fMRI scans were acquired with simultaneous multi-slice gradient-echo EPI (TR/TE = 800/37 ms, flip angle = 52°, 184 frames) and 2.0 mm isotropic voxels that covered the whole brain. During the fMRI scans, participants were to memorize names for a series of faces, beginning with an 22 s encoding block: where the faces and names were shown followed by a 2 second cue to memorize followed by 5 face/name pairs shown for 4s each[6]. This is

followed by a distractor block of 2 seconds followed by a 20 second GO/NoGO task. This is followed by the recall block with a 2s cue and 20s where the faces are shown again. This is repeated twice for each subject[6]. Data Processing The raw BOLD data were preprocessed using FSL for motion correction, slice-timing correction, then normalized and demeaned such that all values in the time series are provided in units of %BOLD. The data were also registered to MNI space. The data were then masked into WM and GM, and the WM data for each subject was further denoised using independent component analysis (ICA) with 30 components being generated and noisy components being visually determined and removed[7]. Masks were generated for the WM and GM networks of the brain using the functionnectome atlas[8], and the GM regions that overlapped with WM were removed from the WM masks, then the masks were eroded by 1 voxel to fully separate the masked regions. Analysis The mean time series of the GM and WM regions were extracted using the masks derived from the functionnectome atlas. The time series within the WM were correlated with each other for each subject using Pearson's correlation coefficient, then the r-value matrices were converted using the Fisher transform to z-standardized matrices and averaged to generate a group-level matrix.

Results: The WM functional connectivity matrix of averaged z-scores is shown in Fig. 1, thresholded at z>2. We can observe that there are high correlations between the activity in distinct WM networks identified from the functionnectome atlas, that are similar to the inter-network connectivity patterns among the corresponding cortical GM regions As shown in Fig. 2, these networks are in deep WM and do not overlap with GM networks.

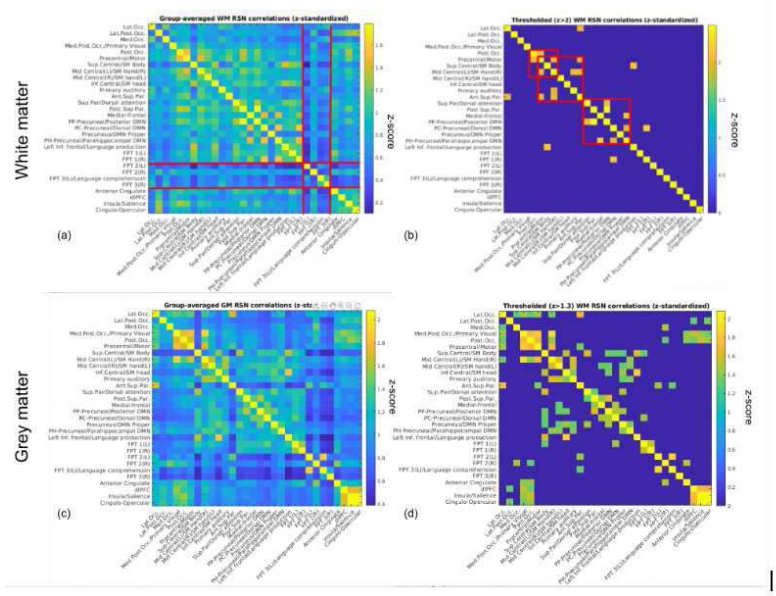

Figure 1. Z-standardized Pearson's correlation matrix for WM network correlations where WM networks and labels are derived from the functionnectome atlas. Networks of high correlation are identified in red boxes on matrix as groups of interest. In (a), the red lines indicate WM networks that are poorly correlated globally, and in (b), the boxes indicate WM networks that are highly correlated with each other. Occ = occipital; FTP=frontal-parietal-temporal network; DMN = default-mode network; L = left; R = right.

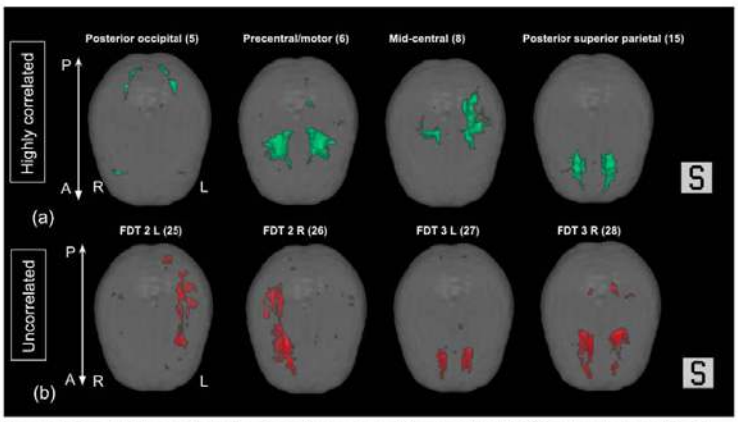

Figure 2. The highly correlated and poorly correlated (uncorrelated) WM networks from Fig. 1 are shown in (a) and (b), respectively. The WM network masks are in deep WM and do not overlap with GM regions. View from superior to inferior. A = anterior, P = posterior.

Conclusions: This study presents an initial investigation of connections between WM networks identified from the functionnectome atlas in fMRI task data. We were able to identify WM networks that were significantly correlated with each other during visual and motor task conditions, and that, by nature of the functionnectome atlas, were separate from GM networks, with a far smaller likelihood of GM effects on the WM analysis.

References

1. Huang, Y. (2020), 'Detection of functional networks within white matter using independent component analysis', NeuroImage, vol. 222, pp.117278.
2. Guo, B.(2022), 'Latency structure of BOLD signals within white matter in resting-state fMRI', Magnetic resonance imaging, vol.89, pp.58–69
3. Peer, M.(2017), 'Evidence for Functional Networks within the Human Brain's White Matter', The Journal of neuroscience : the official journal of the Society for Neuroscience, vol. 37(27), pp.6394–6407
4. Siman-Tov, T. (2017), 'Early Age-Related Functional Connectivity Decline in High-Order Cognitive Networks', Frontiers in aging neuroscience, vol. 8, pp. 330
5. Harms, M. P. (2018), 'Extending the Human Connectome Project across ages: Imaging protocols for the Lifespan Development and Aging projects', NeuroImage, vol. 183, pp. 972–984
6. Bookheimer, S. Y.(2019), 'The Lifespan Human Connectome Project in Aging: An overview', NeuroImage, vol. 185, pp.335–348
7. McKeown, M.(2005), 'ICA Denoising for Event-Related fMRI Studies', Conference proceedings : ... Annual International Conference of the IEEE Engineering in Medicine and Biology Society. IEEE Engineering in Medicine and Biology Society. Annual Conference, 2006, pp. 157–161
8. Nozais, V.(2021), 'Functionnectome as a framework to analyse the contribution of brain circuits to fMRI', Communications biology, vol4(1), pp.1035

Poster No 1788

Explicitly Nonlinear Connectivity-Matrix Independent Component Analysis in Resting fMRI Data

Sara Motlaghian[1], Vince Calhoun[2]

[1]Georgia State University, Atlanta, GA, [2]GSU/GATech/Emory, Decatur, GA

Introduction: Connectivity-matrix independent component analysis (cmICA) is a data-driven method to calculate brain voxel maps of functional connectivity. It is a powerful approach, but one limitation is that it can only capture linear relationships. In this work, we focus on measuring the explicitly nonlinear relationships between the voxel connectivity to identify brain spatial maps which demonstrate explicitly nonlinear dependencies and are typically ignored. We expand cmICA using normalized mutual information (NMI) after removing the linear relationships and find highly structured resting networks which would be completely missed by existing functional connectivity approaches. Results revealed resting fMRI networks that show linear-only, nonlinear-only, and both linear+nonlinear relationships with unique spatial patterns.

Methods: In this work we combined two methods in order to identify maps that show explicitly nonlinear activation. In [https://doi.org/10.1101/2022.06.22.497262], we introduced a method to measure the explicitly nonlinear similarity between two time courses. We want to elaborate that method to find explicitly nonlinear (EN) brain map components. To do so, one of the barriers to implementing ICA is the absence of time variable which cancels during measuring nonlinearity. So we propose to utilize the connectivity matrix (cmICA) method instead, which first was introduced in [https://doi.org/10.1016/j.neuroimage.2018.06.024] to identify spatial map components. We did the following steps: First we canceld the linear correlation between each pair of voxels. Removing the linear information can be done for a given vector x and y, by fitting a linear model $y' = \alpha x + \beta$. Here y' is the best linear estimation of y when x is given, the slope is denoted by α, and β is the y-intercept. We can cancel the linear effect by calculating $z = y - y'$. The explicitly nonlinear dependency of x and z is the same as x and y. Next, we use NMI(x,z) to evaluate the EN dependency of x and y. To assure symmetricity, we took the average of the results when switching x and y. The symmetric matrices from the previous step, next are passed to cmICA. The maps identified by cmICA are divided in matched with linear maps and EN only maps.

Results: We implemented EN-cmICA brain connectivity for 311 rsfMRI datasets resulting in 33 EN spatial maps. These maps reveals a set of maximally independent regions where, in each region, the voxels show a high level of explicitly nonlinear similarity. Each region is considered as one spatial map. We divided EN maps in to two groups of components: Group A) EN components that are not similar to any linear components (i.e., brain networks showing uniquely nonlinear information) Group B) EN components that are highly (spatially) similar to linear maps (i.e., brain networks showing both linear and nonlinear information).

Conclusions: The EN-cmICA process identifies EN maps that are uniqe and are not found from the conventional ICA approach. This findings help to uncover more about brain activities.

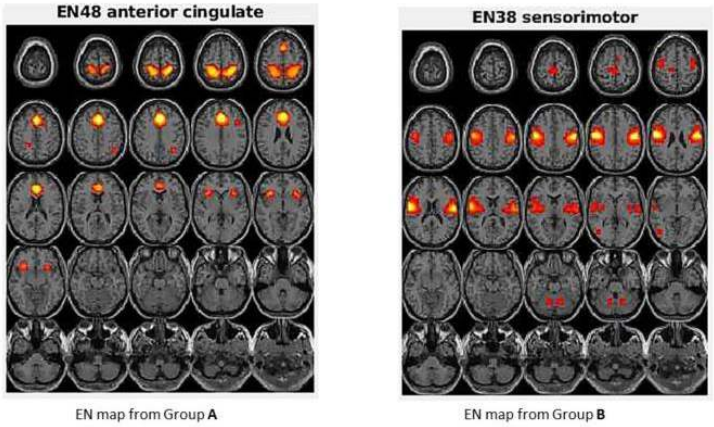

References

1. Explicitly Nonlinear Dynamic Functional Network Connectivity In Resting-State fMRI Data
2. S. M. Motlaghian, A. Belger, J. R. Bustillo, A. Faghiri, J. M. Ford, A. Iraji, K. Lim, D. H. Mathalon, R. Miller, B. A. Mueller, D. O'Leary, G. Pearlson, S. G. Potkin, A. Preda, T.G. van Erp, V. D. Calhoun
3. bioRxiv 2022.06.22.497262; doi: https://doi.org/10.1101/2022.06.22.497262
4. Wu, L., Caprihan, A., Bustillo, J., Mayer, A., & Calhoun, V. (2018). An approach to directly link ICA and seed-based functional connectivity: Application to schizophrenia. NeuroImage, 179, 448-470. https://doi.org/10.1016/j.neuroimage.2018.06.024

Poster No 1789

Relationship Between Structural & Functional Changes for TBI Patients with Chronic Health Symptoms

Xiaojian Kang[1,2], Byung Yoon[3], Maheen Adamson[4,2,5]

[1]WRIISC-Women, VA Palo Alto Health Care System, Palo Alto, CA, [2]Rehabilitation Service, VA Palo Alto Health Care System, Palo Alto, CA, [3]Dept. of Radiology, Stanford School of Medicine, Stanford, CA, [4]WRIISC-Women, VA Palo Alto Healthcare System, Palo Alto, CA, [5]Department of Neurosurgery, Stanford University School of Medicine, Stanford, CA

Introduction: Background/Introduction. Traumatic brain injury (TBI) is among the most frequent causes of death and disability following traumas[1]. Structural (SC) and functional (FC) connectivity to evaluate network properties across the entire spectrum of brain injury from mild[2,3] to moderate and severe TBI[4]. The main aim of the study is to explore the correlation between SC and FC, and detect any differences of SC and FC between TBI patients and control group.

Methods: Methods. A total of forty-six participants were recruited for the study. The participants were divided into 3 groups with matched age and education: (1) Control group (CG) of 13 participants (6 females, age: 33.4 ± 9.8 yrs); 2) Group of 16 TBI patients without cognitive chronic symptoms (TBIncs; 9 females, age: 37.4 ± 13.9 yrs); (3) Group of 17 TBIs with one or more self-reported chronic symptoms (TBIcs; 5 females, age: 37.5 ± 9.4 years). All imaging data were acquired on a GE 3T Discovery MR750 at VAPAHCS. For each participant, one high-resolution T1W image was collected: TR = 7.3 ms, TE = 3.0 ms, flip angle = 11o, voxel size = 0.6 1.05 1.05 mm, 392 sagittal slices. Two DWI scans were acquired: TR = 6600 ms, TE = 80 ms, voxel size = 2.5 x 2.5 x 2.5 mm, b = 3000 s/mm2, 30 non-linear directions, 5 non-diffusion (b = 0) volumes. One resting state functional MRI (rsfMRI) scan was acquired: TR = 2000 ms, TE = 30 ms, flip angle = 80o, voxel size = 3.75 x 3.75 x 4.0 mm, 240 frames/8 min. The T1W anatomical images were processed using FreeSurfer 7.0[5], which provides 34 cortical parcels from the DK parcellations[6] for each hemisphere. The diffusion-weighted images (DWIs) were processed using the software package Mrtrix3[7]. SC data were collected for all the connections between the 68 parcels for all the participants. RsfMRI data were processed using CONN toolbox[8]. FC were obtained for the same 68 DK parcels for all the subjects. The correlation between SC and FC were explored. SC and FC were also compared between subject groups. The significance level was set at $p < .05$. Benjamini-Hochberg algorithm was applied to perform the false discovery rate (FDR) correction for multiple comparisons[9].

Results: Results: Correlation between SC and FC is 11.5% and 11.9% stronger for TBIncs, and TBIcs compared to CG, respectively. SC reduction was observed in 4 parcels and 6 parcel clusters for TBIcs but only one cluster for TBIncs compared to CG. On the other hand, FC reduction was observed only in one cluster for TBIncs but in one parcel and two parcel clusters for TBIncs compared to CG, respectively.

Conclusions: Conclusions: Abnormal FC may be the result of damage to specific functional areas, or damage to the SC between functional areas. Combined assessment of SC and FC may provide a unique predictive model for clinical outcomes based on injury severity.

References

1. Rubiano, A.M., et al., Global neurotrauma research challenges and opportunities. Nature, 2015. 527(7578): p. S193-7.
2. Raizman, R., et al., Traumatic Brain Injury Severity in a Network Perspective: A Diffusion MRI Based Connectome Study. Sci Rep, 2020. 10(1): p. 9121.
3. Yuan, W., et al., Changes in Structural Connectivity Following a Cognitive Intervention in Children With Traumatic Brain Injury. Neurorehabil Neural Repair, 2017. 31(2): p. 190-201.
4. Sours, C., et al., Structural and Functional Integrity of the Intraparietal Sulcus in Moderate and Severe Traumatic Brain Injury. J Neurotrauma, 2017. 34(7): p. 1473-1481.
5. Fischl, B., et al., High-resolution intersubject averaging and a coordinate system for the cortical surface. Hum Brain Mapp, 1999. 8(4): p. 272-84.
6. Desikan, R.S., et al., An automated labeling system for subdividing the human cerebral cortex on MRI scans into gyral based regions of interest. Neuroimage, 2006. 31(3): p. 968-80.
7. Tournier, J.D., et al., MRtrix3: A fast, flexible and open software framework for medical image processing and visualisation. Neuroimage, 2019. 202: p. 116137.
8. Whitfield-Gabrieli, S. and A. Nieto-Castanon, Conn: a functional connectivity toolbox for correlated and anticorrelated brain networks. Brain Connect, 2012. 2(3): p. 125-41.
9. Benjamini, Y. and Y. Hochberg, Controlling The False Discovery Rate - A Practical And Powerful Approach To Multiple Testing. Journal of the Royal Statistical Society. Series B (Methodological), 1995. 57: p. 289-300.

Poster No 1790

Tracing Causal Paths from Prenatal Tobacco Exposure to Adolescent Brain and Behavioral Development

Marvin Yan[1], Malick Abid[2], Erich Kummerfeld[2], Michael Kotlyar[3], Jazmin Camchong[4], Scott Sponheim[4,5], Bonnie Klimes-Dougan[1], David Bond[6], Eric Rawls[4]

[1]University of Minnesota, Department of Psychology, Minneapolis, MN, [2]University of Minnesota, Institute for Health Informatics, Minneapolis, MN, [3]University of Minnesota, Department of Experimental and Clinical Pharmacology, Minneapolis, MN, [4]University of Minnesota, Department of Psychiatry and Behavioral Sciences, Minneapolis, MN, [5]Minneapolis VA Health Care System, Minneapolis, MN, [6]Johns Hopkins University, Department of Psychiatry and Behavioral Sciences, Baltimore, MD

Introduction: In 2021, over 3 million adolescents in the United States were exposed to tobacco prenatally (prenatal tobacco exposure; PTE) (Osterman et al., 2023), a concern given the vital neural development that occurs during the fetal period. PTE is linked to altered neural communication and increased psychopathology (Indredavik et al., 2007; Muller et al., 2013), which is the most proximal risk factor for suicide-related behaviors including suicidical ideation (SI) and non-suicidal self-injury (NSSI). These influences are complicated to unravel, as PTE-related influences extend to physical health, cognitive ability, and intent to try tobacco later in life (future tobacco use; FTU) (Duko et al., 2021; Gonzalez et al., 2023). Existing research on PTE has studied these factors in isolation, but has not examined whether mediated causal paths from PTE to SI and NSSI exist. Traditional analytic techniques can only calculate associations between variables, while effective interventions require causality. Thus, causal discovery analysis (CDA), a statistical approach that uses machine learning to infer causal relationships between observed data, is necessary (Rawls et al., 2021). As part of a project investigating the impact of PTE on FTU, we used CDA to identify causal paths between PTE and neural, behavioral, and clinical factors to unravel the causal paths linking PTE to these factors, thereby illuminating potential intervention targets for NSSI and SI.

Methods: To investigate causal pathways between PTE, SI, and NSSI, we analyzed data from 8,884 adolescents (9-10 years old; 47.9% female), of which 1,142 (12.9%) experienced PTE, from the Adolescent Brain Cognitive Development Study baseline visit. We included measures assessing resting-state functional connectivity within established resting-state brain networks (RSFC), psychopathology, cognitive ability, physical health, PTE, and risk for FTU. A factor analysis was conducted for phenotypic data reduction, which excluded key variables of interest (PTE, SI, NSSI, RSFC).

Factors identified by exploratory factor analysis (left) using phenotypic measures from the ABCD Study (right)

Factor	Phenotypic Measures
Parent-Reported Psychopathology	Child Behavior Checklist Internalizing/Externalizing Subscales; Kiddie Schedule for Affective Disorders and Schizophrenia (K-SADS) parent-reported depression screening items; Sleep Disturbance Scale (SDS) disorder in maintaining sleep subscale
Behavioral Activation	PhenX Behavioral Inhibition/Behavioral Approach System (BIS/BAS): reward responsiveness, drive, and fun seeking subscales
Sleep Problems	SDS: sleep-wake transition disorders, disorder of arousal, sleep hyperhydrosis,sleep breathing disorders, and disorders of excessive somnolence subscales
Impulsivity	UPPS-P for Children - Short Form (ABCD Version): negative/positive urgency subscales
Executive Dysfunction	UPPS-P: lack of planning and lack of perseverance subscales
Cognitive Ability	NIH Toolbox Fluid and Crystallized Composite Scores
Self-Reported Psychopathology	Prodromal Psychosis Scale; K-SADS self-reported depression screening items
Sensation Seeking	UPPS-P: sensitive seeking subscale; Youth Risk Behavior Survey - Exercise

Results: PTE directly decreased RSFC within the cingulo-opercular (CO) network, which had indirect causal effects on outcome measures of interest. Specifically, decreases in CO RSFC causally increased self-reported psychopathology (SRP) (B=-.08), which then causally increased SI (B=.19) and NSSI (B=.15). As such, we can trace a causal path from PTE to psychopathology and suicide-linked behaviors, mediated through functional brain connectivity. PTE also indirectly caused increases in SI by causing increases in sleep problems (B=.09), parent-reported psychopathology (PRP) (B=.11), and impulsivity (B=.04), all of which then separately caused increases in SI (B=.08, .25, .10; i.e., three distinct causal paths). A direct causal relationship between SI and NSSI existed such that SI increased NSSI (B=.23); thus, all paths from PTE to SI also resulted in increased NSSI. Of note, in addition to their indirect causal paths to NSSI through SI, there were also direct causal paths that increased NSSI from impulsivity (B=.09), SRP (B=.15), and PRP (B=.01). Multiple causal paths from PTE also lead to risk for FTU, although due to the young age of the sample, this result should be considered exploratory. All results were adjusted such that p<.001.

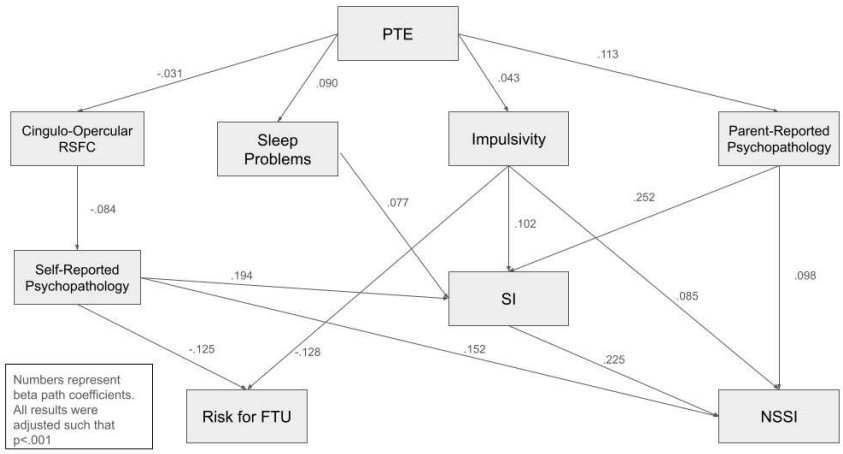

Fig. CDA Model: Numbers represent beta path coefficients. All results were adjusted such that p<.001.

Conclusions: This research illuminates how PTE can initiate a cascade of adverse developmental effects on adolescent brain connectivity, psychological health, and behavior. The findings underscore the impact of PTE on developing brain networks, particularly the salience network, as well as PTE's influences on impulsivity, cognitive control, and psychopathology. Our research implies that interventions focused on sleep problems, psychopathology, and impulsivity may causally reduce SI and NSSI. Finally, a brain-based intervention that increases salience network connectivity may be effective for reducing SI and NSSI. These insights advance our understanding of PTE's far-reaching consequences and pave the way for targeted interventions.

References

1. Duko, B., Pereira, G., Tait, R. J., Nyadanu, S. D., Betts, K., & Alati, R. (2021). Prenatal Tobacco Exposure and the Risk of Tobacco Smoking and Dependence in Offspring: a Systematic Review and Meta-Analysis. Drug and alcohol dependence, 227, 108993. DOI:10.1016/j.drugalcdep.2021.108993
2. Gonzalez, M. R., Uban, K. A., Tapert, S. F., & Sowell, E. R. (2023). Prenatal tobacco exposure associations with physical health and neurodevelopment in the ABCD cohort. Health psychology: official journal of the Division of Health Psychology, American Psychological Association, 42(12), 856–867. DOI:10.1037/hea0001265

3. Indredavik, M. S., Brubakk, A. M., Romundstad, P., & Vik, T. (2007). Prenatal smoking exposure and psychiatric symptoms in adolescence. Acta paediatrica (Oslo, Norway : 1992), 96(3), 377–382. DOI:10.1111/j.1651-2227.2006.00148.x
4. Muller KU, Mennigen E, Ripke S, et al. Altered reward processing in adolescents with prenatal exposure to maternal cigarette smoking. JAMA Psychiatry, 70(8), 847-856. DOI:10.1001/jamapsychiatry.2013.44.
5. Osterman, Michelle J.K. et al. (2023). Births: Final Data for 2021. Center for Disease Control and Prevention. 71(1), DOI:10.15620/cdc:122047.
6. Rawls, E., Kummerfeld, E., & Zilverstand, A. (2021). An integrated multimodal model of alcohol use disorder generated by data-driven causal discovery analysis. Communications Biology, 4(435). DOI:10.1038/s42003-021-01955-z

Poster No 1791

Basic Modes of Spontaneous Activity Capture Spatiotemporal Patterns of the Global Signal at Rest

Xi Chen[1], Xuhong Liao[1,2]

[1]School of Systems Science, Beijing Normal University, Beijing, China, [2]Beijing Key Lab. of Brain Imaging and Connectomics, Beijing Normal University, Beijing, China

Introduction: Recent neuroimaging connectomics has revealed intrinsic human brain functional networks with non-trivial topological properties based on the resting-state functional MRI (R-fMRI)[1]. Of note, connectivity patterns of the functional networks are affected by the data preprocessing and network analysis strategies, among which global signal regression is a longstanding controversial issue[2]. One main concern is that global signal regression better reduces the influence of head motion[3] but induces anti-correlations in networks[4]. However, the spatiotemporal pattern of the global signal itself and how it affects functional connectivity (FC) patterns require further elucidation. Here, we applied a novel eigen-microstate analysis[5,6] on the R-fMRI data from healthy young adults to identify typical activity patterns of the global signal and reveal how the global signal contributes to the functional network organization.

Methods: We selected the minimally preprocessed R-fMRI data from 700 healthy young adults (age range: 21-35 years, M/F: 304/396) in the Human Connectome Project (HCP)[7]. Additional preprocessing steps included removing the first 10-second volumes, linear detrending, nuisance regression, and temporal filtering (0.01-0.08Hz). To assess the potential influence of the global signal, we used two nuisance regression strategies, one with global signal regression (GSR) and the other not (NGSR). After preprocessing, we extracted time courses of 1000 cortical nodes[8] for each participant for the subsequent analysis. First, we constructed group-level FC matrices in GSR and NGSR cases and compared their FC strength distributions and spatial patterns. Second, we performed the eigen-microstate analysis[5,6] on regional time courses to extract basic activity modes in both cases. The basic modes with high ranking are regarded to dominantly contribute to the spatiotemporal variance of spontaneous activity over time. Next, we examined the spatial correspondence of the basic modes between two cases and assumed that the modes specific to the NGSR case capture the global signal influence. We further reconstructed the FC matrix in the GSR case by including basic modes in the NGSR case but excluding the basic modes specific to the NGSR case. Finally, we examined the spatial patterns of the global signal-specific modes by comparing them with that of the principal functional gradient[9]. We further examined the spatial association between the coactivation patterns of this mode and the differences in FC patterns between the two cases.

Results: The FC matrices in the GSR and NGSR cases showed high spatial similarity (Fig. 1A, $r=0.87$, $p<0.001$) but differed in the FC strength (Fig. 1B). Specifically, the GSR strategy induced a leftward shift of the strength distribution (Fig. 1C). We extracted the first ten basic activity modes in two cases and found they showed one-to-one spatial correspondence, except for an additional mode (i.e., first basic mode) identified in the NGSR case (Fig. 2A). The FC matrix reconstructed from the first ten basic modes in NGSR case, but excluding the first mode, was similar with the original FC matrix with GSR in terms of FC patterns ($r=0.81$, $p<0.001$) and strength distributions (Fig. 2B). The global signal-specific first mode showed the same signs of fluctuation amplitudes across regions and exhibited high spatial correlations with the principal functional gradient map (Fig. 2C, $r=-0.83$, $p_{perm}<0.001$, spatial autocorrelation corrected). Moreover, this basic mode corresponded to positive coactivations between regions, which was spatially similar to the differences in FC patterns between the two cases (Fig. 2D, $r=0.70$, $p<0.001$).

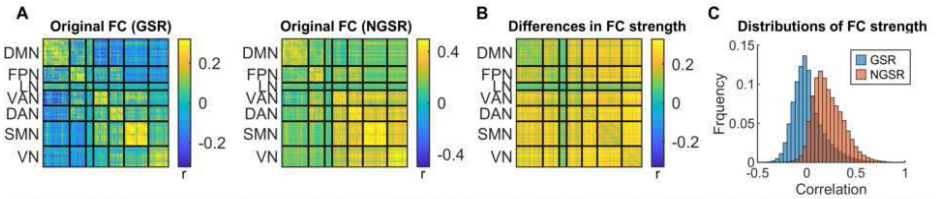

Figure 1. (A) Group-level FC matrices in both GSR and NGSR cases. (B) Differences in the FC strength between two cases (NGSR vs. GSR). (C) Distributions of FC strength in both GSR and NGSR cases. Brain regions are ordered according to their affiliations to seven functional systems defined in Yeo et al [10]. GSR, global signal regression; NGSR, no global signal regression; FC, functional connectivity; DMN, default-mode network; FPN, frontoparietal network; LN, limbic network; VAN, ventral attention network; DAN, dorsal attention network; SMN, somatomotor network; VN, visual network.

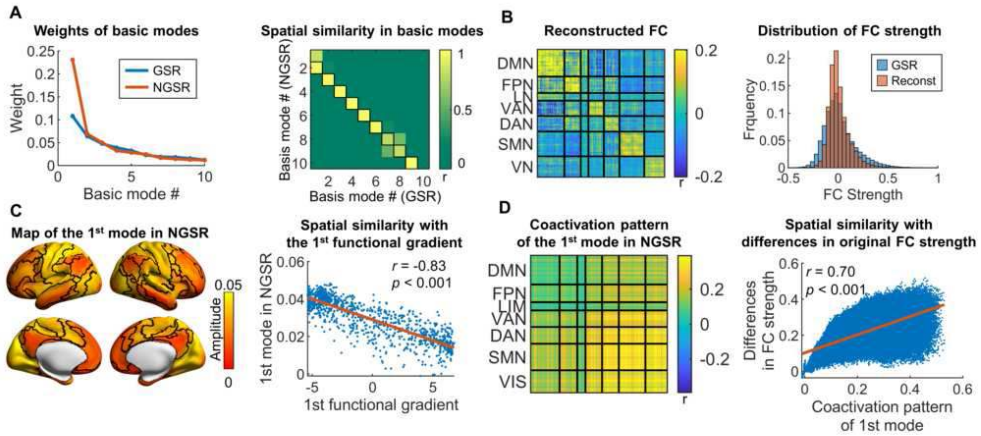

Figure 2. (A) Weights and spatial similarities of the first ten basic modes in GSR and NGSR cases. (B) FC matrix reconstructed from basic modes and its FC strength distribution. The FC matrix was reconstructed from the first ten basic modes in the NGSR case but excluding the global signal-specific first mode. (C) Spatial pattern of the global signal-specific first mode in the NGSR case and its spatial association with the principal functional gradient map. (D) Spatial similarity between the coactivation pattern of the first mode in the NGSR case and the differences in original FC strength between the two cases. Brain regions are ordered according to their affiliations to seven functional systems defined in Yeo et al [10]. GSR, global signal regression; NGSR, no global signal regression; FC, functional connectivity; DMN, default-mode network; FPN, frontoparietal network; LN, limbic network; VAN, ventral attention network; DAN, dorsal attention network; SMN, somatomotor network; VN, visual network.

Conclusions: We identified a global signal-specific basic activity mode, which follows a hierarchical organization and reflects inter-regional positive correlations. We speculate that the GSR strategy will remove the contribution of this mode and thus aggravates anti-correlations in the functional networks.

References

1. Fox, M. D. (2007), 'Spontaneous fluctuations in brain activity observed with functional magnetic resonance imaging', Nature reviews neuroscience, vol. 8, no. 9, pp. 700-711.
2. Murphy, K. (2017), 'Towards a consensus regarding global signal regression for resting state functional connectivity MRI', Neuroimage, vol. 154, pp. 169-173.
3. Yan, C. G. (2013), 'A comprehensive assessment of regional variation in the impact of head micromovements on functional connectomics', Neuroimage, vol. 76, pp. 183-201.
4. Murphy, K. (2009), 'The impact of global signal regression on resting state correlations: are anti-correlated networks introduced?', Neuroimage, vol. 44, no. 3, pp. 893-905.
5. Sun, Y. (2021), 'Eigen microstates and their evolutions in complex systems', Communications in Theoretical Physics, vol. 73, pp.6.
6. Chen, X. (2023), 'Leading basic modes of spontaneous activity drive individual functional connectivity organization in the resting human brain', Communications Biology, vol. 6, no. 892.
7. Van Essen, D. C. (2013), 'The WU-Minn human connectome project: an overview', Neuroimage, vol. 80, pp. 62-79.
8. Schaefer, A. (2018), 'Local-global parcellation of the human cerebral cortex from intrinsic functional connectivity MRI', Cerebral Cortex, vol.28, no. 9, pp. 3095-3114.
9. Margulies, D. S. (2016), 'Situating the default-mode network along a principal gradient of macroscale cortical organization', Proceedings of the National Academy of Sciences, vol. 113, no. 44, pp. 12574-12579.
10. Yeo, B. T. (2011), 'The organization of the human cerebral cortex estimated by intrinsic functional connectivity', Journal of Neurophysiology, vol. 106, no. 3, pp. 1125-1165.

Poster No 1792

An fMRI Study to find aligning Network to the signals related to the Decision making process

Dayoung Yoon[1], Su Hyun Bong[2], Jae Won Kim[3], Bumseok Jeong[4]

[1]KAIST, Daejeon, Daejeon, [2]KAIST, E7 building lobby, Daejeon, [3]Seoul National University College of Medicine, Jongno-gu, Seoul, [4]Korea Advanced Institute of Science and Technology, Daejeon, Daejeon

Introduction: In the extensive study of brain regions crucial for the decision-making process,various behavioral models have been proposed to elucidate their interconnected roles.Notably, dopamine,considered a pivotal neurotransmitter,has garnered significant attention. The prevailing argument suggests that dopamine signals encode the disparity in prediction errors during the observation and inference processes.However the Active Inference, one of the most influential theories in decision-making and action control introduces a novel perspective posits that dopaminergic firing specifically encodes the precision of actions. We aims to scrutinize the validity of this hypothesis in light of the connectivity.

Methods: The fMRI data was collected from 58 participants while they are performing two-armed bandit reinforcement learning task with Pavlovian-instrumental transfer(PIT) paradigm. The task consists of two parts whether subjects get or lose the reward by their choice(Fig1). Participants need to learn which arm is better to get the reward or avoid loss. After preprocessing, we acquire time series from cortex with Schaefer Atlas[1] and subcortex with Melbourne Atlas[2], and to include other regions known to be related to the release of Dopamine and Norepinephrine,we also add some regions in CIT168[3] and Harvard Ascending Arousal Network Atlas[4]. From this, we derived 6 types of timeseries data, each comprising a 3 by 2 structure.3 denotes the hierarchical levels of where the signals are generated, encompassing each node, each edge, and each network. And 2 signifies that one aspect captures the signal changes at each level while the other encapsulates the dynamic changes of intersubject correlation(ISC)[5]. At the node level, the signals correspond to the activation of individual brain regions. Moving to the edge level, these signals represent the connectivity between two nodes and are calculated using phase-locked oscillatory pattern obtained through LEiDA[6]. Finally, at the network level, to estimate the representative networks, we emloyed the graph Laplacian mixture Model[7] and yielded the four most representative brain states. Next, we constructed Active Inference model of two armed bandit task that is neural process theories within the Bayesian framework[8] and fit it to behavioral data of choices and outcomes. As a result we can get two signals from each participants. One is the rate of changes of expected precision value, and the other one is state prediction error. We convolved hemodynamic response function to both signals, and compared them to the above 6 types of neuroimaging data using generalized linear model with both convolved signals as independent variables and neuroimaing data as dependent variables. The coefficients values related to each signal that are derived from the edge level are compared using Network-Based Statistic[9]. And we also performed one-samle test using null distribution which are generated by phase randomization of both signals to coefficients values that are from the other two levels.

Results: Averaged 6 type of timeseries are shown in Fig1. Four extracted states and fractional occupancy of each state are shown in Fig3. The results of one sample test are shown in Table2. Significant nodes and states are indicated.At node level, both signals shares numerous common regions but certain nodes are specific to one of the signals.At the network level, State1,2 are common to both signals, but State3 in the Precision signal is distinctive. At the edge level, the differences are shown in Fig4. While the nodes involved in these connections overlap with those exhibiting significance in the node-level, the connections themselves manifest distinct patterns in both signals.

	EV	NA				SO		dISC		dISC_st	
		Precision		SSPE		P	S	Precision	SSPE	p	S
5	ST Prec SSPE	RH_SomMot_6 GPi-L STN-L GPe-R		LH_Default_PFC_7 RH_SomMot_6 GPe-R DR		X		RH_SomMot_6 GPi-L STN-L GPe-R	LH_Default_PFC_7 RH_SomMot_6 GPe-R DR	X	
12	ST Prec	LH_Vis_2 LH_Vis_5 RH_Vis_2 Pu-L	aThal-R aThal-L VP-L VP-R			2		RH_SomMot_6 GPi-L STN-L GPe-R		X	
13	ST SSPE			LH_Default_Par_2 LH_Default_PFC_7 Pu-R Pu-L	VTA-L VP-L Habe-L		2		RH_SomMot_6 GPe-R DR		X
16	Prec SSPE	LH_Vis_7 LH_Vis_9 LH_SomMot_1 LH_SomMot_2 LH_SomMot_3 LH_SomMot_4 LH_SomMot_5 LH_DorsAttn_Post_6 LH_SalVent_ParOper_1 LH_SalVent_Med_2 LH_Default_Par_2 LH_Default_PFC_2 LH_Default_PFC_5 LH_Default_PFC_7	RH_Vis_8 RH_SomMot_1 RH_SomMot_2 RH_SomMot_3 RH_SomMot_4 RH_SomMot_5 RH_SomMot_7 RH_SalVent_TemOccPar_2 RH_Default_PFCdPFC_3 Pu-R Pu-L Habe-L PBC	LH_Vis_7 LH_Vis_9 LH_SomMot_1 LH_SomMot_2 LH_SomMot_3 LH_SomMot_4 LH_SomMot_5 LH_DorsAttn_Post_6 LH_SalVent_ParOper_1 LH_SalVent_Med_2 LH_Default_Par_2 LH_Default_PFC_2 LH_Default_PFC_5 LH_Default_PFC_7	RH_Vis_8 RH_SomMot_1 RH_SomMot_2 RH_SomMot_3 RH_SomMot_4 RH_SomMot_5 RH_SomMot_7 RH_SalVent_TempOccPar_2 RH_Default_PFCdPFCm_3 Pu-R Pu-L Habe-L PBC	1	1	LH_SalVent_Med_3 RH_SomMot_5 RH_SomMot_8 RH_Cont_Par_1 NAc-L Red-L	LH_SalVent_Med_3 RH_SomMot_5 RH_SomMot_8 RH_Cont_Par_1 NAc-L Red-L	X	X
18	Prec	LH_Vis_2 LH_Vis_5 RH_Vis_2 Pu-L	aThal-R aThal-L VP-L VP-R			2 3		RH_SomMot_6 GPi-L STN-L GPe-R		X	
19	SSPE			LH_Default_Par_2 LH_Default_PFC_7 Pu-R Pu-L	VTA-L VP-L Habe-L		2		LH_Default_PFC_7 RH_SomMot_6 GPe-R DR		X

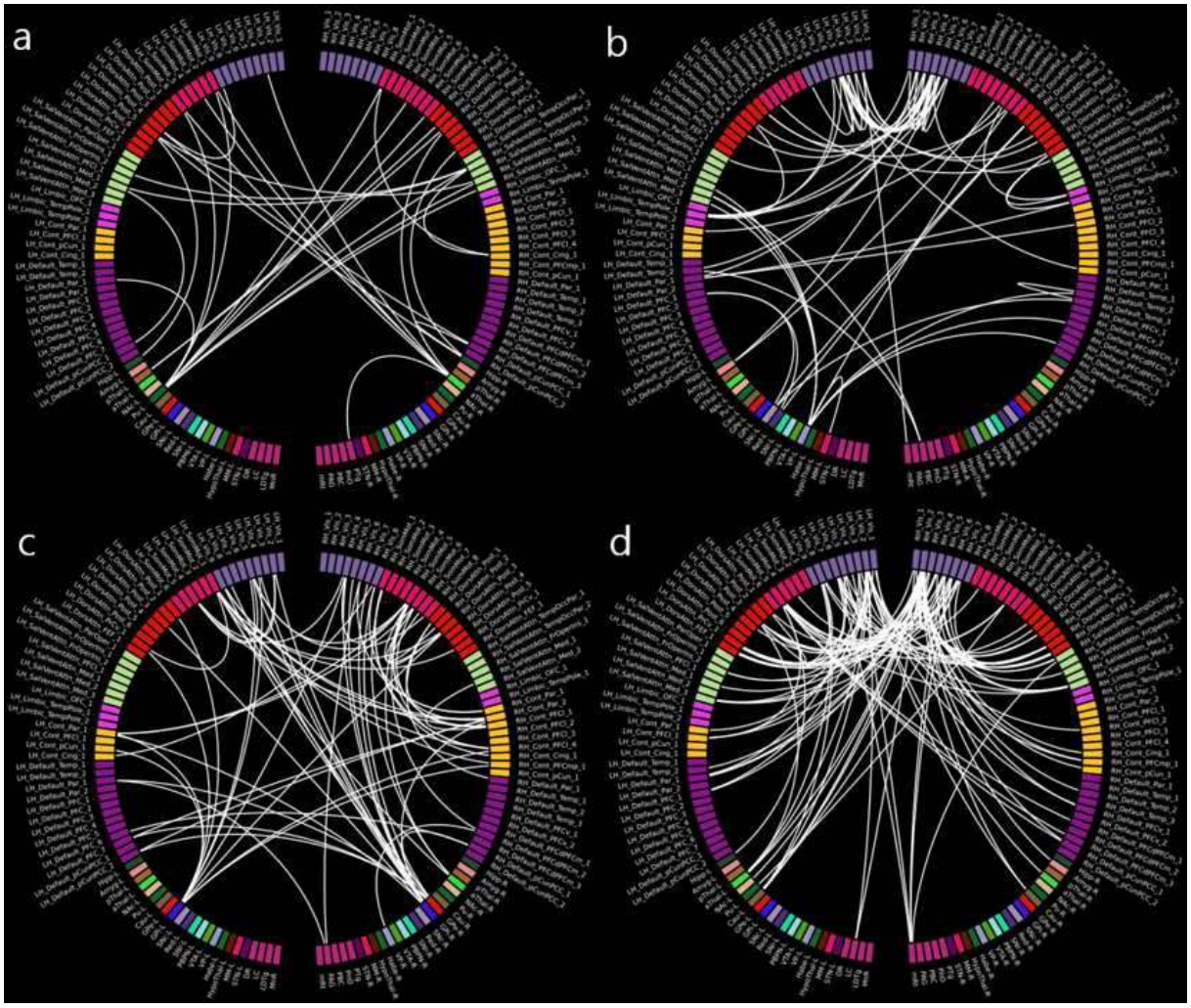

Conclusions: Despite some overlap due to the intimate association between the two signals,we can identify distinct connectivity patterns associated with each signal. and showed that these differences at the edge level were also reflected in the difference in the network level explained by State3.

References
1. Schaefer, A., Kong, R., Gordon, E. M., Laumann, T. O., Zuo, X.-N., Holmes, A. J., ... Yeo, B. T. T. (2018). Local-Global Parcellation of the Human Cerebral Cortex from Intrinsic Functional Connectivity MRI. Cerebral Cortex, 28(9), 3095–3114
2. Tian, Y., Margulies, D. S., Breakspear, M., & Zalesky, A. (2020). Topographic organization of the human subcortex unveiled with functional connectivity gradients. Nature Neuroscience, 23(11), 1421–1432
3. Pauli, W. M., Nili, A. N., & Michael Tyszka, J. (2018). Data Descriptor: A high-resolution probabilistic in vivo atlas of human subcortical brain nuclei. Scientific Data, 5.
4. Edlow, B. L., Takahashi, E., Wu, O., Benner, T., Dai, G., Bu, L., ... Folkerth, R. D. (2012). Neuroanatomic connectivity of the human ascending arousal system critical to consciousness and its disorders. Journal of Neuropathology and Experimental Neurology, 71(6), 531–546
5. Hasson, U., Ghazanfar, A. A., Galantucci, B., Garrod, S., & Keysers, C. (2012). Brain-to-brain coupling: a mechanism for creating and sharing a social world. Trends in Cognitive Sciences, 16(2), 114–121
6. Vohryzek, J., Deco, G., Cessac, B., Kringelbach, M. L., & Cabral, J. (2020). Ghost Attractors in Spontaneous Brain Activity: Recurrent Excursions Into Functionally-Relevant BOLD Phase-Locking States. Frontiers in Systems Neuroscience, 14.
7. Ricchi, I., Tarun, A., Maretic, H. P., Frossard, P., & Van De Ville, D. (2022). Dynamics of functional network organization through graph mixture learning. NeuroImage, 252.
8. Friston, K., FitzGerald, T., Rigoli, F., Schwartenbeck, P., & Pezzulo, G. (2017). Active inference: A process theory. Neural Computation, 29(1), 1–49
9. Zalesky, A., Fornito, A., & Bullmore, E. T. (2010). Network-based statistic: Identifying differences in brain networks. NeuroImage, 53(4), 1197–1207

Poster No 1793

Enhancing Prediction for Depressive Symptoms in Subthreshold Depression by Personalized Parcellation

Liangfang Li[1], Junji Ma[1], Yue Gu[1], Xitian Chen[1], Jiehui Qian[1], Ying Lin[1], Zhengjia Dai[1]

[1]Sun Yat-sen University, Guangzhou, Guangdong

Introduction: Subthreshold depression (SD) is characterized by clinically relevant depressive symptomatology, yet not meet the diagnosis criteria of major depressive disorder (MDD) (Cuijpers & Smit, 2004). Since MDD can be better considered as a continuum and SD is the early stage of MDD, exploring the neuropathology of SD is warranted for understanding the dynamic course of depression-related brain changes from mild to major depression (Hwang et al., 2015), which aids clinical intervention and treatment. However, few studies have studied the SD population and previous works mainly use group-level atlas to assess functional organization and detect case-control difference (Hwang et al., 2015; Zhu et al., 2019), which may ignore the individualized features and miss vital brain-behavior associations that are critical for understanding disease processes (Michon et al., 2022; Zhao et al., 2021).

Methods: We collected the structural MRI (sMRI) and Resting-state fMRI (R-fMRI) data, depression and anxiety scores from 65 SD participants with BDI-II score >13 (Beck et al., 1996). Depressive and anxiety symptoms were measured by Beck Depression Inventory–II (21 items) and Beck Anxiety Inventory scale (21 items). The R-fMRI data was pre-processed using the fMRIprep pipeline (Esteban et al., 2019), including tissue segmentation, surface reconstruction, unstable volumes removal, slice-timing, head motion correction, regressing out nuisance variables, and filtering. After aligning to the structural images, the R-fMRI data was smoothed and projected to fsaverage6 surface space. First, the multi-session hierarchical Bayesian model (Kong et al., 2021) was used to perform individualized parcellation procedure, during which we initialized with the 400-region group-level atlas (Schaefer et al., 2018) and then iteratively refined individualized region boundary. Second, correlations between items and individualized functional connectivity (FC) matrices were calculated to get 42 FC-symptom correlation matrices, which were then clustered into symptom domains using Ward's hierarchical clustering analysis (Murtagh & Legendre, 2014). Third, to identify FCs that were reliably related to a given symptom domain, we ran permutation tests by randomly averaging the equal number of FC-symptom matrices 10000 times. Connection with $p < 0.0001$ was kept as a feature, and the correlation between FC and domain score was set as weight. Last, we used the weighted sum of FC values as the predictive symptom score and assessed the correlation between predicted and actual symptom scores. Same analyses directly using group-level atlas were repeated as a baseline situation.

Results: We identified three symptom domains, all of which can be estimated by related individualized FCs (depressive domain: $r = 0.784$, $p < 0.001$; cognitive and somatic domain: $r = 0.630$, $p < 0.001$; anxiety domain: $r = 0.755$, $p < 0.001$). The contributing individualized FCs to symptom estimation were mainly between-network connections involving the DMN, vATN, and MOT networks (Yeo et al., 2011). Meanwhile, the FC created using group-level atlas also significantly related to these symptom domains (depressive domain: $r = 0.744$, $p < 0.001$; cognitive and somatic domain: $r = 0.610$, $p < 0.001$; anxiety domain: $r = 0.704$, $p < 0.001$). Predictive group-level FCs were also dominated by between-network connections, many of which originate from vATN and primary networks including VIS and MOT. Notably, statistical comparisons of correlation values

showed that prediction performance of individualized FC model outperformed that of group-level FC model (zs > 1.668, ps < 0.048).

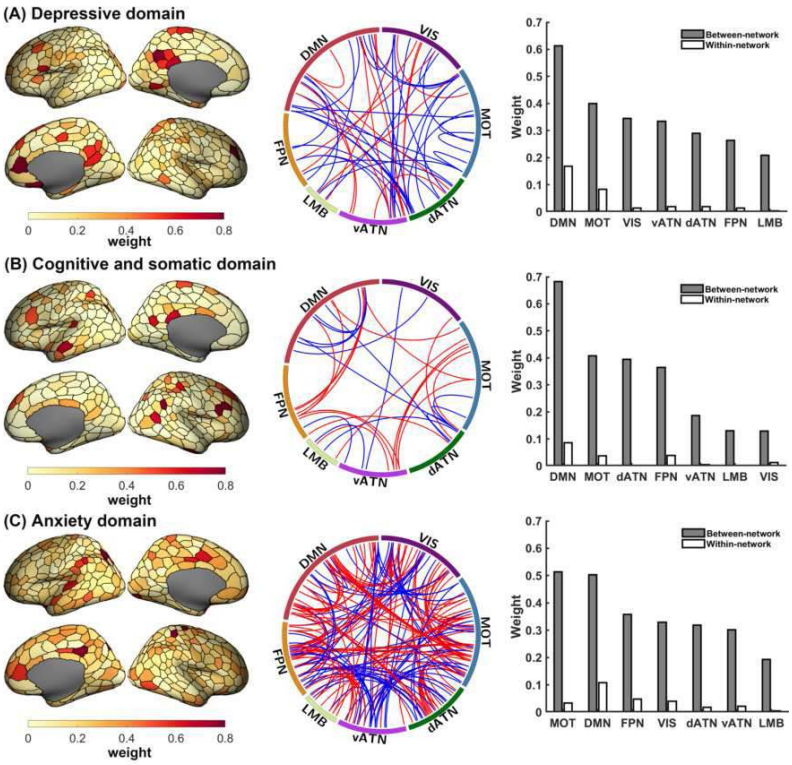

Fig. 1 Predictive individualized FC for estimating three symptom domains. (A) Depressive domain was mainly associated with connections among the DMN, vATN, MOT and VIS. (B) Neural bases for cognitive and somatic domain mainly involved connections in the DMN, MOT, and dATN. (C) Biomarkers for anxiety domain were widely distributed spanning from the MOT, DMN and FPN. Brain surface plots in the left plate demonstrated the spatial distribution of region-level weights; Circular plots in the middle plate displayed the edges with the top 10% absolute weights, with the positive and negative weights colored in red and blue, respectively. The bar plots in the right plate showed the normalized average absolute weights of between-network and within-network connections. Visual (VIS), sensorimotor (MOT), dorsal attention (dATN), ventral attention (vATN), limbic (LMB), frontoparietal control (FPN), and the default mode network (DMN).

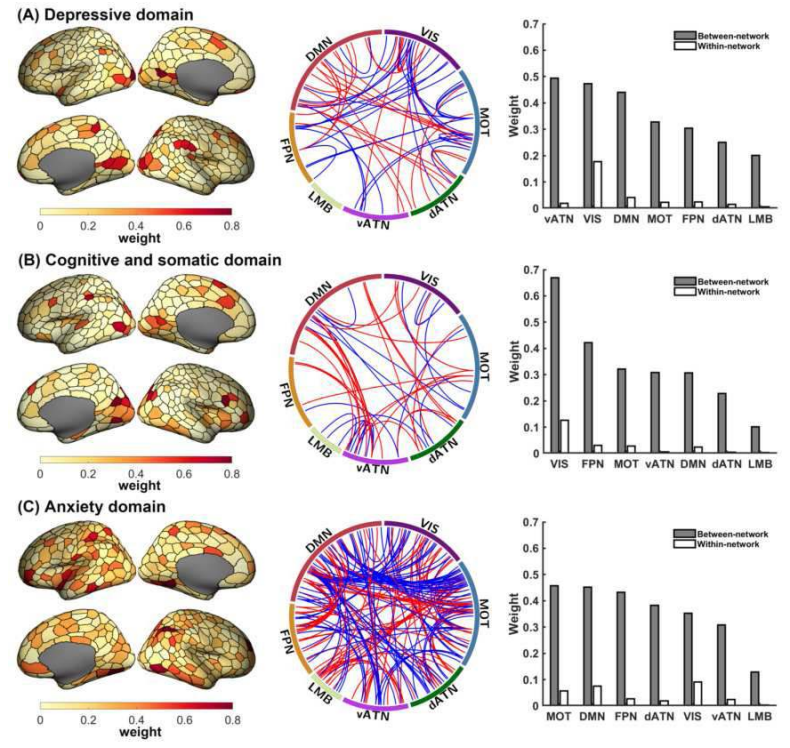

Fig. 2 Contributing group-level FC for estimating three symptom domains. (A) Depressive domain was mainly associated with connections among the vATN, VIS and DMN. (B) Neural bases for cognitive and somatic domain mainly involved connections in the VIS, FPN, and MOT. (C) Biomarkers for anxiety domain were widely distributed spanning from the MOT, DMN and FPN. Brain surface plots in the left plate demonstrated the spatial distribution of region-level weights; Circular plots in the middle plate displayed the edges with the top 10% absolute weights, with the positive and negative weights colored in red and blue, respectively. The bar plots in the right plate showed the normalized average absolute weights of between-network and within-network connections. Visual (VIS), sensorimotor (MOT), dorsal attention (dATN), ventral attention (vATN), limbic (LMB), frontoparietal control (FPN), and the default mode network (DMN).

Conclusions: We identified three different symptom domains for the SD population, and individualized FC estimated the symptom scores with higher accuracy than the group-level FC. These findings highlight the necessity of considering individual variability in brain functional organization, which can facilitate the detection of more effective neural biomarkers for SD and MDD.

References

1. Beck, A. T. (1996), 'Beck depression inventory-II', San. Antonio, vol. 78, pp. 490–498.
2. Cuijpers, P. (2004), 'Subthreshold depression as a risk indicator for major depressive disorder: A systematic review of prospective studies', Acta Psychiatrica Scandinavica, vol. 109, no. 5, pp. 325–331.
3. Esteban, O. (2019), 'fMRIPrep: A robust preprocessing pipeline for functional MRI', Nature Methods, vol. 16, no. 1, pp. 111-116.
4. Hwang, J. W. (2015), 'Subthreshold depression is associated with impaired resting-state functional connectivity of the cognitive control network', Translational Psychiatry, vol. 5, no. 11, pp. e683-e683.
5. Kong, R. (2021), 'Individual-Specific Areal-Level Parcellations Improve Functional Connectivity Prediction of Behavior', Cerebral Cortex, vol. 31, no. 10, pp. 4477–4500.
6. Michon, K. J. (2022), 'Person-specific and precision neuroimaging: Current methods and future directions', NeuroImage, vol. 263, pp. 119589.
7. Schaefer, A. (2018), 'Local-Global Parcellation of the Human Cerebral Cortex from Intrinsic Functional Connectivity MRI', Cerebral Cortex, vol. 28, no. 9, pp. 3095–3114.
8. Yeo, B. T. T. (2011), 'The organization of the human cerebral cortex estimated by intrinsic functional connectivity', Journal of Neurophysiology, vol. 106, no. 3, pp. 1125–1165.
9. Zhao, Y. (2023), 'Individualized functional connectome identified replicable biomarkers for dysphoric symptoms in first-episode medication-naïve patients with major depressive disorder', Biological Psychiatry: Cognitive Neuroscience and Neuroimaging, vol. 8, no. 1, pp. 42-51.
10. Zhu, Y. (2019), 'Connectome-based biomarkers predict subclinical depression and identify abnormal brain connections with the lateral habenula and thalamus', Frontiers in psychiatry, vol. 10, pp. 371.

Poster No 1794

Sequence based clustering of functional brain networks and its association with negative emotions

Dong Yun Lee[1], Seul-Gi Lee[2], Rae Woong Park[2], Bumhee Park[2]

[1]Department of Biomedical Informatics, Ajou University School of Medicine, Suwon, Gyeonggi-Do, [2]Department of Biomedical Informatics, Ajou University School of Medicine, Suwon, Gyeonggi-Do

Introduction: Resting-state functional MRI (rs-fMRI) captures patterns of spontaneous brain activity that can reveal clues about the connectome of the human brain. While many rs-fMRI studies have focused on static measures of functional connectivity, examining the temporal dynamics of rs-fMRI data provides a complementary view of the functional connectome, helping to identify changes in disease, development, and aging[1]. Meanwhile, Studies using rs-fMRI have reported relationships between negative emotions and brain connectivity[2]. This study aimed to propose a sequence-based clustering of rs-fMRI and investigate the relation between clustering and negative emotions.

Methods: For our study, we used the resting state fMRI (rsfMRI) and scales for the US National Institutes of Health (NIH) Toolbox Emotion Battery from 1080 healthy subjects, which were provided by the Human Connectome Project (HCP) S1200 release dataset. The rsfMRI data were canonically preprocessed through realignment, co-registration, normalization, smoothing, regressing out motion related confounding factors, despiking, and band-pass filtering (0.01 ~ 0.1 Hz). Brain regions were then defined with Brainnetome atlas[3] and Schaefer 200[4]. Among these regions, individual inter-regional functional connectivity was calculated using a Pearson correlation coefficient and Fisher's r-to-z transformation. We performed an independent component analysis (ICA) on those brain networks and estimated the time series. Using time series, we did sequence-based clustering using Sequence Graph Transform (SGT) and spectral clustering on acquired brain network sequences[5]. Finally, emotion scales were reduced to meaningful combinations with the principal components analysis and associated with the sequence-based clusters.

Results: From the ICA, we identified several components such as DMN and salience network. Based on this, we obtained a sequence of independent components for each person and further found three clusters (Figure 1). Two principal component scores for negative emotions were significantly different according to clusters (Figure 2, $p < 0.05$).

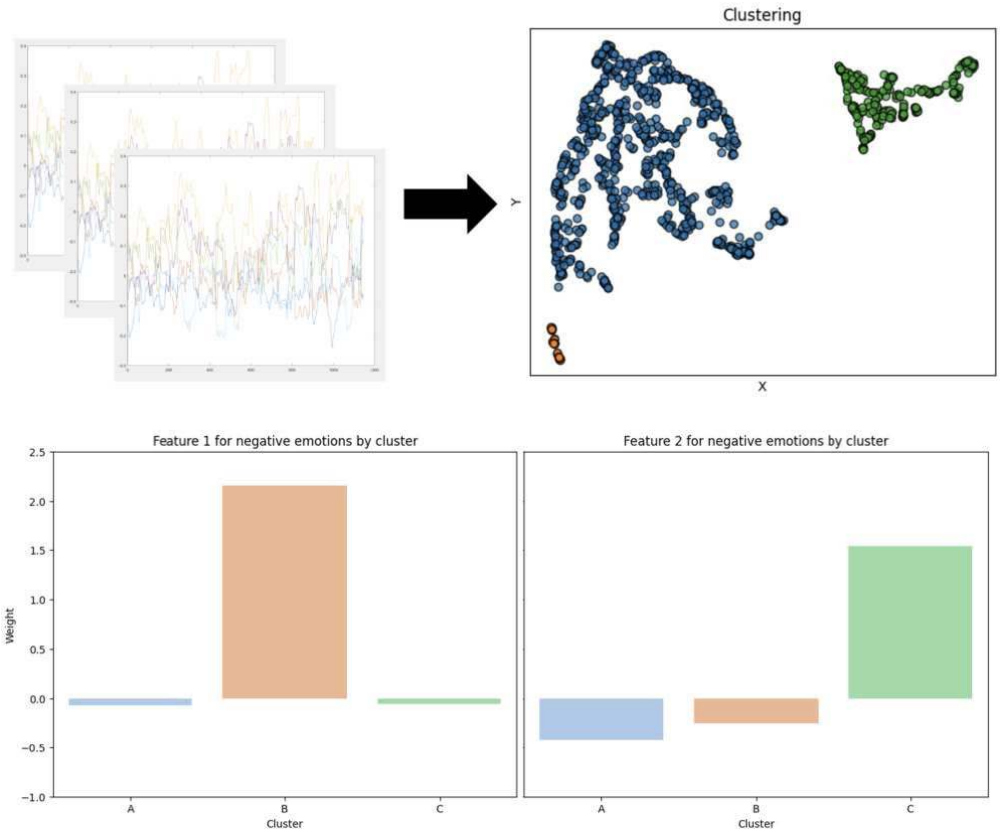

Conclusions: We found that the sequential clusters of rs-fMRI were related to negative emotions. Our findings suggest that the temporal dynamics of rs-fMRI data may be a more useful option for investigating clinical symptoms. Replication of our results from using the temporal approach are needed by other groups.

References

1. Lixia Tian et al. (2018) Changes in dynamic functional connections with aging. Neuroimage, 172:31–39
2. Canario E et al. (2021) A review of resting-state fMRI and its use to examine psychiatric disorders. Psychoradiology. 1(1):42-53.
3. Fan, L., et al. (2016). The human brainnetome atlas: a new brain atlas based on connectional architecture. Cerebral cortex, 26(8), 3508-3526.
4. Kong, R., et al. (2021). Individual-specific areal-level parcellations improve functional connectivity prediction of behavior. Cerebral Cortex, 31(10), 4477-4500.
5. Ranjan C., et al. (2022) Sequence graph transform (SGT): a feature embedding function for sequence data mining. Data Mining and Knowledge Discovery. 36(2):668-708.

Poster No 1795

Transdiagnostic neural correlates of executive dysfunction

Hajer Karoui[1], Danielle Kurtin[1]

[1]Imperial College London, London, London

Introduction: The aetiology of Parkinson's Disease (PD), Obsessive-Compulsive Disorder (OCD), and Huntington's Disease (HD) are distinct, yet all share symptoms of executive dysfunction[1-4], such as challenges in planning, heightened impulsivity, disinhibition, and obsessional tendencies. Functional Magnetic Resonance Imaging (fMRI) studies have revealed comparable neural patterns of executive dysfunction in PD1-2,HD3, and OCD4 patient (PT) groups, including diminished functional connectivity compared to healthy controls (HC). Here, we assess whether the brain state dynamics from each PT group are different from HC and other PT groups. The aim of this work is to evaluate if the cumulative effects of cellular-level pathology converge into similar neural markers of executive dysfunction.

Methods: fMRI data were collected during an executive planning task (Tower of London)[5] from 3 cohorts (PD=68, HD=30, OCD=24) of PTs and their matched HCs. Data preprocessing with fMRIPrep included brain extraction, BBR of BOLD data to T1w subject space using 6 DOF, slice-time correction, and estimation of head motion through 6 rotation and translation

parameters. 14 subcortical regions were identified using Freesurfer, and the 400-region Schaefer cortical atlas was transformed to subject space. Regional timeseries were extracted, z-scored, filtered between 0.02-0.1 Hz, and Hilbert-transformed, enabling the pairwise computation of the cosine of the difference in phase angle, and generating a symmetric coherence matrix for all timepoints. The connectivity matrix for each timepoint was masked with a binarised matrix for the 8 Yeo functional networks 6 and 1 subcortical network. After calculating the mean of the coherence values within each network's mask, the timepoint was labelled with the network with the highest mean coherence, generating a network-based state timeseries (ST) for each subject. State lifetime, Lempel Ziv Complexity (LZC)[7], and Block Decomposition Methods of Complexity (BDMC) of ST were computed. Kruskal-Wallis tests evaluated group effects on state dynamic metrics, with Wilcoxon sign-rank post-hoc pairwise comparisons between PTs, and between PTs and HCs within groups. All p-values were FDR-corrected.

Results: Across all subjects, the limbic state had the highest average percent occupancy, followed by the visual, dorsal attention, subcortical, temporal parietal, somatomotor, control, salience, and DMN states (Fig 1). While the low prevalence of the DMN was expected, the low prevalence of the control state was surprising, given its role in the planning processes engaged in TOL 1-4. The high prevalence of the limbic state was driven by a minority of subjects displaying a total occupancy of their ST by the limbic state. While there was a significant main group effect on LZC and BDMC of ST, post-hoc pairwise differences were not significant (Fig 2). A significant main group effect was also seen for the lifetime of all states (Fig 2). Post-hoc pairwise tests showed PD PTs had significantly higher visual, somatomotor, and DMN lifetime than HCs. Inappropriate DMN engagement during tasks have been associated with poor cognitive task performance 8; thus, we suggest the higher lifetime of the DMN state in PD PTs may contribute to the previously reported worse performance of our PD vs HC subjects 1. PD PTs showed significantly longer lifetimes across all states than OCD PTs, and all states but subcortical ones compared to HD PTs. This is likely due to older age of PD PTs compared to other patient groups, as age disrupts the metastable, flexible neural dynamics associated with healthy cognition[8].

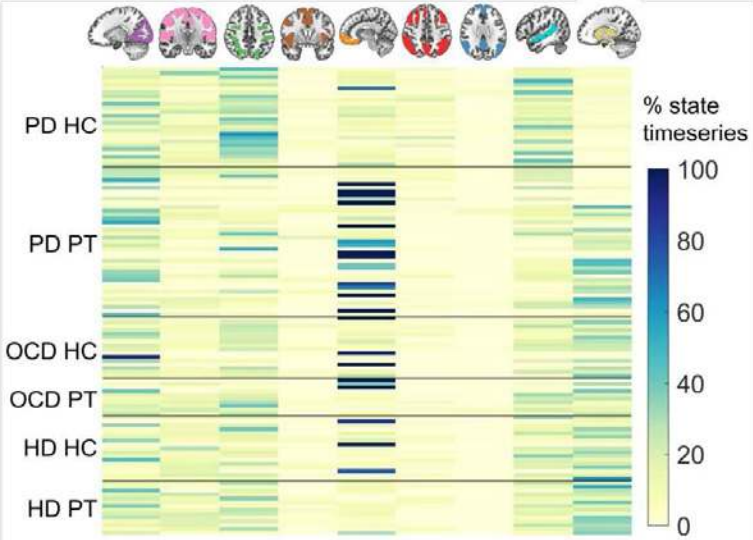

Figure 1: The percent occupancy of each network-based state per subject's lifetime. The figure has one row per subject, with horizontal lines to demarcate boundaries between groups. Each column represents one network-based state. A few participants exhibit total occupancy of the visual or limbic state, generating outliers in state dynamics measures. Since we did not predefine a cutoff for state prevalence as an exclusion criteria, these subjects were kept in all analyses.

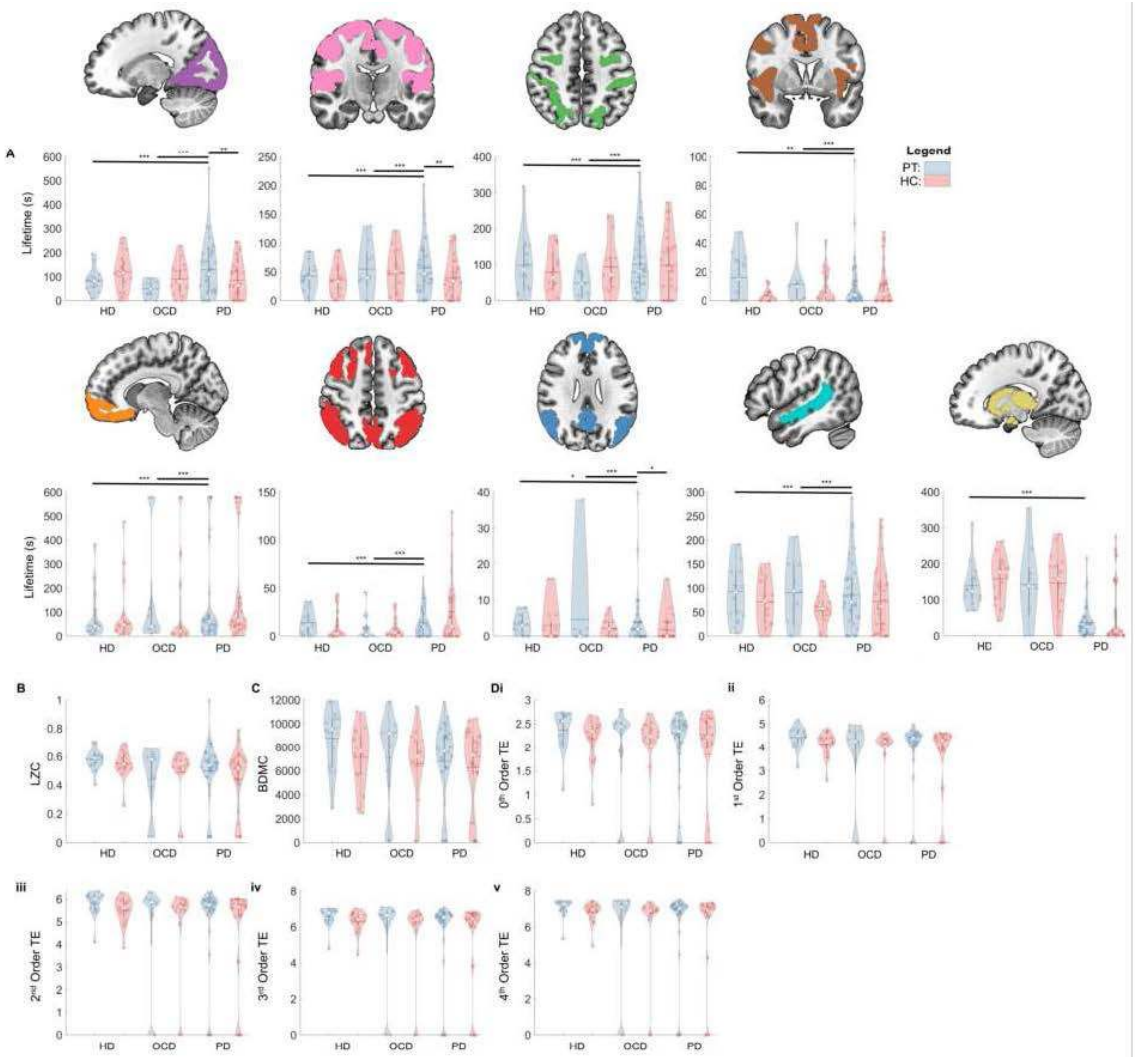

Figure 2: Violin plots of of state dynamics, including **(A)** state lifetime, **(B)** LZC, **(C)** BDMC, and **(Di-v)** 0-4th order transition entropy (TE). The top and bottom edges of the boxes represent the 25th and 75th percentiles, with the mean shown as the white dot and the median by the horizontal line. Extension of the whiskers indicates 1.5 the interquartile range. A kernel density estimate of the data provides the edges to the violin plot. Each point is one subject. * indicates p<0.05 in post-hoc, pairwise Wilcoxon sign-rank comparing information theoretic metrics between groups.

Conclusions: Our results show that metrics of state dynamics capture differences in how neural resources are organised over time to subserve the cognitive demands. Relationships among age, task performance, and measures of state dynamics are currently being investigated.

References

1. Fallon, S. J. (2016). Learning to be inflexible: Enhanced attentional biases in Parkinson's disease. cortex, 82, 24-34.
2. Nombela, C. (2014). Genetic impact on cognition and brain function in newly diagnosed Parkinson's disease: ICICLE-PD study. Brain, 137(10), 2743-2758.
3. Mörkl, S. (2016). Problem solving, impulse control and planning in patients with early-and late-stage Huntington's disease. European Archives of Psychiatry and Clinical Neuroscience, 266, 663-671.
4. Odlaug, B. L. (2016). Abnormal brain activation in excoriation (skin-picking) disorder: evidence from an executive planning fMRI study. The British Journal of Psychiatry, 208(2), 168-174.
5. Shallice, T. (1982). Specific impairments of planning. Philosophical Transactions of the Royal Society of London. B, Biological Sciences, 298(1089), 199-209.
6. Yeo, B. T. (2011). The organization of the human cerebral cortex estimated by intrinsic functional connectivity. Journal of neurophysiology.
7. Lempel, A.(1976). On the complexity of finite sequences. IEEE Transactions on information theory, 22(1), 75-81.
8. Elton, A. (2015). Task-positive functional connectivity of the default mode network transcends task domain. Journal of Cognitive Neuroscience, 27(12), 2369-2381.

Poster No 1797

Alterations in functional connectivity in children with dyslexia

Mingyeong Kim[1], Euisun Kim[2], Jiyoung Park[2], Hae-Jeong Park[2]

[1]Yonsei University, Seoul, Seoul, [2]Yonsei Univ, Seoul, Seoul

Introduction: Dyslexia, a complex neurological disorder, primarily affects reading abilities, distinguishing it from visual impairments or general learning deficits. Recent studies propose dyslexia as a multi-deficit disorder stemming from various independent factors, including challenges in working memory and auditory temporal processing. This study aims to provide neurobiological evidence for this multi-deficit hypothesis by examining resting-state functional connectivity. Specifically, it investigates whether dyslexia involves alterations in functional connectivity, especially in areas related to the visual pathway, working memory, and temporal processing. Additionally, the study compares these alterations in children with dyslexia to those with mathematical disorders, to determine if these connectivity changes are unique to dyslexia.

Methods: 1. Participants Using the Healthy Brain Network dataset from the Child Mind Institute (Data Release 9.0), this study included three groups: 43 children diagnosed with a specific reading impairment (dyslexia group), 41 children in a matched control group, and 43 children with a specific mathematics impairment. 2. Measures and Analysis A functional brain network, comprising 132 regions from the Harvard-Oxford atlas, was established. The study assessed and compared the pairwise correlation of resting-state fMRI time series across these brain regions among the three groups. Preprocessing of the fMRI data utilized SPM software, and the CONN toolbox was employed for functional connectivity analysis.

Results: The analysis revealed notable differences in the dyslexia group compared to the control group, including significant reductions in connectivity between the left and right Posterior Superior Temporal Gyrus and the right caudate nucleus, the Parahippocampal Gyrus (left, posterior division) and the posterior cerebellum, and between the Occipital Cortex and the medial Prefrontal Cortex (mPFC). These diminished connectivity patterns were unique to the dyslexia group and not observed in the mathematics disorder group, highlighting the specificity of these changes to dyslexia.

Conclusions: The findings indicate distinct alterations in brain connectivity within various networks, including those associated with visual and language processing, in children with dyslexia. This reinforces the understanding of dyslexia as a disorder encompassing multiple domains. The study's results are specific to dyslexia, differing from learning disorders related to mathematics. However, it remains unclear whether these changes are primary causes or secondary effects of dyslexia. Improved comprehension of these altered connectivity patterns and their implications on visual pathways, working memory, and temporal processing could inform approaches to other related brain disorders and guide future treatment strategies.

References

1. Fostick, L., & Revah, H. (2018). Dyslexia as a multi-deficit disorder: Working memory and auditory temporal processing. Acta Psychologica, 183, 19-28.
2. Sun, Y-F., Lee, J-S., & Kirby, R. (2010). Brain Imaging Findings in Dyslexia. Pediatrics & Neonatology, 51(2), 89-96.
3. Park, H-J., & Friston, K.J. (2013). Structural and Functional Brain Networks: From Connections to Cognition. Science, 342.
4. Friston, K. J., Holmes, A. P., Worsley, K. J., Poline, J. P., Frith, C. D., & Frackowiak, R. S. (1995). Statistical parametric maps in functional imaging: A general linear approach. Human Brain Mapping, 2(4), 189-210.
5. Whitfield-Gabrieli, S., & Nieto-Castanon, A. (2012). Conn: A functional connectivity toolbox for correlated and anticorrelated brain networks. Journal of Neuroscience Methods, 187(2), 182-193.
6. Alexander, L., et al. (2017). An open resource for transdiagnostic research in pediatric mental health and learning disorders. Scientific Data, 4, 170181.

Poster No 1798

Functional network resilience and its relationship to cognition: A cross-sectional lifespan study

Georgette Argiris[1], Yaakov Stern[2], Christian Habeck[1]

[1]Columbia University, New York, NY, [2]Columbia University Irving Medical Center, New York, NY

Introduction: Functional network studies have shown that healthy brain topology is typically characterized by specific network properties such as high clustering between nodes with a common functionality and short path length between nodal "hubs", purportedly allowing for the efficient and reliable propagation of information across the network[1]. An additional defining feature is resilience, or its ability to retain functionality even when confronted with perturbations, such as lesions, that result in damage or error[2]. Few studies have tested brain network resilience via systematic targeted attack. In the current study, we aimed to assess the impact of virtual nodal lesioning across several network properties of resting BOLD connectivity and to analyze its cross-sectional relationship to age and cognition.

Methods: Four hundred and twenty-five native English participants from the Reference Ability Neural Network and Cognitive Reserve lifespan cohort (mean age= 50.98 ± 16.53; range= 20-80 years) were included in the study. We generated undirected weighted adjacency matrices based on the time series correlations of all nodal pairings from the 400-region parcellation scheme of the Schaefer atlas[3], with matrices thresholded to retain the top 10% of participant-specific connection strength[4]. As a measure of whole-brain network resilience, we adopted a targeted attack approach described by Albert and colleagues[5], whereby nodes were sequentially removed from the connectome in order of their nodal strength. At each iteration, the nodal strength was recomputed to account for the effect of prior lesioning and a series of network metrics- the largest connected component (LCC), mean clustering coefficient, mean characteristic path length, global efficiency, and modularity- were calculated (see Fig for example schematic). Two properties of each metric were considered: (a) the critical point of lesioning curve; and (b) the total area under the curve (AUC) as the integral of each network measure across lesioning iterations. Linear regression analysis was used to first test for age and brain integrity (i.e., cortical thickness) effects on network measure properties after adjusting for sex, education, NART IQ, scrubbing of the signal, and the "static" network measure (e.g., full connectome metric calculation before lesioning). Models were then created to test the utility of each network measure in predicting out-of-scanner behavioral performance in each of four cognitive domains (i.e., episodic memory, fluid reasoning, processing speed, and vocabulary) considered to comprise the breadth of breadth of age-related cognitive changes[6].

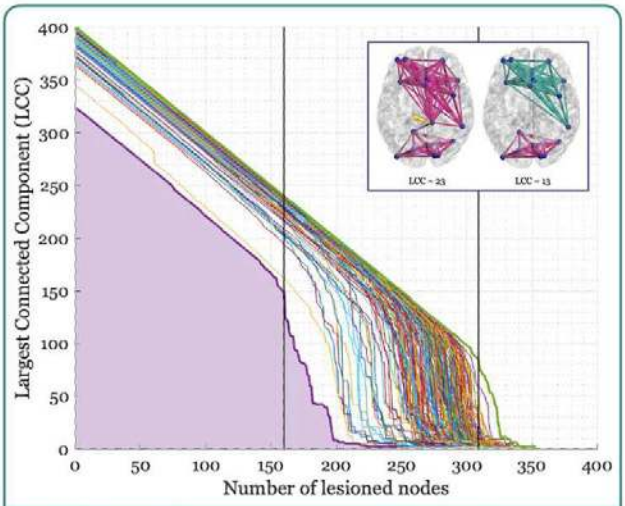

Fig. Schematic of example targeted attack for the LCC metric. The line plot depicts possible curves across nodal lesioning iterations (i = n). Vertical black lines indicate the critical point (e.g., slope of decay) for two example participants, where the early critical point suggests a less resilient individual than one with a late critical point. The toy schematic in the top right depicts the hypothetical lesioning of a node (left) and its consequence on the LCC (right: depicted in green) for a network of n=23, for visibility purposes.

Results: Results from network measure regression models demonstrated age-related declines in the AUC of the mean clustering coefficient, modularity, and global efficiency. Notably, these effects were found after controlling for static network measures. Additionally, the AUC of modularity but not static modularity displayed age-related effects, suggesting unique network information captured by the AUC and not static measure alone. No significant effects were found for the critical point in the lesioning curve. Results from the behavior models demonstrated a significant positive effect of the mean clustering coefficient, global efficiency, and mean characteristic path length on behavioral performance for the fluid reasoning domain such that higher values of AUC predicted more accurate performance. Additionally, critical point of both the mean characteristic path length and global efficiency both positively predicted fluid reasoning performance, independently of the static network measure.

Conclusions: Here, we demonstrated age-related declines in specific network metrics that not only partially corroborates previous findings in the aging network literature[4,7,8], but additionally supports the inclusion of other network metric properties that may be sensitive to capturing both age-related and cognitive declines beyond static measures alone.

References

1. Watts, D. J., & Strogatz, S. H. (1998). Collective dynamics of 'small-world'networks. Nature, 393(6684), 440-442.
2. Gao, J. et al. (2016). Universal resilience patterns in complex networks. Nature, 530(7590), 307-312.
3. Schaefer, A. et al. (2018). Local-global parcellation of the human cerebral cortex from intrinsic functional connectivity MRI. Cerebral Cortex, 28(9), 3095-3114.
4. Menardi, A. et al. (2021). Heritability of brain resilience to perturbation in humans. Neuroimage, 235, 118013.
5. Albert, R. et al. (2000). Error and attack tolerance of complex networks. Nature, 406, 378–382.

6. Salthouse, T. A. (2009). Decomposing age correlations on neuropsychological and cognitive variables. Journal of the International Neuropsychological Society, 15(5), 650-661.
7. Deery, H. A., Di Paolo, R., Moran, C., Egan, G. F., & Jamadar, S. D. (2023). The older adult brain is less modular, more integrated, and less efficient at rest: A systematic review of large-scale resting-state functional brain networks in aging. Psychophysiology, 60(1), e14159.
8. Argiris, G., Stern, Y., Lee, S., Ryu, H., & Habeck, C. (2023). Simple Topological Task-Based Functional Connectivity Features Predict Longitudinal Behavioral Change of Fluid Reasoning in the RANN Cohort. NeuroImage, 120237.

Poster No 1799

Analyzing Thalamocortical Functional Connectivity Differences in COVID Survivors

Sapna Mishra[1], Tapan Gandhi[1], Bharat Biswal[2]

[1]Indian Institute of Technology Delhi, New Delhi, Delhi, [2]New Jersey Institute of Technology, Newark, NJ

Introduction: The long-term neurological impact of COVID-19 has been the subject of intense investigation in the past years. Cognitive symptoms reported by COVID survivors including brain fog, inattention, memory issues, and fatigue may reflect in the functional connectivity patterns of the brain (Li et al. 2023, Hafiz et al. 2022). We hypothesize that the varied range of symptoms in COVID survivor may be linked to abnormalities in the thalamocortical network. Therefore, we conducted this cross-sectional study to investigate the resting state functional connectivity in the thalamocortical networks of COVID-recovered patients (CRPs).

Methods: We acquired T1-weighted MRI and resting state fMRI scans (TR = 2s, 3.75 x 3.75 x 3 mm3) for 72 (17F, mean age=32.12 years) CRPs and 48 Healthy Controls (11F, mean age=31.87 years). The scans were conducted within six months of recovery from COVID-19 infection. The fMRI scans were pre-processed using SPM12 (www.fil.ion.ucl.ac.uk/spm/) including motion correction, slice time correction, coregistration, segmentation and normalization to MNI space. Further, temporal regression was performed with average white matter and CSF signals to minimize physiological contribution to BOLD. After bandpass filtering (0.01-0.1 Hz), an 8 mm FWHM Gaussian filter was used to smooth the fMRI scans. To extract the functional connectivity in the thalamocortical network, six thalamic nuclei were selected as seeds, specified using a spherical region of interest (ROI) of radius 8 mm centered at the respective MNI coordinates. The nuclei studied here are the right and left Mediodorsal nuclei (MD), pulvinar nuclei (PUL), and the Ventral lateral nuclei (VL). The BOLD timeseries for each seed were obtained by averaging the voxels within the ROI. The thalamocortical functional connectivity (FC) of a nucleus with all other voxels in the brain was quantified using the Pearson correlation coefficient to generate a whole-brain FC map for each seed. The correlation values were Fisher-z transformed and then compared across the cohorts. For statistical comparison of thalamocortical connectivity between the cohorts, permutation testing was performed using FSL's randomise (fsl.fmrib.ox.ac.uk/fsl) algorithm and multiple comparison errors were corrected using the voxel-based thresholding (pcorr < 0.05).

Results: Upon comparison of the cohorts, it was observed that the CRPs exhibited significant alterations in thalamocortical FC (CRP > HC) at several regions in the brain. With the seeds in the right and left MD nuclei, significant clusters were observed in the left white matter callosal body, left putamen, and left frontal pole (Figure 1). Further, the right lateral occipital cortex, anterior cingulate gyrus, left sub-callosal orbitofrontal cortex, and the right Heschl's gyrus showed enhanced FC with the PUL nuclei in CRPs (Figure 2). We did not observe any significant changes in thalamocortical FC with the right or left VL nuclei.

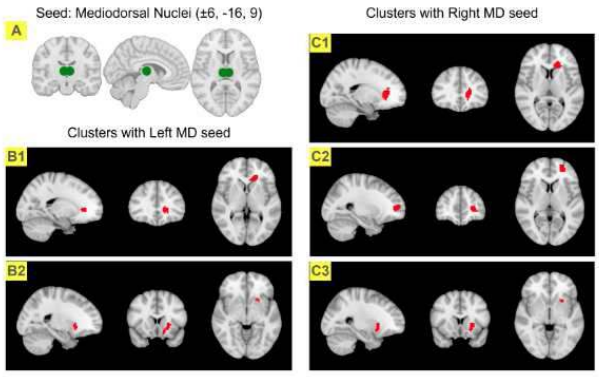

Figure 1. **(A)** Spherical seed ROI centered at the Mediodorsal (MD) nuclei used for analysis. Significant clusters obtained (p_{corr}<0.05) for COVID > HC contrast with left MD seed: **(B1)** Left white matter callosal body, and **(B2)** Left putamen. Significant clusters obtained (p_{corr}<0.05) for COVID > HC contrast with Right MD seed: **(C1)** White matter callosal body, left lateral ventricle, **(C2)** Left cerebral white matter (prefrontal cortex), frontal pole, and **(C3)** Left putamen.

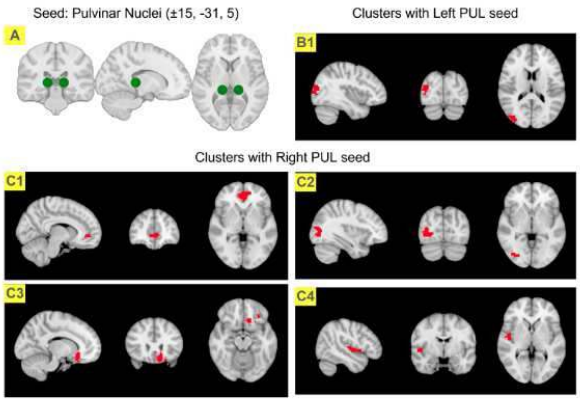

Figure 2. **(A)** Spherical seed ROI centered at the Pulvinar (PUL) nuclei used for analysis. Significant clusters obtained (p_{corr}<0.05) for COVID > HC contrast with left PUL seed: **(B1)** Lateral occipital cortex, inferior and superior division. Significant clusters obtained (p_{corr}<0.05) for COVID > HC contrast with right PUL seed: **(C1)** Cingulate gyrus, anterior division, paracingulate gyrus, **(C2)** Right lateral occipital cortex, inferior division, **(C3)** Left subcallosal cortex, frontal orbital cortex, and **(C4)** Right Heschl's gyrus.

Conclusions: The MD nucleus relays the input from the basal ganglia and the limbic system to the prefrontal cortex and prefrontal association areas and is primarily involved in higher cognitive processes including memory and attention (Mitchell et al. 2013). The PUL nuclei connect the visual cortex with higher association areas in the posterior parietal cortex and temporal lobe. The medial PUL nucleus also connects with the cingulate and is implicated in multisensory integration and visual attention regulation (Cappe et al. 2009). Display of abnormal FC in the MD and PUL thalamocortical circuits in COVID survivors may be linked to symptoms like brain fog, memory loss, fatigue, and inattention. Overall, in this investigation, we observed that vital thalamocortical circuits involved in memory, planning, and attention show abnormal FC in COVID survivors, hinting at possible damage in this network. This can assist in directing future research into the neurological underpinnings of post COVID symptoms.

References

1. Cappe, Céline. (2009), 'The thalamocortical projection systems in primate: an anatomical support for multisensory and sensorimotor interplay,' Cerebral cortex, 19.9, 2025-2037.
2. Hafiz, Rakibul. (2022), 'Assessing functional connectivity differences and work-related fatigue in surviving COVID-negative patients.' bioRxiv.
3. Li, Ruili. (2023), 'Altered intrinsic brain activity and functional connectivity in COVID-19 hospitalized patients at 6-month follow-up,' BMC Infectious Diseases, 23.1, 521.
4. Mitchell, Anna S. (2013). 'What does the mediodorsal thalamus do?' Frontiers in systems neuroscience vol. 7 no. 37.
5. Voruz, Philippe. (2022), 'Functional connectivity underlying cognitive and psychiatric symptoms in post-COVID-19 syndrome: is anosognosia a key determinant?' Brain Communications, 4.2.

Poster No 1800

Connectome-Based Attractor Dynamics underly Brain Activity in Rest, Task, and Disease

Robert Englert[1], Balint Kincses[1], Raviteja Kotikalapudi[1], Giuseppe Gallitto[1], Jialin Li[2], Kevin Hoffschlag[1], Choong-Wan Woo[3], Tor Wager[4], Dagmar Timmann[1], Ulrike Bingel[1], Tamás Spisák[1]

[1]University Medicine Essen, Essen, NRW, [2]Max Planck School of Cognition, Leipzig, Germany, [3]Sungkyunkwan University, Suwon-si, Gyeonggi-do, [4]Dartmouth College, Hanover, NH

Introduction: Brain function is characterized by the continuous activation and deactivation of anatomically distributed neuronal populations, leading to complex fluctuations termed "brain states". These dynamics have been explored using various descriptive techniques, revealing their neuroscientific relevance (Greene et al., 2023, Vidaurre et al., 2017). The intricate nature of understanding brain dynamics persists as we strive to bridge the explanatory gap between biophysical and cognitive perspectives (Breakspear 2017). Here we propose functional connectivity-based Hopfield neural network (fcHNN) as a novel model for macro-scale brain dynamics, incorporating the advantages of large-scale network models and data-driven approaches.

Methods: The fcHNN framework uses the functional connectome to model recurrent activity flow (Cole et al. 2016) across large-scale brain regions and conceptualizes brain dynamics as trajectories on an n-dimensional energy landscape with local minima often referred to as 'attractor states'. Although fcHNNs are a type of artificial neural networks, the network

weights are not explicitly trained, but rather set empirically with the partially correlated, functional connectivity matrix. Through the so-called Hopfield relaxation procedure, fcHNNs naturally converge towards one of the finite number of attractor states, characterized by minimal energy (Hopfield 1982) (Figure 1A). Introducing weak noise during relaxation, referred to as 'stochastic update' (Figure 1B) prevents the system from converging to attractor states and introduces heteroclinic dynamics where the system traverses the energy landscape. This can serve as a high-level generative model of macro-scale brain dynamics, guided by the connectome's topology (Figure 2A). The first two principal components of simulated activity patterns, termed the fcHNN projection, are employed to create a lower-dimensional representation of the state space. This projection effectively separates the attractor state basins and serves as a tool for examining brain dynamics.

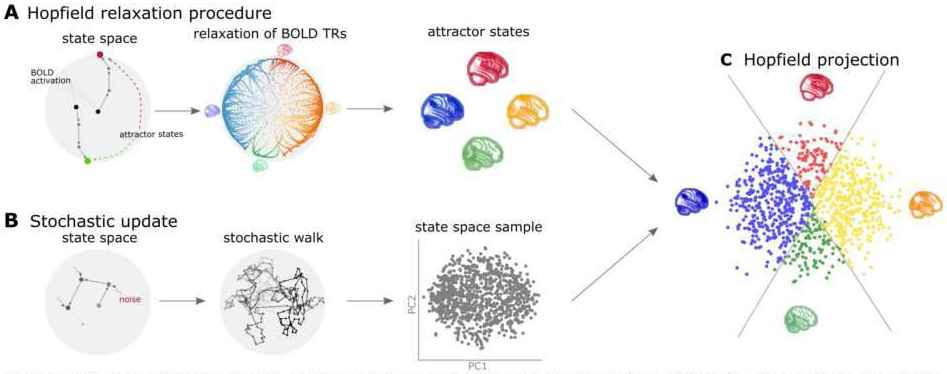

Figure 1, Methods: A Hopfield relaxation, activation patterns converge towards attractor states. **B** Stochastic update: hopfield relaxation is disturbed with noise, resulting in an endless walk across the state space. **C** The first two principal components of the state sample span the hopfield projection, accurately separating the attractor basins.

Results: We found that large-scale attractor states of the brain exhibit significant neuroscientific relevance, closely resembling known large-scale brain systems, showcasing the model's potential in understanding complex brain dynamics. The fcHNN projection, utilizing the first two principal components of the fcHNN state space, demonstrates a notably higher explanatory power ($p<0.0001$) when compared to principal components extracted directly from actual resting state fMRI data. In addition to replicating various aspects of spontaneous brain dynamics, fcHNNs are suitable for modeling responses to perturbations, as demonstrated by their ability to detect changes in neural activity patterns related to pain perception (Woo et al. 2015). Flow analysis on the fcHNN projection (difference in the average timeframe-to-timeframe transition direction), reveals that during pain, brain activity gravitates toward a distinct "ghost attractor" (Figure 2B). To assess clinical relevance of the proposed method, we compared data from autism spectrum disorder (ASD) patients and typically developing controls (Di Martino et al. 2014). Flow analysis predicted increased likelihood of states returning towards the middle on the internal-external axis and transitioning towards the extremes on the action-perception axis in ASD (Figure 2B), findings that were statistically significant and consistent with observed patterns in real data.

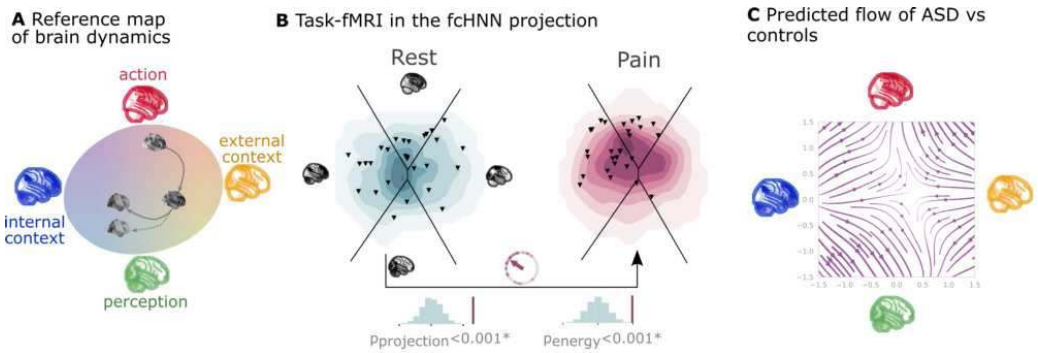

Figure 2, Results: A Attractor states of the fcHNN. **B** fcHNN analysis of pain vs rest data showed significant differences in energy and position in the embedding. **C** Predicted flow of ASD patients vs typically developing controls is highly significant ($p = 0.0009$).

Conclusions: We present the connectome-based Hopfield neural network (fcHNN) model, a lightweight computational framework initialized with empirical functional connectomes, accurately capturing and predicting diverse brain dynamics, offering a mechanistic account for the emergence of brain states, gradients, and autocorrelation structures.

References

1. Vidaurre, D., Smith, S. M., & Woolrich, M. W. (2017). Brain network dynamics are hierarchically organized in time. Proceedings of the National Academy of Sciences, 114(48), 12827-12832.
2. Greene, A. S., Horien, C., Barson, D., Scheinost, D., & Constable, R. T. (2023). Why is everyone talking about brain state?. Trends in Neurosciences.
3. Breakspear, M. (2017). Dynamic models of large-scale brain activity. Nature neuroscience, 20(3), 340-352.
4. Cole, M. W., Ito, T., Bassett, D. S., & Schultz, D. H. (2016). Activity flow over resting-state networks shapes cognitive task activations. Nature neuroscience, 19(12), 1718-1726.

5. Hopfield, J. J. (1982). Neural networks and physical systems with emergent collective computational abilities. Proceedings of the national academy of sciences, 79(8), 2554-2558.
6. Woo, C. W., Roy, M., Buhle, J. T., & Wager, T. D. (2015). Distinct brain systems mediate the effects of nociceptive input and self-regulation on pain. PLoS biology, 13(1), e1002036.
7. Di Martino, A., Yan, C. G., Li, Q., Denio, E., Castellanos, F. X., Alaerts, K., ... & Milham, M. P. (2014). The autism brain imaging data exchange: towards a large-scale evaluation of the intrinsic brain architecture in autism. Molecular psychiatry, 19(6), 659-667.

Poster No 1801

Dynamic network properties from mesoscale iEEG and macroscale BOLD signals link heart rate changes

Saurabh Sonkusare[1], Kartik Iyer[2], Johan van der Meer[2], Vin Thai Nguyen[2], Christine Guo[3], Sasha Dionisio[4], Michael Breakspear[5]

[1]University of Cambridge, Cambridge, United Kingdom, [2]QIMR Berghofer Medical Research Medical Research Institute, Brisbane, Australia, [3]QIMR Berghofer Medical Research Institute, Brisbane, Australia, [4]Advanced Epilepsy Unit, Mater Centre for Neurosciences, Mater Hospitals, Brisbane, Australia, [5]University of Newcastle, Newcastle, N/A

Introduction: The brain's ability to rapidly adapt derives from the flexible reconfiguration of its functional networks (Sporns, Chialvo, Kaiser, & Hilgetag, 2004). The global trade-off between functional integration versus segregation reflects changes in physiological processes including arousal, which in turn depend on ascending neuromodulatory effects acting over multiple (short and long) time scales. However, the association of these dynamic network properties to fluctuations in bodily physiology such as changes in the heart rate (HR) has not been well quantified. Heart rate is modulated by the adrenergic-cholinergic balance has also been proposed to be linked to the neurotransmitter related brain states of integration and segregation (Shine, 2019) and thus provides a good physiological measure to link dynamic network properties.

Methods: Here, we acquired data from two modalities 1) high-fidelity intracranial-EEG recordings from 12 patients undergoing clinical epilepsy evaluation, and 2) functional magnetic resonance imaging (fMRI) data from 18 healthy subjects. Schema of the study approach shown in Figure 1. The participants in both these datasets watched a short unedited emotional movie "The Butterfly Circus" while their respective data was acquired. For iEEG data, we first segment ECG data corresponding to the movie viewing data into 5 second epochs to account for variability in heart rate changes across patients. Subsequently, iEEG high frequency broad band activity (60-140 Hz), a metric of local neuronal firing and which has been found to be correlated wit the BOLD signal, of all the grey matter channels was computed and which was segmented into 5 second epochs. Adjacency matrices were constructed for each 5 second epochs, network properties of integration (global efficiency) and segregation (modularity) properties were obtained for each epoch. For fMRI data, standard pre-processing was employed (van der Meer et al., 2020) and then we extracted BOLD signals using AAL atlas. Subsequently, we used sliding window (~30 seconds) method to construct adjacency matrices and thresholding the matrices to obtain network properties of integration and segregation. Heart rate data corresponding to each TR was obtained using the TAPAS toolbox similar sliding windows used to obtain dynamic HR signal. For testing associations between HR and network properties, we calculated the group mean of the Pearson correlation between HR and integration and HR and segregation. To generate the null distribution, permutation testing with randomly circular shifting the data was used.

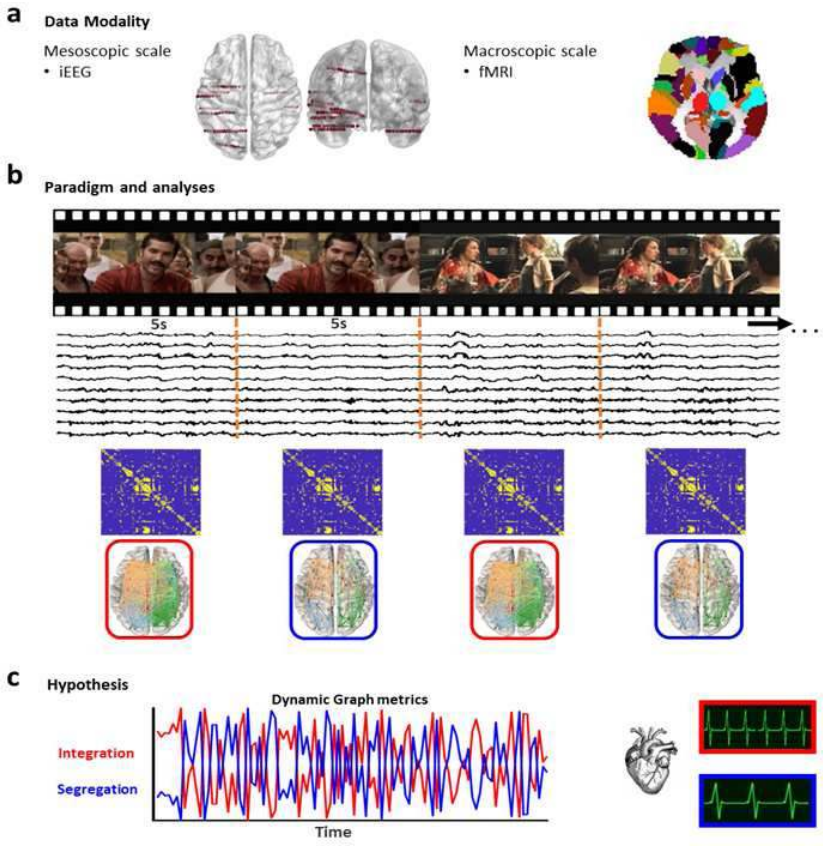

Results: We find dynamic integration states were negatively correlated with HR (r = .14, p<.0001), and segregation states were positively correlated, with HR (r = -.09, p<.0001) (Figure 2 top). In other words, integration or widespread communication was associated with higher heart rate and segregation states associated with lower heart rate. Notably, in fMRI data acquired from the participants viewing the same movie, we find the opposite pattern of results i.e. integration states associated with high heart rate (r = -.17, p<.0001) and segregation states associated with low hear rate (r = .15, p<.0001) (Figure 2 bottom).

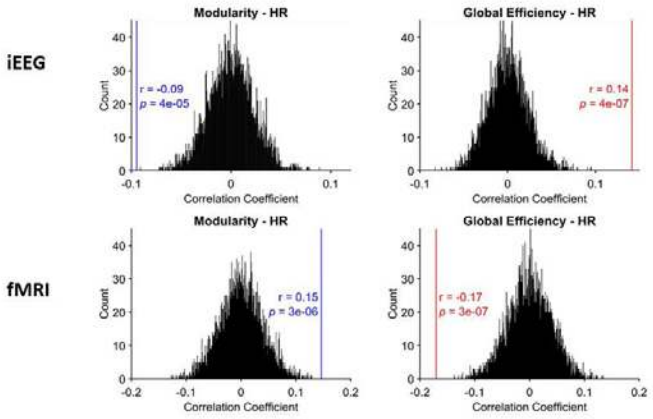

Conclusions: We established with direct neuronal activity that integrations states were linked with higher heart rate and segregation states linked with lower heart rate. Thus our results also indirectly link brain network states to activity in neuromodulatory systems. However we found opposing pattern of results with with fMRI. These opposing findings from iEEG and fMRI highlight the complex relationship between the cortical activity, BOLD signals and cardiac homeostasis.

References

1. Sporns, O., Chialvo, D. R., Kaiser, M., & Hilgetag, C. C. (2004). Organization, development and function of complex brain networks. Trends in cognitive sciences, 8(9), 418-425
2. Shine, J. M. (2019). Neuromodulatory influences on integration and segregation in the brain. Trends in cognitive sciences, 23(7), 572-583
3. van der Meer, J. N., Breakspear, M., Chang, L. J., Sonkusare, S., & Cocchi, L. (2020). Movie viewing elicits rich and reliable brain state dynamics. Nature communications, 11(1), 1-14

Poster No 1802

The insula function via epilepsy-SEEG pattern and fMRI

Yi-Hsiu Chen[1], Cheng-Chia Lee[2,3,4], Cheng-Chen Chou[5], Yi-Hsuan Liu[1], Pei-Lin Lee[6], Kun-Hsien Chou[1,4], Ching-Po Lin[1,6,7]

[1]Institute of Neuroscience, National Yang Ming Chiao Tung University, Taipei, Taiwan, [2]Department of Neurosurgery, Neurological Institute, Taipei Veteran General Hospital, Taipei, Taiwan, [3]School of Medicine, National Yang Ming Chiao Tung University, Taipei, Taiwan, [4]Brain Research Center, National Yang Ming Chiao Tung University, Taipei, Taiwan, [5]Department of Neurology, Neurological Institute,Taipei Veterans General Hospital, Taipei, Taiwan, [6]Center for Healthy Longevity and Aging Sciences, National Yang Ming Chiao Tung University, Taipei, Taiwan, [7]Department of Education and Research, Taipei City Hospital, Taipei, Taiwan

Introduction: The insular cortex, with its concealed location and broad connections to other brain regions, plays a complex role in the spread of epileptic discharges. These discharges often extend from the insula to other lobes, leading to a range of symptoms that can obscure the correct diagnosis of insular epilepsy. Advances in intracranial technology now allow clinicians to precisely identify the epileptogenic zone, including in insular epilepsy cases. Recent clinical reports show a burgeoning interest in the functional mapping of the insula, which is associated not only with visceral-somatic processing but also with a spectrum of sensations such as pain, speech disturbances, and oropharyngeal responses. Specific clinical responses have been correlated with distinct insular subregions[1,2]. A meta-analysis has proposed a functional subdivision of the insula into different four parcellation[3]. In summary, the insula is a multifaceted region whose significance is much greater than previously appreciated. The current study, therefore, aims to utilize a combination of neurophysiological and neuroimaging techniques to explore the FC of the insula.

Methods: We collected electrophysiological mapping data from 42 patients with drug-resistant epilepsy of non-insular origin who had undergone Stereo-encephalography (SEEG). We compiled their electrical stimulation reports to understand the functional characteristics of different subregions within the insular cortex. Additionally, we analyzed rs-fMRI data from 20 control subjects and 16 epilepsy patients with non-insular onset. The rs-fMRI data was used to calculate the functional connectivity (FC) between the insular cortex and other cortical areas. This served to validate the electrical stimulation results and to delineate distinct functional subregions. We defined the motor-premotor (MOT), occipital-parietal (OCC), prefrontal (PRE), somatosensory (SOM), and temporal (TEM) cortical Regions of Interest (ROI) in standard MNI space by combining associated masks from the Harvard-Oxford cortical atlas[4]. The insula mask was derived from the AAL atlas. To compute FC between the left and right cortex and the insular regions, we calculated the Pearson correlation coefficient between the average BOLD time series from each cortical seed and all corresponding insular target voxels. The one-sample t test was done to produce insular-cortical connectivity maps for each group. Lastly, we conducted a nonparametric statistical comparison ($P < 0.05$) between the control group and epilepsy patients, applying a false discovery rate for multiple comparisons

Results: According to our electrophysiological mapping results, insular functions mainly correlated with motor, somatosensory, temporal, oro-pharyngearl responses, which can be corresponded to our FC results. Furthermore, the results demonstrated significantly higher FC in the patient group compared to the normal control group within the insular subregion correlated with the temporal lobe and motor function on both the two sides of the insula. However, there was no statistical difference between groups in the PRE, MOT, SOM, and OCC regions. These findings suggest that epilepsy with a non-insular onset may still affect the FC of the insula, particularly in areas related to the temporal lobe and motor cortex. According to our mapping results, motor responses were primarily associated with the posterior insula, while somatosensory responses were distributed throughout the insula. Temporal lobe functions were mostly mapped to the middle short gyrus and the posterior long gyrus, and oro-pharyngeal responses were asymmetrically localized to the right insula.

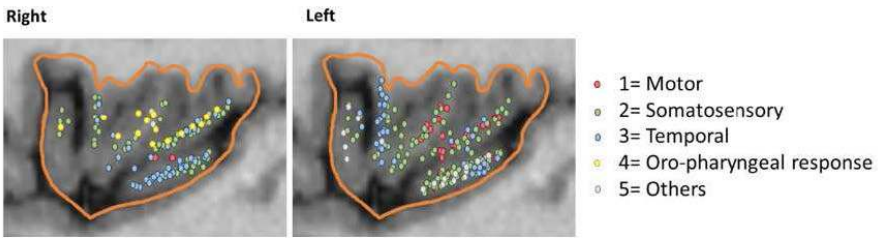

Figure1. Functional mappings by SEEG-guided electrical stimulation are presented.

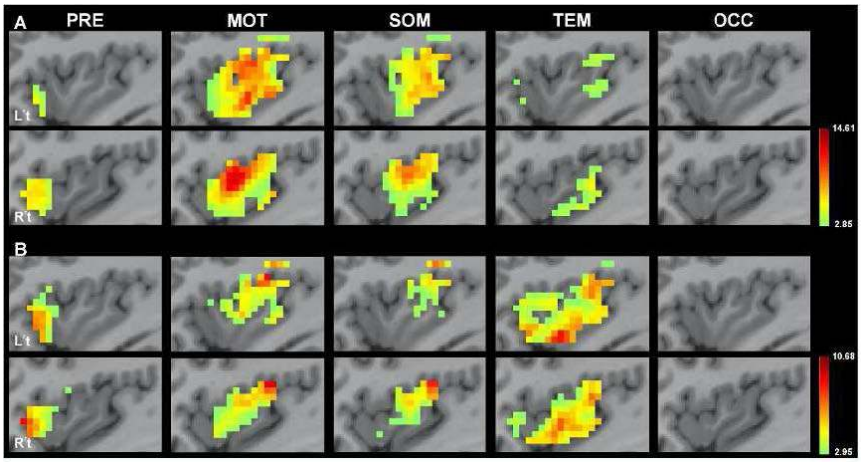

Figure2. Insular-cortical functional connectivity of normal controls (A) and non-insular onset DRE patients (B) are presented (P < 0.05 corrected for multiple comparison by false discovery rate).

Conclusions: Our study combined electrophysiological patterns with FC revealing functions of the insula. Epilepsy with a non-insular onset still influences the epileptic network, including the insula, as evidenced by increased FC within the insula between the temporal lobe and motor cortex.

References

1. J Bancaud, et al. (1969). 'Functional stereotaxic exploration (stereo-electroencephalography) in epilepsies', Rev Neurol (Paris), vol. 120(6), pp. 448
2. Lesser RP et al. (1987). 'Extraoperative cortical functional localization in patients with epilepsy', J Clin Neurophysiol, vol. 4(1), pp. 27–53
3. Kurth F et al. (2010). 'A link between the systems: functional differentiation and integration within the human insula revealed by meta-analysis', Brain Struct Funct, vol. 214, pp. 519-34
4. Hale JR et al. (2015). 'Comparison of functional thalamic segmentation from seed-based analysis and ICA', Neuroimage, vol. 114, pp. 448-465

Poster No 1803

Macroscale angioarchitectural properties of functional and structural networks

Stefano Moia[1], Omer Faruk Gulban[2], Enrico Amico[3], Maria Preti[4], Benedikt A. Poser[5], Dimo Ivanov[5]

[1]Maastricht University, Maastricht, Linburg, [2]Maastricht University, Maastricht, Netherlands, [3]Ecole Polytechnique Federale de Lausanne, Lausanne, Switzerland, [4]University of Geneva, Geneva, Geneva, [5]Maastricht University, Maastricht, Limburg

Introduction: Research with concurrent BOLD fMRI and physiological recordings showed cortical areas correlating with synchronous physiological fluctuations[1,2]; such vascular networks seem to support related functional network activity[2]. Translated to anatomy, capillaries should support neighbouring neurons, with vascular density correlating with neuronal activity[3,4]. We aim at verifying whether angioarchitecture relates to structural connectivity (SC), function-structure coupling (via structural decoupling index, SDI)[5], and total, coupled, and decoupled functional connectivity (FC)[6].

Methods: Data from the Human Connectome Project's (HCP) 100 independent subjects release were preprocessed as per[5]. Resting State (RS) timeseries and diffusion data were used to compute SDI, and node strength (NS) of SC (SCNS) and total, coupled, and decoupled FC (FCNS)[6] within the Glasser atlas (360 parcels) with nigsp[7]. The VENAT atlas[8] density map was adopted to mimic average venous-dominated vascular density for each parcel. The thresholded (.04) VENAT tissue probability map was used to compute average geodesic distance of each parcel from vessels using LayNii. The nodal spatial correlation of all metrics was computed. Preprocessed T1w, T2w, and Time of Flight (ToF) images from the Natural Scenes Dataset[9] (NSD) subject 1 were brain-extracted and their intensity folded on a 2D plane onto which manual clustering was carried out to extract vascular positions with Segmentator[10]. This mask, arteries-dominated, was further manually corrected. Preprocessed fibre tracts and RS timeseries were processed matching steps described above.

Results: Figure 1 shows the metric distributions for the HCP (top) and NSD data (bottom) in the Galsser atlas. Figure 2 shows nodal correlation between different measures for HCP (left) and NSD (right). Nodal correlation between SCNS and all FCNSs is comparable in both datasets. While HCP data feature stronger correlation between FCNS and SCNS and weaker correlation between FCNS and decoupled FCNS than NSD data, the most prominent differences lay in the correlation of FCNS and SCNS with vascular metrics. In HCP data, FCNS weakly but positively correlates with vascular density and negatively with vascular

distance and SDI shows the opposite, suggesting a tendency for areas with more prominent FC to maximise on blood supply redundancy by increasing vascular density and maximise efficiency by lowering the distance from major vessels, in line with previous hypotheses[4]. We expected coupled FCNS to feature strong correlations with vascular properties: coupled FC embeds non-idiosyncratic characteristics of functional organisation[6]. Instead, we found negligible correlation with vascular density and low correlation with vascular distance. In NSD data, correlations of all metrics with vascular properties based on VENAT are negligible, except a weak positive correlation between SDI and vascular distance. Vascular distance based on the subject vascular map weakly correlates negatively with SDI and positively with FCNS and decoupled FCNS. Such opposite relationship of SC and FCs with vascular distance based on VENAT or on the subject-specific vascular map could be attributed to the different nature of the two sets of vessels, venous in the former case and arterial in the latter, being the BOLD contrast mainly a venous effect. The difference between NSD and HCP results indicate how idiosyncratic vascular properties can be.

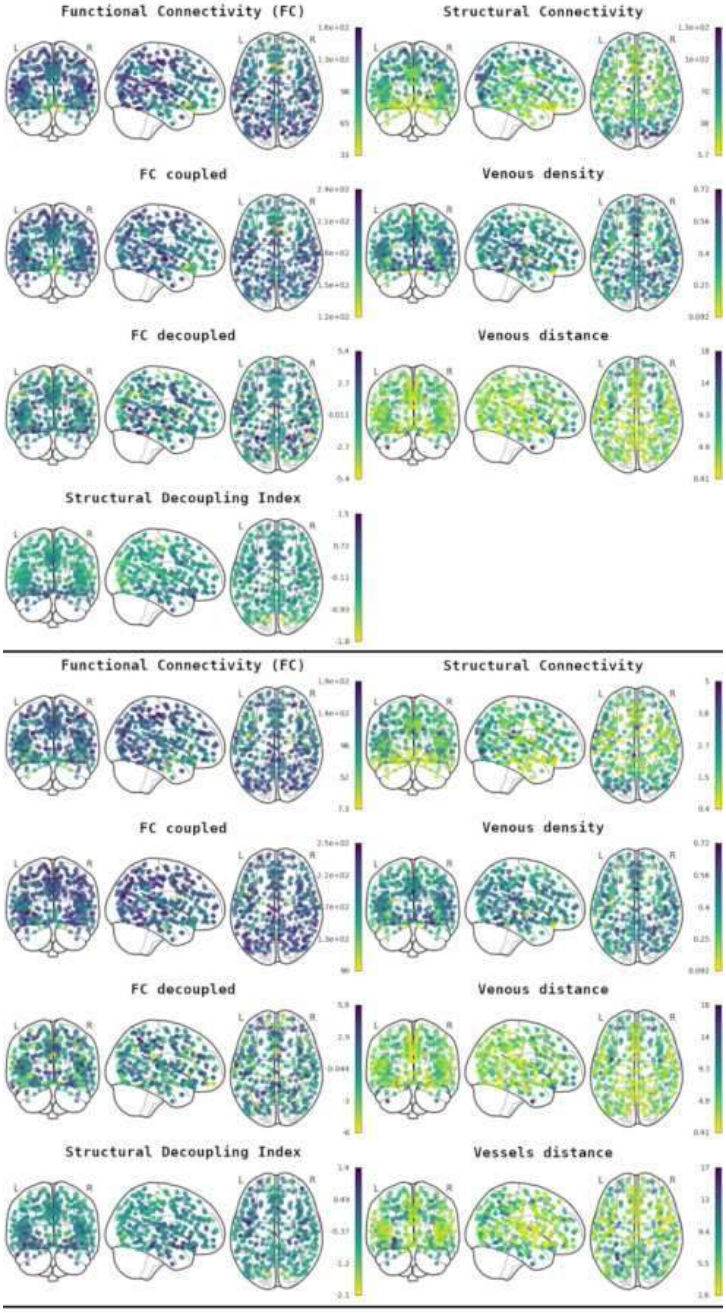

Figure 1 top: Glass brain representation of the group average FC(s) and SC Node Strengths, and SDI (HCP data), as well as veins-dominated vascular density and distance (VENAT atlas).
Figure 1 bottom: Glass brain representation of the single-subject FC(s) and SC Node Strengths, SDI, and arteries-dominated vascular distance (NSD data), as well as veins-dominated vascular density and distance (VENAT atlas).

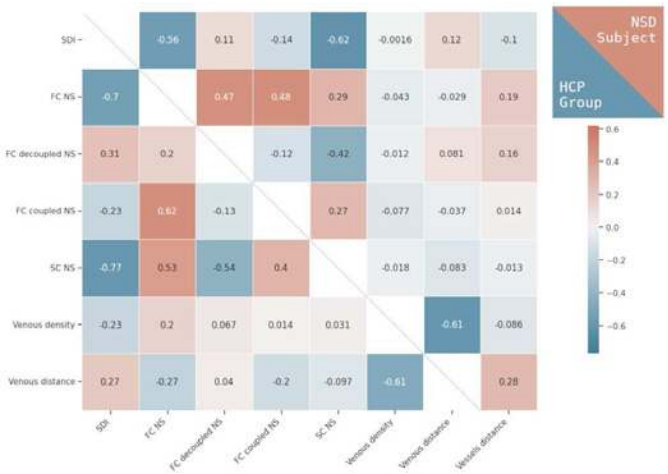

Figure 2: Nodal spatial correlation of connectivity and vascular measures in the two datasets. Upper triangle: NSD data, lower triangle: HCP data. Note the similarity of connectivity correlation across the two datasets, the correlation between veins-dominated vascular properties, FC, and SDI in the HCP dataset but not in the NSD dataset, and the inverse correlation with arteries-sominated vascular properties in the NSD dataset.

Conclusions: Our results provide motivation to suggest to better differentiate and further investigate the type of vasculature (arterial vs. venous) that relate with BOLD-fMRI FC, while paying attention to idiosyncrasies of vascular properties.

References

1. Chen, J. E., Lewis, L. D., Chang, C., Tian, Q., Fultz, N. E., Ohringer, N. A., ... Polimeni, J. R. (2020). Resting-state "physiological networks." NeuroImage, 213(March), 116707. https://doi.org/10.1016/j.neuroimage.2020.116707
2. Bright, M. G., Whittaker, J. R., Driver, I. D., & Murphy, K. (2020). Vascular physiology drives functional brain networks. NeuroImage, 217. https://doi.org/10.1101/475491
3. Harel, N., Bolan, P. J., Turner, R., Ugurbil, K., & Yacoub, E. (2010). Recent Advances in High-Resolution MR Application and Its Implications for Neurovascular Coupling Research. Frontiers in Neuroenergetics, 2(September), 1–8. https://doi.org/10.3389/fnene.2010.001
4. Woolsey, T. A., Rovainen, C. M., Cox, S. B., Henegar, M. H., Liang, G. E., Liu, D., ... Wei, L. (1996). Neuronal units linked to microvascular modules in cerebral cortex: Response elements for imaging the brain. Cerebral Cortex, 6(5), 647–660. https://doi.org/10.1093/cercor/6.5.647
5. Preti, M. G., & Van De Ville, D. (2019). Decoupling of brain function from structure reveals regional behavioral specialization in humans. Nature Communications, 10(1), 1–7. https://doi.org/10.1038/s41467-019-12765-7
6. Griffa, A., Amico, E., Liégeois, R., Van De Ville, D., & Preti, M. G. (2022). Brain structure-function coupling provides signatures for task decoding and individual fingerprinting. NeuroImage, 250(November 2021), 118970. https://doi.org/10.1016/j.neuroimage.2022.118970
7. Moia, S. (2022). NiGSP: A python library (and toolbox!) to run Graph Signal Processing on multimodal MRI data. Zenodo. https://doi.org/10.5281/ZENODO.6855998
8. Huck, J., Wanner, Y., Fan, A. P., Jäger, A. T., Grahl, S., Schneider, U., ... Gauthier, C. J. (2019). High resolution atlas of the venous brain vasculature from 7 T quantitative susceptibility maps. Brain Structure and Function, 224(7), 2467–2485. https://doi.org/10.1007/s00429-019-01919-4
9. Allen, E. J., St-Yves, G., Wu, Y., Breedlove, J. L., Prince, J. S., Dowdle, L. T., ... Kay, K. (2022). A massive 7T fMRI dataset to bridge cognitive neuroscience and artificial intelligence. Nature Neuroscience, 25(1), 116–126. https://doi.org/10.1038/s41593-021-00962-x
10. Gulban, O. F., Schneider, M., Marquardt, I., Haast, R. A. M., & De Martino, F. (2018). A scalable method to improve gray matter segmentation at ultra high field MRI. PLoS ONE (Vol. 13). https://doi.org/10.1371/journal.pone.0198335

Poster No 1804

Gradient-based framework for aging and risk factors

Chen Cheng[1], Xiuhui Chen[2], Samyogita Hardikar[3]

[1]Taiyuan University of Technology, Taiyuan, Shanxi, [2]Max Planck Institute for Human Cognitive and Brain Sciences, Leipzig, Germany, [3]Max Planck Institute for Human Cognitive and Brain Sciences, Department of Neurology, Leipzig, Germany

Introduction: In industrialized societies, blood pressure increases with age, and age-related declines in cardiovascular function may impair cerebral blood flow (CBF) regulation, leading to the disruption of neuronal micro-environmental homeostasis. In addition, previous researches found that aging is considered as a biological process affected by some risk factors such as bmi, ApoE genotype and smoke state. The integration of gradient concepts into fMRI neuroimaging approaches suggests that combining advanced fMRI with cortical gradients could enhance our understanding of brain aging and the pathogenesis of neurodegenerative disorders.

Methods: We will use data from the LIFE-Adult study, a population based cohort study with over 2500 selected participants from Leipzig Germany. The examination was completed in November 2014 and included questionnaires, anthropometry, blood measurements and MRI. The blood measurement was performed after an overnight fast. The study includes participants between 20 - 79 years of age. We plan to derive functional connectivity gradients for each participant via principal component analysis, which is an established technique to linearly reduce the dimensionality of large-scale connectivity data. Then we will use statistical analysis with linear regression models.

Results: The first three group-averaged gradients, projected from established functional communities into a 3D gradient space, were represented in left lateral and medial views. The word clouds representing the results from a meta-analysis to decode the most likely terms used to describe the pattern of gradient, where the size of the word represents the magnitude of the relationship, and the color represents the direction (warmer colors = positive relationship, cooler colors = negative relationship). We also find the association of gradient value with age and cardiovascular risk factors, controlling for sex and head motion.

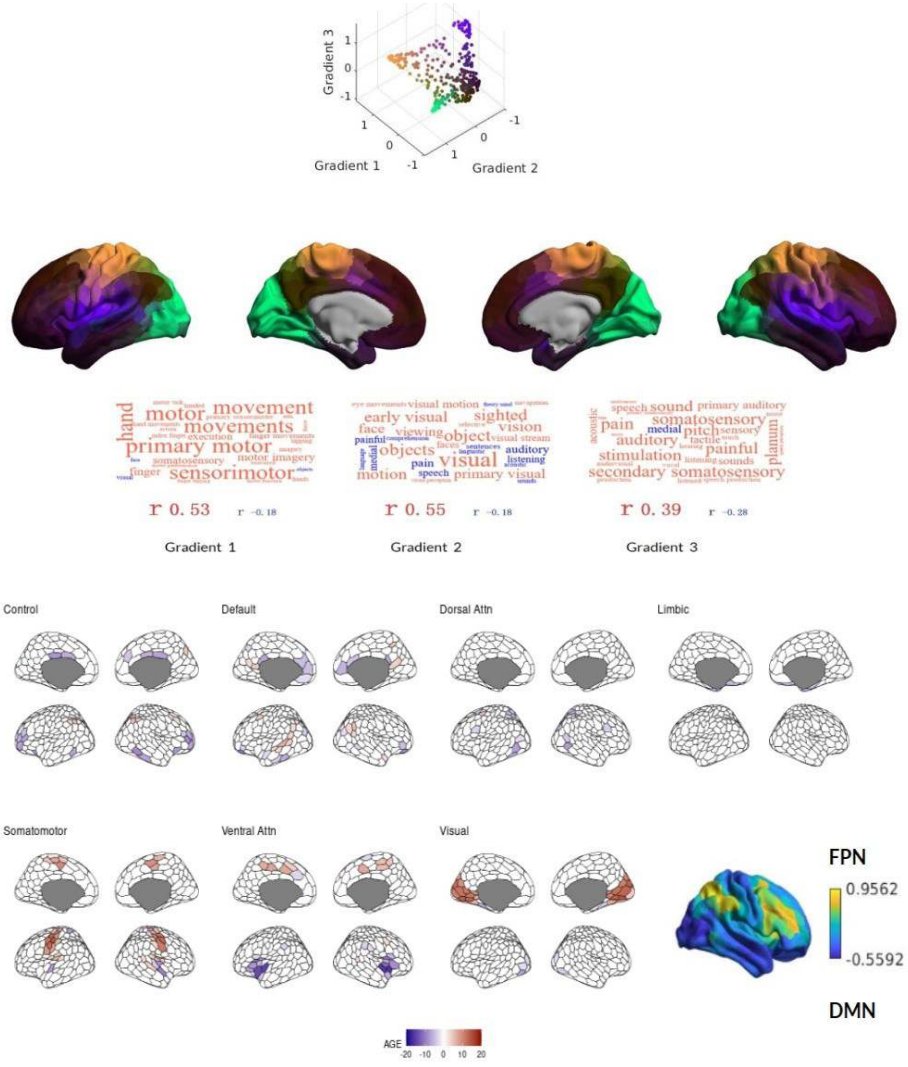

Conclusions: In summary, our study explored global functional gradient using 3D gradient spaces, unveiling compactly localized functional communities. We discovered associations with age, cardiovascular risk factors and the cognitive competence, adjusting for sex and head motion. These findings contribute valuable insights into the complex relationships between functional connectivity gradients and demographic and health factors.

References

1. Loeffler, Markus, Christoph Engel, Peter Ahnert, Dorothee Alfermann, Katrin Arelin, Ronny Baber, Frank Beutner et al. “The LIFE-Adult-Study: objectives and design of a population-based cohort study with 10,000 deeply phenotyped adults in Germany.” BMC public health 15, no. 1: 1-14(2015)

Poster No 1805

Comparing functional connectivity metrics from individualized and group average cortical networks

Diana Perez Rivera[1], Gretchen Wulfekuhle[2], Joanna Hernandez[1], Evan Gordon[3], Caterina Gratton[2,1]

[1]Northwestern University, Evanston, IL, [2]Florida State University, Tallahassee, FL, [3]Washington University, St. Louis, MO

Introduction: The brain is divided into multiple large-scale distributed systems or "networks". Network interactions within and across systems give rise to cognition and behavior. Past research has suggested that these interactions change systematically with age, with networks becoming relatively desegregated from one another (Chan et al., 2014). However, individuals vary widely in the topology of brain networks (Gordon et al., 2017), particularly of higher-order association systems (Seitzman et al., 2019). Yet, most existing research uses a priori network partitions based on a group average (typically from young adult data) to extract measures of functional networks. This approach, while convenient, can introduce further noise by combining signals from different networks when the individual networks deviate from the group average. Obtaining reliable representations of individual-specific network architecture, however, requires large amounts of data per subject; typically more data than is collected in most studies. Here, we compare measures of within- and between-network FC, and a derivative measure of network segregation in highly sampled younger and older adults, using both group-based and individualized networks.

Methods: We leveraged two precision fMRI datasets of younger (n = 16; ages 18-30) and older (n=8; ages 65-75) adults with >90 min. of high-quality rs-FC data per subject. Networks were defined in two ways: 1) based on a priori group-based partition (Gordon et al., 2016), and 2) based on each individual's rs-FC patterns (Gordon et al., 2017). The large amount of data per individual allowed us to produce highly-reliable representations of individual-specific networks. For each network partition, we extracted values for each individual of within-network FC and of between-network FC, and we calculated a segregation index. To determine how these metrics are influenced by individual differences in network topology, we used two-way ANOVAs with age-group and network partition as factors.

Results: Our results indicate that within-network FC shows a main effect of age-group ($p(FDR)<0.013$) and of network partition ($p(FDR)<0.013$). Younger adults showed greater within-network FC compared to older adults and within-network FC was higher when calculated based on individualized networks. Similarly, between-network FC showed a significant main effect of network partition ($p(FDR)<0.013$), where between-network FC was significantly higher when based on a group-based networks compared to individualized networks. Network segregation showed both a main effect of age-group ($p(FDR)<0.013$) and of network partition ($p(FDR)<0.013$). Older adults showed lower segregation index compared to younger adults, replicating previous results, and this pattern was present across both network partitions, though segregation indices were significantly higher for individualized networks.

Conclusions: Our results suggest that FC metrics in both younger and older adults are influenced by individual differences in network topology. In particular, within-network FC and its derivative, network segregation, differ significantly when calculated based on group-based networks compared to individual-specific networks. We attribute this difference to poor fit of group-average networks to individual brains that leads to non-homogenous FC measures.

References

1. Chan, M. Y., et al. (2014). Decreased segregation of brain systems across the healthy adult lifespan. Proceedings of the National Academy of Sciences, 111(46).
2. Gordon, E. M., et al. (2016). Generation and Evaluation of a Cortical Area Parcellation from Resting-State Correlations. Cerebral Cortex, 26(1), 288–303.
3. Gordon, E. M., et al. (2017). Precision Functional Mapping of Individual Human Brains. Neuron, 95(4), 791-807.e7.
4. Seitzman, B. A., Gratton, C., et al. (2019). Trait-like variants in human functional brain networks. Proceedings of the National Academy of Sciences, 116(45), 22851–22861.

Poster No 1806

Connectivity Correlates of Ataxia After Stroke

Asli Akdeniz-Karatay[1], Ana Sofía Ríos[2], Uchralt Temuulen[3], Ahmed Khalil[2], Anna Kufner[2]

[1]Max Planck Institute for Human Cognitive and Brain Sciences, Leipzig, Germany, [2]Center for Stroke Research Berlin (CSB), Berlin, Germany, [3]Freie Universität Berlin, Berlin, Germany

Introduction: Ataxia is a motor coordination impairment primarily related to cerebellar dysfunction.[1] About 50% to 65% of individuals with cerebellar stroke develop ataxia;[2] however ataxia can originate from non-cerebellar injury as well.[3] This could be explained by diaschisis, a term that describes functional impairment beyond focal brain damage in distant but connected

brain areas. The study of diaschisis has broadened the understanding of the intricate dynamics involved in neurological and psychiatric symptoms. Lesion Network Mapping (LNM) is a method for utilizing resting-state functional connectivity measurements to unveil brain circuits underlying symptoms that emerge after injury to the brain. Integrating normative connectome data with symptom mapping after stroke allows LNM to provide insights into the relationship between lesion-inclusive networks and symptoms, as has been shown in conditions like Parkinsonism and tics,[4,5] which can inform targets for neuromodulation therapies.[6] This could be useful for post-stroke ataxia since no treatments for this condition have been approved by the FDA.[6] This study aims to identify a network of functionally interconnected brain regions associated with post-stroke ataxia.

Methods: Here, we retrospectively analyzed a cohort of 380 patients with acute ischemic stroke (140 female, mean age: 65.8 ± 13.4 years) who underwent neurological examination through the National Institutes of Health Stroke Scale (NIHSS).[7] Limb ataxia, specifically assessed using item 7 of the NIHSS scale, was evaluated on both sides through the finger-nose-finger and heel-shin tests, scoring dependent on its manifestation to a degree disproportionate to weakness. For LNM, the stroke lesions were manually delineated from DWI images of the subjects and registered to common space according to Montreal Neurological Institute (MNI152 atlas, 2 × 2 × 2 mm) using the FSL FLIRT function. The resulting lesion masks were used as seeds to calculate functional connectivity from the lesion to every other voxel in the brain, based on a normative connectome from rs-fMRI data from 1,000 healthy subjects,[8] using the lead-mapper tool from lead-dbs.org.[9] The significance of the connections was validated by a non-parametric approach, using randomise from the FSL software.[10] Ataxia scores (NIHSS, item 7) were transformed into binary variables to accommodate cases with or without ataxia and used as the independent variable, while connectivity profiles were used as the dependent variable. Two contrasts were established to compare connectivity to lesions causing ataxia(i) and to lesions not causing ataxia (ii), n=67 and n=313, respectively. We applied the family-wise error rate (FWE) to correct for multiple comparisons. To identify significant connections for each group, regions with $p<0.05$ were considered.

Results: The connections to lesions of patients with ataxia were distributed across all vascular territories of the brain. A map of connectivity to each group was obtained; after thresholding to $pFWE<0.05$ to isolate the significant voxels connected to each group, we found that lesions associated with ataxia were mainly connected to the cerebellum, specifically to Crus I and II, as well as lobule VI in both hemispheres. The group without ataxia lesions showed connectivity to the primary motor cortex, premotor areas, and somatosensory cortex.

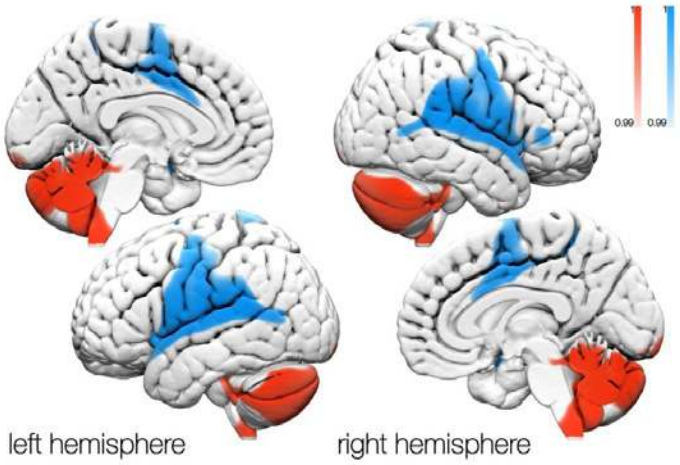

Strongest connections to lesions associated with ataxia after stroke. 3D surface of the brain showing areas most connected to patients with ataxia after stroke ($p < 0.01$) in red, in contrast to patients who did not develop ataxia after stroke ($p < 0.01$) in blue

Conclusions: In conclusion, this study reveals that brain lesions in variable vascular territories of the brain are functionally connected to cerebellar lobules, underlying the importance of this brain structure in ataxic symptoms, providing insights for potential neuromodulatory therapies by understanding the impact of stroke on cortico-cerebellar networks. The study also found that the commonly used NIHSS can detect indirect cerebellar damage effectively.

References

1. Ashizawa T, Xia G. (2016) Movement Disorders, 1208-26.
2. Go S. (2015). Posterior Circulation Ischemic Stroke. 112(3):192-6.
3. Fukutake T. et al. (2023). 63(4):201-208
4. Joutsa J, Horn A, Hsu J, Fox MD. (2018) Brain J Neurol. 141(8):2445-245
5. Ganos C, Al-Fatly B, Fischer JF, et al. (2020) Brain J Neurol. 145(12):4385-4397.
6. Grimaldi G et al. (2014).Cerebellum.13(1):121-38.

7. Malsch C et al. (2018) Outcome after stroke attributable to baseline factors—The PROSpective Cohort with Incident Stroke (PROSCIS). PLOS ONE. e0204285.
8. Holmes, A., Hollinshead, M., O'Keefe, T. et al. (2015). Sci Data 2, 150031.
9. Neudorfer C, Butenko K, Oxenford S, Rajamani N, Achtzehn J, Goede L, Hollunder B, Ríos AS, Hart L, Tasserie J, Fernando KB, Nguyen TAK, Al-Fatly B, Vissani M, Fox M, Richardson RM, van Rienen U, Kühn AA, Husch AD, Opri E, Dembek T, Li N, Horn A. (2023). Neuroimage 268:119862.
10. Eklund A, Nichols TE, Knutsson H. (2016). Proc Natl Acad Sci. 113(28):7900-7905.

Poster No 1807

Topological brain connectomics for task decoding, brain fingerprinting, and behavioral association

Andrea Santoro[1], Federico Battiston[2], Maxime Lucas[3], Giovanni Petri[4], Enrico Amico[5]

[1]Ecole Polytechnique Fédérale de Lausanne, Geneva, Geneva, [2]Central European University, Vienna, Vienna, [3]CENTAI, Turin, Turin, [4]Northeastern University London, London, London, [5]Ecole Polytechnique Federale de Lausanne, Lausanne, Switzerland

Introduction: Traditional models depict human brain activity as a network of pairwise interactions, commonly utilizing functional connectivity (FC). Recent approaches challenge these models by inferring higher-order interactions (HOIs) involving three or more regions from temporal brain signals. This study evaluates whether methods based on inferred HOIs outperform traditional pairwise ones for fMRI data analysis, using a topological approach capable of reconstructing HOI structures in time[1].

Methods: Our method builds on prior work with edge-level signals and extends functional connectivity research beyond pairs[2,3]. It leverages low-order signals to define higher-order ones in four key steps[1], illustrated in Fig. 1(a-d). (i) We standardize the N original fMRI signals through z-scoring; (ii) Compute all possible k-order time series as element-wise products of k + 1 of these z-scored time series, further z-scored for cross-k-order comparability. These k-order time series represent instantaneous co-fluctuation magnitudes of associated (k + 1)-node interactions, like edges and triangles. We assign a sign to the resulting k-order time series at each time based on a strict parity rule: positive for fully concordant group interactions, and negative for discordant interactions. (iii) For each time t, we encode all instantaneous k-order (co-fluctuation) time series into a weighted simplicial complex. Finally, at each time t, we apply computational topology tools to analyze weights of the simplicial complex and extract two local indicators. We aim to assess the performance of higher-order local indicators in different applications, relying on fMRI data of the 100 unrelated subjects from HCP[4].

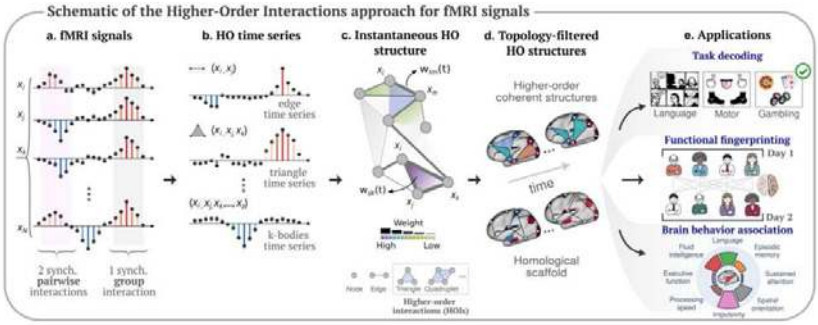

FIG. 1. **Higher-order brain mapping: schematic of the approach and applications. (a)** We start from fMRI brain data, which can be encoded into brain signals (i.e., Blood Oxygen Level Dependent (BOLD) fluctuations) from N regions. Signals can encode synchronized pairwise interactions (highlighted in light purple) and group interactions (highlighted in gray). **(b)** After reconstructing the co-fluctuation time series at each group order (i.e., edges, triangles, k-bodies, etc), **(c)** our instantaneous topological framework enables a time-resolved exploration of the significance of group interactions in comparison to pairwise interactions, encoded within a simplicial structure, using topological data analysis tools. **(d)** From this structure, we then extract instantaneous snapshots of brain dynamics in terms of two different topological structures, namely, the higher-order coherent structures and the homological scaffold. **(e)** To gain more insights into the importance of these higher-order structures during rests or cognitive tasks, we consider three different neuroscience applications, such as: fMRI task decoding, functional brain fingerprinting, and brain-behavior association.

Results: We tested our approach on three brain applications: task decoding, functional brain fingerprinting, and brain-behavior association (two shown). This assessment ran parallel to traditional brain network techniques, including node[5] and edge functional connectivity[2], aiming to unveil the advantages of higher-order methods. For BOLD, edges, triangles, and scaffold signals, we constructed time-time correlation matrices, obtained when concatenating resting-state and seven task fMRI datasets, excluding rest blocks. We then binarized at the 95th percentile, and applied the Louvain algorithm[6] to identify communities. To assess community partitions' effectiveness in decoding task and rest timings, we used the element-centric similarity (ECS) measure[7]. ECS values between 0 and 1 indicate task decoding quality. In Fig. 2, we present the results of computing local higher-order topological indicators on resting-state and task-related fMRI data of HCP[8]. Violating

triangles and homological scaffolds time-time plots effectively decoded individual tasks and rest blocks. In particular, task differentiability increases as we transition from lower-order methods to higher-order ones, as evidenced by the decrease in ECS values (Fig. 2a-d). We conducted Partial Least Square Correlation (PLSC) analyses to evaluate brain-behavior association when considering static connectivity values (FC, eFC, triangles, scaffold) and ten cognitive scores from HCP subjects. When considering whole-brain connections, all four methods performed similarly, explaining brain-behavior covariance within the 10%-20% range (Fig. 2e). By contrast, focusing on connections within specific resting-state functional subsystems (Fig. 2f), distinctions became noticeable. Transitioning from lower-order methods to higher-order ones, such as triangles or scaffolds, resulted in a sharp increase in brain-behavior associations, particularly for somatosensory areas, with triangles reaching approximately 80% of the covariance explained.

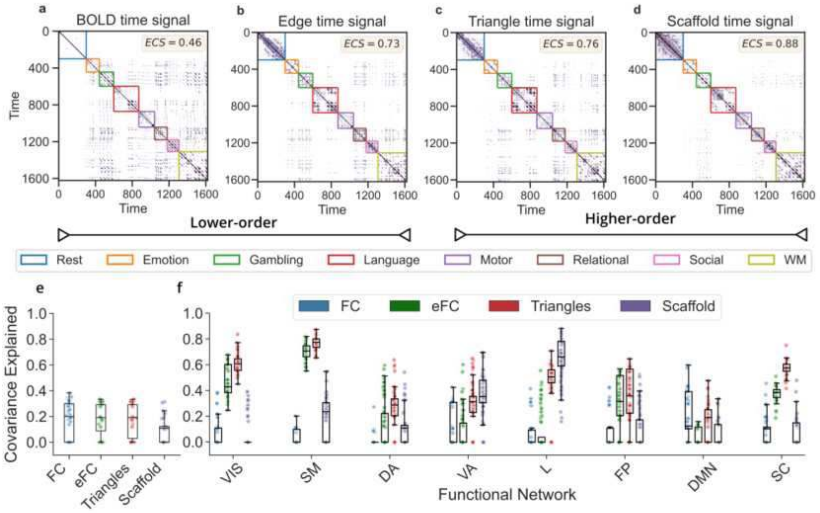

FIG. 2. **Higher-order topological indicators for fMRI task differentiability and brain-behavior association.** (**a**) We compare *local* observables by comparing the temporal recurrence plots (i.e. time-time correlation matrices) for the four methods, from the lower-order ones (BOLD and edge signals) to the higher-order methods (triangle and scaffold time signals). We set a common threshold at the 95th percentile to binarize the data when analyzing an fMRI temporal signal obtained by concatenating resting-state and seven HCP tasks. Colored boxes within the plots denote the ground truth of rest and task segments. When comparing the communities identified with the Louvain algorithm [6] against the ground truth partition, we observed that higher-order methods are able to temporally discriminate the different task blocks better than lower-order ones, as reflected by the higher values of the element-centric similarity (ECS) measure. Results are averaged over the 100 subjects, considering the mean between LR and RL phase encoding. (**e**) Percentage of brain cognition covariance explained by significant multivariate correlation components ($p < 0.05$) obtained from PLSC analyses between the whole-brain functional connections extracted from the different methods and 10 cognitive scores. PLSC components were independently assessed for each method. To obtain a more robust estimate of the covariance explained, we consider a bootstrap procedure randomly subsampling 80 subjects from the total of 100 and repeating the PLSC analysis 100 times. On a whole-brain level, no differences are noticeable. (**f**) We repeat the same PLSC analysis considering only the functional connections extracted from the different methods within specific functional networks (i.e. all interactions between nodes of the same network). Remarkably, higher-order methods perform better in terms of covariance explained, reaching 80% in somatosensory areas.

Conclusions: Overall, our analysis demonstrates that higher-order indicators, extracted from instantaneous topological descriptions of the data, outperform traditional node and edge-based methods[2,3] in task decoding and provide a more robust association between brain activity and behavior.

References

1. A. Santoro, F. Battiston, G. Petri, and E. Amico, Nature Physics 19, 221 (2023), ISSN 1745-2481.
2. J. Faskowitz, F. Z. Esfahlani, Y. Jo, O. Sporns, and R. F. Betzel, Nature Neuroscience 23, 1644 (2020), ISSN 1546-1726.
3. F. Z. Esfahlani, Y. Jo, J. Faskowitz, L. Byrge, D. P. Kennedy, O. Sporns, and R. F. Betzel, Proceedings of the National Academy of Sciences 117, 28393 (2020), ISSN 0027-8424, 1091-6490.
4. D. C. Van Essen, S. M. Smith, D. M. Barch, T. E. Behrens, E. Yacoub, K. Ugurbil, W.-M. H. Consortium, et al., Neuroimage 80, 62 (2013).
5. O. Sporns, G. Tononi, and R. Kötter, PLoS Computational Biology 1, e42 (2005), ISSN 1553- 734X.
6. V. D. Blondel, J.-L. Guillaume, R. Lambiotte, and E. Lefebvre, Journal of Statistical Mechanics: Theory and Experiment 2008, P10008 (2008), ISSN 1742-5468.
7. A. J. Gates, I. B. Wood, W. P. Hetrick, and Y.-Y. Ahn, Scientific Reports 9, 8574 (2019), ISSN 2045-2322.
8. D. C. Van Essen, K. Ugurbil, E. Auerbach, D. Barch, T. E. J. Behrens, R. Bucholz, A. Chang, L. Chen, M. Corbetta, S. W. Curtiss, et al., NeuroImage 62, 2222 (2012), ISSN 1053-8119.

Poster No 1808

Theta-alpha aperiodic dynamics covary with persistence homological scaffolds of hemodynamic networks

Nghi Nguyen[1], Tao Hou[2], Li Shen[3,4], Duy Duong-Tran[4,5]

[1]Gonda Multidisciplinary Brain Research Center, Bar-Ilan University, Ramat Gan, Israel, [2]Department of Computer Science, DePaul University, Chicago, IL, [3]Department of Biostatistics, Epidemiology and Informatics, University of Pennsylvania, Philadelphia, PA, [4]Perelman School of Medicine, University of Pennsylvania, Philadelphia, PA, [5]Department of Mathematics, United States Naval Academy, Annapolis, MD

Introduction: Cortical aperiodic dynamics have recently gained growing interest due to their implicated roles in cognition, consciousness, aging, diseases, and their relevance in theoretical neuronal network models (Gerster, 2022). Several studies have associated such dynamics with resting-state BOLD signals (Jacob, 2021); however, mechanistic models explaining how that association emerges across cortical regions are still inconclusive. This study proposes that the missing element might lie in regional contributions to maintaining the topological structure of the hemodynamic network, especially how these contributions change between resting and excited states. To quantify these contributions, we used persistence strength scaffold centrality (PC) (Lord, 2016) derived from weight-optimal cycles in persistent homology.

Methods: We used the resting-state and task-based 3T fMRI data from the Human Connectome Project Young Adult dataset (Van Essen, 2013) and curated and preprocessed by the Neuromatch Academy (‘t Hart, 2022). We focused on motor and working memory tasks and the following task conditions: left-hand, right-hand, left-foot, right-foot for motor, and 0-back faces, 0-back tools, 2-back faces, and 2-back tools for working memory. Each sample (n=318) represents the Glasser-parcellated BOLD signals of each subject recorded either at rest or during tasks. Functional connectivity maps are obtained by taking the Pearson correlation coefficients between BOLD time series of every pair of regions. From each functional connectivity map, we produced a homological scaffold matrix following the pipeline described by Lord (2016) with Vietoris-Rips filtration to track the persistence of cycles. The group-average scaffold matrix for each task condition (and one for the resting state) was used to calculate regional PCs under that task condition (and the resting state). We also computed degree centrality (DC) vectors from the group-average functional connectivity maps for comparative purposes. To test the relationship between the centrality models and their electromagnetic correlates while ensuring generalizability, we use MEG data from the same HCP dataset under the same task conditions but with different subjects (n = 20). We performed source reconstruction using an LCMV beamformer on BEM surfaces, applied Glasser parcellation, epoched by stimulus onset, and averaged the signals across trials. For the signal from each region, we ran the IRASA algorithm (Wen, 2016) to extract aperiodic activity from 1 Hz to 90 Hz.

Results: By comparing task-evoked changes in PC and those in DC, or ΔPC and ΔDC, respectively, we observed that ΔPC was more correlated with changes in cognitive demand than with the nature of the task, while DC was task-specific (Figure 1). Spatial distributions of ΔPC could also be inferred from resting-state PC while exhibiting robust patterns, such as “sinks” concentrated in the Dorsal-Attention network and “sources” in the Auditory network and part of the Cingulo-Opercular network previously identified as the salience network (Ji, 2019). These observations coincide with aperiodic dynamic patterns outlined in previous fMRI-EEG studies (Jacob, 2021). Further corroborating this correlation, cosine similarities between ΔPC and changes in bandpower ratios (ΔBPRs) within the θ-α range were significantly higher than those between ΔBPRs and ΔDC (Figure 2).

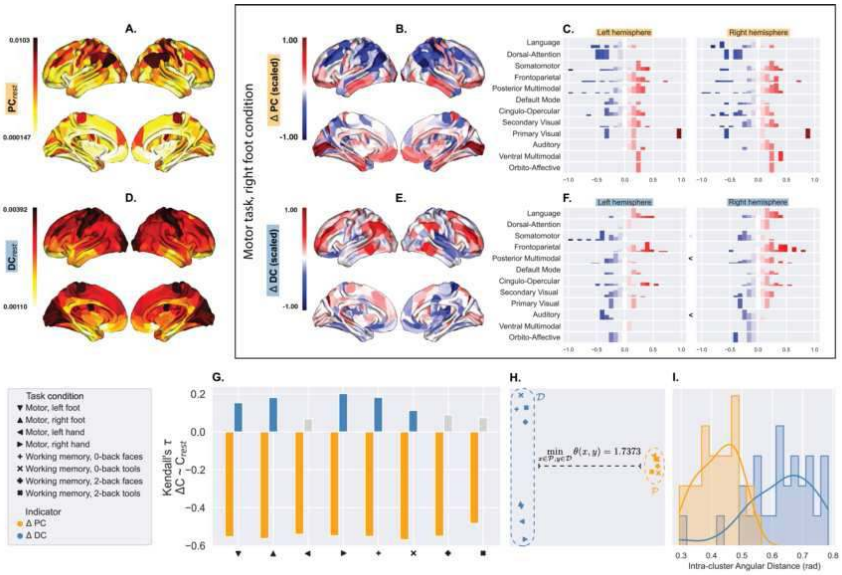

Figure 1. Resting state-subtracted PC (ΔPC) captures task-evoked hemodynamic patterns nonspecific to task conditions, whereas resting state-subtracted DC (ΔDC) is more condition-specific.
In Figures **A** and **D**, the spatial distributions of resting-state PC and DC are portrayed on a Glasser-parcellated surface. Figure **B** maps ΔPC—evoked by the motor task, right foot condition—to the same brain surface, showing a coarse-grained gradient of ΔPC on the global level starting from the deepest ΔPC sinks (in blue) in the dorsal areas to the sources in ventral regions (in red). Notably, this gradient does not exhibit a hemisphere preference (Figure **C**), as evidenced by similar distributions of sinks and sources across hemispheres for each functional network ($p >> 0.05/12$, Welch's t-test, Bonferroni corrected). Figures **E** and **F** demonstrate the ΔDC counterparts of figures **B** and **C**, respectively, revealing a different distribution of sinks and sources. Specifically, ΔDC sinks tend to favor the hemisphere contralateral to the body part engaged in the motor task (e.g., right foot). For instance, left regions in the Posterior Multimodal and Auditory networks display a statistically significant negative shift in ΔDC compared to their right counterparts ($p << 0.05/12$, Welch's t-test, Bonferroni corrected). The Somatomotor network shows a similar trend, although marginally significant (p = 0.0108).
Figure **G** demonstrates the relationship between resting-state PC (or DC) and ΔPC (or ΔDC) evoked by each task condition. All ΔPC vectors have strongly negative correlations with the resting-state PC ($p << 0.05/8$, Kendall's τ, Bonferroni corrected), while their ΔDC counterparts show weak or non-significant correlations. By performing metric multidimensional scaling using pair-wise angular differences, two clusters of ΔPC and ΔDC naturally emerge (figure **H**), between which the minimum angular difference is 1.7373 radians, *i.e.*, nearly orthogonal. Interestingly, ΔDC is composed of 2 sub-clusters, each of which represents response to either the motor or the working memory task. Figure **I** sketches the distributions of angular differences within each cluster, showing that spatial patterns of PC sinks and sources are more persistent across tasks and conditions than those of DC.

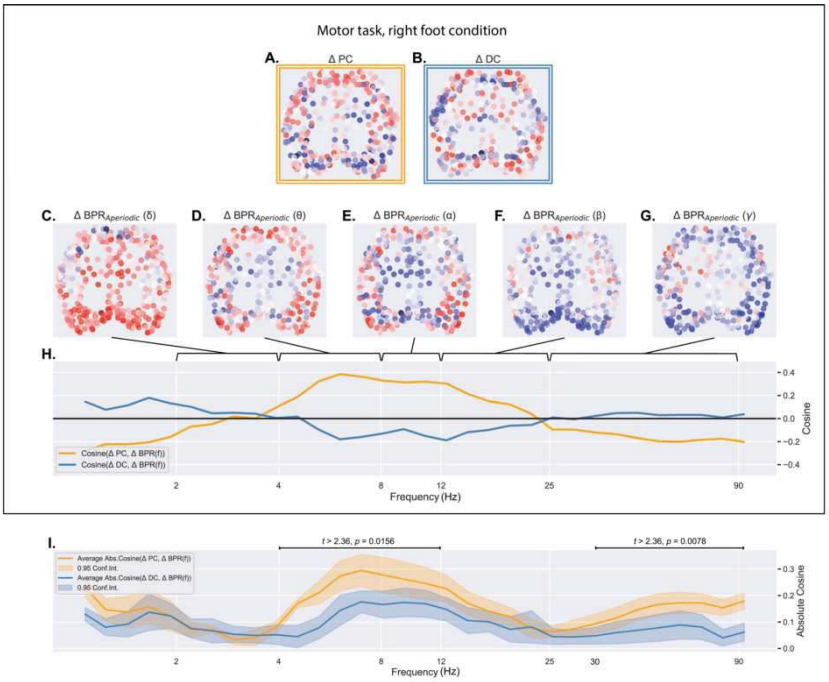

Figure 2. Regional alterations in bandpower ratio (Δ BPR) of cortical aperiodic activity within the θ-α range (4 - 12 Hz) exhibit a stronger alignment with ΔPC compared to ΔDC. Figures **A** and **B** present ISOMAP projections of ΔPC and ΔDC, respectively, evoked by right-foot cues during the motor task. These allow for a visual comparison with the Δ BPR of canonical bands (δ: 2-4 Hz, θ: 4-8 Hz, α: 8-12 Hz, β: 12-25 Hz, γ: 25-90 Hz), also projected using ISOMAP and depicted in figures **C** to **G**. Δ BPR was also computed for 32 frequency bands whose endpoints were logarithmically spaced within the range of 2 to 90 Hz. Cosine similarities between these Δ BPRs and ΔPC (orange) or ΔDC (blue) under the motor, right-foot condition are shown in figure **H**. Absolute cosine similarities averaged across conditions are shown in figure **I**, suggesting that ΔPC better predicts Δ BPRs in the θ-α and γ ranges (p = 0.0156 and p = 0.0078, respectively, cluster-based permutation paired t-test).

Conclusions: This study underscores the spatial and temporal correlation between cortical aperiodic dynamics in the θ-α range and PCs, i.e., levels of participation in cycles scaffolding the hemodynamic networks. This insight helps inform more precise BOLD deconvolution models that account for aperiodic activity, as well as a better mechanistic understanding of lower-level processes simultaneously giving rise to neuronal aperiodic dynamics and brain hemodynamics.

References

1. Gerster, M. (2022). Separating neural oscillations from aperiodic 1/f activity: challenges and recommendations. Neuroinformatics, 20(4), 991-1012.
2. Jacob, M. S. (2021). Aperiodic measures of neural excitability are associated with anticorrelated hemodynamic networks at rest: a combined EEG-fMRI study. NeuroImage, 245, 118705.
3. Ji, J. L. (2019). Mapping the human brain's cortical-subcortical functional network organization. Neuroimage, 185, 35-57.
4. Lord, L. D. (2016). Insights into brain architectures from the homological scaffolds of functional connectivity networks. Frontiers in systems neuroscience, 10, 85.
5. 't Hart, B. (2022). Neuromatch Academy: a 3-week, online summer school in computational neuroscience. Journal of Open Source Education, 5(49), 118.
6. Van Essen, D. C. (2013). The WU-Minn human connectome project: an overview. Neuroimage, 80, 62-79.
7. Wen, H. (2016). Separating fractal and oscillatory components in the power spectrum of neurophysiological signal. Brain topography, 29, 13-26.

Poster No 1809

Thalamic Hubness as a Predictor of Thalamocortical Connectivity Following Locus Coeruleus Activation

LiMing Hsu[1], Patricia Jensen[2], Yen-Yu Shih[1]

[1]University of North Carolina at Chapel Hill, Chapel Hill, NC, [2]NIEHS/NIH, RTP, NC

Introduction: The medial prefrontal cortex (mPFC) is robustly manipulated by the locus coeruleus noradrenergic neurons (LC-NE) and integrates a variety of inputs from limbic thalamus that give rise to goal-directed behaviors (i.e., cognitive and executive functions)[1–3]. To address how thalamus regulates the LC-NE-induced functional connectivity changes, we employed an intersectional chemogenetic approach[4] to modulate LC-NE activity in the mouse brain and examined functional connectivity (FC) and hubness scores using functional magnetic resonance imaging (fMRI). We found that LC-NE neuronal activity driven by chemogenetic stimulation most robustly decreased FC between prelimbic cortex (PrL) and mediodorsal thalamus (MD), and that this observed FC decreases were causally manipulated by baseline hubness of paraventricular thalamic nucleus (PVT). This work suggests a critical role of PVTs thalamus functional integration in regulating the subsequent LC-induced FC changes, which may help explain the individual difference in LC-related behaviors.

Methods: This study utilized transgenic mice with hM3Dq-DREADD receptors selectively expressed in Dbh+ NE neurons, targeting NE neuronal subpopulations in the LC[4]. The experiment involved three groups: LC-NE (n=9), Hoxb1-NE (n=8), and control mice (n=12). Each group was anesthetized and underwent fMRI both before and after chemogenetic stimulation with Clozapine-N-Oxide (CNO). The experimental design incorporated a 10-minute baseline and a subsequent post-CNO segment 20-30 minutes after administration. MRI data acquisition was conducted using a Bruker BioSpec 9.4-Tesla system. The preprocessing of the fMRI data followed protocols established in our previous study[1,2]. All animal procedures were approved from the Institutional Animal Care and Use Committee of the University of North Carolina at Chapel Hill.

Results: Modularity analysis[5] of the mPFC during resting state fMRI identified four functional modules: infralimbic cortex (IL), prelimbic cortex (PrL), anterior cingulate cortex (ACC), and posterior cingulate cortex (PCC) (Fig. 1a and 1b). Following CNO injection, the En1 group exhibited a significant FC reduction between the PrL module and mediodorsal MD, with the most notable effect observed at 30 minutes post-injection (Fig. 1c and 1d). Additionally, the LC-NE group also showed a notable decreasing trend in FC over time (Fig. 1e). Correspondingly, the enhanced green fluorescent protein (EGFP) tracer injections into MD and LH were in line with the peak FC changes identified by ANOVA, with projections to the PrL (Fig. 1f)[6]. To discern the thalamic region influencing mPFC-MD circuit changes, we assessed the thalamus's degree of centrality (DC)[7] at Baseline, identifying the PVT as a hub linked to PrL-MD FC changes (Fig. 2a). Linear mixed-effects (LME) models further confirmed a causal relationship between baseline DC and subsequent FC changes at multiple time points post-CNO (Fig. 2b). Force-directed graphs showed individual thalamic connectivity at Baseline, highlighting the highest, median, and lowest of mean DC in PVT (Fig. 2c). The global efficiency of PVT at Baseline was significantly correlated with PrL-MD FC changes at Post-30 (Fig. 2d) and showed higher global efficiency than other thalamic regions, confirming its hub status (Fig. 2e). These findings suggest that high DC in PVT is associated with its functional integration in the thalamus and contributes to the LC-NE induced decline in PrL-MD FC.

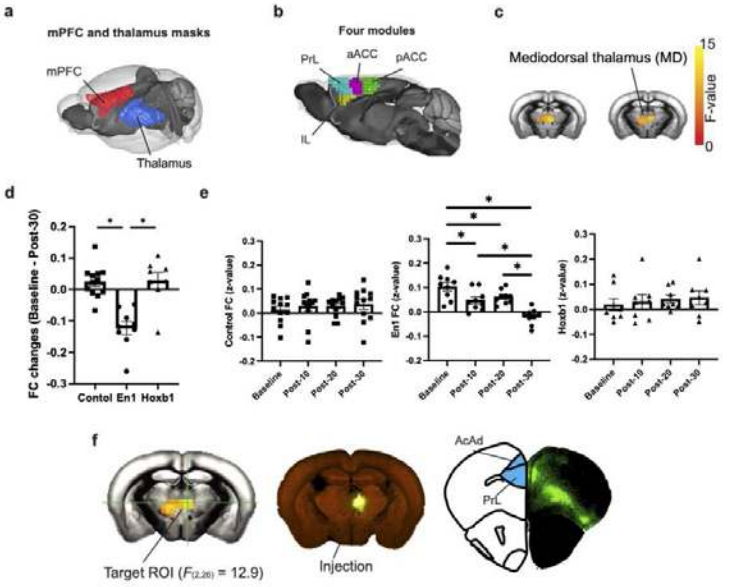

Figure 1(a) Medial prefrontal cortex (mPFC) and thalamus mask. (b) Four functional modules were identified in mPFC using modularity analysis. (c) Significant connection change was found between module of prelimbic cortex (PrL) and MD in thalamus of ANOVA analysis in three groups (En1, control, and Hoxb1). ($p_{corrected}$ < 0.05, 3dClustSim corrected) (c) Mean FC changes of the significant MD in thalamus in three groups. (d) Significant changes of PrL – MD FC were found in En1 group. (Repeated measurement ANOVA F-value = 17.17, p<0.001) while no significant change was found in Control and Hoxb1 groups. (Two sample paired t-test, * $p_{corrected}$<0.05) (e) Neuronal tracing data were adopted from the Allen Mouse Brain Connectivity Atlas. The tracer type is enhanced green fluorescent protein (EGFP) and injected into mediodorsal nucleus of thalamus (MD) lateral habenula (LH) and (https://connectivity.brain-map.org/projection/experiment/294356922, mouse ID: 294356922, volume: 0.086). The crossing green line indicated the peak point of ANOVA analysis ($F_{(2,26)}$ = 12.9) of FC changes in PrL – MD circuit among En1, Hoxb1, and Control.

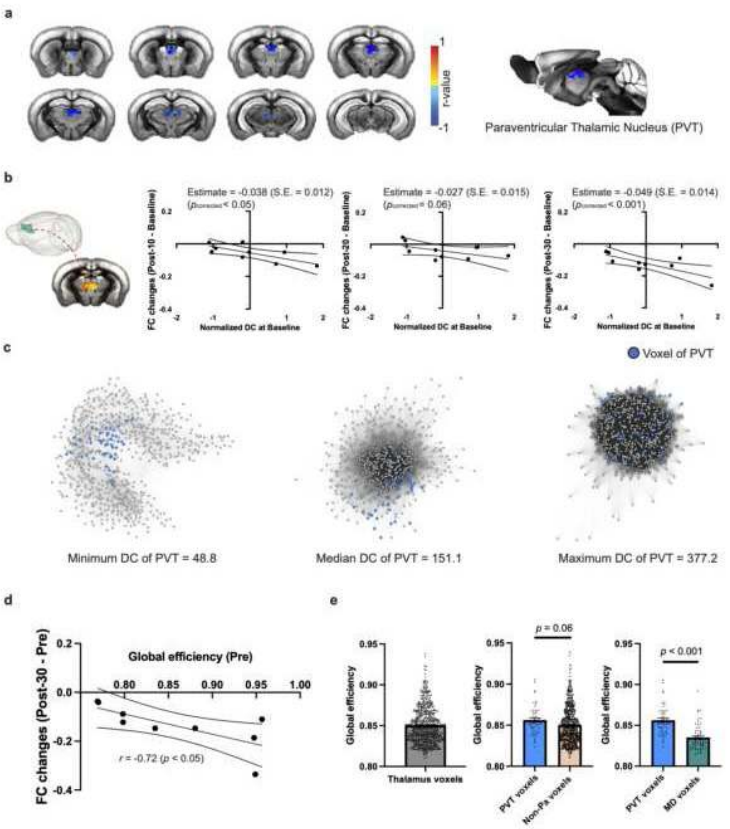

Figure 2 (a) Correlation between the degree of centrality (DC) within thalamus at Baseline and FC changes of PrL – MD circuit. ($p_{corrected}$ <0.05, 3dClustSim corrected, $p_{uncorrected}$ < 0.01, cluster size > 0.324 mm^3) (b) Path analysis shows the significantly causal relationship between the mean DC in identified PVT at Baseline and FC changes of PrL – MD circuit at Post-10 – Baseline, Post-20 – Baseline, and Post-30 – Baseline. (c) Force-directed graph shows the thalamus connection with maximum, median, and minimal mean DC of PVT. Each dot represents a voxel in thalamus, and blue dots show the voxel of PVT. Grey line represents the connection (z > 0.25) between each voxel. (d) Correlation between the mean global efficiency in identified PVT at Baseline and FC changes of PrL – MD circuit at Post-30 – Baseline. (e) The mean global efficiency in identified PVT voxels are higher global efficiency compared to other voxels in thalamus which approached the borderline of significance (p = 0.06) and to MD voxels (p <0.001).

Conclusions: The study elucidates the neuromodulatory role of the LC-NE system in thalamocortical connectivity, highlighting the predictive value of thalamic hubness, particularly of PVT, in LC-NE induced changes[8]. This research provides insights into the mechanisms underlying LC-NE modulation of cognitive functions, with potential implications for understanding disorders involving mPFC and LC-NE system dysfunctions[9,10].

References

1. Hsu, L.-M. (2016). Constituents and functional implications of the rat default mode network. Proceedings of the National Academy of Sciences USA, 113, E4541-7. 10.1073/pnas.1601485113.
2. Oyarzabal, E.A. (2022). Chemogenetic stimulation of tonic locus coeruleus activity strengthens the default mode network. Science Advances, 8, eabm9898. 10.1126/sciadv.abm9898.
3. Lapiz, M.D.S. (2006). Noradrenergic modulation of cognitive function in rat medial prefrontal cortex as measured by attentional set shifting capability. Neuroscience, 137, 1039–1049. 10.1016/j.neuroscience.2005.09.031.
4. Robertson, S.D. (2013). Developmental origins of central norepinephrine neuron diversity. Nature Neuroscience, 16, 1016–1023. 10.1038/nn.3458.
5. Maslov, S. (2002). Specificity and stability in topology of protein networks. Science 296, 910–913. 10.1126/science.1065103.
6. Oh, S.W. (2014). A mesoscale connectome of the mouse brain. Nature, 508, 207–214. 10.1038/nature13186.
7. Wu, G.-R. (2013). Mapping the voxel-wise effective connectome in resting state FMRI. PLoS ONE 8, e73670. 10.1371/journal.pone.0073670.
8. Pinto, A. (2003). Projections from the paraventricular nucleus of the thalamus to the rat prefrontal cortex and nucleus accumbens shell: ultrastructural characteristics and spatial relationships with dopamine afferents. Journal of Comparative Neurology, 459, 142–155. 10.1002/cne.10596.
9. Betts, M.J. (2019). Locus coeruleus imaging as a biomarker for noradrenergic dysfunction in neurodegenerative diseases. Brain, 142, 2558–2571. 10.1093/brain/awz193.
10. Friedman, J.I. (1999). The role of norepinephrine in the pathophysiology of cognitive disorders: potential applications to the treatment of cognitive dysfunction in schizophrenia and Alzheimer's disease. Biological Psychiatry, 46, 1243–1252. 10.1016/s0006-3223(99)0023

Poster No 1810

The role of brain structural connectivity in resting-state networks in fMRI data

Shreyas Harita[1,2], Davide Momi[2], John Griffiths[2,3]

[1]Institute of Medical Science, University of Toronto, Toronto, ON, Canada, [2]Centre for Addiction and Mental Health, Toronto, ON, Canada, [3]Department of Psychiatry, University of Toronto, Toronto, ON, Canada

Introduction: Introduction Resting-state brain activity, as observed through functional magnetic resonance imaging (fMRI), reveals structured neural patterns and resting-state networks (RSNs)[1]. These RSNs, such as visual (VIS), somatomotor (SMT), dorsal attention (DAN), ventral attention (VAN), limbic (LIM), frontoparietal (FPN), and default mode (DMN) networks, consistently emerge in individuals across different contexts[2]. While RSNs' functional connectivity varies, structural connectivity (SC) remains relatively stable and underlies neural coordination[3]. Present Study This study explores the influence of brain structural connectivity (SC), on the existence and interactions of RSNs. Specifically, we examine how inter-network connections affect functional connectivity within and between these networks and investigate how these networks communicate based on their SC.

Methods: Methods We computed SC matrices for 200 randomly selected subjects from the Human Connectome Project[4] using diffusion-weighted imaging data and preprocessing software, including FSL[5], MRtrix3[6], and FreeSurfer[7]. To model mesoscopic brain activity, we utilized the dynamic mean field (DMF) model, characterizing each network node with excitatory and inhibitory neural masses[8,9]. We implemented our brain network model using the WhoBPyT library[10], enabling gradient-based parameter optimization via the ADAM algorithm. This approach bridges physiological brain network models with deep recurrent neural networks. After confirming the replication of resting-state fMRI (rs-fMRI) time series, we selectively lesioned structural connectivity to isolate the seven RSNs. Our goal was to explore how network isolation impacts the relationships between networks, primarily focusing on average functional connectivity (FC) and average SC communicability.

Results: Results Our results reveal a clear distinction between two network groups: lower order networks (LONs) and higher order networks (HONs). LONs encompass VIS, SMT, DAN, and VAN, while HONs include LIM, FPN, and DMN. Following LON lesions, average FC within LONs decreased significantly by 29.2%, with a 12.4% decrease in FC between LONs. Changes between LONs and HONs were not significant. For HON lesions, there was a significant 8.9% decrease in average FC within HONs, while FC between HON networks remained stable. LIM and FPN lesions had no significant effect on FC between HONs and LONs. However, a DMN lesion led to a significant 2.3% increase in average FC within and between LON networks. Regarding SC communicability, we observed a significant reduction within and between LONs and HONs, regardless of whether a LON or HON was lesioned. Following LON lesions, average SC communicability within LONs decreased by 6.9%, with a 2.5% decrease between LONs and a 1.9% decrease between LONs and HONs. HON lesions resulted in an 8.4%

decrease in average SC communicability within HONs, along with a 4.0% decrease between HONs and a 2.9% decrease between HONs and LONs.

Conclusions: Conclusions Our findings provide insights into the emergence and interactions of RSNs in the context of structural connectivity. LON networks exhibit strong interconnections, leading to reduced FC and SC communicability when one LON network is lesioned. Conversely, HON networks appear to operate independently and display limited interdependence among HON networks. This divergence may be attributed to the nature of LON and HON networks. LONs process unimodal information, fostering interactions with similar networks, while HONs are multimodal, processing diverse information[11]. Furthermore, this decrease in FC following network lesioning,particularly for LONs, can also be attributed to reduced SC communicability, affecting efficient information propagation. Our study introduces a novel hypothesis regarding the role of structural connectivity in shaping RSN existence and interactions in fMRI data, contributing to the understanding of brain network dynamics.

References

1. Biswal B, Yetkin FZ, Haughton VM, Hyde JS. Functional connectivity in the motor cortex of resting human brain using echo-planar MRI. Magn Reson Med. 1995;34(4):537-541.
2. Rosazza C, Minati L. Resting-state brain networks: literature review and clinical applications. Neurol Sci. 2011;32(5):773-785.
3. Seguin C, Sporns O, Zalesky A. Brain network communication: concepts, models and applications. Nat Rev Neurosci. Published online July 12, 2023. doi:10.1038/s41583-023-00718-5
4. Van Essen DC, Ugurbil K, Auerbach E, Barch D, Behrens TEJ, Bucholz R, et al. The Human Connectome Project: a data acquisition perspective. Neuroimage. 2012;62(4):2222-2231.
5. Andersson JLR, Sotiropoulos SN. An integrated approach to correction for off-resonance effects and subject movement in diffusion MR imaging. Neuroimage. 2016;125:1063-1078.
6. Tournier JD, Calamante F, Connelly A. MRtrix: Diffusion tractography in crossing fiber regions. Int J Imaging Syst Technol. 2012;22(1):53-66.
7. Fischl B. FreeSurfer. Neuroimage. 2012;62(2):774-781.
8. Deco G, Ponce-Alvarez A, Mantini D, Romani GL, Hagmann P, Corbetta M. Resting-state functional connectivity emerges from structurally and dynamically shaped slow linear fluctuations. J Neurosci. 2013;33(27):11239-11252.
9. Deco G, Ponce-Alvarez A, Hagmann P, Romani GL, Mantini D, Corbetta M. How local excitation-inhibition ratio impacts the whole brain dynamics. J Neurosci. 2014;34(23):7886-7898.
10. Griffiths JD, Wang Z, Ather SH, Momi D, Rich S, Diaconescu A, et al. Deep Learning-Based Parameter Estimation for Neurophysiological Models of Neuroimaging Data. bioRxiv. Published online May 19, 2022:2022.05.19.492664. doi:10.1101/2022.05.19.492664
11. Margulies DS, Ghosh SS, Goulas A, Falkiewicz M, Huntenburg JM, Langs G, et al. Situating the default-mode network along a principal gradient of macroscale cortical organization. Proc Natl Acad Sci U S A. 2016;113(44):12574-12579.

Poster No 1811

Dynamic Brain Coherence Networks Uncovered using Directional Statistics

Anders S. Olsen[1], Anders Brammer[1], Morten Mørup[2]

[1]Technical University of Denmark, Kgs. Lyngby, Denmark, [2]Technical University of Denmark, Kgs. Lungby, Denmark

Introduction: Most fMRI functional connectivity (FC) studies evaluate interregional correlation, either across the entire scan (static) or in sliding windows (time-varying). However, fMRI data are usually filtered within a narrow frequency band, which enables tracking the oscillatory nature of regional signals. This approach may be favourable for investigating FC, since it disregards signal amplitude information, which generally encompasses region-specific activity and transient noise such as motion[1]. Here we characterize interregional, instantaneous phase coherence in the resting human brain. For each volume, we produce a connectivity vector, the pool of which is clustered using mixture models. We uncover time-varying resting-state networks in a cohort of 1003 healthy young adults from the human connectome project (HCP) at fsLR resolution (p=91.282 voxels). To our knowledge, we present the first atlas of instantaneous FC in a large cohort. We provide three versions with varying degrees of mixture model complexity, which may serve as alternatives to existing FC network atlases by relying on instantaneous connectivity rather than time-averages.

Methods: Preprocessed and denoised HCP-fMRI data were decomposed into phase by applying a Hilbert transform, followed by establishing a -dimensional frame-wise phase coherence matrix A_t=cos(\theta_it-\theta_jt) for each region i and j and time point t (see Figure 1). Due to the angle difference identity, A_t has rank 2^2. Thus, the eigendecomposition allows us to capture the majority of the variance in the phase coherence matrix using a px2-dimensional basis. Orthogonal bases are distributed on the Grassmann manifold, while each eigenvector (e.g., the leading eigenvector as in LEiDA[3]) is distributed on the sign-symmetric unit hypersphere[4]. Directional statistics offers suitable statistical distributions for these manifolds, namely the Watson and Angular Central Gaussian (ACG) distributions for the sign-symmetric hypersphere, and matrix ACG (MACG) for the

Grassmann manifold[5-7]. While the Watson distribution is parameterized by a mean direction vector and a scalar precision, the ACG and MACG are parameterized by a full or rank-reduced covariance matrix.

Results: We split the data into a train and test set and evaluated a range of mixture sizes, K={2,...,20}. For Watson mixtures, the test-log-likelihood did not saturate within the evaluated range of K. For ACG/MACG mixtures, K=7 networks were found to be suitable based on an elbow in the test-log-likelihood curve. For simplicity, we present seven Watson networks trained on the full data set (Figure 2). The inferred networks include high-level networks such as the frontoparietal and default-mode networks and some more diffuse background states.

Conclusions: We introduce time-varying high-resolution functional brain networks estimated without assuming any signal stationarity through, e.g., windowing, and by assessing only interregional phase coherence, disregarding potentially spurious amplitude information. For Watson mixtures, we observed states involving brain areas responsible for higher-order cognitive function, while somatosensory regions were less clear. Collectively, the current observations suggest an opportunity to gain complementary information about brain connectomics via time-varying functional coherence based analyses.

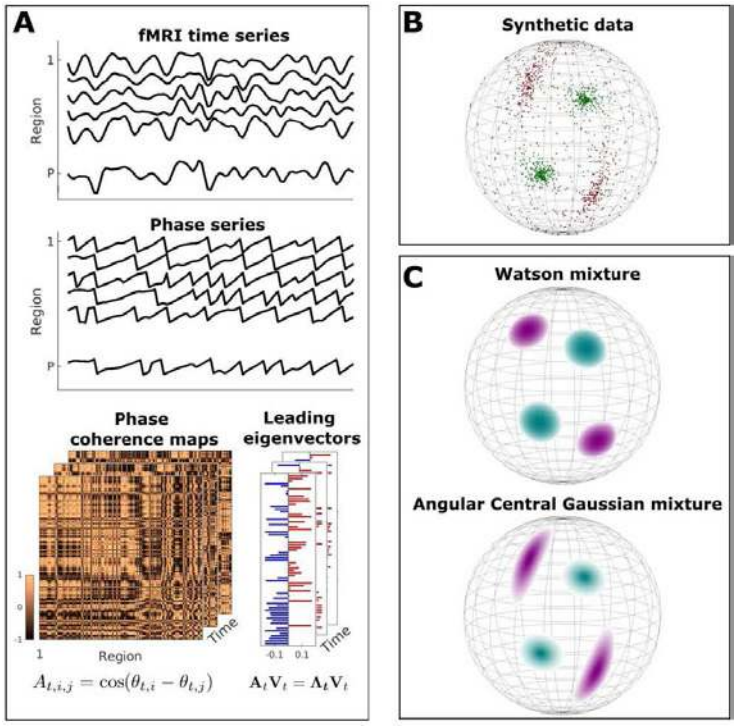

Figure 1: Methodological framework for leading eigenvector dynamics analysis and Watson mixture models

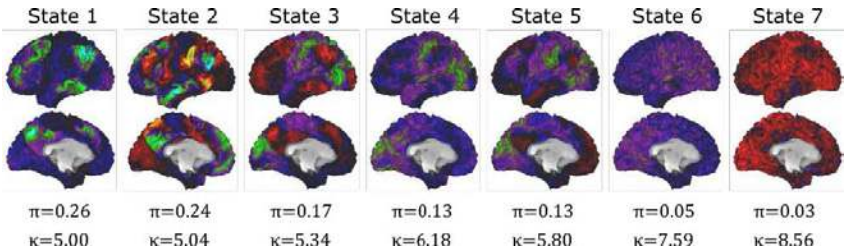

Figure 2: Networks for a K=7 solution for Watson mixture models, including centroids, prior \pi, and precision \kappa.

References

1. Bastos A.M. & Schoffelen J.M. (2016), 'A Tutorial Review of Functional Connectivity Analysis Methods and Their Interpretational Pitfalls', Frontiers in System neuroscience.
2. Olsen A.S. et al. (2022), 'Psilocybin Modulation of Time-Varying Functional Connectivity is Associated with Plasma Psilocin and Subjective Effects', NeuroImage.
3. Cabral J. et al. (2017), 'Cognitive performance in healthy older adults relates to spontaneous switching between states of functional connectivity during rest', Nature Scientific Reports
4. Olsen A.S. et al. (2023), 'Angular Central Gaussian and Watson Mixture Models for Assessing Dynamic Functional Brain Connectivity During a Motor Task', ICASSP2023.
5. Watson G.S. (1965), 'Equatorial Distributions on a Sphere', Biometrika
6. Tyler D.E. (1987), 'Statistical Analysis for the Angular Central Gaussian Distribution on the Sphere', Biometrika.
7. Chikuse Y. (1990), 'The Matrix Angular Central Gaussian Distribution', Journal of Multivariate Analysis.

Poster No 1812

Targeted attacks on occipital-frontal functional connections simulates AD progression

Avalon Campbell-Cousins[1], Federica Guazzo[2], Mario Parra Rodriguez[3], Javier Escudero[4]

[1]Edinburgh University, Edinburgh, Scotland, [2]University of Edinburgh, Edinburgh, Scotland, [3]University of Strathclyde, Glasgow, Scotland, [4]University of Edinburgh, Edinburgh, Midlothian

Introduction: Alzheimer's disease (AD) is the most prominent cause of dementia and causes an immense emotional and financial burden on individuals, families, and health care services. Early stages, namely Mild Cognitive Impairment (MCI), often progresses quickly to AD[1]. Network neuroscience seeks to understand AD progression by studying brain networks constructed from neuroimaging techniques like functional Magnetic Resonance Imaging (fMRI)[2]. Damage to the brain due to AD can result in corresponding changes in functional brain connectivity[3,4]. One such model attacks connections between influential brain regions, providing a mechanism for AD progression in rs-MEG[5]. Inspired by previous research on network attacks, we present a new model to explain AD related changes in fMRI functional networks for a visual short-term memory binding task (VSTMBT). This method preferentially targets long-range connections between key brain regions involved in the task.

Methods: For this pilot study, 5 healthy participants (Age:75.4±4.7, Sex:4F) and 6 MCI that converted to AD (MCIc) after a 2-year follow up (Age:76.3±5.1, Sex:2F) were taken from a longitudinal study which acquired both diffusion and functional MRI during the VSTMBT[6], a task sensitive to memory related changes in early AD[7]. Each subject's 85x85 functional connectivity matrix is constructed using spearman correlation between each brain region's fMRI signal across repetitions of the encoding and maintenance phases of the task. fMRI data and atlas are detailed in[8]. As benchmarks, we implemented the two attack methods in[5]. 1) Random: where edges in each control network are randomly decreased by a factor of 2 until the total edge weight is the same as that of the average MCIc network. 2) Targeted: where edges are preferentially attacked when they exist between high degree nodes. We hypothesized that long-range functional connectivity could be susceptible to damage caused by AD, much like in rs-fMRI[9], and especially those between specific brain regions key to visual short-term memory binding[10]. We devise a novel attack model to simulate the changes in early AD. This consists of attacking the network with a probabilistic approach on the connections in the following groups: occipital-frontal (OF), occipital-parietal/temporal (OPT), frontal-parietal/temporal (FPT), and all others (AO) (method detailed in Fig. 1a). To test the effectiveness of this method, we compare the mean clustering coefficient calculated as in[5], to targeted attacks on the defined groups for a range of probabilities (Fig. 1b). We then compare the results of the random and attack models using various graph measures (Fig. 2), for the best result in Fig. 1b. The clustering coefficient (CC) and path length (PL) are averaged over an ensemble of 50 surrogate networks created by randomly shuffling the network edge weights as in[5], with the addition of modularity (Q).

Results: For each subject, we calculate CC for targeted attacks on the following groups: OF, OPT, FPT, and AO. We start with only attacks on AO, gradually decreasing these while increasing attacks on long-range OF connections (Fig. 1b). As we increase the attacks on OF, we see increases in CC and a closer match with our MCIc group (Fig. 1b). Next we explore the best case from Fig. 1b, comparing it to the original targeted and random attack methods in[5] for a selection of graph metrics. We find that our modified version of the targeted attack model (targeted OF in Fig. 2) clearly outperforms the original in CC and PL, and somewhat in Q.

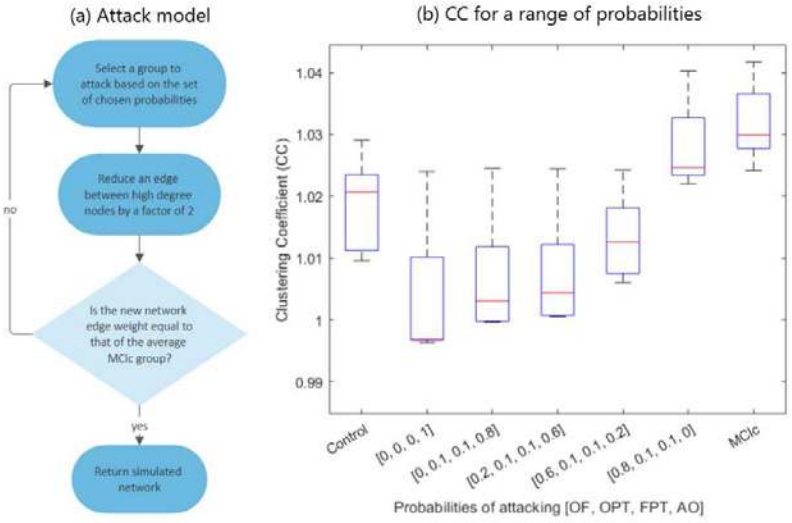

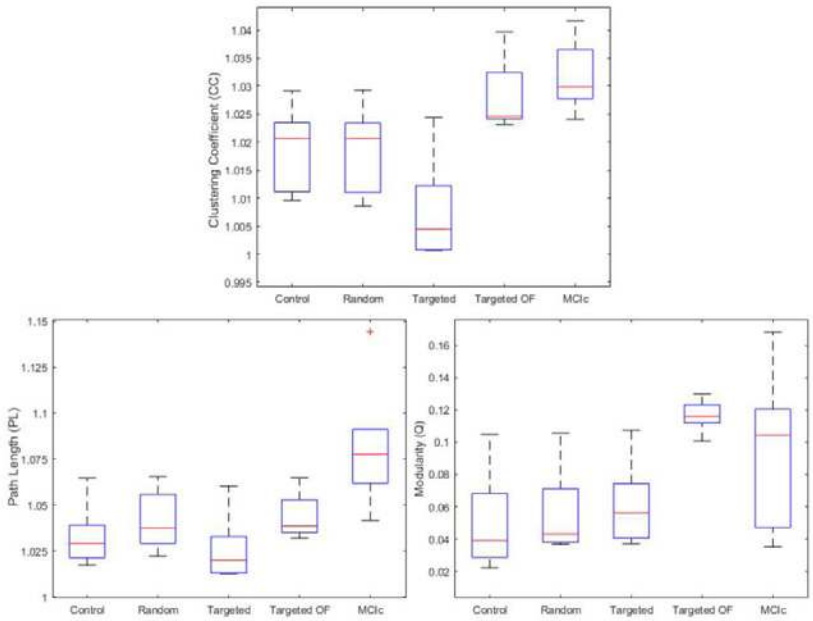

Conclusions: The proposed targeted attack model serves as a way to capture connectivity changes specific to the VSTMBT in early AD. Though limited by sample size, it motivates further research in how we can assess the mechanisms of AD progression. Namely, a refinement of attacks to incorporate further biological or imaging related disease mechanisms, and extensions of targeted attack methods to other imaging modalities like task-EEG.

References

1. Scheltens, P. (2021), 'Alzheimer's disease', The Lancet, vol. 397, no. 10284, pp. 1577-1590.
2. Bassett, D. S. (2018), 'On the nature and use of models in network neuroscience', Nature Reviews Neuroscience, vol. 19, no. 9, pp. 566-578.
3. Pereira, J. B. (2016), 'Disrupted network topology in patients with stable and progressive mild cognitive impairment and Alzheimer's disease', Cerebral Cortex, vol. 26, no. 8, pp. 3476-3493.
4. Sheline, Y. I. (2013), 'Resting state functional connectivity in preclinical Alzheimer's disease', Biological psychiatry, vol. 74, no. 5, pp. 340-347.
5. Stam, C. J. (2009), 'Graph theoretical analysis of magnetoencephalographic functional connectivity in Alzheimer's disease', Brain, vol. 132, no. 1, pp. 213-224.
6. Parra, M. A. (2022), 'Memory markers in the continuum of the Alzheimer's clinical syndrome', Alzheimer's research & therapy, vol. 14 no. 1, pp. 1-16.
7. Parra, M. A. (2010), 'Visual short-term memory binding deficits in familial Alzheimer's disease', Brain, vol. 133, no. 9, pp. 2702-2713.
8. Fabila-Carrasco, J. S. (2023), 'Graph-Based Permutation Patterns for the Analysis of Task-Related fMRI Signals on DTI Networks in Mild Cognitive Impairment', arXiv preprint, arXiv:2309.13083.
9. Liu, Y. (2014), 'Impaired long distance functional connectivity and weighted network architecture in Alzheimer's disease', Cerebral Cortex, vol. 24, no. 6, pp. 1422-1435.
10. Parra, M. A. (2014), 'Neural correlates of shape–color binding in visual working memory', Neuropsychologia, vol. 52, pp. 27-36.

Poster No 1813

Improving behavioral prediction from individual functional connectivity through transfer learning

Alexandre Le Bris[1]

[1]*Inria, Palaiseau, Essonne*

Introduction: Resting-state functional magnetic resonance imaging (rfMRI) enables the exploration of the functional brain organization and its representation via large-scale networks[1]. Summary measures, such as functional connectivity (FC) or networks' spatial topography, present interindividual differences with applications in detecting cognitive disorders or predicting behavioral traits[2,3,4]. However, the limited number of subjects in clinical data can significantly disrupt these estimations and then the accuracy of downstream tasks. We show here that this difficulty can be partially overcome with transfer learning (TL) coupled with Bayesian modeling.

Methods: The dataset comprises 1,000 subjects from the S1200 release of the HCP dataset[5], each going with 2 rfMRI scans acquired on consecutive days. For a given subject and run, the input data represent the functional connectivity of each vertex of the cortical mesh with reference regions provided by the DiFuMo atlas[6]. We considered that each functional connectome

is the combination of two individual-level components: a probabilistic parcellation of the cortex into a finite number of networks and a set of network-specific FC profiles. This is depicted through a Bayesian model, where these components are random variables (RVs) to be inferred. Notably, individual variables are regularized by population priors (Fig. 1A). To estimate the latent RVs, we employed PAVI[7], a variational inference technique leveraging probabilistic graphical models and deep learning techniques like normalizing flows[8]. This approach allows simultaneous estimation of cortical topography and FC at the individual level. Following the extraction of these features, inference performance is evaluated through the regression of 58 behavioral scores provided by the HCP dataset. In a first experiment, we assessed the model's learning capacity by varying the number of subjects used to infer the features and then examining the evolution of mean accuracy when predicting behavioral scores. Secondly, we divided the 1,000 subjects into a large dataset of 750 individuals (the source dataset) and a smaller one ranging from 50 to 200 subjects (out-of-sample or target dataset). We pre-trained a model with the source dataset and used the inferred features to transfer part of the learning to a new model trained on the out-of-sample dataset. We tested two TL approaches. The first, a simple warm start, involves transferring pre-trained parameters in PAVI neural networks to the second model. The second approach, in addition to the warm start, utilizes population priors trained on the source dataset and, as such, is denoted by Bayesian TL (Fig. 1B).

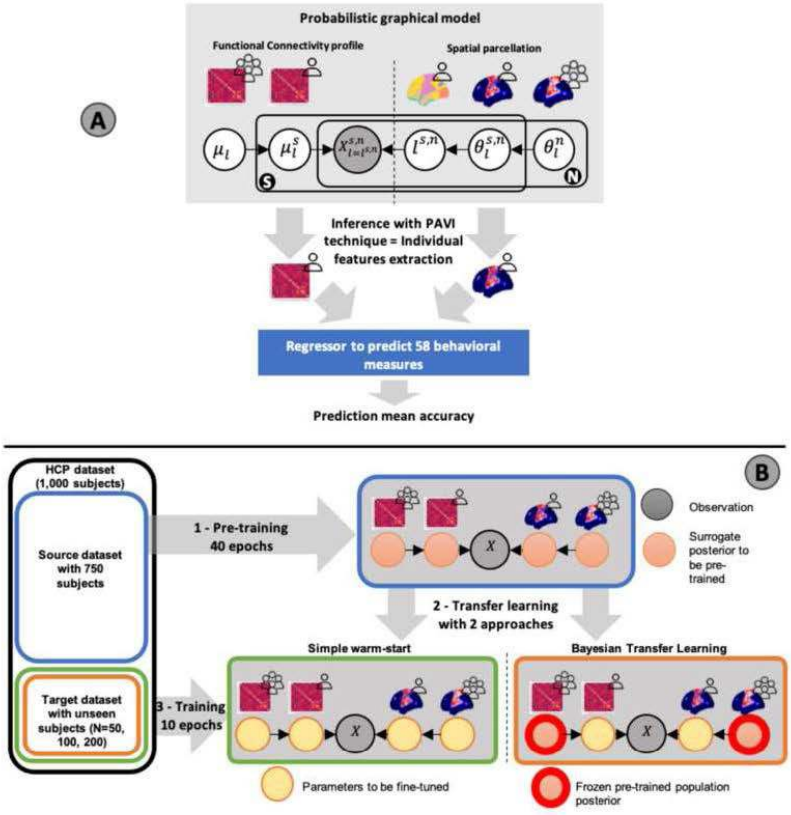

Figure 1 – Panel A: hierarchical Bayesian model used for the inference. The RVs are depicted within circles (grey for the observed variable X and white for latent parameters). μ_l represents the functional connectivity of the network labeled l , θ_l^n the soft parcellation (the probability that vertex n belongs to network l) and l^n the hard parcellation (network label of the vertex n). The upper indice "s" identifies a specific subject; without it, the RV is considered to be a population one, such as the priors. After the individual features inference with PAVI, the behavioral prediction is performed. The accuracy is the r-Pearson correlation between truth and prediction. The mean accuracy was calculated across 20 10-fold cross-validations. **Panel B**: process to evaluate the transfer learning performance with 2 approaches. Once all the models are fitted (pre-trained model + two trained models with TL), the prediction mean accuracy is computed for each of them. The results are plotted in Figure 2.

Results: Evaluating the model's learning capacity reveals a logarithmic growth in prediction accuracy as the number of subjects in the dataset grows. Up to 1,000 subjects, the slope indicates that full learning capacity has not been reached (Fig. 2A). Further subjects are required to enhance prediction performance, justifying the TL approach. The second experiment illustrates the efficiency of TL in inferring individual summary measures, such as subject-specific FC profiles, from a limited dataset. With Bayesian TL and 200 previously unseen subjects, we achieve comparable performance in behavioral prediction as directly inferring with twice as many subjects (Fig. 2A). However, this outcome, averaged across 58 behavioral scores, exhibits considerable variation among the considered behavioral measures. Some even undergo negative TL (Fig. 2B). The reasons for such variability (e.g. summary measures not capturing the underlying neural cause) are yet to be fully understood.

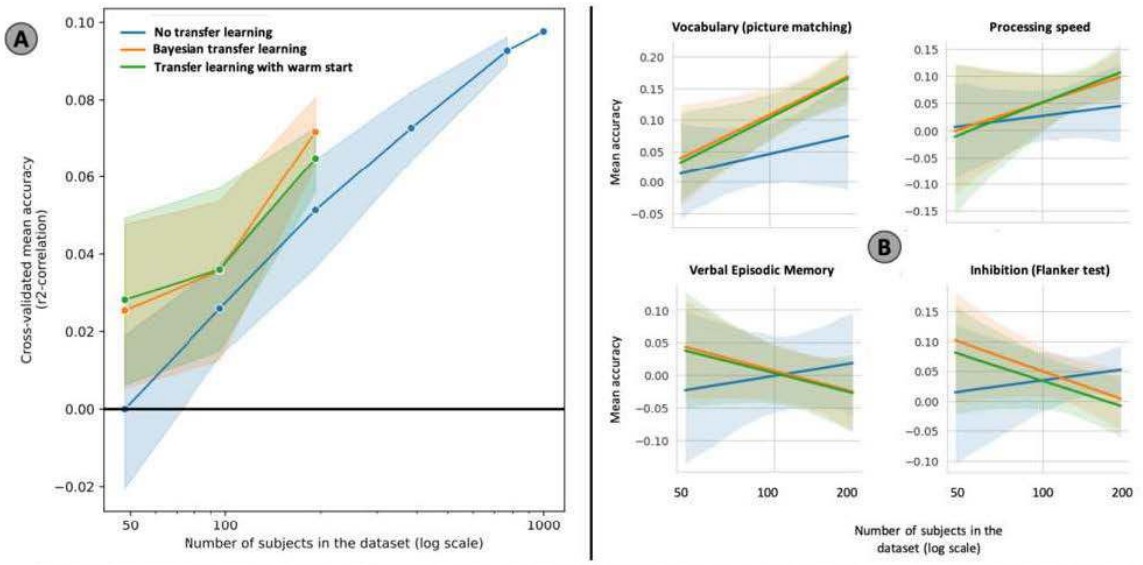

Figure 2 – Panel A: evolution of the mean accuracy over 58 behavioral measures prediction as the number of subjects in the dataset increases. The used features are the individual connectivity profiles μ_i^s and the used predictor is a kernel Ridge regressor with a Laplacian kernel. Each point on the plot was estimated on 10 inferences with different subpopulations in the dataset (except for the blue point with 1,000 subjects, the full dataset). The error band represents the 95% confidence interval. The blue line represents the learning curve of the model without transfer learning. It can be approximated by a logarithmic curve: y = 0.04 . log(x - 50) with a p-value of 10e-11. The learning curves with transfer learning outperform the one without. The Bayesian transfer learning is slightly more efficient than a simple warm start for a number of subjects above 100. For 200 subjects, the performance with transfer learning is comparable to those without transfer learning for 400 subjects. **Panel B** : focuses on 4 behavioral measures. The 2 upper plots are cases where transfer learning proves to be very efficient for predicting these phenotypes. On the other hand, we also can observe a few measures for which the transfer learning deteriorates strongly the performance. The reasons for such variability are yet to be fully understood.

Conclusions: These initial results demonstrate the advantages of TL in deriving individually customized representations of functional brain organization with a limited dataset. However, further confirmation is needed when applying this approach to heterogeneous data from diverse datasets.

References

1. Thomas Yeo, B.T., Krienen, F.M., Sepulcre, J., Sabuncu, M.R., Lashkari, D., Hollinshead, M., Roffman, J.L., Smoller, J.W., Zöllei, L., Polimeni, J.R., Fischl, B., Liu, H., Buckner, R.L., 2011. The organization of the human cerebral cortex estimated by intrinsic functional connectivity. Journal of Neurophysiology 106, 1125–1165. https://doi.org/10.1152/jn.00338.2011
2. Finn, E.S., Shen, X., Scheinost, D., Rosenberg, M.D., Huang, J., Chun, M.M., Papademetris, X., Constable, R.T., 2015. Functional connectome fingerprinting: identifying individuals using patterns of brain connectivity. Nat Neurosci 18, 1664–1671. https://doi.org/10.1038/nn.4135
3. Kaiser, R.H., Andrews-Hanna, J.R., Wager, T.D., Pizzagalli, D.A., 2015. Large-Scale Network Dysfunction in Major Depressive Disorder: A Meta-analysis of Resting-State Functional Connectivity. JAMA Psychiatry 72, 603. https://doi.org/10.1001/jamapsychiatry.2015.0071
4. Kong, R., Li, J., Orban, C., Sabuncu, M.R., Liu, H., Schaefer, A., Sun, N., Zuo, X.-N., Holmes, A.J., Eickhoff, S.B., Yeo, B.T.T., 2019. Spatial Topography of Individual-Specific Cortical Networks Predicts Human Cognition, Personality, and Emotion. Cerebral Cortex 29, 2533–2551. https://doi.org/10.1093/cercor/bhy123
5. Van Essen, D.C., Ugurbil, K., Auerbach, E., Barch, D., Behrens, T.E.J., Bucholz, R., Chang, A., Chen, L., Corbetta, M., Curtiss, S.W., Della Penna, S., Feinberg, D., Glasser, M.F., Harel, N., Heath, A.C., Larson-Prior, L., Marcus, D., Michalareas, G., Moeller, S., Oostenveld, R., Petersen, S.E., Prior, F., Schlaggar, B.L., Smith, S.M., Snyder, A.Z., Xu, J., Yacoub, E., 2012. The Human Connectome Project: A data acquisition perspective. NeuroImage 62, 2222–2231. https://doi.org/10.1016/j.neuroimage.2012.02.018
6. Dadi, K., Varoquaux, G., Machlouzarides-Shalit, A., Gorgolewski, K.J., Wassermann, D., Thirion, B., Mensch, A., 2020. Fine-grain atlases of functional modes for fMRI analysis. NeuroImage 221, 117126. https://doi.org/10.1016/j.neuroimage.2020.117126
7. Rouillard, L., Bris, A.L., Moreau, T., Wassermann, D., 2023. PAVI: Plate-Amortized Variational Inference. https://doi.org/10.48550/ARXIV.2308.16022
8. Papamakarios, G., Nalisnick, E., Rezende, D.J., Mohamed, S., Lakshminarayanan, B., 2021. Normalizing Flows for Probabilistic Modeling and Inference. https://doi.org/10.48550/arXiv.1912.02762

Poster No 1814

Association of Selective Attention and Functional Connectivity in Cerebral Visual Impairment

Negin Nadvar[1], Claire Manley[2], Marie Drottar[1], Lotfi Merabet[2], Corinna Bauer[1,2]

[1]Department of Radiology, Massachusetts General Hospital, Harvard Medical School, Boston, MA, [2]Department of Ophthalmology, Massachusetts Eye and Ear, Harvard Medical School, Boston, MA

Introduction: Cerebral visual impairment (CVI) encompasses any visual deficit due to brain maldevelopment or damage and is a leading cause of visual disorders in the pediatric population in many parts of the world. Higher-order visual processes, such as visual search, are often impacted in individuals with CVI (Boot et al., 2010; Zhang et al., 2022). A recent study investigated performance in a visual search task in individuals with CVI and found an overall impairment in time spent and accuracy in

identifying the test target (Manley et al., 2023). However, the neural correlates of visual search tasks remain unknown in CVI. As a result, in the present study, we examined the association between performance in a selective attention visual task and resting-state functional connectivity (rsFC) in the brain networks involving attention and visual processing.

Methods: Sixteen sighted control (SC: 22.06 years ± 4.17 (sd), 10 females) and 10 CVI (17.70 years ± 5.29 (sd), 4 females) participants were included in the study. Participants completed a conjunction search task with mean performance accuracy and response time as the main outcomes of interest (Manley et al., 2023). For each participant, a T1W image (TR = 6.5 ms, TE = 2.9 ms, resolution = 1 mm3 isotropic), 2 resting-state fMRI (rsfMRI) runs (TR = 800 ms, TE = 30ms, duration = 5 min 15 sec, resolution = 2.25 x 2.25 x 2.4 mm3), and reverse phase-encoded field maps were acquired. Preprocessing steps included brain extraction, Mcflirt, b0 unwarping, 5mm smoothing, removal of motion components using ICA-AROMA, and regression of the white matter and CSF signal using FSL tools. Mean time series were extracted from 54 cortical regions derived from the Glasser atlas (Glasser et al., 2016) and 6 thalamic subdivisions from FreeSurfer (Iglesias et al., 2018). Four networks were considered: the dorsal attention network (DAN, 22 ROIs), ventral attention network (VAN, 26 ROIs), early visual network (VIS, 6 ROIs), and thalamus (Thal, 6 ROIs). Average rsFC was calculated within DAN, VAN, and VIS networks, between each of these networks and the rest of the networks under study (DAN, VAN, VIS, and Thal), as well as between each of the attention networks and Thal. For each of the inter-network and intra-network connections, the Spearman partial correlation was calculated between the task behavioral measures and rsFC across the subjects in each group, while controlling for the potential effects of age and verbal IQ scores. The results were corrected for multiple comparisons using False Discovery Rate (FDR) correction across all the inter- and intra-network study cases.

Results: Our analysis found significant ($p < 0.05$ corrected) correlations between performance accuracy and rsFC within the DAN and VAN networks ($r = 0.78$, $p = 0.007$ and $r = 0.72$, $p = 0.014$, respectively) and between each of the DAN, VAN, and VIS networks and the rest of the networks under study ($r = 0.65$, $p = 0.02$, $r = 0.67$, $p = 0.02$ and $r = 0.63$, $p = 0.02$, respectively), for the SC group. The CVI group did not demonstrate any significant correlations between behavior and rsFC measures. However, the uncorrected results showed a trend for weak rsFC-behavior correlation in the negative direction for the CVI group for the DAN and VAN within-network and DAN, VAN, and VIS between-network analyses, while yielding a positive correlation for the SC group (Figure 1).

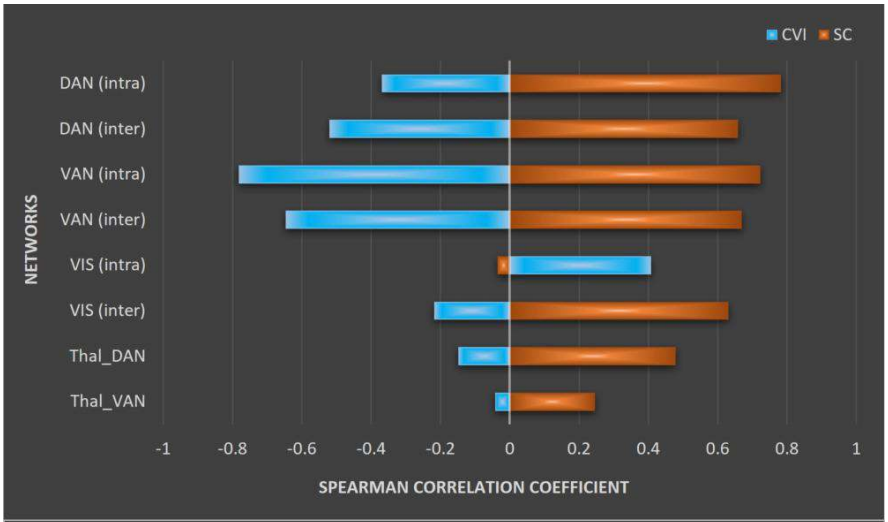

Figure 1 - Correlation between rsFC and Accuracy of Conjunction Visual Search Task. The x-axis shows the raw Spearman partial correlation coefficient values and the y-axis shows various connections within (intra) and between (inter) the networks under study.

Conclusions: Overall, our results indicated a positive correlation between the rsFC involving attention networks and selective attention task in SC (i.e., higher rsFC in these networks is associated with more accurate performance). Our results provided evidence for an aberrant negative association for the CVI group. This change in rsFC-behavior association may be due to the neurological impairment in CVI which has important implications in rehabilitation. This notable hypothesis warrants further investigation in a larger number of individuals affected by CVI.

References

1. Boot, F. H. (2010). Cerebral Visual Impairment: Which perceptive visual dysfunctions can be expected in children with brain damage? A systematic review. Research in Developmental Disabilities, 31(6), 1149–1159. https://doi.org/10.1016/j.ridd.2010.08.001
2. Glasser, M. F. (2016). A multi-modal parcellation of human cerebral cortex. Nature, 536(7615), 171–178. https://doi.org/10.1038/nature18933

3. Iglesias, J. E. (2018). A probabilistic atlas of the human thalamic nuclei combining ex vivo MRI and histology. NeuroImage, 183, 314–326. https://doi.org/10.1016/j.neuroimage.2018.08.012
4. Manley, C. E. (2023). Impaired visuospatial processing in cerebral visual impairment revealed by performance on a conjunction visual search task. British Journal of Visual Impairment, 02646196231187550. https://doi.org/10.1177/02646196231187550
5. Zhang, X. (2022). Assessing visuospatial processing in cerebral visual impairment using a novel and naturalistic static visual search task. Research in Developmental Disabilities, 131, 104364. https://doi.org/10.1016/j.ridd.2022.104364

Poster No 1815

ENIGMA Addiction: Mega-Analysis Results of Alcohol Cue Reactivity

Anthony Juliano[1], Devarshi Pancholi[1], Scott Mackey[2], Patrick Bach[3], Anne Beck[4], Anneke Goudriaan[5], Markus Heilig[6], Andreas Heinz[7], Falk Kiefer[8], Freek Linders[9], Kirsten Morley[10], Irene Perini[11], Haoye Tan[12], Ellen Towers[10], Ruth van Holst[13], Sabine Vollstädt-Klein[8], Adam Yngve[6], Anna Zilverstand[14], Hamed Ekhtiari[15], Hugh Garavan[1]

[1]University of Vermont, Burlington, VT, [2]The University of Vermont, Burlington, VT, [3]Department of Addictive Behavior and Addiction Medicine, Central Institute of Mental Health (CIMH), Mannheim, Germany, [4]Health and Medical University Potsdam, Potsdam, Brandenburg, [5]Amsterdam Institute for Addiction Research, Amsterdam University Medical Center, Amsterdam, Nether, Amsterdam, Netherlands, [6]Center for Social and Affective Neuroscience, Department of Biomedical and Clinical Sciences, Linköping, Sweden, [7]Department of Psychiatry and Psychotherapy, Charité – Universitätsmedizin Berlin, Berlin, Germany, [8]Department of Addictive Behaviour and Addiction Medicine, Central Institute of Mental Health, Mannheim, Germany, [9]Amsterdam University Medical Center, Amsterdam, Netherlands, [10]Clinical School, Sydney Medical School, University of Sydney, Sydney, New South Whales, [11]Linköping University, Linköping, Linköping, [12]Department of Addictive Behavior and Addiction Medicine, Central Institute of Mental Health, Medical, Mannheim, Germany, [13]1Department of Psychiatry, Amsterdam UMC, University of Amsterdam, Amsterdam, Netherlands, [14]University of Minnesota, Minneapolis, MN, [15]Laureate Institute for Brain Research, Tulsa, OK

Introduction: Alcohol use disorder (AUD) is associated with disruption of reward, salience, and cognitive control networks. In cue reactivity paradigms, viewing alcohol cues elicits activation in the anterior cingulate cortex [ACC; Schacht et al., 2013], a primary region of interest (ROI) within the salience network [Seeley, 2019] that is implicated in reward processing[Marsh et al., 2007; Liu, et al., 2011]. Previous work has shown increased effective connectivity [EC] between the ACC and the ventral striatum (VS) and anterior insula in abstinent versus non-abstinent AUD individuals and decreased EC with increased subjective craving ratings [Strosche et al., 2020]. Here, we explored task-based activation and EC patterns in individuals who were diagnosed with an AUD as part of the ENIGMA Addiction Cue Reactivity Initiative (ACRI).

Methods: Datasets from 5 sites were curated by the ENIGMA Addiction working group according to a standardized protocol. Participants included 237 adults ages 18-68 years who were diagnosed with an AUD. Task-based fMRI Alcohol Cue Reactivity data were preprocessed using fMRIPrep version 20.2.5, which is based on Nipype 1.6.1. This pipeline encompasses anatomical (intensity non-uniformity correction, skull stripping, brain tissue segmentation, surface reconstruction, and spatial normalization) and functional (boundary-based registration using six degrees of freedom, estimation of head motion parameters, slice time correction, and generation of confound variables) data workflows. The BOLD time-series was then resampled into MNI152 2mm^3 standard space. Preprocessed data were then parcellated using the Brainnetome atlas (246 ROIs) to extract the timeseries signal for the physiological regressors in bilateral rostral ACC (rACC). Signal cleaning was performed with FSL functions and included the following nuisance covariates: acompcor, tcompcor, cerebrospinal fluid, white matter, three translations/rotations motion parameters and their derivatives, as well as censoring high motion timepoints (standardized DVARS ≥ 1.5). Psychophysiological Interactions (PPI) were tested between the psychological and physiological regressors for the contrast of interest [Alcohol cue vs Neutral cue], in addition to age- and sex-related effects. A linear, mixed-effects model was used to test group-level differences using FSL's PALM. Corrections for multiple comparisons were performed using False Discovery Rate [$p \leq 0.05$].

Results: One sample t-tests of the Alcohol Cue vs. Neutral Cue contrast showed significant BOLD activity in the rostral ACC. For the right rACC, decreased EC was found in the left precuneus and superior temporal gyrus, while the left rACC exhibited decreased EC with the right superior frontal gyrus and right VS. Decreased EC was shown between the right rACC and bilateral central opercula and between the left rACC and the left supramarginal gyrus and right parietal operculum when comparing males and females in the sample. Age-related effects were also found in EC with older individuals showing greater EC with the left anterior insula and bilateral rACC regions.

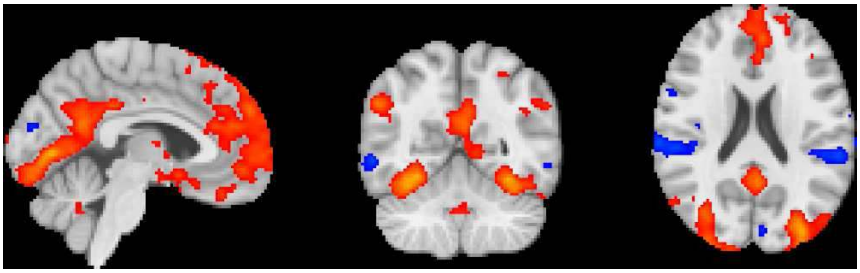

Fig One sample t-test AUD alcohol cue minus neutral cue

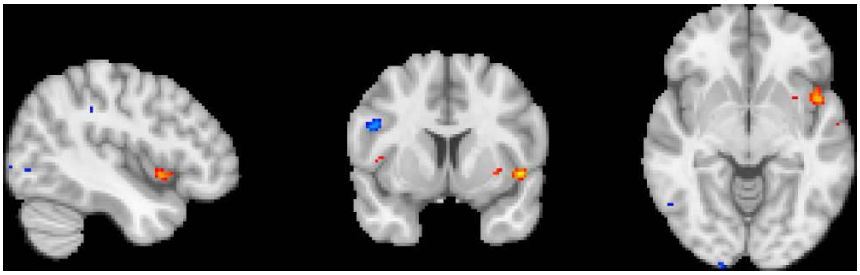

Age-related effects of left rACC EC with left anterior insula

Conclusions: AUD disrupts EC of the rACC, notably when assessing the interaction effects between sex or age. Altered EC between rACC and the left anterior insula between older and younger individuals with AUD holds promise for intervention. Pharmacological [Morley et al., 2021] and psychological [Ewing et al., 2011] interventions have have shown some promise in attenuating the activation of the anterior insula in individuals with AUD, though other interventions, such as repetitive transcranial magnetic stimulation have not [Perini et al., 2020]. Given the need for larger sample sizes to assess interaction effects between sex and a given clinical condition [Galea et al., 2020], as well as interventions more broadly, ENIGMA: Addiction is uniquely positioned to answer the ever-evolving and complex questions being asked of the neuroimaging and healthcare communities.

References

1. Ewing et al., 2011. doi: 10.1111/j.1530-0277.2010.01382.x.
2. Galea et al., 2020. doi: 10.1016/j.yfrne.2019.100817. Epub 2019 Dec 16. PMID: 31837339; PMCID: PMC7050281.
3. Liu et al., 2011. doi: 10.1016/j.neubiorev.2010.12.012. Epub 2010 Dec 24. PMID: 21185861; PMCID: PMC3395003.
4. Marsh et al., 2007. doi: 10.1016/j.neuroimage.2006.11.044. Epub 2007 Feb 9. PMID: 17292631; PMCID: PMC1868682.
5. Morely, et al., 2021. doi: 10.1016/j.euroneuro.2021.02.010.
6. Perini, et al., 2020. doi: 10.1038/s41386-019-0565-7.
7. Schacht et al., 2013. doi: 10.1111/j.1369-1600.2012.00464.x. Epub 2012 May 10. PMID: 22574861; PMCID: PMC3419322.
8. Seeley, 2019. doi: 10.1523/JNEUROSCI.1138-17.2019.
9. Strosche, et al., 2021. doi: 10.1111/adb.12863

Poster No 1816

The Entropy of Task-Induced Centrality Dynamics in Schizophrenia: Novel Applications of Graph Theory

Dhruval Bhatt[1], John Kopchick[2], Dalal Khatib[2], Patricia Thomas[2], Usha Rajan[2], Luay Haddad[2], Alireza Amirsadri[2], Jeffrey Stanley[2], Vaibhav Diwadkar[1]

[1]Wayne State University, Detroit, MI, [2]Wayne State University, Department of Psychiatry, Detroit, MI

Introduction: Both resting and task-evoked brain network dynamics are impaired in schizophrenia (SCZ)(Meram et al., 2023). These dynamics have been explored using Dynamic Functional Connectivity (DFC) primarily applied to resting state fMRI signals (Hutchison et al., 2013). Given that task-induced changes are the most substantive modulators of brain network states (Logothetis, 2008), we introduce a novel framework for the study of centrality dynamics, thereby yoking DFC with graph theory (Rubinov and Sporns, 2010). First, we drove brain networks in SCZ and heathy controls (HC) using an established learning paradigm (Stanley et al., 2017). Next, using a moving window technique (the window width corresponded to the width of each task epoch) we computed a series of stationary functional connectivity matrices (one for each of the 280 partially overlapping windows). Each connectivity matrix (246 functionally derived nodes)(Fan et al., 2016) captures the state of the system in that time window. Next, in each window we estimated the Betweenness Centrality (BC)(Freeman, 1977) of each of the 246 nodes before ranking them (Spearman's rank) for integrative importance. Finally, a 280 point time series (based

on each node's rank in each time window) was formed for each node. Each time series (tBC) captures that node's centrality dynamics across the task. After estimating cross-similarities between tBC, agglomerative clustering was used to cluster regions with similar centrality dynamics. From the analyses of the clustering solutions (and the recovered centrality dynamics in each cluster) we demonstrate a) that the clustering identified different sub-networks in SCZ and HC and b) the centrality dynamics of sub-networks in SCZ were characterized by higher entropy (irregularity).

Methods: fMRI data (Siemens Verio 3T) were collected while participants (n=88, 49 SCZ, ages:18-45) learned nine object-location associations. Learning occurred over eight iterations of a paradigm where each iteration consisted of four distinct epochs (each 27s): Encoding (objects location shown for naming), Post-Encoding Consolidation (instruction-free fixation), Retrieval (locations cued in random order with participants required to name the associate object), and Post-Retrieval Consolidation (instruction-free fixation). fMRI data were preprocessed using typical methods (SPM12). Within each group (HC and SCZ), the 246 tBC were averaged across the respective participants before estimating the cross similarity matrix in centrality dynamics across all 246 nodes (30,135 pairs). Next, the matrix was submitted for agglomerative hierarchical clustering (Ward, 1963)(Figure 1) to cluster regions based on similarities in their centrality dynamics.

Results: Two distinct cluster solutions were observed (Figure 1; five clusters in HC and three in individuals with SCZ) with the averaged time series in each cluster (tCluster) evincing distinct centrality dynamics. Next, we calculated the Approximate Entropy (ApE), over each tCluster to characterize the degree of stochasticity of the cluster's centrality dynamics. ApE is an index of the irregularity of the fluctuations of a time series (Bonal & Marshak, 2019). As seen in Figure 2a, the ApE of each tCluster in the three SCZ clusters were higher than in the five HC clusters. The ApE was also linked to indices relating to network flexibility (Clark & Bjørnstad, 2004) (Figure 2b) and clinical symptoms (Figure 2c).

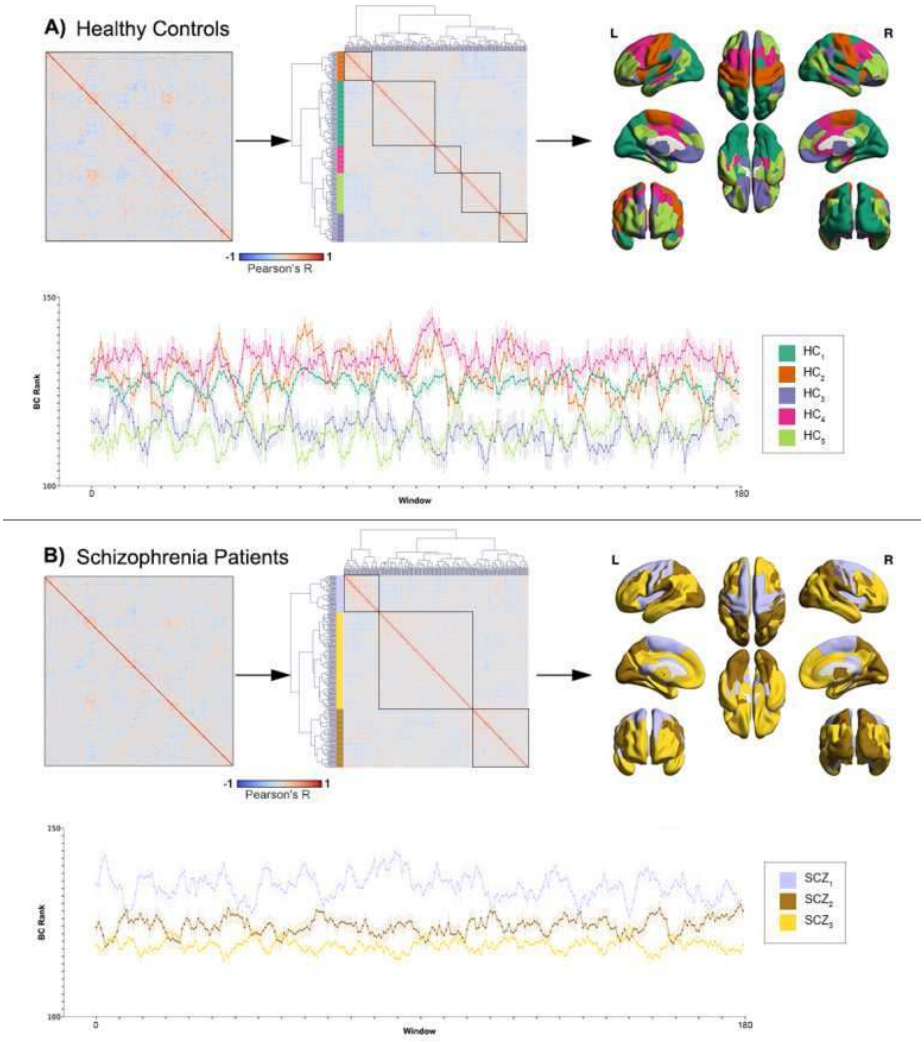

In each sub-figure, the heat map of correlation coefficients between all pairs of averaged t_{BC} captures the similarities in the centrality dynamics between all pairs of nodes in the group. These coefficients formed the data subsequently used for clustering. The choice of Agglomerative Hierarchical Clustering (Ward method) was motivated by its use of similarities (i.e., coefficients) as a basis for clustering, it's robustness in generating clustering solutions independent of cluster size, and its effectiveness in clustering high-dimensional data. The original heat maps are reorganized (to the right) with the order of nodes reorganized to reflect the clustering solution (the optimal numbers of clusters in HC and SCZ to be five and three respectively). Clusters are indicated by color bars on the left of each heat map (the color scheme is maintained). The squares on each heat map represent intra-cluster correlations. Dendrograms show the hierarchical relationship between the observed clusters. In each group, the regions assigned to each cluster were then reverse-mapped to the cerebral surfaces.For subsequent analyses, we computed the average cluster time series, $t_{Cluster}$ (across all regions in the cluster) to represent that cluster's centrality dynamics

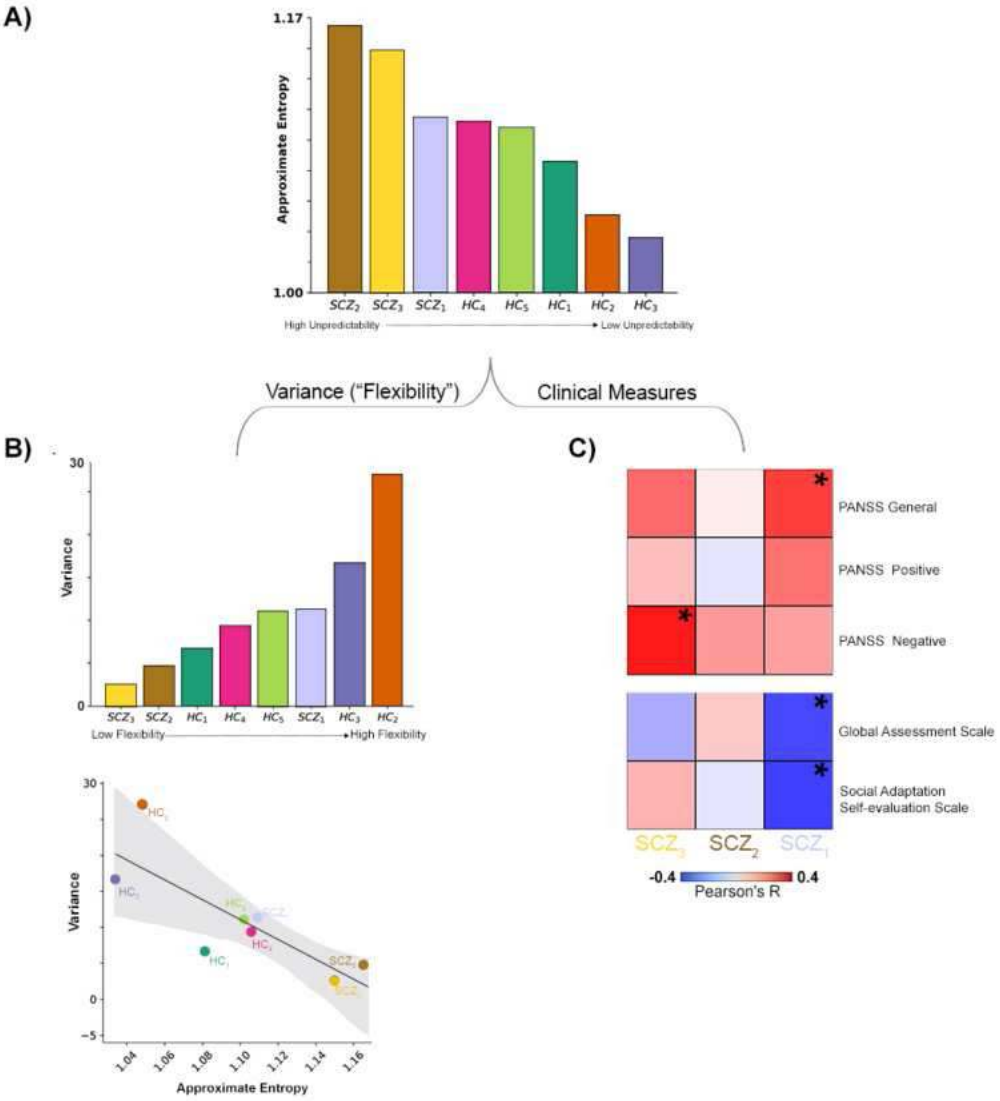

The Approximate Entropy (ApE) values for each of the eight clusters (HC_1-HC_4 and SCZ_1-SCZ_3) are presented in descending order. ApE is an index of the irregularity or the unpredictability over the fluctuation of a time series; thus higher ApE values indicate greater unpredictability (i.e., lower regularity) of a time series. As seen $t_{Cluster}$ in schizophrenia are characterized by higher ApE values than those in healthy controls, indicating that centrality dynamics in schizophrenia were more irregular. The variance for each of the 8 clusters is presented (calculated across the 280 values in each $t_{Cluster}$) in ascending order. A high degree of variability in the centrality dynamics of a time series is indicative of a greater range of dynamics of a sub-network, in turn suggestive of the sub-network's flexibility over the task. As seen by the order of variance of $t_{Cluster}$, this value was on average lower in SCZ, suggestive of lower sub-network flexibility in patients. The negative relationship between ApE and variance was highly significant ($r2$= .64, p<.02, shaded area is 95% confidence interval). In general, clusters in patients were characterized by higher ApE but lower variance compared to those in HC. This summary effect suggests that centrality dynamics in schizophrenia were characterized by high stochasticity, but lower flexibility. SCZ clustering solution was applied on SCZ patient and cluster time series for each of the 3 cluster was calculated for each patient. Approximate Entropy was calculated for each patient cluster time series and was cluster entropies were associated with clinical measures. The stars on the heatmap represents significant association between cluster ApEn and clinical measures (p<0.05). SCZ_1 cluster is significantly positively associated with PANSS General and is significantly negatively associated with Global Assessment Scale and Social Adaptation Self-evaluation Scale. SCZ_3 significantly positively associated with PANSS Negative.

Conclusions: There are many avenues for studying brain dynamics (Heitmann and Breakspear, 2018). Here we derive the concept of centrality dynamics, a new measure that encapsulates (task-driven or spontaneous) changes in the cumulative functional connectome over time. As shown, these dynamics are more stochastic in schizophrenia patients, and this increased stochasticity was linked to salient clinical symptoms. Overall, our findings further highlight the importance of studying dysfunctional network dynamics in complex psychiatric conditions like schizophrenia.

References

1. Clark, J. S. and O. N. Bjørnstad (2004). "Population time series: process variability, observation errors, missing values, lags, and hidden states." Ecology 85(11): 3140-3150.
2. Delgado-Bonal, A. and A. Marshak (2019). "Approximate entropy and sample entropy: A comprehensive tutorial." Entropy 21(6): 541.
3. Fan, L., et al. (2016). "The human brainnetome atlas: a new brain atlas based on connectional architecture." Cerebral cortex 26(8): 3508-3526.
4. Fan, L., et al. (2016). "The Human Brainnetome Atlas: A New Brain Atlas Based on Connectional Architecture." Cereb Cortex 26(8): 3508-3526.
5. Freeman, L. C. (1977). "A set of measures of centrality based on betweenness." Sociometry: 35-41.
6. Heitmann, S. and M. Breakspear (2018). "Putting the "dynamic" back into dynamic functional connectivity." Netw Neurosci 2(2): 150-174.
7. Hutchison, R. M., et al. (2013). "Dynamic functional connectivity: promise, issues, and interpretations." Neuroimage 80: 360-378.
8. Logothetis, N. K. (2008). "What we can do and what we cannot do with fMRI." Nature 453(7197): 869-878.

9. Logothetis, N. K. (2008). “What we can do and what we cannot do with fMRI.” Nature 453(7197): 869-878.
10. Meram, E. D., et al. (2023). “The topology, stability, and instability of learning-induced brain network repertoires in schizophrenia.” Network Neuroscience 7(1): 184-212.
11. Meram, E. D., et al. (2023). “The topology, stability, and instability of learning-induced brain network repertoires in schizophrenia.” Network Neuroscience 7(1): 184-212.
12. Rubinov, M. and O. Sporns (2010). “Complex network measures of brain connectivity: uses and interpretations.” Neuroimage 52(3): 1059-1069.
13. Rubinov, M. and O. Sporns (2010). “Complex network measures of brain connectivity: uses and interpretations.” Neuroimage 52(3): 1059-1069.
14. Stanley, J. A., et al. (2017). “Functional dynamics of hippocampal glutamate during associative learning assessed with in vivo 1H functional magnetic resonance spectroscopy.” Neuroimage 153: 189-197.
15. Ward Jr, J. H. (1963). “Hierarchical grouping to optimize an objective function.” Journal of the American statistical association 58(301): 236-244.

Poster No 1817

Characterizing edge communities within and between neural networks in fetal brains

Lanxin Ji[1], Amyn Majbri[1], Iris Menu[1], Richard Betzel[2], Olaf Sporns[2], Moriah Thomason[1]

[1]NYU School of Medicine, New York, NY, [2]Indiana University, Bloomington, IN

Introduction: Traditional brain network analysis largely relies on node-centric functional connectivity (nFC), in which links between regions are examined using static correlation analysis. However, this method overlooks interactions between edges, missing potentially meaningful features. In this study, we employed an edge-centric network model[1,2], by generating interpretable time series for each edge, in fetal brains. These edge time series enable the estimation of edge-centric functional correlation (eFC), tracking the evolution of communication patterns and assessing simultaneous occurrences in the brain. Unlike nFC, which measures the extent of activity fluctuations between brain regions, eFC unravels co-fluctuations across time, providing moment-by-moment accounts and assessing the similarity between pairs of co-fluctuation time series.

Methods: Imaging data were obtained from 137 fetuses (57 females) aged 25 to 39 weeks gestation (mean = 31.53 ± 3.69) participating in the Perinatal Imaging of Neural Connectivity study. Functional MRI were acquired using a 3 T Siemens Verio 70 cm open-bore system with an abdominal 4-channel Siemens Flex coil. Two sets of multi echo fMRI data were attained with the following scanning parameters: dataset a) TR = 2000ms; TE = 18, 31.07, 44.14ms (3 echoes); flip angle: 83 degrees; voxel size: 3.5 x 3.5 x 3.5 mm3; dataset b) TR = 2000ms; TE = 18, 34, 50ms (3 echoes); flip-angle: 83 degrees; voxel-size: 3.487 x 3.487 x 3.5 mm3. Preprocessing began with automatic fetal brain segmentation using deep learning[3], motion estimation, and censoring with FSL[4]. Participants with fewer than 105 low-motion frames were excluded. Subsequent preprocessing steps included optimal combination across echoes, normalization to standard space (GA = 32 weeks), smoothing, Independent Component Analysis (ICA)[5] and CompCor denoising[6], and regression of motion confounds. Gray matter was divided into 197 functional parcels using Pyclustering package, and regional time series were extracted from concatenated data of all subjects. Calculation of edge-centric functional connectivity (eFC) involved the following steps: 1) z-scoring the time series, 2) calculating the element-wise product of z-scored time series for all pairs of brain regions, and 3) determining the element-wise product between pairs of edge time series, resulting in an eFC matrix. K-means clustering (k = 10) was then applied to eFC, partitioning the eFC network into communities of co-fluctuating edges. The group-representative edge communities, community similarity, and normalized entropy of each network were examined. Edge community similarity represents how similar of the community labels of two regions. Normalized entropy per network is a measure of community overlap. Low entropy indicate that a brain regions’ edges are concentrated among a small number of communities, whereas higher values indicate that edges are uniformly distributed over communities.

Results: We demonstrate that clustering eFC yields communities of edges in fetal brains can naturally divide the brain into overlapping clusters. Regions in subcortical networks (network 12 and 13) exhibiting the greatest levels of norm entropy, indicating that they concentrate to a small number of communities, while the orbital medial prefrontal cortex (network 4) contribute to varied edge communities with lowest entropy.

Conclusions: This is the first study examining the edge-centric functional communities in fetal brains. In future work, we will characterize eFC in fetuses on the individual level, and will examine the developmental and sex effect. An ultimate goal will be leveraging this approach to identify novel biomarkers of disease, characterizing individual variation and mapping the architecture of highly resolved neural circuits.

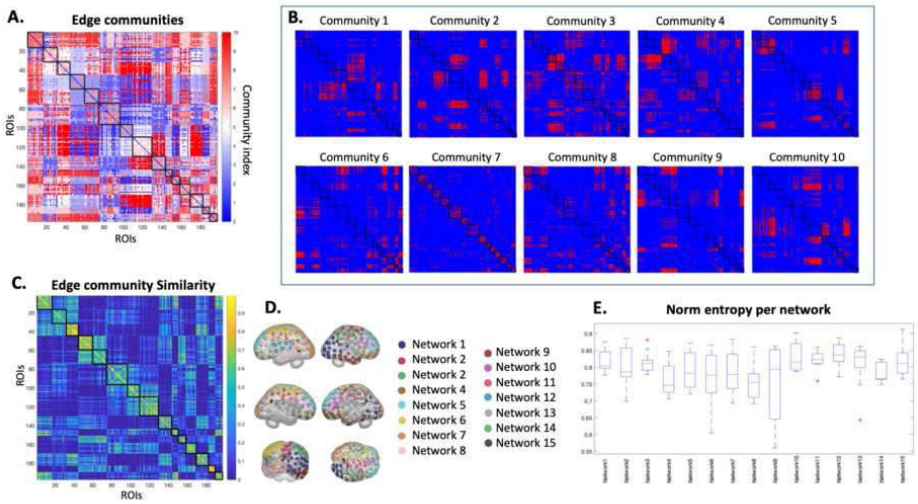

Figure 1. (A) Group-representative edge communities; (B) Community templates. (C) Edge community. (D) ROIs and networks. (E) Normalized entropy per network.

References

1. Faskowitz, J., et al., Edge-centric functional network representations of human cerebral cortex reveal overlapping system-level architecture. Nature neuroscience, 2020. 23(12): p. 1644-1654.
2. Jo, Y., et al., The diversity and multiplexity of edge communities within and between brain systems. Cell reports, 2021. 37(7).
3. Rutherford, S., et al., Automated Brain Masking of Fetal Functional MRI with Open Data. Neuroinformatics, 2021: p. 1-13.
4. Jenkinson, M., et al., Fsl. Neuroimage, 2012. 62(2): p. 782-790.
5. Griffanti, L., et al., ICA-based artefact removal and accelerated fMRI acquisition for improved resting state network imaging. Neuroimage, 2014. 95: p. 232-247.
6. Behzadi, Y., et al., A component based noise correction method (CompCor) for BOLD and perfusion based fMRI. Neuroimage, 2007. 37(1): p. 90-101.

Poster No 1818

Functional Connectome Construction in Very Preterm Infants for Cognitive Biomarker Identification

Junqi Wang[1], Hailong Li[1,2], Kim Cecil[1,2], Mekibib Altaye[1,2], Nehal Parikh[1,2], Lili He[1,2]

[1]Cincinnati Children's Hospital Medical Center, Cincinnati, OH, [2]University of Cincinnati, Cincinnati, OH

Introduction: Infants born very prematurely (<32 weeks, VPT infants) are at risk for cognitive deficits[1]. Early interventions within the first two years post-birth, when neuroplasticity is highest, can notably enhance cognitive outcomes in at-risk infants[2]. Studies have explored resting-state functional connectome (FC) biomarkers of cognitive deficits[3,4]. However, most existing methods have difficulties tackling the high level of signal noise present in neonatal blood–oxygen-level-dependent (BOLD) signals. Brain structural connectome (SC) derived from diffusion tensor imaging (DTI) provides a stable fibrous representation of the brain. There are intrinsic relationships between the SC and FC[5]. Our work introduced an advanced graph learning model that uses SC for improved FC construction. The model, tested on the simulated dataset and a VPT infant cohort, is hypothesized to outperform existing methods in FC construction.

Methods: The IRB-approved study involved 395 VPT infants from five Neonatal Intensive Care Units. All infants were imaged between 39-44 weeks postmenstrual age on a 3T MRI scanner during natural sleep without sedation. We administered standardized Bayley Scales of Infant and Toddler Development (Bayley-III) cognitive tests at the 2-year corrected age, categorizing subjects into low-risk (Bayley-III score > 85) and high-risk (Bayley-III score ≤ 85) for cognitive deficits. We processed rs-fMRI and DTI scans using the developing Human Connectome Project (dHCP) pipeline[6,7] with an 82-region dHCP atlas[8]. We calculated the fractional anisotropy weighed connectome for each infant as the prior knowledge SC. The smoothness property of BOLD signals on the FC has been reported and utilized to estimate the brain FC[9]. Based on the intrinsic coupling between SC and FC, we proposed a putative property that the intrinsic BOLD signals should be smooth on the SC as well. The proposed enhanced FC learning model regulated the intrinsic BOLD signals using the SC, which in turn facilitated the estimation of the deterministic FC. As illustrated in Figure 1, our model contains a Construction block and a Denoising block and is optimized following an alternative manner between the two blocks. where we iteratively performed

FC estimation and signal denoising, incorporating the SC smoothness constraint in the process. The intermediate FCs were constructed from the intrinsic BOLD signals regulated by the SC and intermediate FC from the previous iteration. After multiple iterations, the converged FC from our model is considered optimized FC.

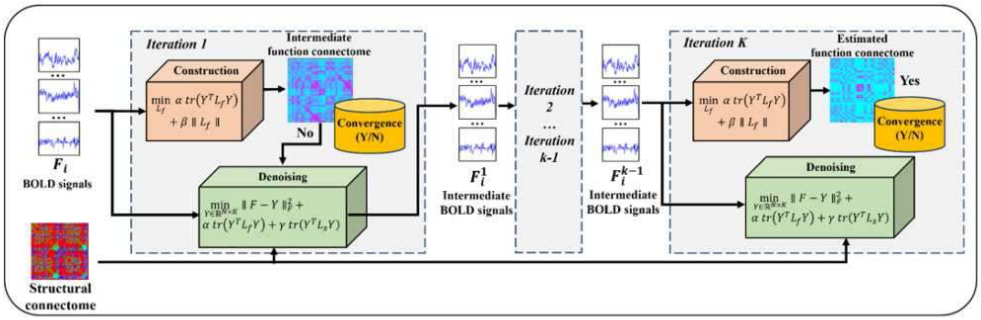

Figure 1. Overview of the enhanced functional connectome construction model. 1) The initial/intermediate FC is constructed based on the smoothness property of BOLD signals on the learned FC; 2) The intrinsic (denoised) BOLD signals are calculated based on the input BOLD signals from the previous iteration, the intermediate FC, and the prior SC. We iteratively estimate the intermediate FC and BOLD signals, until the FC converges.

Results: We simulated the ground truth SC, FC, and BOLD signals and then compared the accuracy of reconstructed FC using our proposed method, the radial basis function kernel (RBF) method, and the graph learning method that does not consider SC (Table 1). Our proposed method achieved superior reconstruction performance over competing methods. We further applied the proposed model to the VPT infant cohort. Based on the enhanced FC, we observed altered functional activation patterns in medial and inferior temporal gyri between low-risk and high-risk groups. These altered regions are not observed in FC constructed using traditional methods.

Table 1. Reconstruction performance using simulated data.

Model	Accuracy (%)	Sensitivity (%)	Specificity (%)
RBF Kernel	82.7 ± 2.6	72.6 ± 4.1	87.4 ± 1.9
Graph Learning	84.0 ± 2.1	74.7 ± 3.4	88.3 ± 1.6
Ours (weak FC-SC coupling)	85.8 ± 2.0	77.5 ± 3.2	89.6 ± 1.5
Ours (strong FC-SC coupling)	**86.8 ± 2.2**	**79.1 ± 3.6**	**90.4 ± 1.6**

We simulated the weak and strong coupling FC-SC pairs. The reconstruction performance goes higher when FC-SC coupling is tighter.

Conclusions: We proposed a novel FC construction algorithm, validated with synthetic data, and applied it to a large cohort of VPT infants. This revealed distinct functional networks between low- and high-risk infants for cognitive deficits.

References

1. He, L. (2020), 'A multi-task, multi-stage deep transfer learning model for early prediction of neurodevelopment in very preterm infants'. Scientific Reports, vol. 10, no. 1, pp. 15072.
2. Morgan, C. (2021) 'Early Intervention for Children Aged 0 to 2 Years With or at High Risk of Cerebral Palsy: International Clinical Practice Guideline Based on Systematic Reviews', JAMA Pediatrics, vol. 175, no. 8, pp. 846-858.
3. Shang, J. (2019), 'A machine learning investigation of volumetric and functional MRI abnormalities in adults born preterm', Humam Brain Mapping, vol. 40, no. 14, pp. 4239-4252.
4. Gozdas, E. (2018), 'Altered functional network connectivity in preterm infants: antecedents of cognitive and motor impairments?', Brain Structure and Function, vol. 223, no.8, pp. 3665-3680.
5. Fjell, A.M. (2017), 'Relationship between structural and functional connectivity change across the adult lifespan: A longitudinal investigation', Human Brain Mapping, vol. 38, no. 1, pp. 561-573.
6. Fitzgibbon, S.P. (2020), 'The developing Human Connectome Project (dHCP) automated resting-state functional processing framework for newborn infants', NeuroImage, vol. 223, pp. 117303.
7. Bastiani, M. (2019), 'Automated processing pipeline for neonatal diffusion MRI in the developing Human Connectome Project'. NeuroImage, vol. 185, pp. 750-763.
8. Makropoulos, A. (2018), 'The developing human connectome project: A minimal processing pipeline for neonatal cortical surface reconstruction', NeuroImage, vol. 173, pp. 88-112.
9. Wang, J. (2023), 'Dynamic weighted hypergraph convolutional network for brain functional connectome analysis', Medical Image Analysis, vol. 87, pp. 102828.

Poster No 1819

Decoding Major Depressive Disorder Neuroconnectivity: Heterogeneity and Demographic Effects

Farzad Farahani[1], Dongnhu Truong[1], Rouhollah Abdollahi[1], Gamal Abdel-Azim[1], Christopher Whelan[1], Shuwei Li[1], Julio Molineros[1]

[1]*Johnson & Johnson, Spring House, PA*

Introduction: Major Depressive Disorder (MDD) affects 3.8% of the global population (GBD Results, 2022), with disrupted functional connectivity playing a key role in its neurobiology. This study utilized ICA-based connectome derived from ~40K patient resting-state functional magnetic resonance imaging (rs-fMRI) data from the UK Biobank (UKB; Miller et al. 2016), a biomedical data repository with 500K voluntary participants aged 40-69 at recruitment. The objectives were to (1) identify connectivity disruptions in MDD, and (2) develop a predictive model for MDD classification against healthy controls (HC), excluding participants with any other mental/neurologic disorders. Additionally, we explored heterogeneity within the HC to further evaluate and enhance model accuracy and generalizability.

Methods: UKB Data (ICA Connectome): Our study included 13,791 subjects (12,656 HC vs. 1,135 MDD) in the UKB with rs-fMRI data and confirmed MDD diagnosis determined by International Classification of Diseases codes. The dataset featured 21 independent components derived through group-ICA decomposition, with 210 edges (correlations) as input features from the lower triangular part of the ICA connectome. To address the imbalanced class distribution, SMOTE (Synthetic Minority Over-sampling Technique) resampling was used to augment the minority class (MDD). Clustering HC: K-means clustering was used to classify controls into two clusters (C1 and C2) because of the observed heterogeneity of the healthy sample. Subsequent analyses explored both the entire dataset and each cluster independently, offering insights into distinctive patterns within the control group that contributed to a more nuanced understanding of factors influencing downstream MDD classification based on the ICA connectome. Classification Models: Various classifiers (including logistic regression, support vector machines, and XGBoost) were used, each followed by 5-fold cross-validation. Stacking classifiers leveraged individual model strengths for enhanced classification performance. Performance was compared across scenarios using metrics such as accuracy, precision, recall, and F1-score.

Results: Deciphering Heterogeneity in MDD Average correlation matrices from rs-fMRI data reveal neuroconnectivity patterns in HC and MDD groups (Fig 1A). There were significant group differences highlighted in the binary matrix through network-based statistics (Fig 1B) (Zalesky et al., 2010). Initial ensemble classification models showed low relative accuracy (Fig 1G; purple bars). The t-SNE projection further emphasized the intricacies of group separation (Fig 1C). Notably, delving into the heterogeneity within the HC group uncovered distinctive clusters (C1 and C2) (Fig 1D). While there are significant differences in age distribution between the full HC group and MDD (Fig 1E), C2 showed a similar age distribution to MDD patients (Fig 1F), which improved prediction performance of MDD vs C2 (Fig 1G). Neural Signatures: SHAP Analysis Unravels Key Edges/Components in MDD Classification SHAP matrix displays edges that significantly contributed to the model's performance upon training on the HC (C2) and MDD groups, as shown in Fig 2A (Lundberg & Lee, 2017). In Fig 2B, the top 20 influential edges are color-coded (red and blue) in the summary plot, indicating their positive and negative effects on the model's performance, respectively. Components 10, 8, 12, and 18 (members of the set of significant edges) had the strongest effect in classification accuracy (as shown in the chord diagram Fig 2C).

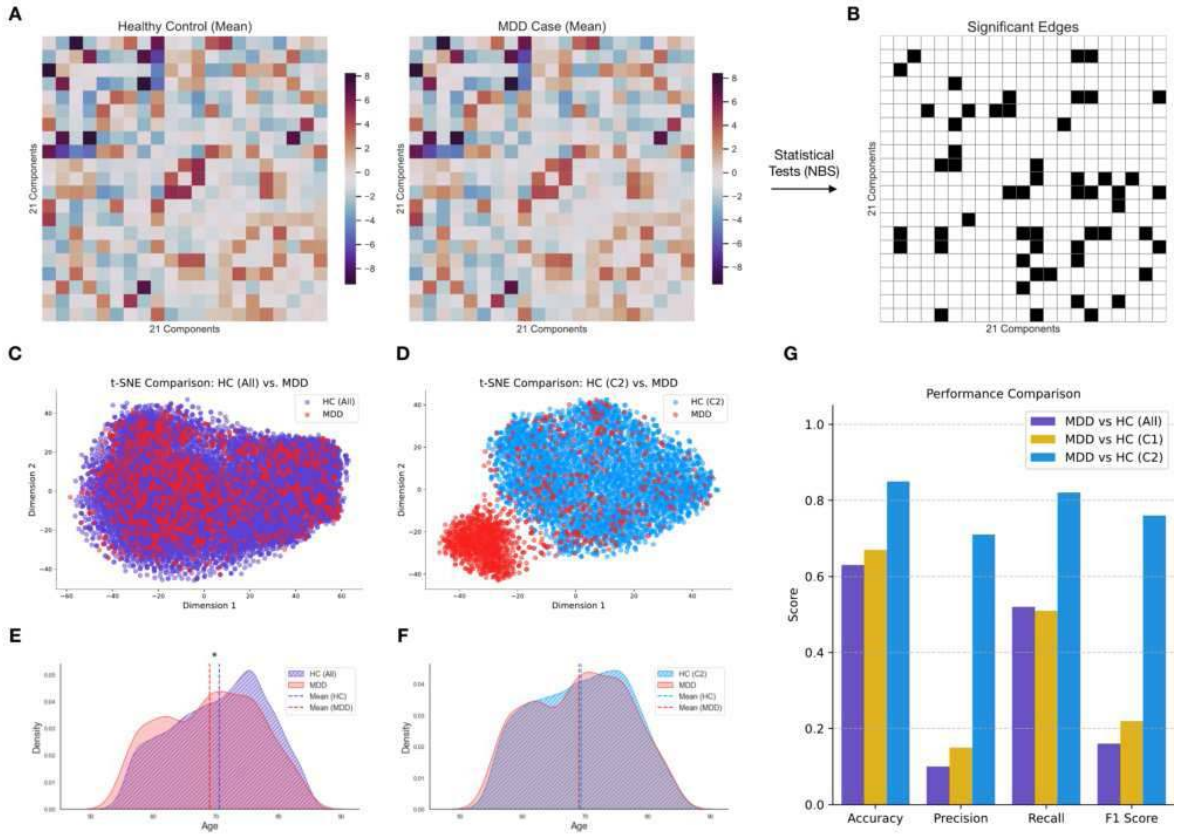

Fig 1. Exploring resting-state connectivity in MDD and HC. (A) Average ICA-based correlation matrices. (B) Binary matrix of significant differences. (C) t-SNE projection highlights group challenges. (D) Improved classification with homogenous HC (C2). Demographics: age disparities (E) reduced in HC (C2) (F). (G) Performance scores in diverse scenarios reveal heterogeneity impact.

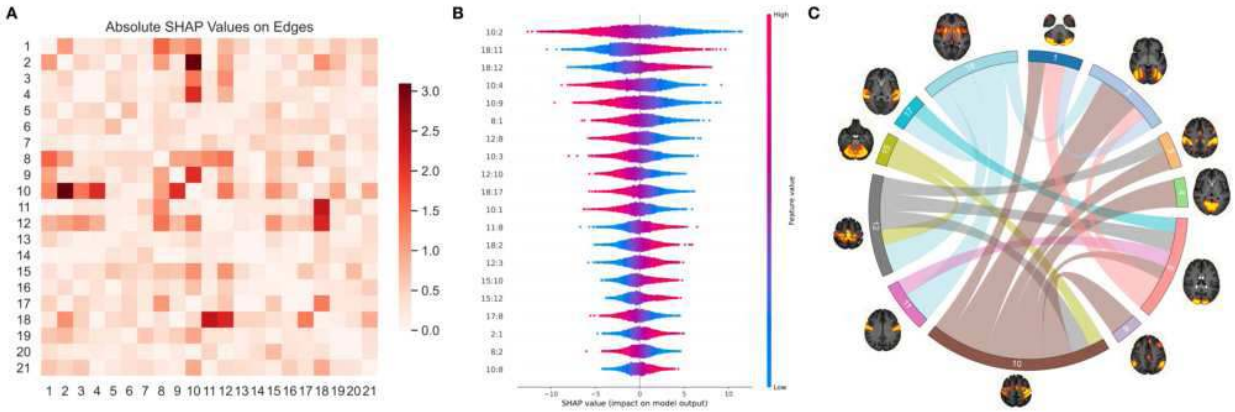

Fig 2. SHAP analysis unveils key connectivity patterns in distinguishing MDD from refined HC (C2). (A) Absolute SHAP values across all edges. (B) Summary plot of the top 20 significant edges, illustrating positive and negative impacts on classification. (C) Chord diagram showing relationships and contributions of significant edges, emphasizing key components in MDD identification.

Conclusions: In conclusion, addressing network heterogeneity within the control group significantly improved prediction performance of MDD. This highlighted the gross network differences between MDD and age-matched HC (C2) in the ICA-based connectome dataset. We identified four major components (8, 10, 12, and 18) from significant edges that significantly impacted MDD classification accuracy based on SHAP analysis of the connectivity patterns.

References

1. Miller, K. L. et al. “Multimodal Population Brain Imaging in the UK Biobank Study.” Nat. Neurosci. 19.11 (2016): 1523-1536.
2. Zalesky, A., Fornito, A., Bullmore, E. T. “Network-based Statistic: Identifying Differences in Brain Networks.” Neuroimage 53.4 (2010): 1197-1207.
3. Lundberg, S. M., Lee, S.-I. “A Unified Approach to Interpreting Model Predictions.” Adv. Neural Inf. Process. Syst. 30 (2017).

Poster No 1820

Certainty in perception, reaction and action, and higher order functional connectivity loss in OCD

Paolo Lorenzo Belleza[1], Hady Saad[2], John Kopchick[3], Phillip Easter[2], David Rosenberg[2], Jeffrey Stanley[3], Vaibhav Diwadkar[2]

[1]Wayne State University, Canton, MI, [2]Wayne State University, Detroit, MI, [3]Wayne State University, Department of Psychiatry, Detroit, MI

Introduction: Predictive processing is partially linked to the certainty (or uncertainty) of the perception-reaction-action cycle (Friston, 2019). In typical control participants, fixed stimulus-response relationships with low uncertainty evoke smooth resonance in network states (Asemi et al., 2015). However, this resonance is distorted when uncertainty is increased (and the predictability of the perception-action-cycle frays). In conditions like Obsessive Compulsive Disorder (OCD), the clinical core of the illness may impact predictive processing and the relationship between perception-reaction-action cycles and brain network interactions (Soriano-Mas, 2021). Such network interactions have usually been assessed on a bivariate basis using methods like stationary functional connectivity based on zero lag correlations (Silverstein et al., 2016). However, the functional properties of brain networks can be captured at several spatial and temporal scales including high-order functional connectivity (HOFC)(Zhang et al., 2016). In any connectome of n nodes, HOFC quantifies the integrative similarity between any pairs of nodes a and b, by estimating the similarity between the connectivity vector of a and all n nodes, and the connectivity vector of b and all n nodes. Here, we provide the first application of studying how certainty and uncertainty in the perception-reaction-action cycle impacts higher order brain network connectivity in OCD youth and typical controls.

Methods: fMRI data (Siemens Verio 3T) were acquired in 63 participants (37 OCD and 26 HC) while they performed a simple perception-reaction-action task. The task required responses (finger tap) to a colored square (green or red). The predictability (certainty or uncertainty) associated with responding was manipulated using two variables: 1) Response mode was either fixed ("respond to every square" i.e. "Go") or contextualized ("respond only to a green square", 75% targets, i.e., "No-Go) and 2) the inter-stimulus interval was either fixed ("periodic", 1 s SOA) or pseudo-randomly varied (SOAs were randomly sample around a distribution with a mean of 1 s and sd of .5 s). The combination of factors and conditions result in ordinal changes in certainty: High certainty ("Go: Periodic") to High Uncertainty ("No-Go : Pseudorandom). fMRI data were processed in SPM 12 (standard methods). In preparation for HOFC analyses, in each participant, time series were extracted from 246 functionally defined cerebral parcels (Fan et al., 2016) for the computation of pairwise functional connectivity in each of the four conditions (30,012 pairs). Next, HOFC was computed between each of the 246 FC vectors. The resultant HOFC matrix encodes integrative similarities between all pairs of parcels. Inter-group differences in HOFC in each condition were identified after comparing the observed HOFC t-value for each pair against a null distribution generated for each pair (3500 simulations following random reordering of time series before the full computation of the HOFC pipeline). Significant t-values (± 2.5 s.d. of the null) were identified.

Results: Results are depicted (and discussed in Figures 1 and 2). Briefly, certainty and uncertainty were expressed differently in driving loss of HOFC in OCD.

Figure 1 (High Certainty)

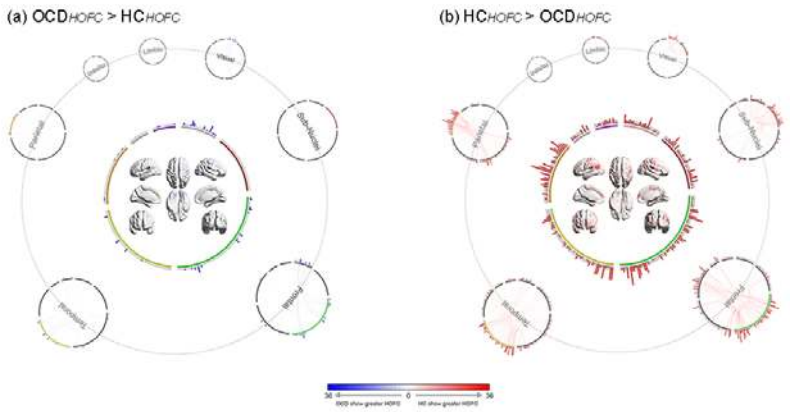

The Figure depicts the two tails of the OCD ≠ HC HOFC comparison during the High Certainty perception, reaction and action condition ("Go Periodic"). In each connectomic ring, the lobar assignments for each of the 246 nodes are clearly separated (in clockwise order, green = frontal; yellow = temporal; orange = parietal; grey = insular, purple = limbic, pink= occipital, maroon = sub-nuclear). The effects specific to each lobe are separated and depicted in the connectomic "satellites" that ring the cumulative connectome. In each ring, a chord represents a pair of regions with a significant difference in HOFC (Blue: OCD > HC; Red: HC > OCD). The circular bar graphs around each connectomic ring quantify the frequency with which any node is part of a significant difference in HOFC. Thus, a higher bar indicates that the node is involved in a higher number of pairs with HOFC differences (see color bar at the bottom). On balance, high certainty in the perception, reaction and action cycle evokes a substantial loss of HOFC in OCD in frontal, parietal, occipital and sub-cortical regions like the thalamus.

Figure 2 (High Uncertainty)

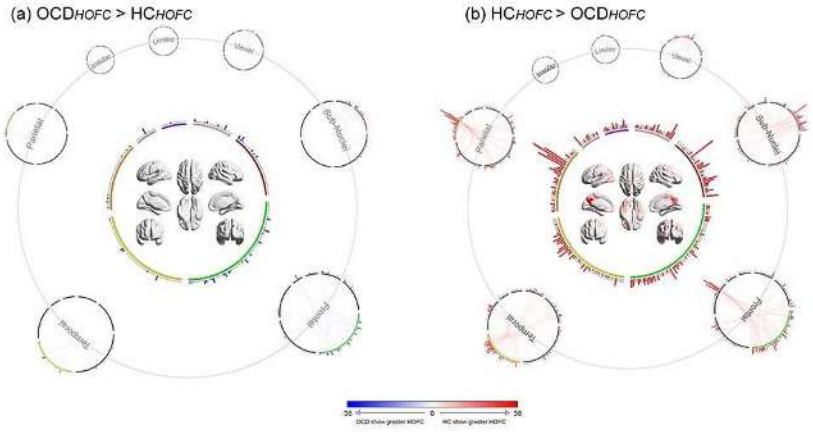

The Figure depicts the two tails of the OCD ≠ HC HOFC comparison during the High Uncertainty perception, reaction and action condition ("No-Go Pseudorandom"). The arrangement of the figure mirrors Figure 1. On balance, high uncertainty in the perception, reaction and action cycle evokes a pattern of HOFC loss that is different than seen in Figure 1. Here, we see a heavy representation of nodes in the parietal cortex and sub-cortical regions like the thalamus.

Conclusions: The brain's ability to implement predictive processing depends on its ability to flexibly recruit cortical hierarchies (Muzik and Diwadkar, 2023), and this ability is likely to be lost in clinical conditions like OCD. We demonstrate that connectivity patterns emergent at higher orders may provide insights on the nexus between a) task evoked network function centered around the construct of certainty b) and functional expressions of neuropsychiatric pathology in conditions like OCD.

References

1. Asemi, A., Ramaseshan, K., Burgess, A., Diwadkar, V.A., Bressler, S.L., 2015. Dorsal anterior cingulate cortex modulates supplementary motor area in coordinated unimanual motor behavior. Front Hum Neurosci 9, 309.
2. Fan, L., Li, H., Zhuo, J., Zhang, Y., Wang, J., Chen, L., Yang, Z., Chu, C., Xie, S., Laird, A.R., Fox, P.T., Eickhoff, S.B., Yu, C., Jiang, T., 2016. The Human Brainnetome Atlas: A New Brain Atlas Based on Connectional Architecture. Cereb Cortex 26 (8), 3508-3526.
3. Friston, K.J., 2019. Waves of prediction. PLoS Biol 17 (10), e3000426.
4. Muzik, O., Diwadkar, V.A., 2023. Depth and hierarchies in the predictive brain: From reaction to action. Wiley Interdiscip Rev Cogn Sci, e1664.
5. Silverstein, B., Bressler, S., Diwadkar, V.A., 2016. Inferring the dysconnection syndrome in schizophrenia: Interpretational considerations on methods for the network analyses of fMRI data. Front Psychiatry 7, 132.
6. Soriano-Mas, C., 2021. Functional Brain Imaging and OCD. Curr Top Behav Neurosci 49, 269-300.
7. Zhang, H., Chen, X., Shi, F., Li, G., Kim, M., Giannakopoulos, P., Haller, S., Shen, D., 2016. Topographical Information-Based High-Order Functional Connectivity and Its Application in Abnormality Detection for Mild Cognitive Impairment. J Alzheimers Dis 54 (3), 1095-1112.

Poster No 1821

A Large Multiscale Neural Model Inversion Framework for Quantifying Excitation-Inhibition Balance

Guoshi Li[1], Pew-Thian Yap[1]

[1]*University of North Carolina at Chapel Hill, Chapel Hill, NC*

Introduction: Excitation-inhibition (E-I) balance is a fundamental property of neuronal circuits and abnormal E-I balance has been hypothesized to be a key driver for multiple neurological and mental disorders. However, no computational models have been established so far to measure E-I balance in large-scale neuronal circuits based on noninvasive individualized neuroimaging. To close this important gap, we developed a large Multiscale Neural Model Inversion (LMNMI) framework for E-I estimation based on resting-state functional MRI (rs-fMRI) by extending a previous small-scale MNMI model (Li et al., 2011). The validity of the LMNMI model was evaluated by both ground-truth simulation and empirical analysis of E-I imbalance in Alzheimer's disease (AD).

Methods: In the LMNMI framework (Fig. 1A) the neural network dynamics is described by a discrete linearized neural mass model (NMM) of Wilson-Cowan type with a time step of Δt (Δt=TR) (Galán, 2008). Each network node contains two mutually coupled excitatory and inhibitory neural populations and the excitatory neural populations are connected via long-range fibers. First, structural connectivity from diffusion MRI is used to construct a sparse network by removing weak inter-regional connections. Second, empirical BOLD signals are Wiener-deconvolved to obtain composite neural activity y ^(t). Third, Kalman filter is applied to estimate neural activity x(t) and the predicted error of composite neural activity is calculated. Lastly,

connection parameters (W) are optimized by minimizing the prediction error using a gradient descent algorithm. For ground-truth simulation, synthetic neural activities were generated using the NMM with model parameters drawn from a uniform distribution. For empirical analysis, we used rs-fMRI data from the ADNI dataset including 48 normal control (NC) (26/22 males/females, 73.4 ± 6.5 years), 48 mild cognitive impairment (MCI) (27/21 males/females, 73.9 ± 10 years) and 48 AD subjects (27/21 males/females, 73.6 ± 8.6 years). Regional BOLD time series were extracted using the Desikan-Killiany atlas (Desikan et al., 2006) based on 46 regions covering the default model, salience, frontoparietal control and limbic networks (Yeo et al., 2011). One-way analysis of variance (ANOVA) was used to compare the E/I means of the three groups followed by post-hoc analysis with two-sample t-test. Multiple comparisons were corrected by controlling FDR with q < 0.05.

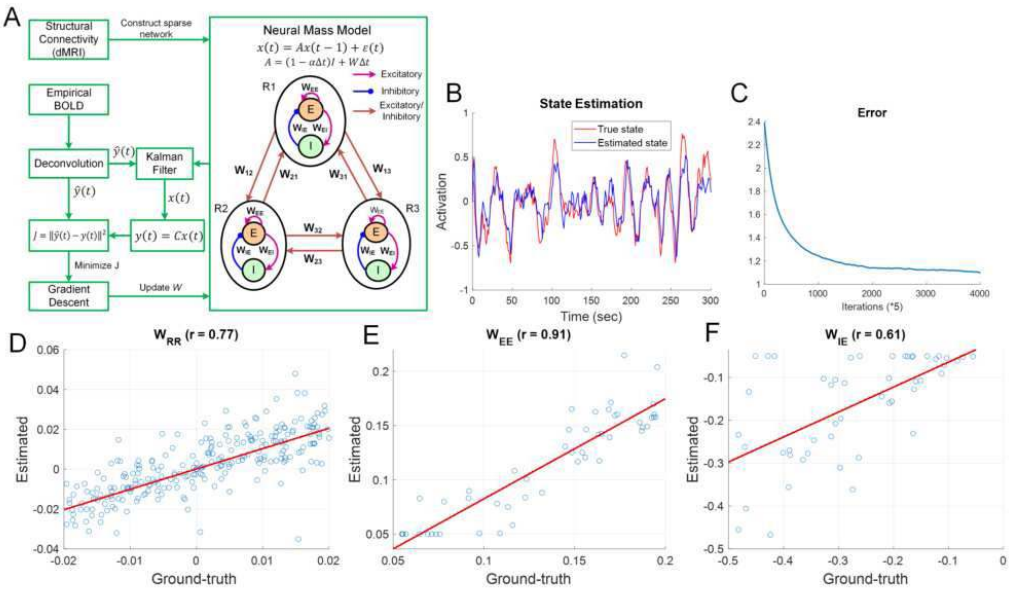

Figure 1. LMNMI framework and ground-truth simulation. (A) LMNMI diagram. **(B)** State estimation using Kalman filter. **(C)** Parameter estimation error computed as the norm of the difference between ground-truth parameters and estimated parameters. **(D)** Scatter plot between ground-truth and estimated inter-regional connection strength (W_{RR}). **(E)** Scatter plot between ground-truth and estimated recurrent excitation strength (W_{EE}). **(F)** Scatter plot between ground-truth and estimated recurrent inhibition strength (W_{IE}).

Results: The Kalman filter was able to accurately track ground-truth neural activity (Fig. 1B) and the parameter estimation error rapidly converged to the minimum (Fig. 1C). The computation time for a network with 50 regions took about 35 minutes (20,000 iterations) when run on a standard computer. The estimated connection parameters closely matched the ground-truth parameters for a representative synthetic subject (r > 0.6; Fig. 1D-F). Application of the LMNMI model to the ADNI dataset indicated that recurrent excitation (WEE) in both MCI and AD significantly decreased compared to NC (p<0.05, FDR corrected) for most of the brain regions (Fig. 2A). In contrast, no significant difference was observed for recurrent inhibition (WIE) among the three groups (Fig. 2B). Consequently, the overall E/I ratio in both MCI and AD was significantly reduced from NC (p<0.05, FDR corrected) in a number of regions including the right precuneus and right putamen (Fig. 2C). The wide-spread reduction in excitation is consistent with the progressive disruption of synaptic transmission during AD progression (Sheng et al., 2012).

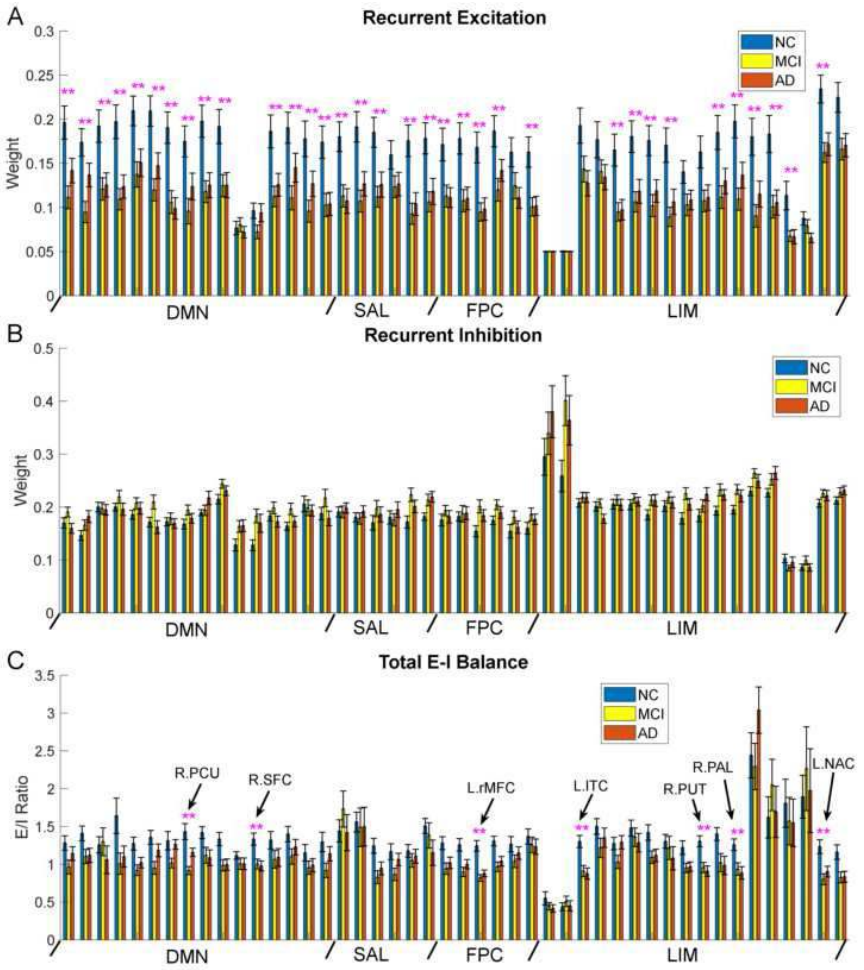

Figure 2. Alterations of E-I balance in MCI and AD. (A) Comparison of recurrent excitation strength among NC, MCI and AD groups. **(B)** Comparison of recurrent inhibition strength among NC, MCI and AD groups. **(C)** Comparison of total E-I balance among NC, MCI and AD groups. Total E-I balance is defined as the ratio between the sum of excitation (recurrent excitation + all incoming positive inter-regional connection strength) and the sum of inhibition (recurrent inhibition + all incoming negative inter-regional connection strength). Double stars indicate the existence of pairwise comparison that passes correction for multiple comparison. R.PCU: Right precuneus; R.SFC: Right superior frontal cortex; L.rMFC: Left rostral middle frontal cortex; L.ITC: Left inferior temporal cortex; R.PUT: Right putamen; R.PAL: Right pallidum; L.NAC: Left nucleus accumbens. DMN: Default mode network; SAL: Salience network; FPC: Frontoparietal control network; LIM: Limbic network.

Conclusions: We developed a new LMNMI framework for large-scale E-I estimation based on rs-fMRI and validated its efficiency and accuracy using both ground-truth simulation and empirical analysis. This framework offers a highly efficient yet biologically realistic method to construct brain-wide individualized neural network for disease diagnosis and the identification of circuit dysfunction in neurological and psychiatric disorders.

References

1. Desikan, R.S. et al. (2006), 'An automated labeling system for subdividing the human cerebral cortex on MRI scans into gyral based regions of interest', Neuroimage, vol. 31, no. 3, pp. 968–980.
2. Galán, R.F. (2008), 'On how network architecture determines the dominant patterns of spontaneous neural activity', PLoS ONE, vol. 3, no. 5, e2148.
3. Li, G. et al. (2021), 'Multiscale neural modeling of resting-state fMRI reveals executive-limbic malfunction as a core mechanism in major depressive disorder', Neuroimage: Clinical vol. 31, 102758.
4. Sheng, M. et al. (2012), 'Synapses and Alzheimer's disease', Cold Spring Harb Perspect Biol, vol. 4, no. 5, a005777.
5. Yeo, B.T. et al. (2011), 'The organization of the human cerebral cortex estimated by intrinsic functional connectivity', Journal of Neurophysiology, vol. 106, no. 3, pp. 1125–1165.

Poster No 1822

Evidence for network compensation to maintain cognitive abilities in clinically impaired individuals

Alexander Simon[1], Xilin Shen[1], Wenjing Luo[1], Saloni Mehta[1], Jagriti Arora[1], Fuyuze Tokoglu[1], Anja Samardzija[1], Corey Horien[1], R Todd Constable[1]

[1]*Yale University, New Haven, CT*

Introduction: Uncovering how abnormalities in functional brain network organization relate to cognition and psychiatric symptoms is an important endeavor of brain- phenotyping. Although extensive work has been done to model how functional network architecture relates to various cognitive processes (Rosenberg, Finn et al. 2016) and symptoms (Xia, Ma et al. 2018), little has been done to examine how functional networks reconfigure to allow individuals with clinically meaningful impairments to maintain cognitive performance. In this study, we tested for evidence supporting the theory that network compensation strategies, detectable in functional connectivity models, are related to maintaining cognitive performance in individuals with clinically relevant impairments. We show that individuals with low levels of self-reported attentiveness and reduced cognitive control network connectivity were able to maintain normal levels of performance on neuropsychiatric evaluations via increased connectivity in a working memory network.

Methods: The relationships between psychiatric symptoms, cognitive performance, and network compensation were analyzed in a transdiagnostic sample consisting of healthy controls and individuals with any combination of 14 different psychiatric diagnoses (n=190). Symptoms were evaluated using the attentiveness scale from the positive and negative affective schedule (PANAS) (Watson, Clark et al. 1988). Functional brain networks were defined for each of the six Research Domain Criteria (RDoC) cognitive constructs (Insel, Cuthbert et al. 2010) using Neurosynth (Yarkoni, Poldrack et al. 2011) to initially identify network nodes. The set of edges within each cognitive construct network was then expanded by including edges with the strongest connections to the nodes within the network constructs. To ensure maximal independence between network constructs, edges shared between networks were removed. This resulted in approximately 200 edges for each construct network. Network connectivity was normalized by performance on the Wechsler Adult Intelligence Scale (WAIS-IV) Symbol Search neuropsychiatric test (Wechsler 2008) by computing the linear relationship between network connectivity and test scores and calculating the distance of each individual's network connectivity from the regression line. Finally, the difference between the normalized working memory network and cognitive control network was correlated with PANAS attentiveness scores.

Results: By calculating differences in connectivity relative to cognitive performance between cognitive construct networks, we developed an approach for evaluating network compensatory strategies to maintain cognitive performance in clinically impaired individuals. The difference between working memory network and cognitive control network connectivity was significantly negatively correlated with PANAS attentiveness scores ($r = -0.184$, $p = 0.011$), such that a larger difference between working memory and cognitive control network connectivity was associated with poorer attentiveness ratings. This finding provides evidence supporting the validity of using this approach to examine network compensation strategies.

Conclusions: The findings suggest that individuals with lower self-reported attentiveness scores can maintain higher levels of neuropsychiatric test performance in part by increased reliance upon a working memory network to compensate for reduced connectivity in a cognitive control network. These results have the potential to advance the applications of neuroimaging in psychiatry by improving our understanding of how cognitive deficits can be compensated for by leveraging networks related to different cognitive constructs. Furthermore, the methodology in this study can be utilized to investigate how other network compensation strategies might contribute to cognitive maintenance in individuals with different psychiatric symptoms.

References

1. Insel, T., B. Cuthbert, M. Garvey, R. Heinssen, D. S. Pine, K. Quinn, C. Sanislow and P. Wang (2010). "Research domain criteria (RDoC): toward a new classification framework for research on mental disorders." Am J Psychiatry 167(7): 748-751.
2. Rosenberg, M. D., E. S. Finn, D. Scheinost, X. Papademetris, X. Shen, R. T. Constable and M. M. Chun (2016). "A neuromarker of sustained attention from whole-brain functional connectivity." Nat Neurosci 19(1): 165-171.
3. Watson, D., L. A. Clark and A. Tellegen (1988). "Development and validation of brief measures of positive and negative affect: the PANAS scales." J Pers Soc Psychol 54(6): 1063-1070.
4. Wechsler, D. (2008). "Wechsler Adult Intelligence Scale--Fourth Edition." APA PsychTests.
5. Xia, C. H., Z. Ma, R. Ciric, S. Gu, R. F. Betzel, A. N. Kaczkurkin, M. E. Calkins, P. A. Cook, A. Garcia de la Garza, S. N. Vandekar, Z. Cui, T. M. Moore, D. R. Roalf, K. Ruparel, D. H. Wolf, C. Davatzikos, R. C. Gur, R. E. Gur, R. T. Shinohara, D. S. Bassett and T. D. Satterthwaite (2018). "Linked dimensions of psychopathology and connectivity in functional brain networks." Nat Commun 9(1): 3003.
6. Yarkoni, T., R. A. Poldrack, T. E. Nichols, D. C. Van Essen and T. D. Wager (2011). "Large-scale automated synthesis of human functional neuroimaging data." Nat Methods 8(8): 665-670.

Poster No 1823

Propriospinal Functional Connectivity During Hand Motor Control in Humans

Matteo Grudny[1], Shahab Vahdat[1]

[1]*University of Florida, Gainesville, FL*

Introduction: Functional magnetic resonance imaging (fMRI) of the brain and spinal cord at the same time allows for novel investigation of the descending motor pathways in humans. The propriospinal pathway in humans is not well characterized and utilizing this innovative acquisition protocol and processing pipeline we report the detection of propriospinal functional connectivity during a motor control task. Specifically, we detect significant partial correlation of C3-C4 ipsilateral ventral horn activity with cortical, subcortical, brainstem, and cerebellar region activation during a motor control task in humans. Additionally, we observed significant functional connectivity with the C3-C4 ipsilateral dorsal horn in a subset of cerebellar and cortical regions. These results validate the sensitivity of our functional connectivity analysis and the importance of the propriospinal motor control pathway in hand motor control. Furthermore, this approach can be applied to gain insight on the dysfunctional descending motor and ascending sensory pathways in stroke patients and help guide therapeutic intervention.

Methods: We collected BOLD fMRI data covering the whole brain and the cervical cord (C1-T1 levels) using simultaneous multi-slice (SMS) EPI sequence on a 3T Prisma Siemens scanner (slice thickness: 4mm, resolution:1.6x1.6 mm2, TR:1.85 s). A MEDIC T2*w image was acquired with similar slice angle and thickness as EPI data (resolution 0.8x0.8 mm2). A T1w image was acquired for registration to the template (PAM50). During functional scans, 17 participants performed a manual grip force control task using their right hand in an event-related design paradigm. We employed a recently developed processing pipeline for analysis of spinal fMRI data called FASB[1]. The pipeline includes: a two-step motion correction procedure, slice-wise centerline alignment to T2*w image, independent component analysis (ICA) of spinal cord data to automatically identify non-neuronal related regressors, and automatic temporal SNR (tSNR) threshold selection based on MAP estimation. Functional connectivity analysis was conducted utilizing ROI based analysis. The ROIs included spinal levels C3-C4 and C5-C8, along with cortical, subcortical, brainstem, and cerebellar regions hypothesized to be involved in upper limb motor control. BASCO (BetA-Series Correlation), Pearson correlation during task-on periods, and partial correlation (by removing the effect of task paradigm presentation) were calculated and tested for significance using a t-statistics and Bonferroni multiple-comparison correction[2].

Results: Our results indicate that unilateral handgrip force control is associated with significant activation clusters at cortical, subcortical, brainstem, cerebellum, C3-C4 cervical spine, and C5-C8 cervical spinal cord ($p < 0.05$, corrected using GRF) (Fig. 1). We additionally report significant functional connectivity at the C3-C4 cervical level ipsilateral ventral horn with cortical (primary motor and premotor cortex), brainstem (pontine and medullary reticular formation, vestibular nucleus), and cerebellar regions consistent with the propriospinal pathway for hand motor control during the task. Lastly, we observed functional connectivity between the C3-C4 ipsilateral dorsal horn and a subset of cerebellar and cortical regions ($p < 0.05$, corrected using Bonferroni) (Fig. 2).

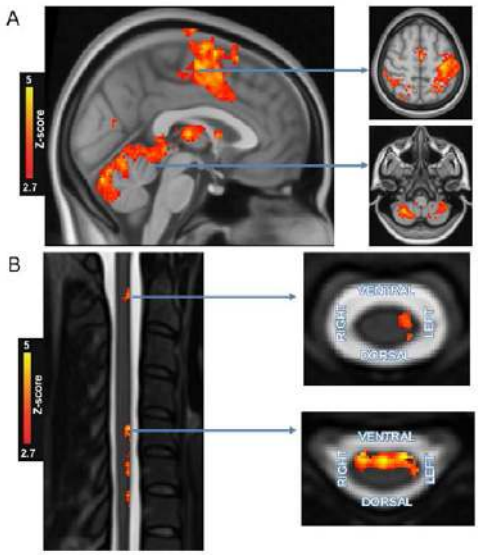

Fig. 1. (A), Unilateral handgrip force control task activates significant clusters at cortical, subcortical, brainstem and cerebellar regions. (B) Unilateral handgrip force control task activates significant clusters at C3-C4 and C5-C8 cervical spine ($p < 0.05$, corrected using GRF).

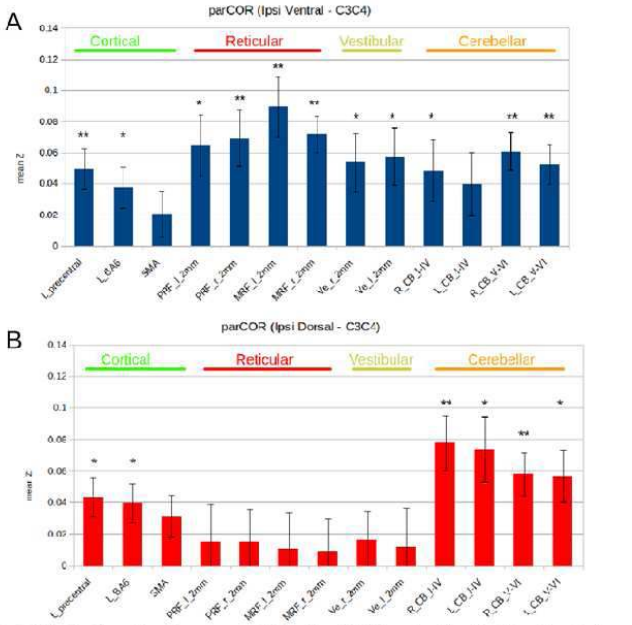

Fig. 2. (A), Significant functional connectivity at the C3-C4 cervical level ipsilateral ventral horn with cortical, brainstem, and cerebellar regions. (B), Significant functional connectivity between the C3-C4 ipsilateral dorsal horn and a subset of cerebellar and cortical regions ($p < 0.05$, corrected using Bonferroni). Left precentral cortex (L_precentral); Left Brodmann area 6 (L_BA6); supplementary motor area (SMA); left and right pontine reticular formation (PRF_l and PRF_r); left and right medullary reticular formation (MRF_l and MRF_r); left and right vestibular nuclei (Ve_l and ve_r); right and left cerebellar lobules 1-4 (R_CB_I-IV and L_CB_I-IV); right and left cerebellar lobules 5-6 (R_CB_V-VI and L_CB_V-VI)

Conclusions: Overall, our analysis results in strong activation at the spinal cord and brain during the motor control task. Our main finding suggests propriospinal functional connectivity is critical during hand motor control and is mainly correlated with the ipsilateral ventral horn of the spine and to a lesser degree with the ipsilateral dorsal horn. These methods will be valuable in characterizing the altered descending motor and ascending sensory pathways of stroke patients.

References

1. Vahdat S "FASB: processing pipeline for Functional Analysis of simultaneous Spinal cord-Brain fMRI", Human Brain Mapping annual meeting, OHBM 2023, Montreal.
2. Rissman J. (2004). Measuring functional connectivity during distinct stages of a cognitive task. Neuroimage 23, 752–763. 10.1016/j.neuroimage.2004.06.035

Poster No 1824

Functional Network Connectivity Dynamics in the Human Fetal Brain

Tanya Bhatia[1], Lanxin Ji[2], Ellyn Kennelly[3], Amyn Majbri[1], Mark Duffy[2], Iris Menu[2], Moriah Thomason[4]

[1]New York University Medical Center, New York, NY, [2]NYU Langone Health, New York, NY, [3]Wayne State University, Detroit, MI, [4]NYU Langone Medical Center, New York, NY

Introduction: The human brain undergoes dramatic transformations during the late fetal stage, with the emergence and organization of brain networks. Fetal MRI has made it possible to map the functional connectivity of the brain during this critical developmental period[9]. Recent literature suggests that dynamic alterations in human brain functional connectivity during an MRI scan may be indicative of large-scale functional capacity and risk for abnormalities and disease[2,4]. However, no studies to date have explored temporally-driven connectivity dynamics in the fetal brain.

Methods: Imaging data were acquired from 101 fetuses (39 females), gestational age 24.00-37.86 weeks (31.19 ± 3.71), who were enrolled in the Perinatal Imaging of Neural Connectivity study. Functional MRI were acquired using a 3T Siemens Verio 70 cm open-bore system with an abdominal 4-channel Siemens Flex coil, with the following gradient multi-echo planar imaging sequence: TR = 2000 ms; TEs = 18, 34.06, 50.12ms; flip-angle: 80-degree, slice-gap: none; voxel-size: 3.4 x 3.4 x 4 mm3. Preprocessing included brain segmentation with deep learning, motion estimation and censoring with FSL FLIRT. Participants with fewer than 105 low-motion frames were excluded. Optimal combination across echoes, normalization to standard space (GA = 32 weeks), smoothing, and ICA and CompCor denoising were subsequently completed. Spatial group independent component analysis (ICA) was implemented in the Group ICA of functional MRI Toolbox[6] to extract functional

brain networks. Each fetus's time course profile was based on the Infomax[1] algorithm. The number of ICs was chosen to be 40 based on MDL criterion[3]. 34 of the 40 components were identified as non-noise and grouped into 9 functional networks: cerebellum, temporoparietal, frontoinsular, frontal pole, DMN, temporal regions, motor, subgenual, and visual (Fig 1). The time courses of 34 ICs were then detrended, despiked, and filtered with a high frequency cut-off of 0.15 Hz[4]. Pair-wise Pearson's correlations between the ICs were then calculated and z-transformed to form the static functional connectivity matrix. Dynamic functional connectivity analysis was then performed using the dynamic functional network connectivity (DFNC) tool in GIFT. A sliding-window approach was first used to investigate time-varying changes in functional connectivity within the 34 IC networks. Time courses were segmented into a 30-repetition time (TR) window, with a step-wise TR of 2 seconds. K-means clustering (k=3) was then conducted to explore recurring states (i.e. functional connectivity patterns). The correlation of the window count of each state was then correlated with fetal sex using point-biserial correlation, and with gestational age at the time of scan using Pearson's correlation.

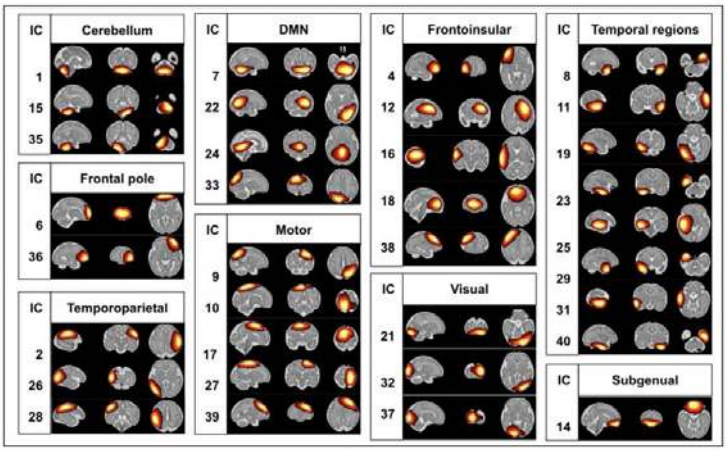

Fig 1. Spatial group independent component analysis results from the GIFT Toolbox, non-noise components grouped into chosen functional networks.

Results: Of the 3 FC states, 2 of them were dominant – 42% in State 1 and 54% in State 2. State 3 was disregarded due to its low frequency of subjects. State 1 was slightly more connected than State 2, both within- and between-networks (Fig 2A). For example, the within-network connectivity of motor, visual, default mode network (DMN), and cerebellar regions is higher in State 1 than State 2. The connectivity between the DMN and visual regions is also higher in State 1. Subjects tended to dwell in State 2 the longest, followed by State 1 (Fig 2B). Subjects tended to dwell in a given state rather than transitioning states, with just 0.4 +/- 0.7 transitions on average (Fig 2C). No significant correlations were found between the count of each state with fetal sex or gestational age at scan.

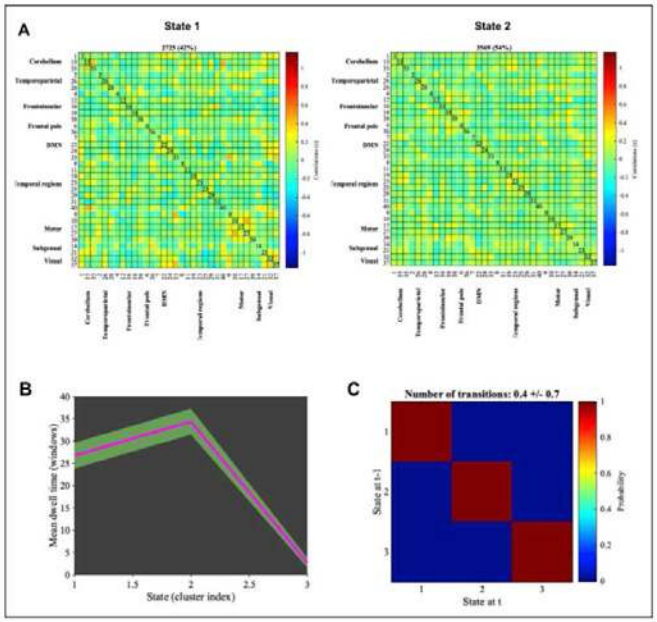

Fig 2. A. Centroid 1 (State 1) and centroid 2 (State 2); functional connectivity patterns of the dominant brain states that emerged from K-means cluster analysis. B. Mean dwell time in windows for each state. C. Probability of being in a given state at t-1 and t.

Conclusions: This exploration of fetal functional connectivity (FC) dynamics revealed two main states with similar FC profiles, and there was minimal state transition, implying low FC dynamics in the fetus. Further work should investigate if these late fetal states persist in varying samples and predictive factors of state characteristics.

References

1. Bell, A. J., & Sejnowski, T. J. (1995). An information-maximization approach to blind separation and blind deconvolution. Neural Computation, 7(6), 1129–1159. https://doi.org/10.1162/neco.1995.7.6.1129
2. Fu, Z., Du, Y., & Calhoun, V. D. (2019). The Dynamic Functional Network Connectivity Analysis Framework. Engineering (Beijing, China), 5(2), 190. https://doi.org/10.1016/j.eng.2018.10.001
3. Grünwald, P. (2000). Model selection based on minimum description length. Journal of Mathematical Psychology, 44(1), 133–152. https://doi.org/10.1006/jmps.1999.1280
4. Kim, J., Criaud, M., Cho, S. S., Díez-Cirarda, M., Mihaescu, A., Coakeley, S., Ghadery, C., Valli, M., Jacobs, M. F., Houle, S., & Strafella, A. P. (2017). Abnormal intrinsic brain functional network dynamics in Parkinson's disease. Brain: A Journal of Neurology, 140(11), 2955–2967. https://doi.org/10.1093/brain/awx233
5. López-Vicente, M., Agcaoglu, O., Pérez-Crespo, L., Estévez-López, F., Heredia-Genestar, J. M., Mulder, R. H., Flournoy, J. C., van Duijvenvoorde, A. C. K., Güroğlu, B., White, T., Calhoun, V., Tiemeier, H., & Muetzel, R. L. (2021). Developmental Changes in Dynamic Functional Connectivity From Childhood Into Adolescence. Frontiers in Systems Neuroscience, 15, 724805. https://doi.org/10.3389/fnsys.2021.724805
6. Rachakonda, S., Egolf, E., Correa, N., & Calhoun, V. (2007). Group ICA of fMRI toolbox (GIFT) manual. Dostupnez [cit 2011-11-5].
7. Thomason, M. E., Hect, J., Waller, R., Manning, J. H., Stacks, A. M., Beeghly, M., Boeve, J. L., Wong, K., van den Heuvel, M. I., Hernandez-Andrade, E., Hassan, S. S., & Romero, R. (2018). Prenatal neural origins of infant motor development: Associations between fetal brain and infant motor development. Development and Psychopathology, 30(3), 763–772. https://doi.org/10.1017/S095457941800072X
8. Towner, D., McGahan, J., Rhee-Morris, L., & Gerscovich, E. (2007). The dynamic fetal brain. Journal of Clinical Ultrasound, 35(5), 238–244. https://doi.org/10.1002/jcu.20320
9. Turk, E., van den Heuvel, M. I., Benders, M. J., de Heus, R., Franx, A., Manning, J. H., Hect, J. L., Hernandez-Andrade, E., Hassan, S. S., Romero, R., Kahn, R. S., Thomason, M. E., & van den Heuvel, M. P. (2019). Functional Connectome of the Fetal Brain. The Journal of Neuroscience, 39(49), 9716–9724. https://doi.org/10.1523/JNEUROSCI.2891-18.2019
10. van den Heuvel, M. I., & Thomason, M. E. (2016). Functional Connectivity of the Human Brain in Utero. Trends in Cognitive Sciences, 20(12), 931–939. https

Poster No 1825

Dynamic Functional Network Connectivity States, Head Motion, and Mental Health Symptoms in Children

Donovan Roediger[1], Andrea Wiglesworth[1], Bonnie Klimes-Dougan[1], Mark Fiecas[1], Monica Luciana[1], Zening Fu[2], Vince Calhoun[2], Bryon Mueller[1], Kathryn Cullen[1]

[1]University of Minnesota, Minneapolis, MN, [2]GSU/GATech/Emory, Atlanta, GA

Introduction: Dynamic functional connectivity analysis is a promising tool for identifying fMRI biomarkers of mental health disorders but is vulnerable to artificial correlations introduced by in-scanner motion (Savaa, 2020). In pediatric imaging, head motion is a common problem and investigations may be further complicated when motion is itself correlated with other measures of interest. Here, we used a sliding window method and k-means clustering algorithm to explore fMRI-derived dynamic "states" and their relationship with head motion and clinical correlates in data from a large-scale adolescent study.

Methods: Using the Adolescent Brain and Cognitive Development dataset, we analyzed baseline data from 11201 participants (ages 9-11) with available data from the Child Behavior Checklist (CBCL), the Kiddie Schedule for Affective Disorders and Schizophrenia (K-SADS), and at least one resting-state scan. Raw fMRI data (first run) were downloaded and preprocessed using previously described methods (Fu, 2023). We then used Neuromark, an ICA-based hybrid framework within the Group ICA of fMRI Toolbox, to derive time series for 53 IC-based ROIs (Du, 2020; Iraji, 2021). These time series were further denoised by applying 6-parameter motion regression, detrending, despiking, and bandpass filtering (0.01 - 0.15Hz). A sliding window approach (40 volumes) was used to calculate dynamic functional network connectivity (dFNC) matrices. Finally, we used a k-means clustering algorithm (k=4) to identify recurring dFNC patterns ("states") across all windows and participants. Initial assessments correlated mean framewise displacement (FD) with the percent of volumes spent in each state to determine the extent of residual motion-related effects that remained after preprocessing and the relationship between mean FD and clinical measures of interest. GLMs were then used to assess how the percentage of scan time spent in each of the four states relates to binary lifetime suicidal ideation (SI; either caregiver or child-report) as well as internalizing, externalizing, and total problems from the CBCL (caregiver report). In addition to time spent in each state, the number of state switch events during the scan was explored as a predictor of clinical outcomes.

Results: Cluster centroids for the four identified dFNC states are shown in Figure 1. Despite efforts to remove motion artifacts, residual motion appeared to heavily influence the proportion of scan time spent in each state, with higher movers spending

more time in States 1 and 4 and lower movers spending more time in States 2 and 3 (Figure 2). Positive correlations were found between mean FD and all clinical measures (r's = 0.1). To account for the confounding effects of motion, all GLMs were adjusted for mean FD. Patterns observed across clinical outcome measures were consistent, where time spent in States 1 and 4 was weakly but consistently associated with higher CBCL scores (more symptoms) and lifetime SI while spending more time in States 2 and 3 was associated with lower CBCL scores and lifetime SI. After Bonferroni correction, only the relationships between time spent in States 1 through 4 and the CBCL "total problems" score remained significant (p's < 0.0025). The frequency of transitions between states was unrelated to any clinical measures.

Figure 1.

Connectivity matrices representing the cluster centroids of four dFNC states and their overall prevalence across the dataset.

Figure 2.

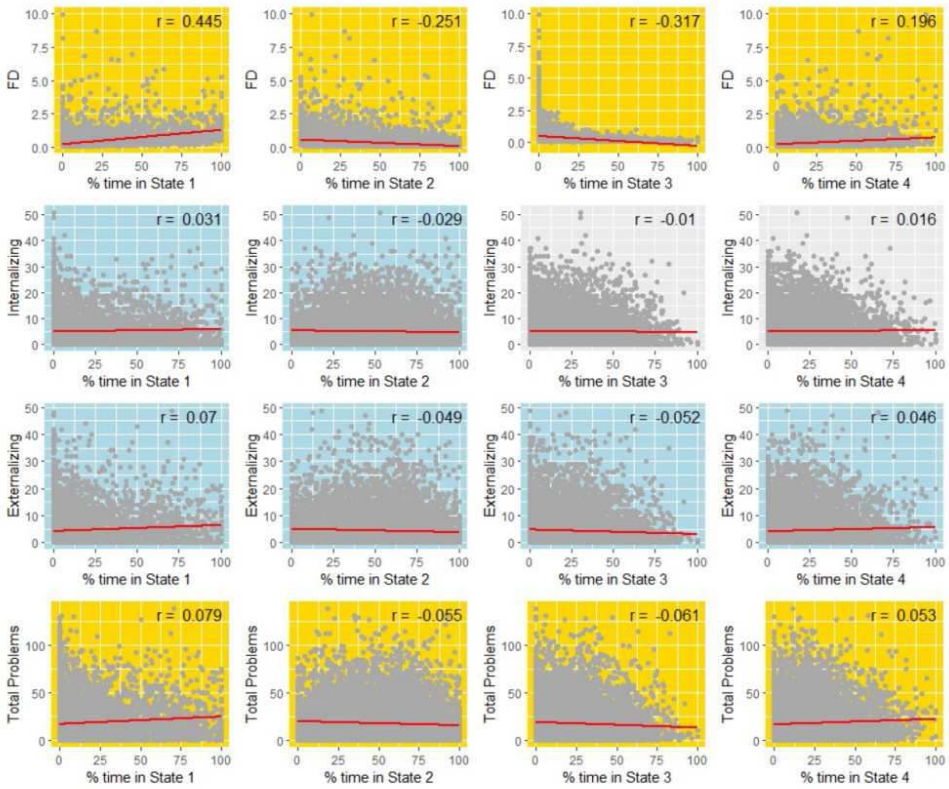

Top row: Linear relationships between average framewise displacement and time spent in each dFNC state. Rows 2-4: Linear relationships between "internalizing", "externalizing", and "total problems" CBCL scores and time spent in each dFNC state. Relationships where $p < 0.05$ are highlighted in blue while relationships where $p < 0.0025$ (Bonferroni-adjusted alpha) are highlighted in yellow.

Conclusions: Motion events appeared to drive windows toward particular dFNC states despite preprocessing methods implemented to limit the impact of motion. This reinforces previous observations that dFNC analyses are especially vulnerable to motion and that steps should be taken during both preprocessing and analysis to identify and control for any motion-related effects (Abrol, 2017). Notably, we also observed significant relationships between dFNC and clinical measures that were robust to this motion, highlighting the utility of dFNC clustering analyses in exploring relationships between fMRI and mental health in children.

References

1. Abrol, A. et al. (2017), 'Replicability of time-varying connectivity patterns in large resting state fMRI samples'. NeuroImage, vol. 163, pp. 160–176.

2. Du, Y. et al. (2020), 'NeuroMark: An automated and adaptive ICA based pipeline to identify reproducible fMRI markers of brain disorders', NeuroImage: Clinical, vol. 28, p. 102375.
3. Fu, Z. et al. (2023), 'Functional connectivity uniqueness and variability? Linkages with cognitive and psychiatric problems in children'. Nature Mental Health, pp. 1–15.
4. Iraji, A. et al. (2021), 'Tools of the trade: Estimating time-varying connectivity patterns from fMRI data', Social Cognitive and Affective Neuroscience, vol. 16(8), pp. 849–874.
5. Savva, A. D. et al. (2020), 'Effects of motion related outliers in dynamic functional connectivity using the sliding window method'. Journal of Neuroscience Methods, vol. 330, p. 108519.

Poster No 1826

Less is more: Importance of long-range exceptions in brain architecture

Jakub Vohryzek[1], Morten Kringelbach[2], Gustavo Deco[3]

[1]Universitat Pompeu Fabra, Barcelona, Barcelona, [2]University of Oxford, Oxford, Oxfordshire, [3]Pompeu Fabra University, Barcelona, Catalonia

Introduction: How brain architecture shapes function is a deep question which has occupied many researchers, from the perspective of network neuroscience (Bullmore and Sporns 2009), brain modelling (Breakspear 2017) and spectral graph theory (Atasoy, Donnelly, and Pearson 2016). Some have even suggested that geometry plays a particularly relevant role in shaping functional activity (Pang et al. 2023a), although see this ongoing discussion (Faskowitz et al. 2023; Pang et al. 2023b). Here we focus on probing the importance of the rare long-range exceptions to the exponential distance rule of brain wiring (Markov et al. 2013). New evidence using turbulence has demonstrated the fundamental role of long-range connectivity in shaping optimal brain information processing (Deco et al. 2021). Here we used Laplacian decomposition of four different graph representations of the underlying anatomy to derive anatomical brain modes: exponential-distance rule (EDR) (Ercsey-Ravasz et al. 2013) and long-range exceptions (EDR+LR), geometry-based modes (geometry) and EDR modes (EDR binary and EDR continuous) (Figure 1 A). Our results show that EDR+LR achieves significantly better reconstruction of long-range functional connectivity (FC) compared to the other mode representations. Furthermore, pertinent to time-critical information processing, we show that a small subset of modes achieves a disproportionately high reconstruction of task MRI activity. When this subset of modes is considered, EDR+LR achieves better reconstruction for the 47 HCP tasks compared to the other mode representations, suggesting that less is more for information processing in the brain.

Methods: We used publicly available data by the Human Connectome Project (HCP) of resting-state and task fMRI of 255 participants. The various modes are derived from applying the laplace decomposition on the graph representation (Figure 1 B, i). These modes are used to reconstruct the fMRI activity by a linear combination of their contributions (Figure 1 B, ii). This serves to reconstruct the resting-state fMRI activity and in particular the long-range connectivity exceptions derived as high-correlation values (<0.5 correlation) and over a long euclidean distance (<40mm) as well as the task fMRI activation maps (Figure 1 B, iii). Four different graph representations were constructed and decomposed into their associated modes (Figure 1 C). Namely, the fitted weighted and binary Euclidean Distance Rule with lambda of 0.18, EDR with long-range connectivity and the geometric modes (Pang et al. 2023a).

Results: An important feature of cortex dynamics are long-range functional connections, defined by high correlation values (<0.5 correlation) and euclidean distance (<40mm) (Figure 2 A). We reconstructed the FC long-range connections for an increasing number of modes (1-200) showing the EDR+LR modes to have the highest reconstruction correlation (Figure 2 B). EDR+LR is statistically higher compared to the other modes (paired t-test, pval<0.05) (Figure 2 C) . For the reconstruction of the 7 activation task fMRI maps lower frequency modes contribute disproportionately more toward the reconstruction error as seen by the elbow around 20 modes (Figure 2 D). We therefore reconstructed the error for the 47 HCP tasks benchmarked against the geometrical modes for the first 20 modes (blue - better reconstruction correlation of the chosen modes, red better for the geometric modes). On average EDR+LR showed the most accurate reconstruction across tasks and number of reconstructed modes 1-20 (Figure 2 E).

Conclusions: Here we show the importance of long-range connectivity as a key feature of shaping brain functional activity both for the spontaneous and task-based fMRI. Moreover, functional brain activity can be shown to be on a lower-dimensional manifold span by a subset of these fundamental modes with the most appropriate representation from the EDR+LR graph, suggesting that less is more for efficient information processing in the brain.

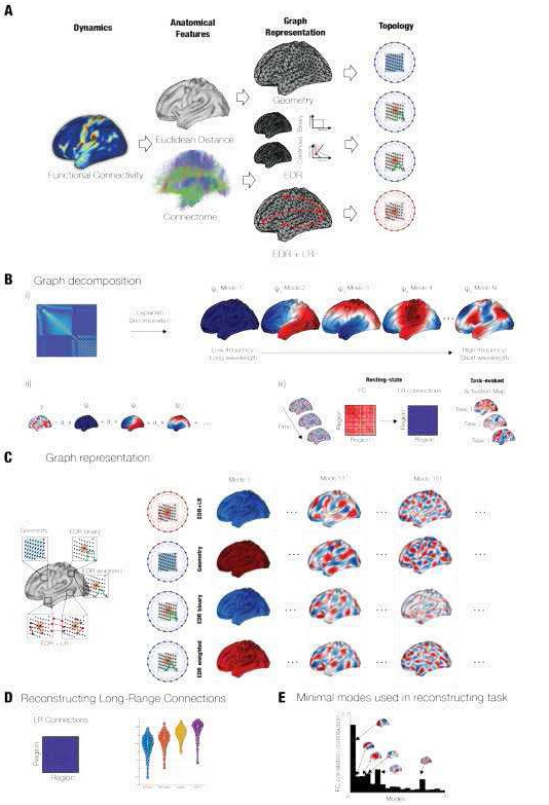

Figure 1: The importance of long-range connectivity for reconstruction of cortical activity. A) Dynamics as represented by Functional fMRI connectivity can be inferred from different anatomical features in terms of how different regions of the neocortex are distant from each other (Euclidean distance) or alternatively by their white-matter wiring contained in the connectome. This information is summarised in a graph representation highlighting the different assumptions on the underlying causes that give rise to the dynamics - the geometrical features, exponential distance rule or the exponential distance rule with long-range exceptions. Consequently, the underlying topology will differ. B) i) The different modes are derived from applying the laplace decomposition on the graph representation by solving the eigenvalue problem. The different modes are in ascending spatial frequency order. ii) These modes are used to reconstruct the fMRI activity by a linear combination of their contributions. iii) This serves to reconstruct the resting-state fMRI activity and in particular the long-range connectivity exceptions derived as high-correlation values (<0.5 correlation) and over a long euclidean distance (<40mm) as well as the task fMRI activation maps. C) Four different graph representations were constructed and decomposed into their associated modes. Namely, the Euclidean Distance Rule with lambda of 0.18, as fitted to the empirically derived connectome, was reconstructed for binary and weighted representation. Furthermore, EDR with long-range connectivity and lastly the geometric modes as described by (Pang et al. 2023a).

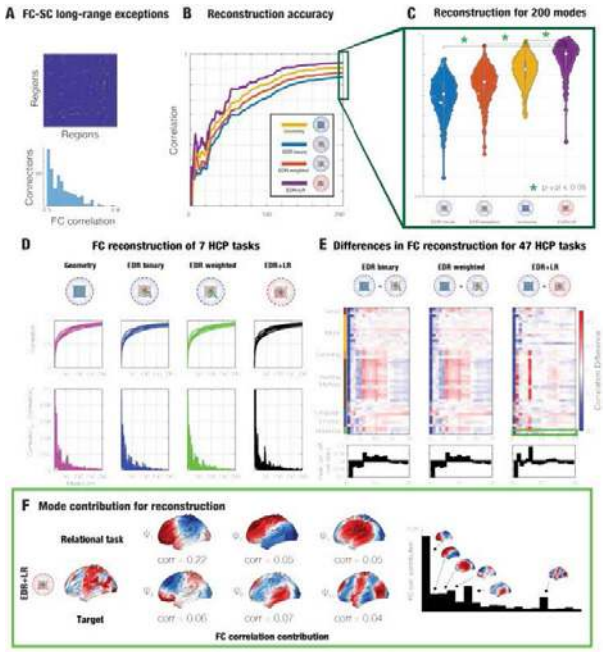

Figure 2 Reconstruction of spontaneous and task fMRI. A) One of the most important features of neocortex dynamics are long-range functional connections, here, defined by high correlation values (<0.5 correlation) and euclidean distance (<40mm). B) Reconstruction of FC long-range connections for increasing number of modes (1-200) for the four representative graphs. The individual lines show an average across 255 HCP participants. C) Correlation values across all the 255 HCP subjects for the reconstruction with 200 modes (EDR+LR statistically higher compared to the other modes paired t-test, pval<0.05). D) Top - Reconstruction of the 7 representative activation task fMRI maps for the four graph representations. Bottom - Lower frequency modes contribute disproportionately more toward the reconstruction error as it can be seen by the elbow around 20 modes. E) Top - Reconstruction error for the 47 HCP taks benchmarked against the geometrical modes for the first 20 modes (blue - better performance of the chosen modes, red better performance of the geometric modes). Bottom - Averaged across the 47HCP task showing overall trend in the benchmarked reconstruction.

References
1. Atasoy, Selen, Isaac Donnelly, and Joel Pearson. 2016. “Human Brain Networks Function in Connectome-Specific Harmonic Waves.” Nature Communications 7 (1): 1–10.
2. Breakspear, Michael. 2017. “Dynamic Models of Large-Scale Brain Activity.” Nature Neuroscience 20 (3): 340–52.
3. Bullmore, Ed, and Olaf Sporns. 2009. “Complex Brain Networks: Graph Theoretical Analysis of Structural and Functional Systems.” Nature Reviews. Neuroscience 10 (3): 186–98.
4. Deco, Gustavo, Yonathan Sanz Perl, Peter Vuust, Enzo Tagliazucchi, Henry Kennedy, and
5. Morten L. Kringelbach. 2021. “Rare Long-Range Cortical Connections Enhance Human Information Processing.” Current Biology: CB 31 (20): 4436–48.e5.
6. Ercsey-Ravasz, Mária, Nikola T. Markov, Camille Lamy, David C. Van Essen, Kenneth Knoblauch, Zoltán Toroczkai, and Henry Kennedy. 2013. “A Predictive Network Model of Cerebral Cortical Connectivity Based on a Distance Rule.” Neuron 80 (1): 184–97.
7. Faskowitz, Joshua, Daniel Moyer, Daniel A. Handwerker, Javier Gonzalez-Castillo, Peter A. Bandettini, Saad Jbabdi, and Richard Betzel. 2023. “Commentary on Pang et Al. (2023) Nature.” bioRxiv. https://doi.org/10.1101/2023.07.20.549785.
8. Markov, Nikola T., Maria Ercsey-Ravasz, Camille Lamy, Ana Rita Ribeiro Gomes, Loïc
9. Magrou, Pierre Misery, Pascale Giroud, et al. 2013. “The Role of Long-Range Connections on the Specificity of the Macaque Interareal Cortical Network.” Proceedings of the National Academy of Sciences of the United States of America 110 (13): 5187–92.
10. Pang, James C., Kevin M. Aquino, Marianne Oldehinkel, Peter A. Robinson, Ben D. Fulcher, Michael Breakspear, and Alex Fornito. 2023a. “Geometric Constraints on Human Brain Function.” Nature 618 (7965): 566–74.
11. Pang, James et al.. 2023b. “Reply to: Commentary on Pang et Al. (2023) Nature.” bioRxiv. https://doi.org/10.1101/2023.10.06.560797.

Poster No 1827

Aging, Emotion, and Inhibition: Neuroimaging Insights into the Automatic Regulation of Affect

Arthur Tsai[1], Kuo Chii-Shyang[2]

[1]Institute of Statistical Science, Taipei, Taiwan, [2]Department of Electrical Engineering, National Central University, Taoyuan, Taiwan

Introduction: Cognitive neuroscience recognizes the profound impact of emotional stimuli on cognitive processes. Research over the past decade has delved into emotional-cognitive interactions, revealing the dual nature of emotional information-capable of enhancing and impairing the cognitive control (Cohen & Henik, 2012; Dolcos, Iordan, & Dolcos, 2011). Negative stimuli, while hindering executive control, paradoxically improve performance when attention is selectively focused (Cohen & Henik, 2012). This study investigates the automatic regulation of affect in young and older adults, employing spectral analysis and directed transfer function. It aims to unravel the nuanced modulation of inhibition across age groups, exploring the effects of age and emotional modulation on response inhibition parameters and underlying neural mechanisms labs (Okon-Singer, Pessoa, & Shackman, 2015). Results suggest older adults may exhibit more automatic regulation of affect compared to their younger counterparts.

Methods: We examined emotional modulation’s impact on response inhibition and associated neural correlates in 35 young and 35 older adults using fMRI and the Emotional Stop-Signal Paradigm (ESSP, Pawliczek et al., 2013; Verbruggen & De Houwer, 2007). Disgusted and neutral expressive faces, selected for age, sex, and valence scores, comprised 140 stimuli from the Taiwanese face database (Tu, Lin, Suzuki, & Goh, 2018). Infomax ICA identified independent components (ICs) in preprocessed ESSP fMRI data, subjected to 20 iterations using ICASSO for reliability. The gRAICAR algorithm (Yang et al., 2012) and unsupervised clustering analyzed IC discriminatory potential between age groups. Spectral analysis and Directed Transfer Function (DTF) assessed cortical network dynamics.

Results: Compared to younger adults, older adults exhibited delayed responses in neutral and disgusting trials. However, the DTF analysis revealed heightened brain connectivity in older adults during emotional response inhibition tasks. Significance was set at $p < 0.05$ with 5000 permutations and TFCE correction (Figure 1). Figure 2 depicts increased connectivity in older adults, complicating our understanding of age-related cognitive control differences. Insights enhance comprehension of emotion, cognitive control, and neural connectivity relationships.

Conclusions: Integrating emotional faces into response inhibition paradigms provides a nuanced perspective on emotion-cognitive control interplay. Patterns emerged - decreased go hits for young and increased for older adults in response to negative emotion contexts. Differential brain activity in older adults, lower parietal and higher frontal activity, further distinguishes inhibition processes (Figure 2). Age-related changes indicate increased connectivity in older adults, potentially augmenting automatic regulation of affect. These findings contribute to understanding emotional influences on cognitive control across age groups.

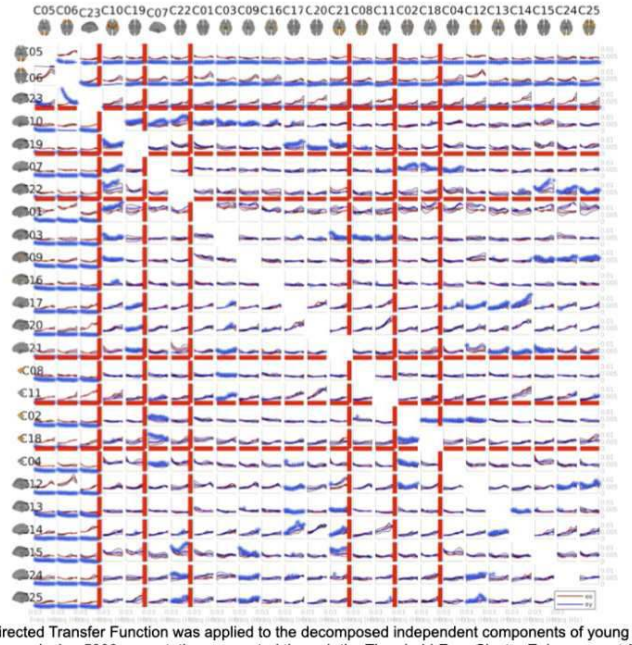

Fig. 1. The Directed Transfer Function was applied to the decomposed independent components of young and older subjects employing 5000 permutations corrected through the Threshold-Free Cluster Enhancement (TFCE) correction.

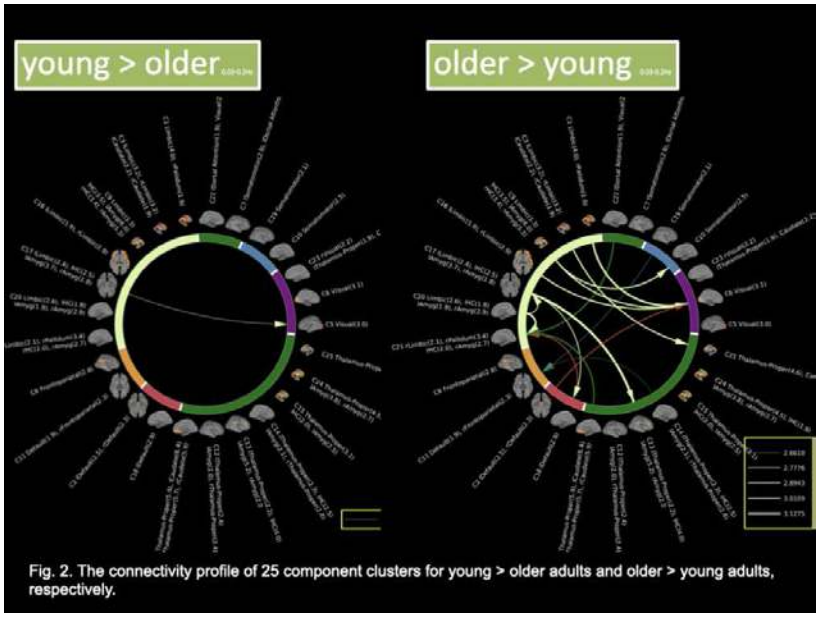

Fig. 2. The connectivity profile of 25 component clusters for young > older adults and older > young adults, respectively.

References

1. Cohen, N., & Henik, A. (2012). Do irrelevant emotional stimuli impair or improve executive control? Frontiers in Integrative Neuroscience, 6, 33.
2. Dolcos, F., Iordan, A. D., & Dolcos, S. (2011). Neural correlates of emotion–cognition interactions: A review of evidence from brain imaging investigations. Journal of Cognitive Psychology, 23(6), 669-694.
3. Okon-Singer, H., Pessoa, L., & Shackman, A. J. (2015). The neurobiology of emotion-cognition interactions: Frontiers Media SA.
4. Pawliczek, C. M., Derntl, B., Kellermann, T., Kohn, N., Gur, R. C., & Habel, U. (2013). Inhibitory control and trait aggression: neural and behavioral insights using the emotional stop signal task. Neuroimage, 79, 264-274.
5. Tu, Y.-Z., Lin, D.-W., Suzuki, A., & Goh, J. O. S. G. (2018). East Asian young and older adult perceptions of emotional faces from an age- and sex-fair East Asian facial expression database. Frontiers in Psychology, 9, 2358.
6. Verbruggen, F., & De Houwer, J. (2007). Do emotional stimuli interfere with response inhibition? Evidence from the stop signal paradigm. Cognition and emotion, 21(2), 391-403.
7. Yang, Z., Zuo, X. N., Wang, P., Li, Z., LaConte, S. M., Bandettini, P. A., & Hu, X. P. (2012). Generalized RAICAR: discover homogeneous subject (sub)groups by reproducibility of their intrinsic connectivity networks. Neuroimage, 63(1), 403-414. doi:10.1016/j.neuroimage.2012.06.060

Poster No 1828

Investigating the somatosensory-motor network heterogeneity associated with higher-order systems

Ziteng Han[1], Jinglong Wu[1], Tianyi Yan[1]

[1]Beijing Institute of Technology, Beijing, Beijing

Introduction: The somatosensory-motor network (SMN) not only plays an important role in primary somatosensory and motor processing but also serves as a transdiagnostic hub, whose upward pathways with the attention and default systems are strongly associated with general psychopathology, cognitive impairment and impulsivity[1,2]. However, the SMN heterogeneity related to higher-order systems still remains unclear. Here, we first delineate a finer-grained cortical parcellation to characterize the SMN substructures in more detail. We then examine how the distinct attention and default streams are carried forward into the functions of SMN, to test for SMN heterogeneity.

Methods: We used ultra-high-field neuroimaging data from the HCP S1200 release. Seventeen of the original 184 subjects with 7T fMRI data were excluded due to major acquisition artifacts or incomplete scans, yielding a total of 167 healthy young subjects (102 female, age range 22–35 years) for further analyses. Then, these individuals were randomly split into two groups, which we termed Dataset 1 (dataset for parcellation, n = 85) and Dataset 2 (dataset for parcellation validation and individual-level analyses, n = 82). (i) First, a hard boundary mapping-based parcellation approach was employed to delineate a finer-grained cortical parcellation[3]. The new population-level parcellation map was then personalized to account for inter-individual variability[4]. (ii) Following this, the network architecture of the parcel-wise graph was assessed using the Infomap algorithm in individuals. For each subject, we identified the SMN, anterior dorsal attention network (aDAN) and anterior frontoparietal control network (aFPCN) by matching the clustering-derived community to the Yeo network[5]. The SMN subnetworks were identified based on task-evoked activity (motor task). (iii) Subsequently, we calculated the resting-state functional connectivity (RSFC) between each SMN subnetwork and the remaining SMN regions, aDAN and aFPCN, respectively. The connector hubness and centrality of each SMN subnetwork were computed to represent their network roles. Furthermore, spectral dynamic causal modelling (DCM) was implemented to infer the effective connections[6]. Finally, a Neurosynth meta-analytic coactivation analysis was performed to validate the generalizability of the SMN fractionation[7].

Results: (i) The new finer-grained cortical parcellation contains 430 parcels (Fig. 1a-b), slightly more than the Gordon333 parcellation. The SMN and its subnetworks are shown in Fig. 1c. (ii) Statistical analyses show that the Hand subnetwork is central within the SMN (Fig. 2a-b) and exhibits stronger RSFC with the attention systems (i.e., aDAN) than the other subnetworks(Fig. 2c), whereas the Tongue subnetwork exhibits stronger RSFC with the default systems (i.e., aFPCN; Fig. 2d). Moreover, both the Hand and Tongue subnetworks serve as connector hubs (Fig. 2e). (iii) Direct interactions were observed between the Hand subnetwork and attention systems, as well as between the Tongue subnetwork and default systems (Fig. 2f). (iv) We further found that two distinct behavioral domains are preferentially associated with specific SMN subnetworks. Perceptual attention processes, such as “visual attention”, load more strongly onto the Hand subnetwork than the Tongue subnetwork, while introspective processes, such as “affective processing”, load more strongly onto the Tongue subnetwork (Fig. 2g).

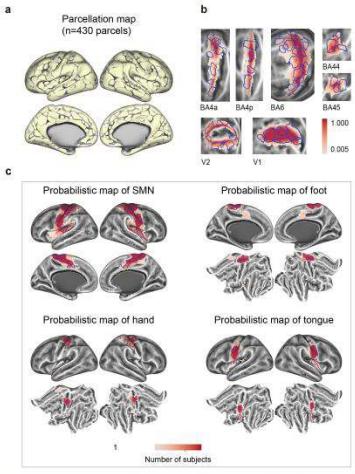

Figure 1. Identification of the SMN and its subnetworks based on the new finer-grained cortical parcellation derived from the 7T resting-state fMRI data. (***a***) The new parcellation map consists of 430 cortical boundary map-derived parcels, with 215 parcels in each hemisphere. (***b***) The boundary map-derived parcels (in blue) spatially match the cytoarchitectonically defined areas, with the auditory areas, motor areas and visual areas illustrated. The vertex color is scaled by the probability that the vertex belongs to the given area. (***c***) Spatial distribution of the SMN and its subnetworks across subjects. The vertex color indicates number of subjects with spatial overlap of matched networks at the vertex. The group-consensus border of the parcel is shown in blue.

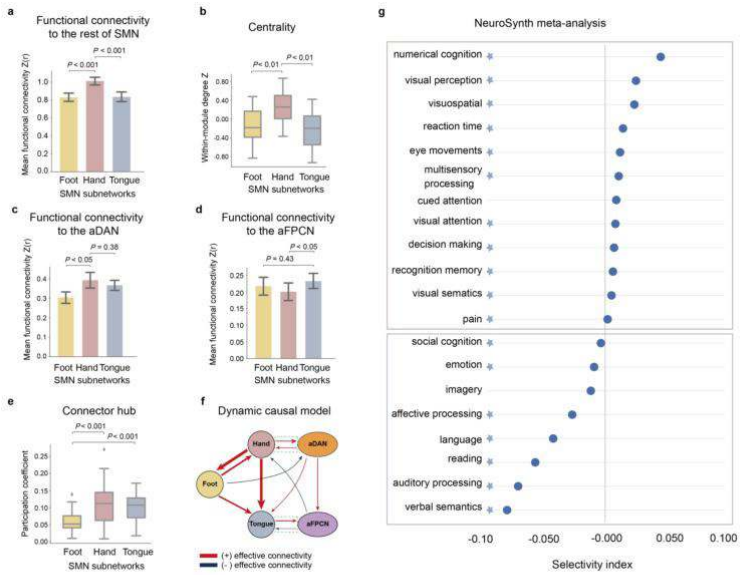

Figure 2. SMN fractionation based on connectivity with the separate attention and default systems. (***a***) The Hand subnetwork exhibited stronger RSFC with the rest of the SMN than the other subnetworks. (***b***) The Hand subnetwork exhibited larger within-module degree Z scores than the other subnetworks. (***c***) The Hand subnetwork exhibited stronger RSFC with the aDAN than the other subnetworks. (***d***) The Tongue subnetwork exhibited stronger RSFC with the aFPCN than the other subnetworks. (***e***) The Hand and Tongue subnetworks had larger participation coefficients than the Foot subnetwork. The error bars indicate the SE across subjects. The box plots show the median, 25th and 75th percentiles, and the whiskers extend to the furthest value within 1.5 times the interquartile range from the quartiles. Benjamini–Hochberg corrections were performed for multiple comparisons. (***f***) Schematic representations of the significant effective connections among the SMN subnetworks, aDAN and aFPCN. The arrows indicate the direction of the influence, and the line widths indicate the strength of the influence. The significant connections in the green rectangles define the Hand–aDAN and Tongue–aFPCN pathways, respectively. (***g***) Neurosynth meta-analyses showing different preferences of cognitive topics to SMN subnetworks. The selectivity index represents the association strength with the Hand subnetwork minus the association strength with the Tongue subnetwork for each topic. A selectivity index greater than 0 indicates that the topic is preferentially associated with the Hand subnetwork, and a selectivity index less than 0 indicates that the topic is preferentially associated with the Tongue subnetwork. The topics with asterisks denote the significance of the association strength ($P < 0.05$) used to compute the selectivity index.

Conclusions: (i) Our parcellation result suggests that ultrahigh spatial resolution (1.6 mm) data, combined with the state-of-the-art algorithm, have the potiential to provide deeper insights into the functional organization of the cortex[8]. (ii) Our findings reveal a heterogeneous SMN organization that may in part emerge from separable attention and default processing streams[9]. The Hand subnetwork may be preferentially involved in exogenous processes, whereas the Tongue subnetwork may be more important in endogenous processes.

References

1. Kebets V, et al. (2019) Somatosensory-motor dysconnectivity spans multiple transdiagnostic dimensions of psychopathology. Biol. Psychiatry 86(10):779-791.
2. Ray D, Bezmaternykh D, Mel'nikov M, Friston KJ, & Das M (2021) Altered effective connectivity in sensorimotor cortices is a signature of severity and clinical course in depression. Proc. Natl. Acad. Sci. U.S.A. 118(40):e2105730118.
3. Gordon EM, et al. (2016) Generation and evaluation of a cortical area parcellation from resting-state correlations. Cereb. Cortex 26(1):288-303.
4. Wang D, et al. (2015) Parcellating cortical functional networks in individuals. Nat. Neurosci. 18(12):1853-1860.
5. Yeo BT, et al. (2011) The organization of the human cerebral cortex estimated by intrinsic functional connectivity. Journal of neurophysiology.
6. Friston KJ, Kahan J, Biswal B, & Razi A (2014) A DCM for resting state fMRI. NeuroImage 94:396-407.
7. Salo T, et al. (2018) NiMARE: a neuroimaging meta-analysis research environment. F1000Research 7.
8. Tian Y, Margulies DS, Breakspear M, & Zalesky A (2020) Topographic organization of the human subcortex unveiled with functional connectivity gradients. Nat. Neurosci. 23(11):1421-1432.
9. Dixon ML, et al. (2018) Heterogeneity within the frontoparietal control network and its relationship to the default and dorsal attention networks. Proc. Natl. Acad. Sci. U. S. A. 115(7):E1598-E1607.

Poster No 1829

The Heritability of Edge-centric Functional Network in Human Brain Activity

Yuanyuan Hu[1,2], Yuening Jin[1,2], Qingchen Fan[1,2], Yuan Zhou[1,2,3]

[1]CAS Key Laboratory of Behavioral Science, Institute of Psychology, Chinese Academy of Sciences, Beijing, China, [2]Department of Psychology, University of Chinese Academy of Sciences, Beijing, China, [3]The National Clinical Research Center for Mental Disorders & Beijing Key Laboratory of Mental Disorders, Beijing Anding Hospital, Capital Medical University, Beijing, China

Introduction: Intrinsic patterns of human brain activity reveal a functional connectivity profile that is intricately linked to behavior, cognitive performance, and disease progression. However, traditional network neuroscience approaches have primarily relied on a node-centric model, which assigns each brain node to a single community, limiting our understanding of interactions among edges and fluctuations of connectivity across time (Betzel et al., 2023). Recently, an edge-centric network model has been proposed to address the aforementioned issues by dividing the cerebral cortex into overlapping communities through examining its edge correlation structure and thus this approach offers new insights into human brain activity (Faskowitz et al., 2020). In the current study, for the first time, we estimate the heritability of the overlapping community features of edge-centric functional connectivity (eFC) and discern the relative contributions of genetic factors and the shared environment among twins.

Methods: A cohort of 102 pairs of same-sex twins was included in the analyses. Their ages ranged from 18 to 24 years (M = 19.60 years, SD = 1.68). Among them, 47 pairs were monozygotic (23 male and 24 female pairs), and 55 pairs were dizygotic (25 male and 30 female pairs). Functional images of this study were preprocessed using fMRIPrep 23.0.2 (Esteban et al., 2019) and were post-processed and noise-regressed by XCP-D (Mehta et al., 2023). Functional regions were defined based on the Schaefer 200 atlas (Schaefer et al., 2018). We calculated the eFC matrix and applied a modified k-means algorithm (k = 10, repeated 250 times) to partition the eFC matrix into non-overlapping communities of co-fluctuating edges. Edge assignments were then mapped back to a single region to calculate normalized entropy, providing overlapping regional community assignments. We then employed a univariate model implemented in the OpenMx package (Boker et al., 2011) in the R programming environment (Version 3.1.2) to estimate the means and genetic (A), shared environmental (C), and nonshared environmental (E) sources of variance for the normalized entropy for each brain region (Figure 1).

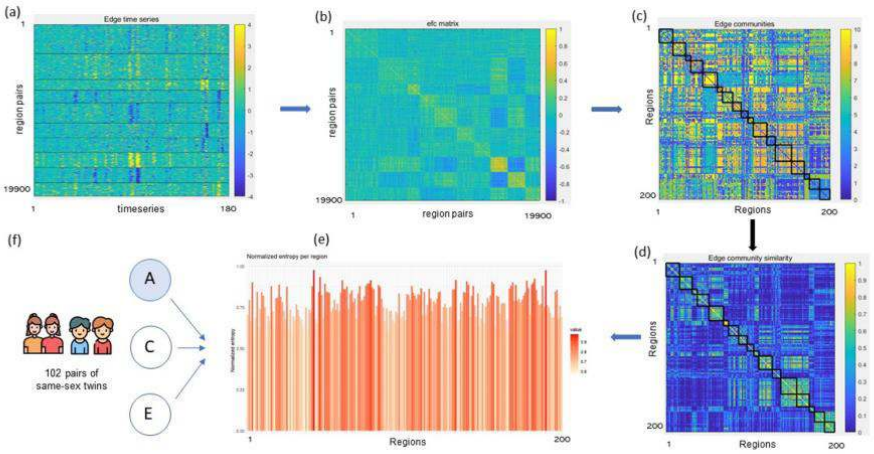

Figure 1. **The workflows used to characterize genetic influences on edge-centric functional connectivity profile.** (*a-b*) Derivation of edge functional connectivity (eFC) matrix. Each element of the eFC matrix is calculated based on the fMRI BOLD activity time series from two pairs of brain regions, resulting in a set of co-fluctuation edge time series. (*c-d*) Edge community similarity refers to the likelihood that pairs of brain regions are jointly assigned to the same community within the *Schaefer 200* Atlas. (*e*) The normalized entropy for each regions, where the range, denoted as [0,1], signifies the consistency of a region's community assignments across all communities. Higher normalized entropy values approaching 1 indicate a more uniform distribution of region community assignments, whereas values closer to 0 suggest that the region belongs to only a single or a few communities. (*f*) The univariate genetic-modeling analyses to normalized entropy for each region.

Results: We found that normalized entropy, a measure of eFC community overlap, exhibits heritability in multiple regions. Notably, the sensorimotor regions displayed the highest heritability (41%, 95%CI = [0.18, 0.59]). We also found a considerable and significant heritability within the default mode regions (20% - 29%), the visual regions (21% - 26%), the control related regions (18% - 28%) (Figure 2.). These findings suggest a substantial genetic influence on the distribution of eFC community affiliations within specific brain regions.

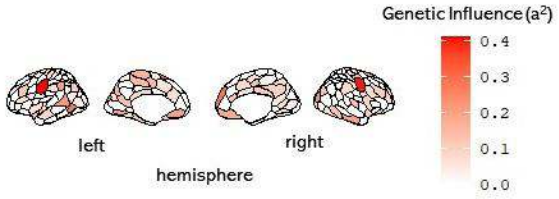

Figure 2. **The percentage of variance explained by genetic (a^2) for normalized entropies.** Among them, the sensorimotor regions display the highest levels of heritability.

Conclusions: In conclusion, our investigation employed an edge-centric network model to examine human brain connectivity beyond individual nodes, offering fresh insights into the heritability of the functional connectivity profile. The identified moderate heritability highlights the genetic impact on community overlap, specifically within the sensorimotor regions. These findings enhance our comprehension of the intricate interplay between genetic and environmental factors in shaping the functional connectivity of the brain.

References

1. Betzel, R. F., Faskowitz, J., & Sporns, O. (2023). Living on the edge: Network neuroscience beyond nodes. Trends in Cognitive Sciences. https://www.cell.com/trends/cognitive-sciences/fulltext/S1364-6613(23)00205-X
2. Boker, S., Neale, M., Maes, H., Wilde, M., Spiegel, M., Brick, T., Spies, J., Estabrook, R., Kenny, S., Bates, T., Mehta, P., & Fox, J. (2011). OpenMx: An Open Source Extended Structural Equation Modeling Framework. Psychometrika, 76(2), 306–317. https://doi.org/10.1007/s11336-010-9200-6
3. Esteban, O., Markiewicz, C. J., Blair, R. W., Moodie, C. A., Isik, A. I., Erramuzpe, A., Kent, J. D., Goncalves, M., DuPre, E., & Snyder, M. (2019). fMRIPrep: A robust preprocessing pipeline for functional MRI. Nature Methods, 16(1), 111–116.
4. Faskowitz, J., Esfahlani, F. Z., Jo, Y., Sporns, O., & Betzel, R. F. (2020). Edge-centric functional network representations of human cerebral cortex reveal overlapping system-level architecture. Nature Neuroscience, 23(12), 1644–1654.
5. Mehta, K. P., Salo, T., Madison, T., Adebimpe, A., Bassett, D. S., Bertolero, M., Cieslak, M., Covitz, S., Houghton, A., & Keller, A. S. (2023). XCP-D: A Robust Pipeline for the post-processing of fMRI data. bioRxiv, 2023–11.
6. Schaefer, A., Kong, R., Gordon, E. M., Laumann, T. O., Zuo, X.-N., Holmes, A. J., Eickhoff, S. B., & Yeo, B. T. (2018). Local-global parcellation of the human cerebral cortex from intrinsic functional connectivity MRI. Cerebral Cortex, 28(9), 3095–3114.

Poster No 1830

Visually demanding tasks show altered sensory network dynamics compared to congruence tasks

Harrison Watters[1], Aleah Davis[2], Lauren Daley[3], Abia Fazili[4], Theodore LaGrow[5], Shella Keilholz[6]

[1]Emory, Atlanta, GA, [2]Agnes Scott College, Atlanta, GA, [3]Emory University-Georgia Institute of Technology, Atlanta, GA, [4]Emory University, Sandy, UT, [5]Georgia Institute of Technology, Beaverton, OR, [6]Georgia Institute of Technology, Atlanta, GA

Introduction: Infraslow resting state brain activity is dominated by a repeating pattern of anti-correlated brain activity between default mode (DMN) and task positive networks (TPN) (Abbas, 2019a). These quasi-periodic patterns (QPPs) of DMN-TPN activity are implicated in cognition, attentional processing of internal vs external stimuli, and complete a cycle about once every 20 seconds in humans (Abbas, 2019b, Bolt et al., 2022). In this study, quasi-periodic patterns (QPPs) were detected on a subject-wise basis using a sliding window-based algorithm (Majeed et al., 2011) in 11 datasets representing different types of tasks and rest. Scans range from neurotypical subjects at rest to subjects engaged in mindfulness meditation, TV watching, congruence tasks, and visually demanding reaction time and working memory tasks. We then calculated correlation during the QPP between 5 attentional and sensory networks and the DMN to see if certain tasks more than others elicit a change of correlation with respect to the DMN. Significant changes were seen in both sensory and visual networks for more visually demanding tasks. While QPPs have been observed widely at rest, task-based studies of QPPs are much more limited. This is one of the first studies connecting such a breadth of datasets for spatiotemporal analysis.

Methods: Functional scans from 11 datasets were obtained from a mix of collaborators and OpenNeuro. All available anatomical and functional scan parameters are shown in figure 1. For uniformity of processing, all fMRI pre-processing and global signal regression was done using the CPAC pipeline (https://fcp-indi.github.io/) and Brainnetome atlas (Fan, 2016). Yeo's 7 canonical networks plus subcortical networks were used for ROI-to-network grouping and network comparisons (Yeo, 2011). QPPs were detected with an in-house algorithm and window lengths (WL) were selected for each dataset based on a TR x WL value that best captured one full cycle of the QPP, most QPPs were in the range of 10-20 seconds depending on scan TRs for each dataset.

A

Anatomical Scan Parameters

Dataset	Scanner	Sequence	TR	TE	FA	FOV	Voxel	Slices
Video Game N=47	3T S Magnetom Prisma MRI scanner	MPRAGE	2530 ms	TE1-4: 1.69-7.27 ms	7°		1x1x1	
Visual Working Memory N=19 (13M 6F) Mean age: 22.4 yr	3 T MRI TrioTim scanner	MPRAGE		2.9 ms	9°		1x1x1	
Flanker N=26	Siemens Allegra 3.0 T scanner	MPRAGE	2500 ms	3.93 ms	8°	256mm		176
Simon N=21	Siemens Allegra 3.0 T scanner	MPRAGE	2500 ms	3.93 ms	8°	256 mm	1x1x1	176
Stroop N=28 (20M 10F) Mean age: 31yr	Siemens Verio 3T scanner	MPRAGE						176
NYU ADHD	3T Siemens Magnetom Allegra Syngo MRI scanner	MPRAGE	2530 ms	3.25 ms		256 mm	1.3x1x1.3	128
MWS (Mind Wandering Scores)N=99 Mean Age: 26yr	Siemens 3 T Trio MRI scanner	MPRAGE	2250 ms	3.98 ms	9°	256 mm	1x1x1	176
Meditators N=14 (3M 11F) Ages 28-66	3-T Siemens Trio scanner	MPRAGE	2600 ms	3.9 ms		240 mm		
Neurotypical Controls N=9	3T	MPRAGE	2300 ms	2.75 ms	8°			
Music Data N=48 (36M 12F)	3T SiemensMRI scanner	MPRAGE	2400 ms		8°	256mm		
Twilight Zone N=24	3T Siemens Skyra scanner	MPRAGE					0.89mm³	

Functional Scan Parameters

Dataset	Scanner	TR	TE	FA	FOV	Voxel Size	Slices
Video Game N=47	3T S Magnetom Prisma MRI scanner	535 ms	30 ms	46°	240 mm	3.6x3.6x4	32
Visual Working Memory N=19 (13M 6F) Mean age: 22.4 yr	3 T MRI TrioTim scanner	2000 ms	30 ms	45°	240 mm	3mm³	36
Flanker N=26	Siemens Allegra 3.0 T scanner	2000 ms	30 ms	80°	192mm	3x3x4mm	40
Simon N=21	Siemens Allegra 3.0 T scanner	2000 ms	30 ms	80°	192mm	3x3x4mm	40
Stroop N=28 (20M 10F) Mean age: 31yr	Siemen's Verio 3T	1500 ms	20 ms	90°	240mm	3.5 mm isotropic	30
NYU ADHD	3T Siemens Magnetom Allegra Syngo MRI scanner	2000 ms	15 ms	90°	240 mm	3x3x4	33
MWS (Mind Wandering Scores)N=99 Mean Age: 26yr	Siemens 3 T Trio MRI scanner	2000 ms	30 ms	90°	240 mm	3x3x3	37
Meditators N=14 (3M 11F) Ages 28-66	3-T Siemens Trio scanner	1500 ms	30 ms	90°	192mm	3x3x4	18
Neurotypical Controls N=9	3T	2000 ms	28 ms	90°			
Music Data N=48 (36M 12F)	3T SiemensMRI scanner	475 ms	30 ms	90°	240 mm	3x3x3 mm³	48
Twilight Zone N=24	3T Siemens Skyra scanner	1500 ms	28 ms	84°	192 mm	4x3x3	27

B

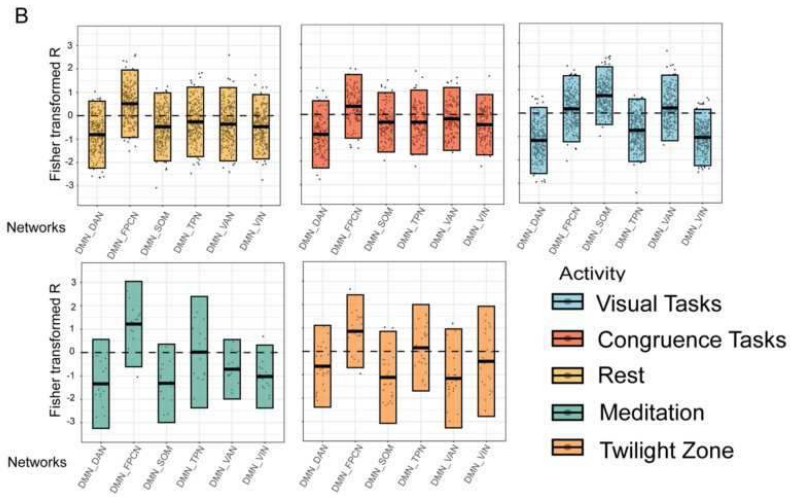

Figure 1: **A**) All available anatomical and functional scan parameters for datasets used. Datasets were obtained from a mix of OpenNeuro and collaborators. **B**) All network-to-DMN correlations during one QPP cycle for QPPs run on a subject-wise basis. Grouped based on task type: rest, congruence, visual, meditation, or TwilightZone watching.

Results: Compared to resting state scans, we found that congruence tasks (Stroop, Flanker, and Simon) did not result in significant changes to alignment with the DMN for any networks. However, visually demanding tasks such as a moving dot reaction time task and a visual working memory task significantly increased correlation with the DMN in the ventral attention network (ANOVA, p=7.6x10-15) and the somatomotor network (p=2.22x10-16). The same visual tasks showed decreased DMN correlation in the dorsal attention network (p=6.1x10-8), frontoparietal network (p=2.8x10-6), and visual network (p=2.22x10-16). Interestingly, the largest changes were seen in sensory networks (figure 2), not cortical networks implicated in attention and executive control. The meditation task and Twilight Zone watching tasks were not grouped with the other tasks or rest groups as the tasks show very different trends and are likely driving more internal rather than external attention (figure 2).

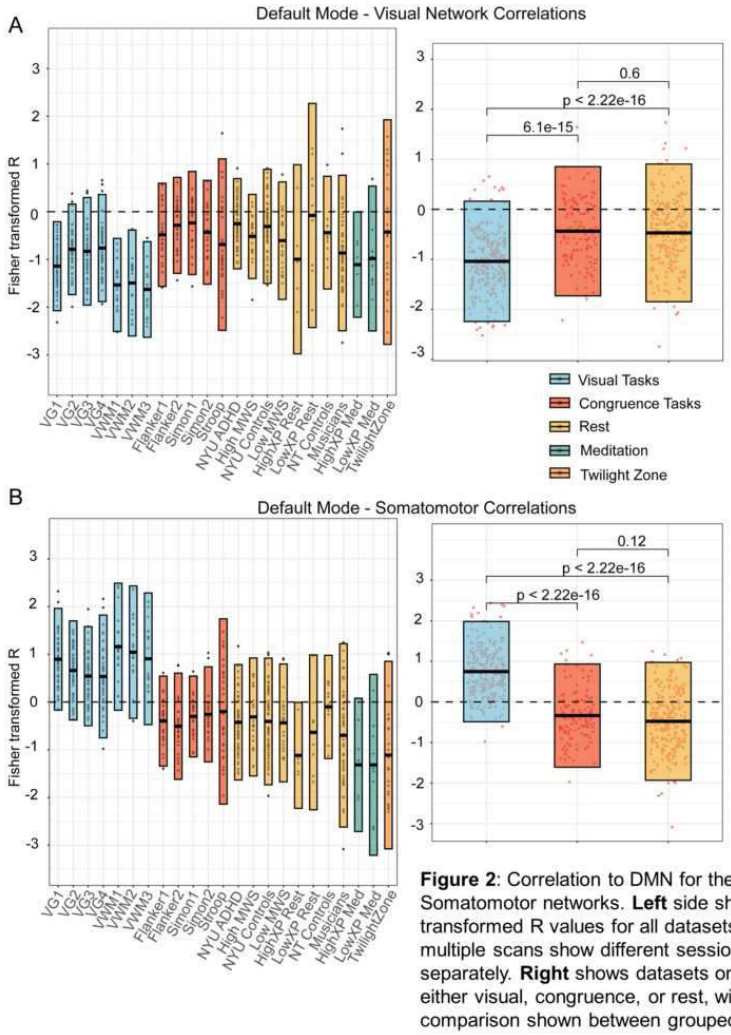

Figure 2: Correlation to DMN for the **a**) Visual and **b**) Somatomotor networks. **Left** side shows fisher transformed R values for all datasets. Datasets with multiple scans show different sessions or states separately. **Right** shows datasets on left grouped as either visual, congruence, or rest, with ANOVA comparison shown between grouped scans.

Conclusions: This is one of the first studies comparing large scale trends in QPP network dynamics across such a breadth of task-rest datasets. We found significant changes in DMN correlation depending on the type of task, with more visually demanding/externally focused tasks showing the largest changes to both attentional and sensory networks. This may represent an axis of attention related to the DMN depending on the type of task and the degree of internal vs external attention. These findings suggest that networks beyond the canonical attention and executive control networks should be considered in studies of brain dynamics related to task, rest, and disorders that affect attention. The sensitivity of QPPs to subject-wise network trends also indicates that dynamic measures of FC such as QPPs are sensitive enough to individual changes to potentially be used in future individual level clinical fMRI applications.

References

1. Abbas, A. (2019a), 'Quasi-periodic patterns contribute to functional connectivity in the brain', Neuroimage, vol. 191, pp. 193-204
2. Abbas, A. (2019b). "Quasi-periodic patterns of brain activity in individuals with attention-deficit/hyperactivity disorder." Neuroimage Clin 21: 101653
3. Bolt, T., Nomi, J.S., Bzdok, D. et al. A parsimonious description of global functional brain organization in three spatiotemporal patterns. Nat Neurosci 25, 1093–1103 (2022). https://doi.org/10.1038/s41593-022-01118-1.
4. Fan, L. (2016). "The Human Brainnetome Atlas: A New Brain Atlas Based on Connectional Architecture." Cereb Cortex 26(8): 3508-3526
5. Majeed, W., Magnuson, M., Hasenkamp, W., Schwarb, H., Schumacher, E. H., Barsalou, L., & Keilholz, S. D. (2011). Spatiotemporal dynamics of low frequency BOLD fluctuations in rats and humans. NeuroImage, 54(2), 1140–1150. https://doi.org/10.1016/j.neuroimage.2010.08.030
6. Yeo, B. T. (2011). "The organization of the human cerebral cortex estimated by intrinsic functional connectivity." J Neurophysiol 106(3): 1125-1165

Poster No 1831

Exploring Multimodal Paths in Time-Varying Brain Graphs: Integrating fMRI-Based FNC with sMRI-Based

Haleh Falakshahi[1], Hooman Rokham[2], Vince Calhoun[3]

[1]Georgia Institute of Technology, Atlanta, GA, [2]Georgia Institue of Technology, Atlanta, GA, [3]GSU/GATech/Emory, Decatur, GA

Introduction: The exploration of multimodal brain network analysis shows potential in uncovering the mechanisms at the core of brain disorders. Previous research has predominantly focused on either unimodal brain graphs or local/global graphic metrics, often neglecting the intricate details of disrupted pathways within patient groups. Our study emphasizes the significance of dynamically integrating multimodal brain graphs with a targeted examination of disrupted paths using a Gaussian graphical model (GGM). This approach reveals profound insights that can aid in identifying time-varying, path-based disease biomarkers.

Methods: In our study, we utilized data from the fBIRN study, incorporating structural MRI (sMRI) and functional MRI (fMRI) data from 160 controls and 151 patients with schizophrenia (SZ). Employing the Neuromark pipeline, we applied a spatially constrained group-independent component analysis to the fMRI data, yielding 53 consistent components representing intrinsic connectivity networks (ICNs). Dynamic functional network connectivity (dFNC) computations were conducted using a sliding window approach, and FNC among segmented ICN time courses was estimated using the GIFT toolbox. Covariance estimation employed a regularized precision matrix obtained through graphical LASSO applied to windowed data, with λ determined via cross-validation. Recurring dFNC patterns were explored using k-means clustering, identifying five states based on the elbow criterion. A univariate test assessed group differences in dFNC, employing t-tests on averaged dFNC values across states and correcting for multiple comparisons using the False Discovery Rate (FDR) method. To create a dynamic multimodal graph, parallel independent component analysis (pICA) was applied to gray matter (GM) and state average features. The optimal number of components, determined using the elbow method, was set at fifteen for GM and fourteen for dFNC states. Loading matrices from pICA were unpacked for each state, and two artifactual GM components were removed. Finally, Gaussian graphical models (GGM) were estimated for control and patient groups for each state, enabling the comparison and analysis of paths between multimodal nodes to identify disconnectors associated with disconnectivity and connectors associated with additional paths (abnormal integration).

Results: In group difference evaluations, the number of significant FDR corrected p values were 173 for State 1, 55 for State 2, 41 for State 3, 57 for State 4, and 34 for State 5. Figure 1 illustrates the results of the multiple comparison test for the control and SZ group. Figure 2 shows the results of applying path analysis to identify missing and additional links for each state. For example, State 2 shows a multimodal disconnector associated with absent paths between the temporal middle component of gray matter and the FNC component which have a high correlation among sensory-motor, visual, and other domains' ICNs. However, state 2 reveals 23 connectors associated with additional paths both within and between modalities.

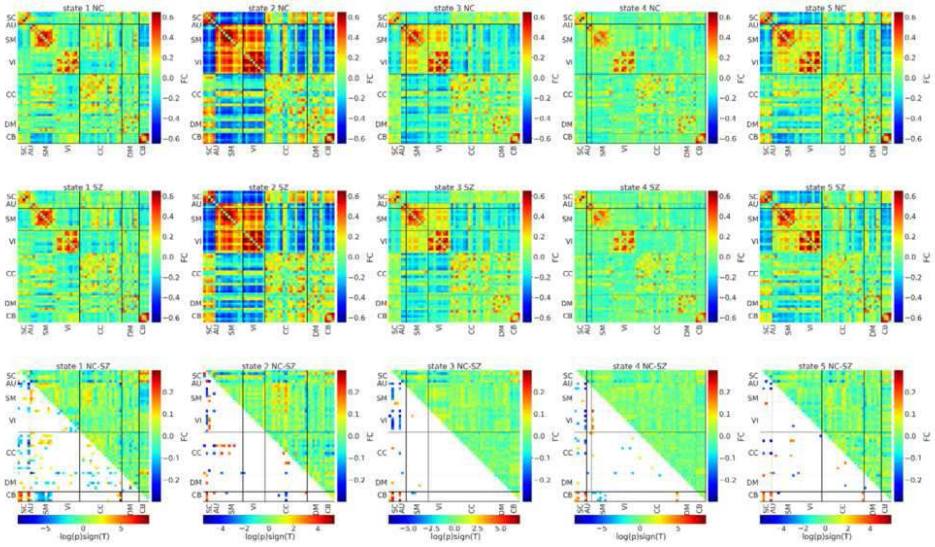

Fig. Averaged functional connectivity matrices for control and SZ and group differences.

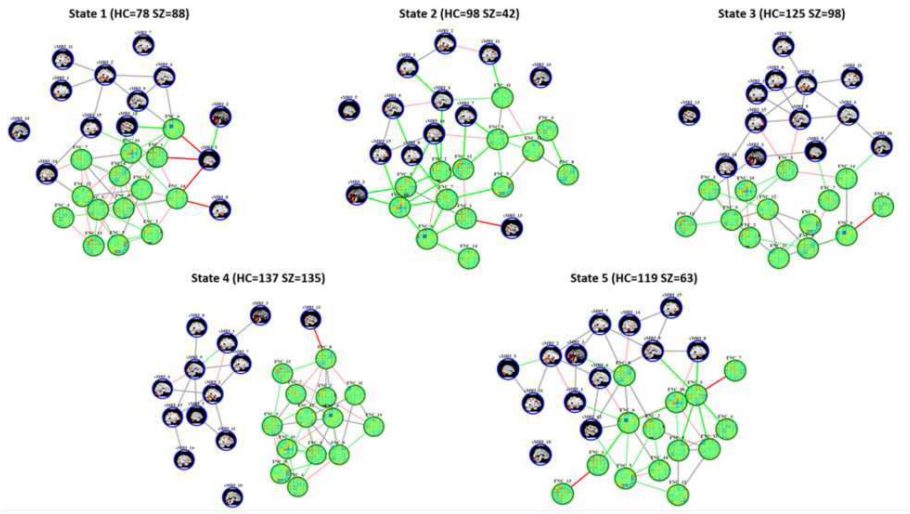

Disconnectors and connectors that were identified in each state.

Conclusions: In summary, we present an approach to estimate and visualize links within and among multimodal data. Subsequently, we scrutinized pathways capable of discerning connections associated with the absence or presence of links in the patient group. Our approach unveils crucial insights into network disruptions related to the disorder-insights often overlooked when focusing solely on a single modality. The absence of multimodal information hinders our ability to identify significant missing connections in SZ patients, playing a pivotal role in the disconnection or abnormal integration among brain components. This underscores the efficacy of our approach and emphasizes the indispensability of employing multimodal imaging methods in studying intricate mental illnesses.

References

1. Du, Y., Fu, Z., Sui, J., Gao, S., Xing, Y., Lin, D., . . . Calhoun, V. D. (2020). NeuroMark: An automated and adaptive ICA based pipeline to identify reproducible fMRI markers of brain disorders. NeuroImage: Clinical, 28, 2213-1582.

Poster No 1832

Time-resolved brain activity during emotion processing in preterm- and full-term-born adolescents

Jenifer Miehlbradt[1], Lorena Freitas[1], Maria Liverani[1], Vanessa Siffredi[1], Cristina Borradori-Tolsa[1], Russia Ha-Vinh Leuchter[1], Dimitri Van De Ville[2], Petra Hüppi[1]

[1]Division of Development and Growth, Department of Pediatrics, University of Geneva, Genève, Switzerland, [2]École Polytechnique Fédérale de Lausanne, Lausanne, Switzerland

Introduction: Premature birth affects 15 million births worldwide every year, with 1% of these infants born before 32 weeks of gestation and considered very preterm (VPT). Long-term neurodevelopmental deficiencies are observed in 35% of the latter, in a wide range of domains including sensory processing, executive functions and emotional regulation, and are accompanied by differences in functional connectivity (FC). While structural features and resting-state FC of VPT adolescents have been described, the relationship between dynamic FC and emotional abilities remains largely unaddressed. Here, we leveraged a time-resolved seed-based approach, psychophysiological interaction of co-activation patterns (PPI-CAPs), to assess the dynamics of brain activity underlying emotion processing and regulation in preterm- and full-term-born teenagers in a naturalistic paradigm.

Methods: 22 VPT (12 +/- 1.3 years old, 14 females) teenagers and 23 full-term born (FT) controls (12 +/- 0.9 years old, 9 females) watched 12 emotionally arousing movie clips, interspersed with intervals dedicated to regulation and breathing. A structural T1-weighted image was acquired with a MP-RAGE (Magnetization Prepared Rapid Gradient Echo) sequences and functional T2*-weighted images were acquired with a multislice gradient echo-planar imaging (EPI) sequence. After preprocessing (realignment, unwarping, coregistration, smoothing, Total Activation deconvolution, MNI normalization via DARTEL), we extracted the PPI-CAPs: using the anterior cingulate cortex (ACC) as a seed, we selected 30% of the frames in which the seed was the most (de)active and performed a consensus clustering (CC) analysis to identify the optimal number of components. Nest, we assessed the main effects of the Seed, Task, and Group as well as their interactions with the sign of the frames composing each PPI-CAP by comparing the determinants of their confusion matrices to a null distribution generated by 4000

random permutations. Lastly, we evaluated the proportion of each of Yeo's 17 functional networks activated or deactivated in each PPI-CAP.

Results: CC yielded an optimal number of 6 PPI-CAPs. All components showed a significant Seed effect, but no Group effect, and PPI-CAPs2-6 showed a Task effect. The Seed x Task interaction (PPI) was significant for PPI-CAPs1-4,6, Group x Seed for all PPI-CAPs, and Group x Task for PPI-CAPs2-6. The overlap with Yeo's networks presented below reveal an important involvement of the limbic and salience networks, areas often associated with emotional processing, in patterns alternating with the Default Mode Network (DMN). This suggests a reduced difference in activation between movie and relaxation in VPT when compared to FT participants. Of note, is the presence of visual and somatomotor areas in PPI-CAPs5-6 : while a main Task effect was expected due to the visual nature of the task and the high movement content of the videos, likely to activate motor-related areas, the contribution of these areas to Group x Task interactions could be associated with the sensorimotor difficulties often experiences by VPT children.

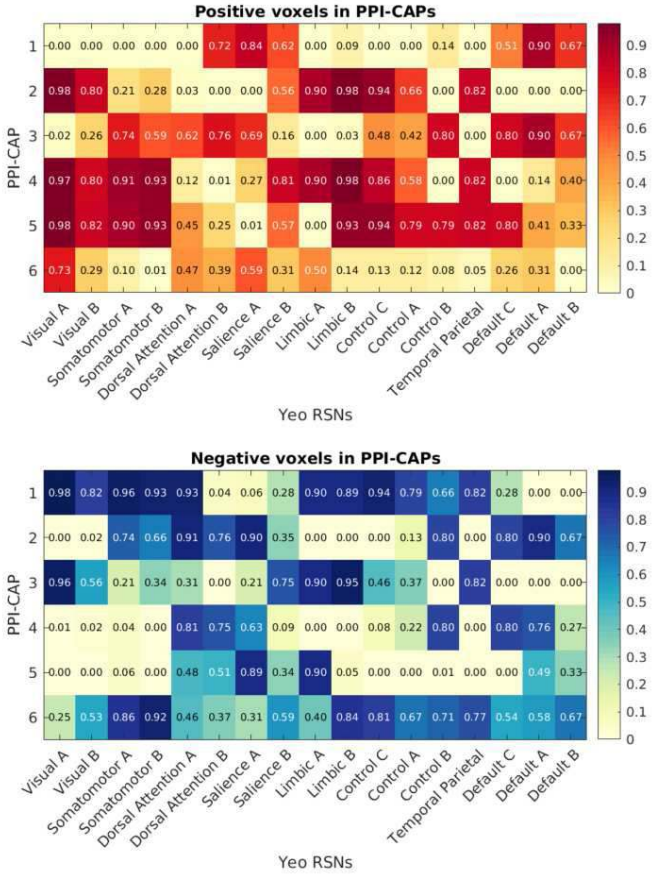

Fig. Similarity between PPI-CAPs and Yeo's 17 networks. The matrices represent the proportion of voxels present in each PPI-CAP, in active (top) or deactive (bottom) form.

Conclusions: Using a time-resolved approach, we identified task-related patterns of brain activation specific to a particular developmental condition. Group x Task interactions revealed that VPT adolescents display different brain activities in response to naturalistic emotional content, with large effects in salience and limbic areas. These results advance the understanding of prematurity and its long-term consequences and highlight the potential of dynamic methods to address brain functions in neurodevelopmental disorders.

References

1. Blencowe, H. et al. (2013) 'Born Too Soon: The global epidemiology of 15 million preterm births', Reproductive Health, 10(1), p. S2.
2. Freitas, L.G.A. et al. (2020) 'Time-resolved effective connectivity in task fMRI: Psychophysiological interactions of Co-Activation patterns', NeuroImage, 212, p. 116635.
3. Karahanoğlu, F.I. et al. (2013) 'Total activation: fMRI deconvolution through spatio-temporal regularization', NeuroImage, 73, pp. 121–134.
4. Thomas Yeo, B.T. et al. (2011) 'The organization of the human cerebral cortex estimated by intrinsic functional connectivity', Journal of Neurophysiology, 106(3), pp. 1125–1165.
5. Wehrle, F.M. et al. (2018) 'Altered resting-state functional connectivity in children and adolescents born very preterm short title', NeuroImage: Clinical, 20, pp. 1148–1156.

Poster No 1833

Evaluating Spatial Correspondence of Multimodal MRI via Anatomical Landmarks

Joy Zhao[1], Alaa Taha[1], Mohamed Abbass[2], Greydon Gilmore[3], Chris Zajner[3], Violet Liu[4], Homa Vahidi[1], Arun Thurairajah[5], Ali Khan[1], Jonathan Lau[6]

[1]University of Western Ontario, London, Ontario, [2]Western Univeristy, London, Ontario, [3]Department of Clinical Neurological Sciences, Division of Neurosurgery, London, Ontario, [4]Western Univeristy, London, MT, [5]Department of Clinical Neurological Sciences, Division of Neurosurgery, Western University, London, ON, [6]Department of Clinical Neurological Sciences, Division of Neurosurgery, London, ON

Introduction: Multimodal fusion involves the combination of two or more datasets acquired using different techniques and parameters to enhance our understanding of brain structure and function [Zhang et al. 2020, 149-187]. It is often common practice to align multimodal images to each other and to a standard neuroimaging template space. Voxel-based overlap metrics, commonly used in neuroimaging analysis, are less sensitive to focal misregistration [Rohlfing 2012, 153-163], compared to a point-based millimetric framework [Lau et al. 2019, 4163-4179]. We validated and released data [Taha et al. 2023] of over 5,000 salient anatomical fiducials (AFIDs) in the human brain across T1w scans with varying MRI field strengths and neurodegenerative diseases (Figure 1). We previously demonstrated the high sensitivity of AFIDs during point-based evaluation of image registration [Abbass et al. 2022, 393-405] which has broad implications in the field and clinical contexts (e.g., pooling deep brain stimulation electrodes for group-level analysis). In this study, we aim to 1) provide an overview of the AFIDs framework and associated data, and 2) extend the AFIDs framework to T2w MRI datasets, enabling evaluation of biases in registration accuracy when using standard neuroimaging software.

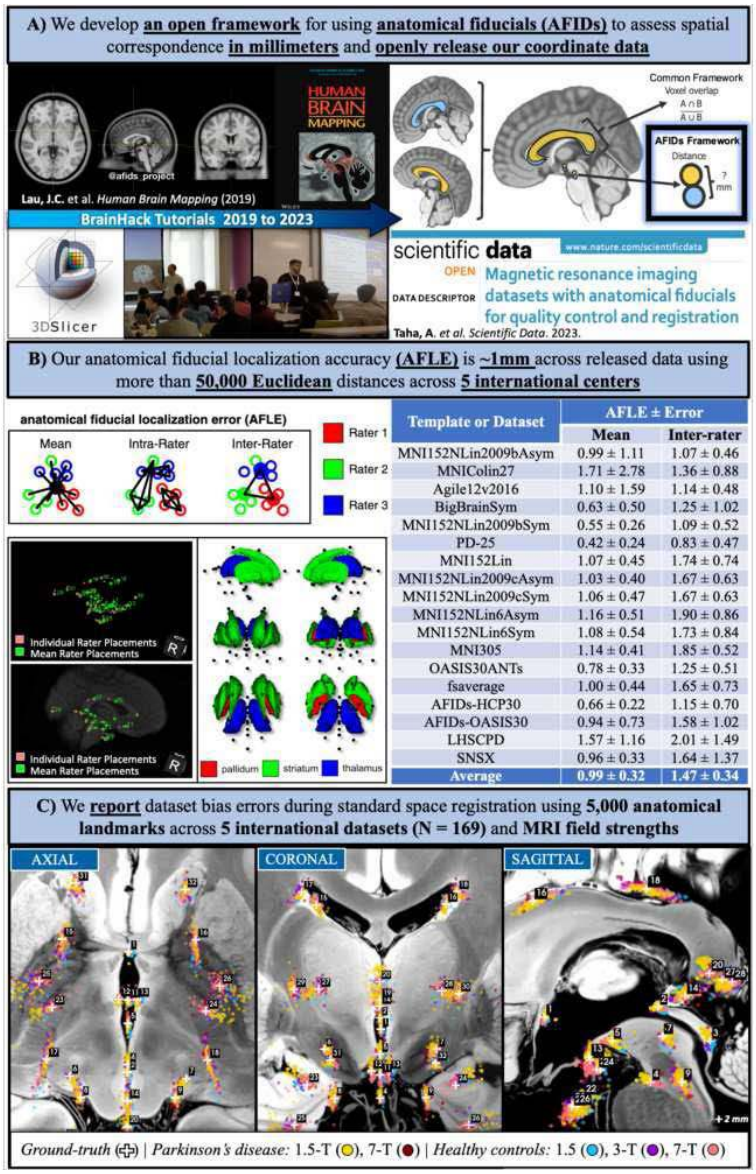

Template or Dataset	AFLE ± Error	
	Mean	Inter-rater
MNI152NLin2009bAsym	0.99 ± 1.11	1.07 ± 0.46
MNIColin27	1.71 ± 2.78	1.36 ± 0.88
Agile12v2016	1.10 ± 1.59	1.14 ± 0.48
BigBrainSym	0.63 ± 0.50	1.25 ± 1.02
MNI152NLin2009bSym	0.55 ± 0.26	1.09 ± 0.52
PD-25	0.42 ± 0.24	0.83 ± 0.47
MNI152Lin	1.07 ± 0.45	1.74 ± 0.74
MNI152NLin2009cAsym	1.03 ± 0.40	1.67 ± 0.63
MNI152NLin2009cSym	1.06 ± 0.47	1.67 ± 0.63
MNI152NLin6Asym	1.16 ± 0.51	1.90 ± 0.86
MNI152NLin6Sym	1.08 ± 0.54	1.73 ± 0.84
MNI305	1.14 ± 0.41	1.85 ± 0.52
OASIS30ANTs	0.78 ± 0.33	1.25 ± 0.51
fsaverage	1.00 ± 0.44	1.65 ± 0.73
AFIDs-HCP30	0.66 ± 0.22	1.15 ± 0.70
AFIDs-OASIS30	0.94 ± 0.73	1.58 ± 1.02
LHSCPD	1.57 ± 1.16	2.01 ± 1.49
SNSX	0.96 ± 0.33	1.64 ± 1.37
Average	**0.99 ± 0.32**	**1.47 ± 0.34**

Methods: Imaging Datasets. We curated across a number of different neuroimaging modalities and resolutions: 1) a previously published dataset [Chen et al. 2023] consistent with healthy paired imaging acquired at 7-T and 3-T MRI employing both T1w and T2w imaging sequences and 2) a local neurosurgical dataset with patients who underwent: a) T1- and T2- weighted MRI (at 1.5- and 7-Tesla), b) contrast-enhanced MRI at 1.5-Tesla, c) contrast- and non-contrast-enhanced CT (peri- and post-operatively), and d) diffusion-weighted imaging (DWI) with quantitative derivatives including fractional anisotropy. Anatomical Landmarks. We made our curated placement protocols publicly available [Lau et al. 2023]. In total, 34 AFIDs (10 midline and 12 bilateral) that survey the brain were applied. To curate AFID ground-truth data, we recruited a total of 20 human raters over the past 4 years, constituting a wide spectrum of expert and novice raters. Novice raters went through the open-access protocol and leveraged our online web app platform "AFIDs Validator" [Kai et al. 2023] during training. Localization Assessment (Figure 2A). We computed the anatomical fiducial localization error (AFLE) of these 34 landmarks across rater applications (i.e., mean AFLE) and also across MRI field-strengths (i.e., inter-scan AFLE) of paired imaging. Registration Assessment (Figure 2B). We quantified the anatomical fiducial registration error (AFRE) when registering a participant's scans to a common standard template, using presets from a nonlinear deformation framework validated via 11,000 non-linear warps across 100 subjects [Ewert et al. 2019]. We focus our reporting here on new findings validating AFIDs for T2w imaging.

Results: Rater demographics. Six human raters were trained and subsequently recruited to place the AFIDs protocol on T2w imaging. AFLE. The mean AFLE across all scans and AFIDs was 1.03 +/- 0.55 mm. Furthermore, the error between AFID localization on 3T and 7T MRI scans was 0.65 +/- 0.35 mm (7 out of 34 AFIDs were localized more accurately on 7T MRI). AFRE. The mean AFRE was statistically higher ($p < 0.001$) on 3T (3.12 +/- 1.93 mm) when compared to 7T scans (2.86 +/- 1.94 mm).

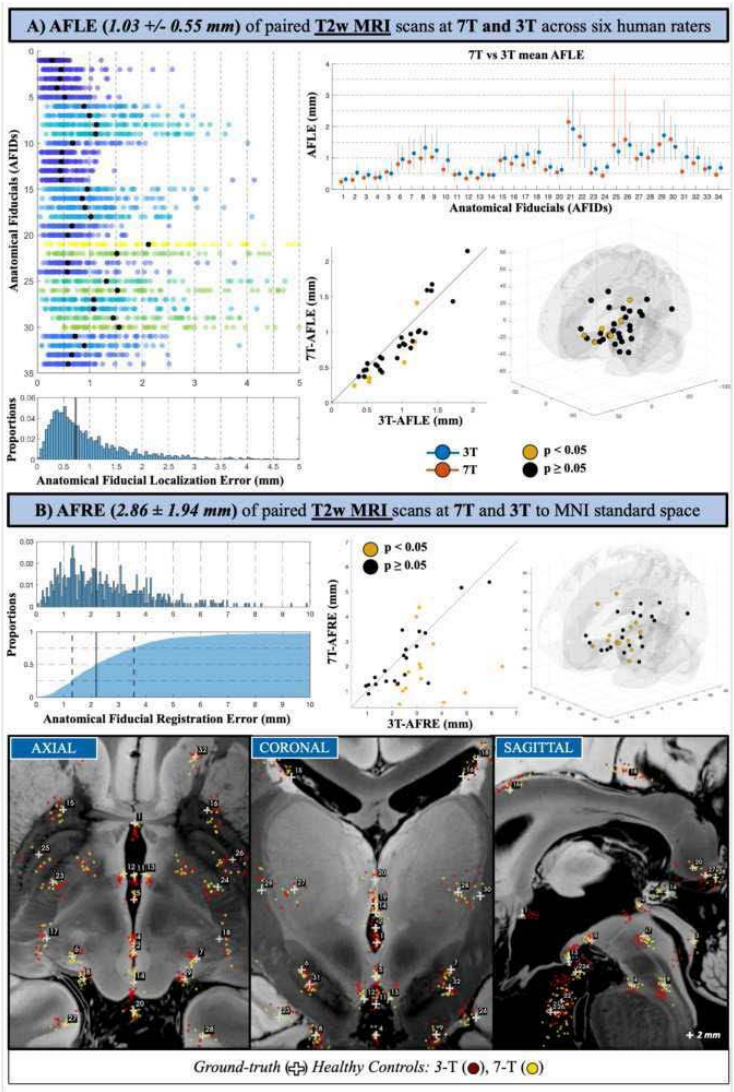

Conclusions: This study validates AFIDs as a reliable and sensitive tool for T2w image registration and strives towards better standardization of intermediate steps taken in a variety of neuroimaging and clinical workflows. Using the curated datasets from this study, future work will expand this protocol to other commonly used imaging modalities (e.g., DWI and CT) and explore approaches that automate AFID localization.

References
1. Abbass, M., et al. (2022), 'Application of the anatomical fiducials framework to a clinical dataset of patients with Parkinson's disease', Brain Structure and Function, vol. 227, pp. 393-405.
2. Chen, X., et al. (2023), 'A paired dataset of T1- and T2-weighted MRI at 3 Tesla and 7 Tesla', Scientific Data, vol. 10, no. 489.
3. Ewert, S., et al. (2019), 'Optimization and comparative evaluation of nonlinear deformation algorithms for atlas-based segmentation of DBS target nuclei' Neuroimage, vol. 184, pp. 586-598.
4. Kai, J., et al. (2023), 'Anatomical Fiducial Placement Validator Tool', Zenodo, vol. 1.2.6.
5. Lau, J.C, et al. (2019), 'A framework for evaluating correspondence between brain images using anatomical fiducials', Human Brain Mapping, vol. 40, no. 14, pp. 4163-4179.
6. Lau, J.C., et al. (2023), 'Source code for: Anatomical Fiducial Placement Protocol', Zenodo, vol. 1.0.0.
7. Rohlfing, T. (2012), 'Image similarity and tissue overlaps as surrogates for image registration accuracy: widely used but unreliable', IEEE Transactions on Medical Imaging, vol. 31, no. 2, pp. 153-163.
8. Taha, A, et al. (2023), 'Magnetic resonance imaging datasets with anatomical fiducials for quality control and registration', Scientific Data, vol. 10, no. 449.
9. Zhang, Y.D., et al. (2020), 'Advances in multimodal data fusion in neuroimaging: Overview, challenges, and novel orientation', Information Fusion, vol. 64, pp. 149-187.

Poster No 1834

Uncovering the asymmetry of common temporal lobe folding variants

Yourong Guo[1,2], Logan Williams[1,2], Matthew Glasser[3,4], Mohamed Suliman[1], Alexander Hammers[5], David van Essen[4], Jonathan O'Muircheartaigh[2,6,7], Emma Robinson[1,2,7]

[1]Department of Biomedical Engineering, King's College London, London, UK, [2]Centre for the Developing Brain, King's College London, London, UK, [3]Department of Radiology, Washington University, St. Louis, MO, USA, [4]Department of Neuroscience, Washington University, St. Louis, MO, USA, [5]King's College London & Guy's and St. Thomas' PET Centre, King's College London, London, UK, [6]Department of Forensic and Neurodevelopmental Sciences, King's College London, London, UK, [7]MRC Centre for Neurodevelopmental Disorders, King's College London, London, UK

Introduction: The asymmetry of the temporal lobe is thought to play a crucial role in language processing, social cognition, and facial recognition[1,2]. Past investigation of asymmetry has largely focused on the superior temporal sulcus (STS), which shows a deeper[3] and less interrupted[4] right STS throughout the lifespan. One of the methodological obstacles to a more detailed evaluation of cortical folding asymmetry has been the difficulty in disentangling true asymmetry from the large natural cortical folding variability[5]. In previous work we have shown that major cortical folding variants may be characterised through hierarchical surface registration (MSM-HT[6]). In this abstract we set out to use these to perform a detailed analysis of more fine-grained structural asymmetries of the whole temporal lobe.

Methods: Starting with the null hypothesis that there is no asymmetry of the temporal lobe, MSM-HT was used to co-register all hemispheres from 1110 subjects from the Young Adult Human Connectome Project (HCP) to each other. This was achieved by first mirror-flipping all right hemispheres; then co-registering all pairs using a fast learning-based surface registration algorithm[7] to construct a 2220 × 2220 matrix of pairwise similarities of cortical folding. Here, cortical folding similarity was assessed by measuring the Dice overlap and correlation of sulcal depth feature separately for each of the frontal, parieto-occipital and temporal lobes. Next, 30 clusters of common folding variants were identified for each lobe, through agglomerative hierarchical clustering on these features (Fig.1A). Multimodal surface matching (MSM)[8] was used to co-register curvature maps of individuals within each cluster to generate a family of templates summarising the clusters. To approach lobar asymmetry, the proportion of left hemisphere examples used to generate each template was calculated; clusters were then categorised as left- or right-biased. Significant asymmetry was tested using Fisher's exact test with Bonferroni correction. To further characterise folding asymmetry of the temporal lobe, surface area of this region was normalised by total ipsilateral hemispheric surface area (Fig.2A, B); this was compared between left- and right-biased folding variants using a two-sample t-test.

Results: The resulting folding variants aligned with the literature[5]. Comparing to frontal and parietal lobe variants (clustered in the same way), a higher proportion of temporal lobe clusters were left-biased (Fig.1B). Left-biased templates present more atypical folding variants, capturing more interruptions on the STS[4]; more branches of the middle segments of the STS extended to inferior temporal sulci (cluster 2,3,4,8 in Fig.1B) and branches of the posterior segments of STS (cluster 4); right-biased templates display a continuous STS with larger cluster sizes compared to the left-biased templates (i.e. patterns were more consistent). Both left and right-biased variants have multiple interruptions of the inferior temporal sulcus. As expected, subjects with larger hemispheric surface area had larger temporal lobe surface areas (Fig.2B), but when comparing the proportions of temporal lobe surface area in the hemisphere, hemispheres in left-biased folding variants were significantly larger than right-biased folding variants (Fig.2C, $P<0.001$), reflecting increased folds and increasingly branched folding.

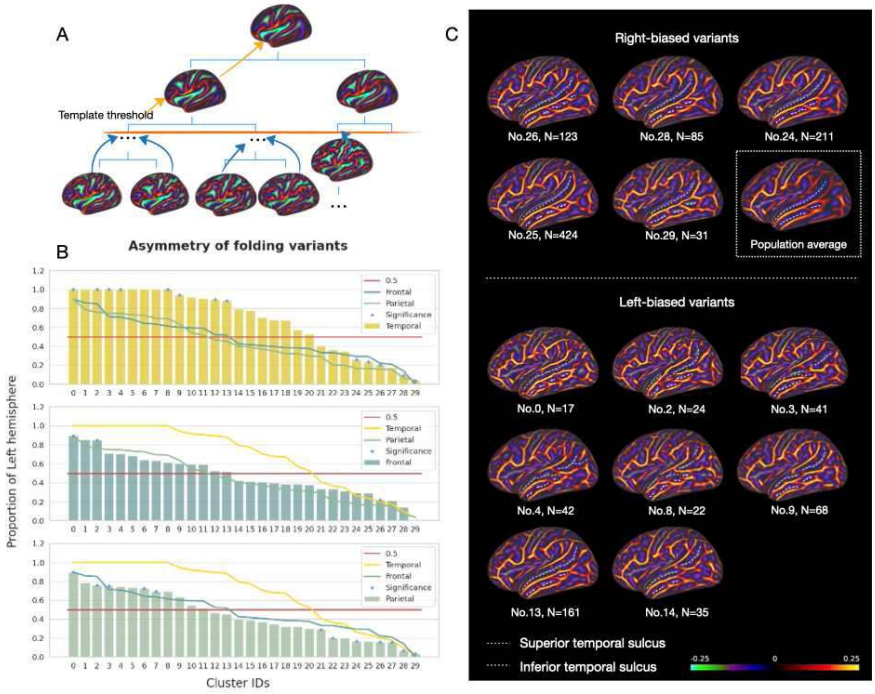

Figure 1: In 1110 subjects from the HCP, all right hemispheres were mirror flipped to the left and we applied MSM-HT [panel A] to co-register all hemispheres (left and right). Relative to asymmetries calculated for frontal and parietal lobes, leftward asymmetric variants were more frequent in the temporal lobe [panel B]. Significantly biased templates were shown in [panel c]. Left-biased templates presented more atypical folding capturing more interruptions on the STS, more branches of the middle segments of STS extending to inferior temporal sulci (cluster 2,3,4,8), and branches of the posterior segments of STS (cluster 4); right-biased templates displayed a continuous STS with larger cluster sizes compared to the left-biased templates (i.e. patterns were more consistent).

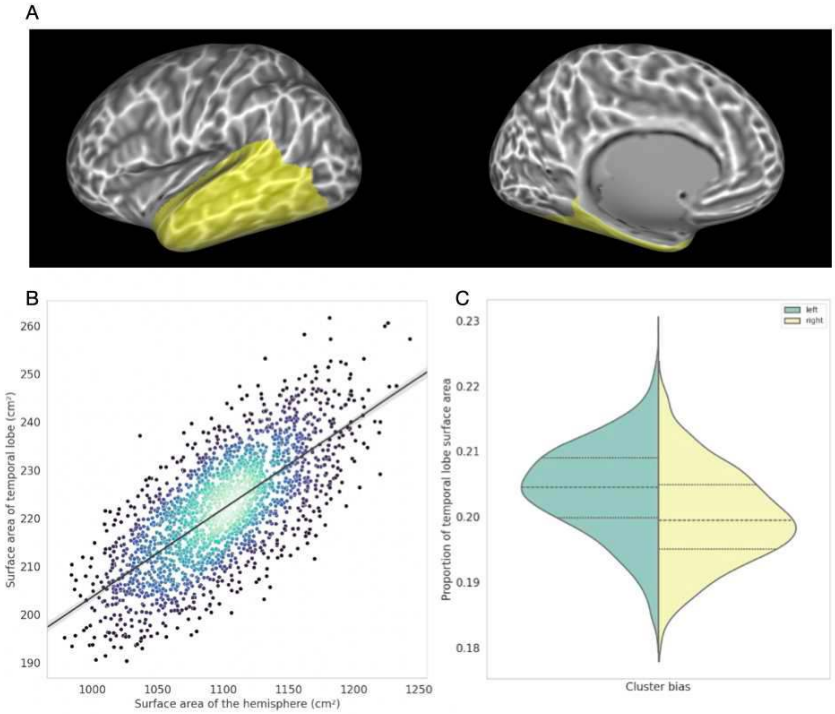

Figure 2: To approach lobar asymmetry, the proportion of left hemisphere examples used to generate each template was calculated and clusters were then categorised as left- or right-biased. The temporal lobe was defined by summing temporal regions of the Desikan-Killiany Atlas [9] [panel A]. Subjects with larger hemispheric surface area had larger temporal lobe surface areas [panel B]. But when comparing the proportions of temporal lobe surface area in the hemisphere, hemispheres in left-biased folding variants are significantly larger than right-biased folding variants [panel C, P<0.001], reflecting increased folds and increasingly branched folding.

Conclusions: Using hierarchical registration and clustering, the present study uncovered strongly lateralised common variants of cortical folding in line with the literature in specific sulci. Differences between left/right-biased folding variants are evident in the temporal lobe, with increased surface area on the left. This aligns with the known higher computational demands of language processing in the left hemisphere, suggesting that MSM-HT offer opportunities for more detailed investigation into the links between lateralised folding variants and function.

References
1. Leroy, F., Cai, Q., Bogart, S. L., Dubois, J., Coulon, O., Monzalvo, K., ... & Dehaene-Lambertz, G. (2015). New human-specific brain landmark: the depth asymmetry of superior temporal sulcus. Proceedings of the National Academy of Sciences, 112(4), 1208-1213.
2. Le Guen, Y. et al., (2018). Genetic influence on the sulcal pits: on the origin of the first cortical folds. Cerebral Cortex, 28(6), 1922-1933.
3. Williams, L. Z. J., Fitzgibbon, S. P., Bozek, J., Winkler, A. M., Dimitrova, R., Poppe, T., ... & Robinson, E. C. (2023). Structural and functional asymmetry of the neonatal cerebral cortex. Nature Human Behaviour, 1-14.
4. Bodin, C. et al., (2021). Plis de passage in the superior temporal sulcus: morphology and local connectivity. Neuroimage, 225, 117513.
5. Ono M, Kubik S, Abernathey CD. Atlas of the cerebral sulci. Stuttgart New York: Georg Thieme Verlag; 1990.
6. Guo, Y. (2023). Uncovering common variants of cortical folding through hierarchical surface registration. OHBM2023.
7. Suliman, M. A. (2022). A deep-discrete learning framework for spherical surface registration. In International Conference on Medical Image Computing and Computer-Assisted Intervention (pp. 119-129). Springer, Cham.
8. Robinson, E. C. (2018). Multimodal surface matching with higher-order smoothness constraints. NeuroImage, 167, 453–465.
9. Desikan, R. S., Ségonne, F., Fischl, B., Quinn, B. T., Dickerson, B. C., Blacker, D., ... & Killiany, R. J. (2006). An automated labeling system for subdividing the human cerebral cortex on MRI scans into gyral based regions of interest. Neuroimage, 31(3), 968-980.

Poster No 1835

Unveiling Dynamics in Standard MRI Sequences through Motion Magnification Techniques

Zhaoying Pan[1], Vidhya Vijayakrishnan Nair[1], Qiuting Wen[2], Yunjie Tong[1], Xiaoqian Wang[1]

[1]Purdue University, West Lafayette, IN, [2]Indiana University School of Medicine, Indianapolis, IN

Introduction: Amplified Magnetic Resonance Imaging (aMRI)[1-3] employs motion magnification techniques[4-8] developed for natural videos in the context of MRI scans, enabling improved observation of nuanced motion cycles within the brain. Previous research[1-3] has experimented with diverse motion magnification methods on cine MRI, a specialized MRI variant offering detailed high-resolution scans. However, due to challenges in the data collection and limitation to specific frequency, the impact of aMRI has been limited. In our study, we developed a new post-processing technique to amplify motion cycles in EPI-based fMRI data. This approach allows for better understanding of minor brain and lateral ventricle movements during both resting state and task-based fMRI scans. Our method, benefiting from the widespread availability of fMRI data, promises broader applicability in both clinical and research contexts.

Methods: MRI data from participants were acquired using a 3T SIEMENS MRI scanner (Magnetom Prisma, Siemens Medical Solutions, Erlangen, Germany) equipped with a 64-channel head coil. Additionally, participants wore chest belts to record respiration signals. Subsequently, extracting slices to enhance lateral ventricle observation and rescaling for higher contrast were applied to 3D brain scan volumes. These slices were then compiled along the temporal axis to construct a video for further magnification. In contrast to utilizing state-of-the-art learning-based methods[7-8], which may be impractical due to the low resolution and limited dataset availability in general MRI, we opted for the phase-based magnification technique[6]. This technique, whose performance stands out among non-learning-based methods[4-6], leveraging complex steerable pyramids, decomposes the video to separate phase from amplitude, enabling the amplification of temporally-bandpassed phases. Evaluating the results of our motion magnification technique is challenging because real-world videos lack a standard for comparison. To address this, we used two methods of assessment: digital simulations and data from a breath-holding experiment, along with the “y-t slices” method[4-8], to visualize motion with static images by extracting one-pixel-width/height slices from a fixed position and concatenating these slices from all frames in a video. For our simulation, we represented brain motion with an oval shape and lateral ventricles with an “X” shape. The motion is simulated with the sum of sine functions at 0.3Hz and 1Hz (respiration and heartbeat), affecting the oval’s size and the “X” shape’s width. Additionally, we used two metrics for simulation results: the structural similarity index measure (SSIM)[9] and mean squared error (MSE). In the breath-holding experiment, we induced 6 cycles of brain dynamics using periodic hypercapnia.

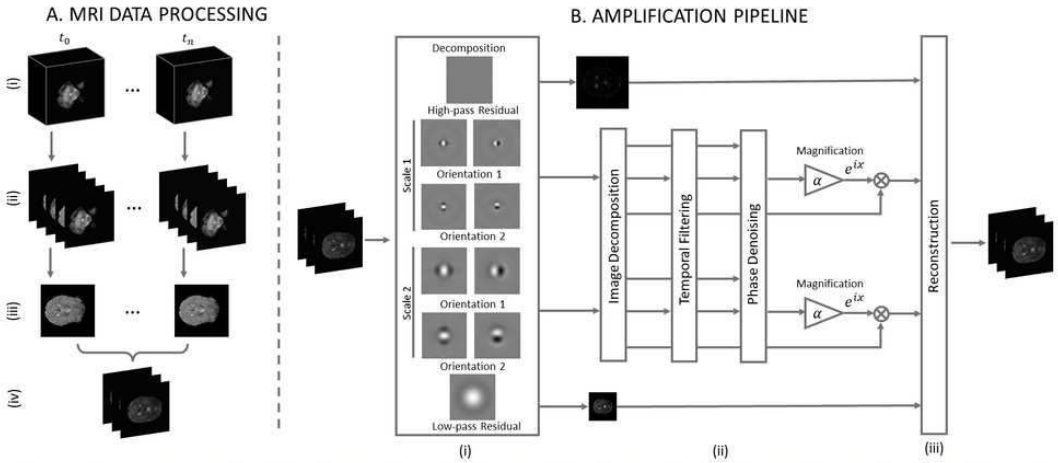

Figure 1: A. In A(i), the MRI volumes along the temporal axis are presented. The processing involves extracting 2D slices from the volumes (ii), resulting in a collection of 2D images from the originally 3D volumes. One slice is selected from each timestamp, and all slices are rescaled to enhance contrast. At last, these rescaled slices compose a video for further amplification. B. The amplification pipeline, as illustrated in B(i), employs the phase-based technique utilizing complex steerable pyramids with multiple levels. In this simplified version with two spatial scales, the input is decomposed into different spatial scales and orientations, along with the separation of amplitudes and phases in (ii). Subsequently, temporal filtering and denoising of the phase occur before amplification (iii). The final step involves reconstructing the magnified video from the amplified phase and other components.

Results: Our simulation results, illustrated in Figure 2, closely matched our simulated standard, achieving an SSIM score of 0.954 and an MSE of 3.186 indicating the similarity between the groundtruth simulation and amplified result. These results confirm our method's ability to effectively magnify motion patterns at different frequency bands. Additionally, in experiments where subjects held their breath, our method successfully identified motion signals corresponding to the exact 6 breath-holding cycles, with precise timing of when the breath-holding started and stopped. By magnifying the data collected from these experiments, we were able to clearly observe breathing patterns. This demonstrates the effectiveness of our method in working with real-world fMRI data.

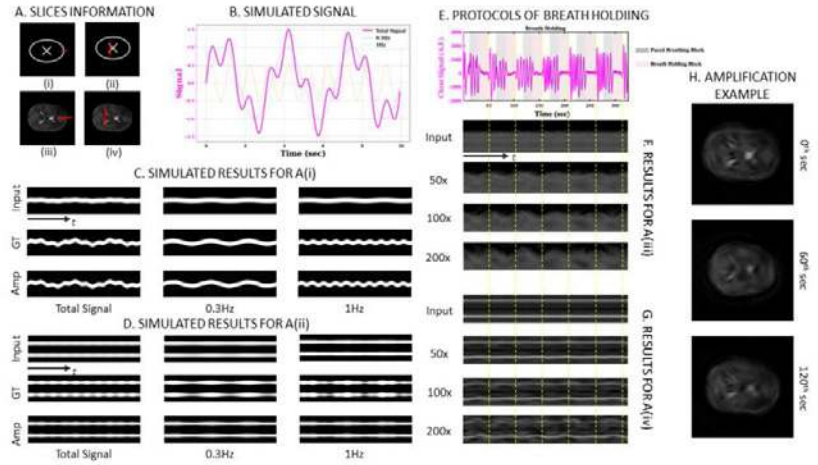

Figure 2: A. Short red lines in A indicate the positions from which slices are selected for amplification visualization. Slices are taken from the boundary of the entire brain (i, iii) and across the lateral ventricles (ii, iv). B. The signal consists of two sine signals with frequencies of 0.3Hz and 1Hz. C. The first row displays slice visualizations of the input data, including the total signal and different frequency bands where subtle motion is challenging to observe. The second row shows the visualization of the ground truth (GT), and the third row presents the visualization of our amplified results (Amp), demonstrating consistency with the ground truth simulation. Note that the visualizations in Figure B are resized to fit in figures. D. Visualizations of slices taken from simulated lateral ventricles are showcased. While some artifacts are present, especially in the 1Hz frequency band, overall, we achieved comparable amplification to the ground truth simulation. E. The signal pattern of data collected with breath-holding protocols is provided. F, G. Slice visualizations of the brain boundary for the input video and amplified videos with different magnification factors (50, 100, and 200) are shown. Yellow dashed lines are used to match the cycles from the signal and the visualizations. Note that we adjusted the brightness and contrast for better visualizations. The visualization displays cycles aligned with the signal from the protocols. H. Frames from 0th, 60th and 120th seconds in the video amplified by 200 times are presented, revealing distinct contraction patterns.

Conclusions: Our results demonstrate the success of the magnification approach in emphasizing minor movements in the brain and lateral ventricles in standard fMRI data, observable across various frequency bands. The adaptability of our approach to fMRI makes it applicable to a wide range of labs and clinics, offering practical benefits for diagnosis and analysis.

References

1. Holdsworth, S. J. (2016). Amplified magnetic resonance imaging (aMRI). Magnetic resonance in medicine, 75(6), 2245-2254.
2. Terem, I. (2018). Revealing sub-voxel motions of brain tissue using phase-based amplified MRI (aMRI). Magnetic resonance in medicine, 80(6), 2549-2559.
3. Terem, I. (2021). 3D amplified MRI (aMRI). Magnetic Resonance in Medicine, 86(3), 1674-1686.
4. Liu, C. (2005). Motion magnification. ACM transactions on graphics (TOG), 24(3), 519-526.
5. Wu, H. (2012). Eulerian video magnification for revealing subtle changes in the world. ACM transactions on graphics (TOG), 31(4), 1-8.
6. Wadhwa, N. (2013). Phase-based video motion processing. ACM Transactions on Graphics (ToG), 32(4), 1-10.

7. Oh, T. H. (2018). Learning-based video motion magnification. In Proceedings of the European Conference on Computer Vision (ECCV) (pp. 633-648).
8. Pan, Z. (2023). Self-Supervised Motion Magnification by Backpropagating Through Optical Flow. In Thirty-seventh Conference on Neural Information Processing Systems.
9. Wang, Z. (2004). Image quality assessment: from error visibility to structural similarity. IEEE transactions on image processing, 13(4), 600-612.

Poster No 1836

CAT faces Python - Combining Deep-Learning with Traditional Segmentation

Christian Gaser[1], Robert Dahnke[1]

[1]Jena University Hospital, Jena, Germany

Introduction: Deep learning (DL) techniques have shown great promise in the analysis and interpretation of medical images, offering unprecedented capabilities in identifying patterns and features indicative of various pathologies. However, while these approaches are remarkably accurate at recognising known conditions, they face significant challenges when confronted with data containing previously unseen or unexpected variations. This phenomenon is a significant barrier to clinical application, as it leads to a form of 'hallucination' where the algorithms generate false positive identifications or misinterpretations when encountering unfamiliar pathologies or abnormal variations[1,2]. Despite the growing interest in the application of DL to medical imaging, the lack of publications addressing this specific challenge is striking.

Methods: We use SynthSeg, a novel deep learning tool capable of segmenting brain scans of any contrast and resolution[3]. SynthSeg does not require retraining and has demonstrated robustness across different populations. It produces a label image and a parcellation (atlas) that are used to generate a skull-stripped and bias-corrected version of the original T1 image. Our proposed hybrid segmentation approach integrates methods from the CAT12 toolbox[4], reimplemented in Python and C to eliminate any dependence on Matlab. Using an adaptive maximum a posteriori (AMAP) segmentation[5], we derived a partial volume estimation (PVE) segmentation from the processed image. This segmentation was then used to estimate cortical thickness and central surface area using projection-based thickness (PBT)[7]. Our comparative analysis involved evaluating our novel approach against (1) a conventional pipeline based on CAT12.8, and (2) a DL-based segmentation using the DL-based result to estimate cortical thickness and central surface.

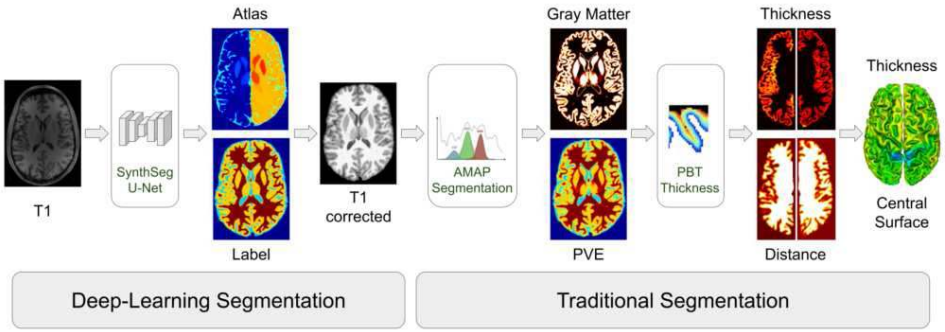

Figure 1 Hybrid Segmentation Pipeline
We use a deep learning tool for segmentation of brain scans of any contrast and resolution, *SynthSeg*, to obtain a tissue label map and a parcellated atlas map. From these maps, a skull-stripped and bias-corrected image is generated, which is segmented using adaptive maximum *a posteriori* (AMAP) segmentation with partial volume estimation (PVE). The result of the AMAP segmentation is used to estimate cortical thickness and the central surface for both hemispheres based on a projection-based thickness (PBT) method.

Results: The DL-based SynthSeg method exhibited a tendency to overestimate thickness values. This overestimation was accompanied by errors in sulcus reconstruction, particularly in regions such as the occipital lobe. In contrast, the hybrid approach showed superior performance, aligning closer to the estimates derived from the CAT12-based reference. In particular, the hybrid method showed improved accuracy in cortical thickness estimation and sulcus delineation, demonstrating its potential for more reliable and accurate neuroimaging analyses.

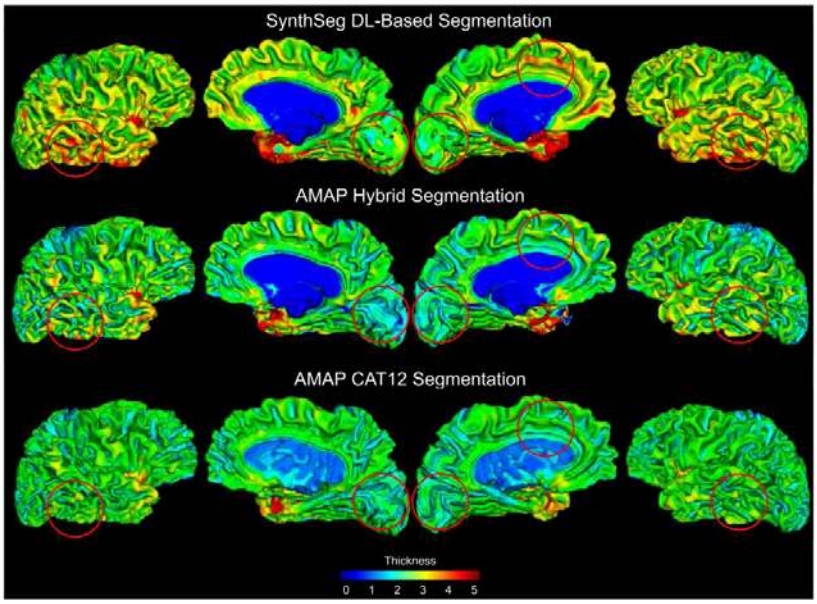

Figure 2 Comparison of Thickness Estimations between DL-Based, Hybrid, and CAT12 Segmentation
Thickness estimation was based on PBT method that used segmentation maps from SynthSeg, the proposed AMAP hybrid method and CAT approach. The example shown is a Parkinson patient from the PPMI study (https://www.ppmi-info.org).

Conclusions: The development and application of our novel hybrid methodology addresses the challenges of DL-based segmentation of brain scans, particularly in clinical contexts involving multiple pathologies. By seamlessly integrating DL with traditional segmentation techniques, our approach mitigates the risk of hallucinations commonly associated with DL algorithms when faced with unexpected variations or pathologies. The observed improvements in accuracy and reliability, particularly in cortical thickness estimation and sulcus delineation, underscore the potential of our hybrid strategy to enhance the robustness of neuroimaging analyses. This hybrid fusion not only provides a more stable segmentation process, but also leverages the strengths of both DL and conventional methods, paving the way for more accurate and clinically relevant neuroimaging assessments.

References

1. S. Bhadra, V.A. Kelkar, F.J. Brooks, M.A. Anastasio (2021). On Hallucinations in Tomographic Image Reconstruction. IEEE Trans Med Imaging. 40(11): 3249–3260.
2. N.M. Gottschling, V. Antun, A.C. Hansen, B. Adcock (2023). The troublesome kernel -- On hallucinations, no free lunches and the accuracy-stability trade-off in inverse problems. arXiv:2001.01258v2.
3. B. Billot, D.N. Greve, O. Puonti, A. Thielscher, K. Van Leemput, B. Fischl, A.V. Dalca, J.E. Iglesias (2023). SynthSeg: Segmentation of brain MRI scans of any contrast and resolution without retraining. Medical Image Analysis, 86:102789.
4. C. Gaser, R. Dahnke, P.M. Thompson, F. Kurth, E. Luders (2023). A Computational Anatomy Toolbox for the Analysis of Structural MRI Data. bioRxiv.
5. J.C. Rajapakse, J.N. Giedd, J.L. Rapoport (1997). Statistical Approach to Segmentation of Single-Channel Cerebral MR Images. IEEE Trans. Med. Imag. 16(2):176-186.
6. J. Tohka, A. Zijdenbos, A. Evans (2004). Fast and robust parameter estimation for statistical partial volume models in brain MRI. Neuroimage 23(1):84-97.
7. R. Dahnke, R.A. Yotter, C. Gaser (2013). Cortical thickness and central surface estimation. Neuroimage 65:336-48.

Poster No 1837

Comparison of MRI normalization strategies for estimating lesion load in multiple sclerosis

Brigitta Malagurski Tortei[1], Hibba Yousef[1]

[1]Technology Innovation Institute, Biotechnology Research Center, P.O.Box: 9639, Masdar City, Abu Dhabi, United Arab Emirates

Introduction: The presence of pathological lesions on structural MRI poses a significant challenge for image registration to standard anatomical spaces[1], which is an essential step for comparison of homologous brain regions in group studies. Multiple sclerosis (MS) is one such pathology, characterized by demyelinated lesions throughout the central nervous system[2]. During registration, geometric distortions are introduced, and erroneous removal or inflation of some lesions may occur[3]. Furthermore, the discrepancies between lesioned brains and the target template can substantially reduce registration

accuracy[4]. This is particularly relevant in lesion-symptom mapping, that is the calculation of the lesion load that reflects the size of the damage and its overlap with a particular region of interest (gray matter or white matter tracts). Thus, our aim was to compare the effects of four registration pipelines with different mitigation strategies and quantify their effect on lesion load in MS.

Methods: A publicly available dataset of 30 MS patients was used for this study, consisting of structural MRI modalities (T1w, T2w, FLAIR) and corresponding lesion masks, which were segmented semi-automatically[5]. For each patient, the T1 images were denoised, bias corrected, brain-extracted (HD-BET;[6]) and normalized to MNI152 space using four different ANTs-based nonlinear (3-stage registration: rigid, affine and SyN) processing pipelines[7]. In the first one, the brain images were registered to MNI space using the default ANTs workflow (Figure 1 – NoMask). In the second one, the inverse of the lesion mask was generated and used during the registration to limit the areas of the mapping within an excluded region (Figure 1 – CFM). In the third and the fourth workflow, we used the SynthSR[8] and the VBG[9] tools, respectively, to generate lesion-free T1-weighted images, which should support further image processing in cases where lesions would interfere with the quality of the output. Lesion load (LL) was calculated using the high-resolution sensorimotor area tract template (SMATT; [10]), which contains 12 bilateral tracts derived from probabilistic tractography based on 6 cortical regions in the primary motor cortex (M1), dorsal premotor cortex (PMd), ventral premotor cortex, supplementary motor area (SMA), pre-supplementary motor area (preSMA), and primary somatosensory cortex. This template was chosen due to the prevalence of MS lesions in white matter and motor disability patterns commonly found in MS patients. Lesion load was defined as the number of lesioned voxels intersecting with a given tract divided by the number of voxels in the tract. The comparison between different registration pipelines and their impact on the SMATT lesion load was evaluated using the Wilcoxon signed-rank test. False discovery rate (FDR) was applied to adjust for multiple comparisons.

Results: Nonparametric paired comparisons were conducted between SMATT lesion loads calculated using four different processing workflows. We did not find any statistically significant differences between any of the registration pipelines (FDR p values > 0.05; Figure 1).

Conclusions: In this preliminary study we showed that the lesion filling and lesion masking, applied during registration to MNI space, didn't have a statistically significant impact on the lesion load calculation within a white matter tract-based template in a small sample of MS subjects. However, further studies should also consider the accuracy of each of these normalization methods, the impact of lesion size and heterogeneity, and the choice of different brain atlases and pathologies (e.g., stroke) on the dis/advantages of each of the preprocessing approaches shown here.

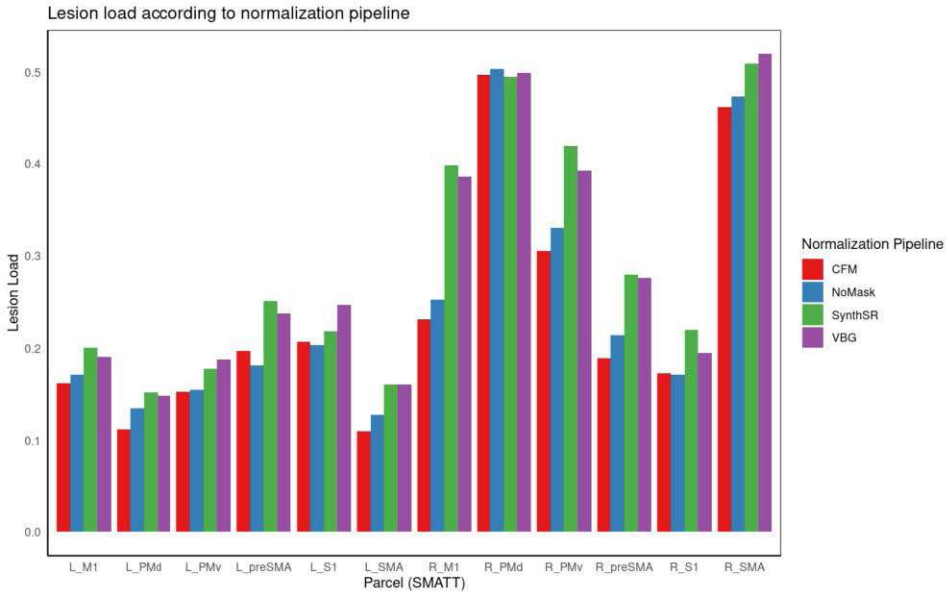

References

1. Visser, M., Petr, J., Müller, D. M. J., Eijgelaar, R. S., Hendriks, E. J., Witte, M., Barkhof, F., van Herk, M., Mutsaerts, H. J. M. M., Vrenken, H., de Munck, J. C., & De Witt Hamer, P. C. (2020). Accurate MR Image Registration to Anatomical Reference Space for Diffuse Glioma. Frontiers in Neuroscience, 14.
2. Lassmann, H. (2018). Multiple sclerosis pathology. In Cold Spring Harbor Perspectives in Medicine (Vol. 8, Issue 3). Cold Spring Harbor Laboratory Press. https://doi.org/10.1101/cshperspect.a028936
3. Andresen, J., Uzunova, H., Ehrhardt, J., Kepp, T., & Handels, H. (2022). Image registration and appearance adaptation in non-correspondent image regions for new MS lesions detection. Frontiers in Neuroscience, 16.

4. Pappas, I., Hector, H., Haws, K., Curran, B., Kayser, A. S., & D'Esposito, M. (2021). Improved normalization of lesioned brains via cohort-specific templates. Human Brain Mapping, 42(13), 4187–4204.
5. Lesjak, Ž., Galimzianova, A., Koren, A., Lukin, M., Pernuš, F., Likar, B., & Špiclin, Ž. (2018). A Novel Public MR Image Dataset of Multiple Sclerosis Patients With Lesion Segmentations Based on Multi-rater Consensus. Neuroinformatics, 16(1), 51–63.
6. Isensee, F., Schell, M., Pflueger, I., Brugnara, G., Bonekamp, D., Neuberger, U., Wick, A., Schlemmer, H. P., Heiland, S., Wick, W., Bendszus, M., Maier-Hein, K. H., & Kickingereder, P. (2019). Automated brain extraction of multisequence MRI using artificial neural networks. Human Brain Mapping, 40(17), 4952–4964.
7. Avants, B. B., Tustison, N. J., Song, G., Cook, P. A., Klein, A., & Gee, J. C. (2011). A reproducible evaluation of ANTs similarity metric performance in brain image registration. NeuroImage, 54(3), 2033–2044.
8. Iglesias, J.E, et al. (2023). SynthSR: A public AI tool to turn heterogeneous clinical brain scans into high-resolution T1-weighted images for 3D morphometry. Sci. Adv.9, eadd3607.
9. Radwan, A.M., Emsell, L., Blommaert, J., Zhylka, A., Kovacs, S., Theys, T., Sollmann, N., Dupont, P., Sunaert, S. (2021). Virtual brain grafting: Enabling whole brain parcellation in the presence of large lesions. Neuroimage, 229:117731.
10. Archer, D.B., Vaillancourt, D.E., Coombes, S.A. (2018). A Template and Probabilistic Atlas of the Human Sensorimotor Tracts using Diffusion MRI. Cereb Cortex, 28(5):1685-1699.

Poster No 1838

Mapping evolutionary cortical expansion with anatomical MSM

Burke Rosen[1], Chad Donahue[1], Timothy Coalson[1], John Harwell[1], Renato Besenczi[2], Emma Robinson[2], Takuya Hayashi[3], David van Essen[1], Matthew Glasser[1]

[1]Washington University in St. Louis, St. Louis, MO, [2]King's College London, London, England, [3]RIKEN Center for Biocystems Dynamics Research, Kobe, Hyogo

Introduction: The surface area of human cortex is ~3-fold greater than that of chimpanzee and >9 times greater than that of the macaque[1]. This enlargement is non-uniform across the cortex. For example, primary visual cortex (V1) is only ~2-fold greater in human vs macaque[2]. However, previously published maps[3–5] of macaque vs human expansion are in poor agreement with one another (Fig. 1A). This may reflect differing registration constraints and algorithms, but one commonality among them is that none have adequately compensated for large areal distortions that arise when projecting anatomical surfaces to the sphere (Fig. 1B). These distortions are particularly deleterious in interspecies registration because the relationship between areal boundaries and cortical folds is very different between species[1,2]. To address this issue, we have applied the anatomical Multimodal Surface Matching[6] (aMSM) algorithm, which was originally designed to enable accurate longitudinal registration of human cortices.

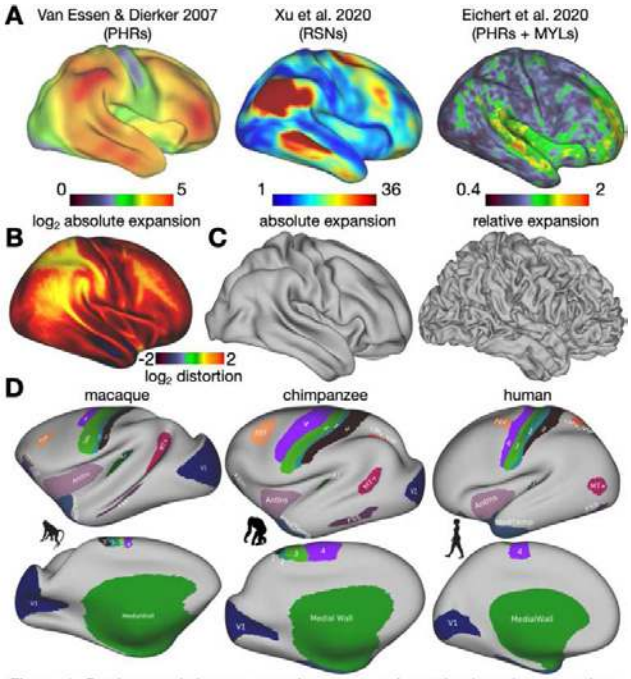

Figure 1. Previous evolutionary expansion maps and putative homologous regions (PHRs). **A.** human vs macaque evolutionary expansion maps from the literature. Features used include landmarks or PHRs, resting state networks (RSNs), and myelin maps (MYLs) **B.** Mean areal distortions introduced by spherical projection of anatomical surfaces **C.** Group average (n=1071) and individual human anatomical surfaces demonstrating the surface area lost during interindividual averaging of anatomical meshes with diverse folding patterns. **D.** PHRs delineated for this study. Labels are shown on inflated group average template surfaces for each species.

Methods: Individuals' cortical surfaces and myelin maps were reconstructed[7] from high-resolution T1 and T2 weighted MR Images for human (n=1071), chimpanzee (n=19), and macaque (n=32)[1,8]. For each species, a group template surface was created with Connectome Workbench[1,7,8]. Interspecies registration between the template surfaces was performed in two stages. The chimpanzee intermediate used for the first stage served to reduce the necessary areal distortion of each species pair registration. Each species pair registration was performed in both directions and results averaged. To compensate for the loss of surface area introduced by inter-subject averaging of human surface meshes with highly variable folding (Fig. 1C), evolutionary expansion was estimated by resampling each human surface to the macaque mesh and averaging vertex areas across subjects. All registrations were performed using 15 putatively homologous regions (PHRs), or landmarks, as registration features. PHRs were delineated based on previous studies and informed by myelin and other features (Fig. 1D). Parameters were tuned to achieve a balance of feature matching while minimizing areal distortions. Tuning was performed separately for spherical MSM[9] and aMSM to ensure fair comparison.

Results: We found that interspecies expansion estimated with anatomical MSM resulted in less folding bias than that estimated by spherical MSM (Fig 2A). The application of aMSM results in smaller areal changes in human posterior middle temporal gyrus, an area disproportionately distorted by spherical projection and differences in expansion between the algorithms. The pattern of expansion in chimpanzee vs macaque is quite different from human vs chimpanzee (Fig. 2B). In the former as compared with the latter, expansion is more pronounced in somatomotor areas and more modest in insula. Resampling human individuals then averaging the resulting expansion maps yields the mean evolutionary expansion ratio without a surface averaging loss effect caused by human interindividual folding variability (Fig. 2C). This procedure resulted in smoother expansion maps and approximately 2 times greater absolute expansion when compared to the group average surface used for regularization during aMSM.

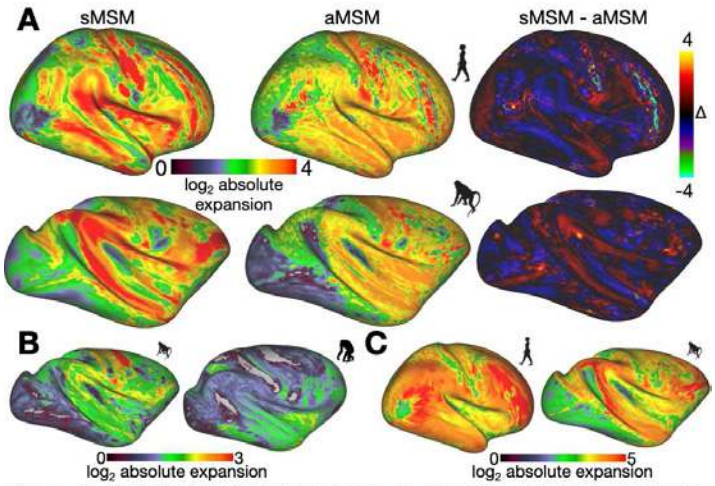

Figure 2. Evolutionary expansion maps. **A.** Template macaque vs human expansion maps for anatomical vs spherical multimodal surface matching (aMSM vs sMSM) registration. Expansion ratio displayed on inflated template human and macaque hemispheres. **B.** Chimpanzee vs macaque expansion displayed on macaque cortex and human vs chimpanzee expansion displayed on chimpanzee cortex. **C.** Average of individual human vs chimpanzee expansion maps. All maps are displayed on inflated template surfaces

Conclusions: Accurate registration of macaque and human cortices is critical for understanding primate brain evolution and for augmenting the clinical and scientific interpretability of animal models. We conclude that using anatomical MSM for interspecies registration and avoiding human surface mesh averaging results in material improvements over prior efforts. Our maps of human vs chimpanzee expansion are consistent with previous findings that a comparatively small somatomotor cortex may be a derived trait in human[10]. Future refinements will incorporate additional features, including myelin maps and fMRI into the registrations.

References

1. Hayashi T, Hou Y, Glasser MF, Autio JA, Knoblauch K, Inoue-Murayama M, Coalson T, Yacoub E, Smith S, Kennedy H, et al. The nonhuman primate neuroimaging and neuroanatomy project. NeuroImage. 2021;229:117726.
2. Donahue CJ, Glasser MF, Preuss TM, Rilling JK, Van Essen DC. Quantitative assessment of prefrontal cortex in humans relative to nonhuman primates. Proceedings of the National Academy of Sciences of the United States of America. 2018;115(22):E5183–E5192.
3. Van Essen DC, Dierker DL. Surface-based and probabilistic atlases of primate cerebral cortex. Neuron. 2007;56(2):209–225.
4. Xu T, Nenning KH, Schwartz E, Hong SJ, Vogelstein JT, Goulas A, Fair DA, Schroeder CE, Margulies DS, Smallwood J, et al. Cross-species functional alignment reveals evolutionary hierarchy within the connectome. NeuroImage. 2020;223.
5. Eichert N, Robinson EC, Bryant KL, Jbabdi S, Jenkinson M, Li L, Krug K, Watkins KE, Mars RB. Cross-species cortical alignment identifies different types of anatomical reorganization in the primate temporal lobe. Elife. 2020;9:e53232.

6. Garcia KE, Robinson EC, Alexopoulos D, Dierker DL, Glasser MF, Coalson TS, Ortinau CM, Rueckert D, Taber LA, Van Essen DC, et al. Dynamic patterns of cortical expansion during folding of the preterm human brain. Proceedings of the National Academy of Sciences. 2018;115(12):3156–3161.
7. Van Essen DC, Smith SM, Barch DM, Behrens TEJ, Yacoub E, Ugurbil K. The WU-Minn Human Connectome Project: An overview. NeuroImage. 2013;80:62–79.
8. Glasser MF, Sotiropoulos SN, Wilson JA, Coalson TS, Fischl B, Andersson JL, Xu J, Jbabdi S, Webster M, Polimeni JR. The minimal preprocessing pipelines for the Human Connectome Project. Neuroimage. 2013;80:105–124.
9. Robinson EC, Garcia K, Glasser MF, Chen Z, Coalson TS, Makropoulos A, Bozek J, Wright R, Schuh A, Webster M, et al. Multimodal surface matching with higher-order smoothness constraints. NeuroImage.
10. Hopkins WD, Meguerditchian A, Coulon O, Bogart S, Mangin JF, Sherwood CC, Grabowski MW, Bennett AJ, Pierre PJ, Fears S, et al. Evolution of the central sulcus morphology in primates. Brain, Behavior and Evolution. 2014;84(1):19–30.

Poster No 1839

Multi-Study Longitudinal Tensor-Based Morphometry Processing Pipelines for Mapping Neurodegeneration

Sunanda Somu[1], Alyssa Zhu[2], Siddharth Narula[1], Iyad Ba Gari[3], Shruti Gadewar[2], Talia Nir[4], Neda Jahanshad[5]

[1]University of Southern California, Los Angeles, CA, [2]USC, Marina Del Rey, CA, [3]University of Southern California, Marina Del Rey, CA, [4]University of Southern California Keck School of Medicine, Marina del Rey, CA, [5]Imaging Genetics Center, Keck School of Medicine of University of Southern California, Los Angeles, California

Introduction: Longitudinal studies offer deep insights into the rate of brain volume changes and their associations with neurodegenerative disease progression, such as Alzheimer's disease (AD). Tensor-Based Morphometry (TBM) quantifies structural brain changes by analyzing deformation field gradients derived from image registrations[1], offering higher regional specificity compared to regional volumetric measurements. TBM results can be influenced by preprocessing and image registration methods[2], necessitating careful workflow consideration in study designs. Longitudinal processing pipelines often use a subject-specific midspace template to minimize bias from any single time point[3,4]. The evaluations of such pipelines have largely focused on the method of calculating the midspace rather than the optimal pre-processing steps, which may vary by dataset. We assessed the sensitivity of four TBM pre-processing pipelines, run in two AD datasets, to detect associations with clinical impairment.

Methods: Baseline (BL) and follow-up (FU) Siemens, GE, and Philips 3T T1-weighted brain MRI (T1w) from ADNI3(N=373) and Prevent-AD(N=213) were used to compare 4 longitudinal TBM pipelines outlined in Fig 1. Two T1w preprocessing options were compared: 1) the default FreeSurfer preprocessing pipeline (FS) or 2) a combination of existing preprocessing tools includingT1w NLM denoising (Denoised)[5–7] (Fig 1B). For each subject, a midspace template was created from their preprocessed BL and FU T1w using ANTs[8]. The BL and FU T1w were warped to the subject template using 2 approaches: 1) the BL, FU, and template were all skull-stripped (Masked) or 2) all images retained the skull (SkullOn). The resulting BL log Jacobian was then subtracted from the FU to quantify net changes, and divided by the scan time interval to obtain the annual rate of volumetric change (Fig 1C). Each subject's BL T1w image was nonlinearly warped to a common BL study-specific minimal deformation template (MDT) using ANTs. Each BL MDT was warped to a common multi-site MDT[9,10](Fig 1D). These transformations were applied to the Jacobian maps to spatially normalize them for pooled statistics across studies. Participants that failed QC in any pipeline (e.g. mis-registration) were excluded from all analyses (i.e. matched N across pipes). Voxel-wise mixed effects linear regressions were run to test for associations between rates of change in brain volume and 1) clinical dementia ratings (CDR), or 2) diagnosis conversion (i.e., stable CN vs cognitive decline). Fixed effects included BL age, sex, and the time interval; scan site was a random effect. FDR was used for multiple comparisons correction across voxels. We compared each model's root mean squared error (RMSE), and the extent and distribution of significant effects across the four pipelines: Denoised+Masked, Denoised+SkullOn, FS+Masked, FS+SkullOn.

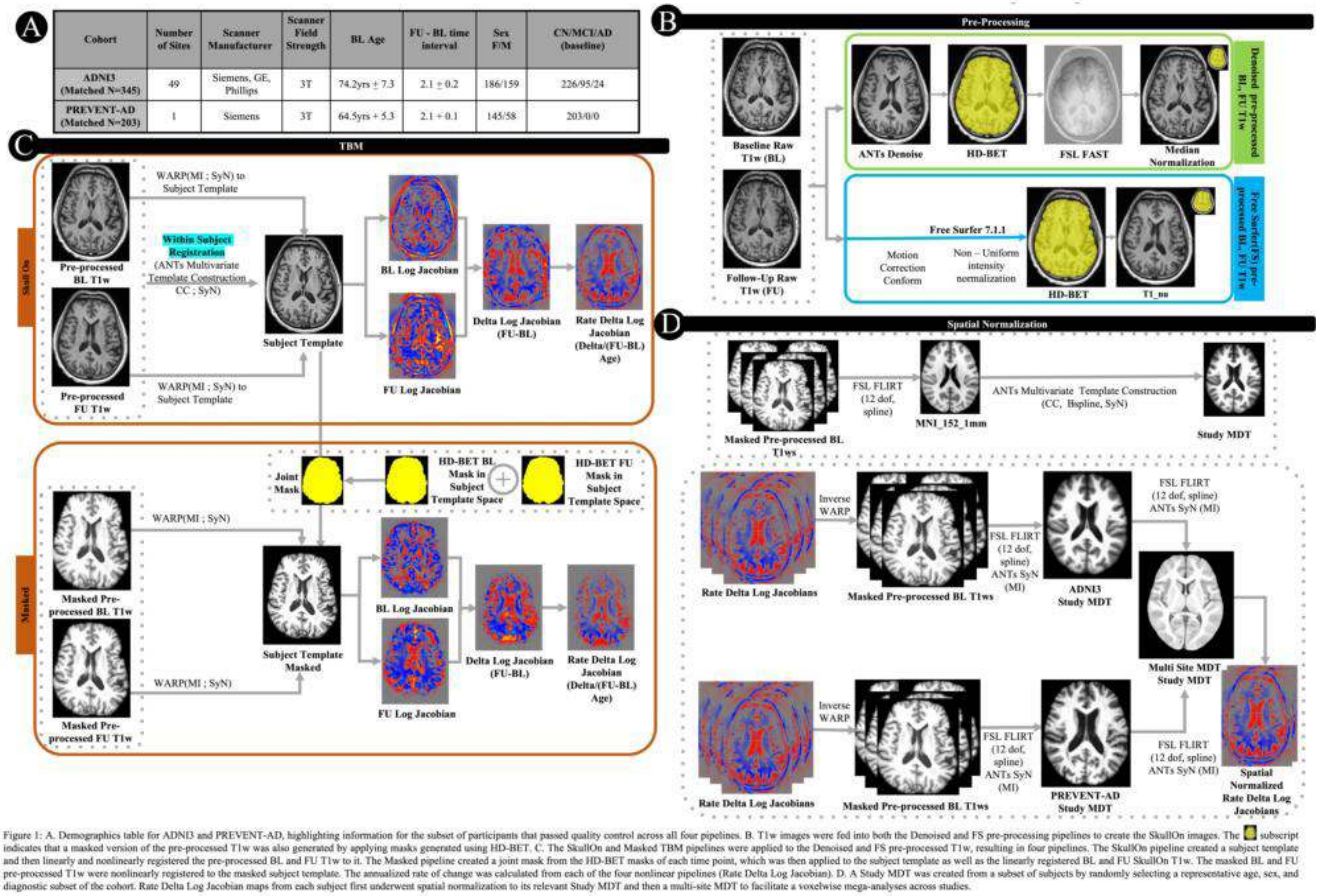

Figure 1: A. Demographics table for ADNI3 and PREVENT-AD, highlighting information for the subset of participants that passed quality control across all four pipelines. B. T1w images were fed into both the Denoised and FS pre-processing pipelines to create the SkullOn images. The subscript indicates that a masked version of the pre-processed T1w was also generated by applying masks generated using HD-BET. C. The SkullOn and Masked TBM pipelines were applied to the Denoised and FS pre-processed T1w, resulting in four pipelines. The SkullOn pipeline created a subject template and then linearly and nonlinearly registered the pre-processed BL and FU T1w to it. The Masked pipeline created a joint mask from the HD-BET masks of each time point, which was then applied to the subject template as well as the linearly registered BL and FU SkullOn T1w. The masked BL and FU pre-processed T1w were nonlinearly registered to the masked subject template. The annualized rate of change was calculated from each of the four nonlinear pipelines (Rate Delta Log Jacobian). D. A Study MDT was created from a subset of subjects by randomly selecting a representative age, sex, and diagnostic subset of the cohort. Rate Delta Log Jacobian maps from each subject first underwent spatial normalization to its relevant Study MDT and then a multi-site MDT to facilitate a voxelwise mega-analyses across studies.

Results: Both higher CDR and disease progression were significantly associated with greater rates of CSF expansion and tissue atrophy across all pipelines. Some of the largest effects were consistently found in the hippocampus, amygdala, ventricles and temporal lobe. Denoised pipelines exhibited lower overall RMSE, with Denoised+SkullOn demonstrating the lowest RMSE (Fig 2). The most widespread associations were detected with Denoised+Masked. In contrast, the largest effect sizes were detected with FS+Masked.

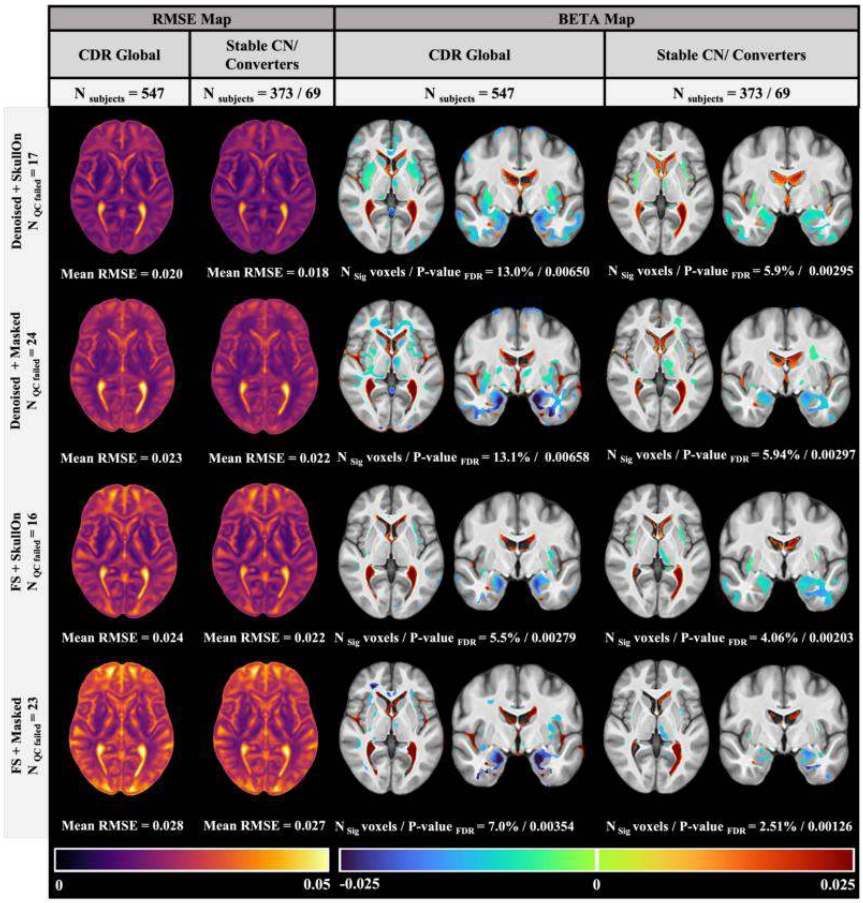

Figure 2: For each of the four pipelines, we report the number of subjects who failed QC, mostly due to mis-registration or bad masks. Here, we show the results after excluding subjects that failed in any pipeline (Total $N_{QC\ failed}$ = 38), but there was little difference when excluding the $N_{QC\ failed}$ of a given pipeline. We also show left) the root mean square error (RMSE) maps after modeling each variable of interest (CDR global scores and diagnosis conversion) and right) beta estimates in regions that survived multiple comparisons correction across voxels (q < 0.05; FDR corrected). Significant effects reveal accelerated tissue atrophy (blue) and ventricular and sulcal expansion (red) are associated with BL clinical impairment and longitudinal clinical decline. To assess differences between the four pipelines across RMSE, Beta and P-value maps obtained from the two regression models, voxel-wise paired t-tests were run. The results of these tests revealed a low p-value of less than 1x10-29 signifying that all the pipelines across all the maps were statistically different.

Conclusions: Longitudinal TBM revealed detailed maps of neurodegeneration and rates of decline. However, no pipeline consistently outperformed the others across comparisons. The Denoised preprocessing pipeline outperformed default FS preprocessing in terms of RMSE and number of passing voxels but not effect sizes. Differences between Denoised SkullOn and Masked pipelines were more subtle. Future work will extend testing to 3 and more timepoints.

References

1. Y. Wang et al., "Surface-based TBM boosts power to detect disease effects on the brain: an N=804 ADNI study," Neuroimage, vol. 56, no. 4, pp. 1993–2010, Jun. 2011.
2. I. Yanovsky, A. D. Leow, S. Lee, S. J. Osher, and P. M. Thompson, "Comparing registration methods for mapping brain change using tensor-based morphometry," Med. Image Anal., vol. 13, no. 5, pp. 679–700, Oct. 2009.
3. N. J. Tustison et al., "The ANTs Longitudinal Cortical Thickness Pipeline," bioRxiv, p. 170209, Aug. 16, 2018. doi: 10.1101/170209.
4. M. Reuter, N. J. Schmansky, H. D. Rosas, and B. Fischl, "Within-subject template estimation for unbiased longitudinal image analysis," Neuroimage, vol. 61, no. 4, pp. 1402–1418, Jul. 2012.
5. F. Isensee et al., "Automated brain extraction of multisequence MRI using artificial neural networks," Hum. Brain Mapp., vol. 40, no. 17, pp. 4952–4964, Dec. 2019.
6. Y. Zhang, M. Brady, and S. Smith, "Segmentation of brain MR images through a hidden Markov random field model and the expectation-maximization algorithm," IEEE Trans. Med. Imaging, vol. 20, no. 1, pp. 45–57, Jan. 2001.
7. J. V. Manjón, P. Coupé, L. Martí-Bonmatí, D. L. Collins, and M. Robles, "Adaptive non-local means denoising of MR images with spatially varying noise levels," J. Magn. Reson. Imaging, vol. 31, no. 1, pp. 192–203, Jan. 2010.
8. B. B. Avants, C. L. Epstein, M. Grossman, and J. C. Gee, "Symmetric diffeomorphic image registration with cross-correlation: evaluating automated labeling of elderly and neurodegenerative brain," Med. Image Anal., vol. 12, no. 1, pp. 26–41, Feb. 2008.
9. M. Jenkinson, P. Bannister, M. Brady, and S. Smith, "Improved Optimization for the Robust and Accurate Linear Registration and Motion Correction of Brain Images," Neuroimage, vol. 17, no. 2, pp. 825–841, Oct. 2002.
10. N. Jahanshad et al., "Multi-Site Meta-Analysis of Morphometry," IEEE/ACM Trans. Comput. Biol. Bioinform., vol. 16, no. 5, Sep. 2019, doi: 10.1109/TCBB.2019.2914905.

Acknowledgments

1. This work is supported in part by NIH grants: R01AG059874, P41EB015922, U01AG068057.

Poster No 1840

Evaluating the quality of brainstem ROI registration using structural and diffusion MRI

Yi-An Chen[1,2], Lars Kasper[1,3], Clement Chow[3], Alexandre Boutet[3,4,5], Andres Lozano[3,4,5], Kamil Uludag[3,6,7], Andreea Diaconescu[2,1], Sriranga Kashyap[3]

[1]Department of Psychology, University of Toronto, Toronto, Canada, [2]Krembil Centre for Neuroinformatics, CAMH, Toronto, Canada, [3]Krembil Brain Institute, University Health Network, Toronto, Canada, [4]Division of Neurosurgery, Toronto Western Hospital, Toronto, Canada, [5]Joint Department of Medical Imaging, University of Toronto, Toronto, Canada, [6]Department of Medical Biophysics, University of Toronto, Toronto, Canada, [7]Center for Neuroscience Imaging Research, Institute for Basic Science & Department of Biomedical Engineering, Sungkyunkwan University, Suwon, Republic of Korea

Introduction: Accurate transformation of regions-of-interest (ROIs) from standard to individual subject space is vital in MRI analyses, such as structural volumetry and BOLD fMRI, particularly for brainstem studies. The small size and dense arrangement of brainstem ROIs mean that minor registration errors can significantly impact results. Typically, ROIs defined on a T1-weighted (T1w) template are transformed to subject space using the participant's T1w image, but this method may not be effective for the brainstem due to limited tissue contrast in T1w images. In contrast, diffusion-weighted imaging (DWI) has demonstrated potential in revealing brainstem nuclei and tracts, suggesting enhanced transformation accuracy. Our study assesses the precision of brainstem ROI transformation using three methods: (1) anatomical T1w, (2) b0, and (3) fractional anisotropy (FA) maps from DWI. We focused on the red nucleus and dorsal raphe nucleus. The red nucleus's consistent anatomical definition facilitates manual delineation and ground-truth comparison, while the dorsal raphe nucleus's location near the cerebral aqueduct and fourth ventricle is ideal for assessing misregistration errors.

Methods: We acquired T1w, DWI, and susceptibility-weighted imaging (SWI) data from 10 healthy participants using a Siemens Prisma 3T scanner. The data were preprocessed using ANTs, Freesurfer, FSL, and MRtrix. Standard ROIs of the red nucleus and the dorsal raphe nucleus were taken from the Brainstem Navigator probabilistic atlas (IIT-space). For each participant, we aligned the IIT T1w template (IIT-T1w) with the subject T1w using whole-brain non-linear registration to generate a primary transform from IIT to subject space. Next, we obtained brainstem masks from Freesurfer and refined them manually. Then, the IIT-T1w to subject T1w registration was refined by three methods: (1) a brainstem-confined, SyN-only registration using cross-correlation cost function. For methods (2)and (3) the same registration algorithm, cost function and brainstem mask was used to warp the IIT-b0 and IIT-FA template to the subject b0 and FA maps, respectively. The three methods yielded three different refined nonlinear transforms, which were then concatenated with IIT-to-subject whole-brain transform to form three spatial transformations of the brainstem ROIs from the IIT to the subject space. All registrations were done using ANTs. To quantify the transformation accuracy of the red nuclei ROIs, ground-truth ROIs were manually delineated using the b0 image and the SWI in ITK-SNAP. Dice coefficients of the ground-truth ROI and the three transformed ROIs were computed for each participant. For the dorsal raphe nucleus, the misregistration fraction was calculated as a proxy of registration accuracy. The mis-registration fraction is the volume of the ROI overlapping with the cerebral aqueduct and the fourth ventricle divided by the total ROI volume. The cerebral aqueduct-fourth ventricle masks were obtained using FreeSurfer, with manual editing in ITK-SNAP. Further analyses were conducted using Python libraries (numpy, nibabel and pandas).

Results: The average combined volume of the manually-delineated left and right red nucleus is 713.58 ± 93.21 mm3, which falls within the range reported in the literature. The average Dice coefficients of the red nuclei ROIs transformed through the three methods are: (1) T1w-based: 0.72 ± 0.02; (2) b0-based: 0.75 ± 0.02; (3) FA-based: 0.76 ± 0.05. The average misregistration fractions for the dorsal raphe nucleus ROIs transformed through the three methods are: (1) T1-based: 0.28 ± 0.06; (2) b0-based: 0.35 ± 0.13; (3) FA-based: 0.18 ± 0.07.

Conclusions: The results suggest that diffusion image-based approaches, particularly the FA-based approach, could outperform the conventional T1w-based approach in achieving higher accuracy of brainstem ROI transformation.

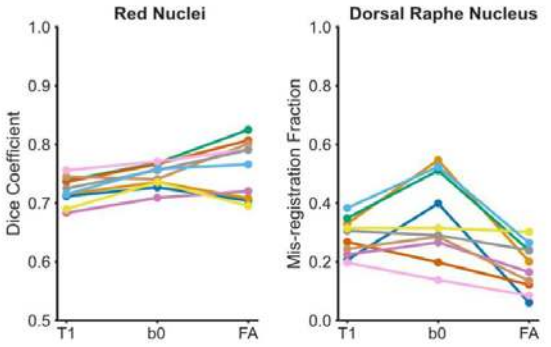

Figure 1. Left panel: The Dice coefficients of the ground-truth red nuclei ROI and red nuclei ROIs transformed through the T1-based, b0-based and FA-based approaches. Right panel: The mis-registration fractions of the dorsal raphe nucleus ROIs transformed through the T1-based, b0-based and FA-based approaches.

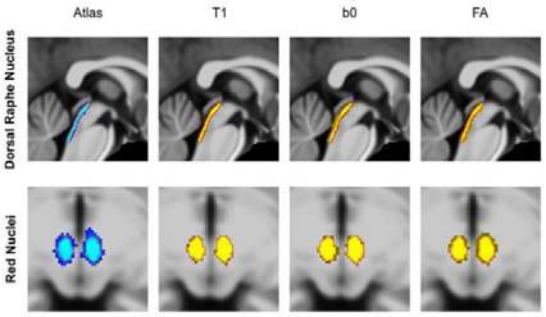

Figure 2. Upper row: The probabilistic map of the dorsal raphe nucleus in the Brainstem Navigator atlas, and maps built from the ten T1-based, b0-based and FA-based ROIs that were inverse-transformed into the IIT space using the same whole-brain transformation. Lower row: The probabilistic maps of the red nuclei in the Brainstem Navigator atlas and those built from ROIs obtained through the three transformation approaches. The probability = 0.35 boundary that defines the binary Brainstem Navigator ROIs used in this study is indicated by the red line superimposed on the map in each panel.

References

1. Bianciardi M. (2015),'Toward an In Vivo Neuroimaging Template of Human Brainstem Nuclei of the Ascending Arousal, Autonomic, and Motor Systems', Brain Connectivity, Dec; 5(10):597-607
2. Colpan, M. E. (2010), 'Subthalamic and red nucleus volumes in patients with Parkinson's disease: do they change with disease progression?', Parkinsonism & related disorders, 16(6), 398-403.
3. Kolpakwar, S. (2021), 'Volumetric analysis of subthalamic nucleus and red nucleus in patients of advanced Parkinson's disease using SWI sequences', Surgical Neurology International, 27-Jul;12:377.
4. Pawlak, M. (2023), 'Red Nucleus Volume Decrease in Healthy Aging (P12-6.003)', Neurology, Apr;100 (17 Supplement 2) 2417.
5. Singh K. (2021), 'Probabilistic Atlas of the Mesencephalic Reticular Formation, Isthmic Reticular Formation, Microcellular Tegmental Nucleus, Ventral Tegmental Area Nucleus Complex, and Caudal-Rostral Linear Raphe Nucleus Complex in Living Humans from 7 Tesla Magnetic Resonance Imaging', Brain Connectivity, Oct;11(8):613-623.

Poster No 1841

Efficient Deep Pyramidal Multi-Residual Network for Brain MRI Registration

Yoonguu Song[1], Seunghyeon Han[2], Min Choi[3], Boreom Lee[4]

[1]Gwangju Institute of Science and Technology, Gwangju, Korea, Republic of, [2]Gwangju Institute of Science and Technology, Gwangju, Jeollanam-do, [3]Gwangju Institute of Science and Technology, Gwangju, Gwangju, [4]Gwangju Institute of Science and Technology(GIST), Gwangju-si, Jellanam-do

Introduction: Deep Learning has recently achieved a significant advance in registering medical images. Traditional methods tackle optimization problems to establish spatial correspondence between images, yielding decent accuracy but demanding significant time to resolve new optimization challenges. In this study, we propose a novel approach for image registration using a robust neural network specifically designed for brain magnetic resonance imaging. This study introduces a deep network called the Multi Residual Laplacian Pyramid Diffeomorphic Registration Network (MR-LapDRN). It efficiently solves the

image registration optimization problem by employing a coarse-to-fine approach, improving spatial feature extraction across various scales. We've progressively increased the number of filters across the following three layers while concatenating the outputs of these layers using a residual connection. We evaluated and compared MR-LapDRN with the classical U-Net and other networks using a brain MRI dataset. While we observed only marginal enhancements in brain MRI images, our model demonstrated that, despite a relatively low total parameter count, it can produce outcomes comparable to cutting-edge algorithms.

Methods: Using the deep learning structure, our aim is to derive the flow field function that establishes a mapping from the domain of the moving image to that of the fixed image. While U-Net[1] utilized convolutional layers exclusively in its encoder-decoder architecture for segmentation, Voxelmorph[2] employed the Spatial Transformer Network[3] to produce the displacement vector field (DVF). We apply a 3-level Laplacian pyramid framework in developing our MR-LapDRN, mirroring the traditional multi-resolution approach through multi-level kernel convolution In the initial pyramidal structure, the input data is reduced by a scale factor of 4. In the second pyramid, the input data is downscaled by a factor of 2, and the last pyramid retains the original dataset to maintain consistent image sizes. Each pyramidal structure features a single encoder-decoder utilizing a multi-residual block. Originally, the multi-residual block consisted of three sequential convolutional blocks employing different kernel sizes to capture diverse spatial features across various scales. To maintain a similar range of spatial characteristics while reducing parameter number, we opted for a 3*3*3 kernel size with dilation size 2,3, instead of 5*5*5 and 7*7*7. Following the passage through various kernel sizes in each layer, the resulting three layers are combined through concatenation to facilitate the influence of diverse spatial features on adjacent channel layers. This concatenated layer is then added to the original input of the multi-residual block, which has passed through a 1*1 convolutional layer. Within the encoder-decoder structure, there are five residual blocks strategically positioned to amplify feature extraction. These blocks operate by enveloping the input value x with identity mapping, ensuring that information preservation, as emphasized in[4], is maintained by passing it through to the output value.

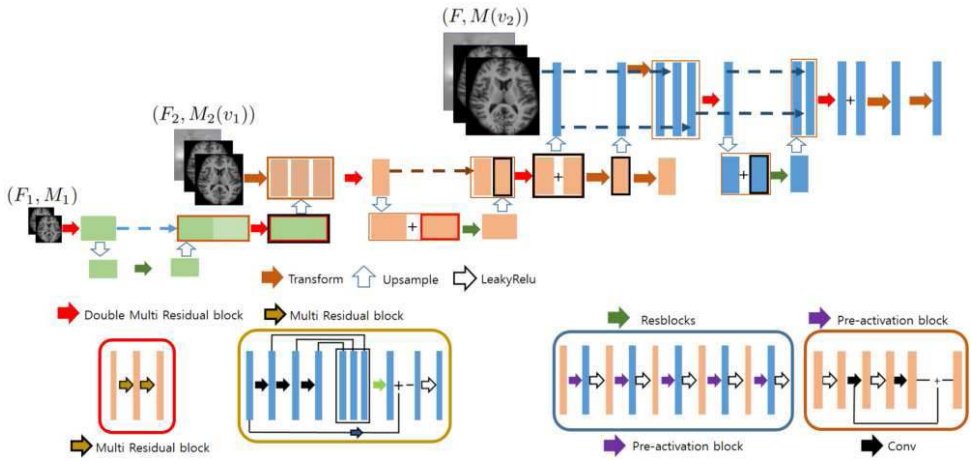

Fig. A simplified 2D depiction instead of 3D to clarify the image registration networks, MR-LapDRN. This model features a 3-level deep Laplacian pyramid and Multi Residual architecture

Results: We trained our model through local normalized cross-correlation (NCC) coupled with a regularization term. Our approach was trained using 414 T1-weighted brain MR scans sourced from the OASIS dataset[5], employing a random split of the dataset into training, validation, and test sets with an 8:1:1 ratio. The evaluation of our method was based on the dice score, using a labeled dataset. In the comparison presented in the table, while U-Net achieves a dice score of 0.569 and LapIRN[6] scores 0.779, our model demonstrates a marginal enhancement despite uti- lizing 90% fewer parameters.

Method	DSC ↑	total param ↓
U-Net	0.569	625530
LapIRN	0.779	634104
Ours	**0.782**	**571914**

Table 1. Registration performances on brain MRI dataset

Conclusions: This research introduces MR-LapDRN, an inventive network that combines Laplacian pyramid networks with a multi- residual module for image registration. Our method show- cases that, despite having fewer total parameters, it achieves comparable results to cutting-edge algorithms.

References

1. Ronneberger, O.(2015), 'U-net: Convolutional networks for biomedical image segmentation'. In Medical Image Computing and Computer-Assisted Intervention–MICCAI 2015: 18th International Conference, Munich, Germany, October 5-9, 2015, Proceedings, Part III 18 (pp. 234-241).
2. Balakrishnan, G. (2019), 'VoxelMorph: a learning framework for deformable medical image registration'. IEEE transactions on medical imaging, 38(8), 1788-1800.
3. Jaderberg, M. (2015). 'Spatial transformer networks'. Advances in neural information processing systems, 28.
4. He, K. (2016). 'Identity mappings in deep residual networks'. In Computer Vision–ECCV 2016: 14th European Conference, Amsterdam, The Netherlands, October 11–14, 2016, Proceedings, Part IV 14 (pp. 630-645)
5. Marcus, D. S.(2010). 'Open access series of imaging studies: longitudinal MRI data in nondemented and demented older adults'. Journal of cognitive neuroscience, 22(12), 2677–2684.
6. Daniel S. Marcus, Tracy H. Wang, Jamie Parker, John G. Csernansky, John C. Morris, and Randy L. Buckner, "Open access series of imaging studies (oasis): Cross- sectional mri data in young, middle aged, nondemented, and demented older adults," J. Cognitive Neuroscience, vol. 19, no. 9, pp. 1498–1507, sep 2007.
7. Mok, T. C. (2020). 'Large deformation diffeomorphic image registration with laplacian pyramid networks'. In Medical Image Computing and Computer Assisted Intervention–MICCAI 2020: 23rd International Conference, Lima, Peru, October 4–8, 2020, Proceedings, Part III 23 (pp. 211-221).

Poster No 1842

Automatic, whole-brain segmentation of cortical layers for the high-resolution anatomical data at 7T

Roman Belenya[1], Gabriel Castrillón[2], Valentin Riedl[3]

[1]Klinikum Rechts der Isar, Technical University of Munich, Munich, Bavaria, [2]Friedrich-Alexander University, Erlangen, Germany, [3]Technical University of Munich, Erlangen, Germany

Introduction: Developments of high-resolution MR imaging at 7 Tesla have allowed researchers to study the brain in unprecedented detail. The increased magnetic field improves the signal-to-noise ratio and the resolution of the images. However, 7T imaging comes with a set of challenges. Among them are magnetic field inhomogeneities and imaging artefacts. They present a common challenge for data preprocessing. Over the years, robust and reproducible preprocessing methods have been well-optimized for standard 3T imaging. However, there are currently no standard optimized pipelines for high-resolution brain images. In this work, we develop a preprocessing pipeline for the 7T hires anatomical data. We focus on performing as few processing steps as possible while maximizing the performance of automatic whole-brain segmentation. Specifically, our end-goal is to maximize the accuracy and reliability of cortical layer segmentation for the analyses of layer fMRI data.

Methods: We processed the anatomical data of 14 participants from the 7T Siemens MAGNETOM Terra.X machine. We collected the 3D T1-weighted MP2RAGE as well as T2-weighted TSE images. The preprocessing pipeline is similar for both modalities: Pre-freesurfer 1. Image denoising using the DenoiseImage program in ANTs. 1a. Gibbs ringing artefacts removal with the mrdegibbs program implemented in mrtrix. We run this step only for the T2w images because they are affected by the artefact the most. 2. Bias field correction using SPM tissue-type segmentation. 3. Brain extraction with HD-BET. Freesurfer 4. Brain surface reconstruction with freesurfer recon-all script. We run the standard processing using the high-resolution (-cm) option and an additional T2w contrast to improve the tissue type segmentation. We entered the combined brain mask from Step 3 using the expert file. Post-Freesurfer 5. To convert brain surfaces generated by the freesurfer to a voxel space rim file required by LayNii, we use the surf-laynii script by Sriranga Kashyap. The script first expands the grey matter and shrinks the white matter surfaces using the mri_expand tool. The mri_fill tool fills the original, expanded and shrunk surfaces, resulting in a set of masks. Subtracting the smaller from a larger mask estimates the boundary between the white matter and the grey matter and the boundary between the CSF and the white matter in voxel space. 6. We use these boundaries as the input to the LayNii LN2_LAYERS program, which estimates cortical layers using an equivolumetric approach.

Results: We run the pipeline on data from 14 subjects. On average, the pre-freesurfer pipeline doubles the spatial SNR and CNR within the grey and white matter masks for T1w and T2w images. Combining the preprocessed contrasts allows for more accurate placement of brain cortical surfaces and estimation of cortical layers. We demonstrate an example of processing steps and their effect on the images in Figure 1.

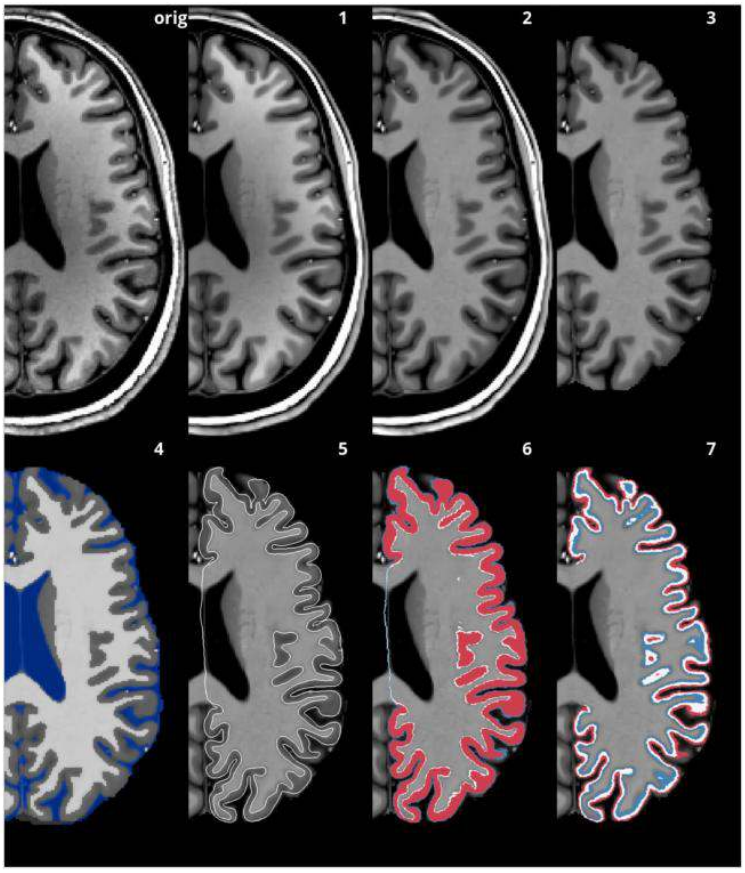

Figure 1
Example of preprocessing steps. Orig) Original T1w MP2RAGE image. 1) Result of the denoising step. 2) Result of the bias correction step. 3) Result of the brain extraction. 4) Tissue type segmentation results. We chose to segment the brain into 4 tissues - the CSF, grey and white matter, and blood vessels. We included the blood vessel as a separate tissue class because of the very bright appearance of blood in 7T imaging. 5) Cortical white and pial surfaces estimated by the freesurfer. 6) Result of surf-laynii script: a rim file with label 1 for the boundary between the grey matter and the cerebrospinal fluid, 2 for the boundary between the grey matter and the white matter and label 3 for the grey matter. 7) 3 cortical layers estimated with LayNii equivolumetric approach.

Conclusions: The accuracy of brain segmentation is crucial in analyzing neuroimaging data. While manual segmentations can be most accurate, they are time-consuming, especially on the whole-brain level. The existing automatic segmentation tools are usually optimized for images from 3T scanners and cannot be used out of the box for high-resolution 7T data. Thus, it is essential to configure the preprocessing pipelines to maximize the accuracy of automatic whole-brain segmentation. Here, we describe the processing pipeline that optimized the performance of cortical layer segmentation for our anatomical data. Accurate automatic layer segmentation can dramatically increase the accessibility of high-resolution data analyses. This work will assist researchers in developing analysis methods for the high-resolution neuroimaging data.

References

1. Huber, L. (2021). LayNii: A software suite for layer-fMRI. NeuroImage, 118091
2. Isensee F. (2019). Automated brain extraction of multi-sequence MRI using artificial neural networks. Human Brain Mapping, 1–13
3. Sriranga Kashyap. Surf-laynii. https://github.com/srikash/surf_laynii
4. Tournier, J.-D. (2019). MRtrix3: A fast, flexible and open software framework for medical image processing and visualisation. NeuroImage, 202, 116137
5. Tustison, N. J. (2014). Large-scale evaluation of ANTs and FreeSurfer cortical thickness measurements. NeuroImage, 99, 166–179

Poster No 1843

Longitudinal MRI in asymptomatic degenerative cervical cord compression

Jan Valosek[1,2,3,4], Petr Hluštík[4], Tomáš Horák[5,6], Magda Horáková[5,6], Josef Bednařík[5,6]

[1]NeuroPoly Lab, Institute of Biomedical Engineering, Polytechnique Montreal, Montreal, Quebec, [2]Mila - Quebec AI Institute, Montreal, Canada, [3]Department of Neurosurgery, Faculty of Medicine and Dentistry, Palacký University Olomouc, Olomouc, Czech Republic, [4]Department of Neurology, Faculty of Medicine and Dentistry, Palacký University Olomouc, Olomouc, Czech Republic, [5]Faculty of Medicine, Masaryk University, Brno, Czech Republic, [6]Department of Neurology, University Hospital Brno, Brno, Czech Republic

Introduction: Spinal cord morphometric measures computed from magnetic resonance (MRI) images, such as cross-sectional area and anteroposterior diameter, are widely used to assess the severity of spinal cord compression (Badhiwala et al. 2020). The longitudinal monitoring of the compression severity might play an important role in the surgical management of participants with asymptomatic degenerative cervical cord compression, particularly prior to the progression to degenerative cervical myelopathy. However, due to difficulties in robustly co-registering spinal cord MRI images across sessions, the longitudinal MRI evaluation is usually performed on morphometric measures aggregated across multiple levels, such as vertebral levels C2-C3 (David et al. 2021). As compression typically occurs in proximity to the intervertebral discs spanning two adjacent vertebral levels, the averaging across levels can thus impact compression parameters. In this study, we perform a longitudinal assessment of compression severity using a recently proposed normalization approach bringing morphometric measures from different sessions into common anatomical dimensions (Valošek et al. 2023).

Methods: 3T T2-weighted images covering the cervical spinal cord were acquired in 59 participants with asymptomatic degenerative cervical cord compression. Participants were scanned longitudinally with an interval of 36 months between measurements. Image processing was done with the Spinal Cord Toolbox (SCT, v6.1) (De Leener et al. 2017). For each participant, the spinal cord was segmented using a deep learning-based algorithm trained on spinal cord injury patients (https://github.com/ivadomed/model_seg_sci), the vertebral levels were identified (Ullmann et al. 2014), and morphometric measures were normalized to the PAM50 anatomical dimensions (Valošek et al. 2023). The following morphometric measures were used: cross-sectional area, anteroposterior diameter, transverse diameter, compression ratio, eccentricity, and solidity.

Results: Figure 1 shows morphometric measures for three participants with asymptomatic degenerative cervical cord compression (A: female, 53 y.o., B: female, 58 y.o., C: male, 53 y.o.). For each participant, the morphometric measures from both sessions are shown in the same anatomical dimensions of the PAM50 spinal cord template. The morphometric measures are plotted across individual axial slices with vertebral levels identified on the plot. The figure also shows (in gray color) normative values computed from a database of 203 healthy controls (Valošek et al. 2023). For the whole patient group, the evolution of morphometric parameters over the follow-up interval of approximately 3 years appears quite heterogeneous. Several scenarios may be observed: First, in ~37% of the patients, the morphometry remains stable, without signs of either worsening or improvement. This may confirm the test-retest stability of the methodology. Second, ~42% of the patients present with worsening cord compression, either more pronounced compression in one segment or a new compression in another segment). Finally, ~20% of patients' compression seems to improve, so that the morphometric measures return to the normal range.

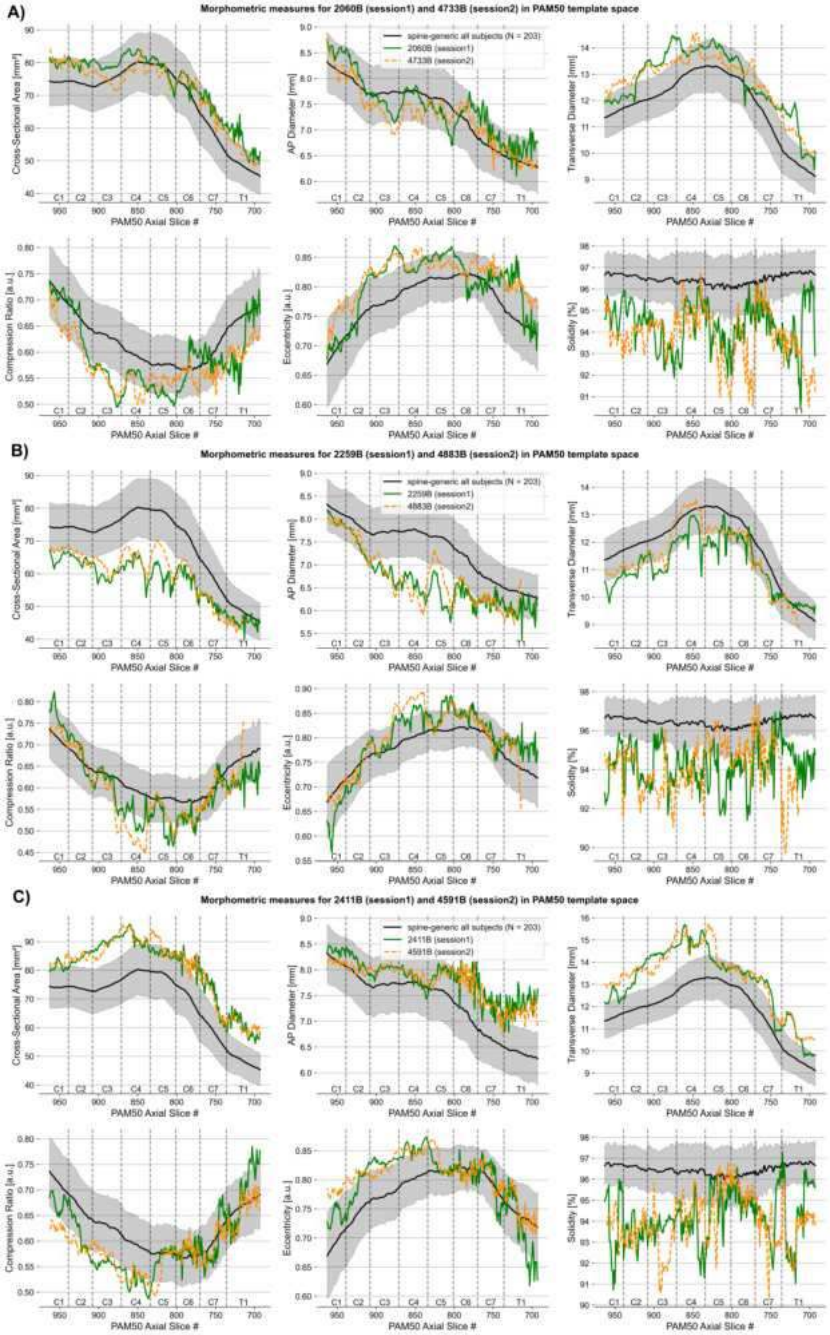

Conclusions: In conclusion, this study employs a normalization approach to longitudinally assess compression severity in participants with cervical spinal cord compression. Bringing morphometric measures from different sessions into common anatomical dimensions facilitates an assessment of all individual axial slices without averaging across levels. Subsequent work will focus on the validation of inter-session variability and correlation with patients' clinical status progression.

References

1. Badhiwala, Jetan H., Christopher S. Ahuja, Muhammad A. Akbar, Christopher D. Witiw, Farshad Nassiri, Julio C. Furlan, Armin Curt, Jefferson R. Wilson, and Michael G. Fehlings. 2020. "Degenerative Cervical Myelopathy - Update and Future Directions." Nature Reviews. Neurology 16 (2): 108–24.
2. David, Gergely, Dario Pfyffer, Kevin Vallotton, Nikolai Pfender, Alan Thompson, Nikolaus Weiskopf, Siawoosh Mohammadi, Armin Curt, and Patrick Freund. 2021. "Longitudinal Changes of Spinal Cord Grey and White Matter Following Spinal Cord Injury." Journal of Neurology, Neurosurgery, and Psychiatry, no. i (August): jnnp – 2021–326337.
3. De Leener, Benjamin, Simon Lévy, Sara M. Dupont, Vladimir S. Fonov, Nikola Stikov, D. Louis Collins, Virginie Callot, and Julien Cohen-Adad. 2017. "SCT: Spinal Cord Toolbox, an Open-Source Software for Processing Spinal Cord MRI Data." NeuroImage 145 (Pt A): 24–43.
4. Ullmann, Eugénie, Jean François Pelletier Paquette, William E. Thong, and Julien Cohen-Adad. 2014. "Automatic Labeling of Vertebral Levels Using a Robust Template-Based Approach." International Journal of Biomedical Imaging 2014: 719520.
5. Valošek, Jan, Sandrine Bédard, Miloš Keřkovský, Tomáš Rohan, and Julien Cohen-Adad. 2023. "A Database of the Healthy Human Spinal Cord Morphometry in the PAM50 Template Space." NeuroLibre 3 (34): 17.

Poster No 1844

Mapping whole-brain communication patterns: An information theoretic approach

Varun Madan Mohan[1], Caio Seguin[2], Thomas Varley[3], Andrew Zalesky[1]

[1]The University of Melbourne, Melbourne, Victoria, [2]Department of Psychological and Brain Sciences, Indiana University, Bloomington, IN, [3]Indiana University, Bloomington, IN

Introduction: The brain relies on fast and accurate communication, or information routing between its various components, for healthy function[1]. However, despite its importance, a lack of methods to systematically investigate empirical communication patterns have led to a notable lack of consensus regarding routing principles in the brain, even with multiple models of communication having been proposed[2,3,4]. In this work, we develop an information-theoretic method to study directional communication patterns in neural recordings. First, we demonstrate the method on a network of three nodes with simple stochastic dynamics. We then apply it to MEG recordings, and exemplify its use in studying principles of inter-regional communication. Specifically, we correlate our measure of information flow with coherence in the alpha and gamma bands: neural-oscillatory metrics previously theorised to shape communication patterns[3,4].

Methods: NETWORK MODEL A system comprising three nodes, with Linear Stochastic Model (LSM) dynamics[5] was defined [Fig2A]. A Poisson process caused two of the regions to "pulse" randomly, with an average frequency of 0.2Hz (source). The noise level of the LSM was systematically varied relative to the pulse amplitude. The system's activity was recorded for 200 seconds. EMPIRICAL DATA Resting-state MEG scans of 30 healthy subjects (13 males, age range 22-35), were obtained from the Human Connectome Project (HCP)[6,7], source localised using the dynamical-SPM method in Brainstorm[8] as per Brainstorm's tutorial on HCP data, and parcellated using the Schaefer 7-Network 100 region atlas[8]. ESTIMATING COMMUNICATION PATTERNS The rationale behind the developed method is that deviations from mean activity of a region should cause a measurable delayed downstream effect on the activities of the rest of the network. Additionally, focusing the information flow estimation around the significant deviations (communication events) excludes the contribution of noisy segments that can cloud true communication patterns. The pipeline is [Fig1]: 1) Regional activities are epoched into 10 second segments; 2) a region is chosen as a source, its activity is z-scored, and timepoints where |z|>3 are marked as events; 3) a "communication window" of 1-second is placed starting at the event. A similar window, delayed in proportion to inter-regional distance, is placed at all other brain regions (targets); 4) The mutual information (MI) between the source and target within the defined windows, conditional upon the target's past, is computed. This captures the directional information flow. In addition to these steps, to test the communication principles: 5) Within the communication window, alpha and gamma band coherence is computed; 6) The Pearson-r values between the MI and coherences is computed, quantifying the dependence of information flow on neural-oscillatory relationships.

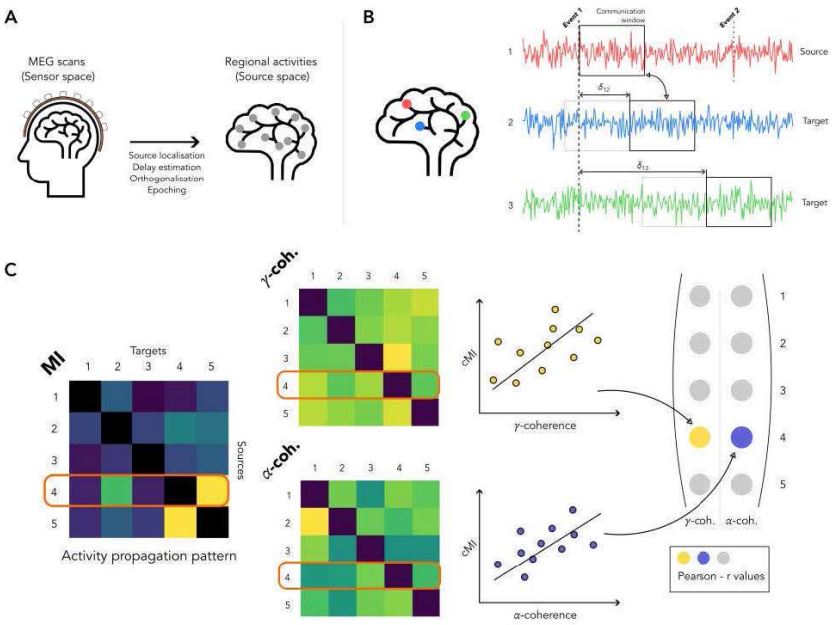

Fig 1: Schematic of the method (as applied to MEG data) (A) Resting-state MEG scans are preprocessed and source localised. **(B)** Significant events are identified from the regional activities. Communication windows (of 1 second) are defined starting at the event (Black solid line box), and at delayed timepoints at all possible targets. The (conditional) mutual information (MI) is computed within the communication windows, conditional upon the target activities in the past 1 second (Grey dashed line box). *In the toy model, only this step is carried out, on the nodes' activities.* **(C)** The MI values are correlated with the gamma coherence and alpha coherence within the communication windows

Results: In the network model, region 2's activity is a mixture of internal dynamics, and inputs from regions 1 and 3. Our method accurately identifies information outflow from both the sources (1 and 3), even at high noise levels. Additionally, estimating the MI around the significant events shows stronger information flow from regions 1 and 3 to 2, compared to when the MI is computed over the entire regional timeseries [Fig2B,C]. Application of the method on source-level MEG and quantifying the dependence of information flow with the alpha and gamma coherence reveals a clear regional variation in the spectral metrics that best correlate with communication. Information flow correlates maximally with alpha coherence in posterior regions, and with gamma coherence in temporal regions [Fig2D,E].

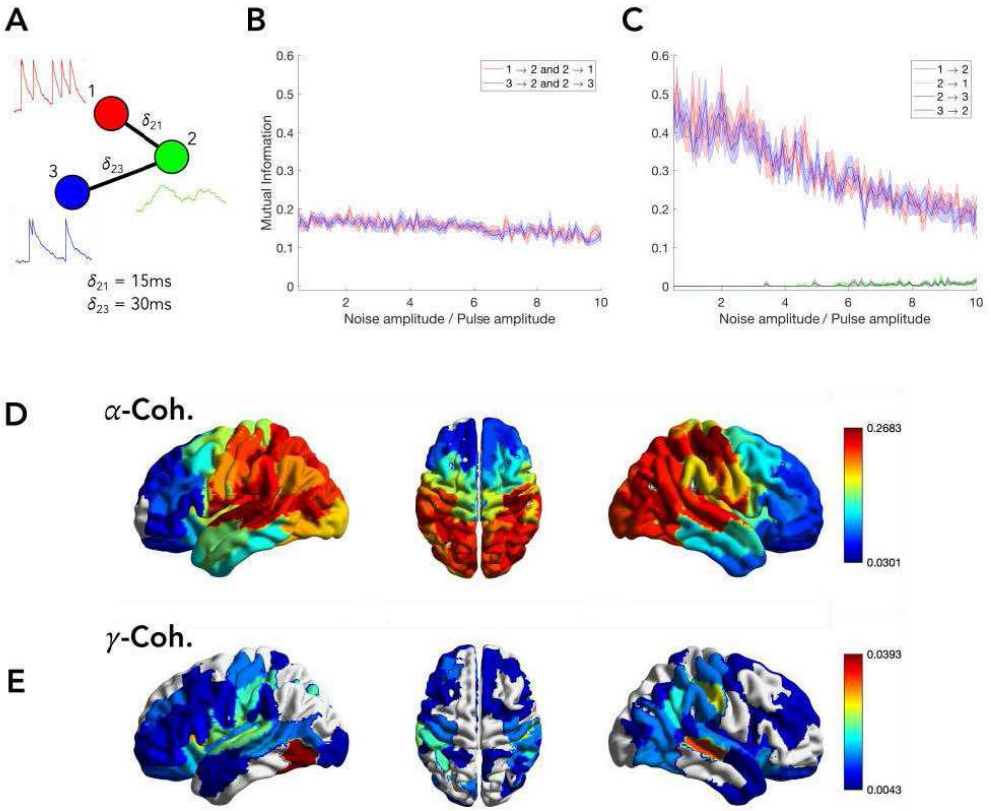

Fig 2: (A) A network model with 3 nodes. The system follows Linear Stochastic Model dynamics with delayed interactions. Regions 1 and 3 show additional Poisson-spiking at 0.2Hz. The delay between regions 1 and 2 is 15ms, and between 2 and 3 is 30ms. **(B)** The mutual information between regions computed over the entire activity time series as function of the ratio between pulse amplitudes at regions 1 and 3, and noise **(C)** *Implementation of the presented method:* The (conditional) mutual information between regions within a communication window of length 1 second, starting at a significant event. The mutual information is conditional upon the past activity of the target region (up to a communication window length), to account for effects of internal dynamics. (Solid line → Mean over 10 trials, Shaded region →±SEM) **(D)** Average cortical distribution of Pearson-r values (30 subjects) capturing correlation between information flow inferred from source-localised resting state MEG and coherence in the alpha band (within the communication windows) **(E)** correlation between information flow and coherence in the gamma band.

Conclusions: In this study, we present an information-theoretic method of estimating directed empirical communication patterns, and showcase its applicability in studying inter-regional communication principles, by revealing a heterogeneous dependence of information flow on neural-oscillatory relationships.

References

1. Avena-Koenigsberger, A. (2018), 'Communication dynamics in complex brain networks', Nature reviews neuroscience, vol. 19, no.1, pp. 17-33.
2. Seguin, C. (2023), 'Brain network communication: concepts, models and applications', Nature Reviews Neuroscience, vol. 24, no. 9, pp. 557-574.
3. Fries, P. (2015), 'Rhythms for cognition: communication through coherence', Neuron, vol. 88, no. 1, pp. 220-235.
4. Jensen, O. (2010), 'Shaping functional architecture by oscillatory alpha activity: gating by inhibition', Frontiers in human neuroscience, vol. 4, 186.
5. Van Essen, D. C. (2013), 'The WU-Minn human connectome project: an overview', Neuroimage, vol. 80, pp. 62-79.
6. Larson-Prior, L. J. (2013), 'Adding dynamics to the Human Connectome Project with MEG', Neuroimage, vol. 80, pp. 190-201.
7. Tadel, F. (2011), 'Brainstorm: a user-friendly application for MEG/EEG analysis', Computational intelligence and neuroscience, vol. 2011, pp. 1-13.
8. Schaefer, A. (2018), 'Local-global parcellation of the human cerebral cortex from intrinsic functional connectivity MRI', Cerebral cortex, vol. 28, no. 9, pp. 3095-3114.

Poster No 1845

Improving Quantification of Aperiodic (1/f) Dynamics: Bayesian Model Selection in SPRiNT

Benjamin Lévesque Kinder[1], Luc Wilson[1], Jason da Silva Castanheira[1], Sylvain Baillet[2]

[1]McGill University, Montreal, Quebec, [2]Montreal Neurological Institute, Montreal, Quebec

Introduction: Neural oscillations are central to the study of neurophysiology (Buzsáki, 2006). These oscillatory dynamics are composed of rhythmic and arrhythmic components. Although the rhythmic components of these signals have been studied extensively, the arrhythmic components have largely been disregarded as noise despite being behaviourally (Albouy et al., 2017) and pathologically (Molina et al., 2020) meaningful. SPRiNT (Spectral Parametrization Resolved in Time; Wilson et al., 2021) characterizes the rhythmic and arrhythmic dynamics of neural oscillations by sequentially applying specparam (Donoghue et al., 2020) to the average of the time series bounded within a sliding window. This method allows users to quantify the evolution of the spectral parameters through time. But, because of its extension into the time-domain, SPRiNT is prone to fitting far more spurious peaks than regular specparam. To remedy this shortcoming, SPRiNT came outfitted with an optional peak post-processing step which uses a heuristic to prune spurious peaks. Although this peak post-processing is moderately effective, it makes the method more obtuse by adding an additional level of user tuning on top of specparam hyperparameter tuning. To improve the method, we implemented Bayesian model selection into SPRiNT (ms-SPRiNT).

Methods: At each time-point, the model selection algorithm initially fits the aperiodic component of the spectra and then creates an additional model for each peak it fits, up to the limit set by the user. Then, it selects the best model by weighting the additional goodness-of-fit provided by fitting the new peak against the loss of parsimony caused by the additional parameters. To accomplish this, the model selection algorithm selects the model with the lowest Bayesian information criterion.

Results: To validate the use of model selection in SPRiNT, we ran SPRiNT and ms-SPRiNT with and without post-processing on 10’000 time series (60s duration each) with temporal dynamics in both the periodic and aperiodic components of the spectra. We used liberal hyperparameters. We found that peak post-processing had a significant impact on SPRiNT’s positive predictive value with relatively small loss in sensitivity; confirming that the amount of post-processing applied has a considerable impact on fit quality. We found that when we applied ms-SPRiNT to the same data ms-SPRiNT provided fits significantly better than SPRiNT without post-processing and provided similar fits to SPRiNT with post-processing. The highest quality fits came from the combination of ms-SPRiNT with post-processing where we saw a 37.5 percentage point increase to PPV as compared to SPRiNT without model selection. Independent of processing applied, the absolute error of the aperiodic exponent and absolute error of the aperiodic offset did not vary. This shows that additional processing does not affect the error in the aperiodic component of the signal. Also, we found that irrespective of processing, SPRiNT does not tend to fit spectra with more than 3 peaks, so it shows root-like trends on simulation-detection matrices.

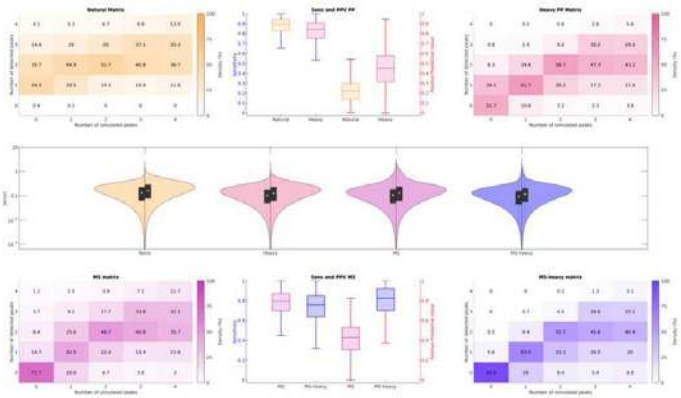

Figure 1: post-processing impacts SPRiNT goodness-of-fit and ms-SPRiNT fits neural power spectra more accurately than SPRiNT alone (synthetic data I)

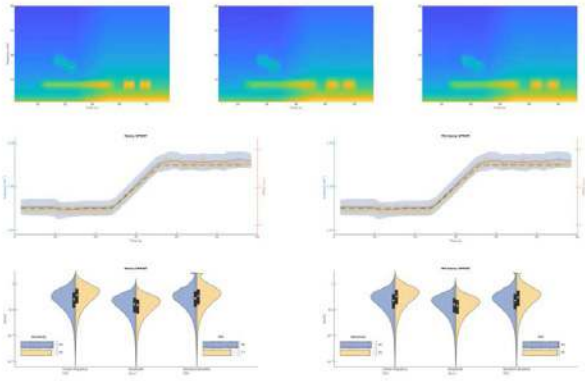

Figure 2: SPRiNT vs ms-SPRiNT performance on naturalistic data (synthetic data II)

Conclusions: We improved upon the original SPRiNT algorithm by implementing Bayesian model selection, and proposed improved hyperparameter and post-processing parameter recommendations. Because SPRiNT is based on specparam, it tends to overfit peaks before post-processing. This issue is compounded by the decrease in signal-to-noise ratio intrinsic to averaging across contiguous time windows. In the original version of SPRiNT judicious selection of hyperparameters and post-processing parameters was crucial to the quality of the fit. This makes analysis and data sharing more difficult. To address this issue, we implemented model selection which allows for far more liberal hyperparameters and rivals optimal post-processing in its performance. This significantly lowers the barrier of entry to using SPRiNT.

References

1. Albouy, P. (2017), 'Selective entrainment of theta oscillations in the dorsal stream causally enhances auditory working memory performance', Neuron, vol. 94, pp. 193–206
2. Buzsáki, G. (2006), 'Rhythms of the Brain'. Oxford University Press.
3. Donoghue, T. (2020), 'Parameterizing neural power spectra into periodic and aperiodic components', Nature Neuroscience, vol. 23, pp. 1655-1665
4. Molina, J. L. (2020), 'Memantine effects on electroencephalographic measures of putative excitatory/inhibitory balance in schizophrenia', Biological Psychiatry: Cognitive Neuroscience and Neuroimaging, vol. 5, no. 6, pp. 562–568
5. Wilson, L. E. (2022), 'Time-resolved parameterization of aperiodic and periodic brain activity', eLife, vol. 11

Poster No 1846

Subject-level segmentation accuracy weights for volumetric studies involving label fusion

Christina Chen[1], Sandhitsu Das[1], M Tisdall[1], Fengling Hu[1], Andrew Chen[2], Paul Yushkevich[1], David Wolk[1], Russell Shinohara[1]

[1]University of Pennsylvania, Philadelphia, PA, [2]Medical University of South Carolina, Charleston, SC

Introduction: Region-specific changes in brain volume accompany many neurological diseases. Delineating these changes can link structural and clinical findings to illuminate disease biology and facilitate clinical management. For example, Alzheimer's disease (AD) is a neurodegenerative disorder characterized by neuropathological deposits that concentrate in regions such as the hippocampus[1,6]. MRI volumetric studies have augmented these findings by establishing correlations between the magnitude of hippocampal atrophy and the severity of clinical disease[3]. Deriving hippocampal volumes from a neuroimaging study entails segmenting the hippocampus in each image. Manual segmentation is cumbersome and prone to errors. Automated atlas-based segmentation borrows information from expert-labeled images (atlases). Multi-atlas label fusion refines single-atlas segmentation by aggregating labels from multiple atlases. One way of testing for group differences in hippocampal volume involves estimating the hippocampal volume for each subject and then regressing these estimates onto the group labels. However, this approach equalizes the contributions of all study subjects. Retaining poorly segmented images can attenuate power or induce bias, but discarding them altogether can potentially deplete the sample size. Ideally, we would like to weight each volume estimate according to its precision. We propose a novel, statistically motivated method of deriving subject-level precision weights by quantifying how resampling different sets of atlases perturbs each subject's volume estimate.

Methods: We used T1-weighted MRIs from the ADNI. In our first experiment, we compared 200 images from controls (CN) to 200 images from AD subjects. In our second experiment, we compared 150 images from amyloid-negative controls to 175 images from subjects with amyloid-positive early mild cognitive impairment (EMCI). We performed neck-trimming, N4 bias

correction, and skull-stripping on each image. For multi-atlas segmentation, we used the 35 OASIS[5] atlases provided for[4]. We fused the labels from the registered atlases via joint label fusion (JLF)[7]. For each image, we obtained 100 bootstrapped atlas collections by sampling from our 35 atlases, derived the hippocampal volume from the JLF segmentation produced by each atlas collection, computed the variance across these 100 volume estimates, and computed the inverse of this variance to weight the hippocampal volume estimate for each subject. We validated our weights by assessing how incorporating them affects the type I error rate and power in detecting a disease status effect on hippocampal volume. To derive a p-value for this effect, we performed the weighted version of the Freedman-Lane permutation test[2]. In all of our experiments, we regressed the subjects' hippocampal volume estimates onto their disease status (CN vs. AD or CN vs. EMCI), ages, and intracranial volumes.

Results: Our weighting and permutation procedure controls the type I error rate. Moreover, it confers significantly increased power compared to OLS. For example, for 160 samples, weighting improves the power to detect a difference in mean hippocampal volume between controls and AD subjects from 0.592 to 0.724 (Fig. 1). The power gain for differentiating between amyloid-negative controls and amyloid-positive EMCI subjects is even more impressive. For example, for 120 samples, weighting improves the power from 0.112 to 0.615 (Fig. 2).

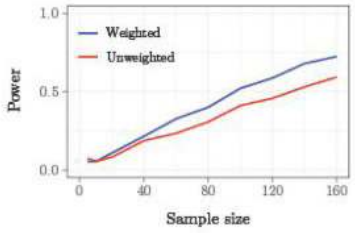

Figure 1: For each sample size n, we sampled with replacement n images from controls and n images from AD subjects and estimated, with and without precision weights, the effect of disease status on hippocampal volume while controlling for age and ICV. We recorded the p-values for both regressions and repeated this procedure 1000 times. Each data point indicates the proportion of these 1000 p-values less than 0.05. Weighting increases the power dramatically.

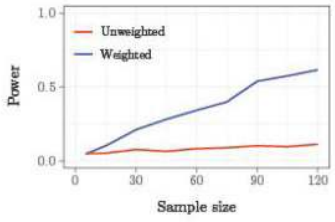

Figure 2: For each sample size n, we sampled with replacement n images from amyloid-negative controls and n images from amyloid-positive EMCI subjects and estimated, with and without precision weights, the effect of disease status on hippocampal volume while controlling for age and ICV. We recorded the p-values for both regressions and repeated this procedure 1000 times. Each data point indicates the proportion of these 1000 p-values less than 0.05. Weighting increases the power dramatically.

Conclusions: We proposed a novel way of deriving subject-level weights that quantify the variability in volume estimates across joint segmentations produced by different atlas collections. We also demonstrated on real data that incorporating these weights significantly improves power for detecting a mean group difference in hippocampal volume. Thus, our method provides definite guidance on how to leverage the uncertainty information extracted from the segmentation procedure to facilitate testing hypotheses motivated by biological questions.

References

1. DeTure, M. A. (2019), 'The neuropathological diagnosis of Alzheimer's disease', Molecular Neurodegeneration, vol. 14, no. 32
2. Freedman, D. (1983), 'A nonstochastic interpretation of reported significance levels', Journal of Business and Economic Statistics, vol. 1, no. 4, pp. 292-298
3. Jack, Jr., C. R. (2011), 'Steps to standardization and validation of hippocampal volumetry as a biomarker in clinical trials and diagnostic criterion for Alzheimer's disease', Alzheimer's and Dementia, vol. 7, no. 4, pp. 474-485
4. Landman, B. (2012), 'MICCAI 2012 workshop on multi-atlas labeling'
5. Marcus, D. S. (2010), 'Open access series of imaging studies (OASIS): Longitudinal MRI data in nondemented and demented older adults', Journal of Cognitive Neuroscience, vol. 22, no. 12, pp. 2677-2684
6. Serrano-Pozo, A. (2011), 'Neuropathological alterations in Alzheimer disease', Cold Spring Harbor Perspectives in Medicine, vol. 1, no. 1
7. Wang, H. (2013), 'Multi-atlas segmentation with joint label fusion', IEEE Transactions on Pattern Analysis and Machine Intelligence, vol. 35, no. 3, pp. 611-623

Poster No 1848

DeepResBat: A residual MRI harmonization framework accounting for covariate distribution differences

Lijun An[1], Chen Zhang[1], Naren Wulan[1], Pansheng Chen[1], Shaoshi Zhang[1], Fang Ji[1], Kwun Kei Ng[1], Christopher Chen[1], Juan Helen Zhou[1], B. T. Thomas Yeo[1]

[1]National University of Singapore, Singapore, Singapore

Introduction: Mega-analysis combining MRI data from multiple sites has significantly advanced neuroimaging research (Miller et al., 2018). When pooling data across multiple sites, MRI harmonization is crucial to reduce undesired site variabilities while preserving effects of covariates of interests (e.g., age). Recently, deep learning has been utilized for addressing harmonization problems (Hu et al., 2023). However, existing deep learning harmonization approaches typically ignore the inclusion of covariates (Zuo et al., 2021; Bashyam et al., 2021). Here, we propose deep learning harmonization models accounting for covariate distribution differences. Furthermore, we demonstrate for the first time that deep learning harmonization algorithms can introduce false positives, which should lead to caution for applying deep learning in neuroimaging.

Methods: In this study, we harmonized T1 MRI between ADNI (adni.loni.usc.edu) and AIBL (aibl.loni.csiro.au), as well as between ADNI and MACC (macc.sg) cohorts. The inputs obtained from FreeSurfer (Fischl et al., 2002; Desikan et al., 2006) are thickness and volumes of cortical ROIs, and volumes of subcortical ROIs. We performed a matching procedure to control for demographics, disease severity, and cognition impairment differences across cohorts. The matched participants served as the testset. The unmatched participants served as training and validation sets. We proposed two deep learning models, coVAE (Figure 1B) and DeepResBat (Figure 1C), which account for covariate distribution differences across datasets. coVAE extends cVAE (Figure 1A; Moyer et al., 2020) by concatenating covariates y and site s with latent representations z. DeepResBat preserves the effects of covariates using machine learning and then eliminates unwanted site differences in covariate-free residuals through a cVAE model. For the baselines, we considered ComBat (Johnson et al., 2007), CovBat (Chen et al., 2021), and cVAE. We considered three evaluation metrics. Firstly, an XGBoost model was applied to predict which dataset a harmonized participant came from. A higher accuracy indicates worse harmonization. Secondly, we tested whether harmonization leads to stronger association between harmonized ROIs and covariates of interests. A stronger association means better harmonization. Finally, we randomly permuted covariates and then harmonized ROIs. The permutation was repeated 1000 times, costing 240,000 GPU and 360,000 CPU hours. For each ROI, a GLM was fitted for each permutation to check association between harmonized ROI and permutated covariates, resulting in 1000 p values; then, we calculated percentage of p values below 0.05 across 1000 p values. The expected percentage across all ROIs is 5%, with a confidence interval of 3.65% to 6.35% (Eklund et al., 2016). A percentage higher than 5% underscores false positives.

Results: Figure 2A shows that deep learning approaches significantly removed more dataset differences than linear approaches (ComBat and CovBat) for harmonizing ADNI and AIBL (Figure 2A1) and harmonizing ADNI and MACC (Figure 2A2) datasets. Figure 2B shows association analysis results between harmonized ROIs and covariates of interests, measured by multivariate ANOVA. We found that coVAE and DeepResBat preserved more biological variabilities than cVAE without considering covariates and linear approaches. Our permutation tests (Figure 2C) show coVAE introduced high false positives, while the DeepResBat achieved expected false positives. The results indicated deep learning harmonization approaches can introduce false positives without careful modeling.

Conclusions: In this study, we proposed deep learning models, coVAE and ResBat, for incorporating covariates during harmonization. coVAE and ResBat outperformed cVAE and linear approaches in removing dataset differences and preserving biological variability. Furthermore, DeepResBat achieved acceptable false positives, which is a novel finding for deep learning harmonization studies.

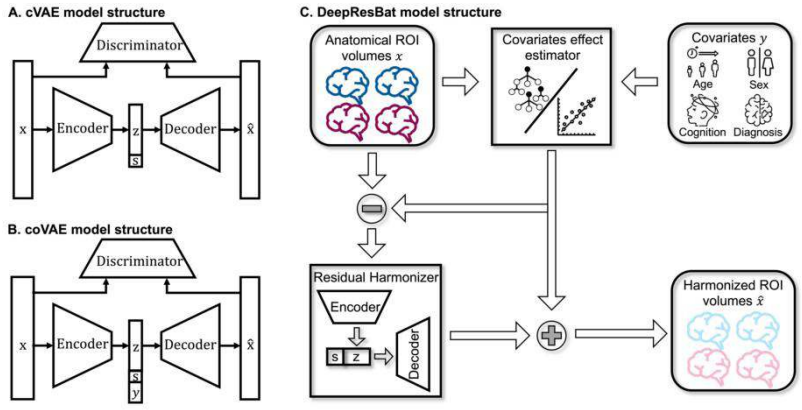

Figure 1. Model structure for cVAE, coVAE, and DeepResBat. (A) Model structure for the cVAE model. Encoder, decoder, and discriminator were all fully connected feedforward DNNs. s was the site we wanted to map the brain volumes to. (B) Model structure for the coVAE model. Covariates y are input into the decoder to preserve covariates effects. (C) Model structure for the DeepResBat model. The covariates effect estimator is an ensemble of XGBoost and linear model, and the residual harmonizer is a cVAE model taking covariate-free residuals as input.

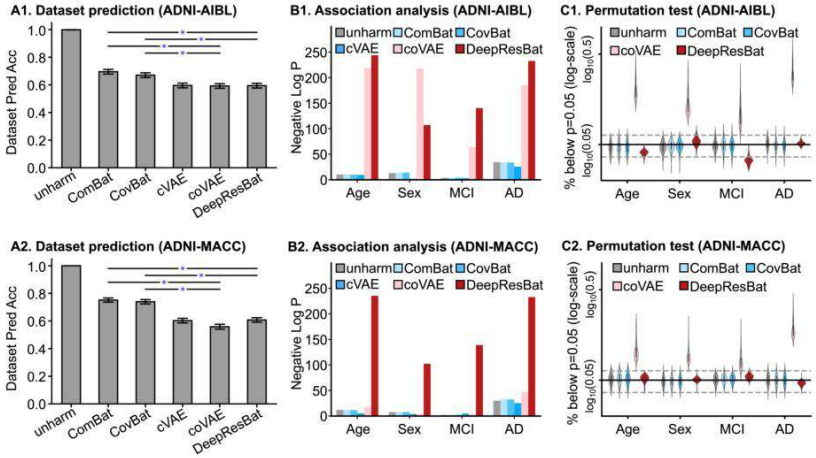

Figure 2. Results for dataset prediction, association analysis and permutation test. (A) Data site prediction accuracies. X axis is unharmonized data and different harmonization models, y axis is dataset prediction accuracy. Blue star indicates statistically significant after FDR correction. Lower accuracy means better harmonization. (B) Association analysis results. X axis is beta in MANOVA, y axis is negative log p values for corresponding beta. Higher negative log of p values suggests better harmonization. (C) Permutation test results. X axis is beta in GLM, y axis is log-scaled percentage of p below 0.05 across 1000 permutations. Each dot in violine plot corresponds to one ROI. The expected percentage of p below 0.05 is 5% across all ROIs, higher percentage than 5% indicates the introduction of false positives.

References

1. Miller, Karla L. (2016), "Multimodal population brain imaging in the UK Biobank prospective epidemiological study." Nature neuroscience 19.11 (2016): 1523-1536.
2. Hu, F. (2023), Image harmonization: A review of statistical and deep learning methods for removing batch effects and evaluation metrics for effective harmonization. NeuroImage, 120125.
3. Zuo, Lianrui. (2021), "Unsupervised MR harmonization by learning disentangled representations using information bottleneck theory." NeuroImage 243 (2021): 118569.
4. Bashyam, Vishnu M. (2021), "Deep Generative Medical Image Harmonization for Improving Cross-Site Generalization in Deep Learning Predictors." Journal of Magnetic Resonance Imaging (2021).
5. Fischl, B. (2002), Whole brain segmentation: automated labeling of neuroanatomical structures in the human brain. Neuron, 33(3), 341-355.
6. Desikan, R. S. (2006), An automated labeling system for subdividing the human cerebral cortex on MRI scans into gyral based regions of interest. Neuroimage, 31(3), 968-980.
7. Moyer, Daniel. (2020), "Scanner invariant representations for diffusion MRI harmonization." Magnetic resonance in medicine 84.4 (2020): 2174-2189.
8. Johnson, W. E. (2007), Adjusting batch effects in microarray expression data using empirical Bayes methods. Biostatistics, 8(1), 118-127.
9. Chen, A. A. (2022), Mitigating site effects in covariance for machine learning in neuroimaging data. Human brain mapping, 43(4), 1179-1195.
10. Eklund, A. (2016), Cluster failure: Why fMRI inferences for spatial extent have inflated false-positive rates. Proceedings of the national academy of sciences, 113(28), 7900-7905.

Poster No 1849

Along-Tract Analysis of White Matter Bundles: Comparing Volumetric and Streamline-based Approaches

Iyad Ba Gari[1], Siddharth Narula[1], Shruti Gadewar[1], Bramsh Chandio[1], Paul Thompson[1], Talia Nir[1], Neda Jahanshad[1]

[1]Imaging Genetics Center, Keck School of Medicine of University of Southern California, Los Angeles, California

Introduction: Along-tract analysis of white matter (WM) bundles can help to map detailed patterns of WM pathway degeneration in Alzheimer's disease and related dementias[1]. Common along-tract methods are often based on simplifying subject bundles to one centroid streamlines and more advanced methods such as Bundle Analytics (BUAN) analyze all possible streamlines in a particular bundle to take anatomical variations into account[2]. While ideal for identifying subtle variations, streamline methods can be computationally intensive, with computation time scaling by the number of streamlines and sample size. As reliable neuroimaging studies require large sample sizes, faster and scalable methods are needed. Here, we present our novel Medial Tractography Analysis (MeTA) method. MeTA aims to minimize partial voluming and microstructural heterogeneity in diffusion MRI (dMRI) metrics by extracting and parcellating the core volume along the bundle length in the voxel-space directly while effectively preserving bundle shape and efficiently capturing the regional variation within and along WM bundles[3]. We evaluated along-tract WM microstructure associations with cognitive impairment using MeTA compared to the established streamline-based BUAN method. We also compared performance efficiency across both methods.

Methods: We used dMRI and clinical data from 714 participants (aged 55-96 years, 52% females) enrolled in ADNI3[4]. The dMRI data were processed using the following steps: denoised using Local PCA[5], deGibbs, and corrected for eddy current and motion artifacts using FSL eddy[6]. The fiber orientation distributions (iFOD2) were estimated using a multi-tissue constrained spherical deconvolution approach[7]. Whole brain probabilistic streamline tractography was generated using the probabilistic iFOD2 method[8]. We used RecoBundles[9] to identify and segment 12 WM bundles. We applied two tractometry methods, MeTA and BUAN, to evaluate the diffusion tensor (DTI) fractional anisotropy (FA) and mean diffusivity (MD) associations with 1) clinical impairment (N=274) compared to cognitively normal (CN) individuals (N=440); and 2) Clinical Dementia Rating Scale Sum of Boxes (CDR-SB). Full details of the tractometry pipelines can be found in Figure 1. We used linear mixed models, where age and sex were modeled as fixed effects, and subjects (as required for BUAN's streamline-based analyses) and scan sites were modeled as nested random variables. We corrected for multiple comparisons across 315 tests (21 bundles x 15 regions) using the false discovery rate (FDR) procedure (q=0.05). We note that BUAN has traditionally been run across 100 segments of a bundle, but we analyze 15 for consistency between the two methods.

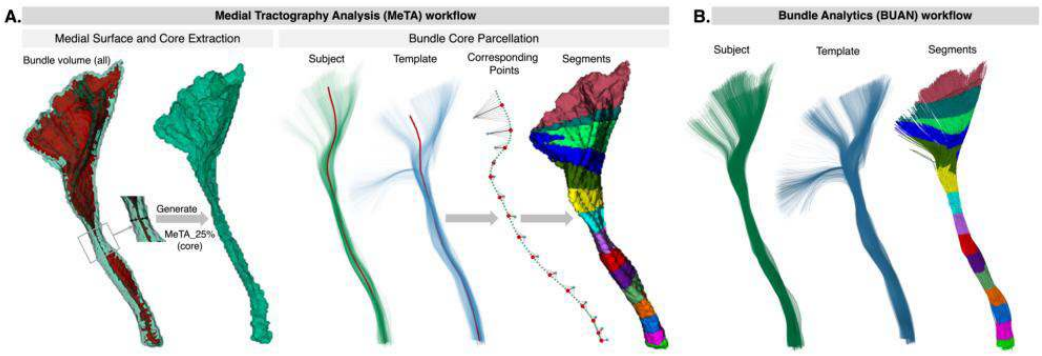

Figure 1: (**A**) ***Medial Tractography Analysis (MeTA) workflow***: Identify and segment 12 white matter (WM) bundles using RecoBundles [9]: the arcuate fasciculus (AF); parahippocampal cingulum (CPH); corticospinal tract (CST); extreme capsule (EMC); inferior fronto-occipital fasciculus (IFOF); inferior longitudinal fasciculus (ILF); middle longitudinal fasciculus (MdLF); optic radiation (OR); uncinate fasciculus (UF); using the left and right hemispheres for each and the corpus callosum (CC), including the forceps major, minor, and mid. Streamlines of the WM bundles are converted to a volume of interest to construct the boundary of the bundle (in green color) and medial surface (in red color) using the CM-Rep method [10]. Then, we generated MeTA_25% (core) using the computed depth from the medial surface. To parcellate the core volume along the bundle length, we generated a centroid (in red color) from the segmented bundle of the subject (in blue color) containing 100 points and the template bundle (in green color) with 14 points. Finally, the parcel bundle core volume was obtained by using corresponding points and calculating the mean of DTI metrics across all voxels within the parcel. This mean of DTI metrics was then used in the linear mixed effects model (LMM). (**B**) **Bundle Analytics (BUAN) workflow:** To segment the subject bundle in a common space, generate a template centroid with N points, then calculate the Euclidean distances between each point on every streamline of the bundle and the template centroid. where each considered point is assigned to the nearest centroid segment. The DTI metrics values within each segment are then aggregated for all the points of each streamline and the bundle's streamlines without subsampling and then used in the LMM model.

Results: MeTA completed statistical tests across 15 segments in a single bundle in about 15 seconds, using 20 MB of memory. In contrast, BUAN took around 15 hours and required 70 GB of memory (expected as it uses rich definitions of bundles). Across both methods participants with cognitive impairment and higher CDR-SB scores showed negative associations with FA values and positive associations with MD measures across bundles such as AF_L, CPH_R, IFOF_R, CST, UF_R, and CC as displayed in Figure 2. However, DTI metrics along the length of the bundles had stronger regional associations using MeTA compared to BUAN.

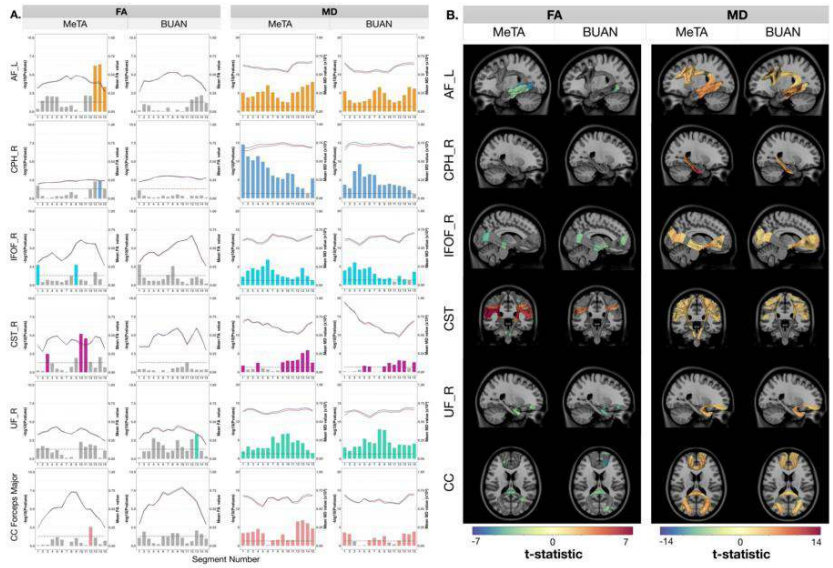

(**A**) Mean bundles profile for DTI metrics (FA and MD) comparing the bundle group differences between individuals with cognitive impairment (represented by the blue line) and the control group (represented by the red line) across 15 segments along the length of the bundles. This analysis was adjusted for age and sex as fixed covariates, and subjects (only in BUAN) and scan sites as nested random variables. In the plot, the x-axis represents the segment number along the tract length. The right y-axis shows the mean values of DTI metrics (FA and MD), while the left y-axis represents the negative logarithm of the p-value. A horizontal line indicates a p-value less than 0.05. A colored bar indicates significant differences between groups that pass the FDR threshold, while a gray bar indicates no significant difference based on the FDR threshold. We find both MeTA and BUAN show similar trends for along-tract mean diffusion metrics between groups. Both methods find significant differences in MD along the majority of all displayed tracts. (**B**) T-values for MeTA_25% core volume vs BUAN along the length of 6 segmented bundles: AF_L, CPH_R, IFOF_R, CST, UF_R, CC. Colored areas indicate significant associations (P_{FDR}<0.05) with CDR-SB scores, while gray color indicates no significant association between DTI metrics and CDR-SB scores. We found that higher CDR-SB scores showed negative associations with FA value (in blue color) and positive associations (in red color) with MD measure. Both methods have similar significant results across most bundles and along the length of tracts.

Conclusions: MeTA is a fast and reliable approach for identifying regional WM brain abnormalities in clinical populations at both the subject and group levels. ADRD associations detected with MeTa were largely consistent with existing along-tract pipelines. While it does not analyze individual streamlines and requires a coarser along-tract parcellation scheme, MeTA is much faster than current state-of-the-art streamline methods with compatible, if not more sensitive findings. Such highly scalable approaches can be complementary to existing methods and applied to large-scale efforts and consortia.

References

1. A. Pichet Binette et al., “Bundle-specific associations between white matter microstructure and Aβ and tau pathology in preclinical Alzheimer’s disease,” Elife, vol. 10, May 2021, doi: 10.7554/eLife.62929.
2. B. Q. Chandio et al., “Bundle analytics, a computational framework for investigating the shapes and profiles of brain pathways across populations,” Sci. Rep., vol. 10, no. 1, p. 17149, Oct. 2020.
3. I. Ba Gari et al., “Along-Tract Parameterization of White Matter Microstructure using Medial Tractography Analysis (MeTA),” in The 19th International Symposium on Medical Information Processing and Analysis, 2023.
4. A. Zavaliangos-Petropulu et al., “Diffusion MRI Indices and Their Relation to Cognitive Impairment in Brain Aging: The Updated Multi-protocol Approach in ADNI3,” Front. Neuroinform., vol. 13, p. 2, Feb. 2019.
5. J. V. Manjón, P. Coupé, L. Concha, A. Buades, D. L. Collins, and M. Robles, “Diffusion weighted image denoising using overcomplete local PCA,” PLoS One, vol. 8, no. 9, p. e73021, Sep. 2013.
6. J. L. R. Andersson and S. N. Sotiropoulos, “An integrated approach to correction for off-resonance effects and subject movement in diffusion MR imaging,” Neuroimage, vol. 125, pp. 1063–1078, Jan. 2016.
7. B. Jeurissen, J.-D. Tournier, T. Dhollander, A. Connelly, and J. Sijbers, “Multi-tissue constrained spherical deconvolution for improved analysis of multi-shell diffusion MRI data,” Neuroimage, vol. 103, pp. 411–426, Dec. 2014.
8. J. D. Tournier, F. Calamante, A. Connelly, and Others, “Improved probabilistic streamlines tractography by 2nd order integration over fibre orientation distributions,” in Proceedings of the international society for magnetic resonance in medicine, John Wiley & Sons, Inc, New Jersey, 2010. Accessed: Dec. 15, 2022. [Online]. Available: https://archive.ismrm.org/2021/1767.html
9. E. Garyfallidis et al., “Recognition of white matter bundles using local and global streamline-based registration and clustering,” Neuroimage, vol. 170, pp. 283–295, Apr. 2018.
10. P. A. Yushkevich, H. Zhang, and J. C. Gee, “Continuous medial representation for anatomical structures,” IEEE Trans. Med. Imaging, vol. 25, no. 12, pp. 1547–1564, Dec. 2006.

Acknowledgments

1. This research was supported by NIH grants P41EB015922, R01AG059874, R01MH134004, and RF1AG057892. Alzheimer’s Disease Neuroimaging Initiative (ADNI) database (adni.loni.usc.edu). As such, the investigators within the ADNI contributed to the design and im

Poster No 1850

Volumetric Fetal Brain Reconstruction from Sensor-free Freehand Ultrasound Videos

Pak Hei Yeung[1], Linde Hesse[1], Moska Aliasi[2], Monique Haak[2], INTERGROWTH-21st Consortium[3], Weidi Xie[1,4], Ana Namburete[5]

[1]University of Oxford, Oxford, Oxfordshire, [2]Leiden University Medical Center, Leiden, Leiden, [3]Oxford Maternal & Perinatal Health Institute (OMPHI), Green Templeton College, University of Oxford, Oxford, United Kingdom, [4]Shanghai Jiao Tong University, Shanghai, China, [5]University of Oxford, Oxford, Oxfordshire

Introduction: Three-dimensional (3D) ultrasound (US) imaging has contributed to our understanding of fetal neurodevelopmental processes by providing rich 3D anatomical and contextual information[3]. However, its use is restricted in clinical settings, due to the high purchasing costs and limited clinical practicality. Freehand 2D US imaging, in contrast, is routinely used in standard obstetric exams, but inherently lacks a 3D representation of the anatomies, which limits its potential for more advanced assessment. 3D representations are challenging to recover from 2D scans even with external tracking devices due to internal fetal movement. Capitalizing on the flexibility offered by freehand 2D US acquisition, we propose ImplicitVol to reconstruct 3D volumes from non-sensor-tracked 2D US sweeps.

Methods: Consider a set of 2D US images capturing different cross-sectional views of a fetal brain. The goal of ImplicitVol (Fig. 1a) is to reconstruct the corresponding 3D brain, such that any 2D cross-sectional view can be generated by inputting the corresponding 3D coordinates of the plane. Plane Localization: We use PlaneInVol[6] to estimate the 3D locations of each of the 2D US images. Not requiring any external tracking, it is trained with 2D slices, sampled from a set of affinely co-registered 3D brain volumes, and their locations in the 3D alignment space[3]. Training: Intuitively, the 3D volume is stored in a deep neural network (DNN). We first derive the 3D coordinates for each pixel of the 2D US images from the predicted 3D locations. By inputting them to the DNN, the corresponding intensity values are predicted. The weights of the DNN can be learned through backpropagation, where the loss is computed by the structural similarity (SSIM)[4] between the predicted intensities and the 2D US images. Since the 3D plane locations predicted by PlaneInVol are imperfect, we further update the 3D locations simultaneously through joint optimization[5]. The DNN weights are also iteratively reinitialized during training to avoid overfitting to a set of sub-optimal 3D locations. Inference: The trained DNN represents a continuous 3D fetal brain captured by the set of 2D images. The 3D volume or any 2D cross-sectional oblique view can be obtained as the output, by feeding the corresponding grid coordinates for the desired slice to the trained DNN.

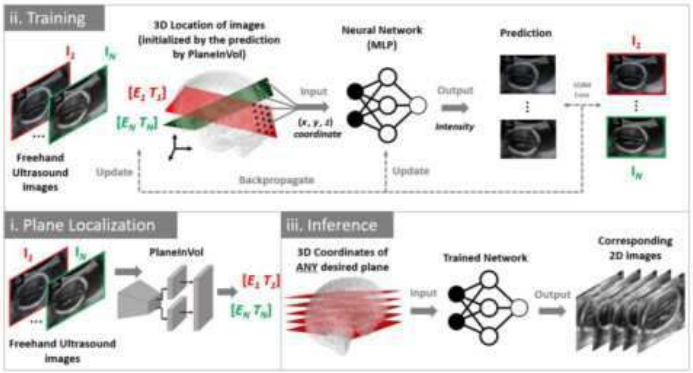

(a) Pipeline of our proposed framework, *ImplicitVol*

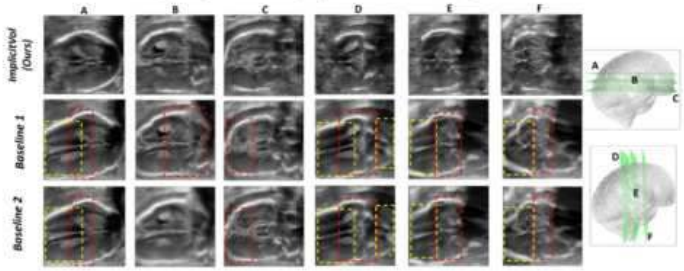

(b) Reconstruction from Native 2D US Images

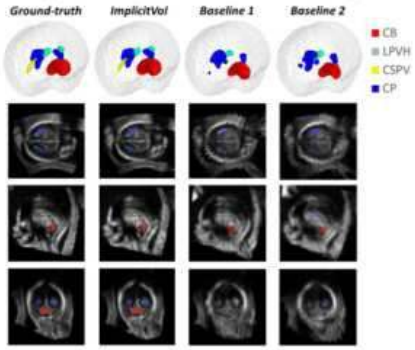

(c) Segmentation on Reconstructed Volumes

Figure 1: **(a)(i)** The 3D locations, $\{\mathbf{E}_i, \mathbf{T}_i\}_{i=1}^N$, of a set of 2D freehand ultrasound images, $\{\mathbf{I}_i\}_{i=1}^N$, are first predicted by PlaneInVol. **(a)(ii)** $\{\mathbf{I}_i\}_{i=1}^N$, and $\{\mathbf{E}_i, \mathbf{T}_i\}_{i=1}^N$ are then used to train a deep neural network to implicitly represent the *continuous* 3D volume from which $\{\mathbf{I}_i\}_{i=1}^N$ are acquired. **(a)(iii)** During inference, images at any planes can be obtained as output, by feeding the corresponding grid coordinates to the network. **(b)** Novel view images sampled from different planes from volumes reconstructed by different approaches are presented. *ImplicitVol*, shows better visual quality in under-sampled region (yellow) and is more robust against inaccurate position estimation (red). **(c)** Segmentation of the choroid plexus (CP), lateral posterior ventricle horns (LPVH), cavum septum pellucidum et vergae (CSPV), and cerebellum (CB) by different approaches are presented in the axial, coronal and sagittal planes.

Results: ImplicitVol, with ablation studies, was compared against an interpolation-based approach (Baseline 1) and Baseline1+SVRTK[2] (Baseline 2). Both 3D volumes acquired from different sites (Dataset A and B) and native 2D freehand video sequences were tested. Reconstruction from Volume-Sampled Images: 2D cross-sectional images were sampled from native 3D volumes. Figure 2a-d demonstrated, with two different evaluation metrics, that the 3D volumes reconstructed from ImplicitVol showed a closer match with the corresponding ground-truth by over 50% (SSIM) and 40% (VIF). Segmentation on Reconstructed Volumes: Using a 3D segmentation DNN[1] to segment four subcortical structures from the brain volumes, ImplicitVol shows a better segmentation accuracy qualitatively (Fig. 1c) and quantitatively by all three evaluation metrics (Fig. 2e-j), suggesting its better performance on semantic level. Reconstruction from Native 2D US Images: Qualitatively, brain volumes reconstructed by ImplicitVol showed better visual quality in motion-corrupted regions and under-sampled regions when compared to Baseline 1 and 2 (Fig. 1b).

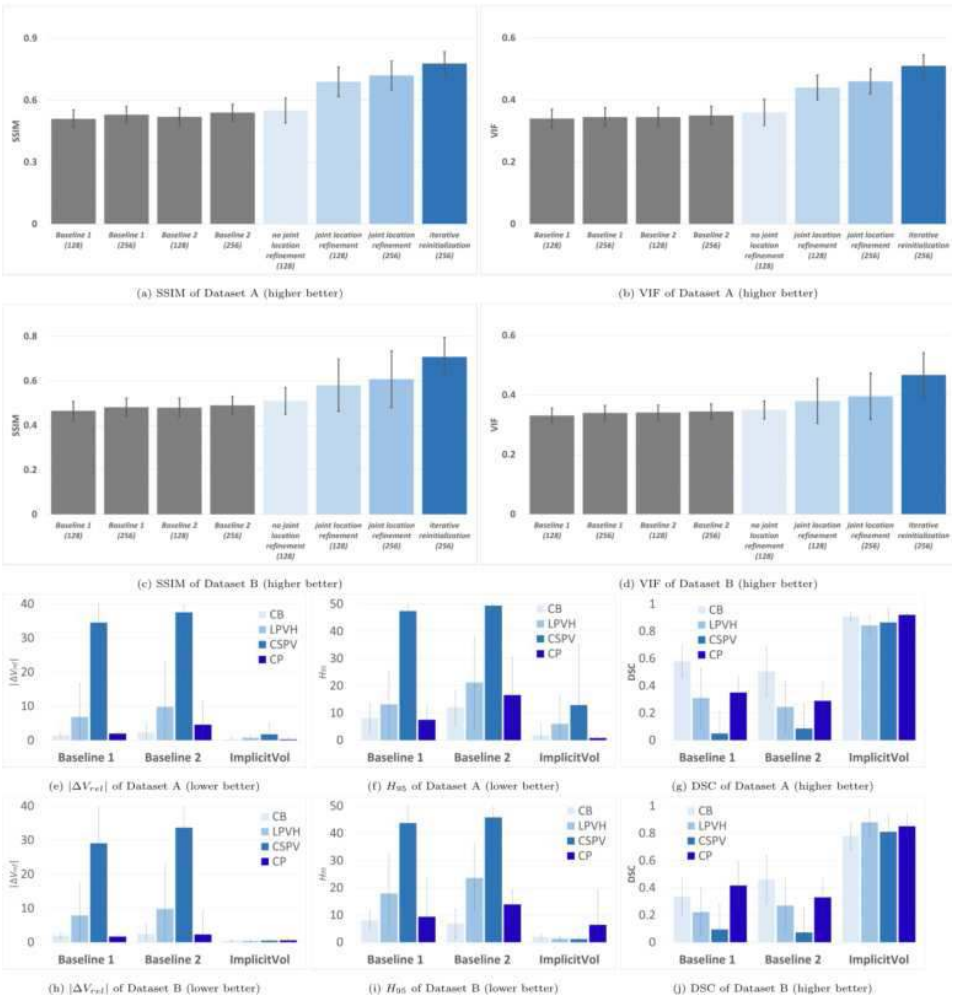

(a) SSIM of Dataset A (higher better) (b) VIF of Dataset A (higher better)

(c) SSIM of Dataset B (higher better) (d) VIF of Dataset B (higher better)

(e) $|\Delta V_{rel}|$ of Dataset A (lower better) (f) H_{95} of Dataset A (lower better) (g) DSC of Dataset A (higher better)

(h) $|\Delta V_{rel}|$ of Dataset B (lower better) (i) H_{95} of Dataset B (lower better) (j) DSC of Dataset B (higher better)

Figure 2: **(a)-(d)** Quantitative volume reconstruction results. The gray bars represent the baseline methods and the blue bars represent *ImplicitVol* with ablation studies. The number in the bracket is the number of 2D slices used for volumetric reconstruction. The 3D version of SSIM was employed to compare the similarity between two 3D volumes. SSIM ranges from 0 to 1, where higher value represents higher similarity. Visual information fidelity (VIF) was also computed to measure the similarity between pair of 2D slices. A higher VIF value represents higher similarity. **(e)-(j)** Quantitative results of segmentation of the choroid plexus (CP), lateral posterior ventricle horns (LPVH), cavum septum pellucidum et vergae (CSPV), and cerebellum (CB) from 3D volumes reconstructed by different approaches. Dice similarity coefficient (DSC), 95^{th} percentile Hausdorff distance (H_{95}) and unsigned relative volume differences ($|\Delta V_{rel}|$) were used to quantify the performance. DSC ranges from 0 to 1, where a higher value corresponds to a better match between the two sets of segmentations, thus suggesting better structural fidelity. For H_{95} and $|\Delta V_{rel}|$, a lower value suggests better performance.

Conclusions: Without requiring extra equipment or substantial changes to the routine scanning procedures, Implicitvol can enhance the diagnostic power of 2D obstetric ultrasound, by extracting volumetric information from standard 2D scanning sequences. This may facilitate the transformation of US from a screening to a powerful diagnostic tool, ultimately offering personalised and advanced monitoring to the most vulnerable members of society, while capitalizing on the affordability and ubiquity of 2D US imaging at the bedside.

References

1. Hesse, L. S. (2022). “Subcortical segmentation of the fetal brain in 3D ultrasound using deep learning.” NeuroImage, 254, 119117.
2. Kuklisova-Murgasova, M. (2012). “Reconstruction of fetal brain MRI with intensity matching and complete outlier removal.” Medical image analysis, 16(8), 1550-1564.
3. Namburete, A. IL. (2023), “Normative spatiotemporal fetal brain maturation with satisfactory development at 2 years.” Nature, 1-9.
4. Wang, Z. (2004). “Image quality assessment: from error visibility to structural similarity.” IEEE transactions on image processing, 13(4), 600-612.
5. Wang, Z. (2021). “NeRF--: Neural radiance fields without known camera parameters.” arXiv preprint arXiv:2102.07064.
6. Yeung, PH. (2021), “Learning to map 2D ultrasound images into 3D space with minimal human annotation.” Medical Image Analysis, 70, 101998.

Poster No 1851

Clarifying the reliability paradox: poor test-retest reliability attenuates group differences

Povilas Karvelis[1], Andreea Diaconescu[1,2,3,4]

[1]CAMH, Toronto, ON, [2]Department of Psychology, University of Toronto, Toronto, ON, [3]Institute of Medical Sciences, University of Toronto, Toronto, ON, [4]Department of Psychiatry, University of Toronto, Toronto, ON

Introduction: Cognitive tasks that produce robust group effects tend to have poor test-rest reliability – a phenomenon known as the reliability paradox (Hedge et al., 2018). This is true for simple summary statistics of task behavior (Hedge et al., 2018), computational measures obtained from modelling task behavior (Karvelis et al., 2023), as well as task-based fMRI activations (Elliott et al., 2020). Most literature on this issue highlights how poor test-retest reliability undermines correlational individual differences research as well as translational personalized and precision psychiatry efforts. Our aim here is to demonstrate that poor test-retest reliability is detrimental not just for studying individual differences, but also for studying group differences (e.g., patients vs controls).

Methods: To illustrate our argument, we ran model simulations. We generated synthetic datasets of varying levels of between-subject and error variance and investigated how it affected test-retest reliability, individual differences, within-subject effects, and between-subject effects. We used intra-class correlation coefficient (ICC) to estimate test-retest reliability, Cohen's d to estimate group difference effect size, and Pearson's r to estimate correlations. While our analysis is general and would apply to any scenario of comparing different groups, to make our demonstration more intuitive, we considered two illustrative cases: 1) comparing patients vs. controls and 2) comparing two groups created via a median split.

Results: First, our simulations reproduce the reliability paradox and provide intuitive clarification that robust group effects are achieved by minimizing overall variance (not just between-subject variance; Fig. 1). Second, and most importantly, our simulations show that test-retest reliability attenuates observed between-subject effects just as much as it attenuates observed correlations – this was equally true in both cases under consideration (patients vs. controls and median split; Fig. 2).

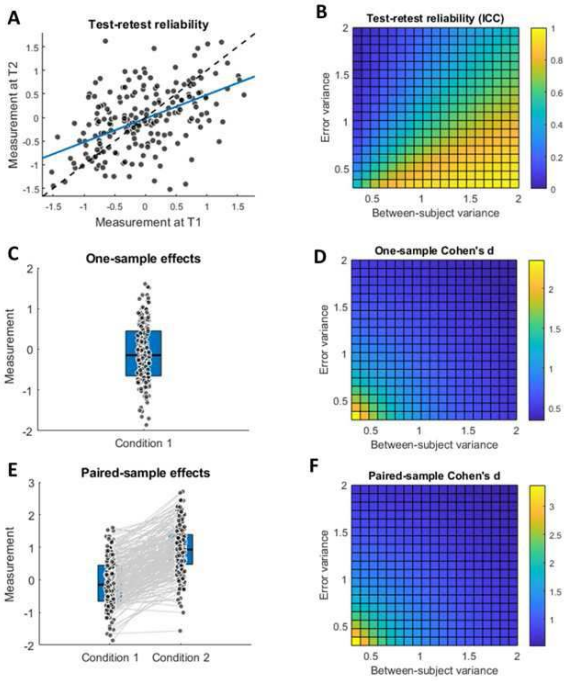

Figure 1. The reliability paradox. Left column panels illustrate the different tests, while the right column panels illustrate the resulting effects under different error and between-subject variance scenarios. Note that test-retest reliability is highest when the error variance is minimized and between-subject variance is maximized (**B**), while the observed effect size for one-sample and paired-sample group effects is maximized when both error and between-subject variances are minimized (**D, F**).

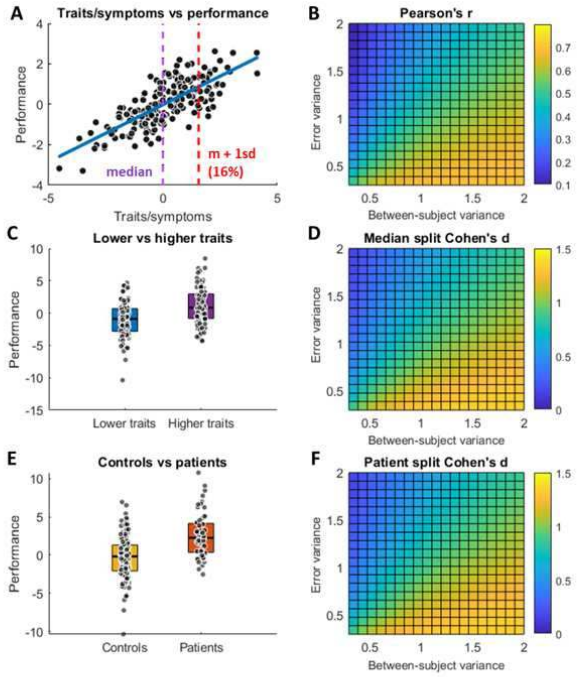

Figure 2. The effects of test-retest reliability on correlational strength and group differences. These results consider a hypothetical scenario where some traits or symptoms are correlated with some task performance measures (**A**). Just like before, we vary error and between-subject variances of the task performance measure and find that minimizing error variance and maximizing between-subject variance (i.e. maximizing test-retest reliability) leads to highest observed correlation strength (**B**). When we perform a median split based on traits and compare the groups (**C**), we also find that the observed effect size is the highest when test-retest reliability is the highest (**D**). We find the same when we assume patients to correspond to individuals with the most severe symptoms (top 16% of the sample) and compare them to the remaining group (**E, F**).

Conclusions: Our work highlights that the reliability paradox has even wider implications than originally stated: low test-retest reliability undermines not only individual differences but also group differences research. Note that this applies not only to studying patient groups but also to many other areas of research: sex differences, ethnic differences, age differences, etc. Overall, our findings further stress that improving test-retest reliability of cognitive measures is of paramount importance for improving the quality of research.

References

1. Elliott, M. L. (2020). What is the test-retest reliability of common task-functional MRI measures? New empirical evidence and a meta-analysis. Psychological science, 31(7), 792-806.
2. Hedge, C. (2018). The reliability paradox: Why robust cognitive tasks do not produce reliable individual differences. Behavior research methods, 50(3), 1166-1186.
3. Karvelis, P. (2023). Individual differences in computational psychiatry: a review of current challenges. Neuroscience & Biobehavioral Reviews, 105137.

Poster No 1853

MultiPAD: a multimodal network biomarker for predicting Amyloid positivity in healthy elderly

Alle Meije Wink[1], Luigi Lorenzini[1], Leonard Pieperhoff[1], Giuseppe Pontillo[2], James Cole[3], Frederik Barkhof[1]

[1]Amsterdam University Medical Centre, Amsterdam, Noord-Holland, [2]Amsterdam University Medical Centre, Amsterdam, Netherlands, [3]University College London, London, London

Introduction: Alzheimer's Disease (AD), the main cause of dementia worldwide,is characterised by a progressive loss of connectivity between brain regions. Different aspects of brain connections are measured with various magnetic resonance (MR) imaging protocols. Diffusion-weighted imaging (DWI) measures the presence of white matter fibres as they guide the diffusion of water, functional MRI (fMRI) measures co-activity between regions as connections, and with anatomical MRI, corresponding morphological properties across the brain are seen as caused by a common factor. Instead of analysing these network measurements in isolation, we propose a new brain network model that incorporates them, and connects the corresponding nodes between them, forming a multiplex network (see figure 1).

Methods: Participants from the European consortium for Prevention of Alzheimer's Dementia (EPAD, https://ep-ad.org) were healthy elderly with no cognitive decline (CDR < 1), some of whom were tested amyloid-positive based on cerebrospinal fluid (CSF) testing. Selected participants underwent anatomical MR imaging, fMRI and DWI. Connectomes (pairwise connections between brain regions) were connected with MIND for anatomical MRI, fmriprep for fMRI and qsiprep for DWI, using the Schaefer brain atlas with 100 regions. Connectomes were stored as matrices, stronger connections being represented by higher values, and missing connections by the value zero. Connections between matrices were only possible within the same region. Mathematically, this corresponds to a block-diagonal matrix of the 3 connectomes, together with diagonals in the rest of the blocks (see figure 2). The values on these diagonals represent the 'connectivity', or the 'cost', of building paths in the network that use more than one connectome (the green connections in figure 1). Keeping the measured connectomes fixed, we computed the optimal weights for predicting the CSF-derived amyloid status as those maximising the difference between the mean group whole-brain centrality of the 10 amyloid-positive subjects with the lowest (most extreme) CSF amyloid levels and the 10 amyloid-negative subjects with the highest CSF amyloid levels, respectively. This optimisation framework was implemented in Python with the lmfit package for nonlinear fitting.

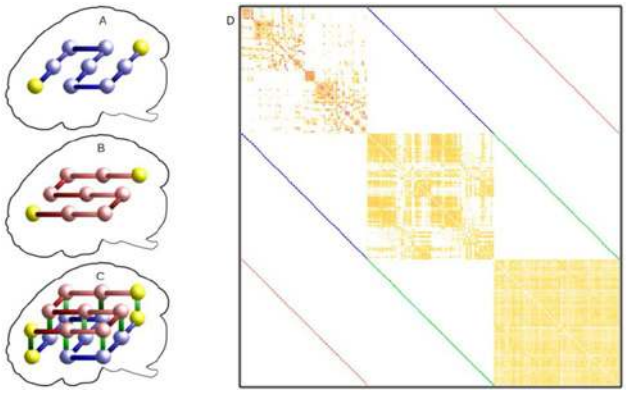

Figure 1: Left: a complete brain network (C) is made by joining connectomes (A and B) within regions. Right: a supra-adjacency matrix made from 3 connectomes.

Results: Different patterns could be seen in the three sets of between-layer connections, when they were optimised to get the highest group-average whole-brain centrality (see Figure 2). The amyloid-negative (A-) and amyloid-positive (A+) groups showed similar patterns of connection weights between the structural and functional connectome layers, with higher weights in the somatomotor cortex. A marked difference between the groups was an area of high frontal between-layer weights in the A- group, which was absent in the A+ group. In the connection channel between the functional and anatomical layers, higher weights were only found in the A- group in the prefrontal, lower visual and occipital lobes. Connections between these layers of similar strength were not found in the A+ group. The channel between the structural and anatomical layers showed higher weights in the left frontal cortex in the A- group. In the A+ group, no pattern of relatively higher weights were found in specific regions, although overall weights were higher than in the A- group.

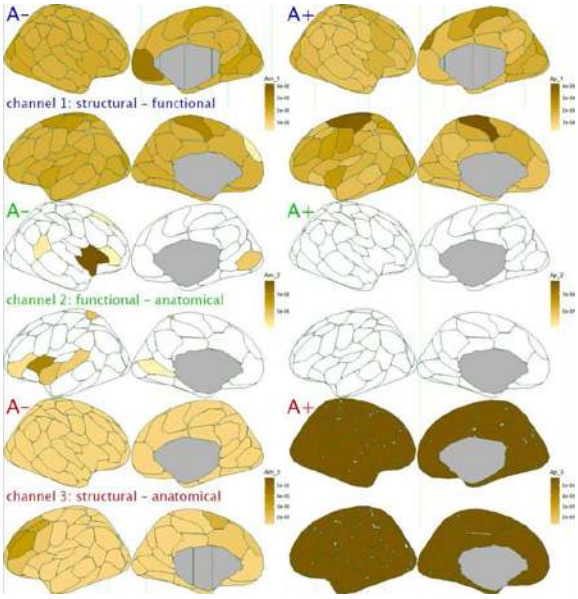

Figure 2: The inter-layer weights in both groups (amyloid negative and positive); top: structral to functional, middle: functional to anatomical, bottom: structural to anatomical.

Conclusions: We have developed a multi-layer brain network model that incorporates connectomes measured with different MR imaging modalities. The interlayer weights between the connectomes of EPAD participants were optimised to maximise their group average whole-brain centrality in the multiplex networks.

References

1. Cieslak, M. et al. (2021), "QSIPrep: an integrative platform for preprocessing and reconstructing diffusion MRI data", Nature Methods 18: 775–78
2. Esteban, O. et al. (2018), "fMRIPrep: a robust preprocessing pipeline for functional MRI", Nature Methods 16: 111–16
3. Newville, M. et al. (2023), "LMFIT: Non-Linear Least-Square Minimization and Curve-Fitting for Python", https://doi.org/10.5281/zenodo.8145703
4. Schaefer, A. et al (2018), "Local-Global Parcellation of the Human Cerebral Cortex from Intrinsic Functional Connectivity MRI", Cerebral Cortex 28: 3095-114
5. Sebenius, I. et al. (2023), "Robust estimation of cortical similarity networks from brain MRI", Nature Neuroscience 26: 1461–71

Poster No 1855

An integrated Bayesian normative and outcome model for brain reserve in MS

Bernd Taschler[1], Samantha Pendleton[1], Stephen Gardiner[1], Piet Aarden[2], Thomas Nichols[1], Dieter Haering[2], Laura Gaetano[2], Habib Ganjgahi[1]

[1]University of Oxford, Oxford, United Kingdom, [2]Novartis Pharma AG, Basel, Switzerland

Introduction: Normative modelling is a standard method to define subject-specific deviations from a reference population. These deviations can then be used as outcomes for prediction, classification, clustering or other tasks. Traditionally, this is done in two steps with separate models for i) the normative component to create deviation scores, and ii) the outcome analysis of the scores. Importantly, derived deviation scores are based on differences of observed data with the normative population mean/median (e.g., developmental charts). In this work we propose two fundamental innovations to how normative modelling is conducted. First, instead of separately deriving a score and modelling that score as an outcome in an analysis, we create a single unified model that integrates the normative and final analyses. Second, instead of defining the deviation score as a difference of noisy observed data and a reference, we propose that a predicted fit replaces the role of the observed data; a sufficiently rich model will produce a prediction that is unbiased and much less variable than the raw data. We apply our integrated model to the concept of "brain reserve" (the neurobiological capacity to cope with pathology; Stern et al., 2020) in a time-to-event analysis of a large cohort of MS patients.

Methods: Normative model. We consider a set of baseline covariates X (e.g. age, sex, medical history, etc.) and a single exposure variable of interest Z (in our case an ordinal score of disease severity, EDSS). The outcome Y is a quantitative MRI-derived measure linked brain reserve (e.g., total brain volume or T2 lesion load). The normative model for Y is based on

Bayesian Additive Regression Trees (BART, Chipman et al., 2010). Deviation scores. We define individual deviation scores d as the difference between predicted outcome and posterior population average for each category in Z. Time-to-event model. We use a Cox proportional hazards (CPH) model with individual deviation scores d as predictor variable. Additionally, the data is stratified into 3 groups of low (d < -1SD), medium (-1SD ≤ d ≤ +1SD) or high (d > +1SD) brain reserve, with the two extreme groups indicating high deviation from the population mean (Sormani et al., 2017). For each of these groups, we estimate the probability of a disease worsening event T (defined as persistent increase in EDSS) occurring within a timeframe of 5 years after baseline. Bayesian hierarchical model. The full model is illustrated in Fig.1. Parameter estimation and model inference is based on draws from the posterior distributions using MCMC techniques. Application. For empirical validation, we use a subset of the NO.MS dataset with 9k subjects from 10 clinical studies and including 7 different treatment arms (Dahlke et al., 2021); 67% female, age (mean±SD) 40.3±10.7 years, median EDSS 3.0.

$$Y_i \sim BART(X_i, Z_i; \Theta) \quad (1)$$

$$d_i = \hat{Y}_i - \hat{\mu}_j | Z_i = z_j \quad (2)$$

$$P(T > t | t_{-1}, d) = CPH(t, d; \Lambda) \quad (3)$$

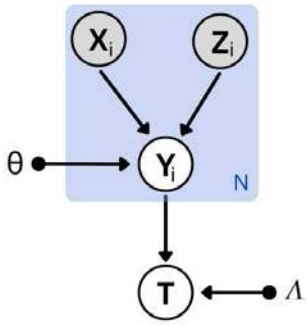

Figure 1. Representation of the Bayesian hierarchical model in the form of a directed acyclic graph. Hollow nodes represent random variables, filled circles represent model parameters, grey shaded variables are observed.

Results: Results from the time-to-event analysis are shown in Fig.2. We use individual deviations of normalised brain volume (conditional on EDSS category) as a proxy for brain reserve. Stratification of the patient population into groups of low, medium and high NBV at baseline shows a strong association of deviation scores derived from the unified model with risk of experiencing a disability worsening event (Fig.2B). Whereas deviation scores based on residuals (Fig.2C) are much less informative.

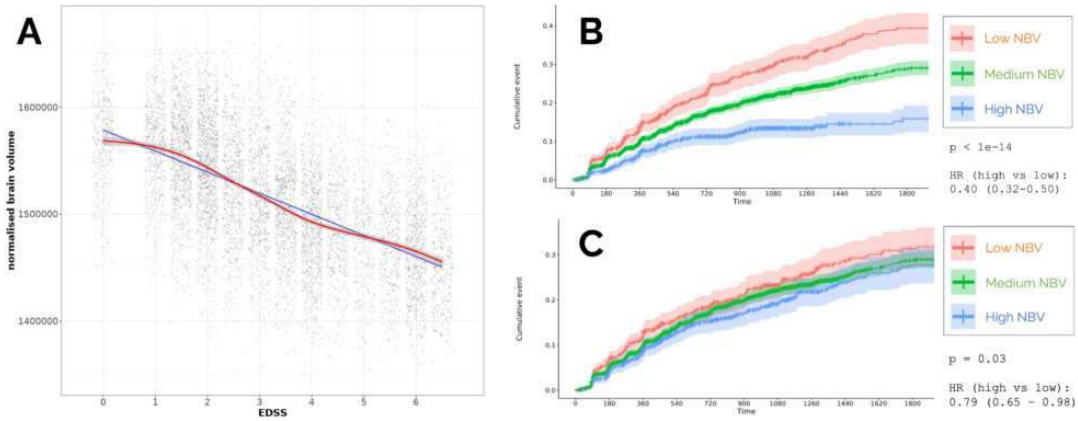

Figure 2. **A)** Normative model of brain volume across disability as measured by EDSS. Dots indicate individual predictions (with jitter), blue/red lines indicate linear/loess fits. **B)** Risk curves using our proposed normative score, a difference of each subject's normalised brain volume (NBV) prediction from the BART model and population mean conditional on their EDSS value. **C)** Risk curves using traditional score, the difference of predicted NBV and observed NBV. Both risk curves are shown over a 5-year period and based on individual deviation in NBV at baseline, grouped by brain reserve (low/medium/high).

Conclusions: Our proposed unified normative modelling approach using a Bayesian hierarchical model that combines normative modelling of brain reserve (individual deviations in brain volume from a reference population of MS patients) with a time-to-event analysis of disability worsening outperforms classical residual based methods. MS patients with low "brain reserve" at baseline have higher risk of accumulating disability compared to patients with higher brain reserve but otherwise similar characteristics (e.g., age, sex, disease duration, etc.).

References

1. Chipman, H.A. (2010). BART: Bayesian Additive Regression Trees. The Annals of Applied Statistics, Vol. 4, No. 1, pp. 266-298. https://www.jstor.org/stable/27801587
2. Dahlke, F. (2021). Characterisation of MS phenotypes across the age span using a novel data set integrating 34 clinical trials (NO.MS cohort): Age is a key contributor to presentation. Multiple Sclerosis Journal, Vol. 27, No. 13. https://doi.org/10.1177/1352458520988637

3. Stern, Y. (2020). Whitepaper: Defining and investigating cognitive reserve, brain reserve, and brain maintenance. Alzheimer's and Dementia, Vol. 16, pp. 1305–1311. https://doi.org/10.1016/j.jalz.2018.07.219
4. Sormani, M.P. (2021). Defining brain volume cutoffs to identify clinically relevant atrophy in RRMS. Multiple Sclerosis Journal, Vol. 23, No. 5. https://doi.org/10.1177/1352458516659550

Poster No 1856

Generating surrogate brain maps through random rotation of geometric eigenmodes

Nikitas Koussis[1], James Pang[2], Jayson Jeganathan[3], Bryan Paton[1], Alex Fornito[2], Peter Robinson[4], Bratislav Misic[5], Michael Breakspear[1]

[1]University of Newcastle, Newcastle, NSW, [2]Monash University, Melbourne, Victoria, [3]The University of Newcastle, Newcastle, NSW, [4]University of Sydney, Sydney, NSW, [5]McGill University, Montreal, Quebec

Introduction: The brain expresses activity in complex spatiotemporal patterns, reflecting cytoarchitectural and genetic influences that possess specific spatial properties. These brain patterns, also known as brain maps, frequently have high smoothness and spatial organization, i.e., spatial autocorrelation (SA), reflecting its central position in modern neuroimaging analyses[1–6]. In regimes of high SA, correlation between two brain maps can be spuriously elevated leading to false positive associations. An appropriate null hypothesis test to exclude false positives requires surrogate brain maps that preserve SA. Here we introduce "eigenstrapping", a technique for generating null hypotheses for maps possessing SA. This method uses geometric eigenmodes derived from various surfaces to produce surrogate brain maps that preserve SA. We show that these surrogate maps appropriately represent the null distribution and control false positives for cortical maps with SA, providing a versatile approach for investigations of cortical and subcortical topography.

Methods: Geometric eigenmodes of the cortical surface, ψ, are first derived by solving the Helmholtz equation on high-resolution surface meshes[7,8]. A generalized linear model is then used to identify the contribution of each mode to an empirical map (coefficients β, Fig. 1A). The cortical eigenmodes are then projected onto the sphere with axes equivalent to eigenvalues μ. The modes are rotated independently per eigengroup Λ (Fig. 1B), preserving orthogonality within groups, while randomly disrupting the orientation of modes between groups. Rotated eigenmodes are projected back onto the cortex and multiplied by the original coefficients β, generating random maps that preserve the eigenspectrum of the original data while destroying the cross spectra (the alignment of modes across groups) (Fig. 1C). An optional amplitude adjustment step can then be performed to retain the empirical amplitude distribution. We then used standard benchmarks to assess whether the ensuing surrogate brain maps represent appropriate null hypotheses for spatially correlated brain maps.

Results: Surrogate brain maps derived from eigenmode rotation retain the variogram of HCP task activation maps[9,10] (Fig. 1E), a measure of local SA. Surrogate maps are uncorrelated with the original brain map (Fig. 1F); and show pairwise correlations that are zero centered and drawn from a Gaussian-like distribution (Fig. 1G). These results show that eigenstrapped brain maps possess core properties necessary for a non-parametric null. We next tested for false positive control by simulating [11,12] 1000 pairs of maps with an average cross-correlation of 0.15 using Gaussian random fields (GRFs) ranging from white spatial noise ($SA \sim 0, \alpha = 0.0$) to strongly autocorrelated ($SA \gg 0$; $\alpha = 4.0$) in steps of 0.5 (Fig. 2A; 9000 pairs of maps in total). When SA is low ($\alpha < 1.5$), these maps fall outside the eigenstrapped null distribution ($p \ll 0.05$) but appropriately within the null ($p > 0.05$) when SA is high ($\alpha \geq 1.5$; Fig. 2C). Random surrogates which do not preserve the SA fail to control these false positives. To quantify a false positive rate (FPR), we randomized pairs of GRFs at each alpha, and performed the same null tests as above. We show in Fig. 2D that when SA is low ($\alpha \leq 1.5$), eigenstrapping performs as expected, with an FPR of around 5%. However, as SA increases ($\alpha \geq 2$), the probability of significant correlations increases dramatically and eigenstrapping FPR increases to a maximum of 14.9% at $\alpha = 3$. Note that the best-performing null to date has an FPR at 13.5% when SA is brain-like ($\alpha \cong 3$), whereas eigenstrapping has a lower FPR at brain-like SA of 12.4%.

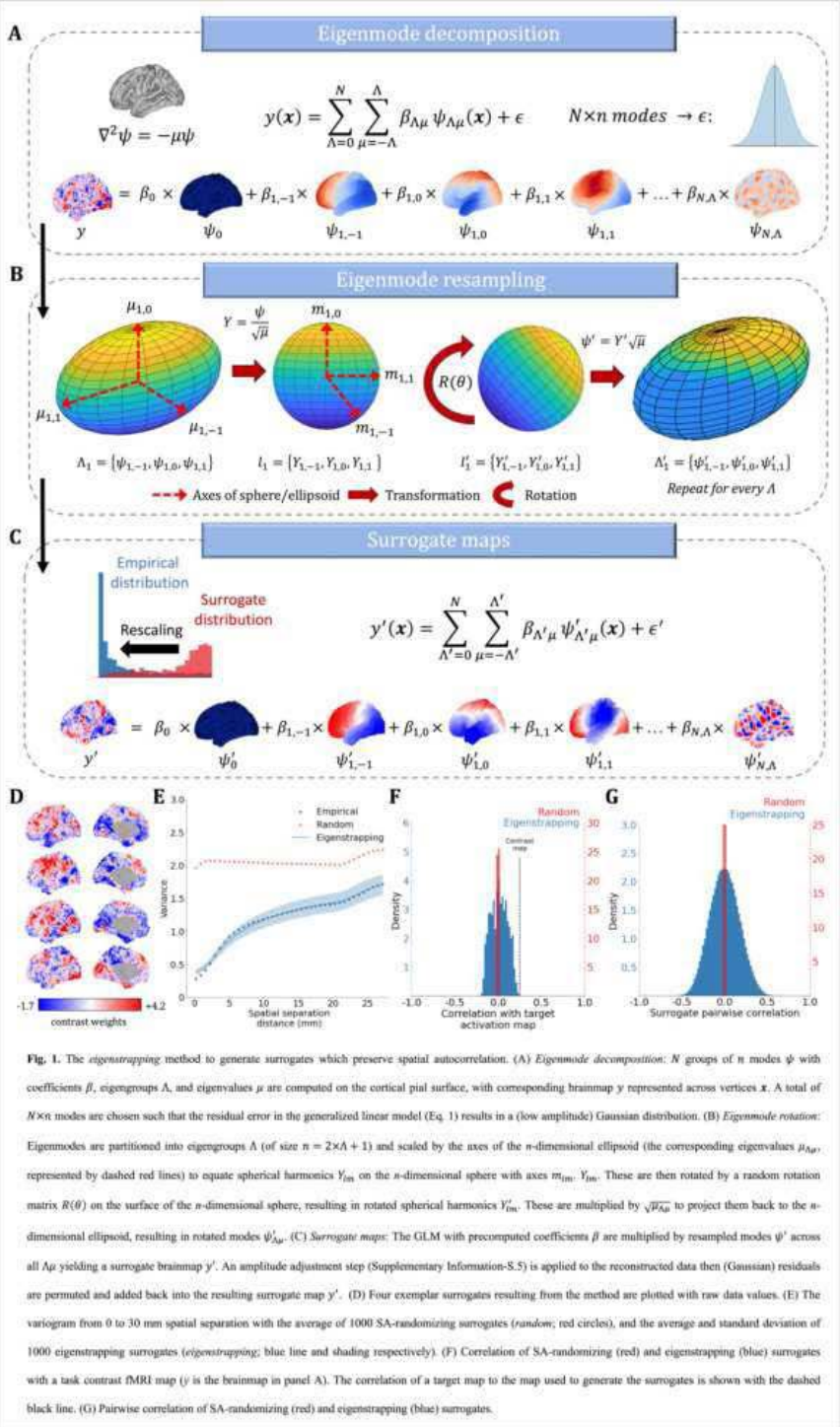

Fig. 1. The *eigenstrapping* method to generate surrogates which preserve spatial autocorrelation. (A) *Eigenmode decomposition*: N groups of n modes ψ with coefficients β, eigengroups Λ, and eigenvalues μ are computed on the cortical pial surface, with corresponding brainmap y represented across vertices $\boldsymbol{x}$. A total of $N \times n$ modes are chosen such that the residual error in the generalized linear model (Eq. 1) results in a (low amplitude) Gaussian distribution. (B) *Eigenmode rotation*: Eigenmodes are partitioned into eigengroups Λ (of size $n = 2\times\Lambda + 1$) and scaled by the axes of the n-dimensional ellipsoid (the corresponding eigenvalues $\mu_{\Lambda\mu}$, represented by dashed red lines) to equate spherical harmonics Y_{lm} on the n-dimensional sphere with axes m_{lm}. Y_{lm}. These are then rotated by a random rotation matrix $R(\theta)$ on the surface of the n-dimensional sphere, resulting in rotated spherical harmonics Y'_{lm}. These are multiplied by $\sqrt{\mu_{\Lambda\mu}}$ to project them back to the n-dimensional ellipsoid, resulting in rotated modes $\psi'_{\Lambda\mu}$. (C) *Surrogate maps*: The GLM with precomputed coefficients β are multiplied by resampled modes ψ' across all $\Lambda\mu$ yielding a surrogate brainmap y'. An amplitude adjustment step (Supplementary Information-S.5) is applied to the reconstructed data then (Gaussian) residuals are permuted and added back into the resulting surrogate map y'. (D) Four exemplar surrogates resulting from the method are plotted with raw data values. (E) The variogram from 0 to 30 mm spatial separation with the average of 1000 SA-randomizing surrogates (*random*; red circles), and the average and standard deviation of 1000 eigenstrapping surrogates (*eigenstrapping*; blue line and shading respectively). (F) Correlation of SA-randomizing (red) and eigenstrapping (blue) surrogates with a task contrast fMRI map (y is the brainmap in panel A). The correlation of a target map to the map used to generate the surrogates is shown with the dashed black line. (G) Pairwise correlation of SA-randomizing (red) and eigenstrapping (blue) surrogates.

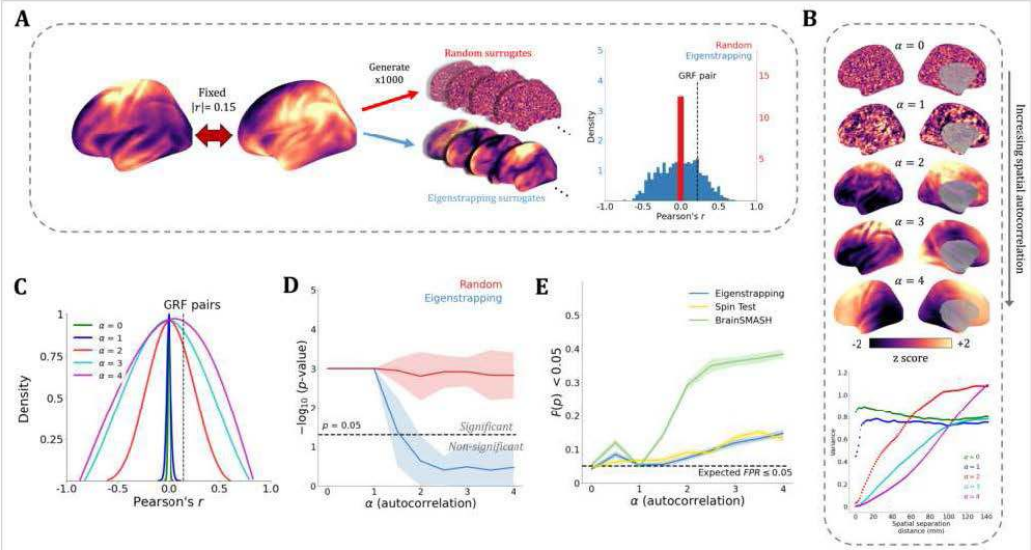

Fig. 2. Eigenstrapping control of false positives. (A) Gaussian random fields (GRFs) with varying SA are used to generate pairs of cortical maps with absolute Pearson correlation $|r| = 0.15 \pm 0.005$. Two GRF maps are plotted at $\alpha = 2$ alongside several random (red) and eigenstrapping (blue) exemplar surrogates. Rightmost panel shows exemplar histogram of SA-randomizing surrogate (red) and eigenstrapping surrogate (blue) correlations. Dashed line shows the ground-truth correlation of the GRF pair. (B) GRFs are plotted with α increasing from 0.0 to 4.0. Variograms derived from the generated maps demonstrate the increase in SA with increase in α (bottom panel). (C) Average null distributions of eigenstrapping for different levels of SA. (D) Mean and standard deviation of two-tailed p-values of 1000 surrogates (SA-randomizing: red; eigenstrapping: blue) per 9000 GRF pairs as a function of SA. Black dashed line shows significance at $p = 0.05$ ($-\log_{10}(p) = 1.3$). Null hypotheses are rejected above this line, not rejected below this line. (E) Each line indicates false positive rate (FPR) of null method as a function of spatial autocorrelation (Eigenstrapping: blue; Spin Test: yellow; BrainSMASH: green). Mean FPRs after 20 randomized sets shown in solid lines. Shaded areas around solid lines correspond to standard deviations. The black dashed line corresponds to expected FPR of $\leq 5\%$.

Conclusions: Resampling of geometric eigenmodes represents a novel method for non-parametric null hypothesis testing. Eigenstrapped nulls pass standard tests of null hypothesis testing including the control of false positives. Extensions include subcortical surrogate maps for cortico-subcortical connectivity gradients.

References

1. Burt JB, Helmer M, Shinn M, Anticevic A, Murray JD. Generative modeling of brain maps with spatial autocorrelation. NeuroImage. 2020;220:117038. doi:10.1016/j.neuroimage.2020.117038
2. Markello RD, Misic B. Comparing spatial null models for brain maps. NeuroImage. 2021;236:118052. doi:10.1016/j.neuroimage.2021.118052
3. Tian Y, Margulies DS, Breakspear M, Zalesky A. Topographic organization of the human subcortex unveiled with functional connectivity gradients. Nat Neurosci. 2020;23(11):1421-1432. doi:10.1038/s41593-020-00711-6
4. Borne L, Tian Y, Lupton MK, et al. Functional re-organization of hippocampal-cortical gradients during naturalistic memory processes. NeuroImage. Published online March 1, 2023:119996. doi:10.1016/j.neuroimage.2023.119996
5. Haak KV, Marquand AF, Beckmann CF. Connectopic mapping with resting-state fMRI. NeuroImage. 2018;170:83-94. doi:10.1016/j.neuroimage.2017.06.075
6. Marquand AF, Haak KV, Beckmann CF. Functional corticostriatal connection topographies predict goal-directed behaviour in humans. Nat Hum Behav. 2017;1(8):1-9. doi:10.1038/s41562-017-0146
7. Lehoucq RB, Sorensen DC, Yang C. ARPACK Users' Guide: Solution of Large-Scale Eigenvalue Problems with Implicitly Restarted Arnoldi Methods. SIAM; 1998.
8. Reuter M, Wolter FE, Shenton M, Niethammer M. Laplace-Beltrami Eigenvalues and Topological Features of Eigenfunctions for Statistical Shape Analysis. Comput Aided Des. 2009;41(10):739-755. doi:10.1016/j.cad.2009.02.007
9. Glasser MF, Sotiropoulos SN, Wilson JA, et al. The minimal preprocessing pipelines for the Human Connectome Project. NeuroImage. 2013;80:105-124. doi:10.1016/j.neuroimage.2013.04.127
10. Van Essen DC, Smith SM, Barch DM, et al. The WU-Minn Human Connectome Project: an overview. NeuroImage. 2013;80:62-79. doi:10.1016/j.neuroimage.2013.05.041
11. Cohen L. The generalization of the Wiener-Khinchin theorem. In: Proceedings of the 1998 IEEE International Conference on Acoustics, Speech and Signal Processing, ICASSP '98 (Cat. No.98CH36181). Vol 3. ; 1998:1577-1580 vol.3. doi:10.1109/ICASSP.1998.681753
12. Yura HT, Hanson SG. Digital simulation of an arbitrary stationary stochastic process by spectral representation. JOSA A. 2011;28(4):675-685. doi:10.1364/JOSAA.28.000675

Poster No 1857

Evaluating the Nonlinear Dynamics of Cerebrovascular Reactivity with Transcranial Doppler Ultrasound

Genevieve Hayes[1], Sierra Sparks[1], Joana Pinto[1], Daniel Bulte[1]

[1]*University of Oxford, Oxford, Oxfordshire*

Introduction: Cerebrovascular reactivity (CVR) describes the dilation and constriction of cerebral blood vessels in response to vasoactive stimuli such as altered PaCO2[1,2]. CVR can be reproducibly assessed using transcranial Doppler ultrasound (TCD) of the middle cerebral artery (MCA)[3]. The current gold-standard for TCD CVR measurement is a 2-point breath hold or gas challenge, however this assumes a linear blood velocity response, neglecting plateaus at the upper and lower bounds of the CVR response[4,5]. Notably, non-linear features of CVR may help distinguish different types of pathology[6,7]. Although advanced alternatives have been developed for CVR mapping using MRI, the high cost and complexity of these setups hinder their application in clinical settings. In this regard, the development of a method to assess a dynamic range of CVR that is feasible and affordable for wide clinical use is warranted[8]. We present a novel breathing protocol in combination with TCD measurements for mapping non-linear CVR.

Methods: Dynamics of the cerebral blood flow (CBF) response to a novel ramped breathing protocol was assessed in 11 healthy participants (5F, aged 33±9 years). Blood flow velocity (CBFv) in the left MCA was measured continuously using a clinical TCD (Doppler-BoxX, DWL). CBFv changes were assessed in response to a ramp protocol consisting of 3 repetitions of 5 deep breaths, followed by 30s of regular breathing on medical air, 40s of 5% CO2 gas, and 40s of 10% CO2 gas. Data processing and analysis were performed using custom Python scripts. A rolling mean of the MCA velocity (MCAv) was applied across the pulsatile MCAv signal. The end-tidal peaks in the CO2 and O2 time-courses were selected automatically. To account for measurement delay, a bulk shift was applied to each PETCO2 trace to maximise its cross-correlation with the mean MCAv signal. MCAvmean was normalised relative to the mean MCAv during the baseline period (breathing air) to account for any variations in probe angle relative to the MCA. To characterise CVR, a 4-parameter sigmoid was fit to the MCAvmean vs. PETCO2 as shown in the equation in Fig 2 where a is the minimum blood velocity, b is the slope of the linear region, c describes the PETCO2 value for the inflection point, and d is the maximum velocity[9].

Results: All 11 subjects successfully completed the ramp protocol. The timeseries of the MCAv, MCAvmean, CO2, and interpolated PETCO2 of a representative subject are presented in Fig 1. The normalised MCAvmean is plotted as a function of PETCO2 for the same subject in Fig 2 along with the sigmoidal fit. Across all subjects, the mean change in PETCO2 from hypocapnia (at the end of the deep breaths) to peak hypercapnia (at the end of the 10% CO2 period) was 28.9±4.7mmHg and the mean baseline PETCO2 was 26.0±5.1mmHg (t-stat>2.61 based on mean to max). The average increase in MCAvmean from hypocapnia to hypercapnia was 0.86±0.27% (t-stat>2.64) and the average baseline MCAvmean was 34.2±2.5cm/s. Changes in blood velocity and PETCO2 are highly correlated with all r-values>0.7 after cross correlation. The linear regression for all 11 subjects was statistically significant ($p<<0.001$, $0.7<r<0.9$), however varying-degrees of plateauing of the blood velocity at the top and bottom of the PETCO2 range is apparent for all subjects. The sigmoidal fit was found to account for the non-linear features in the response with a better residual sum of squares for the sigmoidal fit compared to the linear fit (0.3±0.2 vs. 0.5±0.3 respectively), but refinement of the model bounds is needed to ensure physiologically accurate parameters.

Conclusions: A 4-parameter sigmoidal fit showed a promising model for characterising the full CVR response which may be particularly useful for the identification of vascular pathology. Future work includes developing a more sophisticated non-linear model of CVR and extending the use of a cost-effective ramp protocol and non-linear modelling in MRI.

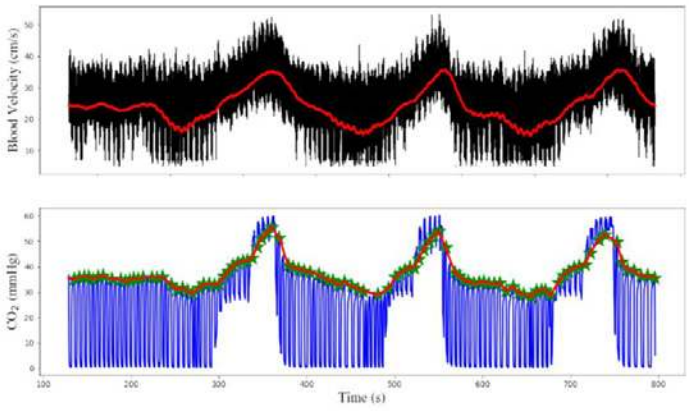

Figure 1: Timeseries of MCA blood velocity in cm/s (top plot, black) overlaid with the rolling mean velocity (red), and CO_2 in mmHg (bottom plot, blue) overlaid with the interpolated $PETCO_2$ peaks (red) for a representative subject (sub-009).

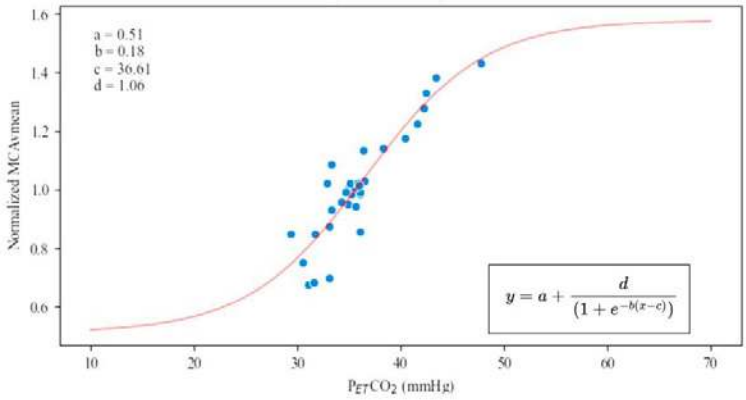

Figure 2: Scatter plot of MCAvmean, normalised with MCAvmean at baseline, as a function of $PETCO_2$ (mmHg), fit with a 4-parameter sigmoid (red line, equation in bottom right) for a representative subject (sub-009). The values for this subject are shown in the top left.

References

1. G. Hayes, J. Pinto, S. N. Sparks, C. Wang, S. Suri, and D. P. Bulte, "Vascular smooth muscle cell dysfunction in neurodegeneration," Front. Neurosci., vol. 16, 2022, doi: 10.3389/fnins.2022.1010164
2. J. Pinto, M. G. Bright, D. P. Bulte, and P. Figueiredo, "Cerebrovascular Reactivity Mapping Without Gas Challenges: A Methodological Guide," Front Physiol, vol. 11, 2021, doi: 10.3389/fphys.2020.608475
3. M. N. McDonnell, N. M. Berry, M. A. Cutting, H. A. Keage, J. D. Buckley, and P. R. C. Howe, "Transcranial Doppler ultrasound to assess cerebrovascular reactivity: reliability, reproducibility and effect of posture," PeerJ, vol. 1, p. e65, Apr. 2013, doi: 10.7717/peerj.65
4. G. D. Mitsis, P. N. Ainslie, M. J. Poulin, P. A. Robbins, and V. Z. Marmarelis, "Nonlinear Modeling of the Dynamic Effects of Arterial Pressure and Blood Gas Variations on Cerebral Blood Flow in Healthy Humans," in Post-Genomic Perspectives in Modeling and Control of Breathing, J. Champagnat, M. Denavit-Saubié, G. Fortin, A. S. Foutz, and M. Thoby-Brisson, Eds., in Advances in Experimental Medicine and Biology. Boston, MA: Springer US, 2005, pp. 259–265. doi: 10.1007/0-387-27023-X_39
5. F. H. R. van der Zande, P. a. M. Hofman, and W. H. Backes, "Mapping hypercapnia-induced cerebrovascular reactivity using BOLD MRI," Neuroradiology, vol. 47, no. 2, pp. 114–120, 2005, doi: 10.1007/s00234-004-1274-3
6. E. B. Ringelstein, C. Sievers, S. Ecker, P. A. Schneider, and S. M. Otis, "Noninvasive assessment of CO2-induced cerebral vasomotor response in normal individuals and patients with internal carotid artery occlusions.," Stroke, vol. 19, no. 8, pp. 963–969, 1988, doi: 10.1161/01.STR.19.8.963
7. C. Wang, G. Reid, C. E. Mackay, G. Hayes, D. P. Bulte, and S. Suri, "A systematic review of the association between dementia risk factors and cerebrovascular reactivity," Neurosci. Biobehav. Rev., vol. 148, p. 105140, 2023, doi: 10.1016/j.neubiorev.2023.105140
8. J. A. H. R. Claassen, R. Zhang, Q. Fu, S. Witkowski, and B. D. Levine, "Transcranial Doppler estimation of cerebral blood flow and cerebrovascular conductance during modified rebreathing," J. Appl. Physiol., vol. 102, no. 3, pp. 870–877, 2007, doi: 10.1152/japplphysiol.00906.2006
9. A. A. Bhogal et al., "Investigating the non-linearity of the BOLD cerebrovascular reactivity response to targeted hypo/hypercapnia at 7T," NeuroImage, vol. 98, pp. 296–305, 2014, doi: 10.1016/j.neuroimage.2014.05.006

Poster No 1859

Individualized Brain MRI Synthesis from a Single Scan: Applications to Aging and Alzheimer's Disease

Jingru Fu[1], Yuqi Zheng[2], Daniel Ferreira[3], Rodrigo Moreno[4]

[1]KTH, Huddinge, Stockholm, [2]KTH, Stockholm, stockholm, [3]Karolinska Institutet, Stockholm, Sweden, [4]KTH, Huddinge, stockholm

Introduction: Simulation of different future appearances of the MRI scans of an individual can provide relevant information to the physicians to select the most appropriate health care. In the last few years, different deep learning- (DL) based medical image generation (MIG) models have been proposed for this task. For example, generative adversarial networks (GANs) have been used for modeling the aging process and the progression of AD[1,2]. Unfortunately, these methods make important simplifications to reduce their computational costs, such as simulating a single slice per subject or downsampling original images. More importantly, GAN-based methods usually lack anatomical plausibility in generated images due to the absence of biologically informed constraints. As an alternative, we used diffeomorphic registration in[3] for this task. The main advantage of our approach compared to GANs is that the anatomical plausibility of the synthetic images is guaranteed by design. However, the main drawback of our method is that it requires two images per subject. In this study, we introduce Individualized Brain Synthesis (InBrainSyn), a MIG to synthesize high-resolution longitudinal MRI scans that faithfully replicate subject-specific neurodegeneration in AD and aging based on a single scan.

Methods: In this study, we used T1-weighted (T1w) MRI from OASIS-3 dataset[4]. Fig.1, shows the proposed pipeline. First, T1w MRI scans were preprocessed and partitioned into cognitive normal (CN) and AD cohorts. Second, AtlasGAN[5], a DL-based template generation method, was employed to produce age-resolved high-quality templates for both the CN and AD cohorts. AtlasGAN uses a diffeomorphic registration model that estimates a stationary velocity field (SVF) that is used to create a diffeomorphic deformation field through an integration layer and a spatial transformer network (STN)[6]. Third, registration was used to estimate SVFs between every follow-up template and age-matched template of the given subject image, independently for the two cohorts. Also, an SVF was estimated between the image of the subject and its age-matched template. Then, parallel transport[7] was used to translate the SVFs from the templates to the SVF computed for the specific subject. This way, the trajectory of the cohort is translated to create the subject-specific trajectory. Lastly, STN and integration were applied to the subject-specific SVFs to generate images that simulate morphological atrophy over time due to normal aging, AD, or both, depending on the used templates.

Results: We used 1,893 T1w MRI scans from 1,020 participants to train the cohort-level models and a separate test set of 473 MRI scans from 398 participants to evaluate it. Fig. 2 shows a comparison between the acquired images and the synthetic images generated using the CN template (InBrainSyn_CN), AD template (InBrainSyn_AD), and both (InBrainSyn_Inter). In the latter case, we use the CN template when the subject had a CDR=0 and the AD template for CDR>0. For comparison, we also show images generated with Simul@trophy[8]. As shown, InBrainSyn_Inter generates sharper images with a closer appearance to the ground truth. We also quantified the quality of synthetic images using two conventional similarity criteria, the structural similarity index (SSIM) and normalized cross-correlation (NCC). The results show the proposed InBrainSyn is superior to a baseline method in both the CN cohort (SSIM: 0.91 (±0.06) vs. 0.80 (±0.02); NCC: 0.98 (±0.02) vs. 0.94 (±0.01)) and the AD cohort (SSIM: 0.91 (±0.04) vs. 0.80 (±0.02); NCC: 0.98 (±0.01) vs. 0.93 (±0.01)).

Conclusions: The proposed framework can synthesize individualized images that simulate normal aging or AD courses from a single scan. The main advantages of the framework are that it is efficient, the generated images are anatomically plausible by design, and it is flexible to simulate transitions from a healthy state to AD, as shown in Fig.2.

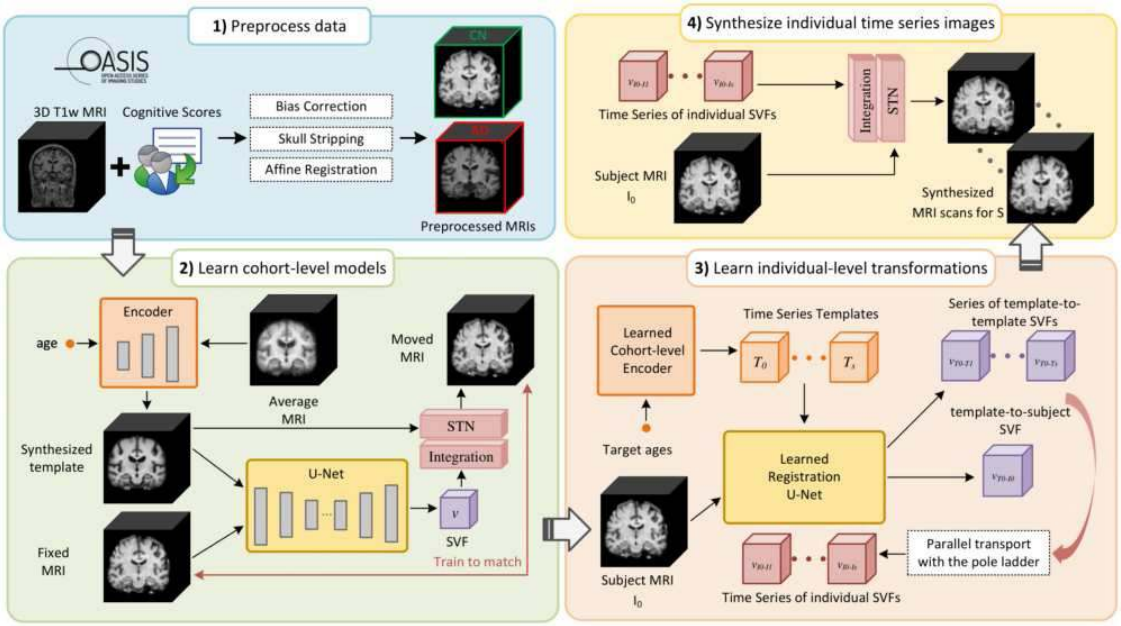

Fig.1: Pipeline of the proposed method.

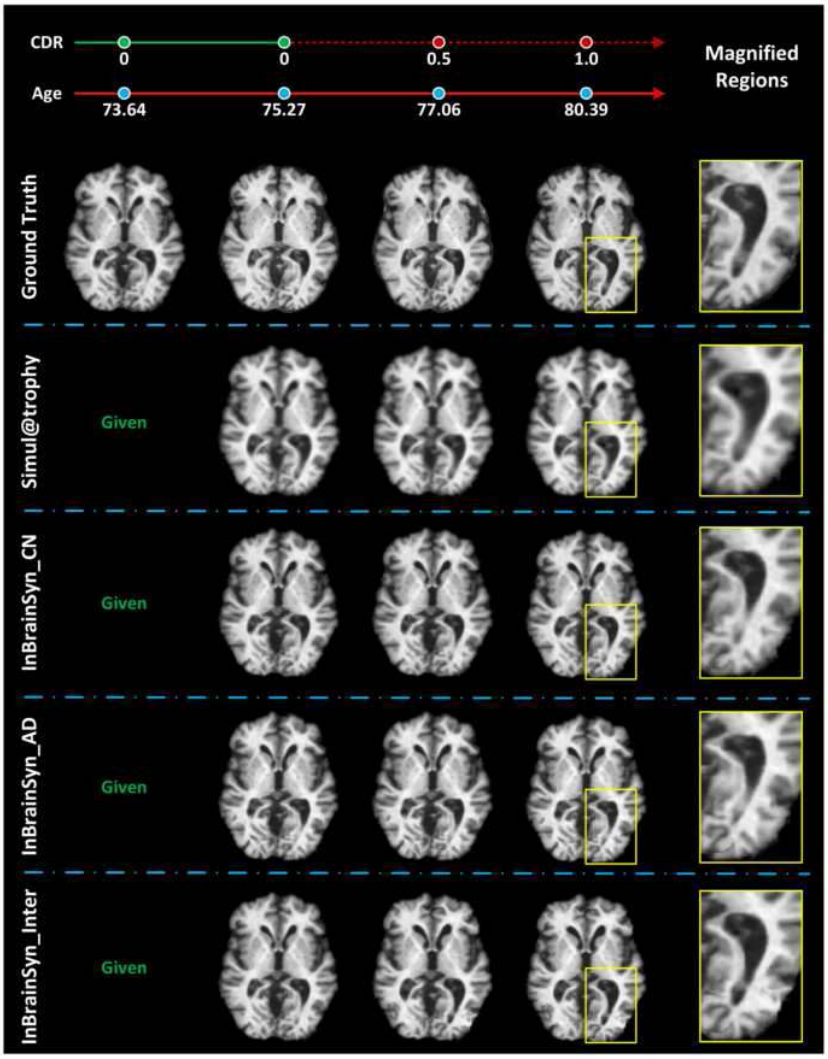

Fig.2: Qualitative comparison. The synthetic MRI scans for a longitudinal representative subject *OASIS30331* between *Simul@trophy* method and three variants of our approach for simulating AD transition case. Clinical Dementia Rating (CDR): CDR = 0 indicates normal cognitive function; CDR = 0.5 indicates very mild cognitive impairment; CDR = 1 indicates mild dementia; and CDR = 2 indicates moderate dementia. The CDR line indicates the two evolutions used in *InBrainSyn_Inter*, where the green solid line indicates CN evolution, and the red dashed line indicates AD evolution.

References

1. Wegmayr et al. (2019), 'Generative Aging of Brain MR-Images and Prediction of Alzheimer Progression', Proc. DAGM German Conference on Pattern Recognition 2019. LNCS, vol 11824. pp. 247–260. Springer, Cham
2. Ravi et al. (2022), 'Generative adversarial neuroimage nets for brain scan simulations: Application in ageing and dementia', Medical Image Analysis, vol. 75, pp. 102257
3. Fu et al. (2023) 'Fast three-dimensional image generation for healthy brain aging using diffeomorphic registration', Human Brain Mapping, vol. 44, no. 4, pp. 1289-1308
4. LaMontagne et al. (2019), 'Oasis-3: longitudinal neuroimaging, clinical, and cognitive dataset for normal aging and alzheimer disease', MedRxiv.
5. Dey et al. (2021), 'Generative adversarial registration for improved conditional deformable templates', Proc. IEEE/CVF International Conference on Computer Vision (ICCV 2021), pp. 3929–3941
6. Jaderberg et al. (2015), 'Spatial transformer networks', In Advances in Neural Information Processing Systems, vol. 28, Curran Associates, Inc.
7. Lorenzi and Pennec. (2014), 'Efficient parallel transport of deformations in time series of images: from schild's to pole ladder', Journal of Mathematical Imaging and Vision, vol. 50, pp. 5–17
8. Khanal et al. (2017), 'Simulating longitudinal brain mris with known volume changes and realistic variations in image intensity', Frontiers in neuroscience, vol. 11

Poster No 1860

FastSurfer-HypVINN: Automated sub-segmentation of the hypothalamus and adjacent structures on HiRes

Santiago Estrada[1,2], David Kügler[1], Emad Bahrami[1,3], Peng Xu[2], Dilshad Mousa[2], Monique Breteler[2,4], N. Ahmad Aziz[2,5], Martin Reuter[1,6,7]

[1]AI in Medical Imaging, German Center for Neurodegenerative Diseases (DZNE), Bonn, NRW, Germany, [2]Population Health Sciences, German Center for Neurodegenerative Diseases (DZNE), Bonn, NRW, Germany, [3]Computer Science Deparment, University of Bonn, Bonn, NRW, Germany, [4]IMBIE, University of Bonn, Bonn, NRW, Germany, [5]Departmet of Neurology, University of Bonn, Bonn, NRW, Germany, [6]A.A. Martinos Center for Biomedical Imaging, Massachusetts General Hospital, Boston, MA, [7]Department of Radiology, Harvard Medical School, Boston, MA

Introduction: The hypothalamus is crucial in regulating a broad range of physiological, behavioral, and cognitive functions. Despite its essential role, only a few small-scale neuroimaging studies have investigated its substructures, primarily due to the lack of fully automated segmentation tools to address the scalability and reproducibility issues of manual segmentation. While a prior attempt to automatically sub-segment the hypothalamus with a neural network showed promise for 1.0 mm isotropic T1-weighted MRI[1], there is a need for an automated tool to sub-segment also high-resolutional (HiRes) MR scans (i.e. sub-millimeter), as they are becoming widely available. To this end, we recently proposed HypVINN[2], a fully automated deep learning method for the sub-segmentation of the hypothalamus and its adjacent structures on 0.8 mm isotropic T1-weighted (T1w) and T2-weighted (T2w) brain MR images that is robust to missing modalities (i.e., hetero-modal segmentation).

Methods: HypVINN utilizes our novel hetero-modal Voxel-Size Independent Neural Network (HM-VINN) architecture at its core. The HM-VINN architecture allows the segmentation of multi-resolution scans in a single model. Furthermore, it also includes the capability of a hetero-modal model, permitting flexibility in the input modalities at inference time (i.e., segmentations can be generated using only a T1w or only a T2w or a T1w/T2w image pair). To train our tool, 44 manually segmented 0.8 mm isotropic scans from the Rhineland Study were used. Manual annotations were performed for eleven hypothalamic subregions and thirteen adjacent structures by an experienced rater using co-registered T1w and T2w images, as presented in Figure 1. HypVINN is extensively validated in terms of segmentation accuracy (dice similarity coefficient (Dice), volume similarity (VS), 95% Hausdorff distance (HD95)) against an unseen test-set, generalizability to 1.0 mm isotropic MRI scans from the UK Biobank (UKB), and in-session test-retest reliability (intra-class correlation (ICC), and VS). Furthermore, we tested the sensitivity of HypVINN to replicate known hypothalamic volume effects with respect to age and sex in two random subsets of the Rhineland Study (RS, n=463) at 0.8mm (HiRes) and the UK Biobank (UKB, n=535) at 1.0 mm.

Results: HypVINN exhibits high segmentation performance both for standalone T1w images (Dice = 0.791, VS = 0.898, HD95 = 1.110 mm) as well as for T1w/T2w image pairs (Dice = 0.795, VS = 0.901, HD95= 1.086 mm). The proposed method can generalize remarkably well (Dice = 0.707, VS = 0.846, HD95= 1.718 mm) to 1.0 mm T1w scans from the UKB, an independent dataset never encountered during training with different acquisition parameters and demographics. Furthermore, HypVINN has an excellent test-retest agreement (ICC(A,1) > 0.95 and VS > 0.95) between in-session volume estimates. Finally, for the age and sex analysis, we observe that the global hypothalamic volume estimates and most sub-structures are negatively associated with age in both the RS and UKB subsets. Moreover, men have larger hypothalamic volumes than women, even after correction for head size (see Figure 2).

Conclusions: HypVINN is the first hetero-modal deep learning method for hypothalamic sub-segmentation and the segmentation of other adjacent structures, such as the hypophysis, epiphysis, and major structures of the central optic system. In contrast to the only other contemporary automated method[1], our tool offers a more detailed parcellation of the hypothalamus. Furthermore, it can accurately generate segmentations from T1w and T2w MR images at isotropic resolutions of 0.8 mm or 1.0 mm. Finally, HypVINN will be integrated into the FastSurfer neuroimaging software suite, providing a user-friendly alternative for the reliable assessment of hypothalamic imaging-derived phenotypes in the neuroimaging community.

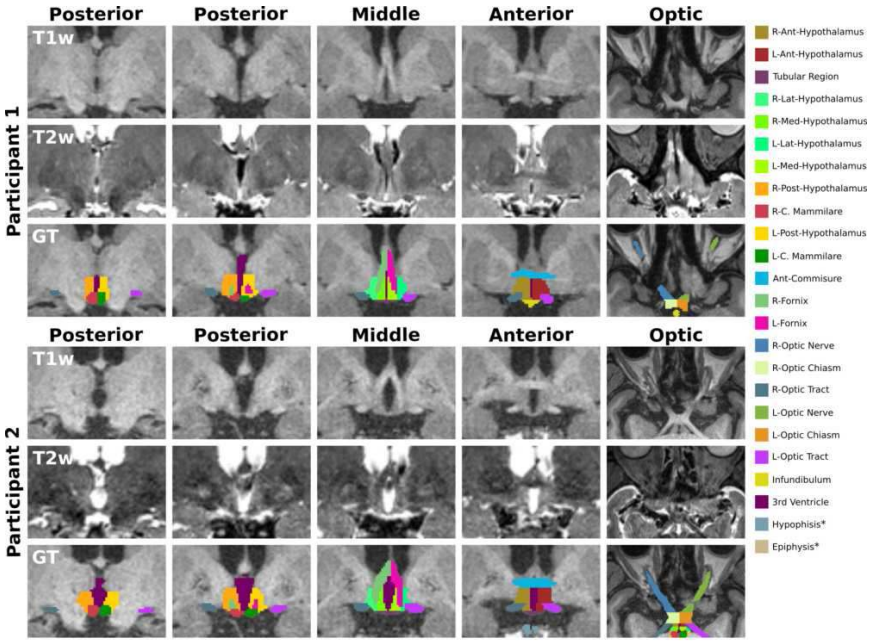

Figure 1. T1-weighted (T1w) and T2-weighted (T2w) images and ground truth (GT) from two participants. The proposed manual segmentation scheme is composed of twenty-four structures divided into three major regions: 1) hypothalamic (anterior, middle, and posterior), 2) optic, and 3) others. The color lookup table* for all structures is presented on the left. *Structures are not visible in the presented snapshots.

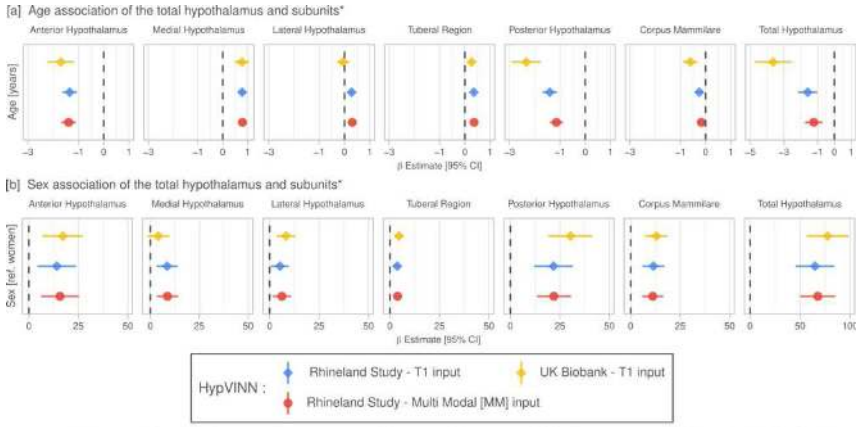

Figure 2. Hypothalamic volume associations with age (a) and sex (b) in participants from the Rhineland Study (n=457) and UK Biobank (N=520) for HypVINN. Age and sex effects on hypothalamic volume estimates in the Rhineland Study from HypVINN, independent of the provided MRI input, follow the same direction trend. Furthermore, our model replicates previous sex findings in both datasets, corroborating the stability and sensitivity of our method. Note: *Effects are obtained after accounting for head size (eTIV) and modality sequence (only Rhineland Study).

References

1. Billot, B., Bocchetta, M., Todd, E., Dalca, A. V., Rohrer, J. D., & Iglesias, J. E. (2020). Automated segmentation of the hypothalamus and associated subunits in brain MRI. Neuroimage, 223, 117287.
2. Estrada, S., Kügler, D., Bahrami, E., Xu, P., Mousa, D., Breteler, M.M.B., Aziz, N.A., & Reuter, M. (2023). FastSurfer-HypVINN: Automated sub-segmentation of the hypothalamus and adjacent structures on high-resolutional brain MRI. Imaging Neuroscience, Advance Publication. https://doi.org/10.1162/imag_a_00034
3. Henschel, L., Conjeti, S., Estrada, S., Diers, K., Fischl, B., & Reuter, M. (2020). Fastsurfer-a fast and accurate deep learning based neuroimaging pipeline. NeuroImage, 219, 117012.

Poster No 1861

From PubMed to a DataFrame: An ecosystem for mining the biomedical literature

Kendra Oudyk[1], Jérôme Dockès[2], Mohammad Torabi[1], Alejandro De La Vega[3], Jean-Baptiste Poline[1]

[1]McGill University, Montreal, Quebec, [2]INRIA, Paris, Paris Region, [3]University of Texas at AUstin, Austin, TX

Introduction: Meta-research is important for summarizing results (as in meta-analyses and reviews) and for pointing out issues with different aspects of research, like methods, authorship, and publishing. Meta-research should be 'living' because the

scientific literature is continuously changing. Further, with thousands of publications each year, we need systematic or (semi-) automated approaches for indexing, aggregating, and summarizing the literature. An important challenge to meta-research projects is the construction of an appropriate dataset (i.e., set of articles). One must download a large number of articles and extract the relevant text, metadata, and often the stereotactic coordinates of results. Ideally this would be done automatically, but doing this well is a software-engineering problem that most researchers are not prepared for. We facilitate living meta-research by providing tools that are as reproducible, scalable, and accessible as possible. Here we introduce a set of inter-operable tools that help with collecting and labelling articles.

Methods: Figure 1 shows the tools that we have created and which stage(s) of a meta-research project they apply to. Pubget is a command-line tool for downloading and processing articles from PubMed Central. It builds upon the code used to create NeuroQuery. Given a search query or a list of PMCIDs, it provides the matching articles in their original XML format, in addition to CSV files containing: (i) metadata such as authors or publication year, (ii) the full text, and (iii) the activation coordinates. Pubget can extract term-frequency features, and run NeuroQuery's or NeuroSynth's analyses. It can prepare a NiMARE (nimare.readthedocs.io) dataset, making a wide range of meta-analysis methods easy to apply. It also can be extended with plugins. Labelbuddy is a simple and lightweight desktop application for labelling texts, which manages annotations with a regular file (a SQLite database). Pubget's output can directly be imported into labelbuddy. Labelbuddy imports and exports its data to a simple JSON format, and offers a command-line interface, making it well-suited for projects organized around a git repository. An example repository containing over 1,800 annotations can be found at https://neurodatascience.github.io/labelbuddy-annotations/. Pubextract is a Python package containing plugins for pubget. Its functions can be called from the command line along with the code to download the papers. This enables a researcher to, for example, automatically extract features from the set of articles they download, such as author genders and locations, demographic information like the number and ages of participants, as well as which papers contain certain user-provided terms (e.g., "FSL" or "UKBioBank").

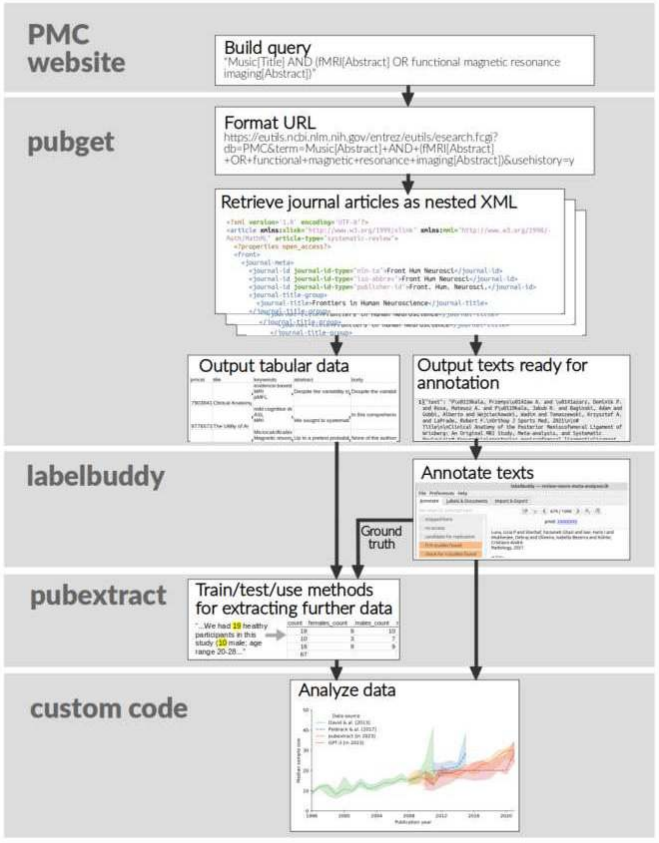

Results: To illustrate the use of this ecosystem, we replicated and extended the investigation of sample sizes from Poldrack et al., (2017). We downloaded articles with pubget, designed a heuristic to extract participant counts and demographics, and validated it on 100 articles that we annotated with labelbuddy. We further compared this heuristic approach to extraction of sample sizes by GPT-3.5 (Figure 2A). As shown in Figure 2C, the median sample size has continued to increase since 2015. We also ran pubget for a query matching a larger number of articles (over 9K), and we produced meta-analytic maps obtained with pubget's --fit_neurosynth option and from neurosynth.org. Results are similar for frequent terms, but for rare terms, pubget's use of the full text produces more powerful analyses.

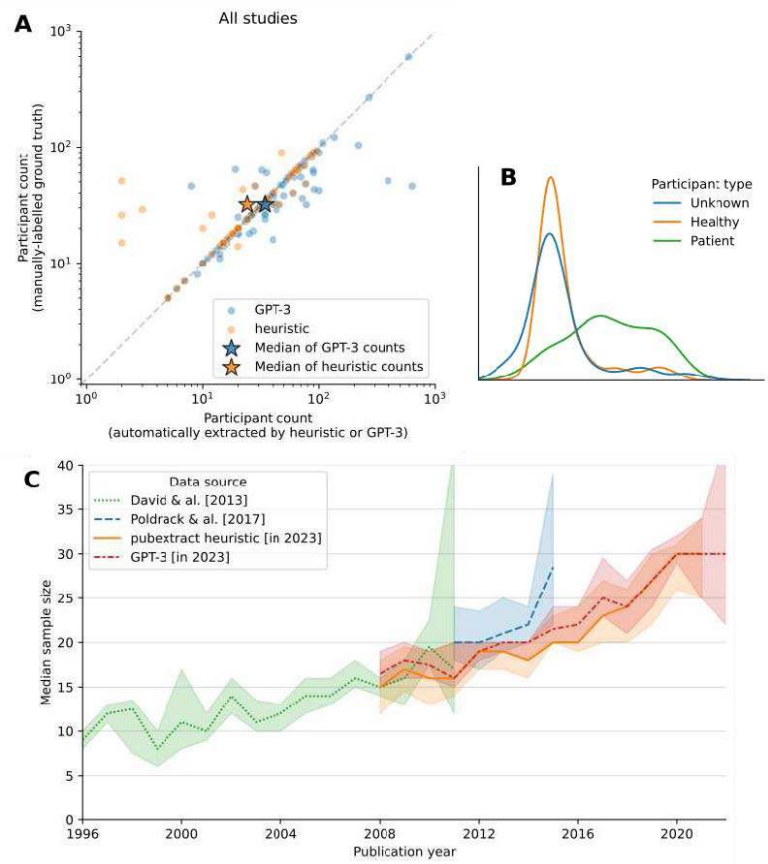

Conclusions: We facilitate downloading, annotating and preparing articles for meta-research in a way that is highly reproducible, scalable, and accessible. This can be key for living meta-research that furthers our understanding of an ever-increasing body of literature. We hope that discussions at the OHBM 2024 meeting will help us tailor them to the needs of the neuroimaging community.

References

1. Poldrack, R. A. et al. (2017). Scanning the horizon: towards transparent and reproducible neuroimaging research. Nature reviews neuroscience, 18(2), 115-126.

Poster No 1862

Nothing but lies: Constructing specific neural predictors of deception

Sangil Lee[1], Runxuan Niu[2], Lusha Zhu[2], Andrew Kayser[3], Ming Hsu[1]

[1]University of California, Berkeley, Berkeley, CA, [2]Peking University, Beijing, Beijing, [3]University of California, San Francisco, San Francisco, CA

Introduction: A fundamental challenge in brain-based lie detection is to distinguish between signals of deception and confounding signals from co-occurring processes. Absent this distinction, a lie detector may well flag innocent but confounded behaviors as deceptive. First, we show that existing methods for constructing neural predictors of deception can lead to overgeneralization, in which the predictors detect not only lies but also innocent behaviors. Second, we identify a general approach to construct a statistical predictor that, by explicitly accounting for a control task, removes confounding signals while predicting the task of interest. Third, we show that this approach can generate a neural predictor of deception that does not overgeneralize, supporting the possibility that signals intrinsic to deception may exist.

Methods: We designed a pair of isomorphic signaling games that differed only in the extent to which players' actions could be assigned a truth value. In both games the participant (the sender) is presented with two potential allocations of monetary gains for themselves and a counterpart (the receiver). On each trial, one outcome provides a larger payoff to the sender, while the other provides a larger payoff to the receiver. Critically, in the deception condition, senders must choose between two messages that are verifiably truthful or false (e.g., "Option A will earn you more money than Option B"). In contrast, in the

preference condition, senders and receivers are faced with identical payoffs, but the senders' messages do not have a truth value (e.g., "I prefer that you choose Option A"). Participants are aware that as the sender, they can see the options but cannot make the choice between them, while the receiver cannot see the options but is responsible for the choice. To establish whether the deceptive choices could be predicted by neural data, we used a leave-one-subject-out cross-validation using the T-PLS whole-brain algorithm to train neural predictors of deception on n-1 subjects and to predict the choices of the left-out subject. Using the criterion for discriminant validity, we also tested the cross-task generalizability of the neural predictor derived from the deception task. Specifically, the predictor that had previously been trained on n-1 subjects in the deception condition was tested on the left-out subject's preference condition.

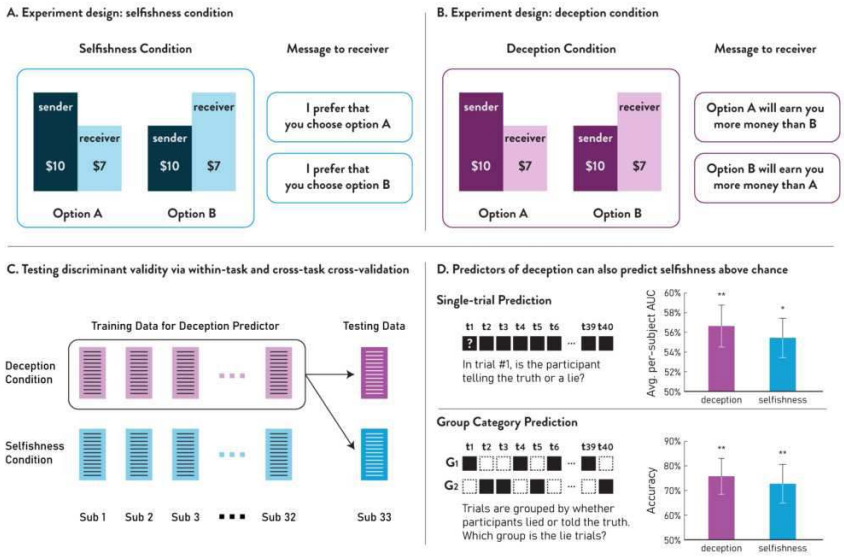

Results: Using whole-brain MVPA, the average prediction accuracy was 75.8% for deception, which was significantly above chance at 50% (t(32) = 3.40, p = 0.0018). However, we also found strong evidence for overgeneralization, as the neural predictor of deception was also able to predict honest but selfish behavior in the preference condition at 72.7% (t(32) = 2.89, p = 0.0069). Accordingly, we propose a dual-goal tuning approach that eliminates this overgeneralization in expectation. Our approach uses a Gram-Schmidt procedure to orthogonalize the predictor with regards to the nuisance signal such that, critically, the inner product between the predictor and the nuisance signal map is expected to be zero for out-of-sample rather than in-sample prediction. To achieve this goal, we dedicate a separate hyperparameter that is tuned to achieve out-of-sample orthogonality, while the prediction algorithm's hyperparameters are tuned to maximize prediction performances, thereby implementing a dual-goal approach. Using the dual-goal tuning approach, our new prediction performances are specific to deception as it can significantly predict deceptive choices at 69.7% (t(32) = 2.42, p = 0.021), but not selfish choices in the preference condition (45.5 %, t(32) = -0.52, p = 0.61).

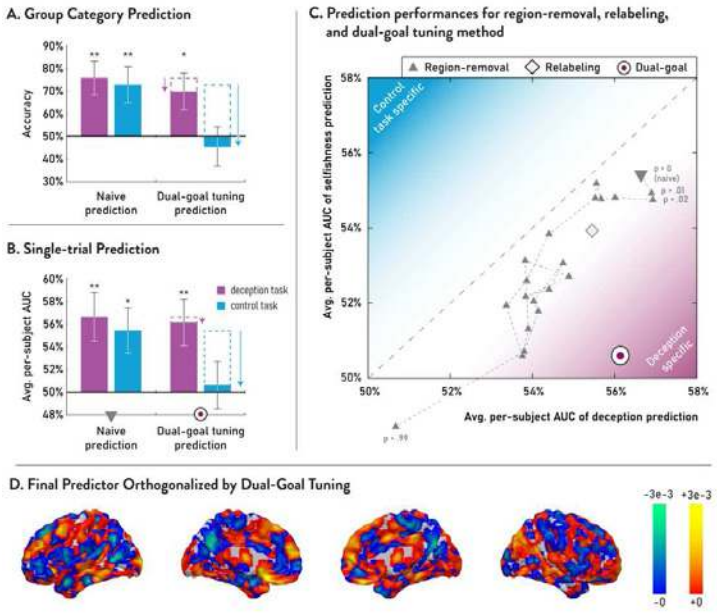

Conclusions: Beyond lie detection, studies have argued for the distinctiveness of mental processes by showing an absence of overgeneralization across datasets with naïve MVPA predictors. However, our results suggest that even when there is a considerable amount of overgeneralization, the underlying mental processes may be distinguishable.

Poster No 1863

Disentangling longitudinal dynamics in schizophrenia using longitudinal normative modelling

Barbora Rehak Buckova[1], Charlotte Fraza[2], Antonín Škoch[3], Marián Kolenič[4], Christian Beckmann[5], Filip Španiel[6], Jaroslav Hlinka[7], Andre Marquand[8]

[1]Radboud UMC, Nijmegen, Netherlands, [2]Donders Institute for Brain, Cognition and Behaviour, Nijmegen, Netherlands, [3]National Institute of Mental Healt of the Czech republic, Klecany, Czech Republic, [4]National Institute of Mental Health of the Czech Republic, Klecany, Czech Republic, [5]Donders Institute for Brain, Cognition, and Behavior, Radboud University Nijmegen, Nijmegen, NL, Nijmegen, Netherlands, [6]National Institue of Mental Health of the Czech Republic, Klecany, Czech Republic, [7]Institute of Computer Science of the Czech Academy of Sciences, Prague, Czech Republic, [8]Radboud University Nijmegen, Nijmegen, Gelderland

Introduction: Despite the raising interest in the analysis of longitudinal dynamics in healthy brain development as well as the course of neuronal and psychiatric diseases, there has not been a substantial progress in the development of methods designed for longitudinal data analysis. We decided to address this issue by introducing a dynamical element into the state-of-the-art normative models creating the first of its kind framework for longitudinal analysis with normative models. We showcase this method on the analysis of two longitudinal samples of schizophrenia subjects. We chose the schizophrenia sample as despite the intensive research into this area, we are still lacking reliable objective neuroimaging biomarkers, which would enable effective outcome prediction and targeted treatment of this condition, in which over 25% of patients do not respond to traditional medication. Thus, an insight into the longitudinal changes is timely.

Methods: We present a method of longitudinal normative modelling which uses the power of pre-trained cross-sectional normative models and combines it with an estimate of longitudinal change to introduce a dynamical element. Using freely available normative models pretrained on over 58,000 samples (Rutherford 2022) and a control cohort for estimating healthy change (Rehak Buckova 2023), we derive a metric known as the z-diff score. This score, the longitudinal analogue to a standard cross-sectionally computed z-score, quantifies the probability of the observed change being statistically significant. We applied this method to two longitudinal datasets of schizophrenia subjects. The first dataset involved a one-year follow-up of 98 young adults with first episode psychosis from the National Institute of Mental Health in the Czech Republic (Rehak Buckova 2023) (Fig. 1A), and the other from the NUSDAST dataset (Wang 2013), featuring 48 adults with schizophrenia and a two-year follow-up (Fig. 1A).

Results: Cross-sectionally, both datasets showed comparable patterns of decreased z-scores in cortical thickness across multiple grey matter regions. This effect was more pronounced in patients in the early stages of psychosis, aligning with recent studies indicating a lag in neurodevelopmental trajectories in schizophrenia followed by a period of normalisation (Fig. 1 B)(Sheffield 2018, Milan 2016). Longitudinally, distinct dynamics emerged in each dataset. While the first episode psychosis sample exhibited higher cortical thickening compared to the general population, the NUSDAST cohort showed cortical thinning in time, although the changes were not statistically significant after correcting for multiple comparisons (Fig. 1C). It is also possible that the size and direction of the changes observed in NUSDAST sample might have been affected by the composition of controls, which were not matched to the patients in terms of age, making it more challenging to reliably estimate the changes. Specifically, adapting the cross-sectional normative models using healthy data with a young and narrow age range makes it difficult to get good estimates of healthy variation across the lifespan, which in turn impacts on your ability to detect disorder-related effects.

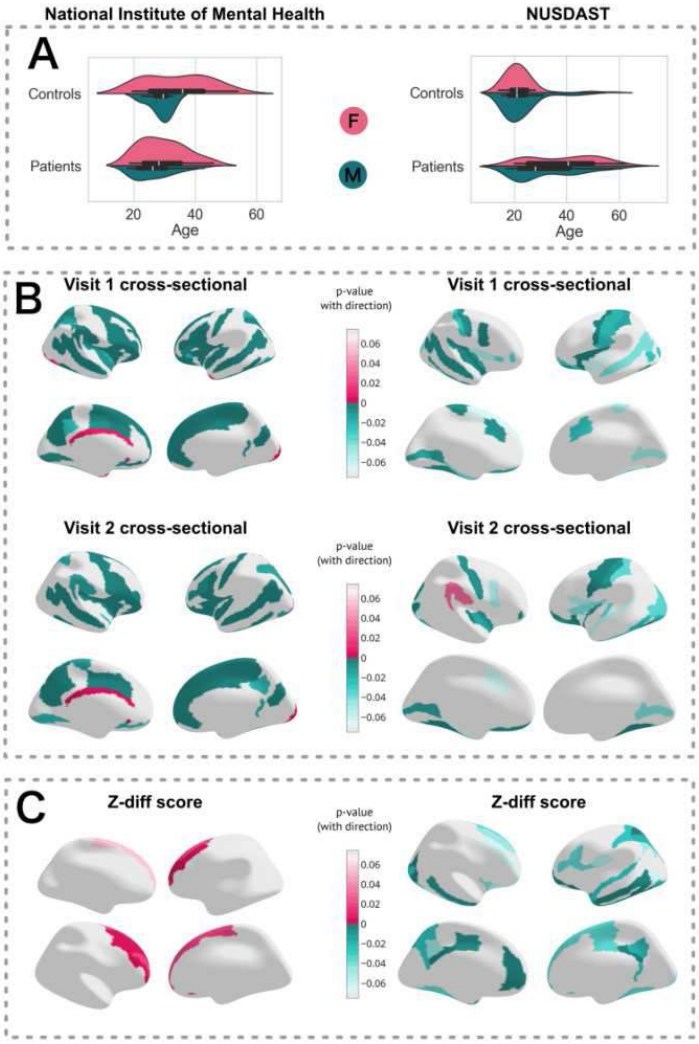

Conclusions: In conclusion, our framework for longitudinal analysis, addresses the critical gap in methods for studying longitudinal brain development. Applying this method to schizophrenia datasets revealed distinct longitudinal patterns in the changes of cortical thickness. The first episode psychosis sample showed increased thickness, while the NUSDAST cohort demonstrated thinning, though not statistically significant after correction for multiple comparisons. Our findings stress the importance of age-matched controls in for reliable longitudinal analyses and offer insights into neurodevelopmental processes in schizophrenia.

References

1. Millan, M. (2016), “Altering the course of schizophrenia: progress and perspectives”, Nature Reviews Drug Discovery, vol. 15, no. 7, pp. 485-515.
2. Rehak Buckova, B. (2023), “Using normative models pre-trained on cross-sectional data to evaluate longitudinal changes in neuroimaging data.” bioRxiv.
3. Rutherford, S. (2022), “Charting brain growth and aging at high spatial precision”, elife, no. 11, pp. e72904.
4. Sheffield, J. M. (2018), “Cognitive deficits in psychotic disorders: a lifespan perspective”, Neuropsychology review, vol. 28, pp. 509-533.
5. Wang, L. (2013), “Northwestern University schizophrenia data and software tool (NUSDAST)”, Frontiers in neuroinformatics, vol. 7.

Poster No 1865

Multi- and Optional-Input Neural Network Architecture for Differential Dementia Detection

Matthew Leming[1], Hyungsoon Im[1]

[1]*Massachusetts General Hospital, Boston, MA*

Introduction: The translation of diagnostic AI models to real-world clinical settings is an area of promise, but the translation of such models to heterogeneous and irregular electronic health record data is a difficult task. One reason for this is the irregular formatting of patient records, which often have varying numbers of imaging and non-imaging data that may be useful for

disease detection, but which cannot be encoded in models that require a fixed format. To overcome this, we present a multi- and optional-input neural network capable of encoding different types of brain MRIs as well as demographic information, which uses an adversarial component to regress confounding factors in imaging data. We apply this to the detection of dementia in multimodal brain imaging data in the Mass General Brigham System. We show that this model is capable of whole-patient differential detection of Alzheimer's, Frontotemporal, Vascular, and Lewy Body in real-world data, and that more data provides better outcomes. In single-modality tests, our regression method leads to better results, indicating that deep learning incentivizes models to focus on disease biomarkers rather than combinations of different modalities.

Methods: We employed a neural network in Pytorch that can take up to 14 three-dimensional images, resized to 96x96x96 arrays, as input, along with encoded demographic information, and output a prediction about the set of data. The model receives a batch of N images that are treated as independent by the encoder and translated to an N x 512 array. These are then padded with a (14-N) x 512 zero array to make a consistently-sized 14xN array. The 14 vectors are then shuffled in a random order and fed into a classifier. In effect, this enables the model to take anywhere from 1 to 14 images, plus two pieces of demographic information (sex and ethnicity) as input. A diagram of this can be seen in Figure 1. Data consists of patient data from Mass General Brigham, separated into Massachusetts General Hospital as a training set and Brigham and Women's and miscellaneous data as a test set. In this dataset, patients often had multiple brain images from one or multiple scanning sessions. ICD-10 codes and medication history were used to determine the presence of four different types of dementia: Alzheimer's, Lewy Body, vascular, and frontotemporal. A confound regression method was used to mask technical and demographic confounds, in a similar method to basic generative adversarial networks. Confounds regressed include sex, age, imaging modality, scanning sequence, MRI modality, image angle, and ethnicity. This translated images into an intermediary feature vector, prior to their being fed into the classifier.

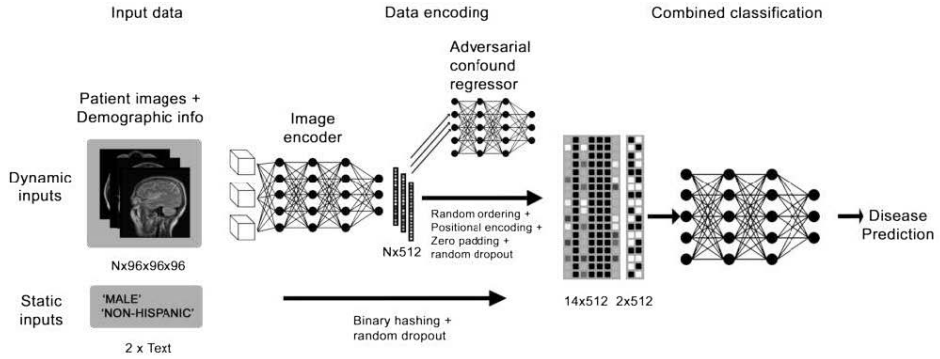

Results: Figure 2 shows the results of each task. Due to differing numbers of data in our dataset for each type of disease, only certain portions of the training set could be used effectively. We also show the effect of varying the number of datapoints input into the model on accuracy, establishing that combining data is a useful initiative, as well as the effects of including static input data on accuracy. Finally, we show the effects of confound regression when only one modality (T1 Axial MRI, the most common type of image) is input in the model, which shows the positive effects of confound regression in the image encoder.

		Vascular (F01)	Alzheimer's (G30)	Frontotemporal (G31.0)	Lewy Body (G31.83)	None
Images in training set (MGH)		905	2149	247	243	60205
Images in test set (BWH/other)		937	1768	203	357	92846
No. unique patients in test sample (BWH/other)		125	258	11	60	459
With confound regression	All modalities (up to 14)	0.810	0.717	0.897	0.940	0.856
	All modalities (up to 10)	0.818	0.670	0.831	0.922	0.830
	All modalities (up to 8)	0.836	0.668	0.832	0.820	0.857
	All modalities (up to 6)	0.808	0.668	0.832	0.820	0.857
	All modalities (up to 4)	0.764	0.627	0.782	0.787	0.839
	All modalities (up to 2)	0.660	0.555	0.614	0.684	0.806
	All modalities (up to 1)	0.568	0.530	0.530	0.493	0.611
	T1 Ax Only (up to 14)	0.699	0.661	0.582	0.657	0.711
Without confound regression	All modalities (up to 14)	0.829	0.684	0.962	0.936	0.830
	All modalities (up to 10)	0.833	0.718	0.917	0.944	0.846
	All modalities (up to 8)	0.825	0.682	0.832	0.937	0.831
	All modalities (up to 6)	0.825	0.714	0.867	0.879	0.846
	All modalities (up to 4)	0.797	0.632	0.838	0.810	0.852
	All modalities (up to 2)	0.696	0.485	0.695	0.497	0.829
	All modalities (up to 1)	0.514	0.478	0.477	0.451	0.532
	T1 Ax Only (up to 14)	0.560	0.526	0.942	0.560	0.619

Conclusions: In this work, we have presented a unique model that is adapted to the unstructured inputs of real-world clinical data. We have shown that these deep learning models are capable of distinguishing between patients with different types of dementia cross-site, and that more data per patient aids in the end diagnosis. While combinations of different modalities may bias the diagnostic results with confounds in many cases, a particularly promising result of the regression method is the improved performance with the method when using one modality in the diagnosis, indicating that the regression incentivizes the model to focus on true disease biomarkers.

References

1. Apostolopoulos, I.D. (2021), 'Multi-input deep learning approach for Cardiovascular Disease diagnosis using Myocardial Perfusion Imaging and clinical data', Physica Medica, vol. 84, pp. 168–177.
2. Bron, E.E. (2015), 'Standardized evaluation of algorithms for computer-aided diagnosis of dementia based on structural MRI: the CADDementia challenge', Neuroimage, vol. 111, pp. 562–579.
3. Gollub, R.L. (2021), 'Use of Medical Imaging to Advance Mental Health Care: Contributions from Neuroimaging Informatics', Mental Health Informatics: Enabling a Learning Mental Healthcare System. 1st ed, pp. 191–216.
4. Klöppel, S. (2012), 'Diagnostic neuroimaging across diseases', Neuroimage, vol. 61, pp. 457–463.
5. Leming, M. (2022), 'Adversarial confound regression and uncertainty measurements to classify heterogeneous clinical MRI in Mass General Brigham', PLOS One, vol. 18, no. 3, pp. e0277572.
6. Leming, M. (2022), 'Construction of a confounder-free clinical MRI dataset in the Mass General Brigham system for classification of Alzheimer's disease', Artificial Intelligence in Medicine, vol. 129.
7. More, S. (2021) 'Confound Removal and Normalization in Practice: A Neuroimaging Based Sex Prediction Case Study', Machine Learning and Knowledge Discovery in Databases, vol. 12461, pp. 3—18.
8. Thung, K.H. (2017), 'Multi-stage Diagnosis of Alzheimer's Disease with Incomplete Multimodal Data via Multi-task Deep Learning', Deep Learning in Medical Image Analysis and Multimodal Learning for Clinical Decision Support: Lecture Notes in Computer Science, vol. 10553.
9. Wen, J. (2020), 'Convolutional Neural Networks for Classification of Alzheimer's Disease: Overview and Reproducible Evaluation', Medical Image Analysis, vol. 63.
10. Yu, M. (2018), 'Statistical harmonization corrects site effects in functional connectivity measurements from multi-site fMRI data', Human Brain Mapping, vol. 39, pp. 4213–4227.
11. Zhao, Q. (2020), 'Training confounder-free deep learning models for medical applications', Nature Communications, vol. 11.

Poster No 1866

In-vivo high-resolution χ-separation (chi-separation) at 7T

Jiye Kim[1], Minjun Kim[1], Sooyeon Ji[1], Kyeongseon Min[1], Seong-Gi Kim[2,3], Jongho Lee[1]

[1]Department of Electrical and Computer Engineering, Seoul National University, Seoul, Korea, Republic of, [2]Center for Neuroscience Imaging Research (CNIR), Institute for Basic Science (IBS), Suwon, Korea, Republic of, [3]Department of Biomedical Engineering, Sungkyunkwan University, Suwon, Korea, Republic of

Introduction: χ-separation[1] can separate paramagnetic and diamagnetic susceptibility distributions related to iron and myelin, respectively[2]. A combination of this new technique and 7T imaging can benefit from increased SNR and susceptibility effects, potentially providing sub-millimeter resolution maps for brain structures[3-4]. However, χ-separation requires an R2 map, which is challenging to acquire due to high SAR, B1 inhomogeneities, and long scan time (> tens of minutes). Recently, a neural network, χ-sepnet-R2*, was developed to remove the necessity for the R2 map but it is designed to work for the input of 3T R2*.[5] Therefore, further work is required to utilize only 7T data (i.e., R2* and local field). This study aims to produce in-vivo high-resolution χ-separation maps at 7T. To achieve this, we introduce a new pipeline that includes a novel deep neural network, an R2* 7T-to-3T conversion network, which converts 7T R2* to match 3T R2*, and QSMnet, χ-sepnet-R2*, and resolution generalization approach[6-7].

Methods: Ten healthy volunteers were scanned at 3 Tesla and 7 Tesla MRI (Siemens Tim Trio and Magnetom Terra, Erlangen, Germany). Sequences include multi-echo GRE, multi-echo SE, and MPRAGE at 3T, and multi-echo GRE at 7T (IRB-approved). Since χ-sepnet-R2* is trained with 3T R2*, a 7T R2* map needs to be converted to that of 3T. This is achieved by an R2* 7T-to-3T conversion network. A dataset of ten R2* pairs at 3T and 7T was used (train:validation: test = 5:1:4). The neural network is trained to take patches of 7T R2* maps as input and patches of 3T R2* maps as labels, utilizing a 3D U-net with L1 and gradient loss as a loss function. The pipeline for high-resolution χ-separation from 7T data is as follows: Initially, a QSM map is reconstructed from a local field map using QSMnet with the resolution generalization method. Secondly, the 7T R2* map is converted using the R2* 7T-to-3T conversion network. Lastly, the QSM map and converted R2* map are applied to χ-sepnet-R2* with resolution generalization, creating χ-separation maps. For χ-separation maps, three methods are compared: i) proposed pipeline, ii) χ-sepnet-R2* with a linearly-scaled 7T R2* map (by B0) as R2* input, and iii) χ-sepnet-R2* with a 3T R2* map as R2* input (not practical because 3T data required). These results were evaluated with respect to the χ-separation-

COSMOS maps at 3T as the reference. The comparison utilizes NRMSE, SSIM, and χ-separation atlas-based ROI anlaysis. The laminar profile of a middle frontal sulcus is conducted in the χpara, χdia, QSM, and R2* maps.

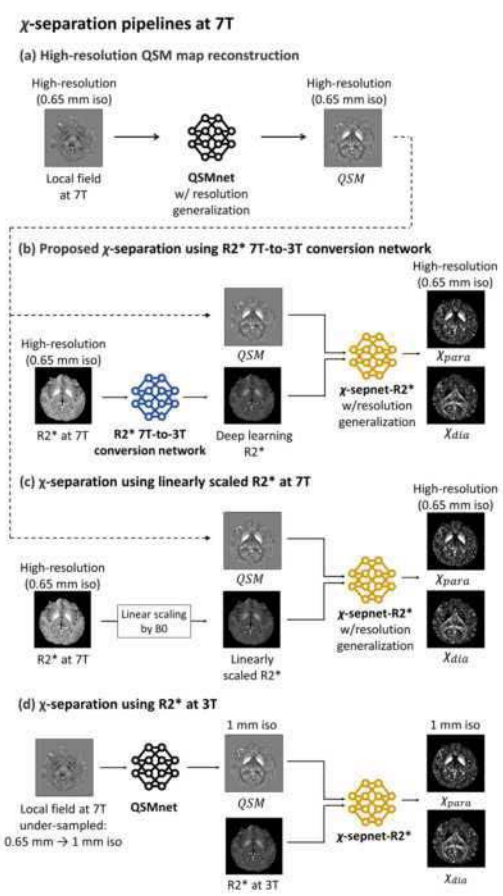

Figure 1. χ-separation pipelines at 7T. (a) A high-resolution QSM map is generated from a local field map at 7T via QSMnet using resolution generalization[10]. (b) Proposed 7T χ -separation pipeline. Because acquiring a whole brain high-resolution R2 map is challenging at 7T, we utilized χ-sepnet-R2*. This network requires an R2* map from 3T, and therefore, an R2* map from 7T is converted to a corresponding R2* map at 3T using a newly developed 7T-to-3T conversion network. Finally, the high-resolution QSM map from (a) and the converted R2* map are used as the input for χ-sepnet-R2*, creating high-resolution χ-separation maps. (c) An alternative pipeline using a linearly-scaled R2* map by B0 is tested for comparison. (d) To evaluate the effect of the conversion network on the resulting maps, another pipeline using an R2* map at 3T and a QSM map from an under-sampled field map at 7T for the input of χ-sepnet-R2*.

Results: The proposed pipeline shows contrasts comparable to those of χ-separation-COSMOS. In contrast, maps from the linearly-scaled R2* input exhibit notably different contrasts and worse metrics. Figure 2 illustrates the capability of the high-resolution χ-separation map to delineate fine structures in the in-vivo human brain such as lamina structures in the globus pallidus, primary visual cortex, transverse pontine fiber and fissures of the cerebellum. These structures are not as distinct at 3T, highlighting the advantage of 7T imaging. Additionally, high-resolution maps enable layer-wise cortex analysis. The results demonstrated consistency with previous findings, the discrepancy between the locations of the peak of QSM and the peak of χpara.

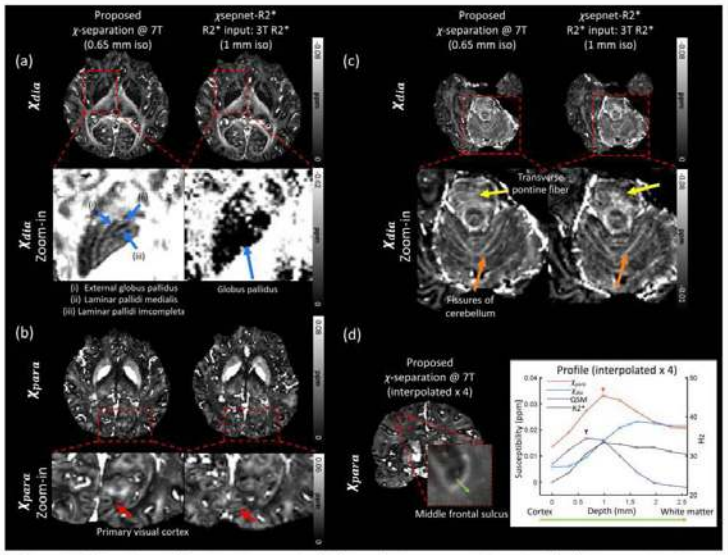

Figure 2. Delineation of fine structures using high-resolution χ-separation at 7T. (a-c) A comparison is made between 0.65 mm iso χ-separation maps at 7T and 1 mm iso χ-sepnet-R2* maps with R2* at 3T in slices of similar locations. (a) Delineation of laminar structures in globus pallidus. In the high-resolution χ_{dia} map, the laminar pallidis are distinct, whereas the low-resolution map does not delineate them (blue arrows). (b) Delineation of visual cortex (red arrows). (c) χ_{dia} maps of the pons and cerebellum indicate that fiber bundles can be distinguished at 7T, whereas these bundles are not as clearly delineated at the lower resolution map (yellow and orange arrows). (d) The depth-wise profiles of χ_{para}, χ_{dia}, QSM, and R2* in the middle frontal sulcus (green arrow) are plotted. The peak of QSM profile is located at a lower cortical depth than that of χ_{para}, confirming QSM does not properly represent layer-wise structures.

Conclusions: In this study, we introduced a novel deep neural network, R2* 7T-to-3T conversion network, to mitigate the discrepancy of R2* along the field strength and utilize χ-sepnet-R2*. By integrating the R2* 7T-to-3T conversion network, QSMnet, χ-sepnet-R2*, and resolution generalization, we generated high-resolution χ-separation maps from GRE data at 7T. Utilizing the proposed high-resolution χ-separation method, it is feasible to delineate more precise brain structures. The proposed method can be applied to layer-wise analysis and examine detailed structures related to iron and myelin accumulation.

References

1. Shin, Hyeong-Geol, et al. “chi-separation: Magnetic susceptibility source separation toward iron and myelin mapping in the brain.” NeuroImage 240 (2021): 118371.
2. Subin, Lee, et al. “Laminar profiling in advanced susceptibility imaging reveals variations in iron and myelin concentrations”, 30th Joint Annual Meeting ISMRM-ESMRMB, 07-12 May 2022.
3. Betts, Matthew J., et al. “High-resolution characterization of the aging brain using simultaneous quantitative susceptibility mapping (QSM) and R2* measurements at 7 T.” Neuroimage 138 (2016): 43-63.
4. Spincemaille, Pascal, et al. “Quantitative susceptibility mapping: MRI at 7T versus 3T.” Journal of Neuroimaging 30.1 (2020): 65-75.
5. Minjoon, Kim, et al. “χ-sepnet: Susceptibility source separation using deep neural network”, 30th Joint Annual Meeting ISMRM-ESMRMB, 07-12 May 2022.
6. Yoon, Jaeyeon, et al. “Quantitative susceptibility mapping using deep neural network: QSMnet.” Neuroimage 179 (2018): 199-206.
7. Sooyeon, Ji, et al. “Resolution generalization of deep learning-based QSM network.”, 31st Joint Annual Meeting ISMRM-ESMRMB, 03-08 June 2023.
8. Dymerska, Barbara, et al. “Phase unwrapping with a rapid opensource minimum spanning tree algorithm (ROMEO).” Magnetic resonance in medicine 85.4 (2021): 2294-2308.
9. Shin, Hyeong-Geol, et al. “chi-separation using multi-orientation data invivo and exvivo brains: Visualization of histology up to the resolution of 350 μm.” Joint Annual Meeting ISMRM-ESMRMB & ISMRT 31st Annual Meeting, London, UK. 2022.
10. Min, Kyeongseon, et al. “A human brain atlas of chi-separation for normative iron and myelin distributions.”, arXiv preprint, https://doi.org/10.48550/arXiv.2311.04468

Poster No 1867

Parsing disease heterogeneity using normative modelling and Generative Adversarial Networks (GANs)

Sai Spandana Chintapalli[1], Sindhuja Govindarajan[1], Haochang Shou[1], Hao Huang[2], Christos Davatzikos[1]

[1]Centre for Biomedical Image Computing and Analytics, University of Pennsylvania, Philadelphia, PA, [2]Department of Radiology, Children’s Hospital of Philadelphia, Philadelphia, PA

Introduction: Neuroimaging studies have documented brain structural and functional heterogeneity in patients with Alzheimer’s disease (AD) and other neurological disorders[1,2,9] This heterogeneity leads to diagnostic and prognostic

uncertainty, confounding clinical treatment planning. One way to parse disease heterogeneity is normative modelling, where individual-level deviations in brain measures from a reference sample are computed to infer personalized effects of disease.[8] Traditional univariate normative modelling techniques like Gaussian process regression (GPR) ignore multivariate interactions between brain measures. On the other hand, multivariate deep-learning based techniques such as adversarial autoencoders (AAE) might have low specificity to disease effects as they are trained solely on the reference sample.[7] In both cases, the computed deviations might incorporate disease irrelevant effects due to inter-individual brain differences. To overcome this, we propose a Generative Adversarial Network (GAN)[5] based normative modelling technique that learns to remove disease-related variations from a subject's brain measures while preserving disease unrelated variations. As illustrated in Fig.1, the proposed model synthesizes patient-specific controls, and the deviation of the patient from the synthesized control acts as an image-based biomarker that is sensitive to disease effects and severity.

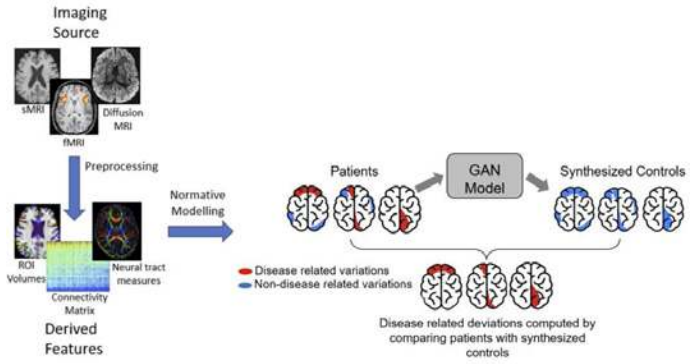

Fig 1: Proposed GAN-based normative modelling technique

Methods: We adapt the pix2pix GAN[5] to translate a subject with disease to a corresponding subject without disease. Training such a network requires paired data i.e. neuroimaging derived brain measures of an individual with and without disease. In reality, only one of these conditions can be satisfied i.e. subjects either have disease or do not. Hence, we synthetically simulate patients from a known reference sample of controls and use the pseudo-synthetic patient and real control pairs for GAN training. To implement this method to study neuroanatomical heterogeneity, we select a reference population of 6000 healthy controls from the ISTAGING consortium[4] without preexisting neurologic disorders. Our neuroanatomical brain measures are the 8 regions of interest (ROI) volumes (the left and right frontal, parietal, occipital and temporal lobe volumes) computed using a multi-atlas segmentation technique.[3] To simulate patients, for each control in the reference sample we introduce 10-30% atrophy or expansion in a random combination of ROIs while preserving clinical covariate effects. The model is optimized to translate pseudo-synthetic patients to real controls. During inference, the model synthesizes a control for each real patient, and the difference between the two relates to real disease effects. For performance assessment, we select 200 controls (CN) and 200 AD participants (PT) from an independent[6] dataset and compute their deviations across the 8 ROI volumes using GAN, GPR, and AAE models (pretrained on the ISTAGING dataset). We then use logistic regression to assess the overall discriminative power of the GAN-derived deviations in AD classification.

Results: We observe that the deviations derived using the GAN model are on average larger than the deviations from the GPR and AAE models for PT. While for CN, the GAN's deviations are on average smaller (Fig.2.a). Larger deviations in PT compared to CN reflects that the deviations capture disease related abnormality in brain measures. Additionally, we note that, GAN's deviations in the 8 ROIs (mean AUC = 0.76) provide a considerable gain over raw ROI volumes (mean AUC = 0.65) in classifying AD participants (Fig.2.b).

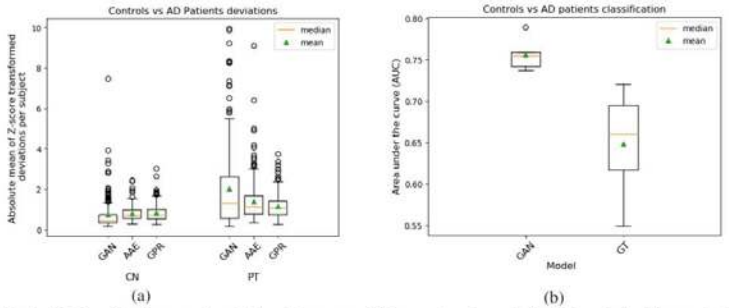

Fig 2: AD classification results. a) Absolute mean of Z-score transformed deviations in healthy controls and AD patients computed using GAN, AAE, and GPR models respectively. b) 5-fold cross-validated AUC (area under the receiver operating characteristic curve) scores for logistic regression based AD classification using deviations measured from GAN. Ground Truth (GT) model uses the raw ROI volumes for AD classification.

Conclusions: GAN-based normative modelling technique introduced here is a useful tool to parse heterogeneity in brain measures at an individual level. We see that self-supervised training of the model using pseudo-synthetically simulated patient data that is agnostic to disease patterns can help detect real disease related effects.

References

1. Covington, N. V. (2021), 'Heterogeneity Is a Hallmark of Traumatic Brain Injury, Not a Limitation: A New Perspective on Study Design in Rehabilitation Research', American Journal of Speech-Language Pathology, 30(2S), pp. 974–985.
2. Dong, A., (2017), 'Heterogeneity of neuroanatomical patterns in prodromal Alzheimer's disease: links to cognition, progression and biomarkers', Brain, 140(3), pp. 735-747.
3. Doshi, J., (2016), 'MUSE: MUlti-atlas region Segmentation utilizing Ensembles of registration algorithms and parameters, and locally optimal atlas selection', Neuroimage, 127, pp. 186-195.
4. Habes, M. (2021), 'The Brain Chart of Aging: machine-learning analytics reveals links between brain aging, white matter disease, amyloid burden, and cognition in the iSTAGING consortium of 10,216 harmonized MR scans', Alzheimer's & Dementia, 17(1), pp. 89-102.
5. Isola, P. (2017), 'Image-to-image translation with conditional adversarial networks', In Proceedings of the IEEE conference on computer vision and pattern recognition, pp. 1125-1134.
6. LaMontagne, P. J. (2019), 'OASIS-3: longitudinal neuroimaging, clinical, and cognitive dataset for normal aging and Alzheimer disease', MedRxiv.
7. Pinaya, W. H. (2021), 'Using normative modelling to detect disease progression in mild cognitive impairment and Alzheimer's disease in a cross-sectional multi-cohort study', Scientific reports, 11(1), pp.15746.
8. Rutherford, S. (2022), 'The normative modeling framework for computational psychiatry', Nature protocols, 17(7), pp. 1711-1734.
9. Segal, A. (2023), 'Regional, circuit and network heterogeneity of brain abnormalities in psychiatric disorders', Nature Neuroscience, 26(9), pp. 1613-1629.

Poster No 1868

FastSurfer-CC: Head Pose Normalization for Consistent Corpus Callosum & Fornix Segmentation

Clemens Pollak[1], Andreas Girodi[1], Kersten Diers[1], Santiago Estrada[1,2], David Kügler[1], Martin Reuter[1,3,4]

[1]AI in Medical Imaging, German Center for Neurodegenerative Diseases (DZNE), Bonn, Germany, [2]Population Health Sciences, German Center for Neurodegenerative Diseases (DZNE), Bonn, Germany, [3]A.A. Martinos Center for Biomedical Imaging, Massachusetts General Hospital, Boston, MA, [4]Department of Radiology, Harvard Medical School, Boston, MA

Introduction: Corpus callosum (CC), fornix (FN), anterior- and posterior commissures (AC, PC) are white matter bundles, central to the communication between hemispheres, memory recall tasks and olfaction. They also play important roles in various diseases, like epilepsy[1], autism[2], and schizophrenia[3]. These bundles have discrete borders to surrounding tissues in the sagittal plane, but not to the left and right hemisphere. Therefore, segmentation is often performed only in midsagittal slices, which are determined a priori. Existing literature frequently treats the head pose normalization and segmentation tasks separately[4,5]. Finding the midsaggital plane (midplane) is challenging, since the border between hemispheres can be curved. Nonetheless, approximating the midplane accurately is required for consistent segmentation, since errors in its orientation can propagate to inaccurate, or even biased measurements w.r.t. CC and FN size and shape. For this reason, we develop a two-step pipeline that first finds the best-suited midplane for CC and FN segmentation, and second, segments CC and FN. Additionally, the second step localizes AC and PC, resulting in the AC-PC line (bicommissural line). We combine this localization with the midplane to standardize the brain orientation on all three axes, which can aid further analysis and quality control.

Methods: We develop and evaluate our methods on a dataset of 280 T1-weighted brain MRIs, from 7T, 3T, and 1.5T scanners of the HCP, ADNI, OASIS, ABIDE-II, MIRIAD, Ia5c, Rhineland-, and in-house studies. To find the midplane, we consider four methods: a) Freesurfer's mri_cc, b) finding the left-right symmetry axis by mid-space registration of Freesurfer's mri_robust_register to a left-right flipped version of the same volume c) registering the center points of segmentation labels to those of a template (centroid_template) d) same as c), but using the flipped segmentation as a template and mapping into mid-space, similar to b) (centroid_flipped). Two blinded experts compared 40 midplanes for each method pair and marked which plane best separates CC, FN, AC, and PC into equal parts. We selected 20 midplane pairs according to the highest difference between them and 20 pairs randomly. The plane-difference was estimated by the volume between planes within the brain, approximated by a left-right oriented cylinder centered at the RAS coordinate origin. As reference standard for the segmentation task, two experts manually segmented CC, FN, AC, and PC in an area 2.5mm around the midplanes derived by mri_cc. The resulting 158 labeled volumes were then split into training (97), validation (31), and test set (30). On these labels, we train a 3D Swin Unet-transformer (S-UNETR)[6] for joint segmentation of CC and FN as well as prediction of heatmaps for the location of AC and PC[8].

a)

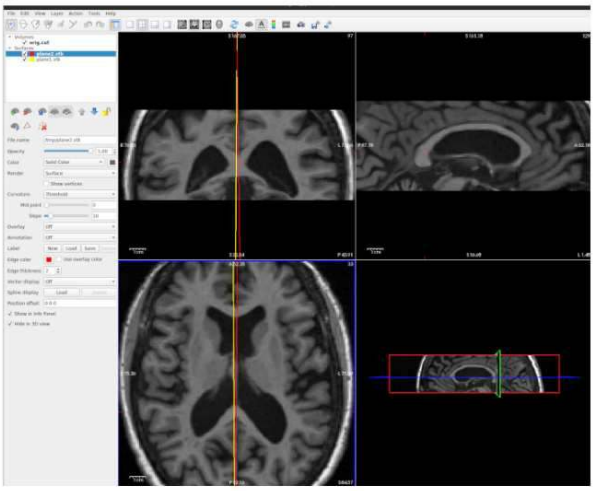

b)

	M1	M2
R1	12	7
R2	13	3
total	25	10

M1: centroid_template
M2: robust_register

	M1	M2
R1	8	5
R2	13	8
total	21	13

M1: mri_cc
M2: centroid_flipped

	M1	M2
R1	6	4
R2	10	12
total	16	16

M1: mri_cc
M2: centroid_template

Figure 1: a) Rating tool with view of two candidate midplanes, **b)** Rating results of the three performed comparisons for the two raters R1 and R2 and two methods M1, M2. Shown are the number of times where a method was visually determined to outperform the other

Results: We compare the four candidate methods (Fig. 1) and conclude that method centroid_template outperforms mri_robust_register and mri_cc outperforms centroid_flipped. No clear ranking can be found between mri_cc and centroid_template. Since the centroid registration is very fast (2 sec. avg.) compared to mri_cc's registration (52 sec. avg.), we choose to include it in our final pipeline. For the joint segmentation and localization sub-task, we find that S-UNETR outperforms other benchmarked architectures and mri_cc (Fig. 2).

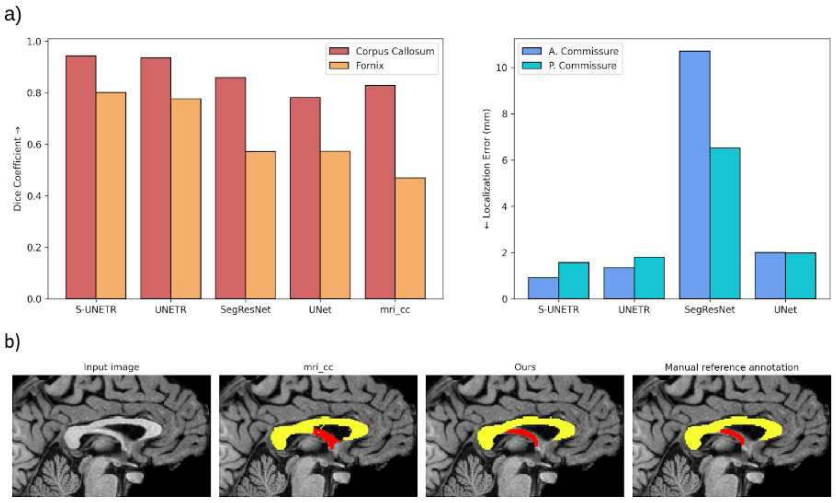

Figure 2: a) comparison of Dice scores for corpus callosum and fornix segmentation (left) and localization error of anterior- and posterior commissure. We compare *mri_cc* (baseline, segmentation only) and the residual U-Net, SegResNet, UNETR and S-UNETR architectures. The networks were adjusted to have similar numbers of parameters. **b)** Visual comparison of corpus callosum (yellow) and fornix (red) segmentation from *mri_cc,* our method and the manual reference labels.

Conclusions: We propose a two-step pipeline for fast and accurate CC and FN segmentation, that includes finding the midplane and performing a joint segmentation and localization. Through localization of AC and PC it also provides an anatomically motivated brain orientation, which matches other standardization techniques, like the rigid registration to the Talairach space. In the future, we aim to predict the midplane with the S-UNETR, further improving upon the existing methods, and to distribute our method as part of the FastSurfer neuroimaging software suite[9].

References

1. Unterberger, I., Bauer, R., Walser, G. and Bauer, G., 2016. Corpus callosum and epilepsies. Seizure, 37, pp.55-60.
2. Piven, J., Bailey, J., Ranson, B.J. and Arndt, S., 1997. An MRI study of the corpus callosum in autism. American Journal of Psychiatry, 154(8), pp.1051-1056.
3. Woodruff, P.W., McManus, I.C. and David, A.S., 1995. Meta-analysis of corpus callosum size in schizophrenia. Journal of Neurology, Neurosurgery & Psychiatry, 58(4), pp.457-461.

4. Brusini, I., Platten, M., Ouellette, R., Piehl, F., Wang, C., Granberg, T., 2022. Automatic deep learning multicontrast corpus callosum segmentation in multiple sclerosis. Journal of Neuroimaging, 32(3), pp.459-470.
5. Chandra, A., Verma, S., Raghuvanshi, A. S., Bodhey, N. K., 2023. PCcS-RAU-Net: Automated parcellated Corpus callosum segmentation from brain MRI images using modified residual attention U-Net. Biocybernetics and Biomedical Engineering, 43(2), pp.403-427.
6. Benear, S.L., Ngo, C.T. and Olson, I.R., 2020. Dissecting the fornix in basic memory processes and neuropsychiatric disease: a review. Brain Connectivity, 10(7), pp.331-354.
7. Hatamizadeh, A., Nath, V., Tang, Y., Yang, D., Roth, H. R., & Xu, D., 2021. Swin unetr: Swin transformers for semantic segmentation of brain tumors in mri images. International MICCAI Brainlesion Workshop, pp. 272-284
8. Edwards, C.A., Goyal, A., Rusheen, A.E., Kouzani, A.Z. and Lee, K.H., 2021. Deepnavnet: Automated landmark localization for neuronavigation. Frontiers in Neuroscience, 15, p.670287.
9. https://github.com/Deep-MI/FastSurfer

Poster No 1869

Multiresolution orthonormal projective nonnegative matrix factorization for large surface data

Sung Min Ha[1], Abdalla Bani[1], Braden Yang[1], Deydeep Kothapalli[1], Thomas Earnest[1], Pan Xiao[1], John Lee[1], Theodore Satterthwaite[2], Janine Bijsterbosch[1], Matthew Glasser[1], Adam Bauer[1], Nico Dosenbach[1], Deanna Barch[1], Aristeidis Sotiras[1]

[1]Washington University in St. Louis, St. Louis, MO, [2]University of Pennsylvania, Philadelphia, PA

Introduction: Recent strides in in vivo neuroimaging technology and image analysis techniques, such as the Human Connectome Project (Glasser et al. 2016), have ushered in an era of high-resolution, large-scale neuroimaging surface data. The availability of such data necessitates the development of data-driven analysis approaches to gain deeper insights into human brain structure and disease from big data. Orthonormal projective nonnegative matrix factorization (opNMF) (Yang et al. 2010) has exhibited promising outcomes in the realm of neuroimaging analysis, yielding interpretable and reproducible patterns (Sotiras et al. 2015). Nevertheless, the application of opNMF on large-scale datasets has been impeded by its computationally intensive nature, characterized by large memory footprint and long runtime. In response, we present a new approach, multiresolution-opNMF (m-opNMF), which leverages graph reduction with spectral guarantees, thereby improving scalability without compromising the performance of opNMF.

Methods: opNMF approximates a nonnegative matrix X as multiplication of two smaller nonnegative matrices, W and H, by minimizing the cost function, frobenius norm of X-WH. Employing a graph coarsening method with preserved spectral properties (Loukas 2019), m-opNMF sequentially reduces the surface in X to progressively lower resolutions. Subsequently, m-opNMF refines the matrices W and H across these resolutions, starting from the coarsest (Fig 1). This strategy enables the implementation of the iterative updates at lower resolutions, resulting in quicker runtime and a reduced memory footprint.

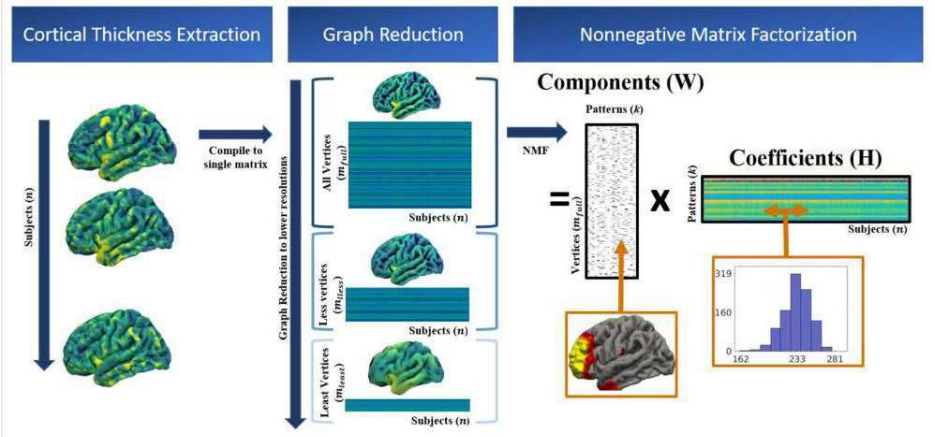

Figure 1. Graphical summary of the m-opNMF method. Left hemisphere cortical thickness of 1,036 subjects in fsaverage template space were vectorized into a vertical vector of length 149,955 vertices after excluding vertices in the medial wall. The data matrix $X \in \mathbb{R}^{(149,955 \times 1,036)}$ was generated by concatenating these vertical vectors side-to-side. Afterwards, graph reduction was applied to reduce the number of vertices to a set ratio $r_{reduction} = \{0.5, 0.75, 0.875\}$ through multiple levels of subsequent lower resolution. opNMF updates were applied with target rank $k = 20$ starting from lowest resolution with lifting to higher resolution in-between, until the original full resolution was reached. $k = 20$ was chosen by user to match previous neuroimaging NMF applications (Sotiras et al. 2015).

Results: We included cortical thickness (CT) from baseline T1 MRI scans of 1,036 subjects (361 males, age 69.77 ± 9.53 years, Clinical Dementia Rating from 0 to 2) of Open Access Series of Imaging Studies 3. (Lamontagne et al. 2019) After undergoing the FreeSurfer pipeline, CT values were vectorized and concatenated to create X∈R^(149,955×1,036). We performed graph coarsening for m-opNMF with rank k=20 and reduction ratios (r_reduction) {0.5, 0.75, 0.875}, each with multiple resolutions and the lowest resolution containing approximately {1/2, 1/4, 1/8} vertices. Frobenius norm of X-WH measured the

reconstruction error, while the sparsity of component W evaluated the spatial specificity. Adjusted Rand Index (ARI), mean and median inner products of W were utilized to measure how well m-opNMF replicated the opNMF W. Total runtime gauged the computational loads. Reconstruction errors were strikingly similar between the two methods (Fig 2a), and the sparsity values were also closely matched (Fig 2b). ARI value greater than 0.6 is typically considered good reproducibility in neuroimaging data. m-opNMF showed ARI≥0.6 for its reproduction of opNMF components for r_reduction=0.875 (Fig 2d). High mean and median inner product values echoed the high reproducibility of m-opNMF to opNMF (Fig 2e, 2f). These results underscored that m-opNMF not only performs on par with opNMF quantitatively, but also generates similar components. Consequently, the W derived from m-opNMF can readily serve as substitutes for opNMF components. Visualizations, where winner-takes-all approach was used to assign most prominent component rank to each vertex to create parcellations, confirmed the component similarity for r_reduction=0.875 (Fig 2j). Most importantly, m-opNMF generated such components with comparable quality and similar composition at reduced runtime of less than a quarter of opNMF (Fig 2c).

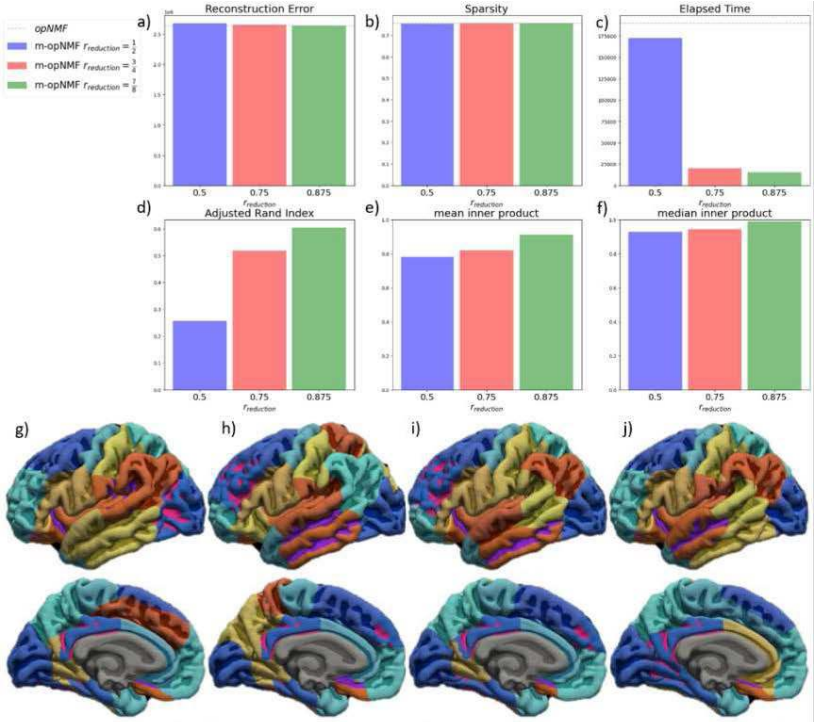

Figure 2. Quantitative and qualitative outputs from comparison of performance of opNMF and m-opNMF. a) Reconstruction error of estimating original $X \approx WH$ using frobenius norm $\|X - WH\|_F^2$. b) Sparsity of the component matrix W. c) Elapsed runtime for full algorithm to run in units of seconds. d) Adjusted Rand Index (ARI) measuring how well m-opNMF components W replicates opNMF W. e) mean of the inner product of W of m-opNMF to that of opNMF to measure how similar the two W matrices are. f) median of the inner product of W of m-opNMF to that of opNMF for measurement of similarity of the two W matrices. For subplots a), b), and c), the dotted black line is the value of opNMF. for all subplots a) through f), the blue, red, and green bars represent m-opNMF runs with different coarsening reduction ratios. Visualizations of opNMF to m-opNMF components W are shown in figures g) through j). A winner-takes-all approach was taken to assign the most prominent rank among the 20 ranks for each vertex, and color coding was matched across the visualizations using Hungarian matching. From left to right, g) opNMF, h) m-opNMF with $r_{reduction} = 0.5$, i) m-opNMF with $r_{reduction} = 0.75$, and j) m-opNMF with $r_{reduction} = 0.875$.

Conclusions: m-opNMF reproduces the interpretable components of opNMF on high-resolution surface data, all the while avoiding the computational burdens associated with opNMF. Quantitative performance is virtually identical, while reproducibility metrics, both quantitative and qualitative, demonstrate sufficient similarity at higher r_reduction to function as drop-in replacement of opNMF. Furthermore, m-opNMF exhibits significantly reduced runtime, promising broader applications to large-scale data.

References

1. Glasser, M. F. (2016), The Human Connectome Project's neuroimaging approach. Nature Neuroscience. vol. 19, no. 9, pp. 1175–1187. doi:10.1038/nn.4361.
2. Lamontagne, P. J. (2019), OASIS-3: Longitudinal Neuroimaging, Clinical, and Cognitive Dataset for Normal Aging and Alzheimer Disease. medRxiv. doi:10.1101/2019.12.13.19014902.
3. Loukas, A. (2019). Graph Reduction with Spectral and Cut Guarantees. Journal of Machine Learning Research. vol. 20, no. 116, pp. 1-42.
4. Sotiras, A. (2015). Finding imaging patterns of structural covariance via Non-Negative Matrix Factorization. NeuroImage. vol. 108, pp. 1-16. doi:10.1016/j.neuroimage.2014.11.045.
5. Yang, Z. (2010). Linear and nonlinear projective nonnegative matrix factorization. IEEE Transactions on Neural Networks. vol. 21, no. 5, pp. 734-749. doi:10.1109/TNN.2010.2041361.

Poster No 1870

Directional Errors with False Discovery Rate on Two-Tailed Tests

Anderson Winkler[1], Paul Taylor[2], Thomas Nichols[3], Chris Rorden[4]

[1]University of Texas Rio Grande Valley, Brownsville, TX, [2]National Institute of Health, Bethesda, MD, [3]University of Oxford, Oxford, United Kingdom, [4]University of South Carolina, Columbia, SC

Introduction: False discovery rate (FDR) is widely used in neuroimaging to address multiple testing. Many of these analyses also involve two-tailed hypotheses. In general, two-sided tests utilize symmetric thresholds (the same threshold for both tails), such that FDR adjustments would be applied symmetrically. However, in practice, effects being examined can be asymmetric, leading to asymmetric false positive rates that can, by large margin, exceed the nominal test level. It remains unclear how to control such directional errors with FDR. Moreover, most analytic software tools do not provide for the use of asymmetrical thresholds, even for corrected data, which limits the ability to investigate directional effects. Here, we investigate various scenarios of asymmetry in estimated results and strategies for performing FDR adjustments, including a novel approach called "split-tails". We apply these methods to both simulations and to a real FMRI dataset.

Methods: We considered four strategies, which we termed "canonical", "combined", "two-tailed", and "split-tails", for handling two-tailed tests with the Benjamini-Hochberg (BH) and Benjamini-Krieger-Yekutieli (BKY) procedures in simulations and on real imaging data. Ten scenarios were simulated with varying proportions of true positive/negative effects, balancedness, and test dependencies. False positives were evaluated globally and separately by direction (i.e., positive and negative). Real data came from a gambling task analysis done as part of the Neuroimaging Analysis Replication and Prediction Study (NARPS).

Results: Simulations demonstrated that, under complete null (no effects), canonical and split-tails controlled false positives at the nominal level when each side was considered separately, but the error rate was doubled when all tests were considered. The combined and two-tailed methods maintained error control globally, but became conservative on each side. With signal in only one side, all strategies were conservative on the side with signal, but two-tailed and combined strategies became invalid in the opposite side, approaching 100% error rate; the canonical and split-tails methods performed well in these cases. Even with balanced effects on both sides, while the strategies controlled the error rate, they leaned towards conservativeness. With unbalanced amounts of signal, the error rate was not controlled for two-tailed and combined strategies in the side opposite to the one with a preponderance of true signal. On real data (Figure), uncorrected thresholds suggested widespread negative and sparse positive activation related to the gambling task. However, among corrected results, no positive effects remained significant with canonical/split-tails approaches, while combined/two-tailed analyses retained some. In light of the simulation results, these effects on the positive side are likely false positives. Similar results were seen with the BKY procedure, although it was generally more powerful than BH.

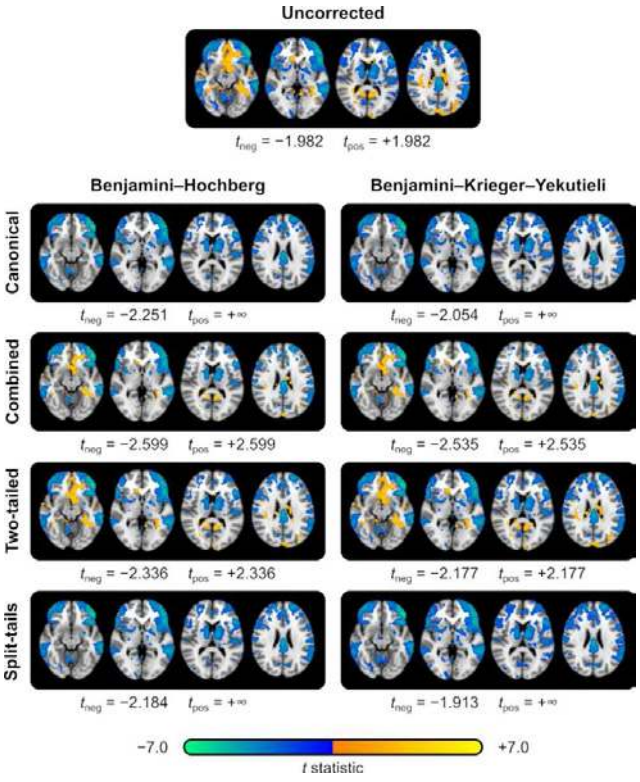

Conclusions: Caution is needed when making directional statements from two-tailed tests with FDR correction, as errors are only controlled globally, not by tail. This is a consequence of FDR lacking localizing power, providing only weak control over the error rate. Asymmetrical thresholds should be used in neuroimaging tools to allow for FDR-based directional analyses even if two-tailed tests are used. Strategies that run FDR separately by side of the original hypotheses or by the sign of the resulting statistical test preserve control over directional error rates, albeit with increased risk of errors under the complete null.

References

1. Benjamini, Y., Hochberg, Y. (1995), 'Controlling the false discovery rate: a practical and powerful approach to multiple testing', Journal of the Royal Statistical Society. Series B (Methodological), vol. 57, pp. 289-300.
2. Benjamini, Y., Krieger, A.M., Yekutieli, D. (2006), 'Adaptive linear step-up procedures that control the false discovery rate', Biometrika, vol. 93, pp. 491-507.

Poster No 1871

Clustersize inference is more informative than TFCE

Samuel Davenport[1], Wouter Weeda[2], Jelle Goeman[3]

[1]University of Calfornia San Diego, LA Jolla, San Diego, CA, [2]Leiden University, Leiden, South Holland, [3]Leiden University Medical Center, Leiden, South Holland

Introduction: Cluster-size inference is one of the most popular approaches in neuroimaging analysis but has been criticized for its dependence on an arbitrary (but important) cluster-forming threshold. Threshold-Free Cluster Enhancement (TFCE) was proposed in Smith (2009) with the aim of 1) decreasing the arbitrariness of the cluster-forming threshold and 2) being more sensitive to brain activation. Here we will show that TFCE does not achieve these aims. First, TFCE introduces more free parameters into the model than cluster-size inference, making it more dependent on researchers' choices. Second, the large clusters of TFCE, often mistakenly interpreted voxel-wise, actually hamper interpretation as the spatial specificity paradox increases. We will show, using recent advances in multiple testing, that cluster-size inference is a more robust way of doing neuroimaging analyses.

Methods: Traditional cluster-size inference makes the weak claim that one voxel within an observed significant cluster above the cluster-defining threshold (CDT) is active. Goeman (2023) showed that cluster-size inference can be embedded into a closed testing procedure. This embedding allows more informative statements to be made. In particular, it provides a 95%-confidence lower bound on the True Discovery proportion (TDP), the proportion of truly active voxels in every cluster. TFCE is often interpreted as making a stronger claim that all voxels in the TFCE-cluster are active. We explicitly refute this claim and prove that TFCE does not even, in general, allow inference that a single voxel is active in the TFCE cluster, but only that such a voxel exists in its surroundings. TFCE aims to reduce the number of free parameters available for the user to select. However it in fact relies on 3 free parameters, E – the power of the cluster extent, H – the power applied to the height and h_0, which we call the TFCE cluster forming threshold. Thus TFCE introduces more parameters for the researcher not less. While users typically use the default parameter configuration when performing inference using TFCE the same is true for cluster size inference.

Results: In order to compare the performance of TFCE and cluster-size inference in practice we compare the results of applying TFCE and cluster-size inference to two different brain imaging datasets, with their default parameter configurations. The first consists of the 80 subjects from the Human Connectome Project (Essen, 2013) who have performed a working memory task. The second consists of 124 subjects from who have undergone an auditory task. The results are shown in Figure 1. They illustrate that clustersize inference is substantially more informative than TFCE. Due to the large size of the TFCE clusters, TFCE is only able to make the weak statement that some voxel is active somewhere in the brain. Instead clustersize inference provides meaningful lower bounds on the proportion of active voxels within each cluster. In Figure 2 we present the results from performing a simulation, adding smooth noise to a signal with two blocks. The results demonstrate the cluster leakage that can occur with TFCE, showing that interpreting TFCE voxelwise can lead to false positives.

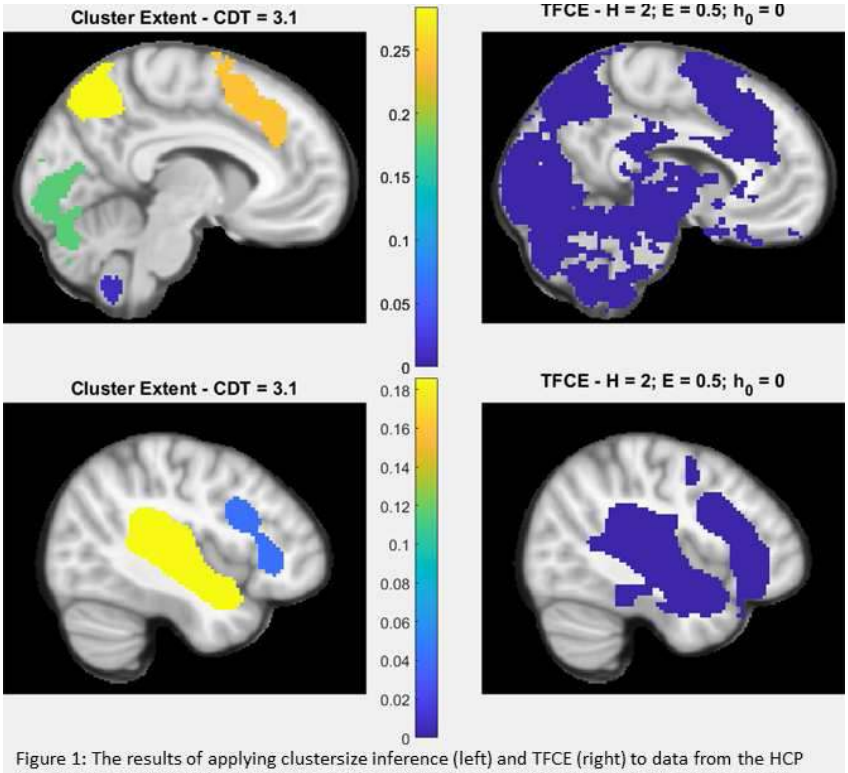

Figure 1: The results of applying clustersize inference (left) and TFCE (right) to data from the HCP (top panel) and 124 subjects from an Auditory dataset collected by Pernet et al (bottom panel). Each cluster is assigned a colour based on the TDP lower bound on the proportion of active voxels. Clustersize inference provides informative bounds on the TDP whereas TFCE provides very weak information about the content within each cluster.

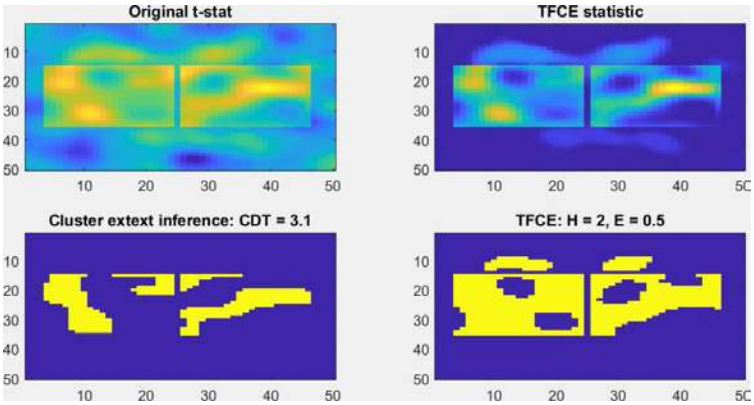

Figure 2: Illustrating TFCE cluster leakage. True signal is the two central blocks.

Conclusions: The information provided by inference using TFCE is quite limited. TFCE clusters can span a large proportion of the brain making it very difficult to localize activation. Instead cluster-size inference is more informative, enabling increased localisation and TDP lower bounds for each cluster. Lower bounds could in principle be derived for TFCE from the embedded closed testing procedure but this seems a priori very difficult. Moreover TFCE is substantially slower than cluster-size inference because it requires that the TFCE statistic be calculated for each permutation. For these reasons we recommend that researchers use cluster-size inference, with lower-bound estimates of the number of active voxels within each cluster, over TFCE when performing brain-imaging analyses.

References

1. Van Essen, David C., et al. (2013) “The WU-Minn human connectome project: an overview.” Neuroimage 80: 62-79.
2. Goeman, Jelle J., et al. (2023): “Cluster extent inference revisited: quantification and localisation of brain activity.” Journal of the Royal Statistical Society Series B: Statistical Methodology 85.4 1128-1153.
3. Pernet, Cyril R., et al. (2015) “The human voice areas: Spatial organization and inter-individual variability in temporal and extra-temporal cortices.” Neuroimage 119: 164-174.
4. Smith, Stephen M., and Thomas E. Nichols (2009) “Threshold-free cluster enhancement: addressing problems of smoothing, threshold dependence and localisation in cluster inference.” Neuroimage 44.1: 83-98.

Poster No 1872

Structural MRI synthesis of human fetal brain using a generative adversarial network

Yunseo Park[1], Yeongjun Park[2], Bo-yong Park[1,3,4]

[1]Department of Data Science, Inha University, Incheon, Republic of Korea, [2]Department of Computer Engineering, Inha University, Incheon, Republic of Korea, [3]Department of Statistics and Data Science, Inha University, Incheon, Republic of Korea, [4]Center for Neuroscience Imaging Research, Institute for Basic Science, Suwon, Republic of Korea

Introduction: Structural magnetic resonance imaging (MRI) facilitates the study of brain anatomy in vivo. Multimodal imaging data, such as T1- (T1w) and T2-weighted (T2w) MRI, provide rich information for understanding the brain; however, obtaining both T1w and T2w MRI is problematic because it is a time-consuming and expensive task. The image synthesis approach can mitigate this issue by generating T1w MRI from the T2w or vice versa. This technique has been conducted in many prior works using medical imaging data (Chira et al., 2022; Nie et al., 2018). For instance, a study utilized a Generative Adversarial Network (GAN) to augment brain MRI scans with tumors, generating other tumor-inclusive MRI modality data (Huang et al., 2021; Osokin et al.,). GAN comprises a generator and discriminator (Goodfellow et al., 2014). The generator is trained to prevent the discriminator from classifying data as fake or real, while the discriminator is trained to improve its accuracy in distinguishing actual from counterfeit images. Thus, the generator and discriminator are trained adversarily. In this study, we propose a synthesis model for generating T1w MRI from T2w images of the fetus using a GAN model.

Methods: We obtained T1w and T2w structural MRI of 418 individuals (mean ± standard deviation [SD] gestational age = 40.60 ± 2.27 weeks; 44.5% female) from the Developing Human connectome Project (dHCP) (Makropoulos et al., 2018). The structural MRI data were preprocessed using HCP minimal preprocessing pipelines (Glasser et al., 2013). We constructed a conditional GAN model to generate T1w MRI from T2w data. We utilized a pix2pix model (Isola et al., 2016), consisting of the generator based on the U-Net and the discriminator based on the PatchGAN, and modified the original two-dimensional (2D) model to 3D architecture (Fig. 1A). Subjects were randomly divided into training (n = 267), validation (n = 67), and test datasets (n = 84). The performance of the model was evaluated using mean squared error (MSE) between the actual and synthesized T1w images after the intensity normalization with the range between 0 and 1.

Results: We observed that the training and validation losses decreased dramatically around ten epochs and saturated around 30 epochs (Fig. 1B). We selected the model at 112 epochs, which showed the minimum test loss. We found that the MSE between the actual and synthesized T1w images of the test subjects was 0.0022 ± 0.001 (mean ± SD).

Conclusions: We proposed a GAN-based model synthesizing T1w data using only T2w MRI, which is optimized for fetal brains. Our pipeline may foster future multimodal neuroimaging studies in fetuses.

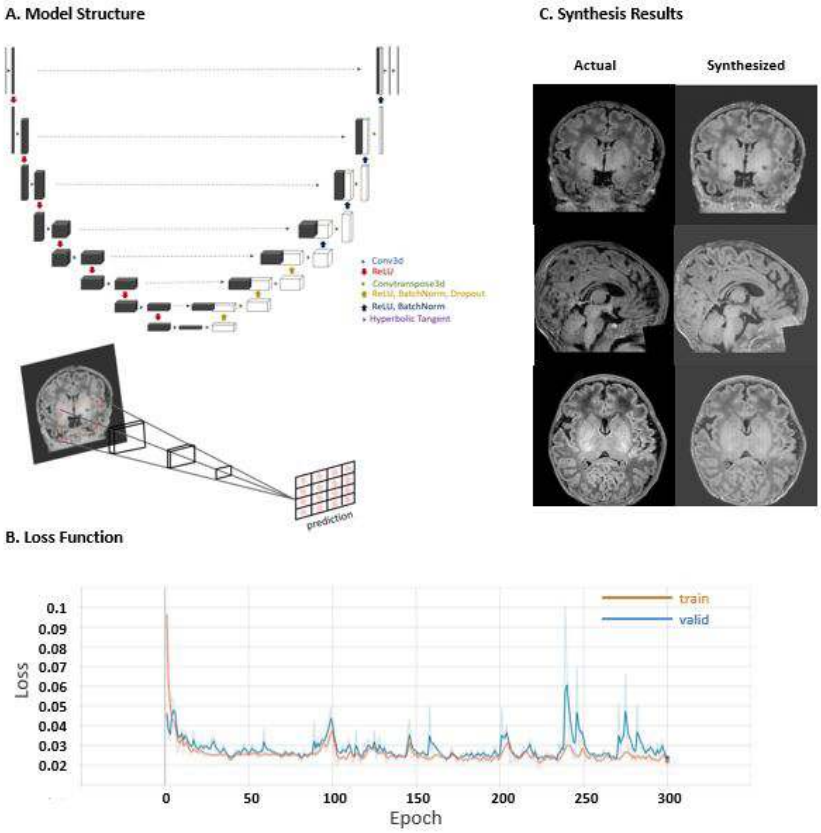

Fig. 1 | Synthesis model for structural MRI. **(A)** The model structure of the generator (top) and discriminator (bottom) are shown. **(B)** Shown are the training and validation losses across epochs. **(C)** We visualized the actual (left) and synthesized (right) T1-weighted images of one representative participant.

References

1. Chira, D., Haralampiev, I., Winther, O., Dittadi, A., & Liévin, V. (2022). Image Super-Resolution With Deep Variational Autoencoders. http://arxiv.org/abs/2203.09445
2. Glasser, M. F., Sotiropoulos, S. N., Wilson, J. A., Coalson, T. S., Fischl, B., Andersson, J. L., Xu, J., Jbabdi, S., Webster, M., Polimeni, J. R., Van Essen, D. C., & Jenkinson, M. (2013). The minimal preprocessing pipelines for the Human Connectome Project. NeuroImage, 80, 105–124. https://doi.org/10.1016/j.neuroimage.2013.04.127
3. Goodfellow, I. J., Pouget-Abadie, J., Mirza, M., Xu, B., Warde-Farley, D., Ozair, S., Courville, A., & Bengio, Y. (2014). Generative Adversarial Networks. http://arxiv.org/abs/1406.2661
4. Huang, P., Liu, X., & Huang, Y. (2021). Data Augmentation For Medical MR Image Using Generative Adversarial Networks. http://arxiv.org/abs/2111.14297
5. Isola, P., Zhu, J.-Y., Zhou, T., & Efros, A. A. (2016). Image-to-Image Translation with Conditional Adversarial Networks. http://arxiv.org/abs/1611.07004
6. Makropoulos, A., Robinson, E. C., Schuh, A., Wright, R., Fitzgibbon, S., Bozek, J., Counsell, S. J., Steinweg, J., Vecchiato, K., Passerat-Palmbach, J., Lenz, G., Mortari, F., Tenev, T., Duff, E. P., Bastiani, M., Cordero-Grande, L., Hughes, E., Tusor, N., Tournier, J.-D., … Rueckert, D. (2018). The Developing Human Connectome Project: a Minimal Processing Pipeline for Neonatal Cortical Surface Reconstruction Europe PMC Funders Group. Neuroimage, 173, 88–112. https://doi.org/10.1101/125526
7. Nie, D., Trullo, R., Lian, J., Wang, L., Petitjean, C., Ruan, S., Wang, Q., & Shen, D. (2018). Medical Image Synthesis with Deep Convolutional Adversarial Networks. IEEE Transactions on Biomedical Engineering, 65(12), 2720–2730. https://doi.org/10.1109/TBME.2018.2814538
8. Osokin, A., Ens, I. /, Hse, F., Anatole, R., Chesseí, C., Salas, R. E. C., & Vaggi, F. (n.d.). GANs for Biological Image Synthesis. https://github.com/soumith/ganhacks

Acknowledgements

Funding: This work was supported by the National Research Foundation of Korea (NRF-2021R1F1A1052303; NRF-2022R1A5A7033499), Institute for Information and Communications Technology Planning and Evaluation (IITP) funded by the Korea Government (MSIT) (No. 2022-0-00448, Deep Total Recall: Continual Learning for Human-Like Recall of Artificial Neural Networks; No. RS-2022-00155915, Artificial Intelligence Convergence Innovation Human Resources Development (Inha University); No. 2021-0-02068, Artificial Intelligence Innovation Hub), and Institute for Basic Science (IBS-R015-D1).

Poster No 1873

Harmonization of multi-site MRI data with dual-projection based Linked ICA model

Huashuai Xu[1], Yuxing Hao[1], Huanjie Li[2], Fengyu Cong[2], Tommi Kärkkäinen[1]

[1]Faculty of Information Technology, University of Jyväskylä, Jyväskylä, Finland, [2]School of Biomedical Engineering, Faculty of Medicine, Dalian University of Technology, Dalian, China

Introduction: Merging magnetic resonance imaging (MRI) data from multiple sites has become increasingly popular. However, measurement biases caused by site differences in scanners represent a barrier while pooling data collected from different sites. The existence of site effects can mask biological effects and lead to false findings[2,4,5]. We proposed a dual-projection (DP) method based on the independent component analysis (ICA) method in our previous study[2]. The method demonstrated superior performance in mitigating site effects while preserving biological signals in the context of unimodal MRI data. This study proposes a novel multimodal denoising approach that implements a linked LICA -based DP method to remove the site effects. This method can separate the signal effects from the identified site effects and remove the site effects more completely. A dataset from Autism Brain Imaging Data Exchange II was used to test the proposed LICA-DP denoising method. The results indicate that the LICA-based DP method can remove site effects while preserving true biological variability.

Methods: Data and preprocess We utilized two modalities of functional MRI data, including amplitude of low frequency fluctuation (ALFF), and regional homogeneity (ReHo). The data were from Autism Brain Imaging Data Exchange II (ABIDE II). There were 795 subjects (including Autism Spectrum Disorder (ASD) patients: 341, Healthy Controls (HC): 454). The raw fMRI data were preprocessed with FSL FEAT (https://fsl.fmrib.ox.ac.uk/fsl/fslwiki/FEAT), including removing the first six volumes, motion correction, and spatial normalization to standard MNI space. Two functional modalities, ALFF and ReHo, were generated from the preprocessed fMRI data with DPABI[6]. For ReHo, spatial smoothing (with Full Width at Half Maximum (FWHM) of 6 mm) was performed after ReHo calculation, but for ALFF, spatial smoothing was completed before the calculation[3]. LICA-DP method The LICA[1] toolbox can be downloaded from the FSL website (https://fsl.fmrib.ox.ac.uk/fsl/fslwiki/FLICA). To preserve the signal effects, the traditional LICA method (LICA-SP) only removes those pure site-related components (related to site effects only), and leaves those mixed components without any process. To eradicate the site effects, we propose the LICA-DP method. Firstly, LICA-DP separates the signal effects out from the mixed components. The left noise contributions of the mixed components and the pure site-related components are regarded as the total site effects, which are then cleaned from the non-denoised data via a second projection procedure.

Results: Figure 1 shows an evaluative exploration of the efficacy of different modalities to attenuate site effects. Compared to a unimodal approach, integrating ALFF and ReHo modalities can more effectively eliminate site effects. The LICA-SP method partially mitigates site effects (ALFF+ReHo > unimodal), whereas the LICA-DP approach can eliminate these effects (not impacted by the number of modalities involved). Figure 2 presents the group-level analyses of age effects. The original data only allowed for detecting positive age effects, while negative age effects went undetected. This limitation can be attributed to site effects, which appear to hinder the detection of the negative age-related influence. After harmonization, notably by LICA-DP, we unveiled negative age effects that were not discernible in the non-denoised data.

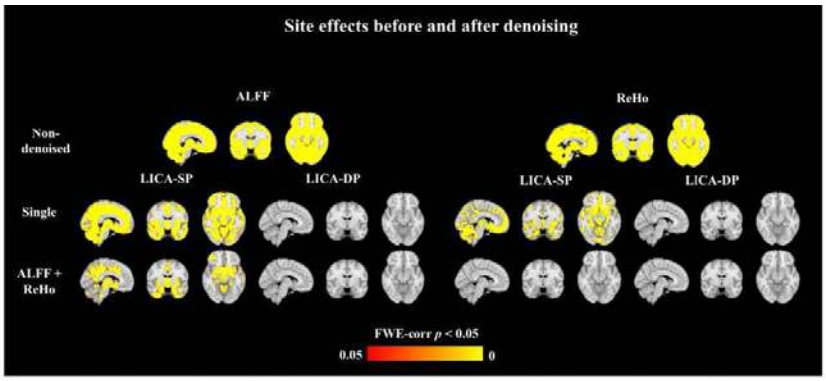

Figure 1. Site effects before and after harmonization. Combining ALFF and ReHo modalities can more effectively eliminate site effects than a unimodal approach. When comparing LICA-SP and LICA-DP, it is observed that LICA-DP consistently achieves complete site effects elimination for unimodal and multimodal data. In contrast, LICA-SP fully removes site effects only in the context of multimodal fusion for ReHo, while in other instances, it achieves only partial site effects reduction.

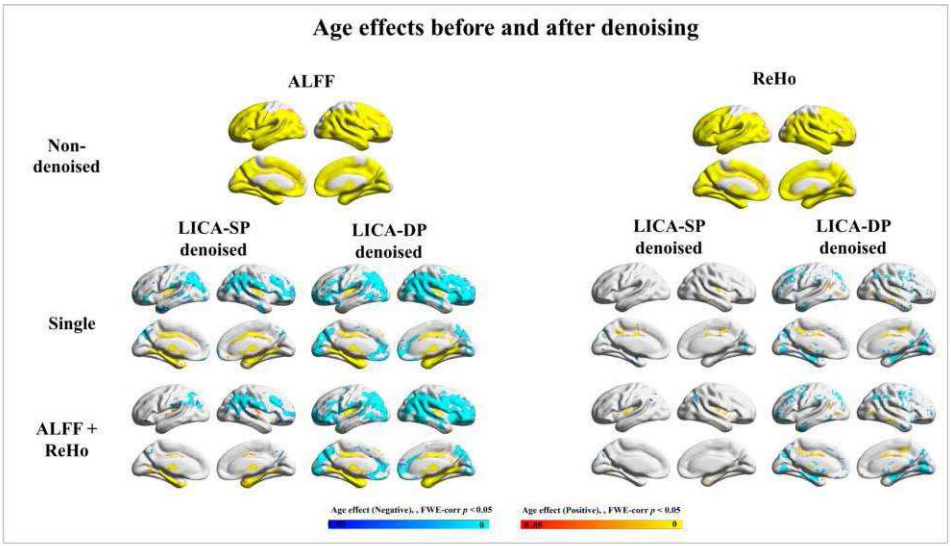

Figure 2. Age effects before and after harmonization. "Positive" association indicates increasing amplitude with increasing age, whereas "Negative" refers to decreasing amplitude with increasing age.

Conclusions: To tackle the shortcomings of not being able to eliminate site effects from the traditional LICA method, we propose a dual-projection data-driven method based on LICA. Compared to traditional LICA methods, which cannot thoroughly eliminate site effects while preserving biological signals, our LICA-DP approach effectively removes site effects and retains biological signals in single and multimodal data scenarios. On the other hand, multimodal fusion yields superior(or at least equivalent) multi-site harmonization results compared to unimodal data.

References

1. Groves, A.R. et al. (2011) 'Linked independent component analysis for multimodal data fusion', NeuroImage, 54(3), pp. 2198–2217. Available at: https://doi.org/10.1016/j.neuroimage.2010.09.073.
2. Hao, Y. et al. (2023) 'Removal of site effects and enhancement of signal using dual projection independent component analysis for pooling multi-site MRI data', European Journal of Neuroscience, 58(6), pp. 3466–3487. Available at: https://doi.org/10.1111/ejn.16120.
3. Jia, X.Z. et al. (2019) 'RESTplus: an improved toolkit for resting-state functional magnetic resonance imaging data processing', Science Bulletin, 64(14), pp. 953–954. Available at: https://doi.org/10.1016/j.scib.2019.05.008.
4. Li, H. et al. (2020) 'Denoising scanner effects from multimodal MRI data using linked independent component analysis', NeuroImage, 208(116388). Available at: https://doi.org/10.1016/j.neuroimage.2019.116388.
5. Xu, H. et al. (2023) 'Harmonization of multi-site functional MRI data with dual-projection based ICA model', Frontiers in Neuroscience, 17. Available at: https://doi.org/10.3389/fnins.2023.1225606.
6. Yan, C.G. et al. (2016) 'DPABI: Data Processing & Analysis for (Resting-State) Brain Imaging', Neuroinformatics, 14(3), pp. 339–351. Available at: https://doi.org/10.1007/s12021-016-9299-4

Poster No 1874

Identification, Characterization, and Mitigation of a Novel Multiband fMRI Signal Artifact

Philip Tubiolo[1], John Williams[2], Jared Van Snellenberg[2]

[1]Stony Brook University, Stony Brook, NY, [2]Stony Brook University Renaissance School of Medicine, Stony Brook, NY

Introduction: Simultaneous multi-slice (multiband; MB) fMRI is an acceleration technique that achieves improved spatiotemporal resolution, leading to its adoption by both individual laboratories and large consortia such as the Human Connectome Project (HCP), Adolescent Brain Cognitive Development (ABCD), and UK Biobank studies. We discovered that unprocessed MB-fMRI images display strongly elevated correlations between the average timeseries in simultaneously acquired (SA) slices, as compared to non-SA (nSA) slices. This indicates the existence of a consequential shared signal between simultaneous slices that cannot be explained by true neural activation patterns. Here, we employ two public datasets (HCP and ABCD) and two in-house datasets to develop an estimation and removal method for this signal, which we term Multiband Artifact Regression in Simultaneous Slices (MARSS).

Methods: We explored resting-state (RS) and working memory (WM) task data from: 1) HCP Young Adult, acquired using a Siemens Connectome Skyra (N=25; MB factor 8); 2) Stony Brook University (SBU) using a Siemens Prisma Fit (N=10; MB factor 6); and 3) New York State Psychiatric Institute (NYSPI) using a GE MR750 (N=10; MB factor 6). We additionally utilized RS data from the ABCD study (N=35; all MB factor 6), which includes data from Siemens Prisma (N=25), GE MR750 (N=3), and Philips

Achieva (N=7) scanners. Data from SBU and NYSPI datasets (in-house) were preprocessed before and after RoMASS using the HCP minimal preprocessing pipeline, with task modeling conducted in SPM12 and Permutation of Linear Models (PALM). MARSS estimates artifact signal separately for each slice as the mean signal across all SA slices (excluding the current slice), orthogonalized with respect to the image's global signal (excluding all SA slices) and motion parameter (MP) estimates (and their squares, derivatives, and squared derivatives). The estimated artifact signal for each slice is then regressed onto each voxel in that slice (in a regression that includes parameters to control for global signal and MPs), and removed from the voxel timeseries via subtraction, to create an artifact-corrected image.

Results: Significantly elevated Pearson correlations between mean slice signals were observed in SA slices as compared to nSA slices in all datasets, and MARSS significantly reduced these correlations in all datasets (all $P < 0.05$). Mean, whole-brain temporal SNR (tSNR) increased following MARSS in all datasets (all $P<0.05$), and the cortical coefficient of variation decreased in 97% and 83% of voxels in the in-house SBU and NYSPI datasets, respectively, resulting in net increases of 1050 and 3838 voxels being included in volume-to-surface mapping during preprocessing. Figure 1 shows the spatial distribution of the artifact estimated by MARSS, calculated as the mean absolute value (over time) of the estimated artifact timeseries, following normalization to MNI space. Single-subject difference images with and without MARSS in un-preprocessed task betas are shown in Figure 2, along with the power spectral density of spatial frequency along the slice direction, demonstrating that MARSS removes spectral power at the fundamental and harmonic frequencies of the spacing between SA slices. In preprocessed group-level data, half of all greyordinates show a t-statistic change after MARSS by a magnitude of at least 0.169 and 0.145 in SBU and NYSPI datasets, respectively, while 10% of t-statistics change by at least 0.490 and 0.415.

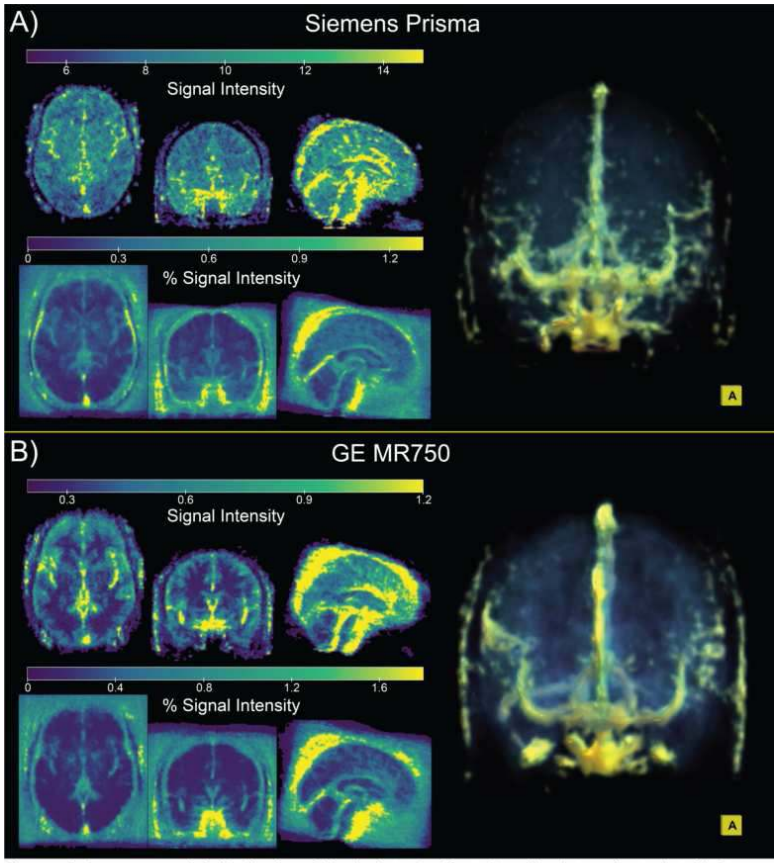

Figure 1. Average spatial distribution of the isolated artifact signal in data collected at A) Stony Brook University (SBU; Siemens Prisma) and B) New York State Psychiatric Institute (NYSPI; GE MR750). Artifact distribution is shown as both raw EPI signal intensity (top left of each panel) and as a percentage of the mean voxelwise EPI intensity (bottom left of each panel). Three-dimensional renders (right of each panel) display anterior view of the raw signal intensity artifact distribution.

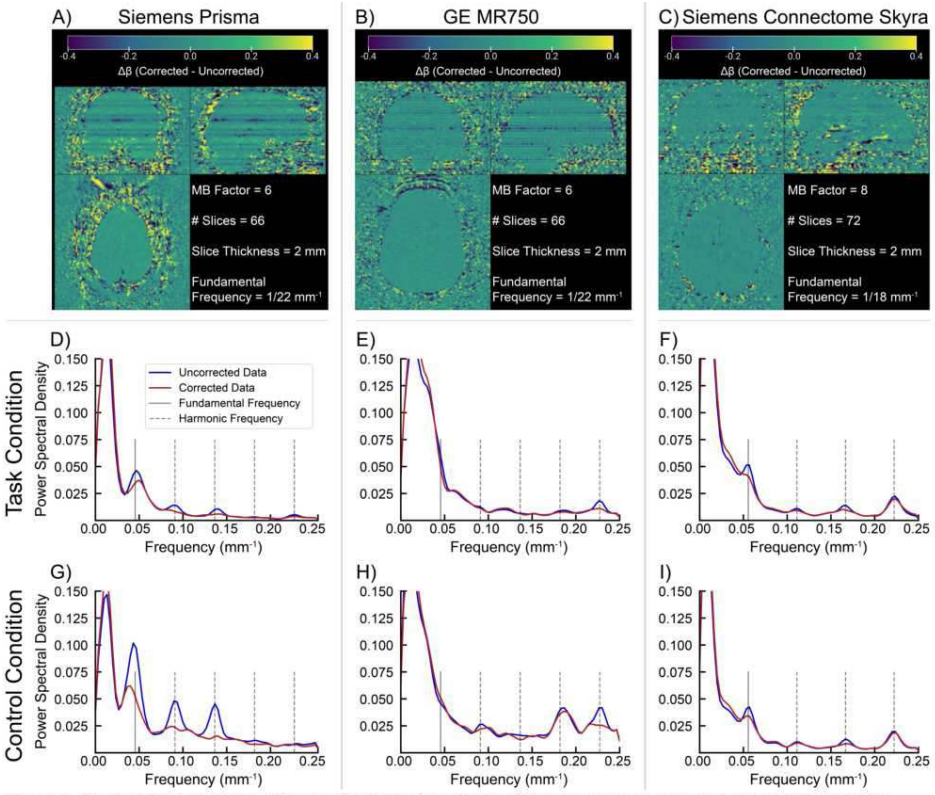

Figure 2. Single-subject examples of the spatial distribution of beta differences between corrected and uncorrected data (Panels A-C), as well as power spectral density (PSD) of average within-subjects betas as a function of spatial frequency (Panels D-I) in uncorrected data (blue line) and corrected data (red line) in data collected from Stony Brook University (SBU; Siemens Prisma; Panels A, D, G), New York State Psychiatric Institute (NYSPI; GE MR750; Panels B, E, H), and the Human Connectome Project (HCP; Siemens Connectome Skyra; Panels C, F, I). In PSD plots, vertical lines denote the fundamental spatial frequency (solid grey line) and harmonic spatial frequencies (dotted grey lines) associated with the simultaneous slice pattern in each dataset. PSD is calculated separately for the task-on condition (D-F) and control condition (G-I) of each task.

Conclusions: These results show that application of MARSS prior to preprocessing: 1) reduces artifactually elevated correlations between the mean signal in each slice of MB fMRI datasets, 2) substantially improves tSNR and the quality of volume-to-surface mapping, and 3) causes dramatic changes in group-level t-statistics that are due to removal of alterations in task betas due to the MB artifact. We recommend that all MB fMRI datasets be cleaned using MARSS prior to standard preprocessing and analysis.

Poster No 1875

A Computational Ontology Framework and Diagnostic Reporting of Brain Atrophy Profiles in Dementia

Devesh Singh[1], Alice Grazia[1], Achim Reiz[2], Andreas Hermann[1,3], Alexander Bernhardt[4,5], Katharina Buerger[4,6], Emrah Düzel[7,8], Klaus Fließbach[9,10], Christoph Laske[11,12], Robert Perneczky[4,13,14,15], Oliver Peters[16,17], Josef Priller[16,18,19,20], Johannes Prudlo[1,21], Anja Schneider[9,10], Annika Spottke[9,22], Matthis Synofzik[11,23], Jens Wiltfang[24,25,26], Frank Jessen[9,27,28], Stefan Teipel[1,29], Martin Dyrba[1]

[1]German Center for Neurodegenerative Diseases (DZNE), Rostock, Germany, [2]Rostock University, Rostock, Germany, [3]Translational Neurodegeneration Section "Albrecht Kossel", Department of Neurology, University Medical Center Rostock, Rostock, Germany, [4]German Center for Neurodegenerative Diseases (DZNE), Munich, Germany, [5]Department of Neurology, University Hospital of Munich, LMU Munich, Munich, Germany, [6]Institute for Stroke and Dementia Research (ISD), University Hospital, LMU Munich, Munich, Germany, [7]Institute of Cognitive Neurology and Dementia Research, Magdeburg, Germany, [8]German Center for Neurodegenerative Diseases (DZNE), Magdeburg, Germany, [9]German Center for Neurodegenerative Diseases (DZNE), Bonn, Germany, [10]University of Bonn Medical Center, Dept. of Neurodegenerative Disease and Geriatric Psychiatry/Psychiatry, Bonn, Germany, [11]German Centre for Neurodegenerative Diseases (DZNE), Tübingen, Germany, [12]Section for Dementia Research, Hertie Institute for Clinical Brain Research and Department of Psychiatry and Psychotherapy, University of Tübingen, Tübingen, Germany, [13]Department of Psychiatry and Psychotherapy, University Hospital, LMU Munich, Munich, Germany, [14]Munich Cluster for Systems Neurology (SyNergy) Munich, Munich, Germany, [15]Ageing Epidemiology Research Unit (AGE), School of Public Health, Imperial College London, London, United Kingdom, [16]German Center for Neurodegenerative Diseases (DZNE), Berlin, Germany, [17]Charité – Universitätsmedizin Berlin, corporate member of Freie

Universität Berlin and Humboldt-Universität zu Berlin-Institute of Psychiatry and Psychotherapy, Berlin, Germany, [18]Department of Psychiatry and Psychotherapy, Charité, Berlin, Germany, [19]School of Medicine, Technical University of Munich; Department of Psychiatry and Psychotherapy, Munich, Germany, [20]University of Edinburgh and UK DRI, Edinburgh, United Kingdom, [21]Department of Neurology, University Medical Centre, Rostock, Germany, [22]Department of Neurology, University of Bonn, Venusberg-Campus 1, Bonn, Germany, [23]Division Translational Genomics of Neurodegenerative Diseases, Hertie Institute for Clinical Brain Research and Center of Neurology, University of Tübingen, Tübingen, Germany, [24]Department of Psychiatry and Psychotherapy, Medical University Göttingen, Göttingen, Lower Saxony, [25]German Center for Neurodegenerative Diseases (DZNE), Göttingen, Germany, [26]Neurosciences and Signaling Group, Institute of Biomedicine (iBiMED), Department of Medical Sciences, University of Aveiro, Aveiro, Portugal, [27]Department of Psychiatry, University of Cologne, Medical Faculty, Cologne, Germany, [28]Excellence Cluster on Cellular Stress Responses in Aging-Associated Diseases (CECAD), University of Cologne, Cologne, Germany, [29]Department of Psychosomatic Medicine, University of Rostock, Rostock, Germany

Introduction: Estimates suggest that the global number of people with dementia could increase to 153 million cases in 2050, with Alzheimer's disease (AD) and frontotemporal lobar degeneration (FTLD) being the most common cause of dementia. The behavioral-variant of frontotemporal dementia (bvFTD) is at times hard to distinguish from AD. Both are marked with regional volumetric loss of grey matter, as visible in T1-weighted MRI scans. Software tools for MRI volumetry can reliably detect and summarize these volumetric findings, however, existing tools often report findings limited to fixed anatomical regions. These tools lack a generalizable framework for aggregating disease pathology at different levels of brain abstractions such as the lobe or hemisphere. They also lack intuitive visualizations for inspecting distinct atrophy profiles in exploratory research. We propose a computational pipeline for quantifying hierarchical volumetric deviations and generating interactive summary visualizations, for the reporting of brain atrophy findings. We also propose a prototypical method of mapping individual MRI scans to possible dementia types.

Methods: The brain segmentation tool FastSurferCNN[1] was utilized as a preprocessing step. We derive anatomical brain region segmentations and associated raw volumes. We used 3433 MRI scans from seven cohorts - two ADNI datasets, AIBL, DELCODE, DESCRIBE, EDSD and NIFD, including healthy control cases, as well as cases with prodromal and clinical AD, and bvFTD. We created a two-step pipeline for disease exploration (Fig. 1). First, we created a semantic model, encoding hierarchical anatomical membership relationships in a Web Ontology Language (OWL) model[2]. The OWL model also includes a computational framework for estimating and aggregating the regional volumetric deviations from normal levels (i.e. w-scores)[3]. Second, we developed a visualization framework, providing visual summary plots implemented with Plotly Sunburst charts. We developed a prototypical framework of similarity quantification, between sample to group averages, to map individual MRI scans to possible dementia types.

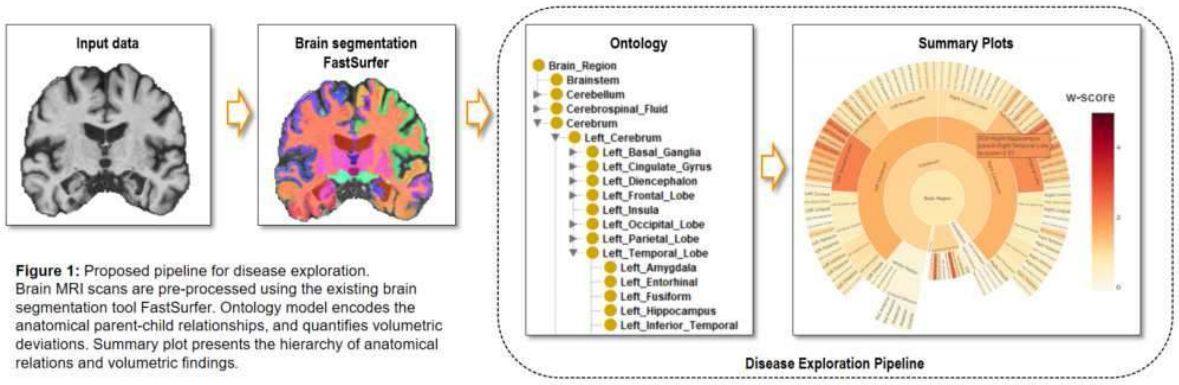

Figure 1: Proposed pipeline for disease exploration. Brain MRI scans are pre-processed using the existing brain segmentation tool FastSurfer. Ontology model encodes the anatomical parent-child relationships, and quantifies volumetric deviations. Summary plot presents the hierarchy of anatomical relations and volumetric findings.

Results: The semantic modeling framework implements computationally efficient calculation of volumetric deviations based on additive linear regression models. The summary plots visualize volumetric deviations at every hierarchical brain abstraction level at once. The summary plots can be used to highlight both mean group characteristics as well as single-subject atrophy profiles, enhancing visual comparison of atrophy profiles with different disease types and phases.

Conclusions: Overall, our pipeline enables an automated and efficient alternative for explorative research and reporting of pathological brain atrophy findings. Our pipeline was able to capture, both visually and numerically, the volumetric changes generally associated with AD progression. The initial results from the prototypical framework for mapping samples to dementia type were also promising. Our pipeline could likely assist clinicians in discovering brain pathologies in an interpretable and reliable manner.

References

1. Henschel, L., Conjeti, S., Estrada, S., Diers, K., Fischl, B., & Reuter, M. (2020), 'FastSurfer - A fast and accurate deep learning based neuroimaging pipeline', NeuroImage, vol. 219.
2. Rosse, C., & Mejino, J. L., Jr (2003), 'A reference ontology for biomedical informatics: the Foundational Model of Anatomy', Journal of biomedical informatics, vol. 36, no. 6, pp. 478–500.
3. Jack, C. R., Jr, Petersen, R. C., Xu, Y. C., Waring, S. C., O'Brien, P. C., Tangalos, E. G., Smith, G. E., Ivnik, R. J., & Kokmen, E. (1997), 'Medial temporal atrophy on MRI in normal aging and very mild Alzheimer's disease', Neurology, vol. 49, no. 3, pp. 786–794.

Poster No 1876

HL-HGAT: A Hodge-Laplacian and Attention Mechanism Approach for Brain Functional Network

Jinghan Huang[1], Anqi Qiu[1,2,3]

[1]Department of Biomedical Engineering, National University of Singapore, Singapore, Singapore, [2]Department of Health Technology and Informatics, Hong Kong Polytechnic University, Kowloon, Hong Kong, [3]Department of Biomedical Engineering, Johns Hopkins University, Baltimore, MD

Introduction: Graph neural networks (GNNs) effectively model complex data relationships and are crucial in fMRI analysis for cognitive and mental disorder studies[1]. Yet, conventional GNNs often overlook complex interrelations beyond node-centric views[2]. Addressing this, our Hodge-Laplacian Heterogeneous Graph Attention Network (HL-HGAT) redefines graphs as simplicial complexes, capturing multi-dimensional data interplay on any k-simplex. We benchmarked HL-HGAT against leading GNN models such as GAT[3], BrainGNN[4], dGCN[5], and Hypergraph NN[6] using the ABCD and OASIS-3 datasets. Our results highlight that HL-HGAT's attention maps offer meaningful insights into neural circuits associated with general intelligence and brain age.

Methods: HL-HGAT combines Hodge-Laplacian (HL) operators and attention mechanisms across k-simplices. Its core consists of three innovative components: HL convolutional filters (HL-filters), multi-simplicial interaction (MSI), and simplicial attention pooling (SAP) operators. The HL-filters, operating within the spectral domain of the k-th HL operators, are enhanced by a novel polynomial approximation method, offering computational efficiency and spatial localization. Although HL-filters primarily operate on specific-dimensional simplices, it is essential to acknowledge that signals on simplices of different dimensions can exhibit intricate interconnections. The MSI module enables signal interaction across distinct dimensional simplices by a simplicial projection operator, which allows signals from k1-simplices to be transformed into k2-simplices, facilitating their fusion and thus facilitating the learning of their interactions. Finally, SAP is designed for efficient spatial dimension reduction of simplices and information pooling. The pooling operator is defined by coarsening the k-simplice and consolidating features associated with these simplices using attention mechanisms. These mechanisms encompass self-attention and cross-attention facilitated through simplicial projection operators and transformers. The simplicial transformers determine the importance of each simplex by learning its weight while gathering signals from its topologically connected simplices, thus evaluating their relevance to a downstream task. For the specific application on brain networks, the k1-simplex and k2-simplex denote node and edge, respectively.

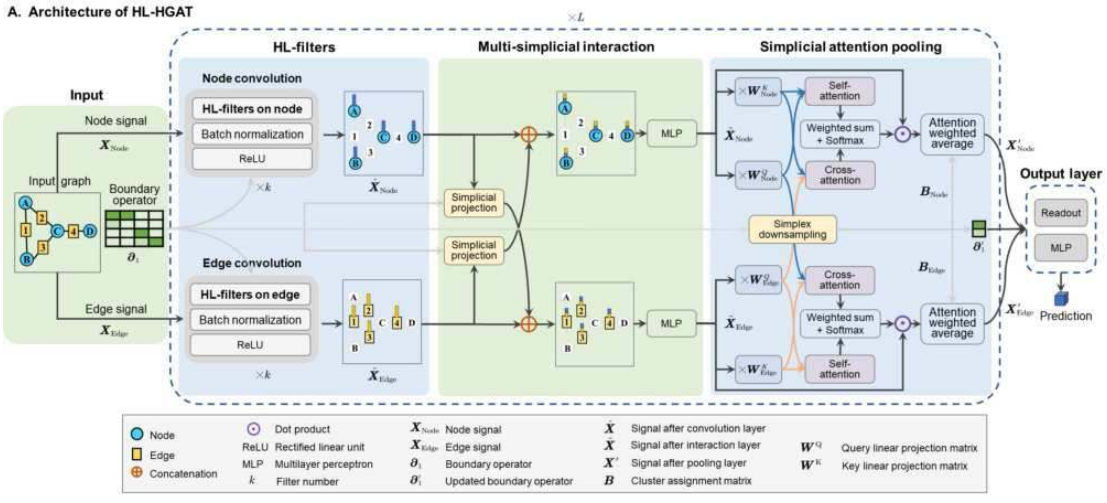

Fig. 1. The Hodge-Laplacian Heterogeneous Graph Attention Network (HL-HGAT) is depicted, revealing three principal components: Hodge-Laplacian filters (HL-filters), multi-simplicial interaction (MSI), and simplicial attention pooling (SAP). Each computational stage commences with HL-filters being applied to the node and edge signals obtained from the previous stage. This is followed by the MSI layer which is responsible for capturing the interactions across nodes and edges. An SAP layer then updates the boundary operator and consolidates features via self- and cross-attention mechanisms. A dedicated output layer is tasked with generating predictions.

Results: We employed two functional MRI datasets, the Adolescent Brain Cognitive Development Study (ABCD, n=7,693)[7] and Open Access Series of Imaging Studies (OASIS-3, n=1,978, https://www.oasis-brains.org/), to predict intelligence and brain age. Our brain graphs utilized 268 regions of interest (ROIs) as nodes[8], linked by edges based on Pearson's correlation across functional time series. Fig. 2(A,B) showcases HL-HGAT's superior performance over baseline models, establishing it as a leading solution in the OASIS and ABCD datasets. For OASIS, HL-HGAT outperforms baseline GNNs like GAT, BrainGNN, and dGCN in node signal processing ($p<0.01$), and eclipses Hypergraph NN in edge signal accuracy ($p=0.02$). ABCD dataset results further confirm HL-HGAT's lower mean absolute errors (MAE) compared to the aforementioned models ($p<0.01$). The last four columns in Fig. 2(A,B) indicate that HL-HGAT's enhanced models (M1 to M4) improve predictive accuracy. Fig. 2(C,D) focuses on the most influential functional connectivities, particularly within the hippocampus and amygdala for brain age, and between prefrontal and parietal regions for intelligence prediction, in line with existing neuroscience research[9-10].

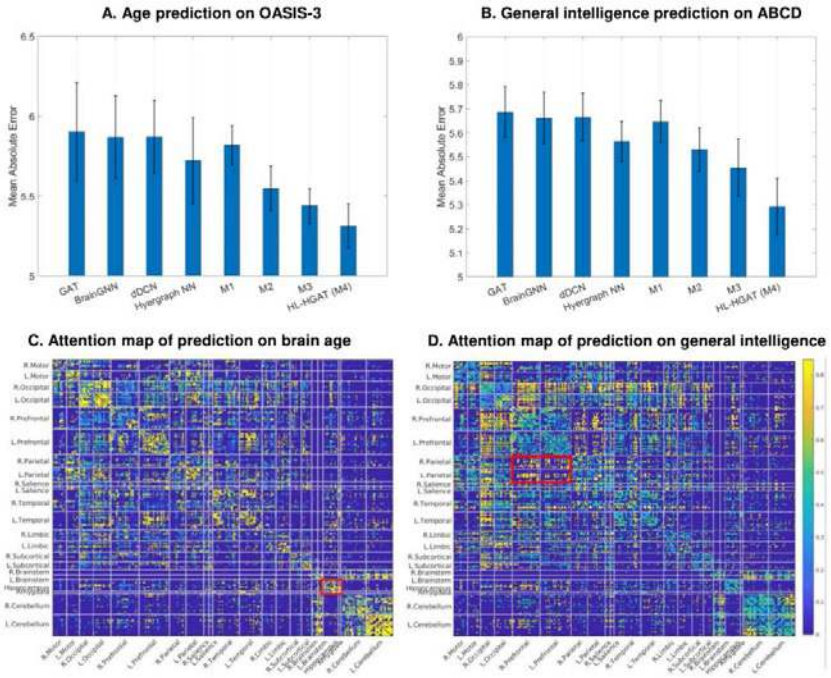

Fig.2. Comparative analysis of our proposed HL-HGAT with leading GNN methodologies on the OASIS-3 (Panel A) and ABCD (Panel B) datasets, illustrating the mean absolute errors complemented by error bars for clarity. An ablation study of HL-HGAT components reveals their individual contributions to enhanced performance: Model 1 (M1) applies HL-filters solely to node signals; Model 2 (M2) extends HL-filters to both node and edge signals; Model 3 (M3) incorporates MSI with node and edge signals; and Model 4 (M4) embodies the complete architecture with all key elements as demonstrated in Fig.1 (A). Panels C and D display averaged attention visualization from the SAP component of HL-HGAT for predicting brain age and general intelligence, respectively. The attention map highlights critical areas and functional connectivity that are essential for understanding age-associated brain changes (Panel C) and the neural activity of intelligence (Panel D), with notable connectivity validated by existing research demarcated in red.

Conclusions: HL-HGAT stands as a substantial advancement in GNN technology. Its proficiency in handling heterogeneous signals, modeling complex interconnections across simplicial dimensions, and ensuring computational efficiency positions it as a versatile tool for brain fMRI analysis.

References

1. Cui, H. et al. Braingb: A benchmark for brain network analysis with graph neural networks. IEEE transactions on medical imaging 42, 493–506 (2022).
2. hou, J. et al. Graph neural networks: A review of methods and applications. AI open 1, 57–81 (2020).
3. Veli ̆ckovic, P. et al. Graph attention networks. International Conference on Learning Representations (2018).
4. Li, X. et al. Braingnn: Interpretable brain graph neural network for fmri analysis. Medical Image Analysis 74, 102233 (2021).
5. Zhao, K. et al. A dynamic graph convolutional neural network framework reveals new insights into connectome dysfunctions in adhd. NeuroImage 246, 118774 (2022).
6. Jo, J. et al. Edge representation learning with hypergraphs. Advances in Neural Information Processing Systems 34, 7534–7546 (2021).
7. Barch, D. M. et al. Demographic, physical and mental health assessments in the adolescent brain and cognitive development study: Rationale and description. Developmental Cognitive Neuroscience 32, 55–66 (2018). URL https://www.sciencedirect.com/science/article/pii/S1878929317300683. The Adolescent Brain Cognitive Development (ABCD) Consortium: Rationale, Aims, and Assessment Strategy.
8. Shen, X. et al. Using connectome-based predictive modeling to predict individual behavior from brain connectivity. nature protocols 12, 506–518 (2017).
9. Nashiro, K., Sakaki, M. & Mather, M. Age differences in brain activity during emotion processing: Reflections of age-related decline or increased emotion regulation. Gerontology 58, 156–163 (2012).
10. Jung, R. E. & Haier, R. J. The parieto-frontal integration theory (p-fit) of intelligence: converging neuroimaging evidence. Behavioral and brain sciences 30, 135–154 (2007).

Poster No 1877

Accelerating multi-echo brain MRI at 7T using variable-density sampling & patch-based regularization

Jyoti Mangal[1], Donovan Tripp[1], Rene Botnar[1,2,3], Claudia Prieto[1,2,3], David Carmichael[1]

[1]School of Biomedical Engineering and Imaging Sciences, King's College London, London, United Kingdom, [2]School of Engineering, Pontificia Universidad Católica de Chile, Santiago, Chile, [3]Institute for Biological and Medical Engineering, Pontificia Universidad Católica de Chile, Santiago, Chile

Introduction: Quantitative mapping is beneficial for a range of neurological applications such as identification and characterisation of small-scale brain architecture[1] but scan times are often long. We previously showed that optimal precision of T2* estimation from multi-echo gradient echo (MEGRE) sequences is achieved at repetition times (TRs) of >30ms at 7T[2]. Even accelerated high-resolution (<0.6mm) multi-parametric maps using parallel imaging[3] with these parameters have clinically infeasible durations and/or remaining aliasing and artefacts at large acceleration factors. Here, we investigated the potential of a patch-based low-rank reconstruction method (HD-PROST)[4] with a variable-density (VD CASPR)[5] undersampling of k-space to efficiently accelerate MEGRE data. We assess the image quality of the reconstructed echo volumes visually and using root mean squared error values.

Methods: Data acquisition: Data acquisition was performed at 7T (Siemens TERRA) for two healthy volunteers (HV). For HV1, a 10-echo GRE at 1mm3 resolution dataset was acquired with the total time of acquisition Tacq =12:26[min:s]. and for HV2, a 7-echo GRE at 0.6mm3 was acquired with Tacq=24:50[min:s]. Both data was fully sampled with an elliptical shutter. The detailed sequence parameters are given in Fig.1 and 2. 'Ground Truth' Reconstruction: The fully sampled data was reconstructed with CG-SENSE[6] for each echo (tolerance=10-10, maxiter=15). Undersampling with VD-CASPR was used in the phase-encoding plane following spiral-like interleaves on the Cartesian grid with denser sampling of k-space centre while maintaining a golden angle step[7] between consecutive spirals. For acceleration factors 6, 8 & 10, two sampling scenarios were considered (a) using identical sampling trajectories for all echo volumes, and (b) sampling the echo volumes such that the spiral interleaves between subsequent volumes were rotated (shifted) to introduce aliasing incoherence. HD-PROST reconstruction: HD-PROST is a regularization framework that performs an iterative low-rank high-order singular value decomposition (HOSVD) of tensors obtained from multiple contrasts (with structural and contrast similarity)[5] which in our case were the multiple echo volumes with different T2* weighting. The low-rank thresholding parameter σ was empirically set to 0.0051. CG-SENSE reconstruction was also performed on the undersampled data for comparison to HD-PROST. Coil compression8 to 16 channels was performed prior all reconstructions. Sensitivity maps for were calculated from the k-space centre using ESPIRiT[8]. Analysis: Visual comparison was made between the undersampling scenarios (a) and (b) for acceleration factor 6, 8 & 10. Root Mean Square Error (RMSE) within the brain (segmented using spm12) quantified differences between each reconstruction and the ground truth (fully sampled CG-SENSE) reconstruction.

Results: Fig 1 shows the results of the reconstructions for HV1 and HV2 for acceleration factors 1,6,8 and 10. The HD-PROST and HD-PROST* reconstructions correspond to the sampling scenario (a) and (b) respectively. Fig. 2 shows the whole brain average RMSE for both HVs. RMSE is reduced for HD-PROST* reconstruction results compared to HD-PROST for all cases showing a clear advantage to altering the phase-encoding between echoes to decrease artifact coherence across the echo-train. Comparison of performance with compressed sensing[9] was not explored but previous work[5] showed HD-PROST was superior.

Conclusions: HD-PROST enables significantly greater acceleration potential than standard parallel imaging approaches owing to the exploitation of information redundancy across contrasts consistent with previous work. We have used redundancy within ME-GRE as the multi-echo images are inherently coregistered and display similar contrast making them suitable for this reconstruction approach.

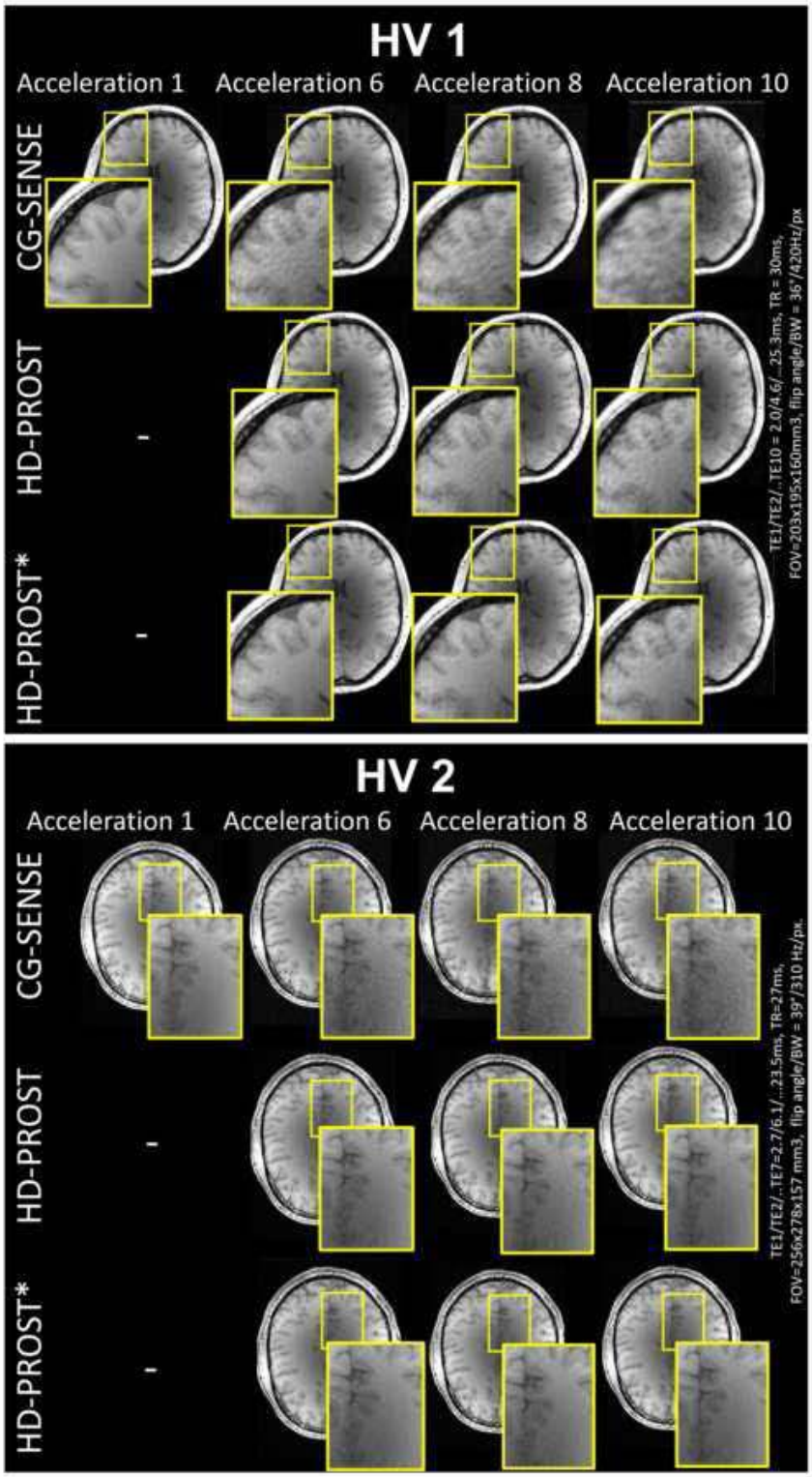

Figure 1 Representative slices showing the reconstruction for HV 1 and 2. The top row corresponds to the CG-SENSE reconstruction for the first echo for each dataset. The second and third row correspond to the HD-PROST reconstruction for sampling scenarios (a) and (b) respectively. The inset shows the representative ROI zoomed in different areas of the cortex. The sequence parameters used for the acquisition of the fully sampled datasets is shown along the right edge of the figure.

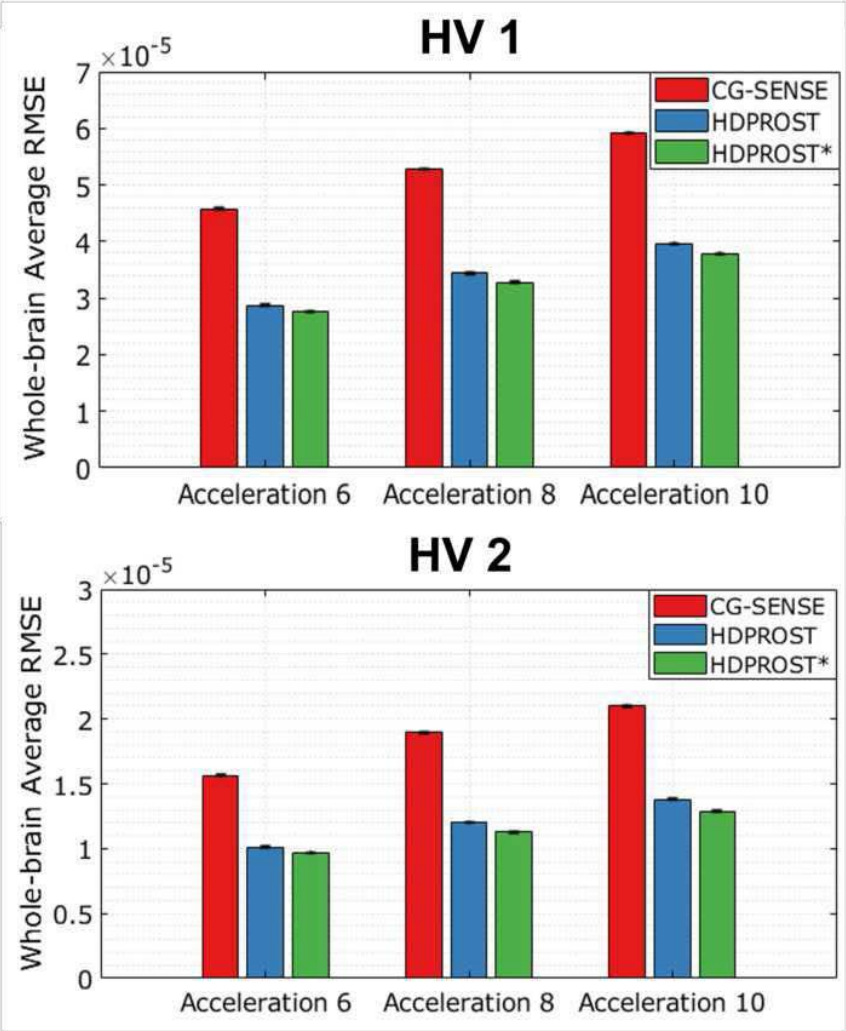

Figure 2. Bar plots showing the whole-brain average RMSE of the reconstructed undersampled first echo volume from the fully sampled CG-SENSE reconstructed volume for acceleration factors 6, 8 and 10. The RMSE for all reconstructions reduces with increase in acceleration factor as expected. The RMSE in the reconstruction for HD-PROST* is clearly lower than RMSE for HD-PROST for all acceleration factors. The errorbar lines represent the standard deviation on the mean of the RMSE.

References

1. Carey, D. (2018), 'Quantitative MRI provides markers of intra-, inter-regional, and age-related differences in young adult cortical microstructure', Neuroimage, 182, 429
2. Mangal J., (2022), ': Simulating the efficiency of Variable Flip Angle (VFA) multi-parametric mapping of T1, PD, and T2* at 7T suggests longer TRs may be optimal', Proceedings of the International Society of Magnetic Resonance
3. Wang, D, (2022), 'Reproducibility of rapid multi-parameter mapping at 3T and 7T with highly segmented and accelerated 3D-EPI', Magnetic Resonance in Medicine,88: 2217-2232
4. Bustin, A (2019), 'High-dimensionality undersampled patch-based reconstruction (HD-PROST) for accelerated multi-contrast MRI', Magnetic Resonance in Medicine, 81: 3705–3719
5. Bustin A (2018), 'Five-minute whole-heart coronary MRA with sub-millimeter isotropic resolution, 100% respiratory scan efficiency, and 3D-PROST reconstruction', Magnetic Resonance in Medicine, 81(1):102-115
6. Pruessmann KP, (1999), 'SENSE: sensitivity encoding for fast MRI', Magnetic Resonance Medicine, 42(5):952-62
7. Prieto, C., (2015), 'Highly efficient respiratory motion compensated free-breathing coronary mra using golden-step Cartesian acquisition', Journal of Magnetic Resonance Imaging, 41: 738-746.
8. Uecker M, (2014), 'ESPIRiT--an eigenvalue approach to autocalibrating parallel MRI: where SENSE meets GRAPPA', Magnetic Resonance in Medicine, 71(3):990-1001
9. Berg RC, (2022), 'Multi-parameter quantitative mapping of R1, R2*, PD, and MTsat is reproducible when accelerated with Compressed SENSE', Neuroimage, 253:119092

Acknowledgements

Funding: This work was supported by EPSRC CDT PhD studentship (JM), Wellcome/EPSRC Centre for Medical Engineering [WT203148/Z/16/Z] and NIHR Biomedical Research Centre based at Guy's and St Thomas' NHS Foundation Trust and King's College London. The views expressed are those of the author(s) and not necessarily those of the NHS, the NIHR or the Department of Health and Social Care. This research was also supported by GOSHCC Sparks Grant V4419 (DC).

Poster No 1878

Physics-informed vessel segmentation for χ-separation (chi-separation)

Taechang Kim[1], Sooyeon Ji[1], Kyeongseon Min[1], Jonghyo Youn[1], Minjun Kim[1], Jiye Kim[1], Jongho Lee[1]

[1]Department of Electrical and Computer Engineering, Seoul National University, Seoul, Korea, Republic of

Introduction: χ-separation offers distributions of paramagnetic and diamagnetic susceptibility sources, presenting valuable information.[6,8] However, both maps show erroneously high susceptibility values in vessels by flow effects[7]. In most studies, vessels are not of interest, interfering accurate quantification of myelin and tissue iron. For a reliable analysis, it is advantageous to remove vessels. In this study, we propose a vessel segmentation method designed for χ-separation.

Methods: The proposed method is illustrated in Fig. 1. [Step 1: Seed generation] For large vessels, we first applied a high pass filter to R2* to suppress non-vessel structures[3]. Then, vesselness[1,2], likelihood of being a vessel, was calculated and thresholded with a high value. For small vessels, maximum intensity projection (MIP) was applied for χpara·|χdia| to enhance the visibility with masking out large vessel seeds from MIP. Then vesselness was calculated and thresholded with a low value. These seeds were backprojected to the original location in 3D. Finally, both large and small vessel seeds are combined, generating the total seed. [Step 2: Vessel geometry characteristics guided-region growing & non-vessel structure removal] If a voxel adjacent to a seed has intensity higher than the upper limit, that voxel was added to the vessel mask. If the intensity is between the upper and lower limit, it was only incorporated into the mask if the condition was satisfied (see Fig. 1, where v is vesselness, Ω is directionality similarity[4], R is intensity ratio between adjacent voxels, and λ2·λ3 is anisotropy (two largest eigenvalues from the Hessian matrix of voxel intensity[2])). To exclude non-vessel structures, connected components (CC) whose average value of anisotropy is lower than threshold (A∈[0.0001,0.004]) were removed assuming high anisotropy in vessels. Evaluation The proposed method was compared with a Frangi filter[2] and REF 10 with and without R2* as input. To test the robustness, the method was applied to various resolutions and field strengths (1.5×1.5×1.5 mm3 and 1×1×1 mm3 at 3 T; 0.8×0.8×1.2 mm3 and 0.65×0.65×0.65 mm3 at 7 T) and χ-separation algorithms (COSMOS[9], MEDI, iLSQR, and χ-sepnet[5]). Applications (1) Using 6 subject data for χ-separation-COSMOS[9], quantitative metrics (RMSE, PSNR and SSIM) were calculated to evaluate the performance of χ-sepnet[5] with, without and within the vessel mask. (2) Using 106 subjects, an χ-separation atlas was developed with and without the vessel mask. Twenty ROIs were analyzed to quantify the proportion of vessel and the population average.

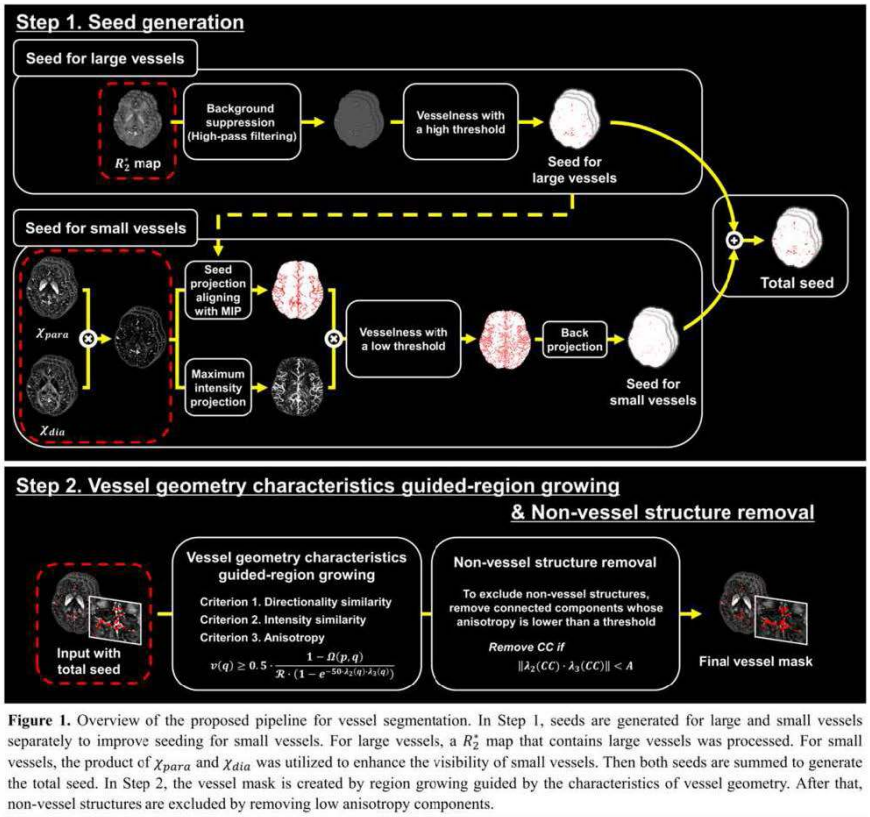

Figure 1. Overview of the proposed pipeline for vessel segmentation. In Step 1, seeds are generated for large and small vessels separately to improve seeding for small vessels. For large vessels, a R_2^* map that contains large vessels was processed. For small vessels, the product of χ_{para} and χ_{dia} was utilized to enhance the visibility of small vessels. Then both seeds are summed to generate the total seed. In Step 2, the vessel mask is created by region growing guided by the characteristics of vessel geometry. After that, non-vessel structures are excluded by removing low anisotropy components.

Results: Our method successfully generated vessel masks for χpara and χdia excluding non-vessel structures (yellow arrows in Fig. 2 (a)), when compared to the conventional methods. When tested for different resolutions, field strengths and

χ-separation algorithms, the proposed method yielded robust outcomes (Fig. 2 (b), (c)). The quantitative metrics computed with the vessel mask reported improved accuracy, suggesting that vessels are the source of variability. (RMSE: 0.0147±0.0015 ppm to 0.0115±0.0010 ppm; PSNR: 36.7260±0.9111 to 38.8034±0.7878; SSIM: 0.9258±0.0071 to 0.9269±0.0070) In the χ-separation atlas, caudate in χpara and genu in χdia revealed the highest vessel occupation (≥1 % voxels), demonstrating statistically significant decrease in the susceptibility values after applying the mask (caudate: 49.6±7.0 ppb to 47.4±6.9 ppb; genu: 30.3±2.4 ppb to 29.3±2.3 ppb; p<0.05/20).

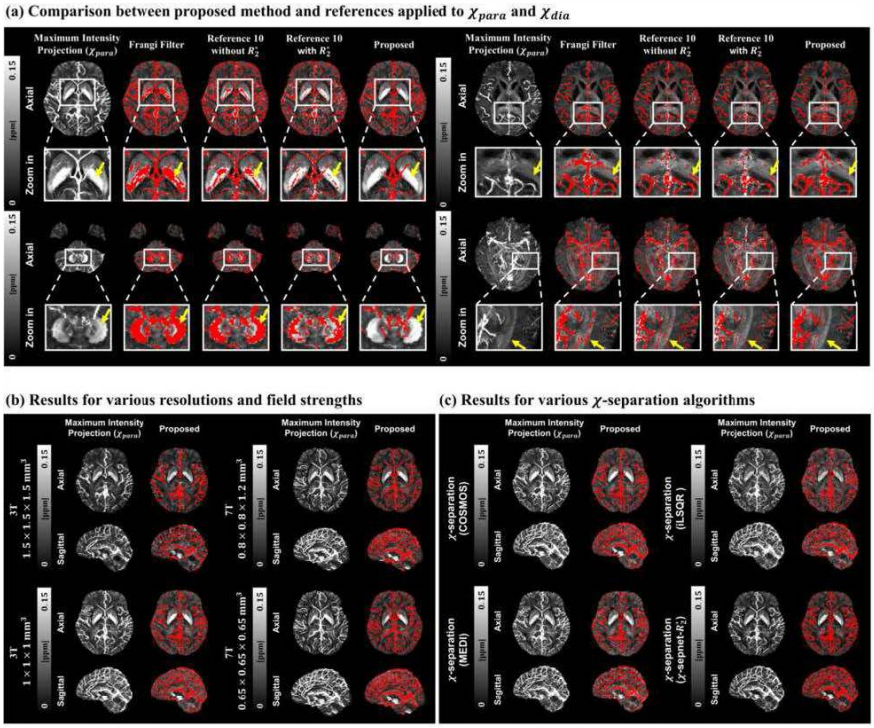

Figure 2. Evaluation of the proposed vessel segmentation algorithms. (a) Comparison of the proposed vessel segmentation algorithm with the conventional methods applied to χ_{para} and χ_{dia}. Deep gray matters such as globus pallidus and dentate nucleus, and white matters including the splenium of corpus callosum and optic radiation are erroneously segmented in the conventional methods (yellow arrows). Vessel segmentation results from various (b) resolutions, field strengths and (c) χ-separation algorithms. All results show successful segmentation of vessels, demonstrating robustness of the proposed method.

Conclusions: The proposed vessel segmentation method shows excellent performance in generating a vessel mask. When the mask is applied for the analysis, it improved the results by reducing variability from vessels.

References

1. Alhasson, H. F. et al. (2019), 2D and 3D Vascular Structures Enhancement via Multiscale Fractional Anisotropy Tensor. arXiv doi:10.48550/arxiv.1902.00550.
2. Frangi, A. et al. (1998), Multiscale Vessel Enhancement Filtering. Medical Image Computing and Computer-Assisted Intervention — MICCAI'98, First International Conference Cambridge, MA, USA, October 11–13, 1998 Proceedings.
3. Jin, Z. et al. (2014), Background-Suppressed MR Venography of the Brain Using Magnitude Data: A High-Pass Filtering Approach. Computational and Mathematical Methods in Medicine, 812785.
4. Kerkeni, A. et al. (2016), A coronary artery segmentation method based on multiscale analysis and region growing. Computerized Medical Imaging and Graphics 48, 49–61.
5. Kim, M. et al. (2022), Chi-sepnet: Susceptibility source separation using deep neural network. Proceedings of International Society of Magnetic Resonance in Medicine 30, 2464.
6. Kim, W. et al. (2023), χ-Separation Imaging for Diagnosis of Multiple Sclerosis versus Neuromyelitis Optica Spectrum Disorder. Radiology 307, e220941.
7. Larson, T. C. et al. (1990), Spatial misregistration of vascular flow during MR imaging of the CNS: cause and clinical significance. American Journal of Neuroradiology 11, 1041–8.
8. Shin, H.-G. et al. (2021), χ-separation: Magnetic susceptibility source separation toward iron and myelin mapping in the brain. NeuroImage 240, 118371.
9. Shin, H.-G. et al. (2022), chi-separation using multi-orientation data in invivo and exvivo brains: Visualization of histology up to the resolution of 350μm. Proceedings of International Society of Magnetic Resonance in Medicine 30, 0771.
10. Straub, S. et al. (2022), A novel gradient echo data based vein segmentation algorithm and its application for the detection of regional cerebral differences in venous susceptibility. NeuroImage 250, 118931.

Poster No 1879

Application of 3D-FFDNet technique for Image Denoising in functional MRI

Hu Cheng[1], Sophia Brink[1], Daniel Kennedy[1]

[1]*Indiana University, Bloomington, IN*

Introduction: Deep learning based denoising methods are more robust compared to conventional ones. Among them, FFDnet[1] has emerged as an effective denoising technique based on a convolutional neural network architecture. One of the advantages is it can handle different noise level and has a tuning parameter to balance the blurring and denoising effects. The original FFDNet method was primarily developed for 2D applications. In order to apply this technique in denoising 3D MRI images, we generalized this method to 3D. To our knowledge, it is still a tradition in fMRI data analysis to reduce the noise through spatial smoothing, which decreases the effective resolution and introduce more partial volume effect. Here we propose the application of 3D-FFDNet to reduce the thermal noise in fMRI images without compromising the resolution significantly.

Methods: Our FFDNet model architecture comprises 5 CNN layers, each with 64 features and a 3-voxel convolution kernel. We trained the model with 61 T1-weight images acquired with the HCP lifespan protocol. Employing a patch size of 44 and a stride of 15, we augmented the dataset, generating 310,000 patches for training. Rician noise was added to the patches for training. The learning rate was initially set to 0.001, and reduced to 0.0001 after 50 epochs. The code was written in pytorch based on the 2D version provided by Tassano et al.[2]. The code is available at https://github.com/huchengMRI. The 3D-FFDNet denoising was applied on higher resolution MPRAGE images (0.6x0.6x0.8 mm3) and EPI images (1 mm isotropic) acquired on a Siemens 3T scanner. We also applied the denoising method on an HCP dataset (ID: 141826) to investigate the impacts on temporal SNR and brain activation of a finger tapping task. All analyses were conducted using SPM, FSL, AFNI, or Matlab codes.

Results: Fig. 1A shows the outcome of FFDNet denoising on a high-resolution T1-weighted image, revealing a visually cleaner result that retains intricate anatomical details. In Fig. 1B, the denoising effect on an EPI image commonly used in fMRI is demonstrated, exhibiting enhanced clarity without compromising sharpness. The difference image underscores variations in denoising performance across different brain regions, suggesting potential challenges in preserving contrast in regions with abrupt signal changes. As a comparison, Fig. 1C presents three smoothed images with Gaussian kernels of 2 mm, 4 mm, and 6 mm. As the kernel size increases, the image gets more blurred. The denoised image maintains superior sharpness. Fig. 2 illustrates the effect of denoising on fMRI activations. First, we conducted a comparative analysis with Gaussian smoothing employing various kernel sizes, quantifying smoothness through AFNI's 3dFWHMx functionality. In Figure 2A, the plot reveals that denoising achieves a level of smoothness equivalent to Gaussian smoothing with a 1.4 mm kernel. However, denoising surpasses Gaussian smoothing in terms of temporal SNR (TSNR) computed on an HCP resting state fMRI dataset (Fig. 2B). Finally, the impact of denoising on fMRI activation during left-hand finger tapping was contrasted with Gaussian smoothing using two different kernels: 1.4 mm and 4 mm. With a 1.4 mm Gaussian kernel, sparse activations were observed in the motor area, whereas the proposed denoising method revealed continuous activation along the gray matter folds. Employing a 4.0 mm Gaussian kernel resulted in continuous activation, but slightly extending into the white matter region.

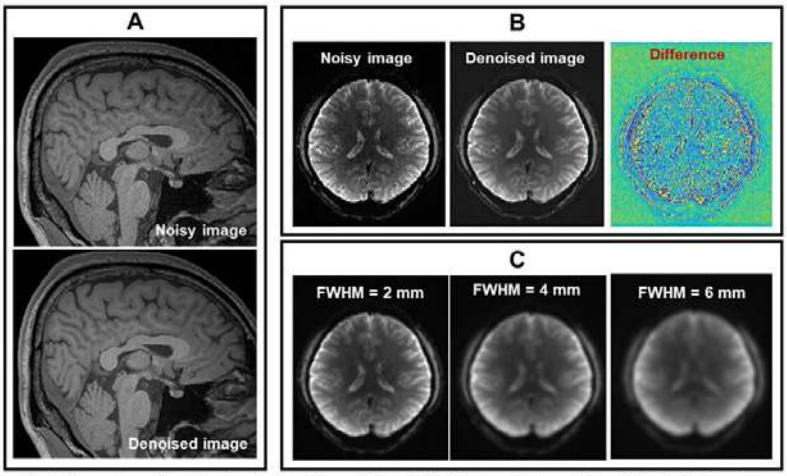

Fig. 1: Examples of the denoiser. A: Denoising of T1-weighted image with voxel size of 0.6x0.6x0.8 mm³. B: Denoising of an EPI image with voxel size of 1x1x1 mm³. The difference between the original image and the denoised one is also shown, indicating potential challenges in areas with abrupt signal changes. C: Gaussian smoothing with different kernel sizes on the noisy image in B. The denoised image clearly shows better resolution than these smoothed images.

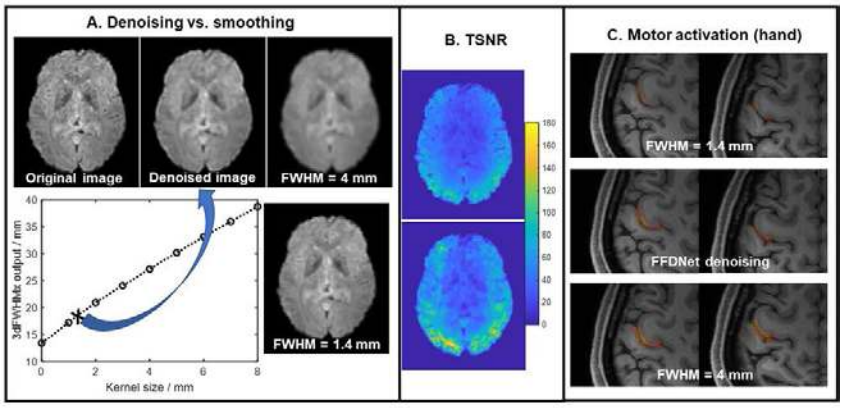

Fig. 2: Denoising results on HCP data. A: The plot illustrates effective smoothness, computed using AFNI's 3dFWHMx functionality, plot against the smoothing kernel size. The denoising process introduces some smoothing, aligning with a kernel size of 1.4 mm on the plot. B: Temporal SNR computed on an HCP resting state fMRI dataset for denoised image (bottom) and smoothed image with 1.4 mm kernel (top). C: The activation pattern of left-hand finger tapping is superimposed on the anatomical image, showcasing the impact of three different noise reduction approaches in preprocessing (Gaussian smoothing with 1.4 mm kernel, FFDNet denoising, and Gaussian smoothing with 4.0 mm kernel).

Conclusions: Our study demonstrates the efficacy of 3D-FFDNet denoising in reducing noise while preserving image resolution. Notably, the model, trained on a relatively small dataset of T1-weighted images, exhibits promising noise reduction capabilities when applied to T2-weighted EPI images, surpassing the performance of spatial smoothing in the context of fMRI. Future work will focus on optimizing the model by increasing sample size and including more contrasts.

References

1. Zhang, K., Zuo, W., Zhang, L. (2018), FFDNet: Toward a Fast and Flexible Solution for CNN based Image Denoising. arXiv:1710.04026.
2. Tassano, M., Delon, J., Veit, T. (2019), An Analysis and Implementation of the FFDNet Image Denoising Method. IPOL, Vol. 9, pp. 1–25. https://doi.org/10.5201/ipol.2019.231.

Poster No 1880

A massive multimodal fMRI dataset bridging naturalistic processes and experimental cognitive tasks

Heejung Jung[1], Maryam Amini[1], Bethany Hunt[2], Eilis Murphy[1], Patrick Sadil[3], Yaroslav Halchenko[1], Zizhuang Miao[1], Philip Kragel[4], Xiaochun Han[5], Mickela Heilicher[6], Bogdan Petre[1], Owen Collins[7], Martin Lindquist[3], Tor Wager[1]

[1]Dartmouth College, Hanover, NH, [2]University of Vermont, Burlington, VT, [3]Johns Hopkins University, Baltimore, MD, [4]Emory University, Atlanta, GA, [5]Beijing Normal University, Beijing, China, [6]University of Wisconsin-Madison, Madison, WI, [7]University of California, Irvine, Irvine, CA

Introduction: Cognitive neuroscience has advanced significantly due to the availability of openly shared datasets. Large sample sizes, large amounts of data per person, and diversity in tasks and data types are all desirable, but are difficult to achieve in a single dataset. Here, we present an open dataset with N = 101 participants and 7.5 hours of scanning per participant, with six multifaceted cognitive tasks including 1.5 hours of naturalistic movie viewing. This dataset's combination of ample sample size, extensive data per participant, and a wide range of experimental conditions – including cognitive, affective, social, and somatic/interoceptive tasks – positions it uniquely for probing important questions in cognitive neuroscience.

Figure 1. Overview of acquired data

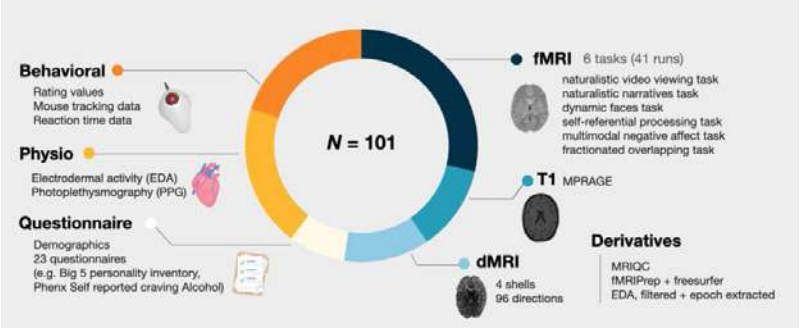

Methods: Six tasks with 20 experimental conditions were administered to adult participants, scanned across four sessions (mean ± s.d. age: 24.7 ± 5.5 years; 69 females, 45 males, 2 other). The dataset includes: 1) a T1-weighted anatomical scan, 2) a multi-shell diffusion weighted MRI (dMRI) scan, 3) functional BOLD echo-planar imaging during cognitive tasks (TR = 460 msec, MB = 8), 4) behavioral and 5) physiological data collected during scanning, and 6) a battery of questionnaires prior to scanning. Tasks completed in the scanner include: a) a naturalistic video viewing task, in which participants watch videos and report their evoked emotions; b) a naturalistic narratives task, in which participants listen/read a series of narratives; c) a dynamic faces task, in which participants view video clips of experimentally manipulated faces with difference age, race, gender, and facial expressions; d) a self-referential processing task, in which participants assess characters in terms of similarity, likability, and mental state attribution; e) a multimodal negative affect task, in which participants experience somatic pain, vicarious pain, and cognitive effort with different levels of predictive cues; and 6) a fractionated overlapping task, in which participants complete two out of four tasks, including text-based theory of mind (i.e. false-belief task; Dodell-Feder et al., 2011), image-based theory of mind (i.e. why/how task; Spunt & Adolphs, 2014), memory (e.g. old/new encoding/retrieval task), and attention reorienting tasks (Posner, 1980). To ensure consistency and reproducibility, we published the experiment presentation code as a package prior to initiating data collection. Furthermore, each experimenter rigorously followed a predefined dialogue script when providing instructions and guidance to participants.

Results: All data conform to Brain Imaging Data Structure (BIDS) conventions and are managed by Datalad, and will be shared publicly on the OpenNeuro archive. The neuroimaging data were preprocessed using fmriprep ver 21.0.2 (Esteban et al., 2019). Regarding quality control, head movement was kept to a minimum, as demonstrated by framewise displacement lower than that of the UK biobank, in spite of the longer scan protocol (Wilcoxon Rank-Sum Test; $W = 49313721$, $p < .001$). Preliminary results from the multimodal negative affect task indicate distinct activation for each modality. Somatic pain activates the canonical pain network, including the insular, somatosensory, and dorsal anterior cingulate cortices. Vicarious pain primarily engages the fusiform gyrus and superior temporal sulcus. Cognitive discomfort involves the attentional network, involving the intraparietal sulcus. Finally, button responses show significant activation in the primary motor cortex.

Figure 2. Contrast of somatic pain, cognitive effort, vicarious pain, and button press. All maps (N=97) are compared against baseline and FDR corrected ($q < .0001$).

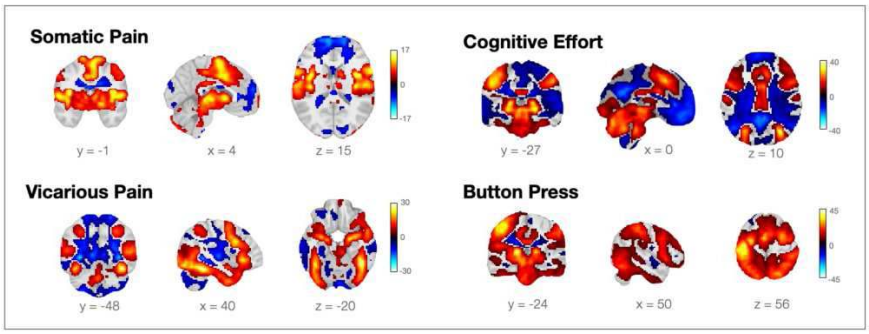

Conclusions: We present a large-scale quality-controlled dataset with multiple cognitive tasks, which provides a testbed to explore novel research questions with a sufficiently large sample size for meaningful effect size. Utilizing this dataset, future studies can construct models of semantic decoding using the naturalistic movie viewing and narratives task or develop markers of affective systems, involving somatic pain, observed pain, and cognitive effort.

References

1. Esteban, O. (2019), 'fMRIPrep: a robust preprocessing pipeline for functional MRI', Nature Methods, 16(1), 111-116.
2. Dodell-Feder, D. (2013), 'Using fiction to assess mental state understanding: a new task for assessing theory of mind in adults', PloS one, 8(11), e81279.
3. Posner, M. I. (1980), 'Orienting of attention', Quarterly Journal of Experimental Psychology, 32(1), 3-25.
4. Spunt, R. P. (2014), 'Validating the why/how contrast for functional MRI studies of theory of mind', Neuroimage, 99, 301-311.

Poster No 1881

Acquisition and evaluation of sub-millimetre resolution GE-BOLD laminar fMRI datasets at 3T and 7 T

Sriranga Kashyap[1], Prathamesh Chopade[2], Seong-Gi Kim[3], Kamil Uludag[1,4,5]

[1]Krembil Brain Institute, University Health Network, Toronto, Ontario, Canada, [2]Center for Neuroscience Imaging Research, Institute for Basic Science, Suwon, Korea, Republic of, [3]Center for Neuroscience Imaging Research, Institute for Basic Science, Sungkyunkwan University, Suwon, Korea, Republic of, [4]Department of Medical Biophysics, University of Toronto, Toronto, Ontario, Canada, [5]Center for Neuroscience Imaging Research, Institute for Basic Science & Department of Biomedical Engineering, Sungkyunkwan University, Suwon, Korea, Republic of

Introduction: The study aims to, first, investigate the feasibility of sub-millimetre functional magnetic resonance imaging (fMRI) in human subjects using gradient-echo BOLD (GE-BOLD) contrast at standard clinical field strengths of 3T, and, second, to characterise the patterns of activation and temporal signal-to-noise ratio (tSNR) values in the same subjects scanned on both 3 and 7T field strengths. The feasibility of sub-millimetre resolution GE-BOLD fMRI enables the investigation of layer-specific differences in wider cohorts than is currently possible at ultra-high field strengths due to the ubiquity of 3T MRI scanners as well as the GE-BOLD fMRI sequence available on all vendor platforms.

Methods: 12 healthy participants were scanned on a Siemens 3T Prisma and 7T Terra using a 2D-EPI sequence at nominal resolutions of 0.6, 0.7, 0.8 and 0.9 mm isotropic, respectively. Data were acquired oblique coronal covering at least V1 and V2 (60 slices). Other sequence parameters were adapted to enable scanning within SAR limits with the TE/TR being 44/3000-3600 ms and 28-35/2500-3000 ms at 3 and 7T, respectively. A 0.6 mm isotropic MP2RAGE acquired at 7T served as the anatomical reference. All participants were shown eight blocks of 20 (on) - 40 (off) flickering checkerboard per run to elicit visual activation (Figure 1). Data from both scanners were corrected for gradient nonlinearities using the HCP's grad_unwarp tool and denoised using NORDIC[1]. A high-resolution slab-optimised pipeline using ANTs[2] was used for data pre-processing and AFNI[3] for statistical analyses.

Results: Fig1b shows that NORDIC improves the activation maps both at 3 and 7T for all resolutions, but has a more significant effect for 3T data demonstrated by activation volume for 3T 0.9 mm being similar to 7T 0.6 mm. Fig1c illustrates on a single subject that tSNR maps for resolutions 0.6-0.9 mm isotropic are highly comparable between 3 and 7T and is indicative of the robust performance of product 2D-EPI sequence. Fig2a shows that robust activation maps can be obtained in a single run in less than 10 min, even at 0.6 mm at 3T. Consistent with expectations, 7T yields increased contrast-to-noise (CNR) of the BOLD signal (z-statistics) compared to 3T as is evident from the histogram difference plots. Laminar profiles in Fig2b show the characteristic GE-BOLD signal increase to the pial surface for all data and consistent with activation maps in Fig2b, 7T has a higher dynamic range across depths than at 3T.

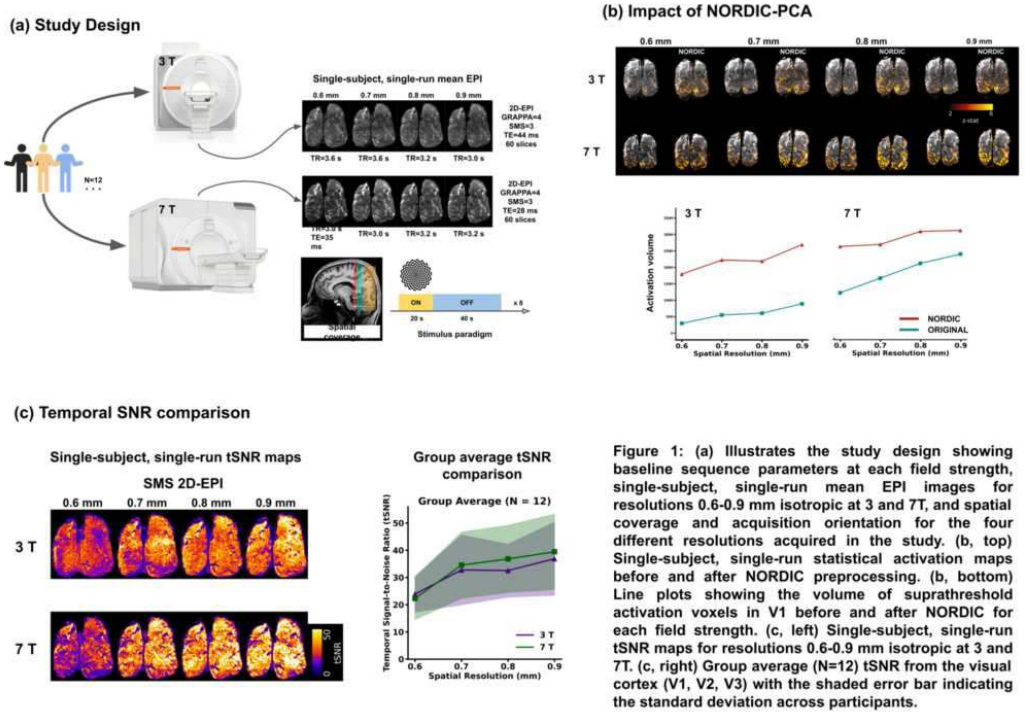

Figure 1: (a) Illustrates the study design showing baseline sequence parameters at each field strength, single-subject, single-run mean EPI images for resolutions 0.6-0.9 mm isotropic at 3 and 7T, and spatial coverage and acquisition orientation for the four different resolutions acquired in the study. (b, top) Single-subject, single-run statistical activation maps before and after NORDIC preprocessing. (b, bottom) Line plots showing the volume of suprathreshold activation voxels in V1 before and after NORDIC for each field strength. (c, left) Single-subject, single-run tSNR maps for resolutions 0.6-0.9 mm isotropic at 3 and 7T. (c, right) Group average (N=12) tSNR from the visual cortex (V1, V2, V3) with the shaded error bar indicating the standard deviation across participants.

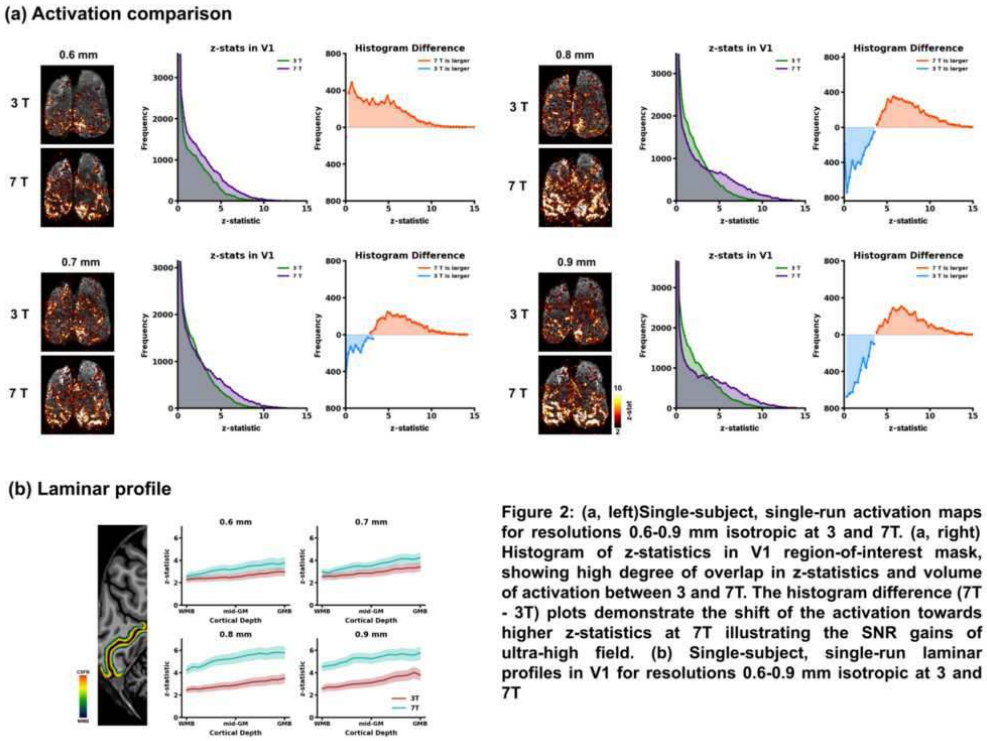

Figure 2: (a, left)Single-subject, single-run activation maps for resolutions 0.6-0.9 mm isotropic at 3 and 7T. (a, right) Histogram of z-statistics in V1 region-of-interest mask, showing high degree of overlap in z-statistics and volume of activation between 3 and 7T. The histogram difference (7T - 3T) plots demonstrate the shift of the activation towards higher z-statistics at 7T illustrating the SNR gains of ultra-high field. (b) Single-subject, single-run laminar profiles in V1 for resolutions 0.6-0.9 mm isotropic at 3 and 7T

Conclusions: Numerous fMRI studies have shown that spatial patterns of neuronal activation can be resolved at a mesoscale (< 1 mm) using the GE-BOLD signal. However, mesoscale fMRI at 3T (and 7T) has been fraught with challenges particularly due to low SNR at sub-millimetre resolutions. While there exists previous work on attempting laminar fMRI at 3T, they often require bespoke coils, offline reconstruction, have limited spatial coverage and/or temporal resolutions[4-9]. We demonstrate the feasibility of acquisition of highest spatial resolution fMRI at 3T (0.6 mm isotropic) using the vendor sequence. We show that novel denoising methods such as NORDIC-PCA enables robust high-resolution fMRI at 3T for resolutions 0.6-0.9 mm isotropic with activation maps that are comparable to those acquired at 7T. The present work successfully pushes the boundary of what has been thus far considered infeasible or difficult to achieve at standard clinical field strengths, showcasing a systematic characterisation of sub-millimetre resolution fMRI data. Our work broadens accessibility to high-resolution fMRI at 3T. Thus, encouraging new directions in neuroimaging and enabling a deeper understanding of human brain function in health and disease, impacting not only neuroscientists but also the broader scientific and medical communities.

References

1. Vizioli, L. (2021), Lowering the thermal noise barrier in functional brain mapping with magnetic resonance imaging, Nature Communciations 12, 5181
2. Avants, B. B. (2009), Advanced Normalization Tools: V1.0, Insight Journal 2.365: 1-35
3. Cox R. W. (1996). AFNI: software for analysis and visualization of functional magnetic resonance neuroimages. Computers and biomedical research, an international journal, 29(3), 162–173
4. Ress, D. (2007). Laminar profiles of functional activity in the human brain. NeuroImage, 34(1), 74–84
5. Koopmans, P. J. (2010). Layer-specific BOLD activation in human V1. Human brain mapping, 31(9), 1297–1304
6. Markuerkiaga, I. (2021). An in-vivo study of BOLD laminar responses as a function of echo time and static magnetic field strength. Scientific reports, 11(1), 1862.
7. Knudsen, L. (2023). Improved sensitivity and microvascular weighting of 3T laminar fMRI with GE-BOLD using NORDIC and phase regression. NeuroImage, 271, 120011
8. Huber L (2023) Evaluating the capabilities and challenges of layer-fMRI VASO at 3T. Aperture Neuro. 2023;3:1-17
9. Chang, W.-T. (2023) Enabling brain-wide mapping of directed functional connectivity at 3T via layer-dependent fMRI with draining-vein suppression. bioRxiv 2023.10.24.563835

Poster No 1882

Synthetic generation of FDG-PET from T1-weighted MRI

Debabrata Mishra[1], Zhaolin Chen[2,3], Kh Tohidul Islam[2], Patrick Kwan[1,4], Meng Law[1,5], Lucy Vivash[1,4], Ben Sinclair[1,4]

[1]Dept. of Neuroscience, Monash University, Melbourne, Australia, [2]Monash Biomedical Imaging, Monash University, Melbourne, Australia, [3]Dept. of DSAI, Monash University, Melbourne, Australia, [4]Dept. of Neurology, The Alfred Hospital, Melbourne, Australia, [5]Dept. of Radiology, The Alfred Hospital, Melbourne, Australia

Introduction: Fluorodeoxyglucose-positron emission tomography(FDG-PET) is a valuable tool for the diagnosis and management of a variety of brain disorders, including Alzheimer's disease (AD), frontotemporal dementia (FTD), and dementia with Lewy bodies (DLB) as well as malignancy[3,5]. However, its high cost and limited availability often pose significant challenges. Using generative AI to synthesise FDG-PET from T1-weighted MRI, a more widely accessible and affordable imaging modality, offers a promising solution to overcome these challenges. This promising technique could provide complementary information latent in the MRI images, that would usually require FDG-PET to attain, thereby enhancing diagnostic accuracy and treatment planning, leading to improved patient outcomes and overall healthcare efficiency.

Methods: Dataset and image preprocessing We acquired MRI and FDG-PET data from 1146 patients from ADNI(Alzheimer's Disease Neuroimaging Initiative) diagnosed as MCI, AD and CN. FDG-PET images with multiple time frames were averaged to give a single FDG-PET per subject. MRI and PET images were resized to a dimension of 170x170x170. Model Training Our study utilised a cycle-consistent Generative adversarial network(GAN)[6] framework with ResNet generator networks comprising of 10 residual blocks and PatchGAN discriminators to unpaired translation of T1-weighted MRI into synthesised FDG-PET scans. The ResNet generator uses skip connections to combine multi-scale features from each residual block, which helps improve detail and image quality in the translation. Compared to previous approaches, this deeper ResNet architecture has increased representational capacity to capture the intricate mappings between MRI and PET modalities. For the discriminator networks we use 128x128x32 PatchGANs, which aim to classify whether overlapping subdivisions (patches) of the full image, of size 128x128x32 are real or fake. Using this architecture, the model will synthesise a FDG-PET from an input MRI and vice-versa. Scoring System A five-point visual grading scale was adapted from equivalent MRI quality rating scales[1,2,4] to measure image quality of FDG-PET: clarity, structural definition, contrast and brightness, and artefacts, on a scale of 1(lowest quality) to 5(highest quality). An imaging scientist (LV) reviewed original/generated pairs of images from randomly selected subjects. Reviewers were blinded to the type of image (real or generated). A nonparametric Mann-Whitney U test was employed to discern any significant differences between the generated and real image groups.

Results: A visual comparison and evaluation of the images using the five-point scoring system was performed on 40 images, with 20 images generated using the GAN and 20 real PET scans(Table 1). The results shows significant statistical differences across two of the criteria : Contrast and Brightness($U=40.0$, $p<0.0001$), Artefacts($U=102.5$, $p=0.001$) than the rest: Image Clarity($U=200.0$, $p=1.0$), Structural Definition($U=200.0$, $p=1.0$) and Overall Diagnostic Usability($U=170.0$, $p=0.08$), indicating improved quality of the synthesised PET images than the original PET scans(Figure 1). This apparent improvement may be due to an implicit denoising i.e. the model doesn't add back in the noise or artefacts, as it cannot predict these from MRI.

Conclusions: The synthesised FDG-PET scans exhibit highly similar image quality metrics as the ground truth images. This is the first step in generating useful images. To determine whether they generate individual level diagnostic information, future work will characterise disease-related FDG-PET abnormalities in the generated images, in e.g. AD and Epilepsy groups, to see if such FDG-PET abnormalities can be extracted from MRI input data alone. By generating surrogate FDG-PET imaging where PET scanners are unavailable, our model has the potential to potentially expand the access, reduce costs, and improve diagnoses.

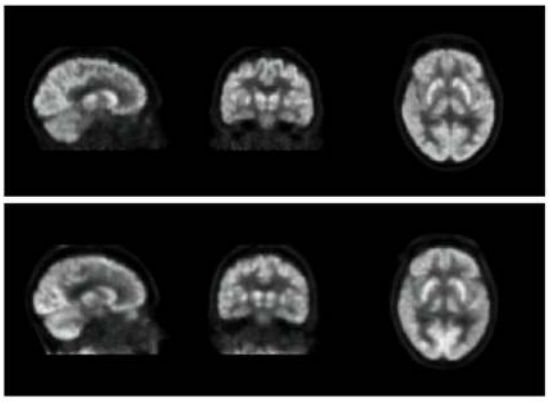

A. Statistics of original images

Statistics	Image Clarity	Structural Definition	Contrast and Brightness	Artefacts	Overall Diagnostic Usability
Min	5	5	2	3	4
Max	5	5	5	5	5
Mean	5	5	3.6	4.15	4.85
Median	5	5	3	4	5
Standard Deviation	0	0	0.882	0.875	0.366

B. Statistics of generated images

Statistics	Image Clarity	Structural Definition	Contrast and Brightness	Artefacts	Overall Diagnostic Usability
Min	5	5	2	3	5
Max	5	5	5	5	5
Mean	5	5	5	4.9	5
Median	5	5	5	5	5
Standard Deviation	0	0	0	0.447	0

References

1. Burmeister, H. P., Baltzer, P. A. T., Möslein, C., Bitter, T., Gudziol, H., Dietzel, M., ... & Kaiser, W. A. (2011), 'Visual grading characteristics (VGC) analysis of diagnostic image quality for high resolution 3 Tesla MRI volumetry of the olfactory bulb', Academic Radiology, 18(5), 634-639.
2. Ludewig, E., Richter, A., & Frame, M. (2010), 'Diagnostic imaging–evaluating image quality using visual grading characteristic (VGC) analysis', Veterinary research communications, 34, 473-479.
3. Mosconi, L., Mistur, R., Switalski, R., Tsui, W. H., Glodzik, L., Li, Y., ... & de Leon, M. J. (2009), 'FDG-PET changes in brain glucose metabolism from normal cognition to pathologically verified Alzheimer's disease', European journal of nuclear medicine and molecular imaging, 36, 811-822.
4. Pawar, K., Chen, Z., Seah, J., Law, M., Close, T., & Egan, G. (2020), 'Clinical utility of deep learning motion correction for T1 weighted MPRAGE MR images', European Journal of Radiology, 133, 109384.
5. Silverman, D. H. (2004), 'Brain 18F-FDG PET in the diagnosis of neurodegenerative dementias: comparison with perfusion SPECT and with clinical evaluations lacking nuclear imaging', Journal of Nuclear Medicine, 45(4), 594-607.
6. Zhu, J. Y., Park, T., Isola, P., & Efros, A. A. (2017), 'Unpaired image-to-image translation using cycle-consistent adversarial networks', In Proceedings of the IEEE international conference on computer vision (pp. 2223-2232).

Poster No 1883

X-separation (chi-separation) toolbox v1.0: updates compared to the beta version and advanced func

Sooyeon Ji[1], Kyeongseon Min[1], Hyeong-Geol Shin[2,3], Junhyeok Lee[4], Minjun Kim[1], Sehong Oh[5], Jongho Lee[1]

[1]Seoul National University, Seoul, Seoul, [2]Johns Hopkins University School of Medicine, Baltimore, MD, [3]Kennedy Krieger Institute, Baltimore, MD, [4]Seoul National University College of Medicine, Seoul, Korea, Republic of, [5]The Cleveland Clinic, Cleveland, OH

Introduction: χ-separation,[Shin et al., 2021] a method to separate para and diamagnetic susceptibility sources, demonstrated the ability to offer clinically valuable information.[Kim et al., 2023] For handy application of χ-separation, there is an increasing need for a toolset that generates high-quality χ-separation. Here, we developed the χ-separation toolbox v1.0 that provides a user-friendly GUI-based χ-separation, including three χ-separation algorithms and four advanced processing options to enhance the quality of the χ-separation results.

Methods: Input/output Complex 3D multi-echo GRE (mGRE) data with DICOM or NIFTI formats are accepted as input. In case of DICOM input, the relevant parameters (i.e., B0, B0 direction, center frequency, voxel size, echo times (TEs), and delta TE) are automatically read from the DICOM header. For NIFTI input, the parameters are manually filled in. An R2' (=R2*-R2) or R2* map and a brain mask may also be inputted. The outputs of the toolbox are the separated χpara and χdia maps (Figure 1). Preprocessing of input data When an R2' or R2* map is not provided, an R2* map is calculated from the mGRE data by fitting an exponential function to the decay curve. The brain mask is calculated using BET (FSL, FMRIB, Oxford, UK) when

not provided. For pipelined phase processing, existing toolboxes must be downloaded. The χ-separation toolbox provides two options for pipelined phase unwrapping according to the consensus [Bilgic et al., 2023]: ROMEO followed by weighted echo averaging, and non-linear complex fit followed by SEGUE. For background field removal, VSHARP[Wu et al., 2012] and PDF[Liu et al., 2011a] are pipelined. Core functionality • χ-sepnet: χ-separation using only mGRE data via a deep neural-network (χ-sepnet-R2*)[Kim et al., 2022] is included. The network is trained using COSMOS QSM and R2* maps as input, and χpara and χdia maps reconstructed using multi-orientation data as output. • χ-separation: When an R2' map is available, two in-house algorithms for optimization-based χ-separation can be used: χ-separation-MEDI and χ-separation-iLSQR. The first option uses the MEDI-regularizer[Liu et al., 2011b], following the original paper.[Shin et al., 2021] The second option calculates χ-separation maps based on iLSQR.[Li et al., 2015] Advanced processing options (Figure 2) • Denoising: Two denoising options are provided for mGRE magnitude data used for R2* mapping. The first is MP-PCA denoising,[Veraart et al., 2016] which takes advantage of the intrinsic redundancy of the multi-echo images. Another option is a deep neural-network trained to denoise MR images. • Background R2* correction: An R2* map is contaminated by background B0 inhomogeneity, due to non-local R2* effects.[Fernández-Seara and Wehrli, 2000] This effect increases with larger effective voxel size related to k-space windowing. An option to apply k-space windowing along with correction of this effect is included to provide accurate χ-separation maps whilst reducing artifacts by k-space windowing. • Resolution generalization for χ-sepnet: An option to utilize the "resolution generalization" pipeline for χ-sepnet is provided, which enables the inference of data that has higher or lower resolution than that of the training data (i.e., 1 mm iso). • Vessel masking: χ-separation maps suffer from vessel artifacts that may hamper accurate calculation of ROI values. The toolbox provides an option to generate vessel masks that can be used to mask out vessels for group analysis.

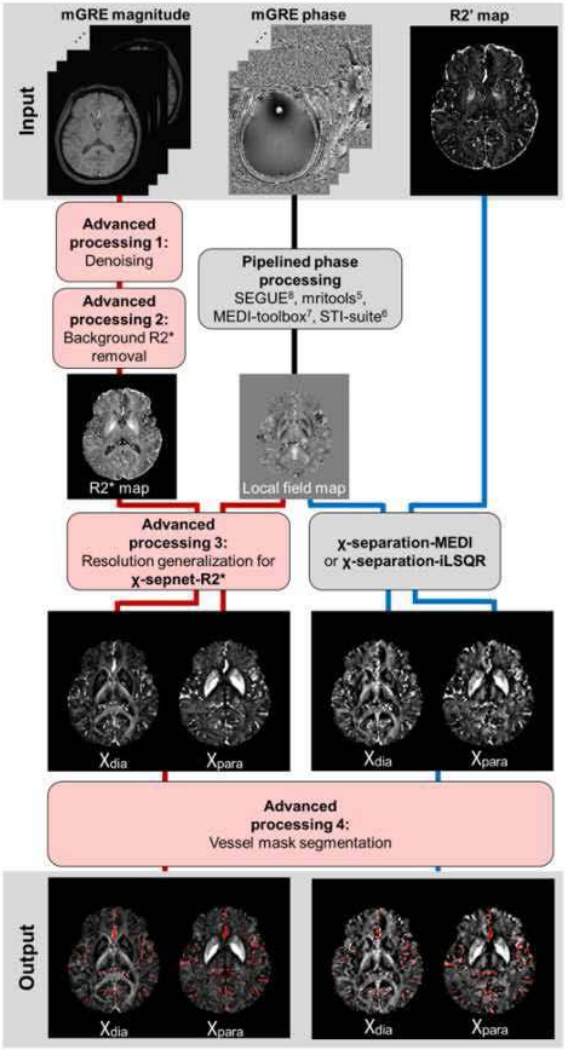

Figure 1. Pipeline for χ-separation including the four advanced processing options, depicted as red colored boxes. The red line is the processing pipeline for χ-separation using only mGRE data, and the blue line is the processing pipeline when an R2' map is provided. The four advanced processing options can be turned on or off by the users by ticking the checkbox (Fig. 1, blue box).

Results: The advanced options offer high-quality χ-separation with fewer artifacts and less noise, and also a tool for more accurate analysis (Figure 2e).

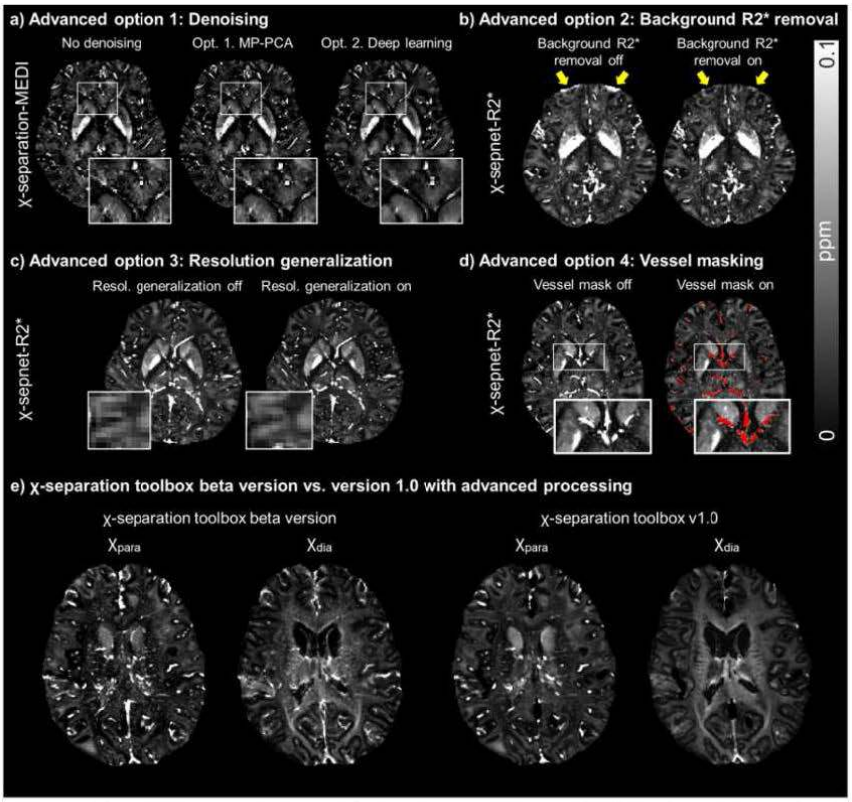

Figure 2. Effect of the four advanced processing options. a) Denoising using MP-PCA algorithm and deep-learning are available. b) Background R2* removal option corrects the R2* error coming from B0 field inhomogeneity, thus correcting χ-separation results (yellow arrows). c) Resolution generalization[21] enables χ-sepnet reconstruction of data with higher/lower resolution compared to trained resolution (1 mm^3) without loss of high frequency information, including anisotropic resolution. d) Vessel masking option is included. e) Comparison between the beta and v1.0 of the χ-separation toolbox. Using the three advanced processing options except for vessel masking, the χ_{para} and χ_{dia} maps reconstructed using χ-separation toolbox v1.0 demonstrate improved quality (χ-sepnet).

Conclusions: With the GUI-based χ-separation toolbox equipped with advanced processing functionalities, reconstruction of high-quality paramagnetic and diamagnetic susceptibility maps becomes readily available, fostering utilization of χ-separation across diverse applications.

References

1. Bilgic B (2023): Recommended Implementation of Quantitative Susceptibility Mapping for Clinical Research in The Brain: A Consensus of the ISMRM Electro-Magnetic Tissue Properties Study Group. arXiv preprint arXiv:230702306.
2. Fernández-Seara MA (2000): Postprocessing technique to correct for background gradients in image-based R*2 measurements. Magnetic Resonance in Medicine 44:358–366.
3. Kim M (2022): Chi-sepnet: Susceptibility source separation using deep neural network. In: . Proceedings of the 30th Annual ISMRM Meeting.
4. Kim W (2023): χ-Separation Imaging for Diagnosis of Multiple Sclerosis versus Neuromyelitis Optica Spectrum Disorder. Radiology 307:e220941.
5. Liu T (2011a): A novel background field removal method for MRI using projection onto dipole fields (PDF). NMR in Biomedicine 24:1129–1136.
6. Liu T (2011b): Morphology enabled dipole inversion (MEDI) from a single-angle acquisition: Comparison with COSMOS in human brain imaging. Magnetic Resonance in Medicine 66:777–783.
7. Li W (2015): A method for estimating and removing streaking artifacts in quantitative susceptibility mapping. NeuroImage 108:111–122.
8. Shin H-G (2021): χ-separation: Magnetic susceptibility source separation toward iron and myelin mapping in the brain. Neuroimage 240:118371.
9. Veraart J (2016): Denoising of diffusion MRI using random matrix theory. Neuroimage 142:394–406.
10. Wu B (2012): Whole brain susceptibility mapping using compressed sensing. Magnetic Resonance in Medicine 67:137–147.

Poster No 1884

CuBNM: GPU-Accelerated Biophysical Network Modeling

Amin Saberi[1,2,3], Kevin Wischnewski[1], Kyesam Jung[1], Leonard Sasse[1], Felix Hoffstaedter[1], Oleksandr Popovych[1], Boris Bernhardt[4], Simon Eickhoff[1], Sofie Valk[2]

[1]INM-7, Research Centre Jülich, Jülich, Germany, [2]Max Planck Institute for Human Cognitive and Brain Sciences, Leipzig, Germany, [3]Institute of Systems Neuroscience, Heinrich Heine University Düsseldorf, Düsseldorf, Germany, [4]Montreal Neurological Institute and Hospital, Montreal, Quebec

Introduction: Biophysical network modeling (BNM) of the brain is a promising technique to bridge macro- and microscale levels of investigation and enables inferences about latent features of brain activity, such as excitation-inhibition balance. Through this approach, personalized models of the brain can be fitted to the imaging data of individual subjects by parameter optimization[1,2]. However, this process typically involves running several thousands of simulations for each subject, and therefore is computationally costly. This limits its scalability to a higher number of subjects and more complex models. Here, we present cuBNM (https://github.com/amnsbr/cuBNM), a toolbox for efficient simulation and optimization of BNMs using GPUs.

Methods: To establish the functionality of our toolbox, we simulated the activity of 100 cortical regions of the Schaefer atlas[3] as network nodes governed by the reduced Wong-Wang model with analytical-numerical feedback inhibition control[4,5] and the Balloon-Windkessel model for calculation of simulated BOLD signals[6]. We used two types of model parameterization, including a homogeneous model with constant local parameters across nodes (3 free parameters) and a heterogeneous model with regionally variable local parameters based on a linear combination of six biological maps (15 free parameters)[5,7,8]. The model fit to empirical data was assessed by comparing the simulated and empirical functional connectivity (FC) and functional connectivity dynamics (FCD) matrices. Model parameters were optimized by either a grid search or covariance matrix adaptation evolution strategy (CMAES). Parallelization within the grid or the sequential iterations of CMAES was done at the level of simulations (across the GPU 'blocks') and nodes (across each block's 'threads'). The calculation of FC and FCD were similarly parallelized across the simulations and matrix entries (Fig. 1). We performed benchmark tests by running N = {1, ..., 215} parallel homogeneous simulations (duration 60s, BOLD TR 1s) on three types of GPU of Nvidia A100, GTX 1080 Ti and T4 GPUs as well as on a supercomputer multi-CPU node (128 cores) and a single core of CPU. Following, as an example use case of the toolbox, we fitted the BNM to the group-averaged data of the Human Connectome Project (HCP; n = 738 training and 317 test subjects) by using grid search and CMAES optimization of the homogeneous and heterogeneous models on A100 GPUs. To match the empirical data, the simulations were run for 900s with a BOLD TR of 0.72s.

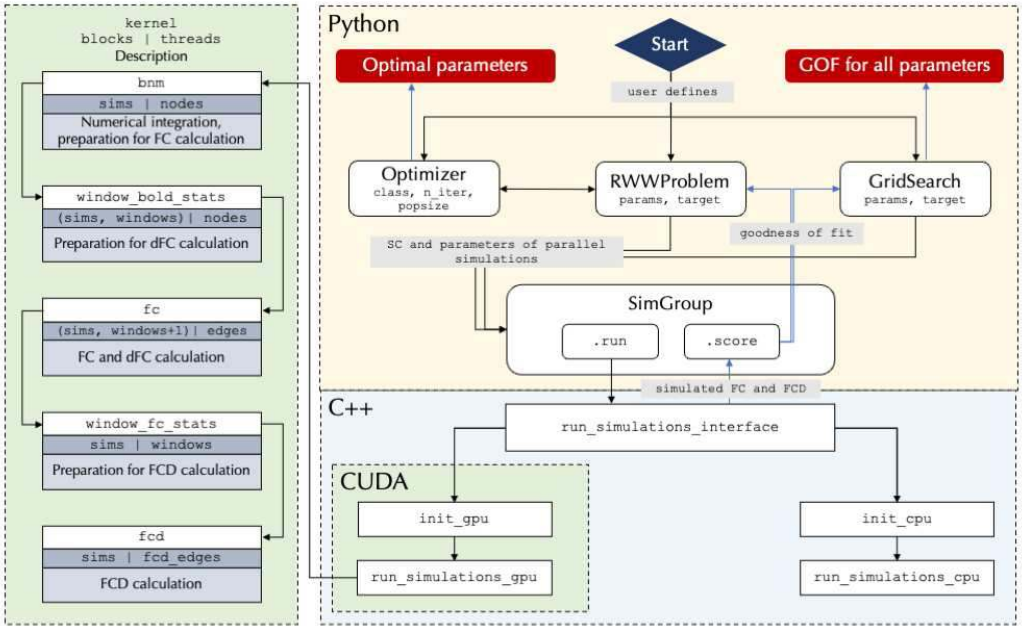

Fig. 1. Program flowchart. The components of the toolbox programmed in Python, C++ and CUDA are shown. The panel in the left shows the CUDA kernels used for the numerical integration of the model as well as functional connectivity (FC) and functional connectivity dynamics (FCD) calculations, along with the number of GPU 'blocks' and 'threads' used by each kernel. The output returned to the user (red boxes) can be goodness of fit (GOF) of all simulations with grid search, or the optimal simulation with optimizers.

Results: Single simulation of the model network corresponding to one minute of real time was faster on GPUs (A100: 4.85s, GTX 1080 Ti: 9.67s, T4: 13.32s) than on CPUs (19.33s). On A100 GPU, running 32768 parallel simulations took 14m41s. The same simulations on a single-core CPU were estimated to take >7 days. We achieved maximum speedups of 180.3 with A100 GPU (32768 simulations), 151.7 with 128-core CPU node (512 simulations), 42.1 with T4 GPU (8192 simulations) and 27.7 with GTX 1080 Ti GPU (1024 simulations; Fig 2A). In our use case, we observed that the goodness-of-fit of the optimal simulations to the group-averaged HCP data was better for the heterogeneous models with 15 free parameters optimized by CMAES with a population size of 256 or 64 particles (training: 0.283, test: 0.276) compared to 3-dimensional homogeneous models fitted using CMAES with 64 particles (training: 0.146, test: 0.138) or grid search with 4096 (training: 0.140, test: 0.132) or 64,000 (training: 0.148, test: 0.134) simulations (Fig 2B).

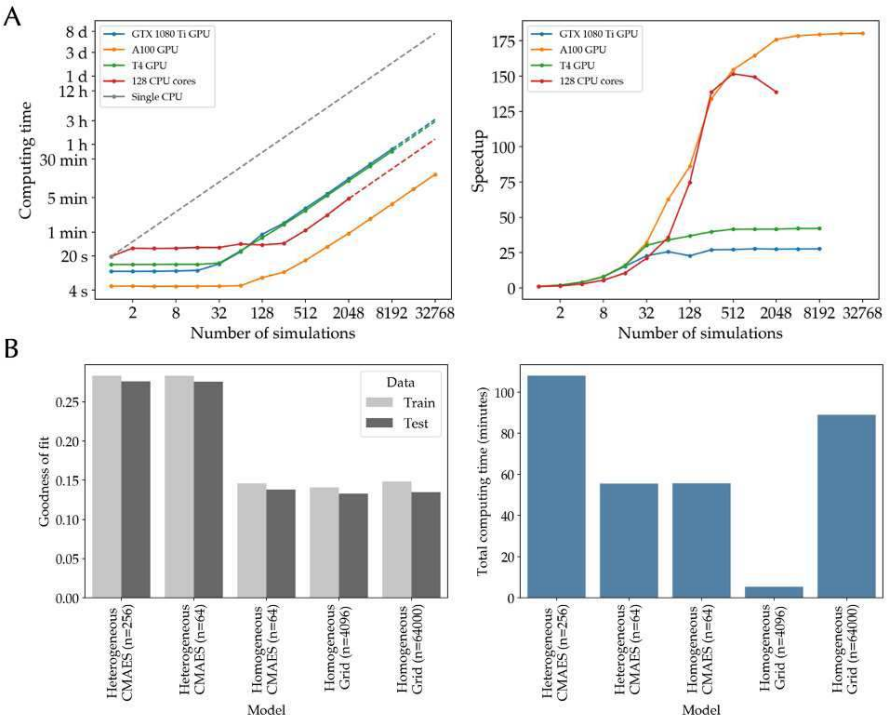

Fig. 2. A) Benchmark results. *left*: The computing time for running N parallel simulations on different devices is shown. Dots and solid lines show measurements and dashed lines show estimations. X- and Y-axes are in $\log_2$ scale. *right*: Speedup of running N parallel simulations on different devices is shown. X-axis is in $\log_2$ scale. B) Example use case results. Goodness of fit of the optimal simulations to the training and test empirical data (*left*) and the total computing time (*right*) of the different types of models and optimization approaches are shown.

Conclusions: The BNM simulations and parameter optimization can be done considerably more efficiently on GPUs compared to CPUs. Our GPU implementation of BNMs enables scaling of this approach to a higher number of subjects as well as more complex and biologically realistic models which can ultimately increase model performance and validity.

References

1. Popovych OV, Manos T, Hoffstaedter F, Eickhoff SB. What Can Computational Models Contribute to Neuroimaging Data Analytics? Frontiers in Systems Neuroscience. 2019;12:68.
2. Ritter P, Schirner M, McIntosh AR, Jirsa VK. The Virtual Brain Integrates Computational Modeling and Multimodal Neuroimaging. Brain Connectivity. 2013;3:121–145.
3. Schaefer A, Kong R, Gordon EM, Laumann TO, Zuo X-N, Holmes AJ, et al. Local-Global Parcellation of the Human Cerebral Cortex from Intrinsic Functional Connectivity MRI. Cereb Cortex. 2018;28:3095–3114.
4. Deco G, Ponce-Alvarez A, Hagmann P, Romani GL, Mantini D, Corbetta M. How local excitation-inhibition ratio impacts the whole brain dynamics. J Neurosci. 2014;34:7886–7898.
5. Demirtaş M, Burt JB, Helmer M, Ji JL, Adkinson BD, Glasser MF, et al. Hierarchical Heterogeneity across Human Cortex Shapes Large-Scale Neural Dynamics. Neuron. 2019;101:1181-1194.e13.
6. Friston KJ, Harrison L, Penny W. Dynamic causal modelling. Neuroimage. 2003;19:1273–1302.
7. Kong X, Kong R, Orban C, Wang P, Zhang S, Anderson K, et al. Sensory-motor cortices shape functional connectivity dynamics in the human brain. Nat Commun. 2021;12:6373.
8. Deco G, Kringelbach ML, Arnatkeviciute A, Oldham S, Sabaroedin K, Rogasch NC, et al. Dynamical consequences of regional heterogeneity in the brain's transcriptional landscape. Science Advances. 2021;7:eabf4752.

Poster No 1885

BrainVolCNN – A Volumetric CNN to Predict Task Contrasts from Resting-State Functional Connectivity

Emin Serin[1], Andre Marquand[2], Kerstin Ritter[3], Henrik Walter[1]

[1]Division of Mind and Brain Research, Department for Psychiatry, Charité–Universitätmedizin Berlin, Berlin, Germany, [2]Radboud University Nijmegen, Nijmegen, Gelderland, [3]Charité – Universitätsmedizin Berlin, Department of Psychiatry and Psychotherapy, Berlin, Germany

Introduction: It is increasingly recognized that large samples are essential for biomarker discovery, cohort stratification, and studying individual differences. While task-based fMRI (tb-fMRI) helps to understand neurocognitive mechanisms and outperforms resting-state fMRI (rs-fMRI) in predicting individuals' cognition (Tik et al., 2023), its cognitive demands present challenges when translating to large samples. However, recent studies have shown a strong correspondence between spontaneous and task-based brain activities (Cole et al., 2016; Tavor et al., 2016), indicating the potential predictability of task-evoked brain activity from resting-state brain activity. This suggests a promising approach to address the limitations of tb-fMRI in large samples. Nevertheless, previous efforts supporting this idea have been overly simplistic, focused only on cortical areas, or lacked transfer learning capabilities (Ngo et al., 2022; Tavor et al., 2016; Zheng et al., 2022). To overcome these limitations, we propose a volumetric-based neural network architecture (BrainVolCNN) that leverages resting-state connectivity of the entire cortex, including subcortical areas, to predict task-based brain activity maps (Fig. 1a).

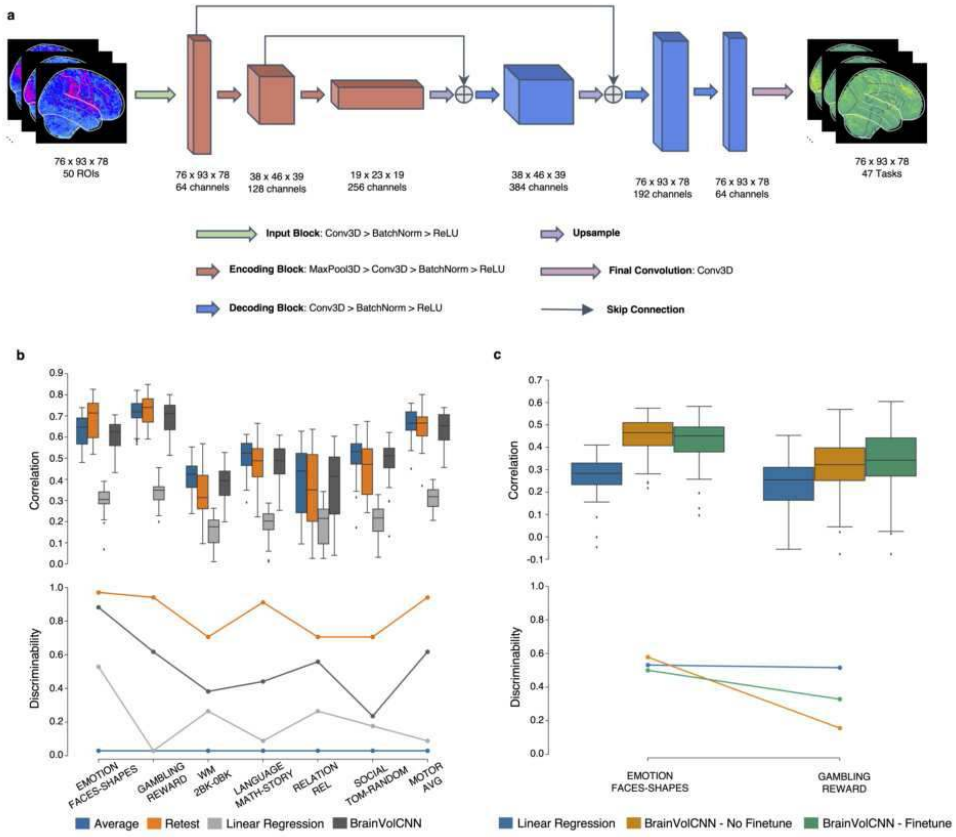

Figure 1. (a) BrainVolCNN architecture. (b) Reconstruction performance (upper) and fingerprinting score (lower) of BrainVolCNN, group average, retest scans, and linear model across seven representative task contrasts on HCP-YA. (c) Reconstruction performance (upper) and fingerprinting score (lower) of various models on HCP-D. Correlation represents the full correlation between predicted and actual task contrasts, while discriminability was computed using fingerprinting score method introduced by Finn et al., 2015.

Methods: Briefly, our study involved several steps. First, we predicted synthetic task contrast maps from resting-state connectivity and compared them to the actual contrast maps in the same training dataset. Second, we employed transfer learning by freezing the final layer of the network and fine-tuning the rest of the network on two held-out datasets that were not part of the training data. Third, we evaluated the performance of actual and predicted contrast maps in predicting age, sex, and fluid intelligence. Specifically, we trained our network using the HCP-Young Adults dataset (HCP-YA) (N = 953) (Van Essen et al., 2013) and evaluated it on HCP-Development (HCP-D) (N = 632) (Somerville et al., 2018) and UK Biobank (N = 20792) (Miller et al., 2016). To validate the predicted images, we assessed the usability of the predicted contrast maps in three machine-learning scenarios: predicting individuals' age, sex, and fluid intelligence based on their predicted and actual

contrast maps. To establish a comprehensive evaluation, we compared the performance of our proposed model with various baselines, such as the linear model (Tavor et al., 2016), group-average contrast maps, and retest scans.

Results: BrainVolCNN outperforms or achieves competitive reconstruction performance compared to baseline methods while preserving individual-specific information, leading to increased discriminability between subjects (Finn et al., 2015) (Fig. 1b). In addition, BrainVolCNN demonstrates superior reconstruction performance when applied to the HCP-D dataset after transfer learning, surpassing the linear model (Fig. 1c). Importantly, we also provide preliminary evidence of the potential value of our synthetic task images as biomarkers in that predicted contrast maps outperformed actual contrast maps in predicting sex and age while showing similar or slightly lower performance in predicting fluid intelligence (Fig. 2). This might be attributed to reduced noise during the synthetic image generation process, leading to an improved signal-to-noise ratio.

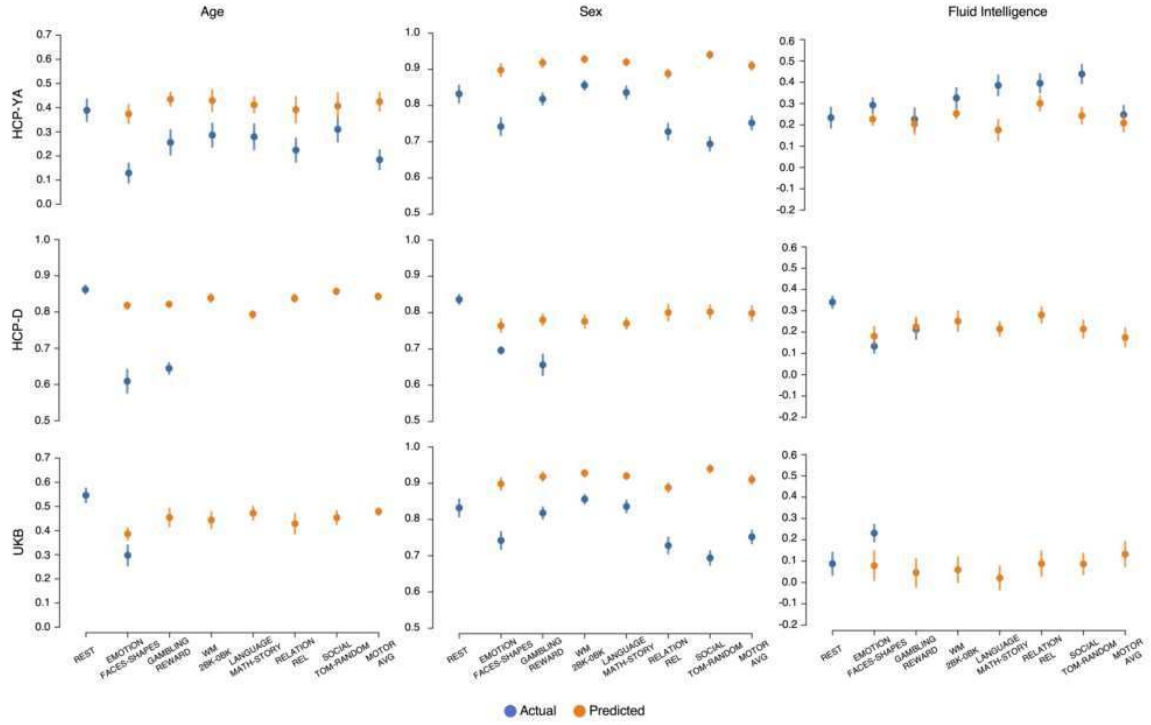

Figure 2. The performance of actual and predicted task contrast maps in predicting individuals' age, sex, and fluid intelligence on the HCP-YA, HCP-D, and UKB datasets. For the HCP-D and UKB datasets, task contrast maps were predicted using a finetuned model. The prediction performance for sex was measured using accuracy, while fluid intelligence and age prediction were assessed using Pearson's correlation coefficient.

Conclusions: The results provide evidence of the partially superior performance of predicting task contrast maps from resting-state connectivity using BrainVolCNN compared to baseline models. This is evident in terms of both reconstruction accuracy and inter-subject discriminability. Our proposed framework facilitates transfer learning, enabling the prediction of contrast maps on datasets that have not been specifically acquired. Consequently, this enables the investigation of task-related biomarkers only requiring rs-fMRI scans.

References

1. Cole, M. W. (2016), 'Activity flow over resting-state networks shapes cognitive task activations.' Nature Neuroscience, 19(12), 1718–1726. https://doi.org/10.1038/nn.4406
2. Finn, E. S. (2015), 'Functional connectome fingerprinting: Identifying individuals using patterns of brain connectivity.' Nature Neuroscience, 18(11), 1664–1671. https://doi.org/10.1038/nn.4135
3. Miller, K. L. (2016). 'Multimodal population brain imaging in the UK Biobank prospective epidemiological study.' Nature Neuroscience, 19(11), 1523–1536. https://doi.org/10.1038/nn.4393
4. Ngo, G. H. (2022), 'Predicting individual task contrasts from resting-state functional connectivity using a surface-based convolutional network.' NeuroImage, 248, 118849. https://doi.org/10.1016/j.neuroimage.2021.118849
5. Somerville, L. H. (2018), 'The Lifespan Human Connectome Project in Development: A large-scale study of brain connectivity development in 5–21 year olds'. NeuroImage, 183, 456–468. https://doi.org/10.1016/j.neuroimage.2018.08.050
6. Tavor, I. (2016), 'Task-free MRI predicts individual differences in brain activity during task performance'. Science, 352(6282), 216–220. https://doi.org/10.1126/science.aad8127
7. Tik, N. (2023), 'Generalizing prediction of task-evoked brain activity across datasets and populations'. NeuroImage, 276, 120213. https://doi.org/10.1016/j.neuroimage.2023.120213
8. Van Essen, D. C. (2013). 'The WU-Minn Human Connectome Project: An overview'. NeuroImage, 80, 62–79. https://doi.org/10.1016/j.neuroimage.2013.05.041
9. Zheng, Y.-Q. (2022). 'Accurate predictions of individual differences in task-evoked brain activity from resting-state fMRI using a sparse ensemble learner', NeuroImage, 259, 119418. https://doi.org/10.1016/j.neuroimage.2022.119418

Poster No 1886

Improving MS lesion segmentation by alleviating the class imbalance and conformal risk control

Yang Sun[1], Bernd Taschler[2], Laura Gaetano[3], Thomas Nichols[4], Dieter Haering[3], Habib Ganjgahi[4]

[1]University of Oxford, Oxford, Oxfordshire, [2]University of Oxford, Goring-on-Thames, South Oxfordshire, [3]Novartis, Basel, Switzerland, [4]University of Oxford, Oxford, United Kingdom

Introduction: Multiple sclerosis (MS) is a chronic and ultimately debilitating disease of the central nervous system that affects approximately 2.5 million individuals worldwide[5]. The accumulated damage from past and ongoing neuroinflammation appears as hyperintense areas in T2-weighted MRI, known as T2 lesions. The count and volume of T2 lesions are an important prognostic factor for MS monitoring and progression[3]. The best detection approach is manual segmentation but it is costly, subject to intra/inter-rater variability, hence there has been growing interest to develop automated tools. Deep learning has been shown to consistently outperform traditional image processing algorithms[4] however class imbalance, the unequal distribution of voxels among foreground (lesion) and background (non-lesion) classes, leads to poor generalizability and inflated false negatives (FN). In this work, we (a)evaluate the performance of different loss functions designed to mitigate the impact of class imbalance, and (b)assess uncertainty using conformal risk control.

Methods: Data resampling and loss function modifications are the common methods to handle class imbalance in image segmentation. It can be addressed by oversampling the minority class or undersampling the majority class during training. Besides, using loss functions that assign higher weights to the minority class and lower weights to the majority class can make the model more robust to class imbalance. The conventional loss functions for image segmentation are Binary Cross-Entropy (BCE), which quantifies the discrepancy between true lesion mask and its prediction, Dice loss, which is a harmonic mean of precision and recall; an alternative is Tversky loss, which is a generalised version of Dice loss that gives different penalty terms to false positives (FP) and FN. In this work, we evaluate the impact of undersampling the majority class (only using lesion slices to train) and the use of combined loss functions to address class imbalance for lesion segmentations: BCE with and without class weights plus Dice; BCE with and without class weights plus Tversky loss with FP and FN penalties of 0.3 and 0.7, respectively; and WBCE plus Tversky loss with FP and FN penalties of 0.7 and 0.3. When used, the weights are proportional to the inverse of class frequency. Conformal inference is an approach to get uncertainty quantification from an arbitrary predictive model. To obtain a conformal risk guarantee in our segmentation task, we manipulate the threshold value to regulate the fraction of misssegmentations[1]. Here, we use the trained model with weighted BCE (WBCE) and Tversky loss (α=0.7&β=0.3) and we target a false negative rate (FNR) less than 0.1 (recall over 0.9). We use the NO.MS dataset[2] for evaluating the performance of different methods. It is currently the largest and most comprehensive clinical trial dataset in MS with more than 35,000 MS patients and over 200,000 MRI scans. We use 11,707 scans, randomly split into 10,571 for training and 1,136 for testing, where the ground truth lesion masks are obtained either manually or semi-automatically.

Results: Our experiments show that resampling has the worst performance in terms of generalizability to test sets, F1 and precision. In addition, up-weighting lesion voxels and down-weighting background voxels in the BCE and Dice improve recall but suffer from inflated FPs. However, Tversky loss that penalizes FPs improves precision while WBCE keeps good recall (see Figure 1). Conformal risk control was used to guarantee FNR is controlled at 0.1 level with high probability.

Conclusions: We have shown WBCE and Tversky loss function improves T2 lesion segmentation by alleviating the class imbalance problem. Tuning the hyperparameters in Tversky can facilitate the efficient balance between recall and precision. Implementing conformal risk control ensures the FNR is managed and consequently improves the recall.

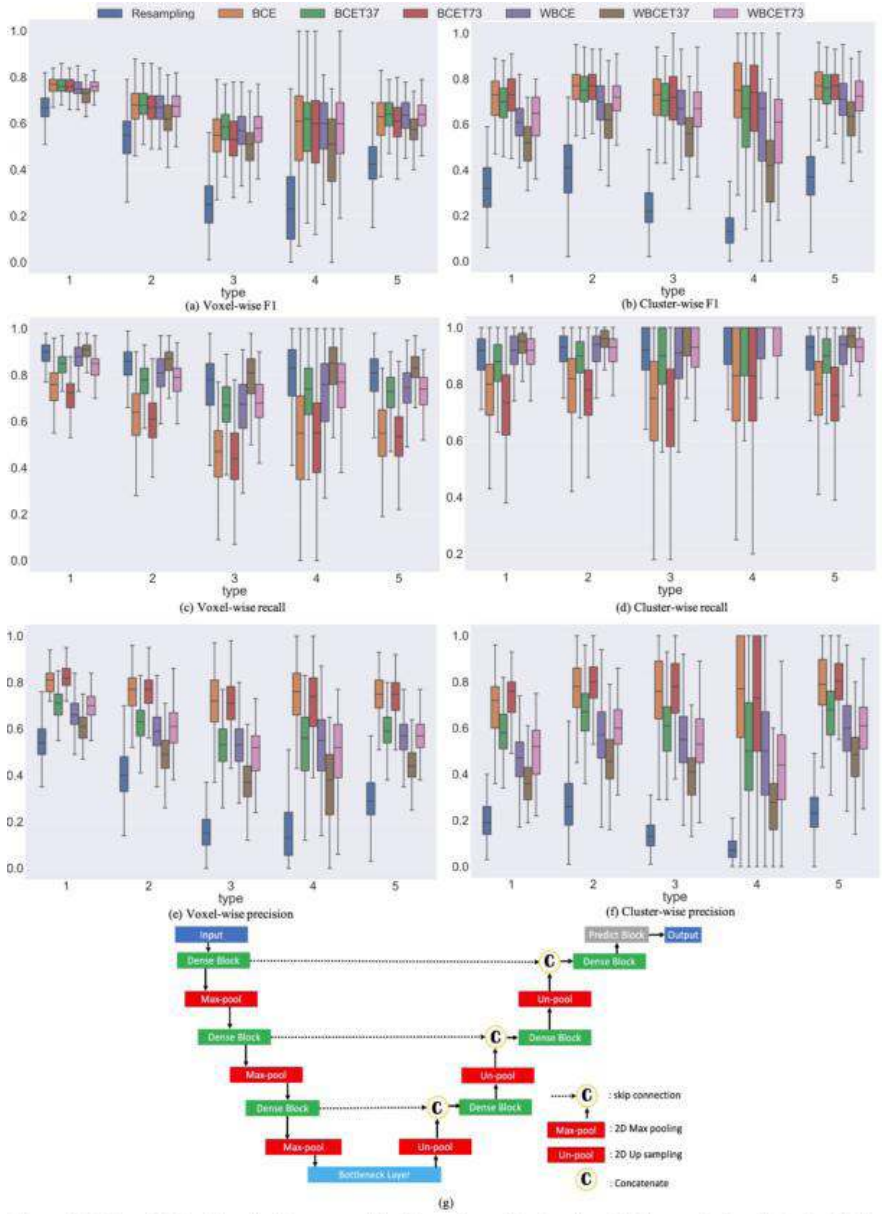

Figure 1:(a-f):Box plots for different performance metrics (F1, recall, precision, from top to bottom; voxel-wise, cluster-wise, left & right), partitioned by 5 distinct types of clusters for testing data. These results show resampling yields the lowest performance in F1 and precision both voxel- and cluster-wise. When up-weighting lesion voxels and down-weighting background voxels in BCE, a higher recall is obtained but also with more FPs. Tversky loss improves the precision through penalizing FPs.
(g): The 2D U-Net model employed for segmentation. T1, T2-weighted (T2), proton density-weighted (PD) and pseudo Fluid-attenuated inversion recovery (generated by T1, T2 and PD) modalities are used as input. All MRI slices are extracted and preprocessed (median absolute deviation normalization and size standardization). MRI slices and their lesion masks are paired to train a U-Net. With the U-Net, the dense block consists of two 3x3 convolutions, each followed by a rectified linear unit (ReLU). Max-pool block has 2D max pooling operation and un-pool block has 2D up sampling operation both with stride 2. In predict block, Sigmoid is used as the output function. The U-net model is trained for 100 epochs using Adam optimizer with an initial learning rate of 0.001 with the Exponential Learning Rate scheduling and a batch size of 256. All the experiments are run on a cluster has six Nvidia Tesla A100 GPUs and 40 GB of RAM.

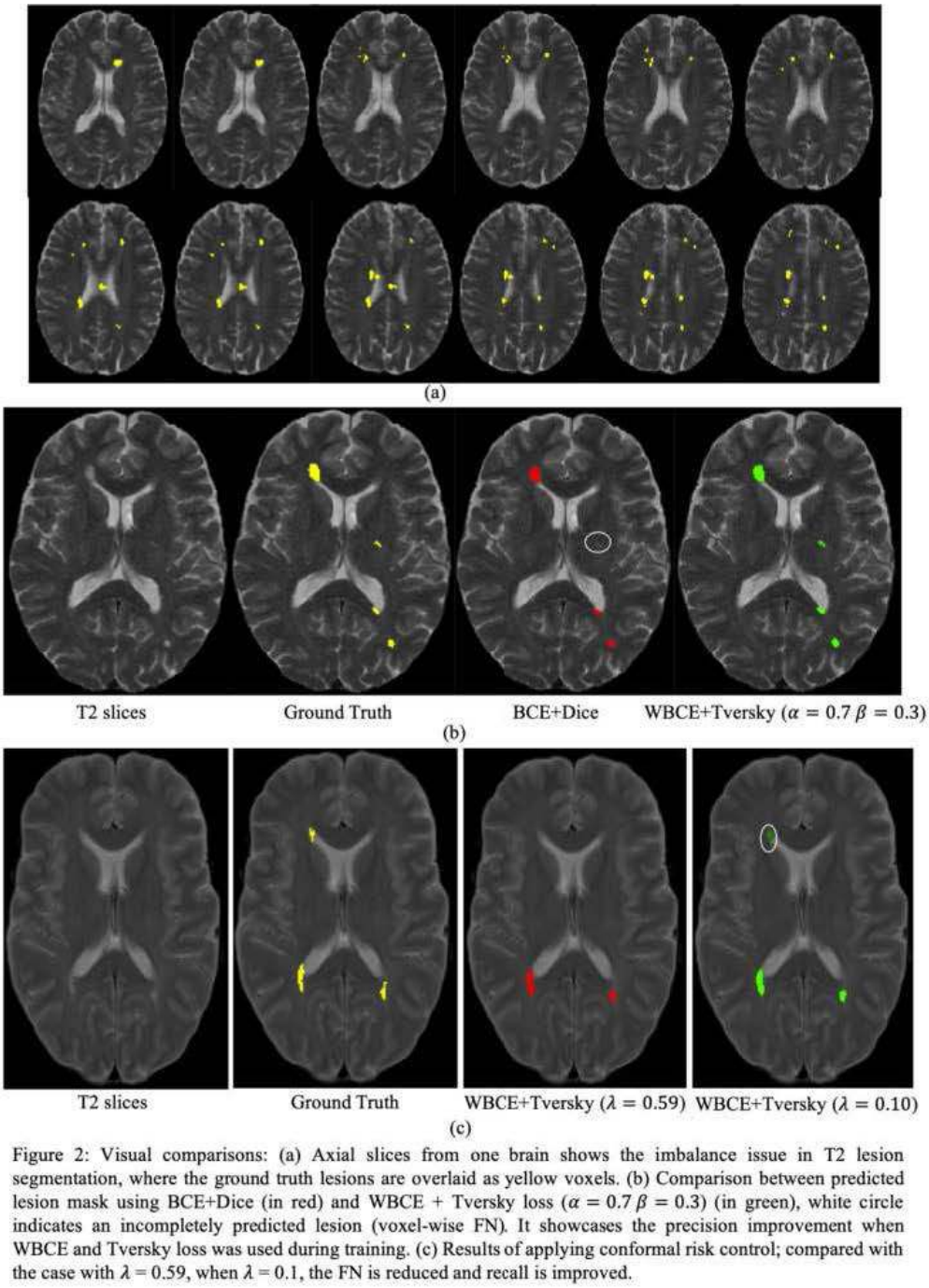

Figure 2: Visual comparisons: (a) Axial slices from one brain shows the imbalance issue in T2 lesion segmentation, where the ground truth lesions are overlaid as yellow voxels. (b) Comparison between predicted lesion mask using BCE+Dice (in red) and WBCE + Tversky loss ($\alpha = 0.7\ \beta = 0.3$) (in green), white circle indicates an incompletely predicted lesion (voxel-wise FN). It showcases the precision improvement when WBCE and Tversky loss was used during training. (c) Results of applying conformal risk control; compared with the case with $\lambda = 0.59$, when $\lambda = 0.1$, the FN is reduced and recall is improved.

References

1. A. N. Angelopoulos, S. Bates, A. Fisch, L. Lei, and T. Schuster,(2023), Conformal risk control. arXiv:2208.02814, Available: https://arxiv.org/abs/2208.02814.
2. F. Dahlke, D. L. Arnold, P. Aarden, H. Ganjgahi, D. A. Haring, J. ˇCuklina, T. E. Nichols, S. Gardiner, R. Bermel, and H. Wiendl. Characterisation of ms phenotypes across the age span using a novel data set integrating 34 clinical trials (no.ms cohort): Age is a key contributor to presentation. (2021), Multiple Sclerosis Journal, 27(13):2062–2076.
3. M. P. McGinley, C. H. Goldschmidt, and A. D. Rae-Grant. (2020), Diagnosis and treatment of multiple sclerosis: A review. JAMA, 325(8):765–779.
4. V. Sundaresan, G. Zamboni, P. M. Rothwell, M. Jenkinson, and L. Griffanti, (2021), Location sensitive deep convolutional neural networks for segmentation of white matter hyperintensities. Medical Image Analysis.
5. M. J. Tullman. (2013), Overview of the epidemiology, diagnosis, and disease progression associated with multiple sclerosis. The American Journal of Managed Care, 19(2 Suppl):S15–20.

Poster No 1887

How to Properly Select Covariates in Neuroimaging Data Analysis

Gang Chen[1], Zhengchen Cai[2], Paul Taylor[1]

[1]National Institutes of Health, Bethesda, MD, [2]The Neuro (Montreal Neurological Institute-Hospital), McGill University, Montreal, Québec

Introduction: The role of covariates is pivotal in data analysis, yet their inclusion often lacks a clear rationale. Recent development has shown how covariates easily lead to biased or spurious estimation, harming interpretation, understanding and reproducibility. We address three common issues: indiscriminate variable inclusion, lack of justification and overlooking reporting nuances. These problems arise when variables like reaction time, height, weight, head size, and cortex thickness are integrated, potentially distorting results. Consider an illustrative scenario involving short-term memory (STM) as the response variable and gray matter density (GMD) as the predictor. Sex, age, intracranial volume (ICV), APOE genotype, and body weight are considered as covariates, leading to four questions: 1) Predictor vs. Response Variable: Is it justifiable to invert the roles of GMD and STM, making GMD the voxel-level response variable for easy implementation? 2) Covariates: Should all five covariates be included? 3) Result Reporting/Interpretability: Is it appropriate to report all parameter estimates from a single GLM? 4) Experimental Design: What variables could be omitted, and what other variables might have been incorporated to improve estimation?

Methods: Common justifications for including covariates encompass availability, precedence, and statistical evidence, often quantified through metrics like p-values or R2. Nevertheless, it is imperative to scrutinize these rationales. For instance, in contexts where the focus is on statistical inference, can the statistical evidence of a covariate justify its inclusion? Furthermore, adding a covariate might either fortify or undermine the statistical evidence for a predictor–what criteria should guide the selection? Can a model be reliably appraised solely based on its output? We advocate for the adoption of independent principles in covariate selection to sidestep circular reasoning or interpretational ambiguities. The incorporation of prior information and domain knowledge is instrumental in guiding this decision-making process. A judicious approach involves a nuanced understanding of causal relationships, aptly depicted through directed acyclic graphs (DAGs)[1,2]. Covariates can be categorized into three types (Fig 1A): confounders (shared causes), colliders (shared effects), and mediators (effects of predictors and causes of response variables). Decisions hinge on three cardinal rules: include confounders, exclude colliders, and include/exclude mediators based on the focus on direct/total effects. For covariates associated with the predictor or response variable, but not both, only consider the parent of the response variable for improved precision (Fig 1B). These rules, deeply rooted in causal inference, have withstood rigorous derivations and validation through simulations[3]. Neglecting them risks biases: underestimation, overestimation, sign reversal, effect suppression, or spurious effects.

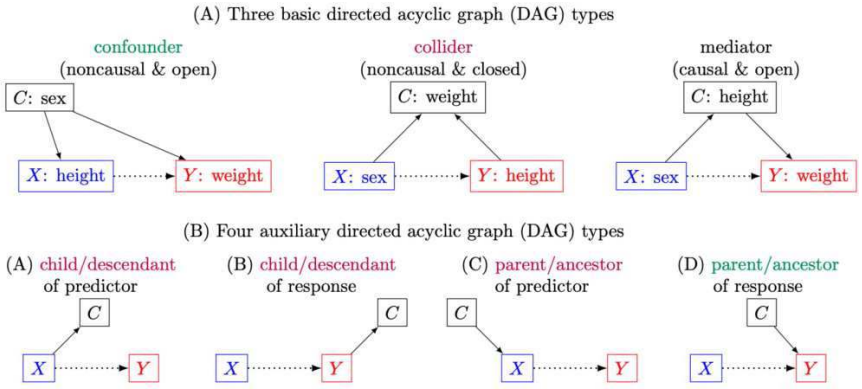

Figure 1: Causal relationships among variables depicted through directed acyclic graphs (DAG). X and Y are predictor and response variable, respectively, while C is a covariate. (A) Three basic DAG types are shown between a predictor X (blue) and a response variable Y (red), as indicated by the dotted arrow. An arrow with a solid line indicates the *a priori* influence direction. A covariate C can be a confounder, a mediator, or a collider. The three variables of sex, height, and weight are used to illustrate the three DAG types. (B) Covariate as a child or parent. The relationship under study is between a predictor X (blue) and a response variable Y (red), as indicated by the dotted arrow. The predictor X or the response Y may single-handedly influence the covariate C. Alternately, C may play the role of a parent, influencing X or Y, but not both.

Results: Using the causal relationships among variables (Fig 2), the four example questions above can be addressed: 1) GMD influencing STM is more plausible. 2) Age and sex (confounders) are included; APOE (influencing only the response variable) improves precision; weight (collider) is excluded; ICV (influencing only GMD) is not considered. 3) Estimation of age and sex effects should not be reported unless their direct effects are the focus. 4) Weight (collider) should be excluded

from data collection when examining the GMD-STM relationship; additional variables like sleep hours would enhance experimental design.

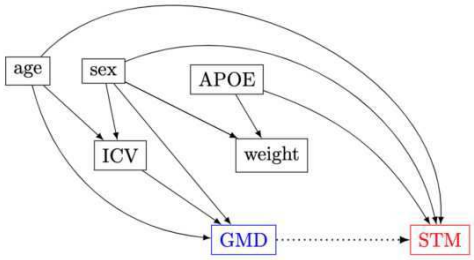

Figure 2: Directed acyclic graph (DAG) for a structure data analysis. Five covariates are considered for the response variable of short-term memory (STM) and the predictor of gray matter density (GMD): sex, age, intracranial volume (ICV), APOE, and weight. The relationships, as represented in this DAG, reflect on the assumptions under which a statistical model can be parametrically constructed to investigate the association (dotted arrow) between GMD (blue) and STM (red). An arrow with a solid line indicates the *a priori* influence direction.

Conclusions: A model reveals associations, but understanding causal relationships is crucial. DAGs aid covariate selection, guiding good experimental design and promoting analytical rigor. Causal thinking fosters theoretical hypotheses, transparency and reproducibility in neuroimaging data analysis. Emphasizing these aspects refines covariate selection, ensuring more robust and meaningful neuroimaging studies.

References

1. Pearl, J., 2009. Causal inference in statistics: An overview. Statistics Surveys 3, 96–146.
2. Pearl J., Mackenzie D., 2018. The Book of Why: The New Science of Cause and Effect. New York: Basic Books
3. Wysocki, A.C., Lawson, K.M., Rhemtulla, M., 2022. Statistical Control Requires Causal Justification. Advances in Methods and Practices in Psychological Science 5, 25152459221095823.

Poster No 1888

A Taxonomy of Seizure Dynamotypes

Maria Luisa Saggio[1], Dakota Crisp[2], Jared Scott[2], Philippa Karoly[3], Levin Kuhlmann[4], Mitsuyoshi Nakatani[5], Tomohiko Murai[6], Matthias Dumpelmann[7], Andreas Schulze-Bonhage[7], Akio Ikeda[8], Mark Cook[3], Stephen Gliske[9], Jack Lin[10], Christophe Bernard[5], Viktor Jirsa[11], William Stacey[12]

[1]Aix Marseille Univ, Inserm, INS, Institut de Neurosciences des Systèmes, Marseille, France, [2]University of Michigan, Ann Arbor, MI, [3]Graeme Clark Institute, The University of Melbourne, Melbourne, Australia, [4]Department of Medicine, St. Vincent's Hospital, The University of Melbourne, Melbourne, Australia, [5]Aix Marseille Univ, Inserm, INS, Institut de Neurosciences des Syst`emes, Marseille, France, [6]Department of Epilepsy, Movement Disorders and Physiology, Kyoto University Graduate School of Medic, Kyoto, Japan, [7]Epilepsy Center, Medical Center – University of Freiburg, Freiburg im Breisgau, Germany, [8]Department of Epilepsy, Movement Disorders and Physiology, Kyoto University Graduate School of Medic, Kyoyo, Japan, [9]Department of Neurology, University of Michigan, Ann Arboor, MI, [10]Department of Neurology, University of Michigan, Ann Arbor, MI, [11]Institut de Neurosciences des Systèmes, Marseille, France, [12]Department of Biomedical Engineering, BioInterfaces Institute, University of Michigan, Ann Arbor, MI

Introduction: Epilepsy is one of the most common neurological disorders and is characterized by spontaneously recurring seizures. Different ways of classifying seizures have been proposed. However, in the absence of fundamental knowledge, the current classification is based on an operational (i.e. practical) system [Fisher et al., 2017a]. A complementary approach leverages on the idea that electrographic seizures can be classified using knowledge from dynamical system theory [Jirsa et al. 2014, Wang et al. 2017]. It is possible to create a taxonomy of sixteen classes, the dynamotypes, based on the bifurcations pair allowing for the transitions between healthy and ictal state and viceversa [Izhikevich 2000, Jirsa et al. 2014]. Based on that initial work, we here expanded and validated the Taxonomy of Seizure Dynamotypes, through the analysis of a large cohort of human data. Our analysis was guided by insights gained from the study of a minimal model for bursting that captures the different dynamotypes in a single mathematical representation [Saggio et al, 2017]. The model establishes a hierarchy among the classes of the taxonomy and introduces relationship among them, with the possibility that patients could exhibit more than one seizure type, with some pairings being more likely too occur.

Methods: We analyzed seizures from 120 patients with focal onset seizures, recorded on intracranial EEG in seven centers worldwide, to identify the bifurcations at onset and offset. The canonical features necessary to distinguish the bifurcations are the trends of the amplitude and interspike intervals (ISI), with some bifurcations exhibiting specific scaling laws, and the presence/absence of a direct current shift. We first validated our procedure, using three human reviewers and an automated algorithm, on a synthetic dataset obtained through the model. We then compared these same methods on 120 human seizures. We found that concordance was also reliable in human data.

Results: We identified 12 different dynamotypes, with some bifurcations being more common than others. To test whether individuals display different types of seizures over time, analysed longitudinal data, with over 2000 seizures from 13 patients. Individual patients displayed different dynamotypes over time. This finding challenges the traditional view of stereotyped seizures, suggesting a more nuanced understanding of seizure dynamics is necessary. In a few cases, we also observed transitions between classes occurring during a single seizure. This findings were reproducible within our model, together with some other 'unusual' seizures, highlighting the role of processes acting on at least three different timescales in the generation, evolution and termination of a seizure.

Conclusions: The introduction of TSD provides a new perspective in the study and classification of epileptic seizures. It does not describe all possible seizure features, but relies on seizure onset and offset classification, complementing existing clinical tools by focusing on the dynamic aspects of seizures. TSD establishes a principled method for characterizing seizure dynamics that has the potential to lead to new branches of research, improved understanding, and better treatment of seizures. The patient specific dynamotype(s) can be used to improve the predictive power of large-scale brain models that are being developed to improve surgery outcome in drug-resistant epilepsy patients. One of these approaches, the Virtual Epileptic Patient (VEP), is currently under clinical trial in France and uses a model encoding one of the most common dynamotypes [Jirsa et al. 2014]. However, our analysis suggests that there is variability among patients and that patient specificity may be improved by modelling the appropriate dynamotype, which which may affect the global dynamics of the VEP and alter predictions on treatment.

References

1. Fisher, R. S. et al. (2017). Operational classification of seizure types by the International League Against Epilepsy: Position Paper of the ILAE Commission for Classification and Terminology. Epilepsia, 58(4), 522-530.
2. Izhikevich, E. M. (2000). Neural excitability, spiking and bursting. Interna- tional journal of bifurcation and chaos, 10(06), 1171-1266.
3. Jirsa, V. K. et al. (2014). On the nature of seizure dynamics. Brain, 137(8), 2210-2230.
4. Wang, Y. et al. (2017). Mechanisms underlying different onset patterns of focal seizures. PLoS computational biology, 13(5), e1005475.
5. Saggio, M. L. et al. (2017). Fast–slow bursters in the unfolding of a high codimension singularity and the ultra-slow transitions of classes. The Journal of Mathematical Neuroscience, 7, 1-47.
6. Saggio, M. L. et al. (2020). A taxonomy of seizure dynamotypes. Elife, 9, e55632.

Poster No 1889

ComBatLS: A location- and scale-preserving method for multi-site image harmonization

Margaret Gardner[1], Russell Shinohara[1], Richard Bethlehem[2], Rafael Romero-García[3], Varun Warrier[4], Sheila Shanmugan[1], Jakob Seidlitz[1], Aaron Alexander-Bloch[1], Andrew Chen[5]

[1]University of Pennsylvania, Philadelphia, PA, [2]Autism Research Centre, Department of Psychiatry, University of Cambridge, Cambridge, United Kingdom, [3]University of Seville, Seville, Spain, [4]University of Cambridge, Cambridge, Cambridgeshire, [5]Medical University of South Caroline, Charleston, SC

Introduction: Recent work has leveraged massive datasets and advanced image harmonization algorithms to construct normative models of imaging-derived phenotypes (IDPs)[1,2]. These brain chart models, which can produce centile or z-scores to benchmark individuals' morphology within a population, are often fit on magnetic resonance imaging data collected across hundreds of scanners. One popular method for harmonizing these data is ComBat, which preserves the effects of specified covariates on the IDPs' means. However, evidence suggests that biological factors, such as sex, also impact an IDP's variance across a population[3]. These scale effects, which directly impact centile and z-score distributions, are not preserved by current harmonization methods. Thus, harmonization may induce error in centile and z-scores, particularly when factors that impact scale are distributed unequally across sites. Here, we propose a new method in the ComBat family of harmonization tools, ComBatLS, that preserves biological variance in IDPs' location and scale. We tested ComBatLS's ability to preserve variation in scale and its impacts on centile and z-scores by harmonizing across sex-imbalanced artificial "sites" in data from the UK Biobank.

Methods: As in all ComBat versions, ComBatLS harmonizes across sites by targeting each IDP to a pooled mean while estimating and preserving the effects of designated covariates. However, prior ComBat models assumed that the variance of each IDP's distribution was consistent across sites. In ComBatLS, we incorporate a log-linear relationship between the error's standard deviation and the covariates[4], enabling the estimation and preservation of covariates' effects on IDP variance. To test this new method, we utilized IDPs derived from the structural MRIs of 28619 participants in the UK Biobank (49.7% female, age 50-80 years), collected across 3 scanners using identical hardware and protocols[5]. T1-weighted structural images, along with T2 for ~98% of subjects, were processed using FreeSurfer v. 6 to extract global volumes for each tissue class (cortical gray matter, subcortical gray matter, white matter, and CSF), as well as surface area, thickness, and volume for each cortical region[6]. Subjects were randomly assigned to one of three simulated sites such that each site had a Male:Female ratio of 1:1, 1:4, and 4:1, respectively. We then harmonized IDPs across the simulated sites using 4 different ComBat configurations: the first preserved no covariate effects, while the remainder preserved the effects of sex and age estimated by a linear model[7], ComBat-GAM[8], and ComBatLS, respectively. Data harmonized by each configuration was then used to fit simple brain charts for each IDP using generalized additive models of location, scale, and shape.

Results: We assessed ComBat configurations' influence by comparing sex effects in scale in each brain chart and, crucially, how the centile and z-scores derived from them were affected by each harmonization technique. Models fit on the complete, unharmonized data showed the true sex effect in scale in this dataset. Despite the confounding of sex- and site-effects in our simulations, ComBatLS accurately preserved the effects of sex on IDP variance (Fig 1). For both centile and z-scores, pairwise t-tests revealed that the magnitude of error for each subject's scores differed significantly across ComBat methods, with ComBatLS producing more accurate scores than the next most accurate method, ComBat-GAM (Fig 2), in 207 of 208 IDPs (pFDR centiles = <0.001 - 0.67, pFDR z-scores = <0.001 - 0.134). These results were stable across 10 permutations of subjects' site assignments.

Figure 1. Standardized effect of male sex on feature variance

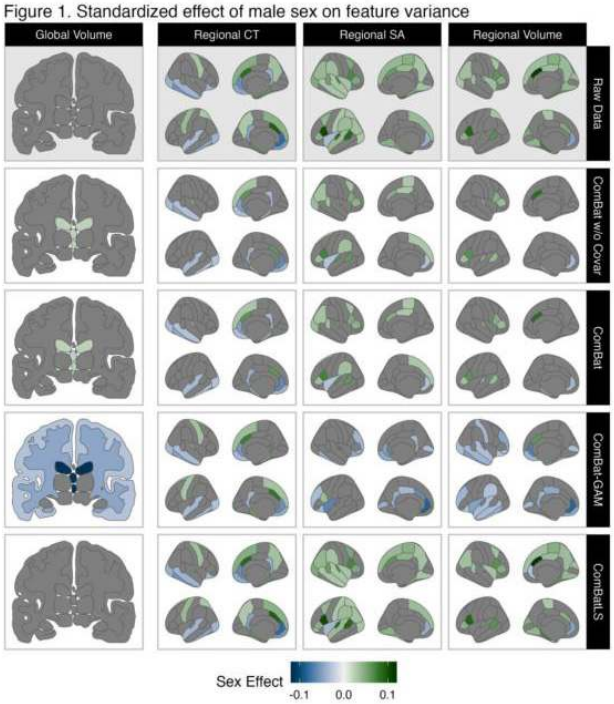

Figure 1. Sex's impact on IDP variance is affected by ComBat configuration and is best preserved by ComBatLS. Shown are significant (FDR-corrected) standardized effects of male sex on each IDP's variance, calculated as the difference in males' and females' predicted variance at age 64.9 years (mean age of the dataset) divided by the predicted variance for females; positive values indicate variance is greater among males than females. The first row displays this effect in the original dataset, while subsequent rows display how brain charts' estimates of sex effects change when different ComBat configurations are applied to sex-imbalanced simulated sites. If ComBat successfully preserves sex effects on variance, harmonized data should reproduce sex effects observed in the raw data. Columns are organized by feature type: global volumes for each tissue class and the cortical thickness, surface area, and volume of cortical regions. (CT = cortical thickness; SA = surface area; ComBat w/o Covar = original ComBat without covariates; ComBat = original ComBat with covariates y ~ age + male; ComBat-GAM = ComBat-GAM with covariates y ~ s(age) + male; ComBatLS = ComBatLS with location covariates y ~ pb(age) + male and scale covariates y ~ age + male)

Figure 2. Absolute errors in centile scores across ComBat processing pipelines

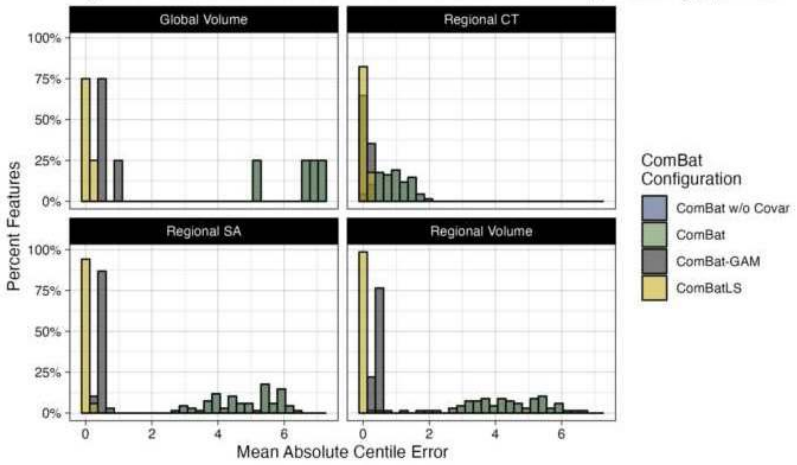

Figure 2. ComBatLS produces the smallest error in centile scores across IDPs. The absolute error in each subject's centile scores, as predicted by brain charts fit on data harmonized using different ComBat configurations relative to those fit on raw data. The average magnitude of error in each region is shown. Note that the error produced by data fitted on ComBat without covariates and data fitted using ComBat with linear covariates is roughly identical. (CT = cortical thickness; SA = surface area; ComBat w/o Covar = original ComBat without covariates; ComBat = original ComBat with covariates y ~ age + male; ComBat-GAM = ComBat-GAM with covariates y ~ s(age) + male; ComBatLS = ComBatLS with location covariates y ~ pb(age) + male and scale covariates y ~ age + male)

Conclusions: We propose ComBatLS as a robust method for harmonizing neuroimaging data across sites while preserving biologically meaningful differences in scale for accurate centile and z-score estimation. ComBatLS is available alongside other ComBat harmonization tools at https://github.com/andy1764/ComBatFamily.

References

1. Frangou, S. (2022). 'Cortical thickness across the lifespan: Data from 17,075 healthy individuals aged 3-90 years', Human Brain Mapping, 43(1), 431–451. https://doi.org/10.1002/hbm.25364
2. Schabdach, J. M. (2023). 'Brain Growth Charts for Quantitative Analysis of Pediatric Clinical Brain MRI Scans with Limited Imaging Pathology', Radiology. https://doi.org/10.1148/radiol.230096
3. Wierenga, L. M. (2022). 'Greater male than female variability in regional brain structure across the lifespan', Human Brain Mapping, 43(1), 470. https://doi.org/10.1002/HBM.25204
4. Harvey, A. C. (1976). 'Estimating Regression Models with Multiplicative Heteroscedasticity', Econometrica, 44(3), 461–465. https://doi.org/10.2307/1913974
5. Littlejohns, T. J., (2020). 'The UK Biobank imaging enhancement of 100,000 participants: Rationale, data collection, management and future directions', Nature Communications, 11(1), Article 1. https://doi.org/10.1038/s41467-020-15948-9
6. Desikan, R. S. (2006). 'An automated labeling system for subdividing the human cerebral cortex on MRI scans into gyral based regions of interest', NeuroImage, 31(3), 968–980. https://doi.org/10.1016/J.NEUROIMAGE.2006.01.021
7. Fortin, J. P. (2018). 'Harmonization of cortical thickness measurements across scanners and sites', NeuroImage, 167, 104. https://doi.org/10.1016/J.NEUROIMAGE.2017.11.024
8. Pomponio, R. (2020). 'Harmonization of large MRI datasets for the analysis of brain imaging patterns throughout the lifespan', NeuroImage, 208. https://doi.org/10.1016/J.NEUROIMAGE.2019.116450

Poster No 1890

A novel approach for quantitative T1 measurements: validation in a longitudinal pediatric sample

Zihan Zhou[1,2], Maya Yablonski[2,3], Xiaozhi Cao[1,4], Mengze Gao[1], Congyu Liao[1,4], Kawin Setsompop[1,4], Jason Yeatman[2,3,5]

[1]Department of Radiology, Stanford University, Stanford, United States, [2]Graduate School of Education, Stanford University, Stanford, United States, [3]Department of Pediatrics, Stanford University School of Medicine, Stanford, United States, [4]Department of Electrical Engineering, Stanford University, Stanford, United States, [5]Department of Psychology, Stanford University, Stanford, United States

Introduction: Developmental cognitive neuroscience aims to shed light on evolving relationships between brain structure and cognitive development. To this end, quantitative methods that reliably measure individual differences are fundamental. Qualitative MR (e.g., T1 weighted images) are influenced by multiple biological factors, along with scan parameters and biases from hardware. In contrast, quantitative T1 mapping measures specific tissue properties[1,2]. Conventional quantitative T1 mapping methods suffer from long scan times, low resolution and sensitivity to field inhomogeneity and motion. To address

these limitations, we adopted a novel MR fingerprinting (MRF) protocol for rapid 1-mm whole-brain T1 maps in 2 minutes which is robust to B1-inhomogeneity[3,4]. This method has yet to be evaluated for cognitive neuroscience research. In this study, we examine the reliability and validity of MRF-based T1 measurements in children scanned longitudinally.

Methods: 49 children aged 8-13y (mean 10y ±1.4) completed two scanning sessions 2-4 months apart. In each session, two multi-axis spiral-projection 3D-MRFs were collected with complementary acquisition trajectories[5]. A separate calibration scan ("PhySiCal")[6] was used to measure B0 inhomogeneity. The total scan time was 4.5 minutes. A subspace recon with locally low-rank constraint was used for MRF reconstruction, followed by pattern matching to generate 1-mm resolution T1 maps. We examined SNR and B0 correction's impact on reliability, comparing single 2-min and combined two 2-min scans, both with and without B0 correction (Figure 1). We used two complementary approaches to evaluate test-retest reliability of T1 values. (A) We compared whole-brain voxel-based T1 values in white matter (WM), using two session data coregistered to a midpoint to avoid bias. (B) We ran an ROI-based comparison using WM and gray matter (GM) segmentations from Freesurfer (Freesurfer was run on a MRF-derived synthetic MPRAGE from each session). For WM, we focused on five corpus callosum (CC) segmentations. For GM analysis, we focused on 6 subcortical ROIs: the caudate, putamen, and thalamus, bilaterally.

Results: Four subjects were excluded due to excessive motion. Figure 1 shows the qualitative effect of the different pipelines on image quality. MRF-derived mean T1 values in the CC range from 795-878 ms, showing the typical inverted-U shape pattern (matching known histology) along the anterior-posterior axis. GM T1 values were 1001-1360ms, in line with[7]. Voxel-based reliability analysis showed that combining two 2-min MRF scans yielded higher reliability (r=0.80) than single 2-min scans (r=0.75). Surprisingly, B0-correction did not significantly improve reliability (r=0.80 vs 0.75 for 4-min and 2-min). ROI-based reliability analysis revealed a similar pattern: reliability was highest when combining the two 2-min scans, with minimal B0 correction impact for both WM (Figure 2A) and GM (Figure 2B). CC ROIs showed r=0.83±0.06 (4-min) vs 0.72±0.09 (2-min) for uncorrected data and r=0.82±0.08 (4-min) vs 0.69±0.11 (2-min) for corrected data. Lastly, age was correlated with T1 values in subcortical ROIs and in the anterior CC ($p<0.05$, fdr corrected; Figure 2C-D), in line with[8].

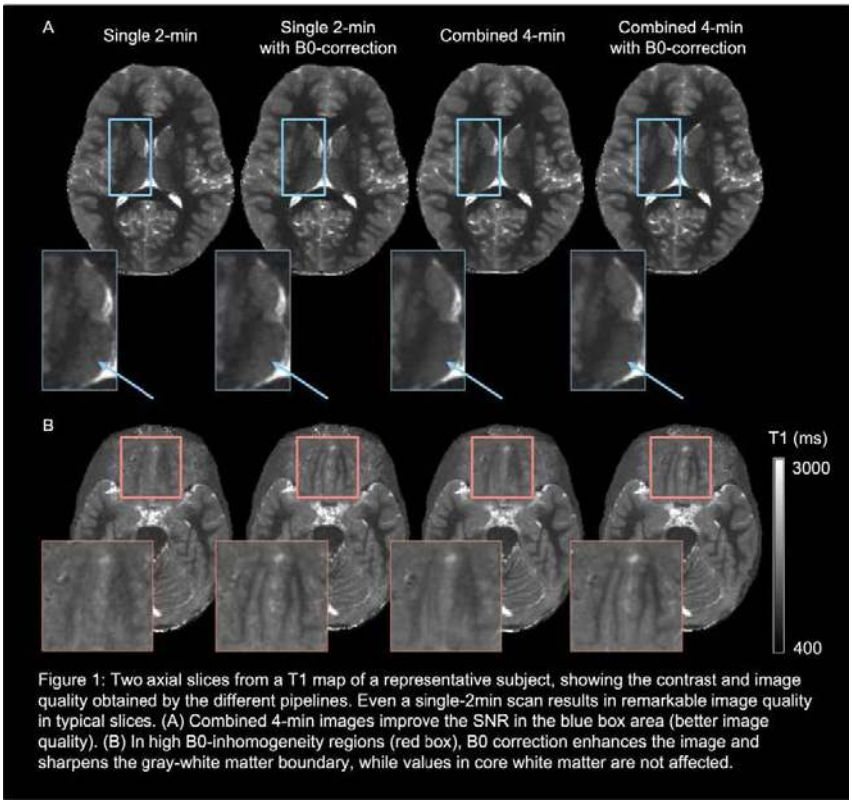

Figure 1: Two axial slices from a T1 map of a representative subject, showing the contrast and image quality obtained by the different pipelines. Even a single-2min scan results in remarkable image quality in typical slices. (A) Combined 4-min images improve the SNR in the blue box area (better image quality). (B) In high B0-inhomogeneity regions (red box), B0 correction enhances the image and sharpens the gray-white matter boundary, while values in core white matter are not affected.

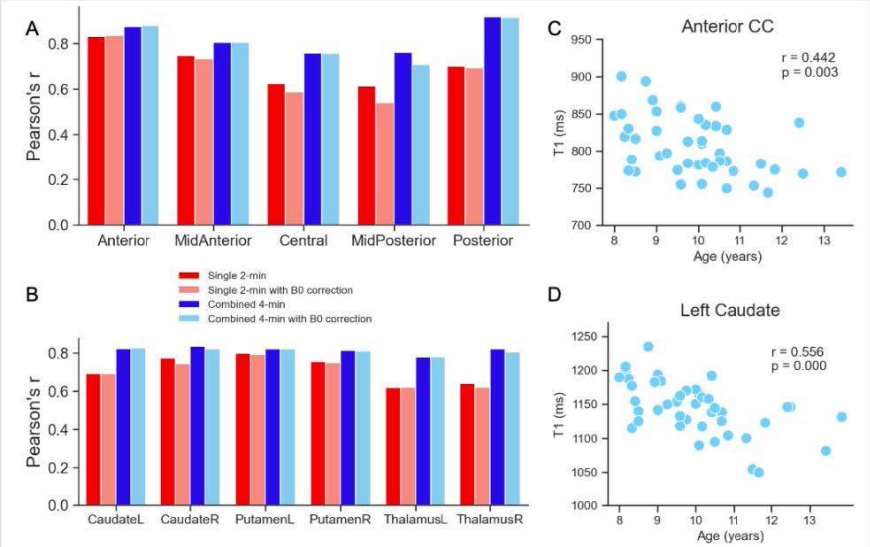

Figure 2: (A-B). Test-retest reliability across white matter (A) and gray matter (B) segmentations. Combining two 2min scans generally improves reliability compared with a single scan, while B0 correction has little to no effect on reliability in these ROIs (compare lighter to darker shades). (C-D) T1 values are negatively correlated with age. Shown are the correlations in the anterior portion of the CC (C) and the left Caudate nucleus (D).

Conclusions: This study assesses the repeatability and reproducibility of MRF-derived quantitative T1 metrics in children scanned longitudinally. We evaluated four MRF reconstruction strategies on data quality and found that longer acquisitions (which result in higher SNR) improve T1 repeatability. Surprisingly, reliability was high even without a B0-correction and did not improve substantially after correction. This highlights the feasibility of rapidly collecting quantitative MRI measures without requiring additional calibrations. In sum, MRF provides a promising methodology for deriving reliable quantitative metrics of brain tissue structure in children and patient populations where scan time and motion are of particular concern.

References

1. Filo S, et al. (2023), 'Non-invasive assessment of normal and impaired iron homeostasis in the brain', Nat Commun, vol. 14, Article number. 5467.
2. Erramuzpe A, et al., (2021), 'A Comparison of Quantitative R1 and Cortical Thickness in Identifying Age, Lifespan Dynamics, and Disease States of the Human Cortex', Cereb Cortex, vol. 31, no. 2, pp.1211-1226.
3. Schauman S, et al., (2023), 'Five clinical contrasts from 1 minute whole brain MRF with B0 correction'. In Proceeding of 31st Annual Meeting of the ISMRM, Toronto, Canada, pp. 2184.
4. Schauman S, et al., (2022), 'Toward a 1-minute high-resolution brain exam- MR Fingerprinting with fast reconstruction and ML-synthesized contrasts'. In Proceeding of 30th Annual Meeting of the ISMRM, London, UK, pp. 0053.
5. Cao X, et al., (2022), 'Optimized multi-axis spiral projection MR fingerprinting with subspace reconstruction for rapid whole-brain high-isotropic-resolution quantitative imaging'. MRM. Vol. 88, no. 1, pp. 133-150
6. Iyer SS, et al (2020), 'PhysiCal: A rapid calibration scan for B0, B1+, coil sensitivity and Eddy current mapping'. In Proceedings of the 28th Annual Meeting of ISMRM, Sydney/Virtual, Australia, pp. 0661.
7. Gräfe D, et al., (2021), 'Quantitative T1 mapping of the normal brain from early infancy to adulthood'. Pediatr Radiol. Vol. 51, no. 3, pp. 450-456.
8. Yeatman J, et al., (2014), 'Lifespan maturation and degeneration of human brain white matter'. Nat Commun. Vol. 5, Article number. 4932.

Poster No 1891

Optical flow GAN-based Translation for Three-Dimensional MRI Harmonization

Jiaying Lin[1], Zhuoshuo Li[1], Youbing Zeng[1], Xiaobo Liu[1], Xinting Ge[2], Minhua Lu[3], Mengting Liu[1]

[1]Sun Yat-sen University, Shenzhen, Guangdong, [2]Shandong Normal University, Jinan, Shandong, [3]Shenzhen University, Shenzhen, Guangdong

Introduction: While pursuing advanced AI-guided MRI diagnostics, there's a growing need for diverse brain imaging datasets. However, variations in data collection methods across sites can introduce biases in subsequent analyses. MRI harmonization methods exist but are primarily tailored for 2D slices, causing inconsistencies when applied to 3D volumes. The extension of 2D MRI harmonization to 3D images poses several challenges: 1) 3D images have a larger voxel count. 2) The availability of 3D training instances is relatively limited compared to 2D. 3) Many machine learning methods are computationally demanding and struggle to stabilize training processes. Our approach uses a GAN-based method integrating optical flow information

to supervise newly generated 2D images. Focusing on slice relationships, we've developed an unsupervised spatial loss to enhance coherence.

Methods: In our study, we introduce an unsupervised model aiming to address inter-slice variations in 3D MRI harmonization. Leveraging optical flow-based translation and GAN, our model effectively aligns MR images. Fig. 1(a) illustrates our model architecture, comprising three key modules: (i) A dual-domain generator synthesizing MR images in the target domain. (ii) A dual-domain discriminator distinguishing real from generated images. (iii) A warping operation W that generates subsequent slices by utilizing the current slice and optical flow. Initially, we segment 3D MR volumes into slices, treating the tissue between neighboring slices as minimally deformed objects. While extracting anatomical details from the source domain, we extract irrelevant biological data from the target domain for harmonized images. Through the generator, our model conducts domain transformation and employs warping operations to generate the next slice. We supervise these operations using Recycle Consistency Loss and Recycle Consistency Loss to enhance the model's effectiveness.

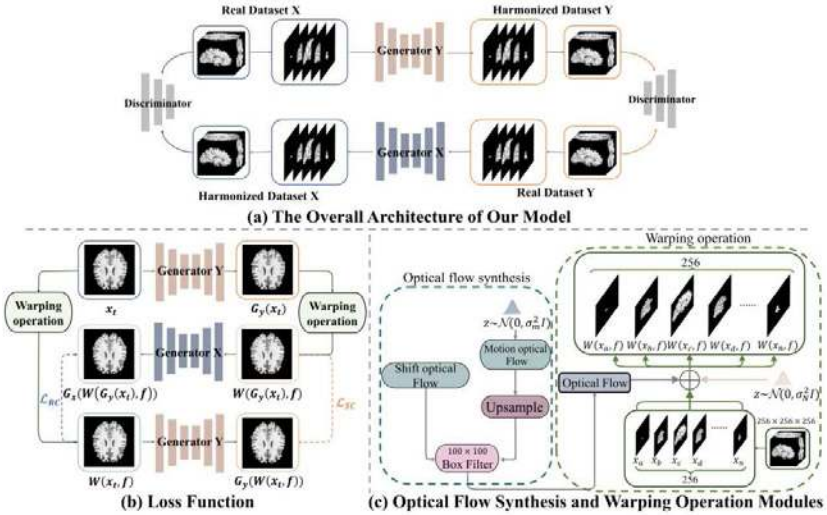

Results: For qualitative and quantitative comparisons, we trained and tested our model using datasets from the Alzheimer's Disease Neuroimaging Initiative (ADNI) (paired and unpaired), UK Biobank (UKBB), and the Nathan Kline Institute-Rockland Sample (NKI-RS). In Fig. 2A, we demonstrate the evaluation of inter-slice stability using the warping error metric to assess our model. It is evident that among the methods considered, the results obtained from our approach surpass those achieved by both 2D techniques and most of the 3D methodologies. In Fig. 2B, we conducted a quantitative evaluation of images from both domains using three image similarity metrics. On average, our model significantly outperforms other methods, showcasing considerable improvements of 1.94dB in Peak Signal-to-Noise Ratio, 27.19% in squared Maximum Mean Discrepancy, and 1.03% in Multi-Scale Structural Similarity.

(A) INTER-SLICE CORRELATION COMPARISON

Dataset	Method	Warping Error(↓) (10^{-5})	Dataset	Method	Warping Error(↓) (10^{-5})
ADNI-traveling subjects	CycleGAN2D	66.7±5.97	ADNI-CN&NKI-RS	CycleGAN2D	67.0±7.31
	ResViT	68.6±4.93		RecycleGAN	68.5±7.27
	RecycleGAN	67.5±4.53		CycleGAN3D	78.5±37.2
	TCGAN	103.5±17.4		Ours	63.4±5.35
	CycleGAN3D	131.7±16.9		No har	64.9±5.38
	Pix2Pix3D	63.9±4.26	ADNI-CN&UKBB	CycleGAN2D	73.6±9.10
	PTNet3D	185.9±4.01		RecycleGAN	81.0±15.8
	Ours	64.2±4.15		CycleGAN3D	62.9±2.44
	No har	63.3±5.83		Ours	61.7±4.86
				No har	61.5±4.39

Inter-slice Correlation comparison for ADNI-traveling subjects(3T, 1.5T), ADNI-CN and UKBB. The symbol ↓ indicates that lower values are better, and the best result is highlighted in bold, while the second-best result is underlined. The term "No har" indicates the absence of harmonization.

(B) IMAGE SIMILARITY COMPARISON

Model	PSNR(↑)		bMMD²(↓)		MS-SSIM(↑)	
	A	B	A	B	A	B
CycleGAN2D	25.13±2.96	25.08±2.91	248.9±173.0	249.9±169.0	0.975±0.0175	0.973±0.0171
ResViT	22.68±2.39	23.19±1.04	**175.2±112.5**	247.8±161.4	0.963±0.0178	0.963±0.0146
RecycleGAN	25.54±1.97	24.74±2.72	205.9±116.4	266.7±173.5	0.977±0.0153	0.972±0.0182
TCGAN	19.37±2.55	24.45±0.68	20252.1±683.2	20254.2±598.9	0.795±0.0323	0.903±0.0041
Pix2Pix3D	26.68±1.97	24.32±3.93	20207.5±2172.7	16000.5±2812.1	0.981±0.0131	0.9666±0.026
CycleGAN3D	18.03±1.55	17.16±2.28	1147.2±358.1	1702.8±905.0	0.8655±0.046	0.8090±0.079
PTNet3D	18.42±2.80	21.47±0.87	563.7±105.1	762.2±256.7	0.8243±0.039	0.8585±0.012
Ours	**26.79±2.60**	**26.47±2.61**	186.2±140.2	**216.3±138.3**	**0.985±0.017**	**0.979±0.017**
No har	24.69±3.027		276.5±183.6		0.972±0.017	

The similarity of image comparison for ADNI-traveling subjects involves the site column. A represents the B→A translation, it involves comparing the ground truth image (A) with generated images (A'), and vice versa for B. The term " No har" category includes the source and target images, indicates the absence of harmonization.

Conclusions: Inspired in[1], we present an unsupervised 3D MRI harmonization method that minimizes inter-slice variations, maintains anatomical details, and ensures consistent MRI styles using optical flow and two consistency losses. Notably, it's computationally efficient for resource-limited settings compared to 3D methods. However, our model currently supports transformations between only two domains and lacks multi-domain capabilities like[2,3,4]. Future work will focus on enhancing this aspect.

References

1. W. Wang, S. Yang, J. Xu, and J. Liu, " Consistent video style transfer via relaxation and regularization," IEEE Transactions on Image Processing, vol. 29, pp. 9125–9139, 2020, DOI: 10.1109/TIP.2020.3024018.
2. Y. Choi, Y. Uh, J. Yoo, and J.-W. Ha, "J.-W. Ha, "StarGAN v2: Diverse image synthesis for multiple domains," in IEEE/CVF Conference on Computer Vision and Pattern Recognition (CVPR), pp. 8185–8194, 2020, DOI: 10.1109/CVPR42600.2020.00821.
3. W. T. Clarke et al., "Multi-site harmonization of 7 tesla MRI neuroimaging protocols," NeuroImage, vol. 206, p. 116335, 2020, DOI:10.1016/j.neuroimage.2019.116335.
4. M. Liu et al., "Style transfer generative adversarial networks to harmonize multisite MRI to a single reference image to avoid overcorrection,"Hum Brain Mapp. 2023, vol. 44(14), pp. 4875-4892, Oct, 2023, DOI: 10.1002/hbm.26422.

Poster No 1892

Effects of cortical heterogeneity on the eigenmodes of brain geometry

Victor Barnes[1], Jace Cruddas[1], Trang Cao[2], James Pang[1], Alex Fornito[3]

[1]Monash University, Melbourne, Victoria, [2]Monash University, Clayton, VIC, [3]Monash University, Clayton, Victoria

Introduction: Brain function is constrained by its underlying structure and anatomy, but explaining the mechanisms behind this link has proven challenging. In many areas of physics and engineering, the dynamics of a system can be understood with respect to the eigenmodes of its structure, representing the fundamental, resonant vibrations of the system. Recent work has shown that a diverse array of functional brain maps derived from task-evoked and resting-state fMRI can be parsimoniously explained as excitations of the eigenmodes of cortical geometry (termed geometric eigenmodes)[1], offering a robust paradigm to explore how the intrinsic geometry of the brain physically constrains emerging dynamics. The success of these geometric eigenmodes is somewhat surprising given that they are estimated using a minimal set of features-simply defining how the shape of the cortex varies through space. However, they treat the cortex as a homogeneous medium, ignoring spatial variations in local cellular and molecular composition (e.g., myelination, cell and neurite density). Here, we developed a framework for deriving geometric eigenmodes that can account for spatial heterogeneities in any arbitrary cortical property.

Methods: We derived geometric eigenmodes with and without spatial heterogeneities, which we termed herein as homogeneous and heterogeneous modes, respectively. We derived the modes by using a triangular mesh representation of the cortical surface from a FreeSurfer template[2] and solving the heterogeneous form of the Helmholtz equation: $\nabla(cs^2\cdot\nabla)\psi=-\lambda\psi$ where ψ are the eigenmodes, λ are the eigenvalues, and cs is the heterogeneous term describing local variations across the cortical mesh and corresponds to the wave speed of the resulting dynamics, as captured in biophysical models such as neural field theory[3]. We define cs as a function of a heterogeneity map, ρ, that encodes spatial variations in cortical properties (e.g. myelination), written formally as: $cs=cmean+\alpha cmean(\rho-\rho mean)$ where cmean=3352.4 mm/s is the mean neural propagation speed taken from physiological estimates[1], ρ is the heterogeneity map normalized between 0 and 1, and α is a free parameter controlling the variance of cs. As an initial case, we derived heterogeneous modes parameterized by the sensory-association (SA) axis, which differentiates sensory and association areas of the cortex and captures spatial variations in a diverse range of anatomical and other properties[4]. We also derived the classical homogeneous modes by solving the above Helmholtz equation with cs set to unity, following[1]. The modes form a complete, orthogonal basis set and can thus be used to decompose data. We used this approach to compare the accuracy with which the heterogeneous and homogeneous modes could reconstruct diverse maps of cortical organisation drawn from the neuromaps repository[5].

Results: Figure 1 shows the homogeneous modes and heterogeneous modes parametrized by the SA axis at varying levels of α. We found that higher levels of α significantly changes the structure of the heterogeneous modes in comparison to the homogeneous modes (see low correlations along the diagonal of the correlation matrices). Figure 2 shows the reconstruction accuracies of key brain maps from the neuromaps repository for both the homogeneous modes and the heterogeneous modes (α=0.3). We found that the heterogeneous modes consistently show a higher accuracy at 5 and 10 modes relative to the homogeneous modes, indicating that they have greater flexibility in capturing the very low-frequency content of the neuromaps data.

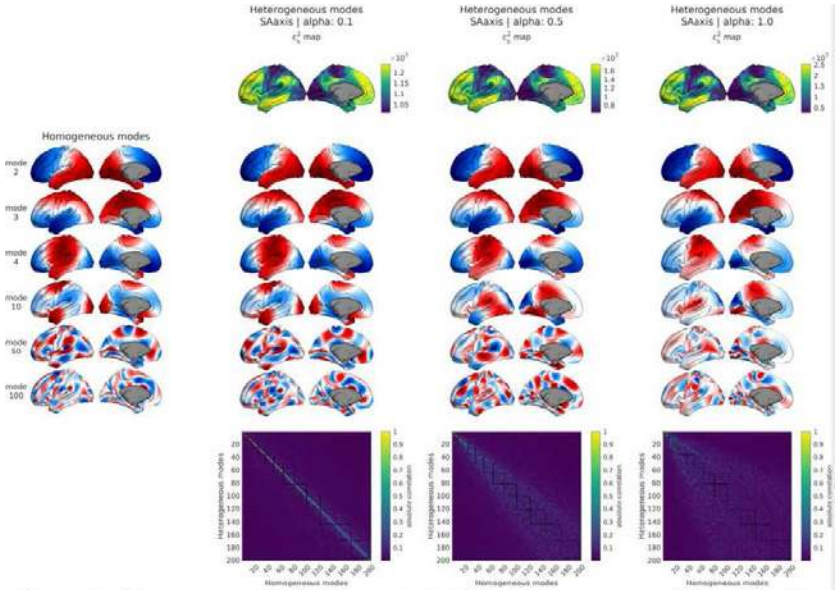

Figure 1. Heterogeneous modes parameterized by the sensory-association axis. The heterogeneous map, the corresponding heterogeneous modes, and the Pearson's correlation between the heterogeneous and homogeneous modes are shown for α values of 0.1, 0.5, and 1.0. The homogeneous modes are shown for reference.

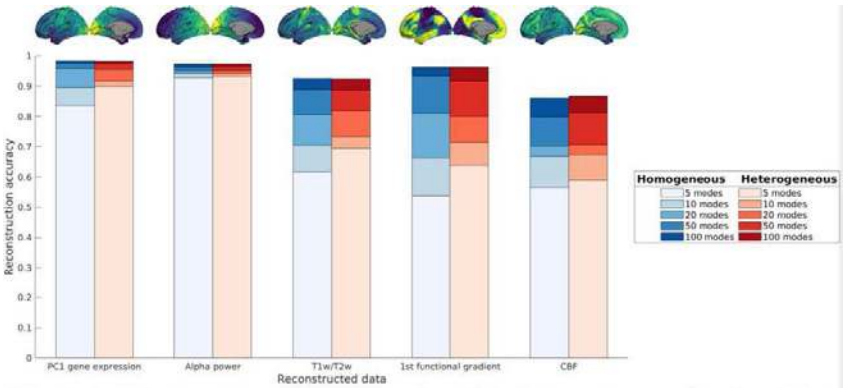

Figure 2. Heterogeneous modes compared against homogeneous modes. Cumulative reconstruction accuracy of key neuromaps data using homogeneous modes (blue) and heterogeneous modes parameterized by the SA axis with α = 0.3 (red). The segments within each bar represent the reconstruction accuracy achieved for the corresponding number of modes used. The target maps being reconstructed are shown above the corresponding reconstruction accuracy bars.

Conclusions: We show that refining the geometric eigenmode model by incorporating information about spatial heterogeneities in cortical tissue can improve reconstruction of very low-frequency aspects of cortical organization. Future work will explore how these heterogeneities influence dynamics.

References

1. Pang, James C., Kevin M. Aquino. 2023. "Geometric Constraints on Human Brain Function." Nature 618 (7965): 566–74.
2. Fischl. 1999. "High-Resolution Intersubject Averaging and a Coordinate System for the Cortical Surface." Human Brain Mapping 8 (4): 272–84.
3. Robinson, P. A. 1997. "Propagation and Stability of Waves of Electrical Activity in the Cerebral Cortex." Physical Review E 56 (1): 826–40.
4. Sydnor. 2021. "Neurodevelopment of the Association Cortices: Patterns, Mechanisms, and Implications for Psychopathology." Neuron 109 (18): 2820–46.
5. Markello, Ross D. 2022. "Neuromaps: Structural and Functional Interpretation of Brain Maps." Nature Methods 19, 1472–1479

Poster No 1893

X-sepnet(chi-sepnet): Susceptibility source separation using deep neural network

Minjun Kim[1], Hyeong-Geol Shin[2], Sooyeon Ji[1], Chungseok Oh[3], Jiye Kim[4], Jinhee Jang[5], Berkin Bilgic[6], Jongho Lee[1]

[1]Seoul National University, Seoul, Seoul, [2]Department of Radiology and Radiological Science, Johns Hopkins University School of Medicine, Baltimore, MD, [3]Department of Electrical Computer Engineering, Seoul National University, Seoul, Korea, Republic of, [4]Seoul National University, Gwanak-gu, Korea, Republic of, [5]Seoul St Mary's Hospital, Seoul, Korea, Republic of, [6]Athinoula A. Martinos Center for Biomedical Imaging, Massachusetts General Hospital, Charlestown, MA

Introduction: Recently, χ-separation has been proposed to separate positive and negative susceptibility source distributions[1,2,3]. These methods should resolve the ill-posed dipole-inversion problem, which creates streaking artifacts. Hence, the results of χ-separation hamper accurate estimation of susceptibility concentrations. The artifacts can be resolved using multiple head orientation datasets as demonstrated in COSMOS QSM[4] or a neural network that is trained using COSMOS dataset as shown in QSMnet[5]. The latter is advantageous because one can infer a COSMOS-quality QSM map from single orientational data once the network is fully trained. In this study, we developed a neural network, χ-sepnet, that generates COSMOS-quality χ-separation results by training the network using multi-orientation χ-separation data. Additionally, another χ-sepnet that only inputs multi-echo GRE data is designed to test the feasibility of using dataset without T2 maps.

Methods: Multi-echo GRE and multi-echo SE data were acquired from six subjects (see REF.1 for scan parameters; 4:1:1 subjects for train:validation:test; IRB-approved). Each subject GRE dataset consisted of six head orientations. These multi-orientation GRE data and multi-echo SE data were processed using a COSMOS-like χ-separation algorithm that created artifact-free positive (χpos) and negative (χneg) susceptibility maps (χ-sep-COSMOS). These maps were utilized as labels to train the two networks (χ-sepnet-R2' that requires R2 and χ-sepnet-R2* that is free from R2). The original χ-separation algorithm that utilized the MEDI prior is also utilized (χ-sepnet-MEDI). The networks had same 3D U-net[6] structure as QSMnet. For the input, not only local field and R2' (or R2*) but also a QSM map generated from QSMnet was concatenated. The loss function had three losses: L1 loss, gradient loss, and model loss which enforces to learn information from local field maps and R2' maps. Data augmentation was performed by rotating the images by random angles relative to B0 direction, resulting in a total of 48 training datasets. For quantitative evaluation, the test subject results were compared for NRMSE, PSNR, and SSIM with the χ-sep-COSMOS results as reference. An ROI analysis performed in 11 ROIs (Fig. 4), reporting the mean and standard deviation of the susceptibility values across the head orientation. Two additional subjects, one multiple sclerosis (MS) patient and the other subject with calcification (IRB-approved) were inferenced for the evaluation of the networks in clinical practice.

Results: The positive and the negative susceptibility maps from all four methods are summarized in Fig. 2(a). The χpos and χneg maps from the two χ-sepnets show high-quality results that are comparable or even cleaner than the reference maps from χ-sep-COSMOS. Streaking artifacts are observed in the χ-sep-MEDI maps but are less noticeable in the other maps. Quantitative metrics report χ-sepnet-R2' generates the best results while χ-sepnet-R2* provides good outcomes (Fig. 2(b)). The three zoomed-in regions reveal well-known structures of the brain in Fig. 2(c,d,e). Deep gray matter regions are clearly delineated in the χpos and χneg maps. In particular, the hand knob region reveals that the positive susceptibility maps report higher values in the motor cortex than in the sensory cortex, which is well-known iron distribution from histology[7].

Conclusions: In this study, χ-sepnets are designed to reconstruct artifact-free susceptibility source distribution maps using deep learning. The methods only require single head orientation data. Furthermore, χ-sepnet-R2* requires only multi-echo GRE data, reducing the requirement of R2 maps in χ-separation at the cost of slightly decreased accuracy. When applied to the patients, the results reveal expected characteristics of lesions.

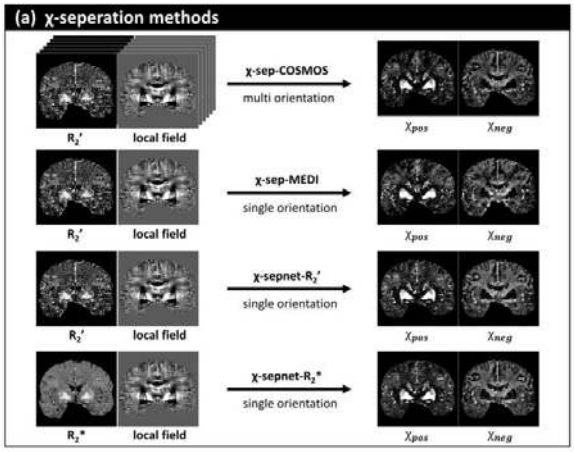

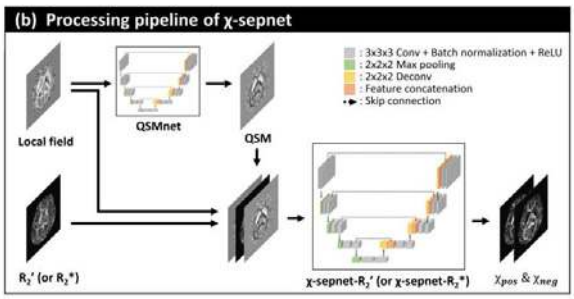

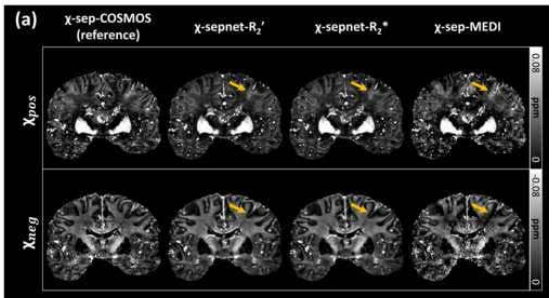

(b)

Metric	Map	χ-sepnet-R2'	χ-sepnet-R2*	χ-sep-MEDI
NRMSE	χpos	32.4 ± 2.9%	36.4 ± 2.6%	48.3 ± 4.8%
	χneg	34.2 ± 2.7%	39.0 ± 2.6%	51.7 ± 4.8%
PSNR	χpos	47.7 ± 0.8	46.7 ± 0.6	44.2 ± 0.9
	χneg	48.1 ± 0.7	46.9 ± 0.6	44.5 ± 0.9
SSIM	χpos	0.93 ± 0.01	0.90 ± 0.01	0.84 ± 0.03
	χneg	0.95 ± 0.01	0.93 ± 0.01	0.91 ± 0.01

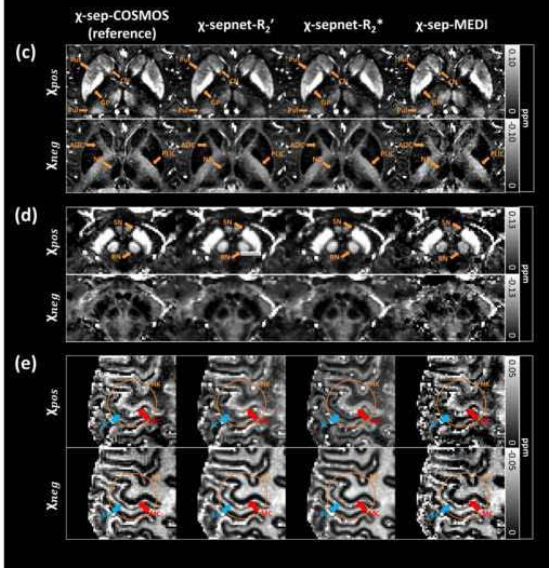

References

1. Shin, H. G., Lee, J., Yun, Y. H., Yoo, S. H., Jang, J., Oh, S. H., ... & Lee, J. (2021). x-separation: Magnetic susceptibility source separation toward iron and myelin mapping in the brain. NeuroImage, 240, 118371.
2. Chen, J., Gong, N. J., Chaim, K. T., Otaduy, M. C. G., & Liu, C. (2021). Decompose quantitative susceptibility mapping (QSM) to sub-voxel diamagnetic and paramagnetic components based on gradient-echo MRI data. NeuroImage, 242, 118477.
3. Emmerich, J., Bachert, P., Ladd, M. E., & Straub, S. (2021). On the separation of susceptibility sources in quantitative susceptibility mapping: Theory and phantom validation with an in vivo application to multiple sclerosis lesions of different age. Journal of Magnetic Resonance, 330, 107033.
4. Liu, T., Spincemaille, P., De Rochefort, L., Kressler, B., & Wang, Y. (2009). Calculation of susceptibility through multiple orientation sampling (COSMOS): a method for conditioning the inverse problem from measured magnetic field map to susceptibility source image in MRI. Magnetic Resonance in Medicine: An Official Journal of the International Society for Magnetic Resonance in Medicine, 61(1), 196-204.
5. Yoon, J., Gong, E., Chatnuntawech, I., Bilgic, B., Lee, J., Jung, W., ... & Lee, J. (2018). Quantitative susceptibility mapping using deep neural network: QSMnet. Neuroimage, 179, 199-206.
6. Ronneberger, O., Fischer, P., & Brox, T. (2015, October). U-net: Convolutional networks for biomedical image segmentation. In International Conference on Medical image computing and computer-assisted intervention (pp. 234-241). Springer, Cham.
7. Deistung, A., Schäfer, A., Schweser, F., Biedermann, U., Turner, R., & Reichenbach, J. R. (2013). Toward in vivo histology: a comparison of quantitative susceptibility mapping (QSM) with magnitude-, phase-, and R2 -imaging at ultra-high magnetic field strength. Neuroimage, 65, 299-314.

Poster No 1894

Best Practices for Advancing Neuroimaging Tools on The Edge

Mohamed Masoud[1], Pratyush Reddy[1], Farfalla Hu[1], Sergey Plis[1]

[1]*Georgia State University, Atlanta, GA*

Introduction: Processing volumetric medical images within web browsers poses unprecedented challenges emerging from the inherent constraints of browser environments. This abstract outlines Brainchop's (https://github.com/neuroneural/brainchop) processing pipeline, an innovative in-browser neuroimaging tool, and evaluates the performance of models across diverse software and hardware configurations, providing best practices for creating client-side neuroimaging tools and analysis of its performance from the lens of Causality. The outcomes highlight the practical viability of client-side processing for volumetric data attributable to the robust MeshNet architecture.

Methods: Brainchop[1] performs MRI segmentation using Meshnet models[2-3] trained in PyTorch with the Human Connectome[4] dataset and converted to tensorflow.js[5] for in-browser inference. It offers a range of volumetric segmentation tasks (Fig. 1a). Table 1 provides a list of the models along with their performance. We analyzed anonymously collected telemetry data to evaluate the tool's performance and identify factors that affect its success rate. Data preprocessing involved cleaning by excluding extreme outliers and removing features with high correlation coefficients (Threshold > 0.95). The selected dataset is devoid of missing values, and categorical data is encoded using a label encoder. For regression models, one-hot encoding is employed to capture the effect of each categorical variable independently. Statistical analysis utilized a 95% confidence interval for null hypothesis testing ($P<0.05$). Brainchop's performance is improved through interventions like patching and cropping applied to input data. Causal analysis to accurately estimate their effects involves treating each intervention as a distinct treatment and isolating its effect from potential confounders. To isolate each effect, the Inverse Probability of Treatment Weighting (IPTW)[6] is used. The Average Treatment Effect (ATE) can be estimated as:: ATE= p(Outcome = 1 | do (Treatment = 1)) − p(Outcome = 1 | do(Treatment = 0)) This represents the probability of success rate when applying the treatment (e.g., patching or cropping) versus when not applying it.

Table 1. Brainchop performance per segmentation model.

Model	Layers	Parameters	Preprocessing Avg. Time(S)	Cropping Avg. Time(S)	Inference Avg. Time(S)	Merging Avg. Time(S)	Postprocessing Avg. Time(S)	Requested Texture Size
Compute Brain Mask (FAST)	20	5598	1.899036	-	7.551620	-	18.739939	9159
Extract the Brain (FAST)	20	5598	2.280892	-	7.870467	-	15.030079	9159
Full Brain GWM (large)	18	23290	1.647580	-	14.011876	-	13.194727	13585
Full Brain GWM (light)	20	5598	2.624046	-	9.935594	-	14.732657	9159
Subvolume GWM (failsafe)	20	96078	2.697981	-	39.773656	1.991998	12.707437	8192
Compute Brain Mask (failsafe)	16	72222	2.124019	-	27.754568	2.161475	16.055606	8192
Compute Brain Mask (High Acc)	18	23290	0.976887	-	17.421975	-	14.490000	13585
Extract the Brain (failsafe)	16	72222	1.932426	-	30.317263	2.163195	12.805639	8192
Extract the Brain (High Acc)	18	23290	1.111473	-	8.232091	-	11.580500	13585
Cortical Atlas 50	20	27132	1.596227	27.202827	8.525125	-	11.803998	16384
FS aparc+aseg Atlas 104 (failsafe)	18	86372	1.710471	29.035294	37.802824	16.573937	19.328529	16384
FS aparc+aseg Atlas 104	18	86372	1.340567	21.924533	13.652400	-	11.471533	32768

Results: Brainchop achieved an 82% success rate from May 2022 to May 2023 despite diverse user-side computational resources. A statistical analysis of the telemetry data using the Chi-square test revealed an adequate sample size with a power of 0.963 (α = 0.05). We incorporated full-volume and sub-volume (Failsafe) models to address edge computational limitations. Our analysis showed that failed statuses were primarily linked to GPU memory limitations. While sub-volume models had higher success rates, they also incurred slower inference times, reduced accuracy, and merge overheads compared to full-volume. Patching treatment, affected by cropping, had an independent effect on the success rate. Estimation of patching effect using IPTW showed a 6.23% success rate increase, a 24.31 second inference time increase, and minimal post processing time change. Our Chi-square tests confirmed a significant correlation (p-value 2-09) between cropping and success rates in full volume inference, with a 99.9% statistical power. IPTW estimates for the cropping effect indicate an 18.12% success rate increase, a 5.26-second decrease in inference time, and a 6.83-second reduction in post processing time. Finally, Fig. 1- b and c depict the interdependence between success rates over time, with GPU and model choice influencing each other.

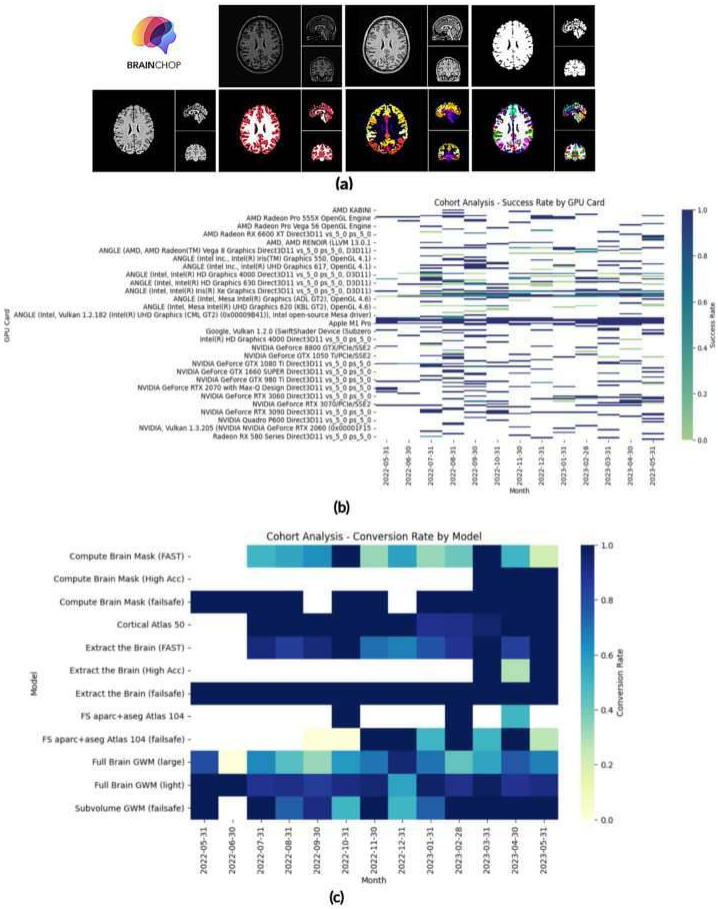

Figure 1. Demonstration of (a) Different brainchop tasks (b) Performance of each task (c) Cohort Analysis for Success Rate by GPU Card Per Month (d) Cohort Analysis for Success Rate by Model.

Conclusions: Our research has identified a statistically significant correlation between the patching and cropping techniques and both the temporal aspects and the success rate of Brainchop. Noteworthy is the observation that Brainchop has demonstrated a high success rate. Our findings highlight the imperative to refine cropping techniques for optimal outcomes and show a potential to reveal more insights that can improve Brainchop's functionality.

References

1. Masoud, M., Hu, F., and Plis, S. (2023), 'Brainchop: In-browser MRI volumetric segmentation and rendering', Journal of Open Source Software, vol. 8, no. 83, p. 5098. doi:10.21105/joss.05098
2. Fedorov, A., Johnson, J., Damaraju, E., Ozerin, A., Calhoun, V., & Plis, S. (2017), "End-to-end learning of brain tissue segmentation from imperfect labeling", IEEE International Joint Conference on Neural Networks (IJCNN). https://doi.org/10.1109/IJCNN.2017.7966333
3. Yu, F., Koltun, V. (2016), "Multi-scale context aggregation by dilated convolutions", arXiv.https://doi.org/10.48550/arXiv.1511.07122
4. D. C. Van Essen, S. M. Smith, D. M. Barch, T. E. Behrens, E. Yacoub, K. Ugurbil, W.-M. H. Consortium et al., (2013), "The wu-minn human connectome project: an overview", Neuroimage, vol. 80, pp. 62–79.
5. Smilkov, D., Thorat, N., Assogba, Y., Yuan, A., Kreeger, N., & et, al. (2019), "TensorFlow.js: Machine learning for the web and beyond", arXiv. https://doi.org/10.48550/arXiv.1901.05350
6. N. Chesnaye, V. Stel, G. Tripepi, F. Dekker, E. Fu, C. Zoccali, K. Jager (2022), An introduction to inverse probability of treatment weighting in observational research, Clinical Kidney Journal

Poster No 1895

Identification of atypical sulcal patterns using prototype-based graph learning

Hyeokjin Kwon[1], Sarah Morton[2,3], Mike Rivkin[4,5,6,7,8], David Wypij[3,9,10], Rick Robertson[7], Jane Newburger[11,10], Ellen Grant[2,7,12], Kiho Im[2,12], Jong-Min Lee[13,14,15]

[1]Department of Electronic Engineering, Hanyang University, Seoul, Korea, Republic of, [2]Division of Newborn Medicine, Boston Children's Hospital and Harvard Medical School, Boston, MA, [3]Department of Pediatrics, Harvard Medical School, Boston, MA, [4]Department of Neurology, Boston Children's Hospital, Boston, MA, [5]Department of Psychiatry, Boston Children's Hospital, Boston, MA, [6]Department of Neurology, Harvard Medical School, Boston, MA, [7]Division of Radiology, Boston Children's Hospital, Boston, MA, [8]Stroke and Cerebrovascular Center, Boston Children's Hospital, Boston, MA, [9]Department of Biostatistics, Harvard T.H. Chan School of Public Health, Boston, MA, [10]Department of Cardiology, Boston Children's Hospital, Boston, MA, [11]Department of Pediatrics, Harvard Medical School, Boston, MA, [12]Fetal Neonatal Neuroimaging and Developmental Science Center, Boston Children's Hospital and Harvard Medical School, Boston, MA, [13]Department of Electronic Engineering, Hanyang University, Seoul, Korea, Republic of, [14]Department of Artificial Intelligence, Hanyang University, Seoul, Korea, Republic of, [15]Department of Biomedical Engineering, Hanyang University, Seoul, Korea, Republic of

Introduction: Recent studies have suggested that identification of early-emerging atypical sulcal folding patterns using a sulcal pit-based graph is effective for characterizing cortical development on patients with congenital heart disease (CHD) (Morton et al., 2020). Particularly, sulcal pattern similarity of a given brain scan with a group of healthy controls can be used for identifying neurodevelopmental risk factors in subjects with CHD (Morton et al., 2021). However, estimation of sulcal pattern similarity relies on the construction of affinity matrix M, which is time-intensive, resulting in a small and even arbitrary reference set of target groups for calculating sulcal pattern similarity (Im et al., 2013). Furthermore, weighting of node features characterizing sulcal pits such as position, sulcal depth, and sulcal area is yet to be generalized for the sulcal pattern analysis. To address these issues, we propose a prototype-based graph neural networks (GNN) framework to identify more general and discriminative atypical sulcal patterns in patients with CHD.

Methods: A total of 248 CHD patients (n [male/female] = 166/84, age [mean ± SD, range]: 15.29 ± 2.21, 10-19 years) and 94 typical controls (n = 47/49, age: 15.42 ± 1.87, 10-19 years) were included from the existing data at the Boston Children's Hospital and approved by the institutional review board. The MRI scans were processed to extract cortical surfaces using the FreeSurfer pipeline[4], and the whole-brain sulcal pattern graphs were represented with sulcal pits using the algorithm from our previous study. We used the popular GraphSage layers as the graph embedding model, to represent node-level hidden feature embeddings[5]. Then we calculate a graph-level embedding vector by applying mean pooling to the resulting matrix. The output embedding is further projected to the trainable class-specific prototype vectors to calculate the pairwise similarity[6]. Finally, a fully-connected layer was utilized to estimate class probability by using the pairwise similarities and Cross-entropy loss is calculated for training the model. For better prototype learning, we utilize the separate loss and cluster loss[6].

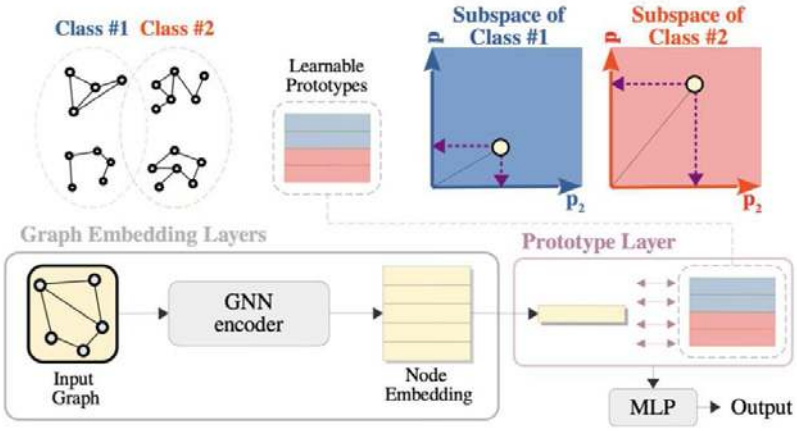

Figure 1. Illustration of the proposed framework.

Results: PyTorch frameworks were used, and we split the samples using the stratified 10-fold cross validation strategy. In each fold, we trained the model for a two-class classification task (CHD vs Control). We used a training strategy based on[9]. To verify the effectiveness, we compared the performance to the three state-of-the-art GNN methods and a multi-layer perceptron (MLP) model, reported in Table 1.

Table 1. Comparison of classification performance

Model	Mean AUC	Std AUC
MLP	53.27	10.86
GCN [7]	61.03	7.17
GraphSAGE [5]	67.8	9.56
GAT [8]	61.93	7.17
Ours	**70.05**	**8.32**

Conclusions: This is first study to identify abnormal sulcal patterns in CHD patients via GNN. Furthermore, the proposed framework is generalizable as it is able to train and use the prototype pattern simultaneously. A possible future work can include more interpretable framework for the prototypes.

References

1. Morton, S.U., et al., Abnormal left-hemispheric sulcal patterns correlate with neurodevelopmental outcomes in subjects with single ventricular congenital heart disease. Cerebral Cortex, 2020. 30(2): p. 476-487.
2. Morton, S.U., et al., Abnormal right-hemispheric sulcal patterns correlate with executive function in adolescents with tetralogy of Fallot. Cerebral Cortex, 2021. 31(10): p. 4670-4680.
3. Im, K., et al., Quantification and discrimination of abnormal sulcal patterns in polymicrogyria. Cerebral cortex, 2013. 23(12): p. 3007-3015.
4. Dale, A.M., B. Fischl, and M.I. Sereno, Cortical surface-based analysis: I. Segmentation and surface reconstruction. Neuroimage, 1999. 9(2): p. 179-194.
5. Hamilton, W., Z. Ying, and J. Leskovec, Inductive representation learning on large graphs. Advances in neural information processing systems, 2017. 30.
6. Zhang, Z., et al. Protgnn: Towards self-explaining graph neural networks. in Proceedings of the AAAI Conference on Artificial Intelligence. 2022.
7. Kipf, T.N. and M. Welling, Semi-supervised classification with graph convolutional networks. arXiv preprint arXiv:1609.02907, 2016.
8. Velickovic, P., et al., Graph attention networks. stat, 2017. 1050(20): p. 10.48550.
9. Dwivedi, V.P., et al., Benchmarking graph neural networks. 2020.

Poster No 1896

Activation Likelihood Estimation: How unbalanced dataset-sizes impact meta-analytic contrasts

Lennart Frahm[1], Simon Eickhoff[2], Robert Langner[3], Veronika Müller[3], Theodore Satterthwaite[4], Peter Fox[5]

[1]Forschungszenturm Jülich, Jülich, North-Rhine Westphalia, [2]Institute for Systems Neuroscience, Medical Faculty, Heinrich-Heine University Düsseldorf, Düsseldorf, North Rhine–Westphalia Land, [3]Inst. Sys. Neurosci., Medical Faculty, HHU Düsseldorf, Düsseldorf, North Rhine-Westphalia, [4]UPenn, Philadelphia, PA, [5]The University of Texas Health Science Center at San Antonio, San Antonio, TX

Introduction: The Activation Likelihood Estimation (ALE) algorithm for neuroimaging meta-analysis has frequently been used to delineate differences in convergence of brain activity between cognitive tasks, domains or groups by virtue of meta-analytic contrasts[1,2,3]. Significance of contrasts is determined by comparing the voxel-wise differences between two ALE maps to an empirical null distribution of ALE score differences. This null distribution is approximated by randomly permuting the experiments between the two datasets 10,000 times and calculating difference scores for each permutation. While being statistically sound and often yielding results with high face validity, there have been concerns that this approach is not suitable when comparing two datasets with very different sizes[4], with contrasts being driven by the larger dataset. To address these concerns, we developed a new, balanced meta-analytic contrast algorithm, in which we calculate 5000 individual contrasts based on same-sized subsamples of the original datasets and then average the results. Such “undersampling” approaches are well established in machine learning literature[5] when dealing with imbalanced class predictions, which are conceptually similar to our use case. Here, we compared the original permutation-based contrasts with the newly developed balanced contrasts, using simulated ALE datasets.

Methods: We simulated datasets with two different sizes, including either 150 or 25 experiments. To manipulate the amount of spatial convergence, 0%, 10%, 20%, 30% or 40% of experiments per dataset were selected to feature a coordinate at a “true location”[6,7]. For each dataset size and amount of convergence we created 100 datasets of experiments whose sample size and number of foci included were randomly sampled from normal distributions similar to what is found in empirical datasets according to the BrainMap database[6,8,9]. We then computed both permutation-based and balanced contrasts for each dataset with 150 experiments against a dataset with 25 experiments. Lastly, we examined the proportion of significant differences at the “true location”, averaging over all contrasts with the same amount of convergence per dataset.

Results: In general, both contrast-algorithms performed reasonably well, reliably detecting large convergence differences independent of dataset size. Both algorithms slightly favored the larger dataset, reporting more contrasts in its favor even for less strong convergence differences. This effect was slightly stronger for the balanced contrasts. The biggest difference between the two algorithms seems to be that the balanced contrast is generally more sensitive, detecting more significant contrasts even if there is only slightly larger convergence in one of the datasets, whereas the unbalanced permutation contrasts would often yield no significant differences in these cases.

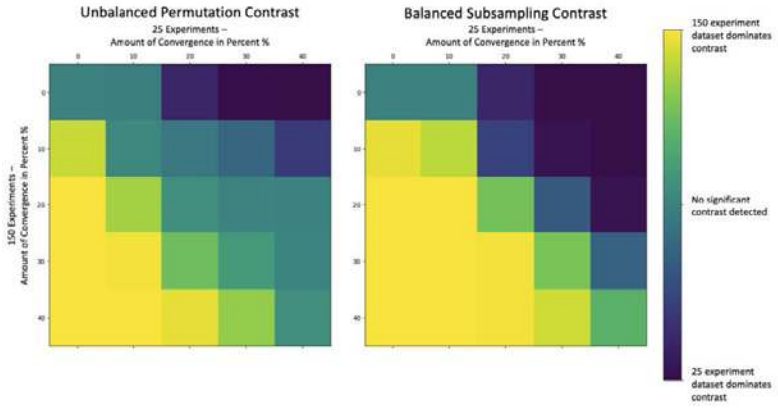

Conclusions: In contrast to previous concerns, we found only little evidence that unbalanced permutation-based contrasts are strongly driven by the larger dataset. This is an important finding, retrospectively validating ALE meta-analyses that employed this methodology. The newly developed balanced subsampling contrast also performed well, reliably detecting differences in convergence between the two datasets. However, its moderately higher sensitivity, relative to the traditional approach, comes at the expense of featuring a somewhat stronger bias toward detecting significant differences in favor of larger datasets. At this moment there is no clearly preferred algorithm choice from our point of view. Future research should look into specific use cases for both contrast algorithm and validate both approaches using a large number of real-life ALE datasets.

References

1. Ardila, A., Bernal, B., & Rosselli, M. (2018). Executive functions brain system: An activation likelihood estimation meta-analytic study. Archives of Clinical Neuropsychology, 33(4), 379-405.
2. Langner, R., & Eickhoff, S. B. (2013). Sustaining attention to simple tasks: a meta-analytic review of the neural mechanisms of vigilant attention. Psychological bulletin, 139(4), 870
3. Worringer, B., Langner, R., Koch, I., Eickhoff, S. B., Eickhoff, C. R., & Binkofski, F. C. (2019). Common and distinct neural correlates of dual-tasking and task-switching: a meta-analytic review and a neuro-cognitive processing model of human multitasking. Brain Structure and Function, 224, 1845-1869.
4. Xu, A., Larsen, B., Baller, E. B., Scott, J. C., Sharma, V., Adebimpe, A., ... & Satterthwaite, T. D. (2020). Convergent neural representations of experimentally-induced acute pain in healthy volunteers: A large-scale fMRI meta-analysis. Neuroscience & biobehavioral reviews, 112, 300-323.
5. Liu, X. Y., Wu, J., & Zhou, Z. H. (2008). Exploratory undersampling for class-imbalance learning. IEEE Transactions on Systems, Man, and Cybernetics, Part B (Cybernetics), 39(2), 539-550.
6. Eickhoff, S. B., Nichols, T. E., Laird, A. R., Hoffstaedter, F., Amunts, K., Fox, P. T., ... & Eickhoff, C. R. (2016). Behavior, sensitivity, and power of activation likelihood estimation characterized by massive empirical simulation. Neuroimage, 137, 70-85.
7. Frahm, L., Cieslik, E. C., Hoffstaedter, F., Satterthwaite, T. D., Fox, P. T., Langner, R., & Eickhoff, S. B. (2022). Evaluation of thresholding methods for activation likelihood estimation meta-analysis via large-scale simulations. Human brain mapping, 43(13), 3987-3997.
8. Fox, P. T., & Lancaster, J. L. (2002). Mapping context and content: the BrainMap model. In Nature Reviews Neuroscience (Vol. 3, Issue 4, pp. 319–321). https://doi.org/10.1038/nrn789
9. Laird, A. R., Lancaster, J. L., & Fox, P. T. (2005). BrainMap: The Social Evolution of a Human Brain Mapping Database. In Neuroinformatics (Vol. 3, Issue 1, pp. 065–078). https://doi.org/10.1385/ni:3:1:065

Poster No 1897

AmygdalaGo-BOLT: Accurate Segmentation of Amygdala Using a Boundary Contrastive Learning Transformer

Bo Dong[1], Quan Zhou[2], Xi-Nian Zuo[3,4,5], Hongjian He[6,7]

[1]College of Biomedical Engineering and Instrument Science, Zhejiang University, Hangzhou, China, [2]Faculty of Psychology, Beijing Normal University, Beijing, China, [3]State Key Laboratory of Cognitive Neuroscience and Learning, Beijing Normal University, Beijing, China, [4]National Basic Science Data Center, Beijing, Beijing, China, [5]Institute of Psychology, Chinese Academy of Sciences, Beijing, China, [6]School of Physics, Zhejiang University, Hangzhou, China, [7]State Key Laboratory of Brain-Machine Intelligence, Zhejiang University, Hangzhou, China

Introduction: The amygdala is involved in various brain functions, and the accurate segmentation of this structure is is a crucial issue in cognitive neuroscience (Avecillas et al. 2023, Chai et al. 2023, Nguyen et al.2023). A major challenge lies in the small volume of the amygdala and the low contrast between the amygdala and the surrounding complex tissues, leading to uncertainty in boundary delineation. To address these issues, we introduced AmygdalaGo-BOLT, a 3D transformer architecture tailored for small structures, incorporating a boundary contrastive learning optimization algorithm. Compared to Freesurfer (Fischl et al. 2002) and Unet (Falk et al. 2019), the proposed method showed superior performance. Additionally, we validated our segmentation approach by applying it to assess volume changes during child development (Zhou et al. 2021).

Methods: The AmygdalaGo-BOLT, innovatively employs 3D transformer to construct the long-range relationships between voxels, thereby enhancing feature and enabling a more holistic comprehension. It is specifically executed by integrating the attention, which considers for the differences between the amygdala and other structures as well as the similarities within the amygdala, as opposed to merely focusing on local regions. Furthermore, to augment the alignment between predicted and actual boundaries, we implement an boundary contrastive learning optimization method. This optimization brings the edges closer to feature points that resemble the amygdala and distances those non-amygdala-like feature points in a high-dimensional feature space to amplify feature differences between the amygdala and surrounding tissue and reducing intra-amygdala variation.

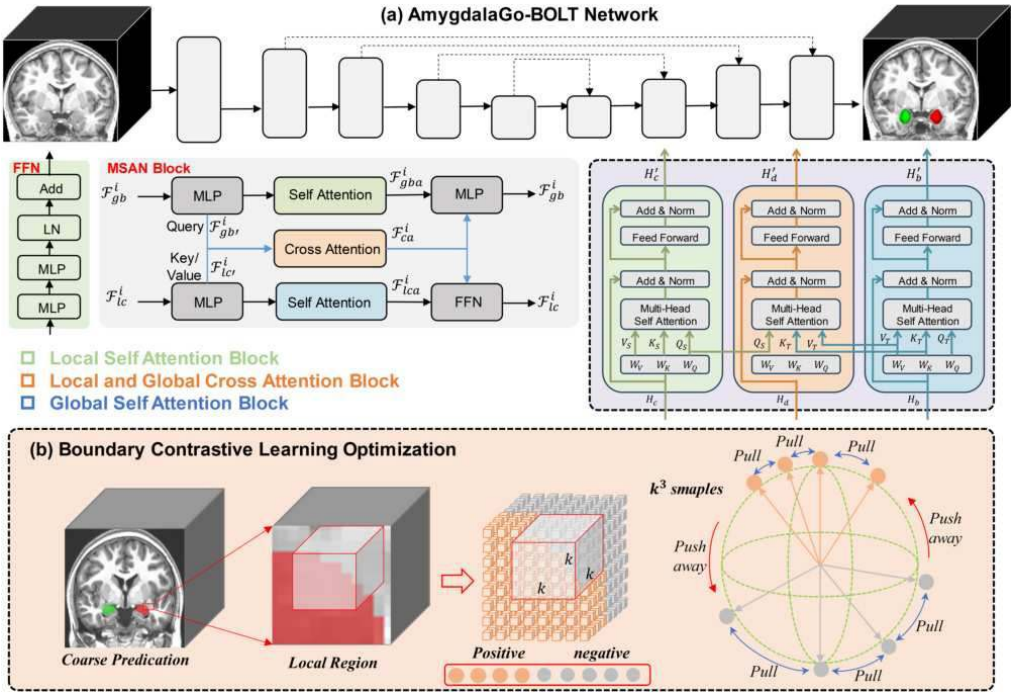

Results: We conducted a comprehensive comparison between our segmentation method and other existing approaches dedicated to the segmentation of the amygdala structure. Notably, our method outperforms both the classical Freesurfer and the widely-used Unet, achieving segmentation results that align closely with human-level performance as illustrated in Figure 2(a). Specifically, our dice score is close to 90%, a substantial improvement over Freesurfer and Unet. The superiority of our amygdala segmentation model is further evident in the precision metric, where we exhibit a significant lead, as illustrated in Figure 2(b). Figure 2(c) displays the growth curve generated by our algorithm, revealing a strong correlation with gender and age and surpassing the performance of alternative algorithms. This emphasizes the robustness and accuracy of our algorithm

in estimating amygdala volume while accounting for variations in sex and age. By closely approximating distribution patterns of amygdala volume across different demographics, our algorithm offers valuable insights into developmental changes in the amygdala. This information enhances our understanding of how the amygdala evolves over time in relation to sex differences and age-related factors. In summary, the ability of our algorithm to precisely capture and represent the distribution of amygdala volume with respect to sex and age underscores its robustness and effectiveness in characterizing changes in amygdala development. This contribution significantly advances the field of neurodevelopmental research.

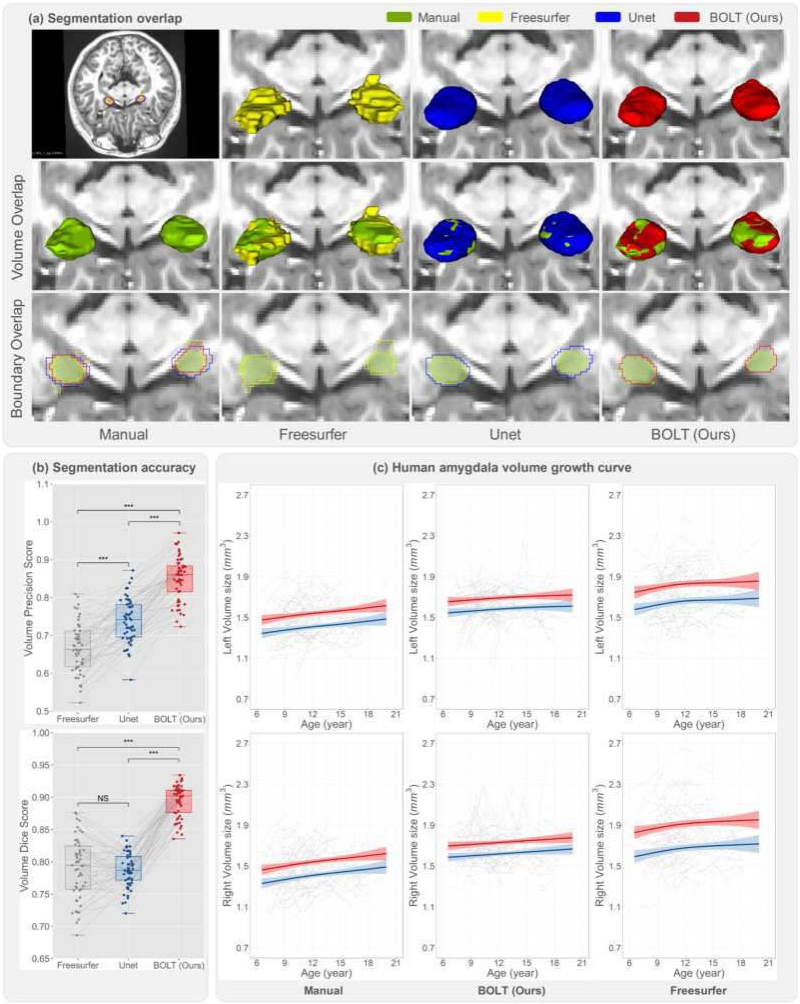

Conclusions: In conclusion, our proposed AmygdalaGo-BOLT achieves accurate amygdala segmentation, as validated across multiple independent datasets. This deep-learning approach with a transformer architecture significantly enhances efficiency, completing the segmentation in just 5 seconds, thus outperforming popular software like Freesurfer. Our targeted network design, tailored for small volume and complex boundary structures, could potentially be extended to other complex brain structure segmentation problems, given sufficient labeled training data. Overall, AmygdalaGo-BOLT offers a valuable tool for morphometric analysis in neuroscience research.

References

1. Avecillas-Chasin JM, Levinson S, Kuhn T, et al (2023) Connectivity-based parcellation of the amygdala and identification of its main white matter connections. Scientific reports 13(1):1305
2. Chai Y, Gehrman P, Yu M, et al (2023) Enhanced amygdala–cingulate connectivity associates with better mood in both healthy and depressive individuals after sleep deprivation. Proceedings of the National Academy of Sciences 120(26):e2214505120
3. Nguyen R, Koukoutselos K, Forro T, et al (2023) Fear extinction relies on ventral hippocampal safety codes shaped by the amygdala. Science Advances 9(22):eadg4881
4. Fischl B, Salat DH, Busa E, et al (2002) Whole brain segmentation: automated labeling of neuroanatomical structures in the human brain. Neuron 33(3):341–355
5. Falk T, Mai D, Bensch R, et al (2019) U-net: deep learning for cell counting, detection, and morphometry. Nature methods 16(1):67–70
6. Zhou Q, Liu S, Jiang C, et al (2021) Charting the human amygdala development across childhood and adolescence: Manual and automatic segmentation. Developmental Cognitive Neuroscience 52:101028

Poster No 1898

Normative discrimination for stratification - proof of concept in the European autism project

Tristan Looden[1], Alberto Llera[2], Dorothea Floris[3], Jan Buitelaar[2], Christian Beckmann[2]

[1]Donders Institute, Nijmegen, Gelderland, [2]Donders Institute for Brain, Cognition, and Behavior, Radboud University Nijmegen, Nijmegen, NL, Nijmegen, Netherlands, [3]Methods of Plasticity Research, Department of Psychology, University of Zürich, Zürich, Switzerland

Introduction: Autism spectrum disorder is a complex neurodevelopmental condition (American Psychiatric Association 2013). Prior work in autism has shown significant multivariate relationships between brain functional connectivity atypicality relative to typically developing controls and cognitive autism-associated measures across different tasks (Looden et al. 2022). The fact that we can identify a relationship between brain functional atypicality and autism-associated measures makes it an interesting target for subtyping. In this project, we investigate whether such subtyping of autistic individuals on the basis of functional connectivity also explains relevant variance in autism measurements. As a crucial methodological step for dimensionality reduction from covariance space to clusters we will introduce and validate Spatial Patterns for Discriminative Estimation (SPADE) an implementation of the Fukunaga-Koontz transform (Llera, A., Chauvin R., Mulders P., Naaijen J., Mennes M. 2019). SPADE finds linear filters in high-dimensional covariance space that optimally separate classes or observations, and furthermore provides visually interpretable spatial maps. We develop an individualized implementation of this framework to characterize individuals with respect to a reference cohort, on the basis of which further analysis is made possible.

Methods: All analyses were based on subsamples from the EU-AIMS/AIMS2TRIALS multisite Longitudinal European Autism Project (LEAP) with participants between 6 and 30 years of age (Charman et al. 2017). This study includes autistic (N=282) and typically developing (N=221) participants and uses data drawn from five different fMRI task paradigms, each sampling brain functional connectivity from different cognitive brain states. The following analysis is done in each of the five tasks. First, SPADE is used on task data to find a single spatial discriminative filter that best separate each autistic individual from the typically developing group (see fig 1). This subject-specific characterization of autistic individuals is then used to form a similarity matrix which is fed into a spectral decomposition to uncover subtype characteristics in the similarity space. The optimal number of clusters in the two-dimensional spectral output is estimated by minimizing the Bayesian Information Criterion (BIC). The resulting clustering solutions are subsequently used in a linear model to explain behaviour in a well-rounded selection of autism-associated measures (corrected for age and sex). We report the variance explained by these clusters in each clinical measure as well as the model F-test for overall significance per measure. Finally, we use the spatial filters learned by SPADE which formed the basis of the clustering to inform us of the most relevant brain regions for each cluster.

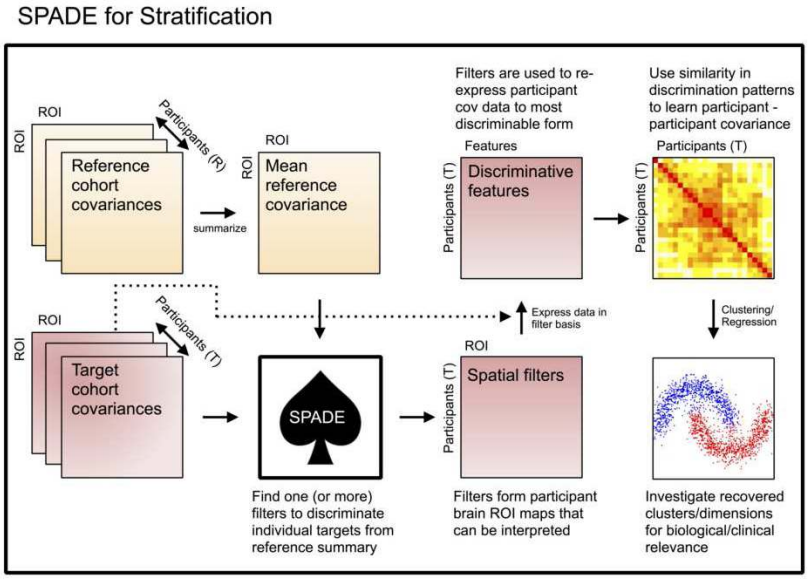

Results: We found a significant relationship between the clustering solution (5 clusters) and one or more clinical autism measures in each of the five tasks (FDR corrected per task). Variance explained for each measure ranges between 7-11% in the significant relationships. Specifically, the cognitive demand induced by the Hariri task formed a fruitful source of covariances on the basis of which clinically relevant clustering could be performed. See figure 2 for more detail in the Hariri task.

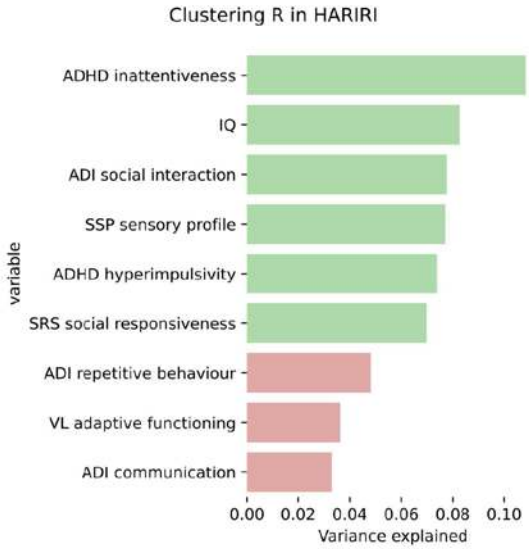

Conclusions: We presented a proof of concept towards a new normative modeling approach for population fmri data with respect to a reference cohort. The SPADE for stratification model uses maximal discrimination filters to find differences from each subject to the reference cohort and we show preliminary results that the process yields behaviouraly relevant stratifications of autistic participants. The clinically validated covariance-based subclusters in autism may furthermore point to groups in autism with differential etiologies as targets for future research.

References

1. American Psychiatric Association. 2013. Diagnostic and Statistical Manual of Mental Disorders (DSM-5®). American Psychiatric Pub.
2. Charman, Tony, Eva Loth, Julian Tillmann, Daisy Crawley, Caroline Wooldridge, David Goyard, Jumana Ahmad, et al. 2017. "The EU-AIMS Longitudinal European Autism Project (LEAP): Methods." Molecular Autism 8 (1): 1–19. https://doi.org/10.1186/s13229-017-0145-9.
3. Llera, A., Chauvin R., Mulders P., Naaijen J., Mennes M., Beckmann C. F. 2019. "Spatial Patterns for Discriminative Estimation (SPADE)." BioArxiv.
4. Looden, Tristan, Dorothea L. Floris, Alberto Llera, Roselyne J. Chauvin, Tony Charman, Tobias Banaschewski, Declan Murphy, et al. 2022. "Patterns of Connectome Variability in Autism across Five Functional Activation Tasks: Findings from the LEAP Project." Molecular Autism 13 (1): 53. https://doi.org/10.1186/s13229-022-00529-y.

Poster No 1899

Segmentation of regional brain volumes from CT images with 3D deep learning models

Aram Salehi[1], Natalia Vilor-Tejedor[2], Juan Domingo Gispert[2], Hieab Adams[1], Tavia Evans[3]

[1]Department of Human Genetics, Radboud UMC, Nijmegen, Netherlands, [2]BarcelonaBeta Brain Research Center, Barcelona, Catalonia, [3]Erasmus University Medical Center, Rotterdam, Zuid Holland

Introduction: Brain imaging is vital for studying the human brain and unraveling key insights into the onset, progression, and prognosis of brain diseases. Magnetic resonance imaging (MRI) provides high detail and soft tissue contrast, however is unfeasible in certain patient populations and many regions lack proper access. Computerized tomography (CT) offers cheaper, faster, and more accessible alternative, but its lower soft tissue contrast makes effective segmentation challenging. In this study, we address this challenge by evaluating deep learning-based models to enhance the accuracy of brain segmentation in CT scans by detecting intricate patterns that may be overlooked by traditional segmentation methods.

Methods: We used 356 paired CT/MRI brain images from the ALFA (ALzheimer and FAmilies) project[4]. Segmentations of regional volumes from MRI images were extracted using FreeSurfer and used as the 'standard of truth' for model training[2]. CT images were aligned to the MRI images and the segmentation labels (FSL, FLIRT)[5]. The CT image voxel intensities were restricted to reflect the brain window of Hounsfield units (0-80). The dataset was split into 70%, 15%, and 15% for training, validation, and testing respectively. We investigated three base 3D deep learning models known to perform well within image segmentation; SwinUNETER, HighResNet, and HRNet[1,3,6]. These networks were trained using CT brain images and paired MRI-derived labels to extract 29 distinct regions. The training of models involved utilizing a combination of the dice score and categorical cross-entropy function as the loss function. The evaluation of segmentation performance was conducted using dice similarity metrics.

Results: SwinUNETR outperformed other models, achieving a mean dice similarity score of 82.71±5.2 (followed by HRNet: 81.08±5.09 and HighResNet: 79.99±5.78) across the 29 regions. The lowest mean dice similarity, 71.49, was observed for the right cerebral cortex (HRNet: 72.85, HighResNet: 68.53), while the mean highest score of 91.58 was achieved for the brain stem (HRNet: right thalamus 89.1, HighResNet: brain-stem 91.72) across the 54 test images (Figures 1 & 2). Our results indicate that SwinUNETR tends to overestimate regional volume segmentations, with a mean deviation of 1.04 and a standard deviation of 0.06 when considering normalized percentage data of the regional volumes. The results demonstrated that for all models larger regions, such as the cerebral cortex (gray matter) and cerebral white matter, displayed a lower mean dice similarity metric, while more internal regions like the thalamus and lateral ventricle exhibited superior performance (Figure 1).

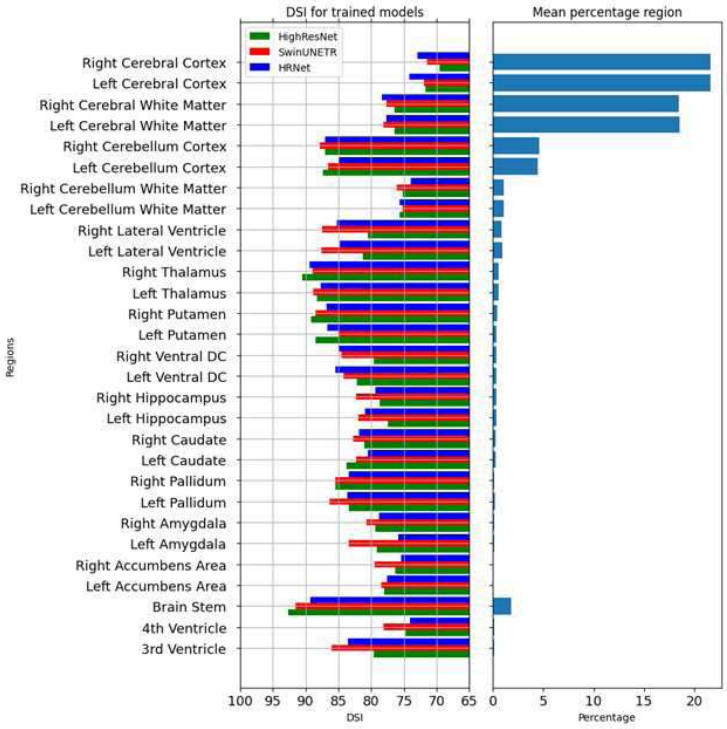

Figure 1. Left; Dice similarity index for HighReNet, SwinUNETR and HRNet, Right; Percentage of the total segmentation for each region.

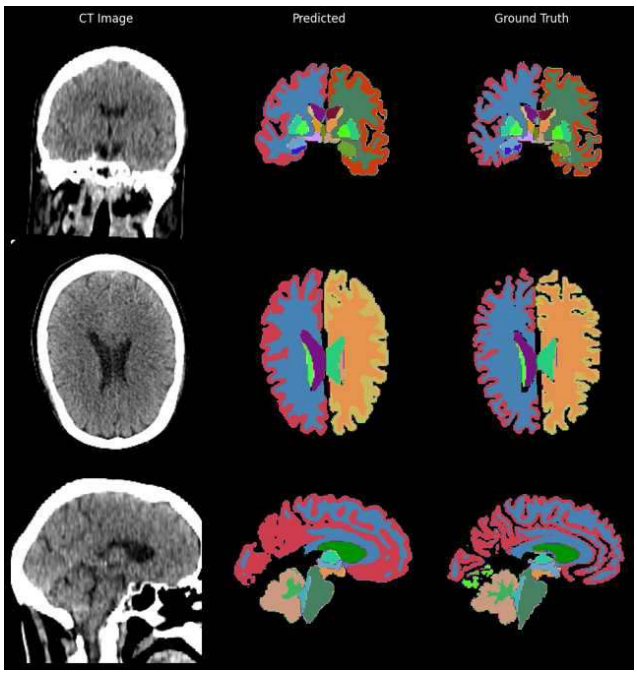

Figure 2. Best performing test case with regards to application of the model. Left to right; Original CT image, predicted segmentation using SwinUNETR, and ground truth from FreeSurfer MRI processing.

Conclusions: Here we show that regional brain volumes can be reliably segmented from CT images using deep learning models. The results showed that SwinUNETER performed the best overall for segmentation of brain CT scans particularly for various subcortical structures. The lowest concordance with MRI segmentations was seen for the cerebral grey and white matter, pointing to the potential inherent difficulty of differentiating between the two because of the low tissue contrast from CT imaging. Future studies could assess whether other models can better distinguish between grey and white matter segmentation, and whether CT images could be used to generate other imaging markers beyond regional volumetry. In conclusion, our approach shows promise for extracting clinically relevant information from CT scans and could be crucial for unlocking the value of CT images in resource-constrained settings, where MRI is not readily available.

References

1. Hatamizadeh A.(2021) Swin unetr: Swin transformers for semantic segmentation of brain tumors in mri images. InInternational MICCAI Brainlesion Workshop (pp. 272-284). Cham: Springer International Publishing.
2. Iglesias, J. E.(2015). A computational atlas of the hippocampal formation using ex vivo, ultra-high resolution MRI: application to adaptive segmentation of in vivo MRI. Neuroimage 115, 117-137.
3. Li W.(2017). On the compactness, efficiency, and representation of 3D convolutional networks: brain parcellation as a pretext task. InInformation Processing in Medical Imaging: 25th International Conference, IPMI 2017, Boone, NC, USA, Proceedings (pp. 348-360). Springer International Publishing.
4. Molinuevo JL.(2016) The ALFA project: a research platform to identify early pathophysiological features of Alzheimer's disease. Alzheimer's & Dementia: Translational Research & Clinical Interventions ;2(2):82-92.
5. Patenaude, B.(2011) A Bayesian model of shape and appearance for subcortical brain segmentation. Neuroimage 56, 907-922.
6. Wang J. (2020).Deep high-resolution representation learning for visual recognition. IEEE transactions on pattern analysis and machine intelligence. ;43(10):3349-64.

Poster No 1900

A Surfaced-based Predictive Model with Interpretability on Cortical Features

Zhuoshuo Li[1], Youbing Zeng[1], Jiaying Lin[1], Duan Xu[2], Hosung Kim[3], Mengting Liu[1]

[1]Sun Yat-sen University, Shenzhen, Guangdong, [2]University of California San Francisco, San Francisco, CA, [3]University of Southern California, Los Angeles, CA

Introduction: Utilizing machine learning models to predict phenotypes, such as age, gender, and brain disease states, based on the highly folded cerebral cortical surface and its morphological features, stands as a crucial method in surface-based analysis and its practical applications. It significantly contributes to investigating brain development/aging trajectories and developments of brain disorders[1]. In the current research, surface-based models exist but have limitations in flexibly identifying the best sub-graph structure or important vertices that contribute best to the prediction task and conducting the interpretable results at the feature level. These limitations are notable because morphological features correspond to numerous phenotypes and functions, and different regions exhibit diverse responses to various predictive demands[2]. To address these, in this study, we propose a surface-based predictive model that focuses on a self-interpretable feature, namely the Surface Graph Neural Network (surfGNN).

Methods: We consider the surface mesh with individual cortical feature as a sparse graph, and the quantity of sparse graphs for each subject is consistent with the number of cortical features extracted for a given task. Based on this, the surfGNN model is constructed, as Fig. 1 shows. The entire framework of surfGNN consists of context-aware learning structures and a regional-specific learning structure for each cortical feature, and a score-weighted fusion structure across all features for prediction. The context-aware learning structure is utilized to condense the topology structure of a low-level surface mesh (with a larger number of vertices). The regional-specific learning structure is employed on a high-level surface mesh (with a lower number of vertices), to accurately identify and emphasize important contributions from various regions. Moreover, a novel score-weighted fusion mechanism is proposed to amalgamate node information derived from individual cortical features within the graph learning framework. This mechanism also facilitates the creation of node scores, providing interpretable results that are specific to each cortical feature.

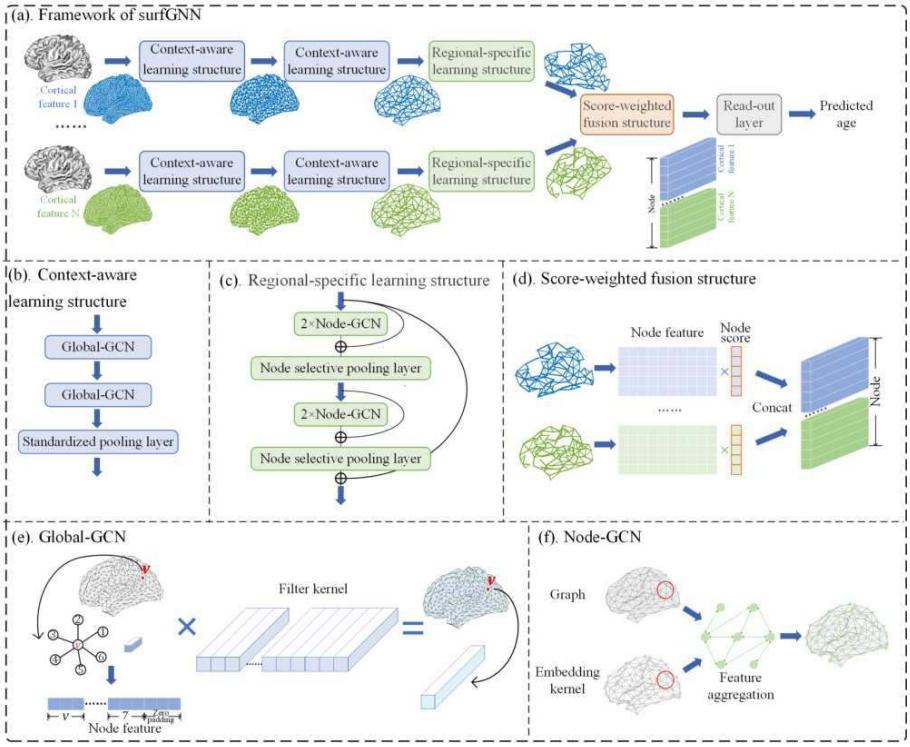

Results: We apply the surfGNN to a neonatal brain age prediction task on a dataset with morphological features including cortical thickness, sulcal depth, and gray matter/white matter (GM/WM) intensity ratio. The dataset consists of harmonized MRI images of 481 subjects (503 scans) from UCSF and dHCP[3] cohorts, where the cortical surface is reconstructed using the NEOCIVET pipeline[4] and downsampled to obtain sparse maps at multi resolutions with distinct quantities of vertices. Our model achieves the best MAE of 0.827±0.562 weeks of post-menstrual age. In Fig. 2(a), we assess our model's predictive performance against state-of-the-art surface-based models. Our surfGNN model demonstrates superior predictive accuracy with sparse graph inputs at each resolution. In Fig.2(b), it provides the activation maps illustrating variations in the response of distinct brain regions to predicted outcomes across various cortical features.

(a)

Method	Number of nodes of the input sparse graphs			
	1,284	5,124	20,484	81,924
SphericalCNN	MAE = 1.085 ± 0.059 PCC = 0.928 ± 0.011 Params = 0.207 M	MAE = 1.056 ± 0.125 PCC = 0.936 ± 0.019 Params = 0.897 M	MAE = 1.036 ± 0.071 PCC = 0.942 ± 0.004 Params = 3.653 M	MAE = 1.058 ± 0.100 PCC = 0.937 ± 0.013 Params = 6.802 M
MoNet	MAE = 1.020 ± 0.042 PCC = 0.944 ± 0.007 Params = 0.230 M	MAE = 0.992 ± 0.024 PCC = 0.946 ± 0.003 Params = 0.231 M	MAE = 0.958 ± 0.025 PCC = 0.951 ± 0.004 Params = 0.239 M	MAE = 0.909 ± 0.015 PCC = 0.955 ± 0.005 Params = 0.241 M
SiT	MAE = 1.031 ± 0.054 PCC = 0.944 ± 0.004 Params = 7.172 M	MAE = 0.980 ± 0.032 PCC = 0.948 ± 0.007 Params = 7.198 M	MAE = 0.963 ± 0.023 PCC = 0.950 ± 0.007 Params = 7.260 M	MAE = 0.977 ± 0.005 PCC = 0.950 ± 0.006 Params = 7.444 M
BrainGNN	MAE = 1.047 ± 0.110 PCC = 0.941 ± 0.010 Params = 0.180 M	MAE = 1.026 ± 0.086 PCC = 0.944 ± 0.006 Params = 0.241 M	MAE = 0.964 ± 0.058 PCC = 0.945 ± 0.013 Params = 0.487 M	\
TSGNN	MAE = 0.896 ± 0.075 PCC = 0.953 ± 0.010 Params = 4.555 M	**MAE = 0.827 ± 0.056** PCC = 0.961 ± 0.006 Params = 4.568 M	MAE = 0.835 ± 0.062 **PCC = 0.961 ± 0.005** Params = 4.571 M	MAE = 0.887 ± 0.040 PCC = 0.958 ± 0.005 Params = 4.609 M

(b)

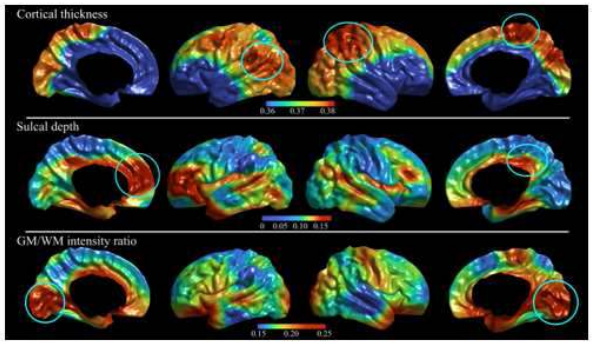

Conclusions: We have presented a novel surface-based predictive model with self-interpretability, which could fully integrate both the topological structure traits and the physiological characteristics of the morphological features on the cortical surface. Our model showcases exceptional predictive performance and generates effective activation maps at a feature level. The limitations of this study encompass the limited scale of the experimental datasets, the lack of tests in diseased cohorts, and the finite precision of the interpretable results. Future work will focus on addressing these issues.

References

1. H. C. Hazlett, et al. 'Early brain development in infants at high risk for autism spectrum disorder.', Nature 542.7641 (2017): 348-351.
2. J. H. Gilmore, et al. 'Imaging structural and functional brain development in early childhood.', Nature Reviews Neuroscience 19.3 (2018): 123-137.
3. A. D. Edwards, et al. 'The developing human connectome project neonatal data release.' Frontiers in Neuroscience 16 (2022): 886772.
4. M. Liu, et al. "Robust cortical thickness morphometry of neonatal brain and systematic evaluation using multi-site MRI datasets." Frontiers in Neuroscience 15 (2021): 650082.

Poster No 1901

ARIbrain: Fast and flexible statistical analysis of fMRI data using True Discovery Proportions

Wouter Weeda[1], Xu Chen[2], Jelle Goeman[3]

[1]Leiden University, Leiden, South Holland, [2]University of Essex, Colchester, CO4 3SQ, [3]Leiden University Medical Center, Leiden, South Holland

Introduction: Statistical analysis of Functional MRI data requires correct control for multiple comparisons. Most often, this is done using cluster-extent based thresholding. One of the drawbacks of this method is that it requires the setting of an arbitrary cluster-forming threshold (usually Z > 3.1) that determines the size/shape of the clusters used for further analysis. Once this threshold is set, researchers are not allowed, statistically, to redo the analysis with a different threshold. Together with the knowledge that the correct interpretation of a significant cluster is: 'there is at least one active voxel in this cluster' and not 'all voxels in this cluster are active', this leads to a (statistically) suboptimal way of analysing fMRI data. Recent advances in statistics have led to a new range of methods based on the True Discovery Proportion (TDP)[1-4]. These methods estimate the lower bound of the number of truly active voxels (TDP) within a cluster, for any cluster in the data, as many times a researcher wants, with full control over multiple comparisons. They do not require the setting of an arbitrary threshold as the TDP provides a simultaneous bound on the number of active voxels over all possible clusters. In practice, these methods thus give the researcher almost unlimited freedom in selecting and analysing clusters. One can use different thresholds for different clusters, calculate the TDP for an a-priori defined cluster, or search for clusters with at least a certain TDP level. This flexibility requires software that goes beyond what is available in current statistical analysis packages like FSL or SPM.

Methods: Here we introduce the improved ARIbrain analysis framework. ARIbrain is an R-package (https://wdweeda.github.io/ARIbrain-project/) that allows for flexible statistical analysis of fMRI data based on True Discovery Proportions (TDPs). It contains both a graphical user interface, allowing for confirmatory and exploratory analyses, as well as command-line functions to integrate with existing analysis pipelines. ARIbrain also incorporates recent improvements of the original Simes based method[1], for example based on permutations[2,4] for better TDP estimates. The package now also includes the option to search for clusters with a least a certain TDP (e.g., 80%). In addition, the interface with output from software packages like FSL and SPM is improved.

Results: Figure 1 and Figure 2 show screenshots of the ARIbrain app. Researchers can upload their images based on z- or t-statistics derived from their analysis (which can be performed using any popular analysis suite like FSL, SPM or AFNI), or load data from a previous analysis from these packages. After the images are loaded, researchers can choose on which clusters the initial analysis is to be performed. This can be based on classical cluster-extent thresholding or based on TDPs. After this initial analysis there is an option to go to the interactive part of the software where researchers can explore clusters, for example, changing the size (threshold) of clusters until a desired TDP level is achieved. In addition to the interactive part, it is also possible to let the ARIbrain return the clusters that have a certain TDP level. In other words, this method will look for all clusters in a brain image with a TDP higher than a certain threshold (e.g., 80%). Using this method, no clusters have to be specified beforehand, only a TDP threshold is required.

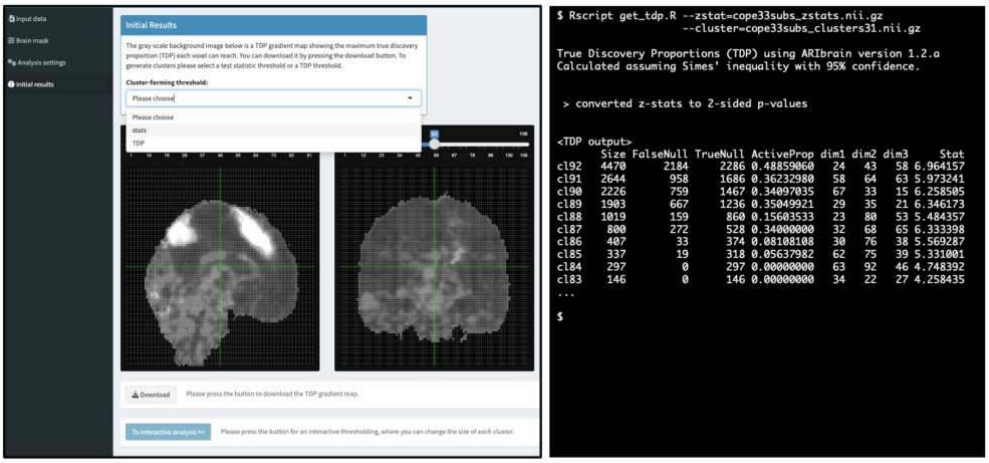

Figure 1. (left) The ARIbrain graphical user interface has multiple options to define clusters. (right) The ARIbrain command-line tools offer a direct way to calculate TDPs for clusters derived from other analysis programs (e.g., FSL).

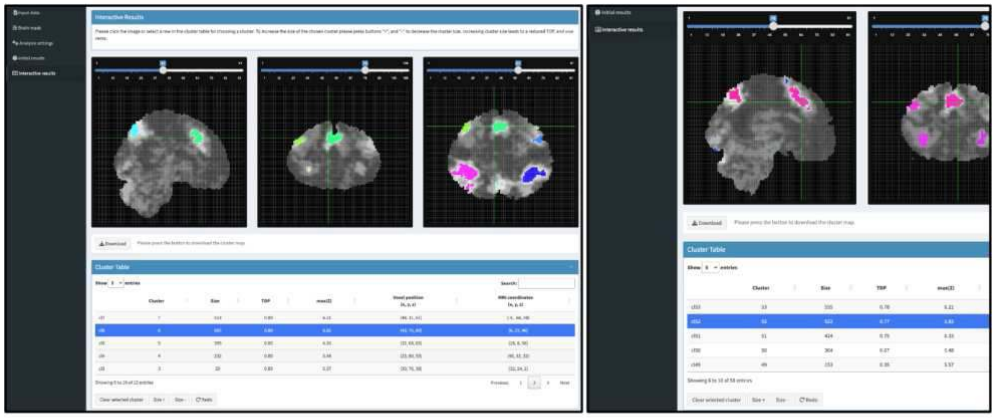

Figure 2. (left) The ARIbrain interactive session allows researchers to define clusters based on a TDP level (e.g., 80%) or based on a pre-defined cluster-forming threshold (right). In both cases the interactive application allows the researcher to change the threshold per cluster until a desired TDP level is reached.

Conclusions: The ARIbrain software allows researchers to perform statistical analyses based on True Discovery Proportions (TDPs) in a flexible manner. The software integrates seamlessly with standard analysis packages and incorporates the latest advantages in statistical methods. It is a useful and statistically sound way to improve cluster-extent based analyses of fMRI data.

References

1. Rosenblatt, J., et al. (2018). All-Resolutions Inference for brain imaging. Neuroimage, 181, 786-796.
2. Andreella, A., et al. (2023). Permutation-based true discovery proportions for fMRI cluster analysis. Statistics in Medicine, 42(14): 2311-2340.
3. Goeman, J.J., et al. (2023). Cluster extent inference revisited: quantification and localization of brain activity. J Roy Stat Soc B, 85(4), 1128–1153.
4. Blain et al. (2022). Notip: Non-parametric true discovery proportion control for brain imaging. Neuroimage, 260, 119492.

Poster No 1902

FEMA: Fast and efficient mixed-effects algorithm for large sample whole-brain imaging data

Pravesh Parekh[1], Chun Chieh Fan[2,3], Oleksandr Frei[1], Clare Palmer[3], Diana Smith[3], Carolina Makowski[3], John Iversen[3], Diliana Pecheva[3], Dominic Holland[3], Robert Loughnan[3], Pierre Nedelec[4], Wesley Thompson[2], Donald Hagler Jr.[3], Ole Andreassen[1], Terry Jernigan[3], Thomas Nichols[5], Anders Dale[3]

[1]University of Oslo, Oslo, Norway, [2]Laureate Institute for Brain Research, Tulsa, OK, [3]University of California San Diego, San Diego, CA, [4]University of California San Francisco, San Francisco, CA, [5]University of Oxford, Oxford, United Kingdom

Introduction: The linear mixed effects (LME) model is a versatile approach for accounting for dependence between observations. In neuroimaging there are sources of such dependence, such as repeated measurements, family structure, or

acquisition site. Not accounting for these covariance patterns can bias standard errors and inflate false positives. However, fitting LMEs for large sample data is computationally challenging. Therefore, there is a need within the neuroimaging community for efficient algorithms for fitting LMEs. We have developed Fast and Efficient Mixed-effects Algorithm (FEMA) that can perform whole-brain LME analyses in a matter of seconds to minutes without sacrificing estimation accuracy. Here, we will introduce FEMA, present its implementation details, and demonstrate its efficiency with respect to standard maximum likelihood (ML)-based solutions.

Methods: A LME estimates fixed effects regression coefficients and random effect variance parameters that capture the dependence. The FEMA estimation procedure starts with an ordinary least squares (OLS) estimation for the fixed effects, producing residuals. The residuals are expanded, creating cross products among all dependent measurements, and this expanded data is regressed on predictors expanded from the random effects design matrix. We then use a non-negativity constrained OLS to estimate these variance parameters. The variance parameters are quantized into discrete bins before the fixed effects coefficients are re-estimated with generalized least squares (GLS), where GLS uses the variance parameters to produce more efficient estimates and more accurate standard errors. FEMA achieves computational efficiency due to i) use of a regression estimator, using the residual cross-products, for the estimation of variance parameters; ii) the binning of random effect parameters (which then allows) iii) the use of efficient vectorized operations over voxels/surface elements.

Results: We have tested FEMA across a wide range of simulations and with real data from the Adolescent Brain Cognitive DevelopmentSM Study (ABCD Study®) and compared the estimates with standard ML estimates (fitlmematrix in MATLAB). Our results show that FEMA provides accurate estimates of fixed effects (Figure 1, top panel) in a fraction of computational time, compared to fitlmematrix or even fitlmematrix invoked in parallel. As a function of number of observations (for 50 outcome variables), FEMA was between 3.8 to 27.1 times faster than MATLAB's fitlmematrix and between 1.3 and 8.7 times faster than the fitlmematrix called in parallel (Figure 2a-c). As a function of number of imaging variables (10,000 observations, up to five family members, and up to five repeated observations), FEMA was between 40.2 and 1020.6 times faster than fitlmematrix and 7.3 and 125 times faster than fitlmematrix called in parallel (Figure 2d). We were able to perform whole-brain vertex-wise cortical thickness analyses for ABCD Study in 11 seconds (6314 subjects, two time points, 18,742 vertices) and connectome-wide analyses in 54 seconds (4994 subjects, two time points, 169,071 pairs of connectivity values). As an application of FEMA, we examined the effect of age on vertex-wise cortical thickness and resting state-derived connectivity values in the ABCD Study, which revealed interesting patterns of the longitudinal effect of age on cortical thickness and functional connectivity values (Figure 1, bottom panel).

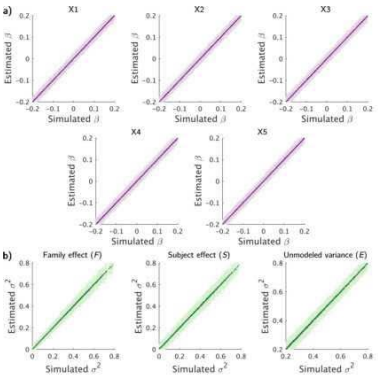

Comparison of estimated parameters against the simulated ground truth for: a) fixed effects, and b) random effects. The light purple and light green dots indicate the estimated parameters for 2000 imaging variables at 50 different repetitions for the fixed and random effects respectively, while the dark purple and dark green dots indicate

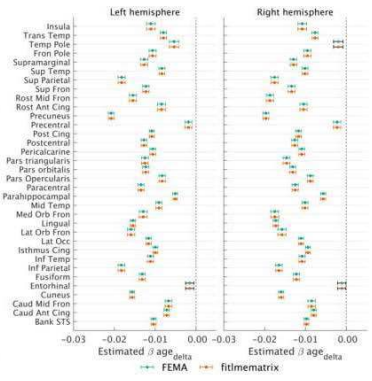

Comparison of the estimated slopes and 95% confidence intervals (CI) for the longitudinal effect of age between MATLAB's fitlmematrix (orange) and FEMA (green) on cortical thickness (6314 ABCD Study subjects, two time points). The statistically significant coefficients (α = 0.05/68) are indicated with filled points and colored CI lines while the non-significant ones are marked with non-filled points and black CI lines; Ant = anterior; Caud = caudal; Cing = cingulate; Fron = frontal; Inf = inferior; Lat = lateral; Med = medial; Mid = middle; Occ = occipital; Orb = orbital; Post = posterior; Rost = rotstral; STS = superior temporal sulcus; Sup = superior; Temp = temporal; Trans = transverse.

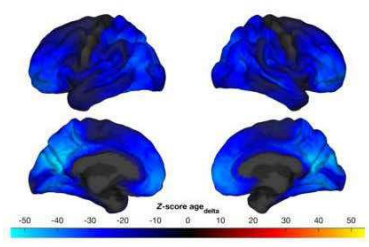

Unthresholded vertex-wise *Z*-scores for the longitudinal effect of age in 6314 ABCD Study subjects (two time points). Performing whole-brain vertex-wise (18,742 vertices) analysis using FEMA took about 11 seconds.

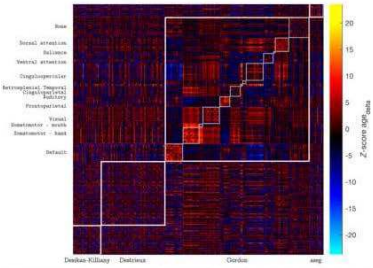

Distribution of *Z*-scores for the longitudinal effect of age across 582 ROIs in 4994 ABCD Study subjects (two time points). Performing connectome-wide analysis (169,071 pairs of connectivity values) using FEMA took about 54 seconds. ROIs were defined using a combination of Desikan-Killiany atlas, Destrieux atlas, Gordon parcellation (further divied into 13 communities), and the aseg atlas.

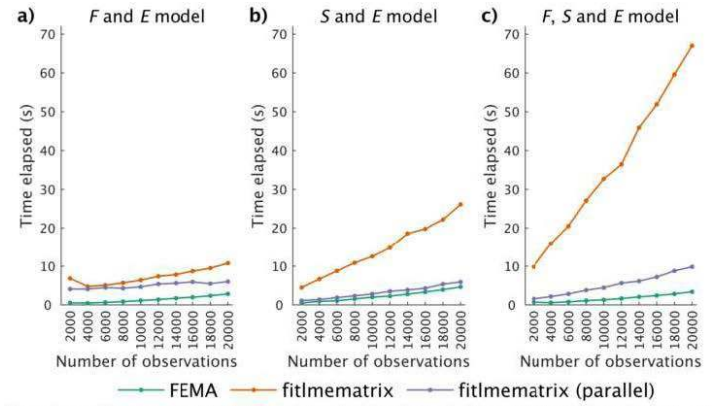

Comparison of time taken to fit different models using FEMA (green), fitlmematrix in MATLAB (orange), and implementation of fitlmematrix using parallel computing (purple) as a function of increasing number of observations for 50 imaging variables and five fixed effects. The random effects included in each model are indicated at the top of each panel: family effect F, subject effect S, and the unmodelec variance term E.

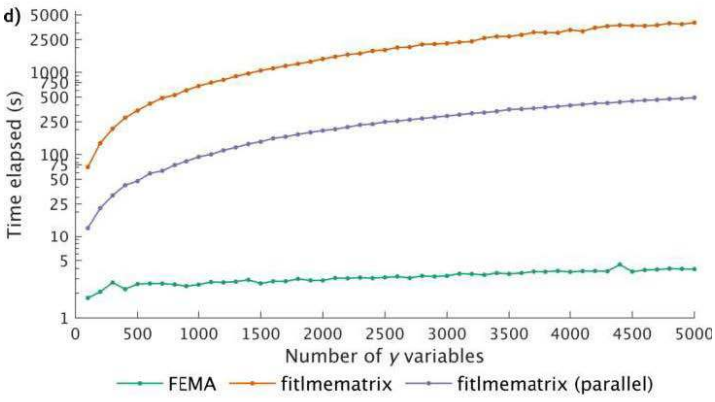

Comparison of time taken by FEMA (green), MATLAB's fitlmematrix (orange), and implementation of fitlmematrix using parallel processing (purple) as a function of increasing number of imaging variables for fitting a model with 10,000 observations, five fixed effects, and the family effect F, subject effect S, and the unmodeled variance term E, specified as random effects. Note that the y-axis is non-linear.

Conclusions: We have developed an efficient solution for performing LME analyses for large sample sizes without compromising estimation accuracy. This opens the possibilities of novel biological applications such as examining neurodevelopmental trajectories, exploration of genetic factors underlying these trajectories, and performing linear and non-linear interaction analyses (of variables of interest like genetic variants) with age/time for longitudinal imaging variables. FEMA is available at: https://github.com/cmig-research-group/cmig_tools/.

References

1. Parekh, P., Fan, C.C., Frei, O., Palmer, C.E., Smith, D.M., Makowski, C., Iversen, J.R., Pecheva, D., Holland, D., Loughnan, R., Nedelec, P., Thompson, W.K., Hagler, D.J., Andreassen, O.A., Jernigan, T.L., Nichols, T.E., Dale, A.M., (2023). FEMA: Fast and efficient mixed-effects algorithm for large sample whole-brain imaging data. https://doi.org/10.1101/2021.10.27.466202

Poster No 1903

Spectral introspection identifies group training dynamics in deep neural networks in neuroimaging

Bradley Baker[1], Vince Calhoun[2], Sergey Plis[3]

[1]TReNDs, Atlanta, GA, [2]GSU/GATech/Emory, Decatur, GA, [3]Georgia State University, Atlanta, GA

Introduction: In this work, we present a novel empirical method for analyzing Deep Neural Network (DNN) learning dynamics, which builds off of previous theoretical work studying changes in gradient rank in auto-differentiation. Our method utilizes the singular values of the gradient and of the component matrices which are used to compute to study evolution of dominant modes during model training. Furthermore, because we analyze gradients dynamically within auto-differentiation, we have the unique opportunity to analyze these dynamics as they adhere to individual samples. Thus, whenever samples have some kind of group labelling, we can perform statistical comparisons of gradient trajectories between groups without breaking normal training behavior. This further allows our method to stand out from post-hoc methods which not only occur outside of training, but can only be evaluated for between different classes in disjoint contexts. To demonstrate the applicability of our method, we identify distinct training dynamics specific to Major Depressive Disorder (MDD), Bipolar Disorder (BPD), Schizophrenia, and

Schizoaffective disorders across multiple studies. We show how these dynamics differ between popular model architectures used in neuroimaging, including convolutional neural networks, transformers and more.

Methods: Reverse-mode auto-differentiation is a computational technique for computing the partial derivatives of complex functions, and has been widely applied to deep learning optimization in the form of back-propagation. Gradients for a neural network's weights are computed by first performing a "forward pass" through the network, and recording the input activations at each layer. Then, a "backward pass" is performed in which the partial derivatives on the output neurons are computed and fed into higher layers. The gradients at each layer are thus computed as an outer product between these accumulated input activations and partial derivatives with respect to the output. To analyze the spectrum of the gradient during training, we compute the singular value decomposition (SVD) of the gradient and its constituent matrices. Because we are working within AD, we can computed the SVD of gradients belonging to particular samples, and thus to particular groups. We then perform statistical tests between singular value trajectories during training to evaluate group differences. We begin with a Multi-Layer perceptron on FreeSurfer volumes. We then analyze functional MRI from the COBRE and FBIRN data sets. To assess dynamics in recurrent models, we perform Spatially Constrained Independent Component Analysis using the NeuroMark template, which provides us with 53 neurologically relevant spatially independent maps and associated time-series. Using the time-series data, we show can reveal group-specific gradient dynamics in 1D and 2D CNNs, LSTMs and the BERT transformer. We then utilize the spatial maps to demonstrate group-specific gradient dynamics in 3D-CNNs.

Results: The MLP autoencoder trained on FSL data shows significant differences between SZ and HC groups in the middle singular values of the output layer, while the corresponding classifier shows more group differences in the input layer. The LSTM, BERT and 1D CNN models all show significant differences between male SZ and HC groups, with the LSTM showing differences mostly in hidden neurons, the 1D CNN showing significant differences at the output layer, and BERT showing differences across the entire model for the autoencoder task with almost no significant differences in the classifier.

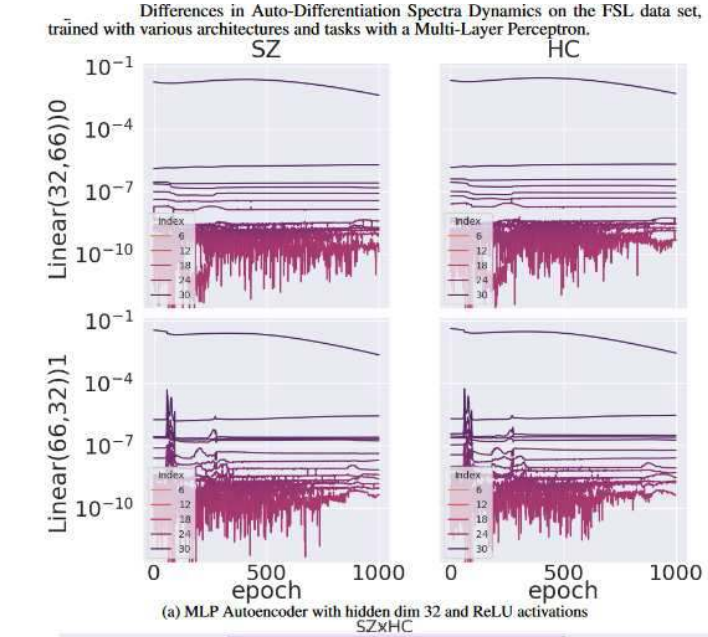

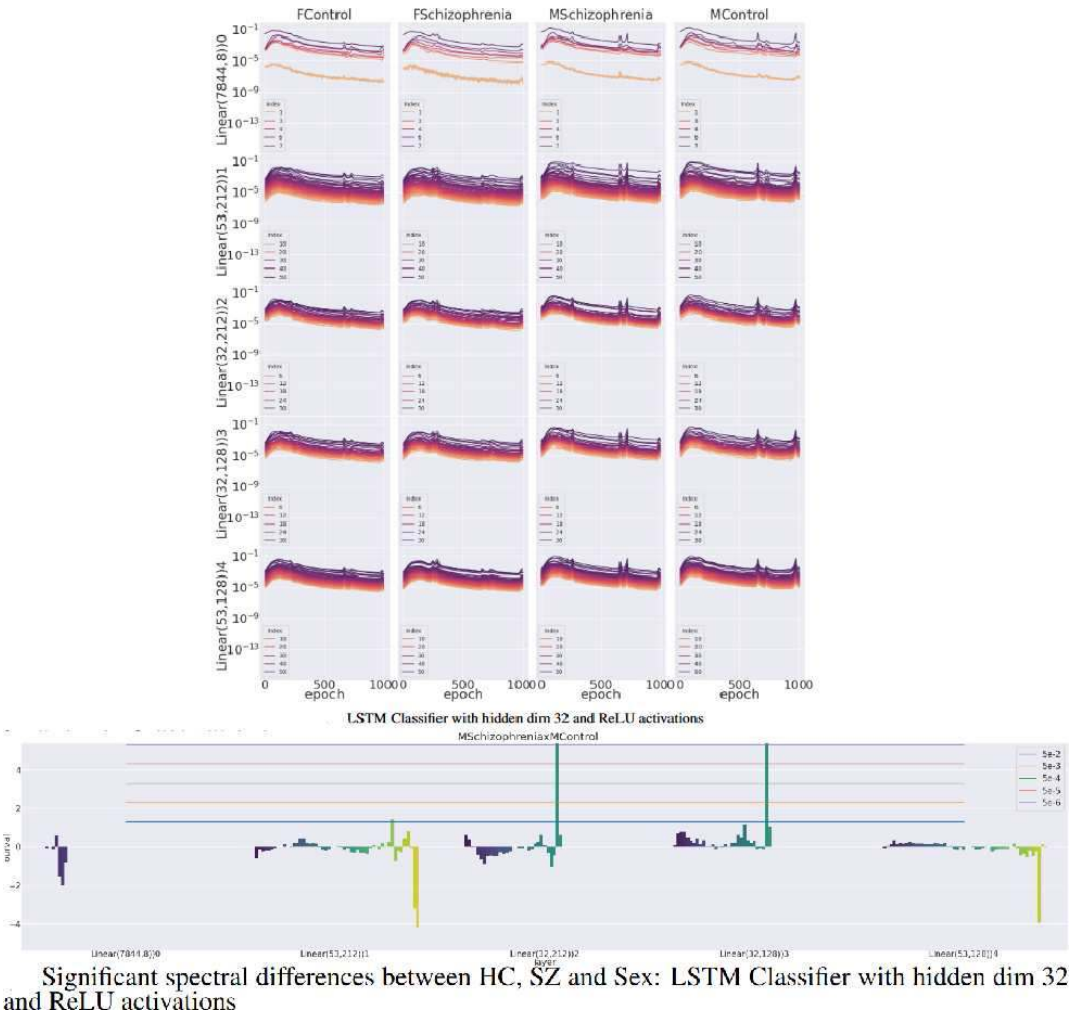

Significant spectral differences between HC, SZ and Sex: LSTM Classifier with hidden dim 32 and ReLU activations

Conclusions: In this work, we have demonstrated a novel, dynamic introspection technique for DNNs applied to neuroimaging. Our method utilizes inherent structure of auto-differentiation to provide analysis which does not affect training, and we can use to compare group differences. We applied the method to multiple neuroimaging studies and demonstrate how group differences appear in different places during training and in the architecture.

References

1. S. Bach, A. Binder, G. Montavon, F. Klauschen, K.-R. Muller, and W. Samek, “On pixel-wise explanations for non-linear classifier decisions by layer-wise relevance propagation,” PloS one, vol. 10, no. 7, e0130140, 2015
2. D. Baehrens, T. Schroeter, S. Harmeling, M. Kawanabe, K. Hansen, and K.-R. Muller, “How to explain individual classification decisions,” The Journal of Machine Learning Research, vol. 11, pp. 1803–1831, 2010.
3. Y. Du et al., “Neuromark: An automated and adaptive ica based pipeline to identify reproducible fmri markers of brain disorders,” NeuroImage: Clinical, vol. 28, p. 102 375, 2020
4. Keator, David B., et al. “The function biomedical informatics research network data repository.” Neuroimage 124 (2016): 1074-1079.
5. A. R. Mayer et al., “Functional imaging of the hemodynamic sensory gating response in schizophrenia,” Human brain mapping, vol. 34, no. 9, pp. 2302–2312
6. J. Oh, B.-L. Oh, K.-U. Lee, J.-H. Chae, and K. Yun, “Identifying schizophrenia using structural mri with a deep learning algorithm,” Frontiers in psychiatry, vol. 11, p. 16, 2020
7. P. Patel, P. Aggarwal, and A. Gupta, “Classification of schizophrenia versus normal subjects using deep learning,” in Proceedings of the Tenth Indian Conference on Computer Vision, Graphics and Image Processing, 2016, pp. 1–6.
8. M. M. Rahman, N. Lewis, and S. Plis, “Geometrically guided saliency maps,” in ICLR 2022 Workshop on PAIR {\textasciicircum} 2Struct: Privacy, Accountability, Interpretability, Robustness, Reasoning on Structured Data, 202
9. R. R. Selvaraju, M. Cogswell, A. Das, R. Vedantam, D. Parikh, and D. Batra, “Grad-cam: Visual explanations from deep networks via gradient-based localization,” in Proceedings of the IEEE international conference on computer vision, pp. 618–626.
10. K. Simonyan, A. Vedaldi, and A. Zisserman, “Deep inside convolutional networks: Visualising image classification models and saliency maps,” arXiv preprint arXiv:1312.6034
11. M. Sundararajan, A. Taly, and Q. Yan, “Axiomatic attribution for deep networks,” in International conference on machine learning, PMLR, 2017, pp. 3319–3328.

Poster No 1904

Emerging Properties Exploration with UMAP Statistics: EMUSE

Chris Foulon[1], Marcela Ovando-Tellez[2], Lia Talozzi[3], Anna Matsulevits[4], Fanny Munsch[5], Igor Sibon[5], Thomas Tourdias[6], Michel Thiebaut de Schotten[7]

[1]Groupe d'Imagerie Neurofonctionnelle (GIN), Institut des Maladies Neurodegeneratives-UMR 5293, CNRS, Bordeaux, France, [2]Institut des maladies neurodégénératives (IMN), Bordeaux, France, [3]Stanford Medical School, Stanford, CA, [4]University Bordeaux, Institut des Maladies Neurodégénératives CNRS UMR 5293 Université de Bordeaux, Bordeaux, Gironde, [5]Université de Bordeaux, Bordeaux, France, [6]University Bordeaux, Bordeaux, Gironde, [7]Groupe d'Imagerie Neurofonctionnelle, Institut des Maladies Neurodégénératives- UMR 5293, CNRS, CEA, Bordeaux, France

Introduction: With the improvement of in-vivo human brain imaging techniques and analyses, it is becoming increasingly clear that cognitive functions are not localised but emerge from the complex interaction between brain areas[1]. Therefore, new tools are required to capture these emergent properties. Uniform Manifold Approximation and Projection (UMAP)[2], a dimensionality reduction technique, is increasingly popular in displaying data structure. Specifically, UMAP creates a morphospace representing different patterns in the input data relative to each other with a proportional distance representing their similarity or dissimilarity-ideal to identify how combining different factors can lead to a unique result. Accordingly, Tallozi et al. proposed a statistical method to associate the disconnection patterns in the UMAP morphospace with psychological deficits[3] that demonstrated high predictive performance and robustness[4]. Here, we propose a new open-source Python tool-EMUSE-that extends the same framework to a more general setting, allowing anyone to build their morphospace and explore its organisation statistically. In a proof-of-concept example, we show that we can associate stroke lesion profiles with cognitive deficits.

Methods: We used the delineated lesion masks in the standard MNI152 space of 187 stroke patients[5]. We train the UMAP model that represents the profile of the lesions, placing similar lesions close together and different lesions far apart in a continuous and unbounded 2D space (Fig 1a). To run statistics on this space, we create a 2D pixelated space with customisable parameters-number of pixels and smoothing-where we can expand the coordinates to represent proximity and explore how this proximity relates to the examined measures (Fig 1b). Then, we ran a pixel-wise Pearson correlation (corrected for multiple comparisons and a p-value threshold of 0.05) and showed the parts of the UMAP space associated with significant variations in the studied psychological test. Finally, we can retrieve which lesions relate to the behavioural changes. We analysed which lesion profiles are associated with a deficit in language and motor tasks in the UMAP morphospace based on the 187 lesion masks. The language task is part of the Montreal Cognitive Assessment (MoCA)[6], and the motor score is part of the Fugl-Meyer test[7]. We chose these two tests to show our method can capture both primary and high-level cognitive impairments that would emerge from complex lesion patterns.

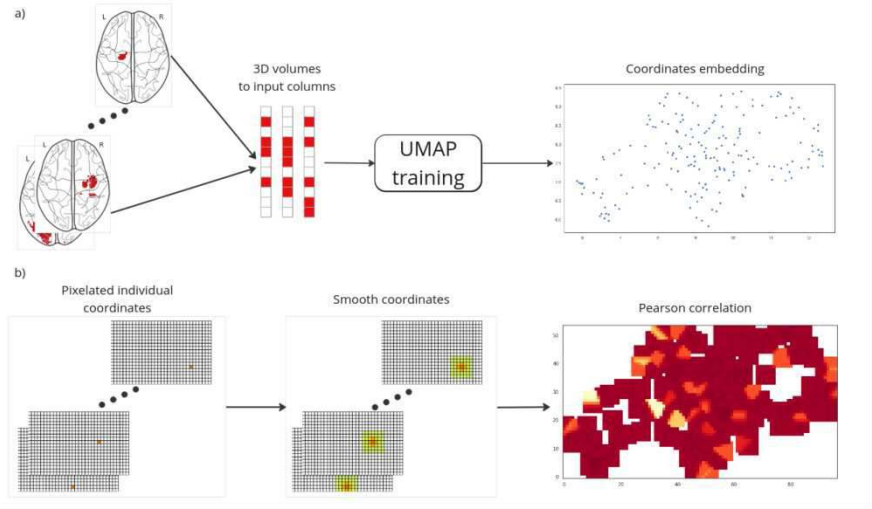

Figure 1: a) Creation of the UMAP space placing points closer proportionally to their similarity. 3D coordinates of the lesion masks are flattened into a vector and combined in a matrix to train de UMAP. b) The embedded coordinates are then pixelated into individual 2D spaces. This allows us to smooth the coordinates to simulate spatial relationships and run statistics on the space. Here, we used a Pearson correlation between the space and different psychological task scores.

Results: We were able to capture the lesion profiles of both motor and language deficits in our dataset (Fig 2). After correction for multiple comparisons, lesion profiles correlated with a motor deficit between 0.32 and 0.39 and a language deficit between 0.318 and 0.324. The comparison of the overlap of the lesions contributing to the correlated lesion profiles in the

UMAP morphospace with the NeuroSynth[8] decoding tool shows that the lesions are consistent with the literature. The lesion profiles associated with a motor deficit were correlated with multiple subcortical structures involved in motor tasks-putamen, basal ganglia, caudate nucleus, striatum-and the insula. The lesions associated with a language deficit were correlated with the superior and middle temporal gyrus and the auditory cortex, as well as the concepts of listening, sounds and speech.

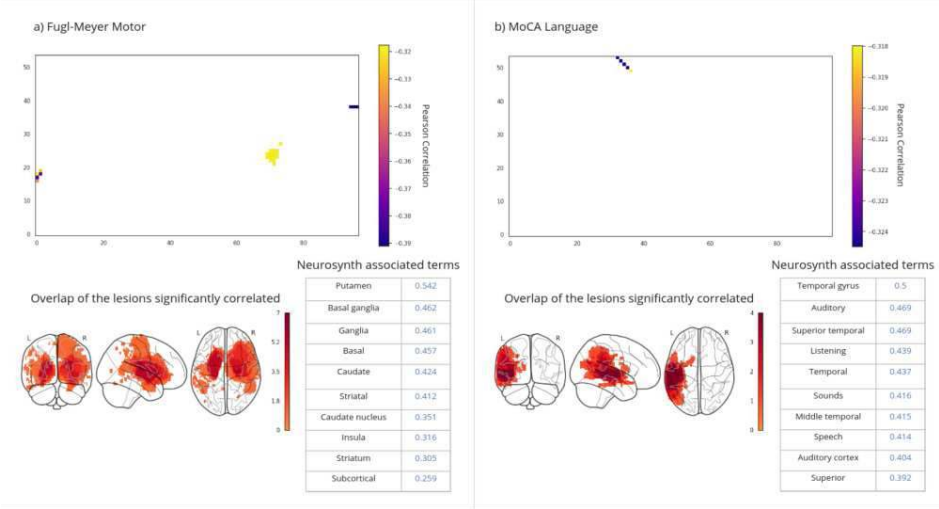

Figure 2: Display of the significant lesion profiles and their association with behaviour in the literature. Upper panels: Pearson correlation (after p-value Bonferroni-Holm corrected < 0.05) between the smoothed embedded coordinates and the psychological tests—a) is the Fugl-Meyer Motor score and b) the language test of MoCA. Lower panels: Overlap of the lesions participating in the correlation display in the top and their correlation value with the meta-analysis decoding tool from NeuroSynth. These terms are the structures and domains most associated with the location of the lesions in the studies referenced in the NeuroSynth database.

Conclusions: Our findings demonstrate that EMUSE is not only able to identify the interaction between complex lesion patterns accurately but also proficiently establish statistical correlations between these interactions and cognitive deficits. This tool has been meticulously crafted for accessibility and user-friendliness, thereby empowering researchers to seamlessly generate and investigate various UMAP morphospaces tailored to their unique datasets. Furthermore, the versatility of EMUSE allows for adaptation to a wide array of data inputs and uses of various statistical techniques, making it a novel asset in neuroscientific research.

References

1. Thiebaut de Schotten, M., & Forkel, S. J. (2022). 'The emergent properties of the connected brain.' Science, 378(6619), 505-510.
2. McInnes, L., Healy, J., & Melville, J. (2018). 'Umap: Uniform manifold approximation and projection for dimension reduction.' arXiv preprint arXiv:1802.03426.
3. Talozzi, L., Forkel, S. J., Pacella, V., Nozais, V., Allart, E., Piscicelli, C., ... & Thiebaut de Schotten, M. (2023). 'Latent disconnectome prediction of long-term cognitive-behavioural symptoms in stroke.' Brain, 146(5), 1963-1978.
4. Hope, T. M., Neville, D., Talozzi, L., Foulon, C., Forkel, S. J., de Schotten, M. T., & Price, C. J. (2023). 'Testing the Disconnectome Symptom Discoverer model on out-of-sample post-stroke language outcomes.' Brain: a journal of neurology, awad352.
5. Munsch, F., Sagnier, S., Asselineau, J., Bigourdan, A., Guttmann, C. R., Debruxelles, S., ... & Tourdias, T. (2016). 'Stroke location is an independent predictor of cognitive outcome.' Stroke, 47(1), 66-73.
6. Nasreddine, Z. S., Phillips, N. A., Bédirian, V., Charbonneau, S., Whitehead, V., Collin, I., ... & Chertkow, H. (2005). 'The Montreal Cognitive Assessment, MoCA: a brief screening tool for mild cognitive impairment.' Journal of the American Geriatrics Society, 53(4), 695-699.
7. Fugel-Meyer, A. R., Jaasko, L., Leyman, I., Ollson, S., & Steglind, S. (1975). 'The post-stroke hemiplegic patient1, a method for evaluation of physical perpormance.' Scand. J. Rahabil. Med, 7, 13-31.
8. Yarkoni, T., Poldrack, R. A., Nichols, T. E., Van Essen, D. C., & Wager, T. D. (2011). 'Large-scale automated synthesis of human functional neuroimaging data.' Nature methods, 8(8), 665-670.

Poster No 1905

Systematic review and evaluation of meta-analysis methods for same data meta-analyses in multiverse

Jeremy Lefort-Besnard[1], Thomas Nichols[2], Camille Maumet[1]

[1]Inria, Empenn team, Rennes, France, [2]University of Oxford, Oxford, United Kingdom

Introduction: Researchers using task-fMRI data have access to a wide range of analysis tools to model brain activity. This diversity of analytical approaches has been shown to have substantial effects on neuroimaging results (Botvinik-Nezer et al., 2020; Bowring et al., 2018; Carp, 2012; Glatard et al., 2015). Combined with selective reporting, this analytical flexibility can lead to an inflated rate of false positives and contributes to the irreproducibility of neuroimaging findings (Poldrack et al., 2017). Multiverse analyses are a way to systematically explore and integrate pipeline variation on a given dataset. We focus on the

setting where multiple statistic maps are produced as an output of a set of analyses. Meta-analysis is a natural approach to extract consensus inferences from these maps, yet the traditional assumption of independence amongst input datasets does not hold. In this work we consider a suite of methods to conduct meta-analysis in the multiverse setting, accounting for inter-pipeline dependence among the results.

Methods: We propose several same data meta-analysis (SDMA) methods based on the traditional 'Stouffer' fixed-effects meta-analysis (Stouffer, 1949): -SDMA Stouffer in which correlation across pipelines is taken into account, -Consensus SDMA Stouffer and Consensus Average methods, where the combined inference is calibrated to be as similar to the input pipelines as possible, and -General Least Squares (GLS) SDMA, where inter-pipeline correlation is used to find the statistically optimal combination of pipeline results. The validity of these models were assessed in a set of simulations. Here, we focus on false positive control in two scenarios: 1/ independent pipelines with no significant results (null case), and 2/ correlated pipelines with no significant results (null correlated case). These meta-analysis models were also evaluated on a real world dataset from NARPS (Botvinik-Nezer et al., 2020), a multiverse analysis with 70 different statistic maps originating from the same data. Finally, given that these SDMA methods assume that the inter-pipeline correlation is the same across the brain, we measured heterogeneity with the Frobenius norm between the whole brain and a set of several brain regions derived from the AAL atlas.

Results: Simulation results under the null setting of no effect and independent pipelines show that all the tested meta-analysis estimators are valid (Fig 1 top row). However, when data are correlated, as typically observed in a multiverse setting, only the SDMA estimators had valid inferences (Fig 1 lower row), while the conventional meta-analysis approach (Stouffer) dramatically overestimated the number of false-positives. On the real world dataset (Fig 2), the GLS method finds more significant voxels while the 3 other methods all have similar sensitivity. Finally, we found that the Frobenius norm was 0.01% across brain regions, supporting the validity of the consistent correlation assumption.

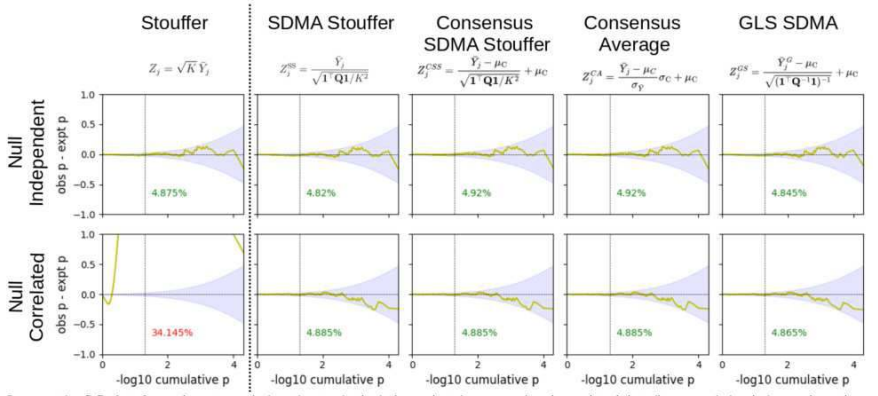

Comparative P-P plots for each meta-analysis estimator in the independent (upper row) and correlated data (lower row) simulations, where the y-axis is the difference in observed and expected sorted -log10 p-value, and the x-axis is the expected sorted p-value. The blue shadow depicts the theoretical confidence interval, and the observed false-positive rate at p<0.05). As expected, only the SDMA methods (right side of the dotted line) perform well in the multiverse setting.

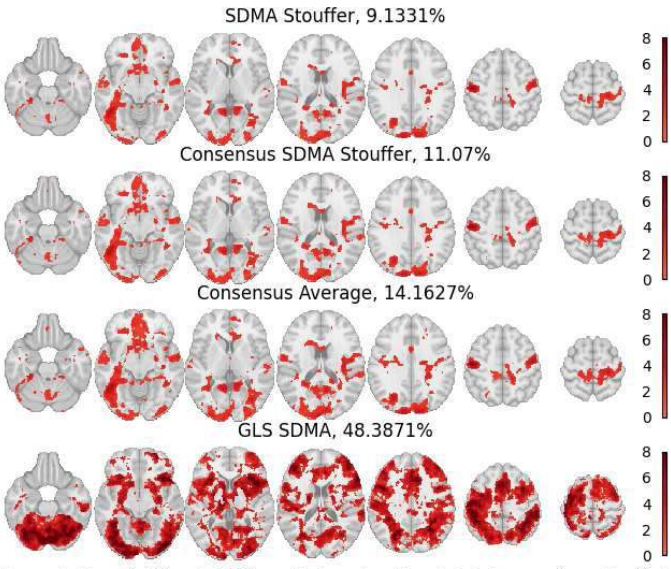

Demonstration of different SDMA methods using the statistical maps from the first hypothesis in the NARPS study (parametric effect of gains in a mixed gambles task). Maps were thresholded at P<0.05 uncorrected to allow for direct comparison. Name of the MA model and percentage of significant voxels are displayed on each map.

Conclusions: We compared several methods for combining multiverse results that account for the dependence among inputs. Our findings demonstrated the validity of the SDMA models under inter-pipeline dependence. As expected, the (traditional) Stouffer's method is liberal while the SDMA methods are all valid and present different levels of significance. These different levels illustrated different types of inference that practitioners can choose based on the assumptions of their analyses. As an illustration, in their work, Botvinik-Nezer and colleagues (2020) implemented the Consensus Average model to combine inferences, striving to align them closely with each of the input pipelines, under the assumption that all pipelines were equally valid and thus contributed equally relevant information. This assumption may not hold true in other multiverse settings.

References

1. Botvinik-Nezer, R. (2020). Variability in the analysis of a single neuroimaging dataset by many teams.
2. Bowring, A. (2018). Same data-different software-different results? Analytic variability of group fmri results. 1–3.
3. Carp, J. (2012). On the plurality of (methodological) worlds: Estimating the analytic flexibility of FMRI experiments. Frontiers in Neuroscience, 6, 149.
4. Glatard, T. (2015). Reproducibility of neuroimaging analyses across operating systems. Frontiers in Neuroinformatics, 9, 12.
5. Poldrack, R. A. (2017). Scanning the horizon: Towards transparent and reproducible neuroimaging research. Nature Reviews Neuroscience, 18(2), 115–126.
6. Stouffer, S. A. (1949). Adjustment during army life. Studies in social psychology in World War II. Princeton Univ. Press.

Poster No 1906

Nilearn: Streamlined neuroimaging analysis with enhanced infrastructure and surface API integration

Yasmin Mzayek[1], Pierre Bellec[2], Ahmad Chamma[1], Alexandre Cionca[3], Jelle Dalenberg[4], Jérôme Dockès[1], Mathieu Dugré[5], Elizabeth DuPre[6], Rémi Gau[7], Nicolas Gensollen[8], Mathias Goncalves[6], Anne-Sophie Kieslinger[9], Alisha Kodibagkar[10], Steven Meisler[11], François Paugam[12], Julio Peraza[13], Jean-Baptiste Poline[7], Patrick Sadil[14], Taylor Salo[15], Kevin Sitek[16], Maximilian Sitter[17], Alexis Thual[1], Mohammad Torabi[7], Konrad Wagstyl[18], Hao-Ting Wang[2], Michelle Wang[7], Bertrand Thirion[19]

[1]Inria, Palaiseau, [2]CRIUGM, Montreal, Quebec, [3]Centre Hospitalier Universitaire Vaudoise, Lausanne, Vaud, [4]University Medical Center Groningen, Groningen, [5]Concordia University, Montreal, Quebec, [6]Stanford University, Stanford, CA, [7]McGill University, Montreal, Quebec, [8]INRIA Paris center, Paris, [9]Max Planck Institute for Human Cognitive and Brain Sciences, Leipzig, Other, [10]University of Pennsylvania, Massachusetts Institute of Technology, Philadelphia, PA, [11]Harvard / MIT, Cambridge, MA, [12]University of Montreal, Montreal, Quebec, [13]Florida International University, Miami, FL, [14]Johns Hopkins Bloomberg School of Public Health, Baltimore, MD, [15]University of Pennsylvania, Philadelphia, PA, [16]Northwestern University, Evanston, IL, [17]University Hospital Cologne, Cologne, [18]UCL, London, London, [19]inria, Palaiseau

Introduction: Nilearn is a widely recognized Python package in the neuroimaging community that offers a comprehensive set of statistical and machine learning tools for analysis of brain images. With over 10 years of ongoing development, it has reached 1000 stars, 576 forks, and over 200 contributors on GitHub, with clear impact as measured by its 163 citations in open access publications[1]. Its continuous growth is backed by its encouraging community, user-friendly API, and comprehensive documentation, solidifying its role as a crucial part of the neuroimaging open-source software ecosystem. Also, Nilearn effectively makes use of powerful Python machine learning libraries, particularly scikit-learn[2], which are extensively utilized by scientific and industrial experts. Recent work in Nilearn has centered on developing a new API to allow users to seamlessly work with surface data in a manner similar to volumetric data, enhancing support for the General Linear Model (GLM), enhancing the BIDS interface, and improving and updating the infrastructure and codebase.

Methods: Nilearn is designed to be accessible for researchers and developers. The documentation (https://nilearn.github.io) comprises a comprehensive user guide and an illustrative example gallery, along with detailed contribution and maintenance guidelines. Moreover, we actively encourage community engagement by welcoming questions, bug reports, enhancement suggestions, and direct involvement in refining the source code. We use several channels of communication including Neurostars, GitHub, Discord, Twitter, and Mastodon for daily communication with both contributors and users. Nilearn follows standard software development practices, including version control, unit testing, and rigorous reviews for contributions. Our automated continuous integration infrastructure ensures constant testing and updates for a streamlined development process. On this end, we have been further improving the code quality of and infrastructure around our codebase to meet best practices and ensure quality as the package grows. Finally, Nilearn is actively showcased in various tutorials and workshops held annually, such as the OHBM Brainhack.

Results: Nilearn supports brain image manipulation, GLM-based analysis, predictive modelling, classification, decoding, and connectivity analysis. It also has tooling for visualizing volumetric and surface brain imaging data. In the latest release (v0.10.2)[3], an experimental surface API has been added to facilitate working with surface data in downstream surface-based analyses. Key features from the release include the addition of LogisitcRegressionCV and LassoCV estimators to the Decoder

module, the ability to compute fixed effects on F contrasts in the GLM module, and the option to enable radiological view for volumetric plotting functions (Fig1). A new surface API has also been released under an experimental module for rapid community feedback. It provides access to a SurfaceImage class that can store mesh and surface data for both hemispheres. This surface object can then be easily passed to other functions for further analysis or visualization (Fig2) mirroring Nilearn's interface for handling volumetric data. Notable maintenance changes were implemented to improve codebase standardization and consistency, including the use of reformatting tools, such as Black and pre-commit for automatic linting and formatting. Ongoing efforts involve codebase restructuring based on new guidelines and writing reusable Pytest fixtures for efficient unit testing.

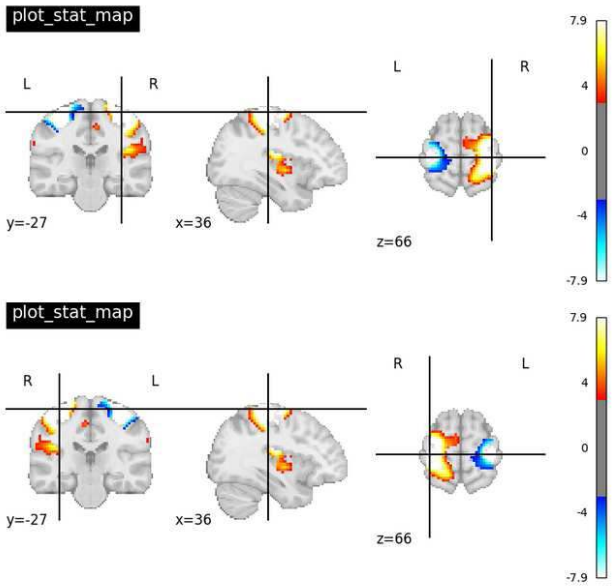

Fig1. Volumetric plotting functions now have a radiological parameter that can be set to True to invert the brain image and the L R labels on the x axis following radiological convention. In this example, the top image shows the default view and the bottom image shows the radiological view.

```
>>> img = surface.fetch_nki()[0]
>>> print(f"NKI image: {img}")
NKI image: <SurfaceImage (895, 20484)>

>>> print(img.data)  # output is truncated
{'left_hemisphere': array([[-0.4938, ..., ]], dtype=object),
'right_hemisphere': array([[-0.5474, ..., ]], dtype=object)}

>>> print(img.mesh)
{'left_hemisphere': <FileMesh with 10242 vertices>,
 'right_hemisphere': <FileMesh with 10242 vertices>}

>>> masker = surface.SurfaceMasker()
>>> masked_data = masker.fit_transform(img)
>>> print(f"Masked data shape: {masked_data.shape}")
Masked data shape: (895, 20484)

>>> first_data = masked_data[0]
>>> first_data = masker.inverse_transform(first_data)
>>> print(f"First timepoint: {first_data}")
First timepoint: <SurfaceImage (20484,)>

>>> plot_surf_img(first_data)
>>> plotting.show()
```

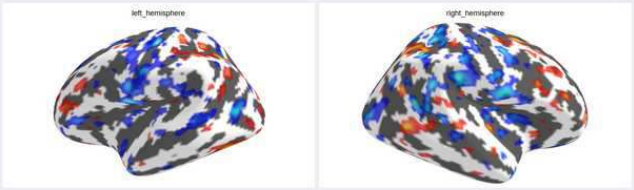

Fig2. Code snippet to demonstrate instantiating an object of the SurfaceImage class and passing it to a SurfaceMasker to perform signal extraction before plotting it with a function that accepts a SurfaceImage object. The SurfaceImage object can store surface data arrays for both hemispheres as well as Mesh objects for each hemisphere. The Mesh objects contain the number of vertices, the coordinates, and the faces for the surface mesh.

Conclusions: The growing reliance on Nilearn underscores its accessibility and utility within the neuroimaging community. Developing the surface API will allow us to better support cortical surface analyses and meet user needs. Further, as the package grows, improved infrastructure and keeping up with new standards will ensure the robustness of this tool.

References

1. NiLearn (RRID:SCR_001362)
2. Pedregosa, F., Varoquaux, G., Gramfort, A., Michel, V., Thirion, B., Grisel, O., Blondel, M., Prettenhofer, P., Weiss, R., Dubourg, V., Vanderplas, J., Passos, A., Cournapeau, D., Brucher, M., Perrot, M., Duchesnay, E. (2011). Scikit-learn: Machine Learning in Python, Journal of Machine Learning Research, 12, 2825-2830.
3. Nilearn contributors, Chamma, A., Frau-Pascual, A., Rothberg, A., Abadie, A., Abraham, A., Gramfort, A., Savio, A., Cionca, A., Thual, A., Kodibagkar, A., Kanaan, A., Pinho, A. L., Idrobo, A. H., Kieslinger, A.-S., Rokem, A., Mensch, A., Vijayan, A., Duran, A., ... Nájera, Ó. (2023). nilearn (0.10.2). Zenodo. https://doi.org/10.5281/zenodo.8397157

Poster No 1907

Polyconnectomic score: a novel quantification of brain signatures in neuropsychiatric disorders

Ilan Libedinsky[1], Koen Helwegen[2], Laura Guerrero Simon[1], Marius Gruber[3], Jonathan Repple[4], Tilo Kircher[5], Udo Dannlowski[6], Martijn van den Heuvel[7]

[1]Vrije Universiteit, Amsterdam, NH, [2]Vrije Universiteit Amsterdam, Amsterdam, North Holland, [3]University Hospital, Goethe University Frankfurt, Frankfurt am Main, Hesse, [4]Department of Psychiatry, Psychosomatic Medicine and Psychotherapy, University Hospital Frankfurt, Frankfurt, Hesse, [5]Department of Psychiatry and Psychotherapy, University of Marburg, Marburg, Hesse, [6]Institute for Translational Psychiatry, Münster, North Rhine Westphalia, [7]Vrije Universiteit, Amsterdam, N/A

Introduction: Emerging evidence has shown that neuropsychiatric disorders have distinct macroscale brain connectivity patterns [Fornito et al., 2015]. Detecting these altered brain patterns with MRI remains challenging, partly due to the numerous tests needed for whole-brain analysis, which increases the risk of missing crucial findings [Helwegen et al., 2023]. To overcome this constraint, we introduce the polyconnectomic score (PCS). Drawing inspiration from polygenic scores [Torkamani et al., 2018], PCS offers an interpretable way to quantify the extent of brain circuitry linked to a disorder that is present within a connectome. We demonstrate the utility of PCS in three applications: detecting individuals with brain disorders, stratifying patients by disease predisposition, and uncovering brain-behaviour associations.

Methods: PCS is based on connectome summary statistics [Nichols et al., 2017], reflecting both the strength and direction of the association between brain connections and a phenotype (Fig. 1). These statistics are derived by estimating connectivity differences between patients and controls (using Cohen's d), either from a prior study or by aggregation from multiple studies via a meta-analytical approach. The PCS for an out-of-sample individual is computed as the weighted average of the summary statistics and the individual's brain connectivity map, resulting in a unique score per subject. Resting-state functional MRI data from a total of 34,570 individuals were used to reconstruct the functional connectivity [De Lange et al., 2023] of controls (n = 5,551) and patients with autism spectrum disorder (n = 1,117), schizophrenia (n = 279), attention deficit hyperactivity disorder (n = 1,064), and Alzheimer's disease (n = 223). In each dataset, we regressed out the effects of covariates such as age, sex, site, and total in-scanner motion from the functional connectivity values. We computed the PCS for each disorder, comparing PCS levels between groups using Cohen's d and FDR-corrected p-values from Student's t-tests. We stratified individuals based on psychosis liability by computing the PCS for schizophrenia and compared PCS levels among patients with schizophrenia, schizoaffective disorder, and bipolar disorder (n = 126, 59, and 72, respectively), their first-degree relatives (n = 113, 71, and 75, respectively), and healthy controls (n = 88) [Ivleva et al., 2013], using Cohen's d and FDR-corrected p-values from Student's t-test statistic. We further explored brain-behaviour associations in the UK Biobank (n = 26,673) [Sudlow et al., 2015] by measuring the Pearson correlation coefficient between PCS for schizophrenia and behavioural measurements (FDR-corrected p-values).

Results: Patients with autism spectrum disorder, schizophrenia, and Alzheimer's disease showed significantly higher PCS compared to controls (Cohen's d range: [0.30, 0.87], $p < 0.05$; Fig. 2). Including the whole-brain connectome led to a better differentiation between groups than including the most significant connections from the summary statistics. PCS enabled stratification of individuals by psychosis predisposition, differentiating patients with schizophrenia from their first-degree relatives (d = 0.42, p = 4 x 10-3), and first-degree relatives from healthy controls (d = 0.34, p = 0.034). PCS also revealed that subjects with brain patterns similar to those with schizophrenia were more likely to show lower fluid intelligence (r = -0.037, p = 1.1 x 10-5), higher neuroticism scores (r = 0.031, p = 1.5 x 10-5), and decreased levels of happiness (r = -0.023, p = 6.4 x 10-4), among other factors.

Conclusions: PCS is a valuable tool for identifying individuals with neuropsychiatric disorders, stratifying disease risk, and uncovering brain-behaviour associations. The potential of PCS to quantify connectivity patterns across the entire connectome could significantly enhance our understanding of both healthy and diseased brain functioning.

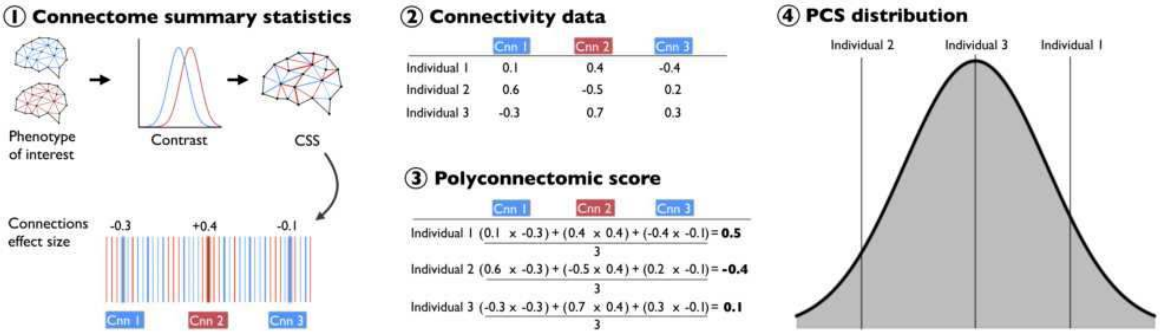

Fig. 1: Computation of polyconnectomic score. *(1)* Computation of the polyconnectomic score (PCS) is based on connectome summary statistics. These statistics capture the strength and direction of the association between brain connections and a phenotype of interest. *(2)* Brain connectivity data are collected from out-of-sample individuals. *(3)* PCS is estimated as the weighted average of the connectome summary statistics and the individual's connectome, quantifying the presence of brain signatures associated with the phenotype of interest in the individual's connectome. *(4)* PCS levels are statistically compared between individuals (e.g., cases and controls). *PCS*, polyconnectomic score; *CSS*, connectome summary statistics; *Cnn*, connection.

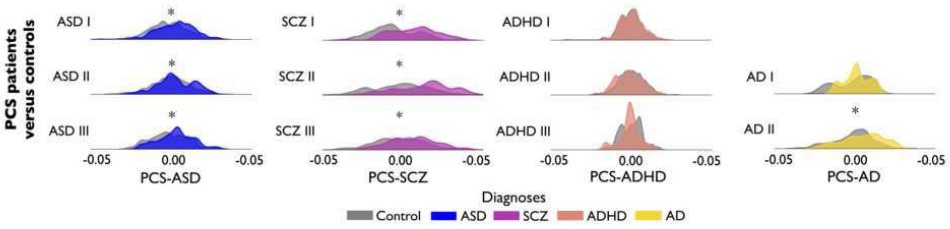

Fig. 2: Polyconnectomic scoring facilitates the identification of patients with neuropsychiatric disorders. PCS levels between patients and controls were compared to assess the efficacy of this method in detecting and quantifying brain signatures associated with the neuropsychiatric disorder of interest. Asterisks denote studies where patients exhibited significantly higher PCS than controls, as estimated by t-test statistics (FDR-corrected) *PCS*, polyconnectomic score; *ASD*, autism spectrum disorder; *SCZ*, schizophrenia; *ADHD*, attention deficit hyperactivity disorder; *AD*, Alzheimer's disease.

References

1. De Lange SC, Helwegen K, Van Den Heuvel MP (2023): Structural and functional connectivity reconstruction with CATO - A Connectivity Analysis TOolbox. NeuroImage 273:120108.
2. Fornito A, Zalesky A, Breakspear M (2015): The connectomics of brain disorders. Nat Rev Neurosci 16:159–172.
3. Helwegen K, Libedinsky I, van den Heuvel MP (2023): Statistical power in network neuroscience. Trends Cogn Sci:S136466132200328X.
4. Ivleva EI, Bidesi AS, Keshavan MS, Pearlson GD, Meda SA, Dodig D, Moates AF, Lu H, Francis AN, Tandon N, Schretlen DJ, Sweeney JA, Clementz BA, Tamminga CA (2013): Gray Matter Volume as an Intermediate Phenotype for Psychosis: Bipolar-Schizophrenia Network on Intermediate Phenotypes (B-SNIP). Am J Psychiatry 170:1285–1296.
5. Nichols TE, Das S, Eickhoff SB, Evans AC, Glatard T, Hanke M, Kriegeskorte N, Milham MP, Poldrack RA, Poline J-B, Proal E, Thirion B (2017): Best practices in data analysis and sharing in neuroimaging using MRI. CO M M E N TA RY 20.
6. Sudlow C, Gallacher J, Allen N, Beral V, Burton P, Danesh J, Downey P, Elliott P, Green J,
7. Landray M, Liu B, Matthews P, Ong G, Pell J, Silman A, Young A, Sprosen T, Peakman T, Collins R (2015): UK Biobank: An Open Access Resource for Identifying the Causes of a Wide Range of Complex Diseases of Middle and Old Age. PLOS Med 12:e1001779.
8. Torkamani A, Wineinger NE, Topol EJ (2018): The personal and clinical utility of polygenic risk scores. Nat Rev Genet 19:581–590.

Poster No 1908

Toward Meta-Connectomic Ergodicity in Neuroimaging

Jonathan Towne[1], Victor Lami[2], Heath Pardoe[3], Jose Cavazos[1], Peter Fox[1]

[1]UT Health San Antonio, San Antonio, TX, [2]UCLA Health, Los Angeles, CA, [3]Florey Institute of Neuroscience and Mental Health, Melbourne, VIC

Introduction: Ergodicity in a dynamical system asserts that group observations at a single time point are equivalent to a single-individual observation over time. In the brain, this would mandate that network properties derived from cross-sectional data will be observed longitudinally in individuals. The implication for neuroimaging, if ergodicity holds, is that meta-analytic sampling can access network architecture (data structures) useful for detecting networks per-subject. Ergodicity has been implicitly shown in healthy subjects by graph theory (Crossley et al., 2013) and other analytics (Smith et al., 2009). In these studies, equivalent functional architecture was identified by connectomic meta-analysis of task-based studies and connectomic analysis of temporally concatenated rs-fMRI. Diseases follow collectively similar yet individually distinct patterns

(shown in trans-diagnostic meta-analyses: Vanasse et al., 2021; Towne et al., 2023), motivating disease-specific ergodic hypotheses. We present evidence of ergodicity in a temporal lobe epilepsy (TLE) cohort.

Methods: A meta-connectomic (cross-sectional) model of TLE pathology was derived from published coordinate data reported in case-control contrasts (n=74 TLE experiments), using Meta-analytic Graph Theory Modeling (M-GTM; Figure 1). For the same set of nodes, connectomic models were derived for from primary (per-subject) rs-fMRI scans (n = 37 patients, 19 healthy controls), using the FMRIB Software Library (FSL) to compute functional connectivity. Models were compared by modularity analysis and node topology metrics (e.g. centrality).

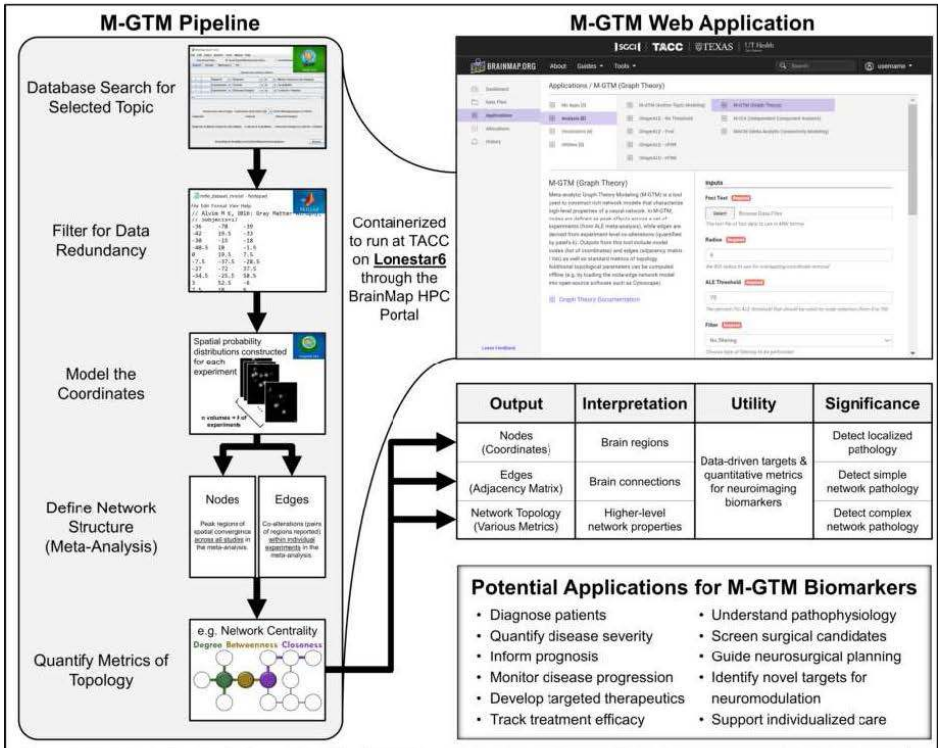

Figure 1. Meta-Analytic Graph Theory Modeling (M-GTM) on the BrainMap Community Portal. The cross-sectional (meta-analytic) model of TLE pathology was constructed using the pipeline. Nodes and edges were derived from published coordinate data reported in voxel-based morphometry and voxel-based physiology disease literature (74 TLE case-control contrasts). Coordinates were modeled as spatial probability distributions proportional to sample size using GingerALE, creating a modeled-alteration (MA) map for each experiment in the meta-analysis (Eickhoff et al., 2016). Nodes were derived by computing the union (spatial convergence) across all MA maps and identifying peaks regions of spatial convergence (Cauda et al., 2018). Edges were derived from pathology co-occurrence patterns observed within individual experiment MA maps; these patterns were computed as Patel's k (Patel et al., 2006) – a Bayesian statistic known to accurately and efficiently identify edge existence (Smith et al., 2011). Note that for the longitudinal models, the same (meta-analytically derived) nodes were used but connectivity was computed directly from primary (per-subject) rs-fMRI scans collected from TLE patients and healthy controls. This M-GTM pipeline has been containerized for use on the BrainMap Community Portal (Fox et al., 2022), an open-source High-Performance Computing environment for meta-analysis and network modeling. The pipeline now is available to the research community, ready for application to the 100+ diseases currently catalogued in the BrainMap Database.

Results: TLE networks identified cross-sectionally (case-control contrasts) were observed longitudinally in TLE, not controls (Figure 2). Two TLE modules were found meta-analytically (limbic & language networks) and present individually. The medial dorsal nucleus was the strongest hub unique to the TLE models (hubness = 0.5); other strong TLE hubs (common to both TLE models) included the hippocampus, MDN thalamus, caudate body, superior temporal gyrus, & inferior parietal lobule.

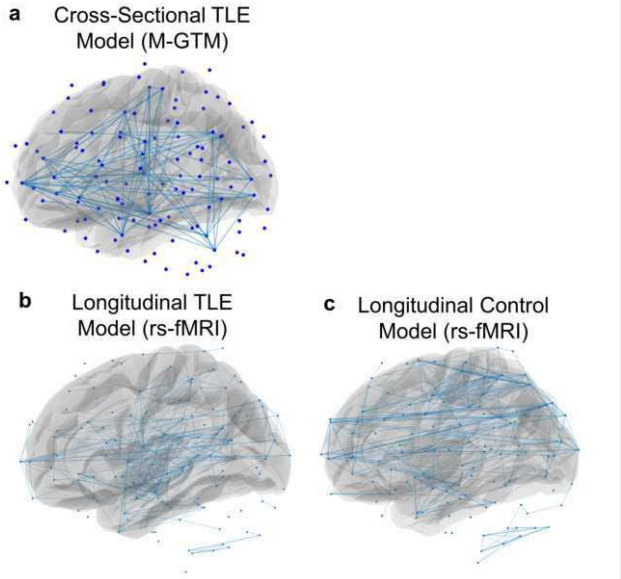

Figure 2. Ergodicity in TLE shown by meta-connectomic and connectomic graph model congruence. a, Meta-connectomic model of TLE co-alteration. **b**, Connectomic model of TLE functional connectivity at rest. **c**, Connectomic model of health functional connectivity at rest. Congruence was quantified by computing topological parameters for each model were: degree centrality, betweenness centrality, closeness centrality, eigenvector centrality, pagerank centrality, clustering coefficient, neighborhood connectivity, average shortest path length, radiality, eccentricity, stress, and topological coefficient. Hubness was quantified by normalizing all values per-metric and then averaging the normalized values (across all metrics) per-node. Clusters of network pathology (modules) were detected offline via a spectral partition method implemented in Cytoscape (Newman et al 2006).

Conclusions: Ergodicity was demonstrated in TLE. Critics purport ergodicity to imply individuals are identical. We suggest network structure is similar cross-sectionally (mean coherent structure) but exhibited ergodically over time. These results motivate the application of meta-analytic functional network models in primary data, to develop per-subject biomarkers.

References

1. Cauda, F. (2018), 'Brain structural alterations are distributed following functional, anatomic and genetic connectivity', Brain, vol. 141, no. 11, pp. 3211–3232
2. Crossley, N.A. (2013), 'Cognitive relevance of the community structure of the human brain functional coactivation network', PNAS, vol. 110, no. 28, pp. 11583–11588
3. Eickhoff, S.B. (2016), 'Behavior, sensitivity, and power of activation likelihood estimation characterized by massive empirical simulation', NeuroImage, vol. 137, pp. 70–85
4. Fox, P.T. (2022), 'BrainMap Community Portal: A Meta-Connectomics Resource', [Keynote Talk], TACCSTER22, Austin, TX
5. Newman, M.E. (2006), 'Modularity and community structure in networks', PNAS, vol. 103, no. 23, pp. 8577–8582
6. Patel, R.S. (2006), 'A Bayesian approach to determining connectivity of the human brain', Human brain mapping, vol. 27, no. 3, pp. 267–276
7. Smith, S.M. (2009), 'Correspondence of the brain's functional architecture during activation and rest', PNAS, vol. 106, no. 31, pp. 13040–13045
8. Smith S.M. (2011), 'Network modelling methods for FMRI', NeuroImage, vol 54, no. 2, pp. 875–891
9. Towne, J.M. (2023), 'BrainMap VBP: Functional Brain Pathology Recapitulates Physiology', [Poster], OHBM, Montréal, Canada
10. Vanasse, T.J. (2021), 'Brain pathology recapitulates physiology: A network meta-analysis', Communications biology, vol. 4, no. 1, pp. 301

Poster No 1909

MiDeFace: A FreeSurfer tool for Minimally Invasive DeFacing of MRI and PET data

Martin Norgaard[1,2], Liam Sennott[3], Teah Serani[3], Nathan Draudt[3], Anthony Galassi[2], Murat Bilgel[4], Cyril Pernet[5], Melanie Ganz[6,1], Douglas Greve[3]

[1]University of Copenhagen, Copenhagen, Denmark, [2]NIMH Intramural Research Program, Bethesda, MD, [3]Martinos Center for Biomedical Imaging at MGH, Boston, MA, [4]NIMH Intramural Research Program, Bethesda, MA, [5]Neurobiology Research Unit, Copenhagen, Denmark, [6]Rigshospitalet, Copenhagen, Copenhagen

Introduction: MiDeFace (https://surfer.nmr.mgh.harvard.edu/fswiki/MiDeFace) is a novel defacing pipeline developed for the FreeSurfer software suite, aimed at removing identifiable facial features from MRI[2,3]. This tool addresses the crucial need for anonymizing MRI data by removing identifiable facial features, thus protecting patient privacy without rendering the data unusable for future analyses.The tool can also be extended to deface multi-modal data (such as PET), allowing for specialized applications to be built for specific multi-modal imaging data.

Methods: The MiDeFace workflow uses the Sequence Adaptive Multimodal Segmentation (SAMSEG) pipeline available in FreeSurfer to segment the entire head, including the skull and eyeballs[1,5]. MiDeFace also uses a surface-based face atlas, where critical facial features (eyes, nose, mouth, cheeks, chin, ears) are labeled and minimally removed in a manner that is hard to reverse (i.e. not able to de-identify). The defacing process includes inward and outward projection of the atlas face, respecting the labeling of the brain and skull.

Results: The MiDeFace defacing pipeline applies random intensity correction within the bounds of the true data's mean and standard deviation, effectively removing the facial surface while retaining statistical similarity (Figure 1). A study involving 41 subjects demonstrated that MiDeFace's defacing workflow, when compared with unaltered FreeSurfer analyses, showed no significant differences in regions of interest, except a minor reduction (0.1%) in estimated intracranial volume. MiDeFace takes less than 8 minutes to run per subject. Finally, MiDeFace can also be extended to multi-modal data applications, such as PETDeface, a BIDS application for removing facial features in PET data (https://github.com/openneuropet/petdeface)[4].

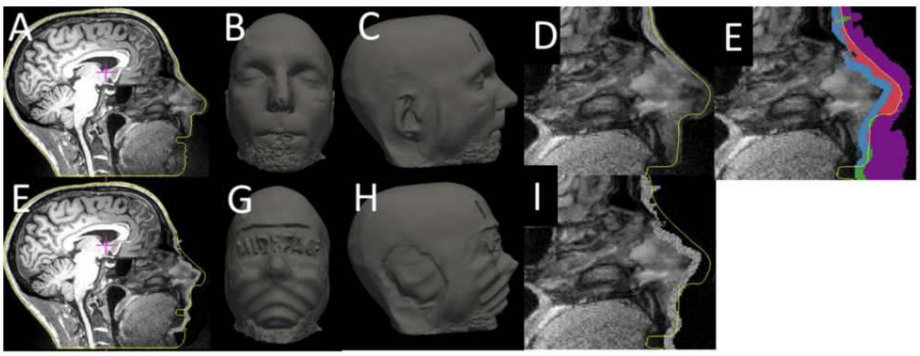

Figure 1: overview of the MiDeFace pipeline showing how the MRI data is first segmented to generate a model of the face, and then subsequently modeled and segmented to minimally remove the outer surfaces of the face.

Conclusions: MiDeFace efficiently anonymizes neuroimaging data, and provides a robust solution for privacy concerns in medical imaging. Its integration into FreeSurfer, along with its capability to work across multiple modalities and create masks applicable to various volumes, makes it a versatile and essential tool for researchers requiring anonymous imaging data while preserving the utility for subsequent neuroimaging analyses.

References

1. Cerri, S. (2023), An open-source tool for longitudinal whole-brain and white matter lesion segmentation, NeuroImage: Clinical, Volume 38, 103354, ISSN 2213-1582, https://doi.org/10.1016/j.nicl.2023.103354.
2. Dale A (1999). Cortical Surface-Based Analysis: I. Segmentation and Surface Reconstruction. Neuroimage. 9(2):179–94. doi:10.1006/nimg.1998.0395.
3. Fischl B. (2012) FreeSurfer. Neuroimage. 15;62(2):774-81. doi: 10.1016/j.neuroimage.2012.01.021. Epub 2012 Jan 10. PMID: 22248573; PMCID: PMC3685476.
4. Gorgolewski, Krzysztof J. (2016). Nipype: a flexible, lightweight and extensible neuroimaging data processing framework in Python. 0.12.0-rc1. Zenodo. 10.5281/zenodo.50186
5. Puonti, O., (2016). NeuroImage Fast and sequence-adaptive whole-brain segmentation using parametric Bayesian modeling. NeuroImage, 143, 235–249. https://doi.org/10.1016/j.neuroimage.2016.09.011

Poster No 1910

Independent VIP: Unveiling spatial patterns in resting-state functional MRI networks

Vaibhavi Itkyal[1], Theodore LaGrow[2], Anees Abrol[3], Vince Calhoun[4]

[1]Emory University, Decatur, GA, [2]Georgia Institute of Technology, Beaverton, OR, [3]Georgia State University, Atlanta, GA, [4]GSU/GATech/Emory, Decatur, GA

Introduction: This study addresses the imperative need for accurate early diagnosis of Alzheimer's Disease (AD) by exploring the synergies between structural magnetic resonance imaging (sMRI) and resting-state functional magnetic resonance imaging (rs-fMRI). The novel approach integrates rs-fMRI networks which are computed using independent component analysis followed by voxelwise intensity projections (i.e., iVIP), with sMRI, surpassing traditional metrics like amplitude of low-frequency fluctuations (ALFF) and fractional ALFF (fALFF). Inspired by AlexNet, a multi-channel convolutional neural network effectively captures both spatial and temporal dependencies, achieving a 93.31% test accuracy and a 97.79 AUC score on the classification task of AD vs cognitively normal (CN) from the Alzheimer's Disease Neuroimaging Initiative (ADNI) dataset. Our multimodal deep learning results outperform unimodal approaches, highlighting crucial differences in neurobiologically relevant regions. Saliency visualizations emphasize distinctions in the hippocampus, amygdala, caudate nucleus, and thalamus, aligning with existing literature. This innovative multimodal deep learning model validated on publicly available data demonstrates superior diagnostic performance, offering valuable insights into AD-related alterations through spatiotemporal information integration.

Methods: We used ADNI data, comprising sMRI and rs-fMRI scans from 466 subjects, including 383 CN and 83 AD individuals. The rigorous preprocessing includes spatial normalization, tissue segmentation, and transformations using SPM 12, with stringent quality control measures applied. The fMRI preprocessing involves motion correction, slice-timing correction, standardization to MNI space, resampling, and Gaussian smoothing. All pre-processing information for this dataset can be found in Du et al. 2020. Spatially constrained independent component analysis generated 53 intrinsic connectivity networks (ICNs) using Neuromark (Du et al. 2020), from which independent voxelwise intensity projection images (iVIPs) are computed. These iVIPs, representing max, abs min, and max abs of ICNs, serve as input for a specialized 3D multimodal deep learning architecture inspired by AlexNet (Abrol et al. 2021; Krizhevsky, Sutskever, and Hinton 2017). The model, operating on rs-fMRI or sMRI data, captures spatial patterns through convolutional layers, adaptive pooling, and dropout for classification. The study achieves a 93.31% test accuracy in discriminating AD and CN, surpassing traditional metrics like ALFF (Turner et al. 2013) and fALFF. Training and saliency maps, generated through guided backpropagation, provide insights into the model's decision-making processes. We did 8-fold cross-validation and used Adam algorithm.

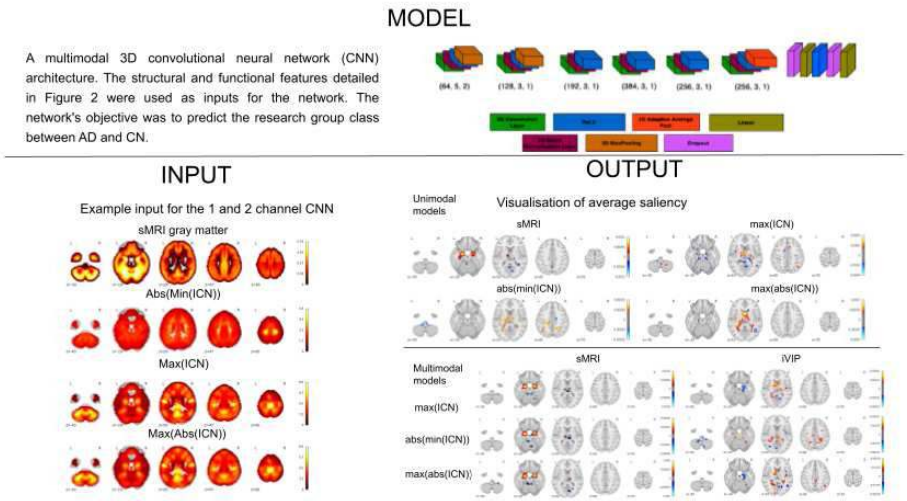

Figure 1: Representation of input which involves the processed sMRI gray matter maps and rs-fMRI iVIPs as max(ICN), abs(min(ICN)), max(abs(ICN)). The model is the modified or adapted version of AlexNet and the outputs are the saliency visualisations after thresholding for unimodal and multimodal models. The multimodal model was a 2-channel 3D CNN with one channel as sMRI and the other as one of the iVIP.

Results: iVIP compared to traditional metrics like ALFF/fALFF, iVIP exhibits quantitative superiority in test accuracy and balanced accuracy, particularly excelling in two-way classification with max(ICN) and max(abs(ICN)). Deep learning models based on iVIP outperform those derived from ALFF/fALFF, achieving an 85.02% peak test accuracy for AD vs CN. Combining sMRI and iVIP in a multimodal model (sMRI + iVIP) achieves the highest accuracy at 93.31%, surpassing unimodal models. Saliency maps highlight distinct spatial patterns, with sMRI emphasizing the hippocampus, amygdala, and caudate nucleus, while max(ICN) reveals variations in the cingulate cortex, thalamus, and caudate nucleus. These findings provide valuable

insights into AD-related brain alterations, emphasizing the synergistic benefits of multimodal approaches in neuroimaging studies (Abbott et al. 2014; Wang et al. 2016; Lee et al. 2020).

Evaluating the predictive performance of iVIP against the established ALFF and fALFF computations in the context of the rs-fMRI dataset

Two-way classification (AD vs CN)			
Different fMRI measures	**Test Accuracy**	**Balanced Test Accuracy**	**AUC**
ALFF	80.25 ± 0.35	64.44 ± 1.6	70.01 ± 0.19
fALFF	80.8 ± 0.5	60.71 ± 3.5	71.96 ± 0.3
max(ICN)	84.81 ± 0.2	71.6 ± 0.95	**83.58 ± 0.53**
abs(min(ICN))	84.05 ± 0.18	66.6 ± 0.63	79.69 ± 0.29
max(abs(ICN))	**85.02 ± 0.17**	71.47± 0.64	83.4 ± 0.49

Quantitative performance for the two-way classification experiment (AD vs CN) with 466 subjects. Note the sMRI + iVIP indicates the multimodal model with each of these modalities used as two different channels in 3D CNN.

	Test Accuracy	**Balanced Test Accuracy**	**AUC**
sMRI	91.18 ± 0.13	86.36 ± 0.69	96.26 ± 0.09
sMRI + **max(ICN)**	91.88 ± 0.18	84.28 ± 0.9	96.88 ± 0.08
sMRI + **abs(min(ICN))**	**93.31 ± 0.11**	88.43 ± 0.67	97.11 ± 0.1
sMRI + **max(abs(ICN))**	91.81 ± 0.25	83.23 ± 1.03	95.59 ± 0.15

Conclusions: The study integrates iVIP with sMRI into a 3D CNN, achieving 93.31% accuracy for early AD diagnosis, surpassing traditional metrics - ALFF/fALFF. Our multimodal approach provides insights into neurobiological changes, emphasizing its potential for effective clinical strategies in AD diagnosis and intervention.

References

1. Abbott, C. C., T. Jones, N. T. Lemke, P. Gallegos, S. M. McClintock, A. R. Mayer, J. Bustillo, and V. D. Calhoun. 2014. "Hippocampal Structural and Functional Changes Associated with Electroconvulsive Therapy Response." Translational Psychiatry 4 (11): e483–e483. https://doi.org/10.1038/tp.2014.124.
2. Abrol, Anees, Zening Fu, Mustafa Salman, Rogers Silva, Yuhui Du, Sergey Plis, and Vince Calhoun. 2021. "Deep Learning Encodes Robust Discriminative Neuroimaging Representations to Outperform Standard Machine Learning." Nature Communications 12 (1): 353. https://doi.org/10.1038/s41467-020-20655-6.
3. Du, Yuhui, Zening Fu, Jing Sui, Shuang Gao, Ying Xing, Dongdong Lin, Mustafa Salman, et al. 2020. "NeuroMark: An Automated and Adaptive ICA Based Pipeline to Identify Reproducible fMRI Markers of Brain Disorders." NeuroImage: Clinical 28 (January): 102375. https://doi.org/10.1016/j.nicl.2020.102375.
4. Krizhevsky, Alex, Ilya Sutskever, and Geoffrey E. Hinton. 2017. "ImageNet Classification with Deep Convolutional Neural Networks." Communications of the ACM 60 (6): 84–90. https://doi.org/10.1145/3065386.
5. Lee, Pei-Lin, Kun-Hsien Chou, Chih-Ping Chung, Tzu-Hsien Lai, Juan Helen Zhou, Pei-Ning Wang, and Ching-Po Lin. 2020. "Posterior Cingulate Cortex Network Predicts Alzheimer's Disease Progression." Frontiers in Aging Neuroscience 12. https://www.frontiersin.org/articles/10.3389/fnagi.2020.608667.
6. Turner, Jessica, Eswar Damaraju, Theo Van Erp, Daniel Mathalon, Judith Ford, James Voyvodic, Bryon Mueller, et al. 2013. "A Multi-Site Resting State fMRI Study on the Amplitude of Low Frequency Fluctuations in Schizophrenia." Frontiers in Neuroscience 7. https://www.frontiersin.org/articles/10.3389/fnins.2013.00137.
7. Wang, Zhiqun, Min Zhang, Ying Han, Haiqing Song, Rongjuan Guo, and Kuncheng Li. 2016. "Differentially Disrupted Functional Connectivity of the Subregions of the Amygdala in Alzheimer's Disease." Journal of X-Ray Science and Technology 24 (2): 329–42. https://doi.org/10.3233/XST-160556.

Poster No 1911

Rsbids: Rapid Indexing of BIDS Datasets with Rust

Peter Van Dyken[1], Mohamed Yousif[1], Ali Khan[2]

[1]Schulich School of Medicine and Dentistry, London, Ontario, [2]University of Western Ontario, London, Ontario

Introduction: The general adoption of the Brain Imaging Data Structure (BIDS) specification (Gorgolewski et al., 2016) has enabled a robust ecosystem of neuroimaging apps that process BIDS formatted datasets (Gorgolewski et al., 2017). Common to these apps is an indexer that reads and parses the dataset files and returns desired files in response to queries. pybids has been the de facto standard library for this purpose (Yarkoni et al., 2019), but is limited by slow runtime, a problem especially evident on large datasets (indexing a 100,000 file dataset can take several minutes). This creates a computational bottleneck for downstream apps and hampers interactive programming. Previous attempts to address this problem, notably ancpbids and bids2table, were also written in Python, fundamentally limiting their speed. To overcome this limitation, we developed rsbids,

a BIDS indexer written in the Rust programming language. Unlike Python, Rust is compiled and can achieve speeds equal to or greater than that of C++ libraries. Unlike C++, rust libraries are relatively easy to compile and the compiler enforces memory safety, making them easier to write and maintain (Bugden & Alahmar, 2022). rsbids can be installed from PyPI and seamlessly used in Python programs. It has a pybids compatible API, allowing its use as a drop-in pybids replacement. Here, we compare the performance of rsbids to previously developed BIDS indexers.

Methods: Benchmarks were measured using the HBN EO/EC task dataset (LM et al., 2022), composed of 177,065 files and available on OpenNeuro. All benchmarks were calculated on a CentOS Linux 7 system with x86_64 architecture, an Intel(R) Xeon(R) CPU E5-2683 v4 @ 2.10GHz, a locally mounted SSD drive, and CPython 3.11.2. Where possible, rsbids was compared to pybids, ancpbids, and bids2table across four tasks, excluding tools from tasks they could not perform. First, the dataset was indexed without metadata (file names were read and parsed, but JSON-sidecar files were not read, bids2table excluded). Second, the dataset was indexed with metadata (as the previous task, but additionally indexing metadata in JSON-sidecar files, ancpbids excluded). Third, a single subject was queried from the indexed dataset (retrieving all the files associated with that subject). Fourth, 14 subjects, one run, and one suffix were queried from the indexed dataset (retrieving all files associated with the intersection of entity values). Benchmarks were measured as the average of five replicates.

Results: When indexing without metadata, rsbids completed in 1.59 s, compared to 30.59 s for ancpbids and 45.80 s for pybids. When metadata was included, rsbids took 11.22 s, compared to 104.2 s for bids2table and 294.7 s for pybids. When indexing a single subject, rsbids took 13.1 ms, slightly slower than bids2table at 7.41 ms, but faster than pybids and ancpbids at 383 ms and 4,300 ms respectively. In the complex query, however, rsbids outperformed all other apps, with 15.1 ms compared to 399 ms for bids2table, 188 ms for pybids, and 40,000 ms for ancpbids.

Fig. Runtime of four BIDS indexing apps in indexing and querying tasks

Conclusions: rsbids achieved 10 - 35-fold speed gains for dataset indexing compared to other libraries. Querying was also generally faster than other libraries, especially ancpbids. Notably, although bids2table was slightly faster querying a single subject, its benchmark was negatively impacted in large queries, unlike rsbids, whose benchmark was relatively unaffected. rsbids is currently in an alpha release and yet to implement the dataset validation supported by pybids. This, along with testing, documentation, and configurability, will be emphasized in the next stages of development. Yet, even at this early stage, rsbids demonstrates it can relieve the indexing bottleneck even for very large datasets, giving it a promising future as the standard bids indexing library.

References

1. Bugden, W. (2022). Rust: The Programming Language for Safety and Performance. arXiv.
2. Gorgolewski, K. J. (2017). BIDS apps: Improving ease of use, accessibility, and reproducibility of neuroimaging data analysis methods. PLOS Computational Biology, 13(3), e1005209.
3. Gorgolewski, K. J. (2016). The brain imaging data structure, a format for organizing and describing outputs of neuroimaging experiments. Scientific Data, 3(1), 160044.
4. LM, A. (2022). HBN EO/EC task. OpenNeuro.
5. Yarkoni, T. (2019). PyBIDS: Python tools for BIDS datasets. Journal of Open Source Software, 4(40), 1294.

Poster No 1912

Network Level Analysis Toolbox for connectome-wide association studies

Muriah Wheelock[1], Ari Segel[1], Andrew Eck[1], Donna Dierker[1], Jim Pollaro[1], Hong Chen[1], Adam Eggebrecht[2]

[1]Washington University in St. Louis, St. Louis, MO, [2]Washington University School of Medicine, St. Louis, MO

Introduction: Determining the mechanisms by which the brain generates cognition, perception, and emotion hinges upon quantifying the relationships between coordinated brain activity and behavior. These brain-behavior association analyses typically consist of several thousand statistical tests which poses a challenge for controlling the false discovery rate. While contemporary connectome research views the brain as an extensive, complex network of non-adjacent, yet functionally and structurally connected brain regions, standard voxel extent cluster correction approaches do not utilize the spatial topology of brain networks when estimating cluster size significance (Friston et al., 1994). Similarly, an edge level Bonferroni or FDR correction on connectomes with thousands of potential connections is unlikely to yield significant findings (Greene et al., 2016). Limited prior work has leveraged the hierarchical network structure of the brain to probe connectome associations with behavior using a variety of statistical approaches (Noble et al., 2022; Sripada et al., 2020). However, a unified, standardized, extensible, and flexible software suite is lacking. Network Level Analysis (NLA) software fills this gap by offering a standardized toolkit that incorporates the hierarchical network structure of the brain to quantify connectome-wide associations with behavior.

Methods: NLA is an extensible MATLAB based software package for the analysis of behavioral associations with brain connectivity data including functional, structural, or task connectivity. NLA utilizes a model-based statistical approach known variously as 'pathway analysis', 'over-representation analysis', or 'enrichment analysis', which was first used to describe behavioral or clinical associations in genome-wide association studies (Subramanian et al. 2005). In this way, NLA diverges from most contemporary tools either focusing on single connection associations (Marek et al., 2022) or cluster correction (Friston et al., 1994; Zalesky et al., 2010). By organizing connectivity-behavior associations according to an a priori model of underlying neurobiology (i.e., systems or networks), NLA leverages the structure of the human connectome and provides a framework for rational interpretation and replication of findings across research methodologies. Finally, the integration of connectome analysis and visualization techniques within a single, extensible MATLAB-based pipeline makes NLA a powerful tool for statistical testing and production of publication quality images all in one package (Figure 1A).

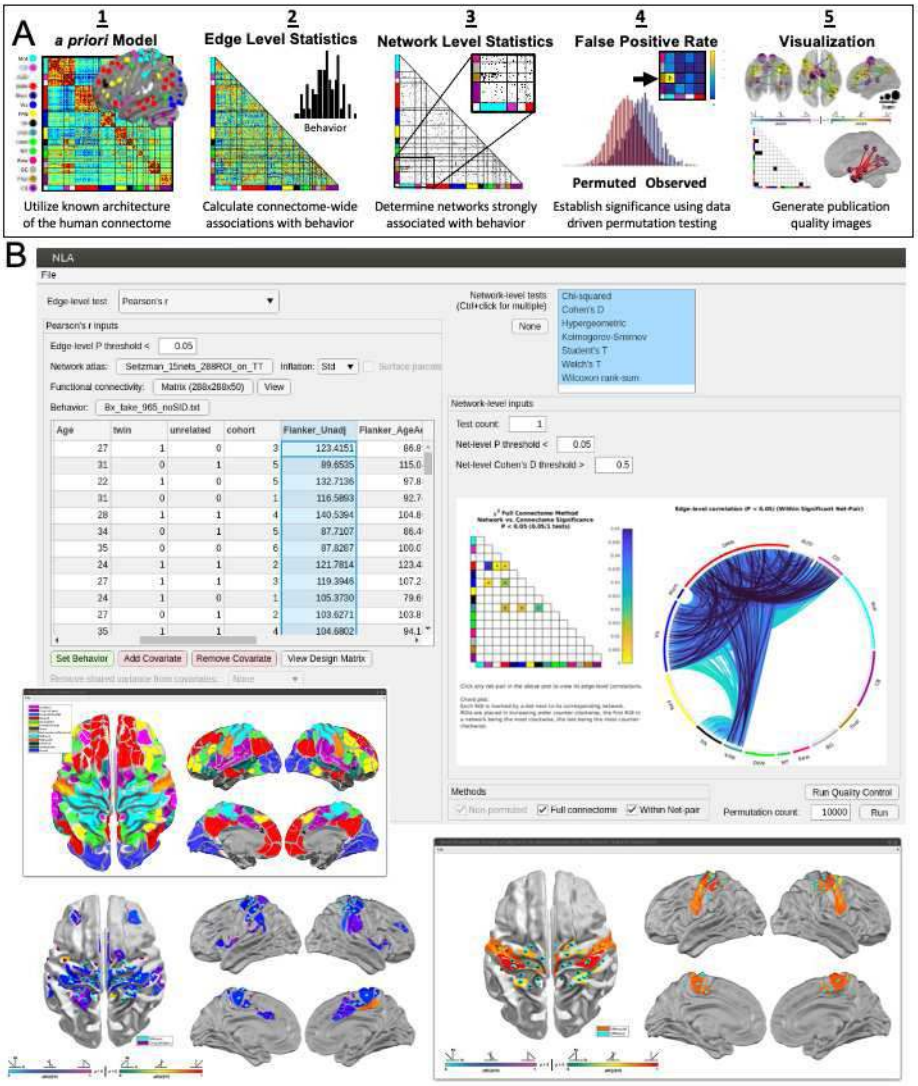

Figure 1. Network Level Analysis (NLA) Toolbox . A) NLA pipeline for analyzing connectome-wide associations with behavior. B) The graphical user interface includes built in diagnostic quality control plots, edge and network level statistical tests, permutation testing, and visualization options including network significance matrix, network level and edge level chord plots, and surface plots.

Results: To date, NLA has been used in several connectome-wide association studies spanning brain development to degeneration (Eggebrecht et al., 2017; Wheelock et al., 2019; Wheelock et al., 2023). Recently, we have developed a graphical user interface to increase accessibility (Figure 1B). We have significantly expanded the number of edge and network level statistical options, included additional quality control diagnostic plots, and incorporated many standard areal and system parcellation atlases (e.g., Schaefer, Gordon, Power, etc.).

Conclusions: The NLA toolbox is a versatile analysis pipeline which leverages the structural and functional architecture of the brain in combination with rigorous statistical testing and validation procedures that can define brain-behavior relationships across species, across the lifespan, and in health and disease. Importantly, NLA uses data-driven permutation testing that respects the underlying covariance structure of connectivity data and leverages the fundamental topological structure of the connectome, affording whole-brain analyses while negating the need for punitive statistical thresholds.

References

1. Friston, K. J., Worsley, K. J., Frackowiak, R. S. J., Mazziotta, J. C. & Evans, A. C. Assessing the significance of focal activations using their spatial extent: Assessing Focal Activations by Spatial Extent. Hum Brain Mapp 1, 210–220 (1994). 34 1.
2. Greene, D. J., Church, J. A., Dosenbach, N. U., Nielsen, A. N., Adeyemo, B., Nardos, B., . . . Schlaggar, B. L. (2016). Multivariate pattern classification of pediatric Tourette syndrome using functional connectivity MRI. Dev Sci, 19(4), 581-598. doi:10.1111/desc.12407
3. Noble, S., Mejia, A. F., Zalesky, A., & Scheinost, D. (2022). Improving power in functional magnetic resonance imaging by moving beyond cluster-level inference. Proc Natl Acad Sci U S A, 119(32), e2203020119. doi:10.1073/pnas.2203020119
4. Sripada, C., Rutherford, S., Angstadt, M., Thompson, W. K., Luciana, M., Weigard, A., . . . Heitzeg, M. (2020). Prediction of neurocognition in youth from resting state fMRI. Mol Psychiatry, 25(12), 3413-3421. doi:10.1038/s41380-019-0481-6

5. Subramanian, A. Gene set enrichment analysis: A knowledge-based approach for interpreting genomewide expression profiles. Proc Natl Acad Sci 102, 15545–15550 (2005).
6. Marek, S., Tervo-Clemmens, B., Calabro, F. J., Montez, D. F., Kay, B. P., Hatoum, A. S., . . . Dosenbach, N. U. F. (2022). Reproducible brain-wide association studies require thousands of individuals. Nature, 603(7902), 654-660. doi:10.1038/s41586-022-04492-9
7. Zalesky, A., Fornito, A. & Bullmore, E. T. Network-based statistic: Identifying differences in brain networks. NeuroImage 53, 1197–1207 (2010).
8. Eggebrecht, A. T., Elison, J. T., Feczko, E., Todorov, A., Wolff, J. J., Kandala, S., . . . Pruett, J. R., Jr. (2017). Joint Attention and Brain Functional Connectivity in Infants and Toddlers. Cerebral Cortex, 27(3), 1709-1720. doi:10.1093/cercor/bhw403
9. Wheelock, M. D., Hect, J. L., Hernandez-Andrade, E., Hassan, S. S., Romero, R., Eggebrecht, A. T., & Thomason, M. E. (2019). Sex differences in functional connectivity during fetal brain development. Dev Cogn Neurosci, 36, 100632. doi:10.1016/j.dcn.2019.100632
10. Wheelock, M. D., Strain, J. F., Mansfield, P., Tu, J. C., Tanenbaum, A., Preische, O., . . . Dominantly Inherited Alzheimer, N. (2023). Brain network decoupling with increased serum neurofilament and reduced cognitive function in Alzheimer's disease. Brain, 146(7), 2928-2943. doi:10.1093/brain/awac498

Poster No 1913

Speed-up pFIC: Deep learning accelerated inversion of parametric feedback inhibition control model

Tianchu Zeng[1], Shaoshi Zhang[1], Fang Tian[2], B. T. Thomas Yeo[1]

[1]National University of Singapore, Singapore, Singapore, [2]National University of Singapore, National University of Singapore, Singapore

Introduction: The efficacy of neural mass models in capturing the neural dynamics is well-established[8]. Prior works[5,8] optimized model parameters by using Covariance Matrix Adaptation Evolution Strategy (CMA-ES) algorithm[4] with forward simulation via Euler integration, referred to as parametric feedback inhibition control model (pFIC). However, pFIC requires solving ordinary differential equations (ODE) for each cortical region simultaneously and each time step sequentially, posing a computational hurdle for model inversion. To tackle this, we propose speed-up pFIC (supFIC) by integrating deep learning to neural mass model framework, leading to a 1500% speed-up of parameter optimization process.

Methods: We use CMA-ES to iteratively optimize local circuit parameters. It starts with sampling several candidate parameters from a Gaussian distribution. Simulated fMRI data are generated by running forward simulations with candidate parameters and structural connectivity (SC) matrices[1]. Evaluation of candidate parameters depends on the agreement between the empirical and simulated static functional connectivity (FC) and FC dynamics (FCD)[3]. We quantify the agreement between empirical and simulated FC using Pearson's correlation (r) and absolute difference between the means (d), as well as empirical and simulated FCD using KS statistics (KS). Parameters with the minimum loss, defined as (1-r)+d+KS, are used to initialize candidate parameters for the next iteration. Our supFIC addresses the computational bottleneck associated with slow forward simulation by utilizing deep learning. To this end, 2 deep networks are trained, including a classifier and a predictor. Only the predictor(Fig 1A) is shown due to their similar network architectures. The classifier determines whether the inputs generate fMRI data within the firing rate range constraints, while the predictor directly generates the loss between simulated and empirical matrices bypassing the process of solving the system ODE, thus speeding up the parameter optimization process. The pFIC was used to generate the ground-truth parameters to train the deep networks and evaluate their performance. After training, we adopt a hybrid procedure to optimize local circuit parameters, which consists of ~67% iterations of deep learning optimization followed by ~33% iterations of forward simulation via Euler integration. The deep learning process speeds up the optimization procedure by 300% while the Euler integration improves the stability of the optimized parameters. To further validate supFIC, we compared its model performance with pFIC using HCP dataset[2,7] and replicated our prior findings on excitation/inhibition ratio (E/I ratio) using a developmental dataset[6].

Results: The loss predicted by supFIC is close to ground-truth loss (r>0.8)(Fig 1B). Furthermore, we compare the 10 sets of parameters with the lowest loss in HCP dataset to that of pFIC. We show supFIC can numerically perform better than pFIC while only using 1 random initialization instead of 5, as originally proposed by pFIC(Fig 2A). This is equivalent to a 1500% (300% x 5) speed-up of parameter optimization process. We then validate supFIC by replicating our previous findings on excitation/inhibition ratio (E/I ratio)[8] using the Philadelphia Neurodevelopment Cohort (PNC) dataset[6]. Like our previous results, E/I ratio decreases during development(Fig 2B) with sensory regions displaying a faster reduction compared to association regions(Fig 2C). After matching the age(Fig 2D left), E/I ratio is significantly lower for high-performance groups compared to low-performance groups(Fig 2D right). E/I ratio differences are more pronounced in association regions than in sensory regions(Fig 2E).

Conclusions: Overall, supFIC substantially accelerates model inversion without sacrificing performance. More importantly, our model replicates prior findings regarding E/I ratio. This opens the possibility to study neural mass model with higher spatial and temporal resolutions.

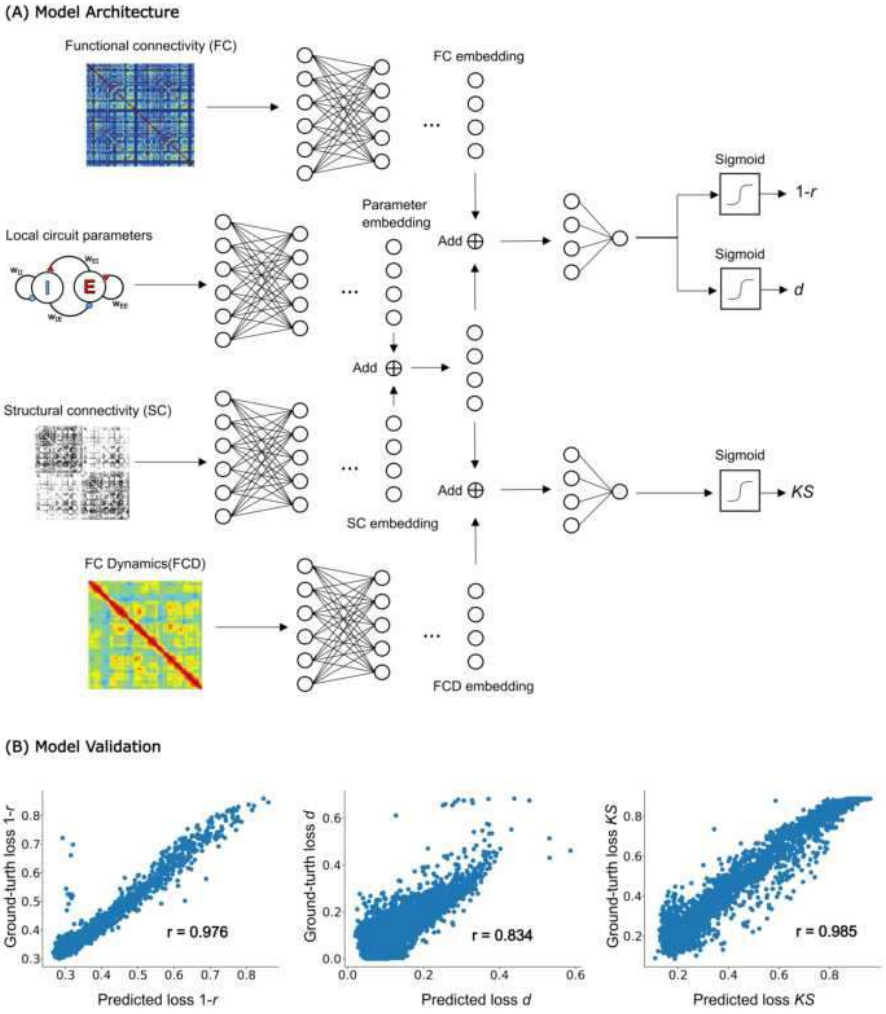

Figure 1. Model architecture and validation. **(A)** Model overview of the predictor. The inputs to this model are local circuit parameters, structural connectivity, static and dynamic functional connectivity. We add these embeddings to predict the disagreement between empirical and simulated fMRI data. We quantify the agreement between empirical and simulated FC using Pearson's correlation (*r*) and absolute difference between the means (*d*), as well as empirical and simulated FCD using KS statistics (*KS*). **(B)** Model evaluation. The plots show the model performance on one example test set. The horizontal axis shows the predicted loss, while the vertical axis shows the ground-truth loss. The overall correlation between the predicted and ground-truth loss are around 0.9 despite the instability at the bottom-left corner.

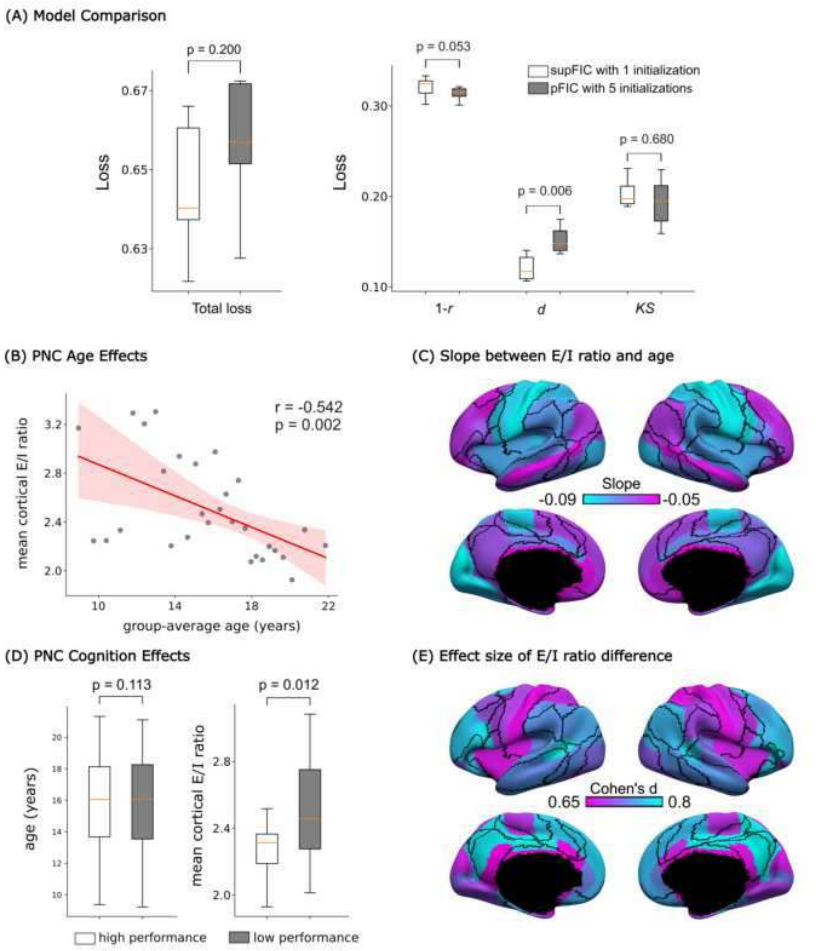

Figure 2. Model evaluations. **(A)** (Left) The total test loss (the sum of 1-*r*, *d* and *KS*) comparison between supFIC and pFIC. Each box plot shows the 10 minimum validation losses corresponding to the best 10 sets of local circuit parameters. supFIC with only 1 random initialization can achieve better numerical results than pFIC with 5 random initializations. (Right) Comparison between supFIC and pFIC for each individual loss term. Overall, supFIC shows comparable performance with the pFIC. **(B)** We utilized Philadelphia Neurodevelopment Cohort (PNC) dataset to study the E/I ratio changes during development. Participants were divided into 29 non-overlapping age groups. Groups with older age exhibited lower E/I ratio ($r = -0.542$, $p = 0.002$). **(C)** Spatial distribution of linear regression slope between regional E/I ratio and age. The values represent the rate of E/I ratio changes during development. All slopes were negative and significant (FDR $q < 0.05$). **(D)** (Left) Boxplots of age (Right) mean cortical E/I ratio of high-performance and low-performance (overall accuracy) groups with 14 subgroups each. The mean cortical E/I ratio of the high-performance group was significantly lower than that of the low-performance group ($p=0.012$). **(E)** Spatial distribution of effect size of regional E/I ratio difference between high-performance and low-performance groups.

References

1. Deco, G., Ponce-Alvarez, A., Hagmann, P., Romani, G. L., Mantini, D., & Corbetta, M. (2014). How local excitation-inhibition ratio impacts the whole brain dynamics. Journal of Neuroscience, 34(23), 7886–7898. https://doi.org/10.1523/JNEUROSCI.5068-13.2014
2. Glasser, M. F., Sotiropoulos, S. N., Wilson, J. A., Coalson, T. S., Fischl, B., Andersson, J. L., Xu, J., Jbabdi, S., Webster, M., Polimeni, J. R., Van Essen, D. C., & Jenkinson, M. (2013). The minimal preprocessing pipelines for the Human Connectome Project. NeuroImage, 80, 105–124. https://doi.org/10.1016/j.neuroimage.2013.04.127
3. Hansen, E. C. A., Battaglia, D., Spiegler, A., Deco, G., & Jirsa, V. K. (2015). Functional connectivity dynamics: Modeling the switching behavior of the resting state. NeuroImage, 105, 525–535. https://doi.org/10.1016/j.neuroimage.2014.11.001
4. Hansen, N. (2006). The CMA Evolution Strategy: A Comparing Review. In J. A. Lozano, P. Larrañaga, I. Inza, & E. Bengoetxea (Eds.), Towards a New Evolutionary Computation (Vol. 192, pp. 75–102). Springer Berlin Heidelberg. https://doi.org/10.1007/3-540-32494-1_4
5. Kong, X., Kong, R., Orban, C., Wang, P., Zhang, S., Anderson, K., … Yeo, B. T. T. (2021). Sensory-motor cortices shape functional connectivity dynamics in the human brain. Nature Communications, 12(1). https://doi.org/10.1038/s41467-021-26704-y
6. Satterthwaite, T. D., Elliott, M. A., Ruparel, K., Loughead, J., Prabhakaran, K., Calkins, M. E., … Gur, R. E. (2014). Neuroimaging of the Philadelphia neurodevelopmental cohort. NeuroImage, 86, 544–553. https://doi.org/10.1016/J.NEUROIMAGE.2013.07.064
7. Van Essen, D. C., Smith, S. M., Barch, D. M., Behrens, T. E. J., Yacoub, E., & Ugurbil, K. (2013). The WU-Minn Human Connectome Project: An overview. NeuroImage, 80, 62–79. https://doi.org/10.1016/j.neuroimage.2013.05.041
8. Zhang, S., Larsen, B., Sydnor, V. J., Zeng, T., An, L., Yan, X., … & Yeo, B. T. (2023). In-vivo whole-cortex estimation of excitation-inhibition ratio indexes cortical maturation and cognitive ability in youth. bioRxiv, 2023-06.

Poster No 1914

CINDERELLA: Computerised INference and DERivation of MRI sequence Linguistic Labelling Algorithm

Ivar Wamelink[1], Joost Kuijer[1], Vera Keil[1], Frederik Barkhof[2], Alle Meije Wink[2]

[1]Amsterdam University Medical Centre, Amsterdam, Netherlands, [2]Amsterdam University Medical Centre, Amsterdam, Noord-Holland

Introduction: Identifying the scanning protocol of MR DICOM datasets by their series descriptions is problematic for two reasons: names for the same sequence may vary between vendors and the series description is a free-form text field prone to inconsistencies. Recent attempts at automatic protocol detection rely on machine learning of image intensities or DICOM header fields. [van der Voort et al., 2021; Bartnik et al., 2023]. This project aims to extract the protocol by exclusively comparing a minimal set of DICOM fields representing common acquisition parameters. Our motivations are that relying on pixel intensities is (i) computationally costly, (ii) will misclassify faulty scans, and (iii): non-acquisition parameters may vary between vendors, institutes, field strengths and software versions. We describe the implementation of our system and demonstrate its performance in a multi-site, multi-vendor, multi-sequencs imaging study.

Methods: Our in-house database contains 206,769 series of 12,712 different scan sessions of 1,384 subjects from scanners of 4 vendors (162 different software versions among all vendors) and with different field strengths (GE: 1.5T and 3T; Siemens: 1T, 1.5T, 3T; Philips: 0.5T, 1T, 1.5T, 3T; Toshiba: 1.5T, 3T). Seven common acquisition-specific DICOM fields were extracted: FieldStrength, EchoTime, FlipAngle, RepetitionTime, InversionTime, DiffusionBValue, and Contrast. We used a manual iterative process guided by expertise to create a vendor and field strength-specific database that could automatically label 16 sequence types (figure 1): 3D FLAIR, 2D FLAIR, 3D T1, 3D T1c, 2D T2, 2D dual-echo T2, DWI, 2D T1, 2D T1c, DSC, SWI, B0, B1, ASL, APT-CEST, and fMRI. Parameters were either matched to values from a set (e.g., vendors) or within a numerical range (e.g., echo time). The selected sequence was the one meeting all parameter criteria. Figure 1 illustrates the iterative process of creating the label database. The protocol identification script was run on our in-house data set and did not classify derived series such as MPR. Correct identification was based on expert comparison of the predicted standardised label with the series description.

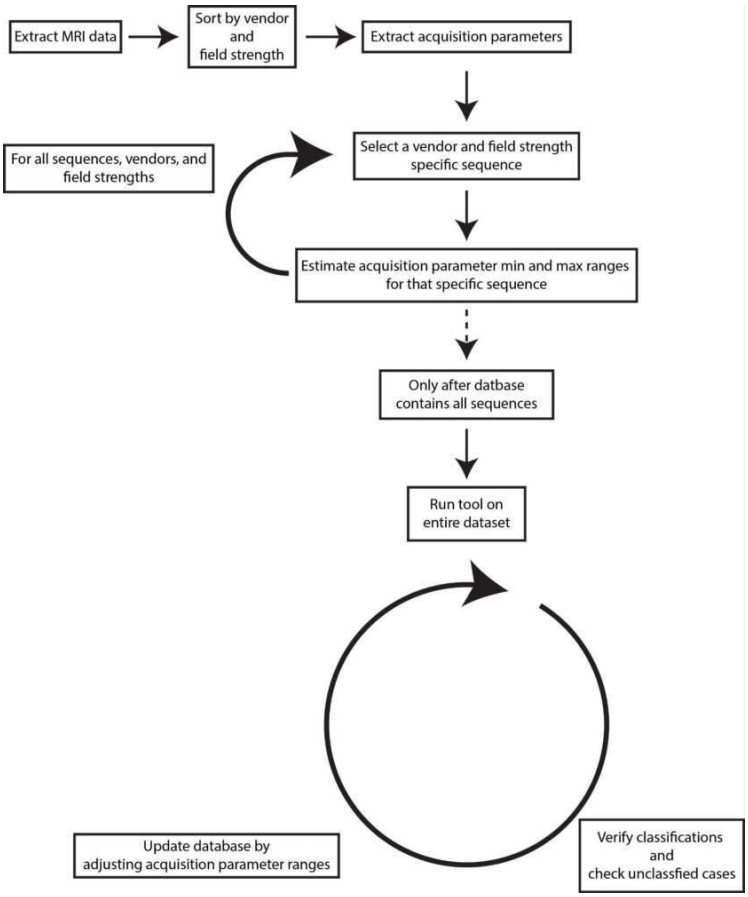

Figure 1. Flowchart that shows the iterative steps for creating the acquisition parameter database fo 16 sequence types.

Results: For our in-house imaging data set, the outcomes were: - Of the total of 206,769 series, 97,748 series were derivatives, e.g. multiplanar reformation (MPR) - Out of the remaining 109,021 series, 89,462 were classified - the remaining 19,559 did not meet the 7 acquisition parameter criteria The majority of this latter group were preparation sequences such as scout (localiser) or calibration scans (12,160), as well as sequences that have not yet been added to the database, such as 3D T2-weighted scans and time of flight angiography. In some cases, the classification by our algorithm did not correspond to the series description. These series turned out to be slices from different acquisitions that had erroneously got the same series identifier. Based on the series description, the algorithm was 99.69%, 99.99% and 94.43% accurate for contrast-enhanced 3D T1-weighted scans, 3D FLAIR, and T2-weighted scans, respectively.

Echo time (TE)	Flip angle	Inversion time (TI)	Repetition time (TR)	Magnetic field strength	manufacturer	diffusion	Series description	Standardised name
3001	12	n/a	7	3	Philips		T13Ddis	3D_T1
4586	8	n/a	9.715	1.5	Philips		3DT1TFE iso	3D_T1
3.04	15	1100	2700	1.5	Siemens		t1_mpr_ns_sag	3D_T1
8	80	n/a	550	3	Toshiba		T1wi ax SE	2D_T1
12	90	n/a	463	1.5	Siemens		T1_SE_SAG	2D_T1
14	90	n/a	620	1.5	GE		Ax T1 SE	2D_T1
278764	90	1650	4800	3	Philips		3d flair SAG	3DFLAIR
132325	90	2336	8000	3	GE		Fat Sat3D LOC	3DFLAIR
401.5	90	2000	6000	3	Toshiba		Flair sg (MPV)	3DFLAIR
84	150	n/a	4940	1.5	Siemens	0	T2_TSE_TRANS	T2
100	90	n/a	3178.37	3	Philips	0	tra T2 TSE	T2
83776	111	n/a	5317	3	GE	0	Ax T2 +c	T2
119	90	n/a	4300	1.5	Siemens	1	ep2d_diff_3scan_t	DWI
95546	90	n/a	5896.393	1.5	Philips	1	SENSE Diffusie s	DWI
84.4	90	n/a	7200	3	GE	1	DTI 24dir-4b0	DWI
25	60	n/a	1037.024	3	Philips		DSC_CTR_perf	DSC
30	90	n/a	1610	1.5	Siemens		ep2d perfusie	DSC
25	90	n/a	2000	3	Toshiba		Perfusion	DSC

Figure 2. Partial table showing predictions for 6 of the 16 sequence types, for all the vendors and field strengths appearing in our in-house imaging study.

Conclusions: We have developed CINDERILLA to label MRI scans from a DICOM data set based upon a limited number of acquisition-related parameters, to correctly label 16 sequences. Focusing on acquisition parameters directly related to image contrast means that, unlike pixel-based protocol prediction, our method is not affected by faulty scans. For performance evaluation, a human expert compared the predicted protocol to the series description. The prediction performance of T2-weighted scans was lower than others, because of overlapping sequence parameters between T2-weighted and diffusion-weighted scans, and requires further development. We will run our software, developed in Python3.9, on further imaging study datasets, to assess prediction performance on new data that was not used to set the parameter ranges. We will make the software available after these additional tests.

References

1. Bartnik A, Singh S, Sum C, Smith M, Bergsland N, Zivadinov R, Dwyer M (2023): An automated tool to classify and transform unstructured MRI data into BIDS datasets. Research Square. https://doi.org/10.21203/rs.3.rs-3328936/v1.
2. van der Voort SR, Smits M, Klein S, for the Alzheimer's Disease Neuroimaging Initiative (2021): DeepDicomSort: An Automatic Sorting Algorithm for Brain Magnetic Resonance Imaging Data. Neuroinformatics 19:159–184.

Poster No 1915

Investigating cortical neural correlates of ipsilateral Silent Period

Costanza Iester[1], Alice Bellosta[1], Elena Monteleone[1], Monica Biggio[1], Ludovico Pedullà[2], Ambra Bisio[3], Sabrina Brigadoi[4], Simone Cutini[4], Laura Bonzano[1], Marco Bove[5]

[1]Department of Neuroscience, DINOGMI, University of Genoa, Genoa, Italy, [2]Italian Multiple Sclerosis Foundation, Genoa, Italy, [3]DIMES, Section of Human Physiology, University of Genoa, Genova, Liguria, Italy, Genova, Italy, [4]Department of Developmental Psychology, University of Padova, Padova, Italy, Padova, Italy, [5]DIMES, University of Genoa, Genova, Italy

Introduction: The ipsilateral silent period (iSP) is employed to investigate the interhemispheric control of voluntary cortical motor output[1]. It involves a brief interruption of voluntary electromyography (EMG) in a hand muscle through focal transcranial magnetic stimulation (TMS) of the ipsilateral primary motor cortex (M1). Given observed differences in iSP outputs across

various studies, variations in dynamics may account for iSP disparities within and between groups. Moreover, it has been observed that the volitional activation of M1, induced by movement of the contralateral hand, leads to an augmentation of interhemispheric motor inhibition[2]. This phenomenon may also be further elucidated by examining iSP cortical correlates. Despite being a frequently measured index of interhemispheric inhibition, the neural dynamics underlying the iSP effect remain unknown. Some insights were discovered using the combination of TMS and EEG, the larger the TMS-evoked potential, occurring approximately 15 ms after the stimulation, the higher the iSP area[3]. However, although EEG provides a global view of brain activity with a precision of milliseconds, it does not allow for the exact localization of the sources of the waves. In this context, functional Near Infra-Red Spectroscopy (fNIRS) could be employed to explore the cortical correlates of iSP. Recent studies emphasize the potential of the combined use of TMS and fNIRS[4]. Consequently, the aim of this study is to develop an experimental protocol able to simultaneously investigate the iSP and the associated neural dynamics using both TMS and fNIRS.

Methods: To investigate the left iSP and its neural correlates, TMS was positioned on the left hemisphere, while fNIRS optodes were arranged on the right hemisphere. To test the protocol, five healthy participants were recruited. The fNIRS array was arranged to obtain 49 standard channels (3cm) and 8 short-separation channels (8mm) (Fig.1). The TMS intensity stimulation was set to the 120% of the passive motor threshold for each subject[2]. Surface EMG activity was recorded both from the right and left first dorsal interosseous muscles to quantify the motor activity. The experiment consisted of three different conditions in which the participant was instructed to maximally contract either the left hand or both hands. The first condition involved TMS stimulation and contraction of the left hand, the second involved TMS stimulation and contraction of both hands, and the third, without TMS stimulation, required contraction of the left hand. In all conditions, fNIRS measured the neural activity of the right hemisphere. For each condition, 25 trials were collected, resulting in a total of 75 trials (task duration: ~1s; rest duration: ~20s). After the acquisition, the fNIRS signal was pre-processed: channels with low signal-to-noise ratio were discarded; intensity data were converted to attenuation changes and motion artifacts were corrected by applying spline[5] and wavelet[6] motion correction techniques; a band-pass filter (0.01-3Hz) was applied, and the mean hemodynamic response for each task block, and channel was recovered using a general linear model approach.

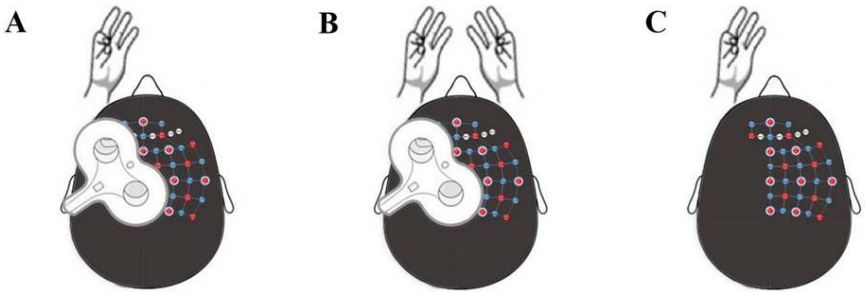

Figure 1: In all conditions, fNIRS records the neural signal in the right hemisphere. A) Maximal contraction with the left hand and TMS stimulation of the left hemisphere; B) Maximal contraction with both hands and TMS stimulation of the left hemisphere; C) Maximal contraction with the left hand and no stimulation.

Results: We propose for the first time a method to assess iSP combining TMS and fNIRS: TMS stimulates a hemisphere while fNIRS records the neural activity of the contralateral one. Standard pipeline used in fNIRS field to preprocess the signal[7] can remove TMS artifacts leading to a reliable result. Some channels related to premotor, motor, and parietal areas seem to be modulated by conditions (Fig. 2). Behavioral data confirms the literature by showing a greater iSP area during the bilateral hand contraction compared to only left-hand contraction.

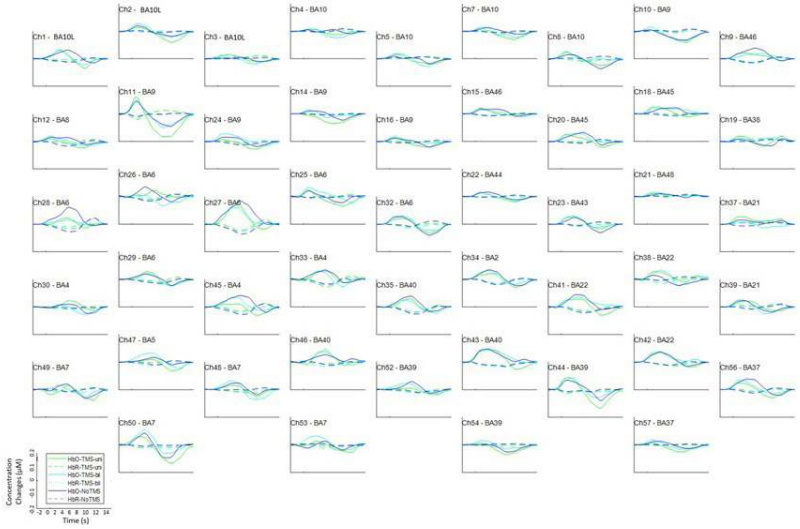

Figure 2: Hemodynamic Function Response of each channel associated with Brodmann area. On the left bottom, the legend of the figure: continued lines represent oxy-haemoglobin concentrations changes (HbO), dashed lined deoxy-haemoglobin concentrations changes (HbR). The color of the lines represents the specific condition (i.e., green is the condition 1, light blue is the condition 2 and blue is the condition 3).

Conclusions: fNIRS is a powerful tool to investigate cortical correlates simultaneously with TMS stimulation. The possibility of studying TMS and fNIRS together can unveil neural mechanisms associated with interhemispheric circuits of motor control.

References

1. Hupfeld, K. E. (2020). TMS-induced silent periods: A review of methods and call for consistency. Journal of Neuroscience Methods, 346, 108950.
2. Giovannelli, F. (2009). Modulation of interhemispheric inhibition by volitional motor activity: an ipsilateral silent period study. The Journal of Physiology, 587(22), 5393-5410.
3. Bortoletto, M. (2021). Asymmetric transcallosal conduction delay leads to finer bimanual coordination. Brain Stimulation, 14(2), 379-388.
4. Curtin, A. (2019). A systematic review of integrated functional near-infrared spectroscopy (fNIRS) and transcranial magnetic stimulation (TMS) studies. Frontiers in Neuroscience, 13, 84.
5. Scholkmann, F. (2010). How to detect and reduce movement artifacts in near-infrared imaging using moving standard deviation and spline interpolation. Physiological Measurement, 31(5), 649.
6. Molavi, B. (2012). Wavelet-based motion artifact removal for functional near-infrared spectroscopy. Physiological Measurement, 33(2), 259.
7. Brigadoi, S. (2014). Motion artifacts in functional near-infrared spectroscopy: a comparison of motion correction techniques applied to real cognitive data. Neuroimage 85, 181–191.

Poster No 1916

The Brain Imaging Statistics (BIS) toolset: C++ libraries and programs for handling brain MRI data

Alle Meije Wink[1]

[1]Amsterdam University Medical Centre, Amsterdam, Noord-Holland

Introduction: Brain image analyses rely on programs to convert, process and analyse the scans stored in DICOM and NIfTI files. Most open-source software packages for these tasks are programmed in either Python or Matlab. Even though these languages often rely on C++ for efficient routines in computation, there is little software that exposes the handling of image data in C++. We present the brain imaging statistics software (BIS) tools, which are built around the Computer Analysis of Brain Imag Statistics (CAnaBIS) library, and include ComBIS, a command-line image processing tool and will include BISkits, a graphical brain image processing tool. The source code of the software is [available at https://github.com/amwink/bis].

Methods: The CAnaBIS library is built around two main features: (i) File I/O and (ii) a flexible data type for scientific analyses. File I/O is handled by wrapping basic routines of the standard DICOM library, DCMTK[1] and the standard NIfTI library, nifticlib[2] into functions that provide an interface to the main CAnaBIS data type. This is the bisimage class template, which supports (a) voxels of multiple data types, (b) variable dimensionality and (c) mathematical operation, e.g. addition and division. More and higher functions are being added, such as watershed and max-tree transformations for segmentation. For file I/O, there is full NIfTI support and increasing DICOM support. We use the following class hierarchy: bisdicomimage :: bisbidsimage ::

bidsniftiimage :: bisimage. The BIDS standard[3], which consists of a directory and file naming convention and a data format where NIfTI images are accompanied by a JSON 'sidecar', is supported by reading and writing the NIfTI/JSON pairs. DICOM images can be read and written as BIDS files (see fig. 1A), the JSON being filled with acquisition-specific information from the DICOM header. The bisimage data type is the parent of the other image types. It is a class template whose pixel data are stored in a 1-dimensional array, with multi-dimensional addressing defined by a sizes array (describing the dimensions), a strides array (describing the offsets for stepping through each dimension) and an addressing operator accepting an initializer_ list argument. This can be an array literal, e.g. {2,3,4}, an array variable, e.g. int [pos[3], or a std::vector of a numerical type (see Fig. 1B). Many images require operations on 2-, 3- and 4-dimensional vectors, and CAnaBIS supports a number of these in the vecN template class (with explicit support for N of 2, 3 and 4). Operations include addition, subtraction, multiplication and division. Vectors operations include inner and cross products, matrix operations include the Hadamard product and eigenvector and -value computation for symmetric matrices (see fig1C).

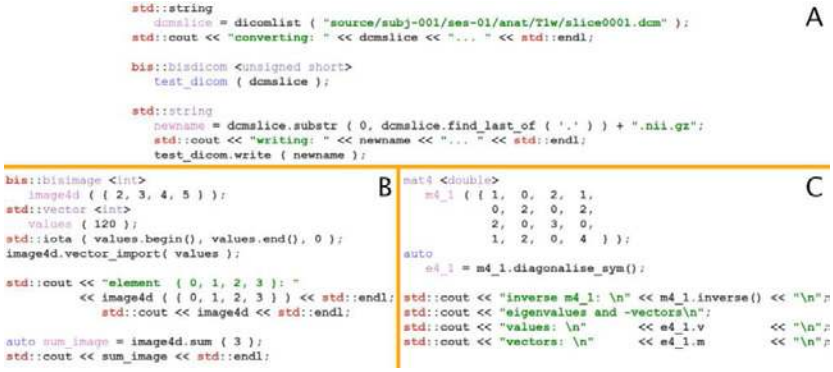

Figure 1: code exmples of the use of the CAnaBIS library

Results: Code example A creates a DICOM image, given the name of a single file. This is usually a 2D slice that is part of a 3D or 4D data set, so the directory where the file is found is scanned for other DICOM files with the same UID. These are sorted by position and converted to a 2D, 3D or 4D image, with an accompanying NIfTI header and JSON record, which are both saved in the write() function. Example B creates a (2x3x4x5)-pixel image with integer values, and imports its values from a 120-value interger array that is filled with the values 0-119. Element (0,1,2,3), which would be row 0 of column 1 in slice 2 of volume 3, is the value at array offset 0*1+1*2+4*(2*3)+5*(2*3*4), so coefficient 86, which also has value 86. The sum over dimension 3 (with size 5) is a new bisimage object of dimensions (2,3,4), see fig. 2A Example C shows the 4x4 matrix, its inverse and its eigenvectors and -values (see fig 2B).

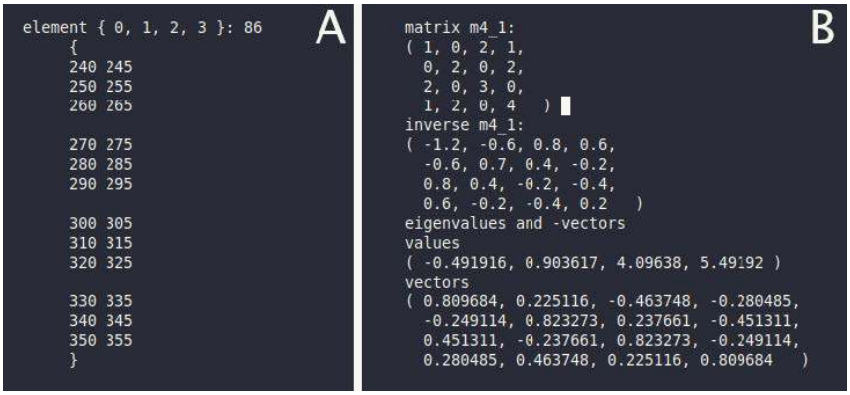

Figure 2: Screen output format of vectors and matrices

Conclusions: We introduce the CAnaBIS library, a C++ library with easy DICOM, BIDS and NIfTI file access and numerical data structures whose behaviour resembles that of MatLab and NumPy matrices. More functionality will be added to the ComBIS and BISkits programs and the code is available on GitHub.

References

1. Eichelberg, M. (2004), "Ten years of medical imaging standardization and prototypical implementation: the DICOM standard and the OFFIS DICOM toolkit (DCMTK)", Proc SPIE vol. 5, DOI 10.1117/12.534853, https://github.com/DCMTK/dcmtk
2. Cox, R.W. (2004), "A (sort of) new image data format standard: NiFTI-1", Proc. OHBM vol. 10, https://nifti.nimh.nih.gov/pub/dist/src/niftilib
3. Gorgolewski K.J. (2016), "The brain imaging data structure, a format for organizing and describing outputs of neuroimaging experiments", Sci Data 3:160044, doi: 10.1038/sdata.2016.44, https://bids.neuroimaging.io

Poster No 1917

Fast and robust structural MRI super-resolution using voxel-size independent CNNs

Walter Adame-Gonzalez[1], Roqaie Moqadam[2], Yashar Zeighami[3], Mahsa Dadar[4]

[1]McGill University, Montreal, Quebec, [2]Cerebral Imaging Center, Douglas Mental Health University Institute, Montreal, Quebec, [3]Douglas Research Centre, Montreal, Quebec, [4]McGill University, Montreal, QC

Introduction: In brain Magnetic Resonance Imaging (MRI) studies, increasing image resolution is an active research field since it can potentially facilitate improved brain morphometry in clinical environments as well as in automatic downstream segmentation pipelines used in research. However, acquiring higher-resolution MRIs comes with increased acquisition times, costs, and patient discomfort, making it prohibitive in large cohort studies. Artificially increasing the MRI resolution is thus beneficial, since it can potentially enhance assessment of the brain through morphometry. We propose a voxel-size independent Generative Adversarial Network (GAN) capable of performing MRI super-resolution.

Methods: We used 1045 randomly selected T1-weighted scans from ABIDE, ADNI, HCP, IXI, LA5c, MIRIAD, and HBA datasets. For all images, we performed preprocessing including Denoising[1], brain segmentation[2], and brain mask generation. To train an MRI super-resolution network, we generated input-target image pairs. The input was generated by a process of downscaling (average pooling 70% and trilinear 30%) - upscaling (cubic BSpline 70%, trilinear 30%) a stack of 2D slices. The input to the network consisted of 9-2D axial slices that were in the high-resolution domain, and the target was a single 2D slice that corresponded to the middle slice of the input, i.e. the ground-truth image. The generator network was a nested UNet++ with upscaling of feature maps through PixelShuffle with a voxel-size normalization step in the latent space[3],[2],[4],[5]. The discriminator was a VGG-based network with the relativistic adversarial loss[6]. The generator loss LG was defined as a combination of L1 norm, learned perceptual image patch similarity (LPIPS)[7], total variation (TV), and relativistic adversarial loss[6]. The network was trained until convergence was reached using OneCycleLR and AdamW with a maximum learning rate of 1e-5 for 10 epochs and batch size of 4. Peak signal-to-noise-ratio (PSNR), structural similarity index measure (SSIM), and LPIPS metrics were used to assess the performance of the model.

Results: To validate our method, we tested its performance on independent subsets of the described datasets (except for HBA), as well as an in-house dataset of ex vivo T1w MRIs with similar resolution as independent validation datasets. We downscaled the whole brain volumes by a factor of 2 using Freesurfer's mri_convert function with cubic interpolation. Then, we compared the upscaled images to the ground-truth native-resolution volumes. For the in vivo validations, SSIM, LPIPS, and PSNR values were improved in 4 out of 6, 3 out of 6, and 1 out of 6 datasets respectively when compared to BSpline of order 3 interpolation (see Fig. 2.). For the ex vivo in-house dataset, we obtained comparable results with the state-of-the-art method NLMUPSAMPLE[8], when upscaled from isotropic voxel size of 1.0mm3 to 0.5mm3. The proposed method yielded 0.0172, 39.6dB, and 0.988 for LPIPS, PSNR, and SSIM metrics respectively. NLMUPSAMPLE performed better in PSNR and SSIM (40.5dB and 0.991) but worse in LPIPS (0.0263). Finally, interpolation obtained 0.0196, 40.6dB, and 0.991 for LPIPS, PSNR and SSIM. The proposed method performed better when upscaling higher-resolution images (Fig. 1). Furthermore, the post-mortem T1w MRI tests showed the generalization capabilities of the proposed model, since the training corpus did not include any post-mortem sample.

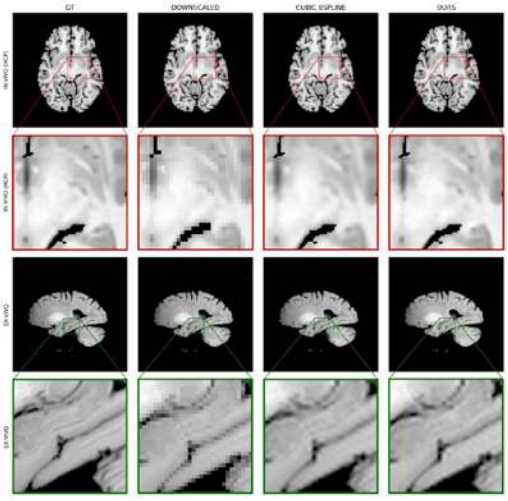

Visual comparison between ground truth (GT), low resolution (DOWNSCALED), BSpline of order 3 interpolation (CUBIC BSPLINE), and the proposed method (OURS).

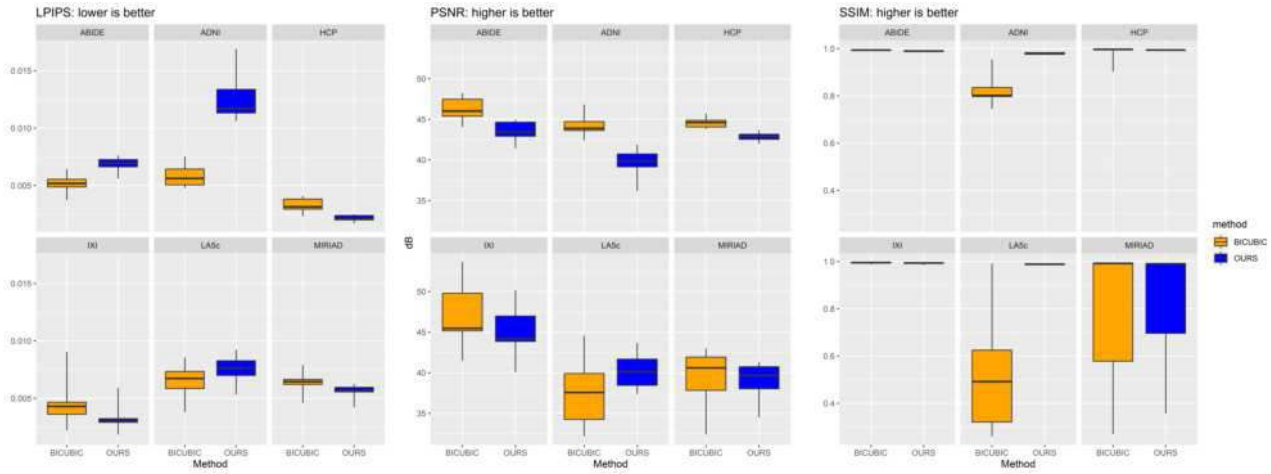

Fig. 2.: Comparison amongst independent samples from 6 of the public datasets used for training the superresolution network.

Conclusions: In general, our method improved sharpness and high-frequency details in MRIs compared to cubic BSpline interpolation. It might over-sharpen the softest textures in the lower-resolution/lower-quality MRIs, which translates to lower PSNR values -a metric that favors softer textures-. Furthermore, since the input to the network is the interpolated version of the low resolution image, artifacts caused by the interpolation such as aliasing can get more evident as they become sharper.

References

1. Adame-Gonzalez, W. et. al. (2023). FONDUE: Robust resolution-invariant denoising of MR Images using Nested UNets [Preprint]. Neuroscience. https://doi.org/10.1101/2023.06.04.543602
2. Henschel, L. et. al. (2020). FastSurfer—A fast and accurate deep learning based neuroimaging pipeline. NeuroImage, 219, 117012. https://doi.org/10.1016/j.neuroimage.2020.117012
3. Henschel, L. et. al. (2022). FastSurferVINN: Building resolution-independence into deep learning segmentation methods—A solution for HighRes brain MRI. NeuroImage, 251, 118933. https://doi.org/10.1016/j.neuroimage.2022.118933
4. Manjón, J. V. et. al. (2015). MRI noise estimation and denoising using non-local PCA. Medical Image Analysis, 22(1), 35–47. https://doi.org/10.1016/j.media.2015.01.004
5. Manjón, J. V. et. al. (2010). Non-local MRI upsampling. Medical Image Analysis, 14(6), 784–792. https://doi.org/10.1016/j.media.2010.05.010
6. Shi, W. et. al. (2016). Real-Time Single Image and Video Super-Resolution Using an Efficient Sub-Pixel Convolutional Neural Network. 2016 IEEE Conference on Computer Vision and Pattern Recognition (CVPR), 1874–1883. https://doi.org/10.1109/CVPR.2016.207
7. Umer, R. M. et. al. (2020). Deep Generative Adversarial Residual Convolutional Networks for Real-World Super-Resolution (arXiv:2005.00953). arXiv. http://arxiv.org/abs/2005.00953
8. Zhang, R. et. al. (2018). The Unreasonable Effectiveness of Deep Features as a Perceptual Metric (arXiv:1801.03924). arXiv. http://arxiv.org/abs/1801.03924

Poster No 1918

HSMM with Gaussian Processes emissions: A method for interpretable modeling of neuroimaging data

Yunier Pieur-Coloma[1,2], David Araya[3,1], Felipe Torres[1], Wael El-Deredy[1,4,5]

[1]Brain Dynamics Laboratory, Universidad de Valparaíso, Valparaíso, Chile, [2]Programa de Doctorado en Ciencias e Ingeniería para la Salud, Universidad de Valparaíso, Valparaíso, Chile, [3]Facultad de Ingeniería, Universidad Andrés Bello, Viña del Mar, Chile, [4]ValgrAI, Valencian Graduate School Research Network of Artificial Intelligence, Valencia, Spain, [5]Department of Electronic Engineering, School of Engineering, Universitat de València, Valencia, Spain

Introduction: Cognitive function emerges from the connectivity of large-scale brain networks. The brain has the ability to adapt to changing cognitive demands and tasks, transitioning between different network configurations (brain states)[1]. Brain states require an efficient coordination between the regions across the whole brain. It is generally agreed that the coordination mechanism involves the synchronization of oscillatory modes among neuronal populations at specific frequencies. Hence, it has been hypothesized that oscillatory modes do not have a local origin, instead they are associated with synchronization among distant neural assemblies[2]. We capitalize on recent advances from interpretable machine learning methods and Hidden Semi Markov Model (HSMM) theory to propose a method for analysis of large-scale brain networks dynamics that provides a plausible interpretation of oscillatory modes from spontaneous neural activity.

Methods: HSMM is a generative parametric model that expresses the beliefs about how a sequence of discrete states gives rise to the observed M/EEG data. Each state emits a sequence of observations through the emission model, which defines

the law governing the generation of observations. In this work, we used emission models based on Multi-Output Gaussian Processes (MOGPs) with spectral kernels whose parameters enable an interpretation of the oscillatory modes in each brain state. Our HSMM implementation assumes that each brain state is represented by a MOGP. MOGPs is a machine learning method for discovering intrinsic patterns in data by modeling statistical interdependencies between channels or brain regions[3]. A MOGPs is parametrized by a mean function, and a kernel or covariance function that express the law governing how the data correlate. We used the Cross-Spectrum Mixture (CSM) kernel to estimate the cross-covariance function between brain regions[4]. The CSM kernel provide us a biophysically consistent formulation by assuming brain regions share the same oscillatory modes. CSM kernel comprises different oscillatory modes, and its hyperparameters provide a plausible description of each one, including its energy across brain regions. To estimate the HSMM-MOGP parameters, we used an Expectation-Maximization iterative procedure. The expectation-step involves sampling observation sequences and their corresponding states jointly, using the Forward Filtering-Backward Sampling algorithm[5]. Afterward, in the maximization step, the HSMM parameters and CSM hyperparameters are updated using the observations and states sampled in the previous expectation-step. The HSMM-MOGP is validated by generating synthetic data from two regions with known parameters a priori, and using it for model training as shown in Figure 1. Subsequently, the oscillatory modes properties estimated by the model are compared with the ground truth.

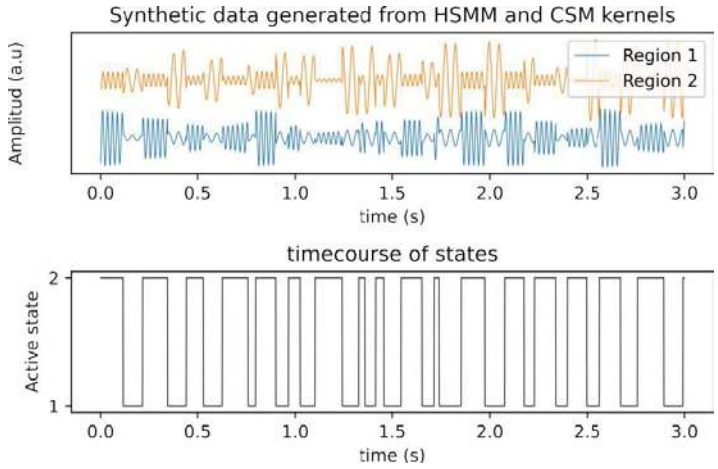

Results: HSMM-MOGP was able to estimate the parameters used to generate the dynamics in synthetic data. The CSM kernels recover the specific properties of the oscillatory modes prevailing in the stationary time segments in which their respective states are active. In Figure 2, the solid line describes the properties of the oscillatory modes considering both regions simultaneously during data simulation, while the dashed line presents the estimation of these properties after training the HSMM-MOGP. The hyperparameters of CSM kernels provided a clear meaning regarding oscillatory modes in all channels.

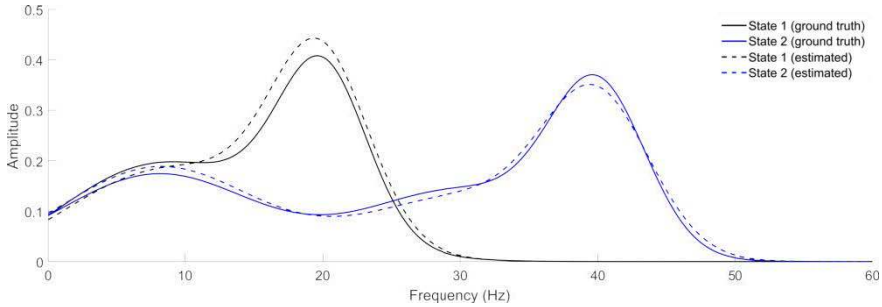

Conclusions: This work presents a method for analysis of large-scale brain networks dynamics using HSMM and MOGPs. The results show the capability of the model to provide parameters that enable the interpretation of brain oscillatory modes.

References

1. A. P. Baker et al., “Fast transient networks in spontaneous human brain activity,” eLife, vol. 3, p. e01867, Mar. doi: 10.7554/eLife.01867.
2. J. F. Hipp, D. J. Hawellek, M. Corbetta, M. Siegel, and A. K. Engel, “Large-scale cortical correlation structure of spontaneous oscillatory activity,” Nat. Neurosci., vol. 15, no. 6, pp. 884–890, Jun. 2012, doi: 10.1038/nn.3101.
3. M. A. Álvarez, L. Rosasco, and N. D. Lawrence, “Kernels for Vector-Valued Functions: A Review,” Found. Trends® Mach. Learn., vol. 4, no. 3, pp. 195–266, Jun. 2012, doi: 10.1561/2200000036.
4. K. R. Ulrich, D. E. Carlson, K. Dzirasa, and L. Carin, “GP Kernels for Cross-Spectrum Analysis,” in Advances in Neural Information Processing Systems, Curran Associates, Inc., 2015. Accessed: Jun. 12, 2023. [Online].
5. Available: https://papers.nips.cc/paper_files/paper/2015/hash/285ab9448d2751ee57ece7f762c39095- Abstract.html
6. S. L. Scott, “Bayesian Methods for Hidden Markov Models,” J. Am. Stat. Assoc., vol. 97, no. 457, pp. 337–351, Mar. 2002, doi: 10.1198/016214502753479464.

Poster No 1919

Beyond Brain Age: A Density-Estimation Approach to Brain Structural Normativity

Ramona Leenings[1], Jan Ernsting[2], Nils Winter[3], Maximilian Konowski[4], Lukas Fisch[3], Daniel Emden[3], Carlotta Barkhau[3], Xiaoyi Jiang[5], Udo Dannlowski[3], Klaus Berger[6], Tim Hahn[3]

[1]University of Münster, Münster, North Rhine Westphalia, [2]University of Münster, Münster, NRW, [3]Institute for Translational Psychiatry, Münster, North Rhine Westphalia, [4]University of Münster, Münster, North-Rhine Westphalia, [5]University of Münster, Münster, Northrine-Westphaila, [6]Institute of Epidemiology and Social Medicine, University of Münster, Münster, NRW, Germany

Introduction: In recent years, Brain Age models have been used to quantify neuro-structural degeneration and the resulting biomarker, the Brain Age Gap (BAG), has been linked to numerous neurological and psychiatric conditions (Cole et al. 2019, Bittner et al. 2021, Wrigglesworth et al. 2021, Blake et al. 2023). The conventional Brain Age concept assumes the existence of discernible, one-year increments of neurostructural changes along the age continuum. In practice, however, a brain age model needs to resolve the conflict of neuro-structurally similar brains with differing age labels and vice versa. In addition, the concept neglects inter-individual variety and implicitly assumes that neurostructural irregularities within one age group are normative in another. We therefore propose to reformulate the learning problem from "how old is this brain?" to "how unusual is this brain structure given its chronological age?". This approach explicitly allows for several prototypical brain structures per age group and overlapping prototypes across several (neighboring) age groups. In addition, this approach offers individual normativity scores for all age groups along the aging continuum, thereby generating an individual aging profile (see Figure 1). We introduce two novel biomarkers termed 'Group Normativity', which describes age-group specific brain structural normativity, and 'Profile Normativity', which describes the normativity of the aging profile with respect to the aging profiles of a same-aged representative sample.

Methods: We utilize a k-Nearest-Neighbor algorithm to estimate the typical regional density for a representative sample of a particular age group. Subsequently, we aggregate the normalized distances to the k=15 nearest neighbors for all training samples, fit a distribution, and derive a normativity score from this process. A total of N=30,047 participants from the German National Cohort (German National Consortium 2014, Peters et al. 2022) was used to derive models for age groups 21 to 72. For simplicity, we describe the brain structures using five global tissue variables (GM, WM, WMH, CSF and TIV) derived with the cat12 toolbox (Gaser, https://neuro-jena.github.io/cat/). To assess detection capabilities for atypical neurostructural degeneration, we evaluate our biomarkers using instances of Mild Cognitive Impairment (MCI) and Alzheimer's Disease (AD) from the ADNI dataset. We compare our novel biomarkers against two Brain Age benchmarks: a SVM-based Brain Age model (BAG-SVM) using the same five variables and a deep learning-based Brain Age model (BAG-DL) trained on full structural T1 images (Hahn et al. 2022, Ernsting et al. 2023). Utilizing a machine learning pipeline implemented in the Python package photonai (Leenings et al. 2021), we classify control subjects (n=351) from those with MCI (n=338) or AD (n=163) with each of the biomarkers.

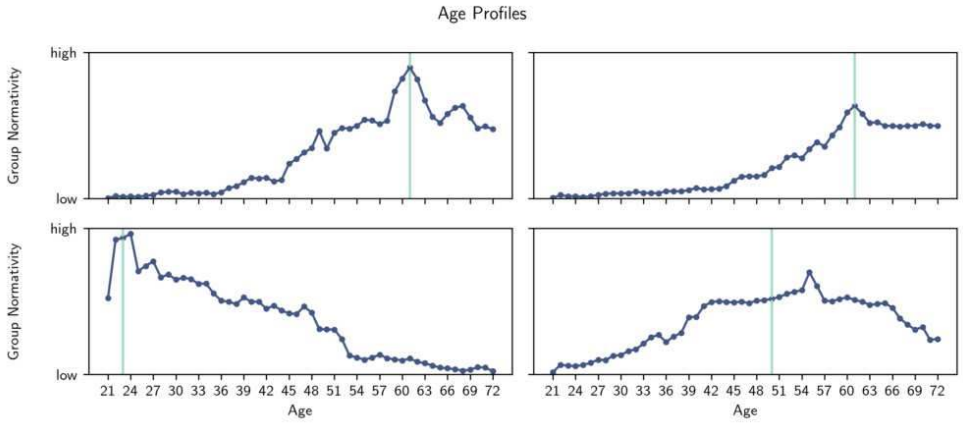

Fig. Actual age (green) and the normativity (blue) of a particular brain structure compared to representative samples of the different age groups.

Results: Both novel biomarkers are able to measure atypical neurostructural degeneration: The Profile Normativity score demonstrates robust performance in distinguishing Alzheimer's Disease (AD) and Mild Cognitive Impairment (MCI), showcasing notably high recall rates of 0.86 for AD and 0.67 for MCI, surpassing BAG-SVM and BAG-DL (see Figure 1). For AD, both novel biomarkers outperform the best Brain Age model (BAG-DL) in terms of balanced accuracy (0.73 and 0.82 vs 0.71) and f1 score (0.64 and 0.7 vs. 0.61). For MCI, the Group Normativity biomarker seems to lack informative value, while the Profile

Normativity biomarker is able to compete with the best Brain Age model (BAG-SVM) in terms of balanced accuracy (0.64 to 0.65) and outperforms the f1 score (0.65 to 0.61).

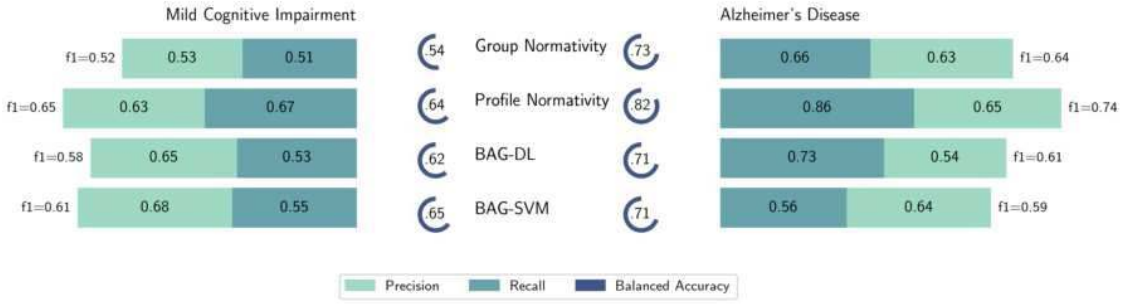

Fig. Benchmarking the detection of atypical neurostructural degeneration for each biomarker.

Conclusions: By focusing on structural deviations relative to chronological age, our approach accommodates the variability in healthy aging trajectories that the current models overlook. The here presented approach was able to compete with or outperform large-scale deep neural networks and yields two promising biomarkers for future scientific pursuits.

References

1. Bittner, N. et al. When your brain looks older than expected: combined lifestyle risk and BrainAGE. Brain Struct. Funct. 226, 621–645 (2021).
2. Blake, K. V. et al. Advanced brain ageing in adult psychopathology: A systematic review and meta-analysis of structural MRI studies. J. Psychiatr. Res. 157, 180–191 (2023).
3. Cole, J. H., Marioni, R. E., Harris, S. E. & Deary, I. J. Brain Age and Other Bodily 'Ages': Implications for Neuropsychiatry. Mol Psychiatr 24, 266–281 (2019).
4. Ernsting, J. et al. From Group-Differences to Single-Subject Probability: Conformal Prediction-based Uncertainty Estimation for Brain-Age Modeling. arXiv (2023)
5. doi:10.48550/arxiv.2302.05304.
6. German National Consortium (GNC). The German National Cohort: aims, study design and organization. Eur. J. Epidemiology 29, 371–382 (2014).
7. Hahn, T. et al. An Uncertainty-Aware, Shareable, and Transparent Neural Network Architecture for Brain-Age Modeling. Sci Adv 8, eabg9471 (2022).
8. Leenings, R. et al. PHOTONAI—A Python API for Rapid Machine Learning Model Development. Plos One 16, e0254062 (2021).
9. Peters, A. et al. Framework and baseline examination of the German National Cohort (NAKO). Eur. J. Epidemiology 37, 1107–1124 (2022).
10. Wrigglesworth, J. et al. Factors associated with brain ageing - a systematic review. BMC Neurol. 21, 312 (2021)

Poster No 1920

Multi-slab whole-brain in vivo 0.35 mm human brain at 7 T to validate acceleration & denoising

Omer Faruk Gulban[1,2], Logan Dowdle[3], Desmond Ho Yan Tse[4], Saskia Bollmann[5], Benedikt A. Poser[1], Rainer Goebel[1,2], Dimo Ivanov[1]

[1]Maastricht University, Maastricht, Netherlands, [2]Brain Innovation, Maastricht, Netherlands, [3]Center for Magnetic Resonance Research, Minneapolis, MN, [4]Scannexus, Maastricht, Netherlands, [5]School of Electrical Engineering and Computer Science, The University of Queensland, Brisbane, Queensland

Introduction: In vivo imaging at mesoscopic scale (0.1-0.5 mm) reveals the intricate details of the brain angioarchitecture[1]. However, there are 3 major constraints to advance the study of human angioarchitecture in vivo: (I) imaging the mesoscopic intracortical vessels in practicable scanning durations, (II) accurate gray matter segmentation, (III) analysis methods to quantify the vascular details. While some work outlined the path [references within 2, 3]; recently we progressed in all 3 aspects by providing a 0.35 mm T2* dataset where the intracortical angioarchitecture details are visible, developing and providing the analyses to start quantifying the mesoscopic intracortical vessels[3]. However, this work only covered a third of the brain while the total scanning lasted 3 hours/subject. Here, we provide two major advancements to increase the brain coverage while decreasing the overall duration: 1. We concatenate partial brain slabs to achieve whole-brain coverage while keeping each scan time around 10 minutes. We "slab-stitch" in the post-processing to have whole-brain images. 2. We apply structure tensor denoising[4] to a single run of 0.35 mm MP2RAGE to achieve SNR similar to averaging 6 runs (used in[6]). As a result, we show that 0.35 mm iso. (near) whole brain in vivo human brain T2*- and T1-weighted contrasts can be achieved with high SNR within 1.5 hours. In addition, our low undersampling dataset provides a testbed for exploring additional acceleration and denoising methods to further reduce the total scanning time in the future.

Methods: Data was acquired as described in[3] using ME GRE[5] at 7 T with pTx[6]. Six bipolar echos at 0.35 mm iso. were obtained using a low undersampling. For the first participant, in 5 sessions totalling 7.5 hours, we piloted: - Different slab positioning and angulations for our partial brain coverage slabs (see Fig1A). - Nr. of averages required for high SNR T2*-weighted contrast in our ME GRE images. - The effect of GRAPPA 3 compared to 2 in ME GRE images. - The effect of structure tensor denoising compared to multi-run MP2RAGE averaging. Based on the quality control, we made the following optimizations: - Instead of 4 ME GRE runs, 2 runs were deemed sufficient for depicting the angioarchitecture. - Instead of GRAPPA 2, GRAPPA 3 was deemed satisfactory also for angioarchitecture visualization. - Instead of 6 MP2RAGE runs, 1 run with structure tensor denoising was deemed sufficient for cortical gray matter segmentation. Combined, these advancements allowed us to acquire "near whole brain" T2* and T1 contrasts at 0.35 mm iso. within 1.5 hours of a single scanning session. With this optimized protocol, two more participants were scanned. The partial brain slabs were stitched by zero filling a central slab and then performing overlap-mask-based affine registration (in ITKSNAP[7]). This step is semi automatic, requiring careful quality control by the user (takes an hour for stitching 5 slabs). Slab-stitching of MP2RAGE images was done using the same method after the UNI contrast after denoising (using "segmentator_filters"[9]).

Results: Fig1B depicts the intricate vascular details easily visible in our T2* weighted images. Fig2A shows the image quality after post-processing and slab-stitching. Fig2B demonstrates that GRAPPA 3 data is to a very large extent indistinguishable from GRAPPA 2 data. Fig2C illustrates that structure tensor denoising helps greatly to increase the SNR of a single run MP2RAGE image. Although there is some loss of fine details around the vessels, the benefits overcompensate the drawbacks, especially for doing cortical gray matter segmentation.

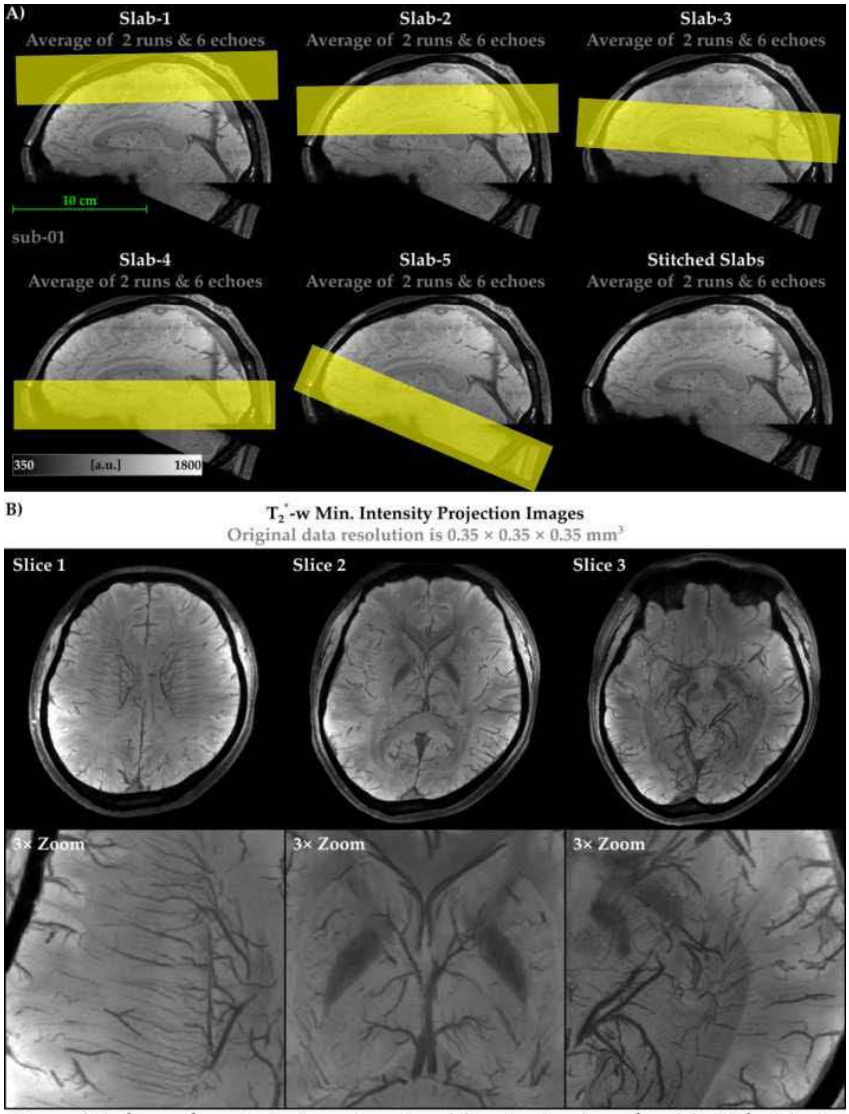

Figure 1A shows the extent of our imaging slabs visualized on the slab-stitched brain image. Nominal voxel resolution is 0.35 mm isotropic. **Figure 1B** shows minimum intensity projection (over 21 slices) images.

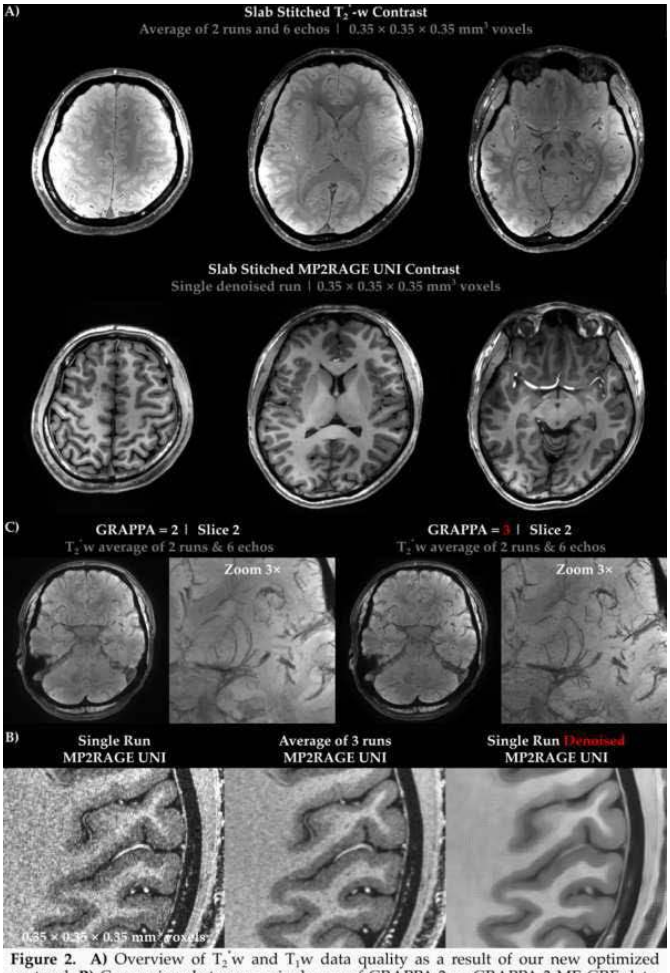

Figure 2. **A)** Overview of T_2^*w and T_1w data quality as a result of our new optimized protocol. **B)** Comparison between a single run of GRAPPA 2 vs GRAPPA 3 ME GRE data. Note that the smoothness of GRAPPA 2 partially is a result of head motion correction that is done in reference to the GRAPPA 3 data. GRAPPA 3 looks indistinguishable to a large extent while decreasing the acquisition time from 14 to 9 min. This seems to help with reducing the head motion artifacts (however note that we had very experienced participants who can stay still for a long time). **C)** Structure tensor denoising helps greatly to increase the SNR of a single run MP2RAGE image. Although there is some loss of fine details around the vessels, the benefit seems to overcompensate drawback for segmenting cortical gray matter.

Conclusions: The results demonstrate excellent data quality despite reducing the total scanning time required 5-fold. However, the in-plane undersampling factor of 3 without partial Fourier is still rather conservative since our additional aim is to provide a reference T2* dataset for future studies employing higher acceleration (e.g. NORDIC[9,10]).

References

1. Duvernoy, H.M., Delon, S., Vannson, J.L., 1981. Cortical blood vessels of the human brain. Brain research bulletin 7, 519–79. https://doi.org/10.1016/0361-9230(81)90007-1
2. Bollmann, S., Mattern, H., Bernier, M., Robinson, S.D., Park, D., Speck, O., Polimeni, J.R., 2022. Imaging of the pial arterial vasculature of the human brain in vivo using high-resolution 7T time-of-flight angiography. eLife 11, 2021.06.09.447807. https://doi.org/10.7554/eLife.71186
3. Gulban, O.F., Bollmann, S., Huber, L. (Renzo), Wagstyl, K., Goebel, R., Poser, B.A., Kay, K., Ivanov, D., 2022. Mesoscopic in vivo human T2* dataset acquired using quantitative MRI at 7 Tesla. NeuroImage 264, 119733. https://doi.org/10.1016/j.neuroimage.2022.119733
4. Weickert, J., 1998. Anisotropic diffusion in image processing. Teubner Stuttgart.
5. Eckstein, K., Dymerska, B., Bachrata, B., Bogner, W., Poljanc, K., Trattnig, S., Robinson, S.D., 2018. Computationally Efficient Combination of Multi-channel Phase Data From Multi-echo Acquisitions (ASPIRE). Magnetic resonance in medicine 79, 2996–3006. https://doi.org/10.1002/mrm.26963
6. Tse, D.H.Y., Wiggins, C.J., Ivanov, D., Brenner, D., Hoffmann, J., Mirkes, C., Shajan, G., Scheffler, K., Uludağ, K., Poser, B.A., 2016. Volumetric imaging with homogenised excitation and static field at 9.4 T. Magnetic Resonance Materials in Physics, Biology and Medicine 29, 333–345. https://doi.org/10.1007/s10334-016-0543-6
7. Yushkevich, P.A., Piven, J., Hazlett, H.C., Smith, R.G., Ho, S., Gee, J.C., Gerig, G., 2006. User-guided 3D active contour segmentation of anatomical structures: significantly improved efficiency and reliability. NeuroImage 31, 1116–28. https://doi.org/10.1016/j.neuroimage.2006.01.015
8. Gulban, O.F., Schneider, M., Marquardt, I., Haast, R.A.M., De Martino, F., 2018. A scalable method to improve gray matter segmentation at ultra high field MRI. PloS one 13, e0198335. https://doi.org/10.1371/journal.pone.0198335
9. Vizioli, L., Moeller, S., Dowdle, L., Akçakaya, M., De Martino, F., Yacoub, E., Uğurbil, K., 2021. Lowering the thermal noise barrier in functional brain mapping with magnetic resonance imaging. Nature Communications 12. https://doi.org/10.1038/s41467-021-25431-8
10. Moeller, S. et al. Locally low-rank denoising in transform domains. in (2023).

Poster No 1921

Phase jolt: 2nd spatial derivative of phase is a new contrast with benefits for SWI type processing

Omer Faruk Gulban[1,2], Andreas Deistung[3], Desmond Ho Yan Tse[4], Saskia Bollmann[5], Renzo Huber[6], Rainer Goebel[1,2], Kendrick Kay[7], Dimo Ivanov[1]

[1]Maastricht University, Maastricht, Netherlands, [2]Brain Innovation, Maastricht, Netherlands, [3]Polyclinic for Radiology, University Hospital Halle, Halle, Germany, [4]Scannexus, Maastricht, Netherlands, [5]School of Electrical Engineering and Computer Science, The University of Queensland, Brisbane, Queensland, [6]National Institutes of Health, Washington, MD, [7]Center for Magnetic Resonance Research, Department of Radiology, University of Minnesota, Minneapolis, MN

Introduction: Unlike magnitude images, even simple averaging is difficult with phase images, because of the circular nature of phase, spanning 2pi radians range. There is a well-developed literature on how to process phase images[1-5]. However, there are also well-known challenges that arise, such as still remaining phase wraps in regions with low signal-to-noise ratio (SNR) after phase unwrapping or removal of background fields. While employing these methods help make phase images more accessible for end users, using phase data is less practical and less commonplace compared to magnitude images. In our own research that uses mesoscopic imaging (<0.5 mm iso.) at 7 T, we need to average multiple acquisitions to increase image signal-to-noise ratio (SNR). To address this problem, we propose to operate on the magnitude of the 2nd spatial derivative of phase images - coining the term “phase jolt”.

Methods: We compute spatial partial derivatives of the phase images through the “circular differences”. This operation accounts for the “phase wraps” at pairwise computations. For each voxel in a 3D MR phase image, we compute the circular differences along x, y, z axes to obtain the first spatial phase derivative image. The 1st spatial derivative is a “vector field”, where each voxel has three values associated with it (as opposed to the initial scalar phase field, where each voxel has a single value associated with it). Note that the circular differences are always in -pi to pi radians range, where the sign indicates clockwise or counterclockwise direction. Once the 1st spatial derivative is computed, we quantify the magnitude of the vectors using the L1 norm divided by 3. We call this spatial operation “phase jump”. The phase jump images highlight tissue edges; however, they also reveal the large-scale phase variations originating from the background field (Fig 1). To account for this, we suggest the 2nd spatial derivative of the phase images. We compute this by taking the spatial derivative of the 1st spatial derivative vector field, resulting in a “tensor field” (where each voxel has 9 values associated). Then, we compute the magnitude of the 2nd spatial derivative using the L1 norm divided by 9. This magnitude calculation again results in a natural 0 to pi radians range. We call this spatial operation “phase jolt”. The benefits of computing the phase jolt are the same as for the phase jump while further mitigating the bias field (Figure1). The downside is that it requires integrating even more information than the phase jump, therefore lowering the effective resolution. We compute the phase jump and jolt on the data acquired as described by[6] using a multi echo gradient echo protocol[7] at 7 T with pTx[8]. Briefly, we have 6 echoes at 0.35 mm isot. resolution, using low acceleration.

Results: Fig 1A shows the phase jump and jolt contrasts compared to the corresponding T2*-weighted magnitude and phase images. Fig 1B highlights that phase images are hard to average due to their circular nature. However, phase jolt images are easy to average due to their numerical range with natural zero and maximum (pi radians). Fig 2 demonstrates the benefit of phase jolt over phase jump, especially for mitigating the background field.

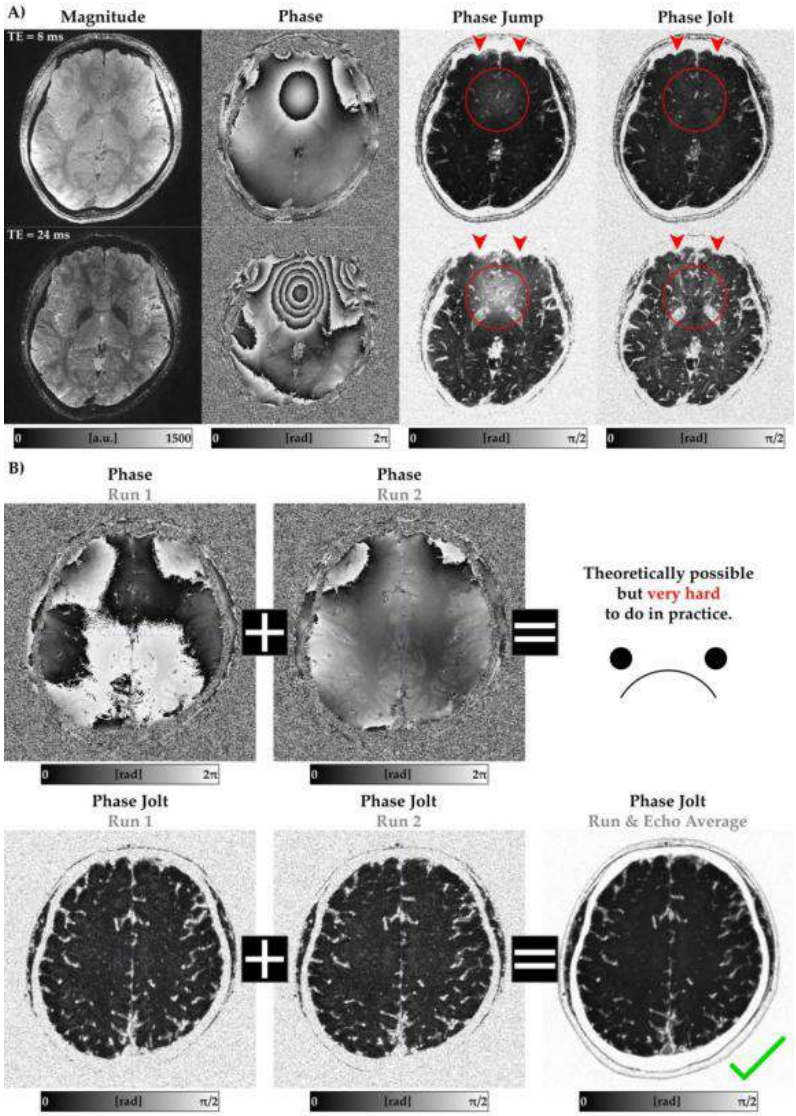

Figure 1A. Magnitude, phase, phase jump and phase jolt images obtained from 0.35 mm isotropic multi-echo GRE in vivo human data. Note that phase jump and phase jolt relate to the first and second spatial derivative of the phase images (see Methods). The natural range of values are positive real numbers in magnitude images, 0 to 2π range for phase images, and 0 to pi in phase jump and jolt images. Note that we prefer to plot 0 to π/2 range in phase jump and phase jolt images because the noise becomes Gaussian and centered around π/2 (see air voxels), and therefore choosing π/2 as the maximum better highlights the brain tissue values. **Figure 1B.** Coil combined phase images cannot be meaningfully averaged voxel-wise without unwrapping and standardizing the phase offsets for each tissue. However, phase jolt images can be easily averaged across acquisitions and echoes because the numerical range is positive real numbers between 0-π rather than the circular 0-π range (see Methods for further explanation).

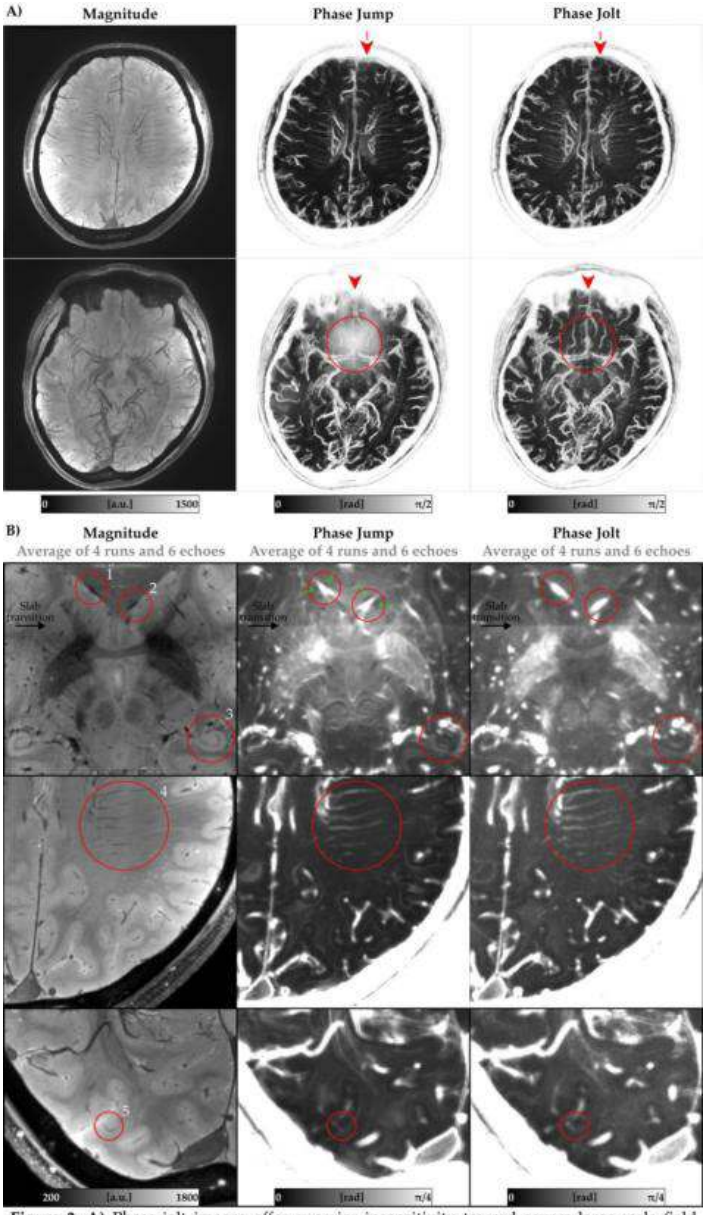

Figure 2. A) Phase jolt images offer superior insensitivity toward severe large-scale field variations over the phase jump images. Red arrows and circles highlight the orbitofrontal cortex where the background field removal benefit is clearly visible. Images here are intensity projected over 7.35 mm (min. intensity projection for T_2^*w and max. intensity projection for phase jump and phase jolt). **B)** Qualitative tissue contrast comparisons for subcortex (1st row), white matter vessels (2nd row), and cortical gray matter details (3rd row) on 0.35 mm isotropic images (no intensity projection). Red circles highlight points of interest. Green arrows indicate the dipole appearances near large vessels in phase jump images are to a larger extent accounted for in phase jolt images. The 2nd row highlights that some white matter vessels are more visible in phase jolt images compared to others. The 3rd row demonstrates the downside of phase jump and jolt, where the visible one voxel wide intracortical vein gets blurred out in the derivative images. Note that we have changed the phase jump and jolt maximum grayscale value to $\pi/4$ in these images to make the brain tissue contrast more visible.

Conclusions: Phase jolt contrast is easy to compute and implement (several voxel-wise circular subtractions, and L1 norm). It provides an informative image where vessels are enhanced while the background field is mitigated. Therefore, phase jolt images may provide an additional contrast in any setting where phase images are recorded. The exquisite contrast of venous vessels in the phase jolt image might be used in a similar setting as susceptibility weighted imaging (SWI) where it may serve to create a phase mask to enhance the sensitivity towards vessels in T2*-weighted images. Additionally, phase jolt images can also be computed on fMRI data. Our implementation is available within the LayNii software package[10] via LN2_PHASE_JOLT program.

References

1. Deistung, A., Rauscher, A., Sedlacik, J., Stadler, J., Witoszynskyj, S., Reichenbach, J.R., 2008. Susceptibility weighted imaging at ultra high magnetic field strengths: Theoretical considerations and experimental results. Magnetic Resonance in Medicine 60, 1155–1168. https://doi.org/10.1002/mrm.21754

2. Haacke, E.M., Mittal, S., Wu, Z., Neelavalli, J., Cheng, Y.-C.N., 2009. Susceptibility-Weighted Imaging: Technical Aspects and Clinical Applications, Part 1. AJNR Am J Neuroradiol 30, 19–30. https://doi.org/10.3174/ajnr.A1400
3. Deistung, A., Schweser, F., Reichenbach, J.R., 2017. Overview of quantitative susceptibility mapping. NMR in Biomedicine 30, e3569. https://doi.org/10.1002/nbm.3569
4. Robinson, S.D., Bredies, K., Khabipova, D., Dymerska, B., Marques, J.P., Schweser, F., 2017. An illustrated comparison of processing methods for MR phase imaging and QSM: combining array coil signals and phase unwrapping. NMR in biomedicine 30. https://doi.org/10.1002/nbm.3601
5. Dymerska, B., Eckstein, K., Bachrata, B., Siow, B., Trattnig, S., Shmueli, K., Robinson, S.D., 2021. Phase unwrapping with a rapid opensource minimum spanning tree algorithm (ROMEO). Magnetic Resonance in Med 85, 2294–2308. https://doi.org/10.1002/mrm.28563
6. Gulban, O.F., Bollmann, S., Huber, L. (Renzo), Wagstyl, K., Goebel, R., Poser, B.A., Kay, K., Ivanov, D., 2022. Mesoscopic in vivo human T2* dataset acquired using quantitative MRI at 7 Tesla. NeuroImage 264, 119733. https://doi.org/10.1016/j.neuroimage.2022.119733
7. Eckstein, K., Dymerska, B., Bachrata, B., Bogner, W., Poljanc, K., Trattnig, S., Robinson, S.D., 2018. Computationally Efficient Combination of Multi-channel Phase Data From Multi-echo Acquisitions (ASPIRE). Magnetic resonance in medicine 79, 2996–3006. https://doi.org/10.1002/mrm.26963
8. Tse, D.H.Y., Wiggins, C.J., Ivanov, D., Brenner, D., Hoffmann, J., Mirkes, C., Shajan, G., Scheffler, K., Uludağ, K., Poser, B.A., 2016. Volumetric imaging with homogenised excitation and static field at 9.4 T. Magnetic Resonance Materials in Physics, Biology and Medicine 29, 333–345. https://doi.org/10.1007/s10334-016-0543-6
9. Huber, L., Poser, B.A., Bandettini, P.A., Arora, K., Wagstyl, K., Cho, S., Goense, J., Nothnagel, N., Morgan, A.T., van den Hurk, J., Müller, A.K., Reynolds, R.C., Glen, D.R., Goebel, R., Gulban, O.F., 2021. LayNii: A software suite for layer-fMRI. NeuroImage 237, 118091. https://doi.org/10.1016/j.neuroimage.2021.118091

Poster No 1922

A new contrast “phase jolt” for analysis of phase-data fMRI reveals strong task-related responses

Omer Faruk Gulban[1,2], Renzo Huber[3], Logan Dowdle[4], Alessandra Pizzuti[1], Chung Kan[3], Rainer Goebel[1,2], Dimo Ivanov[1], Kendrick Kay[4]

[1]Maastricht University, Maastricht, Netherlands, [2]Brain Innovation, Maastricht, Netherlands, [3]National Institutes of Health, Washington, MD, [4]Center for Magnetic Resonance Research, Department of Radiology, University of Minnesota, Minneapolis, MN

Introduction: The vast majority of fMRI studies examine only the magnitude component of the fMRI data while discarding the phase component. Although phase data are known to be sensitive to task activation[1-4], their practical usefulness is impeded by processing difficulty compared to magnitude data. For instance, the circular nature of phase spanning 2π radians range is not handled properly in most preprocessing and analysis programs. Here, we introduce using the second spatial derivative of phase images (“phase jolt”) instead of the phase images themselves as the basis for functional time series analyses. Phase jolt computation casts circular 2π range values of phase with no natural 0 point onto a new range of values with 0 to π range, where noise is centered around π/2. This allows straightforward application of preprocessing and analysis methods developed for magnitude time series on phase jolt time series. We show that there is surprisingly large signal in phase jolt time series corresponding to activation sites in task fMRI experiments.

Methods: We used 6 different 7 T fMRI datasets, all of which included both magnitude and phase data: - Dataset 1: Visual stimulation adapted from github.com/VPNL/fLoc, with data acquisition similar to[5]. Each stimulus lasted 4 s. Functional images were collected with 1.8×1.8×1.8 mm3 voxels at TR=1.6 s using gradient echo EPI (2D). This dataset is provided by K.K. - Dataset 2: Visual stimulation using 4 center-surround probes located in the upper/lower and left/right visual fields. Each stimulus lasted 12 s followed by 8.4 s of rest. Functional images are collected with 1×1×1 mm3 voxels at TR=850 ms using gradient echo EPI (2D). This dataset is provided by L.T.D. (RF1 MH117015 grant). - Dataset 3, 4: Visual stimulation with faces, objects, and their scrambled versions. Each stimulus lasted 10 s. Functional images were collected with 1.6×1.6×1.6 mm3 or 0.8×0.8×0.8 mm3 voxels at TR=650 ms or TR=1850 ms using gradient echo EPI (2D) in experiments 3 and 4, respectively. This dataset is provided by L.T.D. (RF1 MH117015 grant). - Dataset 5: Visual stimulation with flashing checkerboards. Each stimulus lasted 32.7 s with equal amount of rest afterwards. Functional images are collected with 0.8×0.8×0.8 mm3 voxels at TR=8.1 s using T1234 (3D EPI)[6]. This dataset is provided by R.H & C.K. - Dataset 6: Finger tapping stimulation. Each stimulation lasted for 33 s with equal amounts of rest afterwards. Functional images are collected with 0.75×0.75×1.25 mm3 voxels at TR(BOLD)=3.3 s using SS-SI VASO (3D EPI). This dataset is from[7]. Magnitude fMRI time series were only motion corrected and high pass filtered (in BrainVoyager v23[8]). Phase fMRI time series were first subjected to phase jolt computation newly implemented in the LayNii v2.6[9] LN2_PHASE_JOLT program (with ‘-2D’ option for datasets 1-4, and 6). Afterwards, the phase jolt fMRI time series were preprocessed in the same way as the magnitude time series. General linear model was performed to compute the activity maps (stimulation vs baseline).

Results: See Fig1-2 captions.

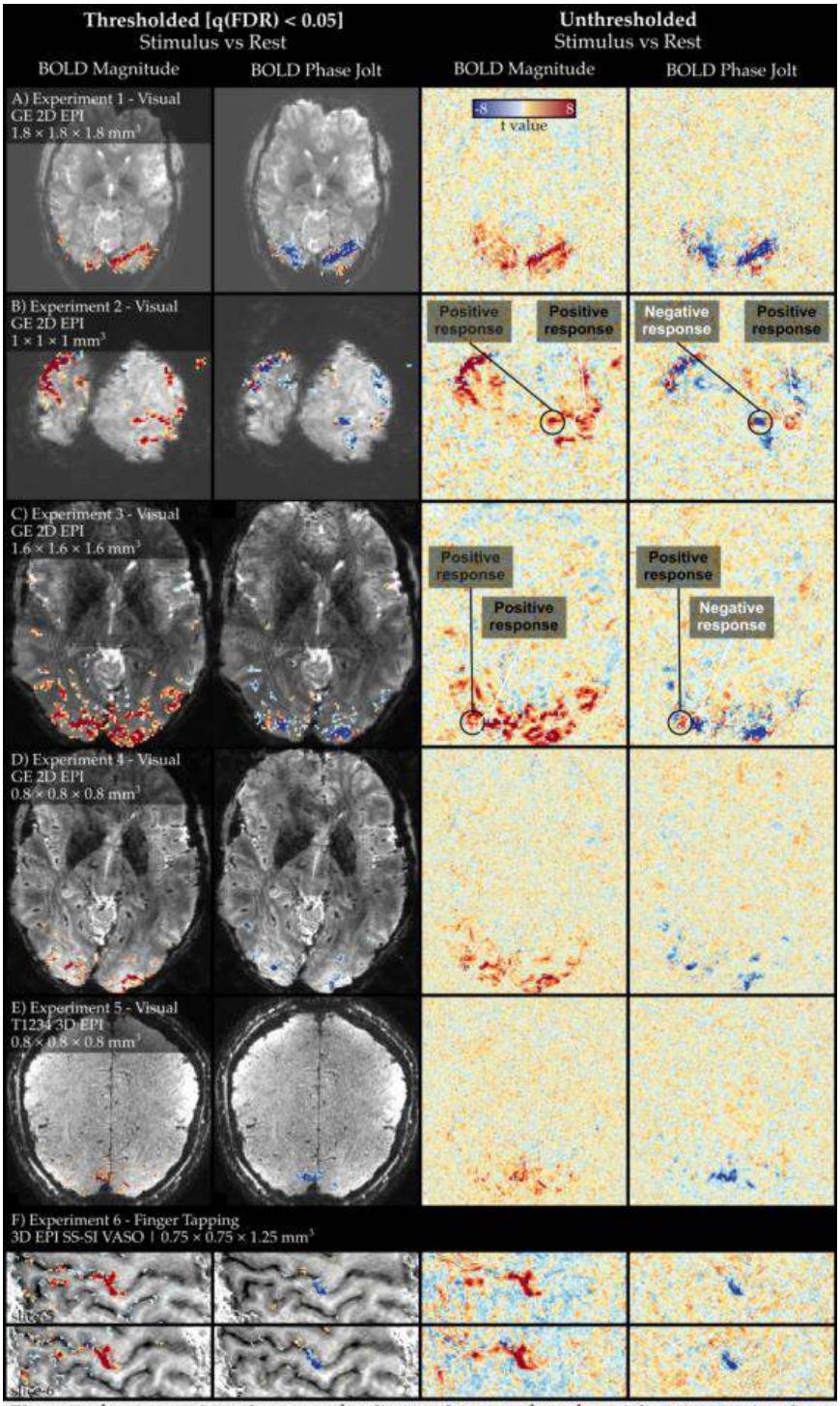

Figure 1 shows, consistently across the diverse datasets, that phase jolt activation is robust and in similar locations to magnitude data activation. However, there are intriguing discrepancies in exact spatial extent of the detected activations.

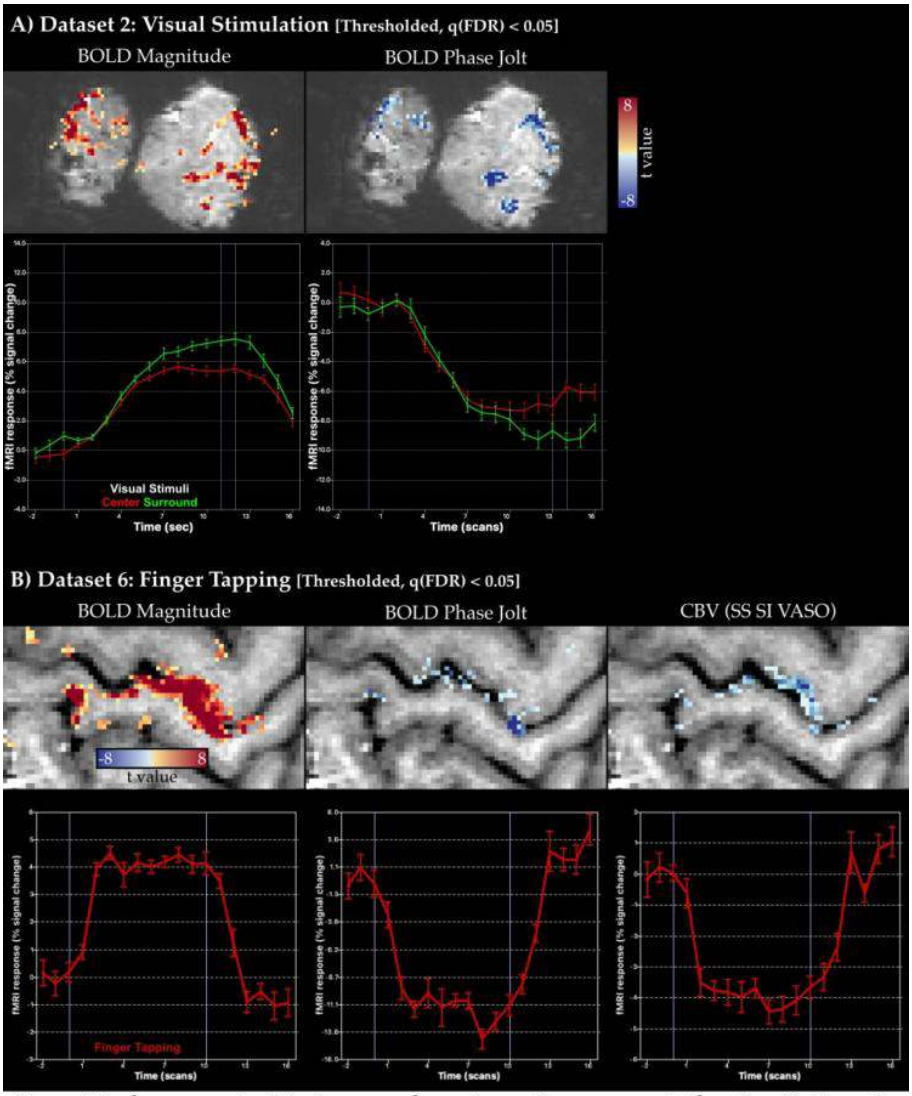

Figure 2A shows event related average hemodynamic responses to the stimuli. It can be seen that phase jolt yields negative signal changes and these are generally larger than those in the magnitude data. **Figure 2B** compares the BOLD phase jolt activity to magnitude and cerebral blood volume. It can be seen that while the responses of CBV and phase jolt look similar, the spatial location of threshold surviving voxels are different.

Conclusions: We have shown that through the simple calculation of phase jolt, phase data can be easily analyzed to reveal substantial task activations. These activations appear to be complementary to standard magnitude time series activations. Phase jolt activity tends to be located near and outside of the cortical gray matter, presumably indicating sensitivity to pial veins. This might be leveraged to detect and mitigate the venous contributions from BOLD magnitude. Alternatively, the strong task-related activity in phase jolt time series might be valuable as an additional information for brain decoding analyses[10]. In the future we will focus on characterizing the biophysical mechanisms underlying phase jolt with respect to MR signal acquisition and noise properties. With further development, we suggest that the effectiveness of phase jolt analysis may spur the usage of phase data in fMRI studies.

References

1. Stanley, O.W., Kuurstra, A.B., Klassen, L.M., Menon, R.S., Gati, J.S., 2021. NeuroImage Effects of phase regression on high-resolution functional MRI of the primary visual cortex. NeuroImage 227, 117631. https://doi.org/10.1016/j.neuroimage.2020.117631
2. Caballero-Gaudes, C., Reynolds, R.C., 2017. Methods for cleaning the BOLD fMRI signal. NeuroImage 154, 128–149. https://doi.org/10.1016/j.neuroimage.2016.12.018
3. Özbay, P.S., Warnock, G., Rossi, C., Kuhn, F., Akin, B., Pruessmann, K.P., Nanz, D., 2016. Probing neuronal activation by functional quantitative susceptibility mapping under a visual paradigm: A group level comparison with BOLD fMRI and PET. NeuroImage 137, 52–60. https://doi.org/10.1016/j.neuroimage.2016.05.013
4. Balla, D.Z., Sanchez-Panchuelo, R.M., Wharton, S.J., Hagberg, G.E., Scheffler, K., Francis, S.T., Bowtell, R., 2014. Functional quantitative susceptibility mapping (fQSM). NeuroImage 100, 112–124. https://doi.org/10.1016/j.neuroimage.2014.06.011
5. Allen, E.J., St-Yves, G., Wu, Y., Breedlove, J.L., Prince, J.S., Dowdle, L.T., Nau, M., Caron, B., Pestilli, F., Charest, I., Hutchinson, J.B., Naselaris, T., Kay, K., 2022. A massive 7T fMRI dataset to bridge cognitive neuroscience and artificial intelligence. Nature Neuroscience 25, 116–126. https://doi.org/10.1038/s41593-021-00962-x

6. Kan, C., Stirnberg, R., Montequin, M., Gulban, O.F., Morgan, A.T., Marrett, S., Bandettini, P.A., Huber, R., 2024. T1234: A distortion-matched structural scan solution to misregistration of high resolution fMRI data, in: ISMRM. p. 54xmrbQ6v.
7. Huber, L., Handwerker, D.A., Jangraw, D.C., Chen, G., Hall, A., Stüber, C., Gonzalez-Castillo, J., Ivanov, D., Marrett, S., Guidi, M., Goense, J., Poser, B.A., Bandettini, P.A., 2017. High-Resolution CBV-fMRI Allows Mapping of Laminar Activity and Connectivity of Cortical Input and Output in Human M1. Neuron 96, 1253-1263.e7.
8. Goebel, R., 2012. BrainVoyager--past, present, future. NeuroImage 62, 748–56. https://doi.org/10.1016/j.neuroimage.2012.01.083
9. Huber, L., Poser, B.A., Bandettini, P.A., Arora, K., Wagstyl, K., Cho, S., Goense, J., Nothnagel, N., Morgan, A.T., van den Hurk, J., Müller, A.K., Reynolds, R.C., Glen, D.R., Goebel, R., Gulban, O.F., 2021. LayNii: A software suite for layer-fMRI. NeuroImage 237, 118091. https://doi.org/10.1016/j.neuroimage.2021.118091
10. Gardner, J.L., 2010. Is cortical vasculature functionally organized? NeuroImage 49, 1953–1956. https://doi.org/10.1016

Poster No 1923

A Generative Model for Missing Data in Large Epidemiological Cohorts

Lav Radosavljevic[1], Thomas Nichols[2], Stephen Smith[1]

[1]University of Oxford, Oxford, Oxfordshire, [2]University of Oxford, Oxford, United Kingdom

Introduction: Large-scale epidemiological cohorts are vital for identifying risk factors of disease and are increasingly including neuroimaging data. Such data inevitably has missing values in two forms, unstructured and structured missingness (Mitra et al., 2023). Unstructured missing data occurs for individual subjects on occasional variables and doesn't reflect a large-scale pattern. Structured missingness occurs when data is missing for a particular set of variables and subjects, often corresponding to follow-up studies that only include a subset of subjects. While much research exists on missing data, it has focused on relatively small datasets and generally omits consideration of structured missingness. We know that participation in studies is correlated to some health- and socio-economic- attributes of the participants (Fry et al., 2017), and there is a need to evaluate missing data methods that account for the type of missing data found in practice to obtain a more accurate picture of the performance of different imputation methods on UK Biobank data. In this work we propose a generative model for mixed type synthetic data that includes structured missingness. The method is applied to non-Imaging Derived Phenotypes (nIDPs) from the UK Biobank brain imaging cohort and we generate synthetic sets to evaluate the performance of commonly used imputation methods.

Methods: We assume that our real data set conforms to these three criteria: 1. There is structured missingness, blocks of missingness caused by non-participation in extension studies, as well as unstructured missingness. 2. There is an association between inter-variable correlation and inter-variable missingness similarity. 3. Missingness is informative in the sense of MAR, where there is a relationship between missingness in a given variable and the observed elements of other variables. We further assume that that the structured missingness is entirely determined by baseline variables through a logistic model that predicts sub-study participation. Also, for the sake of simplicity, we assume that the unstructured missingness is MCAR. Using hierarchical clustering over variable missingness patterns, the sub-studies are identified and parameters for inducing both types of missingness are estimated, giving us our generative model. Crucially, we will have access to ground truth for simulated data, which gives us the ability to evaluate the performance of different methods of handling missing data for analytical tasks.

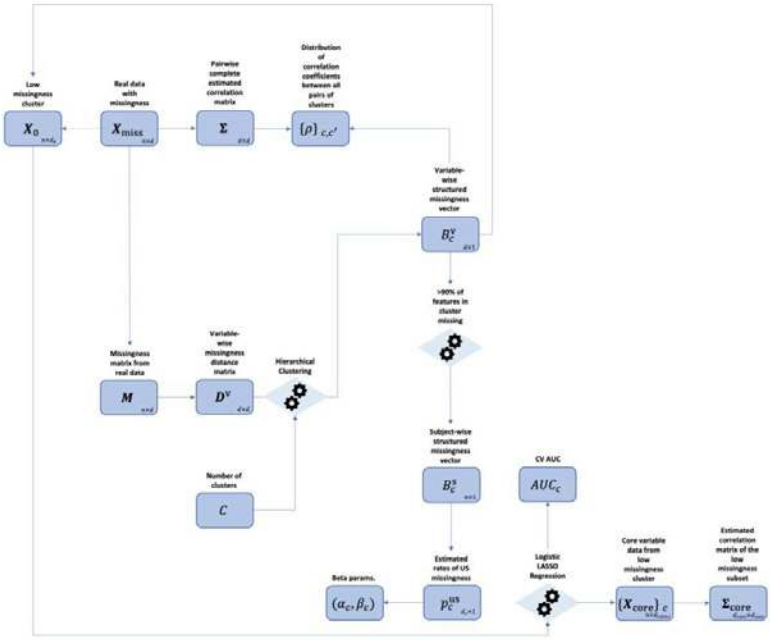

Fig. Analysis Pipeline

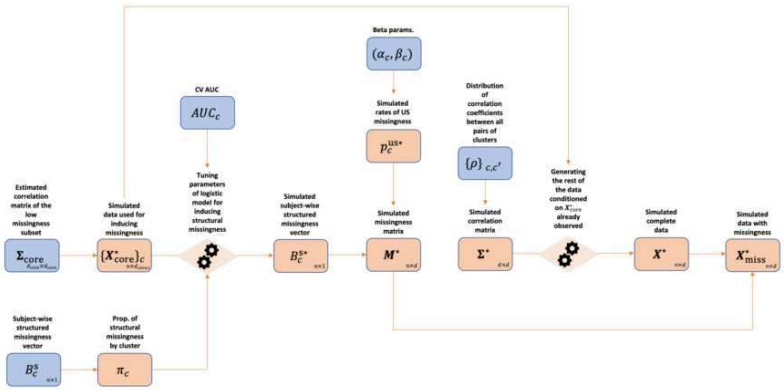

Fig. Generation Pipeline

Results: We evaluated the imputation accuracy of different methods from standard libraries over 20 synthetic data sets. Iterative imputation methods had the best overall performance. It was, however, also shown that it is very difficult to impute structurally missing data, likely due to the fact that highly correlated variables tend to be from the same sub-study, which means that they are mostly jointly missing. This was further demonstrated by comparing the results for our synthetic data sets to data sets with the exact same ground truth, but with completely unstructured missingness. The results from the simulation indicate that standard methods of handling missing data for analysis might give similar results as using mean or median imputation. We illustrated the conclusions of our simulation study by comparing results of variable selection of approx. 15,000 nIDPs for predicting gray matter volume, with imputation as a pre-processing step. Here, iterative imputation again gave the best results, but not much better than those using mean imputation.

Conclusions: The results from our simulation study as well as our illustrative example show that for analytical tasks performed on data with a highly structured missingness pattern, simple methods such as mean imputation will often give results that are similar to more advanced methods found in standard libraries. This means that further research is needed to develop methods that will handle this type of data.

References

1. R. Mitra, S. F. McGough, T. Chakraborti, C. Holmes, R. Copping, N. Hagenbuch, S. Biedermann,
2. J. Noonan, B. Lehmann, A. Shenvi, et al., Learning from data with structured missingness, Nature Machine Intelligence 5 (1) (2023) 13–23.
3. A. Fry, T. J. Littlejohns, C. Sudlow, N. Doherty, L. Adamska, T. Sprosen, R. Collins, N. E. Allen,
4. Comparison of sociodemographic and health-related characteristics of uk biobank participants with those of the general population, American journal of epidemiology 186 (9) (2017) 1026–1034.

Poster No 1924

Efficient Geometric Machine Learning for Brain Functional Connectivity Analysis

Kisung You[1], Hae-Jeong Park[2]

[1]City University of New York, New York, NY, [2]Yonsei Univ, Seoul, Seoul

Introduction: The enhanced availability of large-scale neuroimaging data has laid the foundation for population-level analysis of human brain functional connectivity, where brain network is conceptualized as a correlation matrix among signals from regions of interest. This paradigm, considering functional networks as a unit of analysis for inference, has gained popularity in recent years. Traditional approaches to the analysis of a population of functional networks involve concatenating every element in the lower triangular part of each correlation matrix into a vector. While convenient, this method overlooks the intrinsic association structure among edges of functional networks, failing to respect the perspective of brain as a highly correlation object.

Methods: In response to the intrinsic limitation to naive vectorization, a line of research has addressed the problem by leveraging a mathematical discipline of Riemannian geometry on the space of functional networks. This perspective treats each correlation matrix as a point on a geometric space known as the correlation manifold. Previous studies have explored the plausibility of a specific geometry, the quotient affine metric, applied to functional networks. Although mathematically elegant, this geometry has a practical drawback that even the simplest task of calculating the distance between two correlation matrices involves solving a nonlinear optimization problem, rendering it impractical for extrapolation into a broader class of problems. Recently, two alternative geometries - the Euclidean-Cholesky metric and log-Euclidean-Cholesky metric - have been proposed as alternatives due to their computational efficiency and theoretical soundness. These novel geometries employ diffeomorphism from the correlation manifold onto the Euclidean space, allowing for easily optimized computation. We investigate the comparative performance of these novel geometric formulations against established tools, demonstrating that this approach allows for efficient and robust computation while preserving geometric characterization on the relevant space. Building upon these findings, we introduce a comprehensive toolkit for statistical and machine learning on the space of correlation-based functional networks. Along the development of algorithms, we present theoretical justifications on why our choice of adaptation to the correlation manifold indeed makes sense. Major categories of inferential tasks include computing summary statistics, measuring similarity between two sets of observations, hypothesis testing, cluster analysis, dimensionality reduction for visualization, and regression on scalar responses.

Results: The proposed framework is evaluated on some public datasets including Human Connectome Project (HCP) and ADHD-200. In all experiments, functional networks were defined as partial correlation matrices of the processed functional magnetic resonance imaging signals. To summarize the results, we ran comparative analysis of performances for inferential tasks to predict scalar-valued survey outcomes, identify subtypes of a population, and visualize the distribution of a population of functional networks. In every scenario, we observed that the newly proposed geometries show comparable performance to the incumbent quotient geometry with statistically significant decrease in computational costs.

Conclusions: Our study contributes to the evolving landscape of population-level analysis of human brain functional connectivity by utilizing Riemannian geometry on the correlation manifold. Two geometric structures were introduced to extend our toolbox for machine learning to exploit the computational advantages of the contending geometries. Our contribution adds theoretical justification of geometry-aware inferential methods. Application to the real datasets shows that the new tools makes tremendous reduction in computational resources while maintaining compatible performance metrics at the comparable level.

References

1. David, P. and Gu, W. (2019), 'A Riemannian structure for correlation matrices', Operators and Matrices pp. 607–627.
2. Thanwerdas, Y. and Pennec, X. (2022), 'Theoretically and Computationally Convenient Geometries on Full-Rank Correlation Matrices', SIAM Journal on Matrix Analysis and Applications 43(4), 1851–1872.
3. You, K. and Park, H.-J. (2021), 'Re-visiting Riemannian geometry of symmetric positive definite matrices for the analysis of functional connectivity', NeuroImage 225, 117464.
4. You, K. and Park, H.-J. (2022), 'Geometric learning of functional brain network on the correlation manifold', Scientific Reports 12(1), 17752

Poster No 1925

Brain's Energy Budget: Integrating Information Costs and Metabolic Demand Along the Brain Connectome

Mahnaz Ashrafi Varnosfaderani[1], Gabriel Castrillón[2], Valentin Riedl[3]

[1]Technical University of Munich, Munich, Germany, [2]Friedrich-Alexander University, Erlangen, Germany, [3]Technical University of Munich, Erlangen, Germany

Introduction: The intricate human brain, a dynamic network of connections, dedicates a substantial portion of its energy budget, estimated at up to 90%, to neural signaling processes, especially synaptic transmission and action potentials. This energy-intensive process results in varying energy demands among regions, particularly those connected to highly active neighbors requiring increased signal integration. Traditional neuroimaging techniques, focused on structural and functional network topology, fall short in explaining energy variability across brain regions. Two regions with seemingly identical network topologies can have vastly different energy profiles, underscoring the need for a paradigm shift in brain network analysis. Our research proposes a novel perspective considering the topology and metabolic annotation of connected regions, defining a given region's 'activity importance' within the broader network. By focusing on the energy expended by each target region in integrating information from its connected 'source' regions, we aim to illuminate the complex interplay between connectivity and energy consumption in the brain, offering insights into how neural networks manage limited energy resources for information processing.

Methods: Main data: simultaneous FDG-PET/fMRI of twenty healthy right-handed subjects evenly split between genders, with an average age of 34.45 ± 5.06 years. Data was acquired by a 3T PET/MR scanner. Preprocessing was done by using a standard pipeline of C-PAC. We propose a novel regional information cost (IC) model across the human brain cortex. We hypothesize that regions connected to more influential regions with higher energy consumption demand greater energy costs for information integration. Each region termed the target node, has an IC value based on regional energy consumption and the impact coefficient of its connected nodes called sources. The impact coefficient calculated by the mutual information (MI) network signifies the influence of each source on its respective target. IC for each target (t) is computed by a weighted summation of energy metabolic values of sources (Es) with respective impact coefficients (α(t,s))(Fig 1. a). Energy metabolic values (CMRglc) and MI network acquired from simultaneous fMRI/FDG-PET (Fig.1.b, c).

Results: IC map across the cortex was identified on the group level, with peak values in the angular and frontal cortex (Fig. 1d). It is important to note that the CMRglc of each target is not included in its IC. We found a strong statistically significant correlation between the target's CMRglc and IC values at the group (group: $r = 0.64$, p-value $< 1e\text{-}10$) and individual levels (Fig. 1e, f). This finding indicates that 40% of the variance in the region's CMRglc values can be attributed to external parameters related to sources (Es and α(t,s)). To reinforce the robustness of our findings, we replicated the analysis using two other datasets (TUM.closed-eyes and Wien). We found a significant correlation between IC and CMRglc for targets using group data (scatter plot in Fig.1 g, h) and individual data (box plots in Fig.1 g, h) for two datasets. We did a network analysis and found the IC for each network. Higher cognitive networks such as DMN have higher IC and a stronger correlation with CMRglc.

Conclusions: We employ diverse datasets to demonstrate a highly significant correlation between the target's IC map and its actual CMRglc. This suggests that the IC is a reliable CMRglc map estimate. This model indicates that regions connected to active regions are exposed to higher information rates and demand higher energy. Our network analysis also approves this result, which represents that cognitive regions such as DMN integrating information have higher IC value.

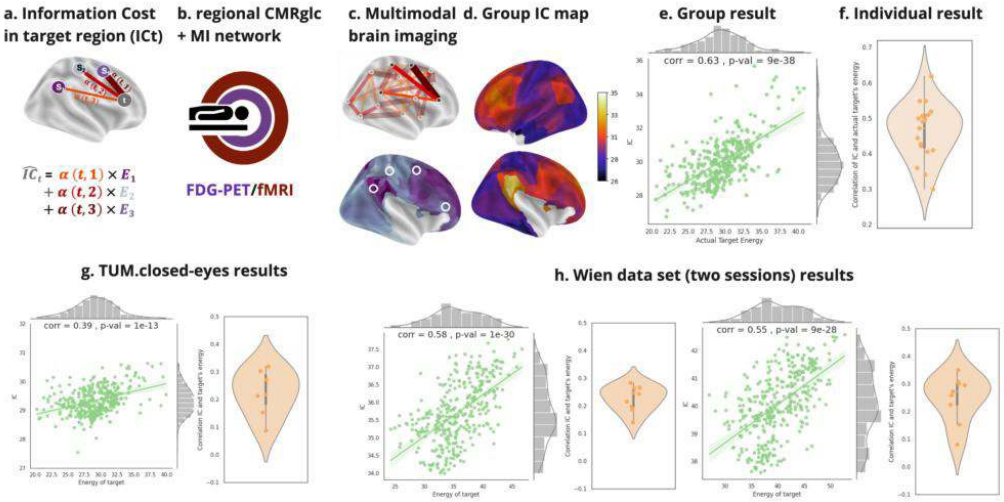

Fig 1. Calculating IC, an estimation of consumed energy for integrating information, for a specific target region and finding its correlation with actual energy consumption. **(a)** The information cost (IC) of a given target region (t) is calculated by combining the energy (Es) derived from PET data and the impact coefficient (*α(t,s)*) derived from fMRI data. IC is defined as the weighted summation of sources' energy, where the weights are the impact coefficient of each source. **(b)** We used simultaneous FDG-PET/fMRI data to implement our model. We did all the analysis in regional space. **(c)** FDG-PET data was used to quantify each region's energy consumption, CMRglc. The CMRglc value for each brain region is obtained by calculating the median of CMRglc values across voxels within that region. The impact coefficient of each connected region or source on its related target region, *α(t,s)*, has been computed using the average BOLD signal of each region (see Methods). **(d)** Average IC map over subjects on the brain surface **(e)** IC estimates energy consumed for integration. To evaluate the model performance, we found the correlation between the IC map and the actual energy, CMRglc, map. This scatter plot presents the average IC values of target regions and their corresponding actual CMRglc consumption values across subjects. A strong significant correlation (corr = 0.63, pval < 1e-10) between IC and CMRglc indicates IC is an appropriate energy consumption estimation at the group level. **(f)** We also extended our analysis to the individual level and found this correlation for each individual subject. All subjects have significant correlations stronger than 0.3. We investigated the reliability of our findings using two external datasets. **(g)** TUM.closed-eyes, the group-level results have been shown in a scatter plot (corr = 0.39, pval < 1e-10), and the box plot illustrates the individual correlation between IC and CMRglc for all subjects. **(h)** Wien datasets with two sessions. Using group-level data, the scatter plot demonstrates the correlation between target IC and CMRglc. The box plot illustrates the individual correlation between IC and CMRglc for all subjects. The correlation coefficients for the two sessions are 0.58 and 0.55, respectively, both demonstrating a statistically significant relationship with a p-value less than 1e-10.

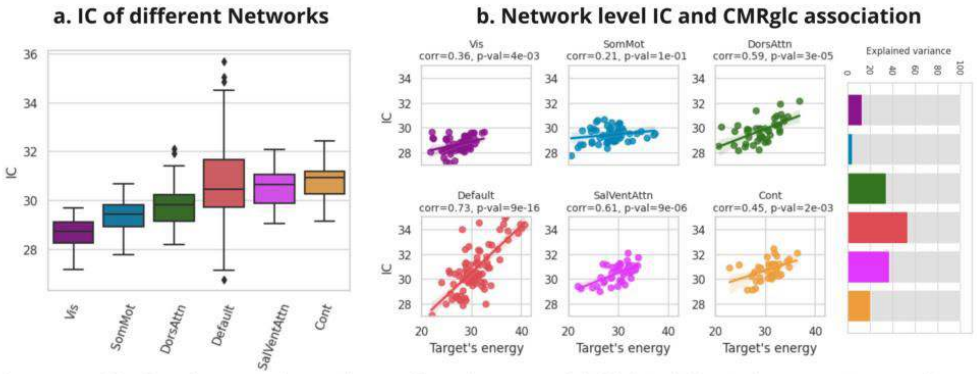

Fig 2. Network-level results. (a) IC values are illustrated for each Yeo network, highlighting higher IC values in cognitive networks, particularly the default mode, compared to sensory-motor networks (Vis and SomMot). **(b)** Correlation values between IC and CMRglc for each network, enabling the ranking of networks as default mode (red), ventral attention (pink), dorsal attention (green), frontoparietal control (orange), visual (purple), and somatomotor (blue). Each network's explained variance of IC has been illustrated on the right side as a bar plot. Higher-order networks can explain the IC variance better than the sensory-motor network; the default mode can explain 53% of the IC variability. Then ventral attention, dorsal attention, and control explain 37%, 35%, and 20% of the IC variability, respectively.

References

1. Attwell, David, and Simon B. Laughlin. "An energy budget for signaling in the grey matter of the brain." Journal of Cerebral Blood Flow & Metabolism 21, no. 10 (2001): 1133-1145.
2. Sporns, Olaf. "The human connectome: a complex network." Annals of the new York Academy of Sciences 1224, no. 1 (2011): 109-125.
3. Telesford, Qawi K., Sean L. Simpson, Jonathan H. Burdette, Satoru Hayasaka, and Paul J. Laurienti. "The brain as a complex system: using network science as a tool for understanding the brain." Brain connectivity 1, no. 4 (2011): 295-308.
4. Bullmore, Ed, and Olaf Sporns. "The economy of brain network organization." Nature reviews neuroscience 13, no. 5 (2012): 336-349.
5. Conrad, Mireille, Elisabeth Engl, and Renaud B. Jolivet. "Energy use constrains brain information processing." In 2017 IEEE International Electron Devices Meeting (IEDM), pp. 11-3. IEEE, 2017.
6. Tomasi, Dardo, Gene-Jack Wang, and Nora D. Volkow. "Energetic cost of brain functional connectivity." Proceedings of the National Academy of Sciences 110, no. 33 (2013): 13642-13647.
7. Aiello, Marco, Elena Salvatore, Arnaud Cachia, Sabina Pappatà, Carlo Cavaliere, Anna Prinster, Emanuele Nicolai, Marco Salvatore, Jean-Claude Baron, and Mario Quarantelli. "Relationship between simultaneously acquired resting-state regional cerebral glucose metabolism and functional MRI: a PET/MR hybrid scanner study." Neuroimage 113 (2015): 111-121.
8. Palombit, Alessandro, Erica Silvestri, Tommaso Volpi, Marco Aiello, Diego Cecchin, Alessandra Bertoldo, and Maurizio Corbetta. "Variability of regional glucose metabolism and the topology of functional networks in the human brain." NeuroImage 257 (2022): 119280.

Poster No 1926

Specialized White and Gray Matter Brain Age Models Using Conditional Variational Autoencoder

Jinghang Li[1], Chang-Le Chen[1], Linghai Wang[1], Shaolin Yang[1], Howard Aizenstein[1], Minjie Wu[1]

[1]*University of Pittsburgh, Pittsburgh, PA*

Introduction: Brain age (BA) prediction models have emerged as valuable tools for understanding individual differences in brain aging trajectory. These models, typically constructed using machine learning techniques, aim to estimate the overall brain health by predicting brain age based on structural MRI data (Lee, Burkett et al. 2022). Using these BA models, women are found to be 1.5-3.5 years younger than men (Lee, Burkett et al. 2022). This obviously does not align with the epidemiologic findings that women are disproportionately affected by dementia (Zhu, Montagne et al. 2021). This suggests that existing BA models are not sufficient to characterize brain aging. Therefore, in this study, we designed and implemented two distinct deep learning-based brain age models with one focusing on the cortical gray matter (GM) while the other on the cerebral white matter (WM). We hypothesize that our WM-BA model can better capture small vessel disease (SVD) related brain aging than GM-BA models.

Methods: Both the gray matter and the white matter brain age prediction models take in 3D volumetric input images. While gray matter model takes in cortical thickness map (Rebsamen, Rummel et al. 2020), the white matter model takes in myelin ratio map (Hannoun, Kocevar et al. 2022). We constructed age conditioned variational autoencoder with 3D convolution blocks for the encoder-decoder component and multilayer perceptron (MLP) for the brain age prediction component (see figure 1 for detailed model schematics). We trained our models on the HCP healthy aging dataset (female, n=396; male, n=316) (Bookheimer, Salat et al. 2019) with an 80-20 training-testing ratio to mitigate overfitting. The trained models' adaptability was tested by conducting model inference on the Cam-CAN healthy aging dataset (Shafto, Tyler et al. 2014), and the credibility of BA predictions was validated through examination of the models' encoded latent space. Additionally, we explored correlations between brain age gaps and white matter lesion burdens (white matter lesion volume/intracranial volume). Both the white matter lesions and the brain segmentations were extracted from FreeSurfer (Fischl 2012). All brain age predictions have been bias corrected via fitted linear regression models (Beheshti, Nugent et al. 2019).

Figure 1. End to end schematics of the implemented brain age prediction models. The models training images were first obtained by running the established pipelines that generates the cortical thickness map and the myelin ratio map respectively. All training images were registered to the 1mm isotropic MNI template before training. The detailed VAE model layout is illustrated in the figure below. Age conditioned generative model output and brain age predictions are also shown here.

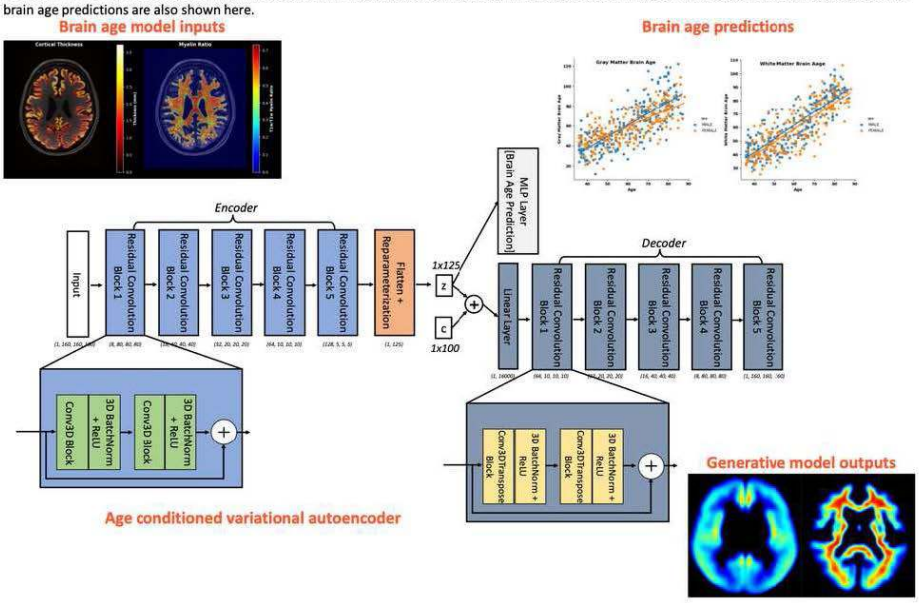

Results: Figure 1 illustrates the generated cortical thickness map and myelin ratio map, along with the model's brain age predictions and reconstructed structural outputs. Figure 2 visualizes the model's latent vectors from the Cam-CAN dataset and revealed effective disentanglement on the age feature, enhancing MLP's predictability (Zhao, Adeli et al. 2019) (figure 2.a., 2.c.). Further, the linear regression models between brain age gap and the white matter lesion burdens illustrates that WM-BA gap correlates with white matter lesions ($p=0.000001$, $r=0.25$) better than GM-BA gap ($p=0.0003$, $r=0.19$), suggesting compared to gray matter brain age model, white matter brain age model can better capture cerebrovascular aging (figure 2.b., 2.d.). Lastly, our brief exploratory analysis showed that women can be more resilient in gray matter decay than men do in healthy aging, suggesting gray matter brain age models fail to capture SVD-related brain aging in women (figure 2.b., 2.d.).

Figure 2. Visualization of the brain age models encoded latent vectors and association of brain age gap with white matter lesion burdens. Figure 2.a. and 2.c. illustrate the disentangled latent vector with respect to age while figure 2.b. and 2.d showcase the two-brain age model's credibility with white matter lesion burdens (gray matter model: p=0.0003, r=0.19; white matter model: r=0.3, p=0.000001). While both models significantly correlate with the aging biomarker, white matter brain age model shows much stronger correlations.

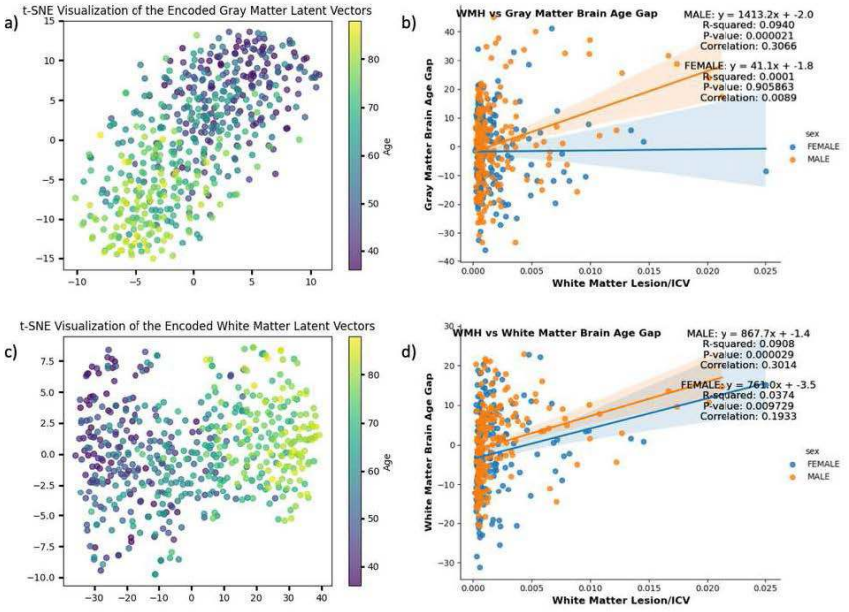

Conclusions: In summary, this work demonstrates the potential avenue for developing specialized brain aging models that facilitate better understanding in brain aging trajectories across different regions as well as across sex.

References

1. Beheshti, I. (2019). "Bias-adjustment in neuroimaging-based brain age frameworks: A robust scheme." Neuroimage Clin 24: 102063.
2. Bookheimer, S. Y. (2019). "The Lifespan Human Connectome Project in Aging: An overview." Neuroimage 185: 335-348.
3. Fischl, B. (2012). "FreeSurfer." Neuroimage 62(2): 774-781.
4. Hannoun, S. (2022). "T1/T2 ratio: A quantitative sensitive marker of brain tissue integrity in multiple sclerosis." J Neuroimaging 32(2): 328-336.
5. Lee, J. (2022). "Deep learning-based brain age prediction in normal aging and dementia." Nature Aging 2(5): 412-424.
6. Rebsamen, M. (2020). "Direct cortical thickness estimation using deep learning-based anatomy segmentation and cortex parcellation." Hum Brain Mapp 41(17): 4804-4814.
7. Shafto, M. A., (2014). "The Cambridge Centre for Ageing and Neuroscience (Cam-CAN) study protocol: a cross-sectional, lifespan, multidisciplinary examination of healthy cognitive ageing." BMC Neurol 14: 204.
8. Zhao, Q. (2019). "Variational AutoEncoder For Regression: Application to Brain Aging Analysis." Med Image Comput Comput Assist Interv 11765: 823-831.
9. Zhu, D. (2021). "Alzheimer's pathogenic mechanisms and underlying sex difference." Cell Mol Life Sci 78(11): 4907-4920.

Poster No 1927

Locating Seed Automatically in PCC for rs-fMRI Data Analysis by Using Unsupervised Machine Learning

Mingyi Li[1], Katherine Koenig[2], Mark Lowe[2]

[1]Cleveland Clinic, Cleveland, OH, [2]The Cleveland Clinic, Cleveland, OH

Introduction: When using seed-based methods to analyze resting state fMRI (rs-fMRI) data, the selection of the seed has large influence on the results. In previous study, we presented a method to automatically produce seed locations from voxel clusters generated by self-organizing map (SOM) whose input was feature vectors formed by combining anatomical and rs-fMRI data[1]. The limitation of the work was bad seed search ROI derived from FreeSurfer brain parcellation in some subjects. To solve the problem, we attempted to propagate template searching ROI to individual subjects by using nonlinear registration. However, the improvement was not obvious compared to FreeSurfer method. Later, we found out SynthSeg, a deep learning based brain parcellation tool, produced obviously better results in brain gray matter parcellation in one of our datasets[2]. In this study, we tested seed searching ROI generated by using SynthSeg[3].

Methods: Data acquisition: Nineteen subjects consisting six healthy controls and thirteen patients were scanned in an IRB-approved protocol at 3T Siemens scanner (Erlangen, Germany) using a bitebar to reduce head motion, in a 12-ch receive

head coil. Scans included T1-MPRAGE (voxel size=1x1x1.2mm, matrix size=256x256x120, TE/TR/TI=1.75/1900/900ms), and rs-fMRI(voxel size=2x2x4mm, matrix size=128x128x31, TR/TE/FA=2800/29/80, 132volumes). Data processing: Each rs-fMRI dataset was motion-corrected, low-pass filtered and spatially filtered. T1 image was parcellated into ROIs by using SynthSeg. The ROIs were registered to rs-fMRI image space by using "align_epi_anat.py" tool in AFNI[4]. The ROI covering the left/right PCC was used as seed searching region for automatic seed generation method (Left side and right side are processed separately). From rs-fMRI data, the global connectivity between each voxel in the seed searching ROI and all other brain cortex voxels were computed and then the connectivity distribution was fitted into a Gaussian distribution[5]. The feature vector was formed by counting the number of voxels whose connectivity value was outside three standard deviations, in the parcellated cortex ROIs. The above feature vector forming step is shown in figure 1. Then the feature vectors of all the voxels in the searching region was feed into a size 4x5 SOM classifier in Matlab. For SOM cluster is further divided into spatially aggregated sub-clusters by using k-means clustering. At last, voxels with weak correlation to other voxels in the same cluster were discarded. The remaining voxels formed the seed clusters. The connectivity map of a seed cluster was the average of the connectivity maps computed for all the voxels in the seed cluster. Using each subject's rs-fMRI data, seeds in PCC were also manually located by experts through the "instacorr" method in AFNI. Seeds comparison: Seeds acquired through the automatic method were compared to those picked through the manual method.

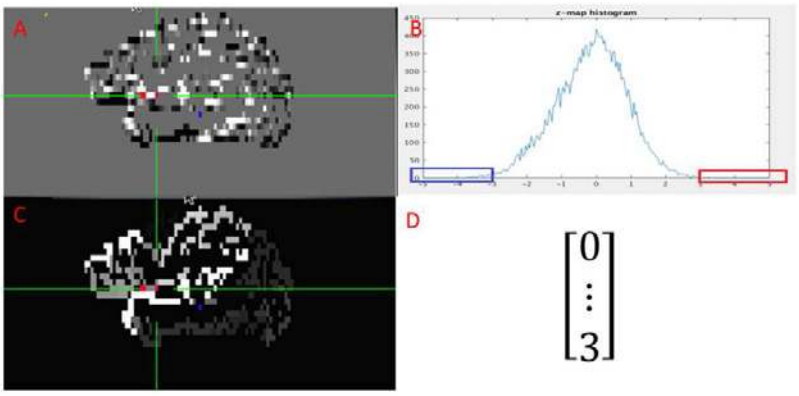

Figure 1. Generating feature vector by combining rs-fMRI connectivity and T1 parcellation. Panel A: Z-map, Panel B: Z-score distribution, Panel C: Brain parcellation, Panel D: feature vectors.

Results: In four out of six control subjects, there was one automatically generated seed overlapping with manually picked seed. There was no matching for the remaining two control subjects. In nine out of thirteen patients, there was one automatically generated seed overlapping with manually picked seed. There was no matching for the remaining four control subjects. SynthSeg apparently did a better job than FreeSurfer on generating seed searching region. For the two unmatched control and three unmatched patients, the manually located seed was partially inside the seed searching ROI of the automatic method. For one unmatched patient, the manually selected seed was outside searching ROI. One matched patient case is shown in figure 2.

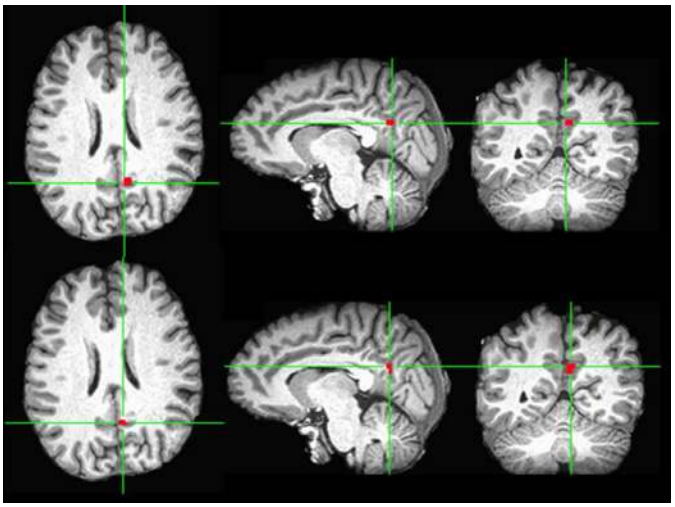

Figure 2. Matched seeds. Top row shows manually picked seed and bottom row shows automatically generated seed.

Conclusions: The performance of the automatic seed generation method was universal across control and patients. We will test out region grow technique on generating seed searching ROI. We will test out the method in a much larger dataset in an ongoing study.

References

1. M. Li, et al (2021), Locating seed automatically in posterior cingulate cortex for resting state fMRI data analysis by using unsupervised machine learning, ISMRM Virtual Conference & Exhibition
2. M. Li, et al (2023), Comparison of 7T MRI Brain Image Parcellation Results Between FreeSurfer and SynthSeg, 29th Annual Meeting of the Organization on Human Brain Mapping
3. Billot B., et al. (2022), Robust Segmentation of Brain MRI in the Wild with Hierarchical CNNs and no Retraining, MICCAI
4. Cox RW. (2012), AFNI: What a long strange trip it's been, NeuroImage, 62(2):743-747
5. Lowe MJ et al. (1998), Functional Connectivity in Single and Multislice Echoplanar Imaging Using Resting-State Fluctuations, NeuroImage, 7(1):119-132.

Poster No 1928

Normative modeling of statistical parameters

Richard Dinga[1], Thomas Wolfers[2], Mostafa Kia[1], Marijn van Wingerden[1]

[1]Tilburg University, Tilburg, Netherlands, [2]Laboratory for Mental Health Mapping, University of Tübingen, Tübingen, BW

Introduction: Normative modeling, inspired by pediatric growth charting, is a method in neuroimaging research to model the distribution of image-derived phenotypes in a reference population[1]. It quantifies individual atypicality by comparing measurements to reference centiles. A complication that hinders the development of normative models in neuroimaging is that, in contrast to body measurements in pediatrics, many variables derived from fMRI images, such as the effects of a stimulus or functional connectivity between regions, are only estimated, which means that they are measured with non-negligible error. This measurement error is not accounted for in standard normative modeling, resulting in the overestimated variance of the normative distribution. In this work, we propose a method to account for the known measurement error in normative modeling, leading to a more accurate estimation of normative models.

Methods: Our goal is to model an estimated neuro-imaging variable, such as the strength of an effect at a specific location or functional connectivity between regions, as a function of one or more variables, such as age and sex, and accurately estimate centiles of the distribution of these variables in a population. For this purpose, we propose a meta-regression random-effects model[2] for the kth subject: $y_k = \theta + \beta_1 x_{1k} + .. .+ \beta_n x_{nk} + \epsilon_k + \zeta_k$ Where θ is an intercept, β_1, ..., β_n are coefficients of independent variables x_1, ... x_n (e.g., age and sex). ζ_k are the between subjects random-effects assumed to be normally distributed with N(0, v), and ϵ_k is a normally distributed residual error term. Estimation of the normative distribution variance equals the estimation of the v from the random-effects model. Centiles are then calculated based on the centiles of the corresponding normal distribution. Experimental validation: We have randomly simulated data for 500 subjects with a uniformly distributed age variable between 20 and 80. The measurement-error-free outcome variable was simulated as 100 - age*0.1 - (age - 50)^2*0.005 + e where e was normally distributed with mean 0 and variance 1. Then, we simulated measurement error by adding a random noise with a mean of 0 and variance of 1.25 to the measurement error-free outcome (Figure 1A). We compared our proposed model with an ordinary least-squares model that did not account for the measurement error.

Results: Results can be seen in Figures 1B and 1C for the proposed method and standard method, respectively. The estimated centiles of the underlying normative distribution using the proposed method closely follow the true centiles, while using the standard method, they are too far apart. The proposed method estimated a variance of 0.99, and the standard method estimated a variance of 1.59. This is because the standard method does not differentiate between the measurement error and the variance of the underlying normative distribution and the estimated variance is estimated based on the mixture of the two distributions.

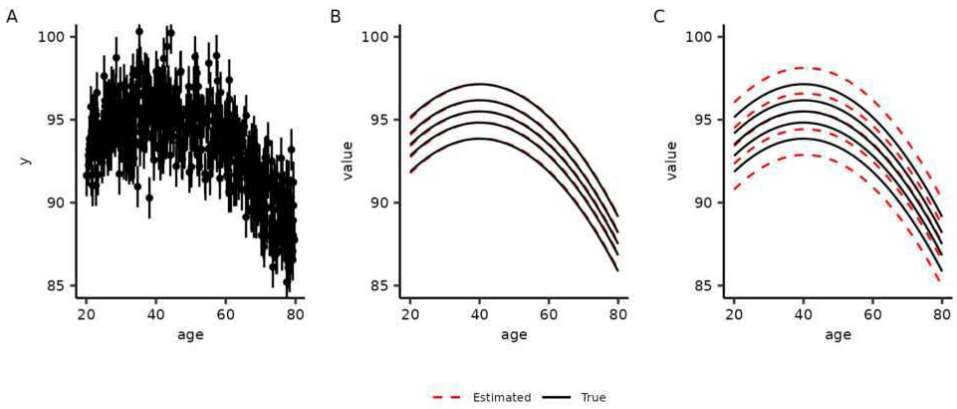

Comparison of an accuracy of estimated centiles using the proposed and standard methods for normative modeling in a simulation in the presence of measurement error.

Conclusions: The proposed method provides a crucial step for valid normative models of task activation data or resting state data, which are measured with noise. The limitation of the method is that it assumes a normal distribution of variables, which might not be the case in neuro-imaging data[3,4], and that the variance of the measurement error needs to be known or estimated beforehand and needs to be reasonably accurate since an underestimation of the measurement error will lead to an overestimation of the normative distribution and vice versa.

References

1. Dinga, Richard, Charlotte J. Fraza, Johanna M. M. Bayer, Seyed Mostafa Kia, Christian F. Beckmann, and Andre F. Marquand. 2021. "Normative Modeling of Neuroimaging Data Using Generalized Additive Models of Location Scale and Shape." bioRxiv. https://doi.org/10.1101/2021.06.14.448106.
2. Fraza, Charlotte J., Richard Dinga, Christian F. Beckmann, and Andre F. Marquand. 2021. "Warped Bayesian Linear Regression for Normative Modelling of Big Data." NeuroImage 245 (December): 118715.
3. Marquand, Andre F., Iead Rezek, Jan Buitelaar, and Christian F. Beckmann. 2016. "Understanding Heterogeneity in Clinical Cohorts Using Normative Models: Beyond Case-Control Studies." Biological Psychiatry 80 (7): 552.
4. Viechtbauer, Wolfgang. 2010. "Conducting Meta-Analyses in R with the Metafor Package." Journal of Statistical Software 36 (August): 1–48.

Poster No 1929

Detection and Segmentation of Enlarged Perivascular Spaces in the Brain

Mariam Zabihi[1], Carole Sudre[1]

[1]University College London (UCL), London, UK

Introduction: Enlarged perivascular spaces (EPVS) are small, fluid-filled cavities in the brain, associated with cognitive decline and dementia. Detecting EPVS is important for understanding cerebral small vessel diseases, but it's challenging due to their small size and variable locations, often confused with white matter hyperintensities in imaging[1-3]. Advances in 3D object detection models in medical imaging have improved the detection of small features like EPVS[4-6]. However, these methods face limitations in accurately capturing the complex morphology of EPVS. This paper presents a model that integrates advanced detection techniques with more representative geometric shapes, aiming to enhance the detection of EPVS. Our approach potentially improves the accuracy in identifying EPVS, contributing to the broader efforts in neurological research and the understanding of cerebrovascular diseases.

Methods: In our study, we employed a 3D Region Convolutional Neural Network (RCNN) for detecting and segmenting Enlarged Perivascular Spaces (EPVS), involving four stages: 1. Feature Learning: A 3D convolutional U-Net architecture[7]was trained on input images to learn key features, using a distance map to enhance feature extraction. 2. Region Proposal Network (RPN): Feature maps from the U-Net fed into an RPN, which generated score maps to identify potential EPVS-containing regions. 3. Non-Maximum Suppression: This stage involved filtering low-confidence regions and eliminating overlapping ellipsoids, using Hellinger[8] and Euclidean distances for optimization. 4. Object Detection and Segmentation: High-confidence ellipsoids were analyzed by another network for precise object detection, integrated with the U-Net's distance map for improved segmentation. For object shape encoding, a simplified seven-parameter ellipsoid was used, focusing on the largest eigenvalue for scale and direction, and fractional anisotropy for spread. The method's pipeline

is shown in Figure 1. For performance assessment in our study, we used the VALDO challenge code, providing four key metrics: two for detection (Absolute element difference and F1 score) and two for segmentation quality (Mean dice over true positive elements and absolute volume difference). An element was deemed a true positive if its Intersection over Union with the ground truth exceeded 0.10. Our experiments focused on: - Segmentation performance based on different imaging modalities (T1, T2, FLAIR, and their combinations). - Performance variability in segmentation and detection based on brain location. - Performance on the VALDO test set (SABRE component). We trained seven distinct models using different modality combinations and assessed them using leave-one-out cross-validation. Each model was trained on random 3D image patches. Data: The Where is VALDO? challenge was run in 2021 as satellite event of MICCAI[9]. It featured 3 tasks focusing on the detection and segmentation of small markers of cerebral small vessel disease namely EPVS, cerebral microbleeds, and lacunes. For this study, we used the six subjects from the SABRE dataset available for training. The elements were segmented manually using structural MR sequences coregistered to the 1mm3 isotropic T1-weighted sequence (T1-weighted, T2-weighted, T2 FLAIR) by two raters. The final label was generated by taking the union of the objects that have been annotated by both raters. Furthermore, only objects larger than 2 voxels were considered, resulting in a database comprising 1864 EPVS elements.

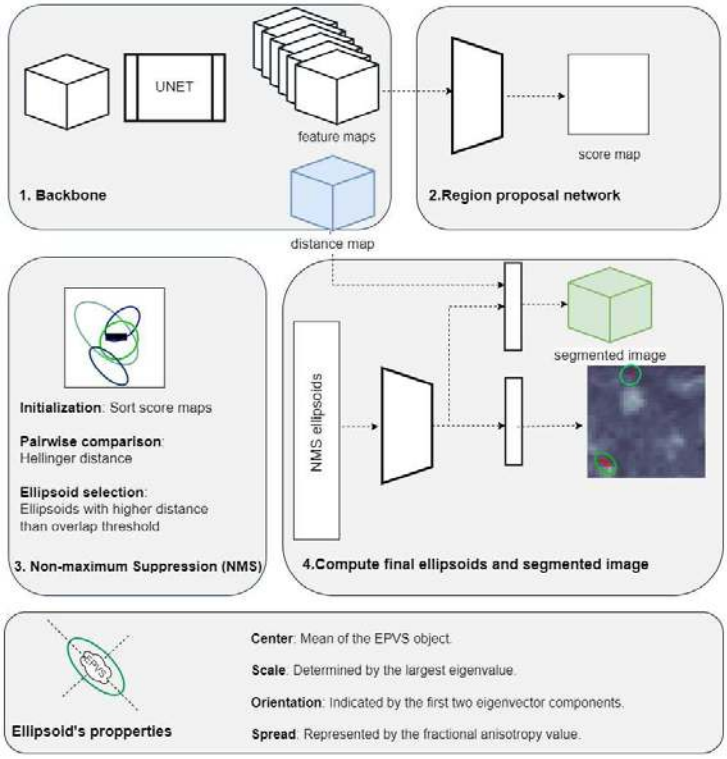

Results: The out-of-sample results presented in Table 1 show the average performance across the cross-validated models for the different modality combinations. Figure 2 shows an example of the gold standard and the model's output in T2 modality.

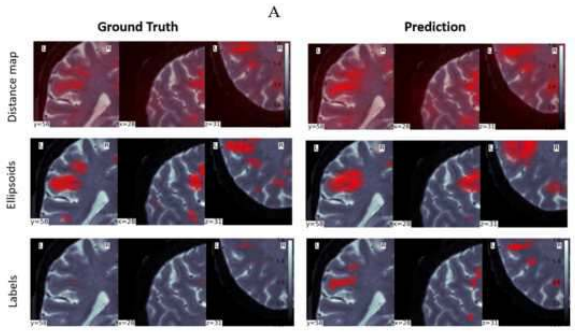

Figure 2: A) Comparative visualization of gold standard and predictive model outputs on an example patch. The first column exhibits the 'gold standard', expert-annotated examples for comparison, the second column displays the corresponding outputs generated by our 3D-UNET (distance map) and 3D RCNN models. All images are overlaid on T2-weighted MR image patch. B) Segmentation visualization Overlaid on a Full 3D T2-weighted MRI Scan

Table 1. Model Performance Summary (mean and standard deviation across six subjects for each measure) for the different modality combinations on the left-out sample in the cross-validation setting.

Modality	Absolute difference	F1	Dice	Absolute volume difference
T1	167 ± 78	0.16 ± 0.04	0.39 ± 0.03	2014 ± 1815
T2	132 ± 80	0.21 ± 0.04	**0.43 ± 0.04**	**2107 ± 1978**
FLAIR	192 ± 105	0.02 ± 0.01	0.21 ± 0.1	2759 ± 225
T1 ⁞ T2	**114 ± 82**	**0.22 ± 0.03**	**0.43 ± 0.04**	2180 ± 1810
T1 ⁞ FLAIR	188 ± 91	0.09 ± 0.09	0.35 ± 0.05	2529 ± 2409
T2 ⁞ FLAIR	151 ± 104	0.13 ± 0.06	0.37 ± 0.04	2366 ± 2109
T1 ⁞ T2 ⁞ FLAIR	140 ± 78	0.20 ± 0.05	**0.43 ± 0.04**	2642 ± 1435

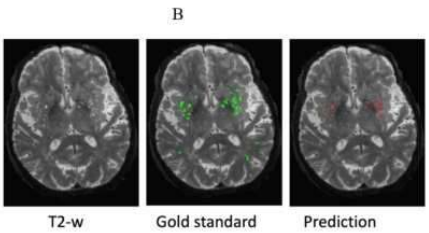

Conclusions: his study adapts advanced object detection methods, using ellipsoid shapes in Fast R-CNN, to improve EPVS detection. Results show that T2 imaging, alone or with T1, enhances detection and segmentaion performance.

References

1. Bown C.W. (2022), 'Physiology and Clinical Relevance of Enlarged Perivascular Spaces in the Aging Brain'. Neurology 98(3) 107-117
2. Paradise M. (2021), ' Association of Dilated Perivascular Spaces With Cognitive Decline and Incident Dementia', Neurology 96(11) 1501-1511
3. Ding J. (2017),' Large Perivascular Spaces Visible on Magnetic Resonance Imaging, Cerebral Small Vessel Disease Progression, and Risk of Dementia: The Age, Gene/Environment Susceptibility–Reykjavik Study. JAMA Neurology74(9)1105–1112 (2017)
4. sgari Taghanaki S.(2021),' Deep semantic segmentation of natural and medical images: a review. Artificial Intelligence', Review54 137–178
5. Ranjbarzadeh R. (2023),'Brain tumor segmentation of MRI images: A comprehensive review on the application of artificial intelligence tools'. Computers in Biology and Medicine 152
6. Ribli D. (2018),' Detecting and classifying lesions in mammograms with Deep Learning'. Scientific Reports8(1: 4165
7. Çiçek, Ö.(2016),' 3D U-Net: Learning Dense Volumetric Segmentation from Sparse Annotation' . Medical Image Computing and Computer-Assisted Intervention – MICCAI
8. Fu, GH.:(2020). Hellinger distance-based stable sparse feature selection for high-dimensional class-imbalanced data. BMC Bioinformatics 21(121)
9. Sudre, C. (2022). Where is VALDO? VAscular lesions detection and segmentation challenge at MICCAI 2021. arXiv preprint arXiv:2208.07167

Poster No 1930

BigBrain Image blind restoration and alignment with generative priors, U-Net and similarity

Mingli Zhang[1], Paule Toussaint[2], Claude Y. Lepage[3], Alan Evans[4]

[1]Mcgill University, Montreal, Quebec, [2]McGill University, Montreal, Quebec, [3]McGill Centre for Integrative Neuroscience (MCIN), Montreal, Quebec, Montreal, Quebec, [4]McGill Centre for Integrative Neuroscience (MCIN), Montreal, Quebec

Introduction: Human brain atlases play a crucial role in providing a spatial framework to organize information derived from diverse research on brains, integrating multimodal and multiresolution images. Recent progress in high-throughput scanning technology, coupled with powerful computing resources, has enabled a higher level of automation in digitizing and analyzing entire sections of the human brain at microscopic resolution. The development of the high-resolution BigBrain model[1] has paved the way for creating comprehensive maps of cytoarchitectonic regions with full microscopic detail, covering extensive image stacks that span thousands of sections. However, many of the scanned BigBrain sections exhibit unknown degradation, low resolution, and noise, resulting in issues like image blurring and misalignment. We present a pipeline that depends on two models to effectively address actual image restoration and realignment when the relationship between high resolution and low resolution images is unknown.

Methods: In the first part, we propose a blind super-resolution model to address the resolution upscaling scenario when the function for mapping high-resolution and low-resolution images is unknown. Our solution relies on three training modules with different learning objectives: 1. a degradation-aware network (U-Net) to synthesize the high resolution image, given a low resolution image and the corresponding blur kernel; 2. a pre-trained generative adversarial network (GAN) to be used as prior, bridged to the U-Net by a latent code mapping and several channel-split spatial feature transforms (CS-SFTs)[2 3]; and 3. a rational polynomial image interpolation into deep convolutional neural networks (CNNs) to retain details. The second aspect of the pipeline considers the generic problem of dense alignment between two images, whether they be two frames of a video, two widely different views of a scene, two paintings depicting similar content, or serial histological sections. While such task is typically addressed with a domain-specific solution, near-duplicates interpolation or alignment, large blurring still challenges existing methods. To address this issue, we adopt a feature extractor that shares weights across the scales and optimize our network with the Gram matrix loss that measures the correlation difference between features. The fine alignment is then learned in an unsupervised manner by a deep network that optimizes a standard structural similarity metric (SSIM) between the two images. We evaluated the performance of this method on degraded 2D sample patches from 10- and 1-micron sections of the BigBrain dataset, and on natural scene images.

Results: Fig 1. Flowchart of the proposed approach (a), applied to image alignment on natural scene images (b), and restoration of 1-micron sections of the BigBrain dataset (c). Generated video with two inputs of 10-micron sections of the BigBrain images. (d) comparisons on PSNR and blind image quality assessment (SoftSplat[3] FILM[4]) Fig 2. Image alignment results on 1-micron (a) and 10-micron sections (b) of the BigBrain dataset. We observed improved detailed structure in the final restored images at cellular resolution. Scores for spatial quality, naturalness, and perception-based image quality evaluation metrics were greatly

improved overall for images restored using our approach compared to the original data. The results for alignment of 1-micron BigBrain images show the superior performance of the proposed approach.

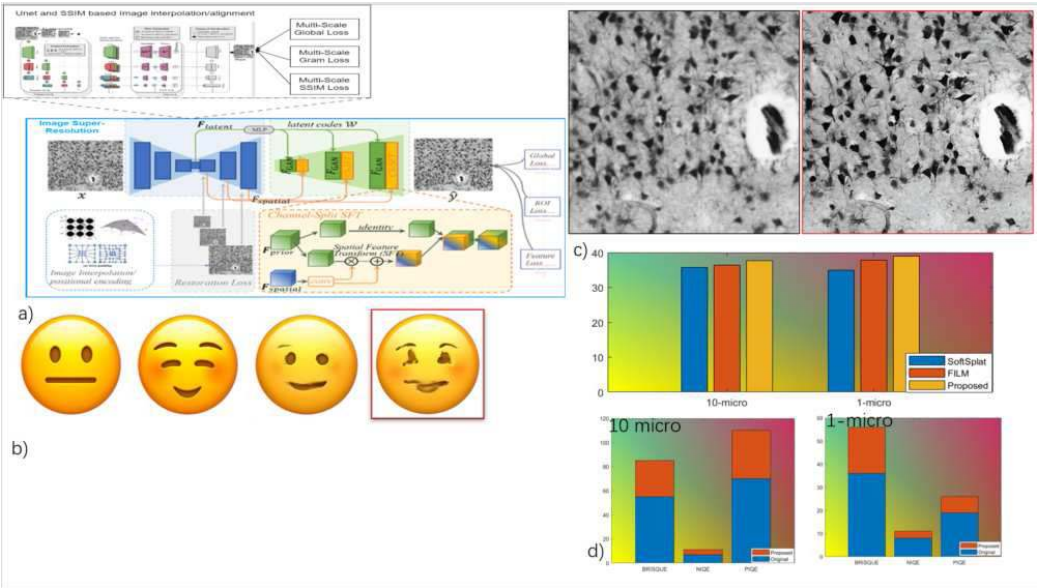

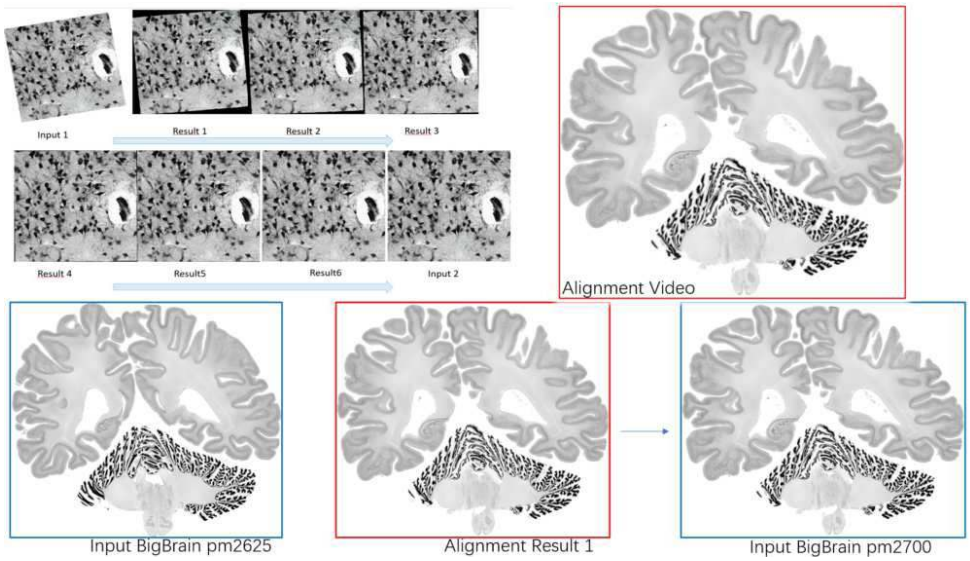

Conclusions: Effective blind preprocessing of the degraded BigBrain images can be used for enhancing their quality, addressing issues related to deterioration and misalignment, and ensuring that subsequent analyses and interpretations are based on reliable and accurate data. The resulting improved image quality consequently supports more robust findings in neuroscientific studies.

References

1. Amunts K, Lepage C, Borgeat L, Mohlberg H, Dickscheid T, Rousseau MÉ, Bludau S, Bazin PL, Lewis LB, Oros-Peusquens AM, Shah NJ, Lippert T, Zilles K, Evans AC. BigBrain: an ultrahigh-resolution 3D human brain model. Science. 2013 Jun 21;340(6139):1472-5. doi: 10.1126/science.1235381.
2. Wang, X., Li, Y., Zhang, H., & Shan, Y. (2021). Towards real-world blind face restoration with generativefacial prior. In Proceedings of the IEEE/CVF Conference on Computer Vision and Pattern Recognition (pp.9168-9178).
3. Bian, S., Xu, X., Jiang, W., Shi, Y., & Sato, T. (2020, October). BUNET: blind medical image segmentation based on secure UNET. In International Conference on Medical Image Computing and Computer-AssistedIntervention (pp. 612-622). Springer, Cham.
4. Niklaus, S., Liu, F.: Softmax splatting for video frame interpolation. In: Proceedings of the IEEE/CVF Conference on Computer Vision and Pattern Recognition. pp. 5437–5446 (2020)
5. Reda, F., Kontkanen, J., Tabellion, E., Sun, D., Pantofaru, C., & Curless, B. (2022, October). Film: Frame interpolation for large motion. In European Conference on Computer Vision (pp. 250-266). Cham: Springer Nature Switzerland.

Poster No 1931

Cluster-aware machine learning of robust brain-behavior associations for precision neuropsychiatry

Amanda Buch[1], Conor Liston[1], Logan Grosenick[1]

[1]*Weill Cornell Medicine, Cornell University, New York, NY*

Introduction: Explainable machine learning of complex multimodal data in neuroscience research is revolutionizing precision neuropsychiatry. Interpretable clustering of patients into distinct subtypes can enhance personalized prognosis, diagnosis, and treatment. However, training on biomedical data poses challenges due to high dimensionality, clustering, and limited sample size. To address this, we propose a scalable approach for cluster-aware embedding, incorporating a convex clustering penalty. This approach facilitates hierarchical clustering of principal component analysis (PCA), locally linear embedding (LLE), and canonical correlation analysis (CCA). Our method improves upon existing techniques and offers a modular framework for interpretable biomarker discovery in precision medicine. We apply this approach to identify neurocognitive subtypes in the Adolescent Brain Cognitive Development (ABCD) and Autism Brain Imaging Data Exchange (ABIDE) datasets.

Methods: Clustering algorithms are often considered difficult optimization problems. However, by relaxing certain constraints, clustering algorithms can be reformulated as convex optimization problems by relaxing the hard clustering constraint ("convex clustering")[3]. Here, we introduce Pathwise Clustered Matrix Factorization (PCMF) and its multi-view extension, incorporating a convex clustering penalty to make embedding methods cluster-aware. PCMF does not require pre-determining the number of clusters and can generate a dendrogram for subtype discovery in biomedical datasets. It fits a path of solutions along a sequence of parameters and estimates split points based on model fit improvement. We extend our PCMF approach to include canonical correlation analysis (CCA) within clusters, introducing pathwise clustered canonical correlation analysis (P3CA). We apply P3CA to discover neurocognitive subtypes in the Adolescent Brain Cognitive Development (ABCD)[5] and Autism Brain Imaging Data Exchange (ABIDE)[6-7] datasets. In the first case study, we use resting state functional connectivity (RSFC) and behavioral (ADOS-2 and verbal IQ) data from N=299 individuals with autism spectrum disorder (ASD) in the ABIDE dataset. In the second case study, we use RSFC and behavioral (NIH Toolbox) data from N=490 adolescents in the ABCD dataset. We implemented a stringent preprocessing of both datasets following or exceeding well-established guidelines[8–9]. Prior to fitting P3CA to the ABIDE and ABCD datasets, we perform robust feature selection as previously described[2]. We evaluated the stability of neurocognitive subtypes by randomly holding out 30% of the data and recalculating P3CA.

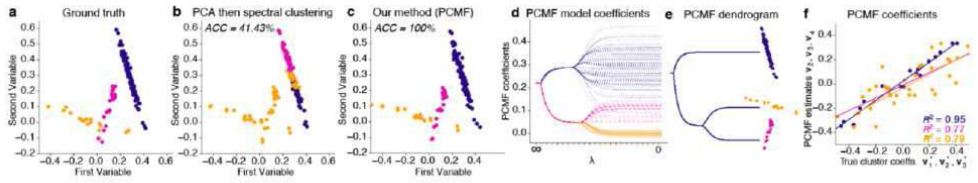

Figure 1: PCMF for explainable joint PCA and hierarchical clustering. **a.** Scatterplot of reconstructed ground truth data (PCA rank $r = 4$) for 3-class problem; $p = 20$; $N_1 = 100$ (blue), $N_2 = 25$ (pink), $N_3 = 25$ (orange), colored by true cluster membership. **b.** PCA ($r = 4$) sequentially followed by spectral clustering on PCA components. **c.** Joint PCA and clustering with PCMF ($r = 4$; $\lambda = 3.0$). Two-step procedures in **b-c** fail to find correct clusters while PCMF succeeds. Color indicates predicted clusters. **d.** PCMF paths for variable 1 fit along decreasing penalty path ($\lambda = \infty$ to $\lambda = 0$). **e.** Interpretable PCMF dendrogram estimated from paths. **f.** PCMF coefficients accurately fit ground truth cluster-specific coefficients used to generate data. PCMF coefficients $\mathbf{v_2}$, $\mathbf{v_3}$, and $\mathbf{v_4}$ approximate true cluster coefficients ("slopes") $\mathbf{v_1^*}$ (blue), $\mathbf{v_2^*}$ (pink), and $\mathbf{v_3^*}$ (orange).

Results: Applying P3CA to the ABIDE dataset, we found strong differences in associations of ASD subtype embeddings with behavior and RSFC (Fig. 2), consistent with known autism subpopulation differences of behaviors with prefrontal cortex to somatosensory cortex, posterior parietal cortex, and middle temporal gyrus[2]. Subject-level P3CA embedding coefficients were robust to data perturbation (cosine similarity: 0.93 ± 0.05 for U estimates; 0.97 ± 0.03 for V estimates). Our method provides clearer cluster separation and improved interpretability. Applying P3CA to the ABCD dataset, we identified cluster-specific brain-behavior embeddings that described two neurocognitive phenotypes (separating high/low crystallized vs. fluid intelligence individuals), which were robust in replication in a second partition of the ABCD dataset.

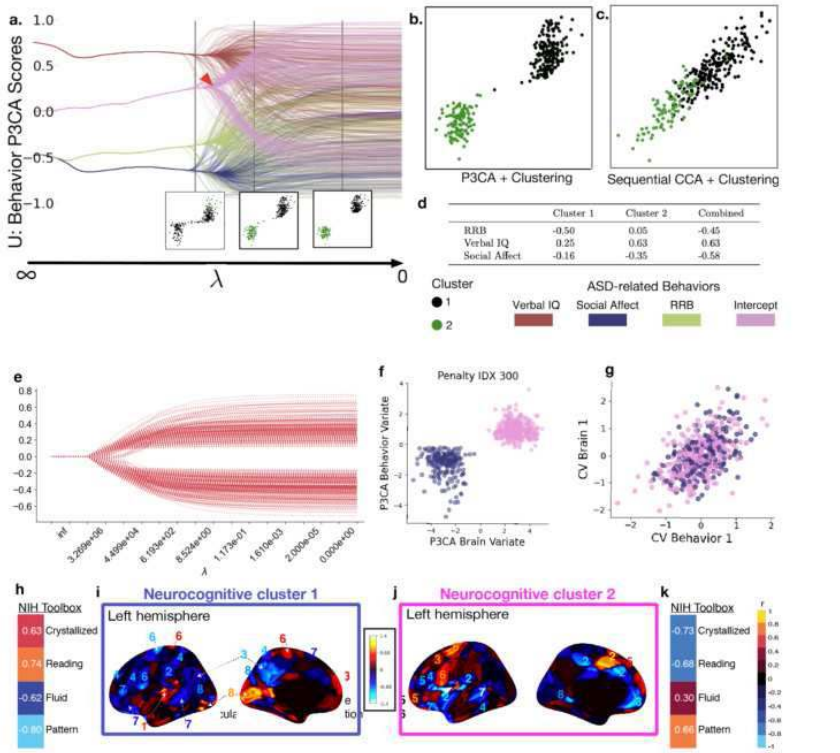

Figure 2. Fitting the cluster-aware embedding method to neuroimaging and behavioral datasets reveals ASD and neurocognitive subtypes. **a-d.** Fit to N=299 individuals with ASD from the ABIDE dataset using behavioral (ADOS-2 social affect and repetitive behavior/restricted interests-RRB and verbal IQ) and resting state functional connectivity (RSFC) data. **a.** P3CA path diagram of behavior-related P3CA scores with clustering solutions at λs indicated by line (see intercept splitting at red arrow). **b.** P3CA clustering solution separates ASD patients along the brain-behavior embedding. **c.** P3CA clusters are much better separated and more robust than sequential CCA followed by K-means clustering. d. Correlations Between ASD Behaviors and P3CA variate. **e-k.** Latent cluster-specific brain-behavior embeddings describe neurocognitive phenotypes. Fit to N=490 individuals from the ABCD dataset using behavioral (NIH toolbox) and RSFC data. e. P3CA path fitting the cluster-aware embedding along convex penalty path. **f.** P3CA embedding at end of path. **g.** Comparison to fitting the dataset using regularized CCA followed by clustering. Correlations between cognition/intelligence and P3CA behavior variate for **h.** cluster 1 and **k.** cluster 2. **h-k.** Benjamini-Hochberg-corrected correlations between resting state functional connectivity and P3CA brain variate for **i.** cluster 1 and **k.** cluster 2. Values were summed across rows for visualization on brain surface and labeled by functional network. NIH Toolbox Abbrev. Cognition fluid composite ("Fluid"); Crystallized composite ("Crystallized"); Oral reading recognition ("reading"); Pattern comparison processing speed ("pattern").

Conclusions: Overall, our approach provides a flexible and effective method for clustering and subtype discovery in biomedical datasets with neuroimaging and behavioral data. We have introduced an interpretable joint clustering and embedding strategy using a modular convex clustering penalty that can be applied in multimodal datasets. We showcased our method in two case studies using the ABCD and ABIDE datasets, which revealed robust neurocognitive subtypes in both adolescents and individuals with autism spectrum disorder.

References

1. Drysdale, Andrew T. et al (2017). "Resting-state connectivity biomarkers define neurophysiological subtypes of depression." Nature Medicine 23 (1): 28–38
2. Buch, Amanda M., et al (2023) "Molecular and Network-Level Mechanisms Explaining Individual Differences in Autism Spectrum Disorder." Nature Neuroscience 26 (4): 650–63.
3. Hocking, Toby Dylan et al (2011) "Clusterpath: An Algorithm for Clustering Using Convex Fusion Penalties." In Proceedings of the 28th International Conference on Machine Learning, 745–52.
4. Buch, Amanda M. et al (2022) "Simple and Scalable Algorithms for Cluster-Aware Precision Medicine." arXiv [cs.LG]. arXiv. http://arxiv.org/abs/2211.16553.
5. Volkow, Nora D. et al. "The Conception of the ABCD Study: From Substance Use to a Broad NIH Collaboration." Developmental Cognitive Neuroscience 32 (August): 4–7.
6. Martino, A. et al (2014), 'The Autism Brain Imaging Data Exchange: Towards a Large-Scale Evaluation of the Intrinsic Brain Architecture in Autism', Molecular Psychiatry, vol. 19, pp. 659-667
7. Martino, A. et al (2017), 'Enhancing Studies of the Connectome in Autism Using the Autism Brain Imaging Data Exchange II', Scientific Data, vol. 4, no. 170010
8. Power, J.D. et al (2012), 'Spurious But Systematic Correlations in Functional Connectivity MRI Networks Arise from Subject Motion', Neuroimage, vol. 59, pp. 2142-2154
9. Yan, C.G. et al (2013) 'Standardizing the Intrinsic Brain: Towards Robust Measurement of Inter-Individual Variation in 1000 Functional Connectomes', Neuroimage, vol. 80, pp. 246-262

Poster No 1932

Exploring Venular Morphological Markers in Cerebral Small Vessel Disease: A 7T MRI Study

Hecheng Jin[1], George Stetten[1], Linghai Wang[1], Yueyang Chi[1], Shaolin Yang[1], Tamer Ibrahim[1], Howard Aizenstein[1], Minjie Wu[1]

[1]*University of Pittsburgh, Pittsburgh, PA*

Introduction: Cerebral small vessel disease (CSVD) is a progressive vascular disease associated with increased risk of cognitive decline, Alzheimer's disease, and clinical dementia[1]. White matter hyperintensities (WMHs) on fluid-attenuated inversion recovery (FLAIR) imaging have been considered as a traditional biomarker of CSVD[2-3]. Compared to WMHs, morphological alterations of the cerebral small vessels may have a potential to serve as a more specific and mesoscopic sign for early CSVD, particularly with the advent of 7T magnetic resonance imaging[4]. In this study, we aim to explore the morphological markers of cerebral small veins as markers of CSVD. We hypothesize that individuals with CSVD will have altered morphological markers of cerebral small veins.

Methods: Fourteen cognitively normal older adults (mean±SD age 71.6±4.4 years, 9 females) were included in this study. MRI images were acquired using a Tic-Tac-Toc 16-ch transmit and 32-channel receive RF head coil system[5] on a 7T MRI scanner (Siemens Magnetom) at University of Pittsburgh. Susceptibility-weighted imaging (SWI) was obtained with voxel size = 0.375 × 0.375 × 0.75 mm, slice number = 352, TR = 24ms, TE = 8.16ms, and flip angle = 20°. T2-weighted FLAIR was obtained with voxel size = 0.75 × 0.75 × 1.5 mm, slice number = 80, TR = 14000ms, TE = 99ms, and TI = 2900ms. WMHs were segmented on T2w FLAIR, and the subjects were divided into two WMHs groups, High WMHs vs. Low WMHs, based on the median split of WMHs volume. Deep medullary veins were segmented on SWI images using a 3D segmentation algorithm, BrainVein[6]. This algorithm identifies continuous vessel branching paths with maximum connectivity (Figure 1). Vessel density index (VDI) and venular tortuosity index (VTI) were employed to evaluate the morphology of deep medullary veins. VDI is defined as the number of veins in a given 3D region of interest (ROI) and VTI represents the ratio of vessel length divided by distance between the two endpoints of the vessel. Due to the blooming effect on SWI, the size of segmented veins does not reflect the actual lumen size. Therefore, to further evaluate effects of CSVD on distal small veins, the segmented veins were assessed at two ROIs, which are proximal or distal to the draining subependymal veins. Linear regression models were performed to test the main effects of WMHs groups (High WMHs vs Low WMHs) and vessel location (distal vs proximal), as well as their interaction (WMHs group x location) on vessel morphological markers.

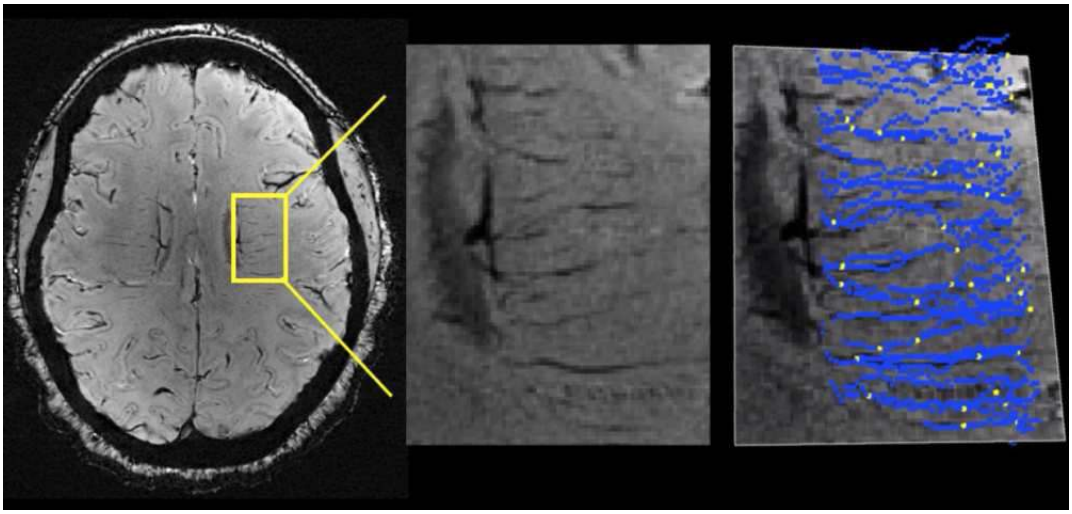

Figure 1. Segmentation of small veins using BrainVein: Segmented veins are represented by blue paths, and branching points are highlighted in yellow.

Results: The result showed that vein density (VDI) ($p < 0.001$) and tortuosity ($p = 0.02$) were significantly higher in the distal veins compared to the proximal veins regardless of WMHs groups (main effect of vein location)(Figure 2). Also, individuals with high WMHs significantly exhibited a higher vein density ($p = 0.02$) and tortuosity ($p = 0.03$) (main effect of WMHs groups). Moreover, individuals with high WMHs exhibited a trend in which there was higher vein density in the distal veins compared to the proximal veins ($p = 0.07$).

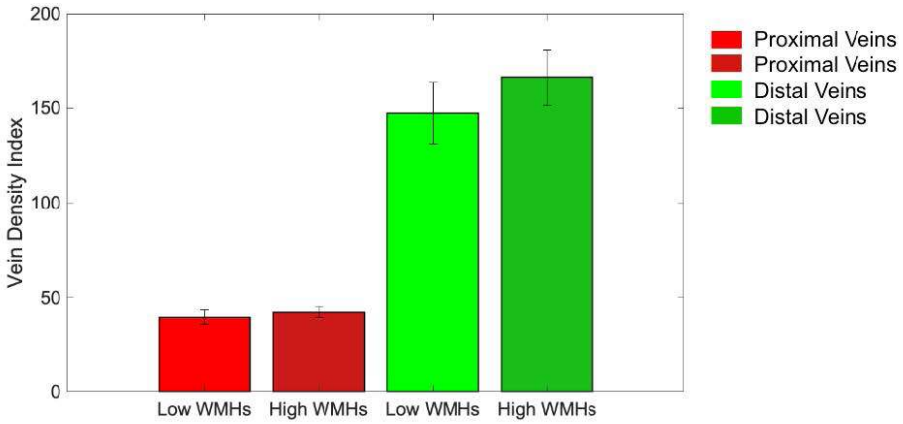

Figure 2. Venous Density Index (VDI) in medullary small deep veins: The bar chart illustrates the mean values, and error bars represent the standard deviation in each group.

Conclusions: This study shows potential in enhancing our comprehension of early CSVD. Utilizing 7T MRI for the characterization of cerebral small vessel morphology may facilitate the development of sensitive biomarkers for early detection of CSVD.

References

1. van Dijk, Ewoud J., et al. "Progression of cerebral small vessel disease in relation to risk factors and cognitive consequences: Rotterdam Scan study." Stroke 39.10 (2008): 2712-2719.
2. Prins, Niels D., et al. "Cerebral white matter lesions and the risk of dementia." Archives of neurology 61.10 (2004): 1531-1534.
3. De Leeuw, F. E., et al. "Prevalence of cerebral white matter lesions in elderly people: a population based magnetic resonance imaging study. The Rotterdam Scan Study." Journal of Neurology, Neurosurgery & Psychiatry 70.1 (2001): 9-14.
4. Shaaban, C. Elizabeth, et al. "In vivo imaging of venous side cerebral small-vessel disease in older adults: an MRI method at 7T." American Journal of Neuroradiology 38.10 (2017): 1923-1928.
5. Santini, Tales, et al. "Improved 7 Tesla transmit field homogeneity with reduced electromagnetic power deposition using coupled Tic Tac Toe antennas." Scientific reports 11.1 (2021): 3370.
6. Stetten, G. et al. Automated Segmentation of Oriented Branching Structures through Dilation Shells using Dynamic Programing. Computer Assisted Radiology and Surgery (CARS) 2019 Congress.

Poster No 1933

Applying Transparent Thresholding to Visualize Data and Highlight Results in suma

Peter Lauren[1], Daniel Glen[2], Paul Taylor[1], Richard Reynolds[1]

[1]National Institute of Mental Health, Bethesda, MD, [2]NIMH, Bethesda, MD

Introduction: AFNI's[1] 3D visualization tool, suma[2], can display neuroimaging data on the anatomical surfaces of an individual's brain or a reference template. To date, thresholding of this overlaid data at some value T has only been performed in a standard all-or-nothing (AON) or "opaque" manner: only information with magnitude >T would be displayed, and none below it. However, there may be times when the user would want to show information below T, and get a sense of how far the data is below T, from a single view without having to interactively adjust T. For example, Allen et al[3] showed that graphical displays can become less informative as data complexity increases; but one can make them more informative by transparently displaying, rather than hiding, subthreshold areas. AON thresholding also hid the degree of uncertainty throughout much of the brain. Showing all areas but making subthreshold ones increasingly transparent provided substantially more information, such as near-significant effects and overall quality of the data. Taylor et al[4] further showed that using AON thresholding in neuroimaging had several negative consequences in reproducibility and understanding and leads to selection bias, giving undue influence to arbitrary filter values. Highlighting, rather than hiding, produced more complete results as information contained in sub-threshold locations is often extremely useful in understanding the supra-threshold ones such as by providing context. Those previous studies only implemented volume-based transparent thresholding, not on surface viewers. suma can now apply transparent thresholding to surface datasets. The opacity for the thresholded value is assigned the maximum value of 1, but can also be between 0 and 1. This allows the sub-T overlay colors to fade, rather than disappear, as their values fall below T.

Methods: An “A” checkbox has been added to the suma surface control menu to turn on transparent threshold (or “Alpha” thresholding, since it is the alpha channel of the displayed coloration that is affected). Consider an underlying surface that has a color U, to which a user adds a color overlay dataset X and threshold dataset Y, which is thresholded at value T. If “A” is unchecked (standard thresholding), then the blended overlay-surface value Z at any location is: X, if |Y|>=T; or U, if |Y|<T. If “A” is checked (transparent thresholding), then the blended value Z at any location is: X, if |Y|>=T (as before); or a*X+(1-a)*U, if |Y|<T, where a=(|Y|/T)**2 is the alpha value, which is always between 0 and 1. In the latter scenario the displayed value in a subthreshold region is a blend of the overlay and underlay, where the blending depends on the square of the ratio of the local value to the global threshold T.

Results: Figure 1 shows two applications of transparent thresholding in suma (each row is a separate overlaid dataset). Within each row, when AON thresholding is applied (Panel C),only suprathreshold overlay values are shown. There is no visible overlay information on the rest of the surface. When transparent thresholding is applied (Panel D), the suprathreshold overlay coloration remains the same, but subthreshold values are also visible globally and interpretable: near-threshold values are nearly opaque, while much lower ones are nearly transparent. This enables all overlay areas to be understood, while the suprathreshold ones remain focally highlighted.

Conclusions: A new option, added to SUMA allows fading, rather than hiding, of subthreshold data on surface overlays. This allows significant (at or above threshold) data to be enhanced while not removing its context which may otherwise be hidden by an arbitrary threshold that does not account for uncertainty or processing errors. For example, this is particularly useful for enhancing understanding when reporting statistics results. Future work will allow multiple overlays to be blended based upon their strength relative to their respective thresholds.

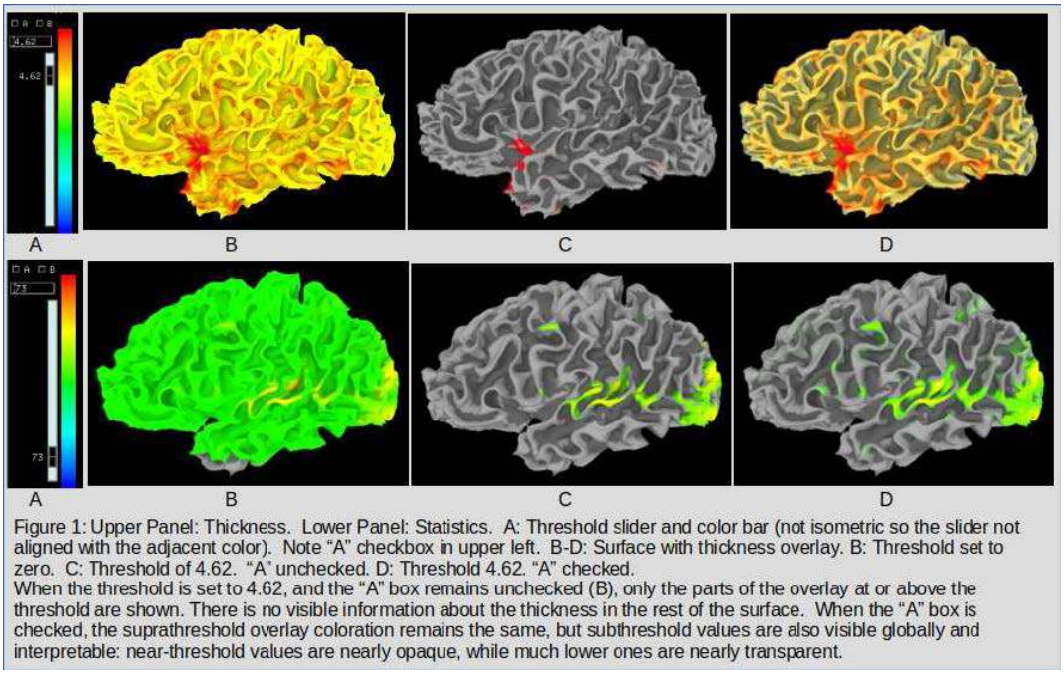

Figure 1: Upper Panel: Thickness. Lower Panel: Statistics. A: Threshold slider and color bar (not isometric so the slider not aligned with the adjacent color). Note “A” checkbox in upper left. B-D: Surface with thickness overlay. B: Threshold set to zero. C: Threshold of 4.62. “A” unchecked. D: Threshold 4.62. “A” checked.
When the threshold is set to 4.62, and the “A” box remains unchecked (B), only the parts of the overlay at or above the threshold are shown. There is no visible information about the thickness in the rest of the surface. When the “A” box is checked, the suprathreshold overlay coloration remains the same, but subthreshold values are also visible globally and interpretable: near-threshold values are nearly opaque, while much lower ones are nearly transparent.

References

1. Cox RW (1996). AFNI: software for analysis and visualization of functional magnetic resonance neuroimages. Comput Biomed Res 29(3):162-173. doi:10.1006/cbmr.1996.0014
2. Saad ZS & Reynolds RC. (2012). Suma. Neuroimage 62(2):768-773.
3. Allen EA, Erhardt EB, Calhoun VD (2012). Data Visualization in the Neurosciences: overcoming the Curse of Dimensionality. Neuron 74:603–608
4. Taylor PA, Reynolds RC, Calhoun V, Gonzalez-Castillo J, Handwerker DA, Bandettini PA, Mejia AF, Chen G (2023). Highlight Results, Don’t Hide Them: Enhance interpretation, reduce biases and improve reproducibility. Neuroimage 274:120138. doi: 10.1016/j.neuroimage.2023.120138

Poster No 1934

Recon-any: A FreeSurfer-based cortical reconstruction tool for any MRI

Karthik Gopinath[1], Oula Puonti[1,2], Douglas Greve[1], Annabel Sorby-Adams[3], Jennifer Guo[3], Sudeshna Das[3], Steve Arnold[3], Colin Magdamo[3], Mark Montine[4], Caitlin Latimer[4], Christine Mac Donald[4], C. Dirk Keene[4], W. Taylor Kimberly[3], Juan Eugenio Iglesias[1]

[1]Athinoula A. Martinos Center for Biomedical Imaging, MGH, HMS, Boston, MA, [2]Danish Research Insttitute for Magnetic Resonance, Hvidovre, Region H, [3]Massachusetts General Hospital, Boston, MA, [4]University of Washington, Seattle, WA

Introduction: Human brain MRI scanning protocols in research almost always include a 1mm isotropic T1 scan for morphometric analysis, and most image analysis pipelines are designed for this specific resolution and MRI contrast. However, there are other imaging modalities that are incompatible with most current tools. Ex vivo MRI is useful for high-resolution mesoscopic studies but does not have T1 contrast[1]. Portable MRI enables affordable large-scale scanning but has low resolution and signal-to-noise ratio[2]. Existing clinical MRI scans are abundant in hospitals and can provide vast amounts of data "for free" but often have large slice spacing and heterogeneous MRI contrast. More recently, 3D-reconstructed dissection photographs enable postmortem morphometry[3] but have large-spacing and heterogeneous image contrast. Here we propose "Recon-any": a deep learning enabled version of FreeSurfer's[4,5] "recon-all" that can handle imaging volumes of any resolution and contrast "out of the box" without retraining.

Methods: Recon-any has two main parts: 1) estimation of isotropic Signed Distance Functions (SDFs) from anisotropic imaging volumes (MRI scans or 3D reconstructed photographs) and 2) placing the white matter (WM) and pial surfaces and subsequent cortical analysis. Learning of SDFs: The learning module simulates synthetic imaging volumes from 3D segmentations, with random orientation, resolution, and contrast. It uses a Gaussian mixture model[6,7] and random bias field, resolution, and noise simulators. The regression targets are voxel-wise SDFs precomputed from WM and pial meshes. A regression convolutional neural network is trained by optimizing weights to minimize the L1 norm of the difference between predicted and ground truth SDFs. At test time, the trained network predicts 1mm isotropic SDFs for any imaging volume. Geometry Processing for Surface Placement: For WM surface reconstruction, we first fill in holes in the WM mask and tessellate it to obtain the initial mesh. Then, we smooth the mesh and use automated manifold surgery[5] to guarantee spherical topology. Next, we iteratively deform the WM mesh by minimizing an objective function consisting of a fidelity term (based on the absolute value of the SDF) and a regularizer. The pial surface is fitted using the predicted SDF of the pial surface. The resulting surfaces undergo FreeSurfer analysis for cortical thickness, parcellation, and registration to an atlas in spherical coordinates.

Results: We evaluate our method's performance on two datasets, HCP[8] (15 subjects, with T1 and T2 scans) and ADNI3[9] (15 subjects, with T1 and FLAIR scans). To evaluate performance as a function of resolution and plane of acquisition, we downsample the initial isotropic data to 2, 4, and 6mm resolution in axial, coronal, and sagittal direction. Subsequently, we quantify the disparity between the regional cortical thicknesses estimated by Recon-any and the ground truth, which is the output of FreeSurfer's recon-all on the 1mm T1 scans. Recon-any achieves a mean absolute error of 0.28mm, 0.26mm, and 0.29mm at 2mm, 4mm, and 6mm for FLAIR scans, and 0.21mm, 0.26mm, and 0.27mm for T2 scans. Additionally, the accuracy of the Desikan-Killiany parcellation[10] of our method against the ground truth reveals Dice scores consistently above 0.91 for every resolution, with an average Dice score of 0.95. We present qualitative results for T2w, ex vivo, 3D photo volume, and portable MRI in Figure 1. Quantitative assessments with paired 1mm T1 data remain as future work.

Conclusions: We have presented a cortical analysis method that works "out of the box" for any MRI contrast and resolution. Future work will seek to replace geometry processing modules with faster learning methods and improve the reliability of thickness measurements. We will make our method publicly available on FreeSurfer, enabling researchers worldwide to perform cortical analysis on large amounts of data which is currently not possible.

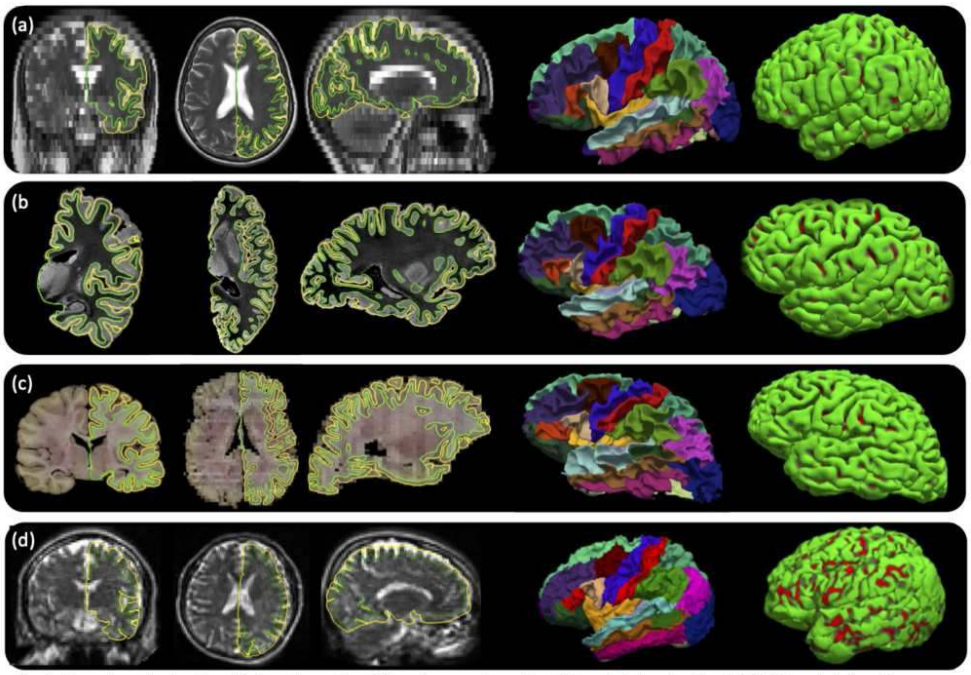

Fig 1. Sample outputs of cortical surfaces for different scans from the different datasets. The left WM and pial surfaces are overlaid on the orthogonal views. The 3D-rendered WM and pial surfaces are shown on the right. The cortical parcellation is overlaid on the WM surface. (a) Axial T2-weighted scan with 0.9×0.9×6mm resolution. (b) Ex vivo MRI scan at 0.5×0.5×0.5mm resolution. (c) A 3D reconstruction of the coronal dissection photograph at 0.5×0.5×4mm. (d) A portable low-field T2 axial scan at 2.5×2.5×2.5mm resolution.

References

1. Edlow, B.L., Mareyam, A., Horn, A., Polimeni, J.R., Witzel, T., Tisdall, M.D., Augustinack, J.C., et al. (2019), '7 Tesla MRI of the ex vivo human brain at 100 micron resolution', Scientific Data, vol. 6, no. 1, 244.
2. Taylor, K.W., Sorby-Adams, A.J., Webb, A.G., Wu, E.X., Beekman, R., Bowry, R., Schiff, S.J., et al. (2023), 'Brain imaging with portable low-field MRI', Nature Reviews Bioengineering, vol. 1, no. 9, pp. 617-630.
3. Gazula, H., Tregidgo, H.F., Billot, B., Balbastre, Y., William-Ramirez, J., Herisse, R., Deden-Binder, L.J., Casamitjana, A., Melief, E.J., Latimer, C.S., and Kilgore, M.D. (2023), 'Machine learning of dissection photographs and surface scanning for quantitative 3D neuropathology', bioRxiv, pp.2023-06.
4. Dale, A.M., Fischl, B., and Sereno, M.I. (1999), 'Cortical surface-based analysis: I. segmentation and surface reconstruction', Neuroimage, vol. 9, pp. 179–19.
5. Fischl, B., Sereno, M., and Dale, A.M. (1999), 'Cortical surface-based analysis: II: inflation, flattening, and a surface-based coordinate system', Neuroimage, vol. 9, pp. 195–207.
6. Billot, B., Greve, D.N., Puonti, O., Thielscher, A., Van Leemput, K., Fischl, B., Dalca, A.V., Iglesias, J.E., et al. (2023a), 'Synthseg: Segmentation of brain MRI scans of any contrast and resolution without retraining', Medical Image Analysis, vol. 86, 102789.
7. Iglesias, J., Billot, B., Balbastre, Y., Tabari, A., et al. (2021), 'Joint super-resolution and synthesis of 1 mm isotropic MP-RAGE volumes from clinical MRI exams with scans of different orientation, resolution & contrast', Neuroimage, vol. 237, 118206.
8. Glasser, M., Sotiropoulos, S., Wilson, J.A., and Coalson, T.S. (2013), 'The minimal preprocessing pipelines for the Human Connectome Project', Neuroimage, vol. 80, pp. 105–24.
9. Jack Jr, C.R., Bernstein, M.A., Fox, N.C., Thompson, P., Alexander, G., et al. (2008), 'The Alzheimer's disease neuroimaging initiative (ADNI)', Journal of Magnetic Resonance Imaging, vol. 27, pp. 685–691.
10. Desikan, R.S., Ségonne, F., Fischl, B., Quinn, B.T., Dickerson, B.C., Blacker, D., Buckner, R.L., Dale, A.M., et al. (2006), 'An automated labeling system for subdividing the human cerebral cortex on MRI scans into gyral based regions of interest', Neuroimage, vol. 31, pp. 968–980.

Poster No 1935

Discovering gain modulation dynamics with dynamic causal modelling

Johan Medrano[1], Noor Sajid[1], Stephanie Mellor[1], Robert Seymour[1], Karl Friston[1], Peter Zeidman[1]

[1]Wellcome Centre for Human Neuroimaging, University College London, London, United Kingdom

Introduction: Gain modulation is an important mechanism related to sensory attenuation or enhancement, e.g., in visual[1,5] or auditory[2,3,4] processing. Discrete changes in synaptic gain can be related to experimental manipulations using dynamic causal modelling (DCM), a statistical framework for inferring the underlying causes of observed data. Here, we use a generic set of temporal basis functions to appropriately model slow continuous dynamics of gain modulation in DCM. Our approach relies on the separation of temporal scales between the dynamics of brain electrophysiological responses and synaptic gain[8]. Our

simulations show that fast effects can be modelled using existing dynamical models while slow effects can only be retrieved using these temporal basis functions. Next, we empirically evaluate this approach using magnetoencephalographic (MEG) data from an auditory roving oddball paradigm collected with Optically-Pumped Magnetometers (OP-MEG) and demonstrate effective recovery of slow modulation of synaptic gain. Our formulation provides a generic method to recover modulatory dynamics from neural activity.

Methods: In DCM, a matrix (i.e., design matrix) is used to map modulatory effects to experimental conditions i.e., relating differences in brain responses to changes in population gain and effective connectivity. We propose to capture the smooth, slow variations of synaptic efficacy between experimental conditions using a generic set of temporal basis functions in the design matrix that can efficiently represent the slow modulatory dynamics. Briefly, each of the modulatory effect matrices now separately models the weight of each of the temporal basis functions. This allows us to retrieve the time course of the slow fluctuations in synaptic gain by projecting the posterior estimates of the modulatory matrices onto the temporal basis functions. Our approach extends the existing DCM formulation and was implemented using standard machinery in SPM.

Results: Face validity: Using a two-region model of electrophysiological responses, we simulated evoked responses for repetition of a stimulus, with slow fluctuations of the synaptic gains over time. Our analysis assumed that conditions were temporally ordered. We used a DCM for event-related potentials[7] with a Fourier basis set to retrieve slow parameter trajectories. Our approach led to successful recovery, i.e., the posterior trajectories attributed a high probability to the true trajectories (Figure 1). Application to gain modulation in auditory repetition with OP -MEG: We investigate the modulatory dynamics in an auditory roving oddball paradigm using this model. Specifically, we asked how changes in evoked response from the first presentation of a tone (deviant) onwards can be explained by the slow evolution of synaptic efficacy. For this, we use OP-MEG data from Ref[8], pre-processed following Ref[10]. Here, two participants listened for approximately 1140 tones dispatched in sequences of 2 to 11 repeated tones with 160 deviants (i.e., tone switches). To model this, we used a DCM for ERP model with a 4th-order cosine set to model the slow evolution of synaptic parameters. Consistent with previous studies[2,6], our results show that changes in evoked response were explained by a decrease in synaptic gain after the first deviant (Figure 2).,We found this effect to be stronger in the right primary auditory cortex, providing a mechanistic hypothesis for the observed repetition suppression.

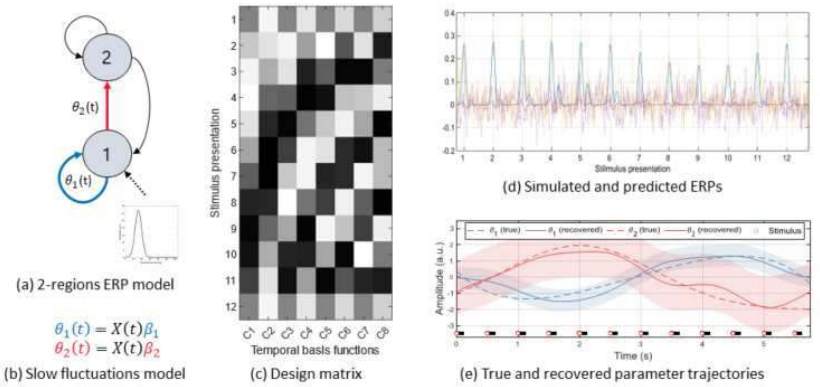

Figure 1: Face validity. (a) 2-regions model used to simulate evoked responses. Each of the two regions is modelled using a canonical microcircuit model. Region 1 has forward connections to region 2 and receives backward connections from it. Input stimuli is modelled as entering region 1. Parameters θ_1 (self-inhibition of superficial pyramidal neurons in region 1) and θ_2 (forward connectivity from region 1 to 2) undergo slow fluctuations over time. (b) Linear model expressing slow fluctuations (resp. of θ_1 and θ_2) as a weighting (resp. by β_1 and β_2) of the design matrix (X). (c) The design matrix consisting of 8 temporal basis functions from a Fourier set for 12 stimulus presentation. (d) Simulated (dotted lines) and predicted (plain lines) ERPs for each stimulus presentation. Simulation and model inversion are conducted using default prior values available in the SPM software. (e) Simulated (dashed lines) and recovered (plain lines) parameter trajectories. Recovered parameter trajectories are obtained by projecting the posterior estimates of β_1 and β_2 onto the design matrix. The shaded area corresponds to the 90% confidence intervals derived from the variance of the posterior.

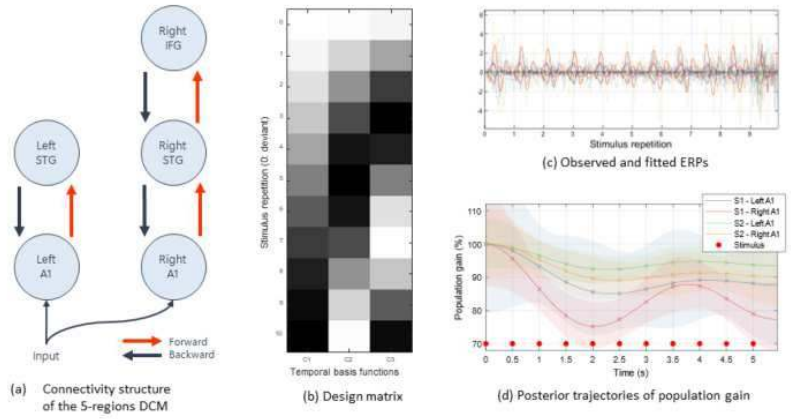

Figure 2: Experimental evaluation. (a) 5-regions DCM used to model the auditory evoked responses. We model both the left and right primary auditory cortices (A1), the left and right superior temporal gyrus (STG) and the right inferior frontal gyrus (IFG). The model architecture and MNI coordinates for each region follows from [8]. (b) Design matrix used to capture the slow modulatory dynamics. The design matrix is constructed from a third-order cosine set. Each row corresponds to the number of repetitions of the tone, with 0 being the deviant. (c) Observed ERPs (dotted lines) and model fits (plain lines). The ERPs presented here correspond to the responses projected over spatial modes. (d) Recovered gain of superficial pyramidal neurons in the primary auditory cortices for both subjects (labelled S1 and S2).

Conclusions: We introduce a new method to model gain modulation, building upon the existing DCM formulation for modelling brain dynamics .We empirically validate it using OP-MEG data. Our results illustrate the relevance of our formulation for recovering slow modulatory dynamics without explicit priors about the shape of the gain modulation. More generally, our method may be useful way to link fast neural activity with slower changes in behaviour, which is of relevance for natural, real-world experiments.

References

1. Adams, R.A. (2016) “Dynamic causal modelling of eye movements during pursuit: confirming precision-encoding in V1 using MEG.” Neuroimage 132: 175-189.
2. Auksztulewicz, R. (2015) “Attentional enhancement of auditory mismatch responses: a DCM/MEG study.” Cerebral cortex 25.11 (2015): 4273-4283.
3. Auksztulewicz, R. (2016) “Repetition suppression and its contextual determinants in predictive coding.” cortex 80: 25-140.
4. Auksztulewicz, R. (2017) “The cumulative effects of predictability on synaptic gain in the auditory processing stream.” Journal of Neuroscience 37.28 (2017): 6751-6760.
5. Bastos, A.M. (2015) “A DCM study of spectral asymmetries in feedforward and feedback connections between visual areas V1 and V4 in the monkey.” Neuroimage 108: 460-475.
6. Garrido M.I., (2009) “Repetition suppression and plasticity in the human brain.” Neuroimage.;48(1):269-79.
7. Kiebel S.J., (2009) “Dynamic causal modeling for EEG and MEG.” Hum Brain Mapp;30(6):1866-76
8. Medrano, J. (2023) “Linking fast and slow: the case for generative models” Network Neuroscience: 1-34.
9. Mellor, S., (2023) “Real-time, model-based magnetic field correction for moving, wearable MEG.” NeuroImage 278: 120252.
10. Seymour, R.A., (2021) “Using OPMs to measure neural activity in standing, mobile participants.” NeuroImage 244 (2021): 118604.

Poster No 1936

Surface Reconstruction for the masses: PialGCN for Efficient Surface Reconstruction

William Ashbee[1], Mohamed Masoud[1], Satrajit Ghosh[2], Sergey Plis[1]

[1]Trends Center, Atlanta, GA, [2]Harvard/MIT, Boston, MA

Introduction: Brain surface reconstruction has evolved from the traditional Freesurfer’s algorithm-based approach, renowned for its accuracy but hindered by lengthy processing times, to embracing deep learning methods[1,3-8]. These advanced methods enhance speeds by utilizing GPU resources, showing promise for web deployment. Our research specifically focuses on optimizing the Pial Surface generation in PialNN through the integration of Graph Convolutional Networks (GCNs). This innovative approach not only sharpens accuracy, as indicated by reduced Hausdorff distances but also lowers memory usage. Our method, differing from PialNN’s standard pointwise deformations, employs graph-aware predictions using GCNs, streamlining both the accuracy and efficiency of the network.

Methods: Our study utilized data from 897 patients, sourced from the Human Connectome Project[2]. The patients were divided into three categories: 732 in the training set, 58 in the validation set, and 107 in the test set. Each patient’s data was processed

using Freesurfer. We aimed to enhance the PialNN model's vertex-independent predictions with GCNs[3]. This enhancement involved integrating Graph Convolutional Networks (GCNs) to incorporate neighborhood data into the prediction process, thereby improving the accuracy and feature recognition across vertices. The depth of the GCNs, critical to the model's performance, was a key aspect of our investigation. In an effort to optimize memory usage, we reduced the number of deformation modules from three to two per forward pass. Our implementation of the GCN component utilized PyTorch Geometric's framework within the Deformation module in figure 1[9]. We also developed graph objects using PyTorch 3D[10] to mirror the mesh connectivity accurately. The inputs for our model included transforming Freesurfer-generated white surfaces into network-generated pial surfaces. To evaluate the effectiveness of our methodology, we conducted both qualitative and quantitative assessments. Qualitatively, we examined the vertex-wise component distances of Hausdorff distances for a single patient across all models. This involved visualizing the differences on vertex-colored brain renderings from test set predictions. Quantitatively, we measured the Hausdorff distances, averaging them over the test set. These analyses allowed us to determine the impact of GCN depth on memory usage and prediction error.

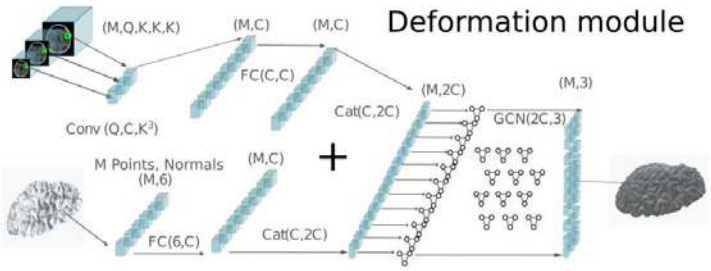

Figure 1: Extension of the PialNN architecture to include Graph Convolutional Networks (GCNs). Image features are gathered from cube sampling in the MRI at mesh coordinates. Mesh features are derived from vertex coordinates and normals. The deformation module is executed twice, transforming a white surface into a pial surface.

Results: Our study revealed significant improvements in brain surface reconstruction using Graph Convolutional Networks (GCNs). We found that GCNs, particularly with 2 to 6 layers, reduced memory usage during training. Moreover, all GCN models outperformed PialNN's MLP methods in accuracy. Additionally, we observed a direct relationship between the depth of GCN layers and memory consumption.

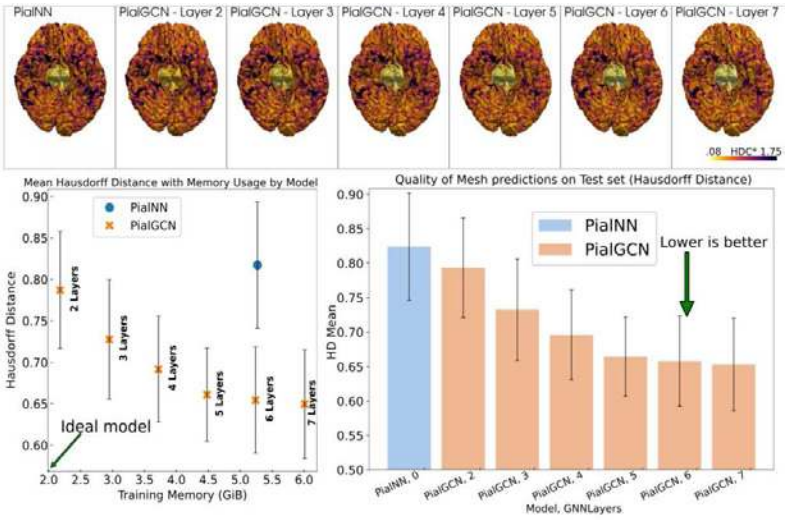

Figure 2: Visualization of per-vertex component distances (HDC*) of the Hausdorff Distance (HD) in rendered brains of a single subject across all models. Incorporating GCNs and reducing deformation modules results in a lower memory footprint (measured in GiB) and error rate (measured by Hausdorff Distance), as shown in the plots.

Conclusions: Our study marks a significant leap in brain surface reconstruction by integrating Graph Convolutional Networks (GCNs) into the PialNN framework. GCN integration has led to substantial improvements in accuracy and error reduction. The adoption of GCNs enhances the model's accuracy, particularly in capturing the intricate details of brain structures, which is crucial for neurological research and clinical applications. However, we also noted a trade-off between increased accuracy and higher memory usage with deeper GCN layers. This balance is particularly important for applications requiring real-time processing and web deployment. Looking ahead, this research paves the way for advanced medical imaging techniques, potentially revolutionizing data processing and interpretation in neuroscience and beyond. Our findings contribute to the

evolving role of deep learning in medical imaging, moving towards more accessible, high-precision imaging solutions in both research and clinical environments.

References
1. Fischl, Bruce. (2012), "FreeSurfer." Neuroimage 62.2: 774-781.
2. Glasser, Matthew F., et al. (2013), "The minimal preprocessing pipelines for the Human Connectome Project." Neuroimage 80: 105-124.
3. Ma, Qiang, et al. (2021), "PialNN: A fast deep learning framework for cortical pial surface reconstruction." International Workshop on Machine Learning in Clinical Neuroimaging. Springer, Cham.
4. Bongratz, Fabian, et al. (2022), "Vox2Cortex: Fast Explicit Reconstruction of Cortical Surfaces from 3D MRI Scans with Geometric Deep Neural Networks." Proceedings of the IEEE/CVF Conference on Computer Vision and Pattern Recognition.
5. Cruz, Rodrigo Santa, et al. (2021), "Deepcsr: A 3d deep learning approach for cortical surface reconstruction." Proceedings of the IEEE/CVF Winter Conference on Applications of Computer Vision.
6. Hoopes, Andrew, et al. (2021), "TopoFit: Rapid Reconstruction of Topologically-Correct Cortical Surfaces." Medical Imaging with Deep Learning.
7. Lebrat, Leo, et al. (2021), "Corticalflow: A diffeomorphic mesh transformer network for cortical surface reconstruction." Advances in Neural Information Processing Systems 34 : 29491-29505.
8. Ma, Qiang, et al. (2022), "CortexODE: Learning Cortical Surface Reconstruction by Neural ODEs." arXiv preprint arXiv:2202.08329.
9. Fey, Matthias and Jan E. Lenssen. (2019), "Fast Graph Representation Learning with PyTorch Geometric." In Proceedings of the ICLR Workshop on Representation Learning on Graphs and Manifolds.
10. Ravi, Nikhila, Jeremy Reizenstein, David Novotny, Taylor Gordon, Wan-Yen Lo, Justin Johnson, and Georgia Gkioxari. (2020), "Accelerating 3D Deep Learning with PyTorch3D." arXiv preprint arXiv:2007.08501.

Poster No 1937

Introducing edge-wise graph signal processing: application to connectome fingerprinting

Thomas Bolton[1], Jagruti Patel[2], Mikkel Schöttner[3], Patric Hagmann[4]

[1]CHUV, Lausanne, Vaud, [2]CHUV, Zurich, Not Specified, [3]Department of Radiology, Lausanne University Hospital and University of Lausanne (CHUV-UNIL), Lausanne, Not Specified, [4]Department of Radiology, Lausanne University Hospital and University of Lausanne (CHUV-UNIL), Lausanne, Switzerland

Introduction: In magnetic resonance imaging (MRI), graph signal processing (GSP) treats brain structural connectivity (SC) as a graph on which functional activity is studied[5]. Given the potential of edge-centric analyses to reveal novel aspects of brain function[3], we assessed whether edge-centric GSP (eGSP) could outperform classical regional GSP (rGSP) in subject fingerprinting, an endeavour tackled by both research lines[4,6].

Methods: We considered S=100 subjects from the Human Connectome Project[10] with T1-weighted (T1W), diffusion MRI (dMRI) and resting-state functional MRI (RS fMRI; four 15-minute scans acquired in pairs over two days) data. Connectome Mapper 3[9] was used to compute SC for each subject. Tractograms were generated from the dMRI data (deterministic tractography, white matter-seeded, order 8 constrained spherical deconvolution, 10 million output streamlines), and SC reflective of normalized fiber density (NFD, normalized by the sizes of both regions at hand) between R=126 brain regions[2] was obtained. RS fMRI data (with ICA-FIX denoising) were detrended, high-pass filtered (0.01 Hz), and regressed for 6 head motion parameters, their derivatives, and average white matter and cerebrospinal fluid signals. Following averaging into regions of interest[2], output time courses were temporally z-scored. For rGSP analysis[5] (Fig. 1A), we computed the normalized Laplacian from average SC across subjects, and its eigendecomposition yielded connectome harmonics (CHs, the eigenvectors) and their associated frequencies (the eigenvalues). A smaller-eigenvalue CH is smoother with respect to SC. Functional signals were expressed as a weighted sum of CHs and filtered to retain their subpart aligned with the underlying SC (i.e., linked to the h smallest-eigenvalue CHs)[8]. The L2-norm was computed over time to yield one feature vector per subject (f, size R). We probed h = {5,10,15,20,⌊0.3R⌋,⌊0.4R⌋,⌊0.5R⌋}. For eGSP analysis, we built a matrix quantifying cross-subject correlations between the NFD of connection pairs. To focus on direct associations, we set to 0 the entries for which both involved connections did not share a common region. We split the resulting matrix in two (with only positive or sign-flipped negative values), and extracted associated CHs. Regional functional time courses were converted into co-fluctuation time courses[3] (one per connection pair), and alignment was quantified (at h = {R, ⌊10E/R⌋,⌊0.1E⌋,⌊0.2E⌋,⌊0.3E⌋,⌊0.4E⌋, ⌊0.5E⌋}) to yield f+ and f- (size E=7264 each). We also computed log(f+/f-). Fingerprinting was assessed on pairs of sessions acquired over separate days. The cross-subject similarity matrix between full feature vectors was used for one-to-one matching[7]. Accuracy was taken as the correct percentage of assignments. We also quantified differential identifiability[1] (DI, average within-subject similarity - average between-subject similarity).

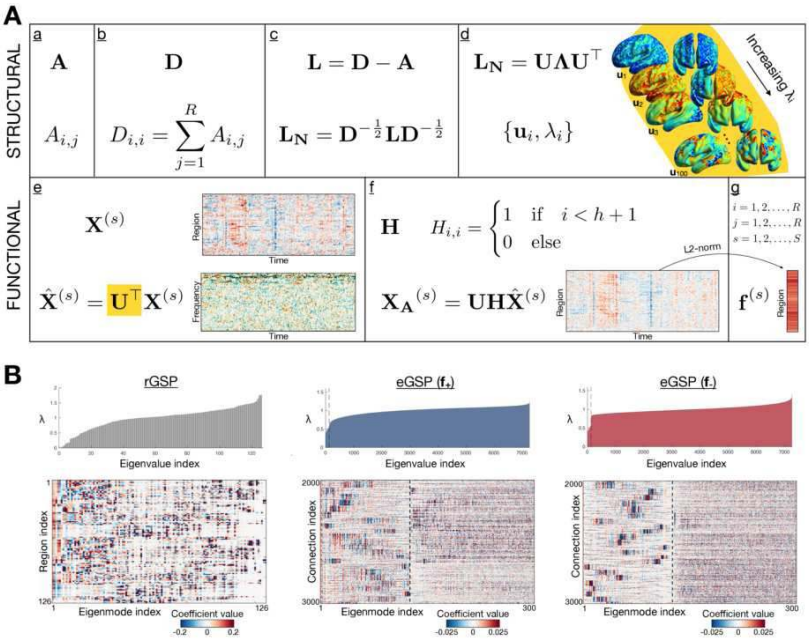

Figure 1. (A) Overview of classical regional graph signal processing (rGSP) analysis. The top row summarises the steps involved in the treatment of structural connectivity (SC) data, which are contained in the matrix **A** (a). Individual entries denote normalised fiber density (NFD) between two regions *i* and *j*. A degree matrix **D** can then be constructed, whose diagonal elements denote regional degree (b). Next, the Laplacian and its normalised variant can be computed (c). The latter enables the extraction of connectome harmonics (CHs) and associated eigenvalues (d). Smaller-eigenvalue CHs are smoother with respect to SC, and thus of lower spatial frequencies (see right hand side illustration for indicative examples). The bottom row highlights the key steps in processing functional data, contained in the matrix **X**. Functional time courses can be expressed as a function of the CHs to yield a spectral representation of brain activity (e). Next, low-pass filtering is performed with a user-defined parameter *h*, so that only the functional signal contributions linked to the first *h* CHs are retained (f). The L2-norm is computed over time to obtain a feature vector for each subject (g). **(B)** (*Top*) Eigenvalue spectra for rGSP (left plot) and ede-wise GSP (eGSP) (**f+**, middle plot, and **f-**, right plot). (*Bottom*) Associated CHs for the same cases. Note that for eGSP displays, only a subset of connections and CHs (the ones linked to the smallest eigenvalues) are shown, and vertical dashed lines highlight the observed sharp transition in smoothness of the CHs.

Results: For eGSP, smoothness sharply decreased from eigenvalue R onwards, paralleled by a switch from CHs contrasting large-scale connection communities to more localized attributes (Fig. 1B). For rGSP and eGSP, fingerprinting accuracy increased to comparable levels (around 60%) as more CHs were retained (Fig. 2A). DI was consistently better for eGSP than for rGSP and reached the largest values for f- (around 10%).

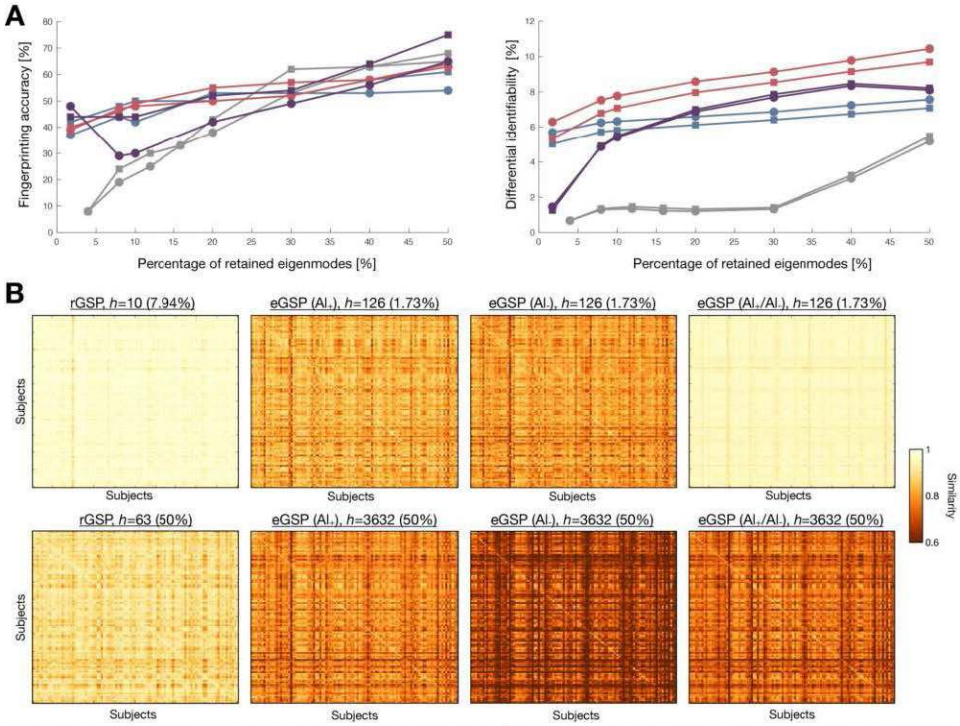

Figure 2. (A) Fingerprinting accuracy (left) and differential identifiability (right) when using alignment for different percentages of retained connectome harmonics, for regional graph signal processing (grey curves) and edge-wise graph signal processing (**f+**, blue curves; **f-**, red curves; log(**f+**/**f-**), purple curves). Squares/circles highlight the results obtained from the first/second pair of available functional magnetic resonance imaging scans. **(B)** Example cross-subject similarity matrices (from the first pair of available scans) for selected percentages of retained connectome harmonics.

Conclusions: Similar accuracy but better DI for eGSP schemes suggests greater robustness to increased data noise. EGSP graphs likely capture neurodevelopmental or experience-induced molecular processes that reshape SC. Connections may be jointly strengthened (as reflected in f+; e.g., if functionally overlapping), or may compete for enhancement (as captured in f-; e.g., due to limited resources to distribute). As f- was the best scheme overall, the uniqueness of one's brain may be more strongly related to competition between structural connections for resources than to their joint strengthening.

References

1. Amico, E. et al. (2018), 'The quest for identifiability in human functional connectomes', Scientific reports, vol. 8, no. 1, p. 8254
2. Cammoun, L. et al. (2012), 'Mapping the human connectome at multiple scales with diffusion spectrum MRI', Journal of neuroscience methods, vol. 203, no. 2, pp. 386-397
3. Faskowitz, J. et al. (2020), 'Edge-centric functional network representations of human cerebral cortex reveal overlapping system-level architecture', Nature neuroscience, vol. 23, no. 12, pp. 1644-1654
4. Griffa, A. et al. (2022), 'Brain structure-function coupling provides signatures for task decoding and individual fingerprinting', NeuroImage, vol. 250, no. 118970
5. Huang, W. et al. (2018), 'A graph signal processing perspective on functional brain imaging', Proceedings of the IEEE, vol. 106, no. 5, pp. 868-885
6. Jo, Y. et al. (2021), 'Subject identification using edge-centric functional connectivity', Neuroimage, vol. 238, no. 118204
7. Kuhn, H.W. (1955), 'The Hungarian method for the assignment problem', Naval research logistics quarterly, vol. 2, no. 1, pp. 83-97
8. Medaglia, J.D. et al. (2018), 'Functional alignment with anatomical networks is associated with cognitive flexibility', Nature human behaviour, vol. 2, no. 2, pp. 156-164
9. Tourbier, S. et al. (2022), 'Connectome mapper 3: a flexible and open-source pipeline software for multiscale multimodal human connectome mapping', Journal of Open Source Software, vol. 7, no. 74, p. 4248
10. Van Essen, D.C. et al. (2013), 'The WU-Minn human connectome project: an overview', Neuroimage, vol. 80, pp. 62-79

Poster No 1938

Explainable brain age predictions to support precision diagnosis in neuropsychiatry

Esten Leonardsen[1], Thomas Wolfers[2], Lars Westlye[3], Yunpeng Wang[1]

[1]University of Oslo, Oslo, Oslo, [2]University of Tübingen, Tübingen, Tübingen, [3]Norwegian Centre for Mental Disorders Research (NORMENT), Oslo University Hospital, Oslo, Norway

Introduction: Over the last decade, brain age has emerged as a promising biomarker to encode generalized brain health based on magnetic resonance imaging (MRI) data (Franke & Gaser, 2019). A multitude of studies have shown reliable increases in the brain age gap (BAG), encoding the difference between apparent brain age and chronological age, in patient cohorts across a multitude of neurological and mental disorders (Kaufmann et al., 2019). However, despite its evident utility, clinical translations of brain age models are lacking. One contributing reason for this is the abstract nature of the measure making it hard to understand exactly what it comprises. Furthermore, while being composite makes it sensitive towards detecting deviations across age-related processes, it also potentially lacks the specificity necessary to support clinical decisions for individual patients. Both issues could be alleviated with explainable artificial intelligence. Here, the brain age predictions originating from a machine learning model would be supplemented with an explanation of what caused the prediction in each individual case. One technique for procuring such explanations is Layerwise Relevance Propagation (LRP), commonly used alongside Convolutional Neural Networks (CNNs), to generate heatmaps indicating how regions of an image contribute to the predictions (Bach et al., 2015). In the brain age case, this would allow for precise inference of how different regions in the brain contribute to its overall apparent age. These heatmaps would be richer than the singular BAGs and could facilitate precision diagnosis of neurological and mental disorders.

Methods: Here we trained CNNs to predict brain age using 114,289 structural MRIs from 83,401 participants with ages spanning from 3 to 97 years old. All models were variants of the state-of-the-art Simple Fully Convolutional Network architecture, tailored specifically towards procuring informative explanations. On top of the models, we implemented LRP to constitute a fully explainable pipeline for brain age predictions. We employed the pipeline in nine patient cohorts with neurological and mental disorders to investigate whether the heatmaps supported better differentiation of patients and controls than BAGs. Furthermore, we associated the heatmaps with measures of disease severity within the disorders, to evaluate whether they could contribute towards fine-grained stratification of the patients.

Results: Our explainable pipeline was able to predict brain age accurately (MAE=2.92), also in test data coming from sites unseen by the model during training (MAE=4.70). For four out of nine disorders we were able to use BAG to differentiate cases from controls meaningfully (AUC>0.5, $p<0.05$). For five out of nine disorders, using the heatmaps instead of BAGs significantly improved the predictive performance ($p<0.05$). Dementia and multiple sclerosis offered the best case-control differentiation both using BAG (AUC=0.75 and 0.63 respectively) and heatmaps (AUC=0.81 and 0.87), but the difference in gain

was substantial, potentially indicating differences in the importance of localizing age-related structural anomalies in the two disorders. In both schizophrenia and bipolar disorder using the heatmaps resulted in predictive performance above chance for case-control differentiation (AUC=0.64 and 0.60), but we were unable to use the heatmaps to differentiate between the patient groups (p>0.05), potentially indicating overlap in the structural anomalies in the two disorders.

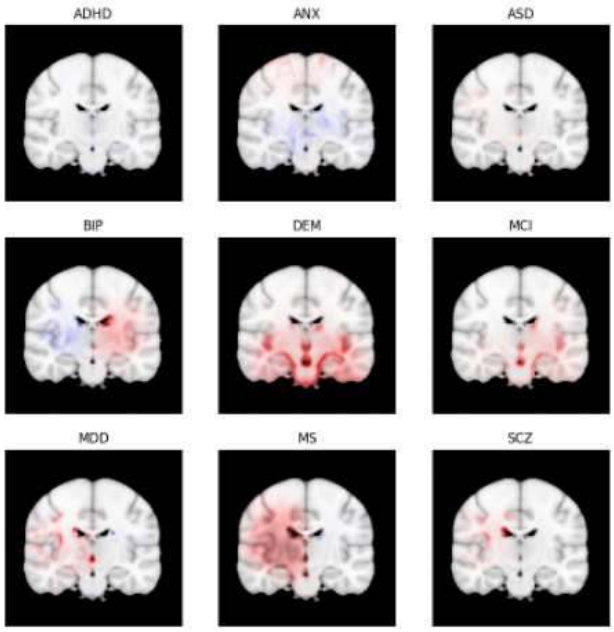

Figure 1: Difference between the mean heatmap for the cases and controls for each patient group

Conclusions: Brain age has the potential to contribute transformatively towards enabling precision medicine in neurological and mental disorders. Our explainable brain age pipeline contributes towards that goal via establishing trust with potential users of the technology by providing explanations of model behaviour, and by increasing its sensitivity through precise localization of age-related structural anomalies.

References

1. Bach, S., Binder, A., Montavon, G., Klauschen, F., Müller, K.-R., & Samek, W. (2015). On Pixel-Wise Explanations for Non-Linear Classifier Decisions by Layer-Wise Relevance Propagation. PLOS ONE, 10(7), e0130140. https://doi.org/10.1371/journal.pone.0130140
2. Franke, K., & Gaser, C. (2019). Ten Years of BrainAGE as a Neuroimaging Biomarker of Brain Aging: What Insights Have We Gained? Frontiers in Neurology, 10. https://www.frontiersin.org/article/10.3389/fneur.2019.00789
3. Kaufmann, T., van der Meer, D., Doan, N. T., Schwarz, E., Lund, M. J., Agartz, I., Alnæs, D., Barch, D. M., Baur-Streubel, R., Bertolino, A., Bettella, F., Beyer, M. K., Bøen, E., Borgwardt, S., Brandt, C. L., Buitelaar, J., Celius, E. G., Cervenka, S., Conzelmann, A., … Westlye, L. T. (2019). Common brain disorders are associated with heritable patterns of apparent aging of the brain. Nature Neuroscience, 22(10), 1617–1623. https://doi.org/10.1038/s41593-019-0471-7

Poster No 1939

Estimating longitudinal analytic flexibility in the UK Biobank with genetic and imaging phenotypes

Brent McPherson[1], Shadi Zabad[1], Yue Li[1], Jean-Baptiste Poline[1]

[1]McGill University, Montreal, Quebec

Introduction: A key goal of clinical neuroscience is to reliably map the health trajectory of an individual at risk of developing a disease. Unfortunately, models developed on cross-sectional data are increasingly failing to reproduce the trends present in longitudinal samples[1,2]. Further, the recruitment of a sufficient number of individuals to a study is largely impossible for all but the largest labs[1]. These challenges have led modern neuroscience to increasingly form large, collaborative, and longitudinally sampled population cohorts to capture comprehensive multimodal phenotypes about individuals[3,4]. The transition to these large population samples changed the kind of quality assessment any observation receives. Many large datasets, like the UK Biobank (UKB), have begun generating a series of image derived phenotypes (IDPs) and observing their distributions for outliers to determine an observation's quality. To evaluate the analytic flexibility of these IDPs we have reproduced many

of them using an equivalent pipeline. Additionally, we explore improving these summaries by incorporating longitudinal observations and additional genetic data as part of the evaluation.[5,6]

Methods: Our goal is to evaluate the analytic flexibility of the IDPs by replicating them with an equivalent pipeline. We will then explore their longitudinal stability and how integrating genetic features in their evaluation may improve their interpretation. The data used for the original quality assessments is available as part of the IDPs released by the UKB. The UKB currently has genetic information available for the majority of the sample (~488k) and neuroimaging data available for the roughly half of the participants that will receive it at time one (~48k) and an initial release of time two (~4k). Using TractoFlow[7] we have produced many of the same IDPs distributed by the UKB. Additionally, we incorporate VIPRS[8], a summary statistics based polygenic risk score to estimate the genetic features associated with change in the IDPs over time.

Results: The comparison of the IDPs reveals that the majority of the features are quite similar (R2 > 0.90). This indicates that these features are largely stable for the use of quality assessment. We want to further explore the quality of these features. To do this, we have modeled each IDP with VIRPS to estimate the genetic contribution to these regions. The VIRPS model takes GWAS summary statistics and estimates a polygenic risk score for an individual imaging phenotype. A key impact of this analysis is to identify an estimate of the variance explained and the heritability by the PRS predictions of IDPs. Additionally, we specifically modeled the change over time of the IDPs to emphasize the genetic contributions associated with longitudinal changes. We believe this will better emphasize the genetic features associated with disease by highlighting their presence in individuals with greater change.

Conclusions: Large population samples are key to facilitating the reliable translation of research findings to clinical practice. Working to maximize the information available to researchers between the modalities of these samples will improve the assessment and validation of data within these databases. We have worked to replicate the existing findings of the UKBB IDPs and have begun exploring their stability longitudinally. Further, we evaluate the performance of VIPRS on the estimation of polygenic risk scores of these longitudinal IDPs. The improvements of modeling a more complex, longitudinal IDPs with VIPRS estimates will better target features that reliably capture the variability in our samples. Following this approach we can better generalize findings to new samples and make better predictions in clinical cohorts. This new information can expand our discussion beyond the generalizability of the features to begin exploring the most effective multimodal features for validating our data.

References

1. Argiris, G., et al. (2021). Quantifying age-related changes in brain and behavior: a longitudinal versus cross-sectional approach. Eneuro, 8(4).
2. Sha, Z., et al. (2023). Genetic architecture of the white matter connectome of the human brain. Science Advances, 9(7).
3. Poldrack, R. A., et al. (2017). Scanning the horizon: towards transparent and reproducible neuroimaging research. Nature reviews neuroscience, 18(2), 115-126.
4. Bycroft, C., et al. (2018). The UK Biobank resource with deep phenotyping and genomic data. Nature, 562(7726), 203-209.
5. Smith, S. M., Douaud, G., Chen, W., Hanayik, T., Alfaro-Almagro, F., Sharp, K., & Elliott, L. T. (2021). An expanded set of genome-wide association studies of brain imaging phenotypes in UK Biobank. Nature neuroscience, 24(5), 737-745.
6. Yang, Xiaochen, et al. "Developing and sharing polygenic risk scores for 4,206 brain imaging-derived phenotypes for 400,000 UK Biobank subjects not participating in the imaging study." medRxiv (2023): 2023-04.
7. Theaud, G., et al. (2020). TractoFlow: A robust, efficient and reproducible diffusion MRI pipeline leveraging Nextflow & Singularity. Neuroimage, 218, 116889.
8. Zabad, S., et al. (2023). Fast and accurate Bayesian polygenic risk modeling with variational inference. The American Journal of Human Genetics, 110(5), 741-761.

Poster No 1940

RepL-fMRI: A Python Library for fMRI Representation Learning

Yaoxin Li[1], Kuan Han[2], Owen MacKenzie[2], Minkyu Choi[2], Zhongming Liu[2], Scott Peltier[2]

[1]Michigan Neuroscience Institute, University of Michigan, Ann Arbor, MI, [2]University of Michigan, Ann Arbor, MI

Introduction: Deep neural networks hold the unique potential for learning low-dimensional representations of high-dimensional fMRI data and supporting functional interpretation of brain activity linked to behavior (Kim 2021; Han 2019). Despite growing literature and large-scale datasets (Ortega 2023; Thomas 2022; Van Essen 2013; Littlejohns 2020; Casey 2018; Markiewicz 2021), there remains a lack of a streamlined pipeline for deep learning in fMRI analysis. To address this gap, we introduce RepL-fMRI: a Python library for building modular, interoperable, and interpretable deep neural networks for fMRI representation learning. This library encapsulates the open-source and pre-trained models for fMRI analysis developed through our prior work, whilst providing a means for extension through containerized software and a web user interface.

Methods: The RepL-fMRI package includes a pre-trained deep foundation model, which converts fMRI data into latent representations, and add-on shallow networks, which further link the representations to human behavior phenotypes. The foundation model uses an encoder-decoder architecture, including two stages of processing: 1) identifying spatial patterns and 2) extracting temporal sequences. The first stage is based on a variational autoencoder (VAE) (Kim 2021). The second stage is based on bi-directional transformer encoder (BERT) (Han 2019). Both of these stages contain paired encoder and decoder models, allowing for compression of brain data into latent representations and decompression of these vectors back to aid analysis of brain networks and dynamics. The foundation model is pre-trained with resting state fMRI data from the Human Connectome Project (HCP) (Van Essen 2013). The embeddings output by the foundation model are used to train a multi-layer perceptron (MLP) model that classifies cognitive and emotional traits from the rich and compressed tokens. Using Python, we define classes to encapsulate these models, as well as their variations, extensions, or linear counterparts. The classes follow the convention of object-oriented programming and build upon a generic set of interfaces for using various models as plug-and-play modules in both forward (encoding) and reverse (decoding) inference. The library also encapsulates existing standards in fMRI preprocessing, including the fMRIPrep (Esteban 2019) and HCP minimal preprocessing pipelines (Glasser 2013). As a framework, RepL-fMRI provides intuitive facilities to manage application of deep learning modules in fMRI analysis.

Results: We tested the Repl-fMRI framework for encoding 2-D (cortical) and 3-D (whole-brain) fMRI activity patterns into an evolving trajectory of latent representation. Through the foundation model, the representations of resting state fMRI activity were distinguishable across individuals (Figure 2a). The model was generalizable to task states, showing comparable encoding and decoding accuracies for both resting and task states. Representations can reveal transitions between different brain states (e.g. from rest to movie watching, Figure 2a). The pre-trained foundation model alongside MLP add-ons could predict the cognitive and emotional traits in terms of both their first principal components and individual measures (see Figure 2b).

Conclusions: Repl-fMRI is an open-source infrastructure to streamline the process of building and using deep learning models as interoperable modules in human fMRI analysis. Its current form and future extensions will contribute to the broader ecosystem for reliable and reproducible fMRI studies, especially for brain-behavior associations.

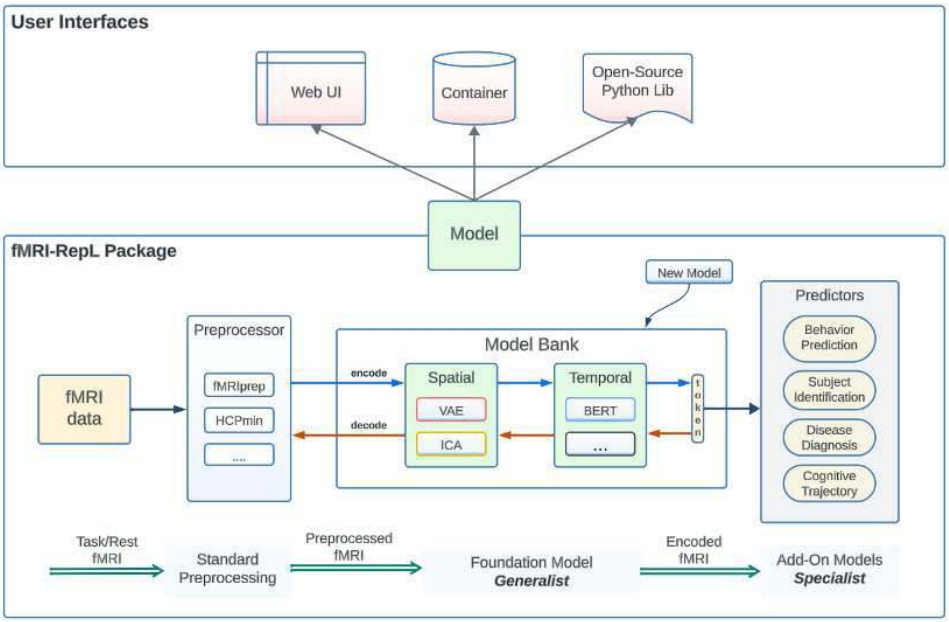

Figure 1. Architecture of the RepL-fMRI framework. The core of RepL-fMRI is an open-source Python library that supports preprocessing and representation learning via modular infrastructure. The library extends intuitive interfaces for the user, such as web application and installable container.

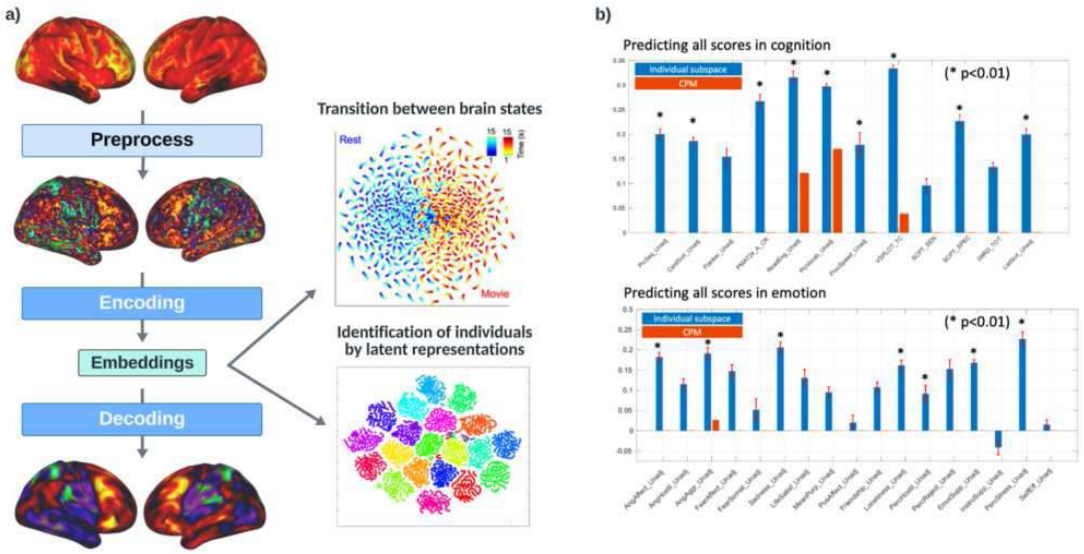

Figure 2. RepL-fMRI encodes latent representations that are effective for downstream predictive analysis. a) Foundation model encodes fMRI data into embeddings that can be decoded into cortical space for visualization. The embeddings highlight cognitive states and individual differences in the original data, as shown by T-SNE trajectories. b) fMRI embeddings effectively predict a multitude of cognitive and emotion task scores as input to downstream predictor models.

References

1. Kim, Jung-Hoon, et al. "Representation learning of resting state fMRI with variational autoencoder." NeuroImage 241 (2021): 118423.
2. Han, Kuan, et al. "Variational autoencoder: An unsupervised model for encoding and decoding fMRI activity in visual cortex." NeuroImage 198 (2019): 125-136.
3. Ortega Caro, Josue, et al. "BrainLM: A foundation model for brain activity recordings." bioRxiv (2023): 2023-09.
4. Thomas, Armin, Christopher Ré, and Russell Poldrack. "Self-supervised learning of brain dynamics from broad neuroimaging data." Advances in Neural Information Processing Systems 35 (2022): 21255-21269.
5. Van Essen, David C., et al. "The WU-Minn human connectome project: an overview." Neuroimage 80 (2013): 62-79.
6. Littlejohns, Thomas J., et al. "The UK Biobank imaging enhancement of 100,000 participants: rationale, data collection, management and future directions." Nature communications 11.1 (2020): 2624.
7. Casey, Betty Jo, et al. "The adolescent brain cognitive development (ABCD) study: imaging acquisition across 21 sites." Developmental cognitive neuroscience 32 (2018): 43-54.
8. Markiewicz, Christopher J., et al. "The OpenNeuro resource for sharing of neuroscience data." Elife 10 (2021): e71774.
9. Esteban, Oscar, et al. "fMRIPrep: a robust preprocessing pipeline for functional MRI." Nature methods 16.1 (2019): 111-116.
10. Glasser, Matthew F., et al. "The minimal preprocessing pipelines for the Human Connectome Project." Neuroimage 80 (2013): 105-124.

Poster No 1941

ARIbrain-SPM: An SPM extension toolbox for All-Resolutions Inference (ARI) for brain imaging

Xu Chen[1], Wouter Weeda[2], Jelle Goeman[3]

[1]University of Essex, Colchester, United Kingdom, [2]Leiden University, Leiden, South Holland, [3]Leiden University Medical Center, Leiden, South Holland

Introduction: Classical random field theory (RFT)-based cluster inference in neuroimaging is hampered by spatial specificity paradox. The findings only suggest that there is at least one voxel activated in statistically significant clusters but the activation extent and location are unknown. Rosenblatt et al. (2018) proposed All-Resolutions Inference (ARI) to alleviate this paradox. ARI is a post-hoc inference approach that quantifies the proportion of truly active voxels, i.e., true discovery proportion (TDP), within any chosen brain regions and measures a simultaneous TDP lower confidence bound for each of such regions. The simultaneity property of ARI ensures that the familywise error rate is always under strong control, even if the regions are chosen post hoc. Furthermore, an ARI-based linearithmic time algorithm was developed by Chen et al. (2023) to guide researchers to quickly localize maximal supra-threshold clusters with a sufficient TDP. When a high enough TDP threshold (e.g., 80%) is used, the paradox is vanished.

Methods: Based on ARI and the almost linear-time algorithm introduced in (Chen et al., 2023), we established the so-called All-Resolutions Inference for brain imaging (ARIbrain) analysis framework, and developed the corresponding ARIbrain-SPM (SPM extension toolbox). The original ARI is based on a closed testing procedure using the Simes local test, which is assumed to be valid but somewhat conservative for the fMRI data. Andreella et al. (2023) improved upon ARI with the use of permutation for a potentially increased detection power, leading to the permutation-based ARI (pARI). Here, our ARIbrain-

SPM toolbox allows both parametric and non-parametric cluster inference by incorporating ARI and pARI. We will illustrate the use of both cluster inference approaches in the ARIbrain framework with an fMRI dataset including 140 healthy subjects, who were asked to distinguish between vocal and non-vocal sounds during the experiment (Pernet et al., 2015). The Vocal>Non-vocal contrasts were derived for group analysis. Given a cluster-forming threshold (CFT), ARIbrain-SPM returns the TDP lower bounds for both parametric and non-parametric approaches. For parametric method, ARIbrain-SPM additionally outputs the maximal clusters, each with the TDP meeting or exceeding a pre-specified TDP threshold.

Results: The running time of ARIbrain-SPM was 0.46 secs and 705.83 secs for parametric and non-parametric approaches, respectively. With the CFT of 3.2 and RFT-based extent threshold of 118, Table 1 displays the estimated TDP bounds for these two approaches. As expected, the permutation-based method is generally more powerful. Given a TDP threshold of 80%, Figure 1 shows the 26 maximal supra-threshold clusters generated using the efficient algorithm introduced in (Chen et al., 2023), where the overall running time was 1.13 secs.

Table 1: Auditory data: supra-threshold clusters obtained by specifying a CFT of 3.2 and a RFT-based cluster extent threshold of 118. The returned TDP lower confidence bounds for parametric and non-parametric approaches are shown in the last two columns.

	MNI coordinates			Statistic	Size	TDP bound (%)	
Cluster	x	y	z	Z_{max}	$\|S\|$	Parametric	Permutation
Right HG/STG/IFG/PT	58	−14	2	7.83	6907	92.4	92.9
Left HG/STG/PT	−60	−22	4	7.51	4607	97.2	97.3
Left IFG	−58	14	30	4.54	385	72.2	73.2
Right precentral gyrus	52	2	52	4.88	249	94.8	94.4
Left amygdala	−18	−8	−10	4.59	168	41.7	41.7

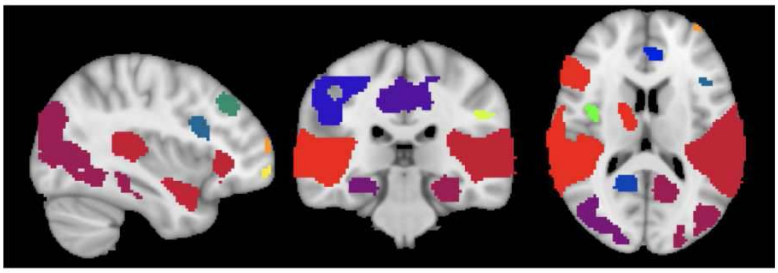

Figure 1: Auditory data: maximal supra-threshold clusters generated by specifying a TDP threshold of 80% using the linearithmic time algorithm detailed in (Chen et al., 2023). Different colours correspond to various clusters.

Conclusions: We developed the ARIbrain-SPM toolbox for cluster inference in neuroimaging, which aims to improve the most commonly used RFT-based cluster inference by resolving the spatial specificity paradox while retaining proper error guarantees. ARIbrain-SPM integrates both parametric and non-parametric approaches, striking the balance between efficiency and effectiveness.

References

1. Rosenblatt, J.D., Finos, L., Weeda, W.D., Solari, A., Goeman, J.J. (2018), 'All-Resolutions Inference for brain imaging', Neuroimage, vol.181, pp. 786-796.
2. Chen, X., Goeman, J.J., Krebs, T.J.P., Meijer, R.J., Weeda, W.D. (2023), 'Adaptive Cluster Thresholding with Spatial Activation Guarantees Using All-resolutions Inference', arXiv:2206.13587.
3. Andreella, A., Hemerik, J., Weeda, W., Finos, L., Goeman, J. (2023), 'Permutation-based true discovery proportions for functional magnetic resonance imaging cluster analysis', Statistics in Medicine, vol. 42, no. 14, pp. 2311-2340.
4. Pernet, C.R., McAleer, P., Latinus, M., et al. (2015), 'The human voice areas: Spatial organization and inter-individual variability in temporal and extra-temporal cortices', NeuroImage, vol. 119, pp. 164-174.

Poster No 1942

Augmented DTI-ALPS for Assessing Interstitial Fluid Dynamics Associated with Glymphatic Function

Chang-Le Chen[1], Sang Joon Son[2], Hecheng Jin[1], Jinghang Li[1], Noah Schweitzer[1], Linghai Wang[1], Chang Hyung Hong[2], Hyun Woong Roh[2], Yong Hyuk Cho[2], Bumhee Park[3], Na-Rae Kim[3], Jin Wook Choi[4], Sang Won Seo[5], So Young Moon[6], Seong Hye Choi[6], Shaolin Yang[1], Howard Aizenstein[1], Minjie Wu[1]

[1]University of Pittsburgh, Pittsburgh, PA, [2]Department of Psychiatry, Ajou University School of Medicine, Suwon, Korea, Republic of, [3]Department of Biomedical Informatics, Ajou University School of Medicine, Suwon, Korea, Republic of, [4]Department of Radiology, Ajou University School of Medicine, Suwon, Korea, Republic of, [5]Samsung Medical Center, Seoul, Korea, Republic of, [6]Department of Neurology, Ajou University School of Medicine, Suwon, Korea, Republic of

Introduction: The perivascular space plays an important role in the glymphatic system of the brain[1,2]. To capture the integrity of the perivascular space, diffusion MRI-based methods such as DTI-ALPS[3,4] have been proposed to quantify interstitial fluid (ISF) dynamics in the deep white matter (WM). However, the original DTI-ALPS focuses only on certain regions of interest (ROI)[5]. Also, it is susceptible to biases in spatial registration when automated methods are used. Thus, we proposed an augmented version of DTI-ALPS to mitigate the limitations, aiming to enhance the validity and better reflect the ISF diffusivity associated with glymphatic function.

Methods: The DTI-ALPS evaluates the perivascular ISF movement along the medullary conduits perpendicular to WM tracts near lateral ventricles (LV). Inspired by this, we established an algorithm to automatically localize the periventricular space (PVS) horizontal to the LV as the target area (Figure 1). In practice, we implemented and tested our analytic pipeline based on a multi-site multi-modal database initiated by Biobank Innovations for Chronic Cerebrovascular Disease with Alzheimer's Disease Study [6.7]. We collected diffusion tensor images (DTI) across 7 sites with different acquisition settings (harmonization was used in further analyses) from 49 healthy controls (age: 71.0[6.0], sex: 24%male, and global clinical dementia rating (CDR): 0.42[0.19]), 295 patients with mild cognitive impairment (MCI) (age: 73.1[6.2], sex: 31%male, and global CDR: 0.51[0.14]) and 134 patients with dementia (age: 74.3[6.9], sex: 37%male, and global CDR: 0.89[0.44]). All DTI data went through standard preprocessing and were then reconstructed to the diffusion tensor in the MNI space using q-space diffeomorphic reconstruction[8], which spatially registers both brain morphologies and fiber orientations. To create a PVS coverage map, we registered a LV prior to the mean diffusivity (MD) map, and it was then expanded along the transverse axis by the region growth algorithm to target the PVS while omitting LV itself and callosal fibers. Moreover, we calculated voxel-wise transverse tensor ratio (TTR, the square of tensor element in the X axis divided by the product of tensor elements in the Y & Z axes) to represent the ISF diffusivity. The average of TTR in the bilateral PVS (namely augmented DTI-ALPS) was estimated to represent the perivascular integrity. To test the biological validity of the augmented DTI-ALPS, we performed partial correlation between diffusion-derived metrics and clinical factors as well as F18-flutemetamol PET-derived measures (adjusting age, sex, and education). Also, we conducted group comparisons (adjusting age, sex, and education) and tested age-by-sex interaction for the original and proposed DTI-ALPS metrics.

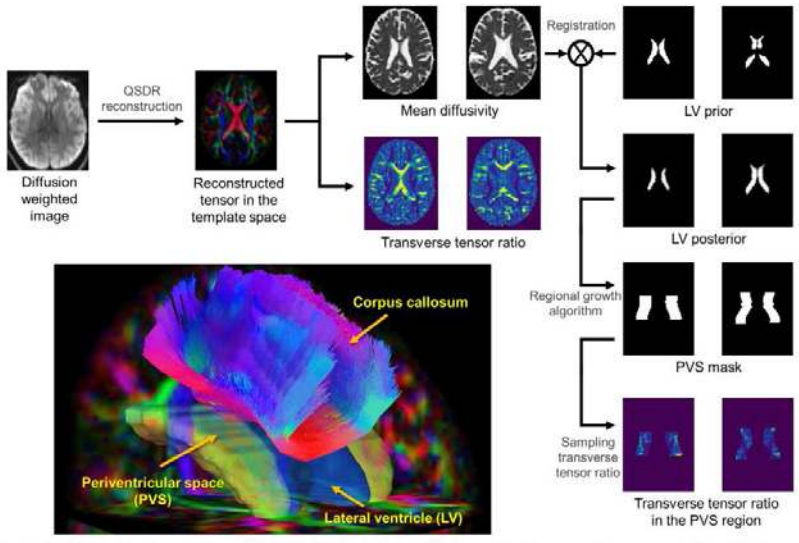

Figure 1. Analytic pipeline of proposed augmented DTI-ALPS analysis. The diffusion weighted images are first reconstructed into diffusion tensors in the MNI space using q-space diffeomorphic reconstruction (QSDR). To sample the periventricular space (PVS) that are horizontal to the lateral ventricles (LV), the LV prior is registered to the mean diffusivity contrast. The registered LV posterior is further transformed to the PVS mask through the regional growth algorithm. This PVS mask is used to sample transverse tensor ratio (the square of the square of tensor element in the X axis divided by the product of tensor element in the Y & Z axes) to obtain overall metrics to represent the interstitial fluid characteristics.

Results: Partial correlation (significance level = 0.01) revealed that the original DTI-ALPS was significantly correlated with both whole WM fractional anisotropy (FA) and MD compared to the proposed one, suggesting the original may share the common information with DTI metrics (Figure 2). Both original and proposed DTI-ALPS were significantly correlated with clinical factors including global CDR, CDR sum of box (CDR-SB), MMSE, Shiraz verbal learning test (SVLT), and hippocampal atrophy. Moreover, the proposed metrics were exclusively significantly correlated with amyloid PET standard uptake value ratio (SUVR) in multiple regions. Both DTI-ALPS metrics showed significant age-by-sex interactions ($p = 0.016$ for the original & 0.014 for the proposed), but only the augmented DTI-ALPS showed significant main effect of age ($p = 0.001$). The proposed metrics showed significant difference ($p < 0.001$) between groups except the pair of HC-MCI.

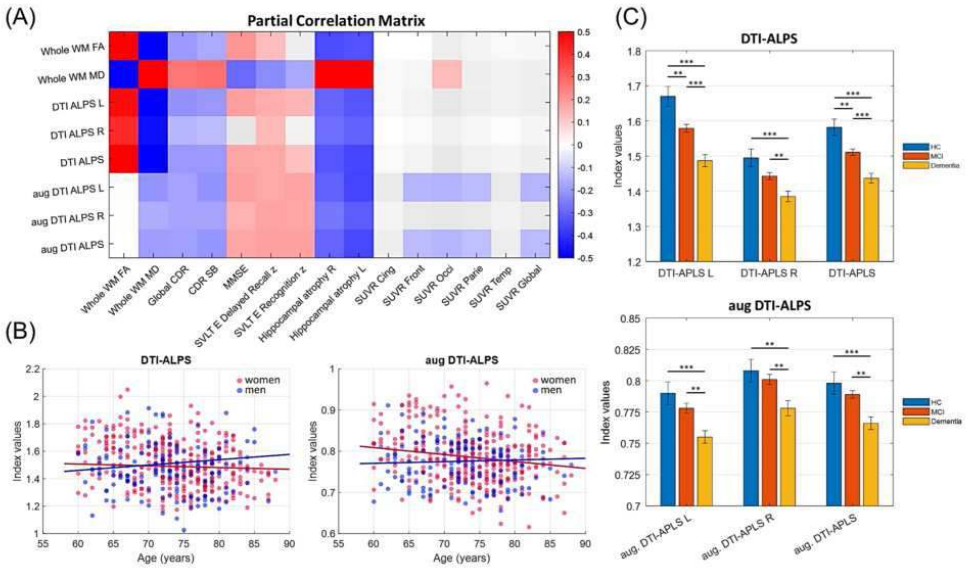

Figure 2. The statistical results of the original DTI-ALPS and proposed DTI-ALPS (augmented DTI-ALPS) metrics. The partial correlation matrix reveals statistical association between diffusion-derived measures and clinical factors as well as PET-derived standard uptake measures. The scatterplots show significant interaction between age and sex for both metrics, and a stronger age effect in the proposed augmented DTI-ALPS metrics. The bar charts demonstrate significant group difference for both metrics (except the HC-MCI pair in the proposed metrics).

Conclusions: We established an automated pipeline to estimate augmented DTI-ALPS metrics in the PVS. This approach is more robust to the registration bias. Moreover, the proposed metrics can provide additional information potentially reflective of glymphatic system integrity.

References

1. Wardlaw, J. M., Benveniste, H., Nedergaard, M., Zlokovic, B. V., Mestre, H., Lee, H., ... & colleagues from the Fondation Leducq Transatlantic Network of Excellence on the Role of the Perivascular Space in Cerebral Small Vessel Disease. (2020). Perivascular spaces in the brain: anatomy, physiology and pathology. Nature Reviews Neurology, 16(3), 137-153.
2. Rasmussen, M. K., Mestre, H., & Nedergaard, M. (2018). The glymphatic pathway in neurological disorders. The Lancet Neurology, 17(11), 1016-1024.
3. Taoka, T., Masutani, Y., Kawai, H., Nakane, T., Matsuoka, K., Yasuno, F., ... & Naganawa, S. (2017). Evaluation of glymphatic system activity with the diffusion MR technique: diffusion tensor image analysis along the perivascular space (DTI-ALPS) in Alzheimer's disease cases. Japanese journal of radiology, 35, 172-178.
4. Taoka, T., Ito, R., Nakamichi, R., Kamagata, K., Sakai, M., Kawai, H., ... & Naganawa, S. (2022). Reproducibility of diffusion tensor image analysis along the perivascular space (DTI-ALPS) for evaluating interstitial fluid diffusivity and glymphatic function: CHanges in Alps index on Multiple conditiON acquIsition eXperiment (CHAMONIX) study. Japanese journal of radiology, 40(2), 147-158.
5. Moses, J., Sinclair, B., Law, M., O'Brien, T. J., & Vivash, L. (2023). Automated methods for detecting and quantitation of enlarged perivascular spaces on MRI. Journal of Magnetic Resonance Imaging, 57(1), 11-24.
6. Son, S. J., Park, B., Roh, H. W., Kim, N., Jo, Y. H., Lee, E., ... & Hong, C. H. (2020). Biobank innovations for chronic cerebrovascular disease with Alzheimer's disease study (BICWALZS) Development of new models and analysis methods/screening studies/platforms. Alzheimer's & Dementia, 16, e042259.
7. Karim, H. T., Aizenstein, H. J., Mizuno, A., Ly, M., Andreescu, C., Wu, M., ... & Son, S. J. (2022). Independent replication of advanced brain age in mild cognitive impairment and dementia: detection of future cognitive dysfunction. Molecular Psychiatry, 27(12), 5235-5243.
8. Yeh, F. C., & Tseng, W. Y. I. (2011). NTU-90: a high angular resolution brain atlas constructed by q-space diffeomorphic reconstruction. Neuroimage, 58(1), 91-99.

Poster No 1943

Group-level inference of fMRI data through non-parametric combination

Matteo Lionello[1], Luca Cecchetti[1]

[1]IMT School for Advanced Studies Lucca, Lucca, Italy

Introduction: A large extent of neuroimaging findings relies on group-level inference, which consists in computing summary statistics and Neyman-Pearson significance from the output of first-level analyses. In this regard, several studies pointed to the importance of using permutation-based null distributions in estimating group-level significance[1,2]. Recombination strategies are available to probe most study designs[3], such as permuting group labels in two-sample tests or sign-flipping. Regarding the latter, in alternative permutation strategies, if the null hypothesis is true, the test variable should have values equally dispersed around the central value of the H0 distribution. This assumption does not hold for unsigned testing variables, such as the R2 in encoding studies. Thus, how can the group-level significance of a multi-column encoding model be assessed? Here, non-parametric combination (NPC), a method conceived to combine multiple neuroimaging modalities within a subject[4], shows to reliably detect group-level effects in encoding studies while controlling for false positives. The code to implement group-level NPC is publicly available at github.com/mlionello/NaPuCco.

Methods: 900 volumes are generated with 27 effected voxels ($R2 \sim U^{0,1}$) while 120 volumes are generated with 8000 non-effected voxels. A synchronised timepoint-shuffling schema is created for 2000 permutations across participants and voxels. Single participant data are then created on effected and non-effected volumes. Parametric p-values are estimated for each voxel and combined into a joint statistic across a variable number of subjects (from 10 to 80) via the Fisher method. In power analysis, 150 experiments are simulated varying the percentage of participants carrying effects. In the clusterbased correction (CFT=0.001), effected volumes are padded by non-effected voxels (padding width=8). Voxel- and cluster-level family-wise false positive rate (FPR) are estimated by simulating 500 and 1000 experiments, respectively. Lastly, in real data, voxelwise FPR are measured with 198 resting-state acquisitions from the Cambridge Buckner dataset[5], a 10-column random noise encoding model, and simulating 1000 experiments. Participants were combined in groups from 5 to 60. All results are reported at pFWC<0.05.

Results: As expected, to maintain statistical power constant, the overall sample size must increase proportionally to the decrease in the number of participants carrying an effect (Fig 1 right). In cluster-based correction, with $R2 \sim N(0.074, 0.17)$, the slope of the power curve at 0.80 increases by 0.06 per participant from 100% down to 70% of effected subjects included, and by 0.05 per participant when considering 60% of individuals carrying an effect (Fig 1 top-centre). Similarly, in the voxelwise correction and $R2 \sim N(0.074, 0.17)$, the slope of the power curve increases by 0.30, 0.15, 0.06, 0.03, 0.01 per participant when 100%, 90%, 80%, 70%, 60% of subject carries an effect(Fig 1 bottom-centre). FPR confidence intervals are in line with the nominal family-wise corrected alpha level (Fig 2). When replicating the same analysis using real data, voxel-level FPR ranges from 4.9% to 6.9% with no association between the number of combined subjects and the number of false positives (p=0.317).

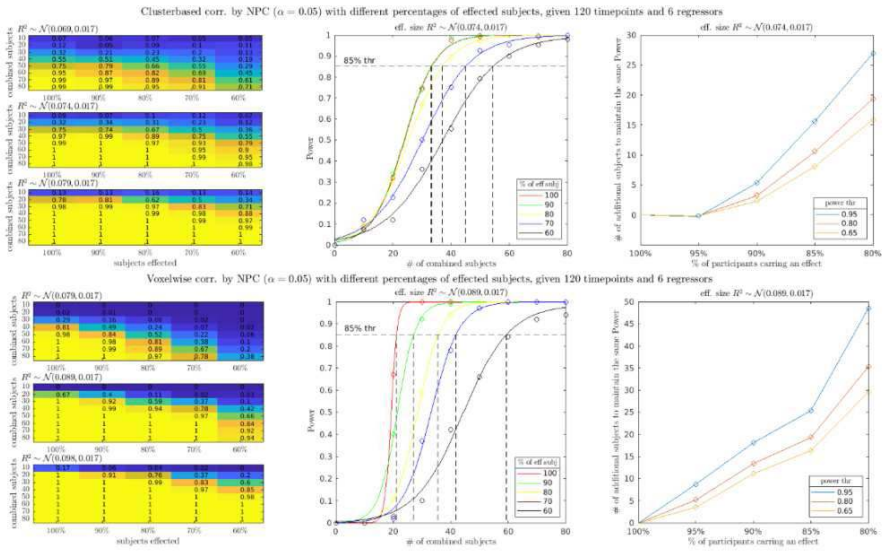

Figure 1: Top: Voxelwise correction; bottom: Clusterbased correction. Left: power estimation grid (number of subjects by percentage of them carrying an effect) across different R^2 distribution; center: power curves for different portions of effected subjects; right: amount of additional subjects needed given power thresholds and portion of effected subjects.

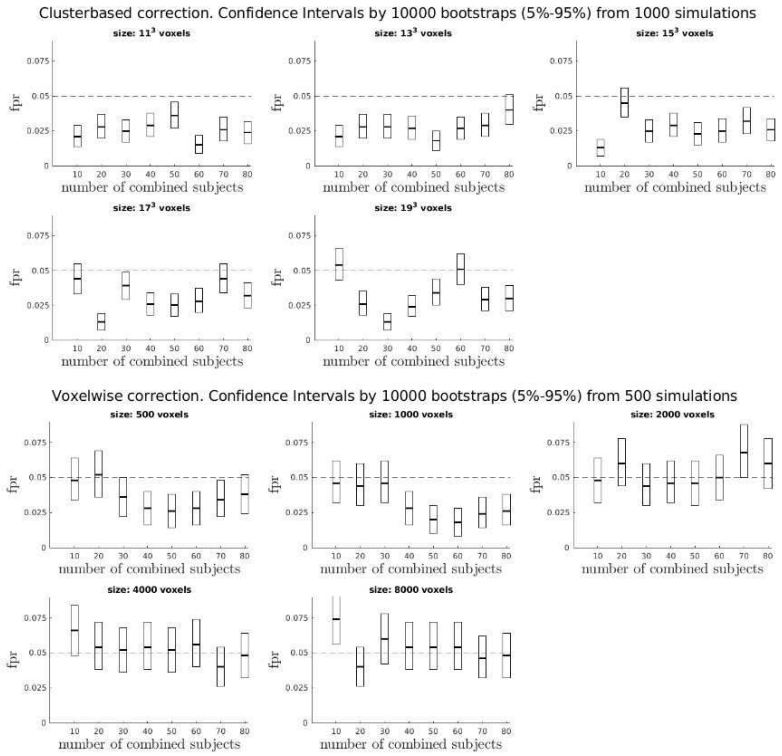

Figure 2: False Positive Rates: confidence intervals at 5% and 95% through bootstrapping (10000 resampling) while varying the number of subjects combined via NPC. Top: Clusterbased correction on 1000 simulated experiments. Bottom: Voxelwise correction on 500 simulated experiments.

Conclusions: This project systematically analyses and validates the use of NPC for group-level inference with unsigned statistics. In line with statistical theory, given a certain power, increasing the number of participants carrying an effect reduces the samples size needed to detect a group-level effect. The FPR aligns with nominal data and with findings in the literature for other permutation methods. In conclusion, the findings suggest that NPC is suitable for establishing group-level significance in encoding studies when the coefficient of determination represents the testing variable. This is crucial, especially when idiosyncrasies exist in how brain activity relates to individual features of an encoding model.

References

1. Nichols, T. E., & Holmes, A. P. (2002), 'Nonparametric permutation tests for functional neuroimaging: a primer with examples', Human brain mapping, vol. 15, no. 1, pp. 1–25.
2. Eklund, A., Nichols, T. E., and Knutsson, H. (2016), 'Cluster failure: Why fmri inferences for spatial extent have inflated false-positive rates', National Academy of Sciences of the United States of America, vol. 113, no. 28, pp. 7900–7905.
3. Winkler, A. M., Ridgway, G. R., Webster, M. A., Smith, S. M., & Nichols, T. E. (2014), 'Permutation inference for the general linear model', NeuroImage, vol. 92, no. 100, pp.381–397
4. Winkler, A. M., Webster, M. A., Brooks, J. C., Tracey, I., Smith, S. M., and Nichols, T. E. (2016), 'Non-parametric combination and related permutation tests for neuroimaging', Human brain mapping, vol. 37, no. 4, pp. 1486–1511.
5. Biswal, B., Mennes, M., Zuo, X.-N., Gohel, S., Kelly, C., Smith, S., Beckmann, C., Adelstein, J., Buckner, R., Colcombe, S., Dogonowski, A.-M., Ernst, M., Fair, D., Hampson, M., Hoptman, M., Hyde, J., Kiviniemi, V., K otter, R.,
6. Li, S.-J., and Milham, M. (2010), 'Toward discovery science of human brain function', Proceedings of the National Academy of Sciences of the United States of America, vol. 107, pp. 4734–9.

Poster No 1944

The dynamic FCT highlights the structure-function association within white matter

Yue Wang[1], Yue Zhang[1], Tianyu Fang[1], Xi Sun[1], Qiuyun Fan[1], Yuanyuan Chen[1]

[1]Academy of Medical Engineering and Translational Medicine, Medical School of Tianjin University, Tianjin, China

Introduction: Plenty of literatures have indicated convergent findings about the brain structure-function coupling between diffusional connectivity and functional connectivity for grey matter. However, less is known for the white matter with the novel aspect of functional activities within white matter. Therefore, the current study aims to examine the association between dynamic functional anisotropy and microstructure within white matter tissue, as well as its potential clinical applications.

Methods: The discovering data included 100 unrelated subjects from Human Connectome Project, with multi-modality MRI data. The two sessions of resting-state fMRI together with emotion and motor task fMRI were used. Then the validation data included 97 hepatopathy patients (40 healthy controls) and 91 nephropathy patients (84 healthy controls), which was collected locally. All subjects were scanned on a 3T MR system. Data processing for HCP went through the minimal preprocessing pipelines, with an additional regression of head movement parameters and CSF signal, temporal band-pass filtering (0.1-0.15Hz), and a 6-mm FWHM spatial smoothing for fMRI; DWI data were non-linearly registered to MNI-152-2mm space and scalar maps of FA were computed. Both datasets shared the standard preprocessing pipelines and registered to MNI space. Classic functional connectivity tensor (FCT) is calculated based on Pearson correlation over whole time which is also a static examination. We extended it to dynamics with a co-fluctuation way between two voxels. This approach allows us to obtain functional correlation tensor at a timescale of single frame. We calculated the dFCT-FA at each time point and got the temporally averaged dFCT-FA value. Pearson correlation coefficients between the mean dFCT-FA and DTI-FA for each tract in JHU-ICBM atlas were calculated as structure-function association index. To determine the values of clinical applications in the association of dFCT-FA and DTI-FA, further group comparisons have done for hepatopathy/nephropathy patients with two-sample t-test. The significance level was established at $p<0.05$ after FDR correction across all white matter tracts.

Results: The dFCT-FA surpassed classic FCT-FA with clear contrast between grey matter and white matter, and both showed high level of repeatability. The mean map of dFCT-FA were illustrated with symmetry across all the tracts, with higher level in the anterior and lower level in the posterior. The association between dFCT-FA and DTI-FA within the white matter tracts showed distinct difference among the varied brain states but not for that of static. The reproducibility of structure-function association with dynamic way showed higher level between sessions than that with static way. Clinical applications further indicated significant lower associations in white matter for patients compared with the healthy. Significant alterations were located at cingulate gyrus for hepatopathy patients and external capsule for nephropathy patients.

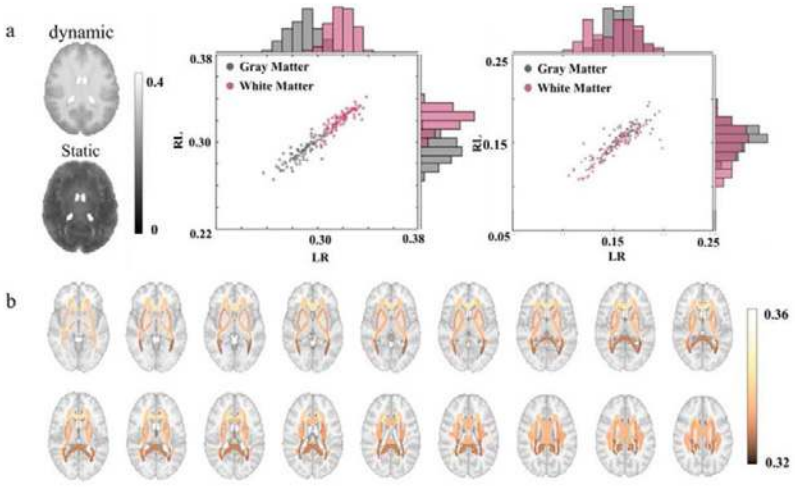

Figure 1. Comparison of dynamic functional tensor temporally averaged FA in gray matter and white matter and visualization of average dFCT-FA within fiber bundles. a. The distribution of functional correlation tensor FA in voxels from white matter and gray matter. Brain slices display group-average dFCT temporal-average FA and classic FCT-FA. Scatter plots with histogram illustrate the distribution of dFCT-FA (left) and classic FCT-FA (right). Each point represents the FA value computed from data of an individual. The horizontal axis represents FCT-FA values of left-to-right phase-encodeding data. The vertical axis represents FCT-FA values of right-to-left phase-encoding data. **b.** Group-average dFCT-FA within each fiber bundle. The image reveal symmetry.

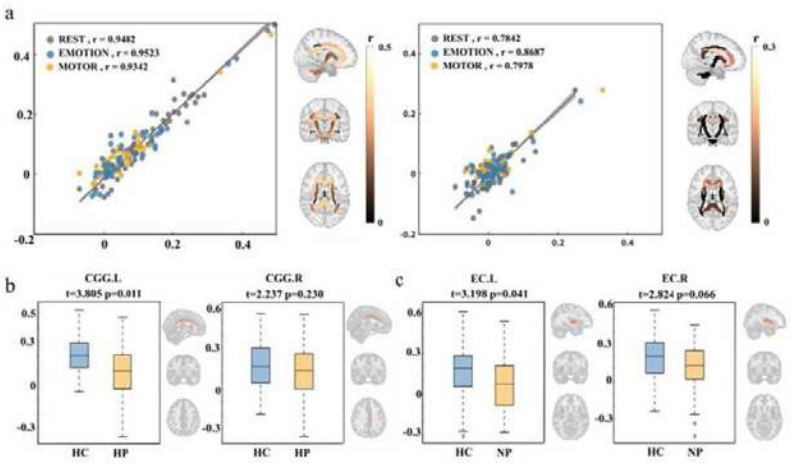

Figure 2. Association of dFCT temporally averaged FA / classic FCT-FA with DTI-FA (a-b) and their application in disease (c-d). a. Repeatability of structure-function association index. Each point in the scatter plot represents group-average Pearson correlation coefficient of dFCT-FA (left) / classic FCT-FA (right) and DTI-FA within a JHU-ICBM ROI (50 ROIs in total). The axis represents structure-function association values calculated from data in different phase-encoding directions (horizontal axis :left-to-right phase-encoding direction; vertical axis: :right-to-left phase-encoding direction). The r values in the upper-right legend show the Pearson correlation coefficient of results from different runs. The brain diagram to the right of each scatter plot shows group-average structure-function association index within each JHU-ICBM ROI. **b.** JHU-ICBM ROI (CGG.L) with significant differences in structure-function association index between hepatopathy patients and healthy control after FDR correction and its contralateral JHU-ICBM ROI (CGG.R). The y axis of box diagram represents structure-function association index. **c.** JHU-ICBM ROI (EC.L) with significant differences in structure-function coupling index between nephropathy patients and healthy control after FDR correction and its contralateral JHU-ICBM ROI (EC.R). The y axis of box diagram represents structure-function association index.

Conclusions: The dFCT-FA is more capable of characterize the functional activities in white matter than the static FCT, and more sensitive to the DTI-FA of microstructural property across different brain states. The proposed method to measure the association of structure-function within white matter exhibited high reliability and clinical value. The reduced association here in patients group probably unveiled the undergoing dysfunctions within that white matter tracts.

References

1. Ding, Z.(2013). Spatio-temporal correlation tensors reveal functional structure in human brain. PloS one, 8(12), e82107.
2. Zamani Esfahlani, F.(2020). High-amplitude cofluctuations in cortical activity drive functional connectivity. Proceedings of the National Academy of Sciences, 117(45), 28393-28401.
3. Zhao, J.(2023). Structure-function coupling in white matter uncovers the abnormal brain connectivity in Schizophrenia. Translational Psychiatry, 13(1), 21.

Poster No 1945

Active Inference Agents: A Proposal for Structural Learning During Sleep

David Araya[1], Leandro Torres[2], Nelson Trujillo-Barreto[3], Yunier Pieur-Coloma[4], Carla Taramasco[5], Wael El-Deredy[6]

[1]Facultad de Ingeniería, Universidad Andrés Bello, Viña del Mar, Región de Valparaiso, [2]Universidad de Playa Ancha, Viña del Mar, Región de Valparaiso, [3]University of Manchester, Manchester, Manchester, [4]Universidad de Valparaíso, Valparaíso, Valparaíso, [5]Universidad Andres Bello, Viña del Mar, Región de Valparaiso, [6]Universidad de Valparaíso, Valparaíso, Valparaíso

Introduction: Active Inference has emerged as a new theory modeling the brain as a predictive machine composed of hierarchically arranged generative models, which continuously make predictions about inputs from the environment[1]. By minimizing a quantity known as variational free energy, an agent based on Active Inference adjusts the parameters of its generative models, enhancing predictions and aiding the agent's adaptation to the specific environment. Traditionally, this model modification does not include altering the model's structure, which is assumed to be predefined and likely formed during the agent's phylogeny. There is only one prior study that addresses structural changes in these models, focusing on varying the number of models by freeing up slots (pruning)[2]. In our approach, however, we discuss altering the underlying structure of the model itself. Inspired by studies suggesting that the brain, during sleep, engages in internal simulations and cognitive restructuring to optimize environmental understanding[3], we propose that an Active Inference-based agent could optimize its models' structure during sleep, by means of variational free energy minimization.

Methods: We implemented an active inference agent based on the partially observable Markov decision process (POMDP)[4]. This agent is designed to identify and classify simple geometric shapes with various rotations in a controlled environment. It uses a repertoire of generative models to represent the geometric shapes in the environment, and parameter estimation is achieved by minimizing the models' free energy. We propose that during night time periods, the agent continues its learning through internal simulations generated by the same generative models, in a cycle of generation and prediction. During this nocturnal phase, the structure of some generative models is modified, employing an evolutionary strategy inspired by neuronal Darwinism[5]. The total number of generative models is kept constant, discarding those models that exhibit the highest variational free energy.

Results: Figure 1 shows changes in free energy corresponding to the agents' simulated behaviour during day and night. During the first day, the free energy decreases, reflecting learning of the models' parameters based on sensory information (geometric figures). During the first night, the free energy remains at the same values, indicating that the sleep simulations are generated using the same models learned during the day, and no further parameters' optimization are made. However, on the second night, a new generative model emerges that simplifies the representation of figure rotations, thereby reducing free energy. The following day, this rotation-invariant model proves its effectiveness in the identification and prediction of geometric figures with various orientations.

Conclusions: In this exploratory study, we propose and test a mechanism by which an active inference agent can modify the structure of its internal generative models. This mechanism is inspired by neurobiological theories about brain simulation during sleep. We hypothesize, that free energy minimization during sleep promotes the creation of generative models with improved generalization capabilities due to a more effective representation of the environment. This hypothesis implies that the brain might be continuously reducing free energy at all times (day and night), even in the presence of minimal sensory information, which could account for the uninterrupted spontaneous activity consistently observed in the brain.

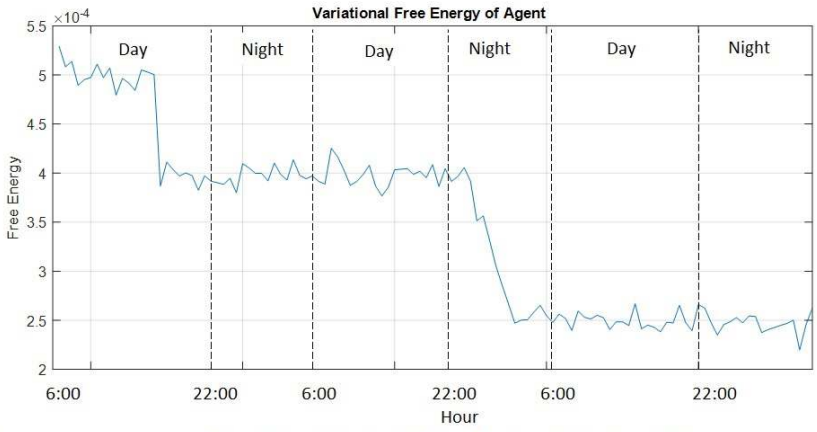

Figure 1: Record of the Agent's Variational Free Energy During Day and Night

References
1. Friston K, FitzGerald T, Rigoli F, Schwartenbeck P, O Doherty J, Pezzulo G. Active inference and learning. Neurosci Biobehav Rev. 2016 Sep;68:862-879. doi: 10.1016/j.neubiorev.2016.06.022. Epub 2016 Jun 29. PMID: 27375276; PMCID: PMC5167251.
2. Smith R, Schwartenbeck P, Parr T, Friston KJ. An Active Inference Approach to Modeling Structure Learning: Concept Learning as an Example Case. Frontiers in Computational Neuroscience. 2020; 14:41. https://doi.org/10.3389/fncom.2020.00041 PMID: 32508611
3. Hobson, J., Hong, C.-H., and Friston, K. (2014). Virtual reality and consciousness inference in dreaming. Front. Psychol. 5:1133. doi: 10.3389/fpsyg.2014.01133
4. Ryan Smith, Karl J. Friston, Christopher J. Whyte, A step-by-step tutorial on active inference and its application to empirical data, Journal of Mathematical Psychology, Volume 107, 2022, 102632, ISSN 0022-2496, https://doi.org/10.1016/j.jmp.2021.102632.
5. Edelman GM. Neural Darwinism: selection and reentrant signaling in higher brain function. Neuron. 1993 Feb;10(2):115-25. doi: 10.1016/0896-6273(93)90304-a. PMID: 8094962.

Poster No 1946

A novel mathematical construction for identifying attractors from task-driven fMRI data

Hassan Abdallah[1], John Kopchick[2], Andrew Salch[1], Vaibhav Diwadkar[1]

[1]Wayne State University, Detroit, MI, [2]Wayne State University, Department of Psychiatry, Detroit, MI

Introduction: Functional brain network data provides a complex and complicated window into dynamics shaping brain function and dysfunction. Conventional connectivity matrices (based on bivariate correlations) can be interpreted as a "connectivity terrain" of the brain's functional state. In principle, we might be able to recover structure in this terrain by traversing it node by node and moving towards its nearest functional neighbor (i.e., its maximally correlated node). If there is meaningful functional structure in this terrain, any such traversal would settle on "attractor nodes." Those nodes that flow into a shared attractor would form an "attractor basin". Extant methods handle global summaries, such as degree distribution and characteristic path length[2], while being unable to effectively identify local structures, such as attractor nodes and basins. Here, we solve this problem by motivating the construction of a new relation from the connectivity terrain (bivariate correlation matrix), which we call transitive maximal correlation (TMC): thus, Node A is transitively maximally correlated to node B if and only if B is an attractor into which A flows. Remarkably, this method identifies attractors whose nearest functional neighbor is their interhemispheric homologue and whose attractor basins are significantly different across conditions during a learning task.

Methods: Data (3T) were acquired during learning[3]. In each subject (n=39), zero-lag undirected functional connectivity was estimated from time series (246 regions)[1] in each condition (Encoding, Post-Encoding Consolidation, Retrieval, Post-Retrieval Consolidation) over eight repetitions (32 matrices per subject). The resulting connectivity terrains are analyzed using transitive maximal correlation (TMC). Region B1 is "transitively maximally correlated" with Bm if there exists a sequence of regions B2, B3, ..., Bm-1 such that B1 is maximally correlated with B2, and B2 is maximally correlated with B3, etc., and Bm-1 is maximally correlated with Bm. We interpret this relation as B1 "flowing" into Bm in the connectivity terrain. We introduce the TMC matrix, a new construction: it is the square matrix whose entry in row x and column y is one if region x is transitively maximally correlated with y and with all regions transitively maximally correlated with y, and zero otherwise. Intuitively, the presence of ones in a column y indicates that region y is an attractor for information flow. The collection of regions that flow into region y form an attractor basin. We develop a test statistic using the Frobenius norm to compare sets of TMC matrices from different conditions in the learning task. A paired permutation test is utilized to determine the p-value for the observed test statistics when comparing conditions pairwise[4].

Results: We apply our statistical test to make pairwise comparisons of TMC matrices between encoding, post-encoding consolidation, retrieval, and post-retrieval consolidation using 10k permutations (see Figure 1). We identified the five percent most influential regions driving these significant results. These eight regions primarily reside in Brodmann areas 1, 2, 3, 6, 28, 34, 35, and 36. We capture the average composition of their attractor basins in Figure 2.

	Encoding	Post-encoding consolidation	Retrieval	Post-retrieval consolidation
Encoding		0.000099	0.000099	0.000099
Post-encoding consolidation	0.000099		0.000099	0.002199
Retrieval	0.000099	0.000099		0.000099
Post-retrieval consolidation	0.000099	0.002199	0.000099	

For each of the experimental conditions (encoding, post-encoding consolidation, retrieval, post-retrieval consolidation), we calculated the TMC matrix of each of the 39 participants during that experimental conditions during each of the 8 iterations of the task, yielding 312 TMC matrices for each of the four experimental conditions. We make pairwise comparisons between encoding, post-encoding consolidation, retrieval, and post-retrieval consolidation using our statistical test with 10k permutations. The null hypothesis is rejected in each comparison using an α-threshold of 0.01. These results stem from significant differences in the dynamics of the TMC matrices associated with each condition, including which regions are attractors, the number of attractor basins, and the composition of attractor basins.

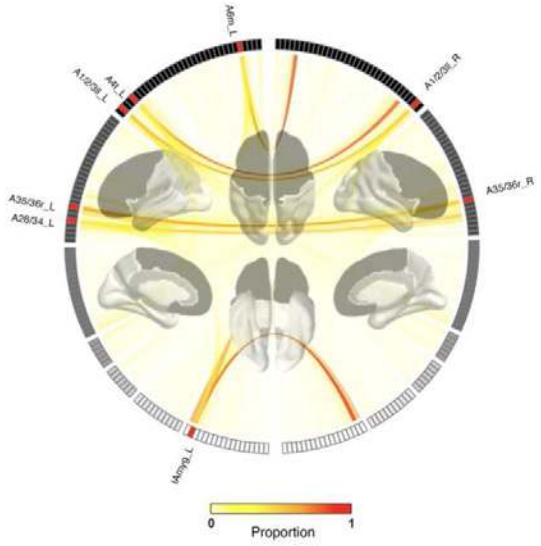

Regions are arranged around the perimeter of the connectome separated by hemisphere, such that each region is horizontally across from its interhemispheric homologue. The lobes are color-coded, and the brain image maintains the color coding. The transitive maximal correlation matrices associated to each experimental condition were compared pairwise using our paired permutation test with significant p-values obtained for all six comparisons. We then identified the five percent most influential regions driving these significant results. These eight regions are marked on the perimeter. A chord is drawn from every region to each of the eight regions. The chords that connect regions are colored to represent the proportion of time that a region "flows" terminally into one of these eight (see color bar). The most striking feature of this diagram is the high-proportionality with which each of these regions' interhemispheric homologue "flows" into it.

Conclusions: Our study employs a novel construction, TMC, to evaluate the structure of the brain's connectivity terrain. TMC enables the identification of attractor nodes and attractor basins, unveiling a nuanced window into information flow within the connectivity terrain. We implement a statistical test on TMC matrices that indicates significant differences across all pairwise comparisons of conditions during a learning task. Our findings highlight attractor nodes with interhemispheric homologues as nearest functional neighbors whose attractor basins exhibit condition-specific variation. These results underscore the efficacy of TMC to capture striking functional properties of the fMRI signal.

References

1. Jiang T. Brainnetome (2013): a new -ome to understand the brain and its disorders. Neuroimage. doi: 10.1016/j.neuroimage.2013.04.002. Epub PMID: 23571422.
2. Shahhosseini Y. (2022): Functional Connectivity Methods and Their Applications in fMRI Data. Entropy (Basel). doi: 10.3390/e24030390. PMID: 35327901; PMCID: PMC8946919.
3. Stanley JA. (2017): Functional dynamics of hippocampal glutamate during associative learning assessed with in vivo 1H functional magnetic resonance spectroscopy. Neuroimage. doi: 10.1016/j.neuroimage.2017.03.051. PMID: 28363835; PMCID: PMC5498221.
4. Winkler AM. (2015): Multi-level block permutation. Neuroimage. doi: 10.1016/j.neuroimage.2015.05.092. PMID: 26074200; PMCID: PMC4644991.

Poster No 1947

Disentangling global brain states from local activity for better classification accuracy

Eloy Geenjaar[1], Vince Calhoun[2]

[1]Georgia Institute of Technology, Atlanta, GA, [2]GSU/GATech/Emory, Decatur, GA

Introduction: Resting-state magnetic resonance imaging (rs-fMRI) is often used to track whole-brain connectivity dynamics[1]. These connectivity dynamics are often computed by dividing the signal into (overlapping) windows and computing the correlation between brain regions over that window. These connectivity matrices effectively summarize the activity in each window. We introduce a more general summarization of the activity in each window using a variational autoencoder (VAE) that summarizes the activity in a window into a low-dimensional representation for the whole window (global) and each timestep in the window (local)[2]. We show that latent space of the global representations is more easily separable into windows belonging to schizophrenia patients and controls than models that only use local information.

Methods: As shown in Figure 1, our model consists of two main sub-models: a global network that summarizes a window of fMRI activity into a low-dimensional global representation, and a local network that uses the global representation and the fMRI activity to summarize each individual timepoint. Just as with dynamic connectivity analyses, we expect that the rs-fMRI signal is non-stationary over time and that this non-stationarity affects the individual timepoints within the window. In the same way, we expect the global representations to capture the underlying brain state a person is in, which influences the latent representation for individual timesteps. By disentangling global and local representations, we expect to find brain states (global representations) that are more common for schizophrenia patients than controls. To explore this research question, we train our model on 53 NeuroMark[4] ICA component timeseries from the fBIRN[5] dataset with 40 second windows (20 seconds of overlap) and compare it to dynamic functional connectivity (dFNC) and a model that only encodes local representations. The local and global representations in our model are both 2-dimensional, and we compare against a model with only 2-dimensional local representations. We train our model and the local-only model across 4 seeds so we can perform a statistical analysis. To evaluate our model against the baselines, we calculate a classification accuracy across windows in the test set to see which method can separate individual windows the best into belonging to schizophrenia patients or controls. Classification is done using a support vector machine with an RBF kernel. To get a representation for a window in the local-only model, we average the latent timesteps in each window, we only use the global representation for the classification in our proposed model and reduce the lower-triangular part of each dFNC matrix to a 2-dimensional vector with PCA. Thus, classifications for our model and the baselines are done in a 2-dimensional space.

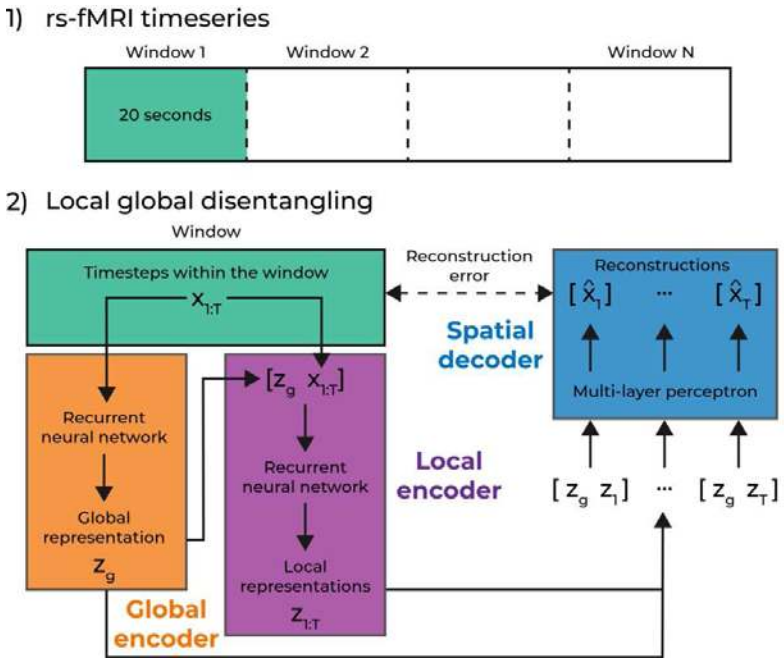

Results: Our experiment in Figure 2a shows that our model significantly (p=2.16E-5) outperforms the local-only baseline, and in Figure 2b, we show how well our model separates out schizophrenia patient windows from control windows. The global and local representations in Figure 2b are both derived from our model.

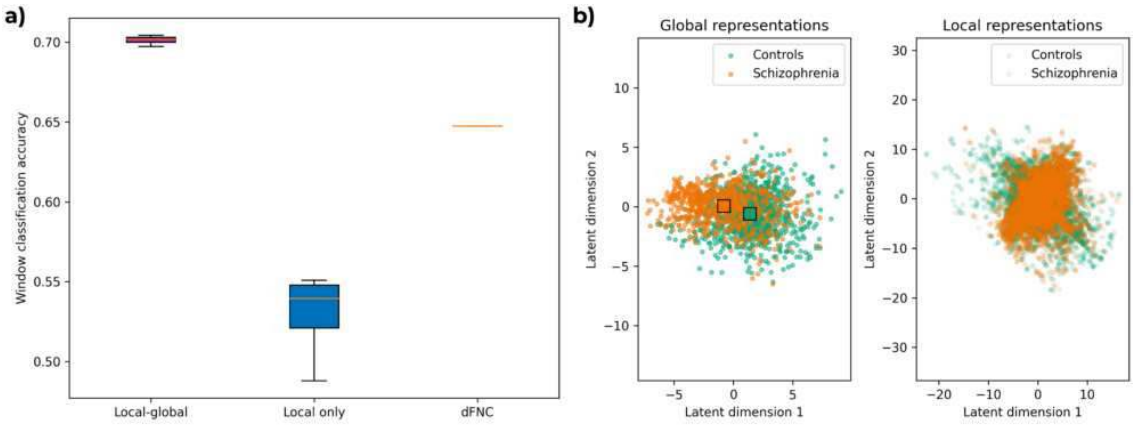

Conclusions: Our results conclude that disentangling local and global representations is a potentially fruitful direction to understand how brain states (global representations) are different for people with a schizophrenia diagnosis as opposed to controls. We compare our model against a baseline, and we find significant differences. In the future, we want to visualize and interpret what these differences look like in the brain. Given that our model is generative, we can ask the question: what would activity in a certain window have looked like if this person was diagnosed with schizophrenia?

References

1. Allen, E. A., Damaraju, E., Plis, S. M., Erhardt, E. B., Eichele, T., & Calhoun, V. D. (2014). Tracking whole-brain connectivity dynamics in the resting state. Cerebral cortex, 24(3), 663-676.
2. Yingzhen, L., & Mandt, S. (2018, July). Disentangled sequential autoencoder. In International Conference on Machine Learning (pp. 5670-5679). PMLR.
3. Chung, J., Gulcehre, C., Cho, K., & Bengio, Y. (2014). Empirical evaluation of gated recurrent neural networks on sequence modeling. arXiv preprint arXiv:1412.3555.
4. Du, Y., Fu, Z., Sui, J., Gao, S., Xing, Y., Lin, D., ... & Alzheimer's Disease Neuroimaging Initiative. (2020). NeuroMark: An automated and adaptive ICA based pipeline to identify reproducible fMRI markers of brain disorders. NeuroImage: Clinical, 28, 102375.
5. Keator, D. B., van Erp, T. G., Turner, J. A., Glover, G. H., Mueller, B. A., Liu, T. T., ... & Potkin, S. G. (2016). The function biomedical informatics research network data repository. Neuroimage, 124, 1074-1079.

Poster No 1948

HistoJS: Web-Based Analytical tool for Advancing Spatial Biology

Mohamed Masoud[1], Sergey Plis[1]

[1]Georgia State University, Atlanta, GA

Introduction: Advances in multiplexed imaging technologies enable us to capture single-cell proteomics and transcriptomics data in unprecedented detail and with high spatial resolution at the single-cell level. This large volume of image data presents a challenge in accurately isolating and quantifying distinct cell types to gain a deeper understanding of brain complexity, neurological disorders, potential biomarkers, and druggable targets for drug development. Therefore, there is an incremental demand and challenges to develop and validate cutting-edge quantitative image analysis tools for diagnosis, prognosis, and therapy response prediction and assessment in neurological and oncological diseases. HistoJS is a newly developed web-based tool that aims to overcome the challenges of utilizing highly-multiplexed immunofluorescence (HMIF) images for Spatial biology research. It provides open-source and extensible tools for analyzing spatial-molecular patterns, enables a deep view into the single-cell spatial relationship, along with machine learning algorithms in an interactive graphical interface that is easy-to-use for non-experts.

Methods: Immunofluorescence images, representing protein type intensities in tissue, are managed and hosted using the Digital Slide Archive (DSA), an open-source platform[1]. DSA, comprising components such as MongoDB, Girder worker, and Girder, serves as a reliable web-based platform for storing and organizing large immunofluorescence image datasets. Installable locally or on the cloud, DSA facilitates user access controls and programmatic data management. HistoJS, utilizing DSA as a backend, enables users to manage and store images along with analysis results based on preferences. OpenSeadragon[2], an open-source viewer, is employed for visualizing Highly-multiplexed immunofluorescence (HMIF)[3-4] images in HistoJS, offering features like panning, zooming, and overlays. HistoJS supports customized protein channel stacking, enabling high-resolution and full-scale composite rendering (Fig. 1). Analytically, HistoJS deploys Flask APIs to encompass cell segmentation[5], phenotyping, classification, correlations, spatial analysis, and cell type quantification for

understanding cell interactions. Real-time challenges are addressed with efficient techniques, including rapid cell boundary extraction and morphological feature analysis (e.g., solidity, eccentricity, orientation). Cell neighbor detection is facilitated through spatial plotting and Delaunay graph computation.

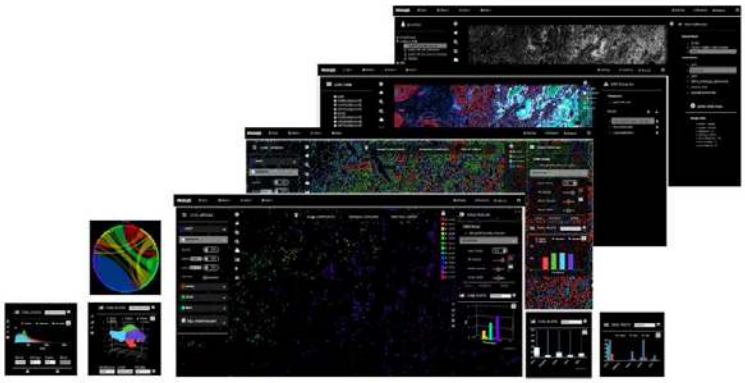

Figure 1. HistoJS Beta version Overview

Results: HistoJS source code is publicly accessible with detailed step-by-step documentation in the GitHub repository https://github.com/Mmasoud1/HistoJS. Multiple DSA online servers can be accessed from HistoJS such as https://styx.neurology.emory.edu/girder/# to load HMIF data samples and test the tool performance (Fig. 2). Researchers could visualize and analyze the expression patterns of key biomarkers associated with neurodegenerative disorders. The platform's interactive features facilitated the identification of disease-specific signatures, providing valuable insights into the molecular basis of brain diseases.

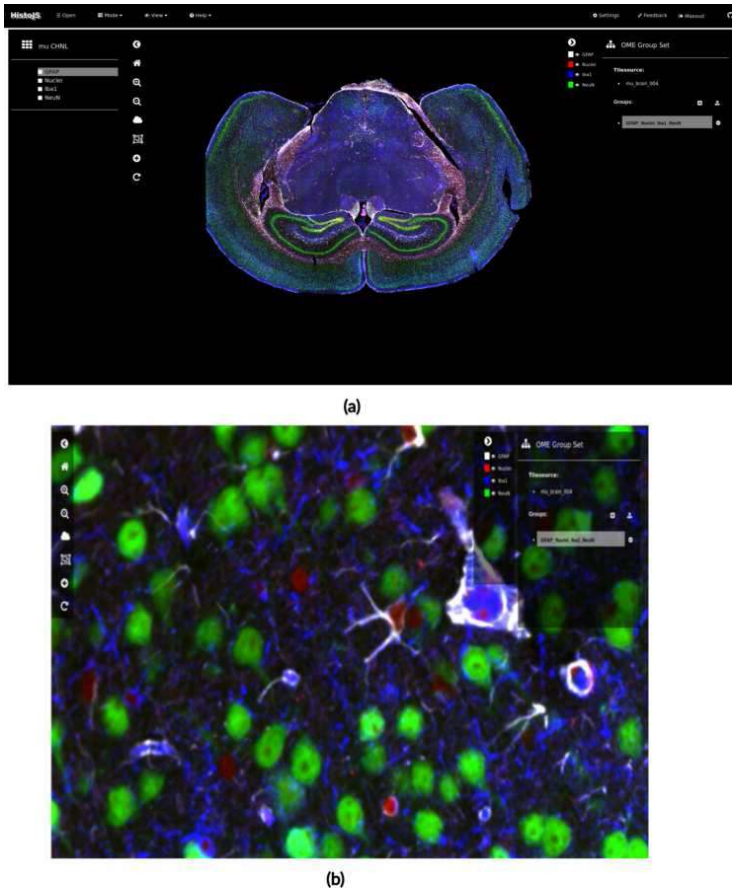

(a)

(b)

Figure 2. *HistoJS visualizes Mouse brain showing* ***Neuronal Nuclei*** *(NeuN- Green),* ***Microglia*** *(Iba1-Blue),* ***Astrocytes*** *(GFAP-White) and* ***DNA****(Red)* (Source: nanoString.com)

Conclusions: HistoJS is among the first web-based tools to visualize and analyze highly-multiplexed immunofluorescence (HMIF) image data while minimizing user inputs. For many researchers, setting up such analytical tasks is a technological barrier, and providing them through an interactive web-based pipeline will help biomedical users and related groups understand the progression of biological diseases and clinical outcomes in an easy-to-use and interactive graphical user

interface. Future developments will focus on expanding the tool's functionalities and enhancing its accessibility to further accelerate advancements in neuroscientific research.

References

1. Gutman, D.A., Khalilia, M., Lee, S., Nalisnik, M., Mullen, Z., Beezley, J., Chittajallu, D.R., Manthey, D. and Cooper, L.A., 2017. The digital slide archive: A software platform for management, integration, and analysis of histology for cancer research. Cancer research, 77(21), pp.e75-e78.
2. OpenSeadragon dev. Team. (2012). OpenSeadragon. In GitHub repository. GitHub. https://github.com/openseadragon/openseadragon
3. Lin, J. R., Fallahi-Sichani, M., & Sorger, P. K. (2015). Highly multiplexed imaging of single cells using a high-throughput cyclic immunofluorescence method. Nature communications, 6(1), 8390.
4. Lin, J.R., Izar, B., Wang, S., Yapp, C., Mei, S., Shah, P.M., Santagata, S. and Sorger, P.K., 2018. Highly multiplexed immunofluorescence imaging of human tissues and tumors using t-CyCIF and conventional optical microscopes. elife, 7.
5. Schmidt, U., Weigert, M., Broaddus, C., & Myers, G. (2018). Cell detection with star-convex polygons. In Medical Image Computing and Computer Assisted Intervention–MICCAI 2018: 21st International Conference, Granada, Spain, September 16-20, 2018, Proceedings, Part II 11 (pp. 265-273). Springer International Publishing.

Poster No 1949

Adaptive Denoising of 3D Structural MR Images using Deep Learning

Lintao Zhang[1], Mingxia Liu[1]

[1]The University of North Carolina at Chapel Hill, Chapel Hill, NC

Introduction: Image denoising is a primary MRI processing step. Many studies exist on MRI denoising, but most rely on 2D methods, ignoring 3D anatomical structures in MRIs. Additionally, multi-site MRIs tend to be affected by inter-site heterogeneity caused by differences in scanners or scanning protocols, resulting in different noise levels. However, previous studies cannot adequately reduce noise across MRIs with varying degrees of noise. To this end, we design a novel adaptive 3D image denoising (A3ID) framework to adaptively remove noise from MRIs. In A3ID, we train a deep learning model to execute adaptive denoising using estimated MRI noise variance. To our knowledge, this is among the first attempts to estimate MRI noise variance and utilize this prior for 3D MRI denoising.

Methods: A novel adaptive 3D image denoising (A3ID) framework (Fig. 1) is designed to adaptively remove noise from MRIs, including 1) noise estimation and 2) noise removal. 1) Noise Estimation. A novel gradient-based 3D MRI noise estimation strategy is proposed, where the gradient map variance of MRI in sagittal, axial, and coronal views is used to estimate the noise level. For MRIs without noise, their gradient maps only contain a small amount of texture information, such as soft tissue boundaries, and its voxel-level data distribution presents zero mean and minimal variance. The noise distribution is relatively independent, and its variance is not reduced by gradient calculation, so the MRI gradient variance can be used to estimate the noise level. 2) Noise Removal. Based on the estimated noise variance, we design a conditional UNet (ConUNet) for image denoising, incorporated by conditional instance normalization[1]. The ConUNet consists of an encoder with 5 convolutional layers, a decoder with 5 deconvolutional layers, and a conditional instance normalization layer for noise estimation. It inputs a perturbed MRI (i.e., 3D MRI+Gaussian noise) and outputs the estimated noise that can be subtracted from the input for denoising. With conditional instance normalization, the ConUNet can adapt to input MRIs with different noise levels. We use the ADAMA optimizer[2] for model training.

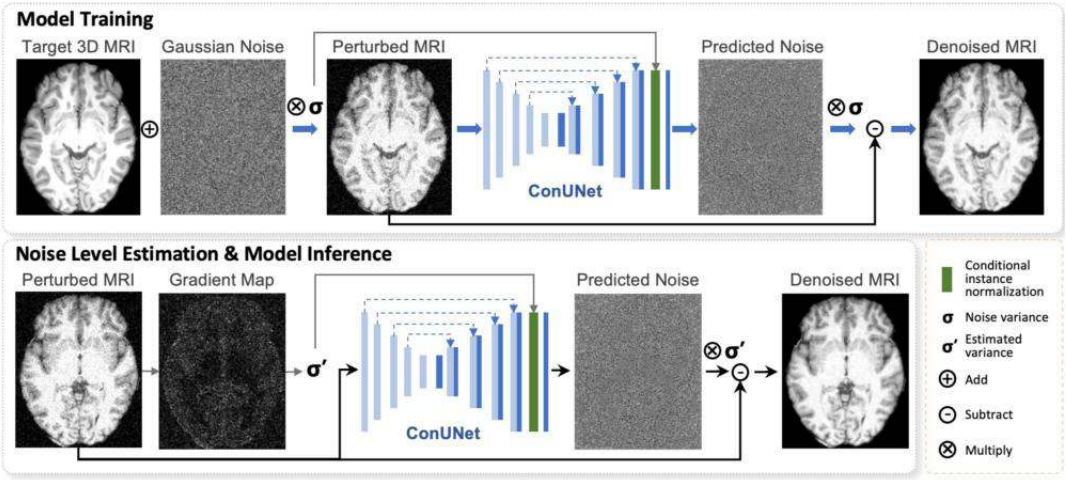

Fig. 1. Illustration of the proposed adaptive 3D image denoising (A3ID) framework

Results: The MR-ART dataset[3] with 148 T1-weighted MRIs is used for evaluation. 70% of the data are used for training and the remaining for test. During training, Gaussian noise with variance randomly distributed in the range of 0~0.2 is added to MRI (image intensity range of 0~1). We add fixed variances of 0.10 and 0.15 noise during test for comparison. 1) At a noise level of 0.10 variance, PSNR, RMSE, and SSIM of our method after denoising on the test set reach 26.50 dB, 0.0481, and 0.8952, which are improved by 3.59dB, 0.0238, and 0.0932, respectively, compared with those before denoising (PSNR=22.91, RMSE=0.0719, SSIM=0.8022). We also compare our method with several state-of-the-arts: FONDUE[4] (PSNR=24.29dB, RMSE=0.0615, SSIM=0.8529), BM4D[5] (PSNR=26.28dB, RMSE=0.0495, SSIM=0.8961), UNet3D[6] (PSNR=26.01dB, RMSE=0.0510, SSIM=0.8896), nnUNet[7] (PSNR=25.96dB, RMSE=0.0511, SSIM=0.8830). 2) At a noise level of 0.15 variance, our method is superior to other methods: A3ID (PSNR=25.50dB, RMSE=0.0537, SSIM=0.8798), FONDUE (PSNR=22.93dB, RMSE=0.0717, SSIM=0.8064), BM4D (PSNR=25.15dB, RMSE=0.0559, SSIM=0.8702), UNet3D (PSNR=23.66dB, RMSE=0.0661, SSIM=0.0091), nnUNet (PSNR=23.15dB, RMSE=0.0700, SSIM=0.8097). Results suggest the effectiveness of our method in 3D MRI denoising with different noise levels.

Conclusions: This work is one of the first attempts to explore adaptive denoising of 3D MRIs. The introduction of conditional instance normalization is crucial to improve the noise estimation ability of our method. Experiment results show that our model outperforms state-of-the-art methods, and this advantage is more apparent when the noise is severe.

References

1. Hou, R. (2022). Truncated residual based plug-and-play ADMM algorithm for MRI reconstruction. IEEE Transactions on Computational Imaging, 8, 96-108.
2. Kingma, D. P. (2014). Adam: A method for stochastic optimization. arXiv preprint arXiv:1412.6980.
3. Nárai, Á. (2022). Movement-related artifacts (MR-ART) dataset of matched motion-corrupted and clean structural MRI brain scans. Scientific Data, 9(1), 630.
4. Adame-Gonzalez. (2023). FONDUE: Robust resolution-invariant denoising of MR Images using Nested UNets. bioRxiv, 2023-06.
5. Mäkinen, Y. (2020). Collaborative filtering of correlated noise: Exact transform-domain variance for improved shrinkage and patch matching. IEEE Transactions on Image Processing, 29, 8339-8354.
6. Falk, T. (2019). U-Net: deep learning for cell counting, detection, and morphometry. Nature Methods, 16(1), 67-70.
7. Isensee, F. (2019). No new-net. In Brainlesion: Glioma, Multiple Sclerosis, Stroke and Traumatic Brain Injuries: 4th International Workshop, BrainLes 2018, Part II 4, 234–244.

Poster No 1950

A Bayesian Covariance Regression Approach to Adjust for Motion Effects in Resting-State fMRI Data

Tianwen Ma[1], Benjamin Risk[1]

[1]Emory University, Atlanta, GA

Introduction: Functional magnetic resonance imaging (fMRI) is a non-invasive tool to measure correlations among brain regions and help characterize neurological disorders, i.e., autism spectrum disorder (ASD). Motion artifact is a major challenge that can create biases. Addressing motion is particularly important for children with ASD because they tend to move more. Classical methods model the first-order effects of motion and other nuisance confounders on the fMRI time series and calculated the covariance of residuals (Ciric et al., 2017). However, the covariates still have time-varying impacts on the correlations among brain regions, known as second-order effects, even after removing the first-order effects. Covariance regression is a statistical approach that models the covariance matrix of multivariate outcomes as functions of covariates (Hoff and Niu, 2012). We aimed to improve functional connectivity estimation by removing the second-order impacts of nuisance confounders on the covariance structure. We propose a novel Bayesian covariance regression (BCR) approach where the time-specific covariance matrix is modeled as a function of time-specific nuisance regressors plus the static functional connectivity.

Methods: Let $y_t \in R^V$, $x_t \in R^{(P+1)}$, V, and P be fMRI data, nuisance covariates with an intercept at time t, numbers of brain regions and nuisance covariates, respectively. Let A and B be two matrices associated with first- and second- orders of motion effects, respectively. The conditional covariance matrix of y given x is $Cov(y|x)=\Psi+Bx(Bx)^T$, where Ψ reflects the static functional connectivity. This model is also parameterized as a mixed-effects model: $y=Ax+\gamma Bx+\epsilon$, where $E(\epsilon)=0$, $Cov(\epsilon)=\Psi$;$E(\gamma)=0$,$Var(\gamma)=1$, and $E(\gamma.\epsilon)=0$. Both γ and ϵ are independent across time t (t ignored to save space). We assume normal priors for ϵ and γ and apply the Gibbs sampling method to update parameters $\{\gamma t\}$,A,Ψ, and B. Most parameters have closed posterior forms. We assign univariate normal priors, matrix normal priors, a Bayesian factor regression model, and matrix-wise horseshoe priors to $\{\gamma t\}$ and A, Ψ, and B, respectively (Ghosh and Dunson, 2009; Carvalho et al., 2010, Li et al., 2019). We conducted 100 simulation studies with true parameters A, B, Ψ, covariates x simulated from multivariate normal distributions with mean and covariance estimated from real data, and outcome y using the mixed-effect representation. We fitted the simulations with BCR and the

classic method (covariance of residuals from linear regression) and compared Ψ:CovReg, Ψ:Classic to Ψ:True. We then fitted BCR to eyes-open 14-minute resting-state fMRI data on a 3T Siemens PrismaFit processed by fMRIprep with a T1 MPRAGE and 4 AP and PA spin-echoes for distortion correction. Time courses were back-constructed from a 30-component group-ICA parcellation. Nuisance regressors included parameters from rigid body motion correction, global, CSF, and white matter signals (9p). We showed results from a 9-yo boy with ASD.

Results: Simulation studies show that covariance and correlation matrix estimates from the classical approach were biased by second-order effects (Figure 1). In the real data analysis, correlations were amplified in the classic approach, particularly negative correlations, while correlations were attenuated in BCR (Figure 2).

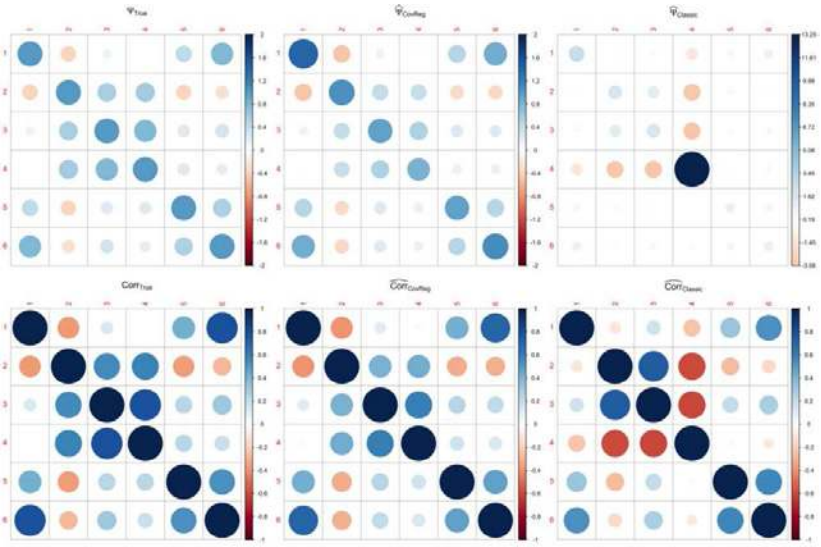

Figure 1. The true, BCR, and classical estimates of covariance matrix (Upper) and correlation matrix (Lower). Original order was used for visualization.

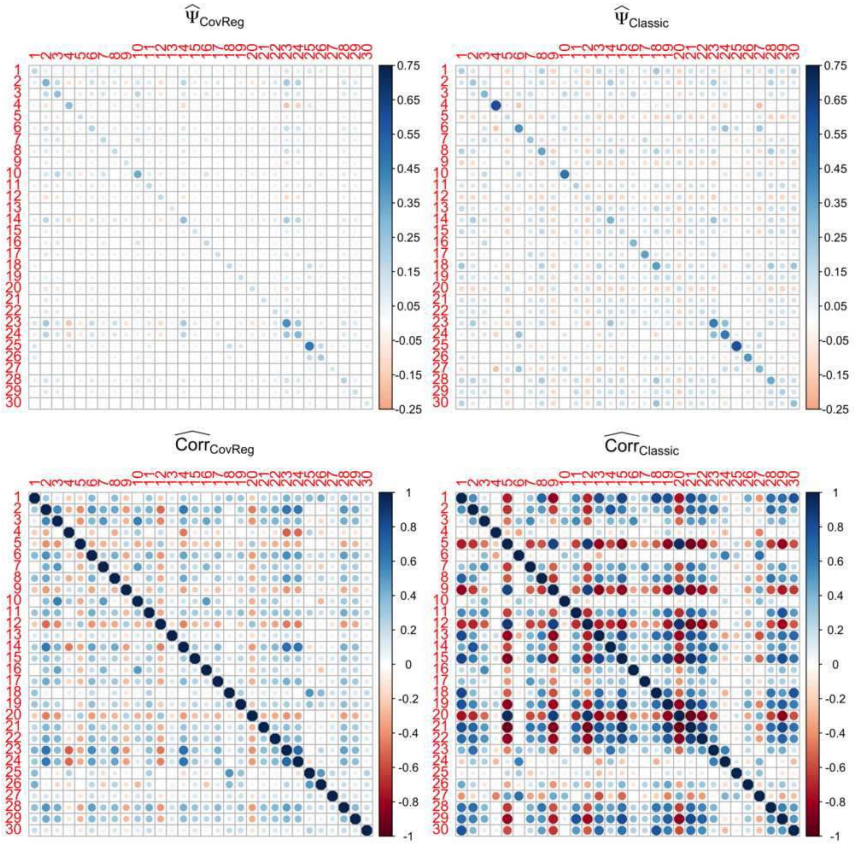

Figure 2. The BCR and classical estimates of covariance matrix (Upper) and correlation matrix (Lower). Original order was used for visualization.

Conclusions: Bayesian covariance regression models the covariance matrix of fMRI data conditional on the motion and nuisance confounders. Our results suggest large second-order impacts of motion bias classic measures of functional connectivity, while BCR removes these second order effects. Future studies should examine whether second-order impacts of nuisance confounders may be spuriously driving dynamic connectivity. We suggest accounting for first- and second-order motion effects to improve functional connectivity estimation. Acknowledgments: The research was funded by R01 MH129855.

References

1. Ciric, R., Wolf, D. H., Power, J. D., Roalf, D. R., Baum, G. L., Ruparel, K., Shinohara, R. T., Elliott, M. A., Eickhoff, S. B., Davatzikos, C., Gur, R. C., Gur, R. E., Bassett, D. S., and Satterthwaite, T. D. (2017). 'Benchmarking of participant-level confound regression strategies for the control of motion artifact in studies of functional connectivity'. Neuroimage, 154, 174-187.
2. Hoff, P. D. and Niu, X. (2012). 'A covariance regression model'. Statistica Sinica, 729-753.
3. Ghosh, J., and Dunson, D. B. (2009). 'Default prior distributions and efficient posterior computation in Bayesian factor analysis'. Journal of Computational and Graphical Statistics, 18(2), 306-320.
4. Carvalho, C. M., Polson, N. G., and Scott, J. G. (2010). 'The horseshoe estimator for sparse signals'. Biometrika, 97(2), 465-480.
5. Li, Y., Craig, B. A., and Bhadra, A. (2019). 'The graphical horseshoe estimator for inverse covariance matrices'. Journal of Computational and Graphical Statistics, 28(3), 747-757.

Poster No 1951

Quantifying the impact of preprocessing strategies on statistical analyses

Brice Ozenne[1], Martin Norgaard[2], Cyril Pernet[1], Melanie Ganz[2]

[1]Neurobiology Research Unit, Rigshospitalet, Copenhagen, Denmark, [2]University of Copenhagen, Copenhagen, Denmark

Introduction: Preprocessing pipelines have become increasingly complex over the years. This multiverse of analytical pipelines naturally leads to a multitude of results. Here, we provide a conceptual framework and a practical tool to aggregate multiple pipeline results beyond simple averaging. The proposed framework is generic and can be applied to any multiverse scenario, but we illustrate its use based on positron emission tomography (PET) data.

Methods: We employ neuroimaging data from a placebo-controlled, double-blinded, clinical study (N=60)[1], measuring cerebral serotonin transporter (SERT) availability following a hormonal treatment. In a previous study[3] multiple valid processing steps (pipelines) were considered to measure SERT availability (see Figure 1). Here we sub-sampled pipelines using the reliability of results in the healthy/placebo arm of[1], while evaluating the results on intervention data (selection independent from testing). Four methods were used to estimate a global effect across pipelines: Ψaverage, average: a naive method would be to compute the mean of the estimated association Ψse, weighted average: the estimated associations are averaged with weight inversely proportional to their standard error ΨGLS, Generalized least squares (GLS): the estimated associations are average with weights accounting for their standard error and correlations. Highly correlated estimates will be given less weights than independent estimates. Ψconstrained, constrained GLS: same as GLS but with weights constrained to be at most one to bound (from above) the influence of a single estimate.

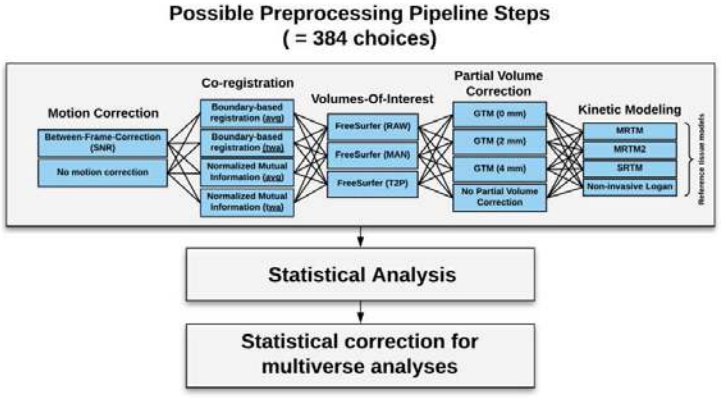

Figure 1. The preprocessing steps include motion correction (with/without), co-registration (4 options), delineation of volumes of interest (3 options), partial volume correction (4 options), and kinetic modeling for quantification of SERT availability (MRTM, SRTM, Non-invasive Logan and MRTM2) leading to a 5 dimensional analysis verse with 384 parallel paths. Next, a statistical analysis is carried out on the data, and then we propose an additional statistical step to correct for multiverse analyses.

Results: We study the behavior of the four statistical estimators to estimate a common effect across pipelines in Figure 2. The dashed vertical line represents the normative value, and all horizontal error bars represent the estimated effect (mean and 95% CI) for a given pipeline and estimator. Across the set of pipelines, 3 of the 8 selected reject the null hypothesis (as indicated by the non-overlapping CI with the normative value) with estimated percent differences between groups ranging between -9% (pipeline 6) and 2.5% (pipeline 1). The Ψaverage, Ψse and Ψconstrained, all fail to reject a common effect across pipelines, whereas the ΨGLS estimator rejects the null hypothesis. However, when inspecting the pipeline weights for the ΨGLS estimator, it assigned a very high weight to four pipelines (i.e. weight above 1 in absolute values) leading to an unreliable estimate. The Ψconstrained estimator did not exhibit this problem.

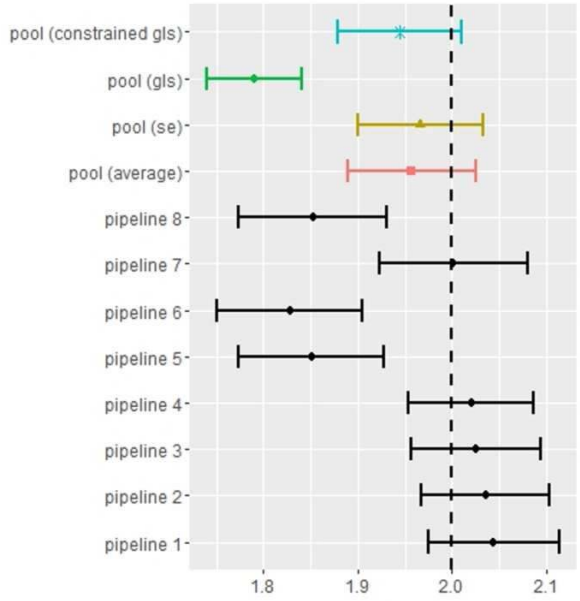

Figure 2. A forest plot of the estimated SERT availability in the amygdala for the intervention group (point and full line) vs. the normative values (dashed line) for each pipeline and the four proposed pooled estimators. The pipelines that were applied were:
Pipeline 1: with motion correction (MC), boundary based registration (BBR) using the time-weighted average PET image (twa), and MRTM2 as kinetic modeling choice.
Pipeline 2: MC, normalized mutual information registration (NMI) using twa, MRTM2.
Pipeline 3: MC, BBR using the average PET image, and MRTM2.
Pipeline 4: MC, NMI using the average PET image, and MRTM2.
Pipeline 5: MC, BBR_{twa}, and MRTM.
Pipeline 6: no motion correction (nMC), BBR_{twa}, and MRTM.
Pipeline 7: nMC, BBR_{twa}, and MRTM2.
Pipeline 8: MC, BBR_{twa}, and SRTM.

Conclusions: Meta-analytical tools were developed mostly for independent data/studies, but in the analytical multiverse results are correlated which imposes constraints on estimations. Here we observed that 'usual' estimators can be readily applied, and three of them performed as expected based on the results from individual pipelines. Only the ΨGLS estimator performed differently, rejecting the null hypothesis hinting at an effect across pipelines. This is though, due to the estimator not being able to fit the weights properly in small sample sizes. Since PET neuroimaging studies are rarely beyond sample sizes of n>50, other estimators should be used. We recommend using Ψse when all pipelines are highly correlated or Ψconstrained when pipelines are not similarly related and the sample size is moderate to large. The framework that we are proposing is not without limitations. The underlying assumption of combining results across pipelines in our analysis is that all pipelines are unbiased. This can however not always be guaranteed. Alternative approaches[4] can be used to reduce the bias of the pooled estimators by assuming a majority of unbiased pipelines or identifying clusters of pipelines and pooling pipeline-specific estimates within clusters.

References

1. Frokjaer, V.G. (2015), 'Role of serotonin transporter changes in depressive responses to sex-steroid hormone manipulation: a positron emission tomography study', Biological psychiatry, vol. 78, no. 8, pp. 534–543
2. Beliveau, V. (2017), 'A high-resolution in vivo atlas of the human brain's serotonin system', Journal of Neuroscience, vol. 37, no. 1, pp. 120–128
3. Nørgaard, M. (2019), 'Optimization of preprocessing strategies in positron emission tomography (PET) neuroimaging: a [11C] DASB PET study', Neuroimage, vol. 199, pp. 466–479
4. Warfield, S.K. (2004), 'Simultaneous truth and performance level estimation (STAPLE): An algorithm for the validation of image segmentation', IEEE Transactions on Medical Imaging, vol. 23, no. 7, pp. 903–921

Poster No 1952

The hidden cost of stringent motion scrubbing

Amanda Mejia[1], Damon Pham[2], Thomas Nichols[3], B. T. Thomas Yeo[4]

[1]Indiana University, Bloomington, IN, [2]Indiana University Bloomington, Bloomington, IN, [3]University of Oxford, Oxford, United Kingdom, [4]National University of Singapore, Singapore, Singapore

Introduction: To mitigate the influence of motion on fMRI analysis, scrubbing is commonly used to exclude volumes with excessive head motion[5,7]. Stringent motion scrubbing (e.g. FD > 0.2mm) is often endorsed, but at what cost? As increasingly subtle noise is removed, the risk of signal loss grows. Introductory statistics teaches us that the error of an estimate is determined by two factors: population variance and sample size. Considering volumes as samples from a population, scrubbing reduces variance while decreasing sample size. These two competing forces may ultimately improve or worsen estimation error. Here, we examine the effect of motion scrubbing on estimation error of FC. We quantify the increase in scan time required to maintain accuracy due to over-scrubbing, with implications for data collection budgets and sample sizes.

Methods: For subject i and edge j, let w(T,i,j) be FC based on T volumes, which is observed with noise: w(T,i,j) = x(i,j) + e(T,i,j) where x(i,j) is the truth. The error variance will be affected by autocorrelation and other factors[2], but we can assume that it is inversely related to T: Var{e(T,i,j)} = v(j)/T The "baseline variance" v(j) reflects noise levels in the underlying data and is reduced by scrubbing. We use the HCP retest set (n=42) to determine this baseline variance for different scrubbing methods. Following the procedure in[4], we establish "ground truth" FC x(i,j) using nearly 2h of rest fMRI (minus a 10-min holdout set), which we stringently scrub using a lagged, filtered version of FD for multi-band data[3,4,6]. We apply different scrubbing methods m to the held-out data to produce FC estimates w(Tmi,i,j). Var{e(T,i,j)} can be estimated based on the squared errors w(Tmi,i,j)- x(i,j), then multiplied by Tmi and averaged over i to estimate the baseline variance v(j,m). We consider FD thresholds of 0.2-0.5mm (FD2-FD5) and the DVARS dual threshold[1]. We assess the impact of scrubbing on accuracy and scan time required. For accuracy, we use mean squared error (MSE) relative to the ground truth. For scan time, we define the budget inflation factor (BIF) of method m versus m' as the increase in total scan time required to achieve the same accuracy. BIF reduces to a simple form: v(j,m)/v(j,m') × d(m)/d(m') d(m) is the average increase in acquired scan time required to have T volumes post-scrubbing. Thus, the BIF is related to the difference between two scrubbing methods' baseline variance and their censoring rates.

Results: Fig. 1 shows that motion scrubbing decreases baseline variance, with stringent motion scrubbing reducing it the most (A). However, stringent motion scrubbing results in substantially greater data loss than other methods (B). As a result, stringent motion scrubbing (FD2) actually worsens FC accuracy, while more lenient motion scrubbing improves it (C, D). There is a U-shaped relationship between data removal and error levels, illustrating the risk of over-scrubbing (E). Fig. 2 shows that over-scrubbing results in the need to collect more data, while more lenient scrubbing can facilitate shorter scans (A-B). The BIF of stringent (FD2) versus more lenient (FD4) motion scrubbing is over 8%.

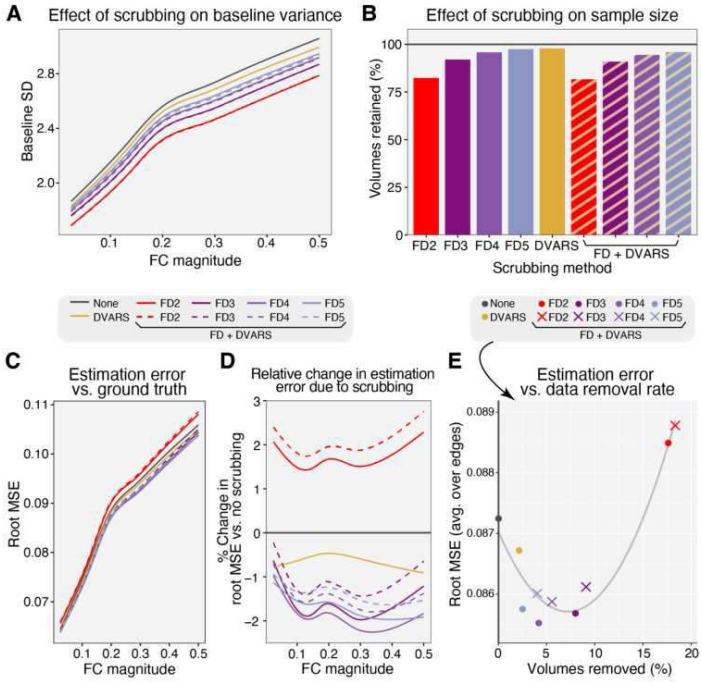

Figure 1. Stringent motion scrubbing reduces baseline variance but also substantially reduces sample size, ultimately leading to worse accuracy. (A) Baseline variance (standard deviation (SD)) of FC for different scrubbing methods. Baseline variance is edge-wise and tends to increase with FC strength. Stringent motion scrubbing with FD > 0.2mm (FD2) achieves the lowest baseline variance, indicating that it most effectively removes noise in the underlying data. **(B)** Stringent motion scrubbing (FD2, FD2+DVARS) censors substantially more volumes than other methods. The percentage of volumes excluded is 17-18% for FD2; 8-9% for FD3; 4-5% for FD4, and 3-4% for FD5. The larger end of each range corresponds to FD + DVARS. **(C)** Estimation error of FC, in terms of root mean squared error (MSE), by scrubbing method. Stringent motion scrubbing worsens accuracy (higher MSE) compared to no scrubbing, while all other scrubbing methods improve accuracy (lower MSE). **(D)** The relative change in accuracy between each scrubbing method versus no scrubbing. Stringent motion scrubbing produces ~2% higher estimation error, while more lenient scrubbing with FD > 0.4mm (FD4) produces ~2% lower estimation error. **(E)** Estimation error as a function of censoring rate. Scrubbing improves accuracy (lower MSE) up to a point, after which more aggressive scrubbing worsens estimation error (higher MSE). *Technical Notes: In panels (A), (C) and (D), each line is a gam smoother across edges for a given scrubbing method. In panel (E), a quadratic fit to the data is shown in gray. For plots showing FC magnitude on the x-axis, the axis range is limited to the middle 90% of the data.*

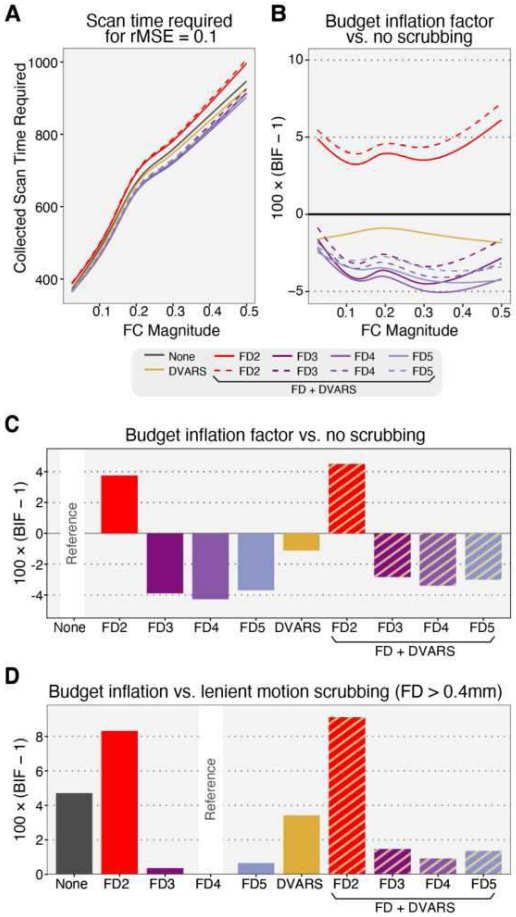

Figure 2. Stringent motion scrubbing requires increased scan time to maintain accuracy to make up for signal loss, with an estimated 8% more scan time over more lenient motion scrubbing. (A) The necessary acquired scan time for different scrubbing methods to achieve a fixed level of accuracy. Stringent motion scrubbing requires longer scans, while more lenient scrubbing could achieve the same accuracy using shorter scans. Note that the target estimation error level of root MSE = 0.1 is arbitrary, and the same patterns would be seen with other values of root MSE. **(B)** Budget inflation factor (BIF) of each scrubbing method versus no scrubbing. The BIF of stringent motion scrubbing is positive, indicating the need for longer scans, while the BIF of more lenient scrubbing is negative, indicating that scan length could be shortened while maintaining accuracy. **(C)** Across all edges, the average BIF of stringent motion scrubbing is around 4%, while the average BIF of more lenient motion scrubbing is around -4%. **(D)** Directly comparing with FD4 (motion scrubbing at FD > 0.4mm), the BIF of stringent motion scrubbing is around 8%, indicating that the total acquired scan time required to make up for data loss is 8% higher if stringent motion scrubbing (FD2 or FD2+DVARS) is adopted over FD4. *Technical Notes: In panels (A) and (B), each line is a gam smoother across edges for a given scrubbing method. For plots showing FC magnitude on the x-axis, the axis range is limited to the middle 90% of the data. Bar plots represent averages across all edges.*

Conclusions: A basic statistical tenant is that the level of error in estimates based on a sample from a population is determined by population variance and sample size. Motion scrubbing affects both factors, and may therefore help or hinder FC, BWAS, and other fMRI analyses. We find that while stringent motion scrubbing reduces baseline variance, it worsens accuracy. This is driven by its high censoring rates: >17% even in the low-motion HCP population. The ultimate consequence of this is the need for longer scans. This reveals that stringent motion scrubbing comes at a real cost, e.g. larger budgets and/or smaller samples. By contrast, more lenient scrubbing is effective and has the opposite effect, ultimately facilitating shorter scans, smaller budgets, and more participants.

References

1. Afyouni, S. (2018), 'Insight and inference for DVARS', NeuroImage, 172, 291-312.
2. Afyouni, S. (2019), 'Effective degrees of freedom of the Pearson's correlation coefficient under autocorrelation', NeuroImage, 199, 609-625.
3. Fair, D. (2020), 'Correction of respiratory artifacts in MRI head motion estimates', NeuroImage, 208, 116400.
4. Phạm, D. Đ. (2023), 'Less is more: balancing noise reduction and data retention in fMRI with data-driven scrubbing', NeuroImage, 270, 119972.
5. Power, J. D. (2012), 'Spurious but systematic correlations in functional connectivity MRI networks arise from subject motion', NeuroImage, 59(3), 2142-2154.
6. Power, J. D. (2019), 'Distinctions among real and apparent respiratory motions in human fMRI data', NeuroImage, 201, 116041.
7. Satterthwaite, T. D. (2019), 'Motion artifact in studies of functional connectivity: Characteristics and mitigation strategies', Human brain mapping, 40(7), 2033-2051.

Poster No 1953

Preprocessing Considerations in fMRI Naturalistic Viewing Paradigms

Menghan Yang[1], Eshin Jolly[1], Luke Chang[1]

[1]Dartmouth College, Hanover, NH

Introduction: Naturalistic stimuli have been increasingly used in brain imaging studies in recent years due to the advantages of enabling researchers to mimic everyday situations, transport individuals into immersive narrative worlds, and evoke neural responses that closely resemble real-life experiences (Chang et al., 2021; Green & Brock, 2002). Compared to resting-state paradigms, naturalistic designs probe a greater variety of cognitive functions (Finn, 2021; Sonkusare et al., 2019), which increases the diversity of mental states (Meer et al., 2020) and the reliability of data (Wang et al., 2017). While naturalistic stimuli have become increasingly popular, most studies rely on traditional preprocessing methods optimized for task or resting-state designs. However, naturalistic viewing paradigms often contain longer range temporal dependencies due to the complexities of the narrative (Hasson et al., 2015) and longer scan times compared to traditional paradigms. If researchers are interested in processes that occur at longer timescales such as emotions (Chang et al., 2021) or memory (Chen et al., 2017), then filtering out slower signals with high pass filters is likely to be undesirable (Lositsky et al., 2016). Therefore, in this study, we examined the impact of different preprocessing steps on intersubject correlations using the Friday Light Nights dataset.

Methods: Participants (N=35) watched a 45-minute episode of Friday Night Lights, a character-driven television drama while undergoing fMRI (Chang et al., 2021). We examined the independent effects of different denoising steps on intersubject correlations (ISC) within 50 different regions of interest (ROIs) from a whole brain parcellation (de la Vega et al., 2016). Specifically, we separately examined the impact of despiking, 24 Volterra expanded head motion covariates, 128s high-pass filter, and average CSF activity compared to a baseline detrended data (intercept, linear, and quadratic).

Results: Overall, we observed a similar pattern of temporal ISC results across the brain reported in prior work in our baseline condition (Fig 1A), with higher ISCs exhibited in sensory cortex compared to heteromodal association cortex. Beyond simply detrending the data, despiking and average CSF activity improved temporal ISC for most brain regions, presumably due to decreasing noise variance in the BOLD signal. However, high-pass filtering dramatically decreased ISC, while motion covariates had mixed results across the brain (Fig 1, B, C, and D). In addition, we also examined spatial ISC within participants by computing pairwise spatial similarity within each ROI across all TRs (Fig 2, A and B). This allowed us to quantify the temporal autocorrelation of spatial patterns for each ROI (Fig 2, C and D). We found that detrending and high-pass filter steps introduced some artifacts in the spatiotemporal signals such as shorter range anti-correlations and longer range correlations, which was particularly notable in the high pass filtering condition. Motion covariates appeared to reduce the impact of these artifacts.

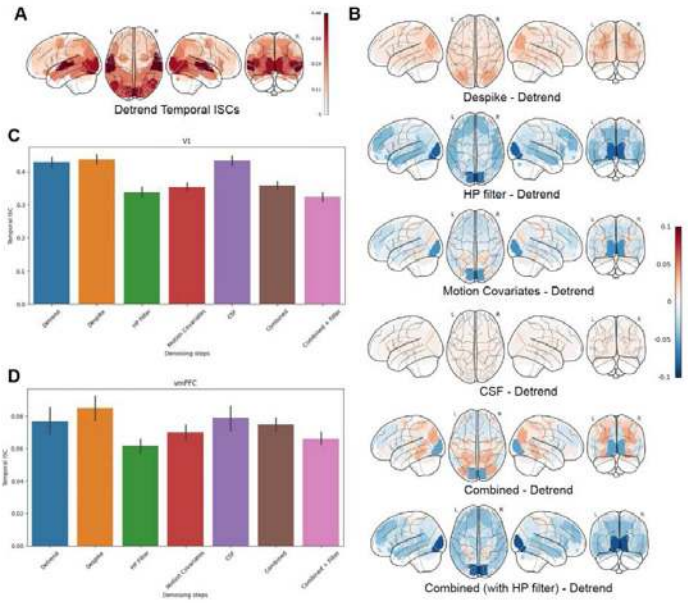

Fig. 1 Effects of Various Denoising Steps on Temporal ISCs Results.

(A) Whole-brain temporal ISCs results after detrending. **(B)** Comparisons between other denoising steps (and their combinations) and detrending over 50 ROIs. HP filter is not included in the combined condition. **(C and D)** Temporal ISCs for V1 and vmPFC after various denoising steps.

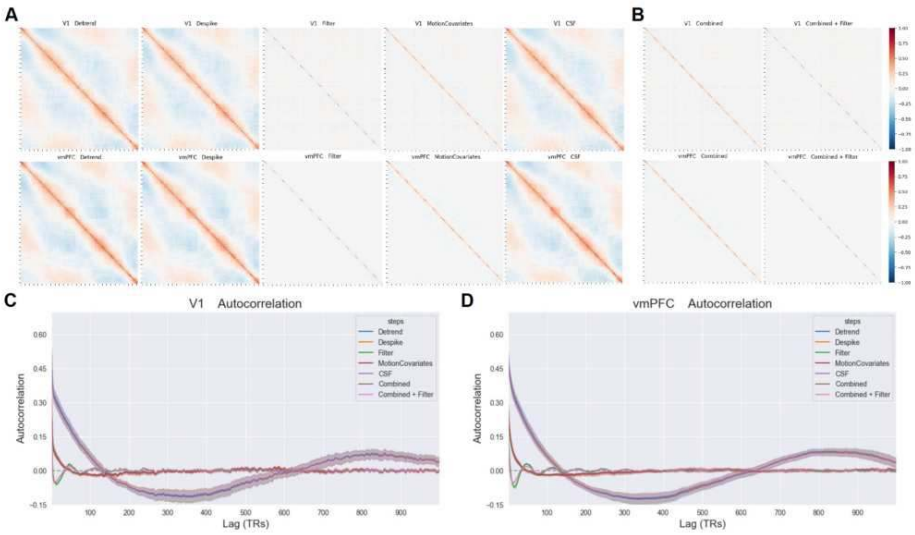

Fig. 2 Spatiotemporal patterns and temporal autocorrelation under different denoising steps.

(A) TR-by-TR spatiotemporal patterns under denoising conditions on V1 and amPFC (averaged across 35 participants). **(B)** Spatiotemporal patterns under combined denoising steps (with and without HP filter). **(C and D)** Temporal autocorrelation function of different steps on V1 and vmPFC.

Conclusions: Together these results suggest that different denoising methods exhibit distinct effects on ISC metrics. For ISC, we recommend that researchers include spikes and motion parameters and optionally CSF activity. High pass filtering is likely to have an adverse impact on analyzing naturalistic data and is not recommended. Future work will continue to assess the impact of these preprocessing methods on other measures beyond ISC such as SNR, connectivity based metrics, and scene classification.

References

1. Chang, L. J., Jolly, E., Cheong, J. H., Rapuano, K. M., Greenstein, N., Chen, P.-H. A., & Manning, J. R. (2021). Endogenous variation in ventromedial prefrontal cortex state dynamics during naturalistic viewing reflects affective experience. Science Advances, 7(17), eabf7129.
2. Chen, J., Leong, Y. C., Honey, C. J., Yong, C. H., Norman, K. A., & Hasson, U. (2017). Shared memories reveal shared structure in neural activity across individuals. Nature Neuroscience, 20(1), 115–125.

3. de la Vega, A., Chang, L. J., Banich, M. T., Wager, T. D., & Yarkoni, T. (2016). Large-Scale Meta-Analysis of Human Medial Frontal Cortex Reveals Tripartite Functional Organization. The Journal of Neuroscience: The Official Journal of the Society for Neuroscience, 36(24), 6553–6562.
4. Finn, E. S. (2021). Is it time to put rest to rest? Trends in Cognitive Sciences, 25(12), 1021–1032.
5. Green, M. C., & Brock, T. C. (2002). In the mind's eye: Transportation-imagery model of narrative persuasion. In M. C. Green (Ed.), Narrative impact: Social and cognitive foundations, (pp (Vol. 373, pp. 315–341). Mahwah, NJ, US.
6. Hasson, U., Chen, J., & Honey, C. J. (2015). Hierarchical process memory: memory as an integral component of information processing. Trends in Cognitive Sciences, 19(6), 304–313.
7. Lositsky, O., Chen, J., Toker, D., Honey, C. J., Shvartsman, M., Poppenk, J. L., Hasson, U., & Norman, K. A. (2016). Neural pattern change during encoding of a narrative predicts retrospective duration estimates. eLife, 5. https://doi.org/10.7554/eLife.16070
8. Meer, J. N. van der, Breakspear, M., Chang, L. J., Sonkusare, S., & Cocchi, L. (2020). Movie viewing elicits rich and reliable brain state dynamics. Nature Communications, 11(1), 5004.
9. Sonkusare, S., Breakspear, M., & Guo, C. (2019). Naturalistic Stimuli in Neuroscience: Critically Acclaimed. Trends in Cognitive Sciences, 23(8), 699–714.
10. Wang, J., Ren, Y., Hu, X., Nguyen, V. T., Guo, L., Han, J., & Guo, C. C. (2017). Test-retest reliability of functional connectivity networks during naturalistic fMRI paradigms. Human Brain Mapping, 38(4), 2226–2241.

Poster No 1954

Semi-automated process for fetal functional brain fMRI isolation, motion correction and censoring

Amyn Majbri[1], Lanxin Ji[2], Ellyn Kennelly[3], Cassandra Hendrix[4], Mark Duffy[2], Iris Menu[2], Tanya Bhatia[5], Moriah Thomason[6]

[1]New York University Grossman School of Medicine, New York, NY, [2]NYU Langone Health, New York, NY, [3]Wayne State University, Detroit, MI, [4]NYU Langone, New York, NY, [5]New York University Medical Center, New York, NY, [6]NYU Langone Medical Center, New York, NY

Introduction: Fetal brain functional MRI is a non-invasive technique that measures correlations of BOLD signals between different brain regions in the developing fetus, providing a unique window into the organization and maturation of the fetal brain networks4.Although well developed in the adult brain, image processing in fetal brains poses more challenges than adult brains due to fetal motion, artifacts, and reduced signal-to-noise. Our research group previously published a manual processing pipeline for fetal brain fMRI, but it is labor intensive and can discards large quantities of fMRI data2This study aims to address these challenges by adapting a novel semi-automated process for fetal functional brain masking, motion correction and censoring.

Methods: Data from 49 fetuses were acquired using a Siemens Verio 70-cm open-bore 3T MR system with a 550 g abdominal 4-Channel Siemens Flex Coil. The data had the following scanning parameters: TR/TE = 2000/18 ms; resolution = 3.4 × 3.4 × 4 mm3), flip angle = 80°. A single mask was manually drawn onto a reference frame within a section of low motion for each acquired run. For every volume in the timeseries, a convolutional neural network-trained model automatically segmented the brain from the maternal compartment, generating a rough 4D mask for the entire timeseries3. The brain was then extracted using this rough mask for motion estimation using FSL mcflirt1, where transformation matrices for mapping each volume to the reference frame were generated. The rough mask is necessary because motion estimation requires a clear background without maternal tissue. We then applied the inverted transformation matrices to the manually drawn mask to generate a more closely defined 4D mask. The raw data was masked again using the improved 4D manual-based mask. We repeated the steps above one time resulting in more refined transformation matrices and a smartly-generated semi-automated mask for the 4D timeseries. Once the final 4D mask is obtained, we apply it to the raw fMRI data for a precise brain extraction and conduct the motion correction on the masked data. See a flowchart in Figure 1. A three-step approach to censoring was adopted. First, frames that not aligned with the reference were identified via Sørensen–Dice coefficient (DC) calculation. Five volumes around the reference volume were averaged and binarized to produce an ideal image-shape mask. The DC between each volume across the whole time series and this mask was calculated. Volumes with a DC below 0.9 were censored. Next, any volume above two standard deviations above the mean framewise displacement (1.5) across all inputted runs was censored. Finally, any volumes with DVARS values greater than two standard deviations above the mean (132) across all inputted runs was censored. The same dataset was pre-processed in parallel with our previously published pipeline for comparison. Retained volumes were calculated for both pipelines and compared.

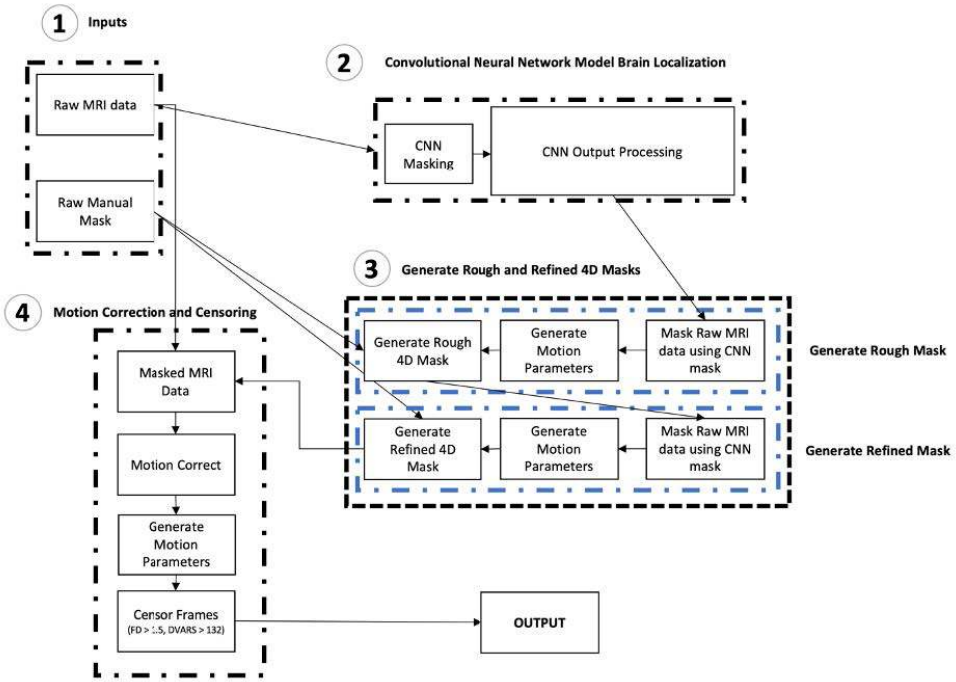

Results: For every run in the dataset, the new approach resulted in an increased number of retrained volumes, while maintaining a low FD. The median number of volumes retained using the legacy method was 157.0 volumes; IQR = 67.0, whereas the novel method proposed here yields a higher median of 264 volumes; IQR = 119.0 volumes (Figure 2). The disparity between the two methods is notable ($p < 0.01$), revealing the new approach increases the median volumes retained, highlighting the effectiveness of the new method in achieving a more consistent and controlled retention of volumes compared to the older approach.

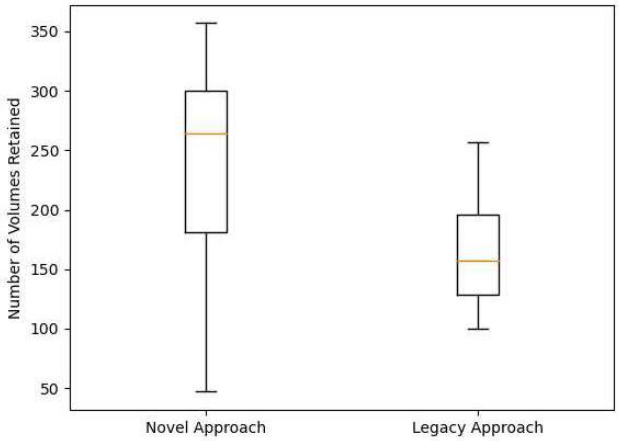

Conclusions: This semi-automated pipeline for fetal fMRI processing improves on previous methods by retaining more volumes. This pre-processing pipeline is also more efficient because it requires a single manual mask per run as opposed to the previous method, which required multiple manually drawn masks per run.

References

1. Jenkinson (2002), 'Improved Optimisation for the Robust and Accurate Linear Registration and Motion Correction of Brain Images', NeuroImage, vol. 17, no. 2, pp. 825-841.
2. Ji (2022), 'Empirical evaluation of human fetal fMRI preprocessing steps', Network Neuroscience, vol. 6, no. 3, pp. 702-721.
3. Rutherford (2022). Automated Brain Masking of Fetal Functional MRI with Open Data. Neuroinformatics. vol. 20 no.1, pp.173-185.
4. Thomason (2021), Interactive relations between maternal prenatal stress, fetal brain connectivity, and gestational age at delivery. Neuropsychopharmacol. vol. 46, pp. 1839–1847.

Poster No 1955

Evaluation of motion censoring in fMRI data using inter-/intra-volume motion corrupted MR data

Wanyong Shin[1], Mark Lowe[1]

[1]*The Cleveland Clinic, Cleveland, OH*

Introduction: Head motion is the one of the main sources of bias sources rs-/fMRI analysis[1-4]. Various motion indexes have been proposed and used to apply thresholds to "censor" motion corrupted volumes in fMRI dataset. In this study, we modify simulated Prospective Acquisition CorrEcted (PACE) EPI sequence[5] and inject different inter- (volume-level) and intra-volume (slice-level) motion to ex-vivo brain phantom during PACE EPI acquisition, referred as Simulated PACE (SIMPACE) data[6]. We test which motion index predicts bad motion corrupted volume effectively and how motion censoring improves fMRI dataset using SIMPACE data.

Methods: We built ex-vivo brain phantom[7] and scanned it using SIMPACE sequence (TR/TE=2s/28ms, voxel size = 2x2x4mm3, 21 slices, 150 vols) with inter-/intra-volume motion patterns injected which were estimated from 10 HCP YA protocol dataset. Two different motion correction and pipelines were used. SIMPACE data was 3d rigid volume motion corrected (VOLMOCO). After VOLMOCO, 6 rigid motion parameters were regressed out with voxelwise partial volume (PV) nuisance regressors[8]. SLOMOCO was applied with 12 volume-/slice-wise motion nuisance and PV regressor[6,9]. We calculate temporal standard deviation (SD) of the residual signal in VOL/SLOMOCO SIMPACE data and averaged SD in grey matter (GM) mask are reported as the quality of fMRI dataset. Time-series of temporal derivative of variance over voxels (DV)[10] in GM and framewise displacement (FD)[11] were calculated. In addition to DV and FD, intra volume motion index, the derivatives of intra-volume volume displacement (iVD) and z component of iVD (iVDz) with the temporal derivative 6 motion parameters at slice-wise time points from SLOMOCO. Time-series of variance over voxels based on the averaged motion corrected images (DVVOL/SLOMOCO) is also calculated, presenting the temporal quality of motion corrected data. Temporal DV, FD, and iVD(z) values were compared to DVVOL/SLOMOCO. Five volumes with top 5 largest FD, DV, iVD(z) value were removed and averaged SD value in GM with each motion censored SIMPACE data were calculated.

Results: Figure 1 shows the temporal characteristic of 10 motion corrected SIMPACE data after VOLMOCO and SLOMOCO and corresponding motion indexes. FD, DV, iVD and iVDz show a high correlation coefficient of 0.32 ($p < 10\text{-}4$), 0.25 ($p < 0.01$), 0.36 ($p < 10\text{-}5$) and 0.48 ($p < 10\text{-}9$) with DVVOLMOCO, respectively, but not showing significant correlation with DVSLOMOCO. It should be noted that DVSLOMOCO is smaller with less spontaneous peak than DVVOLMOCO. Figure 2 shows average SD in GM in VOLMOCO- and SLOMOCO-corrected SIMPACE data with/out censoring 5 volumes. Also shown (horizontal dashed line) is the SD in a SIMPACE acquisition with no motion injected, which can be considered the baseline, or truth. SD in GM is reduced after censoring when using VOLMOCO, but not with SLOMOCO.

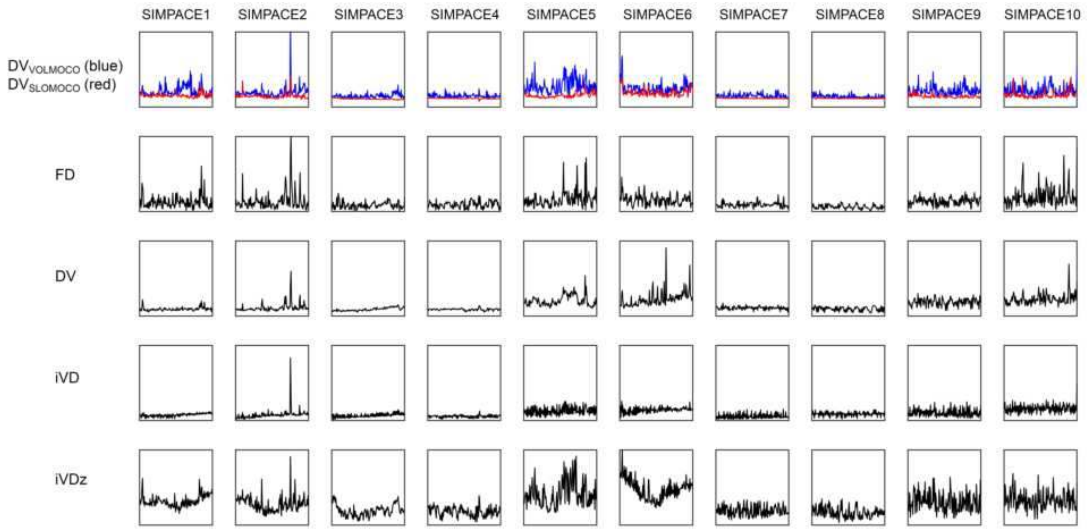

Figure 1. Temporal characteristic of 10 SIMPACE data and different motion indexes. X axes represent time unit (volume number) and Y axes are arbitrary units, but same scaled across SIMPACE datasets.

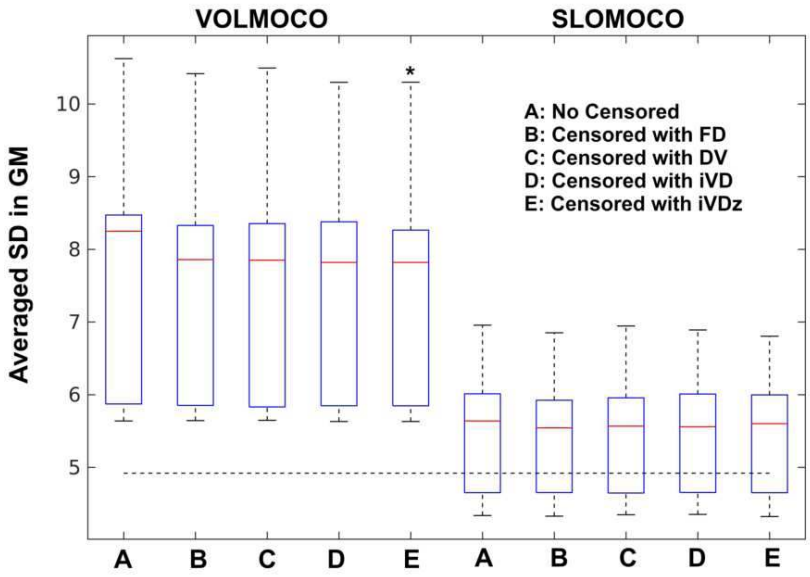

Figure 2. Averaged standard deviation (SD) in grey matter (GM) after VOLMOCO and SLOMOCO in 10 SIMPACE data. * indicates the significant difference from no censoring data (A, $p < 0.05$).

Conclusions: We find that time-series FD, DV and iVD(z) is highly correlated to the residual motion artifact in VOLMOCO SIMPACE data, but not in SLOMOCO, indicating that there is more residual motion artifact when using VOLMOCO as previously presented[12]. Censoring using FD, DV and iVD(z) indexes reduce the residual motion artifact in VOLMOCO-corrected SIMPACE data, but not in SLOMOCO. This result suggests that SLOMOCO-corrected data has minimal levels of residual motion artifact compared to VOLMOCO-corrected data. Average SD in GM for SLOMOCO-corrected data is 5.45±0.84 without censoring. Considering that the baseline SD (i.e. no motion injected) is 4.92 in GM, SLOMOCO output removes the residual artifact from spontaneous inter-/intra-volume motion effectively. Future studies with larger samples of realistic motion simulated data are planned to further validate these results.

References

1. J. V. Hajnal et al., Artifacts due to stimulus correlated motion in functional imaging of the brain. Magn Reson Med 31, 283-291 (1994).
2. A. Jiang et al., Motion detection and correction in functional MR imaging. Human Brain Mapping 3, 224-235 (1995).
3. K. J. Friston, S. Williams, R. Howard, R. S. Frackowiak, R. Turner, Movement-related effects in fMRI time-series. Magn Reson Med 35, 346-355 (1996).
4. S. Grootoonk et al., Characterization and correction of interpolation effects in the realignment of fMRI time series. Neuroimage 11, 49-57 (2000).
5. S. Thesen, O. Heid, E. Mueller, L. R. Schad, Prospective acquisition correction for head motion with image-based tracking for real-time fMRI. Magn Reson Med 44, 457-465 (2000).
6. E. B. Beall, M. J. Lowe, SimPACE: generating simulated motion corrupted BOLD data with synthetic-navigated acquisition for the development and evaluation of SLOMOCO: a new, highly effective slicewise motion correction. Neuroimage 101, 21-34 (2014).
7. S. Kim, K. Sakaie, I. Blumcke, S. Jones, M. J. Lowe, Whole-brain, ultra-high spatial resolution ex vivo MRI with off-the-shelf components. Magn Reson Imaging 76, 39-48 (2021).
8. W. Shin, M. J. Lowe. Effective removal of the residual head motion artifact after motion correction in fMRI data. in 2023 ISMRM & ISMRT Annual Meeting & Exhibition, Toronto, #1821. (2023)
9. W. Shin, M. J. Lowe. The development of Inter-/intra-volume motion correction algorithm for fMRI using a custom MRI acquisition with prospectively injected motion. in 2023 ISMRM & ISMRT Annual Meeting & Exhibition, Toronto, #2001. (2023)
10. C. D. Smyser et al., Longitudinal analysis of neural network development in preterm infants. Cereb Cortex 20, 2852-2862 (2010).
11. J. D. Power, K. A. Barnes, A. Z. Snyder, B. L. Schlaggar, S. E. Petersen, Spurious but systematic correlations in functional connectivity MRI networks arise from subject motion. NeuroImage 59, 2142-2154 (2012).
12. J. D. Power et al., Methods to detect, characterize, and remove motion artifact in resting state fMRI. Neuroimage 84, 320-341 (2014).

Poster No 1956

Optimizing the preprocessing pipeline for multicenter fMRI studies

Marie-Eve Hoeppli[1], Emma Biggs[2], Saül Pascual-Diaz[3], Massieh Moayedi[4], Marina López-Solà[5], Laura Simons[6], Robert Coghill[7]

[1]CCHMC, Cincinnati, OH, [2]Department of Anesthesiology, Perioperative and Pain Medicine, Stanford University School of Medici, Stanford, CA, [3]Universitat de Barcelona, Barcelona, Spain, [4]Centre for Multimodal Sensorimotor and Pain Research, Faculty of Dentistry, University of Toronto, Toronto, Ontario, [5]University of Barcelona, Barcelona, Barcelona, [6]Department of Anesthesiology, Perioperative and Pain Medicine, Stanford University School of Medicin, Stanford, CA, [7]Cincinnati Children's Hospital Medical Center, Cincinnati, OH

Introduction: Today an increasing number of fMRI analyses relies on advanced statistical techniques based on machine learning approaches. These techniques require large sample sizes, which can be challenging to achieve in specific population, e.g. children with chronic musculoskeletal pain. Combining the recruitment efforts of multiple research centers is then needed to successfully complete the required sample size. Due to differences in equipment and practices, this multicenter approach can render the optimization of the protocols and the processing of the data complicated. In this study we aimed at defining the optimal preprocessing pipeline for data acquired in the context of a large-scale study on three different fMRI 3T scanners: Siemens Prisma, GE Premier, and Philips Ingenia Elition (Simons et al., 2022).

Methods: Of 131 teenagers diagnosed with chronic musculoskeletal pain who were enrolled in the main study and underwent an fMRI session, 30 were selected for this substudy. 10 participants from each site were included. Participants were selected on the noise observed in the raw data to ensure an equal representation of noisy and less noisy data. Each participant underwent two resting-state multiband BOLD sequences. Sequence parameters, including reaction time, echo time, flip angle, and voxel size, were constant across centers (Simons et al., 2022). Three main preprocessing pipelines were evaluated: CONN (Whitfield-Gabrieli & Nieto-Castanon, 2012), fMRIprep, and FSL (Jenkinson, Beckmann, Behrens, Woolrich, & Smith, 2012). In addition, three denoising techniques, ICA-AROMA (Pruim et al., 2015), FSL FIX with custom-trained classifier (Salimi-Khorshidi et al., 2014), and aCompCor (Behzadi, Restom, Liau, & Liu, 2007) were tested in a standard FSL pipeline. Finally, a comparison of preprocessing pipelines including temporal high-pass filtering (cut-off: 125sec.) was compared pipelines including temporal bandpass filtering (cut-offs: 125sec. and 11sec.). Signal-to-noise ratios were calculated for each participant and pipeline and compared between pipelines within predefined brain areas, including amygdala, insula, cingulate cortex, ventromedial prefrontal cortex, orbitofrontal cortex, primary and secondary somatosensory cortices, hippocampus, thalamus, cerebrospinal fluid, and white matter.

Results: Results showed that (1) across the three main pipelines (CONN, FSL, and fMRIprep), applying bandpass filtering improved the remaining signal; (2) FSL performed better than fMRIprep or CONN; (3) the application of ICA-based denoising techniques in FSL, and in particular FSL FIX, further improved signal conservation.

Conclusions: In conclusions, our results suggest that an FSL-based preprocessing pipeline including FIX as noise reduction technique and bandpass filtering might be the optimal preprocessing pipeline for multicenter approaches. These results are in line with previous results (Hoeppli et al., 2023), highlighting the benefit of FSL FIX on the quality of preprocessed data. Furthermore, these results demonstrate the advantage of applying bandpass filtering on resting-state BOLD data. In summary, the preprocessing of fMRI data can be particularly challenging in studies relying on acquisitions from different centers and requires careful consideration. Our results are a first attempt to provide guidance to optimize this process.

References

1. Behzadi, Y., Restom, K., Liau, J., & Liu, T. T. (2007). A component based noise correction method (CompCor) for BOLD and perfusion based fMRI. NeuroImage, 37(1), 90–101. https://doi.org/10.1016/j.neuroimage.2007.04.042
2. Hoeppli, M. E., Garenfeld, M. A., Mortensen, C. K., Nahman-Averbuch, H., King, C. D., & Coghill, R. C. (2023). Denoising task-related fMRI: Balancing noise reduction against signal loss. Human Brain Mapping. https://doi.org/10.1002/hbm.26447
3. Jenkinson, M., Beckmann, C. F., Behrens, T. E. J., Woolrich, M. W., & Smith, S. M. (2012). FSL. NeuroImage, 62(2), 782–790. https://doi.org/10.1016/j.neuroimage.2011.09.015
4. Pruim, R. H. R., Mennes, M., Rooij, D. van, Llera, A., Buitelaar, J. K., & Beckmann, C. F. (2015). ICA-AROMA: A robust ICA-based strategy for removing motion artifacts from fMRI data. NeuroImage, 112(C), 267–277. https://doi.org/10.1016/j.neuroimage.2015.02.064
5. Salimi-Khorshidi, G., Douaud, G., Beckmann, C. F., Glasser, M. F., Griffanti, L., & Smith, S. M. (2014). Automatic denoising of functional MRI data: combining independent component analysis and hierarchical fusion of classifiers. NeuroImage, 90, 449–468. https://doi.org/10.1016/j.neuroimage.2013.11.046
6. Simons, L., Moayedi, M., Coghill, R. C., Stinson, J., Angst, M. S., Aghaeepour, N., ... Ruskin, D. (2022). Signature for Pain Recovery IN Teens (SPRINT): Protocol for a multi-site prospective signature study in chronic musculoskeletal pain. BMJ.
7. Whitfield-Gabrieli, S., & Nieto-Castanon, A. (2012). Conn: A Functional Connectivity Toolbox for Correlated and Anticorrelated Brain Networks. Brain Connectivity, 2(3), 125–141. https://doi.org/10.1089/brain.2012.0073

Organization for
Human Brain Mapping

Advancing Understanding of the Human Brain

ORGANIZATION FOR HUMAN BRAIN MAPPING

www.humanbrainmapping.org

1935 County Road B2 W, Ste 165
Roseville, MN 55113
info@humanbrainmapping.org
952-641-2294